SCHOLARLY PUBLICATIONS

A CURRENT AWARENESS BULLETIN
OF RESEARCH OUTPUT

@DTU

(133rd Edition)

JANUARY 2024

BY: CENTRAL LIBRARY

DELHI TECHNOLOGICAL UNIVERSITY
(FORMERLY *DELHI COLLEGE OF ENGINEERING)*
GOVT. OF N.C.T. OF DELHI
SHAHBAD DAULATPUR, MAIN BAWANA ROAD
DELHI 110042

PREFACE

This is the **One Hundred Thirty Three** Issue of Current Awareness Bulletin started by Delhi Technological University, Central Library. The aim of the bulletin is to compile, preserve and disseminate information published by the faculty, students and alumni for mutual benefits. The bulletin also aims to propagate the intellectual contribution of Delhi Technological University (DTU) as a whole to the academia.

The bulletin contains information resources available in the internet in the form of articles, reports, presentations published in international journals, websites, etc. by the faculty and students of DTU. The publications of faculty and student which are not covered in this bulletin may be because of the reason that the full text either was not accessible or could not be searched by the search engine used by the library for this purpose.

The learned faculty and students are requested to provide their uncovered publications to the library either through email or in CD, etc. to make the bulletin more comprehensive.

This issue contains the information published during **January, 2024**. The arrangement of the contents is alphabetical. The full text of the article which is either subscribed by the university or available in the web is provided in this bulletin.

Central Library

CONTENTS

1. 10 Studying wind effect on high-rise building with different cross-section, ***8.Dhruv Chaudhary***, ***8.Dhawal Tayal***, ***8.Devesh Kasana***, ***3.Ritu Raj***, ***3.S. Anbukumar*** and Rahul Kumar Meena, Civil, DTU

2. A Battery Digital Twin From Laboratory Data Using Wavelet Analysis and Neural Networks, Roberta Di Fonso, Remus Teodorescu, Carlo Cecati and ***8.1.Pallavi Bharadwaj***, Electrical, DTU

3. A catalogue of low-mass X-ray binaries in the Galaxy: from the INTEGRAL to the Gaia era, F. Fortin, ***6.A. Kalsi***, F. García, A. Simaz-Bunzel and S. Chaty, DTU

4. A comprehensive energy, exergy, environmental, and economic analysis of dedicated mechanical subcooled vapor compression refrigeration system, Naveen Solanki, ***3.Akhilesh Arora*** and ***3.Raj Kumar Singh***, Mechanical, DTU

5. A comprehensive parametric and structural bond analysis of an actual vapor compression refrigeration system with dedicated mechanical subcooled system, Naveen Solanki, ***3.Akhilesh Arora*** and ***3.Raj Kumar Singh***, Mechanical, DTU

6. A Comprehensive Study on the Closed Loop Performance of a Zeta Converter, ***7.Prashant Singh***, ***3.Alka Singh*** and ***3.Ankita Arora***, Electrical, DTU

7. A Distribution of Nodes in Big Data using Hadoop Open Source System, ***6.Nishant Mathur*** and Mukul Jain, CSE, DTU

8. A feasibility study and cost benefit analysis of an off-grid hybrid system for a rural area electrification, ***6.Upma Singh*** and ***3.M. Rizwan***, Electrical, DTU

9. A single phase Li2Ba5W3O15:Dy3+/Eu3+ phosphor for color tunable devices and non-contact optical thermometry, ***6.Anu***, ***6.Seema***, A. Kumar, Nisha Deopa, Mukesh K. Sahu, Aman Prasad and ***3.A.S. Rao***, Applied Physics, DTU

10. A study on matter accretion onto charged black hole solution in metric-affine gravity, G. Mustafa, A. Ditta, Faisal Javed, S.K. Maurya, ***7.Himanshu Chaudhary*** and Farruh Atamurotov, Applied Mathematics, DTU

11. A Systematic Review on Predicting the Performance of Students in Higher Education in Ofine Mode Using Machine Learning Techniques, ***6.Rahul*** and ***3.Rahul Katarya***, CSE, DTU

12. A Visually Attentive Splice Localization Network with Multi-Domain Feature Extractor and Multi-Receptive Field Upsampler, ***6.Ankit Yadav*** and ***3.Dinesh Kumar Vishwakarma***, IT, DTU

13. Acid hydrolysis of Solanum tuberosum periderm for accumulation of polyhydroxyalkanoates in Pseudomonas putida MTCC 2475, ***6.Sonika Kag***, ***3.Pravir Kumar*** and ***3.1.Rashmi Kataria***, Biotechnology, DTU

14. Advancing Voltage Stability in Half-Bridge Isolated DCDC Converter through the Adoption of PI Controller, ***6.Kumar Gaurav***, ***3.Dheeraj Joshi*** and ***3.Shreyansh Upadhyaya***, Electrical, DTU

15. An overview of cold metal transfer welding of similar materials, ***6.Indra Jeet Singh***, ***3.Paras Kumar*** and ***3.Qasim Murtaza***, Mechanical, DTU

16. Approximate regeneration of image using fragile watermarking for tamper detection and recovery in real time, ***3.Varsha Sisaudia*** and Virendra P. Vishwakarma, IT, DTU

17. Assessment of soil liquefaction potential using genetic programming using a probability-based approach, ***6.Nerusupalli Dinesh Kumar Reddy***, ***3.Prof Ashok Kumar Gupta*** and ***3.Prof Anil Kumar Sahu***, Civil, DTU

18. Bff: Bi-stream feature fusion for object detection in hazy environment, ***3.Kavinder Singh*** and ***3.Anil Singh Parihar***, CSE, DTU

19. Bioactive glass incorporated dressing matrix for rapid hemostatic action with antibacterial activity, Payal Roy, Rupam Saha, Debolina Dattaray, Suman Saha, Tapan Kumar Mandal, ***6.1.Pooja Srivastava*** & Jui Chakraborty, Biotechnology, DTU

20. Blockchain-Based Secure Localization against Malicious Nodes in IoT-Based Wireless Sensor Networks Using Federated Learning, ***6.Gebrekiros Gebreyesus Gebremariam***, ***3.J. Panda*** and ***3.S. Indu***, Electronics, DTU

21. Circular Slot-Based Microstrip Circularly Polarized Antenna for 2.45-GHz RFID Reader Applications, Amit Birwal, ***6.1.Kamlesh Patel*** and Sanjeev Singh, ECE, DTU

22. Datasets, Clues and State-of-the-Arts for Multimedia Forensics: An Extensive Review, ***6.Ankit Yadav*** and ***3.Dinesh Kumar Vishwakarma***, IT, DTU

23. Design and analysis of spider-web photonic crystal fiber in the terahertz regime, ***6.G Singh***, ***6.S Sharma*** and ***3.A Kumar***, Applied Physics, DTU

24. Design optimization of OR-PMSM-IPIM using modified slime mold optimization technique for UAV application, ***3.Monika Verma***, ***3.Mini Sreejeth*** and ***3.Madhusudan Singh***, Electrical, DTU

25. Design, fabrication, and characterization of epsilon negative and near-zero index metasurface, Ankit, ***3.Kamal Kishor*** and ***3.Ravindra Kumar Sinha***, APPLIED PHYSICS, DTU

26. Detecting low-resolution deepfakes: an exploration of machine learning techniques, Mayank Pandey, Samayveer Singh, Aruna Malik and ***3.Rajeev Kumar***, CSE, DTU

27. Evaluating the photocatalytic degradation efficacy of 2,4,6-trichlorophenol: performance evaluation and influencing factors, ***7.Harsh Pipil***, ***6.Shivani Yadav***, Sunil Kumar and ***3.Anil Kumar Haritash***, Environmental, DTU

28. Framework for evaluating sustainability index of a manufacturing system: a case illustration, ***6.Deepak Sharma***, ***3.Pravin Kumar*** and Rajesh Kumar Singh, Mechanical, DTU

29. Gate Engineered Ferroelectric Junctionless BioFET for Label-Free Detection of Biomolecules, ***6.Snehlata Yadav***, ***3.Sonam Rewari*** and ***3.Rajeshwari Pandey***, Electronics, DTU

30. GSMD-SRST: Group Sparse Mode Decomposition and Superlet Transform Based Technique for Multi-Level Classification of Cardiac Arrhythmia, ***6.Shikha Singhal*** and ***3.Manjeet Kumar***, Electronics, DTU

31. High-k dielectric based high performance vertical organic thin film transistor for flexible low power applications, ***6.Sugandha Yadav***, ***3.Poornima Mittal*** and Shubham Negi, Electronics, DTU

32. Impact of tumbling on production of biomethane from household waste, ***6.Pradeep Kumar Meena***, ***3.Amit Pal*** and Samsher Gautam, Mechanical, DTU

33. Impact of various design parameters on solar still systems performance: a review, ***6.Maneesh Kumar Shivhare***, ***3.Samsher*** and ***3.Anil Kumar***, Environment and Mechanical, DTU

34. Innovative Approach to Android Malware Detection: Prioritizing Critical Features Using Rough Set Theory, ***3.Rahul Gupta***, ***3.Kapil Sharma*** and Ramesh Kumar Garg, IT, DTU

35. Intelligent Traffic Light Controller using Verilog and Xilinx Spartan-3e, ***8.Apoorva Banerjee***, Electronics, DTU

36. Interceptor sewer for abatement of pollution in surface water, ***6.Radhey Shyam Tyagi***, ***3.S. K. Singh*** and ***3.P. K. Goyal***, Environment and Civil, DTU

37. IOT BASED SANITIZATION ROBOT USING RASPBERRY PI ZERO W AND UV LAMP, ***8.B Revanth Raj***, ***8.Abhishek Sahani*** and ***8.Ravi Yadav***, Mechanical, DTU

38. Joule-Thomson expansion and tidal force effects of AdS black holes surrounded by Chaplygin dark fluid, Dhruv Arora, Muhammad Yasir, ***7.Himanshu Chaudhary***, Faisal Javed, G. Mustafa, Xia Tiecheng and Farruh Atamurotov, Applied Mathematics, DTU

39. Localization and Detection of Multiple Attacks in Wireless Sensor Networks Using Artificial Neural Network, ***6.Gebrekiros Gebreyesus Gebremariam***, ***3.J. Panda*** and ***3.S. Indu***, Electronics, DTU

40. Matter creation cosmology with generalized Chaplygin gas, ***7.Yogesh Bhardwaj*** and ***3.C.P. Singh***, Applied Mathematics, DTU

41. Mechanistic understanding on the uptake of micro-nano plastics by plants and its phytoremediation, ***6.Megha Bansal***, ***3.Deenan Santhiya*** and ***3.Jai Gopal Sharma***, Biotechnology and Chemistry, DTU

42. MF2 ShrT: Multi-Modal Feature Fusion Using Shared Layered Transformer for Face Anti-Spoofing, ***6.AASHANIA ANTIL*** and ***3.CHHAVI DHIMAN***, ECE, DTU

43. Microplastics influence the functional responses of a tropical estuarine calanoid Pseudodiaptomus annandalei, ***3.Jaigopal Sharma***, Malayaj Rai and Robert S. Guino-o, Biotechnology, DTU

44. Multi-level trust-based secure and optimal IoT-WSN routing for environmental monitoring applications, ***6.Vishal Sharma***, ***3.Rohit Beniwal*** and ***3.Vinod Kumar***, CSE, DTU

45. NLP-enabled Recommendation of Hashtags for Covid Based Tweets Using Hybrid BERT-LSTM Model, ***6.KIRTI JAIN*** and ***3.RAJNI JINDAL***, CSE, DTU

46. Optimization of phytase production by Penicillium oxalicum in solid-state fermentation for potential as a feed additive, ***6.Priya***, Bijender Singh, ***3.Jai Gopal Sharma*** and Bhoopander Giri, Environment and Biotech, DTU

47. Optimizing Reservoir Operation with Artificial Intelligence : A State-of-the-Art Review, ***6.Astha Yadav***, ***3.Prof. Vijay K. Minocha*** and ***3.Prof. Rakesh Kumar***, Civil, DTU

48. Performance Evaluation of Dual-Slope Digitizer for Self-Heating Compensation in Resistive Sensor, ***7.1.Gopal Singh***, Shiraz Sohail, Ashish Dinesh kumar Joshi and Tarikul Islam, Electrical, DTU

49. Performance of an Intelligent Reflecting Mirror Aided Uplink Lightwave Communication System, ***6.Vishal Kumar***, ***3.Rohit Kumar*** and Shankar Prakriya, Applied Mathematics, DTU

50. Potential and Achievement of Floating Solar Photo Voltage in India, ***U Dalal***, ***6.Saksham Rana*** and ***3.Dr J P Kesari***, Mechanical, DTU

51. PV-Fed Single-Phase Induction Motor for Irrigation Application, ***8.Dawda Bojang***, ***8.Eleyde Nhantumbo***, ***3.Monika Verma*** and ***3.Ashish Kulkarni***, Electrical, DTU

52. Recent advancement in the detection of potential cancer biomarkers using the nanomaterial integrated electrochemical sensing technique: a detailed review, ***6.1.Hema Bhardwaj***, Archana, Ashab Noumani, Jayendra Kumar Himanshu, Shreeti Chakravorty and Pratima R. Solanki, Biotechnology, DTU

53. Reconfigurable Low Weight Hybrid PUF Design Against Side Channel Attacks, ***6.Bhagyalakshmi Narayanapuram*** and ***3.Jeebananda Panda***, ECE, DTU

54. Simulation and Computational Study of RING Domain Mutants of BRCA1 and Ube2k in AD/PD Pathophysiology, ***6.Mehar Sahu***, ***6.Neetu Rani*** and ***3.Pravir Kumar***, Biotechnology, DTU

55. Simulation modelling of hydrogen production from steam reforming of methane and biogas, ***6.Ravindra Kumar***, ***3.Anil Kumar*** and ***3.Amit Pal***, Mechanical and Environment, DTU

56. Stress Analysis Of Connecting Rod For Diesel Engine With Different Materials, ***8.Dipanker Meena***, ***8.Kamal Negi*** and ***8.Karan Pradhan***, Mechanical, DTU

57. Structural Investigation and Optical Properties of Dysprosium (Dy3+) Ions Doped Oxyfluoro Antimony Borate Glasses for Photonics Applications, Ch. Pravallika, K. Swapna, Ib Singh Deo, Sk. Mahamuda, M. Venkateswarulu, ***3.A. S. Rao*** and Vijaya Prakash G, Applied Physics, DTU

58. Study of traffic volumes, ***8.Gunjit Gupta***, ***8.Ayush Anand***, ***8.Ayush Raj*** and ***3.Mr. B.R.G Robert***, Civil, DTU

59. Sustainable Concrete: Exploring Fresh, Mechanical, Durability, and Microstructural Properties with Recycled Fine Aggregates, ***6.Harish Panghal*** and ***3.Awadhesh Kumar***, Civil, DTU

60. Synergistic potency of ultrasound and solar energy towards oxidation of 2,4-dichlorophenol: a chemometrics approach, ***7.Harsh Pipil***, ***6.Shivani Yadav***, Sunil Kumar and ***3.Anil Kumar Haritash***, Environment, DTU

61. The utilization of agricultural and industrial waste in the synthesis of AA7075-based novel lightweight composite, ***8.Ashish Kumar***, Virendra Pratap Singh, Akash Mallik, Biraj Kumar Sahoo, ***3.R. C. Singh*** and ***3.Rajiv Chaudhary***, Mechanical, DTU

62. Towards Effective Image Forensics via A Novel Computationally Efficient Framework and A New Image Splice Dataset, ***6.Ankit Yadav*** and ***3.Dinesh Kumar Vishwakarma***, IT, DTU

63. Transition metal induced- magnetization and spin-polarisation in black arsenic phosphorous, ***3.Anurag Chauhan***, ***3.Kapil Sharma*** and Sudhanshu Choudhary, IT, DTU

64. Unveiling the Dynamic Journey from Data Insights to Action in Data Science, Shiva Tyagi and ***7.Riti Rathore***, CSE, DTU

65. Unveiling Xanthine Presence in Rohu Fish Using Ag+-Doped MoS2 Nanosheets Through Electrochemical Analysis, Prateek Sharma, ***6.Deeksha Thakur***, ***3.Devendra Kumar*** and Omprakash Yadav, Applied Chemistry, DTU

66. Voltage and Current Regulation in Cuk DC-DC Converters having Enhanced Closed-Loop Control using PID Controller, ***7.Praanshu Srijan Shandilya***, ***8.Ashutosh Gupta*** and ***3.Dheeraj Joshi***, Electrical, DTU

67. Wire ARC Additive Manufacturing Process for Higher Deposition Rate and Mechanical Strength, ***7.Harshit Bansal***, ***7.Abhiraj Kumar Gupta*** and ***3.Dr. Ashok Madan***, Mechanical, DTU

1. *Vice Chancellor*
2. *Pro Vice Chancellor*
3. *Faculty*
4. *Teaching-cum-Research Fellow*
5. *Asst. Librarian*
6. *Research Scholar*
7. *PG Scholar*
8. *Undergraduate Student*

1.1. *Ex Vice chancellor*
2.1. *Ex Pro Vice Chancellor*
3.1. *Ex Faculty*
4.1. *Alumni*
5.1 *Others*
6.1. *Ex Research Scholar*
7.1. *Ex PG Scholar*
8.1. *Ex Undergraduate Student*

ResearchGate

See discussions, stats, and author profiles for this publication at: https://www.researchgate.net/publication/377625720

Studying wind effect on high-rise building with different cross-section

Conference Paper · January 2024

DOI: 10.1201/9781003450924-10

CITATIONS
0

READS
35

6 authors, including:



Dhruv Choudhary
Delhi Technological University
4 PUBLICATIONS **2** CITATIONS
SEE PROFILE



Dhawal Tayal
Delhi Technological University
4 PUBLICATIONS **2** CITATIONS
SEE PROFILE



Devesh Kasana
Delhi Technological University
4 PUBLICATIONS **2** CITATIONS
SEE PROFILE



Ritu Raj Ahirwar
Delhi Technological University
71 PUBLICATIONS **410** CITATIONS
SEE PROFILE

All content following this page was uploaded by Rahul Kumar Meena on 23 January 2024.

The user has requested enhancement of the downloaded file.

10 Studying wind effect on high-rise building with different cross-section

Dhruv Chaudhary[1,a], Dhawal Tayal[1,b], Devesh Kasana[1,c], Ritu Raj[1,d], S. Anbukumar[1,e] and Rahul Kumar Meena[2,f]

[1]Civil Engineering Department, Delhi Technological University, Delhi, India

[2]Civil Engineering Department, Punjab Engineering College, Chandigarh, India

Abstract

International standard is helpful to design the tall building having regular shape while the irregular shape needs evaluation because wind load is governing the design of the tall building. With the development of technology, composite plan shaped buildings like pentagon, hexagon, etc. have been given consideration by many architects while keeping in mind the building's aesthetics. Hence pressure data is not presented in most of the standards for such shape hence investigation is must for such type of building. Pressure on the upstream side face is nearly same for both buildings while suction magnitude is different in the downstream side face of the high-rise building model having pentagon and square plan shape.

Keywords: ANSYS, CFD, flow patterns, high-rise building, pressure contours

Introduction

Infrastructure of high-rise building is changing the pattern in each decade. Now a days architects have limitations in developing regular plan geometry because of the reason of land shape. Regular shape structure design is possible through the available standards while in case of irregular shape investigation is must hence CFD or wind tunnel tests are used to evaluate the wind effects. With the increment in height of the structure wind load is also increases. Different research studies have already been conducted on different shape with different specification of the building. Some of the studies are as (Bhattacharyya and Dalui, 2018) on "E"-plan shaped; (Nagar et al., 2020) on "H" and square plan (Raj et al., 2020) on "+" shape building; (Pal et al., 2021) evaluated on fish and square plan shape models; and two identical shape building a remodeled triangle shape model; and (Nagar et al., 2021) evaluated the effect on two "Plus" shape model some of the important outcomes from their studies are as pressure contour is symmetrical for symmetrical wind angle. Wind ward face is not much dependent on the shape and size. Suction will mostly be observed in the downstream wake and sides of the buildings.

Wind effects are also investigated using the CFD such as on the rectangular (Paul and Dalui, 2021; octagonal Hajra and Dalui, 2016); rectangular with different corners (Meena et al., 2022); "Y" shape most of the study were validated with experimental studies or with international standards. However, the mesh sizing will significantly affect the results if grid independence test is not performed. K-epsilon model will perform best for the tall building problems.

[a]dhruvchoudhary_2k19ce044@dtu.ac.in, [b]dhawaltayal_2k19ce043@dtu.ac.in, [c]deveshkasana_2k19ce041@dtu.ac.in, [d]rituraj@dtu.ac.in, [e]sanbukumar@dce.ac.in, [f]rahulmeena@pec.edu.in

DOI: 10.1201/9781003450924-10

The present study investigates the wind effects on tall buildings with square and pentagon plan shape. However, the area is keeping constant for both types of buildings so that the architect can decide which shape is most effective in receptive scenario. ANSYS CFX student version is used for post CFD while for simulation purpose ANSYS academic version is used. Different results like pressure contours and streamlines are presented in this chapter.

Numerical model development

Geometric modelling

Present study is performed on two building model H and A having pentagon and square shape are depicted in Figure 10.1. The height of the model is kept constant as 600 mm while the plan area of the model is same for both the model. The geometric scale is 1:350 and buildings are assumed as non-deformable. Wind effects are investigated in virtual wind tunnels and modeling is performed in ANSYS and guidelines are used as available in ASCE report no. 67 wind tunnel manual.

Results and discussions

Pressure contours

The pressure contours for pentagon shape building model-H is presented in Figure 10.2 while for model-A, square shape is presented in Figure 10.3. The pressure on face which is under direct exposure to wind is in positive pressure which is more or less identical and same magnitude. The wind effect in the form of pressure on the side faces are found symmetrical for the symmetrical wind incidence angle and same can be verified with both the Figures 10.2 and 10.3. As the wind crossing the building from its height it is presented that upstream to downstream side wind effects are

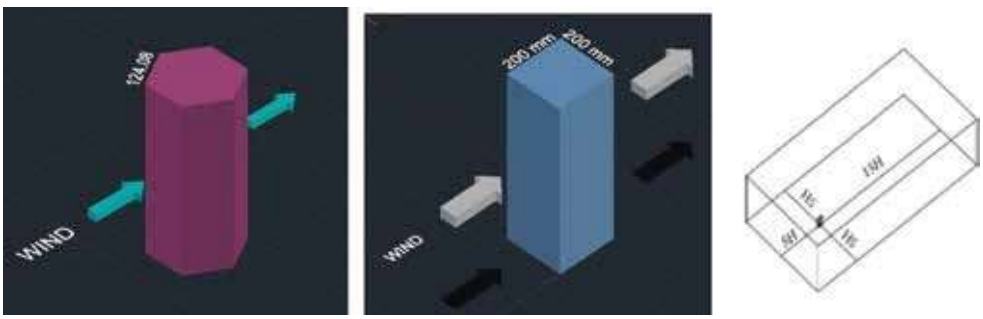


Figure 10.1 Model and domain

Source: Author

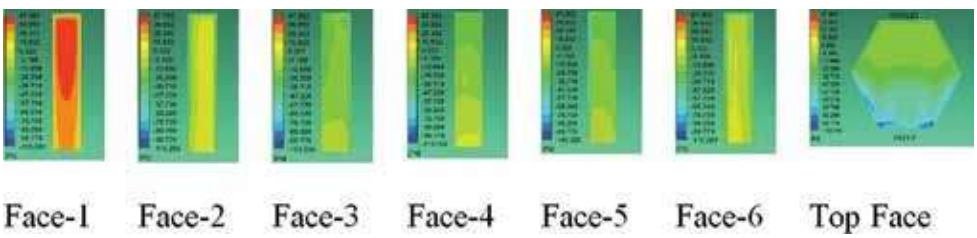


Figure 10.2 Pressure contours for model H

Source: Author

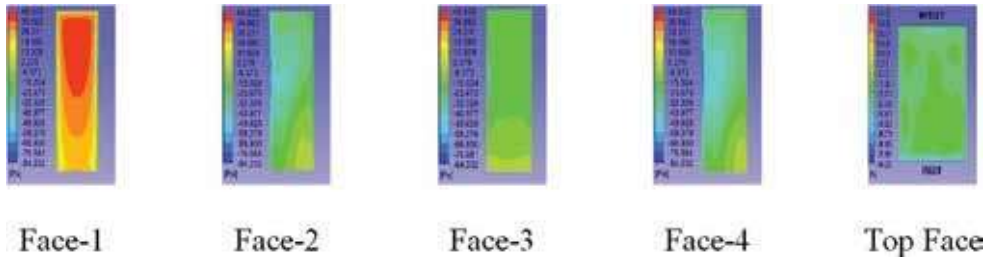


Figure 10.3 Pressure contours for model A

Source: Author

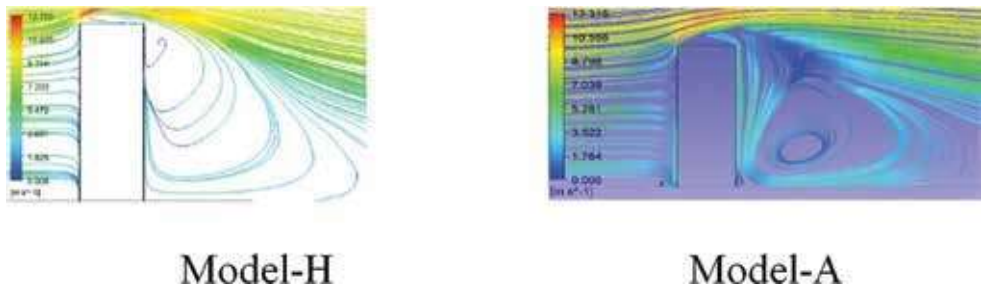


Figure 10.4 Velocity streamlines

Source: Author

changing from pressure to suction it is because of the flow reattachment in the top of the building.

The average coefficient of pressure C_p on faces 1 is +0.54, face 2 is -0.13, face 3 is -0.35, face 4 is -0.30, face 5 is -0.35, face 6 is -0.13. On face 1, the maximum positive Cp is observed 0.54. Similarly negative Cp of 0.35 are observed for Faces 3 and 5. The negative pressure coefficient values for Faces 2 and 6 are also 0.13 for model H. It can be observed that the symmetrical face such as face-2 and face-6 has equal pressure coefficient similarly face-3 and face-5 is under the same or equal pressure distribution and lee ward side face which is face-4 is having less suction than the face-3 and 5 but more suction than the face 2 and 6 it is because of the reason that the wind is incident from face-1 to face-4.

Wind effects in graphical form of pressure contours is presented for building model-A which is having square plan shape. It is clearly presented in Figure 10.3 that the wind ward face is having pressure while rest three faces side face and lee ward face of the building are in suction. The side face 2 and face 4 is having similar pressure distribution also as the wind is passing the building initially face 2 some part on upstream is in positive then the pressure starts to decrease and before leaving the side face it is under the suction and the downmost part of building on down stream of wind, side face is under the more suction then the top of the building.

The average value of C_p on face 1 is 0.68, on face 2 is -0.66, on face 3 is -0.34, on face 4 is -0.66. The maximum positive pressure coefficient value is 0.68 occurred in face 1. Faces 2 and 4 are getting similar negative pressure coefficient values of 0.66.) for building model A.

Streamlines or flow patterns

Streamlines or flow lines are helpful in understanding the flow characteristics in the upstream and downstream, Figure 10.4 is clearly indicating the flow pattern along the height of the building for both model H and A. The flow in the upstream get increases

wind speed in top and ground of the building model while from the top on third position the flow is in stagnation zone for both buildings. The flow reattachment is also presented in the top of the building and the flow reattaches the building at the top part earlier than the square building. The flow is reattaching the square building nearly at the central portion of building along the plan from upstream to downstream.

The wind speed clearly indicating different flow features such as upwash and downwash, upwash wind speed is slightly more than the downwash wind. Also, the vortex shedding in the downstream of wind for both the building is different like for square building strong vortices are observed than the pentagon shape building.

Conclusion

Due to its turbulent and unpredictable nature, wind can create various flow conditions when interacting with tall buildings, making it a complex phenomenon to study. Thus, investigating wind flow characteristics on tall buildings is crucial to understand their behavior. Important outcomes form the present research is summarized as below:

International standard is useful for the regular shape tall building while the designer needs to investigate the wind effect on irregular shape model.

Complex shapes such as hexagon, Model H, ANSYS CFX is employed to interpret wind flow characteristics on high rise structure and results are helpful to the architect in designing such type of tall building.

Effect of wind flow is presented in the form of pressure contours and vertical streamlines, are presented in vertical flow to understand different flow patterns.

The maximum positive pressure was observed on upstream face which is directly comes under the wind exposure and then the side faces as well as the downstream face are in suction.

References

Bhattacharyya, B, and Dalui, S K (2018). Investigation of mean wind pressures on "E" plan shaped tall building. *Wind and Structures, An International Journal*. 26(2), 99–114. Available at: https://doi.org/10.12989/was.2018.26.2.099.

Hajra, S, and Dalui, S K (2016). Numerical investigation of interference effect on octagonal plan shaped tall buildings. *Jordan Journal of Civil Engineering*. 10(4), 462–479.

Meena, R K, Raj, R, and Anbukumar, S (2022). Wind excited action around tall building having different corner configurations. *Advances in Civil Engineering*. 1-22. Available at: https://doi.org/https://doi.org/10.1155/2022/1529416.

Nagar, S K, Raj, R, and Dev, N (2020). Experimental study of wind-induced pressures on tall buildings of different shapes. *Wind and Structures, An International Journal*. 31(5), 441–453. Available at: https://doi.org/10.12989/was.2020.31.5.431.

Nagar, S K, Raj, R, and Dev, N (2021). Proximity effects between two plus-plan shaped high-rise buildings on mean and RMS pressure coefficients. *Scientia Iranica*. 0(0), 28. Available at: https://doi.org/10.24200/sci.2021.55928.4484.

Pal, S, Raj, R, and Anbukumar, S (2021). Comparative study of wind induced mutual interference effects on square and fish-plan shape tall buildings. *Sa¯dhana¯*. 46(2), 86. Available at: https://doi.org/10.1007/s12046-021-01592-6.

Paul, R, and Dalui, S K (2021). Shape optimization to reduce wind pressure on the surfaces of a rectangular building with horizontal limbs. *Periodica Polytechnica Civil Engineering*. 65(1), 134–149. Available at: https://doi.org/10.3311/PPci.16888.

Raj, R, et al. (2020). Response analysis of plus shaped tall building with different bracing systems under wind load. *International Journal of Advanced Research in Engineering and Technology*.11(3), 371–380.Available at: https://doi.org/10.34218/IJARET.11.3.2020.032.

This article has been accepted for inclusion in a future issue of this journal. Content is final as presented, with the exception of pagination.

A Battery Digital Twin From Laboratory Data Using Wavelet Analysis and Neural Networks

Roberta Di Fonso, *Member, IEEE*, Remus Teodorescu, *Fellow, IEEE*, Carlo Cecati, *Life Fellow, IEEE*, and Pallavi Bharadwaj, *Member, IEEE*

***Abstract*—Lithium-ion (Li-ion) batteries are the preferred choice for energy storage applications. Li-ion performances degrade with time and usage, leading to a decreased total charge capacity and to an increased internal resistance. In this article, the wavelet analysis is used to filter the voltage and current signals of the battery to estimate the internal complex impedance as a function of state of charge (SoC) and state of health (SoH). The collected data are then used to synthesize a battery digital twin (BDT). This BDT outputs a realistic voltage signal as a function of SoC and SoH inputs. The BDT is based on feed-forward neural networks trained to simulate the complex internal impedance and the open-circuit voltage generator. The effectiveness of the proposed method is verified on the dataset from the prognostics data repository of NASA.**

***Index Terms*—Battery digital twin (BDT), data-driven modeling, impedance estimation, neural network (NN), wavelet analysis.**

I. Introduction

LITHIUM-ION batteries are the preferred energy source for energy storage applications, ranging from low power in smartphones to high power in electric vehicles (EVs). To accommodate such a wide spectrum of systems, many elementary cells are connected in series/parallel to built a suitable battery pack with required voltage and current capabilities. The overall behavior of the battery is, thus, a function of the behavior of a single cell. During the lifetime, the cell is charged/discharged many times. The internal electrochemical processes are not completely reversible, leading to aging. When a cell ages, its full charged capacity decreases (capacity fade) and its internal resistance rises (power fade), negatively impacting the operational efficiency [1]. For instance, in EV applications, this capacity fade leads to the so called range anxiety and the power fade leads to loss of performance in driving experience and to higher battery temperature, with detrimental effects on battery lifetime. Two important indicators give a compact information of the cell states: state of charge (SoC) and state of health (SoH). SoC is an indicator of the actual charge inside the cell and it can be computed by integrating the current exchanged with the external circuit. SoC is a relative measure of the actual charge, normalized to the full-charge capacity. SoH instead, is a relative measure of the actual full charged capacity, normalized to the full-charge capacity of a fresh built cell. Both indicators are normalized in the range 1 to 0. It is critical to keep monitoring the SoC and SoH of the battery to prevent working conditions that hasten irreversible degradation reactions. SoC and SoH must be estimated from the observation of voltage and current signals at the accessible terminal connections because they cannot be measured directly with sensors on cells.

A. Artificial Intelligence (AI) in Batteries: the Data Challenge

AI has progressively become a very attractive tool to be applied to batteries, mostly to the estimation of battery states and parameters [2], [3], [4], [5], but more recently also to battery modeling [6]. Neural networks (NNs) are broadly used for their capability to infer input–output relationship between data in an automated way, a process known as black-box modeling. A successful application of NN, requires a lot of training data taken from field-specific applications. The input data are usually preprocessed using domain-specific knowledge by researchers. This process requires a great deal of time and effort, since the data need to be fully understood and cleaned of all the parts that are not relevant for the extraction of the data input–output relationship. Despite allowing the creation of accurate models, AI applications are still perceived as opaque since it is usually not easy to understand the reasoning behind the choices made by these black-box models. Therefore, it is of paramount importance to put effort in developing a model that is easily interpretable, thus offering a pragmatic understanding of AI [7].

Manuscript received 8 June 2023; revised 12 September 2023 and 4 December 2023; accepted 24 December 2023. This work was supported in part by the Italian Ministry of University and Research through PRIN2017 project under Grant 2017MS9F49, in part by the SMART BATTERY project, granted by Villum Foundation in 2021 (Project 222860), and in part by the Risorse del Programma Operativo Nazionale Ricerca e Innovazione 2014–2020 under Grant CCI 2014IT16M2OP005. Paper no. TII-23-2082. *(Corresponding author: Roberta Di Fonso.)*

Roberta Di Fonso and Carlo Cecati are with the Department of Information Engineering, Computer Science and Mathematics, University of L'Aquila, 67100 L'Aquila, Italy (e-mail: roberta.difonso@graduate.univaq.it; carlo.cecati@univaq.it).

Remus Teodorescu is with the Department of Energy Technology, Aalborg University, 9220 Aalborg, Denmark (e-mail: ret@energy.aau.dk).

Pallavi Bharadwaj is with the Department of Electrical Engineering, Indian Institute of Technology, Gandhinagar 382055, India (e-mail: pallavib@iitgn.ac.in).

Color versions of one or more figures in this article are available at https://doi.org/10.1109/TII.2024.3355124.

Digital Object Identifier 10.1109/TII.2024.3355124

© 2024 The Authors. This work is licensed under a Creative Commons Attribution-NonCommercial-NoDerivatives 4.0 License. For more information, see https://creativecommons.org/licenses/by-nc-nd/4.0/

This article has been accepted for inclusion in a future issue of this journal. Content is final as presented, with the exception of pagination.

B. Battery Modeling and Related Issues

Different field applications require different aspects of battery modeling. Several models have been developed in the literature, depending on the targeted level of abstraction [8]: empirical models, which use functions to describe the dynamics of the battery [9]; electrochemical models, which offer insight to the internal chemistry of the battery and use complex partial differential equations to describe the dynamics of the battery [10], [11], [12], [13]; equivalent circuit models (ECMs), which model the dynamics of the battery with circuit components, such as voltage generator, resistors (R), and capacitors (C) [14], [15], [16]. ECM models are computationally lighter with respect to other models. The identification of circuit parameters can be done using a variety of methods, such as electrochemical impedance spectroscopy (EIS) [17]. Traditional EIS is a technique to measure the real and imaginary parts of internal impedance Z as a function of frequency. It is an expensive lab activity that requires a scanning sine wave generator, powerful enough to stimulate the battery at different frequencies, from mHz to kHz. The result is a Nyquist plot that is only valid for well-defined values of T, SoC and SoH. The Nyquist plot is then fitted with a circuit containing resistors, capacitors, and even more complex components like Warburg impedance or constant phase element (CPE). However, Z is a function of temperature T, SoC, SoH, and a complete estimation of the components would require an extensive use of EIS. An alternative solution could be the injection of a wide spectrum current signal to the battery. Then, the resulting voltage drop could be analyzed in frequency domain with signal processing techniques [18]. However, as the parameter identification is primarily done offline in EIS, its impedance evaluation approaches are not very helpful for EVs. Since real-time information may be used to operate the battery effectively, an online identification would be more beneficial. Laboratory procedures can take weeks or months to observe the effects of aging on actual batteries and they also call for specialized equipment to ensure safety. Fortunately numerous high-end laboratories have recently made their experimental datasets publicly available for researchers [19]. These data are invaluable, although they are inevitably restricted to a few specific battery cell working conditions, primarily charge–discharge cycles with steady or pulsed currents.

C. Battery Digital Twin

The concept of digital twin has been first introduced by John Vickers from NASA, in 2010 [20] and has gained a lot of interest over recent years both from academia and industry [21], [22]. A digital twin is a digital representation of a unique system of interest. This digital representation is built by using models, information, and data that are representative of the selected characteristics, behaviors, and life cycle of the system that we want to model [23]. In this article, we develop a high-fidelity model that replicates the behavior of a real battery according to its different working conditions. We refer to this model as battery digital twin (BDT). The BDT produces a realistic output voltage signal when receives as inputs a load current waveform of any shape and normalized SoC and SoH parameters, i.e., known charge and aging states. The BDT is essentially a battery simulator that can emulate the cell behavior at different operating conditions. The synthesis of the BDT requires the knowledge of the internal impedance of the real cell as a function of T, SoC, and SoH. In this article, we show that the identification of the internal complex impedance Z can be done by pulsed discharging the cell and then by processing the voltage and current signals. Any lab can easily record pulsed discharge signals of a cell under test. Moreover, in this article, we show that a current pulse applied to the battery, is enough to draw a partial Nyquist plot over at least two decades of frequencies. This allows us to bring the battery testing from the lab to the field of application. After the identification of Z, it is possible to compute the voltage drop across Z and, thus, identify also the open-circuit voltage (OCV) generator as a function of T, SoC, SoH. In summary, the complete ECM model can be extracted from pulsed discharge signals. Afterwards, a realistic BDT can be synthesized and used for many purposes, like the validation of both SoC, SoH estimation algorithms and cell balancing algorithms [24], to name a few. In this article, we use the aging data from the NASA Prognostic Repository [19]. The main contributions of this article are the following:

1) showing how to use the wavelet analysis for online impedance estimation;
2) showing how the wavelet analysis can be used as a tool for automating the preprocessing phase of training data for NN;
3) showing a methodology for OCV extraction;
4) showing how to build a BDT by training NN for the OCV, and the internal impedance circuit elements.

II. Equivalent Circuit Model

Lithium-ion batteries are based on highly complex chemistry that is not easy to understand. However, from the perspective of the application, we need only to know how the battery behaves at the accessible terminals. The ECM it is an electrical model based on common circuit elements, such as voltage generator, resistors, and capacitors. The Randles circuit is based on electrochemical principles [25]:

1) R_0 models the electrolyte resistance;
2) R_1 models the voltage drop over the electrode–electrolyte interface;
3) C_1 models the effect of charges building up in the electrolyte at the electrode surface;
4) Z_W is the Warburg impedance that models diffusion of lithium-ions in the electrodes.

The Warburg impedance

$$Z_W = {}^{A_W}/_{\sqrt{j\omega}} \tag{1}$$

is frequency-dependent and can be thought of the impedance of a semi-infinite transmission line composed only of resistance and capacitance per unit length, where A_W is the Warburg coefficient and ω is the frequency [8]. The precise simulation of a Warburg impedance requires an infinite number of RC pairs and is, thus, not practical. However, Z_W can be modeled well over some frequency range using few RC pairs. The double-layer capacitance

This article has been accepted for inclusion in a future issue of this journal. Content is final as presented, with the exception of pagination.

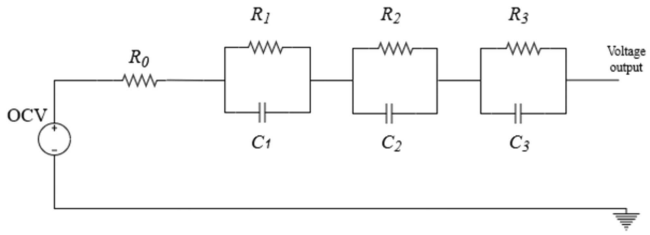


Fig. 1. Complete 3RC ECM model.

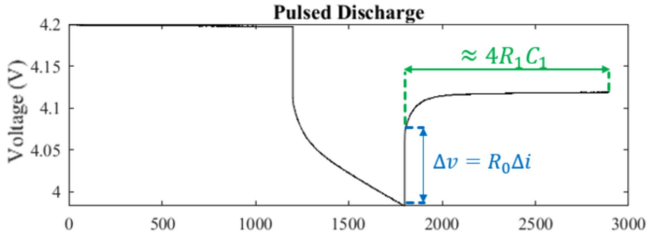


Fig. 2. Battery output voltage response to a 1 A current pulse.

C_1 of the Randles circuit has little effects except at very high frequencies and can, thus, be often omitted. Substituting the Z_W with a small number of RC pairs, the Randles circuit becomes comparable to the one shown in Fig. 1. This ECM model is adopted in this work. Note that the ideal generator, labeled as OCV, R_0 and all RC pairs are nonlinear function of temperature T, SoC, and SoH [8]. To simulate a specific real battery cell, it is first necessary to identify the dependencies of all elements of the ECM model by means of laboratory measurements. Regarding the OCV generator, as the name implies, it can be easily measured at zero or low currents, although the complete function characterization requires a time-consuming process in the lab. The identification of all RC elements is more challenging as they are not accessible from the battery terminals. However, the collective effects of all the RC elements, i.e., of the battery internal impedance, is fully observable as an output voltage drop when the battery supplies current to an external load, as shown in Fig. 2 for a first-order circuit. It is useful to note that the resistance R_0 is linked to the fast change of signal, i.e., to high frequencies, and the RC pair is linked to slow change of signal, i.e., to low frequencies. The traditional identification method of the internal impedance is performed by using EIS, which requires special equipment and time-consuming measurements in the lab. In the following section, we will show that the identification of the internal complex impedance can be done in different ways, by means of signal processing of the battery voltage and current signals.

III. Time-Frequency Analysis of the Battery Signals

We propose to analyze the pulsed discharge signals of a battery in order to recover multiple Nyquist plot, one for each current pulse, corresponding to different SoC. If the process is repeated at different SoH and different T, we obtain a complete characterization of the battery internal impedance as a function of T, SoC, and SoH. The overall frequency analysis of the signals cannot be done with a simple fast Fourier transform (FFT), because this transform locates the signal only in frequency and loses the time information related to SoC. Instead, the frequencies of each pulse must be distinguished by the others in order to build different Nyquist plots at different SoC. The solution is a continuous wavelet transform (CWT) that allows a time-frequency localization of signals [26]. The CWT analyzes a signal with a wavelet, a waveform that is concentrated both in time and in frequency domain. The CWT of a finite energy signal $x(t)$ is [18]

$$W_\Psi(u,s) = \frac{1}{\sqrt{s}} \int_{-\infty}^{+\infty} x(t) \Psi^* \frac{(t-u)}{s} dt \qquad (2)$$

where $\Psi(t)$ represents the mother wavelet, i.e., a complex-valued time-frequency filter; u is the time shift parameter (for time localization) and s is a scaling parameter (for frequency localization). By choosing a suitable mother wavelet, we can compute the time-frequency content of the signal as coefficients of the CWT. The choice of which wavelet to use depends on its time and frequency resolution. Only analytic wavelets will be considered, i.e., wavelets whose spectrum is zero for negative angular frequencies: $\Psi(\omega) = 0, \quad \omega < 0$. Generalized Morse wavelets are a family of complex-valued analytic wavelets whose Fourier transforms are supported on the positive real axis. They are useful for analyzing modulated signals with time-varying amplitude and frequency. Many commonly used analytic wavelets are special cases of the generalized Morse wavelets, as detailed in [27]. In this work, we will use the generalized Morse wavelet [28]

$$\Psi(\omega) = U(\omega) K_{(\beta,\gamma)} \omega^\beta e^{-\omega^\gamma} \qquad (3)$$

where $U(\omega)$ is the Heaviside function, and $K_{(\beta,\gamma)}$ is a normalizing factor and β and γ are two parameters that control the wavelet form. A measure of the concentration is the so called Heisenberg area, defined as the product of standard deviations in the time domain and in the frequency domain, respectively. Unlike other mother wavelets, the generalized Morse wavelet is defined by two parameters $\beta, \gamma > 0$ that allow us to change the wavelet properties, while remaining exactly analytic [18], [27], [29]. By properly choosing β, γ, ω we can tune the frequency and the bandpass resolution. An example of the generalized Morse wavelet is shown in Fig. 3. Here, the parameters γ and β have been chosen in order to obtain a small Heisenberg area. This wavelet in time domain can be thought as the impulse response of a bandpass filter. Then, the CWT output can be thought as a filtered version of the input signal. By changing the wavelet frequency, we perform a time-frequency analysis of a signal. The highest possible wavelet frequency is established by half of the sampling frequency of signals (or $\omega = \pi f_s$). The lowest possible frequency for pulsed discharge signals must be chosen in order to avoid the overlapping of wavelets located at adjacent fronts of current pulses. Fig. 4 shows a zoomed view of a wavelet located at a rising edge of battery voltage signal (falling edge of battery current): the real and imaginary part, as well the absolute value are shown. The absolute value peaks at the rising transition of the voltage signal.

This article has been accepted for inclusion in a future issue of this journal. Content is final as presented, with the exception of pagination.

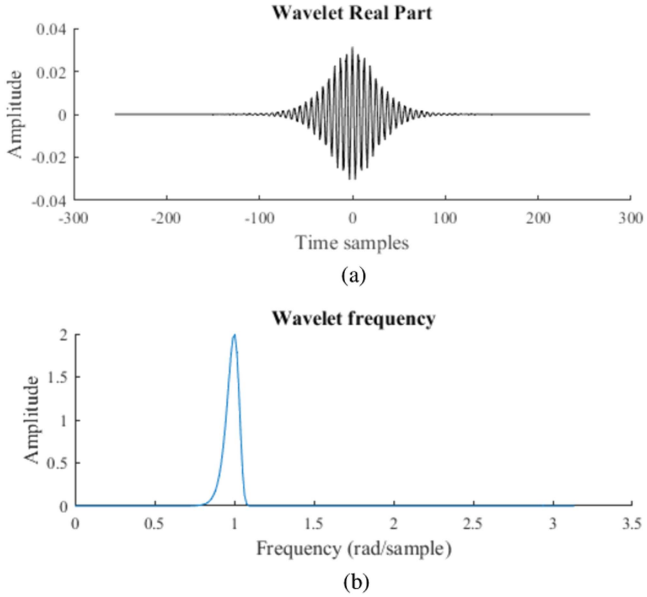


Fig. 3. Generalized Morse Wavelet ($\beta = \gamma = 3,\ \omega = 1$). (a) Wavelet real part. (b) Wavelet frequency.

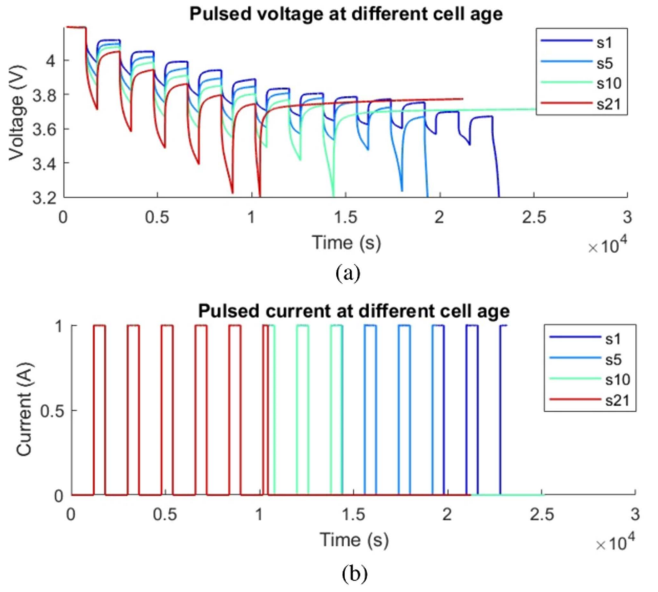


Fig. 5. Selected discharge pulsed voltages and currents from the NASA dataset. (a) Pulsed voltage. (b) Pulsed current.

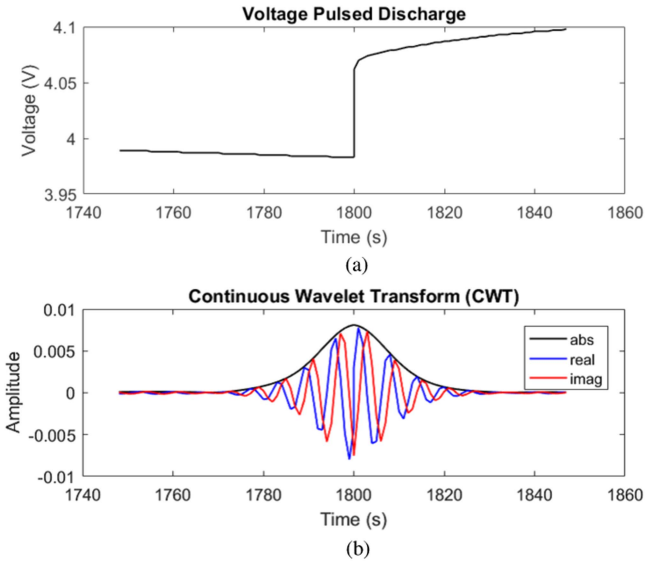


Fig. 4. CWT shown in (a) of the pulsed discharge voltage shown in (b). (a) Pulsed voltage discharge. (b) CWT.

Knowing this behavior, the wavelet transform is applied to voltage and current signals $v(t), i(t)$ of the cell battery in order to obtain a set of coefficients

$$\begin{aligned} W_i(t,\omega) &= \mathrm{Re}\{W_i(t,\omega)\} + j\mathrm{Im}\{W_i(t,\omega)\} \\ W_v(t,\omega) &= \mathrm{Re}\{W_v(t,\omega)\} + j\mathrm{Im}\{W_v(t,\omega)\} \end{aligned} \tag{4}$$

where $W_v(t,\omega)$ is the wavelet transform of the signal $v(t)$ as a function of time t and angular frequency ω. Since the transform is a linear operation, the cell impedance Z can be then identified by a division between the CWT coefficients of voltage and current:

$$Z(t,\omega) = \frac{W_v(t,\omega)}{W_i(t,\omega)}. \tag{5}$$

$Z(t,\omega)$ is the instantaneous amplitude and phase of impedance Z at angular frequency ω. When we divide the CWT of battery voltage and the CWT of battery current at each falling edge, we obtain a single point on multiple Nyquist plots, each corresponding to a falling edge of current, i.e., at different SoC. Changing the wavelet frequency, we can complete all Nyquist plots over a range of frequencies within the limits explained.

IV. Wavelet Analysis of Prerecorded Dataset Under Test

The proposed method has been applied to the NASA dataset [19]. This dataset has 21 pulsed discharge sequences of cell voltage and current, synchronously sampled at 1 Hz and recorded at different ageing times. The maximum Nyquist frequency is thus 0.5 Hz and the CWT can use a wavelet with $\omega_{\max} = 2\pi\, 0.5 = \pi$.

In Fig. 5, only the sequences 1, 5, 10, and 21 are superimposed for a better visualization. A current pulse of 1 A is applied for 10 min, followed by 20 min of rest. Each current pulse extracts from the cell a charge of $1/6$ Ah. The process is repeated until the depletion of the cell. The last current pulse of a sequence can be shorter than 10 min. Integrating the current, we obtain the charge capacity of the cell. The fresh cell has total capacity of 2.1 Ah (sequence 1), the aged cell at end of life has a total capacity of about 0.9 Ah (sequence 21). By applying the CWT to the NASA dataset, we obtain a Nyquist plots at each current front. For visualization clarity, we will show the Nyquist plots computed in correspondence to the falling edge of the third discharge pulse (from the left) of each curve shown in Fig. 5. At the third discharge edge, the total charge extracted from the cell is 0.5 Ah. The Nyquist plots have 30 points each, corresponding to log spaced frequencies from $\omega = 2[\,^{\mathrm{rad}}/_{s}]$ to $\omega = 0.02[\,^{\mathrm{rad}}/_{s}]$ (two decades). Fig. 6 shows the

This article has been accepted for inclusion in a future issue of this journal. Content is final as presented, with the exception of pagination.

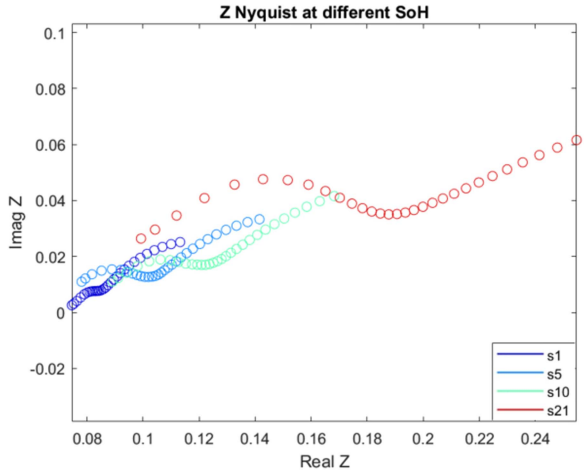


Fig. 6. Nyquist plots of the third discharge pulse computed with the CWT for different SoH.

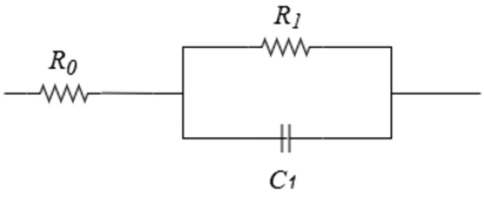


Fig. 7. Single-order ECM.

results for the sequences of Fig. 5, with the same colours for the identification. It is evident the increase of the impedance as the cell ages and the charge capacity fades (decrease of SoH). The Nyquist plots from traditional EIS are computed over a wider frequency range. For example, the intersection with the real axis cannot be computed with CWT due to the limits of the sampling frequency of the cell signals. However, this reduced view of plots has enough information and allows us to successfully extract equivalent circuit elements.

V. Fitting the Nyquist Plots

Nyquist plots show complex impedance values measured at different frequencies. We want to find an equivalent circuit that matches the impedance behavior of the Nyquist plots. We know that for batteries the circuit elements are mainly resistors and capacitors. Small inductances are only due to battery terminals and are present only at high frequencies, which are not considered in this work. Even complex components like Warburg impedance or CPE can be approximated by RC circuits, as they can be modeled by a large number of RC pairs, as in an equivalent transmission line. For batteries, the simplest first-order equivalent circuit is shown in Fig. 7. The corresponding Nyquist plot of the single order simple ECM is a semicircle with center at $R_0 + R_1/2$ and radius $R_1/2$. C_1 has effects on the frequency behavior, as described in detail in [25]. For this simple Nyquist plot, it is possible to write down some formulas to fit the equivalent R_0, R_1, and C_1 circuit elements. Fig. 8 shows some semicircle points computed with the CWT method at known

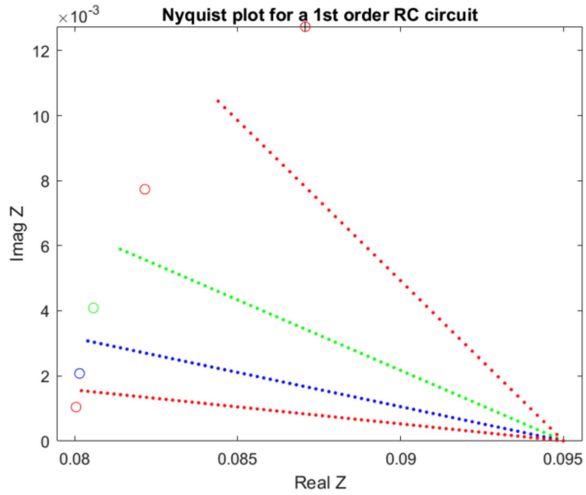


Fig. 8. Selected points computed from Nyquist plot.

frequencies and also the bisects of cords between adjacent points. The bisects intersect at the center of the semicircle, also lying on the real Z-axis. With simple geometric considerations, the following formulas can be written down:

$$Z = R_0 + \frac{R_1}{(1 + sR_1C_1)} \qquad \text{where } s = j\omega \tag{6}$$

the real part $\mathrm{Re}(Z)$ and the imaginary part $\mathrm{Im}(Z)$ are, respectively:

$$\begin{aligned} \mathrm{Re}(Z) &= R_0 + \frac{R_1}{1 + (\omega R_1 C_1)^2} \\ \mathrm{Im}(Z) &= \frac{-\omega R_1^2 C_1}{1 + (\omega R_1 C_1)^2}. \end{aligned} \tag{7}$$

If we consider two different frequencies ω_1 and ω_2, and their respective imaginary parts $\mathrm{Im}(Z_{\omega_1})$ and $\mathrm{Im}(Z_{\omega_2})$, we obtain

$$C_1 = \frac{\frac{\omega_2}{\mathrm{Im2}} - \frac{\omega_1}{\mathrm{Im1}}}{\omega_1^2 - \omega_2^2}. \tag{8}$$

The semicircular Nyquist plot has center $c_N = R_0 + \frac{R_1}{2}$ and radius $r_N = \frac{R_1}{2}$. We know that a perpendicular that bisects a chord passes for the center of the circle. The midpoint P on the chord has the following coordinates:

$$\begin{aligned} p_x &= \mathrm{Re}\,(Z_2) + \tfrac{\mathrm{DR}}{2} \\ p_y &= \mathrm{Im}\,(Z_1) + \tfrac{\mathrm{DI}}{2} \end{aligned} \tag{9}$$

where

$$\begin{aligned} \mathrm{DR} &= abs\,(\mathrm{Re}\,(Z_1) - \mathrm{Re}\,(Z_2)) \\ \mathrm{DI} &= abs\,(\mathrm{Im}\,(Z_1) - \mathrm{Im}\,(Z_2))\,. \end{aligned} \tag{10}$$

The angular coefficient of the perpendicular is

$$\begin{aligned} m &= \tan\left(\frac{\pi}{2} + \arctan\left(\frac{\mathrm{DI}}{\mathrm{DR}}\right)\right) \\ y &= m \cdot (x - p_x) + p_y \end{aligned} \tag{11}$$

This article has been accepted for inclusion in a future issue of this journal. Content is final as presented, with the exception of pagination.

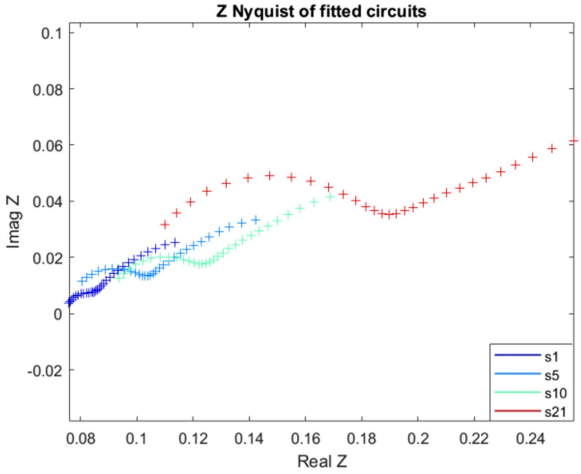


Fig. 9. Third-order ECM fitted values using optimization.

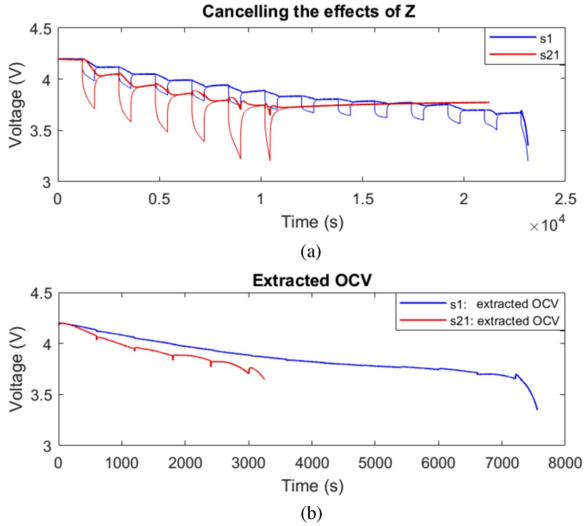


Fig. 10. OCV reconstruction for sequences 1 and 21 of the NASA dataset. (a) Canceling the effects of the impedance Z. (b) Extracted OCV.

and the circle center on the horizontal axis of the Nyquist plot is

$$c_N = \frac{m \cdot (p_x - p_y)}{m}. \tag{12}$$

Finally, we can obtain R_1

$$R_1 = \sqrt{(c_N - \mathrm{Re}\,(Z_1))^2 + \mathrm{Im}\,(Z_2)^2}. \tag{13}$$

These formulas require only two Nyquist points, with better results for bisects near 45°. The component values corresponding to the Nyquist plot of Fig. 8 are: $R_0 = 0.08\ \Omega$; $R_1 = 0.03\ \Omega$; $C_1 = 600\ F$. Real cells have more complicated Nyquist plots and circuit fitting is much more challenging. Nyquist plots computed from the NASA dataset and shown in Fig. 6 require higher order RC circuits for which geometric considerations to derive simple formulas for the components computation are not possible. The solution is to fit RC values with known optimization techniques that minimize the distance between the Nyquist plot and the Z behavior of the ECM circuit. Using the NASA dataset, we will fit the parameters of the ECM model shown in Fig. 1. In the MATLAB environment the fminsearch function can do the job for fitting the Nyquist plots [30]. fminsearch makes a guess for the seven $R_0, R_1, C_1, R_2, C_2, R_3, C_3$ parameters and then call a user callback function that must return a scalar as a measure of distance. The scalar returned has been computed as the unweighted squared distance between the Nyquist points and the corresponding guessed points. Due to the large search space, it is important to start from a good starting guess for a successful fitting. The first guess has been computed with the formulas shown above for a first-order circuit. The fitting results for Nyquist plots of Fig. 6 are shown in Fig. 9, with the same colours for identification.

The $R_0, R_1, C_1, R_2, C_2, R_3, C_3$ have been computed for all the current fronts of all the 21 NASA sequences, obtaining seven functions of cell parameters dependent on SoC, SoH. The dependability from temperature T cannot be computed as all the NASA sequences are taken at room temperature.

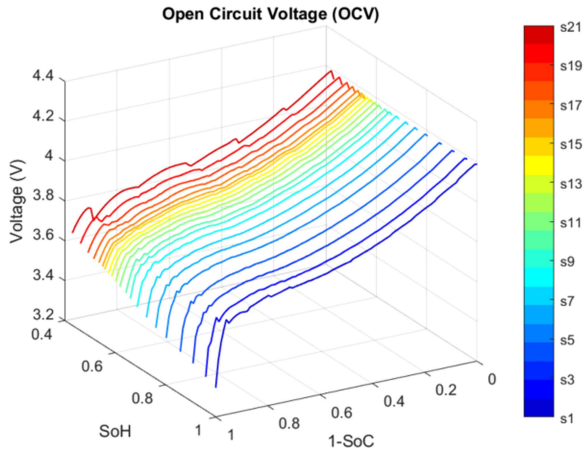


Fig. 11. OCV reconstruction results on the NASA dataset.

VI. OCV Extraction

The OCV of a cell, at a fixed temperature and at a defined aging condition, is a nonlinear function of SoC [31]. This means that the dV drop after the a discharge dQ depends on the SoC. The ratio dQ/dV has a dimension of a capacitance and has a finite value. Thus, the OCV generator can be thought as a nonlinear supercapacitor. Its reactance at the frequencies of the previous Nyquist plots is low, but it has been taken into account by correcting the imaginary part of the internal impedance Z. Here, we want to estimate the OCV generator as a function of SoC and SoH in order to be able to simulate it as a voltage controlled voltage source. Thanks to the previous analysis, we now know the values of the complex internal impedance Z. We can reverse engineer the pulsed voltage discharge signal and subtract the dynamic effects of Z traversed by the pulsed current. The voltage contribution of R_0 is simply the instantaneous product $R_0 i(t)$. The voltage contribution of each pair $R_i C_i$ $(i = 1, 2, 3)$ can be

This article has been accepted for inclusion in a future issue of this journal. Content is final as presented, with the exception of pagination.

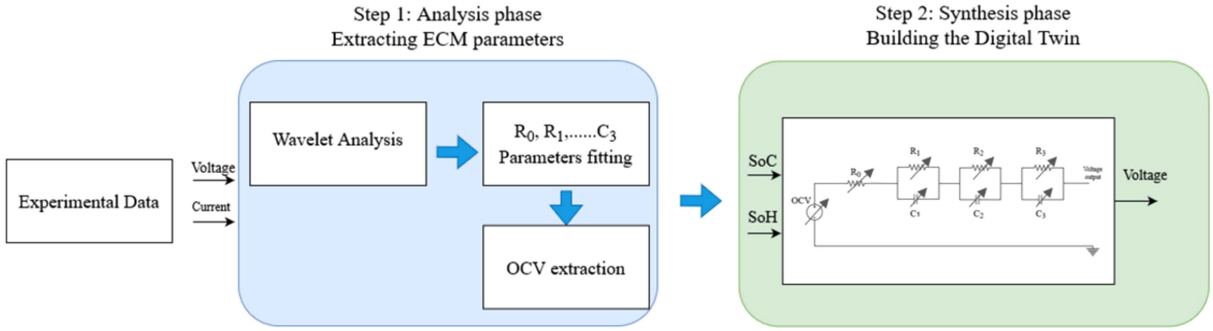


Fig. 12. BDT development block scheme.

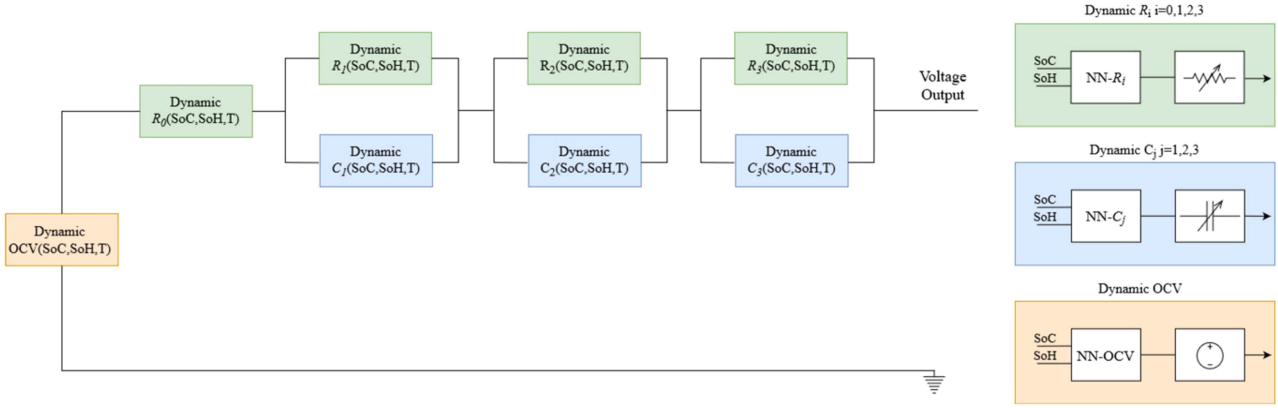


Fig. 13. NN-based dynamic ECM model.

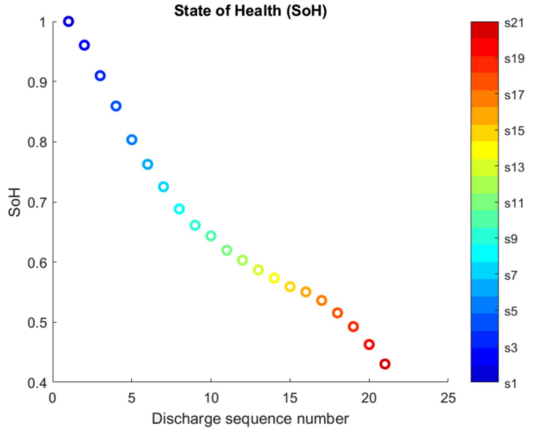


Fig. 14. SoH versus sequence number for the NASA dataset.

computed by the following recursive formula:

$$v_{RC}(k+1) = \exp(-dt/RC)v_{RC}(k) + (1-\exp(-dt/RC))Ri(k) \quad (14)$$

where dt is the sampling period and k is the sample index at time kdt. The total voltage effect of Z is the sum of the four contributions. When this total voltage is summed to the original pulsed voltage of Fig. 5, the results are shown in Fig. 10 (for ease of view, only sequences 1 and 21 are shown).

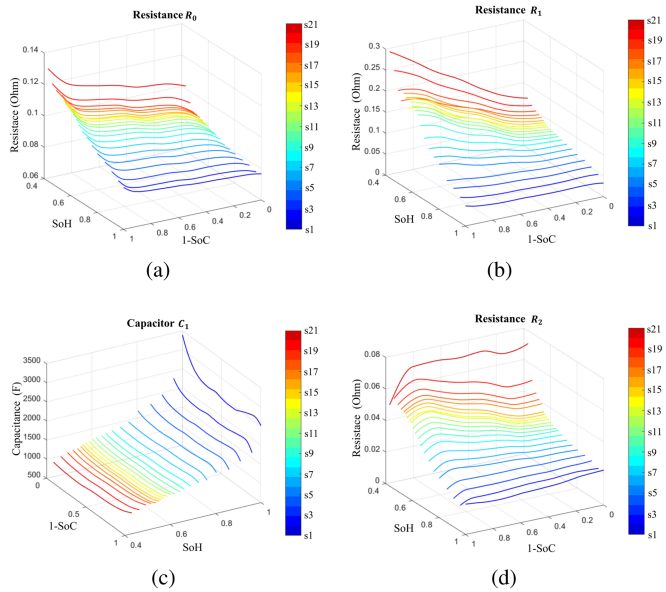


Fig. 15. R_0, R_1, C_1, R_2 ECM parameters values using wavelet analysis on the NASA dataset. (a) R_0(SoC, SoH). (b) R_1(SoC, SoH). (c) C_1(SoC, SoH). (d) R_2(SoC,SoH).

Now, recording the voltage output only when the current is 1 A (i.e., during the current pulses), we obtain the classical OCV plot. The horizontal axis shows time, but it can be easily converted

This article has been accepted for inclusion in a future issue of this journal. Content is final as presented, with the exception of pagination.

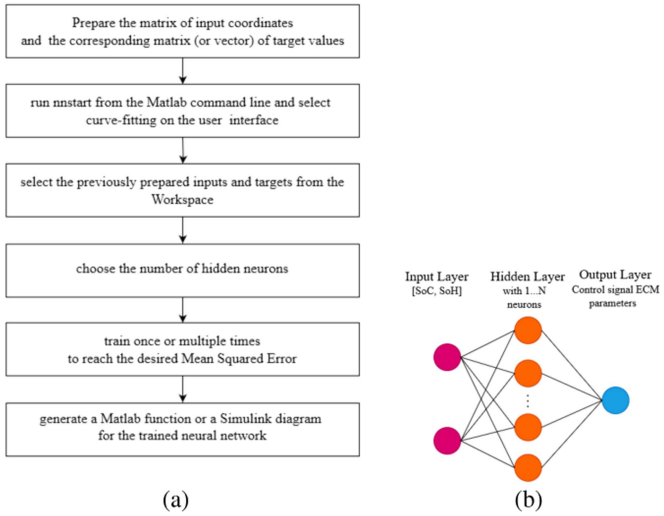


Fig. 16. Training the NNs using deep learning toolbox. (a) Steps to build the NN. (b) NN architecture.

to Ah and thus to SoC. The results for all 21 sequences are shown in Fig. 11. It is worth noting that using the extracted parameters $R_0, R_1, C_1, R_2, C_2, R_3, C_3$ we are able to cancel almost completely the voltage pulses due to internal Z on Fig. 10, obtaining the classical S-shaped curve for the extracted OCV.

VII. Battery Digital Twin

We will synthesize a BDT leveraging on the 3RC ECM model presented in Fig. 1. Developing a BDT starting from pulsed discharge experimental data is a two-step process, as shown in Fig. 12.

In the analysis phase, experimental data are analyzed to extract only the relevant parts needed to train the NN. This phase is performed with wavelet analysis, parameters fitting and by applying the OCV extraction methodology presented in Section VI.

The data coming from the analysis step are used in the synthesis step to train the NNs of the BDT model, as shown in Fig. 13. Each NN will receive as input the SoH and SoC values and compute the present values for the OCV, R_0, R_1, C_1, R_2, C_2, R_3, C_3.

NNs can exactly fit the training points and moreover, they can compute the output for intermediate points, thanks to their interpolation and generalization properties. This simple structure aids the interpretability of the model.

VIII. Training the NNs

At this point, we know all the circuit elements of the ECM model as a continuous function of SoC and at 21 values of SoH (the 21 sequences of NASA dataset). SoH, shown in Fig. 14, is computed as the ratio of the charge capacity of the aged cell over the charge capacity of the fresh cell. Figs. 15 and 17 show the functions for $R_0, R_1, C_1, R_2, C_2, R_3, C_3$. In the side bars, $s1$ colour identifies the pulsed discharge sequence 1 of the fresh cell (longest sequence), $s21$ colour identifies the pulsed discharge sequence 21 of the cell at the end-of-life (shortest sequence). It is easy to accept that internal resistance values increase as the cell ages. Less obvious is the simultaneous decrease of capacitor values, presumably related to the diffusion process inside the cell.

The NN training has been performed in the MATLAB environment using the deep learning Toolbox following the steps shown in Fig. 16(a). After several trials on different partitions of RC elements, it turns out that the best generalization results can be obtained by training an NN for each function $R_0, R_1, C_1, R_2, C_2, R_3, C_3$, OCV. In this way, each NN needs only a few neurons (10–20) and the optimization can be carried out without interference from the other parameters. Other choices lead to bulk NNs with many neurons and with poor generalization.

The chosen NN architecture is a two-layer feedforward network with N sigmoid-activated hidden neurons and linear output neuron, with $10 \leq N \leq 20$. The NN structure is shown in Fig. 16(b).

Each NN has as input the same two row vectors [SoC; SoH] and outputs the control for the corresponding circuit parameter. The networks are trained with the Levenberg–Marquardt backpropagation algorithm [32]. The training can be run several times. The best result must have the lowest mean squared error (MSE) between the NN outputs and the target values. The NNs trained with the data shown in Figs. 11, 15, and 17 have an MSE in the range $10^{-6} \leq \text{MSE} \leq 10^{-4}$.

IX. Results

The Simulink scheme of the cell model is shown in Fig. 18. On the right side of Fig. 18, we can recognize the RC circuit for the realization of the complex internal impedance of the cell. All elements are variable and are controlled by an ensemble of NNs. The OCV generator is realized by a controlled voltage source, again controlled by an NN. All NNs receive in input the same SoC, SoH control signal. All electrical components are taken from the Simscape library and are simulated as physical elements (note the blue colour of the scheme). On the left side of Fig 18, we can see a Simulink test circuit of the cell model. The test performs a pulsed discharge of the cell with a current of 1 A, with the same timings of the NASA signals (10 min ON, 20 minutes OFF). The charged fresh cell has a charge capacity of Q (2.1 Ah in the example). A Coulomb counting function computes the SoC and sends it to the NNs. For simplicity, SoH is fixed as a constant. In a more sophisticated simulation, SoH can be computed from calendar ageing and/or from cycling ageing. The cell model outputs a realistic voltage signal according to the SoC, SoH states. By reversing the input current, the cell model can be used also for charging simulation. The blocks CellC.mat and CellV.mat record the current and voltage signals on files, for later offline postprocessing. The gain blocks between NNs and variable elements determine the actual values of the circuit components. The gains can be set up at the start of the simulation by an init.m program that writes variable values in the MATLAB workspace. The gains are present because the NNs are normalized to the component values at SoC $= 1$, SoH $= 1$ (see values on Figs. 15 and 17). This solution has been

This article has been accepted for inclusion in a future issue of this journal. Content is final as presented, with the exception of pagination.

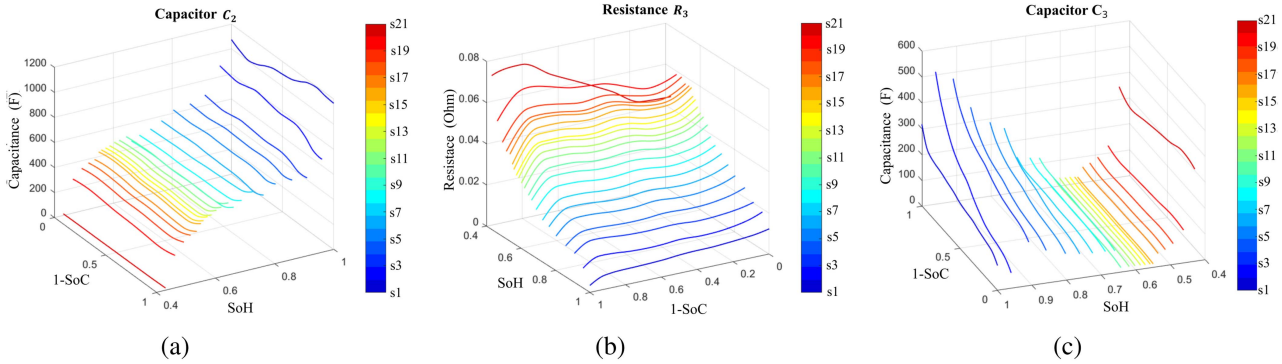


Fig. 17. C_2, R_3, C_3 ECM parameters values using wavelet analysis on the NASA dataset. (a) C_2(SoC, SoH). (b) R_3(SoC, SoH). (c) C_3(SoC,SoH).

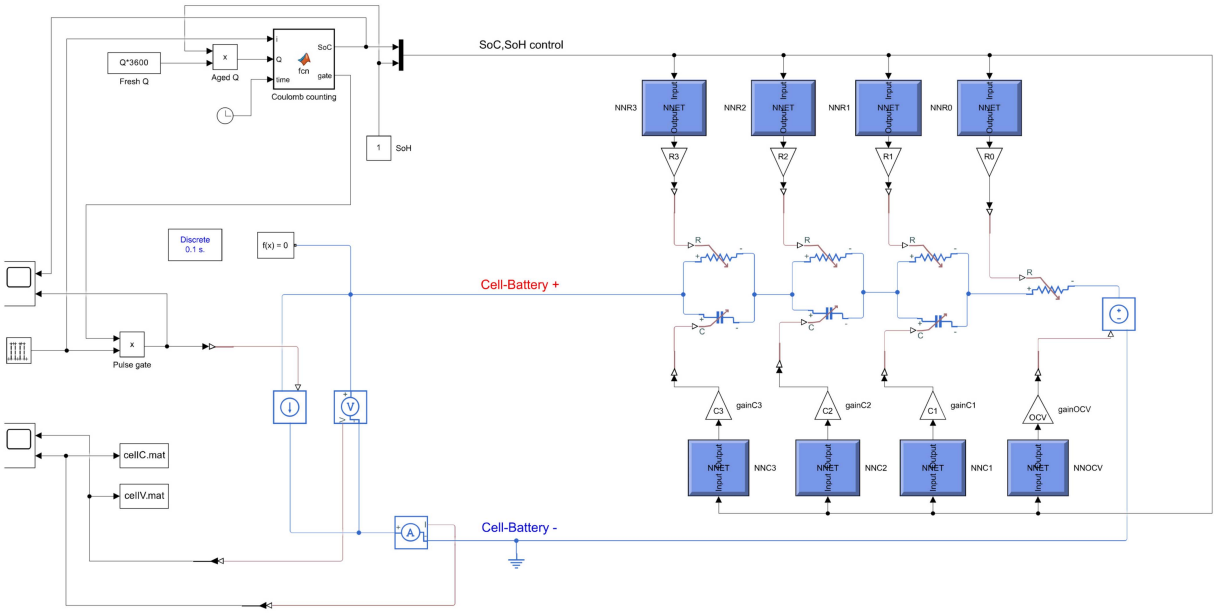


Fig. 18. BDT Simulink model.

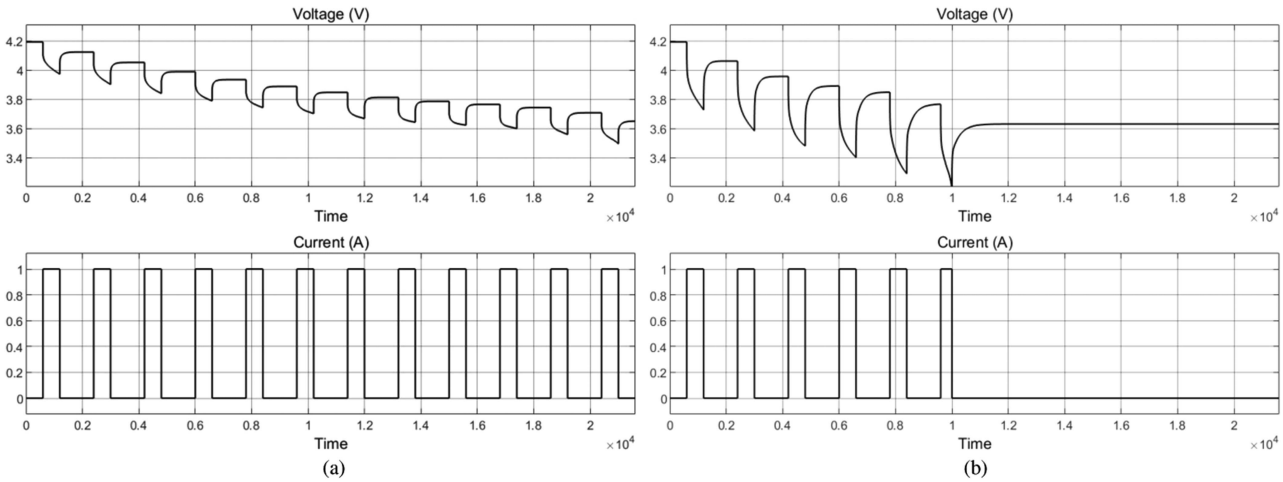


Fig. 19. BDT output voltage and current signals for different SoH: (a) output for SoH=1, (b) output for SoH=0.45. (a) BDT current input and voltage output at SoH $= 1$. (b) BDT current input and voltage output at SoH $= 0.45$.

This article has been accepted for inclusion in a future issue of this journal. Content is final as presented, with the exception of pagination.

adopted in order to allow the BDT to simulate not only a single cell but a complete battery system consisting of a stream of s series connected cells and p parallel connected streams. With the hypothesis of identical cells, the battery can be simulated after multiplying gainOCV by s, gainRi by s/p, and gainCi by p/s (i=1,2,3). In simulations where the cells are not identical and are connected in series, then the BMS must send multiple SoC, SoH control signals. The cell model of Fig. 18 can reproduce the NASA signals with the same pulsed currents and with the same SoH state. Fig. 19 shows the output of the BDT. Fig. 19(a) shows the case of SoH $= 1, 0 \leq$ SoC ≤ 1. Fig. 19(b) shows the case of SoH $= 0.45, 0 \leq$ SoC ≤ 1. As expected, the behavior is the same of sequence 1 and sequence 21 of Fig. 5, respectively. Moreover, the BDT can produce any signal waveform. We can now perform new tests as we had available the same NASA battery but without any hardware equipment.

X. Conclusion

In this article, we showed how to develop a BDT using an ECM and experimental data. The wavelet analysis has been used to analyze the battery output voltage and current signals to estimate the internal impedance of the battery. We also presented a new methodology to extract the OCV from pulsed discharge voltage signals. The nonlinear behavior of the OCV and of the internal impedance parameters versus SoC, SoH are simulated by feedforward NNs, trained with data extracted by wavelet analysis. In this perspective, the wavelet analysis can be viewed as a tool for automating the preprocessing phase of training data for NN. The BDT produces a realistic voltage signal as a function of input current, SoC, and SoH. Simulation results show that the BDT is able to reproduce the original data, and thus, behaves like the original cell tested in the laboratory. This means that a BDT of any battery of interest could be developed by applying our proposed methodology to pulsed discharge data collected in the laboratory. In future work, we will explore the applications of the developed digital twin. The BDT could be used: to produce data signals for testing SoC and SoH algorithms; to simulate a battery pack with cells at different SoC and/or ageing states; to develop and test cell balancing algorithms. Moreover, the BDT could be run in parallel with a real battery for monitoring and diagnostic purposes.

References

[1] S. Barcellona and L. Piegari, "Effect of current on cycle aging of lithium ion batteries," *J. Energy Storage*, vol. 29, 2020, Art. no. 101310.

[2] M. Charkhgard and M. Farrokhi, "State-of-charge estimation for lithium-ion batteries using neural networks and EKF," *IEEE Trans. Ind. Electron.*, vol. 57, no. 12, pp. 4178–4187, Dec. 2010.

[3] Y. Qin, S. Adams, and C. Yuen, "Transfer learning-based state of charge estimation for lithium-ion battery at varying ambient temperatures," *IEEE Trans. Ind. Informat.*, vol. 17, no. 11, pp. 7304–7315, Nov. 2021.

[4] Y. Che et al., "Data efficient health prognostic for batteries based on sequential information-driven probabilistic neural network," *Appl. Energy*, vol. 323, 2022, Art. no. 119663.

[5] H.-T. Lin, T.-J. Liang, and S.-M. Chen, "Estimation of battery state of health using probabilistic neural network," *IEEE Trans. Ind. Informat.*, vol. 9, no. 2, pp. 679–685, May 2013.

[6] R. Di Fonso, P. Bharadwaj, R. Teodorescu, and C. Cecati, "A battery digital twin based on neural network for testing SOC/SOH algorithms," in *Proc. IEEE 20th Int. Power Electron. Motion Control Conf.*, 2022, pp. 655–660.

[7] A. Páez, "The pragmatic turn in explainable artificial intelligence (XAI)," *Minds Mach.*, vol. 29, pp. 441–459, 2019.

[8] G. Plett, *Battery Management Systems, Volume II: Equivalent-Circuit Methods*. Norwood, MA, USA: Artech, 2015..

[9] E. Samadani et al., "Empirical modeling of lithium-ion batteries based on electrochemical impedance spectroscopy tests," *Electroch. Acta*, vol. 160, pp. 169–177, 2015.

[10] W. B. Gu and C. Y. Wang, "Thermal electrochemical modeling of battery systems," *J. Electrochem. Soc.*, vol. 147, Aug. 2000, Art. no. 2910.

[11] C.-H. Chen, F. B. Planella, K. O. Regan, D. Gastol, W. D. Widanage, and E. Kendrick, "Development of experimental techniques for parameterization of multi-scale lithium-ion battery models," *J. Electrochem. Soc.*, vol. 167, May 2020, Art. no. 080534.

[12] Z. Khalik, M. Donkers, J. Sturm, and H. Bergveld, "Parameter estimation of the Doyle-Fuller-Newman model for lithium-ion batteries by parameter normalization, grouping, and sensitivity analysis," *J. Power Sources*, vol. 499, 2021, Art. no. 229901.

[13] I. Korotkin, S. Sahu, S. E. J. O. Kane, G. Richardson, and J. M. Foster, "Dandeliion v1: An extremely fast solver for the newman model of lithium-ion battery (dis)charge," *J. Electrochem. Soc.*, vol. 168, 2021, Art. no. 0605442021.

[14] T. Huria, M. Ceraolo, J. Gazzarri, and R. Jackey, "High fidelity electrical model with thermal dependence for characterization and simulation of high power lithium battery cells," in *Proc. IEEE Intern. Electric Veh. Conf.*, 2012, pp. 1–8.

[15] R. Di Fonso, P. Bharadwaj, R. Teodorescu, and C. Cecati, "Internal resistance estimation of Li-ion batteries using wavelet analysis," in *Proc. IEEE 13th Int. Symp. Power Electron. Distrib. Gener. Syst.*, 2022, pp. 1–5.

[16] H. Sun et al., "Quantitative analysis of degradation modes of lithium-ion battery under different operating conditions," *Energies*, vol. 14, no. 2, 2021, Art. no. 350.

[17] D. Andre, M. Meiler, K. Steiner, C. Wimme, T. Soczka-Guth, and D. Sauer, "Characterization of high-power lithium-ion batteries by electrochemical impedance spectroscopy. I. experimental investigation," *J. Power Sources*, vol. 196, no. 12, pp. 5334–5341, 2011.

[18] G. Nusev, D. Juricic, M. Gaberscek, J. Moskon, and P. Boskoski, "Fast impedance measurement of Li-ion battery using discrete random binary excitation and wavelet transform," *IEEE Access*, vol. 9, pp. 46152–46165, 2021.

[19] B. Saha and K. Goebel, *Battery Data Set*, NASA Ames Prognostics Data Repository, NASA AMES prognostics data repository, 2007.

[20] M. Shafto, M. C. Rich, D. E. Glaessgen, C. Kemp, J. Lemoigne, and L. Wang, "Draft modeling, simulation, information technology & processing roadmap technology area 11," 2010.

[21] F. Tao, H. Zhang, A. Liu, and A. Y. C. Nee, "Digital twin in industry: State-of-the-art," *IEEE Trans. Ind. Informat.*, vol. 15, no. 4, pp. 2405–2415, Apr. 2019.

[22] S. Sierla et al., "Roadmap to semi-automatic generation of digital twins for brownfield process plants," *J. Ind. Inf. Integration*, vol. 27, 2022, Art. no. 100282.

[23] R. Stark and T. Damerau, "Digital Twin," in *CIRP Encyclopedia of Production Engineering*, S. Chatti and T. Tolio, Eds., Berlin, Heidelberg: Springer Berlin Heidelberg, vol. 66, pp. 1–8, 2019. [Online]. Available: https://doi.org/10.1007/978-3-642-35950-7_16870-1

[24] R. Di Fonso, X. Sui, A. B. Acharya, R. Teodorescu, and C. Cecati, "Multidimensional machine learning balancing in smart battery packs," in *Proc. 47th Annu. Conf. IEEE Ind. Electron. Soc.*, 2021, pp. 1–6.

[25] A. Devices, "Cn0510 electrochemical impedance spectroscopy (EIS) for batteries, circuit notes," 2020.

[26] S. Pajevic, "Wavelets an analysis tool," *J. Statist. Phys.*, no. 86, pp. 1399–1400, 1997.

[27] J. M. Lilly and S. C. Olhede, "Higher-order properties of analytic wavelets," *IEEE Trans. Signal Process.*, vol. 57, no. 1, pp. 146–160, Jan. 2009.

[28] J. M. Lilly and S. C. Olhede, "Generalized morse wavelets as a superfamily of analytic wavelets," *IEEE Trans. Signal Process.*, vol. 60, no. 11, pp. 6036–6041, Nov. 2012.

[29] J. M. Lilly and S. C. Olhede, "On the analytic wavelet transform," *IEEE Trans. Inf. Theory*, vol. 56, no. 8, pp. 4135–4156, Aug. 2010.

[30] Mathworks, "Fminsearch function," version R2022a, [Online]. Available: https://www.mathworks.com/help/matlab/ref/fminsearch.html

This article has been accepted for inclusion in a future issue of this journal. Content is final as presented, with the exception of pagination.

[31] R. Xiong, Q. Yu, L. Y. Wang, and C. Lin, "A novel method to obtain the open circuit voltage for the state of charge of lithium ion batteries in electric vehicles by using h infinity filter," *Appl. Energy*, vol. 207, pp. 346–353, 2017.

[32] P. Bharadwaj, K. N. Chaudhury, and V. John, "Sequential optimization for PV panel parameter estimation," *IEEE J. Photovolt.*, vol. 6, no. 5, pp. 1261–1268, Sep. 2016.



Roberta Di Fonso (Member, IEEE) received the B.E. and M.E. degrees in computer science and automation engineering and the Ph.D. degree in systems engineering, telecommunications and HW/SW platforms from the Department of Engineering, Information Science and Mathematics, University of L'Aquila, L'Aquila, Italy, in 2017, 2019, and 2023, respectively.

She is currently a Postdoctoral Researcher with the Energy Department, Aalborg University, Aalborg, Denmark. Her current research interests concern electric mobility with focus on battery modeling and battery management.



Remus Teodorescu (Fellow, IEEE) received the Dipl.-Ing. degree in electrical engineering from the Polytechnical University of Bucharest, Bucharest, Romania, in 1989 and the Ph.D. degree in power electronics from the University of Galati, Galati, Romania, in 1994.

In 1998, he joined the Department of Energy Technology, Aalborg University, Aalborg, Denmark, where he is currently a Full Professor. His main current research interests include modular multilevel converters for HVdc/FACTS, Li-Ion battery SOH estimation with AI, and smart batteries.

Dr. Teodorescu is the IEEE/PELS Fellow since 2012 for contributions to grid converters technology for renewable energy systems. He was the recipient of the Dr. HC from Transilvania University of Brasov, Brasov, Romania, in 2016.



Carlo Cecati (Life Fellow, IEEE) received the Dr.Ing. degree in electrical engineering from the University of L'Aquila, L'Aquila, Italy, in 1983.

Since then, he has been with the University of L'Aquila, where he has been a Professor of Industrial Electronics and Drives since 2006. In 2015–2017, he was Qianren Talents Professor with the Harbin Institute of Technology, Harbin, China. His main research interests include power electronics, distributed generation, e-transportation, smart grids, and related technologies.

Dr. Cecati was a Co-Editor-in-Chief and then was the Editor-in-Chief of the IEEE TRANSACTIONS ON INDUSTRIAL ELECTRONICS, from 2010 to 2015. He was corecipient of the 2012 and 2013 IEEE TRANSACTIONS ON INDUSTRIAL INFORMATICS Best Paper Award, the 2012 IEEE INDUSTRIAL ELECTRONICS MAGAZINE Best Paper Award, and the 2019 IEEE TRANSACTIONS ON INDUSTRIAL ELECTRONICS Outstanding Paper Award. He was the recipient of the 2017 Antony J. Hornfeck Award and the 2021 Eugene Mittlemann Achievement Award from the IEEE Industrial Electronics Society. He is the Chief Technical Officer at DigiPower Ltd., a power electronics research and development company.



Pallavi Bharadwaj (Member, IEEE) received the B.E. degree in electrical engineering from the Delhi College of Engineering, New Delhi, India, in 2012, and the M.E. and Ph.D. degrees from the Department of Electrical Engineering, Indian Institute of Science, Bangalore, India, in 2014 and 2019, respectively.

She then completed her Postdoctoral Research training with the Laboratory for Information and Decision Systems, Massachusetts Institute of Technology, Cambridge, MA, USA, in 2021. She is currently an Assistant Professor with the Department of Electrical Engineering, Indian Institute of Technology, Gandhinagar, Gandhinagar, Gujarat. Her current research interests include renewable energy integration and transportation electrification.

Astronomy & Astrophysics manuscript no. main
January 23, 2024
©ESO 2024

arXiv:2401.11931v1 [astro-ph.HE] 22 Jan 2024

A catalogue of low-mass X-ray binaries in the Galaxy: from the *INTEGRAL* to the *Gaia* era.⋆

F. Fortin[1,2], A. Kalsi[3,4], F. García[5], A. Simaz-Bunzel[5], and S. Chaty[2]

[1] IRAP, CNRS, 9 avenue du Colonel Roche, BP 44346, 31028 Toulouse Cedex 4, France
[2] Université Paris Cité, CNRS, Astroparticule et Cosmologie, F-75013 Paris, France
[3] Delhi Technological University, Delhi 110042, India
[4] Department of Physics and Astronomy "Galileo Galilei", University of Padua, Italy
[5] Instituto Argentino de Radioastronomía (CCT La Plata, CONICET; CICPBA; UNLP), C.C.5, (1894) Villa Elisa, Buenos Aires, Argentina

received ... ; accepted ...

ABSTRACT

Context. Low-mass X-ray binaries (LMXBs) are high-energy sources that require multi-wavelength follow up campaigns to be fully characterized. New transients associated to LMXBs are regularly discovered, and previously known systems are often revisited by astronomers to constrain their intrinsic parameters. All of this information compiled into a catalogue may build up to a useful tool for subsequent studies on LMXBs and their population.
Aims. We provide an update on past LMXB catalogues dating back 16 years and propose to the community a database on Galactic LMXBs with the most complete manually curated set of parameters and their original references. On top of a fixed version accessible through Vizier, we propose to host the catalogue independently on our GitHub collaboration, side-by-side with our previous catalogue on high-mass X-ray binaries. The database will be regularly updated based on new publications and community inputs.
Methods. We build a working base by cross-matching previous LMXB catalogues and supplementing them with lists of hard X-ray sources detected in the past 20 years. We compile information from Simbad on LMXBs as a starting point for a thorough, manual search in the literature to retrieve important parameters that characterize LMXBs. We retrieve newly detected LMXBs and candidates directly from literature searches. Counterparts to these LMXBs are compiled from hard X-rays to infrared and radio domains. Every piece of information presented on the LMXBs is curated and backed by accurate references.
Results. We present a catalogue of 339 Galactic LMXBs listing their coordinates, companion star spectral type, systemic radial velocity, component masses and compact object nature, the presence of type I X-ray bursts as well as orbital data. Coordinates and identifiers of counterparts at various wavelengths are given, including 140 LMXBs detected in *Gaia* DR3.

Key words. stars:binaries:general – catalogues – stars:low mass

1. Introduction

More than 60 years have passed since the identification of the first extrasolar X-ray source (Giacconi et al. 1962). This particular source, Scorpius X-1, belongs to the category of low-mass X-ray binaries (LMXB), which are composed of a compact object – either a black hole (BH) or a neutron star (NS) – that accretes material from a low-mass companion star ($M \lesssim 1\,M_\odot$). LMXBs are soft X-ray emitters powered by mass transfer happening through Roche lobe overflow (see a general review on accreting binaries in Chaty 2022). An accretion disk can form around the compact object and can be responsible for the majority of the radiation emitted during periods of high activity from X-rays down to infrared wavelengths. The formation of relativistic jets commonly occurs during specific phases of activity in microquasars (i.e. BH LMXBs). However, these X-ray systems are but a single phase in the whole evolution of binary stars, from their formation up to their endpoint as compact binaries and gravitational wave sources (see a recent review by Tauris & van den Heuvel 2023).

As a follow-up of our previous work on building an updated catalogue of Galactic high-mass X-ray binaries (HMXBs, Fortin et al. 2023b, now containing 160 sources in HMXBwebcat[1]), we present here our latest catalogue of 339 LMXBs in the Milky Way. Information available on LMXBs in the literature suffers from the same caveat as HMXBs: as these sources are inherently difficult to observe and require multi-wavelength and/or time series campaigns to be properly constrained, most of the discoveries on LMXBs end up spread over several years and can come from many different teams of researchers across the world. This is why the catalogue presented in this paper is centred on two important concepts: firstly, for each parameter listed, we provide the original reference where it was derived : this results in a compilation of more than 600 unique, curated references. Secondly, in parallel to being hosted in Vizier in a fixed version, we host it independently on a dedicated website, LMXBwebcat, on which the database is able to receive updates through our GitHub collaboration[2] as new observations are made, and new or updated parameters of already known sources become available.

⋆ An online version of the catalogue is publicly available at https://binary-revolution.github.io/LMXBwebcat and the database in the associated GitHub repository will be continuously updated based on community inputs.

[1] https://binary-revolution.github.io/HMXBwebcat
[2] https://github.com/Binary-rEvolution/LMXBwebcat

Hence this catalogue is open-source and we invite the community to participate in adding their discoveries and/or updates on LMXBs, or correct any mistake/omission they may identify in our catalogue.

Since the late 90s/early 2000s, X-ray observatories such as *INTEGRAL*[3], *XMM-Newton*[4], *Chandra*, *Swift* and *MAXI*[5] have participated in discovering new LMXBs and gaining in-depth knowledge on their intrinsic parameters such as orbital data, companion mass, or the exact nature of the accreting compact object. All of this information would benefit from being compiled together to facilitate further studies on LMXBs. But the need for such a catalogue is not only motivated by the observational progresses of the past 16 years; it is also the upcoming facilities dedicated to the high energy and transient sky, such as *eROSITA*, LSST[6] and *SVOM*[7], that warrant keeping a constantly up-to-date catalogue in anticipation of the amount of new data that will be available on X-ray binaries. In turn, this will also allow us to better predict the population of gravitational wave sources that LISA[8] will be able to detect (see the white paper Amaro-Seoane et al. 2023).

The first instances of LMXB catalogues date back to the 1980s (Bradt & McClintock 1983; van Paradijs 1983) and counted roughly 33 X-ray systems. Subsequent catalogues were made following the advancements of space-based X-ray observatories, namely the ones presented in van Paradijs (1995), Liu et al. (2001), and finally the latest and most used to date catalogue of 187 Galactic LMXBs by Liu et al. (2007).

In this paper, we first describe the method we followed to build the catalogue (Section 2, which follows a similar structure to what we presented in our HMXB catalogue Fortin et al. 2023b), namely for the recovery of parameters and numerous counterparts to each LMXB. We discuss in Section 3 the catalogue itself and how it compares to previous iterations and other similar catalogues. We also discuss the potential uses of our catalogue, and conclude on this work in Section 4.

2. Building the catalogue

In this section we provide a step-by-step description of the tasks we performed to build the catalogue. We have adopted a very similar approach presented in the twin catalogue dedicated to HMXBs (Fortin et al. 2023b), such as using pre-existing catalogues of high energy sources as a starting base, relying on the services of the Centre de Données Astronomiques de Strasbourg (CDS) such as Simbad and Vizier, and of course minute manual search through references using NASA's Astrophysics Data System (ADS) abstract search engine.

2.1. Reference catalogues and building a working base

More than 16 years after publication, the LMXB catalogue by Liu et al. (2007) is still the most used reference; at that time, the authors listed 187 LMXBs and candidates in the Milky Way. We supplemented this list with the catalogue of *INTEGRAL* detections (Bird et al. 2016) which contains 939 hard X-ray sources of various nature. We only kept the sources labelled LMXB or unidentified, thus adding 345 sources. We identified sources common to both Liu et al. (2007) and Bird et al. (2016) using positional and identifier cross-match performed with TOPCAT (Taylor 2005). We then queried Simbad for all the sources containing the type (or subtype) "LXB"; this returns a list of 674 sources, most of which are extragalactic. These are usually grouped in small clusters around their host galaxy, hence we used the same spatial filtering method as presented in Fortin et al. (2023b), where we check each source for the presence of close neighbours. However, contrary to HMXBs, LMXBs are known to be present in globular clusters, and these structures may hold up to ∼10 LMXBs very close together (as it is the case in NGC 6440 for instance). Hence, we used the list of globular clusters available in Vasiliev & Baumgardt (2021) to check the likelihood of a group of LMXBs to be part of a Galactic globular cluster, before filtering them out if they have neighbours closer than 10′. This way, we retrieved 251 Galactic LMXB candidates from Simbad.

Eventually, after cross-matching the Simbad LXBs with the sample of high energy sources from Liu et al. (2007) and Bird et al. (2016), we obtain a working base of 573 sources. We note that a significant amount (216) were listed in the *INTEGRAL* catalogue as unidentified, and most of them will be discarded through a thorough manual process of checking new information published on these sources in the literature.

2.2. Retrieving binary parameters and new LMXBs

While pieces of information are available on the LMXBs and candidates compiled so far (mainly from the data catalogued in Liu et al. 2007, Ritter & Kolb 2011 and Simbad), our goal for this catalogue is to perform a thorough investigation on each of these sources to, firstly, identify which are interesting LMXB candidates, and secondly, retrieve useful parameters as well as the original studies that derived them (this includes double checking references already compiled by former catalogues). We find that the later point is especially important, as some parameters listed might have been derived using different methods for each source; this information should be readily available for authors of further studies that revisit these sources. Thus, during the individual search for information on each of these sources, we only use already available data as a starting point for the manual search, and always re-check already available references. We compile new and updated data whenever they are available, confirm the already measured parameters by retrieving the original studies, and search for older publications to ensure we have compiled every pieces of information possible on each binary. Hence, none of the parameters or references we list in the catalogue come from an automated, unsupervised query on Simbad. We did use the resources in works that already compiled some useful data on LMXBs, such as spectral types, orbital periods and masses in Yungelson & Lasota (2008); a list of type I X-ray bursts seen be RXTE in Galloway et al. (2008) and its extension to *BeppoSAX* and *INTEGRAL* MINBAR (Galloway et al. 2020); orbital periods in Asai et al. (2022); the catalogue of stellar-mass black holes in X-ray binaries BlackCAT (Corral-Santana et al. 2016); or the latest catalogue of Ultra-Compact X-ray Binaries UltraCompCAT (Armas Padilla et al. 2023, which is also a dynamic database[9]).

Because LMXBs can be highly variable sources, we settled on a list of parameters to look for we reckon are representative of the systems at all times. These are the spectral type of the com-

[3] INTernational Gamma-Ray Astrophysics Laboratory
[4] X-ray Multi-Mirror Mission
[5] Monitor of All-sky X-ray Image
[6] Large Synoptic Survey Telescope
[7] Space Variable Objects Monitor
[8] Laser Interferometer Space Antenna

[9] Available at https://research.iac.es/proyecto/compactos/UltraCompCAT/

panion star, the nature of the accreting compact object, masses of the binary components, the orbital parameters, the radial velocity of the center of mass, the presence of a spin period and its time derivative, and the detection of type-I X-ray bursts. We try not to log any "assumed" values for any parameters –such as when NSs are assumed to be 1.4 $M_\odot$ in orbital solutions or when the LMXBs are being located at 8 kpc by default if they are near the Galactic center– unless they are motivated or indirectly constrained by other measurements.

Lastly, we performed "blind" searches within the literature for newly detected LMXBs and candidates in papers ranging from 2016 to 2023 that may not appear in either catalogues of high energy sources we used or not yet be logged as LMXBs in Simbad. This was mainly done through queries of keywords such as "binary", "transient", "X-rays" in the NASA ADS abstract service. Most new candidates discovered this way come from Astronomer's Telegrams.

We note that at this point, we have made the data in the catalogue as reliable as possible; this kind of curated data-mining is however bound to contain small errors or oversights. This is why the catalogue is hosted on an independent website and, as our previous catalogue already did (Fortin et al. 2023b), will receive gradual updates and new releases as new information is either found by ourselves or brought forward by the community.

2.3. Finding an unambiguous chain of counterparts

As we previously argued in Fortin et al. (2023b), we believe that part of what consists of a secure identification as LMXB or candidate LMXB is having an unambiguous list of counterparts, ideally from hard X-ray to infrared. Having this positional information is also a necessary tool for astronomers to prepare new observations in follow-up campaigns. The automated search for counterparts to each LMXB is not trivial, but still facilitated by positional data already present in Simbad, and also by the stored identifiers which also contain information about the coordinates of the source and their accuracy. Our goal here is to perform a cone search on all the catalogues listed in Table 1 in order to retrieve a proper chain of counterparts from the high energies down to the infrared wavelengths. For this, we need an initial set of coordinates to query around in these catalogues.

These starting coordinates are either the ones listed in Simbad, or the ones that we parsed from the list of identifiers available in Simbad, depending on whichever is most accurate. For instance, the candidate LMXB IGR J17480−2446 has coordinates available in Simbad, but without any information on their accuracy. It does have another identifier, CXOGlb J174804.8−244648, which we can parse into a set of coordinates with an accuracy below the arcsecond scale as it comes from *Chandra* observations. This is a quick method that is capable of automatically retrieving accurate positional data from Simbad, that may not necessarily be available in catalogues but which was for instance derived in Astronomer's Telegrams. In this particular case, this allowed us to instantly find the *Chandra* counterpart of IGR J17480−2446 (2CXO J174804.8−244649) with a cone search in the Chandra CSC 2 database (Evans et al. 2019).

This positional cross-match is still prone to false positives, as we have to purposefully look within the catalogues on a sufficiently large area so that we do not miss any potential counterparts. This is why we also perform a recursive search within the produced list of counterparts, from the poorest to the most accurate catalogues (*XMM-Newton*, *Chandra*, 2MASS, *Gaia*). We note that for LMXBs closely grouped within globular clusters, this method is sometimes unable to automatically separate different chains of counterparts, especially for hard X-rays for which the astrometric precision is not accurate enough to separate closely grouped LMXBs in clusters. Thus, for LMXBs found in clusters, we manually checked the consistency of their counterparts to ensure each have a unique, precise localisation.

Table 1: List of queried catalogues for the counterpart search.

Catalogue	Reference	Radius
HEAO 1	Wood et al. (1984)	20′
Uhuru 4	Forman et al. (1978)	20′
Ariel V 3	Warwick et al. (1981)	20′
INTEGRAL	Bird et al. (2016)	20′
Fermi	Abdollahi et al. (2022)	20′
BeppoSAX	Capitanio et al. (2011)	6′
Einstein 2E	Harris et al. (1990)	4′
ROSAT	White et al. (2000)	35″
Swift 2SXPS	Evans et al. (2020)	8″
4XMM DR11	Webb et al. (2020)	4″
Chandra CSC 2	Evans et al. (2019)	3″
2MASS	Cutri et al. (2003)	120 mas
Gaia DR3	Gaia Collaboration (2022)	20 mas

2.4. Contents of the catalogue

The general characteristics of Galactic LMXBs are presented in Table A.1. The full catalogue provides their Simbad identifier ("Main ID" field from Simbad), as well as a short list of the most used IDs we found in the literature. To build this list, we queried each known IDs from Simbad in ADS and retrieved how many papers used them in their title, abstract or full text. We rank them from most popular to least popular, and thus provide identifiers that should reflect the community's preferred naming convention. In this paper, we list the LMXBs under their most popular identifier, except for a few sources for which no popular ID can be recovered in ADS; in this case, we use their Simbad identifier. The online catalogue provides the full list of identifiers known by Simbad, to facilitate queries in LMXBwebcat. The "Compact" column provides information on the nature of the accreting compact object, and "Spectype" refers to the spectral type of the donor star. When available, we list the distance inferred from *Gaia* EDR3 parallaxes by Bailer-Jones et al. (2021). We also have cross-matched our LMXBs with the list of globular clusters from Baumgardt & Vasiliev (2021), which contains information about their distances inferred from various means, including *Gaia* parallaxes. Hence we provide, in case of a spatial association with a globular cluster, the name of the cluster and the inferred distance in the "Other distance" column. In the text, we only keep the largest error bound for *Gaia* distances and values are voluntarily rounded for the sake of readability; the unaltered numbers are available in the electronic versions of the catalogue. When there is no cluster association, the "Other distance" column may also contain distance estimates from a number of other methods, which are available in the given references. Lastly, we indicate when one or several type I X-ray burst were observed by providing a reference.

In Table A.2 are presented the orbital parameters: orbital period, eccentricity and semi-amplitude of the donor's radial velocity. We also give details on the mass of each binary component –"Mx" for the compact object, "Mo" for the companion star– as well as information on the presence of a pulse period and its time derivative in the case the compact object is a NS. Again,

values are rounded for readability and are available in full in the electronic version of the catalogue.

The electronic version also provides extra information on the counterparts for each binary, namely their numerous identifiers, coordinates and corresponding astrometric precision. The right ascension and declination are given in J2000, and astrometric uncertainties are the 90% positional errors retrieved from the queried catalogues. The full contents of the LMXB catalogue can be queried on Vizier, or viewed and queried from the dedicated website LMXBwebcat[10]. The latter database will be updated regularly and new versions of the catalogue will be published on the website; every changes will be logged to track the evolution of each version, which will remain available alongside the latest upload.

We advise the readers to remain critical of all the parameters we list in this catalogue, and to check the references before using them in their own work. To ease the process, we use a flag system to quickly inform the reader about the reliability of each listed parameter. The flags appear as numbers in dedicated columns in the catalogue database; for the sake of readability, we use daggers in the text:

- 0 / (nothing): directly measured parameter. This flag is not displayed in Tables A.1 and A.2 nor in LMXBwebcat. This includes companion spectral types inferred through spectroscopy, full orbital solutions derived from radial velocity followups, orbital periods from pulse timing or eclipses, dynamical masses, NSs confirmed by the presence of type I bursts or a spin period, or compact object type identified through the measure of the dynamical mass. This also includes distances of globular clusters hosting LMXBs derived via the Gaia parallaxes of the cluster members.
- 1 / (†): caution. The parameter is either indirectly measured or needs better constraints. This includes tentative orbital periods, rough estimations of spectral types from photometry, compact object masses and distances from spectral fitting, radial velocity semi-amplitudes from empirical relations, or compact object types identified through comparison of X-ray spectra. It also includes all parameters for which we only have upper or lower limits on a direct measurement (i.e. most eccentricity measurements).
- 2 / (††): warning. The parameter is assumed in the scope of a model and likely needs proper observational constraints. This also includes indirectly derived parameters with lower or upper limits.

For instance, out of the 75 BH LMXBs we list, only 19 are flagged as reliable BH ("0") since direct evidence of the presence of a BH is hard to get, apart from deriving a dynamical mass greater than $\sim 3\,M_\odot$. Most BHs are thus flagged "1" (N=52) and only a few flagged "2" (N=4) since this identification mostly comes from their X-ray spectrum resembling the one of typical BH LMXBs. The presence of a NS is however much easier to prove through the observation of type I X-ray bursts or the detection of a spin period; hence 146 out of 176 NSs in LMXBs are flagged as being reliable. These flags can be used to quickly identify which LMXBs are worth revisiting to give better constraints on their set of parameters.

2.5. Gaia candidate counterparts

The only parameter flag that slightly differs from the others is the one attributed to the *Gaia* distances in Table A.1. Because LMXBs are generally very faint in optical/nIR, and because there are so many late-type stars in the field, finding the true optical/nIR counterpart to an LMXB can be challenging even in the case sub-arcsecond X-ray localisation is available, as interlopers can be present along with the true counterpart within the X-ray error circles. Hence we propose here candidate *Gaia* counterparts to LMXBs based on astrometric cross-match as well as historical associations in the few cases where both deep and high-resolution optical/nIR imaging has been performed.

The Gaia distance flag does not refer to the reliability of the distance estimation; instead it represents how the *Gaia* counterpart was associated to the LMXB. *Gaia* counterparts that we found compatible with either an *XMM-Newton* or *Chandra* detection (e.g. a sub-arcsecond scale association), and that do not have any other neighbour in the *Gaia* catalogue closer than 1″, are deemed secure and as such we do not flag them. *Gaia* counterparts that were found only based on a *Swift* detection (e.g. an arc-second scale association) are flagged as uncertain ("1"/†). The *Gaia* counterpart flagged as "2"/†† are not necessarily unreliable, but are not based on an association with an accurate soft X-ray detection. Instead, they come from historical association of an optical counterpart. For instance, Sco X-1 has a Gaia counterpart but no soft X-ray position available in the *Swift*, *Chandra* or *XMM* catalogues because of its tremendous X-ray brightness.

These *Gaia* candidate counterparts can be subject to change in further iterations of the database as new X-ray positional constraints and/or deeper optical/nIR imaging becomes available on LMXBs. There are ways to further determine the level of confidence in the *Gaia* counterparts we found, such as comparing their optical magnitudes to previously published survey data. Because LMXBs can be highly variable, we chose to perform a check between the distances inferred by *Gaia* parallax and the distances inferred by other means ("other distance", such as spectral energy distribution fitting or photospheric radius expansion in bursting sources). After removing the LMXBs that lie within clusters (since all of their distance information come from *Gaia* data), we plot in Figure 1 the Gaia distances vs. the other distances from the literature. A linear fitting excluding the data points with lower/upper limits returns a proportional coefficient of 1.03 and a systematic of 50 pc, which is satisfactory since we are comparing two completely independent sets of measurements. We note that this sub-sample is representative of the whole catalogue concerning the *Gaia* flags: we count four flag-0, a single flag-1 and six flag-2 *Gaia* counterparts in the fitted sample. This may indicate that our flagging system is a bit too strict, with the caveat of a low number of sources to work with.

3. Results, discussions, and byproducts

3.1. Catalogue statistics and uses

We present a list of 339 Galactic LMXBs and candidates in this new catalogue, as represented in Figure 2. We note that contrary to the previous catalogue of Liu et al. (2007), we do include quiescent LMXB candidates (qLMXBs hereafter); 25 are present in the current version of our catalogue. Hence, after subtracting these qLMXBs to compare our total sample to Liu et al. (2007), we provide a 67% increase in the total number of LMXBs and candidates in the Milky Way. We have at least a tentative identification of compact object type for more than 250 LMXBs, with a predominance of NSs (70%) compared to BHs (30%). We compile 150 orbital periods and 69 spin periods, which are respectively a 200% and 150% increase compared to the 2007 catalogue, showing the tremendous impact of new detections and

[10] https://binary-revolution.github.io/LMXBwebcat/catalog.html

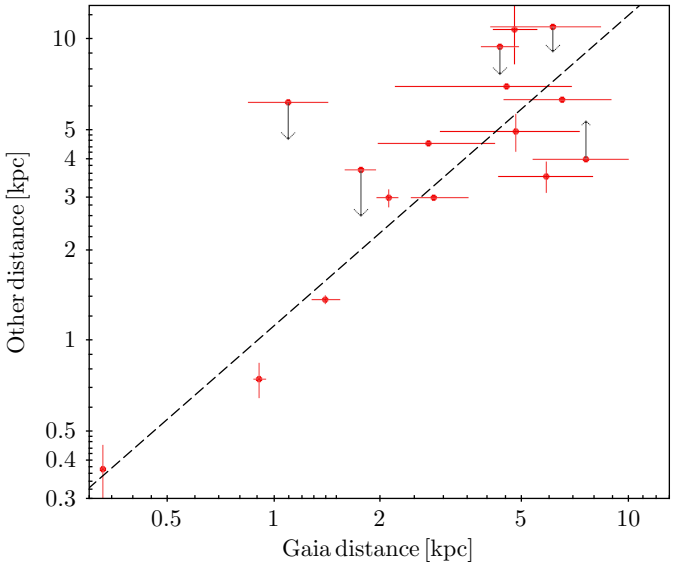


Fig. 1: Comparison between the distances to LMXBs from the literature vs. the distances of the proposed *Gaia* counterparts inferred from their parallax. Only LMXBs that have both information and are not located within a cluster are plotted (N=16); black arrows indicate lower/upper limits. The dashed black line is the best linear fit, excluding sources with only lower/upper limits (N=11).

follow-up studies on LMXBs. Out of the 176 NS LMXBs, 112 are known to be X-ray bursters.

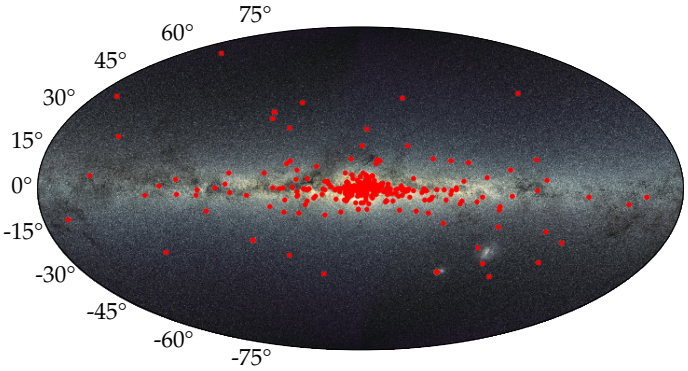


Fig. 2: Edge-on view of the 339 LMXBs in the Galaxy. Galactic latitudes are indicated in degrees. *Background image credits: ESA/Gaia/DPAC.*

In Figure 3 we present the full Corbet diagram of NS XRBs in the Galaxy, compiling the data of the present catalogue for NS LMXBs with both orbital period and spin period derived (N=50) alongside the same data for HMXBs available in Fortin et al. (2023b). In this sample, the majority of the NSs in LMXB have spin periods lower than 10 ms (N=39), a region exclusively dominated by LMXBs contrary to NSs in HMXBs that seldom have spin periods lower than 100 ms. LMXBs and HMXBs are generally well-separated in the Corbet diagram, although some symbiotic LMXBs (where the donor is an evolved, giant star) do overlap with HMXBs as consequence of larger orbital separation and lower efficiency at transferring angular momentum.

In our previous catalogue dedicated to HMXBs, almost 3/4 of the HMXBs were detected by *Gaia* and had sufficient astrometric quality to invert distance from parallax; in this LMXB

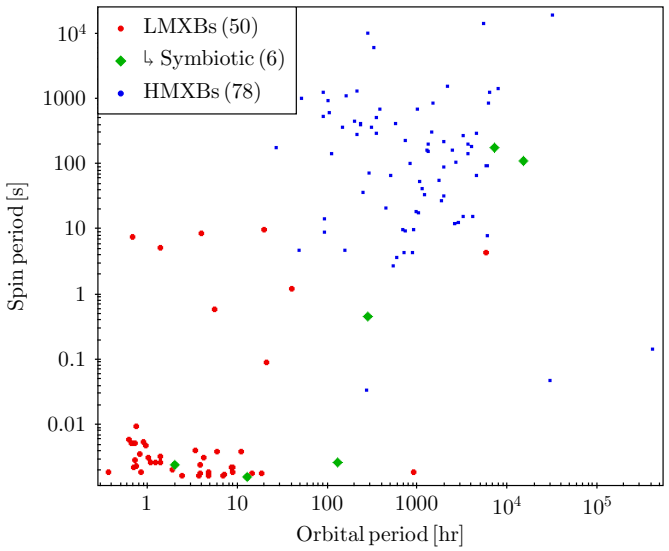


Fig. 3: Corbet diagram of the 50 NS LMXBs in the current catalogue, alongside the 78 NS HMXBs now available in Fortin et al. (2023b) which have both orbital and spin period information (all flags included). Symbiotic LMXBs are indicated in green rhombuses.

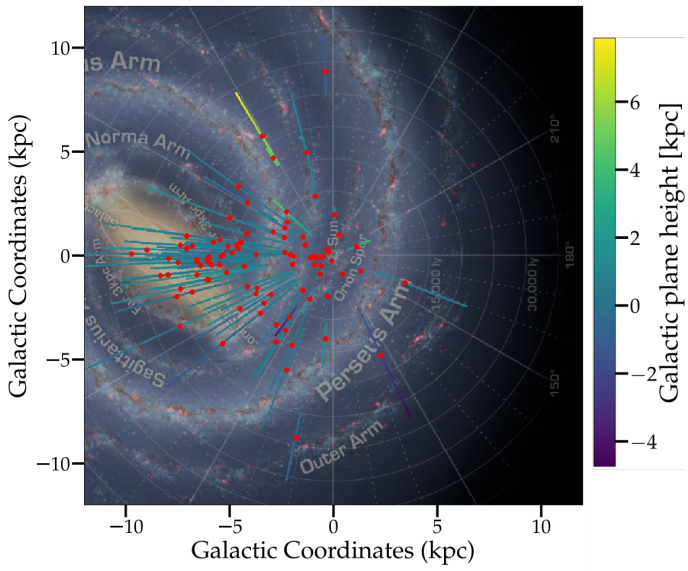


Fig. 4: Face-on view of the 98 Galactic LMXBs with *Gaia* parallaxes. Bars indicate the 68% confidence interval in distance. *Background image credits: NASA/JPL-Caltech/R. Hurt (SSC/Caltech)*

catalogue we note that only about 40% of the sources (140) have a *Gaia* DR3 counterpart and only 98 of them have distance information available in Bailer-Jones et al. (2021). This is explained by the fact that optical counterparts of LMXBs are fainter on average, and also because these are older astrophysical objects that had time to migrate out of the Galactic Plane towards the bulge of the Milky Way, which is too far away for any source to have a reliable *Gaia* parallax even when a counterpart is detected. This still allows us to localise ~30% of our LMXBs within the Galaxy thanks to *Gaia* as shown in Figure 4. If we combine to the *Gaia* distances the ones found in the literature and the distances to

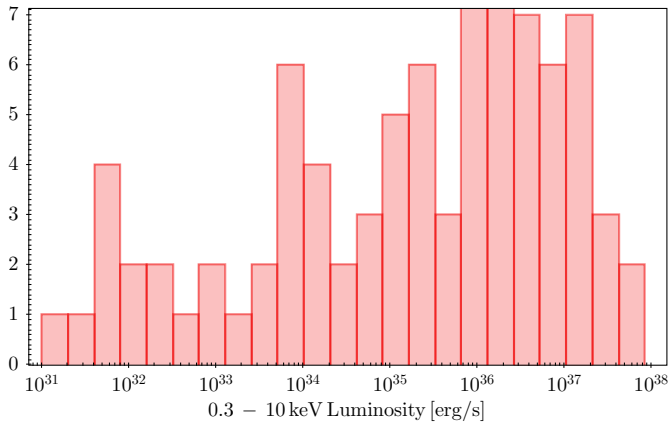


Fig. 5: Distribution of the soft X-ray luminosities of Galactic LMXBs seen by *Swift* and with a distance determination (N=89).

globular clusters, we reach the number of 208 LMXBs with a distance estimation. We note that regardless of the method used for distance estimation (parallax, globular cluster association or X-ray modelling), we advise the users to remain cautious of the determined distance values when considering individual systems as they may be subject to various biases, such as poor parallax quality, wrong association within a globular cluster, foreground star, etc. When considering the whole sample, these biases should at least partly cancel out, but there are bound to be outliers.

To show the potential of the data we aggregated in this catalogue, we constructed the distribution of X-ray luminosities of the Galactic LMXBs using the 2SXPS *Swift* database (Evans et al. 2020). We combined the Unabsorbed 0.3–10 keV Apec Flux (labelled "FAU0" in 2SXPS) with either the *Gaia* distances or, when not available, the "Other distance" determination in the LMXB catalogue. In the case the LMXBs are associated with globular clusters, we use the distance to the cluster. This luminosity distribution, shown in Figure 5, is the first step to get an estimation of the total X-ray budget of LMXBs in the Milky Way, and is only presented here as an example of how this catalogue can be used for. To go further, users may want to consider other methods of flux measurements from the 2SXPS catalogue, combine fluxes from other observatories such as *XMM-Newton* (Webb et al. 2020) or *Chandra* (Evans et al. 2019) and of course discuss the impact of the behaviour of LMXBs from quiescence to outburst on the average flux values available in the aforementioned catalogues.

3.2. Byproducts

A noteworthy byproduct of our work is the retrieval of information about *INTEGRAL* sources marked as unidentified in Bird et al. (2016). We kept five of them as candidate LMXBs, which appear in our catalogue; we also provide in Table B.1 a separate list for the 44 *INTEGRAL* sources for which we found an identification in the literature that is not present in Simbad; most are background Active Galactic Nuclei (AGNs) or Cataclysmic Variables (CVs). The purpose of this table is to provide easily digestible data for the CDS to update references in Simbad.

3.3. Discussion

After the publication of our previous HMXB catalogue and during the writing of this paper, a similar LMXB catalogue was released by Avakyan et al. (2023), where the authors list 349 Galactic LMXBs. We have similar approaches, as the authors also propose to update their database based on community inputs. We did find however notable differences: first and foremost, we do not cite previous catalogues as references for the parameters in our catalogue; instead, we look for the original studies cited in Liu et al. (2007) or Ritter & Kolb (2003) and update them when necessary. This results in a compilation of 570 unique references for the parameters we compile in the present catalogue. Secondly, we carefully review any reference provided by Simbad, as we have found many instances where they do not point to the original study deriving the cited parameter. For example, several companion spectral types are given in Yungelson & Lasota (2008), which is a paper discussing evolutionary models for BH LMXBs that happens to list these spectral types (and some other parameters such as orbital periods or mass ratios) coming from already published data. Thirdly, we are slightly more strict concerning the inclusion of LMXB candidates, as we do not list X-ray sources for which there is no particular indication of them being at least candidate LMXBs. For this reason, we do not include in our catalogue: AX J1824.5−2451, [BSP2003] 24, Swift J174038.1−273712, CXOGC J174538.0−290022, XMM J174544−2913.0, SWIFT J174553.7−290347, CXOGC J174622.2−290634, Swift J175233.9−290952 and NGC 6752 CX19. Thanks to our minute investigation of each LMXB candidates, we were also able to exclude doubloons where one or several counterparts of the same source were listed as independent LMXBs. This was the case for KS 1741−293, IGR J17353−3539, TYC 6824−713−1, [ZGV2011] 9 and 3U 1728−16. Lastly, we provide corrected identifications for some sources that may have been wrongly reported to be LMXBs, such as the HMXB Cir X-1 (Jonker et al. 2007b), the cataclysmic variable OGLE BLG-ELL-12042 (Gomez et al. 2021), and some which are more likely to not be LMXBs ([PLV2002] CX10 is a candidate CV in Pooley et al. 2002).

It is of prime importance for a catalogue to carefully list references. Firstly, this provides at least some insurance to the users that the data was manually curated as, for now, there are no machine learning algorithm that outperform manual data mining in the literature as we present here. Secondly, we also find that it is important to acknowledge all the observational work done on LMXBs and X-ray binaries in general since, as the current catalogue shows, there are still many missing parameters on X-ray binaries that will only be derived thanks to regular proposals for follow up observations by teams of astronomers. Lastly, the main motivator for such catalogues is to untangle the huge amount of information spread within the literature; citing previous catalogues as a source for data goes against this endeavour of making data more accessible to the community.

4. Conclusion

The continuous endeavour of catching X-ray transients and performing multi-wavelength follow ups has brought the discovery of many new LMXBs and helped characterize their properties tremendously in these past 16 years. To bring together all this information, we present a new catalogue of 339 Galactic LMXBs that constitutes a tool for further studies on either individual systems or their whole population. Being hosted on an independent website, LMXBwebcat, this catalogue is also ready

to receive updates/corrections based on new publications or input from the community. Compared to the 187 LMXBs listed in Liu et al. (2007), the current number of known Galactic LMXBs has almost doubled, and given the upcoming observational landscape dedicated to high energies and/or transient sky astronomy (*eROSITA*, LSST or *SVOM* for instance), these numbers are likely to keep growing further.

Thus, it is essential to continue monitoring new discoveries on X-ray binaries so that we are able to better grasp their properties as a population, their role in the Galactic ecology and how, at the endpoint of their evolution, they may become gravitational wave sources detectable by LISA (Tauris 2018). We would also like to note that optical/infrared follow ups are still much needed to complete the set of observables (such as spectral types or orbital solutions from radial velocities) available on LMXBs. We hope this catalogue can also be a tool to identify which parameter needs constraints and to facilitate the identification of ideal targets for astronomers to revisit.

Acknowledgements. We thank the anonymous Referee for their meticulous review of both the manuscript and the database, which allowed us to greatly improve them. The authors were supported by the LabEx UnivEarthS: Interface project I10 "Binary rEvolution: from binary evolution towards merging of compact objects". SC is grateful to the CNES (Centre National d'Études Spatiales) for the funding of MINE (Multi-wavelength *INTEGRAL* Network). FG is a CONICET researcher and acknowledges support from PIP 0113 and PIBAA 1275 (CONICET). This work made use of NASA's Astrophysics Data System (ADS) web services, and of the services associated to the Centre de Données Astronomiques de Strasbourg (CDS) Simbad and Vizier. This work has made use of data from the European Space Agency (ESA) mission *Gaia* (https://www.cosmos.esa.int/gaia), processed by the *Gaia* Data Processing and Analysis Consortium (DPAC, https://www.cosmos.esa.int/web/gaia/dpac/consortium). Funding for the DPAC has been provided by national institutions, in particular, the institutions participating in the *Gaia* Multilateral Agreement. *Software:* Topcat (Taylor 2005), MATPLOTLIB (Hunter 2007), NUMPY (van der Walt et al. 2011), SCIPY (Jones et al. 2001) and PYTHON from python.org

References

Abdollahi, S., Acero, F., Baldini, L., et al. 2022, ApJS, 260, 53
Albayati, A. C., Altamirano, D., Jaisawal, G. K., et al. 2021, MNRAS, 501, 261
Albayati, A. C., Bult, P., Altamirano, D., et al. 2023, MNRAS, 524, 2477
Altamirano, D., Casella, P., Patruno, A., Wijnands, R., & van der Klis, M. 2008a, ApJ, 674, L45
Altamirano, D., Cavecchi, Y., Patruno, A., et al. 2011, ApJ, 727, L18
Altamirano, D., Galloway, D., Chenevez, J., et al. 2008b, The Astronomer's Telegram, 1651, 1
Altamirano, D., Patruno, A., Heinke, C. O., et al. 2010, ApJ, 712, L58
Altamirano, D., Wijnands, R., Heinke, C. O., Sivakoff, G. R., & Pooley, D. 2012, The Astronomer's Telegram, 4264, 1
Amaro-Seoane, P., Andrews, J., Arca Sedda, M., et al. 2023, Living Reviews in Relativity, 26, 2
Anderson, S. F., Wachter, S., Margon, B., et al. 1994, ApJ, 436, 319
Aoki, T., Dotani, T., Ebisawa, K., et al. 1992, PASJ, 44, 641
Archibald, A. M., Stairs, I. H., Ransom, S. M., et al. 2009, Science, 324, 1411
Armas Padilla, M., Corral-Santana, J. M., Borghese, A., et al. 2023, arXiv e-prints, arXiv:2305.07691
Armas Padilla, M., Degenaar, N., Patruno, A., et al. 2011, MNRAS, 417, 659
Armas Padilla, M., Degenaar, N., & Wijnands, R. 2013, MNRAS, 434, 1586
Armas Padilla, M., Rodríguez-Gil, P., Muñoz-Darias, T., et al. 2022, ApJ, 931, L9
Arnason, R. M., Sivakoff, G. R., Heinke, C. O., Cohn, H. N., & Lugger, P. M. 2015, ApJ, 807, 52
Asai, K., Mihara, T., & Matsuoka, M. 2022, PASJ, 74, 974
Ashcraft, T. A., Hynes, R. I., & Robinson, E. L. 2012, MNRAS, 424, 620
Augusteijn, T., Kuulkers, E., & van Kerkwijk, M. H. 2001, A&A, 375, 447
Avakyan, A., Neumann, M., Zainab, A., et al. 2023, A&A, 675, A199
Bagińska, P., Różańska, A., Czerny, B., & Janiuk, A. 2021, ApJ, 912, 110
Baglio, M. C., D'Avanzo, P., Campana, S., et al. 2016, A&A, 587, A102
Baglio, M. C., Mainetti, D., D'Avanzo, P., et al. 2014, A&A, 572, A99
Bahramian, A., Britt, C., & Strader, J. 2018a, The Astronomer's Telegram, 11342, 1
Bahramian, A., Gladstone, J. C., Heinke, C. O., et al. 2014, MNRAS, 441, 640
Bahramian, A., Heinke, C. O., Tudor, V., et al. 2017, MNRAS, 467, 2199
Bahramian, A., Tetarenko, A., Sivakoff, G., et al. 2018b, The Astronomer's Telegram, 11646, 1
Bailer-Jones, C. A. L., Rybizki, J., Fouesneau, M., Demleitner, M., & Andrae, R. 2021, AJ, 161, 147
Bailyn, C. D., Orosz, J. A., McClintock, J. E., & Remillard, R. A. 1995, Nature, 378, 157
Bałucińska-Church, M., Church, M. J., & Smale, A. P. 2004, MNRAS, 347, 334
Bandyopadhyay, R. M., Shahbaz, T., Charles, P. A., & Naylor, T. 1999, MNRAS, 306, 417
Barnes, A. D., Casares, J., Cornelisse, R., et al. 2007, MNRAS, 380, 1182
Barret, D. & Grindlay, J. E. 1995, ApJ, 440, 841
Bassa, C. G., Jonker, P. G., Steeghs, D., & Torres, M. A. P. 2009, MNRAS, 399, 2055
Baumgardt, H. & Vasiliev, E. 2021, MNRAS, 505, 5957
Bayless, A. J., Robinson, E. L., Mason, P. A., & Robertson, P. 2011, ApJ, 730, 43
Becker, W., Swartz, D. A., Pavlov, G. G., et al. 2003, ApJ, 594, 798
Beri, A., Sharma, R., Roy, P., et al. 2023, MNRAS, 521, 5904
Bezayiff, N. 2006, PhD thesis, University of California, Santa Cruz
Bhattacharyya, S. 2020, MNRAS, 498, 728
Bhattacharyya, S., Strohmayer, T. E., Markwardt, C. B., & Swank, J. H. 2006, ApJ, 639, L31
Bird, A. J., Bazzano, A., Malizia, A., et al. 2016, ApJS, 223, 15
Blay, P., Camero, A., Connell, P., et al. 2008, in The 7th INTEGRAL Workshop, 78
Bogdanov, S. & Halpern, J. P. 2015, ApJ, 803, L27
Bogomazov, A. I., Cherepashchuk, A. M., Khruzina, T. S., & Tutukov, A. V. 2022, MNRAS, 514, 5375
Borozdin, K. N. & Trudolyubov, S. P. 2000, ApJ, 533, L131
Bozzo, E., Bahramian, A., Ferrigno, C., et al. 2018, A&A, 613, A22
Bozzo, E., Bazzano, A., Kuulkers, E., et al. 2014, The Astronomer's Telegram, 5765, 1
Bozzo, E., Ferrigno, C., Kuulkers, E., et al. 2009, The Astronomer's Telegram, 2198, 1
Bozzo, E., Pavan, L., Ferrigno, C., et al. 2012, A&A, 544, A118
Bozzo, E., Pjanka, P., Romano, P., et al. 2016, A&A, 589, A42
Bozzo, E., Romano, P., Falanga, M., et al. 2015, A&A, 579, A56
Bozzo, E., Romano, P., Ferrigno, C., et al. 2013, A&A, 556, A30
Bradt, H. V. D. & McClintock, J. E. 1983, ARA&A, 21, 13
Brandt, S., Budtz-Jørgensen, C., & Chenevez, J. 2006a, The Astronomer's Telegram, 778, 1
Brandt, S., Budtz-Jorgensen, C., Chenevez, J., et al. 2006b, The Astronomer's Telegram, 970, 1
Brandt, S., Budtz-Jørgensen, C., Gotz, D., Hurley, K., & Frontera, F. 2007, The Astronomer's Telegram, 1054, 1
Brandt, S., Kuulkers, E., Bazzano, A., et al. 2005, The Astronomer's Telegram, 622, 1
Britt, C. T., Strader, J., Chomiuk, L., et al. 2017, ApJ, 849, 21
Buisson, D. J. K., Altamirano, D., Armas Padilla, M., et al. 2021, MNRAS, 503, 5600
Buisson, D. J. K., Altamirano, D., Bult, P., et al. 2020, MNRAS, 499, 793
Bult, P., Altamirano, D., Arzoumanian, Z., et al. 2022a, ApJ, 935, L32
Bult, P., Altamirano, D., Arzoumanian, Z., et al. 2018, ApJ, 864, 14
Bult, P., Gorgone, N., Younes, G., Kouveliotou, C., & Harrison, F. 2017, The Astronomer's Telegram, 11067, 1
Bult, P., Mancuso, G. C., Strohmayer, T. E., et al. 2022b, ApJ, 940, 81
Bult, P., Markwardt, C. B., Altamirano, D., et al. 2019, ApJ, 877, 70
Bult, P., Strohmayer, T. E., Malacaria, C., Ng, M., & Wadiasingh, Z. 2021, ApJ, 912, 120
Bult, P. M., Ng, M., Iwakiri, W., et al. 2022c, The Astronomer's Telegram, 15425, 1
Cadelano, M., Pallanca, C., Ferraro, F. R., et al. 2017, ApJ, 844, 53
Cadolle Bel, M., Prat, L., Rodriguez, J., et al. 2009, A&A, 501, 1
Camilo, F., Reynolds, J. E., Ransom, S. M., et al. 2016, ApJ, 820, 6
Campana, S., Stella, L., Belloni, T., et al. 2002, A&A, 384, 163
Cantat-Gaudin, T. & Anders, F. 2020, A&A, 633, A99
Cao, H.-M., Migliori, G., Giroletti, M., et al. 2022, A&A, 657, A104
Capitanio, F., Bird, A. J., Fiocchi, M., Scaringi, S., & Ubertini, P. 2011, ApJS, 195, 9
Carotenuto, F., Corbel, S., & Tzioumis, A. 2022, MNRAS, 517, L21
Casares, J. 2016, ApJ, 822, 99
Casares, J., Charles, P., & Kuulkers, E. 1998, ApJ, 493, L39
Casares, J. & Charles, P. A. 1994, MNRAS, 271, L5
Casares, J., Charles, P. A., & Marsh, T. R. 1995, MNRAS, 277, L45
Casares, J., Charles, P. A., & Naylor, T. 1992, Nature, 355, 614
Casares, J., Charles, P. A., Naylor, T., & Pavlenko, E. P. 1993, MNRAS, 265, 834
Casares, J., Cornelisse, R., Steeghs, D., et al. 2006, MNRAS, 373, 1235

Casares, J., Dubus, G., Shahbaz, T., Zurita, C., & Charles, P. A. 2002, MNRAS, 329, 29
Casares, J., González Hernández, J. I., Israelian, G., & Rebolo, R. 2010, MNRAS, 401, 2517
Casares, J., Muñoz-Darias, T., Torres, M. A. P., et al. 2022, MNRAS, 516, 2023
Casares, J., Rodriguez-Gil, P., Zurita, C., et al. 2012, The Astronomer's Telegram, 4347, 1
Casares, J., Yanes-Rizo, I. V., Torres, M. A. P., et al. 2023, MNRAS, 526, 5209
Casares, J., Zurita, C., Shahbaz, T., Charles, P. A., & Fender, R. P. 2004, ApJ, 613, L133
Casella, P., Altamirano, D., Patruno, A., Wijnands, R., & van der Klis, M. 2008, ApJ, 674, L41
Castro-Tirado, A., Gorosabel, J., Walton, N., et al. 1998, IAU Circ., 6931, 1
Chakrabarty, D., Jonker, P. G., & Markwardt, C. B. 2019, The Astronomer's Telegram, 13247, 1
Chakrabarty, D. & Morgan, E. H. 1998, Nature, 394, 346
Charles, P., Thorstensen, J., & Bowyer, S. 1978, MNRAS, 183, 29P
Chatterjee, D., Debnath, D., Chakrabarti, S. K., Mondal, S., & Jana, A. 2016, ApJ, 827, 88
Chaty, S. 2006, in VI Microquasar Workshop: Microquasars and Beyond, 14.1
Chaty, S. 2022, Accreting Binaries; Nature, formation, and evolution (IOP Publishing)
Chaty, S. & Bessolaz, N. 2006, A&A, 455, 639
Chaty, S., Fortin, F., & López-Oramas, A. 2020, A&A, 637, A2
Chaty, S., Mignani, R. P., & Israel, G. L. 2006, MNRAS, 365, 1387
Chelovekov, I. V. & Grebenev, S. A. 2007, The Astronomer's Telegram, 1094, 1
Chelovekov, I. V., Grebenev, S. A., Mereminskiy, I. A., & Prosvetov, A. V. 2017, Astronomy Letters, 43, 781
Chenevez, J., Alizai, K., Lepingwell, V. A., et al. 2018, The Astronomer's Telegram, 11272, 1
Chenevez, J., Altamirano, D., Galloway, D. K., et al. 2011, MNRAS, 410, 179
Chenevez, J., Falanga, M., Kuulkers, E., et al. 2007, A&A, 469, L27
Chenevez, J., Kuulkers, E., Brandt, S., et al. 2012, The Astronomer's Telegram, 4050, 1
Cherepashchuk, A. M., Khruzina, T. S., & Bogomazov, A. I. 2021, MNRAS, 508, 1389
Chevalier, C., Ilovaisky, S. A., & Charles, P. A. 1985, A&A, 147, L3
Chirenti, C. & Jasiulek, M. 2018, MNRAS, 476, 354
Chou, Y. & Jhang, Y.-W. 2023, ApJ, 951, 42
Clavel, M., Tomsick, J. A., Bodaghee, A., et al. 2016, MNRAS, 461, 304
Cocchi, M., Bazzano, A., Natalucci, L., et al. 2001, A&A, 378, L37
Cocchi, M., Bazzano, A., Natalucci, L., et al. 2000, A&A, 357, 527
Cocchi, M., Bazzano, A., Natalucci, L., et al. 1999a, A&A, 346, L45
Cocchi, M., Bazzano, A., Natalucci, L., et al. 1998, ApJ, 508, L163
Cocchi, M., Natalucci, L., in 't Zand, J., et al. 1999b, IAU Circ., 7247, 3
Corbet, R. H. D. 2003, ApJ, 595, 1086
Corbet, R. H. D., Chomiuk, L., Coe, M. J., et al. 2019, ApJ, 884, 93
Corbet, R. H. D., Thorstensen, J. R., Charles, P. A., et al. 1986, MNRAS, 222, 15P
Cornelisse, R., Casares, J., Charles, P. A., & Steeghs, D. 2013, MNRAS, 432, 1361
Cornelisse, R., D'Avanzo, P., Campana, S., et al. 2012, MNRAS, 420, 3538
Cornelisse, R., Verbunt, F., in't Zand, J. J. M., Kuulkers, E., & Heise, J. 2002a, A&A, 392, 931
Cornelisse, R., Verbunt, F., in't Zand, J. J. M., et al. 2002b, A&A, 392, 885
Cornelisse, R., Wijnands, R., & Homan, J. 2007, MNRAS, 380, 1637
Corral-Santana, J. M., Casares, J., Muñoz-Darias, T., et al. 2016, A&A, 587, A61
Corral-Santana, J. M., Torres, M. A. P., Shahbaz, T., et al. 2018, MNRAS, 475, 1036
Coti Zelati, F., de Ugarte Postigo, A., Russell, T. D., et al. 2021, A&A, 650, A69
Coti Zelati, F., Papitto, A., de Martino, D., et al. 2019, A&A, 622, A211
Courvoisier, T. J. L., Peacock, A., & Pakull, M. 1984, IAU Circ., 3932, 2
Cowperthwaite, P. S., Massaro, F., D'Abrusco, R., et al. 2013, AJ, 146, 110
Crawford, F., Lyne, A. G., Stairs, I. H., et al. 2013, ApJ, 776, 20
Cui, W., Heindl, W. A., Swank, J. H., et al. 1997, ApJ, 487, L73
Cutri, R. M., Skrutskie, M. F., van Dyk, S., et al. 2003, VizieR Online Data Catalog, II/246
D'Avanzo, P., Campana, S., Casares, J., et al. 2009, A&A, 508, 297
Davidsen, A., Malina, R., & Bowyer, S. 1977, ApJ, 211, 866
De, K., Chakrabarty, D., Soria, R., et al. 2022a, ApJ, 928, L8
De, K., Mereminskiy, I., Soria, R., et al. 2022b, ApJ, 935, 36
De Cesare, G., Bazzano, A., Stratta, G., et al. 2006, in ESA Special Publication, Vol. 604, The X-ray Universe 2005, ed. A. Wilson, 259
de Martino, D., Casares, J., Mason, E., et al. 2014, MNRAS, 444, 3004
de Martino, D., Papitto, A., Belloni, T., et al. 2015, MNRAS, 454, 2190
Deeter, J. E., Boynton, P. E., & Pravdo, S. H. 1981, ApJ, 247, 1003
Degenaar, N., Altamirano, D., & Wijnands, R. 2012a, The Astronomer's Telegram, 4219, 1
Degenaar, N., Jonker, P. G., Torres, M. A. P., et al. 2010, MNRAS, 404, 1591
Degenaar, N., Linares, M., Altamirano, D., & Wijnands, R. 2012b, ApJ, 759, 8
Degenaar, N., Wijnands, R., & Miller, J. M. 2014a, ApJ, 787, 67
Degenaar, N., Wijnands, R., Reynolds, M. T., et al. 2014b, ApJ, 792, 109
Dehiwalage, D. D., Clavel, M., Petrucci, P. O., & Henri, G. 2022, in SF2A-2022: Proceedings of the Annual meeting of the French Society of Astronomy and Astrophysics. Eds.: J. Richard, ed. J. Richard, A. Siebert, E. Lagadec, N. Lagarde, O. Venot, J. Malzac, J. B. Marquette, M. N'Diaye, & B. Briot, 39–42
Del Santo, M., Chenevez, J., Brandt, S., Bazzano, A., & Ubertini, P. 2007, The Astronomer's Telegram, 1207, 1
Del Santo, M., Sidoli, L., Bazzano, A., et al. 2006, A&A, 456, 1105
Deloye, C. J., Heinke, C. O., Taam, R. E., & Jonker, P. G. 2008, MNRAS, 391, 1619
Deutsch, E. W., Margon, B., & Anderson, S. F. 2000, ApJ, 530, L21
Dieball, A., Knigge, C., Zurek, D. R., et al. 2005, ApJ, 634, L105
Dotani, T., Inoue, H., Murakami, T., Nagase, F., & Tanaka, Y. 1990, Nature, 347, 534
Draghis, P. A., Miller, J. M., Brumback, M. C., et al. 2023, ApJ, 954, 62
Ducci, L., Malacaria, C., Romano, P., et al. 2023, A&A, 674, A100
Echiburú, C. S., Guillot, S., Zhao, Y., et al. 2020, MNRAS, 495, 4508
Elebert, P., Reynolds, M. T., Callanan, P. J., et al. 2009, MNRAS, 395, 884
Engel, M. C., Heinke, C. O., Sivakoff, G. R., Elshamouty, K. G., & Edmonds, P. D. 2012, ApJ, 747, 119
Evans, I. N., Primini, F. A., Glotfelty, C. S., et al. 2019, VizieR Online Data Catalog, IX/57
Evans, P. A., Page, K. L., Osborne, J. P., et al. 2020, ApJS, 247, 54
Ferrigno, C., Bozzo, W., Sanna, A., et al. 2018, The Astronomer's Telegram, 11957, 1
Filippenko, A. V., Leonard, D. C., Matheson, T., et al. 1999, PASP, 111, 969
Filippenko, A. V., Matheson, T., & Ho, L. C. 1995, ApJ, 455, 614
Filippenko, A. V., Matheson, T., Leonard, D. C., Barth, A. J., & van Dyk, S. D. 1997, PASP, 109, 461
Filippova, E., Bozzo, E., & Ferrigno, C. 2014, A&A, 563, A124
Finger, M. H., Koh, D. T., Nelson, R. W., et al. 1996, Nature, 381, 291
Fiocchi, M., Bassani, L., Bazzano, A., et al. 2010, ApJ, 720, 987
Fiocchi, M., Bazzano, A., Natalucci, L., Landi, R., & Ubertini, P. 2011, MNRAS, 414, L41
Focke, W. B., Markwardt, C. B., Swank, J. H., & Taam, R. E. 1999, in American Astronomical Society Meeting Abstracts, Vol. 195, American Astronomical Society Meeting Abstracts, 126.02
Forman, W., Jones, C., Cominsky, L., et al. 1978, ApJS, 38, 357
Fortin, F., Chaty, S., Coleiro, A., Tomsick, J. A., & Nitschelm, C. H. R. 2018, A&A, 618, A150
Fortin, F., Chaty, S., & Tomsick, J. 2023a, The Astronomer's Telegram, 16099, 1
Fortin, F., García, F., Simaz Bunzel, A., & Chaty, S. 2023b, A&A, 671, A149
Foschini, L. 2002, Understanding the nature of the unidentified EGRET source 3EG J1631-4033, Chandra Proposal ID 04508160
Fox, D. & Lewin, W. 1998, IAU Circ., 6964, 2
Fox, D. W., Lewin, W. H. G., Rutledge, R. E., et al. 2001, MNRAS, 321, 776
Gaia Collaboration. 2022, VizieR Online Data Catalog, I/355
Galloway, D. K., Chakrabarty, D., & Lin, J. R. 2009, The Astronomer's Telegram, 2094, 1
Galloway, D. K., Chakrabarty, D., Morgan, E. H., & Remillard, R. A. 2002a, ApJ, 576, L137
Galloway, D. K., Chakrabarty, D., Muno, M. P., & Savov, P. 2001, ApJ, 549, L85
Galloway, D. K., in't Zand, J., Chenevez, J., et al. 2020, ApJS, 249, 32
Galloway, D. K., Markwardt, C. B., Morgan, E. H., Chakrabarty, D., & Strohmayer, T. E. 2005, ApJ, 622, L45
Galloway, D. K., Muno, M. P., Hartman, J. M., Psaltis, D., & Chakrabarty, D. 2008, ApJS, 179, 360
Galloway, D. K., Psaltis, D., Chakrabarty, D., & Muno, M. P. 2003, ApJ, 590, 999
Galloway, D. K., Sokoloski, J. L., & Kenyon, S. J. 2002b, ApJ, 580, 1065
Gambino, A. F., Iaria, R., Di Salvo, T., et al. 2016, A&A, 589, A34
Gandolfi, G., Coletta, A., Ricci, D., et al. 1999, IAU Circ., 7174, 1
Gangopadhyay, T., Li, X.-D., Ray, S., Dey, M., & Dey, J. 2012, New A, 17, 43
Garcia, M., Baliunas, S. L., Doxsey, R., et al. 1983, ApJ, 267, 291
Garcia, M. R., Bailyn, C. D., Grindlay, J. E., & Molnar, L. A. 1989, ApJ, 341, L75
Garcia, M. R. & Grindlay, J. E. 1987, ApJ, 313, L59
Gendre, B., Barret, D., & Webb, N. 2003, A&A, 403, L11
Giacconi, R., Gursky, H., Paolini, F. R., & Rossi, B. B. 1962, Phys. Rev. Lett., 9, 439
Gilfanov, M., Revnivtsev, M., Sunyaev, R., & Churazov, E. 1998, A&A, 338, L83
Gomez, S., Torres, M. A. P., Jonker, P. G., et al. 2021, MNRAS, 502, 48
González Hernández, J. I., Rebolo, R., & Casares, J. 2012, ApJ, 744, L25
González Hernández, J. I., Rebolo, R., Israelian, G., et al. 2008, ApJ, 679, 732
González Hernández, J. I., Rebolo, R., Israelian, G., et al. 2006, ApJ, 644, L49

Goodwin, A. J., Galloway, D. K., in't Zand, J. J. M., et al. 2019, MNRAS, 486, 4149
Goodwin, A. J. & Woods, T. E. 2020, MNRAS, 495, 796
Gorgone, N. M., Kouveliotou, C., Negoro, H., et al. 2019, ApJ, 884, 168
Gosling, A. J., Bandyopadhyay, R. M., Miller-Jones, J. C. A., & Farrell, S. A. 2007, MNRAS, 380, 1511
Göğüş, E., Finger, M. H., Kouveliotou, C., et al. 2004, ApJ, 609, 977
Grebenev, S. A., Molkov, S. V., Revnivtsev, M. G., & Sunyaev, R. A. 2007, in ESA Special Publication, Vol. 622, The Obscured Universe. Proceedings of the VI INTEGRAL Workshop, 3730376
Greenstein, G. 1972, Nature Physical Science, 238, 71
Greiner, J., Dennerl, K., & Predehl, P. 1996, A&A, 314, L21
Grindlay, J., Gursky, H., Schnopper, H., et al. 1976, ApJ, 205, L127
Guillot, S., Rutledge, R. E., Bildsten, L., et al. 2009, MNRAS, 392, 665
Güver, T. & Özel, F. 2013, ApJ, 765, L1
Hammerstein, E. K., Cackett, E. M., Reynolds, M. T., & Miller, J. M. 2018, MNRAS, 478, 4317
Hare, J., Kargaltsev, O., & Rangelov, B. 2018, ApJ, 865, 33
Harlaftis, E. T., Horne, K., & Filippenko, A. V. 1996, PASP, 108, 762
Harris, D. E., Forman, W., Gioia, I. M., et al. 1990, Einstein Observatory Catalog of IPC X-ray Sources, 2
Hasinger, G. & van der Klis, M. 1989, A&A, 225, 79
Heida, M., Jonker, P. G., Torres, M. A. P., & Chiavassa, A. 2017, ApJ, 846, 132
Heinke, C. O., Bahramian, A., Degenaar, N., & Wijnands, R. 2015, MNRAS, 447, 3034
Heinke, C. O., Grindlay, J. E., & Edmonds, P. D. 2005, ApJ, 622, 556
Heinke, C. O., Grindlay, J. E., Lloyd, D. A., & Edmonds, P. D. 2003, ApJ, 588, 452
Hemphill, P. B., Schulz, N. S., Marshall, H. L., & Chakrabarty, D. 2021, ApJ, 920, 142
Hertz, P. & Wood, K. S. 1988, ApJ, 331, 764
Hertz, P., Wood, K. S., & Cominsky, L. R. 1997, ApJ, 486, 1000
Hinkle, K. H., Fekel, F. C., Joyce, R. R., et al. 2006, ApJ, 641, 479
Hjellming, R. M. & Rupen, M. P. 1995, Nature, 375, 464
Hoffman, J. A., Lewin, W. H. G., & Doty, J. 1977, ApJ, 217, L23
Homan, J., Belloni, T., van der Klis, M., et al. 2006, The Astronomer's Telegram, 748, 1
Homan, J., Gendreau, K. C., Sanna, A., et al. 2021, The Astronomer's Telegram, 14606, 1
Homan, J., van den Berg, M., Heinke, C., & Pooley, D. 2022, The Astronomer's Telegram, 15640, 1
Homan, J. & Wijnands, R. 2003, The Astronomer's Telegram, 169, 1
Homer, L., Anderson, S. F., Margon, B., Deutsch, E. W., & Downes, R. A. 2001a, ApJ, 550, L155
Homer, L., Charles, P. A., Hakala, P., et al. 2001b, MNRAS, 322, 827
Horne, K., Verbunt, F., & Schneider, D. P. 1986, MNRAS, 218, 63
Hunter, J. D. 2007, Computing in Science Engineering, 9, 90
Hynes, R. I., Schaefer, B. E., Baum, Z. A., et al. 2016, MNRAS, 459, 3596
Hynes, R. I., Steeghs, D., Casares, J., Charles, P. A., & O'Brien, K. 2003, ApJ, 583, L95
Iaria, R., D'Aí, A., di Salvo, T., et al. 2009, A&A, 505, 1143
Iaria, R., Di Salvo, T., Matranga, M., et al. 2015, A&A, 577, A63
Iaria, R., Gambino, A. F., Di Salvo, T., et al. 2018, MNRAS, 473, 3490
Ilovaisky, S. A., Auriere, M., Koch-Miramond, L., et al. 1993, A&A, 270, 139
in 't Zand, J. J. M., Verbunt, F., Heise, J., et al. 1998, A&A, 329, L37
in 't Zand, J. J. M., Verbunt, F., Strohmayer, T. E., et al. 1999, A&A, 345, 100
in't Zand, J., Linares, M., & Markwardt, C. 2014, The Astronomer's Telegram, 5972, 1
in't Zand, J., Verbunt, F., Heise, J., et al. 2004, Nuclear Physics B Proceedings Supplements, 132, 486
in't Zand, J. J. M., Cornelisse, R., & Méndez, M. 2005a, A&A, 440, 287
in't Zand, J. J. M., Cumming, A., van der Sluys, M. V., Verbunt, F., & Pols, O. R. 2005b, A&A, 441, 675
in't Zand, J. J. M., Galloway, D. K., Kuulkers, E., & Goodwin, A. 2017, The Astronomer's Telegram, 10567, 1
In't Zand, J. J. M., Heise, J., Muller, J. M., et al. 1999, Nuclear Physics B Proceedings Supplements, 69, 228
in't Zand, J. J. M., Hulleman, F., Markwardt, C. B., et al. 2003, A&A, 406, 233
in't Zand, J. J. M., Jonker, P. G., Bassa, C. G., Markwardt, C. B., & Levine, A. M. 2009, A&A, 506, 857
in't Zand, J. J. M., Markwardt, C. B., Bazzano, A., et al. 2002a, A&A, 390, 597
in't Zand, J. J. M., van Kerkwijk, M. H., Pooley, D., et al. 2001, ApJ, 563, L41
in't Zand, J. J. M., Verbunt, F., Kuulkers, E., et al. 2002b, A&A, 389, L43
Ioannou, Z., Robinson, E. L., Welsh, W. F., & Haswell, C. A. 2004, AJ, 127, 481
Iwakiri, W. B., Pottschmidt, K., Falkner, S., et al. 2019, ApJ, 878, 121
Iyer, N., Nandi, A., & Mandal, S. 2015, ApJ, 807, 108
Jain, C. & Paul, B. 2011, MNRAS, 413, 2
Jain, C., Paul, B., & Dutta, A. 2010, MNRAS, 409, 755
Jain, C., Paul, B., Joshi, K., Dutta, A., & Raichur, H. 2007, Journal of Astrophysics and Astronomy, 28, 175
Jaisawal, G. K., Naik, S., Gupta, S., Chenevez, J., & Epili, P. 2018, MNRAS, 478, 448
Jones, E., Oliphant, T., & Peterson, P. 2001
Jonker, P. G., Bassa, C. G., & Wachter, S. 2007a, MNRAS, 377, 1295
Jonker, P. G., Miller-Jones, J., Homan, J., et al. 2010, MNRAS, 401, 1255
Jonker, P. G., Nelemans, G., & Bassa, C. G. 2007b, MNRAS, 374, 999
Jonker, P. G., Steeghs, D., Chakrabarty, D., & Juett, A. M. 2007c, ApJ, 665, L147
Jonker, P. G., Steeghs, D., Nelemans, G., & van der Klis, M. 2005, MNRAS, 356, 621
Jonker, P. G. & van der Klis, M. 2001, ApJ, 553, L43
Jonker, P. G., van der Klis, M., & Groot, P. J. 2003a, MNRAS, 339, 663
Jonker, P. G., van der Klis, M., Homan, J., et al. 2001, ApJ, 553, 335
Jonker, P. G., van der Klis, M., Kouveliotou, C., et al. 2003b, MNRAS, 346, 684
Juett, A. M. & Chakrabarty, D. 2003, ApJ, 599, 498
Kaaret, P., in 't Zand, J. J. M., Heise, J., & Tomsick, J. A. 2002, ApJ, 575, 1018
Kaaret, P., in 't Zand, J. J. M., Heise, J., & Tomsick, J. A. 2003, ApJ, 598, 481
Kaaret, P., Morgan, E. H., Vanderspek, R., & Tomsick, J. A. 2006, ApJ, 638, 963
Kaaret, P., Prieskorn, Z., in 't Zand, J. J. M., et al. 2007, ApJ, 657, L97
Kalamkar, M., Yang, Y., Altamirano, D., et al. 2010, The Astronomer's Telegram, 2881, 1
Kaluzny, J., Rozanska, A., Rozyczka, M., Krzeminski, W., & Thompson, I. B. 2012, ApJ, 750, L3
Kaptein, R. G., in't Zand, J. J. M., Kuulkers, E., et al. 2000, A&A, 358, L71
Karitskaya, E. A. & Bochkarev, N. G. 1987, Astronomicheskij Tsirkulyar, 1477, 1
Kaur, R., Wijnands, R., Kamble, A., et al. 2017, MNRAS, 464, 170
Kaur, R., Wijnands, R., Patruno, A., et al. 2009, MNRAS, 394, 1597
Kennea, J. A. 2018, The Astronomer's Telegram, 11311, 1
Kennea, J. A., Burrows, D. N., Chester, M., et al. 2005, The Astronomer's Telegram, 632, 1
Kennea, J. A., Campana, S., Wijnands, R., et al. 2007, The Astronomer's Telegram, 1209, 1
Kennea, J. A. & Negoro, H. 2019, The Astronomer's Telegram, 12434, 1
Kennea, J. A., Palmer, D. M., Siegel, M. H., et al. 2020, The Astronomer's Telegram, 13452, 1
Kennedy, M. R., Breton, R. P., Clark, C. J., et al. 2020, MNRAS, 494, 3912
Kirsch, M. G. F., Mukerjee, K., Breitfellner, M. G., et al. 2004, A&A, 423, L9
Kitamura, Y., Takahashi, H., & Fukazawa, Y. 2014, PASJ, 66, 6
Klein-Wolt, M., Wijnands, R., Swank, J. H., & Markwardt, C. B. 2007, The Astronomer's Telegram, 1065, 1
Knight, A. H., Ingram, A., & Middleton, M. 2022, MNRAS, 514, 1908
Koo, J. W. C. & Haymes, R. C. 1980, ApJ, 239, L57
Kouveliotou, C., Finger, M. H., Fishman, G. J., et al. 1993, in American Institute of Physics Conference Series, Vol. 280, Compton Gamma-ray Observatory, ed. M. Friedlander, N. Gehrels, & D. J. Macomb, 319–323
Koyama, K., Kunieda, H., Takeuchi, Y., & Tawara, Y. 1991, ApJ, 370, L77
Krimm, H. A., Markwardt, C. B., Deloye, C. J., et al. 2007, ApJ, 668, L147
Krimm, H. A., Tomsick, J. A., Markwardt, C. B., et al. 2011, ApJ, 735, 104
Kuiper, L., Tsygankov, S. S., Falanga, M., et al. 2020, A&A, 641, A37
Kushwaha, A., Jayasurya, K. M., Agrawal, V. K., & Nandi, A. 2023, MNRAS, 524, L15
Kuśmierek, K., Madej, J., & Kuulkers, E. 2011, MNRAS, 415, 3344
Kuulkers, E., Homan, J., van der Klis, M., Lewin, W. H. G., & Méndez, M. 2002, A&A, 382, 947
Kuulkers, E., Kouveliotou, C., van der Horst, A. J., et al. 2011, arXiv e-prints, arXiv:1102.2102
Kuulkers, E. & Levine, A. M. 2006, The Astronomer's Telegram, 837, 1
Kuulkers, E. & van der Klis, M. 1998, A&A, 332, 845
Lamer, G., Schwope, A. D., Predehl, P., et al. 2021, A&A, 647, A7
Landi, R., Bassani, L., Bazzano, A., et al. 2017a, MNRAS, 470, 1107
Landi, R., Bassani, L., Malizia, A., et al. 2010a, MNRAS, 403, 945
Landi, R., Malizia, A., Bassani, L., et al. 2017b, The Astronomer's Telegram, 10467, 1
Landi, R., Masetti, N., Bazzano, A., et al. 2010b, The Astronomer's Telegram, 3065, 1
Langmeier, A., Sztajno, M., Vacca, W. D., Truemper, J., & Pietsch, W. 1986, in NATO Advanced Study Institute (ASI) Series C, Vol. 167, The Evolution of Galactic X-Ray Binaries, ed. J. Truemper, W. H. G. Lewin, & W. Brinkmann, 253
Leahy, D. A., Morsink, S. M., & Chou, Y. 2011, ApJ, 742, 17
Lewin, W. H. G., Clark, G., & Doty, J. 1976a, IAU Circ., 2922, 1
Lewin, W. H. G., Doty, J., Clark, G. W., et al. 1976b, ApJ, 207, L95
Li, Z., Qu, Z., Chen, L., et al. 2015, ApJ, 798, 56
Li, Z., Yu, W., Lu, Y., Pan, Y., & Falanga, M. 2022, ApJ, 935, 123
Liao, N.-H., Chou, Y., Hsieh, H.-E., & Chuang, P.-S. 2015, Publication of Korean Astronomical Society, 30, 593
Lin, D., Altamirano, D., Homan, J., et al. 2009, ApJ, 699, 60
Lin, J. & Yu, W. 2020, ApJ, 903, 37
Lindstrøm, C., Griffin, J., Kiss, L. L., et al. 2005, MNRAS, 363, 882

Liu, Q. Z., van Paradijs, J., & van den Heuvel, E. P. J. 2001, A&A, 368, 1021
Liu, Q. Z., van Paradijs, J., & van den Heuvel, E. P. J. 2007, A&A, 469, 807
López, K. M., Jonker, P. G., Torres, M. A. P., et al. 2019, MNRAS, 482, 2149
Luna, G. J. M. 2023, A&A, 676, L2
Lutovinov, A., Revnivtsev, M., Molkov, S., & Sunyaev, R. 2005, A&A, 430, 997
MacDonald, R. K. D., Bailyn, C. D., Buxton, M., et al. 2014, ApJ, 784, 2
Maeda, Y., Koyama, K., Sakano, M., Takeshima, T., & Yamauchi, S. 1996, PASJ, 48, 417
Maiorano, E., Landi, R., Stephen, J. B., et al. 2011, MNRAS, 416, 531
Majczyna, A., Madej, J., Należyty, M., Różańska, A., & Udalski, A. 2016, in 37th Meeting of the Polish Astronomical Society, ed. A. Różańska & M. Bejger, Vol. 3, 133–136
Makishima, K., Mitsuda, K., Inoue, H., et al. 1983, ApJ, 267, 310
Malizia, A., Landi, R., Bassani, L., et al. 2017, The Astronomer's Telegram, 10468, 1
Malizia, A., Landi, R., Molina, M., et al. 2016, MNRAS, 460, 19
Mandal, M., Pal, S., Chauhan, J., Lohfink, A., & Bharali, P. 2023, MNRAS, 521, 881
Marino, A., Anitra, A., Mazzola, S. M., et al. 2022, MNRAS, 515, 3838
Markwardt, C., Swank, J., & Smith, E. 2001a, IAU Circ., 7707, 2
Markwardt, C. B., Cummings, J., & Krimm, H. 2008a, The Astronomer's Telegram, 1616, 1
Markwardt, C. B., Halpern, J. P., Holland, S. T., et al. 2008b, The Astronomer's Telegram, 1716, 1
Markwardt, C. B., Juda, M., & Swank, J. H. 2003a, IAU Circ., 8095, 2
Markwardt, C. B., Klein-Wolt, M., Swank, J. H., & Wijnands, R. 2007a, The Astronomer's Telegram, 1069, 1
Markwardt, C. B., Krimm, H. A., & Swank, J. H. 2007b, The Astronomer's Telegram, 1108, 1
Markwardt, C. B., Strohmayer, T. E., & Swank, J. H. 1999, ApJ, 512, L125
Markwardt, C. B., Strohmayer, T. E., & Swank, J. H. 2003b, The Astronomer's Telegram, 164, 1
Markwardt, C. B., Strohmayer, T. E., & Swank, J. H. 2008c, The Astronomer's Telegram, 1443, 1
Markwardt, C. B., Strohmayer, T. E., Swank, J. H., & Zhang, W. 2000, IAU Circ., 7482, 2
Markwardt, C. B., Swank, J. H., Krimm, H. A., Pereira, D., & Strohmayer, T. E. 2009, The Astronomer's Telegram, 2107, 1
Markwardt, C. B., Swank, J. H., & Strohmayer, T. E. 2001b, in American Astronomical Society Meeting Abstracts, Vol. 199, American Astronomical Society Meeting Abstracts, 27.04
Markwardt, C. B., Swank, J. H., & Strohmayer, T. E. 2004, The Astronomer's Telegram, 353, 1
Markwardt, C. B., Swank, J. H., Strohmayer, T. E., in 't Zand, J. J. M., & Marshall, F. E. 2002, ApJ, 575, L21
Marsh, T. R., Robinson, E. L., & Wood, J. H. 1994, MNRAS, 266, 137
Marshall, F. E., Ueda, Y., & Markwardt, C. B. 1999, IAU Circ., 7133, 3
Martí, J., Luque-Escamilla, P. L., & Muñoz-Arjonilla, Á. J. 2016, A&A, 596, A46
Marti, J., Mirabel, I. F., Duc, P. A., & Rodriguez, L. F. 1997, A&A, 323, 158
Masetti, N., Bianchini, A., Bonibaker, J., della Valle, M., & Vio, R. 1996, A&A, 314, 123
Masetti, N., Dal Fiume, D., Cusumano, G., et al. 2002, A&A, 382, 104
Masetti, N., Landi, R., Pretorius, M. L., et al. 2007, A&A, 470, 331
Masetti, N., Malizia, A., Landi, R., et al. 2017, The Astronomer's Telegram, 10447, 1
Masetti, N., Parisi, P., Jiménez-Bailón, E., et al. 2012, A&A, 538, A123
Mason, K. O., Bell-Burnell, S. J., & White, N. E. 1976, Nature, 262, 474
Mason, K. O., Middleditch, J., Nelson, J. E., et al. 1980, ApJ, 242, L109
Mason, P. A., Robinson, E. L., Gray, C. L., & Hynes, R. I. 2008, ApJ, 685, 428
Mata Sánchez, D., Muñoz-Darias, T., Casares, J., Corral-Santana, J. M., & Shahbaz, T. 2015, MNRAS, 454, 2199
Mata Sanchez, D., Munoz-Darias, T., Casares, J., et al. 2015, MNRAS, 449, L1
Mata Sánchez, D., Rau, A., Álvarez Hernández, A., et al. 2021, MNRAS, 506, 581
Matsuba, E., Dotani, T., Mitsuda, K., et al. 1995, PASJ, 47, 575
McClintock, J. E. & Remillard, R. A. 1986, ApJ, 308, 110
Mereminskiy, I. A., Grebenev, S. A., Krivonos, R. A., Chelovekov, I. V., & Sunyaev, R. A. 2017a, The Astronomer's Telegram, 10256, 1
Mereminskiy, I. A., Grebenev, S. A., & Sunyaev, R. A. 2017b, Astronomy Letters, 43, 656
Meshcheryakov, A. V., Revnivtsev, M. G., Pavlinsky, M. N., Khamitov, I., & Bikmaev, I. F. 2010, Astronomy Letters, 36, 738
Migliari, S., Di Salvo, T., Belloni, T., et al. 2003, MNRAS, 342, 909
Mignani, R. P., Chaty, S., Mirabel, I. F., & Mereghetti, S. 2002, A&A, 389, L11
Mikhailov, K., van Leeuwen, J., & Jonker, P. G. 2017, ApJ, 840, 9
Mikołajewska, J., Zdziarski, A. A., Ziółkowski, J., Torres, M. A. P., & Casares, J. 2022, ApJ, 930, 9
Miller, J. M., Swihart, S. J., Strader, J., et al. 2020, ApJ, 904, 49
Miller-Jones, J. C. A., Sivakoff, G. R., Rupen, M., & Altamirano, D. 2011, The Astronomer's Telegram, 3628, 1
Molina, M., Landi, R., Bassani, L., et al. 2012, A&A, 548, A32
Molina, M., Malizia, A., Masetti, N., et al. 2021, MNRAS, 507, 3423
Molla, A. A., Chakrabarti, S. K., Debnath, D., & Mondal, S. 2017, ApJ, 834, 88
Mondal, S. 2020, Advances in Space Research, 65, 693
Mondal, S. & Jithesh, V. 2023, MNRAS, 522, 2065
Morgan, E., Kaaret, P., & Vanderspek, R. 2005a, The Astronomer's Telegram, 523, 1
Morgan, E., Swank, J., Markwardt, C., & Gehrels, N. 2005b, The Astronomer's Telegram, 550, 1
Mori, H., Maeda, Y., Pavlov, G. G., Sakano, M., & Tsuboi, Y. 2005, Advances in Space Research, 35, 1137
Morihana, K., Sugizaki, M., Nakahira, S., et al. 2013, PASJ, 65, L10
Motch, C., Pedersen, H., Beuermann, K., Pakull, M. W., & Courvoisier, T. J. L. 1987, ApJ, 313, 792
Motta, S. E., Belloni, T. M., Stella, L., Muñoz-Darias, T., & Fender, R. 2014, MNRAS, 437, 2554
Muñoz-Darias, T., de Ugarte Postigo, A., Russell, D. M., et al. 2013, MNRAS, 432, 1133
Muller, J. M., in 't Zand, J., Smith, M. J. S., et al. 1998a, IAU Circ., 6842, 2
Muller, J. M., Smith, M. J. S., D'Andreta, G., et al. 1998b, IAU Circ., 6867, 2
Muno, M. P., Chakrabarty, D., Galloway, D. K., & Savov, P. 2001, ApJ, 553, L157
Munoz-Darias, T., Motta, S., Stiele, H., & Belloni, T. 2011, The Astronomer's Telegram, 3341, 1
Murakami, T., Inoue, H., Koyama, K., et al. 1983, PASJ, 35, 531
Murdin, P., Allen, D. A., Morton, D. C., Whelan, J. A. J., & Thomas, R. M. 1980, MNRAS, 192, 709
Najar, S., Rangelov, B., & Kargaltsev, O. 2020, in American Astronomical Society Meeting Abstracts, Vol. 235, American Astronomical Society Meeting Abstracts #235, 170.09
Natalucci, L., Bazzano, A., Cocchi, M., et al. 2000a, ApJ, 536, 891
Natalucci, L., Bazzano, A., Cocchi, M., et al. 2000b, ApJ, 543, L73
Natalucci, L., Cornelisse, R., Bazzano, A., et al. 1999, ApJ, 523, L45
Nath, S. K., Debnath, D., Chatterjee, K., et al. 2023, Advances in Space Research, 71, 1045
Nättilä, J., Miller, M. C., Steiner, A. W., et al. 2017, A&A, 608, A31
Negoro, H., Kawase, T., Sugizaki, M., et al. 2017, The Astronomer's Telegram, 10708, 1
Negoro, H., Shidatsu, M., Mihara, T., et al. 2018, The Astronomer's Telegram, 11696, 1
Neilsen, J., Steeghs, D., & Vrtilek, S. D. 2008, MNRAS, 384, 849
Nelson, L. A., Rappaport, S. A., & Joss, P. C. 1986, ApJ, 304, 231
Nespoli, E., Fabregat, J., & Mennickent, R. E. 2010, A&A, 516, A94
Ng, M., Bult, P. M., Sanna, A., et al. 2021a, The Astronomer's Telegram, 14695, 1
Ng, M., Ray, P. S., Bult, P., et al. 2021b, ApJ, 908, L15
Ng, M., Ray, P. S., Strohmayer, T. E., et al. 2020, The Astronomer's Telegram, 14124, 1
Novarino, M. L., Echeveste, M., Benvenuto, O. G., De Vito, M. A., & Ferrero, G. A. 2021, MNRAS, 508, 3812
Oda, S., Shidatsu, M., Nakahira, S., et al. 2019, PASJ, 71, 108
Onori, F., Fiocchi, M., Masetti, N., et al. 2021, MNRAS, 503, 472
Oosterbroek, T., Orlandini, M., Parmar, A. N., et al. 1999, A&A, 351, L33
Orosz, J. A., Groot, P. J., van der Klis, M., et al. 2002, ApJ, 568, 845
Orosz, J. A., Jain, R. K., Bailyn, C. D., McClintock, J. E., & Remillard, R. A. 1998, ApJ, 499, 375
Orosz, J. A. & Kuulkers, E. 1999, MNRAS, 305, 132
Orosz, J. A., Kuulkers, E., van der Klis, M., et al. 2001, ApJ, 555, 489
Orosz, J. A., McClintock, J. E., Remillard, R. A., & Corbel, S. 2004, ApJ, 616, 376
Özbey Arabacı, M., Kalemci, E., Tomsick, J. A., et al. 2012, ApJ, 761, 4
Özel, F., Gould, A., & Güver, T. 2012, ApJ, 748, 5
Özel, F., Güver, T., & Psaltis, D. 2009, ApJ, 693, 1775
Paduano, A., Bahramian, A., Miller-Jones, J. C. A., et al. 2021, MNRAS, 506, 4107
Pahari, M., Misra, R., Dewangan, G. C., & Pawar, P. 2015, ApJ, 814, 158
Paizis, A., Nowak, M. A., Chaty, S., et al. 2007, ApJ, 657, L109
Paizis, A., Nowak, M. A., Rodriguez, J., et al. 2015, ApJ, 808, 34
Paizis, A., Nowak, M. A., Wilms, J., et al. 2011, ApJ, 738, 183
Paliya, V. S., Koss, M., Trakhtenbrot, B., et al. 2019, ApJ, 881, 154
Pan, H. C., Skinner, G. K., Sunyaev, R. A., & Borozdin, K. N. 1995, MNRAS, 274, L15
Papitto, A., Bozzo, E., Ferrigno, C., et al. 2011a, A&A, 535, L4
Papitto, A., Bozzo, E., Ferrigno, C., et al. 2013a, The Astronomer's Telegram, 4959, 1
Papitto, A., D'Aì, A., Motta, S., et al. 2011b, A&A, 526, L3
Papitto, A., di Salvo, T., Burderi, L., et al. 2007, MNRAS, 375, 971

Papitto, A., Ferrigno, C., Bozzo, E., et al. 2011c, The Astronomer's Telegram, 3556, 1
Papitto, A., Ferrigno, C., Bozzo, E., et al. 2013b, Nature, 501, 517
Papitto, A., Riggio, A., di Salvo, T., et al. 2010, MNRAS, 407, 2575
Parikh, A., Wijnands, R., Degenaar, N., & Altamirano, D. 2017, The Astronomer's Telegram, 10612, 1
Park, S. Q., Miller, J. M., McClintock, J. E., & Murray, S. S. 2005, ApJ, 618, L45
Parmar, A. N., Gottwald, M., Haberl, F., Giommi, P., & White, N. E. 1985a, in Recent Results on Cataclysmic Variables. The Importance of IUE and Exosat Results on Cataclysmic Variables and Low-Mass X-Ray Binaries, ed. W. R. Burke, 119
Parmar, A. N., Stella, L., & White, N. E. 1986, ApJ, 304, 664
Parmar, A. N., White, N. E., Giommi, P., et al. 1985b, IAU Circ., 4058, 2
Patel, S. K., Kouveliotou, C., Tennant, A., et al. 2004, Nuclear Physics B Proceedings Supplements, 132, 542
Patel, S. K., Zurita, J., Del Santo, M., et al. 2007, ApJ, 657, 994
Patruno, A., Haskell, B., & D'Angelo, C. 2012, ApJ, 746, 9
Paul, J., Goldwurm, A., Jourdain, E., et al. 1997, IAU Circ., 6746, 2
Pavlinsky, M. N., Grebenev, S. A., Lutovinov, A. A., Sunyaev, R. A., & Finoguenov, A. V. 2001, Astronomy Letters, 27, 297
Peterson, B. A., Wallace, P., Elliott, K. H., Hill, P. W., & Manchester, R. N. 1980, MNRAS, 190, 33P
Pike, S. N., Harrison, F. A., Tomsick, J. A., et al. 2021, ApJ, 918, 9
Pike, S. N., Negoro, H., Tomsick, J. A., et al. 2022, ApJ, 927, 190
Pintore, F., Sanna, A., Riggio, A., et al. 2014, The Astronomer's Telegram, 5901, 1
Ponti, G., Bianchi, S., Muñoz-Darias, T., & Nandra, K. 2018, MNRAS, 481, L94
Ponti, G., De, K., Muñoz-Darias, T., Stella, L., & Nandra, K. 2017, MNRAS, 464, 840
Pooley, D., Lewin, W. H. G., Verbunt, F., et al. 2002, ApJ, 573, 184
Porquet, D., Grosso, N., Bélanger, G., et al. 2005a, A&A, 443, 571
Porquet, D., Grosso, N., Burwitz, V., et al. 2005b, A&A, 430, L9
Priedhorsky, W. 1986, Ap&SS, 126, 89
Prodan, S. & Murray, N. 2015, ApJ, 798, 117
Qiu, H., Zhou, P., Yu, W., Li, X., & Xu, X. 2017, ApJ, 847, 44
Rappaport, S., Nelson, L. A., Ma, C. P., & Joss, P. C. 1987, ApJ, 322, 842
Ratti, E. M., Bassa, C. G., Torres, M. A. P., et al. 2010, MNRAS, 408, 1866
Ratti, E. M., Jonker, P. G., Miller-Jones, J. C. A., et al. 2012a, MNRAS, 423, 2656
Ratti, E. M., Steeghs, D. T. H., Jonker, P. G., et al. 2012b, MNRAS, 420, 75
Ratti, E. M., van Grunsven, T. F. J., Torres, M. A. P., et al. 2013, MNRAS, 431, L10
Ravi, V. 2017, ApJ, 851, 114
Reig, P., Papadakis, I., & Kylafis, N. D. 2003, A&A, 398, 1103
Reis, R. C., Reynolds, M. T., Miller, J. M., et al. 2013, ApJ, 778, 155
Remillard, R., Levine, A. M., Morgan, E. H., Markwardt, C. B., & Swank, J. H. 2006, The Astronomer's Telegram, 714, 1
Revnivtsev, M. & Sunyaev, R. 2003, A&A, 399, 699
Revnivtsev, M. G., Kniazev, A., Karasev, D. I., Berdnikov, L., & Barway, S. 2013, Astronomy Letters, 39, 523
Reynolds, A. P., Quaintrell, H., Still, M. D., et al. 1997, MNRAS, 288, 43
Ritter, H. & Kolb, U. 2003, A&A, 404, 301
Ritter, H. & Kolb, U. 2011, VizieR Online Data Catalog, B/cb
Rout, S. K., Vadawale, S., Garćia, J., & Connors, R. 2023, ApJ, 944, 68
Roy, J., Bhattacharyya, B., & Ray, P. S. 2014, The Astronomer's Telegram, 5890, 1
Rupen, M. P., Dhawan, V., & Mioduszewski, A. J. 2002, IAU Circ., 7893, 2
Russell, D. M., Lewis, F., Doran, R., & Roberts, S. 2011, The Astronomer's Telegram, 3116, 1
Russell, T. D., Del Santo, M., Marino, A., et al. 2022, MNRAS, 513, 6196
Russell, T. D., Miller-Jones, J. C. A., Sivakoff, G. R., Tetarenko, A. J., & JACPOT XRB Collaboration. 2018, The Astronomer's Telegram, 11356, 1
Russell, T. D., Soria, R., Motch, C., et al. 2014, MNRAS, 439, 1381
Saha, D., Mandal, M., & Pal, S. 2023, MNRAS, 519, 519
Sakano, M., Warwick, R. S., Decourchelle, A., & Wang, Q. D. 2005, MNRAS, 357, 1211
Sanna, A., Bahramian, A., Bozzo, E., et al. 2018, A&A, 610, L2
Sanna, A., Bult, P., Ng, M., et al. 2022, MNRAS, 516, L76
Sanna, A., Papitto, A., Burderi, L., et al. 2017, A&A, 598, A34
Sanna, A., Uttley, P., Altamirano, D., et al. 2019, The Astronomer's Telegram, 12447, 1
Sasaki, R., Maeda, T., Tsuboi, Y., et al. 2021, in Astronomical Society of the Pacific Conference Series, Vol. 528, New Horizons in Galactic Center Astronomy and Beyond, ed. M. Tsuboi & T. Oka, 391
Schultz, J. 2003, A&A, 397, 249
Seifina, E., Titarchuk, L., & Shaposhnikov, N. 2014, ApJ, 789, 57
Serino, M., Shidatsu, M., Ueda, Y., et al. 2015, PASJ, 67, 30
Sguera, V., Sidoli, L., Bird, A. J., Paizis, A., & Bazzano, A. 2020, MNRAS, 491, 4543
Shahbaz, T., González-Hernández, J. I., Breton, R. P., et al. 2022, MNRAS, 513, 71
Shahbaz, T., Kuulkers, E., Charles, P. A., et al. 1999, A&A, 344, 101
Shahbaz, T., Russell, D. M., Zurita, C., et al. 2013, MNRAS, 434, 2696
Shahbaz, T., Watson, C. A., & Hernandez-Peralta, H. 2007, MNRAS, 376, 1886
Shaposhnikov, N., Markwardt, C., Swank, J., & Krimm, H. 2010, ApJ, 723, 1817
Shaposhnikov, N., Markwardt, C. B., & Swank, J. H. 2009, The Astronomer's Telegram, 2269, 1
Shaposhnikov, N., Titarchuk, L., & Haberl, F. 2003, ApJ, 593, L35
Sharma, P., Sharma, R., Jain, C., Dewangan, G. C., & Dutta, A. 2021, Research in Astronomy and Astrophysics, 21, 214
Shaw, A. W., Degenaar, N., Maccarone, T. J., et al. 2024, MNRAS, 527, 7603
Shaw, A. W., Heinke, C. O., Degenaar, N., et al. 2017, MNRAS, 471, 2508
Shaw, A. W., Heinke, C. O., Maccarone, T. J., et al. 2020, MNRAS, 492, 4344
Shi, C.-S. & Zhang, S.-N. 2020, MNRAS, 494, 4382
Shidatsu, M., Kobayashi, K., Negoro, H., et al. 2022, ApJ, 927, 151
Sidoli, L., Paizis, A., Mereghetti, S., Götz, D., & Del Santo, M. 2011, MNRAS, 415, 2373
Skinner, G. K., Foster, A. J., Willmore, A. P., & Eyles, C. J. 1990, MNRAS, 243, 72
Smale, A. P. 1991, PASP, 103, 636
Smale, A. P., Church, M. J., & Bałucińska-Church, M. 2001, ApJ, 550, 962
Smith, D. A., Morgan, E. H., & Bradt, H. 1997, ApJ, 479, L137
Smith, D. M., Heindl, W. A., & Swank, J. H. 2002, ApJ, 578, L129
Smith, D. M., Markwardt, C. B., Swank, J. H., & Negueruela, I. 2012, MNRAS, 422, 2661
Soria, R., Ma, R., Tao, L., & Zhang, S.-N. 2022, MNRAS, 515, 3105
Sridhar, N., Bhattacharyya, S., Chandra, S., & Antia, H. M. 2019, MNRAS, 487, 4221
Staubert, R., Klochkov, D., & Wilms, J. 2009, A&A, 500, 883
Steeghs, D. & Casares, J. 2002, ApJ, 568, 273
Steeghs, D. & Jonker, P. G. 2007, ApJ, 669, L85
Steeghs, D., McClintock, J. E., Parsons, S. G., et al. 2013, ApJ, 768, 185
Steiner, J. F., McClintock, J. E., & Reid, M. J. 2012, ApJ, 745, L7
Stoop, M., van den Eijnden, J., Degenaar, N., et al. 2021, MNRAS, 507, 330
Strader, J., Chomiuk, L., Cheung, C. C., et al. 2015, ApJ, 804, L12
Strader, J., Li, K.-L., Chomiuk, L., et al. 2016, ApJ, 831, 89
Strader, J., Swihart, S. J., Urquhart, R., et al. 2021, ApJ, 917, 69
Strohmayer, T. E., Arzoumanian, Z., Bogdanov, S., et al. 2018a, ApJ, 858, L13
Strohmayer, T. E., Jahoda, K., Giles, A. B., & Lee, U. 1997a, ApJ, 486, 355
Strohmayer, T. E. & Markwardt, C. B. 2010, The Astronomer's Telegram, 2929, 1
Strohmayer, T. E. & Markwardt, C. B. 2011, The Astronomer's Telegram, 3121, 1
Strohmayer, T. E., Markwardt, C. B., & Kuulkers, E. 2008, ApJ, 672, L37
Strohmayer, T. E. & Nicer Observatory Science Working Group. 2020, in American Astronomical Society Meeting Abstracts, Vol. 235, American Astronomical Society Meeting Abstracts #235, 159.02
Strohmayer, T. E., Ray, P. S., Gendreau, K. C., et al. 2018b, The Astronomer's Telegram, 11507, 1
Strohmayer, T. E., Zhang, W., & Swank, J. H. 1997b, ApJ, 487, L77
Suleimanov, V. F., Poutanen, J., Nättilä, J., et al. 2017, MNRAS, 466, 906
Suleimanov, V. F., Poutanen, J., & Werner, K. 2020, A&A, 639, A33
Sunyaev, R. 1990, IAU Circ., 5104, 1
Sunyaev, R., Gilfanov, M., Churazov, E., et al. 1991, Pisma v Astronomicheskii Zhurnal, 17, 116
Sunyaev, R. & Kwant Team. 1989, IAU Circ., 4839, 1
Suzuki, K., Fukushima, K., Negoro, H., et al. 2015, The Astronomer's Telegram, 7233, 1
Suzuki, M. & HETE Collaboration. 2005, in American Astronomical Society Meeting Abstracts, Vol. 207, American Astronomical Society Meeting Abstracts, 32.04
Swank, J. H., Becker, R. H., Pravdo, S. H., & Serlemitsos, P. J. 1976, IAU Circ., 2963, 1
Swank, J. H., Strohmayer, T. E., & Markwardt, C. B. 2003, in American Astronomical Society Meeting Abstracts, Vol. 203, American Astronomical Society Meeting Abstracts, 125.01
Sztajno, M., Fujimoto, M. Y., van Paradijs, J., et al. 1987, MNRAS, 226, 39
Sztajno, M., Langmeier, A., Frank, J., et al. 1985, IAU Circ., 4111, 1
Tananbaum, H., Gursky, H., Kellogg, E. M., et al. 1972, ApJ, 174, L143
Tauris, T. M. 2018, Phys. Rev. Lett., 121, 131105
Tauris, T. M. & van den Heuvel, E. P. J. 2023, Physics of Binary Star Evolution. From Stars to X-ray Binaries and Gravitational Wave Sources
Taylor, M. B. 2005, in Astronomical Society of the Pacific Conference Series, Vol. 347, Astronomical Data Analysis Software and Systems XIV, ed. P. Shopbell, M. Britton, & R. Ebert, 29
Tetarenko, B. E., Sivakoff, G. R., Heinke, C. O., & Gladstone, J. C. 2016, ApJS, 222, 15
Thomas, N. T., Gudennavar, S. B., & Bubbly, S. G. 2023, MNRAS, 521, 433
Thorstensen, J., Charles, P., Bowyer, S., et al. 1979, ApJ, 233, L57

Thorstensen, J. R. & Armstrong, E. 2005, AJ, 130, 759
Titarchuk, L. & Seifina, E. 2023, A&A, 669, A57
Tomsick, J. A., Bodaghee, A., Chaty, S., et al. 2020, ApJ, 889, 53
Tomsick, J. A., Bodaghee, A., Chaty, S., et al. 2012, ApJ, 754, 145
Tomsick, J. A., Chaty, S., Rodriguez, J., Walter, R., & Kaaret, P. 2009, ApJ, 701, 811
Tomsick, J. A., Garcia, J., Fabian, A., et al. 2019, The Astronomer's Telegram, 13270, 1
Tomsick, J. A., Halpern, J. P., Kemp, J., & Kaaret, P. 1999, ApJ, 521, 341
Tomsick, J. A., Heindl, W. A., Chakrabarty, D., & Kaaret, P. 2002, ApJ, 581, 570
Torrejón, J. M., Negueruela, I., Smith, D. M., & Harrison, T. E. 2010, A&A, 510, A61
Torres, M. A. P., Casares, J., Jiménez-Ibarra, F., et al. 2020, ApJ, 893, L37
Torres, M. A. P., Casares, J., Jiménez-Ibarra, F., et al. 2019a, ApJ, 882, L21
Torres, M. A. P., Casares, J., Martínez-Pais, I. G., & Charles, P. A. 2002, MNRAS, 334, 233
Torres, M. A. P., Jonker, P. G., Britt, C. T., et al. 2014, MNRAS, 440, 365
Torres, M. A. P., Jonker, P. G., Casares, J., Miller-Jones, J. C. A., & Steeghs, D. 2021, MNRAS, 501, 2174
Torres, M. A. P., Jonker, P. G., Miller-Jones, J. C. A., et al. 2015, MNRAS, 450, 4292
Torres, M. A. P., Jonker, P. G., Steeghs, D., et al. 2008, ApJ, 672, 1079
Torres, M. A. P., McClintock, J. E., Garcia, M. R., & Murray, S. S. 2004, The Astronomer's Telegram, 233, 1
Torres, M. A. P., Repetto, S., Wevers, T., et al. 2019b, MNRAS, 487, 2296
Tse, K., Chou, Y., & Hsieh, H.-E. 2020, ApJ, 899, 120
Tucker, M. A., Shappee, B. J., Holoien, T. W. S., et al. 2018, ApJ, 867, L9
Ubertini, P., Bazzano, A., Cocchi, M., et al. 1999, ApJ, 514, L27
Uemura, M., Kato, T., Matsumoto, K., et al. 2000, PASJ, 52, L15
Urquhart, R., Bahramian, A., Strader, J., et al. 2020, ApJ, 904, 147
Ursini, F., Bassani, L., Malizia, A., et al. 2019, The Astronomer's Telegram, 12840, 1
van den Berg, M. & Homan, J. 2017, ApJ, 834, 71
van den Berg, M., Homan, J., Fridriksson, J. K., & Linares, M. 2014, ApJ, 793, 128
van der Klis, M., Kitamoto, S., Tsunemi, H., & Miyamoto, S. 1991, MNRAS, 248, 751
van der Klis, M., Parmar, A., van Paradijs, J., et al. 1985, IAU Circ., 4044, 1
van der Walt, S., Colbert, C., & Varoquaux, G. 2011, CSE, 13
van Grunsven, T. F. J., Jonker, P. G., Verbunt, F. W. M., & Robinson, E. L. 2017, MNRAS, 472, 1907
van Paradijs, J. 1983, in Accretion-Driven Stellar X-ray Sources, ed. W. H. G. Lewin & E. P. J. van den Heuvel, 192
van Paradijs, J. 1995, in X-ray Binaries, 536–577
van Paradijs, J., Penninx, W., Lewin, W. H. G., Sztajno, M., & Truemper, J. 1988, A&A, 192, 147
van Paradijs, J., van der Klis, M., van Amerongen, S., et al. 1990, A&A, 234, 181
Vargas, M., Goldwurm, A., Denis, M., et al. 1996, A&AS, 120, 291
Vasiliev, E. & Baumgardt, H. 2021, MNRAS, 505, 5978
Vincentelli, F. M., Cavecchi, Y., Casella, P., et al. 2020, MNRAS, 495, L37
Wachter, S. 1997, ApJ, 490, 401
Wachter, S., Hoard, D. W., Bailyn, C. D., Corbel, S., & Kaaret, P. 2002, ApJ, 568, 901
Wagner, R. M., Kreidl, T. J., Howell, S. B., & Starrfield, S. G. 1992, ApJ, 401, L97
Walter, R., Lubiński, P., Paltani, S., et al. 2007, A&A, 461, L17
Wang, L., Steeghs, D., Casares, J., et al. 2017, MNRAS, 466, 2261
Wang, S., Kawai, N., Shidatsu, M., et al. 2022, MNRAS, 514, 5320
Wang, S., Kawai, N., Shidatsu, M., et al. 2018, PASJ, 70, 67
Wang, Z. & Chakrabarty, D. 2004, ApJ, 616, L139
Warwick, R. S., Marshall, N., Fraser, G. W., et al. 1981, MNRAS, 197, 865
Watson, M. G. & Ricketts, M. J. 1978, MNRAS, 183, 35P
Webb, N. A., Coriat, M., Traulsen, I., et al. 2020, A&A, 641, A136
Webb, N. A., Naylor, T., Ioannou, Z., Charles, P. A., & Shahbaz, T. 2000, MNRAS, 317, 528
Welsh, W. F., Robinson, E. L., & Young, P. 2000, AJ, 120, 943
Weng, S.-S., Zhang, S.-N., Yi, S.-X., Rong, Y., & Gao, X.-D. 2015, MNRAS, 450, 2915
Werner, N., in't Zand, J. J. M., Natalucci, L., et al. 2004, A&A, 416, 311
Wetuski, J., Hynes, R. I., Maccarone, T. J., et al. 2021, MNRAS, 506, 5619
White, N. E., Giommi, P., & Angelini, L. 2000, VizieR Online Data Catalog, IX/31
White, N. E., Parmar, A. N., Sztajno, M., et al. 1984, ApJ, 283, L9
Wijnands, R., Homan, J., van der Klis, M., et al. 1997, ApJ, 490, L157
Wijnands, R., Méndez, M., van der Klis, M., et al. 1998, ApJ, 504, L35
Wijnands, R., Rol, E., Cackett, E., Starling, R. L. C., & Remillard, R. A. 2009, MNRAS, 393, 126
Wijnands, R., Strohmayer, T., & Franco, L. M. 2001, ApJ, 549, L71
Wijnands, R., Yang, Y. J., & Altamirano, D. 2012, MNRAS, 422, L91
Williams, D. R. A., Motta, S. E., Fender, R., et al. 2022, MNRAS, 517, 2801
Wilson, R. B., Zhang, S. N., Scott, M., et al. 1995, IAU Circ., 6207, 3
Wood, K. S., Meekins, J. F., Yentis, D. J., et al. 1984, ApJS, 56, 507
Wu, J., Jonker, P. G., Torres, M. A. P., et al. 2015a, MNRAS, 448, 1900
Wu, J., Orosz, J. A., McClintock, J. E., et al. 2016, ApJ, 825, 46
Wu, J., Orosz, J. A., McClintock, J. E., et al. 2015b, ApJ, 806, 92
Xu, Y., Harrison, F. A., Tomsick, J. A., et al. 2020, ApJ, 893, 30
Yadlapalli, N., Ravi, V., Yao, Y., Kulkarni, S. R., & Brisken, W. 2021, ApJ, 909, L27
Yanes-Rizo, I. V., Torres, M. A. P., Casares, J., et al. 2024, MNRAS, 527, 5949
Yanes-Rizo, I. V., Torres, M. A. P., Casares, J., et al. 2022, MNRAS, 517, 1476
Yao, Y., Kulkarni, S. R., Burdge, K. B., et al. 2021a, ApJ, 920, 120
Yao, Y., Kulkarni, S. R., Gendreau, K. C., et al. 2021b, ApJ, 920, 121
Yoshii, T., Kawai, N., Yatsu, Y., et al. 2016, in 41st COSPAR Scientific Assembly, Vol. 41, E1.16–24–16
Yungelson, L. & Lasota, J. P. 2008, New A Rev., 51, 860
Zdziarski, A. A., Ziółkowski, J., Bozzo, E., & Pjanka, P. 2016, A&A, 595, A52
Zhang, S., Chen, Y. P., Wang, J. M., Li, T. P., & Ge, J. Q. 2009, A&A, 497, 347
Zhang, S. N., Harmon, B. A., Wilson, C. A., et al. 1994, IAU Circ., 6096, 1
Zhang, W., Swank, J. H., White, N. E., & Lapidus, I. 1997, in American Astronomical Society Meeting Abstracts, Vol. 190, American Astronomical Society Meeting Abstracts #190, 36.03
Zhong, J. & Wang, Z. 2011, ApJ, 729, 8
Zurita, C., Durant, M., Torres, M. A. P., et al. 2008, ApJ, 681, 1458

Appendix A: Catalogue of Galactic LMXBs

Table A.1: Catalogue of Galactic LMXBs: general information. Confirmed systems are indicated in bold. "Compact object" provides the nature of the accreting compact object; "Companion spec. type" refers to the spectral type of the donor star in the binaries; Right Ascension (RA) and Declination (Dec) are given in J2000 alongside the 90% positional error radius; Gaia Distance is queried from Bailer-Jones et al. (2021); "Type I burst" indicates the presence of type I X-ray bursts; "Globular cluster" gives the host globular cluster in case of association. †/††: reliability flag (see Section 2.4).

Identifier	Compact object	Companion spec. type	R.A. [deg]	Dec. [deg]	Gaia Dist. [kpc]	Other Dist. [kpc]	Type I burst	Globular cluster
NGC 104 125	NS †[1]		5.9749	-72.0639		4.52(3) [2]		NGC104
47 Tuc X-5	NS †[3]		6.00413	-72.08144		4.52(3) [2]		NGC104
47 Tuc X-7	NS †[3]		6.01468	-72.08112		4.52(3) [2]		NGC104
47 Tuc X-9	BH ††[4]		6.01777	-72.0828		4.52(3) [2]		NGC104
NGC 104 37	NS ††[1]		6.02042	-72.08083		4.52(3) [2]		NGC104
NGC 104 17	NS †[1]		6.03437	-72.07555	5(2)	4.52(3) [2]		NGC104
IGR J00291+5934	NS [5]		7.26272	59.57194		2.8(8) ††[6]		
3U 0042+32		G0-8 [7]	11.21	33.02139				
4FGL J0407.7-5702	NS [8]		61.87583	-57.00667		10(3) †[8]		
GRO J0422+32	BH [9]	M4.5V [10]	65.42801	32.90748				
3FGL J0427.9-6704	NS [11]	K7V [12]	66.95686	-67.07641	2.5(5)††			
SRGA J043520.9+552226	BH †[13]		68.84708	55.37611		8(2) †[14]		
4U 0513-40	NS [15]	WD †[16]	78.52654	-40.04372	6(4)††	12.0(1) [2]	[15]	NGC1851
4FGL J0540.0-7552	NS †[17]	KIV-III [17]	85.025	-75.9		>5 †[17]		
MAXI J0556-332	NS †[18]		89.075	-33.13333				
Swift J061223.0+701243.9			93.09583	70.21219				
4U 0614+091	NS [19]		94.27952	9.13233	4(3)†			
1A 0620-00	BH †[20]	K4-5V [21]	95.6856	-0.3456	1.5(3)††			
MAXI J0637-430	BH [22]		99.0983	-42.8678		9(2) †[23]		
SRGt J071522.1-191609			108.84208	-19.26917				
EXO 0748-676	NS [24]		117.1405	-67.7521			[24]	
SAX J0835.9+5118	NS [25]		128.975	51.3			[25]	
4U 0836-429	NS [26]		129.325	-42.88333			[26]	
GRB 200205A	NS †[27]	WD †[28]	130.175	-35.26667				
MAXI J0911-655	NS [29]	WD †[29]	138.00956	-64.86835		10.1(1) [2]		NGC2808
2S 0918-549	NS [30]	WD †[31]	140.1103	-55.2068		4.8(7) †[31]	[30]	
2S 0921-630	NS †[32]	K0III [33]	140.6445	-63.2948	9(2)			
XTE J0929-314	NS [34]		142.33375	-31.38417				
MM Vel	BH [35]	M0V-K6V [35]	153.40168	-45.0757	4(1)††			
PSR J1023+0038	NS [36]	G1-F8 [37]	155.9487	0.6447	1.4(1)	1.37(4) †[38]		
CXOU J110926.4-650224	NS †[39]		167.45186	-64.99025	6(3)††			
XTE J1118+480	BH [40]	K5V-M1V [41]	169.54485	48.03672	3(1)			
IGR J11187-5438			169.58857	-54.62476	0.262(9)††			
GU Mus	BH [42]	K5V [43]	171.6108	-68.6758	5(2)	5.0(7) †[42]		
XSS J12270-4859	NS [44]	G5-F5V [45]	186.99466	-48.8952	2.4(8)††			
1A 1246-588	NS [46]		192.41313	-59.08816	4(3)		[46]	
XB 1254-690	NS [47]		194.4049	-69.2886	5(2)††		[47]	
MAXI J1305-704	BH [48]	KV-IV [49]	196.8	-70.81667		8(2) †[49]		
SAX J1324.5-6313	NS [50]		201.15974	-63.22424	1.1(3)	<6.2 †[51]	[50]	
2E 3049			201.58254	-47.48612		5.47(5) [2]		NGC5139
4U 1323-62	NS [52]		201.65429	-62.13572			[52]	
MAXI J1348-630	BH †[53]		207.05367	-63.27456		3.4(4) †[54]		
SWIFT J1357.2-0933		M4.5V ††[55]	209.3201	-9.5441				
BW Cir	BH [56]	G0-5III [56]	209.54046	-64.7348	4(2)††			
1FGL J1417.7-4407	NS [57]	G-KIII [57]	214.37917	-44.04806		4.4(9) †[57]		
MAXI J1421-613	NS [58]		215.40375	-61.60722		<7 †[59]	[58]	

Table A.1: continued.

Identifier	Compact object	Companion spec. type	R.A. [deg]	Dec. [deg]	Gaia Dist. [kpc]	Other Dist. [kpc]	Type I burst	Globular cluster
IGR J14298-6715			217.49917	-67.24581	2.2(4)[††]			
SAX J1452.8-5949	NS [60]	M-A [††][61]	223.2	-59.81667		<10 [†][61]		
Cen X-4	NS [62]	K3-5V [63]	224.5914	-31.6688				
TrA X-1	BH [64]	K2V [†][64]	232.07054	-61.88276		8.0(9) [†][64]		
MAXI J1535-571	BH [†][65]		233.8325	-57.23		5(2) [†][66]		
AX J1538.3-5541			234.575	-55.68333				
SWIFT J1539.2-6227	BH [†][67]		234.7998	-62.4673				
MAXI J1543-564	BH [†][68]		235.82223	-56.41343				
3FGL J1544.6-1125	NS [69]	K6-7V [†][70]	236.125	-11.45		3.8(7) [†][70]		
4U 1543-47	BH [71]	A0V [71]	236.7845	-47.6695	5(2)			
4U 1543-624	NS [†][72]	WD [73]	236.9775	-62.5684	4(2)[†]	7 [†][74]		
XTE J1550-564	BH [75]	K3III [75]	237.7444	-56.4765	4(3)			
4U 1556-60			240.25884	-60.73865	0.8(2)			
SAX J1603.9-7753	NS [76]		240.975	-77.88333			[76]	
UW CrB	NS [77]		241.44117	25.86254	5(2)[††]		[77]	
4U 1608-52	NS [15]	F-GV-III [†][78]	243.175	-52.41667			[15]	
IGR J16194-2810	NS [79]	M2III [80]	244.88893	-28.12777	2.1(1)[††]	3.0(2) [†][81]		
Sco X-1	NS [82]	K4IV [†][83]	244.9795	-15.6403	2.1(1)[††]			
MAXI J1621-501	NS [84]		245.17078	-49.96776		8(2) [†][85]	[84]	
2MASS J16233414-2631336	NS [†][86]		245.89224	-26.52639	5(2)[††]	1.85(2) [2]		NGC6121
Big Dipper			247.02306	-49.21113	1.04(2)[††]			
IGR J16287-5021			247.1119	-50.3777	4(2)[††]			
IGR J16293-4603		K-MI [††][87]	247.30363	-46.04744	4(3)			
MAXI J1631-479	BH [†][88]		247.975	-47.86667		>4.5 [†][89]		
MAXI J1630-276			248.00083	-27.55972				
4U 1626-67	NS [90]	WD [91]	248.06951	-67.46121	7(4)[††]			
4U 1630-47	BH [†][92]	B-F [††][93]	248.50649	-47.39277		10.0(1) [†][94]		
IGR J16358-4726	NS [95]	K-MIII [96]	248.97374	-47.42773				
KS 1632-477			249.1183	-47.8269				
XTE J1637-498			249.26107	-49.86112	8(6)[††]			
4U 1636-53	NS [97]		250.2317	-53.7514			[97]	
XMMU J164143.8+362758	NS [†][98]		250.43214	36.46638	9(3)[†]	7.42(8) [2]		NGC6205
GX 340+0	NS [†][99]		251.44876	-45.61112				
XTE J1650-500	BH [†][100]	K4V [101]	252.5041	-49.9621				
XTE J1652-453	BH [†][102]		253.08549	-45.34486	4(3)[††]			
GRO J1655-40	BH [103]	F5V [103]	253.46197	-39.85086				
Her X-1	NS [104]	A-F [†][105]	254.45754	35.34232	7.0(6)[††]			
Swift J1658.2-4242	BH [††][106]	K [††][107]	254.55338	-42.69831				
MAXI J1659-152	BH [108]	M2-5V [†][109]	254.757	-15.258				
IGR J16597-3704	NS [110]		254.88648	-37.12088	8(3)[††]			
AX J1659.0-4208	NS/WD [††][111]		255.08	-42.33861		8.5 [†][111]		
XTE J1701-462	NS [112]		255.24359	-46.18572		9(1) [†][113]	[113]	
NGC 6266 CX16			255.30239	-30.10624		6.4(1) [2]		NGC6266
NGC 6266 CX5			255.30451	-30.11189		6.4(1) [2]		NGC6266
NGC 6266 CX4			255.30475	-30.11512		6.4(1) [2]		NGC6266
NGC 6266 CX6			255.30674	-30.1088	8(2)[†]	6.4(1) [2]		NGC6266
XTE J1701-407	NS [114]		255.43478	-40.85821			[114]	
MXB 1659-29	NS [15]		255.48665	-29.94875			[15]	
GX 339-4	BH [115]	K1-2III [116]	255.7058	-48.7897				
GX 349+2	NS [†][117]		256.43538	-36.42309	6(3)[††]			
GX 340-0	NS [15]		256.56381	-43.03575		5.7(6) [†][118]	[15]	
IGR J17062-6143	NS [119]		256.5678	-61.7113	4(4)[††]		[119]	

Table A.1: continued.

Identifier	Compact object	Companion spec. type	R.A. [deg]	Dec. [deg]	Gaia Dist. [kpc]	Other Dist. [kpc]	Type I burst	Globular cluster
4U 1700+24	NS †[120]	M2III [121]	256.6438	23.9718	0.54(2)			
H 1705-25	BH [122]	K7V [122]	257.06042	-25.09175	6(3)			
4U 1705-32	NS [123]		257.2263	-32.31581			[123]	
4U 1705-44	NS [124]		257.22696	-44.10204			[124]	
IGR J17091-3624	BH †[125]		257.28164	-36.40678	6(3)†			
XTE J1709-267	NS [126]		257.32948	-26.70061			[126]	
IGR J17098-3628	BH †[127]		257.44218	-36.46592				
XTE J1710-281	NS [128]		257.55293	-28.13153		15 †[128]	[15]	
SAX J1711.6-3808	BH †[129]		257.9	-38.13333				
4U 1708-40	NS [130]		258.06978	-40.84613			[130]	
SAX J1712.6-3739	NS [131]		258.1512	-37.67613		5.1(5) †[132]	[131]	
SWIFT J1713.4-4219	BH †[133]	KV ††[134]	258.42087	-42.31042		>5.2 †[134]		
NGC 6304 C		III ††[135]	258.54802	-29.53314	0.77(1)	6.2(1) [2]		NGC6304
2S 1711-339	NS [136]		258.58193	-34.0463	7(4)†		[136]	
NGC 6304 B			258.58732	-29.48789	0.72(1)	6.2(1) [2]		NGC6304
XMMU 171433-292747			258.63706	-29.46354	6(3)†	6.2(1) [2]		NGC6304
IGR J17177-3656	BH †[137]		259.25	-36.93333				
1RXS J171824.2-402934	NS [138]		259.60077	-40.49232		6.5(5) †[139]	[138]	
XB 1715-321	NS [140]	MV ††[141]	259.75	-32.26667			[140]	
XMMSL1 J171900.4-353217	BH †[142]		259.75167	-35.53806				
IGR J17191-2821	NS [143]		259.81155	-28.30122	6(2)††	<11 †[144]	[143]	
XTE J1719-291	NS ††[145]		259.82084	-29.07034				
SAX J1719.6-4254			259.9	-42.9				
GRS 1716-249	BH †[146]	K6V †[147]	259.90383	-25.01781		7(1) †[147]		
IGR J17197-3010			259.92917	-30.18				
SWIFT J171951.7-300206		M1-2III [148]	259.96663	-30.03351	6(2)††	6.3 †[148]		
XTE J1720-318	BH †[149]	B-GV ††[150]	259.9958	-31.7503		6(4) †[151]		
PSR J1723-2837	NS [152]	G ††[152]	260.84658	-28.63267	0.90(4)	0.8(1) ††[152]		
XTE J1723-376	NS [153]		260.91471	-37.67907			[153]	
IGR J17254-3257	NS [154]		261.35415	-32.9541		<14 †[155]	[154]	
IGR J17269-4737	BH †[156]		261.5	-47.61667				
4U 1724-307	NS [15]		261.88813	-30.80212		7.8(3) [2]	[15]	Terzan2
MAXI J1727-203	BH †[157]		262.12466	-20.3823		>5.9 †[158]		
IGR J17285-2922	BH †[159]		262.15764	-29.35916	8(2)	>4 †[160]		
MAXI J1728-360	BH †[161]		262.225	-36.21667				
Swift J1729.5-3223			262.375	-32.38333				
GX 9+9	NS †[162]	G5III ††[163]	262.93386	-16.96202	5(1)			
4U 1728-34	NS [164]		262.99041	-33.83358		4.6(2) †[165]	[15]	
IGR J17329-2731	NS [166]	MIII [166]	263.0	-27.51667		3(3) †[166]		
GX 1+4	NS [167]	M6III [168]	263.00895	-24.7456	9(2)††			
Rapid Burster	NS [169]		263.35042	-33.38778		8.1(4) [2]	[170]	Liller1
CXOU J173324.6-332321	NS †[171]		263.35213	-33.38821		8.1(4) [2]		Liller1
KS 1730-312	BH †[172]		263.38167	-31.25611				
4U 1730-22	NS [173]		263.46564	-22.2603		6.9(2) †[174]	[173]	
KS 1731-260	NS [175]	FV †[176]	263.5561	-26.0885		8(1) †[177]	[175]	
IGR J17344-3023	NS [178]		263.60029	-30.39807		7(2) †[178]	[178]	
IGR J17353-3539	NS [179]	G-KIII [180]	263.84894	-35.67129	4.3(6)	<9.5 †[181]	[179]	
AX J1735.8-3207			263.94284	-32.1194	1.11(4)			
SLX 1732-304	NS [182]		263.94577	-30.48258		5.7(2) [2]	[182]	Terzan1
Ter 1 X-1			263.94833	-30.48275	7(6)†	5.7(2) [2]		Terzan1
GRO J1735-27	NS [183]		264.00833	-27.42819				
NGC 6388 X-2			264.07012	-44.73689		11.2(2) [2]		NGC6388

Table A.1: continued.

Identifier	Compact object	Companion spec. type	R.A. [deg]	Dec. [deg]	Gaia Dist. [kpc]	Other Dist. [kpc]	Type I burst	Globular cluster
NGC 6388 X-3			264.07245	-44.73571	7(4)††	11.2(2) [2]		NGC6388
NGC 6388 X-1			264.07338	-44.73783		11.2(2) [2]		NGC6388
CXOGlb J173617.5-444357			264.07342	-44.73265		11.2(2) [2]		NGC6388
CXOGlb J173618.1-444359			264.07579	-44.73349	8(3)†	11.2(2) [2]		NGC6388
IGR J17379-3747	NS [184]		264.49753	-37.77273				
SLX 1735-269	NS [15]		264.57071	-26.99429	5(3)		[15]	
3U 1735-28			264.642	-28.478				
CXOGBS J173838.7-283539			264.66146	-28.59426				
4U 1735-44	NS [185]		264.7427	-44.4502			[185]	
XTE J1739-285	NS [186]		264.97445	-28.49607		<11 †[187]	[186]	
GRS 1737-31	BH †[188]		265.025	-31.03333				
NGC 6397 X-5			265.17299	-53.66783		2.48(2) [2]		NGC6397
IGR J17407-2808		K-MV-IV †[189]	265.17299	-28.14686				
SLX 1737-282	NS [190]		265.1785	-28.3024			[190]	
XTE J1739-278	BH †[191]	B;GK ††[192]	265.66652	-27.74799		7(1) †[193]		
XTE J1743-363	NS ††[194]	M8III [195]	265.75551	-36.37285	8(2)			
CXOGBS J174316.5-274537		F6 ††[196]	265.8189	-27.76035				
XMMU J174445.5-295044	NS ††[197]	M2III [197]	265.97848	-29.74528		3(2) †[197]		
CXOGBS J174405.0-263159			266.02068	-26.53319				
Ginga 1741.6-2849			266.1058	-29.0125				
IGR J17445-2747	NS [198]	K3-5III [199]	266.12673	-27.76682	4(3)		[200]	
GRO J1744-28	NS [201]	G4III [202]	266.1534	-28.76051	5(4)††			
GPS 1742-326			266.15547	-32.53958				
XMM J174457-2850.3	NS [203]		266.23936	-28.8394		6.5(2) †[203]		
KS 1741-293	NS [204]		266.24111	-29.08572			[204]	
IGR J17451-3022	NS ††[205]		266.25	-30.36667				
IGR J17454-2919		K-MIII †[206]	266.25	-29.31667				
Granat 1741.9-2853	NS [207]		266.25973	-28.91378		9.0(5) †[208]	[207]	
SWIFT J174510.8-262411	BH †[209]	K0-M0V ††[210]	266.2952	-26.4035		4(1) †[210]		
AX J1745.6-2901	NS [211]	K3V [21]	266.3985	-29.0261			[211]	
CXOGC J174535.6-285928			266.39875	-28.99141				
1E 1742.7-2902			266.41375	-28.99639				
SWIFT J174540.7-290015			266.41437	-28.99286				
CXOGC J174540.0-290031	BH ††[212]		266.41644	-29.00801				
CXOGC J174540.0-290005			266.41667	-29.00139				
1E 1742.5-2859			266.42042	-29.00389				
1E 1742.5-2845			266.4288	-28.7814				
MXB 1743-29	NS [213]		nan	nan			[213]	
XMMU J174554.4-285456	NS ††[214]		266.47681	-28.91517				
1E 1742.8-2853			266.49975	-28.91384				
GC X-2	NS [215]		266.52128	-29.51493				
1A 1742-294	NS [216]		266.53012	-29.50708			[216]	
CXOGBS J174614.3-321949		III ††[217]	266.56013	-32.33055				
H 1743-322	BH †[218]		266.565	-32.2336		8.5(8) †[219]		
1E 1743.1-2843	NS ††[220]		266.58777	-28.72869				
CXOGBS J174623.5-310550	BH/WD ††[221]	M2-3V [222]	266.59792	-31.09722		1.6(2) ††[222]		
1E 1742.9-2852			266.61	-28.86444				
1E 1742.2-2857			266.61046	-28.98229				
CXOGBS J174627.1-254952			266.61292	-25.83111				
SAX J1747.0-2853	NS [223]		266.70528	-28.87058		8(1) †[224]	[223]	
MXB 1743-28			266.8	-28.5				
XMMU J174716.1-281048	NS [225]		266.81734	-28.17984		8 †[226]	[225]	
IGR J17473-2721	NS [227]		266.825	-27.34389		5.5(8) †[228]	[15]	

Table A.1: continued.

Identifier	Compact object	Companion spec. type	R.A. [deg]	Dec. [deg]	Gaia Dist. [kpc]	Other Dist. [kpc]	Type I burst	Globular cluster
SLX 1744-299	NS [229]		266.85777	-30.00056			[229]	
SLX 1744-300	NS [230]		266.85849	-30.04504			[230]	
GX 3+1	NS [231]	G0–M5V-III [232]	266.98075	-26.56498		10.2(2) †[233]	[231]	
CXOGlb J174804.5-244641			267.01918	-24.77799		6.6(1) [2]		Terzan5
IGR J17480-2446	NS [234]		267.01996	-24.78042	7(3)	6.6(1) [2]	[235]	Terzan5
CXOU J174805.0-244643	BH †[236]		267.0209	-24.77885		6.6(1) [2]		Terzan5
XTE J1748-288	BH †[237]		267.02108	-28.47383				
EXO 1745-248	NS [238]		267.02183	-24.77971		6.6(1) [2]	[239]	Terzan5
MAXI J1747-249	NS [240]		267.02257	-24.77686	7(3)†	6.6(1) [2]	[240]	Terzan5
[ZGV2011] 6			267.03122	-24.78297		6.6(1) [2]		Terzan5
1A 1744-361	NS [241]		267.08	-36.12111			[241]	
NGC 6440 X-13			267.2161	-20.35936		8.2(2) [2]		NGC6440
SAX J1748.9-2021	NS [242]		267.21747	-20.35872		8.2(2) [2]	[243]	NGC6440
NGC 6440 CX3			267.21867	-20.35888		8.2(2) [2]		NGC6440
NGC 6440 CX7			267.21919	-20.36147	7(3)	8.2(2) [2]		NGC6440
NGC 6440 CX1	NS [244]		267.21997	-20.3572		8.2(2) [2]	[244]	NGC6440
NGC 6440 X-3			267.22027	-20.36065		8.2(2) [2]		NGC6440
NGC 6440 CX5			267.22063	-20.36191		8.2(2) [2]		NGC6440
NGC 6440 CX12			267.22131	-20.35751		8.2(2) [2]		NGC6440
NGC 6440 CX2			267.22174	-20.36075		8.2(2) [2]		NGC6440
EXO 1747-214	NS [245]		267.25	-21.31667			[245]	
IGR J17494-3030	NS [246]	WD †[247]	267.34853	-30.49962	8(3)††			
SWIFT J1749.4-2807	NS [248]		267.38206	-28.13471			[249]	
IGR J17497-2821	BH †[250]	KIII ††[251]	267.4085	-28.3549				
SLX 1746-331	BH †[252]		267.4539	-33.2032				
IGR J17498-2921	NS [253]		267.4806	-29.3221			[235]	
1E 1746.7-3224			267.5164	-32.43058				
4U 1746-37	NS [254]		267.55288	-37.05244		12.7(2) [2]	[254]	NGC6441
XTE J1751-305	NS [255]	WD †[256]	267.58614	-30.4477	0.522(5)††			
SAX J1750.8-2900	NS [257]		267.60192	-29.03749		6.3(7) †[258]	[257]	
IGR J17507-2856			267.65	-29.05				
[ZGV2011] 5			267.69479	-31.27498	7(3)††	7.3(4) [2]		Terzan6
IGR J17511-3057	NS [259]		267.72394	-31.09464	0.98(1)		[259]	
MAXI J1749-310	NS [15]		267.725	-31.26667			[15]	
XTE J1752-223	BH †[260]	M ††[261]	268.06222	-22.34182	6(2)††	3.5(4) †[262]		
GX 1.1-1.0			268.0667	-28.5061				
SAX J1752.3-3138	NS [263]		268.0844	-31.6521			[263]	
SWIFT J1753.5-0127	BH †[264]	M2V †[265]	268.3679	-1.4517				
SAX J1753.5-2349	NS [266]		268.3823	-23.82006			[266]	
AX J1754.2-2754	NS [267]		268.55	-27.9			[267]	
MXB 1742-29			268.64999	-29.55828	10(3)			
XTE J1755-324	BH †[268]		268.8692	-32.4775				
AX J1755.7-2818			268.92846	-28.3026	2(1)			
SWIFT J1756.9-2508	NS [269]		269.22488	-25.1332	2.3(4)††			
1RXS J175721.2-304405		III ††[270]	269.33796	-30.73519				
IGR J17585-3057			269.62425	-30.95043	6(2)			
IGR J17586-2129	NS †[271]	KIII [272]	269.64397	-21.38933	6(6)††			
4U 1755-33	BH †[273]		269.6667	-33.8075				
IGR J17591-2342	NS [274]		269.7617	-23.71902		7.6(7) †[275]	[235]	
IGR J17597-2201	NS [276]	G8-K0III [272]	269.93969	-22.02757		5.6 †[272]	[276]	
GX 5-1	NS †[277]		270.2905	-25.0789				
GRS 1758-258	BH †[278]	A5V †[279]	270.30197	-25.74328	5(3)†			

Table A.1: continued.

Identifier	Compact object	Companion spec. type	R.A. [deg]	Dec. [deg]	Gaia Dist. [kpc]	Other Dist. [kpc]	Type I burst	Globular cluster
GX 9+1	NS †[162]	G-KV †[280]	270.38429	-20.52995				
MAXI J1803-298	BH †[281]		270.76162	-29.83046				
1RXS J180408.9-342058	NS [282]	WD †[283]	271.03488	-34.34756			[282]	
SAX J1805.5-2031			271.375	-20.51667				
SAX J1806.5-2215	NS [266]	K †[284]	271.625	-22.38333			[266]	
XTE J1806-246	NS [285]		271.7	-24.58333		<7.3 †[286]	[285]	
XTE J1807-294	NS [287]		271.74958	-29.40724				
MAXI J1807+132	NS [288]		272.03144	13.2515		<12 †[288]	[288]	
SAX J1808.4-3658	NS [289]	IV-III ††[290]	272.11829	-36.97988	6(2)†		[289]	
XMMU J180916-255425			272.31864	-25.90742	5(2)†	5.3(1) [2]		NGC6553
XTE J1810-189	NS [291]		272.5869	-19.0698		6(3) †[292]	[291]	
4U 1807-10	NS [293]		272.675	-10.86667			[293]	
SAX J1810.8-2609	NS [294]		272.68514	-26.15052		4.2(5) †[295]	[294]	
[RPK2014] 1			273.04056	-19.04069				
XMMU J181227.8-181234	NS [296]		273.11653	-18.20977		14(2) †[297]	[296]	
MAXI J1810-222	BH †[298]		273.16585	-22.32383		>6 †[298]		
MAXI J1813-095	BH †[299]		273.39153	-9.5328	5(4)			
XTE J1814-338	NS [300]	MV ††[301]	273.41293	-33.7733	6(2)		[15]	
SRGA J181414.6-225604		M7-8III [302]	273.56292	-22.93806		15(3) †[302]		
GX 13+1	NS [303]	K5III [304]	273.62953	-17.15721			[303]	
4U 1812-12	NS [305]		273.77573	-12.09693			[305]	
GX 17+2	NS [306]		274.0075	-14.03631		8(2) †[307]	[15]	
MAXI J1816-195	NS [308]		274.21808	-19.63214		<8.7 †[309]	[308]	
Swift J181723.1-164300	NS [310]		274.34428	-16.71737			[310]	
XTE J1817-330	BH †[311]		274.4314	-33.0188				
XTE J1818-245	BH †[312]		274.6018	-24.5383		3.5(8) †[312]		
3XMM J181923.7-170616	NS [313]	K3III †[313]	274.63263	-16.94851	4(2)			
SAX J1818.7+1424	NS [50]		274.675	14.4			[50]	
SAX J1819.3-2525	BH [314]	B9III [315]	274.8401	-25.4072	4.7(8)	11(2) †[316]		
MAXI J1820+070	BH †[317]	K4V [318]	275.0914	7.1854	2.8(7)††	3 ††[319]		
4U 1820-30	NS [320]	WD †[321]	275.91743	-30.36172	7(2)††	8.0(1) [2]	[320]	NGC6624
IGR J18245-2452	NS [322]		276.13522	-24.86849		5.3(3) [2]	[322]	NGC6626
CXOGlb J182432.8-245208	NS †[323]		276.13675	-24.86893	5(3)	5.4(1) [2]		NGC6626
4U 1822-000		M4-5V ††[324]	276.34208	-0.01056		6(2) ††[324]		
2A 1822-371	NS [325]	M2-K0V ††[326]	276.44503	-37.10516	6(1)††			
SAX J1828.5-1037	NS [50]		277.14073	-10.61772	1.46(6)†		[50]	
F3R 673			277.22756	-11.449	2.5(8)			
MAXI J1828-249	BH †[327]	A-FV ††[328]	277.24198	-25.02937				
Ginga 1826-238	NS [329]		277.36672	-23.79659			[329]	
Sct X-1	NS [330]	M8-9III [331]	278.8576	-7.614		3.6(8) †[331]	[249]	
MAXI J1836-194	BH †[332]	M2V †[333]	278.925	-19.51667		7(3) ††[334]		
XB 1832-330	NS [335]		278.93208	-32.99086		9.5(1) [2]	[335]	NGC6652
NGC 6652 X-4			278.93309	-32.98194	5(3)†	9.5(1) [2]		NGC6652
CXOGlb J183544.5-325939	NS †[336]	GV †[336]	278.93591	-32.99402		9.5(1) [2]		NGC6652
Ser X-1	NS [337]	M5V ††[338]	279.98966	5.03555			[337]	
SWIFT J1842.5-1124	BH †[339]		280.57247	-11.41802	3(1)††			
Swift J1843.5-0343	NS [340]		280.89527	-3.71572				
EXO 1846-031	BH †[341]		282.07169	-3.17137	3(1)††	4.5 ††[342]		
MAXI J1848-015	BH †[343]		282.20811	-1.49689		3.4(1) †[344]		
SWIFT J185003.2-005627	NS [345]		282.51451	-0.93981	1.8(2)†	<3.7 †[345]	[345]	
4U 1850-087	NS [346]	WD †[347]	283.26985	-8.70577		7.4(2) [2]	[346]	NGC6712
XTE J1856+053	BH †[348]		284.17869	5.30886				

Table A.1: continued.

Identifier	Compact object	Companion spec. type	R.A. [deg]	Dec. [deg]	Gaia Dist. [kpc]	Other Dist. [kpc]	Type I burst	Globular cluster
SWIFT J1858.6-0814	NS [349]	III ††[350]	284.64546	-8.23749		12.8(8) †[349]	[349]	
XTE J1859+226	BH [351]	K5-7V [352]	284.6733	22.6582				
HETE J1900.1-2455	NS [353]		285.025	-24.91667			[354]	
XTE J1901+014		G4III †[355]	285.41748	1.44073		<7 †[355]		
1H 1905+000	NS [356]	M5-WD ††[357]	287.1124	0.1688			[356]	
XTE J1908+094	BH †[358]	A-K †[359]	287.22263	9.38452				
MAXI J1910-057	BH [360]	K-M †[361]	287.595	-5.7989		5(3) †[362]		
Aql X-1	NS [15]		287.8169	0.585	6(3)		[15]	
Granat 1915+105	BH [363]	K-MIII [363]	288.79815	10.94581				
XB 1916-053	NS [364]		289.69975	-5.23863	5(2)††		[364]	
4U 1918+15			290.071	14.705				
SWIFT J1922.7-1716	NS [345]		290.65417	-17.28389		<4.8 †[345]	[345]	
IGR J19308+0530	WD/NS †[365]	F8-G0V-III [272]	292.71148	5.51614	0.328(3)††	0.38(7) †[81]		
NGC 6819 X1			295.53724	40.18748		2.809(3) [366]		
XB 1940-04	NS [367]		295.6583	-3.9			[367]	
MAXI J1957+032	NS [368]	K-MV [369]	299.0	3.43333		5(2) †[369]		
4U 1957+11	BH †[370]		299.85	11.7083				
GS 2000+25	BH [371]	K3-7V [371]	300.70634	25.23629		2.0(6) †[372]		
XTE J2012+381	BH †[373]	F0-3V-III [374]	303.15731	38.18352	5(3)††			
404 Cyg	BH [375]	K0III-V [376]	306.01591	33.86718	3.0(7)††			
SWIFT J2037.2+4151		MIII †[377]	309.3	41.85				
IGR J21188+4901		K7-M4V [378]	319.5	49.01667				
XTE J2123-058	NS [15]	K7V [379]	320.25	-6.11667			[15]	
M15 X-3		V †[380]	322.49229	12.16107		10.7(1) [2]		NGC7078
M15 X-2	NS [381]		322.49237	12.16737		10.7(1) [2]	[381]	NGC7078
4U 2129+12	NS [382]		322.49271	12.16747		10.7(1) [2]	[382]	NGC7078
4U 2129+47	NS [383]	F7V [384]	322.85921	47.29012	2.0(3)		[383]	
CXOGlb J214022.1-231045	NS †[385]		325.09252	-23.17927		8.46(9) [2]		NGC7099
Cyg X-2	NS [386]	A9III [386]	326.17147	38.32141	9(2)††		[15]	
IGR J22014+6034		GIII-IV ††[378]	330.47564	60.63594	1.02(4)			
SAX J2224.9+5421	NS [387]		336.225	54.35		<7.1 †[387]	[387]	
4U 2316+61			350.1422	62.2927				

References. [1]Heinke et al. (2005); [2]Baumgardt & Vasiliev (2021); [3]Heinke et al. (2003); [4]Bahramian et al. (2017); [5]Markwardt et al. (2004); [6]Torres et al. (2008); [7]Charles et al. (1978); [8]Miller et al. (2020); [9]Kouveliotou et al. (1993); [10]Webb et al. (2000); [11]Kennedy et al. (2020); [12]Strader et al. (2016); [13]Yadlapalli et al. (2021); [14]Cao et al. (2022); [15]Galloway et al. (2008); [16]Prodan & Murray (2015); [17]Strader et al. (2021); [18]Russell et al. (2011); [19]Barret & Grindlay (1995); [20]Karitskaya & Bochkarev (1987); [21]Murdin et al. (1980); [22]Tomsick et al. (2019); [23]Soria et al. (2022); [24]Parmar et al. (1985a); [25]Gandolfi et al. (1999); [26]Aoki et al. (1992); [27]Kennea et al. (2020); [28]Coti Zelati et al. (2021); [29]Sanna et al. (2017); [30]Jonker et al. (2001); [31]in't Zand et al. (2005b); [32]Steeghs & Jonker (2007); [33]Shahbaz et al. (1999); [34]Rupen et al. (2002); [35]Filippenko et al. (1999); [36]Archibald et al. (2009); [37]Shahbaz et al. (2022); [38]Bhattacharyya (2020); [39]Coti Zelati et al. (2019); [40]Uemura et al. (2000); [41]González Hernández et al. (2006); [42]Wu et al. (2016); [43]Wu et al. (2015b); [44]Roy et al. (2014); [45]de Martino et al. (2014); [46]Kuulkers & Levine (2006); [47]Courvoisier et al. (1984); [48]Morihana et al. (2013); [49]Mata Sánchez et al. (2021); [50]Cornelisse et al. (2002b); [51]Cornelisse et al. (2002a); [52]van der Klis et al. (1985); [53]Sanna et al. (2019); [54]Lamer et al. (2021); [55]Shahbaz et al. (2013); [56]Casares et al. (2004); [57]Strader et al. (2015); [58]Bozzo et al. (2014); [59]Serino et al. (2015); [60]Oosterbroek et al. (1999); [61]Kaur et al. (2009); [62]Hammerstein et al. (2018); [63]Torres et al. (2002); [64]Yanes-Rizo et al. (2024); [65]Negoro et al. (2017); [66]Sridhar et al. (2019); [67]Krimm et al. (2011); [68]Munoz-Darias et al. (2011); [69]Bogdanov & Halpern (2015); [70]Britt et al. (2017); [71]Orosz et al. (1998); [72]Schultz (2003); [73]Juett & Chakrabarty (2003); [74]Wang & Chakrabarty (2004); [75]Orosz et al. (2002); [76]Muller et al. (1998a); [77]Jonker et al. (2003b); [78]Wachter et al. (2002); [79]Kitamura et al. (2014); [80]Masetti et al. (2007); [81]Ratti et al. (2010); [82]Cherepashchuk et al. (2021); [83]Mata Sanchez et al. (2015); [84]Bult et al. (2017); [85]Chenevez et al. (2018); [86]Kaluzny et al. (2012); [87]Najar et al. (2020); [88]Xu et al. (2020); [89]Rout et al. (2023); [90]Peterson et al. (1980); [91]Hemphill et al. (2021); [92]Parmar et al. (1986); [93]Augusteijn et al. (2001); [94]Kushwaha et al. (2023); [95]Patel et al. (2004); [96]Nespoli et al. (2010); [97]Hoffman et al. (1977); [98]Gendre et al. (2003); [99]Greenstein (1972); [100]Markwardt et al. (2001a); [101]Orosz et al. (2004); [102]Markwardt et al. (2009); [103]Bailyn et al. (1995); [104]Tananbaum et al. (1972); [105]Anderson et al. (1994); [106]Mondal & Jithesh (2023); [107]Bahramian et al. (2018a); [108]Kalamkar et al. (2010); [109]Corral-Santana et al. (2018); [110]Sanna et al. (2018); [111]Revnivtsev et al. (2013); [112]Homan et al. (2006); [113]Lin et al. (2009); [114]Markwardt et al. (2008a); [115]Hynes et al. (2003); [116]Heida et al. (2017); [117]Kuulkers & van der Klis (1998); [118]Nättilä et al. (2017); [119]Degenaar et al. (2012a)

References. [120]Garcia et al. (1983); [121]Masetti et al. (2002); [122]Filippenko et al. (1997); [123]in't Zand et al. (2004); [124]Sztajno et al. (1985); [125]Lutovinov et al. (2005); [126]Cocchi et al. (1998); [127]Grebenev et al. (2007); [128]Markwardt et al. (2001b); [129]in't Zand et al. (2002a); [130]Migliari et al. (2003); [131]Cocchi et al. (1999b); [132]Lin & Yu (2020); [133]Chakrabarty et al. (2019); [134]Onori et al. (2021); [135]Guillot et al. (2009); [136]Torres et al. (2004); [137]Paizis et al. (2011); [138]Kaptein et al. (2000); [139]in't Zand et al. (2005a); [140]Mason et al. (1976); [141]Jonker et al. (2007a); [142]Tetarenko et al. (2016); [143]Klein-Wolt et al. (2007); [144]Markwardt et al. (2007a); [145]Armas Padilla et al. (2011); [146]Masetti et al. (1996); [147]Casares et al. (2023); [148]Masetti et al. (2012); [149]Swank et al. (2003); [150]Chaty & Bessolaz (2006); [151]Chaty (2006); [152]Crawford et al. (2013); [153]Marshall et al. (1999); [154]Brandt et al. (2006a); [155]Chenevez et al. (2007); [156]Kennea et al. (2005); [157]Negoro et al. (2018); [158]Wang et al. (2022); [159]Stoop et al. (2021); [160]Sidoli et al. (2011); [161]Saha et al. (2023); [162]Hasinger & van der Klis (1989); [163]Reig et al. (2003); [164]Strohmayer et al. (1997b); [165]Galloway et al. (2003); [166]Bozzo et al. (2018); [167]Koo & Haymes (1980); [168]Davidsen et al. (1977); [169]Fox et al. (2001); [170]Lewin et al. (1976b); [171]Bahramian et al. (2018b); [172]Vargas et al. (1996); [173]Li et al. (2022); [174]Bult et al. (2022b); [175]Sunyaev & Kwant Team (1989); [176]Mignani et al. (2002); [177]Özel et al. (2012); [178]Bozzo et al. (2015); [179]Degenaar et al. (2010); [180]Shaw et al. (2024); [181]Armas Padilla et al. (2013); [182]Pavlinsky et al. (2001); [183]Wilson et al. (1995); [184]Strohmayer et al. (2018b); [185]van Paradijs et al. (1988); [186]Brandt et al. (2005); [187]Kaaret et al. (2007); [188]Cui et al. (1997); [189]Ducci et al. (2023); [190]in't Zand et al. (2002b); [191]Borozdin & Trudolyubov (2000); [192]Marti et al. (1997); [193]Greiner et al. (1996); [194]Bozzo et al. (2013); [195]Smith et al. (2012); [196]Wu et al. (2015a); [197]Bahramian et al. (2014); [198]Mereminskiy et al. (2017b); [199]Shaw et al. (2020); [200]Mereminskiy et al. (2017a); [201]Finger et al. (1996); [202]Gosling et al. (2007); [203]Degenaar et al. (2014b); [204]De Cesare et al. (2006); [205]Bozzo et al. (2016); [206]Paizis et al. (2015); [207]Cocchi et al. (1999a); [208]Pike et al. (2021); [209]Muñoz-Darias et al. (2013); [210]Chaty et al. (2020); [211]Maeda et al. (1996); [212]Porquet et al. (2005a); [213]Lewin et al. (1976a); [214]Porquet et al. (2005b); [215]Altamirano et al. (2010); [216]Strohmayer et al. (1997a); [217]Wetuski et al. (2021); [218]Molla et al. (2017); [219]Steiner et al. (2012); [220]Del Santo et al. (2006); [221]Torres et al. (2014); [222]Torres et al. (2019b); [223]Natalucci et al. (2000b); [224]Werner et al. (2004); [225]Brandt et al. (2006b); [226]Del Santo et al. (2007); [227]Altamirano et al. (2008b); [228]Chenevez et al. (2011); [229]Skinner et al. (1990); [230]Mori et al. (2005); [231]Makishima et al. (1983); [232]van den Berg et al. (2014); [233]Thomas et al. (2023); [234]Strohmayer & Markwardt (2010); [235]Galloway et al. (2020); [236]Urquhart et al. (2020); [237]Fox & Lewin (1998); [238]Özel et al. (2009); [239]Markwardt et al. (2000); [240]Altamirano et al. (2012); [241]Bhattacharyya et al. (2006); [242]Kaaret et al. (2003); [243]in 't Zand et al. (1999); [244]in't Zand et al. (2001); [245]Parmar et al. (1985b); [246]Ng et al. (2020); [247]Ng et al. (2021b); [248]Wijnands et al. (2009); [249]Albayati et al. (2023); [250]Walter et al. (2007); [251]Paizis et al. (2007); [252]Homan & Wijnands (2003); [253]Papitto et al. (2011c); [254]Sztajno et al. (1987); [255]Chirenti & Jasiulek (2018); [256]Markwardt et al. (2002); [257]Natalucci et al. (1999); [258]Kaaret et al. (2002); [259]Bozzo et al. (2009); [260]Shaposhnikov et al. (2009); [261]Ratti et al. (2012a); [262]Shaposhnikov et al. (2010); [263]Cocchi et al. (2001); [264]Morgan et al. (2005b); [265]Zurita et al. (2008); [266]In't Zand et al. (1999); [267]Chelovekov & Grebenev (2007); [268]Paul et al. (1997); [269]Markwardt et al. (2007b); [270]Sasaki et al. (2021); [271]Dehiwalage et al. (2022); [272]Fortin et al. (2018); [273]Pan et al. (1995); [274]Ferrigno et al. (2018); [275]Kuiper et al. (2020); [276]Brandt et al. (2007); [277]van der Klis et al. (1991); [278]Sunyaev et al. (1991); [279]Martí et al. (2016); [280]van den Berg & Homan (2017); [281]Shidatsu et al. (2022); [282]Chenevez et al. (2012); [283]Baglio et al. (2016); [284]Kaur et al. (2017); [285]Muller et al. (1998b); [286]Cornelisse et al. (2007); [287]Kirsch et al. (2004); [288]Albayati et al. (2021); [289]Gilfanov et al. (1998); [290]Goodwin & Woods (2020); [291]Markwardt et al. (2008c); [292]Weng et al. (2015); [293]Chelovekov et al. (2017); [294]Natalucci et al. (2000a); [295]Suleimanov et al. (2017); [296]in't Zand et al. (2017); [297]Goodwin et al. (2019); [298]Russell et al. (2022); [299]Russell et al. (2018); [300]Markwardt et al. (2003b); [301]Wang et al. (2017); [302]De et al. (2022b); [303]Matsuba et al. (1995); [304]Bandyopadhyay et al. (1999); [305]Cocchi et al. (2000); [306]Wijnands et al. (1997); [307]Kuulkers et al. (2002); [308]Bult et al. (2022c); [309]Mandal et al. (2023); [310]Parikh et al. (2017); [311]Remillard et al. (2006); [312]Cadolle Bel et al. (2009); [313]Qiu et al. (2017); [314]MacDonald et al. (2014); [315]Orosz et al. (2001); [316]Pahari et al. (2015); [317]Tucker et al. (2018); [318]Torres et al. (2019a); [319]Mikołajewska et al. (2022); [320]Grindlay et al. (1976); [321]Rappaport et al. (1987); [322]Papitto et al. (2013a); [323]Becker et al. (2003); [324]Shahbaz et al. (2007); [325]Jonker & van der Klis (2001); [326]Mason et al. (1980); [327]Filippova et al. (2014); [328]Oda et al. (2019); [329]Ubertini et al. (1999); [330]Koyama et al. (1991); [331]De et al. (2022a); [332]Miller-Jones et al. (2011); [333]López et al. (2019); [334]Russell et al. (2014); [335]in 't Zand et al. (1998); [336]Paduano et al. (2021); [337]Swank et al. (1976); [338]Cornelisse et al. (2013); [339]Markwardt et al. (2008b); [340]Strohmayer & Markwardt (2011); [341]Zhang et al. (1994); [342]Williams et al. (2022); [343]Pike et al. (2022); [344]Hare et al. (2018); [345]Degenaar et al. (2012b); [346]in't Zand et al. (2014); [347]Homer et al. (2001a); [348]Suzuki et al. (2015); [349]Buisson et al. (2020); [350]Buisson et al. (2021); [351]Focke et al. (1999); [352]Yanes-Rizo et al. (2022); [353]Morgan et al. (2005a); [354]Suzuki & HETE Collaboration (2005); [355]Torrejón et al. (2010); [356]Chevalier et al. (1985); [357]Jonker et al. (2007c); [358]Göğüş et al. (2004); [359]Chaty et al. (2006); [360]Reis et al. (2013); [361]Yoshii et al. (2016); [362]Nath et al. (2023); [363]Steeghs et al. (2013); [364]Galloway et al. (2001); [365]Ratti et al. (2013); [366]Cantat-Gaudin & Anders (2020); [367]Murakami et al. (1983); [368]Sanna et al. (2022); [369]Ravi (2017); [370]Sharma et al. (2021); [371]Casares et al. (1995); [372]Harlaftis et al. (1996); [373]Campana et al. (2002); [374]Castro-Tirado et al. (1998); [375]Casares & Charles (1994); [376]Casares et al. (1993); [377]Molina et al. (2021); [378]Özbey Arabacı et al. (2012); [379]Casares et al. (2002); [380]Arnason et al. (2015); [381]Homan et al. (2022); [382]Dotani et al. (1990); [383]Garcia & Grindlay (1987); [384]Garcia et al. (1989); [385]Echiburú et al. (2020); [386]Casares et al. (1998); [387]Degenaar et al. (2014a);

Table A.2: Catalogue of Galactic LMXBs: orbital data. Confirmed systems are indicated in bold. Mx and Mo refer respectively to the mass of the compact object and the companion star; $K2$ is the semi-amplitude of the radial velocity curve of the companion star; RV is the systemic radial velocity. †/††: reliability flag (see Section 2.4).

Identifier	Mx [$M_\odot$]	Mo [$M_\odot$]	Period [hr]	Eccentricity	K2 [km/s]	RV [km/s]	Spin period [s]	$\dot{P}/P$ [1/yr]
NGC 104 125								
47 Tuc X-5	1.4 †[1]		8.670(8) [1]					
47 Tuc X-7	1.8 †[1]		5.5 †[1]					
47 Tuc X-9			0.4696(3) [2]					
NGC 104 37			3.087(4) [3]					
NGC 104 17								
IGR J00291+5934		0.07(4) †[4]	2.456692(2) [5]	<2.0e-4 †[5]			0.00166974977400(3) [5]	<-4.2e-8 †[5]
3U 0042+32			2.8(2)$e+02$ [6]					
4FGL J0407.7-5702								
GRO J0422+32	2.7(7) †[7]	0.3(3) †[7]	5.09136(7) [8]		381(6) [8]	9(3) [8]		
3FGL J0427.9-6704	1.9(1) †[9]	0.65(8) †[9]	8.80128(2) [10]		293(4) [10]	79(3) [10]		
SRGA J043520.9+552226		<0.8 †[11]	<16 ††[12]					
4U 0513-40		0.55 †[13]	0.281(4) [14]	0.02 ††[13]				
4FGL J0540.0-7552			2.7 ††[15]					
MAXI J0556-332			16.4(1) [16]		1.9e+2 ††[16]	134(2) [16]		
Swift J061223.0+701243.9								
4U 0614+091			0.75 †[17]				0.00241109(6) [18]	
1A 0620-00	5.9(2) †[19]	0.34(3) †[19]	7.7523(1) [20]		435.4(5) [21]	4(2) [22]		
MAXI J0637-430	5(2) †[23]	0.25(7) †[23]	2.2(8) [23]		7(2)$e+02$ [23]			
SRGt J071522.1-191609								
EXO 0748-676			3.824106869(5) [24]		>4.1e+2 †[25]	44(4) [26]	1.8 †[27]	
SAX J0835.9+5118								
4U 0836-429								
GRB 200205A							9.0e+3 †[28]	
MAXI J0911-655		>0.024 †[29]	0.73887031(1) [29]	<5.0e-3 †[29]			0.002941392643(3) [29]	0.00026(2) [29]
2S 0918-549		0.03 †[30]	0.290(2) [31]					
2S 0921-630	1.4(1) †[32]	0.35(3) †[32]	216.062(2) [33]		99(3) [34]	44(2) [34]		
XTE J0929-314			0.7263183(8) [35]	<7.0e-3 †[35]			0.0054023317900(3) [35]	1.57(7)$e-08$ [35]
MM Vel	>3.9 †[36]		6.84494(3) [36]		475(6) [36]	30(5) [36]		
PSR J1023+0038	1.7(2) †[37]		4.75430885(1) [38]	<2.0e-5 †[38]	268(4) [39]	1(3) [39]	0.0016879874440000(4) [38]	
CXOU J110926.4-650224								
XTE J1118+480	8.3(3) [40]	0.22(7) [40]	4.07841(1) [40]		709(1) [41]	3(1) [41]		
IGR J11187-5438								
GU Mus	11(2) [42]	0.9(2) [42]	10.382460(2) [43]		407(3) [43]	14(6) [43]		
XSS J12270-4859		0.26 †[44]	6.91246(5) [45]				1.7 †[46]	
1A 1246-588								
XB 1254-690	1.9(7) [47]	0.7(2) [47]	3.9334(2) [48]		2.5(3)$e+02$ [47]	185(2) [47]		
MAXI J1305-704	9(2) [49]	0.4(2) [49]	9.5(1) [49]		554(8) [49]	−9(5) [49]		

Table A.2: continued.

Identifier	Mx [$M_\odot$]	Mo [$M_\odot$]	Orbital period [hr]	Eccentricity	K2 [km/s]	RV [km/s]	Spin period [s]	$\dot{P}/P$ [1/yr]
SAX J1324.5-6313								
2E 3049								
4U 1323-62		0.28(3) †† [50]	2.9419156(6) [50]					
MAXI J1348-630	14.8(9) † [51]		<20 †† [52]				9.8e+3 † [53]	
SWIFT J1357.2-0933	12(4) † [54]	0.4 † [55]	3(1) [55]		>7.9e+2 † [56]	-1.5e+2 †† [56]		
BW Cir	>7.8 † [57]	>1 † [57]	61.068(4) [57]		279(5) [57]	103(4) [57]		
1FGL J1417.7-4407	2.0(1) [58]	0.35(4) [58]	128.972(8) [58]	<0.01 † [58]	116(1) [58]	−15.3(9) [58]	0.0026642160(4) [59]	
MAXI J1421-613								
IGR J14298-6715								
SAX J1452.8-5949							437(1) [60]	
Cen X-4	1.5(6) [61]	0.3(3) [62]	15.09719(5) [62]		150(1) [62]	184(2) [62]		
TrA X-1	6(3) [63]	0.5(3) [63]	6.2(2) [63]		$5.0(5)e+02$ [63]			
MAXI J1535-571	10.4(6) † [64]							
AX J1538.3-5541			30(1) † [65]					
SWIFT J1539.2-6227								
MAXI J1543-564	13(1) † [66]	0.66 †† [67]	13(2) †† [67]					
3FGL J1544.6-1125	1.7(3) [68]	<0.7 † [68]	5.796866(9) [68]		39(2) [68]	144(1) [68]		
4U 1543-47	5(2) [69]	0.22(6) [69]	27.0(2) [69]		124(4) [69]	−87(3) [69]		
4U 1543-624		0.03 † [70]	0.303(2) [70]					
XTE J1550-564	9(1) [71]	1.4 † [71]	37.04(2) [71]		$3.5(1)e+02$ [71]	$-7(2)e+01$ [71]		
4U 1556-60			9.137(7) † [72]					
SAX J1603.9-7753								
UW CrB			1.8496120(2) [73]					
4U 1608-52	2.4(2) † [74]		12.89(4) [75]				1.6 † [76]	
IGR J16194-2810						-3.5e+1 †† [77]	14570.3(1) [78]	
Sco X-1	1.5(1) [79]	0.5(2) [80]	18.89550(1) [81]			−114.0(6) [82]		
MAXI J1621-501		0.7(3) †† [83]	12(8) †† [83]					
2MASS J16233414-2631336			6.307718(2) [84]					
Big Dipper		>0.8 † [85]	20.87750(2) [86]					
IGR J16287-5021								
IGR J16293-4603								
MAXI J1631-479	>15 † [87]							
MAXI J1630-276								
4U 1626-67	1 †† [88]	<0.026 † [89]	0.69(2) [90]				8(1) [91]	
4U 1630-47	10.0(1) † [92]							
IGR J16358-4726							$5.97(1)e+03$ [93]	−1.0(6) [93]
KS 1632-477								
XTE J1637-498								
4U 1636-53	1.64(4) † [94]		3.80388(2) [95]				0.0017(2) [96]	

Table A.2: continued.

Identifier	Mx [$M_\odot$]	Mo [$M_\odot$]	Orbital period [hr]	Eccentricity	K2 [km/s]	RV [km/s]	Spin period [s]	$\dot{P}/P$ [1/yr]
XMMU J164143.8+362758								
GX 340+0								
XTE J1650-500	<7.3 †[97]		7.69(2) [97]		4.3(3)$e+02$ [97]			
XTE J1652-453								
GRO J1655-40	5.31(7) [98]	2.3 †[99]	62.4(7) [100]		227(4) [99]	$-1.1(2)e+02$ [99]		
Her X-1	1.5(3) [101]	2.3(3) [101]	40.8040270(2) [102]	0.00042(3) [103]	109(3) [101]	−65(2) [101]	1.2368(6) [104]	
Swift J1658.2-4242	14 ††[105]		4.0(4) ††[105]				8.727(8) †[106]	
MAXI J1659-152	5(2) [107]	0.15(5) †[108]	2.4139(5) [108]		7.5(8)$e+02$ †[107]			
IGR J16597-3704		>6.5e-3 †[109]	0.76617(8) [109]	<0.04 †[109]			0.00950788815(3) [109]	$2.2(2)e-05$ [109]
AX J1659.0-4208								
XTE J1701-462								
NGC 6266 CX16								
NGC 6266 CX5								
NGC 6266 CX4								
NGC 6266 CX6								
XTE J1701-407								
MXB 1659-29		0.9(3) †[110]	7.1161099(3) [110]			$-5(2)e+01$ [111]	0.00175(2) [112]	
GX 339-4	6(4) [113]		42.21(1) [113]		219(3) [113]	26(2) [113]		
GX 349+2		0.78(7) ††[114]	22.53(2) [115]					
GX 340-0	1.9(3) †[116]						0.00303(5) [117]	
IGR J17062-6143		>5.0e-3 †[118]	0.632836(3) [118]	<0.03 †[118]			0.0061103737570(3) [118]	$-7.3(2)e-10$ [119]
4U 1700+24		<2.5 †[120]	$9.70(7)e+03$ [120]	0.3(1) [120]	0.8(1) [120]	−48.7(1) [120]		
H 1705-25	6.7(2) [121]	$0(2)e+01$ [121]	12.5(1) [121]		448(4) [121]	−31(2) [121]		
4U 1705-32								
4U 1705-44								
IGR J17091-3624	12(4) †[122]		>1e+02 ††[123]					
XTE J1709-267								
IGR J17098-3628								
XTE J1710-281			3.281063218(7) [124]					
SAX J1711.6-3808								
4U 1708-40								
SAX J1712.6-3739								
SWIFT J1713.4-4219								
NGC 6304 C								
2S 1711-339								
NGC 6304 B								
XMMU 171433-292747								
IGR J17177-3656								
1RXS J171824.2-402934			<0.12 ††[125]					
XB 1715-321			<1 ††[126]					

Table A.2: continued.

Identifier	Mx [$M_\odot$]	Mo [$M_\odot$]	Orbital period [hr]	Eccentricity	K2 [km/s]	RV [km/s]	Spin period [s]	$\dot{P}/P$ [1/yr]
XMMSL1 J171900.4-353217								
IGR J17191-2821	0.84 †[127]						3.4 †[128]	
XTE J1719-291								
SAX J1719.6-4254								
GRS 1716-249	6(3) †[129]	1.6 †[130]	6.7(2) [129]		5.2(5)$e+02$ †[129]			
IGR J17197-3010								
SWIFT J171951.7-300206								
XTE J1720-318								
PSR J1723-2837		1(2) ††[131]	14.7704753(2) [132]				0.001855732796000(8) [131]	
XTE J1723-376								
IGR J17254-3257								
IGR J17269-4737								
4U 1724-307								
MAXI J1727-203	>12 †[133]							
IGR J17285-2922			<9.3 ††[134]					
MAXI J1728-360	4.6 †[135]							
Swift J1729.5-3223								
GX 9+9			4.19(2) [136]					
4U 1728-34	1.4(2) †[137]		>1.1 ††[138]				0.00275(1) [139]	
IGR J17329-2731							6680(3) [140]	
GX 1+4		<1.2 †[141]	7(2)$e+03$ [142]				176.778(6) [144]	0.01 †[143]
Rapid Burster							3.3 †[145]	
CXOU J173324.6-332321								
KS 1730-312								
4U 1730-22							0.00171(1) [146]	
KS 1731-260	<2.1 †[147]		9.1e+2 †[148]				0.0019087(2) [149]	
IGR J17344-3023								
IGR J17353-3539			1.8e+2 †[150]					
AX J1735.8-3207								
SLX 1732-304								
Ter 1 X-1								
GRO J1735-27							4.45565(3) [151]	
NGC 6388 X-2								
NGC 6388 X-3								
NGC 6388 X-1								
CXOGlb J173617.5-444357								
CXOGlb J173618.1-444359								
IGR J17379-3747			1.8793990(4) [152]				0.0021365(3) [153]	
SLX 1735-269								
3U 1735-28								

Table A.2: continued.

Identifier	Mx [$M_\odot$]	Mo [$M_\odot$]	Orbital period [hr]	Eccentricity	K2 [km/s]	RV [km/s]	Spin period [s]	$\dot{P}/P$ [1/yr]
CXOGBS J173838.7-283539								
4U 1735-44			4.654(5) [154]		3.0(8)e + 02 [155]	−140(3) [155]		
XTE J1739-285							2.6 †[156]	
GRS 1737-31								
NGC 6397 X-5								
IGR J17407-2808								
SLX 1737-282								
XTE J1739-278	11(7) †[157]							
XTE J1743-363								
CXOGBS J174316.5-274537								
XMMU J174445.5-295044								
CXOGBS J174405.0-263159								
Ginga 1741.6-2849								
IGR J17445-2747								
GRO J1744-28			284.009(3) [158]	<1.1e-3 †[158]			0.467033(3) [160]	−2.5(4)e − 05 [159]
GPS 1742-326								
XMM J174457-2850.3			1.4 ††[161]				5.252(1) [162]	
KS 1741-293								
IGR J17451-3022		0.7(1) †[163]	6.284(1) [164]					
IGR J17454-2919								
Granat 1741.9-2853								
SWIFT J174510.8-262411			<11 ††[165]		>2.5e+2 †[166]			
AX J1745.6-2901		0.8 ††[167]	8.3510081(2) [168]					
CXOGC J174535.6-285928								
1E 1742.7-2902								
SWIFT J174540.7-290015								
CXOGC J174540.0-290031	<60 †[169]	<1 †[169]	7.767(1) [169]					
CXOGC J174540.0-290005			0.83 ††[161]					
1E 1742.5-2859								
1E 1742.5-2845								
MXB 1743-29							1.7 †[170]	
XMMU J174554.4-285456							1.7e+5 †[171]	
1E 1742.8-2853								
GC X-2		>6.7e-3 †[172]	0.955(9) [172]				0.0048569117(5) [172]	
1A 1742-294							0.001698(3) [170]	
CXOGBS J174614.3-321949								
H 1743-322	11(2) †[173]		>10 ††[174]					
1E 1743.1-2843								
CXOGBS J174623.5-310550			<2.3 ††[175]					
1E 1742.9-2852								

Table A.2: continued.

Identifier	Mx [$M_\odot$]	Mo [$M_\odot$]	Orbital period [hr]	Eccentricity	K2 [km/s]	RV [km/s]	Spin period [s]	$\dot{P}/P$ [1/yr]
1E 1742.2-2857								
CXOGBS J174627.1-254952								
SAX J1747.0-2853								
MXB 1743-28								
XMMU J174716.1-281048								
IGR J17473-2721								
SLX 1744-299								
SLX 1744-300								
GX 3+1			11(7) [††][176]					
CXOGlb J174804.5-244641								
IGR J17480-2446	1.6(2) [†][177]	>0.4 [†][178]	21.2744(8) [178]	<0.02 [†][178]			0.090539(8) [178]	
CXOU J174805.0-244643								
XTE J1748-288								
EXO 1745-248	1.6(2) [†][177]							
MAXI J1747-249								
[ZGV2011] 6								
1A 1744-361			0.9(4) [†][179]				1.9 [†][179]	
NGC 6440 X-13								
SAX J1748.9-2021	1.8(3) [†][180]	0.77(7) [†][181]	8.700(6) [182]	<1.0e-3 [†][182]			0.002260590(5) [182]	
NGC 6440 CX3								
NGC 6440 CX7								
NGC 6440 CX1		>0.1 [†][182]	8.764(6) [182]	<1.0e-3 [†][182]			0.002260597(5) [182]	
NGC 6440 X-3								
NGC 6440 CX5								
NGC 6440 CX12								
NGC 6440 CX2								
EXO 1747-214								
IGR J17494-3030		>0.015 [†][183]	1.249075(8) [184]	<6.0e-3 [†][184]			0.0026592196450(3) [184]	
SWIFT J1749.4-2807	1.6(6) [†][185]	>0.59 [†][186]	0.3673696(2) [186]	<5.2e-5 [†][186]			0.00193080007200(4) [186]	
IGR J17497-2821								
SLX 1746-331								
IGR J17498-2921		>0.17 [†][187]	3.8432275(3) [187]	<8.0e-5 [†][187]			0.00249382661000(6) [187]	4.9e-9 [†][187]
1E 1746.7-3224								
4U 1746-37	0.4(7) [†][188]		5.16(1) [189]					
XTE J1751-305	1.52(4) [†][94]	>0.015 [†][190]	0.706667(1) [191]	<1.7e-3 [†][191]			0.00229717100000(6) [191]	<-2.0e-8 [†][191]
SAX J1750.8-2900							1.7 [†][192]	
IGR J17507-2856								
[ZGV2011] 5								
IGR J17511-3057		>0.13 [†][193]	3.468753(6) [193]	<8.0e-5 [†][193]			0.004084401000(2) [193]	
MAXI J1749-310			12.3595273(2) [194]					

Table A.2: continued.

Identifier	Mx [$M_\odot$]	Mo [$M_\odot$]	Orbital period [hr]	Eccentricity	K2 [km/s]	RV [km/s]	Spin period [s]	$\dot{P}/P$ [1/yr]
XTE J1752-223	9.6(9) †[195]		>6.5 ††[196]					
GX 1.1-1.0								
SAX J1752.3-3138								
SWIFT J1753.5-0127	12 †[197]	<0.3 †[197]	3.244(1) [197]					
SAX J1753.5-2349			15(4) ††[198]					
AX J1754.2-2754								
MXB 1742-29								
XTE J1755-324								
AX J1755.7-2818								
SWIFT J1756.9-2508		<0.03 †[199]	0.91170(2) [199]	<0.01 †[200]			0.005492519614(2) [200]	$1.3(4)e-10$ [200]
1RXS J175721.2-304405			3.5e+2 †[201]					
IGR J17585-3057								
IGR J17586-2129								
4U 1755-33		0.5 †[202]	4.4(2) [203]					
IGR J17591-2342			8.8013194(1) [204]	<1.0e-5 †[204]			0.00189600165300(7) [204]	$4.2(6)e-09$ [204]
IGR J17597-2201								
GX 5-1							0.0034(1) †[205]	
GRS 1758-258	6(3) †[206]		443(2) †[207]					
GX 9+1								
MAXI J1803-298			7.7 †[208]					
1RXS J180408.9-342058			0.67 ††[209]			$0(1)e+02$ ††[209]		
SAX J1805.5-2031								
SAX J1806.5-2215			4(1) ††[198]					
XTE J1806-246			9 ††[210]					
XTE J1807-294	1.5 †[211]		0.667902(8) [212]				0.0052459427(4) [213]	
MAXI J1807+132								
SAX J1808.4-3658	>1.4 †[214]	0.09(2) †[215]	2.0136000(3) [216]	5.0e-4 †[216]			0.00249391976(5) [216]	
XMMU J180916-255425								
XTE J1810-189								
4U 1807-10			5.8e+3 †[217]				4.4e+3 †[217]	
SAX J1810.8-2609	1.6(2) †[218]						1.9 †[219]	
[RPK2014] 1								
XMMU J181227.8-181234								
MAXI J1810-222								
MAXI J1813-095								
XTE J1814-338	2.0(7) [220]	0.24(7) [220]	4.2746(6) [221]	<2.4e-5 †[221]	$3.9(3)e+02$ [220]	$-3(2)e+01$ [220]	0.0031811058(2) [222]	
SRGA J181414.6-225604		5.2 ††[223]	$3.60(6)e+04$ †[223]					
GX 13+1			577.6(4) [224]					
4U 1812-12			1.91(6) †[225]					

Table A.2: continued.

Identifier	Mx [$M_\odot$]	Mo [$M_\odot$]	Orbital period [hr]	Eccentricity	K2 [km/s]	RV [km/s]	Spin period [s]	$\dot{P}/P$ [1/yr]
GX 17+2			1.4(1) [226]				0.00341(9) [227]	
MAXI J1816-195		0.3(2) [228]	4.834051(1) [228]	<2.0e-4 †[228]			0.00189174988800(4) [228]	
Swift J181723.1-164300								
XTE J1817-330								
XTE J1818-245	4.0(5) †[229]							
3XMM J181923.7-170616							407.904(7) [230]	<8.5e-4 †[230]
SAX J1818.7+1424								
SAX J1819.3-2525	6.4(6) [231]	2.9(4) [231]	67.60(1) [232]		211(1) [232]	73(3) [233]		
MAXI J1820+070	8.5(8) [234]	0.6(1) [234]	16.4518(2) [235]		418(4) [235]	−22(2) [235]		
4U 1820-30	1.3(6) †[236]	0.07(1) †[237]	0.1921(2) [238]					
IGR J18245-2452		>0.17 †[239]	11.025781(2) [239]	<1.0e-4 †[239]			0.003931853(2) [239]	
CXOGlb J182432.8-245208								
4U 1822-000			3.2(1) [240]					
2A 1822-371	1.7(1) †[241]	0.46(2) †[241]	5.5706(4) [242]			5(2)e + 01 [243]	0.59325(2) [244]	−0.000152(2) [244]
SAX J1828.5-1037								
F3R 673								
MAXI J1828-249								
Ginga 1826-238		0.19 †[245]	2.2494(1) [245]					
Sct X-1		4(1) †[246]	1.49(9)e + 04 [246]				111.001(4) [247]	
MAXI J1836-194	8(4) ††[248]	<0.65 ††[248]	<4.9 ††[248]					
XB 1832-330			2.15(2) [249]					
NGC 6652 X-4								
CXOGlb J183544.5-325939			0.73(1) [250]					
Ser X-1			2 †[251]		38(5) [251]	92(4) [251]		
SWIFT J1842.5-1124								
Swift J1843.5-0343							4.2e+4 †[252]	
EXO 1846-031	3.2(2) †[253]							
MAXI J1848-015								
SWIFT J185003.2-005627								
4U 1850-087		0.045 †[254]	0.343(1) [255]	0.018 †[13]	0.01 †[13]			
XTE J1856+053								
SWIFT J1858.6-0814		0.3(1) [256]	21.3448(4) [257]					
XTE J1859+226	8(2) [258]	0.6(2) [258]	6.62(7) [258]		5.5(6)e + 02 [258]	1.1(4)e + 02 [258]		
HETE J1900.1-2455			1.387572(1) [259]	<2.0e-3 †[259]			0.00265020277800(4) [259]	
XTE J1901+014								
1H 1905+000			<1.3 ††[260]					
XTE J1908+094								
MAXI J1910-057	10(4) †[261]		>6.2 †[262]					
Aql X-1			18.71(6) [263]				0.001817275(3) [264]	

Table A.2: continued.

Identifier	Mx [$M_\odot$]	Mo [$M_\odot$]	Orbital period [hr]	Eccentricity	K2 [km/s]	RV [km/s]	Spin period [s]	$\dot{P}/P$ [1/yr]
Granat 1915+105	10.1(6) [265]	0.5(3) [265]	812(4) [265]		126(1) [265]	11(4) [265]		
XB 1916-053		0.047 ††[266]	0.83350(6) [267]				0.003676(3) [268]	
4U 1918+15								
SWIFT J1922.7-1716								
IGR J19308+0530			14.662(1) [269]		91(1) [269]	−46(1) [269]		
NGC 6819 X1								
XB 1940-04								
MAXI J1957+032			1.01473(2) [270]	<0.014 †[270]			0.003188331000(3) [270]	
4U 1957+11	5(1) †[271]		9.331(3) [272]					
GS 2000+25	7(2) [273]	0.3(1) [273]	8.25821(2) [274]		520(5) [275]	19(4) [275]		
XTE J2012+381	>12 †[276]							
404 Cyg	10(2) †[277]	1 †[277]	155.314(2) [278]		208.5(7) [278]	114(6) [279]		
SWIFT J2037.2+4151								
IGR J21188+4901								
XTE J2123-058	1.5(4) †[280]	0.5(4) [280]	5.9562(5) [280]		$2.9(1)e+02$ [281]	−110(8) [281]	0.0039(2) [282]	
M15 X-3		0.44(6) †[283]	4 ††[283]					
M15 X-2			0.376343(3) [284]					
4U 2129+12			17.11296(2) [285]					
4U 2129+47	0.6(2) [286]	0.4(2) [286]	5.2382(7) [287]		$2.3(3)e+02$ [286]			
CXOGlb J214022.1-231045	<1.8 †[288]							
Cyg X-2	1.7(2) [289]	0.6(1) [290]	236.268(5) [289]		86(1) [289]	−210(1) [289]		
IGR J22014+6034								
SAX J2224.9+5421								
4U 2316+61								

References. [1]Heinke et al. (2003); [2]Bahramian et al. (2017); [3]Heinke et al. (2005); [4]Torres et al. (2008); [5]Galloway et al. (2005); [6]Watson & Ricketts (1978); [7]Casares et al. (2022); [8]Filippenko et al. (1995); [9]Kennedy et al. (2020); [10]Strader et al. (2016); [11]Yao et al. (2021a); [12]Yao et al. (2021b); [13]Prodan & Murray (2015); [14]Fiocchi et al. (2011); [15]Strader et al. (2021); [16]Cornelisse et al. (2012); [17]Baglio et al. (2014); [18]Strohmayer et al. (2008); [19]van Grunsven et al. (2017); [20]McClintock & Remillard (1986); [21]Neilsen et al. (2008); [22]Marsh et al. (1994); [23]Soria et al. (2022); [24]Hertz et al. (1997); [25]Bassa et al. (2009); [26]Ratti et al. (2012b); [27]Galloway et al. (2009); [28]Kennea et al. (2020); [29]Sanna et al. (2017); [30]in't Zand et al. (2005b); [31]Zhong & Wang (2011); [32]Steeghs & Jonker (2007); [33]Ashcraft et al. (2012); [34]Jonker et al. (2005); [35]Galloway et al. (2002a); [36]Filippenko et al. (1999); [37]Bhattacharyya (2020); [38]Archibald et al. (2009); [39]Thorstensen & Armstrong (2005); [40]González Hernández et al. (2012); [41]González Hernández et al. (2008); [42]Wu et al. (2016); [43]Wu et al. (2015b); [44]de Martino et al. (2015); [45]de Martino et al. (2014); [46]Roy et al. (2014); [47]Barnes et al. (2007); [48]Motch et al. (1987); [49]Mata Sánchez et al. (2021); [50]Gambino et al. (2016); [51]Titarchuk & Seifina (2023); [52]Carotenuto et al. (2022); [53]Kennea & Negoro (2019); [54]Casares (2016); [55]Mata Sánchez et al. (2015); [56]Torres et al. (2015); [57]Casares et al. (2004); [58]Strader et al. (2015); [59]Camilo et al. (2016); [60]Oosterbroek et al. (1999); [61]Hammerstein et al. (2018); [62]Torres et al. (2002); [63]Yanes-Rizo et al. (2024); [64]Sridhar et al. (2019); [65]Kennea et al. (2007); [66]Chatterjee et al. (2016); [67]Mondal (2020); [68]Britt et al. (2017); [69]Orosz et al. (1998); [70]Wang & Chakrabarty (2004); [71]Orosz et al. (2002); [72]Smale (1991); [73]Mason et al. (2008); [74]Shi & Zhang (2020); [75]Wachter et al. (2002); [76]Muno et al. (2001); [77]Ratti et al. (2010); [78]Luna (2023); [79]Cherepashchuk et al. (2021); [80]Mata Sanchez et al. (2015); [81]Hynes et al. (2016); [82]Steeghs & Casares (2002); [83]Gorgone et al. (2019); [84]Kaluzny et al. (2012); [85]Smale et al. (2001); [86]Liao et al. (2015); [87]Rout et al. (2023); [88]Peterson et al. (1980); [89]Hemphill et al. (2021); [90]Jain et al. (2007); [91]Iwakiri et al. (2019); [92]Seifina et al. (2014); [93]Patel et al. (2007); [94]Chirenti & Jasiulek (2018); [95]van Paradijs et al. (1990); [96]Zhang et al. (1997); [97]Orosz et al. (2004); [98]Motta et al. (2014); [99]Bailyn et al. (1995); [100]Hjellming & Rupen (1995); [101]Reynolds et al. (1997); [102]Deeter et al. (1981); [103]Staubert et al. (2009); [104]Tananbaum et al. (1972); [105]Mondal & Jithesh (2023); [106]Kennea (2018); [107]Torres et al. (2021); [108]Kuulkers et al. (2011); [109]Sanna et al. (2018); [110]Iaria et al. (2018); [111]Ponti et al. (2018); [112]Wijnands et al. (2001); [113]Heida et al. (2017); [114]Iaria et al. (2009); [115]Wachter (1997); [116]Nättilä et al. (2017); [117]Markwardt et al. (1999); [118]Strohmayer et al. (2018a); [119]Bult et al. (2021); [120]Galloway et al. (2002b); [121]Filippenko et al. (1997); [122]Iyer et al. (2015); [123]Wijnands et al. (2012); [124]Jain & Paul (2011); [125]in't Zand et al. (2009); [126]Jonker et al. (2007a); [127]Gangopadhyay et al. (2012); [128]Patruno et al. (2012); [129]Casares et al. (2023); [130]Masetti et al. (1996); [131]Crawford et al. (2013); [132]Novarino et al. (2021); [133]Wang et al. (2022); [134]Stoop et al. (2021); [135]Saha et al. (2023); [136]Hertz & Wood (1988); [137]Shaposhnikov et al. (2003); [138]Vincentelli et al. (2020); [139]Strohmayer et al. (1997b); [140]Bozzo et al. (2018); [141]Hinkle et al. (2006); [142]Majczyna et al. (2016); [143]Sunyaev (1990); [144]Jaisawal et al. (2018); [145]Fox et al. (2001); [146]Li et al. (2022); [147]Özel et al. (2012); [148]Revnivtsev & Sunyaev (2003); [149]Smith et al. (1997); [150]Shaw et al. (2024); [151]Wilson et al. (1995); [152]Bult et al. (2019); [153]Strohmayer et al. (2018b); [154]Corbet et al. (1986); [155]Casares et al. (2006); [156]Beri et al. (2023); [157]Wang et al. (2018); [158]Finger et al. (1996); [159]Pintore et al. (2014); [160]Ng et al. (2021a); [161]Heinke et al. (2015); [162]Sakano et al. (2005); [163]Zdziarski et al. (2016); [164]Bozzo et al. (2016); [165]Chaty et al. (2020); [166]Muñoz-Darias et al. (2013); [167]Bogomazov et al. (2022); [168]Ponti et al. (2017); [169]Porquet et al. (2005a); [170]Strohmayer et al. (1997a); [171]Porquet et al. (2005b); [172]Altamirano et al. (2010); [173]Molla et al. (2017); [174]Jonker et al. (2010); [175]Torres et al. (2019b); [176]van den Berg et al. (2014); [177]Özel et al. (2009); [178]Papitto et al. (2011b); [179]Bhattacharyya et al. (2006); [180]Güver & Özel (2013); [181]Cadelano et al. (2017); [182]Altamirano et al. (2008a); [183]Ng et al. (2020); [184]Ng et al. (2021b); [185]Marino et al. (2022); [186]Altamirano et al. (2011); [187]Papitto et al. (2011a); [188]Li et al. (2015); [189]Bałucińska-Church et al. (2004); [190]D'Avanzo et al. (2009); [191]Markwardt et al. (2002); [192]Kaaret et al. (2002); [193]Papitto et al. (2010); [194]in't Zand et al. (2003); [195]Shaposhnikov et al. (2010); [196]Ratti et al. (2012a); [197]Zurita et al. (2008); [198]Shaw et al. (2017); [199]Krimm et al. (2007); [200]Bult et al. (2018); [201]Sasaki et al. (2021); [202]Park et al. (2005); [203]White et al. (1984); [204]Tse et al. (2020); [205]Wijnands et al. (1998); [206]Bezayiff (2006); [207]Smith et al. (2002); [208]Homan et al. (2021); [209]Baglio et al. (2016); [210]Cornelisse et al. (2007); [211]Leahy et al. (2011); [212]Markwardt et al. (2003a); [213]Kirsch et al. (2004); [214]Elebert et al. (2009); [215]Deloye et al. (2008); [216]Chakrabarty & Morgan (1998); [217]Blay et al. (2008); [218]Suleimanov et al. (2017); [219]Suleimanov et al. (2020); [220]Wang et al. (2017); [221]Papitto et al. (2007); [222]Markwardt et al. (2003b); [223]De et al. (2022b); [224]Corbet (2003); [225]Armas Padilla et al. (2022); [226]Langmeier et al. (1986); [227]Wijnands et al. (1997); [228]Bult et al. (2022a); [229]Bagińska et al. (2021); [230]Qiu et al. (2017); [231]MacDonald et al. (2014); [232]Orosz et al. (2001); [233]Lindstrøm et al. (2005); [234]Torres et al. (2020); [235]Torres et al. (2019a); [236]Kuśmierek et al. (2011); [237]Rappaport et al. (1987); [238]Chou & Jhang (2023); [239]Papitto et al. (2013b); [240]Shahbaz et al. (2007); [241]Iaria et al. (2015); [242]Jain et al. (2010); [243]Jonker et al. (2003a); [244]Jonker & van der Klis (2001); [245]Meshcheryakov et al. (2010); [246]De et al. (2022a); [247]Koyama et al. (1991); [248]Russell et al. (2014); [249]Engel et al. (2012); [250]Deutsch et al. (2000); [251]Cornelisse et al. (2013); [252]Strohmayer & Markwardt (2011); [253]Strohmayer & Nicer Observatory Science Working Group (2020); [254]Homer et al. (2001a); [255]Priedhorsky (1986); [256]Knight et al. (2022); [257]Buisson et al. (2021); [258]Yanes-Rizo et al. (2022); [259]Kaaret et al. (2006); [260]Mikhailov et al. (2017); [261]Nath et al. (2023); [262]Casares et al. (2012); [263]Welsh et al. (2000); [264]Casella et al. (2008); [265]Steeghs et al. (2013); [266]Nelson et al. (1986); [267]Homer et al. (2001b); [268]Galloway et al. (2001); [269]Ratti et al. (2013); [270]Sanna et al. (2022); [271]Sharma et al. (2021); [272]Bayless et al. (2011); [273]Ioannou et al. (2004); [274]Casares et al. (1995); [275]Harlaftis et al. (1996); [276]Draghis et al. (2023); [277]Wagner et al. (1992); [278]Casares & Charles (1994); [279]Casares et al. (1992); [280]Tomsick et al. (2002); [281]Casares et al. (2002); [282]Tomsick et al. (1999); [283]Arnason et al. (2015); [284]Dieball et al. (2005); [285]Ilovaisky et al. (1993); [286]Horne et al. (1986); [287]Thorstensen et al. (1979); [288]Echiburú et al. (2020); [289]Casares et al. (2010); [290]Orosz & Kuulkers (1999);

Appendix B: *INTEGRAL* sources

Table B.1: List of unidentified *INTEGRAL* sources from Bird et al. (2016) with available identification in the literature.

Identifier	R.A. [deg]	Dec. [deg]	Simbad Type	Identification	Ref.
IGR J00486-4241	12.151	-42.719	gamma	AGN ?	[1]
IGR J04069+5042	61.73	50.702	gamma	RS CVn	[2]
IGR J04539+4502	73.46	45.038	gamma	AGN	[3]
IGR J05511-1218	87.776	-12.322	gamma	AGN	[4]
IGR J06552-1146	103.792	-11.77	gamma	RS CVn ?	[2]
IGR J07072-1227	106.801	-12.427	gamma	AGN	[4]
IGR J08004-4309	120.092	-43.166	X	CV	[5]
IGR J08262+4051	126.556	40.855	gamma	AGN	[6]
IGR J10252-6829	156.25204	-68.45758	gamma	early type	[7]
2MASS J10445192-6025115	161.21635	-60.41987	YSO	AGN	[8]
IGR J12341-6143	188.467	-61.796	gamma	SFXT	[9]
IGR J12562+2554	194.05	25.905	gamma	AGN	[10]
IGR J13045-5630	196.13125	-56.51522	gamma	AGN	[11]
IGR J13402-6428	205.05	-64.48	gamma	AGN	[12]
IGR J14043-6148	211.123	-61.789	gamma	blazar ?	[13]
IGR J14059-6116	211.485	-61.275	gamma	Gamma HMXB	[14]
IGR J14385+8553	219.616	85.883	gamma	AGN	[6]
IGR J14466-3352	221.656	-33.875	gamma	AGN ?	[15]
IGR J14557-5448	223.862	-54.786	gamma	AGN ?	[16]
HD 132658	224.99804	12.02395	Star	AGN ?	[5]
IGR J15391-5307	234.82	-53.138	gamma	AGN	[17]
UCAC4 170-140217	238.55406	-56.15832	Star	AGN ?	[18]
IGR J16173-5023	244.314	-50.386	gamma	magnetic CV ?	[17]
IGR J16316-4028	247.9	-40.467	gamma	gamma ray pulsar?	[19]
IGR J16413-4046	250.331	-40.794	gamma	AGN ?	[17]
IGR J16447-5138	251.178	-51.649	gamma	YSO or AGN	[5]
IGR J16460+0849	251.488	8.818	gamma	extragalactic	[20]
IGR J16560-4958	253.989	-49.967	gamma	AGN	[17]
IGR J17259+2603	261.521	25.905	gamma	Type 1 QSO	[4]
IGR J17348-2045	263.745	-20.759	gamma	AGN ?	[21]
IGR J17375-3022	264.3946	-30.3817	gamma	SFXT	[9]
IGR J18293-1213	277.342	-12.222	gamma	CV	[22]
SWIFT J1839.1-5717	279.7762	-57.2511	X	AGN	[5]
IGR J18457+0244	281.42	2.702	gamma	AGN	[8]
IGR J18485-0047	282.106027	-0.776356	gamma	AGN ?	[23]
IGR J18532+0416	283.318	4.297	gamma	AGN	[8]
IGR J19386-4653	294.653	-46.886	gamma	AGN ?	[24]
IGR J20155+3827	303.875	38.45	gamma	HMXB	[25]
IGR J21171+3930	319.306	39.515	gamma	AGN ?	[3]
IGR J21268+6203	321.692	62.062	gamma	AGN ?	[26]
IGR J21485+4306	327.127	43.104	gamma	AGN ?	[1]
2MASX J21561518+1722525	329.06346	17.38128	X	AGN ?	[27]
IGR J22234-4116	335.85	-41.262	gamma	AGN ?	[28]
1SWXRT J230642.8+550817	346.727	55.173	X	CV	[5]

References. [1] Landi et al. (2017b); [2] Özbey Arabacı et al. (2012); [3] Malizia et al. (2017); [4] Masetti et al. (2017); [5] Landi et al. (2017a); [6] Masetti et al. (2012); [7] Fortin et al. in prep; [8] Fortin et al. (2018); [9] Sguera et al. (2020); [10] Fiocchi et al. (2010); [11] Paliya et al. (2019); [12] Fortin et al. (2023a); [13] Cowperthwaite et al. (2013); [14] Corbet et al. (2019); [15] Landi et al. (2010b); [16] Ursini et al. (2019); [17] Tomsick et al. (2012); [18] Tomsick et al. (2020); [19] Foschini (2002); [20] Zhang et al. (2009); [21] Bozzo et al. (2012); [22] Clavel et al. (2016); [23] Tomsick et al. (2009); [24] Molina et al. (2012); [25] Onori et al. (2021); [26] Maiorano et al. (2011); [27] Malizia et al. (2016); [28] Landi et al. (2010a);

Journal of Thermal Analysis and Calorimetry
https://doi.org/10.1007/s10973-023-12761-6

A comprehensive energy, exergy, environmental, and economic analysis of dedicated mechanical subcooled vapor compression refrigeration system

Naveen Solanki[1] · **Akhilesh Arora**[2] · **Raj Kumar Singh**[2]

Received: 7 April 2023 / Accepted: 13 November 2023
© Akadémiai Kiadó, Budapest, Hungary 2023

Abstract

In the modern world, the vapor compression refrigeration (VCR) system is essential in various global applications, including climate control, refrigeration, and food preservation, contributing significantly to energy consumption. The significant energy demands associated with these applications highlight the urgency for sustainable and energy-efficient alternatives that can help diminish our dependence on electrical power. To reduce energy consumption and enhance energy efficiency, a dedicated mechanical subcooled (DMS) system can be integrated with a vapor compression system (VCR) system. This study aims to evaluate and optimize the dedicated mechanical subcooled-vapor compressor refrigeration system (DMS-VCR) system using refrigerant R134a for a 100 kW commercial chiller used for water cooling application. The primary objective is to assess the system from multiple angles which include energy, exergy, environmental, economic analysis (4E's) and optimizing it to enhance its overall effectiveness to reduce the system's annual cost. It is thermo-economically optimized, allowing for independent optimization of the evaporator, condenser-1, condenser-2, and sub-cooler components. The proposed system reduces electrical energy consumption by 17.24% and CO_2 emissions by 12.4%. The DMS-VCR system outperforms the standalone VCR system. The DMS-VCR system's annual operating costs are 6.71% lower than an equivalent VCR system, and optimization further reduces costs by 1.88% (case-I: $i_{rate} = 10\%$, $N_y = 5$ years, and $t_{oper} = 4000$ h) and 16.36% (case-II: $i_{rate} = 2\%$, $N_y = 10$ years, and $t_{oper} = 5000$ h).The study underscores the importance of subcooling within the DMS-VCR system, highlighting its desirability as it varies with the recovery factor and annual operation period. As a result of the DMS-VCR system's better efficiency, design engineers are likely to find it more attractive.

Keywords Energy · Exergy · Economic · Environment · Exergetic efficiency

Abbreviations

COP	Coefficient of performance
DMS	Dedicated mechanical subcooled
DOO	Degree of overlap
DOS	Degree of subcooling
EES	Engineering equation solver
EoS	Element or subsystem
ED	Exergy destruction
LMTD	Logarithmic mean temperature difference
ROI	Rate of interest
VCR	Vapor compression refrigeration

List of symbols

a^c	Capital recovery factor
COP	Coefficient of performance
C_i^{el}	Cost per kilowatt-hour of electricity (\$ kWh^{-1})
C_t	Overall annual cost of the system (\$ $year^{-1}$)
C_{oper}	Operational cost (\$ $year^{-1}$)
C_{env}	Environment damage cost (\$ $year^{-1}$)
c_{sp}	Specific heat (kJ kg^{-1} K^{-1})
i_{rate}	Rate of interest (%)
k	Thermal conductivity of material (kW m^{-2} K^{-1})
$\dot{m}$	Flow rate of mass (kg s^{-1})

✉ Naveen Solanki
naveensolanki@mait.ac.in

Akhilesh Arora
akhilesharora@dce.ac.in

Raj Kumar Singh
rajkumarsingh@dce.ac.in

[1] Mechanical Engineering Department, Maharaja Agrasen Institute of Technology, Sector-22, Rohini, New Delhi 110085, India

[2] Mechanical Engineering Department, Delhi Technological University, Shahbad Daulat Pur, Bawana Road, New Delhi 110042, India

Published online: 29 December 2023

m_{co_2}	Annual emission of carbon dioxide (ton)
N_y	Time frame for repayment (years)
$\dot{Q}$	Heat transfer(kW)
t_{oper}	Per-year operation period (h)
U	Coefficient of overall heat transfer (kW m^{-2} K^{-1})
$\dot{W}$	Power input rate (kW)
Z_k	Capital cost of K subsystem ($)
Z_{total}	Cost of the system ($)
T_m	Mean temperature difference in logarithmic scale (LMTD, in Kelvin)

Greek symbols

ϵ	Effectiveness
η	Efficiency
λ	Conversion factor of Co_2 emission (kg kWh^{-1})
ϕ	The maintenance factor
Ψ	Chemical, potential, kinetic, and physical exergy of matter

Subscripts

1, 2, 3…	State points
comp	Compressor
cond	Condenser
evap	Evaporator
ex	Exergetic
ev	Expansion valve
ef	External fluid
in	Inlet condition
isen	Isentropic
out	State of the outlet
o	Environment condition
ref	Refrigerant
sc	Subcooling
t	Total
k	Kth element of a system

Superscripts

In	Inlet
out	Outlet
Q	Heat
W	Work

Introduction

In today's world, the vapor compression refrigeration (VCR) system plays a vital role in global energy consumption across diverse applications such as climate control, refrigeration, and food preservation. This extensive energy usage emphasizes the need for sustainable and energy-efficient solutions to reduce our reliance on electricity. One promising avenue is the dedicated mechanical subcooled-vapor compressor refrigeration (DMS-VCR) system, which offers the potential to address this challenge. Even modest improvements in electricity consumption within VCR system can translate into substantial global energy savings. The literature on refrigeration technology is extensive and diverse, covering a wide range of studies, innovations, and approaches. Many researchers have worked on DMS-VCR system, which is further explained in the literature survey. The influence of compressor isentropic efficiency (0.1–1.0) and subcooler effectiveness (0.3–1.0) was examined and found that the DMS vapor compression refrigeration cycle out performs the simple VCR cycle by Agarwal et al. [1] and they discovered that the DMS-VCR cycle outperforms the simple VCR cycle based system. Gil et al. [2] examined the energy savings of integrated and dedicated mechanical subcooling systems in CO_2 supporter systems in many supermarket applications. According to Pottker and Hrnjak [3], refrigerants with a higher latent heat of vaporization have a lower propensity for condenser subcooling. Due to its lower latent heat of vaporization, R1234yf (+8.4%) would have a greater opportunity for condenser subcooling in a VCR system than R134a (5.9%), R410A (7.0%), and R717 (2.7%). The impact of condenser subcooling for R134a and R1234yf air conditioning systems with and without internal heat exchangers was examined by Pottker and Hrnjak [4]. They also discovered that an R1234yf air conditioning system performs better when IHX and condenser subcooling are combined. Qureshi and Zubair [5, 6] examined the mechanical subcooling of VCR systems in the condition of optimal operation and management. They also highlighted some recent work in that direction and experimental work to prove the concept of the dedicated subcooling cycle. So they experimented with various refrigerant mixtures using DMS-VCR cycles and found that R134a works better than R717 as the main refrigerant for DMS. Researchers [1–6] conducted an energy and exergy study to improve the performance of the DMS-VCR system but neglected to consider economic and environmental factors, which are essential when deciding how to use energy resources responsibly. Wang and Zhang [7] looked into the energy, exergetic, and economic analysis of the simple single-stage transcritical CO_2 VCR cycle. Jain et al. [8] conducted multi-objective optimization of a 170 kW vapor compression–absorption cascade refrigeration system that simultaneously took into account economic, environmental, and thermodynamic factors. Further, Jain et al. [9] in a separate research investigated the performance of commercially available 170 kW vapor compression-absorption integrated refrigeration system) based on combined energy, exergy, economic and environmental (4E) analysis. They discovered that the annual plant operational costs and CO_2 emissions were significantly lower. It should be emphasized that although there is a substantial quantity of information available on 4E analysis and VCR system optimization, there is relatively little research on a DMS-VCR system based on 4E analysis. The majority of DMS-VCR system studies are introductory in nature and their primary emphasis is on the

energy and exergy evaluations of the system. But for the commercial viability of the system, economic, environmental, and thermodynamic aspects are equally requisite.

In the current study, a novel approach is introduced, which combines insights from four essential domains: energy, exergy, economics, and the environment, collectively referred to as the 4E analysis. The Engineering Equation Solver (EES) software is employed to construct a robust program for the mathematical model of the system using above mentioned 4E principles based on these insights. This 4E analysis not only facilitates in computing the various parameters of the estimation of critical DMS-VCR system characteristics such as cost, size, energy consumption, and exergetic efficiency under various operating conditions over a broad range, but also undergoes a comprehensive 4E analysis that accounts for a broad range of operating variables. A significant finding in our study is the identification of the optimal degree of subcooling, which is determined to be 19 °C. The optimum degree of subcooling is a secured function of capital recovery factor and yearly operating period, which is economically advantageous because exceeding this limit increases the system's annual cost, which is the work's novelty. In a nutshell, the work's unique feature is that it shows a DMS-VCR system performance analysis based on 4E analysis results.

Description and modeling of DMS-VCR system.

The key components of a dedicated subcooled vapor compression refrigeration (DMS-VCR) system, including two condensers, two compressors, two expansion valves, one evaporator, and one subcooler, as are shown in schematically diagram of the system in Fig. 1. The temperature–entropy (T–s) diagram of the cycle is shown in Fig. 2. It illustrates various processes taking place in the VCR system and DMS system. The cycle works between the condensers and evaporator temperatures, respectively.

The subcooling DMS cycle (6–7–8–9) is attached with the VCR cycle (1–2–3–4–5) at the condenser-1 outlet. These components of the two cycles (VCR and DMS) are attached through a piping system in a folded loop with a provision for heat transfer to the environment. This designed system can use the same or different refrigerants in two cycles.

Thermodynamic modeling of system

This section presents the thermodynamic modeling of the system. The assumptions considered in the thermodynamic modeling of the system are:

(i) The system component is in a steady state.

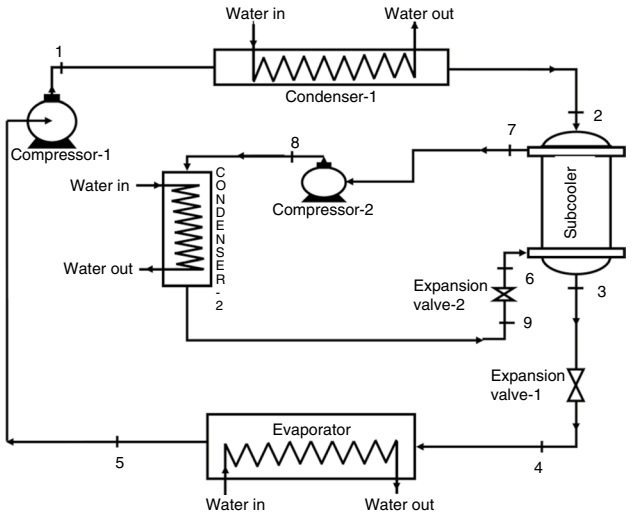


Fig. 1 Flow diagram of dedicated mechanical subcooled VCR system

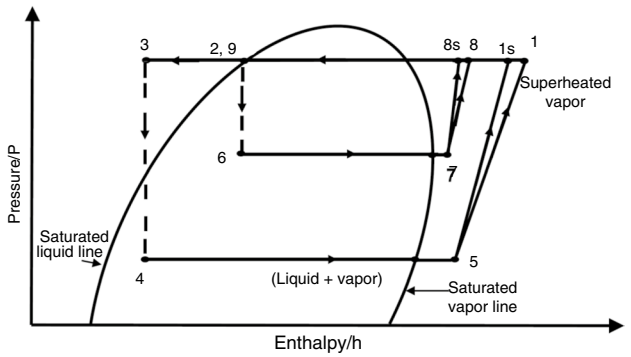


Fig. 2 Pressure–enthalpy diagram of DMS-VCR cycle

(ii) At the exit, the refrigerants in the evaporator and condenser are in a saturated vapor and saturated liquid state.
(iii) The pressure losses in connecting pipelines and other system components are neglected.
(iv) Isentropic efficiency is assumed to be constant for the compressors.
(v) The changes in K.E. and P.E. are neglected.

Energetic and exergetic analysis

In EES software, the DMS-VCR system is thermodynamically simulated for energy and exergy analysis based on the first and second laws, respectively. The mass, energy, and exergy balance concept is applied to each component of the system as the thermophysical refrigerant parameters are derived from built-in EES functions at different state points. The following equations treat the system's components as control volumes with inlet and output streams, heat transfer, and work interactions by Nag [10].

$$\sum \dot{m}_{\mathrm{i}} - \sum \dot{m}_{\mathrm{o}} = 0 \text{ (Mass balance)} \tag{1}$$

$$\sum \dot{Q} - \sum \dot{W} = \sum \dot{m}_{\mathrm{out}} h_{\mathrm{out}} - \sum \dot{m}_{\mathrm{in}} h_{\mathrm{in}} \text{ (Energy balance)} \tag{2}$$

$$\dot{S}_{\mathrm{gen}} = \sum \dot{m}_{\mathrm{out}} s_{\mathrm{out}} - \sum \dot{m}_{\mathrm{in}} s_{\mathrm{in}} - \sum \frac{\dot{Q}}{T} \geq 0 \text{ (Entropy generation)} \tag{3}$$

The rate of heat transmission is significantly influenced by the specific heat and mass flow rate of the fluid streams moving within heat exchangers, specifically the evaporator, condenser-1, condenser-2, and subcooler. The rate of heat transmission particularly in the evaporator is depicted in Eq. (4).

$$\dot{Q}_{\mathrm{evap}} = (\dot{m}_{\mathrm{ef}} \cdot c_{\mathrm{sp}})_{\mathrm{evap}} \left(T_{\mathrm{in,evap}} - T_{\mathrm{out,evap}}\right) = \dot{m}_1 \left(h_5 - h_4\right) \tag{4}$$

$T_{\mathrm{in,evap}}$, as shown in Eq. (4), represents the temperature of the fluid coming from outside and entering the evaporator and Eqs. (5) and (6) shows the compressor's work in the compressor-1 and compressor-2 sections.

$$\dot{W}_{\mathrm{comp1}} = \frac{\dot{W}_{\mathrm{comp1,isen}}}{\eta_{\mathrm{isen1}}} \text{ and } \dot{W}_{\mathrm{comp1,isen}} = \dot{m}_1 \left(h_{1\mathrm{s}} - h_5\right) \tag{5}$$

$$\dot{W}_{\mathrm{comp2}} = \frac{\dot{W}_{\mathrm{comp2,isen}}}{\eta_{\mathrm{isen2}}} \text{ and } \dot{W}_{\mathrm{comp2,isen}} = \dot{m}_2 \left(h_{8\mathrm{s}} - h_7\right) \tag{6}$$

Points 1s and 11s represent the isentropic condition of the refrigerant vapor at the compressor's outlet. A steady-state flow equation is used to calculate the work input needed by the compressor. Furthermore, the coefficient of performance (COP) is determined as the refrigerant effect to compressor power ratio

$$\mathrm{COP} = \frac{\dot{Q}_{\mathrm{evap}}}{\dot{W}_{\mathrm{comp1}} + \dot{W}_{\mathrm{comp2}}} \tag{7}$$

In both commercial and residential systems, fan power consumption is quite low. Therefore, it is not taken into account while calculating COP.

By modifying the design parameters, second law-based analysis aims to improve system performance by identifying energy losses. Exergy analysis is the most accurate way for determining actual losses because the process is irreversible. The irreversibility ($\dot{I}$) of a process indicates the potential loss of useful work (W_{useful}) compared to reversible work.

The following governing equations are part of thermodynamic modeling for a specific system component:

$$\text{Exergy balance, } \dot{I} = E^{\mathrm{in}} - E^{\mathrm{out}} + E^{\mathrm{Q}} - E^{\mathrm{W}} \tag{8}$$

Thus, E^{Q} and E^{W} are the exergy flows connected to heat and work transfer, respectively, and $\dot{I}$ is the total irreversibility or exergy destruction (loss). In $E = \dot{m} * \psi$, ψ is the chemical, potential, kinetic, and physical exergy of matter, and E^{in} and E^{out}, which are matter exergies at the control volume's input and output. The physical specific exergy is calculated after removing chemical, potential, and kinetic exergies.

$$\psi = \left(\mathrm{h} - \mathrm{T_o s}\right) - \left(\mathrm{h_o} - \mathrm{T_o s_o}\right) \tag{9}$$

$$\dot{\mathrm{ED}} = \sum \dot{E}_{\mathrm{in}} - \sum \dot{E}_{\mathrm{out}} + \sum \dot{Q}\left(1 - \frac{T_{\mathrm{o}}}{T}\right) - \sum \dot{W} \tag{10}$$

Here, the temperature of the reference environment is referred to as T_{o}.

By employing the above fundamental equations to all the elements of the DMS-VCR system, the system's entire exergy destruction is indicated by the Eq. (11).

$$\begin{aligned} \dot{\mathrm{ED}}_{\mathrm{t}} = {} & \dot{\mathrm{ED}}_{\mathrm{evap}} + \dot{\mathrm{ED}}_{\mathrm{cond1}} + \dot{\mathrm{ED}}_{\mathrm{cond2}} + \dot{\mathrm{ED}}_{\mathrm{sc}} \\ & + \dot{\mathrm{ED}}_{\mathrm{cond1}} + \dot{\mathrm{ED}}_{\mathrm{cond2}} + \dot{\mathrm{ED}}_{\mathrm{ev1}} + + \dot{\mathrm{ED}}_{\mathrm{ev2}} \end{aligned} \tag{11}$$

Arora et al. [11] Calculated the exergetic efficiency of the VCR system.

$$\eta_{\mathrm{ex}} = \left(1 - \frac{\dot{\mathrm{ED}}_{\mathrm{t}}}{\dot{W}_{\mathrm{t}}}\right) \tag{12}$$

Economic analysis

In this section, economic analysis of the system is presented. The economic analysis assists in minimizing the area of the heat exchangers used in the system and all the costs, i.e., capital, operational, and maintenance costs. The heat exchangers employed in this investigation are the evaporator, condenser-1, condenser-2, and subcooler. Bakhtiari et al. [12], designed the VARS components as well as the water chilling application. In the present work, the evaporator and condenser are of the shell and tube type, whereas the subcooler is of the tube in tube type. Table 1, below shows the additional dimensioning features of different heat exchangers in the current system:

Capital and operational costs

This approach ignores the price of pumps, valves, refrigerants, and connecting pipes, but it does account for the overall price of heat exchangers and compressors, Rubio-Maya [13]. According to Sanaye and Malekmohammadi's [14] estimation, 0.84% of the investment cost is made up of the price of

other products, such as pipes, expansion valves, and refrigerant. According to Kizilkan et al. [15], the cost of investment for each heat exchanger is calculated based on the surface area of the heat exchanger. The DMS system's investment cost is determined by the equations listed below:

$$Z_k = 516.621A_k + 268.45 \tag{13}$$

$$\text{DMS}, \forall k \in \text{EoS} \cap \{\text{Evap}, \text{Cond1}, \text{Cond2}, \text{Subcooler}\}$$

The scroll compressor expenditure cost, on the other hand, is given by Eq. (14).

$$Z_k = \left(\frac{573 \cdot \dot{m}_{ref}}{0.8996 - \eta_{isen}}\right)\left(\frac{P_{cond}}{P_{evap}}\right)\ln\left(\frac{P_{cond}}{P_{evap}}\right) \tag{14}$$

$$\text{DMS}, \forall k \in \text{EoS} \cap \{\text{Compressor}\}$$

Further, the capital recovery factor can be demoed as in Eq. (15).

$$a^c = \frac{i_{rate}\left(1 + i_{rate}\right)^{N_y}}{\left(1 + i_{rate}\right)^{N_y} - 1} \tag{15}$$

Here, interest rate and system lifetime are represented by i_{rate} and N_y.

The isentropic compressor efficiency (Π_{isen}), which is dependent on the pressure ratio, is represented by Eq. (16).

$$\eta_{isen} = 0.85 - 0.046667\left(\frac{P_{cond}}{P_{evap}}\right) \tag{16}$$

Equation (17) calculates the overall cost of the DMS-VCR system and Eq. (18), which represents the system's operational cost, yields the quantity of electric power being provided to the compressor.

$$Z_t = \sum_{k \in \text{EoS}} (Z_k) \tag{17}$$

$$\text{DMS} - \text{VCR}, \forall k \in \text{EoS} \cap$$

$$\{\text{Evap}, \text{Cond1}, \text{Cond2}, \text{Comp1}, \text{Comp2}, \text{Subcooler}\}$$

Table 1 Parameters for sizing the DMS-VCR system heat exchangers

Description	Tube's inner diameter/mm	Tube's outer diameter/mm	Length of tube /m	Number of turns
Evaporator	13.84	15.87	6.09	4
Condenser-1	13.84	15.87	6.09	2
Condenser-2	13.84	15.87	6.09	2
Subcooler	13.84	15.87	6.09	1

$$C_{oper} = t_{oper} * C_i^{el} * \dot{W} \tag{18}$$

The annual operational hours (t_{oper}) and the unit cost of electrical exergy (C_i^{el}) of the DMS-VCR system are assumed as 6000 h and 0.06 USD kWh^{-1}, respectively. The same is referred from Aminyavari et al. [16].

Environment analysis

Many environmentalists believe that carbon pricing, which acts as a penalty for CO_2 emissions, can be used to address issues related to global warming Aminyavari et al. [16]. Equation (19) can be used to calculate this cost.

$$C_{env} = m_{co_2} * C_{co_2} \tag{19}$$

In this context, the cost associated with CO_2 emissions penalty, denoted as, C_{co_2}, is subject to variation across different countries. As stated by Aminyavari et al. [16] and Carlsson et al. [17], the value of this cost ranges from 22 to 117 dollars per ton. However, for the purpose of the current study, the penalty cost (i.e., in 90 USD ton^{-1} of CO_2 emission) is assumed accordingly. Additionally, according to Eq. (20)'s mass of CO_2 emission (m_{co_2}) is given by:

$$m_{co_2} = \lambda * \dot{W}_t * t_{oper} \tag{20}$$

The conversion factor of emissions is denoted by λ, where CO_2 emissions per kWh of electric energy are determined to be 0.968 kg kWh^{-1}. The overall yearly operational cost of the DMS system is calculated by adding the annual electricity cost to the CO_2 penalty cost.

$$C_t = C_{oper} + C_{env} \tag{21}$$

Thermoeconomic optimization

The thermoeconomic optimization of the DMS-VCR system involves a comprehensive approach to enhance both the thermodynamic efficiency and the economic feasibility of the system. This process seeks to identify the optimal operating conditions and system configurations that minimize the overall cost while maximizing performance.

In the context of the DMS-VCR system, thermoeconomic optimization involves fine-tuning various system parameters such as temperatures, pressures, degree of overlap, degree of subcooling, and heat exchanger areas. The objective is to strike a balance between achieving the highest energy efficiency and minimizing operational costs, capital investments, and maintenance expenses.

Equation (22) specifies the economic parameters, which incorporate the annual operational costs of the plant.

$$\min C_t(x) = C_{oper} + C_{env} + a^c \cdot \varnothing \cdot \sum_{k \in EoS} Z_k \quad (22)$$

$$DMS - VCR, \forall k \in EoS \cap \{Evap, Cond1, Cond2, Comp1, Comp2, Subcooler\}$$

The calculation described above is divided into three sections. The first portion denotes the expenditure associated with total energy usage, the second part denotes the penalty for CO_2 emissions, and the final part denotes the cost associated with maintenance and capital investment. In the above Eq. (22), the maintenance component (ϕ), accounts for about 6% of Z_k, which is fluctuating over time. The thermoeconomic optimization of the DMS-VCR system aims to ensure that the system operates in an economically efficient manner while delivering the desired cooling capacity. By systematically evaluating and adjusting various parameters, engineers and researchers can develop systems that are not only environmentally friendly but also economically viable over their operational lifetimes.

Model validation

A program is developed in the EES software based on the model presented above, considering the thermophysical characteristics of the R134a refrigerant. The results of the present work are compared with that of Agarwal et al. [18]. The input data used by Agarwal et al. [18] are $\dot{Q}_{evap} = 3.5167$ kW, $T_{evap}, = -10$ °C, DOS = 5 °C, T_{cond1}, $T_{cond2} = 50$ °C, η_{comp1}, $\eta_{comp2} = 80\%$, $\epsilon_{sc} = 0.8$, $T_o = 25$ °C, $P_o = 101.325$ kPa. The same is used in the current program and the computed results are compared with that of Agarwal et al. [18]. The results depicts that all relevant quantities (COP and exergetic efficiency) are anticipated by EES software effectively with a maximum encountered error of 3.45% but most of the errors are less than 2% (see Figs. 3 and 4).

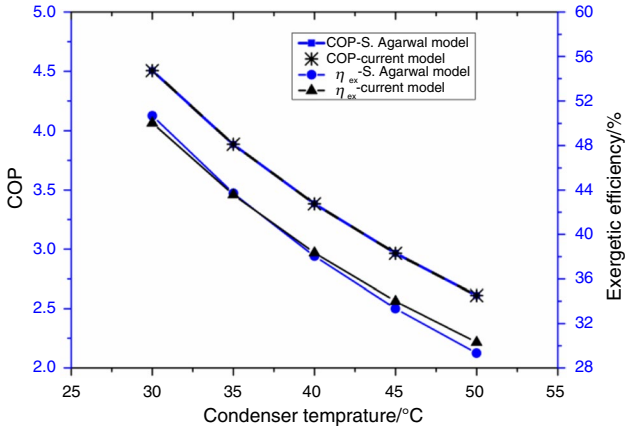


Fig. 3 Performance comparison of Agarwal et al. [18] for effect of condenser temperature with refrigerant R134a ($T_{evap} = -10$ °C)

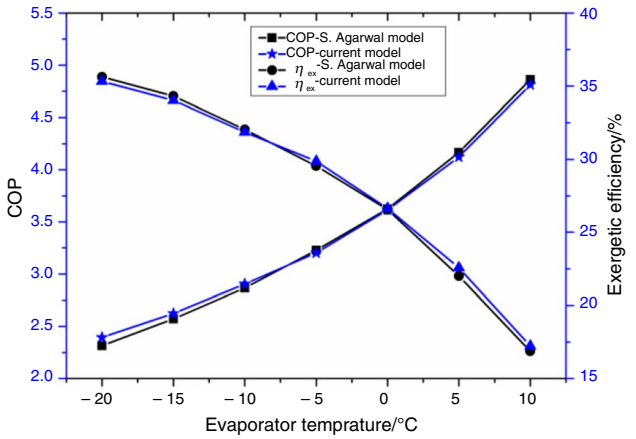


Fig. 4 Performance comparison of Agarwal et al. [18] for effect of evaporator temperature with refrigerant R134a ($T_{cond} = 50$ °C)

Results and discussion

In this section, the results and discussion are presented for different operating parameters of the DMS-VCR system for R134a.

Performance comparison between the equivalent VCR system and DMS-VCR system

A comprehensive comparison is conducted between the DMS-VCR system and an equivalent VCR system designed for industrial water chiller applications. Both systems operate with refrigerant R134a under identical conditions. This assessment encompasses various aspects, including energy, exergy, economic, and environmental considerations. The operational parameters for implementing water cooling within the DMS-VCR system were obtained through research papers [15, 16] and are detailed in Table 2.

Figure 5 shows the variation of total irreversibility and COP with degree of subcooling in DMS-VCR system. It is observed that optimal degree of subcooling is 19 °C as total irreversibility is minimum and COP is maximum for this value of DOS. Consequently, 19 °C as degree of subcooling is considered for computation of subsequent results in Sects. 5.2, 5.3, 5.4, 5.5.1, 5.5.2, and 5.5.3 for enhancing the economic performance of the DMS-VCR system. This innovative approach is a notable contribution of this study to the field.

Table 2 Process data of DMS-VCR system (for Refrigerant R134a)

Parameters		Values
Thermal parameters (Aminyavari et al. [16])	Evaporator cooling capacity ($\dot{Q}_{evap}$, kW)	100
	Evaporator temperature (T_{evap} °C)	0
	Inlet temperature of evaporator coolant ($T_{in,evap}$ °C)	10
	Outlet temperature of evaporator coolant ($T_{out,\ evap}$ °C)	5
	Temperature of Condenser (T_{cond} °C)	45
	Coolant inlet temperature at condenser ($T_{in,\ cond}$ °C)	35
	Coolant outlet temperature at condenser ($T_{out,\ cond}$ °C)	40
	Overlap degree ($T_{overlap}$, °C)	5
	Degree of subcooling ($T_{subcooling}$ °C)	5, 19 (optimal)
	Isentropic efficiency of compressors (η_{isen})	0.66, 0.76
	Environment temperature (T_o °C)	25
	Environment pressure (P_o, kPa)	101.325
	Refrigerants (for both the cycles)	R134a
Economic parameters (Kizilkan et al. [15] and Aminyavari et al. [16])	Interest rate (i_{rate}, %)	10, 2
	Repayment period (N_y, years)	5, 10
	Operation time/year (t_{oper}, hours)	5000, 4000
	Electricity unit cost (C_i^{el} in /$ kWh^{-1})	0.06

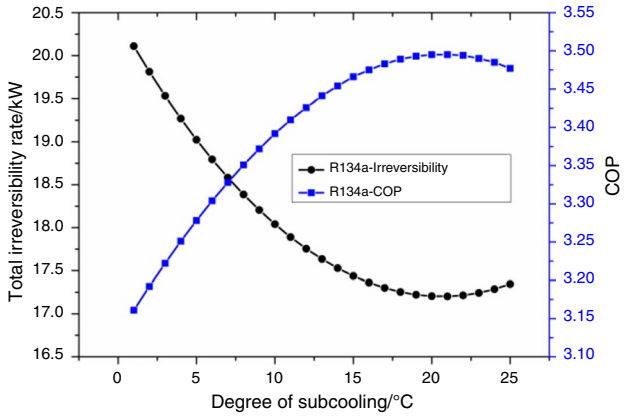


Fig. 5 Effect of degree of subcooling on system's total irreversibility rate and CO

Results of energy analysis

Table 3 displays the outcomes of an energy analysis, which compares the performance of R134a in DMS-VCR system with an equivalent VCR system, both operating under identical conditions. The primary objective of this is to determine COP and electricity consumption in the DMS-VCR system.

As indicated in Table 3, the DMS-VCR system achieves a substantial reduction (17.21%) in electricity consumption while maintaining the same cooling capacity as that in VCR system. Consequently, this reduction leads to decreased compressor-1 work and heat load on the condenser-1. Additionally, the mass flow rate of the refrigerant experienced a reduction of 17.22%. Simultaneously, the COP of the DMS-VCR system shows a noteworthy improvement of 11.67%.

Table 3 Energy analysis results for refrigerant R134a

Performance parameters	R134a		Percentage change /% [(*Y*−*X*)/*X**100]
	VCR system (*X*)	DMS-VCR system (*Y*)	
COP	3.128	3.493	(+) 11.67
$\dot{Q}_{cond1}$ (kW)	131.97	109.28	(−) 17.19
$\dot{Q}_{cond2}$ (kW)	–	19.35	–
$\dot{Q}_{cond,t}$ (kW)	131.97	128.63	(−) 2.53
$\dot{Q}_{sc}$ (kW)	–	17.19	–
$\dot{Q}_{evap}$ (kW)	100	100	–
$\dot{W}_{comp1}$ (kW)	31.97	26.47	(−) 17.20
$\dot{W}_{comp2}$ (kW)	–	2.16	–
$\dot{W}_{comp,\ t}$	31.97	28.63	(−) 10.45
$\dot{m}_{ref,1}$ (kg s^{-1})	0.743	0.615	(−) 17.23
$\dot{m}_{ref,2}$ (kg s^{-1})	–	0.117	–
$\dot{m}_{ref,t}$ (kg s^{-1})	0.743	0.732	(−) 1.48
$\dot{m}_{ef,ev}$ (kg s^{-1}	4.762	4.762	–
$\dot{m}_{ef,cond1}$ (kg s^{-1})	6.315	5.230	(−) 17.18
$\dot{m}_{ef,cond2}$ (kg s^{-1})	–	0.926	–
$\dot{m}_{ef,t}$ (kg s^{-1})	6.315	6.156	(−) 2.52

Results of exergy analysis

The findings of an exergy study performed on the equivalent VCR system and the DMS-VCR system are shown in

Table 4. The study under "Results of energy analysis" section indicates that DMS-VCR system experiences a decrease in compressor work, cooling load of condenser, and mass flow rate of refrigerants, resulting in a 15.71% reduction in the rate of total irreversibility in the DMS-VCR system. Furthermore, the DMS-VCR system's exergetic efficiency increases by 10.38%, which shows the effectiveness of using DMS system for subcooling in VCR system.

Results of economic and environment analysis

Table 5 depicts the comparison of results of economic and environmental analysis for DMS-VCR system and equivalent VCR system operating under the same input conditions.

The DMS-VCR system consumes less electricity since the compressor power required in DMS-VCR system is reduced thereby resulting in cost savings in terms of operational costs. However, it is important to note that DMS-VCR system require a higher initial capital investment due to more number of heat exchangers (resulting in larger heat exchanger area), an additional compressor and expansion valve. Specifically, DMS-VCR system entails a 6.07% increase in the overall heat exchanger area, leading to a corresponding rise in the initial investment cost. However, the DMS-VCR system is more economical since it offers a reduction of 6.72% in total annual cost and 10.44% decrease in annual operational costs when compared with an equivalent VCR system. Moreover, when assessing various performance metrics in comparison to an equivalent VCR system, the DMS-VCR system demonstrates superior performance, as shown in Table 5. The key environmental metric, which is the emission of CO_2 into the atmosphere, demonstrates that the DMS-VCR system emits 10.43% less CO_2 compared to an equivalent VCR system, even though both systems have the same cooling capacity. This reduction is attributed to the DMS-VCR system's lower electricity consumption. As a result, the DMS-VCR system undoubtedly stands out as a highly reliable and energy-efficient cooling system, offering substantial decarbonization benefits.

Table 4 Exergy analysis results for the refrigerants R134a

Performance parameters	R134a		Percentage change /% [(*Y*−*X*)/*X**100]
	VCR system (*X*)	DMS-VCR system (*Y*)	
η_{II} (%)	36.10	39.85	(+) 10.38
$\dot{I}_t$ (kW)	20.43	17.22	(−) 15.71
$\dot{I}_{cond,1}$ (kW)	3.43	2.84	(−) 17.20
$\dot{I}_{cond,2}$ (kW)	–	0.46	–
$\dot{I}_{cond,t}$ (kW)	3.43	3.30	(−) 3.79
$\dot{I}_{evap}$ (kW)	2.85	2.85	–
$\dot{I}_{comp,1}$ kW)	9.69	8.02	(−) 17.23
$\dot{I}_{comp,2}$ (kW)	–	0.48	–
$\dot{I}_{comp,t}$ (kW)	9.69	8.50	(−) 12.28
$\dot{I}_{sc}$ (kW)	–	0.82	–
$\dot{I}_{ev,1}$ (kW)	4.46	1.53	(−) 65.70
$\dot{I}_{ev,2}$ (kW)	–	0.22	–
$\dot{I}_{ev,t}$ (kW)	4.46	1.75	(−) 60.76

Table 5 Comparative analysis results of DMS-VCR system with equivalent VCR system for case-I

Parameters	VCR system (*X*)	DMS-VCR system (*Y*)	Percentage change /% [(*Y*−*X*)/*X**100]
$\dot{C}_t$ (\$ year^{-1})	12,444	11,608	(−)6.72
$\dot{C}_{oper}$ (\$ year^{-1})	7672	6871	(−)10.44
$\dot{m}_{co_2}$ (ton year^{-1})	123.78	110.86	(−)10.43
$A_{cond,1}$ (m^2)	7.73	6.40	(−)17.21
$A_{cond,2}$ (m^2)	–	1.13	–
$A_{cond,t}$ (m^2)	7.73	7.53	(−) 2.58
A_{sc} (m^2)	–	0.98	–
A_{evap} (m^2)	5.12	5.12	–
A_t (m^2)	12.85	13.63	(+)6.07

Parametric analysis of DMS-VCR system

In order to make the DMS-VCR system more feasible, it is important to control the cost and size of the system. This can be achieved by choosing appropriate operating parameters such as evaporator and condenser temperatures, degree of subcooling, and degree of overlap, which can lead to improvements in the system's energy, exergy, economics, and environmental analysis. In this section, a parametric study is carried out to examine the effect of these factors.

Effect of evaporator temperature (T_{evap})

Figure 6 depicts how changes in evaporator temperature impact COP and the overall irreversibility rate. As the evaporator temperature increases from −4 to 4 °C, the refrigerant's specific volume decreases, leading to a 26.03% reduction in compressor power. Moreover, as evaporator temperature increases by 8 °C the system COP improves from 3.0 to 4.1 leading to an increase of 36.67%. This rise in evaporator temperature results in a reduction of heat load on condenser-1 and condenser-2 by 7.12% and 2.85%, respectively, which in turn, decrease the mass flow rate of the external fluid.

As the evaporator temperature increases, the rate of irreversibility in the evaporator section decreases significantly, dropping from 4.5 kW to 1.3 kW. This reduction

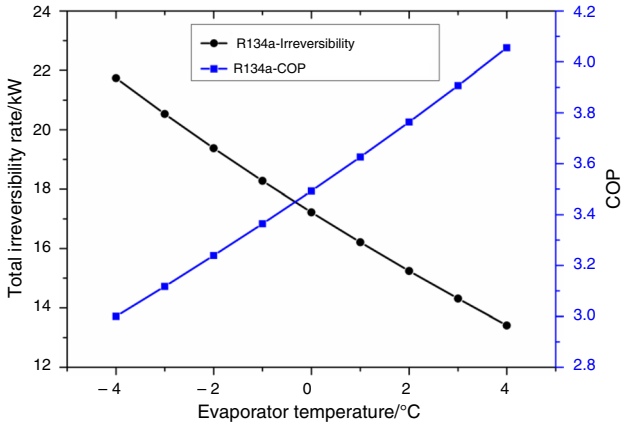


Fig. 6 Effect of evaporator temperature on total irreversibility rate and COP of the system

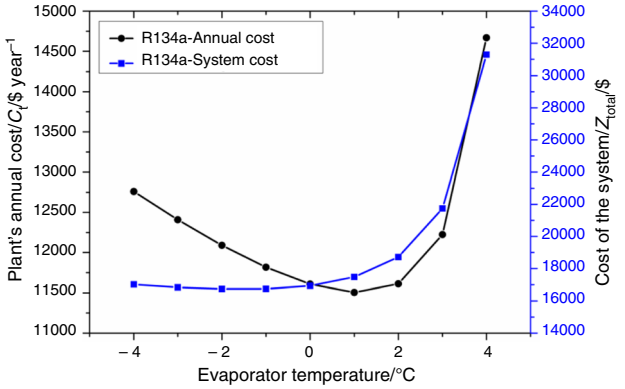


Fig. 7 Effect of evaporator temperature on plant's annual cost and cost of the DMS-VCR system

occurs due to a decrease in the average temperature gradient between the chilled water and the evaporator section. Additionally, the irreversibility rate of the remaining components within the system also decreases, leading to an overall reduction of 38.32% in the irreversibility rate. Consequently, the exergetic efficiency experiences a 31.17% improvement. Hence, a higher evaporator temperature is deemed preferable from both energy and exergy perspectives.

Figure 7 depicts the relationship between the system's evaporator temperature and various expenses connected with system operation, such as the annual cost of the plant (C_t) and overall cost of the system (Z_{total}). The system's overall area rises from 11.28 to 43.70 m^2 with an increase in evaporator temperature of 8 °C owing to a decrease in the overall system's heat transfer coefficient and LMTD.

This causes the system's Z_{total} to increase by 83.82%. However, at an evaporator temperature of 1 °C, the annual plant operation cost (C_t) is found to be at its minimum and begins to increase afterward.

On the other hand, the increase in the evaporator temperature results in a reduction in the system's operational costs (C_{oper}) and environmental damage costs (C_{env}) by about 26%. Since these costs contribute less to the overall plant cost than the initial capital investment, a higher evaporator temperature is financially favorable position from economic view point. A reduced irreversibility rate in a heat exchanger design does not always translate to an optimal outcome, as it leads to an increase in the annual operation cost of the system. Therefore, a refrigeration system with a higher evaporator temperature may not be the best choice.

Effect of condenser temperature (T_{cond})

In Fig. 8, we can see that altering the condenser temperature has a significant effect on both total irreversibility rates and the COP of the system. When we increase the condenser temperature while keeping other conditions constant, the work done by the compressor goes up by 34.7%. This, in turn, leads to a 60.55% increase in total irreversibility rates and a 25.81% decrease in the COP of the system. Additionally, the system's exergetic efficiency drops from 44.97 to 34.42%. As a result of this increased compressor work, the system releases 42 tons of extra CO_2 into the environment when the system is assumed to operate for 5000 h per year. Therefore, from the perspectives of energy, exergy, and environmental analysis, it is more advantageous to maintain a lower temperature in the condenser.

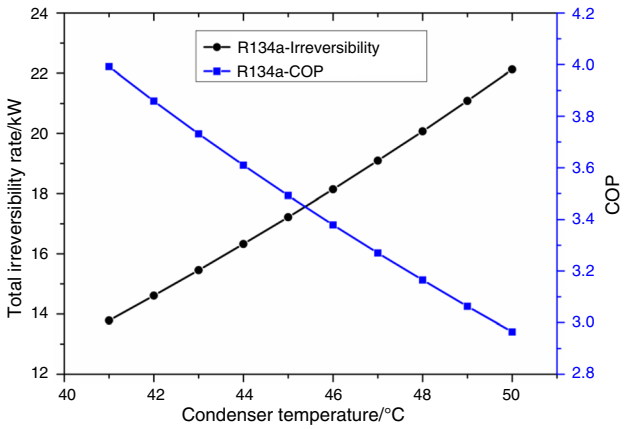


Fig. 8 Effect of condenser temperature on total irreversibility rate and COP of the system

Figure 9 shows how the condenser temperature affect the annual plant costs (C_t) and overall cost of the system (Z_{total}). When the condenser temperature increases, the LMTD is increased from around 3–12 °C, which results in decrease of the condenser area. Consequently, the total system area and overall cost of the system decrease by 63.72% and 29.74%, respectively. The plant attains its most economical operational cost at a temperature of 44 °C, but costs start to increase beyond this optimal point, resulting in an approximately 11.37% increase in annual cost.

The system's economic study supports the use of a low condenser temperature, since it results in lower operating costs (C_{oper}) and environmental damage costs (C_{env}). However, the costs associated with environmental damage and system operation increases as the condenser temperature is increased. This leads to around 35% increase in expense of environmental damage and the system operational cost. Therefore, low condenser temperature value is preferable from economic point of view.

Effect of degree of overlap

The difference in temperature between the fluid exiting the VCR cycle (state 4) after subcooling and the fluid exiting the DMS system (state 9) from the subcooler is referred to as the degree of overlap. Increasing the degree of overlap from 1 to 10 °C (with an effectiveness variation from 95 to 65%) results in a 5.8% increase in heat load over the DMS cycle condenser (condenser-2) while keeping other design factors constant. Figure 10 shows how the degree of overlap affects the system's COP and total irreversibility rate. The performance of compressor of VCR system remains unchanged, while the overall compressor work increases from 28.19 to 29.24 kW as the DMS cycle compressor work increases by nearly 62%. This leads to a 6% increase in total irreversibility and the system's overall COP decreases from 3.547 to 3.420. Hence, considering energy and exergy, it is recommended to have modest degree of overlap values.

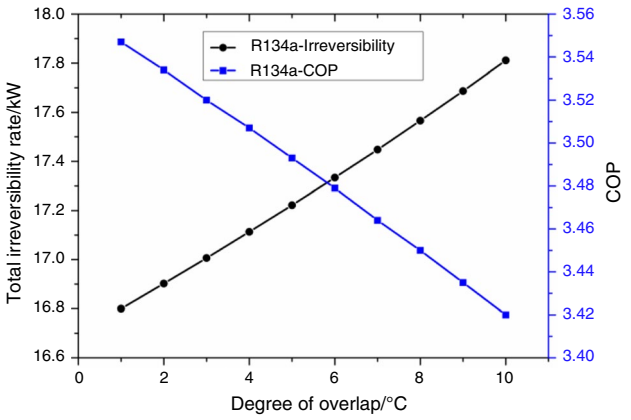


Fig. 10 Effect of overlap degree on total irreversibility rate and COP of the system

The relationship between the degree of overlap and various costs associated with system operation, such as the overall annual cost of the plant (C_t) and overall cost of the system (Z_{total}) is illustrated in the Fig. 11. The area of the subcooler cycle condenser (condenser-2) increases by 5.6%, but the subcooler area decreases rapidly by 95% with a change in the degree of overlap. Consequently, there is a reduction of 41.21% in the system's overall area which results in a decrease in overall cost of the system (Z_{total}) by 20.68%. As depicted in Fig. 11, the optimal point for the objective function concerning the annual cost of the system (C_t) occurs when degree of overlap is 5 °C. However, both the system's

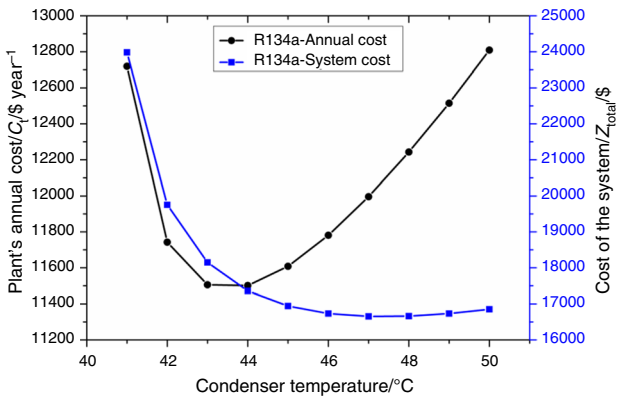


Fig. 9 Effect of condenser temperature on plant's annual cost and cost of the DMS-VCR system

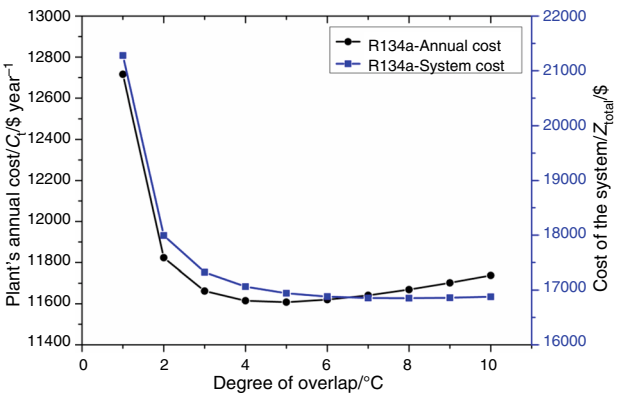


Fig. 11 Effect of overlap degree on plant's annual cost and cost of the DMS-VCR system

operating costs (C_{oper}) and environmental damage costs (C_{env}) increase with variations in the degree of overlap by 3.75%. Therefore, from both an economic and environmental perspective, a lower degree of overlap is recommended.

Effect of degree of subcooling (DOS)

As depicted above in Fig. 5, varying the degree of subcooling affects both the COP and the total irreversibility rate of the system. When we increase the degree of subcooling from 1 °C to 25 °C, it reduces the specific cooling effect, leading to a decrease in the refrigerant's mass flow rate. Consequently, the compressor work is reduced by 9.07%, resulting in a lower heat load on condenser-1 but an increased load on condenser-2. As the degree of subcooling increases, the system's COP rises from 3.161 to 3.477. On the other hand, Fig. 12 shows the changes in the DOS affect the system's annual costs (C_t) and overall cost of the system (Z_{total}).

It is observed that there's an 8.06% increase in the total system area due to a decrease in the overall heat transfer coefficient of the DMS system which increases the cost of heat exchangers; however, there is a reduction in mass flow rate of refrigerant in compressor bringing a huge reduction in compressor cost of VCR system, which acts as a dominating factor in reducing the overall capital cost. Consequently, Z_{total} decreases by 3.33% at degree of subcooling value of 16 °C, after which it increases, as the heat exchanger area cost dominates the reduction in compressor cost.

At 19 °C, the system's annual cost (C_t) reaches its lowest point and begins to increase beyond that point. A reduced compressor workload leads to a 10% decrease in system operating costs (C_{oper}) and environmental damage costs (C_{env}). Beyond this limit, both operating costs and environmental damage costs increase and therefore, values up to this range of the degree of subcooling are encouraged from an economic and environmental perspective.

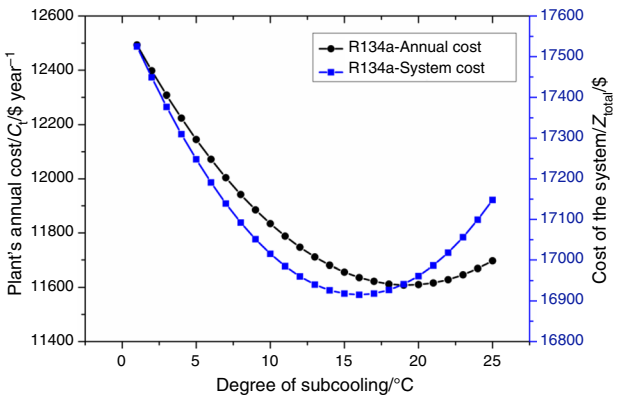


Fig. 12 Effect of degree of subcooling on plant's annual cost and cost of the DMS-VCR system

Thermoeconomic optimization

In this para, two distinct cases are investigated, each characterized by different ROI values, i.e., 10% for case-I and 2% for case-II. The results associated with these cases, including performance indicators, are presented in Table 6. ROI serves as a critical parameter influenced by a nation's economic context, with different countries offering varying ROI rates, typically ranging from 10 (the highest) to 2% (the lowest). Many nations adopt strategies such as subsidies and lower ROI values to promote system acceptance and, in turn, reduce the payback period. It is important to note that these factors undergo changes over time, reflecting evolving economic conditions and policies.

Selecting an optimal point is more important for the system to operate more efficiently both economically and thermodynamically. Finally, by simultaneously modifying the choice variables, the conjugate directions technique is employed to determine the objective functions' ideal value. To perform an economic analysis, a basic compression refrigeration cycle with a 5 °C subcooling is chosen as the base case. For case-I and case-II, Table 6 outlines the optimal values for the decision variables, including T_{evap}, T_{cond}, $T_{subcooling}$, and $T_{overlap}$.

It underlines that, relative to the base case (i.e., $T_{evap} = 0$ °C, $T_{cond} = 45$ °C, $T_{subcooling} = 5$ °C, and $T_{overlap} = 5$ °C), size (area) increases in cases-I and II, yet annual cost greatly lowers in both situations. Consequently, in the optimal scenario, the DMS-VCR system's yearly expenses experience a significant decrease of 6.22% and 20.06% for the two situations with the specified design condition (see Table 6). Compared to the base case (13.05 m^2), the heat exchanger area is increased in case-I (17.62 m^2) and case-II (26.23 m^2). Cases-I and II both show a sizable improvement in the system's total COP. Thus, the total cost of electricity in compressors is reduced by 14.22% in case-I and 22.22% in case-II to generate the same cooling effect. The results indicate that for case-II, there is a lower overall electricity consumption but a higher equipment cost. In case-II, the DMS-VCR system's payback period is less than 5.1 years compared to equivalent VCR system ($20,965 – $17,067 = $3898) due to increased investment costs. It is worth noting that this would result in a payback period for excess expenses that is less than half the system's lifespan.

Table 6 Results of thermoeconomic optimization w.r.t. base case (for Refrigerant R134a)

Performance parameter		Base case	Thermoeconomic optimized	
			Case-I: $i_{rate}=10\%$, $N_y=5$ years and $t_{oper}=4000$ h	Case-II: $i_{rate}=2\%$, $N_y=10$ years and $t_{oper}=5000$ h
Low grade energy	$\dot{Q}_{cond1}$ (kW)	124.95	108.28	106.58
	$\dot{Q}_{cond2}$ (kW)	5.55	17.87	17.14
	$\dot{Q}_{sc}$ (kW)	5.32	16.00	15.48
	$\dot{Q}_{evap}$ (kW)	100	100	100
High-grade energy	$\dot{W}_{comp1}$ (kW)	30.26	24.28	22.07
	$\dot{W}_{comp2}$ (kW)	0.240	1.87	1.65
	$\dot{W}_t$ (kW)	30.50	26.16	23.72
First law analysis	COP_{VCR}	3.30	4.11	4.531
	COP_{DMS}	22.14	8.54	9.37
	$COP_{overall}$	3.278	3.82	4.21
Second law analysis	$\dot{I}_{cond1}$ (kW)	3.24	2.28	1.76
	$\dot{I}_{cond2}$ (kW)	0.129	0.34	0.25
	$\dot{I}_{evap}$ (kW)	2.85	2.41	1.95
	$\dot{I}_{comp1}$ kW)	9.173	7.11	6.24
	$\dot{I}_{comp2}$ (kW)	0.047	0.41	0.36
	$\dot{I}_{sc}$ (kW)	0.121	0.72	0.62
	$\dot{I}_{ev1}$ (kW)	3.44	1.37	1.15
	$\dot{I}_{ev2}$ (kW)	0.015	0.18	0.15
	$\dot{I}_t$ (kW)	19.02	14.85	12.50
	η_{II} (%)	37.64	43.23	47.27
Other parameters	$\dot{m}_{ref1}$ (kg s^{-1})	0.7032	0.6108	0.6023
	$\dot{m}_{ref2}$ (kg s^{-1})	0.0346	0.1078	0.1028
	A_t (m^2)	13.05	17.62	26.23
	Z_t ($)	17,248	18,271	20,965
	C_t ($ $year^{-1}$)	12,145	11,389	9708
Optimized value of operating parameters	Evaporator temperature		Te = 1.084	Te = 2.261
	Condenser temperature		Tc_1 = 43.52	Tc_1 = 42.13
	Degree of overlap		DOO = 4.791	DOO = 3.376
	Degree of subcooling		DOS = 17.87	DOS = 17.61

Conclusions

In this work, the emphasis is laid on energy exergy, environment, and economic analysis of DMS-VCR system and its comparison with VCR system for 100 kW water chiller applications. The following conclusions can be drawn from the present study:

(1) The optimum value of degree of subcooling for DMS-VCR system is 19 °C. The energy analysis shows that the COP of DMS-VCR system is 11.67% higher than that of equivalent VCR system. Moreover, the power consumption of compressors is also reduced by 10.45%, which indicates huge cost savings in terms of electricity consumption cost and simultaneously there is reduction in CO_2 production which also means lower carbon capture cost. Annual CO_2 emissions decrease from 124 to 110 tons $year^{-1}$ with the adoption of the DMS-VCR system. The DMS-VCR system contributes to an 11.30% reduction in the cost of environmental damage. The exergy analysis shows reduction in total irreversibility of the system by 15.71% and an increase of 10.38% in exergetic efficiency of DMS-VCR system in comparison to VCR system.

(2) Environment and economic analysis shows that the area required for heat exchangers in DMS-VCR system is 6.07% more than that required for VCR system. However, this increase in area translates into three positive outcomes, i.e., reduction in total cost by 6.72%, reduc-

tion in operation cost by 10.44%, and 10.43% reduction in mass of CO_2 produced.

The DMS-VCR system emerges as a promising solution, offering substantial energy and environmental benefits in comparison to VCR system.

(3) The parametric analysis shows that with increase in evaporator temperature COP increases, whereas irreversibility decreases and the increase in condenser temperature gives opposite results for COP and irreversibility in comparison to evaporator temperature increase. The evaporator temperature at 1 °C and the condenser temperature at 44 °C optimize the DMS-VCR system's energy, exergy, while maintaining favorable economic and environmental viability.

(4) The parametric analysis further shows that the degree of overlap and degree of subcooling significantly influence the performance and cost of the DMS-VCR system. Increasing the DOO leads to a decrease in the system's COP and an increase in total irreversibility whereas opposite trends are observed with variation of DOS. A modest degree of overlap, around 5 °C and for the degree of subcooling, a value of 19 °C are crucial to achieve optimal performance and cost-effectiveness while minimizing environmental impact.

(5) The overall annual cost of operating the DMS-VCR system is 6.72% more cost-effective compared to an equivalent VCR system, with potential for further cost reductions by 1.88% in case-I and a substantial 16.36% in case-II.

In summary, this research highlights the significance of considering thermodynamic, economic, and environmental aspects when designing efficient and cost-effective cooling systems. It is worth noting that while striving for a high evaporator temperature or low condenser temperature can reduce irreversibility; however, it may lead to higher overall system costs. Similarly, raising the subcooler's (evaporator of DMS system) temperature can improve the COP but may not align with economic and environment considerations. In order to have a feasible and optimum system, it is important to combine thermal, economic, and environmental aspects. This can be achieved through meticulous parametric optimization, i.e., the system can be made economically viable, environmentally sustainable and energy efficient.

References

1. Agarwal S, Arora A, Arora BB. Exergy analysis of dedicated mechanically subcooled vapour compression refrigeration cycle using HFC-R134a, HFO-R1234ze and R1234yf. Lect Notes Civ Eng. 2020. https://doi.org/10.1007/978-981-13-7557-6_3.
2. Catalán-Gil J, Llopis R, Sánchez D, Nebot-Andrés L, Cabello R. Energy analysis of dedicated and integrated mechanical subcooled CO_2 boosters for supermarket applications. Int J Refrig. 2019;101:11–23.
3. Pottker G, Hrnjak P. Effect of the condenser subcooling on the performance of vapor compression systems. Int J Refrig. 2015;50:156–64. https://doi.org/10.1016/j.ijrefrig.2014.11.003.
4. Pottker G, Hrnjak P. Experimental investigation of the effect of condenser subcooling in R134a and R1234yf air-conditioning systems with and without internal heat exchanger. Int J Refrig. 2015;50:104–13. https://doi.org/10.1016/j.ijrefrig.2014.10.023.
5. Qureshi BA, Zubair SM. Mechanical sub-cooling vapor compression systems: Current status and future directions. Int J Refrig. 2013;36:2097–110. https://doi.org/10.1016/j.ijrefrig.2013.07.026.
6. Qureshi BA, Zubair SM. The effect of refrigerant combinations on performance of a vapor compression refrigeration system with dedicated mechanical sub-cooling. Int J Refrig. 2012;35:47–57. https://doi.org/10.1016/j.ijrefrig.2011.09.009.
7. Wang GB, Zhang XR. Thermoeconomic optimization and comparison of the simple single-stage transcritical carbon dioxide vapor compression cycle with different subcooling methods for district heating and cooling. Energy Convers Manag. 2019;185:740–57. https://doi.org/10.1016/j.enconman.2019.02.024.
8. Jain V, Sachdeva G, Kachhwaha SS, Patel B. Thermo-economic and environmental analyses based multi-objective optimization of vapor compression–absorption cascaded refrigeration system using NSGA-II technique. Energy Convers Manag. 2016;113:230–42. https://doi.org/10.1016/j.enconman.2016.01.056.
9. Jain V, Sachdeva G, Kachhwaha SS. Energy, exergy, economic and environmental (4E) analyses based comparative performance study and optimization of vapor compression–absorption integrated refrigeration system. Energy. 2015;91:816–32. https://doi.org/10.1016/j.energy.2015.08.041.
10. Nag PK. Basic and applied thermodynamics by PK Nag: Thermodynamics by PK Nag [Internet]. 2002. bl 781. Opgehaal van: https://books.google.co.uk/books?id=Rq7uBQAAQBAJ&printsec=frontcover&dq=Engineering+thermodynamics+/+P.K.+Nag.+citation&hl=en&sa=X&ved=0ahUKEwiHstjGiKrJAhUIMhoKHYQKCmMQ6wEIJjAB#v=onepage&q&f=false
11. Arora A, Kaushik SC. Theoretical analysis of a vapour compression refrigeration system with R502, R404A and R507A. Int J Refrig. 2008;31:998–1005.
12. Bakhtiari B, Fradette L, Legros R, Paris J. A model for analysis and design of H_2O–LiBr absorption heat pumps. Energy Convers Manag. 2011;52:1439–48. https://doi.org/10.1016/j.enconman.2010.09.037.
13. Rubio-Maya C, Pacheco-Ibarra JJ, Belman-Flores JM, Galván-González SR, Mendoza-Covarrubias C. NLP model of a LiBr–H_2O absorption refrigeration system for the minimization of the annual operating cost. Appl Therm Eng. 2012;37:10–8. https://doi.org/10.1016/j.applthermaleng.2011.12.035.
14. Sanaye S, Malekmohammadi HR. Thermal and economical optimization of air conditioning units with vapor compression refrigeration system. Appl Therm Eng. 2004;24:1807–25.
15. Kizilkan Ö, Şencan A, Kalogirou SA. Thermoeconomic optimization of a LiBr absorption refrigeration system. Chem Eng Process Process Intensif. 2007;46:1376–84.
16. Aminyavari M, Najafi B, Shirazi A, Rinaldi F. Exergetic, economic and environmental (3E) analyses, and multi-objective optimization of a CO_2/NH_3 cascade refrigeration system. Appl Therm Eng. 2014;65:42–50.
17. Carlsson B, Meir M, Rekstad J, Preiß D, Ramschak T. Replacing traditional materials with polymeric materials in solar thermosiphon systems—case study on pros and cons based on a total cost accounting approach. Sol Energy. 2016;125:294–306. https://doi.org/10.1016/j.solener.2015.12.005.

18. Agarwal S. Thermodynamic performance analysis of dedicated mechanically subcooled vapour compression refrigeration system. J Therm Eng. 2019;5:222–33.

Publisher's Note Springer Nature remains neutral with regard to jurisdictional claims in published maps and institutional affiliations.

Springer Nature or its licensor (e.g. a society or other partner) holds exclusive rights to this article under a publishing agreement with the author(s) or other rightsholder(s); author self-archiving of the accepted manuscript version of this article is solely governed by the terms of such publishing agreement and applicable law.

KSME

Springer

Journal of Mechanical Science and Technology 38 (1) 2024

Original Article
DOI 10.1007/s12206-023-1236-5

Keywords:
· Energy
· Exergy
· Exergetic efficiency
· Coefficient of structural bond
· Dedicated mechanical subcooling

Correspondence to:
Naveen Solanki
naveensolanki@mait.ac.in

Citation:
Solanki, N., Arora, A., Singh, R. K. (2024). A comprehensive parametric and structural bond analysis of an actual vapor compression refrigeration system with dedicated mechanical subcooled system. Journal of Mechanical Science and Technology 38 (1) (2024) 439~452. http://doi.org/10.1007/s12206-023-1236-5

Received March 12th, 2023
Revised September 27th, 2023
Accepted October 5th, 2023

† Recommended by Editor Tong Seop Kim

© The Korean Society of Mechanical Engineers and Springer-Verlag GmbH Germany, part of Springer Nature 2024

A comprehensive parametric and structural bond analysis of an actual vapor compression refrigeration system with dedicated mechanical subcooled system

Naveen Solanki[1], Akhilesh Arora[2] and Raj Kumar Singh[3]

[1]Department of Mechanical Engineering, Maharaja Agrasen Institute of Technology, PSP Area Sector-22, Rohini Delhi-110086, India, [2]Department of Mechanical Engineering, Delhi Technological University, Shahbad Daulatpur, Bawana Road, Delhi-110042, India, [3]Department of Mechanical Engineering, Delhi Technological University, Shahbad Daulatpur, Bawana Road, Delhi-110042, India

Abstract This study compares the performance of dedicated mechanical subcooled vapor compression refrigeration (DMS-VCR) system and actual vapor compression refrigeration (VCR) system of same capacity (100 kW), and evaluates them on the basis of energy, exergy, and coefficient of structural bond (CSB) configuration. Results indicate that DMS-VCR system outperforms VCR system at constant condenser temperature (T_{cond} = 40° C) with varying evaporator temperatures (T_{evap} = 0 °C, 5 °C and 10 °C).The most significant results occurs at 0 °C, resulting in a coefficient of performance (COP) 4.60 % higher than actual VCR system's COP and exergetic efficiency 4.38 % higher than actual VCR system's exergetic efficiency, making it a more favourable choice for water chilling applications. Additionally, the study investigates the potential of the CSB method in improving system efficiency by reducing irreversibility rate in a specific component. It finds that improving the efficiency of a component can significantly decrease the total irreversibility rate of the system. The CSB value of condenser-1 and evaporator are observerd to be highest (i.e. 1.96 and 2.27) and hence the performance of DMS-VCR system can be greatly improved by changing the efficiency parameter of evaporator and condenser-1 of the DMS-VCR system.

1. Introduction

The vapor compression refrigeration (VCR) system is widely used technology for heating and cooling purposes in residential, commercial and industrial applications. However, due to the high energy consumption of these systems and rising costs of energy, energy efficiency and its conservation have become a growing concern. The researchers are therefore exploring methods to enhance the performance of these systems so as to address the above issues.

One of the methods to enhance the performance of a VCR system is to subcool the liquid refrigerant leaving the condenser. This can be achieved by incorporating a dedicated mechanical subcooled (DMS) system (which is basically a VCR system only) used in conjunction with the existing VCR system. The sole purpose of DMS system is to subcool the liquid refrigerant leaving the condenser-1 of the VCR system used for cooling or heating application. A number of studies have been conducted on the topic of mechanical and dedicated subcooling of VCR systems as discussed in following paras.

Qureshi and Zubair [1, 2] investigated the mechanical subcooling of VCR systems and explored the most efficient methods of operation and management. They analysed the system at 0 °C of evaporator temperature and 45 °C of condenser temperature. Qureshi et al. [3] conducted experiments to demonstrate the effectiveness of the dedicated subcooling cycle con-

cept and investigated how the efficacy of the DMS-VCR system is affected by considering different combinations of various refrigerants. They also reported that subcooling R22 refrigerant by 5 °C-8 °C in the VCR cycle led to a 0.5 kW increase in the load-bearing capacity of the evaporator. According to Agaro et. al. [4], DMS-VCR system is the most thoroughly studied system and is effectively used to improve the efficiency of the transcritical VCR system. Yang and Yeh [5] examined VCR system that uses various refrigerants (R22, R134a, R410A and R717) to identify ways to enhance their performance and minimize exergy destruction. Wang and Zhang [6] optimised and compared a single-stage transcritical CO_2 VCR cycle with different subcooling methods for district heating and cooling and investigated it on the basis of energy, exergy and economic view point. Agarwal et al. [7] examined the mechanical subcooled VCR system's energy and exergy aspects in order to improve its efficiency. However, they did not take into account the coefficient of structural bonds (CSB) factors, which are crucial in making accurate decisions regarding energy resource utilization. Boer et al. [8] conducted an energy, exergy, and structural analysis of a single effect vapor absorption cooling cycle that utilized ammonia and water. Through exergy analysis, they were able to assess the level of irreversibility within each component of the cycle as well as the overall system. The CSB analysis is also performed to access the impact that how any change in irreversibility within one component of the system would affect the rest of the components and the system as a whole. To assess the actual thermodynamic efficiency of chemical processes and the distribution of irreversibility in a plant, Tekin and Bayramoglu [9] carried out an exergy and CSB analysis. They reported the decrease in total exergy loss is equal to 4.21 % in sugar manufacturing plants. Nikolaidis and Probert [10] analyzed a refrigeration plant that uses a two-stage VCR system and demonstrated that the exergy method is effective for studying its behavior. Misra et al. [11] analyzed an absorption chiller system that is used for air-conditioning purposes and used the CSB technique to assess the economic cost of the product. Their study revealed that the capital cost of the optimal system configuration increased by approximately 33.3 % compared to the base-case, but this additional cost is offset by the reduced fuel cost, making it a cost-effective option in the long run. Solanki et al. [12] theoretically examined the performance of simple vapor compression refrigeration system and DMS-VCR system by CSB analysis and advanced exergy analysis methodologies. Their results reveal that the DMS system can avoid 42.9 % of the overall irreversibility rate using advanced exergy analysis, but they have not considered actual VCR cycle while conducting the analysis. They showed better CSB results for condenser-1, but the current study uncovers a contrasting finding. These outcome differences highlight the unique and distinct research approaches in both studies.

It is thus observed that sustainable and efficient VCR systems should be developed in light of increasing energy costs and energy conservation. The DMS-VCR system is capable of enhancing the energetic and exergetic performance of the system as is evident from the investigations performed by various researchers. Studies have been carried out to evaluate efficacy of DMS-VCR systems. Further, the CSB approach has been observed as a useful tool for assessing the impact of change in irreversibility of a component on the other components and the system. It can thus help the designers to wisely make decisions for changing the design of the component which affects the performance of other components critically.

Previous studies have attempted to improve the performance of mechanical subcooled systems through energy and exergy analyses, but they have overlooked the importance of analyzing the CSB in a system. Most studies on DMS-VCR systems have focused on introductory energy and exergy analyses using typical refrigerants for low cooling capacity systems. In addition to this, the performance analysis studies of DMS-VCR system using specific refrigerants such as R134a for high cooling capacity are observed to be scant in literature. To operate a system efficiently and to reduce energy consumption, it is essential to conduct a CSB analysis so as to find appropriate thermodynamic parameters and improve the design of the component so as to reduce the irreversibility rate. However, the CSB studies of DMS-VCR system are also lacking in literature. In the present study the DMS system is incorporated in a commercial water chiller of 100 kW capacity (which is based on actual vapor compression cycle) and comprehensive energy, exergy and CSB analysis of the combined DMS-VCR system is carried out under different operating conditions. In contrast to Solanki et al. [12], the novelty of current work is that it takes a more practical approach, analyzing an actual DMS-VCR system, providing a comprehensive and applicable perspective of refrigeration systems. The system simulation is carried out for a wide range of various operating parameters using the code developed for the DMS-VCR system using engineering equation solver software (EES) [13]. This research endeavor aims to establish a novel model that stands apart from Solanki et al. [12]. It achieves this by incorporating pivotal factors critical for system analysis, including subcooling within the condenser and dedicated subcooler, evaluation of pressure drops within the evaporator, suction line, condenser and liquid line, examination of superheating within the evaporator and suction line, and a thorough assessment of desuperheating within the discharge line. It's important to note that the effect of these crucial parameters was not analysed in the previous work of Solanki et al. [12]. This unique approach aims to determine the optimal subcooling degree for maximizing coefficient of performance (COP) and exergetic efficiency. The model also investigates the impact of subcooling on the overall irreversibility rate, providing a comprehensive understanding of its impact on system performance. The inclusion of varying evaporator temperatures (0 °C, 5 °C, and 10 °C) in our study significantly enhances its value. By exploring different evaporator temperature scenarios, our research provides a valuable and comprehensive perspective, allowing us to gain deeper insights into the system's

behavior under diverse thermal conditions. This research contributes significant insights into enhancing system performance, making it an essential advancement in the practical field.

2. System description and modeling of DMS-VCR system

2.1 Description of the dedicated subcooled refrigeration system

Fig. 1 shows the schematic diagram of the DMS-VCR system which comprises of two compressors, two condensers, two expansion valves, one evaporator and one sub-cooler. The VCR sub system, of DMS-VCR system, is used for cooling or heating for which DMS sub system is used to subcool the liquid refrigerant leaving the condenser-1 of VCR sub system. The heat exchange between the two sub systems occurs by using the evaporator of DMS sub system as a subcooler heat exchanger in which the liquid refrigerant leaving the condenser-1 of VCR sub system loses heat and the same is utilized to evaporate the refrigerant entering in the evaporator (used as sub-cooler) of VCR sub system.

Fig. 2 displays the pressure-enthalpy (P-h) diagram for DMS-VCR cycle. The P-h diagram is drawn considering that the refrigerant in both cycles is same. Hence the condenser pressure and temperature will be same in both VCR sub system and DMS sub system. However, the evaporator temperature of VCR cycle is lower than that of DMS cycle.

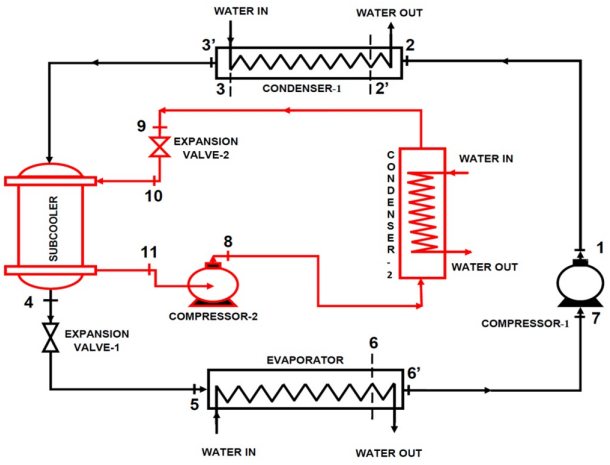


Fig. 1. Schematic diagram of DMS-VCR system.

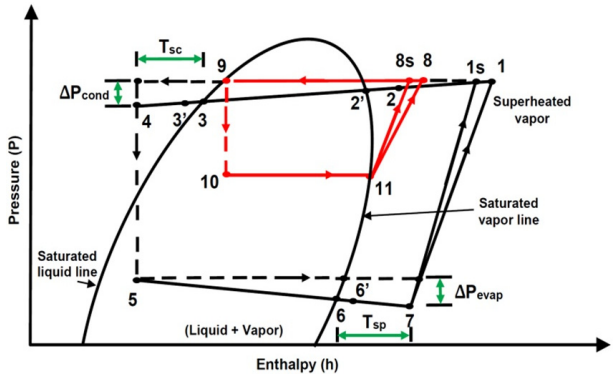


Fig. 2. Pressure - enthalpy diagram of DMS-VCR cycle.

The DMS cycle is shown by state points 8-9-10-11-8 and VCR cycle is depicted by state points 1-2-2'-3-3'-4-5-6-6'-7-1. In VCR cycle, a high-temperature, high-pressure superheated refrigerant vapor at state 1 leaves the compressor and loses heat to surroundings in the desuperheating process 1-2 in the discharge line. Further, desuperheating of the superheated refrigerant occurs in the condenser-1 during the process 2-2' followed by conversion of saturated refrigerant vapour into saturated liquid refrigerant during the process 2'-3 in the condenser due to heat transfer to the surroundings. The process 3-3' shows the subcooling of the refrigerant in the condenser and remaining subcooling takes place in the dedicated subcooler in the process 3'-4. The subcooler section is essentially evaporator of the DMS sub system which operates at a temperature below the condenser outlet temperature (T3'). The corresponding process in the evaporator of DMS sub system is process 10-11 during which the refrigerant in DMS evaporator becomes saturated vapor at state point 11. The refrigerant which leaves the subcooler at state point 4 is expanded to state 5 in the expansion valve-1 to evaporator pressure and temperature of the VCR sub system. The desired cooling goal of the DMS-VCR system is achieved by absorbing heat from the space that needs to be chilled during the process 5-6' in the evaporator. The refrigerant at state point 6 (within the evaporator) is saturated and at state point 6' the refrigerant leaves the evaporator in superheated state. Further superheating takes place in the suction line till state point 7 is achieved just before entry to compressor. The superheated refrigerant is then compressed in the compressor-1 (process 7-1). The VCR sub system cycle includes both subcooling in condenser-1, subcooler, superheating in evaporator and suction line and desuperheating in discharge line. Simultaneously pressure drops in condenser and evaporator are also considered as depicted in Fig. 2 i.e. P-h diagram representing various processes of both the cycles taking place in VCR sub system and DMS sub system of DMS-VCR system. Thus the present work is focused on the analysis of an actual VCR sub system subcooled by DMS sub system. The DMS sub system cycle is assumed to be ideal except compression process which is not assumed reversible adiabatic. Thus the considered DMS-VCR system reasonably follows a real system.

3. Mathematical modeling of system

The current system model in the EES software is created while taking into consideration the thermophysical properties of the refrigerant R134a. Table 1 shows the governing equations for the DMS-VCR system's parts.

The following assumptions apply to the system's thermodynamic modeling:

Table 1. Governing equations for various components of the DMS-VCR system.

S. No.	Component	Energy analysis equations	Exergy analysis equations
1	Evaporator	$\dot{Q}_{evap} = (\in C)_{evap}\left(T_{in,evap} - T_{evap}\right)$ $= \left(\dot{m}_{ef} c_p\right)_{evap}\left(T_{in,evap} - T_{out,evap}\right) = \dot{m}_1\left(h_{6'} - h_5\right)$ $T_{evap} = T_5$ $\dot{Q}_{gain,s1} = \dot{m}_1\left(h_7 - h_{6'}\right)$	$\dot{I}_{evap} = T_0(\dot{m}_1(S_{6'} - S_5) + \left(\dot{m}_{ef} \cdot c_p\right)_{evap} \cdot$ $\ln((T_{out,evap} + 273)/(T_{in,evap} + 273)))$
2	Condenser-1	$\dot{Q}_{cond1} = (\in C)_{cond1}\left(T_{cond1} - T_{in,cond1}\right) = \dot{m}_1\left(h_2 - h_{3'}\right)$ $= \left(\dot{m}_{ef} c_p\right)_{cond1}\left(T_{out,cond1} - T_{in,cond1}\right)$ $T_{cond1} = T_3$ $\dot{Q}_{loss,dl} = \dot{m}_1\left(h_2 - h_1\right)$	$\dot{I}_{cond1} = T_0(\dot{m}_1(S_3 - S_2) + \left(\dot{m}_{ef} \cdot c_p\right)_{cond1} \cdot$ $\ln((T_{out,cond1}+273)/(T_{in,cond1}+273)))$
3	Condenser-2	$\dot{Q}_{cond2} = (\in C)_{cond2}\left(T_{cond2} - T_{in,cond2}\right) = \dot{m}_2\left(h_8 - h_9\right)$ $= \left(\dot{m}_{ef} c_p\right)_{cond2}\left(T_{out,cond2} - T_{in,cond2}\right)$ $T_{cond2} = T_9$	$\dot{I}_{cond2} = T_0(\dot{m}_2(S_9 - S_8) + \left(\dot{m}_{ef} \cdot c_p\right)_{cond2} \cdot$ $\ln((T_{out,cond2}+273)/(T_{in,cond2}+273)))$
4	Compressor-1 [15, 16]	$\dot{W}_{comp1} = \left(\dot{W}_{sc,isen}\right)/\eta_{isen1}$ $\dot{W}_{sc,isen} = \dot{m}_1\left(h_1 - h_7\right)$ $\eta_{isen1} = 0.85 - 0.046667 * \left(\frac{P_{cond1}}{P_{evap}}\right)$	$\dot{I}_{comp1} = T_0\left(\dot{m}_1\left(S_1 - S_7\right)\right)$
5	Compressor-2 [15, 16]	$\dot{W}_{comp2} = \left(\dot{W}_{sc,isen}\right)/\eta_{isen2}$ $\dot{W}_{sc,isen} = \dot{m}_2\left(h_8 - h_{11}\right)$ $\eta_{isen2} = 0.85 - 0.046667 * \left(\frac{P_{cond2}}{P_{sc}}\right)$	$\dot{I}_{comp2} = T_0\left(\dot{m}_2\left(S_8 - S_{11}\right)\right)$
6	Subcooler	$\dot{Q}_{SC} = \in_{sc} \cdot \dot{Q}_{SC,max}$ $\dot{m}_2\left(h_{11} - h_{10}\right) = \dot{m}_1\left(h_{3'} - h_4\right)$ $T_{11} = T_4 - \Delta T_{overlap}$	$\dot{I}_{sc} = T_0\left(\dot{m}_2\left(S_{11} - S_{10}\right) + \dot{m}_1\left(S_4 - S_{3'}\right)\right)$
7	Expansion valve-1	$h_4 = h_5$	$\dot{I}_{cv1} = T_0\left(\dot{m}_1\left(S_5 - S_4\right)\right)$
8	Expansion valve-2	$h_9 = h_{10}$	$\dot{I}_{cv2} = T_0\left(\dot{m}_2\left(S_{10} - S_9\right)\right)$

1) The components of the system are operating at a steady-state condition.
2) The subcooling is assumed to take place in condenser-1 and dedicated subcooler.
3) The superheating takes place in evaporator as well as in suction line.
4) The desuperheating takes place in discharge line.
5) The compression processes in compressors are assumed to be irreversible adiabatic.
6) Water is used as heat exchange fluid in evaporator and condensers.

The components of the DMS-VCR system are analysed by using principles of conservation of mass and energy, and entropy generation [14] and Table 1 displays the governing equations for the DMS-VCR System.

$$\Sigma\dot{m}_{in} - \Sigma\dot{m}_{out} = 0 \quad (1)$$

(Principle of conservation of mass)

$$\Sigma\dot{Q} - \Sigma\dot{W} = \Sigma\dot{m}_{out}h_{out} - \Sigma\dot{m}_{in}h_{in} \quad (2)$$

(Principle of conservation of energy)

$$\dot{S}_{gen} = \Sigma\dot{m}_{out}s_{out} - \Sigma\dot{m}_{in}s_{in} - \Sigma\frac{\dot{Q}}{T} \geq 0 \ . \quad (3)$$

(Principle of increase of entropy)

The following Eqs. (4) and (5) indicate the overall COP of actual VCR system and the DMS-VCR system:

$$COP_{VCR} = \frac{\dot{Q}_{evap}}{\dot{W}_{comp1}} \quad (4)$$

$$COP_{DMS-VCR} = \frac{\dot{Q}_{evap}}{\dot{W}_{comp1} + \dot{W}_{comp2}} \ . \quad (5)$$

A key point for evaluating the cooling impact and energy intake needed in a system is the coefficient of performance (COP). It does not, however, offer information regarding the efficiency of the energy conversion method or point out the elements that are responsible for irreversibility in a process occurring in a particular component and system. In order to assess the exergetic efficiency of the DMS-VCR system and identify the factors that lead to inefficiency, exergetic analysis is

crucial. Exergy analysis can be used to assess the system's exergetic efficiency and encourage energy saving to overcome above restriction. It also pinpoints system's component responsible for irreversibility. The equations are provided in Table 1 for calculating the irreversibility in various components of DMS-VCR system. It is calculated by using the Gouy-Stodola theorem as shown in the Eq. (6).

$$\dot{I} = T_0 \dot{S}_{gen} . \tag{6}$$

Where, T_o is the ambient temperature.

The exergetic efficiency (η_{ex}) of DMS-VCR system is given by [17]:

For DMS-VCR system

$$\dot{I}_t = \dot{I}_{evap} + \dot{I}_{cond1} + \dot{I}_{cond2} + \dot{I}_{comp1} + \dot{I}_{comp2} + \dot{I}_{sc} + \dot{I}_{ev1} + \dot{I}_{ev2} \tag{7}$$

$$\eta_{ex} = \left(\dot{Q}_{evap} \left| 1 - \frac{T_0}{T_e} \right| \right) / \dot{W}_t . \tag{8}$$

where, $\dot{W}_t = \dot{W}_{comp1} + \dot{W}_{comp2}$.

The CSB approach has now been used after determining the irreversibility rate of each system component [11, 18].

$$CSB_n = \left| \frac{\delta \dot{I}_t}{\delta z_i} \right| / \left| \frac{\delta \dot{I}_n}{\delta z_i} \right| \tag{9}$$

$$DMS, \forall \in EoS \cap \{evap, cond1, cond2, comp1, comp2, subcooler\}$$

$$\forall z_i \in \text{system parameter}$$

According to the CSB principle, lowering the irreversibility rate of one component gradually (by changing the system efficiency parameter Z_i) lowers the irreversibility rate of the entire system. Z_i (the system efficiency parameter) in this context may be associated with the system temperature (i.e., evaporator or condenser temperature) or the degree of subcooling or the degree of overlap or the isentropic efficiency of the compressor.

Following are the effects of various CSB values:

In case-1, when $CSB_n > 1$, the system input decreases faster than the irreversibility rate of the n^{th} element. The n^{th} element has a favorable effect on the system's exergetic efficiency, so strengthening it, will increase the system's exergetic efficiency.

In case-2, when $CSB_n < 1$, the system input decreases slower than the n^{th} element's irreversibility rate. In this instance, lowering the irreversibility rate of the n^{th} element has a detrimental effect on the operation of other system components, which in turn has an adverse effect on the performance of the entire system.

In case-3, when $CSB_n = 1$, the performance of the entire system remains unchanged. This is because any enhancement in the n^{th} element's performance is balanced by a decrease in the performance of other components, resulting in a rigid system structure that offers no scope for overall performance enhancement.

Therefore, it is important to consider the value of CSB_n when designing the DMS-VCR system to ensure the overall performance enhancement of the system.

4. Model validation

Model validation of Solanki et al. [12] primarily involved theoretical data, which lacked real-world applicability. However, in the current study, we take a more comprehensive approach by employing a dual validation strategy. This approach combines the comparison of theoretical data of present work with experimental data, significantly enhancing the realism of our analysis. Consequently, our findings are aligned with both theoretical expectations and real-world observations, resulting in a more robust and reliable investigation. The current model is utilized for computation of results corresponding to the input data ($\dot{Q}_{evap}$ = 3.5167 kW, T_{evap}, = -10 °C, DOS = 5° C, T_{cond1}, T_{cond2} = 50 °C C, η_{comp1}, η_{comp2} = 80 %, $\in_{sc}$ = 0.8, T_o = 25 °C, P_o = 101.325 kPa) of Agarwal et al. [19]. The results obtained from the current programme are compared with the results of Agarwal et al. [19] and it is observed that the results obtained from the present model lie within 3.45 % of Agarwal et al. [19], but most of the errors are less than 2 % (see Fig. 3).

The numerical simulation data is also compared with the experimental data from Han et al. [20] in order to assess the accuracy of the existing model and to determine the effect of evaporation temperature on COP for R410A. Fig. 4 compares

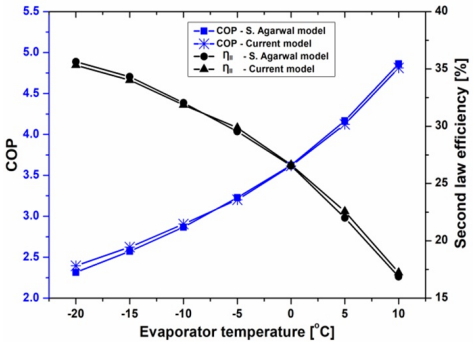


Fig. 3. Performance comparison for effect of evaporator temperature with refrigerant R134a (T_{cond1} = 50 °C).

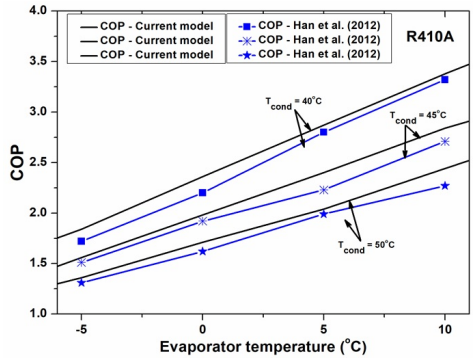


Fig. 4. COP comparison of current model with the experimental data of Han et al. [20] under different condenser temperature.

the coefficient of performance (COP) utilizing fixed superheating (T_{sup} = 8.3 °C) and subcooling (T_{sc} = 11.1 °C) degrees at varied condenser temperatures. The COP value provided by this study is marginally higher than that provided by Han et al. [20] experimental calculations. The experimental results and the theoretical results obtained from the present model corresponding to the data of Han et al. [20] are consistent and they lie between +1.5 % to +5 % of the experimental data reported by Han et al. [20] for coefficient of performance (COP). This level of consistency and accuracy in COP reaffirms the robustness and reliability of our model.

5. Results and discussion

This section presents the results and their discussion based on the process data presented in Table 2 of the DMS-VCR system for water cooling application.

A comparison of the DMS-VCR system with actual VCR system is carried out using the process data values listed in Table 2. As shown in Table 3, the DMS-VCR system's thermodynamic parameters (pressure, temperature, mass flow rate, entropy, and enthalpy) are calculated at the entry and exit of each component. The values of the performance parameters for the DMS-VCR system and actual VCR system are shown in Tables 4 and 5, respectively. For the same cooling capacity of 100 kW at T_{evap} = 5 °C, refrigerant (R134a) has mass flow rates of 0.59 kg/s (VCR sub cycle), 0.08 kg/s (DMS sub cycle), and 0.66 kg/s (actual VCR system). Additionally, the mass flow rates for external fluid (i. e. cooling water) for condensers-1, 2, and evaporator of the DMS-VCR system are 5.33 kg/s, 0.69 kg/s, and 4.77 kg/s, respectively, as compared with 5.84 kg/s in condenser-1 and 4.77 kg/s in evaporator of the actual VCR system. The DMS-VCR system performs better than an actual VCR system.

5.1 Energy analysis results

The results of the energy analysis comparing the use of the refrigerant HFC134a in a DMS-VCR system versus an actual VCR system are shown in Table 4. The primary goal of analysis is to demonstrate how the DMS-VCR system concept improved the COP and decreased compressor power. According to the results in Table 4, with variable evaporator temperatures (T_{evap} = 0 °C, 5 °C, and 10 °C) and constant condenser temperature of 40 °C, the DMS-VCR system reduces compressor-1 power usages by 8.65 %, 8.49 % and 8.31 %, respectively, while maintaining the same cooling capacity. This decrease is also helpful in reducing heat load on the condenser-1 by 8.75 %, 8.68 %, and 8.53 %, respectively. As a result, the COP of the DMS-VCR system increases by 4.60 %, 3.18 % and 1.75 %, respectively. Further, heat exchangers play crucial role in ensuring the overall performance and energy efficiency of the system by effectively transporting heat. It is essential to understand how well the evaporator, condensers, and subcooler work in order to maximize the DMS-VCR system's thermal performance and determine whether it is appropriate for use in real-world situations. The calculated effectiveness values for the evaporator, condenser, and subcooler are 0.80, 0.83, and 0.75, respectively.

5.2 Exergy analysis results

Table 5 displays the outcomes of the exergy analysis performed on the actual VCR system and the DMS-VCR system. The findings show that due to decrease in compressor work, cooling load, and refrigerant mass flow rate, the irreversibility

Table 2. Process data of DMS - VCR system.

	Parameters	Values (range)
Thermal parameters [21]	Evaporator cooling capacity (Q_{evap}, kW)	100 (-)
	Evaporator temperature ($T_{evap,}$ °C)	5 (range 0 to 10)
	Condenser temperature ($T_{cond,}$ °C)	40 (range 35 to 45)
	Evaporator coolant Inlet temperature ($T_{evap,in,}$ °C)	15 (-)
	Evaporator coolant outlet temperature ($T_{evap,out,}$ °C)	10 (-)
	Condenser coolant inlet temperature ($T_{cond,in,}$ °C)	30 (-)
	Condenser coolant outlet temperature ($T_{cond,out,}$ °C)	35 (-)
	Overlap degree ($T_{overlap}$, °C)	5 (-)
	Degree of subcooling in condenser ($T_{sc,}$ °C)	5(-)
	Degree of subcooling in subcooler ($T_{sc,}$ °C)	10 (-)
	Degree of superheating in evaporator (T_{sup}, °C)	5 (-)
	Degree of superheating in suction line (T_{sup}, °C)	10 (-)
	Desuperheating in discharge line (T_{dsup}, °C)	10 (-)
	Environment temperature ($T_{o,}$ °C)	25 (-)
	Environment pressure (P_o, kPa)	101.325 (-)
	Refrigerants (for both cycles)	R134a (-)
	Pressure drop in the evaporator (kPa)	10 (-)
	Pressure drop in the suction line (kPa)	20 (-)
	Pressure drop in the condenser (kPa)	5 (-)
	Pressure drop in the liquid line and subcooler (kPa)	10 (-)

Table 3. Simulation condition data of thermodynamic properties of the DMS-VCR system.

State point	T (°C)	h (kJ/kg)	P (kPa)	s (kJ/kg.K)	$\dot{m}$ (kg/s)	*x*
1	70.67	304.3	1024	1.016	0.599	1
2	60.67	293.8	1024	0.985	0.599	1
2’	39.82	271.3	1021	0.915	0.599	1
3	39.82	108	1016	0.395	0.599	0
3’	34.82	100.6	1012	0.394	0.599	0
4	24.82	86.15	1002	0.323	0.599	0
5	5	86.15	349.9	0.328	0.599	0.14
6	4.17	253.3	339.9	0.929	0.599	1
6’	9.17	252.9	329.9	0.946	0.599	1
7	19.17	266.9	309.9	0.983	0.599	1
8	45.22	277.1	1017	0.934	0.085	1
9	40	108.3	1017	0.395	0.085	0
10	19.82	108.3	568.8	0.399	0.085	0.16
11	19.82	261.5	568.8	0.922	0.085	1

Table 4. Energy analysis results of actual VCR system and DMS-VCR system.

Performance parameters		Actual VCR system			DMS-VCR system		
		T_{evap} = 0 °C	T_{evap} = 5 °C	T_{evap} = 10 °C	T_{evap} = 0 °C	T_{evap} = 5 °C	T_{evap} = 10 °C
First law parameters	COP_{VCR}	3.26	4.08	5.13	-	-	-
	$COP_{DMS-VCR}$	-	-	-	3.41	4.21	5.22
	$\dot{Q}_{cond1}$ (kW)	127.9	122	117.2	116.7	111.4	107.2
	$\dot{Q}_{cond2}$ (kW)	-	-	-	14.70	14.44	14.19
	$\dot{Q}_{evap}$ (kW)	100	100	100	100	100	100
	$\dot{Q}_{sc}$ (kW)	-	-	-	13.34	13.10	12.88
	$\dot{W}_{comp1}$ (kW)	30.64	24.49	19.48	27.99	22.41	17.86
	$\dot{W}_{comp2}$ (kW)	-	-	-	1.36	1.33	1.31
	$\dot{m}_{ref,1}$ (kg/s)	0.67	0.66	0.64	0.61	0.59	0.58
	$\dot{m}_{ref,2}$ (kg/s)	-	-	-	0.08	0.08	0.08
	$\dot{m}_{ef,ev}$ (kg/s)	4.77	4.77	4.77	4.77	4.77	4.77
	$\dot{m}_{ef,cond1}$ (kg/s)	6.12	5.84	5.61	5.58	5.33	5.13
	$\dot{m}_{ef,cond2}$ (kg/s)	-	-	-	0.70	0.69	0.68

rate in the DMS-VCR system is reduced by 4.68 %, 3.17 % and 0.87 %, respectively. In addition, the DMS-VCR system exhibits an increase in exergetic efficiency by 4.38 %, 3.09 % and 1.61 %, respectively (at T_{evap} = 0 °C, 5 °C, and 10 °C), which presents the significance of incorporating DMS sub system.

In Solanki et al. [12], the energy and exergy analysis focused solely on a fixed evaporator temperature of 5 °C. In contrast, the current study introduced a broader spectrum of evaporator temperatures, encompassing 0 °C, 5 °C, and 10 °C, coupled with varying condenser temperatures ranging from 35 °C to 40 °C. This expansive range of evaporator temperatures facilitates a comprehensive analysis across diverse operational conditions, providing deeper insights into the behavior of the system.

5.3 Results of structural analysis

To enhance the DMS-VCR system's performance, it is necessary to minimize the irreversibility rate of each system component. The VCR cycle compressor-1 has the greatest irreversibility rate, making up 41.10 % of the system's overall irreversibility rate. The DMS-VCR system's components are put in sequence of increasing irreversibility rate at T_{evap} = 5 °C, and the outcomes are: expansion valve-2 (0.12 kW i.e. 0.84 %), compressor-2 (0.29 kW i.e. 2.02 %), condenser-2 (0.35 kW i.e.

Table 5. Exergy analysis results of actual VCR system and DMS-VCR system.

Performance parameters		Actual VCR system			DMS-VCR system		
		T_{evap} = 0 °C	T_{evap} = 5 °C	T_{evap} = 10 °C	T_{evap} = 0 °C	T_{evap} = 5 °C	T_{evap} = 10 °C
Second law parameters	$\dot{I}_{cond1}$	3.74	3.36	3.10	3.41	3.07	2.83
	$\dot{I}_{cond2}$	-	-	-	0.36	0.35	0.34
	$\dot{I}_{comp1}$	8.84	6.44	4.72	8.08	5.89	4.33
	$\dot{I}_{comp2}$	-	-	-	0.30	0.29	0.29
	$\dot{I}_{evap}$	5.23	3.17	1.20	5.18	3.13	1.17
	$\dot{I}_{ev1}$	2.49	1.83	1.30	1.35	0.93	0.61
	$\dot{I}_{ev2}$	-	-	-	0.12	0.12	0.11
	$\dot{I}_{sc}$	-	-	-	0.55	0.55	0.54
	$\dot{I}_{t}$	20.30	14.80	10.32	19.35	14.33	10.23
	η_{II} (%)	29.87	29.36	27.19	31.18	30.27	27.63

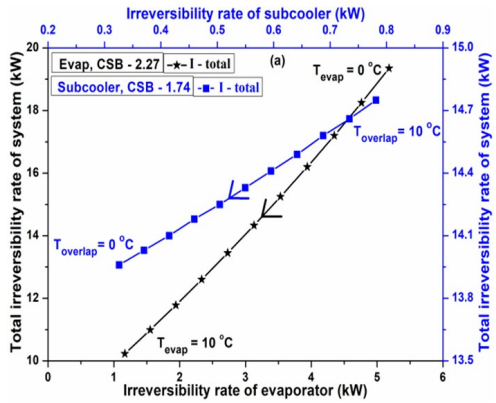
2.44 %), subcooler (0.55 kW i.e. 3.84 %), expansion valve-1 (0.93 kW i.e. 6.49 %), condenser-1 (3.07 kW i.e. 21.42 %), evaporator (3.13 kW i.e. 21.84 %), and compressor-1 (5.89 kW i.e. 41.10 %). Several researchers [11, 17, 18] have proposed the idea of CSB, and in this study, CSB values are calculated for various components of the DSM-VCR system, as presented in Figs. 5(a)-(c). The selected components for the CSB analysis include the subcooler, evaporator, condenser-1, condenser-2, compressor-1, and compressor-2, for which the CSB values are computed. The efficiency parameters (z_i) of the condenser temperature, evaporator temperature, isentropic efficiency, degree of subcooling and degree of overlap are considered for the purpose of CSB analysis.

Fig. 5(a) shows that increase in the evaporator's temperature from 0 °C to 10 °C causes a reduction in the irreversibility rate of evaporator by 77.41 % (from 5.18 kW to 1.17 kW), which reduces the system's overall irreversibility rate by 47.13 % (from 19.35 kW to 10.23 kW). Accordingly, it is appropriate to maintain the evaporator temperature high and the condenser temperature low for optimum performance of DMS-VCR system, depending on the needs of the particular application. However the condenser temperature depends on the surrounding temperature. As shown in Fig. 5(a), by decreasing the degree of overlap from 10 °C to 0 °C leads to a significant decrease of 57.69 % (from 0.78 kW to 0.33 kW) in the subcooler's irreversibility rate, which causes the DMS-VCR system's overall irreversibility rate to decline by 5.35 % (from 14.75 kW to 13.96 kW). Therefore, it is suggested to use a lower degree of overlap, although this would require a larger area of subcooler for effective heat transfer. In addition, if the temperature of the condenser-1 reduces by 10 °C (from 45 °C to 35 °C), it leads to a significant reduction in its irreversibility rate by 70.83 %, (from 5.76 kW to 1.68 kW) and condenser-2 by 79.31 % (from 0.58 kW to 0.12 kW), as illustrated in Fig. 5(b). The total irreversibility rate of the DMS-VCR system also reduces by 43 % (from 18.58 kW to 10.59 kW) when condenser-1 temperature is reduced by 10 °C and similar reduction in the irreversibility rate of DMS-VCR system is 5.23 % (from 14.73 kW to 13.96 kW) for condenser-2.

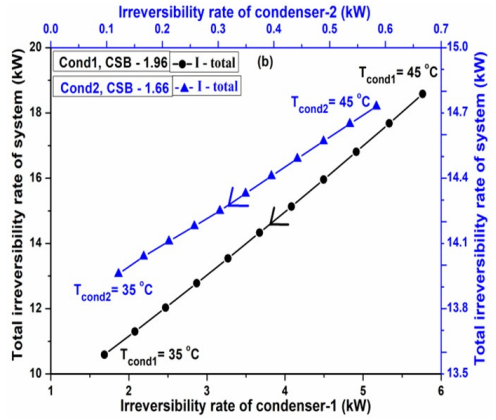
Additionally, the study reveals that achieving 100 % isentropic efficiency in compressor-1 and 2 can lead to a reduction of their irreversibility rates by 100 %, indicating an ideal condition. This would result in a significant decrease in the DMS-VCR system's overall irreversibility rate, with a reduction of 50.24 % in compressor-1 (from 16.02 kW to 7.97 kW) and compressor-2 seeing a reduction of 3.64 % (from 14.56 kW to 14.03 kW), as shown in Fig. 5(c). Compressor-1 has the greatest influence on the DMS-VCR system's total irreversibility rate.

Further, the study shows that, when compared to the other components, compressor-1 adds the most to the overall irreversibility of the DMS-VCR system, accounting for 5.89 kW, or 41.10 %. Therefore, improving the efficiency of compressor-1 is crucial for enhancing the DMS-VCR system's performance. The efficiency of the compressors depends on the pressure ratio as mentioned in equations shown under serial number 4 and 5 of the Table 1. The pressure ratio across compressors depends on the evaporator and condenser pressures and decides the efficiency of compressors. However, the evaporator pressure depends on the evaporator temperature which is dependent on application temperature for which the system is used for and can be varied only in a narrow range whereas condenser temperature depends on the ambient or surrounding conditions and hence it is not feasible to change it at will. Thus DMS-VCR system pressure ratio across compressor-1 can be changed only in a narrow range depending on the small range of the application for which it is being used.

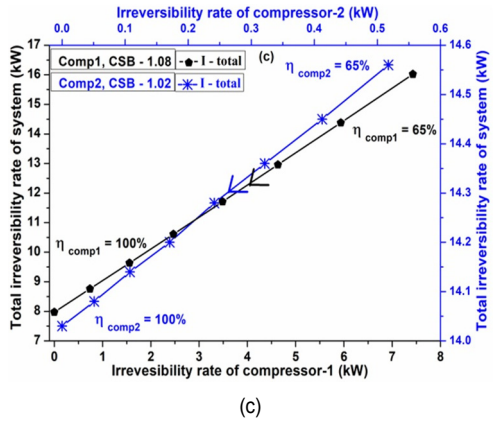
The computed CSB values for the components of DMS-VCR system are shown in Fig. 6. The components can be ranked in ascending order of their CSB values, as follows: compressor-2 (1.02), compressor-1 (1.08), condenser-2 (1.66), subcooler (1.74), condenser-1 (1.96), and evaporator (2.27). All the components have CSB values greater than one which means re-



(a)



(b)



(c)

Fig. 5. Figures showing how the system's overall irreversibility rate has changed in relation to its various components, including: (a) evaporator and subcooler; (b) condenser-1 and condenser-2; (c) compressor-1 and compressor-2.

ducing its value will reduce the component irreversibility rate as well as the system irreversibility rate.

Therefore, modifying these components' efficiency factors would enhance both the performance of the individual component as well as the performance of the entire system. Therefore, even a minor adjustment to the component's operating parameters with a high CSB number could have a big impact on how well the system performs. The component with the highest CSB value is evaporator (2.27), and its contribution to the total irreversibility rate is 21.84 %, followed by the condenser-1 (CSB-1.96) with a contribution of 21.42 %. Compressor-1 has the highest overall contribution to the total irreversibility rate, which is 41.10 %, but it is less sensitive to improvement in exergetic efficiency as its CSB is low i.e.1.08 compared to other components of the DMS-VCR system. The CSB analysis emphasizes the significance of raising the system's overall efficiency, particularly by focusing on components with higher CSB values, such as the evaporator and condenser-1. The overall performance of the DMS-VCR system can be significantly enhanced by increasing the efficiency of these components.

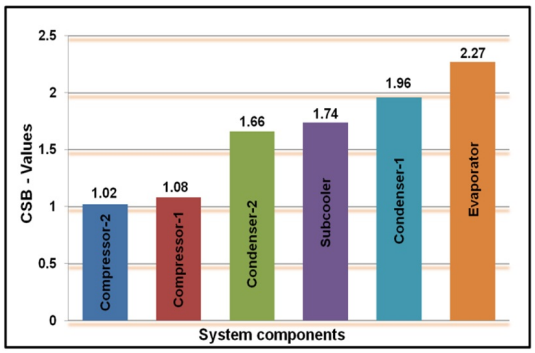


Fig. 6. Comparison of CSB values of DMS-VCR system components.

5.4 Effect of evaporator and condenser temperatures

Fig. 7 illustrates the effect of evaporator temperature on both the coefficient of performance and the total irreversibility rate on DMS-VCR system. Although the working range of the external fluid for the condenser and evaporator is only 5 °C (for example, the evaporator's external fluid intake temperature is 15 °C and its outlet temperature is 10 °C). The DMS-VCR system's evaporator temperature varies between 0 °C and 10 °C while maintaining a constant intake and output temperature for the external fluid and other design parameters. Consequently, the system's overall COP improves from 3.41 to 5.22 on increasing evaporator temperature. The system's total irreversibility rate reduces from 19.35 kW to 10.23 kW, and the exergetic efficiency decreases from 31.18 % to 27.63 %. This decline in irreversibility rate is exclusively because of the reduction in the temperature difference between the evaporator and external fluid, which is caused by an increase in the evaporator temperature. Hence, high evaporator temperature is necessary from an energy point of view and however from exergetic viewpoint, the evaporator temperature should be lower.

Fig. 8 displays the effect of condenser temperature on the DMS-VCR system's total irreversibility rate and coefficient of performance. The DMS-VCR system's condenser temperature is changed from 35 °C to 45 °C while maintaining the same temperatures for the external fluid's inlet and exit as well as

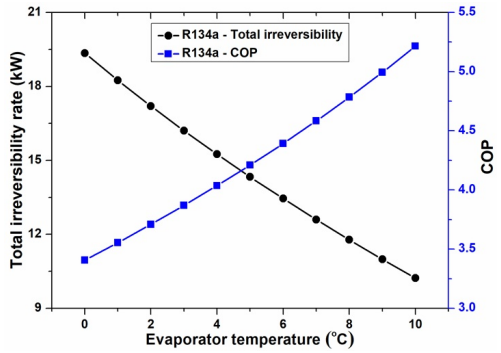


Fig. 7. Effect of evaporator temperature on total irreversibility rate and COP.

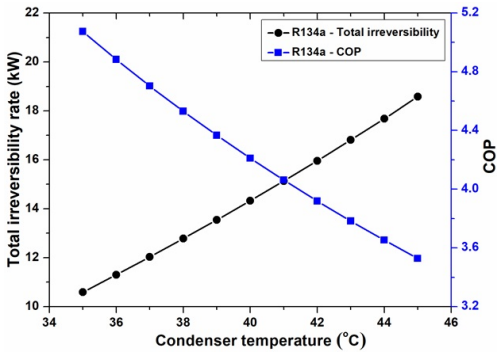


Fig. 8. Effect of condenser temperature on total irreversibility rate and COP.

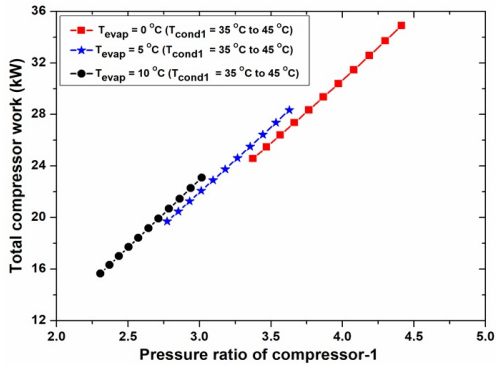


Fig. 9. Effect of pressure ratio of compressor-1 on total compressor work.

other design parameters. It causes the system's overall coefficient of performance to drop from 5.07 to 3.53, while the system's exergetic efficiency declines from 36.48 % to 25.37 % and its total irreversibility rate increases from 10.59 kW to 18.58 kW.

Fig. 9 displays the effect of pressure ratio of compressor-1 on total compressor work of the DMS-VCR system. The pressure ratio across compressor increases at lower evaporator and higher condenser temperatures. The compressor power is dependent on pressure ratio and inlet temperature to compressor. Hence the compressor power is observed to be higher for higher pressure ratio. The current paper explores the effect of compressor pressure ratio on total work at different evaporator temperatures, a critical aspect not addressed in Solanki et al. [12].

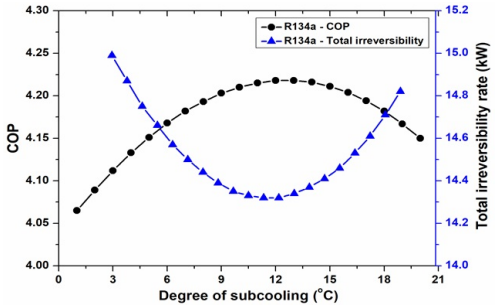


Fig. 10. Variation of COP and total irreversibility rate with respect to degree of subcooling in dedicated subcooler.

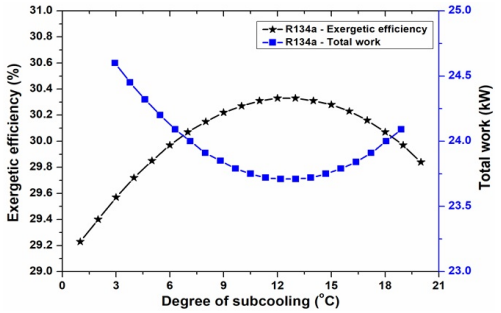


Fig. 11. Variation of exergetic efficiency and total work with respect to degree of subcooling.

The effect of temperature at inlet to compressor is not substantial. In nutshell both the evaporator and condenser temperatures affect pressure ratio and the total compressor work. The higher condenser temperature results in higher total compressor work due to higher pressure ratios. On the other hand, higher evaporator temperatures result in a drop in total compressor work due to reduction in pressure ratio.

5.5 Effect of degree of subcooling and superheating

The degree of subcooling has a significant effect on the effectiveness, efficiency, and overall cooling capacity of the system. Engineers and technicians can increase the cooling efficiency of the system and guarantee its optimal performance by optimizing the degree of subcooling. The current DMS sub system of DMS-VCR system is made to further cool the refrigerant liquid leaving the condenser below its saturation temperature. This additional cooling is accomplished by transferring heat from the refrigerant in VCR section of DMS-VCR system to another secondary refrigerant in DMS section of DMS-VCR system. The degree of subcooling is varied from 1 °C to 20 °C keeping the other design parameters constant (see Table 2). Through various simulations, it has been concluded that the ideal degree of subcooling is 12 °C. According to Figs. 10 and 11, at this subcooling level, the system's overall COP and exergetic efficiency increase, while its total irreversibility rate and total compressor work decreases. Below or above the optimal value of subcooling, the reverse patterns are observed.

Upto ideal degree of subcooling the VCR cycle compressor-1 work decreases from 24.3 kW to 22.04 kW, whereas the DMS cycle compressor work increases from 0.30 kW to 1.67 kW, resulting in a decrease in the total compressor work from 24.60 kW to 23.71 kW. It increases the system's overall COP from 4.06 to 4.22 (an improvement of 4 %). As a result, the system's entire irreversibility drops by 4.5 %.

The superheating is also an important parameter to improve the overall performance of the system, as it increases the temperature of the refrigerant leaving the evaporator by gaining heat from the products to be cooled or surrounding. This indirectly contributes to the protection and longevity of the compressor.

In the current system, the degree of superheat is varied from 1 °C to 20 °C in the evaporator and suction line of the system, keeping other design parameters constant (see Table 2). Figs. 12 and 13 show the effect of degree of superheating on the performance parameters of the DMS-VCR system. The EES simulation results show that the system's overall COP decreases from 4.40 to 4.04 and the system's entire irreversibility rate increases by 8.83 %. Further, the exergetic efficiency decreases from 31.62 % to 29.06 %, while, the total compressor work increases from 22.74 kW to 24.74 kW. Therefore, it is essential to note that superheating in the present case is not beneficial from the performance view point. In order to maximize performance and ensure safe operation, engineering systems must carefully assess the degree of subcooling and superheating.

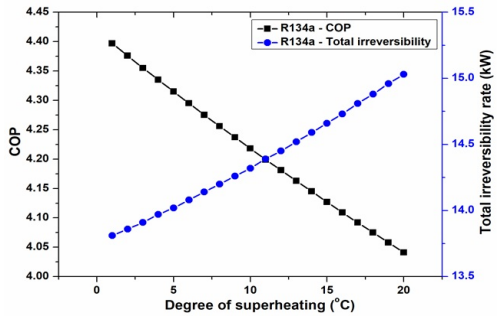


Fig. 12. Variation of COP and total irreversibility rate with respect to degree of superheating.

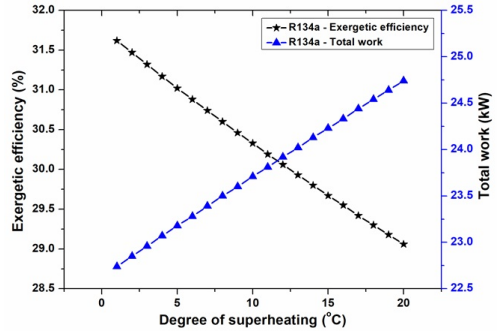


Fig. 13. Variation of exergetic efficiency and total work with respect to degree of superheating.

5.6 Effect of pressure drop in evaporator and condenser

The overall pressure drop in an evaporator is influenced by both the momentum pressure drop and the friction pressure drop. As the vapor flows through the evaporator tubes, it experiences frictional resistance with the interior surfaces, leading to a decrease in pressure. Further, as the vapor velocity increases, the momentum pressure increases in the evaporator. But in a condenser, the vapor condenses into a liquid form, resulting in a decrease in vapor velocity and a decrease in momentum pressure drop. However, friction pressure drop continues to be positive, just like in the evaporator, because the fluid faces resistance as it passes through the evaporator and condenser's interior surfaces. The condenser experiences a marginal overall reduction in pressure as a result of the combination of these pressure drops. The pressure ratio across the compressor rises as the evaporator pressure drop increases, increasing the work required by the compressor; nevertheless, the pressure ratio across the condenser does not vary significantly as discussed above. The COP and exergetic efficiency of the DMS-VCR system decreases as a result of the increased compressor work.

Figs. 14 and 15 depict how a pressure drop in an evaporator affects the COP, total irreversibility rate, exergetic efficiency and total compressor work with variation of pressure drop in evapora-

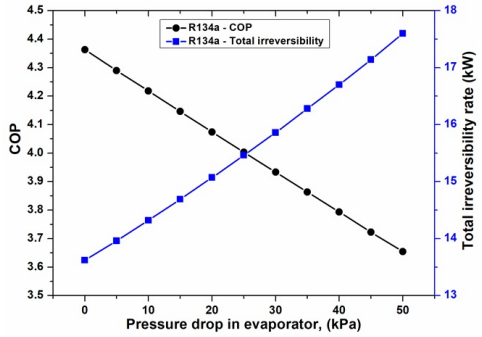


Fig. 14. Variation of COP and total irreversibility rate with respect to pressure drop in evaporator.

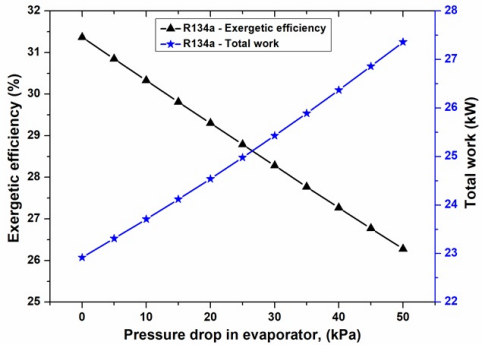


Fig. 15. Variation of exergetic efficiency and total work with respect to pressure drop in evaporator.

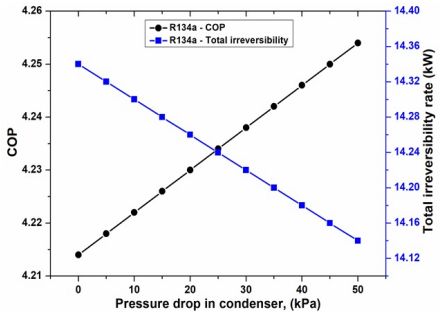


Fig. 16. Variation of COP and total irreversibility rate with respect to pressure drop in condenser.

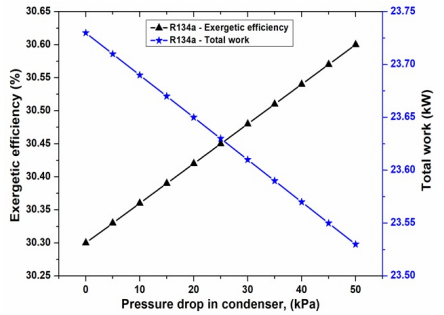


Fig. 17. Variation of exergetic efficiency and total work with respect to pressure drop in condenser.

tor from 0 kPa to 50 kPa. Due to a decrease in the specific refrigerating effect, the cooling capacity decreases as the pressure drop in the evaporator increases, and compressor work increases as the pressure ratio across the compressor rises. Both of these impacts contribute to decrease the COP from 4.36 to 3.65 and an increase in total compressor work by 19.37 %. The total irreversibility rate of the system increases by 29.22 % with a decrease in exergetic efficiency from 31.37 % to 26.28 %.

Contrary to the above the condenser pressure drop exhibits very marginal changes in the values of performance parameters i.e. COP and exergetic efficiency increases from 4.21 to 4.25 and from 30.30 % to 30.60 %, respectively, while total irreversibility rate and total compressor work decreases from 14.34 kW to 14.14 kW, and from 23.73 kW to 23.53 kW, respectively, with variation of pressure drop from 0 kPa to 50 kPa (see Figs. 16 and 17). This therefore implies that the evaporator pressure drop has a more significant effect on the overall performance of the DMS-VCR system.

6. Conclusion

The current study focuses on energy, exergy and CSB analysis of DMS-VCR system. At constant condenser temperature (T_{cond} = 40 °C) and variable evaporator temperatures (T_{evap} = 0 °C, 5 °C, and 10 °C), the results show that the DMS-VCR system works better than an actual VCR system. At 0 °C, the work input for the compressor-1 of the DMS-VCR system is reduced by 8.65 %. The COP and exergetic efficiency of DMS-VCR system both increase by 4.60 % and 4.38 %, respectively. Due to less work being required to provide the same cooling capacity, the DMS-VCR system's operating cost is also reduced. The irreversibility rate of each component is also calculated by exergy analysis, as well as the total irreversibility rate of the DMS-VCR system, which is revealed to be 4.68 % lower than the actual VCR system.

The CSB analysis is then employed to investigate how changes in irreversibility rate of individual components affect the system's overall performance. The values of CSB of evaporator and condenser-1 are most suitable for reducing the irreversibility rate of the overall system and increasing the exergetic efficiency.

Nomenclature

CSB	: Coefficient of structural bonds
COP	: Coefficient of performance
Cp	: Specific-heat (kJ/kg.K)
C	: Thermal capacitance rate (kW/K)
DMS	: Dedicated mechanical subcooling
DOS	: Degree of subcooling
DOO	: Degree of overlap
H	: Enthalpy (specific, kJ/kg)
I	: Irreversibility (rate, kW)
$\dot{m}$	: Mass (flow rate, kg/s)
P	: State point pressure (kPa)
PR	: Pressure ratio
Q	: Rate of heat transfer (kW)
s	: Entropy (specific, kJ/kg.K)
S_gen	: Entropy generation rate (kW/K)
T	: Temperature (°C)
VCR	: Vapor compression refrigeration
W	: Power input rate (kW)

Greek symbols

ϵ	: Effectiveness
η	: Efficiency

Subscripts

o	: Environment condition
dl	: Discharge line
comp	: Compressor
cond	: Condenser
EoS	: Element or subsystem
ef	: External fluid
ev	: Expansion valve
ex	: Exergetic
evap	: Evaporator
in	: Inlet condition
isen	: Isentropic
max	: Maximum
out	: Outlet condition
ol	: Overlap
ref	: Refrigerant
sc	: Subcooling

sup : Superheating
sl : Suction line
t : Total
Z_i : System efficiency parameter
n : Nth element of system
x : Dryness fraction (quality)
1,2,3… : State points

References

[1] B. A. Qureshi and S. M. Zubair, The effect of refrigerant combinations on performance of a vapor compression refrigeration system with dedicated mechanical sub-cooling, *Int. J. Refrig.*, 35 (1) (2012) 47-57.

[2] B. A. Qureshi and S. M. Zubair, Mechanical sub-cooling vapor compression systems: current status and future directions, *Int. J. Refrig.*, 36 (8) (2013) 2097-2110.

[3] B. A. Qureshi et al., Experimental energetic analysis of a vapor compression refrigeration system with dedicated mechanical sub-cooling, *Appl. Energy*, 102 (2013) 1035-1041.

[4] P. D'Agaro, M. A. Coppola and G. Cortella, Effect of dedicated mechanical subcooler size and gas cooler pressure control on transcritical CO_2 booster systems, *Appl. Therm. Eng.*, 182 (2021) 116145.

[5] M. H. Yang and R. H. Yeh, Performance and exergy destruction analyses of optimal subcooling for vapor-compression refrigeration systems, *Int. J. Heat Mass Transf.*, 87 (2015) 1-10.

[6] G. B. Wang and X. R. Zhang, Thermoeconomic optimization and comparison of the simple single-stage transcritical carbon dioxide vapor compression cycle with different subcooling methods for district heating and cooling, *Energy Convers. Manag.*, 185 (2019) 740-757.

[7] S. Agarwal, A. Arora and B. B. Arora, Exergy analysis of dedicated mechanically subcooled vapour compression refrigeration cycle using HFC-R134a, HFO-R1234ze and R1234yf, G. Zhang, N. Kaushika, S. Kaushik and R. Tomar (eds.), *Advances in Energy and Built Environment. Lecture Notes in Civil Engineering*, Springer, Singapore, 36 (2020).

[8] D. Boer, M. Medrano and M. Nogués, Exergy and structural analysis of an absorption cooling cycle and the effect of efficiency parameters, *ECOS 2005 - Proc. 18th Int. Conf. Effic. Cost, Optim. Simulation, Environ. Impact Energy Syst.*, 8 (4) (2005) 337-344.

[9] T. Tekin and M. Bayramoğlu, Exergy and structural analysis of raw juice production and steam-power units of a sugar production plant, *Energy*, 26 (3) (2001) 287-297.

[10] C. Nikolaidis and D. Probert, Exergy-method analysis of a two-stage vapour-compression refrigeration-plants performance, *Appl. Energy*, 60 (4) (1998) 241-256.

[11] R. D. Misra, P. K. Sahoo and A. Gupta, Thermoeconomic optimization of a LiBr/H_2O absorption chiller using structural method, *J. Energy Resour. Technol. Trans. ASME*, 127 (2) (2005) 119-124.

[12] N. Solanki, A. Arora and R. K. Singh, Advance exergy and coefficient of structural bond analysis of dedicated mechanical subcooled vapor compression refrigeration system, *Int. J. Refrig.*, 153 (2023) 266-280, DOI: https://doi.org/10.1016/j.ijrefrig.2023.06.008.

[13] S. A. Klein, *Engineering Equation Solver, Professional Version 10.561*, F-Chart Software, Madison, WI 53744 (2018).

[14] P. K. Nag, *Basic and Applied Thermodynamics*, Tata McGraw-Hill, USA (2002) 781.

[15] V. Jain, G. Sachdeva and S. S. Kachhwaha, NLP model based thermoeconomic optimization of vapor compression-absorption cascaded refrigeration system, *Energy Convers. Manag.*, 93 (2015) 49-62.

[16] H. Sayyaadi and M. Nejatolahi, Multi-objective optimization of a cooling tower assisted vapor compression refrigeration system, *Int. J. Refrig.*, 34 (1) (2011) 243-256.

[17] Ö. Kizilkan, A. Şencan and S. A. Kalogirou, Thermoeconomic optimization of a LiBr absorption refrigeration system, *Chem. Eng. Process. Process Intensif.*, 46 (12) (2007) 1376-1384.

[18] T. J. Kotas, *The Exergy Method of Thermal Plant Analysis 2*, Krieger Publishing Company (1995) 198.

[19] S. Agarwal, A. Arora and B. B. Arora, Thermodynamic performance analysis of dedicated mechanically subcooled vapour compression refrigeration system, *J. Therm. Eng.*, 5 (4) (2019) 222-236.

[20] X. H. Han et al., Cycle performance studies on HFC-161 in a small-scale refrigeration system as an alternative refrigerant to HFC-410A, *Energy Build*, 44 (1) (2012) 33-38.

[21] A. Arora and S. C. Kaushik, Theoretical analysis of a vapour compression refrigeration system with R502, R404A and R507A, *Int. J. Refrig.*, 31 (6) (2008) 998-1005.



Naveen Solanki is currently working as Assistant Professor in the Department of Mechanical Engineering at Maharaja Agrasen Institute of Technology affiliated to Guru Gobind Singh Indraprastha University, Delhi, India. He did his M.E. in thermal engineering from Delhi College of Engineering (DCE), Delhi University, Delhi, India in 2012. He is a research scholar from Delhi Technological University, formerly known as Delhi College of Engineering. His research area is refrigeration and air-conditioning; he has done a lot of work in this field. He has published papers in national and international journals and conferences.



Akhilesh Arora is currently working as a Professor in the Mechanical Engineering Department at Delhi Technological University, Delhi (India). He did his Master's degree in Thermal Engineering from the Indian Institute of Technology (IIT) Delhi. He then went on to pursue his Ph.D. in the same field from the same institute. His research interests lie in the areas of refrigeration and air conditioning, thermal engineering, and energy management. He has published numerous research papers in national and international journals and has presented his work at various conferences and seminars.



Raj Kumar Singh is currently working as a Professor in the Mechanical Engineering Department at Delhi Technological University, Delhi (India). He did his Master's degree in Mechanical and Ph.D. in the field of Fluid Mechanics. His research interests lie in the areas of fluid mechanics, fluid machines, computational fluid dynamics (CFD), biogas utilization, and digital learning. He has published several research papers in national and international journals and has presented his work at various conferences and seminars.

A Comprehensive Study on the Closed Loop Performance of a Zeta Converter

Prashant Singh
Electrical Engineering Department
Delhi Technological University
prashantsingh0719@gmail.com

Alka Singh
Electrical Engineering Department
Delhi Technological University
alkasingh.eed@gmail.com

Ankita Arora
Electrical Engineering Department
Delhi Technological University
aroraankita@dtu.ac.in

2023 11th National Power Electronics Conference (NPEC) | 979-8-3503-1164-8/23/$31.00 ©2023 IEEE | DOI: 10.1109/NPEC57805.2023.10384864

Abstract: **This research study focuses on small signal analysis of the Zeta converter and the design of its control techniques to improve performance and stability. It also compares the effectiveness of voltage mode control (VMC) and current mode control (CMC) strategies in regulating the Zeta converter's output voltage and current. Bidirectional power supplies, motor drives, power factor correction equipment and solar power systems are just some of the many applications where the Zeta converter (inverting SEPIC Converter), a non-isolated DC-DC converter, finds widespread use. By employing state-space averaging and linearization methods, a transfer function is obtained that correlates the converter's input and output parameters. The control scheme is examined for steady-state errors, transient response, and robustness to parameter changes after implementing them in MATLAB/Simulink. In terms of steady-state error and transient response, the results reveal that the current mode control scheme performs better than the Voltage Mode Control (VMC) method. However, the sensitivity of the Current Mode Control (CMC) method to these parameter changes is greater.**

Keywords — Zeta converter, Closed loop control, VMC, CMC, stability.

I. INTRODUCTION

The increasing need for adaptable and effective power electronic systems has led to a new era of research centred on DC-DC converters. Zeta converters have garnered significant interest within the field due to their ability to execute dual voltage steps, namely boost and buck, while simultaneously generating a non-inverted output [1]. The objective of this study is to elucidate the functioning of converters, with a specific focus on their voltage and current mode control mechanisms. The design of Controllers integrating Proportional-Integral-Derivative (PID) will be emphasized, particularly in relation to load and line regulation [2].

Zeta converters, which are a variant of the buck-boost family, offer efficient solutions for applications that require both step-up and step-down capabilities [3]. The distinctive architectural design of these devices provides several advantages, including reduced electromagnetic interference, decreased output ripple, expanded input voltage range, and improved efficiency ranging from 90 to 95 percent. Additionally, their affordability makes them highly suitable for a wide range of power electronic applications such as bidirectional power flow, renewable energy systems, power factor correction, Electric vehicles, portable electronics etc [4]-[6].

However, it is imperative to have a thorough insight into the behaviour of converters under different conditions in order to guarantee their operational stability. The exploration of this topic can be effectively conducted through the utilization of small signal analysis.

The utilization of small signal analysis is highly advantageous in the realm of power converters, as it enables the modelling of dynamic characteristics in the vicinity of an established operating point. The aforementioned approach is crucial in comprehending the stability and transient response of Zeta converters in the presence of disturbances and variations [7]. This paper explores the principles and methodologies of small signal analysis in order to shed light on the operational dynamics and system performance implications of Zeta converters. In addition to the evaluation of small signal model, the investigation of steady state conditions is of the utmost significance for deciding the operational performance of the Zeta converter [8-10].

The careful consideration of suitable control techniques plays a significant role in determining the system's transient response speed and the level of precision in regulating the output voltage Both aspects mentioned are influenced by different operating conditions, and the choice of suitable control method plays a crucial role in defining both aspects.

The primary aim of this research paper is to undertake a comprehensive investigation into the small signal analysis, steady-state analysis, and control technique design pertaining to the Zeta converter. This research paper is organized in the following manner:

Section II of the paper provides a comprehensive examination of the operation modes of the Zeta Converter, as well as an in-depth analysis of its steady state behaviour. Moreover, this paper presents a small signal model for the converter, with particular emphasis on the Continuous Conduction Mode (CCM). Section III of this study delves into control strategies, specifically Voltage Mode Control (VMC) and Current Mode Control (CMC). The section outlines the design process for both VMC and CMC, with a particular focus on the procedure for determining the parameters of the Proportional-Integral-Derivative (PID) controller. Section IV of the work presents the outcomes and inferences derived from the application of voltage mode control and current mode control. This section discusses various aspects, including time response analysis, output parameter comparison, load variation, and line variation. Section V of the paper presents a comprehensive conclusion and examines potential applications and future research prospects in the field of Zeta converter control and optimization.

Authorized licensed use limited to: DELHI TECHNICAL UNIV. Downloaded on February 07,2024 at 06:47:56 UTC from IEEE Xplore. Restrictions apply.

II. OPERATING MODES AND SMALL SIGNAL ANALYSIS OF ZETA CONVERTER

The Zeta converter is a type of DC-DC converter with a non-linear fourth-order configuration. It is designed to efficiently adjust the output voltage either upwards or downwards. The converter is classified as a non-isolated converter, indicating that the input and output voltages share a common ground connection. The Zeta converter comprises two inductors (L_1, L_2), two capacitors(C_1, C_2), and a switch (SW), as shown in Fig. 1.

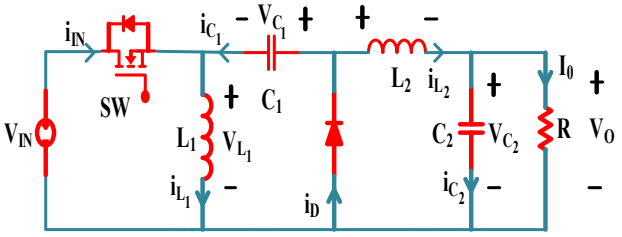


Fig.1 Schematic diagram of Zeta converter

The switching operation of Zeta converter can be categorized into two distinct modes: In mode I, Switch is closed as shown in Fig (2). When SW is On, the diode will be in OFF state. The source voltage appears across the inductor L_1 and causes its current to increase linearly, while the inductor L_2 begins to store energy from the series capacitor C_1 via the load which causes $i_{L_1} and i_{L_2}$ to increase linearly.

In mode II Switch is open as shown in Fig (3). When SW is OFF, the diode will be in ON state. Inductor L_1 charges the capacitor C_1 in series, and Inductor L_2 provides the output power, or discharges through the load which causes $i_{L_1} and\, i_{L_2}$ to decrease linearly. This is how the Zeta converter operates and its output current is continuous.

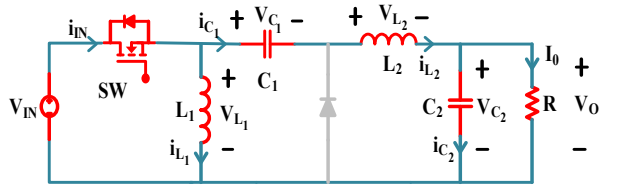


Fig 2: Schematic diagram of Zeta converter in Mode 1 (SW is ON)

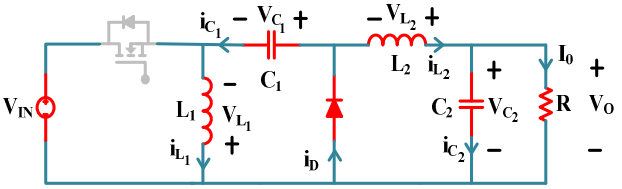


Fig 3: Schematic diagram of Zeta converter in Mode 2 (SW is OFF)

Unlike buck boost and Cuk converters, ZETA converter has same polarity as source polarity and this can be either higher or lower than the input voltage depending upon the duty cycle of the PWM given to the MOSFET switch. The expression relating the input (V_{IN}) and the output (V_O) voltages is given in Eq. (1). where D denotes the duty cycle.

$$V_o = \frac{DV_{IN}}{(1-D)} \tag{1}$$

The values of the inductors (L_1 and L_2) are determined by taking into account both the switching frequency (f_{SW}) and the ripple currents $(\Delta i_{L_1} and\, \Delta i_{L_2})$ that are required. The values of the inductors can be calculated with the help of the following equations:

$$L_1 = \frac{DV_{IN}}{\Delta i_{L_1} f_{SW}} \tag{2}$$

$$L_2 = \frac{V_0(1-D)}{\Delta i_{L_2} f_{SW}} \tag{3}$$

The values of the capacitors (C_1 and C_2) are determined by taking into account both the switching frequency (f_{SW}) and the voltage ripples $(\Delta V_{C_1} and\, \Delta V_{C_2})$ that are required. The values of the capacitors are calculated with the help of the equations (4,5):

$$C_1 = \frac{V_0 D}{R\Delta V_{C_1} f_{s_w}} \tag{4}$$

$$C_2 = \frac{V_0(1-D)}{8L_2\Delta V_{C_2} f_{SW}^2} \tag{5}$$

Considering the ripple current in inductors$(\Delta i_{L_1}, \Delta i_{L_2})$ and ripple in capacitor voltage $(\Delta V_{C_1}, \Delta V_{C_2})$ to be 10%, the design values of Zeta converter are computed as $L_1 = 38.4mH, L_2 = 9.6mH, C_1 = 66.66\mu F, C_2 = 4.166\mu F$ for input voltage of 48V and 12V output voltage. All the design parameter are specified in Table I.

In order to examine the small-signal characteristics of the converter, a small-signal model is developed using state space representation, which is obtained from the circuit equations. The state variables of the Zeta converter are considered as inductor currents (i_{L_1}, i_{L_2}) and capacitor voltages (V_{C_1}, V_{C_2}), in this research paper. The controlled input variable is the input voltage, while the output variable is the output voltage. The Zeta converter is defined by the following equations:

$$x = \begin{bmatrix} i_{L_1} \\ i_{L_2} \\ V_{C_1} \\ V_{C_2} \end{bmatrix}, u = [V_{IN}], y = [V_0] \tag{5}$$

The state space representation of the system is described by the generalized set of equations:

$$\dot{x} = AX + BU \tag{6}$$

$$y = CX + EU \tag{7}$$

where the state matrix is denoted by A, the input matrix is denoted by B, the output matrix is denoted by C, and the input output coupling matrix is denoted by E.

The state space equations of the ZETA converter in mode I are as follows:

Authorized licensed use limited to: DELHI TECHNICAL UNIV. Downloaded on February 07,2024 at 06:47:56 UTC from IEEE Xplore. Restrictions apply.

$$\frac{di_{L_1}}{dt} = \frac{V_{IN}}{L_1} \tag{8}$$

$$\frac{di_{L_2}}{dt} = \frac{V_{IN} + V_{C_1} - V_{C_2}}{L_2} \tag{9}$$

$$\frac{dV_{C_1}}{dt} = -\frac{i_{L_2}}{C_1} \tag{10}$$

$$\frac{dV_{C_2}}{dt} = \frac{i_{L_2}}{C_2} - \frac{V_{C_2}}{RC_2} \tag{11}$$

$$V_0 = V_{C_2} \tag{12}$$

$$\begin{bmatrix} \frac{di_{L_1}}{dt} \\ \frac{di_{L_2}}{dt} \\ \frac{dV_{C_1}}{dt} \\ \frac{dV_{C_2}}{dt} \end{bmatrix} = \begin{bmatrix} 0 & 0 & 0 & 0 \\ 0 & 0 & \frac{1}{L_2} & -\frac{1}{L_2} \\ 0 & -\frac{1}{C_1} & 0 & 0 \\ 0 & \frac{1}{C_2} & 0 & -\frac{1}{RC_2} \end{bmatrix} \begin{bmatrix} i_{L_1} \\ i_{L_2} \\ V_{C_1} \\ V_{C_2} \end{bmatrix} + \begin{bmatrix} \frac{1}{L_1} \\ \frac{1}{L_2} \\ 0 \\ 0 \end{bmatrix} [V_{IN}] \tag{13}$$

$$[V_0] = [0 \quad 0 \quad 0 \quad 1] \begin{bmatrix} i_{L_1} \\ i_{L_2} \\ V_{C_1} \\ V_{C_2} \end{bmatrix} + [0][V_{IN}] \tag{14}$$

The state space equations of the ZETA converter in mode II are as follows:

$$\frac{di_{L_1}}{dt} = -\frac{V_{C_1}}{L_1} \tag{15}$$

$$\frac{di_{L_2}}{dt} = -\frac{V_{C_2}}{L_2} \tag{16}$$

$$\frac{dV_{C_1}}{dt} = \frac{i_{L_1}}{C_1} \tag{17}$$

$$\frac{dV_{C_2}}{dt} = \frac{i_{L_2}}{C_2} - \frac{V_{C_2}}{RC_2} \tag{18}$$

$$V_0 = V_{C_2} \tag{19}$$

$$\begin{bmatrix} \frac{di_{L_1}}{dt} \\ \frac{di_{L_2}}{dt} \\ \frac{dV_{C_1}}{dt} \\ \frac{dV_{C_2}}{dt} \end{bmatrix} = \begin{bmatrix} 0 & 0 & -\frac{1}{L_1} & 0 \\ 0 & 0 & 0 & -\frac{1}{L_2} \\ \frac{1}{C_1} & 0 & 0 & 0 \\ 0 & \frac{1}{C_2} & 0 & -\frac{1}{RC_2} \end{bmatrix} \begin{bmatrix} i_{L_1} \\ i_{L_2} \\ V_{C_1} \\ V_{C_2} \end{bmatrix} + \begin{bmatrix} 0 \\ 0 \\ 0 \\ 0 \end{bmatrix} [V_{IN}] \tag{20}$$

$$[V_0] = [0 \quad 0 \quad 0 \quad 1] \begin{bmatrix} i_{L_1} \\ i_{L_2} \\ V_{C_1} \\ V_{C_2} \end{bmatrix} + [0][V_{IN}] \tag{21}$$

Averaging over one switching period is performed to remove the switching ripple component from the circuit calculations. Averaging these equations over one switching period yields the averaged switching model:

$$A = A_1 d + A_2(1-d) \tag{22}$$

$$B = B_1 d + B_2(1-d) \tag{23}$$

$$C = C_1 d + C_2(1-d) \tag{24}$$

$$E = E_1 d + E_2(1-d) \tag{25}$$

The nonlinear averaged state-space model must be linearized around an operational point before the small-signal model of Zeta converter can be derived. To do this, perturbations are made to the system's state variables, input variables, and parameters. Perturbations refer to small disturbances or changes introduced into these component values, which can lead to significant effects on the overall behaviour and performance of the system.

$$d = D + \hat{d},\ x = X + \hat{x},\ u = U + \hat{u},\ y = Y + \hat{y} \tag{26}$$

Now, substituting the perturbed variables into the averaged state space model Eq. (23-26) and assuming that steady state terms are zero and the effect of higher order terms is neglected.

We get the linearized small signal model is obtained as follows:

$$s\hat{x}(s) = A\hat{x}(s) + B\hat{u}(s) + ((A_1 - A_2)X(s) + (B_1 - B_2)U(s))\hat{d}(s) \tag{27}$$

$$\hat{y}(s) = C\hat{x}(s) + E\hat{u}(s) + ((A_1 - A_2)X(s) + (E_1 - E_2)U(s))\hat{d}(s) \tag{28}$$

$$\frac{\hat{x}(s)}{\hat{d}(s)} = (sI - A)^{-1}((A_1 - A_2)X(s) + (B_1 - B_2)U(s)) \tag{29}$$

Using Equation (28), the output-to-control transfer function can be obtained by substituting the values of the parameters from Table I.

$$\frac{\widehat{v_0}(s)}{\hat{d}(s)} = \frac{(s - Z_1)(s - Z_2)}{(s - P_1)(s - P_2)(s - P_3)(s - P_4)} \tag{30}$$

where,

$$\begin{aligned} Z_1 &= (0.620 + 5.55i) \times 10^2 \\ Z_2 &= (0.620 - 5.55i) \times 10^2 \\ P_1 &= (-3.930 + 0.00i) \times 10^4 \\ P_2 &= (-0.050 + 0.00i) \times 10^4 \\ P_3 &= (-0.003 + 0.05i) \times 10^4 \\ P_4 &= (-0.003 - 0.05i) \times 10^4 \end{aligned} \tag{31}$$

$$\frac{\widehat{i_0}(s)}{\hat{d}(s)} = \frac{(s - Z_A)(s - Z_B)(s - Z_C)}{(s - P_A)(s - P_B)(s - P_C)(s - P_D)} \tag{32}$$

where,

$$\begin{aligned} Z_A &= (-4.0006 + 0.0000i) \times 10^4 \\ Z_B &= (0.0063 + 0.0556i) \times 10^4 \\ Z_C &= (0.0063 - 0.0556i) \times 10^4 \\ P_A &= (-3.93 + 0.000i) \times 10^4 \\ P_B &= (-0.05 + 0.000i) \times 10^4 \\ P_C &= (-0.003 + 0.050i) \times 10^4 \\ P_D &= (-0.003 - 0.050i) \times 10^4 \end{aligned} \tag{33}$$

Authorized licensed use limited to: DELHI TECHNICAL UNIV. Downloaded on February 07,2024 at 06:47:56 UTC from IEEE Xplore. Restrictions apply.

Table I: Parameters specification of Zeta converter		
Parameter	**Symbol**	**Values**
Input Voltage	V_{IN}	48V
Output Voltage	V_0	12V
Duty Cycle	D	0.2
Switching Frequency	f_{SW}	5kHz
Output Power	P_0	24W
Inductor 1	L_1	38.4mH
Inductor 2	L_2	9.6mH
Inductor 1 current	I_{L_1}	2A
Inductor 2 current	I_{L_2}	0.5A
Ripple in inductors	$\Delta i_{L_1}, \Delta i_{L_2}$	$(10\%\, I_{L_1}, 10\% I_{L_2})$
Capacitor 1	C_1	66.66µF
Capacitor 2	C_2	4.166 µF
Ripple in capacitors	$\Delta V_{C_1}, \Delta V_{C_2}$	$(10\%\, V_{C_1}, 10\% V_{C_2})$

III. CONTROL STRATEGIES

The Zeta converter is examined and evaluated in continuous conduction mode (CCM) and design of a closed-loop control mechanism for both voltage and current modes is discussed in this section. The transfer functions of the Zeta converter have been determined in Eq.31 and Eq.33, and a PID controller has been constructed for both the voltage and current loops. The efficacy of the closed-loop voltage and current mode control system is assessed by simulations conducted using MATLAB/Simulink.

A. VOLTAGE MODE CONTROL

The Zeta converter, a non-linear system, is susceptible to variations in the input voltage, load current, and various external factors. Hence, the implementation of a closed-loop control system becomes imperative in order to effectively regulate the output voltage of the Zeta converter. In the absence of a closed-loop control system, it is observed that the output voltage exhibits fluctuations, thereby posing a potential risk of detrimental consequences to both the load and the converter.

The closed-loop voltage mode control technique is employed to effectively regulate the output voltage of the Zeta converter. This control method operates by dynamically adjusting the duty cycle of the converter in response to the error signal, which represents the discrepancy between the desired output voltage and the actual output voltage. By continuously monitoring and adapting the duty cycle, the closed-loop voltage mode control ensures that the Zeta converter maintains a stable and accurate output voltage as shown in fig (4). The closed-loop control system is widely recognised for its ability to deliver exceptional output voltage regulation and rapid transient response, rendering it highly suitable for a diverse range of applications necessitating bidirectional power flow.

The transfer function of PID controller is given as:

$$T_C(s) = K_{pro} + \frac{K_{in}}{s} + K_{der}s \qquad (34)$$

where K_{pro}, K_{in}, K_{der} denote the proportional, integral, derivative gains which are selected as $K_{pro} = 0.8697 \times 10^{-3}, K_{in} = 2.676, K_{der} = 3.005 \times 10^{-8}$

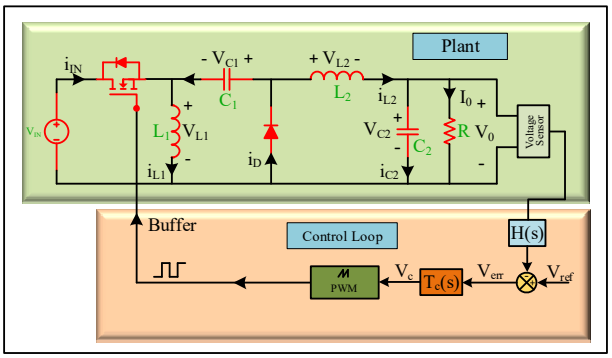


Fig. 4 Voltage mode control loop for Zeta Converter

B. CURRENT MODE CONTROL

The implementation of current mode control in Zeta converters is an essential approach employed to effectively manage the output current and maintain stable and efficient power conversion. The control methodology employed in this system is based on a closed-loop architecture, wherein the inductor current is constantly monitored and compared to a predetermined reference current. The control circuit utilizes contemporary current sensing methods, to provide an error signal that represents the disparity between the intended and real current magnitudes.

The aforementioned error signal is subsequently subjected to processing by a controller, commonly referred to as a Proportional-Integral-Derivative (PID) controller, with the purpose of producing a control signal. The control signal is responsible for modulating the power switch, typically a MOSFET, by means of Pulse Width Modulation (PWM), so effectively altering the duty cycle as shown in fig. (5) Consequently, the Zeta converter exhibits a rapid response to fluctuations in load or input voltage, so ensuring a consistent output current. This characteristic enhances stability and maximizes overall efficiency in a wide range of applications, including power supplies, LED drivers, and renewable energy systems.

The transfer function of PID controller is given as:

$$T_C(s) = K_{pro} + \frac{K_{in}}{s} + K_{der}s \qquad (35)$$

where, the selected values of the gains are $K_{pro} = 1.74 \times 10^{-3}, K_{in} = 18.63, K_{der} = 2.763 \times 10^{-8}$

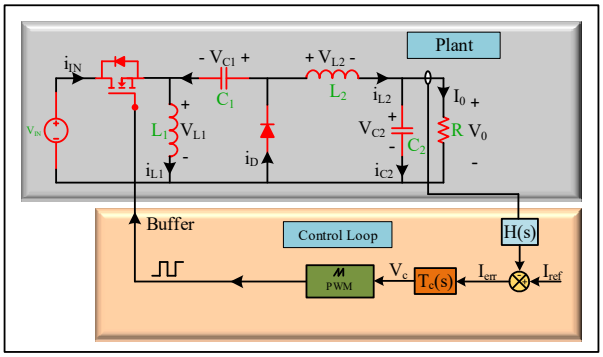


Fig. 5 Current mode control loop for Zeta Converter

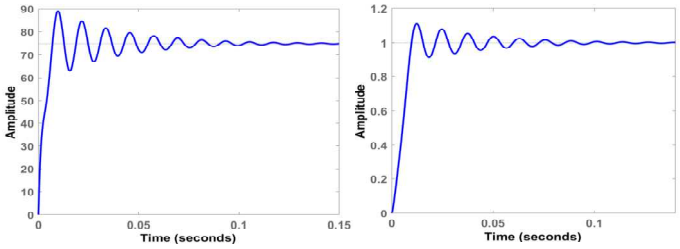
IV. RESULTS AND ANALYSIS

Design and modelling of the Zeta converter has been conducted using MATLAB/Simulink. Additionally, the PID controller was developed and calibrated using the Phase Margin test approach.

Authorized licensed use limited to: DELHI TECHNICAL UNIV. Downloaded on February 07,2024 at 06:47:56 UTC from IEEE Xplore. Restrictions apply.

A. CLOSED LOOP VOLTAGE CONTROL

Step response analysis: The step response of the open loop and closed-loop voltage mode control, which is implemented using PID controller and applied to the Zeta converter, is illustrated in Fig. 6. The results obtained demonstrate that the closed-loop system displays a significant decrease in the percentage overshoot, measuring at 11.2%. The aforementioned decrease indicates a noteworthy enhancement in the performance and stability of the system. The closed loop system exhibits a rise time of 7.28 ms and a settling time of 64.2 ms.



The comparison between open loop and closed loop voltage stability is investigated, Fig.7 illustrates the performance of the Zeta converter under both open and closed-loop scenarios. Under constant load impedance of 6Ω, the converter displays a steady operational state. It is observed that the open-loop system's peak overshoot is 12.32%, the closed-loop application of the ZETA converter remarkably lowers the maximum peak overshoot to a mere 4.07%, signifying an enhanced system performance.

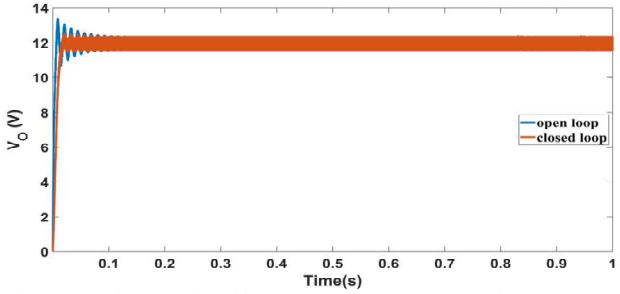


Fig. 7 Open loop vs closed loop Zeta converter output voltage

The regulation of output voltage under load variation is now investigated the control has been designed and developed to ensure a consistent output voltage within predetermined parameters, and it diligently monitors the load and adjusts the duty cycle as required. As depicted in Fig.8, modifying the load resistance from 3Ω to 12Ω results in fluctuations in both the output voltage and load current of the Zeta converter. The data presented in the study provides evidence supporting the converter's capacity to maintain a consistent output voltage of 12V, even when subjected to varying load conditions in wide range.

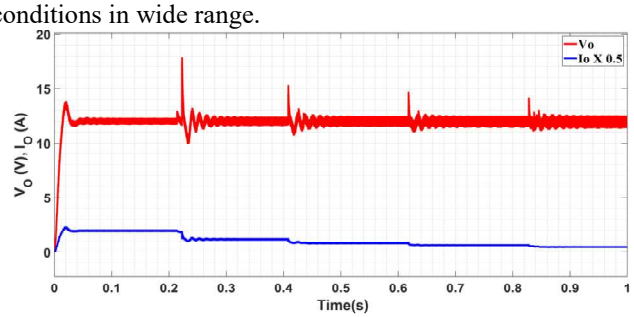


Fig.8 Output Voltage and Current w. r. t. Load Variation

The regulation of load voltage with line variation: The efficiency of power converters can be affected by line variations, which are also known as fluctuations or disruptions in the input voltage. The closed-loop voltage mode control mitigates these effects by adaptively modifying the duty cycle of the converter. The converter commences its operation once the line voltage has achieved stability and has reached a state of equilibrium. In order to replicate power outages, the voltage of the power line is modified in distinct increments ranging from 24V to 48V. Figure 13 illustrates the ability of the control loop to maintain a consistent output voltage despite large fluctuations in the line voltage. This observation further confirms the effectiveness of well-designed control loop.

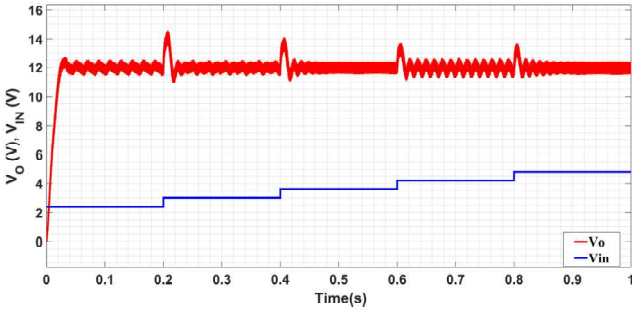


Fig.9 Impact of Line variation on the Output Voltage

B. CLOSED LOOP CURRENT CONTROL

The Zeta converter utilizing a closed-loop current mode control strategy to regulate the inductor current by incorporating a feedback loop is discussed in this section, The automatic regulation of the output current is achieved by regulating the inductor current, as the average value of the inductor current is equivalent to the output current, denoted as I_0. The feedback loop is accountable for measuring the current flowing through the inductor, denoted as i_{L_2}, and subsequently comparing it to a pre-established reference current. The modulation of the duty cycle of the converter is accomplished by leveraging the difference between the two currents, thereby enabling the control of both the inductor current and the output voltage.

Step response analysis: The step response of Zeta converters with open loop control exhibits an unbounded reaction to variations in input conditions. Contrarily, in closed loop current mode control, a feedback loop is implemented to constantly monitor the inductor current and correct the system in real-time. As a result, the Zeta converter under closed loop control exhibits a response time is 8.24ms, settling time of 136ms, and maximum peak overshoot is 7.71% as shown in Fig.10.

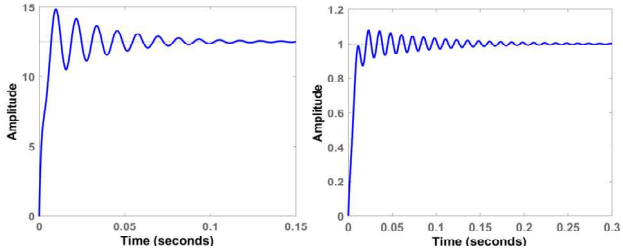


Fig.10 Step Response (a) Open Loop Plant (b) Closed Loop Plant

The comparison between open loop and closed loop current stability: Figure 11 showcases the output current waveform

Authorized licensed use limited to: DELHI TECHNICAL UNIV. Downloaded on February 07,2024 at 06:47:56 UTC from IEEE Xplore. Restrictions apply.

for both open loop and closed loop current control modes, as they operate under a constant load. The simulation, employs a fixed load of 6Ω, reveals that the open-loop system manifests limited regulation abilities, exhibiting a maximum peak overshoot of 12.4%. Conversely, the closed-loop system displays a marked improvement in regulation which is further by evident by a significantly reduced peak overshoot of 9%.

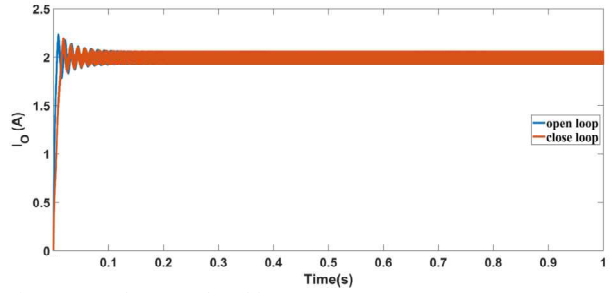


Fig. 11 Open loop vs Closed loop Zeta converter Output current

The regulation of output current under load variation: The comprehensive analysis of the Zeta converter using closed loop current control under varying load conditions has produced significant results. Fig.12 shows the output voltage of the Zeta converter under varying load conditions, ranging from 3Ω to 12Ω. Despite the extensive range in the load values, the Zeta converter with closed loop current control demonstrates an impressive ability to regulate the output current stability throughout at 2A.

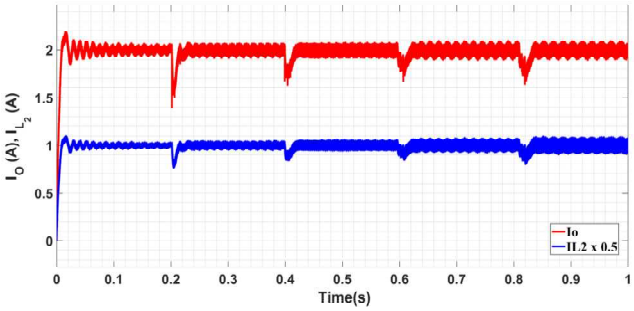


Fig. 12 Load regulation of Zeta converter under Current Mode control

The regulation of load current with line variation: The evaluation of Zeta converter utilizing closed loop current control under varying input is discussed in Fig.13.The Zeta converter was subject to different input voltage levels between 24V to 48V, but control scheme works well to regulate the output current at steady value.

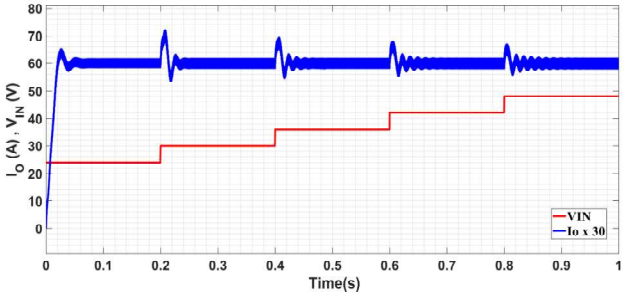


Fig. 13 Impact of Line variation on Output current

V. CONCLUSION

This paper discusses the operating mode of Zeta converter, design aspects and development of small signal model.
Further, the paper investigates and compares two control approaches for Zeta converters: closed-loop voltage mode and closed-loop current mode. Results show that the closed-loop voltage mode is control with its simplicity and ease of implementation, is efficient in regulating Zeta converters' output voltage, ideally suited for applications prioritizing precise voltage regulation. Nevertheless, its ability to handle dynamic load conditions and input voltage fluctuations might be limited compared to alternative methods. On the contrary, closed-loop current mode control effectively tackled challenges stemming from varying load conditions and voltage changes. Continuous current sensing and feedback loop integration resulted in a stable, efficient power conversion, making it a robust option for diverse applications. Future research can focus on integrating cutting edge control algorithms, such as Model Predictive Control (MPC) to enhance the performance of Zeta converters. These algorithms could offer superior control in the face of rapidly changing load and input conditions. Developing adaptive control strategies that can self-adjust to varying operating conditions is a promising area of research. By addressing challenges, exploring innovative control techniques, and prioritizing practical implementation, the field can look forward to a brighter future with Zeta converters at its core.

REFERENCES

[1] P. R. Babu, S. R. Prasath and R. Kiruthika, "Simulation and performance analysis of CCM Zeta converter with PID controller," [ICCPCT-2015].

[2] Verma, Sujata, S. K. Singh, and A. G. Rao, "Overview of control Techniques for DC-DC converters", Research Journal of Engineering Sciences ISSN 2278 (2013).

[3] Niculescu, E., Mioara-Purcaru, D., Niculescu, M. C., Purcaru, I., & Maria, M. (2009, July). A simplified steady-state analysis of the PWM Zeta converter. In *WSEAS International Conference. Proceedings. Mathematics and Computers in Science and Engineering*.

[4] Khaleghi, H., Varjani, A. Y., & Mohamadian, M. (2014, February). A new bidirectional zeta DC/DC converter. In *The 5th Annual International Power Electronics, Drive Systems and Technologies Conference (PEDSTC 2014)*. IEEE.

[5] Mittal, S., Singh, A., & Chittora, P. (2022, October). EV Control in G2V and V2G modes using SOGI Controller. In *2022 IEEE (GCAT)*.

[6] C. Sudhakarababu and M. Veerachary, Zeta Converter for Power Factor Correction and Voltage Regulation, 2004 TENCON Proc.

[7] Durgadevi, S., & Umamaheswari, M. G. (2018). Analysis and design of single-phase power factor correction with DC–DC SEPIC Converter for fast dynamic response using genetic algorithm optimised PI controller. *IET Circuits, Devices & Systems.*

[8] J.-L., Lin, S.-P., Yang, and P.-W. Lin, Small Signal Analysis and Controller Design for an Isolated Zeta Converter with High Power Factor Correction, Electric Power Systems Research 76, © 2005 Elsevier B.V.

[9] Vuthchhay, Eng and Chanin Bunlaksananusorn, "Dynamic modelling of a Zeta converter with State-Space averaging technique", In ECTI-CON 2008, IEEE.

[10] Kochcha, Pijit and Sarawut Sujitjorn, "Isolated zeta converter: principle of operation and design in continuous conduction mode", WSEAS Transactions on Circuits and Systems (2010).

Authorized licensed use limited to: DELHI TECHNICAL UNIV. Downloaded on February 07,2024 at 06:47:56 UTC from IEEE Xplore. Restrictions apply.

A Distribution of Nodes in Big Data using Hadoop Open Source System

Nishant Mathur, Mukul Jain

Abstract*: Apache Hadoop is an free open source Java framework under Apache Software Foundation. It provides storage of large amount of data efficiently with low costing. Hadoop has two main core components one is HDFS (Hadoop Distributed File System) and second Map Reduce. It is basically a file system and has capability of high fault-tolerant and while deploying supports less cost hardware. It provides the high speed admittance to the relevance data. The Hadoop architecture is based on cluster, which consist of two nodes named as Data -Node and Name-Node which perform the internal activity known as heart beat to process data storage on distributed file system and Map reducing is performed internally to show the clustering of distributed data on localhost of ssh serverwebsite. Large quantity of data is needed to store in distributed file structure, for this Hadoop has played important role. Maintaining the large volume storage, making data duplicity for providing security and recovery of big data for its analysis and prediction.

Keywords: Big Data, Hadoop, HDFS, Map Reduce Data-Node, Name-Node, Task-Tracker and Job-Tracker.

I. INTRODUCTION

The term Big Data is used to depict the collection of composite and large data sets such that it is complicated to store, practice and examine. In today's era when we can't wait even for a five seconds to open a Google page or social network page then how can we wait to analyze this much huge amount of data that are generated everyday by different means such as sensors, Facebook, Twitter, flight data, etc. Let us explain what we really want to explain, suppose a team of marketing people have some huge data with them and they want to perform analysis on that data to improve their marketing scheme, back days it use to happen if some famous vendor in the market approach them to analyze that data at that time, it might have taken such as 10 years to analysis it.

What we can conclude that after long 10 years is there any relevance and meaning of that data for the user, obviously not. So we cannot think of such a long duration should be used and followed for analyzing big size of data in present era. So the improvisation we got for such kind of problems like analyzing and storing large size of data, here comes the technology and concept known as Big Data. When we talk about Big Data, the first name comes in mind is "HADOOP" a well known product that introduces as one of the solution for Big Data problems. According to IBM definition of Big Data, it has three components commonly known as three V's they are 1) Volume (data in Exabyte or Petabyte), 2) Variety (Unstructured, Semi Structured and Structured data) and 3) Velocity (data processing speed). By considering every data in these three components we can easily store and retrieve our Big Data.

II. FOUNDATION OF HADOOP

The start of Apache Hadoop Projects was developed from the White paper series which was proposed by Google on Big Table, which uses chunks concepts in GFS from there the idea of Map-Reduce emerged. Google has published whitepaper ice breaking idea for big and distributed file and gave the idea of how to handle Big Data using distributed file system but the code and implementation was never disclosed. Later Yahoo and many other contributors implemented this Google's white paper idea and that's how Hadoop file system framework was proposed. Hadoop is top level Apache Software project led by Yahoo [1][2]. Another term which we have is Hadoop Cluster there might be quite confusion between Hadoop and Hadoop cluster in people's mind. Let us discuss more on their differences.

A. Hadoop

Hadoop is an open source structure, which proposes the functioning of big data sets in a distributed computing surroundings. It has of Map-Reduce, Hadoop Distributed File System (HDFS) and large quantity of interrelated projects like Apache Hive, Hbase, PIG and Zookeeper [11].

B. Hadoop Cluster

Hadoop is unique types of formulated structure for storing, analyzing and managing large amount of structured, semi structured and unstructured files in a distributing atmosphere for computing. These cluster runs on hardware of related and commodity types [11].

III. FOUNDATION WORKINGS OF HADOOP CLUSTER

Hadoop clusture consist three main working components they are Master, Client and Slave. Here Client is neither master nor slave; rather it plays one of the very important roles of loading the data into cluster and submits the jobs to Map Reduce. Also it describes how stored data should be access and retrieves to analyze the reaction after achieving jobs. Master services consist of service like Name-Node and Job-Tracker while Slave services are Data-Node and Task-Tracker which we will be discussing in detail later in this

Revised Manuscript Received on January 05, 2020.
* Correspondence Author
Mr. Nishant Mathur *, Assistant Professor, ICFAI Tech School, ICFAI University, Dehradun , INDIA.
Dr. Mukul Jain, Assistant Professor, ICFAI Tech School, ICFAI University, Dehradun , INDIA.

paper. Master and Slave component of hadoop cluster will be discussed further showing with the specific functioning wherever required.

IV. HADOOP DISTRIBUTED FILE SYSTEM

A. **Introduction-** The Hadoop Distributed File System (HDFS) is a associate venture idea of the Apache Hadoop, the origin of this idea was from Google White paper on Google File System (GFS) [1][2]. It is distributed and extremely error forbearing file system designed to run on less charge commodity hardware. It provides great throughput contact to function of data and also fit for applications with huge data sets [1].

B. **Block Structure-** HDFS is a specifically deliberate file system for managing big data and its sets with the bunch of commodities hardware and analyzing access outline, here streaming access sample works as said in java's slogan i.e. "Write once run anywhere", same way here streaming access pattern in Hadoop means you Write once and read it number of times and never try to change the content of the file. Conceptually, HDFS is a block-controlled file system where connected files are of a fixed size may be of 64Mb or 128Mb broken into blocks.

These blocks with data storage capability are stored crosswise in cluster of one or more equipment [1], as shown in Fig. 1.

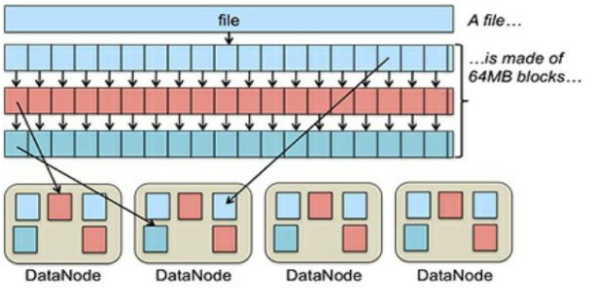


Fig. 1 Example of Block Structure files system

C. **Structural Design-** HDFS is collection of interrelated cluster of point as node where files and directories inhabit. It has two types of services, one is master service and another is slave service. Master services consist of Name Node, Secondary Name-Node and Job-Tracker whereas Data-Node and Task-Tracker consists of Slave services. Each master service can communicate to one other like name node and job tracker can communicate to each other in master service similarly on the other hand each slave service can communicate to each other within here data node and task tracker can communicate to each other, whereas when they have to load and process the data then master can only communicate to its specific slave service, like master's name node can only communicate to slave's data node and master's job tracker can communicate to slave's task tracker ,as shown in Fig. 2.

D. **Name Node-**It is one of the master services. It controlled the data node presents on building blocks in file system. It has meta-data of those data which are stored on data node. If there is any loss of metadata happens in name node and we are unable to access that data from data node this type of failure is known as single point failure. Therefore it requires high reliable hardware for name node.

E. **Data Node-** It is slave service for the name node which is deployed on commodity hardware. It is the location where information is collected and is dependable for managing functions like examine and writes. These services are requested by the clients.

1. Secondary Name Node- As we have already discussed name node in master services, secondary name node is the sub method in master services. Its main responsibility is to perform intermittent checkpoints. At the performance of name node when their failures occur, it can restart the name node utilizing the checkpoint [11].

F. **Job Tracker-** Job-tracker plays one of the important role of master, it is the one to which client request submit performance to carry out the Map Reduce function. Job-tracker submit job to task tracker of slave service and manages overall execution of Map Reduce job.

G. **Task Tracker-** Task tracker plays the role of slave, every task-tracker is accountable to perform and supervise everyone tasks assigned by job-tracker. It manages the data movement. Task-tracker send the heart strike to job-tracker that tells the job-tracker that yes it is alive and process the job that was submitted to it, If it fails to send heart beat then job tracker assumes that task tracker is crashed then again it submit the job to the corresponding task tracker of other nodes in the cluster who so ever have data that client requested.

V. NAME NODE AND DATA NODE: THE BONDING STORY

When client has some data they wants to store in HDFS for effective storage and fast processing client request the name node that it already have some data but they don't know to which data node they will store data, in response of this request the name node send the information to that data node which have enough free space. The data stores in the data node need not to be in serial manner it depends on the free available space in it. As we discussed before that name node can communicate to data node for storing the data. The data-node sends block information and heart hit to let the name-node aware that it is alive and working. In general what happen actually is that data is stored in data node while the name node maintains metadata i.e. data of the data.

This metadata contains information about on which data node client has stored its data and on which data node the replication of data has been made. If the name node fails or crashes sometime then we say it's a loss of metadata, without the metadata we cannot process to store data from data node.

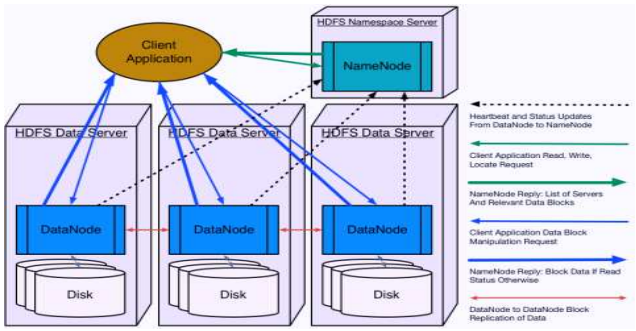


Fig. 2 Example of HDFS Architecture

As we were discussing about the HDFS which is basically a file system, here question arise is, well if it is a file system, so what kind of file organization it has? We can explain this by saying that HDFS managed usual hierarchical file management in which directories was created by users, files renaming was done by user inside the directory and using HDFS commands reposition or deletion can be done in files. It can also manage Cloudera and Amazon Simple Storage System (Amazon's S3) in Amazon web services as a third-party file system [1][5].

A. **Data Replication in HDFS-** When a client loads its data from local file system to HDFS. Its data node makes two more copies of the same data that means maximum we have three copies of every data on different data nodes and if any kind of failure occurs in any of the data node then the user's data will not be lost. It makes replication of data by default.

B. **Block Size-** HDFS is special file system that uses, to store the data in memory, the block size of 64Mb or 128Mb. In local file system the memory block size used is of 4Kb.

C. **Communication-** There is two types of signals sent between data node and name node

1. **Heart Beat-** The data-node and task-tracker used to launch heart beat to name-node and job-tracker to let their master know that they are alive and in working mode. If in case any of data node is crashed or dead no heart beat is sent to data-node and job-tracker. Data stored in dead data-node is not much longer existing to HDFS client from that port, which is proficiently erased from the system. If the casualty of a node happened then the imitation factor drops below to their lowest significance, the name-node starts duplication of data to bring the imitation factor (i.e. three copies of same data) back to the normalized state [1].

2. **Block Report-** Whenever client stores the block into data node it sends the proper block report to name node. By the help of this block report map reduce is performed on HDFS stored data.

VI. THE IMPLEMENTATION

The implementation of Single Node Hadoop Cluster on Ubuntu operating system is explained in following steps:

Step 1: *D*ownload and install JAVA JDK1.8.0_31 from website [14].

Then moved that file to directory created for JAVA

step 2: JDK installation.

Code: sudo mvjdk1.8.0_31/*/usr/lib/nishant/jvm/jdk1.8.0_31

Now run the following command to enable JAVA JDK,

Code: sudo update-alternatives –-install "/usr/nishant/bin/java" "java" "/usr/lib/jvm/jdk1.8.0_31 bin/java" 1

sudo update-alternatives –install "/usr/bin/nishant/javac" "javac" "/usr/lib/jvm/jdk1.8.0_31/bin/javac" 1

sudo update-alternatives –install "/usr/bin/nishant/javaws" "javaws"

"/usr/lib/jvm/jjdk1.8.0_31 /bin/nishant/javaws" 1

After running these commands set java path under .bashrc file by creating a JAVA_HOME variable.

Code: #JAVA_HOME directory setup

export JAVA_HOME="/usr/lib/nishant/jvm/jdk1.8.0_31"

set PATH="$PATH:$JAVA_HOME/bin/nishant"

export PATH

Step 3: Now Install Apache Hadoop free open source.

For this download Apache Hadoop free open source latest Version from its official website [3]

Then edit hadoop-env.sh inside the /home//nishant/user/Downloads/hadoop-1.2.1/conf_by adding following code.

Code:

export JAVA_HOME="/usr/lib/nishant/jvm/jdk1.8.0_31"

After this now pass the path address of Hadoop inside .bashrc file link again by adding the below code.

Code:

export HADOOP_HOME="Downloads/hadoop"

PATH=$PATH:$HADOOP_HOME/bin/nishant

Type the export PATH

Then reconfigured core1-site.xml, hdfs1-site.xml and mapred1-site.xml by adding the following code to respective .xml file.

Code: core1-site.xml

<name>fs.default.name</name>

<value>hdfs://localhost:8000</value>

Code: hdfs1-site.xml

<name>dfs.replication</name>

<value>1</value>

Code: mapred1-site.xml

<name>mapred.job.tracker</name>

<value>localhost: 9001</value>

***Step 4*:** Installation of ssh server

Code: sudo apt-get install ssh

***Step 5*:** To Connecting ssh server

Code: ssh localhost

Step 6: Enter password

Step 7: For the first time formate the name node before starting it

Code: hadoop namenode -format

Step 8: To Start all services

Code: start-all.sh

Step 9: To check connection services has been established or not, enter the following address to browser [3]. You get the following Screen as output, as shown in following screenshot when you enter the following address to browser.

http://localhost:50070/, as shown in Fig. 3.

http://localhost:50030/, as shown in Fig. 4.

http://localhost:50060/, as

shown in Fig. 5.

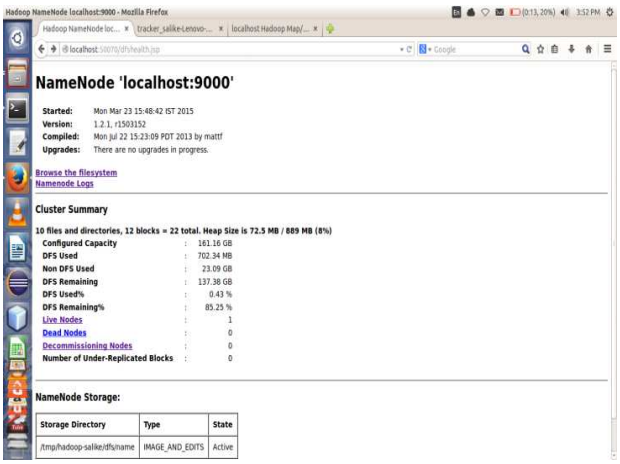


Fig. 3 Example of localhost: 50070

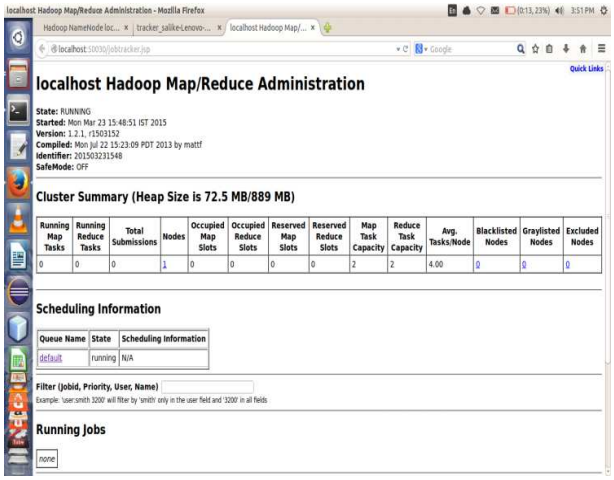


Fig. 4 Example of localhost:: 50030

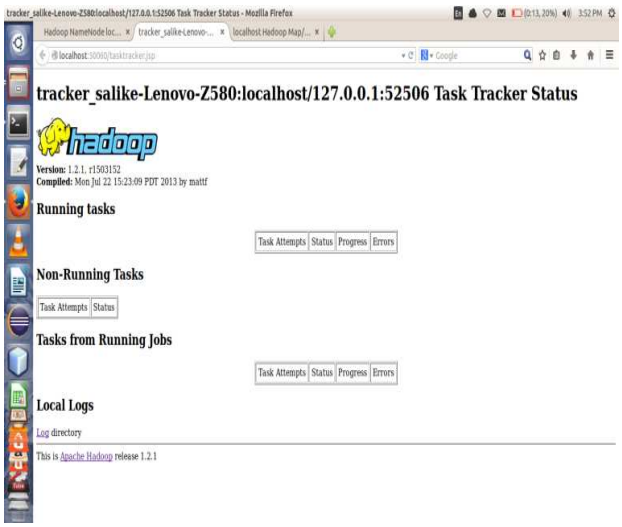


Fig. 5 Example of localhost: 50060

The above screenshot shows the successfully configured Hadoop single node using local host on Ubuntu.

VI. RESULTS

After performing single node implementation on Apache Hadoop, the file which we uploaded as sample data is movie file of size 730.7 Mb with .mkv format that was much heavy file we used as compared to the normal text file, this has been distributed on eleven number of blocks of size 64 Mb each and there time calculation has been optimized and access of data after distribution on different has become fast and easy. If we could have used normal file system of 4 Kb block size then this same file of 730.7 Mb should have used 299307.2 numbers of blocks in memory. This is one of the main reasons why we are using block size of 64 Mb or 128 Mb in HDFS, so we can say by our experiment that lesser the number of memory block used by data, lesser the number of meta data in name node.

Output of file distribution in 11 blocks of 64 Mb file sized, is shown in Fig. 6.

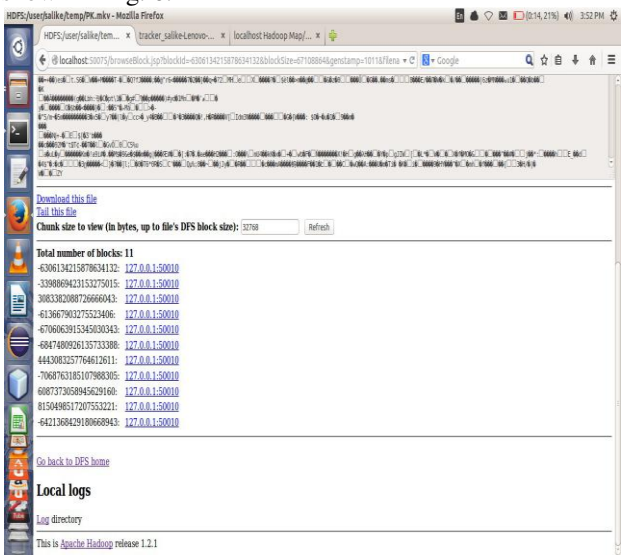


FIG. 6 Example Showing Distribution Of 730.7 Mb Files In 11 Hdfs Block

VII. CONCLUSION

Apache Hadoop is an open source disseminated file structure and data managing project that is used for keeping and managing huge data sets. It has two core components first HDFS for storage of data and second Map Reduce for processing of data. Hadoop is not a database. The Hadoop platform was designed to solve Big Data three V's problem. Also it is used 1) For search as in Yahoo, Amazon, Zevents. 2) For log processing as in Facebook, Yahoo etc 3) For Data Warehouse as for Facebook, AOL. 4) For Video-Image examination like New York Times, Eyealike[2]. The Hadoop structure mostly written in JAVA programming language, with some indigenous code in C and control written in shell-script is useful for data management and its analysis for managing big size data and hence can be utilized for data extraction and foretelling.

VIII. FUTURE WORK

Our present work shows block size of 64 Mb has been used, for further we can manage to use the block size to 128 Mb by

which we can further reduce the space for Metadata in memory allocation as we can have big data to implement the modified version of algorithm. Also further the working on Hadoop Multi Node cluster's implementation can be achieved which will explore the power of distributed computing on multiple systems by using Apache Hadoop and Apache nutch indexing concept on open source system.

REFERENCES

1. J. Jeffrey Hanson, CTO MAX"An Introduction to the Hadoop Distributed File System" by IBM developer works 01 February 2011.
2. (2015) The Hadoop Apache homepage on wikipedia. [Online]. Available: http://en.wikipedia.org/wiki/Apache_Hadoop
3. (2015) The Hadoop Distributed File System project website. [Online]. Available: https://hadoop.apache.org/
4. (2012) The Big Data University website. [Online]. Available: https://bigdatauniversity.com/wpcourses/
5. (2011) S3 infrastructure homepage on Amazon [Online]. Available: http://aws.amazon.com/s3
6. Agrawal, R., Rajagopalan, S., Srikant, R. and Xu, Y, "Mining Newsgroups using Networks Arising from Social Behavior" in *12th International World Wide Web Conference (WWW 2003)*,(pp. 529-535), Budapest, Hungary, May 2003.
7. Aktas, M. S., Nacar, M. A. and Menczer.F, "Personalizing Page Rank Based on Domain Profiles" in Workshop on Web Mining and Web Usage Analysis, Seattle, WA, Aug 2004.
8. (2004) Search Kit Reference homepage on Apple Developer Connection.[Online]. Available:https://developer.apple.com/library/mac/documentation/UserExperience/Reference/SearchKit/index.html
9. Arasu, A., Cho, J., Garcia-Molina, H., Paepcke, A. andRaghavan, S. Searching the Web in ACM TOIT, 2001
10. Joachims, T. Optimizing, "Search Engines Using Click through Data" in ACM Knowledge Discovery and Data Mining, 2002.
11. (2014) Sap hana and Hadoop homepage on saphanatutorial [Online].Available:http://saphanatutorial.com/sap-hana-online-courses
12. (2014) Hadoop cluster on homepage search business analytics's TechTarget[Online].Available:http://searchbusinessanalytics.techtarget.com/definition/Hadoop-cluster
13. (2016) Tsai, Cheng-Fa, and Yao Chiang, "Enhancement of data clustering using TSS-DBSCAN approach for data mining," International Conference on Machine Learning and Cybernetics (ICMLC), IEEE, Vol. 2, pp. 535-540.
14. (2017) Charu C. Aggarwal, "Introduction to special issue on the Best paper from KDD 2016," IBM T.J. Watson Research Center, Vol.11, Issue 4, pp. 39.

AUTHORS PROFILE



Mr. Nishant Mathur received B.Tech, M.E. (Computer Science and Engineering) degree from Delhi College of Engineering and Ph.D.(Pursuing). His specialized fields are Database Systems, Data Mining, Machine Learning and Big Data Analysis. He published several research papers in reputed conferences & Journals. He is Assistant Professor of Computer Science and Engineering at ICFAI Tech School, The ICFAI University, Dehradun.



Dr. Mukul Jain (Assistant Professor) is Doctorate from H.N.B Gharwal University in the field of Operational Research. He earned his Bachelor degree in Mathematics with First Division in 1997 and completed his Masters Degree in Mathematics in 1999 from Gharwal University, Uttarakhand, Dehradun. He has published more than 6 papers in peer reviewed international/national journals and conferences. He is Department In charge at ICFAI Tech School, The ICFAI University, Dehradun.

Solar Compass 3–4 (2022) 100031

Contents lists available at ScienceDirect

Solar Compass

journal homepage: www.elsevier.com/locate/solcom

A feasibility study and cost benefit analysis of an off-grid hybrid system for a rural area electrification

Upma Singh[a,b,*], M. Rizwan[a]

[a] Department of Electrical Engineering, Delhi Technological University, Delhi 110042, India
[b] Department of Electronics and Communication Engineering, Maharaja Surajmal Institute of Technology, Delhi 110058, India

ARTICLE INFO

Keywords:
Renewable energy
HOMER
Biogas
Solar photovoltaic
Hybrid renewable energy sources (HRES)

ABSTRACT

Off-grid power production utilizing renewable sources of power has become more significant and viable to meet the limited demands of remote locations. The primary goal of this study is to develop an economic and optimal hybrid PV/Biogas configuration for power production for rural common facilities including one Primary school, Junior school, and Panchayat Ghar buildings of Sarai Jairam village in Uttar Pradesh, India. Data on the electric load was gathered for two schools and Panchayat Ghar. The PV/biogas hybrid configuration was designed utilizing the Hybrid Optimization Model for Electric Renewable (HOMER) and techno-economic analysis is carried out to fulfill the load requirements. The available biomass potential and the data on solar irradiance of the study area were utilized in the HOMER software to carry out the analysis. The HOMER analysis produced a solution that included total net present cost (NPC) and cost of electricity (COE), and these results were then further improved using sensitivity analysis. The sensitivity analysis employed sensitivity parameters like biomass potential, biomass pricing, solar irradiance, and variation in loads. Based on the NPC and COE, this analysis evaluates the system performance and demonstrates that it is techno-economically feasible.

1. Introduction

The unavailability or shortage of electrical networks in remote locations, the excessive cost of grid extension, and the harsh topography frequently lead to the exploration of other alternatives. One of the most promising approaches to meet these areas' need for electrification now involves standalone hybrid systems [1]. The grid-connected electricity for power delivery does not always benefit people. For instance, individuals who live in isolated villages, distant farms, and rural locations must rely on autonomous power supply systems that are based on the burning of fossil fuels [2]. The issue is that these systems increase greenhouse gas (GHG) emissions, which in turn lead to air pollution [3]. By utilizing renewable energy sources like solar, wind, biofuels, and others, GHG emissions may be decreased. Rural electrification is crucial to improving the economic and social conditions of rural residents and, eventually, to the development of the country [4–5]. The bulk of the population in India lives in isolated rural regions where they do not have access to grid energy and expanding the grid is not practical. Furthermore, those remote locations with grid connections only receive a restricted supply once every six to nine hours [6]. In addition, using a diesel generator to get an electric supply is not a practical alternative due to the expense of fuel, maintenance, and operation, as well as the emission of greenhouse gases, etc [7–8]. Additionally, the Government of India is working to promote renewable energy sources by offering various programs, incentives, etc. The Indian government has also set a target of increasing the amount of electricity produced by RES to 450 GW by 2022 [9].

Due to the stochastic nature of RES, a hybrid system that combines two or more sources is a more advantageous and sustainable alternative [10]. Utilizing a variety of simulation and optimization tools and approaches, a great deal of work has been done in this regard.

Flavio Odoi- Yorke et al. examined the possibility of using a hybrid solar PV/biogas/battery energy system to provide power to distant areas in Ghana. The objective is to employ locally accessible renewable energy sources to reduce greenhouse gas emissions while achieving a Levelized Cost of Electricity (LCOE). The results show that in terms of cost and pollution savings, PV/biogas/battery systems outperform PV/diesel/battery and diesel-only systems [11]. Endeshaw Solomon Bayu et al. conducted a study to incorporate wind turbines, microhydro systems, solar photovoltaic (PV) systems, and battery systems to check the feasibility of hybrid systems to electrify the remote place [12]. Paul et al. examined the economic viability and feasibility of utilizing a hybrid-electricity system in rural areas. The findings show that, when compared to PV/Diesel Generator (DG)/B and isolated DG systems, the photovoltaic (PV)/battery (B) system based on renewable energy (RE) has the lowest net profit cost (NPC) and cost of energy (COE). Although the COE and NPC values of the diesel generator (DG) hybrid-electric sys-

* Corresponding author.
E-mail addresses: upma@msit.in (U. Singh), rizwan@dce.ac.in (M. Rizwan).

https://doi.org/10.1016/j.solcom.2022.100031
Received 11 November 2022; Accepted 30 November 2022
2772-9400/© 2022 Published by Elsevier Ltd on behalf of International Solar Alliance. This is an open access article under the CC BY-NC-ND license (http://creativecommons.org/licenses/by-nc-nd/4.0/)

tem (HES) are lower than those of the PV/DG/B system, the DG system still emits the most substantial pollution [13].

Similarly, Nyagong Santino et al. evaluated the viability of a hybrid power system for a remote South Sudanese community without electricity access. Based on the community's energy requirements, average energy consumption profiles were created over the course of a year. The system was configured and optimized using the HOMER pro application, and based on the standalone mode of operation, six potential combinations were modeled and examined technically and economically. Due to the significant solar potential, the Battery/DG/PV system has the minimum Net Present Cost (NPC) and Cost of Energy (COE) and provides a 22.94% investment return [14]. For the Atacama Desert in Chile, Francisco et al. conducted a cost-benefit analysis of the TEG-HPV system under actual environmental and market circumstances. The economic, electrical, and thermal models of the TEG-HPV system are constructed and examined in MATLAB. With regard to system costs, energy losses, ordinal efficiencies of TEG and PV modules, and their contributions to the economical viability of TEG-HPV systems, five distinct cases are taken into consideration. Payback durations for every scenario are calculated at maximum and minimum PV temperatures for the Atacama Desert, taking into account the industrial and residential prices of electricity [15]. Laetitia et al. conducted a feasibility study with the goal of incorporating renewable energy sources into Popova Island's energy system. It takes an analytical strategy that entails using an energy systems model and the Monte Carlo method before assessing the financial results [16]. Ahmad et al. investigated the feasibility of meeting the load demand with the best system that produces the least amount of CO_2 and net present cost (NPC) emissions. The modeling results demonstrate that the NPC of the proposed grid/PV system is more sufficient than other configurations at the present grid tariff, resulting in a renewable proportion of more than over 50%, a payback period of 17 years, and a 54.3% decrease in CO_2. The outcomes further demonstrate that the integration of a 62 kW PV array with the primary grid is the optimal configuration that results in a minimal COE of 0.0688 $/kWh and sale back power of 9.16% of Al Baha University's total electricity consumption [17]. Mohammad Amin et al. developed the best renewable energy system possible to power a small community using only renewable energy sources. Like many remote Iranian communities, this one experiences regular power shortages. A hybrid stand-alone and on-grid renewable energy system using fuel cells, biogas generators, wind turbines and photovoltaics, is suggested. In addition to the fuel cells, batteries, a hydrogen tank, an electrolyzer or reformer, and other backup and storage components are employed. The major objective is to identify the best design that can fulfill the demand for power while being acceptable from an environmental and an economic standpoint. The findings demonstrate that the cheapest option is to use biogas, wind and solar rather than adding a fuel cell to this design would raise prices by 33–37% while simultaneously increasing the scalability of the system [18].

It is clearly revealed from the literature that a hybrid energy system with a diesel engine has several benefits over one that is solely powered by a diesel engine, including a longer engine lifespan, lower O&M (Operation and Maintenance) costs, lower fuel consumption and less of an adverse impact on the environment. Such systems still depend on fossil fuel, which is unfriendly to the environment and necessitates logistical arrangements for delivering the fuel to the community, which is the problem with them. Local fuel availability is frequently poor because of expensive transit expenses and theft danger.

The diesel engine may be totally replaced with a biogas engine to solve the aforementioned issues, and its fuel can be produced locally in a limited digester. Utilizing locally generated biogas from dung can resolve issues associated with diesel fuel.

Furthermore, the literature survey also indicates that HRES is a more reliable and cost-effective source of power than conventional grid systems. Additionally, the aforesaid research mostly focused on household electrification of rural areas while ignoring the need for power for schools and panchayat ghar. To the author's knowledge, there is no thorough study on the techno-economic analysis of such HRES in using HOMER on the selected location. Also, the creation of such models relied on the use of solar and wind energy, and there are only a small number of studies in which biogas and biomass energy sources were regarded as important sources for generating electricity. İn this regard, an HRE-based power producing system is suggested for supplying continuous electricity to two schools and Panchayat ghar, located in Sarai Jairam village, district Agra, Uttar Pradesh, India. As a consequence, the major goal of this study is to offer the most feasible and most optimized alternative for electrifying panchayat ghar and primary schools situated in distant areas without access to grid electricity. To create the HRES, local RES from the research region is employed. Data on electrical load, solar radiation and biogas were utilized to apply techno-economic analysis utilizing HOMER pro simulations based on sensitivity.

The organizational structure of the paper is planned as follows. Section 2 discusses the method of modeling of hybrid systems. Section 3 describes the assessment of electrical load. Section 4 briefly explains the system design and its assessment. Section 5, contains results and discussion and Section 6 presents the conclusions.

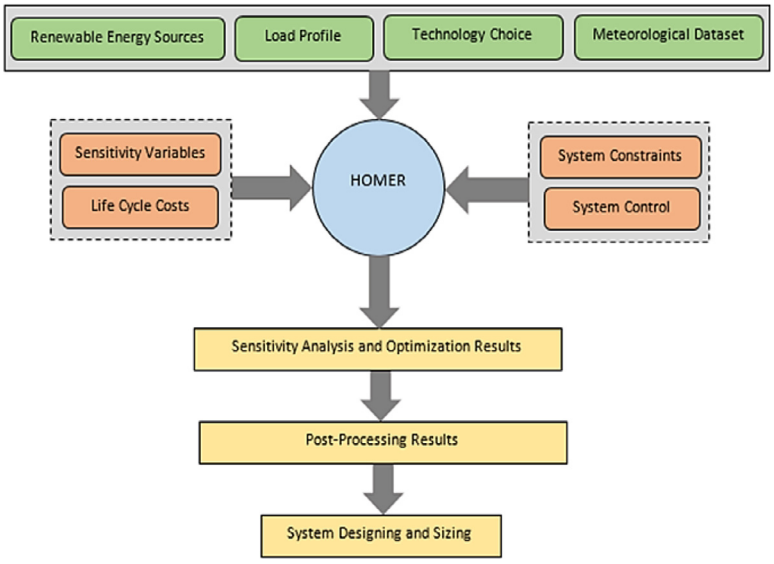


Fig. 1. Process and proposed framework for system modeling and analysis.



Fig. 2. The geographic view of the research location.

2. Method of modeling hybrid systems

For the design and construction of an optimum hybrid system for a rural region, a systematized modeling technique is an integral step since it ensures that the rural population has reliable, consistent and dependable access to electricity [19]. The HOMER pro software has been utilized as a tool to identify the set of optimum systems that meet the load demand under specific system restrictions and input assumptions [20]. HOMER pro is a distributed power optimization tool designed by the National Renewable Energy Laboratory in the United States [21]. Due to the uncertainties, a sensitivity analysis is conducted to investigate the influence of input assumptions on the optimization outcomes. Fig. 1 depicts the process and proposed framework for system modeling and analysis. In the current study, a modeling technique that is shown in the following sections includes a description of the selected location, assessment of renewable energy sources potential, electrical load estimation and system design and optimization procedure.

2.1. Location description

The site for this study was Sarai Jairam village in Uttar Pradesh, India. The abundance of renewable energy and the region's strategic significance was taken into consideration while choosing the location. The location is identified by the coordinates at the longitude of 78° 10.7'E and latitude of 27° 20.2'N and time zone (GMT+05:30) from NASA meteorological data. Fig. 2 shows the geographic view of the research location.

2.2. Assessment of wind and solar resources potential at the selected site

From NASA meteorological data, the solar and wind energy data for Sarai Jairam village have been extracted, and the data are shown in Table 1 with their latitude and longitude (27° 20.2'N, 78° 10.7'E), and time stamp (GMT+05:30). Figs. 3 and 4 provide graphical representations of the specifics of solar radiation throughout the course of the year and wind data over the same period. Table 1 provides data on the selected site's annual average daily radiation (kWh/m^2/day), clearness index and wind speed (m/s).

2.3. Assessment of biomass energy resource potential at the selected location

In Sarai Jairam village animal dung may be simply used to produce biogas through the digestion and combustion processes, respectively. Anaerobic digesters are used to treat the manure produced by cattle and

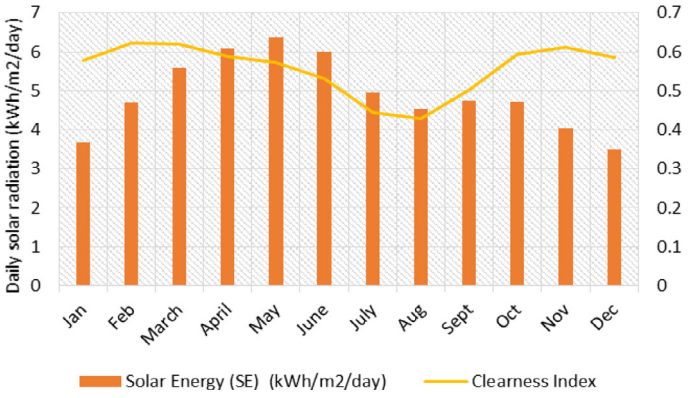


Fig. 3. Monthly average solar irradiance throughout the year.

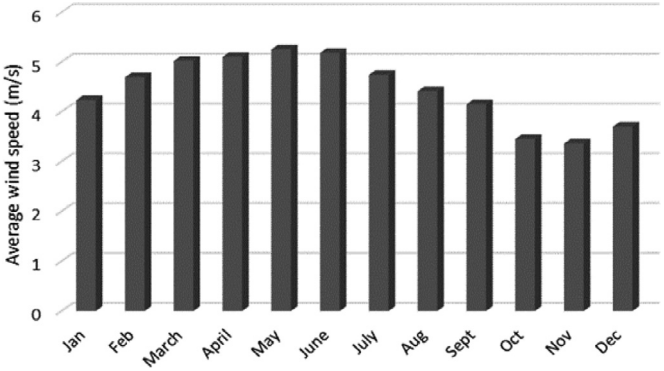


Fig. 4. Monthly average wind speed throughout the year.

produce power. The total dung produced annually from the community is calculated by Eq. (1);

$$M_n = \sum_{n=1}^{j} N_j m_j \tag{1}$$

where, M_n is the annual total amount of manure produced, N_j is the number of the selected group of animals, n is the overall number of cattle and m_j shows manure produced per cattle [21].

Table 2 lists the number of animals and the availability of animal manure in the village of Sarai Jairam. The total amount of manure produced by all the animals is estimated to be 6.425 tons/day, which may

Table 1
Average monthly daily radiation, clearness index and wind speed.

Month	Solar Energy (SE) (kWh/m^2/day)	Clearness Index	Wind Speed (WS) (m/s)
Jan	3.670	0.578	4.230
Feb	4.690	0.623	4.690
March	5.590	0.620	5.020
April	6.080	0.589	5.100
May	6.360	0.574	5.250
June	6.010	0.531	5.180
July	4.960	0.444	4.740
Aug	4.540	0.430	4.410
Sept	4.750	0.503	4.150
Oct	4.730	0.595	3.450
Nov	4.030	0.611	3.360
Dec	3.490	0.585	3.700

Table 2
Total amount of manure produced by all animals.

Description	Number of animals	Dung (kg/day/cattle)	Dung availability (kg/day)
Buffaloes	310	15	4650
Cow	175	10	1750
Goat	25	1	25

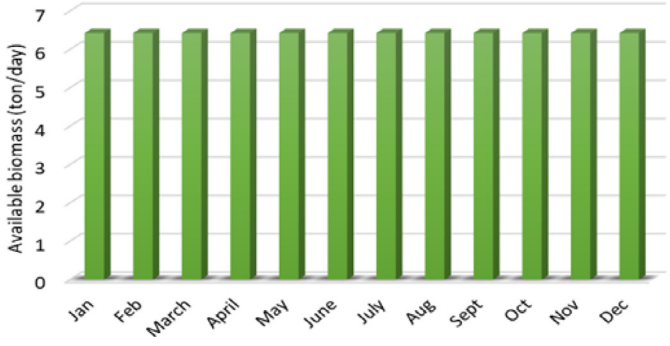


Fig. 5. Technical potential of biomass (animal manure).

be used to produce 166667.76 kWh of power annually. The total potential of biomass is shown in Fig. 5.

3. Assessment of electrical load

In this work, a hybrid system that employs energy from solar and biogas has been designed to meet the electrical demands of one Primary school, Junior school and Panchayat ghar. The panchayat ghar has two rooms with two fans and four tube lights. The primary school contains six rooms with twelve fans, twelve tube lights, two computers and one submersible pump, while, five rooms, ten fans, ten tube lights, two computers and one submersible pump make up the junior high school.

Table 3 provides the quantity, power ratings and power consumption for each load. Fig. 6 depicts the electricity load of the proposed region taking into account future expansion. The data has been gathered from the school and panchayat ghar employees.

4. System design and assessment

The system configuration shown in Fig. 7 includes a PV panel, biogas engine generator, and battery storage with a bidirectional converter. An electric load and biogas generator are connected to the AC bus. The battery storage and PV module are connected to the DC bus. Additionally, the converter is coupled with the AC and DC buses. Table 4 shows the technical specifications and capital costs of components.

5. Results and discussion

5.1. System sensitivity analysis outcomes

For technical and economical assessment purposes, the system must be designed with certain constraints or control variables that have an impact on the operating costs and output of the HRES system. Because the developed system is sustainable and the possibilities like the changes in solar radiations and biomass supply were taken into account for the sensitivity analysis. Since animal dung is a free source of biomass, hence, the biomass price was not considered in the system design. It enables planners and designers in selecting a very efficient and cost-effective method for the specified design parameters. To find out how variations in solar radiation and biomass supply might affect the system economy, both variables were varied. As the supplied biomass was 6.43 tonnes per day, it varied between 6.43-6.50 tonnes per day for the sensitivity analysis, and the solar radiation varied between 4.91–4.99 kWh/m^2/day. The sensitivity analysis outcomes of the HRE system are displayed in Table 5, which highlights how changes in the supply of biomass and

Table 3
Electricity load calculation for the selected communities.

S.no.		1	2	3	4
Load		Fan	Tube light	Computer	Water pump
Power rating (watts)		60	30	100	500
Panchayat ghar	No. in use	2	4	0	0
	Utilization hours	10	10	0	0
Primary school	No. in use	12	12	2	1
	Utilization hours	8	8	8	1
Junior school	No. in use	10	10	2	1
	Utilization hours	8	8	8	1
Total energy Consumed (Watt)		11760	6480	3200	1000
Total load		22.440kWh			

Table 4
Technical specifications and cost of components.

Hybrid system components	Specifications	Value
Solar PV	Capital cost	650$/kW
	O&M cost	1$/kW
	Replacement cost	0$/kW
	Sizes	0,1,1.5,2,2.5,3,3.5,4,4.5,5,6,7,7.5,8,9,10
	Tracking system	No
	Ground reflectance	20%
	Derating factor	80%
	Life span	25 years
	Azimuth,Slope	0
Converter	Capital cost	190$/kW
	Replacement cost	190$/kW
	Sizes	0,1,1.5,2,2.5,3,3.5,4,4.5,5
	Rectifier efficiency	85%
	Capaicity relative to inverter	100%
	Inverter efficiency	95%
	Life span	20 years
	Annual rate of interest	0%
Battery	Capital cost	150$/kW
	Replacement cost	30$/kW
	Nominal capacity	1kWh
	Float life	5 years
	Round trip efficiency	80%
	Mninmum state of charge	40%
	Lifetime throughput	917kWh
Biogas generator	Capital cost	250$/kW
	O&M cost	0.08$/kW
	Sizes	0, 1, 1.5, 2, 2.5, 3, 3.5, 4, 4.5, 5
	Replacement cost	150$/kW
	Biomass cost	$3.75/tone
	Lowest load ratio	30%
	Life span	20000 h

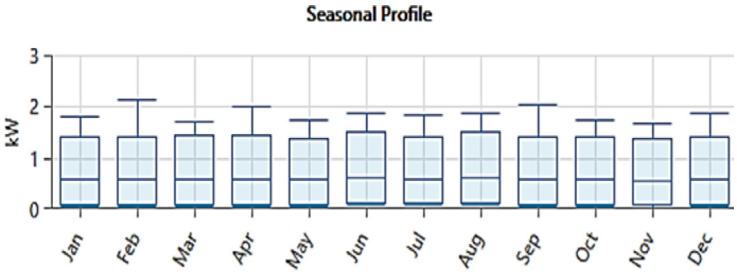


Fig. 6. Monthly load profile during the whole yea.

Table 5
Sensitivity outcomes for the hybrid PV/biogas system.

Sensitivity		Architecture				Cost			
Solar Scaled Average (kWh/m^2/day)	Biomass Scaled Average (t/d)	PV (kW)	Bio (kW)	1kWh LA	Converter (kW)	NPC ($)	COE ($)	Operating cost ($/yr)	Initial capital ($)
4.91	6.43	5	1.5	30	3.25	57283	0.614	4547	8743
4.92	6.44	5	1.5	32	3.25	56901	0.610	4483	9043
4.95	6.46	5	1.5	32	3.25	55964	0.600	4396	9043
4.97	6.48	5	1.5	32	3.26	55345	0.594	4337	9044
4.99	6.5	5	1.5	32	3.25	54762	0.587	4283	9043

solar radiation affect the NPC, COE, and operating costs. The findings reveal that as biomass is increased and solar radiation changes are taken into account, net present and operating costs also rise.

5.2. System optimization outcomes

The developed hybrid Photovoltaic/biogas system with sensitivity inputs was modeled in HOMER Pro software by ranging the potential of the biogas generator and solar radiance in order to determine the most efficient, optimized, and cost-effective system for the Primary school, Junior school, and Panchayat ghar in rural areas. To maximize the system's ability to meet the electricity demand, the capacity range of the biomass generator varied between 1 kW to 5 kW, while the capacity range of the PV system varied between 4 kW to 6 kW. In this study, a 1.50 kW biogas generator, a 5 kW PV array, a 3.25 kW converter, and 30 storage batteries were the optimal and most economically viable configurations evaluated for the hybrid system. This configuration is depicted in Fig 9.

The developed hybrid Photovoltaic/biogas system with sensitivity inputs was modeled in HOMER Pro software by ranging the potential of the biogas generator and solar radiance in order to determine the most efficient, optimized, and cost-effective system for the Primary school,

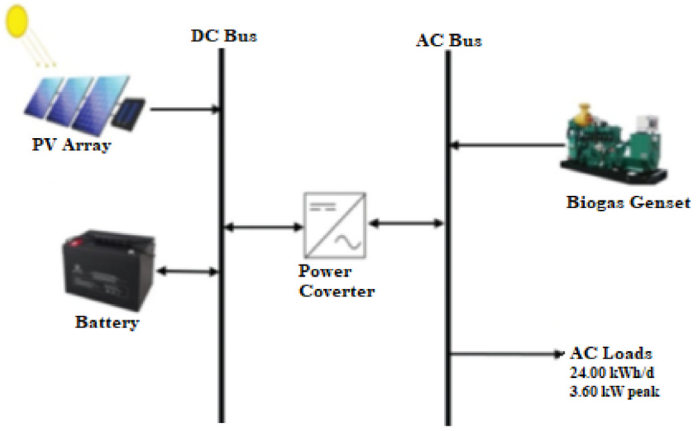


Fig. 7. Configuration of off-grid hybrid PV-biogas system.

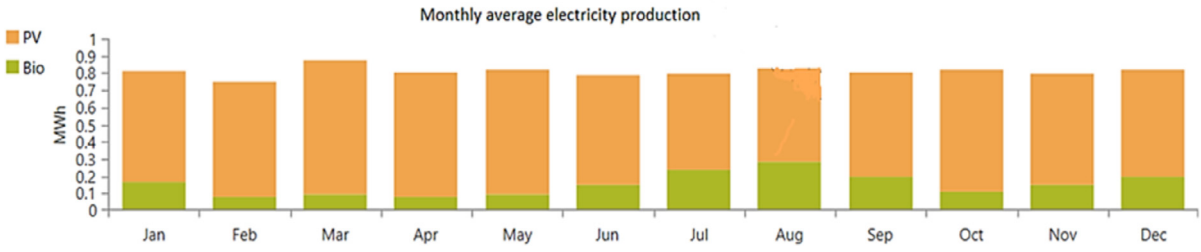


Fig. 8. Monthly average electricity generation from the hybrid system.

Table 6
Various different optimized system configurations with economic parameters.

Various Configuration	NPC ($)	COE ($)	Operating Cost ($)	Initial Cost ($)
PV/Biogas/Battery/Converter	57283	0.6145	4547	8743
PV/Biogas/Converter	169188	1.8107	15458	4178
Biogas/Battery/Converter	213798	2.3475	19884	1539
Biogas	260688	2.8009	24362	625

Table 7
Electricity generation of different feasible system designs.

Parameters	PV/Biogas/Battery/Converter	PV/Biogas/Converter	Biogas/Battery/Converter	Biogas
PV array (kWh/year)	7,868 (81.1%)	7,868 (56.2%)	-	-
Biogas generator (kWh/year)	1,830 (18.9%)	6,128 (43.8%)	9,013 (100%)	10,185 (100%)
Total electricity generation (kWh/year)	9,698 (100%)	13,996 (100%)	9,013 (100%)	10,185 (100%)
Renewable fraction (%)	100	100	100	0
Capacity shortage (kWh/year)	0.212 (0%)	143 (1.63%)	2.11 (0.1%)	111 (1.27%)
Excess electricity (kWh/year)	65.0 (0.67%)	5,055 (36.1%)	0	1,466 (14.4%)
Unmet electric load (kWh/year)	0.0000267 (0%)	6.77 (0.0773%)	1.10 (0%)	41.0 (0.468%)

Junior school, and Panchayat ghar in rural areas. To maximize the system's ability to meet the electricity demand, the capacity range of the biomass generator varied between 1 kW to 5 kW, while the capacity range of the PV system varied between 4 kW to 6 kW. In this study, an 1.50 kW biogas generator, 5 kW PV array, a 3.25 kW converter and 30 storage batteries were the optimal and most economically viable configurations evaluated for the hybrid system. This configuration is depicted in Fig. 9. As NPC, COE, and beginning capital investment are used to sort HOMER's optimum results. The total capital cost, NPC and COE for the best optimized PV-Biogas configuration are, respectively $8,743, $57,283, and $0.614. Other designs with varying equipment sizing that can meet the same energy load have low initial capital costs but high NPC, COE, and operating costs over the lifetime of the project. The various system designs with their significant economic parameters are shown in Table 6. Table 7 also depicts the share of power production of each component throughout a year, total electricity production, renewable percentage, and excess electricity with unmet load for all different system designs. Fig. 8 depicts the average monthly electricity production from a hybrid PV-Biogas system, where orange bars show the power supplied by the photovoltaic panel and green bars show the power generated by a biogas generator.

The total initial cost is calculated at $8,743 as shown in Table 6. This is the first investment needed to start the project. The initial cost of Lead acid battery and photovoltaic panels are more as compared to other components as shown in Fig. 9. This higher cost is a result of the substantial battery storage capacity, which is intended to offer reliable electricity dispatch when the electricity produced by the power systems is not enough to fulfill the load. In addition, the photovoltaic panels, which are less expensive once installed than a biogas generator, as biomass is available for free, which is why the fuel category has not been presented. Fig. 10 displays the power generated by each component and the total electrical load served is represented in the above plot

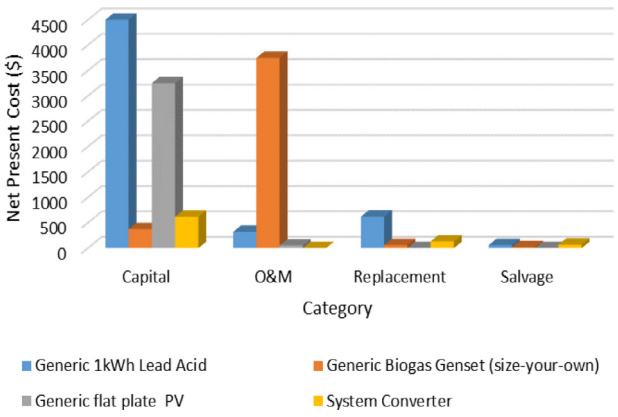


Fig. 9. Cost summary of the hybrid PV/Biogas system.

Table 8
Annual generation and consumption of electricity by a hybrid system.

Generation	kWh/year	%	Consumption	kWh/year	%
PV Modules	7,868	81.1	AC primary load	8,733	100
Biogas Generator	1,830	18.9	DC primary load	0	0
Total	9,698	100	Total	8,733	100

while the lower plot shows the unmet electrical load, total renewable power output, ac primary load served, input power and state of chage of battery over the course of July 9 to July 18 to help with a better understanding of how the system operates.

Table 8 and Fig. 8 make it clear that the photovoltaic system consistently outperforms biogas in terms of electricity production. Being off the grid, the system uses solar and biogas as resources to meet the load demands because our maximum demand hours are during the daytime for community load (schools and panchayat ghar) purposes. The capacity factor of the PV modules is about 81.1%, and it operates throughout the year depending on load requirements, producing about 7,868 kWh/year, compared to 1,830 kWh/year from the biomass generator having a capacity factor of 18.9%. Due to the lack of biomass availability throughout the day, biogas power generation is reduced. Furthermore, the system is producing more power than it needs to satisfy its annual power usage of 8,733 kWh, which can be saved or used for other productive purposes.

6. Conclusion

This study offers a technical and economical assessment of different stand-alone solutions for Primary school, Junior school and Panchayat Ghar buildings of Sarai Jairam village in Uttar Pradesh, India. HOMER pro analyzed several hybrid PV-biogas system configurations by modeling a dynamic hybrid model. An ideal solution was suggested based on the cost analysis after these hybrid designs underwent sensitivity analysis using variables such as solar radiation, biomass resource, and system sizing. In this study, the combination of a 1.50 kW biogas generator, 5 kW PV array, a 3.25 kW converter and 30 storage batteries was found to be the most cost-effective option with a total capital cost of $8,743, Net Present Cost (NPC) of $57,283 and Cost of Energy (COE) $0.61, respectively. This hybrid renewable energy system produces roughly 9,698 kWh per year, with an additional 965 kWh per year being generated to make the study area grid-independent. Additionally, the system has an estimated payback period of 0.41 years and a favorable net current cost for a projection timeframe of 25 years. By providing rural areas with these hybrid renewable energy systems, the Indian government may significantly contribute to resolving the country's current energy crisis. Additionally, the existing legislation that supports the use of such systems only offers tax breaks or reductions, which is insufficient to allow low-income populations to make use of these systems. The government may alter its supporting policies, offer rewards for system employment, and launch a national electrification campaign. Similar studies could be undertaken for other rural places in order to electrify them, which would also help the Indian government achieve its goal of "Power to all."

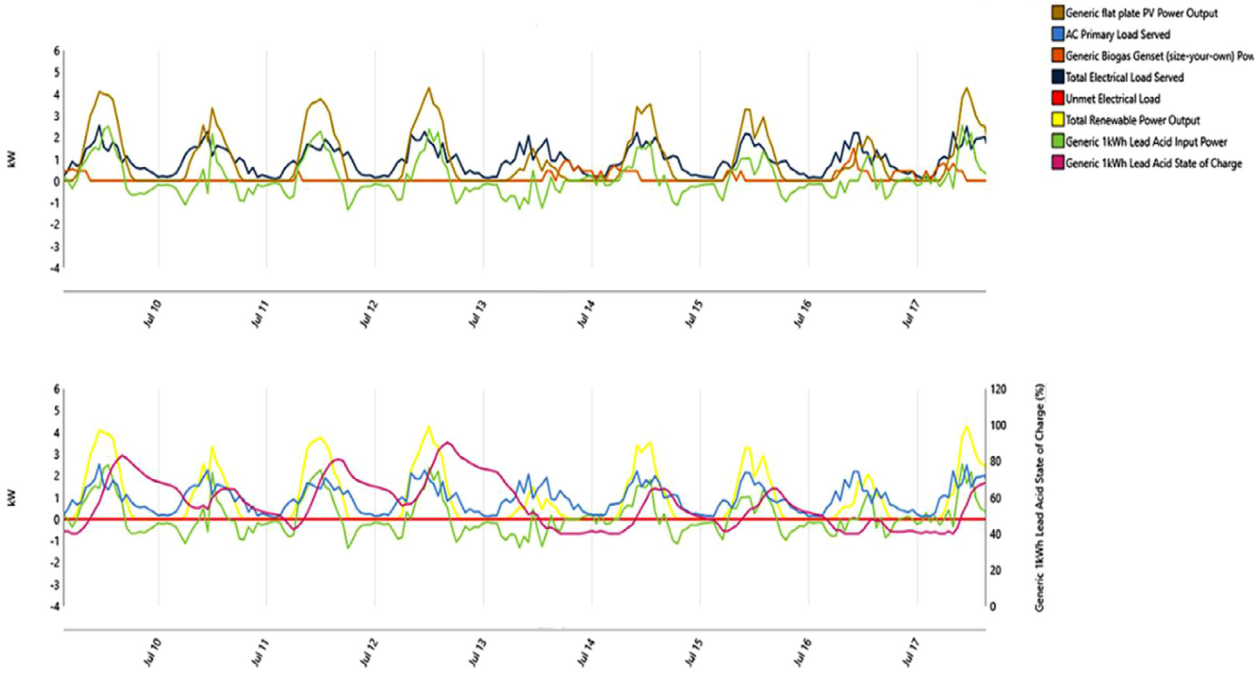


Fig. 10. Total electrical load served, unmet electrical load, total renewable power output, state of charge of the battery, ac primary load served and generated power by each component during July 9 to July 18.

Compliance with ethical standards

The authors declare that they have no competing financial interest.

Dataset Availability Statement

Dataset analysis and forecasting have been performed utilizing publicly available data that has been gathered from Yalova wind firm in the north-western region of Turkey.

Funding

No specific grant has been given to this research by any funding agency/organizations.

Declaration of Competing Interest

The authors declare that they have no known competing financial interests or personal relationships that could have appeared to influence the work presented in this paper.

CRediT authorship contribution statement

Upma Singh: Methodology, Investigation, Data curation, Software, Validation, Visualization, Writing – original draft, Writing – review & editing. **M. Rizwan:** Conceptualization, Supervision.

References

[1] K. Kusakana, J.L. Munda, A.A. Jimoh, Feasibility study of a hybrid PV-micro hydro system for rural electrification, in: AFRICON 2009, IEEE, Sep. 2009, pp. 1–5.
[2] F. Rinaldi, F. Moghaddampoor, B. Najafi, R. Marchesi, Economic feasibility analysis and optimization of hybrid renewable energy systems for rural electrification in Peru, Clean Technol. Environ. Policy 23 (3) (2021) 731–748.
[3] J. Ahmed, K. Harijan, P.H. Shaikh, A.A. Lashari, Techno-economic feasibility analysis of an off-grid hybrid renewable energy system for rural electrification, J. Electr. Electron. Eng. 9 (1) (2021) 7.
[4] A.K. Awopone, Feasibility analysis of off-grid hybrid energy system for rural electrification in Northern Ghana, Cogent Eng. 8 (1) (2021) 1981523.
[5] F. Rashid, M.E. Hoque, M. Aziz, T.N. Sakib, M.T. Islam, R.M. Robin, Investigation of optimal hybrid energy systems using available energy sources in a rural area of Bangladesh, Energies 14 (18) (2021) 5794.
[6] A.H. Eisapour, K. Jafarpur, E. Farjah, Feasibility study of a smart hybrid renewable energy system to supply the electricity and heat demand of Eram Campus, Shiraz University; simulation, optimization, and sensitivity analysis, Energy Convers. Manage. 248 (2021) 114779.
[7] S. Iqbal, M.U. Jan, A.U. Rehman, A. Shafiq, H.U. Rehman, M. Aurangzeb, Feasibility study and deployment of solar photovoltaic system to enhance energy economics of King Abdullah Campus University of Azad Jammu and Kashmir Muzaffarabad, AJK Pakistan, IEEE Access 10 (2022) 5440–5455.
[8] Q. Ma, X. Huang, F. Wang, C. Xu, R. Babaei, H. Ahmadian, Optimal sizing and feasibility analysis of grid-isolated renewable hybrid microgrids: effects of energy management controllers, Energy 240 (2022) 122503.
[9] F. Eze, J. Ogola, R. Kivindu, M. Egbo, C. Obi, Technical and economic feasibility assessment of hybrid renewable energy system at Kenyan institutional building: a case study, Sustain. Energy Technol. Assess. 51 (2022) 101939.
[10] M.M. Seedahmed, M.A. Ramli, H.R. Bouchekara, M.S. Shahriar, A.H. Milyani, M. Rawa, A techno-economic analysis of a hybrid energy system for the electrification of a remote cluster in western Saudi Arabia, Alex. Eng. J. 61 (7) (2022) 5183–5202.
[11] F. Odoi-Yorke, S. Abaase, M. Zebilila, L. Atepor, Feasibility analysis of solar PV/biogas hybrid energy system for rural electrification in Ghana, Cogent Eng. 9 (1) (2022) 2034376.
[12] E.S. Bayu, B. Khan, I.G. Hagos, O.P. Mahela, J.M. Guerrero, Feasibility analysis and development of stand-alone hybrid power generation system for remote areas: a case study of Ethiopian rural area, Wind 2 (1) (2022) 68–86.
[13] P.C. Okonkwo, E.M. Barhoumi, W. Emori, M.I. Shammas, P.C. Uzoma, A.M. Amer Mohamed, A.M. Abdullah, Economic evaluation of hybrid electrical systems for rural electrification: a case study of a rural community in Nigeria, Int. J. Green Energy 19 (10) (2022) 1059–1071.
[14] N.S.D. Ladu, R. Samikannu, K.G. Gebreslassie, M. Sankoh, L.E.R Hakim, A. Badawi, T.P..B Latio, Feasibility study of a standalone hybrid energy system to supply electricity to a rural community in South Sudan, Sci. Afr. 16 (2022) e01157.
[15] F.J. Montero, R. Kumar, R. Lamba, R.A. Escobar, M. Vashishtha, S. Upadhyaya, A.M. Guzmán, Hybrid photovoltaic-thermoelectric system: economic feasibility analysis in the Atacama Desert, Chile, Energy 239 (2022) 122058.
[16] L. Uwineza, H.G. Kim, C.K. Kim, Feasibility study of integrating the renewable energy system in Popova Island using the Monte Carlo model and HOMER, Energy Strategy Rev. 33 (2021) 100607.
[17] A. Tazay, Techno-economic feasibility analysis of a hybrid renewable energy supply options for university buildings in Saudi Arabia, Open Eng. 11 (1) (2021) 39–55.
[18] M.A.V. Rad, R. Ghasempour, P. Rahdan, S. Mousavi, M. Arastounia, Techno-economic analysis of a hybrid power system based on the cost-effective hydrogen production method for rural electrification, a case study in Iran, Energy 190 (2020) 116421.
[19] O. Babatunde, I. Denwigwe, O. Oyebode, D. Ighravwe, A. Ohiaeri, D. Babatunde, Assessing the use of hybrid renewable energy system with battery storage for power generation in a University in Nigeria, Environ. Sci. Pollut. Res. 29 (3) (2022) 4291–4310.
[20] L. Ji, Z. Liu, Y. Wu, G. Huang, Techno-economic feasibility analysis of optimally sized a biomass/PV/DG hybrid system under different operation modes in the remote area, Sustain. Energy Technol. Assess. 52 (2022) 102117.
[21] D.T. Hermann, N. Donatien, T.K.F. Armel, T. René, Techno-economic and environmental feasibility study with demand-side management of photovoltaic/wind/hydroelectricity/battery/diesel: a case study in Sub-Saharan Africa, Energy Convers. Manage. 258 (2022) 115494.



Upma Singh received her BTech degree in electronics and communication engineering from Uttar Pradesh Technical University, India in 2010 and MTech degree in instrumentation and control from Deenbandhu Chhotu Ram University, Haryana, India in 2012. She is currently pursuing PhD at the Department of Electrical Engineering, Delhi Technological University, Delhi, India. Her areas of interest are artificial intelligence, machine learning, Modelling and Optimization of Hybrid Renewable Energy Systems and Applications, Conventional & Renewable Energy Sources and Intelligent Techniques.



Prof Mohammad Rizwan did his post-doctoral research at Virginia Polytechnic Institute and State University, USA. He is presently working as an Associate Professor at the Department of Electrical Engineering, Delhi Technological University, Delhi, India. Dr. Rizwan has successfully completed three research projects in the area of renewable energy systems and published and presented more than 150 research papers in reputed international/national journals including IEEE transactions and conference proceedings. Recently, Dr. Rizwan has received a research project from the Science and Engineering Research Board, DST, Govt. of India in the area of energy management system. He is the recipient of Raman Fellowships for Post-Doctoral Research for Indian Scholars in the USA for the Year 2016-17, DST Start Up Grants (Young Scientists) and many other grants. His areas of interest include power system engineering, renewable energy systems particularly solar photovoltaic, building energy management, smart grid and soft computing applications in renewable energy systems.

Journal of Luminescence 269 (2024) 120444



Contents lists available at ScienceDirect

Journal of Luminescence

journal homepage: www.elsevier.com/locate/jlumin



Full Length Article

A single phase $Li_2Ba_5W_3O_{15}$:Dy^{3+}/Eu^{3+} phosphor for color tunable devices and non-contact optical thermometry

Anu [a], Seema [a,b], A. Kumar [c], Nisha Deopa [c], Mukesh K. Sahu [d], Aman Prasad [e], A.S. Rao [a,*]

[a] Department of Applied Physics, Delhi Technological University, Bawana Road, New Delhi, 110 042, India
[b] Department of Physics, Govt. College Nagina, Nuh, Haryana, 122108, India
[c] Department of Physics, Chaudhary Ranbir Singh University, Rohtak Bypass Road, Jind, Haryana, 126102, India
[d] Department of Electronics and Communication Engineering, GLA University, Mathura UP 281406, India
[e] Department of Physics and Computer Science, Dayalbagh Educational Institute (DEI), Deemed University, Agra UP 282005, India

ARTICLE INFO

Keywords:
Phosphors
Reisfeld approximation
Color tunability
Energy transfer

ABSTRACT

A set of warm white phosphor samples $Li_2Ba_5W_3O_{15}$ (LBW):xDy^{3+}, yEu^{3+} were prepared via a high-temperature solid-state process. Field emission scanning electron microscopy (FE-SEM) and Energy-dispersive X-ray analysis (EDX) with X-ray diffraction (XRD) are the structural analyses that show the incorporation of Dy^{3+} and Eu^{3+} ions into the LBW host matrix, without causing any damage to the lattice structure. Fourier Transform Infrared Spectroscopy (FT-IR) approves the presence of distinct vibrational characteristics of the proposed phosphors. The band gaps of the prepared phosphor samples were determined using diffused reflectance spectral (DRS) data. The energy transfer between Dy^{3+} and Eu^{3+} ions was observed, contributing to the adjustable luminescence of the LBW:Dy^{3+}/Eu^{3+} phosphors. By varying the activator doping levels while keeping the excitation wavelength constant, the emission colors of LBW:Dy^{3+}/Eu^{3+} phosphors shift from natural white with negligible color purity to a relatively pure orange-red region. The decay curves follow the bi-exponential behavior of decreasing lifetime with increasing concentration of the activator ions. A temperature measurement model using fluorescence intensity ratio (FIR) was developed using D3E0.75 phosphor demonstrating excellent optical temperature measurement properties, with a maximum value of S_r (=0.97 % K^{-1}). Therefore, all the experimental results indicate that the prepared Dy^{3+}/Eu^{3+} co-doped LBW phosphors can be a suitable choice for UV-excitable warm white lighting devices with color tunability and non-contact optical thermometry measurements.

1. Introduction

Photonic devices based on rare earth or transition metal induced luminous materials are currently rapidly expanding and have made huge advancements all over the world. To meet the demands of the necessary applications, this worldwide innovation generates an ever-increasing demand for transformative photonic devices [1,2]. The use of photonic devices is widespread in all fields, from cutting-edge science and technology to many industries and activities of daily life. Researchers have been motivated to enhance the properties of phosphors due to the continual increase in demand and the wide range of uses for luminous materials. These luminous materials are used in a variety of industries, including sensing, solid-state lighting, lasers, sophisticated displays, optical storage, and many more [3]. The temperature has a critical and fundamental characteristic use for biological, chemical, and physical processes. One of the main uses of photonic devices is to sense the real-time temperature with great accuracy [4,5]. Also, with the advancement of science and technology, biological imaging and large-scale integrated circuits (LSI) created new demands for temperature measurement tolerance, high spatial resolution and remote detection [6]. Currently, there are two types of temperature measurement technologies, one is common contact temperature dimensions and another is non-contact. Yet, in some unique circumstances such as electromagnetically or thermally demanding areas and organisms, the conventional contact temperature measurements are carried out [7,8]. The usage of contact temperature measuring instruments are challenging by virtue of its condition of contact. Therefore, the study of non-contact thermometers is very important not only from the point of view of non-contact but also from financial viability. Non-contact phosphor thermometers have been a focus of research in the field of

* Corresponding author.
E-mail address: drsrallam@gmail.com (A.S. Rao).

https://doi.org/10.1016/j.jlumin.2024.120444
Received 21 November 2023; Received in revised form 13 December 2023; Accepted 5 January 2024
Available online 6 January 2024
0022-2313/© 2024 Elsevier B.V. All rights reserved.

temperature measurement because of its assets such as great selectivity, high accuracy, sensitivity and prolonged lifetime [8,9]. Further, non-contact thermometers, compared to conventional contact thermometers, are better suited to measure the temperature of inaccessible objects in environments with strong electromagnetic fields, high pressures, or corrosive conditions with high precision, high sensitivity, and a large relevant temperature range [10,11]. The investigation of non-contact optical thermometers has also received a great deal of attention since they have the potential to solve the shortcomings of standard thermometers, such as their slow response time and imprecision. One of the most sophisticated methods for measuring surface temperature is phosphor thermometry, which makes use of the PL properties of materials with rare earth (RE) elements and transition metals inclusions in both crystalline and amorphous form [12,13].

The sensitivity of the luminescence properties of RE ions doped luminous materials is the basis for temperature measurement. One of the most popular approaches in this research field is temperature measurement based on FIR, originating due to the Boltzmann distribution of two separate excitation energy stages which vary with change in temperature [14]. Contrarily, the ambient factors that affect temperature measurement are unaffected by FIR temperature measuring technology and minimises or eliminates the external interference. This matters for the consistency, precision, and dependability of the non-contact thermometers [15]. RE ions provide the best circumstances to their various energy levels and characteristic 4f electron structure for thermally coupled level pairs (TCLs), which are valuable for use in the FIR temperature measurement [16]. The trivalent RE ions, such as Tb^{3+} ($^5D_4 \rightarrow {}^7F_5$ and $^5D_3 \rightarrow {}^7F_J$) [17], Sm^{3+} ($^4G_{5/2} \rightarrow {}^6H_{5/2}$ and $^4G_{5/2} \rightarrow {}^6H_{7/2}$) [18], Dy^{3+} ($^4F_{9/2} \rightarrow {}^6H_{15/2}$ and $^4F_{9/2} \rightarrow {}^6H_{15/2}$) [19], Eu^{3+} ($^5D_0 \rightarrow {}^7F_J$ and $^5D_1 \rightarrow {}^7F_3$) [14], Yb^{3+} ($^2F_{5/2} \rightarrow {}^2F_{7/2}$) & Tm^{3+} ($^3H_4 \rightarrow {}^3H_6$) [20] and Er^{3+} ($^2H_{11/2} \rightarrow {}^4I_{15/2}$ and $^4S_{3/2} \rightarrow {}^4I_{15/2}$) [21,22] are used frequently in this field. All the aforementioned research results prompted us for a comprehensive investigation on trivalent RE ions (in present research work, Dy^{3+} and Eu^{3+} ions) together LBW host matrix to understand their usefulness in non-contact temperature sensing applications using FIR temperature statistics.

In recent years, there has been a growing interest in the development of single-phased white light-emitting phosphors [23–25]. However, creating a novel single-phase phosphor that emit "white and bright" light having relatively high luminescence efficiency and color purity; and then exploring their practical implications, remains a significant challenge. The morphology, composition, structure, and crystal phase of the host materials are all strongly related to the luminous characteristics of the inorganic phosphors. Additionally, the stability and luminous efficiency of the phosphors are influenced by the activation sites, crystal field strength, and energy transfer behaviour of the activator ions. The previously discussed parameters can be efficiently controlled by the host matrix selection [26], therefore, the choice of suitable host materials is pivotal in determining the performance of these substances. Many researchers have directed their attention to inorganic host materials for lanthanide activator ions, such as titanates [27], silicates [28], tungstate [29], phosphates [30], and many more. Tungsten oxide is a popular choice among these substrates for achieving red emission. One of the reasons for this preference is that the WO^{-6} or WO^{-4} polyhedral groups in a tungstate host can efficiently absorb ultraviolet (UV) and near-ultraviolet (n-UV) light, facilitating energy transfer from WO^{-6} or WO^{-4} to the dopant ions.

In the present research work, we analysed the phase purity, microscopic morphology, luminescence properties, and fluorescence intensity ratio (FIR) optical thermometry properties of the warm white phosphors prepared by co-doping of Dy^{3+} and Eu^{3+} in $Li_2Ba_5W_3O_{15}$ (LBW) host material.

1.1. Synthesis method

The as-prepared phosphor samples can be made using various processes, including solid state reaction, sol-gel, combustion method, co-precipitation etc. In the current study, the high temperature solid-state reaction method is used to prepare the phosphor samples.

Dy^{3+}/Eu^{3+} singly doped ($LBWDy:Li_2CO_3+(5-x)BaCO_3+3WO_3+xDy_2O_3$; ($0.01 \leq x \leq 0.05$, $\Delta x = 0.01$), ($LBWEu:Li_2CO_3+(5-y)BaCO_3+3WO_3+yEu_2O_3$($y = 0.01$) and Dy^{3+}/Eu^{3+} co-doped (($Li_2CO_3+(5-x-y)BaCO_3+3WO_3+xDy_2O_3+yEu_2O_3$, ($x = 0.03$, and $0.0025 \leq y \leq 0.0125$, $\Delta x = 0.0025$) multicomponent lithium barium tungstate phosphors (LBWDE) were prepared. The initial ingredients were obtained as finely ground powder. In an agate mortar, 5 gm of each batch composition were vigorously mixed until homogeneity was reached. After that, the thoroughly mixed sample was heated in an alumina crucible for 6 h at 1200 °C with 5 °C/min of heating rate. The mixture was then let to cool naturally to room temperature and then the final products were re-ground again for further characterizations.

1.2. Characterization techniques

Various characterisation techniques were used to study the structural, optical and thermal properties of the prepared phosphor samples. X-ray diffraction (XRD) was used to analyse the structure of the prepared Dy^{3+}/Eu^{3+} co-doped phosphor samples with Bruker D-8 Model Advance diffractometer (least count of ±0.01) having a nickel-based filter and Cu-K_α as radiation source. With a wavelength (λ) of 1.5406 Å, the XRD measurements were conducted for 2θ angles between 20° and 70°. FE-SEM recordings were done for surface morphology by using JEOL JSM-6490 operated at an accelerating voltage of 10 kV. The FT-IR spectrum for the as prepared phosphors has been recorded in the range 4000 to 400 cm^{-1} by means of PerkinElmer Frontier FT-IR spectrometer. A Jasco V-770 spectrophotometer (resolution of ±0.1 nm), which uses halogen and deuterium light sources for UV and Visible range, was used to analyse the DRS. A Jasco 8300 FP spectrofluorophotometer (resolution of ±1.0 nm) with a Xenon lamp (300 W) as the excitation source was used to validate the PL excitation and emission spectra. The time resolved PL studies were conducted using 150 MHz digital oscilloscope (HM 1507 Hameg Instruments). All the measurements were taken at room temperature. Ocean optics Flame-S-XR1-ES spectrometer was utilised to study the thermal behaviour of the optimised sample using TDPL analysis.

2. Results and their discussion

2.1. Structural and morphological analysis

To emphasis the structural and morphological properties of the as-prepared phosphor samples, various techniques has been performed, for instance, XRD, FE-SEM, EDX & FT-IR.

2.1.1. XRD analysis

X-ray diffraction for all the powdered samples un-doped LBW, 3 mol % concentration of Dy^{3+} (D3), 1 mol% of Eu^{3+} (E1) and 3 mol% of Dy^{3+}, 0.75 mol% of Eu^{3+} ions co-doped (D3E0.75) LBW phosphors were recorded in the 2θ range from 20° to 70° with a step size of 0.02° to obtain all crystalline peaks and depicted in Fig. 1. All the samples belong to a hexagonal crystal structure with $P6_3mc$ space group (186). For all the different compositions of dopant (Dy^{3+} & Eu^{3+}) ions, the crystalline single-phase hexagonal structure of LBW phosphor was formed without any secondary phase which are in good agreement with the Joint Committee on Powder Diffraction Standards (JCPDS) card no. 01-072-1717. Therefore, doping of RE^{3+} (Dy^{3+} and Eu^{3+}) ions into LBW host lattice does not distort the crystal structure. This indicates that the dopant ions (Dy^{3+} and Eu^{3+}) has been correctly accumulated within the host matrix in place of Ba^{2+} lattice position.

Further the Williamson-Hall (W–H) plot formalism was used to compute the strain (∈) and crystallite size (D) for un-doped LBW, D3, E1 and D3E0.75 phosphors [31]:

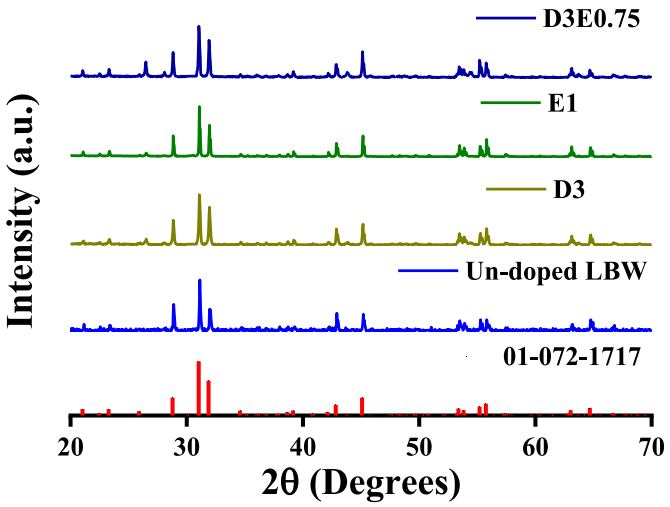


Fig. 1. The XRD patterns for un-doped LBW, D3, E1 and D3E0.75 phosphors.

$$\beta_{hkl}\, cos\, \theta = \frac{k\lambda}{D} + 4 \in sin\, \theta \quad (1)$$

The structure factor K has a value of 0.94, and the average crystallite size is denoted by the letter 'D'. '2θ' is the diffraction angle corresponding to the XRD diffraction peaks and the parameter β_{hkl} denotes FWHM (full width half maxima) of the diffraction for the intense XRD peaks. Here, parameter '∈' and 'λ' are the lattice micro-strain connected to the phosphor samples and the wavelength of CuK_α source, respectively. As indicated by the W–H plot in Fig. 2, a graph (straight line) is produced between $\beta_{hkl}\, cos\, \theta$ (along the y-axis) and 4 $sin\, \theta$ (along the x-axis) in order to determine the values of parameters 'D' and '∈ ' for un-doped LBW, D3, E1 and D3E0.75 phosphors. The observed crystallite size and lattice strain presented in Table 1.

Crystallite size along with strain from XRD analysis is found to be varying with the concentration of RE element and allows for tunability in the emission colors. Smaller crystallites may exhibit blue-shifted emissions, while larger ones might have red-shift. Strain is due to smaller size and strongly affect the environment and tends to change the particle size. Despite of crystallite size, particle size also changes the luminescence efficiency of phosphors. Smaller particle size of phosphor provides higher surface to volume ratio and this increases in surface area and provides smooth environment for more interaction tend to increase in luminescence efficiency. The probability of formation of surface

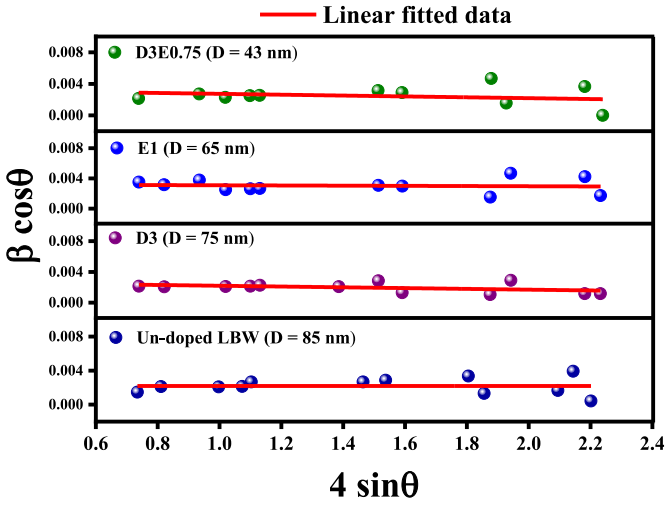


Fig. 2. A graph between $\beta_{hkl}\, cos\, \theta$ and $sin\, \theta$ for un-doped LBW, D3, E1 and D3E0.75 phosphors.

Table 1
Crystallite size D (nm) and Strain (∈) values for un-doped LBW, D3, E1 and D3E0.75 phosphors.

Sample Name	Crystallite size D (nm)	Strain (∈)
Un-doped LBW	85	0.00045 ± 0.00005
D3	75	0.00013 ± 0.00004
E1	65	0.0027 ± 0.0004
D3E0.75	43	0.0033 ± 0.0008

defects increases due to the increase in surface area and this leads to the non-radiative emission [32].

2.1.2. FE-SEM and EDX

FE-SEM and EDX employed to better understand the surface morphology of the prepared samples. The FE-SEM image of an D3E0.75 phosphor is shown in Fig. 3. As can be observed, the phosphor's shape and particle size are not consistent. However, because of the high-temperature synthesis, the prepared materials show an agglomeration phenomenon. The FE-SEM picture displayed in Fig. 3 indicates that the average particle size of the as-prepared phosphor samples is within the range of 5–7 μm.

As depicted in Fig. 4 (a), EDX analysis was employed to monitor the elemental composition of the prepared phosphor material. In this figure, distinct peaks are evident, corresponding to Ba, W, O, Dy, and Eu, respectively. The comprehensive element distribution map, presented in Fig. 4 (b), illustrates the uniform distribution of these elements across the external surface. Fig. 4(c–g) display element points in different colors against a dark background; i.e., Ba, W, O, Dy, and Eu are represented by violet, magenta, green, red, and yellow, respectively. These findings confirm that the components of the prepared phosphors are evenly distributed, indicating the successful preparation of Dy^{3+}/Eu^{3+} co-doped LBW phosphors. It is important to note, as mentioned in the literature [33], elements with low-energy characteristic radiation, such as Li, do not exhibit any peaks in their EDX spectrum.

2.1.3. FT-IR spectral analysis

Infrared spectroscopy (IR) analysis was conducted to gain insights into the bonding characteristics of the singly and co-doped LBW phosphor samples. Fig. 5 shows the FT-IR spectrum of D3 and D3E0.75 phosphor in the range 4000–400 cm^{-1}, represents various vibrational bands. The FT-IR spectrum has bands near 530, 574, 680, 807, 1062, 1247, 1416, 2901, 2991 and 3673 cm^{-1}, shown in Fig. 5. The tungstate group's W–O symmetric and antisymmetric stretching and O–W–O symmetric and antisymmetric stretching deformation vibrations are

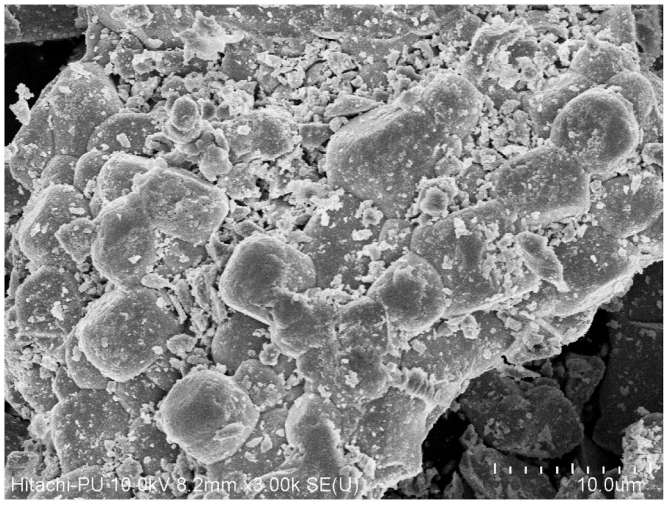


Fig. 3. The SEM picture of an D3E0.75 phosphor.

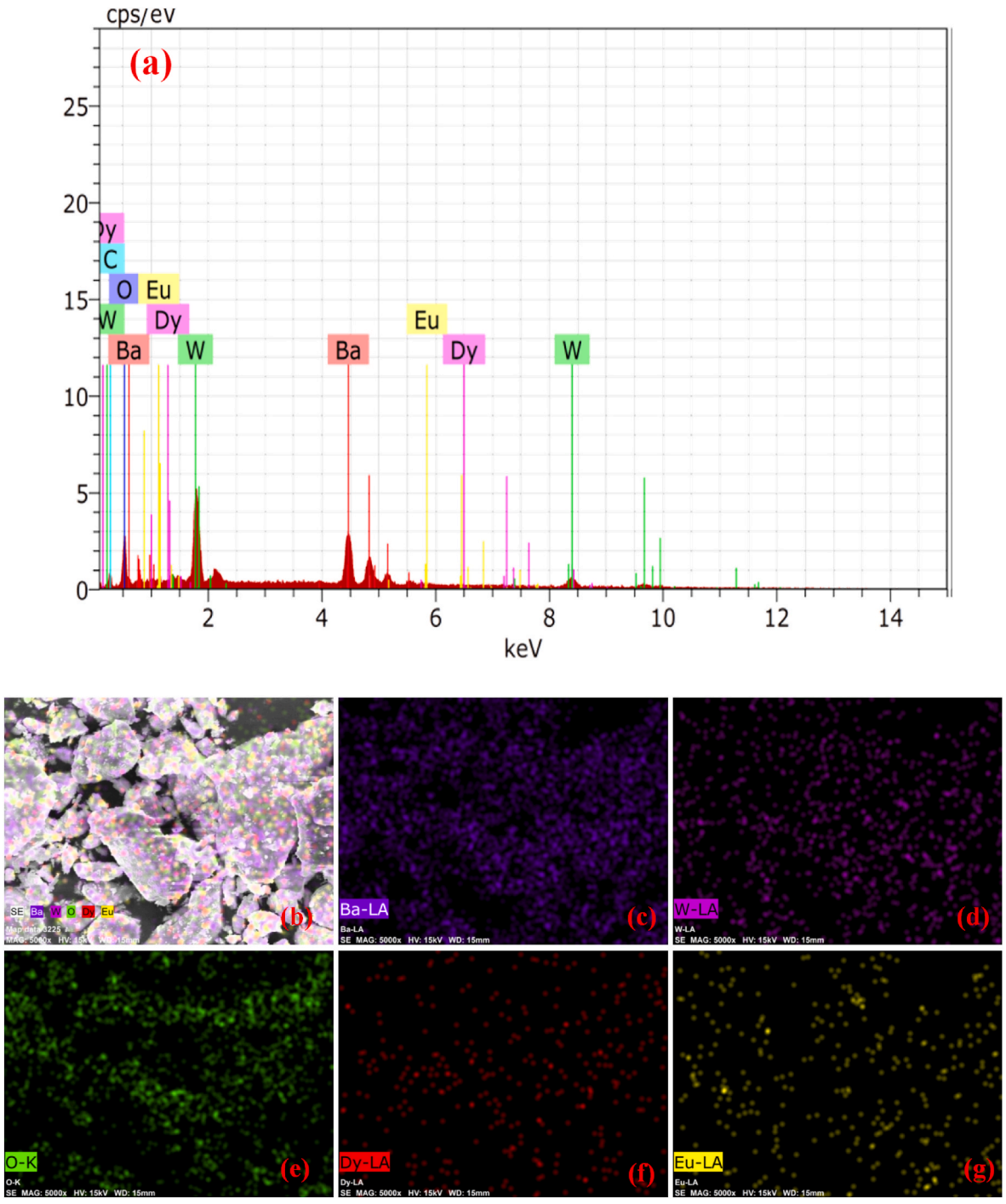


Fig. 4. (a) The elemental composition, (b) elements' consistent distribution over the outside surface, (c–g) shows the relative element points of various colors against a dark background; blue, purple, green, and red correspond to Ba, W, O, Dy and Eu, respectively.

linked to the bands at 500-807 cm^{-1} [34]. Peak intensities vary slightly depending on the doping concentration. These changes in the W–O stretching vibration at 807 and 574 cm^{-1} are related to the altered local symmetry of the Dy^{3+} ion. However, XRD study showed no change in the phosphor's geometry. The presence of tungstate groups is also indicated by the bands in the shorter wavelength range (807 and 574 cm^{-1}) [34, 35]. The W–O bond's asymmetric stretching vibration is most likely the cause of the peak seen at roughly 1062 and 1247 cm^{-1} [34]. The existence of surface CO32- species is responsible for another band, which is situated at 1416 cm^{-1} [34]. The spectral peak at 2901 cm^{-1} analogous to the existence of hydroxyl radicals, whereas the peak at 2991 cm^{-1} represents the antisymmetric stretching of water molecules. Lastly, the peak at 3673 cm^{-1} is associated with the stretching vibration of the hydroxyl group [36]. An increase in the OH content leads to higher non-radiative losses, which in turn reduces the quantum efficiency of materials doped with rare earth elements. But as shown in Fig. 5, the OH band have comparatively very less intensity which indicates the presence of low OH content in the as-prepared phosphor material. The distinctive bonding found in the prepared LBW phosphors was therefore validated by the FT-IR spectrum shown in Fig. 5.

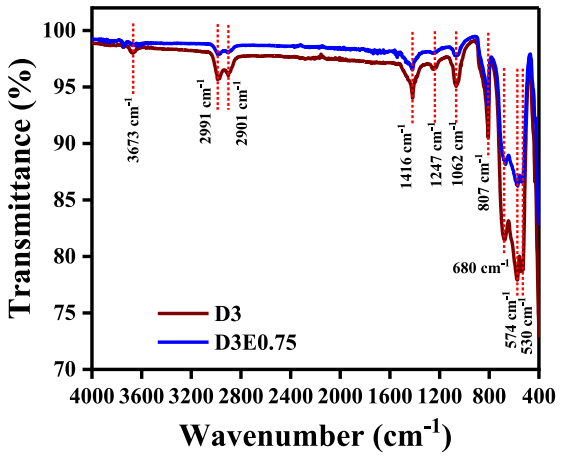


Fig. 5. FT-IR spectrum of D3 and D3E0.75 phosphors.

2.2. Optical parametric analysis

2.2.1. DRS analysis and band gap energy

The DRS of LBW phosphors co-doped with Dy^{3+}/Eu^{3+} ions and un-doped LBW is shown in Fig. 6 (a). At room temperature, the DRS were detected in the 200–1600 nm range. The absorbance at 412 nm in the spectra linked to the Eu^{3+} ion's transition from $^7F_0$–$^5L_6$ [37]. Transitions from the ground state $^6H_{15/2}$ to other excited states $^6F_{3/2}$, $^6F_{5/2}$, $^6F_{7/2}$, $^6H_{5/2}$, $^6F_{9/2}$, and $^6F_{11/2}$ are represented by the remaining peaks, related to Dy^{3+} ions [38,39].

The Kubelka-Munk function, which represents the optical absorption close to the band edge, can be used to solve for the band gap (E_g) [40]:

$$\alpha h\nu = A\left(h\nu - E_g\right)^{n/2} \tag{2}$$

where α, $h\nu$, E_g and A denotes the absorption coefficient, energy of a photon, energy band gap and a constant. In equation (2), $n = 1$ and 4 represents for direct transition and indirect transition, respectively.

The $F(R)$ function can be written as [41]:

$$F(R) = \frac{(1-R^2)}{2R} = \frac{A}{S} \tag{3}$$

where R stands for reflectance, A for absorbance, and S for scattering coefficient. The linear part of the plot between $[F(R)\,h\nu]^2$ and $h\nu$ was extrapolated to compute the band gap value as shown in Fig. 6 (b). The optical band gap for un-doped LBW, D3 and D3E0.75 phosphors was determined and found to be equal to 3.74, 3.64 and 3.62 eV, respectively. With the doping of RE ions, the E_g value slightly decreases from 3.74 to 3.62 eV, which may be due to the 4f energy level of Dy^{3+} and Eu^{3+} ions [42]. On the other hand, the little decrease also suggests that the samples under consideration crystallised efficiently [39].

2.2.2. PL excitation and emission spectra analysis

2.2.2.1. PLE and PL properties of Dy^{3+} ions doped LBW phosphor. Fig. 7 (a) and (b) represents the PLE and PL emission spectra of Dy^{3+} ions doped LBW phosphors, respectively. By choosing PL emission wavelength (Em) of 493 nm, Fig. 7 (a) depicts the PLE spectra for the entire series of Dy^{3+} substituted LBW in the spectral range from 320 to 460 nm. As a result nine PL excitation bands were observed from the ground state $^6H_{15/2}$ to various excited states $^6P_{3/2}$, $^6P_{7/2}$, $^4I_{13/2}$, $^6P_{5/2}$, $^4K_{17/2}$, $^4F_{7/2}$, $^4G_{11/2}$, $^4I_{15/2}$ and $^4F_{9/2}$ at 338, 347, 357, 368, 378, 396, 425, 447 and 456 nm respectively [43,44]. The strongest excitation band, $^6P_{5/2}$, is located around 368 nm. As a result, PL emission spectra were recorded monitoring the excitation wavelength (Ex) at 368 nm, shown in Fig. 7 (b). Three emission peaks were visible in the PL spectra at wavelengths of 493 nm (blue), 583 nm (yellow), and 684 nm (red), which corresponded to the ($^4F_{9/2} \rightarrow {}^6H_{15/2}$), ($^4F_{9/2} \rightarrow {}^6H_{13/2}$) and ($^4F_{9/2} \rightarrow {}^6H_{11/2}$) transitions, respectively. The emission intensities gradually increased and reached their maximum value as the concentration of Dy^{3+} ions increased from 1 to 3 mol%. Due to concentration quenching, the emission intensity significantly decreased as the concentration of Dy^{3+} ions further increased. This is because the distance between luminous centres reduces as the number of Dy^{3+} ion rises, which can result in the non-radiative energy transfer [36]. According to Blasse, the following expression could be used to determine the critical separation between the adjacent dopant (Dy^{3+}) ions, govern the energy transfer process between two adjacent Dy^{3+}-Dy^{3+} ions [31];

$$R_c \approx 2\left[\frac{3V}{4\Pi X_c N}\right]^{1/3} \tag{4}$$

In this case, "N" denotes the number of atoms, " X_c" is the optimum concentration of Dy^{3+} ions, and " V " denotes the unit cell volume. The critical distance for $X_c = 0.03$, $V = 681.182$ Å3, and $N = 2$ is evaluated

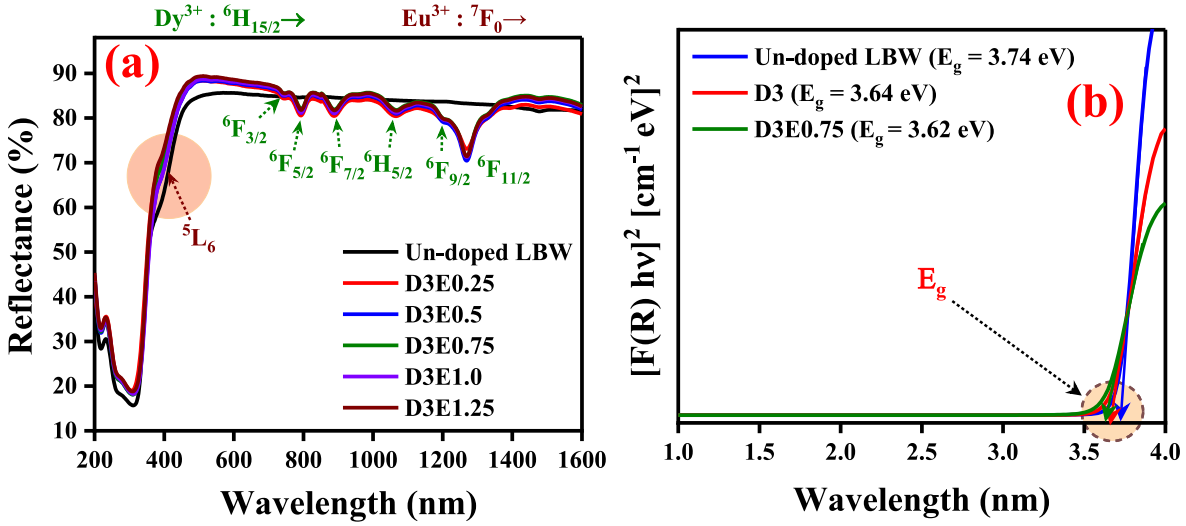


Fig. 6. (a) UV–vis DRS of the un-doped LBW, LBW:xDy^{3+}/yEu^{3+} (x = 3.0 mol% and 0 ≤ y ≤ 1.25, Δy = 0.25 mol%) phosphors, **(b)** Band gap variations of an un-doped LBW, LBWD3, D3E0.75 phosphors.

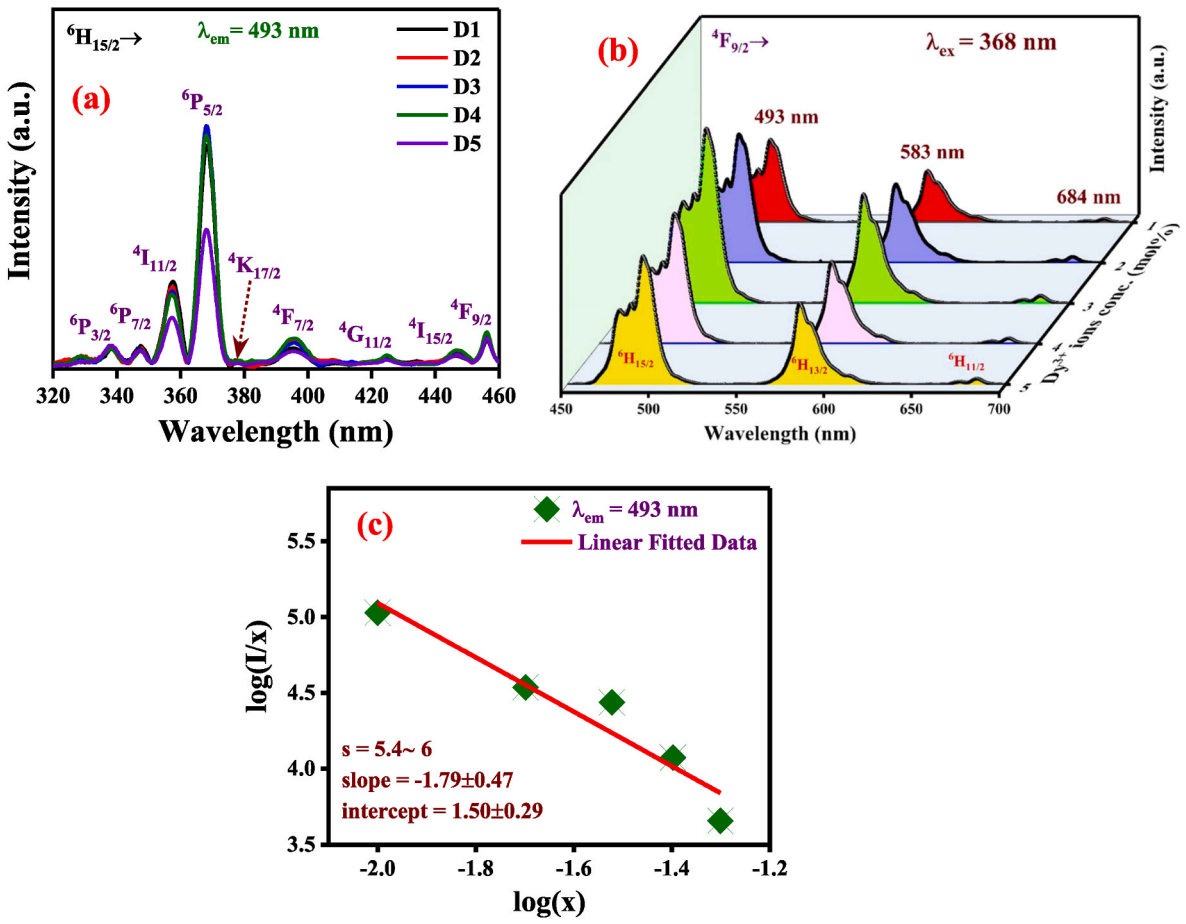


Fig. 7. (a) PL excitation and **(b)** PL emission spectra, **(c)** Dexter plot for LBW:xDy^{3+} ($0.01 \leq x \leq 0.05$, $\Delta x = 0.01$) phosphors.

and found to be 27.88 Å after analysis of the experimental data. According to Van Uitert, the phenomenon of energy exchange, reabsorption of radiation, and multipolar interactions, etc. are all related to energy transfer [45]. The evaluated value of the critical distance between adjacent Dy^{3+} ions in the current investigation was found to be more than 5 Å, therefore, multipolar interactions rather than exchange interactions will be more significant [46]. According to Dexter's concept, the expression below could represent a corelation between the PL intensity (I) and the activator ions mole fraction (x) [47];

$$log\frac{I}{x} = -\frac{Q}{3}log\,x + A \tag{5}$$

here, " Q " refers to the kind of interaction that occurs between the rare-earth ions (may be equal to 6 for electric dipole-dipole (d-d), 8 for dipole-quadrupole (d-q), and 10 for quadrupole-quadrupole (q-q) interaction) [48] and " A " is a constant. Fig. 7 (c) provides a good representation of the relation amid $log\,I/x$ and $log\,x$, for Dy^{3+} ions doped LBW phosphors under Ex = 368 nm for Em = 493 nm. The fact that the values for the " Q " parameter, using Em = 493 under Ex = 368 nm, are obtained at 5.4, which is near to 6, therefore represents that electric d-d interaction is the cause of energy transfer between adjacent Dy^{3+} ions and therefore, concentration quenching occurs.

2.2.2.2. PL properties of Dy^{3+}/Eu^{3+} co-doped LBW phosphor. The absence of red colour was identified in the study of phosphors doped with Dy^{3+} ions. To solve this problem, co-doping was carried out in combination with Dy^{3+} ions using Eu^{3+}, Mn^{2+}, and Mn^{4+} red-emitting ions. When exposed to the proper excitation, this co-doping technique produced white light emission [49]. In the present study, the host matrix LBW was altered by adding various Eu^{3+} ion concentrations in addition to the previously optimised 3.0 mol% Dy^{3+} ions concentration. The purpose of this alteration was to study the energy transfer (ET) mechanism that exists between these two RE ions. Energy is transmitted from the ion in relatively high-energy state to the ion lying in a lower-energy state in RE ions, resulting in luminescence through ET-based down-conversion. Since the energy state of the Dy^{3+} ions are higher than that of the Eu^{3+} ions, the ET process is most likely to occur from Dy^{3+} to Eu^{3+} ions. The key criterion for the investigation of the ET process is the spectral overlap between the donor (Dy^{3+}) emission and the acceptor (Eu^{3+}) excitation [49]. The alignment between the excitation band of Eu^{3+} ions at 469 nm (from $^7F_0$ to $^5D_2$) and the emission band of Dy^{3+} ions at 493 nm (from $^4F_{9/2}$ to $^6H_{15/2}$) is demonstrated in Fig. 8 (a). These discoveries prompted additional research into the ET process from Dy^{3+} to Eu^{3+} by introducing different concentrations of Eu^{3+} ions (ranging from 0.25 to 1.25 mol% in increments of 0.25 mol%) alongside the optimal concentration of Dy^{3+} ions. Prior to conducting this study, the excitation spectra of the co-doped Dy^{3+}/Eu^{3+} phosphor samples were assessed at emission wavelengths of 583 nm for Dy^{3+} and 615 nm for Eu^{3+} ions. The obtained spectrum was then compared with those of the singly Dy^{3+} and Eu^{3+} ions doped LBW phosphors, as shown in Fig. 8 (b). Different bands were observed in the excitation spectrum of the singly Dy^{3+}, Eu^{3+}, and Dy^{3+}/Eu^{3+} co-doped systems at emission wavelengths of 583 nm and 615 nm. These bands correspond to the transitions such as $^6H_{15/2}$ to $^6P_{5/2}$ (at 368 nm) and $^6F_{7/2}$ (at 394 nm), which are consistent with the excitation bands of Dy^{3+} ions, as well as Eu^{3+} bands assigned to $^7F_0$ to $^5L_6$ (394 nm), $^5D_3$ (410 nm), $^5D_2$ (466 nm), and a charge transfer band (CTB) at 329 nm. Hence, both Dy^{3+} ions (by Em = 583 nm) and Eu^{3+} ions (by Em = 615 nm) have the capacity to contribute towards the overall emission in as-prepared co-doped LBW

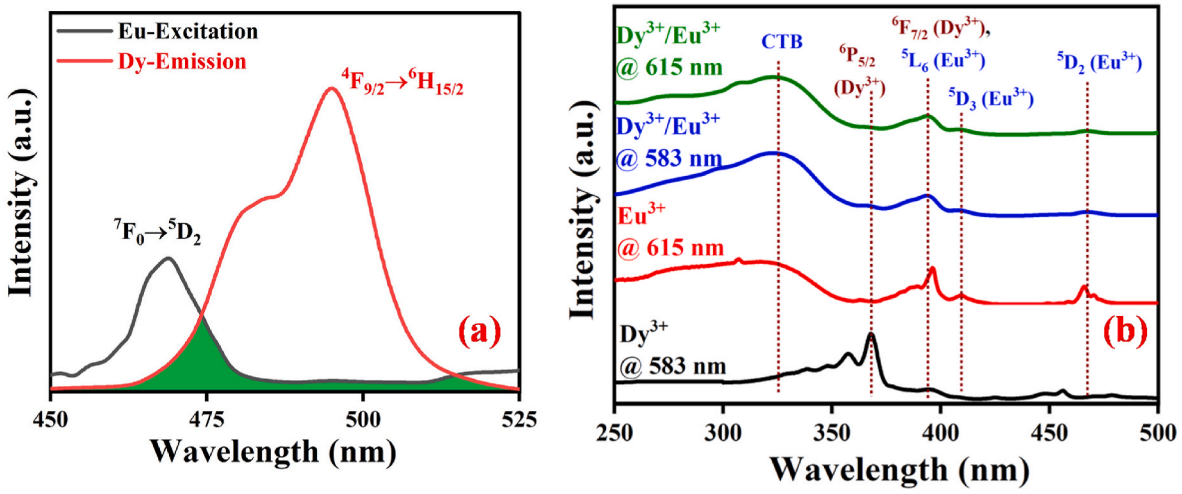


Fig. 8. (a) The overlapped region between the Eu^{3+}excitation band and Dy^{3+} emission band, **(b)** The excitation spectra for the Dy^{3+}/Eu^{3+} co-doped system is observed at Em = 583 nm (Dy^{3+}) and 615 nm (Eu^{3+}) and correlated with the singly Dy^{3+} and Eu^{3+} doped LBW phosphors.

phosphor samples.

Based on the excitation spectra, the PL emission spectra of the Dy^{3+}/Eu^{3+} co-doped LBW phosphor were measured at two distinct wavelengths (Ex = 329 nm and 394 nm), shown in Fig. 9. The PL emission spectra obtained at Ex = 329 nm show many strong peaks ranging from 450 to 700 nm, shown in Fig. 9 (a). Of these peaks, two are ascribed to the Dy^{3+} ion transitions from $^4F_{9/2}$ to $^6H_{15/2}$ (493 nm) and $^6H_{13/2}$ (583 nm). The transitions of Eu^{3+} ions from $^5D_0$ to $^7F_1$ (595 nm), $^7F_2$ (615 nm), and $^7F_3$ (661 nm) are responsible for the remaining peaks. As the concentration of the Eu^{3+} ions rise, the change in PL emission intensity of Dy^{3+} ions indicates that energy is transferred from Dy^{3+} to Eu^{3+} ions, which causes decrement in the PL emission intensity of Dy^{3+} ions and increment in PL emission intensity of Eu^{3+} ions. Similar patterns were observed with an Ex = 394 nm, shown in Fig. 9 (b). The above observations implies that Eu^{3+} ions are sensitised by Dy^{3+} ions and energy is transferred from Dy^{3+} ions to Eu^{3+} ions, leading to optical emission [49,50].

2.2.2.3. Energy level diagram. Energy transfer can take place either between dissimilar luminescent centres or identical luminescent centres. In the scenario of involving dissimilar luminescent centres, there are two distinct centres: a sensitizer (S) and an activator (A), separated in a solid by a distance R. It is assumed that R is sufficiently short for S and A to have a non-negligible interaction. This implies that when S is in an excited state and A is in the ground state, the relaxed excited state of S can transfer its energy to A. Resonance needs to be satisfied, indicating that the energy differences between the ground and excited states must be equal, and a suitable interaction must exist for energy transfer to occur. This interaction could be an exchange interaction with wave function overlap, as shown in Fig. 8 (a), or an electric/magnetic multipolar interaction as shown in Fig. 11.

Dexter's MEI formula and Reisfeld's approximation are used to determine the specific multipolar interaction mechanism present in the prepared co-doped phosphor samples [49,51]:

$$\frac{\eta_0}{\eta} = C^{n/3} \tag{6}$$

here, the radiant quantum efficiencies in the absence of a sensitizer (Eu^{3+}) and in the presence of one are denoted by the symbols η_0 & η, respectively. The variable ' n ' indicates the type of multipolar interaction; i.e., $n = 6$ for d-d, 8 for d-q, and 10 for q-q [52]. The variable C indicates the total concentration of sensitizer and activator ions in moles. The relationship between the luminous intensities and the values

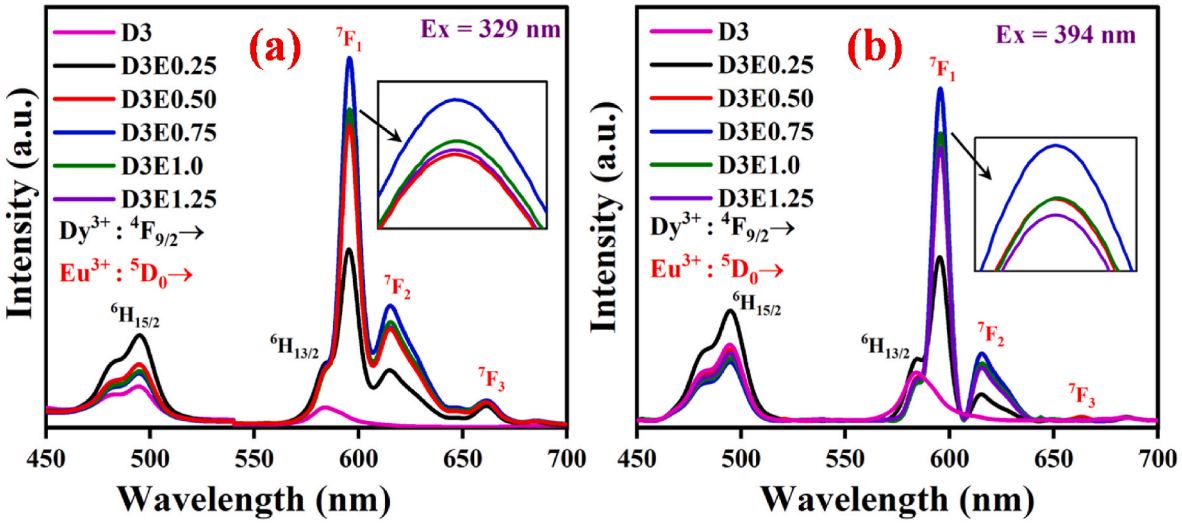


Fig. 9. (a) & **(b)** represent the PL emission spectra for the as-prepared LBW:xDy^{3+}/yEu^{3+} (x = 3.0 mol% and $0 \leq y \leq 1.25$, $\Delta y = 0.25$ mol%) phosphors at two different excitation wavelengths (329 and 394 nm), respectively.

of η_0 & η is as follows [49]:

$$\frac{I_{S0}}{I_S} \propto \frac{\eta_0}{\eta} = C^{n/3} \quad (7)$$

The PL emission intensities of Dy^{3+} ions in the absence and presence of activator ions (Eu^{3+}) are denoted by I_{S0} & I_S, respectively. With excitation at 394 nm, Fig. 10 shows the variation in the ratio I_{S0}/I_S as a function of $C^{n/3}$, where n might take values of 6, 8, or 10. The data demonstrated the best linear fit for $n = 6$, indicating that non-radiative energy transfer via d-d interaction. Carnall's publication [53] was referenced in order to identify the energy levels for the dopant ions.

On the other hand, energy transfer between identical luminescent centres leads to concentration quenching of luminescence, and a weak-coupling scheme or a strong coupling scheme can be applied. Strong coupling is notably observed in groups like tungstates and vanadates, which are oxidic anions with a central metal ion lacking d electrons (e.g., WO_4^{2-}, WO_6^{6-}, VO_4^{3-}, MoO_4^{2-}). The luminescent species' nature determines the strength of the electron-lattice coupling. In the case of weak coupling, the zero-phonon line dominates, resulting in narrow peaks, as seen in Eu^{3+} emission. In the excited state, the electronic charge moves from the oxygen ligands to the central metal ion, forming a CT (charge transfer) state. Although the CT is typically small, a significant amount of electronic reorganization occurs, promoting electrons from bonding orbitals in the ground state to antibonding orbitals in the excited state. This leads to a large value of ΔR in the configurational coordinate diagram and broad spectral bands [54,55].

Jorgensen was the first to attribute the broad and strong absorption bands in the spectra of trivalent lanthanides to either CT or 4f→5d transitions. As a general rule, CT bands shift to lower energies with increasing oxidation state, while Rydberg transitions, such as 4f→5d transitions, shift to higher energies. The lowest absorption bands of tetravalent ions are expected to relate to CT transitions, and those of divalent lanthanide ions are related to 4f→5d transitions. Depending on the number of f-electrons in the ground state, the first allowed transition in trivalent lanthanide ions may be either a CT transition or a 4f→5d transition. The stability of half-filled and completely filled shells is used to predict which of the two transitions is expected. CT transitions involve ligands and/or central ions, causing a change in charge configuration [55,56].

In the present case, Fig. 11 represents the energy transfer process from Dy^{3+} ions to Eu^{3+} ions in the co-doped LBW phosphors. During this process, a particular n-UV light source activated the prepared phosphor samples, causing non-radiative transitions amid different energy levels of Dy^{3+} and Eu^{3+} ions. Two strong PL emission peaks are seen at 493 and 583 nm of Dy^{3+} ions. Some of this energy is then transferred to Eu^{3+} ions, causing red light emission. Fig. 11 shows that the energy of the Dy^{3+} ions at the $^4F_{9/2}$ level is about 21,144 cm^{-1}, which is slightly more than the energies of the Eu^{3+} ions at the $^5D_0$ (nearly 17,393 cm^{-1}) and $^5D_1$ (nearly 19,077 cm^{-1}) levels. There is a 2067 cm^{-1} energy difference between the $^4F_{9/2}$ and $^5D_1$ levels and about 3751 cm^{-1} between the $^4F_{9/2}$ and $^5D_0$ levels. These small energy differences imply that energy transfer from Dy^{3+} to Eu^{3+} ions can be facilitated by Dy^{3+} ions acting as an effective sensitizer of Eu^{3+} ions.

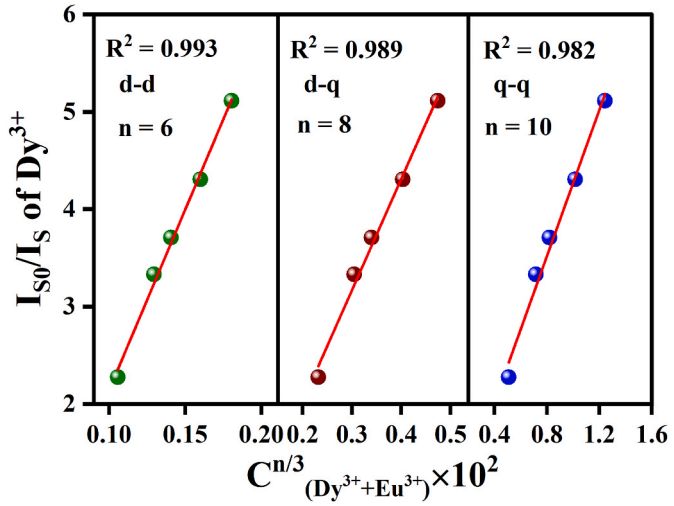


Fig. 10. Plot between I_{S0}/I_S and $C^{n/3}$, at Ex = 394 nm with n = 6, 8 and 10.

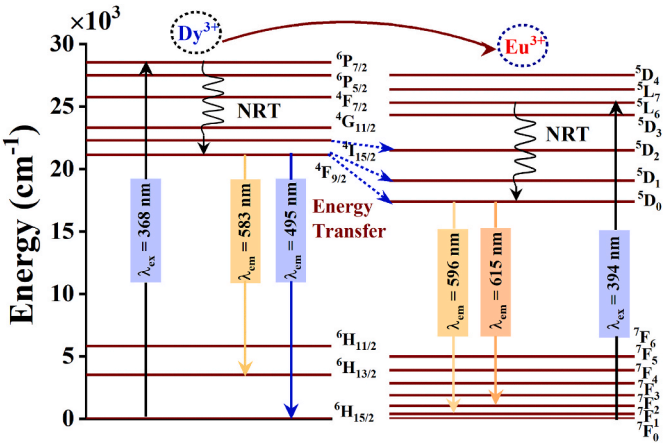


Fig. 11. The schematic ET process between Dy^{3+} and Eu^{3+} ions of the co-doped LBW phosphors.

2.2.2.4. Evaluations of CIE chromaticity coordinates. CIE color chromaticity coordinates for the as-prepared Dy^{3+}/Eu^{3+} co-doped LBW phosphors were evaluated using the emission spectra under Ex = 394 nm and presented in Table 2 and shown in Fig. 12 (a), by employing the formula given in literature [49].

The evaluated CIE color coordinates were lie in red region and shows a color tunability with the varying concentration of Eu^{3+} ions. The color coordinates were shifted from white to red region in co-doped LBW phosphors as the Eu^{3+} ions concentration changes from 0 to 1.25 mol%. Thus, Dy^{3+}/Eu^{3+} co-doped LBW phosphors may be a suitable choice for red emitter useful to fabricate n-UV driven w-LEDs. In Fig. 12 (b), CIE X shows a noticeable variation, however, CIE Y remains nearly constant. Therefore, the overall variation of the color chromaticity coordinates with the variation of the europium ions confirm the color tunability of the prepared phosphors.

Moreover, the McCamy relation is employed to evaluate the Correlated Colour Temperature (CCT), which is an essential measure for characterising white light [57]. CCT (in Kelvin (K)) offers a measurement of the perceived "warmth" or "coolness" of the light, therefore it can be used to divide natural white light into two categories [58]. The addition of Eu^{3+} ions caused the computed CCT values in the prepared phosphor samples to change from a colder to a warmer white light. This suggests that when excited by n-UV LEDs, these phosphors can potentially rely on to generate warm white light and making the prepared

Table 2
CIE chromaticity coordinates, CCT and CP values of as-prepared Dy^{3+}/Eu^{3+} co-doped LBW phosphors.

System	CIE		CCT (K)	CP (%)
	X	Y		
D3	0.329	0.366	5626	7.91
D3E0.25	0.421	0.366	2955	26.02
D3E0.50	0.514	0.367	1824	50.57
D3E0.75	0.540	0.368	1734	57.96
D3E1.0	0.524	0.366	1772	53.25
D3E1.25	0.515	0.368	1824	52.15

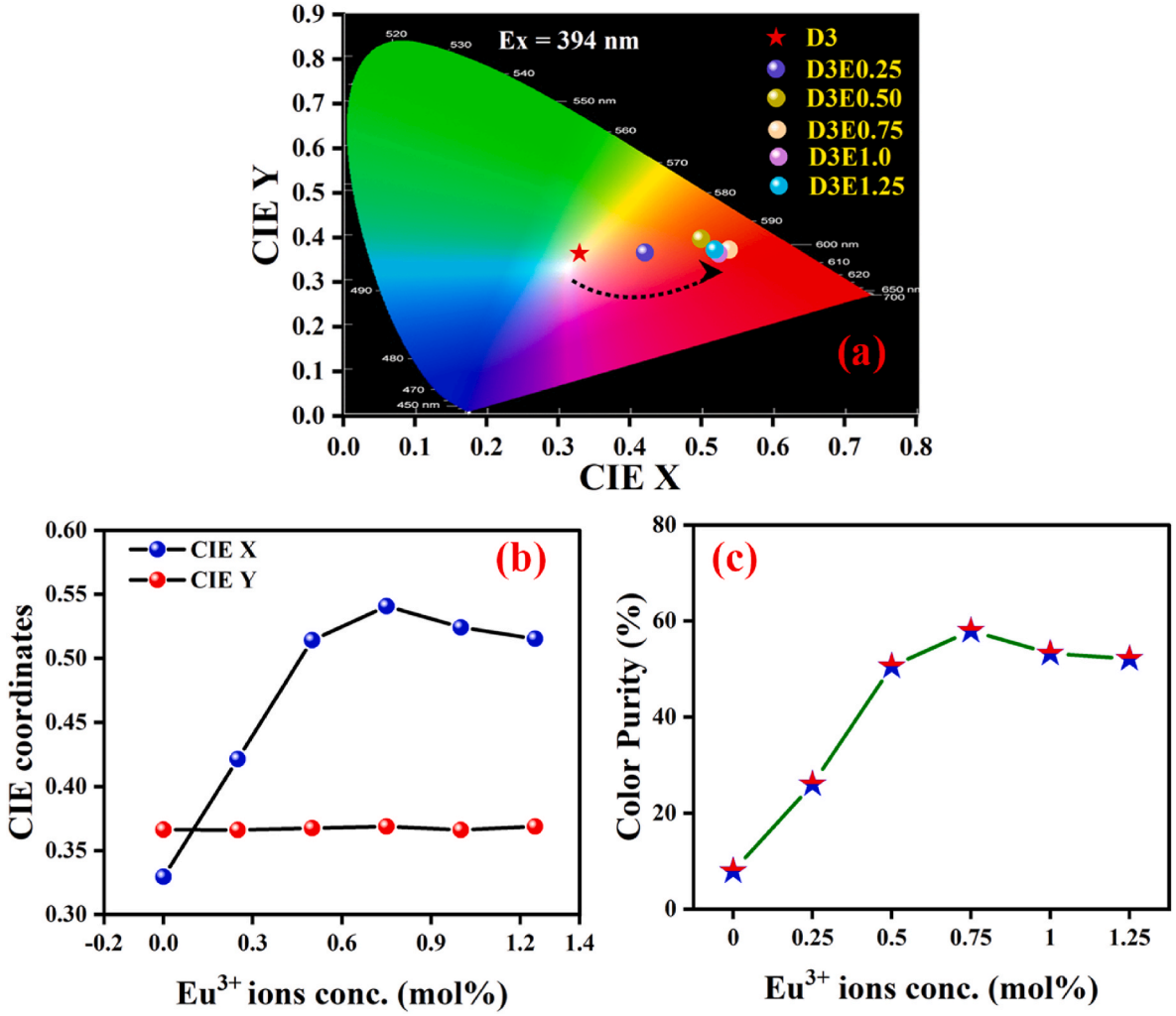


Fig. 12. (a) CIE color coordinates, **(b)** the variation of CIEX & CIEY & **(c)** CP values with Eu^{3+} ions of LBW:xDy^{3+}/yEu^{3+} (x = 3.0 and 0 ≤ y ≤ 1.25, Δy = 0.25 mol %) phosphors.

phosphor samples suitable for indoor lighting applications.

Another important parameter to further investigate the prepared LBW:xDy^{3+}/yEu^{3+} (x = 3.0 mol% and 0 ≤ y ≤ 1.25, Δy = 0.25 mol%) phosphors is the color purity (CP) [58]. Fig. 12 (c) represents the variation of CP values with the co-dopant Eu^{3+} ions. The color purity for the optimised D3E0.75 phosphor is maximum amid all the samples and is nearly equal to 60 %. The evaluated CIE chromaticity coordinates, CCT (K) and CP (%) values are presented in Table 2.

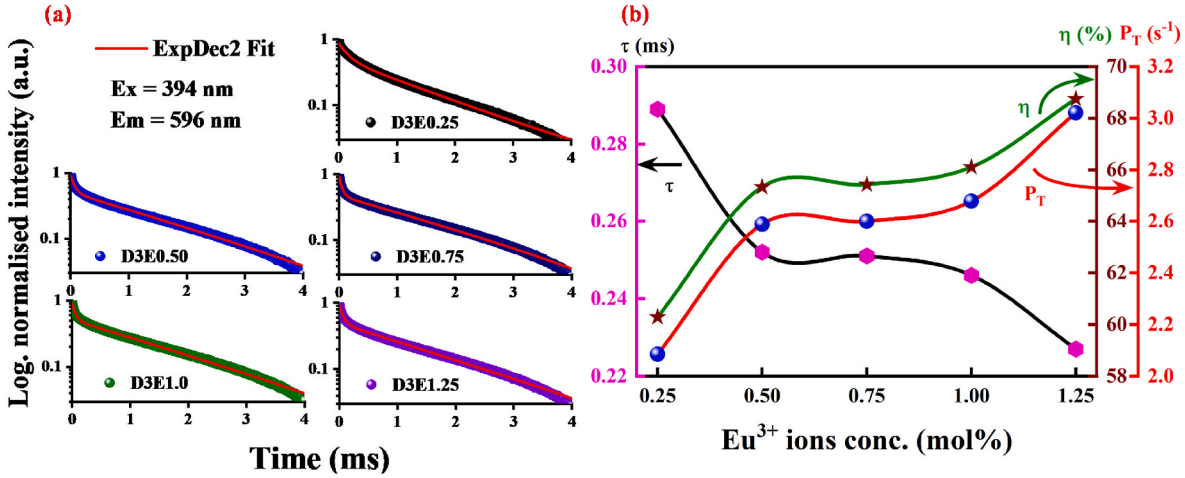


Fig. 13. (a) The decay curves at Em = 596 nm & Ex = 394 nm, **(b)** variation of τ_{av}, η_T and P_T with the Eu^{3+} ions concentration for all the as-prepared Dy^{3+}/Eu^{3+} co-doped LBW phosphor samples.

2.2.2.5. Decay analysis and exponential fitting. A greater understanding of the energy transfer mechanism was obtained by study the PL decay. As shown in Fig. 13 (a), the decay curves for all the prepared LBW phosphor samples co-doped with Dy^{3+} and Eu^{3+} were measured at an Ex = 394 nm and an Em = 596 nm. The decay curves were seen to have non-exponential behaviour, and the following bi-exponential equation provides the best description [58]:

$$I_t = A_1 \exp\left(\frac{t}{\tau_1}\right) + A_2 \exp\left(\frac{t}{\tau_2}\right) \quad (8)$$

I_t denotes the luminous intensity at time t, A_1 and A_2 denote the fitted constants, τ_1 and τ_2 mean the decay time. The average lifetime (τ_{av}), which ranges from 0.289 ms to 0.252 ms, decreases as the concentration of Eu^{3+} ions increase. The following formula is used to find the values of τ_{av} [49]:

$$\tau = \frac{A_1\tau_1^2 + A_2\tau_2^2}{A_1\tau_1 + A_2\tau_2} \quad (9)$$

The findings are displayed in Table 3. The reduction in τ as the concentration of Eu^{3+} increases offer additional evidence of the energy transfer from Dy^{3+} to Eu^{3+} ions. Moreover, the increase in energy transfer efficiency with higher concentrations of Eu^{3+} ions is attributed to non-radiative energy transfer rates. Moreover, the energy transfer efficiency (η_T) is determined using the following relation [59]:

$$\eta_T = 1 - \frac{\tau}{\tau_0} \quad (10)$$

Table 3 presents data that demonstrates a noticeable increase in η_T values with increasing Eu^{3+} ions concentration. The observed pattern provides additional evidence in favour of the theory that energy is transferred from donors (Dy^{3+}) to acceptors (Eu^{3+}) ions. Interestingly, the sample labelled D3E1.25 has an efficiency more than 68 %, which is comparatively higher than previous studies [60–63], presented in Table 4. The following given formula is employed for calculating the energy transfer probability (P_T), which quantifies the likelihood of energy transfer occurring from the donor ions to the acceptor ions [59]:

$$P_T = \frac{1}{\tau} - \frac{1}{\tau_0} \quad (11)$$

Table 3 provides an overview of all the evaluated parameters, and Fig. 13 (b) shows the variation of τ_{av}, η_T and P_T with the concentration of Eu^{3+} ions.

2.2.2.6. TDPL studies. As temperature rises, UV/blue LED chips lose optical performance. Consequently, TDPL tests were conducted, as seen in Fig. 14, for all as-prepared phosphor samples at Ex = 394 nm in order to examine their temperature sensitivity by adjusting the temperature from room temperature (303 K) to 443 K.

The relative emission intensities with variation of temperature for the $^4F_{9/2} \rightarrow {}^6H_{15/2}$ (495 nm), $^6H_{13/2}$ (585 nm), and $^5D_0 \rightarrow {}^7F_1$ (596 nm), $^7F_2$ (615 nm) transitions is shown in Fig. 15, with the greatest integrated emission intensity being 100 % at room temperature. Due to the increase in non-radiative transitions with rise in temperature, the emission peak intensity appears to be decreasing [64].

However, with the rise in temperature, there is little decrement in the

Table 3
Variation of lifetime (τ) (ms), energy transfer efficiency (η_T) (%) and energy transfer probability (P_T) (s^{-1}) with Dy^{3+}/Eu^{3+} co-doped LBW phosphors.

Sample	τ (ms)	η_T (%)	P_T (s^{-1})
D3E0.25	0.289	60.28	2.08
D3E0.50	0.252	65.33	2.58
D3E0.75	0.251	65.42	2.59
D3E1.0	0.246	66.10	2.67
D3E1.25	0.227	68.74	3.02

Table 4
Comparison of energy transfer efficiency (η_T) of the present sample with some previously reported literature.

Sample	η_T (%)	References
D3E1.25	68.74	**This work**
D2E7	39.6	[60]
D9E15	51.0	[61]
D5E3	51.2	[62]
D5E20	60.1	[63]

PL emission intensities of $^4F_{9/2} \rightarrow {}^6H_{15/2}$ and $^5D_0 \rightarrow {}^7F_2$ transitions, whereas the PL emission intensities of $^4F_{9/2} \rightarrow {}^6H_{13/2}$ and $^5D_0 \rightarrow {}^7F_1$ transitions decrease dramatically, can be seen in Fig. 15. Therefore, $^5D_0 \rightarrow {}^7F_2$ and $^4F_{9/2} \rightarrow {}^6H_{13/2}$ transitions can be assumed as thermally coupled energy levels (TCLs). Temperature has an impact on the relative population of various emission levels, which follows a Boltzmann-type distribution. Using the temperature-dependent emission spectra of all the prepared phosphors (Fig. 14) under the 394 nm excitation, the Fluorescence intensity ratio (FIR) theory was applied to evaluate its performance as a luminescent thermometer. The ratio of the population between the two TCLs, *FIR*, is determined by a population distribution of the Boltzmann type and is given by the equation [65]:

$$\boldsymbol{FIR} = \frac{\boldsymbol{I_{596\ nm}}}{\boldsymbol{I_{615\ nm}}} = \boldsymbol{A}exp\left(\frac{-\Delta \boldsymbol{E}}{\boldsymbol{KT}}\right) \quad (12)$$

here $\boldsymbol{K}$ represents the Boltzmann constant, $\boldsymbol{A}$ denotes a proportional parameter, and $\Delta\boldsymbol{E}$ is the energy separation of two TCLs.

The measured plot of $\boldsymbol{FIR}$ vs $\boldsymbol{T}$ (temperature) is nicely matched by equation (12), as seen in Fig. 16 (a) and presented in Table 5. For temperature control purposes, it is crucial to know the rate of change in $\boldsymbol{FIR}$ with temperature. The sensor sensitivity, which illustrates the material's sensitivity, is the rate at which the $\boldsymbol{FIR}$ changes for a specific change in temperature. Relative Sensitivity ($\boldsymbol{S_r}$) value, which can be computed using the calculation below, is used in practical applications to recognize the thermometric capability of a phosphor sample [46]:

$$\boldsymbol{S_r} = \frac{\mathbf{1}}{\boldsymbol{FIR}} \frac{\boldsymbol{d(FIR)}}{\boldsymbol{dT}} \times \mathbf{100\%} = \left(\frac{\Delta \boldsymbol{E}}{\boldsymbol{KT^2}}\right) \times \mathbf{100\%} \quad (13)$$

The calculated relative sensitivity for TCLs is dependent on the absolute temperature. Fig. 16 (b) represents the values of S_r for all the prepared phosphors having maximum value at 303 K and subsequently exhibits monotonic diminishing behaviour as the temperature rises.

It is evident that the evaluated value of the S_r is maximum with a value of 0.96 % K^{-1} at 303 K, for D3E0.75 (i.e., 3.0 mol% of Dy^{3+} ions and 0.75 mol% of Eu^{3+} ions co-doped LBW) phosphor amid all the samples, shown in Fig. 16 (c). This phosphor was found to have the highest observed sensor sensitivity for the low-temperature range, when compared with the previous literature [66–70], presented in Table 6.

3. Conclusion

In summary, the crystal $Li_2Ba_5W_3O_{15}$ has been employed as a host material for integrating lanthanide activator ions. The various features of the prepared co-doped LBW:Dy^{3+}/Eu^{3+} phosphors, including their structure, composition, luminescence properties, and temperature-dependent behavior, were thoroughly examined using different characterisation methods such as XRD, FE-SEM, EDX, FT-IR, PL, PL decay, and TDPL. XRD analysis, in combination with W–H plot, demonstrated that Dy^{3+} and Eu^{3+} ions primarily occupy the Ba^{2+} lattice sites within the LBW host lattice. The little variation of bandgap with the dopant ions in the host matrix indicated the incorporation of dopant (Dy^{3+}/Eu^{3+}) ions in the LBW host without causing any excessive crystal defects. A luminescence spectroscopy study was conducted on single Dy^{3+} doped and Dy^{3+}/Eu^{3+} co-doped LBW samples. The incorporation of Dy^{3+} and Eu^{3+} activator ions into the LBW host allowed for adjustable

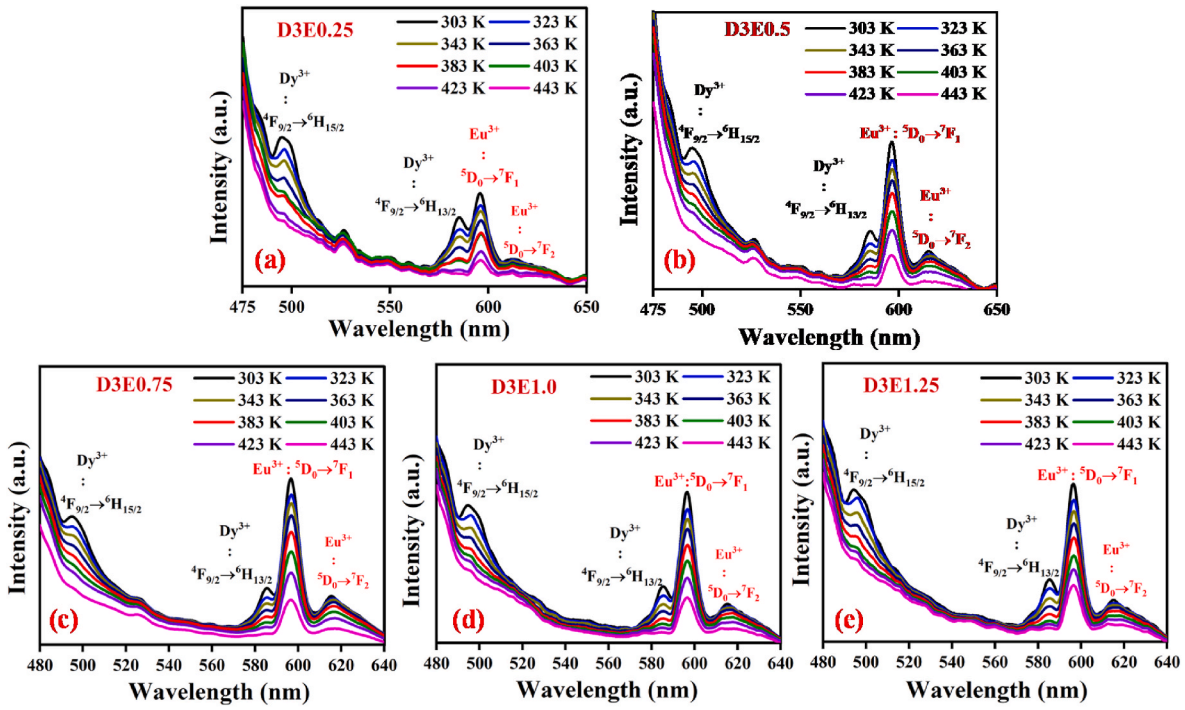


Fig. 14. The temperature-dependent emission spectra of LBW:xDy^{3+}/yEu^{3+}(0.25 ≤ x ≤ 1.25, Δx = 0.25 mol%) phosphors.

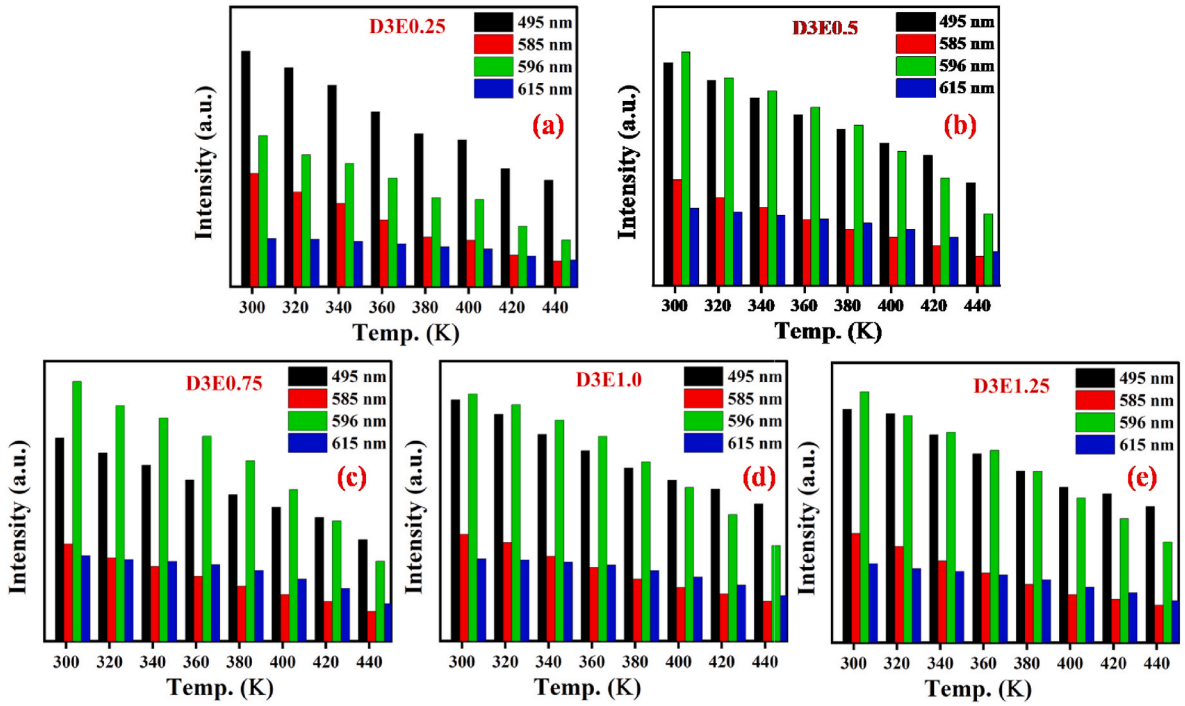


Fig. 15. The variation of PL intensities of various peaks of LBW:xDy^{3+}/yEu^{3+}(0.25 ≤ x ≤ 1.25, Δx = 0.25 mol%) phosphors with temperature.

luminescent performance at a specific excitation wavelength, resulting in the emission of multiple colors. By simply varying the concentration of Eu^{3+}, the luminescent colors could be shifted from natural white to orange-red, achieving warm white light emission with a low Correlated Color Temperature (CCT), making it suitable for indoor lighting applications. The Reisfeld approximation suggested that energy transfer from Dy^{3+} to Eu^{3+} ions occur through dipole-dipole interactions. As the concentration of Eu^{3+} ions increased, the decay time decreased due to an increase in the non-radiative transitions. The luminescence decay kinetics revealed that energy transfer from Dy^{3+} to Eu^{3+} ions happened with a maximum energy transfer efficiency of 68.74 % for D3E1.25 phosphors. Furthermore, by adjusting the Dy^{3+}/Eu^{3+} ions concentrations and excitation wavelengths; the CIE chromaticity coordinates, CCTs and energy transfer efficiency (η_T) can be effectively modified. The two emission peaks in the prepared phosphor samples exhibited different temperature-dependent trends. Finally, an FIR model was established, yielding a maximum relative sensitivity (S_r) of 0.97 % K^{-1} for the D3E0.75 phosphor sample at 303 K. Therefore, all the

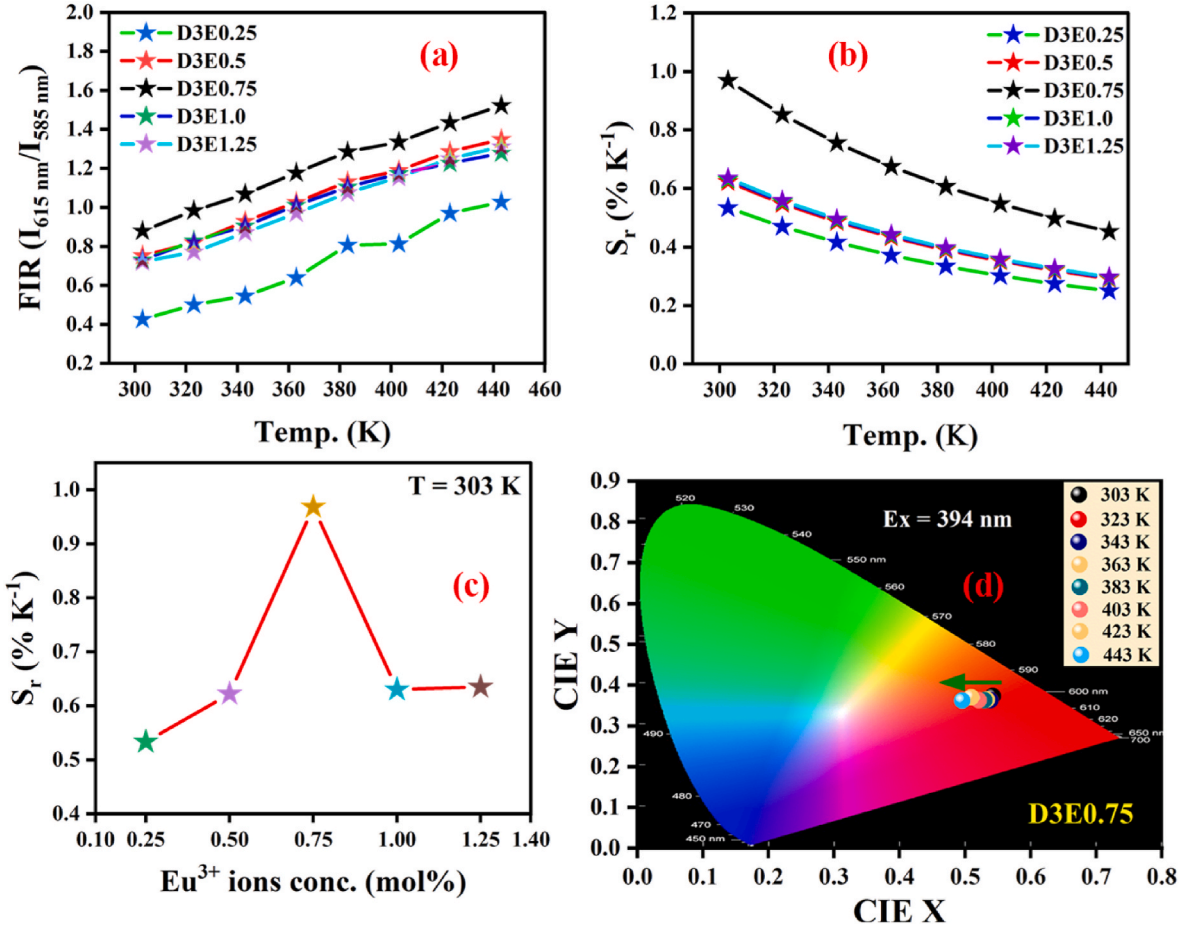


Fig. 16. (a) The temperature dependency of the FIR curve and **(b)** the temperature sensitivity curves and **(c)** Variation of S_r (% K^{-1}) with Eu^{3+} ions concentration at 303 K temperature, **(d)** variation of CIE color coordinates with temperature for D3E0.75 phosphor.

Table 5
The variation of FIR and S_r values of D3E0.75 with change in temperature (303–443 K).

Temperature (K)	FIR	S_r (% K^{-1})
303	0.81	0.97
323	0.98	0.85
343	1.07	0.75
363	1.18	0.67
383	1.28	0.61
403	1.33	0.55
423	1.43	0.50
443	1.52	0.45

Table 6
Optical parameters comparison of temperature sensing materials.

Sensing material	Temperature range (K)	S_r (% K^{-1})	References
$Tb_{0.99}Eu_{0.01}(BDC)_{1.5}(H_2O_2)$	300–320	0.37–318	[66]
CYSO:Bi^{3+}/Eu^{3+}	298–523	0.95–423	[67]
SYF:Er^{3+} glass ceramic	300–500	0.62–560	[68]
LaOBr:Ce^{3+}/Tb^{3+} phosphor	293–433	0.42–433	[69]
NLF:Ho^{3+}/Yb^{3+} phosphor	360–780	0.83–500	[70]
D3E0.75 phosphor	303–**443**	**0.97–298**	**This work**

experimental results indicated that the prepared Dy^{3+}/Eu^{3+} co-doped LBW phosphors can be a suitable choice for UV excitable warm white lighting devices with color tunability and non-contact optical thermometry measurements.

The estimated CIE coordinate values for D3E0.75 at various temperatures, taking Ex = 394 nm, are shown in Fig. 16 (d), confirm the tunability of the luminous colouring pattern from orange-red to yellowish-orange region. The values of FIR, S_r parameters for D3E0.75 phosphor with variation of temperature are presented in Table 5.

CRediT authorship contribution statement

Anu: Writing - original draft, Software, Methodology, Investigation, Conceptualization. **Seema:** Writing - original draft, Methodology, Conceptualization. **A. Kumar:** Formal analysis. **Nisha Deopa:** Formal analysis. **Mukesh K. Sahu:** Writing - review & editing. **Aman Prasad:** Formal analysis. **A.S. Rao:** Writing - review & editing, Visualization, Validation, Supervision.

Declaration of competing interest

The authors declare that they have no known competing financial interests or personal relationships that could have appeared to influence the work reported in this paper.

Data availability

Data will be made available on request.

Acknowledgement

Ms. Anu is very much thankful to CSIR/UGC for the award of a Junior Research Fellowship (JRF) (UGC Ref.1352: CSIR-UGC NET DEC. 2018) to her. The authors are also thankful to the authorities of Delhi Technological University, New Delhi, INDIA for providing the necessary infrastructure facilities to carry out the present research work.

References

[1] J. Brübach, C. Pflitsch, A. Dreizler, B. Atakan, On surface temperature measurements with thermographic phosphors: a review, Prog. Energy Combust. Sci. 39 (2013) 37–60.
[2] R. Vaz, M.F. Frasco, M.G.F. Sales, Photonics in nature and bioinspired designs: sustainable approaches for a colourful world, Nanoscale Adv. 2 (2020) 5106–5129.
[3] C. Zhang, J. Lin, Defect-related luminescent materials: synthesis, emission properties and applications, Chem. Soc. Rev. 41 (2012) 7938.
[4] B. Hou, M. Jia, P. Li, G. Liu, Z. Sun, Z. Fu, Multifunctional optical thermometry based on the rare-earth-ions-doped up-/Down-Conversion $Ba_2TiGe_2O_8$:Ln (Ln = Eu^{3+}/Er^{3+}/Ho^{3+}/Yb^{3+}) phosphors, Inorg. Chem. 58 (2019) 7939–7946.
[5] Z. Feng, L. Lin, Z. Wang, Z. Zheng, Highly efficient and wide range low temperature sensing of upconversion luminescence of $NaYF_4$:Er^{3+} nanoparticles: Effects of concentration of active or sensitive ions, excitation power and particle size on temperature sensing sensitivity, Opt Commun. 491 (2021) 126942.
[6] X. Wang, O.S. Wolfbeis, R.J. Meier, Luminescent probes and sensors for temperature, Chem. Soc. Rev. 42 (2013) 7834.
[7] C.D.S. Brites, A. Millán, L.D. Carlos, Lanthanides in Luminescent Thermometry 49 (2016) 339–427.
[8] S.F. Collins, G.W. Baxter, S.A. Wade, T. Sun, K.T.V. Grattan, Z.Y. Zhang, A. W. Palmer, Comparison of fluorescence-based temperature sensor schemes: Theoretical analysis and experimental validation, J. Appl. Phys. 84 (1998) 4649–4654.
[9] S.W. Allison, G.T. Gillies, Remote thermometry with thermographic phosphors: Instrumentation and applications, Rev. Sci. Instrum. 68 (1997) 2615–2650.
[10] J. Zhao, S.X. Huang, D. Zhao, C.H. Huang, M.J. Ma, R.J. Zhang, Y.C. Fan, B.Z. Liu, J.W. Gao, Q. Zong, Y.P. Yu, Sm^{3+} doped $K_3Gd_3B_4O_{12}$: an orange-emitting phosphor for white light-emitting diodes, Optik 159 (2018) 115–122.
[11] W. Xu, Y. Hu, L. Zheng, Z. Zhang, W. Cao, H. Liu, X. Wu, Enhanced NIR-NIR luminescence from $CaWO_4$: Nd^{3+}/Yb^{3+} phosphors by Li^+ codoping for thermometry and optical heating, J. Lumin. 208 (2019) 415–423.
[12] D. Chen, Z. Wan, Y. Zhou, X. Zhou, Y. Yu, J. Zhong, M. Ding, Z. Ji, Dual-phase Glass Ceramic: structure, dual-Modal luminescence, and temperature sensing behaviors, ACS Appl. Mater. Interfaces 7 (2015) 19484–19493.
[13] R. Ao, L. Xing, W. Yang, A high-brightness phosphor based on Yb^{3+}/Er^{3+} codoped Y2O3 micro-crystals and controllable temperature sensing sensitivity via rare earth ions, Opt Commun. 492 (2021) 126967.
[14] Q. Liu, M. Wu, B. Chen, X. Huang, M. Liu, Y. Liu, K. Su, X. Min, R. Mi, Z. Huang, Optical thermometry based on fluorescence intensity ratio of Dy^{3+}-Doped oxysilicate apatite warm white phosphor, Ceram. Int. 49 (2023) 4971–4978.
[15] S. Zhou, S. Jiang, X. Wei, Y. Chen, C. Duan, M. Yin, Optical thermometry based on upconversion luminescence in Yb^{3+}/Ho^{3+} co-doped $NaLuF_4$, J. Alloys Compd. 588 (2014) 654–657.
[16] M. Que, Z. Ci, Y. Wang, G. Zhu, Y. Shi, S. Xin, Synthesis and luminescent properties of $Ca_2La_8(GeO_4)_6O_2$:RE^{3+} (RE^{3+}=Eu^{3+}, Tb^{3+}, Dy^{3+}, Sm^{3+}, Tm^{3+}) phosphors, J. Lumin. 144 (2013) 64–68.
[17] N. Pasberg, D. den Engelsen, G.R. Fern, P.G. Harris, T.G. Ireland, J. Silver, Structure and luminescence analyses of simultaneously synthesised $(Lu_{1-x}Gd_x)_2O_2S$:Tb^{3+} and $(Lu_{1-x}Gd_x)_2O_3$:Tb_{3+}, Dalton Trans. 46 (2017) 7693–7707.
[18] Q. Wang, M. Liao, Q. Lin, M. Xiong, Z. Mu, F. Wu, A review on fluorescence intensity ratio thermometer based on rare-earth and transition metal ions doped inorganic luminescent materials, J. Alloys Compd. 850 (2021) 156744.
[19] Z. Li, X. Geng, Y. Wang, Y. Chen, Synthesis and luminescence properties of $NaBaPO_4$:Tm^{3+},Dy^{3+} white-light emitting phosphors with enhanced brightness by Li^+ co-doping, J. Lumin. 240 (2021) 118428.
[20] M. Runowski, P. Woźny, N. Stopikowska, I.R. Martín, V. Lavín, S. Lis, Luminescent Nanothermometer operating at very high temperature-sensing up to 1000 K with Upconverting nanoparticles (Yb^{3+}/Tm^{3+}), ACS Appl. Mater. Interfaces 12 (2020) 43933–43941.
[21] T. Zheng, M. Runowski, P. Woźny, B. Barszcz, S. Lis, M. Vega, J. Llanos, K. Soler-Carracedo, I.R. Martín, Boltzmann vs. non-Boltzmann (non-linear) thermometry-Y^{3+}-Er^{3+} activated dual-mode thermometer and phase transition sensor via second harmonic generation, J. Alloys Compd. 906 (2022) 164329.
[22] M. Runowski, P. Woźny, S. Lis, V. Lavín, I.R. Martín, Optical Vacuum sensor based on lanthanide upconversion-luminescence thermometry as a Tool for ultralow pressure sensing, Adv. Mater. Technol. 5 (2020) 1901091.
[23] H. Kong, G. Jia, N. Zhang, Z. Meng, H. Li, C. Zhang, Facile synthesis, novel structure, and tunable luminescence properties of $K_6Bi_{13}(PO_4)_{15}$:Dy^{3+}, Eu^{3+} phosphors for ultraviolet converted white light-emitting diodes, Ceram. Int. 49 (2023) 19373–19383.
[24] A. Khan, F. Song, X. Gao, Z. Chen, X. Sang, M. Feng, L. Liu, Introduction of Molybdenum into the lattice of single-host $CaZrO_3$:Dy^{3+}/Eu^{3+} to enhance luminescence intensity of the phosphor for white light emission, J. Alloys Compd. 881 (2021) 160652.
[25] G. Xie, J. Si, G. Li, G. Cai, Environment-dependent Eu^{2+}-activated $Ba_3CaK(PO_4)_3$ toward white-light emission by chemical cosubstitution of the $(BO_3)^{3-}$ anion group, Inorg. Chem. 61 (2022) 14845–14856.
[26] X. Qin, X. Liu, W. Huang, M. Bettinelli, X. Liu, Lanthanide-activated phosphors based on 4f-5d optical transitions: theoretical and experimental aspects, Chem. Rev. 117 (2017) 4488–4527.
[27] X. Tian, S. Lian, C. Ji, Z. Huang, J. Wen, Z. Chen, H. Peng, S. Wang, J. Li, J. Hu, Y. Peng, Enhanced photoluminescence and ultrahigh temperature sensitivity from NaF flux assisted $CaTiO_3$:Pr^{3+} red emitting phosphor, J. Alloys Compd. 784 (2019) 628–640.
[28] H. Liu, H. Liang, W. Zhang, Q. Zeng, D. Wen, Improving the thermal stability and luminescent efficiency of $(Ba,Sr)_3SiO_5$:Eu^{2+} phosphors by structure, bandgap engineering and soft chemistry synthesis method, Chem. Eng. J. 410 (2021) 128367.
[29] Q. Cheng, F. Ren, Q. Lin, H. Tong, X. Miao, High quantum efficiency red emitting α-phase $La_2W_2O_9$:Eu^{3+} phosphor, J. Alloys Compd. 772 (2019) 905–911.
[30] Y. Zheng, Z. Wang, D. Yang, Z. Fang, Y. Xiang, T. Yang, S. Yang, Y. Mao, K. Xiong, J. Zhu, Highly thermostable white-emitting $Ca_9ZnK(PO_4)_7$:Ce^{3+}, Dy^{3+} single-phase phosphor with tunable photoluminescence and energy transfer, Dalton Trans. 51 (2022) 2770–2781.
[31] S. Jana, A. Mondal, J. Manam, S. Das, Pr^{3+} doped $BaNb_2O_6$ reddish orange emitting phosphor for solid state lighting and optical thermometry applications, J. Alloys Compd. 821 (2020) 153342.
[32] O. Madkhali, Ü.H. Kaynar, S. Cam Kaynar, M. Ayvacikli, N. Can, Dy^{3+} and Eu^{3+} co-activated gadolinium aluminate borate phosphor: synthesis, enhanced luminescence, energy transfer and tunable color, Mater. Res. Bull. 164 (2023) 112282.
[33] C. Kumari, A. Kumar, S.K. Sharma, J. Manam, Sr_3LiSbO_6:Er^{3+} phosphors for green LEDs and solar cell applications, Vacuum 207 (2023) 111599.
[34] E. Sreeja, V. Vidyadharan, S.K. Jose, A. George, C. Joseph, N. V Unnikrishnan, P. R. Biju, A single-phase white light emitting Pr^{3+} doped Ba_2CaWO_6 phosphor : synthesis , photoluminescence and optical properties, Opt. Mater. 78 (2018) 52–62.
[35] S.K. Hussain, J.S. Yu, Citrate-based sol-gel synthesis of blue- and green-emitting $BaLa_2WO_7$:Tm^{3+} or Er^{3+} phosphors and their luminescence properties, Mater. Res. Bull. 95 (2017) 229–234.
[36] Anu, N. Deopa, A.S. Rao, Structural and luminescence characteristics of thermally stable Dy^{3+} doped oxyfluoride strontium zinc borosilicate glasses for photonic device applications, Opt. Laser Technol. 154 (2022) 108328.
[37] D. Jiang, L. Geng, S. Zhou, Y. Wang, Photoluminescence properties and energy transfer in the Sm^{3+} and Eu^{3+} co-doped $Ca_3Bi(PO_4)_3$ red phosphor, Inorg. Chem. Commun. 142 (2022).
[38] Z.P. Ning Liu, Lefu Mei, Jianxiong Bin, Ze Zhang, Effect of Anionic Group $[SiO_4]^{4}$/$[PO_4]^{3-}$ on the Luminescence Properties of Dy^{3+}-Doped Tungstate Structural Compounds, 2021, pp. 843–851.
[39] Y. Xiang, Y. Zheng, L. Yang, M. Li, Y. Mao, J. Zhu, Exploring a new Dy^{3+}-activated borotellurate phosphor with thermally stable photoluminescence, J. Alloys Compd. 919 (2022) 165837.
[40] H. Huang, Y. He, Z. Lin, L. Kang, Y. Zhang, Two novel Bi-based borate photocatalysts: crystal structure, electronic structure, photoelectrochemical properties, and photocatalytic activity under simulated solar light irradiation, J. Phys. Chem. C 117 (2013) 22986–22994.
[41] P. Rohilla, A.S. Rao, Synthesis optimisation and efficiency enhancement in Eu^{3+} doped barium molybdenum titanate phosphors for w-LED applications, Mater. Res. Bull. 150 (2022) 111753.
[42] V.V. Shanbhag, S.C. Prashantha, T.R.S. Shekhar, H. Nagabhushana, R. Naik, K. M. Girish, S. Ashwini, D. Rangappa, D.S. Prasanna, Enhanced photoluminescence of SiO^2 coated $CaTiO^3$:Dy^{3+}, Li^+ nanophosphors for white light emitting diodes, Ceram. Int. 47 (2021) 10346–10354.
[43] D.L. Monika, H. Nagabhushana, R.H. Krishna, B.M. Nagabhushana, S.C. Sharma, T. Thomas, Synthesis and photoluminescence properties of a novel Sr_2CeO_4:Dy^{3+} nanophosphor with enhanced brightness by Li+ co-doping, RSC Adv. 4 (2014) 38655–38662.
[44] W.T. Carnall, P.R. Fields, K. Rajnak, Electronic energy levels in the trivalent lanthanide aquo ions. I. Pr^{3+}, Nd^{3+}, Pm^{3+}, Sm^{3+}, Dy^{3+}, Ho^{3+}, Er^{3+}, and Tm^{3+} (1968) 4424.
[45] L.G. Van Uitert, J.E. Soc, I.G. Van Uitert, Characterization of energy transfer interactions between rare earth ions characterization of energy transfer interactions between rare earth ions, J. Electrochem. Soc. 114 (1967) 1048–1053.
[46] Anu, A.S. Rao, Luminescence and optical thermometry strategy based on emission spectra of $Li_2Ba_5W_3O_{15}$:Pr^{3+} phosphors, Opt. Mater. 145 (2023) 114476.
[47] N. Deopa, S. Saini, S. Kaur, A. Prasad, A.S. Rao, Spectroscopic investigations on Dy^{3+} ions doped zinc lead alumino borate glasses for photonic device applications, J. Rare Earths 37 (2019) 52–59.
[48] H. Li, R. Zhao, Y. Jia, W. Sun, J. Fu, L. Jiang, S. Zhang, R. Pang, C. Li, $Sr_{1.7}Zn_{0.3}CeO4$:Eu^{3+} novel red-emitting phosphors: synthesis and photoluminescence properties, ACS Appl. Mater. Interfaces 6 (2014) 3163–3169.
[49] Anu, A. Kumar, Ravina, N. Deopa, A.S. Rao, Efficient tunable photoluminescence of Dy^{3+}/Eu^{3+} co-doped OFSZBS glasses for warm white LEDs, J. Non-Cryst. Solids 616 (2023) 122421.
[50] N. Deopa, M.K. Sahu, P.R. Rani, R. Punia, A.S. Rao, Realization of warm white light and energy transfer studies of Dy^{3+}/Eu^{3+} co-doped Li_2O-PbO-Al_2O_3-B_2O_3 glasses for lighting applications, J. Lumin. 222 (2020) 117166.

[51] J. Zhou, Y. Yao, Y. Chen, B. Wang, X. Huang, Y. Lai, Y. Zhang, Q. Wu, Synthesis, energy transfer mechanism, and tunable emissions of novel $Na_3La(VO_4)_2:Re^{3+}$ (Re^{3+} = Dy^{3+}, Eu^{3+}, and Sm^{3+}) vanadate phosphors for near-UV-excited white LEDs, Ceram. Int. 46 (2020) 6276–6283.
[52] X. Zhang, H. Zou, C. Xu, Z. An, R. Dong, K. Zheng, Y. Sheng, Y. Song, Energy transfer and luminescence properties of Dy^{3+}/Eu^{3+} doped silicoaluminate phosphors, Opt. Mater. 89 (2019) 512–520.
[53] W.T. Carnall, P.R. Fields, K. Rajnak, Electronic energy levels of the trivalent lanthanide aquo ions. IV. Eu^{3+}, J. Chem. Phys. 49 (1968) 4450–4455.
[54] E.M.J. Weber, A.A. Kaminskii, M.J. Weber, M.J. Weber, M.J. Weber, Phosphor Handbook, 2018.
[55] G. Blasse, B.C. Grabmaier, Luminescent Materials, Springer Berlin Heidelberg, Berlin, Heidelberg, 1994.
[56] H.A. Höppe, Recent developments in the field of inorganic phosphors, Angew. Chemie Int. Ed. 48 (2009) 3572–3582.
[57] S. Kumari, Anu, A. Prasad, P. Rohilla, A.S. Rao, Prospective applications of thermally stable Dy^{3+} doped potassium zinc strontium borate (KZSB) glasses in w-LEDs, J. Mater. Sci. Mater. Electron. 34 (2023) 1–17.
[58] Anu, A.S. Rao, Synthesis, Structural and fluorescence investigations of novel $Li_2Ba_5W_3O_{15}:Sm^{3+}$ phosphors for photonic device applications, J. Fluoresc. (2023). https://link.springer.com/article/10.1007/s10895-023-03449-z.
[59] A.S. Ravita, Rao, Effective sensitization of Eu^{3+} visible red emission by Sm^{3+} in thermally stable potassium zinc alumino borosilicate glasses for photonic device applications, J. Lumin. 244 (2022) 118689.
[60] A. Kumar, J. Manam, Color tunable emission and temperature dependent photoluminescence properties of Eu^{3+} co-doped $Gd_2Zr_2O_7:Dy^{3+}$ phosphors, Opt. Mater. 96 (2019) 109373.
[61] E.A. Rathnakumari, S.M.M. Kennedy, Photoluminescence properties of certain trivalent RE ions (Dy/Sm/Eu) activated $NaSrBi_2(PO_4)_3$ phosphors and cool to warm white color tuning in Dy^{3+}-Sm^{3+} and Dy^{3+}-Eu^{3+} codoped $NaSrBi_2(PO_4)_3$ phosphors for indoor lighting applications, J. Lumin. 235 (2021) 118018.
[62] S.K. Hussain, H.S. Go, J.J. Han, H. Patnam, G. Nagaraju, J.S. Yu, Energy transfer mechanism and tunable emissions from $K_3La(VO_4)_2:Dy^{3+}/Eu^{3+}$ phosphors and soft-PDMS-based composite films for multifunctional applications, J. Alloys Compd. 805 (2019) 1271–1281.
[63] W. Wang, J. Li, Z. Zhang, Z. Liu, The synthesis and luminescent properties of Dy/Re (Re = Tb or Eu) co-doped $Gd_2(WO_4)_3$ phosphor with tunable color via energy transfer, J. Lumin. 207 (2019) 114–122.
[64] J.A. Jiménez, Temperature dependent spectroscopic properties of Cu^+ and Dy^{3+} Co-doped phosphate glass: band gap analysis and Cu nanocluster-enhanced Dy^{3+} luminescence, ChemPhysChem (2018) 399–404.
[65] Z. Liang, F. Qin, Y. Zheng, Z. Zhang, W. Cao, Noncontact thermometry based on downconversion luminescence from Eu^{3+} doped $LiNbO_3$ single crystal, Sensors Actuators A Phys 238 (2016) 215–219.
[66] A. Cadiau, C.D.S. Brites, P.M.F.J. Costa, R.A.S. Ferreira, J. Rocha, L.D. Carlos, Ratiometric nanothermometer based on an emissive Ln^{3+}-organic framework, ACS Nano 7 (2013) 7213–7218.
[67] K. Li, R. Van Deun, Site-Bi^{3+} and Eu^{3+} dual emissions in color-tunable $Ca_2Y_8(SiO_4)_6O_2:Bi^{3+}$, Eu^{3+} phosphors prepared via sol-gel synthesis for potentially ratiometric temperature sensing, J. Alloys Compd. 787 (2019) 86–95.
[68] X. Li, J. Cao, Y. Wei, Z. Yang, H. Guo, Optical thermometry based on up-conversion luminescence behavior of Er^{3+} -doped transparent Sr_2YbF_7 glass-ceramics, J. Am. Ceram. Soc. 98 (2015) 3824–3830.
[69] X. Zhang, Y. Huang, M. Gong, Dual-emitting Ce^{3+}, Tb^{3+} co-doped LaOBr phosphor: luminescence, energy transfer and ratiometric temperature sensing, Chem. Eng. J. 307 (2017) 291–299.
[70] X. Chen, Z. Zheng, L. Teng, R. Wei, F. Hu, H. Guo, Self-calibrated optical thermometer based on luminescence from $SrLu_2O_4$:Bi^{3+}, Eu^{3+} phosphors, RSC Adv. 8 (2018) 35422–35428.

arXiv:2312.16857v1 [gr-qc] 28 Dec 2023

A study on matter accretion onto charged black hole solution in metric-affine gravity

G. Mustafa,[1,*] A. Ditta,[2,†] Faisal Javed,[1,‡] S.K. Maurya,[3,§]
Himanshu Chaudhary,[4,5,6,¶] and Farruh Atamurotov[7,8,9,**]

[1]*Department of Physics, Zhejiang Normal University, Jinhua 321004, People's Republic of China*
[2]*Department of Mathematics, The Islamia University of Bahawalpur, Bahawalpur-63100, Pakistan*
[3]*Department of Mathematical and Physical Sciences, College of Arts and Sciences, University of Nizwa, Nizwa 616, Sultanate of Oman*
[4]*Department of Applied Mathematics, Delhi Technological University, Delhi-110042, India*
[5]*Pacif Institute of Cosmology and Selfology (PICS), Sagara, Sambalpur 768224, Odisha, India*
[6]*Department of Mathematics, Shyamlal College, University of Delhi, Delhi-110032, India,*
[7]*Central Asian University, Milliy Bog' Street 264, Tashkent 111221, Uzbekistan*
[8]*University of Tashkent for Applied Sciences, Str. Gavhar 1, Tashkent 100149, Uzbekistan*
[9]*Institute of Theoretical Physics, National University of Uzbekistan, Tashkent 100174, Uzbekistan*

(Dated: December 29, 2023)

This study deals with astrophysical accretion onto the charged black hole solution, which is sourced by the dilation, spin, and shear charge of matter in metric affine gravity. The metric affine gravity defines the link between torsion and nonmetricity in space-time geometry. In the current analysis, we study the accretion process of various perfect fluids that are accreting near the charged black hole in the framework of metric affine gravity. Within the domain of accretion, multiple fluids have been examined depending on the value of f_1. The ultra-stiff, ultra-relativistic, and sub-relativistic fluids are considered to discuss the accretion. In the framework of equations of state, we consider isothermal fluids for this investigation. Further, we explore the effect of polytropic test fluid in relation to accretion discs, and it is presented in phase diagrams. Some important aspects of the accretion process are investigated. Analyzing the accretion rate close to a charged black hole solution, typical behavior is created and discussed graphically.

keywords: Black Hole; Hamiltonian approach; Accretion; Metric affine gravity.

I. INTRODUCTION

Modified Einstein gravity refers to theories that modify or extend Einstein's general relativity (GR). These modifications are introduced to address certain shortcomings or limitations of the original theory, such as the inability to explain the accelerated expansion of the universe or the existence of dark matter and dark energy. These modifications often involve introducing additional fields, modifying the equations of motion, or considering higher-dimensional spacetimes. The non-metricity of spacetime is explained by extra components introduced in modified Einstein field equations, such as metric affine gravity (MAG) [1]. The purpose of these changes is to provide a more complete account of gravity beyond GR by including the effects of torsion and non-metricity into the gravitational field equations. Metric affine gravity sheds light on the underlying characteristics of gravity and its interactions with matter and energy by taking into account geometric features of spacetime other than curvature.

The sources of torsion in matter are specifically found to be the spin angular momentum [2, 3], while the sources of nonmetricity are found to be the so called dilation and shear currents of matter [4, 5]. Development of new models in the field of MAG that provide precise solutions with torsion and nonmetricity beyond GR is especially important, since there are currently insufficient better understandings and empirical evidence for the existence of these variables. Unfortunately, the main obstacle to finding such models is the computational complexity resulting from the simultaneous inclusion of curvature, torsion, and nonmetricity in the computations. Furthermore, the order of the corresponding field strength tensors in the gravitational action determines the dynamics of these post-Riemannian quantities. For material sources with inherent hypermomentum [6], the torsion and nonmetricity tensors are connected to non-propagating linear combinations of the curvature tensor. Conversely, the introduction of dynamics to these

*Email:gmustafa3828@gmail.com
†Email:adsmeerkhan@gmail.com
‡Email:faisaljaved.math@gmail.com
§Email:sunil@unizwa.edu.om
¶Email:himanshuch1729@gmail.com
**Email:atamurotov@yahoo.com

fields through higher-order curvature corrections results in a notable rise in theoretical complexity [7]. Despite these difficulties, from the beginning of MAG, a great deal of work has been done to comprehend the physical effects of the field equations and to identify and examine different kinds of solutions [8–16]. Notably, recent research has investigated the use of MAG in gravitational waves, black hole (BH) physics, and cosmology [17–27].

The first BH solutions with torsion and nonmetricity were found by looking at a basic Lagrangian form and applying mathematical restrictions to these tensors. These limitations, which significantly simplify the field equations, include the triplet ansatz and other limits produced via prolongation techniques [28, 29]. These simplifications, however, lead to BH configurations that do not adequately display the dynamic link among the coframe, the metric, and the independent post-Riemannian structures found in the connection. A novel model was recently developed in the context of Weyl-Cartan geometry, integrating nonmetricity and dynamical torsion and establishing a relationship between these components [30]. Investigating the dynamic role of the traceless component of the nonmetricity tensor and its relation to shears is the main focus of study by Bahamonde and others [31]. They have created a model that takes this dynamic into account, leading to a novel BH solution with shear charges. This extension is shown to provide, upon the introduction of dynamical torsion and a Weyl vector, the largest known set of static and spherically symmetric BH solutions with spin, dilation, and shear charges in Metric-Affine Gravity [31]. Recently, the dynamical configurations of thin-shell developed from BHs in MAG filled with massless and massive scalar fields were studied in [32]. Also, the thermodynamics and Joule-Thomson expansion of charged anti-de Sitter (AdS) BHs in MAG are studied in [33]. A. Ditta et al. were investigated testing BH in MAG with its parameters using particle dynamics and photon motion in details [34].

A BH accretion disc is a swirling disk of gas and dust that forms around a BH as it pulls in surrounding matter through its strong gravitational pull. This disc is often made up of hot, ionized gas that emits intense radiation as it spirals inward towards the BH's event horizon. The accretion disc plays a crucial role in understanding the dynamics and energy release mechanisms associated with BHs. Exploration of accurate and analytical answers has led to continuous advancements in accretion theory [35]. These answers provide a framework to define different astrophysical circumstances, which is essential to understanding the events under study. Moreover, because they act as benchmark tests for numerical codes, analytical solutions are useful tools in the area [36]. The Bondi model provides an explanation of the uniform flow of a spherically symmetric fluid falling onto a BH in the context of Newtonian gravity [35]. This model was expanded by Michel to the relativistic regime using a Schwarzschild BH as a framework [37]. Furthermore, Tejeda and Aguayortiz produced analytic solutions for a Schwarzschild BH [38], while Bondi and Hoyle created analytic solutions for wind accretion situations in the Newtonian theory[39]. Many studies using both analytical and numerical methods have improved our understanding of spherical and wind accretion [40–45]. The studies of various BH spacetimes are explored in [46]-[60].

Researchers have investigated phantom accretion inside a certain type of BHs [61–64]. Furthermore, utilizing massless and massive scalar fields, a number of research publications have examined the dynamic configurations of particles at the boundary of different BH geometries [65–68]. In [69–71], Ditta and Abbas have additionally demonstrated efficacious outcomes concerning accretion while taking into account various kinds of BHs. In the setting of nonlinear electrodynamics BHs, Ditta et al. recently examined circular orbits and accretion disks [72]. Furthermore, researchers have investigated modified theories of gravity, including noncommutative theory [74], quantum gravity corrections [75], and accretion flows onto scalar-tensor-vector gravity [73]. It has also been explored [76, 77] for heteroclinic and cyclic accretion processes onto $f(R)$ and $f(T)$ BHs. Furthermore, studies have been conducted [80]-[87] utilizing dynamical systems and BH thermodynamics to analyze accretion flows onto static BHs. Researchers have also carried out fascinating research on alternative BH geometries, including [88]-[98]. Quasi-periodic oscillations were computed and tested by Liu and colleagues [100, 101] with observational data from various compact objects.

The settlement of this paper is as follows: section **2** is devoted to present BH solution in MAG. In section **3**, we determine the generic expressions of accretion of BH solutions in MAG. The speed of sound at the sonic points are evaluated in the section **4** by considering Hamiltonian system for the accretion by the equation of state (EoS). Moreover, in section **5**, we obsere the physical configurations of accretion flow near a considered BH in MAG for numerous cases of fluids such as ultra-stiff fluid (USF), ultra-relativistic fluid (URF), radiation fluid (RF) and sub-relativistic fluid (SRF). The polytropic test fluid accretion has been analyzed in section **6**. The accretion rate for polytropic fluid and mass accretion rate for different fluid distributions are presented in **7** and **8**, respectively. The last section presents the final outcomes of the our manuscript.

II. METRIC-AFFINE GRAVITY AND BLACK HOLE SOLUTION WITH SPIN, DILATION AND SHEAR CHARGES

The MAG is a gravitational theory that expands beyond GR by accommodating non-zero torsion and nonmetricity. The literature around a non-holonomic connection $w_\epsilon \in g[(4, \mathrm{R})$ explains the concepts of the spin, dilation and shear

currents of matter, and fulfils via a vector bundle isomorphism, or coframe field, which is further defined by the following relation $e^{a}_{epsilon}$. The relation of an affine-exhibiting metric spacetime is expressed as [31]:

$$w^{a}{}_{b\epsilon} = e^{a}{}_{\lambda} e_{b}{}^{\rho} \tilde{\Gamma}^{\lambda}_{\rho\epsilon} + e^{a}{}_{\lambda} \partial_{\epsilon} e_{b}{}^{\lambda}, \tag{1}$$

which is fully quantified by the torsion and nonmetricity tensors as [31]

$$T^{\lambda}_{\epsilon\psi} = 2\tilde{\Gamma}^{\lambda}_{[\epsilon\psi]}, \quad Q_{\lambda\epsilon\psi} = \tilde{\nabla}_{\lambda} g\epsilon\psi.$$

Let us start from the modified action in the form of dynamical nonmetricity tensor, which is provided as: [31]

$$S = \int d^{4}x\sqrt{-g}\left\{\mathcal{L}_{\mathrm{m}} + \frac{1}{16\pi}\left[-R + 2f_{1}\tilde{R}_{(\lambda\rho)\epsilon\psi}\tilde{R}^{(\lambda\rho)\epsilon\psi} + 2f_{2}\left(\tilde{R}_{(\epsilon\psi)} - \hat{R}_{(\epsilon\psi)}\right)\left(\tilde{R}^{(\epsilon\psi)} - \hat{R}^{(\epsilon\psi)}\right)\right]\right\}, \tag{2}$$

where $\mathcal{L}_{\mathrm{m}}$ represents the matter Lagrangian. The nonmetricity field in the action within the scope of symmetric part of the curvature tensor and its contraction is defined as [31]

$$\begin{aligned} \tilde{R}^{(\lambda\rho)}{}_{\epsilon\psi} &= \tilde{\nabla}_{[\psi} Q_{\epsilon]}{}^{\lambda\rho} + \frac{1}{2} T^{\sigma}_{\epsilon\psi} Q^{\lambda\rho}_{\sigma}, \\ \tilde{R}_{(\epsilon\psi)} - \hat{R}_{(\epsilon\psi)} &= \tilde{\nabla}_{(\epsilon} Q^{\lambda}_{\psi)\lambda} - \tilde{\nabla}_{\lambda} Q_{(\epsilon\psi)}{}^{\lambda} - Q^{\lambda\rho}{}_{\lambda} Q_{(\epsilon\psi)\rho} + Q_{\lambda\rho(\epsilon} Q_{\psi)}{}^{\lambda\rho} + T_{\lambda\rho(\epsilon} Q^{\lambda\rho}_{\psi\rho}. \end{aligned} \tag{3}$$

Now, by varying the action by Eq. (2) with respect to the anholonomic connection and co-frame field, one can find the following set of equations, which can be found in detail in the appendix part of Ref. [31]

$$Y1^{\psi}_{\epsilon} = 8\pi\theta_{\epsilon}{}^{\psi}, \tag{4}$$

$$Y2^{\lambda\epsilon\psi} = 4\pi\Delta^{\lambda\epsilon\psi}, \tag{5}$$

where $Y1_{\epsilon}{}^{\psi}$ and $Y2^{\lambda\epsilon\psi}$ provides the tensor quantities. Also, $\Delta^{\lambda\epsilon\psi}$ and $\theta_{\epsilon}{}^{\psi}$ express hyper-momentum density tensor and the canonical energy-momentum tensor as

$$\begin{aligned} \theta_{\epsilon}{}^{\psi} &= \frac{e^{a}{}_{\epsilon}}{\sqrt{-g}} \frac{\delta\left(\mathcal{L}_{m}\sqrt{-g}\right)}{\delta e^{a}\psi}, \\ \Delta^{\lambda\epsilon\psi} &= \frac{e^{a\lambda} e_{b\epsilon}}{\sqrt{-g}} \frac{\delta\left(\mathcal{L}_{m}\sqrt{-g}\right)}{\delta w^{a}{}_{b\psi}}. \end{aligned} \tag{6}$$

For MAG, the anholonomic connection by Eq. (1) in the Lie-algebra of the linear group $GL(4,\mathcal{R})$ separated into hyper-momentum showing its formal decay into spin, dilation, and shear currents [102]. The necessary presence of shear gives rise to a dynamical traceless nonmetricity tensor within the composition of the special linear group $SL(4,\mathcal{R}) \subset GL(4,\mathcal{R})$ [103]. Finally, the effective gravitational action for these above quantities has the following form [31]:

$$\begin{aligned} S = \frac{1}{64\pi}\int d^{4}x\sqrt{-g}\Big[&-4R - 6d_{1}\bar{R}_{\lambda[\rho\epsilon\psi]}\bar{R}^{\lambda[\rho\epsilon\psi]} - 9d_{1}\bar{R}_{\lambda[\rho\epsilon\psi]}\bar{R}^{\epsilon[\lambda\psi\rho]} + 8d_{1}\bar{R}_{[\epsilon\psi]}\bar{R}^{[\epsilon\psi]} + 4e_{1}\tilde{R}^{\lambda}{}_{\lambda\epsilon\psi}\tilde{R}^{\rho}{}_{\rho}\epsilon\psi \\ &+8f_{1}\tilde{R}_{(\lambda\rho)\epsilon\psi}\tilde{R}^{(\lambda\rho)\epsilon\psi} - 2f_{1}\left(\tilde{R}_{(\epsilon\psi)} - \hat{R}_{(\epsilon\psi)}\right)\left(\tilde{R}^{(\epsilon\psi)} - \hat{R}^{(\epsilon\psi)}\right) + 18d_{1}\bar{R}_{\epsilon[\lambda\rho\psi]}\tilde{R}^{(\epsilon\psi)\lambda\rho} - 6d_{1}\bar{R}_{[\epsilon\psi]}\bar{R}^{\epsilon\psi} \\ &-3d_{1}\tilde{R}_{(\lambda\rho)\epsilon\psi}\tilde{R}^{(\lambda\rho)\epsilon\psi} + 6d_{1}\tilde{R}_{(\lambda\rho)\epsilon\psi}\tilde{R}^{(\lambda\epsilon)\rho\psi} + \frac{9}{2}d_{1}\tilde{R}_{\epsilon\psi}\tilde{R}^{\epsilon\psi} + 3\left(1-2a_{2}\right)T_{[\lambda\epsilon\psi]}T^{[\lambda\epsilon\psi]}\Big], \end{aligned} \tag{7}$$

which provides the following independent field equations (the main calculations can be seen in appendix of Ref. [31]):

$$X1^{\psi}_{\epsilon} = 0, \tag{8}$$

$$X2^{\lambda\epsilon\psi} = 0, \tag{9}$$

where $X2^{\lambda\epsilon\psi}$ and $X1^{\psi}_{\epsilon}$ express the tensor quantities [31]. As a result, the tetrad field equations (8-9) help us to define the Reissner-Nordström-like BH geometry with spin, dilation, and shear charges. Finally, we have the following lapse function, i.e., g_{tt} metric component for Reissner-Nordström-like BH geometry as [31, 32],

$$f(r) \;=\; 1 - \frac{2m}{r} + \frac{d_{1}\kappa_{\mathrm{s}}^{2} - 4e_{1}\kappa_{\mathrm{d}}^{2} - 2f_{1}\kappa_{\mathrm{sh}}^{2}}{r^{2}}. \tag{10}$$

In the metric function $f(r)$, the parametric representation is as follows: d_1 and f_1 denote the Lagrangian coefficients; e_1 is a constant whereas k_{sh}, k_s and k_d are the shear, spin and dilation charges, respectively. In this setup, one

can produce three kinds of solutions, namely: (i) $d_1 = 8f_1$, (ii) $d_1 = -8f_1$ and (iii) $d_1 \neq 8f_1$ for which $f_1 \leq 0$. The conventional Reissner-Nordström solution of General Relativity may be derived from this geometric framework. Instead of assuming an electromagnetic component, the solution is constructed using a traceless nonmetricity field in the given context. To study the accretion properties of BHs, we just consider two cases of solutions, that is, $d_1 = 8f_1$ and $d_1 = -8f_1$. The horizon radii for the metric function (2) can be found as

$$r_{\pm} = M - \sqrt{4e_1k_d^2 - d_1k_s^2 + 2f_1k_{sh}^2 + M^2}. \tag{11}$$

For the horizon analysis of the metric-affine gravity black hole (MAGBH), we plot $f(r) = 0$ by varying the values of f_1 for both cases $d_1 = \pm 8f_1$ in Fig. 1, which behaves differently. The effect of f_1 is important and makes a constant contribution to the horizon analysis. Therefore, the MAGBH horizon has the following structure: As seen in Fig. 1 (left plot),

- We observe that an event horizon is formed by the effected parameter f_1 of MAGBH at $f_1 = 0.25$ (red dotes).
- Two horizons are formed at the initial value of he MAGBH parameter $f_1 = 0.2$ (black dotes).
- The other two curves have no horizon.
- Subsequently, the curves go away from the BH as the parameter f_1 increases.

As seen in Figure (1), the right plot exhibits different behaviour compared to the left plot while varying the values of f_1. The maximum portion of the curve is negative. In this portion, the radius increased by increasing f_1 and vice versa. The bottom plots are significant because they support our observation of the light emitted by accreting MAGBH. This understanding can be used to characterize the nature of accretion and constrain the parameters of BH.

III. SPHERICAL ACCRETION FLOW AND SOME FUNDAMENTAL EQUATIONS

In this section, our aim is to find the general solutions of accretion onto MAGBH, which explain the motion of particles around the horizon. To do this, we are assuming the basic conservation laws in the context of the spherically symmetric metric. During the accretion process, there is no mass annihilation, and creation leads to the law of mass conservation, which is expressed as

$$\nabla_\eta J^\eta = 0. \tag{12}$$

As, $J^\eta = \varepsilon u^\eta$ in which ε denotes the number of particles and $u^\eta = \frac{dx^\eta}{d\tau}$ is the velocity of the fluid. Now, by introducing the energy-momentum tensor $T^{\eta\zeta} = (\rho + p)u^\eta u^\zeta + pg^{\eta\zeta}$, we can setup the current problem. Further, the expression $u^\eta = \frac{dx^\eta}{d\tau} = (u^t, u^r, 0, 0)$, is the four velocity of the particle used in the conservation of energy, which is provided as

$$\nabla_\eta T^{\eta\zeta} = 0. \tag{13}$$

By applying the normalization condition $u^\mu u_\mu = -1$, it is easy to find a required relation, which is defined as

$$\Big[u^t\Big]^2 = \frac{1}{f^2(r)}\Big[u^2 + f(r)\Big], \tag{14}$$

also

$$\Big[u^t\Big]^2 = u^2 - f(r). \tag{15}$$

For equatorial plane, we assume $(\theta = \pi/2)$, the mass conservation law by Eq. (12) can be rewritten as

$$\Big[\frac{1}{r}\Big]^2 \frac{d}{dr}\Big[\varepsilon u r^2\Big] = 0. \tag{16}$$

Now, by integrating, we get the following expression

$$\varepsilon u r^2 = A_1, \tag{17}$$

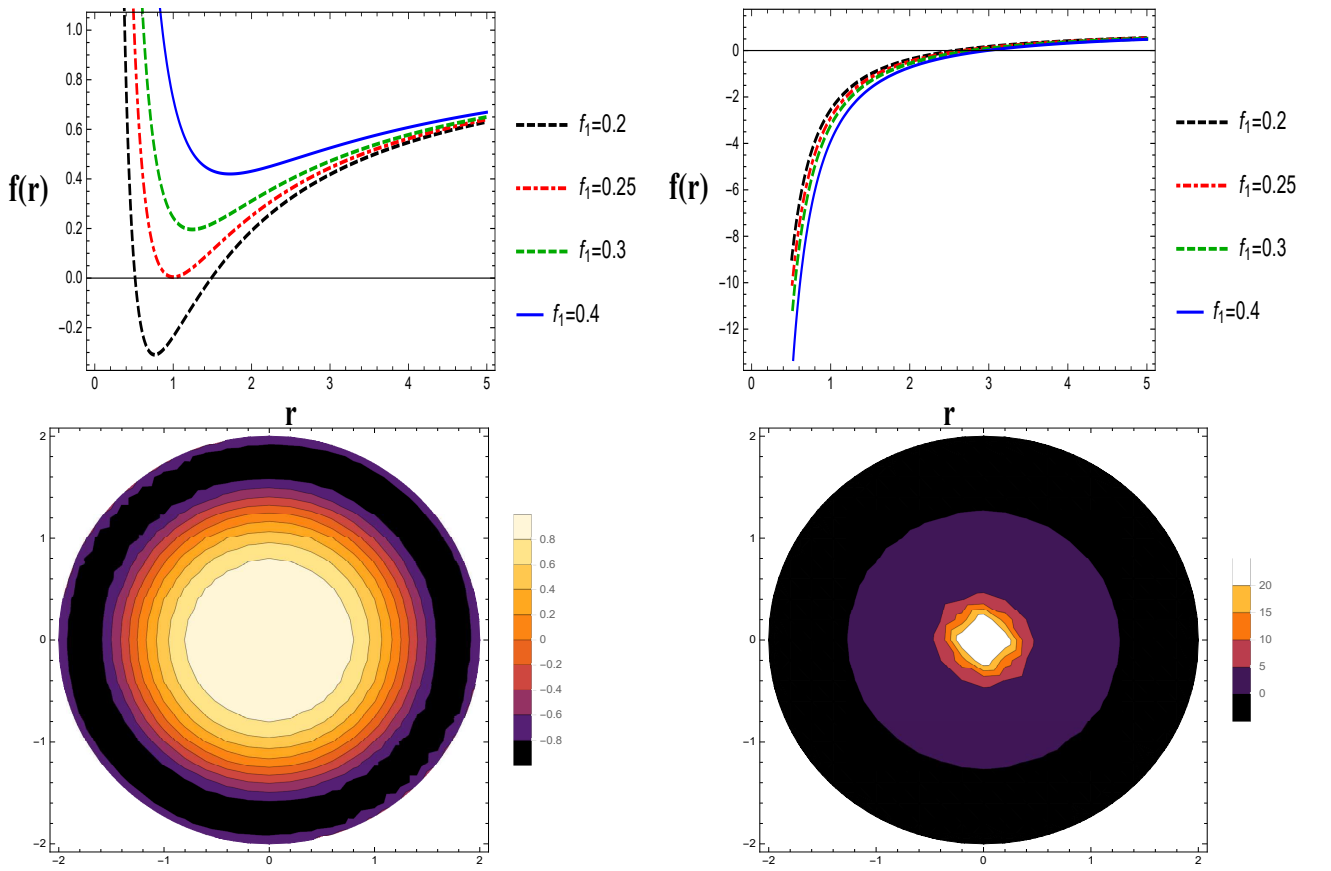


FIG. 1: Horizon display using the MAGBH parameters. Left plot is for $d_1 = 8f_1$ in the lapse function $f(r) = 0$ with the variation in f_1. Right plot is for $d_1 = -8f_1$ in the lapse function $f(r) = 0$ with the variation in f_1. The fixed parameters are $m = 1$, $e_1 = 0.1$, $k_s = 0.85$, $k_d = 0.7$ and $k_{sh} = 0.7$. The bottom plots are for mass of MAGBH with the conditions $d_1 = 8f_1$ and $d_1 = -8f_1$.

where A_1 is integration constant. Since accretion belongs to the fluid velocity $u^r = u < 0$, we define the enthalpy, which is the ratio between the density of the fluid and the total energy of its structure at a constant pressure (as $h(\rho, p, \varepsilon) = \frac{\rho+p}{\varepsilon}$). Since the flow of fluid is smooth, therefore Eq. (9) yields

$$\varepsilon u^\eta \nabla_\eta (h u^\zeta) + g^{\eta\zeta} \partial_\eta p = 0. \tag{18}$$

Next, if the entropy of a moving fluid along a streamline is constant, then the fluid flow must be isotropic [42]. The above equation gives the following relationship:

$$u^\eta \nabla_\eta (h u^\eta) + \partial_\zeta h = 0. \tag{19}$$

Now, by putting the zeroth component, we obtain

$$\partial_r (h u_t) = 0. \tag{20}$$

On integrating, one can get the following expression

$$\left[h^2 (f(r) + (u)^2)\right]^{1/2} = A_2, \tag{21}$$

where A_2 is integration constant. These fundamental relations by Eq. (17) and Eq. (21) exploring the critical flow of fluid in the framework of spherically symmetric MAGBH.

IV. DYNAMICAL ANALYSIS

In this current section, we shall discuss about sonic points and isothermal test fluid.

A. Sonic Points

The dark compact object achieves maximum accretion when the flow passes through the sonic point. This is a critical point where the velocity of falling matter is equal to the speed of sound. To determine these points under MAGBH, we consider barotropic matter with constant enthalpy as $h = h(\varepsilon)$. The EoS for barotropic matter is given by [76]

$$\frac{1}{h}dh = \mathbf{s}^2\frac{d\varepsilon}{\varepsilon}, \tag{22}$$

where $\mathbf{s}$ is the speed of sound, and the EoS becomes $\ln h = \mathbf{s}^2 \ln \varepsilon$. Using Eqs. (10), (21) and (22), we have the following relation

$$\left[\left(\frac{u}{u_t}\right)^2 - \mathbf{s}^2\right](\ln u)_{,r} = \frac{1}{r(u_t)^2}\left[2\mathbf{s}^2(u_t)^2 - \frac{1}{2}rf'(r)\right]. \tag{23}$$

To determine the value of the speed of sound at the sonic point, we take both sides of the above Eq. (23) equal to zero, which leads us

$$\mathbf{s}_c^2 = \left(\frac{u_c}{u_{tc}}\right)^2. \tag{24}$$

From the right hand side of Eq. (23), we have

$$2\mathbf{s}_c^2(u_{tc})^2 - \frac{1}{2}r_c f'_{r_c} = 0. \tag{25}$$

Using (24) and (25), attaining the critical radial velocity, given by the following relation

$$(u_c)^2 = \frac{1}{4}r_c f'_{r_c}. \tag{26}$$

Further, from Eqs. (15), (25) and (26), one can get following expression

$$r_c f'_{r_c} = 4\mathbf{s}_c^2[f(r_c) + (u_c)^2]. \tag{27}$$

Hence, the final value of the speed of sound is calculated as

$$\mathbf{s}_c^2 = \frac{r_c f'_{r_c}}{r_c f'_{r_c} + 4f(r_c)}. \tag{28}$$

The Eqs. (26) and (28) provide the sonic points as $(r_c, \pm u_c)$, when we have the value of speed of sound.

B. Isothermal Test Fluid Background

The isothermal test fluid is a significant process which provides us a better understanding to explain the accretion flow for MAGBH at a constant temperature. Throughout the process, the speed of matter remains very fast, and it is exposed as adiabatic. In this process, considering $\mathbf{s}^2 = \frac{dp}{d\rho}$, to determine analytic solutions of the equations of moving matter. Now, by introducing the EoS $p = \omega\rho$, for these solutions, where ρ is the energy density and ω is the state parameter with conditions $(0 < \omega \leq 1)$, defined in [104]. By using $p = \omega\rho$ and $\mathbf{s}^2 = \frac{dp}{d\rho}$, one can obtain $\mathbf{s}^2 = \omega$. According to the first law of thermodynamics, we have

$$\frac{1}{dn}d\rho = \frac{\rho + p}{\varepsilon} = h. \tag{29}$$

By limit of integration from the sonic point to any point of the fluid, which is inside, is calculated as

$$\frac{\varepsilon}{\varepsilon_c} = \exp\left(\int_{\rho_c}^{\rho}\frac{1}{\rho' + p(\rho')}d\rho'\right). \tag{30}$$

By applying $p=\omega\rho$, the Eq. (30) becomes

$$\frac{\varepsilon}{\varepsilon_c}=\left(\frac{\rho}{\rho_c}\right)^{\frac{1}{\omega+1}}. \tag{31}$$

By taking enthalpy as $h(\rho,p,\varepsilon)=\frac{\rho+p}{\varepsilon}$, into Eq. (31), one can obtain a following relation

$$\frac{(\omega+1)\rho_c}{\varepsilon_c}\left(\frac{\varepsilon}{\varepsilon_c}\right)^{\omega}=h. \tag{32}$$

Now, by putting $A_3=\frac{A_2\varepsilon_c^{1-\omega}}{(\omega+1)\rho_c}$ into Eq. (32) and Eq.(21), we obtain the following result

$$\varepsilon^{\omega}\sqrt{f(r)+(u)^2}=A_3. \tag{33}$$

The Eq. (29) and Eq. (10), lead us to

$$\left(f(r)+(u)^2\right)^{1/2}=A_3r^{2\omega}(u)^{\omega}. \tag{34}$$

Therefore, we take the following Hamiltonian, which is defined in [42, 43]

$$H=\frac{f^{1-\omega}(r)}{(1-v^2)^{1-\omega}v^{2\omega}r^{4\omega}}, \tag{35}$$

where $v\equiv\frac{dr}{f(r)dt}$, is three-dimensional speed of a particle with the radial motion in equatorial plane, and it is defined as

$$v^2=\left(\frac{u}{f(r)u^0}\right)^2=\frac{u^2}{u_0^2}=\frac{u^2}{f(r)+u^2}. \tag{36}$$

The main critical solutions are explored at the sonic points, from Eqs. (26) and (27), which is given as

$$(u_c)^2 = \frac{1}{4}r_cf_c'(r), \tag{37}$$

$$(u_c)^2 = \omega\left(f_c(r)+\frac{1}{4}r_cf_c'(r)\right). \tag{38}$$

This generalized result can be analyzed by taking the any value of ω. In this work, we will use some interesting fluids such as UST ($\omega=1$), URF ($\omega=1/2$), RF ($\omega=1/3$) and SRF ($\omega=1/4$) in the accretion flow around a MAGBH.

V. TESTING OF FLUIDS

The current section of this study deals with the Hamiltonian of different kinds of fluids, say USF, URF, RF, and SRF.

A. The Hamiltonian of USF

One can be found that pressure is equal to the energy density that is $p=\rho$ for the USF by using the EoS ($\omega=1$). The critical radius r_c is equal to the horizon that is $r_h=r_c$, at the metric potential $f_c=0$. The Hamiltonian (35) for this case is given by

$$H=\left(\frac{1}{\nu r^2}\right)^2. \tag{39}$$

TABLE I: The sonic points for URF with respect to MAGBH parameter f_1

$d_1 = 8f_1$			
f_1	r_c	v_c	H_c
0.10	3.83118	0.197643	0.174527
0.20	3.65052	0.262114	0.1504
0.30	3.15069	0.21385	0.19167
0.40	2.49156	0.15296	0.29775
0.50	2.61044	0.16219	0.33483
0.60	2.72054	0.174106	0.361829

TABLE II: The sonic points for URF with respect to MAGBH parameter f_1

$d_1 = -8f_1$			
f_1	r_c	v_c	H_c
0.10	4.2604	0.203247	0.139826
0.20	3.1308	0.235270	0.14999
0.30	2.5966	0.20587	0.18544
0.40	2.19952	0.187071	0.24782
0.50	1.68072	0.15573	0.29761
0.60	1.32235	0.24478	0.321652

B. The Hamiltonian of URF

It can be seen that the energy density in the URF is greater than the pressure, where the pressure is given by the equation $p = \rho/2$ and the parameter ω is equal to $1/2$. By the relation $r_c f_c'(r) - 4f_c(r) = 0$, the critical radius for URF may be derived by solving the Eqs. (37) and (38).

$$\frac{-6d_1k_s^2 + 12f_1k_{sh}^2 + 10mr - 4r^2 + 24e_1k_d^2}{r^2} = 0. \tag{40}$$

So, we choose only useful numerical value by the parameters $d_1 = 8f_1$, $f_1 = 1$, $e_1 = 1$, $m = 1$ and $k_s = 1$, $k_d = 0.7$ $k_{sh} = 2$.

$$r_c = 3.37191. \tag{41}$$

In second condition $d_1 = -8f_1$, the critical radius is $r_c = 6.58877$. Using the critical radius r_c, into (36), we get another critical value v_c. Then, by using the critical values $(r_c, \pm v_c)$, with the result $s_c^2 = v_c^2$, the critical Hamiltonian H_c is obtained. The general Hamiltonian (35) reduces into the form

$$H = \frac{f(r))^{1/2}}{r^2 v(1-v^2)^{1/2}}. \tag{42}$$

This implies that

$$H = \frac{\left(1 - \frac{2m}{r} + \frac{d_1k_s^2 - 4e_1k_d^2 - 2f_1k_{sh}^2}{r^2}\right)^{1/2}}{r^2 v(1-v^2)^{1/2}}. \tag{43}$$

By choosing the suitable value of $H = H_c$, one can see the graphical analysis of v and r_c. Continuing from (42), we have

$$v^2 = \frac{1 \pm \left(1 - 4x(r)\right)^{1/2}}{2}, \tag{44}$$

where $x(r) = \frac{\left(1 - \frac{2MG}{r} + \frac{Q^2}{2\alpha r^2} - \frac{(1-\alpha)}{24\pi G c_0} r^2\right)}{Hr^4}$.

TABLE III: The sonic points for RF with respect to MAGBH parameter f_1

$d_1 = 8f_1$			
f_1	r_c	v_c	H_c
0.10	4.50832	0.0886502	0.557103
0.20	4.24872	0.0866521	0.55996
0.30	3.87663	0.0786564	0.567354
0.40	3.29723	0.182596	0.58534
0.50	2.18278	0.186002	0.64298
0.60	1.99231	0.177754	0.757143

TABLE IV: The sonic points for RF with respect to MAGBH parameter f_1

$d_1 = -8f_1$			
f_1	r_c	v_c	H_c
0.10	2.8875	0.55024	0.87174
0.20	2.24675	0.84666	0.65916
0.30	2.07655	0.47641	0.60384
0.40	1.9228	0.27785	0.98581
0.50	1.62674	0.187054	0.74223
0.60	1.19866	0.07375	0.58631

C. The Hamiltonian of RF

One can find that the energy density is greater than three times of isotropic pressure that is $(3p = \rho)$ in the radiation fluid. By the relation $r_c f_c'(r) - 2f_c(r) = 0$, the critical equation is given by

$$-\frac{2\Big(2d_1k_s^2 - 4f_1k_{sh}^2 - 3mr - r^2 - 8e_1k_d^2\Big)}{r^2} = 0. \tag{45}$$

So, we choose only useful numerical values by the parameters $d_1 = 8f_1$, $f_1 = 1$, $e_1 = 1$, $m = 1$ and $k_s = 1$, $k_d = 0.7$ $k_{sh} = 2$.

$$r_c = 3.98395. \tag{46}$$

In the second condition $d_1 = -8f_1$, the critical radius is $r_c = 7.67819$. For this case, the general Hamiltonian (35) is given by

$$H = \frac{f(r)^{2/3}}{r^{\frac{4}{3}}v^{\frac{2}{3}}(1-v^2)^{\frac{2}{3}}}. \tag{47}$$

This implies that

$$H = \frac{\Big(1 - \frac{2m}{r} + \frac{d_1k_s^2 - 4e_1k_d^2 - 2f_1k_{sh}^2}{r^2}\Big)^{\frac{2}{3}}}{r^{\frac{4}{3}}v^{\frac{2}{3}}(1-v^2)^{\frac{2}{3}}}. \tag{48}$$

D. The Hamiltonian of SRF

One can be found that the energy density is equal to four times an isotropic pressure $(4p = \rho)$. By the relation $4f_c(r) - 3r_c f_c'(r) = 0$, the critical equation is given by

$$\frac{2\Big(5d_1k_s^2 - 10f_1k_{sh}^2 - 7mr + 2r^2 - 20e_1k_d^2\Big)}{r^2} = 0. \tag{49}$$

So, we choose only useful numerical values by the parameters $d_1 = 8f_1$, $f_1 = 1$, $e_1 = 1$, $m = 1$ and $k_s = 1$, $k_d = 0.7$ $k_{sh} = 2$.

$$r_c = 0.256956. \tag{50}$$

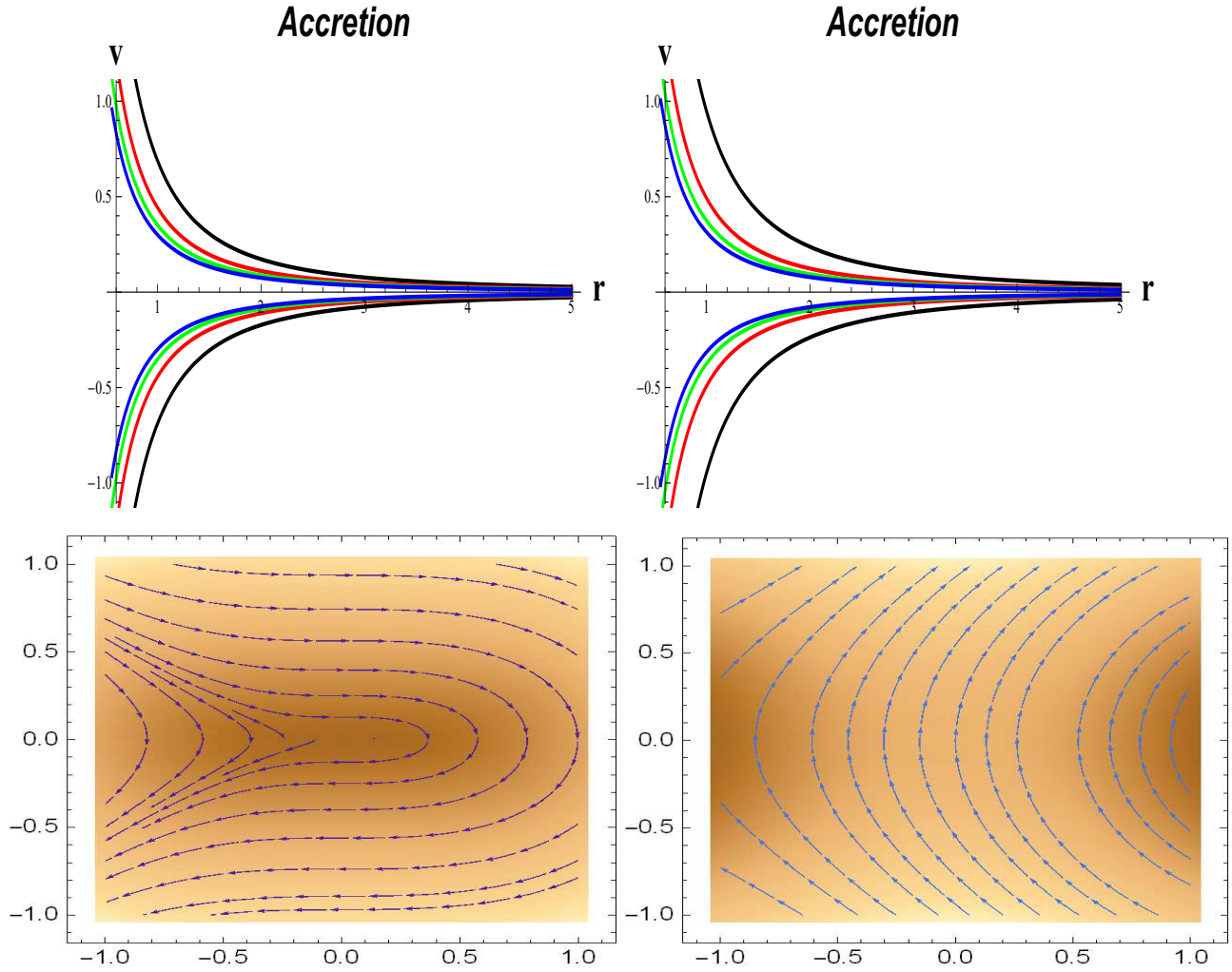


FIG. 2: Accretion display of stiff fluid using the MAGBH parameters. The left plot is for $d_1 = 8f_1$ in the lapse function $f(r)$ with the variation in H_c. The right plot is for $d_1 = -8f_1$ in the lapse function $f(r)$ with the variation in H_c. The fixed parameters are $m = 1$, $e_1 = 0.1$, $k_s = 0.85$, $k_d = 0.7$ and $k_{sh} = 0.7$. The bottom plots represent the streamlines accretion of stiff fluid around the MAGBH.

Similarly, using the critical points, the general Hamiltonian takes the form

$$H = \frac{f(r)^{3/4}}{rv^{\frac{1}{2}}(1-v^2)^{\frac{3}{4}}}. \tag{51}$$

This implies that

$$H = \frac{\left(1 - \frac{2m}{r} + \frac{d_1 k_s^2 - 4e_1 k_d^2 - 2f_1 k_{sh}^2}{r^2}\right)^{3/4}}{rv^{1/2}(1-v^2)^{3/4}}. \tag{52}$$

The sonic points from Tables I-VI, we observe that the critical radius decreased as increasing the MAGBH parameter f_1, but the other critical values behave differently.

VI. RESULTS AND DISCUSSION FOR ALL TEST FLUIDS

This section provides the significance of USF, URF, RF and SRF in the framework of MAGBH.

TABLE V: The sonic points for SRF with respect to MAGBH parameter f_1

$d_1 = 8f_1$			
f_1	r_c	v_c	H_c
0.10	4.15211	0.17865	0.95713
0.20	3.44891	0.28675	0.76952
0.30	3.07338	0.27214	0.66359
0.40	2.87238	0.18874	0.47655
0.50	2.38475	0.18777	0.42776
0.60	1.29876	0.18733	0.70872

TABLE VI: The sonic points for SRF with respect to MAGBH parameter f_1

$d_1 = -8f_1$			
f_1	r_c	v_c	H_c
0.10	2.6675	0.70711	0.45102
0.20	2.44634	0.61743	0.53374
0.30	2.12917	0.76422	0.73612
0.40	2.03375	0.70550	0.75843
0.50	1.32833	0.48709	0.14497
0.60	1.11763	0.53515	0.08771

A. Pictorial analysis of USF for MAGBH

The accretion for the USF is depicted in Fig. 2 for the Hamiltonian (39). We observe from the system that there are two types of accretion flow. The first is the supersonic accretion that informed us, the fluid motion directed towards outside the horizon in the region ($v > 0$). The other one is subsonic accretion, where the fluid motion is directed towards the horizon in the region ($v < 0$). Both the plots (left and right) have the same analysis without the sonic points. The stream line accretion is represented in the bottom plot of Fig. 2. From this information, we understand that the stream lines are closed near the BH and open far from the BH.

B. Pictorial analysis of URF for MAGBH

The accretion for the URF is depicted in Fig. 3 for the Hamiltonian (42). We observe from the system that there are different types of accretion flow around the MAGBH. The curves associated with the critical points (r_c, v_c) and $(r_c, -v_c)$ informed us that the fluid outflow and inflow start from the event horizon, which remains very close to the BH and causes the high pressure. The purely supersonic accretion flow is observed in the neighbourhood $v < v_c$ (red dotes and blue) near the horizon, and purely subsonic accretion is observed in the neighbourhood $v > v_c$ (red dotes and blue) far from the horizon. The bottom plots in Fig. 3 illustrate the streamlines of the accretion flow in various fluid motion patterns inside the MAGBH system.

C. Pictorial analysis of RF for MAGBH

Fig. 4 illustrates the accretion for RF with the MAGBH parameters and variation in H_c. We noted that the supersonic accretion of the fluid motion in the region $v > v_c$ is far from the BH for $H < H_c$ (doted curves). While the subsonic accretion of the fluid motion in the region $v < v_c$ is closest to the BH for $H > H_c$ (thick curves). We observe that the fluid motion is directed towards the BH in the form of an accretion disk at the maximum radius. The purely supersonic accretion is seen far from the source mass. The right plot of Fig. 4, indicates that the curves are away from the horizon for $H = H_c$ and $H > H_c$. But the supersonic and subsonic accretions are the same as seen in the left plot. The bottom plots of Fig. 4, depict the stream lines accretion flow in several different types of fluid motion in the MAGBH.

D. Pictorial analysis of SRF for MAGBH

The Fig. 5 illustrates the accretion for SRF with the MAGBH parameters and variation in H_c. We noted that the supersonic accretion of the fluid motion in the region $v > v_c$ is far from the BH for $H < H_c$ (doted curves). While the subsonic accretion of the fluid motion in the region $v < v_c$ is closest to the BH for $H > H_c$ (thick curves). We

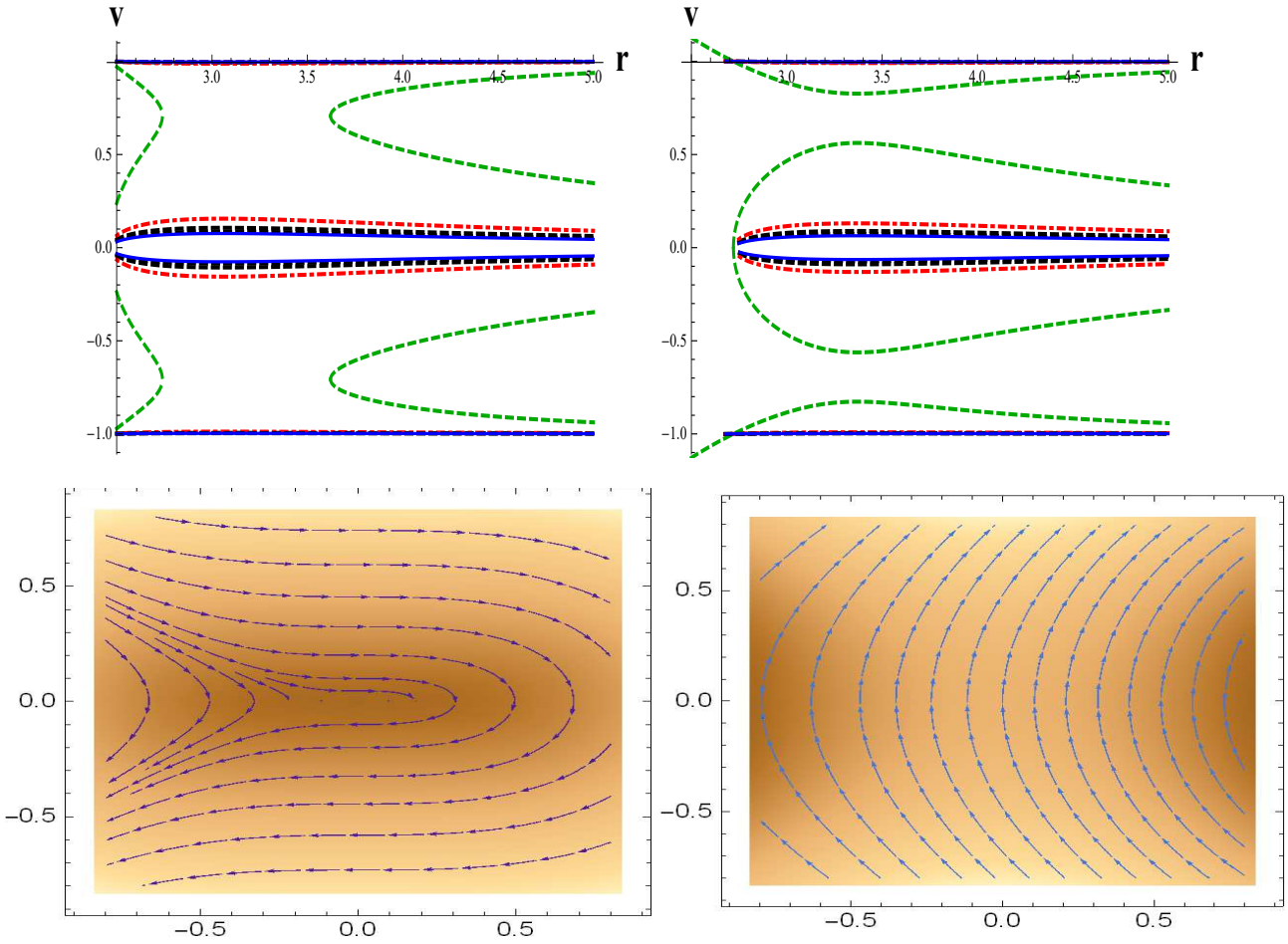


FIG. 3: Accretion display of ultra radiation fluid using the MAGBH parameters. Left plot is for $d_1 = 8f_1$ in the lapse function $f(r)$ with the variation in H_c. Right plot is for $d_1 = -8f_1$ in the lapse function $f(r)$ with the variation in H_c. The fixed parameters are $m = 1$, $e_1 = 0.1$, $k_s = 0.85$, $k_d = 0.7$ and $k_{sh} = 0.7$. The bottom plots represent the stream lines accretion of ultra radiation fluid around the MAGBH.

observe that the fluid motion is directed towards the BH in the form of an accretion disk at the maximum radius. The purely supersonic accretion is seen far from the source mass. The right plot of Fig. 5, indicates that the curves are away from the horizon for $H = H_c$ and $H > H_c$. But the supersonic and subsonic accretions are the same as seen in the left plot. The bottom plots of Fig. 5, depict the stream lines accretion flow in several different types of fluid motion in the MAGBH. The accurate depiction of Fig. 5 illustrates the accretion flow in various fluid motion patterns for the MAGBH.

VII. POLYTROPIC FLUID ACCRETION

In this section, we consider the EoS for polytropic test fluid as considered by [42–44],

$$p = \Gamma\, n^{\gamma}, \tag{53}$$

where Γ and γ are only constants. For an ordinary fluid, the authors considered the general constraint $\gamma > 1$. Adopting the procedure [44], we obtain the following specific enthalpy

$$\chi = B + \frac{\Gamma\gamma n^{\gamma-1}}{\gamma - 1}, \tag{54}$$

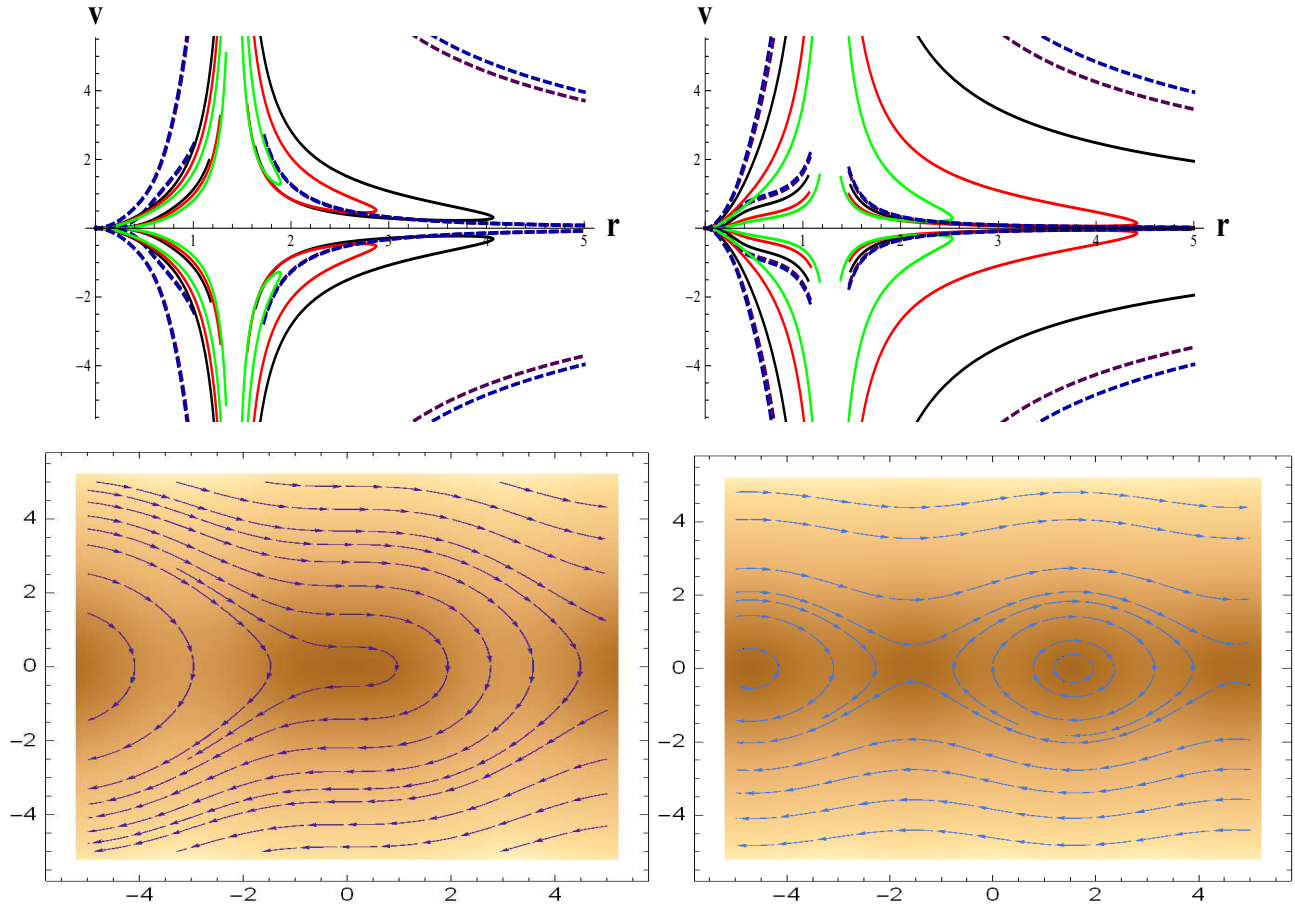


FIG. 4: Accretion display of radiation fluid using the MAGBH parameters. Left plot is for $d_1 = 8f_1$ in the lapse function $f(r)$ with the variation in H_c. Right plot is for $d_1 = -8f_1$ in the lapse function $f(r)$ with the variation in H_c. The fixed parameters are $m = 1$, $e_1 = 0.1$, $k_s = 0.85$, $k_d = 0.7$ and $k_{sh} = 0.7$. The bottom plots represent the stream lines accretion of radiation fluid around the MAGBH.

The symbol B represents the integration constant. The determination of three-dimensional sound speed may be achieved by the use of specific enthalpy as,

$$\mathbf{s}^2 = \frac{(\gamma-1)U}{B(\gamma-1)+U} \qquad (U \equiv \Gamma\gamma n^{\gamma-1}). \tag{55}$$

Following expression is obtained by using the speed of sound

$$\chi = B\frac{\gamma-1}{\gamma-1-a^2}, \tag{56}$$

now we have

$$\chi = B\left(1 + X\left(\frac{1-v^2}{r^4 f(r) v^2}\right)^{(\gamma-1)/2}\right), \tag{57}$$

where

$$Z \equiv \frac{\Gamma\gamma n_c^{\gamma-1}}{B(\gamma-1)}\left(\frac{r_c^5 f'(r_c)}{4}\right)^{(\frac{\gamma-1}{2})} = const > 0. \tag{58}$$

Here, Z is a positive constant, which sustains on the BH parameters as well as on certain test fluids. Hamiltonian can be evaluated by inserting Eq. (57) into (35)

$$H = \frac{f(r)}{1-v^2}\left[1 + X\left(\frac{1-v^2}{r^4 f(r) v^2}\right)^{(\gamma-1)/2}\right]^2. \tag{59}$$

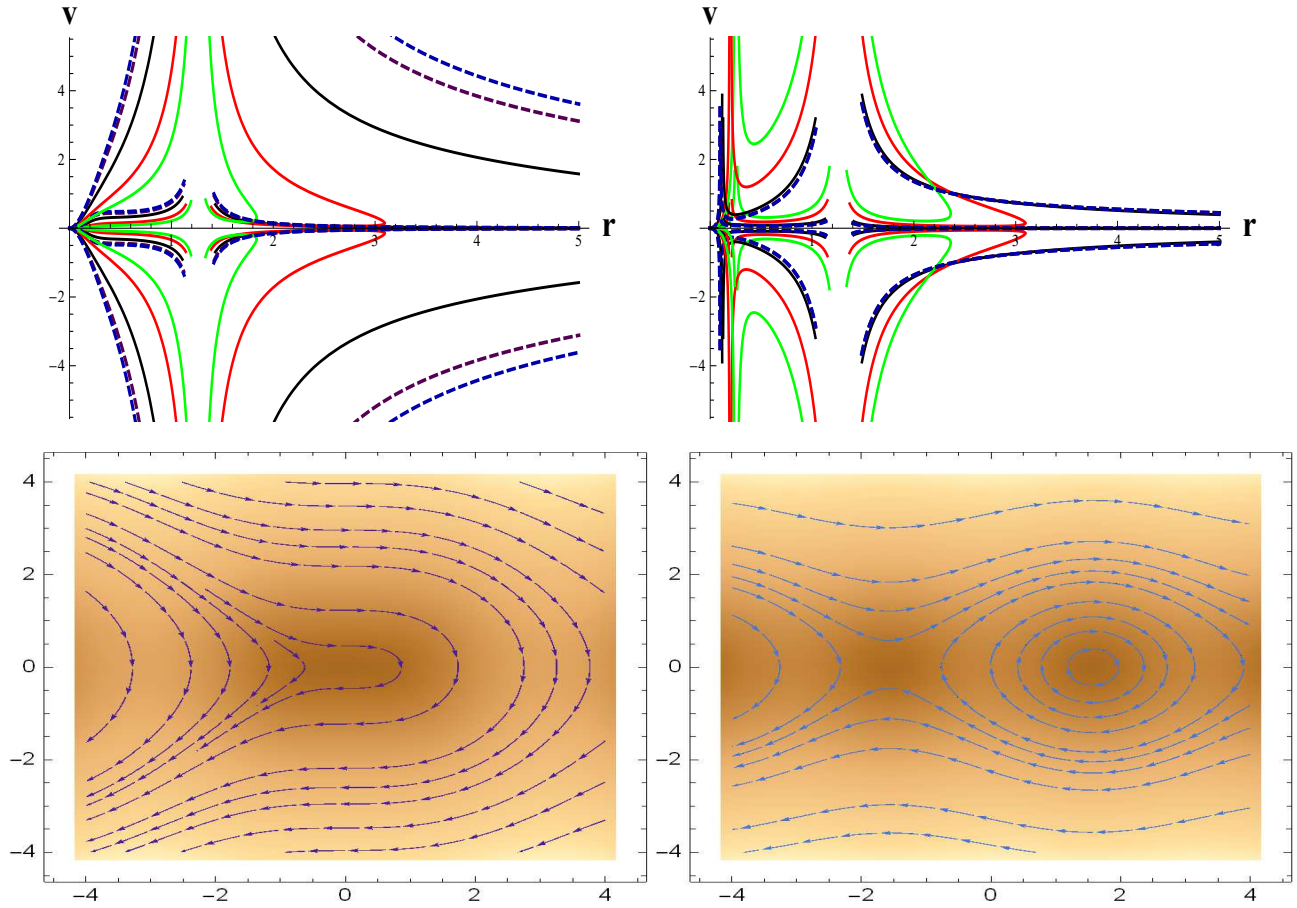


FIG. 5: Accretion display of sub-relativistic fluid using the MAGBH parameters. Left plot is for $d_1 = 8f_1$ in the lapse function $f(r)$ with the variation in H_c. Right plot is for $d_1 = -8f_1$ in the lapse function $f(r)$ with the variation in H_c. The fixed parameters are $m = 1$, $e_1 = 0.1$, $k_s = 0.85$, $k_d = 0.7$ and $k_{sh} = 0.7$. The bottom plots represent the stream lines accretion of sub-relativistic fluid around the MAGBH.

This implies that

$$H = \frac{\left(1 - \frac{2m}{r} + \frac{d_1 k_s^2 - 4e_1 k_d^2 - 2f_1 k_{sh}^2}{r^2}\right)}{1 - v^2} = \left[1 + X\left(\frac{1 - v^2}{r^4 v^2 \left(1 - \frac{2m}{r} + \frac{d_1 k_s^2 - 4e_1 k_d^2 - 2f_1 k_{sh}^2}{r^2}\right)}\right)^{(\gamma-1)/2}\right]^2. \tag{60}$$

We examined from (60), that $\frac{d}{dr} f(r) > 0$, for all r. However, the coefficient of $\frac{f(r)}{1-v^2}$, diverges when $r \to \infty$, and the denominator $1 - v^2$, assume the domain $(0, 1)$, hence the Hamiltonian diverges.

Following the procedure [42–44], we obtain the following relations

$$(\gamma - 1 - v_c^2)\left(\frac{1 - v_c^2}{r_c^4 f(r_c) v_c^2}\right)^{\frac{\gamma-1}{2}} = \frac{n_c}{2X}\left(r_c^5 f'(r_c)\right)^{\frac{1}{2}v_c^2}, \tag{61}$$

$$v_c^2 = \frac{r_c f'_{r_c}}{r_c f'_{r_c} + 4f(r_c)}. \tag{62}$$

The accretion of polytropic test fluid around the MAGBH with extra constants $B = 0.15$, $Z = 7$, $\gamma = 5/3$ is depicted in Fig. 6. This analysis is important because it gives us a better understanding of the circular disks produced by the accreting BH. We observe that the critical flow begins on a subsonic path, then follows a supersonic path, escaping the sonic point, and ends at the killing horizon. As the critical flow towards the BH, it develops into the accretion disks. These disks are below the critical velocities and at the maximum radius. From the bottom contour, there are the same types of accretion flow for polytropic test fluid with parameter γ in the stream lines.

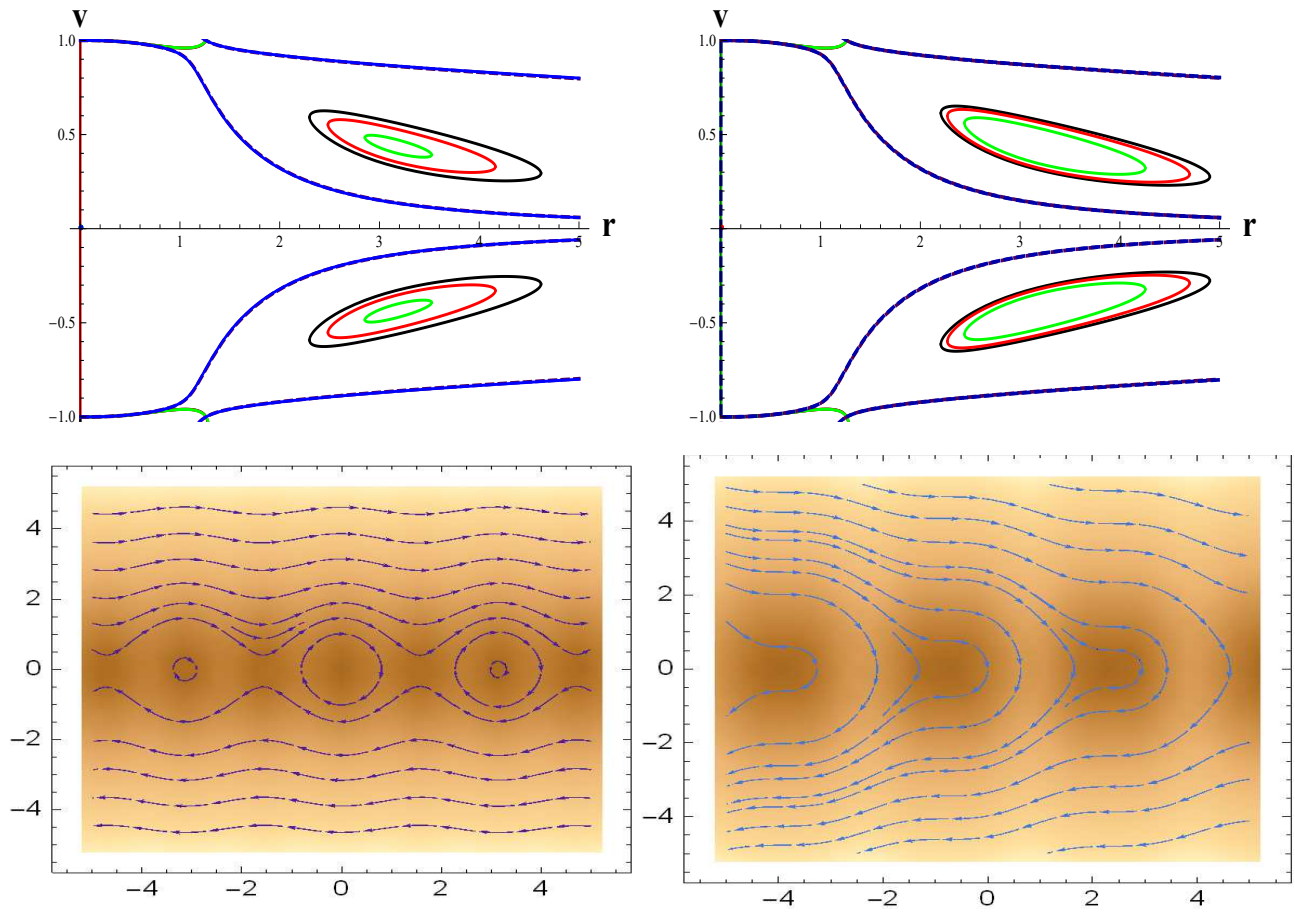


FIG. 6: Accretion display of polytropic test fluid using the MAGBH parameters. Left plot is for $d_1 = 8f_1$ in the lapse function $f(r)$ with the variation in H_c. Right plot is for $d_1 = -8f_1$ in the lapse function $f(r)$ with the variation in H_c. The fixed parameters are $m = 1$, $e_1 = 0.1$, $k_s = 0.85$, $k_d = 0.7$ and $k_{sh} = 0.7$. The bottom plots represent the stream lines accretion of polytropic test fluid around the MAGBH.

VIII. MASS ACCRETION RATE SIGNIFICANCE

Since the mass of a BHs as well as a dark compact object is increased by the accreting matter falling onto them. The mass rate of change or accretion rate of a MAGBH dark compact object can be explored through $\dot{M}\mid_{rh}= 4\pi r^2 T^r_t\mid_{rh}$ [77]. For this, we consider $T^r_t = (\rho + p)u_t u^r$ [78, 79] and the conserved elements $\Delta_\eta J^\eta = 0$ and $\nabla_\zeta T^{\eta\zeta} = 0$. Using the Eqs. (17) and (21), we get

$$r^2 u(\rho + p)\Big(f(r) + (u)^2\Big)^{1/2} = A_0, \tag{63}$$

where A_0 represents an arbitrary constant. The energy flow and the equation of state, denoted as $p = p(\rho)$, lead us to

$$\frac{1}{\rho + p}d\rho + \frac{1}{u}du + \frac{2}{r}dr = 0. \tag{64}$$

Integrating Eq. (64), we get

$$\exp\left[\int_{\rho\infty}^{\rho}\frac{d\rho'}{\rho' + p(\rho')}\right] ru = -A_1, \tag{65}$$

where A_1 is an integration constant and ρ_∞ shows a fluid density at infinity. The Eqs. (63) and (65), yield

$$A_3 = -\frac{A_0}{A_1} = (\rho + p)\Big(f(r) + (u)^2\Big)^{1/2}\exp\left[-\int_{\rho\infty}^{\rho}\frac{d\rho'}{\rho' + p(\rho')}\right], \tag{66}$$

where A_3 is constant of integration. While, $A_3 = \rho_\infty + p(\rho_\infty) = -\frac{A_0}{A_1}$, with $A_0 = (\rho+p)u^0 ur^2 = -A_1(\rho_\infty + p(\rho_\infty))$ at infinity. The given problem is static and spherically symmetric at equatorial plane, so, $\nabla_\eta J^\eta = 0$, we get

$$r^2 u\varepsilon = A_2, \tag{67}$$

where A_2 is constant of integration. The Eqs. (63) and (67), give the relation

$$\frac{\rho+p}{\varepsilon}\Big(f(r)+(u)^2\Big)^{1/2} = \frac{A_0}{A_2} \equiv A_4, \tag{68}$$

and A_4 is any constant as $A_4 = \frac{(\rho_\infty + p_\infty)}{\varepsilon_\infty}$. Keeping the Eq. (63), the mass of BH takes the form

$$\dot{M} = -4\pi r^2 u(\rho+p)\Big(f(r)+(u)^2\Big)^{1/2} = -4\pi A_0. \tag{69}$$

This implies that

$$\dot{M} = 4\pi A_1(\rho_\infty + p(\rho_\infty)). \tag{70}$$

This Eq. (70) yields the valid outcome for any nature of fluid. Therefore

$$\dot{M} = 4\pi A_1(\rho+p)|_{r=r_h}, \tag{71}$$

Using EoS ($p = \omega\rho$), into the Eq. (65), we get

$$\rho = \left[-\frac{A_1}{r^2 u}\right]^{1+\omega}. \tag{72}$$

Now using this expression into (63), we obtain

$$(u)^2 - \frac{A_0^2 A_1^{-2(1+\omega)}}{(1+\omega)^2} r^{4\omega}(-u)^{2\omega} + f(r) = 0. \tag{73}$$

This result is valid for fluid velocity u for any value of ω. Simply, one can be found the energy density ρ by using this result.

A. Mass Accretion Rate for USF

One can find the radial velocity and the energy-density keeping $\omega = 1$ in Eqs. (68) and (72), we have

$$u = \pm A_1^2\sqrt{\frac{f(r)}{A_0^2 r^4 - 4A_1^4}}, \tag{74}$$

and

$$\rho = \frac{(A_0^2 r^4 - 4A_1^4)}{4A_1^2 r^4 f(r)}. \tag{75}$$

Thus, from (71) and (75), we evaluate the mass accretion rate for MAGBH, which is given by

$$\dot{M} = \frac{2\pi(A_0^2 r^4 - 4A_1^4)}{A_1 r^4 f(r)}. \tag{76}$$

$$\dot{M} = \frac{2\pi(A_0^2 r^4 - 4A_1^4)}{A_1 r^4\Big(1 - \frac{2m}{r} + \frac{d_1 k_s^2 - 4e_1 k_d^2 - 2f_1 k_{sh}^2}{r^2}\Big)}. \tag{77}$$

The accretion rate $\dot{M}$ versus the radius r for USF around the MAGBH is analyzed in Fig. 7. In the left plot, the accretion rate remains the same at the maximum position ($\dot{M} = 10$) for distant observers. The radius increased as increasing the parameter f_1. In the right plot, the same behavior is observed as in the left plot, but the observer position is fixed at $r = 1.91$.

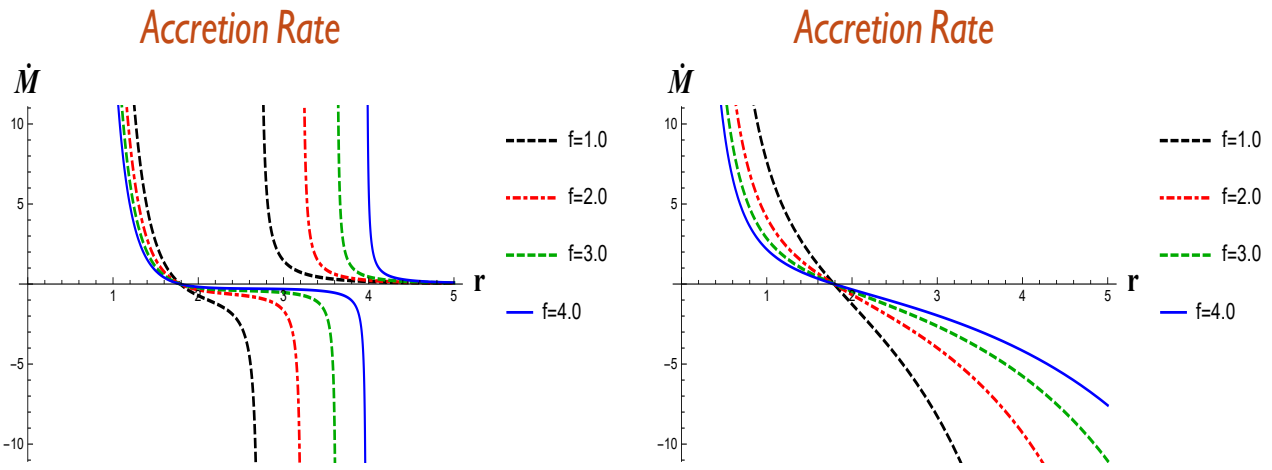


FIG. 7: Accretion rate display of stiff fluid using the MAGBH parameters. Left plot is for $d_1 = 8f_1$ in the lapse function $f(r)$ with the variation in f_1. Right plot is for $d_1 = -8f_1$ in the lapse function $f(r)$ with the variation in f_1. The fixed parameters are $m = 1$, $e_1 = 0.1$, $k_s = 0.85$, $k_d = 0.7$ and $k_{sh} = 0.7$.

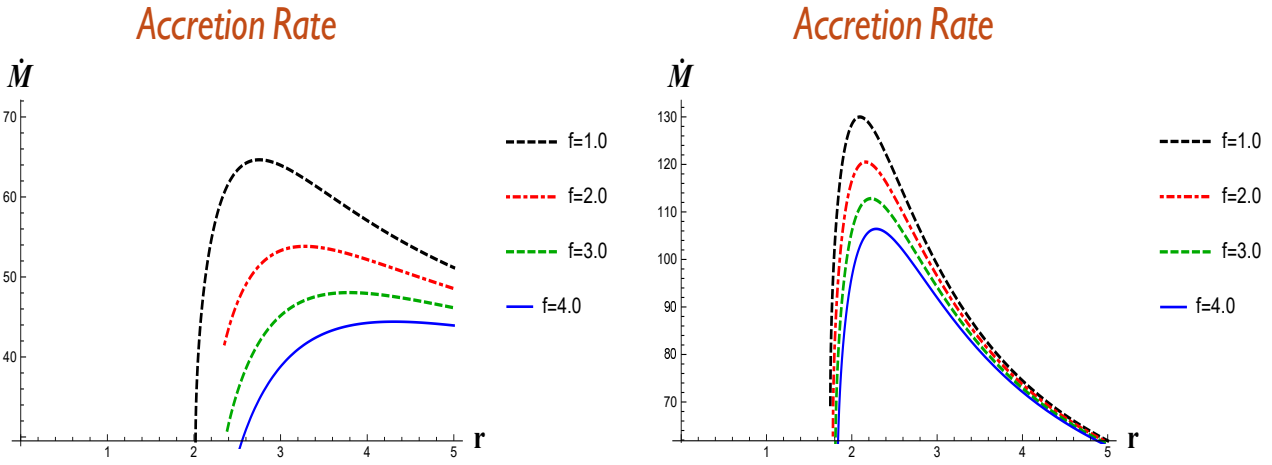


FIG. 8: Accretion rate display of ultra radiation fluid using the MAGBH parameters. Left plot is for $d_1 = 8f_1$ in the lapse function $f(r)$ with the variation in f_1. Right plot is for $d_1 = -8f_1$ in the lapse function $f(r)$ with the variation in f_1. The fixed parameters are $m = 1$, $e_1 = 0.1$, $k_s = 0.85$, $k_d = 0.7$ and $k_{sh} = 0.7$.

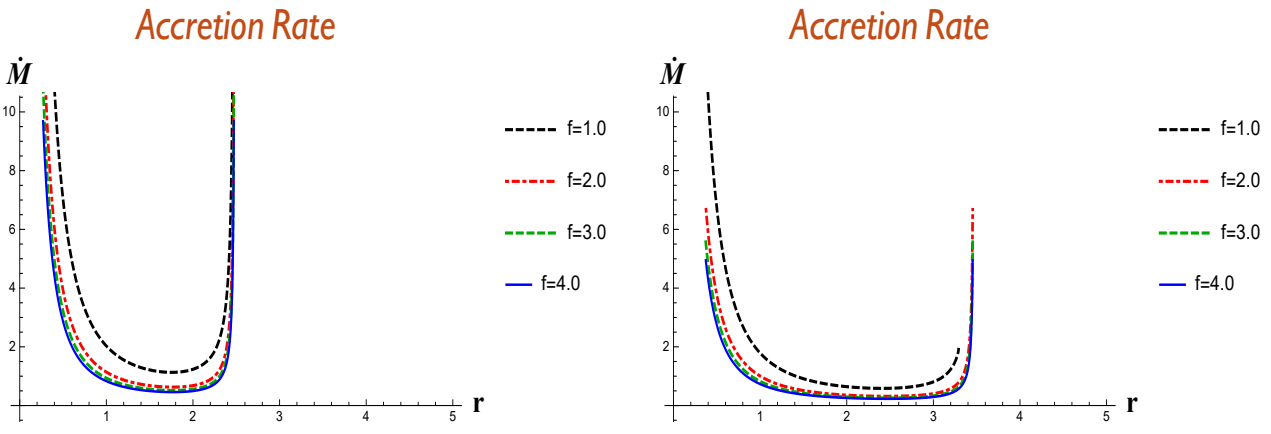


FIG. 9: Accretion rate display of radiation fluid using the MAGBH parameters. Left plot is for $d_1 = 8f_1$ in the lapse function $f(r)$ with the variation in f_1. Right plot is for $d_1 = -8f_1$ in the lapse function $f(r)$ with the variation in f_1. The fixed parameters are $m = 1$, $e_1 = 0.1$, $k_s = 0.85$, $k_d = 0.7$ and $k_{sh} = 0.7$.

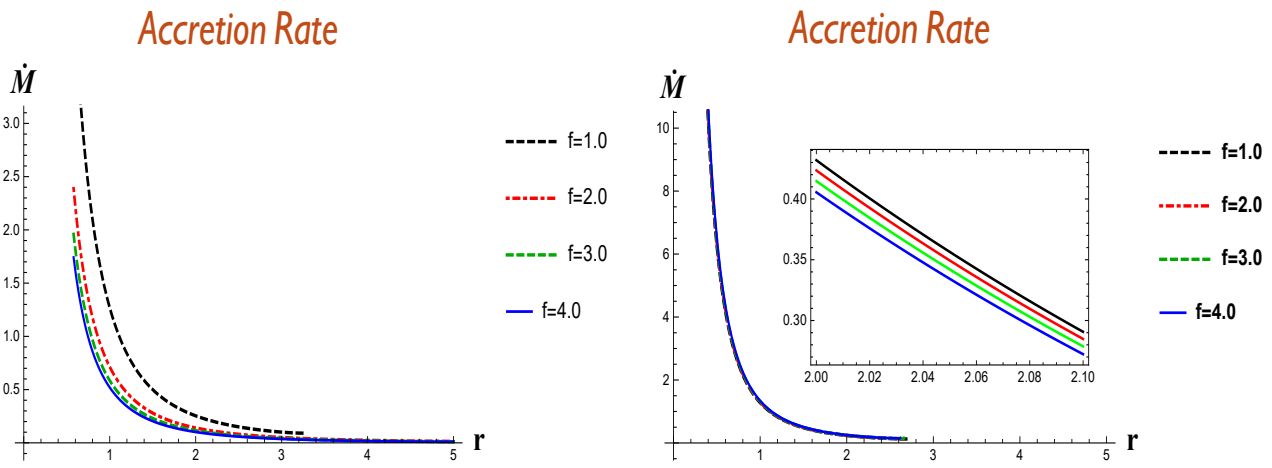


FIG. 10: Accretion rate display of sub-relativistic fluid using the MAGBH parameters. Left plot is for $d_1 = 8f_1$ in the lapse function $f(r)$ with the variation in f_1. Right plot is for $d_1 = -8f_1$ in the lapse function $f(r)$ with the variation in f_1. The fixed parameters are $m = 1$, $e_1 = 0.1$, $k_s = 0.85$, $k_d = 0.7$ and $k_{sh} = 0.7$.

B. Mass Accretion rate for URF

One can find the radial velocity and the energy density keeping $\omega = 1/2$ in Eqs. (68) and (72), we have,

$$u = \frac{2r^2A_0^2 + \sqrt{4r^2A_0^4 - 81f(r)A_1^6}}{9A_1^3}, \tag{78}$$

$$\rho = 27\left(\frac{A_1^4}{r^2\left(2r^2A_0^2 + \sqrt{4r^2A_0^4 - 81f(r)A_1^6}\right)}\right)^{3/2}, \tag{79}$$

$$\dot{M} = 216\pi A_1\left(\frac{A_1^4}{r^2\left(2r^2A_0^2 + \sqrt{4r^2A_0^4 - 81f(r)A_1^6}\right)}\right)^{3/2}. \tag{80}$$

This implies that

$$\dot{M} = 216\pi A_1\left(\frac{A_1^4}{r^2\left(2r^2A_0^2 + M_1\right)}\right)^{3/2}, \tag{81}$$

where,

$$M_1 = \sqrt{4r^2A_0^4 - 81\Big(1 - \frac{2m}{r} + \frac{d_1k_s^2 - 4e_1k_d^2 - 2f_1k_{sh}^2}{r^2}\Big)A_1^6}.$$

C. Mass Accretion rate for RF

One can find the radial velocity and the energy density keeping $\omega = 1/3$ in Eqs. (68) and (72), we have

$$u = \Big[\frac{\Big(-32f(r)A_1^4 + \Psi_{11}(r)\Psi_{11}(r)\Big)^{1/3}}{4A_1^2} + \frac{3r^{4/3}A_0^2}{4A_1^{2/3}\Big(\Psi_{11}(r) - 32f(r)A_1^4\Big)^{1/3}}\Big]^{2/3}, \tag{82}$$

and

$$\rho = \Big[\frac{A_1}{r^2}\Big]^{\frac{4}{3}}\Big[\frac{\Big(-32f(r)A_1^4 + \Psi_{11}(r)\Big)^{1/3}}{4A_1^2} + \frac{3r^{4/3}A_0^2}{4A_1^{2/3}\Big(\Psi_{11}(r) - 32f(r)A_1^4\Big)^{1/3}}\Big]^{\frac{-8}{9}}. \tag{83}$$

where, $\Psi_{11}(r)=\sqrt{1024f(r)^2A_1^8-27r^4A_0^6}$. The mass accretion rate of BH is given by

$$\dot{M}=\Big[\frac{8\pi A_1^{\frac{7}{3}}}{r^{\frac{8}{3}}}\Big]\Big[\Big(\Psi_{11}(r)-32f(r)A_1^4\Big)^{1/3}\Big(4A_1^2\Big)^{-1}+\frac{3r^{4/3}A_0^2}{4A_1^{2/3}}\Big(\Psi_{11}(r)-32f(r)A_1^4\Big)^{-1/3}\Big]^{\frac{-8}{9}}. \tag{84}$$

This implies that

$$\begin{aligned}\dot{M}=&\Big[\frac{8\pi A_1^{\frac{7}{3}}}{r^{\frac{8}{3}}}\Big]\Big[\Big(-32\Big(1-\frac{2m}{r}+\frac{d_1k_s^2-4e_1k_d^2-2f_1k_{sh}^2}{r^2}\Big)A_1^4+\sqrt{M_2-27r^4A_0^6}\Big)^{1/3}\Big(4A_1^2\Big)^{-1}\\&+\frac{3r^{4/3}A_0^2}{4A_1^{2/3}}\Big(-32\Big(1-\frac{2m}{r}+\frac{d_1k_s^2-4e_1k_d^2-2f_1k_{sh}^2}{r^2}\Big)A_1^4+\sqrt{M_2-27r^4L_0^6}\Big)^{-1/3}\Big]^{\frac{-8}{9}}.\end{aligned} \tag{85}$$

where,

$$M_2=1024\Big(1-\frac{2m}{r}+\frac{d_1k_s^2-4e_1k_d^2-2f_1k_{sh}^2}{r^2}\Big)^2A_1^8.$$

D. Mass Accretion rate for SRF

Herein this subsection, we shall find the radial velocity and the energy density by considering $\omega=1/4$ in Eqs. (68) and (72), one can get the following expression for radial velocity:

$$u=\frac{\sqrt{u_2}}{5\sqrt{3}}-\frac{1}{2}\Bigg(-\frac{256\sqrt{3}A_0^4r^2}{125B^5\sqrt{u_2}}-\frac{100\ 5^{2/3}A_1^5f^2}{3\sqrt[3]{u_1}}-\frac{4\sqrt[3]{u_1}}{75\ 5^{2/3}A_1^5}-\frac{8f}{3}\Bigg)^{\frac{1}{2}} \tag{86}$$

where

$$\begin{aligned}u_1&=13824A_0^8A_1^5r^4+96\sqrt{3}\Big(6912A_0^{16}A_1^{10}r^8-390625A_0^8A_1^{20}f^3r^4\Big)^{\frac{1}{2}}-390625A_1^{15}f^3,\\u_2&=\frac{625\ 5^{2/3}A_1^5f^2}{\sqrt[3]{u_1}}+\frac{\sqrt[3]{u_1}}{5^{2/3}A_1^5}-25f.\end{aligned}$$

The energy density for SRF fluid is calculated as:

$$\rho=\left(-\frac{A_1}{r^2\left(\frac{\sqrt{\frac{u_2\sqrt[3]{u_1}}{5^{2/3}A_1^5}}}{5\sqrt{3}}-\frac{1}{2}\sqrt{\rho_1-\frac{256\sqrt{3}A_0^4r^2}{125A_1^5\sqrt{\frac{u_2\sqrt[3]{u_1}}{5^{2/3}A_1^5}}}}\right)}\right)^{5/4}, \tag{87}$$

where

$$\rho_1=-\frac{100\ 5^{2/3}A_1^5f^2}{3\sqrt[3]{u_1}}-\frac{4\sqrt[3]{u_1}}{75\ 5^{2/3}A_1^5}-\frac{8f}{3}. \tag{88}$$

Finally, acceration rate is calculated as

$$\dot{M}=5\pi A_1\left(-\frac{A_1}{r^2\left(\frac{\sqrt{\frac{u_2\sqrt[3]{u_1}}{5^{2/3}A_1^5}}}{5\sqrt{3}}-\frac{1}{2}\sqrt{\rho_1-\rho_2}\right)}\right)^{5/4}, \tag{89}$$

where

$$\rho_2=\frac{256\sqrt{3}A_0^4r^2}{125A_1^5\sqrt{\frac{u_2\sqrt[3]{u_1}}{5^{2/3}A_1^5}}}. \tag{90}$$

Fig. 8 illustrates the accretion rate for URF near the MAGBH. In both cases, we observe that the accretion rate decreased as the parameter f_1 increased and vice versa. In Fig. 9, it is decreased towards the BH and increased far from the BH for RF as increasing values of f_1. For SRF in Fig. 10, it is a decreasing function of r as increasing the parameter f_1.

IX. CONCLUSION

Within the context of the traceless nonmetricity tensor, we have examined the MAG in the current study, which is predicated on the metricity of space-time and the affine relationship. Stated differently, it illustrates the relationship between the metric tensor and the affine connection derived from the Levi-Civita connection. In fact, MAG, a theory of gravity that extends GR by permitting non-zero torsion and nonmetricity, heavily relies on the traceless nonmetricity tensor. It is interesting to note that these extra geometric objects are related, respectively, to the spin of matter fields and the existence of a preferred direction in space-time. The presence of nonmetricity assists in the computation of the geodesic equation for test particles, resulting in departures from the GR-predicted acceleration. Further, we have explored some interesting aspects of matter accretion onto charged BH solutions in the framework of MAG. For this purpose, we have discussed general accretion by using different kinds of fluids. Further, we have used the Hamiltonian approach to discuss the accretion in the current study. Some important insights from the present analysis are listed below:

- As we have discussed Reissner-Nordström-like BH geometry with spin, dilation, and shear charges. In the considered BH solution, we have two different cases, i.e., $d_1 = 8f_1$, (ii) $d_1 = -8f_1$ and (iii) $d_1 \neq 8f_1$ for which $f_1 \leq 0$. The horizon structure for the considered BH solution is shown in Fig. 1. It has been noted that singularities exist in both cases of the BH solution.

- We have developed the fundamental formulas for general accretion to exploring the critical flow of fluid in the background of spherically symmetric MAGBH. We have also provided the basic background for sonic points and isothermal test fluid.

- Four different kinds of fluids as, USF ($\omega = 1$), URF ($\omega = 1/2$), RF ($\omega = 1/3$) and SRF ($\omega = 1/4$) have been considered in the accretion flow around a MAGBH. It is necessary to mention that we have successfully calculated these four different kinds of fluids for the considered MAGBH solution.

- For the Hamiltonian through Eq. (39), the accretion for the USF is shown in Fig. 2. Two different forms of accretion flow are visible in the system. The first one is the fluid motion oriented towards the outside of the horizon in the region ($v > 0$), which is what the supersonic accretion told us about. An alternative scenario involves subsonic accretion, in which fluid motion is directed towards the horizon within the region ($v < 0$). The bottom plot of Fig. 2 shows the accretion through stream lines. From these stream lines, we are able to understand that the stream lines are closed near the BH and they are open far from the BH.

- The URF's accretion is given in Fig. 3. We can see from the system that the accretion flow surrounding the MAGBH is diverse. The critical point curves (r_c, v_c), $(r_c, -v_c)$ showed us that the high pressure is caused by the fluid outflow and inflow starting at the event horizon and continuing quite close to the BH. Several different kinds of fluid motion in the MAGBH are depicted in the bottom plots of Fig. 3.

- The accretion for RF with the MAGBH settings and change in H_c is shown in Fig. 4. For $H < H_c$, we observed that the supersonic accretion of the fluid motion is located far from the BH in the area $v > v_c$ (dot curves). For $H > H_c$ (thick curves), the subsonic accretion of the fluid motion is closest to the BH in the region $v < v_c$. We note that the fluid motion at the maximum radius is directed towards the BH as an accretion disk. Fig. (4) bottom plots show the stream lines accretion flow in various forms of fluid motion in the MAGBH.

- The accretion for SRF with the MAGBH parameters and change in H_c are provided in Fig. 5. We note that the fluid motion at maximum radius is directed towards the BH as an accretion disk. The accretion is completely supersonic and observed far from the source mass. For both $H = H_c$ and $H > H_c$, the curves are away from the horizon, according to the right plot of same figure. However, from the left plot, it has been confirmed that the supersonic and subsonic accretions are the same. Fig. 5 bottom plots show the stream lines accretion flow in various forms of fluid motion in the MAGBH.

- The Fig. 6 shows the accretion for polytropic test fluid around the MAGBH with the introduced constants $B = 0.15$, $Z = 7$, and $\gamma = 5/3$. This study is significant because it helps us comprehend the circular disks that the accreting BH produces. As we can see, the crucial flow starts on a subsonic course, escapes the sonic point

by taking a supersonic path, and finishes at the killing horizon. The accretion disks form when the critical flow moves closer to the BH. These disks are at the maximum radius and below the critical velocities.

- The mass accretion rates for USF, URF, RF, and SRF in the background of the MAGBH solution are provided graphically in the Figs. 7-10, respectively. For distant observers, the accretion rate is constant at the maximum position ($\dot{M} = 10$). As the parameter f_1 increased, the radius also increased. One can see similar behavior in the right plot for USF. In both scenarios, we see that when we increased the parameter f_1, the accretion rate fell within the context of URF, and vice versa. For RF, it decreases near the BH and increases further from the BH as f_1 values grow. In the SRF fluid, the accretion rate decreases as the parameter f_1 increases.

The study has examined the effects of parameter f_1 on a MAGBH's horizon structure. Within the domain of accretion, multiple fluids have been examined depending on the value of f_1. Using a variety of models of fluids, including the USF, URF, RF, and SRF, the behavior of accretion flow has been investigated. The identification of critical points and flow patterns revealed supersonic and subsonic accretion in various places. The investigation produced well-behaved and physically realistic outcomes. These studies provide a new perspective regarding the accretion of BH.

[1] F. W. Hehl, J. D. McCrea, E. W. Mielke, and Y. Neeman, Phys. Rept. **258**(1995)1.
[2] F. W. Hehl, P. von der Heyde, G. D. Kerlick, J. M. Nester, Rev. Mod. Phys. **48**(1976)393.
[3] Y. Obukhov, V. Ponomarev, and V. Zhytnikov, Gen. Rel. Grav. **21** (1989) 1107.
[4] Y. N. Obukhov.: arXiv:2206.05205 [gr-qc].
[5] F. Cabral, F. S. Lobo, and D. Rubiera-Garcia, Universe **6**(2020)238.
[6] P. Baekler, F. W. Hehl, and E. W. Mielke, Nonmetricity and torsion: facts and fancies in gauge approaches to gravity, in 4th Marcel Grossmann Meeting on the Recent Developments of General Relativity. 6, 1985.
[7] F. Gronwald and F. W. Hehl, On the gauge aspects of gravity, in International School of Cosmology and Gravitation: 14th Course: Quantum Gravity, pp. 148-198, 5, 1995: arXiv:gr-qc/9602013.
[8] W. Adamowicz.: General Relativity and Gravitation **12**(1980)677.
[9] P. Baekler.: Phys. Lett. B **99**(1981)329.
[10] H. Gonner and F. Mueller-Hoissen.: Class. Quantum Grav. 1(1984)651.
[11] P. Baekler, M. Gurses, F. W. Hehl, and J. D. McCrea.: Phys. Lett. A **128**(1988)245.
[12] R. Tresguerres.: Z. Phys. C **65**(1995)347.
[13] R. Tresguerres.: Physics Letters A **200**(1995)405.
[14] F. W. Hehl and A. Macias.: Int. J. Mod. Phys. D **8**(1999)399.
[15] A. Garcia, A. Macias, D. Puetzfeld, and J. Socorro.: Phys. Rev. D **62**(2000)044021.
[16] D. Puetzfeld and R. Tresguerres.: Class. Quantum Grav. **18**(2001)677.
[17] H. Chen, F.H. Ho, J. M. Nester, C.H. Wang, and H.J. Yo.: JCAP **10**(2009)027.
[18] J. Lu and G. Chee.: JHEP **05**(2016)024.
[19] J. Boos and F. W. Hehl.: Int. J. Theor. Phys. **56**(2017)751.
[20] J. A. R. Cembranos and J. Gigante Valcarcel.: JCAP **01**(2017)014.
[21] J. A. R. Cembranos and J. Gigante Valcarcel.: Phys. Lett. B **779**(2018)143.
[22] M. Blagojevic and B. Cvetkovic.: Phys. Rev. D **95**(2017)104018.
[23] M. Blagojevic, B. Cvetkovi´c, and Y. N. Obukhov.: Phys. Rev. D **96**(2017)064031.
[24] Y. N. Obukhov.: Universe **5**(2019)127.
[25] M. Guerrero, G. Mora-Perez, G. J. Olmo, E. Orazi, and D. Rubiera-Garcia.: JCAP **07**(2020)058.
[26] Y. N. Obukhov.: Phys. Rev. D **102**(2020)104059.
[27] D. Iosifidis.: Eur. Phys. J. C **80**(2020)1042.
[28] C. Heinicke, P. Baekler, and F. W. Hehl.: Phys. Rev. D **72**(2005)025012.
[29] P. Baekler and F. W. Hehl.: Int. J. Mod. Phys. D **15**(2006)635.
[30] S. Bahamonde and J. Gigante Valcarcel.: JCAP **09**(2020)057.
[31] S. Bahamonde, J. Chevrier, J. G. Valcarcel.: JCAP **02**(2023)018.
[32] F. Javed.: Annals of Physics **458**(2023)169464.
[33] M. Yasir, X. Tiecheng, F. Javed, G. Mustafa.: arXiv:2305.13709.
[34] A. Ditta, X. Tiecheng, S. Mumtaz, F. Atamurotov, G. Mustafa and A. Abdujabbarov,: Phys. Dark Univ. **41**(2023)101248.
[35] H. Bondi.: Mon. Not. Roy. Astron. Soc. **112**(1952)195.
[36] L. Rezzolla, O. Zanotti.: Relativistic Hydrodynamics. Oxford University Press, London (2013).
[37] C. F. Michel.: Astrophys. Space Sci. **15**(1972)153.
[38] F. Hoyle, R. A.: Lyttelton, Proc. Camb. Philos. Soc. **35**1939)405.
[39] H. Bondi, F. Hoyle.: Mon. Not. R. Astron. Soc. **104**(1944)273.
[40] J. Karkowski, E. Malec.: Phys. Rev. **87**(2013)044007.
[41] P. Mach, E. Malec.: Phys. Rev. **88**(2013)084055.
[42] E. Chaverra, O. Sarbach.: Class. Quantum Grav. **32**(2015)15.

[43] R. Hunt.: Mon. Not. R. Astron. Soc. **154**(1971)141.
[44] M. Ruffert.: Astrophys. J. **427**(1994)342.
[45] F. D. Lora-Clavijo, F. S. Guzman.: Mon. Not. R. Astron. Soc. **429**(2013)3144.
[46] J. Ovalle,: Phys. Rev. D **107**(2023)104005: doi:10.1103/PhysRevD.107.104005.
[47] R. Casadio, A. Giusti and J. Ovalle,: JHEP **05**(2023)118; doi:10.1007/JHEP05(2023)118.
[48] J. Ovalle,: Eur. Phys. J. C **82**(2022)170.
[49] J. Ovalle, E. Contreras and Z. Stuchlik,: Phys. Rev. D **103**(2021)084016.
[50] J. Ovalle, R. Casadio, E. Contreras and A. Sotomayor,: Phys. Dark Univ. **31**(2021)100744.
[51] E. Contreras, J. Ovalle and R. Casadio,: Phys. Rev. D **103**(2021)044020.
[52] J. Ovalle, R. Casadio, R. d. Rocha, A. Sotomayor and Z. Stuchlik,: Eur. Phys. J. C **78**(2018)960.
[53] R. Casadio and J. Ovalle,: Phys. Lett. B **715**(2012)251-255.
[54] P. Bargueño and E. Contreras,: Phys. Rev. D **107**(2023)066013.
[55] R. Avalos, P. Bargueño and E. Contreras,: Fortsch. Phys. **71**(2023)2200171.
[56] R. Avalos and E. Contreras,: Eur. Phys. J. C **83**(2023)155.
[57] E. López, P. Bargueño and E. Contreras,: doi:10.1142/s0218271822501255.
[58] P. Bargueño and E. Contreras,: Phys. Rev. D **105**(2022)046003.
[59] Á. Rincón, E. Contreras, P. Bargueño, B. Koch and G. Panotopoulos,: Phys. Dark Univ. **31**(2021)100783.
[60] E. Contreras and P. Bargueño,: Eur. Phys. J. C **78**(2018)985.
[61] M. Sharif, G. Abbas.: Mod. Phys. Lett. A **26** (2011) 1731.
[62] M. Sharif, G. Abbas, Chin. Phys. Lett. A **29** (2012) 010401.
[63] M. Sharif, S. Iftikhar, Eur. Phys. J. C **76** (2016) 147.
[64] M. Sharif, M. Shahzadi, Eur. Phys. J. C **77** (2017) 363.
[65] M. Sharif, F. Javed, Int. J. Mod. Phys. D **28** (2019) 1950046; Ann. Phys. **407** (2019) 198.
[66] M. Sharif, F. Javed, Mod. Phys. Lett. A **35**(2019)1950350; Ann. Phys. **416**(2020)168146.
[67] F. Javed, Euro. Phys. J. C **83**(2023)513.
[68] F. Javed, G. Mustafa, A. Ovgün, Eur. Phys. J. Plus **138**(2023)706.
[69] A. Ditta, G. Abbas, Gen. Relat. Gravit. **52**(2020)77.
[70] A. Ditta, G. Abbas, Chinese Journal of Physics **65**(2020)325.
[71] A. Ditta, G. Abbas, New Astronomy **81**(2020)101437.
[72] A. Ditta et al, JCAP 08(2023)002.
[73] A.J. John, Monthly Notices of the Royal Astronomical Society **490**(2019)3824.
[74] S. Gangopadhyay, B. Paik, R. Mandal, Int. J. Mod. Phys. A **33**(2018)1850084.
[75] R. Yang, Phys. Rev. D **92**(2015)084011.
[76] A. K. Ahmad, M. Azreg-Ainou, M. Faizal, M.Jamil, Eur. Phys. J. C. **76**(2016)280.
[77] A. K. Ahmad, M. Azreg-Ainou, S. Bahamonde, S. Capozziello, M. Jamil, Eur. Phys. J. C. **76**(2016)269.
[78] M. Jamil, M.A. Rashid, A. Qadir, Eur. Phys. J. C 58 (2008) 325.
[79] U. Debnath, Eur. Phys. J. C 75 (2015) 129.
[80] A. Jawad, M. U. Shahzad., Eur. Phys. J. C **77** (2017) 515.
[81] G. Abbas, A. Ditta, Gen. Relat. Gravit. **51** (2019) 43; Gen. Relat. Gravit. **51** (2019) 136.
[82] G. Abbas, A. Ditta, Eur. Phys. J. C **80**(2020)1212.
[83] S. Umair, R. Ali, A. Jawad, S. Rani, Chinese Physics C**44**(2020)065106.
[84] Y. Liu, et al, Eur. Phys. J. C **83**(2023)584.
[85] M. Yasir, et al, arXiv:2305.13709.
[86] G. Rakhimova, et al, Nuclear Physics B **996**(2023)116363.
[87] A. Ditta, F. Javed, S. K. Maurya, G. Mustafa and F. Atamurotov, Phys. Dark Univ. **42**(2023)101345.
[88] C. Bambi, K. Freese, S. Vagnozzi, L. Visinelli, Phys. Rev. D **100**(2019)044057.
[89] F. Atamurotov, I. Hussain, G. Mustafa, A. Ovgun, Chin. Phys. C **47**(2023)025102.
[90] S. Vagnozzi, C. Bambi, L. Visinelli, Class. Quantum Grav. **37**(2020)087001.
[91] M. Khodadi, A. Allahyari, S. Vagnozzi, D.F. Mota, J. Cosmol. Astropart. Phys. **2020**(2020)026.
[92] A. Allahyari, M. Khodadi, S. Vagnozzi, D.F. Mota, JCAP **02**(2020)003.
[93] F. Atamurotov, U. Papnoi, K. Jusufi, Class. Quantum Grav. **39**(2022)025014.
[94] R. Roy, S. Vagnozzi, L. Visinelli, Phys. Rev. D 105(2022)083002.
[95] F. Sarikulov, F. Atamurotov, A. Abdujabbarov, B. Ahmedov, Eur. Phys. J. C **82**(2022)771.
[96] U. Papnoi, F. Atamurotov, Phys. Dark Univ. **35**(2022)100916.
[97] Y. Chen, R. Roy, S. Vagnozzi, L. Visinelli, Phys. Rev. D **106**(2022) 043021.
[98] Sunny Vagnozzi et al, Class. Quantum Grav. **40**(2023)165007.
[99] H. Rehman, G. Abbas, Chinese Physics C **47**(2023)12.
[100] Y. Liu et al, Phys. Dark Univ. **42**(2023)101311.
[101] Y. Liu et al, Eur. Phys. J. C **83**(2023)584.
[102] F.W. Hehl, J.D. McCrea, E.W. Mielke, Y. Neeman, Phys. Rep. **258**(1995)1.
[103] Y. Ne'eman and D. Sijacki, Annals Phys. **120**(1979)292.
[104] P. Mach, E. Malec, Phys. Rev. D 88, 084055 (2013). arXiv:1309.1546 [gr-qc]

Wireless Personal Communications
https://doi.org/10.1007/s11277-023-10838-x

A Systematic Review on Predicting the Performance of Students in Higher Education in Offline Mode Using Machine Learning Techniques

Rahul[1] **· Rahul Katarya**[1]

Accepted: 21 December 2023
© The Author(s), under exclusive licence to Springer Science+Business Media, LLC, part of Springer Nature 2024

Abstract
For scholarly organizations, students' academic performance (AP) computes student achievements in different academic subjects. Therefore, a systematic literature review based on machine learning approaches to improve student performance is proposed. This field creates a way to discover hidden examples from instructive information. Machine learning (ML) techniques are used for performance prediction. It is become a challenge due to its imbalanced dataset. This review aims to identify the best proposals that focus on various ML methods used for the performance analysis of students. This review will become helpful to the teachers in identifying the weak students, and it helps to improve their performance through proper guidance. Thus, it reflects in the student's background and boosts their growth. It also brings benefits to students, teachers, and institutions. This study focused on applying machine learning techniques to predict students' performance in recent times. With a systematic approach, the research identified the existing prediction methods and tools used to predict students' performance and observed the researchers' type of variables in this research area. In this study, almost more than 100 papers were analyzed to reveal various modern techniques that are commonly used to predict student performance and the goals they need to achieve in this field. The results from the various research will help improve students' academics and monitor the student's performance, which would also improve their literacy rate.

Keywords Educational data mining · Student performance prediction · Classification · Regression · Clustering

1 Introduction

Today, ML techniques, Artificial Intelligence, and automation are increasing in every sector. The growth of these concepts can be realized from the fact that robots used to be defined only by a mechanical arm and have now moved to teach pendant techniques and

✉ Rahul
rahulzhere023@gmail.com

[1] Big Data Analytics and Web Intelligence Laboratory, Department of Computer Science and Engineering, Delhi Technological University, New Delhi, Delhi 110042, India

Published online: 26 January 2024

even programmable robots. Education Mining has been used in much work to enhance performance prediction. This field creates a way to discover hidden examples from instructive information. This technique is used in the educational system to analyze the performance of students (POS) to create a development in the educational system. This paper tried to analyze the techniques performed in analyzing the POS. This review helps to identify the result of some basic questions. India currently spends less than 5% of its Gross Domestic Product (GDP) on Education, while countries like Denmark spend nearly 9% of their GDP. Therefore, the usage of technology in the education system is more important. Information technology is used to analyze POS to identify the students with poor performance and the teachers and professors trying to improve their scores. Since the volume of research is enlarging day by day, it can be challenging for research scholars to find and analyze the studies of POS based on ML algorithms.

An important way to contribute to the scientific community is to support practitioners by using ML methods to study/track student performance (SP) to provide the foundations for acquiring key concepts and works in state-of-the-art research. The techniques removed from the Educational Data Mining (EDM) regulation [1] have been used to understand students, including their learning behavior, and predict their academic presentation based on various student-related attributes such as demographic, academic and external details. The results of this learning identify an explanatory structure that unifies multiple dimensions to make the prediction convincing. The ML models outperform current predictable approaches. More effort is expected to produce well-formulated and generalizable results. ML techniques are the most extensive way to analyze the POS. This review article aims at showcasing a detailed SLR of students' performance prediction. Different techniques involve studies such as Adaptive Neuro-Fuzzy Inference Systems (ANFIS), Artificial Neural Networks (ANN), and Recurrent Neural Networks (RNN). In the context of studying POS, ML techniques are used to provide instructors with better tips for constructing powerful ML models. About 109 studies were considered, and other relevant works from other sources were also considered. It might be observed that many articles included more than one ML Technique. In many cases, datasets do not contain only the performance in exams but also the performance of the quizzes and assignments [2].

The various ML algorithms are classified into supervised ML (SML) and Unsupervised ML (UML). SML can be further categorized into Classification and Regression, and UML can be further categorized into Clustering. Classification algorithms can be Support Vector Machine (SVM), Naïve Bayes (NB), K Nearest Neighbour (KNN), and Neural Networks (NN). Regression Algorithms can be Logistic Regression (LR) and Decision Tree (DT). Clustering can be classified into K-means, Hierarchical, and Fuzzy C-means. Various classification algorithms classify the target variable [3]. Attributes considered for these studies include Academic achievements during preclinical, school Data, Internal marks, Sessional Marks, Admission scores, CGPA, Online questionnaire filled out by students themselves, Student Images, Course Difficulty, External Assessment, Average National Exam Score, School Attended or not, Socio-Demographic Academic Variables, Personal life details and much more.

The grades in these studies are predicted through various parameters like their Graduate Results, Graduate Degree, and past results. Some datasets also include Registration Number, Program, Duration, Program Code, Gender, Address, etc. [4]. Early prediction of student performance in the right fashion will improve student retention and the testing methods used for students. This practice will also aid educators and education policymakers by giving them better information about their student's learning abilities and how best they can help students.

In today's fast growing society, it is crucial for an institution to predict student performance, classify people according to their abilities, and work to improve their performance in upcoming exams. To improve academic performance, students should be encouraged early on to focus their efforts on a specific subject. By using this type of study, an institution can reduce its failure rates. This study predicts students' performance based on their previous performance in related courses. Data mining is a group of methods to find hidden patterns in massive amounts of pre-existing data. These trends could be useful for analysis and forecasting. Data mining applications in education are called education data mining. The focus of these programs is on the analysis of student and teacher data [5].

In educational data mining, ML is crucial. It enables forecasting in the field of education. This method has the benefit of being able to spot recurrent inquiries. The average weight of each topic may be calculated by analyzing question papers from competitive exams. Every course offers a selection of topics throughout a semester or year. Some problems are interrelated, whereas others are not. It is common knowledge that students who do not study in foundational classes perform badly in advanced courses. Finding such an interrelated set of disciplines is made easier with the help of education data mining [6, 7]. Students can use this knowledge to determine which subjects will be important.

The paper's content is summarized in the next section; Sect. 2 includes the research questions and the search criteria in education for predicting the POS with various methods and attributes. Section 3 discusses the factors which are used in predicting the POS. Section 4 discusses the results, and lastly, Sect. 5 concludes the paper. Table 1 lists the abbreviations used in this review paper are given below.

2 Methodology

The next subsections contain key research questions (RQs) that this SLR aims to answer.

3 Research Questions

Given below are some RQs that were acknowledged:

- *RQ1* What are the most distinguished Conferences and Journals with published articles?
- *RQ2* Which ML techniques and datasets have been used for SP prediction studies?
- *RQ3* Which year of publication has the most studies?
- *RQ4* Which are the frequently used ML techniques for studies on SP prediction?
- *RQ5* Which key performance metrics are used for estimating the applied methods?

The required information was collected from the chosen literature by reviewing the article's content to answer the research questions. This review paper classified the chosen articles according to the machine learning algorithm, year, and attributes.

3.1 Search Criteria

The review paper includes 109 reference papers, and these works are mainly from 2010 to 2020. These papers provide the information for the review. New trends were analyzed from

Table 1 Abbreviations used in this review

Abbreviation	Full form
ANFIS	Adaptive Network Based Fuzzy Inference System
ANN	Artificial Neural Network
AP	Academic Performance
AUC	Area Under Curve
BFGS	Broyden-Fletcher-Goldfarb-Shanno
BN	Bayesian Networks
BPNN	Back Propagation Neural Network
DM	Data Mining
DT	Decision Tree
EDM	Educational Data Mining
FGA	Fuzzy Genetic Algorithm
FN	False Negative
FP	False Positive
FPNN	Fuzzy Probabilistic Neural Network
GDP	Gross Domestic Product
K-NN	K-Nearest Neighbour
LR	Linear Regression
MAE	Mean Absolute Error
ML	Machine Learning
MSE	Mean Square Error
NB	Naïve Bayes
RF	Random Forest
RMS	Root Mean Square
RMSE	RMS Error
RT	Random Tree
SLR	Systematic Literature Review
SP	Student Performance
SPNN	Student Performance Prediction Network
SVM	Support Vector Machine
TN	True Negative
TP	True Positive
TEL	Technology Enhanced Learning

the following databases: IEEE Explore the digital library, science direct, ACM Library, and Springer Link Portal. The examination of the paper includes the identification of a specific algorithm used for the review. The keywords used for the base paper identification are "predicting student performance" and "machine learning." The filters eliminate the results of the articles published earlier than 2010. Different tools were used to perform different analyses. Machine learning and data mining are useful tools like SPSS, WEKA, MATLAB, and Python.

4 Factors Used in Predicting Student Performance

4.1 Attributes Used for Prediction

The most commonly used attribute for student performance prediction is the CGPA, and some authors select the attribute as an internal assessment [8]. The attributes used for the review are listed in Fig. 1.

4.2 Techniques Used for Prediction

Different techniques, such as ML, ANN, RS, and CF, predict POS using different data. The first study was proposed by the Hellenic Open University [9], in which a particular dataset is used to analyze different machine-supervised learning algorithms. The results showed that the NB algorithm accurately predicted student performance. Also, different techniques have their nature; therefore, these can be used for different applications in the POS.

The different techniques used in predicting POS can be classified into four groups: Unsupervised ML, Supervised ML, ANN, and CF, as shown in Fig. 2. Figure 3 represents the weighting of the group of techniques in the review. This figure shows that half of the cases were based on supervised ML, 40% were based on CF technique, and unsupervised ML techniques were used in very few cases [10].

4.2.1 Machine Learning

It is referred to as a set of techniques that help learn a computer's ability without using human programming [11, 12]. ML has been used in many applications such as stock market analysis, medical diagnosis, predictive analysis, Robotics, Games, etc. There are complex models used for prediction purposes, and these models help users provide relevant data for decision making. ML algorithms are mainly classified into two: supervised and unsupervised learning.

4.2.2 Supervised Learning

Supervised Machine Learning (SL) helps identify the algorithm for a general hypothesis to predict future instances [13]. In general, the main objective of this algorithm is to categorize the data from the prior information.

The prediction of POS in nursing courses from 3978 records on 528 students was proposed by [14]. An efficient SL method is the rule induction, which helps to make predictions and has an accuracy of about 94%. The selection of classification techniques is to be careful due to its unbalanced nature. This unbalanced nature of the dataset leads to accuracy misleading. Different techniques were implemented to identify these dataset types [15]. These techniques can be used to evaluate different factors such as POS prediction, attribute selection, effectiveness evaluation, etc. The classifier algorithms used for this review are C 4.5, One-R, NB, AD Trees, BN, and RBN (Radial Basis Networks). Different algorithms were applied, and compared the performance results to identify the better performance.

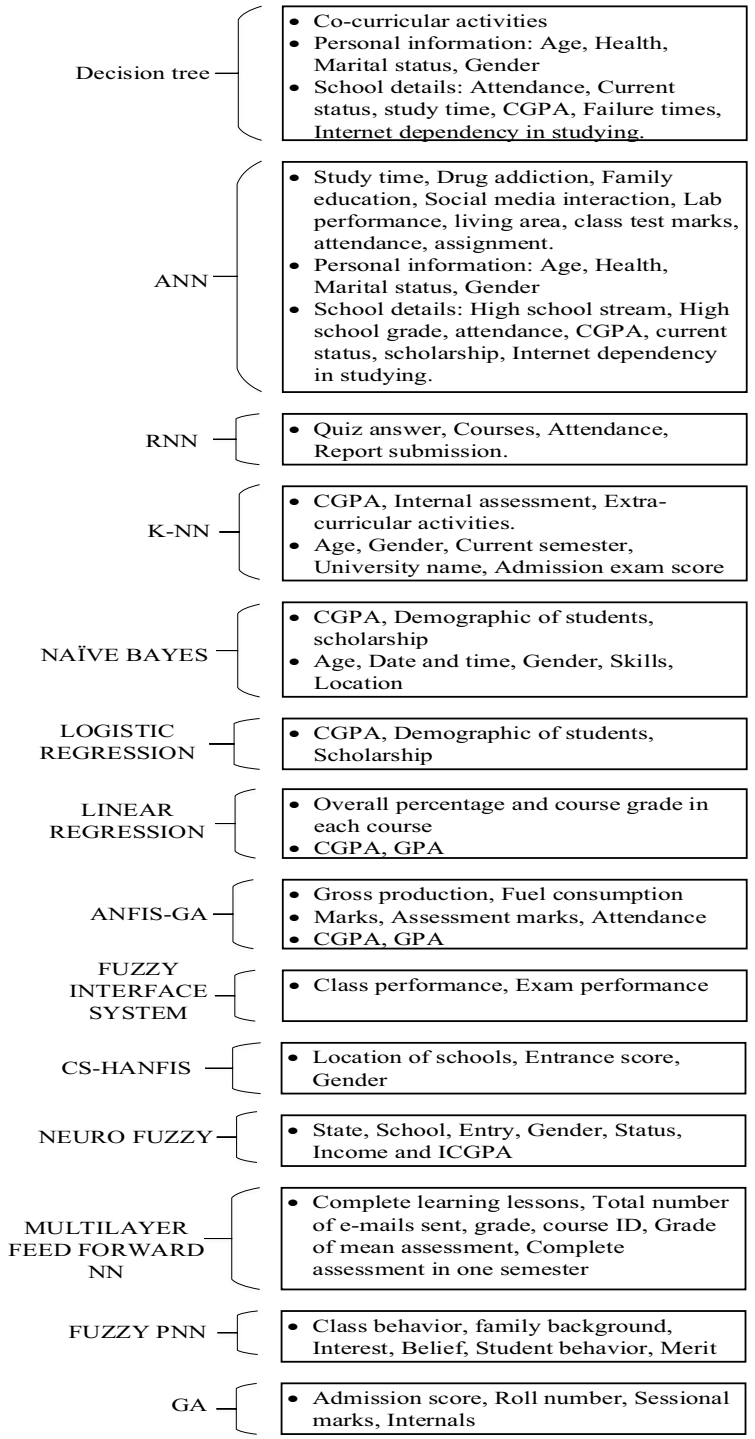


Fig. 1 Attributes used for SP prediction [8]

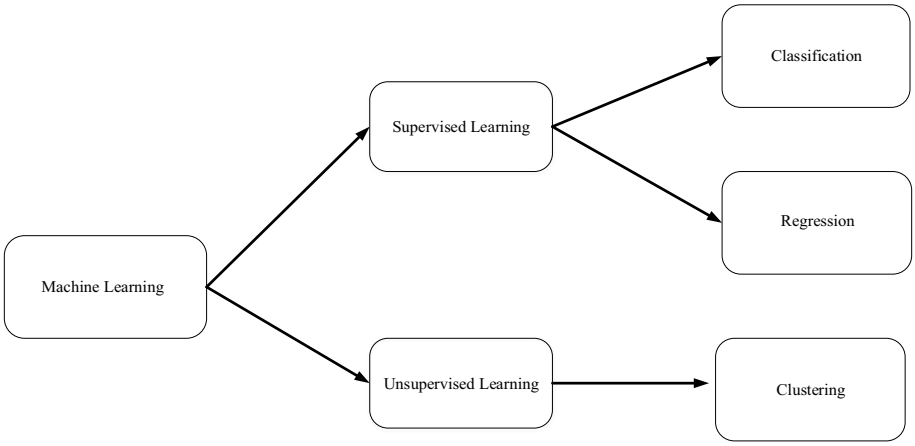


Fig. 2 Classification of Machine learning algorithm

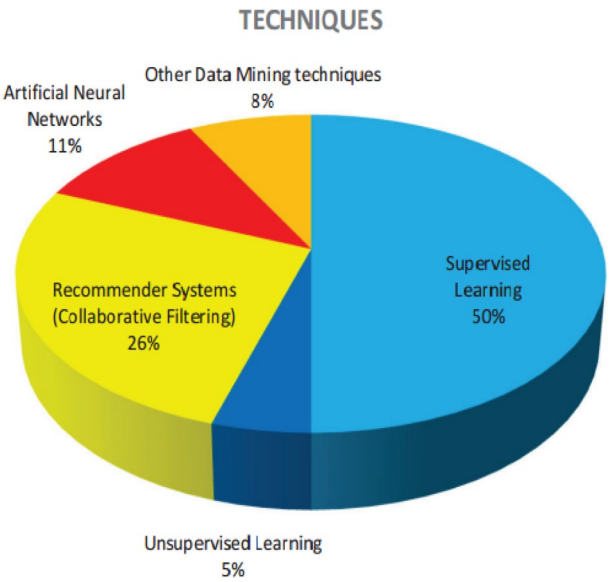


Fig. 3 Distribution of articles based on various ML methods

In [16], four classification algorithms as Logistic Regression (LR) [17], DT, ANN, and SVM were compared with the data balancing techniques such as Over-Sampling, Under-Sampling, and Synthetic Minority Over-Sampling (SMOTE). The results showed that the SMOTE with SVM had the best accuracy for performance prediction.

In [18], a new technique was proposed to predict risk at the early stages of online courses. The number of drop-outs is a major problem at the university level. The proposed technique is based on three ML techniques: KNN, RBN, and SVM, and it uses 28 attributes per student. The student's personal characteristics and academic performance were considered in [19] to predict POS. A set of three ML algorithms (ANN, BN, and DT) was used for the evaluation. The effectiveness was evaluated using indicators like

accuracy, recovery rate, etc. In addition to the personal characteristics, the cognitive characteristics were included to increase the prediction accuracy using DT [20].

An SA framework was developed in [21] for the early identification of at-risk students, where the proposed technique was compared with the other ML techniques. The results showed that 60% of drop-outs occurred in the first 2 years, mainly in science, technology, and mathematics. Similarly, in [22], other ML algorithms such as DT, NB, KNN, Deep Learning, linear models, and GBT (Gradient Boosted Tree) were used for the same purpose. From this, the DL and GBT techniques show the best accuracy. Some of the studies were used to identify the quality of the SL technique for performance prediction. In [23], SVM and NB were used to predict individual performance, and in [24], classifiers like Sequential Forward Selection (SFS), RF, KNN, C4.5, and NB were used to analyze the performance prediction with 97% accuracy. Random Forests (RF) showed better performance in the prediction of POS. Various performance metrics can predict binary classification performance [25]. ANN, LR, DT, SVM, and NB were used for the same application using data recorded by e-learning tools [26].

In [11], different algorithms were compared to predict new student performance. NB showed the best accuracy in a web tool. Moreover, in [27], SVM shows better performance than the remaining techniques for predicting student performance. In [28], the Bayesian Belief Network (BNN) was developed for early detection of student performance. SVM and LR were applied to this situation [29]. By implementing different algorithms, the classification accuracy of the system can be improved. Therefore pre-processing techniques can be done along with the classification algorithms to increase the accuracy of the prediction [30].

Different techniques for the prediction were proposed in [31]. RF and SVM developed the prediction models for this technique. Also, the characteristics were identified from the daily interaction events of a student, and RF showed the best results. Similarly, other SL techniques are used to analyze the dataset from the website to predict POS [32]. Software in e-learning platforms analyzes algorithms' results and helps decide educational approaches [33].

The data analysis method was proposed in [34] that helps determine the performance in the courses of the next trimesters. Various ML techniques were used to predict student performance, which helped construct Markov Decision Process (MDP) transition probabilities. In [35], student performance was identified using the Jacobian Matrix-Based Learning Machine (JMLM). Similarly, the AdaBoost assembly algorithm was proposed to predict POS [36], showing the best performance. Adaboost was the best meta-decision classifier to predict student performance [37].

Some other SL algorithms were used effectively for predicting student performance. Bayesian Additive Regressive Trees (BART) were used to predict the final grade of students in the sixth week [38]. There are three types of results from the weekly prediction: low, medium, or high performance [39]. A new method was proposed in [40] describing Latent Dirichlet Allocation (LDA) to predict POS. This technique involves describing the learning condition of the students.

4.2.3 Unsupervised Learning

The unsupervised Learning (UL) algorithm does not contain a dataset for processing. It is also known as class discovery. Therefore, it is not used in cross-validation [41].

Most clustering algorithms were expressed in terms of optimal criterion, but there is no chance for an optimal solution in the case of UL.

A new method was proposed in [42] to predict the POS. This method includes the development of a UL Sparse Auto-Encoder for automatically learning algorithms. Moreover, clustering and classification algorithms such as Hierarchial and K-means Clustering were used to evaluate the performance prediction [43]. In [44], the recursive clustering technique for the evaluation was applied to a group of students.

4.2.4 Recommender Systems

This type of system collects information from the user preferences. The information can be collected explicitly or implicitly for student performance evaluation [45]. The RS performed the predictions with the help of different sources.

4.2.4.1 Collaborative Filtering Collaborative Filtering (CF) methods are used for recommendations, and these methods are also combined with other filtering methods like knowledge based, content based, or social [46]. CF use the same way as humans for the prediction and recommendation by considering the knowledge and past experiences. There are some studies to predict student performance.

In [46, 47], the evaluation is based on the similarities within the students, and the grades from the previous courses represented the student's knowledge. CF generated personalized student grade predictions using improved similarities [48]. Student groups were helped to make predictions on grade models for CF based approaches. The prediction accuracy is not good due to the large dataset. Therefore, in [49], the CF approach was implemented in small universities.

CF methods are also used to improve the results in some particular environments. A novel method was proposed in [50], in which a new model, PSFK was developed with the combination of user-based CF and a user modelling method (Bayesian Knowledge Tracing (BKT)). Similarly, a new method for prediction was proposed in [51]. The developed Hints-Model model combines the factorization method called Regularized Single-Element Based Non-Negative Matrix Factorization, which helps to attain greater prediction accuracy. The grades in upcoming courses are predicted using a Grade Prediction Advisor (pGPA) [52]. The Expectation–Maximization procedure was implemented to solve the problems that occurred with the CF approach [53]. With personalized study planning and orientation for students, the CF technique allows performance prediction of grades [54]. A CF tool helped predict the unknown performance by analyzing the performance database for different tasks [55]. The parameters of the CF technique were selected with great accuracy. CF combined with knowledge based techniques for better accuracy and helped to suggest new methods that help new students [56].

In the prediction of POS, matrix factorization is the best technique. In [57], the Singular Value Decomposition MF technique was applied to improve efficiency. This method is compared with simple baseline techniques such as Uniform Random, Mean of Means, and Global Mean [58]. Predict student performance on multiple-choice questions using two reference methods. It was achieved by comparing MF and biased MF with other CF methods [59].

4.2.5 Artificial Neural Networks

Processing elements are a set of highly interconnected entities. These are the basic elements of Artificial Neural Networks (ANN). This structure is developed based on the biological central nervous system, especially the brain. The processing elements structure is based on the neuron [60]. The processing elements contain a set of weighted inputs and the corresponding outputs. ANN has been used in many prediction technologies, particularly in evaluating student performance.

In [61], the author proposed a feed forward ANN technique to predict the scores of tests by considering half scores during the course. In [62], the cumulative Grade Point Average was used along with ANN to predict the POS. There are two models for ANN: Generalized Regression Neural Network and Multilayer Perception. These two were compared to identify the accurate model to predict the POS [63]. In medical education, the learning results were compared with a multivariate LR model to predict the performance [64].

The POS prediction was improved using basic students' cognitive and non-cognitive measures information. Also, the performance evaluation was done by three ANN models [65]. The relationship between cognitive and psychological variables influenced student performance. In [60], students are effectively grouped into different classes with expected results. Considering the value of focusing the subject on the final exam, a new technique, ELM, was used to predict POS [66].

4.2.6 Effect of Techniques

The techniques had different accuracies to the students' behaviour. The SVM and ANN were the most applied techniques, followed by CF, NB, and DT. The performance of SVM is better than other techniques. For the selection of techniques, there is a guide for decision making [67]. Figure 4 shows the ML methods which are used for SP prediction. The summary of ML approaches is given in Table 2.

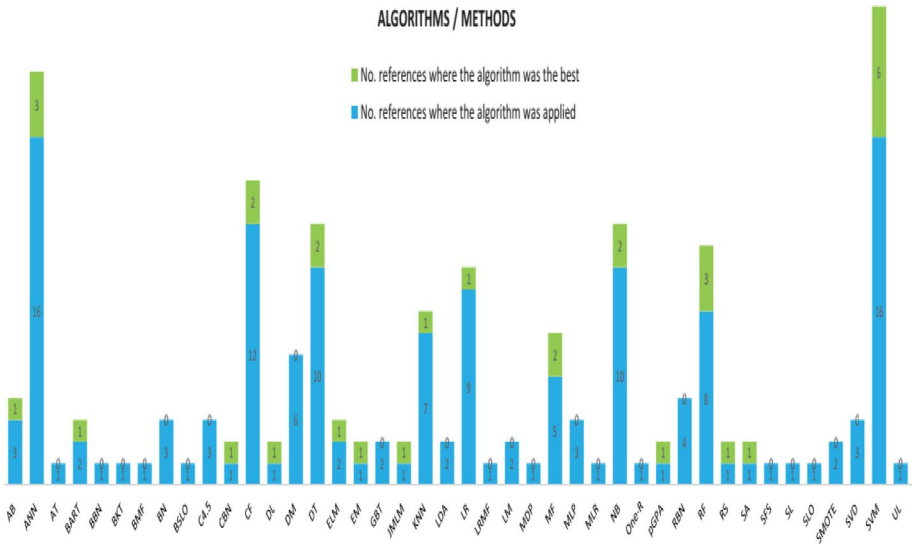


Fig. 4 ML techniques used for SP prediction

Table 2 Summary of ML techniques (Katarya [8])

Technique	Year	Authors	Attributes	Achieved performance
K-Nearest Neighbour	2015	Mayilvaganan et al. [68]	ECA, IA, CGPA	MKNN—45% (slow learner), 10% (Average learner), 5% (good learner) and 40% (excellent learner) MKNN takes less time to classify student performance
	2015	Shahiri et al. [69]	ECA, IA, CGPA	In comparison to neural networks and decision trees, NB provided the best accuracy. This is because when utilizing NB as a prediction approach, the attributes employed are significant with respect to one another
	2012	Kabakchieva et al. [4]	Age, Gender, Admission year, Current semester, University name, Birth year	The K-NN attains 70.5% accuracy for both classes – Weak and Strong
Naïve Bayes	2019	Tomasevic et al. [70]	Past exam grades, Deck commenting, Age, Date and Time, Skills, Gender, Location, Exam attempts	For classification and regression tasks, the ANN has achieved efficient results in time analysis
	2015	Jishan et al. [71]	CGPA	Neural Network and NB classification using SMOTE oversampling and ideal equal width binning have the highest accuracy, around 75%. The neural Network Backpropagation approach is computationally slower than Naive Bayes classification
	2015	Mayilvaganan et al. [68]	ECA, IA, CGPA	Naïve Bayes shows 40% (good learner), 20% (Average learner), 30% (slow learner), and 10% (excellent learner) from the required quantitative data set based on speciality
	2015	Shahiri et al. [69]	Scholarship, CGPA, Student demographic	In comparison to neural networks and decision trees, naive Bayes provided the best accuracy

Table 2 (continued)

Technique	Year	Authors	Attributes	Achieved performance
Decision Tree	2019	Alsalman et al. [72]	Personal Information: Age, Gender, Health, Marital Status School details: Scholarship, Attendance, Study time, Current status	DT attains 66% accuracy for the selected data
	2016	Hamsa et al. [73]	EA, Personal Details, Co-curricular activities	DT analyses the risk barriers and improves the lecture's point of view to improve the results of average students
	2019	Tomasevic et al. [70]	Age, Location, Gender, Date and Time, Exam Attempts, Past exam grades	RMSE is 0.9507
	2015	Mayilvaganan et al. [68]	ECA, IA, CGPA	Achieved better accuracy but not the same as a neural network
	2015	Jishan et al. [71]	CGPA	The AUC of DT is found to be less than other existing models
	2015	Shahiri et al. [69]	CGPA	DT method's performance accuracy is 91%. DT method's most accurate indicator of a student's achievement is their CGPA
Linear Regression	2012	Abidin et al. [3]	Final Exam Exit Score, CGPA, GPA	–
	2006	Chamillard [74]	Grade in each course, Overall percentage	It analyses which attributes are major key factors for later academic performance
Logistic Regression	2018	Rusli et al. [75]	CGPA, Social network interaction, Scholarship, Demographic of students	RMSE is 0.33

Table 2 (continued)

Technique	Year	Authors	Attributes	Achieved performance
Artificial Neural Network	2019	Alsalman et al. [72]	Personal Information: Age, Health, Gender, Marital status School details: Scholarship, High school stream, Attendance, Study time, Failure times, CGPA	ANN attains an accuracy of 97% while applying the testing and training data at the same time
	2019	Tomasevic et al. [70]	Age, Gender, Skills, Location, Number and Duration of Activity participation, Past exam grades,	ANN model (three layered network) provided the best results in each case. RMSE—12.34
Neural network	2016	Sikder et al. [76]	Study time, Assignment, Class Test Marks, Attendance, Location, Social media usage, Drug addiction	RMSE is 0.1765, and accuracy is more than 80%, which is better than existing methods
	2015	Pathak et al. [77]	Location of school, Gender, Past exam results	It enables the instructor to become aware of the weak students in the middle of the school year and to pay closer attention to such children
	2013	Do et al. [78]	Gender, Exam Result	ANFIS model is used to assist in student admission procedures and strengthen the service system in educational institutions
Recurrent Neural Network	2017	Okubo et al. [79]	Attendance, Report Submission, Courses, Quiz answer	An RNN has proven successful in early grade prediction compared to multiple regression analysis
Multilayer Feed-forward Neural Network	2019	Altaf et al. [80]	Grades, Total number of emails sent, Course ID, All session length average	When performance indicators are taken into account, it can be concluded that the neural network is a great classifier for predicting student performance and may be used to determine whether a student needs academic support
Genetic Algorithm	2016	Hamsa et al. [73]	Internal, Roll no, Admission score, Sessional marks	Results achieved by fuzzy based genetic algorithm have achieved sufficient performance for passed students by considering risk and safety constraints

Table 2 (continued)

Technique	Year	Authors	Attributes	Achieved performance
Fuzzy Probabilistic Neural Network	2013	Arora et al. [81]	Study behaviour, merit, Interest, Belief, family background	It achieves an average of 98.56% classification accuracy

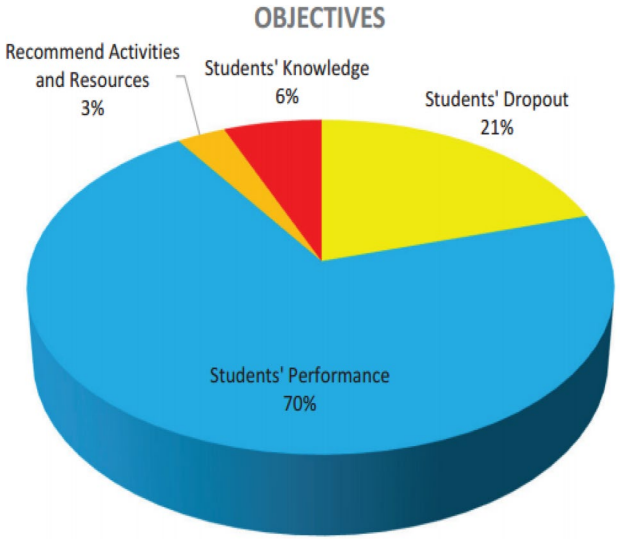


Fig. 5 Distribution of articles based on various objectives

4.3 Objectives Used for Prediction

The objectives are classified into four groups: student drop-out, student knowledge, performance, and recommended activities and resources. Figure 5 shows the weight of each objective in this review. It indicates the importance of the objectives. This analysis analyses the major prediction part using student performance (70%), followed by student drop-out (21%). Students' knowledge and recommended activities affected the prediction of low demand (6% and 3%).

4.3.1 Student Drop-Out

Various studies were developed based on the drop-out rate, which helps predict the POS. In [82], IBM SPSS Answer Tree (AT) software was developed to predict drop-out. Family history, socioeconomic status of families, exam results, and school grades are the important factors affecting the prediction of school drop-out, as described in [15]. In [16], it was found that imbalanced class data is a problem in predicting POS. This problem is reduced by comparing different data balancing techniques.

High school institutions use the data from university systems to analyze performance. In [83], the analysis was done based on the Moodle Engagement Analytics Plugin learning analysis tool. A new technique was proposed by combining multiple classifiers to identify the students' activities within time [18]. Some authors used personal characteristics for evaluation [19]. The prediction models were created by using DT, BN, and ANN. Exploratory Data Analysis was applied to identify the commitment to using online sources. It was represented in [84] to predict drop-out.

4.3.2 Student Knowledge

The information generated by students was used to analyze the prediction checker [85]. This proposed method helps to improve efficiency through the analysis of POS. The student performance analysis was automatically detected in [86]. It is based on the student's behaviour and the response analysis to the learning style.

The test results were a major factor in determining the students' characteristics [87]. In [88], machine learning applications were developed to gain students' knowledge and identify the learning's behavioural indicators.

4.3.3 Student Performance

The prediction of POS is the most challenging issue faced by educational institutions. Several approaches were developed for POS prediction. This was very useful for the e-learning environment.

A machine supervised algorithm is developed with the characteristics of the students and their grades in some tasks [9]. In [27], four mathematical models were compared to predict the POS. There is a relationship between geographic environment, ethnicity, and student performance. This relationship is explained in [11].

In [46, 89], the performance is predicted by the student's history on particular first semester courses. In the proposed method, students' knowledge is represented as a set of grades from the passed courses. The research was carried out with the help of large matrices in courses with few students and small universities. Accuracy is an important factor in educational applications, and it helps to save the effort and time of educators and the resources [59]. Therefore, in [30], an additional pre-processing technique was used with a classification algorithm to improve the accuracy of the prediction.

In [39], the proposed system stated that the weekly ranking performance of each student is classified into three levels: Low, Medium, and High. The performance analysis based on non-cognitive characteristics was presented in [90]. The result showed that students' cognitive and non-cognitive characteristics increased the prediction technique. It can increase the prediction accuracy [37].

ML techniques were also included in this application. The recursive clustering algorithm helps to group the students with their performance. The main objective of [44] is to move the students from lower to higher groups. In [47], a new method based on personalized prediction is presented. In this, the student's performance was done by a personalized prediction. It helped to find the appropriate specialization for each student.

4.3.4 Recommended Resources and Activities

These systems are used to improve the teacher and student experience. The interests and preferences of the students are the factors considered for the RS system. In [29], the RS was developed considering the previously-stored experiences and compared with the present POS. Also, in [91], POS is identified using an online forum. It contains a "Like" button, similar to the button on Facebook. Table 3 illustrates the summary of the papers.

Table 3 Summary of papers

Paper	Attributes	Machine Learning Algorithm	Achievements
Altaf et al., [80]	Course ID, Total learning sessions, number of quizzes made, Mean assessment grade	Multilayer Feed-Forward NN Architecture	Average accuracy—97.1%
Guleria et al. [92]	Class performance, Attendance, Lab work, Assignment, Sessional Performance	DT	To learn more about each student's academic performance and to determine which pupils need more support
Burman and Som [93]	Psychological features of students, collected using Questionnaire like Personality, Motivation, Learning strategies, Psychosocial contextual influences, Socioeconomic status and Approach to learning	Multi-classifier SVM using Linear Kernel and Radial Basis Kernel	Radial Basis Function kernel gives more accurate results than Linear Kernel, which is approximately 90%
Arsad et al., [62]	Grades	ANN	The results show that the NN model is valid and may be applied to forecast student academic success
Gray et al. [24]	Aptitude, Motivation, Personality, Learning strategies	NB, DT, SVM, KNN, ANN, Logistic Regression	More than 97% accuracy has been attained. It reduces the number of children who get unnecessary intervention as well as the number of pupils whose outcomes were mistakenly anticipated to be favorable
Mohammadi et al. [94]	Gender, category, First Language, Family details, Location, Transportation, Grade Point Average, Studying hours, Friends quantity	KNN, DT and NB	This procedure can make it easier for teachers to assess student performance and plan more effective strategies for their academic growth
Ketui et al. [95]	Registration data: year, semester, subject id, subject name, department name, department id, grade, and credit	DT, Random Tree (RT), DT Weight-Based, ID3 and GBT	GBT attains 92.41% accuracy and F-measure—84.59%
Hussain et al. [26]	Performance, Gender, Caste, coaching, Class ten and twelve education, medium, Class X/XII Percentage, Mother occupation, Father occupation	a) Association Rule Mining using Orange b) NB, NN and DT using Weka c) K-means, Hierarchical Clustering and Partitioning around Medoids using Orange and R Studio	Findings demonstrate that ANNs and SVMs outperform other algorithms in terms of accuracy. The TEL system can be readily connected with ANNs and SVMs, therefore it anticipates instructors to report increased student performance during the following session

Table 3 (continued)

Paper	Attributes	Machine Learning Algorithm	Achievements
Jamil et al. [96]	Nationality, Stage ID, Grade ID, Gender, Topic, Section ID, Semester, Relation, Place of Birth, raised hands, Visited Resources, Announcements View, discussion, etc	NB, RF, J48 and REP tree	RF achieves better results than other algorithms
Rustia et al. [97]	General Weighted Average and the passed and failed remarks on the LET (Licensure Examination for Teachers) results	NN, SVM, NB, C4.5 and LR	C4.5 is the most suitable model, achieving 73.10% accuracy, 0.730 AUC, and 62.53% F-measure value
Hamsa et al. [73]	Internal marks, sessional marks, admission score	DT and FGA	Results achieved by fuzzy based genetic algorithm have achieved sufficient performance for passed students by considering risk and safety constraints
Chaudhury et al. [30]	School attended, Age, Family size, Parent's status (Together/Separated), Gender, Mother's Education, Mother's job, Rural/Urban background, Family support, Father's job, a reason to choose a school	SVM, DT and NB	These models can be used to provide the target pupils with advice or caution. Thus, providing these target students with tailored learning techniques can decrease the number of students who fail university examinations
Sikder et al. [76]	Family education, drug addiction, social media interaction, Academic Details, etc	BPNN	RMSE is 0.1765, and accuracy is more than 80%, which is better than existing methods
Hasan et al. [98]	CGPA	DT, NB, and NN	RF was considered the best suitable based on the lower mean absolute error and relative absolute error
Tanuar et al. [99]	Result of 1st semester of 6 subjects	GLM, Deep Learning and DT	The simplest model to correctly introduce to consumers is the DT because it achieves less error in less time duration
Bharara et al. [100]	Demographic features, Academic Features, Parental Involvement Features, Interaction Features	K-means Clustering	The final analysis showed that the mother's involvement in the student's academic education resulted in them performing better than the father

Table 3 (continued)

Paper	Attributes	Machine Learning Algorithm	Achievements
Okubo et al. [79]	Submit a report each week to answer quizzes, write a log of lectures and read slides for preview	RNN	An RNN hasproven successful in early grade prediction compared to multiple regression analysis
Kaur et al. [101]	Student's Sex, Type of board, Medium of instruction, Institution at high level, Type of school, Area at school level, Student having mobile, Private tuition, Computer at home, etc	MLP, NB, J48, SMO and REPTree	MLP achieves the highest with a 75% accuracy rate across all data mining classifiers, making MLP a potentially useful and efficient classifier technique
Pathak et al. [77]	10th and 12th percentage of a student, Another competitive exam status, gender, etc	BFGS and LMA	It enables the instructor to become aware of the weak students in the middle of the school year and to pay closer attention to such children
Shaleena et al. [102]	Student's marks, along with social, economic, and cultural attributes	DT	These techniques produce outcomes that are simpler to comprehend since they may use IF–THEN principles to explain predictions at a higher level. As a result, it is quite simple for a teacher or other non-expert data miner to understand the categorization outcome
Jishan et al. [71]	CGPA, Quiz marks, Mid-term marks, Attendance marks	NB, DT and NN	Neural Network and NB classification using SMOTE oversampling and ideal equal width binning have the highest accuracy, around 75%
Mayilvaganan et al. [68]	Internal assessment, CGPA, Extra-curricular activities	DT, NBC and MultiLabeled K-NN	MKNN takes less time to classify student performance
Márquez- vera et al. [103]	Demographics, social, family, educational or cultural background etc	DT and Induction Algorithms	The accuracy of the algorithm is increased by choosing the optimal features, using cost-sensitive categorization, and balancing the data

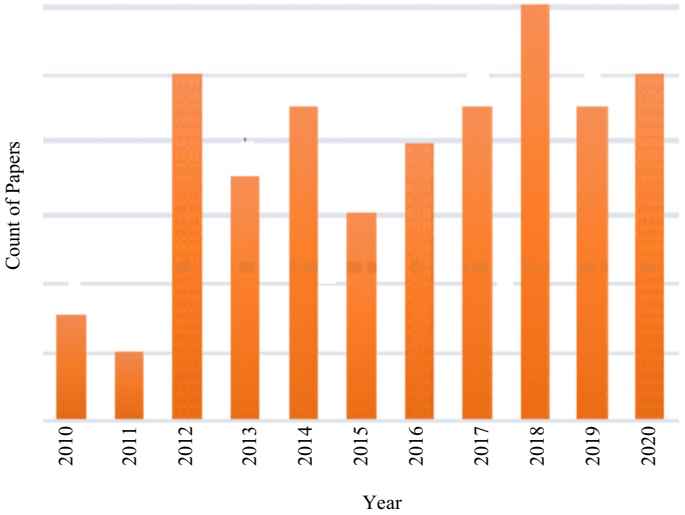


Fig. 6 The count of papers reviewed per year

5 Publication Distribution Over the Years

Figure 6 represents different articles published from 2010 to 2020 on SP prediction. Since 2010, several papers have been proposed to study POS using ML techniques. Further, the researcher's interest grew, and the publication raised to 30% until 2015. In 2018, the number of articles increased unbelievably. Until 2020, the average amount of publications in a constant manner generates new ML techniques by solving the problem of SP and measuring them with different metrics. From 2010 to 2020, important articles related to EDM were collected. Therefore, the trend line shows up and downs. In the year 2018, the highest number of research papers was developed.

6 Citation Analysis

Citation analysis is very beneficial for finding out the effect of a solitary article on a given field by identifying the number of others who have referred to the article. It allows scholars to see how often work has been cited in articles and is a priceless tool for any literature review. The Google Scholar engine was chosen to determine the number of citations of the nominated papers in this study to accomplish a citation breakdown. Table 4 lists the summary of all studied cited articles from the Google Scholar database.

7 Performance Assessment of ML Models

The major goal of this review is to identify the complexity of various performance prediction techniques. A variety of metrics are used in SP predictive analysis to achieve the efficiency of ML approaches [111]. The different metrics are:

Table 4 Summary of all studied cited articles from the Google Scholar database

Relevant studies	Publication year	Number of citations
Kaur et al. [101]	2015	167
Márquez- vera et al. [103]	2013	112
Kabakchieva [4]	2012	84
Thai-Nghe, et al. [104]	2009	81
Şen, et al. [105]	2012	80
Jishan et al. [71]	2015	77
Mayilvaganan et al. [68]	2014	75
Guo et al. [42]	2015	64
Hamsa et.al. [73]	2016	60
Okubo et al. [79]	2017	48
Do et al. [78]	2013	39
Arora et al. [81]	2013	32
Arsad et al. [62]	2015	29
Ahmed et al. [106]	2016	27
Shaleena et al. [102]	2015	22
Guleria et al. [92]	2014	20
Bharara et al. [100]	2017	19
Rana and Garg [43]	2016	17
Widyahastuti et al. [107]	2017	15
Sivasakthi [108]	2017	15
Arsad et al. [62]	2012	13
Hasan et al. [98]	2018	12
Hussain et al. [26]	2019	12
Sikder et al. [76]	2016	12
Sekeroglu et al. [109]	2019	10
Chaudhury et al. [30]	2016	7
Abidin et al. [3]	2012	4
Burman and Som [93]	2019	4
Mohammadi et al. [94]	2019	4
Ketui et al. [95]	2019	4
Alsalman et al. [72]	2019	3
Dimililer et al. [67]	2017	3
Altaf et al. [80]	2019	2
Rustia et al., [97]	2018	2
Jamil et al. [96]	2018	1
Kaunang et al. [110]	2018	1
Tanuar et al., [99]	2018	1
Pathak et al. [77]	2015	1

Accuracy: This metric is used for classification performance. It is the proportion of several right forecasts to add input samples. It operates admirably even if there are equal samples in each class. In our study, accuracy is the most used metric for performance prediction.

$$Accuracy = \frac{TP + TN}{TP + TN + FP + FN} \times 100 \tag{1}$$

RMSE: A popular way to calculate the error in a set of regression predictions is RMSE. It is the RMS of the squared difference between real and anticipated results.

F-Measure: F-Measure, also known as the F1 score, is utilized to test exactness, which is known as a weighted consonant mean of precision and recall. 1 is considered to be the best value for F- Measure.

MAE: It is the mean of the contrast between the underlying initial and anticipated values. It measures the distance between the predicted outputs and the actual outputs.

Precision: It is one of the efficient performance metrics to predict the exactness of the proposed methods.

Recall: It is the number of right positive outcomes divided by every single significant example (TP and FP).

Coefficient Correlation: Correlation coefficients identify the relationship between two variables. Pearson's correlation is frequently used in LR.

TPR: It is also referred to as Sensitivity, which is defined as the part of positive data points which are accurately considered as positive with respect to all positive data points.

Area under Curve (AUC): The area under the receiver operating characteristic (ROC) curve is stated as AUC. It measures the overall performance of the binary classifier. It is the average value of Sensitivity for every possible value of specificity and vice versa.

$$Specificity = \frac{TN}{TN + FP} \times 100 \tag{2}$$

$$Sensitivity = \frac{TP}{TP + FN} \times 100 \tag{3}$$

Confusion Matrix: As the name suggests, it gives us a matrix and depicts the total execution of the model. It works on four terms: TN, TP, FN, and FP. It can calculate the accuracy by taking an average of the values in the diagonal of the matrix, i.e., the proportion of the whole of FN and TP to the absolute amount of tests.

Kappa: Cohen's kappa coefficient is a statistical degree of agreement for categorical items. It processes the agreement of the prediction to the true class. It is generally considered more robust since it considers the agreement arising by chance. The performance metrics used in the review are given in Table 5. The performance evaluation of ML models is shown in Fig. 7.

8 Discussion

This section includes a discussion of the main objective of our review paper. It helps to give the advantage to the researchers with the identification of different classification techniques used for predicting POS. This article has reviewed many papers aimed at predicting student behaviour in the academic environment. Some conclusions can be drawn from the analysis of these papers. There is a tendency for SP prediction to be high at the school level. Around 60% of the articles included in this review are used for this application. Here, the outcomes were obtained as results of the RQs. The mapping of examination articles to the respective RQs.

Table 5 Performance metrics used in this review

Used Metric	Relevant studies
Accuracy	Ahmed et al. [106], Saa et al. [112], Şen et al. [105], Guo et al. [42], Sekeroglu et al. [109], Sivasakthi [108], Altaf et al. [80], Rustia et al. [97], Bharara et al. [100], Dimililer et al. [67], Mohammadi et al. [94], Agarwal et al. [113], Burman and Som [93], Shaleena et al. [102], Hasan et al. [98], Jishan et al. [71], Márquez- vera et al. [103], Ketui et al. [95], Hamsa et al. [73]
RMSE	Hussain et al. 2018 [114], Tanuar et al. [99], Widyahastuti, et al. [107], Dimililer [115], Sikder et al. [76], Chaudhury et al. [30], Chen et al. [116], Do et al. [78]
F Measure	Rustia et al. [97], Kaunang [110], Jishan et al. [71], Kabakchieva [4], Thai-Nghe [104], Kaur et al. [101], Ketui et al. [95]
MAE	Hussain, S. [26], Widyahastuti [107], Chaudhury et al. [30], Chen [116], Do et al. [78]
Precision	Jamil et al. [96], Kaunang [110], Jishan et al. [71], Kabakchieva [4], Thai-Nghe [104], Kaur et al. [101], Ketui et al., 2019
Recall/ Sensitivity/ TPR	Jamil et al. [96], Burman and Som [93], Kaunang [110], Jishan et al. [71], Kabakchieva [4], Márquez- vera et al. [103], Kaur et al. [101], Ketui et al. [95]
Correlation coefficient (R Value)	Chen [116], Do et al. [78]
ROC Area	Jamil et al. [96], Chaudhury et al. [30], Kabakchieva [4]
AUC	Rustia et al. [97], Jishan et al. [71], Thai-Nghe [104]
Confusion Matrix	Guleria et al. [92], Shaleena et al. [102]
Kappa	Jamil et al. [96], Hasan et al. [98]
TNR/ Specificity	Burman and Som [93], Márquez- vera et al. [103]
Remaining Metrics	Chen [116], Jamil et al. [96], Do et al. [78], Kabakchieva [4]

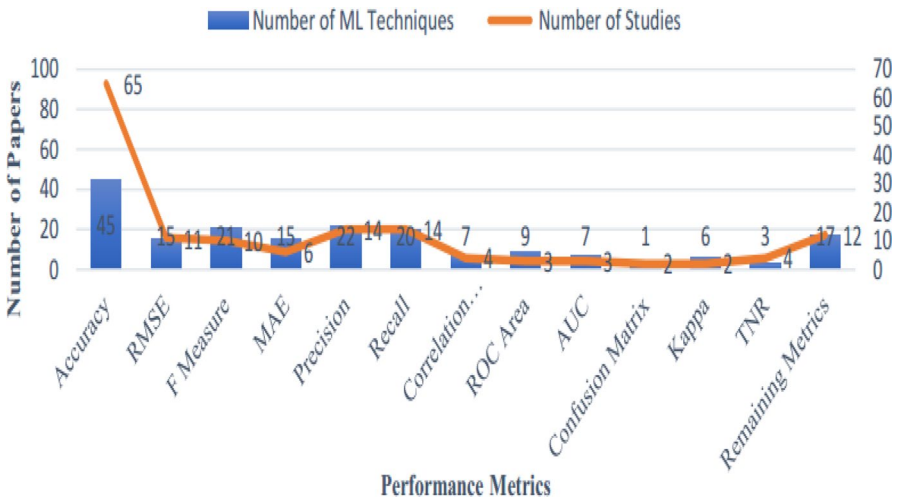


Fig. 7 Performance estimation of ML models used in the articles

The most well-known and significant journals and conferences with published articles (RQ1)

The quality research papers for the review were extracted using synthesis. A total 109 papers have been taken into account, including conference papers, journals, and transaction papers from various libraries such as IEEE, Springer, Science Direct, ACM, etc. Table 4 represents the author and publication year, with several citations for each paper. These results have been taken from the Google Scholar database.

On which ML Techniques and datasets the studies for SP forecast have been performed? (RQ2)

It was seen that various ML Techniques had been used in Educational Mining to analyze students' performance. Datasets are based on education-focused or those attributes that would define a student and his performance. These attributes can be either publicly available or data fetched from a college/school academic database, a random set of questionnaires/ surveys on selective topics related to students' personal like age, gender, caste, etc. and academic details like CGPA of various subjects, entrance exam score, etc. Their Internet usage [76] has often been viewed as parental reporting to see how much time a parent devotes to their child [26, 30].

Which publication year shows the highest number of studies from extracted papers? (RQ3)

The graph depicted in Fig. 6 shows different techniques worked upon each year starting from 2010. It can be seen that among 109 studies extracted, the year which witnessed a high number of publications is 2018, including studies mainly on techniques like SVM, NN, KNN NB, Clustering, DT, and Regression.

Which is the most frequently used ML technique for studies on AP prediction? (RQ4)

RQ4 can be answered by representing various ML techniques using a pie chart (Fig. 3). It concludes that the widely used ML techniques are SVM, k-NN, and NB. The most commonly used attributes for students' learning mechanisms for predicting their performance are their demographic features, academic performance, and social information. The widely used technique for analyzing SP is supervised learning by analyzing the data used for this review. It helps to generate accurate results and provide good predictions. Also, SVM, DT, RF, and NB provide accurate results. The next suitable method is the collaborative filtering algorithm.

Widely used performance measures (RQ5)

Furthermore, different metrics such as Accuracy, F-Measure, RMSE, Correlation Coefficient, Recall, Precision, TP Rate, MAE, AUC, confusion matrices, and many more have been depicted and used as a measure in various papers (Table 5, Fig. 7). According to our research, the most used metric is accuracy.

This review can be useful to obtain a wide application of machine learning techniques to predict student performance. This practice will help educators and education policymakers by giving them better information about their student's learning abilities and how best they can help students. Many researchers will probably tackle this problem in the coming years by considering other and new ML tools since this problem has attracted a high degree of interest.

9 Conclusion

The expanded utilization of innovation in education is producing a lot of information consistently, which has to be an objective for some stakeholders all over the globe. The field of instructive DM is emerging rapidly and has the advantage of containing new calculations. EDM is an emerging discipline worried about creating techniques for investigating the

exceptional and progressively huge scale information acquired from academic settings and utilizing those strategies to recognize students more readily and the situations they acquire. Below are some stakeholders as indicated by their goals for utilizing EDM:

- *Students/Learners* Enhancing singular learning styles, learning resources and learning encounters, or suggesting them.
- *Instructors* Analyzing understudies' learning practices, picking up the steadiest guidance, and anticipating understudies figuring out how to expand education adequacy.
- *Associations* Increasing the productivity and cost-effectiveness of basic leadership forms in higher education foundations, such as the admissions process, confirmation forms, and budgetary asset distribution.
- *Specialists/Developers* Evaluating learning materials, improving learning frameworks, and surveying information-digging strategies for adequacy.

This work is collective research of the work studied worldwide regarding Educational Mining and predicting student performance considering various attributes and employing different ML techniques for classifying performance using various metrics. This paper follows an SLR methodology that includes different phases and steps: arranging the survey, shaping the study-based questions, and setting up the incorporated and avoided criteria until determining the data extraction tactic. Additionally, EDM tools are straightforward and interfaced with different strategies. Teachers with no ability in DM can also apply their hands in these fields.

Researchers can get beneficial help from this systematic literature review to work ahead in this field. This paper will help them understand the different work covered in the respective years from 2010 to 2020. As an inadequacy, this research has engrossed on a few databases only in provisions of article gathering. Furthermore, upcoming potential endeavours may reflect on different search engines and databases for article assemblage to influence the amount of investigated research. The results of the investigation show that RF has higher generality on all chosen datasets. Additionally, the effectiveness of DT and ANN models on the chosen datasets suggests that they are potentially suitable candidates to resolve challenges involving predicting student performance.

9.1 Future Scope

The reader can trace concepts of the various things after predicting scores, e.g., Designing a system for tracking student behaviour and shopping patterns to study what kind of person he/she is and the reason for the decrease in performance. Finally, a Student recommender system may be designed for the student, which gives them accurate and functional tips for their personal life and recommends new studying patterns and techniques to actually up their grade. If properly designed and implemented in educational institutions, this would be a huge breakthrough. An automatic system that describes the students' issues and problems based on an AI would be remarkable. This technically proves the worthiness of our article and SLR.

The future scope includes the consideration of factors like the confidence of the student while performing a practical exam, nervousness during a viva voce or an interview, the stage fright of a student while presenting slides, personal and family problems at home for the SP analysis. These parameters would produce more results and improve this study and, more importantly, what factors this study implies. Some political and social records of

understudies with more cases can be considered. New features can be included in the dataset that may affect the POS.

More attention should be paid by researchers to the interpretability of the prediction process and results. In order to improve the interpretability of the prediction process and results and help instructors and students more, it is imperative to make full use of modern teaching and learning theories and ML interpretability theories and approaches. Additionally, it is important to continually raise the standard of educational data used to develop models to predict student performance. The performance of predictive models developed in different studies cannot be evaluated and compared, and these models cannot be transferred between other sites and systems due to the limited size and inconsistent educational data used by researchers in previous studies. In order to predict student performance, it is necessary to create a unified and optimized data set, expand the number of data sources, and improve the portability and evaluability of the prediction model. The world's most active online data mining and machine learning community is Kaggle. Through competitions, many academics and technology experts regularly improve the technology and effectiveness of ML tasks of various types and purposes. By conducting competitions like those run by the Kaggle community, researchers could further improve data mining techniques for predicting student success.

Authors Contributions All authors have equal contributions in this work.

Funding No funding is provided for the preparation of the manuscript.

Data Availability Data sharing not applicable to this article.

Declarations

Conflict of interest Authors declare that they have no conflict of interest.

Ethical Approval This article does not contain any studies with human participants or animals performed by any authors.

Consent to Participate All the authors involved have agreed to participate in this submitted article.

Consent to Publish All the authors involved in this manuscript give full consent for publication of this submitted article.

References

1. Yağcı, M. (2022). Educational data mining: Prediction of students' academic performance using machine learning algorithms. *Smart Learning Environments, 9*(1), 11.
2. Peña-Ayala, A. (2014). Educational data mining: A survey and a data mining-based analysis of recent works. *Expert systems with applications, 41*(4), 1432–1462.
3. Abidin, B., & Dom, R. M. (2012). Prediction of preclinical academic performance using ANFIS model. *Int Proc Econ Dev Res, 41*, 105–109.
4. Kabakchieva, D. (2012). Student performance prediction by using data mining classification algorithms. *International Journal of Computer Science and Management Research, 1*(4), 686–690.
5. Pallathadka, H., Wenda, A., Ramirez-Asís, E., Asís-López, M., Flores-Albornoz, J., & Phasinam, K. (2023). Classification and prediction of student performance data using various machine learning algorithms. *Materials today: Proceedings, 80*, 3782–3785.

6. Hicham, A., Jeghal, A., Sabri, A., & Tairi, H. (2020). A survey on educational data mining [2014–2019]. In *2020 international conference on intelligent systems and computer vision (ISCV) IEEE*. pp 1–6.
7. Manne, R., & Kantheti, S. C. (2021). Application of artificial intelligence in healthcare: Chances and challenges. *Current Journal of Applied Science and Technology, 40*(6), 78–89.
8. Katarya, R. (2019). A review: Predicting the performance of students using machine learning classification techniques. In *2019 Third International conference on I-SMAC (IoT in Social, Mobile, Analytics and Cloud) (I-SMAC), IEEE*, 36–41.
9. Kotsiantis, S., Pierrakeas, C., & Pintelas, P. (2004). Predicting students' performance in distance learning using machine learning techniques. *Applied Artificial Intelligence, 18*(5), 411–426.
10. Verma, U., Garg, C., Bhushan, M., Samant, P., Kumar, A., & Negi, A. (2022). Prediction of students' academic performance using Machine Learning Techniques. In *2022 International Mobile and Embedded Technology Conference (MECON) IEEE*. pp 151–156.
11. Navamani, J. M. A., & Kannammal, A. (2015). Predicting performance of schools by applying data mining techniques on public examination results. *Research Journal of Applied Sciences, Engineering and Technology, 9*(4), 262–271.
12. Feng, G., Fan, M., & Chen, Y. (2022). Analysis and prediction of students' academic performance based on educational data mining. *IEEE Access, 10*, 19558–19571.
13. Singh, A., Thakur, N., & Sharma, A. (2016). A review of supervised machine learning algorithms. In *2016 3rd International Conference on Computing for Sustainable Global Development (INDIACom), IEEE*, 1310–1315.
14. Rastrollo-Guerrero, J. L., Gomez-Pulido, J. A., & Duran-Dominguez, A. (2020). Analyzing and predicting students' performance by means of machine learning: A review. *Applied sciences, 10*(3), 1042.
15. Nandeshwar, A., Menzies, T., & Nelson, A. (2011). Learning patterns of university student retention. *Expert Systems with Applications, 38*(12), 14984–14996.
16. Thammasiri, D., Delen, D., Meesad, P., & Kasap, N. (2014). A critical assessment of imbalanced class distribution problem: The case of predicting freshmen student attrition. *Expert Systems with Applications, 41*(2), 321–330.
17. Hosmer, D. W., Lemeshow, S., & Sturdivant, R. X. (2013). *Applied logistic regression*. John Wiley & Sons.
18. Dewan, M.A.A., Lin, F., & Wen, D. (2015). Predicting dropout-prone students in e-learning education system. In *2015 IEEE 12th Intl Conf on Ubiquitous Intelligence and Computing and 2015 IEEE 12th Intl Conf on Autonomic and Trusted Computing and 2015 IEEE 15th Intl Conf on Scalable Computing and Communications and Its Associated Workshops (UIC-ATC-ScalCom)* 1735–1740.
19. Tan, M., & Shao, P. (2015). Prediction of student drop-out in e-Learning program through the use of machine learning method. *International Journal of Emerging Technologies in Learning*. https://doi.org/10.3991/ijet.v10i1.4189
20. Fonteyne, L., Duyck, W., & De Fruyt, F. (2017). Program-specific prediction of academic achievement on the basis of cognitive and non-cognitive factors. *Learning and Individual Differences, 56*, 34–48.
21. Chen, Y., Johri, A., & Rangwala, H. (2018). Running out of stem: A comparative study across stem majors of college students at-risk of dropping out early. In *Proceedings of the 8th international conference on learning analytics and knowledge*. pp 270–279.
22. Nagy, M., & Molontay, R. (2018). Predicting drop-out in higher education based on secondary school performance. In *2018 IEEE 22nd international conference on intelligent engineering systems (INES)* 000389–000394.
23. Serra, A., Perchinunno, P., & Bilancia, M. (2018). Predicting student drop-outs in higher education using supervised classification algorithms. In *International Conference on Computational Science and Its Applications, Springer, Cham*, 18–33.
24. Gray, C. C., & Perkins, D. (2019). Utilizing early engagement and machine learning to predict student outcomes. *Computers & Education, 131*, 22–32.
25. Chung, J. Y., & Lee, S. (2019). Drop-out early warning systems for high school students using machine learning. *Children and Youth Services Review, 96*, 346–353.
26. Hussain, M., Zhu, W., Zhang, W., Abidi, S. M. R., & Ali, S. (2019). Using machine learning to predict student difficulties from learning session data. *Artificial Intelligence Review, 52*(1), 381–407.
27. Huang, S., & Fang, N. (2013). Predicting student academic performance in an engineering dynamics course: A comparison of four types of predictive mathematical models. *Computers & Education, 61*, 133–145.

28. Slim, A., Heileman, G. L., Kozlick, J., & Abdallah, C. T. (2014). Predicting student success based on prior performance. In *2014 IEEE symposium on computational intelligence and data mining (CIDM)*. pp 410–415.
29. Zhao, C., Yang, J., Liang, J., & Li, C. (2016). Discover learning behavior patterns to predict certification. In *2016 11th International Conference on Computer Science & Education (ICCSE), IEEE*, pp 69–73.
30. Chaudhury, P., Mishra, S., Tripathy, H. K., & Kishore, B. (2016). Enhancing the capabilities of student result prediction system. In *Proceedings of the Second International Conference on Information and Communication Technology for Competitive Strategies*. pp 1–6.
31. Nespereira, C. G., Elhariri, E., El-Bendary, N., Vilas, A. F., & Redondo, R. P. D. (2016). Machine learning based classification approach for predicting students performance in blended learning. In *The 1st International Conference on Advanced Intelligent System and Informatics (AISI2015), November 28–30, 2015, Beni Suef, Egypt Springer, Cham*, pp 47–56.
32. Sagar, M., Gupta, A., & Kaushal, R. (2016). Performance prediction and behavioral analysis of student programming ability. In *2016 International Conference on Advances in Computing, Communications and Informatics (ICACCI) IEEE*, pp 1039–1045.
33. Ghorbani, R., & Ghousi, R. (2020). Comparing different resampling methods in predicting Students' performance using machine learning techniques. *IEEE Access, 8*, 67899–67911.
34. Backenköhler, M., & Wolf, V. (2017). Student performance prediction and optimal course selection: An MDP approach. In *International conference on software engineering and formal methods Springer, Cham*, pp 40–47.
35. Hsieh, Y. Z., Su, M. C., & Jeng, Y. L. (2017). The Jacobian matrix-based learning machine in student. In *International Symposium on Emerging Technologies for Education, Springer, Cham*, pp 469–474.
36. Han, M., Tong, M., Chen, M., Liu, J., Liu, C. (2017). Application of ensemble algorithm in students' performance prediction. In *2017 6th IIAI International Congress on Advanced Applied Informatics (IIAI-AAI), IEEE*, pp 735–740.
37. Shanthini, A., Vinodhini, G., & Chandrasekaran, R. M. (2018). Predicting students' academic performance in the university using meta decision tree classifiers. *Journal of Computer Science, 14*(5), 654–662.
38. Howard, E., Meehan, M., & Parnell, A. (2018). Contrasting prediction methods for early warning systems at undergraduate level. *The Internet and Higher Education, 37*, 66–75.
39. Villagrá-Arnedo, C. J., Gallego-Durán, F. J., Compañ, P., Largo, F.L., & Molina-Carmona, R. (2016). Predicting academic performance from behavioural and learning data.
40. Sorour, S. E., Goda, K., & Mine, T. (2015). Estimation of student performance by considering consecutive lessons. *In 2015 IIAI 4th International Congress on Advanced Applied Informatics, IEEE*, pp 121–126.
41. Alloghani, M., Al-Jumeily, D., Mustafina, J., Hussain, A., & Aljaaf, A. J. (2020). A systematic review on supervised and unsupervised machine learning algorithms for data science. *Supervised and Unsupervised Learning for Data Science*. https://doi.org/10.1007/978-3-030-22475-2_1
42. Guo, B., Zhang, R., Xu, G., Shi, C., & Yang, L. (2015). Predicting students performance in educational data mining. In *2015 International Symposium on Educational Technology (ISET), IEEE*, pp 125–128.
43. Rana, S., & Garg, R. (2017). Prediction of students performance of an institute using Classification via Clustering and Classification via Regression. In *Proceedings of International Conference on Communication and Networks Springer, Singapore*. Pp 333–343.
44. Anand, V. K., Rahiman, S.A., George, E.B., & Huda, A. S. (2018). Recursive clustering technique for students' performance evaluation in programming courses. *In 2018 Majan International Conference (MIC), IEEE*. pp 1–5.
45. Bobadilla, J., Ortega, F., Hernando, A., & Gutiérrez, A. (2013). Recommender systems survey. *Knowledge-Based Systems, 46*, 109–132.
46. Bydžovská, H. (2015). Student performance prediction using collaborative filtering methods. In *International Conference on Artificial Intelligence in Education, Springer, Cham*. pp 550–553.
47. Park, Y. (2018). Predicting personalized student performance in computing-related majors via collaborative filtering. In *Proceedings of the 19th Annual SIG Conference on Information Technology Education*. pp 151–151.
48. Elbadrawy, A., & Karypis, G. (2016). Domain-aware grade prediction and top-n course recommendation. In *Proceedings of the 10th ACM Conference on Recommender Systems*. pp 183–190.
49. Pero, Š., & Horváth, T. (2015). Comparison of collaborative-filtering techniques for small-scale student performance prediction task. In *Innovations and Advances in Computing, Informatics, Systems Sciences, Networking and Engineering Springer, Cham*. pp 111–116.

50. Song, Y., Jin, Y., Zheng, X., Han, H., Zhong, Y., & Zhao, X. (2015). PSFK: A student performance prediction scheme for first-encounter knowledge in ITS. In *International Conference on Knowledge Science, Engineering and Management Springer, Cham*. pp 639–650.
51. Xu, K., Liu, R., Sun, Y., Zou, K., Huang, Y., & Zhang, X. (2017). Improve the prediction of student performance with hint's assistance based on an efficient non-negative factorization. *IEICE Transactions on Information and Systems, 100*(4), 768–775.
52. Sheehan, M., & Park, Y. (2012). pGPA: A personalized grade prediction tool to aid student success. In *Proceedings of the sixth ACM conference on Recommender systems* 309–310.
53. Lorenzen, S., Pham, N., & Alstrup, S. (2017). On predicting student performance using low-rank matrix factorization techniques. In *European Conference on e-Learning, Academic Conferences International Limited*. pp 326–334.
54. Houbraken, M., Sun, C., Smirnov, E., & Driessens, K. (2017). Discovering hidden course requirements and student competences from grade data. In *Adjunct Publication of the 25th Conference on User Modeling, Adaptation and Personalization*. pp 147–152.
55. Gómez-Pulido, J.A., Cortés-Toro, E., Durán-Domínguez, A., Crawford, B., & Soto, R. (2018). Novel and classic metaheuristics for tunning a recommender system for predicting student performance in online campus. In *International Conference on Intelligent Data Engineering and Automated Learning, Springer, Cham*. pp 125–133.
56. Chavarriaga, O., Florian-Gaviria, B., & Solarte, O. (2014). A recommender system for students based on social knowledge and assessment data of competences. In *European Conference on Technology Enhanced Learning, Springer, Cham*. pp 56–69.
57. Jembere, E., Rawatlal, R., & Pillay, A. W. (2017). Matrix factorization for predicting student performance. In *2017 7th World Engineering Education Forum (WEEF), IEEE*. pp 513–518.
58. Sweeney, M., Lester, J., & Rangwala, H. (2015). Next-term student grade prediction. In *2015 IEEE International Conference on Big Data (Big Data)*. pp 970–975.
59. Adán-Coello, J.M., & Tobar, C.M. (2016). Using collaborative filtering algorithms for predicting student performance. In *International Conference on Electronic Government and the Information Systems Perspective Springer, Cham*. pp 206–218.
60. Adewale, A. M., Bamidele, A. O., & Lateef, U. O. (2018). Predictive modelling and analysis of academic performance of secondary school students: Artificial Neural Network approach. *International Journal of Science and Technology Education Research, 9*(1), 1–8.
61. Gedeon, T.D., & Turner, H.S. (1993). Explaining student grades predicted by a neural network. In *Proceedings of 1993 International Conference on Neural Networks (IJCNN-93-Nagoya, Japan), IEEE*, *1*, pp 609–612.
62. Arsad, P. M., & Buniyamin, N. (2013). A neural network students' performance prediction model (NNSPPM). In *2013 IEEE International Conference on Smart Instrumentation, Measurement and Applications (ICSIMA)*. pp 1–5.
63. Iyanda, A. R., Ninan, O. D., Ajayi, A. O., & Anyabolu, O. G. (2018). Predicting student academic performance in computer science courses: A comparison of neural network models. *International Journal of Modern Education & Computer Science, 10*(6), 1–9.
64. Dharmasaroja, P., & Kingkaew, N. (2016). Application of artificial neural networks for prediction of learning performances. In *2016 12th International Conference on Natural Computation, Fuzzy Systems and Knowledge Discovery (ICNC-FSKD) IEEE*. pp 745–751.
65. Musso, M. F., Kyndt, E., Cascallar, E. C., & Dochy, F. (2013). Predicting general academic performance and identifying the differential contribution of participating variables using artificial neural networks. *Frontline Learning Research, 1*(1), 42–71.
66. Rochman, E. M. S., Rachmad, A., & Damayanti, F. (2018). Predicting the final result of student national test with extreme learning machine. *Pancaran Pendidikan, 7*(2), 5–10.
67. Dimililer, K., Ever, Y. K., & Ergun, F. (2017). A preliminary framework using bpnn for performability modelling and analyses of a kerberos server. In *2017 International Conference on Advances in Computing, Communications and Informatics (ICACCI), IEEE*. pp 698–700.
68. Mayilvaganan, M., & Kalpanadevi, D. (2014). Comparison of classification techniques for predicting the performance of students academic environment. In *2014 International Conference on Communication and Network Technologies IEEE*. pp 113–118.
69. Shahiri, A. M., & Husain, W. (2015). A review on predicting student's performance using data mining techniques. *Procedia Computer Science, 72*, 414–422.
70. Tomasevic, N., Gvozdenovic, N., & Vranes, S. (2020). An overview and comparison of supervised data mining techniques for student exam performance prediction. *Computers & Education, 143*, 103676.

71. Jishan, S. T., Rashu, R. I., Haque, N., & Rahman, R. M. (2015). Improving accuracy of students' final grade prediction model using optimal equal width binning and synthetic minority over-sampling technique. *Decision Analytics, 2*(1), 1–25.
72. Alsalman, Y. S., Halemah, N. K. A., AlNagi, E. S., & Salameh, W. (2019). Using decision tree and artificial neural network to predict students academic performance. In *2019 10th International Conference on Information and Communication Systems (ICICS) IEEE*. pp 104–109.
73. Hamsa, H., Indiradevi, S., & Kizhakkethottam, J. J. (2016). Student academic performance prediction model using decision tree and fuzzy genetic algorithm. *Procedia Technology, 25*, 326–332.
74. Chamillard, A. T. (2006). Using student performance predictions in a computer science curriculum. *ACM SIGCSE Bulletin, 38*(3), 260–264.
75. Rusli, N. M., Ibrahim, Z., & Janor, R. M. (2008). Predicting students' academic achievement: Comparison between logistic regression, artificial neural network, and Neuro-fuzzy. In 2008 International Symposium on Information Technology IEEE, 1: 1–6.
76. Sikder, M. F., Uddin, M. J., & Halder, S. (2016). Predicting students yearly performance using neural network: A case study of BSMRSTU. In *2016 5th International Conference on Informatics, Electronics and Vision (ICIEV) IEEE*. pp 524–52.
77. Pathak, P., Bansal, N., & Singh, S. (2015). Mulyankan: A prediction for student's performance using Neural Network. In *2015 2nd International Conference on Computing for Sustainable Global Development (INDIACom), IEEE*, pp 46–49.
78. Do, Q. H., & Chen, J. F. (2013). A comparative study of hierarchical ANFIS and ANN in predicting student academic performance. *WSEAS Transactions on Information Science and Applications, 10*(12), 396–405.
79. Okubo, F., Yamashita, T., Shimada, A., & Ogata, H. (2017). A neural network approach for students' performance prediction. In *Proceedings of the seventh international learning analytics & knowledge conference*. pp 598–599.
80. Altaf, S., Soomro, W., & Rawi, M. I. M. (2019). Student performance prediction using multilayers artificial neural networks: A case study on educational data mining. In *Proceedings of the 2019 3rd International Conference on Information System and Data Mining*. pp 59–64.
81. Arora, N., & Saini, J. R. (2013). A fuzzy probabilistic neural network for student's academic performance prediction. *International Journal of Innovative Research in Science, Engineering and Technology, 2*(9), 4425–4432.
82. Moseley, L. G., & Mead, D. M. (2008). Predicting who will drop out of nursing courses: A machine learning exercise. *Nurse education today, 28*(4), 469–475.
83. Liu, D., Richards, D., Froissard, C., & Atif, A. (2015). Validating the effectiveness of the moodle engagement analytics plugin to predict student academic performance. In *21st Americas Conference on Information Systems, AMCIS 2015, Americas Conference on Information Systems*. pp 1–10.
84. Saqr, M., Fors, U., & Tedre, M. (2017). How learning analytics can early predict under-achieving students in a blended medical education course. *Medical teacher, 39*(7), 757–767.
85. Villegas-Ch, W., Lujan-Mora, S., Buenaño-Fernandez, D., & Roman-Canizares, M. (2017). Analysis of web-based learning systems by data mining. In *2017 IEEE Second Ecuador Technical Chapters Meeting (ETCM)*. pp 1–5.
86. Costa, E. B., Fonseca, B., Santana, M. A., de Araújo, F. F., & Rego, J. (2017). Evaluating the effectiveness of educational data mining techniques for early prediction of students' academic failure in introductory programming courses. *Computers in Human Behavior, 73*, 247–256.
87. Masci, C., Johnes, G., & Agasisti, T. (2018). Student and school performance across countries: A machine learning approach. *European Journal of Operational Research, 269*(3), 1072–1085.
88. Johnson, W. G. (2018). Data mining and machine learning in education with focus in undergraduate cs student success. In *Proceedings of the 2018 ACM Conference on International Computing Education Research*. pp 270–271.
89. Bydžovská, H. (2015). Are collaborative filtering methods suitable for student performance prediction?. In *Portuguese Conference on Artificial Intelligence, Springer, Cham*. pp 425–430.
90. Sultana, S., Khan, S., & Abbas, M. A. (2017). Predicting performance of electrical engineering students using cognitive and non-cognitive features for identification of potential drop-outs. *International Journal of Electrical Engineering Education, 54*(2), 105–118.
91. Liou, C. H. (2016). Personalized article recommendation based on student's rating mechanism in an online discussion forum. In *2016 49th Hawaii International Conference on System Sciences (HICSS), IEEE*. pp 60–65.
92. Guleria, P., Thakur, N., & Sood, M. (2014). Predicting student performance using decision tree classifiers and information gain. In *2014 International conference on parallel, distributed and grid computing, IEEE*. pp 126–129.

93. Burman, I., & Som, S. (2019). Predicting students academic performance using support vector machine. In *2019 Amity International Conference on Artificial Intelligence (AICAI), IEEE*. pp 756–759.
94. Mohammadi, M., Dawodi, M., Tomohisa, W., & Ahmadi, N. (2019). Comparative study of supervised learning algorithms for student performance prediction. In *2019 International Conference on Artificial Intelligence in Information and Communication (ICAIIC), IEEE*. pp 124–127.
95. Ketui, N., Wisomka, W., & Homjun, K. (2019). Using classification data mining techniques for students performance prediction. In *2019 Joint International Conference on Digital Arts, Media and Technology with ECTI Northern Section Conference on Electrical, Electronics, Computer and Telecommunications Engineering (ECTI DAMT-NCON) IEEE*. pp 359–363.
96. Jamil, A., Ahsan, M., Farooq, T., Hussain, A., & Ashraf, R. (2018). Student performance prediction using algorithms of data mining. In *2018 International Conference on Computing, Engineering, and Design (ICCED), IEEE*. pp 244–249.
97. Rustia, R. A., Cruz, M. M. A., Burac, M. A. P., & Palaoag, T. D. (2018). Predicting student's board examination performance using classification algorithms. In *Proceedings of the 2018 7th International Conference on Software and Computer Applications*. pp 233–237.
98. Hasan, R., Palaniappan, S., Raziff, A. R. A., Mahmood, S., & Sarker, K.U. (2018). Student academic performance prediction by using decision tree algorithm. *In 2018 4th international conference on computer and information sciences (ICCOINS) IEEE*. pp 1–5.
99. Tanuar, E., Heryadi, Y., Abbas, B. S., & Gaol, F. L. (2018). Using machine learning techniques to earlier predict student's performance. In *2018 Indonesian Association for Pattern Recognition International Conference (INAPR), IEEE*. pp 85–89.
100. Bharara, S., Sabitha, S., & Bansal, A. (2018). Application of learning analytics using clustering data Mining for Students' disposition analysis. *Education and Information Technologies, 23*(2), 957–984.
101. Kaur, P., Singh, M., & Josan, G. S. (2015). Classification and prediction based data mining algorithms to predict slow learners in education sector. *Procedia Computer Science, 57*, 500–508.
102. Shaleena, K. P., & Paul, S. (2015). Data mining techniques for predicting student performance. In *2015 IEEE international conference on engineering and technology (ICETECH)*. pp 1–3.
103. Márquez-Vera, C., Morales, C. R., & Soto, S. V. (2013). Predicting school failure and drop-out by using data mining techniques. *IEEE Revista Iberoamericana de Tecnologias del Aprendizaje, 8*(1), 7–14.
104. Thai-Nghe, N., Busche, A., & Schmidt-Thieme, L. (2009). Improving academic performance prediction by dealing with class imbalance. In *2009 Ninth international conference on intelligent systems design and applications, IEEE*. pp 878–883.
105. Şen, B., Uçar, E., & Delen, D. (2012). Predicting and analyzing secondary education placement-test scores: A data mining approach. *Expert Systems with Applications, 39*(10), 9468–9476.
106. Ahmed, A. M., Rizaner, A., & Ulusoy, A. H. (2016). Using data mining to predict instructor performance. *Procedia Computer Science, 102*, 137–142.
107. Widyahastuti, F., & Tjhin, V.U. (2017). Predicting students performance in final examination using linear regression and multilayer perceptron. In *2017 10th International Conference on Human System Interactions (HSI), IEEE*. pp 188–192.
108. Sivasakthi, M. (2017). Classification and prediction based data mining algorithms to predict students' introductory programming performance. In *2017 International Conference on Inventive Computing and Informatics (ICICI), IEEE*. pp 346–350.
109. Sekeroglu, B., Dimililer, K., & Tuncal, K. (2019). Student performance prediction and classification using machine learning algorithms. In *Proceedings of the 2019 8th International Conference on Educational and Information Technology*. pp 7–11.
110. Kaunang, F.J., & Rotikan, R. (2018). Students' academic performance prediction using data mining. In *2018 Third International Conference on Informatics and Computing (ICIC) IEEE*, pp 1–5.
111. Poudyal, S., Mohammadi-Aragh, M. J., & Ball, J. E. (2022). Prediction of student academic performance using a hybrid 2D CNN model. *Electronics, 11*(7), 1005.
112. Saa, A. A., Al-Emran, M., & Shaalan, K. (2019). Factors affecting students' performance in higher education: A systematic review of predictive data mining techniques. *Technology, Knowledge and Learning, 24*(4), 567–598.
113. Agarwal, K., Maheshwari, E., Roy, C., Pandey, M., & Rautray, S.S. (2019). Analyzing student performance in engineering placement using data mining. In *Proceedings of International Conference on Computational Intelligence and Data Engineering, Springer, Singapore*. pp 171–181.
114. Hussain, S., Atallah, R., Kamsin, A., & Hazarika, J. (2018). Classification, clustering and association rule mining in educational datasets using data mining tools: A case study. *In Computer Science Online Conference, Springer, Cham*. pp 196–211.

115. Dimililer, K. (2018). Use of Intelligent Student Mood Classification System (ISMCS) to achieve high quality in education. *Quality & quantity, 52*(1), 651–662.
116. Chen, J. F., & Do, Q. H. (2014). A cooperative cuckoo search–hierarchical adaptive neuro-fuzzy inference system approach for predicting student academic performance. *Journal of Intelligent & Fuzzy Systems, 27*(5), 2551–2561.

Publisher's Note Springer Nature remains neutral with regard to jurisdictional claims in published maps and institutional affiliations.

Springer Nature or its licensor (e.g. a society or other partner) holds exclusive rights to this article under a publishing agreement with the author(s) or other rightsholder(s); author self-archiving of the accepted manuscript version of this article is solely governed by the terms of such publishing agreement and applicable law.



Rahul currently designated as a Ph.D. scholar in the Department of Computer Science and Engineering, Delhi Technological University (DTU), Delhi, India. He is also working as Assistant Professor in the Department of Software Engineering, Delhi Technological University (DTU), Delhi, India. He has completed his Master of Technology in Information Security from the Department of Computer Science and Engineering, Ambedkar Institute of Technology (Now NSUT East Campus). He has completed his Bachelor of Technology in Computer Science and Engineering from GGSIPU, Delhi. He has published more than 40 research papers in International Conferences and Journals. He has more than 8 years of experience in teaching and research. His research area of interest includes Artificial Intelligence, Machine learning, Deep Learning and Social Networking.



Rahul Katarya is working in the Department of Computer Science & Engineering, Delhi Technological University (DTU) (formerly Delhi College of Engineering), New Delhi, India. He was selected World's top 2% Scientist in 2020, 2021, 2022 and 2023 by Stanford University, USA. His h-index as per google scholar is 25. He is also Associate Editor for various SCI/SCIE Journals. He also delivered many Expert Talks at National and International level. He has more than 13 years of experience in teaching and research. He is the Officer-in-charge of "Big Data Analytics and Web Intelligence" (BDAWI) research Laboratory. His research interests are Data Science, Deep Learning, Big Data analytics, Web Mining, IoT, Social Networks Analysis, Recommender Systems, Machine learning, Software Engineering, Multimedia Systems, Internet Technologies, Data Mining, Software Quality and Testing, Human Behavior, Evolutionary Computing, Artificial Intelligence, NLP, Computational Intelligence, Healthcare, Climate Change, Disaster Management, Blockchain Technology.

A Visually Attentive Splice Localization Network with Multi-Domain Feature Extractor and Multi-Receptive Field Upsampler

Ankit Yadav, Dinesh Kumar Vishwakarma *Senior Member, IEEE*

***Abstract*—Image splice manipulation presents a severe challenge in today's society. With easy access to image manipulation tools, it is easier than ever to modify images that can mislead individuals, organizations or society. In this work, a novel, "Visually Attentive Splice Localization Network with Multi-Domain Feature Extractor and Multi-Receptive Field Upsampler" has been proposed. It contains a unique "visually attentive multi-domain feature extractor" (VA-MDFE) that extracts attentional features from the RGB, edge and depth domains. Next, a "visually attentive downsampler" (VA-DS) is responsible for fusing and downsampling the multi-domain features. Finally, a novel "visually attentive multi-receptive field upsampler" (VA-MRFU) module employs multiple receptive field-based convolutions to upsample attentional features by focussing on different information scales. Experimental results conducted on the public benchmark dataset CASIA v2.0 prove the potency of the proposed model. It comfortably beats the existing state-of-the-arts by achieving an IoU score of 0.851, pixel F1 score of 0.9195 and pixel AUC score of 0.8989.**

***Index Terms*—Splice Localization; Image Tampering; Image Manipulation; Multi-Domain; Receptive Field;**

I. INTRODUCTION

IN an age where the alteration of digital content has become effortlessly easy, the authenticity and integrity of visual information have faced substantial hurdles. Image splicing is a very deceitful method of modification that is prevalent in the digital world. Image splicing is the covert practice of merging different visual components from diverse origins to produce an artificial image, typically tricking or misleading onlookers. The ubiquity of image editing tools and the ease of access to digital media have amplified the risks associated with image splicing, exacerbating the propagation of misleading information across various domains, including journalism, forensic analysis, and social media. Consequently, the urgent need for robust and efficient methods to detect these manipulations has become increasingly apparent.

(Corresponding author: Ankit Yadav). Ankit Yadav and Dinesh Kumar Vishwakarma are with the Department of Information Technology, Delhi Technological University, Bawana Road, Delhi-110042, India. (email: ankit4607@gmail.com; dvishwakarma@dtu.ac.in;).

Traditional handcrafted feature-based methods have proven ineffective especially for accurate localization of forgery regions within an image. However, the growth of deep-learning models and the rise of visual attention mechanisms have solved this problem to a great extent.

Several research works are dedicated for this purpose. Zhang et al. [1] propose a novel multi-task squeeze and excitation network (SE-Network) developed explicitly for splicing localization in images. The network incorporates two streams, namely label mask and edge-guided, inside a convolutional encoder-decoder architecture. The method effectively utilises picture edges, label masks, and mask edges to provide thorough supervision. It combines low-level and high-level feature maps and incorporates squeezing and excitation attention modules.

Sun et al. [2] introduce an Edge-enhanced Transformer (ET) for precise tampered region localization in images by effectively integrating splicing edge clues into a two-branch edge-aware transformer. It addresses the challenge of accurately detecting tampered regions without false alarms by enhancing forgery features with edge information and incorporating a feature enhancement module.

Huang et al. [3] develop DS-UNet, a new dual-stream UNet architecture particularly developed for the purpose of detecting picture manipulation and accurately identifying the exact locations of manipulated regions. The DS-UNet algorithm uses an RGB stream to roughly determine the location of tampered items and a Noise stream to accurately detect them. It combines both streams in a hierarchical manner to detect tampered objects of different sizes.

Deng et al. [4] propose MSD-Nets to solve the $QF_1 > QF_2$ case problem by using a *discriminative module* comprising of a CNN trained on $QF_1 > QF_2$ examples exclusively. Multi-scale features are first extracted from DCT histograms which are then fused in a weighted manner. Then, the discriminative module is utilized for the challenging scenario of $QF_1 > QF_2$. Localization results prove the high robustness of the proposed architecture.

The major contributions of this manuscript are:

- Proposed a novel splice localization network with

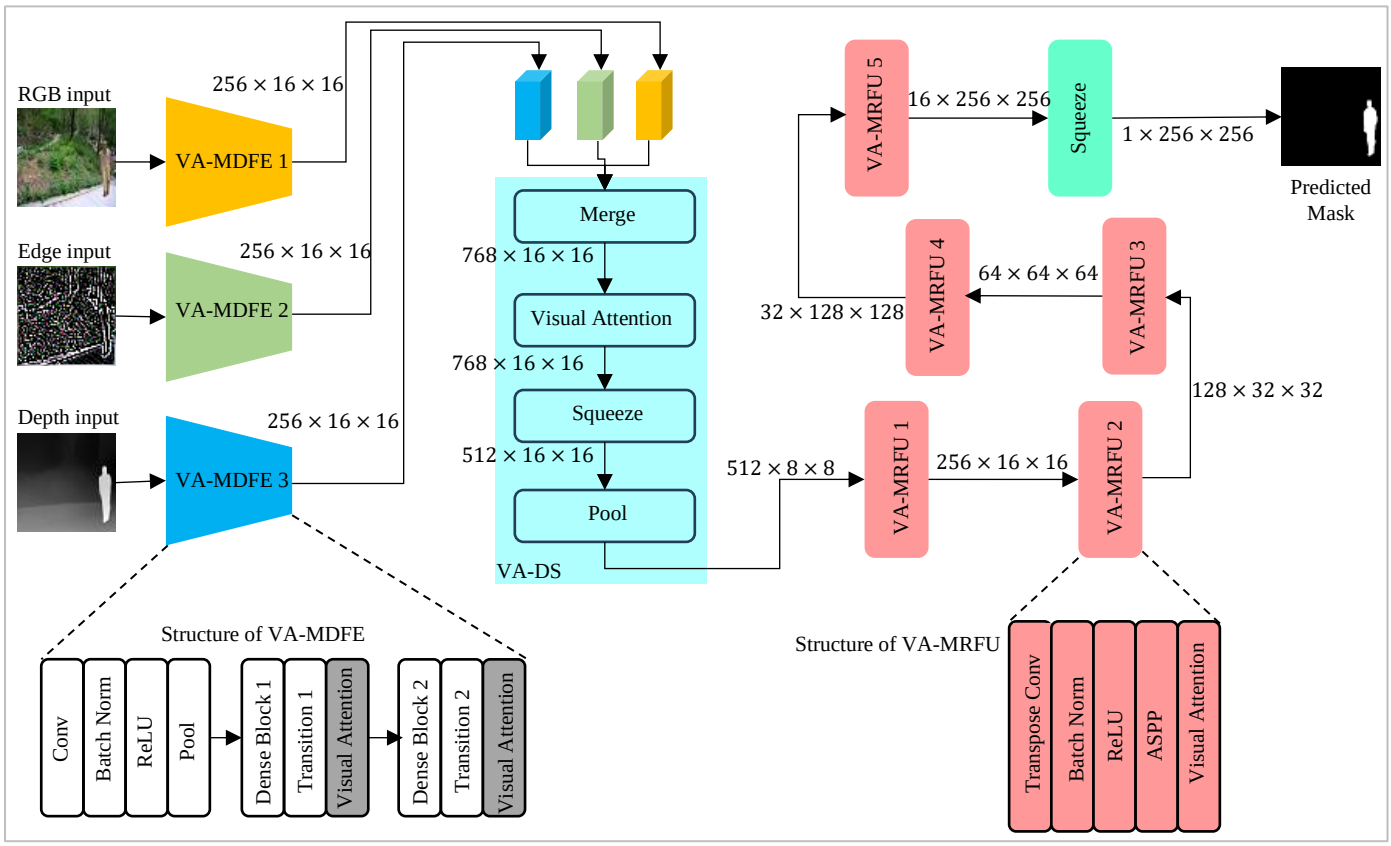


Fig. 1 The structure of the proposed splice localization model. VA-MDFE stands for "visually attentive multi-domain feature extractor". VA-DS stands for "visually attentive downsampler". VA-MRFU stands for "visually attentive multi-receptive field upsampler".

"visually attentive multi-domain feature extractor" (VA-MDFE) and "visually attentive multi-receptive field upsampler" (VA-MRFU).

- The VA-MDFE extracts multi-domain features from the RGB, edge and depth domain aided by the visual attention layer.
- The VA-MRFU is responsible for upsampling features by using multiple receptive field-based convolution operations. This is achieved by varying the dilation rate of convolutional kernels.
- Experimental results on the public benchmark dataset CASIA v2.0 prove that the proposed model outperforms several state-of-the-art methods by achieving an IoU score of 0.851, pixel F1 score of 0.9195 and pixel AUC score of 0.8989.

The rest of the paper is organized as follows. Section II presents the proposed splice localization model. Section III describes the experimental setup. Section IV presents the performance of the proposed model. Section V gives the conclusion, and Section VI includes the references cited in this research work.

II. Proposed Architecture

This section presents the architecture of the proposed model.

A. Visually Attentive Multi-Domain Feature Extractor (VA-MDFE)

This section describes the visually attentive multi-domain feature extractor of the proposed model. Specifically, a baseline model aided with visual attention extracts features from the input image's RGB, edge and depth domain.

The design proposed in [5] serves as the foundational architecture in this paper. The system promotes the reuse of features by allowing a layer to access feature maps from all preceding levels, hence enhancing the overall flow of information throughout the network., as shown in Eq. 1:

$$\mathfrak{y}_L = \emptyset_L([\mathfrak{y}_0, \mathfrak{y}_1, \mathfrak{y}_2, \mathfrak{y}_3 \dots \dots \mathfrak{y}_{L-1}]) \quad (1)$$

The baseline contains four dense blocks and three transition blocks. The last two dense blocks and transition blocks are discarded for computational efficiency.

Each of the two remaining dense blocks of this baseline is appended with a visual attention layer [6] that employs a three-branch design using a 'rotational' module to detect distinct elements in three different orientations. This approach ensures efficient computation with a minimal parameter count of just 300.Two branches handle the input of shape $\mathcal{X} \in \mathbb{R}^{H \times W \times C}$ and employ a distinct Z-pool mechanism to extract important channel characteristics along the height H and W dimensions. Meanwhile, the a traditional spatial attention is computed in the third branch.

Three instances of VA-MDFE is used to create a three-branch architecture for multi-domain feature extraction as shown in Fig. 1. The three input domains are RGB, edge and depth.

B. Visually Attentive Downsampler (VA-DS)

The proposed model contains a novel "visually attentive downsampler" (VA-DS). VA-DS is responsible for aggregating features from each domain. VA-DS has two stages namely 'merge' and 'downsample'. The following equation describes the operations of VA-DS:

$$f_{down} = \mathcal{P}(\mathcal{Sq}(\mathcal{VA}(\mathcal{M}(f_i)))) \quad (2)$$

Here f_i refers to the input features from each of the three domains. $\mathcal{M}(.)$ stands for the merge operation and it is achieved by concatenating features along the channel dimension. $\mathcal{VA}(.)$ refers to the visual attention layer applied after merging to highlight important regions within the features fused from multiple domains. $\mathcal{Sq}(.)$ means 'squeeze' operation, which reduces the number of channels via 1×1 convolution. $\mathcal{P}(.)$ is the pool operation to reduce the spatial resolution of features

C. Visually Attentive Multi-Receptive Field Upsampler (VA-MRFU)

The proposed model contains a novel "visually attentive multi-receptive field upsampler" (VA-MRFU). VA-MRFU is responsible for upsampling the multi-domain features extracted from VA-MDFE. The following equation can describe this module:

$$f_{up,i} = \mathcal{VA}(\mathcal{ASPP}(\mathcal{Re}(\mathcal{BN}(\mathcal{TC}(f_{multi}))) \quad (3)$$

Here $f_{up,i}$ are the upsampled features from one VA-MRFU module. f_{multi} represents the multi-domain features extracted from VA-MDFE. $\mathcal{TC}(.)$ stands for transpose convolution with kernel size and stride taken as 2. $\mathcal{BN}(.)$ and $\mathcal{Re}(.)$ represent batch normalization and ReLU activation, respectively.

The multi-receptive field mechanism has been implemented via the atrous spatial pyramid pooling module represented here as $\mathcal{ASPP}(.)$. Specifically, it is a three-branch architecture that performs convolution over the input with varying receptive fields. This is achieved by varying the 'dilation' parameter of the convolution operation to change the receptive fields without increasing the computational cost. Dilation rates of 2, 3 and 4 are used in this experiment in each VA-MRFU module.

Finally, $\mathcal{VA}(.)$ represents the attention layer similar to the ones used in the above modules.

III. Experimental Setup

This part outlines the specific experimental parameters employed in this study to assess the efficacy of the proposed approach.

A. Dataset

The CASIA v2.0 is a challenging image tampering dataset containing 7491 original and 5123 tampered images [7]. The manipulated images are created through various techniques like copy-move, splicing, and removal. The manipulated images aim to simulate real-world tampering scenarios, providing researchers with comprehensive data to develop and evaluate algorithms for detecting and analyzing image forgeries.

B. Preprocessing, Hyperparameters, Hardware & Loss Function

All images are resized to the resolution of 256×256. Each pixel value is normalized to the range of $[0,1]$.

All experiments are run for 20 epochs. Adam optimizer is used for weight updation. The learning rate is initialized to 0.0001 and is decayed linearly by 10% after every epoch.

Two 24GB NVIDIA RTX A5000 GPUs are run in parallel for this experiment.

The 'focal loss' from [8] has been used to train the proposed model. This loss is ideally suited for the background-foreground class imbalance problem in object detection scenarios.

C. Evaluation Metrics

The following metrics have been to measure the localization capabilities of the proposed model.

The *Intersection over Union* (IoU) quantifies the degree of overlap between the predicted and ground truth masks by calculating the ratio of the intersection area to the union area of these areas. Higher iou scores suggest superior alignment and accuracy in localization tasks, where a value of 1 signifies complete overlap.

Pixel-level accuracy measures the correctness of localised image modifications by determining the proportion of properly identified pixels out of the total number of pixels in a picture. Greater pixel-level accuracy ratings suggest more alignment and precision in localised alterations.

Pixel-level F1 score is a quantitative measure employed to assess the precision and memory of localised picture alterations at the individual pixel level. The F1 score quantifies the trade-off between correctly identified manipulated pixels (true positives) and the accuracy of the localised manipulation compared to the ground truth annotations. Higher F1 scores indicate better overall accuracy in capturing manipulated regions.

Pixel-level AUC, also known as Area Under the Curve, is a quantitative metric utilised to evaluate the effectiveness of detecting localised image modification at different thresholds. It assesses the balance between the rate of correctly identified manipulated areas and the rate of incorrectly identified manipulated regions at the individual pixel level. A greater pixel-level AUC signifies superior differentiation between manipulated and non-manipulated areas, demonstrating the efficacy of the detection system.

IV. Experimental Results

This section presents the experimental results obtained for the proposed model on the benchmark datasets.

A. Performance on Benchmark Dataset CASIA v2.0

Fig. 2 presents the performance on the CASIA v2.0 dataset in terms of the IoU, pixel accuracy, pixel F1 and pixel AUC scores. The proposed model achieves excellent scores, highlighting its strong localization capability.

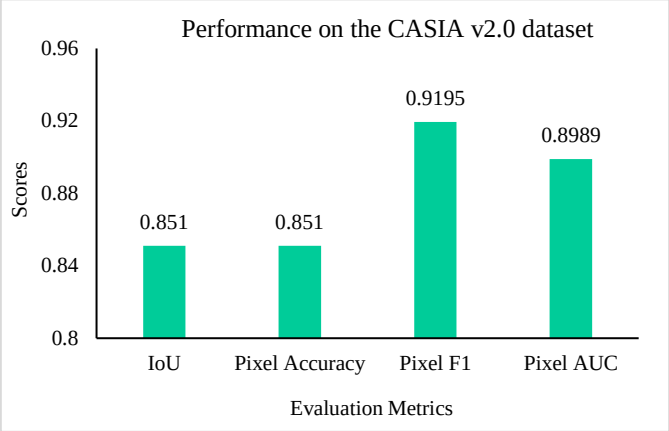


Fig. 2 Performance of the proposed model on CASIA v2.0 dataset. All metrics are pixel-level except IoU.

B. *Comparison Against the State-of-the-Arts*

Table I compares the proposed model against the existing state-of-art methods. The proposed model easily outperforms other methods, demonstrating its superiority.

Table I Comparison of the Proposed Model against existing state-of-the-art methods. The best scores are highlighted in bold.

Methods	IoU	Pixel F1	Pixel AUC
Zhang et al. [1]	0.7139	0.7653	-
Sun et al. [2]	0.5157	0.6805	-
Huang et al. [3]	-	0.6100	0.749
Nazir et al. [9]	-	0.8469	-
Yin et al. [10]	-	0.5840	0.8950
RRU-Net [11]	0.4752	0.5333	-
ManTra-Net [12]	0.1261	0.2009	-
Chen et al. [13]	0.4386	0.6097	-
Proposed Model	**0.8510**	**0.9195**	**0.8989**

C. *Qualitative Analysis*

This section presents a visual comparison of the forgery masks predicted by the proposed model.

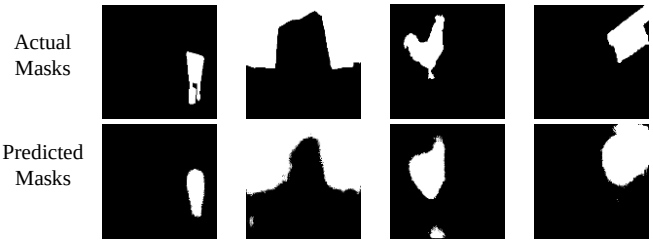


Fig. 3 A comparison of the actual and predicted masks from the proposed model.

D. *Ablation Study*

This section presents an ablation study of the proposed model. Specifically, each of the individual domains are evaluated separately. This means that the proposed model is compared against single domain feature extractors with RGB, edge and depth images as input.

Table II Comparison of single-domain vs the proposed multi-domain model.

Methods	IoU	Pixel	Pixel F1	Pixel AUC
		Accuracy		
RGB Only	0.5494	0.7245	0.6201	0.637
Edge Only	0.5164	0.614	0.652	0.5497
Depth Only	0.4633	0.6681	0.6332	0.5804
Proposed Model	**0.851**	**0.851**	**0.9195**	**0.8989**

Table II presents the performance of single-domain approaches against the proposed model. Specifically, each domain from the RGB, edge and depth is used as an individual feature extractor in the single domain models.

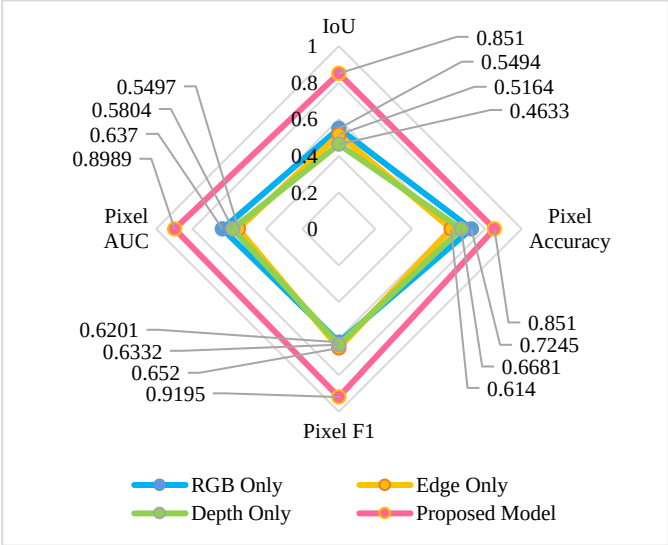


Fig. 4 A visual comparison of single domain (RGB, edge and depth) against the proposed multi-domain feature extractor. The proposed model (pink) achieves the highest IOU, pixel accuracy, pixel F1 and pixel AUC score.

Fig. 4 visually compares the ablation study conducted where single domain architectures are compared against the proposed model. The proposed model (pink) outperforms the individual domains of RGB (blue), edge (orange) and depth (green) across all metrics, namely IoU, pixel accuracy, pixel F1 and pixel AUC. This clearly states the benefit of having a multi-domain feature extractor.

V. Conclusion

In this manuscript, a novel image splice localization network is proposed. The proposed model contains a novel "visually attentive multi-domain feature extractor" that extracts attentional features from the RGB, edge and depth domain. A novel "visually attentive multi-receptive field upsampler" is responsible for the upsampling of features using multiple receptive field-based convolution operation. Experimental results on the CASIA v2.0 public benchmark dataset prove the potency of the proposed model as it easily beats the existing research approaches of splice localization.

VI. References

[1] Y. Zhang, G. Zhu, L. Wu, S. Kwong, H. Zhang and Y. Zhou, "Multi-Task SE-Network for Image Splicing Localization," *IEEE Transactions on Circuits and Systems for Video Technology* , vol. 32, no. 7, pp. 4828 - 4840, 2022.

[2] Y. Sun, R. Ni and Y. Zhao, "ET: Edge-Enhanced Transformer for Image Splicing Detection," *IEEE Signal Processing Letters*, vol. 29, pp. 1232 - 1236, 2022.

[3] Y. Huang, S. Bian, H. Li, C. Wang and K. Li, "DS-UNet: A dual streams UNet for refined image forgery localization," *Information Sciences*, vol. 610, pp. 73-89, 2022.

[4] C. Deng, Z. Li, X. Gao and D. Tao, "Deep Multi-scale Discriminative Networks for Double JPEG Compression Forensics," *ACM Transactions on Intelligent Systems and Technology*, vol. 10, no. 2, 2019.

[5] G. Huang, Z. Liu, L. V. D. Maaten and K. Q. Weinberger, "Densely Connected Convolutional Networks," in *IEEE Conference on Computer Vision and Pattern Recognition (CVPR)*, Honolulu, 2017.

[6] D. Misra, T. Nalamada, A. U. Arasanipalai and Q. Hou, "Rotate to Attend: Convolutional Triplet Attention Module," in *IEEE Winter Conference on Applications of Computer Vision (WACV)*, Waikoloa, HI, USA, 2021.

[7] J. Dong, W. Wang and T. Tan, "CASIA Image Tampering Detection Evaluation Database," in *IEEE China Summit and International Conference on Signal and Information Processing*, Beijing, 2013.

[8] T.-Y. Lin, P. Goyal, R. Girshick, K. He and P. Dollár, "Focal Loss for Dense Object Detection," *IEEE Transactions on Pattern Analysis and Machine Intelligence*, vol. 42, no. 2, pp. 318 - 327, 2020.

[9] T. Nazir, M. Nawaz, M. Masood and A. Javed, "Copy move forgery detection and segmentation using improved mask region-based convolution network (RCNN)," *Applied Soft Computing*, vol. 131, 2022.

[10] Q. Yin, J. Wang, W. Lu and X. Luo, "Contrastive Learning based Multi-task Network for Image Manipulation Detection," *Signal Processing*, vol. 201, 2022.

[11] X. Bi, Y. Wei, B. Xiao and W. Li, "RRU-Net: The Ringed Residual U-Net for Image Splicing Forgery Detection," in *IEEE/CVF Conference on Computer Vision and Pattern Recognition Workshops (CVPRW)*, Long Beach, 2019.

[12] Y. Wu, W. AbdAlmageed and P. Natarajan, "ManTra-Net: Manipulation Tracing Network for Detection and Localization of Image Forgeries With Anomalous Features," in *IEEE/CVF Conference on Computer Vision and Pattern Recognition (CVPR)*, Long Beach, 2019.

[13] X. Chen, C. Dong, J. Ji, J. Cao and X. Li, "Image Manipulation Detection by Multi-View Multi-Scale Supervision," in *IEEE/CVF International Conference on Computer Vision*, Montreal, 2021.

[14] B. Li, H. Zhang, H. Luo and S. Tan, "Detecting double JPEG compression and its related anti-forensic operations with CNN," *Multimedia Tools and Applications*, vol. 78, p. 8577–8601, 2019.

[15] I. Amerini, T. Uricchio, L. Ballan and R. Caldelli, "Localization of JPEG Double Compression Through Multi-domain Convolutional Neural Networks," in *IEEE Conference on Computer Vision and Pattern Recognition Workshops (CVPRW)*, Honolulu, 2017.

[16] Q. Wang and R. Zhang, "Double JPEG compression forensics based on a convolutional neural network," *EURASIP Journal on Information Security*, 2016.

frontiers | Frontiers in Bioengineering and Biotechnology

TYPE Original Research
PUBLISHED 07 February 2024
DOI 10.3389/fbioe.2024.1343540

Check for updates

OPEN ACCESS

EDITED BY
Carlos Peña Malacara,
National Autonomous University of Mexico, Mexico

REVIEWED BY
Pinaki Dey,
National Institute for Interdisciplinary Science and Technology (CSIR), India
Venkata Giridhar Poosarla,
Gandhi Institute of Technology and Management (GITAM), India

*CORRESPONDENCE
Rashmi Kataria,
rashmikataria@gmail.com,
rashmi.kataria@vit.ac.in

RECEIVED 23 November 2023
ACCEPTED 17 January 2024
PUBLISHED 07 February 2024

CITATION
Kag S, Kumar P and Kataria R (2024), Acid hydrolysis of *Solanum tuberosum* periderm for accumulation of polyhydroxyalkanoates in *Pseudomonas putida* MTCC 2475. *Front. Bioeng. Biotechnol.* 12:1343540. doi: 10.3389/fbioe.2024.1343540

COPYRIGHT
© 2024 Kag, Kumar and Kataria. This is an open-access article distributed under the terms of the Creative Commons Attribution License (CC BY). The use, distribution or reproduction in other forums is permitted, provided the original author(s) and the copyright owner(s) are credited and that the original publication in this journal is cited, in accordance with accepted academic practice. No use, distribution or reproduction is permitted which does not comply with these terms.

Acid hydrolysis of *Solanum tuberosum* periderm for accumulation of polyhydroxyalkanoates in *Pseudomonas putida* MTCC 2475

Sonika Kag[1], Pravir Kumar[1] and Rashmi Kataria[1,2]*

[1]Department of Biotechnology, Delhi Technological University (DTU), Delhi, India, [2]School of Bio Sciences and Technology, Vellore Institute of Technology (VIT), Vellore, Tamil Nadu, India

Polyhydroxyalkanoates are a class of biodegradable, biocompatible polymers composed of polyesters of R-hydroxyalkanoic acids and deposited intracellularly by a variety of microorganisms which have potential to serve as alternative to commercial plastic. Bioplastics are gaining attention due to sustainability, biodegradability, biocompatibility, and lower carbon footprint. Nevertheless, the commercialization of PHA is predominantly hindered by the elevated production expenses arising primarily from the use of a pure sugar substrate. Our study has established a feasible method for bioplastic formation applying *Pseudomonas putida* MTCC 2475 and *Solanum tuberosum* periderm as a carbon source. To optimize the sugar yield response surface methodology was used, which released 69.34% ± 0.25% reducing sugar. PHA production experiments were performed in hydrolysate containing media as well as commercial sugar containing mineral salt media. After 48 h of fermentation of using this sugar, a biomass concentration of 2.19 gL^{-1}, with a PHA production of 0.60 gL^{-1} (28.71% ± 0.55%) was obtained which was comparatively similar with synthetic media (2.56 gL^{-1} cell dry weight and 29.97% ± 0.45% PHA). Furthermore, the monomers of PHA produced by hydrolysate were characterized using Gas chromatography-mass spectrometry, Fourier transform infrared spectroscopy, differential scanning calorimetry, and nuclear magnetic resonance. This investigation has identified three distinct monomers of medium-chain PHAs, namely, methyl 3-Hydroxydodecanoate, 3-Hydroxytetradecanoate, and Hexadecanoic acid 3-Hydroxy methyl esters. Hence this study concludes a sustainable production of bioplastics from *S. tuberosum* periderm waste.

KEYWORDS

acid hydrolysis, fermentation, *Solanum tuberosum* peiderm, *Pseudomonas putida*, polyhydroxyalkanoate, potato peel waste

1 Introduction

According to "Food and Agricultural Organization of the United Nations," globally, annual *Solanum tuberosum* or potato production exceeds 40 million tons, resulting in substantial quantities of *S. tuberosum* waste. Approximately 40% of which is generated as byproducts in the food processing industry, including products such as fries, chips, and other packaged food (Rodríguez-Martínez et al., 2023). Commonly *S. tuberosum* periderm waste (potato peel waste) is utilized for generating low-value animal fodder, compost, or raw

substrate for biogas production, resulting in the squandering of valuable nutritional resources within it. *S. tuberosum* periderm possess antioxidant, antibacterial, and anti-inflammatory and further more properties (Khanal et al., 2023). However, the fundamental principle of the current study remains the efficient disposal of waste with the economic viability of processing advancement. In various studies *S. tuberosum* periderm was utilized for animal feed but proper treatment is required before subjecting it as a fodder for non-ruminants as it contains high amount of fibres to be digested (Akter et al., 2023). Despite lacking economic value, *S. tuberosum* periderm waste holds promise due to its significant carbohydrate content, making it an attractive feedstock to produce valuable compounds (Almeida et al., 2023).

The ongoing quest for sustainable and biodegradable alternatives to non-renewable, petrochemical plastics has been a driving force in scientific research within the field of biobased plastics, particularly polyhydroxyalkanoates (PHA). PHAs are intracellularly decomposable polyesters that various types of microbes accumulate as reserve food materials under stressful conditions (Wang et al., 2023). PHA is categorized based on its carbon chain length, with two main categories: short-length (3–5) and medium-length (6–12). Both types exhibit biodegradable properties, but medium-chain-length PHA (mcl PHA) holds significant industrial value due to its elastomeric and thermoplastic characteristics (Zhou et al., 2023). Large-scale production of Polyhydroxyalkanoates has become possible by selecting highly potent microbial strains to ferment refined feedstocks (de Souza Reis et al., 2020). While fatty acids and sugars are commonly used carbon sources for PHA production. Hence, carbon-rich waste materials can serve as cost-effective, sustainable, and economical substrates for industrial-scale PHA production (Kacanski et al., 2023).

S. tuberosum biomass contains 40%–80% sugar/gram of dry weight in the form of starch, cellulose, and hemicellulose. Worldwide production of *S. tuberosum* is consistently on the rise, reaching approximately around 390 million tons in the year 2021 and its industrial processing generates large volume nearly 78–195 million tons (20%–50%) raw material (Remedios and Domingues, 2023). It has been explored to produce various renewable metabolites, including bioethanol (Rodríguez-Martínez et al., 2023), biobutanol (Abedini et al., 2020), lactic acid (Liang et al., 2014), and bacterial cellulose (Abdelraof et al., 2019). Additionally, research has demonstrated the potential for bioplastic production from potato peel starch, both through chemical methods (Bezirhan Arikan and Bilgen, 2019), and through microbial routes, such as SCL polymer production using *Bacillus megaterium* (Vu et al., 2021), and mcl PHA production using various strains of *Pseudomonas* (Tanikkul et al., 2020a; Mahato et al., 2021; Pan et al., 2021).

To the best of author's knowledge, this study marks the first report of polyhydroxyalkanoate (mcl PHA) production using *S. tuberosum* periderm sugar as a carbon source by *Pseudomonas putida MTCC* 2475. The research was designed to maximize the extraction of reducing sugar by optimizing sugar concentration through response surface methodology, followed by bacterial fermentation for PHA production. Furthermore, the study explores the capacity of *Pseudomonas putida* (MTCC 2475) to produce PHA in various growth media and over different time frames. Additionally, the produced PHA was characterized using FTIR, DSC, and NMR.

2 Material and methods

2.1 Sample collection

S. tuberosum periderm biomass was obtained from the canteen of Delhi Technological University (DTU) (Figure 1). The processing involved washing the periderm and subsequently drying them at 40°C. A constant weight was achieved using Matrix Scientific Instrument. To achieve biomass size reduction in the range of 0.5–1 mm, a physical pretreatment involving grinding was applied.

2.2 Microorganism procurement and maintenance

The bacterium used in this research, *Pseudomonas putida* 2475, was procured from the Microbial Type Culture Collection (MTCC) in Chandigarh, India. Upon procurement, a mother culture was established on nutrient agar medium composed of the following components per liter: beef extract (0.1 g), yeast extract (2 g), peptone (5 g), NaCl (5 g), and agar (15 g), The pH of the medium maintained to be 7.

2.3 Acid hydrolysis of *Solanum tuberosum* periderm biomass

S. tuberosum periderm biomass is composed of various components, including starch, cellulose, lignin, protein, cellulose, and hemicellulose. To release fermentable sugars from these polysaccharides, an appropriate treatment strategy is necessary before subjecting the biomass to fermentation. Thermochemical treatment involving dilute acid at high temperatures is employed to convert the carbohydrates into monomer units and enhance sugar yield. For the optimization of sugar yield, a chemical treatment was carried out using varying HCl concentrations (0.25, 1.15, and 2%), and times (15, 55, and 95 min) at autoclave condition (121°C/15psi). For acid hydrolysis stock solution of 10% HCl (3.2 M) was prepared and then working solutions of 0.25%, 1.15%, and 2% of acid concentrations were prepared from it. Reaction volume was taken 1L and biomass loading was 100 g in 1,000 mL of aqueous phase in every single combination. After cooling centrifugation was done to separate liquid hydrolysate from unhydrolyzed solid part. After centrifugation liquid hydrolysate was subjected for detoxification with dry calcium carbonate until the pH of sample reaches up to neutral value (6.8–7).

2.3.1 Design of experiment by response surface methodology for acid hydrolysis

To optimize the highest yield of reducing sugar, statistical software (Minitab) was employed for regression analysis. Thirteen successive trials were outlined using a Central Composite Design, involving two factors: acid concentration [0.2, 1.125% and 2% (w/v)] and time (15, 55, 95 min), with five central points for the single response variable (reducing sugar yield). Each of the 13 trials was conducted in triplicate with 10% biomass loading, and the standard deviation was recorded.

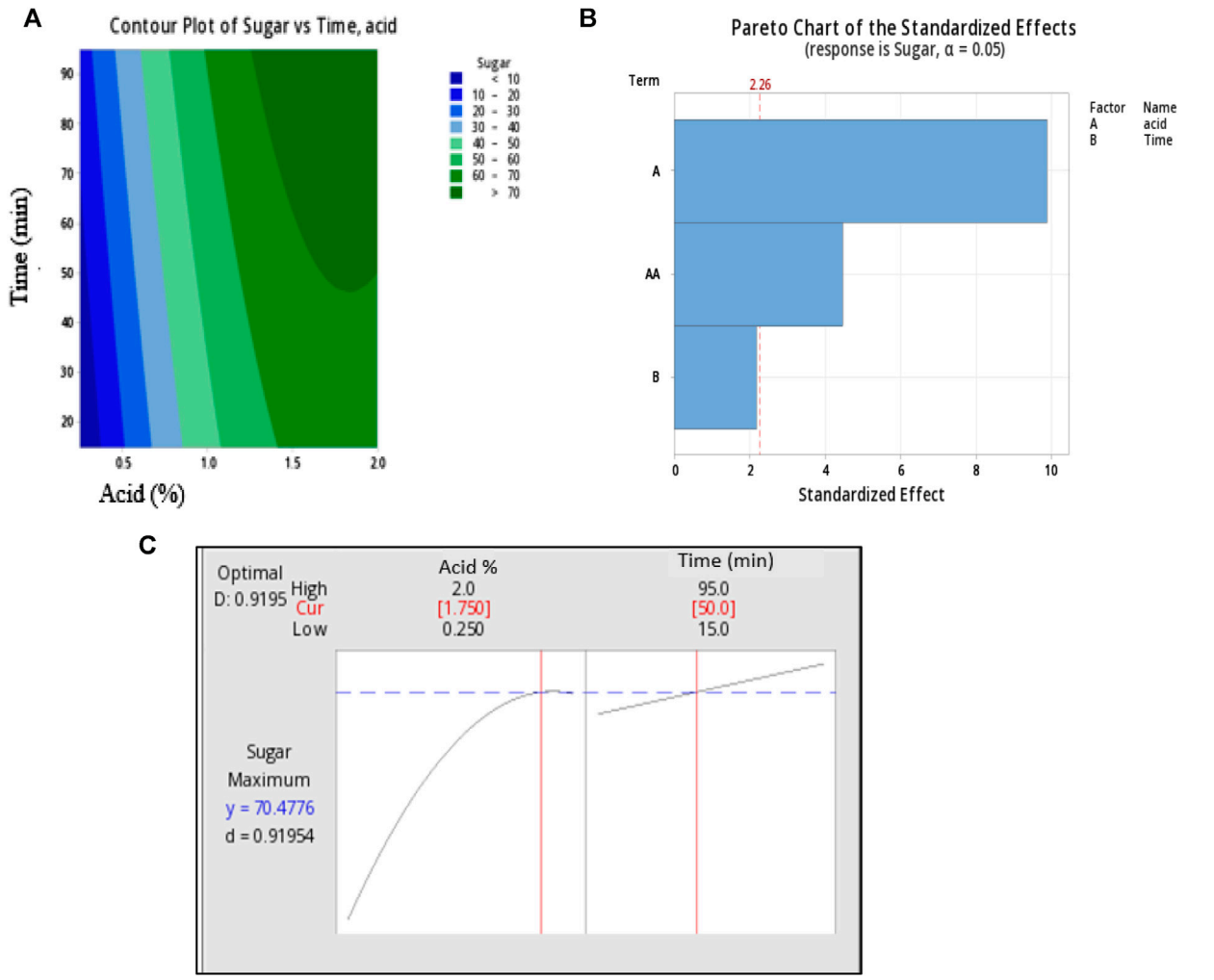


FIGURE 1
Response surface plots of two independence factors acid (X_1) Acid concentration and Time (X_2) where **(A)** is pareto chart of standardized effect, **(B)** counter plots and **(C)** optimum condition parameters.

A regression equation was utilized to summarize the combined results of the two independent variables: acid percentage ($\mathbf{X_1}$) and time in minutes ($\mathbf{X_2}$). The equation, represented as Y (the response, expressed as a percentage of reducing sugar), was used to interpret the observed outcomes.

To account for unexpected variations in the acquired data, the trials were randomized. Model fitness, the $\mathbf{R^2}$ value, and the F-test results were employed to assess the model's effectiveness, using data from ANOVA. The interaction between the two independent variables was examined through counterplots and a Pareto chart. Model efficacy was evaluated by comparing experimental results with the model's predicted values.

2.4 Composition analysis of raw *Solanum tuberosum* periderm biomass

The chemical composition of *S. tuberosum* periderm, including proximate analysis (total solid, moisture, and ash), was determined using techniques developed by the National Renewable Energy Laboratory (NREL) (Fatmawati et al., 2023). Briefly for total solid analysis 1 g biomass was kept in oven at 105°C till constant weight achieved. For the ash content analysis, the sample was subjected to a temperature of 575°C in a muffle furnace for a duration of 6 hours. Subsequently, the crucibles were taken out directly from the furnace and transferred into a desiccator, where they were allowed to cool for a designated period. Following this, the crucibles and ash were weighed and analyzed gravimetrically using prescribed formula $\%\ Ash = weight\ crucible\ plus\ ash - weight\ crucible \div Oven\ dry\ weight\ sample \times 100$.

Starch and total phenolics were quantified spectroscopically, following methods found in the literature (Lafont-Mendoza et al., 2018). In the starch analysis method 1 mL sample was taken in a test tube and 0.33 mL of potassium iodide (KI) solution was subsequently added. The blue color intensity was measured at 600 nm using spectrophotometer against KI blank. The amount of starch in the sample was determined by the standard curve (1 mg/mL). For total phenolics 1 gm sample was subjected to methanol extraction (1:10) and then subjected to incubation with Folin reagent (0.5 mL) and sodium carbonate (1 mL) for 2 h at room temperature

and then subjected to spectrophotometric assay at 765 nm against the gallic acid standard (1 mg/mL) (Samarin et al., 2012). Cellulose and hemicellulose content was estimated using the chlorite method. Briefly holocellulose content was determined using treatment with sodium chlorite. 17.5% NaOH was used to extract the cellulose compound from the holocellulose. Hemicellulose was determined by subtracting the value of cellulose from holocellulose (Zhou et al., 2015).

2.5 Total reducing sugar estimation

After dilute acid treatment, Hydrolysate was used for reducing sugar analysis by the Dinitro salicylic acid method briefly 1 mL of extracted hydrolysate with equal amount of DNS solution (3,5 dinitro salicylic acid 1 gm, Na_2SO_3 0.05 g, sodium potassium tartarate 18.2 g, NaOH 1 gm, and phenol 0.2 gm per 100 mL of H_2O) were subjected to heating for 10 min at 100°C and optical density at 540 nm was recorded upon cooling using standard glucose curve (1 mg/mL). Total reducing sugars (glucose, fructose, and xylose) present in the biomass has been considered for estimation (Shangdiar et al., 2023).

$$Sugar\ recovered\left(\frac{mg}{mL}\right) = Volume\ of\ liquid\ hydrolysate\ recovered \div Amount\ of\ sample\ taken\ for\ hydrolysis \times 100$$

2.6 Physicochemical characterization of *S. tuberosum* periderm biomass

Functional group analysis of both raw and acid hydrolyzed *S. tuberosum* periderm waste was conducted using Fourier-transform infrared (FTIR) spectroscopy with KBr pelleting (PEIR SUBTECH SPECTRUM ASCII PEDS 4.00). Thermogravimetric analysis (TGA) of the *S. tuberosum* periderm was carried out to observe decomposition peaks at various heating rates under an inert nitrogen environment, using a PerkinElmer analyzer. The analysis covered temperatures ranging from 30°C to 900°C with a heating rate of 10°C min^{-1}. The surface structure of both raw and treated *S. tuberosum* periderm biomass was observed using a Scanning Electron Microscope (ZEISS EVO 18) at a beam accelerating voltage of 20 kV.

2.7 PHA production using *S. tuberosum* periderm biomass hydrolysate by *P. putida*

Pseudomonas putida (strain 2475) was procured from MTCC, Chandigarh, India. The culture was periodically revived by transferring it to fresh Luria Bertani media (comprising 5 g/L yeast extract, 10 g/L NaCl, 15 g/L agar, and 10 g/L tryptone) and storing it at a low temperature of 4°C. To develop the inoculum, bacterial colonies from the pure culture were transferred to 150 mL of nutrient broth and incubated at 30°C with continuous shaking at 180 rpm for 24 h. Initially, we assessed the growth pattern of *P. putida* by measuring its optical density at 600 nm using a GENESYS 50 UV-visible spectrophotometer from Thermo Fisher. This assessment was conducted in mineral salt media containing $Na_2HPO_4{\cdot}7H_2O$ (30 g/L), KH_2PO_4 (15 g/L), NaCl (5 g/L), NH_4Cl (1 g/L), $MgSO_4$ (2 g/L), $CaCl_2$ (0.1 g/L), and synthetic glucose (10 g/L), as the carbon source. For nitrogen limitation, the quantity of NH_4Cl was reduced to 1 g/L. In media containing hydrolysates, 0.1% tryptone was used as nitrogen limitation.

TABLE 1 Composition analysis of *S. tuberosum* periderm waste.

Parameters	% (W/W)
Total solid	90.366 ± 0.40
Moisture	09.633 ± 0.40
Ash	14.033 ± 0.05
Total lignin	06.564 ± 0.20
Starch	64.44 ± 0.26
Total phenolics	0.6 ± 0.09
Cellulose	9.01 ± 0.48
Hemicellulose	1.89 ± 0.48
Total solid	90.366 ± 0.40

For inoculation, 1% of the freshly prepared seed culture, prepared in Luria Bertani media with an optical density of 0.8 and a concentration of 312 × 10^6 colony-forming units (cfu) was employed. The study involved three different media conditions for PHA production, each conducted in 2 L conical flasks containing 1 L of modified medium: **(A)** Modified medium comprised a specified volume (1%) of acid treated liquid hydrolyzed *S. tuberosum* periderm hydrolysate at a concentration of 10 g/L (after neutralization with calcium carbonate), 5 g/L NaCl, and 1 g/L tryptone. Incubation was carried out in a shaking incubator (180 rpm) at 30°C for 24, 36, 48, and 72 h. **(B)** Pure hydrolysate medium at a concentration of 10 g/L. **(C)** Mineral salt medium, as described in the literature (Sriyapai et al., 2022). PHA production values were averaged after each experiment, which was conducted in duplicate.

2.8 Cell dry weight measurement and extraction of PHA

After incubation, the culture broth was subjected to centrifugation at 10,000 rpm using an Eppendorf 5810 centrifuge for 15 min at 4°C. Following centrifugation, the supernatant was carefully drained, and the cell pellet was recovered. Recovered cell pellet was subsequently washed sequentially with 25 mL deionized water, 25 mL acetone, and 25 mL ethanol, and then dried at 40°C until a constant weight was achieved. This recovered cell biomass, referred to as cell dry mass, was determined gravimetrically, as per the method outlined in the literature (Tanikkul et al., 2020b). Polymer extraction was carried out using the chloroform extraction method with slight modifications, following the procedure described by Filippi et al. (2021). 2.1 g cell pellet was crushed with the help of mortar pestle and then incubated in 20-fold chloroform (43.8 mL) at 60°C in a water bath for 2 h. The resulting mixture was filtered using Whatman filter paper (1), and the liquid was concentrated through evaporation. PHA was obtained by precipitation of whole recovered solution obtained after heating with 22 mL ice-chilled methanol and subsequently analyzed using GC-MS, following the

TABLE 2 Experimental conditions, sugar recovery (%) and severity factor of acid hydrolysed *S. tuberosum* periderm by central composite design.

Run order	Time (X1)	Conc. (X2)	Sugar (%)	Combined severity factor
1	55	2	65.12 ± 0.17	0.18
2	95	0.25	16.45 ± 0.30	1.26
3	55	0.25	5.49 ± 0.16	1.52
4	15	0.25	0.05 ± 0.04	0.75
5	95	2	70.80 ± 0.27	1.83
6	55	1.125	61.39 ± 0.23	1.83
7	95	1.125	67.36 ± 0.41	1.83
8	55	1.125	60.99 ± 0.11	1.83
9	15	1.125	35.72 ± 0.26	1.83
10	55	1.125	61.58 ± 0.06	2.09
11	15	2	76.64 ± 0.17	0.99
12	55	1.125	59.82 ± 0.13	2.07
13	55	1.125	63.67 ± 0.28	2.33

X1 and X2 are the coded coefficients of time (min) and acid concentration (%), respectively. And combined severity factors LogR0 = Log [t· exp ((Hydrolysis temperature → reference temperature)/14.75)]- PH where t represents time (min), the hydrolysis temperature (°C) and Tref the reference temperature, which is usually set to 100°C (Liang et al., 2014).

previously established protocol (de Souza Reis et al., 2020). Briefly For the analysis of monomer composition, we performed GC MS-MS. First, 20 mg of dry cell biomass was subjected to acidic methanolysis. Methyl esters were prepared by combining 15% sulfuric acid in 85% methanol (2 mL) with chloroform (2 mL) in a screw-capped culture tube and heating it at 100°C for 2 h and 20 min (de Souza Reis et al., 2020).

2.9 Monomer identification GCMS-MS analysis

After cooling, 2 mL of water was added to separate the organic layer from the aqueous layer. The GC-MS-MS analysis was conducted using the Triple quadrupole 7000D GC/TQ Agilent, equipped with a triple-axis detector. For the analysis, PHA was used in the form of hydroxy alkanoic acid methyl esters, following the method reported by Mahato et al. (2021). A sample of 2 µL at a split ratio of 1:50 was automatically injected into the GC and injection temperature was 200°C. Helium served as the carrier gas at 48 mL^{-1}min and 0.42 bar pressure (Hierro-iglesias et al., 2023). Monomer identification was performed using the NIST 17 library.

2.10 Preparation and characterization of PHA film

The extracted PHA film was prepared in a fume hood by dissolving 200 mg extracted PHA in 20 mL of chloroform at room temperature and subsequently pouring the solution into Petri dish till complete evaporation of solvent. To determine the melting temperature of the PHA film, we conducted Differential Scanning Calorimetry (DSC) using a temperature-regulated system (DSC 8000, Perkin Elmer). We took 5 mg of extracted PHA in an aluminum pan and subjected it to a nitrogen flux rate of 10 mL/min, heating it from 30°C to 250°C, following the procedure outlined in the literature (Kacanski et al., 2023) with some modifications.

TABLE 3 *Solanum tuberosum* periderm experimental range of levels of independent process variables and coded values in CCD.

Variables	Level		
	−1	0	1
Time (min)	15	55	95
Acid concentration (%)	0.2	1.125	2

For the analysis of functional groups, we recorded Infrared (IR) spectra in the range of 4,000 to 450 cm^{-1}. This was done by preparing KBr pellets and using a (Perkin Elmer Frontier Shelton CT08484). In brief potassium bromide (KBr) was subjected to drying at 110°C for 2 h for moisture removal. 5 mg sample was mixed with 200 mg of powdered KBr. After pulverization, mixture (sample and KBr) placed in to pellet forming machine and resulting pellet was taken for IR analysis (Cerrone et al., 2023). To analyze the chemical shift of the PHA, we utilized 1H Nuclear Magnetic Resonance (NMR) by dissolving a 5 mg sample in 600 µL of $CDCl_3$, employing a (BRUKER Proton NMR 500 MHz), as described by Kacanski et al. (2023). The chemical shift of PHA was recorded in parts per million (ppm).

3 Results and discussion

3.1 Composition analysis

The composition analysis of *S. tuberosum* periderm collected during winter was conducted, and the findings are presented in

Table 1. One gram of the sample was used for composition analysis, and the results were reported in triplicate.

The composition of the *S. tuberosum* periderm was as follows: starch 64.44%, ash 14%, total lignin 6.5%, phenolics at 0.6% of *S. tuberosum* periderm, cellulose 9.01%, hemicellulose 1.89%, and the total solid content was found to be 90% (w/w).

In comparison, Malakar et al. (2020) reported 76% moisture and 8% ash in S. tuberosum periderm, Arapoglou et al. (2010) reported starch content at 52.14%, Lima et al. (2021) reported cellulose and hemicellulose content ranging from 10% to 30%, and Samarin et al. (2012) reported a total phenolic content of 522 µg GAE/g dry weight. These findings support the results of our study. However, it is worth noting that the composition of *S. tuberosum* periderm can vary among different *Solanum tuberosum* species (Sampaio et al., 2020).

3.2 Acid hydrolysis of the biomass

Different concentrations of dilute acid and time variation for hydrolysate development were used in this study which resulted in a varied amount of reducing sugar and their combined severity factor ($LogR_o$). Based on the above parameters, results presented in Table 2. From the obtained results it can be concluded that very low acid concentration (0.25), is unable to liberate high sugar at any time. Briefly 0.25% acid at 15 min extracted 0.05% reducing sugar. However, at 55 and 95 min sugar yield was 5.49% and 16.45%, respectively. Center point (1.12% acid and 55 min time) was obtained through the software and the sugar yield in all the five runs was between 59% and 63%. While High acid concentration (2%) releases the highest amount of sugar such as 76% at 15 min, and 70% at 95 min. From the above observations it can be said that sugar yield increases with the increase in acid concentration. However, time is not very significant factor in terms of sugar removal as 2% acid at 15 min can extract more sugar as compare to 95 min. The reason behind the diversity in sugar removal is high acid concentration and longtime combinedly generate toxic metabolites which leads to degrade sugar molecule. Therefore, a comparatively low acid concentration was optimized from response surface methodology the for maximum sugar with low toxicity. Further the optimized condition was used for acid hydrolysis.

3.3 Optimization of hydrolysis condition through RSM

This study was designed to establish a linear equation based on thirteen experimental runs, including five center points, all subjected to analysis of variance (ANOVA). Two factors, time and acid concentration, were optimized through Central Composite Design (CCD) and further analyzed using regression analysis and analysis of variance. The independent variables and their respective values are presented in Table 3.

Following the completion of thirteen trial runs, the optimal conditions for achieving the highest yield of reducing sugars were determined using Minitab software and graphically represented in Figure 2. The Pareto chart illustrates the standardized effects of individual factors: (A) acid concentration, (B) time, and the combined effects of both factors. The Pareto chart indicates that factor (A) exerts the most significant influence on sugar extraction, while the impact of time is relatively negligible. Furthermore, the combined influence of acid and time explains a smaller portion of sugar extraction.

The contour plot displays the region of maximum sugar yield, falling within the ranges of 1.5%–2% for acid concentration and 50–90 min for time. Based on above observations, this study was aimed to exact the maximum sugar at mild acid concentration. At 2% acid concentration and after 95 min of hydrolysis time, sugar was observed to be 70.80 ± 0.27, however, the acid concentration and time was a bit higher. While at 2% acid and 15 min of time sugar yield was maximum (76%) but acid concentration was higher. Hence, the maximum sugar liberation and milder condition were established to obtain optimized condition. The predicted optimal conditions from the model were determined for 1.75% acid concentration and 50 min of reaction time, resulting in a predicted sugar yield of 70.47%. To validate the accuracy of the predicted response, a hydrolysis experiment was conducted under the specified parameters, and the trials were conducted in triplicate. The average sugar yield obtained was 69.34% ± 0.25%, which closely matched the predicted value. Further this extracted sugar used as a carbon source for PHA production by *P. putida* in through this study.

The combined severity factor ($LogR_o$) under the optimized conditions was calculated to be 1.99. In a study, 5% hydrochloric acid, yielding 62 g L^{-1} of sugars (Khanal et al., 2023). In a two stage hydrolysis study, 32 g of potato peel in 400 mL of 1% w/w H_2SO_4 at 180°C for 60 min was performed, For second stage hydrolysis with cellulase, α-amylase and glucoamylase 36 g L^{-1} glucose was obtained (Abedini et al., 2020). In another two-step hydrolysis process of potato peels, 141 g L^{-1} of sugar obtained with 3% w/w H_2SO_4 in an autoclave condition for 15 min, The second stage enzymatic hydrolysis was done with the crude enzyme complex produced by *Aspergillus* sp. For 72 h at 50°C and 150 rpm (Soni et al., 2023). In an experiment, potato peel waste underwent pretreatment with 1% H_2SO_4 at 121°C for 30 min, with a substrate loading of 10%. In the subsequent hydrolysis step, 10 g of the pretreated substrate were exposed to enzymatic hydrolysis using cellulase, hemicellulose and amylase (at concentration of 30 U, 5 U, and 70 U/g of substrate, respectively). This hydrolysis process occurred at 50°C in a rotatory shaker incubator, with agitation at 700 rpm for 48 h. The outcome of this process revealed the presence of 77 g/L of reducing sugar (Kalafat et al., 2018).

In the current study, we achieved a considerably high yield of reducing sugars at 1.75% HCl, which is milder in terms of the generation of toxic byproducts such as furfural and hydroxymethylfurfural. Details regarding the responses after the trial runs and their Coefficient of Standard Deviation (CSD) are provided in Table 2.

RSM (Response Surface Methodology) was employed to assess the combined impact of two independent variables: Acid concentration ($\mathbf{X_1}$) and Time ($\mathbf{X_2}$), From the numerical data obtained in this study, the simplified linear regression model for sugar yield from S. tuberosum periderm can be expressed as follow

$$-24.19 + 93.8\mathbf{X_1} + 0.1758\,\mathbf{X_2} - 25.54\,\mathbf{X_1} \times \mathbf{X_1}$$

where $\mathbf{X_1}$ = Acid concentration (%) and $\mathbf{X_2}$ = Time (min).

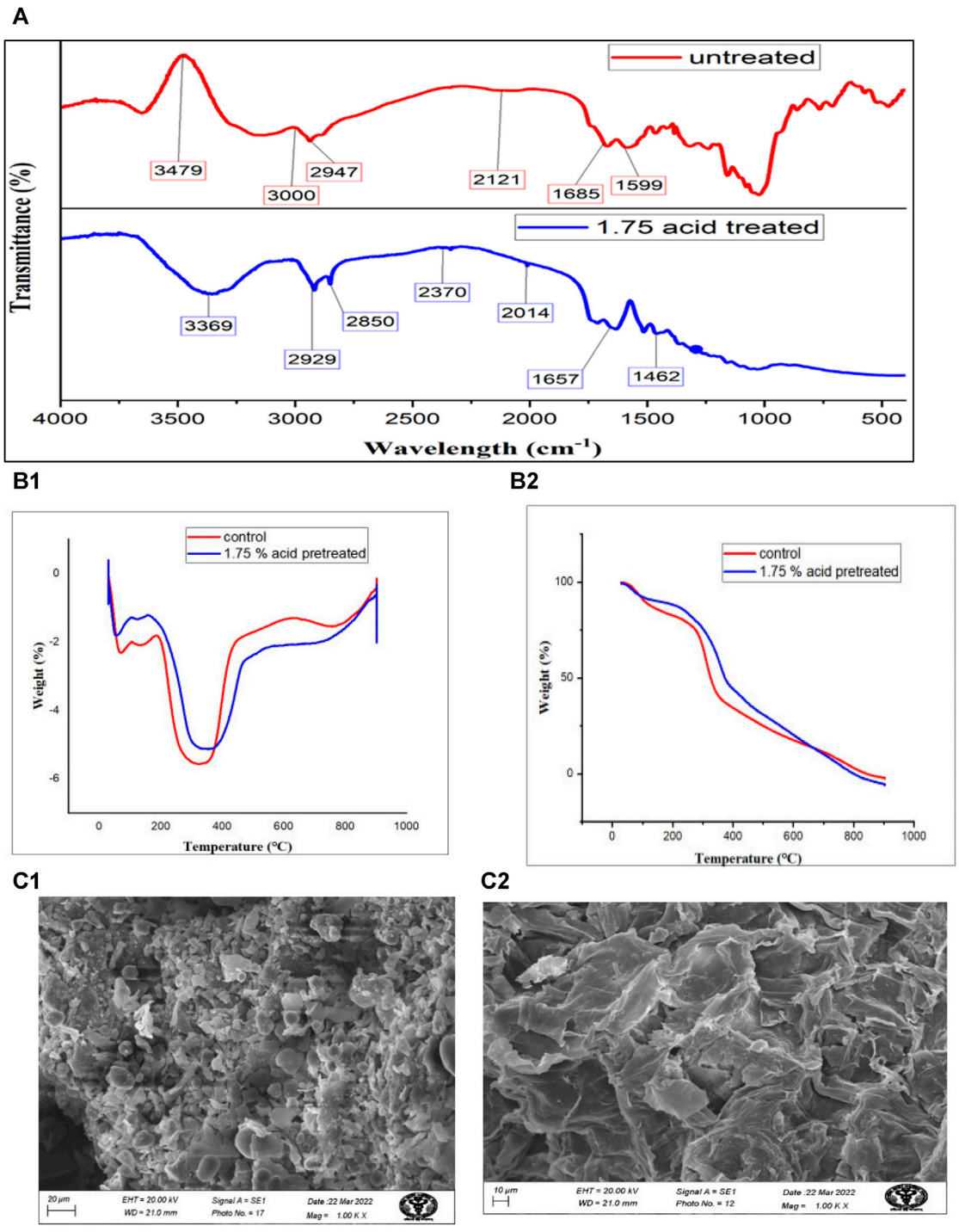


FIGURE 2
Thermochemical characterization of *S. tuberosum* periderm waste before and after acid hydrolysis **(A)** represents the FTIR of untreated and treated sample while, **(B1,B2)** belong to TGA and DGA, respectively and **(C1,C2)** are images obtained from scanning electron microscopy.

The regression analysis of the trial runs yielded a statistically significant result, with an R-squared value of 93.14%, indicating a strong fit of the model. Additionally, the lack-of-fit for the model was found to be negligible. The output of the regression analysis for glucose yield is presented in Table 2, where a *p*-value greater than 0.05 indicates the significance of the model.

To create the best-fit model and eliminate irrelevant conditions (those with *p*-values greater than 0.05), a linear equation for regression was applied. So, a model for the optimization of reducing sugar yield from *S. tuberosum* periderm was successfully generated. Based on obtained values, the sequence of relevance for the two factors on acidic hydrolysis was acid concentration > time.

The counterplots and Pareto chart were used to visually depict the effects of individual variables and the combined interactions of acid concentration (X_1) and Time (X_2) on sugar yield.

These statistical analyses and graphical representations are valuable tools for understanding the impact of the variables on the hydrolysis process and optimizing the yield of reducing sugars from *S. tuberosum* periderm waste.

3.4 Thermochemical characterization of biomass

3.4.1 FTIR

Infrared (IR) studies were conducted to assess the chemical modifications in *S. tuberosum* periderm waste before and after acid hydrolysis treatment. Key peaks in the FTIR spectra of treated and untreated biomass are depicted in Figure 3A. Treated samples exhibited lower peak intensities compared to untreated ones, indicating the efficient removal of various biomass constituents.

In the untreated sample, a peak at 3,480 cm^{-1}, corresponding to the free and intermolecular O-H stretch, suggests the presence of starch. However, in the case of treated biomass, a reduction in peak intensity and a shift in the band to 3,369 cm^{-1} indicate the conversion of starch into glucose.

In the untreated sample, the peak at 3,000 cm^{-1} corresponds to the free hydrogen-bonded OH stretching of cellulose. The band at 2,947 cm^{-1} represents the stretching of functional groups, methyl and methylene of cellulose. Post-treatment, there is a significant reduction in cellulose content, as evidenced by the low-intensity peak at 2,850 cm^{-1} as compared to untreated sample (3,000 cm^{-1})

Sharp peaks observed between 1,657 and 1,463 cm^{-1} in treated *S. tuberosum* periderm are attributed to the C=C stretching of the aromatic structure of suberin. This peak distribution pattern is consistent with findings from previous studies, such as the work of Malakar et al. (2020) on acid-treated *S. tuberosum* periderm waste and the research conducted by Liang and McDonald (2014), which compared raw biomass with its residue after fermentation. Both studies reported similar patterns in O-H stretching, C-H (indicative of carbohydrate presence), C=O, and C-O-C (related to hydroxy fatty acid and suberin).

3.4.2 TGA

Acid hydrolyzed (1.75%) and unhydrolyzed *S. tuberosum* periderm underwent thermogravimetric analysis to compare their thermal decomposition rates, as illustrated in Figure 3B. The Differential Thermogravimetric (DTG) analysis of peel biomass revealed two distinct weight loss regions in all samples.

The first weight loss peak, observed at 100°C, can be attributed to dewatering processes. Weight loss occurring between 200°C–300°C indicates the depolymerization of cellulose and hemicellulose, key components of the biomass. Additionally, a peak in the temperature range of 350°C–380°C corresponds to the cleavage of glycosidic bonds within starch molecules.

In the case of unhydrolyzed (raw) samples, the TGA (Thermogravimetric Analysis) curve exhibited a peak at 354°C, resulting in a 59.941% weight loss. However, under optimized conditions of 1.75% acid concentration and approximately 50 min of treatment, a more significant weight loss of approximately 60% was observed at 429°C. This peak signifies the effective removal of starch from *S. tuberosum* periderm due to acidic hydrolysis.

The thermal decomposition behavior, as assessed through TGA and DTG, in our *S. tuberosum* periderm samples exhibited similarities with the findings of Liang et al. (2014) Notably, distinct peak areas corresponding to starch, cellulose, and hemicellulose (within the range of 220°C–400°C) were evident. In contrast, lignin and suberin displayed notable peaks at temperatures between 250°C–290°C.

Investigating the thermal properties of *S. tuberosum* periderm through Thermogravimetric Analysis (TGA) revealed noteworthy findings. The TGA analysis demonstrated distinct decomposition peaks for cellulose and hemicellulose in the temperature range of 200°C–375°C, while lignin exhibited a degradation peak spanning from 180°C to 450°C, consistent with the observations made by Osman et al. (2019). In a separate study conducted by Liang et al. (2015), bio-oil was produced from *S. tuberosum* periderm, and it was observed that the thermal degradation of the material occurred at temperatures below 450°C. These findings further corroborate the presence of these specific biomolecules within the *S. tuberosum* periderm sample. This alignment between the identified peaks and their corresponding thermal degradation patterns is consistent with the existing literature.

3.4.3 SEM

The surface morphology of both pre-treated and untreated *S. tuberosum* periderm waste was analyzed using scanning electron microscopy (SEM), as depicted in Figure 3C. The images reveal distinct disparities between the pre-treated and untreated samples. In contrast to the untreated sample, which appears compact and smooth, the pre-treated sample exhibits noticeable structural alterations.

These structural changes can be attributed to the acidic treatment, which appears to have resulted in the breakdown of bonds between lignin and carbohydrates. This structural modification likely played a role in facilitating the release of maximum sugars from the *S. tuberosum* periderm waste. In a recent study conducted (Soni et al., 2023), the authors examined both untreated and pretreated *S. tuberosum* periderm samples using scanning electron microscopy (SEM). Their observations closely parallel the findings of our current study. In their investigation, the untreated *S. tuberosum* periderm samples displayed an intact and solid structure. In contrast, the acid-pretreated samples, treated with 3% H_2SO_4, exhibited noticeable changes, characterized by cracking and fragmentation of the biomass.

3.5 Growth of *Pseudomonas putida* for PHA production and it is extraction in different production media

3.5.1 Growth pattern of *Pseudomonas putida* in different media

The growth pattern of *Pseudomonas putida* was monitored in various production media denoted as A, B, and C as illustrated in Figure 4. Cell biomass was collected at distinct time intervals: 24, 36, 48, and 72 h, across the four different media mentioned above. An

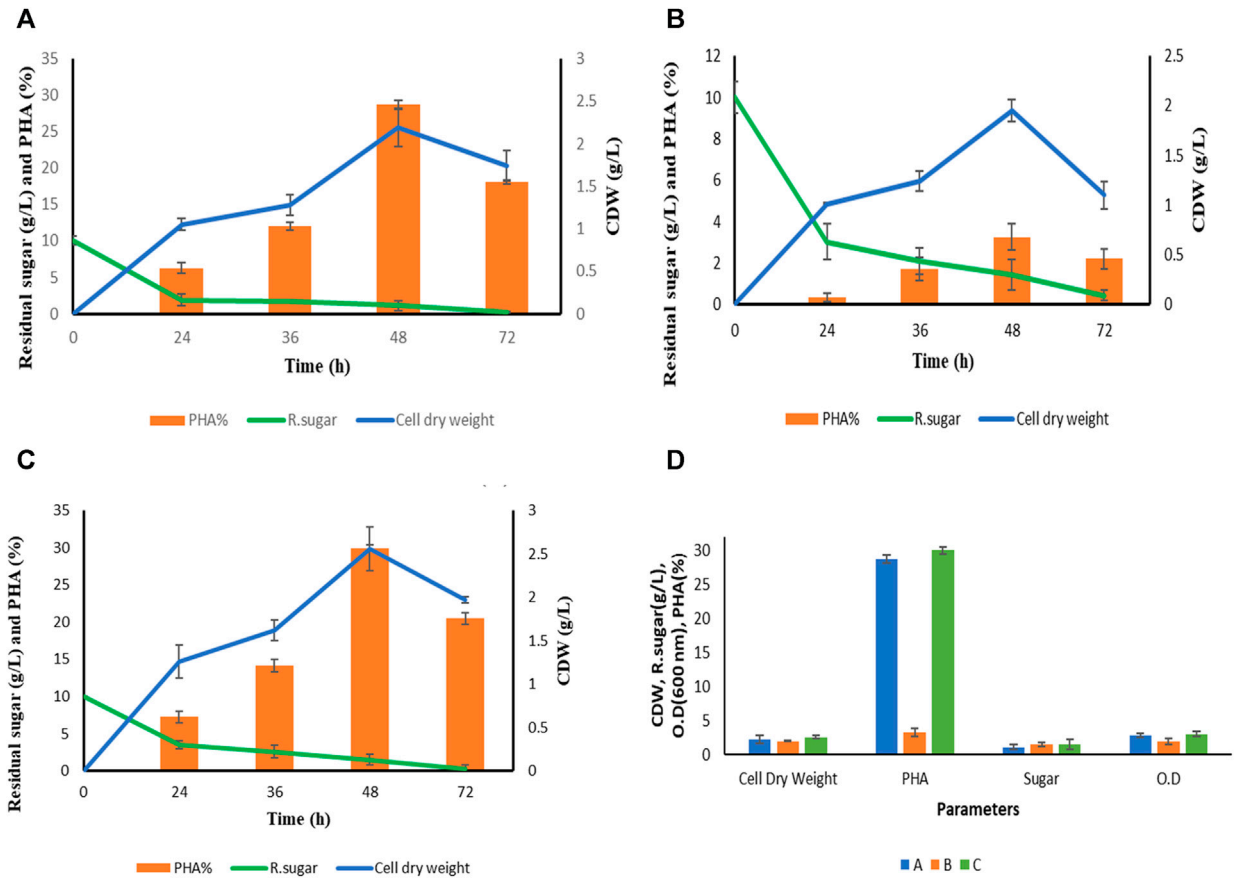


FIGURE 3
Summary of growth pattern of *P. putida* in terms of optical density (OD), cell dry weight (cdw) and residual sugar in three different media. In media **(A)** This includes extracted hydrolysate from *S. tuberosum* periderm, NaCl, and tryptone. In media **(B)** This involve pure hydrolysate at a concentration of 10 g L^{-1} without the addition of any other components. In media **(C)** Mineral salt media containing $Na_2HPO_4.7H_2O$, KH_2PO_4, NaCl, NH_4Cl, $MgSO_4$, $CaCl_2$ and Synthetic glucose. **(D)** Growth pattern of *P. putida* in terms of cell dry weight, PHA, residual sugar and optical density at optimized condition (48 h).

interesting trend emerged where biopolymer accumulation within the bacterial cells decreased after 48 h of fermentation in all media. This reduction can be attributed to the depletion of the carbon source. Notably, deposited Polyhydroxyalkanoates (PHA) within the cells serve as an energy source, allowing the cells to persist in carbon-depleted conditions, as discussed by Maheshwari et al. (2018). The highest Cell Dry Weight (CDW) was recorded at the 48-h mark in each production medium.

Figure 4 provides comprehensive data on the type of media, time (in hours), cell dry weight (in grams), PHA content (%), and residual sugar levels after each fermentation experiment. Mineral salt media containing synthetic glucose emerged as the most efficient PHA accumulator, with a PHA content of 29.97% ± 0.45%. This is attributed to the presence of the desired salt concentration, which optimally supports the growth of *P. putida*. However, it is important to note that the primary objective of this study is to utilize a sustainable carbon source, specifically *S. tuberosum* periderm, to reduce the production cost of PHA. Carbon source costs typically account for approximately 50% of the overall production expenses, as discussed by Jiang et al. (2016).

Hence, mineral salt media **(C)** was included primarily for comparative purposes, as it contains synthetic glucose, while the focus remains on evaluating *S. tuberosum* periderm hydrolysate (extracted sugar) as a potential carbon source for PHA production. Comparing the media types, it is observed that aside from mineral salt media, cell dry weight was slightly higher in the modified media **(A)**, which includes *S. tuberosum* periderm hydrolysate, tryptone, and NaCl, as compared to media **(B)** consisting solely of hydrolysate (1%). While **(D)** represents the O.D at 600 nm, cell dry weight, PHA, and residual sugar of all the three media (A, B, and C) at optimum condition (48 h).

Significant differences in PHA accumulation among these media types indicate that PHA-producing bacteria require a specific balance between nutritional stress and carbon abundance to foster PHA production. In contrast, when using only *S. tuberosum* periderm hydrolysate, while the carbon content was at the desired level (1%), the absence of NaCl to maintain osmotic balance and nitrogen led to biomass that lacked biopolyester components, specifically Polyhydroxyalkanoates (PHA), as reported by Passanha et al. (2014).

These findings underscore the importance of optimizing the carbon source, nutritional conditions, and osmotic balance to achieve efficient PHA production, particularly when utilizing sustainable carbon sources such as *S. tuberosum* periderm waste.

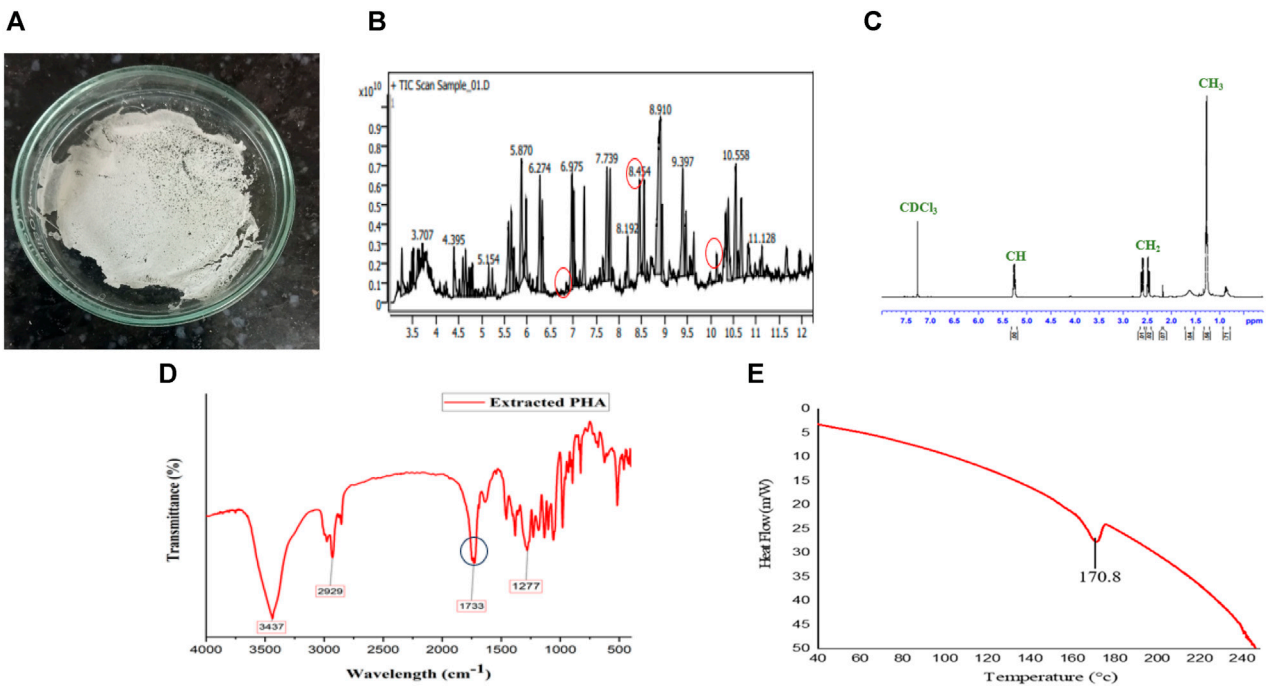


FIGURE 4
Extracted PHA characterization, Figure depicts **(A)** PHA film, **(B)** monomer confirmation of MCL PHA by GCMS-MS, **(C)** NMR spectra, **(D)** FTIR, and **(E)** DSC of PHA extracted from *Pseudomonas putida*.

TABLE 4 Comparison of PHA production by different strains of *Pseudomonas putida* on the basis of fermentation parameters such as carbon source, incubation time, agitation speed and results were obtained in the form of cell dry mass, PHA% and monomer composition.

S. No	Bacteria used	Carbon source	Fermentation condition	Cell dry weight	PHA % in CDW	Monomer	Reference
1	*P. putida* KT2440	Glycerol (1%)	Incubation time 72 h at 28°C	2.6 g L–1	20.70%	Methyl 3-Hydroxyhexadecanoic acid, methyl 3-hydroxyoctadecanoic acid, methyl 3-hydroxydecanoic acid, methyl 3-hydroxydodecanoic acid, methyl 3-hydroxytetradecanoic acid	(Xu et al., 2021)
2	*P. putida* GO19	Terephthalic acid	E2 media containing 0.42% carbon source at 30°C and at 200 rpm	—	23%	3-hydroxyhexanoic acid, 3-hydroxyoctan-oic acid, 3-hydroxy-dodecanoic acid, 3-hydroxydodecenoic acid	(Kenny et al., 2008)
3	*P. putida* (MTCC 2475)	*Solanum tuberosum* periderm	Modified media containing 1% sugar hydrolysate at 30°C for 48 h	2.19	28.71% ± 0.55% (0.60 g/L)	Methyl 3-hydroxydodecanote methyl 3 hydroxytetradecanote hexadecanoic 3 hydroxy methyl esters	Present study

3.5.2 PHA accumulation in *Pseudomonas putida* in different media

The percentage of extracted PHA is calculated gravimetrically in each media which is shown in Figure 4 but for GCMS MS analysis only media **(A)** However, PHA production from *S. tuberosum* periderm waste is reported for the first time in this study with 0.60 g/L (28.71% ± 0.55%) PHA production at 48 h with media **(A)** which is close to PHA accumulation in media **(C)** mineral salt media (29.97% ± 0.45%) media (A) contained hydrolysate (1%) along with tryptone (0.1%) and NaCl (0.5%) while media (B) confined pure hydrolysate without any other nutrients. 0.5 NaCl was added in media (A) for the osmotic balance of bacteria and the stress was given in the form of 0.1% organic nitrogen (tryptone). However, Nitrogen limited media triggers the bacteria to store excess carbon in the form of PHA but for bacterial growth and physiological activity small amount of nitrogen is required. Although complete omit of nitrogen may interfere with PHA accumulating activity of bacteria. Therefore, in media (B) no significant PHA accumulation observed. In case of media (C) 1% synthetic glucose along with other minerals and for nitrogen stress inorganic nitrogen (0.1% NH_4Cl was added. Therefore, higher PHA accumulation was seen in synthetic media also. Although, it is assumed that acid-hydrolyzed sugar has its stress

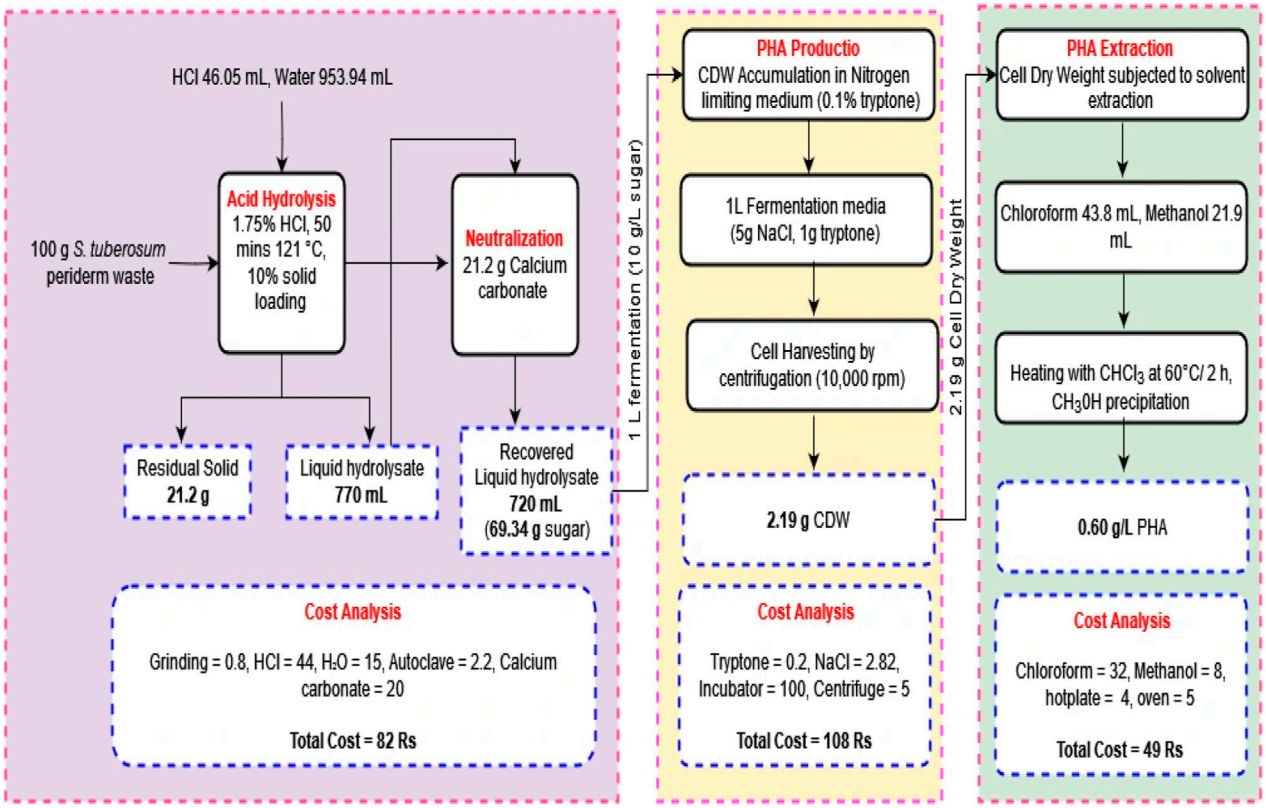


FIGURE 5
Mass balance study of PHA production from *S. tuberosum* periderm waste.

factors (phenolics) which are responsible for the accumulation of high percentage of PHA. Sharma et al. (2012) reported 22.6% mcl PHA of CDW from an isolated strain of *Pseudomonas putida* LS46 which is closely related to KT2440 (a potent PHA-producing recombinant strain) by using synthetic glucose (2%) as a carbon source.

In a study by Sikkema et al. (2023), three distinct strains of *Pseudomonas putida*, namely, NRRL B-14875, KT2440, and GN112, were employed as microbial cultures for the assimilation of fatty acids as the carbon source. The growth medium consisted of 20 mM ammonium sulfate, 50 mM potassium phosphate, 140 μM calcium carbonate, 2 μM copper sulfate, and 0.1 mL of a trace element solution. The incubation was carried out at 30°C, with constant agitation at 200 rpm, for a duration of 68 h. The investigation yielded significant results, with NRRL B-14875 producing 29% Polyhydroxyalkanoates (PHA), KT2440 contributing 34% PHA, and GN112 strain yielding the highest PHA content at 35%. In a literature 6 g/L MCL PHA was obtained using *Pseudomonas* putida KT2442. In first step bacterial was subjected to grow in organic fraction of municipal solid waste 1 L along with 5 g yest extract, 2 g glucose, 1 g KCl, (NH_4) SO_4 1 g and trace element solution and fed batch fermentation and second step was ethanol was added as a substrate of PHA production (de Vrije et al., 2023).

This study shows a satisfactory amount of PHA production using only sugar hydrolysate (1%) NaCl (0.5%) and a negligible amount of tryptone (0.1%). At economic point of view, high amount of sugar (~70%) can be extracted from *S. tuberosum* periderm biomass which is comparatively higher than other lignin and complex sugars containing organic waste. The comparative study with *P. putida* with other carbon sources is discussed in Table 4. However, extracted sugar % can vary in different species of *S. tuberosum* periderm and applied peeling method but considerable amount of starch is present in *S. tuberosum* periderm, could be used for biodegradable bioplastic (PHA) production which is discarded otherwise.

3.6 PHA monomer conformation

Based on the GC-MS-MS analysis, using *S. tuberosum* periderm waste hydrolysate as the sole carbon source resulted in the formation of medium-chain length polyhydroxyalkanoates (mcl PHA) containing three distinct monomers: 3-hydroxydodecanoate (3HDD) with a retention time (RT) of 6.99 min and a peak area of 1.75%., 3-hydroxydecanoate (3HD) with an RT of 10.34 min and a peak area of 1.72% and 3-hydroxytetradecanoate (3HTD) with an RT of 8.52 min and a peak area of 19.2% (Figure 5B).

These identified monomers demonstrate the feasibility of producing industrially important mcl PHA with carbon sources of low cost, such as *S. tuberosum* periderm hydrolysate. This approach enables the construction of mcl PHA with chain lengths ranging from 5 to 14 carbons, making it an economically attractive option.

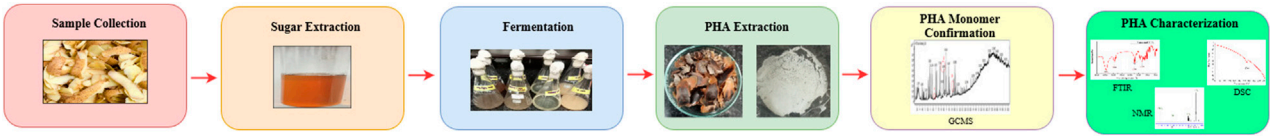


FIGURE 6
Steps involved in PHA production using *Solanum tuberosum* periderm.

This finding aligns with the work of Mahato et al. (2021), who reported the presence of beta-3-hydroxybutyric acid (7.41%), 3-hydroxytetradecanoic acid methyl esters, and 3-hydroxyhexadecanoate (5.03%) in PHA produced by *Pseudomonas aeruginosa*. However, it is important to note that their PHA production was observed in mineral salt media containing different oils as carbon sources, which may not be as sustainable and could potentially incur higher costs compared to the approach used in the present study. In a study Ciesielska et al. (2017) reported mcl PHA monomers such as 3- hydroxyhexadecanoate and 3- hydroxyoctadecanoate from *Pseudomonas putida* KT2440 using oleic acid as a carbon source.

By comparing PHA monomers produced by *Pseudomonas* from different studies it is evident that PHA extracted from *P. putida* MTCC 2475 (present study) is mcl PHA.

3.7 Preparation and characterization of extracted PHA film

The PHA film was created by adding extracted PHA in solvent (chloroform) and stored securely under aseptic conditions at room temperature (Figure 5A). The Differential Scanning Calorimetry (DSC) thermogram presented in Figure 5D reveals the melting temperature (T_m) of the produced Polyhydroxyalkanoates (PHA), which was found to be approximately 170°C. This temperature closely aligns with the melting temperature of 3-hydroxydecanoic acid (166°C), as reported in the literature (Sharma et al., 2017).

The identification of functional groups within the extracted PHA was accomplished through Fourier Transform Infrared Spectroscopy (FTIR), as illustrated in Figure 5C. The spectral pattern of functional groups closely resembled findings from Mahato et al. (2021), who identified different forms of decanoic acid methyl esters, including Methyl 3-hydroxytetradecanoate and hexadecanoic acid methyl ester, from *Pseudomonas aeruginosa*. Notable absorption bands included: 1) A band at 3,437 cm^{-1}, attributed to the O-H stretching of the hydroxyl group in PHA. 2) The band at 2,929 cm^{-1}, assigned to the CH_2 group. 3) An absorption band at 1,733 cm^{-1}, indicating C=O stretching vibration, confirming the presence of an ester bond in the PHA monomer. 4) A band at 1,277 cm^{-1}, associated with the asymmetric C–O–C stretching vibration.

Furthermore, the Proton Nuclear Magnetic Resonance (NMR) spectrum of the PHA film is depicted in Figure 5E. The complex multiple resonance bands between 1.26 and 1.33 ppm (peak no. 1) suggest the presence of methyl groups ($–CH_3$) in the PHA film. Multiple resonance spectra observed between 2.17 and 2.60 ppm (peak no. 2) confirm the existence of methylene groups ($–CH_2$). The band position ranging from 5.22 to 5.27 ppm (peak no. 3) indicates the presence of methane (–CH) in the PHA polymer. Peak no. 4 corresponds to the solvent $CDCl_3$. These observed peaks align with prior studies on medium-chain length PHA produced by *Pseudomonas* strains, as reported by Gumel et al. (2014). Comparing the results of the present study with findings from various previous investigations, it can be confidently affirmed that the extracted polymer is indeed medium-chain length Polyhydroxyalkanoates (PHA).

4 Mass balance and economic analysis of the study

The experiment commenced with 100 g of *S. tuberosum* periderm waste used for sugar extraction, with a solid loading of 10%. This extraction process yielded 69.34% ± 0.25%, of sugar. Out of the total sugar obtained, 10 g were used for the fermentation process per liter, resulting in the production of 2.19 g of dry cell weight and 0.60 g/L PHA. Conducting an economic assessment revealed that the production of 1 L media with a concentration of 0.60 g/L of PHA incurred a cost of 239 Rs. In contrast, the acid hydrolysis method utilized a total of 100 g of biomass, yielding approximately 70 g of sugar. For the subsequent fermentation, only 10 g of this sugar were utilized, allowing the preparation of an additional 6 L fermentation media. Scaling down the acid hydrolysis process for a single liter production media has the potential to decrease cost. Moreover, the cost of PHA can not be compared with conventional plastic because along with packaging material it possesses biodegradable, sustainable, eco-friendly, medical application properties.

Based on these results, it can be estimated that approximately 4.35 g of PHA can be produced from 100 g of *S. tuberosum* periderm waste. Figure 6 provides an operational flow diagram of mass balance and economic analysis, illustrating the process of PHA production from *S. tuberosum* periderm waste.

5 Conclusion

The data obtained from this study holds significant potential for enhancing the economic sustainability of Polyhydroxyalkanoates production from *S. tuberosum* periderm using *Pseudomonas putida*. The optimization of sugar concentration, achieved through RSM represents a critical step in PHA production, enabling higher sugar yields. While this study successfully demonstrated the production of MCL PHA 0.60 g/L within 48 h. The results encourage the concept of waste valorisation and its potentiality to donate to a more circular

and sustainable environment. Although PHA production can be upgraded by optimizing certain parameters such as Carbon to nitrogen ratio and inoculum size. In summery the extent of the research extends further than the laboratory, motivating scientific community and industries to think about *Solanum tuberosum* periderm waste as a valuable feedstock in the endeavour of eco-friendly substitute to conventional plastic.

Data availability statement

The original contributions presented in the study are included in the article/supplementary material, further inquiries can be directed to the first and corresponding author.

Author contributions

SK: Conceptualization, Data curation, Formal Analysis, Investigation, Methodology, Validation, Writing–original draft. PK: Supervision, Writing–review and editing. RK: Conceptualization, Funding acquisition, Project administration, Supervision, Writing–review and editing.

Funding

The authors declare that financial support was received for the research, authorship, and/or publication of this article. This work was supported by Department of Biotechnology, Govt. of India (DBT) (BT/RLF/Re-entry/40/2017; SAN No. 102/IFD/SAN/1276/2019-20). Science and Engineering Research Board, India (SERB) File No. EEQ/2020/000614, Govt. of India. Council of Scientific & Industrial Research (CSIR), Govt. of India for the fellowship of SK (File No.08/133(0041)/2019-EMR-I).

Acknowledgments

The authors would like to acknowledge the grant agencies, Department of Biotechnology, India (DBT) [BT/RLF/Re-entry/40/2017; SAN No. 102/IFD/SAN/1276/2019-20] and Science and Engineering Research Board, India (SERB) File No. EEQ/2020/000614, Govt. of India for providing the financial support for this work. Special thanks to Council of Scientific & Industrial Research (CSIR), Govt. of India for fellowship of SK [File No. 08/133(0041)/2019-EMR-I]. Authors would also like to thank Department of Biotechnology and Department of Chemistry, Delhi Technological University (DTU) for the support and providing analysis facilities.

Conflict of interest

The authors declare that the research was conducted in the absence of any commercial or financial relationships that could be construed as a potential conflict of interest.

Publisher's note

All claims expressed in this article are solely those of the authors and do not necessarily represent those of their affiliated organizations, or those of the publisher, the editors and the reviewers. Any product that may be evaluated in this article, or claim that may be made by its manufacturer, is not guaranteed or endorsed by the publisher.

References

Abdelraof, M., Hasanin, M. S., and El-Saied, H. (2019). Ecofriendly green conversion of potato peel wastes to high productivity bacterial cellulose. *Carbohydr. Polym.* 211, 75–83. doi:10.1016/j.carbpol.2019.01.095

Abedini, A., Amiri, H., and Karimi, K. (2020). Efficient biobutanol production from potato peel wastes by separate and simultaneous inhibitors removal and pretreatment. *Renew. Energy. Elsevier Ltd.* 160, 269–277. doi:10.1016/j.renene.2020.06.112

Akter, M., Anjum, N., Roy, F., Yasmin, S., Sohany, M., and Mahomud, M. S. (2023). Effect of drying methods on physicochemical, antioxidant and functional properties of potato peel flour and quality evaluation of potato peel composite cake. *J. Agric. Food Res.* 11, 100508. doi:10.1016/j.jafr.2023.100508

Almeida, P. V., Gando-Ferreira, L. M., and Quina, M. J. (2023). Biorefinery perspective for industrial potato peel management: technology readiness level and economic assessment. *J. Environ. Chem. Eng.* 11, 110049. doi:10.1016/j.jece.2023.110049

Arapoglou, D., Varzakas, T., Vlyssides, A., and Israilides, C. (2010). Ethanol production from potato peel waste (PPW). *Waste Manag.* 30, 1898–1902. doi:10.1016/j.wasman.2010.04.017

Bezirhan Arikan, E., and Bilgen, H. D. (2019). Production of bioplastic from potato peel waste and investigation of its biodegradability. *Int. Adv. Res. Eng. J.* 03, 93–97. doi:10.35860/iarej.420633

Cerrone, F., Zhou, B., Mouren, A., Avérous, L., Conroy, S., Simpson, J. C., et al. (2023). Pseudomonas umsongensis GO16 as a platform for the *in vivo* synthesis of short and medium chain length polyhydroxyalkanoate blends. *Bioresour. Technol.* 387, 129668. doi:10.1016/j.biortech.2023.129668

Ciesielska, J. M., Dabrowska, D., Palasz, A. S., and Ciesielski, S. (2017). Medium - chain - length polyhydroxyalkanoates synthesis by Pseudomonas putida KT2440 relA/spoT mutant: bioprocess characterization and transcriptome analysis. *Amb. Express* 7, 92. doi:10.1186/s13568-017-0396-z

de Souza Reis, G. A., Michels, M. H. A., Fajardo, G. L., Lamot, I., and de Best, J. H. (2020). Optimization of green extraction and purification of PHA produced by mixed microbial cultures from sludge. *WaterSwitzerl.* 12, 1185. doi:10.3390/W12041185

de Vrije, T., Nagtegaal, R. M., Veloo, R. M., Kappen, F. H. J., and de Wolf, F. A. (2023). Medium chain length polyhydroxyalkanoate produced from ethanol by Pseudomonas putida grown in liquid obtained from acidogenic digestion of organic municipal solid waste. *Bioresour. Technol.* 375, 128825. doi:10.1016/j.biortech.2023.128825

Fatmawati, A., Nurtono, T., and Widjaja, A. (2023). Thermogravimetric kinetic-based computation of raw and pretreated coconut husk powder lignocellulosic composition. *Bioresour. Technol. Rep.* 22, 101500. doi:10.1016/j.biteb.2023.101500

Filippi, S., Cinelli, P., Mezzetta, A., Carlozzi, P., and Seggiani, M. (2021). Extraction of polyhydroxyalkanoates from purple non-sulfur bacteria by non-chlorinated solvents. *Polym. (Basel)* 13, 4163. doi:10.3390/polym13234163

Gumel, A. M., Annuar, M. S. M., and Heidelberg, T. (2014). Growth kinetics, effect of carbon substrate in biosynthesis of mcl-PHA by Pseudomonas putida Bet001. *Braz. J. Microbiol.* 45, 427–438. doi:10.1590/S1517-83822014000200009

Hierro-iglesias, C., Fatokun, C. O., Chimphango, A., Bayitse, R., Helena, P., Thornley, P., et al. (2023). u rn a l P. *J. Environ. Chem. Eng.* 111815. doi:10.1016/j.jece.2023.111815

Jiang, G., Hill, D. J., Kowalczuk, M., Johnston, B., Adamus, G., Irorere, V., et al. (2016). Carbon sources for polyhydroxyalkanoates and an integrated biorefinery. *Int. J. Mol. Sci.* 17, 1157. doi:10.3390/ijms17071157

Kacanski, M., Stelzer, F., Walsh, M., Kenny, S., O'Connor, K., and Neureiter, M. (2023). Pilot-scale production of mcl-PHA by Pseudomonas citronellolis using acetic acid as the sole carbon source. *N. Biotechnol.* 78, 68–75. doi:10.1016/j.nbt.2023.10.003

Kalafat, E., Laoreti, A., Khalil, A., Costa, F. D. S., and Thilaganathan, B. (2018). Ophthalmic artery Doppler for prediction of pre-eclampsia: systematic review and meta-analysis. *J. Fish. Biol.* 1, 731–737. doi:10.1002/uog.19002

Kenny, S., Nikodinovic-Runic, J., Kaminsky, W., Woods, T., Babu, R., Keely, C., et al. (2008). Up-Cycling of PET (Polyethylene Terephthalate) to the Biodegradable Plastic PHA (Polyhydroxyalkanoate). *Environ. Sci. Technol.* 42, 7696–7701. doi:10.1021/es801010e

Khanal, S., Karimi, K., Majumdar, S., Kumar, V., Verma, R., Bhatia, S. K., et al. (2023). Sustainable utilization and valorization of potato waste: state of the art, challenges, and perspectives. *Biomass Convers. Biorefinery*. doi:10.1007/s13399-023-04521-1

Lafont-Mendoza, J. J., Severiche-Sierra, C. A., and Jaimes-Morales, J. (2018). Evaluation of the starch quantification methods of *Musa paradisiaca, Manihot esculenta,* and *Dioscorea trífida* using factorial experiments. *Int. J. Food Sci.* 2018, 1–7. doi:10.1155/2018/5901930

Liang, S., and McDonald, A. G. (2014). Chemical and thermal characterization of potato peel waste and its fermentation residue as potential resources for biofuel and bioproducts production. *J. Agric. Food Chem.* 62, 8421–8429. doi:10.1021/jf5019406

Liang, S., Han, Y., Wei, L., and McDonald, A. G. (2015). Production and characterization of bio-oil and bio-char from pyrolysis of potato peel wastes. *Biomass Convers. Biorefinery* 5, 237–246. doi:10.1007/s13399-014-0130-x

Liang, S., McDonald, A. G., and Coats, E. R. (2014). Lactic acid production from potato peel waste by anaerobic sequencing batch fermentation using undefined mixed culture. *Waste Manag.* 45, 51–56. doi:10.1016/j.wasman.2015.02.004

Lima, M. de A., Andreou, R., Charalampopoulos, D., and Chatzifragkou, A. (2021). Supercritical carbon dioxide extraction of phenolic compounds from potato (Solanum tuberosum) peels. *Appl. Sci.* 11, 3410. doi:10.3390/app11083410

Mahato, R. P., Kumar, S., and Singh, P. (2021). Optimization of growth conditions to produce sustainable polyhydroxyalkanoate bioplastic by *Pseudomonas aeruginosa* EO1. *Front. Microbiol.* 12, 711588. doi:10.3389/fmicb.2021.711588

Maheshwari, N., Kumar, M., Thakur, I. S., and Srivastava, S. (2018). Production, process optimization and molecular characterization of polyhydroxyalkanoate (PHA) by CO2 sequestering B. cereus SS105. *Bioresour. Technol.* 254, 75–82. doi:10.1016/j.biortech.2018.01.002

Malakar, B., Das, D., and Mohanty, K. (2020). Optimization of glucose yield from potato and sweet lime peel waste through different pre-treatment techniques along with enzyme assisted hydrolysis towards liquid biofuel. *Renew. Energy* 145, 2723–2732. doi:10.1016/j.renene.2019.08.037

Osman, A. I., Blewitt, J., Abu-Dahrieh, J. K., Farrell, C., Al-muhtaseb, A. H., Harrison, J., et al. (2019). Production and characterisation of activated carbon and carbon nanotubes from potato peel waste and their application in heavy metal removal. *Environ. Sci. Pollut. Res.* 26, 37228–37241. doi:10.1007/s11356-019-06594-w

Pan, L., Li, J., Wang, R., Wang, Yu, Lin, Q., Li, C., et al. (2021). Biosynthesis of polyhydroxyalkanoate from food waste oil by *Pseudomonas alcaligenes* with simultaneous energy recovery from fermentation wastewater. *Waste Manag.* 131, 268–276. doi:10.1016/j.wasman.2021.06.008

Passanha, P., Kedia, G., Dinsdale, R. M., Guwy, A. J., and Esteves, S. R. (2014). The use of NaCl addition for the improvement of polyhydroxyalkanoate production by Cupriavidus necator. *Bioresour. Technol.* 163, 287–294. doi:10.1016/j.biortech.2014.04.068

Remedios, Y., and Domingues, L. (2023). Potato peels waste as a sustainable source for biotechnological production of biofuels. *Process Optim.* 155, 320–328. doi:10.1016/j.wasman.2022.11.007

Rodríguez-Martínez, B., Coelho, E., Gullón, B., Yáñez, R., and Domingues, L. (2023). Potato peels waste as a sustainable source for biotechnological production of biofuels: process optimization. *Waste Manag.* 155, 320–328. doi:10.1016/j.wasman.2022.11.007

Samarin, A. M., Hematyar, N., and Elhamirad, A. H. (2012). Phenolics in potato peels: extraction and utilization as natural antioxidants phenolics in potato peels: extraction and utilization as natural antioxidants. *World Appl. Sci. J.* doi:10.5829/idosi.wasj.2012.18.02.1057

Sampaio, S. L., Petropoulos, S. A., Alexopoulos, A., Heleno, S. A., Santos-buelga, C., Barros, L., et al. (2020). Potato peels as sources of functional compounds for the food industry: a review. *Trends Food Sci. Technol.* 103, 118–129. doi:10.1016/j.tifs.2020.07.015

Shangdiar, S., Cheng, P., Chen, S., Amesho, K. T., Ponnusamy, V. K., and Lin, Y. C. (2023). Enhancing sugar yield for bioconversion of rice straw: optimization of Microwave-assisted Pretreatment using dilute acid hydrolysis. *Environ. Technol. Innov.* 32, 103313. doi:10.1016/j.eti.2023.103313

Sharma, P. K., Fu, J., Cicek, N., Sparling, R., and Levin, D. B. (2012). Kinetics of medium-chain-length polyhydroxyalkanoate production by a novel isolate of pseudomonas putida LS46. *Can. J. Microbiol.* 58, 982–989. doi:10.1139/W2012-074

Sharma, P. K., Munir, R. I., Blunt, W., Dartiailh, C., Cheng, J., Charles, T. C., et al. (2017). Synthesis and physical properties of polyhydroxyalkanoate polymers with different monomer compositions by recombinant Pseudomonas putida LS46 expressing a novel PHA SYNTHASE (PhaC116) enzyme. *Appl. Sci.* 7, 242. doi:10.3390/app7030242

Sikkema, W. D., Cal, A. J., Hathwaik, U. I., Orts, W. J., and Id, C. C. L. (2023). Polyhydroxyalkanoate production in Pseudomonas putida from alkanoic acids of varying lengths. *Plos One* 15, e0284377. doi:10.1371/journal.pone.0284377

Soni, S. K., Sharma, B., Sharma, A., Thakur, B., and Soni, R. (2023). Potato peels to bioethanol: evaluation of different pre-treatment strategies for low-cost saccharification using in-house produced multi-enzyme system. *Biol. Biotechnol.* 19, 1. doi:10.20944/preprints202305.0635.v1

Sriyapai, T., Chuarung, T., Kimbara, K., Samosorn, S., and Sriyapai, P. (2022). Production and optimization of polyhydroxyalkanoates (PHAs) from Paraburkholderia sp. PFN 29 under submerged fermentation. *Electron. J. Biotechnol.* 56, 1–11. doi:10.1016/j.ejbt.2021.12.003

Tanikkul, P., Sullivan, G. L., Sarp, S., and Pisutpaisal, N. (2020a). Biosynthesis of medium chain length polyhydroxyalkanoates (mcl-PHAs) from palm oil. *Case Stud. Chem. Environ. Eng.* 2, 100045. doi:10.1016/j.cscee.2020.100045

Tanikkul, P., Sullivan, G. L., Sarp, S., and Pisutpaisal, N. (2020b). Biosynthesis of medium chain length polyhydroxyalkanoates (mcl-PHAs) from palm oil. *Case Stud. Chem. Environ. Eng.* 2, 100045. doi:10.1016/j.cscee.2020.100045

Vu, D. H., Wainaina, S., Taherzadeh, M. J., Åkesson, D., and Ferreira, J. A. (2021). Production of polyhydroxyalkanoates (PHAs) by Bacillus megaterium using food waste acidogenic fermentation-derived volatile fatty acids. *Bioengineered* 12, 2480–2498. doi:10.1080/21655979.2021.1935524

Wang, J., Liu, S., Huang, J., Cui, R., Xu, Y., and Song, Z. (2023). Genetic engineering strategies for sustainable polyhydroxyalkanoate (PHA) production from carbon-rich wastes. *Environ. Technol. Innov.* 30, 103069. doi:10.1016/j.eti.2023.103069

Xu, Z., Pan, C., Li, X., Hao, N., Zhang, T., Gaffrey, M. J., et al. (2021). Enhancement of polyhydroxyalkanoate production by co-feeding lignin derivatives with glycerol in Pseudomonas putida KT2440. *Biotechnol. Biofuels* 14, 11. doi:10.1186/s13068-020-01861-2

Zhou, C., Jiang, W., Via, B. K., Fasina, O., and Han, G. (2015). Prediction of mixed hardwood lignin and carbohydrate content using ATR-FTIR and FT-NIR. *Carbohydr. Polym.* 121, 336–341. doi:10.1016/j.carbpol.2014.11.062

Zhou, W., Bergsma, S., Colpa, D. I., Euverink, G. J. W., and Krooneman, J. (2023). Polyhydroxyalkanoates (PHAs) synthesis and degradation by microbes and applications towards a circular economy. *J. Environ. Manage.* 341, 118033. doi:10.1016/j.jenvman.2023.118033

Advancing Voltage Stability in Half-Bridge Isolated DC-DC Converter through the Adoption of PI Controller

Kumar Gaurav
Electrical Engineering Department
Delhi Technological University
kgaurav000999@gmail.com

Dheeraj Joshi
Electrical Engineering Department
Delhi Technological University
joshidheeraj@dce.ac.in

Shreyansh Upadhyaya
Electrical Engineering Department
Delhi Technological University
shreyansh@dtu.ac.in

2023 11th National Power Electronics Conference (NPEC) | 979-8-3503-1164-8/23/$31.00 ©2023 IEEE | DOI: 10.1109/NPEC57805.2023.10384896

Abstract: **For efficient, reliable, and precise regulation methods in DC-DC converters, the field of power electronics has seen a sharp increase in demand. This study focuses on half-bridge DC-DC buck converter closed-loop voltage mode regulation. A control strategy that assures precise and reliable voltage regulation in the converter output is what is intended to be designed and analysed. Starting with the derivation of a mathematical model, state-space averaging, linearization method, assessment of the open loop bode plot at various input voltage dividing capacitors, and closed-loop voltage mode control are all characterized by their exceptional load regulation abilities. The findings of this research contribute to the enhancement of half-bridge DC-DC buck converter in general and highlight the importance of closed loop voltage mode control, which successfully maintains the target output voltage even in the presence of load changes and disturbances. The controller demonstrates stable output voltage according to the specification required. Comparing the control strategy to open loop control, it also shows improved transient response and decreased steady-state error.**

Keywords — Isolated DC-DC Converter, Small Signal Modelling, PI Controller, Voltage Control mode (VCM), Half bridge buck converter (HBBC)

I. INTRODUCTION

The demand for efficient and reliable power electronic converters has experienced substantial growth in recent years. This growth can be attributed to the increasing integration of renewable energy sources and the necessity for enhanced energy conversion systems. One of the primary obstacles encountered in the field of power electronics pertains to the formulation of resilient control methodologies for converters, with the aim of creating a trade-off between stability and performance. The half-bridge converter is a widely used topology that strikes an optimal balance between cost-effectiveness and performance throughout various applications [1]-[4]. Closed-loop control methods have increasingly gained interest due to their capacity to enhance control performance. This research paper's primary goal is to scrutinize the voltage-mode control of a half-bridge converter, using a Proportional-Integral (PI) controller. Voltage mode control is used to maintain the output voltage by adjusting the duty cycle of the switches in the converter. The Proportional-Integral (PI) controller, presents a valuable solution for maintaining the converter's output voltage while preserving ideal stability and dynamic response traits [5]-[7].

The main focus of this investigation is to analyse the efficiency and resilience of the closed-loop control system using a proportional-integral (PI) controller in conjunction with voltage-mode control in a half-bridge converter. This study's objective is to explore the influence of distinct system parameters, particularly the proportional and integral gains of the PI controller, on the converter's transient and steady-state behaviour Furthermore, the present study offers a comparative analysis of the closed-loop control system in contrast to the open-loop control system, with the aim of explaining the benefits and constraints associated with the implementation of closed-loop control. In order to accomplish these objectives, a MATLAB simulation was conducted on a prototype of a half bridge buck DC-DC converter. The performance metrics examined in this study encompass output voltage regulation, transient response and system stability. The findings of this study carry substantial implications for the design and advancement of control strategies pertaining to voltage-mode control in half-bridge converters [8]-[9]. The findings will enhance comprehension regarding the behaviour of the proportional-integral (PI) controller and its influence on the performance of the converter. Furthermore, the discovered results will contribute to the establishment of criteria for the selection of optimal values for the proportional-integral (PI) controller's gains, thereby facilitating the efficient attainment of the desired control objectives [10]-[12].

The structure of this research paper is neatly organized as follows:

Section II presents the workings of the Half-Bridge DC-DC buck Converter, its operational modes, and the derivation of its small signal model which is a mathematical representation of its dynamic behaviour. Section III explains the crucial process of controller parameters design for the converter, detailing the subsequent formation of the closed-loop system. Furthermore, this section imparts a comparative analysis of the converter's frequency responses, by varying input capacitor values, revealing their impact on the system's dynamics. Section IV deals with MATLAB based simulation for validation of results. The results show the efficacy of the designed controller parameters, upholding stable output voltage regulation while also expediting response time to disturbances—an emphatic testament to the half-bridge DC converter's robustness under the closed-loop arrangement.

II. MODELLING OF HALF BRIDGE BUCK CONVERTER

A third-order isolated half-bridge buck DC-DC converter is composed of two switches, S_{w1} and S_{w2}, two input capacitors, C_a and C_b, one output capacitor C_o and a transformer and inductor for energy transfer as shown in fig.1.

Authorized licensed use limited to: DELHI TECHNICAL UNIV. Downloaded on February 07,2024 at 06:48:32 UTC from IEEE Xplore. Restrictions apply.

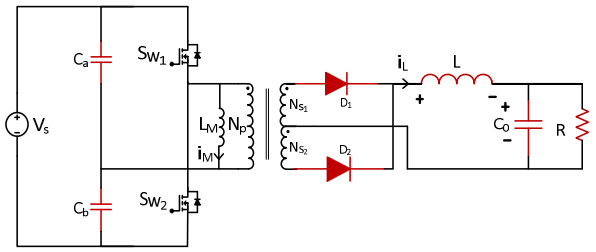


Fig.1 Half Bridge DC-DC Buck Converter Circuit Diagram

The state space averaging method is utilized to conduct the small signal modelling of isolated HBBC. The analysis of the converter modelling is based on the following assumptions. In steady state condition output voltage and current are constant. The transformer's leakage inductance L and the parasitic capacitance Co of switches can be considered insignificant. The duration of the inactive period between the two switch transitions is significantly smaller in comparison to the switching time period and can be neglected. The components L_m, L, and C_o does not have any series resistance. All components within the circuit show no losses, meaning that there is no voltage drop across MOSFETs, diodes, inductors, or capacitors. A small -signal model is derived from the circuit equation to analyse circuit dynamics. The transformer magnetizing inductor current (i_M), output inductor current (i_L), input capacitor voltage (V_{C_a}) and output capacitor voltage (V_{C_o}) are state variables. Input voltage, output voltage are controlled input variable and output variable respectively of the HBBC as shown in Eq. (1).

$$x = \begin{bmatrix} V_{C_a} \\ i_M \\ i_L \\ V_{C_o} \end{bmatrix}, \quad u = [V_s], \quad y = [V_o] \tag{1}$$

The subsequent equation presents the state space representation of a converter system:

$$\begin{aligned} \dot{x} &= Ax + Bu \\ y &= Cx + Du \end{aligned} \tag{2}$$

where A is the state transition matrix, B is the input matrix, C is the output matrix and E is the direct transmission matrix. During the positive half cycle, the upper switch (S_{w1}) is turned on, the lower switch (S_{w2}) is off, allowing current to flow through the positive half of the input DC source, charging the load inductor and delivering power to the output as shown in fig.2(a). Conversely, during the negative half cycle, the lower switch (S_{w2}) turns on, and the upper switch (S_{w1}) turns off, transferring the power stored in the inductor to the load and ensuring continuous power flow to the output.

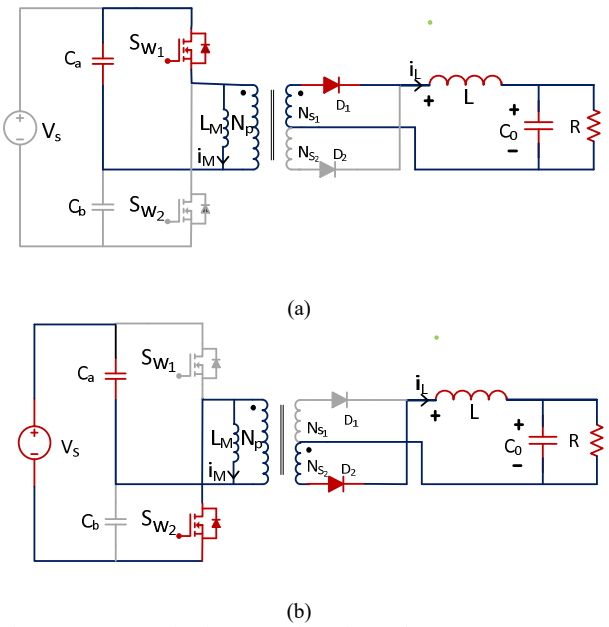


Fig.2. HBBC operation in: (a) Mode 1, (b) Mode 2

The differential equations for Mode 1 operation are given by:

$$\frac{dV_{C_a}}{dt} = -\frac{i_M}{2C_a} - \frac{i_L}{2N_1C_a} \tag{3}$$

$$\frac{di_M}{dt} = \frac{V_{C_a}}{L_M} \tag{4}$$

$$\frac{di_L}{dt} = \frac{V_{C_a}}{N_1 L} - \frac{V_{C_o}}{L} \tag{5}$$

$$V_{C_o} = \frac{i_L}{C_o} - \frac{V_{C_o}}{RC_O} \tag{6}$$

$$\begin{bmatrix} V_{C_a} \\ i_M \\ i_L \\ V_{C_o} \end{bmatrix} = \begin{bmatrix} 0 & -\frac{1}{2C_a} & -\frac{1}{2N_1C_a} & 0 \\ \frac{1}{L_M} & 0 & 0 & 0 \\ \frac{1}{N_1 L} & 0 & 0 & -\frac{1}{L} \\ 0 & 0 & \frac{1}{C_o} & -\frac{1}{RC_O} \end{bmatrix} \begin{bmatrix} V_{C_a} \\ i_M \\ i_L \\ V_{C_o} \end{bmatrix} + \begin{bmatrix} 0 \\ 0 \\ 0 \\ 0 \end{bmatrix} V_s \tag{7}$$

The differential equations for Mode 2 operation are given by:

$$\frac{dV_{C_a}}{dt} = -\frac{i_M}{2C_a} - \frac{i_L}{2N_2C_a} \tag{8}$$

$$\frac{di_M}{dt} = \frac{V_{C_a}}{L_M} - \frac{V_s}{L_M} \tag{9}$$

$$\frac{di_L}{dt} = -\frac{V_{C_a}}{N_2 L} - \frac{V_{C_o}}{L} + \frac{V_s}{N_2 L} \tag{10}$$

$$V_{C_o} = \frac{i_L}{C_o} - \frac{V_{C_o}}{RC_O} \tag{11}$$

$$\begin{bmatrix} V_{C_a} \\ i_M \\ i_L \\ V_{C_o} \end{bmatrix} = \begin{bmatrix} 0 & -\frac{1}{2C_a} & -\frac{1}{2N_2C_a} & 0 \\ \frac{1}{L_M} & 0 & 0 & 0 \\ -\frac{1}{N_2 L} & 0 & 0 & -\frac{1}{L} \\ 0 & 0 & \frac{1}{C_o} & -\frac{1}{RC_O} \end{bmatrix} \begin{bmatrix} V_{C_a} \\ i_M \\ i_L \\ V_{C_o} \end{bmatrix} + \begin{bmatrix} 0 \\ -\frac{1}{L_M} \\ \frac{1}{N_2 L} \\ 0 \end{bmatrix} V_s \tag{12}$$

Authorized licensed use limited to: DELHI TECHNICAL UNIV. Downloaded on February 07,2024 at 06:48:32 UTC from IEEE Xplore. Restrictions apply.

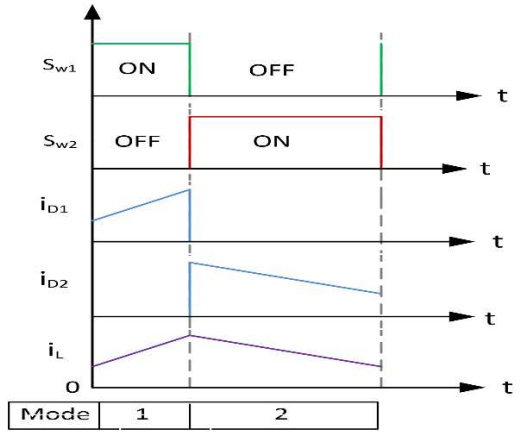


Fig. 3. Switching waveform for switches, diodes and inductor.

To mitigate the impact of the switching ripple component on the circuit equations, a technique of averaging across a single switching period is employed. The averaged switching model is obtained by calculating the average of the aforementioned equations over a single switching period according to fig.3.

$$A = A_1 d + A_2(1-d) \quad (13)$$
$$B = B_1 d + B_2(1-d) \quad (14)$$
$$C = C_1 d + C_2(1-d) \quad (15)$$
$$D = D_1 d + D_2(1-d) \quad (16)$$

In order to obtain the small signal model of the isolated half bridge DC-DC buck converter, it is essential to linearize the nonlinear averaged state-space model in relation to a specified operating point. The introduction of perturbations is employed to modify the state variables (i_m, i_L, V_{Ca}, V_{Co}), input variables (V_s), output variables (V_o), and duty cycle (D).

$$\begin{aligned} d &= D + \hat{d} \\ x &= X + \hat{x} \\ u &= U + \hat{u} \\ y &= Y + \hat{y} \end{aligned} \quad (17)$$

The linearized small signal model is obtained by incorporating the perturbed variables into the averaged state-space model Eq. (13) – Eq. (16) while disregarding the higher order terms.

$$s\hat{x}(s) = A\hat{x}(s) + B\hat{u}(s) + \big((A_1 - A_2)X(s) + (B_1 - B_2)U(s)\big)\hat{d}(s) \quad (18)$$

$$\hat{y}(s) = C\hat{x}(s) + D\hat{u}(s) + \big((C_1 - C_2)X(s) + (D_1 - D_2)U(s)\big)\hat{d}(s) \quad (19)$$

By substituting the parameters values from Table 1, the control to output transfer function can be derived using Eq. (18) as shown below:

$$\frac{\hat{V_o}(s)}{\hat{d}(s)} = (sI - A)^{-1}\big((A_1 - A_2)X(s) + (B_1 - B_2)U(s)\big) \quad (20)$$

$$\frac{\hat{V_o}(s)}{\hat{d}(s)} = \frac{\alpha_{12}s^2 + \alpha_{11}s + \alpha_{10}}{s^4 + \beta_3 s^3 + \beta_2 s^2 + \beta_1 s + \beta_0} \quad (21)$$

Where the constant values are given as follows:

$$\begin{aligned} &\alpha_{12} = 4.7 \times 10^8 \quad \alpha_{11} = 4.273 \times 10^{10} \\ &\alpha_{10} = 9.4 \times 10^{15} \\ &\beta_3 = 126.3 \quad \beta_2 = 1.578 \times 10^7 \\ &\beta_1 = 1.514 \times 10^9 \quad \beta_0 = 3.788 \times 10^{13} \end{aligned} \quad (22)$$

Table I Design parameter of half bridge DC-DC buck converter

Parameters	Symbols	Values
Input Voltage	V_s	220 V
Output Voltage	V_o	48 V
Switching Frequency	f_{sw}	100 kHz
Duty Cycle	D	.218
Magnetising Inductance	L_m	500µH
Filter Inductor	L	800µH
Filter Capacitor	C_0	300µF
Load Resistance	R	24Ω
Secondary Winding 1	N_{s_2}	1
Secondary Winding 2	N_{s_1}	1
Current Ripple	ΔI_o	20% I_o
Voltage Ripple	ΔV_o	10%V_o

III. CONTROL METHOD

For the isolated half bridge DC-DC buck converter to achieve the desired voltage regulation, improve dynamic response, and increased system stability, closed-loop control must be used. In this study, the proportional integral (PI) controller utilized in closed-loop half bridge DC-DC converter with voltage mode control is thoroughly studied, and its effects on the converter's overall performance is evaluated.

A. Voltage mode control

Voltage mode control is a widely used technique in half-bridge DC-DC buck converter for regulating the output voltage. It involves comparing the output voltage with a reference voltage and adjusting the duty cycle of the switching signals to achieve the desired output voltage as shown in fig.4. This control method provides stable and reliable regulation of the output voltage, this section primarily focuses on the control design factors, stability analysis, and performance evaluation of voltage mode control strategies

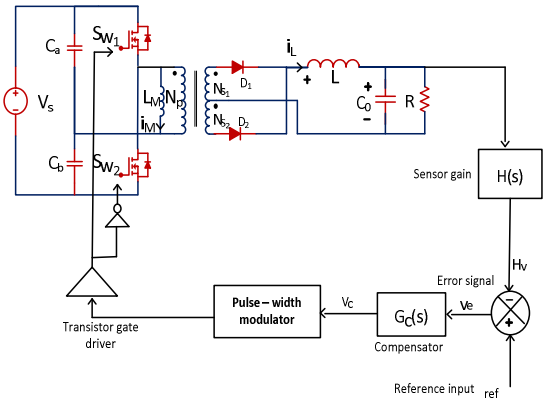


Fig. 4. Voltage mode control of Half bridge buck converter

The transfer function of the PI controller is given by:

$$G_c(s) = K_{prop} + \frac{K_{int}}{s} \quad (23)$$

$$G_c(s) = 1.8344 \times 10^{-2} + \frac{0.56521}{s} \quad (24)$$

The reference to the output closed-loop transfer function is given by:

Authorized licensed use limited to: DELHI TECHNICAL UNIV. Downloaded on February 07,2024 at 06:48:32 UTC from IEEE Xplore. Restrictions apply.

$$\frac{V_{ref}}{V_o} = \frac{\alpha_{23}s^3+\alpha_{22}s^2+\alpha_{21}s+\alpha_{20}}{s^5+\beta_4 s^4+\beta_3 s^3+\beta_2 s^2+\beta_1 s+\beta_0} \quad (25)$$

Where the constant values are given as follows:

$$\alpha_{23} = 8.622\times10^{6} \quad \alpha_{22} = 1.049\times10^{9}$$
$$\alpha_{21} = 1.725\times10^{14} \quad \alpha_{20} = 5.313\times10^{15} \quad (26)$$
$$\beta_4 = 126.3 \quad \beta_3 = 2.44\times10^{7} \quad \beta_2 = 2.563\times10^{9}$$
$$\beta_1 = 2.103\times10^{14} \quad \beta_0 = 5.313\times10^{15}$$

Fig.4. displays the bode plot of the open loop plant, illustrating the variations resulting from different input capacitor values, C_a. Three different capacitance values were used for C_a are 100µF, 200µF, and 330µF. The presented figure illustrates that alterations in the values of capacitors result in variations in the phase margin of the open loop system. The phase margin for a 100µF capacitor is -0.773 degrees, indicating a high level of instability in the open loop system. However, when using a 200µF capacitor, there is a slight improvement in the phase margin, which increases to 5.96 degrees. The phase margin for a capacitor with a capacitance of 330 µF is measured to be 6.54 degrees. An increase in the value of capacitor C_a leads to an enhancement in the phase margin of the open loop system. This study helps in selection of C_a capacitor value

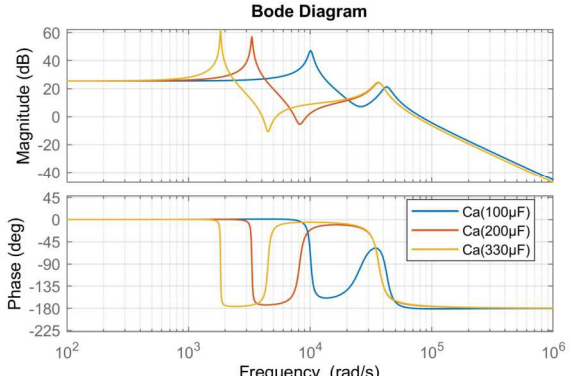


Fig. 5 Open loop frequency response with variation in C_a of Half bridge DC-DC buck Converter

While it is true that the stability of a system increases with an increase in phase margin, this improvement is accompanied by a trade-off in the form of a slower response time. In order to achieve optimal response time and system stability, the value of C_a is selected as 200 µF for the design of the closed-loop system, as indicated by Eq. (24).

Fig.6. illustrates the frequency response of the closed loop system. The closed loop system exhibits a phase margin of 78 degrees, indicating a significantly higher level of stability in comparison to its open loop counterpart.

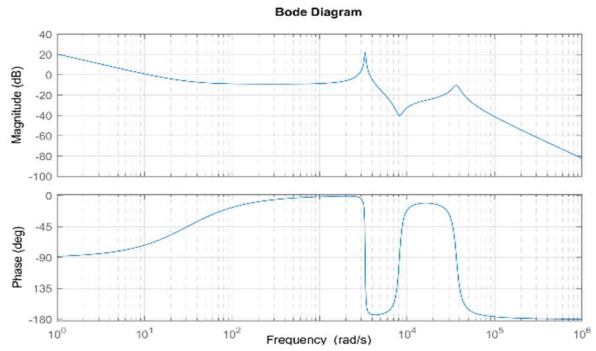


Fig. 6 Bode plot of closed loop system of half bridge DC-DC buck converter

IV. RESULTS AND DISCUSSION

The design and modeling of the Half bridge DC-DC buck converter in conducted using MATLAB/Simulink. Additionally, the PI controller was developed and calibrated using the Phase Margin test methodology.

Open loop Vs Closed Loop Voltage Comparison: Fig. 7 depicts the output voltage characteristics of the half bridge buck converter in both open and closed loop configurations. The open loop system exhibits a maximum peak overshoot of 51%, whereas the closed loop system demonstrates a maximum peak overshoot of 9.85%. This observation suggests a clear correlation between the phase margin and the maximum peak overshoot. Increasing the phase margin of the system results in a reduction in the peak overshoot.

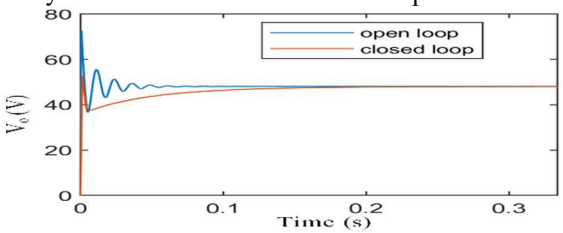


Fig. 7 Open loop vs closed loop Half bridge DC-DC buck converter output voltage

Load Regulation: The evaluation of the steady load regulation performance involves a step variation of the resistive load within the range of 20Ω to 100Ω. This process is accompanied by continuous monitoring of the output voltage, as illustrated in Fig. 8. The simulation findings illustrate the converter's capacity to sustain a consistent output voltage within a desired load, thereby regulating output voltage precisely.

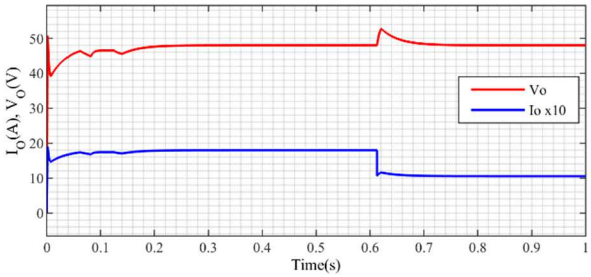


Fig. 8 Load Regulation response of Half bridge DC-DC buck converter

V. CONCLUSION AND FUTURE SCOPE

In conclusion, this research underscores the substantial merits of employing closed-loop voltage mode control in half-bridge DC converter. Through a thorough investigation, including a small-signal analysis, we have assessed the system's stability, transient step response, and bandwidth characteristics. In the course of the investigation, the system's response to different input capacitor values is examined. This in-depth analysis proved instrumental in identifying the most suitable input capacitor with a capacitance of 200 µF, thereby enhancing the overall stability of the system, resulting a phase margin of 78 degrees. These findings both inform and propel the design, optimization, and effective application of this control strategy in numerous power electronic contexts.

Dependable output voltage of 48V is maintained via voltage mode control, even when faced with sudden load variations from 20Ω to 100Ω. It's critical to recognize, however, that achieving superior performance is

Authorized licensed use limited to: DELHI TECHNICAL UNIV. Downloaded on February 07,2024 at 06:48:32 UTC from IEEE Xplore. Restrictions apply.

fundamentally contingent upon appropriate selection of controller parameters. Additionally, the efficiency of this control approach may be modulated by different power levels or applications.

To effectively address the impact of load and line voltage variations, it is advisable to encourage further research in this domain. Subsequent investigations could centre their attention on optimizing controller parameters to suit diverse operating conditions, as well as engaging in comparative analyses of alternative control strategies. Moreover, future research endeavours may delve into the exploration of non-linear controllers, such as sliding mode or model predictive controllers, to tackle the inherent non-linearities within the system. This avenue of research holds the promise of deepening our understanding and uncovering the most efficient controller strategies tailored for half-bridge DC-DC buck converters

REFERENCES

[1] Xinyu Xu, A. M. Khambadkone and R. Oruganti, "An asymmetrical half bridge DC-DC converter: close loop design in frequency domain," 2004 IEEE 35th Annual Power Electronics Specialists Conference (IEEE Cat. No.04CH37551), Aachen, Germany, 2004, pp. 1642-1647 Vol.2, doi: 10.1109/PESC.2004.1355672.

[2] B. Choi, W. Lim, Sanghyun Bang and Seungwon Choi, "Small-signal analysis and control design of asymmetrical half-bridge DC-DC converters," in IEEE Transactions on Industrial Electronics, vol. 53, no. 2, pp. 511-520, April 2006, doi: 10.1109/TIE.2006.870715.

[3] A. J. Perin and I. Barbi, "A new isolated half-bridge soft-switching pulse-width modulated DC-DC converter," [Proceedings] APEC '92 Seventh Annual Applied Power Electronics Conference and Exposition, Boston, MA, USA, 1992, pp. 66-72, doi: 10.1109/APEC.1992.228429.

[4] W. Eberle and Yan-Fei Liu, "A zero voltage switching asymmetrical half-bridge DC/DC converter with unbalanced secondary windings for improved bandwidth," 2002 IEEE 33rd Annual IEEE Power Electronics Specialists Conference. Proceedings (Cat. No.02CH37289), Cairns, QLD, Australia, 2002, pp. 1829-1834 vol.4, doi: 10.1109/PSEC.2002.1023076.

[5] F. F. Linera, J. Sebastian, M. A. Perez Garcia, J. Diaz and A. Fontan, "Closing the feedback loop in the half-bridge complementary-control DC-to-DC converter," Proceedings of APEC 97 - Applied Power Electronics Conference, Atlanta, GA, USA, 1997, pp. 977-982 vol.2, doi: 10.1109/APEC.1997.575766.

[6] T. Ninomiya, N. Matsumoto, M. Nakahara and K. Harada, "Static and dynamic analysis of zero-voltage-switched half-bridge converter with PWM control," PESC '91 Record 22nd Annual IEEE Power Electronics Specialists Conference, Cambridge, MA, USA, 1991, pp. 230-237, doi: 10.1109/PESC.1991.162681.

[7] Erickson, R. W., Maksimovic, D. (2001). Fundamentals of Power Electronics. Springer.

[8] D.W. Hart, "Power Electronics," McGraw-Hill, New York, NY, USA, 2011.

[9] O. Tahmaz and A. B. Yıldız, "Efficient Modeling Technique for Analysis of the Half Bridge DC-DC Converter," 2021 23rd European Conference on Power Electronics and Applications (EPE'21 ECCE Europe), Ghent, Belgium, 2021, pp. P.1-P.10, doi: 10.23919/EPE21ECCEEurope50061.2021.9570626.

[10] Hong Mao, Songquan Deng, Yangyang wen and Issa Batarseh, "Unified steady-state model and DC analysis of half-bridge DC-DC converters with current doubler rectifier," Nineteenth Annual IEEE Applied Power Electronics Conference and Exposition, 2004. APEC '04., Anaheim, CA, USA, 2004, pp. 786-791 vol.2, doi: 10.1109/APEC.2004.1295912.

[11] Xinyu Xu, A. M. Khambadkone and R. Oruganti, "Analysis and design of an optimized asymmetrical half-bridge DC-DC converter," The Fifth International Conference on Power Electronics and Drive Systems, 2003. PEDS 2003., Singapore, 2003, pp. 120-125 Vol.1, doi: 10.1109/PEDS.2003.1282697.

[12] P. Imbertson and N. Mohan, "Asymmetrical duty cycle permits zero switching loss in PWM circuits with no conduction loss penalty," in IEEE Transactions on Industry Applications, vol. 29, no. 1, pp. 121-125, Jan.-Feb. 1993, doi: 10.1109/28.195897.

Authorized licensed use limited to: DELHI TECHNICAL UNIV. Downloaded on February 07,2024 at 06:48:32 UTC from IEEE Xplore. Restrictions apply.

International Journal on Interactive Design and Manufacturing (IJIDeM)
https://doi.org/10.1007/s12008-023-01719-5

REVIEW

An overview of cold metal transfer welding of similar materials

Indra Jeet Singh[1] · **Paras Kumar**[1] · **Qasim Murtaza**[1]

Received: 24 September 2023 / Accepted: 11 December 2023
© The Author(s), under exclusive licence to Springer-Verlag France SAS, part of Springer Nature 2024

Abstract
This review paper offers a comprehensive analysis of the cold metal transfer (CMT) welding process in the context of similar metals and alloys. With a focus on recent advancements and key research contributions, the paper synthesizes a wealth of information to provide an understanding of the technique's applicability and potential in welding similar metals and alloys. By delving into the intricate interplay of process parameters, such as welding current, wire feed speed and shielding gas composition, the paper elucidates their influence on critical aspects of weld quality, including bead morphology, microstructure, and mechanical properties. In summation, this review consolidates the collective knowledge surrounding CMT welding of similar metals and alloys, providing researchers, practitioners, and industries with a comprehensive resource to navigate the intricacies of this technique. As the industrial landscape seeks to elevate welding standards, minimize post-weld processing, and optimize resource utilization, the insights presented in this review pave the way for the continued evolution and widespread adoption of CMT welding in the field of similar metals and alloys.

Keywords Cold metal transfer welding · Similar metals · Microstructure · Bead morphology · Mechanical properties

1 Introduction

Cold metal transfer (CMT) welding is a novel technique for joining similar and dissimilar metals. It offers advantages such as reduced heat input, clear weld morphology, and high reproducibility. CMT welding has been successfully used for joining aluminum alloy to galvanized low carbon steel, resulting in visually acceptable welds with clear fish-scale ripples [1]. Friction stir welding (FSW) is another non-fusion process that has been employed for steel-aluminium joining, offering a viable alternative for dissimilar welding [2]. CMT welding technique, an improvised version of gas metal arc welding (GMAW), has been found to be ideal for joining thin sheets and plates, with reduced spatter and distortion [3]. The growth of intermetallic compounds (IMCs) in Al/steel dissimilar joints, particularly the Fe2Al5 layer, significantly affects joint strength and reliability [4]. Twin-wire CMT with Al–Si filler has been used for dissimilar joining of stainless steel and aluminum, resulting in satisfactory joint performance with the presence of IMCs [5]. The use of cold metal transfer (CMT) welding technique for dissimilar metal welding has gained significant attention due to its ability to produce improved weld bead aesthetics, controlled metal deposition, and low heat input [6]. This method has been particularly effective in joining dissimilar metals, such as aluminum and steel, with better results than other welding techniques [7]. The process parameters and material properties play a crucial role in achieving a good welding joint [8]. Recent advancements in CMT welding have focused on enhancing the mechanical properties of aluminum alloys and improving the efficiency of the welding system [9]. However, further research is needed to address the challenges and improve the methods for joining dissimilar metals using CMT welding.

CMT stands for cold metal transfer and is known for its ability to minimize distortion and reduce the risk of effects in welded joints. It achieves this by using a controlled short-circuiting transfer mode, resulting in precise and controlled heat input. Additionally, CMT offers improved control over the welding process, making it suitable for applications requiring high-quality welds with minimal spatter. Contrary to conventional welding, CMT welding utilizes an

✉ Indra Jeet Singh
iindrajeett@gmail.com

Paras Kumar
paraskumar@dtu.ac.in

Qasim Murtaza
qasimmurtaza@dce.ac.in

[1] Delhi Technological University, New Delhi, India

Published online: 24 January 2024

inverter, digital signal processing (DSP), and analogue to digital converter (ADC). Galvanised steel, aluminium alloys, magnesium alloys, and other materials can all be used using CMT technology. For combining aluminium pieces made of comparable and different alloys, cold metal transfer (CMT) is probably a revolutionary welding procedure that offers versatility, eco-friendly, and energy efficiency [10, 11]. The CMT technique has been successfully used in certain reports to weld components constructed from similar aluminium alloys [12–16]. CMT has also been used in joining different grades of steel in the fabrication industry because of its economical and ideal means of joining process [17]. Moreover, for many applications, including the repair of welds in Al alloys, CMT is an alternative to thermal spray techniques due to its higher deposition rate [18].

The development of the current scenario in the advanced welding process of aluminum to automotive steel with the help of the CMT welding process has been investigated in several studies. One study focused on the use of advanced CMT variants in joining galvannealed steel and AA6061-T6 aluminum. The influence of current and voltage characteristics on the thermal profile, joint profile, IMC layer morphology, and mechanical properties of the joint was studied [19]. Another study explored the welding of zinc-coated steel using the CMT process, which successfully joined the zinc-coated steels without defects due to its controlled heat input [20]. Additionally, a study analyzed the welded joint of DX51D steel with an Aluzinc layer and AlMg3 alloy sheet using CMT welding, resulting in a weld with considerable porosity [21]. Furthermore, a research paper described a new joining technology based on resistance welding for joining ultra-high strength steel with aluminum sheets, which showed successful results for joining dissimilar steel-aluminum compounds [22]. Finally, an invention provided a CMT welding process for joining 1Cr18Ni9Ti stainless steel and 5A06 aluminum alloy, solving the technical problem of low argon arc welding strength and improving connection strength [23].

In 2019, Çömez et al. [24] investigated the effect of varying different welding parameters, like heat input, welding speed, etc., on the strength, microstructure, and corrosion behaviour of AA6061 aluminium alloy sheets welded by the CMT process. Ola and Doern [25] proposed the CMT technique for low-dilution clads and Inconel 718 repair in turbine applications. Rajeev et al. [26] studied the effect of dynamic correction and the arc length correction parameters on the deposition of Sterilite 6 filler wire on AISI H13 steel by CMT. In their result they found lower heat input in lower dilution and finer microstructure resulting in high hardness of the bead.

In this review paper different behavior of similar joints have been discussed along with their welding parameters. The microstructure, tensile strength, micro hardness and other analysis are investigated and from them certain conclusions are made on the basis of their weld quality.

2 Experimental process of CMT along their parameters

The mechanism of the CMT welding process involves a continuous process of arc heating, mass transfer, short-circuit, and spreading. This process is characterized by the deliberate retraction of the filler metal wire during the short circuit, which aids in the disengagement of droplets and their transfer into the molten pool without the support of electromagnetic force [9]. The input of heat is greatly reduced, resulting in lower spatter and distortion of joints, making CMT welding ideal for joining thin sheets and plates [3]. The stability of the arc is maintained through mechanical means, allowing for easy control of the arc length and making CMT welding suitable for all positions and applications [27]. The welding width can be analyzed and predicted using calculation equations based on the CMT model, which simplifies the complex welding process into continuous physical behaviour [28]. The CMT welding process has gained attention for its ability to join dissimilar metals with minimal heat input and rapid heating and cooling [29].

CMT welding is a process used to join metal plates using a MIG wire. The effects of various parameters such as current, distance between nozzle and tip, and welding speed on the strength, hardness, and surface roughness of the welded zone have been investigated in several studies. The results show that current has a significant effect on the output variables, and its interaction with welding speed also influences the tensile strength, hardness, and surface roughness [30] In addition, the CMT process has been applied in additive manufacturing, specifically in the deposition of copper overlays on different substrates. Post heat-treatment of the weld overlays has been found to improve their electrical conductivity [31]. Furthermore, the alloy composition of hot-work steels has been tailored using metal-cored wires in a modified CMT process for wire arc additive manufacturing. The addition of nickel to the hot-work tool steel alloys has been shown to reduce the phase fraction of delta ferrite and improve the mechanical properties of the fabricated structures [32].

3 Effect of filler wire in CMT process

CMT welding has various effects on the mechanical and microstructure properties of welded joints. In the case of AA7475-T7351 alloy, the weld metal (WM) has lower hardness compared to the base metal (BM) [33]. Cu-based filler metals in Cu/SS dissimilar metal joints can lead to Cu penetration cracks in the heat-affected zone (HAZ) on

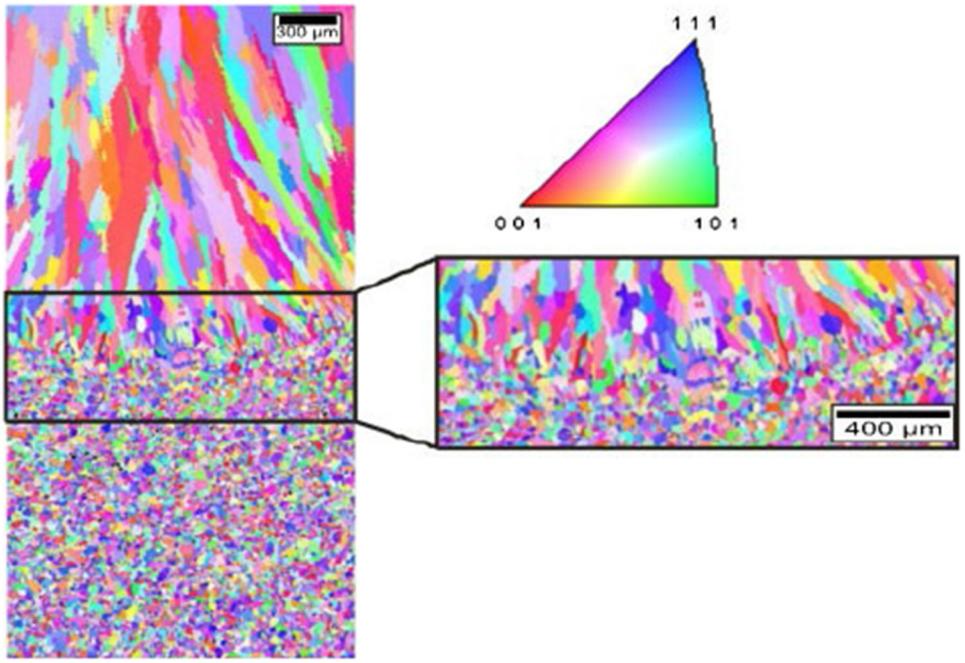


Fig. 1 Displays the electron backscatter diffraction (EBSD) maps acquired at the center of the weld

the steel side, while Ni-based filler metals can effectively eliminate these cracks [34]. In dissimilar joints of aluminum-galvanized steel, increasing the heat input improves the corrosion resistance and strength of the joints due to reduced solidification defects and the establishment of an appropriate intermetallic layer thickness [35]. In the case of 7050-T6 aluminum alloy, the weld zone has equiaxed crystal and dendrite structures, and the hardness of the weld zone is the smallest [36]. Friction stir welded joints of 7075 aluminum alloy with CO2-assisted cooling exhibit finer grain size and precipitation hardening, resulting in softened joints at room temperature [37].

4 CMT welding of similar metals

Joints of similar metals/metal alloys have been accomplished by the CMT welding technique giving a better weld appearance and joint strength. Some of the similar metal/metal alloy joints are briefly discussed below:

4.1 Inconel 718 alloy

The microstructure of the welded workpiece showed no lack of fusion. HAZ formed with the CMT technique was small (0.5 mm) compared to MIG HAZ. The residual stresses found by Benoit et al. [38] were minimum. With low process temperature, some intrinsic properties of the weld got enhanced. The small size of HAZ and reduced residual stresses were the main reasons for increasing the weld quality.

Figure 1 displays the electron backscatter diffraction (EBSD) maps acquired at the center of the weld. Two primary microstructures are observable. The parent metal at the bottom exhibits small equiaxed grains, which are typical of a hot rolled sheet. In contrast, the weld zone at the top is characterized by columnar grains. This structure is commonly observed during the solidification phase. Crystallite growth is influenced by temperature gradients, resulting in the formation of elongated grains. The average length of the grains is 120 mm, and the average dimension of the substrate grains is 12 mm. In conclusion, the presence of lack of fusion was examined during the microstructure analysis. EBSD analysis was performed on the weld edges. Figure 2 displays the electron backscatter diffraction (EBSD) map located in the left corner of the weld. The absence of defects is observable, and the fusion line exhibits satisfactory quality. The presence of multicolour points on the left side of the weld is attributed to the absence of indexation. No cracks or lack of fusion were observed in this area during SEM investigations.

4.2 Aluminum 7075 alloy

The implementation of CMT welding resulted in the creation of spatter-free joints characterized by the absence of cracks and reduced porosity, as illustrated in Fig. 3. As observed by Elrefaey et al. [39], this welding technique effectively mitigated the typical issues associated with spatter and porosity formation during the welding process. However, despite the joint formation's overall success, the mechanical properties of the welded joint exhibited variations across different regions. Notably, joint failure predominantly occurred in the

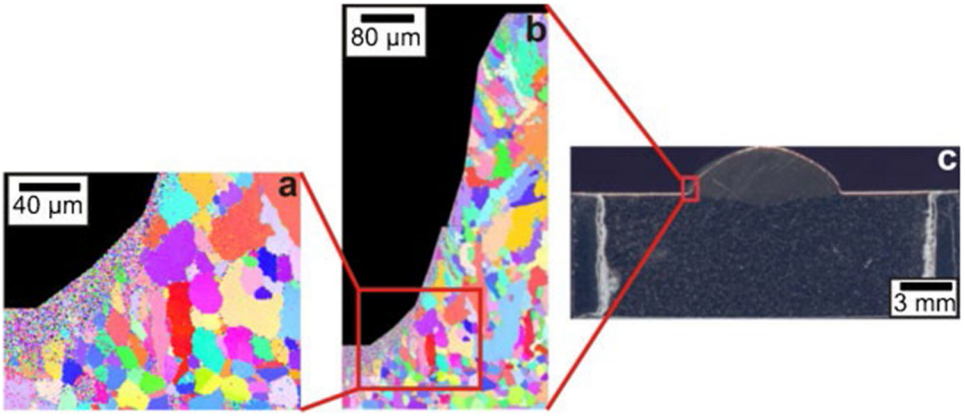


Fig. 2 Displays the electron backscatter diffraction (EBSD) map located in the left corner of the weld

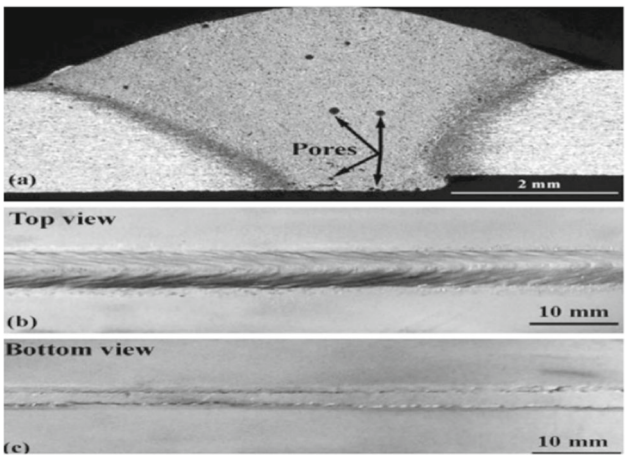


Fig. 3 Weld bead microstructure cross-section (**a**), top view (**b**) and bottom view (**c**) [39]

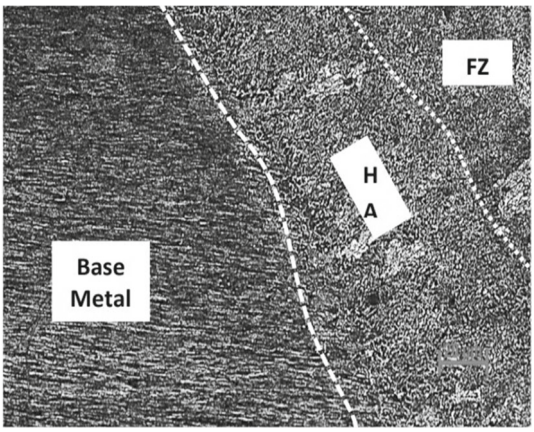


Fig. 4 Microstructure of Al 6061 alloy seen from optical microscopy [40]

weld metal zone, emphasizing the significance of understanding the microstructural changes induced by the welding process. In terms of microhardness, it was observed that the weld metal zone exhibited the minimum hardness, while the heat-affected zone (HAZ) experienced a slight decrease in hardness. This variation in hardness across different joint zones indicates differences in material properties, which can influence the joint's overall mechanical performance. The joint achieved mechanical property coefficients of 77%, 60%, and 69% for yield strength, ultimate tensile strength, and elongation, respectively. These coefficients highlight the joint's capability to withstand applied forces, resist deformation, and exhibit ductility. The observed decrease in microhardness in the HAZ, coupled with joint failure in the weld metal zone, underscores the importance of optimizing welding parameters to achieve a well-balanced distribution of mechanical properties across the entire welded joint. This optimization process is essential for ensuring the welded component's overall structural integrity and performance.

4.3 Aluminium AA6061 alloy

Kumar et al. [40] found out that the weld obtained was remarkable when the current is maintained between 60 and 70A and weld speed at 8–10 mm/s. Figure 4 shows the microstructure of aluminum 6061 alloys obtained from optical microscopy. At the joints, the microstructure revealed fine recrystallization. A clear-cut distribution of grain and its size were visible. CMT spot welding was done on AA6061-T6 aluminum alloy. The joints fabricated from the CMT mode have superior mechanical properties and very few defects among other arc modes. With a chill block at the bottom of the weld zone, the strength and toughness were improved, and HAZ was reduced, as found by Lei et al. [41]. In Pramod et al. [42] investigation, the tensile strength and the elongation of weld metal were less than the parent metal. The fracture position of reinforced and without reinforced tensile specimens was found in the base and weld metal regions, respectively. The fracture formed in the sample was because of the presence of dimples and empty voids.

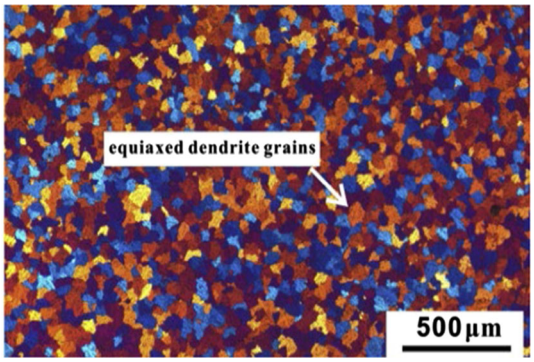


Fig. 5 Grain morphology of the sample [43]

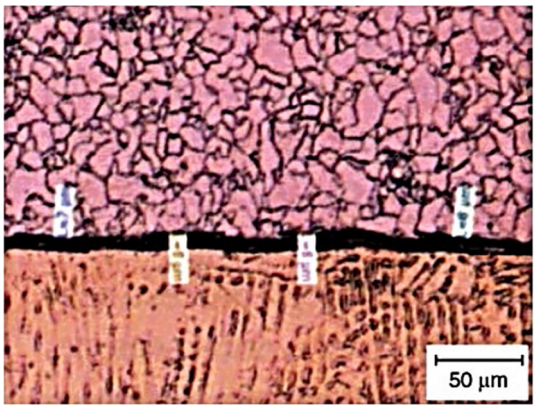


Fig. 6 Diffusion of copper in the parent metal [44]

4.4 H111-5083 aluminum alloy

The microstructural analysis revealed the formation of refined equiaxed grains with reduced pores, as illustrated in Fig. 5. This outcome indicates a favorable welding condition in the Wire Arc Additive Manufacturing (WAAM) process. However, a notable observation by Zhang et al. [43] showed a sudden increase in grain size in the top layer. This phenomenon was attributed to differences in heat accumulation. The heat input during welding is crucial in determining microstructural characteristics. A gradual decrement of heat input in the initial layers of WAAM contributes to refining the microstructure. This refinement is associated with the formation of refined, equiaxed grains, enhancing the overall mechanical properties of the structure. The abrupt increase in grain size observed in the top layer may result from variations in the heat accumulation process. These differences can influence the cooling rate and, subsequently, the grain growth. The corresponding microhardness values reflected this trend, decreasing from 98.7 to 76.4 HV. The connection between heat input, microstructure, and mechanical properties underscores the importance of precise control over welding parameters in WAAM to achieve desired material characteristics.

4.5 Galvanized steel

In A. Magda et al. investigation, Macro- and microscopic metallographic examination confirmed the high quality of brazed joints, showing a copper diffusion area and the undamaged zinc layer in areas adjacent to the weld. As shown in Fig. 6, the copper diffusion zone increased the strength of the brazed joint and the durability of the zinc coating [44]. Selvamani et al. also investigated galvanized steel's microstructure and mechanical properties. The joint quality was improved using the advanced CMT technique compared with the joints formed with the conventional CMT technique. The combined ferrite-pearlite microstructures, fine bainitic ferrite phases, and acicular ferrite and martensite with an average size of 9.4 µm in the FZ were responsible for improved mechanical properties [45].

4.6 AISI 304 stainless-steel

In the CMT (Cold Metal Transfer) welding process, a butt joint of AISI 304 was created, and the microstructure and mechanical properties of the welded joint were analyzed. The microhardness in the heat affected zone (HAZ) decreased due to the metal's softening effect and the presence of coarser grains, as illustrated in Fig. 7. The decrease in microhardness was approximately 16% and 25% in the weld metal zone compared to the parent metal. HAZ is the material region that experiences changes in microstructure and properties due to the heat generated during welding. Coarser grains in HAZ contribute to the reduction in microhardness, as larger grains are often associated with a softer material. The softening effect in HAZ is a common phenomenon in welding processes and is influenced by factors such as heat input and cooling rates. Roy et al. [28] achieved the highest tensile strength of 723 MPa in the welded joint. The welding parameters used for this achievement were a 95 A current, 4 mm/s welding speed, and a 7 mm contact tip-to-workpiece distance. Tensile strength is a crucial mechanical property that indicates the material's ability to withstand axial loads without breaking. The welding conditions and parameters employed by J. G. Roy et al. demonstrate the optimization of the CMT process for achieving high tensile strength in the welded joint. The detailed analysis of microhardness and tensile strength provides valuable information about the mechanical behavior of the welded joint, offering insights essential for ensuring the structural integrity and performance of the weld.

4.7 2A12 aluminum alloy

In the fabrication of a double-sided joint using 2A12 aluminum alloy with a 2 mm sheet thickness, welding played

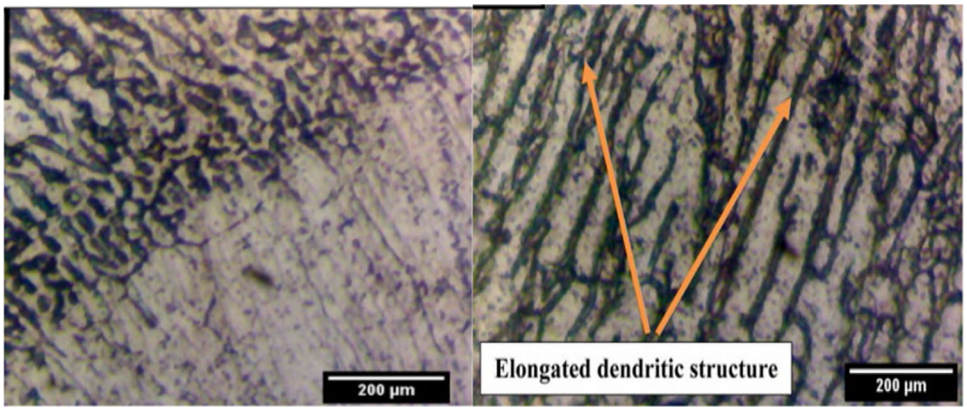


Fig. 7 Microstructure of fusion line and HAZ, respectively [28]

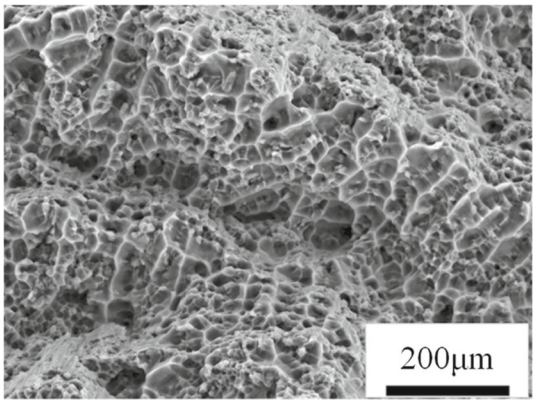


Fig. 8 Fracture morphology of welded workpiece [46]

a critical role in determining the weld's appearance and microstructure. Increasing the heat input to 651.75 J/mm contributed to notable improvements in both aspects.

The weld's appearance, which refers to its visual characteristics, such as bead geometry and surface quality, is a key factor in assessing the quality of the welding process. Higher heat input often enhances fusion and penetration, resulting in a more refined and aesthetically pleasing weld appearance. Microstructural changes are crucial in understanding a welded joint's mechanical properties and performance. With the elevated heat input, the microstructure of the weld likely underwent modifications that influenced its properties. However, specific details about the alterations in the microstructure were not provided. The coefficient of strength, recorded at approximately 70%, indicates a substantial level of strength retention in the welded joint. This coefficient measures the joint's strength compared to the base material, with a higher percentage indicating a more robust welded joint. As depicted in Fig. 8, the fracture surface analysis revealed dimples on the fractured surface [46]. Dimples are characteristic of ductile fracture modes, suggesting that the failure occurred progressively through plastic deformation rather than sudden rupture. Ductile fractures are typically desirable in structural components as they allow for some deformation before failure, providing a warning sign and enhancing the overall safety of the structure.

4.8 AA2219-T851 alloy

The study by Cong et al. [47] focused on investigating the impact of multiple cold metal transfer (CMT) arc modes on weld geometry. The CMT process is a welding technique known for minimizing heat input and reducing spatter. Different CMT arc modes were employed, and their effects on the weld geometry were observed.

In the conventional CMT mode, the researchers noted the weld's narrow, finger-shaped geometry, characterized by many pores in both the lower and upper parts of the bead. Pores can be detrimental to weld quality, affecting its mechanical properties. The finger-shaped geometry may indicate uneven heat distribution or insufficient fusion. Transitioning to the CMT + P mode, there was an effective increase in the weld metal area. This mode likely introduced some modifications to the process, resulting in a more desirable weld metal distribution. Reducing gas pores in this mode suggests improving the overall weld quality.

A finger-shaped geometry was again observed in the CMT-Advance mode but with reduced gas pores. This indicates that the CMT-Advance mode might offer improvements in porosity compared to the conventional CMT mode. The CMT-PADV mode exhibited a distinctive spherical-shaped bead geometry with the elimination of pores shown in Fig. 8. The spherical shape is often desirable as it indicates more uniform heat distribution and better fusion. The absence of pores further enhances the weld quality, as pores can act as stress concentrators and compromise the mechanical properties of the weld.

4.9 G115 steel

CMT-P arc mode was used in the fabrication of G115 steel. Cai et al. [48] investigated the effect of varying heat input on the microstructure and mechanical properties of the joint. A

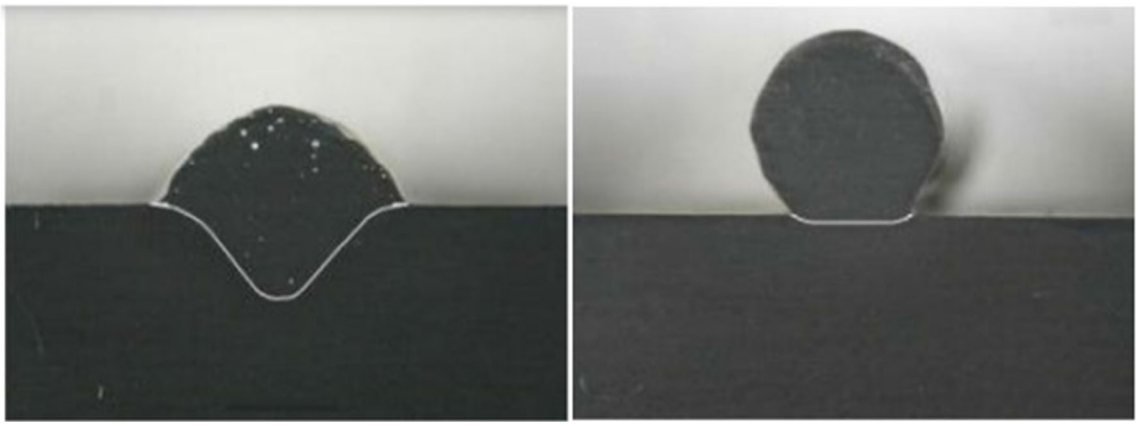


Fig. 9 Cross-section of weld bead formed by conventional CMT mode and CMT-PADV mode, respectively [47]

higher heat input increased the high-temperature time period, which was the reason for precipitate formation, which is why the joint's hardness and strength were improved. The toughness of the joint was reduced due to the coarsening of grains caused by high heat input. At 0.89 kJ/mm heat input, maximum hardness and maximum tensile strength (777 MPa) were recorded at room temperature.

4.10 UNS S32750

Different forms of austenite and ferrite were observed in the welding process, as depicted in Fig. 9. Austenite and ferrite are two distinct phases in the steel microstructure, and their formation is influenced by temperature and alloy composition. The specific arrangement of these phases plays a crucial role in determining the mechanical properties of the welded joint. According to the observations made by Arun et al. [49] hardness was slightly increased in the fusion zone (FZ), the region of the welded joint where the base materials have melted and fused. The tensile fracture formation in the FZ suggests that the welding process had an impact on the mechanical behavior of the joint. The efficiency of the joints welded using the cold metal transfer (CMT) technique was recorded as 98.5%. This indicates that the CMT technique, known for its ability to reduce heat input and minimize spatter, resulted in highly effective joints with a high percentage of weld efficiency. Weld efficiency measures how well the welded joint performs compared to the base material. A change in fracture mode was observed when the temperature decreased from 24 to − 196 °C. The transition from ductile to brittle fracture behavior suggests that the mechanical response of the welded joint is temperature-dependent. Ductile fractures are characterized by plastic deformation and energy absorption, while brittle fractures involve little to no plastic deformation and are associated with sudden and catastrophic failure (Fig. 10).

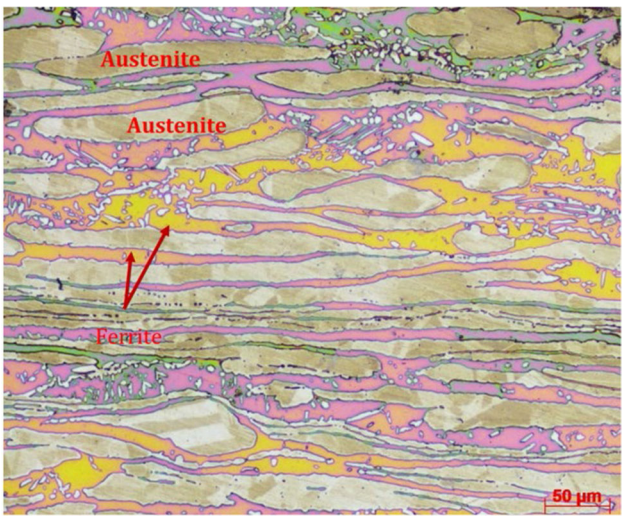


Fig. 10 Optical microscopy image of ferrite and austenite islands [49]

4.11 AISI430 ferritic stainless steel

A butt joint of respective stainless steel was fabricated with the help of CMT. The microstructure of weld metal contained ferrite and austenite phases. The microhardness of the welded joint first increased from weld metal to HAZ and then decreased from HAZ to the base metal. The fracture occurred, was in the base metal region. The dimple formation on the fractured surface depicted in Fig. 11 was characterized as ductile fracture mode. The number and size of dimples showed the strength of the base metal. The X-ray diffraction (XRD) analysis seen in Fig. 10 provides evidence that the base metal consisted solely of a single-phase ferrite structure [50].

Similar metal or metal alloy joint properties and their failures found during the experiment are written in Table 1 and their corresponding authors. The properties could be their tensile strength, microstructure, and microhardness that they

Table 1 CMT welding is used in similar metals with their parameters and key findings

Author	Metal used	Filler used	Shielding gas used	Parameter used	Key findings
[38]	Inconel 718 alloy	1.2 mm diameter Inconel 718 wire	Composed of Argon, 5% H_2 Flow rate 15 l/min	6.5 mm thick plate of Inconel 718 Weld speed 0.3 m/min Wire-speed 4.5 m/min	1. By analyzing the macrostructure, it was found that there is no lack of fusion, so it showed a good weld quality 2. HAZ is small, i.e., 0.5 mm, compared to MIG welding 3. The residual stresses were found to be minimum
[39]	Aluminum 7075 alloy	ER5356	Argon gas Flow rate 15 l/min	2 mm thick sheet of alloy 7075 in the T6 condition weld speed 15 mm/s wire feed rate 5.5 m/min	1. Joints were formed without spatter or crack and with very low porosity 2. There was minimum microhardness in the weld metal, causing all joint failure and hardness slightly decreases in the HAZ compared to the base metal 3. The joint's yield strength, ultimate tensile strength, and elongation mechanical property coefficients were 77%, 60%, and 69%, respectively
[40]	Aluminum AA6061 alloy	Al 6061	Argon gas Flow rate 18 l/min	2 mm thick sheet Welding speed 400–600 mm/min Welding current 50–70A Welding voltage 11.7–13.7	1. The weld obtained was remarkable when the current was maintained between 60 to 70A and weld speed at 8–10 mm/sble 2. For filler metal same material as a base metal was used, which showed a quasi-binary mixture that is less susceptible to solidification cracking, narrower HAZ, and reduced intermetallic phase area 3. At the joints, the microstructure reveals fine recrystallization 4. The base metal and HAZ showed a clear grain size distribution

Table 1 (continued)

Author	Metal used	Filler used	Shielding gas used	Parameter used	Key findings
[41]	AA6061-T6 aluminum alloy	ER4043 wire with a 1.2 mm diameter	Argon gas Flow rate 15 l/min	1 mm thick sheet Wire feed rate 6.6 m/min	1. CMT arc mode generated welds with the best mechanical properties and few defects among other welding arc modes 2. The partial tearing defects were eliminated with a chill block under the bottom sheet; it also increased the strength and toughness of the joint 3. The heat-affected zone was reduced with the chill block
[42]	AA6061-T6 aluminum alloy	ER4043 wire with a 1.2 mm diameter	Argon gas Flow rate 15 l/min	A 3.5 mm thick sheet of AA60661-T6 was used Welding speed 450 mm/min Wire feed rate 4.9 m/min Current 110 A Voltage 19.4 V	1. The tensile strength and elongation of weld metal were lesser than the parent metal 2. The mean microhardness of base metal was the highest (64.9HV), the weld zone had the least (59.7HV), and 61.8HV was recorded in the HAZ 3. The fracture position of reinforced and without reinforced tensile specimens was found in the base metal region and weld metal zone, respectively 4. The formation of fracture was because of dimples and voids
[43]	H111-5083 aluminum alloy	ER5183 wire with a 1.2 mm diameter	Argon gas Flow rate 25 l/min	A 5 mm thick H111-5083 aluminum alloy substrate was used Welding speed 0.5 m/min Wire feed rate 7.2 m/min	1. Fine equiaxed grains and negligible pores were formed 2. Because of the heat accumulation difference, there was a sudden and extreme increase in the grain size found in the top layer from 37 to 52 μm. The corresponding microhardness was also decreased from 98.7 to 76.4HV 3. In the end, it was concluded that to gain refined microstructure and properties in WAAM, the heat input should be gradually decreased in the first few layers

Table 1 (continued)

Author	Metal used	Filler used	Shielding gas used	Parameter used	Key findings
[44]	Galvanized steel sheet	$CuSi_3$	Mixture of Ar + 30%He + 1%CO_2	1 mm thick sheet Welding speed of 2 m/min	1. Macro- and microscopic metallographic examination confirmed the high quality of the brazed joints 2. The above point confirms the existence of both, i.e., copper diffusion area and the undamaged zinc layer in areas adjacent to the weld
[45]	Galvanized steel sheet	ER70 S-6 wire with a 1.2 mm diameter	80% of Ar and 20% of CO_2 Flow rate 15 l/min	3 mm thick sheet Welding speed 6 mm/s Current 210–260 A Voltage 15.9–16.9 V Heat input 0.56–0.73 kJ/mm	1. The mechanical and metallurgical properties of the joint got enhanced by employing the CMT technique when compared with the conventional welding process 2. The enhanced mechanical characteristics were due to the mixed ferrite-pearlite microstructures, fine bainitic ferrite phases, acicular ferrite, and martensite, with an average size of 9.4 m in the FZ
[28]	AISI 304 Stainless-Steel	ER 308L wire with a 1.2 mm diameter	Argon gas Flow rate 14 l/min	A 2 mm thick sheet was used Welding speed 4–8 mm/s Current 85–95 A Voltage 10–20.8 V	1. Approximately 16% decrement in microhardness of heat affected zone and 25% in the weld metal zone was observed compared to the parent metal. The reason behind it was the softening effect of the material and the presence of coarser grains in the HAZ 2. With welding conditions of 95 A current, 4 mm/s welding speed, and 7 mm of contact tip-to-workpiece distance of the welded sample, the highest tensile strength recorded was 723 MPa

Table 1 (continued)

Author	Metal used	Filler used	Shielding gas used	Parameter used	Key findings
[46]	2A12 Aluminum alloy	ER2319 with a diameter of 1.2 mm	Argon gas Flow rate 15 l/min	8 mm thick sheet Welding speed 2–8 mm/sec Welding current 145-165A Welding voltage 10.2–15.8 V Heat input 184.87–1303.5 J/mm	1. A double-sided joint was formed in which a better weld appearance was obtained when the heat input was increased up to 651.75 J/mm 2. By increasing the heat input, the size of the microstructure was also increased 3. The welded joint's strength coefficient was approximately 70% 4. After doing a fracture analysis, a ductile fracture mode was obtained
[47]	AA2219-T851 alloy	ER2319 with a diameter of 1.2 mm	Argon gas Flow rate 25 l.min	19 mm thick plate Wire feed speed 7.5 m/min Varying welding speed and heat	1. A narrow finger-shaped geometry was observed using the conventional CMT process 2. There were a considerable amount of gas pores in the lower and upper parts of the weld 3. The porosity was reduced effectively with the help of CMT welding
[48]	G115 steel	GER-95 wire with a 1.2 mm diameter	97.5% Ar + 2.5% CO_2	15 mm thick plate Welding speed 5 mm/s Wire feed rate 4.5–5.5 m/min Heat input 0.51–0.89 kJ/mm	The weldability issue was resolved by using CMT + P with GER-95 filler wire A higher heat input increased the high-temperature duration, because of which precipitates were formed, thereby increasing the hardness and strength Increasing the heat input also made the grains more coarser, thereby inducing poor toughness At 0.89 kJ/mm heat input maximum hardness(310HV10) and maximum tensile strength (777 MPa) were recorded at room temperature

Table 1 (continued)

Author	Metal used	Filler used	Shielding gas used	Parameter used	Key findings
[49]	UNS S32750	Inox 2509 MoW B wire with a 1.2 mm diameter	Argon gas Flow rate 15–18 l/min	3 mm thick plates Welding speed 320 mm/min Wire feed rate 4.9 m/min Current 130 A Voltage 14.5 V Heat input 0.302 kJ/mm	1. No harmful precipitation phases were found in the FZ of the weld except for different forms of austenite 2. Tensile fracture occurred in the FZ, and a little increase in the hardness was observed 3. The efficiency of the CMT welded joint was recorded as 98.5% 4. A change in fracture mode from ductile to brittle was observed at the time of impact loading while decreasing the temperature from 24 to − 196 °C
[50]	AISI430 ferritic stainless steel	ER308L wire with a 1.2 mm diameter	97.5% Ar + 2.5% CO_2 Flow rate 15 l/min	1 mm thick plates were used Welding speed 10 mm/s Wire feed rate 3.4–4.2 m/min Heat input 208.03–274.57 J/mm	1. The microstructure of the welded joint had ferrite and austenite phases 2. The coarse grain zone of HAZ contained ferrite grain and a considerable amount of intergranular martensite and carbides; conversely, the fine grain zone consisted of ferrite grains and a small amount of intergranular martensite 3. The microhardness of the welded joint first increased from weld metal to HAZ and then decreased from HAZ to the base metal 4. The fracture was observed in the parent metal region

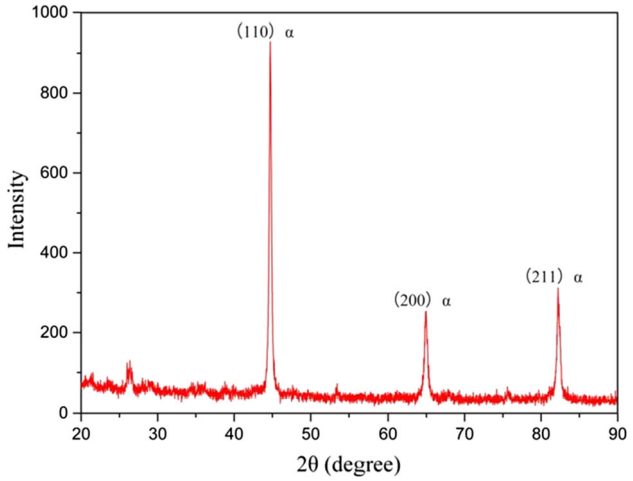


Fig. 11 Base metal XRD pattern

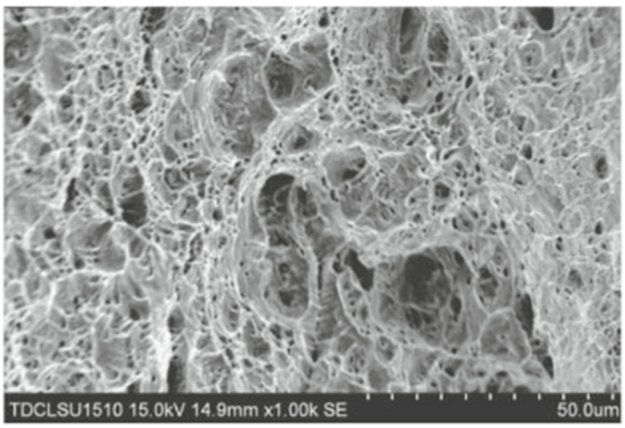


Fig. 12 Fracture morphology of the fractured sample [50]

exhibit with some particular welding parameters like welding speed, heat input, and wire feed rate.

5 Effect of intermetallic compound on similar alloys

The formation of IMC layers at the weld interface plays a crucial role in the microstructural characteristics and mechanical properties of welded joints. In the context of the given information, IMC layers were observed near the AZ31B side of the welded joints, and three intermediate layers were identified: Mg_2A_{l3} layer, $Mg_{17}Al_{12}$ layer, and a $Mg_{17}Al$ + α-Mg solid solution eutectic layer.

The Mg_2A_{l3} layer indicates a specific intermetallic compound formed at the interface. This layer is often associated with magnesium–aluminum alloy systems and plays a role in determining the mechanical properties of the welded joint revealed in Fig. 12a. The $Mg_{17}Al_{12}$ layer is another distinct intermetallic phase that contributes to the overall composition of the IMC layer. Additionally, the $Mg_{17}Al$ + α-Mg solid solution eutectic layer represents a combination of phases, further influencing the microstructure. The given information highlights the effect of the EP/EN ratio (energy per pulse to energy per unit length) on the IMC layer thickness and tensile strength. As the EP/EN ratio decreases from 4:1 to 1:4, the thickness of the entire IMC layer gradually increases. This suggests that the welding process parameters, specifically the energy input, significantly impact the growth and characteristics of the IMC layer.

The correlation between the thickness of the IMC layer and tensile strength is noteworthy. A decrease in the EP/EN ratio leads to an increase in both the IMC layer thickness and tensile strength. This relationship indicates that the welding conditions play a crucial role in influencing the mechanical properties of the welded joints. Furthermore, it is mentioned that all samples were fractured in the hard, brittle IMC layer, emphasizing the importance of understanding and controlling the IMC layer characteristics to enhance the overall integrity of the weld. Two key criteria were proposed in evaluating structural integrity at the interface between steel and aluminum: the maximum principle stress and deformation energy for interface failure and plastic strain for fusion line failure. These criteria are essential for assessing the interface's structural response and potential failure modes.

The maximum principle stress criterion indicates the highest stress experienced at a given point in the structure. It plays a crucial role in determining potential failure areas and is employed as a criterion for interface failure, providing insights into the stress distribution at the steel–aluminum interface.

Simultaneously, the deformation energy criterion assesses the energy absorbed or released during the deformation process. This criterion is particularly relevant for understanding the structural response and predicting failure patterns associated with the interface. Additionally, plastic strain, proposed as a criterion for fusion line failure, highlights the importance of considering strain-induced plastic deformation in the region where steel and aluminum are fused. Plastic strain becomes a key factor in assessing the failure mechanism at the fusion line. The information establishes a multi-criteria approach to comprehensively evaluate the steel–aluminum interface's structural behavior and potential failure modes. Figure 12b visually represents the interface, serving as a reference for analyzing and interpreting the proposed criteria in the context of stress, deformation energy, and plastic strain (Fig. 13).

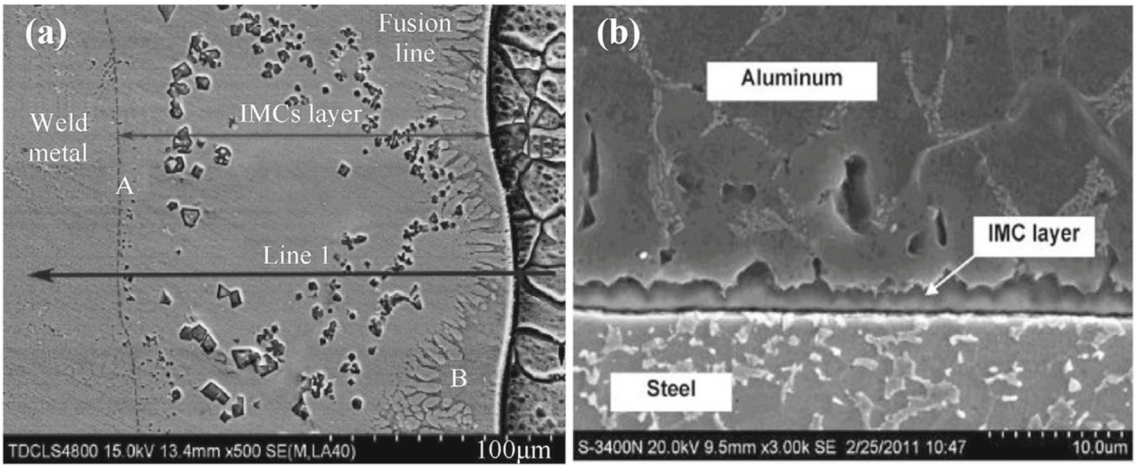


Fig. 13 **a** Weld interface, **b** aluminium-steel interface [6]

6 Effect of dimples and facets on welded joint

The effect of big dimples, small dimples, and cleavage facets on the mechanical properties of the welded joint in cold metal transfer welding process has been studied in various papers. The presence of big dimples and small dimples in the fracture surfaces of the welded joints indicates a ductile fracture behaviour [28, 51]. Cleavage facets, on the other hand, are associated with brittle fracture behaviour [48]. The mechanical properties of the welded joint are influenced by the interfacial microstructure. The thickness and distribution of intermetallic compounds, such as AlCu2Ti phases, play a significant role in the fracture behavior and tensile strength of the joint [52]. The hardness distribution of the joint is also affected by the welding process parameters and heat input [36]. Overall, the presence of big dimples and small dimples indicates a more ductile fracture behavior, while cleavage facets suggest a brittle fracture behavior in the welded joint. The interfacial microstructure and heat input also influence the mechanical properties of the joint.

7 Comparison of CMT with MIG

CMT welding and MIG welding differ in their results due to various factors. CMT welding exhibits a higher electrode melting coefficient compared to pulsed MIG welding, making it suitable for welding aluminum alloys [53]. Additionally, CMT welding is characterized by low heat input and no-spatter welding, which is ideal for joining metals and results in reduced distortions, high welding speed, good tensile performance, and increased productivity [54, 55]. Compared to regular MIG short-circuit welding, CMT emits about 90% less heat into the workpiece, making it suitable for working with thin gauge metal prone to warping from high heat input [56]. Furthermore, CMT welding is known for producing less spatter, slag, fumes, and smoke compared to MIG welding, resulting in a cleaner welding process [6].

In summary, CMT welding and MIG welding differ in their suitability for thin and thick metals, cleanliness, energy efficiency, ease of learning, and the welding process itself. These differences make each technique suitable for different applications in metal fabrication.

8 Comparison of CMT with FSW

Cold metal transfer (CMT) welding and friction stir welding (FSW) are two different welding processes that produce different results. CMT welding is characterized by low heat input and no-spatter welding, resulting in reduced distortions, high welding speed, good tensile performance, and increased productivity [9, 54]. CMT welding is also considered a cleaner type of welding, producing less spatter, slag, fumes, and smoke compared to MIG welding [53] On the other hand, FSW welding is a solid-state welding process that produces high-quality welds with no porosity, low distortion, and excellent mechanical properties. FSW welding is ideal for joining aluminum and its alloys, and it is particularly useful for welding large structures, such as shipbuilding, aerospace, and automotive industries [57–59]. The FSW welding also produces a narrow heat-affected zone, which reduces the risk of cracking and distortion.

In summary, CMT welding and FSW welding differ in their results, with CMT welding being characterized by low heat input, no-spatter welding, and high productivity, while FSW welding produces high-quality welds with no porosity, low distortion, and excellent mechanical properties. The choice of welding process depends on the specific application and the desired results.

9 Conclusions

- With the help of post-weld heat treatment, the softening issue in the HAZ got resolved along with an increment in the tensile strength and hardness of the material in the case of the butt joint of AA6061-T6 Al alloy.
- By preheating 7075 aluminum and galvanized steel plates, the wetting angle decreased and the bead width increased.
- The microstructure and mechanical characteristics of the corresponding materials altered as the heat input increased during joining.
- CMT welding is a highly significant and innovative method for joining similar and dissimilar metals. Its ability to provide controlled material transfer, low heat input, and improved weld quality makes it a preferred choice in various industries. Whether it is joining similar metals like aluminum alloys or dissimilar combinations of metals, CMT welding offers numerous benefits such as reduced distortions, high welding speeds, and enhanced mechanical properties.
- The results of CMT welding and MIG welding differ in terms of heat input, spatter, distortion, and productivity, making each technique suitable for different applications in metal fabrication.
- CMT welding a preferred choice over FSW welding for various applications, especially when working with thin metals, aiming for cleaner and more efficient welding processes, and requiring lower heat input.

Declarations

Conflict of interest The authors declare that they have no conflict of interest.

References

1. Peng, M., Liu, H., Liang, Y., Xu, W., Zhao, Y., Chen, S., Weng, J., Yang, J.: CMT welding-brazing of al/steel dissimilar materials using cycle-step mode. J. Mater. Res. Technol. **18**, 1267–1280 (2022). https://doi.org/10.1016/j.jmrt.2022.03.043
2. Dwivedi, D.K.: Dissimilar metal joining of steel-aluminium alloy by friction stir welding. In: Dissimilar Metal Joining pp. 269–285 (2023). https://doi.org/10.1007/978-981-99-1897-3_10
3. Srinivasan, D., Sevvel, P., John Solomon, I., Tanushkumaar, P.: A review on cold metal transfer (CMT) technology of welding. Mater. Today Proc. **64**, 108–115 (2022). https://doi.org/10.1016/j.matpr.2022.04.016
4. Xu, P., Hua, X., Shen, C., Huang, Y., Li, F., Zhang, Y.: Dynamic growth model of Fe2Al5 during dissimilar joining of Al to steel using the variable polarity cold metal transfer (VP-CMT). J. Mater. Process. Technol. (2022). https://doi.org/10.1016/j.jmatprotec.2021.117477
5. Xu, W., He, H., Yi, Y., Wang, H., Yu, C., Fang, W.: Dissimilar joining of stainless steel and aluminum using twin-wire CMT. Weld. World **65**, 1541–1551 (2021). https://doi.org/10.1007/s40194-021-01089-0
6. Selvi, S., Vishvaksenan, A., Rajasekar, E.: Cold metal transfer (CMT) technology—an overview. Def. Technol. **14**, 28–44 (2018). https://doi.org/10.1016/j.dt.2017.08.002
7. Venukumar, S., Cheepu, M., Vijayababu, T., Venkateswarlu, D.: Cold metal transfer (Cmt) welding of dissimilar materials: an overview. Mater. Sci. Forum **969**, 685–690 (2019). https://doi.org/10.4028/www.scientific.net/MSF.969.685
8. Burhanuddin, N.M., Redzuan, N., Ahmad, N., Sudin, I., Zaharuddin, M.F.A.: Brief review on dissimilar welding using cold metal transfer. IOP Conf. Ser. Mater. Sci. Eng. (2020). https://doi.org/10.1088/1757-899X/884/1/012115
9. Shanker, H., Wattal, R.: A comprehensive survey on the cold metal transfer process in welding similar and dissimilar materials and for cladding. Proc. Inst. Mech. Eng. Part C Mech. Eng. Sci. **237**, 2360–2391 (2023). https://doi.org/10.1177/09544062221139947
10. Elrefaey, A., Ross, N.G.: Microstructure and mechanical properties of cold metal transfer welding similar and dissimilar aluminum alloys. Acta Metall. Sin. (Engl. Lett.) **28**, 715–724 (2015). https://doi.org/10.1007/s40195-015-0252-6
11. Miguel, P., Almeida, S., Titanium, N.: Innovations in arc welding. 5° Congr. Luso-Moçambicano Eng. (2011)
12. Frappier, R., Benoit, A., Paillard, P., Baudin, T., Le Gall, R., Dupuy, T.: Quantitative infrared analysis of welding processes: temperature measurement during RSW and CMT-MIG welding. Sci. Technol. Weld. Join. **19**, 38–43 (2014). https://doi.org/10.1179/1362171813Y.0000000158
13. Shu, F., Lv, Y., Liu, Y., Xu, F., Sun, Z., He, P., Xu, B.: Residual stress modeling of narrow gap welded joint of aluminum alloy by cold metal transferring procedure. Constr. Build. Mater. **54**, 224–235 (2014). https://doi.org/10.1016/j.conbuildmat.2013.12.056
14. Gungor, B., Kaluc, E., Taban, E., Aydin, S.I.K.: Mechanical and microstructural properties of robotic cold metal transfer (CMT) welded 5083–H111 and 6082–T651 aluminum alloys. Mater. Des. **54**, 207–211 (2014). https://doi.org/10.1016/j.matdes.2013.08.018
15. Ahmad, R., Bakar, M.A.: Effect of a post-weld heat treatment on the mechanical and microstructure properties of AA6061 joints welded by the gas metal arc welding cold metal transfer method. Mater. Des. **32**, 5120–5126 (2011). https://doi.org/10.1016/j.matdes.2011.06.007
16. Omiyale, B.O., Olugbade, T.O., Abioye, T.E., Farayibi, P.K.: Wire arc additive manufacturing of aluminium alloys for aerospace and automotive applications: a review. Mater. Sci. Technol. (United Kingdom) **38**, 391–408 (2022). https://doi.org/10.1080/02670836.2022.2045549
17. Kannan, R.A., Shanmugam, N.S., Naveenkumar, S.: Effect of arc length correction on weld bead geometry and mechanical properties of AISI 316L weldments by cold metal transfer (CMT) process. Mater. Today Proc. **18**, 3916–3921 (2019). https://doi.org/10.1016/j.matpr.2019.07.331
18. Rajeev, G.P., Kamaraj, M., Bakshi, S.R.: Al-Si-Mn alloy coating on aluminum substrate using cold metal transfer (CMT) welding technique. Jom **66**, 1061–1067 (2014). https://doi.org/10.1007/s11837-014-0970-7
19. Kumar, T., Kiran, D.V., Arora, N., Kumar, P.S.: Study of steel-aluminium joining under the influence of current waveforms using advanced CMT process variants. Mater. Manuf. Process. (2022). https://doi.org/10.1080/10426914.2022.2030879
20. Selvamani, S.T., Velmurugan, S., Palanikumar, K.: Heat transfer analysis on advanced CMT welded low carbon steel joints. Proc. Mater. **7**, 683–689 (2021). https://doi.org/10.1007/978-981-15-6267-9_78
21. Dobrocky, D., Dostal, P., Sustr, M., Pokorny, Z., Studeny, Z.: Analysis of weld joint of DX51D steel with AlMg3 alloy made by CMT

welding method. Manuf. Technol. **18**, 215–221 (2018). https://doi.org/10.21062/ujep/80.2018/a/1213-2489/MT/18/2/215
22. Zvorykina, A., Sherepenko, O., Jüttner, S.: Novel projection welding technology for joining of steel–aluminum hybrid components—part 1: technology and its potential for industrial use. Weld. World **64**, 317–326 (2020). https://doi.org/10.1007/s40194-019-00833-x
23. Jingsong, G.: CMT welding process for 1Cr18Ni9Ti stainless steel and 5A06 aluminum alloy. CN10806770 (2018)
24. Çömez, N., Durmuş, H.: Effect of heat input on the microstructure, strength and corrosion behavior of sheets of alloy AA6061 after cold metal transfer welding. Met. Sci. Heat Treat. **61**, 421–427 (2019). https://doi.org/10.1007/s11041-019-00440-z
25. Ola, O.T., Doern, F.E.: A study of cold metal transfer clads in nickel-base INCONEL 718 superalloy. Mater. Des. **57**, 51–59 (2014). https://doi.org/10.1016/j.matdes.2013.12.060
26. Rajeev, G.P., Kamaraj, M., Bakshi, S.R.: Effect of correction parameters on deposition characteristics in cold metal transfer welding. Mater. Manuf. Process. **34**, 1205–1216 (2019). https://doi.org/10.1080/10426914.2019.1628260
27. Yang, S., Xing, Y., Yang, F., Cao, J.: Complex behavior of droplet transfer and spreading in cold metal transfer. Shock. Vib. (2020). https://doi.org/10.1155/2020/6650155
28. Roy, J.G., Yuvaraj, N.: Vipin: effect of welding parameters on mechanical properties of cold metal transfer welded thin AISI 304 stainless-steel sheets. Trans. Indian Inst. Met. **74**, 2397–2408 (2021). https://doi.org/10.1007/s12666-021-02326-2
29. Balasubramanian, M., Choudary, M.V., Nagaraja, A., Sai, K.O.C.: Cold metal transfer process—a review. Mater. Today Proc. **33**, 543–549 (2020). https://doi.org/10.1016/j.matpr.2020.05.225
30. Ainapurapu, S.B., Devulapalli, V.A.R., Theagarajan, R.P.: Experimental investigation and process parameter optimization in cold metal transfer welding for SS304L using response surface method. Eng. Res. Express. (2023). https://doi.org/10.1088/2631-8695/acbd86
31. Zhang, A., Xing, Y., Yang, F., Zhang, X., Wang, H., Yu, T.: Development of a new cold metal transfer arc additive die manufacturing process. Adv. Mater. Sci. Eng. (2021). https://doi.org/10.1155/2021/9353820
32. Kannan, A.R., Kumar, S.M., Pramod, R., Kumar, N.P., Prakash, K.S., Shanmugam, N.S., Vishnukumar, M.: Metallurgical aspects and electrical resistivity of hardfaced pure copper layers over AISI 347 with cold metal transfer process. Proc. Inst. Mech. Eng. Part C J. Mech. Eng. Sci. **237**, 95–102 (2023). https://doi.org/10.1177/09544062221115578
33. Shanker, H., Wattal, R.: Mechanical and microstructure characteristics of 7475–T7351 aluminium alloy joints welded by robot cold metal transfer. Proc. Inst. Mech. Eng. Part B J. Eng. Manuf. (2023). https://doi.org/10.1177/09544054231178956
34. Xiao, P., Wang, L., Tang, Y., Tu, X., Song, X., Chen, L., Liu, F., Zhang, Y.: Effect of wire composition on microstructure and penetration crack of laser-cold metal transfer hybrid welded Cu and stainless steel joints. Mater. Chem. Phys. (2023). https://doi.org/10.1016/j.matchemphys.2023.127480
35. Selvamani, S.T., Yoganandan, G., Bakkiyaraj, M., Sivaraman, V.: Influence of heat input on cold metal transfer welded joints. Mater. Manuf. Process. (2022). https://doi.org/10.1080/10426914.2022.2030877
36. Zhu, M., Yang, S., Xie, C., Bai, Y., Fan, C.: Research on microstructure and fatigue properties of 7050–T6 high-strength aluminum alloy cold metal transfer welded joint. J. Mater. Eng. Perform. **30**, 7461–7471 (2021). https://doi.org/10.1007/s11665-021-05885-z
37. Luo, L., Yang, B.H., Quan, Q.Q., Yang, X.R., Liu, X.Y., Wang, J.Z.: Effect of rapid cooling on the microstructure and properties of fine-grained 7075 aluminium alloy under friction stir welding. Mater. Res. Express (2022). https://doi.org/10.1088/2053-1591/ac6da5
38. Benoit, A., Jobez, S., Paillard, P., Klosek, V., Baudin, T.: Study of inconel 718 weldability using MIG CMT process. Sci. Technol. Weld. Join. **16**, 477–482 (2011). https://doi.org/10.1179/136217181 1Y.0000000031
39. Elrefaey, A.: Effectiveness of cold metal transfer process for welding 7075 aluminium alloys. Sci. Technol. Weld. Join. **20**, 280–285 (2015). https://doi.org/10.1179/1362171815Y.0000000017
40. Kumar, N.P., Arungalai Vendan, S., Siva Shanmugam, N.: Investigations on the parametric effects of cold metal transfer process on the microstructural aspects in AA6061. J. Alloys Compd. **658**, 255–264 (2016). https://doi.org/10.1016/j.jallcom.2015.10.166
41. Lei, H.Y., Li, Y.B., Carlson, B.E.: Cold metal transfer spot welding of 1 mm thick AA6061-T6. J. Manuf. Process. **28**, 209–219 (2017). https://doi.org/10.1016/j.jmapro.2017.06.004
42. Pramod, R., Shanmugam, N.S., Krishnadasan, C.K.: Studies on cold metal transfer welding of aluminium alloy 6061-T6 using ER 4043. Proc. Inst. Mech. Eng. Part L J. Mater. Des. Appl. **234**, 924–937 (2020). https://doi.org/10.1177/1464420720917175
43. Zhang, B., Zhang, L., Wang, C., Wang, Z., Gao, Q.: Microstructure and properties of Al alloy ER5183 deposited by variable polarity cold metal transfer. J. Mater. Process. Technol. **267**, 167–176 (2019). https://doi.org/10.1016/j.jmatprotec.2018.12.011
44. Magda, A., Popescu, M., Codrean, C., Mocuta, E.G.: Possibilities of joining galvanized sheet steel using the CMT method (cold metal transfer). Weld. Int. **27**, 665–667 (2013). https://doi.org/10.1080/09507116.2011.606137
45. Selvamani, S.T., Velmurugan, S., Balasubramanian, V., Palanikumar, K.: Effects of heat distribution during cold metal transfer arc welding on galvanized steel using volumetric heat source model. J. Mater. Res. Technol. **9**, 10097–10109 (2020). https://doi.org/10.1016/j.jmrt.2020.07.004
46. Chen, C., Sun, G., Zhao, Y., Chen, F., Zhang, H., Liu, J.: Microstructure and mechanical properties of 2A12 aluminum alloy welded joint through CMT double side welding. CIRP J. Manuf. Sci. Technol. **37**, 258–266 (2022). https://doi.org/10.1016/j.cirpj.2022.02.006
47. Cong, B., Ouyang, R., Qi, B., Ding, J.: Influence of cold metal transfer process and its heat input on weld bead geometry and porosity of aluminium–copper alloy welds. Xiyou Jinshu Cailiao Yu Gongcheng/Rare Met. Mater. Eng. **45**, 606–611 (2016). https://doi.org/10.1016/s1875-5372(16)30080-7
48. Cai, H., Xu, L., Zhao, L., Han, Y., Pang, H., Chen, W.: Cold metal transfer plus pulse (CMT+P) welding of G115 steel: Mechanisms, microstructure, and mechanical properties. Mater. Sci. Eng. A (2022). https://doi.org/10.1016/j.msea.2022.143156
49. Arun, D., Ramkumar, K.D.: Microstructural and mechanical characteristics of cold metal transfer weld joints of UNS S32750. J. Mater. Eng. Perform. **30**, 8095–8107 (2021). https://doi.org/10.1007/s11665-021-06015-5
50. Zhou, J., Shen, J., Hu, S., Zhao, G., Wang, Q.: Microstructure and mechanical properties of AISI 430 ferritic stainless steel joints fabricated by cold metal transfer welding. Mater. Res. Express. (2019). https://doi.org/10.1088/2053-1591/ab4770
51. Brezinová, J., Hašuľ, J.: Evaluation of fillet welds properties performed by cold metal transfer robotic metal active gas welding technology. Transport **38**, 44–51 (2023). https://doi.org/10.3846/transport.2023.19084
52. Huang, L., Dong, H., Ma, Y., Li, P., Wang, J., Yang, J., Wu, B.: Interfacial layer regulation and its effect on mechanical properties of Ti6Al4V titanium alloy and T2 copper dissimilar joints by cold metal transfer welding. J. Manuf. Process. **75**, 1100–1110 (2022). https://doi.org/10.1016/j.jmapro.2022.01.056

53. Pickin, C.G., Young, K.: Evaluation of cold metal transfer (CMT) process for welding aluminium alloy. Sci. Technol. Weld. Join. **11**, 583–585 (2006). https://doi.org/10.1179/174329306X120886
54. Kurşun, T.: Cold metal transfer (Cmt) welding technology. Sci. Tecnol. **8**, 35–39 (2018)
55. Cornacchia, G., Cecchel, S.: Study and characterization of EN AW 6181/6082-T6 and EN AC 42100–T6 aluminum alloy welding of structural applications: metal inert gas (MIG), cold metal transfer (CMT), and fiber laser-MIG hybrid comparison. Metals (Basel) (2020). https://doi.org/10.3390/met10040441
56. Cornacchia, G., Cecchel, S., Panvini, A.: A comparative study of mechanical properties of metal inert gas (MIG)-cold metal transfer (CMT) and fiber laser-MIG hybrid welds for 6005A T6 extruded sheet. Int. J. Adv. Manuf. Technol. **94**, 2017–2030 (2018). https://doi.org/10.1007/s00170-017-0914-9
57. Ramnath, B.V., Elanchezhain, C., Vignesh, C., Sudharsan, V., Ganesh, C.S.: A review on friction stir welding and it's processes. IOP Conf. Ser. Mater. Sci. Eng. (2020). https://doi.org/10.1088/1757-899X/923/1/012030
58. Mohan, D.G., Wu, C.S.: A review on friction stir welding of steels. Chin. J. Mech. Eng. (Engl. Ed.) (2021). https://doi.org/10.1186/s10033-021-00655-3
59. Liu, F.C., Hovanski, Y., Miles, M.P., Sorensen, C.D., Nelson, T.W.: A review of friction stir welding of steels: tool, material flow, microstructure, and properties. J. Mater. Sci. Technol. **34**, 39–57 (2018). https://doi.org/10.1016/j.jmst.2017.10.024

Publisher's Note Springer Nature remains neutral with regard to jurisdictional claims in published maps and institutional affiliations.

Springer Nature or its licensor (e.g. a society or other partner) holds exclusive rights to this article under a publishing agreement with the author(s) or other rightsholder(s); author self-archiving of the accepted manuscript version of this article is solely governed by the terms of such publishing agreement and applicable law.

Multimedia Tools and Applications
https://doi.org/10.1007/s11042-024-18247-3

Approximate regeneration of image using fragile watermarking for tamper detection and recovery in real time

Varsha Sisaudia[1] · **Virendra P. Vishwakarma**[2]

Received: 18 May 2023 / Revised: 3 November 2023 / Accepted: 9 January 2024
© The Author(s), under exclusive licence to Springer Science+Business Media, LLC, part of Springer Nature 2024

Abstract
Digital Image Watermarking has been rigorously used for image authenticity problems. Fragile watermarking is sensitive to even slight modifications and can detect tampering. This paper proposes a real-time tamper detection algorithm and regenerates an approximate image for the tampered locations. The image is divided into 4 parts and pair-wise correspondence is formed. This correspondence is used for marking the authenticity of parts of images and helps in the reconstruction of tampered parts. For every part, sub-blocks of size 4×4 are formed. Upon calculating the average of 4 inner pixels of these 4×4 blocks, a Local Binary Pattern (LBP) is constructed for that sub-block. Using XOR operation on 12-bit LBP, a 6-bit watermark for that sub-block is generated. This watermark is used for block authentication. Next, for recovery information, the 4×4 sub-block is divided into four 2×2 parts, and their average is calculated. This information is used for the recovery of tampered regions in the image. The watermark along with the average is then embedded into the corresponding sub-block in the pair-wise section of the image. This helps ensure the authenticity of the sub-block and helps in storing information needed for regeneration in case a part of the watermarked image has been tampered with. The imperceptibility and extent of degradation of the original image upon embedding the watermarking bits are calculated using the peak signal-to-noise ratio and structural similarity index. The approach is tested against a variety of attacks and shows its applicability in real-time applications with quick approximate reconstruction.

Keywords Fragile watermarking · Tamper detection · Local binary pattern · Image reconstruction

✉ Varsha Sisaudia
sisaudia.varsha@gmail.com

[1] Delhi Technological University, Delhi, India

[2] University School of Information Communication & Technology, GGSIPU, Delhi, India

Published online: 22 January 2024

1 Introduction

Watermarking [1–3] is the process of embedding additional information into the original media in order to later extract it to check the authenticity and ownership of the media in question. Digital image watermarking is a method of inserting digital information into the cover image/original image or the source image with the intent of embedding copyright information [4] and owner information, or with the intent of detecting fraud [5]. It has been a popular subject of research for more than two decades now and is still a relevant field for today's world, where the digital platform is a ruling platform for sharing data, content, reports, and almost everything. With the world having witnessed a pandemic that is still impacting some parts of our everyday lives, even after more than three years since the first case was detected, everything has migrated to digital platforms. Digital content has never been more valuable than today. Hence, the need for protecting the digital content has also grown. Along with the huge volume of data being generated, the risk of obtaining false and unauthentic information has also risen [6–8]. A lot of digital content online today is in the form of images that are being shared on social and public platforms. These images may be of critical importance or national security. Hence, it is of paramount importance to know whether the image has been forged before it hits public records. Thus, to prevent such scenarios from happening, digital image watermarking has been proposed by many researchers as a solution. It aims at signing an image to check its authenticity later in time. Copyrights and ownership help in establishing the authenticity of the media. It prevents illegal use of images by embedding robust watermarks that can withstand attacks and do not get degraded while the image is modified using filters, resizing, rotation, and many more attacks [9, 10].

Fragile watermarking [11–14] is another type of image watermarking in which the watermark is sensitive to any kind of modification after being embedded in the watermarked image. Such a watermark gets corrupted because of intentional or unintentional attacks. It has been widely researched for its applicability in temper detection and information recovery. Multiple spatial and transform-based fragile watermarking have been proposed for digital images. The amount of information required at the time of extraction is dependent on the type of watermarking used. Blind watermarking [15, 16] does not require any information for watermark extraction, semi-blind [17, 18] may require the position of the watermark and some additional information, whereas non-blind [19] watermarking requires position as well as the original image as reference for extraction of watermark.

1.1 Motivation

A lot of work has been done on tamper detection and reconstruction of images. But, in order to achieve better results in terms of imperceptibility and quality of watermarked images, researchers propose complicated techniques, combining optimization algorithms, machine learning algorithms, and transform domains like DWT, DCT, etc. This all compromises the time required to detect and reconstruct images that have been tampered with. Minute details might not always be needed unless it is a matter of national security. Hence, reconstruction of an approximate image to give a fair idea of the original image can help us with quick and easy solutions that work. This research work is motivated by a similar idea of regenerating an approximate image in real-time.

1.2 Contribution

In this paper, fragile watermarking has been implemented on gray-scale images to detect tampered regions of an image and have a quick approximate recovery of the tampered regions as an initial step of investigation. The major contributions of the proposed algorithm to fragile watermarking are as follows:

1. Increased speed because the proposed technique uses spatial domain fragile watermarking. No transformation is required to embed the watermark.
2. LBP is easy to compute effective feature extraction strategy. It captures the information of an entire block concerning the center pixel.
3. The watermark information embedded in the cover image is self-generating. So, no external image or stream of information is required. The watermark is generated from every 4×4 sub-block of the cover image.
4. The least significant bits are susceptible to modifications. Hence, watermarking bits as well as regeneration bits for every 4×4 block are embedded into 2 LSBs of the image.
5. The proposed watermarking technique achieves good approximate recovery of tampered regions without the use of machine learning algorithms that are time-intensive. Hence, the entire recovery process is fast.

1.3 Organization

The rest of the paper is organized as follows: Section 2 highlights the related research based on fragile watermarking. The following section details the watermark generation, embedding, and extraction steps. Experimental results are elaborated in Section 4 followed by a conclusion in Section 5.

2 Related research

Previous literature related to fragile watermarking has been briefly discussed in this section. Fragile watermarking, as the name suggests is delicate in handling any kind of changes made to the host images. Such a high level of susceptibility is naturally achieved in the spatial domain where any change in pixel intensity can be easily detected. Hence, a lot of fragile watermarking techniques for tamper detection and recovery have been implemented in the spatial domain. To improve imperceptibility, transform domain techniques are also becoming popular.

Rakhmawati et al. [20] have proposed a dual, self-embedding, and robust blind watermarking technique for image authentication, image recovery as well and copyright protection all in a single host image. A total of 3 watermarks are embedded in the cover image, out of which a robust watermark is embedded in the DCT domain and 2 others are self-embedding in nature for image authentication and recovery. It is a block-based approach in which first robust watermarking is carried out followed by the insertion of fragile watermarks. The proposed scheme withstands attacks efficiently and also reconstructs tampered regions of the watermarked image. Another hybrid technique engaging both robust and fragile watermarking is proposed by Rahman et al. [21]. They have proposed a spatial domain technique with embedded security features for medical images. The host image is fragile and unrecoverable

whereas the watermark is robust. Here the image is divided into two regions, one is the region of interest (ROI) and the other of non-interest (RONI). The watermark information is embedded in RONI and the scheme uses two watermarks. The technique is evaluated in terms of fragility, robustness, and security and proves its effectiveness.

Quin et al. [22] have proposed a vector quantization-based self-embedding fragile watermarking technique where the principal components of the cover image are first calculated and they are represented using VQ indices. Next, using a random binary matrix, the binary bits of VQ indices are extended to generate reference bits. The watermark bits and reference bits are then embedded in the cover image for tampering localization and content recovery respectively. The tampered regions can thus be detected and reconstructed with the help of quantization index reconstruction. Another technique used is Huffman coding and moment block truncation code for designing a fragile watermarking technique that works on pixel pairwise watermarking [23]. Here, two LSBs of the original image have been used for embedding the recovery information into the cover image using a turtle shell-based data hiding technique and a matrix that has been predetermined. Upon doubts of tampering, the compressed image generated using block truncation can be used for detecting tampers and restoration.

In numerous fragile image watermarking methods, the original image undergoes division into non-overlapping sub-blocks. Each sub-block receives a watermark comprising both authentication and recovery bits. Authentication bits serve the role of tampering detection, confirming the block's integrity when successfully extracted. The recovery process relies on the retrieved bits to restore tampered blocks [24]. Singh et al. [25] present a novel self-embedding block-wise fragile image watermarking method for enhanced authentication, localization, and recovery accuracy. It divides the host image into non-overlapping 2×2 blocks, deriving restoration and authentication bits from the five most significant bit planes. In the watermarked image, each block contains authentication bits and restoration bits from other partner blocks, offering redundancy for recovery. A three-level tampered detection approach is employed to confirm block authenticity. Experimental results showcase the scheme's effectiveness, achieving high-quality restoration even at a 50% tampering rate, while minimizing blocking artifacts and enhancing tampered region localization accuracy. The authors in [26] present a fragile watermarking method for pinpointing unauthorized digital image alterations effectively. This technique identifies changes at the block level, focusing on pairs of adjacent pixels. The image is divided into non-overlapping (1×2) pixel blocks, and an authentication code is generated from the most significant bits of adjacent pixels in each block using averaging and modulus operations. The code is encrypted with a chaotic key sequence and embedded into the same block's two consecutive pixels. Any tampering in the watermarked image is detectable by comparing the extracted and regenerated authentication codes. Renklier and Öztürk present a novel self-embedding watermarking method inspired by Sudoku puzzles, enabling recovery of up to 80% of tampered images in [27]. Initially, the grayscale host image is divided into twenty-five blocks, following a 5×5 Sudoku grid. These blocks are further split into non-overlapping 5×5 sub-blocks, with recovery data extracted from their average pixel values. Within each group, they discreetly embed four copies of the sub-block recovery data into the second least significant bits (LSBs) of other group blocks, employing Sudoku-based placement. We also generate authentication data for each 5×5 sub-block using the MD5 hash algorithm, considering block position, pixel values, and a secret key. The resulting 25-bit authentication data is subtly embedded into the first LSBs of the sub-blocks. The experiments reveal the method's resilience against various attacks, such as cropping,

splicing, copy-move, salt-pepper noise, histogram equalization, sharpening, blurring, and text addition in different image regions. Furthermore, the approach effectively mitigates the coincidence problem, yielding high-quality recovered images.

In some instances, watermark bit generation includes frequency-domain transformations like the discrete cosine transform (DCT) [28–30], discrete Fourier transform (DFT) [31, 32] or the discrete wavelet transform (DWT) [24, 33, 34] introduces a novel reversible fragile digital watermarking method, tailored for tamper localization and safeguarding authenticity and integrity in medical images. The process commences with the division of the host image into non-overlapping 8×8 blocks. Following this, a Discrete Wavelet Transform translates the image into the frequency domain, allowing for watermark embedding. Subsequently, the image is reverted from the frequency domain to the spatial domain using inverse Discrete Wavelet Transform. Throughout this transformation, an intelligent optimization technique corrects rounding errors, preserving the watermarked image's imperceptibility. Experimentation verifies the method's capacity to maintain high imperceptibility, facilitate lossless host image extraction during watermark retrieval, and offer precise tamper localization.

LBP has also been a popular method in fragile watermarking techniques [35–37]. In [38], using a 2-level wavelet transform, first, the image has been transformed, and then for extracting features, LBP has been applied. To detect copy-move attacks, a feature matrix has been generated from all the extracted binary patterns. This helps in detecting duplicate features of the image, the duplicity can thus be removed. In a study described in [29], a combination of Local Binary Pattern (LBP) and Discrete Cosine Transform (DCT) is recommended for processing of colored images. This method involves converting the image from the RGB channel to the YCbCr channel and dividing it into overlapping sub-blocks. Subsequently, LBP is employed on these sub-blocks, followed by the application of DCT. To enhance forgery detection, a support vector machine is trained using a two-class classification approach.

A secure fragile watermarking technique based on a secure hashing algorithm has been proposed in [39]. The technique uses a spatial domain block-based embedding technique for watermark embedding. The technique can handle varied sizes of tampering. Gul and Ozturk [13] have proposed a self-embedding fragile watermarking process for image authentication. In addition to incorporating tamper detection, the authors introduced a recovery mechanism within their approach. The paper suggests a pixel-based authentication scheme, departing from the conventional block-based approach, which proves effective in countering attacks such as salt and pepper noise insertion.

3 Proposed technique

The methods of generating a watermark using LBP, watermark embedding, watermark extraction, tamper detection, and image reconstruction are explained in this section.

3.1 Watermark generation

LPB is usually calculated for an odd-sized block. It establishes a relation between the central pixel and its neighborhood (of varying size, say 9 with radius 1 or 16 with radius 2). However, in the proposed watermarking method, LBP is calculated for a 4×4 sized block. First, an average of 4 internal pixels is calculated and stored for the generation of LBP. The neighborhood pixel values are compared with the average value to generate a 12-bit LBP. If

the neighborhood pixel value N_i is less than the average, then 0 is generated in LBP for that pixel, else 1. This process has been detailed in Fig. 1 with an example. The 4 internal pixel intensities are denoted by M_1, M_2, M_3, and M_4 and are highlighted in gray. The neighboring pixel intensities are denoted by N_1, N_2, …, and N_{12} (Fig. 1(a)). Sample calculation of LBP for a block is shown in Fig. 1(b)-(d). Thus, after applying LBP to a 4×4 block, we obtain a 12-bit binary pattern represented by X:

$$X = \{X_1, X_2, X_3, \ldots, X_{12}\}$$

From this pattern, a 6-bit watermark $w = \{w_1, w_2, w_3, w_4, w_5, w_6\}$ is generated for each block using Eq. (1) – Eq. (6).

$$w_1 = X_1 \oplus X_7 \tag{1}$$

$$w_2 = X_2 \oplus X_8 \tag{2}$$

$$w_3 = X_3 \oplus X_9 \tag{3}$$

$$w_4 = X_4 \oplus X_{10} \tag{4}$$

$$w_5 = X_5 \oplus X_{11} \tag{5}$$

$$w_6 = X_6 \oplus X_{12} \tag{6}$$

Here $\oplus$ represents the XOR operator. This process is repeated for every 4×4 sub-block to generate its 6-bit watermark.

3.2 Recovery information generation

If a 4×4 sub-block is detected as tampered, then additional information is required to regenerate the tampered sub-block. For this purpose, the 4×4 sub-block is further divided into 4 equal parts. The average of each of these parts is calculated. The average is then converted into binary representation of 8 bits and 5 MSBs from each part are concatenated to form 20-bit recovery information of the block. The average of the entire 4×4 sub-block is not used as recovery information because the image texture may change rapidly. In such a case, an average of 4×4 sub-block will regenerate a more distorted image as compared to 2×2 blocks. The smaller the regeneration blocks, the more the possibilities

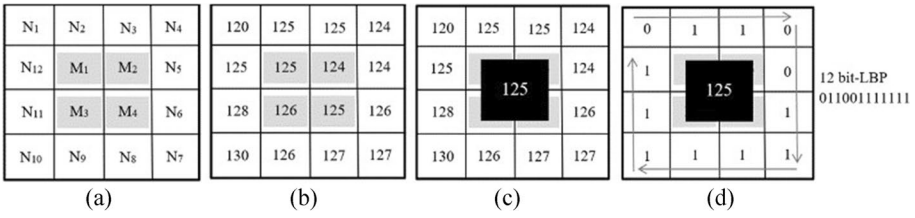


Fig. 1 Sample image block for LBP calculation (**a**) 4×4 block (**b**) Sample intensities (**c**) Average value of 4 internal pixels (**d**) 12-bit LBP

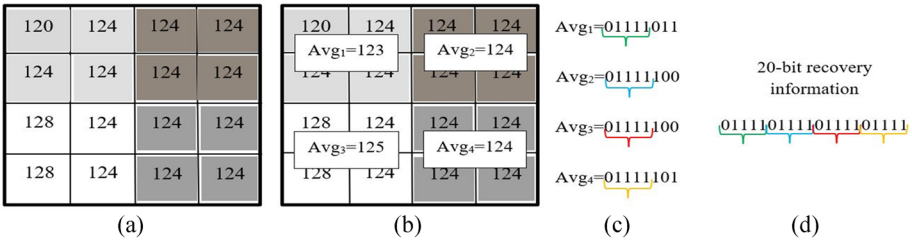


Fig. 2 Recovery Information Generation (**a**) 4×4 block (**b**) Average pixel intensities (**c**) Binary representation of Average intensities (**d**) 20-bit recovery information

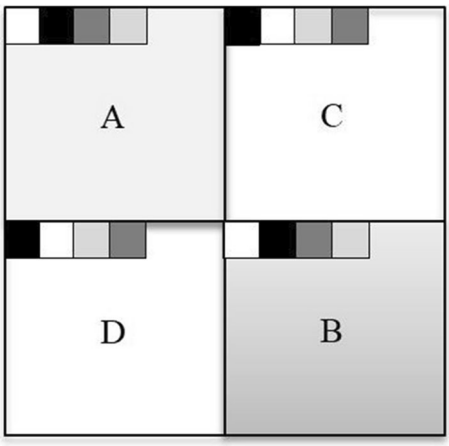


Fig. 3 Correspondence between sub-blocks of **A** & **B** and **C** & **D**

of reconstructing a tampered image with finer details. Also, it does not leave scales on the image, and the transition from one sub-block to another seems a lot smoother. The process of construction of 20-bit recovery information from a 4×4 sub-block is shown in Fig. 2.

Figure 2(a) shows a sample 4×4 sub-block divided into four parts (each of size 2×2) marked by different colors. The values shown depict the pixel intensities for a 4×4 sub-block. The averages for the four parts are calculated as depicted in Fig. 2(b) and they are converted into 8-bit binary representations. From each 8-bit representation, 5 MSBs are selected (Fig. 2(c)) and concatenated to generate 20-bit recovery information for that sub-block (Fig. 2(d)).

3.3 Embedding algorithm

The steps for embedding a fragile watermark as well as recovery information into the cover image I of size $m \times n$ are given below:

1. Convert the 2 LSBs of every pixel intensity in the cover image to 0 and generate an image I^*.
2. Divide image I^* into 4 equal blocks of size $(m/2) \times (n/2)$. Form a block-wise correspondence pair namely {A, B} and {C, D}. These pairs are diagonally opposite to each other. This ensures maximum distance between A & B and C & D (Fig. 3).

3. Divide each of the blocks i.e. A, B, C, and D further into non-overlapping sub-blocks of size 4×4. There is a one-to-one mapping between the positions of these sub-blocks of A & B and C & D. Figure 3 shows the correspondence and mapping between sub-blocks in the pair of blocks. The ones with the same color in A & B are sharing the correspondence and so are sub-blocks in C & D.
4. Generate a 6-bit watermark for every sub-block using LBP and XOR operations, as explained in Section 3.1. The watermark is thus generated at the time of watermarking and is different for every sub-block, depending on the pixel values.
5. Obtain 20-bit recovery information for the sub-blocks as per Section 3.2.
6. Modify the 2nd LSB and 1st LSB for pixels P_1, P_2, P_3 respectively (Fig. 4) to embed 6-bit watermark $\{w_1, w_2, w_3, w_4, w_5, w_6\}$ generated for that sub-block.
7. For double authenticity and recovery of a tampered sub-block, store the 6-bit watermark and 20-bit recovery information of the sub-block generated in Step 4 and Step 5 in the respective sub-block of pair-wise correspondence. The watermark bits are embedded in P_4, P_5 and P_6 at 2nd and 1st LSB positions and the 20-bit information at 2nd and 1st LSB of pixels P_7, P_8, P_9, P_{10}, P_{11}, P_{12}, P_{13}, P_{14}, P_{15} and P_{16} represented in binary notation. In Fig. 4, a dummy matrix of size 16×16 is shown representing pixels from P_1 to P_{16} in every sub-block of size 4×4. Here, for clarity, sub-blocks of A and B are marked in the same color to mark one-on-one correspondence. Thus, 20-bit recovery information generated for a sub-block in A is embedded in the corresponding sub-block in B in pixels P_7 to P_{16}. 10-pixel values are modified at 2 LSB positions to embed 20-bit recovery information of a corresponding sub-block.

The sub-blocks are combined again to form a watermarked image I_w of the original dimension $m \times n$ containing both authentication information and regeneration information, in case the sub-block is found tampered.

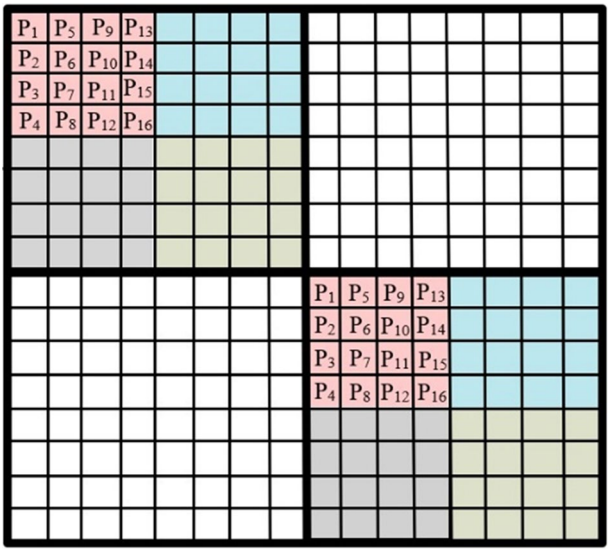


Fig. 4 Sample 16×16 matrix showing Pixel numbering for embedding and extraction purpose

3.4 Watermark extraction and tamper detection

Since the proposed watermarking scheme is blind, it does not require any prior information to extract watermarks. The following steps are followed for extracting watermarks from the marked image:

1. Divide the watermarked image I_w into 4 equal parts A_w, B_w, C_w, and D_w as done in Step 3 of the previous sub-section.
2. Create sub-blocks of size 4×4 for every part and extract watermark bits $e = \{e_1, e_2, e_3, e_4, e_5, e_6\}$ from 2nd LSB and 1st LSB of pixels P_1, P_2 and P_3 (Fig. 4) for each of the sub-block.
3. Now, set the two LSBs of all the pixels of the 4×4 sub-block to 0.
4. Apply LBP and XOR operator to every sub-block, and generate watermark bits $g = \{g_1, g_2, g_3, g_4, g_5, g_6\}$ for each one of them using the same procedure as discussed in Section 3.1.
5. Compare e with g for every sub-block. If equal, the sub-block is marked as 1 level authentic, otherwise tampered.
6. Also, check if the corresponding sub-block in pair-wise correspondence is 1 level authentic. If found authentic, extract the watermark embedded in pixels P_4, P_5, and P_6 for double authentication. Let this be $d = \{d_1, d_2, d_3, d_4, d_5, d_6\}$. If $g = d$, then the sub-block is marked as double-authentic.

3.5 Image reconstruction

The steps for approximate reconstruction of tampered regions of the image are done as follows:

1. Mark every sub-block that passes both the authenticity levels as a valid sub-block.
2. For a sub-block of size 4×4 that did not pass Step 5 of the previous section or failed 2-level authenticity, check the first-level authenticity of the one-on-one corresponding sub-block in the corresponding pair. If the corresponding sub-block storing reconstruction information is found to be authentic, extract the recovery information stored in it, i.e., 20-bit recovery information.
3. Segregate the 20-bit information into 4 parts of 5-bit each and convert each into an 8-bit representation by adding three 0 s at the LSB end. Convert the binary bits to decimal representation and replace the 2×2 blocks' pixel values with their corresponding average. This would range between 0 and 255 for gray-scale images.
4. After regenerating the tampered sub-blocks, the complete image is combined to form the whole recovered image.

4 Experiments and results

This section discusses the experimentation carried out and the results obtained with the proposed approach. It also compares the results with other state -of-the-art techniques for fragile watermarking.

4.1 Experimental setup

The proposed technique for tamper detection and quick image reconstruction has been coded in Matlab 2022b release. The system used for the research is a Windows 11 OS based machine with 6 GB RAM, i7 intel processor and 512 GB solid state drive (SSD). The experimentation has been performed on 6 grayscale images: Lena, Sailboat, Baboon, Boat, Peppers, and Cameraman of size 512×512. These images are standard watermarking test images that can be downloaded from USC SIPI dataset.

4.2 Metrics for performance evaluation

The original images (I) and watermarked images (I_w) are shown in Fig. 5. Various metrics have been used in the manuscript to depict the quality of watermarking approach. The similarity between I and I_w is measured using the peak-signal-to-noise ratio (PSNR) and structural similarity index (SSI) where PSNR is calculated using Eq. (7)

$$PSNR = 10log_{10}\frac{255^2}{MSE}\ (dB) \tag{7}$$

where MSE represents the error (mean-square) calculated by squaring the difference between the corresponding pixel (p,q) of the two images and dividing by the size of the image ($m \times n$) as given in Eq. (8).

$$MSE = \frac{\sum_{p=1}^{m}\sum_{q=1}^{n}\left(I(p,q) - I_w(p,q)\right)^2}{m \times n} \tag{8}$$

SSI is calculated over different windows of fixed size on patches of two images x and y by using Eq. (9) where μ_x, μ_y, σ_x^2, σ_y^2, and $\sigma_{x,y}$ are mean of x, mean of y, variance of x, variance of y and covariance of x and y respectively. $L1$ and $L2$ are coefficients.

$$\mathrm{SSI}(x,y) = \frac{\left(2\mu_x\mu_y + L1\right)\left(2\sigma_{xy} + L2\right)}{\left(\mu_x^2 + \mu_y^2 + L1\right)\left(\sigma_x^2 + \sigma_y^2 + L2\right)} \tag{9}$$

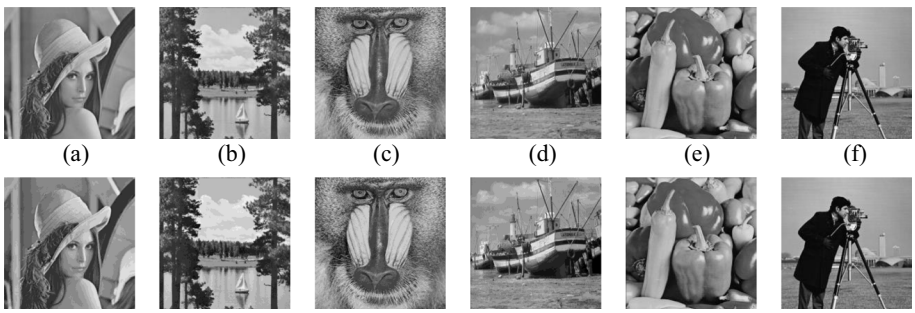


Fig. 5 (**a**)-(**f**) Original Lena, Sailboat, Baboon, Ship, Peppers and Cameraman respectively (**g**)-(**l**) Corresponding Watermarked Images

Table 1 PSNR, SSI, and Time for Watermarking Algorithm

Image	PSNR	SSI	Embedding time (s)	Extraction time (s)
Lena	44.776	0.986	3.18	0.46
Sailboat	44.949	0.992	3.05	0.47
Baboon	44.890	0.993	3.28	0.43
Ship	44.793	0.989	3.07	0.45
Peppers	44.233	0.983	3.13	0.43
Cameraman	44.869	0.991	3.29	0.47

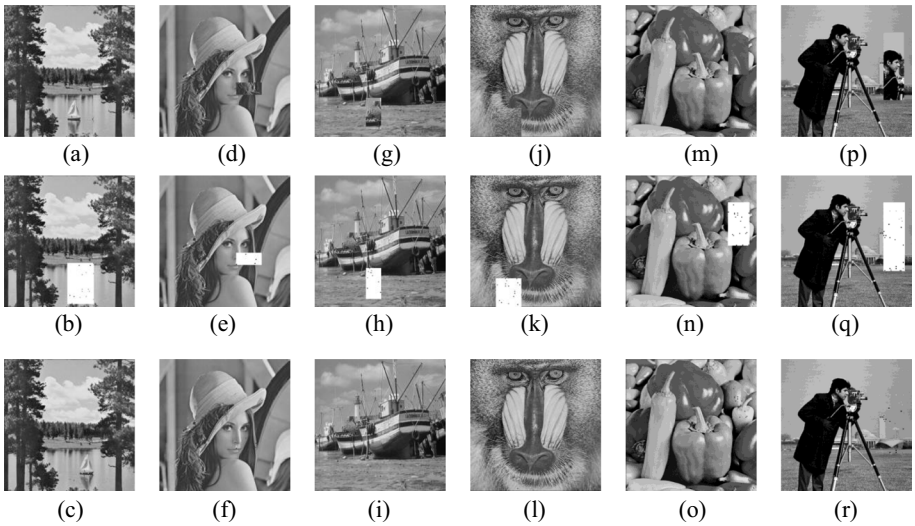


Fig. 6 Copy-Move Attacked Image, Tamper Localization and Image Reconstruction (**a**)-(**c**) Sailboat (**d**)-(**f**) Lena (**g**)-(**i**) Ship (**j**)-(**l**) Baboon (**m**)-(**o**) Peppers (**p**)-(**r**) Cameraman

Time required to embed self-generated watermark and that of tamper detection and reconstruction of image are noted for the proposed technique. The PSNR values, SSI values, and time consumed by the watermarking algorithm are shown in Table 1. Time has been calculated by taking the average of ten runs per image.

4.3 Attacks on watermarked images

The images are subjected to several attacks namely copy-paste, copy-move attack, cropping, text insertion, histogram equalization, and blurring using average filter. The quality of reconstructed image after tamper detection is assessed by PSNR.

Figure 6 shows a Copy-move attack which is a commonly forged attack to circulate misleading content over the internet. It is carried out by copying and pasting a part of the image over the original image. Such attacks can represent incorrect information and thus need to be detected efficiently. First, the image in every column is the tampered image, followed by an image that shows regions detected as tampered and last the approximate reconstruction of the image. The white region in the second row shows the region detected as tampered. Table 2 shows results for Copy-move attacks with varying

Table 2 PSNR and Recovery Percentage with varying Tampering Rate for Copy-Paste Attack

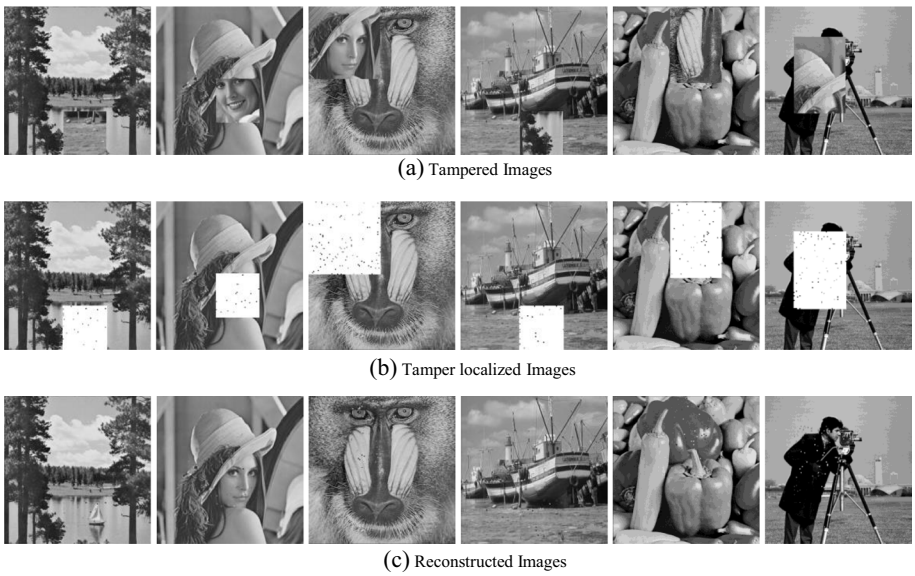
	Sailboat			Lena			Ship			Baboon		
Tampering % (No. of sub-blocks tampered)	Recovered Sub-blocks	Percentage Recovery	PSNR (in dB)	Recovered Sub-blocks	Percentage Recovery	PSNR (in dB)	Recovered Sub-blocks	Percentage Recovery	PSNR (in dB)	Recovered Sub-blocks	Percentage Recovery	PSNR (in dB)
5% (820)	810	98.78%	42.10	819	99.87%	44.95	804	98.05%	38.43	808	98.54%	36.71
10% (1640)	1613	98.35%	36.26	1630	99.39%	38.61	1609	98.11%	34.89	1615	98.47%	33.48
15% (2460)	2424	98.54%	33.66	2443	99.31%	37.91	2418	98.29%	33.78	2422	98.46%	31.65
20% (3280)	3228	98.41%	31.15	3256	99.27%	36.30	3234	98.60%	31.44	3240	98.78%	31.33
25% (4096)	4044	98.73%	30.80	4070	99.36%	35.45	4044	98.73%	30.70	4055	98.99%	30.67
30% (4920)	4847	98.51%	29.42	4882	99.22%	34.63	4852	98.61%	30.03	4857	98.71%	29.81
40% (6560)	6558	98.52%	27.81	6592	99.04%	32.52	6563	98.60%	30.12	6542	98.28%	27.05
50% (8192)	8074	98.54%	26.60	8107	98.96%	32.14	8091	98.71%	29.42	8095	98.81%	26.16

percentages of tampering. It depicts the PSNR value post-recovery of tampered regions of the watermarked image. It shows the number of sub-blocks that were actually tampered (column 1) and the count of blocks that were detected by the proposed method as tampered and recovered through the recovery process. The efficiency of detecting tampered sub-blocks does not go below 98% for the images.

Copy-paste is another attack that is commonly performed to forge an image to represent incorrect information. A part of some other image is pasted on the original image to seem like it belonged to the image. Detection of such attacks can be useful for surveillance systems. Figure 7 shows the results obtained for this attack with varied sizes and locations of tampering for all six images namely Sailboat, Lena, Baboon, Ship, Peppers, and Cameraman. The white portion in images shows tamper localization which is then reconstructed using regeneration bits stored in the image at the time of watermarking.

A cropping attack is another popular category of attack where a portion of the image is removed altogether. Figure 8 shows the results of the cropping attack with different portions of cropping for Baboon and Lena images. The images are arranged in increasing order of cropping attack. Here, the blacked region denotes the cropped area and the white region depicts tamper localization. As can be observed from Fig. 8(c), (d), (g), and (h), as the area cropped goes beyond 50%, recovery of the complete image becomes impossible as recovery information gets corrupted.

Forging signatures or text addition in images is also a critical challenge. Illegally signed medical reports and scans can pose a problem. Some unauthorized testing centers may forge a doctor's signature on their scans and imaging X-rays to authenticate a report by a qualified professional. Such discrepancies should be detected by fragile watermarks, and if possible, reconstruction adds an advantage, giving a proper idea about underlying information. Thus, Fig. 9 shows results for text attacks with different content and quantity on 3 test images- Baboon, Lena, and Ship.



(a) Tampered Images

(b) Tamper localized Images

(c) Reconstructed Images

Fig. 7 Copy-Paste Attacked Image, Tamper Localization and Image Reconstruction

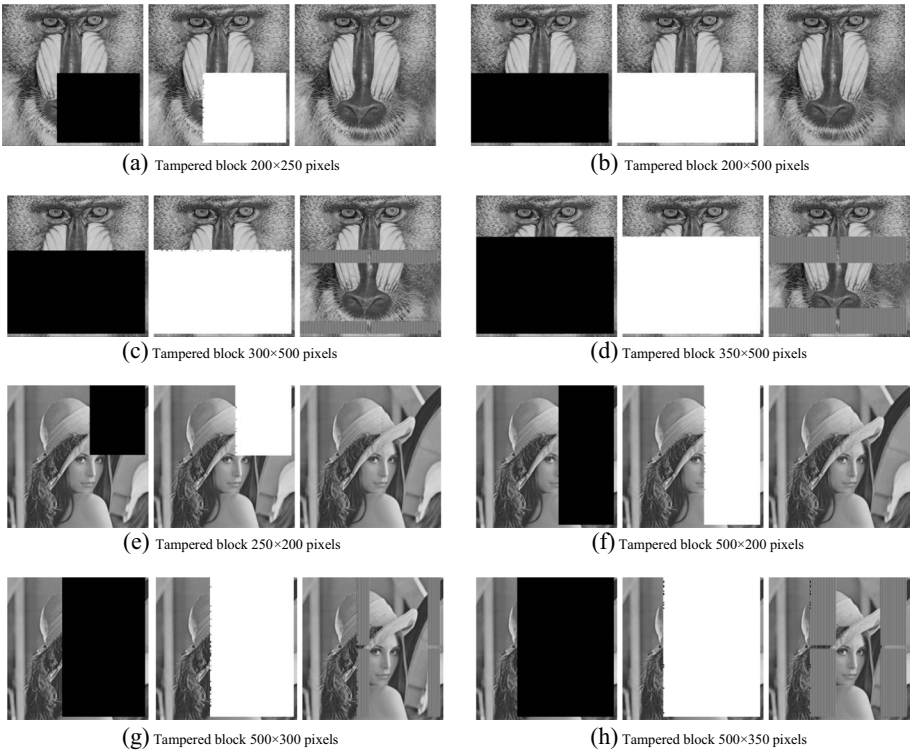


Fig. 8 Cropping Attacked Image, Tamper Localization and Image Reconstruction (**a**)-(**d**) Baboon (**e**)-(**h**) Lena

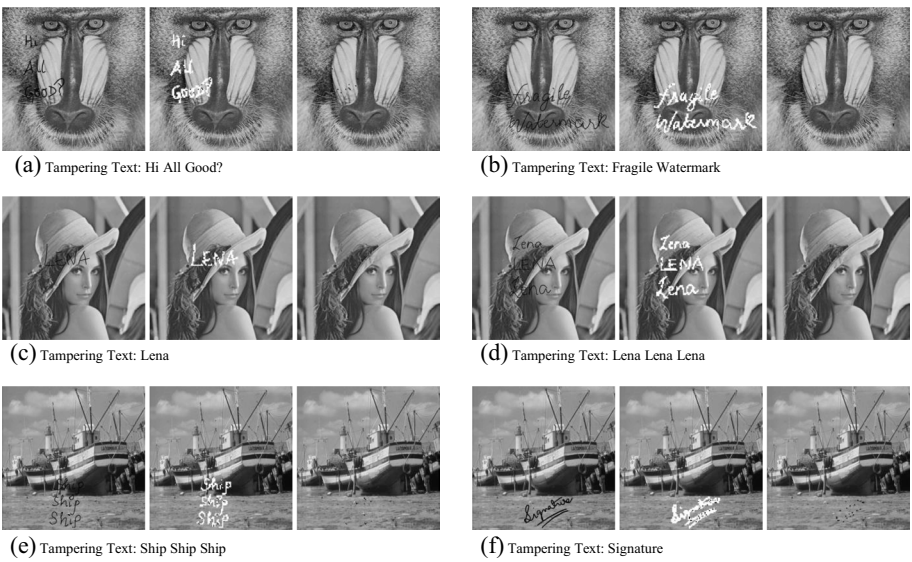


Fig. 9 Text Attacked Image, Tamper Localization and Image Reconstruction (**a**)-(**b**) Baboon (**c**)-(**d**) Lena (**e**)-(**f**) Ship

Another attack that may be commonly used is histogram equalization which adjusts the contrast of the image. A portion of the image may be adjusted for brightness and toning of the image. PSNR of the reconstructed image with varying tampering portions is listed in Table 3 along with the number of recovered sub-blocks against the count of tampered sub-blocks mentioned in column 1 of the table.

Table 4 lists the results of the blurring attack. It is a common practice to blur a portion of the image to bring focus on the important part or feature of an image. Average filtering is a blurring attack that can be performed to have different blurring impacts based on the window size. We have tested the watermarking algorithm using 3 window sizes, 3×3, 5×5, and 7×7. The results depict that the recovery percentage is high with the lowest value being 93% approximately.

4.4 Comparisons

The proposed technique has been compared with existing state-of-the-art techniques (SOTA) in this sub-section. These techniques apply block-based watermarking technique for storing watermarking information and reconstruction of tampered image. The comparison of PSNR values and SSI or normalized correlation (NC) is carried out with techniques proposed in [27, 40], and [25] in Table 5. The PSNR value obtained by the proposed algorithm is better than [40] and [25] and comparable with [27]. Further, SSI is better than [27] and NC is better than [25]. For [40] even though the SSI is pretty high (almost approaching 1), their PSNR is lesser than our scheme.

Further, since the proposed scheme focuses on quick reconstruction of the tampered regions, the time of embedding and extraction are also compared with other SOTA techniques. Table 6 shows the comparison results. Because of the simplicity of proposed technique, the time requirements are low as compared to other spatial domain techniques.

5 Limitations of the research approach

The proposed technique achieves an average time of 0.47 s for tamper detection. However, this detection and reconstruction is limited to a maximum of 50% attack percentage. Beyond that, there are visible unconstructed or wrongly constructed blocks in the image. Also, since the proposed technique is a block-based tamper detection scheme, it suffers from block artifacts as compared to pixel-based technique. Hence, some minute details may be missed while reconstruction. Thus, the proposed technique is only a quick solution to regenerate approximate image where intricate details may not be of utmost importance. Some techniques have further achieved higher PSNR values at the cost of time by using transform domain techniques along with Machine Learning algorithms. Our technique achieves an average PSNR of 44 dB.

6 Conclusions

This research article introduces an innovative digital watermarking scheme that serves as a fragile and blind method. It employs self-generated distinctive watermarks based on block-level information, which are instrumental for tamper detection and image reconstruction. The evaluation of the watermarked image quality is conducted through metrics like PSNR

Table 3 PSNR and Recovery Percentage with varying Tampering Rate for Histogram Equalization Attack

Tampering % (approx.)	Sailboat		Lena		Ship		Baboon		Peppers		Cameraman	
	Recovered Sub-blocks	PSNR (in dB)	Recovered Sub-blocks	PSNR (in dB)	Recovered Sub-blocks	PSNR (in dB)	Recovered Sub-blocks	PSNR (in dB)	Recovered Sub-blocks	PSNR (in dB)	Recovered Sub-blocks	PSNR (in dB)
5% (820)	790	35.95	803	39.09	805	39.99	798	36.70	789	37.21	805	41.32
10% (1640)	1597	34.63	1586	35.50	1612	36.94	1606	34.24	1603	37.88	1608	38.72
15% (2460)	2409	36.13	2382	36.58	2386	33.94	2412	33.85	2373	34.92	2423	35.47
20% (3280)	3197	33.93	3184	35.94	3176	32.54	3207	32.86	3166	33.49	3129	33.98
25% (4096)	4007	32.98	3965	34.45	3942	31.19	3992	30.67	3927	32.88	3995	32.98
30% (4920)	4808	32.30	4757	33.77	4758	30.85	4790	30.77	4730	32.13	4760	32.85
40% (6560)	6473	30.23	6295	28.70	6406	29.78	6465	27.45	6441	32.55	6488	32.16
50% (8192)	7998	29.48	7890	28.69	7941	29.16	8005	26.77	7944	30.65	8001	31.20

Table 4 PSNR and Recovery Percentage with varying Tampering Rate for Average Filtering of different window size

	Sailboat		Lena		Ship		Baboon		Peppers		Cameraman	
Window size—>	[3×3]											
Tampering % (approx.)	% Recovery	PSNR (in dB)	% Recovery	PSNR (in dB)	% Recovery	PSNR (in dB)	% Recovery	PSNR (in dB)	% Recovery	PSNR (in dB)	% Recovery	PSNR (in dB)
10%	97.25%	41.51	99.07%	43.11	97.68%	36.36	98.53%	34.49	98.80%	35.51	97.02%	43.86
20%	98.01%	36.41	98.10%	38.86	98.20%	33.21	97.98%	33.30	98.22%	33.96	96.45%	41.34
25%	97.83%	34.04	98.68%	37.68	98.02%	32.33	98.31%	31.93	97.26%	31.65	96.16%	39.65
30%	97.88%	33.37	98.41%	36.95	98.04%	31.72	98.25%	31.22	96.98%	31.04	95.49%	37.65
Window size—>	**[5×5]**											
Tampering % (approx.)	% Recovery	PSNR (in dB)	% Recovery	PSNR (in dB)	% Recovery	PSNR (in dB)	% Recovery	PSNR (in dB)	% Recovery	PSNR (in dB)	% Recovery	PSNR (in dB)
10%	95.18%	40.34	97.13%	42.72	97.37%	36.12	97.86%	34.38	97.83%	35.15	96.77%	42.83
20%	96.82%	35.92	97.25%	38.67	97.65%	33.09	97.56%	33.14	97.11%	33.94	95.49%	40.62
25%	97.48%	33.83	97.38%	37.31	97.85%	32.24	97.90%	31.84	96.24%	31.10	94.98%	39.06
30%	97.27%	33.17	97.19%	36.66	97.59%	31.39	97.92%	31.12	95.86%	30.07	94.27%	37.97
Window size—>	**[7×7]**											
Tampering % (approx.)	% Recovery	PSNR (in dB)	% Recovery	PSNR (in dB)	% Recovery	PSNR (in dB)	% Recovery	PSNR (in dB)	% Recovery	PSNR (in dB)	% Recovery	PSNR (in dB)
10%	94.69%	40.77	95.67%	42.34	96.58%	36.20	98.04%	34.35	97.59%	35.48	95.43%	43.20
20%	95.97%	35.87	96.55%	38.61	97.13%	33.10	97.37%	33.11	96.57%	33.93	94.90%	40.55
25%	96.45%	33.75	96.48%	37.03	96.75%	32.14	97.50%	31.78	95.88%	32.06	93.76%	39.56
30%	96.35%	32.30	96.32%	36.49	96.88%	31.53	97.59%	31.09	95.08%	30.75	93.24%	38.96

Table 5 Comparison of PSNR and SSI/NC with SOTA techniques

Image	Proposed			Prasad and Pal [40]		Renklier and Öztürk [27]		Singh et al. [25]	
	PSNR (dB)	SSI	NC	PSNR (dB)	SSI	PSNR (dB)	SSI	PSNR (dB)	NC
Lena	44.776	0.986	0.9993	42.01	0.999	44.2716	0.981	39.77	0.9977
Baboon	44.890	0.993	0.9994	42.29	0.999	44.2244	0.992	39.86	0.9976
Ship	44.793	0.989	0.9994	42.11	1.000	44.463	0.988	-	-
Cameraman	44.869	0.991	0.9997	41.62	0.999	-	-	39.56	0.9986
Peppers	44.233	0.983	0.9996	42.21	0.999	-	-	-	-

Table 6 Comparison of time with other SOTA techniques

Procedure	Proposed	Renklier and Öztürk [27]	Singh et al. [25]
Watermark embedding	3.16 s	3.61 s	6.7 s
Tamper detection & recovery for 20%	0.55 s	4.45 s	-

(Peak Signal-to-Noise Ratio) and SSI (Structural Similarity Index). High PSNR and SSI values indicate that the watermarking process is imperceptible to human observers, ensuring minimal image degradation.

The embedding of the watermark and recovery data into the least significant bits (LSBs) maintains a high PSNR value while rendering the watermark sensitive to alterations. Furthermore, the article explores a strategy involving pair-wise correspondence between four major image blocks, optimizing the distances between sub-blocks in corresponding pairs. This approach increases the likelihood of preserving recovery information during image attacks, such as cropping, copy-paste, copy-move, or text insertion.

The proposed scheme excels in tamper localization and provides a rapid method for approximating the restoration of tampered areas in attacked images. Additionally, the utilization of Local Binary Pattern (LBP) is an effective means of capturing patterns within sub-blocks, which, in turn, aids in watermark generation.

In the future, machine learning-based techniques along with LBP will be explored so that the tampered regions can be regenerated by the machine, instead of hiding regeneration information into the image. This will improve PSNR further.

Abbreviations *LBP*: Local Binary pattern; *XOR*: Exclusive OR; *ROI*: Region of interest; *RONI*: Region of non-interest; *DCT*: Discrete cosine transform; *VQ*: Vector quantization; *RGB*: Red green blue; *PSNR*: Peak signal-to-noise ratio; *SSI*: Structural similarity index; *MSE*: Mean-squared error; *NC*: Normalized correlation; *SOTA*: State-of-the-art

Data availability The test images used in the manuscript are standard watermarking images found at sipi.usc.edu.

Further, no new custom algorithms have been created for this work.

Declarations

Conflict of interest The authors declare that they have no conflict of interest.

References

1. Haouzia A, Noumeir R (2008) Methods for image authentication : a survey. Multimed Tools Appl 39:1–46. https://doi.org/10.1007/s11042-007-0154-3
2. Anand A, Singh AK (2021) Watermarking techniques for medical data authentication: a survey. Multimed Tools Appl 80:30165–30197
3. Kumar S, Kumar B, Mohit S (2020) A Recent Survey on Multimedia and Database Watermarking. Multimed Tools Appl 79:20149–20197
4. Tao H, Zain JM, Ahmed MM, Abdalla AN, Jing W (2012) A wavelet-based particle swarm optimization algorithm for digital image watermarking. Integr Comput Aided Eng 19(1):81–91. https://doi.org/10.3233/ICA-2012-0392
5. Sisaudia V, Vishwakarma VP (2021) Tamper detection using self-generating watermarks based on local binary patterns. International conference on smart generation computing, communication and networking (SMART GENCON), Pune: IEEE, pp. 1–6. https://doi.org/10.1109/SMARTGENCON51891.2021.9645894
6. Shih FY, Zhong X, Chang I (2017) An adjustable-purpose image watermarking technique by particle swarm optimization. Multimed Tools Appl 77:1623–1642. https://doi.org/10.1007/s11042-017-4367-9
7. Belferdi W, Behloul A, Noui L (2019) A Bayer pattern-based fragile watermarking scheme for color image tamper detection and restoration. Multidimens Syst Signal Process 30:1093–1112. https://doi.org/10.1007/s11045-018-0597-x
8. Balasamy K (2019) An intelligent reversible watermarking system for authenticating medical images using Wavelet and PSO. Cluster Comput 22:4431–4442. https://doi.org/10.1007/s10586-018-1991-8
9. Evsutin O, Dzhanashia K (2022) Watermarking schemes for digital images: Robustness overview. Signal Process Image Commun 100:116523. https://doi.org/10.1016/j.image.2021.116523
10. Savakar DG, Ghuli A (2019) Robust Invisible Digital Image Watermarking Using Hybrid Scheme. Arab J Sci Eng 44(4):3995–4008. https://doi.org/10.1007/s13369-019-03751-8
11. Prasad KSVK (2018) Fragile watermarking schemes for image authentication : a survey. Int J Mach Learn Cybern 9(7):1193–1218. https://doi.org/10.1007/s13042-017-0641-4
12. Di Martino F, Sessa S (2019) Fragile watermarking tamper detection via bilinear fuzzy relation equations. J Ambient Intell Humanized Comput 10:2041–2061
13. Gul E, Ozturk S (2019) A novel hash function based fragile watermarking method for image integrity. Multimed Tools Appl 73:17701–17718
14. Gul E, Ozturk S (2021) A novel pixel-wise authentication-based self-embedding fragile watermarking method. Multimed Syst 27(3):531–545
15. Yuan Z, Su Q, Liu D, Zhang X (2021) A blind image watermarking scheme combining spatial domain and frequency domain. Vis Comput 37(7):1867–1881. https://doi.org/10.1007/s00371-020-01945-y
16. Rawat S, Raman B (2012) A blind watermarking algorithm based on fractional Fourier transform and visual cryptography. Signal Process 92(6):1480–1491. https://doi.org/10.1016/j.sigpro.2011.12.006
17. Mishra A, Rajpal A, Bala R (2018) Journal of Information Security and Applications Bi-directional extreme learning machine for semi-blind watermarking of compressed images. J Inf Secur Appl 38:71–84. https://doi.org/10.1016/j.jisa.2017.11.008
18. Rajpal A, Mishra A, Bala R (2016) Multiple scaling factors based Semi-Blind watermarking of gray-scale images using OS-ELM neural network, ICSPCC 2016 - IEEE International conference on signal processing, communications and computing, conference proceedings, Hong Kong, China, pp. 1-6. https://doi.org/10.1109/ICSPCC.2016.7753622
19. Dharwadkar NV, Amberker BB, Gorai A (2011) Non-blind watermarking scheme for color images in RGB space using DWT-SVD. In 2011 International conference on communications and signal processing, IEEE, pp. 489–493. https://doi.org/10.1109/ICCSP.2011.5739368
20. Rakhmawati L, Suwadi S, Wirawan W (2020) Blind robust and self-embedding fragile image watermarking for image authentication and copyright protection with recovery capability. Int J Intell Eng Syst 13(5):197–210
21. Rahman AU, Sultan K, Musleh D, Aldhafferi N, Alqahtani A, Mahmud M (2018) Robust and fragile medical image watermarking: a joint venture of coding and chaos theories. J Healthcare Eng. https://doi.org/10.1155/2018/8137436
22. Qin C, Ji P, Wang J, Chang CC (2017) Fragile image watermarking scheme based on VQ index sharing and self-embedding. Multimed Tools Appl 76(2):2267–2287. https://doi.org/10.1007/s11042-015-3218-9

23. Lin CC, He SL, Chang CC (2021) Pixel-based fragile image watermarking based on absolute moment block truncation coding. Multimed Tools Appl 80(19):29497–29518. https://doi.org/10.1007/s11042-021-10598-5
24. Ramos AM, Artiles JAP, Chaves DPB, Pimentel C (2023) A Fragile Image Watermarking Scheme in DWT Domain Using Chaotic Sequences and Error-Correcting Codes. Entropy 25(3):508. https://doi.org/10.3390/e25030508
25. Singh D, Singh SK, Udmale SS (2023) An efficient self-embedding fragile watermarking scheme for image authentication with two chances for recovery capability. Multimed Tools Appl 82(1):1045–1066. https://doi.org/10.1007/s11042-022-13270-8
26. Prasad S, Pal AK, Paul S (2022) A Block-Level Image Tamper Detection Scheme Using Modulus Function Based Fragile Watermarking. Wirel Pers Commun 125(3):2581–2619. https://doi.org/10.1007/s11277-022-09675-1
27. Renklier A, Öztürk S (2023) Image authentication and recovery: sudoku puzzle and MD5 hash algorithm based self-embedding fragile image watermarking method. Multimed Tools Appl. https://doi.org/10.1007/s11042-023-15999-2
28. Sivasubramanian N, Konganathan G (2020) A novel semi fragile watermarking technique for tamper detection and recovery using IWT and DCT. Computing 102(6):1365–1384. https://doi.org/10.1007/s00607-020-00797-7
29. Alahmadi A, Hussain M, Aboalsamh H, Muhammad G, Bebis G, Mathkour H (2017) Passive detection of image forgery using DCT and local binary pattern. Signal Image Video Process 11(1):81–88. https://doi.org/10.1007/s11760-016-0899-0
30. Singh D, Singh SK (2015) DCT based efficient fragile watermarking scheme for image authentication and restoration. Multimed Tools Appl 76:953–977. https://doi.org/10.1007/s11042-015-3010-x
31. Ouyang J, Huang J, Wen X (2023) A semi-fragile reversible watermarking method based on qdft and tamper ranking, Multimed Tools Appl. https://doi.org/10.1007/s11042-023-16963-w
32. Ouyang J, Huang J, Wen X, Shao Z (2023) A semi-fragile watermarking tamper localization method based on QDFT and multi-view fusion. Multimed Tools Appl 82(10):15113–15141. https://doi.org/10.1007/s11042-022-13938-1
33. Wu HC, Fan WL, Tsai CS, Ying JJC (2022) An image authentication and recovery system based on discrete wavelet transform and convolutional neural networks. Multimed Tools Appl 81(14):19351–19375. https://doi.org/10.1007/s11042-021-11018-4
34. Azizoglu G, Toprak AN (2023) A novel reversible fragile watermarking method in DWT domain for tamper localization and digital image authentication. Biomed Signal Process Control 84:105015. https://doi.org/10.1016/j.bspc.2023.105015
35. Srivastava V, Yadav SK (2022) Digital Image Tampering Detection Using Multilevel Local Binary Pattern Texture Descriptor. J Appl Secur Res 17(1):62–79. https://doi.org/10.1080/19361610.2021.1883397
36. Pal P, Jana B, Bhaumik J (2021) An Image Authentication and Tampered Detection Scheme Exploiting Local Binary Pattern Along with Hamming Error. Wirel Pers Commun 121(1):939–961. https://doi.org/10.1007/s11277-021-08666-y
37. Park JY, Kang TA, Moon YH, Eom IK (2020) Copy-move forgery detection using scale invariant feature and reduced local binary pattern histogram. Symmetry (Basel) 12(4):492
38. Kalsi DK, Rai P (2017) A Copy-move forgery detection system using approximation image local binary pattern. In 2017 International conference on recent innovations in signal processing and embedded systems (RISE), IEEE. pp. 284–288. https://doi.org/10.1109/RISE.2017.8378168
39. Bhalerao S, Ahmad I, Anil A (2021) A secure image watermarking for tamper detection and localization. J Ambient Intell Humaniz Comput 12(1):1057–1068. https://doi.org/10.1007/s12652-020-02135-3
40. Prasad S, Pal AK (2020) A tamper detection suitable fragile watermarking scheme based on novel payload embedding strategy. Multimed Tools Appl 79(3–4):1673–1705

Publisher's Note Springer Nature remains neutral with regard to jurisdictional claims in published maps and institutional affiliations.

Springer Nature or its licensor (e.g. a society or other partner) holds exclusive rights to this article under a publishing agreement with the author(s) or other rightsholder(s); author self-archiving of the accepted manuscript version of this article is solely governed by the terms of such publishing agreement and applicable law.

Assessment of soil liquefaction potential using genetic programming using a probability-based approach.

Nerusupalli Dinesh Kumar Reddy* , Prof Ashok Kumar Gupta[2] , Prof Anil Kumar Sahu[3]

Department of Civil Engineering, Delhi Technological University, 110042, India.

Email: dkumarreddy_phd2k18@dtu.ac.in

Email: akgupta@dtu.ac.in

Email: Kumar.civil2018@gmail.com

*Corresponding Author: (dkumarreddy_phd2k18@dtu.ac.in)

Abstract

Soil liquefaction is a substantial seismic hazard that endangers both human life and infrastructure. This research specifically examines the occurrence of soil liquefaction events in past earthquakes, with a special emphasis on the 1964 Niigata, Japan and 1964 Alaska, USA earthquakes. These occurrences were important achievements in the comprehension of harm caused by liquefaction. Geotechnical engineers often use in-situ experiments, such as the standard penetration test (SPT) to evaluate the likelihood of liquefaction. The attraction for this option arises from the difficulties connected in acquiring undisturbed samples of superior quality, as well as the related expenses. Geotechnical engineering specialists choose the deterministic framework for liquefaction assessment because of its clear mathematical approach and low needs for data, time, and effort. This work emphasises the need of integrating probabilistic and reliability methodologies into the design process of crucial life line structures to enable well-informed risk-based decision-making. The objective of this project is to create models that use deterministic, probabilistic, and reliability-based methods to evaluate the likelihood of soil liquefaction. The work presents a new equation that combines Bayes conditional probability with Genetic Programming (GP). and also in study is to identify the most suitable method for liquefaction analysis based on factor of safety and Performance Fitness Error Metrics (PFEMs), Rank analysis, Gini index, etc. The information provided in study data include soil and seismic characteristics, including the corrected blow count $(N1)60cs$, fines content (FC), mean grain size ($D50$), peak horizontal ground surface acceleration ($amax$), earthquake magnitude (M), and $CSR7.5$. The parameters are derived from the SPT measurements conducted at many global locations, together with field performance observations (LI) and probability of liquefaction has been assessed through the use of Gini Index (GI). A comparison was made between the novel methodology and the techniques proposed by Juang et al. (2002), Toprak et al. (1999), and Idriss and Boulanger (2006) status of case history data using Performance Fitness Error Metrices. The comparison included employing a confusion matrix for binary classification and doing a score analysis based on factor ranking. The proposed model exhibited superior performance, as the outputs of the constructed model increased for all positive factors and decreased for negative indicators.

1. Introduction

Seismic hazards include many threats such as ground shaking, structural vulnerabilities, liquefaction, landslides, failures of retaining structures, dangers to essential infrastructure, and tsunamis. The primary cause of both human casualties and infrastructure damage is the liquefaction of soil triggered by seismic activity. Terzhagi and Peck (1948) were the first to recognise and describe the occurrence of soil liquefaction, which refers to the abrupt decrease in strength of loose sand deposits. This discovery played a crucial role in the early development of soil mechanics. The key factor leading to slope collapse in saturated sand deposits was identified. However, it was the occurrence of severe earthquakes in various parts of the world, such as Niigata and Alaska (1964), Loma Prieta (1989), Kobe (1995), Kocaeli (1999), and Chi-Chi (1999), that drew the attention of engineers, seismologists, and the scientific community to this phenomenon (Baziar and Jafarian, 2007). Subsequent research conducted in both field and laboratory settings has demonstrated that soil liquefaction can be better characterised as a disastrous failure event. This occurs when saturated soil experiences a loss of strength caused by a rise in pore water pressure and a decrease in effective stress due to rapid loading. As a result, the soil becomes mobile enough to move over distances ranging from metres to kilometres. Soil liquefaction may cause ground failure, such as the emergence of sand boils, large landslides, surface sinking, lateral spreading, movement of bridge supports, settling and swaying of buildings, collapse of marine structures, and extensive damage to lifeline systems, among other consequences.

The simplified approach based on the Standard Penetration Test (SPT), first devised by Seed and Idriss in 1971, At the same time, Tsuchida and Hayashi (1971) developed a relation between the grain-size distribution and liquefaction susceptibility of soils using the Japanese liquefaction sites. In the later stage, based on this “simplified procedure” researchers have attempted to build more accurate deterministic and probabilistic triggering correlations using the SPT data (Seed and Idriss 1982; Seed et al. 1983; Seed et al. 1985; Youd et al. 2001), It remains the most often used method globally. Robertson and Campanella (1985) pioneered the development of a CPT-based technique for assessing the likelihood of liquefaction, this method involves converting the SPT-based approach by using an empirical correlation between SPT-CPT, it follows a stress-based approach similar to the one proposed by Seed and Idriss (1971). Further Several improvements done for on cone penetration testing (CPT) by using statistical and regression analysis techniques methods (Seed and de Alba (1986), Olsen (1988), Shibata and Teparaksa (1988), Mitchell and Tseng (1990), Stark and Olson (1995), Suzuki et al. (1995), Olsen (1997), Robertson and Wride (1998), and Youd et al. (2001).) Multiple simpler procedures using shear wave velocity VS have been developed (Stokoe et al. 1988; Tokimatsu and Uchida 1990; Addo and Robertson 1992; Kayen et al. 1992; Andrus and Stokoe 2000; Juang et al. 2000; Juang et al. 2001; Andrus et al. 2004). There are only a limited number of simpler techniques based on the BPT (Becker Penetration Test) technique which was proposed by Harder and Seed (1986). These methods, however, are only applicable to soils with a gravelly composition.

The boundary curve provides the liquefaction resistance of a soil, usually stated as the cyclic resistance ratio (CRR), for a certain index of soil resistance, such as the corrected SPT impact count. The evaluation of a soil's liquefaction potential under seismic loading involves assessing the factor of safety (Fs), which is determined by the ratio of the cyclic resistance ratio (CRR) to the cyclic stress ratio (CSR). The seismic loading is commonly

stated as CSR. The deterministic technique, which involves quantifying the liquefaction potential of soil in terms of the factor of safety (Fs), is preferred by geotechnical specialists for its simplicity in implementation. Parametric and model inaccuracies may lead to situations where Fs>1 does not always indicate the absence of soil liquefaction, nor does it guarantee a complete absence of the risk of liquefaction. Furthermore, it should be noted that Fs does not always result in liquefaction and does not guarantee complete liquefaction, as stated by Juang et al. (2000). In deterministic methodologies, the interface between liquefaction and non-liquefaction scenarios is known as a performance function or "limit state function." This function is often designed to be conservative, including the majority of liquefied instances.

In recent decades, some geotechnical researchers have successfully forecasted the probability of liquefaction by using reliability analysis, taking into consideration mistakes in models and parameters (Haldar and Tang 1979; Liao et al. 1988; Toprak et al. 1999; Juang et al. 2006; Idriss and Boulanger 2006.) performed a logistic regression analysis on the available case histories in order to ascertain the probability of liquefaction (P_L). These studies propose a simple regression equation that may be used to estimate the nominal probability, which is a measure of the model's level of uncertainty.

Juang et al. (1999) developed a dependable technique for estimating the likelihood of liquefaction (P_L) using a Bayesian mapping function. Juang et al. (2002) further developed their previously suggested approach for creating a mapping function that relates P_L and Fs. This mapping function was constructed using the methodology proposed by Youd and Idriss (2001). Goharzay et al. (2017) built upon the first proposal of the first order reliability-based Bayes probability function by Muduli and Das (2015). The Bayesian network (BN) approach has been shown to be a very effective method for engineers to assess the probability of earthquake-induced liquefaction. Hu (2021a) introduced an innovative approach for forecasting the liquefaction of soil containing gravel this technique relies on the use of two Bayesian network models. Hu et al. (2022) developed a hybrid Bayesian network (BN) model to predict liquefaction caused by earthquakes. The model is based on shear wave velocity (Vs) and builds upon previous studies by Hu and Liu (2019); Hu (2021b); Hu et al. (2022); Pirhadi et al. (2023). In their study, used Cetin et al. (2004) database of case histories to establish a new collection of probabilistic and deterministic connections. Their objective was to predict the likelihood of liquefaction start by using the maximum likelihood function inside a Bayesian framework. Subsequently, Idriss and Boulanger (2010) and Boulanger and Idriss (2014) devised a method that combines deterministic and probabilistic approaches using SPT data, therefore enhancing the methodology established by Seed and Idriss (1971). The determination of liquefaction potential relies on a set of assumptions and approximations, which form the basis of all suggested conventional techniques and empirical linkages.

Fundamentally, difficulties related to assessing liquefaction are very nonlinear. Some of geotechnical researchers developed machine learning methods to overcome the challenges posed by nonlinearity and other complexities in forecasting the likelihood of liquefaction. Goh (1994) developed a neural network model to predict and evaluate the likelihood of liquefaction in saturated, cohesionless soil. The Artificial Neural Network (ANN) model, which is widely recognised as a leading machine learning approach in this field, has shown good use in the prediction of liquefaction (Samui and Sitharam 2011; Ramakrishnan et al. 2008). Subsequently, additional scholars in the geotechnical domain developed various machine learning techniques, such as neural networks, support vector machine (SVM), genetic programming (GP), least square support vector machine (LSSVM), and stochastic

gradient boosting (SGB), for the purpose of conducting liquefaction analysis (Pal 2006; Samui and Karthikeyan 2013; Hanna et al. 2007; Samui et al. 2011; Samui and Hariharan 2015; Xue and Liu 2017). Zhang et al. (2016) devised a non-parametric, multivariate adaptive regression spline (MARS) method to assess the likelihood of liquefaction in sands and granular soils using the energy concept. Zhang et al. (2021a) used CPT data to introduce the extreme learning machine (ELM) as a method for assessing the susceptibility of soil deposits to liquefaction. These basic models have some significant limitations, such as limited generalisation capacity, slow convergence rate, and susceptibility to overfitting. These shortcomings may adversely affect the accuracy of result prediction. The existing liquefaction assessment methods based on machine learning are fundamentally opaque since they favour accuracy at the expense of explainability. The existing liquefaction datasets are quite small and have a higher percentage of liquefaction events compared to non-liquefaction events. As a result, these models exhibit distinct performance characteristics when compared to databases from other areas of the world. Subsequently, additional scholars have introduced novel machine learning techniques such as random forest (RF) (Kohestani et al 2015), Jas and Dodagoudar (2023) proposed an explainable machine learning model for liquefaction potential assessment of soils using XGBoost-SHAP to address the issue of interpretability in the machine learning model, and gradient boosting machine (GBM) shown better adoptability to the low amount of data (Kumar et al. 2022a; Zou et al. 2019). Zhang and Wang (2021) have devised an improved ensembled and hybrid method using genetic algorithms and GWO, while Zhang et al. (2021b) have developed a hybrid model by incorporating SVM-GWO. Machine learning (ML) models that already exist are better options for handling enormous amounts of data and enhancing the accuracy of predictions. Every machine learning approach has its own limitations and constraints due to parameters and model ambiguity (Momeni et al., 2015).

2. Methodology

2.1 Introduction of prediction model and data base

A stress-based technique to evaluate the likelihood for liquefaction triggering was first devised by Seed and Idriss (1967). This methodology has been employed extensively over the course of the previous 45 years (Seed and Idriss 1971; Tokimatsu and Yoshimi 1983; *NRC* 1985; Seed et al. 1985; Youd et al. 2001; Cetin et al. 2004; Idriss and Boulanger 2004, 2008). The correlation between the cyclic resistance ratio (CRR) adjusted to a magnitude of 7.5 (M = 7.5) and the effective vertical stress ($\sigma_v' = 1$) and the corresponding value of the normalised cone penetration resistance $(N_1)_{60CS}$ for cohesionless soils, as determined by Idriss and Boulanger (2004, 2008), can be expressed as:

$$CSR_{7.5} = 0.65\frac{\sigma_v}{\sigma_y'}\frac{a_{max}}{g}r_d/MSFK_\sigma K_\propto \qquad (1)$$

$$CRR_{M=7.5,\sigma_v'=1atm} = exp\left(\left(\frac{(N_1)_{60cs}}{14.1}\right) + \left(\frac{(N_1)_{60cs}}{126}\right)^2 - \left(\frac{(N_1)_{60cs}}{23.6}\right)^3 + \left(\frac{(N_1)_{60cs}}{25.4}\right)^4 - 2.8\right) \qquad (2)$$

Where:

$amax$= surface peak acceleration

σv= total overburden pressure

$\sigma' y$= effective overburden pressure

rd= reduction in shear stress in depth z

$K\sigma$, Ka= correction factors

MSF= magnitude scaling factor

$(N1)60CS$= corrected SPT no

2.1.1 Deterministic methods (F_S)

In the approach, the F_S parameter, which signifies the ratio of CRR to CSR, is determined by forecasting individual values of load (CSR) and resistance (CRR) without considering the uncertainty related to the prediction of loading and resistance. Figure 2.8 illustrates this. The computed CRR and CSR are considered to have a probability of occurrence of 100%. Within a deterministic approach, a factor of safety (F_S) beyond 1 signifies the absence of liquefaction, whereas a F_S value of 1 or below indicates the occurrence of liquefaction. The "simplified procedure" first introduced by Seed and Idriss (1971), and further explained in preceding sections, is the most definitive method for assessing the likelihood of liquefaction at a given site. This technique has been modified and improved several times to make it suitable for different in-situ testing scenarios (Seed et al., 1983; Seed et al., 1985; Robertson and Campanella, 1985; Shibata and Teparaksa, 1988; Olsen, 1997; Robertson and Wride, 1998). The 1998 workshop conducted by the National Centre for Earthquake Engineering Research ($NCEER$) resulted in a comprehensive assessment of deterministic methods that use in-situ testing to evaluate the potential occurrence of soil liquefaction (Youd et al., 2001). The equation may be used to compute the factor of safety (Fs) against liquefaction during an earthquake.

$$F_S = \left(\frac{CRR_{M=7.5,\sigma'_v=1atm} K_\sigma K_\alpha}{\text{CSR}*\text{MSF}}\right) \quad (3)$$

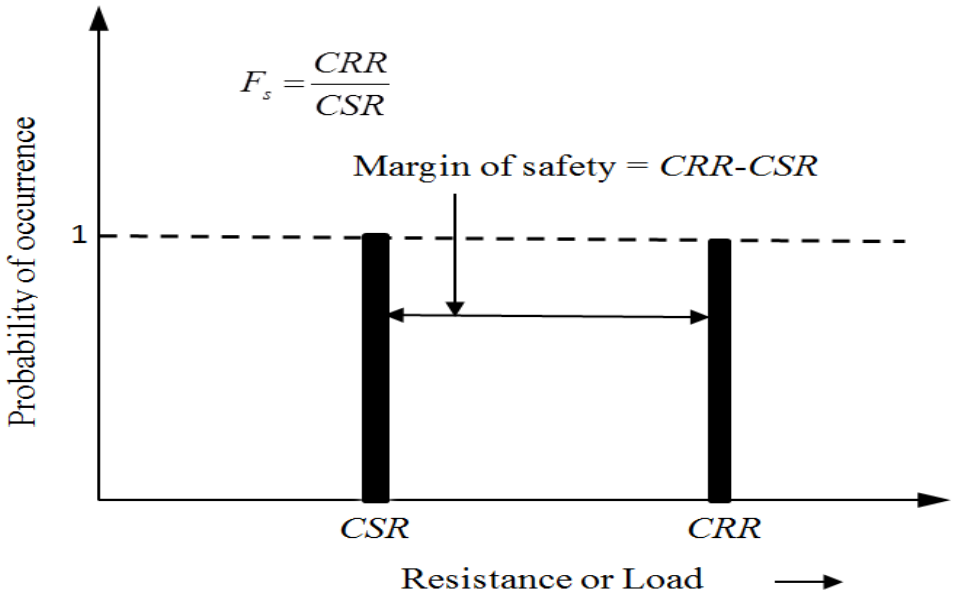


Figure 1. illustrates the deterministic technique used to evaluate liquefaction potential, as described by Becker (1997)

2.1.2 Data collection and processing

The current analysis used a dataset of measures acquired from the Standard Penetration Test (SPT). The collection included post-liquefaction case studies spanning from the Tohnankai earthquake in 1944 to the Chi Chi earthquake in 1999 in Taiwan. The dataset for the study included 286 instances of liquefaction and 210 instances of non-liquefaction. In addition, to verify the accuracy of the models, a set of 30 Standard Penetration Test (SPT) borehole data collected from Faridabad a region in the National Capital District (NCR) of Delhi. In the Figure .2 shown collection of sample setup and split spoon sampler. The bore hole data and the model data for the study are shown in Table 1 and Table 2, respectively.



Figure 2. (a) SPT field set up and (b) split spoon sample

Table 1 Sample bore hole data

Avg Depth	WT	σ_v (kPa)	σ'_v (kPa)	N_m	$(N_1)_{60}$	C_B	C_E	C_N	C_R	C_S	FC	$(N_1)_{60c}$	$\Delta(N_1)_{60cs}$	γ_{total}	γ'_{total}

2.3	1.2	43	32	4	6.1	1	1.13	1.70	0.8	1	69	11.7	5	18.5	19.1
3.0	1.2	57	39	6	9.2	1	1.13	1.59	0.85	1	33	14.6	2	18.5	19.1
3.4	1.2	63	42	3	4.6	1	1.13	1.60	0.85	1	33	10.1	1	18.5	19.1
3.7	1.2	69	45	6	8.6	1	1.13	1.49	0.85	1	33	14.1	2	18.5	19.1
3.8	1.2	72	46	13	17.4	1	1.13	1.39	0.85	1	20	21.9	5	18.5	19.1
4.3	1.2	81	51	11	14.4	1	1.13	1.37	0.85	1	20	18.9	2	18.5	19.1
4.6	1.2	87	54	10	14.3	1	1.13	1.33	0.95	1	20	18.8	5	18.5	19.1
4.9	1.2	92	56	4	5.8	1	1.13	1.36	0.95	1	33	11.3	2	18.5	19.1
5.2	1.2	98	59	4	5.7	1	1.13	1.33	0.95	1	33	11.2	1	18.5	19.1
5.3	1.2	101	61	6	8.3	1	1.13	1.29	0.95	1	33	13.8	5	18.5	19.1
5.5	1.2	104	62	10	13.4	1	1.13	1.25	0.95	1	33	18.9	2	18.5	19.1
6.1	1.2	116	68	9	11.7	1	1.13	1.21	0.95	1	33	17.1	1	18.5	19.1
7.1	1.2	133	76	14	16.9	1	1.13	1.13	0.95	1	33	22.4	2	18.5	19.1
7.6	1.2	87	54	7.1	10.3	1	1.13	1.36	0.95	1	30	15.7	5.4	18.5	19.1

Table 2. sample trained and test data

Liquefaction	Magnitude (M)	Critical Depth (d)	Fine Content (%)	D50 (mm)	Water Table (m)	PGA (g)	r_d	(N1)60cs	CSR
Yes	7.300	6.000	61.000	0.075	2.300	0.428	0.942	8.470	0.451
Yes	7.300	4.200	24.000	0.200	2.700	0.789	0.959	3.580	0.378
Yes	7.300	9.000	42.000	0.100	2.300	0.789	0.886	6.380	0.714
Yes	7.300	2.400	41.000	0.095	2.300	0.789	0.972	8.710	0.514
Yes	7.300	5.000	22.000	0.065	2.200	0.428	0.952	3.670	0.379

Yes	7.300	4.200	62.000	0.100	1.800	0.211	0.959	4.050	0.417
Yes	7.300	7.700	16.000	0.220	3.800	0.165	0.915	10.190	0.132
Yes	7.300	8.100	16.000	0.190	3.100	0.165	0.907	8.480	0.136
Yes	7.300	5.700	16.000	0.170	2.800	0.165	0.945	8.820	0.139
Yes	7.300	8.100	19.000	0.170	2.800	0.165	0.907	10.710	0.148
Yes	7.300	3.700	11.000	0.190	2.300	0.165	0.962	11.570	0.128
Yes	7.300	10.000	45.000	0.080	3.000	0.165	0.850	7.250	0.145
Yes	7.300	7.700	18.000	0.170	3.000	0.165	0.915	6.720	0.142
No	7.300	5.000	14.000	0.200	0.600	0.124	0.952	23.860	0.137
No	7.300	10.000	15.000	0.220	0.600	0.124	0.850	21.980	0.128
No	7.300	9.000	12.000	0.200	0.600	0.124	0.886	21.090	0.133
No	7.300	5.000	14.000	0.200	0.600	0.124	0.952	18.680	0.138
No	7.300	6.000	19.000	0.190	0.600	0.124	0.942	21.970	0.138
No	7.300	10.000	16.000	0.170	1.300	0.124	0.850	20.420	0.122
No	7.300	18.000	22.000	0.104	2.700	0.165	0.730	9.340	0.142
No	7.300	6.000	8.000	0.200	2.700	0.165	0.942	12.070	0.142
No	7.300	16.000	18.000	0.140	2.700	0.165	0.760	12.080	0.145
No	7.300	18.000	32.000	0.100	2.700	0.165	0.730	10.770	0.142
No	7.300	16.000	18.000	0.140	2.700	0.165	0.760	9.060	0.145
No	7.300	4.000	43.000	0.090	2.700	0.165	0.960	7.460	0.124
No	7.300	12.000	8.000	0.201	2.700	0.165	0.820	10.200	0.149

The sample bore hole data depth spans from 2.3 to 7.3 and has a water table depth of 1.2 metre, and SPT has been done and registered SPT no at different depths, and all adjustments are computed according to standard protocols supplied by previous studies. After calculating all variables, the corrected blow count $(N1)60cs$, fines content (FC), mean grain size ($D50$), peak horizontal ground surface acceleration (amax), magnitude of earthquake (M), shear stress reduction factor (rd), water table depth (WT), critical depth (d), and $CSR7.5$ were selected for further investigation.

The information provided in study data include soil and seismic characteristics, including the corrected blow count $(N1)60cs$, fines content (FC), mean grain size ($D50$), peak horizontal ground surface acceleration ($amax$), earthquake magnitude (M), and $CSR7.5$. The parameters are derived from the SPT measurements conducted at many global locations, together with field performance observations (LI). The soil in these circumstances may include sand, silty sand, sandy silt, and clayey silt. In terms of the database, the documented depths of SPT measurements range from 1.3 metres to 20.3 metres. The water table depth ranges from 0 to 15.30 metres. The range of values among $(N1)60cs$, is 0.93 to 35.22. The fines content (FC) number range from 0 to 92%. Conversely, the PGA value ranges from 0.052 to 1, while the $CSR7.5$ value ranges from 0.041 to 0.822. Based on the data, a total of 347 instances are randomly selected for training, while the remaining 149 cases are allocated for testing the developed model.

2.1.3 Data cleaning, normalization

Prior to constructing the model, it is necessary to preprocess the data in order to guarantee the precision of the model's predictions. The dataset has a minimal number of null values this time, and the conventional approach to address missing data is by using the empty value filling technique. To optimize the use of existing data and maintain the quantity and quality of samples, the 496 datasets may be enhanced by replacing the missing characteristic values with null values. By using statistical measures such as the average, median, quantile, complex, and random values of the whole dataset, one may assess the impact of various filling strategies. Ultimately, this article employs the most precise form of filling, which is the mean filling. All 10 parameters in the soil liquefaction dataset are numerical and exhibit varying ranges of values, which may fluctuate significantly in magnitude. The variability of values in the dataset might impact the rate at which the model converges. The features undergo min-max normalization to get precise classification outcomes and guarantee that each feature contributes significantly. Hence, data normalization guarantees that features with varying dimensions possess equal significance, hence enhancing the accuracy, speed of convergence, and stability of the model. Consequently, this leads to an improvement in the performance of machine learning algorithms. Every characteristic of the whole dataset is transformed to a range of values between 0 and 1 in order to minimize the influence of feature size and magnitude on the model. The min-max normalizing approach reduces the values of the features in a linear manner, while preserving the linear properties of the original dataset. The equation is as stated.

$$X' = \frac{X - Min(X)}{Max(X) - Min(X)} \tag{4}$$

2.1.4 Data Visualization and correlation analysis

The use of data visualization facilitates the comprehension of data trends, the interrelationships and distinctions among several variables employed in the study, and the level of disorder or randomness within the data. This understanding aids in determining appropriate methodologies for data analysis.

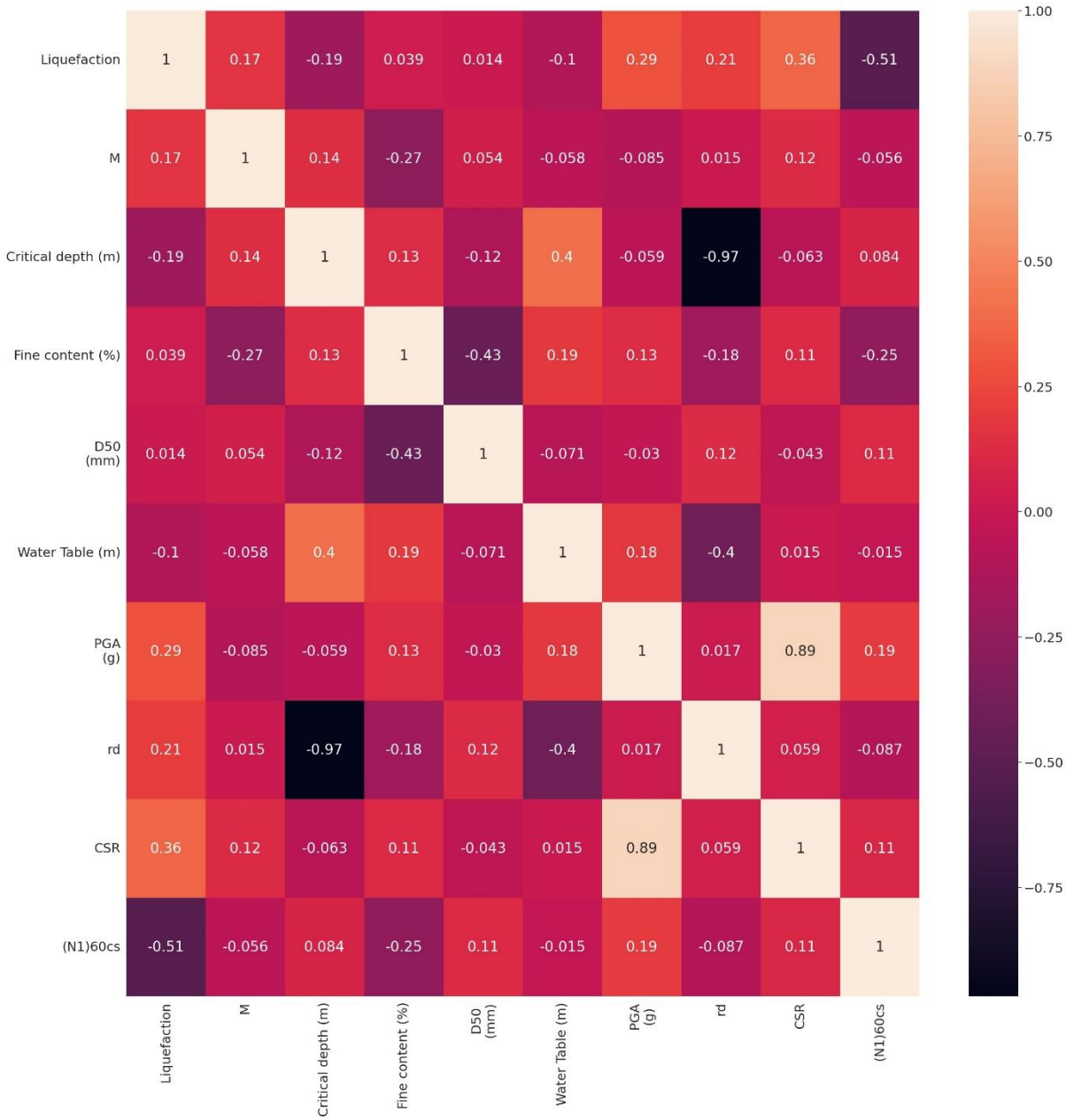


Figure 3. heat map of the Spearman's rank correlation coefficient matrix

A heat map of the Spearman's rank correlation coefficient matrix for the input variables is shown in Figure 3, with the corresponding correlation coefficients and diagonal element shown the target variable. It can be seen that parameters (Generally speaking, |R|= 0 implies an uncorrelated relationship; |R|< 0.2 implies a very weak correlation; 0.2 <|R|< 0.4 stands for a weak correlation; 0.4 <|R|< 0.6 stands for a moderate correlation; 0.6 <|R|<0.8 implies a strong correlation; 0.8 <|R|<1 implies a very strong correlation; |R|= 1 implies fully correlated.)

The formula for spearman's rank correlation coefficient is follows:

$$R = \frac{COV(rank\,(X) rank\,(Y))}{\sigma_{rank\,(X)} \sigma_{rank\,(Y)}} = \frac{\Sigma_i (R_X\,(i) - \overline{R_X})(R_Y\,(i) - \overline{R_Y})}{\sqrt{\Sigma_i (R_X\,(i) - \overline{R_X})^2} \sqrt{\Sigma_i (R_Y\,(i) - \overline{R_Y})^2}} \quad (5)$$

Where: $rank\,(X) rank\,(Y)$ are the ranks of variables X, Y, respectively COV denotes covariance and $\sigma_{rank\,(X)} \sigma_{rank\,(Y)}$ are the standard deviations of $rank\,(X) rank\,(Y)$, R_X, R_Y represents the average ranks for $rank\,(X) rank\,(Y)$, respectively.

Multicollinearity arises when predictor variables exhibit either positive or negative correlation. Positive correlation, as observed between variables X and Y, implies that they move in the same direction; when X increases, Y tends to increase. In regression, this strong positive relationship can lead to multicollinearity, hindering the model's ability to distinguish individual effects. Similarly, negative correlation, such as between variables A and B, involves opposite movements; as A increases, B tends to decrease. High negative correlations in regression may also result in multicollinearity issues, making it challenging to differentiate the impact of A and B on the outcome variable and potentially leading to unreliable estimates.

The variables Cyclic Stress Ratio (CSR) and Peak Ground Acceleration (PGA) exhibit a substantial positive correlation with a value of 0.89. This high correlation raises concerns about multicollinearity, suggesting the need to eliminate one of the variables. However, both variables are indispensable in liquefaction studies, necessitating their retention despite the correlation issue. Similarly, the Reduction Factor (rd) and Critical Depth (d) display a notable negative correlation of -0.97, which may also indicate multicollinearity. Despite this challenge, both variables remain crucial in liquefaction studies, and therefore, the decision is to retain both variables while acknowledging the potential impact of their high correlation.

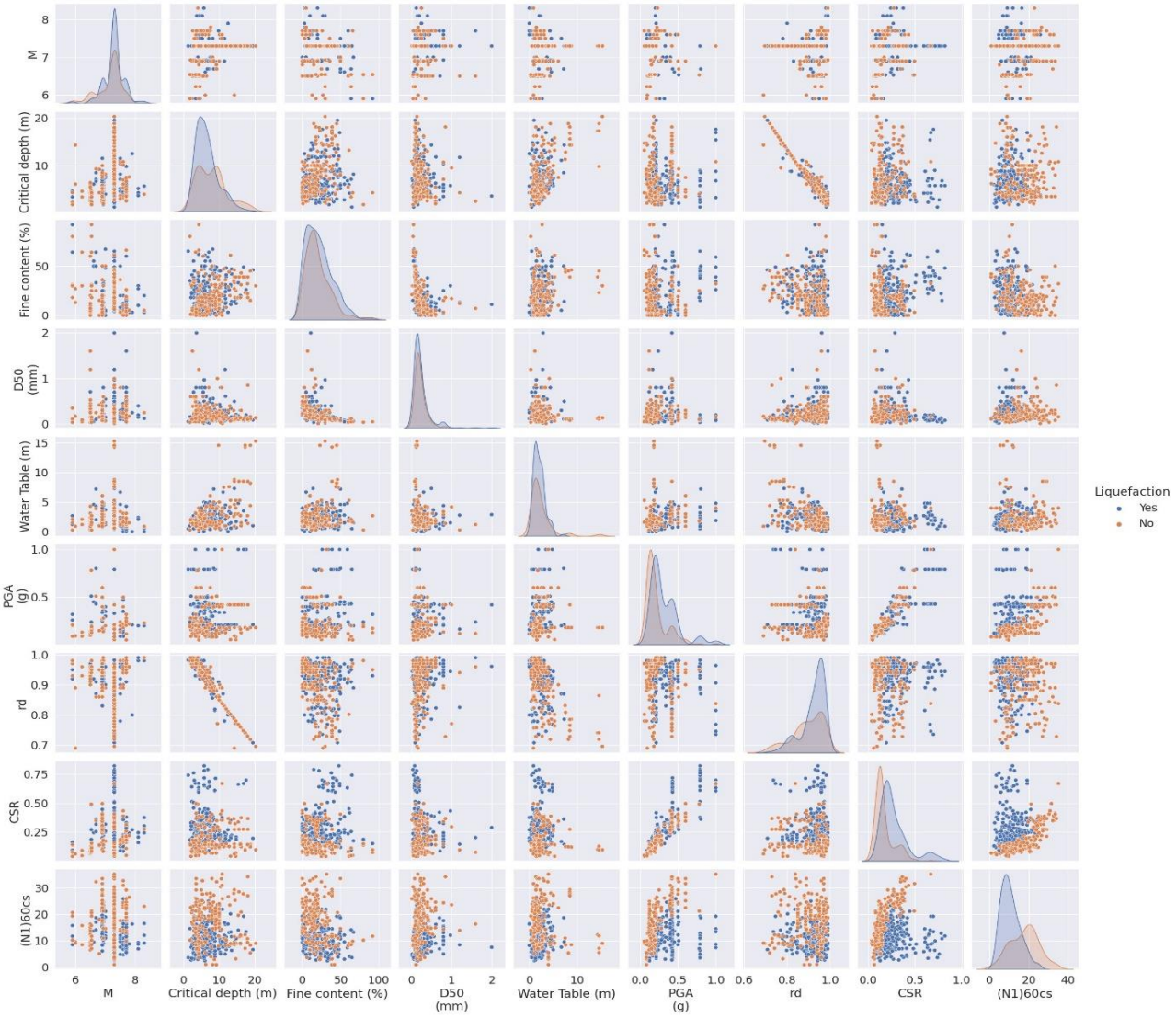


Figure 4. Pair plot to determine entropy of variables

Pair plot graphs are often used to assess the entropy of data, a lower entropy number indicates a substantial level of segregation or classification within the data, but a lower entropy value signifies a higher degree of information transmission. This entropy metric may provide a deeper comprehension of the selection of models, considering their categorization complexity and information transmission capabilities**.** Figure 4 depicts the contrast between data that has been liquefied and data that has non-liquefied, with respect to changes in the values of two variables. The Figure 4 clearly shows that there is no clear differentiation between the two types of data, suggesting a high level of complexity. Therefore, basic models are inadequate for analysing such intricate data. When faced with such a high degree of complexity, it is advisable to use more advanced models, such as genetic programming and advanced deep learning models, to get beneficial results.

2.2 GEP model

The computational approach known as GEP is applied to generate computer programs that contain the capacity to tackle difficult issues. Dr. Candida Ferreira first proposed the idea in 1992 as part of her PhD research at the University of Coimbra in Portugal. The GEP technique is based on the basic principles of genetics and natural

selection. The operating method of this system comprises the repeated development of a set of computer programs via a sequence of mutation and selection procedures. The GEP technique entails representing each program as a sequence of symbols that may undergo different genetic processes, such as combination and modification. By selecting programs with higher performance on a specific challenge in each generation and propagating them to the next generation, their overall fitness is improved over time. The capacity of GEP to manage numerous objectives concurrently renders it a valuable tool in the domain of optimization. The GEP has been extensively utilized in various domains, encompassing but not limited to data analysis, classification, and modelling. Empirical evidence suggests that GEP exhibits superior performance compared to other evolutionary computation techniques, including genetic programming and evolutionary strategies, in specific problem domains (Ferreira 2002). In addition, the GEP methodology has been expanded to accommodate intricate data structures, including trees and graphs, by implementing altered genetic operators (Oliveira et al. 2016).

The present investigation employs a modelling method that represents the objective value as CRR, while considering the five independent components as input variables. The model's structure was developed using GeneXproTools 5.0 (2023) in conjunction with the four fundamental arithmetic operators (+, −, ×, and /). The modelling process used high-quality datasets that were randomly distributed throughout two distinct periods. Table 3 displays many distinct models that were created for the present study. These models were generated by using varying ratios of training and testing datasets, employing diverse programme dimensions, and employing distinct generations. The root-mean-squared error (RMSE), denoted as Ei, was used as the fitness function in this specific experiment. The fitness (fi) was calculated by using an equation derived from the expression tree. This equation accounted for the overall number of errors relative to the desired value. The method of addition was used to form a link between the genetic components. The expression tree (ET) for the CRR of the GP model 3 may be visualised in Figure 6. In this particular case, the input parameters are represented by the letters d0 through d5, while the constant value for gene one is represented by the symbol G1c8. To facilitate the interpretation of the expression tree, a mathematical equation derived for model 3. This equation establishes a connection between the input variables and the output variables. This research analysed five independent factors and one target variable. Equation 4 as derived using just two independent variables, namely (N1)60cs and D50. This was conducted to ascertain the relationship between CRR and input components, which was derived from the Spearman's rank correlation matrix of variables shown in Figure 5.

During the process of Genetic Programming (GP), a multitude of potential models are created at random. Subsequently, every model undergoes training and evaluation utilising the appropriate training and testing data. Each model's fitness is evaluated by minimizing the root mean square error ($RMSE$) between the predicted and observed values of the output variable (LI) through the employment of the objective function (f).

$$RMSE = \sqrt{\frac{\sum_{i=1}^{n}(LI - LI_{Pre})^2}{n}} \quad (6)$$

Let n be the total amount of incidences within the fitness group. If the errors calculated using Equation (3.1) for all models in the present population don't satisfy the termination criteria, the cycle of generating a new population continues until the desired optimal model is attained, as previously detailed.

The current study's GP-based model is presented in the following general manner:

$$LI_P = \sum_{i=1}^{n} F[X, f(X), C_i] + C_o \quad (7)$$

where LI_P represents the predicted value of the liquefaction performance index, F is the liquefaction index function created by the GP, X is the vector of input variables, Ci is a constant, f represents the user-defined functions, n is the number of terms in the target expression, and $C0$ is the bias term. The GP, as described by Searson et al. (2010), is used in the development and implementation of the current models utilising gene expo 5.0.

After simplifying, the following algebraic equation has been obtained for CRR:

$$CRR = \tanh\left(tanh\left(\frac{1}{7.19+6.02(N_1)_{60cs}-min(3.471,(N_1)_{60cs}}\right)\right) + \frac{((N_1)_{60cs})^{\frac{1}{3}}}{2} + tan^{-1}\left(\frac{\max(D_{50},6.364)\times 3.89(N_1)_{60cs}}{4}\right) - 1.8221 \quad (8)$$

Table 3 genetic programming (GP) models

Model	**Training data (in percent)**	**Testing data (in percent)**	**No. of chromosomes**	**Head size**	**No. of genes**	**Gene size**	**Program size**	**Literals**	**No. of generations**
M1	60	40	30	12	6	38	106	41	356684
M2	50	50	30	12	6	38	96	37	270413
M3	70	30	30	12	6	38	104	38	163511
M4	80	20	30	12	6	38	104	40	260010
M5	90	10	30	12	6	38	100	39	275015

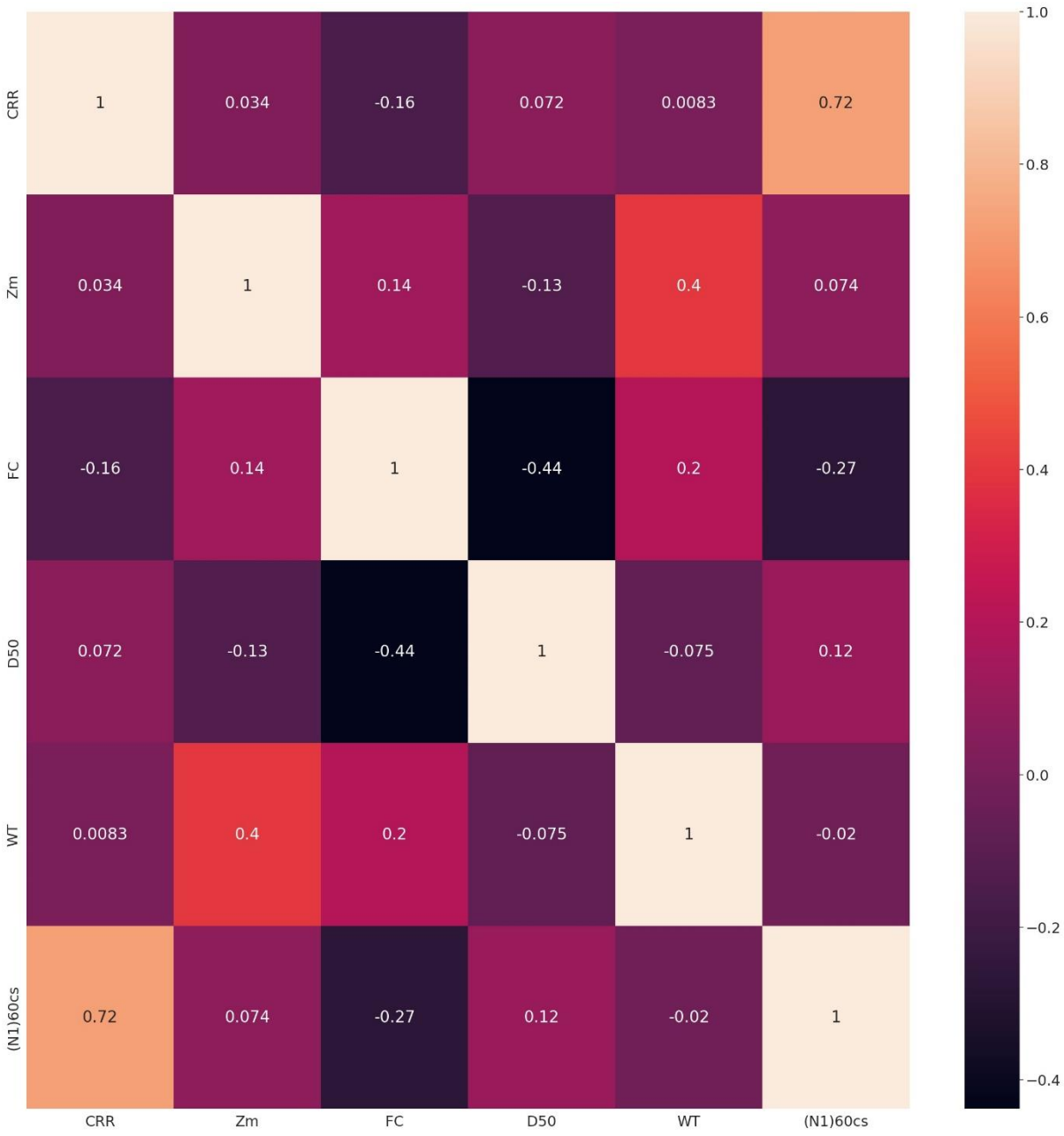


Figure 5. the Spearman's rank corelation matrix of variables used for GP

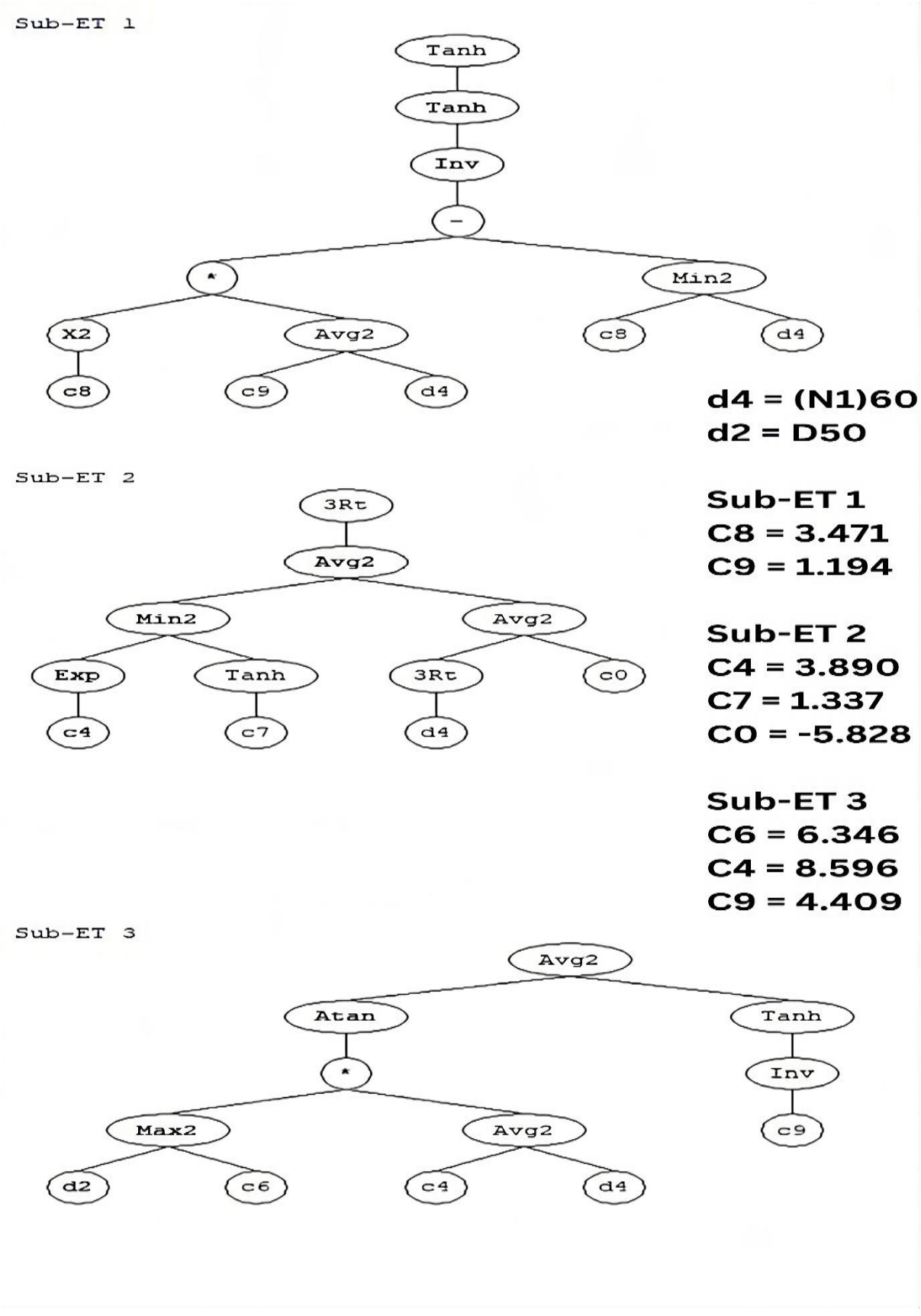


Figure 6. Expression tree for cyclic resistance ratio (CRR)

2.3 Probabilistic methods

Uncertainties in parameters and models make it clear that having a factor of safety (Fs) greater than 1 in liquefaction potential assessment does not provide total protection against liquefaction. Similarly, a Fs value less than or equal to 1 does not necessarily imply that liquefaction would occur. The ambiguity is resolved by taking into account the fluctuation of CRR and CSR, as seen in Figure 7. If Fs is calculated using the average values of CRR and CSR, it might exceed 1.0. Nevertheless, considering the distributions of CSR and CRR shown in Figure 7, there exists a likelihood that CRR may be lower than CSR, as indicated by the shaded area in the Figure 7, leading to Fs values below 1. This contradicts prior forecasts, in which a case originally deemed non-liquefied may ultimately be determined to be liquefied. Therefore, recent study has concentrated on evaluating the likelihood of liquefaction by estimating its probability (PL).

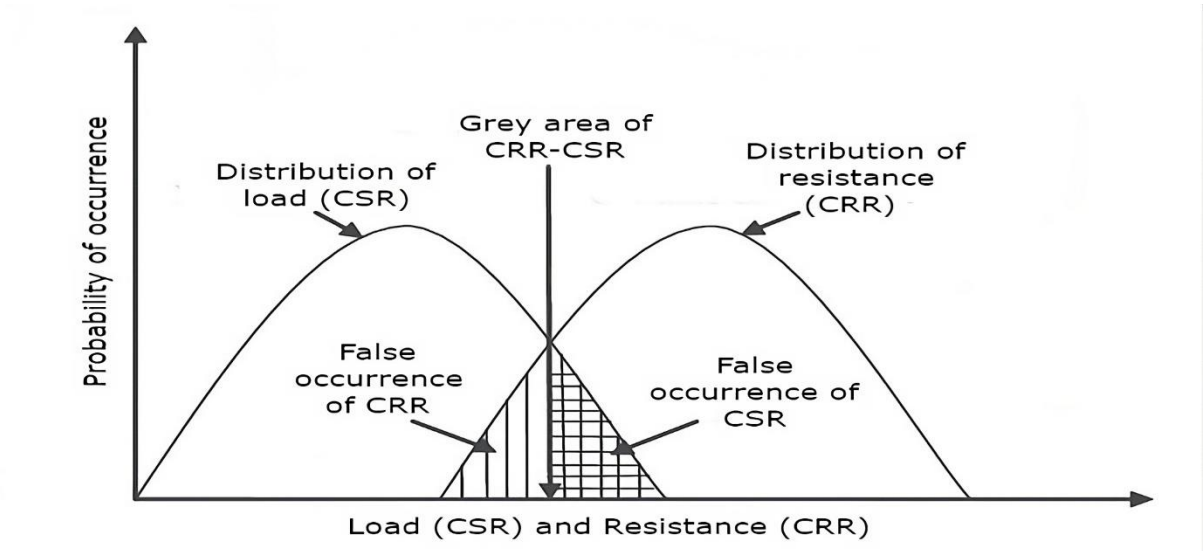


Figure 7. illustrates the prospective distribution of CRR (Cyclic Resistance Ratio) and CSR (Cyclic Stress Ratio) in the assessment of liquefaction potential

2.3.1 Implementation of Bayesian mapping function

Based on the research conducted by Juang et al. (1999), the probability of a case in the database undergoing liquefaction may be estimated using Bayes' theorem of conditional probability, given that the Fs has been calculated.

$$P\left(L/F_s\right) = \left(\frac{P\left(F_s/L\right)P(L)}{P\left(F_s/L\right)P(L)+P\left(F_s/NL\right)P(NL)}\right) \quad (9)$$

The equation $P\left(L/F_s\right)$ represents the probability of liquefaction given a certain value of Fs. $P\left(F_s/L\right)$ represents the probability of Fs assuming that liquefaction did occur. $P\left(F_s/NL\right)$ represents the probability of Fs assuming that liquefaction did not occur. $P(L)$ represents the prior probability of liquefaction, and $P(NL)$represents the prior probability of non-liquefaction. $P\left(F_s/L\right)$and $P\left(F_s/NL\right)$may be derived using equations (10) and (11) correspondingly.

$$P\left(F_s/L\right) = \int_{F_s}^{F_s+\Delta F_s} f_L(x)dx \quad (10)$$

$$P\left(F_s/NL\right) = \int_{F_s}^{F_s+\Delta F_s} f_{NL}(x)dx \quad (11)$$

$f_L(x)$ and $f_{NL}(x)$represent the probability density functions of Fs for examples in the database where liquefaction occurred and where liquefaction did not occur, respectively. As the change in Fs approaches zero, Equation (9) may be rewritten as Equation (12).

$$\left(L/F_s\right) = \left(\frac{f_L(F_s)P(L)}{f_L(F_s)P(L)+f_{NL}(F_s)P(NL)}\right) \quad (12)$$

Given the established prior probabilities $P(L)$ and $P(NL)$, one may use Equation (5.3) to compute the probability of liquefaction for a certain value of Fs. Without knowing the values of P(L) and P(NL), may deduce that $P(L)$ is likely to be equal to $P(NL)$ based on the principle of maximum entropy (Juang et al. 1999). Thus, if we assume that the likelihood of L is equivalent to the probability of NL, we may express Equation (12) as Equation (13).

$$P_L = \frac{f_L(F_s)}{f_L(F_s)+f_{NL}(F_s)} \quad (13)$$

The Fs values, calculated using the SPT-based deterministic approach, are computed for different cases in the collected database in this research. The examples are classified according to their observed field performance as either liquefaction (L) or non-liquefaction (NL).

Various distributions are performed for the factor of safety, and Weibull probability density function is determined to provide the most optimal fitting curves for both the L and NL groups. Figures 10 and 11 depict this. And Figure 8 and 9 shows the different percentage of each factor of safety values. The factor of safety of both groups is best described by the Weibull distribution, with scale parameter (λ) and shape parameter (k) values of 0.580 and 2.437, respectively. The probability density functions (PDF) of these Weibull distributions are seen in Figures 5.1 to 5.4 and may be expressed using Equation (14).

$$f(x;\lambda,k) = \frac{k}{\lambda}\left(\frac{x}{\lambda}\right)^{k-1} e^{-\left(\frac{x}{\lambda}\right)^{k}}, \qquad x \geq 0 \tag{14}$$

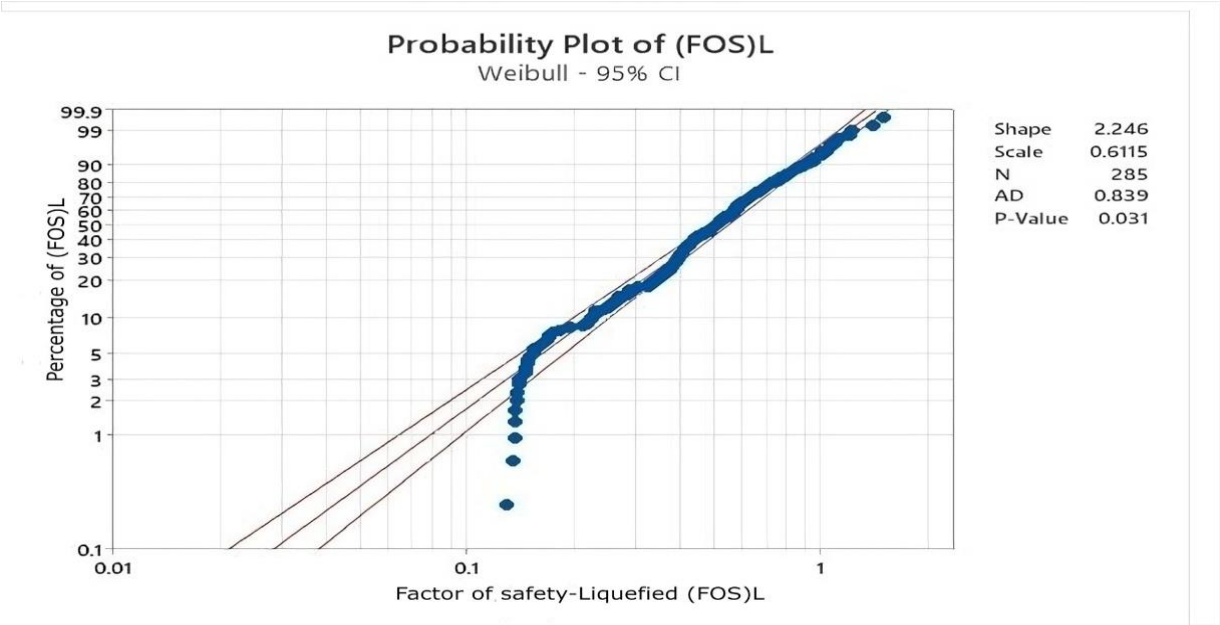


Figure 8 Percentage of probability of factor of safety liquefied data

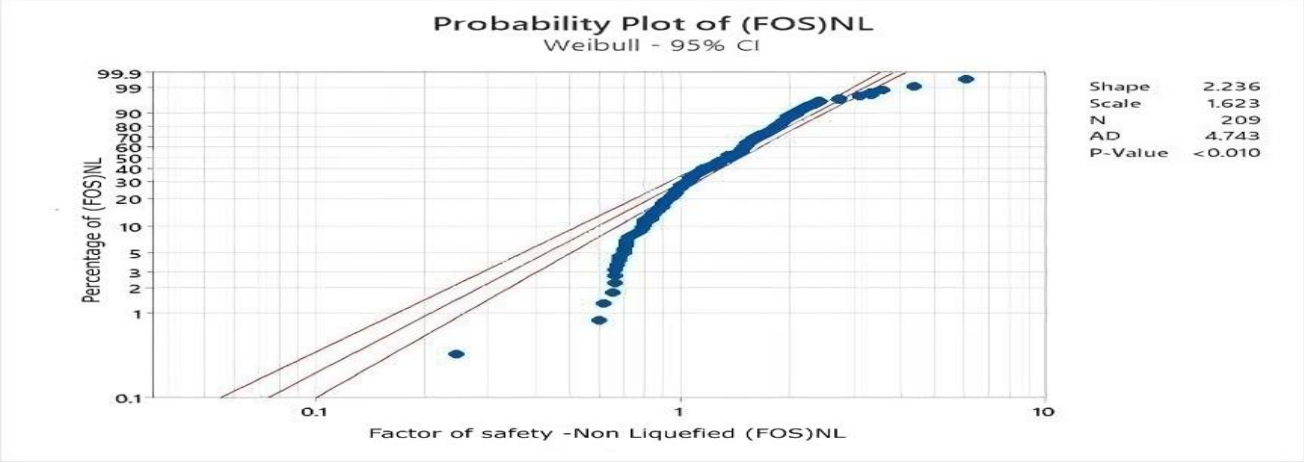


Figure 9 Percentage of probability of factor of safety non-liquefied data

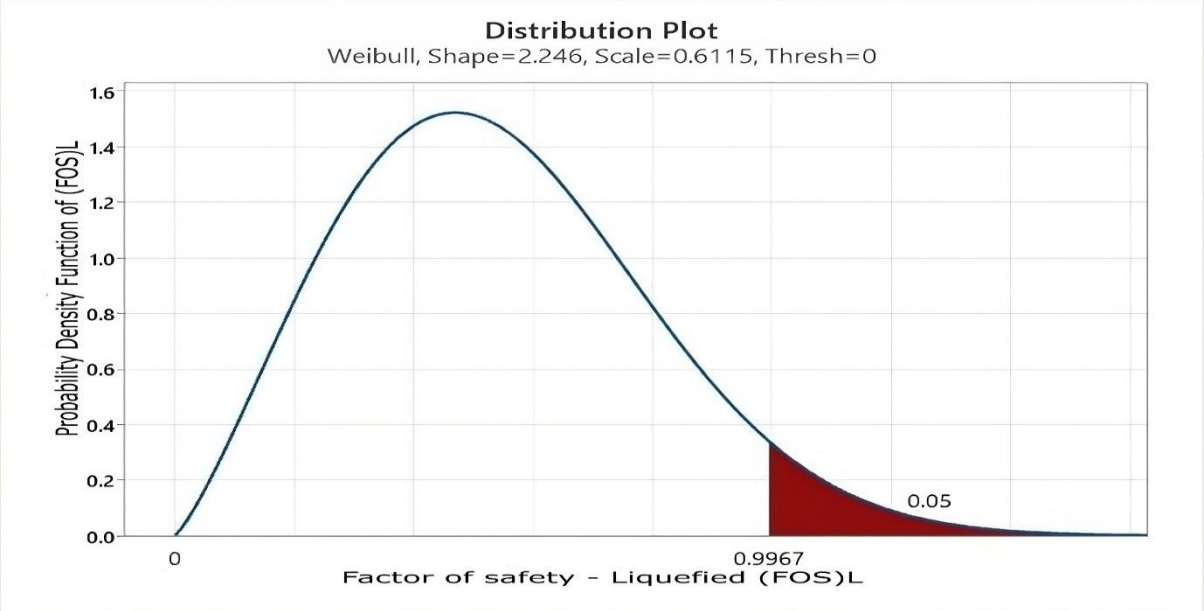


Figure 10. Weibull distribution of probability density function of liquefied data

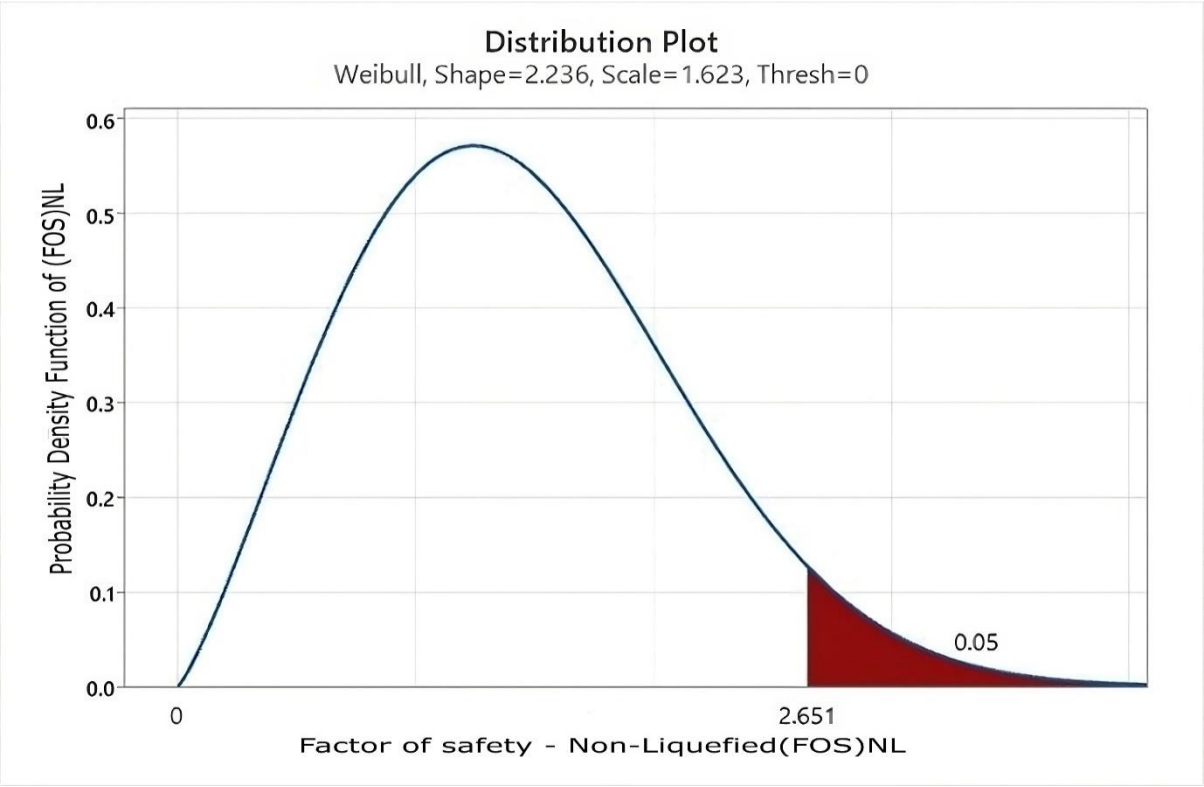


Figure 11. Weibull distribution of probability density function of non-liquefied data

3. Results and discussion

3.1 Formulation of equation by Bayesian mapping function

The probability of liquefaction (P_L) and probability of non-liquefaction (P_{NL}) for each case in the database is calculated using Equation (13), which depends on the probability density functions. The values of the factor of

safety (Fs) and probability of liquefaction (P_L) and probability of non-liquefaction (P_{NL}) for each of the 496 samples in the database are shown in Figure 12. A mapping function is obtained by the use of curve-fitting methodologies. The equation was formulated using the logistic curve fitting methodology. The derived equation has a coefficient of determination (R^2) value of 0.93. The equation (15) formulation presents the coefficients and variables, as seen in Figure 13. The derived equation is compared to the equations proposed by Toprak et al. (1999), Juang et al. (2002), and Idriss and Boulanger (2006).

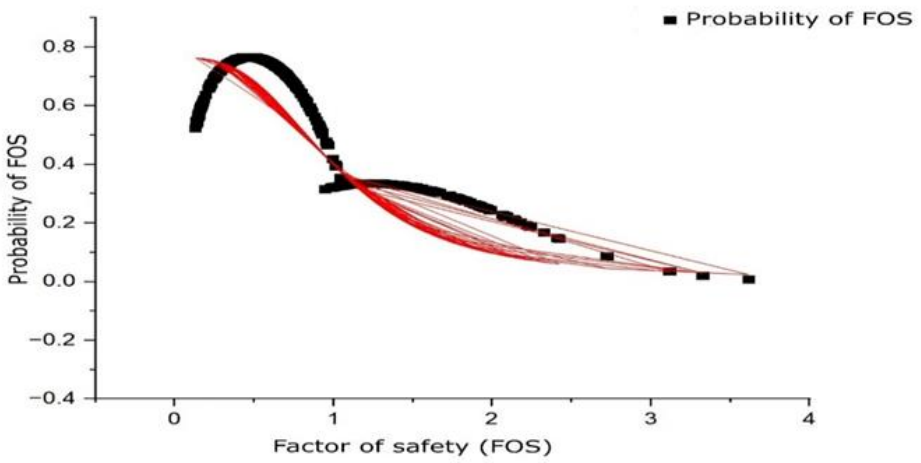


Figure 12. Curve fitting of probability of factor of safety

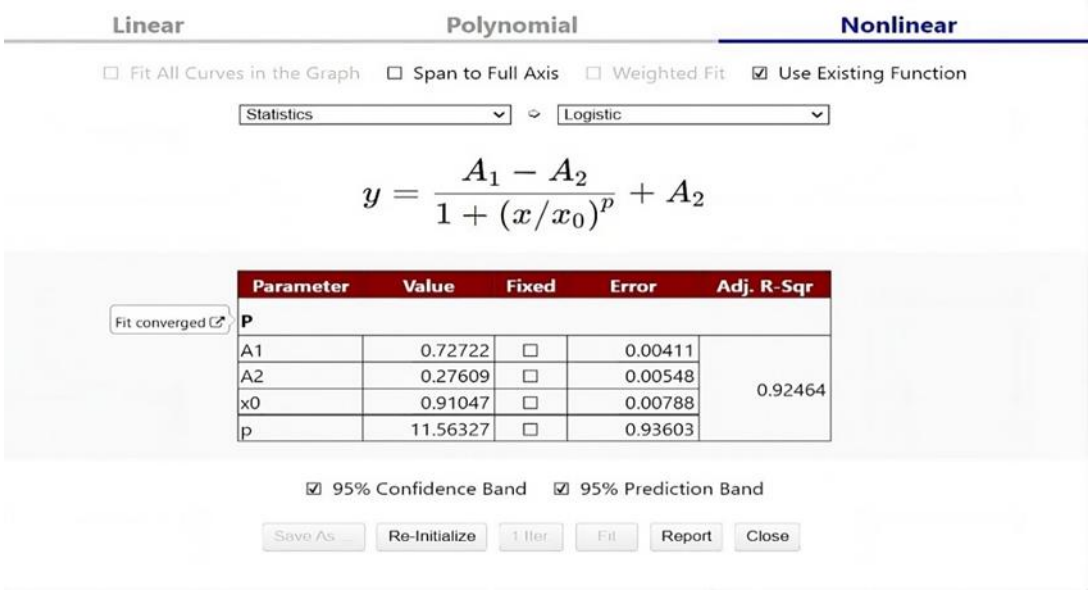


Figure 13 Curve fitting equation with constants and variables

$$P = \frac{0.45113}{1+\left(\frac{FOS}{0.91049}\right)^{11.5632}} + 0.27609 \qquad (15)$$

3.2 Comparison with existing methods using independent database

Regularly assessing the efficacy of a recently developed method in relation to existing methods is crucial. The present study examines the efficacy of the GP −based probabilistic approach in forecasting liquefied and non-liquefied scenarios, in comparison to the equations proposed by Toprak et al. (1999), Juang et al. (2002), and Idriss & Boulanger (2006), with respect to their success rate. There are 30 databases gathered in the NCR area utilizing SPT tests, and these databases are used to assess the efficacy of the model.

Liquefaction probability (P_L) is determined by calculating its value, where a P_L more than 0.5 indicates liquefied soil, while a P_L less than 0.5 indicates non-liquefied soil.

Table 4 Classification criteria for liquefied and non-liquefied (Kumar et al. 2022b)

Criteria	Probability of Liquefaction	Liquefaction Classification	Non-Liquefaction Classification
A	P_L> 0.85	High Chances of Liquefaction	
B	P_L > 0.65	Intermediate Chances of Liquefaction	
C	P_L> 0.5	Low Chances of Liquefaction	
D	P_L < 0.15		High Chances of Non-Liquefaction
E	P_L < 0.35		Intermediate Chances of Non-Liquefaction
F	P_L < 0.5		Non-Low Chances of Liquefaction

The effectiveness of the suggested techniques, based on real-world data, is assessed by calculating the probability of liquefaction using the three endorsed approaches. The present research assesses the accuracy of the suggested methods based on three criteria (A-C): High probability of liquefaction 0.85-1.0), Intermediate probability of liquefaction (0.65-1.0), and Low probability of liquefaction (0.65-1.0). The range is between 0.5 and 1.0. Criteria (D) is defined as having a high probability of non-liquefaction with a range of 0.15 to 0. Criteria (E) is defined as having an intermediate probability of non-liquefaction with a range of 0.35 to 0. Criteria (F) is defined as having a low probability of non-liquefaction with a range of 0.5 to 0. These criteria are applicable to cases when liquefaction does not occur. The categorization criteria are shown in Table 4.

5.5.1 Probability categorization

Table 5 Classification results of different models

Criteria	Models							
	Proposed Model		Toprak et al. (1999)		Juang et al. (2002)		Idriss and Boulanger (2006)	
	Count of successful prediction	Rate (%)	Count of successful prediction	Rate (%)	Count of successful prediction	Rate (%)	Count of successful prediction	Rate (%)
Total observed liquefied (285)								
A (P_L > 0.85)	214	75	199	70	208	73	210	74
B (P_L > 0.65)	242	85	208	73	230	81	239	84
C (P_L > 0.5)	254	89	228	80	239	84	242	85
Total observed non-liquefied (211)								
D (P_L < 0.15)	127	60	65	31	105	50	91	43
E (P_L < 0.35)	137	65	89	42	120	57	108	51
F (P_L < 0.5)	154	73	120	57	139	66	129	61

The results are shown in Table 5 , which classifies the soil that has the potential to liquefy (Criteria A-C) and the soil that does not have the potential to liquefy (Criteria D-F) based on the predictive accuracy of each recommended approach.

The findings from Table 5 show that the Proposed Model, which is based on certain criteria, has a higher success rate in predicting liquefaction cases compared to the models developed by Idriss & Boulanger (2006), Juang et al. (2002), and Toprak et al. (1999). Specifically, the Proposed Model achieved success rates of 75% for A, 85% for B, and 89% for C, whereas the other models achieved lower success rates ranging from 70% to 84%. Furthermore, compared to Idriss & Boulanger (2006) (A = 74%, B = 84% and C= 85%), Juang et al. (2002) (A = 73%, B = 81% and C= 84%) And Toprak et al. (1999) (A = 70%, B = 73% and C= 80%) proposed model has a greater success rate of non-liquefiable case prediction.

5.5.2 Performance fitness and error metrics (PFEMs)

Table 6 Comparative analysis of the proposed approach with existing techniques for binary classification

Matrices	Models				
	Proposed Model	Toprak et al. (1999)	Juang et al. (2002)	Idriss and Boulanger (2006)	Range
TPR	0.89	0.762	0.84	0.85	1.0
FNR	0.108	0.237	0.161	0.15	0.0
PPV/Precision	0.817	0.714	0.768	0.746	1.0

NPV	0.832	0.628	0.751	0.75	1.0
FPR	0.270	0.431	0.341	0.388	0.0
FDR	0.183	0.285	0.231	0.253	0.0
FOR	0.168	0.372	0.249	0.25	0.0
F_1 Score	0.852	0.737	0.802	0.794	1.0
MCC	0.634	0.3851	0.508	0.478	-1.0 to + 1.0
Accuracy	0.822	0.682	0.762	0.747	1.0
Sensitivity/Recall	0.891	0.762	0.838	0.849	1.0
Specificity	0.729	0.568	0.658	0.611	---------
G mean error	0.193	0.342	0.257	0.279	0.0
BA	0.81	0.665	0.748	0.730	1.0

Utilising Performance Fitness and Error Metrics ($PFEMs$) for binary classification. In order to fully evaluate the efficacy of the proposed approaches for classifying liquefaction problems, several Performance Fitness and Error Metrics ($PFEMs$) are used in this section. Within the binary classification scenario, including both liquefied and non-liquefied instances, there are four distinct possible outcomes for a single prediction. The terms "true negative" (TN) and "true positive" (TP) refer to accurate classifications. A false positive (FP) occurs when the output is erroneously predicted to be negative, whereas a false negative (FN) arises when the outcome is mistakenly classified as negative. The 2 × 2 confusion matrix seen in Figure 5.7 may be used to assess these matrices. $PFEMs$ are used to elucidate the correspondence between probabilistic forecasts of suggested methodologies and the actual outcome. These measures often pertain to the discrepancy in variance between the predicted and actual data. In this study, we used specific Performance Fitness and Error Metrics ($PFEMs$) to evaluate categorization issues (Naser and Alavi 2021). The mathematical representation of these $PFEMs$ is provided below:

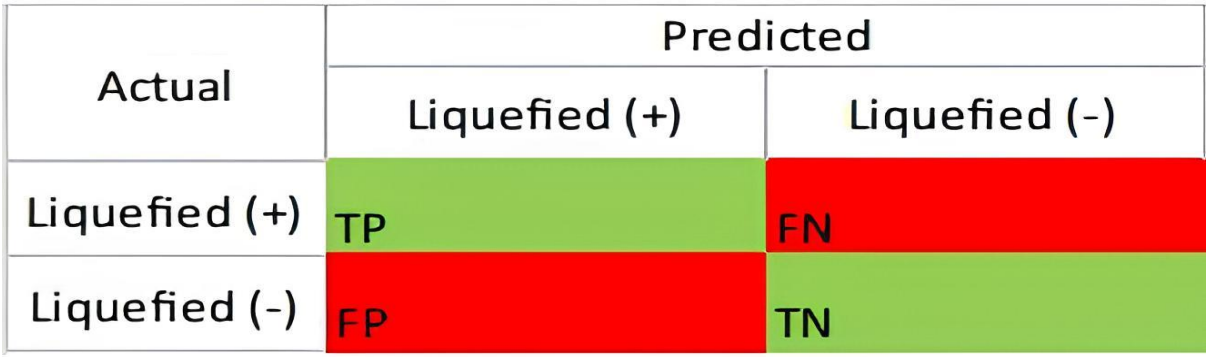


Figure 14 Illustration of confusion matrix (2 × 2) for classification problem

$$TPR = \frac{TP}{TP+FN} \tag{5.7}$$

$$FNR = \frac{FN}{FN+TP} \tag{5.8}$$

$$PPV = \frac{TP}{TP+FP} \quad (5.9)$$

$$NPV = \frac{TN}{TN+FN} \quad (5.10)$$

$$FPR = \frac{FP}{FP+TN} \quad (5.11)$$

$$FDR = \frac{FP}{FP+TP} \quad (5.12)$$

$$FOR = \frac{FN}{FN+TP} = 1 - NPV \quad (5.13)$$

$$F_{1\,SCORE} = \frac{2TP}{2TP+FP+FN} \quad (5.14)$$

$$MCC = \frac{TP \times TN - FP \times FN}{\sqrt{(TP+FP)(TP+FN)(TN+FP)(TN+PN)}} \quad (5.15)$$

$$Accuracy = \frac{TP+TN}{FN+TP+FP+TN} \quad (5.16)$$

$$Sensitivity = \frac{TP}{FN+TP} \quad (5.17)$$

$$Specificity = \frac{TN}{FP+TN} \quad (5.18)$$

$$G_{(mean)error} = 1 - \sqrt{Sensitivity \times Specificity} \quad (5.19)$$

$$BA = 0.5 \times \left(\frac{TP}{TP+FN} + \frac{TN}{TN+FP}\right) \quad (5.20)$$

Table 7 Score analysis of the proposed method and existing methods

Matrices	Proposed Model	Toprak et al. (1999)	Juang et al. (2002)	Idriss and Boulanger (2006)
TPR	4	1	2	3
FNR	4	1	2	3
PPV	4	1	3	2
NPV	4	1	3	2
FPR	4	1	3	2
FDR	4	1	3	2
FOR	4	1	3	2
F_1 Score	4	1	3	2
MCC	4	1	3	2
Accuracy	4	1	3	2
Sensitivity	4	1	2	3
Specificity	4	1	3	2
$G_{\text{mean error}}$	4	1	3	2

BA	4	1	3	2
Total Score	56	14	39	31
Rank	1	4	2	3

Within this particular framework, TP denotes the count of positive examples that were accurately assigned to their respective categories, TN denotes the count of negative instances that were correctly classified, FN denotes the count of positive instances that were erroneously classified, and FP denotes the count of negative instances that were inaccurately classified. The binary classification predictions and actual observations were compared by analysing the $PFEMs$ data shown in Table 6.

The true positive rate (TPR) measures the ratio of accurately detected positive cases to the total number of actual positive cases. This exercise does not consider indeterminate outcomes. The TPR values of the suggested model (0.89) were found to be higher than those of the Idriss and Boulanger (2006) (0.85), Toprak et al. (1999) (0.762), and Juang et al. (2002) (0.84) approaches. The positive predictive value (PPV) is a measure that represents the percentage of positive observations that actually result in true positive values. The PPV value obtained for the proposed model (0.817) is higher than the values obtained by Juang et al. (2002) (0.764), Idriss and Boulanger (2006) (0.746), and Toprak et al. (1999) (0.714) techniques. The optimal and suboptimal values for the Negative Predictive Value (NPV) are 1 and 0, correspondingly. It computes the ratio of incorrect positive results among observations that seem to be negative. The suggested model (0.832) outperforms the Juang et al. (2002) (0.751), Idriss and Boulanger (2006) (0.75), and Toprak et al. (1999) (0.628) approaches. A perfect prediction accuracy would include a False Positive Rate (FPR) of zero, indicating that no negative instances are incorrectly categorised as positive ones. Although the FPR score of the suggested model (0.270) is lower than that of Juang et al. (2002) (0.341), Idriss and Boulanger (2006) (0.388), and Toprak et al. (1999) (0.431) approaches. The False Discovery Rate (FDR) refers to the proportion of individuals who have a positive test result while not having the real ailment. The false discovery rate (FDR) obtained in this study for the proposed model (0.183) is lower than that reported by Juang et al. (2002) (0.231), Idriss and Boulanger (2006) (0.253), and Toprak et al. (1999) (0.285). This indicates that the proposed method outperformed the methods employed by Idriss and Boulanger (2006), Toprak et al. (1999), and Juang et al.

The False Omission Rate (FOR) quantifies the proportion of individuals whose test results indicated a negative outcome, although really having a positive condition. The suggested technique (0.168) has a lower value compared to the procedures used by Toprak et al. (1999) (0.372), Juang et al. (2002) (0.249), and Idriss and Boulanger (2006) (0.25). The suggested approaches' accuracy is evaluated using the F1 score. The $F1$-score obtained for the suggested approach (0.852) is greater than that for the Idriss and Boulanger (0.794), Toprak et al. (1999) (0.737), and Juang et al. (2002) methodologies. This indicates that the proposed method is more accurate in forecasting the possibility of liquefaction. Furthermore, the assessment of a binary classifier's effectiveness involves the use of Balanced Accuracy (BA), miss or false negative rate (FNR), $Gmean$ error, and the Matthews correlation coefficient (MCC). The definitions of balanced accuracy and G(mean) error may be found in Equation (5.17) and Equation (5.19) accordingly. The miss rate indicates the quantity of liquefied or non-liquefied substances that could have been incorrectly classified as not having the potential to cause tsunamis. $Gmean$ is often used when each class's performance is both remarkable and anticipated to be excellent simultaneously (Kubat and Matwin

1997; Yuan and Liu 2011). The given value is the geometric mean of the correctness of each instance inside each class. To assess the efficacy of the classifier model, some studies have used $Gmean$ as a measure of error rate, in addition to the $F1$-score. Matthews (1975) established the Matthews Correlation Coefficient (MCC) to measure the effectiveness of a model when there is a significant difference between the percentage of positive and negative data. The MCC is particularly valuable in such scenarios. The MCC value must fall between the range of -1.0 and +1.0. Conversely, a preference for the greater number indicates a more accurate forecast.

When compared to the criteria established by Toprak et al. (1999) (0.385), Juang et al. (2002) (0.508), and Idriss and Boulanger (2006) (0.478), the suggested method's MCC value (0.634) indicates that it outperforms these criteria in predicting liquefaction likelihood. The False Negative Rate (FNR) accurately predicts cases of liquefaction turning into non-liquefaction. FNR provides a clearer understanding of where sudden failure occurs. In this study, the proposed method (0.108) demonstrates lower FNR values compared to Toprak et al. (1999) (0.237), Juang et al. (2002) (0.161), and Idriss and Boulanger (2006) (0.15). Score analysis is performed to assess the effectiveness of the suggested methods. The score is calculated for each strategy by considering their performance fitness and error matrices. The score value range is defined by the total number of approaches used in this study, which is 1-4 (with a total of 4 procedures applied). The score value in this study is calculated based on the obtained value of PFEMs. The procedures that possess the most worth for any particular $PFEMs$, with an optimal value of 1.0, are assigned a maximum score of 4.0. On the other hand, the methods that have the greatest significance for any particular PFEMs with an optimal value of 0.0 are assigned a minimum score of 0. The proposed methodology in this research has received the highest score of 56, as shown in Table 7. Thus, the suggested approach has obtained the highest ranking, with Juang et al. (2002), Idriss and Boulanger (2006), and Toprak et al. (1999) methods following in subsequent positions. Scatter plots are shown for both liquefied and non-liquefied samples, demonstrating all the recommended methods for the parameters $(N1)$,$60cs$, and CSR. The scatter plots in Figures 15, 16, 17, and 18 illustrate the correlation between the total number of liquefied and non-liquefied instances for the Proposed Model, Toprak et al. (1999), Idriss and Boulanger (2006), and Juang et al. (2002) techniques. These charts illustrate the comparison between the observed and forecasted values. The scatter plot of the Proposed Model exhibits distinct and improved segregation, aligning closely with the projected value ranges in contrast to the other models. Conversely, the scatter plot for Toprak et al. (1999) demonstrates a substantial degree of inaccuracy in forecasting both liquefied and non-liquefied instances.

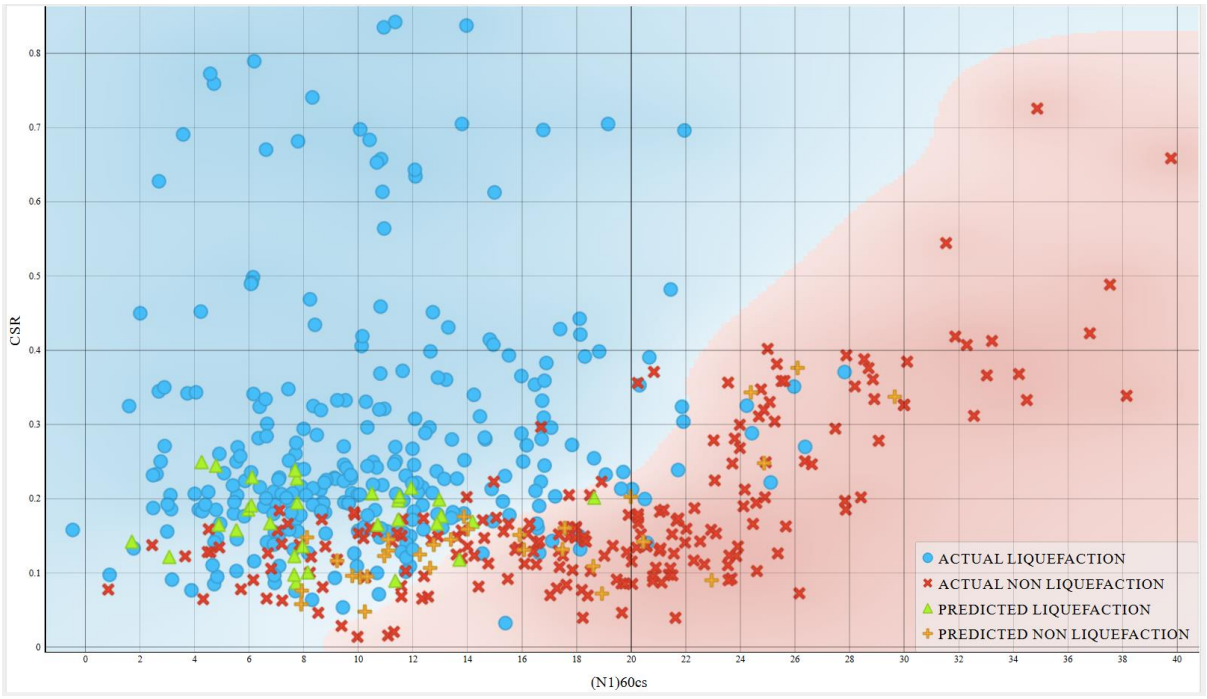


Figure 15 Visualisation of observed and forecasted instances using the suggested methodology

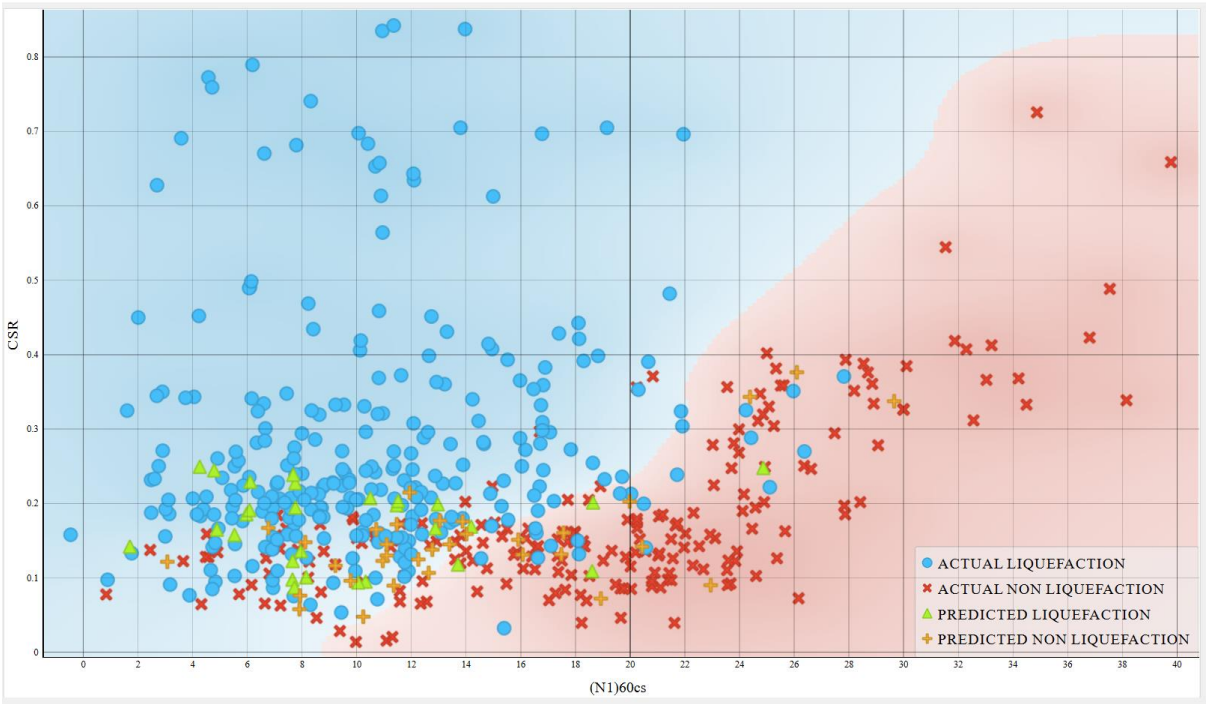


Figure 16 Visualisation of observed and forecasted instances of Juang et al. (2002) method

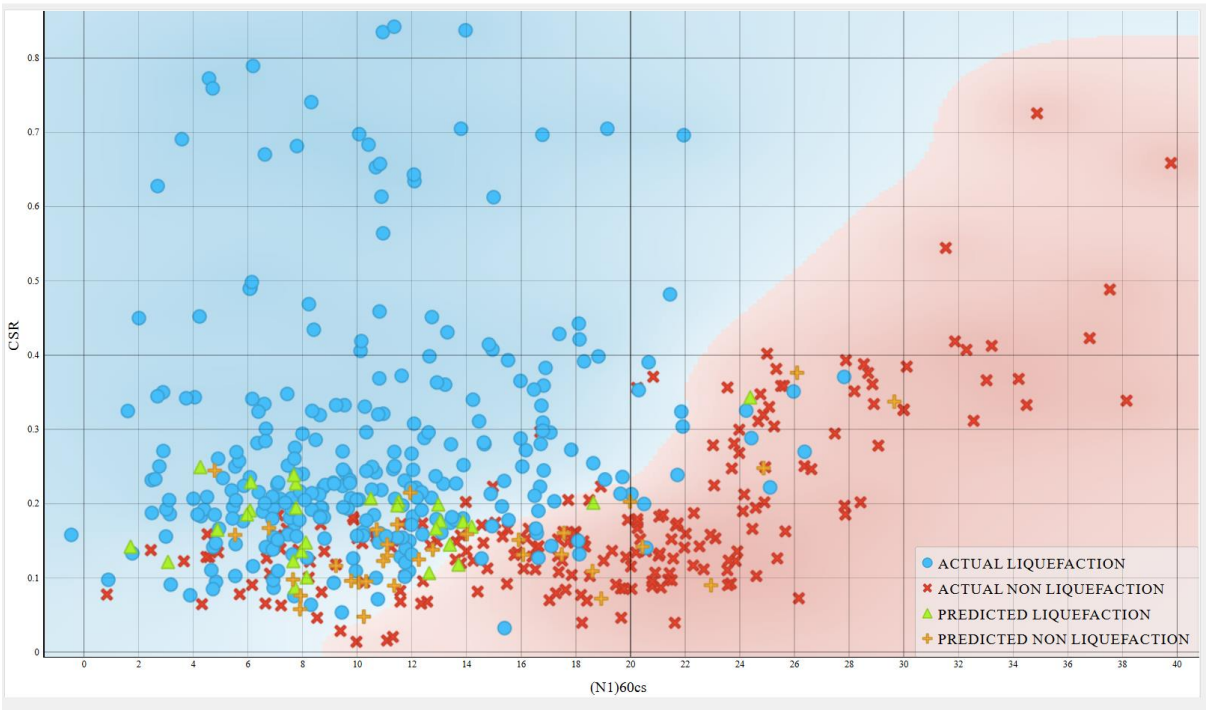


Figure 17 Visualisation of observed and forecasted instances of Idriss and Boulanger (2006) method

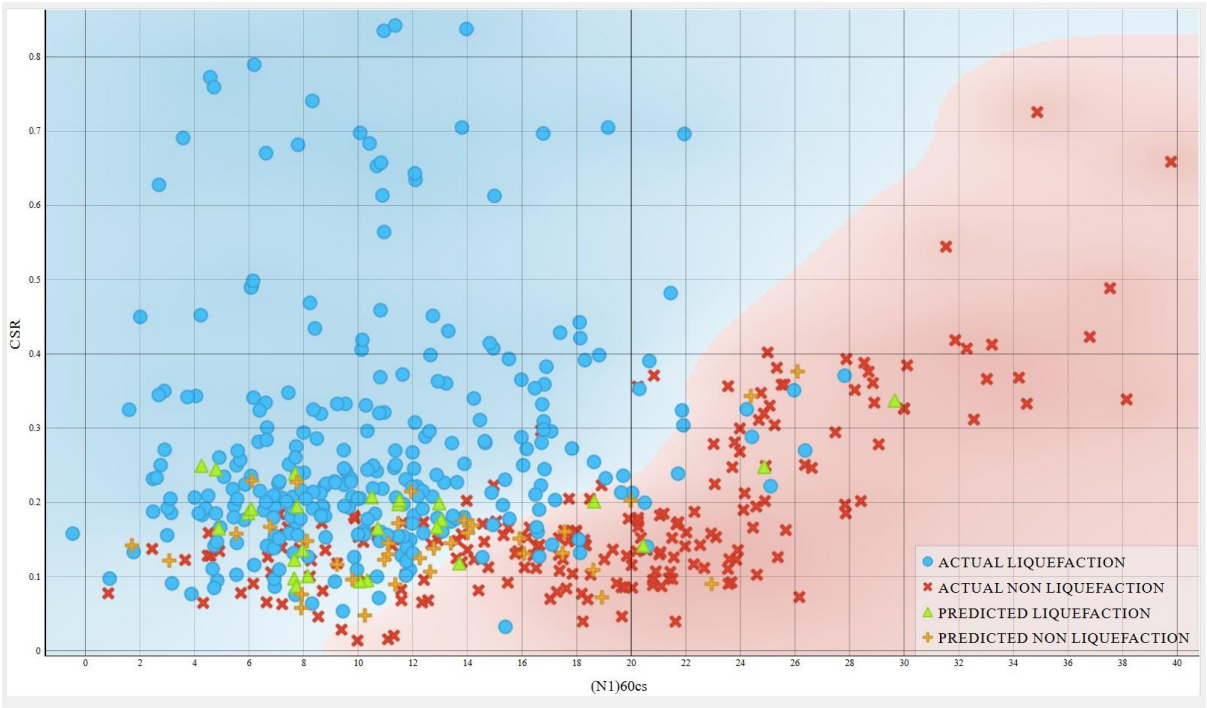


Figure 18 Visualisation of observed and forecasted instances of Toprak et al. (1999) method

3.3 Evaluating the proportional impact of various criteria on the computation of PL using the Gini Index (GI)

The Gini index (GI) is used to evaluate the relative significance of independent variables in predicting the likelihood of soil deposit liquefaction. The Gini index has been computed for each independent variable, and their relative significance has been evaluated. A higher Gini index value signifies a stronger influence of individual independent elements in forecasting the likelihood of soil liquefaction in a deposit. The Gini index is calculated using the following mathematical equation:

$$GI = \left|\sum_{i=2}^{n} Cum\ X_{i-1} Cum\ P_{Li} - \sum_{i=2}^{n} Cum\ X_i Cum\ P_{Li-1}\right| \qquad (5.21)$$

Here, $CumX$ denotes the cumulative value of independent variables, whereas CumPL represents the cumulative value of liquefaction probability for a set of n observed data points. The Gini index values for all three approaches, considering various input variables such as Critical depth, $FC, D50, PGA, rd,$ Water Table $(W.T), CSR$, and $(N1)60CS$, are shown in Table 5.5.

The results shown in Table 8 demonstrate that the Gini index value for each independent variable in the proposed technique is lower than the values obtained in the methods used by Juang et al. (2002), Toprak et al. (1999), and Idriss and Boulanger (2006). These findings indicate that each component has a substantial impact on the capacity to estimate the likelihood of liquefaction using the suggested approach.

Table 8 Gini index value for all proposed and existing methods

Variables	Proposed Model	Toprak et al. (1999)	Juang et al. (2002)	Idriss and Boulanger (2006)
Critical depth	150.763	208.26	593.07	553.543
FC	336.26	314.6	979.8	811.6
D50	3.1259	4.7289	18.6078	17.0856
Water Table	140.165	177.05	296.85	288.44
PGA	2.56265	4.3765	22.9305	20.828
rd	34.0271	37.116	18.033	10.0435
CSR	1.85031	1.0921	7.4296	13.1889
$(N_1)_{60CS}$	1849.761	2180.662	1523.244	1678.829

4. conclusions

The study attempts to develop a probabilistic liquefaction method using updated cyclic resistance ratio (CRR) and cyclic stress ratio (CSR) by the application of Bayes' conditional probability theorem. The study used a dataset that included several instances of post-liquefaction occurrences, including the time period from the 1944 Tohnankai earthquake to the 1999 Chi Chi earthquake in Taiwan. The dataset included 286 occurrences of liquefaction and 210 occurrences of non-liquefaction. Furthermore, a set of 30 borehole data obtained from the Standard Penetration Test (SPT) were collected in the Faridabad area, which is situated in the National Capital area (NCR) of Delhi, India. These acquired 30 borehole data were used to verify the accuracy of both the proposed and current models.

(1) Data visualization is essential for improving comprehension of data patterns, the relationships and distinctions among several variables used in research, and the level of disorder or unpredictability inherent in the data. The correlation coefficient between (PGA) and (CSR) is 0.89, indicating a strong positive link. Similarly, there is a strong negative correlation of -0.97 between the overburden correction factor (rd) and critical depth. Based on theoretical research, it is essential to eliminate one of these aspects from each combination. However, this study acknowledges the importance of both variables and acknowledges their distinct contributions to the analysis of liquefaction studies.

(2) The analysis of entropy reveals, via the use of pair plots, a significant lack of clear separation between the two data groups, hence indicating a substantial level of complexity. Thus, the analysis of complex datasets may require more sophisticated models to address this complex problem, it is recommended to use advanced techniques like Genetic Programming (GP) and advanced deep learning models to get improved results.

(3) Through the use of variables, the present work used genetic programming (GP) to produce several models, each characterized by unique combinations of training and testing datasets, program dimensions, and generations. The current investigation used the root-mean-squared error (RMSE) as the fitness function, and the measure of fitness was obtained by using an equation formed from the expression tree. The expression tree generated by the GP model 3 resulted in a mathematical equation that demonstrated improved performance for the input and output variables.

(4) After formulating the new equation for cyclic resistance ratio (CRR), the factor of safety (Fs) has been determined by using the new CRR equation and cyclic stress ratio (CSR). Subsequently, several probability density functions are applied to the calculated factor of safety. It has been observed that the Weibull probability density functions provide the most accurate fitting curves for both liquefied (L) and non-liquefied (NL) conditions.

(5) The probability of the liquefied equation was determined by using probability density curves and the Bayes' conditional probability theorem. The values derived from the Bayes' conditional probability theorem were further used in logistic curve fitting to formulate an equation, which was further compared to pre-existing probabilistic models. A comparison was made between the novel methodology and the techniques proposed by Juang et al. (2002), Toprak et al. (1999), and Idriss and Boulanger (2006). The comparison included employing a confusion matrix for binary classification and doing a score analysis based on factor ranking. The proposed model exhibited superior performance, as the outputs of the constructed model increased for all positive factors and decreased for negative indicators.

(6) The Gini index was finally calculated for the proposed method and the existing methods by Juang et al. (2002), Toprak et al. (1999), and Idriss and Boulanger (2006). It was observed that all the existing methods were biased towards a limited number of variables. However, the proposed method demonstrated the significance of all variables in predicting the probability of liquefaction.

References

Addo, K. O., & Robertson, P. K. (1992). Shear-wave velocity measurement of soils using Rayleigh waves. *Canadian Geotechnical Journal*, 29(4), 558-568.

Andrus, R. D., & Stokoe II, K. H. (2000). Liquefaction resistance of soils from shear-wave velocity. Journal of geotechnical and geoenvironmental engineering, 126(11), 1015-1025.

Andrus, R. D., Stokoe, K. H., & Hsein Juang, C. (2004). Guide for shear-wave-based liquefaction potential evaluation. Earthquake Spectra, 20(2), 285-308.

Baziar, M. H., & Jafarian, Y. (2007). Assessment of liquefaction triggering using strain energy concept and ANN model: capacity energy. *Soil Dynamics and Earthquake Engineering*, 27(12), 1056-1072.

Becker, D. E. (1997). Eighteenth Canadian geotechnical colloquium: Limit states design for foundations. Part I. An overview of the foundation design process. *Canadian Geotechnical Journal*, *33*(6), 956-983.

Boulanger, R. W., & Idriss, I. M. (2014). CPT and SPT based liquefaction triggering procedures. Report No. UCD/CGM.-14, 1.

Cetin, K. O., and Seed, R. B. (2004). "Nonlinear shear mass participation factor (rd) for cyclic shear stress ratio evaluation." *Soil Dynamics and Earthquake Engineering*, Elsevier, 24: 103-113.

Ferreira, C. (2002). Gene expression programming in problem solving. In *Soft computing and industry: recent applications* (pp. 635-653). London: Springer London.

Goh, A. T. (1994). Seismic liquefaction potential assessed by neural networks. Journal of Geotechnical engineering, 120(9), 1467-1480.

Goharzay, M., Noorzad, A., Ardakani, A. M., & Jalal, M. (2017). A worldwide SPT-based soil liquefaction triggering analysis utilizing gene expression programming and Bayesian probabilistic method. Journal of Rock Mechanics and Geotechnical Engineering, 9(4), 683-693.

Haldar, A., & Tang, W. H. (1979). Probabilistic evaluation of liquefaction potential. Journal of the Geotechnical Engineering Division, 105(2), 145-163.

Hanna, A. M., Ural, D., & Saygili, G. (2007). Evaluation of liquefaction potential of soil deposits using artificial neural networks. Engineering Computations, 24(1), 5-16.

Harder, L. F., & Seed, H. B. (1986). Determination of penetration resistance for coarse-grained soils using the Becker hammer drill. Berkeley, CA, USA: College of Engineering, University of California.

Hu J, Liu H (2019) Bayesian network models for probabilistic evaluation of earthquake-induced liquefaction based on CPT and Vs databases. Eng Geol 254:76–88.

Hu J (2021a) A new approach for constructing two Bayesian network models for predicting the liquefaction of gravelly soil. *Comput Geotech* 137:104304.

Hu, J. (2021b). Data cleaning and feature selection for gravelly soil liquefaction. *Soil Dynamics and Earthquake Engineering*, *145*, 106711.

Hu J, Wang J, Zhang Z, Liu H (2022) Continuous-discrete hybrid Bayesian network models for predicting earthquake-induced liquefaction based on the Vs database. *Comput Geosci* 169:105231.

Idriss, I. M., and Boulanger, R. W. (2004). Semi-empirical procedures for evaluating liquefaction potential during earthquakes, in Proceedings, *11th International Conference on Soil Dynamics and Earthquake Engineering, and 3rd International Conference on Earthquake Geotechnical Engineering,* D. Doolin et al., eds., Stallion Press, Vol. 1, pp. 32–56.

Idriss, I. M., and Boulanger, R. W. (2006). Semi-empirical procedures for evaluating liquefaction potential during earthquakes, *J. Soil Dynamics and Earthquake* Eng. 26, 115–30.

Idriss, I. M., and Boulanger, R. W. (2008). Soil liquefaction during earthquakes. Monograph MNO-12, Earthquake Engineering Research Institute, Oakland, CA, 261 pp.

Idriss IM, Boulanger RW (2010) Spt-based liquefaction triggering procedures. Rep. UCD/CGM-10. 2, 4–13.

Jas, K., & Dodagoudar, G. R. (2023). Explainable machine learning model for liquefaction potential assessment of soils using XGBoost-SHAP. *Soil Dynamics and Earthquake Engineering*, *165*, 107662.

Juang, C. H., Rosowsky, D. V., & Tang, W. H. (1999). Reliability-based method for assessing liquefaction potential of soils. *Journal of Geotechnical and Geoenvironmental Engineering*, 125(8), 684-689.

Juang, C. H., Chen, C. J., Jiang, T., & Andrus, R. D. (2000). Risk-based liquefaction potential evaluation using standard penetration tests. Canadian Geotechnical Journal, 37(6), 1195-1208.

Juang, C. H., Chen, C. J., & Jiang, T. (2001). Probabilistic framework for liquefaction potential by shear wave velocity. *Journal of geotechnical and geoenvironmental engineering*, 127(8), 670-678.

Juang CH, Jiang T, Andrus RD (2002) Assessing probability-based methods for liquefaction potential evaluation. J Geotech Geoenviron Eng 128:580–589

Juang, C. H., Fang, S. Y., & Khor, E. H. (2006). First-order reliability method for probabilistic liquefaction triggering analysis using CPT. *Journal of Geotechnical and Geoenvironmental Engineering*, 132(3), 337-350.

Kayen, R. E., Mitchell, J. K., Seed, R. B., Lodge, A., Nishio, S. Y., & Coutinho, R. (1992, May). Evaluation of SPT-, CPT-, and shear wave-based methods for liquefaction potential assessment using Loma Prieta data. *In Proceedings of the 4th Japan-US Workshop on Earthquake Resistant Design of Lifeline Facilities and Countermeasures for Soil Liquefaction*, Hamada, M. and O'Rourke, TD, eds.

Kohestani, V. R., Hassanlourad, M., & Ardakani, A. J. N. H. (2015). Evaluation of liquefaction potential based on CPT data using random forest. Natural Hazards, 79(2), 1079-1089.

Kumar, D. R., Samui, P., & Burman, A. (2022a). Prediction of probability of liquefaction using soft computing techniques. *Journal of The Institution of Engineers* (India): Series A, 103(4), 1195-1208.

Kumar, D. R., Samui, P., & Burman, A. (2022b). Determination of best criteria for evaluation of liquefaction potential of soil. Transportation Infrastructure Geotechnology, 1-20.

Liao, S. S., Veneziano, D., & Whitman, R. V. (1988). Regression models for evaluating liquefaction probability. *Journal of Geotechnical Engineering*, 114(4), 389-411.

Mitchell, J. K., & Tseng, D. J. (1990, May). Assessment of liquefaction potential by cone penetration resistance. In Proc., H. Bolton Seed Memorial Symp. Duncan (pp. 335-350). Vancouver, Canada: JM BiTech.

Momeni, E., Armaghani, D. J., Hajihassani, M., & Amin, M. F. M. (2015). Prediction of uniaxial compressive strength of rock samples using hybrid particle swarm optimization-based artificial neural networks. Measurement, 60, 50-63.

Muduli, P. K., & Das, S. K. (2015). First-order reliability method for probabilistic evaluation of liquefaction potential of soil using genetic programming. *International Journal of Geomechanics,* 15(3), 04014052.

National Research Council (NRC) (1985). Liquefaction of Soils During Earthquakes, National Academy Press, Washington, DC, 240 pp.

Naser, M. Z., & Alavi, A. H. (2021). Error metrics and performance fitness indicators for artificial intelligence and machine learning in engineering and sciences. *Architecture, Structures and Construction*, 1-19.

Oliveira, L. O. V., Otero, F. E., & Pappa, G. L. (2016, July). A dispersion operator for geometric semantic genetic programming. In *Proceedings of the Genetic and Evolutionary Computation Conference 2016* (pp. 773-780).

Olsen, R. S. (1988, June). Using the CPT for dynamic site response characterization. In Earthquake Engineering and Soil Dynamics II—Recent Advances in Ground-Motion Evaluation (pp. 374-388). ASCE.

Olsen, R. S. (1997, December). Cyclic liquefaction based on the cone penetrometer test. In Proceedings of *the NCEER Workshop on Evaluation of Liquefaction Resistance of Soils* (pp. 225-276). Buffalo: State University of New York.

Pal, M. (2006). Support vector machines-based modelling of seismic liquefaction potential. *International Journal for Numerical and Analytical Methods in Geomechanics*, 30(10), 983-996.

Pirhadi N,Wan X, Lu J, Hu J, AhmadM, Tahmoorian F (2023) Seismic liquefaction resistance based on strain energy concept considering fine content value effect and performance parametric sensitivity analysis. C Model Eng Sci 135:733–754.
Ramakrishnan, D., Singh, T. N., Purwar, N., Barde, K. S., Gulati, A., & Gupta, S. (2008). Artificial neural network and liquefaction susceptibility assessment: a case study using the 2001 Bhuj earthquake data, Gujarat, India. *Computational Geosciences*, 12, 491-501.

Robertson, P. K., & Campanella, R. G. (1985). Liquefaction potential of sands using the CPT. Journal of geotechnical engineering, 111(3), 384-403.

Robertson, P. K., & Wride, C. E. (1998). Evaluating cyclic liquefaction potential using the cone penetration test. *Canadian geotechnical journal*, 35(3), 442-459.

Samui, P., & Hariharan, R. (2015). A unified classification model for modeling of seismic liquefaction potential of soil based on CPT. *Journal of advanced research*, 6(4), 587-592.

Samui, P., & Karthikeyan, J. (2013). Determination of liquefaction susceptibility of soil: a least square support vector machine approach. International Journal for Numerical and Analytical Methods in Geomechanics, 37(9), 1154-1161.

Samui, P., & Sitharam, T. G. (2011). Machine learning modelling for predicting soil liquefaction susceptibility. *Natural Hazards and Earth System Sciences*, 11(1), 1-9.

Seed, H. B., and Idriss, I. M. (1967). "Analysis of liquefaction: Niigata earthquake." Proc., ASCE, 93(SM3), 83-108.

Seed, H. B., & Idriss, I. M. (1971). Simplified procedure for evaluating soil liquefaction potential. *Journal of the Soil Mechanics and Foundations division*, 97(9), 1249-1273.

Seed H. B., and Idriss, I. M. (1982). Ground Motions and Soil Liquefaction During
Earthquakes, Earthquake Engineering Research Institute, Oakland, CA, 134.

Seed, H. B., Idriss, I. M., & Arango, I. (1983). Evaluation of liquefaction potential using field performance data. Journal of geotechnical engineering, 109(3), 458-482.

Seed, H. B., Tokimatsu, K., Harder, L. F., & Chung, R. M. (1985). Influence of SPT procedures in soil liquefaction resistance evaluations. Journal of geotechnical engineering, 111(12), 1425-1445.

Seed, H. B., & De Alba, P. (1986). Use of SPT and CPT tests for evaluating the liquefaction resistance of sands. In Use of in situ tests in geotechnical engineering (pp. 281-302). ASCE.

Shibata, T., & Teparaksa, W. (1988). Evaluation of liquefaction potentials of soils using cone penetration tests. Soils and Foundations, 28(2), 49-60.

Stark, T. D., & Olson, S. M. (1995). Liquefaction resistance using CPT and field case histories. *Journal of geotechnical engineering*, 121(12), 856-869.

Stokoe, K. H., Roesset, J. M., Bierschwale, J. G., & Aouad, M. (1988, August). Liquefaction potential of sands from shear wave velocity. In Proceedings, 9nd World Conference on Earthquake (Vol. 13, pp. 213-218).

Suzuki, Y., Tokimatsu, K., Koyamada, K., Taya, Y., & Kubota, Y. (1995). Field correlation of soil liquefaction based on CPT data. In Proceedings of *the International Symposium on Cone Penetration Testing* (Vol. 2, pp. 538-588).

Terzaghi K, Peck RB (1948) Soil mechanics in engineering practice. Wiley, New York

Tsuchida, H. and Hayashi, S. (1971): "Estimation of liquefaction potential of sandy soils," Third Joint Meeting of U.S. and Japan Panel on Wind and Seismic Effects, UJNR, Tokyo, pp.1-16.

Tokimatsu, K., & Uchida, A. (1990). Correlation between liquefaction resistance and shear wave velocity. Soils and foundations, 30(2), 33-42.

Tokimatsu, K., and Yoshimi, Y. (1983). "Empirical correlation of soil liquefaction based on SPT N-value and fines content." Soils and Foundations, 23(4), 56-74.

Toprak, S., Holzer, T. L., Bennett, M. J., & Tinsley III, J. C. (1999, August). CPT-and SPT-based probabilistic assessment of liquefaction. In Proc., 7th US–Japan Workshop on Earthquake Resistant Design of Lifeline Facilities and Countermeasures against Liquefaction (pp. 69-86). Buffalo, NY: Multidisciplinary Center for Earthquake Engineering Research.

Xue, X., & Liu, E. (2017). Seismic liquefaction potential assessed by neural networks. Environmental Earth Sciences, 76, 1-15.

Youd, T. L., & Idriss, I. M. (2001). Liquefaction Resistance of Soils: Summary Report from the 1. Geotechnical and Geoenvironmental Eng. In ASCE (Vol. 127, No. 10, pp. 817-33).

Zhang, W., & Goh, A. T. (2016). Evaluating seismic liquefaction potential using multivariate adaptive regression splines and logistic regression. *Geomech. Eng*, *10*(3), 269-284.

Zhang, Y. G., Qiu, J., Zhang, Y., & Wei, Y. (2021a). The adoption of ELM to the prediction of soil liquefaction based on CPT. *Natural Hazards*, *107*(1), 539-549.

Zhang, Y., Qiu, J., Zhang, Y., & Xie, Y. (2021b). The adoption of a support vector machine optimized by GWO to the prediction of soil liquefaction. Environmental Earth Sciences, 80, 1-9.

Zhou, J., Huang, S., Wang, M., & Qiu, Y. (2021). Performance evaluation of hybrid GA–SVM and GWO–SVM models to predict earthquake-induced liquefaction potential of soil: a multi-dataset investigation. *Engineering with Computers*, 1-19.

Zhou, J., Li, E., Wang, M., Chen, X., Shi, X., & Jiang, L. (2019). Feasibility of stochastic gradient boosting approach for evaluating seismic liquefaction potential based on SPT and CPT case histories. Journal of Performance of Constructed Facilities, 33(3), 04019024.

Signal, Image and Video Processing
https://doi.org/10.1007/s11760-023-02973-6

ORIGINAL PAPER



Bff: Bi-stream feature fusion for object detection in hazy environment

Kavinder Singh[1] · **Anil Singh Parihar**[1]

Received: 17 October 2023 / Revised: 21 November 2023 / Accepted: 15 December 2023
© The Author(s), under exclusive licence to Springer-Verlag London Ltd., part of Springer Nature 2024

Abstract
In hazy environments, the computer vision system may require to perform object detection. The performance of the object detection methods degrades in a hazy environment. To overcome this issue, we propose a Bi-stream feature fusion (BFF) network for object detection in a hazy environment. The BFF network consists of three modules: hybrid input, Bi-stream feature extractor (BFE), and multi-level feature fusion. We present the notion of hybrid input to extract features from the hazy images in an effective manner. This paper leverages the hybrid input for feature extraction from the hazy images to avoid the requirement of enhancement in hazy object detection. The proposed BFE network extracts multi-level features from the hazy image and hybrid input. The multi-level feature fusion (MFF) network performs the convolution-based adaptive feature fusion and processes the extracted features. The proposed BFF model outperforms other state-of-the-art methods in hazy environments while achieving competitive performance in normal conditions. Another challenge in hazy object detection is the unavailability of a dataset with sufficient samples and classes. In this work, we developed a synthetic object detection dataset for a hazy environment (DHOD). The DHOD dataset contains twenty object classes with more than twenty thousand samples.

Keywords Object detection · Feature fusion · Hazy images · Feature extraction

1 Introduction

Most object detection methods perform well in normal environments. However, the performance of these methods degrades significantly in hazy environments because of the lesser visibility, faded details, or color distortion. Many computer vision applications (like, object tracking [2, 11, 15], action recognition [3, 8, 29], surveillance [6, 56], self-driving cars [14, 43, 57], and others [4, 5, 7, 9, 42, 45]) may encounter hazy environments in real-world applications. Thus, object detection in a hazy environment becomes crucial. For object detection in a hazy environment, the obvious solution [32, 58] is to apply image dehazing (as pre-processing) [41, 54] before the object detection method. However, such an approach requires additional time and computation to enhance the image. Moreover, the performance of object detection relies highly on the performance of the dehazing algorithm in such an approach. Alternatively, some researchers [60, 63] used domain adaptation (DA) for object detection in a hazy environment. DA-based approaches attempt to learn haze-relevant features from an image-dehazing dataset to achieve better performance. In general, DA-based approaches have poor generalization across the datasets. A single-step solution, i.e., direct object detection in a hazy environment, is always desirable.

In this work, we developed an end-to-end trainable model for object detection in a hazy environment. The existing object detection model for hazy environments uses the image-dehazing dataset to learn haze-relevant features using domain adaptation. There are benchmark datasets available for evaluation of the performance. The presently available dataset [31, 49] contains samples of five to eight classes. To train a deep learning-based end-to-end trainable method, we require a large amount of data. The performance of DL-based approaches is primarily governed by the quality and quantity of data samples along with the model. In this work, we develop a synthetic dataset for hazy object detection (DHOD) with twenty classes and more than twenty thousand annotated images. DHOD is synthesized using the Pascal-VOC dataset

✉ Anil Singh Parihar
parihar.anil@gmail.com

Kavinder Singh
kavinder85@gmail.com

[1] Machine Learning Research Laboratory, Department of Computer Science and Engineering, Delhi Technological University, Delhi, Delhi, India

Published online: 23 January 2024

[16]. The DHOD contains annotated hazy images with distinct level of haze. We used the developed DHOD dataset to train the proposed model and the benchmark RTTS dataset to test the performance and generalization.

We propose a novel architecture, namely, Bi-stream feature fusion (BFF) for object detection in the hazy environment. BFF consists of a Bi-stream feature extractor (BFE) and multi-level feature fusion (MFF). The Bi-stream feature extractor uses two streams with inputs as a hazy image in one stream and a hybrid image in the other stream. The hybrid image is a combination of the min-channel, gradient, and max-channel of the hazy image. The hybrid image facilitates the BFE network in extracting appropriate features from hazy images. The proposed BFE network extracts multi-level features from the hazy image and hybrid image. Further, we propose the MFF network to perform the fusion of extracted features at multiple levels and process the extracted features. The BFF uses BFE for feature extraction, and MFF for feature fusion and processing. Finally, the proposed approach leverages the class subnetwork (subnet) and box subnet for object localization and classification. The major contributions of the proposed work are summarized as follows:

1. We proposed a novel Bi-stream feature extraction (BFE) network. The BFE extracts features at multiple levels from the hazy image and hybrid image.
2. We proposed a multi-level adaptive feature fusion (MFF) network to perform the fusion of adequate features. MFF provides attention to appropriate features across the streams.
3. We developed a new dataset for hazy object detection (DHOD) to train the object detection models in the hazy environment based on the Pascal-VOC dataset.
4. We proposed an object detection model for the hazy environment, namely, Bi-stream feature fusion network, which outperforms state-of-the-art object detection models in a hazy environment.

The remaining paper organization is as follows. Section 2 contains related work. Section 3 describes the proposed methodology. Section 4 presents the results and analysis. Section 5 contains the conclusion.

2 Related work

The proposed method focuses on object detection in hazy environments based on deep learning. The related work includes the available object detection methods and adaptation-based object detection in the hazy environments.

2.1 Object detection

Object detection is mainly classified into two classes: two-stage and one-stage. In two-stage detectors, the first-stage is responsible for region proposal (like [59, 68]). The second-stage is responsible for the classification of the objects with improved bounding box. Two-stage detectors (like R-CNNs [18, 47] and SPPnet [22]) require a comparably higher amount of time and less efficient than one-stage detectors. Furthermore, many researchers attempted to enhance the performance of two-stage detectors by multi-layer exploitation [34], contextual reasoning [17], training strategies [52], and architectural designs [10].

Due to better efficiency, one-stage detectors gained popularity. YOLO [46] enhanced detection speed by developing an end-to-end model to perform detection in the regression manner. SSD [37] attempted to improve the performance by using multiple aspect ratios and scales for detection of different size of objects. Based on SSD, various fundamentals [50, 67] are developed for training of object detectors from scratch. The unequal number of samples for all classes in the datasets creates class imbalance. RetinaNet [35] developed focal loss to manage the weightage of easy negatives and hard examples to deal with class imbalance. STOD [64] presented scale-transfer for explicit exploration of consistency between multiple scales. SSDES [62] developed location-agnostic, and semantic segmentation module for feature enrichment in one-stage detectors. DFPR [27] presented the local reconfiguration and global attention in the feature pyramid. RFBN [36] enhanced the ability of feature discrimination by developing receptive field block. PFPN [26] developed a wide-width network for parallel feature pyramids to improve the detection process.

The above-discussed methods are developed and trained for object detection in normal environment. The performance of the above-discussed methods degrades while dealing with images captured in hazy environment.

2.2 Object detection in hazy environment

Object detection in a hazy environment is less explored as compared to general object detection. The existing methods for object detection in hazy conditions focus on image dehazing [1, 21, 54] before detection. Another set of methods attempted to solve detection tasks in hazy environments by using domain adaptation. Sindagi et al. [53] developed domain adaptive object detection using transmission map as the domain prior. Kumar et al. [28] presented the object detection after dehazing the image using dark channel prior [21] for autonomous vehicles. Kalwar et al. [25] presented a domain agnostic network by gated differentiable image processing to plug it into existing object detection models. Liu et al. [38] developed image enhancement guided object detection to

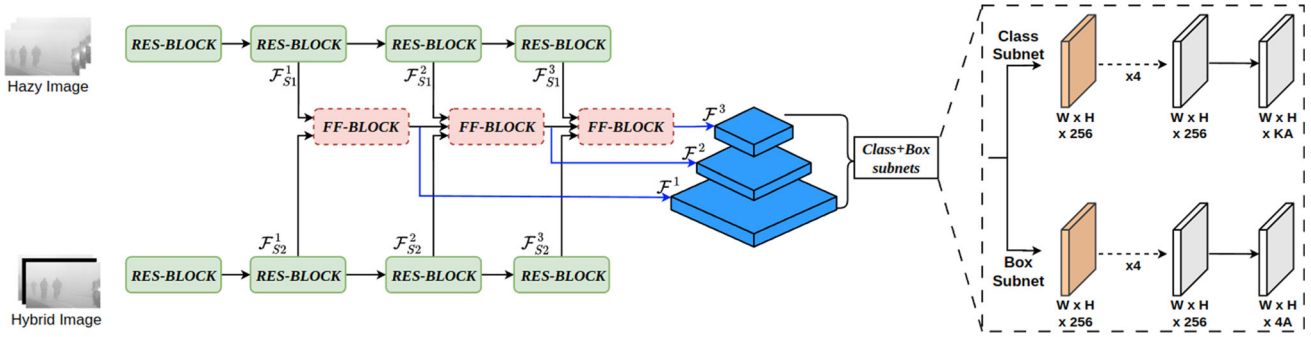


Fig. 1 Framework of Bi-stream feature fusion for object detection in hazy environment

refine the detection model with an enhancement branch. Li et al. [30] presented enhancement to dehaze image before detection. Tanwar et al. [58] presented an image-dehazing model for object detection. Qin et al. [44] proposed a detection-driven enhancement network which combines low-frequency and high-frequency components for multi-scale features. Li et al. [32] combined the dehazing and detection networks to propose detection-friendly dehazing.

3 The proposed approach

The existing object detection models are developed and trained to deal with images captured in normal environments. The existing models perform poorly in a hazy environment as such methods are not capable of dealing with hazy conditions. Thus, we propose a Bi-stream feature fusion (BFF) model for object detection in a hazy environment. The proposed model involves three sub-modules: Hybrid input, Bi-stream feature extractor, and feature fusion block. The framework of proposed BFF network is shown in Fig. 1.

The proposed Bi-stream feature extractor is developed with a combination of two streams (rather than a single stream) that leverages res-blocks in each stream. Each res-block contains a set of convolution, batch-norm, and skip-connection to extract the features from the input image. In between each res-block, there is a pooling layer to reduce the size of the feature map. The set of res-blocks helps in the extraction of multi-level features from the hazy image and hybrid input. The feature fusion block (FF-block) performs convolution-based and multi-level fusion to process the feature map in an appropriate manner. The feature fusion block is developed to perform an adaptive feature fusion, as shown in Fig. 2. The fused features are processed with the help of class and box subnets to detect the location of the object along with the class. The class and box subnets are two distinct convolution networks which generate the class and bounding box, respectively. The detailed discussion is given in the following sections.

3.1 Hybrid image formation

Images captured in a hazy environment contain less visible and faded details, which degrades the performance of object detection. The existing object detection models use single stream (i.e., only hazy images as input) for feature extraction and detection. Feature extraction from hazy images is a challenging task due to lesser details. Thus, we introduced the notion of hybrid input which to facilitate the feature extraction from the hazy image. Further, we propose the BFF model with two distinct streams to deal with the hazy image (haze-stream) and the hybrid image (hybrid stream). The feature extraction from haze-stream and hybrid stream uses pre-trained backbones which requires three-channels input; thus, we develop a hybrid input with three-channels.

The notion of hybrid input is to facilitate the feature extraction from hazy images. The dehazed image as the hybrid input may help the feature extraction; however, image-dehazing techniques have their own limitations and require a large amount of computational time. Thus, we considered three such components as channels which help in haze-related domains and require less computational time to restrict computational overhead. In DCP [21], the method uses a dark channel prior which uses window-based element-wise minimum to perform image dehazing. We considered the simple element-wise minimum pixel (min-channel) as the first channel of hybrid input. The min-channel of hazy image is influenced by the airlight which assist the hybrid stream in extraction of haze-relevant feature. The min-channel used in the hybrid image is represented as:

$$\mathscr{H}_1 = \min_{c \in \{R,G,B\}} (\mathbf{I}^c_{hazy}) \tag{1}$$

where $\mathbf{I}$ denotes the hazy image, c denotes the channels of the image (i.e., red, green, and blue channel), and $\mathscr{H}_1$ denotes the first channel of the hybrid image.

The second channel of hybrid input contains the gradient of the hazy image. Image edges are important to detect an object. However, it is difficult to extract features related

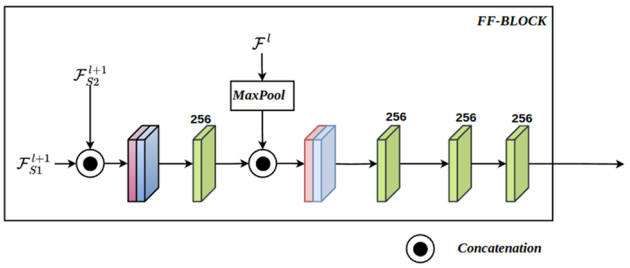


Fig. 2 Architecture of feature fusion block

to edges from the hazy image because hazy images contains faded details. Many dehazing methods [54, 55] focus on improvement of gradient information to enhance the image. Thus, we leverage the gradient information as the second channel of our hybrid input to provide the textural-details for facilitating the feature extraction. The second channel of hybrid image $\mathscr{H}_2$ is represented as:

$$\mathscr{H}_2 = max(\max_{c\in\{R,G,B\}}(\nabla_h \mathbf{I}^c), \max_{c\in\{R,G,B\}}(\nabla_v \mathbf{I}^c)) \tag{2}$$

where ∇_h and ∇_v denote the first-order derivative across horizontal and vertical directions of the image $\mathbf{I}$.

Many approaches consider the inverted hazy images as the low-light images to enhance the image quality. The element-wise maximum is used in many low-light image enhancement methods. Moreover, min-channel is an assumption-based consideration for the hybrid input and it can have minor limitations. Thus, we considered the max-channel as the third channel to counter the limitations of the min-channel in the hybrid channel. The max-channel can be represented as:

$$\mathscr{H}_3 = \max_{c\in\{R,G,B\}}(\mathbf{I}^c) \tag{3}$$

where $\mathscr{H}_3$ denotes the third channel of the hybrid input. The final hybrid input ($\mathbf{I}_{hybrid}$) is a combination of the three derived channels, i.e., $[\mathscr{H}_1, \mathscr{H}_2, \mathscr{H}_3]$.

3.2 Bi-Stream feature extraction

The existing feature extractors perform poorly in a hazy environment. Thus, a new feature extraction paradigm for object detection in hazy images is required. We propose a novel feature extractor, namely, a Bi-stream feature extraction (BFE) network for hazy images with two distinct streams. We introduce two streams in BFE, namely, haze-stream and hybrid stream, to deal with distinct input separately. The haze-stream facilitates the feature extraction from the input hazy images. The hybrid stream assists the haze-stream in extracting appropriate features from the hazy images. The framework of BFF is shown in Fig. 1. The BFE extracts multi-level features from the above-mentioned streams. We denote multi-level features of hazy-stream as $\mathscr{P}_{\mathscr{S}_1}$, and hybrid stream as $\mathscr{P}_{\mathscr{S}_2}$. The multi-level features of j^{th} stream ($\mathscr{P}_{\mathscr{S}_j}$) can be represented as:

$$\mathscr{P}_{\mathscr{S}_j} = [\mathscr{F}^3_{\mathscr{S}_j}, \mathscr{F}^2_{\mathscr{S}_j}, \mathscr{F}^1_{\mathscr{S}_j}] \tag{4}$$

where $\mathscr{S}_j$ denotes the j^{th} stream, and $\mathscr{F}^l_{\mathscr{S}_j}$ denotes the feature map of l^{th} level of $\mathscr{P}_{\mathscr{S}_j}$. The extraction of l^{th} level features in the j^{th} stream can be represented as:

$$\mathscr{F}^l_{\mathscr{S}_j} = \psi^k(|\mathbf{I}|_{\mathscr{S}_j}) \tag{5}$$

where $l = k - 1$ and k is the block number of ResNet-like architecture (ψ) [23], $\mathbf{I}$ denotes the input image (mean normalized), and $\mathscr{S}_j \in [hazy, hybrid]$ denotes the input to the stream.

The streams of BFE attempt to extract features from the hazy images and hybrid input. However, the problem of irrelevant features may still occur due to noise amplification, saturation, and other artifacts in the hybrid input, and suppressed details in the hazy image. Thus, we perform an adaptive feature fusion at multiple levels to extract the appropriate features for object detection. We propose an adaptive feature fusion for the features of the proposed Bi-stream model. The proposed fusion focuses on the appropriate features which help in effective object detection in hazy images. The convolution-based adaptive feature fusion is used in the proposed feature fusion block, discussed in the next section.

3.3 Feature fusion block

The extracted multi-level features of the Bi-stream feature extraction network can be processed separately to detect the objects. However, such an approach processes the undesired features along with the appropriate features which degrade the performance of object detection as discussed in section 4.3. The multi-level features of both streams may contain appropriate features from distinct regions of images. Thus, we perform the adaptive feature fusion of the Bi-stream features. We propose the feature fusion network for the fusion and processing of the Bi-stream features. The detailed architecture of the feature fusion network is shown in Fig. 2. The simplest fusion approach can be given by considering the weighted sum, which can be expressed as:

$$\mathscr{F}^l = w_1 * \mathscr{F}^l_{\mathscr{S}_1} + w_2 * \mathscr{F}^l_{\mathscr{S}_2} \tag{6}$$

where $\mathscr{F}^l$ denotes the fused feature map, w_1 denotes weights for the first feature map, and w_2 denotes the weights of the second feature maps. The weighted sum strategy provides equal importance to the complete feature map. However, feature fusion is required to combine adequate features from

distinct streams. The weighted sum of the feature maps is unable to fuse the adequate features based on the characteristics. However, the feature maps may contain adequate features in one region while having irrelevant features in others. Thus, we proposed an adaptive feature fusion to fuse the multi-level features. The proposed multi-level adaptive feature fusion approach is represented as:

$$\mathscr{F}^l = conv(\mathscr{F}^l_{\mathscr{S}_1} \odot \mathscr{F}^l_{\mathscr{S}_2}) \tag{7}$$

where $\mathscr{F}^l$ denotes the fused feature map, $conv$ denotes convolution, and $\odot$ denotes the concatenation of feature maps.

We perform multi-level fusion with the feature maps of the previous feature fusion block to further improve the fused feature maps ($\mathscr{F}^l$). The feature fusion network performs the multi-level fusion by using the fused features of $(l+1)^{th}$ and l^{th} block. The multi-level fusion in the MSPF network can be expressed as:

$$\mathscr{F}^l = conv(\mathscr{F}^{l+1} \odot MaxPool(\mathscr{F}^l)) \tag{8}$$

where $MaxPool$ denotes the max pooling operation with a kernel and stride of two. The multi-level fusion is used in all the levels of the proposed methods except the first level. After fusion, the feature fusion network uses three convolution layers for processing the features, which can be expressed as:

$$\mathscr{F}^l = conv(conv(conv(\mathscr{F}^l))) \tag{9}$$

Finally, the proposed feature fusion block generates fused multi-level features $\mathscr{P}_{ff}$, which can be expressed as:

$$\mathscr{P}_{ff} = [\mathscr{F}^3, \mathscr{F}^2, \mathscr{F}^1] \tag{10}$$

To process the fused multi-level features, we use the detection approach which is similar to RetinaNet. The training of the proposed network uses generalized focal loss [33]. The summary of the overall proposed BFF network is discussed in the following section.

3.4 Bi-stream feature fusion for object detection in hazy environment

The framework of the proposed BFF network for object detection in hazy environment is shown in Fig. 1. The BFF network extracts multi-level features from a hazy image and hybrid input, then feeds into a feature fusion network. The feature fusion network performs a multi-level adaptive feature fusion to generate a fused feature pyramid. The fused feature pyramid requires processing for object detection and localization. We leveraged the class subnet and box subnet [33] to obtain the object class and localization, respectively. The class subnet processes each feature map of the fused pyramid using a convolution-network to detect the object classes from an image. Another convolution-network (i.e., box subnet) processes the feature maps to improve the quality of bounding boxes. The training of class and box subnets along with the feature extraction and fusion block is performed using the generalized focal loss. The class and box subnets use distinct sets of convolution layers to process the features from the fused feature pyramid, which can be represented as:

$$x = conv(conv(\mathscr{F}^l)) \tag{11}$$

where $\forall \mathscr{F}^l \in \mathscr{P}_{ff}$. The class and box subnet uses the feature of all the levels from the fused feature pyramid for prediction. The loss function ($\mathscr{L}$) is expressed as:

$$\mathscr{L} = -\sum_{m=1}^{c} \alpha_m (1 - p^n_m)^\gamma log(p^n_m) \tag{12}$$

where α_m represents weights of m^{th} class, p^n_m represents the probability of class c for sample t, c represents the overall class number, and γ controls the degree of weights of samples.

4 Experimental results and analysis

4.1 Dataset

The existing object detection method for hazy images uses the pre-trained models and attempts to learn the haze-relevant features using domain adaptation. The models leverage either the RESIDE dataset or the foggy-cityscapes dataset to learn haze characteristics. Further, the validation of the object detection methods for a hazy environment uses the RTTS dataset [31] which is a subset of the RESIDE dataset. In such scenarios, the object detection methods tend to learn features which are similar to the features of RTTS dataset. Thus, such detectors perform well on the RTTS dataset and fail to generalize in the real-world scenario (or images of other datasets). In the Foggy-cityscapes dataset, there are eight object classes and three levels of haze for both training and validation. To perform end-to-end training and demonstrate the generalization capabilities of our proposed BFF model, we develop a new dataset which contains hazy images based on the images of Pascal-VOC dataset for training the object detection methods in a hazy environment. Our synthesized dataset is used to train the proposed model and then validation is performed using the datasets available for validation: RTTS dataset, Foggy-cityscapes, and Foggy-driving dataset.

The synthetic haze generation for our DHOD (dataset for hazy object detection) uses two approaches. In both

Table 1 Quantitative results of state-of-the-art methods in the hazy environment on RTTS dataset. The values in bold depict the best performance and the values in underlined depict the second best

Method	Person	Car	Bus	Bike	Bicycle	mAP
Faster R-CNN [47]	46.6	39.8	11.7	19.0	37.0	30.9
DA-Faster [12]	42.5	43.7	16.0	18.3	32.8	30.7
SWDA [48]	40.1	44.2	16.6	23.2	41.3	33.1
SCL [51]	33.5	48.1	18.2	15.0	28.9	28.7
PBDA [53]	37.4	54.7	17.2	22.5	38.5	34.1
SADA [13]	37.9	52.7	14.5	16.1	26.2	29.5
DA-ODFS [61]	47.7	53.4	19.1	30.2	49.3	39.9
Proposed BFF-50	71.3	52.5	26.4	43.8	49.1	48.6
Proposed BFF-101	**74.0**	**55.2**	**28.4**	**46.9**	**51.6**	**51.2**

Table 2 Details of the datasets used for experimentation

Dataset	Classes (instances)	Total samples
Synthetic	airplane, bicycle, bird, boat, bottle, bus, car, cat, chair, cow, dining table, dog, horse, motorbike, person, potted plant, sheep, sofa, train, tvmonitor	24,640
RTTS	Person, Car, Bus, Bike, Bicycle	4,322
Foggy-cityscapes	Person, Rider, Car, Truck, Bus, Train, Bike, Bicycle	5000
Foggy Driving	Person, Rider, Car, Truck, Bus, Train, Bike, Bicycle	101

approaches of haze generation, DHOD leverages the annotated images of pascal-VOC dataset. The first approach of haze generation is based on the physical image formation model [39, 54], which requires depth map and atmospheric light to generate haze in an image. The depth map is used in the estimation of transmission map with the aid of a beta parameter to control the haze in the depth. Further, the atmospheric light also controls the haze in an image. The variation of beta parameter and the atmospheric light helps in synthesizing the images with distinct variations of haze. The depth map is not available for the images. Thus, the estimation of depth map from a single image is performed using monodep [19]. The estimated depth is utilized for transmission map synthesis using the beta parameter. We used random values for atmospheric light and beta parameters to vary the level of haze in the images in a random manner. The discrete haze characteristics are not suitable for real-world scenarios. The value of atmospheric light and beta is in the range of 0.7 to 0.95. The second approach uses a generative method based on Cycle-GAN [66] to synthesize haze controlled by the generator. In the second approach of haze generation for DHOD, we developed a cycle-GAN to generate hazy to haze-free and haze-free to hazy samples. We trained the developed model on an unpaired set of hazy and normal images collected from distinct sources. The Cycle-GAN is used to generate haze in the samples. The final DHOD contains sixty percent of hazy images from the first approach and the forty percent of hazy images from the second approach. The training of the proposed model on our developed DHOD dataset and validation on the other datasets shows the superiority and generalization of the proposed model. The details of the datasets used for experimentation are given in Table 2.

4.2 Implementation details

The proposed BFF is implemented using the PyTorch framework. Both streams of the BFE network use pre-trained ResNet-101 in all experiments. The BFF network is trained for ten epochs using stochastic gradient descent (SGD). The learning rate for the SGD optimizer is 0.01 for all experiments with decay at 8^{th} and 11^{th} epochs. During training, the model uses a batch size of 4 samples per GPU on the machine with two Titan-RTX GPUs and 128GB RAM. The proposed BFF model is trained on the synthesized DHOD dataset and validated on the RTTS dataset to analyze the performance in a hazy environment. In multi-scale training, we resized the shorter side of the input image into multiple scales between 360 to 640. In the ablation study, the BFF uses ResNet-101 in both streams of the BFE network. Further, the models are trained for twelve epochs during ablation with a batch size of eight.

Table 3 Ablation study of the hybrid input

X_{min}	X_{max}	X_{delta}	mAP
✓	✓	–	48.4
✓	–	✓	50.3
–	✓	✓	49.3
✓	–	–	47.9
–	✓	–	48.7
–	–	✓	49.6
✓	✓	✓	51.2

Table 4 Ablation study of multi-level feature fusion

BFF model	mAP
without fusion	46.9
with fusion	51.2

4.3 Ablations

In this subsection, we analyzed the effectiveness of hybrid input and multi-level feature fusion. Table 3 shows the analysis of distinct components of the hybrid image. We have used three components in the hybrid image since the BFE network uses pre-trained backbone which can deal with three-channel input. Each component in the hybrid image is analyzed to evaluate its impact on the overall performance. The mean average precision measure is used for analysis. Firstly, we evaluated the impact of individual components (i.e., x_{min}, x_{max}, and x_{delta}) by processing just one component in the hybrid frame and having other components as zero. The results shown in Table 3 show that only one component in the hybrid input reduces the overall mAP. The exclusion of two components from the hybrid input reduces the performance of the proposed methods by at least 1.6 mAP value. Further, the exclusion of a single component from the hybrid frame decimates the performance by at least 0.9 mAP value.

Table 4 shows the impact of multi-level fusion in the proposed method. We developed two alternative configurations, one with multi-level fusion and the other one without fusion. The BFF model with the proposed multi-level fusion outperforms the variant of our model without fusion. Direct detection using the distinct level of features from both streams is unable to process the features adequately. Thus, the BFF model without fusion results in a lesser mAP. On the other hand, the processing of Bi-stream features using the proposed approach helps the proposed model in achieving better performance. This analysis shows the importance of proposed multi-level features in our BFF model. Our BFF model performs the fusion of appropriate features within and across the stream which results in a better performance.

4.4 Quantitative analysis

This section presents an exhaustive quantitative analysis of the proposed BFF and state-of-the-art methods on the RTTS dataset, Foggy-cityscapes dataset, and Foggy-driving dataset. The values of quantitative measures for other methods are taken from the source provided by the authors for a fair comparison. The class-wise average precision and mean average precision of each method are used for quantitative comparison. State-of-the-art methods (used for comparison) use ResNet-50, ResNet-101, and VGG-16 as the backbones. The RTTS dataset, Foggy-cityscapes dataset, and Foggy-driving dataset are widely used for the assessment of object detection methods in hazy environments. The proposed method outperforms the other methods in hazy conditions as well as normal conditions.

4.4.1 Validation on RTTS dataset

The performance comparison of the proposed BFF with other contemporary methods on the RTTS dataset is given in Table 1. RTTS is a part of RESIDE (a well-known image-dehazing dataset). It contains more than four thousand hazy images to assess the performance of object detection in a hazy environment. The images are annotated for five classes in RTTS, namely, bicycle, bike, bus, car, and person. The RTTS dataset is not used for training the proposed method. Pascal-VOC dataset is used for warm-up training of the proposed model. Then, we used the synthesized DHOD dataset for training the model to deal with hazy object detection. The trained model is validated on the RTTS dataset. The contemporary methods are trained on the RESIDE dataset for adaptation of the haze in the detection model. The supervised training on RESIDE helps the existing models in learning the haze-relevant characteristics which are similar to the RTTS dataset. Table 1 shows that the proposed BFF-101 (with ResNet-101 backbone) outperforms the other state-of-the-art methods. Further, the BFF-50 model achieves second best for most of the classes. For the bicycle class, the BFF-50 achieves the third-best score. The mAP shows the superior performance of the proposed BFF network.

4.4.2 Validation on foggy-cityscapes dataset

Another widely used dataset for performance analysis of object detection methods in hazy environments is Foggy-cityscapes. The cityscapes dataset is processed to add foggy conditions and generate foggy-cityscapes. Many methods attempted domain adaptation of the cityscapes dataset to the foggy-cityscapes dataset for object detection in a hazy environment. The existing models are finetuned on the foggy-cityscapes to learn the haze-relevant features for object detection in hazy environments. The foggy-cityscapes dataset

Table 5 Quantitative results of state-of-the-art methods in the hazy environment on Foggy-cityscapes dataset. The values in bold depict the best performance and the values in underlined depict the second best

Method	Person	Rider	Car	Truck	Bus	Train	Bike	Bicycle	mAP
Faster R-CNN [47]	32.0	39.5	36.2	19.4	32.1	9.4	23.3	33.2	28.1
DA-Faster [12]	37.2	46.8	49.9	28.2	42.3	30.9	32.8	40.0	38.5
SWDA [48]	29.9	42.3	43.5	24.5	36.2	32.6	30.0	35.3	34.3
SCL [51]	30.7	44.1	44.3	30.0	47.9	42.9	29.6	33.7	37.9
PBDA [53]	34.9	46.4	51.4	29.2	46.3	43.2	31.7	37.0	40.0
Mega-CDA [60]	37.7	49.0	52.4	25.4	49.2	46.9	34.5	39.0	41.8
UaDAN [20]	36.5	46.1	53.6	28.9	49.4	42.7	32.3	38.9	41.1
MEAA [40]	34.2	48.9	52.4	30.3	42.7	46.0	33.2	36.2	40.5
SADA [13]	48.5	<u>52.6</u>	62.1	29.5	50.3	31.5	32.4	45.4	44.0
CaCO [24]	38.3	46.7	48.1	33.2	45.9	37.6	31.0	33.0	39.2
MGA [65]	43.9	49.6	60.6	29.6	50.7	39.0	38.3	42.8	44.3
DA-ODFS [61]	39.9	51.6	59.0	**39.7**	**58.0**	<u>49.1</u>	<u>39.2</u>	45.1	47.6
Proposed BFF-50	<u>48.9</u>	52.1	<u>65.5</u>	35.1	56.8	47.8	38.6	<u>46.2</u>	<u>48.9</u>
Proposed BFF-101	**51.7**	**54.2**	**66.8**	<u>37.3</u>	<u>57.8</u>	**51.2**	**41.1**	**48.5**	**51.1**

contains seven classes: bicycle, bike, bus, car, person, rider, train, and truck. The proposed BFF network is finetuned on the foggy-cityscapes dataset to learn the features related to the new classes rider and truck. The proposed methods and other contemporary methods are validated on the images of foggy-cityscapes and results are shown in Table 5. The mAP shows that the proposed BFF-101 outperforms the existing methods for most of the classes. Further, it achieves the second best result for the truck and bus class. The overall mAP shows the superior performance of the proposed method on the foggy-cityscapes dataset.

4.4.3 Validation on foggy-driving dataset

One of the widely used datasets for the validation of object detection methods in a hazy environment is Foggy driving. The Foggy driving depicts driving scenes from real-world foggy environments. The images are captured in a foggy environment with the mobile phone and web. Many approaches use Foggy-driving dataset to test the real-world generalization of their methods. The validation of different methods on the real-world Foggy-driving dataset is shown in Table 6. Various methods have shown the performance analysis on synthetic datasets and their codes are unavailable to test on the real-world dataset. The performance analysis on the Foggy-driving dataset shows that the proposed BFF-101 can generalize on real-world scenes.

Table 6 Quantitative results of state-of-the-art methods in the hazy environment on Foggy-driving dataset. The values in bold depict the best performance and the values in underlined depict the second best

Method	mAP
Faster R-CNN	26.4
DA-Faster	31.6
SWDA	33.5
SCL	33.5
SADA	32.3
DA-ODFS	<u>34.6</u>
Proposed BFF-101	**36.4**

4.5 Computational time

We analyzed the computational time of the proposed method and other contemporary methods [12, 40, 47, 48, 51, 61]. The codes and parameters are used as given by the authors for computational time analysis. We used images of size 1000 $\times$ 600 for the analysis. Most of the methods are focused on dehazing or its variants for adaptation. Further, the contemporary methods use the two-stage detection mechanism to achieve better accuracy in hazy conditions. The methods [12, 40, 47, 48, 51, 61] require different amounts of time for training; however, the time required for the inference is approximately the same. These methods process seven frames per second. The proposed method leverages a single-stage detection mechanism with BFE and feature fusion block. The proposed method with ResNet-101 processes fourteen frames per second. Further, our method with ResNet-50 processes eighteen frames per second. The proposed method achieves better detection performance than the other contemporary methods.

5 Conclusion

This paper presents a new BFF model for object detection in hazy environments. The proposed BFF consists of a Bi-stream feature extractor and a multi-level feature fusion. The proposed model outperforms state-of-the-art methods in a hazy environment. The Bi-stream feature extractor is capa-

ble of extracting effective features from the hazy image and the hybrid input. The proposed multi-level feature fusion performs a fusion of appropriate features across and within both streams and achieves superior performance in a hazy environment. The existing object detection model uses an image-dehazing dataset to learn haze-relevant characteristics. To address this issue, we developed a DHOD dataset for training the object detection model directly on hazy annotated images. We showed the validation on the RTTS dataset after training on our DHOD dataset. The extensive experimentation on distinct benchmark datasets shows that the proposed BFF model outperforms other state-of-the-art object detection models in a hazy environment.

Author Contributions KS and ASP have equal contributions to the manuscript.

Funding In this research, there is no funding involved from any agency.

Data Availability Data will be made available on reasonable request.

Declarations

Conflict of interest The authors declare that they have no conflicts of interest.

Ethical Approval Not applicable.

References

1. Akhtar, M.S., Ali, A., Chaudhuri, S.S.: Mobile-unet gan: a single-image dehazing model. Signal Image Video Process pp. 1–9 (2023)
2. Ali, A., Ghosh, A., Chaudhuri, S.S.: Real-time tracking of moving objects through efficient scale space adaptation and normalized correlation filtering. Signal Image Video Process (2023)
3. Alzahrani, M.S., Jarraya, S.K., Ben-Abdallah, H., Ali, M.S.: Comprehensive evaluation of skeleton features-based fall detection from microsoft kinect v2. Signal Image Video Process **13**, 1431–1439 (2019)
4. An, G., Guo, J., Wang, Y., Ai, Y.: Egbnet: a real-time edge-guided bilateral network for nighttime semantic segmentation. Signal Image Video Process pp. 1–9 (2023)
5. Aote, S.S., Wankhade, N., Pardhi, A., Misra, N., Agrawal, H., Potnurwar, A.: An improved deep learning method for flying object detection and recognition. Signal Image Video Process pp. 1–10 (2023)
6. Bhatnagar, G., Liu, Z.: A novel image fusion framework for night-vision navigation and surveillance. Signal Image Video Process **9**, 165–175 (2015)
7. Bhatt, D., Patel, C., Talsania, H., Patel, J., Vaghela, R., Pandya, S., Modi, K., Ghayvat, H.: Cnn variants for computer vision: history, architecture, application, challenges and future scope. Electronics **10**(20), 2470 (2021)
8. Bi, S., Hu, Z., Zhao, M., Zhang, H., Di, J., Sun, Z.: Self-supervised pretext task collaborative multi-view contrastive learning for video action recognition. Signal Image Video Process **58**, 1–8 (2023)
9. Bulugu, I.: Gesture recognition system based on cross-domain csi extracted from wi-fi devices combined with the 3d cnn. Signal Image Video Process **24**, 1–9 (2023)
10. Cai, Z., Vasconcelos, N.: Cascade r-cnn: high quality object detection and instance segmentation. IEEE Trans. Pattern Anal. Mach. Intell. **43**(5), 1483–1498 (2019)
11. Cakir, S., Cetin, A.E.: Visual object tracking using fourier domain phase information. Signal Image Video Process **16**(1), 119–126 (2022)
12. Chen, Y., Li, W., Sakaridis, C., Dai, D., Van Gool, L.: Domain adaptive faster r-cnn for object detection in the wild. Proc. Conf. Comput. Vis. Pattern Recognit. **25**, 3339–3348 (2018)
13. Chen, Y., Wang, H., Li, W., Sakaridis, C., Dai, D., Van Gool, L.: Scale-aware domain adaptive faster r-cnn. Int. J. Comput. Vis. **129**(7), 2223–2243 (2021)
14. Devipriya, A., Prabakar, D., Singh, L., Oliver, A.S., Qamar, S., Azeem, A.: Machine learning-driven pedestrian detection and classification for electric vehicles: integrating bayesian component network analysis and reinforcement region-based convolutional neural networks. Signal Image Video Process **17**(8), 4475–4483 (2023)
15. Elafi, I., Jedra, M., Zahid, N.: Tracking occluded objects using chromatic co-occurrence matrices and particle filter. Signal Image Video Process **12**, 1227–1235 (2018)
16. Everingham, M., Van Gool, L., Williams, C.K., Winn, J., Zisserman, A.: The pascal visual object classes (voc) challenge. Int. J. Comput. Vis. **88**(2), 303–338 (2010)
17. Gidaris, S., Komodakis, N.: Object detection via a multi-region and semantic segmentation-aware cnn model. In: Proceedings of the IEEE international conference on computer vision, pp. 1134–1142 (2015)
18. Girshick, R.: Fast r-cnn. In: IEEE International Conference on Computer Vision, pp. 1440–1448 (2015)
19. Godard, C., Aodha, O.M., Firman, M., Brostow, G.: Digging into self-supervised monocular depth estimation. In: IEEE/CVF International Conference on Computer Vision, pp. 3827–3837 (2019)
20. Guan, D., Huang, J., Xiao, A., Lu, S., Cao, Y.: Uncertainty-aware unsupervised domain adaptation in object detection. IEEE Trans. Multimedia. **24**, 2502–2514 (2021)
21. He, K., Sun, J., Tang, X.: Single image haze removal using dark channel prior. IEEE Trans. Pattern Anal. Mach. Intell. **33**(12), 2341–2353 (2011)
22. He, K., Zhang, X., Ren, S., Sun, J.: Spatial pyramid pooling in deep convolutional networks for visual recognition. IEEE Trans. Pattern Anal. Mach. Intell. **37**(9), 1904–1916 (2015)
23. He, K., Zhang, X., Ren, S., Sun, J.: Deep residual learning for image recognition. In: Proc. IEEE/CVF Conf. Comput. Vis. Pattern Recognit., pp. 770–778 (2016)
24. Huang, J., Guan, D., Xiao, A., Lu, S., Shao, L.: Category contrast for unsupervised domain adaptation in visual tasks. In: Proc. IEEE/CVF Conf. Comput. Vis. Pattern Recognit., pp. 1203–1214 (2022)
25. Kalwar, S., Patel, D., Aanegola, A., Konda, K.R., Garg, S., Krishna, K.M.: Gdip: Gated differentiable image processing for object-detection in adverse conditions. arXiv preprint arXiv:2209.14922 (2022)
26. Kim, S.W., Kook, H.K., Sun, J.Y., Kang, M.C., Ko, S.J.: Parallel feature pyramid network for object detection. In: European conference on computer vision, pp. 234–250 (2018)
27. Kong, T., Sun, F., Tan, C., Liu, H., Huang, W.: Deep feature pyramid reconfiguration for object detection. In: European Conference on Computer Vision, pp. 169–185 (2018)
28. Kumar, B., Mishra, A., Talesara, A., Kumar, S., Dey, S., Vyas, Vyas, R.: Object detection for autonomous vehicle in hazy environment using optimized deep learning techniques. In: Proceedings of the 2022 Fourteenth International Conference on Contemporary Computing, pp. 242–249 (2022)

29. Kumar, N., Sukavanam, N.: A weakly supervised cnn model for spatial localization of human activities in unconstraint environment. Signal Image Video Process **14**(5), 1009–1016 (2020)
30. Li, B., Hua, Y., Lu, M.: Object detection in hazy environment enhanced by preprocessing image dataset with synthetic haze. In: 2020 International Conference on Computational Science and Computational Intelligence (CSCI), pp. 1618–1623. IEEE (2020)
31. Li, B., Ren, W., Fu, D., Tao, D., Feng, D., Zeng, W., Wang, Z.: Benchmarking single-image dehazing and beyond. IEEE Trans. Image Process. **28**(1), 492–505 (2019)
32. Li, C., Zhou, H., Liu, Y., Yang, C., Xie, Y., Li, Z., Zhu, L.: Detection-Friendly Dehazing: Object Detection in Real-World Hazy Scenes. IEEE Trans. Pattern Anal. Mach, Intell (2023)
33. Li, X., Lv, C., Wang, W., Li, G., Yang, L., Yang, J.: Generalized focal loss: towards efficient representation learning for dense object detection. IEEE Trans. Pattern Anal. Mach. Intell. **45**(3), 3139–3153 (2023)
34. Lin, T.Y., Dollar, P., Girshick, R., He, K., Hariharan, B., Belongie, S.: Feature pyramid networks for object detection. In: Proc. IEEE/CVF Conf. Comput. Vis. Pattern Recognit. (2017)
35. Lin, T.Y., Goyal, P., Girshick, R., He, K., Dollár, P.: Focal loss for dense object detection. IEEE Trans. Pattern Anal. Mach. Intell. **42**(2), 318–327 (2020)
36. Liu, S., Huang, D., et al.: Receptive field block net for accurate and fast object detection. In: European conference on computer vision, pp. 385–400 (2018)
37. Liu, W., Anguelov, D., Erhan, D., Szegedy, C., Reed, S., Fu, C.Y., Berg, A.C.: Ssd: Single shot multibox detector. In: European Conference on Computer Vision, pp. 21–37. Springer (2016)
38. Liu, W., Ren, G., Yu, R., Guo, S., Zhu, J., Zhang, L.: Image-adaptive yolo for object detection in adverse weather conditions. In: Proceedings of the AAAI Conference on Artificial Intelligence, vol. 36, pp. 1792–1800 (2022)
39. Nayar, S., Narasimhan, S.: Vision in bad weather. In: Proceedings of IEEE Conference on Computer Vision, vol. 2, pp. 820 – 827 vol.2 (1999)
40. Nguyen, D.K., Tseng, W.L., Shuai, H.H.: Domain-adaptive object detection via uncertainty-aware distribution alignment. In: Proceedings of the 28th ACM international conference on multimedia, pp. 2499–2507 (2020)
41. Parihar, A.S., Verma, O.P., Khanna, C.: Fuzzy-contextual contrast enhancement. IEEE Trans. Image Process. **26**(4), 1810–1819 (2017)
42. Patel, C., Bhatt, D., Sharma, U., Patel, R., Pandya, S., Modi, K., Cholli, N., Patel, A., Bhatt, U., Khan, M.A., et al.: Dbgc: dimension-based generic convolution block for object recognition. Sensors **22**(5), 1780 (2022)
43. Priyadharshini, G., Ukrit, M.F.: Cso-cnn: circulatory system optimization-based cascade region cnn for fault estimation and driver behavior detection. Signal Image Video Process pp. 1–9 (2023)
44. Qin, Q., Chang, K., Huang, M., Li, G.: Denet: Detection-driven enhancement network for object detection under adverse weather conditions. In: Asian Conf. on Computer Vision, pp. 2813–2829 (2022)
45. Rathee, N., Ganotra, D.: An efficient approach for facial action unit intensity detection using distance metric learning based on cosine similarity. Signal Image Video Process **12**, 1141–1148 (2018)
46. Redmon, J., Divvala, S., Girshick, R., Farhadi, A.: You only look once: Unified, real-time object detection. In: Proc. IEEE/CVF Conf. Comput. Vis. Pattern Recognit., pp. 779–788 (2016)
47. Ren, S., He, K., Girshick, R., Sun, J.: Faster r-cnn: towards real-time object detection with region proposal networks. IEEE Trans. Pattern Anal. Mach. Intell. **39**(6), 1137–1149 (2017)
48. Saito, K., Ushiku, Y., Harada, T., Saenko, K.: Strong-weak distribution alignment for adaptive object detection. In: Proc. IEEE/CVF Conf. Comput. Vis. Pattern Recognit., pp. 6956–6965 (2019)
49. Sakaridis, C., Dai, D., Van Gool, L.: Semantic foggy scene understanding with synthetic data. Int. J. Comput. Vis. **126**(9), 973–992 (2018)
50. Shen, Z., Liu, Z., Li, J., Jiang, Y.G., Chen, Y., Xue, X.: Dsod: Learning deeply supervised object detectors from scratch. In: IEEE International Conference on Computer Vision, pp. 1937–1945 (2017)
51. Shen, Z., Maheshwari, H., Yao, W., Savvides, M.: Scl: Towards accurate domain adaptive object detection via gradient detach based stacked complementary losses. arXiv preprint arXiv:1911.02559 (2019)
52. Shrivastava, A., Gupta, A., Girshick, R.: Training region-based object detectors with online hard example mining. In: Proceedings of the IEEE conference on computer vision and pattern Recognition pp. 761–769 (2016)
53. Sindagi, V.A., Oza, P., Yasarla, R., Patel, V.M.: Prior-based domain adaptive object detection for hazy and rainy conditions. In: European Conference on Computer Vision, pp. 763–780. Springer (2020)
54. Singh, K., Parihar, A.S.: Variational optimization based single image dehazing. J. Vis. Commun. Image Represent. **79**, 103241 (2021)
55. Singh, K., Parihar, A.S.: Illumination estimation for nature preserving low-light image enhancement. The Visual Computer pp. 1–16 (2023)
56. Soumya, T., Thampi, S.M.: Self-organized night video enhancement for surveillance systems. Signal Image Video Process **11**, 57–64 (2017)
57. Tammvee, M., Anbarjafari, G.: Human activity recognition-based path planning for autonomous vehicles. Signal Image Video Process **15**(4), 809–816 (2021)
58. Tanwar, R., Verma, S., Kumar, M., et al.: Object detection using image dehazing: A journey of visual improvement. In: International Conference on Intelligent Technologies, pp. 1–8. IEEE (2022)
59. Uijlings, J.R., Van De Sande, K.E., Gevers, T., Smeulders, A.W.: Selective search for object recognition. Int. J. Comput. Vis. **104**, 154–171 (2013)
60. Vs, V., Gupta, V., Oza, P., Sindagi, V.A., Patel, V.M.: Mega-cda: Memory guided attention for category-aware unsupervised domain adaptive object detection. In: Proc. IEEE/CVF Conf. Comput. Vis. Pattern Recognit., pp. 4516–4526 (2021)
61. Yang, X., Mi, M.B., Yuan, Y., Wang, X., Tan, R.T.: Object detection in foggy scenes by embedding depth and reconstruction into domain adaptation. Conference on Computer Vision, pp. 1093–1108 (2022)
62. Zhang, Z., Qiao, S., Xie, C., Shen, W., Wang, B., Yuille, A.L.: Single-shot object detection with enriched semantics. Proceedings of the IEEE conference on computer vision and pattern Recognition pp. 5813–5821 (2018)
63. Zhang, Z., Zhao, L., Liu, Y., Zhang, S., Yang, J.: Unified density-aware image dehazing and object detection in real-world hazy scenes. In: Asian Conference on Computer Vision (2020)
64. Zhou, P., Ni, B., Geng, C., Hu, J., Xu, Y.: Scale-transferrable object detection. In: Proc. IEEE/CVF Conf. Comput. Vis. Pattern Recognit., pp. 528–537 (2018)
65. Zhou, W., Du, D., Zhang, L., Luo, T., Wu, Y.: Multi-granularity alignment domain adaptation for object detection. In: Proceedings of the IEEE Conference on Computer Vision and Pattern Recognition, pp. 9581–9590 (2022)

66. Zhu, J.Y., Park, T., Isola, P., Efros, A.A.: Unpaired image-to-image translation using cycle-consistent adversarial networks. In: IEEE International Conference on Computer Vision, pp. 2242–2251 (2017)
67. Zhu, R., Zhang, S., Wang, X., Wen, L., Shi, H., Bo, L., Mei, T.: Scratchdet: Training single-shot object detectors from scratch. In: Proceedings of the IEEE Conference on Computer Vision and Pattern Recognition, pp. 2263–2272 (2019)
68. Zitnick, C.L., Dollár, P.: Edge boxes: Locating object proposals from edges. In: European Conference on Computer Vision, pp. 391–405. Springer (2014)

Publisher's Note Springer Nature remains neutral with regard to jurisdictional claims in published maps and institutional affiliations.

Springer Nature or its licensor (e.g. a society or other partner) holds exclusive rights to this article under a publishing agreement with the author(s) or other rightsholder(s); author self-archiving of the accepted manuscript version of this article is solely governed by the terms of such publishing agreement and applicable law.

Materials Chemistry and Physics 315 (2024) 128942

Contents lists available at ScienceDirect

Materials Chemistry and Physics

journal homepage: www.elsevier.com/locate/matchemphys

Bioactive glass incorporated dressing matrix for rapid hemostatic action with antibacterial activity

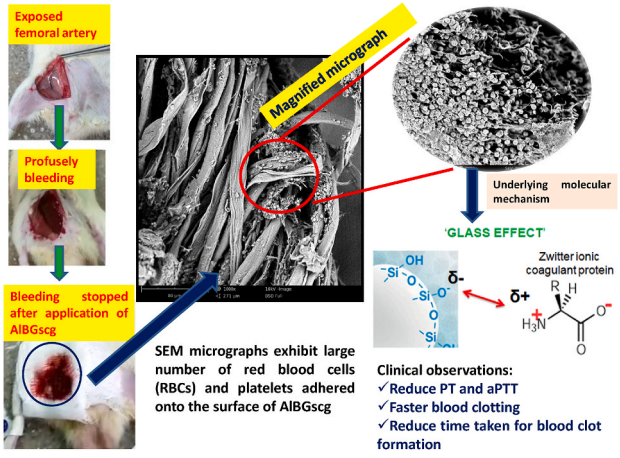
Payal Roy [a], Rupam Saha [a,b], Debolina Dattaray [c], Suman Saha [a], Tapan Kumar Mandal [c], Pooja Srivastava [d], Jui Chakraborty [a,b,*]

[a] Bioceramics and Coating Division, CSIR-Central Glass and Ceramic Research Institute (CSIR- CGCRI), 196, Raja S. C. Mullick Road, Kolkata, 700 032, India
[b] Academy of Scientific and Innovative Research (AcSIR), Ghaziabad, 201002, India
[c] Department of Veterinary Pharmacology and Toxicology, West Bengal University of Animal and Fishery Sciences, Belgachia, Kolkata, 700 037, India
[d] Institute of Nuclear Medicine & Allied Sciences, Brig SK Mazumdar Marg, Timarpur, Delhi, 110054, India

HIGHLIGHTS

- AlBGscg is cytocompatible, **has** rapid hemostasis **and** antibacterial activity.
- It can **initiate** both intrinsic and extrinsic coagulation **cascades.**
- It shows **rapid** thrombin generation and **improves** hemostasis *in* ***vivo.***

GRAPHICAL ABSTRACT



ARTICLE INFO

Keywords:
AlBGscg
Platelet adhesion
PT-aPTT
Antibacterial activity
Thrombin generation
In-vivo hemostatic efficacy

ABSTRACT

Uncontrolled bleeding stands as a leading cause of preventable death in both civilian trauma and military battlefield scenarios. Existing hemostatic dressings like HemCon, Celox, and QuickClot, often lack instant hemostasis at the bleeding site and may have biodegradability and exothermic issues. To address the above in this communication, we have synthesized a hemostatic glass (acronym AlBG, $CaO\text{-}SiO_2$ system, incorporated with Al_2O_3 and ZnO) by sol gel route and carried out detail physicochemical characterizations, e.g., XRD, FESEM, FTIR, BET and particle size analysis etc. The AlBG of particle size range 140–253 nm was incorporated into the nonwoven surgical cotton gauze to obtain AlBGscg. *In vitro* biological assays including cytocomtability, hemocompatibility assays of the above coated gauze was undertaken using NIH3T3 of which, the later showed optimum hemocompatibility with <6 % lysis of red blood cells. Potent antibacterial action on both gram positive

* Corresponding author. Bioceramics and Coating Division, CSIR-Central Glass and Ceramic Research Institute (CSIR- CGCRI), 196, Raja S. C. Mullick Road, Kolkata, 700 032, India.
E-mail address: jui@cgcri.res.in (J. Chakraborty).

https://doi.org/10.1016/j.matchemphys.2024.128942
Received 3 May 2023; Received in revised form 8 January 2024; Accepted 11 January 2024
Available online 13 January 2024
0254-0584/© 2024 Elsevier B.V. All rights reserved.

and gram negative strains were obtained with significant zone of inhibition of 17 ± 0.34 mm and 16 ± 0.56 mm, respectively. Importantly, significant reduction of the clotting time (31.81 ± 0.12 % for P time and 33.3 ± 0.23 % for aPTT) compared to the control group, indicated activation of both intrinsic and extrinsic coagulation pathways. Scanning electron microscope (SEM) images exhibited an enhanced *in vitro* blood clot formation in case of AlBGscg in comparison to the control (uncoated surgical cotton gauze), visually. Additionally, a noticeable reduction of ~30 % in the time required for the blood clot formation, in case of AlBGscg, was observed. The *in vivo* hemostatic potential of AlBGscg was evaluated in Wistar rats through femoral artery injury and was compared with commercially available surgical cotton gauze. The results demonstrated substantial reduction in the time required for hemostasis (approximately 50 % reduction), a lower amount of blood loss (7.33 % with AlBGscg compared to 22.31 % with surgical cotton gauze), and importantly, there were no incidents of re-bleeding observed with AlBGscg, highlighting its promise as a candidate for effective hemostasis.

1. Introduction

Exsanguinating blood loss, a leading cause of potentially preventable mortality in civilian and military injuries, poses a significant challenge [1]. Market available hemostatic gauze and dressings such as HemCon [2], Celox [3], and QuickClot [4], while effective to some extent, often fall short in providing instant hemostasis at the bleeding site, and they may have issues with biodegradability and generate heat during clotting [5,6]. HemCon, Celox, and other hemostatics e.g., chitosan (natural polymer) are patient specific, exhibit allergic response, lack adhesion at the wound bed, and cause blood to re-drain when the dressing is changed [7]. Most importantly, there is evidence of a difference in action between batches in indigenous brands such as chitosan based Axiostat; consequently, these dressings are not reliable for controlling hemorrhage in coagulopathy [8]. Ordinary surgical gauge do not adhere to the injury site and as a result they can not hold fluids at the damage site also fall off anytime. Also, it needs to be refreshed frequently, thereby reducing the patient compliance [7]. Addressing these limitations there is an ongoing area of research and development for rapid hemostatic action, improved biodegradability and reduced adverse effects, with the aim of saving lives in severely bleeding cases [6]. Hence, the development of an ideal hemostatic material is still a challenge and herewith, bioactive glass (BG) with significantly high specific surface area can induce hemostasis via activation of factor XII and other clotting proteins such as prekallikrein, and high-molecular-weight kininogen, due to the high concentration of polar silanol groups and negative charges at their surfaces [9]. With their inherently polar surfaces on account of the difference in electronegativity between oxygen and metallic atoms, the glass surfaces with surface energy >60 dyne/cm are more likely to be accelerators of clot formation [10], resulting in the term 'glass effect' [11]. The hemostatic properties of BGs with an 80 % SiO_2, 15 % CaO, and 5 % P_2O_5 composition enhances hemostatic activity, reducing R times and promoting faster coagulation [12–14]. 'R' represents the Reaction Time, is one of the parameters measured in thromboboelastogram (Thromboelastography/TEG is a viscoelastic hemostatic assay that assesses the global viscoelastic properties of whole blood clot formation under conditions of low shear stress), which provides information about the time it takes for the initial formation of a blood clot after the activation of coagulation. It is often used to assess the early stages of clot formation. This effect is attributed to the "glass effect, " which triggers the autocatalytic activation of clotting factors XII, XI, prekallikrein, and high-molecular-weight kininogen, leading to thrombin enzyme association and fibrin polymerization [15]. Surface area is crucial for immobilizing participants in surface-dependent clotting reactions, while Ca^{2+} ions serve as cofactors for orienting protein assemblies and enzymes involved in fibrin production. Upon hydration and release of Ca^{2+} ions actively supports thrombosis. These characteristics make BGs a promising material for hemostasis and clot formation in medical applications [16]. Silver (Ag^{+}), zinc (Zn^{2+}), magnesium (Mg^{2+}), cobalt (Co^{2+}), gallium (Ga^{3+}), cerium (Ce^{3+}), titanium (Ti^{4+}), tantalum (Ta^{5+}), and other trace elements have recently emerged and are incorporating into the glass network in order to achieve unique characteristics that can be beneficial for applications in healthcare, such as hemostasis [17–21]. Inorganic aluminum based salt, generally known as alum is broadly utilized in dentistry and furthermore applied in bladder hemorrhagic condition [22,23]. When high-ionic Al^{3+} comes into contact with blood, its strength helps to promote hemostasis and neutralize anionic-charged plasma [22]. Blood clotting is a complex process that involves a series of reactions to stop bleeding when blood vessels are injured. One of the key steps in hemostasis is the activation of the coagulation cascade, a series of enzymatic reactions that ultimately lead to the formation of a blood clot. Al^{3+} ions can promote hemostasis by interaction with various coagulation factors such as fibrinogen and prothrombin, which are essential for clot formation. The electropilic tendencies of Al^{3+} basically neutralized the coagulation proteins as above, thereby reducing the electrostatic repulsion, facilitating enhanced interaction and coagulation thereafter. Further, Al^{3+} ions influence the platelet activation, leading to formation of platelet plug at the site of injury [22]. The Zn^{2+} in the composition plays a significant role in cell replication, proliferation, and coagulation by enhancing platelet aggregation and improving interactions with plasma proteins that are anionic [24,25]. The hemostatic activity of BG reveals that the release of Ca^{2+} ion upon hydration, is able to concentrate blood constituents through capillary absorption of fluid-phase media, and is composed of an insoluble inorganic core that could provide an effective support for thrombosis [26].

Also, they perform the dual role of supplying calcium ions that are cofactors for the blood clotting cascade, which under physiological conditions provide negatively charged siliceous oxide as a support for surface-dependent thrombotic reactions and there is an optimum ratio of SiO_2 to CaO in bioactive glass for the fastest hemostatic response [27].

In view of the above, we synthesized aluminum-based hemostatic bioactive glass (AlBG) and incorporated it into nonwoven surgical cotton gauze (AlBGscg) to obtain a hemostatic dressing matrix. *In vitro* material and biological characterization and an *in vivo* animal study were carried out and the pertinent parameters e.g., water vapour transmission rate (WVTR), contact angle, water absorption capacity, platelet adhesion, thrombin generation, Prothrombin time/activated partial thromboplastin time (PT/aPTT), blood clot formation, hemocompatibility, apart from good cell viability and antibacterial potential followed by *in vivo* hemostatic efficacy study established good efficacy of AlBGscg that might have potential to replace existing market brands possibly.

2. Materials

Tetraethyl orthosilicate (98 %, TEOS: $Si(OC_2H_5)_4$), calcium nitrate tetrahydrate [$Ca(NO_3)_2.4H_2O$, >99.0 %], aluminium nitrate nonahydrate [$Al((NO_3)_3.9H_2O$,>99.0 %), zinc nitrate hexahydrate [$Zn((NO_3)_2.6H_2O$, >99.0 %], polyethylene glycol 4000 [Sigma-Aldrich, CAS No. 25322-68-3] and ethanol (EtOH) were used. Reagent grade hydrochloric acid (HCl) was diluted to 1 N using distilled water. All reagents were obtained from M/S Sigma Aldrich, USA.

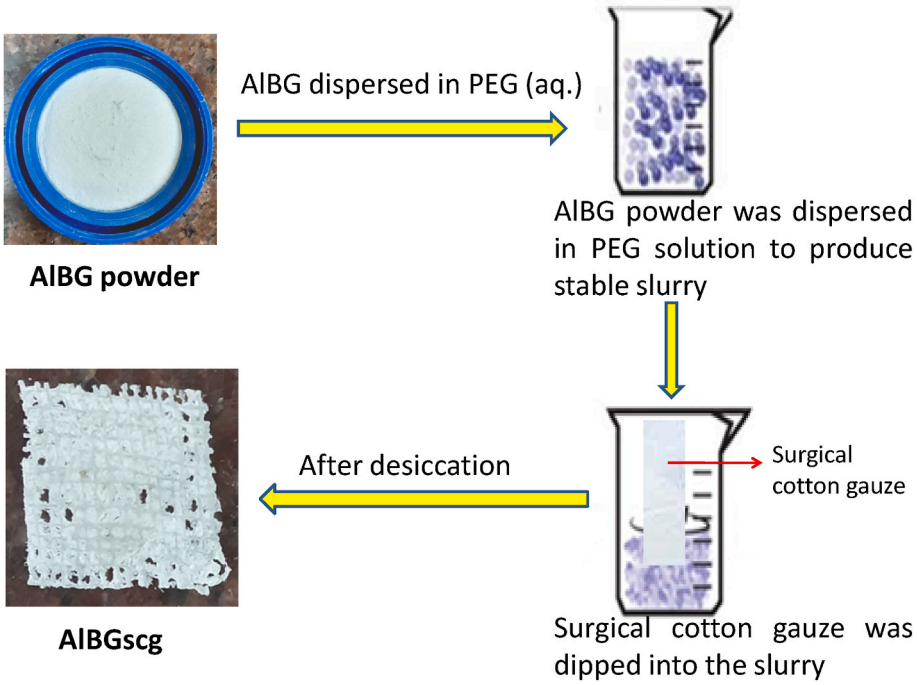


Fig. 1. The fabrication of AlBG incorporated surgical cotton gauze (AlBGscg) by slurry dipping technique.

3. Experimental

3.1. Synthesis of AlBG

The sample of AlBG powder (70 SiO_2: (30-x-y) CaO: x.Al_2O_3: y.ZnO, where x = 10–18 mol% of Al_2O_3 and y = 0–8 mol % of ZnO) was made by sol-gel method [25]. Herewith, tetraethyl orthosilicate (TEOS), calcium nitrate tetrahydrate ($Ca(NO_3)_2.4H_2O$), aluminum nitrate nonahydrate ($Al(NO_3)_3.9H_2O$) and zinc nitrate hexahydrate [$Zn(NO_3)_2.6H_2O$] were added one at a time to the 40 ml of ethanol, comprising 1 N HCl in 9:1 ratio v/v. The final sol was kept at 60 °C in BOD incubator for 3 days followed by calcination/heat treatment as per a predefined program up to 650 °C for 4h [28,29]. [Fig. 1(a)]. The as prepared glass obtained were ground manually and passed through geological sieve no.140 to obtain particle size in the range 75–106 μm. The resulting glass was milled using a planetary milling machine (Retsch, Germany) for reducing the particle size.

3.2. Fabrication of AlBG incorporated nonwoven surgical cotton gauze (AlBGscg)

The AlBGscg was fabricated using slurry dipping technique [30,31]. For the same, AlBG slurry was made by mixing it with FDA-approved polymer polyethylene glycol (PEG, MW-4000). PEG-4000 powder was added DI water to obtain 10 % w/v PEG-4000 polymer solution. To produce stable slurries, a requisite amount of AlBG powder was dispersed in 15 ml PEG-4000 solution, and the mixture was continuously stirred with a magnetic stirrer at 200 rpm to prevent sedimentation. In order to minimize the expansion of the micro-cracks onto the coating, a defined size (2 × 2 cm^2) of surgical cotton gauze was dipped into the slurry and then desiccated on glass plates at room temperature in a stability chamber [Fig. 1(b)].

3.3. Collection of blood

Healthy donors within the age range of 25–45 years underwent the blood collection procedure with utmost care, utilizing "butterfly" needles (0.9 mm) through venipuncture. The process was carried out in a sterile environment, and an appropriate anticoagulant, such as sodium citrate was used to ensure the safety and integrity of the collected blood samples.

3.4. Microstructural characterization

The AlBGscg was characterized using a variety of methods, including analytical and physiochemical methods. The AlBG and AlBGscg were characterized by X-Ray diffraction (XRD) technique[X'Pert Pro MPD diffractometer (Panalytical, Almero, Netherland] using CuK_α radiation [32]. At 2θ ranging from 10° to 80°, the AlBG powder and AlBGscg samples were examined for 2° with a step size of 0.03°. The fourier transform infrared spectroscopy (FTIR) spectra of the AlBGscg were demonstrated by means of the KBr (Sigma Aldrich, 99 %) pellet method. The instance: The FT varian 3600 spectrometer from the United States has a KBr ratio of 1:100, a resolution of 4 cm^{-1}, an average of 50 scans, and a wavelength range of 400–4000 cm^{-1} [31]. N_2 adsorption-desorption isotherms were generated at 77 K using a Nova Station A instrument to assess the textural characteristics of bioactive glass, AlBG. The surface area was determined using the Brunauer-Emmett-Teller (BET) method, while the pore size distribution was analyzed using the Barret-Joyner-Halenda method (BJH). Particle size of AlBG was determined using laser Doppler electrophoresis, employing the Zetasizer Nano ZS instrument from Malvern Instruments Ltd, England. The surface morphology of the AlBGscg was examined by using field emission scanning electron microscope (FESEM) [Carl Zeiss SUPRA 35VP, Germany]. The AlBGscg samples were coated with gold via sputtering; before imaging, the coating should have a thickness of 12 nm and operate at a voltage of 5 kV [32].

3.5. Determination of water vapour transmission rate (WVTR)

The ASTM E96 protocol was used to evaluate WVTR [33]. Briefly, round samples were cut and placed in an elastic band-sealed 1.5 cm-diameter cylindrical vial containing 10 mL of deionized water (dH_2O). After that, it was placed in a chamber with a temperature of 37 °C and a relative humidity (RH) of 75 % for 24 h, and the WVTR was estimated using formula (1) below:

$$\text{WVTR}\left(\text{g}/\text{m}^2/\text{day}\right) = (\Delta m/\Delta t) \quad (1)$$

Where, $(\Delta m/\Delta t)$ is the change of mass for 24h (gram per day) and A is the area of the transfer.

3.6. Water contact angle, surface free energy and water absorption capacity of AlBGscg

Using the sessile drop method, the KRÜSS Drop Shape Analyzer (GmbH) was used to calculate the AlBGscg's wettability. The AlBGscg was cut into square pieces (e.g., 1 cm^2) and inserted into a specific holder for the measurements (as per ASTM D7334-08) [34]. The container containing the liquid (water and diiodo methane) was raised prior to the procedure until the sample edge touched the liquid surface. During the water adsorption phase, the change in the sample mass as a function of time (t) was evident. The contact angle is calculated using the function of the initial slope known as capillary velocity [34].

AlBGscg's initial weight was recorded as W_{dry} for the purpose of determining its water absorption capacity. After being immersed in water for 15 min and kept in an incubator, AlBGscg's final weight was recorded as W_{wet}. Here, uncoated surgical cotton gauze was used as the 'control'. The *in vitro* water absorption capacity (percent) was analyzed in the following manner (Equation (2)):

$$\text{Water absorption capacity}(\%) = \left[\left(W_{wet} - W_{dry}\right)/W_{dry}\right] \times 100\% \quad (2)$$

3.7. Tensile strength of AlBGscg

AlBGscg's tensile strength was measured in accordance with ASTM D882-91 using Universal Testing machine, Instron, 5500R, USA [35]. For the test, the AlBGscg sample was cut into (2.5 × 8) cm^2 pieces. The sample was held using pneumatic grips and subjected to elongation to determine the mechanical properties, viz. tensile strength, Young's Modulus and elongation at break at a rate of 10 mm/min (equation (3) and (4)). Slope of the initial linear stretch of the typical stress-strain plot is used to calculate the modulus of the sample and provides important insight regarding its flexibility. All measurements were carried out in triplicates and are presented as mean with standard deviation.

$$\textbf{Young's Modulus (Y)} = \text{Longitudinal stress / longitudinal strain.} \quad (3)$$

$$\textbf{Dimension of Young modulus, Y} = [ML^{-1}T^{-2}] \quad (4)$$

Where, M = Mass, L = Length and T = Time.

3.8. Determination of in vitro loading of AlBG into AlBGscg

The loading of AlBG in surgical cotton gauze was measured by obtaining the mass of the gauze before and after immersion in the AlBG containing polymer solution [36]. Briefly, 1.5 g of AlBG was dispersed into 15 ml of an aqueous solution that contained an optimal concentration (10 % w/v) of an FDA-approved polymer (i.e., Polyethylene glycol, PEG, M.W. 4000) in an incubator for a predefined time (e.g., 15min) at 37 °C. Equation (5) was used to calculate the loading percentage:

$$(\text{AlBG} + \text{PEG})\ \text{loading}\ (\%) = [(W_D\text{-}W_d)/W_d] \quad (5)$$

Where, W_d and W_D are the mass of dried surgical cotton gauze before and after immersion in polymer solution containing AlBG. The AlBG and PEG were mixed into a specific w/w ratio. From here, we derived the AlBG loading % by simple mathematical calculation.

3.9. In vitro biological characterization

3.9.1. Culture of NIH3T3

The NIH3T3 cell line was grown in Dulbecco's Modified Eagles Medium (DMEM) with pen-streptomycin, 10 % (v/v) fetal bovine serum (FBS, HIMEDIA), and 1 mM sodium pyruvate. The cultured cells were kept in a T_{75} flask in an incubator at 37 °C and 5 % CO_2.

3.9.2. Sample preparation and MTT assay at 24, 48 and 72 h

The *in vitro* cytotoxicity assay was carried out as per standard protocol of ISO 10993-5: 2009 [37]. The NIH3T3 cell line was cultured up to 90 % confluence at 37 °C and 5 % CO_2 for the MTT assay. After being cut into circles with a diameter of 3-4 mm that coated with AlBG and PEG polymer, the hemostatic gauze was sterilized for 20 min under UV light. The material was then placed in the 96-well plate. In each well, a volume of 200 μl of cell suspension with a cell density of 10^4 cells per ml was kept at 37 °C and 5 % CO_2 for three different time intervals (24, 48, and 72 h). The cell culture medium was restored with 200 μl of MTT solution after the above-mentioned intervals of time and incubated for 4 h. After discarding the MTT solution, 100 μl of DMSO were added and were incubated for 15 min. Then absorbance at 595 nm was measured with a Bio-Rad ELISA microplate reader The positive "control" was cell (NIH3T3) in media [37].

3.10. Hemocompatibility assay

To create a standard curve, 2 ml of blood with sodium citrate (3.2 % w/v) was mixed with 5 ml of deionized water. After incubating at 37 °C for 60 min and centrifuging at 2500 G for 10 min, the resulting supernatant containing plasma was collected. Dilutions of 100 %, 50 %, 25 %, 10 %, and 1 % were prepared to establish the standard curve. In the experiment, 500 μl of blood was kept in contact with the AlBGscg, following the ISO 10993-4 standard protocol, and incubated at 37°C for 60 min before centrifugation at 2500 G for 10 min [38]. A control group involved incubating 500 μl of blood without the sample, under the same conditions. The supernatant from both the sample-treated and control blood was collected. To measure hemolysis, 100 μl of the supernatant were mixed with 900 μl of PBS, and 200 μl of this solution was placed in a 96-well plate to measure absorbance at 540 nm. PBS served as the negative control, and the "no treatment" group acted as a control. Hemolysis percentage was calculated using Equation (6) as follows:

$$\text{Haemolysis}\ (\%) = (\text{Sample absorbance - negative control}) / (\text{positive control - negative control}) \times 100 \quad (6)$$

The absorbance values were then used to determine hemolysis percentages by referencing them to the standard curve. The reported results are the average values with the standard error of the mean.

3.11. Antibacterial study

The *in vitro* antibacterial activity of AlBGscg and uncoated surgical cotton gauze were assessed using the disc diffusion method against the standard microbial strains, namely, the gram-positive strain *S. aureus* (ATCC 25923) and the gram-negative strain *E. coli* (ATCC 252922) [39]. The bacterial strains were briefly incubated in Luria-Bertani medium at 37 °C in a shaking incubator set at 150 rpm. AlBGscg samples, each measuring 1 cm^2, were sterilized via UV irradiation for 30 min. Bacterial suspensions were adjusted to match the OD_{600} and 0.5 McFarland standards. Inoculums were streaked onto nutrient agar plates and allowed to incubate for 15 min at 37 °C. The antibacterial efficacy of AlBGscg was determined by measuring the zone of inhibition (ZOI) after the samples were carefully placed on *S. aureus* and *E. coli* culture plates, followed by a 24h incubation at 37 °C.

3.12. In-vitro blood coagulation assay

AlBGscg was used to measure prothrombin time (PT) and activated partial thromboplastin time (aPTT) to assess the activation of blood plasma coagulation. The results were analyzed by a coagulation analyzer (BIO-MERIEUX, France). To obtain platelet poor plasma (PPP),

the heparinized blood was centrifuged at 2500 G for 10 min at 37 °C. For the PT experiment, 50 μL of PPP and 100 μL of PT reagent were mixed at 37 °C for 3 min. The $CaCl_2$ solution and AlBGscg were added as a sample or uncoated surgical cotton gauze as a control, and the PT was measured. For the aPTT experiment, 100 μL of aPTT reagent and 50 μL of PPP were incubated at 37 °C for 3 min. After that, the mixture was added to $CaCl_2$ solution and AlBGscg/control, and the aPTT was measured [40–42].

3.13. In-vitro thrombin generation

The human thrombin and antithrombin complex (TAT) indicates that thrombin has been formed and antithrombin has been neutralized over time. AlBGscg (1 cm^2) and uncoated surgical cotton gauze were incubated with 1 ml of EDTA-blood for 30 min at 37 °C. To prevent the formation of thrombin-antithrombin complexes,20ml of a solution of sodium citrate was added. An ELISA kit (ImmunoTag, Cat: ITLK01049) was utilized to measure the TAT levels in the blood [43,44].

3.14. Blood clot formation

Blood samples were obtained from a healthy human volunteer, and an anticoagulant, EDTA was introduced into the blood to prevent the clotting during collection. The collected blood was then subjected to centrifugation at 2500 G for duration of 10 min at 37 °C, which effectively separated the plasma. In the experimental group, AlBGscg was applied to the blood to induce clot formation. The control group, on the other hand, employed uncoated surgical cotton gauze. The process of clot formation was meticulously observed over time after both AlBGscg and the uncoated surgical cotton gauze came into contact with the blood, and the clotting time was recorded. For scanning electron microscope (SEM) studies, the samples were initially fixed in 3.7 % paraformaldehyde and then underwent a dehydration process. Subsequently, the samples were dried and coated with gold before SEM analysis [PHENOM Pro- X] [45].

3.15. In vitro assessment of platelet adhesion

To assess platelet adhesion, lactate dehydrogenase (LDH) assay was undertaken. Human blood samples were freshly collected from volunteers and anticoagulated with 3.2 % sodium citrate. After that, the citrated blood samples underwent centrifugation at 1500 rpm for 10 min to eliminate white blood cells and red blood cells. This process produced platelet-rich plasma (PRP), which was further centrifuged at 3000 rpm for 10 min, resulting in a platelet pellet and platelet-poor plasma as the supernatant. The platelet pellet was resuspended in PBS to achieve a concentration of 4 × 10^8 platelets/ml. AlBGscg was exposed to the

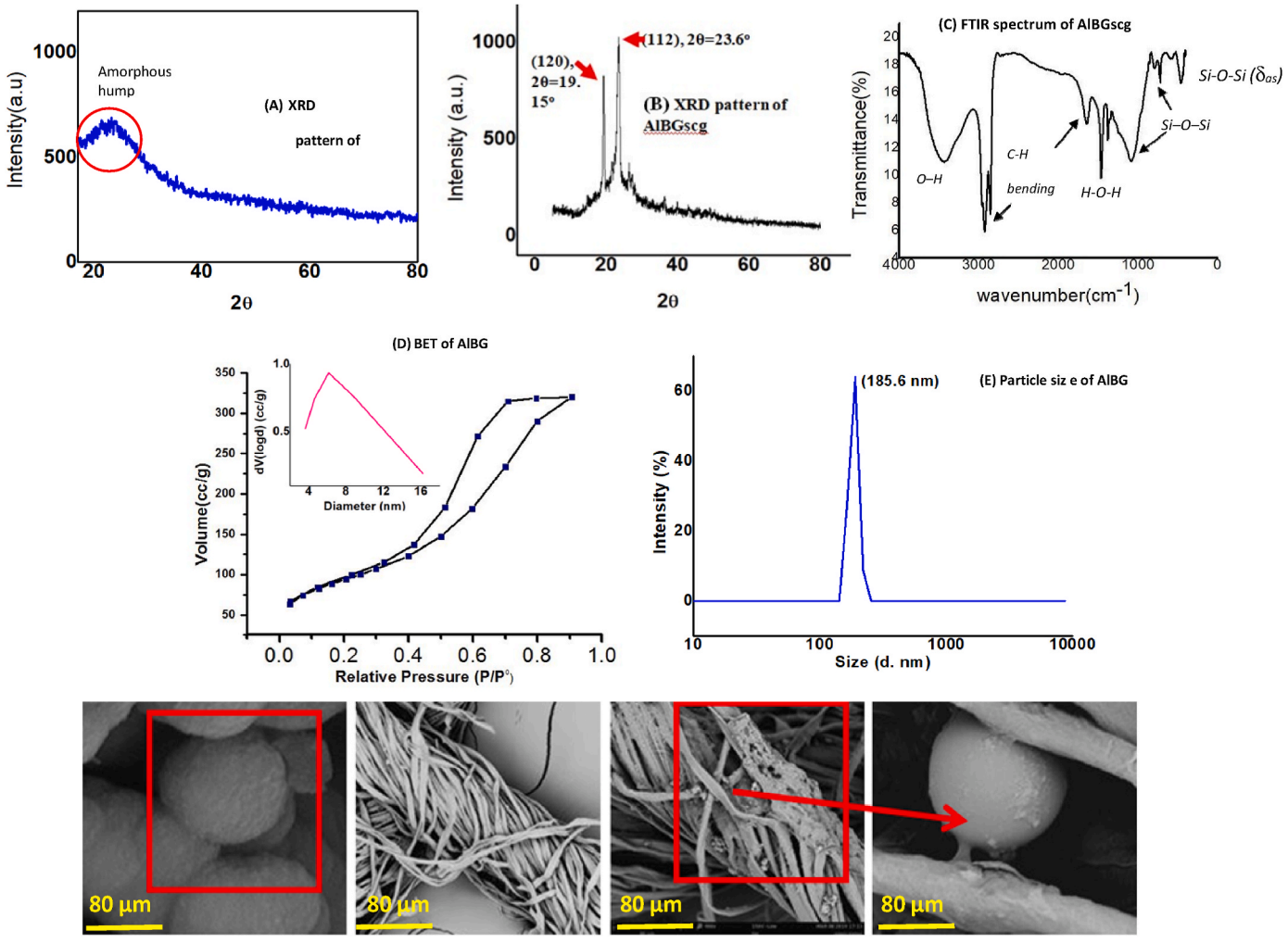


Fig. 2(A). AlBG XRD pattern, as shown by Si-O-Si linkage, at a 2θ value of 23°;
(B) The AlBGscg XRD pattern has two significant, sharp peaks at 19.15° and 23.61°, which represent the PEG-4000's crystallinity. (C) FTIR spectrum of AlBGscg. (D) Displays the N_2 adsorption-desorption isotherm and its associated pore size distribution for AlBG [inset of 2(D)]. (E) Particle size distribution measurement of AlBG. (F) FESEM image of (1) the prepared AlBG; (2) the surgical cotton gauze; (3) the AlBG with a surgical gauze dressing (AlBGscg); and (4) A discrete AlBG particle on coated strands of theAlBGscgThe scale bar represents 80 μm and 1000x magnification.

platelets and incubated at 37 °C for three different durations (15, 30, and 60 min). At the end of each time interval, the samples were removed and rinsed 10 times in PBS to eliminate non-adherent platelets. Subsequently, the samples were immersed in PBS containing 1 % Triton X-100 for 1 h at 37 °C to lyse the adherent platelets. The number of platelets adhering to the surface matrix was quantified using an LDH assay kit. A platelet calibration curve was established by performing serial dilutions of a known number of platelets and measuring the optical density (OD) at 450 nm with a BioRad microplate reader. Each measurement was conducted at least three times. Following the assessment of platelet adhesion, the interaction between platelets and AlBG was observed using scanning electron microscopy (SEM). To prepare the samples for SEM studies, they were first fixed in 3.7 % paraformaldehyde and then dehydrated through a series of ascending ethanol concentrations up to 100 % [21]. Finally, the samples were dried and coated with gold via sputter coating [21].

3.16. Whole blood clotting and determination of blood clotting index (BCI)

The blood clot indexing (BCI) protocol proposed by Shih et al. has been changed slightly for the current research purpose [43]. Anticoagulant containing whole blood (0.2 ml) was distributed to the coated and uncoated samples, 20 μL of 0.25 M $CaCl_2$ solution was added to initiate coagulation, and the samples were incubated at 37 °C with shaking at 100 rpm. The uncoated surgical cotton gauze (the "control") and the AlBGscg (1 cm^2) were placed into tubes and kept at 37 °C. After 10 min of osmotic lysis of RBCs that were not attached to the clot, a BioRad Microplate Reader was used to measure the optical density (OD) at 540 nm. The BCI was measured using formula (7) [46]:

$$BCI = 100 \times (Absorbance\ of AlBGscg\ /\ Absorbance of\ control). \quad (7)$$

3.17. In-vivo hemostatic efficacy study

In an *in vivo* study conducted in accordance with the ISO 10993-4 standard [38], Wistar rats (n = 3), having weight range of 200–250 g, aged 7–8 weeks, were subjected to surgically induced hemostasis injuries as described in Ref. [47]. The study was approved by Institutional Animal Ethics Committee (IAEC) of the West Bengal University of Animal and Fishery Sciences (WBUAFS). These injuries were treated with AlBGscg, comprising AlBG loading of 167 mg/kg bw based on our previous finding [28]. AlBG scg was sterilized for 20 min via UV radiation.

The Wistar rats were anaesthesized via intravenous injections of ketamine (40 mg/kg bw) and xylazine (5 mg/kg bw), respectively. The animals were positioned on their backs with their hind limbs extended to expose their groins for the experiment. Using a scalpel, an incision was made to expose the thigh's soft tissues, including the skin and underlying muscles. Subsequently, a 24-gauze needle was used to puncture the femoral artery to induce profuse bleeding from the artery. The experiment involved three separate runs, during which the capacity of the dressing to absorb blood and the time it took for bleeding to cease were measured and compared to a control group, which consisted uncoated surgical cotton gauze (without AlBG). The evaluation of the hemostatic potential involved the study of the following parameters:

a. Adherence strength of AlBGscg and uncoated surgical cotton gauze
b. Time required for complete hemostasis
c. Percentage of blood absorption
d. Incidence of re-bleeding, if any
e. Survival of the animals

Following the experiment, the injuries on the animals were cleaned using normal saline, and market brand medicine was applied for healing the injury. The animals were then kept under observation for a period of one week.

Table 1

Sample name	Surface area (m^2/g)	Average pore diameter (nm)	Pore volume (cc/g)
AlBG	333.744	4.617	0.45

3.18. Statistical analysis

Representative mean standard deviations from three experiments conducted in duplicate were used to present all of the data. The statistical analysis of the data yielded a 95 % confidence interval (CI) with a p value of 0.05.

4. Results

4.1. Material characterizations

The AlBG XRD pattern displays a Si-O-Si linkage at a 2θ value of 23°, a broad hump in the sample indicates material's amorphorus characteristics. In the XRD pattern of AlBG and PEG-4000 polymeric surgical cotton gauze, sharp diffraction peaks at $2\theta = 19.15^0$ and 23.61^0 for PEG-4000 signify crystallinity, corresponding to (120) and (112) planes [48] [Fig. 2 (A, B)].

FTIR results reveal significant peaks indicating local structural changes. The glass exhibits absorption peaks at 1083.33 and 792.95 cm^{-1}, representing Si–O–Si asymmetric stretching mode and symmetric Si–O–Si stretching or vibrational modes of the silica network. A peak at 453 cm^{-1} is attributed to Si-O-Si bending mode. The appearance of a minor peak at approximately 589 cm^{-1} was assigned to Si-O-Al [28]. The peak observed at ~1373 cm^{-1} is corresponding to the O-H bending vibration of the chemically adsorbed hydroxyl group. Absorbed water's O–H bonds stretch at 3453 cm^{-1}, while structural hydroxyl group's H-O-H bonds stretch at 1648 cm^{-1}.The presence of a distinct peak at approximately 2939 cm^{-1} signifies the stretching vibration associated with alkyl (-CH_2) groups. Simultaneously, a broad peak observed at 1084 cm^{-1} suggests the stretching of the ether (C-O-C) group [Fig. 2(C)]. Notably, this particular stretching vibration band overlaps with the Si-O-Si asymmetric stretching mode [49,50], as well. Fig. 2(D) displays the N_2 adsorption-desorption isotherm and its associated pore size distribution for AlBG [inset of 2(D)]. Table 1 provides key textural characteristics of AlBG determined through N_2 adsorption porosimetry. As shown in Fig. 2(D), AlBG exhibited a type IV isotherm with a type H1 hysteresis loop. The specific surface area of AlBG measured 333.744 m^2/g, and the average pore size was 4.617 nm. The particle size of AlBG is obtained in the range 140 nm–253 nm having D_{50} of 185.6 nm [Fig. 2 (E)].

Key textural characteristics of AlBG determined through N_2 adsorption porosimetry. The AlBG's adhesion to the gauze's coated strands and the microstructure of the AlBG-incorporated surgical gauze dressing (AlBGscg) are depicted in a FESEM image [Fig. 2(F)].

4.2. Water vapour transmission rate (WVTR)

The impact of AlBGscg at the application site is significantly influenced by the water vapour transmission rate (WVTR). When the dressing allows for faster transmission, it can lead to tissue dehydration, potentially resulting in scarring at the site. Conversely, if the dressing hinders transmission, it may slow down the healing process and increase the risk of bacterial colonization [51]. In the case of AlBGscg and control (surgical cotton gauze), their respective WVTR values were measured at 1944 ± 30 g/m^2/day and 2055 ± 31 g/m^2/day, as illustrated in Fig. 3 (a–c). It was observed that an ideal moist microenvironment for epidermal and fibroblast proliferation is maintained when a dressing has a WVTR of approximately 2000 g/m^2/day [51]. Our findings indicate that the WVTR values for AlBGscg and the uncoated surgical cotton gauze closely align with this optimal range, making them suitable

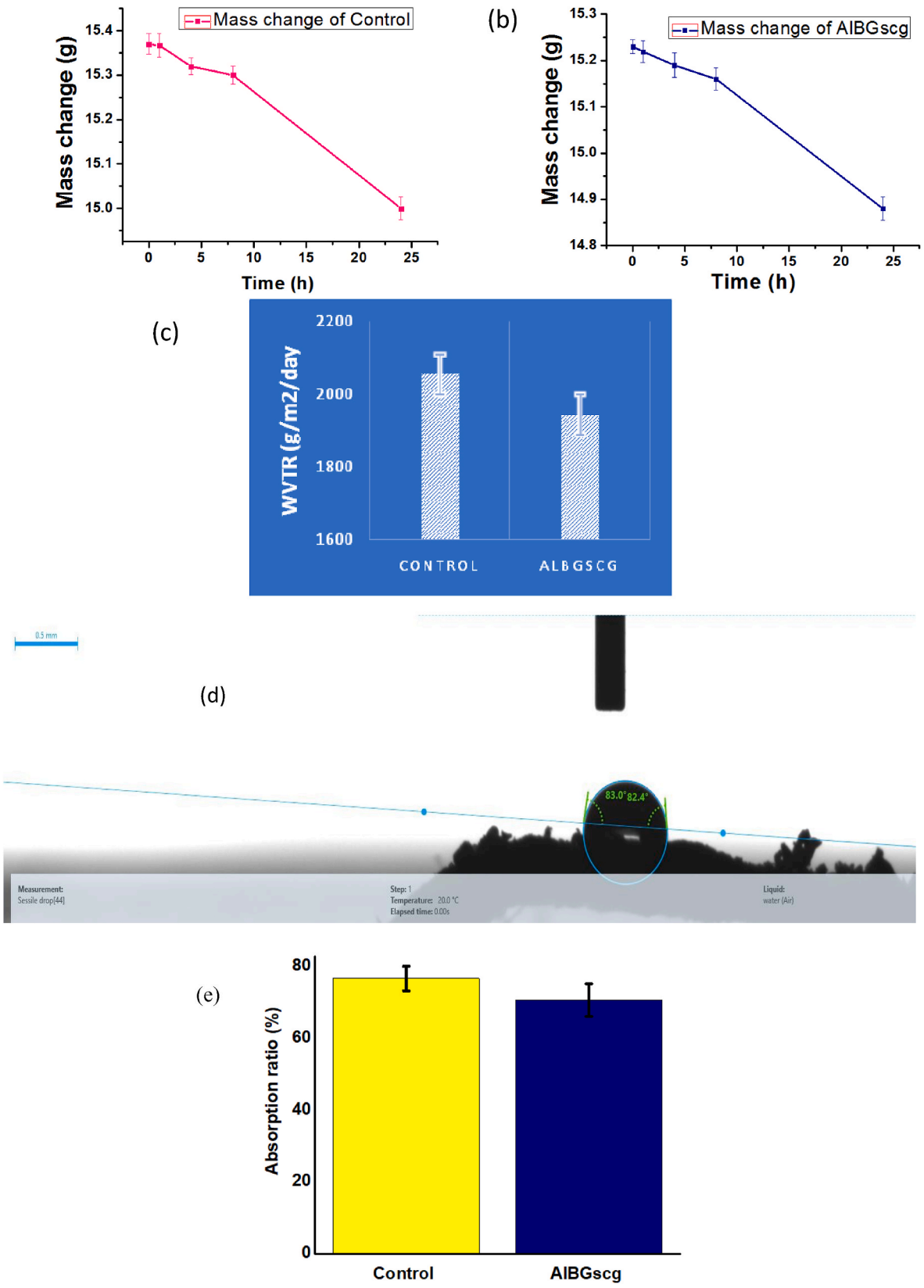


Fig. 3. Physical properties of AlBGscg, (a) mass change of surgical cotton gauze, (b) mass change of AlBGscg, (c) water vapour transmission rate (WVTR) (d) water contact angle and (e) water absorption capacity.

Table 2
Assessment of ultimate tensile strength, elongation at break (%) and modulus of samples.

Sample name	Ultimate Tensile strength (MPa)	Elongation at break (%)	Modulus (MPa)
1. Uncoated surgical cotton gauze	2.00 ± 0.13	7.23 ± 1.30	18.12 ± 1.12
2. AlBG incorporated surgical cotton gauze (AlBGscg)	2.14 ± 0.93	9.15 ± 1.51	19.00 ± 1.24

choices for hemostatic applications.

4.3. Water contact angle, surface energy and water absorption capacity

The static water contact angle of the AlBGscg was measured (82.7°) to confirm its hydrophilicity [Fig. 3(d)]. The surface energy was calculated using the water contact angle. The surface free energy of AlBGscg was 73.10 ± 1.76 mN/m. The water absorption capacity of AlBGscg was assessed and compared to uncoated surgical cotton gauze. The findings indicated that AlBGscg exhibited a water absorption rate of 70.67 (±3.4)%, whereas uncoated surgical cotton gauze demonstrated a slightly higher absorption rate of 76.60(±4.5)% [Fig. 3(e)].

4.4. Mechanical properties

Ultimate tensile strength, elongation at break (%) and modulus did not differ significantly between the AlBGscg and uncoated surgical cotton gauze. The obtained results from the tensile

tests are enumerated in Table 2 and Fig. 4 showed the stress-strain curve of (a) uncoated surgical cotton gauze and (b) AlBG incorporated surgical cotton gauze (AlBGscg).

4.5. MTT assay

The cytotoxicity of the AlBGscg was determined by directly contacting the NIH3T3 cells for 24, 48, and 72 h. This allowed for the evaluation of the cells' viability. The MTT assay indicated that the cell viability of NIH3T3 cells in the presence of AlBGscg was enhanced slightly with the culture time, suggesting that the AlBGscg is non-cytotoxic to the above cells [Fig. 5].

4.6. Hemocompatibility assay

In order to evaluate potential of AlBGscg to cause the lysis of red blood cells (RBCs), we conducted hemolysis test. This test is designed to assess the extent to which the sample may lead to the undesirable lysis, or rupture of RBCs, taken at a wavelength of 540 nm. It was observed that 4.2(±1.4)% RBCs [Fig. 6] were lysed in a period of 15 min, which is a recommended range as per standard protocol.

4.7. Antibacterial study

The antibacterial properties of AlBG incorporated surgical gauze (AlBGscg) were evaluated against

S.aureus and *E. coli*. Fig. 7 demonstrates that a zone of inhibition (ZOI) of 17 ± 0.34 mm for *S. aureus* [Fig. 7(a)] and 16 ± 0.56 mm for *E. coli* [Fig. 7(b)] This is due to the fact that Zn-containing AlBG can significantly release Zn^{2+} ions, which are likely to be capable of disruption by attacking the negatively charged bacterial cell wall [52].

4.8. In vitro loading of AlBG in the surgical gauze

The AlBG loading percentage in the surgical cotton gauze was determined as following: the loading can be a critical factor in understanding the material's performance in potential application. AlBG +

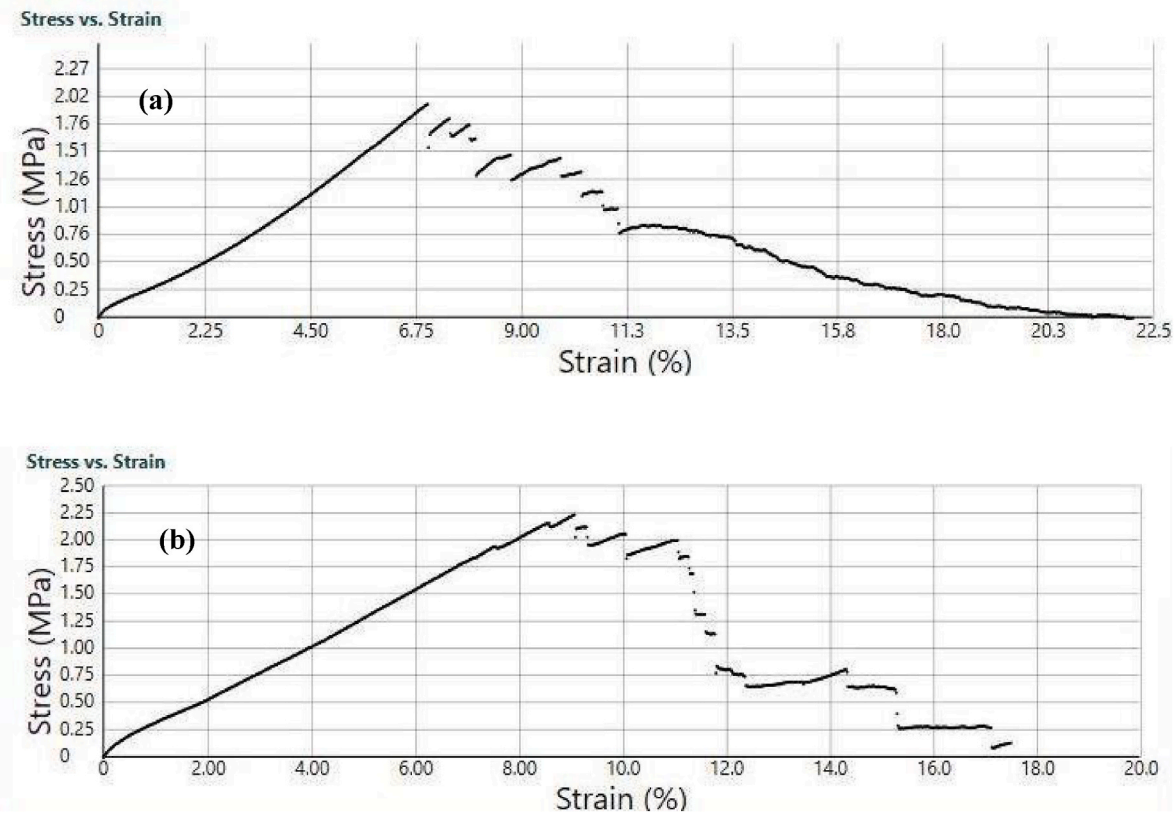


Fig. 4. Stress-strain curve of (a) Uncoated surgical cotton gauze and (b) AlBG incorporated surgical cotton gauze (AlBGscg).

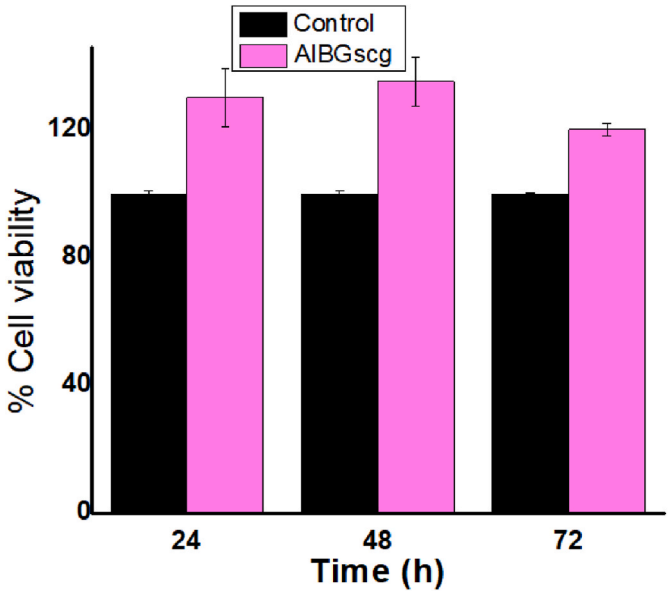


Fig. 5. *In vitro* cytotoxicity assay of AlBG incorporated surgical gauze (AlBGscg) showing excellent cell viability (direct method), using NIH3T3 skin fibroblast cell line [ISO 10993–5:2009].

PEG loading (%) = $[(W_D - W_d)/W_d] \times 100$.

Here, W_d represents the weight of the dry surgical cotton gauze before it was immersed in the AlBG and polymer solution, and this weight was measured 34 mg. W_D, on the other hand, stands for the weight of the same sample after it has been immersed in the above-mentioned solution, (AlBG and polymer solution) and this weight was found to be 86.6 mg.

By putting these values into the formula, the calculation exhibits an AlBG + PEG loading percentage of approximately 154.70 %. This means that around 154.70 % of the AlBG + PEG have been successfully integrated into the surgical cotton gauze. From simple mathematical calculation, AlBG loading % was derived and was found that about 11 % of AlBG was loaded into the AlBGscg. Such loading percentage indicates the presence of AlBG within the surgical cotton gauze, which may be desirable for hemostatic applications where the properties of AlBG are intended to be harnessed. It's important data for evaluating the efficacy and performance of the gauze in its intended use, particularly in relation to hemostasis, as mentioned in the previous discussion.

4.9. In-vitro blood coagulation assays (PT and aPTT)

In Fig. 8, a comparison is presented between the results of Prothrombin Time (PT) and Activated Partial Thromboplastin Time (aPTT) tests conducted on AlBGscg in plasma and an uncoated surgical cotton gauze, which serves as the control. In Fig. 8(a), the plasma, separated from the blood and in its liquid state. Following the agglutination

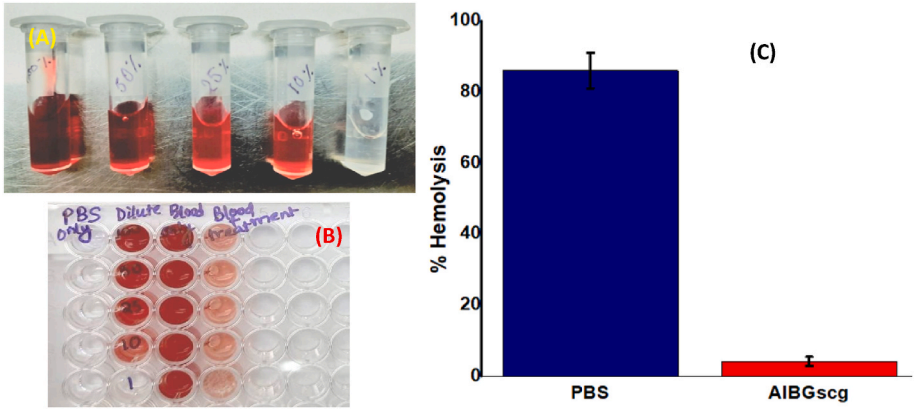


Fig. 6. (A) 100 %,50 %,25 %,10 % and 1 % dilutions were made to create a line of best fit. (B) Performance of the Hemolysis Test.(C) Graphical representation of the hemolysis assay, treated with AlBGscg and PBS (as control).

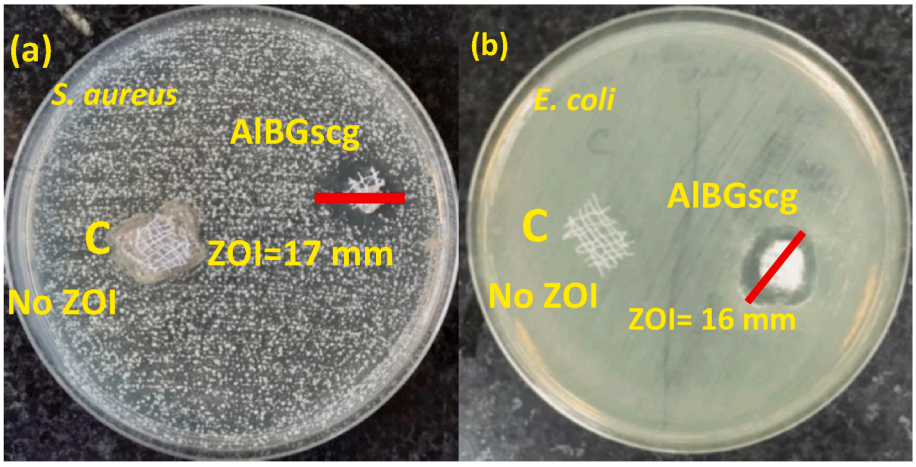


Fig. 7. Antibacterial activity of AlBG incorporated surgical cotton gauze (AlBGscg) (showing ZOI) compared with control, uncoated surgical cotton gauze (no ZOI) after 24h incubation on agar plate at 37 °C against (a) *S. aureus* and (b) *E. coli.*

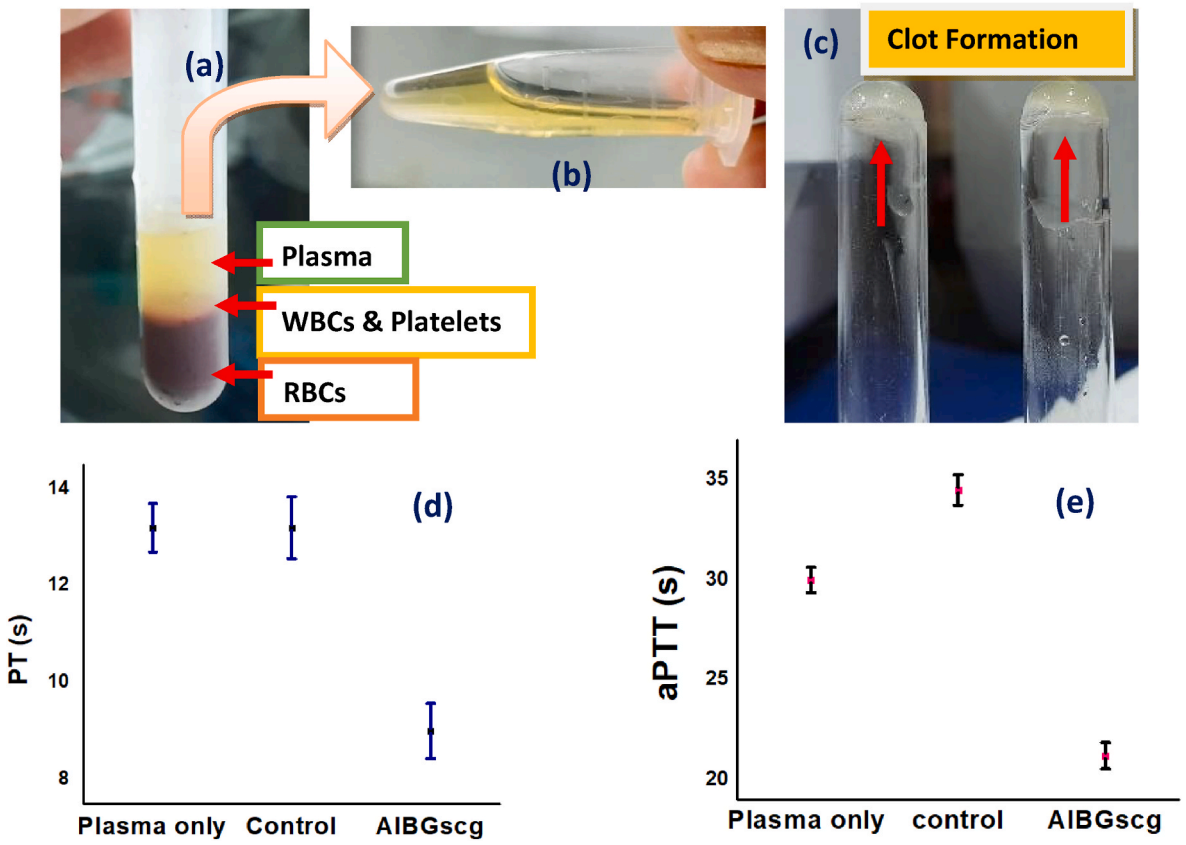


Fig. 8. (a) Plasma was separated from whole blood; (b) Plasma was collected in different vial; (c) Clot formation after agglutination reaction, in the presence of AlBGscg; (d) Prothrombin time (PT) and (e) activated partial thromboplastin time (aPTT) of AlBGscg.

reaction, the plasma solidified, as illustrated in Fig. 8(c).

The clotting times in plasma for PT and aPTT were measured at 9 ± 1.5 s and 21.2 ± 1.5 s, respectively, as shown in Fig. 8(d–e). Notably, AlBGscg exhibited significantly shorter clotting times, with PT and aPTT times found to be 31.81 ± 0.12 % and 33.3 ± 0.23 % reduction than those of the control (with PT at 13.2 ± 1.5 s and aPTT at 30 ± 1.5 s, respectively). These findings demonstrate that AlBGscg accelerates the clotting process compared to the control, making it a promising option for promoting hemostasis in a medical context.

4.10. *In-vitro thrombin generation*

In order to determine the amount of thrombin that was produced over time, TAT was measured in whole blood that was incubated with AlBGscg. The level of TAT in blood contacted with AlBGscg was significantly higher, at 62.58 pg/ml ($p < 0.05$), compared to the control 6.00 pg/ml (uncoated surgical cotton gauze) [Fig. 9].

4.11. *Determination of blood clot formation*

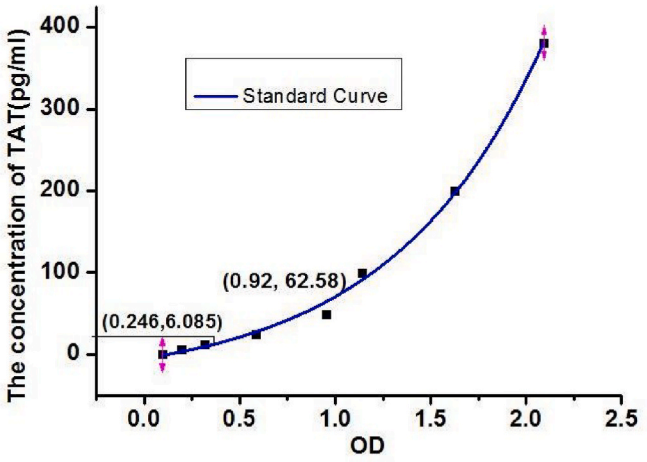
SEM analysis revealed that uncoated both surgical cotton gauze (control) and AlBGscg, are absorbed plasma proteins and blood cells [Fig. 10]. Despite the fact that SEM images are able to quantify the adhered platelets, they are still useful for observing the dressing surface following platelet aggregation and adhesion. Platelet adhesion was significantly lower in uncoated surgical cotton gauze [Fig. 10(a)], and adhesion formed clusters (marked with a red arrow). In addition, the AlBGscg sample demonstrated significantly better platelet attachment, albeit less uniformly distributed (some areas are indicated by a yellow arrow mark) [Fig. 10(b-c)]. The blood clot formation time was noted and found 590(±4) s and 410(±5) s for control and AlBGscg, respectively [Fig. 10(d)].

4.12. *In vitro assessment of platelet adhesion*

To investigate the impact of AlBG on promoting platelet adhesion and aggregation in a laboratory setting, AlBG with surgical cotton gauze (AlBGscg) and uncoated surgical cotton gauze (used as a control) were combined with a platelet suspension for three different time periods (15, 30, and 60 min). The quantitative assessment of platelet adhesion was carried out using an LDH assay kit. Fig. 11 illustrates both the qualitative and quantitative outcomes of platelet adhesion on AlBGscg. The results indicate that AlBG has a notable capacity to significantly enhance the adhesion of platelets over varying time intervals. No significant differences in the number of adherent platelets on the surfaces were observed after a 15 min incubation period. The most significant changes in platelet numbers occurred during 30 and 60 min [Fig. 11(A)]. The images revealed that the AlBG surface displayed a greater coverage of platelets, accompanied by the presence of fibrin with a silky appearance, as well as numerous pseudopodia of platelets on the AlBG surface, suggesting enhanced platelet activation and aggregation.

4.13. *Whole blood clotting and determination of blood clotting index (BCI)*

The AlBGscg and the uncoated surgical cotton gauze, used as the control, were exposed to whole blood to assess whether AlBGscg could accelerate blood clot formation. The presence of hemolyzed, untrapped red blood cells not adhering to the dressing surface is directly associated with slower clotting, resulting in higher absorbance. The outcomes revealed that AlBGscg exhibited a lower absorbance ($p < 0.05$), signifying a shorter clotting time compared to the control. The Blood Clotting



Sample	Concentration of TAT (pg/ml)
1. Uncoated surgical cotton gauze (control)	6.00
2. AlBGscg	62.58

Fig. 9. Thrombin generation over time as measured by the levels of thrombin-antithrombin complex $p < 0.05$ by AlBGscg compared to control, analyzed by one-way ANOVA with post hoc Scheffe test, n = 4.

Index (BCI), determined using the provided equation, was approximately 47(±2.3)%. The notably low BCI value suggests that AlBGscg promotes quick clotting [Fig. 12].

4.14. *In-vivo hemostatic activity study*

The previous discussion centered on the assessment of the composition's biocompatibility and histocompatibility, which was documented in Ref. [28]. In an experiment conducted following the ISO 10993-4 standard, Wistar rats (n = 3) were subjected to surgically induced hemostasis injuries. AlBGscg demonstrated fairly good clot retention when the dressing was removed for checking incidence of re-bleeding in the animals at the site of injury, indicating the likelihood of clot being stable within the dressing. Other parameters, included in the study like incidence of re-bleeding and survival of animals, are summarized in Table 3. Fig. 13 visually illustrates the impact of AlBGscg on hemostasis, bleeding time, and blood absorption capacity (as presented in Table 3). In the control group, the average time for hemostasis was approximately 180 ± 5 s, while in the case of AlBGscg, it was notably shorter (less than 50 %), at around 79 ± 5 s. This rapid reduction in the time for hemostasis indicates that AlBGscg is highly effective in initiating the coagulation cascade, highlighting its significant hemostatic properties.

5. Discussion

AlBG was synthesized in sol gel method and incorporated into surgical cotton gauze to form a hemostatic dressing AlBGscg, and further characterized using XRD, FTIR, BET, particle size and FESEM, among other techniques. Characteristic peaks corresponding to the amorphous phase exhibited the presence of AlBG. [Fig. 2A]. Notwithstanding, the sharp peaks were detected due to the presence of PEG- 4000 in AlBGscg [Fig. 2(A-B)]. In the FTIR study, the glass exhibits absorption peaks at 1083.33 and 792.95 cm^{-1}, representing Si–O–Si asymmetric stretching mode and symmetric Si–O–Si stretching modes of the silica network. A peak at 453 cm^{-1} is attributed to Si-O-Si bending mode. The appearance of a minor peak at approximately 589 cm^{-1} was assigned to Si-O-Al bonds [28]. Absorbed water's O–H bonds stretch at 1373 and 3453 cm^{-1}, while structural hydroxyl group's H-O-H bonds stretch at 1648 cm^{-1}. The presence of a distinct peak at approximately 2939 cm^{-1} signifies the stretching vibration associated with alkyl ($-CH_2$) groups. Simultaneously, a broad peak observed at 1084 cm^{-1} suggests the stretching of the ether (C-O-C) group [Fig. 2(C)]. Notably, this particular stretching vibration band overlaps with the Si-O-Si asymmetric stretching mode [49,50], as well. In the BET analysis, AlBG displayed type IV isotherms in conjunction with H1 hysteresis loops [Fig. 2(D)]. The inset in Fig. 2 (D) presented a pore size distribution curve derived from the adsorption using the BJH model. AlBG exhibited a notably higher surface area (333.744 m^2/g) and pore volume (0.450 cc/g). This property is particularly valuable as it enables the material to capture and retain a significant volume of water within its pores, primarily due to electrostatic interactions with Ca^{2+} ions residing in these pores. These interactions result in the hyperconcentration of coagulation factors and cellular components within the plasma, consequently expediting the coagulation cascade and the subsequent formation of a fibrin clot. In essence, the porous structure of AlBG, with its inherent properties, plays a pivotal role in enhancing the blood coagulation process. Smaller particle sizes provide a larger surface area per unit mass. This increased surface area allows for more efficient interaction with blood components, especially platelets and coagulation factors, can trigger platelet activation more efficiently, leading to a faster and more robust platelet plug formation at the site of the injury, which is a crucial step in hemostasis which is the particle size of AlBG is 185.6 nm [Fig. 2(E)]. Further correlated with quantitative and qualitative outcomes of the platelet adhesion experiment [Fig. 11]. Morphological analysis with FESEM demonstrated that the AlBG was successfully incorporated into the surgical cotton gauze [Fig. 2F]. Additionally, the surface free energy, water absorption capacity, and water contact angle of the AlBGscg were measured to assess its hydrophilicity [Fig. 3]. In our case, the water contact angle is $< 90^o$, hence is hydrophilic in nature. Surface Free Energy (SFE) comprises polar and dispersive components, with the polar component significantly influencing cellular behavior. Cell-material interactions are predominantly driven by polar forces. Surfaces with high polar SFE components exhibit small contact angles with polar liquids like water, leading to increased wettability and improved cell attachment. The current study's results indicate that the surface of AlBGscg possesses notable wettability (water contact angle 82^0) and a substantial polar SFE (73.10 ± 1.76 mN/m). This may result in the favorable adhesion of platelets to AlBGscg. In order to assess how the modification process impacted the mechanical properties of the surgical cotton gauze, tensile strength and elongation at break were conducted. The initial, uncoated surgical cotton gauze exhibited a tensile elongation at break of 7.23 ± 1.30 % and a tensile strength of 2.00 ± 0.13 MPa. Subsequent to the incorporation of AlBG into the surgical cotton gauze (AlBGscg), the tensile elongation at break increased to 9.15 ± 1.51 %, and the tensile strength was enhanced to 2.14 ± 0.93 MPa. These findings indicate a shift in both tensile strength and tensile elongation at break after the modification process. Importantly, these changes in mechanical properties demonstrate that the modification process did not have an adverse impact on the surgical cotton gauze's ability to withstand tensile forces and elongation, suggesting that its mechanical integrity remained unaffected [Fig. 4]

Hemostasis is a complex physiological process that involves the interplay of blood coagulation, platelet plug formation, and vasoconstriction to effectively prevent excessive blood loss [53]. In the context of this study, our focus was on the hemostatic dressing created by incorporating AlBG into surgical cotton gauze. Before assessing its hemostatic capabilities, we conducted a cytocompatibility assay of AlBGscg using the NIH3T3 cell line, which revealed excellent cellular

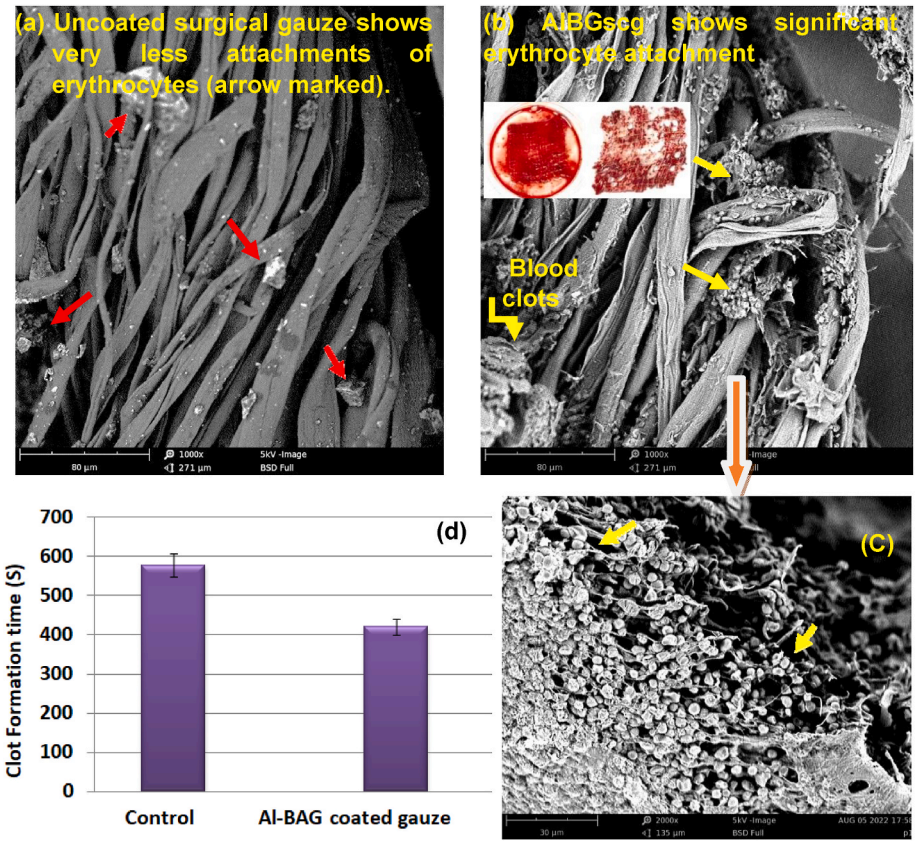


Fig. 10. SEM micrographs exhibit more red blood cells (RBCs) and platelets adhered onto the AlBGscg (b, yellow arrow marked) compared to control (a, red arrow marked); scale bar represents 80 μm and 1000x magnification [Inset original image]. Fig. (c) represent the higher magnification (2000× and scale bar represents 30 μm) (d) represents the clot formation time, contact with whole blood in the presence of AlBGscg as well as control (n = 5). (For interpretation of the references to colour in this figure legend, the reader is referred to the Web version of this article.)

response as depicted in Fig. 5. Similarly, AlBGscg also exhibited moderate hemocompatibility, exhibiting 4.2(±1.4)% hemolysis, corresponding to the rupture of erythrocytes (Fig. 6). This in turn also reveals that AlBGscg is unlikely to interfere significantly with the metabolic activity of these cells. Additionally, the AlBGscg has significant ZOI value of 17 ± 0.34 and 16 ± 0.56 mm, respectively against *S. aureus* and *E. coli* [Fig. 7]. The antibacterial potential is necessary for the hemostatic agents for addressing the secondary bacterial infections at the wound bed [39,54]. We have also carried out a number of experiments using blood to determine the *in vitro* coagulation activity. PT and aPTT were performed to explore the coagulation potential of AlBGscg via both the intrinsic and extrinsic pathways [39,40]. As shown in Fig. 8(d–e), in contact with AlBGscg, the time required for PT and aPTT significantly decreased, indicating that it could have activated both the intrinsic and extrinsic pathways of the coagulation cascade. When a negatively charged substance comes in is contact to body fluids like blood or plasma, triggering the coagulation factors, rapid ion exchange and protonation (H^+ or $^{H}3^{O+)}$ occurs on the surface. These protonated groups attracted the negatively charged residues on

the membranes of red blood cells, resulting in increased platelet aggregation and strong hemagglutination [55–60]. AlBGscg also increased the quantity of thrombin produced and reduced the delay in thrombin generation [Fig. 9]. The study involved the measurement of thrombin-antithrombin complex (TAT) formation in whole blood samples that had been exposed to AlBGscg and uncoated surgical cotton gauze. The objective was to understand how the presence of AlBG influenced the generation of thrombin, a pivotal factor in blood coagulation. Elevated levels of thrombin trigger the formation of the TAT complex. When treated with AlBGscg, TAT levels were substantially higher, measuring at 62.58 pg/ml. In contrast to the control group, which used uncoated surgical cotton gauze, produced only 6.00 pg/ml of TAT, signifying a considerably lower response compared to AlBGscg [Fig. 9]. This discrepancy in TAT levels demonstrated that AlBGscg had a pronounced effect on inducing thrombin generation compared to the surgical cotton gauze control. It was hypothesized that the presence of specific ions such as Al^{3+}, Ca^{2+} and Zn^{2+} within the AlBG of AlBGscg played a role in initiating the blood clotting process, contributing to an increase in thrombin production. Consequently, the study suggested that the porous structure of AlBG was effective in managing hemostasis by entrapping red blood cells (RBCs), and the presence of AlBG facilitated and accelerated the clotting process [43]. The study further confirmed its findings by employing scanning electron microscopy (SEM) to investigate the formation of a thrombus and the time required for clot formation, as illustrated in Fig. 10. The results demonstrated that AlBGscg significantly reduced the time needed for clot formation by approximately 29.31 ± 0.12 % compared to the control, as shown in Fig. 10(d). This remarkable capability was attributed to AlBGscg's ability to convert prothrombin into thrombin, thereby accelerating clot formation, as depicted in Fig. 10(c). Moreover, AlBGscg exhibited an impressive capacity to adhere to red blood cells (RBCs) within the clot, as seen through the entrapment of hemoglobin by fibrin. As the clot formed, the levels of free hemoglobin decreased, while the hemoglobin entrapped by fibrin increased [61]. Furthermore, the platelets on the surface of AlBGscg display platelet activation in dendritic and early spread states, signifying an activated state. This positive platelet response is likely linked to the wettability of AlBGscg [Fig. 11]. A 47 % reduction in BCI corresponded to a faster clot formation, while a decrease in BCI was associated with an increase in the rate of clotting. These findings were further supported by absorbance measurements (OD values). A lower absorbance (OD value) for AlBGscg indicated a

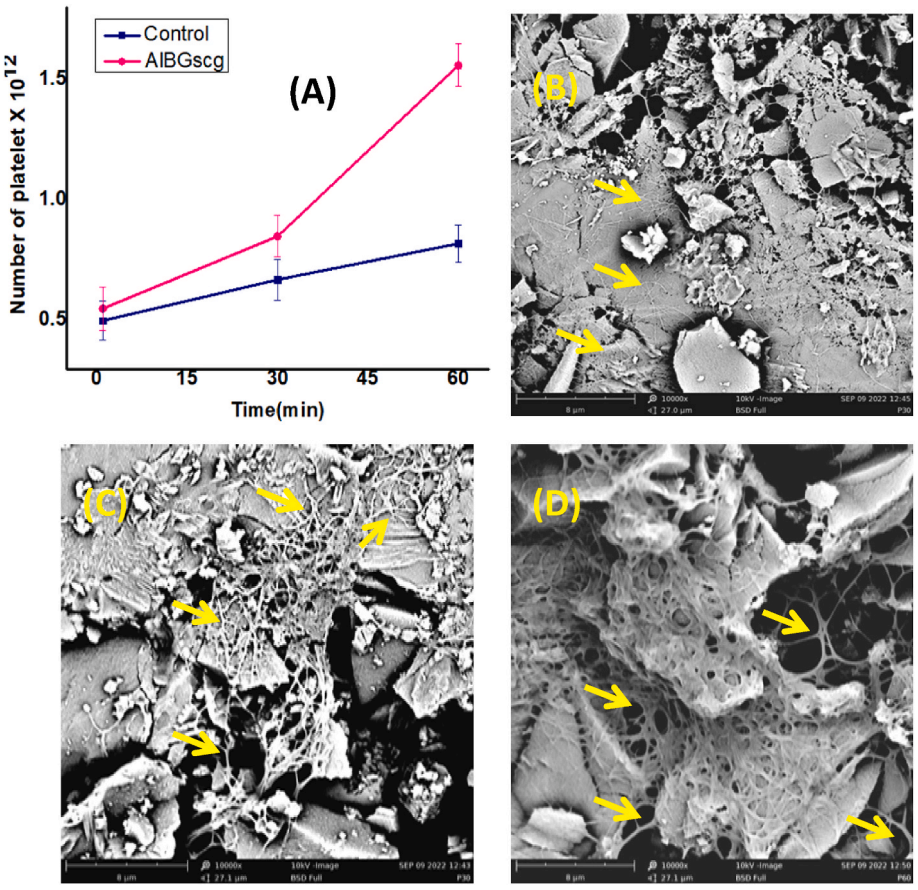


Fig. 11. (A) Quantification of platelet adhesion on the AlBG surface. (Represented a significant difference, $p > 0.05$).
(B), (C) and (D) SEM images illustrating platelet adhesion on the AlBG surface at 15, 30, and 60 min (magnification 10000× and scale bar 8 μm).The arrows indicate the dendrites connecting the platelets.

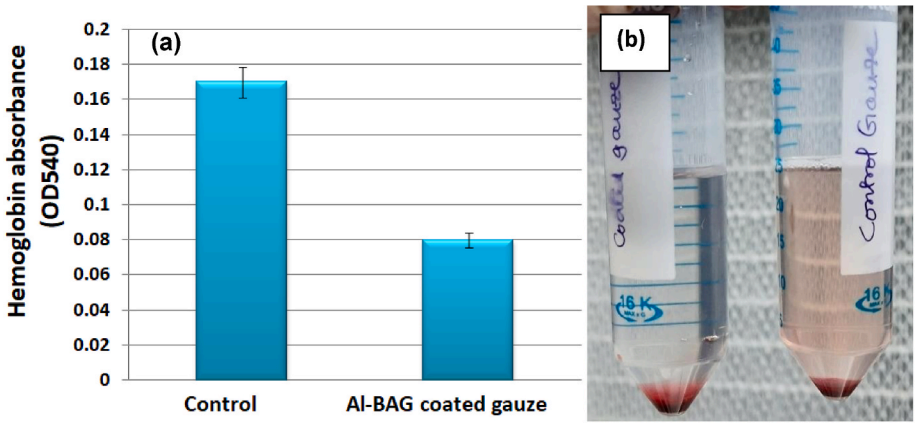


Fig. 12. (a) Effect of the AlBGscg on blood clotting rates, as calculated by absorbance of haemoglobin from lysed untrapped RBCs. $p < 0.05$ with respect to the uncoated surgical gauze, estimated by one-way ANOVA with post hoc Scheffe test, n = 4. (b) Photograph showing almost negligible amount of untrapped RBCs in case of AlBGscg compared to the control.

faster clotting rate, while a higher absorbance (OD value) for the control (uncoated surgical cotton gauze) indicated a slower clotting rate, as demonstrated in Fig. 12(a) and visually examined in Fig. 12(b). In summary, the study employed SEM, absorbance measurements, and visual observations to reinforce the finding that AlBGscg greatly accelerates the clot formation process, demonstrating its considerable potential as a hemostatic dressing material for applications where rapid and effective hemostasis is essential [41]. Fig. 13(a–e) displayed visual representations of the hemostatis process in a rat femoral injury, while Table 3 provided data on the time required for complete hemostasis. *In vivo* experiments clearly demonstrated the effectiveness of AlBGscg in comparison to surgical cotton gauze. The ability to absorb blood, particularly for aggregating blood cells such as platelets at the injury site, is considered crucial for a hemostatic agent. Interestingly, AlBGscg absorbed less blood compared to surgical cotton gauze because it facilitated quicker blood clotting. The key parameters for evaluation were the time needed to achieve hemostasis and the amount of blood loss during treatment; AlBGscg significantly outperformed surgical

Table 3
The parameters related to the *in vivo* hemostatic activity study.

Parameters	Uncoated surgical cotton gauze (control)	AlBGscg
Number of animals	3	3
Blood absorption capacity (%)	110 ± 3	90 ± 5
Total blood volume (in ml)	13	13.65
Blood loss (in ml)	2.9	1
% Blood loss	22.31	7.33
Time for hemostasis (s)	180 ± 5	79 ± 5
Adherent strength of test agent	Low	High
Incidence of re-bleeding	Yes	No
Survival of animal	Yes	Yes

cotton gauze. While surgical cotton gauze absorbed a notable amount of blood, it failed to induce clot formation at the injury site. Conversely, AlBGscg effectively adhered to erythrocytes, platelets, and components of the coagulation cascade on its surface, and the presence of calcium ions played a role in activating the coagulation factors, thus aiding in fast clot formation. The notable observation was that AlBGscg achieved significantly faster hemostasis compared to the control, underscoring its potential as an effective hemostatic dressing material.

Investigations into hemostatic materials, specifically those derived from bioactive glass, are receiving international attention. Pourshahrestani et al. successfully developed Ga-MBG and assessed its hemostatic potential, antihemorrhagic effects, biocompatibility, and antibacterial properties. Ga-MBG was found to accelerate the intrinsic pathway of the coagulation cascade, responsible for thrombus formation and platelet adhesion [5]. In another study, Nagrath et al. conducted research using a porcine liver injury model with severe hemorrhage. They synthesized Ta-MBG and demonstrated its superior hemostatic efficacy compared to Arista™, a commercial hemostatic agent. Ta-MBG not only absorbed the fluid component of blood but also provided a matrix for concentrating clotting factors and promoting blood clot formation. Additionally, Ta-MBG offered negatively charged surfaces that initiated coagulation [62]. A different group, led by Zheng et al. employed the layer-by-layer (LBL) method to coat bovine serum albumin (BSA) and chitosan (CS) on the surface of synthesized macroporous and mesoporous bioactive glass (MBG). They created a bioactive glass-based membrane-like structure called MBG@BSA/CS. This substance effectively promoted hemostasis by rapidly aggregating coagulation factors, erythrocytes, and activating platelets. It facilitated the formation of a fibrin network, demonstrating a significant hemostatic effect for both internal irregular and deep bleeding in a liver injury model and surface irregular bleeding in a tail-amputation model in

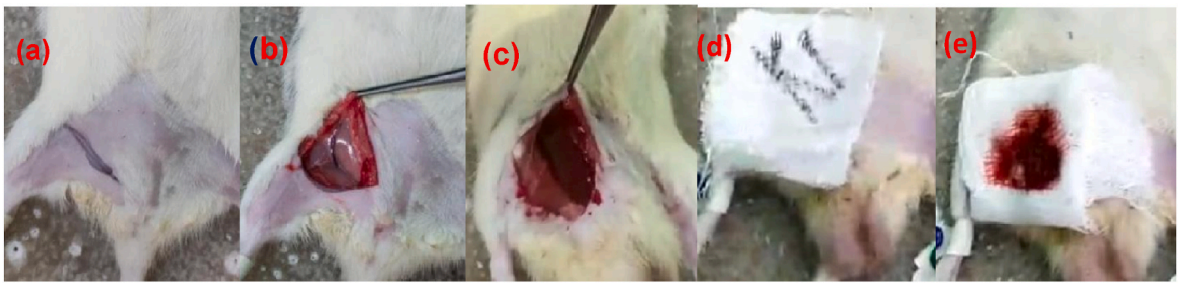


Fig. 13. Hemostasis following femoral artery injury in rats. (a) exposing the femoral artery by opening the skin above; (b) Exposed femoral artery; (c) Profusely bleeding was immediately started after the injury was created; (d) The injury site was treated with AlBGscg; (e) Bleeding stopped in a faster rate compared to the control ($p < 0.05$).

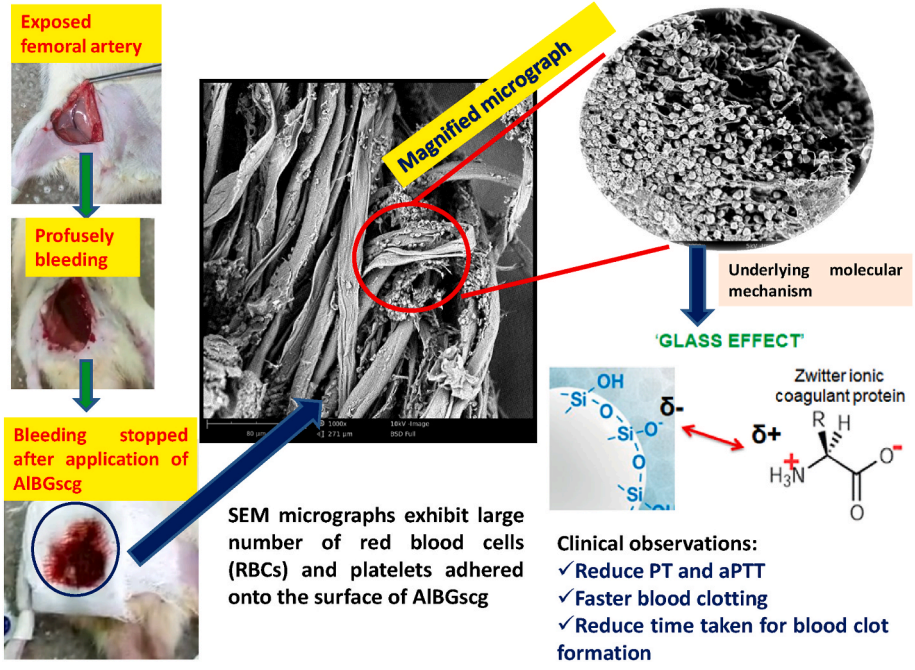


Fig. 14. The possible mechanism of hemostatic action by AlBGscg.

Sprague-Dawley rats [63,64]. These studies reflect the ongoing research efforts to develop innovative hemostatic materials based on bioactive glass. The findings indicate the potential for these materials to offer enhanced hemostatic capabilities and improved outcomes in managing bleeding in various clinical scenarios.

The active ingredient in the present study, AlBG, when incorporated into the surgical cotton gauze (AlBGscg), exhibited significant hemostatic activity. Notably, it demonstrated the capability to activate both the intrinsic and extrinsic pathways of the coagulation cascade. This unique feature sets it apart from previous research in this area.

While the detailed mechanism of action is still complex and not fully elucidated, a proposed representation of the potential mechanism is illustrated in Fig. 14. This visual depiction aims to provide an overview of how AlBG, when integrated into the surgical cotton gauze, may interact with the coagulation cascade to achieve its hemostatic effects. This mechanism may open new avenues for developing effective hemostatic materials with improved coagulation pathway activation.

6. Conclusion

In this comprehensive study, AlBG was produced through the sol-gel method and incorporated into surgical cotton gauze, resulting in a novel hemostatic dressing known as AlBGscg. The properties and functionality of AlBGscg were extensively characterized to assess its potential as an effective hemostatic agent.

In conclusion, this study provides a comprehensive assessment of the material properties, cytocompatibility, hemocompatibility, and hemostatic efficacy of AlBG-incorporated surgical cotton gauze (AlBGscg). The material exhibited a complex structure with amorphous and crystalline features, which was validated by XRD and FTIR. Its high surface area, and pore volume, as demonstrated by BET analysis, was shown to enhance water retention and coagulation factor concentration, expediting the coagulation process. The small particle size of AlBG played a vital role in promoting efficient interaction with blood components, contributing to faster and more robust hemostasis. FESEM analysis confirmed the successful incorporation of AlBG into the gauze, and mechanical tests indicated that its mechanical properties were unaffected. Importantly, AlBGscg demonstrated excellent cytocompatibility and moderate hemocompatibility, making it a safe option for medical use. Finally, the AlBGscg's remarkable hemostatic properties were highlighted by its ability to activate coagulation pathways, reduce clot formation time, and induce higher thrombin generation. These findings suggest that AlBG-incorporated surgical cotton gauze holds significant promise as an effective hemostatic material with potential applications in clinical scenarios requiring rapid and reliable hemostasis.

CRediT authorship contribution statement

Payal Roy: Conceptualization, Data curation, Formal analysis, Methodology, Writing – original draft. **Rupam Saha:** Data curation, Formal analysis, Methodology. **Debolina Dattaray:** Data curation, Methodology. **Suman Saha:** Conceptualization, Data curation, Formal analysis, Methodology. **Tapan Kumar Mandal:** Investigation, Supervision, Visualization. **Pooja Srivastava:** Funding acquisition, Resources, Writing – review & editing. **Jui Chakraborty:** Conceptualization, Funding acquisition, Investigation, Project administration, Resources, Supervision, Validation, Visualization, Writing – review & editing.

Declaration of competing interest

The authors declare that they have no known competing financial interests or personal relationships that could have appeared to influence the work reported in this paper.

Data availability

Data will be made available on request.

Acknowledgement

We are grateful to the Director of CSIR-CGCRI for providing the facilities for this work. Additionally, we are grateful to the Government's Defence Research and Development Organization (DRDO) Project number: LSRB-356, India and Council of Scientific and Industrial Research (CSIR, File No. **31/015(0154)/2019-EMR-I**) the Government of India for support funding our research. We are indebted to Dr. Samar Chakraborty for generously providing us with bacterial strains for our research.

References

[1] R.F. Bellamy, The causes of death in conventional land warfare: implications for combat casualty care research, Mil. Med. 149 (2) (1984 Feb) 55–62. PMID: 6427656.
[2] S. Kargozar, F. Baino, S. Hamzehlou, R.G. Hill, M. Mozafari, Bioactive glasses: sprouting angiogenesis in tissue engineering, Trends Biotechnol. 36 (4) (2018) 430–444.
[3] R.J. Huey, D. Lo, D.J. Burns, G. Basadonna, F.X. Hursey, Clay Based Hemostatic Agents and Devices for the Delivery Thereof, US Patent No. US8114433B2, Wallingford, USA, 2006.
[4] L. Lucchesi, H. Xie, US Patent No. US9205170B2. Wound Dressing Devices and Methods, Oregon, USA, 2008.
[5] S. Pourshahrestani, et al., Gallium-containing mesoporous bioactive glass with potent hemostatic activity and antibacterial efficacy, J. Mater. Chem. B 4 (2016) 71–86.
[6] K.H. Waibel, B. Haney, M. Moore, B. Whisman, R. Gomez, Safety of chitosan bandages in shellfish allergic patients, Mil. Med. 176 (10) (2011 Oct) 1153–1156, https://doi.org/10.7205/milmed-d-11-00150. PMID: 22128651.
[7] H.E. Achneck, B. Sileshi, R.M. Jamiolkowski, D.M. Albala, M.L. Shapiro, J. H. Lawson, A comprehensive review of topical hemostatic agents: efficacy and recommendations for use, Ann. Surg. 251 (2) (2010 Feb) 217–228, https://doi.org/10.1097/SLA.0b013e3181c3bcca. PMID: 20010084.
[8] C. Vichery, J.M. Nedelec, Bioactive glass nanoparticles: from synthesis to materials design for biomedical applications, Materials 9 (4) (2016) 288.
[9] Y. Wang, M. Luo, T. Li, C. Xie, S. Li, B. Lei, Multi-layer-structured bioactive glass nanopowder for multistage-stimulated hemostasis and wound repair, Bioact. Mater. 25 (2023) 319–332.
[10] T.A. Ostomel, Q. Shi, P.K. Stoimenov, G.D. Stucky, Metal oxide surface charge mediated hemostasis, Langmuir 23 (22) (2007) 11233–11238.
[11] Galen Stucky, et al., US 2010/0209531 A2, Oxides for Wound Healing and Body Repair, 2010. United States.
[12] M. Kilbourne, K. Keledjian, J.R. Hess, T. Scalea, G.V. Bochicchio, Hemostatic efficacy of modified amylopectin powder in a lethal porcine model of extremity arterial injury, Ann. Emerg. Med. 53 (6) (2009 Jun) 804–810, https://doi.org/10.1016/j.annemergmed.2008.12.041. Epub 2009 Mar 25. PMID: 19321227.
[13] P. Rhee, C. Brown, M. Martin, A. Salim, D. Plurad, D. Green, L. Chambers, D. Demetriades, G. Velmahos, H. Alam, QuikClot use in trauma for hemorrhage control: case series of 103 documented uses, J. Trauma 64 (4) (2008 Apr) 1093–1099, https://doi.org/10.1097/TA.0b013e31812f6dbc. PMID: 18404080.
[14] F. Arnaud, T. Tomori, W. Carr, A. McKeague, K. Teranishi, K. Prusaczyk, R. McCarron, Exothermic reaction in zeolite hemostatic dressings: QuikClot ACS and ACS+, Ann. Biomed. Eng. 36 (10) (2008 Oct) 1708–1713, https://doi.org/10.1007/s10439-008-9543-7. Epub 2008 Aug 20. PMID: 18712606.
[15] G.C. Velmahos, et al., Models for hemostatic agent testing: control versus fidelity, J. Trauma 66 (4) (2009) 984–988.
[16] D.R. Hospenthal, et al., J. Trauma Inj. Infect. Crit. Care 71 (2) (2011) 210–234.
[17] P. Jiang, F. Qu, H. Lin, X. Wu, R. Xing, J. Zhang, Macroporous/mesoporous bioglasses doped with Ag/TiO_2 for dual drug action property and bone repair, IET Nanobiotechnol. 6 (3) (2012) 93–101.
[18] A.J. Salinas, S. Shruti, G. Malavasi, L. Menabue, M. Vallet-Regí, Substitutions of cerium, gallium and zinc in ordered mesoporous bioactive glasses, Acta Biomater. 7 (9) (2011) 3452–3458.
[19] S. Shruti, A.J. Salinas, E. Ferrari, G. Malavasi, G. Lusvardi, A.L. Doadrio, L. Menabue, M. Vallet-Regi, Curcumin release from cerium, gallium and zinc containing mesoporous bioactive glasses, Microporous Mesoporous Mater. 180 (2013) 92–101.
[20] N. Gargiulo, A.M. Cusano, F. Causa, D. Caputo, P.A. Netti, Silver-containing mesoporous bioactive glass with improved antibacterial properties, J. Mater. Sci. Mater. Med. 24 (9) (2013) 2129–2135.
[21] S. Pourshahrestani, E. Zeimaran, N.A. Kadri, N. Gargiulo, S. Samuel, S.V. Naveen, T. Kamarul, M.R. Towler, Gallium-containing mesoporous bioactive glass with potent hemostatic activity and antibacterial efficacy, J. Mater. Chem. B 4 (1) (2016) 71–86.
[22] S.K. Dentel, J.M. Gossett, Mechanisms of Coagulation with Aluminium Salts, AWWA, 1988, pp. 187–198.

[23] P. Tarighi, M. Khoroushi, A review on common chemical hemostatic agents in restorative dentistry, Dent. Res. J. 11 (2011) 423–428.
[24] P. Meng, Z. Tang, J. Tu, Z. Wang, Q. Chen, R. Xiao, H. Liu, Porous chitosan microspheres containing zinc ion for enhanced thrombosis and haemostasis, Mater. Sci. Eng. C 85 (2018) 27–36.
[25] T.T. Vu, J.C. Fredenburgh, J.I. Weitz, Zinc: an important cofactor in haemostasis and thrombosis, Thromb. Haemostasis 109 (3) (2013) 421–430.
[26] X. Yan, X. Huang, C. Yu, H. Deng, Y. Wang, Z. Zhang, S. Qiao, G. Lu, D. Zhao, The in-vitro bioactivity of mesoporous bioactive glasses, Biomaterials 27 (18) (2006) 3396–3403.
[27] V.M. Villapún, et al., Antibacterial metallic touch surfaces, Materials 9 (2016) 736–759.
[28] P. Roy, R. Saha, J. Chakraborty, A novel composition of bioactive glass with potent haemostatic action and antibacterial competence, Ceram. Int. 49 (2023) 6389–6400.
[29] M. Zhu, J. Shi, Q. He, L. Zhang, F. Chen, Y. Chen, An emulsification–solvent evaporation route to mesoporous bioactive glass microspheres for bisphosphonate drug delivery, J. Mater. Sci. 47 (5) (2012) 2256–2263.
[30] J.A. Roether, A.R. Boccaccini, L.L. Hench, V. Maquet, S. Gautier, R. Jérôme, Development and in vitro characterisation of novel bioresorbable and bioactive composite materials based on polylactide foams and Bioglass® for tissue engineering applications, Biomaterials 23 (18) (2002) 3871–3878.
[31] A.G. Stamboulis, A.R. Boccaccini, L.L. Hench, Novel biodegradable polymer/bioactive glass composites for tissue engineering applications, Adv. Eng. Mater. 4 (3) (2002) 105–109.
[32] P. Roy, R. Saha, S. Saha, D. Dattaray, T.K. Mandal, N. ElShazly, M.K. Marei, J. Chakraborty, Facile synthesis of electrospun antibacterial bioactive glass based micronanofibre (ABGmnf) for exalted wound healing: *In vitro* and *in vivo* studies, Mater. Chem. Phys. 305 (2023) 127874.
[33] ASTM E96/E96M, Standard Test Methods for Water Vapour Tansmission of Materials, 2016.
[34] ASTM D7334-08, Standard Practice for Surface Wettability of Coatings, Substrates and Pigments by Advancing Contact Angle Measurement, 2022.
[35] ASTM D882-12, Tensile Strength of Thin Plastic Sheeting.
[36] N.M. Ranjha, U.F. Qureshi, Preparation and characterization of crosslinked acrylic acid/hydroxypropyl methyl cellulose hydrogels for drug delivery, Int. J. Pharm. Pharmaceut. Sci. 6 (4) (2014) 400–410.
[37] International Standard-ISO 10993-5, Biological Evaluation of Medical Devices-Part-5: Tests for *In-Vitro* Cytotoxicity, third ed., 2009.
[38] ISO 10993-4, Biological Evaluation of Medical Devices- Part-4: Selectionof Tests for Interactions with Blood, second ed., 2002.
[39] A. Turlybekuly, A.D. Pogrebnjak, L.F. Sukhodub, Liudmyla B. Sukhodub, A. S. Kistaubayeva, I.S. Savitskaya, D.H. Shokatayeva, et al., Synthesis, characterization, in vitro biocompatibility and antibacterial properties study of nanocomposite materials based on hydroxyapatite-biphasic ZnO micro-and nanoparticles embedded in Alginate matrix, Mater. Sci. Eng. C 104 (2019) 109965.
[40] J.W. Carraway, D. Kent, K. Young, A. Cole, R. Friedman, K.R. Ward, Comparison of a new mineral based hemostatic agent to a commercially available granular zeolite agent for hemostasis in a swine model of lethal extremity arterial hemorrhage, Resuscitation 78 (2008) 230–235.
[41] C. Dai, Y. Yuan, C. Liu, J. Wei, H. Hong, X. Li, X. Pan, Degradable, antibacterial silver exchanged mesoporous silica spheres for hemorrhage control, Biomaterials 30 (2009) 5364–5375.
[42] C.W. Wang, H.Y. Zhou, H.Y. Niu, X.Y. Ma, Y. Yuan, H. Hong, C.S. Liu, Tannic acid-loaded mesoporous silica for rapid hemostasis and antibacterial activity, Biomater. Sci. 6 (2018) 3318–3331.
[43] J. Chen, L. Qiu, Q. Li, J. Ai, H. Liu, Q. Chen, Rapid hemostasis accompanied by antibacterial action of calcium crosslinking tannic acid-coated mesoporous silica/silver Janus nanoparticles, Mater. Sci. Eng. C 123 (2021) 111958.
[44] A. Diquelou, S. Lemozy, D. Dupouy, B. Boneu, K. Sakariassen, Y. Cadroy, Effect of blood flow on thrombin generation is dependent on the nature of the thrombogenic surface, Blood 84 (1994) 2206–2213.
[45] Shin-Yeu Ong, Jian Wu, M. Shabbir, Moochhala, Mui-Hong Tan, Jia Lu, Development of a chitosan-based wound dressing with improved hemostatic and antimicrobial properties, Biomaterials 29 (2008) 4323–4332.
[46] C. Wiegand, M. Abel, Uta-Christina Hipler, P. Elsner, M. Zieger, J. Kurz, H. P. Wendel, S. Stoppelkamp, Hemostatic wound dressings: predicting their effects by in vitro tests, J. of Biomaterials applications (2019) 1–13.
[47] M.F. Shih, M.D. Shau, M.Y. Chang, S.K. Chiou, J.K. Chang, J.Y. Cherng, Platelet adsorption and haemolytic properties of liquid crystal/composite polymers, Int. J. Pharm. 327 (2006) 117–125.
[48] Hu, Antibacterial hemostatic dressings with nanoporous bioglass containing silver, et al. Int. J. Nanomed. 7 (2012) 2613–2620.
[49] M.A. Hussien, E. Essa, S.A. El Gizawy, Investigation of the effect of formulation additives on telmisartan dissolution rate: development of oral disintegrating tablets, Eur. J. Biomed. Pharmaceut. Sci. 6 (4) (2019) 12–20.
[50] M. Suhail, I.-H. Chiu, I.-L. Lin, M.-J. Tsai, P.-C. Wu, A novel approach of polyethylene glycol-4000 hydrogels as controlled drug carriers, Micro 3 (2023) 578–590.
[51] F.C. Kenechukwu, E.C. Ibezim, A.A. Attama, M.A. Momoh, J.D.N. Ogbonna, P. O. Nnamani, S.A. Chime, C.E. Umeyor, E.M. Uronnachi, Preliminary spectroscopic characterization of PEGylated mucin, a novel polymeric drug delivery system, Afr. J. Biotechnol. 12 (47) (2013) 6661–6671.
[52] Xu R, Xia H, He W and Li Z, Controlled water vapour transmission rate promotes wound- healing via wound re-epithelialization and contraction enhancement. Sci. Rep., 6(1): 24596.
[53] D.A. Hickman, C.L. Pawlowski, U.D.S. Sekhon, J. Marks, A.S. Gupta, Biomaterials and advanced technologies for hemostatic management of bleeding, Adv. Mater. 30 (2018) 1700859.
[54] Y.Z. Bu, L.C. Zhang, J.H. Liu, L.H. Zhang, T.T. Li, H. Shen, X. Wang, F. Yang, P. F. Tang, D.C. Wu, Synthesis and properties of hemostatic and bacteria-responsive in situ hydrogels for emergency treatment in critical situations, ACS Appl. Mater. Interfaces 8 (2016) 12674–12683.
[55] M.T. Matter, F. Starsich, M. Galli, M. Hilber, A.A. Schlegel, S. Bertazzo, S. E. Pratsinis, I.K. Herrmann, Developing a tissue glue by engineering the adhesive and hemostatic properties of metal oxide nanoparticles, Nanoscale 9 (2017) 8418–8426.
[56] Z. Chen, F. Li, C. Liu, J. Guan, X. Hu, G. Du, X. Yao, J. Wu, F. Tian, Blood clot initiation by mesoporous silica nanoparticles: dependence on pore size or particle size? J. Mater. Chem. B 4 (2016) 7146–7154.
[57] T.A. Ostomel, Q. Shi, P.K. Stoimenov, G.D. Stucky, Metal oxide surface charge mediated hemostasis, Langmuir 23 (2007) 11233–11238.
[58] S.E. Baker, A.M. Sawvel, N. Zheng, G.D. Stucky, Controlling bioprocesses with inorganic surfaces: layered clay hemostatic agents, Chem. Mater. 19 (2007) 4390–4392.
[59] C. Dai, Y. Yuan, C. Liu, J. Wei, H. Hong, X. Li, X. Pan, Degradable, antibacterial silver exchanged mesoporous silica spheres for hemorrhage control, Biomaterials 30 (2009) 5364–5375.
[60] M. Nagrath, A.R. Yazdi, A. Rafferty, D. Daly, S.U. Rahman, R.C. Gallant, H. Ni, P. R. Arany, M.R. Towler, Tantalum-containing meso-porous glass fibres for hemostatic applications, Mater. Today Commun. 27 (2021) 102260.
[61] M. Long, Y. Zhang, P. Huang, S. Chang, Y. Hu, Q. Yang, L. Mao, H. Yang, Emerging nanoclay composite for effective hemostasis, Adv. Funct. Mater. 28 (2018) 1–9.
[62] M. Mohammadi Aria, A. Erten, O. Yalcin, Technology advancements in blood coagulation measurements for point-of-care diagnostic testing, Front. Bioeng. Biotechnol. 7 (2019) 395.
[63] M. Nagrath, D. Bince, C. Rowsell, D. Polintan, J. Rezende-Neto, M. Towler, Porcine liver injury model to assess tantalum-containing bioactive glass powders for hemostasis, J. Mater. Sci. Mater. Med. 33 (6) (2022) 53.
[64] C. Zheng, J. Liu, Q. Bai, Y. Quan, Z. Li, W. Chen, Q. Gao, Y. Zhang, T. Lu, Preparation and hemostatic mechanism of bioactive glass-based membrane-like structure camouflage composite particles, Mater. Des. (2022) 111116.



Payal Roy is a PhD scholar in Bio-ceramics and Coating Division (BCCD), CSIR-Central Glass and Ceramic Research Institute (CSIR-CGCRI), Kolkata, India. She is pursuing her PhD thesis under the supervision of Dr. Jui Chakraborty. She has received fellowship from Council of Scientific and Industrial Research (CSIR, **File No. 31/015(0154)/2019-EMR-I**) Govt. of India, India for her PhD. Her basic background is Zoology, and her research interest focuses on inter-disciplinary area to serve healthcare related problems.



Rupam Saha is a PhD Scholar of AcSIR-IDDP programme, under the supervision of Dr. Jui Chakraborty in Bio-ceramics and Coating Division (BCCD), CSIR-Central Glass and Ceramic Research Institute (CSIR-CGCRI), Kolkata, India. Her background is B. Sc. in Chemistry and Post B. Sc., B. Tech. in Chemical Technology, and her research interest focuses on sol-gel chemistry, nanoparticle synthesis and bioactive glass in healthcare application.



Dr. Debolina Dattaray, Ph.D. scholar in Department of Veterinary Pharmacology and Toxicology (VPT), West Bengal University of Animal and Fishery Sciences (WBUAFS), Kolkata, India. I have pursued my MVSc in VPT from GADVASU, Ludhiana and BVSc & A.H.from C.V.Sc. and A.H., R.K. Nagar, West Tripura. I have received NEC Merit scholarship during my Undergraduate programme and have qualified my ICAR NET in Veterinary Pharmacology & Toxicology in the year 2021. My Ph.D. research is mostly based on toxicological aspect which focuses on various toxicity studies of newly derived compounds for health care benefits.



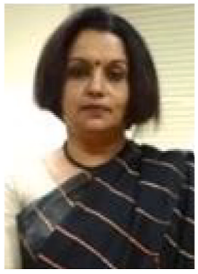
Suman Saha is DST INPIRE fellow and PhD student under the supervision of Dr. Jui Chakraborty. His background is M. Pharm. (Clinical Pharmacy). His research interest focuses on ceramics, drug delivery, and development of biopharmaceutical products in healthcare application.



Prof. Tapan Kumar Mandal works in the Department of Veterinary Pharmacology and Toxicology (VPT), West Bengal University of Animal and Fishery Sciences (WBUAFS), Kolkata, India and one of his well known works are Assemblages of Total Mercury in the Tropical Macrotidal Bidyadhari Estuarine Stretches of Indian Sundarban Mangrove Eco-Region.



Dr Pooja Srivastava is Scientist "E" at Institute of Nuclear Medicine and Allied Sciences, Delhi. She has done her integrated M.Sc. in Chemistry from IIT Kharagpur, M.Tech. in Material Science from IIT Kanpur and PhD in Biotechnology from Delhi Technological University. She also holds MBA degree from Purdue University, USA. Her research interest includes development of materials for wound care and radiopharmaceutical for molecular imaging and member of various professional societies such as Society of Nuclear Medicine, Indian Science Congress and Indian Society of Nanomedicine. She received 'Laboratory Technology Group Award-2011' for significant contribution towards implementation of quality management system and 'Director's commendation (Group award, 2019) for contribution in the area of Project Management. She also received 'Commendable Research Award' from Delhi Technological University in 2020.



Jui Chakraborty is a Principal Scientist at Bio-ceramics and Coating Division (BCCD) of CSIR- Central Glass and Ceramic Research Institute, Kolkata, India. Her research activity encompasses application of bioactive glass in healthcare and development of inorganic nanoconjugate to deliver drugs/biomolecules. She pursued her doctoral studies from National Institute of Technology, India. She has authored many papers in high impact journals along with several patents to her name. She has been conferred with several prestigious scientific research awards and serves as reviewer of many eminent international journals. She looks forward to solve healthcare problems by developing new approaches and impactful inventions.

Hindawi
Wireless Communications and Mobile Computing
Volume 2023, Article ID 8068038, 27 pages
https://doi.org/10.1155/2023/8068038

Research Article

Blockchain-Based Secure Localization against Malicious Nodes in IoT-Based Wireless Sensor Networks Using Federated Learning

Gebrekiros Gebreyesus Gebremariam,[1,2] **J. Panda**,[2] **and S. Indu**[2]

[1]*Department of Electronics and Communication Engineering, Raya University, Maychew, 7020 Tigray, Ethiopia*
[2]*Department of Electronics and Communication Engineering, Delhi Technological University, Shahbad Daulatpur, Main Bwana Road, Delhi 110042, India*

Correspondence should be addressed to Gebrekiros Gebreyesus Gebremariam; kiros2004comp@gmail.com

Received 11 November 2022; Revised 9 January 2023; Accepted 13 January 2023; Published 31 January 2023

Academic Editor: Javier Prieto

Copyright © 2023 Gebrekiros Gebreyesus Gebremariam et al. This is an open access article distributed under the Creative Commons Attribution License, which permits unrestricted use, distribution, and reproduction in any medium, provided the original work is properly cited.

Wireless sensor networks are the core of the Internet of Things and are used in healthcare, locations, the military, and security. Threats to the security of wireless sensor networks built on the Internet of Things (IoT-WSNs) can come from a variety of sources. This study proposes secure attack localization and detection in IoT-WSNs to improve security and service delivery. The technique used blockchain-based cascade encryption and trust evaluation in a hierarchical design to generate blockchain trust values before beacon nodes broadcast data to the base station. Simulation results reveal that cascading encryption and feature assessment measure the trust value of nodes by rewarding each other for service provisioning and trust by removing malicious nodes that reduce localization accuracy and quality of service in the network. Federated machine learning improves data security and transmission by merging raw device data and placing malicious threats in the blockchain. Malicious nodes are classified through federated learning. Federated learning combines hybrid random forest, gradient boost, ensemble learning, K-means clustering, and support vector machine approaches to classify harmful nodes via a feature assessment process. Comparing the proposed system to current ones shows an average detection and classification accuracy of 100% for binary and 99.95% for multiclass. This demonstrates that the suggested approach works well for large-scale IoT-WSNs, both in terms of performance and security, when utilizing heterogeneous wireless senor networks for the providing of secure services.

1. Introduction

Technology and network advancements have created a new environment where the Internet of Things (IoT) is flourishing, fostering several positive social and economic changes [1]. The Internet of Things (IoT) are the networked and interconnected systems, devices, applications, and people that process data [2]. The Internet of Things makes it possible for physical objects to communicate with one another and share critical information while also making decisions and completing important tasks. As a result, these objects now have the capacity to see, hear, think, and carry out significant acts [3]. IoT-WSNs are important and popular research areas in recent applications, including military, smart cities, healthcare, and environmental [4]. The rapid growth of the Internet of Things (IoT) is largely due to the contributions of wireless sensor networks (WSNs), which have both practical and academic importance. Ad hoc networks, or WSNs, are made up of a swarm of devices, or "sensor nodes," each of which is equipped with some form of sensing technology. Sensor nodes should be able to self-organize, be deployed at random, be fault-tolerant, and monitor a wide region with high precision. IoT-WSNs are self-organizing networks with different parameters for monitoring and collecting environmental data. The sensor nodes cooperate and evaluate each other for effective data transmission and detection and removal of malicious nodes in the network. The malicious attacks can be internal or external for exploiting information and creating wrong routing information between the sensor node and base station by compromising the beacon node in the cluster region. The malicious node degrades the network performance by

broadcasting wrong information and creating mistrust between the nodes and end users. The trust evaluation process continuously uses threshold and signal strength values between the sensor nodes to detect and analyze the network's malicious nodes.

The integrity of bitcoin networks is ensured by blockchain, a distributed ledger technology [5]. This groundbreaking architecture is now often utilized in a variety of distributed contexts, including healthcare and automotive ad hoc networks (VANET). There are three primary reasons why blockchain technology is well-suited to addressing IoT security concerns, according to a number of studies. As with an IoT network, the data associated with blockchain technology is stored and handled in a decentralized fashion by all of the agents in the network. Distributed blockchain technology offers many advantages over traditional centralized management approaches, including the elimination of a potential single point of failure and a significant reduction in the cost of keeping a large number of Internet of Things devices up and running. Lack of trust between IoT devices is a commonplace because of the energy-limited nature of these devices. As a result, sensitive information stored on these devices is at risk of being exposed or stolen. Due to blockchains unique immutability, it allows parties to exchange information without having to rely on one other's integrity. In the blockchain design, data is saved in blocks, each of which has a hash backup of the data in the preceding block. In many instances, it is also necessary for the devices to be completely untraceable. However, most gadgets have a low setup and are not suited for the complexity of standard encryption methods. With the blockchain architecture of IoT-WSNs, entities connect with one another using transactions as the fundamental unit of information exchange. In the first iteration of the blockchain, every piece of data pertaining to a client's commercial exchange is considered a transaction.

Many fields, including medicine, computer vision, and wireless communication, have benefited from the significant progress made in recent years in machine learning (ML) techniques and especially in deep learning (DL) models. ML also encompasses shallow models [6]. It can provide means for detecting certain forms of attacks without requiring intensive human engagement. Intrusion detection systems (IDS) that employ ML techniques can train themselves by observing and comparing "normal" and "abnormal" flows of traffic. It can be used to detect harmful traffic patterns in a dataset or in an actual environment. Although these approaches have been put to good use for IDS, they often necessitate a centralized organization to process and aggregate data from all users on the network and found that high packet loss rate reduces prediction accuracy at larger network size. In this study, we proposed blockchain-based hybrid federated machine learning techniqe for locating and identifying the origin of assaults in IoT-WSNs, using the immutable and distributed ledger technology blockchain.

1.1. Blockchain Applications in IoT-WSNs. Blockchain is a distributed database for storing transactions' records to provide trust in unknown nodes in the network with the same edge. A blockchain, as its name implies, is a series of linked blocks. The structure for storing bargaining data is a chain of blocks, each of which has its own hash value and contains a specified quantity of transaction data. All the data on the blockchain is secure because each block contains a unique hash value for the one before it [5]. The blockchain is a distributed, unchangeable ledger of all transactions that have been validated by a majority of the network's peers. Distributed ledger is a term for the system of decentralized data storage it describes [7]. Whenever a ledger transaction is performed, it is validated with the approval of the majority of the network users. The most well-known application of blockchain technology in the real world is Bitcoin. Connecting blockchain technology with the Internet of Things has many benefits. For example, a decentralized blockchain storage architecture can synchronize IoT devices and deliver real-time data to each IoT node. However, the data produced by these applications is enormous, leading to problems associated with big data. Therefore, artificial intelligence (AI) functions as an analytical tool and contributes to decision-making, categorization, prediction, and detection in a blockchain-enabled IoT network to solve this problem. Further, the analysis in the current blockchain-based architecture is performed on a cloud server. However, there are limitations associated with using a centralized server, including slow speeds and accuracy, as well as low latency and limited computational storage. Fog computing, a new distributed paradigm that may be able to meet these needs, warrants extensive study. Fog computing, which Cisco first defined in 2012, is a distributed architecture that brings cloud services to the network's periphery. Fog computing's principles offer extensive assistance to blockchain-based applications, including but not limited to location awareness, support for heterogeneity, low latency, mobility, and geodistribution. In addition to these load-balancing and data-gathering benefits, fog computing has found application in other areas. As a result, this research combines fog computing with AI to create a distributed security mechanism that can identify DoS attacks directed at mining pools in a blockchain-enabled IoT network. The integrated secure attack detection model using blockchain, IoT, AI, and fog computing is depicted in Figure 1 for various applications.

Blockchain is an up-and-coming technology that is being implemented in numerous sectors to facilitate security and distributed trust among peer nodes [8]. The following sections cover some literature that has utilized blockchain technology to safeguard IoT applications. For authentication and authorization in IoT-based WSNs, blockchain technology was integrated into IoT. To solve this problem, we propose a blockchain-based decentralized localization technique, a pseudonymous permission management framework that gives users complete authority over their own information while also protecting their privacy. Blockchain models are decentralized access control managers that store access permissions to resources. A new subfield of study is exploring the use of blockchain technology in IoT based-WSNs [9].

Some academics have recently included blockchain in WSNs to solve problems with processing capability, data storage, node failure, and user access management. The mobile edge computing (MEC) server can store encrypted

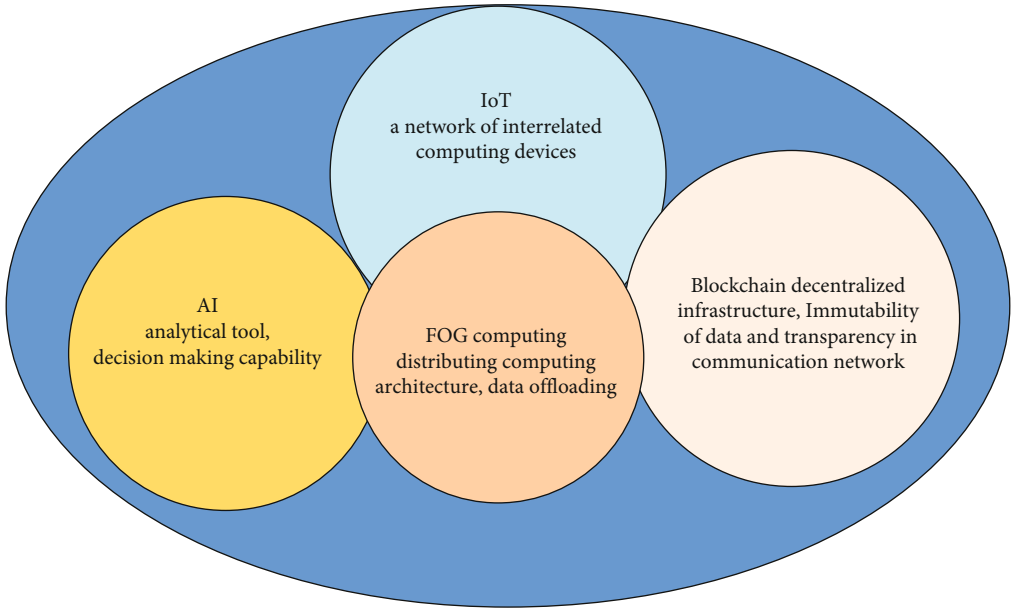


Figure 1: Illustrating of secure IoT-based WSNs showing the use of a detection model incorporating blockchain, IoT, AI, and fog computing [7].

block hashes in memory and delegate computationally difficult mining work to the edge computing nodes. The blockchain uses census algorithms to achieve agreement between unknown nodes using proof-of-work (PoW), proof-of-state, and proof-of-authority (PoA). The blockchain establishes trust in the network by storing the transactions in the block in chronological order consisting of headers and bodies. The headers contain the hash elements, including the transaction root, previous blocks, and timestamp. Blockchain techniques are applied in different domains in IoT-based wireless sensor networks for effective localization of the beacon nodes in the network. Sensor nodes sense and collect data containing precise location and identity to the sink node in the network. However, malicious nodes' presence affects the location and position of sensor nodes by compromising the beacon nodes and sending wrong information to the sink node. The blockchain-based secure localization scheme provides reliable service to the client nodes using the nonrepudiation model.

A sensor node's location can be determined by a global positioning system (GPS) or via other means of precise localization [10]. One approach is to centralize the management of information about the network as a whole, employing mathematical techniques to determine the locations of individual nodes. In WSN, the support vector machine is primarily used for securing nodes and determining their locations. The mobile node localization strategy uses support vector machines and information about network accessibility. It determines the node's position by measuring the strength of the incoming signal or RSSI. Fast and widespread localization is possible with localized SVM, although it is still vulnerable to outliers in the training data. Support vector regression (SVR), a unique data extraction method for localization models, has led to more accurate localization. Without increasing the price of the necessary gear, it enhances localization's precision. Using SVM-based learning with a small number of anchor nodes, we can precisely pinpoint the location of the unknown node. Grid cells of finite size guarantee precision. SVM-based DV-hop works well for large-scale networks. Some AI capabilities are made available to sensor nodes by use of a localization method based on a self-organizing map (SOM). SOM can learn classification on its own without human input. Each sensor node's location is calculated using a self-organizing map. The input layer consists of the spatial coordinates of eight anchor nodes close to the unknown node. After training, the network's output layer provides the unidentified node's unique 2D spatial coordinates. This approach has the drawback that nodes must be uniformly distributed across the monitored area.

This study presents a fog computing-based distributed intrusion detection system (IDS) for mining pools in blockchain-enabled IoT networks, complete with safe planning and simulation, attack detection, and classification. Hybrid federated machine learning algorithms are used to train the suggested IDS. Figure 2 depicts a high-level view of the suggested distributed paradigm. Sensing nodes are the building blocks of the detection system, and it is their job to track and identify any moving objects that come within range. Based on their performance in training and testing, all IoT sensors belong to one of several groups, each with the same capabilities for detection. This cluster sends its data to nearby fog nodes. Since fog nodes act as a gateway or access point for IoT devices, they must incorporate an intrusion detection system as part of their security infrastructure. Incoming traffic is analyzed by IDS, and actions are done based on its results. Assuming a typical influx of data, the transaction is broadcast throughout the mining pool's memory. In a blockchain network hosted in the cloud, miners choose which transactions to mine and create new blocks.

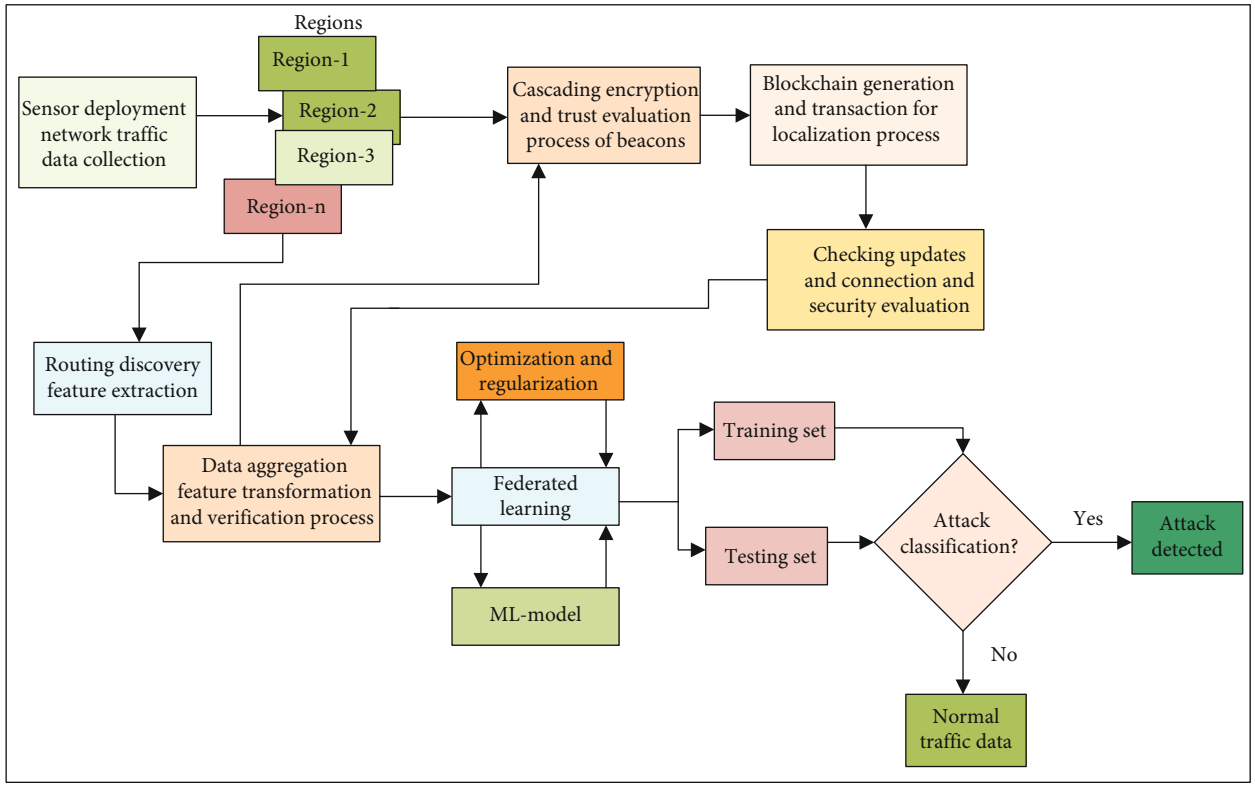


Figure 2: Blockchain-based secure localization detection of attacks for IoT-based wireless sensor networks using federated learning.

To alert the administrator to take corrective action in the event of malicious or invalid transactions, the IDS will sound an alarm. Scalability and detection performances for routing threats in IoT-based WSNs are two advantages of the proposed approach. It functions well in IoT systems that incorporate several wireless sensor networks.

1.2. Motivation and Contribution. The literature reveals a wide variety of security issues and concerns related to the design, development, and implementation of IDS, detection, and classification attacks utilizing blockchain technology in IoT-based wireless sensor networks. As the number of distributed denial of service (DDoS) attacks in the blockchain-IoT ecosystem rises, all IoT networks supported by blockchain will become increasingly at risk. Protecting a blockchain-based Internet of Things network requires a complex distributed security architecture, making sure a security mechanism can deal with the massive amounts of data produced by IoT devices and applies the right analytical tools in a decentralized framework. It is not easy to make an IDS that can tell the difference between safe and dangerous online transactions. Not much is known about how to prevent distributed denial of service (DDoS) attacks against mining pools in blockchain-enabled Internet of Things (IoT) wireless sensor networks once the corresponding model has been implemented. Because of these issues, we presented a hybrid federated machine learning-based technique for detecting and localizing routing attacks in WSNs-IoT by analyzing representative datasets.

In light of these problems, we proposed the use of a secure blockchain enabled by federated learning (FL) in Internet of Things (IoT) wireless sensor networks in order to identify and localize assaults. With FL, devices can work together to learn without transmitting information to a central hub. That is to say, ML/DL can be trained in a distributed fashion, requiring several devices and servers to process data over multiple rounds of training. The two main components of this approach are local learning and model transmission, which together provide for the privacy preservation and cost reduction typical of more traditional centralized machine learning approaches. When using FL, the entire ML/DL model can be refined over time. The FL server picks a subset of clients at the start of each round to take part in the learning process and shares its most recent global model with them. The contributions of the proposed secure localization based on blockchain technique in IoT-based wireless sensor network are bulleted as follows:

(1) Explore blockchain techniques for detecting and localizing malicious nodes in IoT-based wireless senor networks

(2) Enhance detection and localization of malicious nodes in IoT-based wireless sensor networks to improve service quality

(3) Explore the effectiveness of federated learning techniques using performance metrics to evaluate the attack detection performance

(4) Provide secure routing and data transmission in a hierarchical IoT-based wireless sensor network for secure service provisioning

(5) Effective detection and localization of malicious nodes by computing the unknown nodes based on the blockchain technique with the help of beacon node

(6) Secure data aggregation and trust value computation of beacon nodes using a trust management model based on blockchain for malicious node removal and ensuring service provision

(7) Design and plan secure range-free localization processing using blockchain technology-based selection of trust value of the miner beacon nodes

(8) Explore the blockchain secure data aggregation and localization of unknown nodes for malicious node detection and localization using federated learning approaches

The other parts of this paper are organized in the following sections. Section 2 contains previous literature works on secure blockchain-based localization in IoT-based wireless sensor networks. Sections 3 and 4 detail the network models, proposed methods, and simulation techniques of the scheme using blockchain techniques. Sections 5 details simulation results and analysis. Section 6 is about performance evaluation and validation followed by Section 7 containing conclusion and future work.

2. Related Works

Several related works and techniques have been reviewed for detecting and localizing malicious nodes in IoT-based wireless sensor networks. The schemes in the literature include the following:

(i) Secure localization of malicious nodes in low power sensor node networks

(ii) Routing schemes for effective resource consumption and network life time

(iii) Authentication and encryption processes for establishing trust among nodes

(iv) Blockchain-based localization technique for improving quality of services in WSNS

(v) Techniques for achieving optimized and secure data storage in IoT-WSNs

(vi) Secure and optimized models for the next-generation IoT-based WSNs

(vii) Federated machine learning and classification techniques

Kim et al. [1] conducted research on blockchain techniques based on a trust management model for detecting malicious nodes by enhancing relationships among beacon nodes using various evaluation metrics, including closeness, honesty, detection rate, average energy consumption, frequency of interaction, and intimacy. The beacon nodes are selected based on the trust values and broadcast information to the base station, forming a trust evaluation model for detecting and localizing malicious nodes in WSNs. Abubaker et al. [4] presented blockchain-based for detection and localization of malicious nodes in IoT-based wireless sensor networks using federated random forest and support vector machine techniques. They also discussed secure service provisioning using feature evaluation and cascading encryption for detecting and removing malicious nodes in the network. Security and performance metrics, including accuracy, node honesty, and end-to-end delay of the packet transmission, measured the performance of the malicious node detection and secure provisioning approaches. Ming et al. [5] suggested an authenticated group key agreement mechanism using blockchain technology for the Internet of Things. The suggested protocol includes a novel concept called the device manager, whose job is mediating communications between Internet of Things gadgets and blockchain infrastructures. The proposed protocol has been shown to be secure after being subjected to various assaults, as shown by the security analysis. The simulation results demonstrate that the time expenditures of protocol operations are fair and appropriate for IoT settings. Kumar et al. [7] proposed a new distributed intrusion detection system (IDS) leveraging fog computing for detecting DDoS assaults against mining pools in blockchain-enabled IoT networks. Random forest (RF) and a gradient tree boosting system (XGBoost) are trained on fog nodes, and their performances are compared. A real-world IoT dataset is used to evaluate the proposed model's performance, containing the most recent assaults discovered in a blockchain-enabled IoT network. The system for detecting DDoS attacks was connected to a mining pool in a blockchain-enabled IoT network. Three distinct mechanisms power the suggested distributed detection system. First, there is the traffic processing engine, which employs fog nodes to preprocess network data by standardizing its features with the help of the aforementioned Standard Scaler. Goyat et al. [11] examined a secure and novel range-free localization-based blockchain technique in wireless sensor networks against a malicious node in two-dimensional environments. They also discussed the implementation of blockchain technology using beacon nodes' trust value for the mining process of blocks to form a localization process for the unknown nodes with neighbor node list, mobility, residual energy, and repudiation value. The location and precise positions of the unknown nodes are computed using the trusted beacon nodes based on the blockchain-based generated trust values. The malicious nodes broadcast false localization information by compromising the beacon and reporting the false energy information. Awan et al. [12] proposed blockchain-based encryption and trust evaluation model for detection and secure data transmission. The authentication of the sensor nodes and aggregator nodes is in a private and public blockchain, respectively, for detection of the activities of malicious nodes, including transmitting wrong information

of routing and energy by compromising the aggregating node that degrades the network performance by increasing resource consumption and packet loss. The trust values and residual energy of the sensor nodes were computed after authentication based on the detection rate for removing the malicious nodes from the secure routing in the network. Honar Pajooh et al. [13] proposed a multilayer-based distributed and decentralized blockchain security model for a secure IoT model. IoT devices operate under multihop cellular networks using a self-clustering hybrid evolutionary algorithm combining simulated annealing and genetic algorithm approaches by clustering the unknown sensor nodes in the network. The cluster head authenticates and authorizes locally for effective communication between the cluster head and the base station using a private lightweight balanced blockchain with better throughput and network latency. Otoum et al. [14] presented an adaptive framework using integrated blockchain and federated learning using reinforcement support vector federated learning for a secure trust evaluation process in the network. The reinforcement learning occurs at the end devices, and the models were trained for communication with fog and creating a global model. They also evaluated and verified the model through simulation techniques using performance metrics, including trust value, energy consumption, and network lifetime. The model also achieved a detection rate and accuracy of 96% and 93%, respectively, for detecting and localizing malicious nodes using federated learning. She et al. [15] proposed a blockchain trust model framework for detecting malicious nodes in IoT-based wireless sensor networks by constructing blockchain data structure in three-dimensional space using a localization scheme. The detection of malicious nodes is realized using intelligent contact and wireless sensor networks quadrilateral measurement to localize and detect attacks. The sensor nodes are authenticated and recorded in the blockchain network to remove and prevent loss of routing information. Fan et al. [16] proposed a decentralized topology-based blockchain scheme for secure IoT systems during synchronization for detection and analysis attacks using multiple time resources. The scheme solved the problem of time announcement in IoT-based distributed wireless sensor networks using a closed blockchain for recording and broadcasting time for attack detection with adaptive topology for reducing communication overhead. The scheme also avoids centralization using block structure adaptable topology and multiple time sources. Friha et al. [17] presented secure IoT infrastructure using federated learning based on intrusion detection system agricultural applications for data protection producing an improved attack detection model. The scheme utilized a convolutional neural network, recurrent neural network, and deep neural network using benchmark datasets to detect and classify attacks and performance metrics. They also discussed the performance metrics, including recall, precision, F1-score, and accuracy for the multiclass classification federated deep learning model. Javaid [18] examined and designed the Dijkstra algorithm-based routing protocol for secure and efficient communication between the sensor and sink nodes without hole attacks in IoT-based WSNs. The scheme also provided transparency for transaction by the sensor nodes based on the network's blockchain technique for detecting malicious nodes. The transactions were added into blocks using the poof of authority consensus technique to validate the trust model in terms of the energy and detection metrics. Wu and Ansari [19] proposed blockchain-based secure and trust evaluation process for detection of malicious nodes in industrial Internet of Things for information sharing and access control list. The security of access control list is protected and stored by the blockchain. They also designed a voting technique with trust evaluation for access control list for high probability of malicious node detection and authentication in the network. Khan et al. [20] described the implementation of a low-energy, energy-temperature-degree-adaptive, hierarchical routing protocol. One advantage of the protocol is that it reduces the amount of energy used by nodes during data transmission, which in turn increases the lifespan of the network. The cluster heads (CHs) that will be used to carry out routing are chosen by the proposed protocol based on their degree, temperature, and energy. More importantly, the blockchain is used to eliminate the risk of a centralized failure point. Since several nodes are required for a blockchain to function, the CHs and BSs use it to store and record all of the data transactions that take place between them. Blockchain transactions are hashed using the 256-bit secure hashing method (SHA-256). To top it all off, the ETD-LEACH protocol uses a real-time message content validation (RMCV) mechanism to identify rogue nodes before they cause any damage during routing.

Goyat et al. [21] addressed IoT-WSN security issues and trusted architecture of secure localization attacks. In particular, it examines the trust evaluation method and the process of creating a blockchain. Trust values of each beacon node are calculated using several trust metrics, and the weights associated with those values are dynamically changed during the localization process. That is why only the most reliable beacon nodes are chosen during the mining procedure. This two-stage process guarantees an always up-to-date blockchain regarding reliability and the trust values of all beacon nodes. Minoli and Occhiogrosso [22] proposed and implemented a method of protection in the context of a defense-in-depth/castle approach based on blockchain mechanisms (BCMs) playing a role in protecting numerous IoT-oriented applications by becoming part of a security mosaic. A blockchain is an immutable digital ledger that records each completed transaction or piece of data in sequential order in a distributed ledger that outside parties cannot alter. All of the users in the network then have access to these exchanges. Every node in the system keeps the same ledger as all other nodes in the network; the information is saved and published in a public ledger. A full-fledged blockchain-secured network may not always be practical for all IoT applications. The typical limitations of IoT nodes are critical or institutional applications such as smart grids, ITSs, e-health, insurance, and banking that may require nodes with sufficient capabilities to support the necessary peer-to-peer functionality. Ma et al. [23] presented a blockchain-based

secure sharing scheme using ITS as an example for IoV data. It uses smart contracts to enable features like automated registration, speedy authentication, and a reliable sharing mechanism for IoV data. The private information is protected through homomorphic encryption and zero-knowledge proof processing performed by the smart contract and stored as ciphertext on the distributed ledger. We use a tamper-proof Merkle tree-based block to permanently record all IoV data processing and usage procedures and a PBFT consensus mechanism to guarantee the integrity of the entire network's ledger. The IoV chain method maintains the integrity, accessibility, and tamper resistance of the IoV data under the premise of privacy and security, allowing for the data to be traced if and when required.

Yang et al. [24] addressed the issue of centralized anomaly detection in WSNs, and the authors describe a blockchain-based ensemble anomaly detection (BCEAD) system that stores the model of a common anomaly detection method on the distributed ledger. Once a suitable block structure and consensus method have been developed, the scheme changed iteratively to increase detection and classification accuracy. The detection approach is safe from system-level attacks since the blockchain guarantees a trustworthy network environment. In conclusion, the findings demonstrate that BCEAD is superior to competing schemes in terms of performance, cost, and other parameters. Abnormality detection across all network domains is the responsibility of the sink layer. A decentralized ledger stores the isolation forest detection model (tangle). In this study, we also compare and contrast experimental data to show that BCEAD has better detection performance than previous methods. Sarhan et al. [25] presented a federated learning architecture built on a blockchain-based hierarchy to ensure that collaborative IoT intrusion detection is safe and private. The proposed machine learning-based intrusion detection system employs a federated learning architecture with a hierarchical structure to safeguard the confidentiality of the training and company information. There are several potential advantages to using machine learning (ML) skills in the security against IoT cyberattacks. However, the existing framework proposals do not consider data privacy, safe architectures, or scalable deployments of IoT ecosystems. A trusted distributed ledger will manage all business processes and transactions, and the smart contract will ensure that all obligations are met. Hsiao and Sung [26] proposed a method that employed blockchain technology to improve the safety of wireless sensor networks' data transmissions (WSNs). This research combines distributed ledger technology (blockchain) with data transmission to establish a highly reliable WSN infrastructure. Today's wireless network is founded on IoT design principles and uses a blockchain-based approach to ensure the integrity of all transmitted data. The blockchain-based transaction ledger is adapted in this research strategy to store information gathered by sensors. The suggested system collects and analyses sensor data to improve the dependability of the wireless sensing network architecture. To establish a connection between blocks, every blockchain must undergo cryptographic processing and the decryption of public keys. Even more so, before any data can be transmitted in a newly created blockchain, the prior and subsequent sequences of the link must be confirmed. Abbas et al. [27] presented a lightweight blockchain-based authentication solution to store the credentials of standard sensors. Because IoT nodes have a certain amount of time before they die from battery exhaustion, lightweight authentication is achieved by storing only a small number of credentials in the blockchain. Furthermore, a genetic algorithm-enabled software-defined network controller performs the route calculation and is also utilized for on-demand routing to minimize the nodes' energy usage in an IoT network. In addition, we present a route correctness technique to validate the absence of harmful nodes in the suggested path. Abualsauod [28] proposeda peer-reviewed research on UAV IoT frameworks and to analyse it to find answers to problems with the frameworks' overall security and privacy. An optimal solution is provided in the paper for the many security and reliability issues that arise in UAV-enabled IoT applications by integrating different ways based on blockchain technologies. Multiple metrics, including processing speed, latency, accuracy, and overall system usefulness, are used to evaluate and contrast the acquired results.

3. IoT-Based Network Model

The network model comprises various types of wireless sensor nodes operating under different computational processing and clustered into ten regions. Each region is partitioned into clusters, as shown in Figure 3. The nodes are classified into sink nodes, cluster heads, and sensor nodes based on the computational power and data processioning capabilities. The sensor nodes are assumed to be randomly deployed and are unaware of their location and position. At the same time, the beacon nodes and sink nodes are aware of their locations and positions, and they assist the unknown sensor nodes in locating the sensor nodes and identifying the malicious nodes by computing the distance between each node and its position, with each node having its own distinctive identifier [29]. The network model incorporates challenging design requirements and assumptions for efficient performance. The requirements include the following:

(i) Randomly deployed sensor nodes are assumed to be homogeneous, with mobility changing in the topology framework

(ii) Each device in the Internet of Things has its distinct IP address

(iii) The storage and processing power of the cluster's head nodes and base stations, which can be used to implement a smart contract, are described

(iv) The existence of a continuous malicious node in the network makes the framework overconscious

(v) All sink nodes are trustworthy and generate keys to all the nodes in the network

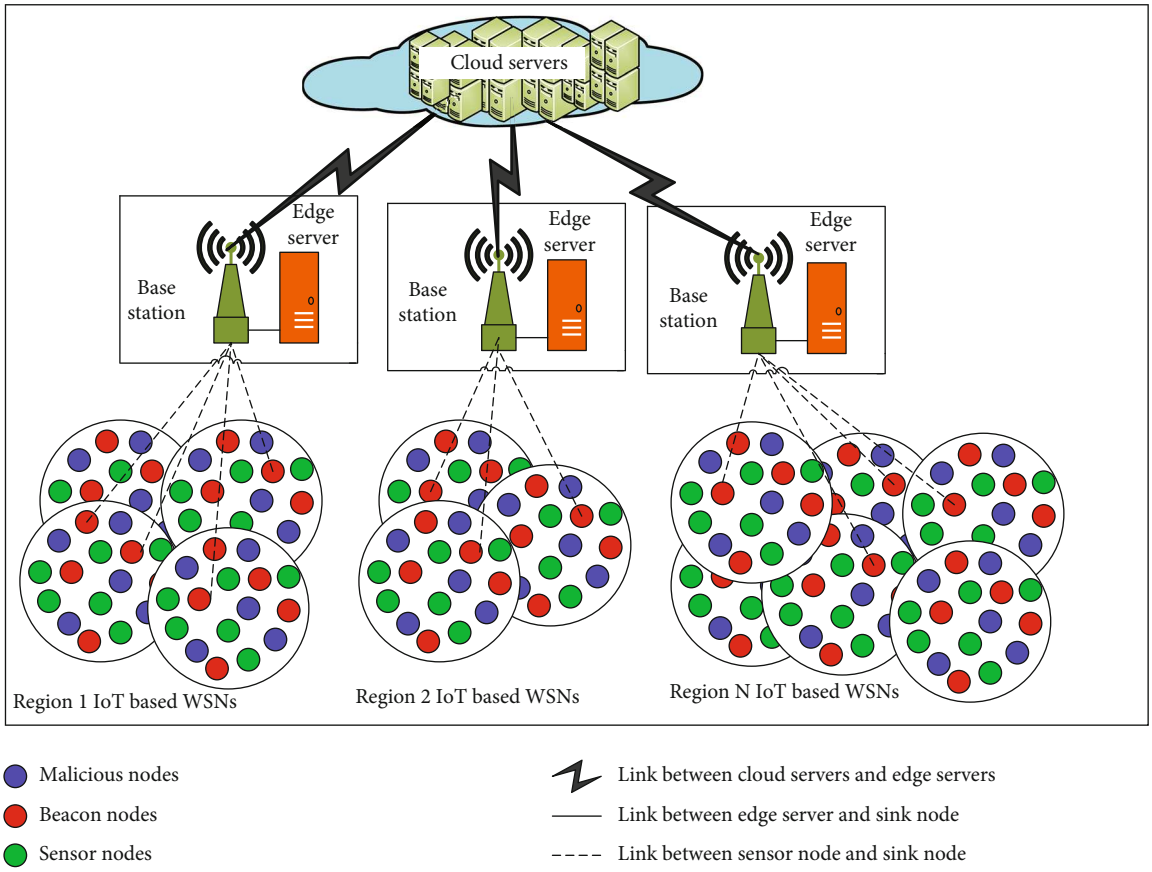


Figure 3: Proposed hierarchical IoT-based wireless sensor network model for secure localization of malicious nodes.

(vi) All sink nodes have high computational and data processing capabilities for data aggregation

(vii) The servers provide reliable and secure storage for the data in the network

The two requirements in IoT-based wireless sensor networks make the sensor nodes broadcast malicious information by gaining control over the other nodes and wrong information about energy and localization that affect the precise localization accuracy. This paper proposed blockchain-based secure localization using a trust evaluation process and cascading encryption for effective network transaction and malicious node detection. The randomly deployed sensor nodes face security threats during the localization process since malicious nodes affect the localization approach's accuracy in IoT-based wireless sensor networks. The blockchain-based technique overcomes this problem through the cascading encryption and effective transaction and trust evaluation process of the beacon nodes. The blockchain receives the trust value list and localizes the malicious nodes using the distributed consensus.

The nodes that send data to the cluster head without knowing their location are unknown and disrupt the normal functioning of the network. To avoid this problem, beacon node having their precise location helps find the accurate location of unknown nodes of their deployment before sending data. The reliable beacon nodes are selected by computing the trust value of beacon nodes without considering the malicious node. The presence of the malicious node is solved by using blockchain-based localization techniques using federated learning without compromising the beacon node and privacy. In this proposed model, each region has its network with multiple clusters for monitoring the environmental conditions. Nodes in the network cooperate to accomplish specified tasks, and the interaction between nodes needs to assure the legitimacy of node identity [30]. One of the crucial ways to safeguard the IoT is through identity authentication. In the network model presented here, two-factor authentication is required to set up encrypted channels between nodes before any communication can occur, or end users can have access to the resources hosted by a node.

4. Proposed System

The proposed system for detecting and localizing malicious nodes, as shown in Figure 2, consists of various phases for identifying and removing attacks in IoT-based wireless sensor networks using hybrid and federated learning-based blockchain technology. The proposed scheme ensures client and service provisioning using hybrid machine federated machine learning models, feature evaluation, and cascading

encryption for effective transaction and localization. The proposed system utilized federated machine learning model for detecting and classifying malicious nodes by training and testing the dataset received from the blockchain trust value lists with suitable data format using preprocessing techniques. In a WSN, the localization process relies on the accuracy of information relayed by beacon nodes; therefore, ensuring their reliability can be difficult [31]. Since IoT-based WSNs' range-free localization method does not rely on any specialized hardware, it is susceptible to mistakes when malicious attacks are present in the network. During the localization procedure, the malicious nodes provide false location data. There is a single point of failure in typical localization strategies for WSNs because they rely on a centralized body. For attack detection and localization, the efficacy of the trust evaluation based on secure blockchain using hybrid federated machine learning, reinforcement learning, and maximum likelihood estimation needs to be put to the test. One application of the blockchain is in the realm of trust administration. Furthermore, just a small set of criteria are employed to determine whether or not to trust a beacon node. For this reason, the trustworthiness of both behaviors and data must be factored into the ultimate trustworthiness assessment. From there, the data is gathered and processed by the blockchain infrastructure that was provided to it by the trusted nodes.

4.1. Sensor Deployment and Routing. The proposed system consists of N number of total sensor nodes deployed with random mobility in two-dimensional environments with B beacon nodes and U unknown nodes. The base stations are located outside the clusters in each region connected to the edge servers. The beacon's network size and communication radius are computed as in the following equations shown below.

$$|N| = |B| + |U|. \tag{1}$$

The transmission range (T_R) of the beacon nodes is computed with the maximum ($T_{\max}$) and minimum ($T_{\min}$) communication ranges as shown below:

$$T_R = (T_{\max} - 1) + \text{random}(0, 1) \times [(T_{\min} - 1) - (T_{\max} - 1)] + 1. \tag{2}$$

Randomly deployed wireless sensor networks face security threats by computing the location estimation and position of unknown nodes in the network. Detecting malicious sensor nodes provides information for calculating the location and enhancing the localization accuracy in WSNs based on beacon nodes. The beacon node is selected from the sensor nodes using the selection three criteria:

(i) The minimum distance of the node from the base station computed using the distance-vector protocol

(ii) The residual energy of the node for activation

(iii) The strength of the received signal from the sensor node

The number of neighbor nodes is close to it. Using the distance vector method, as indicated in equation (3) below, we are able to calculate the distance, denoted by D, that separates any two sensor nodes.

$$D = \sqrt{(u_i - u_j)^2 + (v_i - v_j)^2}. \tag{3}$$

Any node that has a small distance from the base stations (where u and v are the coordinates for nodes i and j, respectively) is probably the cluster head.

Threshold parameters are determined using the multipath model strategy, which is then used to assess the energy expenditure involved in network model communication and activation. In the steady-state phase, each cluster head (CH) communicates with the other nodes to keep their receivers on and respond to its CH [32]. For a data transmission of k bits across a distance D and a threshold distance D_o, we have (4) as the energy required for transmission E_{TX}:

$$E_{\text{TX}} = \begin{cases} k \times E_e + k \times E_f \times D^2, & \text{if } D \le D_o, \\ k \times E_e + k \times E_m \times D^4, & \text{if } D > D_o. \end{cases} \tag{4}$$

For one-bit data transmission, we get where E_{TX} is the energy being sent, E_f is the energy being received, and E_e is the power being lost somewhere along the line [29]. Signal propagation, filtering, modulation, and channel coding all play a role in the amount of energy lost in the process. With a data length of k, we have the following expression for the minimum acceptable transmission distance, d_o:

$$D_o = \sqrt{\frac{E_f}{E_m}}. \tag{5}$$

Energy used by the receiving node for k-bit messages is calculated as

$$E_{\text{RX}(k)} = k \times E_e. \tag{6}$$

4.2. Selection of Miner Node and Localization Process. Methods for computing behavioural trust, data-based trust, and feedback trust, and as well as calculating the overall trust beacon nodes in WSNs, are used. The most trustworthy beacon nodes are picked based on their trust levels when trust is calculated for each node. For mining and trilateration, these beacon nodes are trusted. Our blockchain network's PoA consensus is based on this group of miners. On the sink and beacon nodes, a private blockchain is being used in this network. On the blockchain, the trustworthiness beacon nodes are permanently recorded. In addition, the network's nodes encrypt the trade data and store it on the blockchain. The miner node is the anchor node having its own location with the most significant trusted values for verifying communications and putting the blocks for the next transactions. Figure 1 depicts the architecture of the proposed network model containing block. After this, the translation process begins. Trilateration is used to determine the precise

location of each unknown node. Here, unknown nodes determine their approximate location by calculating the distance between themselves and the three anchor nodes with the highest trust ratings and then utilizing that information to solve for their coordinates using the following equation:

$$D_{\text{tri}} = \begin{cases} \sqrt{(u_a - u_i)^2 + (v_a - v_i)^2} \\ \sqrt{(u_a - u_j)^2 + (v_a - v_j)^2}, \\ \sqrt{(u_a - u_k)^2 + (v_a - v_k)^2} \end{cases} \tag{7}$$

where D_{tri} is the trilateration process for finding the distance of any node a, and (u_a, v_a), (u_i, v_i), (u_j, v_j), and (u_k, v_k) are the positions of the ordinary sensor nodes with respect to i, j, and k beacon nodes.

Finding the nodes' locations and strengths of connections, as well as evaluating their positions, is tasks for which specific algorithms are required. The system is broken down into two types of categories, range-based and range-free localization methods [29]. The second option is more practical financially, but it needs specialized hardware. Accurate positioning and positioning of wireless sensor nodes are evaluated using the received signal strength indicator (RSSI) and the distance vector hop localization techniques. To determine where sensor nodes and cluster leaders are in relation to beacon (base station) nodes, a distance vector localization process is required [33]. Position and separation between the unknown nodes can be calculated and manipulated with the help of the scheme. Beacon nodes in a WSN can be located using the distance vector hop process. The average hop size is used in the distance vector approach to determine the minimal distance. In [34], this algorithm was discovered for the first time. Here are the steps of the range-free distance vector localization scheme [35]:

4.2.1. Routing Initialization. The beacon node transmits a message to all sensor nodes. As soon as it enters the network, the hop count associated with its position data is set to 0 [35]. A node that gets such a message will determine where the beacon node is located, append its own identifier to the message, and then broadcast it to its neighbours while increasing the hop count [36].

4.2.2. Calculating Distance. With the help of the beacon node, we can determine the average hop size and the distance to the unknown node.

4.2.3. Position Estimation. Geometric calculations like triangulation, the polygon technique, and trilateration are frequently employed as the underlying basis for determining the locations of unknown nodes [29]. There are a number of methods that can be used to calculate the separation of two nodes; they include synchronization, radio signal intensity, and the physical features of the carrying wave [37].

4.3. Registration and Authentication Process. Sensor nodes, aggregation nodes, and base stations are the three main categories of WSNs in the proposed network model [12]. Intelligent communications confirm the aggregation, and data processing node exists by using its MAC address and the base station's authentication procedures to verify its identification as in Figure 4. In order to gain access to the model and the public blockchain that is being utilized, the sensor nodes need to be authenticated and given permission [38]. It is essential that the privacy of the nodes be preserved, and in order to do this, our model made use of a layered security architecture. The IoT-WSN framework that has been presented needs to have the capability of establishing trust between different IoT members in order to identify and localize threats. Node placements in wireless sensor networks are shown in Figure 4(a).

In Figures 4(b) and 4(c), we can see that the cluster head (CHs) gathers a large message size, while the sensor nodes (SNs) spend a disproportionate amount of time doing data execution during deployment, registration, and authentication. The cluster heads that are location and position aware are regarded as beacon nodes. The data forwarding, retrieval, processing, and aggregation to the base station are shown in Figure 4(d).

In WSNs, the aggregated node's data and the public blockchain records of certified nodes make it possible to have faith in authentication techniques. After the registration procedure has been finalized, sensor nodes are given permission to join the blockchain, which helps to protect WSNs from outside threats. After being randomly dispersed around the playing field, the sensor nodes eventually form aggregation nodes. As the aggregation nodes communicate with the sensor nodes, they verify and identify sensor nodes via a private blockchain, and the base station verifies the identity of the aggregate node via a public blockchain. Mutual authentication is used for all of the aggregate nodes' internode communications.

4.4. Benchmark Datasets. The evaluation of the proposed system's ability to detect and classify the attack type using machine learning models is conducted against a benchmark consisting of the CICIDS2017 and UNSW-NB15 sample datasets. The dataset was captured and executed using tools for intrusion detection and network attack scenario purposes with seven categories of attacks, as shown in Figure 5(a), with the frequency distribution of the attack samples. The dataset contains normal and common classes of attacks that materialize real-world data, including network traffic analysis. The dataset is also heterogeneous, having diversified attacks with 80 feature sets generated using CICFlowMeter available online.

The UNSW-NB15 is an advanced benchmark dataset for intrusion detection widely used for recent research and many previous works. The raw data traffic packets were generated using the cyber range laboratory IXIA PerfectStorm tool from the Australia Center for cyber security (ACCS) [39], creating hybrid normal and abnormal network traffic packets. The Tool simulates nine classes of attacks and continuously updates the information security vulnerabilities and exposures of captured packets. The dataset consists of 42 attributes, three categorical features, and 39 numerical attributes. The dataset has ten classes of attacks, and the

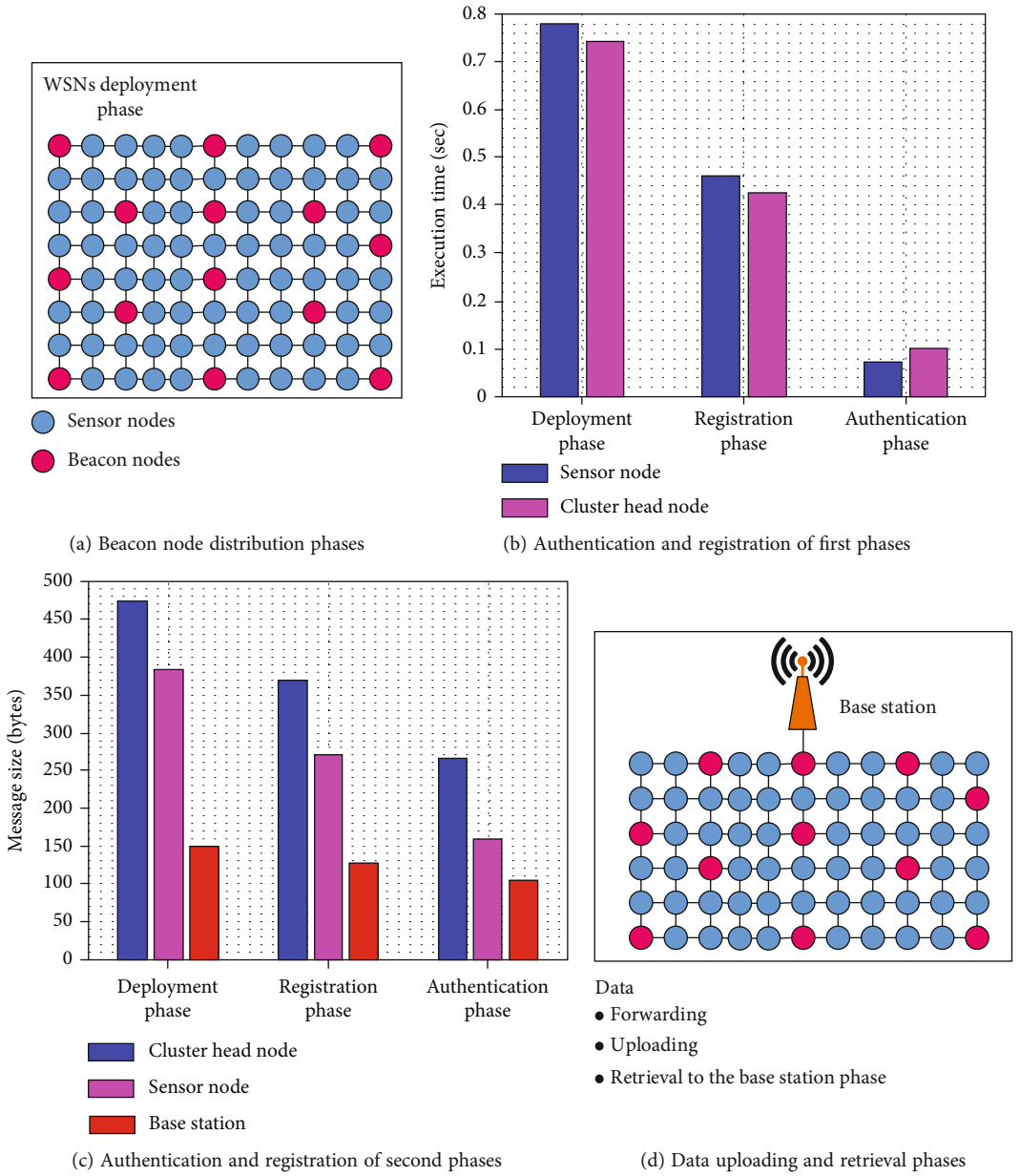
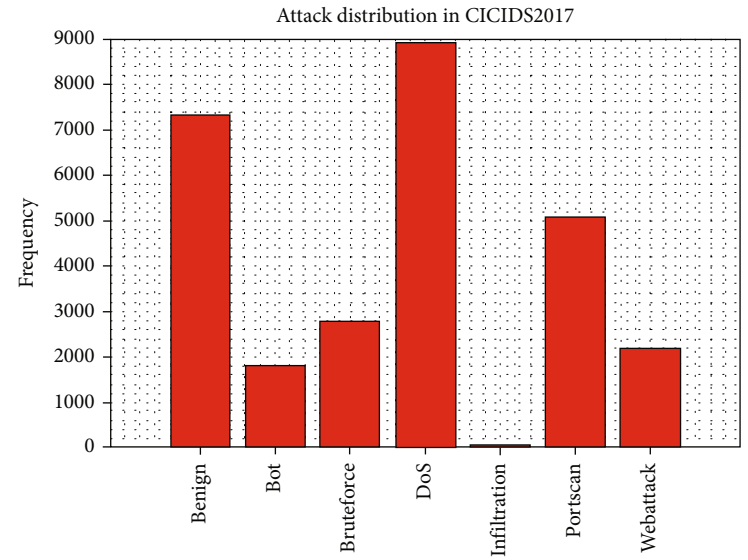


FIGURE 4: Secure data collection and transfer via IoT-WSNs that entail multiple steps, including authentication, registration, and transmission.

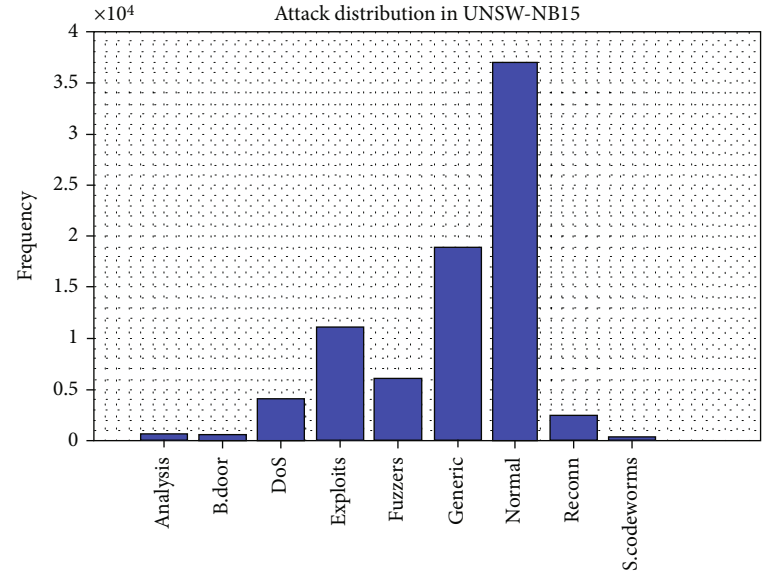
frequency distribution of these attacks is depicted in Figure 5(b). The dataset is divided into 80% training and 20% testing samples for building the predictive models for classification and regression tasks using machine learning models.

4.4.1. Data Preprocessing and Feature Selection. The traffic data can be collected from a local network or the benchmark dataset using the Data collection module [40]. The preprocessing module receives these data and filters them before they are used. These details are also supplied to the cluster and the trust-based safer routing module for more efficient data transmission. The data preprocessing agent makes excellent use of available data preparation methods. Data cleansing, integration, and modification are also undertaken before preprocessing. The data preprocessing step starts with data cleaning and normalization to improve the data quality for training and testing for building the predicting machine learning models. The preprocessing is important for vectorizing, consisting of feature extraction, feature selection, and dimensional reduction [41]. The dataset can be cleaned by removing the duplicated values, replacing the mission data, and removing and fixing unwanted structures from the samples. After cleaning the dataset, it is essential to normalize using the minimum and maximum scaling values as in the following equations:

$$Z_{\text{norm}} = \frac{Z - \min(z)}{\max(z) - \min(z)}, \tag{8}$$



(a) Frequency distribution of attacks in CICIDS2017



(b) Frequency distribution of attacks in UNSW_NB15

Figure 5: Attack occurrences in the CICIDS2017 and UNSW_NB15 benchmark datasets were plotted as a frequency distribution.

where min (z) is the minimum value, and max (z) is the maximum value of the attribute Z, respectively. Z_{norm} is a normalized feature value, and Z is an original feature value [42].

K-means cluster sampling is utilized to improve the classification and detection accuracies of the machine learning model by generating a small K-number of clusters of the original dataset to reduce the training complexity [43]. The K-means sampling technique generates highly representative small groups by removing redundant data to increase efficiency, computational power, and resource. The synthetic minority oversampling process (SMOTE) creates high-quality samples to avoid class imbalance. After the data preprocessing technique, a feature engineering technique is applied to produce sensitive, high-quality features, reduce dimensionality, and remove redundant features by computing the correlation features between features.

4.5. Federated Learning and Security. Currently, the federated cybersecurity (FC) model communicates and collaborates at several levels to provide security solutions for IoT applications. However, privacy and security risks are associated with the standard method of transmitting data within the cluster and across different groups. As a result, federated learning (FL) has emerged as a viable option for exchanging data and information in a method that is both secure and private as in Figure 6. To ensure the security of the IoT network, an FC model that works in tandem with FL to share and discuss data at any level is essential. Most FC strategies based on FL as a cyberdefense mechanism have concentrated

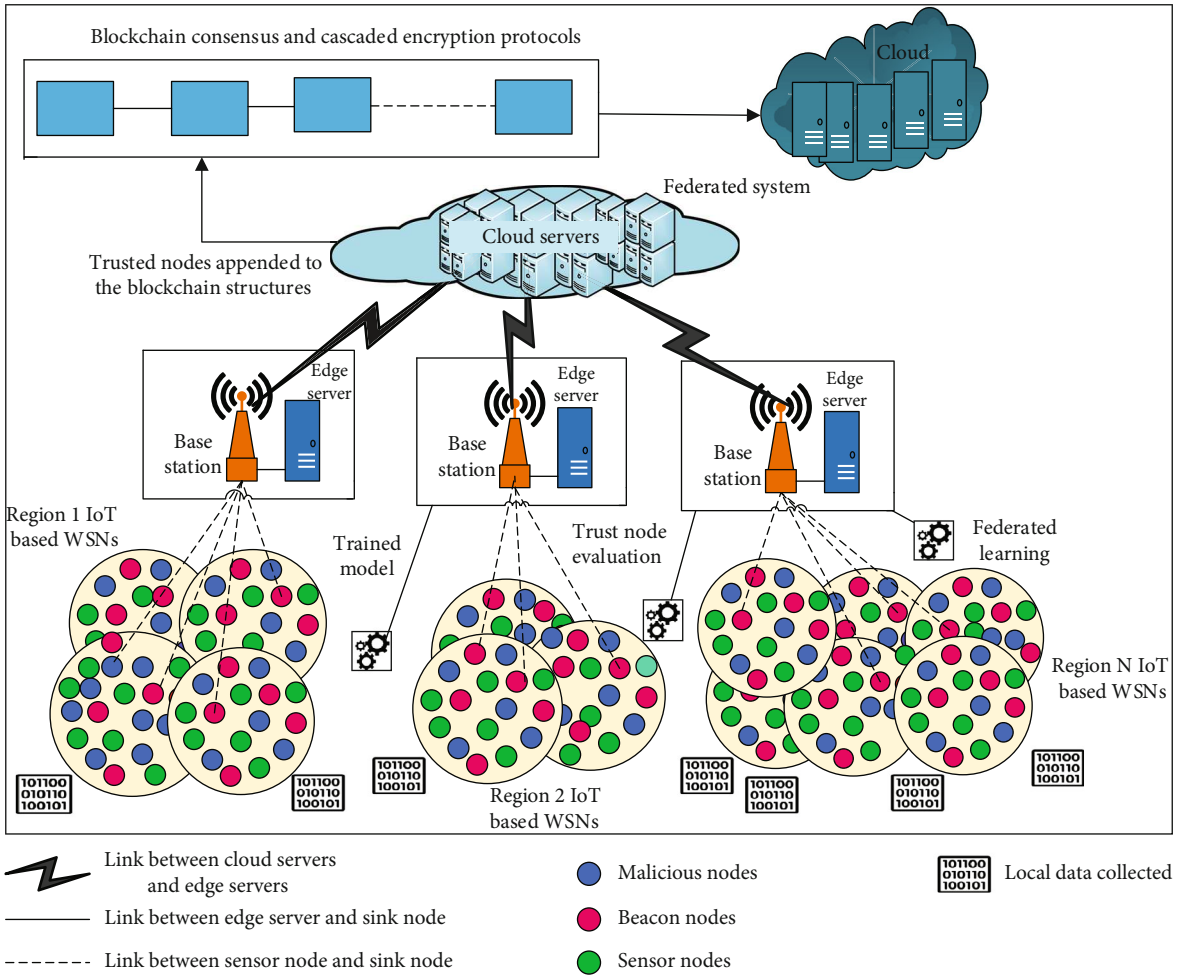


Figure 6: Secure hybrid federated IoT-based WSN model for detection and localization of malicious attacks.

on protecting IoT networks while assuming a unified, worldwide service offering. The method has been developed for a single global model managed by a single service provider; however, it may be readily generalized to a collaborative scenario with several global models managed by numerous service providers. Only a tiny amount of study has developed a federated security model that integrates different international approaches [44]. Machine learning techniques identify resource allocation, security and privacy, communication cost, localization of malicious nodes, and enhancing network lifetime in IoT-based WSNs [45].

Some of the learning techniques utilized in this work include a support vector machine, XGBoost, random forest, and ensemble stacking to improve the performance and evaluate the effectiveness of the proposed system using various evaluation metrics. They are effective and practical techniques for knowledge extraction and finding the relations in wireless sensors that make detecting malicious nodes in the network more accessible. Trusted nodes valuated by the beacon nodes and base station are allowed to enter the block structure as shown in Figure 6 in IoT-based WSNs.

Machine learning models are statistical algorithms with the ability to infer meaningful insights about future data by learning complex patterns in existing data [25]. These ML models are designed using a training procedure in which the learning models glean relevant meanings from the accessible data logs. Training log sets in an IoT ecosystem are produced locally by a wide variety of digital endpoints including smartphones, smart appliances, sensors, and the like. The efficacy of ML-based IDSs is directly impacted by the quality and quantity of data utilized in training and evaluating learning models. The first type, known as localized learning, involves training a model locally using data sets generated by a single endpoint; the second, known as centralized learning, involves training a model centrally using data sets collected from multiple endpoints, and the third, known as federated learning, involves training a model across multiple endpoints using local data sets without exchanging them.

4.5.1. Random Forest. Random forest (RF) is an ensemble learning model that operates by constructing many decision trees for predicting a class [46]. Random forest manages high-dimensional data by judging the importance of the features for solving overfitting and stability problems by reducing the variance. This makes the random forest technique effective for detecting and classifying malicious attacks using

a heterogeneous benchmark dataset in wireless sensor networks. The random forest also handles the missing values and is robust to outliers with less effect for nosy data. The scheme also needs more computational power and more resources due to the construction of many trees. Random forest constructs a forest of several decision trees to predict the model's detection accuracy [47]. It is successful in detecting and classifying attacks using a benchmark dataset.

4.5.2. Gradient Boost. Extreme gradient boosting (XGBoost) is a classification technique for large datasets with a minimum amount of time, making it popular nowadays [48]. The gradient boosting technique uses the extraction of essential features to improve the computational speed and provides a precise output for intrusion detection by reducing memory consumption during the training and testing of the dataset for classification [49]. It is an efficient machine learning technique for optimizing the loss function and computed features, as shown below:

$$\phi(\mathrm{X}) = \sum_{k=1}^{K} f_k(X) \quad f_k \epsilon F, \tag{9}$$

where $\phi(X)$ is the final result of the K sequential classifier and f_k is the decision tree for the K number of iterations in the gradient descent algorithm. The technique also performs parallel computing for getting results in classifying the target results. The XGBoosting improves the gradient descent and regularization strategy for optimizing and managing the process and overfitting factor. The parameters of the classifiers are related as in the following equation shown below:

$$\mathscr{L}(\phi)_{\mathrm{t}} = \sum l(f_{t-1} + f_t) + \Omega(f_t), \tag{10}$$

where $\mathscr{L}(\phi)_t$ is the loss function and $\Omega(f_t)$ is the regularization term to optimize the step size t. The gradient boosting technique uses feature metrics to retrieve the scores according to the features for each attribute.

4.5.3. Ensemble Learning. Ensemble machine learning techniques are classifiers with averaged accuracy to reduce the risk of overfitting and bias from a single classifier [50]. The classification machine learning models are set of tree structures and enhance the overall accuracy. Ensemble techniques are meta-algorithms combining various machine learning techniques into a unified machine learning prediction model for evaluating variation and stacking [51]. The ensemble technique integrates different machine learning results into a single robust model and improves the overall performance. Stacking, bagging, and boosting are the essential ensemble technique concepts. In this scheme, stacking is used for combining and increasing the prediction power of the machine learning models.

4.5.4. Support Vector Machine. The term "support vector machine" (SVM) refers to a family of statistical methods for categorizing network activity under the guidance of an experienced teacher [52]. The fundamental purpose of a support vector machine (SVM) classifier is to build a hyperplane in the feature spaces using a set of vectors called support vectors. Here, we use a dispersed binary classifier for normal and abnormal, which enables the detection of any harmful behavior.

$$w = \sum_{i=1}^{n} a_i y_i x_i \quad \min \left\{ \frac{\|w\|^2}{2} + \mathrm{C} \sum_{i=1}^{n} \varepsilon_i \right\}. \tag{11}$$

$\sum_{i=1}^{n} \varepsilon_i$ is the bounds on the learning vectors, C is the constant that determines the tradeoff between the number of false positives and the margin, and a_i is the Lagrange multiplier. The input and output variables, x and y, are for the demo data set.

Support vector machine (SVM) is a technique for classification, outlier detection, and regression of data samples using hyperplane mapping the data into feature space [47]. It is used for multiclass classification techniques using nonlinear data as a benchmark for evaluation. The SVM technique is used to detect and classify attacks in WSNs to improve the performance and detection accuracy of the system. The SVM has some key features, including more training time, nonlinear data usage, and a higher false alarm rate. It is most beneficial for the classification and prediction of performance evaluation.

4.6. Optimization Techniques. To further enhance the classification of machine learning models for the proposed method on the benchmark dataset, we combine two hyperparameter optimization strategies with Bayesian optimization using a tree based on the Parzen estimation (BO-PTE). Hyperparameters are used by every machine learning method in order to fine-tune the settings and achieve the best possible results. Machine learning performance is enhanced while human labour is reduced thanks to hyperparameter optimization (HPO) [53]. Hyperparameter optimization is also utilized in a black box and global optimization for enhancing functional evaluation. This enables us to describe the black box Bayesian optimization techniques. Bayesian optimization (BO) is a framework for global optimization with expensive black box functions gaining attraction in HPO for deep neural networks. Bayesian optimization is an iterative technique with an acquisition function and probabilistic surrogate model evaluating the decision-making points by applying the Gaussian process. The hyperparameters are handled by tree-based methods, including random forest and tree Parzen estimators (PTE). In this proposed work, Bayesian-based optimization is used with tree Parzen estimators (BO-PTE) for evaluating the best point of evaluation for automatic machine learning.

5. Simulation Results

The validation of the proposed system model is presented using simulation results with different simulation scenarios. The simulation results confirmed that the proposed scheme effectively detects and localizes malicious nodes in IoT-based wireless sensor networks. Our suggested approach employs a

Table 1: Simulation setup for the proposed network model.

Parameter	Values	Parameter	Values
Software	MATLAB	Total sink nodes	10
Number of sensors	1600	Number of clusters	53
Total unknown nodes	1480	Sink position	500, 2000
Protocol type	Clustering and routing	Attacks	Routing
Deployment area	$20000 \times 20000\,m^2$	Mobility	Random
Total beacon nodes	110	Transmission radius	250
Total edge servers	10	Data size	4000 KB

trust evaluation mechanism to pinpoint malicious sensor nodes in the network. In addition, we have included an authentication method to prevent unauthorized access to our network. An energy-efficient and real-time routing system between SNs and BSs is also proposed. Based on authentication, the proposed model is contrasted with the current paradigm. Since authentication's impact is difficult to see in real-time, we measure it in terms of how long a network lasts, how much power it uses, and how fast it can transfer data. In addition, Solidity is employed in the creation of the smart contract. PoW and PoA are used together as part of a consensus process to verify the integrity of the network. The implemented algorithms are compared based on their gas consumption and transaction delay [12].

In our experiments, we used Python 3 and MATLAB as the primary language of code [17]. Popular libraries like NumPy, which facilitates the manipulation of multidimensional arrays and matrices, have been used to implement the proposed strategy. These matrices and arrays are used in the analysis and classification of attacks. Pandas python library provides easy access to advanced data structure modification and analysis tools. Frameworks like TensorFlow and Keras have become increasingly common in deep learning and machine learning. Both supervised and unsupervised ML techniques can be developed with the scikit-learn toolkit. SMOTE was created to oversample people from underrepresented groups systematically. The network planning and simulation of the models were conducted using MATLAB R2021a running on a machine having a Processor Intel(R) Xeon(R) Silver 4214 CPU @ 2.20GHz 2.19 GHz (2 processors), Installed RAM 128 GB (128 GB usable), windows ten 64-bit operating system, and ×64-based processor. Python is also used for data processing and analysis. Table 1 shows the parameters of the simulation setup for network deployment and performs a comprehensive security analysis. Solidity programming language is also employed for creating smart contacts and consensus processes. Both proof-of-work and proof-of-audit are used as network-wide consensus techniques for validation. Measures such as gas consumption, transaction delay, geolocation accuracy, and classification precision are used to evaluate the developed algorithms.

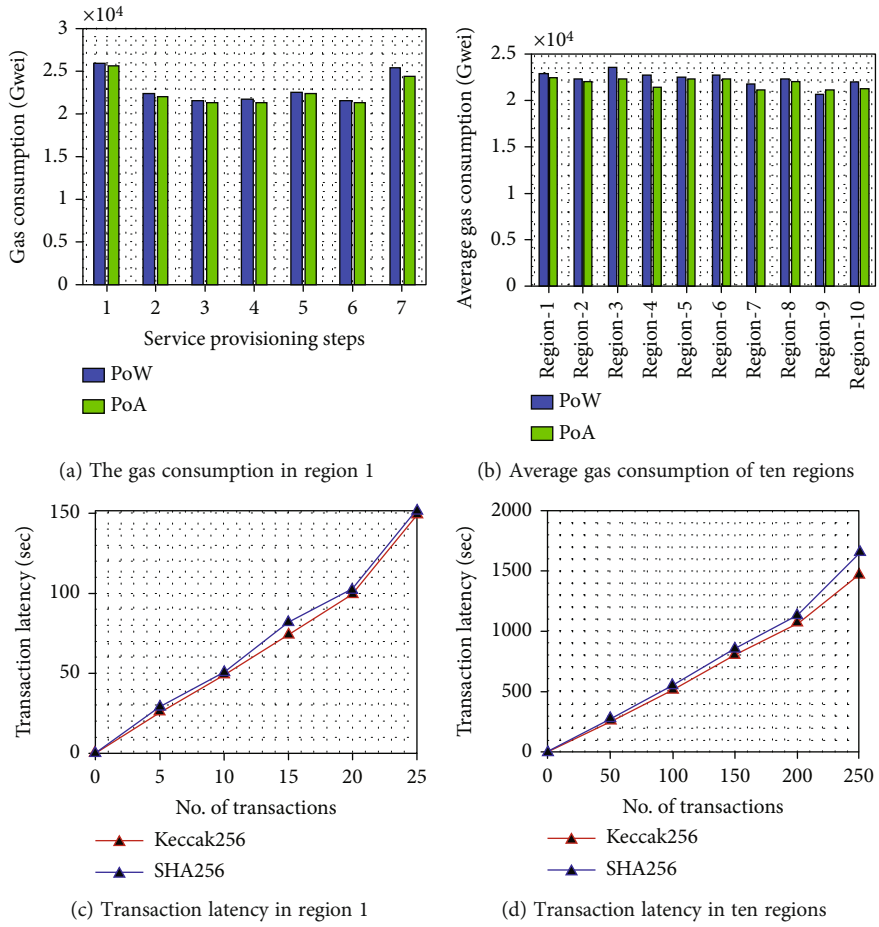
The proposed localization technique uses blockchain for detecting malicious attacks, and the models are deployed into ten independent IoT-based regions for IoT-based WSNs. The PoW and PoA consensus algorithms are used in the region for validating the transactions and adding blocks for detecting malicious nodes and service provisioning. Minor nodes validate the transactions and add blocks for localization of the unknown nodes so that attacks can be removed. This blockchain-based technique enables localizing routing attacks that degrade the network performance and lifetime.

Table 1 also contains the simulation parameters for the models we have proposed. Ten distinct IoT-WSN areas have implemented in this proposed blockchain-based localization for detecting malicious attacks and various simulation parameters for the proposed models. Predesignated nodes are liable for approving transactions and putting blocks onto the blockchain under these models, which use the PoA consensus method Figure 7(a) illustrates how IoT-WSN gas usage varies by power level and area in region 1 IoT-WSNs for service provisioning. For example, Figure 7(b) compares the average gas consumption of the IoT-WSNs in all ten regions to that of PoW and PoA. PoW uses more gas than PoA, as evidenced by these numbers. This is because in proof-of-work (PoW), the miner nodes in charge of validating transactions are chosen through a rigorous mathematical process. On the other hand, in PoA, miners are selected based on their stakes rather than their qualifications. A group of miners is chosen to validate and run blockchain transactions and add new blocks.

5.1. Evaluation Metrics. A trust value is determined for each beacon node to choose the most reliable and secure beacon nodes [4]. According to the trust value calculation, the network has numerous nodes that do not know their specific location. These nodes cannot locate themselves without the help of nearby beacon nodes why they should be the most reliable and trustworthy in a network. The confidence of each anchor node is calculated using the triangulation process and distance vector routing to identify the most reliable beacon nodes. Behavioural, feedback, and trusted data values contribute to the total trust level. Four criteria are used to measure behavioural trust:

(1) Frequency of interaction: anchor nodes' interactions with other anchor nodes are counted as the rate of interactions

(2) Friend nodes and list of neighbors: the ratio of the total amount of one-hope nodes in any beacon node



(a) The gas consumption in region 1

(b) Average gas consumption of ten regions

(c) Transaction latency in region 1

(d) Transaction latency in ten regions

FIGURE 7: The gas consumption and transaction latency of different regions in IoT-based wireless sensor networks.

to the whole number of nodes except for this particular beacon node is an essential statistic for calculating behavioural trust. It is the quickest route from the beacon node to the rest of the network. The number of nodes in the vicinity of anchor node is called its range

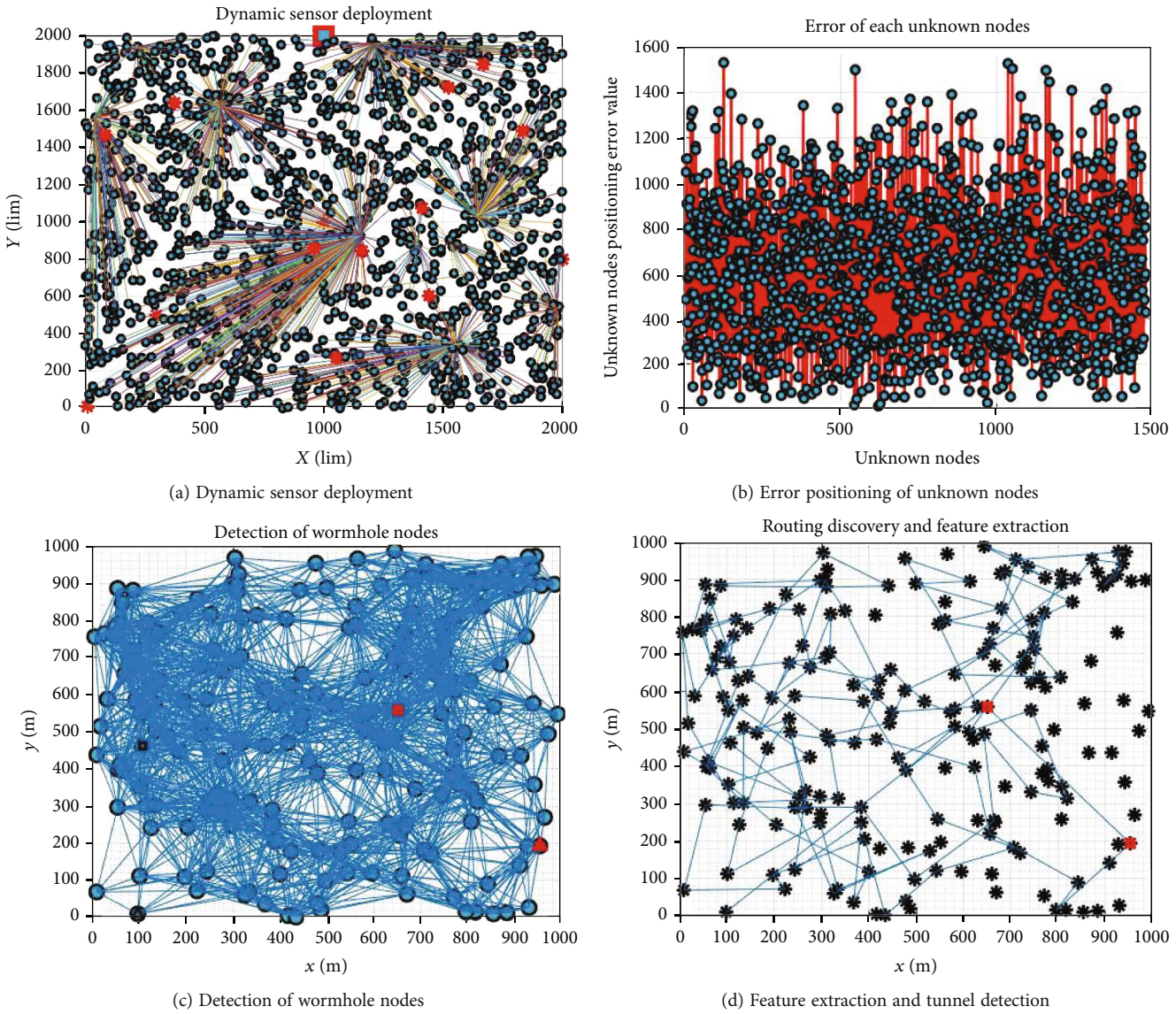
5.1.1. Localization Accuracy. The performance of the proposed system is measured using localization error (LE), average localization error (ALE), localization accuracy of the unknown sensor nodes, and the confusion matrix taking the CICIDS2017 benchmark dataset for classification of attacks. The localization error measures how far away the estimated position is from the true position [54]. To facilitate a standard means of comparison, localization errors are normalized to the radio range of sensor nodes. The average localization accuracy measures how precisely the nodes in the study area are located [55]. The average error localization (ALE) [34] is computed as in equations (12)-(14), respectively. The average detection rate, accuracy, precision, and recall are also used to evaluate the effectiveness the proposed system. In order to calculate the ALE, add up the LE of all the unknown nodes and divide by the total number of unknown nodes [29].The LE represents the discrepancy between the estimated and true locations of any undiscovered nodes.

$$\mathrm{LE} = \sqrt{\left(u_i' - u_i\right)^2 + \left(v_i' - v_i\right)^2},$$

$$\mathrm{ALE} = \sum_{i=1}^{n} \frac{\sqrt{\left(u_i' - u_i\right)^2 + \left(v_i' - v_i\right)^2}}{\mathrm{nR}},$$

$$\mathrm{ALA} = \left(1 - \left(\sum_{i=1}^{n} \frac{\sqrt{\left(u_i' - u_i\right)^2 + \left(v_i' - v_i\right)^2}}{\mathrm{nR}}\right)\right) \times 100\%, \tag{12}$$

where (u'_i, v'_i) and (u_i, v_i) are the real and computed coordinates of the anonymous node I, respectively; n represents unknown nodes, and R represents the communication radius of the network. In Figure 8(b), we can see the deviation of the unknown sensor nodes (b). Using the localization scheme, the positions and deviations of all nodes are calculated. The performance of the proposed scheme is evaluated using the performance metrics including detection rate, false



(a) Dynamic sensor deployment

(b) Error positioning of unknown nodes

(c) Detection of wormhole nodes

(d) Feature extraction and tunnel detection

Figure 8: Dynamic deployment and clustering of sensor nodes for computing unknown node positioning in IoT-based WSNs.

alarm, precision, and recall. Equations (15)-(17) provide a mathematical representation of this:

$$\begin{aligned} \text{Accuarcy} &= \frac{\text{TP} + \text{TN}}{\text{TP} + \text{TN} + \text{FP} + \text{FN}}, \\ \text{Detection rate} &= \frac{\text{TP}}{\text{TP} + \text{FN}}, \\ \text{F1} - \text{score} &= \frac{2 \times \text{TP}}{2 \times \text{TP} + \text{FP} + \text{FN}}. \end{aligned} \tag{13}$$

Accuracy determines how well the learning model functions are [56]. We put the proposed method to the test by doing experiments and comparing the outcomes to those obtained using an established secure blockchain based on federated hybrid machine learning models. To accomplish this, we must first determine the proportion of attacks that were correctly classified as true positive, trusted nodes that were correctly classified as true negative, false positives that were incorrectly classified as true negative, and false negatives that were incorrectly classified as true positive.

The detection rate is a measure of correctively classified normal traffic and is regarded as a positive value over the total samples in the dataset. The detection rate is the same as the actual positive rate computed in equation (14). The precision is the number of correctly classified attacks over the total number of instances of attacks in the networks.

$$\text{Precision} = \frac{\text{TP}}{\text{TP} + \text{FP}}, \tag{14}$$

where true positive (TP) is the number of attacks correctly classified as attacks [57, 58], and false positive (FP) is the number of attacks incorrectly classified in the network [59]. The true negative (TN) is the legitimate nodes organized as

legitimate, and the false negative is the honest nodes incorrectly as malicious nodes in the network traffic.

The detection accuracy is the fraction of trusted sensor nodes that correctly identify malicious nodes relative to the total number of harmful nodes in the network [6]. When compared to the false negative rate (FNR), which is the total number of malicious nodes that are incorrectly classified as legitimate nodes by the suggested model, it is computed by the following equation:

$$\mathrm{FNR} = \frac{\mathrm{FN}}{\mathrm{FN} + \mathrm{TP}}. \tag{15}$$

5.1.2. Intimacy. It is one way to gauge the behavioural trusted values of the anchor nodes. It is the time consumed that anchor nodes spend for communicating. It is computed by using the following formula:

$$\mathrm{In} = \frac{t_i}{t_i + t_a}, \tag{16}$$

where t_a is the time consumed for node to communicate with the a anchor node and t_i is the collaboration time of a particular node with beacon i.

5.1.3. Honesty. Another metric that is used to calculate behavioural trust is honesty. The equation used to calculate it is presented below.

$$h_{\mathrm{o}} = \frac{P_s}{P_n}. \tag{17}$$

There are P_n interactions between source and destination nodes and P_s interactions between source and destination nodes that result in successful outcomes. Truthfulness tells the overall amount of interactions between nodes, both successful and unsuccessful. The interactions take into account end-to-end delay for classifying interactions among nodes. The amount of time it takes, on average, for data packets to be transported from source nodes to sinks, including both valid and faulty data packets, is referred to as end-to-end latency [60]. It is the amount of time required for a data packet to travel from its point of origin to the location where it will be stored permanently.

When malicious nodes are inside the radius of any anchor node, the behavioural trust in those beacons is compromised. Beacon nodes' overall trust is impacted, resulting in an incorrect selection of anchor node and cluster head nodes for accurate localization malicious nodes in WSNs. The number of neighbour nodes, distance error, security, mobility, and localization techniques all plays a role in determining where rogue nodes can be found in WSNs [61].

After calculating behavioural trust, each beacon node's feedback trust is determined. A beacon or an unknown node must supply the other with its coordinates to figure it out. After verifying that the sender beacon node gave it the correct coordinates, this node provides feedback on the sender beacon node. Last, each beacon node's data-based trust is calculated by comparing the actual distance of the beacons to their anticipated distance. Equation (18) gives the Euclidean theorem to calculate the exact distance for estimating distance.

$$D_{\mathrm{ac}} = \sqrt{\left(u_i - u_j\right)^2 + \left(v_i - v_j\right)^2}, \tag{18}$$

where D_{ac} is the actual distance, u_i and v_i denote the positions of the sender anchor node, and u_j and v_j are the positions of the destination anchor node.

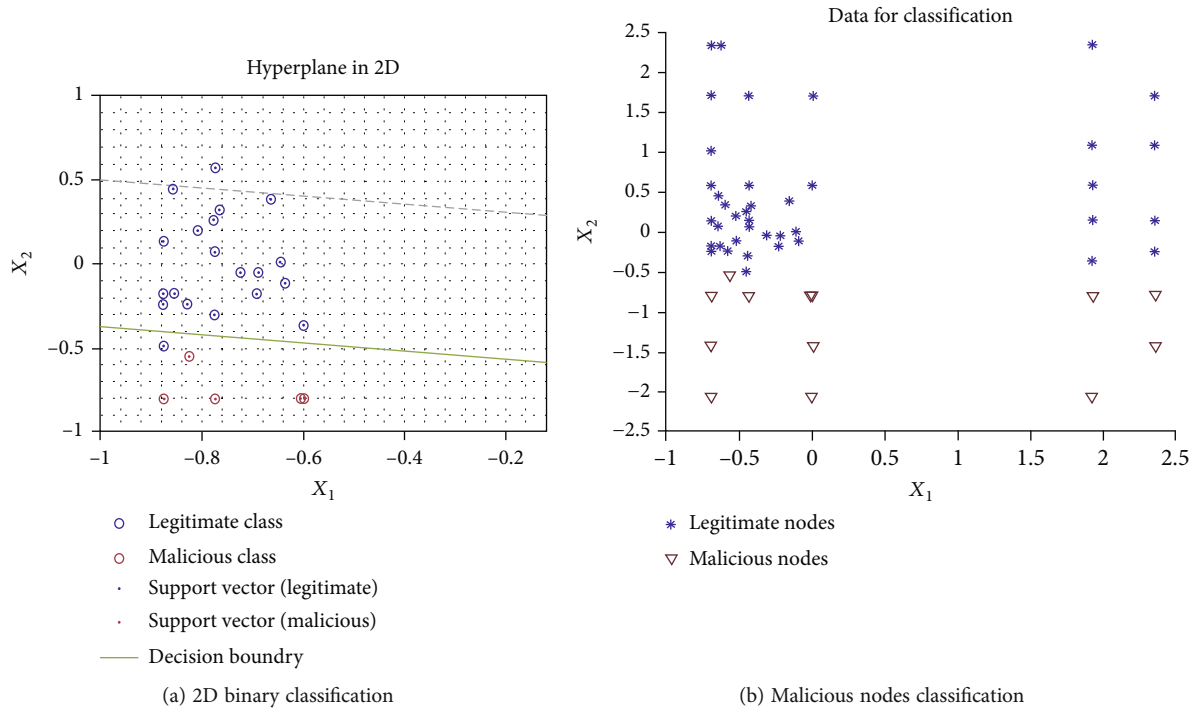
The novelty of the proposed methodology is scalability and chain of trust evaluation using intelligent communication of the wireless sensor nodes within a given region. The security performance of the system is independent for each area; hence, the DoS attacks cannot manipulate and access multiple religions simultaneously.

6. Performance Evaluation and Validation

The evaluation and validation of the proposed system are computed through simulating and classification of hybrid and federated machine learning models. Our simulation results demonstrate the efficacy of the proposed system's federated-based machine learning algorithms for identifying, localizing, and classifying malicious nodes in the simulated network. The proposed model has been simulated to determine its gas consumption, delay, time response, data aggregation, remaining network energy, and dropped packet count.

The practical steps of our model are deployment, as shown in Figure 8(a) and computing in Figure 8(b), for localization error of unknown nodes, registration, authentication, routing calculation, and malicious node detection and classification using hybrid federated machine learning models. The wormhole attacks were detected by computing the distances and position of the sensor nodes marked with red colors as in Figure 8(c). Wormhole tunnels were created and detected using routing discovery and feature extraction between two malicious nodes as depicted in Figure 8(d).The simulation result shows that the proposed system achieved the localization accuracy of the routing attacks is 99.14% by training the extracted features as shown in Figure 8(d). This shows that the localization accuracy of the wormhole attack is effective compare to Kim et al. [1] with localization accuracy of 82.17%.

As a result of this research, the network's malicious nodes have been located and deleted. XGBoost, random forest, extra tree, and ensemble stacking are utilized for evaluating the performance and test the effectiveness of the proposed system utilizing benchmark datasets with various evaluation metrics to classify genuine and malicious nodes. Hyperplanes are used by SVM to classify data points into one of two categories. As a result of this model, a line (hyperplane) is generated that splits the data samples into two distinct categories. A hyperplane is constructed for comparing these data point. The SVM model then determines the class of each data point. SVM's primary goal is to build a decision border that is effective for separating the data samples of each course, as shown in Figure 9(a), for malicious node classification as in Figure 9(b).



(a) 2D binary classification

(b) Malicious nodes classification

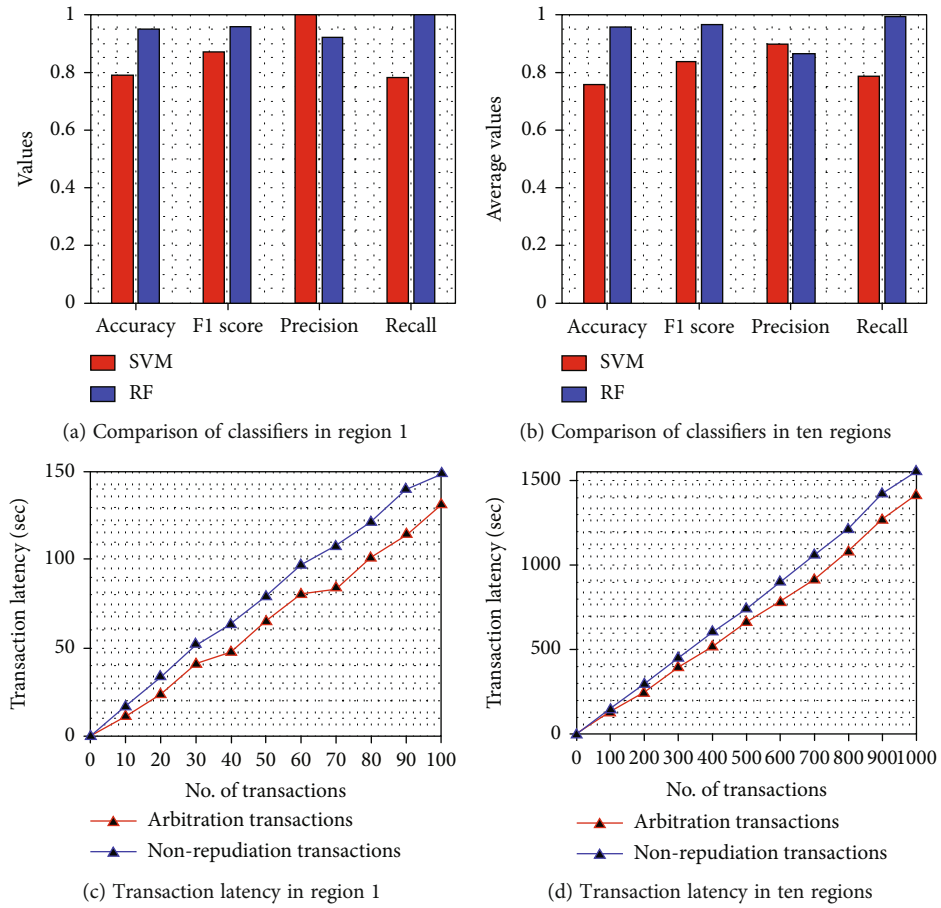
Figure 9: Classification of legitimate nodes from malicious nodes using decision boundary with SVM.

The dataset is imported and labelled when the honesty and end-to-end delay calculations are completed. After that, it is separated into datasets for training and testing. Following the division of the dataset, the model is trained to predict the node categorization based on its predictions. The benchmark dataset demonstrates the SVM model's extensive methodology for detecting malicious nodes.

The results also show that the proposed approach is efficient for malicious node detection using the blockchain technique for ten independent and nonrepudiation regions in IoT-based wireless sensor networks. Preselected network nodes, as depicted in Figure 7(a) and Figure 7(b), in the next generation's IoT-based wireless sensor networks will use the proof-of-authority (PoA) consensus process to validate transactions and add blocks to the block. The majority of consortium blockchains use the PoA consensus technique. To add new blocks to the blockchain, PoA chooses a set of validators. Validators are chosen according to their standing in the system. Since validators can be preselected using PoA, it uses far fewer computing resources than PoW. Contrary to PoW, the PoA consensus technique does not include any form of mining. Proof-of-work (PoW) is a consensus technique utilized by public blockchains like Bitcoin and Ethereum. A cryptographic problem is broadcast over the network to determine a miner in proof-of-work (PoW). The node chosen will be the one that figures out the solution to the challenge quickly and accurately. The chosen miner verifies the transactions and creates the block hash. The hash is then sent across the network to establish an agreement. Figure 7(a) compares the gas consumption in the secure service provisioning method between PoW and PoA in region 1 of an IoT-based wireless sensor network. The gas consumption is a small amount of cryptocurrency, as shown in Figure 7(a). The amount is deducted from the user's account performing the transaction on the Ethereum blockchain [62]. The cryptocurrency is removed from the user account. Figure 7(a) shows the gas consumption of events of the secure service provisioning process in gas units.

Similarly, Figure 7(b) compares the average gas consumption of IoT-based wireless sensor networks between PoW and PoA in all ten regions. PoW uses more gas than PoA, as evidenced by these numbers. This is because in proof-of-work (PoW), the miner nodes in charge of validating transactions are chosen through a rigorous mathematical process. On the other hand, in PoA, miners are selected based on their stakes rather than their qualifications. A group of miners is chosen to validate transactions and add new blocks to keep the blockchain running. Since all transactions depend on a limited number of miners, the PoA process weakens distributed nature of the blockchain. This is partly because PoA makes blockchain networks more centralized. The transaction delay of Keccak-256 and SHA-256 hashing algorithms in region 1 IoT-based wireless sensor networks and across all ten IoT sensor networks is shown in Figures 7(c) and 7(d). The secure hashing method has been expanded, and the Keccak256 hashing algorithm is the result (SHA3). There is a built-in implementation of the Keccak256 algorithm in the Solidity programming language. Keccak256 may hash any data into a hexadecimal value of a predetermined size.

Because the hashing process is irreversible, this hash cannot be used to retrieve the original data. When compared to other hashing algorithms like SHA256 and RIPEMD160, Keccak256 offers a lower cost profile. Hence, we choose to



(a) Comparison of classifiers in region 1

(b) Comparison of classifiers in ten regions

(c) Transaction latency in region 1

(d) Transaction latency in ten regions

FIGURE 10: Performance compression of classifiers and transaction latency using blockchain technique for detecting and localizing malicious nodes in IoT-based WSNs.

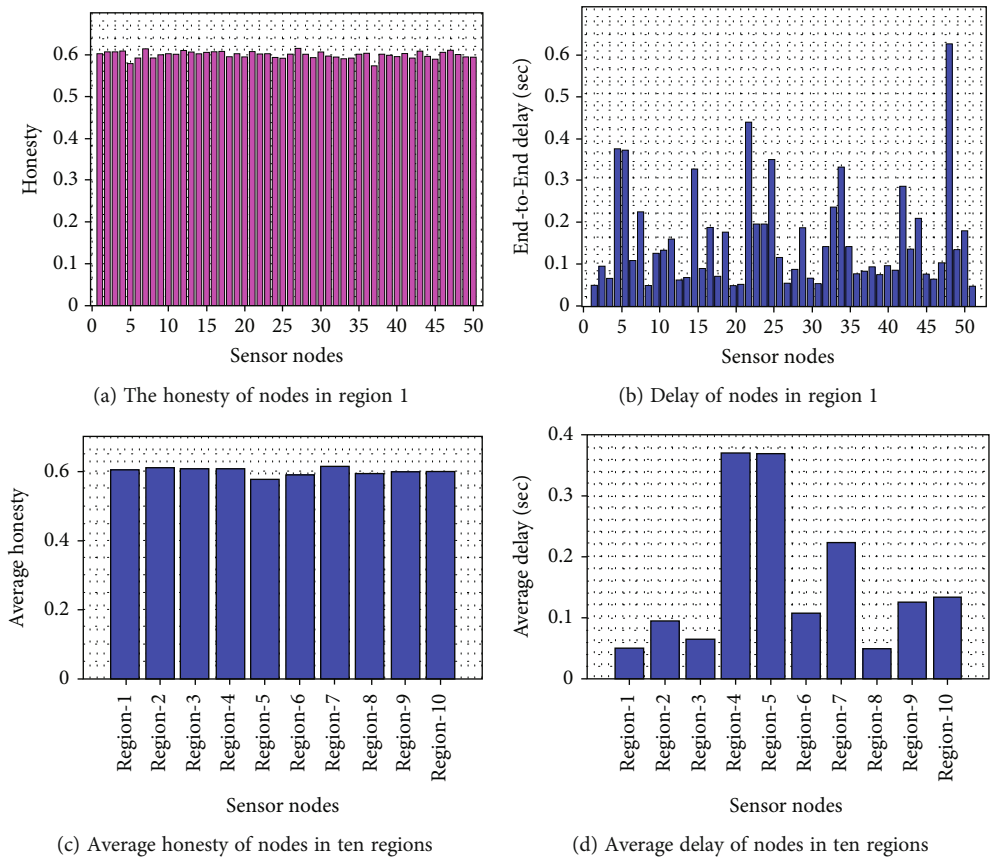
employ it. Network sensors in region 1 of Figure 7 perform 25 transactions per second, while all Figure 7 sensors perform 250 transactions per second (d).

Figures 7(c) and 7(d) depict a network with one and ten areas of IoT sensors, respectively. SHA-256 and Keccak-256 hashing methods behave identically in both figures. It can be deduced from the data that SHA-256 takes almost twice as long as Keccak-256 to execute. SHA-256 lacks an infinite input space, which makes it easier for Keccak-256 to do hashing. A nonrepudiation model based on a support vector machine, XGBoost, random forest, and ensemble stacking classifiers is effectively used for scalable and large networks. The model also provides effective actions for detecting and localizing malicious nodes in the network model using federated machine learning techniques. Linear separability in the SVM hyperplane allows for categorizing data points into two distinct categories.

As a genuine class, the one with the highest honesty value and the least delay from beginning to end is considered the best candidate. However, malicious nodes have a high end-to-end delay and a poor integrity rating. The recall, precision, accuracy, and F1 score of RF and SVM in IoT-based wireless sensor networks are shown in Figures 10(a) and 10(b). IoT wireless sensor networks with rogue nodes can be detected more effectively by using radio frequency identification (RFID) technology. Figure 10(a) shows that SVM has an accuracy of 89%, but RF has an accuracy of 99%.

It shows that support vector machine (SVM) has an average accuracy of 86%, and RF has an average accuracy of 99.3% in all ten regions of interest. According to the findings, RF outperforms SVM in detecting malicious nodes across several regions' networks based on honesty and end-to-end latency. Ensemble learning multiple decision trees are another explanation for RF's better accuracy. Many trees are produced for training and testing to solve the same problem of identifying malicious nodes. Figure 10(a) shows that the F1 score of SVM in a single region is 87.95%, while RF has a 96% F1 score. As depicted in Figure 10(b), SVM and RF have an average F1 score of 84% and 97% in all ten regions of IoT based WSNs, respectively. Because of this, hostile nodes in sensor networks, whether in a single part or over numerous areas, are less likely to be mistaken for legitimate nodes via RF.

In addition, as shown in Figures 10(a) and 10(b), SVM's recall score is lower than RF's because RF is better at predicting harmful nodes. In addition, these results show that SVM's precision is superior to RF's. As a result, SVM can correctly identify the positive observations thanks to its support vector. Our suggested nonrepudiation model was shown to be effective in all ten clusters of the regions of



(a) The honesty of nodes in region 1

(b) Delay of nodes in region 1

(c) Average honesty of nodes in ten regions

(d) Average delay of nodes in ten regions

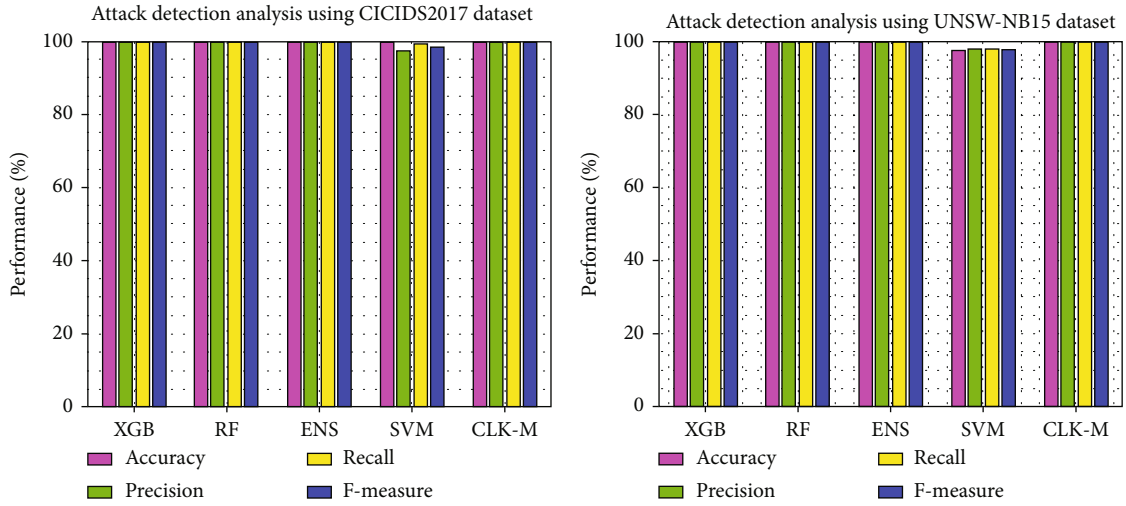
Figure 11: Honesty of wireless sensor nodes and end-to-end delay of nodes in IoT-WSNs.

IoT-WSNs, as shown in Figures 10(c) and 10(d). A varied number of disagreements are reflected in the numbers. Transaction latency is the time it takes a network to process a transaction. Client and service provider latency for arbitration transactions is also depicted. Both the service provider and the customer are found to be vicious in these transactions. According to the diagrams in Figure 10, our suggested system can process a high number of transactions in a short period. As a result, no data is exchanged between the features indicated and the service supplied during these transactions, allowing for a fair comparison. It demonstrates that the arbitration transactions use the bare minimum of network resources including throughput and bandwidth. In addition, the results reveal that the nonrepudiated transactions have relatively low latency. This proves that our suggested nonrepudiation strategy is effective to protect a large number of users over a wide area of IoT-WSNs while being efficient in terms of quality of services and security.

Nodes from region 1 IoT-WSNs are shown to be honest in Figure 11(a). From the region 1 IoT-WSNs, a random sample of fifty nodes is chosen randomly. Shown in the graph are various levels of trustworthiness for each node. For this reason, each node has a varied number of successful interactions. All ten areas' IoT-WSNs' honesty is calculated in the same method, as illustrated in Figure 11(c). Nodes with a high honesty rating are more likely to be legitimate.

This indicates that the node has many interactions and connections with other sensor nodes in WSNs. Honesty is a critical criterion for determining the authenticity of nodes in our networks. Nodes' validity can also be verified by looking at the end-to-end delay, transmission delay, propagation delay, processing delay, and queuing delay and can all be calculated. The malicious nodes are those that have end-to-end delays that are higher than the predefined threshold value. Nodes are not responding quickly enough when other nodes send them messages. Furthermore, their limited processing skills cannot process the data packet, resulting in service denial.

There is a high end-to-end delay with this type of node that broadcasts this information (latency). Figure 11 shows the end-to-end latency of region 1 IoT-WSNs and the average end-to-end delay of all ten regions' IoT-WSNs (Figures 11(b) and 11(d)). Figure 11 depicts the random selection of fifty ordinary nodes from each location. Figure 11(b) shows that the end-to-end delay for each node varies. This is because each node responds to requests in a different period. The malicious nodes in the network are those that have a higher end-to-end delay than a predetermined threshold. Another interesting finding from Figure 11 is that different IoT-WSN region networks have varied range of honesty and end-to-end delay average values, demonstrating the performance of different IoT-WSN region networks in providing secure services.



(a) Hybrid machine learning models using CICIDS2017

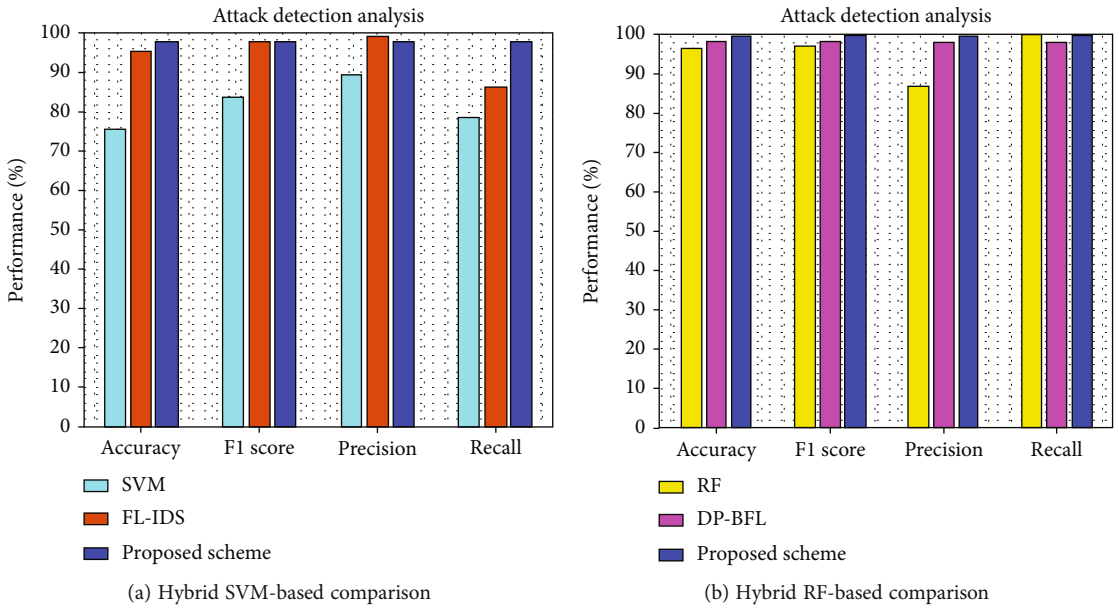
(b) Hybrid machine learning models using UNSW_NB15

Figure 12: The utilization of CICIDS2017 and UNSW_NB15 benchmark datasets for comparison performance of several machine learning models is conducted based on a variety of performance measures.

6.1. Attack Detection Analysis. The performance of the proposed system is evaluated using machine learning models using a benchmark dataset containing a class of attacks in WSNs. The hybrid optimized machine learning also utilizes the same benchmark dataset to evaluate the proposed routing attack localization and detection effectiveness in wireless sensor networks. Figure 12(a) shows the comparative performance of the various machine learning schemes. The performance of the proposed system is further improved with the application of cluster labeling (CL) *K*-means binary classification techniques.

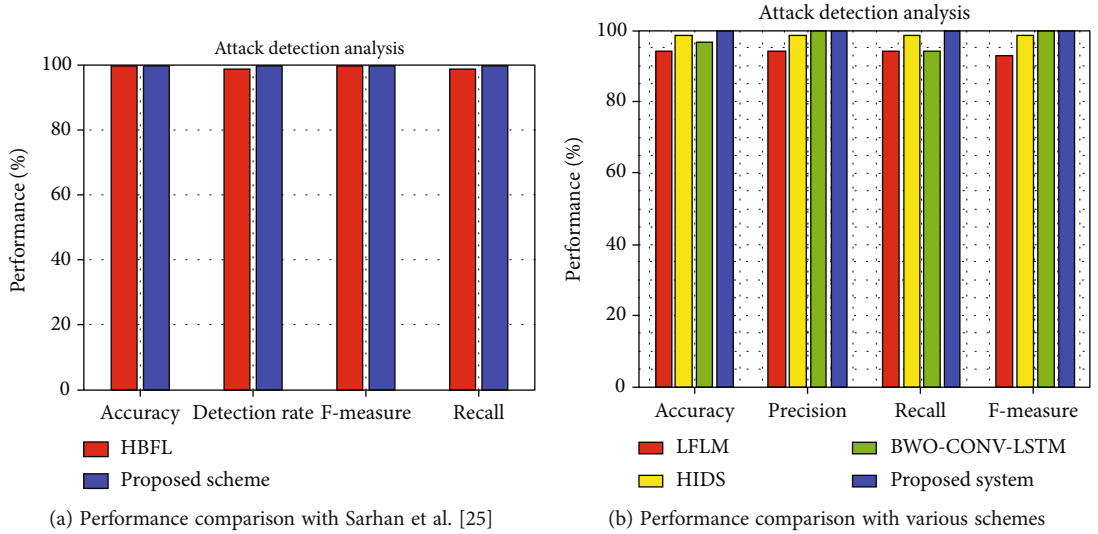
The performance of the proposed scheme is also evaluated using a UNSW_NB15 benchmark dataset with the application of various machine learning models, as shown in Figure 12(b). The binary classification technique using hybrid cluster labeling *K*-means achieves better classification accuracy of 100% using the benchmark dataset. As shown in Figure 12, the proposed system's performance is adequate for detection and localization attacks in IoT-based wireless sensor networks using benchmark datasets. This can be validated and confirmed by comparing the simulation and experimental results with other research works. Abubaker et al. [4] proposed blockchain-based malicious node detection and localization using federated machine learning using SVM and RF in IoT-based WSNs, as depicted in Figures 13(a) and 13(b). Figure 11 shows that the proposed approach effectively detects and localizes malicious nodes in IoT-WSNs using a hybrid federated machine learning approach. Using the dynamic power of SM 3.0 networks and MNSIT datasets as a benchmark evaluation method, Salim et al. [63] present a differentially privacy blockchain-based explainable FL (DP-BFL) architecture as shown in Figure 13(b). Any Internet-connected device can now contribute data to a globally secure model thanks to this platform. Rehman et al. [64] explored the interplay between blockchain technology and federated learning in healthcare and provides a thorough analysis of the results 5.0. The goal of this research is to build a safe healthcare monitoring system 5.0 by using a blockchain-enabled, federated-learning-based intrusion detection system (FL-IDS) to detect any malicious activity within a healthcare network and allowing doctors to keep tabs on patients via sensors and take preventative measures on a regular basis by foreseeing diseases, as shown in Figure 13(a). The results of the suggested system show that the method is well suited to healthcare monitoring.

The results show that the proposed scheme is better compared to Awan et al. [12] which presented a trust evaluation process based on blockchain for storing the identities of the sensor nodes (SN) and aggregator nodes (AN). The scheme utilized the private and public blockchains for detecting malicious nodes with the detection accuracy of 75% taking malicious nodes 20-80, whereas the proposed technique achieves a detection accuracy of 95%, bringing the number of malicious nodes to 5-30. Otoum et al. [14] proposed a framework using blockchain and federated learning for trust evaluation and security and achieved average detection rate accuracy of 96% and 93%, respectively. Kim et al. [1] achieved average localization detection accuracy and average localization error of 96.5% and 6.97 using secure blockchain based on trust management and evaluation, respectively. Friha et al. [17] designed DNN, CNN, and RNN learning techniques and achieved average detection accuracy of 98.63%, 99.71%, and 99.05% for FELIDS using a benchmark dataset for measuring the detection performance of the system. Kim et al. [41] presented collaborative security system-based federated learning for the internet of things. They achieved a training accuracy of 98.47% using the NSL-KDD benchmark dataset with various classes of attacks for training and testing. This suggests that the proposed scheme is enhanced for detecting and localizing attacks in IoT-based WSNs. The proposed blockchain-based technique for attack detection and localization enhances security. It reduces energy consumption and



(a) Hybrid SVM-based comparison (b) Hybrid RF-based comparison

Figure 13: Performance comparison of the proposed scheme with various evaluation metrics for identification of malicious nodes in IoT-WSNs using benchmark dataset.



(a) Performance comparison with Sarhan et al. [25] (b) Performance comparison with various schemes

Figure 14: Performance comparison of the proposed scheme using various evaluation metrics and benchmark dataset with previous works.

effective data aggregation using the trust values of the beacon nodes for improved network lifetime compared to Ahmed et al. [45]. Mahmood and Jusas [65] proposed blockchain-enabled federated learning for data security and privacy in IoT-WSNs and decentralized nodes and sent global data sharing and achieved average detection accuracy of 95%. The scheme also aggregates the data from the local model to the global model for secure transactions. This shows that the proposed method achieves better classification accuracy. Sarhan et al. [25] proposed a hierarchical blockchain-based federated learning (HBFL) for a secure collaborated intrusion detection system in IoT-based wireless sensor networks as shown in Figure 14(a). The scheme achieves an average detection accuracy of 99.71% using a benchmark dataset UNSW-NB15 containing various classes of attacks. Hassan et al. [66] proposed self-learning and the adaptive protocol to transmit multiuser data automatically by efficiently using channel spectral features and achieved average attack classification accuracy of 98.98 using a nonlinear SVM classification model for IoT-based WSNs. Nasser et al. [67] presented a lightweight federated learning model (LFLM) to learn medical symptoms with high accuracy from data collected by individuals utilizing ambient IoT based-sensors and wearable devices for the COVID-19 response in a collaborative yet private manner with evaluation metrics a shown in Figure 14(b). Roy et al. [68] present a two-layer hierarchical intrusion detection system (HIDS) based on machine learning to successfully detect intrusions

in IoT networks while meeting the IoT resource restrictions. Kanna and Santhi [69] proposed a MapReduce-based black widow optimized convolutional-long short-term memory (BWO-CONV-LSTM) networks for building a hybrid IDS model that efficiently addresses these problems in IoT-based WSNs.

Kumar et al. [56] proposed a federated machine learning-based intrusion detection system for detecting and localizing malicious nodes. They achieved an average detection accuracy of 92.7% using KDD-99 in IoT-based WSNs. The proposed approach is further compared with Mohar et al. [70], and Kumar et al. [71] performed an average localization error of 0.43 with four beacon nodes using a hybrid scalable, secure collaborative localization technique for WSNs. Sajid et al. [72] presented models based on genetic algorithms are presented for identifying malicious nodes, specifically the GA-SVM and GA-DT. After a rogue node has been identified, the Dijkstra algorithm is used to determine the most efficient route through the network. Both GA-DT and GA-SVM are highly accurate, with a 96% and 98% success rate, respectively. The GA-DT and GA-SVM each score 94% and 96%, respectively, when it comes to their accuracy. Nagalakshmi et al. [73] designed and presented detection and localization of black hole attacks based on machine learning models using 114 samples and achieved localization accuracy of 98.01% for WSNs. This demonstrates that the suggested approach performance is more sufficient for identifying and categorising attacks in IoT-based WSNs.

7. Conclusion

The proposed solution utilizes a blockchain-based security technique to detect and localize malicious nodes in hierarchically distributed IoT-WSNs. Using XGBoost and CLK-means machine learning federated classifiers for multiclass and binary classification approaches, the blockchain technique successfully identifies and pinpoints rogue nodes in IoT-based wireless sensor networks. Service delivery without the risk of attack and improved network speed was other goals of this technique, which also made use of feature evaluation and cascading encryption techniques. Results from simulation and classification demonstrate that the proposed system is sufficient for malicious node detection and localization, with average detection accuracies of 99.95% and 100% for XGBoost and CLK-means, respectively, based on the multiclass and binary classification approach with the CICIDS2017 benchmark dataset. Detecting and localizing attacks in IoT-WSNs with the use of a hybrid federated machine learning approach are a novel approach. The outcomes demonstrate that random forest is superior to other methods for classifying diverse network traffic data and detecting malicious nodes. Node honesty, end-to-end delay, and transaction latency are also measured to gauge the effectiveness of the proposed paradigm in delivering services safely and promptly. Since sensor nodes are typically placed in unattended environments where they are susceptible to various routing attacks, more research into how to identify the location of malicious nodes is warranted.

In the future, we want to investigate and develop cutting-edge blockchain-based secure IoT-WSNs with hybrid federated and hybrid machine learning methodologies for massive, safe, and intelligent IoT-WSN deployments in the near future. To locate and identify malicious nodes in IoT-WSNs, we will investigate blockchain-based sophisticated hybrid access control mechanisms. In addition, we will implement cutting-edge multiclass and binary classification evaluation metrics utilizing a wide range of benchmark datasets and hybrid routing protocols.

Data Availability

Data used in this article are available from the corresponding author upon request.

Conflicts of Interest

Authors confirm that they have no financial or personal ties to any parties that might influence the results of this study.

Authors' Contributions

Compiling, writing, and conceptualizing are done by Gebrekiros. Prof. J. Panda, and Prof. S. Indu did the discussion, validation, and evaluation.

References

[1] T. H. Kim, R. Goyat, M. K. Rai et al., "A novel trust evaluation process for secure localization using a decentralized blockchain in wireless sensor networks," *IEEE Access*, vol. 7, pp. 184133–184144, 2019.

[2] A. Sagu, N. S. Gill, and P. Gulia, "Hybrid deep neural network model for detection of security attacks in IoT enabled environment," *International Journal of Advanced Computer Science and Applications*, vol. 13, no. 1, pp. 120–127, 2022.

[3] R. Bharathi, S. Kannadhasan, B. Padminidevi, M. S. Maharajan, R. Nagarajan, and M. M. Tonmoy, "Predictive model techniques with energy efficiency for iot-based data transmission in wireless sensor networks," *Journal of Sensors*, vol. 2022, Article ID 3434646, 18 pages, 2022.

[4] Z. Abubaker, N. Javaid, A. Almogren, M. Akbar, M. Zuair, and J. Ben-Othman, "Blockchained service provisioning and malicious node detection via federated learning in scalable Internet of Sensor Things networks," *Computer Networks*, vol. 204, article 108691, 2022.

[5] C. Ming, C. Xiaoting, D. Wensheng, and G. Jiahui, "A secure blockchain-based group key agreement protocol for IoT," *The Journal of Supercomputing*, vol. 77, no. 8, pp. 9046–9068, 2021.

[6] S. Agrawal, S. Sarkar, O. Aouedi et al., "Federated learning for intrusion detection system: concepts, challenges and future directions," *Computer Communications*, vol. 195, pp. 346–361, 2022.

[7] R. Kumar, P. Kumar, R. Tripathi, G. P. Gupta, S. Garg, and M. M. Hassan, "A distributed intrusion detection system to detect DDoS attacks in blockchain- enabled IoT network," *Journal of Parallel and Distributed Computing*, vol. 164, pp. 55–68, 2022.

[8] O. Cheikhrouhou and A. Koubaa, "BlockLoc: secure localization in the Internet of Things using blockchain," in *2019 15th International Wireless Communications & Mobile Computing Conference (IWCMC)*, pp. 629–634, Tangier, Morocco, 2019.

[9] S. Algarni, F. Eassa, K. Almarhabi et al., "Blockchain-based secured access control in an IoT system," *Applied Sciences*, vol. 11, no. 4, article 1772, 2021.

[10] M. P. Nath, S. N. Mohanty, and S. B. B. Priyadarshini, "Application of machine learning in wireless sensor network," in *2021 8th International Conference on Computing for Sustainable Global Development (INDIACom)*, pp. 7–12, New Delhi, India, 2021.

[11] R. Goyat, G. Kumar, M. K. Rai, R. Saha, R. Thomas, and T. H. Kim, "Blockchain powered secure range-free localization in wireless sensor networks," *Arabian Journal for Science and Engineering*, vol. 45, no. 8, pp. 6139–6155, 2020.

[12] S. Awan, N. Javaid, S. Ullah, A. U. Khan, A. M. Qamar, and J. G. Choi, "Blockchain based secure routing and trust management in wireless sensor networks," *Sensors*, vol. 22, no. 2, pp. 1–24, 2022.

[13] H. Honar Pajooh, M. Rashid, F. Alam, and S. Demidenko, "Multi-layer blockchain-based security architecture for Internet of Things," *Sensors*, vol. 21, no. 3, pp. 1–26, 2021.

[14] S. Otoum, I. A. Ridhawi, and H. Mouftah, "Securing critical IoT infrastructures with blockchain-supported federated learning," *IEEE Internet of Things Journal*, vol. 9, no. 4, pp. 2592–2601, 2022.

[15] W. She, Q. Liu, Z. Tian, J. Sen Chen, B. Wang, and W. Liu, "Blockchain trust model for malicious node detection in wireless sensor networks," *IEEE Access*, vol. 7, pp. 38947–38956, 2019.

[16] K. Fan, S. Wang, Y. Ren et al., "Blockchain-based secure time protection scheme in IoT," *IEEE Internet of Things Journal*, vol. 6, no. 3, pp. 4671–4679, 2019.

[17] O. Friha, M. A. Ferrag, L. Shu, L. Maglaras, K. K. R. Choo, and M. Nafaa, "FELIDS: federated learning-based intrusion detection system for agricultural Internet of Things," *Journal of Parallel and Distributed Computing*, vol. 165, pp. 17–31, 2022.

[18] N. Javaid, "A secure and efficient trust model for wireless sensor IoTs using blockchain," *IEEE Access*, vol. 10, pp. 4568–4579, 2022.

[19] D. Wu and N. Ansari, "A trust-evaluation-enhanced blockchain-secured industrial iot system," *IEEE Internet of Things Journal*, vol. 8, no. 7, pp. 5510–5517, 2021.

[20] A. U. Khan, M. B. E. Sajid, A. Rauf, M. N. Saqib, F. Zaman, and N. Javaid, "Exploiting blockchain and RMCV-based malicious node detection in ETD-LEACH for wireless sensor networks," *Wireless Communications and Mobile Computing*, vol. 2022, Article ID 7281872, 15 pages, 2022.

[21] R. Goyat, G. Kumar, M. Alazab, R. Saha, R. Thomas, and M. K. Rai, "A secure localization scheme based on trust assessment for WSNs using blockchain technology," *Future Generation Computer Systems*, vol. 125, pp. 221–231, 2021.

[22] D. Minoli and B. Occhiogrosso, "Blockchain mechanisms for IoT security," *Internet of Things*, vol. 1-2, pp. 1–13, 2018.

[23] Z. Ma, L. Wang, and W. Zhao, "Blockchain-driven trusted data sharing with privacy protection in IoT sensor network," *IEEE Sensors Journal*, vol. 21, no. 22, pp. 25472–25479, 2021.

[24] X. Yang, Y. Chen, X. Qian, T. Li, and X. Lv, "BCEAD: a blockchain-empowered ensemble anomaly detection for wireless sensor network via isolation forest," *Security and Communication Networks*, vol. 2021, Article ID 9430132, 10 pages, 2021.

[25] M. Sarhan, W. W. Lo, S. Layeghy, and M. Portmann, "HBFL: a hierarchical blockchain-based federated learning framework for a collaborative iot intrusion detection," 2022, https://arxiv.org/abs/2204.04254.

[26] S. J. Hsiao and W. T. Sung, "Employing blockchain technology to strengthen security of wireless sensor networks," *IEEE Access*, vol. 9, pp. 72326–72341, 2021.

[27] S. Abbas, N. Javaid, A. Almogren, S. M. Gulfam, A. Ahmed, and A. Radwan, "Securing genetic algorithm enabled SDN routing for blockchain based Internet of Things," *IEEE Access*, vol. 9, pp. 139739–139754, 2021.

[28] E. H. Abualsauod, "A hybrid blockchain method in Internet of Things for privacy and security in unmanned aerial vehicles network," *Computers and Electrical Engineering*, vol. 99, article 107847, 2022.

[29] G. G. Gebremariam, J. Panda, and S. Indu, "Localization and detection of multiple attacks in wireless sensor networks using artificial neural network," *Wireless Communications and Mobile Computing*, vol. 2023, Article ID 2744706, 29 pages, 2023.

[30] Z. Cui, F. Xue, S. Zhang et al., "A hybrid blockchain-based identity authentication scheme for multi-WSN," *IEEE Transactions on Services Computing*, vol. 13, no. 2, pp. 241–251, 2020.

[31] A. U. Khan, N. Javaid, M. A. Khan, and I. Ullah, "A blockchain scheme for authentication, data sharing and nonrepudiation to secure internet of wireless sensor things," *Cluster Computing*, vol. 112, pp. 1–16, 2022.

[32] Z. Ullah, "A survey on hybrid, energy efficient and distributed (HEED) based energy efficient clustering protocols for wireless sensor networks," *Wireless Personal Communications*, vol. 112, no. 4, pp. 2685–2713, 2020.

[33] S. Messous and H. Liouane, "Online sequential DV-hop localization algorithm for wireless sensor networks," *Mobile Information Systems*, vol. 2020, Article ID 8195309, 14 pages, 2020.

[34] S. Dong, X. G. Zhang, and W. G. Zhou, "A security localization algorithm based on DV-hop against Sybil attack in wireless sensor networks," *Journal of Electrical Engineering & Technology*, vol. 15, no. 2, pp. 919–926, 2020.

[35] A. Hadir, K. Zine-Dine, M. Bakhouya, and J. El Kafi, "An improved DV-hop localization algorithm for wireless sensor networks," in *2018 13th IEEE Conference on Industrial Electronics and Applications (ICIEA)*, pp. 330–334, Wuhan, China, 2014.

[36] H. Chen, W. Lou, Z. Wang, J. Wu, Z. Wang, and A. Xi, "Securing DV-hop localization against wormhole attacks in wireless sensor networks," *Pervasive and Mobile Computing*, vol. 16, pp. 22–35, 2015.

[37] F. Khelifi, A. Bradai, A. Benslimane, P. Rawat, and M. Atri, "A survey of localization systems in Internet of Things," *Mobile Networks and Applications*, vol. 24, no. 3, pp. 761–785, 2019.

[38] R. Jeet, S. S. Kang, S. S. Hoque, and B. N. Dugbakie, "Secure model for IoT healthcare system under encrypted blockchain framework," *Security and Communication Networks*, vol. 2022, Article ID 3940849, 11 pages, 2022.

[39] S. M. Kasongo, "An advanced intrusion detection system for IIoT based on GA and tree based algorithms," *IEEE Access*, vol. 9, pp. 113199–113212, 2021.

[40] S. Subramani, *Deep learning based IDS for secured routing in wireless sensor networks using fuzzy genetic approach*, Research Square, 2022.

[41] S. Kim, H. Cai, C. Hua, P. Gu, W. Xu, and J. Park, "Collaborative anomaly detection for Internet of Things based on federated learning," in *2020 IEEE/CIC International Conference on Communications in China (ICCC)*, pp. 623–628, Chongqing, China, 2020.

[42] Y. Kayode Saheed, A. Idris Abiodun, S. Misra, M. Kristiansen Holone, and R. Colomo-Palacios, "A machine learning-based intrusion detection for detecting Internet of Things network attacks," *Alexandria Engineering Journal*, vol. 61, no. 12, pp. 9395–9409, 2022.

[43] L. Yang, A. Moubayed, and A. Shami, "MTH-IDS: a multitiered hybrid intrusion detection system for Internet of Vehicles," *IEEE Internet of Things Journal*, vol. 9, no. 1, pp. 616–632, 2022.

[44] B. Ghimire and D. B. Rawat, "Recent advances on federated learning for cybersecurity and cybersecurity for federated learning for Internet of Things," *IEEE Internet of Things Journal*, vol. 9, no. 11, pp. 8229–8249, 2022.

[45] A. Ahmed, S. Abdullah, M. Bukhsh, I. Ahmad, and Z. Mushtaq, "An energy-efficient data aggregation mechanism for IoT secured by blockchain," *IEEE Access*, vol. 10, pp. 11404–11419, 2022.

[46] P. Roy and C. Chowdhury, "A survey of machine learning techniques for indoor localization and navigation systems," *Journal of Intelligent & Robotic Systems*, vol. 101, no. 3, pp. 1–34, 2021.

[47] G. Kocher and G. Kumar, "Machine learning and deep learning methods for intrusion detection systems: recent developments and challenges," *Soft Computing*, vol. 25, no. 15, pp. 9731–9763, 2021.

[48] S. Pande, A. Khamparia, and D. Gupta, "Feature selection and comparison of classification algorithms for wireless sensor networks," *Journal of Ambient Intelligence and Humanized Computing*, vol. 2021, pp. 1–13, 2021.

[49] D. Upadhyay, J. Manero, M. Zaman, and S. Sampalli, "Gradient boosting feature selection with machine learning classifiers for intrusion detection on power grids," *IEEE Transactions on Network and Service Management*, vol. 18, no. 1, pp. 1104–1116, 2021.

[50] S. Taleb, A. Al Sallab, H. Hajj, Z. Dawy, R. Khanna, and A. Keshavamurthy, "Deep learning with ensemble classification method for sensor sampling decisions," in *2016 International Wireless Communications and Mobile Computing Conference (IWCMC)*, pp. 114–119, Paphos, Cyprus, 2016.

[51] M. Sri Vidya and G. R. Sakthidharan, "Accurate anomaly detection using various machine learning methods for IoT devices in indoor environment," in *2021 Fifth International Conference on I-SMAC (IoT in Social, Mobile, Analytics and Cloud) (I-SMAC)*, pp. 308–316, Palladam, India, 2021.

[52] L. Moulad, H. Belhadaoui, and M. Rifi, "Implementation of a hierarchical hybrid intrusion detection mechanism in wireless sensors network," *International Journal of Advanced Computer Science and Applications*, vol. 8, no. 10, pp. 270–278, 2017.

[53] M. Feurer and F. Hutter, *Hyperparameter optimization*, Springer, 2019.

[54] M. Farooq-I-Azam, Q. Ni, and E. A. Ansari, "Intelligent energy efficient localization using variable range beacons in industrial wireless sensor networks," *IEEE Transactions on Industrial Informatics*, vol. 12, no. 6, pp. 2206–2216, 2016.

[55] S. Karagol and D. Yildiz, "A novel path planning model based on nested regular hexagons for mobile anchor-assisted localization in wireless sensor networks," *Arabian Journal for Science and Engineering*, vol. 47, no. 8, pp. 9833–9848, 2022.

[56] K. P. S. Kumar, S. A. H. Nair, D. Guha Roy, B. Rajalingam, and R. S. Kumar, "Security and privacy-aware artificial intrusion detection system using federated machine learning," *Computers and Electrical Engineering*, vol. 96, article 107440, 2021.

[57] Z. Tan, A. Jamdagni, P. Nanda, X. He, and R. P. Liu, "Evaluation on multivariate correlation analysis based denial-of-service attack detection system," in *SecurIT '12: Proceedings of the First International Conference on Security of Internet of Things*, pp. 160–164, Kollam India, 2012.

[58] Z. Tan, "Detection of Denial-of-Service Attacks Based on By," pp. 1–14, University of Technology Sydney Australia, 2013.

[59] M. Nivaashini and P. Thangaraj, "Computational intelligence techniques for automatic detection of Wi-Fi attacks in wireless IoT networks," *Wireless Networks*, vol. 27, no. 4, pp. 2761–2784, 2021.

[60] C. Lyu, X. Zhang, Z. Liu, and C. H. Chi, "Selective authentication based geographic opportunistic routing in wireless sensor networks for Internet of Things against DoS attacks," *IEEE Access*, vol. 7, pp. 31068–31082, 2019.

[61] B. Kaur and D. Prashar, "Localization in wireless sensor network: techniques, algorithms analysis and challenges," in *2021 9th International Conference on Reliability, Infocom Technologies and Optimization (Trends and Future Directions) (ICRITO)*, pp. 1–7, Noida, India, 2021.

[62] T. A. Alghamdi, I. Ali, N. Javaid, and M. Shafiq, "Secure service provisioning scheme for lightweight IoT devices with a fair payment system and an incentive mechanism based on blockchain," *IEEE Access*, vol. 8, pp. 1048–1061, 2020.

[63] S. Salim, B. Turnbull, and S. Member, "A Blockchain-Enabled Explainable Federated Learning for Securing Internet-of-Things-Based Social Media 3. 0 Networks," *IEEE Transactions on Computational Social Systems*, pp. 1–17, 2021.

[64] A. Rehman, S. Abbas, M. A. Khan, T. M. Ghazal, K. Muhammad, and A. Mosavi, "A secure healthcare 5.0 system based on blockchain technology entangled with federated learning technique," *Computers in Biology and Medicine*, vol. 150, article 106019, 2022.

[65] Z. Mahmood and V. Jusas, "Blockchain-enabled: multi-layered security federated learning platform for preserving data privacy," *Electronics*, vol. 11, no. 10, p. 1624, 2022.

[66] T. Hassan, S. Aslam, and J. W. Jang, "Fully automated multi-resolution channels and multithreaded spectrum allocation protocol for IoT based sensor nets," *IEEE Access*, vol. 6, pp. 22545–22556, 2018.

[67] N. Nasser, Z. M. Fadlullah, M. M. Fouda, A. Ali, and M. Imran, "A lightweight federated learning based privacy preserving B5G pandemic response network using unmanned aerial vehicles: a proof-of-concept," *Computer Networks*, vol. 205, article 108672, 2022.

[68] S. Roy, J. Li, and Y. Bai, "A two-layer fog-cloud intrusion detection model for IoT networks," *Internet of Things*, vol. 19, article 100557, 2022.

[69] P. R. Kanna and P. Santhi, "Hybrid intrusion detection using MapReduce based black widow optimized convolutional long short-term memory neural networks," *Expert Systems with Applications*, vol. 194, article 116545, 2022.

[70] S. S. Mohar, S. Goyal, and R. Kaur, "Localization of sensor nodes in wireless sensor networks using bat optimization algorithm with enhanced exploration and exploitation characteristics," *The Journal of Supercomputing*, vol. 78, no. 9, pp. 11975–12023, 2022.

[71] A. Kumar, "A hybrid fuzzy system based cooperative scalable and secured localization scheme for wireless sensor networks," *International Journal of Wireless & Mobile Networks*, vol. 10, no. 3, pp. 51–68, 2018.

[72] M. B. E. Sajid, S. Ullah, N. Javaid, I. Ullah, A. M. Qamar, and F. Zaman, "Exploiting machine learning to detect malicious nodes in intelligent sensor- based systems using blockchain," *Wireless Communications and Mobile Computing*, vol. 2022, Article ID 7386049, 16 pages, 2022.

[73] T. J. Nagalakshmi, A. K. Gnanasekar, G. Ramkumar, and A. Sabarivani, "Machine learning models to detect the black-hole attack in wireless adhoc network," *Materials Today: Proceedings*, vol. 47, pp. 235–239, 2021.

Circular Slot-Based Microstrip Circularly Polarized Antenna for 2.45-GHz RFID Reader Applications

Amit Birwal, *Member, IEEE*, Kamlesh Patel, *Member, IEEE*, and Sanjeev Singh

***Abstract*—The paper presents a new design for a mobile 2.45-GHz passive Radio Frequency Identification (RFID) reader, featuring a compact, broadband, and circularly polarized antenna. The antenna proposed consists of two stacked square patches separated by an air gap for a wide-band impedance bandwidth. The antenna is printed on a double-sided 1.6 mm FR4 substrate with an overall dimension of $65\times65\times11.27$ mm^3. By introducing and optimizing a pair of symmetrical ring slots in both the square patches, a good Axial-Ratio Bandwidth (ARBW) and symmetrical broadside radiation patterns are achieved. The reader antenna shows a measured S_{11} bandwidth ($S_{11}<-10$ dB) from (2.3–2.7 GHz) and ARBW (< 3 dB) from (2.39-2.48 GHz). The peak gain of the proposed antenna is 6.2 dBi and is obtained at the center frequency of 2.45 GHz. Measurements of the proposed antenna are discussed to obtain the read range and field of view, which confirms its suitability for RFID Reader Applications and other Internet of Things (IoT) based applications.**

***Index Terms*—Axial ratio (AR), circular polarization (CP), RFID, reader antenna, return loss.**

I. Introduction

IN RECENT years, Radio Frequency Identification (RFID) technology has gained significant attention due to its wide range of applications in various fields such as inventory management, supply chain logistics, and asset tracking. One of the key components of an RFID system is the antenna, which plays a crucial role in ensuring reliable and efficient communication between the RFID reader and the tags. Among the various types of antennas used in RFID systems, microstrip patch antennas have gained popularity due to their compact size, low profile, ease of fabrication, and cost-effectiveness. However, conventional microstrip patch antennas often suffer from limitations such as narrow bandwidth and linear polarization, which can lead to reduced performance and reliability in certain RFID applications [1]. RFID systems are operated in different frequency ranges, namely Low frequency (LF), High frequency (HF), Ultra - high frequency (UHF), microwave frequencies etc. In recent years, significant advancements have been made in RFID technology, especially in the HF and UHF bands. Concurrently, with the growing popularity of smart devices, the utilization of Wireless Fidelity (Wi-Fi) for indoor communication has also increased. Therefore, it is crucial to explore RFID antennas within these domains, emphasizing their utmost significance. In practical applications, RFID tags are typically positioned without a specific orientation, while their antennas are predominantly Linearly Polarized (LP) [2].

When compared to LP waves, Circularly Polarized (CP) waves offer more flexibility for readers and tags in terms of their angular positions. Consequently, the utilization of CP reader antennas has become the primary approach for enhancing the reliability of communication in RFID systems. Typically, CP waves are generated by simultaneously activating two or more orthogonal LP modes with equal amplitude and a phase difference of 90° between them [3], [4]. In [5], a wearable Quasi-Yagi antenna is presented to detect tagged objects very close to the human palm and hand for UHF-RFID and 2.4 GHz applications. In [2], the authors presented the development of microstrip-type single-band CP reader antennas tailored for universal RFID applications. Two dual-band CP microstrip antennas, utilizing parasitic patches and cross slots, are developed in a single-fed configuration [7], [8]. In [9], a dual-band CP antenna features two sets of cross dipoles. To achieve CP, the first set of dipoles is connected with an arrowhead-shaped trace, enabling resonance at 915 MHz. The second set of rectangular dipoles generates CP resonance at 2.45 GHz. Several studies [10], [11], [12], [13] have demonstrated numerous dipole configurations for investigating CP antennas with dual-band capabilities. Novel asymmetric-circular shaped slotted microstrip patch antennas with slits are reported for CP radiation and RFID reader applications, which has a measured 3-dB axial-ratio (AR) bandwidth in 903 – 909 MHz band (RO4003C) and 918-929 MHz band (FR4) with 17.0 MHz impedance bandwidth [12]. A wideband CP stacked slotted microstrip patch antenna operating in the 835-955 MHz band is reported in [13]. Nonetheless, the frequency of these antennas is relatively limited, making them unsuitable for microwave ranges, as required for RFID technology with Wi-Fi connectivity. By utilizing microstrip antennas based on CP technology, a plethora of practical applications can be developed within the microwave band specifically allocated for Industrial, Scientific, and Medical (ISM) purposes. A majority of the RFID reader antenna proposed in [5], [7], [8], [9], [10], [11] are of dual-and type

Manuscript received 6 September 2023; revised 18 October 2023, 9 December 2023, and 11 January 2024; accepted 11 January 2024. Date of publication 16 January 2024; date of current version 1 February 2024. This work was supported in part by the Faculty Research Programme (FRP) of the Institute of Eminence (IoE) Scheme of the University of Delhi under Grant IoE/2023-24/12/FRP dated 31/08/2023. *(Corresponding author: Kamlesh Patel.)*

Amit Birwal and Kamlesh Patel are with the Department of Electronic Science, University of Delhi South Campus, New Delhi 110021, India (e-mail: amit.birwal@south.du.ac.in; kpatel@south.du.ac.in).

Sanjeev Singh is with the Institute of Informatics and Communication, University of Delhi South Campus, New Delhi 110021, India (e-mail: sanjeev@south.du.ac.in).

Digital Object Identifier 10.1109/JRFID.2024.3354515

2469-7281 © 2024 IEEE. Personal use is permitted, but republication/redistribution requires IEEE permission.
See https://www.ieee.org/publications/rights/index.html for more information.

Authorized licensed use limited to: DELHI TECHNICAL UNIV. Downloaded on February 07,2024 at 06:37:37 UTC from IEEE Xplore. Restrictions apply.

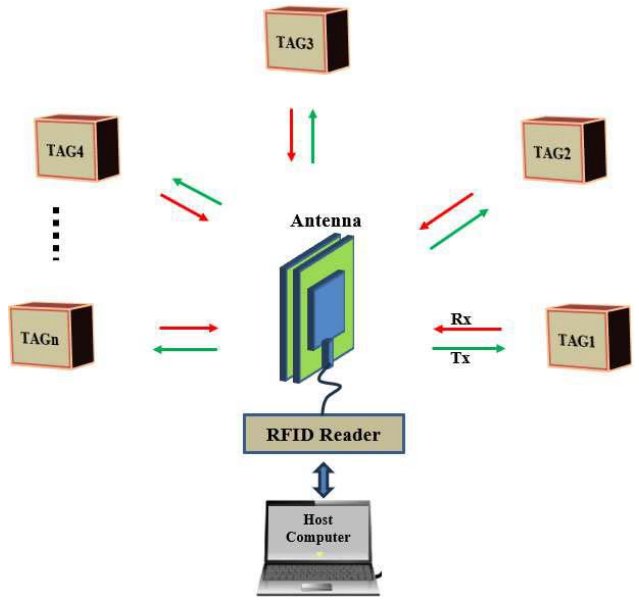


Fig. 1. Antenna with RFID system architecture.

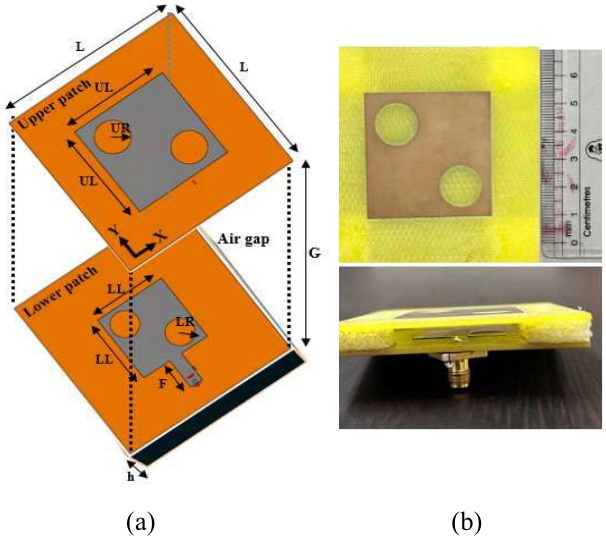


Fig. 2. Geometrical view of the proposed antenna (a) Upper patch, Air gap, Lower patch, (b) side view of fabricated prototype.

targeting UHF-RFID and 2.4 GHz bands together on the same antenna structure. This approach makes the antenna structure complex as well as electrically large and bulky. So, the proposed work is based on designing a dedicated reader antenna for a 2.4 GHz band with slot rings.

To seamlessly incorporate the reader antenna into various Internet of Things (IoT) applications, a wideband CP antenna is necessary, which must be capable of accommodating a wide range of frequencies around 2.45 GHz, as illustrated in Fig. 1. Previously, a square shape CPW-fed antenna providing a circular polarization and bidirectional radiation pattern was presented for RFID reader applications in the ISM band at 2.45 GHz [1]. This antenna is made of the low-cost FR4 substrate with an overall dimension of $60\times60\times1.5$ mm^3 and offers wideband CP in 2.03 – 2.7 GHz, and is also tested as a reader antenna in transmit mode using a wireless communication system. This design suffers from a lower gain of 3.17 dBi in the 2.45 GHz band. Although few CP antenna designs offering higher gain from about 4 dBic to 15.2 dBic are reported [14], [15], [16], [17], [18], the size of these antennas is still large and involves multilayers and design complexities. So, in this work, a broadband and compact microstrip stacked square patch antenna with circular polarization (CP) is designed to cover the microwave RFID range of 2.45 GHz. By incorporating a pair of circular slots in both the upper patch and lower patch, an axial-ratio bandwidth (<3 dB) of 90 MHz around 2.45 GHz is achieved. The antenna gain is enhanced by incorporating an air dielectric layer and the upper-patch layer acting as a parasitic patch due to single-side radiation, instead of bidirectional radiation for CPW fed antenna reported in [1]. It is believed that the reader antenna holds potential for applications in mobile vehicle identification systems, such as community parking management.

This paper is organized as follows. Section II explains the proposed antenna design and its simulated results of S_{11}, axial ratio with change in slot dimensions along with surface current distribution. Section III presents the measured results of S_{11}, axial ratio, and radiation patterns for the proposed antenna. Section IV covers a thorough application of the proposed antenna used as a reader antenna with previously reported 2.4 GHz antennas as a receiving antenna for the determination of a field of view (FOV). Section V discusses the proposed antenna integration with a Raspberry-Pi 4 model B using a digital modulation technique, while Section VI gives concluding remarks.

II. Antenna Design

The proposed reader antenna consists of three layers, i.e., upper-patch, air-gap, and lower-patch. Both the upper and lower patches consist of a square microstrip antenna with a pair of slotted rings as shown in Fig. 2(a), which illustrates its cross-sectional view under well-matched conditions for the ISM 2.45-GHz band. The slotted ring radius and diagonal axis position are fine-tuned to optimize wideband circularly polarized radiation. The upper-patch layer is printed on single-sided FR4 board ($\epsilon_r = 4.4$, h = 1.6 mm and tan $\delta = 0.04$), while the lower-patch layer is printed on double-sided board with a dimension of $65\times65\times1.6$ mm^3. A side view of the fabricated antenna is shown in Fig. 2(b). To ensure excellent impedance matching across the desired frequency range, the lower square slotted patch is fed by the microstrip line of length F which is connected to a coaxial feed of 50Ω via a probe-fed SMA connector.

The orthogonal modes of a circularly polarized antenna are commonly generated by creating perturbations across the diagonal axis, i.e., 45° angle relative to the feed location axis. So, based on this approach, two symmetric circular slots are created as perturbations along the diagonal axis of both the square microstrip patches to generate two orthogonal modes. The location of the circular slot along the diagonal patch is selected relative to the length (LL or UL) of the lower and

Authorized licensed use limited to: DELHI TECHNICAL UNIV. Downloaded on February 07,2024 at 06:37:37 UTC from IEEE Xplore. Restrictions apply.

TABLE I
DIMENSIONS OF THE PROPOSED ANTENNA

Parameter	Value (mm)	Parameter	Value (mm)
L	65	LL	26
UL	35	F	11.7
UR	6.5	G	8
LR	5.5	W_f	4.7
h	1.6	T	0.035

upper square patch, which is approximately one-quarter of the square patch length. Here, the radius of both the circular slots is kept the same in each layer to make it diagonally symmetric. The process of designing, optimizing, and simulating the antenna is carried out using the commercial software CST Microwave Studio tool. The optimized parameters of the antenna, as determined through this process, are provided in Table I, where, F = length of feed line in lower patch, G = air gap between upper and lower patches, Wf = width of feed line, and T = thickness of copper strip.

Further, the radius of both lower- and upper-layer circular slots is optimized to LR = 5.5 mm and UR = 6.5 mm, which can be used to control the resonant length of the two orthogonal modes to get circularly polarized radiation.

Fig. 3 shows the parametric variation of the radius of the circular slots present in both layers. Firstly, the radius of the lower circular slot LR is varied from 4 to 6 mm keeping UR fixed to 5 mm and the return loss and axial ratio are monitored as shown in Fig. 3(a) and (b). As can be seen from Fig. 3(a) for LR = 4 mm, a good impedance bandwidth (IBW) is observed but the corresponding axial ratio (AR) is poor in the operating band, i.e., greater than 4 dB. On further increasing LR = 5 mm, there is a minor improvement in the AR. At this point, the LR is increased in the step of 0.5 mm, which reduces the AR up to 1 dB around 2.45 GHz, and the corresponding impedance bandwidth also increases slightly at this band. On increasing the LR further to 6 mm, the AR started to fall, so further LR variation was stopped. The final optimized value of LR is then fixed to 5.5 mm. Fig. 3(c) shows the variation of UR from 5 mm to 7.5 mm keeping LR fixed to 5.5 mm. It is observed that the AR is further enhanced to 0.5 dB at 2.4 GHz by varying the UR to 6.5 mm and deteriorates on further increasing UR. At these optimized values of UR and LR, a smoother AR response is obtained with more frequency sweep points shown in Fig. 5(b).

A parametric study of the air gap (G) between two stacked square patches is also studied from 4 to 10 mm as shown in Fig. 4. A narrow IBW is observed for G = 4 mm, which gradually enhanced with increasing the gap from 6 to 8 mm where a wide-band IBW is achieved. On further increasing the gap to 10 mm, the IBW deteriorates so the final optimized value of G is fixed to 8 mm. The total efficiency of the proposed antenna is found from 85% to 98% in the 2.3-2.7 GHz band.

Fig. 5 illustrates the distribution of surface current on the proposed antenna when the port is excited at a frequency of 2.45 GHz with a coaxial feed of 50Ω. When a phase zero

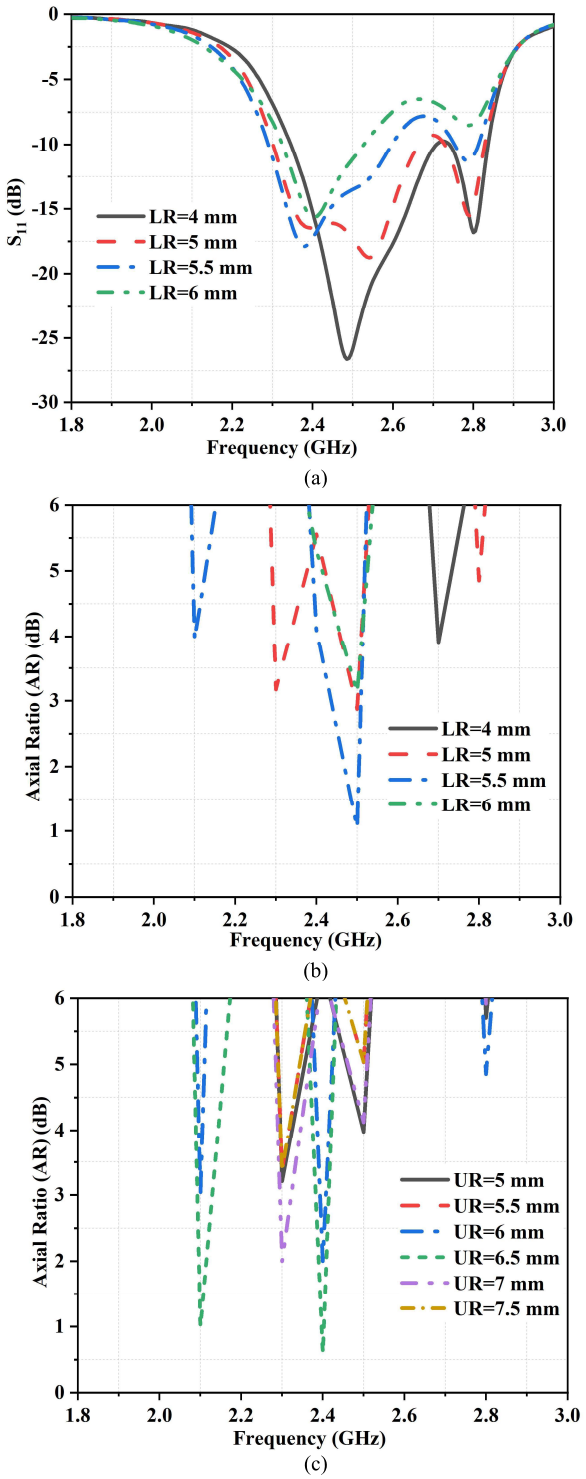


Fig. 3. Antenna parametric variation (a) S_{11} (dB), (b) AR (dB) when LR is varied, and (c) AR (dB) when UR is varied keeping LR fixed.

signal is applied, the predominant current vector, indicated by the black color, is observed along the positive X direction. As the phase angle changes to 90^0, the current vector shifts its orientation to the positive Y direction. Similarly, for phase angles of 180^0 and 270^0, the orientation changes to negative X and Y directions, respectively. By observing the rotation of this resultant current vector from the top of the antenna

Authorized licensed use limited to: DELHI TECHNICAL UNIV. Downloaded on February 07,2024 at 06:37:37 UTC from IEEE Xplore. Restrictions apply.

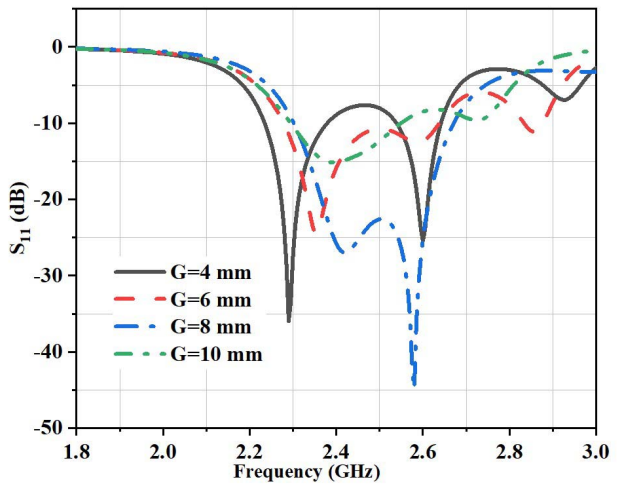


Fig. 4. Antenna parametric variation of S_{11} (dB) when G is varied using the optimized value of UR and LR.

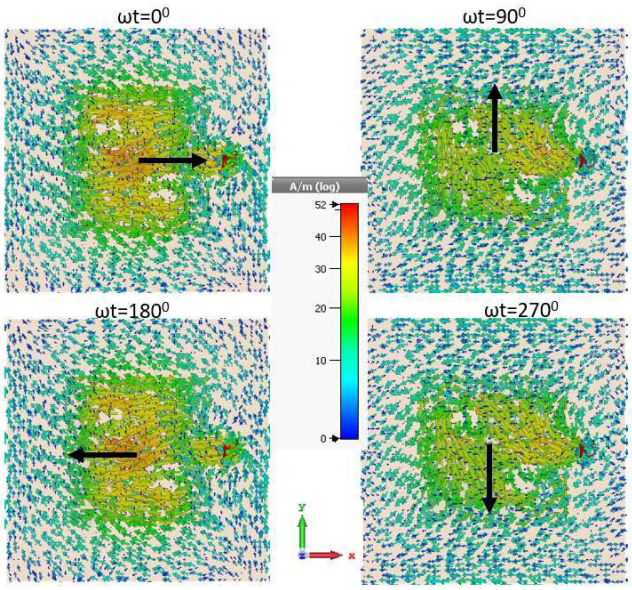


Fig. 5. Surface current distribution on the proposed antenna at 2.45 GHz for four different angles.

(positive Z), it can be determined that the rotation follows a counterclockwise direction. This rotation corresponds to Right-Hand Circular Polarization (RHCP).

III. Antenna Measurement Results

After the antenna dimensions are optimized for the 2.45 GHz band with CP, the DXF file of both layers is exported from the CST studio suite and imported into the LPKF ProtoMat S100 PCB milling machine for the fabrication of each layer. Each layer is printed on the FR4 board separately and placed one over the other with the help of a supporting foam structure as shown in Fig. 2 (b). Finally, an SMA connector is soldered at the optimized feed location on the bottom side of the lower patch. To conduct the measurement, the Rohde & Schwarz ZVH8 handheld vector network analyzer is used. Figs. 6(a-b) compares the measured and simulated outcomes for return loss and the axial ratio

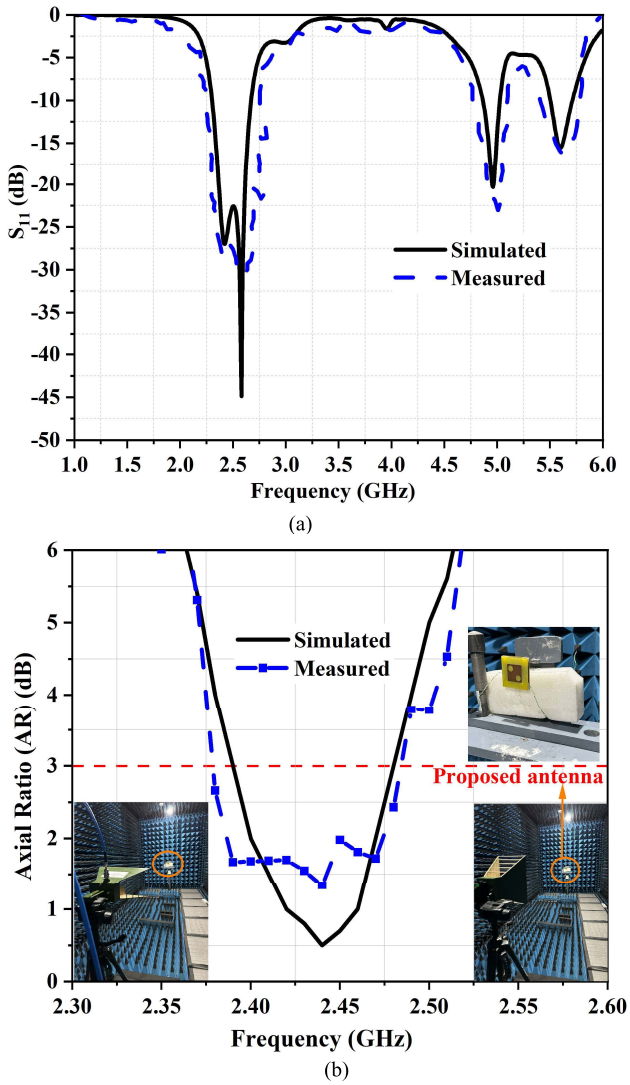


Fig. 6. Simulated and measured result (a) S_{11} (dB), (b) axial ratio (dB) of the proposed antenna.

at the boresight. The simulated 10-dB return loss bandwidth of 380 MHz (2.30–2.68 GHz), 350 MHz (4.68–5.03 GHz), and 240 MHz (5.49–5.73) are obtained. Since the proposed antenna is optimized for RFID reader application at 2.45 GHz, only the first band (2.30–2.68 GHz) is considered, where circular polarization is also obtained.

To evaluate the circularly polarized performance of the antenna, a rotating linearly polarized transmitting standard horn antenna is used and the proposed antenna is placed at the receiving end in the same orientation. The received power is measured by changing the frequency from 2.3 to 2.6 GHz on the R&S spectrum analyzer model FSL6. Then the orientation of the standard horn antenna is changed by 90° and the received power is measured again in the same frequency points. The difference of two received powers is taken as the axial ratio in dB. The measured 3-dB axial-ratio bandwidth (ARBW) was 90 MHz (2.39–2.48 GHz). Comparing the measured results with the simulations, an agreement was observed.

Authorized licensed use limited to: DELHI TECHNICAL UNIV. Downloaded on February 07,2024 at 06:37:37 UTC from IEEE Xplore. Restrictions apply.

TABLE II
COMPARISON OF ANTENNA FEATURES

Ref	Size (mm^3)	IBW (GHz)	AR Bandwidth (GHz)	Gain (max. or range) (dBic)	Radiation Efficiency (%)	Substrate used
[1]	60×60×1.6	2.18-3.28	2.03-2.7	3.17	-	FR-4
[6]	210×210×33	2.424 – 2.472	2.423 – 2.470	6.25	74.31	FR-4
[7]	134×134×3.2	2.08-2.65 (meas)	2.42 –2.47 (meas)	2.5 (meas)	-	FR-4
[8]	85.0×85.0×1.6	2.16-2.80	2.35-2.58	3.1-3.8 (sim) 1.8-2.6 (meas)	97.0 (simu) 70.4 (meas)	FR-4
[14]	110×110×6.6	2.22-2.57 (simu) 2.18-2.59 (meas)	2.27- 2.62 (simu) 2.11-2.64 (meas)	8.9 (meas)	-	FR-4
[15]	100×160×1.6	2.28-2.57 (sim) 2.34-2.67 (meas)	-	4.37 (simu) 3.97 (meas)	94.8	FR-4
[16]	104×104×1.524	2.19-2.85	2.19-2.85	15.2	>90	Rogers 4003
[17]	80×80×7.76	2.4-2.48	2.42-2.468	5		Rogers RO4350
[18]	109×109×15	2.1- 2.85	2.25-2.86	13.3	-	FR-4, Arlon AR1000, Two Rogers 4003
This work	**65×65×11.27**	**2.3–2.7**	**2.39-2.48**	**6**	**85 – 98**	**FR-4**

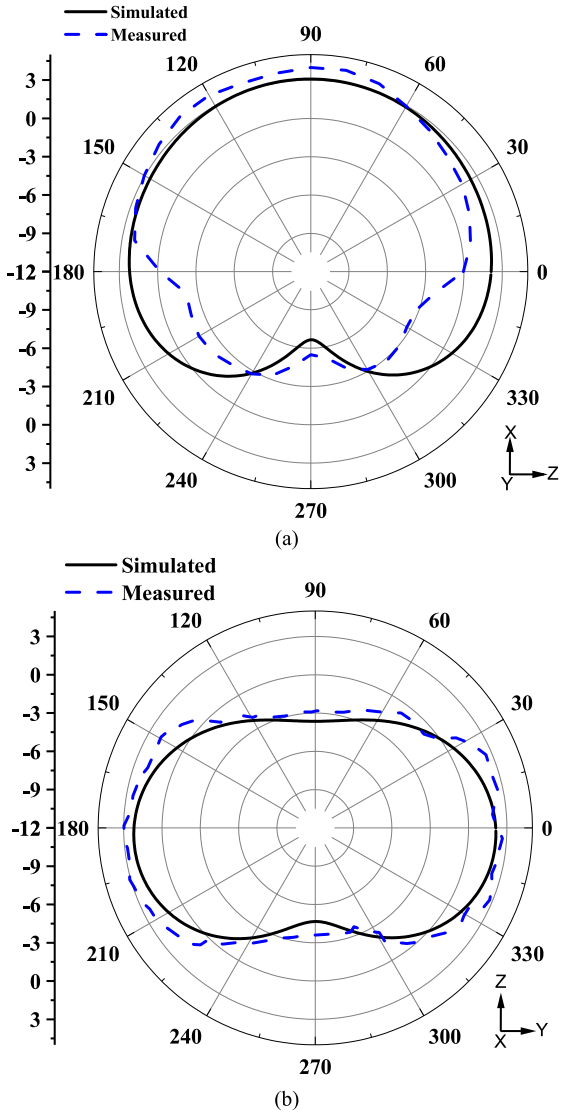


Fig. 7. Simulated and measured RHCP 2D radiation pattern of the antenna at 2.45 GHz, (a) XZ-plane, (b) YZ-plane.

The measured gain of this circularly polarized antenna is averaged around 6 dBi, with a minimal gain variation of approximately ±0.2 dB within the 3-dB ARBW. The high gain of the antenna was a result of the additional air dielectric layer and the parasitic patch element. These findings demonstrate that the proposed antenna is capable of covering the entire 2.45GHz microwave RFID band used worldwide.

Also, in comparison to a stacked square slotted microstrip antenna containing a circular slot on both patches of size 200.0×200.0×29.8 mm^3 [12] and four asymmetrical circular slots on the top layer of a single patch with a coaxial feed of size 90.0×90.0×4.8 mm^3 [13], the proposed antenna with two symmetrical circular slots achieved a gain of about 6 dBi with 90 MHz axial ratio bandwidth over a comparatively much lower size of 65.0×65.0×11.27 mm^3 including 8 mm of the air gap. In Table II. the reported features of previously published antennas at 2.45 GHz band only are taken for comparison. Thus, the proposed antenna is simplified, compact, and offers wide impedance and axial ratio bandwidth with good gain in the 2.45 GHz band compared to most of these antennas made on the same substrate.

Fig. 7 displays the comparison between RHCP simulated and measured radiation patterns at the 2.45 GHz microwave RFID band for both principal axes. The symmetry of the radiation patterns is observed in both the XZ and YZ planes. It is observed that the proposed antenna provides a very stable radiation pattern in the broadside direction.

IV. ANTENNA APPLICATION AS RFID READER

To check the capability of the proposed RFID reader antenna, the read range with any tag antenna is to be obtained. Knowledge of the antenna gain is required to verify the read range in the operational mode of the RFID system. There are many techniques for measuring the gain of an antenna, with the majority involving a reference antenna of known gain. However, in this work, a three-antenna gain method is used which requires only three antennas without prior knowledge about their gains.

To implement this technique, two previously reported tag antennas as receiving antenna are used. The first receiving antenna is a Hexagonal Split Ring Resonator (HSRR) antenna

Authorized licensed use limited to: DELHI TECHNICAL UNIV. Downloaded on February 07,2024 at 06:37:37 UTC from IEEE Xplore. Restrictions apply.

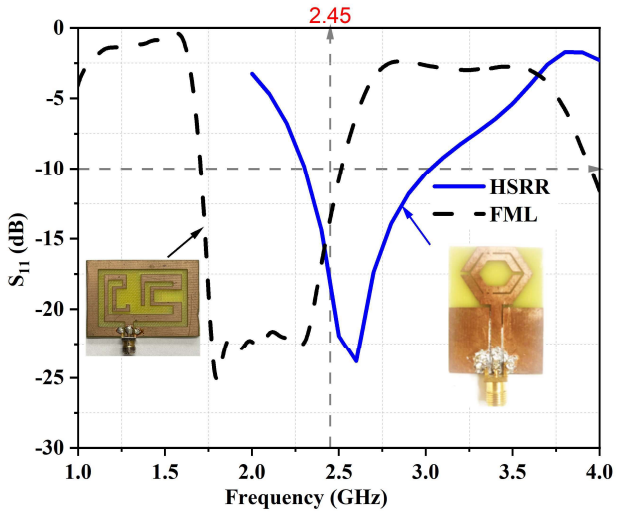


Fig. 8. Measured return loss S_{11} (dB) of receiving antennas used in this work.

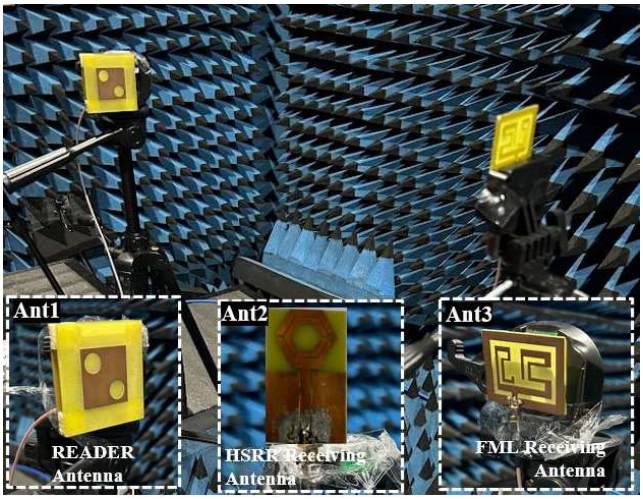


Fig. 9. Measurement setup for the three-antenna gain method inside an anechoic chamber.

of dimension 43×26 mm^2 [19], and the second receiving antenna of dimension of 49×39 mm^2 is a Folded Microstrip Line (FML) antenna reported in [20]. Both the receiving antennas resonate at 2.45 GHz within the range of the proposed RFID reader antenna as confirmed by their measured return loss as shown in Fig. 8.

The gain measurement method is based on the popular Friis equation, which can be modified and after converting to dB is written as equation (1), (2), and (3) for three different antennas:

$$G_{Ant1}(dB) + G_{Ant2}(dB) = [S_{21}(dB)]_{1-2} - FSL\ (dB) \quad (1)$$

$$G_{Ant2}(dB) + G_{Ant3}(dB) = [S_{21}(dB)]_{2-3} - FSL\ (dB) \quad (2)$$

$$G_{Ant1}(dB) + G_{Ant3}(dB) = [S_{21}(dB)]_{1-3} - FSL\ (dB) \quad (3)$$

Here, $G_{Ant1}(dB)$ is the gain of our proposed RFID reader antenna (Ant1), $G_{Ant2}(dB)$ is the gain of the HSRR antenna (Ant2) and $G_{Ant3}(dB)$ is the gain of the FML antenna (Ant3). S_{21}(dB) represents the ratio of transmit power (P_T) and received power (P_R) in dB for the respective sets of antennas (Ant1, Ant2 and Ant3). FSL (dB) is the Free Space Loss in dB and is obtained using $(\frac{\lambda}{4\pi R})^2$, where λ is the operating wavelength, and R is the distance between the transmitting and receiving antennas, respectively.

As shown in Fig. 9, Ant1 and Ant2 are connected at port 1 and port 2 of the VNA, and S_{21} (dB) is measured by maintaining a far-field distance of R = 210 cm between the antennas in the first setup. The trigger power of VNA is set to −10 dBm. By subtracting the S_{21} (dB) and FSL (dB), equation (1) is used to obtain gain. Similarly, for equation (2) setup between Ant2 and Ant3 is used, and for equation (3) setup is made utilizing Ant1 and Ant3. By solving three equations with three unknowns, the measured gains of all three antennas are obtained as shown in Fig. 10. The measured gain (G_{Ant1}) of the proposed reader antenna is 6.2 dB at 2.45 GHz, while for receiving antennas it is found to be G_{Ant2} = 1.9 dB and G_{Ant3} = 2.1 dB at 2.45 GHz. Since the gain of Ant3 (FML) is slightly higher than Ant2 (HSRR), Ant3 is planned

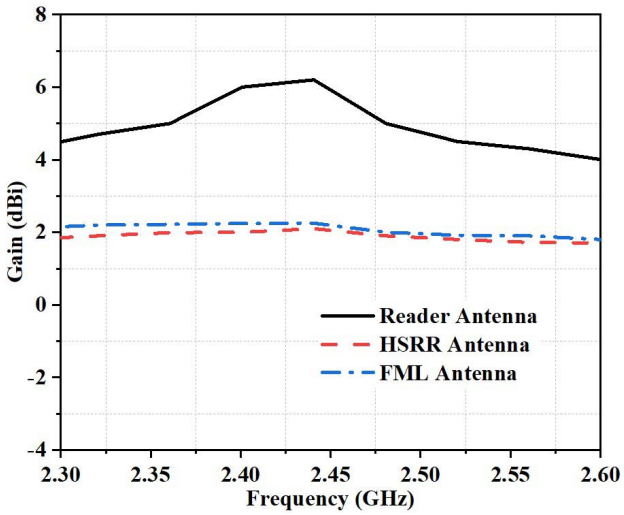


Fig. 10. Measured gain (dBi) using three antenna method.

to be used as a receiving antenna for further studies. As shown in Fig. 11, the reader antenna (proposed) is connected to the RIGOL®DSG3060 signal generator and the receiving antenna (FML) is connected to the R&S® FSL6 spectrum analyzer. This existing setup is capable of measuring up to 6 GHz. For this study, the reader antenna is placed in the Line of Sight (LOS) to the receiving antenna.

A transmit power of P_T (0 dBm) is selected at a frequency of 2.45 GHz and a corresponding received power P_R (dBm) is measured by varying the distance R (read range in cm) in a step distance of 5 cm in +Z direction keeping the position of transmit antenna fixed [21]. The received power at the receiving side is also known as the Received Signal Strength Indicator (RSSI), which is used to estimate the read range. In the first case, the proposed reader antenna acting as a transmitter is kept at an angle of 0^0 and the received power P_R (in dBm) is measured by varying the distance from 5 cm to 200 cm in the step of 5 cm. Then, this process is repeated

Authorized licensed use limited to: DELHI TECHNICAL UNIV. Downloaded on February 07,2024 at 06:37:37 UTC from IEEE Xplore. Restrictions apply.

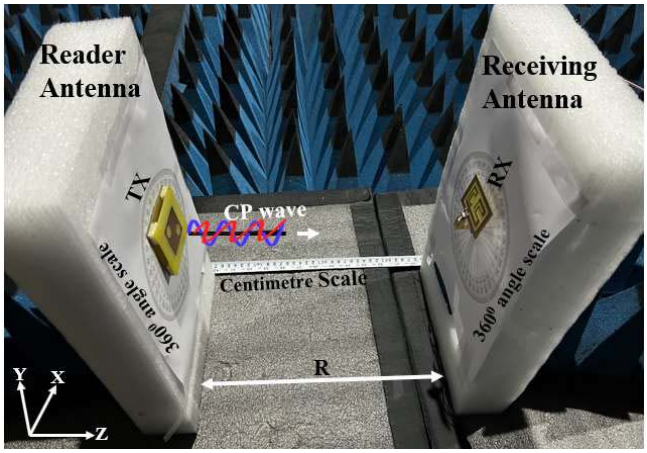


Fig. 11. Read range measurement setup between receiving and reader antennas in the lab environment.

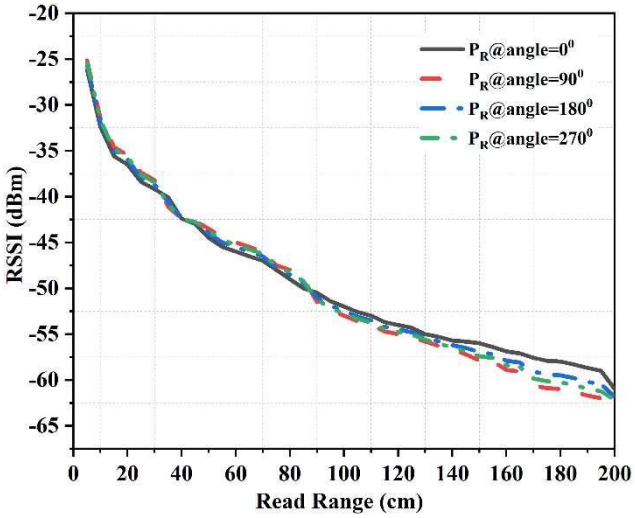


Fig. 12. Measured RSSI (dBm) as a function of the distance between the reader and the receiving antenna.

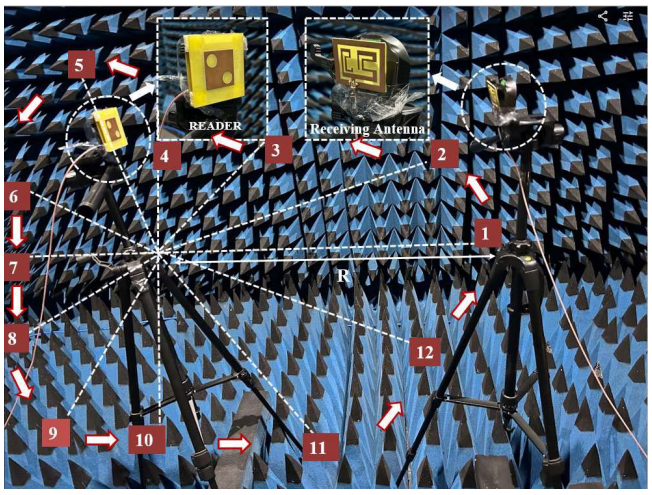


Fig. 13. Measurement setup when receiving antenna is rotated around reader antenna in azimuthal axis.

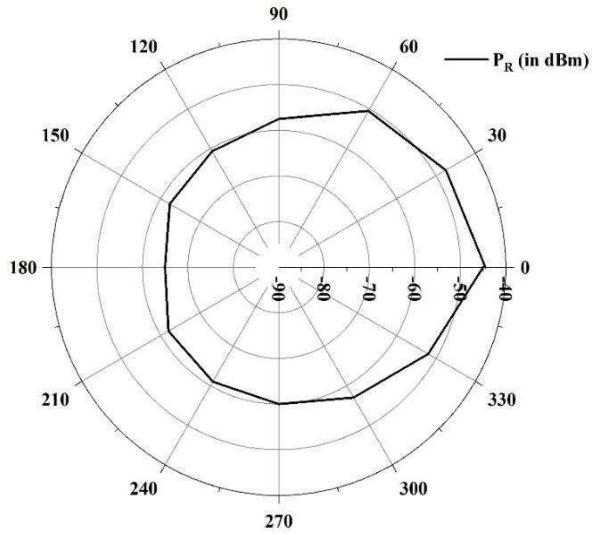


Fig. 14. Polar plot of the received power at different angular locations from the reader antenna.

for angles, i.e., 90^0, 180^0, and 270^0 and the received power is obtained for these cases.

Fig. 12 shows the variation of RSSI as a function of distance. Since the receiving antenna used is linearly polarized and the proposed reader antenna is circularly polarized, the received power is found almost similar in all the cases even though the polarization mismatch exists between the circularly polarized reader and the linearly polarized receiving antenna. At a distance of almost 200 cm, the received power falls close to the noise floor of the spectrum analyzer, i.e., −62 to −65 dBm, which limits the read range up to 200 cm. This can further be increased by enhancing the transmit power. So, based on the RFID chip sensitivity of the receiving antenna, i.e., the minimum received power to the receiving antenna, the read range can be controlled.

Now, to check a 360^0 coverage of the proposed antenna, the receiving antenna is physically moved from angular location 1 to 12 in the azimuthal axis as shown in Fig. 13. At each location like 1 to 2, 2 to 3, 3 to 4 and so on, received power is measured, while the receiving antenna is rotated in different angular locations from 0^0 to 360^0 anticlockwise in a step of 30^0 around the reader antenna. These locations are marked as 1 to 12 as shown in Fig. 13, which shows the read range in various directions away from the reader antenna. A plot between this received power obtained by varying angles is shown in Fig. 14, where the detected power by receiving antenna at larger distances gives the front Field of View (FOV), which is approximately 120^0 horizontally on both sides of the reader antenna, whereas using a frequency beam-scanning leaky-wave antenna and selecting two appropriate RFID channels at 902.75 MHz and 927.25 MHz, a wide FOV of 130° is obtained by a novel RSSI-based Angle of Arrival (AoA) estimation RFID system [22]. The read range at the side and the back side of the reader antenna is mostly affected due to minimum radiation in the side and back side of the antenna and the directional radiation pattern of the reader antenna in the XZ-plane, i.e., front side (Fig. 6a).

Authorized licensed use limited to: DELHI TECHNICAL UNIV. Downloaded on February 07,2024 at 06:37:37 UTC from IEEE Xplore. Restrictions apply.

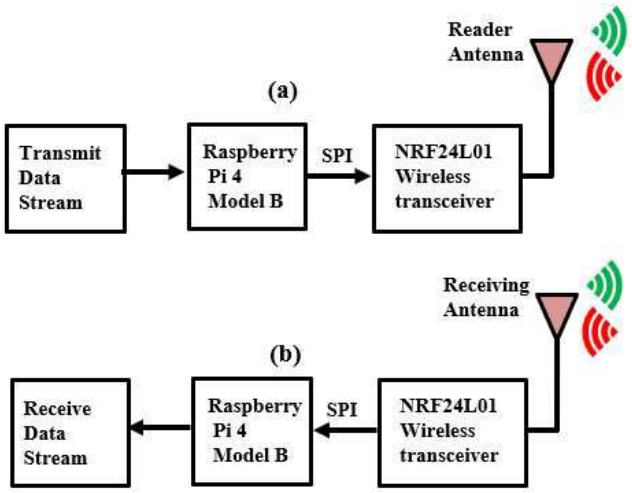


Fig. 15. Antenna integration setup for (a) reader, and (b) receiving antenna.

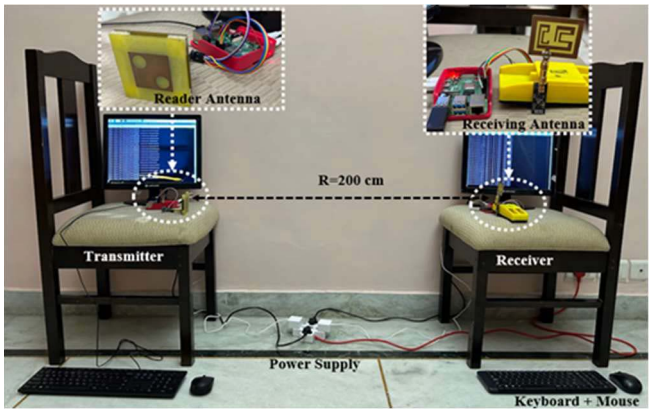


Fig. 16. Transmit and receive setup of the proposed antenna with Raspberry-Pi.

V. Antenna Integration

To further assess the potential of the suggested antenna for deployment as a reader antenna employing digital modulation technique and to mimic the RFID reader electronics using the proposed antenna with digitally modulated messages, a test setup configuration is created which employs a Raspberry-Pi 4 model B, a small single-board computer equipped with a microprocessor, memory and input/output (I/O) [23] as shown in Fig. 15. To test the wireless data, transmit/receive functionality of reader and receiving antenna, a wireless transceiver NRF24L01 module [24] operating at 2.45 GHz is used, with the flexibility to connect external antenna. For this setup, two NRF24L01 modules are used which are connected to the I/O pins of two Raspberry-Pi, one acting as a transmitter and the second as a receiver as shown in Fig. 16. The distance between the reader and receiving antennas is kept at R = 200 cm.

The Raspberry-Pi microprocessor board comes with 40 input-output pins that are specifically designed for connecting external circuits. In our case, these pins are employed to establish a connection with the NRF24L01 module using the Serial Peripheral Interface (SPI). This wireless module, known as NRF24L01 can function at a frequency of 2.45 GHz and uses Gaussian FSK modulation for data transmission at maximum output power of 0 dBm using an external antenna. A pair of Python scripts given in [25] is used to program the transmitter and receiver. These scripts are designed to emulate a continuous transmit data stream with every 10-second interval based on digital modulation technology. The monitors connected to the Raspberry-Pi are used to display these emulated text messages generated from the reader antenna and received from the receiving antenna and vice versa. This study confirms that the proposed antenna is suitable for sending and receiving by emulating the transceiver reader module using digital modulation technology.

VI. Conclusion

In this work, a circularly polarized antenna using two circular slots suitable for a 2.45-GHz RFID reader is presented. The air gap between two stacked square patches is optimized to achieve a wide-band impedance bandwidth. By inserting only two symmetric circular slots in both patches, a good axial-ratio bandwidth of about 90 MHz is obtained. The measurement result is found to be in close agreement with the simulated. The antenna offers a gain of 6.2 dBi and a wider impedance bandwidth of 400 MHz ($S_{11}<-10$ dB) in the 2.45 GHz band. The overall dimension of the proposed antenna is $65\times65\times11.27$ mm^3, which is compact in comparison to the other reported antennas made on the FR4 substrate. The maximum read range of the proposed antenna is found to be about 200 cm for satisfactory detection, while its field of view is a total of 120°. Hence, this antenna has the potential for use in RFID readers and other IoT integrations, such as Wi-Fi.

References

[1] A. Birwal, V. Kaushal, and K. Patel, "Investigation of circularly polarized CPW fed antenna as a 2.45 GHz RFID reader," *IEEE J. Radio Freq. Identif.*, vol. 6, pp. 593–600, May 2022, doi: 10.1109/JRFID.2022.3172691.

[2] Z. N. Chen, X. Qing, and H. L. Chung, "A universal UHF RFID reader antenna," *IEEE Trans. Microw. Theory Techn.*, vol. 57, no. 5, pp. 1275–1282, May 2009.

[3] Y.-X. Guo, K.-W. Khoo, and L. C. Ong, "Wideband circularly polarized patch antenna using broadband baluns," *IEEE Trans. Antennas Propag.*, vol. 56, no. 2, pp. 319–326, Feb. 2008.

[4] W. J. Yang, Y. M. Pan, and S. Y. Zheng, "A low-profile wideband circularly polarized crossed-dipole antenna with wide axial-ratio and gain beamwidths," *IEEE Trans. Antennas Propag.*, vol. 66, no. 7, pp. 3346–3353, Jul. 2018.

[5] R. K. Singh, A. Michel, P. Nepa, and A. Salvatore, "Wearable dual-band quasi-yagi antenna for UHF-RFID and 2.4 GHz applications," *IEEE J. Radio Freq. Identif.*, vol. 4, no. 4, pp. 420–427, Dec. 2020.

[6] S. Sarkar and B. Gupta, "A dual-band circularly polarized antenna with a dual-band AMC reflector for RFID readers," *IEEE Antennas Wireless Propag. Lett.*, vol. 19, pp. 796–800, 2020.

[7] T. N. Chang and G. Y. Ni, "Dual-band circularly polarized antenna with a QUAD-EMC structure," *Microw. Opt. Technol. Lett.*, vol. 49, no. 3, pp. 645–647, 2007.

[8] F.-P. Lai, J.-F. Yang, and Y.-S. Chen, "Compact dual-band circularly polarized antenna using double cross dipoles for RFID handheld readers," *IEEE Antennas Wireless Propag. Lett.*, vol. 19, pp. 1429–1433, 2020.

[9] K. Saurav, D. Sarkar, and K. V. Srivastava, "Dual-band circularly polarized cavity-backed crossed-dipole antennas," *IEEE Antennas Wireless Propag. Lett.*, vol. 14, pp. 52–55, 2015.

Authorized licensed use limited to: DELHI TECHNICAL UNIV. Downloaded on February 07,2024 at 06:37:37 UTC from IEEE Xplore. Restrictions apply.

[10] S. X. Ta and I. Park, "Dual-band low-profile crossed asymmetric dipole antenna on dual-band AMC surface," *IEEE Antennas Wireless Propag. Lett.*, vol. 13, pp. 587–590, 2014.
[11] H. H. Tran and I. Park, "A dual-wideband circularly polarized antenna using an artificial magnetic conductor," *IEEE Antennas Wireless Propag. Lett.*, vol. 15, pp. 950–953, 2016.
[12] Nasimuddin, Z. N. Chen, and X. Qing, "Asymmetric-circular shaped slotted microstrip antennas for circular polarization and RFID applications," *IEEE Trans. Antennas Propag.*, vol. 58, no. 12, pp. 3821–3828, Dec. 2010.
[13] Nasimuddin, X. Qing, and Z. N. Chen, "A wideband circularly polarized stacked slotted microstrip patch antenna," *IEEE Antennas Propag. Mag.*, vol. 55, no. 6, pp. 84–99, Dec. 2013.
[14] Q. Liu, J. Shen, J. Yin, H. Liu, and Y. Liu, "Compact 0.92/2.45-GH dual-band directional circularly polarized microstrip antenna for handheld RFID reader applications," *IEEE Trans. Antennas Propag.*, vol. 63, no. 9, pp. 3849–3856, Sep. 2015.
[15] A. Romputtal and C. Phongcharoenpanich, "IoT-linked integrated NFC and dual band UHF/2.45 GHz RFID reader antenna scheme," *IEEE Access*, vol. 7, pp. 177832–177843, 2019.
[16] R. Xu et al., "Dual-band circularly polarized antenna with two pairs of crossed-dipoles for RFID reader," *IEEE Trans. Antennas Propag.*, vol. 69, no. 12, pp. 8194–8203, Dec. 2021.
[17] C. Bajaj, D. K. Upadhyay, S. Kumar, and B. K. Kanaujia, "A dual-band circularly polarized hexagonal ring antenna for handheld RFID readers," *Wireless Pers. Commun.*, vol. 125, pp. 3101–3115, Apr. 2022.
[18] R. Xu and Z. Shen, "Dual-band circularly polarized RFID reader antenna with combined dipole and monopoles," *IEEE Trans. Antennas Propag.*, vol. 71, no. 12, pp. 9593–9600, Dec. 2023, doi: 10.1109/TAP.2023.3326945.
[19] P. Sehgal and K. Patel, "Dual-band hexagonal SRR antennas and their applications in SIMO and MISO-based WLAN/WiMAX systems," *Prog. Electrom. Res. B*, vol. 99, no. 2, pp. 139–157, 2023.
[20] A. Birwal, S. Singh, and B. K. Kanaujia, "Smart compact-folded microstrip antenna for GSM, LTE, and WLAN applications," in *Smart Systems and IoT: Innovations in Computing* (Smart Innovation, Systems and Technologies), vol. 141, A. K. Somani, R. S. Shekhawat, A. Mundra, S. Srivastava, and V. K. Verma, Eds. Singapore, Springer, 2020, pp. 475–481. [Online]. Available: https://doi.org/10.1007/978-981-13-8406-6_45
[21] B. Molina-Farrugia, A. Rivadeneyra, J. Fernández-Salmerón, F. Martínez-Martí, J. Banqueri, and M. A. Carvajal, "Read range enhancement of a sensing RFID tag by photovoltaic panel," *J. Sens.*, vol. 2017, May 2017, Art. no. 7264703.
[22] A. Gil-Martínez, M. Poveda-García, J. García-Fernández, M. M. Campo-Valera, D. Cañete-Rebenaque, and J. L. G. Tornero, "Direction finding of RFID tags in UHF band using a passive beam-scanning leaky-wave antenna," *IEEE J. Radio Freq. Identif.*, vol. 6, pp. 552–563, Jun. 2022.
[23] "Raspberry Pi 4 tech specs." Accessed: Aug. 27, 2023. [Online]. Available: https://www.raspberrypi.com/products/raspberry-pi-4-model-b/
[24] (Nordic Semicond. Co.,Trondheim, Norway). *nRF24 Series*. Accessed: Aug. 27, 2023. [Online].Available: https://www.nordicsemi.com/Products/nRF24-series
[25] "Python scirpt for interfacing NRF24L01 with Raspberry Pi, Version 2.0.0." Accessed: Aug. 27, 2023. [Online]. Available: https://github.com/bjarne-hansen/py-nrf24



Amit Birwal (Member, IEEE) received the B.Tech. degree in electronics and communication engineering from Guru Gobind Singh Indraprastha University, Delhi, India, in 2003, and the M.Tech. degree in microwave electronics and the Ph.D. degree from the University of Delhi, New Delhi, India, in 2006 and 2021, respectively. He worked at various levels in the development and test phases of telecom devices with Ericsson India. He is currently an Assistant Professor with the Department of Electronic Science, University of Delhi South Campus, India. His main research interests are designing and optimizing planar antennas for IoT-based systems and communications systems.



Kamlesh Patel (Member, IEEE) received the M.Sc. degree in electronics from Rani Durgavati Vishwavidyalaya, Jabalpur, in 1999, the M.Tech. degree in microwave electronics from the University of Delhi, India, in 2003, and the Ph.D. degree from Delhi Technological University, Delhi. He was a Scientist with CSIR—National Physical Laboratory from 2004 to 2013. He is currently an Associate Professor with the Department of Electronic Science, University of Delhi South Campus, New Delhi. His research interests include microwave components, material characterization, and planar antennas for mobile communications.



Sanjeev Singh received the M.Sc. degree in physics from Chaudhary Charan Singh University, Meerut, India, in 1992, and the Doctoral degree in electronics from the University of Delhi in 1997. He is currently a Professor with the Institute of Informatics and Communication, University of Delhi and has published more than 50 research articles in various international/national journals and conferences. His current research areas are IoT-based system design, security models, and cyber–physical systems. He is a Fellow of the EU-India Cross Cultural Innovation Network.

Authorized licensed use limited to: DELHI TECHNICAL UNIV. Downloaded on February 07,2024 at 06:37:37 UTC from IEEE Xplore. Restrictions apply.

Datasets, Clues and State-of-the-Arts for Multimedia Forensics: An Extensive Review

Ankit Yadav[1,*], Dinesh Kumar Vishwakarma[2]
Department of Information Technology, Delhi Technological University, Bawana Road, Delhi-110042, India
ankit4607@gmail.com[1,*], dvishwakarma@gmail.com[2]

Abstract: With the large chunks of social media data being created daily and the parallel rise of realistic multimedia tampering methods, detecting and localising tampering in images and videos has become essential. This survey focusses on approaches for tampering detection in multimedia data using deep learning models. Specifically, it presents a detailed analysis of benchmark datasets for malicious manipulation detection that are publicly available. It also offers a comprehensive list of tampering clues and commonly used deep learning architectures. Next, it discusses the current state-of-the-art tampering detection methods, categorizing them into meaningful types such as deepfake detection methods, splice tampering detection methods, copy-move tampering detection methods, etc. and discussing their strengths and weaknesses. Top results achieved on benchmark datasets, comparison of deep learning approaches against traditional methods and critical insights from the recent tampering detection methods are also discussed. Lastly, the research gaps, future direction and conclusion are discussed to provide an in-depth understanding of the tampering detection research arena.

Keywords: Tampering Detection, Localization, Forgery, Manipulation, Deep Learning, Convolutional Neural Networks

1 INTRODUCTION

Manipulation of multimedia content poses a serious threat to society today. Several research contributions have been made to counter these manipulation attacks and this review summarises their key aspects. This section discusses why manipulation detection approaches are highly desirable in the present times of booming social media popularity and big data. Then it describes the commonly occurring multimedia manipulations. Finally, it explains the major contributions of this review.

1.1 The Need for Tampering Detection

Growing Popularity of Social Media Platforms: The last decade has witnessed a tremendous rise in social media platforms. An extensive online presence has become a normal part of daily human lives. The number of active users on social media has grown tremendously, from just over 2 million active users at the beginning of 2015 to almost 4 million active users by the end of 2020 (Dean, 2020). Also, the average person had about 8.6 social media accounts in 2020 (Dean, 2020). It is an understatement to say that social media has become integral to everyday life. The importance of social media is discussed as follows:

* Corresponding Author

- Social media connects people together.
- Social media provides a platform for sharing information, exchanging ideas, expressing opinions, etc.
- Social media also attracts a large number of passive information consumers. Users create and share multimedia data and view and explore data shared by other users of their community, group, organization, etc.
- Social media has a large impact on individuals' mental and emotional state.

Role of Big Data: With the growth of social media platforms, massive amount of multimedia content is being created every hour. This massive and ever-increasing amount of multimedia data has been termed as '*Big Data'.* Users on different platforms freely share different aspects of their lives via images, videos and text posts. The large amount of content, especially visual content having images and videos creates a fast-changing, dynamic and yet very impactful impression on society as a whole. Some *critical aspects of big data* are:

- Big Data is a massive collection of multimedia content, including text, audio, images and videos.
- Such a massive collection of multimedia data was never created before in human history and is largely due to the growing social media platforms.
- Big Data provides a clear picture into the personal lives of individuals, the functioning of organizations and about the collective psyche of society as a whole.

Creation of Multimedia Manipulation Tools and Approaches: Several tools like Adobe Photoshop, Adobe Premier Pro, and Adobe Illustrator allow for the modification of multimedia content including images and videos. Such tools provide an extensive list of options to modify content and create enhanced and yet realistic manipulations. While these tools are primarily meant to modify multimedia content to improve the visual quality of samples, they can be easily used to harm individuals, groups or society. Same applies to the endless number of mobile applications targeted specifically to modify and manipulate multimedia content.

Several recent state-of-the-art (SOTA) methods have been developed in the research domain to create realistic manipulations on images and videos. Manipulations such as deepfakes (Mirsky & Lee, 2022) provide serious identity manipulations that are so realistic that it is humanly difficult to distinguish between an original and a deepfake. Other manipulation includes splicing (Horváth, Montserrat, Hao, & Delp, 2020), (Johnston, Elyan, & Jayne, 2020), copy-move (Zhu, Chen, Yan, Guo, & Dong, 2020), (Islam, Long, Basharat, & Hoogs, 2020) and many more.

In this era of widespread social media popularity, the design and development of methods for malicious multimedia manipulation are proving harmful to society. While social media is the main engine behind producing massive amounts of multimedia data or big data, several malicious manipulation approaches can be enforced to use this unending source of images

and videos to inflict harm upon individuals/organizations and promote the spread of misinformation.

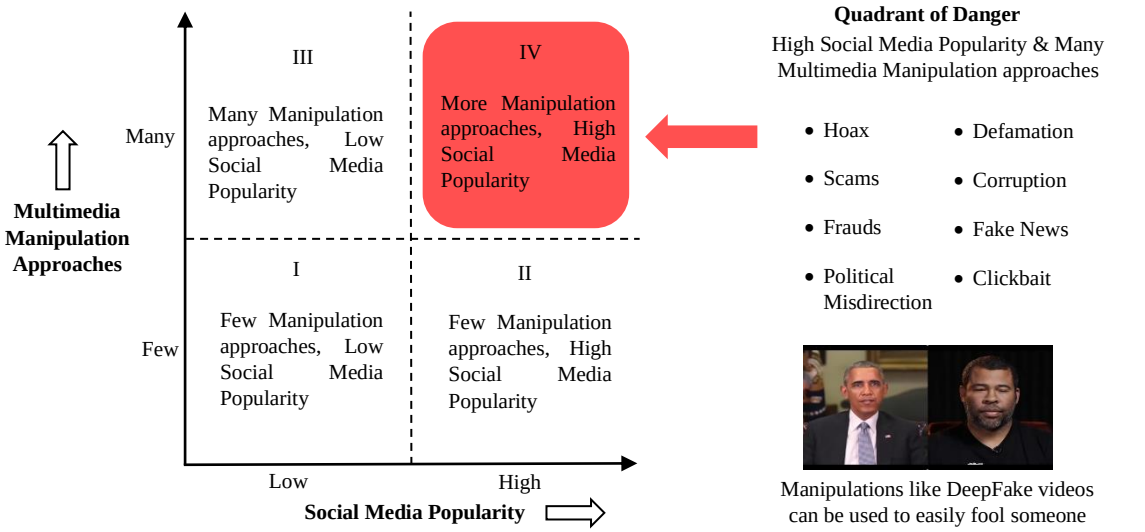


Figure 1 Quadrant IV with high social media popularity and creation of numerous multimedia manipulation approaches has given rise to a dangerous scenario in current times where it is easy to mislead, lie, defame and cause harm to an individual/organization.

Harmful Impacts of Multimedia Manipulation: Some harmful effects of manipulation approaches are discussed below:

- **Defamation:** An individual or an organization can be defamed by posting their maliciously manipulated images/videos that create a false impression of wrong doings.
- **Frauds:** Facial manipulation methods facilitate faking identities. By pretending to be someone else in an image/video, fraudsters attempt to cause monetary losses to an unsuspecting individual.
- **Misdirection:** Manipulated multimedia can also be used to create misdirection and sway public opinion, often times to gain political advantage.
- **Fake News:** Maliciously editing images or repurposing an old multimedia sample to promote untrue news or rumours causes panic and distress in society.
- **Other Manipulations:** While the list of possible manipulations is endless, most of these can be used in some form or another to mislead, lie, manipulate and cause harm to individuals/organizations.

Figure 1 clearly demonstrates the sensitive nature of the present time. Given the scenario of rising social media presence and the development of numerous malicious manipulation approaches for images and videos, undesirable communications such as hoaxes, scams, frauds, defamation, misdirection, etc., have become quite common and robust detection systems are required to prevent the damage caused to society through such manipulations. Hence, it is a matter of paramount important to develop novel manipulation detection approaches that are capable of detecting and finding tampered regions within multimedia

images and videos (Tyagi & Yadav, 2022), (Kaur, Singh, Kaur, & Lee, 2022), (Bharathiraja, Kanna, & Hariharan, 2022), (Suratkar & Kazi, 2022).

Motivations for Tampering Detection: There are several motivations behind proposing tamper detection methods:

- *Preventing Financial Fraud*: One of the key reasons for forgery detection systems in the financial sector is to avoid fraud. This includes identifying fake checks, counterfeit cash, and fraudulent credit card transactions.
- *Protection of Intellectual Property:* In the domain of intellectual property, forgery detection is used to safeguard copyrights, trademarks, and patents from being counterfeited or exploited.
- *Ensuring Document Authenticity:* Forgery detection technologies are critical in legal and government contexts for validating the validity of documents such as passports, driver's licences, birth certificates, and immigration paperwork.
- *Art Authentication:* In the art world, artwork authentication is vital to preventing art fraud. Forgery detection methods aid in determining if a work of art is genuine or a forgery.
- *Maintaining Data Integrity:* Forgery detection methods ensure data integrity in the digital era. Detecting falsified digital signatures, changed electronic documents, and modified photos or videos is part of this.
- *Protecting Brand Reputation:* Companies and brands use forgery detection to safeguard their reputation by identifying and blocking counterfeit items from entering the market.
- *Securing Identification and Access Control:* Forgery detection methods are used in security applications for biometric authentication (e.g., fingerprint, face recognition) and access control systems to prevent unauthorised access.
- *Ensuring Trust in Digital Transactions:* Forgery detection aids in establishing trust between parties in e-commerce and online financial transactions by confirming the legitimacy of digital identities and transactions.
- *Regulation Compliance:* Various sectors are required by rules to deploy forgery detection technologies as part of their compliance activities. Financial institutions, for example, are frequently required to implement anti-money laundering (AML) and know-your-customer (KYC) procedures.
- *Legal and Forensic Investigations:* Forgery detection procedures are used by law enforcement agencies and forensic professionals to gather evidence, create cases, and solve crimes involving forged papers, signatures, or identities.
- *Identity Theft Prevention:* Forgery detection is crucial in preventing identity theft, which occurs when people's personal information is faked or taken for fraud.
- *Improving Cybersecurity:* Forgery detection methods are used in the cybersecurity arena to identify and prevent many sorts of cyberattacks, such as email spoofing, phishing, and malware that attempt to fool or mimic people.

"It is both urgent and critical to develop capable, robust, generalized manipulation detection approaches that help to identify and exclude manipulated multimedia content and thereby prevent them from harming our society."

Multimedia forensics has several applications such as Forgery Detection, Digital Document Authentication, Medical Imaging, Video Surveillance and Security, Agricultural Engineering, Environmental Engineering (Feng, et al., 2022), Manufacturing Quality Control (Tang, et al., 2022) etc.

1.2 Common Manipulation Types

This section describes the common manipulations methods in images and videos.

Deepfakes: Image splicing combines parts, objects, or areas from many source pictures into a single composite image. Examples of these elements are people, objects, backdrops, and other visual components. Image splicing may be used for various objectives, ranging from artistic inventiveness and photo editing to generating deceiving or misleading images for nefarious goals such as disinformation dissemination or digital forgeries. Deep learning techniques, namely generative adversarial networks (GANs) and deep neural networks, enable deepfakes. GANs comprise two neural networks—a generator and a discriminator—that work in tandem to generate extremely realistic synthetic material. Deepfake technology enables for the amazingly accurate modification of faces, sounds, or whole scenarios. This includes modifying facial expressions, swapping faces, adjusting lip-syncing in films, and more. Deepfakes aren't just for visual content. They may also be used to make false audio recordings or voiceovers by synthesising sounds that resemble a certain person's voice.

Splicing*:* Image splicing is a digital image alteration method that combines various bits or aspects from numerous source pictures to generate a new composite image. Cutting or copying portions from one or more source pictures and pasting them into a destination image is what this method entails. Image splicing can be used for legal objectives like image editing and composition, or for deceitful ones like generating misleading or fraudulent visual information. Image splicing combines parts, objects, or areas from many source pictures into a single composite image. Examples of these elements are people, objects, backdrops, and other visual components. Image splicing may be used for various objectives, ranging from artistic inventiveness and photo editing to generating deceiving or misleading images for nefarious goals such as disinformation dissemination or digital forgeries.

Copy-Move*:* Copy-move forgery is a digital image forgery or manipulation in which a specific picture section is copied and pasted within the same image, frequently to fool viewers or modify the content. This sort of forgery is especially prevalent in the digital arena, where it is used to produce duplicate or cloned objects or pieces inside an image. The duplicated piece is generally pasted over another image area to hide or reproduce an item or scene, making the original information look intact. A part of the picture is reproduced in a

copy-move fake. Copying an object, text, or any other visual element is an example of this. The copied section is then put into another part of the same picture. This frequently entails changing the location, orientation, or size of the cloned element. The main purpose of copy-move forgery is to trick people into thinking the edited image is authentic and unaltered. It may be used to conceal or add things, eliminate undesired features, or change the image's composition.

Object Removal: In the context of digital image processing and computer vision, object removal refers to removing or concealing certain objects or areas within an image while keeping the picture's visual coherence and consistency. This approach is extensively used in picture editing, image modification, and computer vision applications for various goals, including improving an image's attractiveness, deleting undesired items, and changing the content. It has applications in a variety of disciplines, but its usage in particular settings necessitates careful evaluation of the ethical implications.

Other Manipulations: Several other manipulations are also possible including recolouring, resampling, seam carving, inpainting, shadow removal etc.

Several research contributions have been proposed to counter these common manipulations such as copy-move detection methods (Alhaidery, Taherinia, & Shahadi, 2023), (Abdulwahid , 2023), (Zhu, Chen, Yan, Guo, & Dong, 2020) (Islam, Long, Basharat, & Hoogs, 2020), splice detection approaches (Horváth, Montserrat, Hao, & Delp, 2020) (Johnston, Elyan, & Jayne, 2020), facial manipulation detection contributions (Wu, Xie, Gao, & Xiao, 2020) (Agarwal, Farid, Fried, & Agrawala, 2020), facial retouching detection (Sharma, Singh, & Goyal, 2023) etc.

This review studies deep learning-based manipulation detection approaches in images and videos. Because of the explosive rise of social media platforms in recent years and the development of harmful manipulation techniques, it is now easier than ever to generate and change multimedia material. Deep learning-based approaches have proven superior to hand-crafted feature-designing methods in computer vision applications. This review analyses deep approaches for manipulation detection in images and videos.

Figure 2 describes a novel taxonomy for deep learning-based manipulation detection and localization approaches.

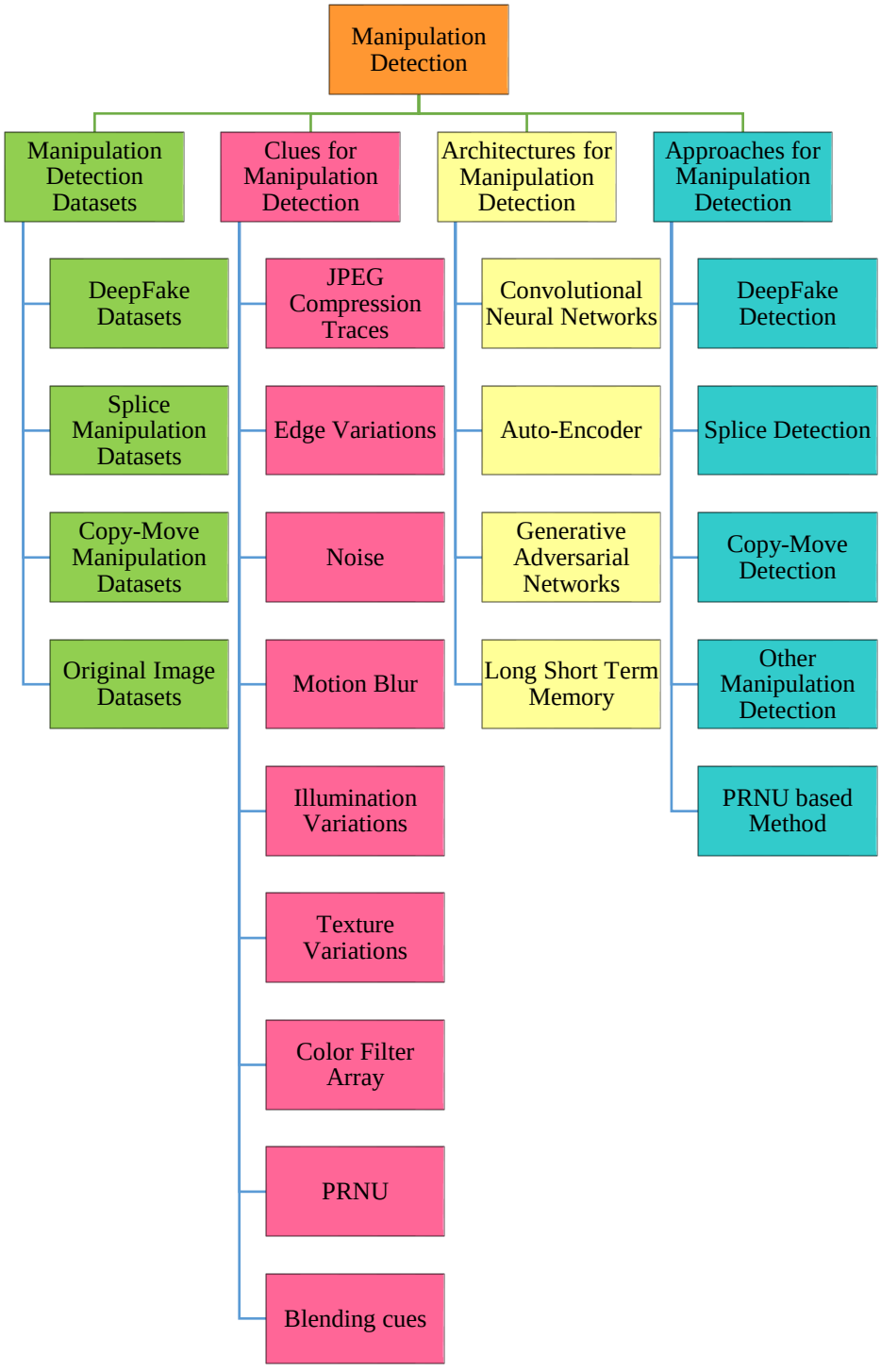


Figure 2 Taxonomy of Malicious Manipulation Detection in Multimedia

This review presents the following major contributions:

- Present a thorough review of the latest manipulation detection approaches based on deep learning from top journals and conferences covering diverse approaches towards tampering detection in images and videos.
- Present the most significant publicly available benchmark datasets for manipulation detection, specifying their characteristics like number of samples, manipulation types, resolution of media files, file format etc (Section 3).
- Demonstrate the common clues and popular deep architectures (Table 3) used for manipulation detection.
- Conduct an in-depth study of deep learning-based manipulation detection approaches (Section 6) by comparing them against traditional methods, providing detailed descriptions of architectural novelties, their advantages, visual block diagrams (Figure 9-20), etc.
- Also presents an exhaustive tabular representation of the latest deep learning-based contributions for manipulation detection (Table 4), highlighting the manipulation types under focus (deepfakes, splicing, copy-move etc), proposed novelty of methods, approach type (detection or localization), manipulation clues extracted, deep architectures used and detection scores achieved on publicly available benchmark datasets.
- Discuss research gaps of existing state-of-the-arts and possible future trends in manipulation detection (Section 8)

The novel manipulation detection approaches have been classified into deepfake detection, splice detection, copy-move detection, and other manipulation detection approaches.

The rest of this review is organised as follows. Section 2 explains the approach followed in preparation of this review. Section 3 describes the publicly available benchmark datasets for manipulation detections and evaluation metrics used to measure their performance. Section 4 describes the common manipulation clues. Section 5 talks about the fundamental deep learning architectures used for manipulation detection. Section 6 is dedicated to an in-depth review of the SOTA manipulation detection methods by describing deepfake detection methods, splice detection methods, copy-move detection methods, and other methods. Section 7 presents a detailed discussion of the manipulation detection research ecosystem. Section 8 specifies the research gaps and possible future trends and Section 9 specifies the conclusion section.

2 RESEARCH METHODOLOGY

This section highlights the approach used to prepare this review. This review includes the research papers from top journals, conferences and workshops of several popular repositories like IEEE Xplore, Science Direct, Springer, ACM and Google Scholar. Relevant publications were included using keyword searches for “forgery detection”, “manipulation detection”, “images”, “videos”, “deep”, “review”, “survey” etc. High-quality journals such as ACM Transactions, IEEE Transactions and top computer vision

conferences such as European Conference on Computer Vision (ECCV), Conference on Computer Vision and Pattern Recognition (CVPR), IEEE International Conference on Acoustics, Speech and Signal Processing (ICASSP), International Conference on Computer Vision (ICCV) were prioritized while including research contributions. Finally, a novel taxonomy of manipulation detection approaches (Figure 2) is formulated based on the included research papers.

Figure 3 shows the year-wise distribution of contributions, demonstrating that the major contributions are from recent years.

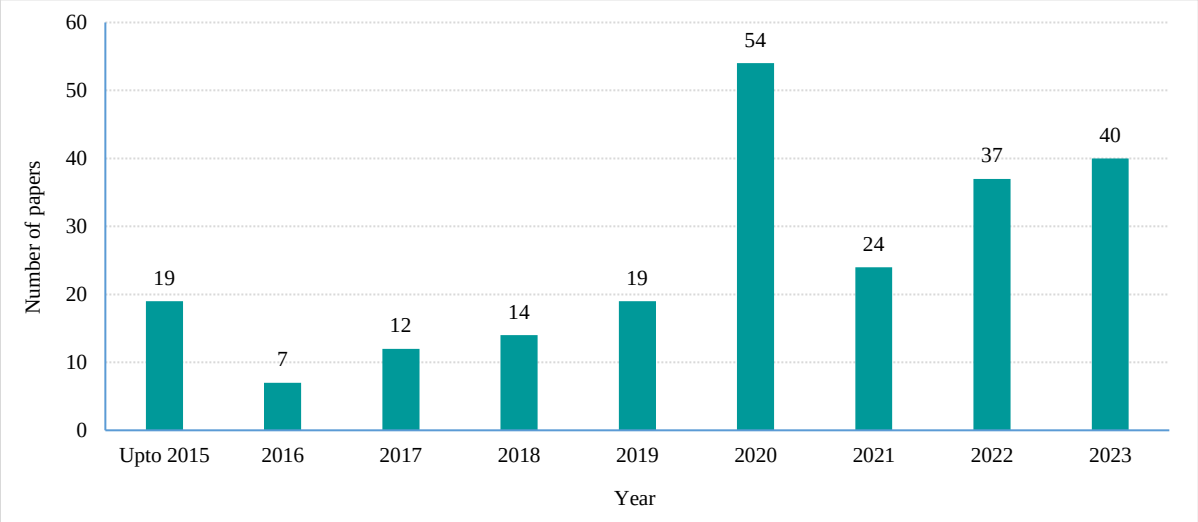
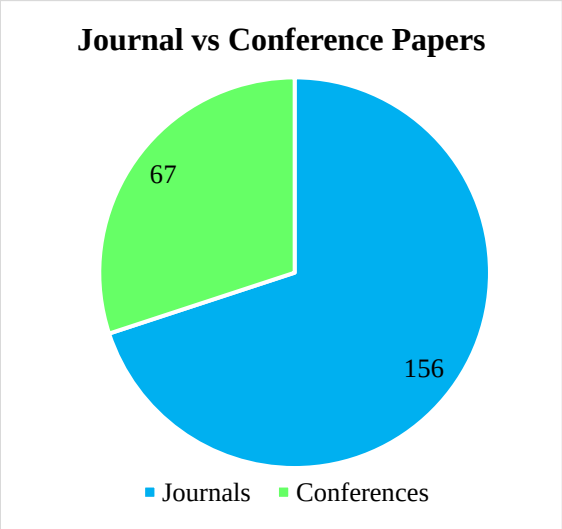
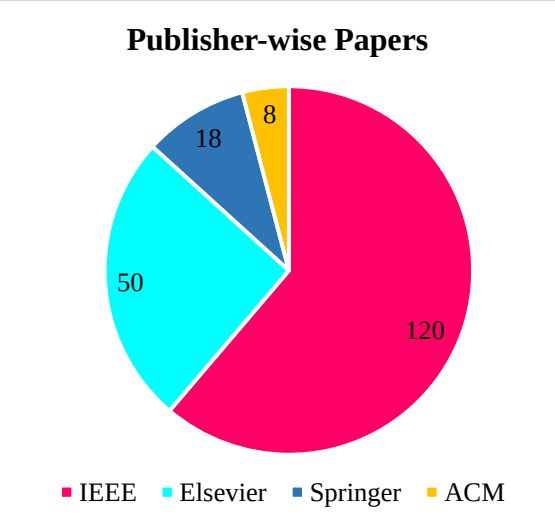


Figure 3 Year-wise Papers of Manipulation Detection Literature





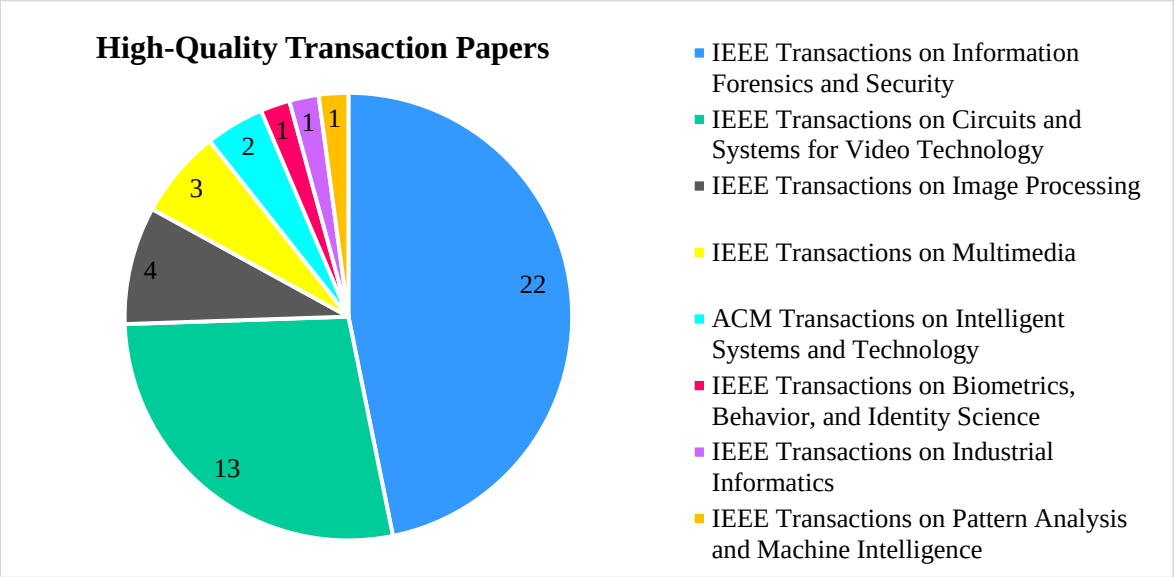


Figure 4 The distribution of papers discussed in this paper is presented in the above pie charts. The first graph gives the comparison of the number of conference and journal papers cited in this paper. The second graph shows the publisher-wise distribution of papers. The third graph shows the number of high-quality research papers from trasaction journals.

Figure 4 shows the distribution of papers cited in this manuscript. The first graph presents the number of conference and journal papers cited in this manuscript. Next, the second graph shows the publisher-wise distribution of papers. And last, the third pie chart shows the number of papers from high-quality transaction journals.

3 TAMPERING DETECTION DATASETS

This section highlights the properties of the most prominent tampering detection datasets for images and videos in the research community. Following that, the assessment measures utilised to assess the performance of many cutting-edge manipulation detection and localization algorithms are explained.

The most commonly used Image manipulation datasets are Columbia, CASIA, MICC and FORENSIC datasets. For video manipulations, novel approaches are commonly trained and evaluated on the FaceForensics, FaceForensics++ and VTD datasets. IMD2020, DeeperForensics 1.0 and DFDC are large-scale manipulation datasets proposed in recent times.

Table 1 provides a comprehensive overview of these popularly used manipulation detection datasets for images and videos.

Table 1 Manipulation Detection Datasets for Images and Videos

Ref.	Year	Dataset	Modality	Manipulation Type	Original Samples	Manipulated Samples	Resolution	Format	Mask
(Ng, Hsu, & Chang, 2004)	2004	Columbia Gray	Image	Splicing	933	912	128*128	BMP	No
(Schaefer & Stich, 2004)	2004	Uncompressed Color Image Database (UCID)	Image	-	1338 uncompressed color images		512 × 384	-	-
(Hsu & Chang, 2006)	2006	Columbia Color	Image	Splicing	183	180	757*568 / 1152*768	TIFF	Yes
(Dong, Wang, & Tan, 2013)	2009	Casia v1.0	Image	Splicing	800	921	384*256	JPEG	No
(Dong, Wang, & Tan, 2013)	2009	Casia v2.0	Image	Splicing	7491	5123	240*160 / 900*600	TIFF / JPEG	No
(Amerini, Ballan, Caldelli, Bimbo, & Serra, 2011)	2011	MICC-F2000	Image	Copy-Move	1300	700	2048 * 1536	JPEG	No
(Christlein, Riess, Jordan, Riess, & Angelopoulou, 2012)	2011	IMD	Image	Copy-Move	48	48	3000 * 2300	JPEG / PNG	Yes
(Amerini, Ballan, Caldelli, Bimbo, & Serra, 2011)	2011	MICC-F220	Image	Copy-Move	110	110	722 * 480 or 800 * 600	JPEG	No
(Bas, Filler, & Pevný, 2011)	2011	BOSSbase v1.01	Image	-	10000 uncompressed gray scale images		512*512	PGM	-
(Chingovska, Anjos, & Marcel, 2012)	2012	Replay Attack	Video	Face Spoofing	200	1000	320*240 @ 25fps	QVGA	-
(Amerini, et al., 2013)	2013	MICC-F600	Image	-	440	160	800*533 / 3888*2592	JPEG / PNG	Yes
(Tralic, Zupancic, Grgic, & Grgic, 2013)	2013	CoMoFoD	Image	Copy-Move	260	260	512*512	JPEG / PNG	Yes
(Carvalho, Riess, Angelopoulou, Pedrini, & Rocha, 2013)	2013	DSO-1	Image	Person Splicing	100	100	2048*1536	PNG	-
(Carvalho, Riess, Angelopoulou, Pedrini, & Rocha, 2013)	2013	DSI-I	Image	Person Splicing	25	25	Variable	-	-
(Image Forensics Challenge Dataset, 2014)	2014	Image Forensic Challenge Dataset	Image	Splicing	144	144	2018*1536	PNG	-
(Chen, Tan, Li, & Huang, 2015)	2015	SYSU-OBJFORG dataset	Video	Copy-Move, Splicing	100	100	1280*720 @ 25fps	H.264 / AVC	-
(Dang-Nguyen, Pasquini, Conotter, & Boato, 2015)	2015	Raw Images Dataset (RAISE)	Image	-	8156 raw images		3008*2000 / 4288*2848 / 4928*3264	-	-
(Cozzolino, Poggi, & Verdoliva, 2015)	2015	GRIP	Image	Splicing	80	80	1024*768	JPEG	Yes
(Sanjary, Ahmed, & Sulong, 2016)	2016	Video Tampering dataset (VTD)	Video	Copy Move, Slicing, Swapping Frames	33 manipulated videos from YouTube		1280*720 @ 30 fps	-	Yes
(Wen, et al., 2016)	2016	Coverage	Image	Copy Move	100	100	Variable	TIFF	Yes
(Taimori, Razzazi, Behrad, Ahmadi, & Zadeh, 2016)	2016	Raw Color Image Database (RCID)	Image	-	208 raw images		5184*3456	TIFF	-
(Zhou, Han, Morariu, & Davis, 2017)	2017	FaceSwap	Image	Facial Swapping	2300	1005	Variable	JPEG	-
(Rössler, et al., 2018)	2018	FaceForensic	Video	Face2Face manipulation	500000 frames from 1004 videos		YouTube videos greater than 480p	-	Yes
(Rössler, et al., 2019)	2019	FaceForensics++	Image	DeepFake, Face2Face, FaceSwap, NeuralTextures	1.8 million images		858 x 480 / 1280 x 720 / 1920 x 1080	-	Yes

Ref.	Year	Dataset	Modality	Manipulation Type	Original Samples	Manipulated Samples	Resolution	Format	Mask
(Novozámský, Mahdian, & Saic, 2020)	2020	IMD2020 (synthetic)	Image	Copy Paste, Splicing, Retouching	35000	35000	Variable	JPEG	Yes
(Novozámský, Mahdian, & Saic, 2020)	2020	IMD2020 (manual)	Image	Copy Paste, Splicing, Retouching	2000	2000	Variable	JPEG	Yes
(Jiang, Li, Wu, Qian, & Loy, 2020)	2020	DeeperForensics 1.0	Video	Facial Manipulations	50000	10000	1920 x 1080	-	-
(Li, Yang, Sun, Qi, & Lyu, 2020)	2020	Celeb DF dataset	Video	DeepFake	590	5639	13 second videos @ 30 fps	MPEG-4	-
(Dolhansky, et al., 2020)	2020	DeepFake Detection Challenge dataset (DFDC)	Video	FaceSwap, NTH, FSGAN, StyleGAN,	124K videos		Most videos shot at 1080p	-	-

3.1 DeepFake Datasets

This section discusses the popular image and video-based datasets for deepfake detection. Several popular benchmarks have been proposed to train deepfake detection frameworks. The most widely used deepfake datasets are discussed below:

Deepfake Detection Challenge (DFDC) dataset: The DFDC is a massive deepfake video dataset proposed in 2020. It contains two variants, namely, *DFDC-preview* and DFDC dataset. The preview dataset includes 5214 videos featuring two facial manipulation algorithms. Original videos were shot by using 66 actors and the ratio of tampered to original samples is 1:0.28. The main DFDC dataset has 124k videos, including eight facial manipulation variations(Dolhansky, et al., 2020). Original videos are recorded from as many as 3426 actors and is the most widely used deepfake detection dataset owing to the large number of samples. It is one of the research community's oldest and most widely used deepfake datasets. It provides two variants, the first is ideally suited for designing lightweight samples, while the larger variant with 124K videos is used to train more extensive and comprehensive face tampering detection models. All videos are labelled, making it the standard dataset for supervised learning-based methods.

FaceForensics++ dataset: Another popularly used dataset for deepfake detection is FaceForenscis++. It presents four variations of facial manipulations, namely, face swap (FS), face-to-face (F2F), deepfakes (DF) and Neural Textures (NT) (Rössler, et al., FaceForensics++: Learning to Detect Manipulated Facial Images, 2019). This dataset contains 1.8 million images from 1000 videos. Videos are available at three compression levels: raw (no compression), high-quality (low compression) and low-quality (high compression). This dataset is widely used for *cross-dataset* performance evaluation of novel deepfake detection methods. Methods trained only one of the four manipulations are later evaluated on other manipulations, demonstrating the generalization capability of proposed approaches. Its main advantage is the incorporation of multiple types of facial modifications that truly test a given model's forgery identification capabilities.

Celeb-DF dataset: The Celeb-DF dataset contains 5639 high-quality deepfake videos of celebrities generated from 600 original videos collected from YouTube. The average video length is 13 seconds and the frame rate is 30 fps (Li, Yang, Sun, Qi, & Lyu, 2020). The main advantage of using this dataset is that compared to other deepfake datasets, it specializes in providing high-quality deepfakes. The face-tampered samples are very realistic and not distinguishable to human eyes. Hence, a deep learning model is forced to extract discriminative non-semantic image features that are not obvious is the visible domain.

DeeperForensics 1.0 dataset: This deepfake dataset has 60000 videos with 17.6 million frames and fake samples are generated using the latest end-to-end face swapping frameworks. Original videos are shot using 100 paid actors, and seven types of attacks are applied with five intensity levels each, making the total number of manipulation combinations 35. The ratio of real to fake videos is 5:1 (Jiang, Li, Wu, Qian, & Loy, 2020). Containing as many as 60000 videos with 17.6 million frames, it is another giant dataset for face manipulation detection models. Its main highlight is the utilization of 100 actors selected from diverse backgrounds. Thirty-five different perturbations are used to prepare the tampered face videos. Generated from an end-to-end face-swapping framework, it contains the highest video quality for manipulated videos.

3.2 Splice Manipulation Datasets

Several publicly available datasets are developed towards splice detection. The most widely used splice datasets are discussed here:

CASIA v1.0 and v2.0: Casia datasets are used to train deep models to detect splice manipulation. Casia v1.0 contains 800 authentic and 921 splice images. Spliced samples are prepared using Adobe Photoshop software and all images are jpeg compressed. Several pre-processing attacks are performed before pasting such as rotation, resize, distortion or any combination of the three. Casia v2.0 is a larger variation of splice dataset with 7200 authentic and 5123 spliced images with variable image resolutions. Casia v2.0 also contains uncompressed images (TIF format), unlike the previous version. The main benefit of choosing the CASIA datasets is that they present real-world image tampering examples not focused on specific domains, such as deepfake datasets focusing explicitly on facial manipulations. The CASIA datasets are the very first image tampering datasets that have led the research field of image forensics. With multiple pre and post-processing attacks and multiple file formats in the v2.0 variant, it is still a favourite for evaluating models for generic image manipulation.

COLUMBIA: The Columbia dataset contains 363 images 183 authentic images from four camera models and 180 spliced samples. No post-processing is performed on spliced samples. While most image datasets are built around the commonly used jpeg format, this dataset contains TIFF image files, which is a lossless compression standard. It is ideally

suited for evaluating models that do not rely on compression artefacts for forgery detection. It contains high-resolution images with binary masks that aid detection and localization models.

3.3 Copy-Move Manipulation Datasets

Several publicly available datasets are developed towards copy-move detection. The most widely used datasets are discussed here:

MICC-F200 and F2000: The MICC datasets include samples manipulated with copy-move forgery. MICC-F220 contains 110 ground truth and 110 forged images, while the MICC-F2000 contains 1300 original and 700 tampered images. The resolution of images varies from 722 x 480 to 800 x 600 in MICC-F220 while MICC-F2000 has higher resolution images (2048 x 1536). These datasets are the benchmark datasets for detecting copy-move forgery. The higher resolution images in MICC-F2000 helps to uncover copy-move forgery in realistic real-world images.

CoMoFoD: The CoMoFoD dataset contains 260 original and 260 copy-move tampered images. The main advantage of this dataset is the presence of several manipulations such as rotation, scaling, distortion, combination etc. Post-processing methods such as compression, blurring, noise addition, color modification are applied to both the original and manipulated. Hence, it is ideally suited to check model robustness against various attacks and post-processing steps that ideally hide the image tampering clues.

3.4 Original Image Datasets

Several existing manipulation datasets are small-scale i.e., they have very few samples. However, deep learning architectures require large-scale datasets with high diversity to effectively learn discriminative features. Hence, several manipulation detection approaches have used raw image-based datasets to create their own manipulated samples and evaluated their proposed methods on the newly created datasets. To this end, several raw image-based datasets such as BOSSbase, RAISE, UCID etc have become crucial in developing novel manipulation datasets (Li , Feng, He, Weng, & Lu, 2023), (Misra, Rohil, Moorthi , & Dhar, 2023).

Yang et al. (Yang, Li, & Zhang, 2020) use BOSSbase image dataset to create cloning and splicing manipulated samples. Li et al. (Li, Zhang, Luo, & Tan, 2019) use BOSSbase image dataset to prepare doubly compressed samples with jpeg compression standard to detect double compression, an indicator of forgery. Nam et al. (Nam, et al., 2019) use UCID and BOSSbase to prepare a dataset for image resizing detection.

Similarly, the dataset RAISE has also been used to prepare forged samples for semantic segmentation of jpeg blocks (Alipour & Behrad, 2020), prevent anti-forensic attacks on images that are median filtered (Tariang, Chakraborty, & Naskar, 2019) etc.

Some samples from DFDC and DeeperForensics 1.0 datasets are shown in Figure 5.

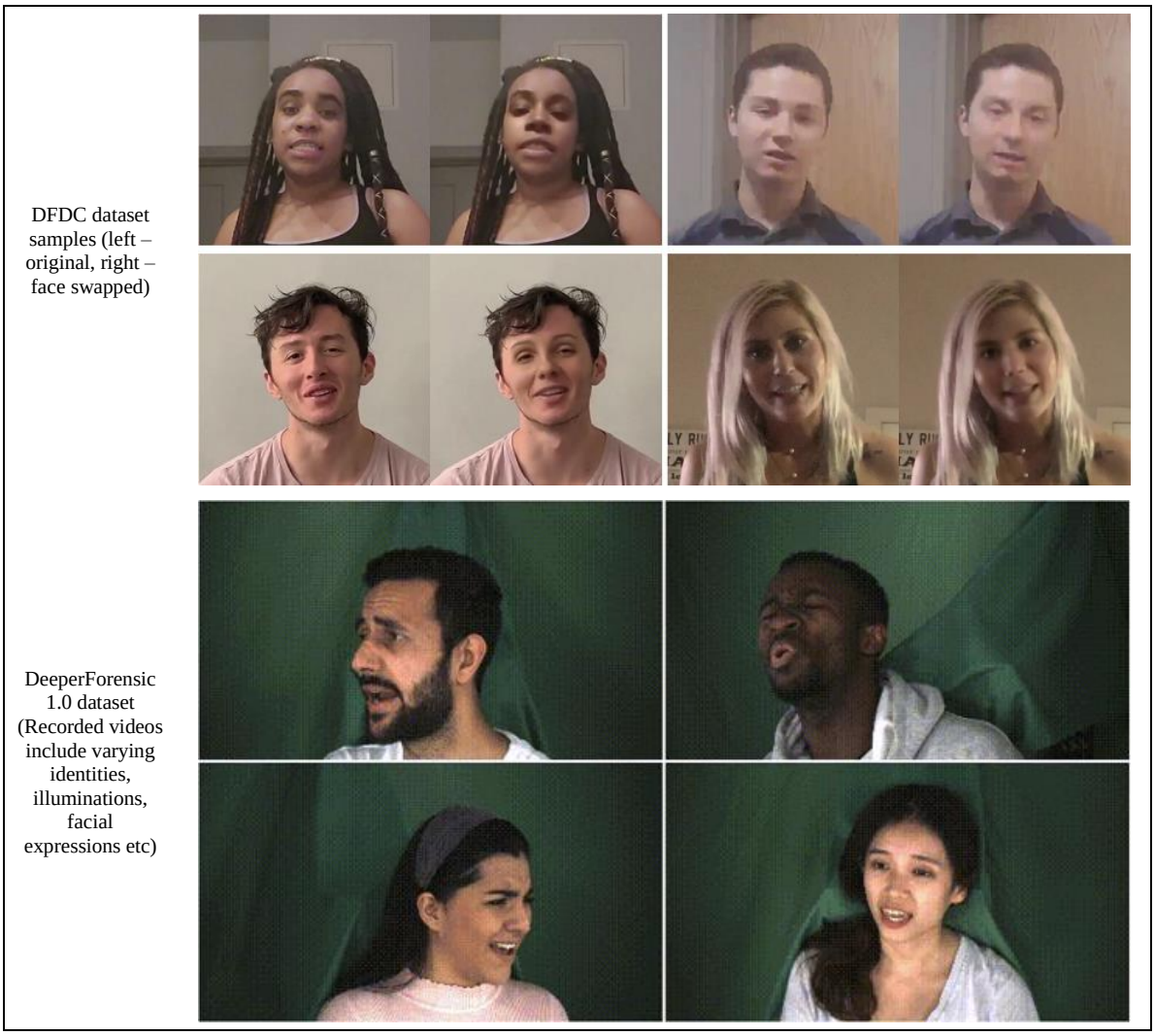


Figure 5 Samples from DFDC and DeeperForensics 1.0 datasets

Metrics for Performance Evaluation

This section describes the commonly used evaluation metrics to illustrate the performance measures of state-of-the-art methods for manipulation detection in images and videos. Concerning classification models, the following terms are defined - **True Positive** ($\mathcal{TP}$) where manipulated samples are classified as manipulated. **False Positive** ($\mathcal{FP}$) where original inputs are classified as manipulated. **True Negative** ($\mathcal{TN}$) where original inputs are

classified as original. **False Negative** ($\mathcal{FN}$) where manipulated samples are classified as original.

Accuracy (Mi, Jiang, Sun, & Xu, 2020), (Mayer & Stamm, 2020) defines the ratio of correct predictions to all predictions. It is the most commonly used metric for performance evaluation of classification models.

$$Accuracy = \frac{\mathcal{TP}+\mathcal{TN}}{\mathcal{TP}+\mathcal{TN}+\mathcal{FP}+\mathcal{FN}} \qquad (1)$$

Precision (Zhu, Chen, Yan, Guo, & Dong, 2020), (Islam, Long, Basharat, & Hoogs, 2020) metric measures the proportion of manipulated samples correctly classified out of all samples classified as manipulated. It is the ratio of $\mathcal{TP}$ samples to total number of positively predicted samples i.e., $\mathcal{TP} + \mathcal{FP}$.

$$Precision = \frac{\mathcal{TP}}{\mathcal{TP}+\mathcal{FP}} \qquad (2)$$

Recall (Zhu, Chen, Yan, Guo, & Dong, 2020), (Islam, Long, Basharat, & Hoogs, 2020) is the ratio of correctly classified manipulated samples to all actual manipulated samples.

$$Recall = \frac{\mathcal{TP}}{\mathcal{TP}+\mathcal{FN}} \qquad (3)$$

F1 score (Zhu, Chen, Yan, Guo, & Dong, 2020), (Islam, Long, Basharat, & Hoogs, 2020) maintains the balance between precision and recall. A good classification model must have a high chance of identifying a manipulated sample (high precision) and also identify most of the actual manipulated samples (high recall). F1 score lies between 0 and 1.

$$\mathbb{F}1\ Score = 2 * \frac{Precision*Recall}{Precision+Recall} \qquad (4)$$

Mathews Correlation Coefficient (Cun & Pun, 2018), (Cozzolino & Verdoliva, Noiseprint: A CNN-Based Camera Model Fingerprint, 2020) computes the correlation coefficient of the two classes (original and manipulated). It is a relatively less popular but robust classification metric. It overcomes other metrics' challenges, such as class imbalance problems for accuracy and asymmetric problems of precision, recall and F1.

$$\mathcal{MCC} = \frac{\mathcal{TP}*\mathcal{TN}-\mathcal{FP}*\mathcal{FN}}{\sqrt{(\mathcal{TP}+\mathcal{FP})(\mathcal{TP}+\mathcal{FN})(\mathcal{TN}+\mathcal{FP})(\mathcal{TN}+\mathcal{FN})}} \quad (5)$$

Receiver Operating Characteristic (ROC) curve plots the 'true positive rate' ($\mathcal{TPR}$) against 'false positive rate' ($\mathcal{FPR}$) by taking different threshold values for the positive class (manipulated class). The AUC score (Horváth, Montserrat, Hao, & Delp, 2020), (Yan, Ren, & Cao, 2019) measures the area under this ROC. The aim is to maximize the $\mathcal{TPR}$ while keeping the $\mathcal{FPR}$ to a minimum.

$$\mathcal{TPR} = \frac{\mathcal{TP}}{\mathcal{TP}+\mathcal{FN}} \qquad (6)$$

$$\mathcal{FPR} = \frac{\mathcal{FP}}{\mathcal{TN}+\mathcal{FP}} \quad (7)$$

Table 4 illustrates the performance measures of several state-of-the-art manipulation detection and localization approaches. The metrics Accuracy, Precision, Recall, F1-score, Area-Under-Curve, and Mathews Correlation Coefficient have been mentioned as 'acc', 'precision', 'recall', 'F1', 'auc' and 'mcc' respectively.

Advantages and Limitations of Performance Metrics

Accuracy is one of the most widely used metrics for classification-based tasks. However, the accuracy metric is suitable for use only when no class imbalance exists in the training data. High accuracy for an imbalanced dataset is a misleading indication of the model's goodness as the model may be wrongfully classifying all data samples as the majority class and still achieve a high accuracy score.

Precision is a more robust measure for detecting manipulated images/videos since it highlights the 'goodness' of a given deep model in identifying image manipulation. *Recall* measures the proportion of 'truly manipulated' samples that were correctly identified. *F1-score* measures the balance between the precision and recall capability of a model. Although precions, recall, and F1-scores are proven metrics, they are asymmetric and focus only on the model's ability to identify the positive or manipulated images.

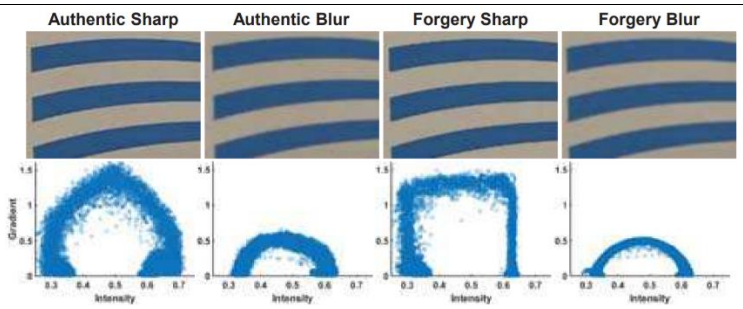
MCC score is the most robust classification metric as it focuses on identifying the positive class and the negative class. This gives a more robust evaluation of the model under study. A model that is good at identifying only manipulated images can have good precision, recall and F1-score but may still have a low MCC score if it cannot recognize negative images accurately.

4 CLUES FOR TAMPERING DETECTION

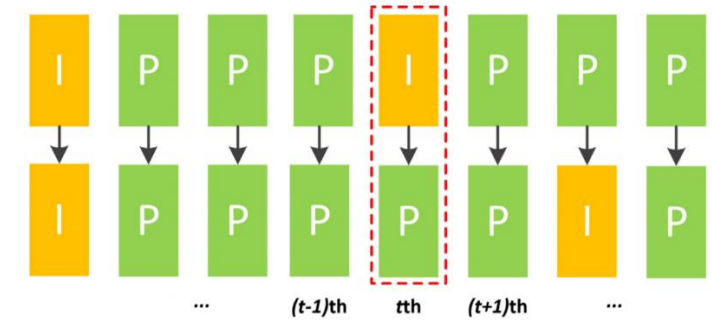
Manipulation of images and videos leaves different kinds of traces that can be used to detect forgery. These traces form the basis of different manipulation detection approaches. It is essential to analyse the nature of these traces and how they help evaluate if a given image or video is tampered. This section discusses such manipulation clues. Table 2 demonstrates these common manipulation clues.

Table 2 Demonstration of Common Manipulation Clues

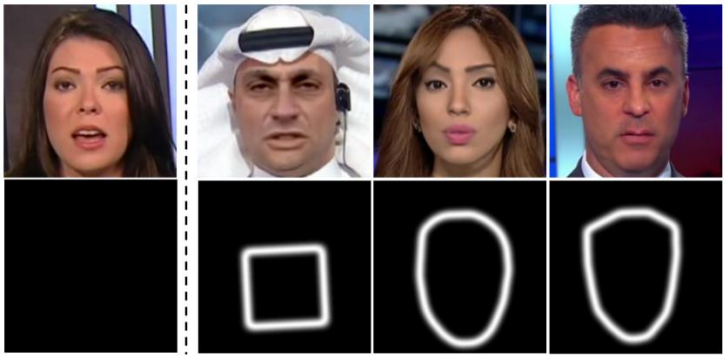
Edges
Gradient vs Intensity plots demonstrate distinct plot distributions for authentic sharp, authentic blur, forgery sharp and forgery blur edges. (Chen, McCloskey, & Yu, 2017)



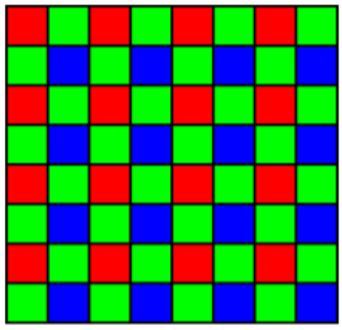
Relocated I-Frames
Video double compression leads to misalignment of I-Frames within manipulated videos. (He, et al., 2017)



Blending
Detecting facial manipulation by the localization of blending boundaries. First image is original and others are manipulated. (Li, et al., 2020)



Color Filter Array (CFA)
The Bayer matrix is the most commonly used CFA matrix where each pixel is sampled in the color represented. Misaligned CFA is a sign of tampering. (Bammey, Gioi, & Morel, 2020)



Inconsistent Object Edges: The border areas around a spliced object frequently show anomalies. Edge information retrieved using an edge convolution kernel can be used to identify whether or not edge areas have been tampered with. Edges also aid in distinguishing between original and acquired photos (Anjum & Islam , 2020), (Wang, Ni, Liu, Luo, & Jha, 2020), (Cun & Pun, 2018).

Camera Noise Cues: Camera noise, also known as image or sensor noise, is the appearance of undesired and unpredictable changes in brightness and colour in a photograph or digital image. This is mostly caused by erratic sensor sensitivity or by boosting the ISO level on a camera to capture photographs in low-light circumstances, which can increase the sensor's sensitivity. When a picture contains portions from another image, many noise differences may be discovered using frequency domain analysis (Chen, et al., 2023), (Liu & Pun, 2018), (Liu & Pun, 2020), (Xiao, Wei, Bi, Li, & Ma, 2020).

Image Seam Carving: Seam carving, also known as information-aware image resizing or retargeting, is a digital image processing technique for scaling a picture so that the most relevant material is preserved while distortion or loss of visual information is minimised. Unlike standard picture resizing algorithms that merely scale an image, seam carving intelligently discovers and eliminates or adds pixel seams from the image. Image manipulation is sometimes accompanied by seam carving operation and hence it can be used to identify tampering (Nam, et al., 2020), (Nam, et al., 2019).

Color Filter Array (CFA): A Color Filter Array, often known as a Bayer filter, is a critical component of most digital image sensors used in cameras and camcorders. It collects colour information in a single image sensor that is generally monochromatic or light intensity sensitive. A grid of small colour filters is put over individual photosensitive components (pixels) on the image sensor to form the CFA. The most prevalent Bayer CFA is characterised by a mosaic pattern of red, green, and blue filters organised in a precise repeating pattern. It is a filter camera sensors use to sample pixels in one color and interpolate other color channels from adjacent pixels, leaving different interpolation traces behind. Image manipulation results in non-aligned mosaic patches (Bammey, Gioi, & Morel, 2020).

Contrast Enhancement Traces: To hide manipulation traces, contrast enhancement is typically employed, and a GLCM matrix (gray-level co-occurrence matrix) containing enhancement traces is used to locate it (Shan, Yi, Huang, & Xie, 2019), (Sun, Kim, Lee, & Ko, 2018).

Shadow Misalignment Clues: Depending on the lighting source, all objects in a given image cast a shadow at a fixed angle which is uniform for its containing objects. Traces of shadow removal or uneven shadow direction is a good indicator of image tampering (Yarlagadda, et al., 2019).

Phoneme Viseme Mismatch: A phoneme is the smallest distinguishable element of sound in a language that may alter the meaning of a word. Phonemes are the building elements of spoken language and are utilised to distinguish between words. Because numerous phonemes can cause the same or comparable lip motions, they are classified as visemes. This makes animating lip movements in time with speech or training voice recognition systems to read lip movements easier. In deepfake movies, there are inconsistent mouth

shape imprints while pronouncing particular phonemes (Agarwal, Farid, Fried, & Agrawala, 2020).

Face Motion Amplitude: Face motion amplitude usually refers to the amount or degree of movement or displacement displayed by various facial features or components of a person's face. It quantifies how much the face moves during facial emotions, gestures, and other facial movements. Compared to real recorded videos, AI produced fake facial videos with significant distortions and flickering in facial regions that lead to unnatural facial movements. Hence, this is usually a good indicator of face forgery (Fei, Xia, Yu, & Xiao, 2020), (Li , Xie, & Wang, 2023).

Video Codec and coding quality: A video codec or "compression-decompression", is a software or hardware technique used to compress and decompress video files or streams. Video codecs are vital for effectively storing and transmitting digital video data because they minimise file size while retaining acceptable visual quality. Codecs compress video data by encoding it more compactly for storage or transmission and then decoding it to show or replay the video. In manipulated videos, video frame splicing can leave indications of numerous codecs and quality (Verde, et al., 2018).

Relocated I-Frames: An I-frame, short for "Intra-frame," is a frame in video compression that serves as a keyframe or reference frame. Unlike P-frames (Predictive frames) and B-frames (Bi-directional frames), I-frames do not rely on information from previous or subsequent frames. They are instead self-contained and represent an entire image in the video sequence. The relocation of I-frames is caused by video frame manipulation, which leaves various compression traces (He, et al., 2017).

Texture Information: If there are differences in illumination across distinct picture sections, the sample has been spliced. The textural disparity between areas directly proves manipulation (Shi, Shen, Chen, & Lyu, 2020).

Photo Response Non-Uniformity (PRNU): PRNU is an intrinsic feature of the camera used to take pictures that may be used to identify spliced sections with different PRNU traces than the original regions within the image (Wang, Ni, Liu, Luo, & Jha, 2020).

JPEG Compression Artefacts: When a jpeg picture is altered and saved as a jpeg image again, the image has a twofold quantization effect due to two compressions. (Liu & Pun, 2018), (Amerini, Uricchio, Ballan, & Caldelli, 2017), (Deng, Li, Gao, & Tao, 2019), (Jiang, Xu, Sun, Li, & He, 2020), (He, et al., 20202), (Qian, Yin, Sheng, Chen, & Shao, 2020).

YcbCr Inconsistencies: The color space YcbCr is utilised in digital image and video processing to separate the luminance (brightness) and chrominance (colour) information in an image or video stream. This separation enables more effective visual data compression and processing, making it a popular choice in various multimedia applications. YCbCr

characteristics specify the brightness and chrominance detail and differences in these values indicate splice manipulation (Wang, Ni, Liu, Luo, & Jha, 2020).

Source Camera Model: Each camera sensor leaves distinct traces in the acquired picture, and many source camera traces in an instance suggesthe possibility of manipulation (Cozzolino & Verdoliva, 2020).

Blending Cues: Blending processes are used in several facial modification techniques, such as face swapping, to smooth out manipulated borders. Tampering is detected immediately by detecting blending borders (Li, et al., 2020).

Motion Blur Cues: Based on the relative motion between the scene and the camera, an originally taken image has the same motion blur traces across the image. A picture with several motion blur trails indicates image manipulation (Song, et al., 2019).

Illumination Inconsistency: If there are differences in illumination across distinct picture sections, the sample is likely to have been spliced. (Mazumdar & Bora, 2019), (Cun & Pun, 2018), (Zhou, Sun, Yacoob, & Jacobs, 2018).

5 ARCHITECTURES FOR TAMPERING DETECTION

This section details several deep learning based architectural components commonly used in the manipulation detection approaches. Figure 6 illustrates these commonly used deep architectures.

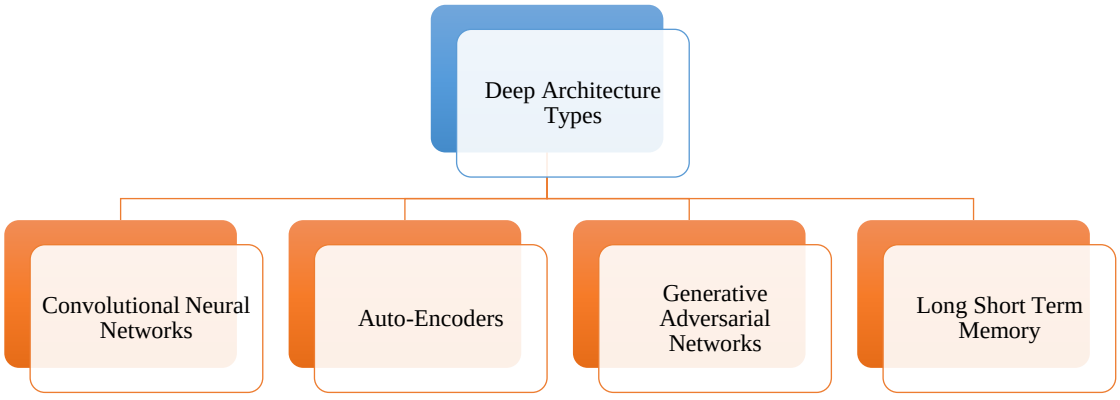


Figure 6 Commonly used Deep Architectural Components for Manipulation Detection

Table 3 gives a detailed overview about the commonly used deep architectural components, its description, and benefits.

Table 3 Commonly used Deep Architectural Components for Manipulation Detection

Architecture	Description	Benefit	Limitation	Ref.
Convolutional Neural Network (CNN)	Extracts features automatically from labelled samples	Highly capable of learning discriminative features of	Prone to data overfitting, vanishing gradient and	(Cozzolino & Verdoliva, 2020), (Bammey, Gioi, & Morel, 2020),

Architecture	Description	Benefit	Limitation	Ref.
		manipulation clues for detection and localization	exploding gradient problem	(Agarwal, Farid, Fried, & Agrawala, 2020)
Auto-Encoder (AE)	Learns efficiently compressed feature representation in an unsupervised fashion	Learn lower dimensional representation of higher dimensional input data to classify them as real or manipulated	Imperfect data reconstruction, missing important data dimensions due to narrow bottleneck layer	(Bappy, Simons, Nataraj, Manjunath, & Chowdhury, 2019), (Zhang & Thing, 2018), (Zhu, Qian, Zhao, Sun, & Sun, 2018), (Wu, Almageed, & Natarajan, 2018)
Generative Adversarial Network (GAN)	Uses two neural nets to generate fake samples that closely resemble a real data distribution	Can be trained to output the pixel wise likelihood of manipulation for localization of forgery	Mode Collapse, vanishing gradient	(Yarlagadda, et al., 2019), (Islam, Long, Basharat, & Hoogs, 2020), (Zhuang & Hsu, 2019), (Neves, et al., 2020)
Recurrent Neural Network (RNN)	Can learn the short-term dependencies of individual inputs from a sequence of input samples	Detect temporal inconsistencies between video frames	Difficult to train, vanishing gradient, exploding gradient, unable to learn from long input sequences	(Wu, Xie, Gao, & Xiao, 2020), (Chintha, et al., 2020)
Long-Short Term Memory (LSTM)	Can learn long term dependencies of individual inputs from a sequence of input samples	Can memorize features to learn correlation between frames in temporal data	Prone to overfitting, difficult to implement dropout regularization, affected by different weight initialization strategies	(Bappy, Simons, Nataraj, Manjunath, & Chowdhury, 2019), (Cun & Pun, 2018), (Shi, Shen, Chen, & Lyu, 2020), (Chintha, et al., 2020), (Fei, Xia, Yu, & Xiao, 2020)

Convolutional Neural Network (CNN): A Convolutional Neural Network (CNN) is a form of deep neural network that is designed to analyse structured grid data like photos and videos (Cozzolino & Verdoliva, 2020). CNNs are extremely effective in various computer vision applications, including picture classification, object identification, image segmentation, and others (He, Wang, Dong, & Tan, 2023). They are inspired by human visual processing and are particularly well-suited for problems extracting hierarchical characteristics from visual input. The key characteristics of CNNs are convolutional layers, pooling layers and activation functions. Convolutional layers are the main building elements of CNNs. Convolution is running a tiny filter (kernel) over input data (e.g., an image) to extract local patterns and features. These filters are learnt during training and aid the network in recognising elements such as edges, textures, and shapes. The benefit of CNNs is that they can learn the discriminative features of manipulation clues for detection and localization (Bammey, Gioi, & Morel, 2020), (Agarwal, Farid, Fried, & Agrawala, 2020). Their limitation includes being prone to data overfitting, vanishing gradient and exploding gradient problem.

Auto-Encoder (AE): AE are a form of artificial neural networks used in unsupervised machine learning and dimensionality reduction. Its primary applications are data reduction and feature learning. The basic idea behind an autoencoder is to learn a compact representation (encoding) of input data in a lower-dimensional space and then use this representation to recreate the original data (decoding) reliably. For the problem of tampering detection, they can learn lower dimensional representation of higher dimensional input data to classify them as real or manipulated (Bappy, Simons, Nataraj, Manjunath, & Chowdhury, 2019), (Zhang & Thing, 2018), (Zhu, Qian, Zhao, Sun, & Sun, 2018), (Wu, Almageed, & Natarajan, 2018). However, they sometimes suffer from imperfect data reconstruction and

missing important data dimensions due to a narrow bottleneck layer design. Autoencoders have various applications. Autoencoders can be used to decrease data dimensions while retaining critical characteristics. This is especially beneficial for situations requiring high-dimensional data to be visualised or analysed more effectively. Autoencoders can be used to detect anomalies. If the reconstruction loss for a single data point is much larger, it may suggest that the data point is an abnormality or outlier.

Recurrent Neural Network (RNN): A Recurrent Neural Network (RNN) is a form of artificial neural network intended to analyse sequential or temporal input. Unlike standard feedforward neural networks, RNNs can store and utilise information from prior time steps, which analyse incoming data in a single pass and do not recall past inputs. This makes them ideal for applications requiring sequences, such as natural language processing, speech recognition, and time series analysis. RNNs can be trained to output the pixel-wise likelihood of manipulation for localization of forgery in images (Wu, Xie, Gao, & Xiao, 2020), (Chintha, et al., 2020). But they are difficult to train and suffer from problems like vanishing gradient, exploding gradient, thereby making them ineffective in learning long input sequences. RNNs are neural network topologies that are especially built for processing sequential input. They have recurrent connections and hidden states, which allow them to capture and recall information from previous time steps, making them suited for a wide range of sequential data analysis applications.

Long-Short Term Memory (LSTM): Long Short-Term Memory is a subset of recurrent neural network (RNN) architecture developed to overcome the vanishing gradient problem and better capture long-term relationships in sequential data. Natural language processing, speech recognition, time series analysis, and other activities requiring sequential data are particularly well suited to LSTMs. They were developed to address some of the shortcomings of traditional RNNs. LSTMs can memorize features to learn correlation between frames in temporal data of videos (Bappy, Simons, Nataraj, Manjunath, & Chowdhury, 2019), (Cun & Pun, 2018). This acts as a temporal feature consistency network that learns the inconsistencies in a manipulated video (Shi, Shen, Chen, & Lyu, 2020), (Chintha, et al., 2020), (Fei, Xia, Yu, & Xiao, 2020). But they are also prone to overfitting, are difficult to implement with dropout regularization and are easily affected by different weight initialization strategies. They use memory cells and gate mechanisms that govern information flow, making them extremely effective for a wide range of sequential data analysis applications.

Generative Adversarial Networks (GAN): A Generative Adversarial Network is an unsupervised machine learning architecture that generates new data that resembles a given dataset. GANs comprise two neural networks, the generator and the discriminator, trained jointly in a competitive environment. GANs have received much attention for their capacity to generate high-quality synthetic data, making them useful in various applications such as picture synthesis, style transfer, data augmentation, and so on (Preeti, Kumar, & Sharma, 2023). GAN uses two neural nets to generate fake samples resembling a real data distribution. GANs can be trained to output the pixel-wise likelihood of manipulation for

localization of forgery (Yarlagadda, et al., 2019), (Islam, Long, Basharat, & Hoogs, 2020), (Zhuang & Hsu, 2019), (Neves, et al., 2020) but suffer from mode collapse and vanishing gradient problems.

6 APPROACHES FOR TAMPERING DETECTION

This section comprehensively examines deep learning-based manipulation detection and localization approaches. These approaches can be broadly classified into deepfake detection, splice detection approaches, copy move detection approaches and other approaches of tampering detection. Each category has been explored further by describing novel contributions that fall under it. Table 4 presents an exhaustive tabular representation of several novel contributions towards deep learning-based manipulation detection and localization.

6.1 DeepFake Detection Methods

Deepfake is any multimedia content synthesized using an artificially-intelligent approach (Mirsky & Lee, 2022), (Lee, Tariq, Shin, & Woo, 2021), (Montserrat, et al., 2020). Deepfakes are identity manipulations that are ultra-realistic and cannot be differentiated by a human manually (Rana, Nobi, Murali, & Sung, 2022), (Chamot, Geradts, & Haasdijk,

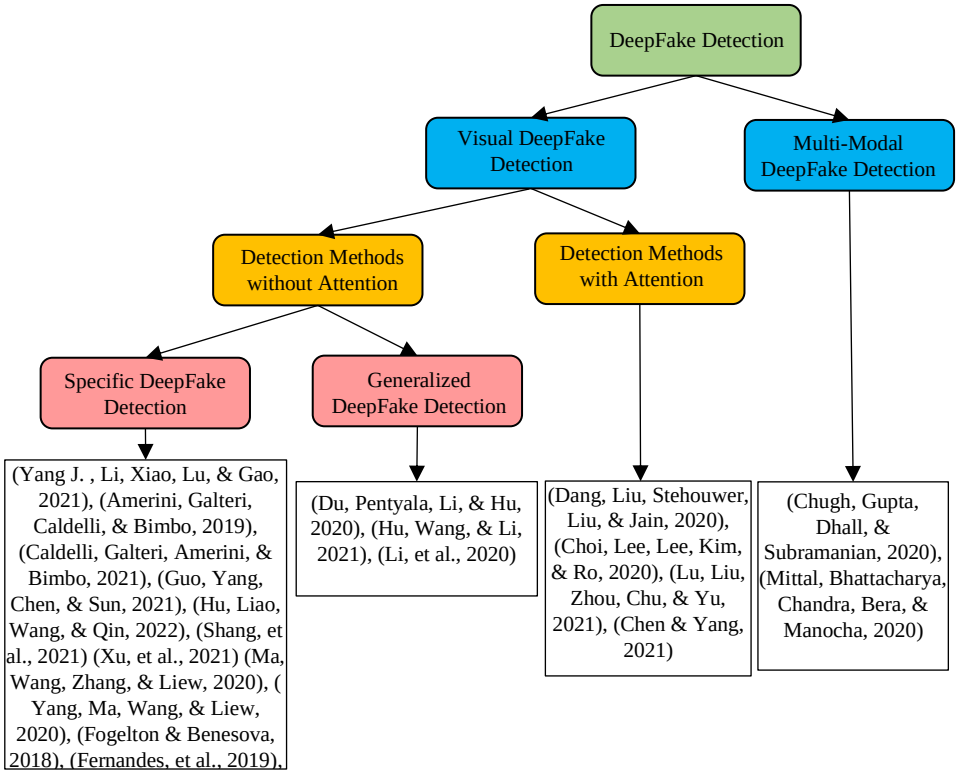


Figure 7 Categories of DeepFake Detection Methods

2022). These manipulations commonly include swapping of facial regions, transferring

facial pose/expression or synthesizing a complete artificial face (Malik, Kuribayashi, Abdullahi, & Khan, 2022), (Khalifa, Zaher, Abdallah, & Fakhr, 2022), (Mustak, Salminen, Mäntymäki, Rahman, & Dwivedi, 2023), (Yadav & Vishwakarma, 2023).

Some contributions have used handcrafted feature-based methods to detect deepfake videos such as texture analysis from Local Derivative Patterns on Three Orthogonal Planes (Bonomi, Pasquini, & Boato, 2021). While these methods claim to achieve good detection scores, they seriously lack localisation capabilities and require comprehensive manual feature designing, a classic drawback of handcrafted feature methods. The most effective deepfake detection/localization methods are based on deep architectures learning discriminative features automatically using a variety of novelties in input pre-processing, architectures or both.

Figure 7 gives an overview of the different deepfake detection methods covered in this review.

6.1.1 Visual Deepfake Detection

The most common approach towards deepfake detection is to use visual information from images or video frames as input and employ novel deep architectures to learn discriminative features. This section describes deepfake detection methods trained on visual input data and includes methods with and without attention mechanism (Ke & Wang, 2023), (Yang, Liang, Xu, Zhang, & He, 2023), (Xu, Yang, Fang, & Zhang, 2023).

6.1.1.1 Detection Methods without Attention

This section presents deepfake detection methods without an attention mechanism (Pang, Zhang, Teng, Qi, & Fan, 2023).

Specific DeepFake Detection: Yang et al. (Yang J. , Li, Xiao, Lu, & Gao, 2021) extract multi-scale textural features and demonstrate their high relevance in detecting deepfakes. Authors propose a novel “central difference convolution” (CDC) operator to compute texture difference from pixel gradient information. The texture difference is combined at multiple scales using “atrous spatial pyramid pooling” (ASPP). The CNN based on the novel CDC and ASPP shows strong generalization capability and high robustness to distorted test data. Some methods have targeted optical flow to detect deepfakes. Amerini et al. (Amerini, Galteri, Caldelli, & Bimbo, 2019) propose to learn inter-frame dissimilarities from optical flow. Guo et al. (Guo, Yang, Wang, & Zhang, 2023) extract structure forgery clues dividing face into strong and weak correlation regions and highlighting potential tampering areas. VGG16 and ResNet50 architectures are trained on optical flow frames to classify input as original or fake, achieving 81.61% and 75.46% accuracy, respectively, on the FaceForensics++ dataset.

Caldelli et al. (Caldelli, Galteri, Amerini, & Bimbo, 2021) propose another similar approach where optical flow frames form the basis of deepfake detection. Authors employ bi-directional optical flow to train a ResNet50 architecture for binary classification. Experiments indicate that the proposed model is an improvement over the traditional RGB input-based model in the case of cross-forgery detection, indicating that optical flow-based methods have strong generalizability capabilities. Chen et al. (Chen H. , Li, Lin, Li, & Wu, 2023) expose bi-granularity artefacts caused by convolutional upsampling and post-processing blen operation to detect deepfakes. Guo et al. (Guo, Yang, Chen, & Sun, 2021) propose a novel deep architecture highlighting manipulation traces by suppressing semantic image content. This is achieved by subtracting the input image matrix from the output of first convolutional layer, followed by the feature reuse idea of DenseNets to concatenate any layer's output with that of the previous layer. The proposed model shows high generalization capabilities against compression and media filtering attacks. Most of the visual data shared on social media includes compressed images and videos. But compression adds unwanted noise that hinders in detecting manipulation traces.

Hu et al. (Hu, Liao, Wang, & Qin, 2022) work towards deepfake detection in compressed videos by proposing a dual-branch architecture. First branch learns from video I-frames instead of all frames, reducing training complexity. Optional connections are pruned via greedy search to reduce the impact of compression noise. The second branch is trained on three segments from video to learn temporal inconsistencies. The proposed model scores well on same as well as cross-manipulation evaluation and performance is enhanced further via data augmentation. Shang et al. (Shang, et al., 2021) propose a novel PRRNet that captures relationships of visual data on two levels, pixel level and region level. Using spatial attention, a novel Pixel-wise Relation (PR) module finds pixel correlation in local neighbourhoods. Then, another novel Region-wise Relation (RR) module measures statistical inconsistencies using inner product, cosine distance and Euclidean distance between regions of original and manipulated content to provide a final binary prediction. The proposed model outperforms Xception architecture on CelebDF dataset.

Xu et al. (Xu, et al., 2021) consider faces from different video frames as a set and propose a novel set convolutional neural network that performs multi-frame feature aggregation to detect deepfakes. Kong et al. (Kong, et al., 2022) utilize segmentation and noise maps to detect and localize facial manipulations. Tan et al. (Tan, Yang, Miao, & Guo, 2022) propose a novel transformer-based architecture for feature compensation and aggregation, fusing global transformer and local convolutional features and reducing redundant feature learning. Chen et al. (Chen, Li, & Ding, 2022) use a spatiotemporal attention-based Xception-LSTM architecture for tamper detection. Ganguly et al. (Ganguly, Ganguly, Mohiuddin, Malakar, & Sarkar, 2022) utilise a transformer in one branch and Xception CNN in another branch to highlight face tampering artefacts. Pu et al. (Pu, et al., 2022) combine frame level and video level inconsistencies to detect facial manipulation. Xia et al. (Xia, Qiao, Xu, Zheng, & Xie, 2022) utilize textual statistical disparities between real and fake samples in each color

channel and extract discriminative features from the co-occurance matrix to detect deepfake manipulation. Kingra et al. (Kingra, Aggarwal, & Kaur, 2022) exploit LBP-based texture differences to detect manipulation.

Several approaches have targeted inconsistencies in biological clues such as visual lip movements (Wang, Liu, & Wang, 2023), (Ma, Wang, Zhang, & Liew, 2020), (Yang, Ma, Wang, & Liew, 2020), (Lin, et al., 2023), eye blinking (Fogelton & Benesova, 2018), heartbeat information (Fernandes, et al., 2019), (Qi, et al., 2020), face context (Nirkin, Wolf, Keller, & Hassner, 2021) as an indicator for deepfake manipulations. Yang et al. (Yang, Ma, Wang, & Liew, 2020) aim for speaker authentication by proposing a novel deep architecture based on novel lip feature representation. A novel "Fundamental Lip Feature Extraction" (FFE-Net) subnet captures lip motion patterns, reducing the impact of static lip features such as lip shape and appearance. Another novel, "Representative Lip Feature Extraction and Classification" (RC-Net) subnet, captures a person's talking habits by extracting high-level lip features.

Ma et al. (Ma, Wang, Zhang, & Liew, 2020) also target to extract robust lip features for visual speaker authentication to discriminate between human and computer-generated imposters. A novel Dynamic Response block suppresses static lip information and another novel Dynamic Response block fully temporal pixel level dynamic lip features. The two blocks learn complimentary information towards deepfake detection. Fogelton et al. (Fogelton & Benesova, 2018) propose an RNN-based architecture to learn temporal features from eye blinking speed and duration and provide a three-class classification: no blink, completely blinked and partial blink. Motion vector capturing eye movements gives the best classification results. Fernandes et al. (Fernandes, et al., 2019) train "Neural Ordinary Differential Equations Model" (NODE) with heart rate of original videos to predict heart rate variations occurring in deepfakes. Heart rate is obtained from three approaches: skin color variations, average optical intensity and Eulerian video magnification.

Qi et al. (Qi, et al., 2020) infer that since heartbeat rhythms can be estimated from visual photoplethysmography and hence can be used as sequential feature to differentiate real videos from fake where the heartbeat rhythms will be disrupted. Authors propose a dual spatio-temporal attention network based on a novel "motion magnified spatial temporal representation" (MMSTR) to extract discriminative deepfake features. Nirkin et al. (Nirkin, Wolf, Keller, & Hassner, 2021) infer that face swapping and other similar facial manipulations leave distinct differences between face regions and their context including hairs, ears, neck etc in images. Two recognition networks (XceptionNet architecture) are pre-trained to extract facial and context features respectively. Then, a face discrepancy network is used to predict whether the face and context from an image indicate face swapping. Given the distinct difference between swapping and reenactment manipulation methods, another network is optionally trained to detect face reenactment, i.e., manipulated facial pose and expressions. The proposed model achieves high accuracy scores on

FaceForensics++ dataset for seen and unseen manipulation, suggesting high generalizability.

GANs have been widely to create totally new images/video from scratch. With the growing ability of GANs to emulate a given data distribution, the quality and realism of generated facial samples is so real that it is no longer possible to differentiate between a genuine manually and an AI-generated facial image/video (Zhang L. , Yang, Qiu, & Li, 2022). Several contributions have targeted to detect such visually perfect deepfake samples. Wang et al. (Wang, Wang, Zhang, Owens, & Efros, 2020) show that fully synthesized deepfakes created from a variety of architectures such as ProGAN, StyleGAN, CycleGAN etc can be detected efficiently by merely training with just one such GAN. Specifically, careful pre and post-processing operations combined with robust augmentations reveal that fully synthesized images are easily classified by a standard ResNet50 architecture pre-trained on ImageNet and trained on images generated by ProGAN. Augmentations include horizontal flipping, gaussian blur, compression attack or their combinations. Experimental results demonstrate that augmentations improve generalizability and robustness against post-processing attacks.

Guarnera et al. (Guarnera, Giudice, & Battiato, 2020) show that all generative CNNs leave a sort of fingerprint during the image generation process and this can be uncovered using an "expectation maximization" algorithm that extracts a feature vector representing the structure of Transpose Convolution used to upscale features during image generation. Chen et al. (Chen, et al., 2021) target the same goal of detecting fully synthesized deepfakes by using a modified Xception architecture in which four residual blocks are removed to avoid the overfitting problem, strided convolution is used to extract multi-scale features and a feature pyramid is used to obtain multi-level features. Huang et al. (Huang, Xu, Guo, Liu, & Pu, 2022) localize GAN-based manipulation using a grey-scale fakeness map. Other such methods include (Liu, Ding, Zhu, & Yu, 2023), (Guo, Yang, Chen, & Sun, 2023), (Kiruthika & Masilamani, 2023).

Generalized DeepFake Detection: Several contributions have been made towards generalizations of deepfake detection. Wang et al. (Wang, Guo, & Zuo, 2022) use pixel-wise Gaussian blurring and a novel adversarial training practise to train models on adversarially crafted inputs to boost generalization capability. Korshunov et al. (Korshunov & Marcel, 2022) propose to boost generalized deepfake detection by trying several data augmentation techniques, including a novel data farming approach. The authors also demonstrate the effectiveness of a few-shot tuning approaches to achieve the same. Wang et al. (Wang, Sun, & Tang, 2022) prevent a drop of detection performance against compression degradation by training on a siamese network setup that processes input image and its degraded quality equivalent in pairs. In (Du, Pentyala, Li, & Hu, 2020), authors propose a Locality Aware Autoencoder (LAE) that uses a pixel-level mask to learn discriminative features from forged regions instead of finding superficial correlations. Hu et

al. (Hu, Wang, & Li, 2021) use disentangled representation learning (DRL) to separate forgery-relevant information from other non-forgery-based noise features. Ablation study indicates that the disentanglement module plays a significant role in detecting deepfakes.

Li et al. (Li, et al., 2020) also propose a generalized deepfake detection method by assuming that blending operation follows any facial manipulation. Hence, there is no requirement for any knowledge about manipulation type. Authors propose a novel image representation, Face X-ray (Figure 8) and detect the noticeable blending artefacts introduced in any manipulated image. Another contribution towards generalized deepfake detection is proposed by comparison of forensic traces from two image patches without any prior knowledge about existing manipulations (Mayer & Stamm, 2020). Kang et al. (Kang, Ji, Lee, Jang, & Hou, 2022) boost generalized deep fake detection by training on traces of warping artefacts, blur traces and residual noise. Miao et al. (Miao, Tan, Chu, Yu, & Guo, 2022) boost model generalization capabilities by employing frequency domain-based attention on RGB features to highlight manipulation regions. Both CNN and transformer architectures extract local details and global contextural information, respectively. Kong et al. (Kong, et al., 2022) target extracting original facial attributes from a manipulated video sample by utilizing both fake facial features and audio domain features. Several other contributions have aimed to achieve better generalization of deepfake detection by achieving high cross-dataset scores (Yu, et al., 2023), (Shang, et al., 2021), (Yang J. , Li, Xiao, Lu, & Gao, 2021), (Caldelli, Galteri, Amerini, & Bimbo, 2021), (Guo, Yang, Chen, & Sun, 2021), (Zhao, et al., 2023).

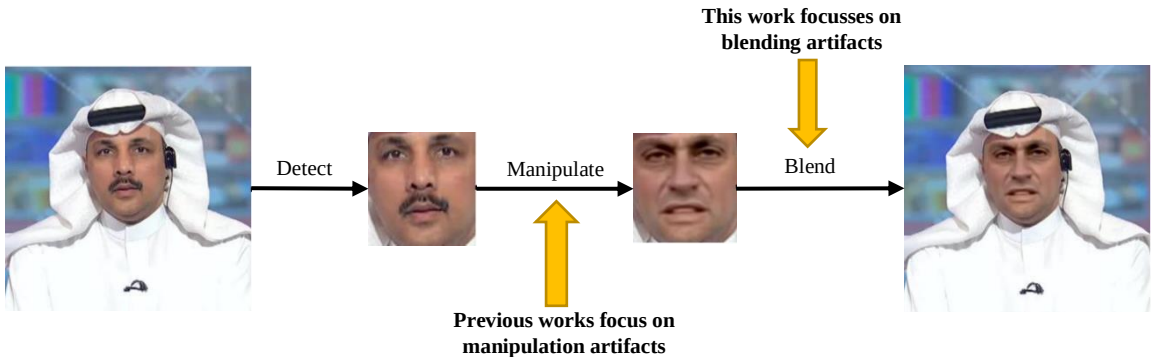


Figure 8 Face X ray detects blending traces (Li, et al., 2020)

6.1.1.2 Detection Methods with Attention

The recently proposed “attention-mechanism” has greatly enhanced the learning capability of deep models in detecting manipulation of images/videos (Vaswani, et al., 2017). Several novel contributions have used attention to highlight discriminative regions within input that helps to refine deepfake localization. Dang et al. (Dang, Liu, Stehouwer, Liu, & Jain, 2020) improve the binary classification capability of CNN by using attention mechanism. A novel attention-layer is proposed that takes any high dimensional CNN feature map $\mathbb{F}$ as input and

produces an attention map $\mathbb{M}_{att}$ using a novel "manipulation appearance model" (MAM) and then perform channel-wise multiplication with $\mathbb{F}$ to produce $\widetilde{\mathbb{F}}$. Equation 18 and 19 show the computation of $\widetilde{\mathbb{F}}$ and $\mathbb{M}_{att}$ respectively. $\bar{\mathbb{M}}$ and $\mathbb{A}$ are pre-defined and represent average map and basis functions of maps while $\propto$ is the weight parameter. The learnt attention maps improve deepfake detection capability of CNN network.

$$\widetilde{\mathbb{F}} = \mathbb{F} \odot Sigmoid(\mathbb{M}_{att}) \quad (18)$$

$$\mathbb{M}_{att} = \bar{\mathbb{M}} + \mathbb{A}.\propto \quad (19)$$

Choi et al. (Choi, Lee, Lee, Kim, & Ro, 2020) use attention to uncover key video frames that have high impact in the final prediction score. A certainty-aware attention map is generated that computes the certainty of frame level prediction from a video and then certainty-attentive features are generated based on the previously learnt attention map to produce binary classification. Experimentation results suggest that the attention mechanism improves the auc scores from 0.92 to 0.94 and accuracy score from 0.89 to 0.92.

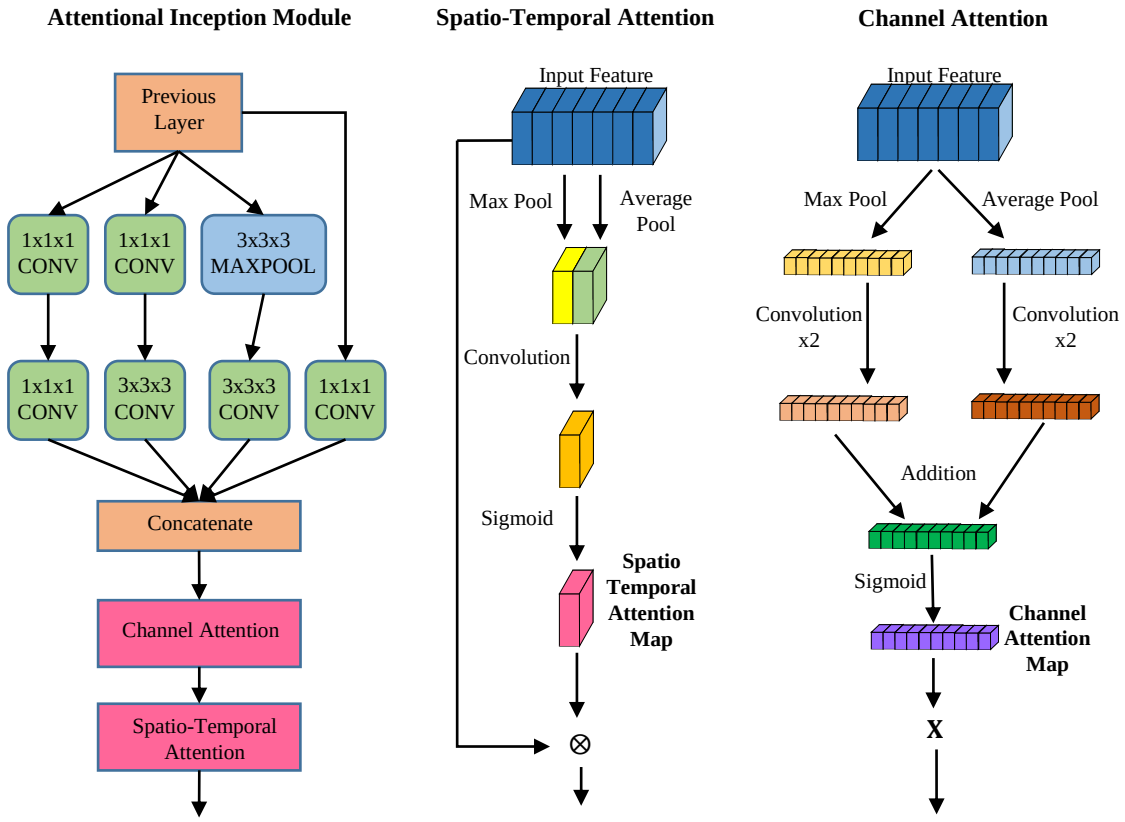


Figure 9 The novel Attentional Inception Module having a spatio-temporal attention module and a channel attention module (Lu, Liu, Zhou, Chu, & Yu, 2021)

Lu et al. (Lu, Liu, Zhou, Chu, & Yu, 2021) use 3D CNN combined with a novel attention-inception module (Figure 9) to detect deepfake videos. The proposed attention-inception module integrates channel attention by using inter-channel relationship to highlight

meaningful channels and spatio-temporal attention to highlight the distinct regions of input feature maps. The proposed model is trained on different variety of malicious tampering such as frame shuffling, frame level and video level data augmentation including flipping, cropping, adding Gaussian noise etc. The best score is reported on the model trained on video-level data augmentation suggesting increased robustness in comparison to other variants tried.

Chen et al. (Chen & Yang, 2021) divide an input image into six region-based fragments namely, eyes, nose, mouth, face, background, complete picture and employ a combination of a novel Local Attention Module (LAMs) to find generalized discriminative regions and a novel Semantic Attention Module (SAM). Six LAM modules input the fragments from an input sample and then use a CNN to compute binary classification scores from the six fragments. Then SAM modules track how each fragment is contributing to the final prediction. Experimental results indicate that the proposed model has strong generalization ability in unknown-dataset evaluation. Luo et al. (Luo & Chen, 2022) employ two novel attentional blocks namely, forgery feature attention block and spatial reduction attention block to boost CNN capability in detecting deepfakes. Wang et al. (Wang, Yang, You, Zhou, & Chu, 2022) use semantic masks to generate facial attention and extract features from relevant regions like hair, eyes etc. Cao et al. (Cao, Chen, Huang, Huang, & Ye, 2022) propose a novel attention module which finds real-fake clues and identity-changing forgery clues separately.

6.1.2 Multi-Modal Deepfake Detection

While most deepfake detection methods have focused on using visual data, some contributions include multi-modal approaches. Chugh et al. (Chugh, Gupta, Dhall, & Subramanian, 2020) infer that fake videos will have dissimilarities in their audio and video channels. A two-branch architecture extracts features from visual and audio channels of 1-second videos. The two branches are trained individually on binary cross-entropy loss. The contrastive loss enforces the dissimilarities between audio and visual information of fake samples. A novel “Modality Dissonance Score” (MDS) measures the aggregate dissimilarity of visual-audio modality. Building up on a similar idea, Mittal et al. (Mittal, Bhattacharya, Chandra, Bera, & Manocha, 2020) not only utilize the audio-visual channel but also learn perceived emotions from the audio and visual channels to detect deepfakes. Chu et al. (Chu, You, Yang, Zhou, & Wang, 2022) extract facial expression representations and lip motion patterns using Action Unit Transformer and Temporal Convolutional Network, respectively to predict deepfake manipulation.

Other novel deepfake detection approaches include using attribution metric to detect deepfakes (Fernandes, et al., 2020), training only on original videos and treating deepfakes as anomalies (Khalid & Woo, 2020), using geometry to highlight lack of facial symmetry in deepfakes (Li, Cao, & Zhao, 2021), separating irrelevant features from forgery relevant

features (Zhang, Ni, & Xie, 2021), using neural ordinary differential equations (Luo, Kamata, & Sun, 2021), using successive subspace learning (Chen, et al., 2021) etc.

6.2 Splice Detection Methods

Splice manipulation involves copying pasting region(s) of one image onto another. Fundamentally, all splice detection approaches rely on the simple idea that the pasted region and the original region of a spliced sample hold distinct properties and any competent splice detection framework must highlight this difference. The most common splice detection clues include 1) Noise variations 2) Compression traces 3) Source camera property differences 4) Illumination inconsistencies (Figure 10).

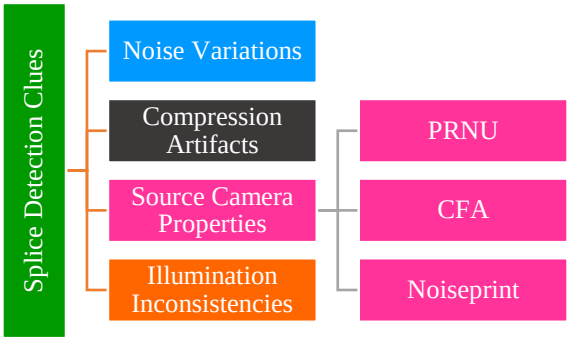


Figure 10 Common Splice Detection Clues

Traditional Splice Detection Methods: Traditional splice detection methods primarily focused on designing handcrafted features that highlight discriminative differences between original and spliced samples. Some methods are based on *image characteristics* such as detecting sharp transitions of edges and corners (Chen, Shi, & Su, 2007), chroma information (Zhao, Li, Li, & Wang, 2010) etc. Methods based on *source device identification* such as (Hsu & Chang, 2006), (Gou, Swaminathan, & Wu, 2007) proved ineffective when the extracted camera signal was weak. Certain *hash-based methods* such as (Tang, Zhang, Li, & Zhang, 2016), (Wang, et al., 2015) have been also attempted to solve splice manipulation but cannot be regarded as blind splice manipulation detection methods.

Deep Learning-based Splice Detection methods: Several recent deep learning-based approaches are highlighted in Table 4 detailing the approach, clues, architectural novelties, datasets used and results obtained. Deep learning-based approaches for splice detection are dividied into two categories namely, 1) *Deep Spatial Splice Detection Methods* 2) *Deep Hybrid Splice Detection Methods*.

Deep Spatial Splice detection methods directly input pixel information from image/video and employ architectural novelties to automatically extract discriminative features for manipulation detection and localization of spliced region (Cun & Pun, 2018), (Bi, Wei, Xiao, & Li, 2019). Deep Hybrid Splice detection methods perform automatic feature

extraction from a variety of input information including spatial information (Liu & Pun, 2018), CbCr channels (Zhang, Zhang, Zhou, & Luo, 2018), illumination maps (Pomari, Ruppert, Rezende, Rocha, & Carvalho, 2018), resampling features (Bappy, Simons, Nataraj, Manjunath, & Chowdhury, 2019), DCT histograms (Deng, Li, Gao, & Tao, 2019), residual features (Zhang & Ni, 2020), source device patterns (Bondi, et al., 2017) etc to obtain robust classification of manipulated samples. Some approaches combine these distinct inputs with spatial pixel data to obtain higher metric scores (Amerini, Uricchio, Ballan, & Caldelli, 2017), (Bappy, Simons, Nataraj, Manjunath, & Chowdhury, 2019), (Saddique, et al., 2020) etc.

Splice Detection Discussion: Challenges & Solutions

- Traditional splice manipulation detection methods focus on extracting specific discriminative features to classify the original and spliced samples.
- Traditional splice manipulation methods are mainly based on:
  - ✓ Image Characteristics
  - ✓ Source Device Properties
  - ✓ Hashing
  - ✓ Watermarking
- Traditional splice manipulation methods suffer from several drawbacks. *Image Characteristic* based methods prove weak if forgery is followed by a post-processing operation. *Source Device Properties* methods fail if the signals extracted are dilute and provide very little discriminative information. *Hash methods* for splice detection require hash of original non-forged image which defeats the purpose of blind splice manipulation detection. *Watermarking* methods like (Podilchuk & Delp, 2001) also require original image which presents the same problem as in the case of hash-based splice detection methods.
- Another serious drawback of traditional splice manipulation detection methods is that while these methods are able to classify original and spliced samples to some degree, they demonstrate very weak localization ability. Hence, the automatic feature extraction capability of deep learning proves paramount towards accurate splice detection and localization.
- Splice manipulation leaves distinct compression artifacts and several contributions have targeted to exploit this (Li, Zhang, Luo, & Tan, 2019), (Amerini, Uricchio, Ballan, & Caldelli, 2017). Specifically, if an original single-compressed image is spliced and is recompressed a second time, the double compression leaves distinct traces. The DCT histograms of doubly compressed image obtain a distinct shape by exhibiting a higher frequency of missing values as compared to histograms from original single compressed image (Wang & Zhang, 2016).

- Some contributions combine spatial and compression information to detect/localize splice manipulation. In (Li, Zhang, Luo, & Tan, 2019), authors train a novel deep model by combining DCT coefficients and uncompressed pixel information for splice detection and beat traditional hand-crafted based splice detection methods. In (Amerini, Uricchio, Ballan, & Caldelli, 2017), researchers prove that spatial and DCT compression information prove complimentary in detecting double jpeg compression that indicates splice forgery. A dual-branch deep architecture is trained on spatial and DCT features and attain high accuracy scores (93 to 99% accuracy) for cases when first compression quality (QF_1) is less than second compression quality (QF_2) i.e., $QF_1 < QF_2$. However, these model performances suffer for the case $QF_1 > QF_2$ due to small statistical differences. This is still a persistent research gap that needs to be addressed by upcoming tampering detection models.
- Deng et al. (Deng, Li, Gao, & Tao, 2019) propose MSD-Nets (Figure 11) to solve the $QF_1 > QF_2$ case problem by using a *discriminative module* comprising of a CNN trained on $QF_1 > QF_2$ examples exclusively. Multi-scale features are first extracted from DCT histograms which are then fused in a weighted manner. Then, the discriminative module is utilized for the challenging scenario of $QF_1 > QF_2$. Localization results prove the high robustness of the proposed architecture.

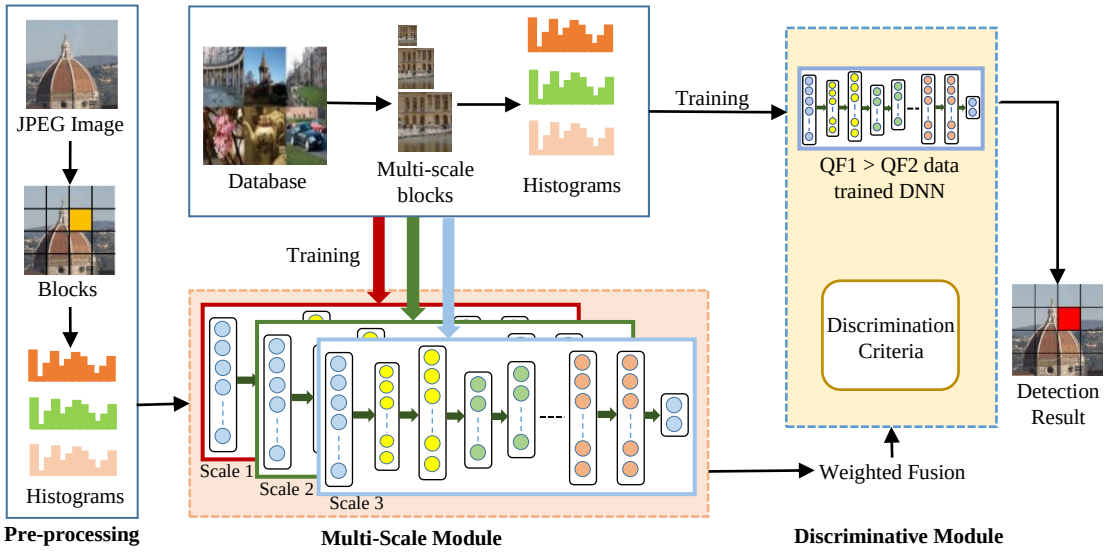


Figure 11 MSD-Nets (Deng, Li, Gao, & Tao, 2019)

- Some splice detection frameworks separate double JPEG compression detection (DJPG) into *aligned* (A-DJPG) and *non-aligned* (NA-DJPG) category depending on whether the second compression grid is aligned with the first or not. Barni et al. (Barni, et al., 2017) target accurate splice localization over small image patches with sizes as small as 64 x 64. Authors trained three different CNNs based on DCT data, noise data and pixel values, respectively. Results demonstrate that DCT-based CNN is well suited for detecting and localizing only A-DJPG, while pixel and noise domain CNNs do well for both A-DJPG and NA-DJPG. Unlike other methods that

use pre-processing to compute DCT information, authors in (Alipour & Behrad, 2020) estimate jpeg block boundaries using semantic pixel segmentation to detect and localize NA-DJPG in small local regions of size 8 x 8 pixels. The proposed architecture achieves 92.66% accuracy on jpeg images constructed from UCID, RCID and RAISE datasets. However, the method is prone to fail when forged boundaries lie near block boundaries.

- Liu et al. (Liu & Pun, 2020) propose a fusion of noise and compression information for splice detection. Specifically, the proposed Fusion-net contains two blocks of the novel DenseNet architecture. A novel residual loss is proposed that enforces the network to learn forensic features of noise and compression and a novel discrepancy loss is used to enhance the traces from multiple sources within an image patch. The two novel losses combined with classification loss help the proposed model to achieve 0.97 and 0.90 auc scores on the Columbia and Realistic Tampering datasets respectively, make it highly robust for splice localization. Another similar method utilizing noise and compression features is proposed in (Liu & Pun, 2018).
- Since splice manipulations copy an image region onto a different image, the spliced sample contains source device traces of multiple cameras. Several splice detection methods exploit this characteristic by judging if a given image contains patterns from multiple cameras, thereby indicating splice forgery.
- Bondi et al. (Bondi, et al., 2017) use a pre-trained CNN to extract features from non-overlapping image patches and then utilize a clustering algorithm to decide if each patch includes traces from single or multiple cameras. A patch confidence score indicating the contribution of a given patch in finding discriminative source camera information helps the clustering algorithm to choose correct patches for splice detection results but it contributes little in the localization process. The proposed model achieves 0.91 accuracy for known camera images and 0.81 accuracy for unknown camera category.
- Unlike most splice detection methods, Mayer et al. (Mayer & Stamm, 2020) propose a generalized *forensic similarity* (Figure 12) method to detect known and unknown forensic traces. Instead of training on specific forensic traces, the proposed method

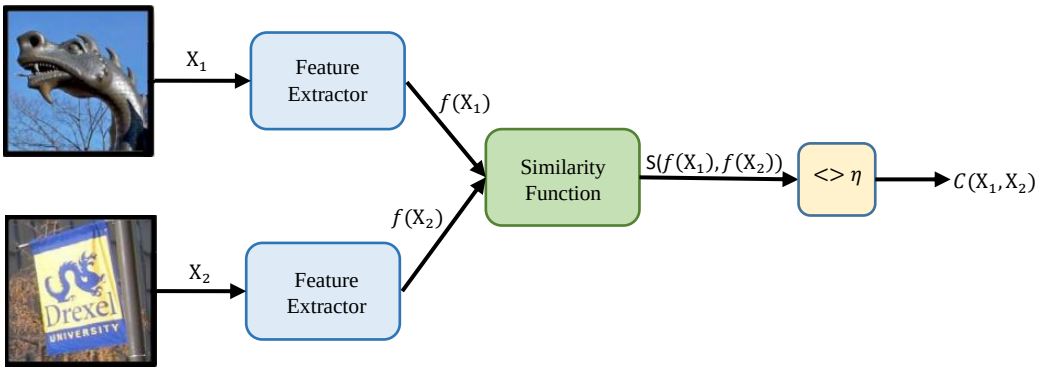


Figure 12 Forensic Similarity System (Mayer & Stamm, 2020)

evaluates whether two image patches contain similar forensic traces, be it known or unknown. A Siamese setup of CNNs extract patch-wise features and a three-layer similarity neural network is trained to output a similarity score of the two patches. The proposed method can identify patches with known source cameras with an accuracy of 95.93%. Showing strong generalization capability, the model also achieves 93.72% accuracy for known vs unknown camera model patches and 92.41% for unknown vs unknown camera model patches.

- PRNU pattern is a popular source camera characteristic that aids in splice detection. But estimating PRNU requires a large number of images from a given camera. Also, rich semantic image content interferes with PRNU estimation. Cozzolino et al. (Cozzolino & Verdoliva, 2020) propose a novel camera model fingerprint called *noiseprint* that outputs camera residual signals much stronger than PRNU. The main novelty of noiseprint lies in the fact that the uncovered camera patterns don't match over the entirety of two images from same camera but only when the patches are from same spatial regions within the images since camera artifacts vary spatially within images. Two CNNs with same architecture and weights are trained to suppress image content and highlight discriminative noise residual using a *distance-based logistic loss*. The proposed noise residual extraction method achieves splice detection and localization scores. However, experimental results suggest that the extracted pattern is not robust to training with uncompressed image data or resizing operation on test images as both scenarios lead to significant drops in performance. Another study combines noiseprint with PRNU for device source identification (Cozzolino, Marra, Gragnaniello, Poggi, & Verdoliva, 2020).
- Wang et al. (Wang, Ni, Liu, Luo, & Jha, 2020) propose an architecture based on a novel *weight combination module* that combines YCbCr, Edge and PRNU features in a weighted manner. Four such modules are connected in serial and the weight parameters are autotuned with backpropagation. The ablation study reveals that individual PRNU features are more discriminative than YCbCr or Edge features. However, the best results are obtained by a weighted combination of the three, scoring 99.45% accuracy on CASIA v1.0 and 99.32% on CASIA v2.0 for size 64×64.
- Another splice detection approach includes using illumination information (Carvalho, Faria, Pedrini, Torres, & Rocha, 2016). Pomari et al. (Pomari, Ruppert, Rezende, Rocha, & Carvalho, 2018) leverage illumination map inconsistencies by training over an ImageNet pre-trained ResNet-50 architecture to produce *Deep Splicing Features* and classifying them using an SVM classifier. The proposed method also predicts splice localization masks using the final convolution layer gradient information.

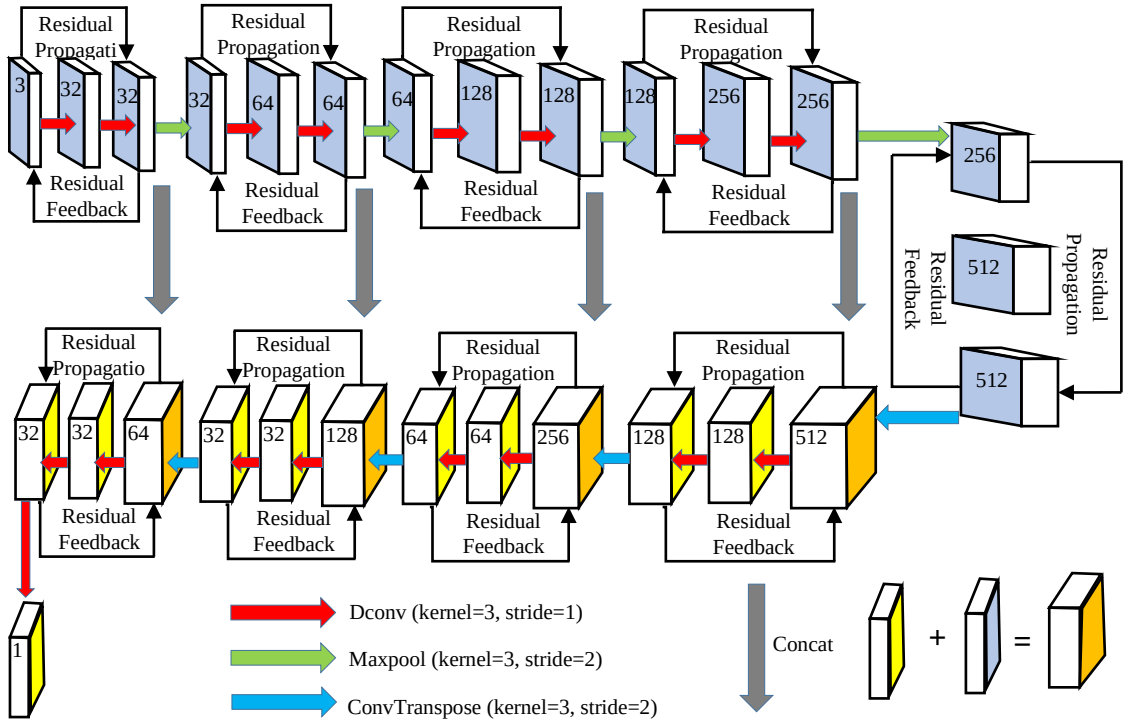


Figure 14 RRU-Net architecture (Bi, Wei, Xiao, & Li, 2019)

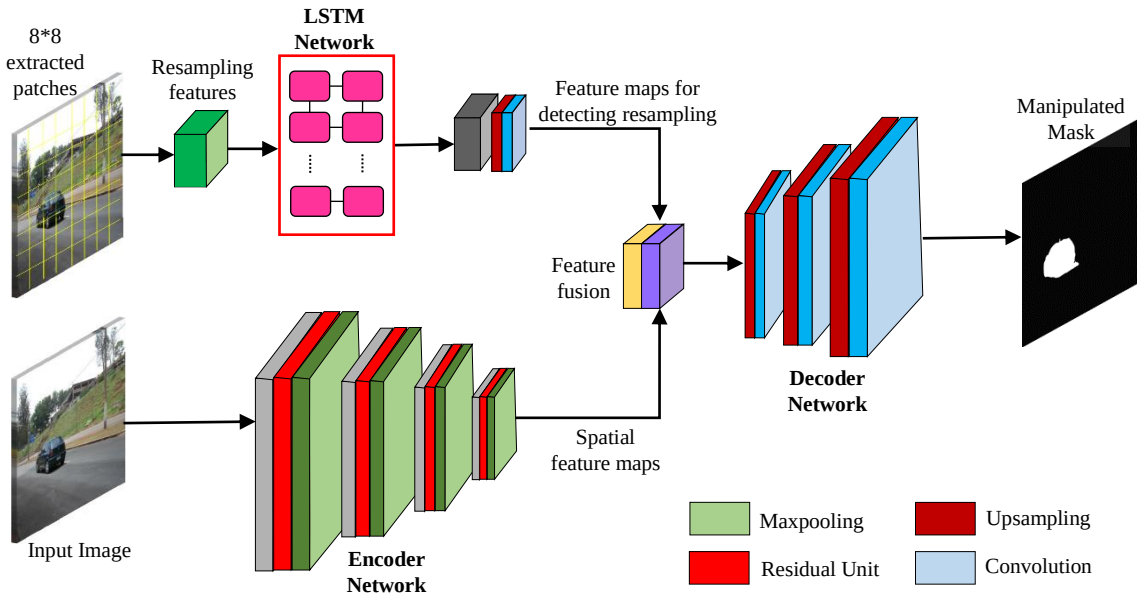


Figure 13 Hybrid LSTM and Encoder Decoder architecture for Image Splice Detection (Bappy, Simons, Nataraj, Manjunath, &

- Other splice detection novelties include using SRM filters to initialize the first convolution layer for better splice classification (Zhang & Ni, 2020), improving CNN learning and preventing gradient degradation through *ringed residual* structures (Bi, Wei, Xiao, & Li, 2019) (Figure 13), training LSTM cells to learn correlation between forged and pristine image blocks in frequency domain (Bappy, Simons, Nataraj, Manjunath, & Chowdhury, 2019) (Figure 15), combining local patch-level feature (like edges) learning with global feature (such as illumination) learning (Cun & Pun, 2018) (Figure 14) etc.

6.3 Copy-Move Detection Methods

Copy Move is one of the most popular types of image tampering, in which a portion of a picture is copied onto one or more parts of the same image.

Table 4 presents several recent research contributions towards copy move manipulation detection (Zhu, Chen, Yan, Guo, & Dong, 2020), (Zhong & Pun, 2020), (Zhang & Ni, 2020), (Islam, Long, Basharat, & Hoogs, 2020), (Saddique, et al., 2020), (Wu, Almageed, & Natarajan, 2018), (Bunk, et al., 2017). A detailed analysis of copy move manipulation detection and localization methods is presented in this section.

Traditional Copy-Move Detection Methods: Traditional copy-move manipulation detection methods primarily focused on handcrafted features such as discrete cosine transform (DCT) (Ye, Sun, & Chang, 2007), chroma features (Cozzolino, Poggi, & Verdoliva, 2015), discrete wavelet transform (DWT) (Bashar, Noda, Ohnishi, & Mori, 2010), principle component analysis (PCA) (Huang, Huang, Hu, & Chou , 2017), Zernike

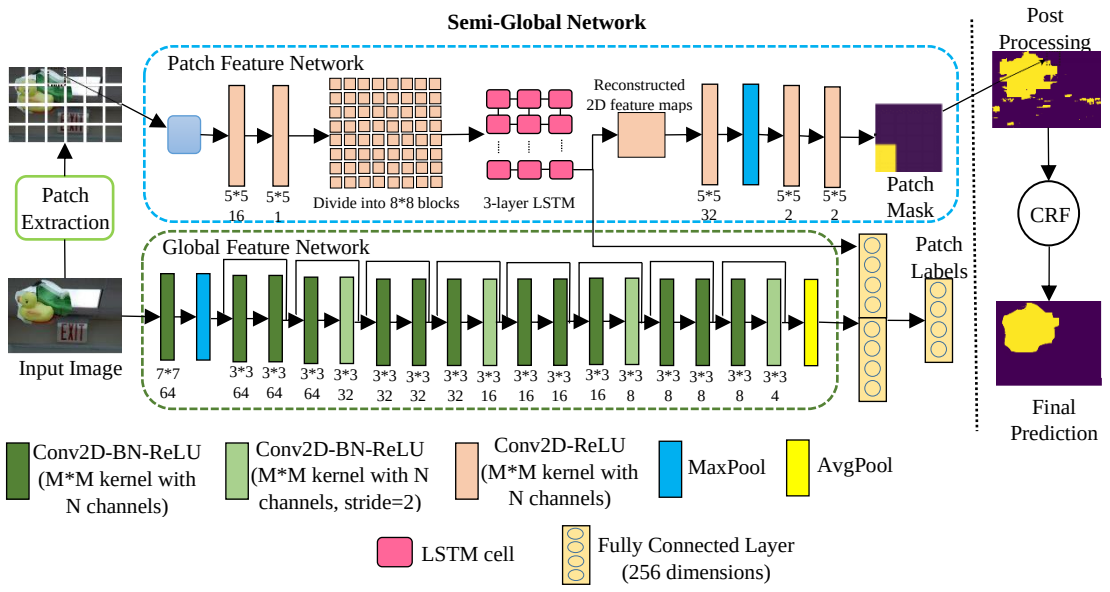


Figure 15 Image Splice Localization via Semi-Global Network and Fully Connected Conditional Random Fields (Cun & Pun, 2018)

moments (Ryu, Lee, & Lee, 2010), Blur moments (Mahdian & Saic, 2007), Local Binary Pattern (LBP) (Chingovska, Anjos, & Marcel, 2012), Oriented Fast and Rotated Brief (ORB) (Zhu, Shen , & Chen, 2016), Speeded up Robust Features (SURF) (Shivakumar & Baboo, 2011), Scale-Invariant Feature Transform (SIFT) (Costanzo, Amerini, Caldelli, & Barni, 2014), Color Filter Array (CFA) (Bammey, Gioi, & Morel, 2020).

The traditional copy-move detection approaches are categorized as: *block-based approaches* and *keypoint-based approaches.* In block-based detection approaches, an image is broken down into overlapping blocks. Then handcrafted features such as DWT, DCT, chroma features, PCA etc, are extracted for each block and finally, a block matching algorithm compares the uncovered features from each block. In keypoint algorithms, features are extracted to compare only high-entropy regions within images using local descriptors like SIFT, SURF and ORB.

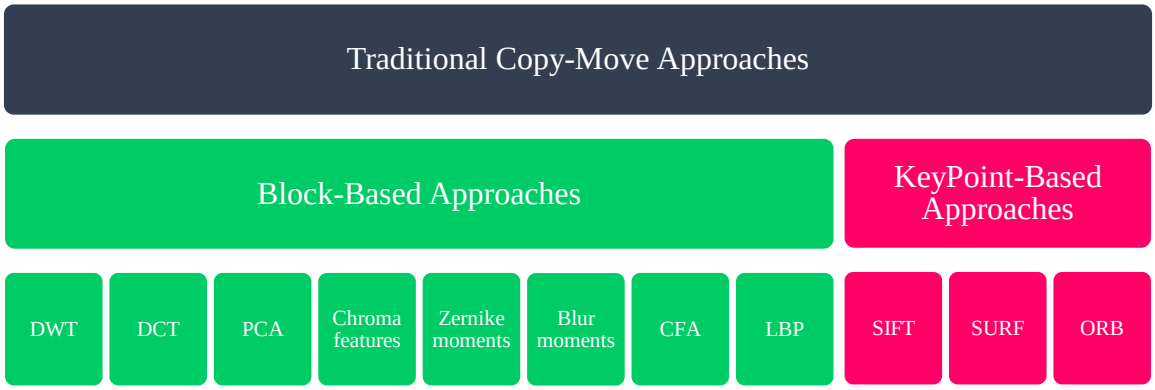


Figure 16 Traditional Copy-Move Detection Approaches

Deep learning-based Copy-Move Detection methods: Most of the recent deep learning-based copy-move detection/localization methods have been described in Table 4, highlighting their approach, manipulation clues, architectural components implemented, datasets used and results obtained.

Copy-Move Detection Discussion: Challenges & Solutions

- Copy-move manipulation can be *plain, affine* or *complex* (Wu, Almageed, & Natarajan, 2018). Plain copy-move comprises of a simple copy-paste operation with no transformations and is easy to detect. Affine copy-move includes scaling and rotation transformation before pasting the object. Complex copy-move includes not only affine transformations but also utilizes extra image processing steps such as blending edges of pasted objects and color/brightness enhancements to suppress the manipulation artifacts. Affine copy-move requires advanced tools such as Adobe Photoshop.

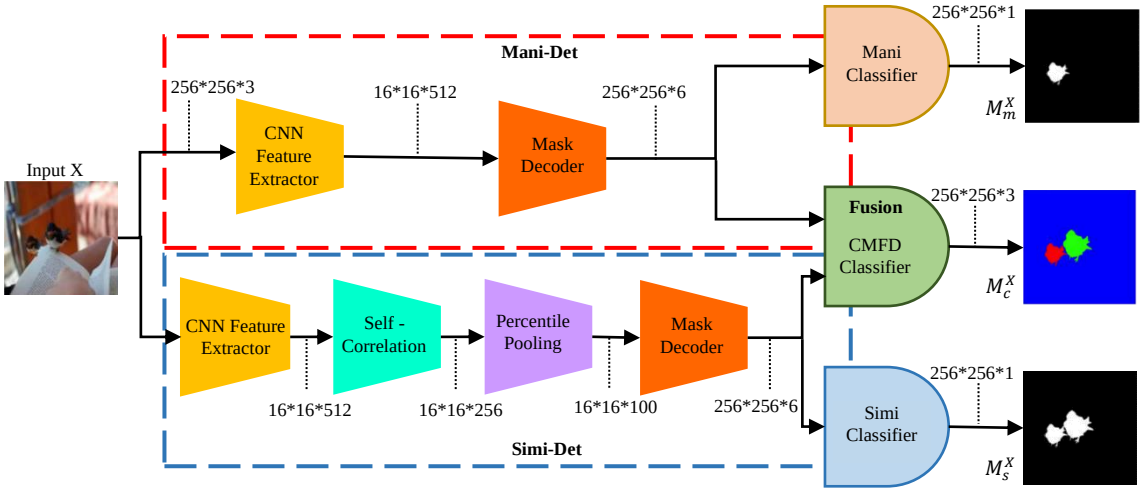


Figure 17 Buster-net (Wu, Almageed, & Natarajan, BusterNet: Detecting Copy-Move Image Forgery with Source/Target Localization, 2018)

- Though effective, traditional block-based copy-move detection methods are computationally expensive and not robust to geometric transformations such as scaling pasted objects. (Zhu, Chen, Yan, Guo, & Dong, 2020)
- Traditional keypoint-based copy-move detection methods are computationally efficient when compared to block-based methods since they avoid an exhaustive comparison of all overlapping regions within an image and only aim to match extracted keypoint features. However, these methods demonstrate poor localization capabilities and cannot solve the smoothing manipulation snippet (Zhong & Pun, 2020)
- BusterNet (Wu, Almageed, & Natarajan, 2018) is the first major end-to-end deep learning architecture to detect and localize copy-move manipulation. It comprises of a dual-branch CNN network utilizing the first four VGG16 architecture (Figure 17).

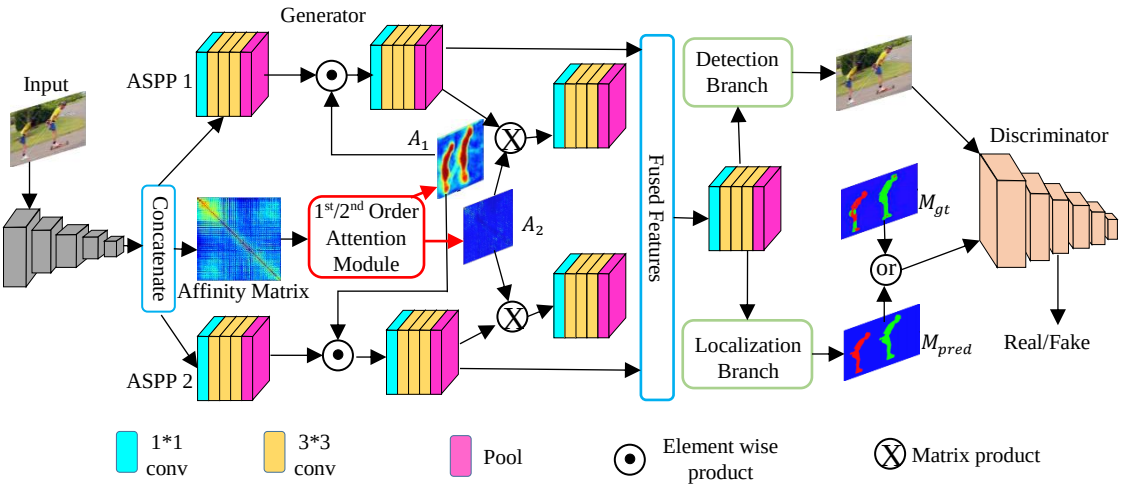


Figure 18 Structure of DOA-GAN (Islam, Long, Basharat, & Hoogs, 2020)

A ‘manipulation detection’ branch predicts regions of possible manipulation. A ‘similarity detection’ branch is responsible for finding copy-move regions using self-correlation by measuring region-wise similarity and percentile pooling for additional statistical analysis. Pretrained on ImageNet dataset and fine-tuned on a synthetically prepared dataset with attacks including blending, rotation, scaling and translation, a three-stage training strategy ensures that the branches learn to maximize their feature extraction capability before training the model end-to-end. BusterNet outperforms the then state-of-the-arts, achieving a high image level auc score of 0.8 on the CASIA dataset. It proves robust against most attacks or postprocessing methods of the CoMoFoD dataset.

- One key challenge in copy-move manipulation detection is identifying and distinguishing between original image regions with similar textural data and copy-move manipulated regions, since both cases have identical visual information. Islam et al. (Islam, Long, Basharat, & Hoogs, 2020) try to solve this problem by using a dual-attention-based architecture. The authors compute an *affinity matrix* (Figure 18) with second-order statistics on features extracted from a CNN. Then a first-order attention module highlights all similar regions within an image and a second-order attention module separates similar-looking original regions from copy-moved regions. High values in off-diagonal elements indicate copy-move forgery. The proposed method is designed for adversarial training where a generator produces copy-move forgery mask and a discriminator is trained to differentiate generated masks from actual ground truths.
- Zhu et al. (Zhu, Chen, Yan, Guo, & Dong, 2020) propose a novel *Adaptive Attention and Residual Refinement Network* (AR-Net) that utilizes positional and channel attention (Figure 19) to highlight discriminative parts of features. Deep matching is used to learn self-correlation among feature maps and atrous spatial pyramid pooling is used to obtain multi-scale features. Zhong et al. (Zhong & Pun, 2020) propose the Dense InceptionNet network having a pyramid feature extractor (PFE) to extract multi-dimensional and multi-scale features, feature correlation matching (FCM) to learn the correlation of dense features and hierarchical post-processing (HPP) to improve training through a combination of entropies.

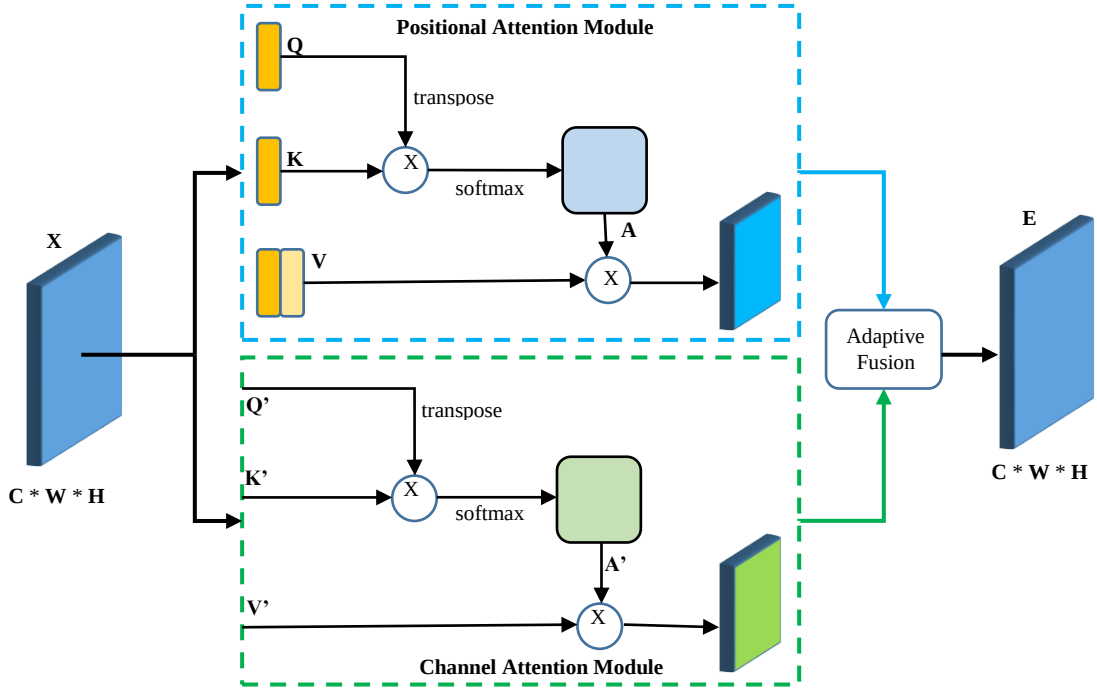


Figure 19 Adaptive Attention Module having a) positional attention b) channel attention and their fusion (Zhu, Chen, Yan, Guo,

6.4 Other Manipulation Detection Methods

While copy move, splicing and facial tampering are the most common forms of manipulations, several other types of manipulation detection and localization approaches have also been proposed. Some of these manipulations are discussed below.

Nam et al. (Nam, et al., 2020) tackle *seam carving* by proposing an ILFNet architecture containing five blocks to detect local artefacts caused by seam insertion or removal operation. Li et al. (Li & Huang, 2019) handle *inpainting* manipulation through a C-based architecture with four ResNet blocks trained on image residuals to localize the inpainting region. Yan et al. (Yan, Ren, & Cao, 2019) approach recoloring detection using a CNN with three feature extraction blocks and one feature fusion block. To identify recoloring, the picture is used as input, along with illumination consistency and inter-channel correlation Yarlagadda et al. (Yarlagadda, et al., 2019) take the issue of *shadow removal detection* by training a cGAN to output localization mask of shadow removal region. Long et al. (Long, Smith, Basharat, & Hoogs, 2017) perform *frame deletion detection* in videos by using 3D convolutions in the network that thresholds L2 distance of color histograms, optical flow and motion energy of two consecutive frames to detect deleted frames.

6.5 Photo Response Non-Uniformity (PRNU) based Detection

Due to inevitable inaccuracies in camera manufacturing processes, certain camera sensor cells tend to generate different pixel interpolations for same light intensity. This noise pattern caused by inaccurate pixel values leaves a Photo Response Non-Uniformity (PRNU) noise pattern. PRNU patters are unique for each sensor device and all images from a given camera sensor contain the same PRNU pattern. Hence, PRNU is considered an effective source device estimation strategy. PRNU also works well for splice manipulation detection applications in images since an image containing more than one PRNU noise pattern is a clear indication of splice forgery (Cozzolino, Marra, Gragnaniello, Poggi, & Verdoliva, 2020). Let $\mathcal{I}_0$ represent a true image (without PRNU noise). An image $\mathcal{I}$ captured from a camera having PRNU pattern $\mathcal{H}$ and external noise $\otimes$ can be specified as:

$$\mathcal{I} = \mathcal{I}_0(\mathcal{H} + 1) + \otimes \tag{20}$$

PRNU of a camera $\mathcal{C}^i$ can be computed by utilizing a number of images, say $\mathcal{I}_{i,1}, \mathcal{I}_{i,2}, \ldots \mathcal{I}_{i,N}$ from camera $\mathcal{C}^i$. The noise residual can be computed using any de-noising algorithm $\mathcal{f}(.)$:

$$\mathcal{W}_{i,n} = \mathcal{I}_{i,n} - \mathcal{f}(\mathcal{I}_{i,n}) \tag{21}$$

The PRNU $\mathcal{H}_i$ is then estimated by taking plain average:

$$\mathcal{H}_i = \frac{1}{N}\sum_{i=1}^{N} \mathcal{W}_{i,n} \tag{22}$$

If the true PRNU $\mathcal{H}_i$ of a camera $\mathcal{C}^i$ is known, it can be checked for an image $\mathcal{I}_m$, whether it was captured from $\mathcal{C}^i$ using normalized cross-correlation ($\mathbb{NCC}$) where $\|.\|$ and $\langle . \rangle$ represent Euclidean norm and inner product respectively:

$$\mathbb{NCC}(\mathcal{W}_m, \mathcal{H}_i) = \frac{1}{\|\mathcal{W}_m\| \cdot \|\mathcal{H}_i\|}\langle \mathcal{W}_m, \mathcal{H}_i \rangle \tag{23}$$

By using Eq. 23, it can be determined whether an image contains more than one PRNU noise traces thereby implicating splicing manipulation.

PRNU is a unique fingerprint of digital cameras and image sensors that may be utilised in digital forensics and image processing applications for source identification, forgery detection, and picture authentication. It establishes a sensor's distinctive signature by relying on small non-uniformities in pixel responses throughout its surface. The PRNU has several applications such as source identification, forgery detection, image authentication etc. There are several challenges related to PRNU analysis. *Firstly*, PRNU is extremely sensitive to image noise and hence needs robust noise removal techniques to be effective. *Secondly*, compression and post-processing operations interfere with PRNU patterns, making verifying its legitimacy difficult. Such limitations restrict the use of PRNU for tampering

detection in isolation. Consequently, PRNU analysis is often used as supplementary feature which is combined with other discriminative information to enhance the performance of tampering detection methods.

6.6 Multi-Modal Multi-Branch Based Fusion Methods for Tampering Methods

This section presents multi-modal approaches for tampering detection based on the fusion of features. Specifically, several multi-branch models have been proposed that extract discriminative features from more than one domain. The features extracted from the multi-branch architecture are then fused together before making the final prediction.

(Guo, Yang, Zhang, & Xia, 2023) offer a dual branch architecture for feature refinement, including a unique 'tensor pre-processing unit and a 'manipulation trace attention' module. The authors use the gradient operator with CNNs, and the newly suggested plug-and-play modules may readily integrate with any conventional CNN architecture. On five picture datasets, the proposed modules improve model performance. (Liang, et al., 2023) extract and merge depth and RGB information using a dual branch triplet network-based model. The RGB branch catches typical manipulation spatial hints, whereas depth characteristics capture illumination and blur discrepancies.

(Lin, Huang, Luo, & Lu, 2023) offer a dual-subnetwork to extract multi-scale features and MBConv blocks from the EfficientNet model to extract higher dimensions semantic face representation. The two characteristics are merged and put into a transformer network for final categorization. The results of the experiments show that the suggested model excels at categorising both high and low-quality input samples and has significant generalisation abilities. (Ilyas, Javed, & Malik, 2023) combine spatial and auditory domain data to generate the final forecast. By training just on I-frames, (Hu, Liao, Wang, & Qin, 2022) minimise the complexity of the face modification detection model. To reduce noise overfitting, the proposed model includes a trimmed frame stream. The second stream learns elements of temporal consistency between video frames. The proposed model scores 0.8700 AUC score on the CelebDF dataset.

(Xu, et al., 2021) employ multi-frame feature aggregation by training in sets, each including a collection of frames from a movie. On the DFDC dataset, the learnt features are merged, and the model achieves an accuracy of 0.8453. (Chen & Yang, 2021) divide input photos into six categories: eyes, mouth, face, nose, backdrop, and entire image. A new local attention module focuses on these six locations independently, while another semantic attention module collects each region's contribution to the final prediction.

Heartbeat is treated as sequential data predicted by visual photoplethysmography (Qi, et al., 2020). The authors devise a new motion-magnified spatial-temporal representation for discriminative categorization. (Kumar, Vatsa, & Singh, 2020) present a five-branch architecture to process four local and one global face area, with the learnt characteristics concatenated to create the final prediction. (Zhou, Han, Morariu, & Davis, 2017) To create

the final prediction, offer a dual-branch network with face categorization in one branch and triplet architecture in the other.

While multi-branch architectures are ideally adapted to learning complimentary features from many domains, they frequently suffer from a problem during the feature fusion step. The majority of techniques rely on feature concatenation. Other fusion strategies, such as taking the sum or mean, have been tried in several works (Chen & Yang, 2021). However, regardless of the fusion approach utilised, the domain characteristics are always fused proportionally (Zhao, Zhang, Ding, & Cui, 2023), (Mohiuddin, Sheikh, Malakar, Velásquez, & Sarkar, 2023).

6.7 Transformer-Based Tampering Detection Methods

Transformers are a pioneering deep learning architecture first described in the paper "Attention Is All You Need" (Vaswani, et al., 2017). Transformers have had a significant influence on natural language processing (NLP) and have been expanded to various other fields, including computer vision and reinforcement learning, since its introduction. They are well-known for their ability to handle sequential data effectively and have been the foundation for several cutting-edge models. The key components of transformers include self-attention mechanism that enables the model to weigh the significance of various input sequence elements while processing a specific piece. This allows the model to incorporate long-term relationships in the data, which was difficult for previous recurrent neural networks (RNNs). Self-attention is frequently implemented in Transformers with *multi-head attention*, each collecting a particular connection in the data. These numerous heads simultaneously learn different elements of the input, resulting in richer representations. Because Transformers, unlike RNNs and CNNs, do not have a built-in notion of order or position in the input data, *positional encodings* are added to the input embeddings to supply the model with information about the location of each element in the sequence.

Several recent tampering detection methods have used the transformer architecture. Li et al. (Li Y. , et al., 2023) propose an enhanced transformer-based architecture to detect image inpainting manipulation. The proposed model captures both short and long-term pixel dependencies. Shi et al. (Shi, Chen, & Zhang, 2023) utilize a stacked multi-scale transformer model to extract pixel irregularities between patches of variable sizes. The proposed transformer-based model shows strong manipulation localization capabilities in images. Liu et al. (Liu, Lv, Jin, Chen, & Zhang, 2023) create a two-branch transformer model called ‘TBFormer’ for image forgery localization. The two transformer branches have identical structures and extract discriminative RGB and noise features combined using an attentional hierarchical fusion module. Yu et al. (Yu, et al., 2023) use a novel ‘Multiple SpatioTemporal Views Transformer’ to capture spatio-temporal features locally and globally. Specifically, vision-transformer encoders capture the temporal relationships extracted from a CNN backbone both locally within a video clip and globally across all video frames. Bai et al. (Bai, Liu, Zhang, Li, & Hu, 2023) detect facial forgery by defining an ‘action units relation

transformer' that captures the relationships between distinct facial action units and improves the performance of forgery detection. The proposed model is also capable of localizing the region of facial forgery. Ilyas et al. (Ilyas, Javed, & Malik, 2023) propose a Swin Transformer-based deepfake detection model that combines the audio and visual modalities, making the proposed model multi-modal. Zhao et al. (Zhao, et al., 2023) focus on the interpretability of deepfake detection by designing a transformer-based spatio-temporal model. The proposed model contains a novel 'spatio-temporal based self-attention' and a 'self-subtract' operator crucial for capturing spatial and temporal inconsistency clues of face manipulation. Miao et al. (Miao, et al., 2023) propose a 'high-grequency fine-grained transformer' model for face forgery detection. The proposed model contains a high-frequency wavelet sampler that searches for forgery clues in high-frequency features and ignores the confusing lower frequency bands.

Additionally, a central difference attention is utilized to focus on texture gradient information crucial in identifying forgery. Li et al. (Li, Yao, Le, & Qin, 2023) detect recaptured screen images by using a vision transformer to extract global features whila CNN extracts local features. The two networks are cascaded before making a final prediction.

Table 4 Deep Learning based Manipulation Detection and Localization Contributions. Performance metrics such as accuracy, F1 score, area under curve and Mathews Correlation Coefficient have been mentioned as 'acc', 'F1', 'auc' and 'mcc' respectively.

Ref.	Medium	Manipulation Type	Approach	Detection / Localization	Clues	Model Type	Datasets & Results
Cozzolino et al. (Cozzolino & Verdoliva, 2020)	Image	-	Propose a novel forgery localization approach that ignores scene content and extracts camera model fingerprint "NOISEPRINT" to compare source camera model and camera position of image patches from same or different images.	Localization	Noiseprint (Camera footprint)	CNNs	DSO-1 – 0.7800 F1, 0.7580 mcc
Mi et al. (Mi, Jiang, Sun, & Xu, 2020)	Image	DeepFake	Propose a novel multi-head self-attention-based algorithm that detects fake GAN generated facial images. The proposed approach highlights the lack of global information from the transposed convolution operation in fake GAN generated samples.	Detection	-	CNNs + Self-Attention	*Human Face Images – 0.9930 acc *Bedroom Images – 0.9900 acc *Cat Images – 0.9880% acc
Qian et al. (Qian, Yin, Sheng, Chen, & Shao, 2020)	Image	-	Propose a novel architecture F3-net that utilizes frequency information to find facial manipulation. The proposed network learns from frequency aware image decomposition and local frequency statistics through cross attention to obtain discriminative features.	Detection	Frequency artifacts	CNNs	FaceForensics++: LQ – 0.9302 acc and 0.9580 auc HQ – 0.9895 acc and 0.9930 auc Raw – 0.9999 acc and 0.9999 auc
Mayer et al. (Mayer & Stamm, 2020)	Image	-	Propose a novel approach of comparing the "FORENSIC SIMILARITY" of two image patches using a CNN feature extractor and a three-layered neural net based on forensic traces including camera model, editing operations and editing parameters to detect both known and unknown manipulations. (**Figure 12**)	Detection	Forensic traces – camera, editing operation	CNNs	*Self-created dataset of 47785 images – 0.9400 acc
Zhu et al. (Zhu, Chen, Yan, Guo, & Dong, 2020)	Image	Copy Move	Propose a novel ADAPTIVE ATTENTION AND RESIDUAL REFINEMENT NETWORK (AR-Net) that uses fused positional and channel wise feature maps from adaptive attention mechanisms to extract rich representations, computes self-correlation of features maps using deep matching and uses "atrous spatial pyramid pooling" (ASPP) to generate manipulation mask. (**Figure 19**)	Localization	-	CNNs	CASIA II – 0.5832 precision, 0.3733 recall and 0.4552 F1 CoMoFoD – 0.5421 precision, 0.4655 recall and 0.5009 F1 Coverage – 0.8488 auc
Zhong et al. (Zhong & Pun, 2020)	Image	Copy Move	Propose a novel "Dense InceptionNet" network that contains a pyramid feature extractor (PFE) to extract multi-dimensional and multi-scale features, feature correlation matching (FCM) to learn the correlation of dense features and hierarchal post processing (HPP) module that obtains a combination of cross entropies for better training.	Detection	-	Dense Inception Net (CNN)	CASIA – 0.7085 precision, 0.5885 recall and 0.6429 F1 CoMoFoD – 0.4610 precision, 0.4220 recall and 0.4410 F1
Singhal et al. (Singhal, Gupta, Tripathi, & Kothari, 2020)	Image	-	Propose a novel RF-CNN model that utilizes RESIDUAL and FREQUENCY pre-processing layers to detect manipulations in low resolution images. Frequency representation is input to the CNN having two convolutional layers and two classifiers namely softmax and extremely randomized trees. Frequency information gives visual cues of manipulations while image residual features are more discriminative to detect manipulations than raw features.	Detection	Frequency Representation	CNNs	*Self-created images from IEEE IFS-TC image forensics challenge – 0.9710 acc
Horvath et al. (Horváth, Montserrat, Hao, & Delp, 2020)	Image	Splicing	Propose a one-class splice detection through deep belief networks (DBN) to detect and localize manipulation in satellite images. DBN containing two Restricted Boltzmann Machines tries to reconstruct patches from input patches of satellite images and error heatmaps are used to localize manipulation.	Localization	-	DBN	*Self-created dataset – 0.8960 auc

* Corresponding Author

Ref.	Medium	Manipulation Type	Approach	Detection / Localization	Clues	Model Type	Datasets & Results
Bammey et al. (Bammey, Gioi, & Morel, 2020)	Image	-	Propose a novel CNN based manipulation detection approach that utilizes inconsistency in color filter array (CFA) or "mosaic" to detect manipulations in unlabeled data	Localization	mosaic inconsistency	CNNs	*Dataset created from Dresdan Image Database – 0.8210 auc
Zhang et al. (Zhang & Ni, 2020)	Image	Copy Move, Splicing, Removal	Propose a novel forgery detection and localization architecture utilizing DenseNets and CNN. Dense U-Net undergo cross layer intersection mechanism and Spatial Rich Model (SRM) filters are used to extract residual signals from tampered images. Feature maps from fully connected layers are used for image segmentation for localization purpose.	Localization	-	Dense U-Net	CASIA v1.0 – 0.9421 acc CASIA v2.0 – 0.9739 acc NC2016 – 0.8509 acc Columbia – 0.9917 acc
Li et al. (Li, et al., 2020)	Image	DeepFake	Propose a novel face representation approach "Face X-ray" to detect and localize facial manipulation in images. Face X-ray assumes the presence of blending operation after any kind of facial manipulation and looks for inconsistencies along the blending boundary to localize region of forgery. (**Figure 8**)	Localization	Blending operation traces	CNNs	FaceForensics++ - 0.9917 auc DFD – 0.9540 auc DFDC – 0.8092 auc Celeb DF – 0.8058 auc
Islam et al. (Islam, Long, Basharat, & Hoogs, 2020)	Image	Copy Move	Propose a Dual-Order Attentive Generative Adversarial Network (DOA-GAN) where the first attention module explores copy move aware location info while the second attention module captures patch inter dependencies. Discriminator fine tunes the predicted localization mask. (**Figure 18**)	Localization	-	GAN	CASIA – 0.6339 precision, 0.7700 recall and 0.6953 F1 CoMoFoD – 0.6038 precision, 0.6598 recall and 0.6305 F1
Wu et al. (Wu, Xie, Gao, & Xiao, 2020)	Video	DeepFake	Propose a face manipulation detection framework SSTNet that utilizes spatial, steganalysis and temporal features. Spatial features look for irregularities in color, shape and texture. Steganalysis features look for inconsistencies in statistical information and temporal features help in finding tampering amongst frames.	Detection	Inconsistent color, shape, texture, statistics, frames	CNNs, RNN	FaceForensics++: LQ – 0.9011 acc HQ – 0.9857 acc
Nam et al. (Nam, et al., 2020)	Image	Seam Carving (Other manipulation)	Propose a CNN based architecture ILFNet containing five network blocks capable of detecting local artefacts caused by seam carving. First block contains convolutional layers with stride 1, second includes skip connections, third block helps to learn refined features generated from previous block. Next block learns high level representation of features from previous block and the last block performs classification of three classes (original, seam insertion, seam removal).	Localization	Local Artefacts of Seam Carving	CNNs	*Self-created dataset from BOSSbase and UCID datasets – 0.9656 acc
Tarasiou et al. (Tarasiou & Zafeiriou, 2020)	Image	DeepFake	Propose a novel local image feature that can be used for automatic detection of facial manipulation in images. Preprocessing step includes extracting manipulation mask as zeros mask, ones mask and convex hull mask. A lightweight CNN architecture along with dense classification tasks boosts detection results.	Detection	Local features	CNNs	FaceForensics++: DF (c23) – 0.9790 acc F2F (c23) – 0.9858 acc FS (c23) – 0.9832 acc DF (c40) – 0.9240 acc F2F (c40) – 0.8711 acc FS (c40) – 0.9126 acc
Agarwal et al. (Agarwal, Farid, Fried, & Agrawala, 2020)	Video	DeepFake	Propose a unique method for detecting deepfake movies by leveraging anomalies in mouth shape (viseme) in deepfake videos when pronouncing specified phonemes. In a given video frame, a CNN is taught to recognise whether the mouth is open or closed.	Detection	Phoneme Viseme Mismatches	CNNs	*Self-created dataset: Audio2Video – 0.9690 acc Text2Video (Long) – 0.7110 acc Text2Video (Short) – 0.8070 acc In-the-Wild – 0.9700 acc

Ref.	Medium	Manipulation Type	Approach	Detection / Localization	Clues	Model Type	Datasets & Results
Chintha et al. (Chintha, et al., 2020)	Video	DeepFake	Propose a RECURRENT CONVOLUTIONAL STRUCTURE for deepfake video detection. For each frame, a convolutional architecture extracts facial vector representations, which are then input into a bidirectional LSTM to train representations capable of distinguishing between real and fake face vectors using an entropy-based loss function.	Detection	-	CNNs, LSTM	FaceForensics++ - 1.0 acc Celeb DF – 0.9783 acc
Kohli et al. (Kohli, Gupta, & Singhal, 2020)	Video	Object Forgery (Other manipulation)	Propose a novel spatio-temporal CNN network for manipulation detection and localization in videos that is trained on motion residual of videos and contains a temporal CNN to extract forged frames and a spatial CNN to localize manipulated region within forged frames.	Localization	Compression traces	CNNs	SYSU-OBJFORG – 0.9173 acc
Johnston et al. (Johnston, Elyan, & Jayne, 2020)	Video	Splicing	Propose a CNN-based method for detecting and localizing video splice forgery using three H.264/AVC compression features: quantization parameter, intra/inter frame, and deblock modes.	Localization	Compression traces	CNNs	FaceForensics – 0.6700 mcc, 0.8100 F1 VTD – 0.0820 mcc, 0.0650 F1
Fei et al. (Fei, Xia, Yu, & Xiao, 2020)	Video	DeepFake	Propose a novel CNN-LSTM based approach to detect AI generated fake videos. The proposed architecture detects distorted facial movements in videos pre-processed with the “Eulerian Motion Magnification” method that amplifies facial motion in videos.	Detection	Facial Movement Inconsistencies	CNNs, LSTM	FaceForensics++ - 0.9925 acc
Saddique et al. (Saddique, et al., 2020)	Video	Splicing, Copy Move	Propose a network to detect video tampering using a “motion residual” (MR) layer to calculate the motion residual of each channel of a video frame, CNN layers pretrained on ImageNet dataset to extract hierarchical features and “parasitic layers” based on extreme learning theory act as classifier.	Detection	Traces of object insertion or removal	CNNs	*Self-created dataset – 0.9889 acc, 0.9912 TPR
Li et al. (Li & Huang, 2019)	Image	Inpainting (Other Manipulation)	Propose a novel CNN based architecture having four concatenated ResNet blocks that are trained on image residual extracted using high pass pre-filtering module to localize deep inpainting.	Localization	Image residual	ResNet Blocks (CNN)	*Self-created dataset from ImageNet dataset images: QF:96 – 0.9689 recall, 0.9797 precision, 0.9728 F1 QF:75 – 0.8984 recall, 0.9522 precision, 0.9153 F1
Deng et al. (Deng, Li, Gao, & Tao, 2019)	Image	Splicing	Present an innovative DEEP MULTI-SCALE DISCRIMINATIVE NETWORK (MSD-Nets) that can automatically extract a variety of characteristics from the DCT coefficient histograms of jpeg images at various scales without the need to estimate the initial quality factor of the compression method. A probability map is used to show where manipulations have been made. (**Figure 11**)	Localization	JPEG double compression traces	CNNs	*Synthetic Dataset – 0.9880 acc Florence – 0.9526 acc
Yan et al. (Yan, Ren, & Cao, 2019)	Image	Recoloring (Other Manipulation)	Propose a CNN based recoloring detection approach having three blocks of feature extraction and one block for fusion that uses image along with illumination consistency and inter-channel correlation information as input to detect recoloring.	Detection	Inter-channel correlation and Illumination inconsistencies	CNNs	VOC PASCAL 2012 – 0.8689 acc, 0.9429 auc
Bappy et al. (Bappy, Simons, Nataraj,	Image	Splicing	Propose a novel architecture for manipulation localization that employs resampling features like jpeg quality loss, upsampling, downsampling, rotation, and shearing to find tampering clues, an encoder-decoder network to capture spatial information, and an	Localization	JPEG quality loss, rotation and shearing traces,	LSTM, Encoder-Decoder	NIST 2016 – 0.9480 acc, 0.7936 auc IEEE Forensics – 0.9119 acc, 0.7577 auc

Ref.	Medium	Manipulation Type	Approach	Detection / Localization	Clues	Model Type	Datasets & Results
Manjunath, & Chowdhury, 2019)			LSTM network that learns correlation between original and manipulated blocks in frequency domain. (**Figure 15**)		frequency domain correlation		Coverage – 0.7124 auc
Yarlagadda et al. (Yarlagadda, et al., 2019)	Image	Shadow Removal (Other Manipulation)	Propose a conditional GAN (cGAN) based method to detect and localize shadow removal. The cGAN is trained to generate a localization mask that outputs pixelwise probability of region containing the shadow before removal.	Localization	Shadow removal traces	GAN	*Dataset created from Image Shadow Triplets Dataset – 0.7880 auc
Bi et al. (Bi, Wei, Xiao, & Li, 2019)	Image	Splicing	Propose a novel Ringed Residual U-Net (RRU-Net) that accomplishes splice detection and localization without any pre-processing or post-processing by improving the learning ability of CNNs using the residual propagation to solve gradient degradation problem and residual feedback widen the gap of features from original and manipulated samples. (**Figure 13**)	Localization	-	CNNs	CASIA – 0.8480 precision, 0.8340 recall and 0.8410 F1 Columbia – 0.9610 precision, 0.8730 recall and 0.9150 F1
Wu et al. (Wu, AbdAlmageed, & Natarajan, 2019)	Image	-	Propose MANTRA-NET, a novel end-to-end network that requires no preprocessing or postprocessing. Proposed network takes input of arbitrary size and is trained on 385 different types of manipulations. LSTM is used for forgery localization which is considered as an anomaly detection problem.	Localization	-	CNNs, LSTM	NIST 2016 – 0.7950 auc Columbia – 0.8240 auc Coverage – 0.8190 auc CASIA – 0.8170 auc
Zhuang et al. (Zhuang & Hsu, 2019)	Image	DeepFake	Propose a novel COUPLED DEEP NEURAL NETWORK (CDNN) with two-step learning that takes facial images generated by GAN, pairwise info and label information to learn "common fake features" (CFF) using a triplet loss. A classifier is trained using binary cross entropy loss to classify input as original or fake.	Detection	Common Fake Features (CFF)	CNNs	*GAN generated image dataset – 0.9860 precision and 0.9860 recall
Mazumdar et al. (Mazumdar & Bora, 2019)	Image	DeepFake	Propose a novel Siamese CNN having twin CNNs sharing parameters that process input image to create and compare illumination maps and compare facial regions in a pair wise fashion.	Detection	Lightning inconsistencies	CNNs	DSO-1 – 0.9700 acc DSI-1 – 0.9400 acc
Nam et al. (Nam, et al., 2019)	Image	Resizing (Other Manipulation)	Propose a novel CNN based approach for content aware resizing detection and localization. Proposed CNN contains four types of block, first type has convolutional layers, second type has convolutional layers with skip connections, third block is responsible for dimensionality reduction and last block for classification into original, seam inserted and seam removed classes.	Localization	Resizing artefacts	CNNs	*Self-created dataset from BOSSbase and UCID images – 0.9539 acc
Nguyen et al. (Nguyen, Yamagishi, & Echizen, 2019)	Video	DeepFake	Using a network of capsules with three primary capsules and two output capsules for authentic and forged frames, respectively, propose a novel approach to detect forged videos. Capsule network inputs features extracted by a VGG19 network and uses routing algorithm to boost the performance of manipulation detection.	Detection	-	Capsule Network (CNNs)	FaceForensics: No Compression – 0.9937 acc C23 – 0.9713 acc C40 – 0.8120 acc
Liu et al. (Liu & Pun, 2018)	Image	Splicing	Propose a novel FUSION NET network which is a fusion of pre-trained layers from several CNN based "base net" networks focused on learning different manipulation clues such as noise inconsistencies and jpeg double compression traces.	Localization	Noise, JPEG double compression traces	CNNs	*No numeric results reported
Cun et al. (Cun & Pun, 2018)	Image	Splicing	Propose a SEMI GLOBAL NETWORK for image splice localization that contains two subnetworks, "patch feature network" that extracts local features like spliced edges and "global feature network" that learns global features like illumination variations. CRF is used to refine manipulation mask estimation. (**Figure 14**)	Localization	Edges and Illumination variations	CNNs, CRF	NC2016 – 0.9900 auc, 0.7900 F1 DSO-1 – 0.8300 auc, 0.5006 F1 Columbia – 0.6700 auc, 0.6482 F1

Ref.	Medium	Manipulation Type	Approach	Detection / Localization	Clues	Model Type	Datasets & Results
Verde et al. (Verde, et al., 2018)	Video	Splicing	Propose to train a pair of CNNs to derive the video codec and perform coding quality estimation on individual video frames. Inconsistent codec and coding traces are marked as manipulated frames.	Localization	Variations in video codec and coding quality	CNNs	*Self-created dataset – 0.9600 auc
Zhou et al. (Zhou, Sun, Yacoob, & Jacobs, 2018)	Image	DeepFake	Propose a novel lightning regression network LABEL DENOISING ADVERSARIAL NETWORK (LDAN) that trains to denoise auto-generated lightning labels and performs estimates Spherical Harmonics of environment lightning in facial images.	Detection	Facial Lightning Inconsistencies	GAN	*Self-created dataset: Top 1 acc – 0.6573 Top 2 acc – 0.8475 Top 3 acc – 0.9243
Pomari et al. (Pomari, Ruppert, Rezende, Rocha, & Carvalho, 2018)	Image	Splicing	Propose a novel approach of combing powerful illumination maps with CNN features utilizing SVM classifier for splice detection and localization. The proposed model's final decision is supervised by a gradient-based technique.	Localization	Lightning Inconsistencies	CNNs	DSO-1 – 0.9600 acc DSI-1 – 0.9200 acc Columbia – 0.8900 acc
Zhang et al. (Zhang, Zhang, Zhou, & Luo, 2018)	Image	Splicing	Propose a SHALLOW CONVOLUTIONAL NEURAL NETWORK (SCNN) that detects splice boundaries using saturation and chroma details. SCNN based Sliding Window Detection (SWD) and Fast SCNN are proposed for manipulation detection and localization respectively.	Localization	Abnormal changes in saturation and chroma boundaries	CNNs	CASIA v2.0: JPEG images – 0.8535 acc TIFF images – 0.8293 acc
Wu et al. (Wu, Almageed, & Natarajan, 2018)	Image	Copy Move	Propose BUSTER-NET, a novel end-to-end network with two subnetworks, “mani-det” which detects manipulated regions and “simi-det” to detect cloned regions. Features fused from both subnetworks is used to estimate manipulation mask (**Figure 17**).	Localization	-	CNNs	CASIA v2.0 – 0.7822 precision, 0.7389 recall, 0.7598 F1, 0.8000 auc CoMoFoD – 0.5734 precision, 0.4939 recall, 0.4926 F1
Bondi et al. (Bondi, et al., 2017)	Image	Splicing	Propose a novel approach of clustering source camera footprints. A CNN extracts features from an image patch which is then forwarded along with patch position and confidence score to the clustering algorithm that estimates a binary mask with 0 intensity indicating original pixels and 1 intensity represents manipulation.	Localization	Source Camera footprint variations	CNNs	*Self-created dataset from Dresdan Image Database: Known – 0.9080 acc, 0.94440 auc Unknown – 0.8100 acc, 0.8550 auc
Amerini et al. (Amerini, Uricchio, Ballan, & Caldelli, 2017)	Image	Splicing	To localize jpeg double compression, authors suggest a unique MULTI-DOMAIN CONVOLUTIONAL NEURAL NETWORK that uses two CNNs to extract both spatial domain and frequency domain characteristics.	Localization	JPEG double compression traces	CNNs	*Self-created dataset from UCID dataset images: Uncompressed – 0.9990 acc Singly Compressed – 0.9160 acc Doubly Compressed – 0.9720 acc
Chen et al. (Chen, McCloskey, & Yu, 2017)	Image	Splicing	Propose a novel approach of analyzing camera response function (CRF) to detect and localize copy move and splice manipulation. CRF is capable of differentiating between authentic edges and forged spliced boundaries including artificially blurred and artificially sharp transitions.	Localization	Variations in blur shape of original and forged boundary	CNNs	*Self-created SpLogo dataset – 0.9900 acc Columbia – 0.9700 acc
Bunk et al. (Bunk, et al., 2017)	Image	Copy Move, Splicing, Removal	Two methods for the localization and detection of tampering using deep learning and resampling characteristics are proposed. First approach has deep classifier and Gaussian CRF to generate heat maps of resampling feature radon transforms. Random Walker	Localization	Resampling traces	CNN, LSTM	Nist Nimble 2016 – 0.9486 acc, 0.9138 auc

Ref.	Medium	Manipulation Type	Approach	Detection / Localization	Clues	Model Type	Datasets & Results
			segmentation method is used for localization. Second method utlilizes LSTM on resampling features to detect and localize forgery.				
Long et al. (Long, Smith, Basharat, & Hoogs, 2017)	Video	Video Manipulation	Present a novel frame deletion detection method that thresholds the L2 distance of color histograms, the average moving direction (optical flow), and the difference of the Y channel in the YCrCb color space (motion energy) for two consecutive video frames using a 3D convolutional network.	Detection	Optical flow, motion energy, and colour histogram traces.	CNNs	*Videos from YFCC100m dataset – 0.9818 acc
He et al. (He, et al., 2017)	Video	Video Manipulation	Propose a novel video tampering detection method that uses a lightweight architecture having as few as 29K parameters which outperforms AlexNet CNN having 58M parameters and uses 1X1 convolutions plus average pooling to avoid overfitting. The authors propose to extract double compression traces by finding relocated I-frames.	Detection	Video compression traces (relocated I-frames)	CNNs	*Self-Created dataset: TNR – 0.9710 TPR – 0.9635 Acc – 0.9673

7 DISCUSSION

This section presents discussions regarding different aspects of manipulation detection. It covers the top results obtained on publicly available manipulation detection datasets. It compares deep learning-based manipulation detection methods with traditional ones. It identifies the popular clues and architectures commonly used for manipulation detection. It also presents crucial insights from existing state-of-the-art methods.

7.1 Tampering Datasets & Results

Datasets lie at the heart of deep learning approaches for manipulation detection. Table 1 discusses various publicly available datasets for deepfake detection, splice detection, copy move detection etc. The size and variety of these datasets play a crucial role in the manipulation detection process since deep architectures require comprehensive training from diverse examples. When it comes to splicing and copy-move detection, the publicly available datasets are very small in size. Table 1 clearly shows small datasets like Columbia Gray, Columbia Color, Casia v1.0, MICC-F220, MICC-F2000, MICC-F600, CoMoFoD, etc. Hence there is an obvious need to create larger splicing and copy-move datasets for better generalization and preventing the overfitting problem commonly found in deep learning models. However, the publicly available datasets for deepfake detection do not suffer from this problem as plenty of large-scale datasets like DFDC (124K videos), DeeperForensics 1.0 (60000 videos), FaceForensics++ (1.8 million facial images) exist having multiple kinds of facial manipulations.

The classification scores reported on these publicly available datasets have improved with the growing number of state-of-the-art approaches. Contributions such as (Qian, Yin, Sheng, Chen, & Shao, 2020), (Wu, Xie, Gao, & Xiao, 2020) have scored more than 0.98 accuracy on the FaceForensics++ dataset and models like (Zhang & Ni, 2020) have scored 0.97 accuracy on the Casia v2.0 dataset. A similar trend can be observed in other publicly available datasets as more and more novel approaches are proposed. (Li, et al., 2020) scores AUC score of 0.8092 on DFDC, 0.8058 on Celeb DF and 0.9540 on DFD dataset. (Mazumdar & Bora, 2019) achieve accuracy score of 0.9700 on DSO-1 and 0.9400 on DSI-1 datasets.

Building new manipulation datasets poses several challenges. Manipulation detection datasets can either be created manually or synthetically. Manual manipulation requires tremendous amount of time and manpower. Synthetic tampering restricts the variety of manipulations possible. Size of initial image or video-based manipulation detection datasets was very small. For example, Columbia Color dataset contains merely 183 original and 183 tampered images. Such small-scale datasets lead to limited diversity which bottlenecks training of deep networks. For effective facial manipulation detection, datasets require actors providing diversity across identities, race, facial shape & alignments, expressions etc. However, it remains a challenge to find many such actors with diverse characteristics who

* Corresponding Author

also agree to participate in manipulating their images and videos to be used publicly for research. Supervised learning demands labelled samples in manipulation detection datasets. Again, this is a challenge as manual annotations are more accurate but less feasible in large scale datasets than automatic labelling.

7.2 Traditional vs Deep Learning based Tampering Detection

Several traditional methods exist for manipulation detection. Manipulation detection methods utilizing image characteristics are prone to post-processing attacks (Chen, Shi, & Su, 2007), (Zhao, Li, Li, & Wang, 2010). Source device information fail when the extracted signal is weak (Hsu & Chang, 2006), (Gou, Swaminathan, & Wu, 2007) and methods using hashing and watermarking require the presence of untampered images (Tang, Zhang, Li, & Zhang, 2016), (Wang, et al., 2015). The block based traditional copy-move detection methods are computationally expensive (Zhu, Chen, Yan, Guo, & Dong, 2020). Traditional methods generally suffer from severe flaws and demonstrate poor manipulation localization capability.

The primary benefit of manipulation detection using deep learning approaches is that they do not require any feature engineering. Deep architectures are capable of extracting discriminative features on their own. Section 6 discusses the latest state-of-the-art manipulation detection methods. Recent deepfake detection models are based on learning from different modality inputs such as spatial (Shang, et al., 2021), textural (Yang J. , Li, Xiao, Lu, & Gao, 2021), optical flow (Amerini, Galteri, Caldelli, & Bimbo, 2019), (Caldelli, Galteri, Amerini, & Bimbo, 2021) etc. Other methods leverage biological clues such as visual lip movements (Ma, Wang, Zhang, & Liew, 2020), (Yang, Ma, Wang, & Liew, 2020), eye blinking consistency (Fogelton & Benesova, 2018), heartbeat patterns (Fernandes, et al., 2019), (Qi, et al., 2020) and face context (Nirkin, Wolf, Keller, & Hassner, 2021). Deep architectures have also proven their high capability in identifying fully synthesized fake facial images generated from GANs (Wang, Wang, Zhang, Owens, & Efros, 2020), (Guarnera, Giudice, & Battiato, 2020), (Chen, et al., 2021). The recently proposed attention mechanism has boosted the model classification capabilities even further (Dang, Liu, Stehouwer, Liu, & Jain, 2020), (Choi, Lee, Lee, Kim, & Ro, 2020), (Lu, Liu, Zhou, Chu, & Yu, 2021), (Chen & Yang, 2021).

Novel architectures also detect splice manipulation from compression traces (Li, Zhang, Luo, & Tan, 2019), (Amerini, Uricchio, Ballan, & Caldelli, 2017), (Deng, Li, Gao, & Tao, 2019), inconsistent noise patterns (Cozzolino & Verdoliva, 2020), (Cozzolino, Marra, Gragnaniello, Poggi, & Verdoliva, 2020), illumination maps (Pomari, Ruppert, Rezende, Rocha, & Carvalho, 2018) etc. These diverse novel architectures have achieved high classification scores on publicly available datasets, are robust against compression and noise attacks and show strong generalization capabilities when the nature of manipulation is unknown.

7.3 Important Clues and Architectures for Tampering Detection

Table 4 presents an exhaustive tabular representation of the recently proposed novel SOTA approaches for manipulation detection and states the clues and architectures associated with each method. Since compression is necessary before sharing multimedia files online, so it has played a significant role in tamper detection. Several contributions highlight the inconsistent compression artifacts caused by multimedia manipulation (Amerini, Uricchio, Ballan, & Caldelli, 2017), (Liu & Pun, 2018), (Deng, Li, Gao, & Tao, 2019), (Kohli, Gupta, & Singhal, 2020). Source camera noise patterns prove discriminative when manipulation involves pasting objects from another image; hence, manipulated sample contains traces from multiple source devices (Bondi, et al., 2017), (Cozzolino & Verdoliva, 2020). Optical flow-based features have provided strong generalization capabilities in deepfake detection (Amerini, Galteri, Caldelli, & Bimbo, 2019), (Caldelli, Galteri, Amerini, & Bimbo, 2021).

Various CNNs have demonstrated tremendous capability in extracting discriminative features towards manipulation detection. The novelties in such CNN architectures include extracting multi-scale features (Yang J. , Li, Xiao, Lu, & Gao, 2021), novel textural difference operator (Yang J. , Li, Xiao, Lu, & Gao, 2021), highlighting manipulation trace by suppressing image semantic content (Guo, Yang, Chen, & Sun, 2021), dual branch architectures to learn multi-modal features (Hu, Liao, Wang, & Qin, 2022), (Chugh, Gupta, Dhall, & Subramanian, 2020), (Wang, Ni, Liu, Luo, & Jha, 2020), (Wu, Almageed, & Natarajan, 2018), neural ordinary differential equation model (Fernandes, et al., 2019), training separate neural nets on different facial regions (Nirkin, Wolf, Keller, & Hassner, 2021), integrating inception module with attention (Lu, Liu, Zhou, Chu, & Yu, 2021), etc. Some approaches have focussed on extracting temporal features across video segments or entire video to highlight manipulation (Hu, Liao, Wang, & Qin, 2022), (Lu, Liu, Zhou, Chu, & Yu, 2021) etc.

7.4 Insights from SOTA Tampering Detection Methods

The following important inferences can be drawn based on the contributions presented in Section 6. Several appearance-preserving manipulations significantly modify frequency information, leaving distinct tampering clues in the frequency domain (Singhal, Gupta, Tripathi, & Kothari, 2020). CNNs can extract discriminative forensic features from picture patches by mapping them to a low-dimensional feature space (Mayer & Stamm, 2020). Spatial and Channel wise adaptive attention can extract global features specifying long-term dependence of global pixels (Zhu, Chen, Yan, Guo, & Dong, 2020). DenseNets demonstrate high potential for feature reuse, keeping the number of parameters to a minimum and conducting efficient, deeper and accurate training (Zhong & Pun, 2020). Image residual-based features are more discriminative in highlighting tampered regions than raw image features (Singhal, Gupta, Tripathi, & Kothari, 2020). Deep Belief Networks can utilize layers of Restricted Boltzmann Machines to learn data distribution in an unsupervised

fashion and highlight unusual (tampered) data points (Horváth, Montserrat, Hao, & Delp, 2020).

Variation of noise residuals between a given pixel and its neighbours can be used to highlight manipulation by using high-pass convolutional filters that magnify high-frequency information like noise (Wu, Xie, Gao, & Xiao, 2020). CNNs can be trained to predict whether a facial video frame contains an open mouth (Agarwal, Farid, Fried, & Agrawala, 2020). Deep matching helps to find copy-move forgery by finding a high correlation between the copied region and the original region from where it was copied compared to the correlation with other genuine regions (Zhu, Chen, Yan, Guo, & Dong, 2020). Weighted multi-scale features extracted from histograms of DCT coefficients extract double JPEG compression forensics for highlighting tampering detection (Deng, Li, Gao, & Tao, 2019). Ringed residual structures help in CNN training by preventing the vanishing gradient problem commonly occurring in deeper CNNs to extract meaningful discriminative features for tampering detection (Bi, Wei, Xiao, & Li, 2019).

8 RESEARCH GAPS AND FUTURE TRENDS

This section discusses the research gaps and possible future trends based on research contributions reviewed in this manuscript:

Research Gaps: Most datasets for manipulation detection are too small to provide robust training for deep models (Hsu & Chang, 2006), (Amerini, Ballan, Caldelli, Bimbo, & Serra, 2011), (Chen, Tan, Li, & Huang, 2015). More comprehensive datasets are required to prevent overfitting of deep architectures targeting manipulation detection. Since the size of manipulation detection datasets is not large, hence deep models tend to overfit while training. Approaches of manipulation detection must consider improving the learning capability of CNNs such as in (Bi, Wei, Xiao, & Li, 2019). While most manipulation detection approaches are focussed on finding traces of specific kind of tampering, few generic methods exist that can find manipulation without prior knowledge of the modification operation (Cozzolino & Verdoliva, 2020), (Singhal, Gupta, Tripathi, & Kothari, 2020). More of such generic methods are required since it is unreasonable to know the kinds of manipulations a sample undergo. The number of possible manipulations to any image or video is endless and it is not feasible to create comprehensive labelled datasets for each type of tampering. No single approach is capable of detecting all types of manipulations. For example, noiseprint (Cozzolino & Verdoliva, 2020) which is highly effective for camera model identification, fails in device identification problems. Fusion-based approaches are needed to enhance robustness of research contributions towards tampering detection. DeepFakes have created more realistic fake images and videos than ever before, and they can seriously harm society. Some GAN-based approaches (Zhou, Sun, Yacoob, & Jacobs, 2018) have shown promising results in detecting such identity tampering methods and more such methods need to be developed and fine-tuned.

Post-Processing Attacks: Another research gap is the performance degradation of forgery detection methods due to post-processing attacks such as compression, filtering, blending, etc. These post-processing operations suppress the discriminative clues in tampered multimedia samples and make it harder for models to differentiate original images from tampered ones. Recent forgery detection models emphasize on the importance of minimizing this performance drop due to such post-attack operations.

Adversarial Training is can be used to increase the robustness and effectiveness of tampering detection methods. Specifically, adversarial training entails using two neural networks in an adversarial situation, the generator and the discriminator. The generator seeks to produce as convincing fake content (such as falsified photos, movies, or documents) as feasible. The discriminator, on the other hand, has been educated to recognise authentic and fabricated content. Adversarial training teaches forgery detection algorithms to recognise minor artefacts and patterns in fabricated information. As the generator improves at making plausible forgeries, so does the discriminator at recognising them. This adversarial process increases the forgery detection model's capacity to recognise increasingly sophisticated forgeries over time.

Future Trends: The use of attention-based approaches in recent times (Mi, Jiang, Sun, & Xu, 2020), (Zhu, Chen, Yan, Guo, & Dong, 2020), (Islam, Long, Basharat, & Hoogs, 2020) etc, have proven greater localization capabilities of tampered regions in images/videos. More and more novel attention mechanisms are being proposed such as Triplet Attention (Misra, Nalamada, Arasanipalai, & Hou, 2021), Shuffle Attention (Zhang & Yang, 2021), Coordinate Attention (Hou, Zhou, & Feng, 2021), ParNet (Mehta & Rastegari, 2022) etc, and these can be utilized in manipulation detection approaches. While convolution operator lies at the heart of CNNs, a novel operator Involution (Li D. , et al., 2021) has been proposed recently that achieves competent classification results with fewer trainable parameters. Involution-based neural nets may be able to improve manipulation detection with reduced computational costs. The rise of vision transformer architectures (Dosovitskiy, et al., 2021) are also becoming increasingly popular in computer vision tasks. The initial versions of these transformers required more training data than CNNs but showed superior classification capabilities. As newer and lighter transformers such as (Han, et al., 2021) are proposed, these self-attention-based architectures are strong contenders to replace CNNs for tampering detection. The interpretability of deep architectures has always been in question. However, with the recent rise of class activation map (CAM) methods such as (Selvaraju, et al.), (Jiang, Zhang, Hou, Cheng, & Wei, 2021) CAM maps can be used for better interpretability of deep architecture trained to identify manipulated images/videos.

9 CONCLUSION

Solution to Research Gaps: Larger tampering datasets with more samples are needed to develop effective and robust detection approaches. Especially from the point of deep learning, both the size and variety of tampering of datasets need to be comprehensive. Visual

attention-based methods have boosted the performance of neural networks and these can be used effectively to improve the forgery identification capability of various methods. Generalized tampering detection methods such as (Guo, Yang, Chen, & Sun, 2021), (Zhao, et al., 2023) need to be developed to identify tampering without prior knowledge. Specifically, these methods should be capable of uncovering unnatural patterns from images' spatial or frequency domain. In videos, temporal consistency is a key indicator for verifying the authenticity of visual data. Hence, unsupervised manipulation detection is a promising research direction to handle known and unknown modifications within samples. Multi-modal multi-branch methods as discussed in Section 6.6 have performed better than single-branch approaches. This is mainly due to the complementary feature learning provided by information from multiple input domains. Such methods can boost model performance for forgery detection. Realistic face manipulations are a real threat in today's world and Section 6.1 extensively covers various approaches that can be used to identify facial tampering detection. Adversarial training can also be an effective tool in identifying forgery in images and videos.

This review thoroughly studies manipulation detection approaches for images and videos using deep learning methods. **Figure 2** provides a tampering detection taxonomy defining the categories for manipulation detection datasets, clues, architectures and SOTA approaches. *Firstly*, this review describes the common manipulation detection datasets for both images and videos (Section 3). Table 1 provides comprehensive details for these datasets, including the media type, manipulation type, number of original and tampered samples, media sample resolution, file format and presence of ground truth masks. Evaluation metrics used to measure manipulation detection approaches' performance are also described. *Secondly*, common manipulation clues are presented that form the basis of various tampering detection approaches. *Thirdly*, the review explains the commonly used deep learning architectures for forgery detection in Section 5. Most approaches utilize one of the numerous versions of CNNs due to their superior automatic feature extraction capability in a supervised environment. *Finally*, state-of-the-art manipulation detection approaches based on deep learning are discussed in Section 6. The approaches can be broadly classified into deepfake detection, splice detection, copy-move detection and other approaches. Table 4 presents an exhaustive tabular representation of manipulation detection methods specifying the type of input files involved, the type being detected, the key idea behind the novel approaches for tampering detection, manipulation clues utilized, the deep architectures used, and results reported on publicly available manipulation detection datasets. Section 7 presents an in-depth discussion of the manipulation detection ecosystem, diving into important aspects such as top results reported on publicly available datasets, traditional versus deep learning-based manipulation detection approaches, important clues, deep architectures, and insights from existing state-of-the-art manipulation detection approaches. Section 8 explores the existing research gaps and possible future trends based on the new upcoming research ideas.

DECLARATIONS

Ethical Approval: Not applicable.
Supporting Data Availability: No datasets were utilized in this study, and hence data availability statement is not applicable.
Statement of Competing Interests: The authors affirm that they have no known financial or interpersonal conflicts that would have seemed to have an impact on the research presented in this study.
Statement of Funding: For the creation of this manuscript, no funding was given.
Statement of Author Contribution: Ankit Yadav – Conceptualization, Investigation , Implementation, Writing – Original Draft, Visualization. Dinesh Kumar Vishwakarma - Conceptualization, Supervision, Formal Analysis, Review and Editing.
Acknowledgements: Not applicable

10 REFERENCES

Kohli, A., Gupta, A., & Singhal, D. (2020). CNN based localisation of forged region in object-based forgery for HD videos. *IET Image Processing, 14*(5), 947-958.

Kosuru, S., Swain, G., Kumar, N., & Pradhan, A. (2022). Image tamper detection and correction using Merkle tree and remainder value differencing. *Optik, 261*.

Selvaraju, R., Cogswell, M., Das, A., Vedantam, R., Parikh, D., & Batra, D. (n.d.). Grad-CAM: Visual Explanations from Deep Networks via Gradient-based Localization. *https://arxiv.org/abs/1610.02391*.

Sun, J.-Y., Kim, S.-W., Lee, S.-W., & Ko, S.-J. (2018). A novel contrast enhancement forensics based on convolutional neural networks. *Signal Processing: Image Communication, 63*, 149-160.

Tariang, D., Chakraborty, R., & Naskar, R. (2019). A Robust Residual Dense Neural Network For Countering Antiforensic Attack on Median Filtered Images. *IEEE Signal Processing Letters, 26*(8), 1132-1136.

Wu, Y., AbdAlmageed, W., & Natarajan, P. (2019). ManTra-Net: Manipulation Tracing Network for Detection and Localization of Image Forgeries With Anomalous Features. *IEEE/CVF Conference on Computer Vision and Pattern Recognition (CVPR).* Long Beach.

Yang, C.-Z., Ma, J., Wang, S., & Liew, A.-C. (2020). Preventing DeepFake Attacks on Speaker Authentication by Dynamic Lip Movement Analysis. *IEEE Transactions on Information Forensics and Security, 16*, 1841-1854.

Abdulwahid , S. (2023). The detection of copy move forgery image methodologies. *Measurement: Sensors , 26*.

Agarwal, S., Farid, H., Fried, O., & Agrawala, M. (2020). Detecting Deep-Fake Videos from Phoneme-Viseme Mismatches. *IEEE/CVF Conference on Computer Vision and Pattern Recognition Workshops (CVPRW).* Seattle.

Alhaidery, M., Taherinia, A., & Shahadi, H. (2023). A robust detection and localization technique for copy-move forgery in digital images. *Journal of King Saud University - Computer and Information Sciences, 35*(1), 449-461.

Alipour, N., & Behrad, A. (2020). Semantic segmentation of JPEG blocks using a deep CNN for non-aligned JPEG forgery detection and localization. *Multimedia Tools and Applications volume, 79*, 8249–8265.

Amerini, I., Ballan, L., Caldelli, R., Bimbo, A., & Serra, G. (2011). A SIFT-Based Forensic Method for Copy–Move Attack Detection and Transformation Recovery. *IEEE Transactions on Information Forensics and Security , 6*(3), 1099 - 1110.

Amerini, I., Ballan, L., Caldelli, R., Bimbo, A., Tongo, L., & Serra, G. (2013). Copy-move forgery detection and localization by means of robust clustering with J-Linkage. *Signal Processing: Image Communication, 28*(6), 659-669.

Amerini, I., Galteri, L., Caldelli, R., & Bimbo, A. (2019). Deepfake Video Detection through Optical Flow Based CNN. *IEEE/CVF International Conference on Computer Vision Workshop (ICCVW).* Seoul.

Amerini, I., Uricchio, T., Ballan, L., & Caldelli, R. (2017). Localization of JPEG Double Compression Through Multi-domain Convolutional Neural Networks. *IEEE Conference on Computer Vision and Pattern Recognition Workshops (CVPRW).* Honolulu.

Anjum, A., & Islam , S. (2020). Recapture detection technique based on edge-types by analysing high-frequency components in digital images acquired through LCD screens. *Multimedia Tools and Applications, 79*, 6965–6985.

Bai, W., Liu, Y., Zhang, Z., Li, B., & Hu, W. (2023). AUNet: Learning Relations Between Action Units for Face Forgery Detection. *Conference on Computer Vision and Pattern Recognition (CVPR).*

Bammey, Q., Gioi, R., & Morel, J.-M. (2020). An Adaptive Neural Network for Unsupervised Mosaic Consistency Analysis in Image Forensics. *Proceedings of the IEEE/CVF Conference on Computer Vision and Pattern Recognition (CVPR).* Seattle.

Bappy, J., Simons, C., Nataraj, L., Manjunath, B., & Chowdhury, A. (2019). Hybrid LSTM and Encoder–Decoder Architecture for Detection of Image Forgeries. *IEEE Transactions on Image Processing, 28*(7), 3286 - 3300.

Barni, M., Bondi, L., Bonettini, N., Bestagini, P., Costanzo, A., Maggini, M., . . . Tubaro, S. (2017). Aligned and non-aligned double JPEG detection using convolutional neural networks. *Journal of Visual Communication and Image Representation, 49*, 153-163.

Bas, P., Filler, T., & Pevný, T. (2011). "Break Our Steganographic System": The Ins and Outs of Organizing BOSS. *International Workshop on Information Hiding.* Prague.

Bashar, M., Noda, K., Ohnishi, N., & Mori, K. (2010). Exploring Duplicated Regions in Natural Images. *IEEE Transactions on Image Processing*.

Bharathiraja, S., Kanna, B., & Hariharan, M. (2022). A Deep Learning Framework for Image Authentication: An Automatic Source Camera Identification Deep-Net. *Arabian Journal for Science and Engineering*.

Bi, X., Wei, Y., Xiao, B., & Li, W. (2019). RRU-Net: The Ringed Residual U-Net for Image Splicing Forgery Detection. *IEEE/CVF Conference on Computer Vision and Pattern Recognition Workshops (CVPRW).* Long Beach.

Bondi, L., Lameri, S., Güera, D., Bestagini, P., Delp, E., & Tubaro, S. (2017). Tampering Detection and Localization Through Clustering of Camera-Based CNN Features. *IEEE Conference on Computer Vision and Pattern Recognition Workshops (CVPRW).* Honolulu.

Bonomi, M., Pasquini, C., & Boato, G. (2021). Dynamic texture analysis for detecting fake faces in video sequences. *Journal of Visual Communication and Image Representation, 79*.

Bunk, J., Bappy, J., Mohammed, T., Nataraj, L., Flenner, A., Manjunath, B., . . . Peterson, L. (2017). Detection and Localization of Image Forgeries Using Resampling Features and Deep Learning. *IEEE Conference on Computer Vision and Pattern Recognition Workshops (CVPRW).* Honolulu.

Caldelli, R., Galteri, L., Amerini, I., & Bimbo, A. (2021). Optical Flow based CNN for detection of unlearnt deepfake manipulations. *Pattern Recognition Letters, 146*, 31-37.

Cao, Y., Chen, J., Huang, L., Huang, T., & Ye, F. (2022). Three-classification Face Manipulation Detection Using Attention-based Feature Decomposition☆. *Computers & Security*.

Carvalho, T., Faria, F., Pedrini, H., Torres, R., & Rocha, A. (2016). Illuminant-Based Transformed Spaces for Image Forensics. *IEEE Transactions on Information Forensics and Security, 11*(4), 720-733.

Carvalho, T., Riess, C., Angelopoulou, E., Pedrini, H., & Rocha, A. (2013). Exposing Digital Image Forgeries by Illumination Color Classification. *IEEE Transactions on Information Forensics and Security , 8*(7), 1182 - 1194.

Chamot, F., Geradts, Z., & Haasdijk, E. (2022). Deepfake forensics: Cross-manipulation robustness of feedforward- and recurrent convolutional forgery detection methods. *Forensic Science International: Digital Investigation, 40*.

Chen, B., Ju, X., Xiao, B., Ding, W., Zheng, Y., & Albuquerque, V. (2021). Locally GAN-generated face detection based on an improved Xception. *Information Sciences, 572*, 16-28.

Chen, B., Li, T., & Ding, W. (2022). Detecting deepfake videos based on spatiotemporal attention and convolutional LSTM. *Information Sciences, 601*, 58-70.

Chen, C., McCloskey, S., & Yu, J. (2017). Image Splicing Detection via Camera Response Function Analysis. *IEEE Conference on Computer Vision and Pattern Recognition (CVPR).* Honolulu.

Chen, H., Li, Y., Lin, D., Li, B., & Wu, J. (2023). Watching the BiG artifacts: Exposing DeepFake videos via Bi-granularity artifacts☆. *Pattern Recognition, 135*.

Chen, H.-S., Rouhsedaghat, M., Ghani, H., Hu, S., You, S., & Kuo, C.-C. (2021). DefakeHop: A Light-Weight High-Performance Deepfake Detector. *IEEE International Conference on Multimedia and Expo (ICME).* Shenzhen.

Chen, J., Liao, X., Wang, W., Qian, Z., Qin, Z., & Wang, Y. (2023). SNIS: A Signal Noise Separation-Based Network for Post-Processed Image Forgery Detection. *IEEE Transactions on Circuits and Systems for Video Technology*, *33*(2), 935 - 951.

Chen, S., Tan, S., Li, B., & Huang, J. (2015). Automatic detection of object-based forgery. *IEEE Transactions on Circuits and Systems for Video Technology , 26*(11), 2138 - 2151.

Chen, W., Shi, Y., & Su, W. (2007). Image splicing detection using 2-D phase congruency and statistical moments of characteristic function. *Security, Steganography, and Watermarking of Multimedia Contents IX*. San Jose.

Chen, Z., & Yang, H. (2021). Attentive Semantic Exploring for Manipulated Face Detection. *IEEE International Conference on Acoustics, Speech and Signal Processing (ICASSP).* Toronto.

Chingovska, I., Anjos, A., & Marcel, S. (2012). On the effectiveness of local binary patterns in face anti-spoofing. *International Conference of Biometrics Special Interest Group (BIOSIG).* Darmstadt.

Chintha, A., Thai, B., Sohrawardi, S., Bhatt, K., Hickerson, A., & Wright, M. (2020). Recurrent Convolutional Structures for Audio Spoof and Video Deepfake Detection. *IEEE Journal of Selected Topics in Signal Processing , 14*(5), 1024-1037.

Choi, D., Lee, H., Lee, S., Kim, J., & Ro, Y. (2020). Fake Video Detection With Certainty-Based Attention Network. *IEEE International Conference on Image Processing (ICIP).* Abu Dhabi.

Christlein, V., Riess, C., Jordan, J., Riess, C., & Angelopoulou, E. (2012). An Evaluation of Popular Copy-Move Forgery Detection Approaches. *IEEE Transactions on Information Forensics and Security , 7*(6), 1841 - 1854.

Chu, B., You, W., Yang, Z., Zhou, L., & Wang, R. (2022). Protecting World Leader Using Facial Speaking Pattern Against Deepfakes. *IEEE Signal Processing Letters , 29*, 2078 - 2082.

Chugh, K., Gupta, P., Dhall, A., & Subramanian, R. (2020). Not made for each other- Audio-Visual Dissonance-based Deepfake Detection and Localization. *28th ACM International Conference on Multimedia.* Lisboa.

Costanzo, A., Amerini, I., Caldelli, R., & Barni, M. (2014). Forensic Analysis of SIFT Keypoint Removal and Injection. *IEEE Transactions on Information Forensics and Security, 9*(9), 1450 - 1464.

Cozzolino, D., & Verdoliva, L. (2020). Noiseprint: A CNN-Based Camera Model Fingerprint. *IEEE Transactions on Information Forensics and Security, 15*, 144 - 159.

Cozzolino, D., Marra, F., Gragnaniello, D., Poggi, G., & Verdoliva, L. (2020). Combining PRNU and noiseprint for robust and efficient device source identification. *EURASIP Journal on Information Security*.

Cozzolino, D., Poggi, G., & Verdoliva, L. (2015). Efficient Dense-Field Copy–Move Forgery Detection. *IEEE Transactions on Information Forensics and Security, 10*(11), 2284-2297.

Cun, X., & Pun, C.-M. (2018). Image Splicing Localization via Semi-global Network and Fully Connected Conditional Random Fields. *European Conference on Computer Vision (ECCV).* Munich.

Dang, H., Liu, F., Stehouwer, J., Liu, X., & Jain, A. (2020). On the Detection of Digital Face Manipulation. *IEEE/CVF Conference on Computer Vision and Pattern Recognition (CVPR).* Seattle.

Dang-Nguyen, D.-T., Pasquini, C., Conotter, V., & Boato, G. (2015). RAISE: a raw images dataset for digital image. *6th ACM Multimedia Systems Conference, 219-224.* Portland .

Dean, B. (2020, August). *Social Network Usage & Growth Statistics: How Many People Use Social Media in 2020?* (BackLinko) Retrieved from https://backlinko.com/social-media-users

Deng, C., Li, Z., Gao, X., & Tao, D. (2019). Deep Multi-scale Discriminative Networks for Double JPEG Compression Forensics. *ACM Transactions on Intelligent Systems and Technology, 10*(2).

Dolhansky, B., Bitton, J., Pflaum, B., Lu, J., Howes, R., Wang, M., & Ferrer, C. C. (2020). The DeepFake Detection Challenge (DFDC) Dataset. *arXiv:2006.07397*.

Dong, J., Wang, W., & Tan, T. (2013). CASIA Image Tampering Detection Evaluation Database. *IEEE China Summit and International Conference on Signal and Information Processing.* Beijing.

Dosovitskiy, A., Beyer, L., Kolesnikov, A., Weissenborn, D., Zhai, X., Unterthiner, T., . . . Houlsby, N. (2021). An Image is Worth 16x16 Words: Transformers for Image Recognition at Scale. *International Conference on Learning Representations (ICLR).* Austria.

Du, M., Pentyala, S., Li, Y., & Hu, X. (2020). Towards Generalizable Deepfake Detection with Locality-aware AutoEncoder. *29th ACM International Conference on Information & Knowledge Management.* Atlanta.

Fei, J., Xia, Z., Yu, P., & Xiao, F. (2020). Exposing AI-generated videos with motion magnification. *Multimedia Tools and Applications*.

Feng, W., Wang, Y., Sun , J., Tang, Y., Wu, D., Jiang, Z., . . . Wang, X. (2022). Prediction of thermo-mechanical properties of rubber-modified recycled aggregate concrete. *Construction and Building Materials, 318*.

Feng, Z., Zeng, Z., Guo, C., & Li, Z. (2023). Temporal Multimodal Graph Transformer With Global-Local Alignment for Video-Text Retrieval. *IEEE Transactions on Circuits and Systems for Video Technology, 33*(3), 1438 - 1453.

Fernandes, S., Raj, S., Ewetz, R., Pannu, J., Jha, S., Ortiz, E., . . . Salter, M. (2020). Detecting Deepfake Videos using Attribution-Based Confidence Metric. *IEEE/CVF Conference on Computer Vision and Pattern Recognition Workshops (CVPRW).* Seattle.

Fernandes, S., Raj, S., Ortiz, E., Vintila, L., Salter, M., Urosevic, G., & Jha, S. (2019). Predicting Heart Rate Variations of Deepfake Videos using Neural ODE. *IEEE/CVF International Conference on Computer Vision Workshop (ICCVW).* Seoul.

Fogelton, A., & Benesova, W. (2018). Eye blink completeness detection. *Computer Vision and Image Understanding, 176-177*, 78-85.

Ganguly, S., Ganguly, A., Mohiuddin, S., Malakar, S., & Sarkar, R. (2022). ViXNet: Vision Transformer with Xception Network for deepfakes based video and image forgery detection. *Expert Systems with Applications, 210*.

Goodfellow, I., Abadie, J., Mirza, M., Xu, B., Farley, D., Ozair, S., . . . Bengio, Y. (2014). Generative Adversarial Nets. *Advances in Neural Information Processing Systems (NIPS 2014).* Montreal.

Gou, H., Swaminathan, A., & Wu, M. (2007). Noise Features for Image Tampering Detection and Steganalysis. *IEEE International Conference on Image Processing.* San Antonio.

Guarnera, L., Giudice, O., & Battiato, S. (2020). DeepFake Detection by Analyzing Convolutional Traces. *IEEE/CVF Conference on Computer Vision and Pattern Recognition Workshops (CVPRW).* Seattle.

Guo, Z., Yang, G., Chen, J., & Sun, X. (2021). Fake face detection via adaptive manipulation traces extraction network. *Computer Vision and Image Understanding, 204*.

Guo, Z., Yang, G., Chen, J., & Sun, X. (2023). Exposing Deepfake Face Forgeries with Guided Residuals. *IEEE Transactions on Multimedia*, 1 - 14.

Guo, Z., Yang, G., Wang, D., & Zhang, D. (2023). A data augmentation framework by mining structured features for fake face image detection. *Computer Vision and Image Understanding, 226*.

Guo, Z., Yang, G., Zhang, D., & Xia, M. (2023). Rethinking gradient operator for exposing AI-enabled face forgeries. *Expert Systems with Applications, 215*.

Han, K., Xiao, A., Wu, E., Guo, J., XU, C., & Wang, Y. (2021). Transformer in Transformer. *Advances in Neural Information Processing Systems 34 (NeurIPS 2021).* Virtual.

He, P., Jiang, X., Sun, T., Wang, S., Li, B., & Dong, Y. (2017). Frame-wise detection of relocated I-frames in double compressed H.264 videos based on convolutional neural network. *Journal of Visual Communication and Image Representation, 48*, 149-158.

He, P., Li, H., Wang, H., Wang, S., Jiang, X., & Zhang, R. (20202). Frame-wise Detection of Double HEVC Compression by Learning Deep Spatio-temporal Representations in Compression Domain. *IEEE Transactions on Multimedia*.

He, Z., Wang, W., Dong, J., & Tan, T. (2023). Temporal sparse adversarial attack on sequence-based gait recognition. *Pattern Recognition, 133*.

Horváth, J., Montserrat, D., Hao, H., & Delp, E. (2020). Manipulation Detection in Satellite Images Using Deep Belief Networks. *IEEE/CVF Conference on Computer Vision and Pattern Recognition Workshops (CVPRW).* Seattle.

Hou, Q., Zhou, D., & Feng, J. (2021). Coordinate Attention for Efficient Mobile Network Design. *IEEE/CVF Conference on Computer Vision and Pattern Recognition (CVPR).* Nashville, TN, USA.

Hsu, Y.-f., & Chang, S.-f. (2006). Detecting Image Splicing using Geometry Invariants and Camera Characteristics Consistency. *IEEE International Conference on Multimedia and Expo.* Toronto.

Hu, J., Liao, X., Wang, W., & Qin, Z. (2022). Detecting Compressed Deepfake Videos in Social Networks Using Frame-Temporality Two-Stream Convolutional Network. *IEEE Transactions on Circuits and Systems for Video Technology, 32*(3), 1089 - 1102.

Hu, J., Liao, X., Wang, W., & Qin, Z. (2022). Detecting Compressed Deepfake Videos in Social Networks Using Frame-Temporality Two-Stream Convolutional Network. *IEEE Transactions on Circuits and Systems for Video Technology, 32*(3), 1089 - 1102.

Hu, J., Wang, S., & Li, X. (2021). Improving the Generalization Ability of Deepfake Detection via Disentangled Representation Learning. *IEEE International Conference on Image Processing (ICIP).* Anchorage.

Huang, D.-Y., Huang, C.-N., Hu, W.-C., & Chou , C.-H. (2017). Robustness of copy-move forgery detection under high JPEG compression artifacts. *Multimedia Tools and Applications, 76*, 1509–1530.

Huang, Y., Xu, F., Guo, Q., Liu, Y., & Pu, G. (2022). FakeLocator: Robust Localization of GAN-Based Face Manipulations. *IEEE Transactions on Information Forensics and Security , 17*, 2657 - 2672.

Ilyas, H., Javed, A., & Malik, K. (2023). AVFakeNet: A unified end-to-end Dense Swin Transformer deep learning model for audio–visual deepfakes detection. *Applied Soft Computing*.

Image Forensics Challenge Dataset. (2014). Retrieved from https://signalprocessingsociety.org/newsletter/2014/01/ieee-ifs-tc-image-forensics-challenge-website-new-submissions

Islam, A., Long, C., Basharat, A., & Hoogs, A. (2020). DOA-GAN: Dual-Order Attentive Generative Adversarial Network for Image Copy-Move Forgery Detection and Localization. *IEEE/CVF Conference on Computer Vision and Pattern Recognition (CVPR).* Seattle.

Jiang, L., Li, R., Wu, W., Qian, C., & Loy, C. (2020). DeeperForensics-1.0: A Large-Scale Dataset for Real-World Face Forgery Detection. *IEEE/CVF Conference on Computer Vision and Pattern Recognition (CVPR).* Seattle.

Jiang, P.-T., Zhang, C.-B., Hou, Q., Cheng, M.-M., & Wei, Y. (2021). LayerCAM: Exploring Hierarchical Class Activation Maps for Localization. *IEEE Transactions on Image Processing , 30*, 5875 - 5888.

Jiang, X., Xu, Q., Sun, T., Li, B., & He, P. (2020). Detection of HEVC Double Compression With the Same Coding Parameters Based on Analysis of Intra Coding Quality Degradation Process. *IEEE Transactions on Information Forensics and Security, 15*, 250 - 263.

Johnston, P., Elyan, E., & Jayne, C. (2020). Video tampering localisation using features learned from authentic content. *Neural Computing and Applications, 32*, 12243–12257.

Kang, J., Ji, S.-K., Lee, S., Jang, D., & Hou, J.-U. (2022). Detection Enhancement for Various Deepfake Types Based on Residual Noise and Manipulation Traces. *IEEE Access, 10*, 69031 - 69040.

Kaur, S., Singh, S., Kaur, M., & Lee, H.-N. (2022). A Systematic Review of Computational Image Steganography Approaches. *Archives of Computational Methods in Engineering, 29*, 4775–4797.

Ke, J., & Wang, L. (2023). DF-UDetector: An effective method towards robust deepfake detection via feature restoration. *Neural Networks, 160*, 216-226.

Khalid, H., & Woo, S. (2020). OC-FakeDect: Classifying Deepfakes Using One-class Variational Autoencoder. *IEEE/CVF Conference on Computer Vision and Pattern Recognition Workshops (CVPRW).* Seattle.

Khalifa, A., Zaher, N., Abdallah, A., & Fakhr, M. (2022). Convolutional Neural Network Based on Diverse Gabor Filters for Deepfake Recognition. *IEEE Access, 10*, 22678 - 22686.

Kingra, S., Aggarwal, N., & Kaur, N. (2022). LBPNet: Exploiting texture descriptor for deepfake detection. *Forensic Science International: Digital Investigation, 42-43*.

Kiruthika, S., & Masilamani, V. (2023). Image quality assessment based fake face detection. *Multimedia Tools and Applications, 82*, 8691–8708.

Kong, C., Chen, B., Li, H., Wang, S., Rocha, A., & Kwong, S. (2022). Detect and Locate: Exposing Face Manipulation by Semantic- and Noise-Level Telltales. *IEEE Transactions on Information Forensics and Security, 17*, 1741 - 1756.

Kong, C., Chen, B., Yang, W., Li, H., Chen, P., & Wang, S. (2022). Appearance Matters, So Does Audio: Revealing the Hidden Face via Cross-Modality Transfer. *IEEE Transactions on Circuits and Systems for Video Technology*, *32*(1), 423 - 436.

Korshunov, P., & Marcel, S. (2022). Improving Generalization of Deepfake Detection With Data Farming and Few-Shot Learning. *IEEE Transactions on Biometrics, Behavior, and Identity Science, 4*(3), 386 - 397.

Kumar, P., Vatsa, M., & Singh, R. (2020). Detecting Face2Face Facial Reenactment in Videos. *Winter Conference on Applications of Computer Vision.*

Lee, S., Tariq, S., Shin, Y., & Woo, S. (2021). Detecting handcrafted facial image manipulations and GAN-generated facial images using Shallow-FakeFaceNet. *Applied Soft Computing, 105*.

Li , G., Feng, B., He, M., Weng, J., & Lu, W. (2023). High-capacity coverless image steganographic scheme based on image synthesis. *Signal Processing: Image Communication, 111*.

Li , Z., Xie, L., & Wang, G. (2023). Deep learning features in facial identification and the likelihood ratio bound. *Forensic Science International, 344*.

Li, B., Zhang, H., Luo, H., & Tan, S. (2019). Detecting double JPEG compression and its related anti-forensic operations with CNN. *Multimedia Tools and Applications, 78*, 8577–8601.

Li, D., Hu, J., Wang, C., Li, X., She, Q., Zhu, L., . . . Chen, Q. (2021). Involution: Inverting the Inherence of Convolution for Visual Recognition. *Computer Vision and Pattern Recognition (CVPR).* Nashville.

Li, G., Cao, Y., & Zhao, X. (2021). Exploiting Facial Symmetry to Expose Deepfakes. *IEEE International Conference on Image Processing (ICIP).* Anchorage.

Li, G., Yao, H., Le, Y., & Qin, C. (2023). Recaptured screen image identification based on vision transformer. *Journal of Visual Communication and Image Representation, 90*.

Li, H., & Huang, J. (2019). Localization of Deep Inpainting Using High-Pass Fully Convolutional Network. *IEEE/CVF International Conference on Computer Vision (ICCV).* Seoul.

Li, L., Bao, J., Zhang, T., Yang, H., Chen, D., Wen, F., & Guo, B. (2020). Face X-Ray for More General Face Forgery Detection. *2020 IEEE/CVF Conference on Computer Vision and Pattern Recognition (CVPR).* Seattle.

Li, Y., Hu, L., Dong, L., Wu, H., Tian, J., Zhou, J., & Li, X. (2023). Transformer-Based Image Inpainting Detection via Label Decoupling and Constrained Adversarial Training. *IEEE Transactions on Circuits and Systems for Video Technology*.

Li, Y., Yang, X., Sun, P., Qi, H., & Lyu, S. (2020). Celeb-DF: A Large-Scale Challenging Dataset for DeepFake Forensics. *IEEE/CVF Conference on Computer Vision and Pattern Recognition (CVPR).* Seattle.

Liang, B., Wang, Z., Huang, B., Zou, Q., Wang, Q., & Liang, J. (2023). Depth map guided triplet network for deepfake face detection. *Neural Networks, 159*, 34-42.

Lin, H., Huang, W., Luo, W., & Lu, W. (2023). DeepFake detection with multi-scale convolution and vision transformer. *Digital Signal Processing, 134*.

Lin, K., Han, W., Li, S., Zhao, H., Ren, J., Zhu, L., & Lv, J. (2023). IR-Capsule: Two-Stream Network for Face Forgery Detection. *Cognitive Computation, 15*, 13-22.

Liu, B., & Pun, C.-M. (2018). Deep Fusion Network for Splicing Forgery Localization. *European Conference on Computer Vision (ECCV).* Munich.

Liu, B., & Pun, C.-M. (2020). Exposing splicing forgery in realistic scenes using deep fusion network. *Information Sciences, 526*, 133-150.

Liu, B., Ding, M., Zhu, T., & Yu, X. (2023). TI2Net: Temporal Identity Inconsistency Network for Deepfake Detection. *2023 IEEE/CVF Winter Conference on Applications of Computer Vision (WACV).* Waikoloa, HI, USA .

Liu, Y., Lv, B., Jin, X., Chen, X., & Zhang, X. (2023). TBFormer: Two-Branch Transformer for Image Forgery Localization. *IEEE Signal Processing Letters, 30*, 623 - 627.

Long, C., Smith, E., Basharat, A., & Hoogs, A. (2017). A C3D-Based Convolutional Neural Network for Frame Dropping Detection in a Single Video Shot. *IEEE Conference on Computer Vision and Pattern Recognition Workshops (CVPRW).* Honolulu.

Lu, C., Liu, B., Zhou, W., Chu, Q., & Yu, N. (2021). Deepfake Video Detection Using 3D-Attentional Inception Convolutional Neural Network. *IEEE International Conference on Image Processing (ICIP).* Anchorage.

Luo, Y.-X., & Chen, J.-L. (2022). Dual Attention Network Approaches to Face Forgery Video Detection. *IEEE Access, 10*, 110754 - 110760.

Luo, Z., Kamata, S.-I., & Sun, Z. (2021). Transformer And Node-Compressed Dnn Based Dual-Path System For Manipulated Face Detection. *IEEE International Conference on Image Processing (ICIP).* Anchorage.

Ma, J., Wang, S., Zhang, A., & Liew, A.-C. (2020). Feature Extraction For Visual Speaker Authentication Against Computer-Generated Video Attacks. *IEEE International Conference on Image Processing (ICIP).* Abu Dhabi.

Mahdian, B., & Saic, S. (2007). Detection of copy–move forgery using a method based on blur moment invariants. *Forensic Science International, 171*(2-3), 180-189.

Malik, A., Kuribayashi, M., Abdullahi, S., & Khan, A. (2022). DeepFake Detection for Human Face Images and Videos: A Survey. *IEEE Access, 10*, 18757 - 18775.

Mayer, O., & Stamm, M. (2020). Forensic Similarity for Digital Images. *IEEE Transactions on Information Forensics and Security, 15*, 1331 - 1346.

Mazumdar, A., & Bora, P. K. (2019). Deep Learning-Based Classification of Illumination Maps for Exposing Face Splicing Forgeries in Images. *2019 IEEE International Conference on Image Processing (ICIP).* Taipei.

Mehta, S., & Rastegari, M. (2022). MobileViT: Light-weight, General-purpose, and Mobile-friendly Vision Transformer. *Tenth International Conference on Learning Representations.* Virtual.

Mi, Z., Jiang, X., Sun, T., & Xu, K. (2020). GAN-Generated Image Detection With Self-Attention Mechanism Against GAN Generator Defect. *IEEE Journal of Selected Topics in Signal Processing, 14*(5), 969 - 981.

Miao, C., Tan, Z., Chu, Q., Liu, H., Hu, H., & Yu, N. (2023). F2Trans: High-Frequency Fine-Grained Transformer for Face Forgery Detection. *IEEE Transactions on Information Forensics and Security, 18*, 1039 - 1051.

Miao, C., Tan, Z., Chu, Q., Yu, N., & Guo, G. (2022). Hierarchical Frequency-Assisted Interactive Networks for Face Manipulation Detection. *IEEE Transactions on Information Forensics and Security, 17*, 3008 - 3021.

Mirsky, Y., & Lee, W. (2022). The Creation & Detection of Deepfakes - A Survey. *ACM Computing Surveys, 54*, 1-41.

Misra, D., Nalamada, T., Arasanipalai, A., & Hou, Q. (2021). Rotate to Attend: Convolutional Triplet Attention Module. *IEEE Winter Conference on Applications of Computer Vision (WACV).* Waikoloa, HI, USA.

Misra, I., Rohil, M., Moorthi , S., & Dhar, D. (2023). SPRINT: Spectra Preserving Radiance Image Fusion Technique using holistic deep edge spatial attention and Minnaert guided Bayesian probabilistic model. *Signal Processing: Image Communication, 113*.

Mittal, T., Bhattacharya, U., Chandra, R., Bera, A., & Manocha, D. (2020). Emotions Don't Lie: An Audio-Visual Deepfake Detection Method using Affective Cues. *28th ACM International Conference on Multimedia.* Lisboa.

Mohiuddin, S., Sheikh, K., Malakar, S., Velásquez, J., & Sarkar, R. (2023). A hierarchical feature selection strategy for deepfake video detection. *Neural Computing and Applications*, 9363–9380.

Montserrat, D., Hao, H., Yarlagadda, S., Baireddy, S., Shao, R., Horváth, J., . . . Delp, E. (2020). Deepfakes Detection with Automatic Face Weighting. *IEEE/CVF Conference on Computer Vision and Pattern Recognition Workshops (CVPRW).* Seattle.

Mustak, M., Salminen, J., Mäntymäki, M., Rahman, A., & Dwivedi, Y. (2023). Deepfakes: Deceptions, mitigations, and opportunities. *Journal of Business Research, 154*.

Nam, S.-H., Ahn, W., Yu, I.-J., Kwon, M.-J., Son, M., & Lee, H.-K. (2020). Deep Convolutional Neural Network for Identifying Seam-Carving Forgery. *IEEE Transactions on Circuits and Systems for Video Technology* .

Nam, S.-H., Ahn, W., Mun, S.-M., Park, J., Kim, D., Yu, I.-J., & Lee, H.-K. (2019). Content-Aware Image Resizing Detection Using Deep Neural Network. *IEEE International Conference on Image Processing (ICIP).* Taipei.

Neves, J., Tolosana, R., Rodriguez, R., Lopes, V., Proença, H., & Fierrez, J. (2020). GANprintR: Improved Fakes and Evaluation of the State of the Art in Face Manipulation Detection. *IEEE Journal of Selected Topics in Signal Processing, 14*(5), 1038 - 1048.

Ng, T.-T., Hsu, J., & Chang, S.-F. (2004). *Columbia Image Splicing Detection Evaluation Dataset*. (Columbia University) Retrieved from https://www.ee.columbia.edu/ln/dvmm/downloads/AuthSplicedDataSet/AuthSplicedDataSet.htm

Nguyen, H., Yamagishi, J., & Echizen, I. (2019). Capsule-forensics: Using Capsule Networks to Detect Forged Images and Videos. *IEEE International Conference on Acoustics, Speech and Signal Processing (ICASSP).* Brighton.

Nirkin, Y., Wolf, L., Keller, Y., & Hassner, T. (2021). DeepFake Detection Based on Discrepancies Between Faces and their Context. *IEEE Transactions on Pattern Analysis and Machine Intelligence*.

Novozámský, A., Mahdian, B., & Saic, S. (2020). IMD2020: A Large-Scale Annotated Dataset Tailored for Detecting Manipulated Images. *IEEE Winter Applications of Computer Vision Workshops (WACVW).* Snowmass Village.

Otum, H., & Ellubani, A. (2022). Secure and effective color image tampering detection and self restoration using a dual watermarking approach. *Optik, 262*.

Pang, G., Zhang, B., Teng, Z., Qi, Z., & Fan, J. (2023). MRE-Net: Multi-Rate Excitation Network for Deepfake Video Detection. *IEEE Transactions on Circuits and Systems for Video Technology, Early Access*.

Podilchuk, C., & Delp, E. (2001). Digital watermarking: algorithms and applications. *IEEE Signal Processing Magazine , 18*(4), 33-46.

Pomari, T., Ruppert, G., Rezende, E., Rocha, A., & Carvalho, T. (2018). Image Splicing Detection Through Illumination Inconsistencies and Deep Learning. *IEEE International Conference on Image Processing (ICIP).* Athens.

Preeti, Kumar, M., & Sharma, H. (2023). A GAN-Based Model of Deepfake Detection in Social Media. *Procedia Computer Science, 218*, 2153-2162.

Pu, W., Hu, J., Wang, X., Li, Y., Hu, S., Zhu, B., . . . Lyu, S. (2022). Learning a deep dual-level network for robust DeepFake detection. *Pattern Recognition, 130*.

Qi, H., Guo, Q., Xu, F., Xie, X., Ma, L., Feng, W., . . . Zhao, J. (2020). DeepRhythm: Exposing DeepFakes with Attentional Visual Heartbeat Rhythms. *28th ACM International Conference on Multimedia.* Lisboa.

Qian, Y., Yin, G., Sheng, L., Chen, Z., & Shao, J. (2020). Thinking in Frequency: Face Forgery Detection by Mining Frequency-aware Clues. *arXiv:2007.09355*.

Rana, M., Nobi, M., Murali, B., & Sung, A. (2022). Deepfake Detection: A Systematic Literature Review. *IEEE Access, 10*, 25494 - 25513.

Rezaei, M., & Taheri, H. (2022). Digital image self-recovery using CNN networks. *Optik, 264*.

Rössler, A., Cozzolino, D., Verdoliva, L., Riess, C., Thies, J., & Nießner, M. (2018). FaceForensics: A Large-scale Video Dataset for Forgery Detection in Human Faces. *https://arxiv.org/abs/1803.09179*.

Rössler, A., Cozzolino, D., Verdoliva, L., Riess, C., Thies, J., & Niessner, M. (2019). FaceForensics++: Learning to Detect Manipulated Facial Images. *IEEE/CVF International Conference on Computer Vision (ICCV).* Seoul.

Ryu, S.-J., Lee, M.-J., & Lee, H.-K. (2010). Detection of Copy-Rotate-Move Forgery Using Zernike Moments. *International Workshop on Information Hiding.* Calgary: Springer.

Saddique, M., Asghar, K., Bajwa, U., Hussain, M., Aboalsamh, H., & Habib, Z. (2020). Classification of Authentic and Tampered Video Using Motion Residual and Parasitic Layers. *IEEE Access, 8*, 56782 - 56797.

Sanjary, O., Ahmed, A., & Sulong, G. (2016). Development of a video tampering dataset for forensic investigation. *Forensic Science International, 266*, 565-572.

Schaefer, G., & Stich, M. (2004). UCID: an uncompressed color image database. *Storage and Retrieval Methods and Applications for Multimedia.*

Shan, W., Yi, Y., Huang, R., & Xie, Y. (2019). Robust contrast enhancement forensics based on convolutional neural networks. *Signal Processing: Image Communication, 71*, 138-146.

Shang, Z., Xie, H., Zha, Z., Yu, L., Li, Y., & Zhang, Y. (2021). PRRNet: Pixel-Region relation network for face forgery detection. *Pattern Recognition, 116*.

Sharma, K., Singh, G., & Goyal, P. (2023). IPDCN2: Improvised Patch-based Deep CNN for facial retouching detection. *Expert Systems with Applications, 211*.

Shi, Z., Chen, H., & Zhang, D. (2023). Transformer-Auxiliary Neural Networks for Image Manipulation Localization by Operator Inductions. *IEEE Transactions on Circuits and Systems for Video Technology , 33*(9), 4907 - 4920.

Shi, Z., Shen, X., Chen, H., & Lyu, Y. (2020). Global Semantic Consistency Network for Image Manipulation Detection. *IEEE Signal Processing Letters, 27*, 1755 - 1759.

Shivakumar, B., & Baboo, S. (2011). Detection of region duplication forgery in digital images using SURF. *International Journal of Computer Science, 8*(4).

Singhal, D., Gupta, A., Tripathi, A., & Kothari, R. (2020). CNN-based Multiple Manipulation Detector Using Frequency Domain Features of Image Residuals. *ACM Transactions on Intelligent Systems and Technology, 11*(4).

Song, C., Zeng, P., Wang, Z., Li, T., Qiao, L., & Shen, L. (2019). Image Forgery Detection Based on Motion Blur Estimated Using Convolutional Neural Network. *IEEE Sensors Journal, 19*(23), 11601 - 11611.

Suratkar, S., & Kazi, F. (2022). Deep Fake Video Detection Using Transfer Learning Approach. *Arabian Journal for Science and Engineering*.

Taimori, A., Razzazi, F., Behrad, A., Ahmadi, A., & Zadeh, M. (2016). A novel forensic image analysis tool for discovering double JPEG compression clues. *Multimedia Tools and Applications, 76*, 7749–7783.

Tan, Z., Yang, Z., Miao, C., & Guo, G. (2022). Transformer-Based Feature Compensation and Aggregation for DeepFake Detection. *IEEE Signal Processing Letters, 29*, 2183 - 2187.

Tang, Y., Wang, Y., Wu, D., Liu, Z., Zhang, H., Zhu, M., . . . Wang, X. (2022). An experimental investigation and machine learning-based prediction for seismic performance of steel tubular column filled with recycled aggregate concrete. *REVIEWS ON ADVANCED MATERIALS SCIENCE, 61*(1).

Tang, Z., Zhang, X., Li, X., & Zhang, S. (2016). Robust Image Hashing With Ring Partition and Invariant Vector Distance. *IEEE Transactions on Information Forensics and Security, 11*(1), 200-214.

Tarasiou, M., & Zafeiriou, S. (2020). Extracting Deep Local Features to Detect Manipulated Images of Human Faces. *IEEE International Conference on Image Processing (ICIP).* Abu Dhabi.

Tralic, D., Zupancic, I., Grgic, S., & Grgic, M. (2013). CoMoFoD — New database for copy-move forgery detection. *International Symposium on Electronics in Marine (ELMAR).* Zadar.

Tyagi, S., & Yadav, D. (2022). A Comprehensive Review on Image Synthesis with Adversarial Networks: Theory, Literature, and Applications. *Archives of Computational Methods in Engineering, 29*, 2685–2705.

Vaswani, A., Shazeer, N., Parmar, N., Uszkoreit, J., Jones, L., Gomez, A., . . . Polosukhin, I. (2017). Attention is All you Need. *Advances in Neural Information Processing Systems 30 (NIPS 2017).* Long Beach.

Verde, S., Bondi, L., Bestagini, P., Milani, S., Calvagno, G., & Tubaro, S. (2018). Video Codec Forensics Based on Convolutional Neural Networks. *IEEE International Conference on Image Processing (ICIP).* Athens.

Wang, H., Liu, Z., & Wang, S. (2023). Exploiting Complementary Dynamic Incoherence for DeepFake Video Detection. *IEEE Transactions on Circuits and Systems for Video Technology, 33*(8), 4027 - 4040.

Wang, J., Ni, Q., Liu, G., Luo, X., & Jha, S. (2020). Image splicing detection based on convolutional neural network with weight combination strategy. *Journal of Information Security and Applications, 54*.

Wang, J., Sun, Y., & Tang, J. (2022). LiSiam: Localization Invariance Siamese Network for Deepfake Detection. *IEEE Transactions on Information Forensics and Security, 17*, 2425 - 2436.

Wang, Q., & Zhang, R. (2016). Double JPEG compression forensics based on a convolutional neural network. *EURASIP Journal on Information Security*.

Wang, R., Yang, Z., You, W., Zhou, L., & Chu, B. (2022). Fake Face Images Detection and Identification of Celebrities Based on Semantic Segmentation. *IEEE Signal Processing Letters , 29*, 2018 - 2022.

Wang, S.-Y., Wang, O., Zhang, R., Owens, A., & Efros, A. (2020). CNN-Generated Images Are Surprisingly Easy to Spot… for Now. *IEEE/CVF Conference on Computer Vision and Pattern Recognition (CVPR).* Seattle.

Wang, X., Pang, K., Zhou, X., Zhou, Y., Li, L., & Xue, J. (2015). A Visual Model-Based Perceptual Image Hash for Content Authentication. *IEEE Transactions on Information Forensics and Security , 10*(7), 1336 - 1349.

Wang, Z., Guo, Y., & Zuo, W. (2022). Deepfake Forensics via an Adversarial Game. *IEEE Transactions on Image Processing, 31*, 3541 - 3552.

Wen, B., Zhu, Y., Subramanian, R., Ng, T.-T., Shen, X., & Winkler, S. (2016). COVERAGE — A novel database for copy-move forgery detection. *IEEE International Conference on Image Processing (ICIP).* Phoenix.

Wu, X., Xie, Z., Gao, Y., & Xiao, Y. (2020). SSTNet: Detecting Manipulated Faces Through Spatial, Steganalysis and Temporal Features. *IEEE International Conference on Acoustics, Speech and Signal Processing (ICASSP).* Barcelona.

Wu, Y., Almageed, W., & Natarajan, P. (2018). BusterNet: Detecting Copy-Move Image Forgery with Source/Target Localization. *European Conference on Computer Vision (ECCV).* Munich.

Xia, Z., Qiao, T., Xu, M., Zheng, N., & Xie, S. (2022). Towards DeepFake video forensics based on facial textural disparities in multi-color channels. *Information Sciences, 607*, 654-669.

Xiao, B., Wei, Y., Bi, X., Li, W., & Ma, J. (2020). Image splicing forgery detection combining coarse to refined convolutional neural network and adaptive clustering. *Information Sciences, 511*, 172-191.

Xu, K., Yang, G., Fang, X., & Zhang, J. (2023). Facial depth forgery detection based on image gradient. *Multimedia Tools and Applications*.

Xu, Z., Liu, J., Lu, W., Xu, B., Zhao, X., Li, B., & Huang, J. (2021). Detecting facial manipulated videos based on set convolutional neural networks. *Journal of Visual Communication and Image Representation, 77*.

Yadav, A., & Vishwakarma, D. (2023). MRT-Net: Auto-adaptive weighting of manipulation residuals and texture clues for face manipulation detection. *Expert Systems with Applications, 232*.

Yan, Y., Ren, W., & Cao, X. (2019). Recolored Image Detection via a Deep Discriminative Model. *IEEE Transactions on Information Forensics and Security , 14*(1), 5-17.

Yang, B., Li, Z., & Zhang, T. (2020). A real-time image forensics scheme based on multi-domain learning. *Journal of Real-Time Image Processing, 17*, 29-40.

Yang, J., Li, A., Xiao, S., Lu, W., & Gao, X. (2021). MTD-Net: Learning to Detect Deepfakes Images by Multi-Scale Texture Difference. *IEEE Transactions on Information Forensics and Security, 16*, 4234 - 4245.

Yang, Z., Liang, J., Xu, Y., Zhang, X.-Y., & He, R. (2023). Masked Relation Learning for DeepFake Detection. *IEEE Transactions on Information Forensics and Security, 18*, 1696 - 1708.

Yarlagadda, S., Güera, D., Montserrat, D., Zhu, F., Delp, E., Bestagini, P., & Tubaro, S. (2019). Shadow Removal Detection and Localization for Forensics Analysis. *IEEE International Conference on Acoustics, Speech and Signal Processing (ICASSP).* Brighton.

Ye, S., Sun, Q., & Chang, E.-C. (2007). Detecting Digital Image Forgeries by Measuring Inconsistencies of Blocking Artifact. *IEEE International Conference on Multimedia and Expo.* Beijing.

Yu, Y., Ni, R., Zhao, Y., Yang, S., Xia, F., Jiang, N., & Zhao, G. (2023). MSVT: Multiple Spatiotemporal Views Transformer for DeepFake Video Detection. *IEEE Transactions on Circuits and Systems for Video Technology, 33*(9), 4462 - 4471.

Yu, Y., Zhao, X., Ni, R., Yang, S., Zhao, Y., & Kot, A. (2023). Augmented Multi-Scale Spatiotemporal Inconsistency Magnifier for Generalized DeepFake Detection. *IEEE Transactions on Multimedia, Early Access*, 1-13.

Zhang, J., Ni, J., & Xie, H. (2021). DeepFake Videos Detection Using Self-Supervised Decoupling Network. *IEEE International Conference on Multimedia and Expo (ICME).* Shenzhen.

Zhang, L., Yang, H., Qiu, T., & Li, L. (2022). AP-GAN: Improving Attribute Preservation in Video Face Swapping. *IEEE Transactions on Circuits and Systems for Video Technology, 32*(4), 2226 - 2237.

Zhang, Q.-L., & Yang, Y.-B. (2021). SA-Net: Shuffle Attention for Deep Convolutional Neural Networks. *IEEE International Conference on Acoustics, Speech and Signal Processing (ICASSP).* Toronto, ON, Canada.

Zhang, R., & Ni, J. (2020). A Dense U-Net with Cross-Layer Intersection for Detection and Localization of Image Forgery. *IEEE International Conference on Acoustics, Speech and Signal Processing (ICASSP).* Barcelona.

Zhang, Y., & Thing, V. (2018). A semi-feature learning approach for tampered region localization across multi-format images. *Multimedia Tools and Applications volume, 77*, 25027–25052.

Zhang, Z., Zhang, Y., Zhou, Z., & Luo, J. (2018). Boundary-based Image Forgery Detection by Fast Shallow CNN. *IEEE International Conference on Pattern Recognition (ICPR).* Beijing.

Zhao, C., Wang, C., Hu, G., Chen, H., Liu, C., & Tang, J. (2023). ISTVT: Interpretable Spatial-Temporal Video Transformer for Deepfake Detection. *IEEE Transactions on Information Forensics and Security, 18*, 1335 - 1348.

Zhao, L., Zhang, M., Ding, H., & Cui, X. (2023). Fine-grained deepfake detection based on cross-modality attention. *Neural Computing and Applications, 35*, 10861–10874.

Zhao, X., Li, J., Li, S., & Wang, S. (2010). Detecting Digital Image Splicing in Chroma Spaces. *International Workshop on Digital Watermarking.* Seoul.

Zhao, Y., Jin, X., Gao, S., Wu, L., Yao, S., & Jiang, Q. (2023). TAN-GFD: generalizing face forgery detection based on texture information and adaptive noise mining. *Applied Intelligence, 53*, 19007–19027.

Zhong, J.-L., & Pun, C.-M. (2020). An End-to-End Dense-InceptionNet for Image Copy-Move Forgery Detection. *IEEE Transactions on Information Forensics and Security, 15*, 2134 - 2146.

Zhou, H., Sun, J., Yacoob, Y., & Jacobs, D. (2018). Label Denoising Adversarial Network (LDAN) for Inverse Lighting of Faces. *2018 IEEE/CVF Conference on Computer Vision and Pattern Recognition.* Salt Lake City.

Zhou, P., Han, X., Morariu, V., & Davis, L. (2017). Two-Stream Neural Networks for Tampered Face Detection. *IEEE Conference on Computer Vision and Pattern Recognition (CVPR) Workshops.* Honolulu.

Zhou, P., Han, X., Morariu, V., & Davis, L. (2017). Two-Stream Neural Networks for Tampered Face Detection. *IEEE Conference on Computer Vision and Pattern Recognition Workshops (CVPRW).* Honolulu, HI, USA.

Zhu, X., Qian, Y., Zhao, X., Sun, B., & Sun, Y. (2018). A deep learning approach to patch-based image inpainting forensics. *Signal Processing: Image Communication, 67*, 90-99.

Zhu, Y., Chen, C., Yan, G., Guo, Y., & Dong, Y. (2020). AR-Net: Adaptive Attention and Residual Refinement Network for Copy-Move Forgery Detection. *IEEE Transactions on Industrial Informatics, 16*(10), 6714 - 6723.

Zhu, Y., Shen , X., & Chen, H. (2016). Copy-move forgery detection based on scaled ORB. *Multimedia Tools and Applications, 75*, 3221–3233.

Zhuang, Y.-X., & Hsu, C.-C. (2019). Detecting Generated Image Based on a Coupled Network with Two-Step Pairwise Learning. *IEEE International Conference on Image Processing (ICIP).* Taipei.

Indian J Phys
https://doi.org/10.1007/s12648-023-03038-7

ORIGINAL PAPER

Design and analysis of spider-web photonic crystal fiber in the terahertz regime

G Singh, S Sharma and A Kumar*

Advanced Photonics Simulation Research Laboratory, Department of Applied Physics, Delhi Technological University, Bawana Road, New Delhi, Delhi 110042, India

Received: 08 August 2023 / Accepted: 16 November 2023

Abstract: In this paper, we have proposed a novel photonic crystal fiber (PCF) design having a spider-web (SW) cladding. The finite element method (FEM)-based COMSOL Multiphysics software has been used to investigate the guiding properties and performance of the fiber in the terahertz radiation regime. Detailed numerical analyses ensure that proposed fiber design possesses a low confinement loss ($\sim 10^{-17}\text{cm}^{-1}$)) and low effective material loss (EML). *The high core power fraction of* 99% *and the effective mode area of* $1.06 \times 10^{-5}\text{m}^2$ *make this fiber an exception. V*-parameter confirms the single-mode behavior of fiber over 0.1–3.0-THz frequency range. Thus, we can say that the proposed fiber can be useful in various applications of terahertz propagation such as broadband transmission, biosensors, and chemical sensors.

Keywords: Photonic crystal fiber; Terahertz; Spider-web; Confinement loss; Effective mode area

1. Introduction

The terahertz frequency lies between the microwave and infrared on the electromagnetic spectrum, ranging from 0.1 to 10 THz [1]. Due to numerous applications in the medical field [2], biosensing and chemical sensing [3, 4], biotechnology, security, imaging, and telecommunications [5, 6], it has gained a significant attention from researchers in the past decade [7]. The emerging industry of PCF, also known as micro-structured fibers, has been introduced in terahertz wave transmission due to various applications of these combinations. Different types of PCF cores, such as solid, hollow, and porous, can be designed to minimize material loss and confinement loss [8]. Solid core PCF works on the principle of total internal reflection (TIR) where the core is made up of dielectric material, and the cladding has periodically arranged air holes with a lower refractive index [9, 10].

In the past decade, multiple articles on photonic crystal fiber in terahertz regime have been published for seeking low effective material loss (EML), low confinement loss, and large effective mode area (EMA). Islam et al. [11] designed an elliptical array-shaped rectangular PCF and culminated EML, confinement loss, power fraction, and effective mode area of $0.06\ \text{cm}^{-1}$, $5.45 \times 10^{-13}\text{cm}^{-1}$, 43%, and $1.20 \times 10^{-7}\text{m}^2$, respectively at 1 THz. However, they did not calculate an important *V*-parameter and failed to increase the frequency region. Zhang et al. [12] proposed the porous core PCF for terahertz communication. They evaluated EML, confinement loss, core power fraction, and effective mode area of 0.08cm^{-1}, $3.2 \times 10^{-13}\text{cm}^{-1}$, 57%, and $1.20 \times 10^{-7}\text{m}^2$, respectively. Porous core PCF design enhances the power fraction in the core significantly from 43 to 57%. Abdullah-Al-Shafi et al. [13] suggested octagonal core PCF and calculated confinement loss, effective mode area, and core power fraction of $2.28 \times 10^{-16}\text{cm}^{-1}$, $1.49 \times 10^{-7}\text{m}^2$, and 77%, respectively. This design further reduced the confinement loss and improved the power fraction significantly. Eid et al. [14] analyzed hollow-core PCF for confinement loss, EML, NA, effective mode area, and *V*-parameter of $3.80 \times 10^{-13}\text{cm}^{-1}$, $1.5 \times 10^{-2}\text{cm}^{-1}$, 0.50, $5.0 \times 10^{-8}\text{m}^2$, and 3.00, respectively. In the same year, Jibon et al. [15] proposed a porous core PCF. They calculated EML, confinement loss, core power fraction, effective mode area, *V*-parameter, and NA of $5.0 \times 10^{-2}\text{cm}^{-1}$, $8.01 \times 10^{-7}\text{cm}^{-1}$, 55%, $1.5 \times 10^{-6}\text{m}^2$, 4.5, and 0.37, respectively.

In this paper, we have proposed a unique single-mode spider wave PCF for terahertz communication. A detailed

*Corresponding author, E-mail: ajeetdph@dtu.ac.in; jeetdph@gmail.com

Published online: 31 December 2023

© 2023 IACS

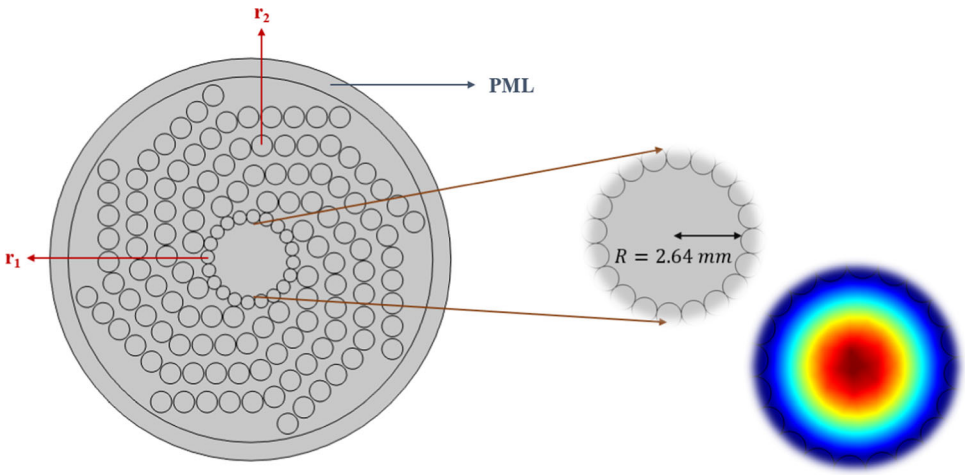


Fig. 1 Cross-sectional view of the SW PCF with the fundamental mode at 1 THz

analyse has been made to investigate its performance by calculating various important parameters such as confinement loss, effective material loss, effective mode area, nonlinearity coefficient, numerical aperture (NA), core power fraction, and *V*-parameter.

2. Proposed design

The schematic cross-sectional view of the proposed SW-PCF is shown in Fig. 1. In the cladding region, the air holes are arranged in the spider-web manner that can be formed by rotating a triangular structure of air holes at an angle of $\theta_n = \frac{360n}{8}$, where $n = 1, 2, 3, 4, 5, 6,$ and 7. The structure turns into a spider-web arrangement by placing the centralized air hole some distance away. In addition to this, the air holes surrounded the core region arranged in a form to approximate the core in a circular shape. In cladding, the air holes nearer to the core have a radius of $r_1 = 213\mu m$, and the rest has a radius of $r_2 = 332.5\mu m$, with the air-filling fraction (AFF) of 0.45 and 0.7, respectively. The fused silica is used as core material in this design due to its broad transparent transmission range, which is stretched from the ultraviolet to infrared range [16]. The perfectly matched layer has been used to estimate losses of the proposed fiber.

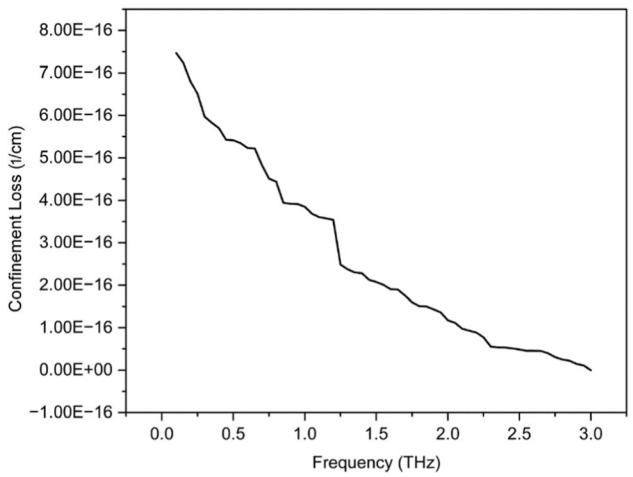


Fig. 2 Confinement loss as a function of frequency

3. Numerical analysis

In order to evaluate the optical characteristics of the proposed SW-PCF design, FEM-based computational analyses are completed using COMSOL Multiphysics software. Effective mode index and losses in PML region are essential to characterize any PCF design. The more the radiation is confined in the core-cladding region, the better the PCF. The mode at a particular frequency consists of two factors, one is the real part $\mathrm{Re}(n_{\mathrm{eff}})$ which can be used to study the guiding properties of the mode, and another is the imaginary part $\mathrm{Im}(n_{\mathrm{eff}})$ from which confinement loss is evaluated. The confinement loss is estimated using the following equation [17]:

$$L = 8.686 k_0 \mathrm{Im}(n_{\mathrm{eff}}) \times 10^{-2} \quad (1)$$

where $k_o = \frac{2\pi v}{c}$, k_o is the wave number, v is the frequency of radiation used, c is the speed of light in the free space, and $Im(n_{eff})$ is the imaginary part of effective mode index. The proposed PCF has been formed using the super-fine transparent fused silica. However, at higher frequencies, these materials can absorb some radiation which comes as effective material loss or EML. It can be calculated using the following [18]:

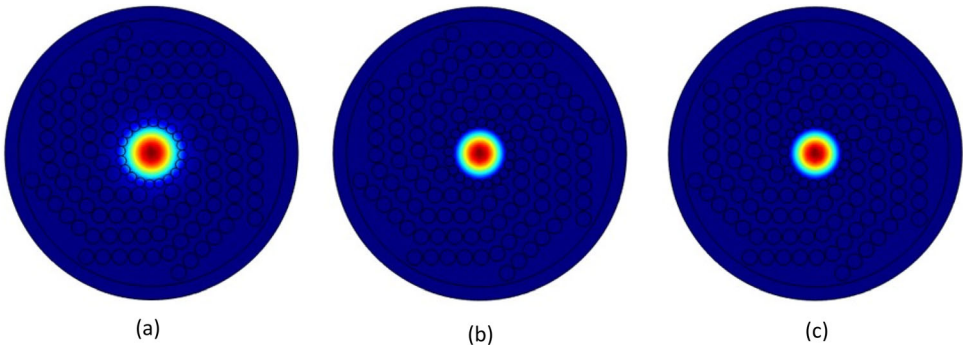


Fig. 3 Field profile variation in core at the frequency (**a**) 0.1 THz, (**b**) 1 THz, and (**c**) 3 THz

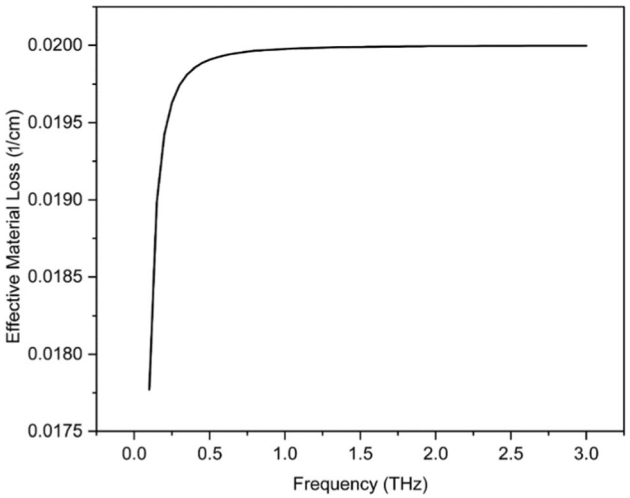


Fig. 4 Effective material loss as a function of frequency

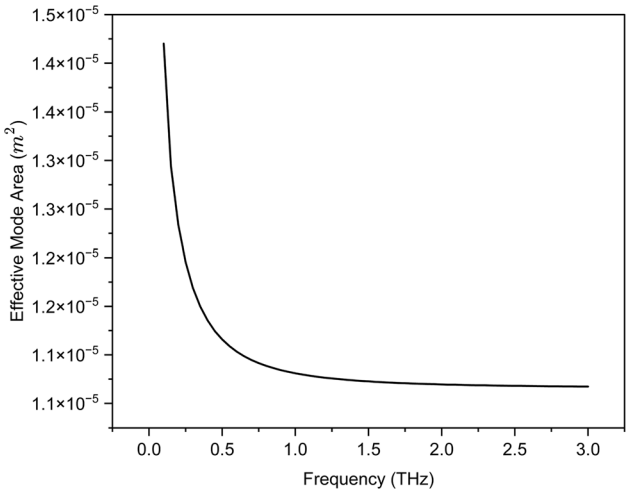


Fig. 5 Effective mode area as a function of frequency

$$\alpha_{\text{eff}} = \sqrt{\frac{\epsilon_0}{u_0}} \frac{\int_{\text{mat}} n_{\text{mat}} \alpha_{\text{mat}} |E|^2 \mathrm{d}A}{2\left|\int_{\text{all}} s_z \mathrm{d}A\right|} \tag{2}$$

where α_{mat} is the bulk material absorption loss, n_{mat} is the refractive index of material, ϵ_0 is the electric permittivity in free space, u_0 is the magnetic permeability in free space,

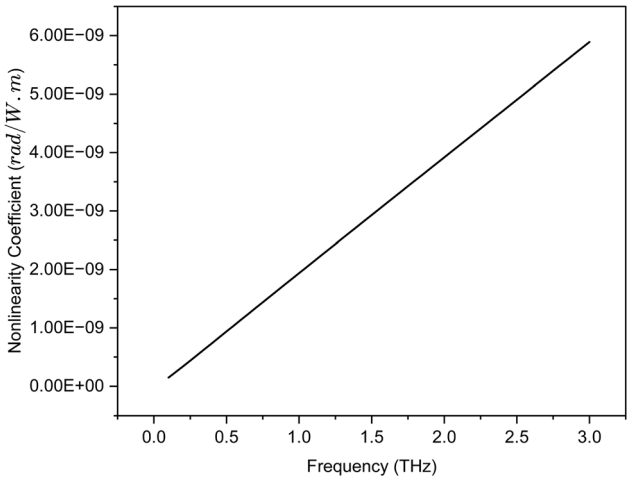


Fig. 6 Nonlinearity coefficient as a function of frequency

and S_z is the Poynting's vector. The effective mode area (A_{eff}) of the fundamental mode can be evaluated [19]:

$$A_{\text{eff}} = \frac{\left[\int I(r)\mathrm{d}r\right]^2}{\left[\int I^2(r)\mathrm{d}r\right]} \tag{3}$$

A_{eff} plays an important role in calculation of the nonlinearity coefficient (γ) and numerical aperture (NA) of the fiber that governs the acceptance or emission of radiation by the core [20, 21],

$$\gamma = \frac{2\pi n_2}{\lambda A_{\text{eff}}} = \frac{2\pi \nu n_2}{c A_{\text{eff}}} \tag{4}$$

$$\text{NA} = \frac{1}{\sqrt{1 + \frac{\pi A_{\text{eff}} \nu^2}{c^2}}} \tag{5}$$

where n_2 is nonlinear refractive index of the material.

To know the power confined inside the core of the fiber, power fraction (P) can be to be calculated [22]:

$$P = \frac{\int_i S_z \mathrm{d}A}{\int_{\text{All}} S_z \mathrm{d}A\prime} \times 100\% \tag{6}$$

In the end, V-parameter of the fiber is examined. The V-parameter can be estimated using the following [23]:

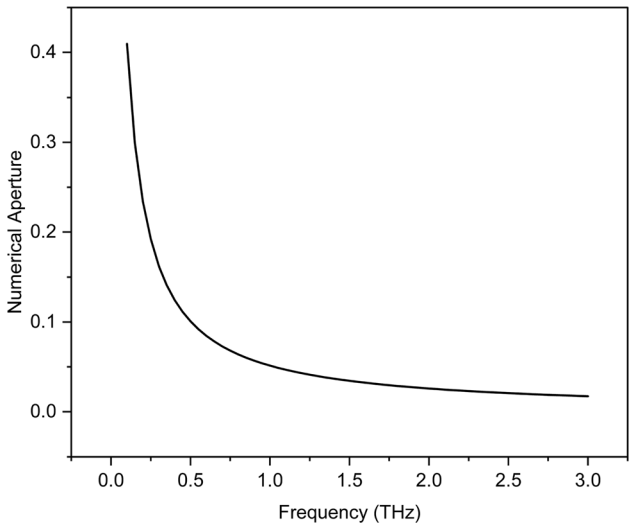


Fig. 7 Numerical aperture as a function of frequency

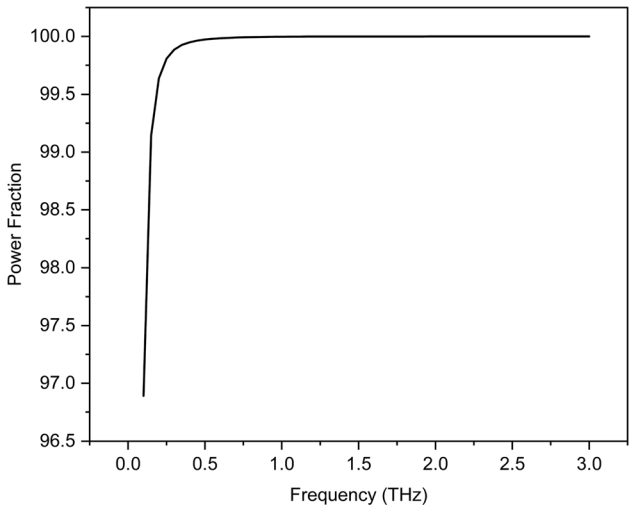


Fig. 8 Power fraction as a function of frequency

$$V = \frac{2\pi r v}{c}\sqrt{n_{\mathrm{co}}^2 - n_{\mathrm{cl}}^2} = \frac{2\pi r v}{c}(\mathrm{NA}) \tag{7}$$

where r is the radius of the core, n_{co} is the refractive index of core, and n_{cl} is the effective refractive index of cladding. n_{cl} is calculated by solving the fundamental cladding mode which is also known as space-filling mode [24, 25]. It is also worth to mention that frequency-dependent behavior of *NA* keeps the $V < 2.4048$ which ensures the single-mode operation of the proposed SW-PCF in frequency range $0.1 < v < 3.0$ THz.

4. Simulation results

In the proposed design, initially, the PML is taken as the 10% part of the whole PCF, which is used to estimate the EML and confinement losses of the fiber. The finite element method is implemented by using the triangular physics-controlled mesh. In the whole of SW-PCF, 24,134 elements are used including a dense meshing in the core region because most of the radiation is confined within the core and a minimal meshing near the boundary.

Figure 2 depicts the confinement loss with terahertz wave transmission frequency variation. The light is confined tightly in the core region and ensures a negligible amount of confinement loss. At 1 THz, the confinement loss is found to be $3.85 \times 10^{-16}\mathrm{cm}^{-1}$. It reaches the minimum value of $1.07 \times 10^{-17}\mathrm{cm}^{-1}$, which is the lowest among the previous [11–15] results.

In this design, the confinement loss decreases as frequency increases. Figure 3a shows that the field is getting distributed outside the core which results in high confinement loss at 0.1 *THz*, whereas the radiation is getting confined within the core as the frequency increases which governs the low confinement loss at preceding frequencies. Figure 3(a)–(c) depicts the situation for increasing frequency of 0.1 THz, 1 THz, and 3 THz, respectively.

In Fig. 4, the EML of the fused silica material with frequency has been evaluated. At 1 THz, it is reported as $1.99 \times 10^{-2}\mathrm{cm}^{-1}$. The material loss is said to reach the value of bulk material absorption loss (α_{mat}) for fused silica.

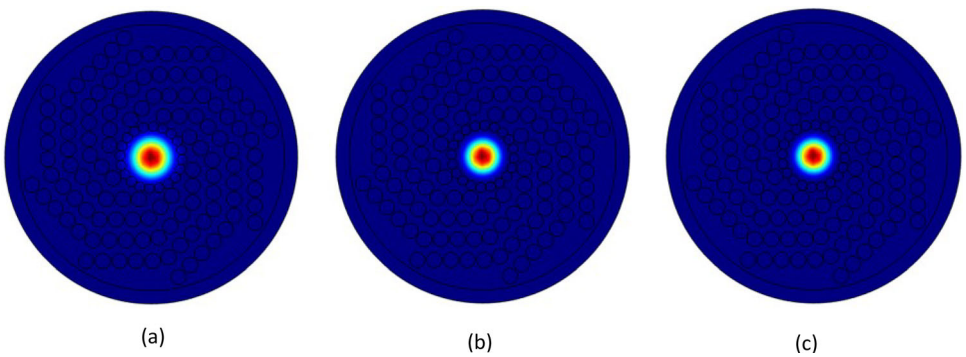


Fig. 9 Power profile variation in core at the frequency (**a**) 0.1 THz, (**b**) 1 THz, and (**c**) 3 THz

Table 1 Performance comparison of the proposed design with existing PCF designs

References	EML (cm^{-1})	L (cm^{-1})	A_{eff} (m^2)	γ (rad/W m)	NA	Power%
[11]	6.0×10^{-2}	5.45×10^{-13}	1.20×10^{-7}	–	–	44
[12]	8.0×10^{-2}	3.20×10^{-13}	1.20×10^{-7}	–	–	57
[13]	–	2.28×10^{-16}	1.49×10^{-7}	–	–	77
[14]	1.5×10^{-2}	3.80×10^{-13}	5.00×10^{-8}	–	0.50	–
[15]	5.0×10^{-2}	8.01×10^{-7}	1.50×10^{-6}	–	0.37	55
This work	1.99×10^{-2}	6.22×10^{-17}	1.08×10^{-5}	2.03×10^{-9}	0.41	99

Figure 5 shows the variation of effective mode area with frequency. At 1 THz, effective mode area has the most significant value of $1.08 \times 10^{-5}m^2$ that reaches to the minimum value of $1.06 \times 10^{-5}m^2$ at 3 THz frequency. The large effective mode area is crucial for a fiber for a huge power transmission [26]. Corresponding to effective mode area, the nonlinearity coefficient varies inversely, which is shown in Fig. 6, at 1 THz, nonlinearity coefficient has the minimum value of 2.03×10^{-9}rad/W m.

The NA in a fiber represents the radiation acceptance or emission through the PCF. Figure 7 illustrates the NA varying with the frequency. The higher value of NA is reported at 0.1 THz of 0.41, which is a threshold value for fused silica-based fibers.

Figure 8 illustrates the variation of power fraction that is confined in the core region with frequency. A tightly packed core surrounded by air holes confine most of the radiation in the core region and ensured 99% of the power fraction confinement at 1 THz frequency.

Moreover, the power fraction increases as frequency increases. Figure 9(a) shows that the power is getting trapped inside the core at 0.1 *THz*; however, at preceding frequencies, it is densely packed within the core which governs the high-power transmission. Figure 9(a)–(c) depicts the situation for increasing frequency of 0.1 THz, 1 THz, and 3 THz, respectively.

We have calculated the *V*-parameter of proposed SW-PCF and observed that the value of the *V*-parameter is approximately equal to 2.4048 [27] and made the proposed SW-PCF a fundamental mode fiber. Table 1 shows the performance comparison of the proposed design with existing PCF designs.

For fabrication purposes, it is important to investigate the tolerance of the proposed design with respect to its design parameters. We have investigated the effect of variation in values of r_1 and r_2. We have seen that 1% variation in r_1 changes 2% change in confinement loss, 2% change in EML, 1% change in effective mode area, and 0.05% change in power fraction. Similarly, 1% variation in r_2 changes 1% change in confinement loss, 1% change in EML, 1% change in effective mode area, and 0.05% change in power fraction. The above tolerance study confirms that the proposed design has suitable design parameters for fabrication.

5. Fabrication possibilities

The most challenging and complex part of PCFs is always the fabrication [28]. The fabrication challenges majorly depend on the number of air holes and the air-filling fraction. In the proposed SW-PCF, two types of different air holes are used. Several methods are offered to fabricate fibers such as stack and draw, drilling method, sol–gel casting method, etc. Honeycomb lattices, one of the simplest structures, can be fabricated using the stack and draw method, while the drilling method is used for adjusting the size and spacing of air holes, but it is limited to a minimal amount of air holes that have circular shapes. Sol–gel technique, proposed by Hamzausi et al. [29], can be used to fabricate the proposed SW-PCF because it provides the freedom to adjust the size, shape, and spacing of air holes. Hence, SW-PCF can be fabricated by the sol–gel technique.

6. Conclusions

A unique design of SW-PCF has been proposed and simulated for various optical parameters. Simulated results have shown low confinement loss and EML of $\sim 10^{-17}cm^{-1}$ and $1.99 \times 10^{-2}cm^{-1}$, respectively. Moreover, our numerical analysis also confirms the single-mode propagation with large effective mode area, high core power fraction, and NA in the broad range of terahertz radiation. This fiber can, indeed, be used in broadband transmission, biosensing, chemical sensing, and other terahertz applications because of its fundamental properties.

Acknowledgements This work was supported by the Delhi Technological University, Bawana Road, New Delhi, Delhi 110042, India.

References

[1] W Biao, C Jia, J Yang, Z Di, J Yao and J Zhang *IEEE Photo. J.* **13** 1 (2021)
[2] M K Khodzitsky et al. *J. Phys. Conf. Ser.* **8** 76 (2021)
[3] A A Rifat et al. *IEEE Photon. Technol. Lett.* **27** 1628 (2015)
[4] M F Arif, S Asaduzzaman, M J Biddut and K Ahmed *Int. J. Technol* (2016)
[5] S Shuvo, M Abdullah-Al-Shafi, A S Sikder, M S Hossain and M M Azad *Sens. Bio-Sens. Res.* **31** 100393 (2021)
[6] G K M Hasanuzzaman, S Rana and M S Habib *IEEE Photon. Technol. Lett.* **28** 899 (2016)
[7] W Zhiqing, Z Shi, H Xia, X Zhou, Q Deng, J Huang, X Jiang and W Wu *IEEE Photon. J.* **8** 1 (2016)
[8] M Abdullah-Al-Shafi, N Akter, S Sen and M S Hossain *Optik* **243** 167519 (2021)
[9] A Huseyin *Optik* **125** 6274 (2014)
[10] A Kawsar and M Morshed *Sens. Bio-Sens. Res.* **7** 687 (2016)
[11] M S Islam, J Sultana, A Dinovitser, M Faisal, M R Islam, W-H Brian and D Abbott *Appl. Opt.* **57** 336 (2018)
[12] Z Yani, L Xue, D Qiao and Z Guang *Optik* **207** 163817 (2020)
[13] M Abdullah-Al-Shafi and S Sen *Sens. Bio-Sens. Res.* **29** 100372 (2020)
[14] M A M Eid, M A Habib, M S Anower and A N Z Rashed *Braz. J. Phys.* **51** 1017 (2021)
[15] J R Habib, B A Al-Mamun, N Abdullah-Al, S Faragallah Osama, Md Baz, M A Eid Mahmoud and A N Z Rashed *Opt. Rev.* **28** (2021)
[16] T Danh, G Sigel and B Bendow *J. Lightwave Technol.* **2** 566 (1984)
[17] L Shaopeng, H Liu, N Huang and Q Sun *J. Opt.* **16** 105102 (2014)
[18] M S Islam, J Sultana, A A Rifat, A Dinovitser, N B H Brian and D Abbott *IEEE Sens. J.* **18** 4073 (2018)
[19] K Shubi Felix, Z Ouyang and X Jin *IEEE Photon. Technol. Lett.* **25** 1454 (2013)
[20] A Patrick Atsu and E Kofi Akowuah *Sci. Rep.* **10** 21182 (2020)
[21] M S Islam, J Sultana, K Ahmed, M Rakibul-Islam, A Dinovitser, N W H Brian and D Abbott *IEEE Sens. J.* **18** 575 (2017)
[22] M Saiful, J Sultana, A Dinovitser, N W H Brian and D Abbott *Opt. Commun.* **413** 2426 (2018)
[23] W Zhiqing, X Zhou, H Xia, Z Shi, J Huang, X Jiang and W Wu *Appl. Opt.* **56** 2288 (2017)
[24] M Midrio, M P Singh and C G Someda *J. Lightwave Technol* **18** 1031 (2000)
[25] Z Zhu and T G Brown *Opt. Express* **8** 547 (2001)
[26] A Kawsar et al. *Appl. Opt.* **56** 3477 (2017)
[27] A Ghatak and K Thyagarajan. *An Introduction to Fiber Optics* (Cambridge University Press) (1998)
[28] M I Islam, K Ahmed, S Asaduzzaman, B Kumar Paul, T Bhuiyan, S Sen, M S Islam and S Chowdhury *Sens. Bio-Sens. Res.* **13** 55 (2017)
[29] H El Hamzaoui et al. *Opt. Express* **28** 29751 (2012)

Publisher's Note Springer Nature remains neutral with regard to jurisdictional claims in published maps and institutional affiliations.

Springer Nature or its licensor (e.g. a society or other partner) holds exclusive rights to this article under a publishing agreement with the author(s) or other rightsholder(s); author self-archiving of the accepted manuscript version of this article is solely governed by the terms of such publishing agreement and applicable law.

Electrical Engineering
https://doi.org/10.1007/s00202-023-02194-7

ORIGINAL PAPER

Design optimization of OR-PMSM-IPIM using modified slime mold optimization technique for UAV application

Monika Verma[1] · **Mini Sreejeth**[1] · **Madhusudan Singh**[1]

Received: 12 September 2023 / Accepted: 1 December 2023
© The Author(s), under exclusive licence to Springer-Verlag GmbH Germany, part of Springer Nature 2024

Abstract
Extensive research in the traction component of unmanned aerial vehicles (UAV) reveals that selection of electric motor is paramount to enhance its endurance flight time with high efficiency. This can be achieved by employing a motor with light weight, low losses, high efficiency and efficient speed—torque characteristics. For addressing the above-mentioned requirements, an outer-rotor-permanent-magnet-synchronous-motor with inner-periphery-inset-magnet (OR-PMSM-IPIM) structure is selected, as it has eminent electromagnetic performance. To optimize structural design of such geometries, it is important to utilize the better exploration and exploitation of search space of design parameters. Hence, inspired by the high accuracy of optimization obtained by slime mold optimization (SMO) technique, a modified version of this algorithm is developed by introducing its collective behavior and swarm intelligence in the environment. In order to avoid collapsing for local optimal spots and enhance diversity in the population, the introduction of complex group interaction patterns is carried out in the traditional SMO algorithm. In order to verify the effectiveness and convergence speed of proposed methodology, few comparative experiments are administered using Benchmark functions. Through experiments using different integrated collective behaviors (CBs) to SMO, it is found that nearly 10% lesser values are obtained for unimodal and multimodal functions. Also, the convergence profiles are improved by the proposed novel CB-SMO algorithm, when compared to existing SMO technique. The application of proposed method is tested by developing design optimization problem (DOP) for OR-PMSM-IPIM. The analysis results show that the torque-per-unit-weight performance of optimized model of OR-PMSM-IPIM has been increased by 6% through proposed CB-SMO design optimization.

Keywords Collective behavior disturbances (CB) · OR-PMSM-IPIM · Slime mold inspired optimization (SMO) · Traction device · Unmanned aerial vehicle (UAV)

1 Introduction

The energy conversion system of UAVs grabbed the attention of researchers as it plays an important role in the performance of UAV in terms of its efficiency and flight time. As electric motor dominates the energy conversion system, the selection of appropriate motor with optimized design, which ensures light weight (an absolute necessity for flight operation), high efficiency and suitable speed-torque characteristics, is of paramount importance. In order to drive the traction system of UAV such as electric aircraft, quadcopter and multi-copters, etc., the employment of OR-PMSM-IPIM is practiced to enhance its endurance flight time with high efficiency.

This article was submitted on 12th September, 2023 to Electrical Engineering, Springer. This work was supported by Centre of Excellence for Electric Vehicles and Related Technologies, Electrical Engineering Department, Delhi Technological University, Delhi, 110042.

✉ Monika Verma
monikaverma_phd2k17@dtu.ac.in

Mini Sreejeth
minisreejeth@dce.ac.in

Madhusudan Singh
madhusudan@dce.ac.in

[1] Electrical Engineering Department, Delhi Technological University, Delhi, India

Published online: 06 January 2024

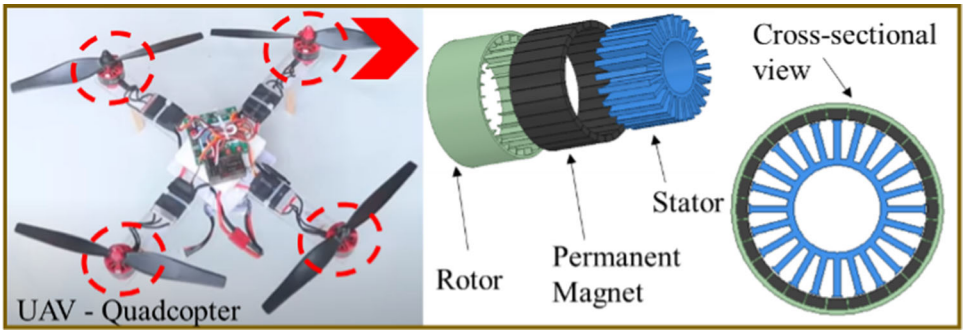


Fig. 1 UAV—quadcopter energy conversion system design outline

(1) *Background*

Among various structures of PMSM, such as interior type, surface type, multilayer type, interior-exterior type; one of the majorly utilized configuration has been OR-PMSM with inner-periphery-inset-magnet structure. This design is endurance-focused motor configuration, specifically designed for numerous surveying applications [1, 2]. It is also used for aerial photography in various fields. This configuration has been chosen as reference configuration for the energy conversion system in order to obtain high performance of the motor [3, 4]. As can be seen in Fig. 1, as a part of UAV-Quadcopter, OR-PMSM-IPIM structure is shown in dissembled form as well as cross-sectional view.

The design optimization helps in investigating the viability of accomplishing highly efficient, fully electric motor traction system for quadcopter UAV, which is capable of performing Vertical Take Off and Landing (VTOL) operation [5].

(2) *Literature review*

Until now, only small UAV exhibits fully electrical system as its propulsion system, whereas large quadcopter UAV have dependence on traditional engines. The main reasons are low efficiency of electric motors along with the lack of high energy density of batteries. Due to this, the short operational range and short flight time of UAV traction system is obtained. Hence, to achieve smooth VTOL operation of UAV, it is necessary that the electric energy conversion device perform distortion-less operation. Since the variation in design variables of OR-PMSM showcases its capability of delivering smooth and efficient operation. In other words, the search of optimized design parameters of the motor has direct influence over the VTOL operation of UAV [6, 7]. Therefore, the design optimization of OR-PMSM-IPIM is carried out in this paper by introducing novel optimization technique. Table 1 shows the attempts and their respective research gaps related to design optimization of OR-PMSM.

(3) *Research gap and motivation*

Based on the "survival of the fittest" concept, the bio-inspired optimization methodologies having swarm intelligent algorithms are being progressively used in diverse fields. Out of the streak of such tools like modified artificial bee colony [16], particle swarm optimization [17], genetic algorithm [18], wind driven optimization [19], brain storm optimization [20], the bio-inspired optimization techniques can be governed by environmental as well as evolutionary mediums. The discontinuous and nonlinear type of optimization problems can be efficiently solved using characteristic interactive behavior of such tools. The bio-inspired algorithms are strongly robust since the overall optimization problem is not influenced by variation in individual characteristic behavior. The absence of faction-level patterns in the formation of conventional SMO algorithm highlights the research gap. Hence, the implementation of collective behavior (CB) along with the singular-level behaviors has been the motivation behind the development of modified version of slime mold algorithm, in this work

Primarily, the study of collective behavior (CB) has been carried out in various animal organizations, such as bird flocking, fish schooling and insect colonies. As per the studies, the disturbance due to CB is also encountered in microorganisms. *This work argues that slime molds, having CBs integrated with them, can play a dominant role to deal with several outstanding problems*. For developing the novel CB-SMO algorithm, particularly, the clue of behaviors of slime mold leading to the linkage of group-level mechanisms has been followed.

(4) *Challenges*

Prior to this article, many researchers have proposed modifications in the SMO algorithm. Table 2 exhibits the till-today versions of modified SMO algorithm. From the discussed literature, it is quite noticeable that the inclusion of CB and utilization outline are not addressed in any of them. Therefore, a novel CB-based SMO technique called "CB-SMO" is developed in this paper. This proposed method is tested by

Table 1 Literature related to prior work of design optimization of OR-PMSM

References	Application	Pros	Cons
Mutluer [8]	Direct drive mixer	Cost reduction and efficiency improvement is obtained	Multi-objective optimization increases complexity
Mbadiwe et al. [9]	Automotive industry	PM flux is increased to enhance torque performance	No definite method of optimization is used
Guerroudj et al. [10]	Wind turbine	Doubly salient PM generator is optimized	Large cogging torque
Taha et al. [11]	Electric bicycle	Inner and outer configurations are compared	Method of optimization is absent
Shi et al. [12]	Low speed campus patrol electric vehicle (EV)	Efficiency and torque density is improved	Limited working area of EV
Chau et al. [13]	In-wheel EV	Torque performance is improved	Speed is reduced, ripples are more
Ahmad et al. [14]	Direct drive EV	OR-PMSM gives better performance than inner rotor PMSM	Low speed operation is considered
Boldea et al. [15]	Home applications use	FEA analysis is embedded within the optimization process	High variation of efficiency at different ratings of load due to inaccurate modeling of material properties
Ahn et al. SPS:refid::bib2[2]	UAV high endurance	Geometry of PMSM is optimized with reduced cogging	Introduces more stochastic behavior in conventional PSO

Table 2 Literature showing historical background of modified SMO

References	Strategy
Tang et al. [21]	Introduced chaotic-opposition strategy, spiral search technique and adaptive parameter control schemes in the traditional SMO for global optimization [18]
Naik et al. [22]	Infused adaptive opposition based learning concept
Xiao et al. [23]	Tent Chaotic map functions and inertial weights are inculcated
Hamed et al. [24]	The application of traditional SMO to lay best size and location of DSTATCOM and PV to improve its voltage and current profile
Jones et al. [25]	The multi-agent based approach has been introduced to comment on the performance of SMO in material computation
Liu et al. [26]	Integration of chaotic maps and Nelder–Mead simplex technique and implemented it for photovoltaic (PV) parameters selection
Jia et al. [27]	Merged mutation and restart schemes with SMO for increasing accuracy and aid the feature selection
Basset et al. [28]	A hybrid version of whale optimization technique with SMO was implemented to solve the problem of image segmentation in paramedics
Cui et al. [29]	The search space was improved using levy flight distribution with SMO
Gao et al. [30]	Combined with support vector machine technique for predicting stability in postgraduate employment
Naik et al. [31]	The concept of three best leaders inspired by Grey Wolf Optimizer has been introduced
Liu et al. [32]	The hybridization of differential evolution along with SMO has been proposed for performance improvement in multilevel image segmentation field

solving various Benchmark functions. Thereafter, CB-SMO is utilized for its implementation in the application to UAV energy conversion device analysis. At last, the performance of model, having optimized design parameters, is compared with that of the model without optimized parameters.

(5) *Contribution*

This work makes following contributions to the related field: (1) The absence of Collective Behavior of Slime Mold is removed from the traditional SMO and thus, a complete novel CB-SMO is developed by introducing social behavior of slime mold in a group. (2) The proposed new CB-SMO is tested using few Unimodal and Multimodal Benchmark functions. (3) The performance analysis is also carried out by undertaking its comparison with few classical metaheuristic algorithms. (4) The problem of contradiction in obtaining lighter weight along with the efficient flight operation of UAVs is solved using the proposed CB-SMO technique.

(6) *Paper organization*

Organization of the paper is as given: Sect. 1 shows the introductory literature survey. Section 2 shows the technical details of proposed CB-SMO technique. Section 3 presents the design of DPO. Section 4 contains all the results and the related discussion. It also presents the achievements obtained by implementing the novel CB-SMO method to the developed DOP. Section 5 shows the concluding remarks and future scope of this work.

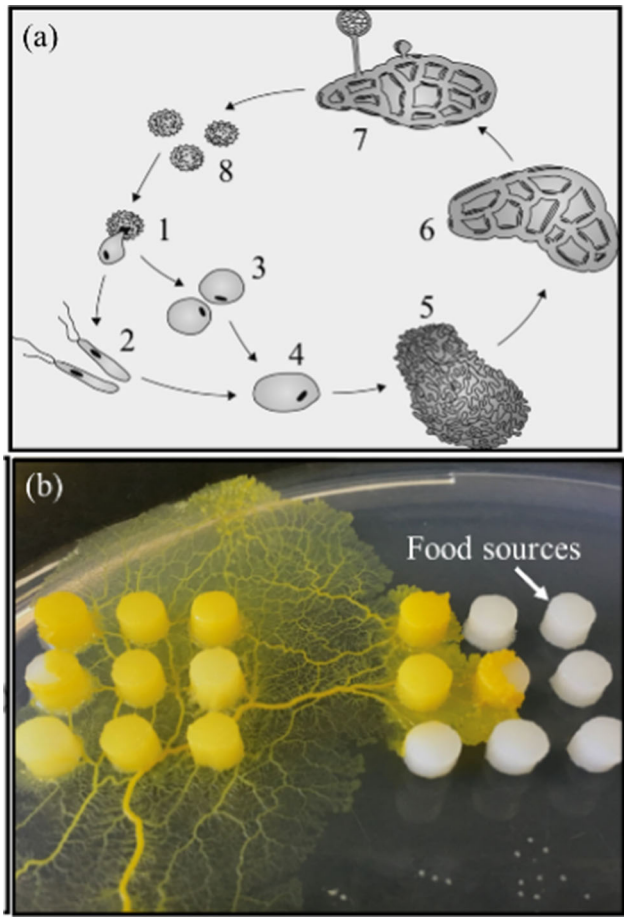


Fig. 2 **a** Life cycle of Physarum Polycephalum; **b** Food engulfing by slime mold as problem solving segment [Picture Courtesy: [33]]

2 Proposed collective behavior based SMO

The slime molds, of class Myxogastria, are multinucleate unicells, can grow up to 900 squared centimeters during plasmodium stage. The morphological life cycle structure of Physarum Polycephalum consisting of (1) germination, (2) flagellation, (3) amoeboid, (4) fusion of haploid, (5) microplasmodium, (6) mature plasmodium, (7) sporangium, (8) dispersal is shown in Fig. 2a. The food engulfing stage of slime mold during search of source is presented in Fig. 2b.

The CB possesses conceptual origin in the investigation of coherent physical systems that involves the essential exchange of individual particles. The relatively state-of-the-art understanding of cell behavior, driven by intercellular operations in slime molds, make them, conceivably, powerful model systems for implementation of CB [33].

The upcoming subsections describe the observed CB behaviors of Physarum Polycephalum (Slim mold), that are considered to develop novel CB-SMO technique. The corresponding display chart is shown in Fig. 3.

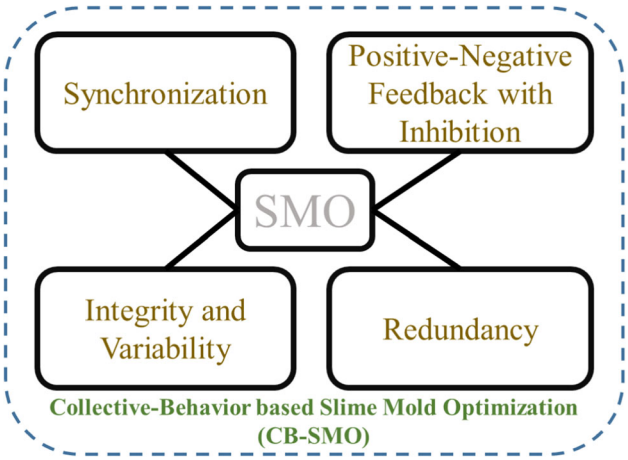


Fig. 3 The display chart of the proposed CB-SMO technique, consisting of four CBs combined with traditional SMO

(1) *Synchronization*

The first behavior is *Synchronization.* Plasmodium slime molds are collective of oscillators. The food discovery and interaction between neighboring oscillators govern the frequency of oscillations.

The *synchronization* behavior is carried out by slime through cytoplasmic flow. This CB follows simple steps:

- Food Source is recognized (by surface receptors of cell).
- Frequency of the oscillators (nearest to the food attractant) increases.
- The cytoplasmic flow leads to amoeboid migration in the direction of food attractant.
- Neighboring oscillators gets informed (due to existence of physical coupling) about the qualitative aspect of local environment.
- This encoded information is dispatched to the secluded cell parts, causing *synchronization*.

Thus, the new solution $x^{\text{syn}}(i+1)$, at ith index, is updated using the randomly selected neighbor, $x^{\text{ran}}(i)$ (see Eq. (1)). This process is "recruitment." Then comes the "communication."

The information is shared with the coupled oscillators which select and update its position based on the probability data. These probability data are computed from the fitness of the previous solution, fitness$(x^{\text{syn}}(i))$. The probability, p_i^{syn}, is computed using Eq. (2). During "communication", if ran $< p_i^{\text{syn}}$, the solution is updated using Eq. (1) again. The solutions which are not improved by *synchronization* behavior or they exceed pre-determined limit (called abandoned oscillators), the solution is updated using Eq. (3). They are thus determined to search new food source randomly [16].

$$x^{\text{syn}}(i+1) = x^{\text{syn}}(i) + r^{\text{ran}}\left(x^{\text{syn}}(i) - x^{\text{ran}}(i)\right) \tag{1}$$

$$p_i^{\text{syn}} = \frac{\text{fitness}(x^{\text{syn}}(i))}{\sum_{i=1}^{N} \text{fitness}(x^{\text{syn}}(i))} \tag{2}$$

$$x^{\text{syn}}(i+1) = lb + \text{ran}(ub - lb) \tag{3}$$

where r^{ran} is random number from -1 to 1, to ensure randomness in the recruitment of neighbor. Here, ranϵ [0, 1] is random number, lb is the lower bound of solution and ub is upper bound of solution.

(2) *Positive–Negative feedback with inhibition*

The second behavior is *Positive–negative feedback with Inhibition*. The traditional SMO makes use of weights in order to simulate positive–negative feedback produced during foraging. The weights of Slime Mold are computed using Eq. (4), [where, bestF= best fitness, worstF= worst fitness during current iteration, so(i) = first half of sorted population, sx(i) = index of sorted synchronized fitness of population, N = population size].

So, due to positive–negative feedback, the updated position of oscillators, $x^{pn}(i+1)$, is computed using Eq. (5). [where, z = constant to control exploration and exploitation, bestS(i) = The so far best solution, $x^a(i)$ and $x^b(i)$= two randomly selected oscillators, $x^{pn}(i)$ = old position of oscillator]. Factors v_b and v_c = vectors consisting of random numbers, are specified by Eqs. (6) and (7), respectively. [where, t = current iteration, T = total iteration, p = control parameter, gbestF = global optimal fitness value (see Eq. (8))].

However, in Physarum, poly-L-malate like polyanions can have interaction with polymerase and other histones of Physarum resulting in the "*inhibition*" of activities of nuclei of Physarum plasmodia. It is observed that the severity of inhibition depends upon the distance between the number of cleft atoms [34]. To model this CB, three randomly selected fragments ($x^i(i)$, where *superscript i* indicates the ith fragment) are chosen to form *inhibiting* solution vector.

Depending upon the inhibiting probability factor, p_i, the position of inhibited oscillator is computed using Eq. (9). The inhibiting solution vector, $x^{inh}(i+1)$, is calculated using Eq. (10), where f^i indicates the inhibition factor, set by the designer [18, 19].

$$W^{pn}(sx(i)) = \left\{ \begin{array}{l} 1 + \text{ran} \log\left(\frac{\text{bestF}-so(i)}{\text{bestF}-\text{worstF}} + 1\right);\ i \le N/2 \\ 1 - \text{ran} \log\left(\frac{\text{bestF}-so(i)}{\text{bestF}-\text{worstF}} + 1\right);\ i > N/2 \end{array} \right\} \tag{4}$$

$$x^{pn}(i+1) = \left\{ \begin{array}{c} lb + \text{ran}(ub - lb);\ r < z \\ \text{bestS}(i) + v_b\left(W^{pn}.x^a(i) - x^b(i)\right);\ r < p \\ v_c.x^{pn}(i);\ r > p \end{array} \right\} \tag{5}$$

$$v_b \epsilon \left[-\tanh^{-1}\left(-\frac{t}{T}+1\right),\ -\tanh^{-1}\left(-\frac{t}{T}+1\right)\right] \tag{6}$$

$$v_c \epsilon [-\left(1-\frac{t}{T}\right),\ \left(1-\frac{t}{T}\right)] \tag{7}$$

$$p = \tanh\left|\text{fitness}\left(x^{pn}(i)\right) - \text{gbestF}\right| \tag{8}$$

$$x^{inh}(i+1) = \{ \begin{array}{ll} I^i(i); & \text{ran} \le p_i \\ x^{pn}(i); & \text{otherwise} \end{array} \tag{9}$$

$$I^i(i) = x^1(i) + f^i(x^2(i) - x^3(i)) \tag{10}$$

(3) *Integrity and variability*

The third important collective behavior added here is *Integrity and Variability*. While oscillating, the venous structure of SM retains the "*integrity"* of keeping the track of its previous optimum food location. However, the same sized fragments (obtained from common plasmodium) showcase preferences of food search differently during propagation, due to intra-plasmodium "*variability."*

Thus, the oscillators' journey proceeds towards the global optimum independently, on the basis of reporting done by the other fragments. The mathematical modeling of this behavior is expressed in Eq. (11). [For *integrity,* the inertial weight (of fragment), W^{iv}, and its speed, V^{iv}, are introduced to reach global optimum, bestS(i); a_p and a_g are acceleration coefficients; popt= individual optimum location (representing *variability* in CB of SM)]. The updated and previous position of oscillators due to *integrity and variability* are expressed as $x^{iv}(i+1)$ and $x^{iv}(i)$, respectively [17].

$$x^{iv}(i+1) = x^{iv}(i) + W^{iv}V^{iv} + a_p \text{ran}\left(\text{popt}(i) - x^{iv}(i)\right) + a_g \text{ran}\left(\text{bestS}(i) - x^{iv}(i)\right) \tag{11}$$

(4) *Redundancy*

The epitome of *redundant* behavior is also presented by Physarum plasmodia, due to the presence of the syncytial property. The *redundancy* CB undergoes two phases; "serving at prime cell level" and "sharing information at individual level independently." The position of fragments is updated using Eq. (12) for first phase and using Eq. (13) for second phase, respectively.

[where, $x^{r1}(i+1)$ = updated position of oscillator for serving phase; $x^{r2}(i+1)$ = updated position of oscillator for sharing phase; $x^r(i)$ = previous location; sf = serving factor (randomly chosen for a particular fragment undergoing *redundancy*); meanS(i) = mean of current solution vector; $x^p(i)$ = randomly selected partner attractant].

Once the "serving phase" updates the position, the "sharing phase" ensures the interconnection in the foraging network, ensuring the linkage to each food source. However, depending upon the fitness of the partner, "sharing phase" updates the position using + or − in Eq. (13) [20].

$$x^{r1}(i+1) = x^r(i) + \text{ran}(\text{bestS}(i) - sf(\text{meanS}(i)) \tag{12}$$

$$x^{r2}(i+1) = x^r(i) \pm \text{ran}(x^{r1}(i) - x^p(i)) \tag{13}$$

(5) *Complexity analysis*

The analysis of computation complexity of SMO and CB-SMO is performed using the mathematical notations. Let the input cells of Physarum be expressed as N for each instance, D be the size of dimension and T be the upper bound of iterations or total number of iterations for the fitness model.

In traditional SMO, the initialization complexity is $O(D)$, fitness and sorting complexity is $O(N + N\log N)$, weight update complexity is $O(ND)$ and location update complexity is $O(ND)$. Thus, the overall computational complexity of conventional SMO is $O(D + TN(1 + \log N + 2D))$.

In CB-based SMO with "*synchronization*" behavior, the location update complexity is $O(N)$ using Eq. (1), conditional (Eq. (2)) location update complexity is $O(N^2)$, sorting complexity is $O(D)$ and abandoned oscillators' location update (Eq. (3)) has the complexity of $O(N\log N)$. Synchronization behavior-based SMO has complexity of $O(T(N + N^2 + D + N\log N)) \approx O(N^2)$.

In CB-based SMO with "*positive–negative feedback including inhibition"* behavior, the location update complexity (Eqs. (9)–(10)) is $O(TN(1 + D))$.

CB-based SMO with "*integrity and variability"* behavior has location update complexity of $O(TN)$ (Eq. (11)).

With "*redundancy"* behavior in CB based SMO, the location of each oscillator is updated using Eqs. (12) and (13) with complexity of $O(TN)$.

3 Development of design optimization problem

There are few assumptions considered for modeling of OR-PMSM in this paper; (1) the three phase star connection is identical and symmetrical, (2) the magnetic material used in rotor magnets have uniform properties and (3) the stator winding has coincident inductance and resistance in winding.

(1) *UAV-Quadcopter dynamics*

The UAV—Quadcopter Energy Conversion system follows four rotating propellers. They have clockwise (exhibited by motor 1 and motor 3) as well as anti-clockwise (motor 2 and motor 4) rotating directions (Fig. 4).

The three-degree-of-freedom movement of quadcopter occurs in three axes; x, y and z. It forms three Euler angles, i.e., roll, pitch and yaw angle. The roll, pitch and yaw angular acceleration are related to the moment of inertia on the corresponding axis and the lifting forces.

The moment of inertia depends upon center of mass (M) of UAV, distance (R) of middle tip from center of mass, height (H) of quadrotor's central part, radius (r) of OR-PMSM,

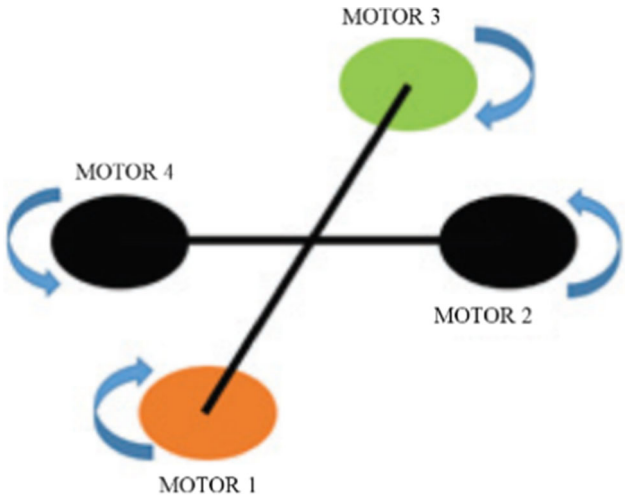


Fig. 4 Representation of rotational direction of UAV motors

mass (m) of OR-PMSM and height (h) of OR-PMSM, etc. The relationships of three angular accelerations of pitch, roll and yaw ($\ddot{\phi}$, $\ddot{\theta}$ and $\ddot{\psi}$) are presented as follows (Eq. (14)):

$$\ddot{\phi} = \frac{l}{\left(\frac{mr^2}{4} + \frac{mh^2}{6} + 2mr^2 + \frac{MR^2}{4} + \frac{MH^2}{12}\right)} b(\omega_4^2 - \omega_2^2)$$

$$\ddot{\theta} = \frac{l}{\left(\frac{mr^2}{4} + \frac{mh^2}{6} + 2mr^2 + \frac{MR^2}{4} + \frac{MH^2}{12}\right)} b(\omega_3^2 - \omega_1^2)$$

$$\ddot{\psi} = \frac{l}{\left(\frac{MR^2}{2} + 4mr^2\right)} d(\omega_2^2 + \omega_4^2 - \omega_1^2 - \omega_3^2) \quad (14)$$

where l = length of quadcopter arm; b = thrust factor; d = drag factor; ω_1, ω_2, ω_3, ω_4 = angular velocities of motor 1, 2, 3, 4. By keeping constant values of M, R, b and angular velocities, angular accelerations are re-written as follows (Eq. (15); where k_1 and k_3 are constants).

$$\ddot{\phi} = \ddot{\theta} = f\left(\frac{1}{\frac{mr^2}{4} + \frac{mh^2}{6} + 2mr^2 + k_1} . k_{2\left(\frac{\phi}{\theta}\right)}\right)$$

$$\ddot{\psi} = f\left(\frac{1}{4mr^2 + k_3} . k_{2(\psi)}\right) \quad (15)$$

(2) *DOP Development procedure—Polynomial regression-based surrogate modeling.*

There appear numerous rotor positions in a single revolution of motor where the rise in cogging torque is observed. For smoother VTOL operation, cogging situation is needed to be suppressed. To save the unnecessary time wasted in re-designing of model, the surrogate model of cogging torque is designed using polynomial regression to develop the desired DOP [35].

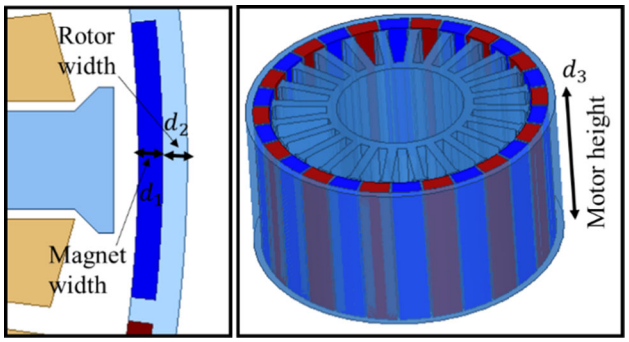


Fig. 5 Description of Design parameter for developing DOP

The predicted or target output (here it is cogging torque), P_o, with respect to design parameters, d_α or d_l of motor based on Response Surface Modeling (RSM) [36] is related as follows Eq. (16):

$$P_o = \beta_0 + \sum_{\alpha=1}^{3} \beta_\alpha d_\alpha + \sum_{\alpha=1}^{3} \sum_{l=\alpha+1}^{3} \beta_{\alpha l} d_\alpha d_l + \sum_{\alpha=1}^{3} \beta_{\alpha\alpha} d_\alpha^2 + \epsilon \quad (16)$$

where β_0 = offset coefficient; β_α = individual coefficient of αth variable; $\beta_{\alpha l}$ = associative coefficient of αth and lth variable; $\beta_{\alpha\alpha}$ = non-linear coefficient; ϵ = error between predicted and actual output.

Since, magnet thickness, rotor yoke thickness and motor height are factors which majorly contribute towards the production of unwanted cogging torque. Also, these parameters have influence over the parameters m, h and r of OR-PMSM. The angular accelerations of pitch, roll and yaw ($\ddot{\phi}$, $\ddot{\theta}$ and $\ddot{\psi}$) are related to these design parameters, as can be seen from Eq. (15).

For smooth and efficient VTOL operation, the values of angular accelerations of pitch, roll and yaw ($\ddot{\phi}$, $\ddot{\theta}$ and $\ddot{\psi}$) should be optimum. Hence, these three are chosen as design variables for designing the DOP (Fig. 5).

The samples obtained by FEM analysis with variation in αth design variable are listed in Appendix A (Table 7). The β coefficients of surrogate models are computed using Least Square Method (LSM). The surrogate model obtained for cogging torque is given by Eq. (17):

$$\begin{aligned} T_c = {} & 447.166 - 151.1875d_1 + 16.1289d_2 \\ & - 13.1771d_3 + 4.36d_1d_2 - 0.3875d_1d_3 \\ & - 0.1433d_2d_3 + 24d_1^2 - 5.6556d_2^2 + 0.2625d_3^2 \end{aligned} \quad (17)$$

The root-mean-square error (RMSE) value obtained for the formulated DOP equation to obtain minimum cogging torque T_c is 0.1322. This RMSE value shows that the formulated surrogate models are accurate in nature and does

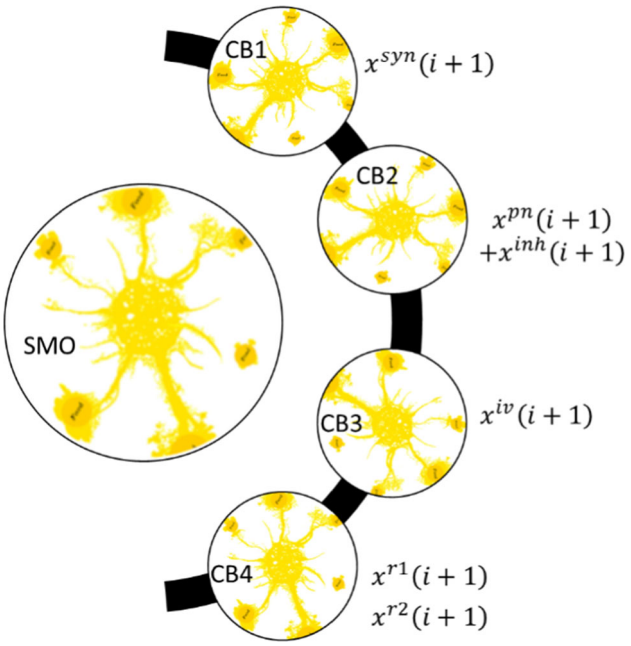


Fig. 6 Descriptive view of SMO along with proposed CBs [Picture Curtsey: [29]]

not contain any undesired input variable [37]. This surrogate model has been assigned as objective function to the proposed CB-SMO for obtaining the optimal parameters of OR-PMSM for least cogging torque.

4 Results and discussion

This section presents the performance analysis of the proposed modified SMO technique, "CB-SMO" by incorporating CB disturbances one by one. Then, the proposed CB-SMO is utilized in order to solve the formulated DOP.

(1) *Performance Analysis of CB-SMO*

The proposed CB-SMO is pictorially represented in Fig. 6. Here, CB1 suggests the addition of "Synchronization" behavior to SMO; CB2 suggests the addition of "Positive–Negative Feedback with Inhibition" behavior to SMO, CB3 suggests the addition of "Integrity and Invariability" behavior to SMO and CB4 suggests the addition of "Redundancy" behavior to SMO. The comparative study of performance shown by different algorithms is shown in Table 3 for various Benchmark Functions.

From this study, it is observed that:

Adding "only CB1 to SMO" will mostly have negative effect over nonlinear problems involving trigonometric functions.

Addition of "only CB2 to SMO" has increased the efficiency of SMO.

Addition of CB3 has negative effect while solving problems containing trigonometric functions (exhibits the similar effect as that of adding "CB1 to SMO").

By adding CB4, the SMO produces better results (~ 98% lesser than SMO result) or similar results for Rosenbrock, Sum of different powers, Quartic and Schwefel functions. While for Penalized1 and Levy N.13 functions, SMO produces better result than "SMO with CB4 only".

Overall effect of "adding all CBs to the SMO" always shows the positive effect over the performance of SMO.

Table 4represents analysis results for testing the proposed CB-SMO with other traditional and popular MH techniques. The results report that CB-SMO produces precise optimal values for all the Benchmark functions. The convergence profiles, exhibited by different "CB added to SMO" are presented in Fig. 7. It reveals that although adding individual CB behaviors to SMO, can produce sluggishness in the convergence of SMO. However, the proposed CB-SMO, having incorporated all the CB behaviors, can search the space area thoroughly while going through the computational iterations and can converge to the better optimal value than that produced by SMO.

(2) *Solution to DOP via proposed CB-SMO*

In this subsection, the proposed CB-SMO and other techniques solves DOP to obtain least cogging torque (Eq. (17)), the optimal design parameters are analyzed and compared. The comparative analysis results, obtained by proposed technique and few conventional MH techniques, are presented in Table 5. The 'Rank' represents the effectiveness of their performances for getting the solution of the designed DOP.

The successful implementation of proposed CB-SMO secures rank 1 in producing the least value of cogging torque T_c, of 41mNm. While GOA and TLBO secures ranks <4 and AGO, ABC, AO, PSO, DE secures ranks from 4 to 8, respectively. Also the dimensions of initial and final models are presented in 2-D and 3-D FEM models of Quadcopters in Fig. 8. Further, for verification of influence over the performance of UAV, the "*optimal*" model of OR-PMSM-IPIM is thus designed for Quadcopter application, by assigning the rotational directions as discussed in Fig. 4 previously.

(3) *Computational analysis.*

The computational analysis results for initial and optimal models are presented in Table 6. It compares the Initial and Optimal model and their respective weights, t-p-w values and cogging torques with respect to the initial and optimized

Table 3 Definitions of Benchmark Functions and comparative analysis results with overall CB and individual CB behaviors added with SMO

	Names	Description	Range	f_{min}	CB-SMO	SMO with CB1	SMO with CB2	SMO with CB3	SMO with CB4	SMO
Unimodal	Rosenbrock	$f(x) = \sum_{i=1}^{n-1}[100\left(x_i^2 - x_{i+1}\right)^2 + \left(1 - x_i\right)^2]$	[−30, 30]	0	3.2343e−04 (+)	2.5361e−02 (+)	3.2576e−03 (+)	4.020e−02 ( )	1.8342e−03 (+)	1.7308e−01
	Sum of different powers	$f(x) = \sum_{i=1}^{n}(\lvert x_i + 0.5\rvert)^2$	[−100, 100]	0	7.7404e−09 (+)	7.8283e−07 (0)	3.0450e−07 (0)	2.4682e−07 (0)	2.1504e−07 (0)	2.3727e−07
Multimodal	Quartic	$f(x) = \sum_{i=0}^{n} i x_i^4 + random[0, 1)$	[−128, 128]	0	4.5931e−05 (+)	3.7890e−05 (+)	1.6178e−04 (0)	2.6782e−04 (0)	2.7006e−06 (+)	2.7007e−04
	Schwefel	$f(x) = \sum_{i=1}^{n}(-x_i \sin(\sqrt{\lvert x_i \rvert}))$	[−500, 500]	−418.982n	−1291.5806 (+)	−1299.4384 (−)	−1256.9486 (0)	−1217.6031 (−)	−1256.9485 (0)	−1256.9487
	Penalized1	$f(x) = \frac{\pi}{n}\{10\sin(\pi y_1)\}$ $+\sum_{i=1}^{n-1}(y_i - 1)^2\left[1 + 10\sin^2\left(\pi y_{i+1}\right) + \sum_{i=1}^{n} u\left(x_i, 10, 100, 4\right)\right];$ where $y_i = 1 + \frac{x_i+1}{4}$, $u\left(x_i, a, k, m\right)\begin{cases} K(x_i - a)^m; & \text{for } x_i > a \\ 0; & \text{for } -a \le x_i \le a \\ K(-x_i - a)^m; & \text{for } x_i \le -a \end{cases}$	[−50, 50]	0	1.4611e−10 (+)	7.153e−08 (0)	4.1413e−08 (0)	1.271e−08 (0)	1.6075e−07 (−)	4.1297e−08
	Levy N.13	$f(x) =$ $0.1(\sin^2(3\pi x_1) + \sum_{i=1}^{n}\left(x_i - 1\right)^2\left[1 + \sin^2\left(3\pi x_i + 1\right)\right] +$ $(x_n - 1)^2\left[1 + \sin^2(2\pi x_n)\right) + \sum_{i=1}^{n} u\left(x_i, 5, 100, 4\right)$	[−50, 50]	0	6.6909e−08 (+)	8.3077e−04 (−)	2.6601e−05 (0)	1.9595e−04 (−)	2.2119e−04 (−)	1.0168e−05

(+) shows positive effect: produces better result, ( ) shows negative effect: fails to produce better result, (0) shows null effect: produces similar result

Table 4 Definitions of Benchmark Functions and comparative analysis results with other classical MH techniques; Aquila Grasshopper Optimization (AGO), Aquila Optimizer (AO), Grasshopper Optimization Algorithm (GOA), Artificial Bee Colony (ABC) method, Particle Swarm Optimization (PSO) method, Teaching Learning Based Optimization (TLBO) method and Differential Evolution (DE)

	Names	Description	Range	f_{min}	CB-SMO	AGO	AO	GOA	ABC	DE	PSO	TLBO
Unimodal	Rosenbrock	$f(x) = \sum_{i=1}^{n-1}[100\left(x_i^2 - x_{i+1}\right)^2 + \left(1 - x_i\right)^2]$	[−30, 30]	0	3.2343e−04	8.222e−04	8.306e−04	1.011e+00	0.401e+00	0.000e+00	0.000e+00	0.000e+00
	Sum of different powers	$f(x) = \sum_{i=1}^{n}(\lvert x_i + 0.5\rvert)^2$	[−100, 100]	0	7.7404e−09	2.152e0−5	4.556e−06	1.012e−07	0.500e+00	0.000e+00	4.264e−08	1.080e−08
Multimodal	Quartic	$f(x) = \sum_{i=0}^{n} i x_i^4 + random[0, 1)$	[−128, 128]	0	4.5931e−05	5.318e−03	2.661e−03	5.812e−03	0.098e+00	3.292e−05	0.004e+00	0.011e+00
	Schwefel	$f(x) = \sum_{i=1}^{n}(-x_i \sin(\sqrt{\lvert x_i\rvert}))$	[−500, 500]	−418.982n	−1291.5806	−1213.586	−1212.784	−1217.336	−1202.968	−1208.229	−1200.868	−1362.886
	Penalized1	$f(x) = \frac{\pi}{n}\{10\sin(\pi y_1)\} + \sum_{i=1}^{n-1}(y_i - 1)^2\left[1 + 10\sin^2\left(\pi y_{i+1}\right) + \sum_{i=1}^{n} u\left(x_i, 10, 100, 4\right)\right]$; where $y_i = 1 + \frac{x_i+1}{4}$, $u\left(x_i, a, k, m\right) = \begin{cases} K(x_i - a)^m; & \text{for } x_i > a \\ 0; & \text{for } -a \le x_i \le a \\ K(-x_i - a)^m; & \text{for } x_i \le -a \end{cases}$	[−50, 50]	0	1.4611e−10	1.498e−06	1.505e−05	5.519e−06	1.000e+00	4.711e−03	4.326e−04	3.110e+00
	Levy N.13	$f(x) = 0.1(\sin^2(3\pi x_1) + \sum_{i=1}^{n}\left(x_i - 1\right)^2\left[1 + \sin^2\left(3\pi x_i + 1\right)\right] + (x_n - 1)^2\left[1 + \sin^2(2\pi x_n)\right) + \sum_{i=1}^{n} u\left(x_i, 5, 100, 4\right)$	[−50, 50]	0	6.6909e−08	1.537e−07	1.353e−06	1.327e−06	1.000e+00	1.349e−02	6.816e−03	0.019e+00

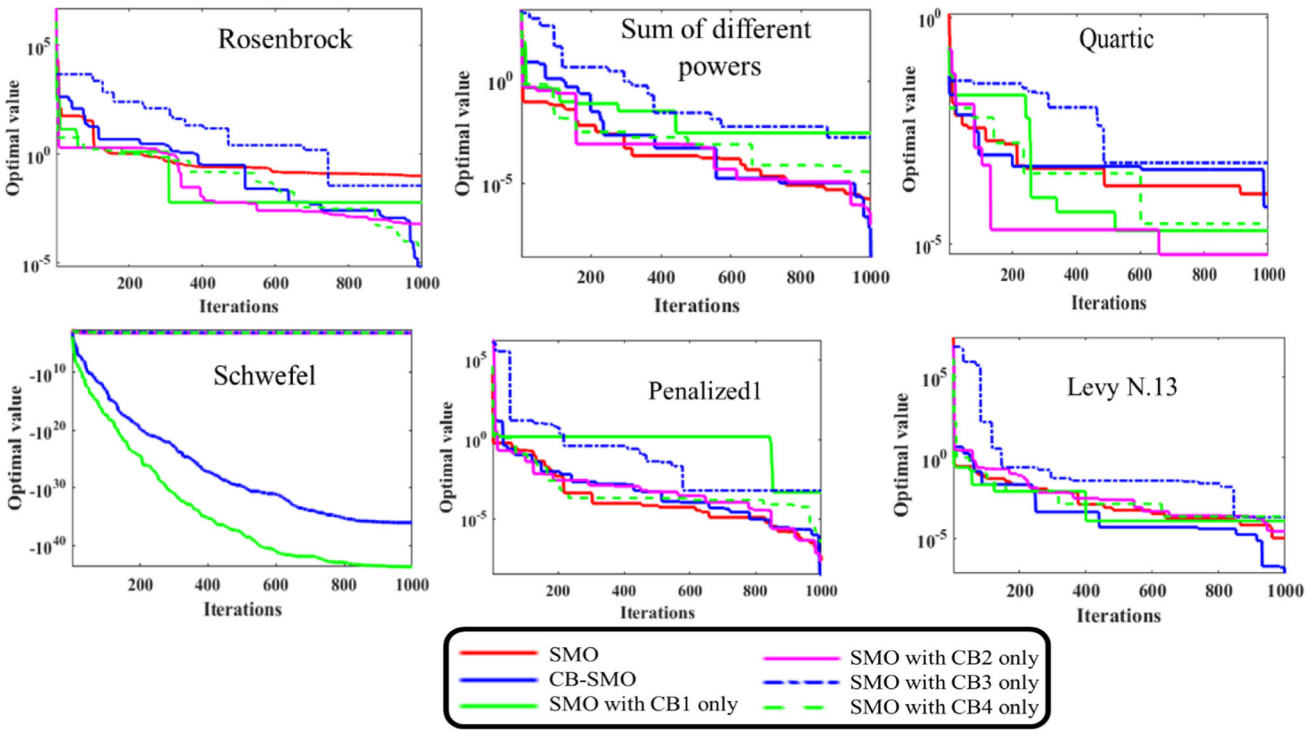


Fig. 7 Comparative representation of convergence profiles by introducing CB behavior in SMO

Table 5 Comparative analysis of optimal models obtained by proposed CB-SMO and other classical MH techniques

Algorithm	OR-PMSM-IPIM		Rank
	Parameter values (d_1, d_2, d_3)	T_c(mNm)	
CB-SMO	(3.3, 1.5, 31.9)	41	1
AGO	(3.6, 2, 31)	42.107	4
AO	(3.7, 1.84, 31.34)	42.523	6
GOA	(3.4, 1.9, 31)	41.959	2
ABC	(3.4, 1.8, 31)	42.297	5
PSO	(3.2, 1.2, 30.8)	42.637	7
TLBO	(3.2, 1.5, 32)	42.051	3
DE	(3.2, 1.5, 32)	42.836	8

design parameters. Thus, comparison of different essential aspects of Initial and optimal model are shown in the form of Bar graph in Fig. 9. Initially, the OR-PMSM-IPIM has weight of 2.151 N (0.484 lbs) producing 2.615 Nm/N of torque per weight (t–p–w) ratio. The cogging torque is 19.99 mNm per unit weight. The optimized OR-PMSM-IPIM model, when operated at rated speed, possesses 1.885 N (0.423 lbs) of weight (12.4% reduction). It produces 18.04 mNm of cogging torque per unit weight (9.8% reduction). The t-p-w for the optimized model is found to be 2.779 Nm/N (6.3% increase). This enables UAV device to have better propeller efficiency. The reduced weight of motor ensures reduction in moment of inertia. This helps in obtaining lesser values of radius of gyration. The lesser the value of radius of gyration, lesser is the deflection in pitch, roll and yaw angle. This ensures the ease of overcoming the thrust in lifting load along three dimensional axes. It becomes easier to control such advantageous models in UAV drive system.

5 Conclusion

Inspired by accuracy results obtained by brainless slime mold optimizer, a novel modified version of SMO is introduced in this paper. By introducing all CBs, which were not present in conventional SMO, a complete version of CB-SMO technique is presented and implemented. Using this algorithm,

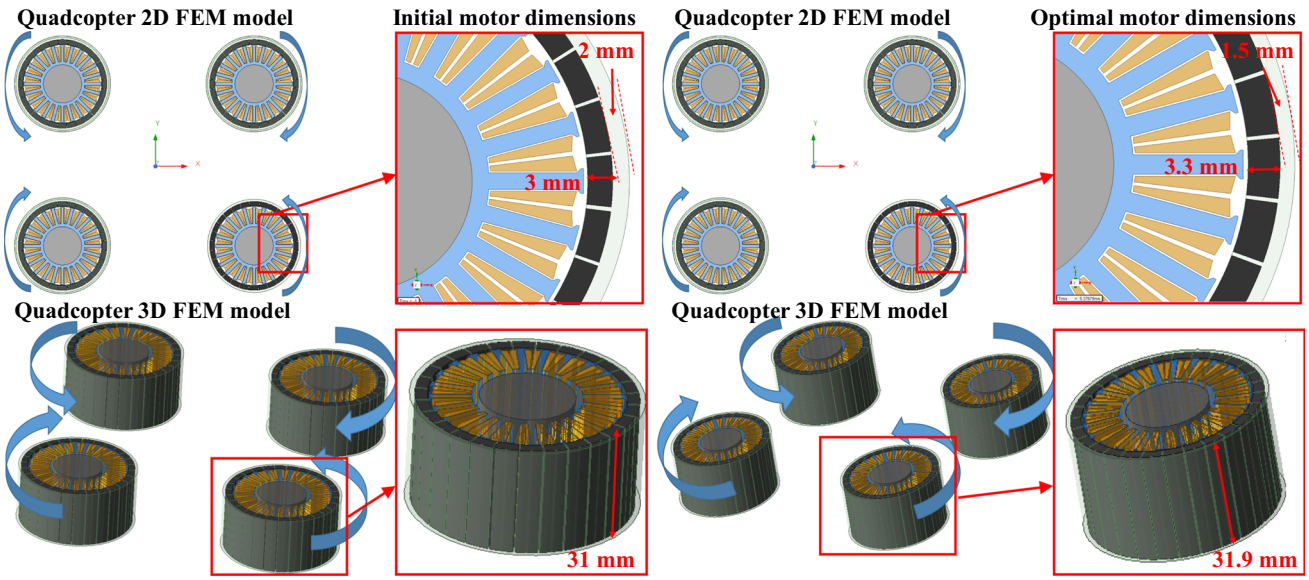


Fig. 8 Comparative Representation of initial and optimal 2D and 3D FEM model designs in Quadcopters

Table 6 Computational analysis results of Initial and optimal models obtained by proposed CB-SMO

Model	OR-PMSM-IPIM				Remark
	Parameter values (mm) (d_1, d_2, d_3)	T_c (mNm)	Weight (N)	t–p–w (Nm/N)	
Initial model	(3, 2, 31)	43	2.151	2.615	–
Optimal model	(3.3, 1.5, 31.9)	41 (4.6% reduction)	1.885 (12% decrease)	2.779 (6% increase)	Improved performance

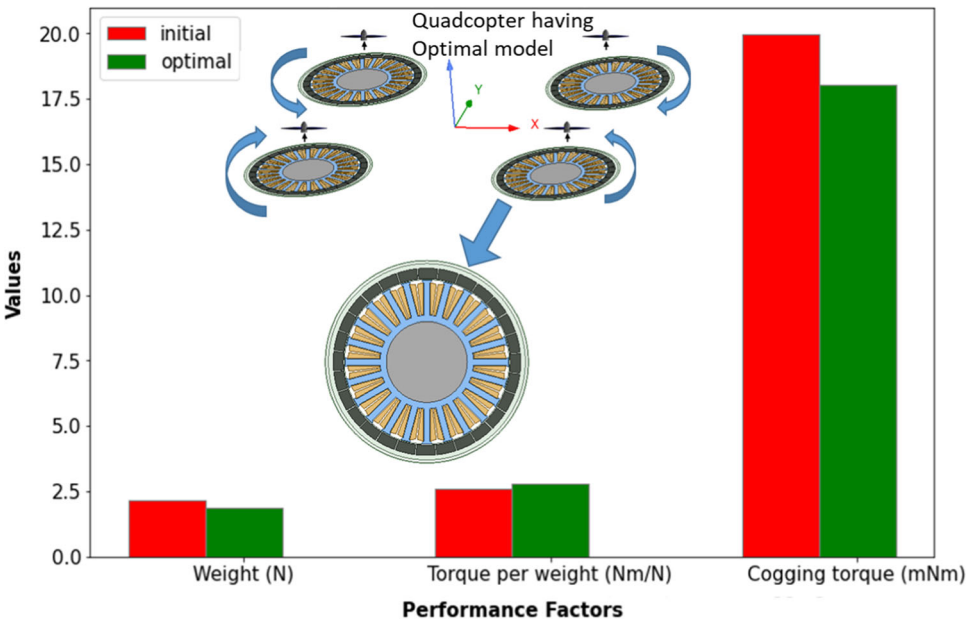


Fig. 9 Comparison of different essential electromagnetic performance aspects of Initial and optimal model for UAV performance improvement

the OR-PMSM geometry, having unique IPIM structure, has been optimized in this article.

The performance analysis of conventional SMO by adding individual CBs is tested for various Benchmark functions. By comparing their convergence profiles and complexity, it is found that the novel CB-CMO method is able to achieve better optimization results of the Benchmark functions. Thus, the performance of CB-SMO is compared with few popular MH techniques. It is found that CB-SMO produces convincingly better results for unimodal as well as multimodal Benchmark functions.

Furthermore, for implementation of the proposed CB-SMO to practical field, the DOP of OR-PMSM-IPIM is designed in order to optimize its performance. For designing DOP, LSM technique is implemented for obtaining cogging torque, as a function of three design parameters, i.e., magnet width, rotor width and motor height. Then, this DOP is solved by proposed CB-SMO as well as few classical MH techniques, in order to minimize the cogging torque. It is found that CB-SMO outperforms other techniques to supply the least cogging torque by obtaining optimized value of design parameters.

Thereafter, these optimized values of design parameters are utilized to design the overall quadcopter model in order to compare the t-p-w ratios of initial and optimal models.

In UAV application, the energy conversion system should have high propeller efficiency, in order to obtain better performance while undergoing VTOL operation [3, 4, 7]. The propeller efficiency is affected by angle of propeller and advance ratio, which is the ratio of freestream air speed to propeller tip speed of quadcopter. Here, since the scope of this work has been the comparison of electromagnetic performance analysis only. Therefore, by comparing electromagnetic performance of initial and optimal models, it is found that following achievements are noticeable out of this work:

In optimal model, there is nearly 12% reduction in weight. It leads to almost 10% reduction in cogging torque per unit weight. This ensures reduction in noise and enhancement in "*smoothness*" of VTOL operation.

The overall t-p-w of the optimal model is enhanced by nearly 6%, as compared to the initial model. This enables UAV device to have better propeller efficiency.

The reduced weight of motor ensures reduction in moment of inertia. This helps in obtaining lesser values of radius of gyration. (*The lesser the value of radius of gyration, lesser is the deflection in pitch, roll and yaw angle*.)

This ensures the ease of overcoming the thrust in lifting load along three dimensional axes.

It becomes easier to control such advantageous models in UAV drive system.

Based on the above observations, the future directions for this work can be to produce the optimized model of OR-PMSM-IPIM and monitor the performance with respect to powertrain operation for VTOL operation. By developing the real-time environment of the quadcopter model, the computer-aided design (CAD) can be studied for different environment conditions.

Acknowledgement This work has been supported by Centre of Excellence for Electric Vehicles and Related Technologies, Electrical Engineering Department, Delhi Technological University, Delhi, India, 110042.

Author contributions Monika Verma performed the modeling cum analysis work and wrote the main manuscript. Mini Sreejeth and Madhusudan Singh reviewed the manuscript.

Declarations

Conflict of interest The authors have no conflict of interest.

Appendix A: Samples collected from FEM experiments and impact of selection of prescribed design parameters

For UAV application, electric motor should be reliable, i.e., its critical efficiency should be higher and the motor should be of lighter weight. However, it is contradictory to obtain minimized weight and maximized efficiency of the motor simultaneously. To compensate this adversity, the optimal designing of related parameters of OR-PMSM is essential for designers. This is the reason why parameters d_1, d_2 and d_3 (specified in Fig. 5) are selected as design parameters for minimizing cogging torque. Impact of selecting above mentioned design parameters are discussed below:

- The designer should compute the motor design approximately. The electric as well as magnetic loading of motor are related to size and motor's endurance.
- From theoretical point of view, the increase in stack length results in the improvement of motor's efficiency but at the cost of increased mass of the motor.
- The radial length of magnets in OR-PMSM leads to increase in intensity of magnetic induction in rotor magnetic circuit of motor. Thus, increment in magnetic length results in obtaining the condition of magnetic saturation. Therefore, the optimization of radial length of magnets in rotor can rectify magnetic saturation condition.
- However, it may increase the cost and mass of motor. Also, the increased current density in stator winding leads to enhanced copper loss causing reduced efficiency and increment in the temperature of motor (Table 7).

Table 7 Design of experiment sample data for T_c (COGGING TORQUE)

No.	d_1(mm)	d_2(mm)	d_3(mm)	T_c(mNm)
1	3	2	31	43.0
2	3	0.5	31	23.4
3	3	0.5	30	22.6
4	4	0.5	32	31.9
5	4	0.5	31	30.9
6	4	0.5	30	29.9
7	3.5	0.5	32	31.0
8	3.5	0.5	31	30.0
9	3.5	0.5	30	29.1
10	3	1.5	32	46.9
11	3	1.5	31	45.4
12	3	1.5	30	44.0
13	4	1.5	32	42.1
14	4	1.5	31	40.8
15	4	1.5	30	39.6
16	3.5	1.5	32	40.8
17	3.5	1.5	31	39.5
18	3.5	1.5	30	38.2
19	3	2	32	44.4
20	3	0.5	32	29.9
21	3	2	30	41.6
22	4	2	32	65.9
23	4	2	31	63.9
24	4	2	30	61.7
25	3.5	2	32	45.9
26	3.5	2	31	44.4
27	3.5	2	30	43.0
28	3	1	32	39.0
29	3	1	31	37.7
30	3	1	30	36.5
31	4	1	32	58.8
32	4	1	31	56.9
33	4	1	30	55.1
34	3.5	1	32	35.1
35	3.5	1	31	34.0
36	3.5	1	30	32.9

References

1. Bozkurt A, Baba AF, Oner Y (2021) Design of outer–rotor permanent–magnet-assisted synchronous reluctance motor for electric vehicles. Energies 14(3739):1–12. https://doi.org/10.3390/en14133739
2. Ahn JM, Son JC, Lim DK (2020) Optimal design of Outer rotor surface mounted permanent magnet synchronous motor for cogging torque reduction using territory particle swarm optimization. J Electr Eng Technol. https://doi.org/10.1007/s42835-020-00599-z
3. Masson PJ, Luongo CA, Nam T, Kim HD, Mavris D, Brown GV, Hall D, Waters M (2009) Next generation more electric aircraft: a potential application for HTS superconductors. IEEE Trans Appl Supercond 19(3):1055–1068
4. Rosu M, Zhou P, Lonol D, Popescu M, Lin D, Blaabjerg F, Rallabandi V, Staton D (2018) Multi-physics simulation by design for electrical machines, power electronics and drives. Wiley, IEEE Press, Hoboken, NJ
5. Akash A, Raj VSJ, Sushmitha R, Prateek B, Aditya S, Sreehari VM (2021) "Design and analysis of VTOL operated intercity electrical vehicle for urban air mobility. Electronics 11(1):20
6. Finger DF, Braun C, Bil C (2019) Impact of electric propulsion technology and mission requirements on the performance of VTOL UAVs. CEAS Aeronaut J 10:827–843. https://doi.org/10.1007/s13272-018-0352-x
7. Cao W, Mecrow BC, Atkinson GJ, Bennett JW, Atkinson DJ (2012) Overview of electric motor technologies used for more electric aircraft (MEA). IEEE Trans Ind Electron 59(9):3523–3531
8. Mutluer M (2021) Analysis and design optimization of permanent magnet synchronous motor with external rotor for direct driven mixer. J Electr Eng Technol. https://doi.org/10.1007/s42835-021-00706-8
9. Mbadiwe EI, Sulaiman EB (2020) Design and optimization of outer rotor permanent magnet flux switching motor using transverse segmental rotor shape for automotive applications. Ain Shams Eng J 12:507–516
10. Guerroudj C, Karnavas YL, Charpentier JF, Chasiotis ID, Bekhouche L, Saou R, Zaim EH (2021) Design optimization of outer rotor toothed doubly salient permanent magnet generator using symbiotic organisms search algorithm. Energies 14:1–25
11. Taha HM, Talnaab IR (2019) Designs of PMSMs with inner and outer rotors for electric bicycle applications. Kurd J Appl Res 4(1):20–25
12. Shi Z, Sun X, Cai Y, Tian X, Chen L (2020) Design optimization of an outer rotor permanent magnet synchronous hub motor for a low speed campus patrol EV. IET Electr Power Appl 14(11):2111–2118
13. Chau KT, Zhang D, Jiang JZ, Liu C, Zhang Y (2007) Design of a magnetic geared outer rotor permanent magnet brushless motor for electric vehicles. IEEE Trans Magn 43(6):2504–2506
14. Ahmed MZ, Sulaiman E, Romalan GM, Haron ZA (2015) Optimal torque investigation of outer rotor hybrid excitation flux Switching machine for in wheel drive EV. ARPN J Eng Appl Sci 10(19):8839–8845
15. Isfanuti A-S, Tutelea LN, Boldea I, Staudt T, da Silva PE (2020) Outer ferrite-PM-rotor BLAC motor characterization: FEM-assisted optimal design and preliminary experiments. IEEE Trans Ind Appl 56(3):2580–2589. https://doi.org/10.1109/TIA.2020.2979672
16. Ho SL, Yang S, Ni G, Machado JM (2006) A modified ant colony optimization algorithm modeled on tabu-search methods. IEEE Trans Magn 42(4):1195–1198
17. Brandslatter B, Baumgartner U (2002) Particle swarm optimization-mass spring system analogon. IEEE Trans Magn 38(2):997–1000
18. Im CH, Jung HK, Kim YJ (2003) Hybrid genetic algorithm for electromagnetic topology optimization. IEEE Trans Magn 39(5):2163–2169
19. Bayraktar Z, Komurcu M, Bossard JA, Warner HD (2013) The wind driven optimization technique and its application in electromagnetics. IEEE Trans Antenna Propag 61(5):2745–2757

20. Shi Y (2011) Brain storm optimization algorithm. In: Proceedings of the 2nd international conference on swarm intelligence, Chongqing, China, Jun 2011, pp 303–309
21. Tang AD, Tang SQ, Han T, Zhou H, Xie L (2021) A modified slime mould algorithm for global optimization. Comput Intell Neurosci 21:1–22
22. Naik MK, Panda R, Abraham A (2021) Adaptive opposition slime mold algorithm. Soft Comput 25:14297–14313
23. Xiao Y, Sun X, Zhang Y, Guo Y, Wnag Y, Li J (2021) An improved slime mould algorithm based on tent chaotic mapping and nonlinear inertia weight. Int J Innov Comput Inf Control 17(6):2151–2176
24. Hamed A, Ebeed M, Refai A, Sattar M, Elbaset A, Ahmed T (2021) Application of SMO for optimal allocation of DSTATCOM and PV system in real Egyptian radial network. Sohag Int J 1(1):16–24
25. Jones J (2015) Applications of multi-agent slime mold computing. Int J Parallel Emerg Distrib Syst 31(5):1–34
26. Liu Y, Heidari A, Ye X, Liang G, Chen H, He C (2021) Boosting slime mould algorithm for parameter identification of photovoltaic models. Energy 234:121164
27. Jia H, Zhang W, Zheng R, Wang S, Leng X, Cao N (2021) "Ensemble mutation slime mold algorithm with restart mechanism for feature selection. Int J Intell Syst 37:2335–2370
28. Basset MA, Chang V, Mohamed R (2020) "HSMA_WOA: A hybrid novel slime mold algorithm with whale optimization for tackling the image segmentation problem of chest X-ray images. Appl Soft Computi 95:106642
29. Z. Cui, H. Hou, H. Zhou, W. Lian and J. Wu, "Modified Slime mold algorithm via Levy Flight", International Congress on Image and Signal Processing, BioMedical Engineering and Informatics, 2020.
30. Gao H, Liang G, Chen H (2022) Multi-Population Enhanced Slime Mould Algorithm and with Application to Postgraduate Employment Stability Prediction". Electronics 11:209
31. Naik MK, Panda R, Abraham A (2020) Normalized square difference based multilevel thresholding technique for multispectral images using leader slime mould algorithm. J King Saud Univ-Comput Inf Sci 34:4524–4536
32. Liu L, Zhao D, Yu F, Heidari AA, Ru J, Chen H, Mafarja M, Turabieh H, Pan Z (2021) Performance optimization of differential evolution with slime mouldalgorithm for multilevel breast cancer image segmentation. Comput Biol Med 138:1–5
33. Reid CR, Latty T (2016) Collective behavior and swarm intelligence in slime moulds. FEMS Biol Rev Oxford 40:798–806
34. Latty T, Beekman M (2019) Food quality affects search strategy in the a cellular slime mould, *Physarum polycephalum*. Behav Ecol 20:1160–1167
35. Singh R, Ranjan S, Pradhan T, Raju Dhenuvakonda K (2022) Calibration and frequency estimation in sensors for electrical parameter measurement using regression and metaheuristic based models. Expert Syst. https://doi.org/10.1111/exsy.13208
36. Khuri AI, Mukhopadhyay S (2010) Response surface methodology. Wiley Interdiscipl Rev: Comput Stat 2(2):128–149
37. Chai T, Draxler RR (2014) Root mean square error (RMSE) or mean absolute error (MAE)? Arguments against avoiding RMSE in the literature. Geosci Model Dev 7:1247–1250

Publisher's Note Springer Nature remains neutral with regard to jurisdictional claims in published maps and institutional affiliations.

Springer Nature or its licensor (e.g. a society or other partner) holds exclusive rights to this article under a publishing agreement with the author(s) or other rightsholder(s); author self-archiving of the accepted manuscript version of this article is solely governed by the terms of such publishing agreement and applicable law.

Applied Physics A (2024) 130:98
https://doi.org/10.1007/s00339-023-07239-z

Applied Physics A
Materials Science & Processing

Design, fabrication, and characterization of epsilon negative and near-zero index metasurface

Ankit[1] · Kamal Kishor[1] · Ravindra Kumar Sinha[1,2]

Received: 1 August 2023 / Accepted: 15 December 2023
© The Author(s), under exclusive licence to Springer-Verlag GmbH, DE part of Springer Nature 2024

Abstract
This paper delves into the intricacies of designing, fabricating, and characterizing a metasurface exhibiting epsilon-negative (ENG) and near-zero index (NZI) properties. Specifically, it focuses on an eye-shaped coupled circular split ring resonator (CC-SRR) metasurface, crafted from copper on an epoxy resin fiber (FR-4) dielectric substrate material. The design is further optimized to induce resonance frequencies at approximately 7.5, 8.8, and 13.4 GHz within the C, X, and Ku bands, respectively. Utilizing the COMSOL Multiphysics and CST Microwave Studio simulation tools, the structural design is developed to ascertain its electromagnetic properties across the 1–15 GHz frequency spectrum. Experimental measurements of the transmission characteristics of the fabricated metasurface align closely with the simulated results. The electromagnetic field distributions of the proposed metasurface structure are scrutinized, revealing tunable characteristics contingent upon variations in the thickness (t_s) of the dielectric substrate material and the copper resonator thickness (t_m). Additionally, a theoretical model employing an equivalent circuit, featuring various inductor (L) and capacitor (C) components, is presented to compare against simulated results for the targeted resonance frequencies.

Keywords Coupled circular split ring resonator (CC-SRR) · Dielectric · Epsilon negative (ENG) · Finite element method (FEM) · Metasurface · Near-zero index (NZI)

1 Introduction

Metasurfaces have indeed earned significant attention from experts worldwide due to their unique properties and potential applications, particularly in the microwave frequency spectrum. These are artificial structures designed to exhibit properties not found in naturally occurring materials [1]. They are two-dimensional artificial structures created by arranging subwavelength unit cells in a specific pattern to achieve the desired electromagnetic properties. The unit cell configuration of the metasurface typically involves a periodic array of metal-dielectric or metal-dielectric-metal structures on a host substrate [2]. The metal components, often in the form of split-ring resonators (SRR) or wire structures, provide the desired electromagnetic response, while the dielectric materials help control and manipulate the propagation of electromagnetic waves. In 1968, Russian physicist Victor Veselago first proposed the theoretical concept of Double negative (DNG) metamaterial or Left-handed metamaterial (LHM), which is a hypothetical "ε-negative and μ-negative" metamaterial [3]. In 1996, Pendry et al. introduced thin metal wire-based structures to realize negative permittivity [4]. In 1999, Pendry et al. [5] also introduced SRR metamaterial unit cells which could provide negative permeability and were easy to construct. Depending on the values of the effective permittivity and effective permeability parameters of the designed metasurface structure, it can be categorized as single-negative (SNG), DNG, and double-positive materials. The SNG materials show either negative permeability or negative permittivity, whereas double-negative (DNG) materials show both negative characteristics [6]. Another type of metamaterial category is near-zero index (NZI) metamaterials which represent a fascinating class of engineered materials that exhibit an effective refractive index close to zero. Unlike conventional materials,

✉ Ravindra Kumar Sinha
dr_rk_sinha@yahoo.com

[1] TIFAC-Center of Relevance and Excellence in Fiber Optics and Optical Communication, Department of Applied Physics, Delhi Technological University, Delhi 110042, India

[2] Gautam Buddha University, Gautam Budh Nagar, Greater Noida, UP 201312, India

Published online: 16 January 2024

which have positive refractive indices, these metasurfaces have the remarkable ability to manipulate light in unprecedented ways. By harnessing their unique optical properties, these metasurfaces have the potential to revolutionize various fields, from optics and photonics to telecommunications, imaging and cloaking [7]. By manipulating the geometric arrangement and composition of the metasurface unit cells, it is possible to engineer the effective permittivity and effective permeability of these structure.

Further, with a finite length of metasurface, shorter than the microwave frequency, the electromagnetic field allows for the calculation of reflection and transmission coefficients [8]. Within the microwave frequency range, the SRR's geometrical structural arrangement can be used to predict electric permittivity and magnetic permeability. Sub-wavelength metasurfaces are currently receiving significant attention in structural research due to their ability to exhibit unique electromagnetic properties [9, 10]. These materials are lightweight, and compact, and offer optimal output properties, making them highly desirable. The versatility and potential of sub-wavelength metasurface make them a promising field of study in various domains. They have contributed to the development of applications such as invisibility cloaking [11], refractive index and temperature sensors [12], wavelength-tunable reflectors [13], absorbers [14], tunable negative refractive index materials [15], nano absorbers [16], superlenses [17], microwave antennas [18], filters [19–21], multi-mode propagation filter [22, 23] and energy harvesting techniques [24]. Sabah et al. proposed an S-shaped resonator-based metamaterial and its sensor applications in L-band [25]. Faruque et al. created a dual-band (X and Ku-bands) flexible metamaterial impinges on a substrate i.e., nickel aluminate with dimensions equal to 12.5×10 mm^2 [26]. An SNG metamaterial with triple band resonance for microwave applications was introduced by Islam et al. [27]. An SRR embedded in an epsilon-negative delta-shaped metamaterial displayed triple resonance covering the C and X bands discussed by Marathe et al. [28]. Previously existing single, dual, or triple-band metamaterial structures must find a metamaterial structure that can operate in a triple band, including Ku-band applications with ENG and NZI characteristics.

In the present research article, we designed an eye-shaped CC-SRR metasurface unit cell for triple-band applications in microwave regions. The proposed structure exhibits the ENG along with the NZI characteristics in the frequency range of 1–15 GHz. The NZI characteristics are observed within the frequencies of 5.70–7.55 GHz, 7.90–9.00 GHz, and 13.20–14.10 GHz, respectively, while the ENG characteristics are observed at 4.85–7.60 GHz, 7.80–9.15 GHz and 10.35–14.0 GHz, respectively. The proposed copper resonator is fabricated on the FR-4 dielectric substrate with $16 \text{ mm} \times 16 \text{ mm} \times 1.6 \text{ mm}$ dimension. The simulated results using FEM-based COMSOL Multiphysics software, which were further verified by CST Microwave Studio. The equivalent circuit modeling results using the Advanced Design Simulation (ADS) tool and experimentally measured results show excellent harmony with the simulated results for the proposed metasurface structure. The designed structure manifests the triple resonance frequencies corresponding to the C, X, and Ku-band of the microwave region. Hence, a novel metasurface structure is introduced and analyzed using both experimental, theoretical, and simulated methods.

2 Fabrication and modelling of the designed metasurface structure

Figure 1a demonstrates the simulated designed metasurface unit cell structure and Fig. 1b shows the fabricated prototype array of the same structure. The proposed structure comprises a circular split ring resonator (CSRR), two interconnected circular shapes, and coupled metallic elements adjacent to two circular shapes. The outer circular SRR

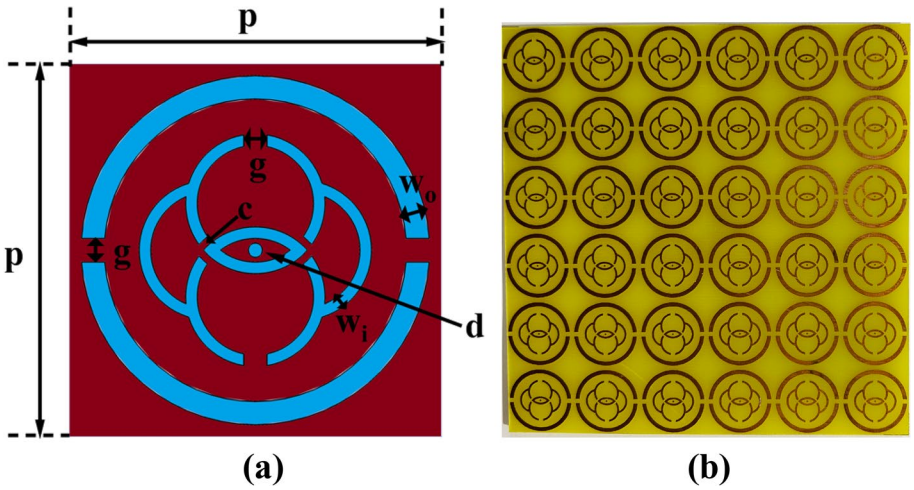


Fig. 1 **a** Unit cell (orthogonal view) and **b** fabricated array prototype of the simulated metasurface design

consists of a split gap 'g' with the width of the resonator 'w_o'. The interconnected circles have a gap "g", making an eye of diameter "d" in the center of the structure with a resonator width of 'w_i' along with four gaps 'c' around the eye shape. The unit cell of the proposed metasurface with dimensions of 16 mm × 16 mm consists of a copper resonator fabricated (6 × 6 array) on FR-4 dielectric substrate (thickness (t_s) = 1.6 mm) with the automated base CNC machine, shown in Fig. 1b. All the necessary parameters are listed in Table 1.

The proposed structure is also designed and simulated using the finite element method (FEM) based COMSOL Multiphysics 4.3b simulation tool, shown in Fig. 1b. The physics-controlled mesh with extra fine element size is utilized in simulation which will examine the physics to automatically determine size attributes and sequence operations needed to create a mesh adapted to the problem. The copper material patch has a thickness (t_m) of 0.35 mm and electrical conductivity $\sigma = 5.8 \times 10^7$ S/m [29]. The dielectric constant (ε_r) and loss tangent (tan δ) of epoxy resin fiber (FR-4) substrate material are 4.3 and 0.025, respectively [30]. The dielectric constant represents the material's electrical energy storage capacity in the presence of an electric field whereas the dielectric loss tangent represents the energy lost when an electric field is applied in the form of heat. Due to the high value of the dielectric constant of FR-4, there is stronger electric field confinement inside the substrate material.

Table 1 The parameters of the fabricated and simulated designed unit cell metasurface structure

Parameter	Value (mm)	Description
p	16	Period of the unit cell
g	1	Circular split gap
c	0.3	Gap between circular and eye-shaped
d	0.6	Diameter of an inner small circle
w_i	0.5	Width of the inner resonator
w_0	1	Width of the outer resonator

3 Optimization of the designed CC-SRR metasurface geometry

3.1 Methodology of the design structure

Figure 2 illustrates the design progression from the initial stages to the final evaluation of the proposed structure with the transmission coefficient response to the different designs. Design evaluation for the proposed system aims to meet the properties of ENG and NZI with maximum frequency bands. As a result, multiple steps are taken to achieve a satisfactory outcome.

One CSRR with a split gap 'g' of 1 mm is built on the dielectric substrate in step 1, resulting in the two parts depicted in Fig. 2a. These two circular arcs act as two inductors, and the gaps between them act as two capacitors. This stage results in the achievement of a single resonance frequency in a single band, i.e., around 9 GHz, as illustrated in Fig. 2e. In the second step, two circular-shaped SRR circles are interconnected with a split gap 'g' of 1 mm and gap 'c' of 0.1 mm resulting in dual-band resonance in X and Ku-band as shown in Fig. 2b, e. In this part, the four circular arcs act as four inductors along with the middle inductor and the gaps act as capacitors. In the third step, the CSRRs are coupled together using an arc on the backside (Fig. 2c), resulting in a shift in resonance within the microwave region. Due to the coupling, there is an increase in the magnitude of S_{21} up to the desired maximum magnitude due to the addition of two more capacitors and inductors in the third step, but unable to reach our goal of triple band resonance, as shown in Fig. 2e. In the final step, a small circle with a diameter 'd' of 0.6 mm is placed in the center of the resonator, resulting in three frequency bands i.e., C-band (7.5

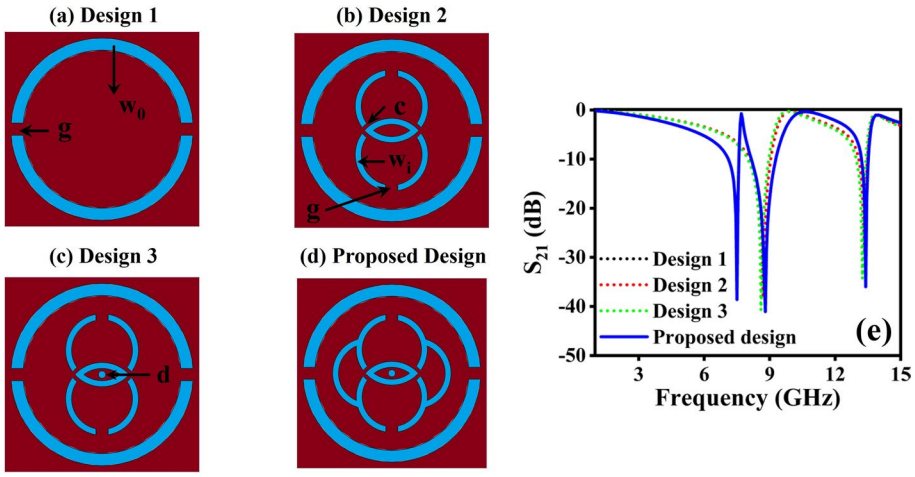


Fig. 2 Step-by-step design evolution **a**–**d** of the designed CC-SRR metasurface unit cell and **e** transmission coefficient corresponding to the various designed structures using simulation

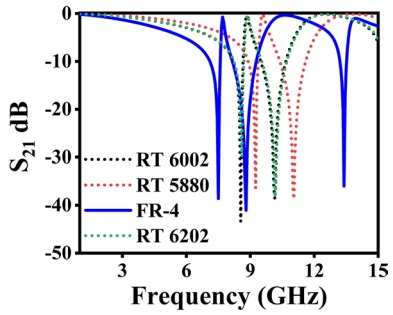


Fig. 3 Transmission coefficient (S_{21}) concerning the frequency for different substrate dielectric materials

GHz), X-band (8.8 GHz), and Ku-band (13.4 GHz), aligning with the desired outcome of our objective for the proposed design, shown in Fig. 2d, e. This circle aims to make the proposed design to be eye-shaped. In all design configurations, there is the addition of gaps resulting in changing the resonance frequency due to the addition of capacitors and inductors in the structure i.e., $f = \frac{1}{2\pi\sqrt{LC}}$.

3.2 Simulation-based parametric analysis of the proposed metasurface

(1) Impact of various substrate materials on the resonance frequency: Several dielectric materials including FR-4, RT 6002, RT 5880, and RT 6202 have been taken under consideration as substrates for the proposed metasurface structure. The obtained transmission coefficient (S_{21}) concerning the above-mentioned dielectric materials is represented in Fig. 3.

When Roger's versions are utilized as the substrate material for the proposed structure, the resonance frequencies do not correspond to the desired resonance within the triple band (i.e., C-, X-, and Ku-band). Figure 3 clearly illustrates the discrepancy between the desired and obtained resonance frequencies when using Roger's versions as the substrate material. FR-4 remains a highly suitable and advantageous choice for the proposed structure compared to Roger's version because it offers a high dielectric constant, is more cost-effective, has a lower loss tangent, and also indicates reduced signal loss. This emphasizes the importance of choosing an alternative substrate material, such as FR-4, to achieve the desired resonance characteristics in the triple band with minimum losses. All the findings corresponding to different substrate materials are listed in Table 2.

(2) Effect of different thicknesses of FR-4 substrate and copper resonator on the resonance frequency: The substrate material FR-4 thickness (t_s), and copper resonator thickness (t_m) are varied with a step size of 0.2 mm and the corresponding variation is shown in Fig. 4.

The substrate thickness (t_s) is increased from 1.2 to 2.0 mm, and there was a slight shift in the resonance frequency towards the lower side displaying a blue shift for the proposed structure as shown in Fig. 4a. Correspondingly, when the copper resonator thickness (t_m) varied from 0.15 to 0.95 mm, there was a shift in resonance frequency towards the higher side signifying a redshift, shown in Fig. 4b. The solid blue lines in Fig. 4a, b represent the optimized values of the substrate thickness (t_s) and copper

Table 2 Various properties and S_{21} parameters result from different substrate materials

Sr. no.	Substrate	Electric permittivity	Tangent loss	Resonance frequency of S_{21} (GHz)	Frequency band
1	Roger's RT6002	2.94	0.0012	8.5, 10.1	X
2	Roger's RT6202	2.90	0.0015	8.6, 10.1	X
3	Roger's RT5880	2.20	0.0009	9.2, 11.0	X
4	FR-4	4.30	0.025	7.5, 8.8, 13.4	C, X, and Ku

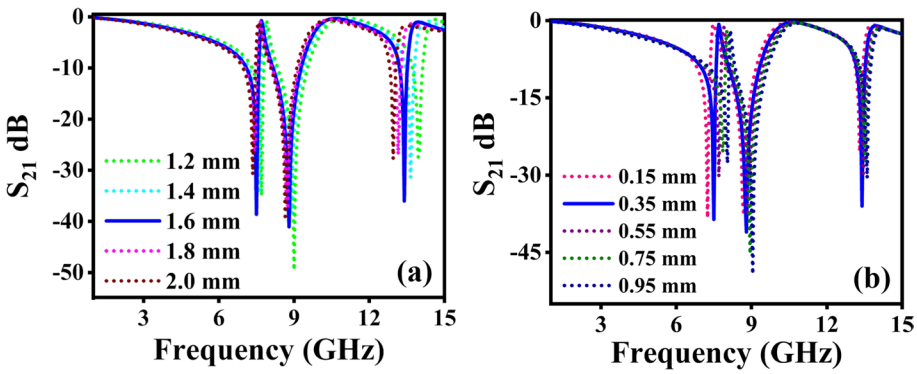


Fig. 4 Variation of resonance frequency with the thickness of **a** FR-4 substrate material and **b** copper resonator of the designed metasurface structure

resonator thickness (t_m) ($t_s = 1.6$ mm and $t_m = 0.35$ mm) for the proposed designed metasurface. The observed shift in resonance frequencies also imparts tunability characteristics of the designed metasurface structure. The designed tunable metasurface can be used in a range of frequencies. By modifying the substrate material FR-4 thickness (t_s), and copper resonator thickness (t_m) of the metasurface, we can switch between different operational frequencies, making them versatile in applications like reconfigurable antennas [31] and communication systems. These can be engineered to manipulate the transmission, scattering, and absorption of electromagnetic waves. By designed metasurface tunable properties, it is possible to render objects invisible to specific frequencies for potential applications in military and security purposes [32].

(3) Geometrical parameters of the proposed metasurface: The design parameters of the proposed metasurface were optimized, i.e., d, w_o and g to achieve resonance frequencies in the triple band (C, X, and Ku bands) as shown in Fig. 5.

The diameter of the center eye circle (d) is optimized to the value 0.3 mm as it shows triple resonance in C, X, and Ku bands with a high magnitude of transmission coefficient (S_{21}) as shown in Fig. 5a. Similarly, in Fig. 5b, c, the high magnitude of S_{21} corresponds to the optimized value of w_0 and g parameters, 1 mm each. When we increase or decrease the value of any of the parameters from the optimized value, then the magnitude of the transmission coefficient (S_{21}) decreases, leading to a lower value of transmittance.

4 Results and discussion

The properties of the proposed metasurface design were extracted and studied thoroughly. This study involved calculations and analysis of the effective electromagnetic parameters as well as studying the distribution of electromagnetic fields. Additionally, equivalent circuit modeling was conducted, and compared with the corresponding simulation and fabrication results to calculate the resonance frequency. These comprehensive analyses provided valuable insights into the behavior and characteristics of the proposed metasurface structure using theoretical and experimental results.

4.1 Metasurface unit cell scattering parameter

The scattering parameter of the metasurface unit cell includes the transmission coefficient (S_{21}). Using FEM-based simulation tools, the Drude–Lorentz variables were employed to evaluate the scattering parameters. A two-waveguide port configuration was employed in the simulation process. Port 1 served as the transmitter of the signal, while port 2 functioned as the receiver, as depicted in Fig. 6a. The periodic boundary conditions along with perfect magnetic conductor (PMC) in the x-axis and perfect electric conductor (PEC) in the y-axis were equipped in the simulation. In the simulation, first geometry is created using the defined parameters and then the material is assigned to the designed structure. Electromagnetic wave in the frequency domain along with boundary conditions is assigned to the structure.

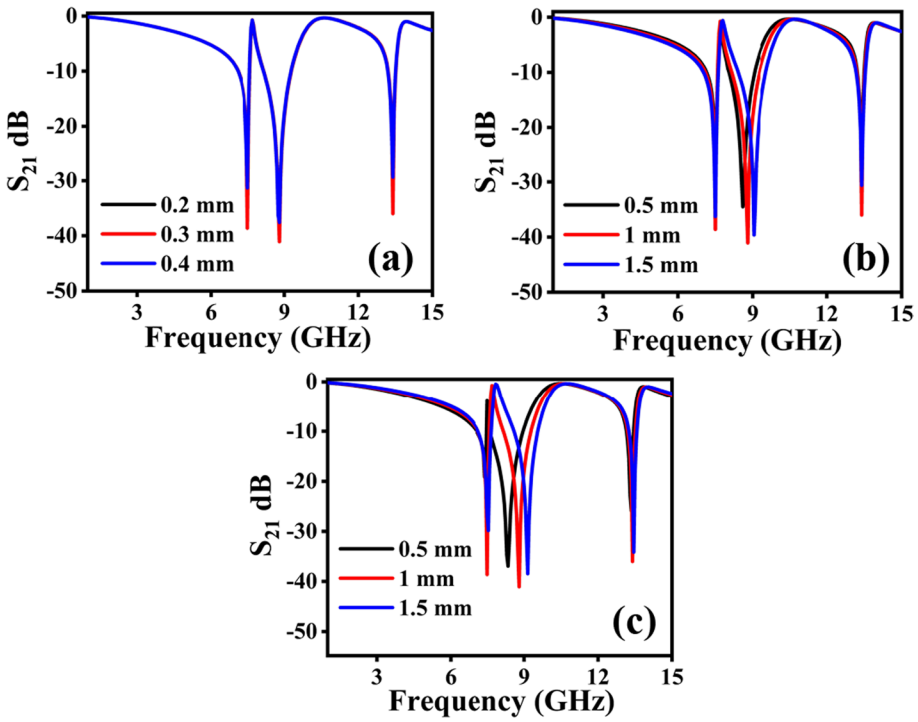


Fig. 5 Optimization of the proposed designed metasurface parameter **a** diameter of center eye circle "d", **b** width of outer CSRR "w_0", and **c** circular split gap "g"

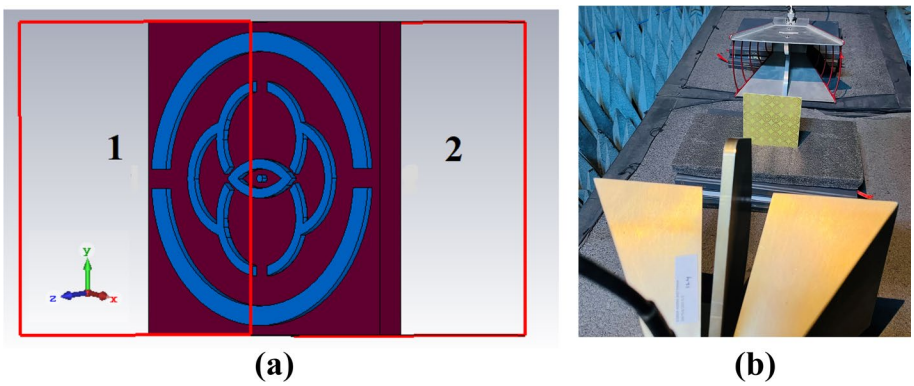


Fig. 6 **a** Simulation analysis and **b** experimental measurement setup of the designed metasurface

Lastly, the required meshing is done with the defined study. The simulation parameters used in FEM simulations include meshing, geometry, and physics, etc. The electromagnetic wave propagated vertically along the z-axis. This setup facilitated accurate simulations and analysis of the electromagnetic behavior of the proposed design.

The experimental setup used for the measurement of S_{21} is an Antenna test setup as shown in Fig. 6b. The setup includes connectors, RF cables, and necessary standards for calibration. This measurement is performed using a Vector Network Analyzer (VNA-MS2028C). In this, the DUT (Device Under Test), i.e., fabricated sample, which is a planar Frequency Selective Surface (FSS), is placed in the test setup. The VNA measures the signal transmitted (S_{21}) through the DUT. One port of the VNA is connected to the transmitting horn antenna and the other end is attached to the receiver horn antenna and DUT is placed in between the two horn antennas. This whole antenna setup is placed in an anechoic chamber to minimize external interference and reflections. VNA calibration is crucial to obtain accurate measurements. The calibration standards include short-open-load-through (SOLT) calibration, and these are connected to the VNA's ports for accurate reference. The VNA generates a swept RF signal, which is transmitted through the DUT. That transmitted signal is measured via VNA in terms of magnitude and phase (in dB). Figure 7 shows the comparison of the response of transmission coefficient (S_{21}) (a) using simulation and measurement of the fabricated design and (b) using two simulation software i.e., COMSOL Multiphysics and CST Microwave Studio.

As seen in Fig. 7a, there is a slight obvious discrepancy between measured and simulated results. This discrepancy may arise due to fabrication tolerance, signal leakage, reflection noise, etc. The experimental setup has constraints because the desired performance can only be obtained by properly aligning the two horn antennas. To avoid calibration errors compromising experiment findings, the network analyzer must be properly calibrated. The cumulative effect of all these constraints can be seen in the measurement results with a slight shift in resonance frequencies. Nevertheless, simulated and measured results include the C (4–8 GHz), X (8–12 GHz), and Ku (12–18 GHz) bands. The experimental observations were confirmed with the simulation results obtained from the COMSOL Multiphysics within the experimental limits. During the simulation process, the proposed structure demonstrated triple resonance frequencies at 7.5, 8.8, and 13.4 GHz, with maximum magnitude values of − 38.6, − 41.0, and − 35.9 dB, respectively. However, in the experimental results, the resonance frequencies were slightly shifted to 7.2, 9.0, and 13.1 GHz, with maximum magnitude values of − 34.3, − 33.9, and − 27.3 dB, respectively. Notably, a left shift was observed between the simulated and experimental results at 7.5 to 7.2 GHz

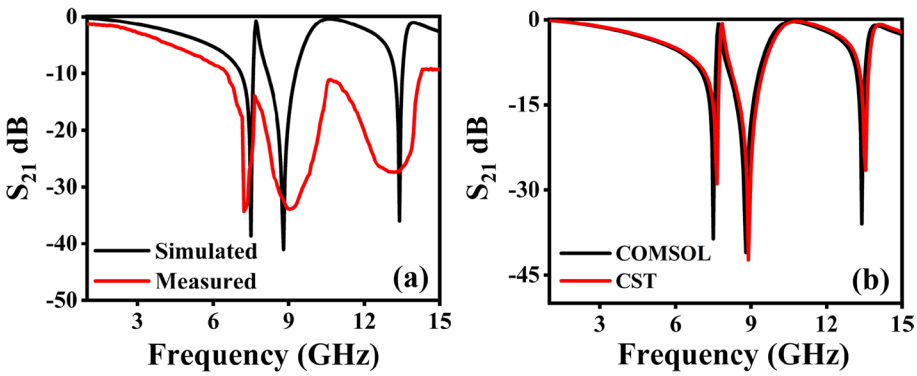


Fig. 7 Transmission coefficient (S_{21}) of the proposed metasurface structure for **a** the simulated and measured response and **b** COMSOL Multiphysics and CST Microwave studio response

and 13.4 to 13.1 GHz, while a right shift was observed at 8.8 to 9.0 GHz. The results of S_{21} obtained from both the simulators, COMSOL Multiphysics and CST, were compared and presented in Fig. 7b. Remarkably, the simulation results from both platforms exhibited a high degree of similarity, thereby confirming the accuracy of the designed structure for the proposed metasurface unit cell in triple bands (C, X and Ku).

Almutairi et al. [33], Islam et al. [34], and Ramachandran et al. [35] introduced metasurface unit cells based on CSRR (Circular Split Ring Resonator), GCHSRR (Gap-Coupled Hexagonal Split Ring Resonator), and CSR (Circular and Square Ring) shapes, respectively. These designs offer compact sizes but only cover one or two frequency bands. Ali et al. [36] presents a CCRR (Closed Circular Ring Resonator) design structure, which has larger dimensions compared to other authors but only covers the single frequency X-band. Another design, the square-enclosed split-maze-shaped (SE-SMS) metasurface unit cell, was discussed by Hannan et al. [37] which covers two frequency bands, namely the S and Ku bands. In 2023, Hossain et al. presented an SSRR (Square Split Ring Resonator) structure [38], which exhibits triple-band functionality in the S, C, and X bands but does not cover the Ku-band. In contrast, the proposed CC-SRR structure presented in the present study demonstrates triple band functionality, specifically in the C, X, and Ku bands. This unique design allows for applications across a wider frequency range, making it advantageous compared to the previous literature [33—38], presented in Table 3.

The provided Table 3 illustrates prior discoveries in metasurface research, indicating that the structures resembling the one examined resonate across three bands, specifically S, C, and X-bands. However, the resonance does not extend to the Ku-band, which is crucial for high-data-rate satellite communications. This study aims to push the boundaries of current metasurface research in satellite communication by developing devices that resonate across all three bands, addressing the demand for triple-band resonance with Ku-band applications.

4.2 Effective electromagnetic parameters measurements

The Nicolson–Ross–Weir (NRW) method is used for the measurement of the effective parameters such as the effective permittivity ($\varepsilon_{eff.}$), effective permeability ($\mu_{eff.}$) and effective refractive index ($\eta_{eff.}$) using the transmission (S_{21}) and reflection (S_{11}) coefficients, and the results are shown in Fig. 8. The effective parameters of the designed metasurface unit cell can be derived using the following equations [39, 40]:

$$S_{11} = \frac{R_{01}(1 - e^{i2\eta k_0 d})}{1 - R_{01}^2 e^{i2\eta k_o d}} \tag{1}$$

$$S_{21} = \frac{(1 - R_{01}^2)e^{i\eta k_0 d}}{1 - R_{01}^2 e^{i2k_o d}} \tag{2}$$

where $R_{01} = \frac{z-1}{z+1}$, $k_0 = \frac{2\pi\nu}{c}$ is the wave vector, and d is the thickness of the metasurface slab.

The metasurface is identified as a non-passive medium. In such a situation, the real and imaginary components of impedance (Z) and refractive index ($\eta_{eff.}$) satisfy the conditions given in the literature [39]. The usual extraction procedure is applied to calculate the effective parameter values for the designed metasurface structure [41]. From the effective parameter analysis, the resonance frequencies can be easily analyzed. The $\varepsilon_{eff.}$, $\mu_{eff.}$, $\eta_{eff.}$ and normalized impedance (Z) can be calculated using the following equations [42, 43]:

$$\varepsilon_{eff.} = \frac{2}{jk_0 d} \times \frac{(1 - V_1)}{(1 + V_1)} = \frac{c}{j\pi\nu d} \frac{(1 - S_{21} - S_{11})}{(1 + S_{21} + S_{11})} \tag{3}$$

$$\mu_{eff.} = \frac{2}{jk_0 d} \times \frac{(1 - V_2)}{(1 + V_2)} = \frac{c}{j\pi\nu d} \times \frac{(1 - S_{21} + S_{11})}{(1 + S_{21} - S_{11})} \tag{4}$$

$$\eta_{eff.} = \sqrt{\varepsilon_{eff.} \times \mu_{eff.}} = \frac{c}{j\pi\nu d} \sqrt{\frac{(S_{21} - 1)^2 - (S_{11})^2}{(S_{21} + 1)^2 - (S_{11})^2}} \tag{5}$$

Table 3 Comparison of the metasurface shape, dimension of the unit cell, and frequency bands of the proposed designed metasurface structure with some previously reported data

References	Year of Publication	Metasurface shape	Dimension of the unit cell mm^2	Frequency bands
[33]	2019	CSRR	5.5×5.5	C-band
[34]	2020	GCHSRR	10×10	S-band, X-band
[35]	2020	CSR	22×22	C-band, Ku-band
[36]	2022	CCRR	22×22	X-band
[37]	2022	SE-SMS	10×10	S-band, Ku-band
[38]	2023	SSRR	15×15	S, C, and X-band
This work	2023	CC-SRR	16×16	C, X, and Ku-band

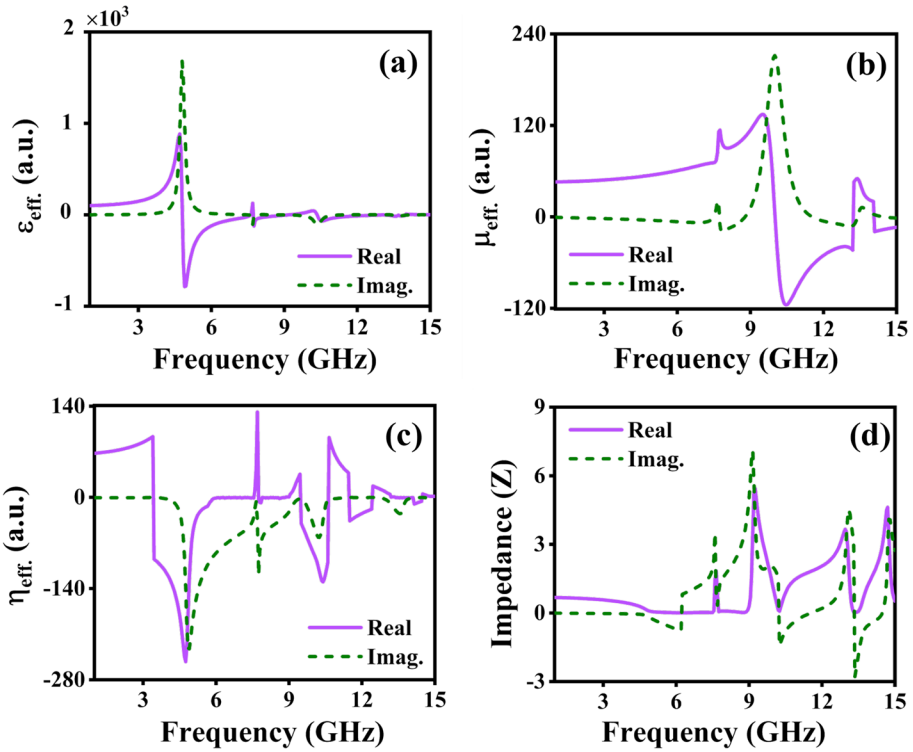


Fig. 8 Variation of **a** effective permittivity ($\varepsilon_{eff.}$), **b** effective permeability ($\mu_{eff.}$), **c** effective refractive index ($\eta_{eff.}$) and **d** impedance (Z) with the frequency of the designed metasurface structure

$$Z = \sqrt{\frac{(1+S_{11})^2 - S_{21}^2}{(1-S_{11})^2 - S_{21}^2}} \tag{6}$$

where $V_1 = |S_{21}| + |S_{11}|$, $V_2 = |S_{21}| - |S_{11}|$, and c is the speed of light in a vacuum.

Figure 8a shows the negative permittivity at three resonance frequencies i.e., at 7.5, 8.8, and 13.4 GHz with magnitudes of − 18.64, − 8.89, and − 8.20, respectively. In Fig. 8b, the permeability graph is plotted in which at the resonance frequencies, the $\mu_{eff.}$ is positive indicating the designed structure to be an SNG (Single negative) metasurface. Although the plot of $\eta_{eff.}$ in Fig. 8c shows the near zero characteristics i.e., at 7.5 GHz it is − 0.53, at 8.8 GHz it is − 0.36 and at 13.4 GHz it is − 0.46, respectively. These findings indicate that the proposed design satisfies the near zero index (NZI) along with epsilon negative (ENG) properties. In Fig. 8d, the impedance characteristics are illustrated. Table 4 provides a summary of the overall parameter properties for the designed metasurface structure.

4.3 Analysis of E-field and H-field distribution

The suggested metasurface structure has resonant copper assemblies made up of split gaps and metallic strips (conductors) in the top layer. Conductors and split gaps function as inductors and capacitors, respectively. The interaction of time-varying electromagnetic fields with the designed structure causes an electromagnetic force to be delivered to the resonators. Produced electric and magnetic moments affect a material's capacity for transmission and alter properties like effective permittivity ($\varepsilon_{eff.}$) and effective permeability ($\mu_{eff.}$). According to Ampere's law and Faraday's law of induction, time-varying charge flow is primarily responsible for producing a magnetic field, which then results in an electric field as a result of electromagnetic interaction. Maxwell's curl equation can be used to examine the induced E-field and H-field given by (7)–(11) [44].

Table 4 Effective parameter property

Parameters	Operating frequency (GHz)	Extracted property
Effective permittivity ($\varepsilon_{eff.}$)	4.85–7.60, 7.80–9.15 and 10.35–14.0	$\varepsilon_{eff.} < 0$ (ENG)
Effective permeability ($\mu_{eff.}$)	1.00–10.00 and 13.25–14.05	$\mu_{eff.} > 0$ (SNG)
Refractive index ($\eta_{eff.}$)	5.70–7.55, 7.90–9.00 and 13.20–14.10	$\eta \sim 0$ (NZI)
Impedance (Z)	4.9–7.55, 7.8–8.9 and 13.3–13.55	$Z \sim 0$

Horizontal magnetic field component:

$$\nabla \times H = J + \frac{\partial D}{\partial t} \tag{7}$$

The electric field produced is related to the magnetic field:

$$\nabla \times E = -\frac{\partial B}{\partial t} \tag{8}$$

where,

$$\nabla = \hat{i}\frac{\partial x}{\partial t} + \hat{j}\frac{\partial y}{\partial t} + \hat{k}\frac{\partial z}{\partial t} \quad \text{is the vector operator.} \tag{9}$$

Equations (7) and (8) describe the interaction of the H and E vectors with the material. It is insufficient to explain why the two fields interact with materials from the magnetic flux and electric flux densities given by B and D, respectively. When determining the magnetic flux density (B), permeability can be employed, whereas permeability is used to estimate the electric flux density (D). To get beyond these constraints that define the relationship between B and D, two more equations are needed [38]:

$$\varepsilon(t) = \frac{D(t)}{E(t)} \tag{10}$$

$$\mu(t) = \frac{B(t)}{H(t)} \tag{11}$$

Using (7)–(11) following relations can be achieved which can be used to express Maxwell's curl equations [38]:

$$\nabla \times E = -j\omega\mu H \tag{12}$$

$$\nabla \times H = j\omega\varepsilon E \tag{13}$$

Throughout the simulation, electromagnetic waves pass through the CC-SRR metasurface unit cell and respond to reflection and transmission coefficients, respectively.

The surface current, magnetic field, and electric field distributions of the proposed metasurface were analyzed for triple resonance frequency and are shown in Figs. 9, 10, and 11 respectively. The electric and magnetic field distributions identify the resonance happenings inside the designed metasurface. This enables us to identify the frequencies at which strong field enhancements or interactions are present on the designed metasurface. The electric field confinement emerges from the interaction of the electromagnetic fields within the designed metasurface.

The MTM surface current distribution is shown in Fig. 9a–c. Figure 9a reveals that at 7.5 GHz, a clockwise current flow in the right half and an anticlockwise current flow in the left half of the circular coupled SRR structure. The even current distribution is seen in the inner coupled SRR structure. It is relatively high in the inner circular edges of Fig. 9a compared to the remaining portion. A decrease in current is observed at 8.8 GHz, as shown in Fig. 9b, due to the current distribution in outer CSRR along with inner coupled SRR. Furthermore, the surface current intensity shown by the color bar again increases at the frequency of 13.4 GHz as compared to the 8.8 GHz frequency. The outer region of CRRR shows the maximum amount of the current, shown in Fig. 9c however, the remaining portion has negligible current distribution. The magnetic field distribution for the three resonance frequencies is shown in Fig. 10a–c.

Magnetic field and surface current density are correlated, as shown in Eq. (7). In Fig. 10a, high magnetic field intensities are shown in those regions where a larger current density is observed; this satisfies Maxwell's equation represented by Eq. (7). The H-field distribution of the proposed structure is of the order of 345 A/m in the inner layer of the circular coupled ring for the 7.5 GHz resonance frequency as shown in Fig. 10a. Figure 10b shows a low-intensity magnetic field owing to the low current intensity at this frequency due to the current getting more distributed in outer CSRR. In contrast, in Fig. 10c, the outer circular edges exhibit significant magnetic field intensity due to knowledgeable current distribution. However, the field intensity is low in other parts of the metasurface structure. The magnetic field distributions at the 8.8 and 13.4 GHz resonance frequencies show lesser accumulation of the field as compared to the magnetic field at 7.5 GHz resonance frequency as shown in Fig. 10b, c. The distributions of the electric and magnetic fields are in contradiction to one another, with the magnetic field being the largest where the electric field is minimum and vice versa. Figure 11a–c displays the electric field distribution.

Equation (8) states that changes in the magnetic field affect the induced electric field. An intense electric field is observed in the areas where the rate of change in the magnetic field is maximum, as per the comparison of Figs. 10a and 11a. Due to the capacitive effect, a strong electric field is detected near the gap in the metasurface structure. In the proposed designed metasurface, the gap regions 'g' and 'c' denote the capacitance of the resonator structure [45]. The capacitance is inversely dependent on the gap region of the resonator. The electric field is more confined in the gap region which indicates the capacitance region in metasurface. The capacitance is given as, $C = \frac{\varepsilon_0 A}{d}$, where ε_0 is the dielectric constant, A is the area between the plates, and d is the distance between the plates. A strong electric field near the gaps 'c' of the central coupled circular ring of the order of 1.4×10^5 V/m at the resonance frequency of 7.5 GHz is depicted in Fig. 11a. As we shift towards the higher resonance frequency i.e., 8.8 GHz the electric field gets accumulated on the gap region of the circle 'c' as well as in the gap 'g' of CSRR of the reduced order of 4.19×10^4 V/m

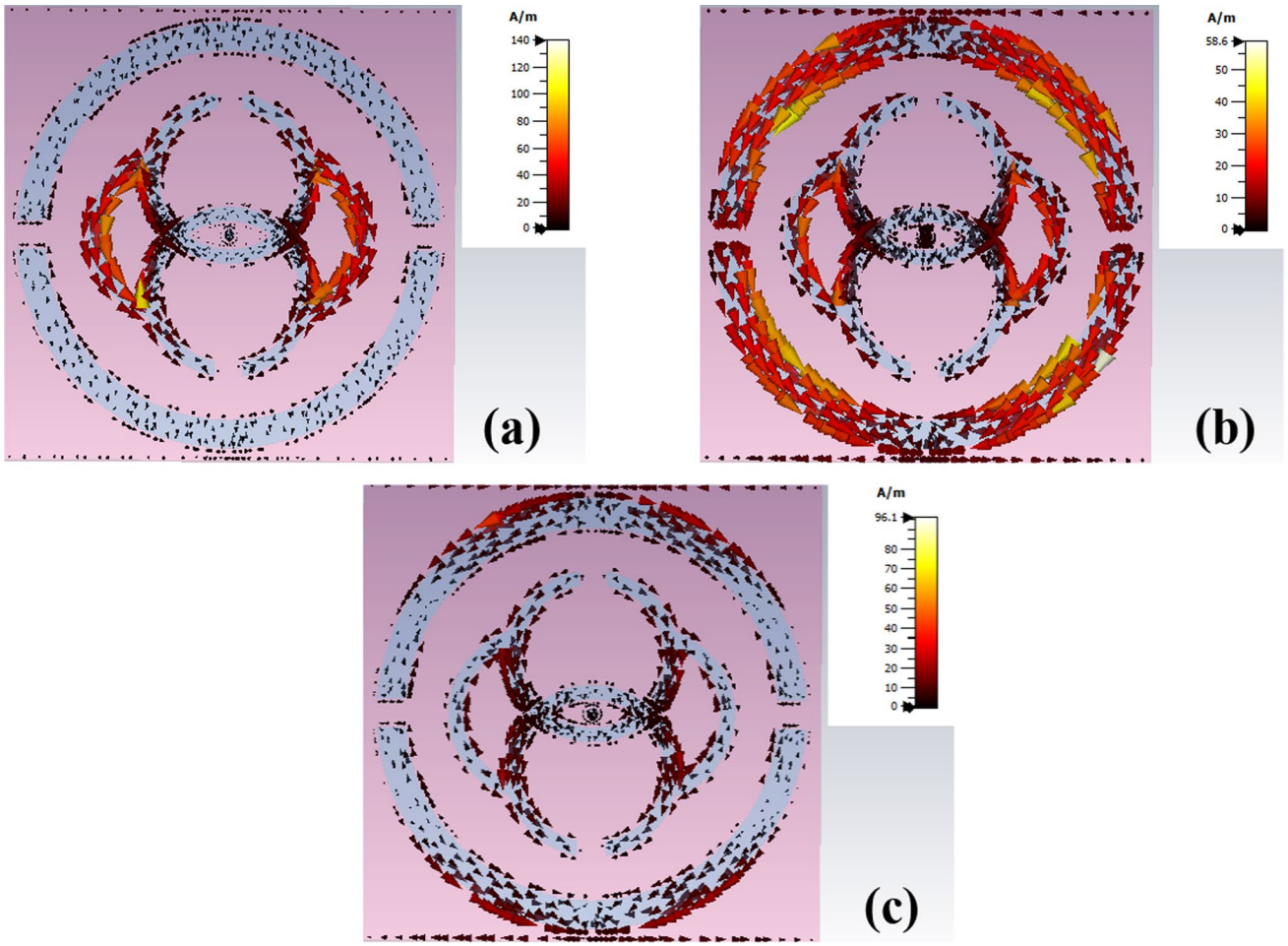


Fig. 9 Surface current distribution at **a** 7.5 GHz, **b** 8.8 GHz, and **c** 13.4 GHz resonance frequency, respectively

as shown in Fig. 11b. Consequently, at the 13.4 GHz resonance frequency, the electric field accumulation magnitude is slightly higher than that at 8.8 GHz, order of 6.09×10^4 V/m shown in Fig. 11c. The low electric field intensity is observed due to low electric current resulting in less magnetic field intensity. Further, the electric field is neutralized when the magnetic field is constant in the resonator. Due to the interconnected nature of electromagnetic fields and currents, both play a vital role in the resonances at the frequencies mentioned above.

4.4 Equivalent circuit model of the designed metasurface

To verify the COMSOL Multiphysics results of the designed metasurface, ADS generates and executes an estimated electrical equivalent circuit model. The components in the equivalent circuit model correspond to the capacitance and inductance of the individual resonators in the designed metasurface. Metal strips and split gaps are used to construct the unit cell. In the proposed metasurface, these resonators are copper metallic patches, and their capacitance and inductance are determined by their physical dimensions and material properties. Each metal strip is an inductor, and each split gap is a capacitor [45]. The proposed design along with gaps indicating capacitor and metal strip as inductor is already discussed in section III-A. To ensure proper coupling of electromagnetic waves with the metasurface, impedance-matching components have been included in the equivalent circuit model. These components help optimize the reflection and transmission properties of the metasurface. The equivalent circuit model predicts the resonance frequencies in the proposed structure because in this model we have connected the inductor and capacitor which becomes an LC circuit like an LCR tank circuit. These components are connected in series or parallel to create circuit configurations. The resonance frequency of an LCR circuit is the frequency at which the inductive and capacitive reactance are equal, canceling each other out, and leaving only the resistance

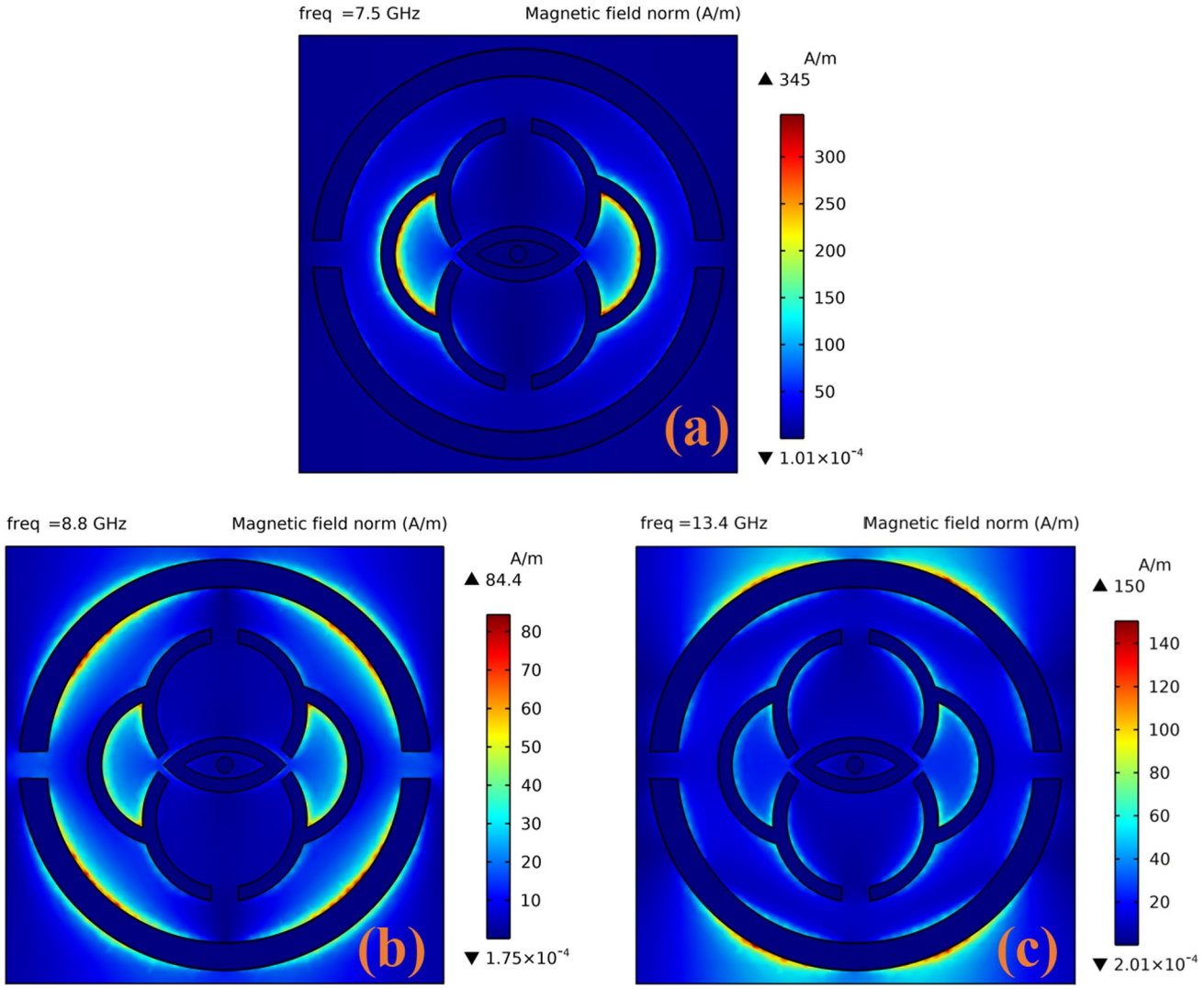


Fig. 10 Magnetic field distribution at **a** 7.5 GHz, **b** 8.8 GHz, and **c** 13.4 GHz resonance frequency, respectively

in the circuit. At resonance, the impedance of the circuit becomes purely resistive, and the circuit responds most strongly to the applied frequency. As a result, an LC resonance circuit is employed to represent the entire unit cell, with inductance (L) and capacitance (C) acting as the fundamental variables to calculate the resonance frequency (f).

The impedance (Z) of an LCR circuit is a complex quantity that considers the resistance (R), inductive reactance (X_L), and capacitive reactance (X_C) which is given as, $Z = R + j\,(X_L - X_C)$, where j is the imaginary unit. At resonance, $X_L = X_C$, so the reactive components cancel each other out, and Z becomes purely resistive. The imaginary part of the impedance is zero, and the impedance is purely resistive. The frequency at which the impedance is minimized (equal to the resistance) is the resonance frequency. The resonance frequency (f) can be found using the formula [46]:

$$f = \frac{1}{2\pi\sqrt{LC}} \tag{14}$$

Figure 12a shows the proposed metasurface resonator equivalent LC circuit model and Fig. 12c represents the obtained results from the simulated structure and the equivalent circuit model of the proposed metasurface. The L_1C_1 and L_2C_2 correspond to the outer ring of the circular-shaped split ring resonator LC combination. The C_3 and C_4 correspond to the upper and lower split gap 'g', L_8 and L_9 represent the coupled circular arc inductors, L_3 C_5 L_5 and

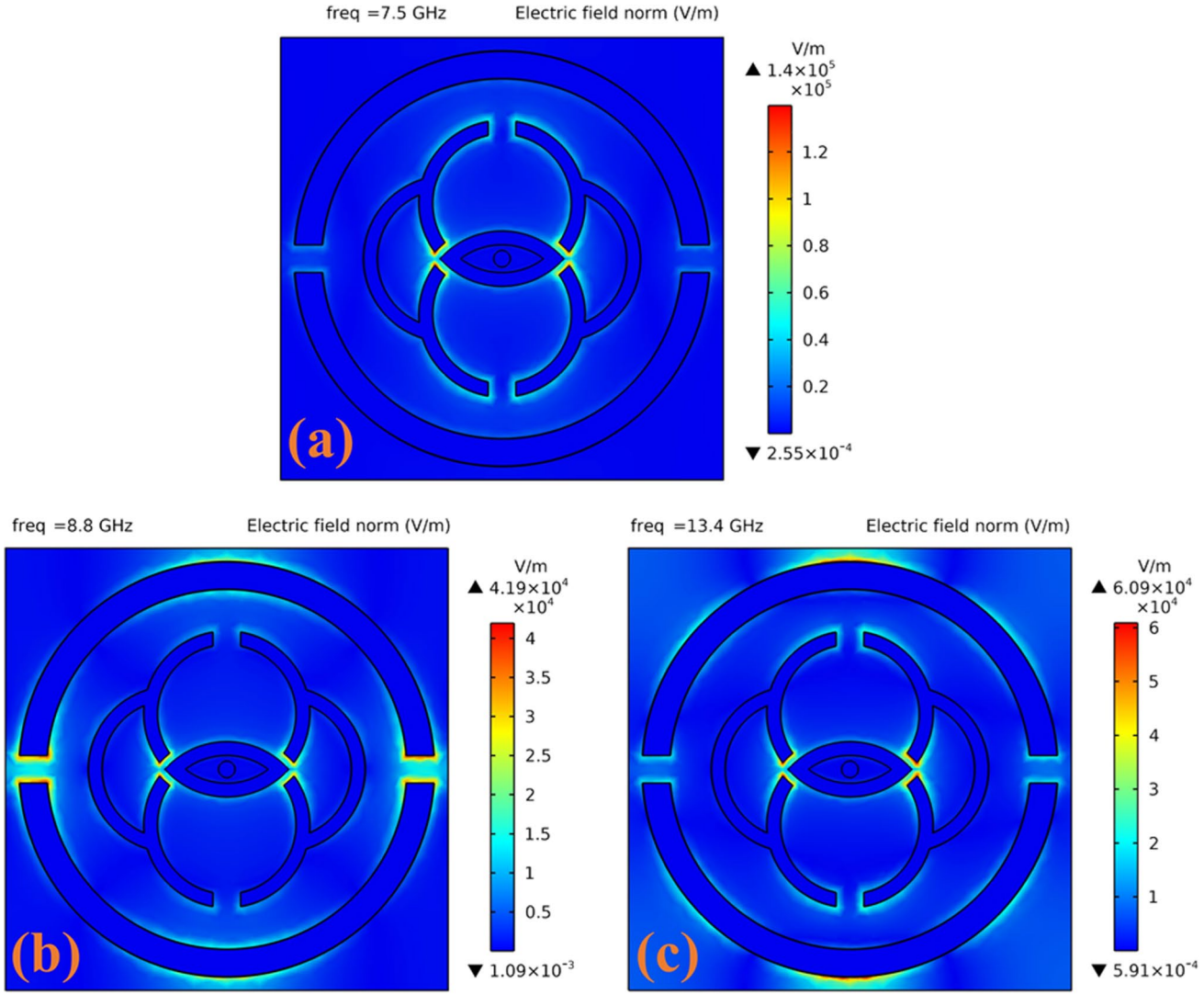


Fig. 11 Electric field distribution at **a** 7.5 GHz, **b** 8.8 GHz, and **c** 13.4 GHz resonance frequency, respectively

L_4 C_6 L_6 represent the centered cross circle and L_{10} C_8 L_7 C_7 corresponds to the centered eye shaped, and circle shaped respectively as shown in Fig. 12b. It is evident from Fig. 12c that the result for the equivalent LC circuit modeling of the proposed metasurface unit cell structure resonates in the triple band which matches the simulated result. The corresponding values of all lumped elements are listed in Table 5.

4.5 Potential future applications

The designed metasurface has numerous applications and potential future research directions in emerging technologies and specific engineering applications. Designed metasurface can be used to make antennas having properties such as high gain, reduced size, and improved directivity [47]. The designed metasurface can also enable beamforming and beam-steering capabilities in antennas, which are crucial for wireless communication systems [48, 49]. The designed metasurface can be used to create cloaking devices that can hide objects from radar and microwave detection [32]. This has applications in military stealth technology and could be used to protect sensitive equipment. The designed metasurface can be engineered to create highly efficient filters for specific microwave frequencies [50]. They can also be used to design microwave absorbers, which are essential for reducing electromagnetic interference and improving signal-to-noise ratios in microwave devices [51, 52]. Designed metasurface can enable the miniaturization of microwave patch antennas, making them suitable for compact and portable devices like smartphones and wearable technology [53].

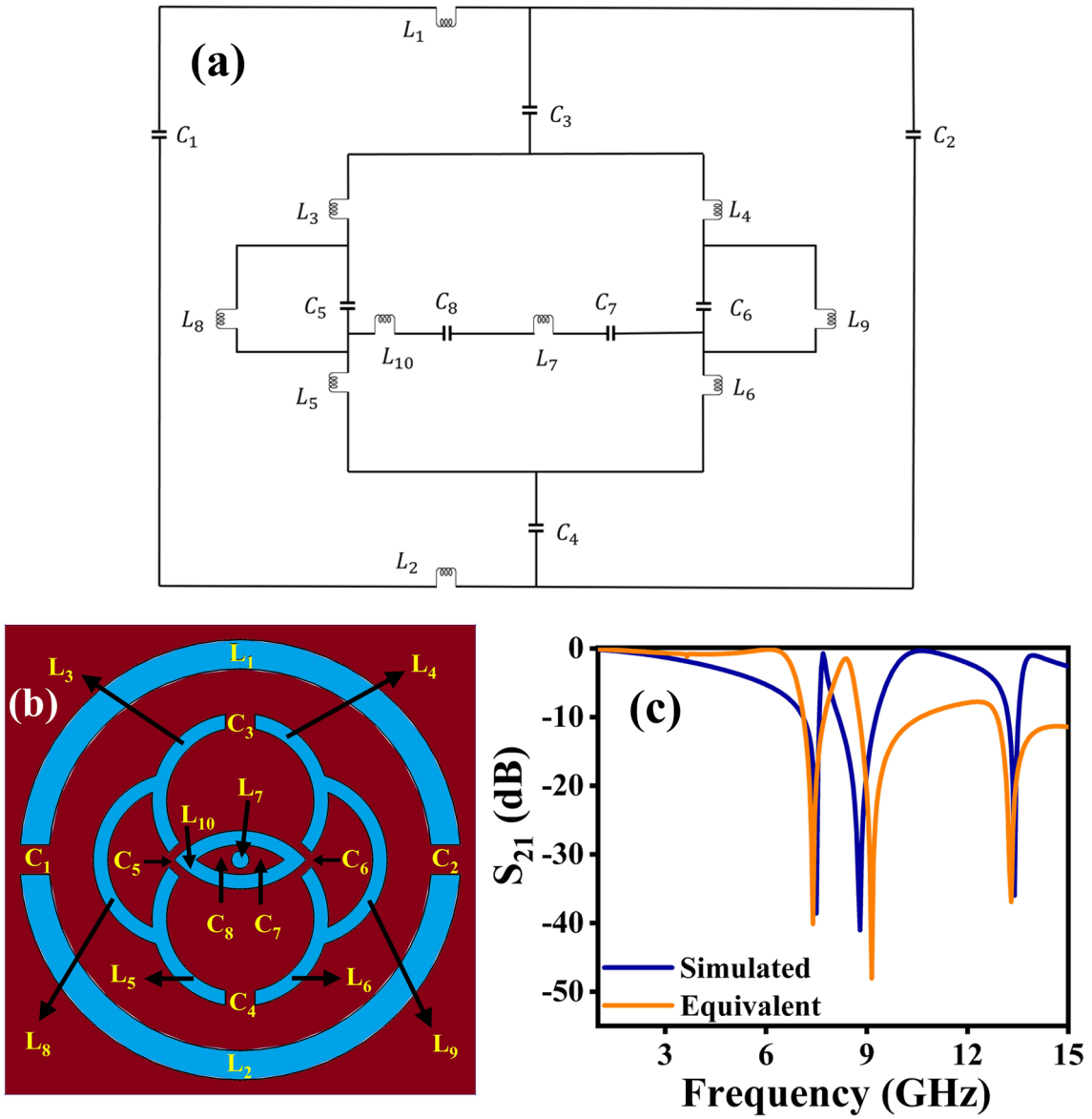


Fig. 12 **a** Equivalent circuit model with lumped elements, **b** inductance (L) and capacitance (C) representation of the equivalent circuit model, and **c** corresponding results of S_{21} (transmission coefficient) from the simulated structure and the equivalent structure of the proposed metasurface

5 Conclusion

The present study involves the fabrication and simulation of an eye-shaped CC-SRR metasurface structure on the FR-4 dielectric substrate, revealing ENG and NZI characteristics in the frequency range of 1–15 GHz. The results from experimental measurements were compared with the simulated results. A good match between the two was observed, with minimum frequency shift, suggesting that any deviations between the simulated and measured resonance frequencies are within the acceptable range. The structure also shows tunable characteristics with variations in the thickness of dielectric substrate material (t_s) and copper resonator thickness (t_m). The simulated results were also validated by using different simulation software and equivalent electrical circuit model. The electric and magnetic field distributions were investigated to observe the electromagnetic characteristics at different resonant frequencies. The above results suggest that the designed metasurface structure may be an excellent aspirant for microwave components and devices in C, X, and Ku-band applications.

Table 5 Corresponding values of all lumped components of the equivalent circuit for the proposed metasurface design

Lumped components	Value (nH)	Lumped components	Value (pF)
L_1	1.04	C_1	0.85
L_2	0.534	C_2	0.265
L_3	0.98	C_3	0.406
L_4	0.8	C_4	1.38
L_5	1.19	C_5	0.59
L_6	1.5	C_6	2.525
L_7	0.86	C_7	0.9
L_8	1.136	C_8	1.5
L_9	0.156		
L_{10}	0.3		

Acknowledgements Authors gratefully acknowledge the initiatives and support from the TIFAC-Centre of Relevance and Excellence in Fiber Optics and Optical Communication at Delhi College of Engineering, now DTU, Delhi, under the Mission REACH program of Technology Vision-2020, Government of India. One of the authors, Mr. Ankit, would like to acknowledge (i) the Central Research Facility (CRF) of IIT-Delhi for facilitating with measurement of fabricated design using RF and Antenna Measurement setup, (ii) Delhi Technological University, Delhi, for support in terms of Research Fellowship and (iii) Dr. Monu Nath Baitha of Yonsei University, South Korea for critical and useful discussions on this research work.

Author contributions All authors have contributed to the study conception and design. Ankit: conceptualization, methodology, software, fabrication, calculations, and writing-original draft. KK: writing-reviewing and verification of results. RKS: conceptualization, validation, and supervision editing. All authors read and approved the final manuscript.

Data availability Data will be made available on request.

Declarations

Conflict of interest There is no conflict of interest. The authors declare that they have no known competing financial interests or personal relationships that could have appeared to influence the work reported in this paper.

Ethical approval We approved all ethics.

References

1. R. Liu, C. Ji, Z. Zhao, T. Zhou, Engineering **1**, 179 (2015)
2. R.W. Ziolkowski, IEICE Trans. Electron. **E89-C**, 1267 (2006)
3. V.G. Veselago, Sov. Phys. Uspekhi **10**, 509 (1968)
4. J.B. Pendry, A.J. Holden, W.J. Stewart, I. Youngs, Phys. Rev. Lett. **76**, 4773 (1996)
5. J.B. Pendry, A.J. Holden, D.J. Robbins, W.J. Stewart, IEEE Trans. Microw. Theory Tech. **47**, 2075 (1999)
6. N. Engheta, R.W. Ziolkowski, IEEE Trans. Microw. Theory Tech. **53**, 1535 (2005)
7. N. Shankhwar, R.K. Sinha, *Zero Index Metamaterials* (Singapore, Springer Singapore, 2021), pp.57–82
8. T. Koschny, P. Markoš, D.R. Smith, C.M. Soukoulis, Phys. Rev. E **68**, 065602 (2003)
9. M.J. Hossain, M.R.I. Faruque, S.S. Islam, M.T. Islam, Microw. Opt. Technol. Lett. **58**, 3004 (2016)
10. H. Jeong, T.T. Nguyen, S. Lim, Sci. Rep. **8**, 16774 (2018)
11. D. Schurig, J.J. Mock, B.J. Justice, S.A. Cummer, J.B. Pendry, A.F. Starr, D.R. Smith, Science (80-) **314**, 977 (2006)
12. P. Agarwal, K. Kishor, R.K. Sinha, Opt. Commun. **522**, 128667 (2022)
13. Ankit, K. Kishor, R.K. Sinha, Results Opt. **10**, 100366 (2023)
14. H. Zhu, Y. Zhang, L. Ye, Y. Li, Z. Dang, R. Xu, B. Yan, IEEE Trans. Microw. Theory Tech. **70**, 5383 (2022)
15. K. Kishor, M.N. Baitha, R.K. Sinha, B. Lahiri, J. Opt. Soc. Am. B **31**, 1410 (2014)
16. F. Tavakoli, F.B. Zarrabi, H. Saghaei, Appl. Opt. **58**, 5404 (2019)
17. S. Haxha, F. AbdelMalek, F. Ouerghi, M.D.B. Charlton, A. Aggoun, X. Fang, Sci. Rep. **8**, 16119 (2018)
18. H.O. Yilmaz, F. Yaman, IEEE Trans. Instrum. Meas. **69**, 1775 (2020)
19. H. Saghaei, P. Elyasi, B.J. Shastri, J. Appl. Phys. **132**, 064501 (2022)
20. H. Saghaei, Appl. Opt. **57**, 5591 (2018)
21. H. Saghaei, P. Elyasi, R. Karimzadeh, Photon. Nanostruct. Fundam. Appl. **37**, 100733 (2019)
22. N. Benmostefa, M. Meliani, H. Ouslimani, J. Electromagn. Anal. Appl. **05**, 250 (2013)
23. I.C. Hunter, J.D. Rhodes, M.Y. Sandhu, R.V. Snyder, M. Meng, IEEE Trans. Microw. Theory Tech. **64**, 4204 (2016)
24. E. Karakaya, F. Bagci, S. Can, A.E. Yilmaz, B. Akaoglu, Int. J. RF Microw. Comput. Eng. **29**, e21644 (2019)
25. C. Sabah, T. Nesimoglu, Opt. Eng. **55**, 027107 (2016)
26. M.R.I. Faruque, E. Ahamed, M.A. Rahman, M.T. Islam, Results Phys. **14**, 102524 (2019)
27. M. Shahidul Islam, M.T. Islam, N. Mohd Sahar, H. Rmili, N. Amin, M.E.H. Chowdhury, Results Phys. **18**, 103292 (2020)
28. D. Marathe, K. Kulat, Int. J. Antennas Propag. **2017**, 1 (2017)
29. M. Bellal Hossain, M. Rashed Iqbal Faruque, A.S. Alshammari, M. Tariqul Islam, Results Phys. **37**, 105511 (2022)
30. M.B. Hossain, M.R.I. Faruque, M.T. Islam, Alex. Eng. J. **69**, 193 (2023)
31. H.L. Zhu, X.H. Liu, S.W. Cheung, T.I. Yuk, IEEE Trans. Antennas Propag. **62**, 80 (2014)
32. K. Srilatha, B.T.P. Madhav, B.A. Babu, S. Das, M.C. Rao, Appl. Phys. A **128**, 1091 (2022)
33. A.F. Almutairi, M.S. Islam, M. Samsuzzaman, M.T. Islam, N. Misran, M.T. Islam, Results Phys. **15**, 102675 (2019)
34. M. Shahidul Islam, M. Samsuzzaman, G.K. Beng, N. Misran, N. Amin, M.T. Islam, IEEE Access **8**, 68239 (2020)
35. T. Ramachandran, M.R.I. Faruque, M.T. Islam, Results Phys. **16**, 102942 (2020)
36. H.O. Ali, A.M. Al-Hindawi, Y.I. Abdulkarim, M. Karaaslan, Opt. Commun. **503**, 127457 (2022)
37. S. Hannan, M.T. Islam, S.H.A. Almalki, M.R.I. Faruque, M.S. M, M.S. Islam, Sci. Rep. **12**, 3740 (2022)
38. I. Hossain, M. Tariqul Islam, N. Binti Mohd Sahar, A. Mohamed Moubark, M.S. Soliman, M. Samsuzzaman, J. Magn. Magn. Mater. **565**, 170226 (2023)
39. R. Sifat, M.R.I. Faruque, M.B. Hossain, M. Abdullah, M.T. Islam, M.U. Khandaker, N. Tamam, A. Sulieman, Crystals **12**, 836 (2022)
40. Z. Szabó, G.-H. Park, R. Hedge, E.-P. Li, IEEE Trans. Microw. Theory Tech. **58**, 2646 (2010)

41. D.R. Smith, D.C. Vier, T. Koschny, C.M. Soukoulis, Phys. Rev. E **71**, 036617 (2005)
42. X. Chen, T.M. Grzegorczyk, B.I. Wu, J. Pacheco, J.A. Kong, Phys. Rev. E Stat. Phys. Plasmas Fluids Relat. Interdiscipl. Top. **70**, 7 (2004)
43. S.S. Islam, M.R.I. Faruque, M.T. Islam, Curr. Sci. **109**, 337 (2015)
44. M.S.U. Afsar, M.R.I. Faruque, S. Abdullah, M.T. Islam, M.U. Khandaker, K.S. Al-Mugren, Materials (Basel). **16**, 1137 (2023)
45. Y. Guo, J. Zhou, Sci. Rep. **5**, 8144 (2015)
46. M. Moniruzzaman, M.T. Islam, N. Misran, M. Samsuzzaman, T. Alam, M.E.H. Chowdhury, Sci. Rep. **11**, 11950 (2021)
47. H.-P. Li, G.-M. Wang, X.-J. Gao, J.-G. Liang, H.-S. Hou, IEEE Trans. Antennas Propag. **66**, 3706 (2018)
48. D. Rotshild, A. Abramovich, Electronics **10**, 2165 (2021)
49. H. Li, G. Wang, L. Zhu, X. Gao, H. Hou, Opt. Commun. **466**, 124601 (2020)
50. H. Badgujar, A. Khan, F. Carvalho, A. Kotrashetti, S. Ghosh, S. Bhattacharyya, in *2022 IEEE Reg. 10 Symp.* (IEEE, 2022), pp. 1–5
51. Y. Khanna, Y.K. Awasthi, Int. J. Microw. Wirel. Technol. **14**, 573 (2022)
52. C. Barde, A. Choubey, R. Sinha, J. Appl. Phys. **126**,175104 (2019)
53. H.L. Zhu, S.W. Cheung, T.I. Yuk, Microw. Opt. Technol. Lett. **57**, 2050 (2015)

Publisher's Note Springer Nature remains neutral with regard to jurisdictional claims in published maps and institutional affiliations.

Springer Nature or its licensor (e.g. a society or other partner) holds exclusive rights to this article under a publishing agreement with the author(s) or other rightsholder(s); author self-archiving of the accepted manuscript version of this article is solely governed by the terms of such publishing agreement and applicable law.

Multimedia Tools and Applications
https://doi.org/10.1007/s11042-024-18235-7

Detecting low-resolution deepfakes: an exploration of machine learning techniques

Mayank Pandey[1] · Samayveer Singh[1] · Aruna Malik[1] · Rajeev Kumar[2]

Received: 4 July 2023 / Revised: 31 October 2023 / Accepted: 8 January 2024
© The Author(s), under exclusive licence to Springer Science+Business Media, LLC, part of Springer Nature 2024

Abstract
Deep generative models, especially Generative Adversarial Networks (GANs), have recently demonstrated outstanding performance in real-world applications such as image generation and content production for large-scale public datasets and social media platforms, enabling high-resolution compelling fake content generation. Deepfakes have raised global concerns and disbelief due to the potential implications of misleading multimedia. Several algorithms to detect deepfakes have emerged; however, most rely on deep learning and video datasets. So, an automated approach is needed to detect the generated deepfakes. This paper presents a deepfake detection technique employing simple machine learning to identify low-resolution deepfakes and introduces a dataset that contains high-resolution, low-resolution, and mixed images. The method utilizes classification algorithms and an ensemble model in the frequency domain. K-fold cross-validation determines an average detection accuracy of 99.97% for high-resolution datasets using random forest, 98.27% for low-resolution datasets using SVM polynomial, and 98.72% for mixed datasets using voting classifier.

Keywords Generative adversarial networks · Deepfake · Low-resolution images · Machine learning

✉ Samayveer Singh
samayveersingh@gmail.com

Mayank Pandey
pandeym444@gmail.com

Aruna Malik
malika@nitj.ac.in

Rajeev Kumar
rajeevgargnsit@gmail.com

[1] Department of Computer Science & Engineering, Dr. B R Ambedkar National Institute of Technology, Jalandhar, Punjab, India

[2] Delhi Technological University, New Delhi, India

Published online: 22 January 2024

1 Introduction

Artificial intelligence is advancing rapidly, enhancing machines' capability to emulate human behavior. Notably, deep learning algorithms, such as GANs are making significant strides [1]. GANs generate synthetic samples from original datasets. Deep learning marked a pivotal shift in the creation of Deepfakes [2]. In 2017, an anonymous Reddit user pioneered the first deepfakes by superimposing celebrity faces onto explicit films without consent. Deepfakes are produced by training two competing deep learning models using genuine data. The automated nature of deepfakes makes these falsified representations challenging to identify. Figure 1 provides an example.

Research on deepfakes predominantly centers on the detection of fabricated images and videos. These deceptive media are exploited for purposes such as pornography, identity theft, and false authorization. Figure 2a depicts the exponential surge in deepfake production, doubling approximately every six months. Figure 2b illustrates the geographical transition of deepfakes from the western to the eastern parts of the world.

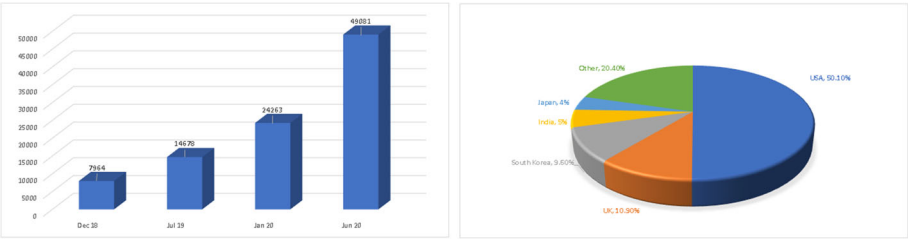
Deep learning, a subset of AI that employs deep neural networks (DNNs), is instrumental in the creation of deepfakes. DNNs consist of numerous interconnected artificial neurons. Individually, each neuron handles a basic computation, but when combined, they can manage intricate tasks. By optimizing connection weights and understanding hidden task features, these computations can be enhanced, though such refinement demands a wealth of data.

The production of deepfakes typically involves outlining the original image, subsequently feeding this outlined image into the deep neural network, and then superimposing the generated images back onto the original ones. DNNs, a prominent method in AI/ML, stand as multi-layered artificial neural networks positioned between the input and output. These "deep" networks often have a range of layers, from 10 to well over 100.

An autoencoder is a type of deep neural network designed to recreate input images by condensing them into essential properties and subsequently reproducing them [5]. As these



Fig. 1 Example of deepfakes [3]



(a) Trend of deepfake contents. (b) Distribution of deepfake contents.

Fig. 2 Illustration of the exponential surge in deepfake production and the geographical transition of deepfakes [4]

networks focus on accurate reconstruction, another class of models, known as Generative Adversarial Networks, emerges with a different approach. GANs are advanced generative modeling techniques in machine learning. These systems excel at detecting patterns in input data and can craft new instances that bear a striking resemblance to the original dataset. Central to GANs are two primary sub-models: the Generator (G) and the Discriminator (D). While the generator conceives new data instances from random noise, the discriminator assesses the authenticity of each instance. The ultimate aim is refining the generator until it produces instances so authentic that the discriminator struggles to distinguish real from fake, achieving a state of equilibrium where it's deceived approximately half the time. This intricate balance, exemplified in Fig. 3, underscores the core architecture of GANs.

Deepfakes have gained significant attention due to their potential implications in diverse areas, from entertainment to the dissemination of misinformation [6]. Broadly, deepfakes can be segmented into four primary categories. Photo Deepfakes predominantly focus on still images where facial alterations are executed by substituting them with another person's face, such as swapping both the body and face of an individual in a photograph with someone else's [5]. Audio Deepfakes venture into sound manipulation, with techniques like Voice Swapping, where an individual's voice is modified to resemble someone else's, and Text-to-Speech,

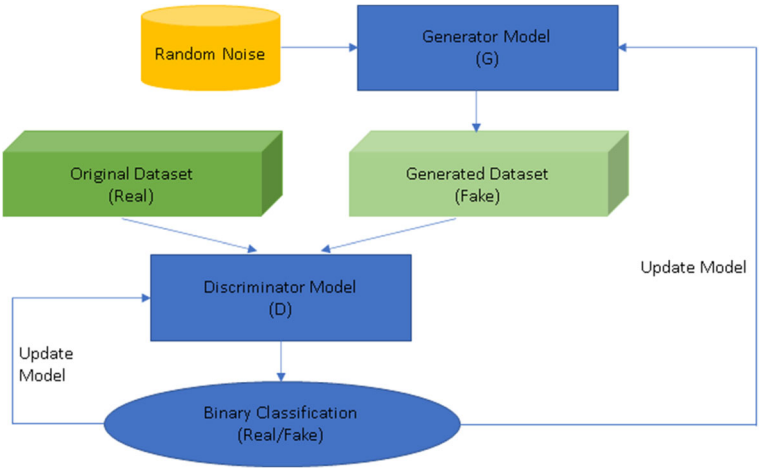


Fig. 3 Generative adversarial networks architecture

which amends audio content to make the spoken discourse diverge from the original. Video Deepfakes concentrate on video manipulations, including techniques like Face Swapping, which applies the concept of photo deepfakes to videos, and Face Morphing, allowing one face to gradually morph into another within a video sequence. The combined category of Audio& Video Deepfakes represents a fusion of both audio and video alterations, such as modifying a "talking head" video where the subject's lip movements and spoken utterances are synchronized with different audio content to craft a fabricated message [7].

Given the rapid expansion of digital content in today's age, discerning genuine information from falsified data has become increasingly challenging. The advent of deepfakes in 2018 has further blurred the lines, making the distinction between authentic and fabricated content nearly indistinguishable. This technology has paved the way for a myriad of online malpractices, encompassing areas such as non-consensual pornography, identity theft, the propagation of counterfeit documents, and the spread of disinformation. There is, thus, an acute need for a more robust and reliable deepfake detection system to differentiate between real and manipulated materials. Such a system would greatly mitigate the dissemination of false content and the associated cybercrimes. However, a limitation of the current research is its reliance on a deepfake detection technique that primarily targets low-resolution deepfakes using basic machine learning. This is addressed in this paper, which introduces a dataset comprising high-resolution, low-resolution, and mixed images. Employing classification algorithms and an ensemble model in the frequency domain, the proposed approach aims to overcome this limitation, enhancing the accuracy and reliability of deepfake detection. The main contribution of the research is delineated as follows:

- The article introduces a dataset tailored for deepfake detection that encompasses high-resolution, low-resolution, and mixed images.
- Proposed and develop a classification-based approach that leverages algorithms and an ensemble model operating in the frequency domain for deepfake detection.
- The research notably achieved deepfake detection accuracies of 99.97% for high-resolution datasets with Random Forest, 98.27% for low-resolution datasets with SVM polynomial, and 98.72% for mixed datasets using voting classifier.

The remaining sections of this paper are organized as follows: Section 2 discusses the tools and techniques utilized in the current research. Section 3 details the methodology, which includes implementation steps (3.1), the proposed architecture (3.2), and subsections on the chosen datasets (3.2.1), image pre-processing (3.2.2), segmentation (3.2.3), augmentation (3.2.4), and classification (3.2.5). Section 4 presents the results and evaluation of the proposed approach, and the paper concludes with Section 5.

2 Related work

In this section, we provide an overview of recent research efforts in deepfake detection. McCloskey and Albright [8] in 2018 analyzed the generative network structure of GANs, highlighting the differences in color treatment between real cameras and such networks. The identified color cues could help distinguish real camera images from GAN-generated fakes. In 2019, Marra, Saltori, et al. [9] introduced an incremental learning-based method for classifying and detecting GAN-produced images. This technique adeptly discriminated between images when presented with new GANs, attributing its efficiency to the continuous evolution facilitated by incremental learning. The same year, Yu et al. [10] investigated GAN fingerprints for image attribution. Their findings suggested that GANs leave distinctive fin-

gerprints on generated images, enabling image source attribution. The study emphasized that even minor changes in GAN training can produce unique fingerprints, allowing precise model verification. Marra, Gragnaniello, et al. [11] further emphasized in 2019 that GANs imprint unique fingerprints on images, paralleling real image acquisition devices that embed signature patterns. Their experiments validated the forensic utility of these fingerprints derived from various GANs. Durall et al. [12] in 2019 opted for a more straightforward approach, employing frequency domain analysis and a basic classifier for deepfake detection. This method excelled even with limited training datasets and showcased impressive accuracy in unsupervised settings. In 2020, Jung et al. [13] unveiled a deepfake detection technique focusing on the human eye's blinking patterns, a variable influenced by individual biology, cognitive activities, and information processing. Their method, DeepVision, analyzed anomalies in eye blink frequency and duration over short durations, achieving an accuracy rate of 87.5%. Kietzmann et al. [14] in 2020 presented a comprehensive review of deepfake technologies and proposed the R.E.A.L. framework to counter deepfake threats: Record original content, Expose deepfakes early, Advocate for legal protection, and Leverage trust. The article underscored two primary factors facilitating the rise and success of deceptive deepfakes: the increasing believability of fake content and the growing accessibility to user-friendly deepfake creation tools. Hosler and Salvi [15] in 2023 analyzed the micro-expressions and minute facial movements that deepfake algorithms often overlook. Their research highlighted that while GANs can replicate broader facial movements, they struggle with intricate, rapid facial changes that occur naturally. Building on this, Tian et al. [16] in 2021 proposed a deepfake detection framework that operates on thermal imaging. Since GANs generate images based on visible light datasets, the thermal inconsistencies between genuine human faces and deepfakes become evident. Lastly, Pashentsev in 2020 embarked on the political aspects of deepfakes. They conducted surveys and social experiments to gauge public perception, deducing that societal awareness can be a potent tool in deepfake mitigation. In 2020, Guarnera et al. [17] delved into the analysis of deepfakes focusing on human faces, aiming to develop a novel detection method that identifies forensic traces concealed within images. These traces act as fingerprints, remnants of the image-generation process. Their proposed method leverages the Expectation Maximization (EM) algorithm to pinpoint local features characteristic of the convolutional generation process. Validation was rigorously conducted using naive classifiers across five distinct architectures: GDWCT, STARGAN, ATTGAN [18], STYLEGAN [19], and STYLEGAN2 [20]. The outcomes demonstrated the method's proficiency in discerning between various architectures and their respective creation processes. While this approach is adept at detecting realistic facial images produced by modern GANs, its application needs expansion to cater to video deepfakes.In 2021, Zhao et al. [21] proposed a multi-attentional deepfake detection network, framing deepfake detection as a fine-grained classification challenge. Their approach consists of three main components: multiple spatial attention heads that direct the network towards specific regions, a texture block designed to highlight superficial artifacts, and attention maps that consolidate both low- and high-level textural and semantic information. To enhance the network's learning capabilities, they integrated regional independence loss and attention-driven data augmentation. While this method showed improvement in certain scenarios, it didn't prove universally effective across all cases. In 2021, Nirkin et al. [22] introduced a technique that combines a face identification network with precise semantic segmentation and a context recognition network targeting features like hair, ears, and neck. This approach detects inconsistencies by merging signals from both networks, offering a detection capability superior to standard real vs. fake classifiers. It excels in detecting alterations to inner facial regions, but might be less effective when an entire head is algorithmically generated.

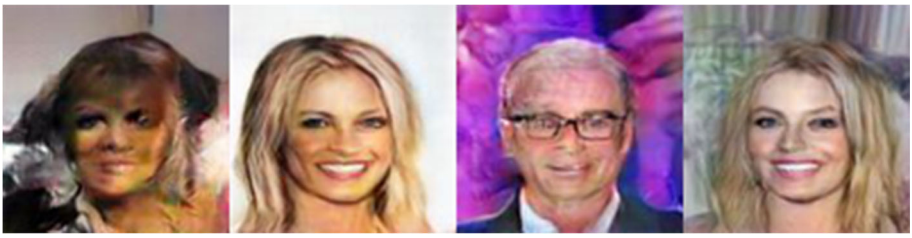


Fig. 4 Old existing dataset sample

In conclusion, the related work underscores the evolving landscape of deepfake detection techniques and their associated challenges. This article contributes significantly to this domain by introducing a specialized dataset for deepfake detection, which includes high-resolution, low-resolution, and mixed images. Building on the foundations set by previous research, we propose a classification-based approach that harnesses specific algorithms and an ensemble model, functioning within the frequency domain, to detect deepfakes. A testament to the efficacy of our method is the remarkable detection accuracy achieved: 99.97% for high-resolution datasets using Random Forest, 98.27% for low-resolution datasets via SVM polynomial, and 98.72% for mixed datasets employing voting classifier. This holistic approach positions our research as a pivotal step towards more reliable deepfake detection solutions.

3 Proposed dataset

In the current landscape of deepfake detection, popular datasets such as Faces-HQ [23], FaceForensics++ [24], and CelebA-fake [25] are often referenced, but they come with inherent limitations. Notably, these datasets are primarily derived from cropped fake video sequences, rendering them less suitable for systems explicitly designed to detect fake images. Furthermore, the CelebA-fake dataset presents many noisy images that are readily distinguishable even to the untrained human eye. To address these shortcomings, we introduce a new dataset in this work. The fake images in our dataset are derived from the website "This Person Does Not Exist", leveraging the sophisticated StyleGAN2 [20] algorithm renowned for generating exceptionally realistic face images. Real images, in contrast, have been meticulously sourced from Flickr. Intriguingly, our dataset incorporates specially designed low-resolution images, produced by employing inter-area interpolation techniques on their high-resolution equivalents. Furthermore, to provide a comprehensive dataset, mixed images amalgamate



Fig. 5 New proposed dataset sample

Table 1 Proposed Dataset Structure

Type	Number of Images	Class	Label
Low Resolution	15000	Real	0
	15000	Fake	1
High Resolution	15000	Real	0
	15000	Fake	1
Mixed Resolution	30000	Real	0
	30000	Fake	1

high-resolution photos with their degraded renditions, derived from applying known degradation processes to the original high-definition images. Consequently, we set a threshold resolution to categorically differentiate between low and high-resolution images, ensuring a discernible distinction. This proposed dataset promises a balanced distribution amongst high-resolution, low-resolution, and mixed images, catering extensively to the evaluation needs of deepfake detection systems. For a nuanced comparative insight, exemplar images from both the conventional datasets and our novel proposition are showcased in Figs. 4 and 5, respectively.

Table 1 provides a summary of the recently suggested dataset for quick reference. Three sets of datasets are used in the proposed method, starting with a low-resolution dataset made up of 15,000 real and 15,000 fake images of 128x128 pixels, followed by a high-resolution dataset made up of 15,000 real and 15,000 fake images of 1024x1024 pixels. Finally, a mixed-resolution dataset made up of all 30,000 real and 30,000 fake images of both low-resolution and high-resolution.

4 Proposed method

A majority of existing deepfake detection techniques primarily target video content, some methods differentiate between deepfake images and real ones. However, these often fall short in terms of efficiency when applied to lower resolution content. This section introduces a methodology adept at detecting deepfake images, even those of low resolution, using machine learning. The technique starts by transforming the input image into the frequency domain and computing its 1-D power spectrum. Subsequently, multiple machine learning classification algorithms operate on this spectrum to optimize detection results.

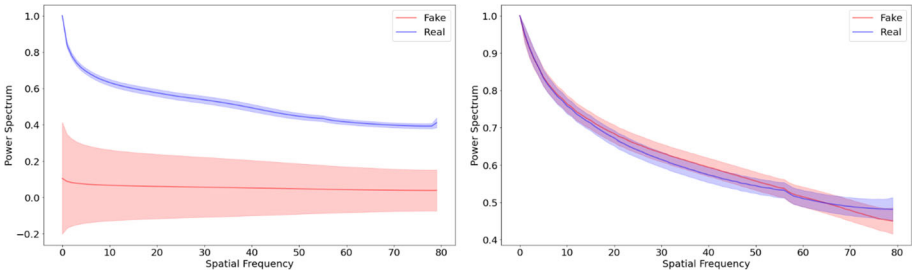


Fig. 6 Power spectrum-Spatial frequency analysis of (a) high-resolution (b) low-resolution dataset

To ensure objectivity, a balanced dataset is curated, eliminating potential biases. Prior to the core detection process, we engage in several preprocessing measures. Initially, the entire dataset is segmented into two categories: high-resolution and low-resolution. Each image in these subsets receives a label indicating whether it's 'real' or 'fake'. The next stage involves feature extraction; images are transitioned into the frequency domain using the Discrete Fourier Transform (DFT). An azimuthal averaging process then computes a 1-D power spectrum for each image.

Figure 6 depicts the analysis of the power spectrum over spatial frequency for both high- and low-resolution datasets. The detection and classification of high-resolution images seem evident from the graphs. However, classifying low-resolution images presents a challenge, as indicated by the overlapping graphs. This underscores the need for a technique proficient in detecting not just high-resolution deepfake images, but also producing accurate results for low-resolution ones.

The proposed methodology adopts a novel approach. Initially, two 'weak learner' models are trained separately using high- and low-resolution datasets. An aggregation function subsequently merges these models, creating a 'strong learner'. The workflow of this technique is illustrated in Fig. 7.

In Fig. 7, part (a) illustrates the generation of weak learners. These learners are created by segregating the high- and low-resolution datasets. These datasets are then subjected to preprocessing to perform feature extraction, as elaborated earlier in this chapter. Upon completing the preprocessing, the extracted features undergo training with various machine learning classification algorithms, culminating in the derivation of weak learner models A and B. In Fig. 7, part (b), a flowchart delineates the process of formulating a robust learner model, C,

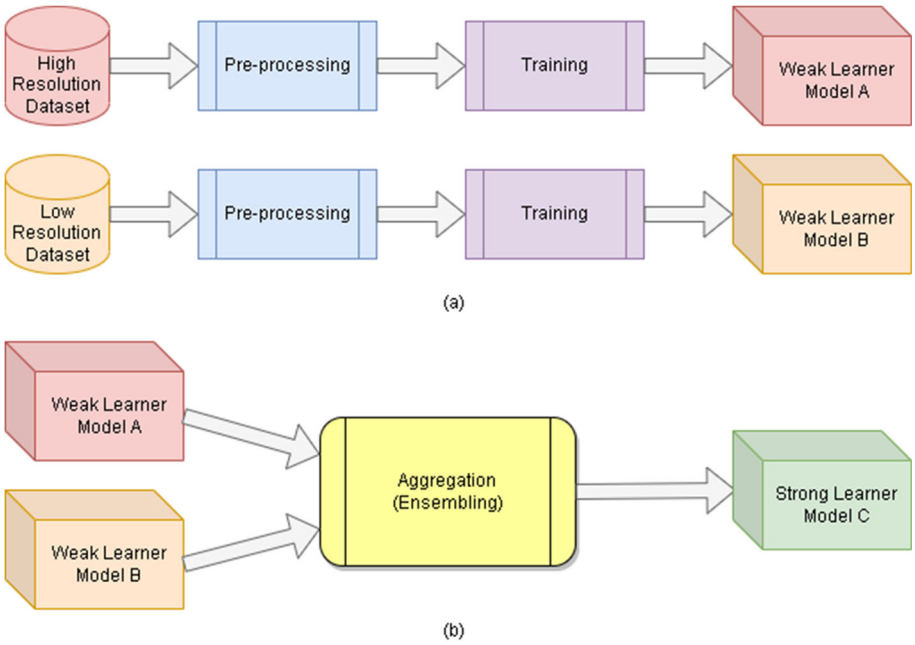


Fig. 7 Process flow for proposed method

which emerges from aggregating weak learner models A and B using an ensemble learning approach, specifically, the voting classifier algorithm.

Delving deeper into the process detailed in part (a), the internal architecture is further elucidated in Fig. 8. Here, the journey of an input image is clearly mapped: initially, it traverses through a Discrete Fourier Transformation (DFT) block, transitioning the image into the frequency domain. This results in a 2-D amplitude spectrum. Subsequently, a function block imposes azimuthal averaging on this spectrum, distilling it into a 1-D amplitude spectrum. This processed data is then channelled into machine learning classification algorithms, which are honed to distinguish real images from deepfakes.

The dataset used in this research is systematically partitioned into two distinct subsets. Firstly, 80% is allocated to the training set, which is employed to instruct the model according to specific criteria. The remaining 20% forms the testing set, designed to evaluate the model's adherence to predefined expectations. This research primarily aims to classify images into two distinct categories, labeled as 'real' (represented by 0) and 'fake' (represented by 1). To accomplish this binary classification challenge, we have harnessed a suite of machine learning algorithms, encompassing logistic regression, support vector machine (with configurations including linear, RBF, and polynomial), decision tree, random forest, XGBoost, and the Naive Bayes algorithm. As the training progresses, the model is fed with preprocessed features from the images, a step introduced to optimize efficiency and curtail processing duration. Notably, careful consideration was given to maintaining a balanced dataset during training to ensure objectivity and negate potential biases. Throughout this phase, we have constantly monitored an array of performance metrics, including validation accuracy, loss, precision, recall, and the f1-score. These metrics provide insights into the model's classification prowess. Based on our experimental observations, validation accuracy emerged as the most indicative metric of the model's classification effectiveness.

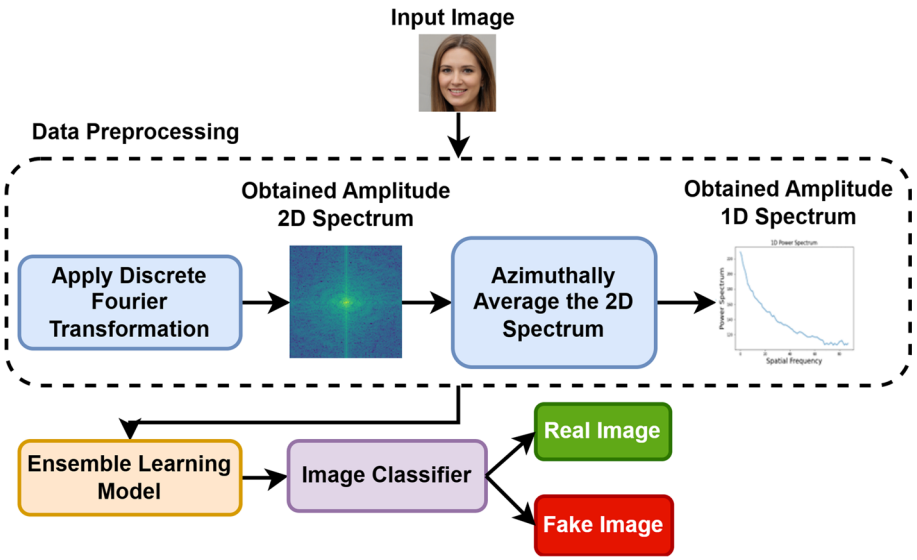


Fig. 8 Architecture of the proposed algorithm

5 Experimental results

This section offers a comprehensive examination of the outcomes produced by the proposed method, assessing them using various performance metrics. Furthermore, it furnishes an in-depth comparison between the proposed technique and multiple machine learning classification algorithms. Recognizing the inherent challenge in detecting low-resolution deepfake images, this section underscores various facets of the proposed approach, supplemented with visual representations. The efficacy of the method concerning high-resolution deepfake images is also probed, as well as its behavior when a dataset, a fusion of both high- and low-resolution images, is input to the system.

Given that data forms the crux of any machine learning model, the effectiveness of such systems is intrinsically linked to the training data. In light of this, a meticulously balanced dataset has been introduced to negate potential biases during the model training phase. Consequently, this dataset exhibits robustness across varied scenarios, be it classifying high-resolution real vs. fake images, discerning between low-resolution real and fabricated images, or when presented with a blend of both high- and low-resolution inputs. Figures 9 and 10 offer a glimpse of some real and fake image samples, highlighting their 1-Dimensional and 2-Dimensional amplitude from the novel dataset, elucidating the algorithm's function within the frequency domain.

Evaluating the effectiveness of various algorithms necessitates more than just a singular metric; a suite of distinct evaluation criteria is typically utilized for comprehensive comparison. While certain algorithms might outshine others in terms of accuracy and precision, some might excel by maintaining a low error rate. It's imperative to assess an algorithm against a broad spectrum of metrics to identify those that consistently perform well across the board. In this study, the primary metrics under consideration are accuracy, recall, precision, and the F1 score. The terminologies used are defined as follows: True Positive (TP) refers to instances where an image is correctly predicted as fake, False Positive (FP) pertains to situations where a real image is incorrectly predicted as fake, True Negative (TN) denotes correct predictions

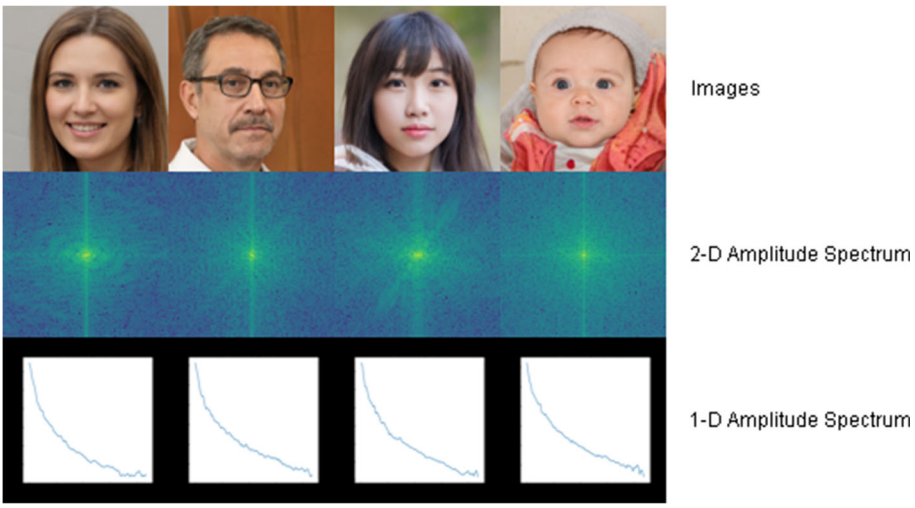


Fig. 9 Fake Dataset Samples

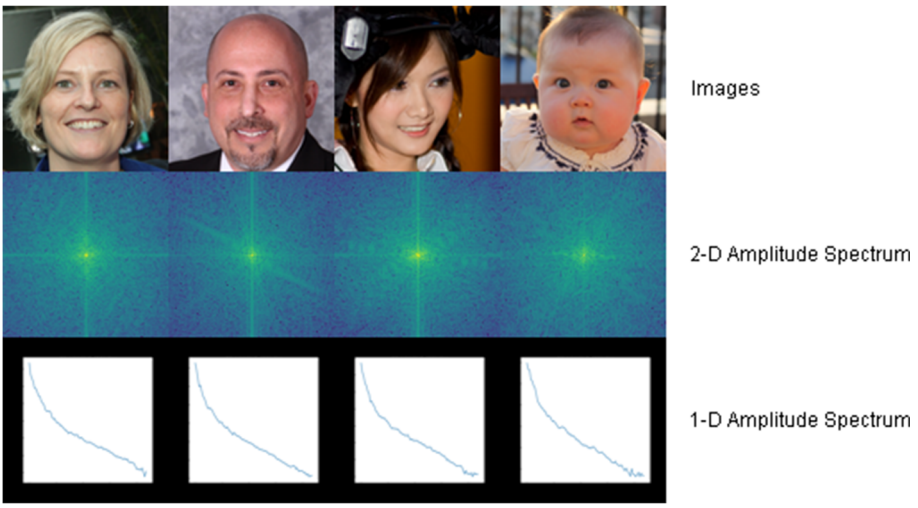


Fig. 10 Real Dataset Samples

of real images, and False Negative (FN) occurs when a fake image is inaccurately identified as real.

The current study delves into the significance of frequency domain analysis and its potential use in tandem with machine learning to detect deepfakes. Consequently, the analysis was structured around three specific scenarios. In the first scenario, systems were provided solely with high-resolution images for model training. In the second, only low-resolution images were used as inputs for model training. Lastly, in the third scenario, the proposed system was fed with a combination of both high- and low-resolution images for training purposes.

In the scenario where only high-resolution image datasets were utilized, it was observed that almost all the algorithms, with the exception of the decision tree, achieved the maximum value of 1 for the precision parameter. Additionally, the random forest algorithm stood out with values of 0.9993 for recall, 0.9997 for accuracy, and 0.9997 for the f1-score. A comprehensive analysis of this high-resolution dataset is available in Table 2.

For the scenario where only low-resolution image datasets were the focus, the SVM Polynomial algorithm yielded the highest values: 0.9848 for precision, 0.9801 for recall,

Table 2 Result Analysis for High Resolution Dataset

Model	Precision	Recall	Accuracy	F1-Score
Logistic Regression	1.0000	0.9510	0.9745	0.9749
SVM Linear	1.0000	0.9809	0.9903	0.9903
SVM Polynomial	1.0000	0.9914	0.9957	0.9957
SVM RBF	1.0000	0.9964	0.9982	0.9982
Decision Tree	0.9973	0.9977	0.9975	0.9975
Random Forest	1.0000	0.9993	0.9997	0.9997
XGBoost	1.0000	0.9987	0.9993	0.9993
Naive Bayes	1.0000	0.9024	0.9458	0.9487

Table 3 Result Analysis for Low Resolution Dataset

Model	Precision	Recall	Accuracy	F1-Score
Logistic Regression	0.7440	0.7766	0.7650	0.7600
SVM Linear	0.8620	0.8760	0.8700	0.8690
SVM Polynomial	0.9848	0.9801	0.9827	0.9824
SVM RBF	0.9841	0.9745	0.9795	0.9793
Decision Tree	0.9292	0.9286	0.9300	0.9289
Random Forest	0.9709	0.9614	0.9665	0.9661
XGBoost	0.9770	0.9710	0.9743	0.9740
Naive Bayes	0.8053	0.6535	0.6940	0.7215

0.9827 for accuracy, and 0.9824 for the f1-score. It's worth noting that while the SVM RBF also produced values closely aligned with the SVM Polynomial, repeated trials often showed the SVM RBF outperforming the SVM Polynomial. Therefore, they can be deemed roughly equivalent in this context. A detailed analysis using the low-resolution dataset can be found in Table 3.

In the scenario where mixed-resolution image datasets were utilized, it was observed that Naive Bayes algorithm achieved the maximum value of 0.9984 for the precision parameter. Additionally, the proposed Voting Classifier algorithm stood out with values of 0.9937 for precision, 0.9748 for recall, 0.9838 for accuracy, and 0.9842 for the f1-score. A comprehensive analysis of this mixed-resolution dataset is available in Table 4. It can be observed that no single model excels in all the performance parameters. A Voting Classifier amalgamates predictions from diverse models, deciding outcomes based on majority vote or average, thereby capitalizing on the strength of multiple architectures. In contrast, Bagging, like the Random Forest, uses bootstrapped samples to train similar models, targeting variance reduction. Boosting, seen in AdaBoost and Gradient Boosted Trees, emphasizes the correction of prior model mistakes to mitigate bias. While Bagging and Boosting employ homogenous base learners with specialized sampling or weighting, a Voting Classifier's advantage lies in its model diversity, enabling a richer ensemble decision from varied patterns in data. Therefore, to address this, an ensemble model, known as the voting classifier, is proposed. This classifier aggregates models from both high- and low-resolution datasets to form a robust

Table 4 Result obtained from Voting Classifier on Mixed Resolution

Model	Precision	Recall	Accuracy	F1-Score
Logistic Regression	0.8720	0.8638	0.8698	0.8674
SVM Linear	0.9310	0.9284	0.9302	0.9296
SVM Polynomial	0.9860	0.9693	0.9776	0.9776
SVM RBF	0.9904	0.9802	0.9853	0.9853
Decision Tree	0.9672	0.9608	0.9642	0.9640
Random Forest	0.9859	0.9783	0.9822	0.9821
XGBoost	0.9909	0.9835	0.9872	0.9872
Naive Bayes	0.9984	0.6428	0.7239	0.7821
Voting Classifier	0.9937	0.9748	0.9838	0.9842

Table 5 Result Analysis for Mixed Resolution Dataset using the Ensemble Model

Iteration	Precision	Recall	Accuracy	F1-Score
1	0.9870	0.9847	0.9858	0.9858
2	0.9846	0.9852	0.9847	0.9849
3	0.9891	0.9828	0.9861	0.9860
4	0.9867	0.9860	0.9863	0.9864
5	0.9880	0.9851	0.9865	0.9866
6	0.9848	0.9848	0.9850	0.9848
7	0.9882	0.9865	0.9872	0.9874
8	0.9842	0.9862	0.9853	0.9852
9	0.9868	0.9805	0.9838	0.9837
10	0.9873	0.9853	0.9863	0.9863
Avg.	0.9867	0.9847	0.9857	0.9857

model capable of producing superior results irrespective of the dataset presented for prediction. The values in Table 5 indicate that the voting classifier consistently offers commendable performance across various parameters.

The confusion matrix for the voting classifier, as illustrated in Fig. 11 for mixed datasets, shows that this classifier has the lowest false negative rate. In simpler terms, it seldom predicts an image to be real when it is actually fake. Given that the primary objective is to detect deepfakes, it's crucial not to misjudge in this context. While occasionally misclassifying a genuine image as a fake can be overlooked, misinterpreting a fake image as real can have grave implications. Such mispredictions can result in significant damages, from fostering forgery and the spread of false news to potential security breaches.

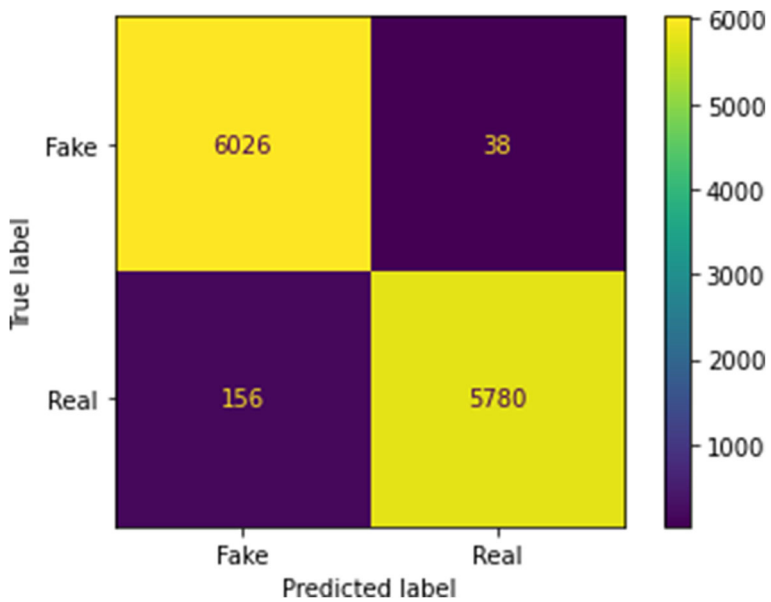


Fig. 11 Confusion matrix for voting classifier with mixed resolution datasets

The K-Fold cross-validation technique has also been applied to ascertain that the proposed approach doesn't succumb to biases that could cause underfitting or overfitting of the model. Table 5 showcases the comprehensive K-Fold analysis with a K value of 10. This value was chosen because a K value of 10 is often recommended for achieving a balance between computational efficiency and reliable estimation of model performance. For the final result, the mean values of these K-Fold iterations, represented in the last row of Table 4, are taken into account.

The proposed method can accurately identify fake images across all resolutions, be it high, low, or mixed. Handling various types of images poses a significant challenge for any machine learning model, primarily due to the stark differences in their frequency distributions. Recognizing that no solitary algorithm can deliver the pinnacle of accuracy coupled with a minimized error rate, the proposal suggests constructing weak learner models with high- and low-resolution datasets separately. These can then be amalgamated through an ensemble model to foster a powerful learner model. Furthermore, the K-Fold technique aids in discerning any inherent biases in this approach. The research also uncovers a distinct correlation between the frequency domains of genuine and counterfeit images.

Looking forward, the current analysis aims to serve as a foundation, motivating more comprehensive evaluations of future GANs. Addressing this evolving challenge becomes even more complex considering the possibility of encountering images produced by newer GANs, especially when there's limited knowledge about the underlying architecture. Future research endeavors will focus on this intricate task, striving to pinpoint the subtleties of images crafted by these advanced GANs and enhance detection mechanisms.

6 Conclusion

In this paper, insights are provided into the understanding of deepfakes and their generation processes. The study also delves into significant research conducted over the past decade on detecting deepfakes and the emerging challenges. To address some of these challenges, a novel approach to deepfake detection is introduced, framing it as a fine-grained classification problem. This method employs machine learning algorithms, capitalizing on the frequency domain. Considering the limited availability of deepfake image datasets, a new dataset comprising both fake and real images in high and low resolutions is introduced. The images in this dataset are generated using StyleGAN2. A machine learning strategy for deepfake detection proves effective for both high-resolution and low-resolution images. Various deepfake detection machine learning models are assessed based on precision, recall, accuracy, and the F1 score, with the inclusion of K-fold cross-validation. As deceptive techniques evolve, this analysis is poised to encourage continued evaluations of emerging GANs, contributing to the mitigation of an escalating societal issue.

Author Contributions Mayank Pandey: Methodology, Software, Investigation, Writing original draft.
Samayveer Singh: Conceptualization, Methodology, Writing - review & editing, Validation.
Aruna Malik: Conceptualization, Methodology, Writing - review & editing, Validation.
Rajeev Kumar: Conceptualization, Methodology, Writing - review & editing, Validation.

Funding There is no funding for this research.

Availability of data and materials The data set will be available on a request basis, if required, contact to Mr. Mayank Pandey (pandeym444@gmail.com).

Declarations

Conflict/Competing of Interest The authors declare that they have no conflict/competing of interest

Ethical standard This study does not include both human and/ or animal.

References

1. Goodfellow I, Pouget-Abadie J, Mirza M, Xu B, Warde-Farley D, Ozair S, Courville A, Bengio Y (2014) Generative adversarial nets. Advances in neural information processing systems 27
2. Chesney R, Citron D (2019) Deepfakes and the new disinformation war: The coming age of post-truth geopolitics. Foreign Aff 98:147
3. Siarohin A, Lathuilière S, Tulyakov S, Ricci E, Sebe N (2019) First order motion model for image animation. Advances in neural information processing systems 32
4. Gil R, Virgili-Gomà J, López-Gil J-M, García R (2023) Deepfakes: evolution and trends. Soft Comput 1–24
5. Baldi P (2012) Autoencoders, unsupervised learning, and deep architectures. In: Proceedings of ICML Workshop on Unsupervised and Transfer Learning, pp 37–49. JMLR Workshop and conference proceedings
6. Masood M, Nawaz M, Malik KM, Javed A, Irtaza A, Malik H (2023) Deepfakes generation and detection: State-of-the-art, open challenges, countermeasures, and way forward. Appl Intell 53(4):3974–4026
7. Nguyen TT, Nguyen QVH, Nguyen DT, Nguyen DT, Huynh-The T, Nahavandi S, Nguyen TT, Pham Q-V, Nguyen CM (2022) Deep learning for deepfakes creation and detection: A survey. Comput Vis Image Underst 223:103525
8. McCloskey S, Albright M (2018) Detecting gan-generated imagery using color cues. arXiv preprint arXiv:1812.08247
9. Marra F, Saltori C, Boato G, Verdoliva L (2019) Incremental learning for the detection and classification of gan-generated images. In: 2019 IEEE International workshop on information forensics and security (WIFS), pp 1–6. IEEE
10. Yu N, Davis LS, Fritz M (2019) Attributing fake images to gans: Learning and analyzing gan fingerprints. In: Proceedings of the IEEE/CVF international conference on computer vision, pp 7556–7566
11. Marra F, Gragnaniello D, Verdoliva L, Poggi G (2019) Do gans leave artificial fingerprints? In: 2019 IEEE Conference on multimedia information processing and retrieval (MIPR), pp 506–511. IEEE
12. Durall R, Keuper M, Pfreundt F-J, Keuper J (2019) Unmasking deepfakes with simple features. arXiv preprint arXiv:1911.00686
13. Jung T, Kim S, Kim K (2020) Deepvision: Deepfakes detection using human eye blinking pattern. IEEE Access 8:83144–83154
14. Kietzmann J, Lee LW, McCarthy IP, Kietzmann TC (2020) Deepfakes: Trick or treat? Business Horizons 63(2):135–146
15. Hosler B, Salvi D, Murray A, Antonacci F, Bestagini P, Tubaro S, Stamm MC (2021) Do deepfakes feel emotions? a semantic approach to detecting deepfakes via emotional inconsistencies. In: Proceedings of the IEEE/CVF conference on computer vision and pattern recognition, pp 1013–1022
16. Tian L, Wang Z, Liu W, Cheng Y, Alsaadi FE, Liu X (2021) A new gan-based approach to data augmentation and image segmentation for crack detection in thermal imaging tests. Cogn Comput 13:1263–1273
17. Guarnera L, Giudice O, Battiato S (2020) Deepfake detection by analyzing convolutional traces. In: Proceedings of the IEEE/CVF conference on computer vision and pattern recognition workshops, pp 666–667
18. Sharma N, Sharma R, Jindal N (2022) Comparative analysis of cyclegan and attentiongan on face aging application. Sādhanā 47(1):33
19. Karras T, Laine S, Aila T (2019) A style-based generator architecture for generative adversarial networks. In: Proceedings of the IEEE/CVF conference on computer vision and pattern recognition, pp 4401–4410
20. Karras T, Laine S, Aittala M, Hellsten J, Lehtinen J, Aila T (2020) Analyzing and improving the image quality of stylegan. In: Proceedings of the IEEE/CVF conference on computer vision and pattern recognition, pp 8110–8119
21. Zhao H, Zhou W, Chen D, Wei T, Zhang W, Yu N (2021) Multi-attentional deepfake detection. In: Proceedings of the IEEE/CVF conference on computer vision and pattern recognition, pp 2185–2194

22. Nirkin Y, Wolf L, Keller Y, Hassner T (2021) Deepfake detection based on discrepancies between faces and their context. IEEE Trans Pattern Anal Mach Intell 44(10):6111–6121
23. Beniaguev D (2022) Synthetic Faces High Quality (SFHQ) dataset. GitHub. https://doi.org/10.34740/kaggle/dsv/4737549. https://github.com/SelfishGene/SFHQ-dataset
24. Rössler A, Cozzolino D, Verdoliva L, Riess C, Thies J, Nießner M (2019) FaceForensics++: Learning to detect manipulated facial images. In: International conference on computer vision (ICCV)
25. Zhang Y, Yin Z, Li Y, Yin G, Yan J, Shao J, Liu Z (2020) Celeba-spoof: Large-scale face anti-spoofing dataset with rich annotations. In: European conference on computer vision (ECCV)

Publisher's Note Springer Nature remains neutral with regard to jurisdictional claims in published maps and institutional affiliations.

Springer Nature or its licensor (e.g. a society or other partner) holds exclusive rights to this article under a publishing agreement with the author(s) or other rightsholder(s); author self-archiving of the accepted manuscript version of this article is solely governed by the terms of such publishing agreement and applicable law.

Uncorrected Proof

Journal of
Water & Climate Change

© 2024 The Authors

Journal of Water and Climate Change Vol 00 No 0, 1 doi: 10.2166/wcc.2024.483

Evaluating the photocatalytic degradation efficacy of 2,4,6-trichlorophenol: performance evaluation and influencing factors

Harsh Pipil[a], Shivani Yadav[a,*], Sunil Kumar[b] and Anil Kumar Haritash[c]

[a] Environmental Microbiology & Bioremediation Laboratory, Department of Environmental Engineering, Delhi Technological University, Delhi 110042, India
[b] Research and Development, Solaris Chemtech Industries, Bhuj 370001, Gujarat, India
[c] Department of Environmental Engineering, Delhi Technological University, Delhi 110042, India
*Corresponding author. E-mail: shivaniyadav_phd2k19@dtu.ac.in

SY, 0000-0001-5135-4624

ABSTRACT

Chlorophenols are the organic compounds that have garnered considerable attention in recent years because of their prevalent occurrence in the environment and associated harmful effects on ecosystems and human health. The current work investigated the photocatalytic oxidation of 2,4,6-trichlorophenol as a potential treatment option. The effects of different process conditioning parameters were studied. Analytical grade commercially available TiO_2 reported 80% degradation, whereas nano-grade TiO_2 resulted in complete removal in the same time duration. Furthermore, the study assessed the use of Degussa P-25 nano-TiO_2 at varying doses for the optimization of treatment. Under the optimal dose of 250 mg/L of nano-TiO_2, the complete removal of 2,4,6-trichlorophenol was observed within 210 min of the reaction period. The addition of H_2O_2 to further increase the rates of treatment did not yield any benefit. Under solar irradiation, almost 95% degradation of 2,4,6-trichlorophenol was observed in 315 min at an optimized photocatalyst dose. Moreover, the comparison of the operational cost of UV-photocatalysis (UV/nano-TiO_2), photocatalysis with H_2O_2 (UV/nano-TiO_2/H_2O_2) and solar-photocatalysis revealed the cost of US$ 0.27 per litre, US$ 0.30 per litre and US$ 0.16 per litre, respectively, during the experimentation, thus making solar-photocatalysis the best option.

Key words: Degussa P-25 nano-TiO_2, H_2O_2, mineralization, photocatalysis, solar-photocatalysis, trichlorophenol

HIGHLIGHTS

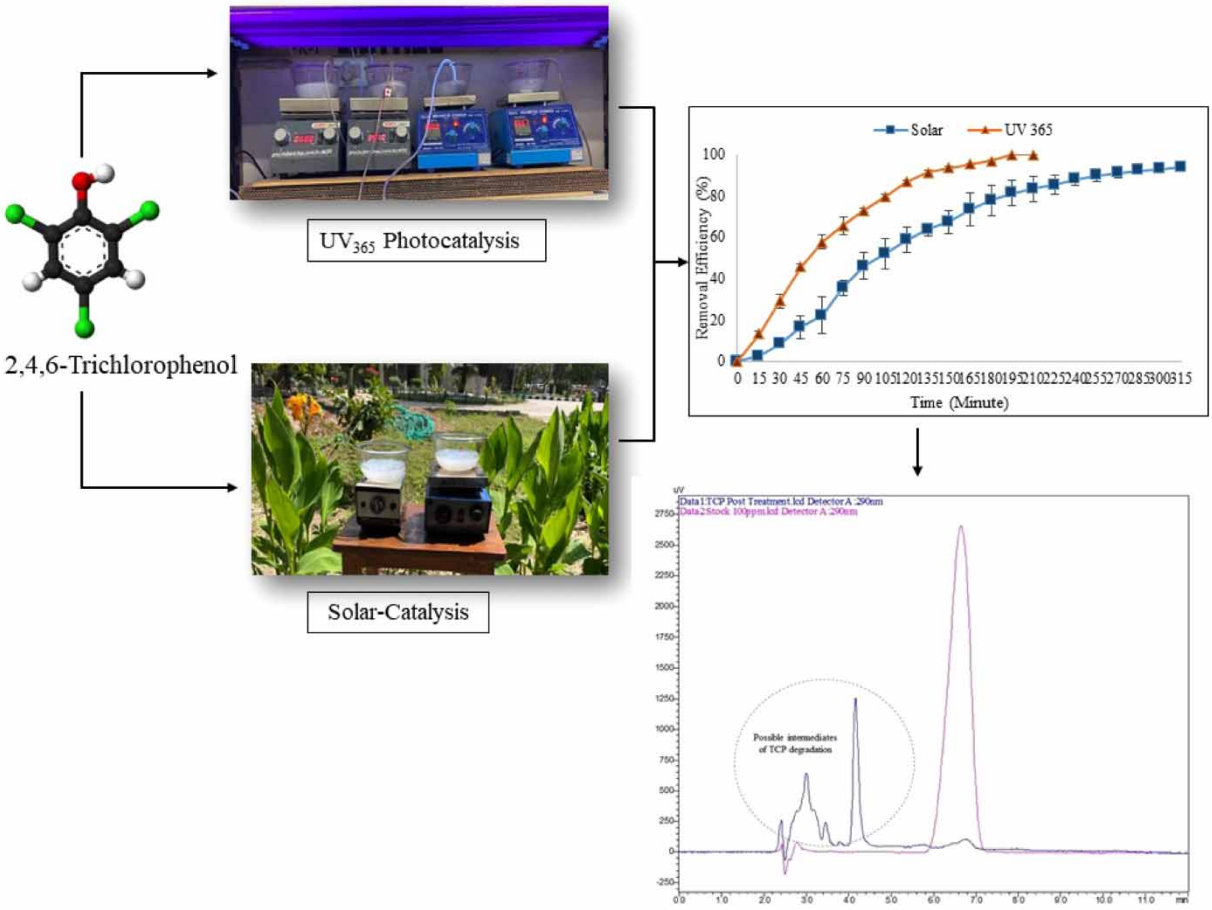
- Photochemical oxidation of 2,4,6-trichlorophenol (TCP) using nano-TiO_2 is a potential treatment method.
- The degradation method reported 71% mineralization of TCP based on analysis of total organic carbon.
- High-performance liquid chromatography confirmed 99% degradation of TCP and revealed the formation of a few intermediates during the photocatalytic oxidation.

This is an Open Access article distributed under the terms of the Creative Commons Attribution Licence (CC BY 4.0), which permits copying, adaptation and redistribution, provided the original work is properly cited (http://creativecommons.org/licenses/by/4.0/).

Downloaded from http://iwaponline.com/jwcc/article-pdf/doi/10.2166/wcc.2024.483/1355560/jwc2024483.pdf
by DELHI TECHNOLOGICAL UNIVERSITY (DTU) user

Uncorrected Proof

GRAPHICAL ABSTRACT



ABBREVIATIONS

AOPs	advanced oxidation processes
CPs	chlorophenols
DCPs	dichlorophenols
eV	electron volt
HPLC	high-performance liquid chromatography
MCPs	monochlorophenols
TCP	2,4,6-trichlorophenol
TOC	total organic carbon
USEPA	United States Environmental Protection Agency

1. INTRODUCTION

The continuous release of organic pollutants from industrial units is deteriorating the quality of aquatic ecosystems. The widespread use of chlorinated organics in the industrial and manufacturing processes has resulted in the introduction of toxicity in the aquatic environment. The bleaching unit in the textile industry and pulp & paper industry generates effluent loaded with chlorinated aromatic organics (Ahlborg & Thunberg 1980). According to a report, the production of 1 ton of paper requires 100 kg of colour-imparting materials and around 2–5 kg of organochlorides to the bleaching section, resulting in the introduction of chlorophenols (CPs) in the wastewater generated (Nagarathnamma *et al.* 1999). CPs possess broad-spectrum bactericidal properties and, thus, find an application as preservatives in the wood processing industry, paints, leather, vegetable fibres, and as disinfectants. The 2,4,6-trichlorophenol (TCP) is one of the most commonly formed chlorinated

Downloaded from http://iwaponline.com/jwcc/article-pdf/doi/10.2166/wcc.2024.483/1355560/jwc2024483.pdf
by DELHI TECHNOLOGICAL UNIVERSITY (DTU) user

Uncorrected Proof

compounds during dechlorination of water. These compounds are widely applied in the agricultural fields as herbicides, pesticides and insecticides. Health organizations and environmental pollution agencies have recommended 0.1 and 200 μg/l as the maximum permissible concentrations of CPs in drinking water and wastewater, respectively (ASTDR 1999). Owing to their widespread use of CPs, residues of such compounds are continuously detected in soils, sediments, surface water, groundwater and in the trophic levels of a food chain. There has been an increasing concern towards the adverse effects of CPs towards environmental damage and human health (Mukherjee *et al.* 2022). CPs are categorized as the priority toxic pollutants listed by the United States Environmental Protection Agency (USEPA) (ASTDR 2007) and can bioaccumulate in organisms (de Souza *et al.* 2021). The toxicity of CPs increases with an increase in the number of chlorine atoms present at ortho- and para-positions and is more stable than chlorine present at the meta-position. These compounds absorb light with a wavelength of less than 300 nm (a lesser fraction of sunlight), resulting in environmental stability (Bandara *et al.* 2001). At the same time, conventional treatment methods fail to degrade the pollutant as biological treatment is inefficient towards decomposition due to the complex structure of the pollutant. On the other hand, advanced oxidation processes (AOPs) have emerged as a promising approach towards the treatment of such recalcitrant organic pollutants (Yadav *et al.* 2022). The application of AOPs is reported successful in the treatment of wastewater generated from pharmaceuticals (Verma & Haritash 2019), textile (Sharma *et al.* 2016; Pipil *et al.* 2022), pesticide, pulp & paper sector (Cameselle & Gouveia 2018), etc. The processes are governed by the principle of *in situ* generation of highly reactive oxidizing species in the form of hydroxyl radicals (Verma & Haritash 2020). Because of the high reduction potential of $OH^{\cdot}$ (2.8 electron volt (eV)), they can oxidize toxicants such as CPs to non-toxic forms such as CO_2 and H_2O. Among AOPs, heterogeneous catalysis has gained popularity because of its inherent destructive potential towards the complete mineralization of organic pollutants. TiO_2 is the most common semiconductor used in the photocatalysis process (Aljuboury *et al.* 2016; Balzani *et al.* 2019). The high photocatalytic activity, high photochemical reactivity, high stability and lesser toxicity towards the environment make it compatible with its use (Thirunavukkarasu *et al.* 2020). When irradiated with a light source, it absorbs photons of energy equivalent to or more than its bandgap width of 3.2 eV. Electrons from the valence band are excited to the conduction band leaving behind holes. Thus, the formation of an electron–hole pair takes place (Equation (1)). Electrons directly react with organic pollutant to form reduction products, whereas holes either react directly with organic compound or react with water to form hydroxyl radicals which carry out oxidation of harmful organics (Equations (2)–(7)) (Ahmad *et al.* 2016). The following reactions take place during the TiO_2-based photocatalysis:

$$TiO_2 \xrightarrow{hv} e^- + h^+ \tag{1}$$

$$e^- + O \rightarrow O_2^{-\bullet} \tag{2}$$

$$h^+ + H_2O \rightarrow OH\bullet + H^+ \tag{3}$$

$$h^+ + OH^- \rightarrow OH\bullet \tag{4}$$

$$h^+ + \text{organic compound} \rightarrow \text{end product} \tag{5}$$

$$OH\bullet + \text{organic compound} \rightarrow \text{end product} \tag{6}$$

$$e^- + \text{organic compound} \rightarrow \text{end product} \tag{7}$$

There have been several studies on the removal of polychlorophenols using photocatalysis and Fenton's treatment *in silo* (Pera-Titus *et al.* 2004; Kusvuran *et al.* 2005), but the studies on degradation/mineralization of TCP are very limited. The studies on monochlorophenols and dichlorophenols reported the removal of the contaminants, but the studies on the degradation of TCPs and the removal of toxicity are not targeted in most of the studies done so far. Since the toxicity of CPs is higher as Cl is attached at ortho- and para-positions, the degradation of TCP in textile and pulp & paper industry effluent is pertinent (Yadav *et al.* 2023).

Although the removal efficiency of photocatalytic oxidation is high, the chemical and energy input is also high. To minimize the cost of treatment, optimization of regulating/input parameters should be performed. The present study dealt with the optimization of nano-TiO_2, an option of removing the use of H_2O_2, and the possibility of visible light excitation. In the present study, effort has been made to study the mineralisztion (degradation) of TCP based on analysis of intermediates of degradation, if any, supported by the analysis of total organic carbon (TOC) before and after photocatalytic oxidation.

Downloaded from http://iwaponline.com/jwcc/article-pdf/doi/10.2166/wcc.2024.483/1355560/jwc2024483.pdf
by DELHI TECHNOLOGICAL UNIVERSITY (DTU) user

Uncorrected Proof

Finally, the operational cost of treatment was evaluated for all the options tested for the treatment of TCP-contaminated wastewater.

2. MATERIALS AND METHODS

2.1. Chemicals

2,4,6-TCP (purity 98%) was obtained from Thermo Fisher Scientific (USA) and was used for the degradation experiments in the present study. The Degussa P25 nano-TiO_2 (anatase to rutile ratio: 80:20) was obtained from Evonik Industries, Germany; hydrogen peroxide H_2O_2 (30% w/v) that was used as an oxidant was obtained from Central Drug House (CDH), India; and high-performance liquid chromatography (HPLC) grade methanol was procured from Merck & Co (India).

2.2. Experimental setup

The photocatalytic degradation of TCP was carried out by varying the dose of TiO_2 and H_2O_2, and optimized conditions were noted. Figure 1 illustrates the treatment system setup of TCP. Keeping the concentration of TCP constant (100 mg/L), varying doses of TiO_2 (50.0–750.0 mg/L) and oxidant (H_2O_2 – 680, 1,700 and 3,400 mg/L) were used to study the removal profile for TCP. The removal study was performed using 200 mL of the synthetic stock solution of TCP of (100 mg/L) in a glass beaker. As the solubility of model pollutant (TCP) is less in water, methanol was used to solubilize the salt, while ultrapure water was later used to top-up the required volume. Prior to photocatalytic degradation, the solution was kept under dark conditions to establish the adsorption/desorption equilibrium of TCP with TiO_2. The aqueous suspension of TCP and photocatalyst was then irradiated under UV light (λ – 365 nm) with continuous stirring and air sparging. The experiments were carried out in a fabricated UV chamber with eight UV tubes (Phillips 36 W each) of wavelength 365 nm. The cumulative source intensity of the UV chamber as calculated by Verma & Haritash (2019) is 672 W/m^2 with an accumulated energy of 535.1 kJ/L. A sample volume of 5 mL was extracted for analysis using a pre-rinsed syringe at regular intervals of 15 min and was then

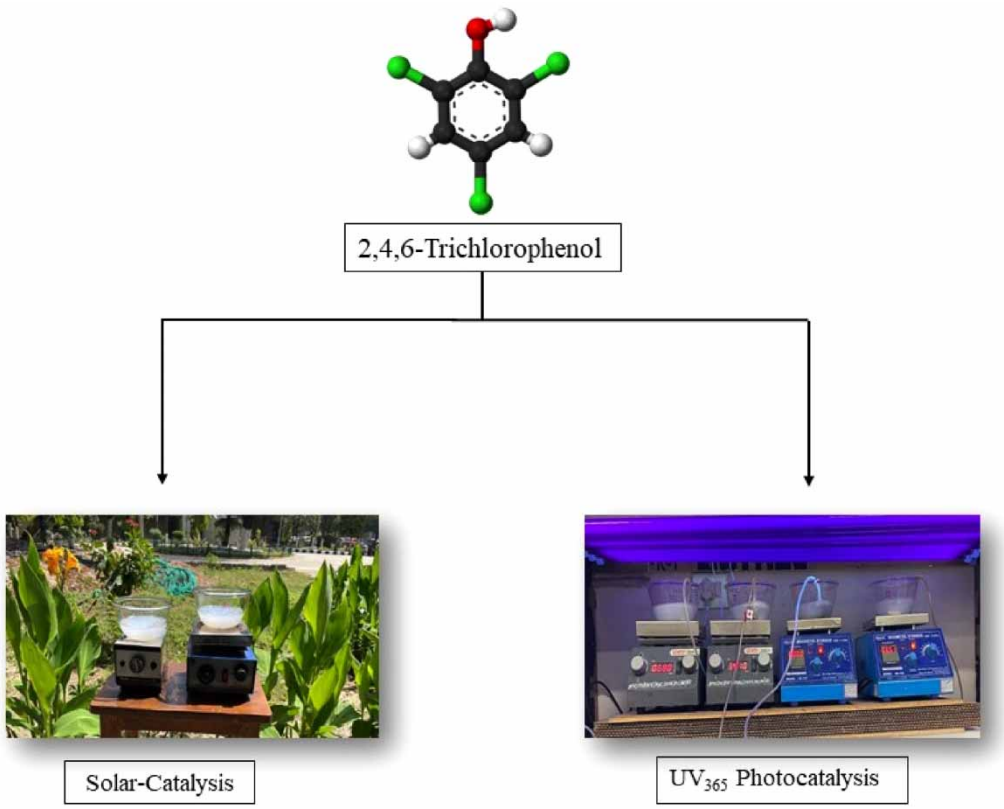


Figure 1 | Treatment system setup of TCP.

Downloaded from http://iwaponline.com/jwcc/article-pdf/doi/10.2166/wcc.2024.483/1355560/jwc2024483.pdf
by DELHI TECHNOLOGICAL UNIVERSITY (DTU) user

Uncorrected Proof

subjected to centrifugation at 5,000 rpm for 5 min. The above procedure was repeated until the residual concentration of TCP became constant. All the experiments were carried out in triplicates to ensure the accuracy of the analysis.

2.3. Analysis of 2,4,6-TCP

For continuous detection of the degradation of TCP, a double-beam UV–Vis spectrophotometer (Lab India make UV 3092 model) was used. An absorption spectrum of 2,4,6-TCP was plotted in the wavelength range of 190–800 nm and the wavelength of maximum absorption (λ_{max}) was obtained at 290 nm. The calibration graph for TCP was plotted in the concentration range of 10–100 mg/L at 10 mg/L intervals. The removal efficiency of TCP was calculated using the following equation (Equation (8))

$$\text{Efficiency } (\%) = \left[\frac{C_i - C_t}{C_i}\right] \times 100 \tag{8}$$

where C_i is the initial concentration of TCP and C_t is the concentration of TCP at time 't'.

In addition to this, the residual concentration of TCP was confirmed over HPLC (Shimadzu, Japan). The chromatographic investigation was also used to determine the residual reaction intermediates during the photocatalytic oxidation of TCP. The HPLC system (Shimadzu, LC-20AD) equipped with an UV/VIS detector (SPD-20A) and C-18 column (Inertsil® ODS-3 V, 5 μm 4.6 × 250 mm) was used for the analysis. A standard curve of the model compound (TCP) was plotted in the concentration range of 0–100 mg/L at intervals of 10 mg/L in the HPLC system. Methanol and water (70:30 v/v) were used as a mobile phase at a flow rate of 1.5 mL/min for separation by HPLC, and the response was recorded at 290 nm. Mineralization of TCP was analysed over a TOC Analyser too (TOC-L Shimadzu Make, Japan) to confirm the observation of UV–Vis spectrophotometer and HPLC.

3. RESULTS AND DISCUSSION

Photocatalytic oxidation of TCP using TiO_2 as a catalyst was found efficient in the removal of the aforementioned pollutant. The study undertook the effect of regulating parameters such as catalyst dose, catalyst size, source of light and the presence of oxidizing agent on the removal efficiency of TCP. The pH of the TCP solution was kept neutral since earlier studies have reported optimum degradation of organic impurities using Degussa P-25 TiO_2 at pH 6.8 (Aljuboury *et al.* 2016).

3.1. Effect of catalyst type

Commercially available analytical grade TiO_2 was analysed against nano-TiO_2 (Degussa P-25) towards the degradation of TCP. It was observed that nano-TiO_2 exhibited greater potential towards the removal of TCP. Nano-TiO_2 reported nearly complete degradation (~97%) of TCP within 210 min (3.5 h), whereas analytical grade TiO_2 was able to degrade only 75% of model pollutant during the same irradiation time (Figure 2). The effectiveness of nano-TiO_2 is attributed because of increased surface area and absorption of energy as well as increased internal recombination of electrons and holes and surface active sites (Chen *et al.* 2020).

It could also be observed that in the absence of photocatalyst, UV_{365} alone removed a significant proportion of TCP (~30%), indicating that photolysis also plays a role in the removal of TCP. Considering the edge of nano-TiO_2 over analytical grade TiO_2, further experimentation was conducted using nano-TiO_2 for the degradation of TCP.

3.2. Effect of catalyst dose and H_2O_2

The photocatalytic oxidation of TCP (100 mg/L) with different doses of nano-TiO_2 was varied substantially (Figure 3). It can be observed from Figure 3 that the removal rate increased upon increasing the dose of the photocatalyst. At a concentration of 250 mg/L of TiO_2, complete degradation was achieved after 210 min of irradiation. However, TiO_2 concentration when increased beyond 250 mg/L, i.e., 275, 300, 500 and 750 mg/L, the degradation rate decreased (Figure 3).

This can be rationalized concerning the availability of active sites on the surface of TiO_2 and the effective penetration of photoactivating light in TCP–TiO_2 suspension. At higher doses of TiO_2, a turbid suspension inhibits the effective penetration of light. Furthermore, a lesser number of photons are absorbed causing fewer generations of hydroxyl radicals to oxidize TCP, thereby affecting the degradation efficiency, as observed in other literature studies as well (Verma & Haritash 2020; Pipil *et al.* 2022). The higher degradation efficiency while increasing the dose of TiO_2 is because of the electron–hole pairs generated. The Degussa P-25 nano-TiO_2 consists of rutile and anatase phases (anatase to rutile ratio: 80:20). Anatase TiO_2 exhibits a

Downloaded from http://iwaponline.com/jwcc/article-pdf/doi/10.2166/wcc.2024.483/1355560/jwc2024483.pdf
by DELHI TECHNOLOGICAL UNIVERSITY (DTU) user

Uncorrected Proof

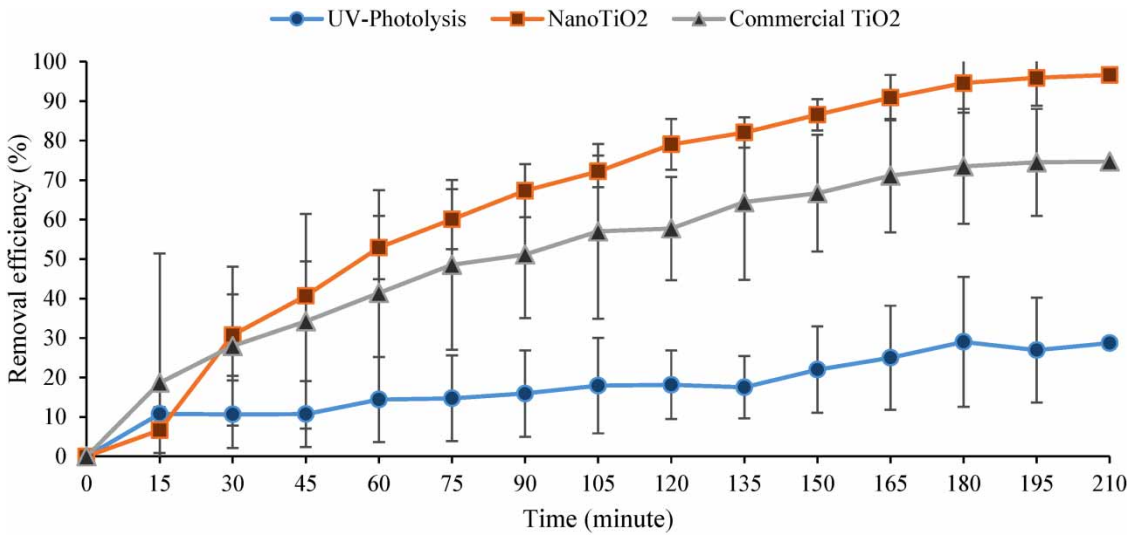


Figure 2 | UV_{365}-induced degradation of 2,4,6-TCP using commercial-TiO_2 and nano-TiO_2.

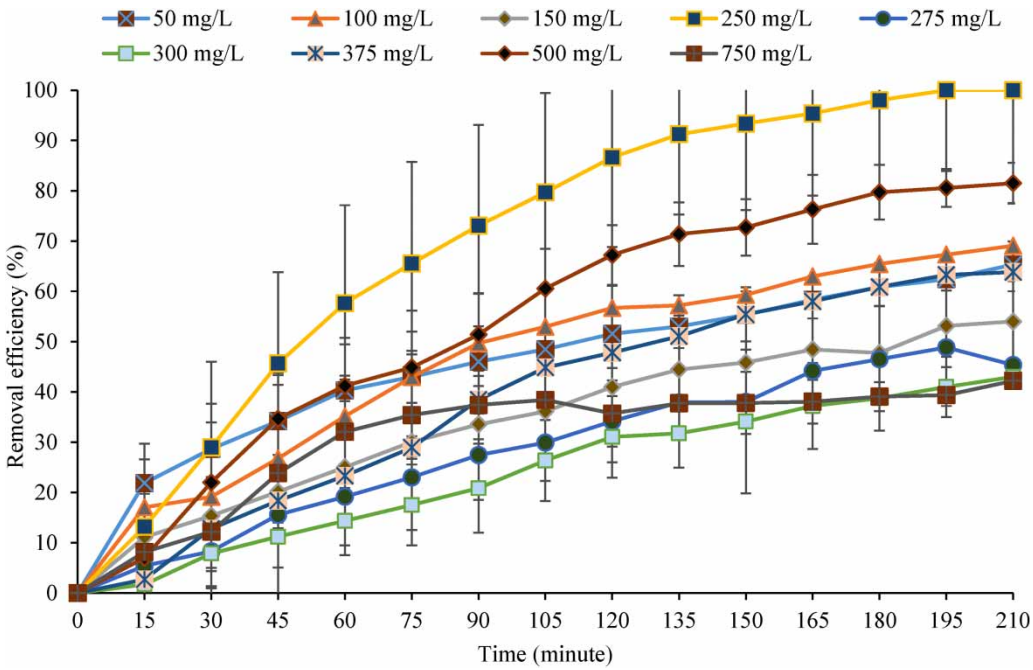


Figure 3 | Removal efficiency of 2,4,6-TCP (C_i – 100 mg/L) at varying catalyst doses.

longer period of electron holes with lower recombination of charge carriers. This causes mass migration of electrons and holes from the interior to the surface of anatase TiO_2. Whereas, the rutile TiO_2 part has a smaller band gap that generates electron–hole pairs when irradiated with low-energy photons making it advantageous for anatase TiO_2 to utilize these electron–hole pairs (Bagbi *et al.* 2017). Thus, the synergetic effect of rutile and anatase phases of TiO_2 plays a crucial role in photocatalytic efficiency. The generated electron–hole pair reacts either directly with the organic pollutant or with surface-bound water to produce hydroxyl radicals. Increasing the amount of TiO_2 increases the availability of active sites, thus increasing the adsorption process too. Hence, the more the binding of electron–hole pairs with water, the more the production of the hydroxyl radicals.

Downloaded from http://iwaponline.com/jwcc/article-pdf/doi/10.2166/wcc.2024.483/1355560/jwc2024483.pdf
by DELHI TECHNOLOGICAL UNIVERSITY (DTU) user

Uncorrected Proof

Earlier studies on photocatalytic degradation of TCP revealed that the time for the complete removal of TCP remains extended if optimization for TiO_2 dose is not taken into account. The degradation of TCP (C_i – 50 mg/L) at a TiO_2 dose of 500 mg/L reported 100% degradation in 240 min (Shoneye & Tang 2020), whereas the present study reports 100% degradation within 210 min for an initial concentration of 100 mg/L TCP but at an optimized TiO_2 dose of 250 mg/L. It may be important to note that optimization resulted in the degradation of two-fold concentrated wastewater with half the amount of TiO_2 in a relatively short time. This may favour the treatment of more volume/concentration of effluent efficiently with reduced cost of treatment based on the results of the present study. It is also important to mention that reaction conditions should be optimized to achieve enhanced treatment efficiency. Some studies report lesser reaction time (Rengaraj & Li 2006; Choi *et al.* 2019) compared to this study, but it is because the initial concentration of TCP was significantly less (20–50 mg/L) than the one used (100 mg/L) in the present study. The other reason in few studies is relatively higher doses of TiO_2 being used for photocatalysis (Pandiyan *et al.* 2002; Choi *et al.* 2019), which adds to the cost of treatment.

H_2O_2 is a strong oxidizing agent, which was added in the experiment to increase the generation of OH radicals and to further enhance the rate of degradation. The effect of the addition of H_2O_2 was studied by varying the concentration at 20, 50 and 100 mM at optimized dose of TiO_2 (250 mg/L) for the removal of TCP. However, the addition of H_2O_2 did not result in any significant improvement towards the removal of TCP in the present study. The efficacy of photocatalytic degradation in the presence of H_2O_2 was reported less than 80% in 3.5 h among all the above-mentioned experimental setups.

3.3. Solar-induced photocatalysis

The enormity of solar energy consumption is almost four times the total solar energy irradiating the surface of the earth (Balzani *et al.* 2019). As no alteration can take place in the solar spectrum, the solar energy could be exploited and harnessed to increase the efficiency of the treatment system. Although the proportion of UV light is 3–5% in natural sunlight, the degradation profile of TCP under natural sunlight (solar-catalysis) using nano-TiO_2 at a concentration of 250 mg/L was also investigated. It was observed that 95% degradation efficiency was attained in 300 min (5.0 h) of sunlight exposure (Figure 4).

It was also noted that with the increase in the solar intensity, the rate of degradation also increased. The average solar influx radiation intensity was 655.5 W/m^2 with accumulated energy of 522.2 kJ/L. Figure 5 represents the degradation profile of TCP as a function of accumulated energy for every 15 min. It has been reported that the rate of electron excited from the valence band to the conduction band is influenced by the intensity of light affecting the rate of photocatalytic reaction and photocatalyst activation. Thus, higher intensity is directly proportional to photocatalytic oxidation (Yadav *et al.* 2023).

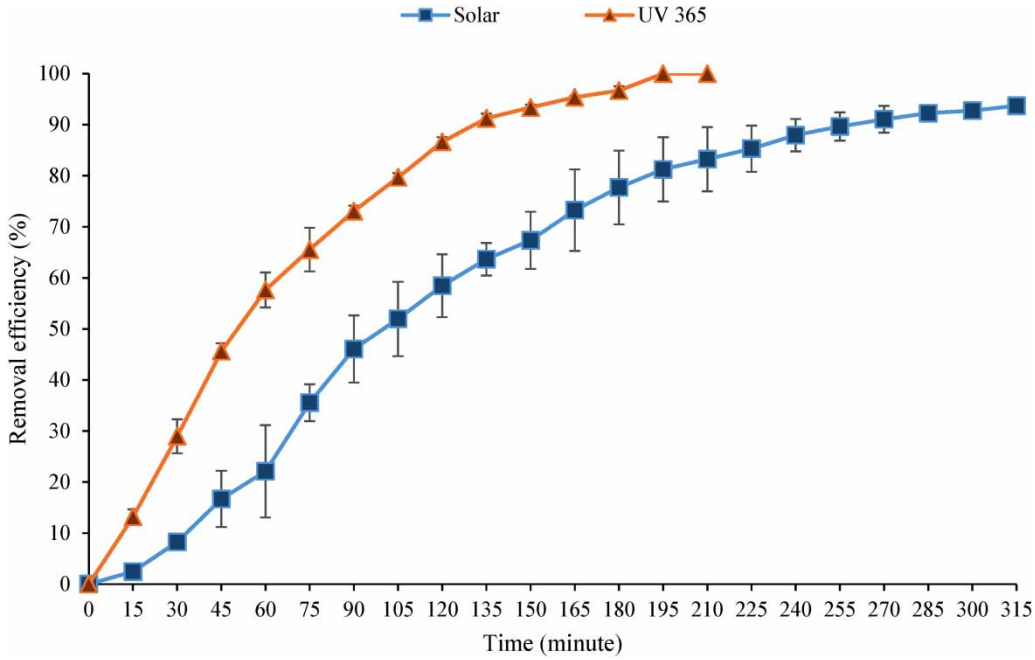


Figure 4 | Removal efficiency of TCP under solar and UV light as a function of time.

Downloaded from http://iwaponline.com/jwcc/article-pdf/doi/10.2166/wcc.2024.483/1355560/jwc2024483.pdf
by DELHI TECHNOLOGICAL UNIVERSITY (DTU) user

Uncorrected Proof

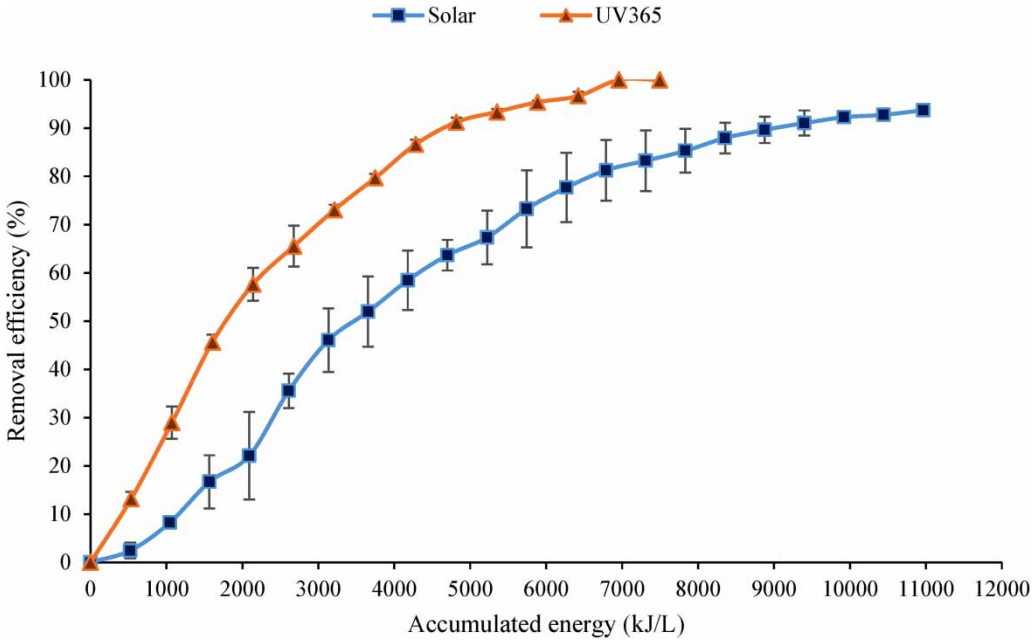


Figure 5 | Removal efficiency of TCP under solar and UV light as a function of accumulated energy.

However, the rate of photocatalysis is no longer affected by the intensity of light beyond the optimum level because of the limited availability of active sites on the surface of the photocatalyst (Blake *et al.* 1991). Based on the results of the present study, it is seen that photo exposure and catalyst (based on size) can significantly regulate the removal efficiency of TCP during photocatalysis.

3.4. Mineralization of TCP

The degradation of TCP was studied using a spectrophotometer in terms of absorbance of residual concentration at regular intervals. To further confirm the mineralization of the organic compound, TOC analysis was done. The degradation profile revealed that approximately 71% of TCP was mineralized based on analysis of TOC. To monitor the feasibility of the formation of any intermediates, HPLC analysis of TCP pretreatment and post-treated samples was done. The analysis over HPLC (Rt: 6.8 min) confirmed 99% degradation of TCP, but it reported the formation of a few intermediates during the photocatalytic oxidation, thus confirming that there are about 29% TOC leftovers in the form of intermediates (Figure 6).

3.5. Economic analysis and recovery of TiO_2

TiO_2 was added as a catalyst in the experiment and is not consumed in the reaction; however, some fraction of TiO_2 was lost during analysis, sample centrifugation, sample transfer, etc. At the end of the reaction process, the leftover TiO_2 was recovered and oven-dried at 105°C. The recovery of TiO_2 was calculated using the following formula:

$$TiO_2 \text{ recovered} = \frac{w_2}{w_1} \times 100 \tag{9}$$

where w_1 is the initial known weight of TiO_2 added and w_2 is the residual weight of recovered TiO_2. In the present study, ~80% of the TiO_2 added in the experiment was recovered under optimized conditions. Thus, the use of optimized TiO_2 reduces the overall cost of the treatment, making the process environment and energy-efficient. The economic analysis was conducted after maximal degradation of TCP, *w.r.t.* photocatalysis, solar-photocatalysis and photocatalysis with H_2O_2, and a comparative analysis of operational cost was done (Table 1).

Photocatalysis was carried out in a fabricated UV chamber having eight UV tubes, each having a power rating of 36 W making together 288 W; also power rating of the magnetic stirrer and air sparger are 8.5 and 3.5 W, respectively. Therefore, the overall power consumption is 300 W or 0.3 kWh. In the case of solar-photocatalysis, only magnetic stirrer and air sparger

Downloaded from http://iwaponline.com/jwcc/article-pdf/doi/10.2166/wcc.2024.483/1355560/jwc2024483.pdf
by DELHI TECHNOLOGICAL UNIVERSITY (DTU) user

Uncorrected Proof

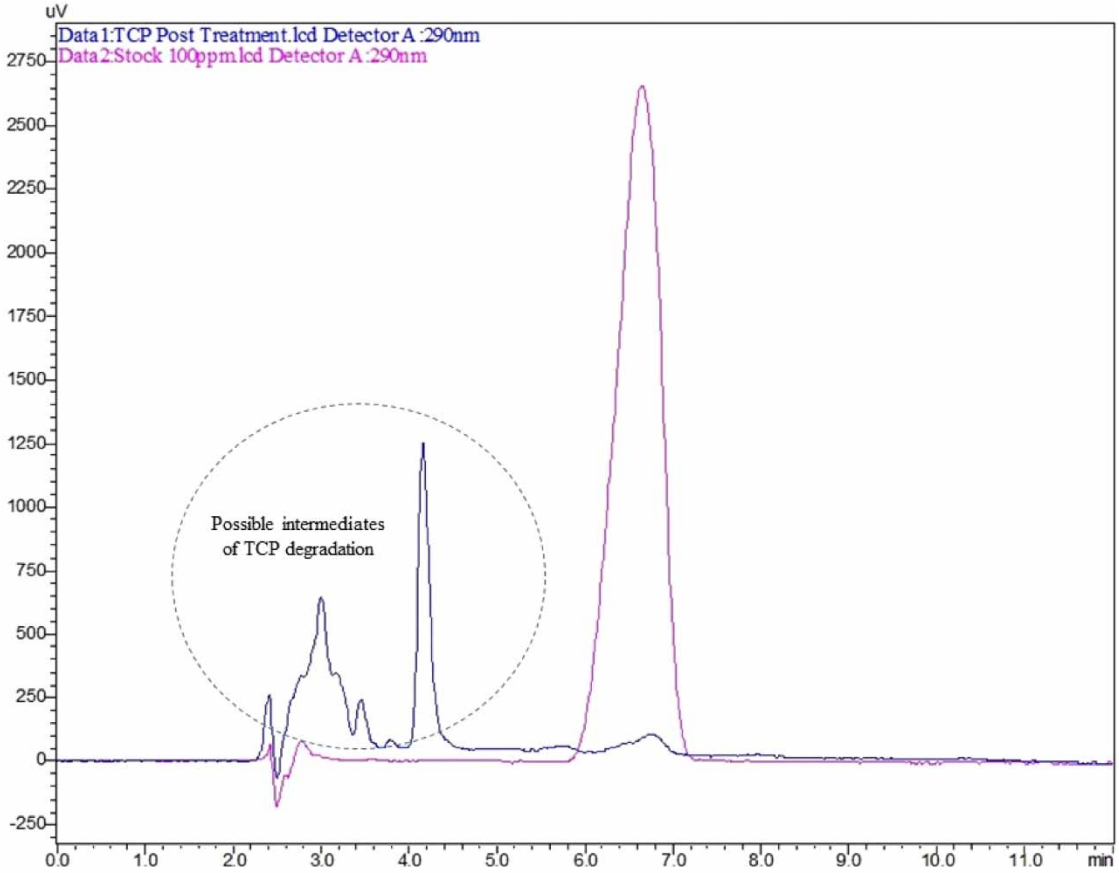


Figure 6 | Chromatogram of TCP before and after degradation depicting the intermediate formation.

Table 1 | Economic analysis of the operating cost of UV_{365} photocatalysis, solar-photocatalysis and UV-photocatalysis with H_2O_2 (with 80% TiO_2 recovery)

Treatment method	Energy per hour (kWh)	Time for treatment (min)	Rate of energy (per kWh) (INR)	Cost of electricity (INR)	Chemical consumed	Cost of chemical per litre (INR)	Cost of treatment per litre (UD$)
UV_{365} photocatalysis	0.3	210	8.50	8.9	Nano-TiO_2	11.34	0.27
Solar-photocatalysis	0.012	300	8.5	0.51	Nano-TiO_2	11.34	0.16
UV-photocatalysis with H_2O_2	0.3	210	8.5	8.9	Nano-TiO_2 H_2O_2 (30% w/v)	13.62	0.30

were used, thus making power consumption of 12 W or 0.012 kWh. The electricity cost for industrial supply in most of the states in India is INR 8.5 per unit kWh. The complete degradation efficiency of TCP under the UV/TiO_2 system was observed in 210 min with a photocatalyst dose of 250 mg/L. The cost of nano-size TiO_2 (P25) is INR 22,680 per 100 g but only 20% of it was consumed while 80% is recovered. Therefore, the cost of the photocatalyst is INR 11.34 per litre for synthetic wastewater treatment (for 250 mg/L dose of TiO_2) in UV/TiO_2, UV/H_2O_2/TiO_2 and solar/TiO_2 system. Thus, the overall operational cost of the UV/TiO_2 treatment process is INR 14.57 or US$ 0.27. In the case of UV/H_2O_2/TiO_2, the additional cost of oxidant chemicals occurred making together the cost of treatment per litre US$ 0.30. However, a considerable cost of the treatment was saved in the case of solar-photocatalysis (US$ 0.16 per litre).

Downloaded from http://iwaponline.com/jwcc/article-pdf/doi/10.2166/wcc.2024.483/1355560/jwc2024483.pdf
by DELHI TECHNOLOGICAL UNIVERSITY (DTU) user

Uncorrected Proof

4. CONCLUSION

CPs have significant environmental concerns owing to their toxicity, carcinogenicity and bioaccumulation potential, especially in the aquatic environment. Inefficient treatment of these xenobiotics in industrial effluents and discharge of partially treated wastewater further aggravates the environmental and health issues. The present study reported the efficacy of photocatalytic oxidation as a potential method for the removal/degradation of 2,4,6-TCP. The removal efficiency of the treatment methods follows the order of 80% < 95% < 100% for UV/nano-TiO_2/H_2O_2 < solar-photocatalysis < UV-photocatalysis, respectively. The rate of reaction was faster in the case of UV-photocatalysis; however, it may be replaced by solar for low-strength or low-volume wastewater, further reducing the burden of cost. Despite the non-avoidable cost associated with chemicals and energy input, optimization of such chemical oxidation methods can significantly reduce the operational cost as observed in the case of catalyst optimization. Compared to the limited removal rate of conventional treatment and perseverance of CPs in the environment, photochemical oxidation using nano-TiO_2 is a promising treatment approach, since it leads to the mineralization of TCP and elimination of associated residual toxicity apart from bringing down the organic load in wastewater. Additionally, the cost of treatment of effluent is a governing factor for industries and solar-induced removal of such contaminants could be a cost-effective approach. As no modification in the solar spectrum can take place, the solar energy could be exploited and harnessed to increase the efficiency of the treatment system. Thus, solar-photocatalytic oxidation can serve as a sustainable treatment option for the degradation of 2,4,6-TCP considering its benefits to the environment and health.

ACKNOWLEDGEMENT

The authors are grateful to Mr Harsh Pipil, Research Scholar, Department of Environmental Engineering at DTU for the assistance during this study.

CONSENT TO PARTICIPATE

Authors provide the consent to participate.

CONSENT TO PUBLISH

Authors provide the consent to publish the manuscript.

AUTHORS' CONTRIBUTION

H. Pipil and A. K. Haritash contributed to the conceptualization, execution, data compilation and draft writing of this research. S. Kumar and A. K. Haritash contributed to the conceptualization as well as supervising, reviewing and editing the manuscript.

DATA AVAILABILITY STATEMENT

All relevant data are included in the paper or its Supplementary Information.

CONFLICT OF INTEREST

The authors declare there is no conflict.

REFERENCES

Ahlborg, U. G. & Thunberg, T. M. 1980 Chlorinated phenols: Occurrence, toxicity, metabolism and environmental impact. *Crit Rev Toxicol.* **7**(1), 1–35. doi:10.3109/10408448009017934.

Ahmad, R., Ahmad, Z., Khan, A. U., Mastoi, N. R., Aslam, M. & Kim, J. 2016 Photocatalytic systems as an advanced environmental remediation: Recent developments, limitations and new avenues for applications. *J Environ Chem Eng.* **4**(4), 4143–4164. doi:10.1016/j.jece.2016.09.009.

Aljuboury, D. A. D. A., Palaniandy, P., Abdul Aziz, H. B., Feroz, S. & Abu Amr, S. S. 2016 Evaluating photo-degradation of COD and TOC in petroleum refinery wastewater by using TiO_2/ZnO photo-catalyst. *Water Sci Technol.* **74**(6), 1312–1325. doi:10.2166/wst.2016.293.

ASTDR 1999 *Toxicological Profile for Chlorophenols*. US Department of Health and Human Services, Atlanta, GA.

ASTDR 2007 Comprehensive Environmental Response, Compensation, and Liability Act (CERCLA) Priority List of Hazardous Substances.

Downloaded from http://iwaponline.com/jwcc/article-pdf/doi/10.2166/wcc.2024.483/1355560/jwc2024483.pdf
by DELHI TECHNOLOGICAL UNIVERSITY (DTU) user

Uncorrected Proof

Bagbi, Y., Sarswat, A., Mohan, D., Pandey, A. & Solanki, P. R. 2017 Lead and chromium adsorption from water using L-cysteine functionalized magnetite (Fe_3O_4) nanoparticles. *Sci Rep.* **7** (1), 1–15.

Balzani, V., Pacchioni, G., Prato, M. & Zecchina, A. 2019 Solar driven chemistry: Towards new catalytic solutions for a sustainable world. *Rend Fis Acc Lincei.* **30**(3), 443–452. doi:10.1007/s12210-019-00836-2.

Bandara, J., Mielczarski, J. A., Lopez, A. & Kiwi, J. 2001 Sensitized degradation of chlorophenols on iron oxides induced by visible light. *Appl Catal B Environ.* **34**(4), 321–333. doi:10.1016/S0926-3373(01)00225-9.

Blake, D. M., Webb, J., Turchi, C. & Magrini, K. 1991 Kinetic and mechanistic overview of TiO_2-photocatalyzed oxidation reactions in aqueous solution. *Sol Energy Mater.* **24**(1–4), 584–593. doi:10.1016/0165-1633(91)90092-Y.

Cameselle, C. & Gouveia, S. 2018 Electrokinetic remediation for the removal of organic contaminants in soils. *Curr Opin Electrochem.* **11**, 41–47. doi:10.1016/j.coelec.2018.07.005.

Chen, D., Cheng, Y., Zhou, N., Chen, P., Wang, Y., Li, K., Huo, S., Cheng, P., Peng, P., Zhang, R. & Wang, L. 2020 Photocatalytic degradation of organic pollutants using TiO_2-based photocatalysts: A review. *J Clean Prod.* **268**, 121725. doi:10.1016/j.jclepro.2020.121725.

Choi, K. H., Min, J., Park, S. Y., Park, B. J. & Jung, J. S. 2019 Enhanced photocatalytic degradation of tri-chlorophenol by Fe_3O_4@TiO_2@Au photocatalyst under visible-light. *Ceram Int.* **45**(7), 9477–9482. doi:10.1016/j.ceramint.2018.09.104.

De Souza, L. P., Graça, C. A. L., Teixeira, A. C. S. & Chiavone-Filho, O. 2021 Degradation of 2, 4, 6-trichlorophenol in aqueous systems through the association of zero-valent-copper-mediated reduction and UVC/H_2O_2: Effect of water matrix and toxicity assessment. *Environ Sci Pollut Res.* **28**, 24057–24066. doi:10.1007/s11356-020-11885-8.

Kusvuran, E., Samil, A., Atanur, O. M. & Erbatur, O. 2005 Photocatalytic degradation kinetics of di-and tri-substituted phenolic compounds in aqueous solution by TiO_2/UV. *Appl Catal B Environ.* **58**(3–4), 211–216. doi:10.1016/j.apcatb.2004.11.023.

Mukherjee, D., Ferreira, N. G. & Saha, N. C. 2022 Effects of 2, 4, 6-trichlorophenol on *Clarias batrachus*: A biomarkers approach. *Environ Sci Pollut Res.* 1–14. doi:10.1007/s11356-022-19213-y.

Nagarathnamma, R., Bajpai, P. & Bajpai, P. K. 1999 Studies on decolourization, degradation and detoxification of chlorinated lignin compounds in kraft bleaching effluents by *Ceriporiopsis subvermispora*. *Process Biochem.* **34**(9), 939–948. doi:10.1016/S0032-9592(99)00021-7.

Pandiyan, T., Rivas, O. M., Martínez, J. O., Amezcua, G. B. & Martínez-Carrillo, M. A. 2002 Comparison of methods for the photochemical degradation of chlorophenols. *J Photochem Photobiol A Chem.* **146**(3), 149–155. doi:10.1016/S1010-6030(01)00606-2.

Pera-Titus, M., García-Molina, V., Baños, M. A., Giménez, J. & Esplugas, S. 2004 Degradation of chlorophenols by means of advanced oxidation processes: A general review. *Appl Catal B: Environ.* **47**(4), 219–256. doi:10.1016/j.apcatb.2003.09.010.

Pipil, H., Yadav, S., Chawla, H., Taneja, S., Verma, M., Singla, N. & Haritash, A. K. 2022 Comparison of TiO_2 catalysis and Fenton's treatment for rapid degradation of Remazol Red Dye in textile industry effluent. *Rend Fis Acc Lincei.* **33**, 105–114. doi:10.1007/s12210-021-01040-x.

Rengaraj, S. & Li, X. Z. 2006 Enhanced photocatalytic activity of TiO_2 by doping with Ag for degradation of 2, 4, 6-trichlorophenol in aqueous suspension. *J Mol Catal A Chem.* **243**(1), 60–67. doi:10.1016/j.molcata.2005.08.010.

Sharma, A., Verma, M. & Haritash, A. K. 2016 Degradation of toxic azo dye (AO7) using fenton's process. *Adv Environ Res.* **5**(3), 189–200. doi:10.12989/aer.2016.5.3.189.

Shoneye, A. & Tang, J. 2020 Highly dispersed FeOOH to enhance photocatalytic activity of TiO_2 for complete mineralisation of herbicides. *Appl Surf Sci.* **511**, 145479. doi:10.1016/j.apsusc.2020.145479.

Thirunavukkarasu, A., Nithya, R. & Sivashankar, R. 2020 A review on the role of nanomaterials in the removal of organic pollutants from wastewater. *Rev Environ Sci Biotechnol.* **19**(4), 751–778. doi:10.1007/s11157-020-09548-8.

Verma, M. & Haritash, A. K. 2019 Degradation of amoxicillin by Fenton and Fenton-integrated hybrid oxidation processes. *J Environ Chem Eng.* **7**(1), 02886. doi:10.1016/j.jece.2019.102886.

Verma, M. & Haritash, A. K. 2020 Photocatalytic degradation of amoxicillin in pharmaceutical wastewater: A potential tool to manage residual antibiotics. *Environ Technol Innov.* **20**, 101072. doi:10.1016/j.eti.2020.101072.

Yadav, S., Pipil, H., Chawla, H., Taneja, S., Kumar, S., Haritash, A. K, . 2022 Textile industry wastewater treatment using eco-friendly techniques. In: *Proceedings of International Conference on Innovative Technologies for Clean and Sustainable Development (ICITCSD – 2021)* (Kanwar, V.S., Sharma, S.K. & Prakasam, C, eds). Springer, Cham. doi:10.1007/978-3-030-93936-6_6.

Yadav, S., Kumar, S. & Haritash, A. K. 2023 A comprehensive review of chlorophenols: Fate, toxicology and its treatment. *J Environ Manage.* **342**, 118254. doi:10.1016/j.jenvman.2023.118254.

First received 23 August 2023; accepted in revised form 10 January 2024. Available online 23 January 2024

Downloaded from http://iwaponline.com/jwcc/article-pdf/doi/10.2166/wcc.2024.483/1355560/jwc2024483.pdf
by DELHI TECHNOLOGICAL UNIVERSITY (DTU) user

Operations Management Research
https://doi.org/10.1007/s12063-023-00438-0

Framework for evaluating sustainability index of a manufacturing system: a case illustration

Deepak Sharma[1,2] · **Pravin Kumar**[1] · **Rajesh Kumar Singh**[3]

Received: 22 November 2022 / Revised: 6 November 2023 / Accepted: 20 December 2023
© The Author(s), under exclusive licence to Springer Science+Business Media, LLC, part of Springer Nature 2024

Abstract
A traditional manufacturing system leads to rapid exploitation of natural resources, global warming, and a decline in biodiversity. Sustainable practices are essential for the conservation of natural resources and environmental protection. A reluctant attitude of manufacturing organizations towards sustainable practices has been observed due to the lack of exposure to sustainability-specific indicators and frameworks. Therefore, relying on the concepts of stakeholder theory, resource-based theory, and institutional theory, this study has proposed a framework to evaluate the sustainability index. There are two aspects of the study: one is to explore the indicators of sustainability considering all dimensions of the triple-bottom-line and validation through a questionnaire survey, and another is prioritization and indexing of the sustainability performance using the Delphi method and Graph Theory Matrix Approach (GTMA). Finally, forty-five indicators have been considered for this study. The GTMA-based framework is proposed for evaluating the sustainability index. Its application is illustrated in the context of an Indian manufacturing organization. The findings of the study unveiled that 'employees and customers welfare', 'material & energy consumption', and 'value creation' possess a strong contribution to the sustainable operations of an organization. This study will assist the concerned professionals in gauging their industrial sustainability performance.

Keywords Sustainable manufacturing systems · Triple bottom line · Structural equation modelling · GTMA · Sustainability index

1 Introduction

Manufacturing organizations have been perceived as a strong pillar in strengthening the nation's economy by generating employment and enhancing gross domestic product (GDP) for many years (Virmani et al. 2021). Globally, it acts as a driving force for economic building and social progress. But, it is accompanied by high consumption of materials and energy with rapid depletion of natural resources (Wang and Yang 2021). The manufacturing sector is facing a few sustainability challenges like greenhouse gas emissions, global warming, and a decline in biodiversity (Aktaş and Demirel 2021; Agrawal et al. 2023). United Nations (UN) estimated that almost three planets' natural resources will be required to sustain human life of up to ~9.6 billion by 2050 (Haleem et al. 2021).

The responsive solution to such endangering population growth, environmental deterioration, societal, and technological imbalance lies with sustainable practices for overall development (Mathiyazhagan et al. 2018). In the era of competitive dynamic technology, sustainable manufacturing (SM) practices have become a meaningful alternate approach with optimized economic concurrence and balanced societal aspects-along with a healthy environment (Mishra et al. 2019). SM is an eco-friendly concept, inclined towards efficiently designed products with economic benefits, and better quality (Gouda and Saranga 2020). Therefore, manufacturing industries will have to transform their traditional manufacturing practices into SM practices considering all facets of the triple bottom line (TBL), i.e., environmental, social, and economic (Singh et al. 2019; Mengistu and Panizzolo 2022).

With the same objective, Apple and Dell have adopted a refurbishing policy for their electronic products to minimize

✉ Deepak Sharma
deep241087@gmail.com; deepak.sharma@gla.ac.in

[1] Department of Mechanical Engineering, Delhi Technological University, 110042 Delhi, India

[2] Department of Mechanical Engineering, GLA University, 281406 Mathura, U.P, India

[3] Management Development Institute, 122007 Gurgaon, Haryana, India

Published online: 26 January 2024

toxic seepage through buried solid wastes. In Wiesbaden, the first electric bus named 'eCitaro' was introduced by Mercedes as a 'Sustainable Bus' operated on solid-state batteries. Recently, Iceland has developed a concept of carbon capture and storage (CCS) which involves capturing and separating CO_2 from other gases, transporting it deep underground, and turning it into stone. The above-discussed examples give an insight into adopted SM practices as the key step of survival for these organizations and are considered a viable production approach (Ahmad and Wong 2018). The robustness of SM practices can empower organizations to stand out in a competitive market (Eslami et al. 2019). The harmful impact on human health and safety leading to quality of life can easily be eliminated including sustainable practices in product and process development,(Singh et al. 2019). SM operations also enhance the productivity, profitability of firms, and the upcoming opportunities for new product development and market expansion (Brones et al. 2014).

In developing nations, the diffusion of SM practices is relatively very low despite the high potential in world economics and workforce deployment (Ngan et al. 2019). SM adoption in manufacturing organizations of developing countries is getting set back issues due to improper performance measurement framework and unavailability of consistent, quantified, practically applicable sustainability indicators (Jamwal et al. 2021). Sustainability indicators (SI) assist in managing the processes of industrial operations avoiding the damages to its TBL aspects for an organizational transition towards sustainability. It also helps to anticipate the possible conditions, trends, occurrences, and situations (Feil et al. 2019). Sartal et al. (2020) emphasized the unavailability of accepted standards and assessment procedures to measure organizational sustainability. Some companies have been pursuing sustainability with unclear strategies and policies (Ihlen and Roper 2014). Elkington with his team conducted a research study in North America and Europe, which concluded that companies had to face a high possibility of medium and long-term losses if they didn`t pay equal attention to environmental and social aspects with economic (Henao and Sarache 2022). Some researchers highlighted that stakeholder pressure can affect the behaviour of SMEs by encouraging environmental commitment (Nguyen and Adomako 2022). Moldavska and Welo (2019) found the absence of suitable assessment frameworks and indicators as decision-making tools for SM. Danese et al. (2019) found that customers presume enhanced environmental and social commitment from the industry, and they can even pay more for their products, resulting in improved financial and operational performance. Baah et al. (2021) proposed that developing institutional pressure (coercive, mimetic, and normative) can motivate manufacturing organizations towards the implementation of sustainability practices. Swarnakar et al. (2021) highlighted the absence of environmental and social SI, giving the primal need for the identification of a structured set of SI from a TBL perspective.

Previous research studies reveal an imbalance in the application of TBL within the manufacturing sector and give unequal emphasis on the economic and environmental aspects, while the social is comparatively neglected (Yip et al. 2023). Based on the availability of literature, indicators that are used in industries are purely generic, not viable concerning activities and size, and not so fully matured to monitor specific manufacturers (Wilson et al. 2007). Consequently, it becomes difficult to gauge the sustainability performance of an organization. The deficit of practical application and quantifiable indicators is responsible for discouragement among practitioners for not undertaking their sustainability assessment. The selection of the indicators should be able to evaluate all critical parameters (product, process & policy) considering three facets of sustainability (*viz.*, environmental, economic, and social). Based on the literature review, the following research gaps were observed:

- Limited research papers are available on a balanced assessment of SM practices with three-dimensional synchronization of the environmental, social, and economic controls (Jamwal et al. 2021; Yip et al. 2023).
- The notable imbalance between the management theories and practical approach to the SM concept has held back the adoption strategies of execution of SM systems in manufacturing organizations (Sabat et al. 2022).

To guide manufacturing organizations toward the adoption & connection of theoretical aspects with a practical paradigm of SM practices, this study addresses the following research questions (RQs):

RQ1: What are the indicators influencing the sustainability of manufacturing sector?
RQ2: How to compare the importance of sustainability indicators?
RQ3: How to prepare the sustainability index of an organization?

To answer the aforementioned questions, this research study explored the indicators of sustainability through a literature review and categorized them using factor analysis. The sustainability index is produced using GTMA to measure the sustainability of manufacturing organizations. All the indicators were rated on a five-point rating scale by the respondents and factor analysis has been used to make the cluster of indicators. All the clusters of sustainability indicators were indexed with the help of factor loadings of the indicators and GTMA. The indices for different clusters show their relative importance. The overall sustainability index of an organization has been calculated considering the

indices of different clusters of the indicators. This study is based on the integrated concept of stakeholder theory (ST), resource-based theory (RBT), and Institutional Theory (IT). The theoretical concept of these theories has been pivotal in shaping the understanding of the organization for the combination of external and internal factors for achieving sustainable development. Many studies mentioned the adoption of the Resource-based view and institutional theory combination for better comprehension of organizational strategies (Peng et al. 2009; Sabat et al. 2022). The novel contribution of this study is given below:

(i) The combined theory of ST, RBT, and IT is utilized for the selection of SM indicators and for developing a framework for achieving sustainability in manufacturing organizations.
(ii) The framework and sustainability indicators proposed within this study can serve as a benchmark to excel in the adoption of sustainability in manufacturing organizations with the creation of more values and satisfaction among the stakeholders, society, and industries while diminishing the environmental effects.
(iii) The result outcomes significantly assist in achieving business sustainability and targets of Sustainable Development Goals, which are optimal units for gauging and evaluating the progress of sustainable development across all levels.

It is observed that in developing countries like India, economic sustainability is more important than environmental and social sustainability. The difference in the importance of environmental and social sustainability is not significant.

The remaining part of this study is outlined as follows: Section 2 represents the literature review of SM indicators considering the triple-bottom-line perspective. Section 3 describes the research methodology framework. Section 4 represents the data analysis and its results. Section 5 represents the discussion and managerial/practitioners and academic implications. Section 6 provides the conclusions of the study with its limitations and the future scope.

2 Literature review

The Manufacturing sector is characterized by high energy consumption, waste generation, and greenhouse gas emissions, creating a void, that necessitates a shift toward energy-efficient SM practices (Cai et al. 2022). In view of organizations` quest for sustainable development, the prominent role of the manufacturing sector is widely acknowledged. In recent years, the manufacturing sector has seen a rising emphasis on sustainability. To effectively embrace sustainability, manufacturers encourage SM practices to maintain economic advantage with minimal impact on the environment and society (Huang and Badurdeen 2017). Sarkis et al. (2010) specified in their study that pressure from organizational stakeholders, including customers, employees, suppliers, and shareholders, plays a significant role in driving firms to adopt and implement proactive green production practices. This research work proposed a framework for evaluating the sustainability index of a manufacturing organization with the help of a case study.

Limited literature exists on the assessment and determination of the environmental and social impacts of production (Ahmad et al. 2019; Wu and Su 2020). However, the taxonomy of sustainability metrics and industrial units lacks uniformity. This necessitates the adoption of relevant measures and indicators for achieving the objectives of sustainable production processes and products (Chaim et al. 2018). Amidst a vast pool of indicators, it becomes tedious to define and implement comprehensive, standardized, and usable SM indicators (Singh et al. 2007). Therefore, the identification, categorization, and assessment of an exhaustive list of indicators are highly desirable for modelling manufacturing sustainability (Park and Kremer 2017; Bui et al. 2017; Sikdar 2019). A distinct set of indicators has been utilized and proposed by various researchers, because of diversity in the manufacturing sector (Gani et al. 2022). In this study, we initially identified fifty-two sustainability indicators through an extensive literature review, as shown in Table 1. After the questionnaire survey and the experts' opinions, seven indicators (volatile organic compounds, tool materials, particulate suspended matter, turnover, payback period, personal protective equipment, and workload) were removed. Insights from industry experts indicated, that these seven indicators are not significant for enhancing the sustainability of manufacturing organizations. 'Volatile organic compounds' and 'particulate suspended matter' are mostly significant in chemical industries. 'Turnover' and 'payback period' are related to management financial strategies and are not much influencive to economic sustainability. 'Personal protective equipment' and 'workload' have already been considered indirectly under the social sustainability indicators. The rest 45 indicators utilized in this study are presented in Table 2.

2.1 Literature search

In this study, a detailed literature review has been conducted to evaluate the status of sustainability in the manufacturing sector. The process involves the review of past literature with appropriate search keywords, properly selected databases, and filtering the search database to access the most relevant research articles available (Rizvi et al. 2023). This research work follows processes for the data collection, thematic

Table 1 Sustainability indicators

	Acronym	Indicators	References
Environmental Sustainability	EN1	Recycling of used materials	Sala (2020), Beng and Omar (2014), Bonvoisin et al. (2014), Pinto et al. (2020)
	EN2	Consumption of recycled/refurbished materials/components	Sala (2020), Bonvoisin et al. (2014), Peralta Álvarez et al. (2017), Feil et al. (2019)
	EN3	Non-Hazardous materials consumption	Sala (2020), Eastwood and Haapala (2015), Feil et al. (2019), Hegab et al. (2023)
	EN4	Economic water consumption	Chaim et al. (2018), Razmjoo et al. (2020), Sharma (2021), Hegab et al. (2023)
	EN5	Green packaging materials	Bereketli and Erol Genevois (2013), Jin et al. (2017)
	EN6	Green transportation/ fuel economy and emission control	Badurdeen and Jawahir (2017), Feil et al. (2019), Sangwan et al. (2018)
	EN7	Reuse and recycling of wastewater	Sala (2020), Razmjoo et al. (2020), Pinto et al. (2020), Sharma (2021)
	EN8	Renewable energy Consumption	Cobut et al. (2015), Sharma (2021), Feil et al. (2019), Ahmad et al. (2019)
	EN9	Elimination of landfills & contamination	Sala (2020), Chaim et al. (2018), Pinto et al. (2020), Feil et al. (2019)
	EN10	Water Contamination	Sala (2020), Akbar and Irohara (2018), Razmjoo et al. (2020)
	EN11	Prevention of water pollution	Razmjoo et al. (2020), Pinto et al. (2020), Feil et al. (2019), Ahmad et al. (2019)
	EN12	Green Initiatives	Bracke et al. (2017), Moktadir et al. (2018)
	EN13	Emission control	Akbar and Irohara (2018), Eastwood and Haapala (2015), Pinto et al. (2020)
	EN14	Volatile organic compounds	Samuel et al. (2013), Ahmad et al. (2019)
	EN15	Labels and certificates (ISO 14001 & ISO 9001)	Beng and Omar (2014), Ghobadian et al. (2020), Urbaniak et al. (2022), Hegab et al. (2023)
	EN16	Quality control	Beng and Omar (2014), Moktadir et al. (2018)
	EN17	Materials of tools	Zhang and Haapala, (2015), Ahmad et al. (2019)
	EN18	Particulate suspended matters	Ahmad et al. (2019)
Economic Sustainability	EC1	Wages and operating cost	Ghobadian et al. (2020), Moktadir et al. (2018), Sharma (2021)
	EC2	Pollution control cost	Kim et al. (2013), Feil et al. (2019), Ahmad et al. (2019)
	EC3	Environmental treatment cost	Kim et al. (2013), Feil et al. (2019), Ahmad et al. (2019)
	EC4	Expenses on corporate social responsibility (CSR)	Badurdeen and Jawahir (2017), Moktadir et al. (2018), Sharma (2021)

Table 1 (continued)

	Acronym	Indicators	References
	EC5	Sales promotion	Borchardt et al. (2011), Feil et al. (2019), Ahmad et al. (2019)
	EC6	Facility expansion	Badurdeen and Jawahir (2017), Ocampo et al. (2016), Ahmad et al. (2019)
	EC7	Revenue generation	Feil et al. (2019), Ahmad et al. (2019), Sharma (2021)
	EC8	Investment in research and development	Butnariu and Avasilcai (2015), Feil et al. (2019), Ahmad et al. (2019)
	EC9	Profit earned	Butnariu and Avasilcai (2015), Ocampo et al. (2016), Feil et al. (2019)
	EC10	Annual Productivity	Feil et al. (2019)
	EC11	New Product Design and Development	Butnariu and Avasilcai (2015), Ahmad et al. (2019)
	EC12	Market share	Borchardt et al. (2011), Feil et al. (2019)
	EC13	Liability and Debt payment	(Singh et al. 2009), Sharma (2021)
	EC14	Depreciation	Feil et al. (2019), Ahmad et al. (2019)
	EC15	Maintenance	Kim et al. (2013), Ahmad et al. (2019)
	EC16	Prevention of scrap production	Kim et al. (2013), Ahmad et al. (2019)
	EC17	Turnover (selling inventory)	Butnariu and Avasilcai (2015), Ahmad et al. (2019)
	EC18	Payback period	Ahmad et al. (2019)
Social Sustainability	SC1	Job security and employee retention	Chaim et al. (2018), Ahmad et al. (2019), Sharma (2021)
	SC2	Health and Safety	Feil et al. (2019), Ahmad et al. (2019), Peruzzini et al. (2017)
	SC3	Human rights protection	Chaim et al. (2018), Holm (2018), Ahmad et al. (2019), Peruzzini et al. (2017), Sharma (2021)
	SC4	Employee performance	Bortolotti et al. (2015), Holm (2018), Sharma (2021)
	SC5	Employee satisfaction	Ocampo et al. (2016), Feil et al. (2019), Ahmad et al. (2019)
	SC6	Training and Development	Chaim et al. (2018), Holm (2018), Ahmad et al. (2019), Sharma (2021)
	SC7	Risk identification and employee feedback management	Badurdeen and Jawahir (2017), Chaim et al. (2018), Moreira et al. (2018)
	SC8	Customer satisfaction and relationship	Ghobadian et al. (2020), Feil et al. (2019), Ahmad et al. (2019), Sharma (2021)

Table 1 (continued)

	Acronym	Indicators	References
	SC9	Product quality	Chaim et al. (2018), Moktadir et al. (2018), Sharma (2021)
	SC10	Trust development	Gebisa and Lemu (2017), Ahmad et al. (2019)
	SC11	Customer feedback	Chaim et al. (2018), Ahmad et al. (2019), Sharma (2021)
	SC12	Personal protective equipment	Ahmad et al. (2019)
	SC13	Community feedback	Chaim et al. (2018), Peralta Álvarez et al. (2017), Sharma (2021)
	SC14	The social and political aspects	Chaim et al. (2018), Holm (2018)
	SC15	Technology development and support	Chaim et al. (2018), Ahmad et al. (2019), Peruzzini et al. (2017), Sharma (2021)
	SC16	Work load	Zhang and Haapala (2015), Peruzzini et al. (2017), Ahmad et al. (2019)

evaluation focused on depicting concerned published papers, and segregation for identifying the most relevant sustainability indicators from the perspective of the manufacturing sector. The detailed literature review revealed that the sustainability aspects of manufacturing systems are mostly assessed by three main indicators, which are termed environmental, social, and economic (Akbar and Irohara 2018). The theoretical structure of the study and the three different clusters of sustainability indicators are reviewed subsequently.

2.2 Theoretical foundation

Predominantly, the performance measuring framework for an SM system is multifaceted. Organizations aiming to transform their system should combine external and internal factors to attain sustainable development and enhance the firm's performance. In an organization, resources cannot be combined independently, they need some form of temporary commitment by a governing entity (Stout 2012). McGahan (2021) stated that "stakeholders bind resources". Stakeholder theory views resource development in the organization from two aspects, one is the development of human capital, and the second is the interaction between customers, communities, investors, and government, leading to sustainability. The resource-based theory leads to the utilization of the resources developed using the stakeholder theory. The institutional theory puts pressure on the management to fulfill the various parameters of environmental, social, and economic sustainability. To fulfill these needs, resources are required and effectively utilized. Consequently, these three theories are collectively utilized to enhance the capacity of the organization to fulfill the sustainability criteria. In the past, various research studies have employed an integrated theoretical framework to promote sustainable development and address issues related to environmental degradation and climate change. Horbach et al. (2023) utilized the concepts of three theoretical theories namely ST, IT, and resource-based view to identify the antecedents of firms` greenness. Ozdemir et al. (2023) applied ST, RBT, and the knowledge-based view theory to promote innovation collaboration in a Spanish technological panel industry, emphasizing the effectiveness of resource utilization through collaborations with multiple stakeholders. Ijaz Baig and Yadegaridehkordi (2023) employ RBT, ST, and TBL theory as a foundation for assessing the sustainable performance of a Malaysian manufacturing enterprise. They underscored the positive impact of organizational capabilities, stakeholder pressure, and green orientation and marketing on organizational sustainability. The adopted theoretical lenses for this study have been sequentially elucidated.

The stakeholder theory is most popular among sustainability researchers because it widens the perspective of business from the firm, itself, to a larger society and environment with an objective of 'creation of value for all stakeholders' (Freeman

2010). The encouragement of sustainable development by harnessing the synergies among stakeholders is the fundamental step to achieving sustainability on both local and global scales (Beck and Ferasso 2023). The stakeholder constitutes customers, regulators, governments, NGOs, media, etc. The rationale is that a lack of meeting the requirements of stakeholders can lead to economic and reputation loss (Hermundsdottir and Aspelund 2022) while meeting their needs can induce an increase in reputation, customer satisfaction, economic gains, and increase in market share (Liao 2018). ST also explains, how firms can implement sustainability innovations, can enhance market goodwill, and diminish business risk (Hermundsdottir and Aspelund 2022). Previous studies have found that stakeholder pressure significantly leads the top management to establish sustainable operations and steers organizational intentions toward green innovation within the manufacturing context (Shahzad et al. 2023). The engaged participation of stakeholders within the organization can enhance operational efficiencies by embracing environmentally conscious and sustainable practices.

RBT visualizes the organization as an array of resources and capabilities that develop a basis for the incorporation of sustainability (Barney 1991). Resources mean the assets that the organization embraced, i.e., employees, financial equity, skills, and organizational (social) processes (Ramadani et al. 2022). Analogously, RBT is an inside-out frame of approach, which means that the firm available resources utilization approach, routines, and policies can yield desired outcomes. The organization production system is a well-thought example of an internal resource with inference for economic, and environmental performance. The logical thought is that the waste generation, emissions, and other environmental impacts are simply indications of an inefficient production system. The firm can reduce the cost by diminishing those environmental footprints.

Institutional theory (IT), also referred as regulatory pressure, can drive the adoption of sustainable practices within the organization. IT has been used primarily in many studies as a theoretical framework elaborating how pressure can change the implementation of green practices in the supply chain of manufacturing organizations (Fontana et al. 2022). From an institutional perspective, stakeholders can exert coercive, normative, or mimetic pressure on organizations to promote sustainability (Yuen et al. 2017). Coercive pressures emerge from governmental agencies, industry associations, and departmental trade and industry policies, while normative pressure arises from professionalization, and mimetic pressure reflects the tendency of firms to imitate others (Dubey et al. 2019). These pressures exhibit a significant and positive correlation with tangible resources and the development of workforce skills (Bag and Pretorius 2022). The institutional perspective can induce motivation in the firm to practice sustainability, as evident in numerous sustainability studies that have employed institutional theory as a precursor (León-Bravo et al. 2019; Khurshid et al. 2021).

The integrated theoretical framework based on the application of ST, RBT, and IT is depicted in Fig. 1.

2.3 Environmental sustainability indicators

The environmental dimension of sustainability focuses on the ecosystem in terms of total energy consumption, exploitation of natural resources, and self-restoration limits. Environmental assessment of manufacturing organizations is measured in terms of the use of green material (Di Foggia 2018), energy consumption (Feil et al. 2019), and optimal water utilization throughout the product life cycle (Eslami et al. 2019). Ogunmakinde (2019) acknowledged 'buy green' and 'act green' as effective acquisition strategies for waste minimization. The organization should be capable to integrate, build, and reconfigure resources to embed environmental sustainability into new product development as per the market requirements. The Resource-based view derives two SM capabilities named "product stewardship", and "pollution prevention" as vital strategies for the company (Barletta et al. 2021).

A well-maintained and self-sustained ecosystem requires a dynamic equilibrium to prevent environmental degradation such as air pollution, global warming, climate change, water pollution, land contamination, etc. (Bereketli and Erol Genevois 2013). Gedam et al. (2021) emphasized carbon footprints, green production practices, green logistics, green packaging, and green accounting for building a sustainable ecosystem in supply chain networks. The prime focus lies on the consumption of materials, energy, water, and biomass, in addition to their environmental impacts involved in logistics (packaging, storage & transportation), and certification (environmental laws & regulations) of the process (Bonvoisin et al. 2014; Ogunmakinde et al. 2022). To counter the hazardous effects of manufacturing activities on the environment, the World Economic Forum (WEF) promoted the circular economy to imply the reuse/recycling of products without affecting biodiversity. Khan and Haleem (2021) recommended the optimized reuse of products, parts, and materials leading to increased profit and reduced environmental distraction. Environmental sustainability can also be achieved through energy consumption, emissions, waste, water, and carbon footprint (Mani et al. 2014). Bhutta et al. (2021) reviewed green packaging, distribution, and inculcation of environmental standards (ISO 14000-14001), and observed that sustainable procurement strategies are the prominent areas of environmental sustainability practices with enhanced financial performance (Wang and Mao 2020).

2.4 Economic sustainability indicators

The assessment of economic performance stands as a key factor in gauging the financial prosperity of any

manufacturing unit (Borchardt et al. 2011). The economic attributes for any manufacturing organization lie in its capacity to deliver superior value to customers rather than competitors. Within the economic context, the emphasis rests on identifying indicators that can effectively gauge progress in acquiring financial gains for the organization (Mengistu and Panizzolo 2022). It is noteworthy that many manufacturing organizations often lack a well-defined and comprehensive set of mature indicators when it comes to evaluating financial activities (Swarnakar et al. 2021). The economic facet of sustainability encompasses its effects on the economic health of stakeholders, local communities, and national economic systems (Butnariu and Avasilcai 2015). It considers the generation and dissemination of direct economic benefits, including operational costs, sales, administrative expenses, employee remuneration, contributions, as well as investments incurred in the safety, stakeholders` health, net profits, expenditure on various sanctions, approvals, and fines. The financial risks and implications due to the value depreciation of the products, repair, and maintenance are also assessed.

Furthermore, the assessment also takes into account substantial financial aid or subsidies obtained for the industrial setup and distribution of manufactured goods (Riayatsyah et al. 2017). The competitive strategies, recruiting procedures, and amount of expenditure on local vendors and senior-level management at significant operational sites are considered to assess the financial position and stability of the unit (Wu and Su 2020). Xu et al. (2017) indicated that taxation over carbon emissions is one of the followed global initiatives for reducing GHG emissions in developing and developed nations, highlighting the significance of economic indicators designed to analyze industrial operations and their influence on a wide variety of stakeholders.

2.5 Social sustainability indicators

The National Institute of Standards and Technology (NIST) has identified that manufacturing activities and products can pose challenges to the social dimension of sustainability, which encompasses the well-being of employees, customers, and communities (Kibira et al. 2018). Social indicators, such as the health & safety of both employees and customers, have been employed to assess the societal impacts of various manufacturing processes and products (Chaim et al. 2018). SM expects a workplace that is sustainable and promote an empowered, informed, and willing workforce, despite of factors like age, gender, abilities, and individual growth in light of a diminishing recruiting pool (Gebisa and Lemu 2017). Fundamental principles like equality, empowerment, inclusion, engagement, sharing, cultural identity, and institutional cohesion form the foundation of social sustainability (Henao et al. 2017). Diversity, Equity, and Inclusion (DEI) related perspectives are considered under the dimension of Human rights protection. It emphasizes society's solidarity and its ability to work towards shared objectives while addressing the health and well-being, nutrition, housing, education, and cultural expression of individuals (Holm 2018). These proactive visions are vital for the potential growth of the industries, not only to ensure demographic continuity and meet employee requirements but also to promote work-life balance, and the welfare of all stakeholders. Moreover, they rely on enhancing customer satisfaction and community relations through effective feedback mechanisms (Zhou et al. 2016).

Manufacturing industries can boost productivity and sustainability, gaining a competitive edge by incorporating human resource management aspects, such as training, employee engagement, skill development, rewards, incentives, and commitment (Muduli et al. 2020). A healthy workplace, proper training, risk identification, feedback mechanism, financial support, suitable working hours, and medico-legal benefits promote employee satisfaction and their ability to perform effectively (Reiman and Pietikäinen 2010). Employee satisfaction plays a key role in improving the productivity of manufacturing organizations considering aspects like organizational culture, work environment, equality policies, and the provision of rewards and incentives, among others (Lee et al. 2014; Swarnakar et al. 2020). Transparent, confidential, and proactive feedback mechanisms involving various stakeholders (employees, customers, and community) serve as a guiding source for a company`s growth (Moreira et al. 2018). In a broader context, stakeholders such as customers, employees, the public, suppliers, and shareholders can exert various forms of institutional pressure - mimetic, coercive, and normative pressure to influence firms to adopt sustainable practices.

The major works done on all three dimensions of sustainability in manufacturing systems are summarized in Table 1.

3 Research methodology

The identification, categorization, and evaluation of SM indicators were executed in three phases. At first, the most adequate, and leading indicators of SM were explored and incorporated through an exhaustive literature review. The depicted indicators were then assessed through the administration of a questionnaire, whose content was validated by academic and industrial experts. We have approached 15 experts from both industry and academia for the pilot study. Out of this group, only two industry experts and three academics have expressed their interest in taking part in our questionnaire survey and interview. Both the industrial experts are having an average experience of 10 years, one serves as a General Manager in production, while the other holds the position of Deputy General Manager in the Research & Development Department. As for the academic experts, two

are esteemed professors with a research focus on the renewable energy sector, while the third member is an Associate Professor with expertise in non-conventional manufacturing processes. These experts meticulously evaluated and confirmed the validity and acceptability of our proposed scale. The response data collected was initially subjected to scrutiny based on mean values, leading us to select only those factors whose mean values exceeded the threshold of 3.

In the second phase, the scrutinized 45 sustainability indicators were categorized, i.e., 15-environmental, 16-economic, and 14-social into 10-subgroups using exploratory factor analysis (EFA), with subsequent validation via confirmatory factor analysis (CFA). The nomenclature assigned to these 10 subgroups was influenced by the defining characteristics of the factors lying in that corresponding group. The third and final phase involves a detailed discussion with the experts' panel, utilizing the Delphi technique. This phase facilitated pairwise comparisons of the indicators across all 10 subgroups, leading to a sustainability index tailored for manufacturing organizations using GTMA.

To ensure minimum ambiguity among expert opinions, the following selection criteria were considered:

- Experts should have substantial experience within the manufacturing industry and be concerned with the application of sustainable practices.
- Experts should be working in the field of sustainability and CSR initiatives within their respective organizations.

The experts' panel comprised 12 members having managerial experience as Head-R&D, Head-PPC, General Manager Operations, Quality Managers, Production Managers, etc. Among these experts, 5 were from the automobile sector, 4 from the iron & steel sector, and 3 from the chemical and pharmaceutical sector. Given the constraints imposed by the COVID-19 pandemic, opinions were gathered through a series of online interactive video conferencing sessions. The consensus formed during these sessions among the indicators was incorporated within the GTMA framework. The process flow chart of the research methodology is shown in Fig. 2.

3.1 Questionnaire administration and data collection

A questionnaire was prepared in consultation with academic experts and professionals/practitioners from the manufacturing sector for data collection. The questionnaire comprised 52 distinct indicators. These indicators were systematically assessed using a 5-Point-Likert scale, wherein a score of 5 indicates strongly agree and a score of 1 indicates strongly disagree. The questionnaire was communicated among manufacturing firms operating in the northern region of India. To ensure accuracy and effectiveness, data has been collected across different age groups, distinct experienced professionals, and varying academic qualifications. In total, we received 444 completed responses, while 12 responses were found to be incomplete and were consequently excluded from our analysis. The demographic characteristics of the respondents are shown in Table A1 (Appendix).

3.2 Data reliability/validation

The data collected through the questionnaire survey was initially analyzed based on mean values, because of a large number of indicators. The indicators whose mean values come out to be less than 3, as per the descriptive analysis of the respondent data, were ignored from further consideration, shown in Table A2 (Appendix). The less mean value (<3) indicators (volatile organic compounds, tool materials, particulate suspended matter, turnover, payback period, personal protective equipment, and workload) were also discussed with the experts, and they suggested to overlook them for further analysis. The remaining set of 45 indicators was then validated using Bartlett's test of sphericity, also known as the correlation test, and Kaiser-Meyer-Olkin (KMO) analysis to check the adequacy of the sample. The KMO value greater than 0.6 and the significance level value less than 0.05 signified that factor analysis could be applied to the given data set (Kumar et al. 2021a). Furthermore, the reliability of the dataset was assessed through the Cronbach alpha test, which measures the internal consistency of the data. A Cronbach Alpha value equal to or greater than 0.7 is considered indicative of high reliability (Agrawal et al. 2017).

Using EFA, the SM indicators were categorized into the respective groups/criteria based on common patterns, nature, and similarities (Mittal and Sangwan 2014). The factor analysis technique has been widely used for data minimization, development of scale measurement, and sorting. EFA encompasses three segments; factor extraction, rotation, and interpretation (Thompson 2004). Factor interpretation is executed to calculate underlying factors that completely explain the observed correlation among the indicators (Williams et al. 2010).

3.2.1 Confirmatory factor analysis

CFA is performed for the detailed quantification of principal latent variable structure, and to validate the results obtained during EFA. The principal aim of CFA is to check the unidimensionality aspects of the data (Mittal and Sangwan 2014). CFA is employed to verify the structure of the factors and to compute the covariance weights between latent factors (identified from EFA) and their variables. The formulated model is validated in terms of statistical measures for checking its goodness of fit, shown in Table A3 (Appendix).

$$
\begin{aligned}
permI = & \prod_{i=1}^{6} F_i + \sum_{i=1}^{5}\sum_{j=i+1}^{6}\sum_{k=1}^{3}\sum_{l=k+1}^{4}\sum_{m=l+1}^{5}\sum_{n=m+1}^{6} (r_{ij}r_{ji})I_kI_lI_mI_n \\
& + \sum_{i=1}^{4}\sum_{j=i+1}^{5}\sum_{k=j+1}^{6}\sum_{l=1}^{4}\sum_{m=l+1}^{5}\sum_{n=m+1}^{6} (r_{ij}r_{jk}r_{ki} + r_{ik}r_{kj}r_{ji})I_lI_mI_n \\
& + \left[\begin{array}{l} \sum_{i=1}^{3}\sum_{j=i+1}^{6}\sum_{k=j+1}^{5}\sum_{l=i+2}^{6}\sum_{m=1}^{5}\sum_{n=m+1}^{6} (r_{ij}r_{jk})(r_{kl}r_{lk})_lI_mI_n \\ + \sum_{i=1}^{3}\sum_{j=i+1}^{5}\sum_{k=i+1}^{6}\sum_{l=j+1}^{6}\sum_{m=1}^{5}\sum_{n=m+1}^{6} (r_{ij}r_{jk}r_{kl}r_{li} + r_{il}r_{kjji})_lI_mI_n \end{array} \right] \\
& + \left[\begin{array}{l} \sum_{i=1}^{4}\sum_{j=i+1}^{5}\sum_{k=j+1}^{6}\sum_{l=1}^{5}\sum_{m=l+1}^{6}\sum_{n=1}^{6} (r_{ij}r_{jk}r_{ki} + r_{ik}r_{kj}r_{ji})(r_{lm}r_{ml})_lI_m \\ + \sum_{i=1}^{2}\sum_{j=i+1}^{5}\sum_{k=i+1}^{6}\sum_{l=i+1}^{6}\sum_{m=j+1}^{6}\sum_{n=1}^{6} (r_{ij}r_{jk}r_{kl}r_{lm}r_{mi} + r_{im}r_{ml}r_{lk}r_{kj}r_{ji})I_n \end{array} \right] \\
& + \left[\begin{array}{l} \sum_{i=1}^{3}\sum_{j=i+1}^{5}\sum_{k=i+1}^{6}\sum_{l=i+1}^{6}\sum_{m=1}^{6}\sum_{n=m+1}^{6} (r_{ij}r_{jk}r_{kl}r_{li} + r_{il}r_{lk}r_{kj}r_{ji})(r_{mn}r_{nm}) \\ + \sum_{i=1}^{1}\sum_{j=i+1}^{5}\sum_{k=j+1}^{6}\sum_{l=1}^{4}\sum_{m=l+1}^{5}\sum_{n=m+1}^{6} (r_{ij}r_{jk}r_{ki} + r_{ik}r_{kj}r_{ji})(r_{lm}r_{mn}r_{nl} + r_{\ln}r_{nm}r_{ml}) \\ + \sum_{i=1}^{1}\sum_{j=i+1}^{6}\sum_{k=i+1}^{3}\sum_{l=i+2}^{6}\sum_{m=k+1}^{5}\sum_{n=k+2}^{6} (r_{ij}r_{ji})(r_{kl}r_{lk})(r_{mn}r_{nm}) \\ + \sum_{i=1}^{1}\sum_{j=i+1}^{5}\sum_{k=i+1}^{6}\sum_{l=i+1}^{6}\sum_{m=i+1}^{6}\sum_{n=j+1}^{6} (r_{ij}r_{jk}r_{kl}r_{lm}r_{mn}r_{ni} + r_{in}r_{nm}r_{ml}r_{lk}r_{kj}r_{ji}) \end{array} \right]
\end{aligned} \tag{1}
$$

3.2.2 Graph theory matrix approach (GTMA)

The graph theory matrix (digraph) approach is used for evaluating the intensity of indicators for environmental, economic, and social sustainability by computing a permanent matrix. It is a systematic and powerful tool for converting qualitative preferred opinions into quantitative values by providing a single mathematical index. The other multi-criteria decision-making techniques like the best-worst method, the Analytic network process (ANP), the Analytical Hierarchical process (AHP), and the Technique for order preference by similarity to the ideal solution (TOPSIS), technically give similar results. Although, these methods lack in capturing interdependency among variables while doing pairwise comparisons. GTMA has no such constraints, as it is based on digraphs and permanent matrix value computation which doesn't need a hypothesis formulation about interdependency (Tuljak-Suban and Bajec 2020). GTMA can solve a few complex problems, resulting in its widespread applications in many fields of science and engineering (Kek and Gurumurthy 2018), such as logistics service providers (Gupta and Singh 2020), supply chain flexibility index (Singh and Kumar 2019), roadblocks of Industry 4.0 (Virmani et al. 2021), for evaluating the maintainability index (Singh et al. 2015). In this study, we used it to measure the sustainability index for an SM system. GTMA methodology consists of the following steps:

- Digraph formulation between indicators based on mutual correlations.
- Matrix formulation for different groups and subgroups of indicators.
- Computation of permanent function for each sustainable dimension.
- Construct inheritance and interdependency matrix for indicators with expert's opinion based on the rating scale.
- Calculation of permanent function for an SM system.

Hence, the permanent function is calculated by formulating a permanent matrix by using a generalized equation written as:

Matrices are formulated on a rating scale of 0-10 (shown in Table A4, Appendix) to define the relative importance of indicators using experts' opinions.

Based on the matrices, directed graphs are prepared for all the groups and subgroups of the indicators. A directed graph consists of nodes and edges. Nodes represent the SM indicators and edges represent their interconnections. I_i shows the inheritance of indicators and r_{ij} shows the influence of i_{th} indicator on j_{th} indicator.

Figure 3 shows a schematic representation of environmental sustainability and its sub-group indicators showing their interdependencies. The sub-group indicator includes material and energy consumption ($I1_1$), water consumption ($I1_2$), environmental factor ($I1_3$), and global certification and control ($I1_4$). The indicators permanent matrix (IPM) of environmental sustainability shown in Fig. 3. is written as:

$$
Per(Environmental) = IPM(Environmental) = \begin{pmatrix} I1_1 & r_{12} & r_{13} & r_{14} \\ r_{21} & I1_2 & r_{23} & r_{24} \\ r_{31} & r_{32} & I1_3 & r_{34} \\ r_{41} & r_{42} & r_{43} & I1_4 \end{pmatrix}
$$

The units of the matrix obtain values from the digraph. The units shown on the diagonal constitute the nodes of the digraph, which are permanent matrix values of the sub-factors of the respective dimension of SM indicators. The non-diagonal units show the interdependencies among the indicators. Correspondingly, the IPM of the remaining dimensions can be formulated. The overall interaction among SM indicators, i.e., environmental (I1), economic (I2), and social (I3). The IPM of the SM system represents the resultant value of sustainability for an organization, computed as:

$$
Per(IPM)\left[SMsystem\right] = \begin{pmatrix} I1 & r_{12} & r_{13} \\ r_{21} & I2 & r_{23} \\ r_{31} & r_{32} & I3 \end{pmatrix}
$$

4 Data analysis and results

The results of the study are analyzed and discussed in the succeeding two sub-sections. The first sub-section covers the exploratory and CFA of SM indicators, and the second sub-section discusses the outcomes of GTMA.

4.1 Exploratory factor analysis and confirmatory factor analysis

In this study, the responses of considered forty-five (45) SM indicators whose mean values are greater than 3, were analyzed through EFA for estimating their dimensionality, and to frame the factorial structure of GTMA. The construct`s reliability test was conducted using Cronbach's alpha. The calculated value of Cronbach alpha was 0.917 which is considered a good indicator of reliability, i.e. greater than the threshold of 0.7 (Vinodh and Joy 2012). Further Kaiser-Meyer-Olkin's (KMO) assessment of sampling adequacy is 0.857 which is more than the recommended level of 0.80 (Kaiser 1970). Bartlett's test of sphericity ($p < 0.01$) calculates the overall correlation among the indicators (Lučić 2020). The KMO and Bartlett`s test results are shown in Table A5 (Appendix) with acceptable values.

In this study, we successfully grouped the 45 indicators into 10 latent factors, consisting of 4 latent factors for environmental sustainability (EN), 3 for economic sustainability (EC), and 3 for social sustainability (SC) by factor analysis as presented in Table 2. These ten latent factors were formulated based on eigenvalues exceeding one and collectively explained 69.44% of the total variance. Notably, the first group contributed 22.87 % to the total variance, while the subsequent latent factors contributed as follows: the second (8.80%), the third (7.67%), the fourth (6.74%), the fifth (5.27%), the sixth (5.02%), the seventh (4.27%), the eighth (4.00%), the ninth (2.54%), and the tenth (2.26%). All 45 indicators were meticulously categorized with their corresponding labeled rotated factor loadings and Cronbach`s alpha value exceeding 0.7. Table 2 shows that the internal consistency among the indicators under each dimension (environmental, economic, and social) was strong, with reliability ratings of more than 0.67 for all factors (Thorndike 1995).

CFA is used to confirm the loadings of the identified indicators and assess the relationships between individual criteria. EFA alone can`t be adequate for getting all the requisite constructs (Pathak et al. 2020). In this study, CFA was run on the assessment model comprising ten factors, composed of sustainability indicators for an SM system. This analysis was employed in gauging the validity of the developed structure, testing construct validity, assessing discriminant validity, and evaluating the goodness of fit of the model. The outcomes pertaining to the goodness of fit measures are shown in Table A6 (Appendix), indicating their alignment with acceptable values.

The Chi-square ($\chi 2$) test provides evidence that a CMIN/DF value closer to zero signifies a good fit (Thompson 2004). In our developed structure, the CMIN/DF value stands at 2.715, falling within the acceptable threshold of 3. The value of RMSEA is 0.062, which is within the acceptable limit of 0.1. The standardized RMR (root mean square residual) is .0460, which is calculated by the square root of the variation between the model and sample covariance matrices (Coughlan et al. 2008). RMSR value less than 0.14 is considered allowable. The developed model has a Goodness of fit Index (GFI) = 0.817, comparative fit index (CFI) = 0.871, parsimony comparative fit index (PCFI) = 0.792, and PGFI (Parsimony Goodness of Fit Index) = 0.710. Importantly, all these calculated values fall within the approved threshold limits (Bentler 1990; Hair 2014).

We also calculated the average variance extracted (AVE) for each latent factor, all of which exceeded 0.50, surpassing the recommended threshold (shown in Table 2) and showing adequate convergence (Fornell and Larcker 1981). To further validate the constructs, we determined the composite reliability (CR) for each factor, with values consistently exceeding 0.7, indicating statistical significance. The CFA diagram, generated using AMOS 23.0, illustrates ten factors/criteria with a total of forty-five indicators, as depicted in Fig. 4. We also checked and determined discriminant validity for the constructs, presented in Table A7 (Appendix). Discriminant validity reveals that indicators should be more strongly related to their latent factor than to others (Fornell and Larcker 1981). As a consequence of the above discussions and the results from Table 2, A6, A7, and Fig. 4, we have successfully classified and confirmed in total ten factors; four from environmental sustainability, named as material and energy consumption, water consumption, environmental factor, and global certification and control; three from economic sustainability, namely, initial investment & operating cost, value creation, indirectly-associated expenses; and lastly three from social sustainability, named employees, customers, and the community.

4.2 Evaluation of SM index by GTMA: case illustration

The manufacturing sector's contribution is about 17 % of India's GDP (Virmani et al. 2021). In this study, a company having global headquarters in the National Capital Region of India is considered for the case analysis. The company is dealing with auto components & their systems, electric vehicles, charging infrastructure, and renewable energy. It supplies the components and services to all major giants of the automobile industry in India and abroad (Germany, Italy, the USA, China, and Spain). The company has a worth of $1.8 billion in 18 locations in 8 countries across the world with 21,000 global workforces. GTMA is applied to evaluate the sustainability index of

Table 2 EFA and CFA results of SM indicators

			Factor Loadings											
			Environmental sustainability				**Economic sustainability**			**Social sustainability**			Cronbach Alpha	AVE	CR
Sub Category	**Indicators**	**Notation**	**$I1_1$ (MEC)**	**$I1_2$ (WC)**	**$I1_3$ (EF)**	**$I1_4$ (GCC)**	**$I2_1$ (IIOC)**	**$I2_2$ (VC)**	**$I2_3$ (IAE)**	**$I3_1$ (EM)**	**$I3_2$ (CU)**	**$I3_3$ (CO)**			
Materials and Energy consumption (MEC)	EN1	$I1_1^1$	0.714										0.858	0.502	0.858
	EN2	$I1_1^2$	0.683												
	EN3	$I1_1^3$	0.693												
	EN5	$I1_1^4$	0.735												
	EN6	$I1_1^5$	0.706												
	EN8	$I1_1^6$	0.779												
Water consumption (WC)	EN4	$I1_2^1$		0.735									0.913	0.782	0.915
	EN10	$I1_2^2$		0.724											
	EN7	$I1_2^3$		0.749											
Environmental Factors (EF)	EN11	$I1_3^1$			0.862								0.854	0.663	0.855
	EN9	$I1_3^2$			0.854										
	EN13	$I1_3^3$			0.855										
Global Certification and Control (GCC)	EN15	$I1_4^1$				0.670							0.793	0.562	0.794
	EN12	$I1_4^2$				0.741									
	EN16	$I1_4^3$				0.701									
Initial Investment & Operating Cost (IIOC)	EC1	$I2_1^1$					0.830						0.831	0.502	0.834
	EC13	$I2_1^2$					0.722								
	EC3	$I2_1^3$					0.723								
	EC4	$I2_1^4$					0.738								
	EC5	$I2_1^5$					0.693								
Value Creation (VC)	EC7	$I2_2^1$						0.821					0.916	0.643	0.914
	EC9	$I2_2^2$						0.832							
	EC10	$I2_2^3$						0.791							
	EC11	$I2_2^4$						0.720							
	EC12	$I2_2^5$						0.778							
	EC6	$I2_2^6$						0.765							
Indirectly-Associated Expenses (IAE)	EC14	$I2_3^1$							0.774				0.860	0.561	0.863
	EC15	$I2_3^2$							0.746						
	EC2	$I2_3^3$							0.775						
	EC8	$I2_3^4$							0.772						
	EC16	$I2_3^5$							0.756						

Table 2 (continued)

Sub Category	Indicators	Notation	Factor Loadings										Cronbach Alpha	AVE	CR
			Environmental sustainability				Economic sustainability			Social sustainability					
			$I1_1$ (MEC)	$I1_2$ (WC)	$I1_3$ (EF)	$I1_4$ (GCC)	$I2_1$ (IIOC)	$I2_2$ (VC)	$I2_3$ (IAE)	$I3_1$ (EM)	$I3_2$ (CU)	$I3_3$ (CO)			
Employees (EM)	SC1	$I3_1^1$								0.829			0.890	0.576	0.890
	SC2	$I3_1^2$								0.771					
	SC4	$I3_1^3$								0.737					
	SC6	$I3_1^4$								0.829					
	SC7	$I3_1^5$								0.835					
	SC5	$I3_1^6$								0.702					
Customers (CU)	SC8	$I3_2^1$									0.795		0.837	0.563	0.837
	SC9	$I3_2^2$									0.776				
	SC11	$I3_2^3$									0.778				
	SC10	$I3_2^4$									0.746				
Community (CO)	SC14	$I3_3^1$										0.859	0.879	0.651	0.882
	SC15	$I3_3^2$										0.812			
	SC3	$I3_3^3$										0.833			
	SC13	$I3_3^4$										0.784			

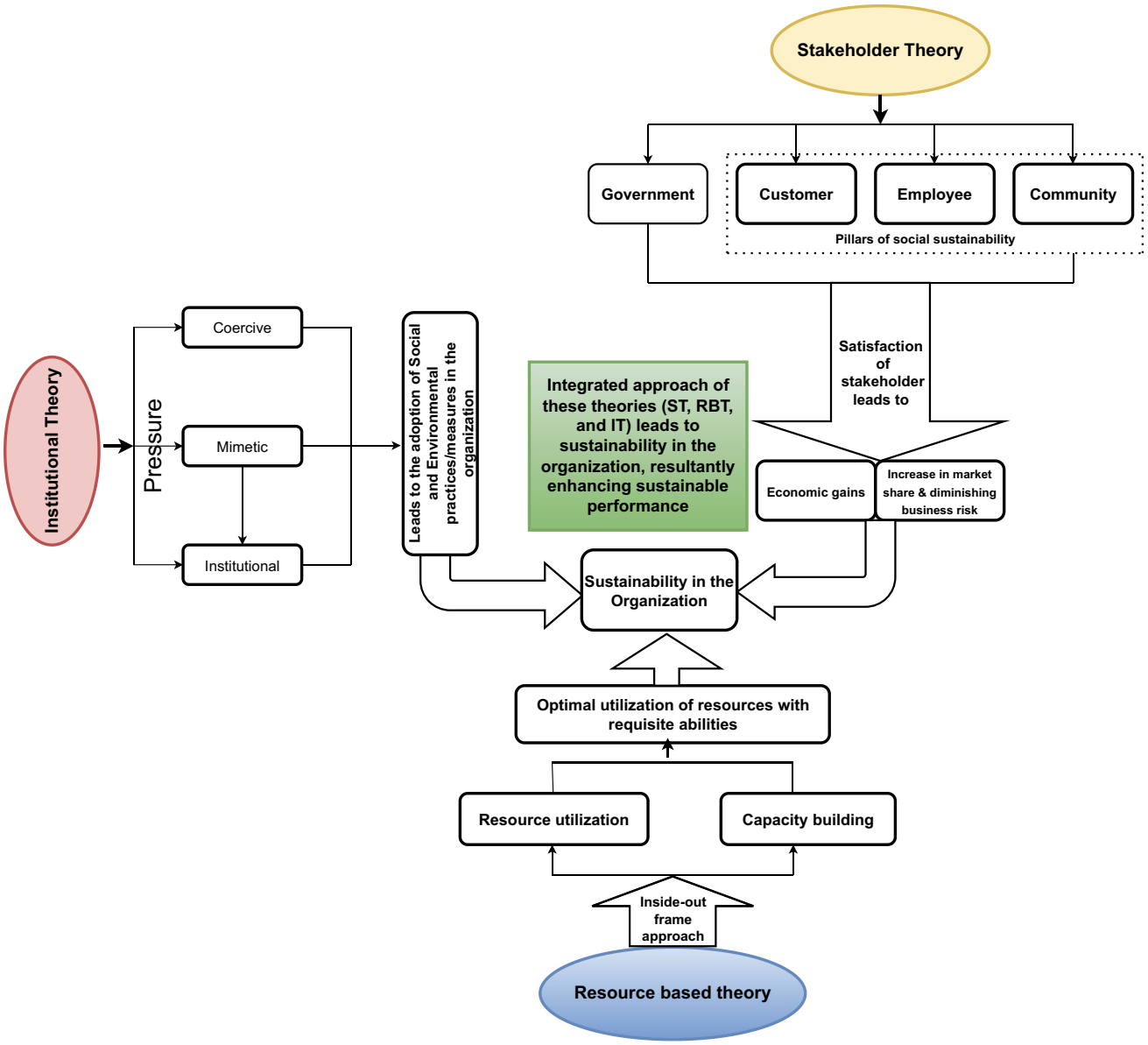


Fig. 1 The integrated theoretical framework based on the application of ST, RBT, and IT

this manufacturing organization. The panel of experts (details discussed in the methodology section) was consulted for data collection.

4.2.1 Indicators permanent matrix (IPM) for sustainability index evaluation

In this section, the IPM of each sub-category and major category of indicators is evaluated as per the GTMA description, given in section 3.1.1. Quantification of the matrix is achieved by an expert's score based on a rating scale (shown in Table A4, Appendix). Notations used for the main categories are I1 (environmental sustainability), I2 (economic sustainability), and I3 (social sustainability). The step-by-step result of IPM calculation for each SM dimension is shown below by applying equations (2) to (3).

Environmental sustainability index evaluation:

$$Per\left[i1_1(MEC)\right] = ()$$

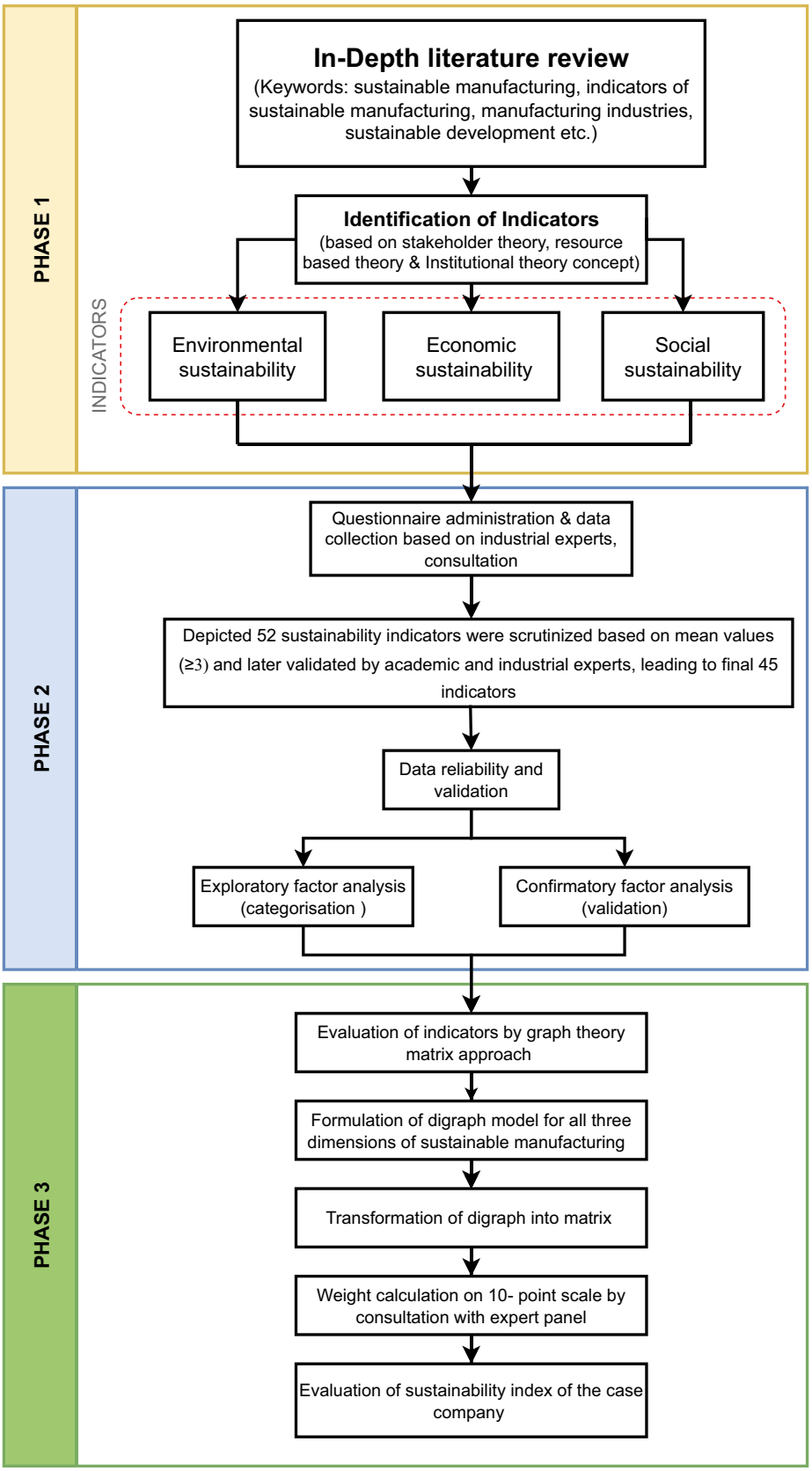


Fig. 2 A framework used for the research methodology

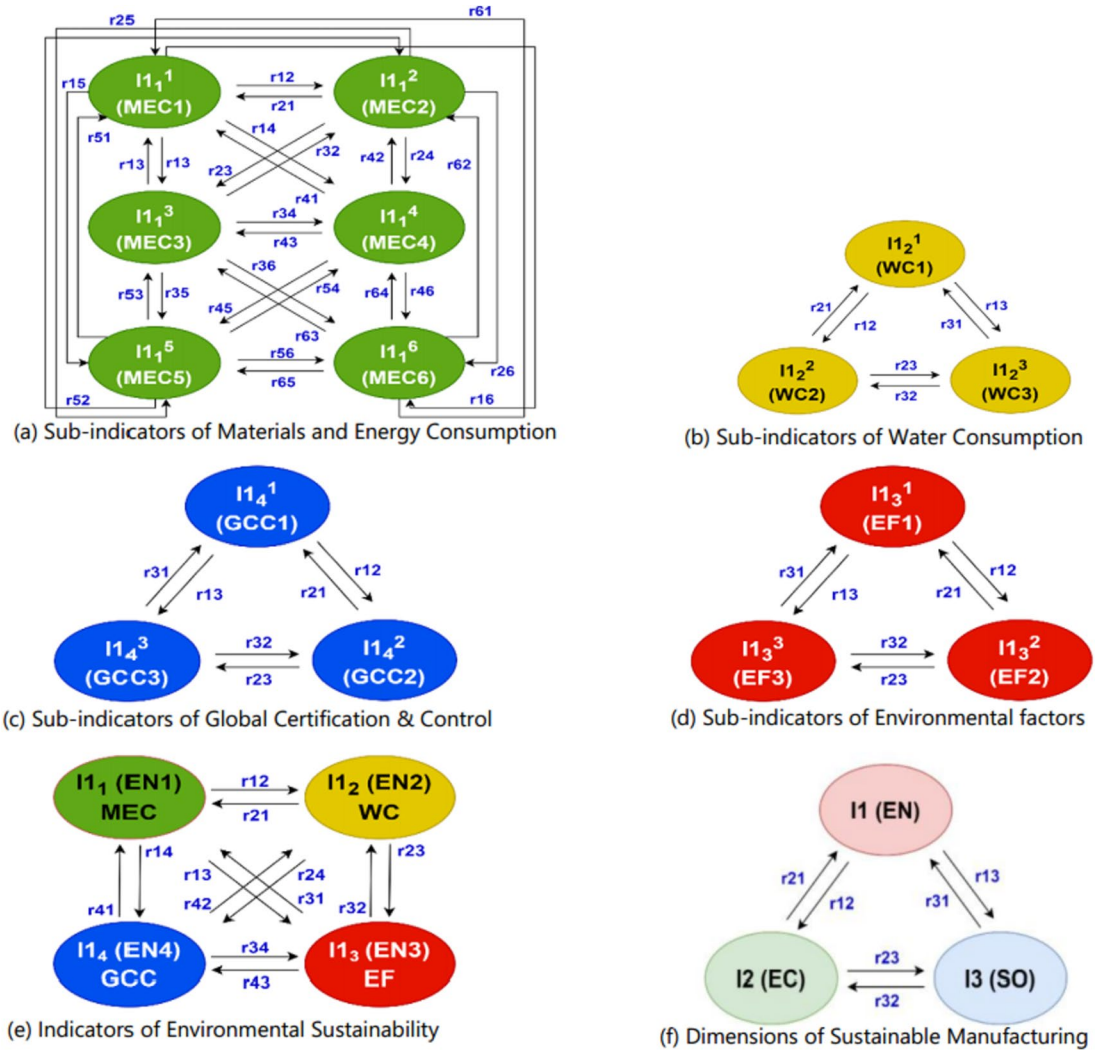


Fig. 3 Digraph related to environmental sustainability and its subgroup indicators

$$Per[I1_1(MEC)] = \begin{pmatrix} I1_1^1 & r_{12} & r_{13} & r_{14} & r_{15} & r_{16} \\ r_{21} & I1_1^2 & r_{23} & r_{24} & r_{25} & r_{26} \\ r_{31} & r_{32} & I1_1^3 & r_{34} & r_{35} & r_{36} \\ r_{41} & r_{42} & r_{43} & I1_1^4 & r_{45} & r_{46} \\ r_{51} & r_{52} & r_{53} & r_{54} & I1_1^5 & r_{56} \\ r_{61} & r_{62} & r_{63} & r_{64} & r_{65} & I1_1^6 \end{pmatrix} = \begin{bmatrix} 5 & 5 & 7 & 6 & 6 & 5 \\ 5 & 3 & 7 & 6 & 6 & 5 \\ 3 & 3 & 2 & 4 & 3 & 3 \\ 4 & 4 & 6 & 4 & 6 & 4 \\ 4 & 4 & 7 & 4 & 2 & 4 \\ 5 & 5 & 7 & 6 & 6 & 4 \end{bmatrix} = 6766664 \tag{2}$$

$$Per[I1_2(WC)] = \begin{bmatrix} I1_2^1 & r_{12} & r_{13} \\ r_{21} & I1_2^2 & r_{23} \\ r_{31} & r_{32} & I1_2^3 \end{bmatrix} = \begin{bmatrix} 3 & 6 & 5 \\ 4 & 2 & 4 \\ 5 & 6 & 4 \end{bmatrix} = 482 \tag{3}$$

$$Per[I1_3(EF)] = \begin{bmatrix} I1_3^1 & r_{12} & r_{13} \\ r_{21} & I1_3^2 & r_{23} \\ r_{31} & r_{32} & I1_3^3 \end{bmatrix} = \begin{bmatrix} 3 & 6 & 5 \\ 4 & 2 & 4 \\ 5 & 6 & 4 \end{bmatrix} = 482 \tag{4}$$

$$Per[I1_4(GCC)] = \begin{bmatrix} I1_4^1 & r_{12} & r_{13} \\ r_{21} & I1_4^2 & r_{23} \\ r_{31} & r_{32} & I1_4^3 \end{bmatrix} = \begin{bmatrix} 2 & 4 & 5 \\ 6 & 4 & 5 \\ 5 & 5 & 3 \end{bmatrix} = 496 \tag{5}$$

After the computation of IPM values for each subcategory, the final score of the dimension is calculated by using the above permanent values as a diagonal element, and off-diagonal elements represent interdependence values assigned by experts, as shown in equation (6).

$$Per[I1(Environmental\ sustainability)] = \begin{bmatrix} I1_1 & r_{12} & r_{13} & r_{14} \\ r_{21} & I1_2 & r_{23} & r_{24} \\ r_{31} & r_{32} & I1_3 & r_{34} \\ r_{41} & r_{42} & r_{43} & I1_4 \end{bmatrix} = \begin{bmatrix} 6766664 & 7 & 6 & 5 \\ 3 & 482 & 4 & 3 \\ 4 & 6 & 482 & 5 \\ 5 & 7 & 5 & 496 \end{bmatrix} = 77.99 \times 10^{13} \quad (6)$$

Similarly, the final IPM score is calculated for economic, and social sustainability dimensions (shown by equations 7 to 15), then these scores are used to determine the sustainability index score for manufacturing organizations trying to structure their SM system.

Economic sustainability evaluation:

$$\text{Per } [I2_1 \text{ (IIOC)}] = 214097 \quad (7)$$

$$\text{Per } [I2_2 \text{ (VC)}] = 6708522 \quad (8)$$

$$\text{Per } [I2_3 \text{ (IAE)}] = 205420 \quad (9)$$

$$Per[I2(Economic\ sustainability)] = \begin{bmatrix} 214097 & 4 & 3 \\ 6 & 6708522 & 3 \\ 7 & 7 & 205420 \end{bmatrix} = 29.5 \times 10^{16} \quad (10)$$

Social sustainability evaluation:

$$\text{Per } [I3_1 \text{ (EM)}] = 7139994 \quad (11)$$

$$\text{Per } [I3_2 \text{ (CU)}] = 9431 \quad (12)$$

$$\text{Per } [I3_3 \text{ (CO)}] = 9716 \quad (13)$$

$$Per[I2(Social\ sustainability)] = \begin{bmatrix} 7139994 & 5 & 6 \\ 5 & 9431 & 6 \\ 4 & 4 & 9716 \end{bmatrix} = 65.42 \times 10^{13} \quad (14)$$

Overall sustainability index score (SIS) for selected manufacturing system

$$Per(SMsystem) = \begin{bmatrix} 77.99 \times 10^{13} & 5 & 6 \\ 5 & 29.5 \times 10^{16} & 6 \\ 4 & 4 & 65.42 \times 10^{13} \end{bmatrix} = 15.05 \times 10^{46} \quad (15)$$

4.2.2 Theoretical best and worst-case values

After the calculation of SIS, we further examined the range to gain insights into hypothetical scenarios, characterized by maximum and minimum values. In the case of the maximum index value, the manufacturing organization needs to excel in all three dimensions of sustainability. Hence, in this context, the inheritance score is maintained at its maximum value, i.e.

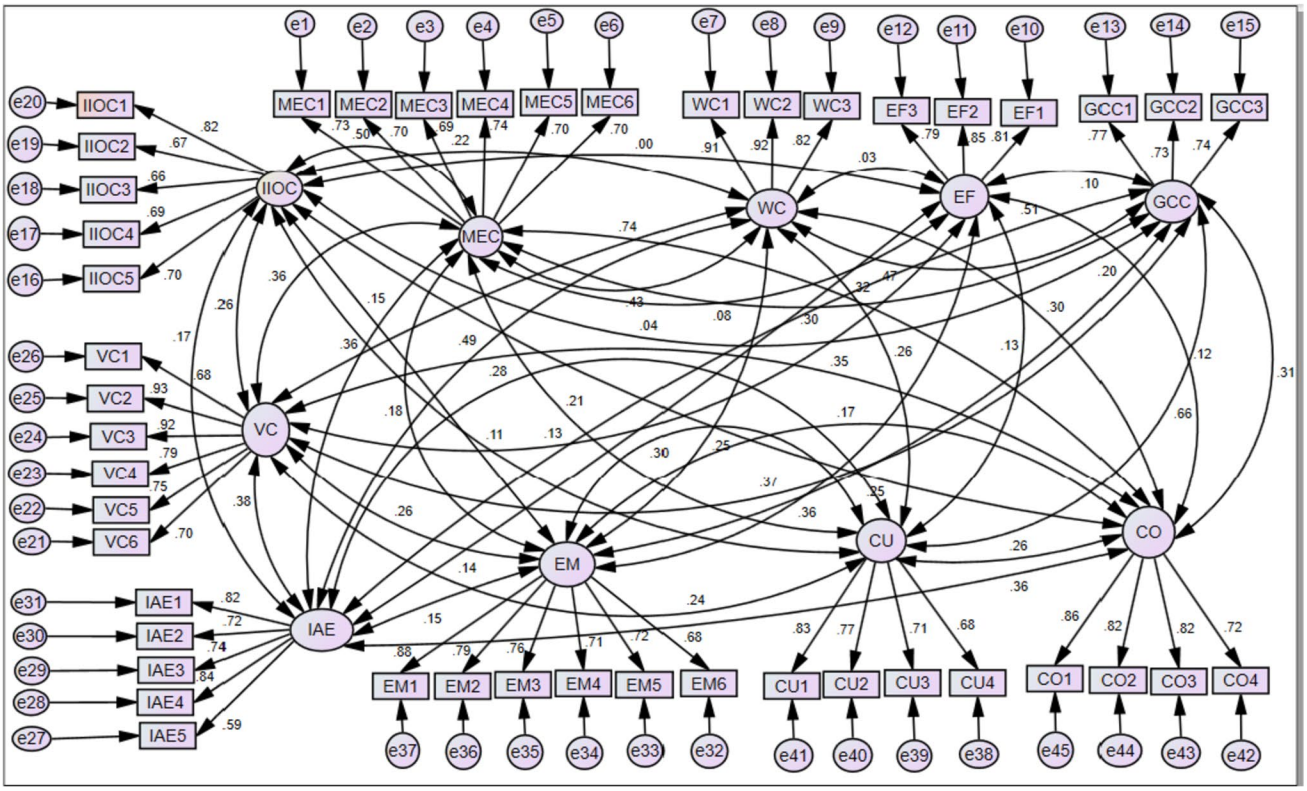


Fig. 4 Measurement model of SM indicators

5. Conversely, in the scenario with the minimum index value, it becomes evident that the organization has a low existence of sustainability indicators. In such cases, the inheritance value is assigned as '1'. This situation occurs in those, who have just started the implementation of SM practices. The summary of GTMA results for all dimensions of sustainability with the computed permanent values for actual, maximum, and minimum scenarios, is presented in Table A8 (Appendix). Additionally, corresponding logarithmic values for each category were also computed to facilitate an easier interpretation of the results.

Best case scenario permanent values of the SM indicators:

$$\text{Per [I1(Environmental sustainability)]} = 38.27 \times 10^{14}$$

$$\text{Per [I2(Economic sustainability)]} = 93.15 \times 10^{16}$$

$$\text{Per [I3(Social sustainability)]} = 22.42 \times 10^{14}$$

$$\text{Per (SM system) or SIS} = 97.94 \times 10^{47}$$

Worst case scenario permanent values of the SM indicators:

$$\text{Per [I1(Environmental sustainability)]} = 13.54 \times 10^{13}$$

$$\text{Per [I2(Economic sustainability)]} = 76.43 \times 10^{15}$$

$$\text{Per [I3(Social sustainability)]} = 20.13 \times 10^{13}$$

$$\text{Per (SM system) or SIS} = 20.84 \times 10^{44}$$

The existing permanent matrix values (Table A8 Appendix) show the relative importance of the indicators, category-wise as well as subcategory-wise. The ranks of the SM dimensions in descending order are prioritized as economic sustainability, environmental sustainability, and social sustainability. These rankings guide the significance of each indicator, assisting organizations in making informed decisions about their sustainability priorities. The relative scores assigned to the indicators show a clear indication of where emphasis should be placed on achieving sustainability within an organization. Consequently, the final SIS can be used to assess the sustainable development of an organization. Based on the IPM score and SIS, we can conduct valuable comparisons with other organizations and establish rankings from an SM perceptive.

5 Discussion and implications

As per the results summarized in Table A8 (Appendix), the following five sub-groups of sustainable manufacturing indicators, i.e., employee (6.854), materials and energy consumption (6.830), value creation (6.827), initial investment & operating cost (5.331), and indirectly associated expenses (5.313) have been observed the most vital and influential from the adoption perspective of sustainability in manufacturing organizations.

Among the social sustainability indicators, the employee (EM) factor has the highest potential to enhance the performance of the organization as they are fully responsible for manufacturing processes, product development, and designing parts. The employee management category includes job security and employee retention, health and safety, employee performance, training and development, risk identification and employee feedback management, and employee satisfaction. Lin et al. (2020) also observed that employees are the key resources in the manufacturing process for the smooth adoption of sustainability. Manufacturing organization has to impart regular training and development for the empowerment of their employees to achieve excellence in business, goals, and sustainable competitive gains (Ghosh 2013). Under the social dimensions of sustainability, customer feedback (SC11), community feedback (SC13), and the social and political aspects (SC14) play an important role in enhancing the sustainability of an organization. Also, it is observed that the factor loading of the social and political aspects is highest (0.859) in the community-related subsection of the social dimensions. However, most organizations have not indicated much interest in these areas which are to be one of the important aspects of social sustainability. Resource-based theory advocates the proper utilization of the human resource and other resources and the enhancement of the capability. In India, many enterprises are engaging heavily in delivering training programs.

The second most important indicator category is materials and energy consumption, a subcategory of environmental sustainability. It includes recycling of used materials, consumption of recycled/refurbished materials/components, non-hazardous material consumption, green packaging materials, green transportation/fuel economy and emission control, and renewable energy consumption. Legitimacy pressures from different institutions accelerate the firm actions towards environmental compliance activities which leads to Institutional theory (Gupta and Gupta 2021). The manufacturing sector, over the years, has been the backbone of Indian GDP by creating ample opportunities for their stakeholders, at the expense of a large amount of waste generation, environmental degradation, GHG emissions, and biodiversity deterioration. Thus, it becomes imperative for industries to inculcate materials and energy consumption indicators. In most countries, the organization must get a certificate of environmental compliance from the regional environmental compliance departments, which triggers the organization for the adoption of necessary environmental measures, leading to economic benefits, enhanced employee engagement, internal production efficiencies, customer satisfaction, and branding (Govindan et al. 2015). Abbas (2020) also supported that the implementation of new technologies in synchronization with

green manufacturing and total quality management enables a reduction in pollution, energy consumption, and waste generation, correspondingly amplifying the organization's performance, product quality, and services.

The third, fourth, and fifth important indicators categories are value creation (VC), initial investment and operating cost (IIOC), and indirectly associated expenses (IAE), which need to be followed by manufacturing organizations for sustainability. All the above indicators are concerned with economic sustainability. Value creation aims in designing and developing a product of good functionality, and high quality at low input cost. It comprised revenue generation, profit earned, annual productivity, new product design and development, market share, and facility expansion. In today`s competitive scenario, the organization adopts those indicators that can outreach its revenue generation, annual productivity, and market share. Disruptions like pandemics and natural calamities are unpredictable and unforeseen, but firms can minimize the effect by becoming prudent towards sustainability practices. The implementation of SM practices can ensure market competitiveness and an organization's reputation during such a critical time (Nader et al. 2022). IIOC category includes indicators carried by industries in the form of wages and operating costs, liability and debt payment, environmental treatment cost, expenses as a philanthropist on CSR activities, and sales promotion. Eslami et al. (2019) confirmed in their study that economic indicators constituted process input cost (raw materials and operating), process output cost (environmental treatment cost), and capital cost. The indirectly associated expenses (IAE) category is composed of indicators that higher management of the organization counts before any transformation in manufacturing processes. It includes depreciation, maintenance, pollution control costs, investment in research and development, and prevention of scrap production.

Overall, it has been found that economic sustainability with an indicator permanent matrix score of 17.470 is the most important dimension, followed by environmental (14.892) and social (14.816). Hariyani and Mishra (2022) have also observed that organizations are not able to enforce SM practices due to price competition and quality standard issues. In a developing country like India, it requires a huge takeout from an individual in the form of high capital, skilled manpower, and government help to transform the existing system. In the current business environment of economic slowdown, manufacturers are noticing waste reduction and value creation; and customers assre seeking products of high quality at low cost (Kumar et al. 2021b). In the last five years, we have observed very slow growth in the economy, setting foot back of manufacturers for any new change. Thus, it can comply that acceptance of indicators for sustainability adoption in manufacturing industries will be perceived by giving an extra edge to economic in comparison to environmental, and social. Shubham and Murty (2018) discussed that institutional pressure from industrial associations and regulatory bodies critically influenced organizations to adopt SM practices. Tu and Wu (2021) highlighted that pressure from stakeholders (consumers and communities), policies, and regulations have a highly positive effect on sustainability and creating enterprise competitive advantage. Stakeholder theory leads to the fulfillment of the vested interests of all the stakeholders of the organization. Thus, it is concerned with all three dimensions of sustainability.

5.1 Managerial implications

This study has identified a realistic set of sustainability indicators that will help managers in the decision-making process, and allow them to fully commit to their use for achieving sustainability in manufacturing processes. The distinctive contribution of the study is its mathematical model. The sustainability indicators will be positively perceived by the managers at a business level. The relative priority of indicators will assist industry professionals and practitioners in putting the efforts on the right path for achieving sustainability in their organizations and developing necessary strategies correspondingly. Appolloni et al. (2022) also highlighted that sustainability is an essential need for manufacturing companies to cope with times of economic crisis and uncertainty. It can develop a competitive edge in manufacturing. Manufacturing organizations should primarily have to empower and develop their employees to achieve sustainability, excellence in business, and economic gains. The findings offer valuable insights to manufacturers, guiding them in developing effective strategies for attaining sustainable development within their organizations. To promote sustainability, business excellence, and economic growth, manufacturing organizations must prioritize the empowerment and development of their employees. Management at higher levels should actively promote the use of recycling, non-hazardous materials, and renewable energy to assess and improve sustainability performance. In today's dynamic and competitive landscape, policymakers should focus on key indicators such as organizational value enhancement, initial investment for operations, and indirectly related expenses to drive economic growth toward sustainable development.

5.2 Academic implications

This study basis is not underpinned by the concept of a single theory, but utilizes the integrated contributions of three theories Resource-based theory, Stakeholder theory, and Institutional theory. The combination effect suggests that to gain competitive advantage, an organization must be focused primarily on internal strengths and weaknesses, bonded by stakeholders, and motivated by legitimacy. This study may motivate researchers and practitioners to explore some more management theories to address sustainability indicators. Also, they can use this framework to determine

sustainability and other performance-related indices. GTMA and other indexing models may be used to scale the sustainability of an organization. The theoretical maximum and minimum values of the different sustainability indicators can be used as a benchmarking of the performed values using GTMA. The researchers can also compare the sustainability performance of an organization with other organizations and improve the different sustainability parameters accordingly.

6 Conclusion, limitation, and future scope

In this study the sustainability indicators are grouped into ten clusters using factor analysis and indexing of these clusters has been prepared using GTMA. These clusters are arranged in decreasing order of importance as: *employee-related issues, material and energy consumption, value creation, initial investment and operating cost, indirectly associated expenses, community, customer, global certification and control, water consumption, and environmental factors.* Among these clusters of indicators, the five most important indicators are *non-hazardous materials consumption, green packaging materials, green transportation/ fuel economy & emission control, renewable energy consumption, and recycling of used materials.* This underscores the significance of environmental sustainability as a key pillar of the triple bottom line. This research utilized the theoretical foundation of stakeholder theory, resource-based theory, and institutional theory applied for the analysis of sustainability indicators, explored through the in-depth literature review. The sustainability index has been developed with the help of experts from the automobile sector, iron & steel sector, and chemical & pharmaceutical sector as a case study, however, the sustainability indicators are selected based on the opinions of the respondents from different manufacturing industries. Therefore, the findings are more suitable for the automobile sector, iron & steel sector, and chemical & pharmaceutical sector, and also applicable for the other manufacturing sectors.

Future research can be focused on diverse industrial sectors for other developing economies like China and Malaysia for comparative analysis and validation. In the future, sample size can be extended and statistical and causal analysis can be applied to enhance result reliability. Exploring sustainability within the context of a net-zero economy, and incorporating additional relevant indicators into the framework, could be a valuable aspect of forthcoming investigations. Additionally, broadening the application of MCDM methods through multiple case studies would contribute to improving the generalizability of the outcomes.

Appendix

Table A1 Respondent's profile

Category	Item	Frequency	Percentage
Gender	Male	396	89.18
	Female	48	10.81
Age	≤29	95	21.39
	30-39	149	33.56
	40-49	121	27.25
	50-59	58	13.06
	≥60	21	4.73
Experience	<1 year	28	6.31
	1–5 years	84	18.92
	5–10 years	93	20.95
	10–15 years	101	22.75
	15–20 years	87	19.59
	≥ 20 years	51	11.48
Organization type	Automobile	147	33.13
	Sheet Metal processing	56	12.61
	Iron and Steel	68	15.32
	Chemical and industrial fertilizer	39	8.78
	Pharmaceutical	52	11.71
	Textile Industries	34	7.66
	Electrical and Electronics	29	6.53
	Others	19	4.28
Position held	Lower management	191	43.02
	Middle management	167	37.61
	Higher management	86	19.37
Education	Graduate	232	52.25
	Post Graduate	165	37.16
	Doctorate	47	10.58

Table A2 Descriptive analysis of the depicted indicators

SM Dimensions	Acronym	Indicators	Mean	Standard Deviation
Environmental Sustainability	EN1	Recycling of used materials	3.73	0.974
	EN2	Consumption of recycled/refurbished materials/components	3.65	0.988
	EN3	Non-Hazardous materials consumption	3.77	0.966
	EN4	Economic water consumption	3.38	1.225
	EN5	Green packaging materials	3.76	0.995
	EN6	Green transportation/ fuel economy and emission control	3.76	0.952
	EN7	Reuse and recycling of wastewater	3.25	1.191
	EN8	Renewable energy Consumption	3.74	0.948
	EN9	Elimination of landfills & contamination	3.15	1.094
	EN10	Water Contamination	3.28	1.314
	EN11	Prevention of water pollution	3.13	1.211
	EN12	Green Initiatives	3.42	1.178
	EN13	Emission control	3.18	1.129
	EN14	Volatile organic compounds	2.11	0.891
	EN15	Labels and certificates (ISO 14001 & ISO 9001)	3.41	1.235
	EN16	Quality control	3.53	1.151
	EN17	Materials of tools	1.75	0.777
	EN18	Particulate suspended matters	1.98	0.796
Economic Sustainability	EC1	Wages and operating cost	3.20	1.259
	EC2	Pollution control cost	3.30	1.092
	EC3	Environmental treatment cost	3.28	1.152
	EC4	Expenses on corporate social responsibility (CSR)	3.28	1.220
	EC5	Sales promotion	3.20	1.239
	EC6	Facility expansion	3.18	1.275
	EC7	Revenue generation	3.32	1.232
	EC8	Investment in research and development	3.28	0.969
	EC9	Profit earned	3.19	1.240
	EC10	Annual Productivity	3.18	1.273
	EC11	New Product Design and Development	3.18	1.188
	EC12	Market share	3.16	1.231
	EC13	Liability and Debt payment	3.18	1.218
	EC14	Depreciation	3.33	1.056
	EC15	Maintenance	3.34	1.074
	EC16	Prevention of scrap production	3.30	1.139
	EC17	Turnover (selling inventory)	2.47	1.092
	EC18	Payback period	2.50	1.103
Social Sustainability	SC1	Job security and employee retention	3.51	1.199
	SC2	Health and Safety	3.25	1.061
	SC3	Human rights protection	3.26	1.079
	SC4	Employee performance	3.21	1.152
	SC5	Employee satisfaction	3.41	1.104
	SC6	Training and Development	3.30	1.191
	SC7	Risk identification and employee feedback management	3.32	1.195
	SC8	Customer satisfaction and relationship	3.24	1.282
	SC9	Product quality	3.26	1.245
	SC10	Trust development	3.23	1.239
	SC11	Customer feedback	3.29	1.185
	SC12	Personal protective equipment	2.17	0.928
	SC13	Community feedback	3.20	1.231
	SC14	The social and political aspects	3.18	1.269
	SC15	Technology development and support	3.22	1.242
	SC16	Work load	1.69	0.779

Table A3 Structural model fit Indices

Model fit measures	Acceptance level
Absolute measures	
CMIN/DF	<2 (good) 5 (acceptable)
GFI (Goodness of Fit Index)	>0.9 (good) 0.95 (very good)
RMSEA	<0.05 (very good) 0.08 (good) 0.1 (poor)
RMR (Root mean square residual)	< 0.10
Relative measures	
CFI (Comparative fit index)	>0.9 (good) 0.95 (very good)
Parsimony measures	
PCFI (Parsimony Comparative Fit Index)	>0.6 (reasonable) 0.8 (good)
PGFI (Parsimony Goodness of Fit Index)	>0.6 (reasonable) 0.8 (good)

Table A4 Rating scale for Interdependency estimation of Indicators

Qualitative description	Relative Dependence	
	Sij	Sji = (10- Sij)
Exceptionally low influencing	0	10
Extremely low influencing	1	9
Very low influencing	2	8
Below average influencing	3	7
Average influencing	4	6
Above-average influencing	5	5
Moderate influencing	6	4
High influencing	7	3
Very high influencing	8	2
Extremely high influencing	9	1
Exceptionally high influencing	10	0

Table A5 KMO and Bartlett's Test results

Kaiser-Meyer-Olkin Measure of Sampling Adequacy		.857
Bartlett's Test of Sphericity	Approx. Chi-Square	12495.710
	df	990
	Sig.	0.000

Table A6 Goodness of fit measures of SM indicators

Fit Indices	Calculated values	Accepted values
CMIN/DF	2.715	<2 (good) 5 (acceptable)
GFI (Goodness of Fit Index)	0.817	>0.8 (average), >0.9 (good), 0.95 (very good)
RMSEA	0.062	<0.05 (very good) 0.08 (good) 0.1 (poor)
RMR (Root mean square residual)	0.062	< 0.10
CFI (Comparative fit index)	0.871	>0.85 (good) 0.95 (very good)
PCFI (Parsimony Comparative Fit Index)	0.792	>0.6 (reasonable) 0.8 (good)
PGFI (Parsimony Goodness of Fit Index)	0.710	>0.6 (reasonable) 0.8 (good)

Table A7 Correlation and discriminant validity of SM indicators

Constructs	EM	MEC	VC	CU	IIOC	CO	IAE	EF	GCC	WC
EM	0.759									
MEC	0.183	0.708								
VC	0.262	0.360	0.802							
CU	0.300	0.211	0.243	0.751						
IIOC	0.153	0.496	0.260	0.114	0.709					
CO	0.166	0.323	0.349	0.260	0.246	0.807				
NAE	0.153	0.362	0.376	0.283	0.168	0.358	0.749			
EI	0.361	0.082	0.133	0.133	-0.002	0.117	0.138	0.814		
GCC	0.199	0.303	0.371	0.661	0.041	0.309	0.515	0.103	0.750	
WC	0.253	0.432	0.736	0.262	0.216	0.304	0.485	0.033	0.470	0.884

Table A8 Permanent matrix values for the actual, best- and worst-case scenario

Dimension	Indicators	Actual Case (Permanent matrix values)	Log_{10} (Actual case)	Best case (Permanent matrix values)	Log_{10} (Best case)	Worst case (Permanent matrix values)	Log_{10} (Worst case)
Environmental	Per (MEC)	6766664	6.830	9639906	6.984	4223858	6.626
	Per (WC)	482	2.683	730	2.863	314	2.497
	Per (EF)	482	2.683	730	2.863	314	2.497
	Per (GCC)	496	2.695	745	2.872	325	2.512
Per (Environmental)		7.99×10^{13}	14.892	38.27×10^{14}	15.583	13.54×10^{13}	14.132
Economic	Per (IIOC)	214097	5.331	311955	5.494	135367	5.132
	Per (VC)	6708522	6.827	9852802	6.994	4335218	6.637
	Per (IAE)	205420	5.313	303065	5.482	130237	5.115
Per (Economic)		29.5×10^{16}	17.470	93.15×10^{16}	17.970	76.43×10^{15}	16.883
Social	Per (EM)	7139994	6.854	10375846	7.016	4605190	6.663
	Per (CU)	9431	3.974	14851	4.172	6699	3.826
	Per (CO)	9716	3.987	14550	4.163	6526	3.815
Per (Social)		65.42×10^{13}	14.816	22.42×10^{14}	15.351	20.13×10^{13}	14.304
Per (SM system)		15.05×10^{46}	47.178	79.94×10^{47}	48.903	20.84×10^{44}	45.319

Data availability statements The datasets generated during and/or analysed during the current study are not publicly available, but are available from the corresponding author on reasonable request.

Declarations

Ethical statements The authors have no relevant financial or non-financial interests to disclose. All authors certify that they have no affiliations with or involvement in any organization or entity with any financial interest or non-financial interest in the subject matter discussed in this manuscript.

Competing interest The authors have no competing interests to declare that are relevant to the content of this article.

References

Abbas J (2020) Impact of total quality management on corporate green performance through the mediating role of corporate social responsibility. J Clean Prod 242:118458. https://doi.org/10.1016/j.jclepro.2019.118458

Agrawal R, Majumdar A, Kumar A, Luthra S (2023) Integration of artificial intelligence in sustainable manufacturing: current status and future opportunities. Oper Manag Res. https://doi.org/10.1007/s12063-023-00383-y

Agrawal V, Agarwal S, Agrawal AM (2017) Perception of employees toward e-learning service quality: exploratory factor analysis. Ind Commer Train 49:350–356. https://doi.org/10.1108/ICT-06-2017-0042

Ahmad S, Wong KY (2018) Sustainability assessment in the manufacturing industry: a review of recent studies. Benchmarking Int J 25:3162–3179. https://doi.org/10.1108/BIJ-08-2017-0214

Ahmad S, Wong KY, Rajoo S (2019) Sustainability indicators for manufacturing sectors: A literature survey and maturity analysis from the triple-bottom line perspective. J Manuf Technol Manag 30:312–334. https://doi.org/10.1108/JMTM-03-2018-0091

Akbar M, Irohara T (2018) Scheduling for sustainable manufacturing: A review. J Clean Prod 205:866–883. https://doi.org/10.1016/j.jclepro.2018.09.100

Aktaş N, Demirel N (2021) A hybrid framework for evaluating corporate sustainability using multi-criteria decision making. Environ Dev Sustain 23:15591–15618. https://doi.org/10.1007/s10668-021-01311-5

Appolloni A, Chiappetta Jabbour CJ, D'Adamo I et al (2022) Green recovery in the mature manufacturing industry: The role of the green-circular premium and sustainability certification in innovative efforts. Ecol Econ 193:107311. https://doi.org/10.1016/j.ecolecon.2021.107311

Baah C, Opoku-Agyeman D, Acquah ISK et al (2021) Examining the correlations between stakeholder pressures, green production practices, firm reputation, environmental and financial performance: Evidence from manufacturing SMEs. Sustain Prod Consum 27:100–114. https://doi.org/10.1016/j.spc.2020.10.015

Badurdeen F, Jawahir IS (2017) Strategies for Value Creation Through Sustainable Manufacturing. Procedia Manuf 8:20–27. https://doi.org/10.1016/j.promfg.2017.02.002

Bag S, Pretorius JHC (2022) Relationships between industry 4.0, sustainable manufacturing and circular economy: proposal of a research framework. Int J Organ Anal 30:864–898. https://doi.org/10.1108/IJOA-04-2020-2120

Barletta I, Despeisse M, Hoffenson S, Johansson B (2021) Organisational sustainability readiness: A model and assessment tool for manufacturing companies. J Clean Prod 284:125404. https://doi.org/10.1016/j.jclepro.2020.125404

Barney J (1991) Firm Resources and Sustained Competitive Advantage. J Manag 17:99–120. https://doi.org/10.1177/014920639101700108

Beck D, Ferasso M (2023) Bridging 'Stakeholder Value Creation' and 'Urban Sustainability': The need for better integrating the Environmental Dimension. Sustain Cities Soc 89:104316. https://doi.org/10.1016/j.scs.2022.104316

Beng LG, Omar B (2014) Integrating axiomatic design principles into sustainable product development. Int J Precis Eng Manuf-Green Technol 1:107–117. https://doi.org/10.1007/s40684-014-0015-2

Bentler PM (1990) Comparative fit indexes in structural models. Psychol Bull 107:238–246. https://doi.org/10.1037/0033-2909.107.2.238

Bereketli I, Erol Genevois M (2013) An integrated QFDE approach for identifying improvement strategies in sustainable product development. J Clean Prod 54:188–198. https://doi.org/10.1016/j.jclepro.2013.03.053

Bhutta MKS, Muzaffar A, Egilmez G et al (2021) Environmental sustainability, innovation capacity, and supply chain management practices nexus: A mixed methods research approach. Sustain Prod Consum 28:1508–1521. https://doi.org/10.1016/j.spc.2021.08.015

Bonvoisin J, Lelah A, Mathieux F, Brissaud D (2014) An integrated method for environmental assessment and ecodesign of ICT-based optimization services. J Clean Prod 68:144–154. https://doi.org/10.1016/j.jclepro.2014.01.003

Borchardt M, Wendt MH, Pereira GM, Sellitto MA (2011) Redesign of a component based on ecodesign practices: environmental impact and cost reduction achievements. J Clean Prod 19:49–57. https://doi.org/10.1016/j.jclepro.2010.08.006

Bortolotti T, Boscari S, Danese P (2015) Successful lean implementation: Organizational culture and soft lean practices. Int J Prod Econ 160:182–201. https://doi.org/10.1016/j.ijpe.2014.10.013

Bracke S, Yamada S, Kinoshita Y et al (2017) Decision Making within the Conceptual Design Phase of Eco-Friendly Products. Procedia Manuf 8:463–470. https://doi.org/10.1016/j.promfg.2017.02.059

Brones F, de Carvalho MM, de Senzi Zancul E (2014) Ecodesign in project management: a missing link for the integration of sustainability in product development? J Clean Prod 80:106–118. https://doi.org/10.1016/j.jclepro.2014.05.088

Bui NT, Kawamura A, Kim KW et al (2017) Proposal of an indicator-based sustainability assessment framework for the mining sector of APEC economies. Resour Policy 52:405–417. https://doi.org/10.1016/j.resourpol.2017.05.005

Butnariu A, Avasilcai S (2015) The Assessment of The Companies' Sustainable Development Performance. Procedia Econ Finance 23:1233–1238. https://doi.org/10.1016/S2212-5671(15)00422-0

Cai W, Wang L, Li L et al (2022) A review on methods of energy performance improvement towards sustainable manufacturing from perspectives of energy monitoring, evaluation, optimization and benchmarking. Renew Sustain Energy Rev 159:112227. https://doi.org/10.1016/j.rser.2022.112227

Chaim O, Muschard B, Cazarini E, Rozenfeld H (2018) Insertion of sustainability performance indicators in an industry 4.0 virtual learning environment. Procedia Manuf 21:446–453. https://doi.org/10.1016/j.promfg.2018.02.143

Cobut A, Beauregard R, Blanchet P (2015) Reducing the environmental footprint of interior wood doors in non-residential buildings – part 2: ecodesign. J Clean Prod 109:247–259. https://doi.org/10.1016/j.jclepro.2015.05.068

Coughlan J, Hooper D, Mullen M (2008) Structural equation modelling: guidelines for determining model fit. https://doi.org/10.21427/D7CF7R

Danese P, Lion A, Vinelli A (2019) Drivers and enablers of supplier sustainability practices: a survey-based analysis. Int J Prod Res 57:2034–2056. https://doi.org/10.1080/00207543.2018.1519265

Di Foggia G (2018) Energy efficiency measures in buildings for achieving sustainable development goals. Heliyon 4:e00953. https://doi.org/10.1016/j.heliyon.2018.e00953

Dubey R, Gunasekaran A, Childe SJ et al (2019) Big Data and Predictive Analytics and Manufacturing Performance: Integrating Institutional Theory, Resource-Based View and Big Data Culture. Br J Manag 30:341–361. https://doi.org/10.1111/1467-8551.12355

Eastwood MD, Haapala KR (2015) A unit process model based methodology to assist product sustainability assessment during design for manufacturing. J Clean Prod 108:54–64. https://doi.org/10.1016/j.jclepro.2015.08.105

Eslami Y, Dassisti M, Lezoche M, Panetto H (2019) A survey on sustainability in manufacturing organisations: dimensions and future insights. Int J Prod Res 57:5194–5214. https://doi.org/10.1080/00207543.2018.1544723

Feil A, Schreiber D, Haetinger C et al (2019) Sustainability Indicators for Industrial Organizations: Systematic Review of Literature. Sustainability 11:854. https://doi.org/10.3390/su11030854

Fontana E, Atif M, Heuer M (2022) Implementing social sustainability through market pressures: an inter-organizational network analysis in the Pakistani apparel supply chain. Int J Phys Distrib Logist Manag. https://doi.org/10.1108/IJPDLM-07-2021-0265

Fornell C, Larcker DF (1981) Structural Equation Models with Unobservable Variables and Measurement Error: Algebra and Statistics. J Mark Res 18:382. https://doi.org/10.2307/3150980

Freeman RE (2010) Stakeholder theory: the state of the art. Cambridge University Press, Cambridge, New York

Gani A, James AT, Asjad M, Talib F (2022) Development of a manufacturing sustainability index for MSMEs using a structural approach. J Clean Prod 353:131687. https://doi.org/10.1016/j.jclepro.2022.131687

Gebisa AW, Lemu HG (2017) Design for manufacturing to design for Additive Manufacturing: Analysis of implications for design

optimality and product sustainability. Procedia Manuf 13:724–731. https://doi.org/10.1016/j.promfg.2017.09.120
Gedam VV, Raut RD, de Sousa Lopes, Jabbour AB et al (2021) Sustainable manufacturing and green human resources: Critical success factors in the automotive sector. Bus Strategy Environ 30:1296–1313. https://doi.org/10.1002/bse.2685
Ghobadian A, Talavera I, Bhattacharya A et al (2020) Examining legitimatisation of additive manufacturing in the interplay between innovation, lean manufacturing and sustainability. Int J Prod Econ 219:457–468. https://doi.org/10.1016/j.ijpe.2018.06.001
Ghosh PS (2013) An Enigma that is South Asia: India versus the Region. Asia-Pac Rev 20:100–120. https://doi.org/10.1080/13439006.2013.788336
Gouda SK, Saranga H (2020) Pressure or premium: what works best where? Antecedents and outcomes of sustainable manufacturing practices. Int J Prod Res 58:7201–7217. https://doi.org/10.1080/00207543.2020.1717010
Govindan K, Rajendran S, Sarkis J, Murugesan P (2015) Multi criteria decision making approaches for green supplier evaluation and selection: a literature review. J Clean Prod 98:66–83. https://doi.org/10.1016/j.jclepro.2013.06.046
Gupta A, Singh RK (2020) Developing a framework for evaluating sustainability index for logistics service providers: graph theory matrix approach. Int J Product Perform Manag 69:1627–1646. https://doi.org/10.1108/IJPPM-12-2019-0593
Gupta AK, Gupta N (2021) Environment Practices Mediating the Environmental Compliance and firm Performance: An Institutional Theory Perspective from Emerging Economies. Glob J Flex Syst Manag 22:157–178. https://doi.org/10.1007/s40171-021-00266-w
Hair JF (ed) (2014) Multivariate data analysis, 7. ed., Pearson new internat. ed. Pearson, Harlow
Haleem A, Khan S, Luthra S et al (2021) Supplier evaluation in the context of circular economy: A forward step for resilient business and environment concern. Bus Strategy Environ 30:2119–2146. https://doi.org/10.1002/bse.2736
Hariyani D, Mishra S (2022) Organizational enablers for sustainable manufacturing and industrial ecology. Clean Eng Technol 6:100375. https://doi.org/10.1016/j.clet.2021.100375
Hegab H, Shaban I, Jamil M, Khanna N (2023) Toward sustainable future: Strategies, indicators, and challenges for implementing sustainable production systems. Sustain Mater Technol 36:e00617. https://doi.org/10.1016/j.susmat.2023.e00617
Henao R, Sarache W (2022) Sustainable performance in manufacturing operations: The cumulative approach vs. trade-offs approach. Int J Prod Econ 244:108385. https://doi.org/10.1016/j.ijpe.2021.108385
Henao R, Sarache W, Gomez I (2017) Social Performance Metrics for Manufacturing Industry. 24th EurOMA Conf 1–10
Hermundsdottir F, Aspelund A (2022) Competitive sustainable manufacturing - Sustainability strategies, environmental and social innovations, and their effects on firm performance. J Clean Prod 370:133474. https://doi.org/10.1016/j.jclepro.2022.133474
Holm M (2018) The future shop-floor operators, demands, requirements and interpretations. J Manuf Syst 47:35–42. https://doi.org/10.1016/j.jmsy.2018.03.004
Horbach J, Prokop V, Stejskal J (2023) Determinants of firms' greenness towards sustainable development: A multi-country analysis. Bus Strategy Environ 32:2868–2881. https://doi.org/10.1002/bse.3275
Huang A, Badurdeen F (2017) Sustainable manufacturing performance evaluation: integrating product and process metrics for systems level assessment. Procedia Manuf 8:563–570. https://doi.org/10.1016/j.promfg.2017.02.072
Ihlen Ø, Roper J (2014) Corporate reports on sustainability and sustainable development: 'we have arrived': corporate reports. Sustain Dev 22:42–51. https://doi.org/10.1002/sd.524
Ijaz Baig M, Yadegaridehkordi E (2023) Exploring moderating effects of industry 4.0 adoption on sustainable performance of Malaysian manufacturing organizations. J Ind Prod Eng 40:271–286. https://doi.org/10.1080/21681015.2023.2190766
Jamwal A, Agrawal R, Sharma M, Kumar V (2021) Review on multi-criteria decision analysis in sustainable manufacturing decision making. Int J Sustain Eng 14:202–225. https://doi.org/10.1080/19397038.2020.1866708
Jin M, Tang R, Ji Y et al (2017) Impact of advanced manufacturing on sustainability: An overview of the special volume on advanced manufacturing for sustainability and low fossil carbon emissions. J Clean Prod 161:69–74. https://doi.org/10.1016/j.jclepro.2017.05.101
Kek V, Gurumurthy A (2018) Modelling and analysis of sustainable manufacturing system using a digraph-based approach. Int J Sustain Eng 11:397–411. https://doi.org/10.1080/19397038.2017.1420108
Kaiser HF (1970) A second generation little jiffy. Psychometrika 35:401–415. https://doi.org/10.1007/BF02291817
Khan S, Haleem A (2021) Investigation of circular economy practices in the context of emerging economies: a CoCoSo approach. Int J Sustain Eng 14:357–367. https://doi.org/10.1080/19397038.2020.1871442
Khurshid A, Muzaffar A, Bhutta MKS (2021) Institutional pressures and supplier involvement: a perspective on sustainability. Oper Manag Res 14:123–137. https://doi.org/10.1007/s12063-021-00181-4
Kibira D, Brundage MP, Feng S, Morris KC (2018) Procedure for Selecting Key Performance Indicators for Sustainable Manufacturing. J Manuf Sci Eng 140:011005. https://doi.org/10.1115/1.4037439
Kim S, Kim G-H, Lee Y-D (2013) Sustainability Life Cycle Cost Analysis of Roof Waterproofing Methods Considering LCCO2. Sustainability 6:158–174. https://doi.org/10.3390/su6010158
Kumar N, Kumar G, Singh RK (2021) Analysis of barriers intensity for investment in big data analytics for sustainable manufacturing operations in post-COVID-19 pandemic era. J Enterp Inf Manag ahead-of-print: https://doi.org/10.1108/JEIM-03-2021-0154
Kumar N, Kumar G, Singh RK (2021) Big data analytics application for sustainable manufacturing operations: analysis of strategic factors. Clean Technol Environ Policy 23:965–989. https://doi.org/10.1007/s10098-020-02008-5
Lee JY, Kang HS, Noh SD (2014) MAS2: an integrated modeling and simulation-based life cycle evaluation approach for sustainable manufacturing. J Clean Prod 66:146–163. https://doi.org/10.1016/j.jclepro.2013.11.029
León-Bravo V, Caniato F, Caridi M (2019) Sustainability in multiple stages of the food supply chain in Italy: practices, performance and reputation. Oper Manag Res 12:40–61. https://doi.org/10.1007/s12063-018-0136-9
Liao Z (2018) Corporate culture, environmental innovation and financial performance. Bus Strategy Environ 27:1368–1375. https://doi.org/10.1002/bse.2186
Lin CJ, Belis TT, Caesaron D et al (2020) Development of sustainability indicators for employee-activity based production process using fuzzy delphi method. Sustainability 12:6378. https://doi.org/10.3390/su12166378
Lučić A (2020) Measuring sustainable marketing orientation-Scale development process. Sustain Switz 12:9–11. https://doi.org/10.3390/su12051734
Mani M, Madan J, Lee JH et al (2014) Sustainability characterisation for manufacturing processes. Int J Prod Res 52:5895–5912. https://doi.org/10.1080/00207543.2014.886788

Mathiyazhagan K, Sengupta S, Poovazhagan L (2018) A decision making trial and evaluation laboratory approach to analyse the challenges to environmentally sustainable manufacturing in Indian automobile industry. Sustain Prod Consum 16:58–67. https://doi.org/10.1016/j.spc.2018.05.007

McGahan AM (2021) Integrating Insights From the Resource-Based View of the Firm Into the New Stakeholder Theory. J Manag 47:1734–1756. https://doi.org/10.1177/0149206320987282

Mengistu AT, Panizzolo R (2022) Analysis of indicators used for measuring industrial sustainability: a systematic review. Environ Dev Sustain. https://doi.org/10.1007/s10668-021-02053-0

Mishra S, Singh SP, Johansen J et al (2019) Evaluating indicators for international manufacturing network under circular economy. Manag Decis 57:811–839. https://doi.org/10.1108/MD-05-2018-0565

Mittal VK, Sangwan KS (2014) Development of a model of barriers to environmentally conscious manufacturing implementation. Int J Prod Res 52:584–594. https://doi.org/10.1080/00207543.2013.838649

Moktadir MA, Rahman T, Rahman MH et al (2018) Drivers to sustainable manufacturing practices and circular economy: A perspective of leather industries in Bangladesh. J Clean Prod 174:1366–1380. https://doi.org/10.1016/j.jclepro.2017.11.063

Moldavska A, Welo T (2019) A Holistic approach to corporate sustainability assessment: Incorporating sustainable development goals into sustainable manufacturing performance evaluation. J Manuf Syst 50:53–68. https://doi.org/10.1016/j.jmsy.2018.11.004

Moreira S, Vasconcelos L, Silva Santos C (2018) Occupational health indicators: Exploring the social and decent work dimensions of green jobs in Portugal. Work 61:189–209. https://doi.org/10.3233/WOR-182792

Muduli K, kanta, Luthra S, Kumar Mangla S et al (2020) Environmental management and the "soft side" of organisations: Discovering the most relevant behavioural factors in green supply chains. Bus Strategy Environ 29:1647–1665. https://doi.org/10.1002/bse.2459

Nader J, El-Khalil R, Nassar E, Hong P (2022) Pandemic planning, sustainability practices, and organizational performance: An empirical investigation of global manufacturing firms. Int J Prod Econ 246:108419. https://doi.org/10.1016/j.ijpe.2022.108419

Ngan SL, How BS, Teng SY et al (2019) Prioritization of sustainability indicators for promoting the circular economy: The case of developing countries. Renew Sustain Energy Rev 111:314–331. https://doi.org/10.1016/j.rser.2019.05.001

Nguyen NP, Adomako S (2022) Stakeholder pressure for eco-friendly practices, international orientation, and eco-innovation: A study of small and medium-sized enterprises in Vietnam. Corp Soc Responsib Environ Manag 29:79–88. https://doi.org/10.1002/csr.2185

Ocampo LA, Clark EE, Promentilla MAB (2016) Computing sustainable manufacturing index with fuzzy analytic hierarchy process. Int J Sustain Eng 1–10. https://doi.org/10.1080/19397038.2016.1144828

Ogunmakinde OE (2019) A Review of Circular Economy Development Models in China. Germany and Japan. Recycling 4:27. https://doi.org/10.3390/recycling4030027

Ogunmakinde OE, Egbelakin T, Sher W (2022) Contributions of the circular economy to the UN sustainable development goals through sustainable construction. Resour Conserv Recycl 178:106023. https://doi.org/10.1016/j.resconrec.2021.106023

Ozdemir S, Arroyabe Carlos Fernandez De, J, Sena V, Gupta S, (2023) Stakeholder diversity and collaborative innovation: Integrating the resource-based view with stakeholder theory. J Bus Res 164:113955. https://doi.org/10.1016/j.jbusres.2023.113955

Park K, Kremer GEO (2017) Text mining-based categorization and user perspective analysis of environmental sustainability indicators for manufacturing and service systems. Ecol Indic 72:803–820. https://doi.org/10.1016/j.ecolind.2016.08.027

Pathak P, Singh MP, Badhotiya GK (2020) Performance obstacles in sustainable manufacturing – model building and validation. J Adv Manag Res 17:549–566. https://doi.org/10.1108/JAMR-03-2020-0031

Peng MW, Sun SL, Pinkham B, Chen H (2009) The institution-based view as a third leg for a strategy tripod. Acad Manag Perspect 23:63–81. https://doi.org/10.5465/amp.2009.43479264

Peralta Álvarez ME, Marcos Bárcena M, Aguayo González F (2017) On the sustainability of machining processes. Proposal for a unified framework through the triple bottom-line from an understanding review. J Clean Prod 142:3890–3904. https://doi.org/10.1016/j.jclepro.2016.10.071

Peruzzini M, Gregori F, Luzi A et al (2017) A social life cycle assessment methodology for smart manufacturing: The case of study of a kitchen sink. J Ind Inf Integr 7:24–32. https://doi.org/10.1016/j.jii.2017.04.001

Pinto LFR, de Venturini G, FP, Digiesi S et al (2020) Sustainability assessment in manufacturing under a strong sustainability perspective—an ecological neutrality initiative. Sustainability 12:9232. https://doi.org/10.3390/su12219232

Ramadani V, Agarwal S, Caputo A et al (2022) Sustainable competencies of social entrepreneurship for sustainable development: Exploratory analysis from a developing economy. Bus Strategy Environ bse.3093. https://doi.org/10.1002/bse.3093

Razmjoo A, Khalili N, Majidi Nezhad M et al (2020) The main role of energy sustainability indicators on the water management. Model Earth Syst Environ 6:1419–1426. https://doi.org/10.1007/s40808-020-00758-1

Reiman T, Pietikäinen E (2010) Indicators of safety culture – selectionand utilization of leading safetyperformance indicators. 72

Riayatsyah TMI, Ong HC, Chong WT et al (2017) Life cycle cost and sensitivity analysis of reutealis trisperma as non-edible feedstock for future biodiesel production. Energies 10. https://doi.org/10.3390/en10070877

Rizvi SWH, Agrawal S, Murtaza Q (2023) Automotive industry and industry 4.0-Circular economy nexus through the consumers' and manufacturers' perspectives: A case study. Renew Sustain Energy Rev 183:113517. https://doi.org/10.1016/j.rser.2023.113517

Sabat KC, Bhattacharyya SS, Krishnamoorthy B (2022) Circular economy in pharmaceutical industry through the lens of stimulus organism response theory. Eur Bus Rev. https://doi.org/10.1108/EBR-02-2022-0037

Sala S (2020) Triple bottom line, sustainability and sustainability assessment, an overview. In: Biofuels for a More Sustainable Future. Elsevier, pp 47–72

Samuel VB, Agamuthu P, Hashim MA (2013) Indicators for assessment of sustainable production: A case study of the petrochemical industry in Malaysia. Ecol Indic 24:392–402. https://doi.org/10.1016/j.ecolind.2012.07.017

Sangwan KS, Bhakar V, Digalwar AK (2018) Sustainability assessment in manufacturing organizations: Development of assessment models. Benchmarking Int J 25:994–1027. https://doi.org/10.1108/BIJ-08-2017-0227

Sarkis J, Gonzalez-Torre P, Adenso-Diaz B (2010) Stakeholder pressure and the adoption of environmental practices: The mediating effect of training. J Oper Manag 28:163–176. https://doi.org/10.1016/j.jom.2009.10.001

Sartal A, Bellas R, Mejías AM, García-Collado A (2020) The sustainable manufacturing concept, evolution and opportunities within Industry 4.0: A literature review. Adv Mech Eng 12:168781402092523. https://doi.org/10.1177/1687814020925232

Shahzad M, Qu Y, Ur Rehman S et al (2023) Impact of stakeholders' pressure on green management practices of manufacturing organizations under the mediation of organizational motives. J Environ

Plan Manag 66:2171–2194. https://doi.org/10.1080/09640568.2022.2062567
Sharma D (2021) Strategies for assessment and implementation of sustainable manufacturing. J Eng Res. https://doi.org/10.36909/jer.ICARI.15267
Shubham CP, Murty LS (2018) Int J Sustain Dev World Ecol 25:23–34. https://doi.org/10.1080/13504509.2016.1258373
Sikdar SK (2019) Fractured state of decisions on sustainability: An assessment. Sustain Prod Consum 19:231–237. https://doi.org/10.1016/j.spc.2019.04.004
Singh RK, Kumar P (2019) Measuring the flexibility index for a supply chain using graph theory matrix approach. J Glob Oper Strateg Sourc 13:56–69. https://doi.org/10.1108/JGOSS-04-2019-0027
Singh RK, Kumar P, Joseph B, Sharma H (2015) Evaluation of Maintainability Index of a Mechanical System using Graph Theoretic Approach. Procedia - Soc Behav Sci 189:303–313. https://doi.org/10.1016/j.sbspro.2015.03.226
Singh RK, Modgil S, Tiwari AA (2019) Identification and evaluation of determinants of sustainable manufacturing: a case of Indian cement manufacturing. Meas Bus Excell 23:24–40. https://doi.org/10.1108/MBE-08-2018-0056
Singh RK, Murty HR, Gupta SK, Dikshit AK (2007) Development of composite sustainability performance index for steel industry. Ecol Indic 7:565–588. https://doi.org/10.1016/j.ecolind.2006.06.004
Singh RK, Murty HR, Gupta SK, Dikshit AK (2009) An overview of sustainability assessment methodologies. Ecol Indic 9:189–212. https://doi.org/10.1016/j.ecolind.2008.05.011
Stout LA (2012) The shareholder value myth: how putting shareholders first harms investors, corporations, and the public, 1st edn. Berrett-Koehler, San Francisco
Swarnakar V, Singh AR, Antony J et al (2021) Development of a conceptual method for sustainability assessment in manufacturing. Comput Ind Eng 158:107403. https://doi.org/10.1016/j.cie.2021.107403
Swarnakar V, Tiwari AK, Singh AR (2020) Evaluating critical failure factors for implementing sustainable lean six sigma framework in manufacturing organization: A case experience. Int J Lean Six Sigma 11:1069–1104. https://doi.org/10.1108/IJLSS-05-2019-0050
Thompson B (2004) Exploratory and confirmatory factor analysis: Understanding concepts and applications. American Psychological Association, Washington
Thorndike RM (1995) Book review : psychometric theory (3rd ed.) by jum nunnally and Ira Bernstein New York: McGraw-Hill, 1994, xxiv + 752 pp. Appl Psychol Meas 19:303–305. https://doi.org/10.1177/014662169501900308
Tu Y, Wu W (2021) How does green innovation improve enterprises' competitive advantage? The role of organizational learning. Sustain Prod Consum 26:504–516. https://doi.org/10.1016/j.spc.2020.12.031
Tuljak-Suban D, Bajec P (2020) Integration of ahp and gtma to make a reliable decision in complex decision-making problems: application of the logistics provider selection problem as a case study. Symmetry 12:766. https://doi.org/10.3390/sym12050766
Urbaniak M, Rogala P, Kafel P (2022) Expectations of manufacturing companies regarding future priorities of improvement actions taken by their suppliers. Oper Manag Res. https://doi.org/10.1007/s12063-022-00307-2
Vinodh S, Joy D (2012) Structural equation modeling of sustainable manufacturing practices. Clean Technol Environ Policy 14:79–84. https://doi.org/10.1007/s10098-011-0379-8
Virmani N, Salve UR, Kumar A, Luthra S (2021) Analyzing roadblocks of industry 4.0 adoption using graph theory and matrix approach. IEEE Trans Eng Manag 1–10. https://doi.org/10.1109/TEM.2020.3048554
Wang J, Mao Y (2020) Pains and gains of environmental management system certification for the sustainable development of manufacturing companies: Heterogeneous effects of industry peer learning. Bus Strategy Environ 29:2092–2109. https://doi.org/10.1002/bse.2489
Wang Y, Yang Y (2021) Analyzing the green innovation practices based on sustainability performance indicators: a Chinese manufacturing industry case. Environ Sci Pollut Res 28:1181–1203. https://doi.org/10.1007/s11356-020-10531-7
Williams B, Onsman A, Brown T (2010) Exploratory factor analysis: A five-step guide for novices. Australas J Paramed 8:. https://doi.org/10.33151/ajp.8.3.93
Wilson J, Tyedmers P, Pelot R (2007) Contrasting and comparing sustainable development indicator metrics. Ecol Indic 7:299–314. https://doi.org/10.1016/j.ecolind.2006.02.009
Wu Y, Su D (2020) Social Life Cycle Assessment. Sustainable Product Development. Springer International Publishing, Cham, pp 127–152
Xu Z, Elomri A, Pokharel S et al (2017) Global reverse supply chain design for solid waste recycling under uncertainties and carbon emission constraint. Waste Manag 64:358–370. https://doi.org/10.1016/j.wasman.2017.02.024
Yip WS, Zhou H, To S (2023) A critical analysis on the triple bottom line of sustainable manufacturing: key findings and implications. Environ Sci Pollut Res 30:41388–41404. https://doi.org/10.1007/s11356-022-25122-x
Yuen KF, Wang X, Wong YD, Zhou Q (2017) Antecedents and outcomes of sustainable shipping practices: The integration of stakeholder and behavioural theories. Transp Res Part E Logist Transp Rev 108:18–35. https://doi.org/10.1016/j.tre.2017.10.002
Zhang H, Haapala KR (2015) Integrating sustainable manufacturing assessment into decision making for a production work cell. J Clean Prod 105:52–63. https://doi.org/10.1016/j.jclepro.2014.01.038
Zhou G, Hu W, Huang W (2016) Are Consumers Willing to Pay More for Sustainable Products? A Study of Eco-Labeled Tuna Steak. Sustainability 8:494. https://doi.org/10.3390/su8050494

Publisher's Note Springer Nature remains neutral with regard to jurisdictional claims in published maps and institutional affiliations.

Springer Nature or its licensor (e.g. a society or other partner) holds exclusive rights to this article under a publishing agreement with the author(s) or other rightsholder(s); author self-archiving of the accepted manuscript version of this article is solely governed by the terms of such publishing agreement and applicable law.

Journal of Electronic Materials (2024) 53:683–692
https://doi.org/10.1007/s11664-023-10862-4

ORIGINAL RESEARCH ARTICLE

Gate Engineered Ferroelectric Junctionless BioFET for Label-Free Detection of Biomolecules

Snehlata Yadav[1] · Sonam Rewari[1] · Rajeshwari Pandey[1]

Received: 14 September 2023 / Accepted: 27 November 2023 / Published online: 31 December 2023
© The Minerals, Metals & Materials Society 2023

Abstract

A gate engineered ferroelectric junctionless field-effect transistor biosensor (BioFET) is proposed and investigated for label-free detection of various biomolecules. A nanocavity is created by etching a part of the gate oxide material on the top and bottom of the device, which allows biomolecules to get immobilized. The immobilization of biomolecules in the cavity causes changes in electrostatic characteristics such as surface potential, input and output characteristics, transconductance, output conductance, gate capacitance, and cutoff frequency used as sensing metrics. The biosensor is also examined at different biomolecule concentrations (-1×10^{12} cm^{-2}, 0 cm^{-2}, and 1×10^{12} cm^{-2}). The transistor's sensitivity is then understood by looking at the fluctuation in threshold voltage, subthreshold swing, and switching ratio. The performance is compared between the ferroelectric junctionless BioFET and the gate engineered ferroelectric junctionless BioFET. The results indicate that the gate engineered ferroelectric junctionless BioFET shows the maximum improvement for protein (1202.4%, 111%, and 565%) and DNA (787.5%, 117.3%, and 600%). The gate engineered ferroelectric junctionless BioFET is shown to be suitable for ultrasensitive bio-sensing applications.

Keywords Biosensor · ferroelectric · junctionless · sensitivity · biomolecules · immobilization

Introduction

The current research focus has been addressing challenges that conventional complementary metal–oxide–semiconductor (CMOS) technology faces, including voltage scaling and short-channel effects (SCEs).[1] The junctionless dual-gate metal–oxide–semiconductor field-effect transistor (MOSFET), immune to short-channel effects and possessing several unique features, is an outstanding alternative device architecture for CMOS technology.[2] The most prominent challenge in fabricating short-channel devices is forming source/channel and channel/drain junctions in typical MOSFETs.[3] Several advantageous qualities of junctionless (JL) MOSFETs include the absence of sharp junctions, which is challenging to achieve, along with a streamlined fabrication technique and other benefits.[4] Field-effect transistor-based electrochemical biosensors have garnered the most attention in the research community because they have numerous benefits over other biosensors, including compatibility with CMOS technology, label-free detection, increased scaling, and inexpensive production costs. They could be suitable for use in upcoming biosensor applications because of these qualities. FET-based biosensors have many applications, including label-free detection of charged bio-analytes.[5] Biomolecules change the sensors' electrical responses by modifying the gate terminals' functioning. Dielectrically regulated field-effect transistors, which exploit the dielectric constant of biomolecules, have recently sparked much attention.[6] This technology can detect charged and uncharged biomolecules at various concentrations. Advancement in the technology and device engineering has a huge impact on the evolution of biosensors and their designing principles.[7–9] Various biosensors have been designed and reported, such as surrounding-gate MOSFETs, gate-all-around tunnel FETs, and Ge/Si-interfaced label-free nanowire field-effect transistor biosensors (BioFETs). These biosensors have improved sensitivity and serve in different sensing applications.[10–14] There have been numerous FET-based nanoscale sensors presented recently, and to improve sensitivity and detection, more design parameter optimization is required.[15,16]

✉ Sonam Rewari
rewarisonam@gmail.com

[1] Department of Electronics and Communication Engineering, Delhi Technological University, New Delhi, India

Larger sensitivity in terms of current is required to detect biomolecule species at very low concentrations. The maximum current sensitivity for FET-based biosensors can be achieved when the device is operated in the subthreshold range.[17,18] On the other hand, the so-called Boltzmann tyranny limits the subthreshold swing (SS) in typical FET-based biosensors to a minimum of 60 mV/decade at ambient temperature, lowering the maximum current sensitivity.[19] As technology has improved, the demand for efficiency has increased substantially. Therefore, shifting to an advanced technology that can handle these difficulties is mandatory. Negative-capacitance field-effect transistors (NCFETs), a form of the steep-switching device based on ferroelectrics, offer a potential solution to overcome the Boltzmann limit of SS and achieve a swing of less than 60 mV/decade.[19] Recent research shows that HfO_2 exhibits ferroelectric behavior when doped with elements such as Y, Zr, Al, Si, and others at different mole concentrations and annealing temperatures.[20] It has been found in previous research that the mechanical encapsulation of thin sheets of zirconium-doped hafnium oxide (HZO) forms an orthorhombic phase. It possesses a piezoelectric response, and polarization tests have proved that it is ferroelectric. According to studies, HZO has a low dielectric constant (about 30), indicating that it can be scaled down to meet existing technological nodes.[21] As a result, these materials are excellent candidates for application as ferroelectric materials. The benefits of the ferroelectric layer and junctionless structures, as well as the creation of cavities in the oxide regions for inserting the biomolecules, is what distinguishes our work. A dielectric-modulated FET can be used to implement this form of a biosensor.[22] Even though simulation and modeling of dielectric-modulated FETs have been documented in many publications, they are typically used for sensing biomolecules in dry environments.[22–24] The key novelty of this work is the incorporation of the ferroelectric layer in the junctionless structures, as well as the creation of cavities in the oxide regions for inserting the biomolecules. Our suggested study is more innovative because there are no ferroelectric junctionless FET-based biosensors in the literature. Therefore, a gate engineered ferroelectric junctionless BioFET (GE-FJ-BioFET) capable of detecting diverse biomolecules such as enzymes, proteins, and DNA[25] is described in this study. Ferroelectric material used as gate oxide material improves the subthreshold swing, improves the gate control over the channel, and establishes its applicability in low-power biosensor design. The proposed biosensor provides advantages such as high sensitivity, selectivity, label-free detection, compatibility, and fabrication feasibility. These qualities make them well suited for various medical applications. This device could be a significant contender for CMOS technology in the future since it can overcome the critical limitations of complex fabrication methods and operate at lower voltage limits, thereby eliminating the problem of excessive chip heating.[26] Analysis of ballistic transistors is not intended to allow for accurate prediction of actual device characteristics. A ballistic transistor is an ideal device that can never be achieved.[27] From the literature, it has been reported that the internal gate capacitance in the ballistic case worsens the capacitance matching and in turn reduces the voltage amplification effect of the negative capacitance (NC).[28] Therefore, these models have not been considered in this work. Furthermore, various studies have outlined fabrication methods for JL transistors and ferroelectric FETs (FeFETs);[29–31] as a result, the suggested device may be produced using current technologies. The section "Device Structure, Simulation, and Calibration" describes the device structure, simulation of the gate engineered ferroelectric junctionless BioFET, and calibration with experimental work. The results and discussion are covered in the "Results and Discussion" section. The "Conclusion" section concludes the work.

Device Structure, Simulation, and Calibration

Figure 1 depicts a two-dimensional (2D) schematic cross-sectional view of the GE-FJ-BioFET. The device employs an *n*-type doped, symmetric double-gate junctionless transistor with a ferroelectric layer and two biomolecule nano-cavities. The doping concentrations are assumed to be 10^{19} cm^{-3} across the source, drain, and channel. The thicknesses of the ferroelectric (t_{fe}), oxide (t_{ox}), and channel (t_{ch}) are 5 nm, 2 nm, and 20 nm, respectively. The GE-FJ-BioFET analyzes each dielectric constant to identify biomolecules, including biotin, APTES, protein, and DNA.[32] The biomolecules are inserted into the gate stack's nano-cavities. The dielectric constant of each of the biomolecules is shown in Table I. The biomolecules are placed in the nano-cavities created in the gate stack. The cavity region is filled with air in the absence of biomolecules, i.e., $\varepsilon = 1$, and when the dielectric constant $\varepsilon > 1$, the cavity region is infused with biomolecules. The calibration of the simulated work with the experimental work[33] is shown in Fig. 2a. The simulations are performed using the Silvaco ATLAS technology computer-aided design (TCAD) simulator, with the Lombardi concentration, voltage, and temperature (CVT) model, Shockley–Read–Hall (SRH) recombination, Fermi, and Landau–Khalatnikov (LK) models[34] explained in Table II.

Figure 3 depicts the contour plots for electron concentration in the channel region at different dielectric constants. When biomolecules are added to the cavity region, charges are induced in the channel below the cavity. As shown in Fig. 3, the amount of charge produced depends on the biomolecule's dielectric constant.

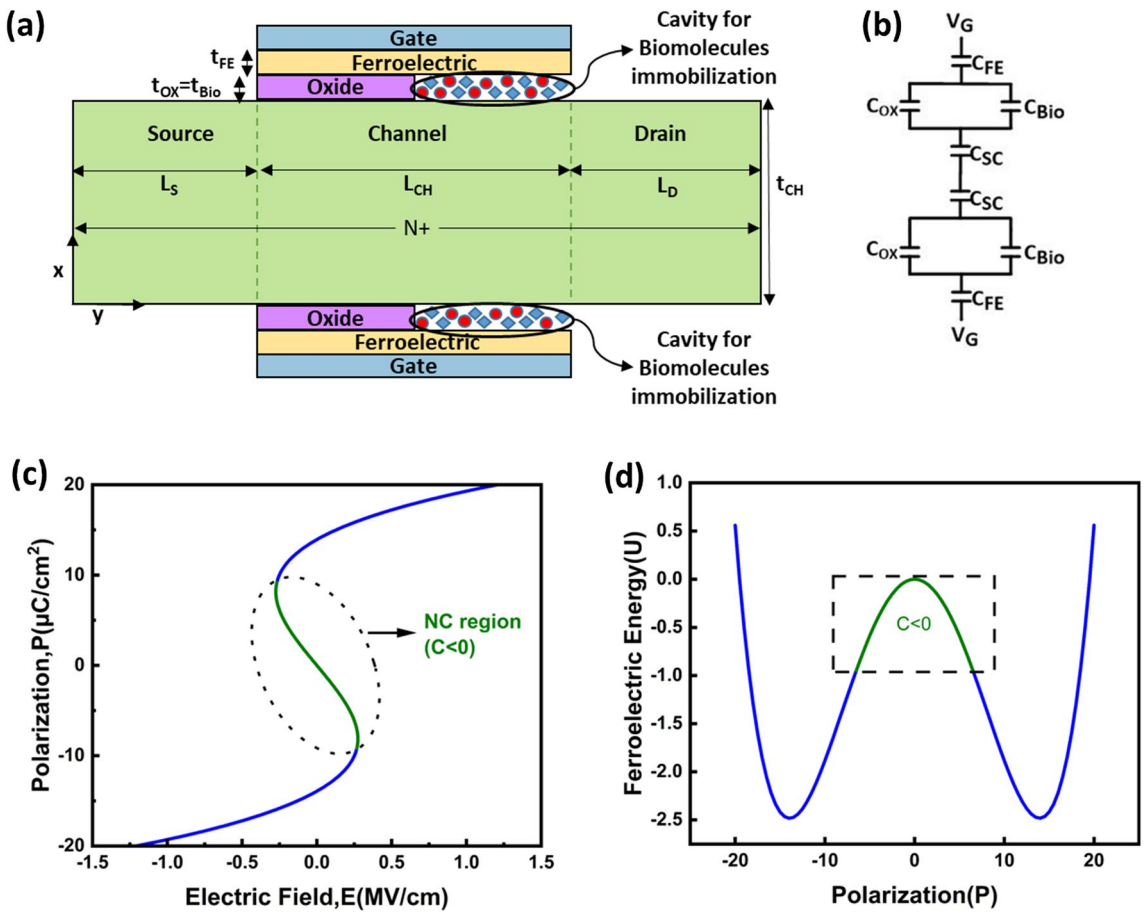


Fig. 1 (a) Schematic of gate engineered ferroelectric junctionless BioFET (GE-FJ-BioFET), (b) equivalent capacitance model, (c) the double-well ferroelectric energy versus polarization using LK theory, and (d) ferroelectric polarization as a function of electric field.

Table I Biomolecule with dielectric constant variations

Biomolecule	Dielectric constant
Biotin[35]	2.63
APTES[36]	3.57
Protein[37]	6
DNA[38]	8

Results and Discussion

Biomolecules have dielectric properties as well as charge concentration. Variations of biomolecule species and their concentrations have been investigated for biomolecule detection. The dielectric variation of biomolecules is considered when examining the electrical characteristics of the GE-FJ-BioFET for biomolecules with dielectric properties and concentrations. The biomolecule concentrations

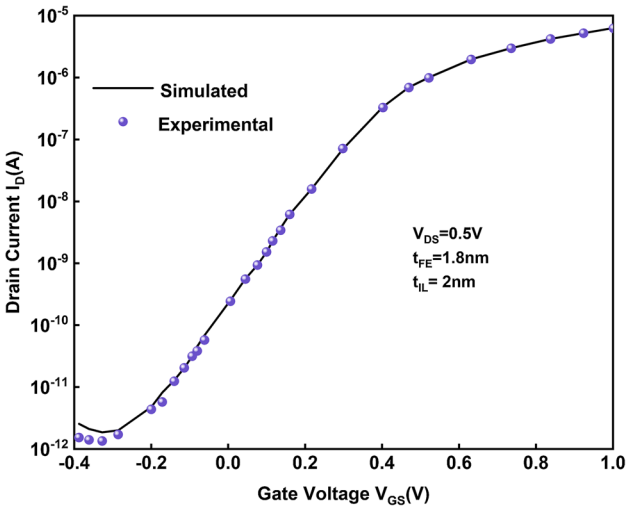


Fig. 2 Calibration with the experimental work.

used to analyze the electrical properties of GE-FJ-BioFET

with charge density variation and constant dielectric are -1×10^{12} cm^{-2}, 0 cm^{-2}, and 1×10^{12} cm^{-2}.

GE-FJ-BioFET as a Biomolecule Species Sensor

As seen in Fig. 4a, changes in the dielectric constant have an impact on the surface potential of the GE-FJ-BioFET. As illustrated, a drop in the potential is observed as the biomolecule with n increasing dielectric constant is introduced. A drop in the potential reduces the drain current in the device and raises the threshold voltage.

The effectiveness of the GE-FJ-BioFET as a biomolecule species sensor can be determined by the device electrical parameters, investigated using the device transfer characteristics, transconductance (gm), threshold voltage (V_{th}), I_{on}/I_{off} ratio, and subthreshold swing (SS). Figure 5a and b demonstrate the drain current and transconductance fluctuation for different biomolecule species. The drain current reduces as the biomolecule dielectric increases because of a fall in the surface potential of the device in the channel region. Also, as shown in Fig. 5b, the transconductance decreases as the dielectric constant increases. Figure 6 depicts the changes in output characteristics and output conductance

Table II Physical models used for the simulations

Model	Description
Lombardi CVT model	This model overrides any other mobility models which may be specified in the MODELS statement
Shockley–Read–Hall (SRH) recombination model	The Shockley–Read–Hall (SRH) recombination model with concentration-dependent lifetimes accounts for the recombination of minority carriers
Fermi model	This model introduces Fermi statistics recombination into intrinsic concentration calculation
Landau–Khalatnikov ferroelectric model	The model is enabled by specifying the flag LKFERRO on the INTERFACE statement, along with the LKCORECIVE and LKREMNANT parameters

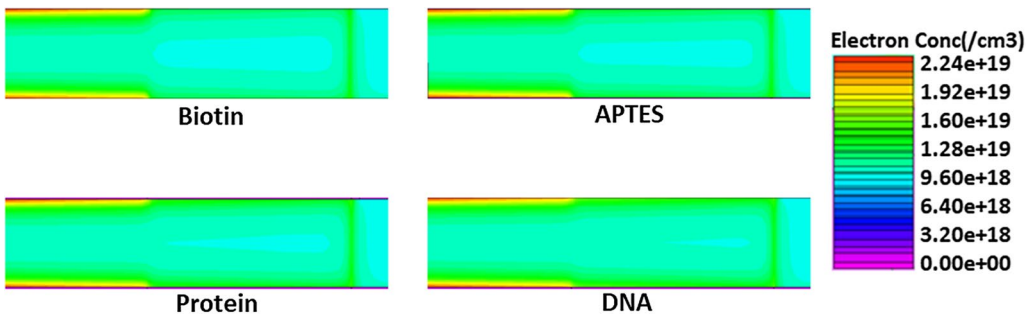


Fig. 3 Electron concentration in the channel region of the GE-FJ-BioFET at different dielectric constants.

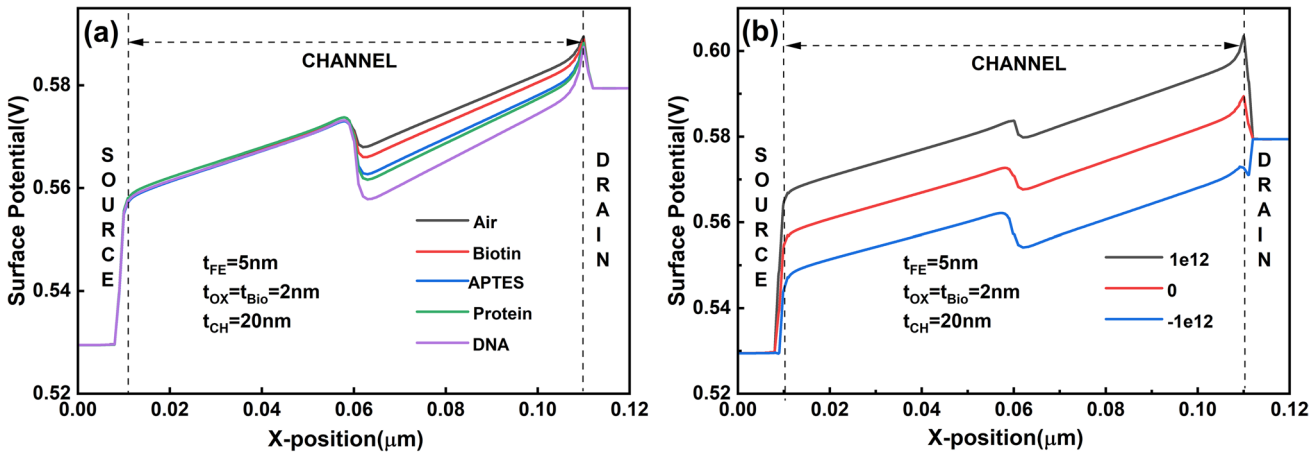


Fig. 4 Surface potential of GE-FJ-BioFET at varying (a) dielectric constants and (b) biomolecule concentrations.

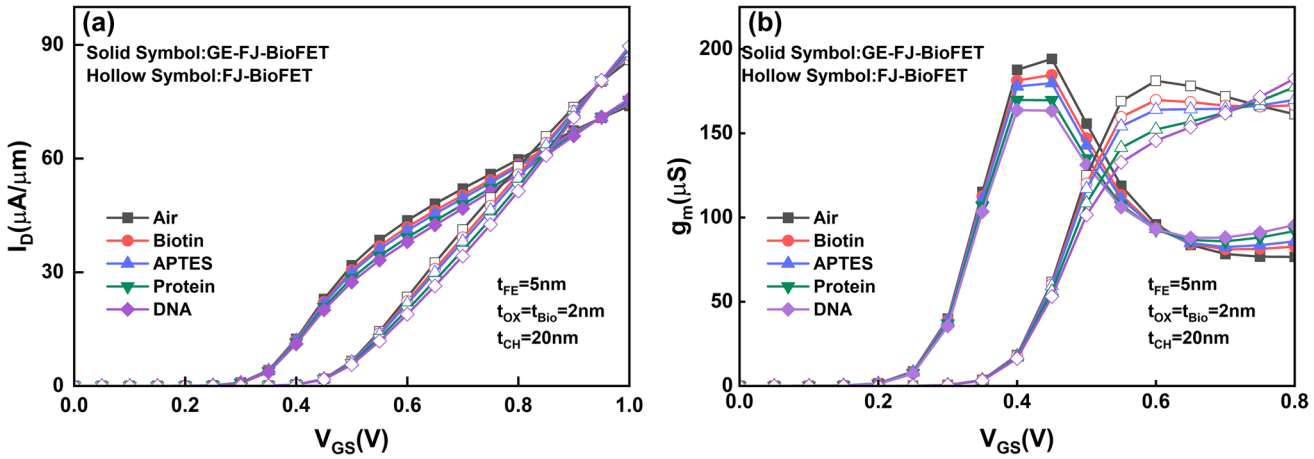


Fig. 5 (a) Transfer characteristics and (b) transconductance of devices with variations in the dielectric constant.

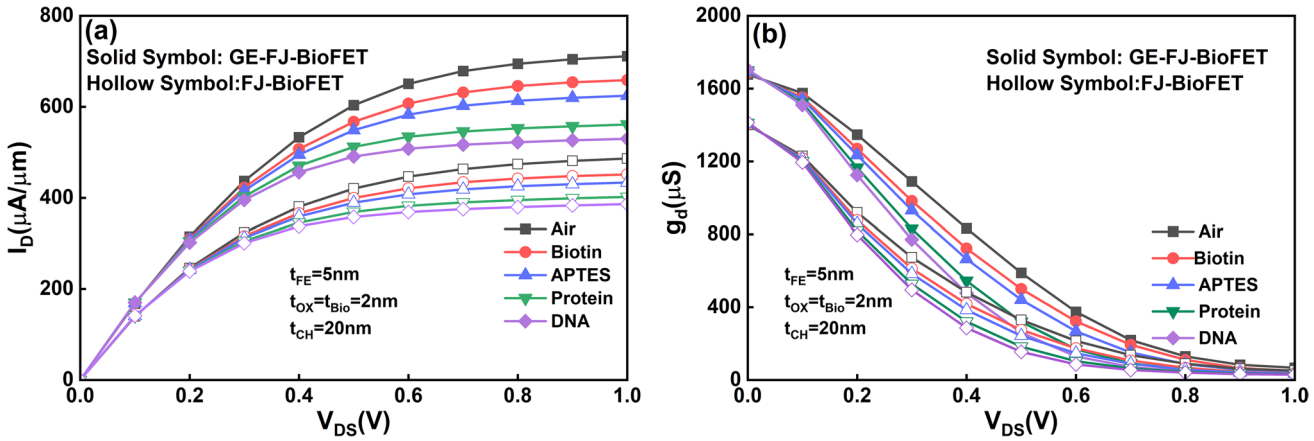


Fig. 6 (a) Output characteristics and (b) output conductance for different biomolecule dielectric constants.

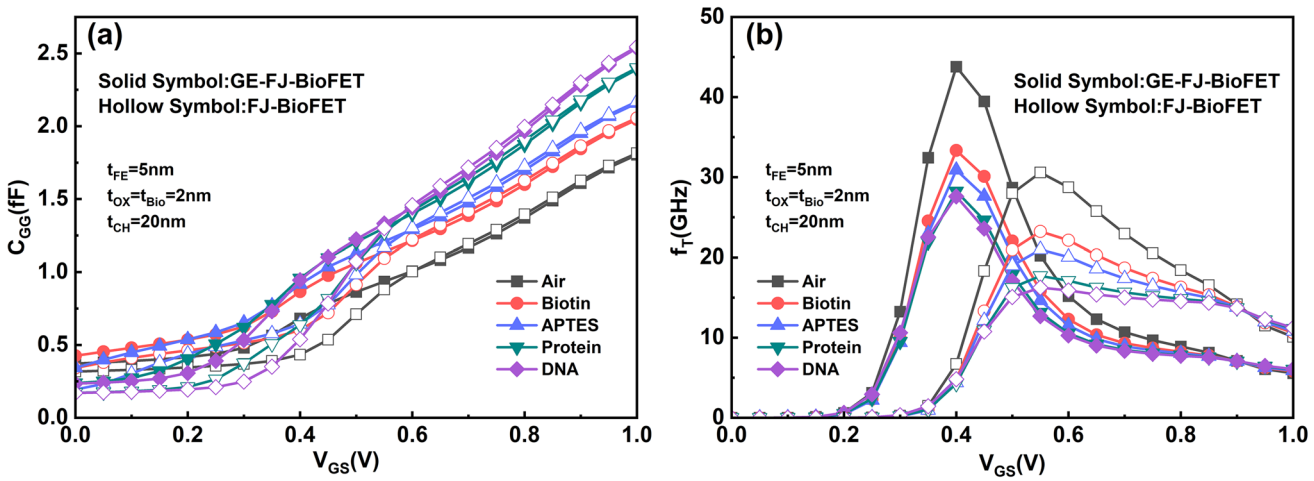


Fig. 7 (a) Total gate capacitance and (b) cutoff frequency of the devices for different biomolecule species.

with different biomolecule dielectric constants. As observed, the output characteristics decreases with an increase in the dielectric constant. It is also evident from the figures that the performance of the GE-FJ-BioFET is high when compared to the FJ-BioFET. Figure 7a and b show the total gate capacitance (C_{GG}) and cutoff frequency (f_T), which shows that both parameters increase when the dielectric constant increases. The threshold voltage sensitivity is investigated with increasing dielectric constant with regard to air in the cavity, and the results are depicted in Fig. 8a. The figure shows that the threshold voltage sensitivity increases as the dielectric constant increases, allowing biomolecules to be detected. Furthermore, the GE-FJ-BioFET biosensor's sensitivity concerning the SS and I_{on}/I_{off} is illustrated in Fig. 8b and c. The sensitivity can be formulated as follows[39]:

$$S_{V_{th}} = \frac{V_{th,bio} - V_{th,air}}{V_{th,air}} \tag{1}$$

$$S_{SS} = \frac{SS_{bio} - SS_{air}}{SS_{air}} \tag{2}$$

$$S_{I_{on}/I_{off}} = \frac{I_{on}/I_{offbio} - I_{on}/I_{offair}}{I_{on}/I_{offair}} \tag{3}$$

As is evident from the figure, the GE-FJ-BioFET is highly sensitive for protein and DNA when compared with the other device. The sensitivity in terms of V_{th}, SS, and I_{on}/I_{off} with variations in dielectric constants are listed in Table III.

The protein and DNA biomolecules show a more significant sensitivity improvement. The % improvement for protein is 1202.4%, 111%, and 565%, whereas for DNA, it is 787.5%, 117.3%, and 600%. The devices are compared, and it is found that the GE-FJ-BioFET is highly sensitive and constitutes a good choice for biosensing applications.

GE-FJ-BioFET as a Biomolecule Concentration Sensor

The biomolecule concentration affects the device surface potential, as shown in Fig. 4b. Negatively charged biomolecules decrease the device's potential in the channel region, while positively charged biomolecules increase it. When the potential increases, the current flow increases, and the threshold voltage decreases, but when the potential decreases, the current flow decreases, and the threshold voltage increases. The influence of biomolecule charge concentration fluctuation on the device electrical parameters including device transfer characteristics, transconductance (gm), threshold voltage (V_{th}), I_{on}/I_{off} ratio, and subthreshold swing (SS) was investigated.

The fluctuation in the device transfer characteristics and transconductance with biomolecule charge concentration is depicted in Fig. 9a and b. The drain current is

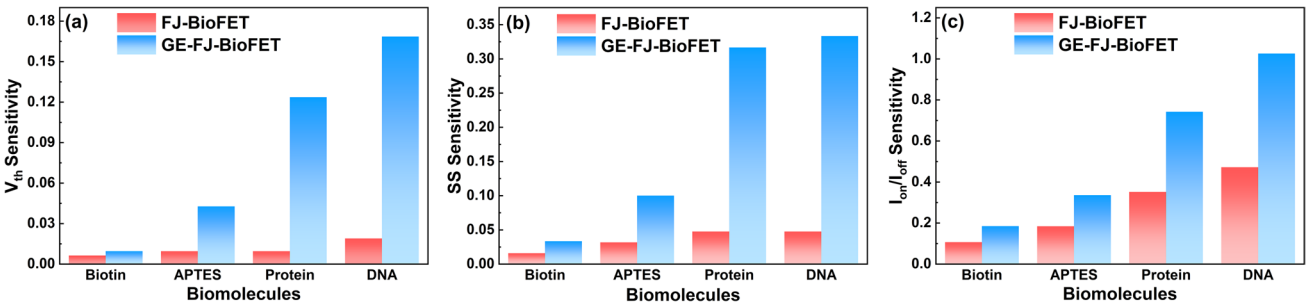


Fig. 8 Sensitivity comparison in terms of (a) V_{th}, (b) SS, and (c) I_{on}/I_{off} ratio for different biomolecule species.

Table III Device sensitivity with dielectric constant variation

Dielectric constant (ε)	S_{Vth}			$S_{Ion/Ioff}$			S_{SS}		
	FJ-BioFET	GE-FJ-BioFET	% improvement (%)	FJ-BioFET	GE-FJ-BioFET	% improvement (%)	FJ-BioFET	GE-FJ-BioFET	% improvement (%)
Biotin	0.00633	0.00949	50	0.1066	0.18488	73.4	0.01587	0.03333	110
APTES	0.00949	0.0427	350	0.18441	0.33564	82	0.03175	0.1	215
Protein	0.00949	0.1236	1202.4	0.35151	0.74205	111	0.04762	0.31667	565
DNA	0.01899	0.16854	787.5	0.4720	1.02601	117.3	0.04762	0.33333	600

higher for positively charged biomolecule because the surface potential is higher in the channel region and lower for negatively charged biomolecules because the surface potential is lower in the channel region. Additionally, the transconductance is also higher for positively charged biomolecules. The output characteristics are depicted in Fig. 10a and b, which shows that the performance of the GE-FJ-BioFET is better than that of the FJ-BioFET. The sensitivity in terms of V_{th}, SS, and I_{on}/I_{off} with positively and negatively charged biomolecules about neutral biomolecules in the cavities is illustrated in Fig. 11a, b, and c, which shows higher sensitivity for the GE-FJ-BioFET

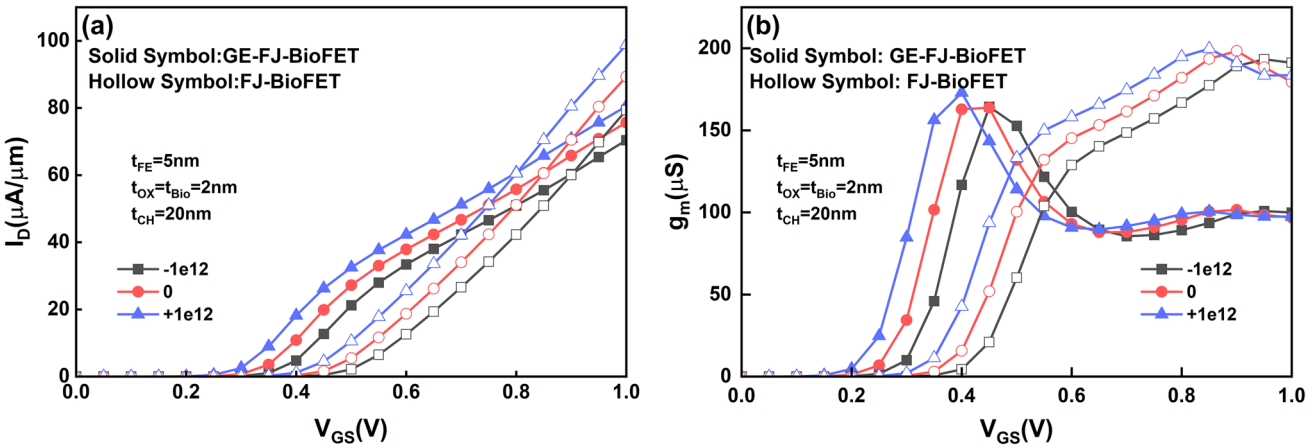


Fig. 9 (a) Transfer characteristics and (b) transconductance at different biomolecule concentrations.

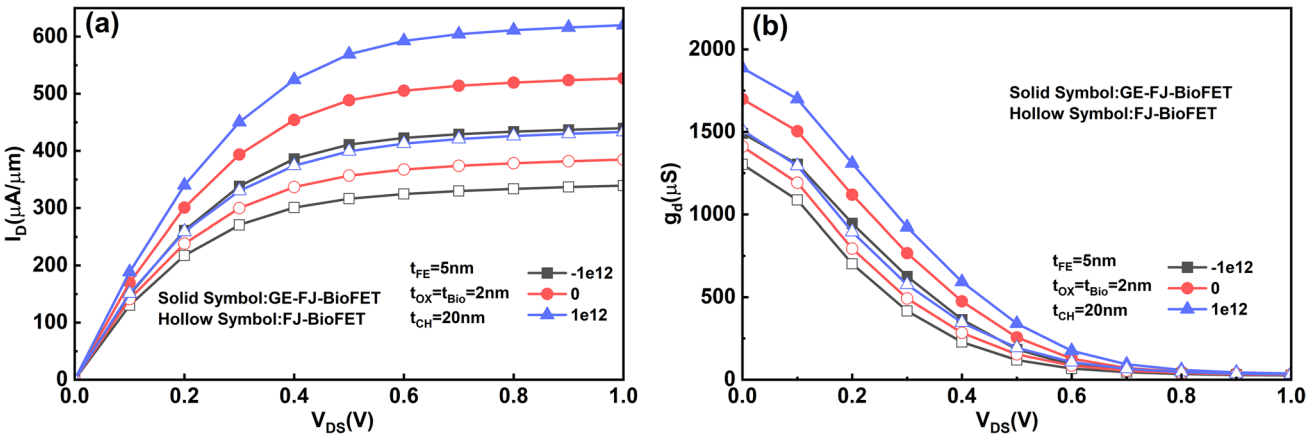


Fig. 10 (a) Output characteristics and (b) output conductance at different biomolecule concentrations.

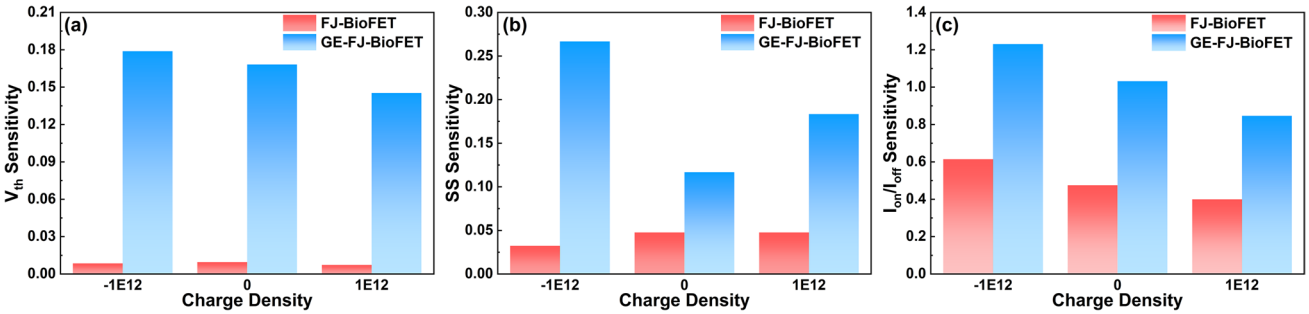


Fig. 11 Sensitivity comparison in terms of (a) V_{th}, (b) SS, and **c** I_{on}/I_{off} ratio at different biomolecule concentrations.

Table IV Device sensitivity with respect to biomolecule charge concentration

Charge density	S_{Vth}			$S_{Ion/Ioff}$			S_{SS}		
	FJ-BioFET	GE-FJ-BioFET	% improvement (%)	FJ-BioFET	GE-FJ-BioFET	% improvement (%)	FJ-BioFET	GE-FJ-BioFET	% improvement (%)
−1e12	0.0085	0.17879	2003.4	0.61403	1.22997	100.3	0.03226	0.26667	726.6
0	0.00946	0.16816	1677.5	0.47436	1.03164	117.5	0.04762	0.11667	145
1e12	0.00719	0.14528	1920.5	0.39914	0.84623	112	0.04762	0.18333	285

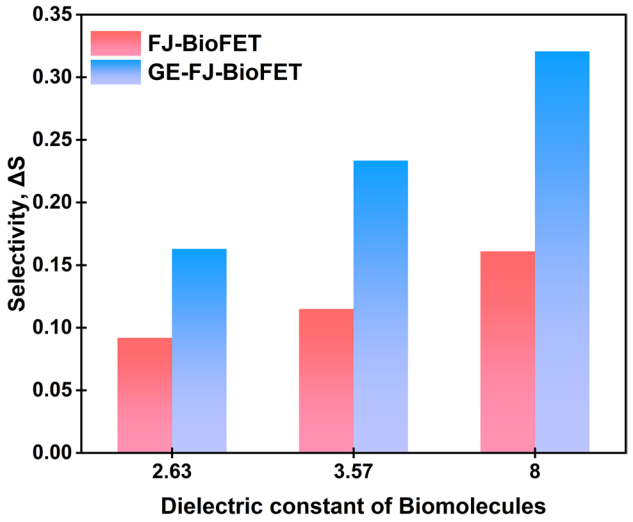


Fig. 12 Selectivity of the proposed biosensor.

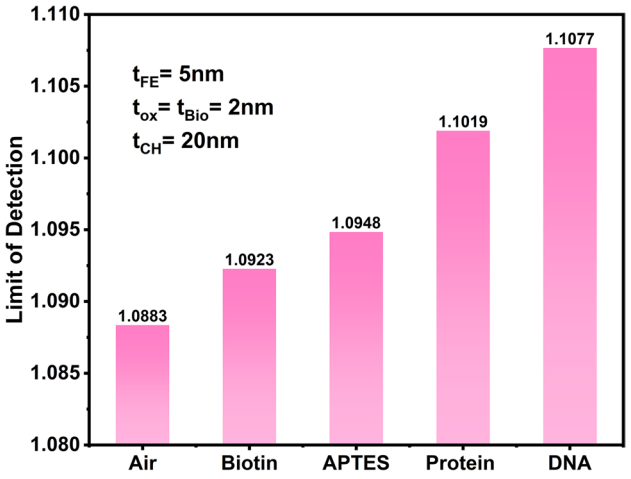


Fig. 13 Limit of detection (LOD) plot for different biomolecules with a standard deviation of 3.039E−05 for air, 3.012E−05 for biotin, 2.999E−05 for APTES, 2.976E−05 for protein, and 2.963E−05 for DNA.

in terms of V_{th}, SS, and I_{on}/I_{off} for negatively charged biomolecules.

Table IV shows the comparison of the GE-FJ-BioFET and FJ-BioFET at different biomolecule concentrations with respect to V_{th}, SS, and I_{on}/I_{off}. Improvement in the sensitivity is 2003.3% for V_{th}, 100.3% for I_{on}/I_{off}, and 726.6% for SS in a DNA biomolecule. Therefore, it can be concluded that the GE-FJ-BioFET is more sensitive than the FJ-BioFET.

Selectivity Analysis, Limit of Detection, and Hot Carrier Effect on Biosensor

A key characteristic of biosensors is selectivity, which describes how well a biosensor can bind to the desired target biomolecule while actively rejecting or excluding all other biomolecules. Mathematically, selectivity is determined by calculating the relative ratio of the drain current at various dielectric constants, which corresponds to different biomolecules.[40] This calculation is expressed in Eq. 4.

$$\text{Selectivity, } \Delta S_{I_{on}/I_{off}} = \frac{I_{on}/I_{off}(\varepsilon = 2.63, 3.57, 8) - I_{on}/I_{off}(\varepsilon = 6)}{I_{on}/I_{off}(\varepsilon = 6)} \quad (4)$$

Figure 12 presents a comparison of selectivity between the proposed and conventional devices. It is evident that the selectivity of the proposed device significantly surpasses that of the conventional device, ranging from two to three times, depending on the specific target biomolecules. The selectivity of the biomolecules has been calculated using Eq. 4, with a parameter value of $\varepsilon = 6$, and the results are displayed in Fig. 12.

Figure 13 shows the plot of limit of detection (LOD) for different biomolecules with a standard deviation of 3.039E−05 for air, 3.012E−05 for biotin, 2.999E−05 for APTES, 2.976E−05 for protein, and 2.963E−05 for DNA. The LOD of the biosensor is elevated when a biomolecule is present, signifying a greater concentration of the analyte in the sample that can be identified, though not necessarily precisely measured.[5] These results provide insights into the importance of regulating parameters to enhance sensitivity and reduce operational variability in the design and production of FET-based biosensors.

The hot carrier effect is a phenomenon observed in field-effect transistors, including negative-capacitance FETs, and it has implications for the reliability and performance of

these devices. To mitigate the hot carrier effect in our device, several strategies have been employed such as the selection of an appropriate ferroelectric material having high polarization and high breakdown voltage, and gate stack engineering which helps in reducing the impact of hot carriers on the device. Hence, from the whole analysis of the proposed biosensor, it is evident that key performance metrics, including threshold voltage, SS, and I_{on}/I_{off} ratio, demonstrate enhancements compared to conventional devices. This renders the recommended device more resilient to the effects associated with hot carriers.

Conclusion

A gate engineered ferroelectric junctionless BioFET (GE-FJ-BioFET) sensor has been investigated owing to its strong sensing capability. Various sensing parameters such as input and output characteristics, g_m, V_{th}, SS, I_{on}/I_{off}, C_{gg}, and f_T have been considered for detecting the immobilized biomolecules in the cavity area. Sensitivity has been obtained by varying the dielectric of biomolecule species and their concentration. A comparison between the GE-FJ-BioFET and FJ-BioFET shows that the GE-FJ-BioFET transistor exhibits an excellent improvement in sensitivity. The % improvement in V_{th}, SS, and I_{on}/I_{off} for protein is 1202.4%, 111%, and 565%, whereas for DNA it is 787.5%, 117.3%, and 600%, respectively. As a result, the research presented in this study demonstrates that the GE-FJ-BioFET is better suited for applications requiring ultrasensitive biosensing. Additionally, techniques like material engineering using different channel materials, such as silicon–germanium and III-V compound semiconductors, can be employed to enhance carrier mobility and further improve the performance of the device.

Acknowledgments Not applicable.

Funding The authors declare that no funds, grants, or other support were received during the preparation of this manuscript.

Conflict of interest The authors declare that they have no conflict of interest.

References

1. IRDS Systems and Architectures Team, *International Roadmap for Devices and Systems: Executive Summary* (2020)
2. P. Kumar, M. Vashishath, and N. Gupta, Analytical modeling and performance analysis of surface potential for junctionless MOSFET. *J. Phys.: Conf. Ser.* 1916, 012026 (2021).
3. N. Gupta, J. B. Patel, and A. K. Raghav, A study of conventional and junctionless MOSFET using TCAD simulations, in *International Conference on Advanced Computing and Communication Technologies, ACCT*, vol. 2015-April (IEEE, 2015), pp. 53–56
4. S. Sahay and M.J. Kumar, Fundamentals of junctionless field-effect transistors, *Junctionless Field-Effect Transistors*, Vol. 67. ed. S. Sahay, and M.J. Kumar (New York: Wiley, 2019).
5. D. Sadighbayan, M. Hasanzadeh, and E. Ghafar-Zadeh, Biosensing based on field-effect transistors (FET): recent progress and challenges. *TrAC Trends Anal. Chem.* 133, 116067 (2020).
6. P. Dwivedi, *Influence of Transistor Architecture on the Performance of Dielectric Modulated Biosensor* (2021)
7. A. Das, S. Rewari, B.K. Kanaujia, and R.S. Gupta, Recent technological advancement in surrounding gate MOSFET for biosensing applications—a synoptic study. *SILICON* 14, 5133 (2022).
8. A. Das, B. K. Kanaujia, S. S. Deswal, S. Rewari, and R. S. Gupta, Doping induced threshold voltage and I_{ON}/I_{OFF} ratio modulation in surrounding gate MOSFET for analog applications, in *2022 IEEE International Conference of Electron Devices Society Kolkata Chapter (EDKCON)* (IEEE, 2022), pp. 1–6
9. A. Das, S. Rewari, B.K. Kanaujia, S.S. Deswal, and R.S. Gupta, Analytical modeling and doping optimization for enhanced analog performance in a Ge/Si interfaced nanowire MOSFET. *Phys. Scr.* 98, 074005 (2023).
10. A. Das, B. K. Kanaujia, V. Nath, S. Rewari, and R. S. Gupta, Impact of reverse gate oxide stacking on gate all around tunnel FET for high frequency analog and RF applications, in *2020 IEEE 17th India Council International Conference (INDICON)* (IEEE, 2020), pp. 1–6
11. A. Das, S. Rewari, B.K. Kanaujia, S.S. Deswal, and R.S. Gupta, Ge/Si interfaced label free nanowire BIOFET for biomolecules detection-analytical analysis. *Microelectronics J.* 138, 105832 (2023).
12. A. Das, S. Rewari, B.K. Kanaujia, S.S. Deswal, and R.S. Gupta, Analytical investigation of a triple surrounding gate germanium source metal–oxide–semiconductor field-effect transistor with step graded channel for biosensing applications. *Int. J. Numer. Model. Electron. Netw. Devices Fields* 36, e3106 (2023).
13. A. Das, S. Rewari, B.K. Kanaujia, S.S. Deswal, and R.S. Gupta, Physics based numerical model of a nanoscale dielectric modulated step graded germanium source biotube FET sensor: modelling and simulation. *Phys. Scr.* 98, 115013 (2023).
14. A. Das, S. Rewari, B.K. Kanaujia, S.S. Deswal, and R.S. Gupta, Numerical modeling of a dielectric modulated surrounding-triple-gate germanium-source MOSFET (DM-STGGS-MOSFET)-based biosensor. *J. Comput. Electron.* 22, 742 (2023).
15. K. Baruah and S. Baishya, Numerical assessment of dielectrically-modulated short- double-gate PNPN TFET-based label-free biosensor. *Microelectron. J.* 133, 105717 (2023).
16. P. Kumar and B. Raj, Design and simulation of junctionless nanowire tunnel field effect transistor for highly sensitive biosensor. *Microelectron. J.* 137, 105826 (2023).
17. S.K. Parija, S.K. Swain, S.M. Biswal, S. Adak, and P. Dutta, Performance analysis of gate stack DG-MOSFET for biosensor applications. *SILICON* 14, 8371 (2022).
18. D. Singh and G.C. Patil, Dielectric-modulated bulk-planar junctionless field-effect transistor for biosensing applications. *IEEE Trans. Electron Devices* 68, 3545 (2021).
19. T. Manimekala, R. Sivasubramanian, and G. Dharmalingam, Nanomaterial-based biosensors using field-effect transistors: a review. *J. Electron. Mater.* 51(5), 1950 (2022).
20. H. Mulaosmanovic, E.T. Breyer, S. Dünkel, S. Beyer, T. Mikolajick, and S. Slesazeck, Ferroelectric field-effect transistors based on HfO_2: a review. *Nanotechnology* 32, 502002 (2021).
21. T. Ali, P. Polakowski, S. Riedel, T. Büttner, T. Kämpfe, M. Rudolph, B. Pätzold, K. Seidel, D. Löhr, R. Hoffmann, M. Czernohorsky, K. Kühnel, X. Thrun, N. Hanisch, P. Steinke, J. Calvo, and J. Müller, Silicon doped hafnium oxide (HSO) and hafnium zirconium oxide (HZO) based FeFET: a material relation to device physics. *Appl. Phys. Lett.* 112, 222903 (2018).

22. K.N. Priyadarshani, S. Singh, and M.K.A. Mohammed, Dielectric/charge density modulated junctionless FET based label-free biosensor. *Inorg. Chem. Commun.* 148, 110350 (2023).
23. P. Kaur, A.S. Buttar, and B. Raj, Design and performance analysis of proposed biosensor based on double gate junctionless transistor. *SILICON* 14, 5577 (2022).
24. D. Sen, A. De, B. Goswami, S. Shee, and S.K. Sarkar, Noise immune dielectric modulated dual trench transparent gate engineered MOSFET as a label free biosensor: proposal and investigation. *J. Comput. Electron.* 20, 2594 (2021).
25. A. Goel, S. Rewari, S. Verma, S.S. Deswal, and R.S. Gupta, Dielectric modulated junctionless biotube FET (DM-JL-BT-FET) bio-sensor. *IEEE Sens. J.* 21, 16731 (2021).
26. M. Singh, G. Kumar, S. Bordoloi, and G. Trivedi, A study on modeling and simulation of multiple- gate MOSFETs. *J. Phys. Conf. Ser.* 759, 012093 (2016).
27. A. Rahman, J. Guo, S. Datta, and M.S. Lundstrom, Theory of ballistic nanotransistors. *IEEE Trans. Electron Devices* 50, 1853 (2003).
28. A. D. Gaidhane, G. Pahwa, A. Dasgupta, A. Verma, and Y. S. Chauhan, Compact modeling of negative capacitance nanosheet FET including quasi-ballistic transport, in *2020 4th IEEE Electron Devices Technology & Manufacturing Conference (EDTM)* (IEEE, 2020), pp. 1–4
29. M. Hoffmann, B. Max, T. Mittmann, U. Schroeder, S. Slesazeck, and T. Mikolajick, Demonstration of high-speed hysteresis-free negative capacitance in ferroelectric $Hf_{0.5}Zr_{0.5}O_2$. *Tech. Dig. Int. Electron Devices Meet. IEDM* (2019)
30. Q. Xu, K. Chen, G. Xu, J. Xiang, J. Gao, X. Wang, J. Li, X. He, J. Li, W. Wang, and D. Chen, Physical thickness 1.5-Nm HfZrO negative capacitance nmosfeTs. *IEEE Trans. Electron Devices* 68, 3696 (2021).
31. L. Stucchi-Zucchi, A. R. Silva, and J. A. Diniz, Junctionless-FET device fabrication using silicon etching in NH_4OH solution: device behaviour according to etching time, in *SBMicro 2019 34th Symposium on Microelectronics Technology and Devices*, vol. 2 (2019)
32. A. Dixit, D.P. Samajdar, and V. Chauhan, Sensitivity analysis of a novel negative capacitance FinFET for label-free biosensing. *IEEE Trans. Electron Devices* 68, 5204 (2021).
33. Q.H. Luc, C.C. Fan-Chiang, S.H. Huynh, P. Huang, H.B. Do, M.T.H. Ha, Y.D. Jin, T.A. Nguyen, K.Y. Zhang, H.C. Wang, Y.K. Lin, Y.C. Lin, C. Hu, H. Iwai, and E.Y. Chang, First experimental demonstration of negative capacitance InGaAs MOSFETs with $Hf_{0.5}Zr_{0.5}O_2$ ferroelectric gate stack. *Dig. Tech. Pap. Symp. VLSI Technol.* 2018, 47 (2018).
34. D. S. Software, *Atlas User Manual*, 567 (2019).
35. R. Gautam, M. Saxena, R.S. Gupta, and M. Gupta, Numerical model of gate-all-around MOSFET with vacuum gate dielectric for biomolecule detection. *IEEE Electron Device Lett.* 33, 1756 (2012).
36. S.I. Amin, L. Gajal, and S. Anand, Analysis of dielectrically modulated doping-less transistor for biomolecule detection using the charge plasma technique. *Appl. Phys. A Mater. Sci. Process.* 124, 1 (2018).
37. A. Chattopadhyay, S. Tewari, and P.S. Gupta, Dual-metal double-gate with low-k/high-k oxide stack junctionless MOSFET for a wide range of protein detection: a fully electrostatic based numerical approach. *SILICON* 13, 441 (2021).
38. S.A. Hafiz, Iltesha, M. Ehteshamuddin, and S.A. Loan, Dielectrically modulated source-engineered charge-plasma-based Schottky-FET as a label-free biosensor. *IEEE Trans. Electron Devices* 66, 1905 (2019).
39. A. Chakraborty and A. Sarkar, Analytical modeling and sensitivity analysis of dielectric-modulated junctionless gate stack surrounding gate MOSFET (JLGSSRG) for application as biosensor. *J. Comput. Electron.* 16, 556 (2017).
40. S. Rashid, F. Bashir, F.A. Khanday, and M.R. Beigh, L-Shaped high performance Schottky barrier FET as dielectrically modulated label free biosensor. *IEEE Trans. Nanobiosci.* 21, 542 (2022).

Publisher's Note Springer Nature remains neutral with regard to jurisdictional claims in published maps and institutional affiliations.

Springer Nature or its licensor (e.g. a society or other partner) holds exclusive rights to this article under a publishing agreement with the author(s) or other rightsholder(s); author self-archiving of the accepted manuscript version of this article is solely governed by the terms of such publishing agreement and applicable law.

This article has been accepted for publication in IEEE Sensors Journal. This is the author's version which has not been fully edited and content may change prior to final publication. Citation information: DOI 10.1109/JSEN.2024.3354113

GSMD-SRST: Group Sparse Mode Decomposition and Superlet Transform Based Technique for Multi-Level Classification of Cardiac Arrhythmia

Shikha Singhal, *Manjeet Kumar*, *Member, IEEE*

***Abstract*—** Cardiac arrhythmia is caused due to the irregularity of the heartbeat, and heart rhythm, which increases the complications leading to the risk of heart strokes. Atrial fibrillation and ventricular fibrillation are the most prevalent cardiac arrhythmia. Timely and precise detection of arrhythmia reduces mortality rates which are essential to prevent various heart diseases. The proposed framework utilizes the Group Sparse Mode Decomposition (GSMD) technique for decomposing the non-stationary ECG signals into the intrinsic mode functions (IMFs). Then, the super-resolution technique is applied to obtain frequency domain spectrograms corresponding to IMFs of the input electrocardiogram (ECG) record. The SLT is a high-resolution technique used to reshape the 1D ECG signal into a 2D ECG signal. The spectrograms obtained through SLT, are fed to the deep neural networks for arrhythmia classification. ECG records are fetched from different databases like MIT-BIH arrhythmia, MIT-BIH malignant ventricular ectopy, MIT-BIH CU ventricular tachyarrhythmia, MIT-BIH atrial fibrillation and Mendeley-II dataset. Different deep neural models like VGG19, RESNET-18, GoogleNet, and AlexNet are used for the classification of arrhythmia from the ECG signals. The proposed method with VGG19 shows the best results with an overall accuracy of 98.2% on physionet dataset whereas, for the combined dataset (Physionet+Mendely-II), the proposed model achieved an accuracy of 99.2% using GoogleNet. The classification is done between healthy heart, atrial fibrillation, and ventricular fibrillation. The proposed system minimizes the overall intricacy as it reduces the requirement of an extra step for noise removal and peak detection.

***Index Terms*—** Group Sparse Mode Decomposition, SLT, Deep Neural Networks, Arrhythmia classification, Electrocardiogram.

I. INTRODUCTION

Cardiovascular disease (CVD) is an immense destroyer of human health. Due to an unanticipated and high possibility of CVD, it is required to monitor and examine the electrocardiogram (ECG) signals to detect heart disease efficiently and effectively [1]. Handling the ECG data manually reflects a time-consuming process. To overcome this, an automatic classification of ECG data is a well-organized way to conduct and detect the disease early to avoid any mishap. An arrhythmia is one of the features of CVD that shows an irregularity in heartbeat or rhythm. As an important ceaseless disease, CVD can be caused by the accumulative effects of tobacco usage, deleterious diet, and inadequate physical activities that degrade the overall health status [2]. Regular monitoring is required to reduce the probability of heart disease to some extent. However, some wearable devices like bands and watches can be implemented to avoid any calamity at an early stage. To recognize the irregularities in ECG signals, arrhythmia detection regulates the classification process using ECG signals and helps to determine the occurrence of the disease [3]. Various noises of ECG signal like power line interference, baseline wander, and others deteriorate the performance of the overall system, therefore, some denoising techniques can be implemented to minimize the effect and upgrade the efficacy of the system. In [4], the generative module is used to convert the 1D data to the 2D image which is then fed to the dense convolutional networks for classification purposes. In [5], ECG classification belonging to five classes of heartbeat is done using 2D convolutional neural network (CNN), after generating the spectrograms by implementing short-time Fourier transform (STFT), which calculates the Fourier spectra on consecutive sliding windows. In [6], spiking neural networks are applied for the real-time operation of ECG classification. In [7], introduced a probabilistic process neural network for multi-channel time-varying signal classification using a SoftMax classifier. Several schemes of deep learning have been put forward to manage the arrhythmia classification [4]-[7]. Here, the main focus is on the decomposition techniques to decompose the non-stationary ECG signals effectively and can be utilized for further processing. The most prevalent method is empirical mode decomposition (EMD), used to decompose the ECG signal into intrinsic mode functions (IMFs) [8] resulting in the recursive sifting scheme. There is an issue of mode mixing or mode splitting in EMD which causes uncertainty in explaining the acquired modes. To deteriorate the effects of mode mixing or mode splitting and end effects, compact EMD (CEMD) is introduced in [9]. The decomposition of noise signals in successive variational mode decomposition (SVMD) [10] results in the extraction of extra signals that leads to the generation of excess noise, due to which SVMD suffers from mode splitting of wideband modes. Above all, to analyze the non-linear data, a set of a small number of band-limited Fourier Intrinsic Band Functions (FIBFs) is generated by a Fourier Decomposition Method (FDM) [11]. A detailed discussion of decomposition techniques for non-linear ECG signals is given in [8]-[11]. As Fourier analysis is not the best method for decomposition, so, for accurate results, the group sparse mode decomposition (GSMD) technique [12] is

S. Singhal is with the Delhi Technological University, Delhi- 110042, India. (e-mail: ggshikha12@gmail.com).

M. Kumar, is with the Delhi Technological University, Delhi, 110042, India. (e-mail: manjeetchhillar@gmail.com).

Authorized licensed use limited to: DELHI TECHNICAL UNIV. Downloaded on February 07,2024 at 06:07:56 UTC from IEEE Xplore. Restrictions apply.
© 2024 IEEE. Personal use is permitted, but republication/redistribution requires IEEE permission. See https://www.ieee.org/publications/rights/index.html for more information.

This article has been accepted for publication in IEEE Sensors Journal. This is the author's version which has not been fully edited and content may change prior to final publication. Citation information: DOI 10.1109/JSEN.2024.3354113

evolved where IMFs are estimated utilizing a set of ideal filters in the frequency domain. The idea of this paper comes with the development of a research area in the detection and classification of arrhythmia is as follows:

1) The GSMD technique is employed to decompose the non-stationary ECG signal into a set of basic function, IMFs and employs a set of ideal filters with the weighted l_0 norm as a penalty term to develop an efficient model.
2) A high-resolution technique, SLT is applied for denoising purposes, detection of QRS complexes, and to transform the non-linear data into 2D time-frequency representation that will be useful for arrhythmia detection and classification.
3) A combination of GSMD with SLT on physionet and the combined dataset (physionet + Mendeley-II) is proposed to categorize the ECG data into Healthy Heart, CU Ventricular, and Atrial Fibrillation classes.
4) Deep neural network models (VGG19, RESNET-18, GoogleNet, and AlexNet) are implemented on transformed signals for arrhythmia classification.

The paper is structured into the following sections: Section II commences with an introduction to the GSMD technique with the mathematical background involved and a brief of the Superlet transform. In Section III, the proposed work, the database, and the overall process involved in arrhythmia classification are discussed. Section IV elaborates on the analysis of existing decomposition techniques, and the results corresponding to the proposed technique. The conclusion with the future scope is discussed in Section V.

II. Description of GSMD and SLT

A. Group Sparse Mode Decomposition Technique

A method based on the decomposition of non-linear signals is utilized, resulting in the generation of intrinsic mode functions, which have a smaller bandwidth, and the frequency bands of IMFs are displaced from each other. It has been proposed to calculate the IMFs using a set of ideal filters and utilizing the weighted penalty l_0-norm. On the basis of energy detection over short windows, weighting parameters and regularization parameters are calculated. A non-linear signal $z(t)$ is represented in this script [12] utilizing the equation

$$z(t) = p(t) + q(t), \qquad t = 1, \ldots . N \tag{1}$$

Here, N denotes the count of samples, $q(t)$ shows the additive white noise with variance σ_v^2 having zero mean, and $p(t)$ is a non-linear signal comprised of a set of F basis functions, termed as intrinsic mode function [13], IMFs represented by

$$\{h_f(t)\}_{f=1}^{F}, \text{ i.e } p(t) = \sum_{f=1}^{F} h_f(t), \quad t = 1, \ldots . N \tag{2}$$

Here, $\tau(.)$ has been chosen as the Discrete Cosine Transform (DCT) [14]. DCT is used due to a property of energy compaction and deals with reflective boundary conditions that help to remove the artifacts during the analysis of the signal as compared to the DFT [15]. The coefficients of DCT are real-valued as compared to DFT which is normally complex. Mentioning $\tau(.)$, a linear transformation on eq. (1) and (2), we obtain the corresponding calculation in the frequency domain,

$$d_z = d_p + d_q = \sum_{f=1}^{F} d_{h_f} + d_q \tag{3}$$

where the DCT coefficients of d_z, d_p, d_q, and d_{h_f} are $d_z \in S^N, d_p \in S^N, d_q \in S^N$, and $d_{h_f} \in S^N$ respectively. Referring $R_f \subset [1, \mathrm{N}]$ as a support to d_{h_f} represent the indices of non-zero entries and the total of indices in R_f is shown by $|R_f|$. The mode $h_f(t)$ is primarily estimated as

$$\widehat{h_f}(t) = \tau^{-1}(r_f \circ d_z), f = 1, \ldots . F, \tag{4}$$

where $\circ$ shows the Hadamard product (multiplication of element to element) and the DCT coefficient vector of an ideal filter is r_f mentioned as $r_f[i] = \begin{cases} 1, & i \in R_f \\ 0, & \text{otherwise} \end{cases}$

From eq. (3) and (4), the estimated value of d_p is discussed as

$$\widehat{d_p} = \sum_{f=1}^{F} d_{h_f} = \sum_{f=1}^{F} d_z \circ r_f = d_z \circ r \tag{5}$$

where $r := \sum_{f=1}^{F} r_f = \begin{cases} 1, & i \in R_f \\ 0, & \text{otherwise} \end{cases}$ and the support of d_p is $R := \bigcup_{f=1}^{F} R_f$.

It is recommended to calculate the estimated value of the general filter r as an ideal filter which reduces $\left\| d_z - \widehat{d_p} \right\|_2^2 = \| d_z - d_z \circ r \|_2^2$ with the limitation that r is an on-off group sparse vector that comprises zeros and ones, where ones tend to focus in clusters. Every single filter r_f can be approximated as a category of contiguous samples in r, in total, they are equal to one. With this, an estimated number of modes F can be done directly with the number of groups r and the bandwidth of each filter r_f is modified accordingly.

By resolving the optimum value, it is recommended to evaluate the ideal filter bank r, is defined as

$$\hat{r} = arg \min_{r} \tau(r) := \| d_z - d_z \circ r \|_2^2 + \lambda \| r \|_{o,w} \tag{6}$$

where λ denotes the regularization parameter, that limits the trade-off between accuracy of the regular data, recorded by $(\| d_z - d_z \circ r \|_2^2)$ and the on-off group sparsity of the filter bank calculated by the weighted l_0 norm, $(\| r \|_{o,w} := \sum_{i=1}^{N} w_i \pi_{\{r_i\}})$ and a group of positive weighting conditions is denoted by $\{w_i\}$. The value of λ is chosen wisely for attaining the desired outcome of the filtered signal. Some of the key features of GSMD are discussed.

- To observe the presence of IMFs in the frequency domain, the opinion of group sparsity was applied.
- To strengthen the on-off group sparsity of the ideal filters, utilized the weighted l_0-norm as a penalty term.
- Based on the energy concentration of every single IMF, bandwidth is automatically modified by selecting the weighting parameters.

B. Superlet Transform

A super-resolution technique, SLT [16] can be defined by a Morlet wavelet representing the multiplication of plane waves with a Gaussian envelope. The normalization constant of the Morlet wavelet is used to remove its mean and becomes negligible when the wavelet is broad. It is suggested to merge Fourier-based spectrograms acquired with the varying lengths of the window, and the technique was named "Super-resolution" because it can localize oscillation packets in both time and frequency simultaneously. To upgrade the resolution, various spectrograms are merged by calculating their Geometric Mean which is analogous to the Minimum Mean Cross-Entropy (MMCE). The QRS complex detection and application of SLT in various research areas is discussed in

Authorized licensed use limited to: DELHI TECHNICAL UNIV. Downloaded on February 07,2024 at 06:07:56 UTC from IEEE Xplore. Restrictions apply.
© 2024 IEEE. Personal use is permitted, but republication/redistribution requires IEEE permission. See https://www.ieee.org/publications/rights/index.html for more information.

This article has been accepted for publication in IEEE Sensors Journal. This is the author's version which has not been fully edited and content may change prior to final publication. Citation information: DOI 10.1109/JSEN.2024.3354113

detail in [17]-[21].

III. Proposed Work

In this article, the GSMD algorithm is utilized to break down the non-stationary ECG signals into IMFs, which have finite bandwidth and the frequency bands are disjoint. IMFs are calculated using a set of ideal filters with a weighted penalty term. The two datasets are used in the study to demonstrate the robustness, reliability, and efficiency of the proposed algorithm. The first dataset is fetched from the physionet and the second dataset is the combination of the physionet and the Mendeley-II dataset. The data is categorized into three classes, Healthy (Normal), AF (Atrial Fibrillation), and VF (Ventricular Fibrillation). Initially, segmentation is performed on the records of both the datasets and segmented into a 10-second duration. The obtained signal is then applied to the GSMD algorithm that generates several decomposition levels. Various combinations are made on these levels to obtain the noiseless data which is used further for transforming the time domain signal into a time-frequency (TF) energy spectrogram. A high-resolution technique, Superlet is applied which is a combination of Fourier-based spectrograms acquired with a long and short window, or with a set of windows of different sizes [16].

It is used to convert the 1D ECG signals into 2D energy diagrams and the resolution of an obtained image is increased after combining the multiple spectrograms by calculating their geometric mean, which is identical to the minimum mean cross entropy. With these representations, the details on time, frequency, and energy characterization related to arrhythmia diseases are evaluated. The obtained spectrograms are then fed to the deep neural network for arrhythmia detection and classification. A multilevel classification is performed which classifies the data into multiple classes, Healthy, AF, and VF. A few points are mentioned as follows.

(i) The requirement of an extra denoising step of pre-processing is eliminated by the use of SLT after decomposition by GSMD. The noise including the baseline drift, electrode motion artifacts, and powerline interference is suppressed which reduces the overall complexity and increases the efficiency.

(ii) The dislocation of ECG peaks is recovered, thus, the detection of QRS complexes is fulfilled by the use of SLT.

The implementation of GSMD+SLT generates the spectrograms from calculated IMFs is described in Algorithm 1. The computational complexity of the method describes the number of resources required to run it. The time complexity of the methods is discussed in Table 1. The various steps involved in arrhythmia classification are represented in Fig 1. which shows the data acquisition, segmentation of ECG records, implementation of GSMD+SLT followed by the classification using deep neural networks. From the literature, it is noted that the non-linear ECG signal shows the occurrence of noisy data mixed with the original signal, due to which there are more chances of missing out of QRS peaks. To verify the existence of several peaks at specific points, a frequency spectrum is calculated of every individual intrinsic mode.

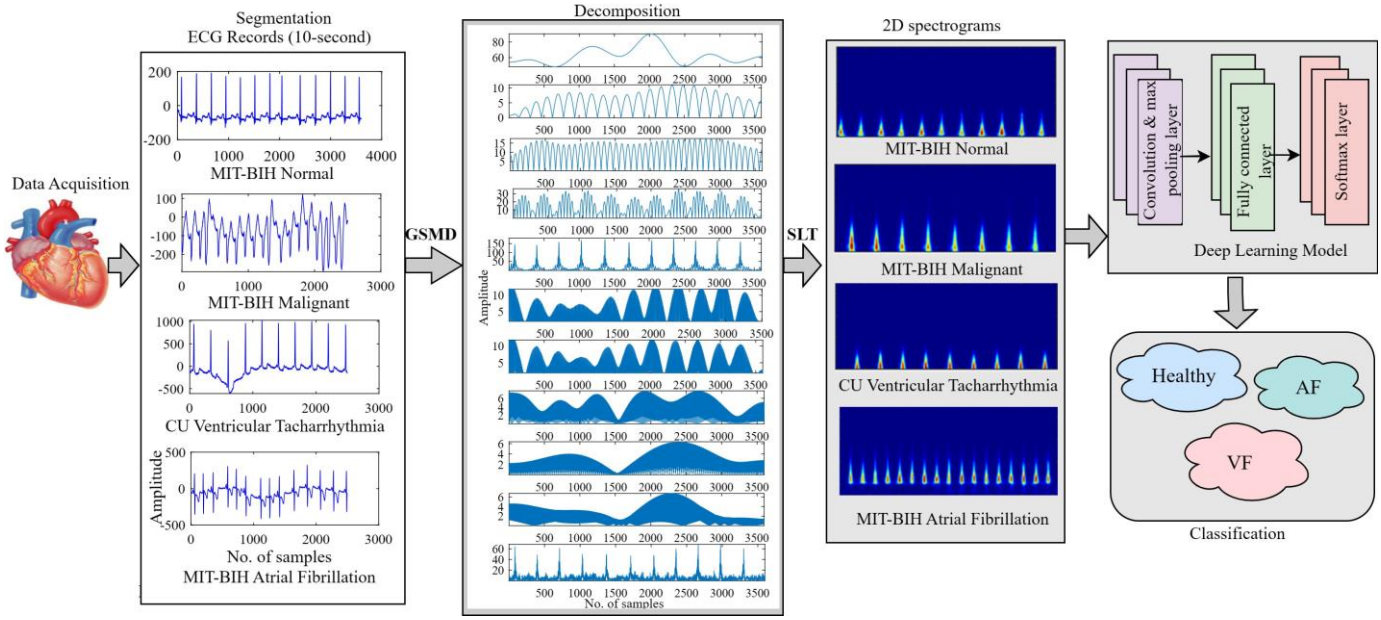


Fig 1. The proposed method GSMD+SLT for arrhythmia classification using deep neural networks

Algorithm 1: The proposed technique GSMD with SLT for decomposition and denoising of ECG signal

START program; LOAD ECG data

INITIALISE function GSMD

For $k = 1 : k_{max}$

Calculate $g = \frac{1}{B_t}\sum_{t-b_t^k}^{t+b_t^k} d_z^2[\tau]$ where $B_t = 2b_t^k + 1$

Evaluate $\lambda = \left(\frac{2\widehat{\sigma_v}^2}{B_t}\right) \Gamma^{-1}\left(\frac{B_t}{2}, \alpha\Gamma\left(\frac{B_t}{2}\right)\right)$

Update $r_t^k := \begin{cases} g > \lambda, r_t^k = 1 \\ r_t^k = 0, otherwise \end{cases}$

Update k: $k_t = kurtosis(d_z[t - b_t^k : t + b_t^k])$

Adjust $r^k, d_z^2, \widehat{\sigma_v}^2, \alpha$

CONSTRUCT the f ideal filter r_f; Set $r_f = 0$, update $r_f = 1$

Construct the DCT coefficient vector of

$\widehat{h_f}(t)$: $\widehat{d_{h_f}} = r_f \circ d_z$

FORMULATE the matrix of IMFs

Authorized licensed use limited to: DELHI TECHNICAL UNIV. Downloaded on February 07,2024 at 06:07:56 UTC from IEEE Xplore. Restrictions apply.
© 2024 IEEE. Personal use is permitted, but republication/redistribution requires IEEE permission. See https://www.ieee.org/publications/rights/index.html for more information.

This article has been accepted for publication in IEEE Sensors Journal. This is the author's version which has not been fully edited and content may change prior to final publication. Citation information: DOI 10.1109/JSEN.2024.3354113

$H \in S^{\hat{F}\times N}: H = [\widehat{h_1}(t); \widehat{h_2}(t); \ldots..; \widehat{h_{\hat{F}}}(t)]$
CONSTRUCT the denoised signal: $\hat{p}(t) = \sum_{f=1}^{\hat{F}} \widehat{h_f}\,(t)$
INITIALISE function SLT.
Calculate the response of SL, $R[SL_{f,o}] = \sqrt[o]{\prod_{i=1}^{o} R[\Psi_{f,s_i}]}$
INITIALISE frequency resolution ranges from [10 to 90] CALCULATE Geometric Mean and the wavelet coefficient of the revised spectrogram of individual wavelets.

Table 1. The Computational Complexity of the proposed method GSMD+SLT

(i) Kurtosis: TC$(k\bar{v}) = 4nADD + 2nMUL + 2DIVI$
n → number of samples, k→ number of iterations.
ADD → Addition; MUL→ Multiplication
DIVI→ Division; COMP → Comparison
Variance: $TC(\widehat{\sigma_v^2}) = 3nADD + nMUL + 2DIVI$
(ii) Total time-complexity of GSMD
$\cong [11k + 4\hat{J} + 4 + (7M_l + 12L_{max} + 20).k_{max}).n]$
$\boldsymbol{TC \cong (7M_l + 12L_{max} + 20).k_{max}.n}$
k_{max}→ the maximum number of iterations
L_{max} → maximum number of blocks used in filter bank.
$\hat{J}$ → the number of estimated IMFs,
$M_l := 2m_l + 1$, where m_l is the largest value of m.
Time-complexity of SLT:
(i) Morlet wavelet complexity:
$\boldsymbol{TC = (4n + 6)MUL + (4n + 2)ADD}$,
n→ the shaping factor in Morlet wavelet.

From the above characterization, it has been shown that GSMD with SLT demonstrates a better result that can be seen in a 2D image in all the cases. The various steps involved in the overall process of classification are represented in Fig 2.

A. DATABASE

In this manuscript, two datasets are utilized for experimentation. The first dataset is taken from physionet [22] and the second is the combined dataset created from (Physionet+Mendeley-II). The MIT-BIH Atrial Fibrillation [23], MIT-BIH Malignant Ventricular Ectopy [24], CU Ventricular Tachycardia [25], and MIT-BIH Arrhythmia [26] are the supreme databases utilized for decomposition, denoising, and classification of ECG signals, available at physionet. The ECG recordings taken from the above databases are attainable at some sampling frequency and resolution. In the physionet dataset, CU Ventricular and Malignant are combined for efficient classification results.

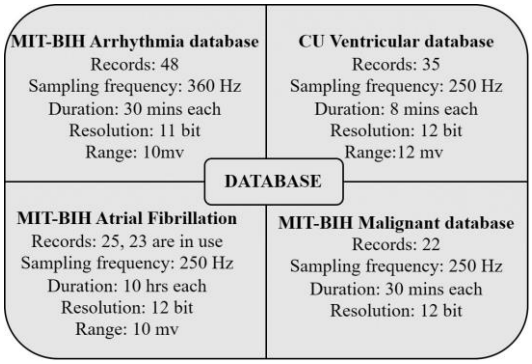
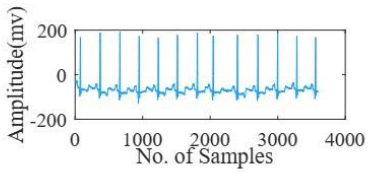
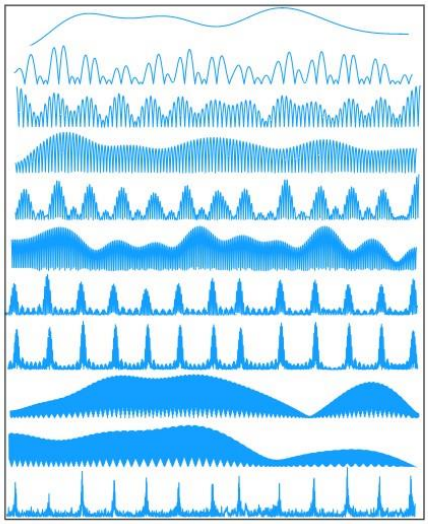


Fig 3. Summary of the Physionet database used for decomposition, denoising, and classification of ECG signal

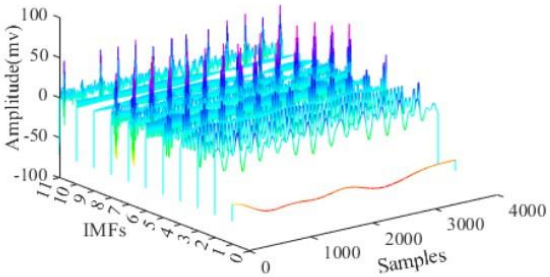
The same classes have been fetched from the Mendeley-II [27] dataset for experimentation on the combined dataset. The physionet database used in the study is mentioned in Fig 3 along with the features of the database. The dataset of Mendeley-II is collected from 45 patients of 10-second duration and only lead II is utilized to measure the records.



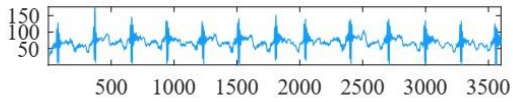
(a) MIT-BIH arrhythmia of record 100



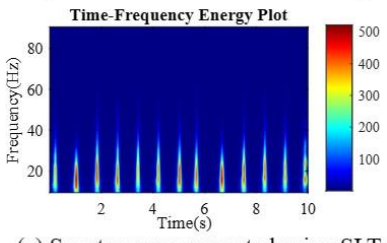
(b) Decomposition levels obtained by GSMD



(c) Representation of IMFs in 3D



(d) Denoised signal after combination of decomposition levels



(e) Spectrogram generated using SLT

Fig 2. (a) The uppermost panel reflects the noisy ECG signal of record 100 from MIT-BIH arrhythmia database. (b) Depicts the IMFs generated from GSMD. (c) A 3D view of IMFs is shown. (d) Depicts a denoised signal estimated from different combinations of IMFs. (e) 2D spectrogram generated from SLT.

Authorized licensed use limited to: DELHI TECHNICAL UNIV. Downloaded on February 07,2024 at 06:07:56 UTC from IEEE Xplore. Restrictions apply.
© 2024 IEEE. Personal use is permitted, but republication/redistribution requires IEEE permission. See https://www.ieee.org/publications/rights/index.html for more information.

This article has been accepted for publication in IEEE Sensors Journal. This is the author's version which has not been fully edited and content may change prior to final publication. Citation information: DOI 10.1109/JSEN.2024.3354113

A. *Classification Techniques*

VGG19: A convolution neural network, CNN commenced in 2014 by Simonyan and Zisserman [28], comprises 19 layers in which 16 convolutional layers are adequate to extricate the features with three fully connected layers, used to label the images into 1000 object classes and infused on the database of ImageNet [29]. It is an appropriate method for image classification by utilising 3×3 kernels and a stride size of 1 pixel in each convolutional layer, shown in Fig 4. The five max-pooling layers are placed between the 16 feature layers which are divided into different groups and the final layer is equivalent to a SoftMax layer. To identify the image, an RGB input image of size 224×224 is applied to the model, shows the matrix of shape $(224 \times 224 \times 3)$.

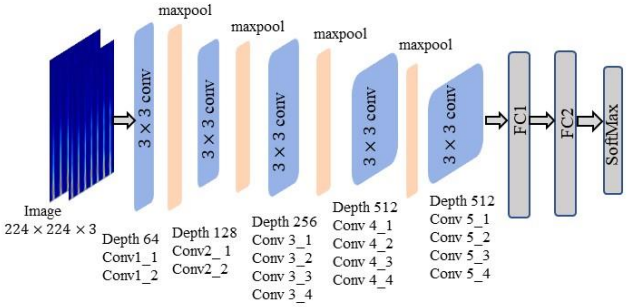


Fig 4. Representation of VGG19 architecture

RESNET-18: The CNN emphasizes millions of images from the ImageNet database. The input image of 224×224 size is applied at the input terminal, and a skip connection is maintained after the first layer [30]. The connection between input and output is obtained by 2 convolutional sheets each of 64 kernels with size 3×3, showing the first residual block is shown in Fig 5. The third block consists of the output of the second block through a skip connection and the output of two convolutional layers with a 3x3 filter size and 256 filters. The final block includes the 512 filters with convolutional layer output through a skip connection. In the last stage, average pooling is executed on the output, applied the fully connected layers followed by the SoftMax layer to attain the desired outcome.

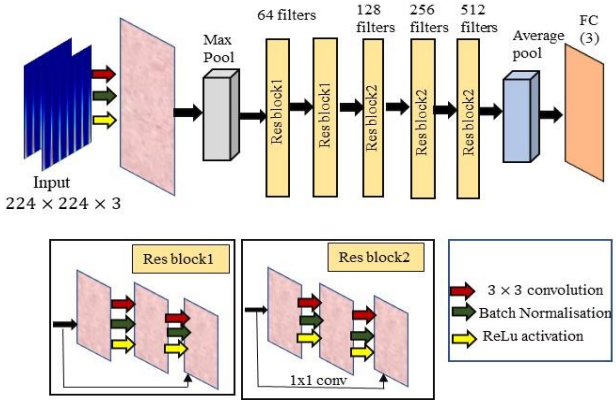


Fig 5. Representation of RESNET-18 architecture

GoogleNet: It is a 22-layered structure based upon the Inception architecture [31]. It utilizes distinct techniques like global average pooling and 1x1 pooling to enhance the architecture. The deep CNN, Inception is introduced at the 2014 ImageNet Large Scale Visual Recognition Challenge (ILSVRC14). The auxiliary classifiers used in training have an average pooling layer of 5×5 filter size and a stride of 3. The input is passed through the normalization layer, max pooling layer to reach the second convolutional layer. The same procedure is followed by the remaining layers and the output is obtained from SoftMax layer.

AlexNet: The CNN is designed to categorize 1.2 million images in the ImageNet LSVRC-2010 into 1000 different classes [32]. The architecture consists of five convolutional layers followed by two fully connected layers and a SoftMax layer of 1000 as an object as output. The size of an input image is $227 \times 227 \times 3$ applied to the input of the convolutional layer with a stride of four.

IV. Results and Discussion

In the study, the arrhythmia classification is being performed and categorized into three distinct classes, Healthy, AF, and VF, by utilizing the Physionet dataset and the combined dataset (Physionet+Medeley-II). The evaluation parameters like accuracy, sensitivity, specificity, precision, and F1-score are calculated using the formulas as given in eq. (7) to (11).

$$acc.(\%) = \left(\frac{Tp + Tn}{Tp + Tn + Fp + Fn}\right) \times 100 \tag{7}$$

$$sen.(\%) = \left(\frac{Tp}{Tp + Fn}\right) \times 100 \tag{8}$$

$$spe.(\%) = \left(\frac{Tn}{Tn + Fp}\right) \times 100 \tag{9}$$

$$pre.(\%) = \left(\frac{Tp}{Tp + Fp}\right) \times 100 \tag{10}$$

$$F1 - sc(\%) = \left(\frac{2 \times pre. \times sen.}{pre. \times sen.}\right) \times 100 \tag{11}$$

The accurate classification of the positive class is referred as True positive Tp; True negative Tn represents that the class is correctly classified as negative; wrong classification of positive class is denoted by False positive Fp; and the False negative Fn shows the misclassification of negative class. Here, the existing decomposition methods (EMD and FDM) using SLT are compared with the proposed method GSMD+SLT and depicted in Fig 6. In the study, the count of 2214 images using physionet dataset is generated from SLT where each class contains 738 images of which 15% is used for validation. For testing purposes, a set of 147 images is preserved separately. The count of 615 images is generated using combined dataset (Physionet+Mendeley-II) where each class has 165 training images and 40 images are used for testing purposes. Several iterations are performed on the hyperparameters (optimizer, learning rate, number of epochs, mini-batch size) of the deep learning models to attain the higher classification results. From the study, it has been observed that the best results of arrhythmia classification acquired from VGG19 with an accuracy of 98.2% using Stochastic gradient descent optimizer under 60 epochs with learning rate 10^{-5} having a loss of 0.07 and a batch size of 32. The generated 2D signal is fed to the deep neural networks, VGG19, RESNET-18, GoogleNet, and

Authorized licensed use limited to: DELHI TECHNICAL UNIV. Downloaded on February 07,2024 at 06:07:56 UTC from IEEE Xplore. Restrictions apply.
© 2024 IEEE. Personal use is permitted, but republication/redistribution requires IEEE permission. See https://www.ieee.org/publications/rights/index.html for more information.

This article has been accepted for publication in IEEE Sensors Journal. This is the author's version which has not been fully edited and
content may change prior to final publication. Citation information: DOI 10.1109/JSEN.2024.3354113

AlexNet for the acute classification results, out of which VGG19 and RESNET-18 shown the best results for physionet dataset whereas the proposed method GSMD+SLT using GoogleNet shows the highest accuracy for combined dataset.

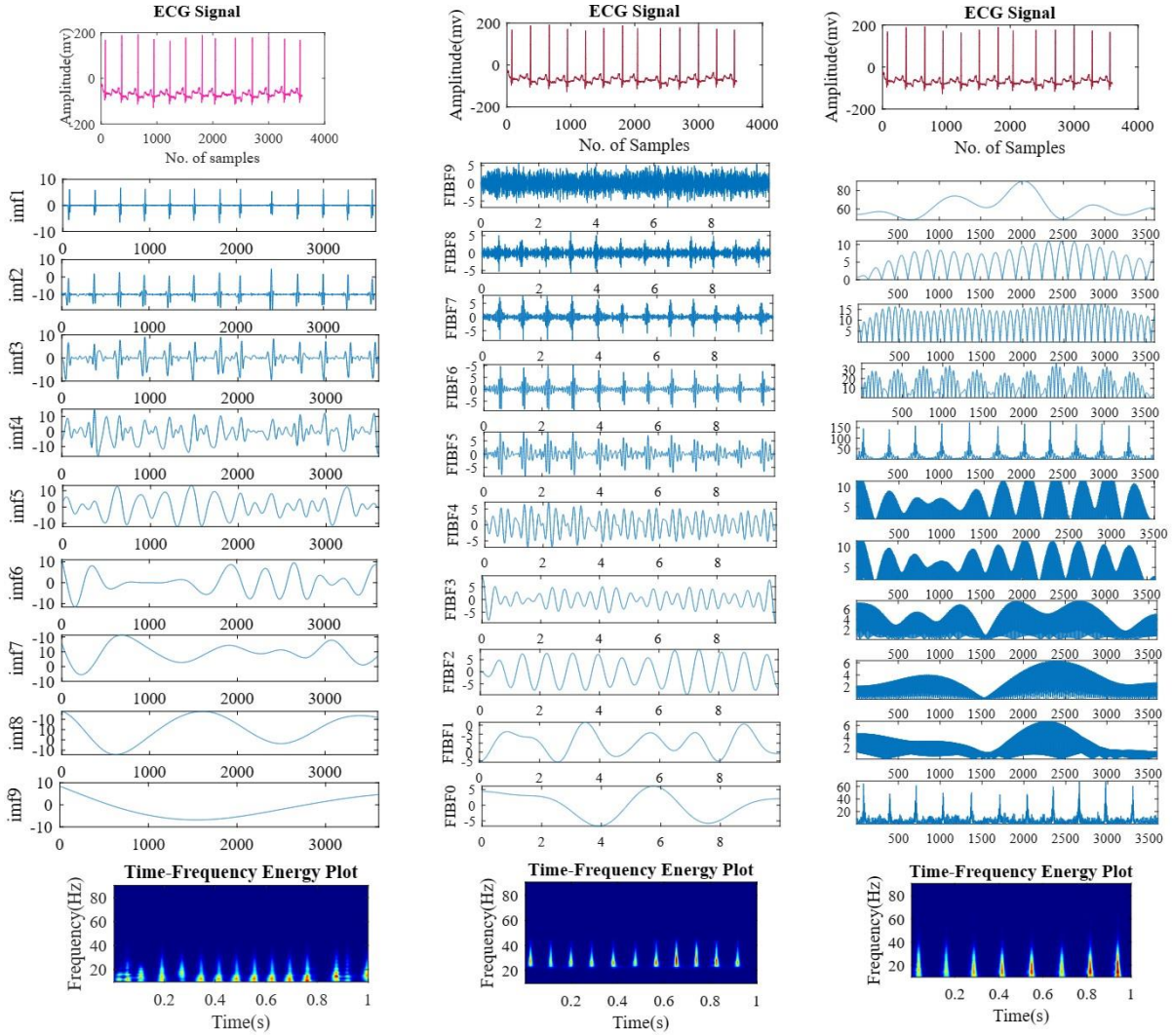


Fig 6. (a) The decomposition levels with the corresponding spectrogram are shown by implementing EMD and SLT on MIT-BIH Arrhythmia record-100 respectively. (b) FDM is applied to an ECG signal generates the perfect oriented intrinsic band functions, FIBFs, and correspondingly energy graph is plotted. (c) The GSMD technique reflects the different intrinsic mode functions with high-resolution 2D image transformed by SLT.

As per the size of necessity of the model, the images of the dataset are rescaled to $224 \times 224 \times 3$. The multilevel classification is done between classes Healthy, AF, and VF. The confusion metrics allow the visualization of the performance of an algorithm for classification. The confusion metrices of validation and testing records using VGG19 on physionet dataset is shown in Fig 7. It is noticed that 142 images corresponding to 32.3% are correctly classified as AF, whereas 3 images of Healthy section are wrongly named as AF. 144 and 146 images are accurately categorized as Healthy and VF respectively. The next model RESNET-18 achieved the validation and testing accuracy of 95.1% and 98% respectively on physionet dataset shown in Fig 8. It is noted that 141 images are accurately classified as AF signifies to 32%, and 2 images of Healthy class are wrongly categorized as AF.

A count of 145 images is perfectly classified as Healthy and AF both. The multiclassification is performed on the combined dataset using various deep learning models (RESNET-18, AlexNet, VGG19, and GoogleNet) out of which GoogleNet performed best with validation and testing accuracy of 98.0% and 99.2% respectively. The confusion metrics obtained using GoogleNet on the combined dataset is reported in Fig 9. The comparison between the proposed method GSMD+SLT on both datasets (Physionet and combined dataset) and the existing decomposition methods of non-linear signals are reported in Table 2. that achieved the accuracy, sensitivity, and specificity of 98.2%, 98.1%, and 99.09%, respectively using VGG19 on physionet dataset. The performance is also measured on the combined dataset using GoogleNet, attained an accuracy of 99.2%. The FDM+SLT shows an accuracy of 97.3% on VGG19 which is better than the existing FDM technique.

The performance of the proposed method GSMD+SLT on both datasets using deep learning models is represented by histogram in Fig 10. A performance comparison of Atrial Fibrillation is reported between the proposed method and the existing methods on the physionet dataset discussed in Table 3. The highest accuracy of 98.18% is achieved on VGG19, RESNET-18, and AlexNet. The other evaluation parameters (sensitivity,

Authorized licensed use limited to: DELHI TECHNICAL UNIV. Downloaded on February 07,2024 at 06:07:56 UTC from IEEE Xplore. Restrictions apply.
© 2024 IEEE. Personal use is permitted, but republication/redistribution requires IEEE permission. See https://www.ieee.org/publications/rights/index.html for more information.

This article has been accepted for publication in IEEE Sensors Journal. This is the author's version which has not been fully edited and content may change prior to final publication. Citation information: DOI 10.1109/JSEN.2024.3354113

specificity, precision, and F1-score) are also mentioned. Table 4 represents the comparison of the proposed method with the existing ones for the detection of Ventricular Fibrillation on physionet dataset. The value of specificity is 100%, 99.6%, 98.9%, and 100% obtained using VGG19, RESNET-18, GoogleNet, and AlexNet respectively. The AlexNet and GoogleNet performed better in terms of precision. The simulation results of proposed method using VGG19 and RESNET-18 on physionet dataset are listed in Table 5.

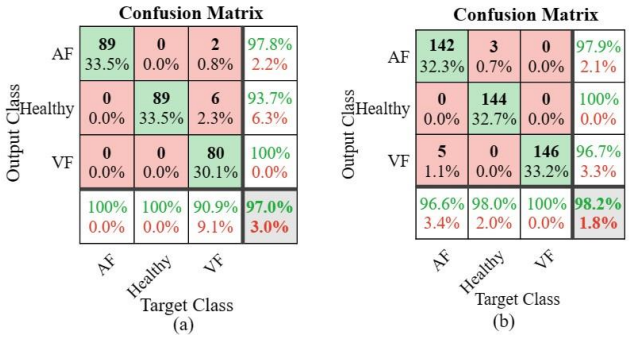


Fig 7. (a) The confusion metrics of validation accuracy using VGG19 (b) The confusion metrics of test accuracy using VGG19 on the physionet dataset

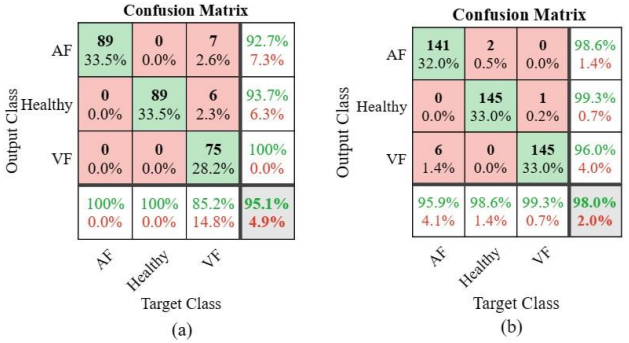


Fig 8. (a) The confusion metrics of validation accuracy using RESNET-18. (b) The confusion metrics of test accuracy using RESNET-18 on physionet dataset.

The highest value of 100% sensitivity is recorded in case of healthy class. Table 6 represents the comparison in multilevel classification between the proposed and the existing methods. The highest accuracy of 98% and 99.2% is achieved with GSMD+SLT+VGG19 on physionet dataset and GSMD+SLT+GoogleNet on combined dataset respectively. The various existing methods with multilevel classification are listed in Table 6.

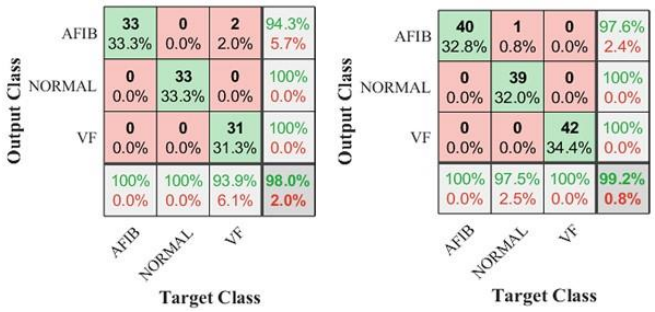


Fig 9. (a) The confusion metrics of validation accuracy using GoogleNet. (b) The confusion metrics of test accuracy using GoogleNet on combined dataset

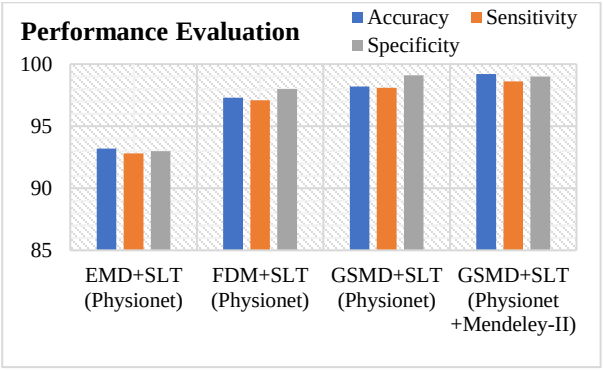


Fig 10. The performance of the proposed method (GSMD+SLT) on both datasets with existing methods

Table 2. Summary of various existing decomposition techniques with the proposed method (GSMD+SLT) on both datasets.

Author	Dataset	Method	Class	Acc(%)	Sen (%)	Spec (%)
Setiawan and Lin (2022) [33]	Physionet Apnea ECG	EMD+SMOTE+ 1D CNN	2	91.8	91	92.6
Proposed	**Physionet**	**EMD+SLT**	**3**	**93.2**	**92.8**	**93**
Kumar et al. (2020) [34]	Physionet	FDM+Support Vector Machine	2	99.5	NR	NR
Proposed	**Physionet**	**FDM + SLT**	**3**	**97.3**	**97.1**	**98**
Proposed	**Physionet**	**GSMD + SLT + VGG19**	**3**	**98.2**	**98.1**	**99.09**
Proposed	**Combined (Physionet+ Mendeley-II)**	**GSMD+SLT+ GoogleNet**	**3**	**99.2**	**98.6**	**99**

Table 3. The performance comparison between the proposed method with existing methods for Atrial Fibrillation on physionet dataset.

Author	Method	Acc (%)	Sen (%)	Spec (%)	Prec (%)	F1-sc (%)
Tripathi et al. (2022) [17]	SLT+ DenseNet – 201	97.1	100	95.7	92.1	95.8
Mathunjwa et al. (2021) [35]	Recurrent plot + CNN	86.97	86.79	NA	73.61	79.65
Lai et al. (2020) [36]	Patch-based lead + CNN	93.1	93.1	93.4	NA	NA
Dang et al. (2019) [37]	CNN-BLSTM	96.59	99.93	97.03	NR	NR
Fan et al. (2018) [38]	MS-CNN	97.19	80.26	98.84	87.14	88.78
Proposed Method	**GSMD+SLT+ VGG19**	**98.18**	**97.93**	**98.30**	**96.59**	**97.32**
Proposed Method	**GSMD+SLT+ RESNET-18**	**98.18**	**98.60**	**97.97**	**95.91**	**97.21**
Proposed Method	**GSMD+ SLT+ GoogleNet**	**93.63**	**95.41**	**92.88**	**85.03**	**89.89**
Proposed Method	**GSMD+ SLT+ AlexNet**	**98.18**	**100**	**97.34**	**94.55**	**97.20**

Table 4. Comparison of the proposed method with existing methods for Ventricular Fibrillation on physionet dataset.

Author	Method	Acc (%)	Sens (%)	Spec (%)	Precision (%)	F1-sc (%)
Tripathi et al. (2022) [17]	SLT+ DenseNet-201	97.1	92.8	99.2	NR	95.6
Rajeshwari & Kavitha (2022) [39]	Ensemble method	97.02	92.71	NR	NR	NR
Xia et al. (2014) [40]	EMD + Lempel Ziv complexity	97.08	NR	NR	NR	NR
Reddy et al. (2022) [41]	SVRF	98.2	NR	NR	NR	NR

Authorized licensed use limited to: DELHI TECHNICAL UNIV. Downloaded on February 07,2024 at 06:07:56 UTC from IEEE Xplore. Restrictions apply.
© 2024 IEEE. Personal use is permitted, but republication/redistribution requires IEEE permission. See https://www.ieee.org/publications/rights/index.html for more information.

This article has been accepted for publication in IEEE Sensors Journal. This is the author's version which has not been fully edited and content may change prior to final publication. Citation information: DOI 10.1109/JSEN.2024.3354113

Eltrass et al. (2022) [42]	Gabor transform + DL features	98.75	98.18	99	NR	NR
Proposed Method	**GSMD+ SLT+VGG19**	**98.8**	**96.6**	**100**	**100**	**98.3**
Proposed Method	**GSMD+SLT+ RESNET18**	**98.4**	**96.02**	**99.6**	**99.3**	**97.6**
Proposed Method	**GSMD+ SLT+ GoogleNet**	**94.31**	**86.6**	**98.9**	**97.9**	**91.93**
Proposed Method	**GSMD+ SLT+ AlexNet**	**97.72**	**93.58**	**100**	**100**	**96.68**

DNN: Deep Neural Network; SVRF: Sampling vector Random Forest; DL: Deep Learning

Table 5. Simulation result of the proposed GSMD+SLT method using VGG19 and RESNET18 on physionet dataset.

Class	Acc (%)		Sen (%)		Spec (%)		Precision (%)		F1-sc (%)	
	VGG19	RESNET18	VGG19	RESNET18	VGG19	RESNET18	VGG19	RESNET18	VGG19	RESNET18
AF	98.18	98.18	97.93	98.60	98.30	97.97	96.59	95.91	97.32	97.21
Healthy	98.86	99.31	100	99.31	98.98	99.31	97.95	98.63	98.98	98.98
VF	98.86	98.40	96.68	96.02	100	99.65	100	99.31	98.32	97.64

Table 6. Comparison of the proposed method for multilevel classification with existing methods.

Author	Dataset	Method	**Classes**	**Acc. (%)**
Tripathi et al. (2022) [17]	AF termination challenge, CU VT, MIT-BIH MV, and MIT-BIHA.	SLT+ AlexNet	3	92.9
		SLT+ GoogleNet		93.8
Baygin et al. (2021) [43]	Zheng et al dataset	HIT patten + SVM	7	92.95
Llamedo and Martnez (2012) [44]	MAHB	LDC+ EMCA	3	95.42
Essa and Xie (2022) [45]	MIT-BIH dataset	CNN-LSTM + RRHOS-LSTM	4	95.81
Proposed	MIT-BIH Atrial Fibrillation, MIT-BIH CU Ventricular Tachycardia, MIT-BIH Malignant Ventricular Ectopy, and MIT-BIH arrhythmia	GSMD+ SLT+ AlexNet	3	97.7
Proposed		GSMD+SLT+VGG19		98.2
Proposed		GSMD+ SLT+ RESNET-18		98.0
Proposed		GSMD+ SLT+ GoogleNet		94.5
Proposed	Combined dataset (Physionet + Mendeley II)	GSMD+SLT+VGG19	3	94.3
Proposed		GSMD+SLT+GoogleNet		99.2
Proposed		GSMD+SLT+AlexNet		93.4
Proposed		GSMD+SLT+RESNET-18		96.7

HIT: Homeomorphically Irreducible Tree; LDC: Linear Discriminant Classifier; EMCA: Expectation-Maximization Clustering Algorithm; VT: Ventricular Tachycardiac; MV: Malignant Ventricular.

V. Conclusion and Future Scope

In this article, we initiated a framework that proposes a combined technique of GSMD and high-resolution, SLT, to detect and perform the multilevel classification which categorizes the cardiac arrhythmia into Healthy, AF, and VF classes using ECG signal. The GSMD technique decomposes the complex ECG signal into a set of intrinsic mode functions, assuming an IMF has a finite bandwidth and the frequency bands of several IMFs are disjoint. By grouping them in several combinations, the denoised signal is acquired with the use of filters integrated with GSMD. The high-resolution technique, SLT, is employed that transformed the obtained signal from GSMD into a 2D spectrogram which is then fed to the deep neural networks for arrhythmia classification. The models, VGG19, RESNET-18, GoogleNet, and Alexnet are utilized for classifying the ECG signal and achieved an accuracy of 98.2%, 98%, 94.5%, and 97.7% respectively on the physionet dataset. The combined dataset (Physionet+Mendeley-II), attained an accuracy of 94.3%, 94.3%, 99.2%, and 93.4% respectively from the above deep learning models. The results show that the proposed method (GSMD+SLT) is reliable and efficient for arrhythmia classification. In the future, a more focused technique for the detection and classification of arrhythmia for real-time ECG signals will be implemented.

References

[1]. X. Peng et al., "DSCSSA: A Classification Framework for Spatiotemporal Features Extraction of Arrhythmia Based on the Seq2Seq Model With Attention Mechanism," in IEEE Transactions on Instrumentation and Measurement, vol. 71, pp. 1-12, 2022, Art no. 2515112, doi: 10.1109/TIM.2022.3194906.

[2]. Y. -T. Zhang, Y. -L. Zheng, W. -H. Lin, H. -Y. Zhang and X. -L. Zhou, "Challenges and Opportunities in Cardiovascular Health Informatics," in *IEEE Transactions on Biomedical Engineering*, vol. 60, no. 3, pp. 633-642, March 2013, doi: 10.1109/TBME.2013.2244892.

[3]. S. Singhal, and M. Kumar, "A Systematic Review on Artificial Intelligence-Based Techniques for Diagnosis of Cardiovascular Arrhythmia Diseases: Challenges and Opportunities", Archives of Computational Methods in Engineering (Springer), Volume 30, Pages 865–888, March 2023.

[4]. M. M. Al Rahhal, Y. Bazi, H. Almubarak, N. Alajlan and M. Al Zuair, "Dense Convolutional Networks With Focal Loss and Image Generation for Electrocardiogram Classification," in IEEE Access, vol. 7, pp. 182225-182237, 2019, doi: 10.1109/ACCESS.2019.2960116.

[5]. J. Huang, B. Chen, B. Yao and W. He, "ECG Arrhythmia Classification Using STFT-Based Spectrogram and Convolutional Neural Network," in IEEE Access, vol. 7, pp. 92871-92880, 2019, doi: 10.1109/ACCESS.2019.2928017.

[6]. A. Amirshahi and M. Hashemi, "ECG Classification Algorithm Based on STDP and R-STDP Neural Networks for Real-Time Monitoring on Ultra Low-Power Personal Wearable Devices," in IEEE Transactions on Biomedical Circuits and Systems, vol. 13, no. 6, pp. 1483-1493, Dec. 2019, doi: 10.1109/TBCAS.2019.2948920.

[7]. N. Feng, S. Xu, Y. Liang and K. Liu, "A Probabilistic Process Neural Network and Its Application in ECG Classification," in IEEE Access, vol. 7, pp. 50431-50439, 2019, doi: 10.1109/ACCESS.2019.2910880.

[8]. N.E Huang et al., "The Empirical Mode Decomposition and the Hilbert Spectrum for Nonlinear and Non-Stationary Time Series Analysis", Proceedings of the Royal Society of London A: Mathematical, Physical and Engineering Sciences, vol. 454, 1998, pp- 903-995. https://doi.org/10.1098/rspa.1998.0193.

[9]. P. Chu, C. Fan, N. Huang, "Compact empirical mode decomposition: an algorithm to reduce mode mixing, end effect, and detrend uncertainty". Adv. Adapt. Data Anal., vol. 4, 2012, 1250017, doi:10.1142/S1793536912500173.

[10]. M. Nazari, and S.M. Sakhaei, "Successive variational mode decomposition", Signal Process., vol. 174, 2020, pp- 107610.

[11]. P. Singh, SD. Joshi, RK. Patney, K. Saha, "The Fourier decomposition method for nonlinear and non-stationary time series analysis", Proceedings of the Royal Society of London A, vol. 473, 2017, 20160871. http://dx.doi.org/10.1098/rspa.2016.0871.

Authorized licensed use limited to: DELHI TECHNICAL UNIV. Downloaded on February 07,2024 at 06:07:56 UTC from IEEE Xplore. Restrictions apply.
© 2024 IEEE. Personal use is permitted, but republication/redistribution requires IEEE permission. See https://www.ieee.org/publications/rights/index.html for more information.

This article has been accepted for publication in IEEE Sensors Journal. This is the author's version which has not been fully edited and
content may change prior to final publication. Citation information: DOI 10.1109/JSEN.2024.3354113

[12]. N. Mourad, "Group-sparse mode decomposition: A signal decomposition algorithm based on group-sparsity in the frequency domain", Digital Signal Processing, vol. 122, 2022, 103375, doi: https://doi.org/10.1016/j.dsp.2021.103375.

[13]. E. H. S. Diop, R. Alexandre and A. O. Boudraa, "Analysis of Intrinsic Mode Functions: A PDE Approach," in IEEE Signal Processing Letters, vol. 17, no. 4, pp. 398-401, April 2010, doi: 10.1109/LSP.2009.2038770.

[14]. N. Ahmed, T. Natarajan and K. R. Rao, "Discrete Cosine Transform," in IEEE Transactions on Computers, vol. C-23, no. 1, pp. 90-93, Jan. 1974, doi: 10.1109/T-C.1974.223784.

[15]. M.J. Buckley, "Fast computation of a discretized thin-plate smoothing spline for image data", Biometrika, vol. 81 (2), 1994, pp-247–258.

[16]. V.V. Moca, H. Bârzan, A.N. Dăbâcan, and R.C. Muresan "Time-frequency super-resolution with superlets. Nature Communications, vol.**12,** 337 Jan 2021. https://doi.org/10.1038/s41467-020-20539-9

[17]. P. M. Tripathi, A. Kumar, M. Kumar and R. Komaragiri, "Multilevel Classification and Detection of Cardiac Arrhythmias With High-Resolution Superlet Transform and Deep Convolution Neural Network," in IEEE Transactions on Instrumentation and Measurement, vol. 71, pp. 1-13, 2022, Art no. 4006113, doi: 10.1109/TIM.2022.3186355.

[18]. Pankaj, A. Kumar, M. Kumar and R. Komaragiri, "STSR: Spectro-Temporal Super-Resolution Analysis of a Reference Signal Less Photoplethysmogram for Heart Rate Estimation During Physical Activity," in IEEE Transactions on Instrumentation and Measurement, vol. 71, pp. 1-10, 2022, Art no. 4006910, doi: 10.1109/TIM.2022.3192831

[19]. Pankaj, Kumar, A., Kumar, M. et al. Optimized deep neural network models for blood pressure classification using Fourier analysis-based time–frequency spectrogram of photoplethysmography signal. Biomed. Eng. Lett. (2023). https://doi.org/10.1007/s13534-023-00296-6.

[20]. Kumar, Ashish, Rama Komaragiri, and Manjeet Kumar. "A novel CS-NET architecture based on the unification of CNN, SVM and super-resolution spectrogram to monitor and classify blood pressure using photoplethysmography." *Computer Methods and Programs in Biomedicine* 240 (2023): 107716.

[21]. C. Nayak, S. K. Saha, R. Kar and D. Mandal, "An Efficient and Robust Digital Fractional Order Differentiator Based ECG Pre-Processor Design for QRS Detection," in IEEE Transactions on Biomedical Circuits and Systems, vol. 13, no. 4, pp. 682-696, Aug. 2019, doi: 10.1109/TBCAS.2019.2916676.

[22]. Ary L. Goldberger et al., "PhysioBank, PhysioToolkit, and PhysioNet: components of a new research resource for complex physiologic signals," Circulation, vol. 101, no. 23, pp. e215-e220, 2000.

[23]. Moody GB, Mark RG. A new method for detecting atrial fibrillation using R-R intervals. Computers in Cardiology. 10:227-230 (1983), https://www.physionet.org/.

[24]. Greenwald SD, Albrecht P, Moody GB, Mark RG. Estimating confidence limits for arrhythmia detector performance. Computers in Cardiology 1985; 12:383–386.

[25]. Nolle FM et al., "a new concept in computerised arrhythmia monitoring systems", Computers in Cardiology 13:515-518 (1986).

[26]. G. B. Moody and R. G. Mark, "The impact of the MIT-BIH Arrhythmia Database," IEEE Engineering in Medicine and Biology Magazine, vol. 20, no. 3, pp. 45-50, May-June 2001, doi: 10.1109/51.932724.

[27]. Plawiak, Pawel (2017), "ECG signals (1000 fragments)", Mendeley Data, V3, doi: 10.17632/7dybx7wyfn.3.

[28]. M. Bansal, M. Kumar, M. Sachdeva and A. Mittal, "Transfer learning for image classification using VGG19" Caltech-101 image data set. J Ambient Intell Human Comput (2021). https://doi.org/10.1007/s12652-021-03488-z.

[29]. J. Deng, W. Dong, R. Socher, L. -J. Li, Kai Li and Li Fei-Fei, "ImageNet: A large-scale hierarchical image database," 2009 IEEE Conference on Computer Vision and Pattern Recognition, Miami, FL, USA, 2009, pp. 248-255, doi: 10.1109/CVPR.2009.5206848.

[30]. K. He, X. Zhang, S. Ren, and J. Sun, "Deep residual learning for image recognition," in Proceedings of the IEEE conference on computer vision and pattern recognition, 2016, pp. 770–778, https://doi.org/10.1109/CVPR.2016.90.

[31]. C. Szegedy et al., "Going deeper with convolutions," In Proceedings of the IEEE conference on computer vision and pattern recognition, pp. 1-9, 2015.

[32]. Alex Krizhevsky, Ilya Sutskever, and Geoffrey E. Hinton, "Imagenet classification with deep convolutional neural networks," Advances in Neural Information Processing Systems 25 (2012): 1097-1105.

[33]. F Setiawan, C-W Lin, "A Deep Learning Framework for Automatic Sleep Apnea Classification Based on Empirical Mode Decomposition Derived from Single-Lead Electrocardiogram", *vol. 12,* 2022, https://doi.org/10.3390/life12101509.

[34]. A. Kumar, V. K. Mehla, H. Tomar, M. Kumar and R. Komaragiri, "Classification of Normal and Abnormal ECG signals using Support Vector Machine and Fourier Decomposition Method," *2020 IEEE International Symposium on Smart Electronic Systems (iSES) (Formerly iNiS)*, 2020, pp. 161-166, doi: 10.1109/iSES50453.2020.00044.

[35]. BM. Mathunjwa, Y-T Lin, C-H Lin, MF. Abbod, and J-S Shieh, "ECG arrhythmia classification by using a recurrence plot and convolutional neural network," Biomedical Signal Processing and Control, vol. 64, pp. 102262, Feb. 2021, doi: 10.1016/J.BSPC.2020.102262.

[36]. D. Lai, Y. Bu, Y. Su, X. Zhang and C. -S. Ma, "Non-Standardized Patch-Based ECG Lead Together With Deep Learning Based Algorithm for Automatic Screening of Atrial Fibrillation," IEEE Journal of Biomedical and Health Informatics, vol. 24, no. 6, pp. 1569-1578, June 2020, doi: 10.1109/JBHI.2020.2980454.

[37]. H. Dang, M. Sun, G. Zhang, X. Qi, X. Zhou and Q. Chang, "A Novel Deep Arrhythmia-Diagnosis Network for Atrial Fibrillation Classification Using Electrocardiogram Signals," in IEEE Access, vol. 7, pp. 75577-75590, 2019, doi: 10.1109/ACCESS.2019.2918792.

[38]. X. Fan, Q. Yao, Y. Cai, F. Miao, F. Sun and Y. Li, "Multiscaled Fusion of Deep Convolutional Neural Networks for Screening Atrial Fibrillation From Single Lead Short ECG Recordings," IEEE Journal of Biomedical and Health Informatics, vol. 22, no. 6, pp. 1744-1753, Nov. 2018, doi: 10.1109/JBHI.2018.2858789.

[39]. M.R. Rajeshwari, K. Kavitha, "Arrhythmia ventricular fibrillation classification on ECG signal using ensemble feature selection and deep neural network", Cluster Comput vol. **25**, 2022, pp-3085–3102, https://doi.org/10.1007/s10586-022-03547-w.

[40]. D. Xia, Q. Meng, Y. Chen, and Z. Zhang, "Classification of Ventricular Tachycardia and Fibrillation Based on the Lempel-Ziv Complexity and EMD", In: Huang, DS., Han, K., Gromiha, M. (eds) Intelligent Computing in Bioinformatics. ICIC 2014. Lecture Notes in Computer Science (), vol 8590. Pp- 322- 329, https://doi.org/10.1007/978-3-319-09330-7_39.

[41]. S.D. Reddy, R. Murugan, A. Nandi, T. Goel, "Classification of arrhythmia disease through electrocardiogram signals using sampling vector random forest classifier", Multimed Tools Appl, vol. 851, 2022, pp- 675-687, https://doi.org/10.1007/978-981-16-9154-6_62.

[42]. A.S. Eltrass, M.B. Tayel, and A.I. Ammar, "Automated ECG multi-class classification system based on combining deep learning features with HRV and ECG measures", Neural Comput & Applic, vol. **34**, 2022, pp-8755–8775, https://doi.org/10.1007/s00521-022-06889-z.

[43]. M. Baygin, T. Tuncer, S. Dogan, P. D. Barua, O. Faust, N.A. Kumar, E.W. Abdulhay, E.E. Palmer, and U.R. Acharya, "Automated arrhythmia detection with homeomorphically irreducible tree technique using more than 10,000 individual subject ECG records," Information Sciences, vol. 575, pp. 323-337, Oct. 2021, doi: 10.1016/J.INS.2021.06.022.

[44]. M. Llamedo and J. P. Martinez, "An Automatic Patient-Adapted ECG Heartbeat Classifier Allowing Expert Assistance," in IEEE Transactions on Biomedical Engineering, vol. 59, no. 8, pp. 2312-2320, Aug. 2012, doi: 10.1109/TBME.2012.2202662.

[45]. E. Essa and X. Xie, "An Ensemble of Deep Learning-Based Multi-Model for ECG Heartbeats Arrhythmia Classification," in IEEE Access, vol. 9, pp. 103452-103464, 2021, doi: 10.1109/ACCESS.2021.3098986.

Authorized licensed use limited to: DELHI TECHNICAL UNIV. Downloaded on February 07,2024 at 06:07:56 UTC from IEEE Xplore. Restrictions apply.
© 2024 IEEE. Personal use is permitted, but republication/redistribution requires IEEE permission. See https://www.ieee.org/publications/rights/index.html for more information.

Physica Scripta

INCLUSIVE PUBLISHING
TRUSTED SCIENCE

PAPER

High-k dielectric based high performance vertical organic thin film transistor for flexible low power applications

To cite this article: Sugandha Yadav *et al* 2024 *Phys. Scr.* **99** 025940

View the article online for updates and enhancements.

You may also like

- Dosimetry impact of gating latency in cine magnetic resonance image guided breath-hold pancreatic cancer radiotherapy
Panpan Hu, Xiaoyang Li, Wei Liu et al.
- Empirical formulation for small circular electron fields
Imran Khan, Sunil Kumar, Sushil Kumar et al.
- Towards high performance near infrared sensitive multilayer organic phototransistors: effects of the acceptor and its position
Chenyu Tang, Chengyu Lu, Qingyong Dai et al.

This content was downloaded from IP address 14.139.251.98 on 07/02/2024 at 07:16

Physica Scripta

PAPER

High-k dielectric based high performance vertical organic thin film transistor for flexible low power applications

Sugandha Yadav[1], **Poornima Mittal**[1,*] **and Shubham Negi**[2]

[1] Department of Electronics & Communication Engineering, Delhi Technological University, New Delhi, 110042, India
[2] Department of Electronics and Communication Engineering, Chandigarh University, Mohali Punjab, 140413 India
[*] Author to whom any correspondence should be addressed.

E-mail: sugandhayadav555@gmail.com, poornimamittal@dtu.ac.in and shubhamnegi0192@gmail.com

RECEIVED
31 January 2023

REVISED
9 September 2023

ACCEPTED FOR PUBLICATION
2 January 2024

PUBLISHED
15 January 2024

Keywords: organic semiconductors, organic thin film transistor (OTFT), vertical OTFT

Abstract

The basic performance parameters such as threshold voltage, drain current and saturation mobility play an important role for any transistor-based devices. The planar organic TFT provides a good performance but it is still not satisfactory. Therefore, in this paper, a vertical channel TFT (D_5) is proposed that exhibits a significant improvement for threshold voltage V_t, drain current I_{Dmax} and saturation mobility μ_{sat} in comparison to planar devices. The proposed vertical device (D_5) is 44 and 24 times enhanced in comparison with planar device D_1 in terms of I_{Dmax} and μ_{sat}, correspondingly. Furthermore, this paper compares five different vertical-channel device architectures (D_2, D_3, D_4, D_5, D_6 & D_7). Out of these structures, our proposed novel structure (D_5) shows remarkable performance in terms of drain current (528 μA) and saturation mobility (80.8 cm^2/V.s). As compared to the best mentioned vertical devices D_2, D_3 and D_7, the proposed device exhibits 41.8 %, 15.6 % and 27.8 %, increment in drain current, respectively. Additionally, the proposed device exhibits about 2.7, 5.2 and 3.5 times improvement in comparison with D_2, D_3 and D_7 correspondingly. The reasons for this better performance of the proposed device have been explained by vertical and horizontal cutline analysis.

1. Introduction

In the last decade, the performance of thin film transistors (OTFTs) has been enhanced remarkably [1, 2]. Various deposition techniques, in-depth analysis of physical structure and novel materials have played major role in this significant progress. In conventional OTFTs overlapping of capacitances and higher threshold voltage restrict the performance of device. Also, need of charge carrier injection and shorter channel length [3–7] has been highlighted. Therefore, researchers have made several efforts in scaling down the dimensions of TFTs by keeping the electric field constant [8, 9]. Even so, these methods are not enough to make significant improvement in cut-off frequency and transconductance of conventional horizontal organic TFTs. On the other hand, by incorporating additional injection layer and decreasing the parasitic capacitances the fabrication process becomes complex [10, 11]. The straightforward solution to improve the TFT transconductance is to decrease the channel length to the submicron regime [12]. However, submicron channels require sophisticated and often expensive patterning techniques such as electron-beam lithography or stencil mask patterning [13], which cannot be adopted to a possible low-cost fabrication process on flexible substrates. An alternative device concept, offering submicron channel lengths but without the compromise of using complex patterning techniques, is the vertical organic thin film transistor (VOTFT) [14–16].

In vertical TFTs, gate electrode, source electrode, organic semiconductor and drain electrode are arranged vertically which lead to a vertical channel instead of horizontal. The major difference between common lateral TFTs and vertical TFTs is the distance between source and drain. This distance is usually defined as the length of channel. This length is provided by the thickness of layer and so, ultra-short channel (<1 μm) can be easily achieved in VOTFTs. Many researchers have suggested various structures where vertical channels are incorporated. In 2008, Kim *et al* [17] fabricated a VOTFT using tris-(8-hydroxyquinoline) aluminium (Alq3) as

© 2024 IOP Publishing Ltd

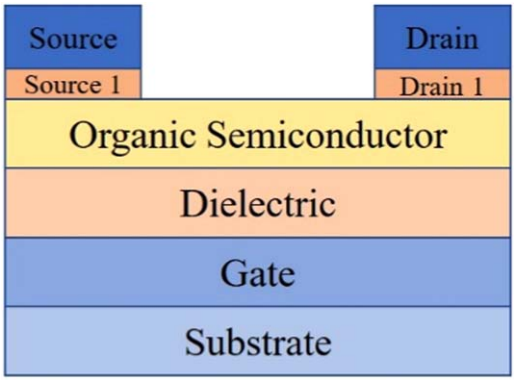


Figure 1. Structure of BGTC planar TFT (D_1) [21].

an n-type active material. The deposition rate of active layer and surface temperature are varied. Eventually, it is concluded that deposition conditions of active layer play a major role to enhance the performance of VOTFTs based on Alq_3. Afterwards, in 2013, Kleemann *et al* [3] presented high performance novel vertical TFTs having channel length of 50 nm where C60 is used for *n-type* operation and pentacene for *p-type*. The manufacturing of the transistors is done by photolithography. These devices exhibited very high I_{on}/I_{off} greater than 10^6 along with higher transconductance ($> 50\ \mu S\ mm^{-1}$). Also, pentacene based p-type device shows on-state current densities of ($\sim 50\ mA\ cm^{-2}$).

In 2018, Rathi *et al* [18] compared the performance of single and dual gate VOTFTs. It is reported here that dual gate vertical transistor is showing much enhanced performance and exhibited higher I_{on}/I_{off}. Furthermore, in 2019, Chen *et al* [19] reported a vertical quantum-dot light emitting transistor (VQLET) using a VOTFT. The device exhibited very high performance in terms of current density and current efficiency. The maximum current efficiency is reported as 37 cd/A. Thereafter, in 2021, Kneppe *et al* [20] fabricated a first solution-processed pentacene based VOTFT and compared it with small molecule-based vertical transistors. The fabricated device showed extremely high performance and showed charge carrier mobility of 4.8 cm^2/V.S.

In this paper, a vertical TFT is proposed which provides significantly improved performance parameters such as maximum drain current, I_{on}/I_{off} and saturation mobility. The proposed device is also compared in terms of the mentioned parameters with the other planer and vertical TFTs. In this work, first of all, a fabricated bottom gate top contact (BGTC) device [21] is validated using Silvaco Atlas simulator tool. Herein, we first try to set the boundaries for the simulation work by the validation of the BGTC device. Afterwards, a vertical-channel TFT is proposed using same simulation tool with the same materials and same possible thickness as taken in the validated device. Hence, it can be considered that the proposed device is feasible for experimental purpose as well.

The complete paper is distributed in 5 sections. Section 1 is about the introduction of vertical TFTs. Their importance and role are discussed in this section. Section 2 is depicting the validation of planar transistor. Thereafter, the comparison of planar and vertical TFTs are incorporated in section 3. Furthermore, section 4 provides the proposed device. In this section, cutline analysis is also being performed on the proposed vertical TFT. Eventually, section 5 highlights the conclusion of the research.

2. Characteristic analysis and parameters extraction of single gate planar transistor

A low power BGTC (bottom gate top contact) thin film transistor [21] having 2,7-dioctyl[1] benzothieno[3,2-b] [1]benzothiophene (C8-BTBT) as an active layer is simulated using Silvaco Atlas 2D device simulator. A high-k ultrathin polymer is used as a gate dielectric to realize the stable operation of a flexible, low-power device. MoO_3/Au bilayer electrodes having thickness of 20 nm and 70 nm, respectively, are utilized as source and drain. The layer of MoO_3 is situated between Au source/drain electrodes and C8-BTBT to make smooth charge injection as shown in figure 1 [22–24].

Table 1 is depicting the materials and thickness of the different regions such as source, gate, drain, semiconductor and dielectric. The channel length and width of the device structure are 200 μm and 1000 μm, correspondingly. Table 2 is highlighting the properties of semiconductor.

The simulator predicts the electrical characteristics by utilizing a set of differential equations that are derived from Maxwells laws. This set of equations contains some equation for device simulator such as Poison's, transport and continuity equations. These equations are applied onto 2D/3D grid which consists of many grid

Table 1. Materials and thickness of different regions.

Region	Material	Thickness (nm)
Source/Drain	Gold	70
Source1/Drain1	MoO_3	20
Active Layer	C8-BTBT	30
Gate Dielectric	pC1B5	29
Gate	Aluminium	50

Table 2. Material's specification for different layers.

Parameter	Value
Band gap	2.0
Density of conduction band	1×10^{21} cm^{-3}
Density of valence band	1×10^{21} cm^{-3}
Acceptor doping concentration	6.5×10^{17} cm^{-3}
Dielectric constant of C8-BTBT	5
Dielectric constant of pC1b5	7.5

Table 3. Parametric comparison of simulated and experimental [21] device.

Parameters	Experiment [21]	Simulation (D_1)
Threshold Voltage V_t (V)	−1.8	−1.7
Maximum Drain Current I_{Dmax} (μA)	12	11
I_{on}/I_{off}	$>10^6$	1×10^6
Saturation Mobility μ_{sat}(cm^2/V.s)	3.3	3.1

points called nodes. This process is used to simulate the carrier's transportation in a device structure. Further, the device electrical performance can be modelled in DC, AC or transient modes of operation. Eventually, Poole-Frenkel mobility model, proposed by Frenkel in 1938 is included to obtain the results under specified boundary conditions. This model is given as:

$$\mu(E) = \mu_0 e^{\left[-\frac{\Delta}{kT}+\left(\frac{\beta}{kT}-\gamma\right)\sqrt{|E|}\right.} \quad (1)$$

Where μ, μ_0 and E are field dependent mobility, zero field mobility, and electric field, correspondingly. Besides this Δ, k, T, β and γ represent activation energy at zero electric field, Boltzmann constant, effective temperature for charge carriers, hole Pool–Frenkel factor and fitting parameter, respectively.

The performance parameters such as threshold voltage V_t, maximum drain current I_{Dmax}, I_{on}/I_{off} and saturation mobility μ_{sat} are compared with the experimental device [21] and it is clearly seen in table 3 that the obtained results are closely matched with the maximum error of 10%.

Figure 2(a) is demonstrating the planar device structure obtained by using Tolyplot in Silvaco Tool. Figure 2(b) is depicting the current flowlines in the structure. Here, it is seen that channel is forming just above the dielectric layer between source and drain.

The transfer and drain characteristics of planar device are highlighted in figures 3(a) and (b), respectively. In figure 3(a) the maximum $\sqrt{I_D}$ value is obtained as 3.3 $\sqrt{(10^{-3}\ A^{0.5})}$ at drain voltage of −5 V. The threshold voltage is also obtained by plotting a straight line on current-voltage slope towards x-axis as mentioned in the figure. The maximum drain current is obtained as 11 μA at gate voltage of −5 V.

3. Parameters comparison of vertical and planar transistor

In this section, performance of planar and vertical TFTs will be compared keeping same material and thickness for both devices. As mentioned above, a planar device (D_1) is validated and compared with experimental devices. Now, keeping the same materials and thickness as in planar device [21], a vertical OTFT device [20] is presented. Figure 4 is outlining the structure of vertical device (D_2). In D_2, vertical stacking of source and drain electrodes are incorporated. These electrodes are separated by an insulating spacer and a semiconductor layer.

Table 4 is highlighting the comparison of planar and vertical device in terms of V_t, I_{Dmax}, I_{on}/I_{off} and μ_{sat}. The table shows that vertical device (D_2) is exhibiting the remarkable improvement as drain current, threshold

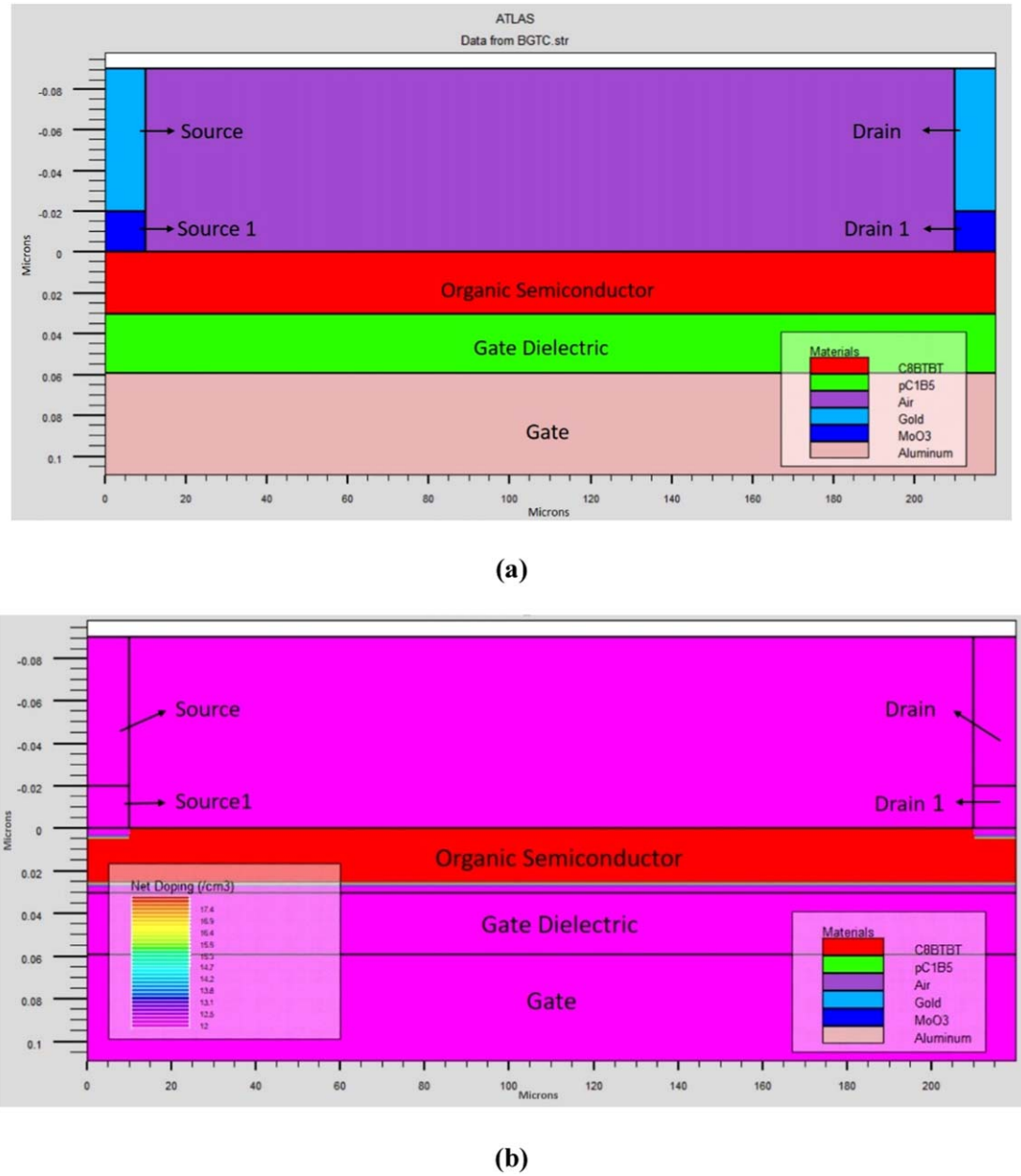


Figure 2. (a) Simulated device structure of BGTC (planar) transistor (b) representation of layers with current flow-lines from source to drain.

voltage and saturation mobility are improved by 18, 2 and 9 times, correspondingly in comparison with planar device D_1.

Figure 5(a) below is illustrating the comparison of transfer curves of D_1 and D_2 devices along with the threshold voltage. Figure 5(b) is depicting the drain characteristics of D_2 devices at different gate voltages from 0 to −5 V. The maximum drain current is achieved as 221 μA at $V_{GS} = -5$ V.

Figures 6(a) and (b) are illustrating device structure and current flowlines of D_2, respectively. In figure (b) it is clear that the channel is formed in a very small region of active layer between source and drain. This results in shorter channel length in nano-meters. Hence, the drain current is achieved 18 times higher than the planar device.

3.1. Internal device comparison of vertical and planar TFTs

In this section, internal analysis is performed for both D_1 and D_2 devices. In device D_1, a horizontal cutline is drawn at 1 nm above the dielectric layer as mentioned in figure 6(b). This device contains a horizontal channel as it is a planar TFT. On the other hand, in device D_2, horizontal cutline is drawn at 5 nm (Y-axis) for better results. In this device current is flowing like a U-shape from source to drain. Hence, in this device two different channel

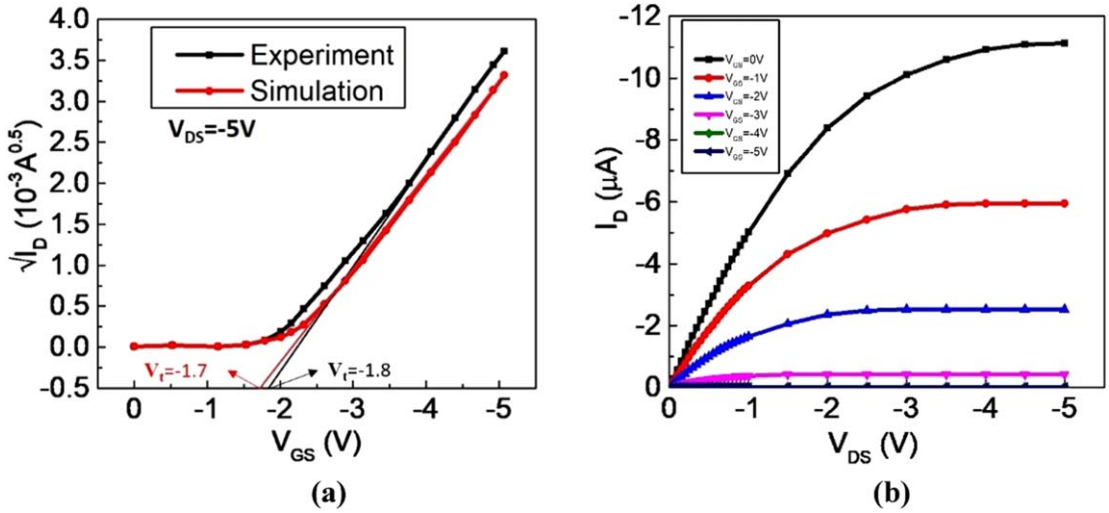


Figure 3. (a) Comparison of transfer characteristics of experimental [21] and simulated planar devices along with threshold voltages (b) drain characteristics of planar (simulated) device.

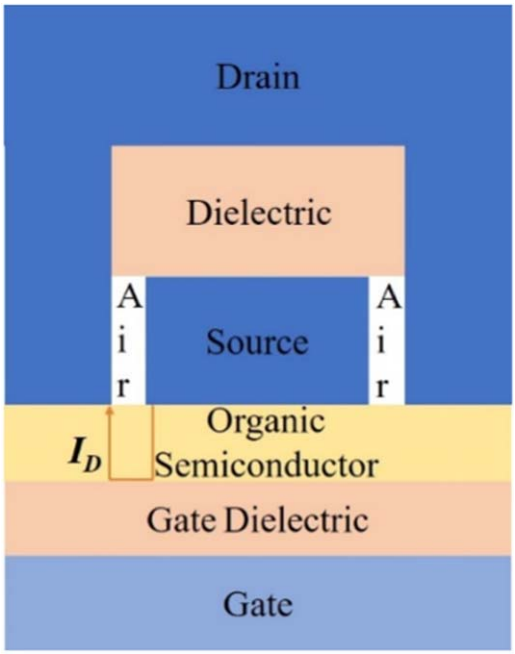


Figure 4. Vertical device [20].

Table 4. Comparison of planar and vertical device.

Parameters	Planar device (D_1)	Vertical device (D_2)
Threshold Voltage V_t (V)	−1.8	−0.9
Maximum Drain Current I_{Dmax} (μA)	12	221
I_{on}/I_{off}	$>10^6$	2.3×10^{10}
Saturation Mobility μ_{sat}(cm^2/V.s)	3.3	30.2

will develop due to the structural variation. Here, channel length is measured in vertical as well as in horizontal direction as illustrated in figure 4. Also, it is clear from the figure that the D_2 device will provide significant enhancement in performance parameters as ultra-short channel (in nano-meters) is achieved in D_2.

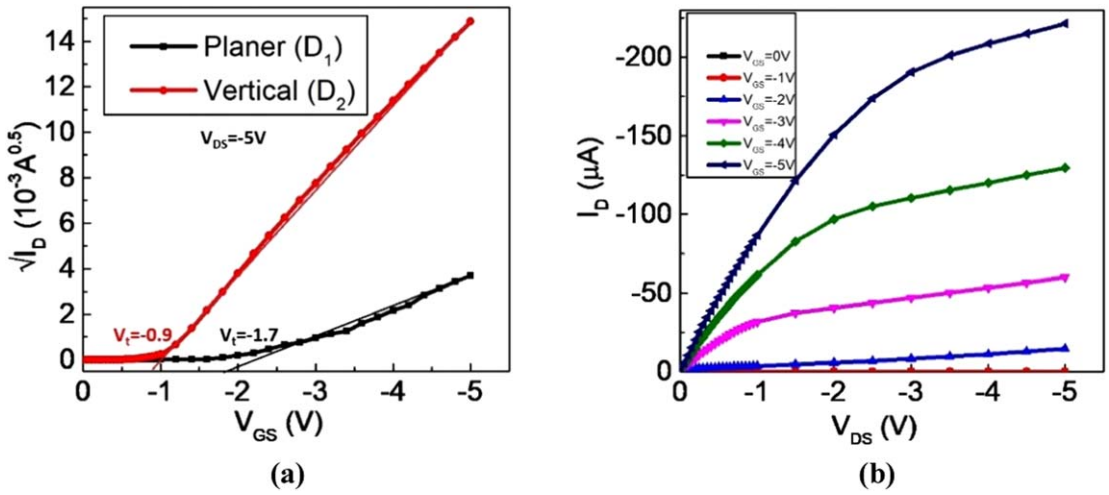


Figure 5. (a) Comparison of transfer characteristics of D_1 (planar) and D_2 (vertical) devices along with threshold voltages (b) drain characteristics of D_2 device.

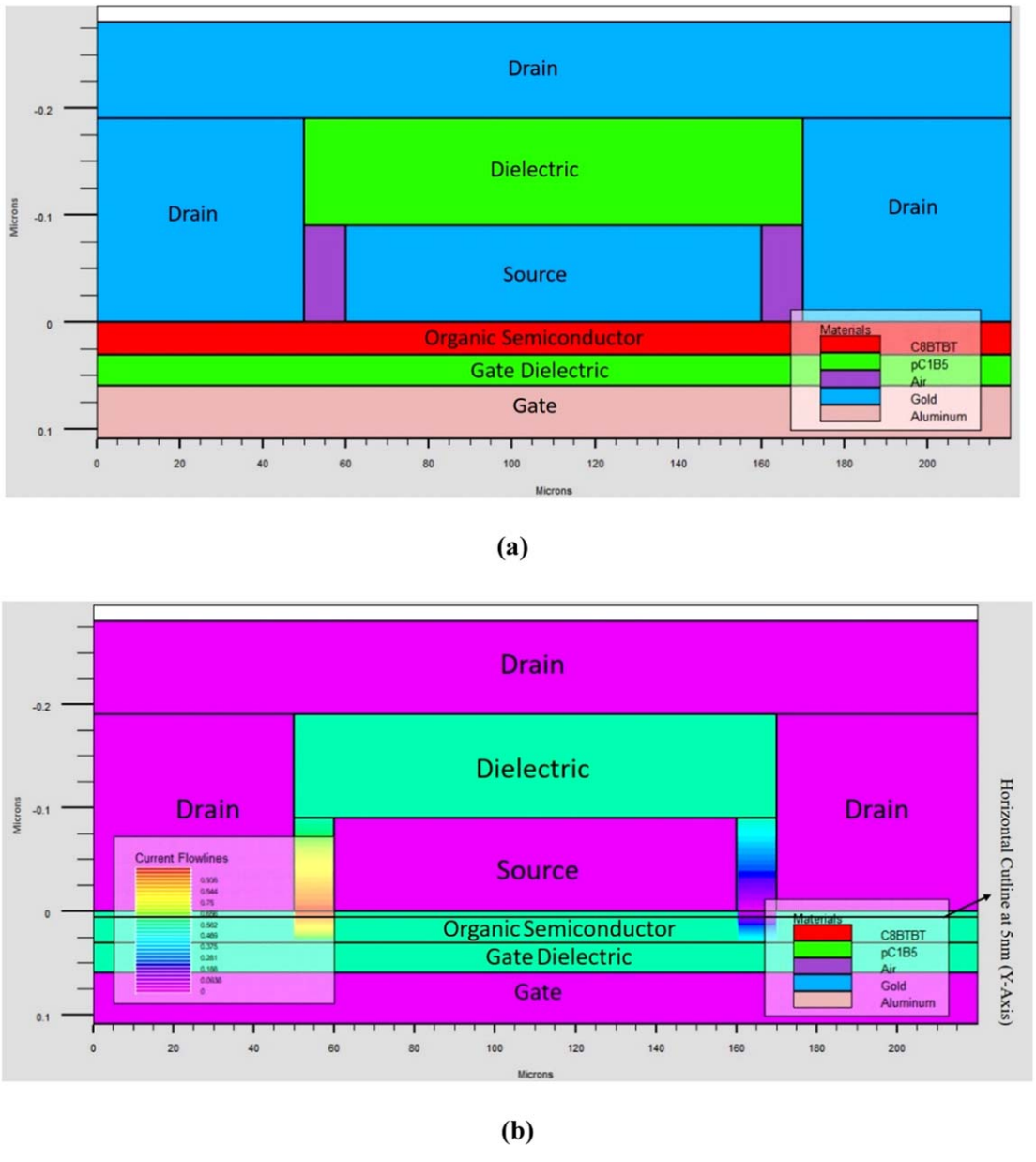


Figure 6. (a) Simulated vertical device structure (D_2) and (b) current flowline of D_2.

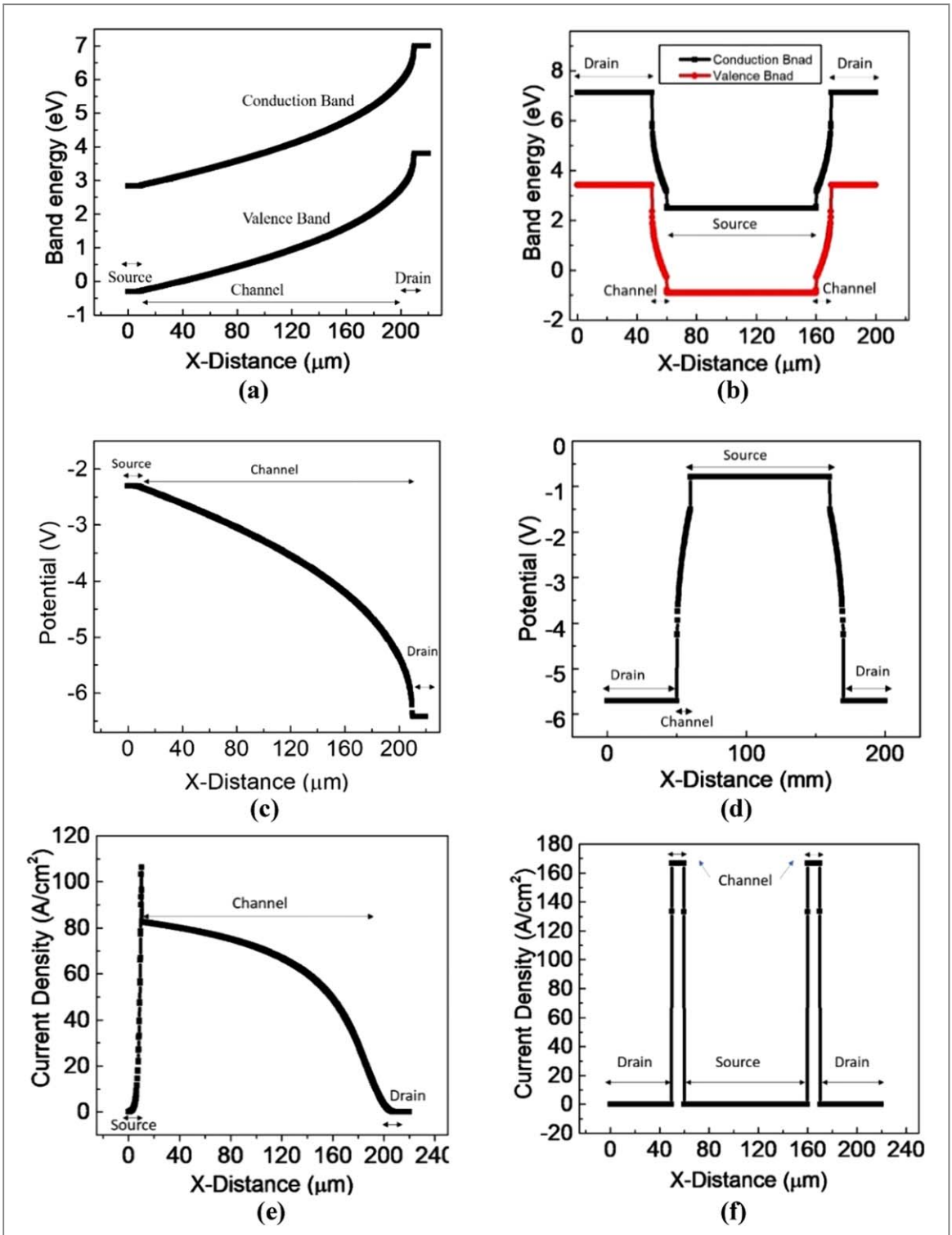


Figure 7. (a) Band energy of D_1 device (b) band energy of D_2 device (c) potential of D_1 device (d) potential of D_2 device (e) total current density of D_1 (f) total current density of D_2.

Figures 7(a) and (b) are highlighting the band energy profile of D_1 and D_2 device in terms of valence and conduction band energies, respectively. In above figures, X-distance is representing the total device length i.e. 220 μm. In figure 7(b), two different band are demonstrated as two channels are formed at both side of source electrode. Further, the potential distribution of planar (D_1) and vertical (D_2) devices are shown in figure 7(c) and (d), correspondingly. In both figures, it is observed that drain is at highest potential and source is at lowest potential value. Addition to this, figures 7(e) and (f) are respresenting the total current density of D_1 and D_2, respectively. Device D_1 is exhibitting the maximum current density of 109 A cm^{-2} at X = 10 nm. This value further keeps decreasing towards the drain electrode and becomes zero at X = 200 nm. Here, the distance

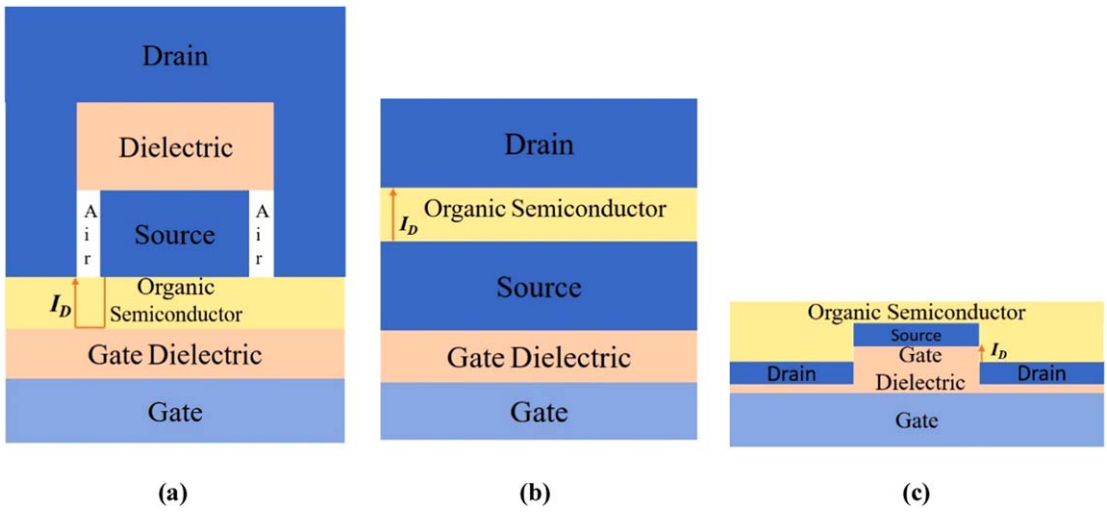


Figure 8. Device structures of (a) D_2 [20], (b) D_3 [25] and (c) D_4 [26].

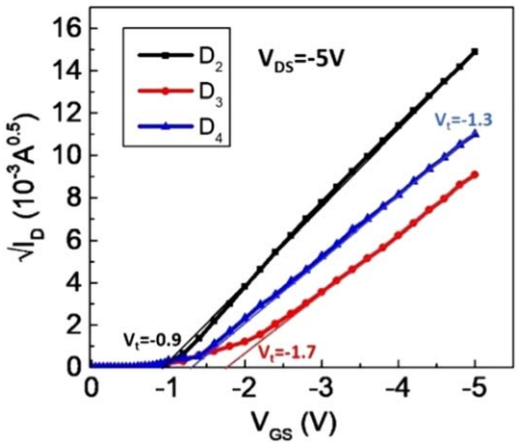


Figure 9. Comparison of transfer curve of D_2, D_3 and D_4 along with threshold voltages.

Table 5. Materials and thickness of different regions of vertical devices.

		Thickness (nm)		
Layer	Material	D_2	D_3	D_4
OSC	C8-BTBT	30	30	30
Source	Gold	90	90	10
Drain	Gold	90	90	10
Gate dielectric	pC1B5	29	29	29
Gate	Aluminium	50	50	50

Table 6. Comparison of performance parameters of vertical devices.

Parameters	(D_2) [20]	(D_3) [25]	(D_4) [26]
Threshold Voltage V_t (V)	−0.9	−1.5	−1.2
Maximum Drain Current I_{Dmax} (μA)	221	82.5	120
I_{on}/I_{off}	2.3×10^{10}	0.8×10^{10}	0.1×10^{11}
Saturation Mobility μ_{sat}(cm^2/V.s)	30.2	9.7	15.2

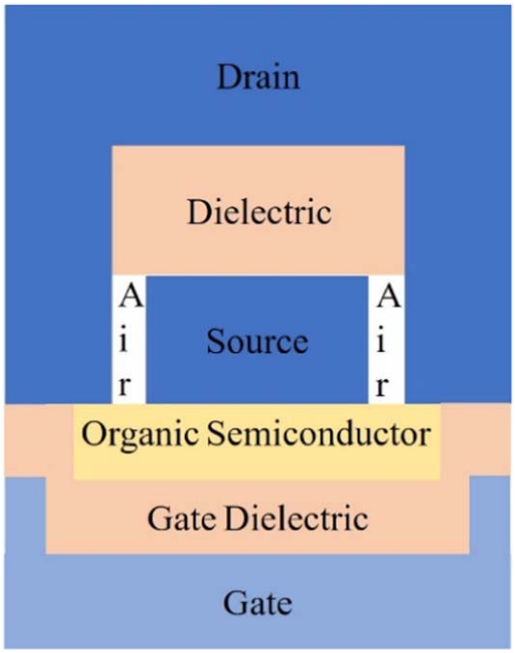


Figure 10. Proposed vertical structure.

Table 7. Materials and thickness of different regions of D_2 and D_5.

		Thickness (nm)	
Layer	Material	D_2	D_5
OSC	C8-BTBT	30	30
Source	Gold	90	90
Drain	Gold	90	90
Gate dielectric	pC1B5	29	59
Gate	Aluminium	50	80

between source and drain is the channel length. The total current density of D_2 is highlighted in figure 7(e). It is noticed from the figure that current density is higher from 50 nm to 60 nm and 160 nm to 170 nm as at these values of X-axis channel is formed. The maximum values obtained here is 169 A cm^{-2} which leads to higher current in D_2 device as compared with D_1.

3.2. Performance analysis of different vertical structures

After getting precise results of planar (D_1) and vertical (D_2) devices, D_2 device is now compared with two other vertical devices D_3 [25] and D_4 [26]. The materials of the regions in all three vertical TFTs devices D_2, D_3 and D_4 are kept same as in planar device with the same possible thickness. The performance of vertical TFTs in terms of maximum drain current, Ion/off ratio, threshold voltage and mobility saturation are compared with the BGTC TFT. In D_2 device, source and drain electrodes are placed vertically which are separated by an insulating spacer and a semiconductor layer as shown in figure 8(a).

On the other hand, in D_3 device, source is placed above the dielectric and drain is placed above the OSC layer as depicted in figure 8(b). As the channel is vertical and developing between source and drain, hence it will completely depend on the thickness of the active layer which in nano-meters. Next, in device D_4, the source and drain electrodes are situated below the OSC layer in vertical manner. Here, the drain electrode is utilized in split form. The channel length is determined by the distance between source and drain as shown in the figure 10(c). All D_2, D_3 and D_4 devices exhibit ultra-short channel which encounters the drawbacks of conventional organic TFTs.

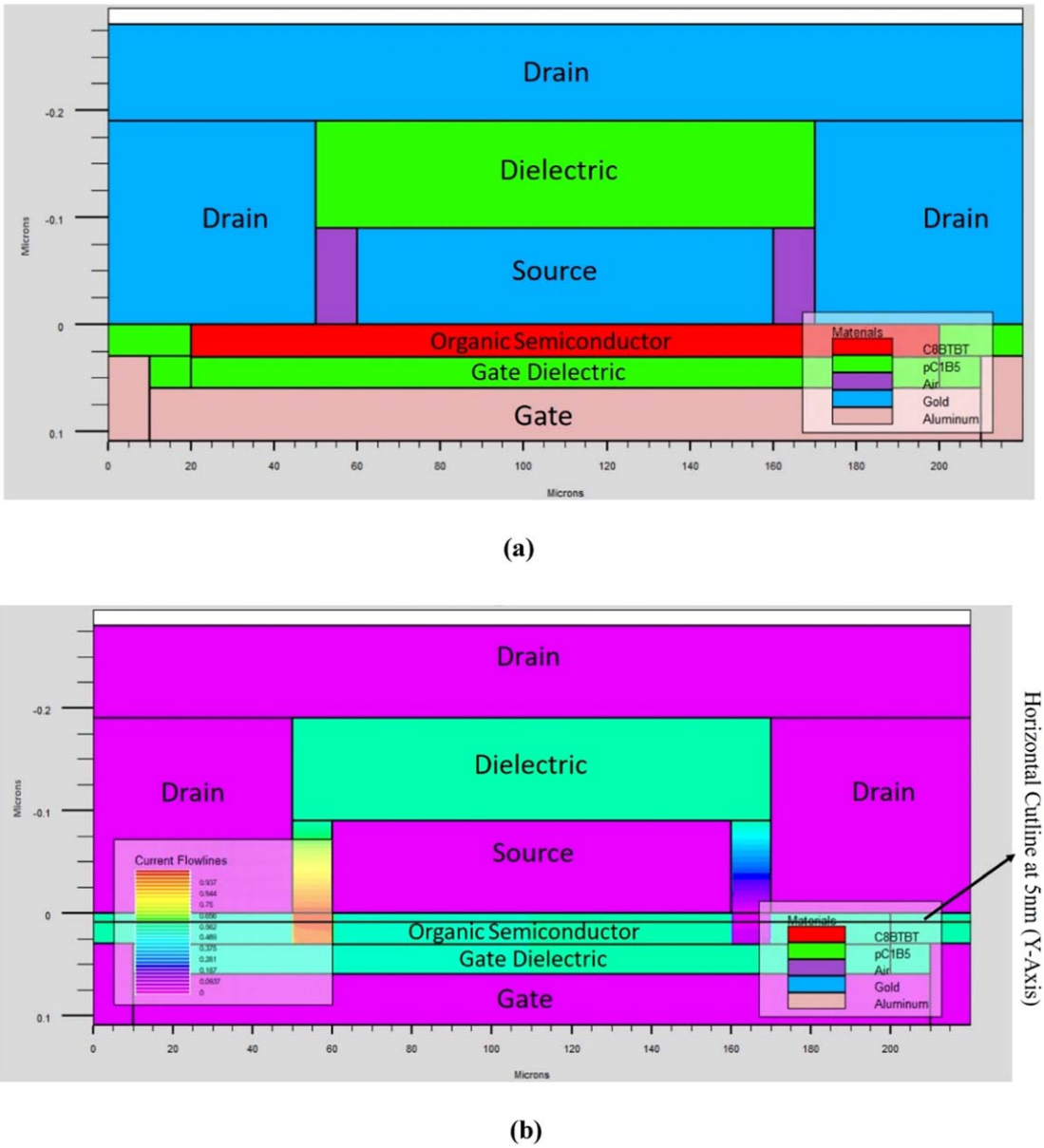


Figure 11. (a) Simulated structure of proposed device (D_5) and (b) current flowlines along with horizontal cutline.

Table 8. Performance parameters of D_2 and D_5.

Parameters	Device		
	D_2	D_2^* (at gate = 80 nm, dielectric = 59 nm)	D_5 (Proposed)
Threshold Voltage V_t (V)	−0.9	−0.8	−1.5
Maximum Drain Current I_{Dmax} (μA)	221	161	528
I_{on}/I_{off}	2.3×10^{10}	7.8×10^{6}	1.1×10^{9}
Saturation Mobility μ_{sat}(cm^2/V.s)	30.2	18.7	80.8

The thickness of layers is highlighted in table 5. In device D_4, source and drain are considered of 10 nm each due to the structural variation. However, change in thickness does not affect the performance of the transistor as performance parameters are independent of the thickness of source/drain electrodes.

Table 6 represents the performance parameters of D_2, D_3 and D_4 devices. D_4 is showing the best results as compared with other devices. The parameters of device D_2 such as V_t, I_{Dmax}, and μ_{sat} are 0.6, 2.6 and 3.1 times improved in comparison with D_3 device and 0.75, 1.8 and 1.9 times better than D_4 device.

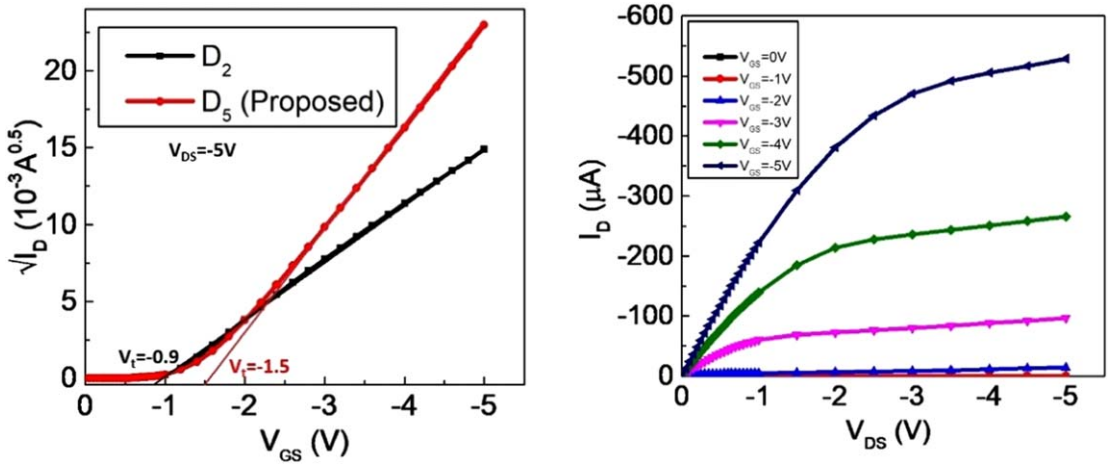


Figure 12. (a) Comparison of transfer characteristics of D2 and D5 devices (b) drain characteristics of D5 device.

Figure 9 is showing the comparison of transfer curves of D_2, D_3 and D_4 devices with the threshold voltages. Among all, D_2 device is exhibiting the best performance in terms of V_t, I_{Dmax}, and μ_{sat}. The $\sqrt{I_{Dmax}}$ of D_2, D_3 and D_4 are 14.9, 10.9 and 9.0 $\sqrt{(10^{-3}\ A^{0.5})}$, respectively at $V_{GS} = V_{DS} = -5$ V. Addition to this, D_2 is operating at threshold voltage of −0.9 V which is smaller than D_3 and D_4.

4. Proposed novel vertical structure

In this section, a novel vertical structure (D_5) is proposed. The materials and thicknesses of D_5 are kept same as of D2, D3 and D4 to make a fair comparison as depicted in figure 10. The proposed vertical TFT is completely a novel structure with ditch like shapes of gate and dielectric. The proposed novel structure (D_5) is showing significantly a higher performance in comparison to other devices; D_1, D_2, D_3 and D_4 as illustrated in table 8. Also, the proposed TFT is analysed internally using horizontal and vertical cutline to understand internal device physics associated for its improved parameters. In cutline analysis, various parameters such as, potential, current density, band energy for conduction and valence band and hole concentration around the channel are explored deeply to justify the outperformance of this novel device.

The reason for the performance improvement in case of D_5 is very clear. Here, all the organic TFTs are of p type. In D_2, on applying negative potential at gate terminal, electrons start repelling from gate side and moving towards source. Hence, current starts flowing in the opposite direction. It can be seen in figure 4 that the complete channel is developing in both the directions (vertical and horizontal). Here, from source to OSC, the channel is strongly induced but it is comparatively weak as we move from OSC to drain. On the other hand, in case of D_5, the gate layer is twisted towards OSC. This results in additional charge carriers into the vertical channel created from OSC to drain side which automatically enhances the current density and mobility of the proposed device.

Table 7 is demonstrating the materials and thickness of D_2 and D_5 device. The thicknesses of OSC, source and drain are same in both devices. Although, the thickness of gate dielectric and gate are varied from 29 to 59 nm and 50 to 80 nm, correspondingly due to the structural changes incorporated in D_5 device. Addition to this, figures 11(a) and (b) is showing the device structure and current flowlines of proposed novel VOTFT.

4.1. Results and discussion

Table 8 highlights that the proposed device is exhibiting I_{Dmax} and μ_{sat} as 528 μA and 80.8 cm^2/V.s which are approximately 2.4 and 2.6 times greater than the performance of D_2 device, respectively. Also, I_{on}/I_{off} is also improved by 10 times. In the table, D_2^* is highlighting the results of D_2 device where only dielectric and gate layers are varied in terms of the thickness as 59 nm and 80 nm, respectively.

Figures 12(a) and (b) are illustrating the transfer and drain characteristics of proposed device. The maximum $\sqrt{I_D}$ is obtained as 22.9 $\sqrt{(10^{-3}\ A^{0.5})}$ with the threshold voltage of −1.5 V at drain voltage of −5 V.

4.2. Internal analysis of proposed device

Here, internal analysis of proposed device D_5 is performed by creating horizontal and vertical cutline as this structure contains the channel in both horizontal and vertical direction. The cutlines are providing the detailed analysis of band energy, potential distribution, and total current density.

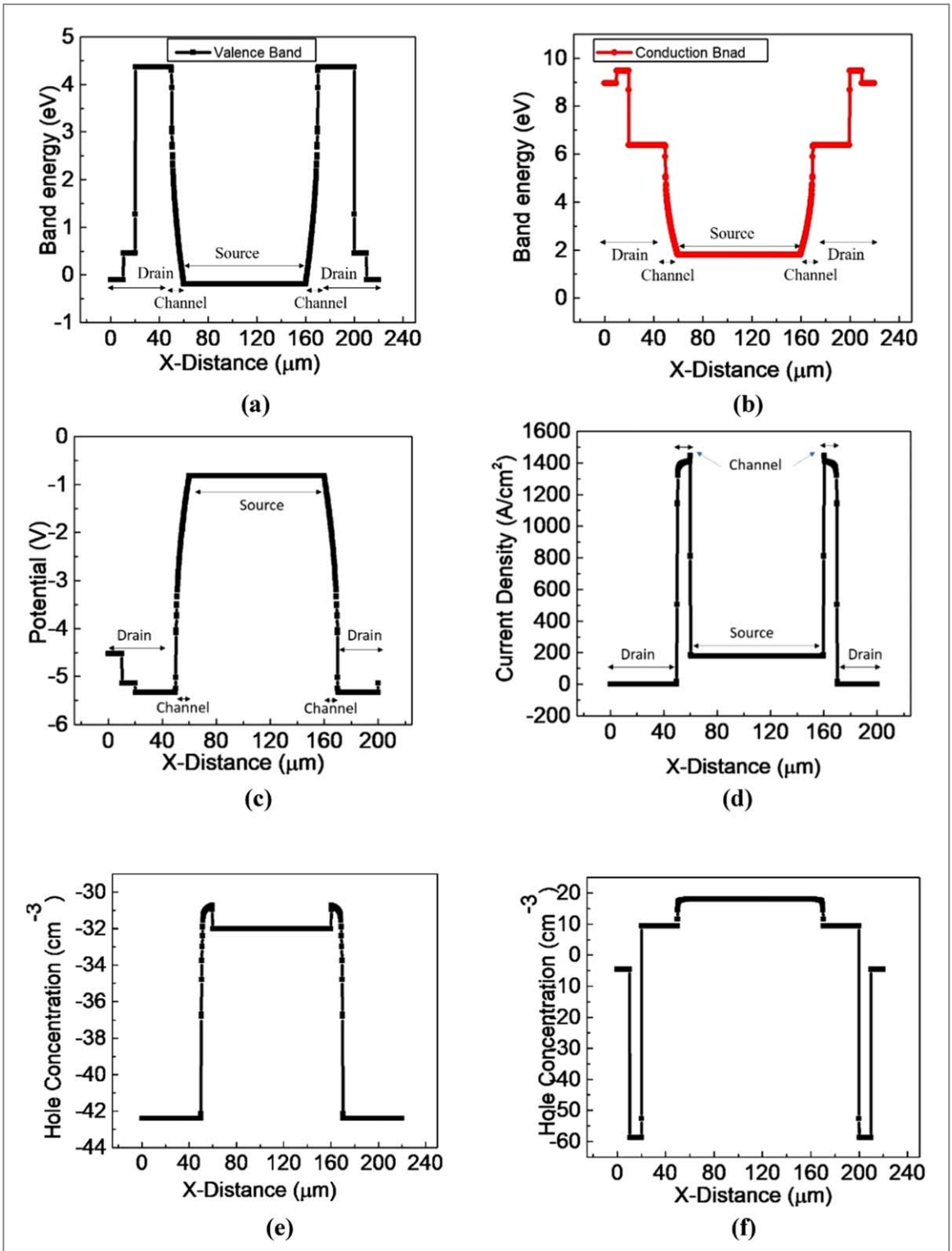


Figure 13. Horizontal cutline analysis of (a) valence band, (b) condution band (c) potential distribution. (d) total current density of D_5 Device (e) hole concentration of D_2 and (f) hole concentration of D_5.

4.2.1. Horizontal cutline analysis

A horizontal cutline is drawn at 5 nm below the source electrode as highlighted in figure 11 (b).

Figures 13(a) and (b) are depicting the energy bands of valence and conduction band, respectively. Figure 13(c) is highlighting the data for potential distribution of D_5. It can be observed from the figure that potential is lower at source i.e. around −1 V and is higher (∼−5 V) at drain electrodes. Addition to this, the figure 13(d) is demonstrating the total current density of the device. The device is achieving the maximum current density at the channel i.e. 1451 A cm^{-2} and minimum at drain electrodes. Furthermore, figures (e) and (f) are demonstrating the hole concentration of D_2 and D_5 devices, correspondingly. It is clearly visible from the

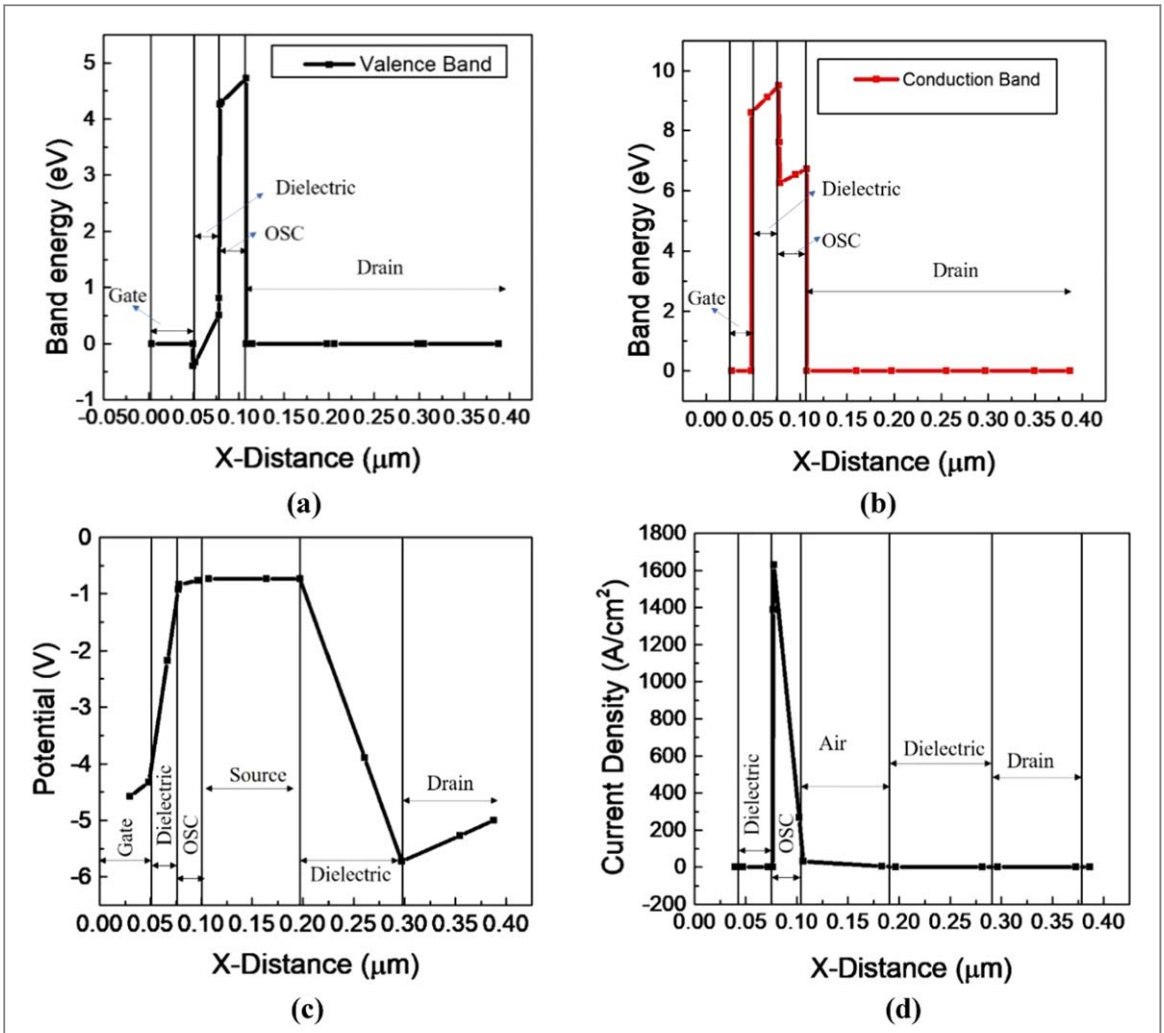


Figure 14. Vertical cutline analysis of (a) valence band, (b) condution band (c) potential distribution (d) total current density of D_5 Device.

figures that the proposed structure (D_5) is exhibiting extremely good performance as compared with D_2 device. The reason behind this is the presence of the ditches of gate dielectric and gate in the proposed device which improved the charge injection. Hence, the performance of the device is enhanced significantly.

4.2.2. Vertical cutline analysis

A vertical cutline is drawn here at X = 58 nm. This cutline reveals the vertical information of different layers on the basis of band energy, potential graph and current density. Figures 14(a) and (b) are illustrating the band energies in terms of valence and conduction band, correspondingly. Thereafter, figure 14(c) is showing the potential distribution of the device in vertical manner.

The value of potential is dropping from drain to source as −5 V to −1 V. As well as there is another fall in potential from gate to dielectric layer. Additionally, figure 14(d) is depicting the total current density which is maximum at semiconductor layer as 1625 A cm^{-2}. At dielectric, air and drain electrode the value of current density is approximately zero.

4.3. Comparison of real existing vertical TFTs with the proposed device

In this sub-section, the proposed device (D_5) is compared with the real existing devices D_2 [20], D_3 [25], D_4 [26], D_6 [27] and D_7 [28] in terms of various important parameters such as maximum drain current, saturation mobility, I_{on}/I_{off}, and threshold voltage. The comparison is highlighted in two ways. In Table 9, D_5 is compared with the reported results of the real devices. On the other hand, table 10 is depicting the comparison of D_5 with simulated results of the real devices at common materials and common possible thicknesses.

It can be clearly observed from the table 10, that the proposed device is exhibiting the best performance as compared to the other mentioned devices. To be precise, the obtained drain current of the proposed novel structure (D_5) is 2.38, 6.4, 4.4, 44, 3.59 times enhanced on comparing with D_2, D_3, D_4, D_6 and D_7,

Table 9. Comparison of the proposed device with real devices (reported results).

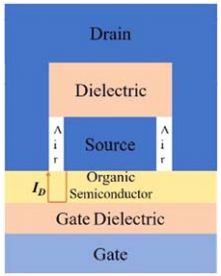
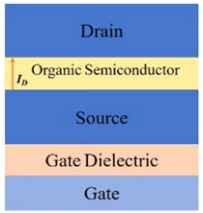
Sr no.	Real existing device structures	Fabricated results along with the materials	
		Materials	Parameters
1.	D_2 [20] 	Source/Drain: Gold Gate: Al	$V_{GS} = -5$ V $V_{DS} = -10$ V
2.	D_3 [25] 	OSC: TIPS-Pentacene Gate Dielectric: Al_2O_3 Source: Silver nanowires Drain: Al	$I_{Dmax} = 150$ μA $\mu_{sat} = 4.8$ cm^2/V.s $V_{GS} = 10$ V $V_{DS} = 30$ V
		Gate: Indium Tin Oxide (ITO) OSC: VTP (vanadyl 3,10,17,24-tetra-tert-butyl-1,8,15,22-tetrakis (dimethylamino) −29H,31H-phthalocyanine)	$I_{Dmax} = 37$ mA cm^{-2} $I_{on}/I_{off} = 10^5$

Table 9. (Continued.)

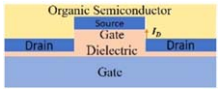
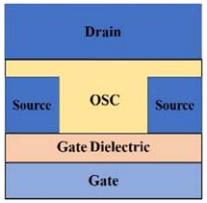
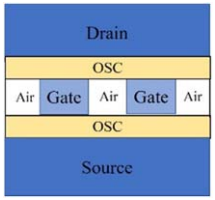
Sr no.	Real existing device structures	Fabricated results along with the materials	
		Materials	Parameters
3.	D_4 [26] 	Gate Dielectric: PVDF-TrFE OSC: Pentacene Gate Dielectric: Tantalum	$V_t = 7.1$ V $V_{GS} = -20$ V $V_{DS} = -20$ V
4.	D_6 [27] 	Source/Drain: Palladium/Titanium, Gate: Silicon OSC: Pentacene	$I_{Dmax} = 0.2$ μA $V_{GS} = -40$ V $V_{DS} = -40$ V
5.	D_7 [28] 	Gate Dielectric: SiO_2 Source: Al Drain: ITO	$I_{Dmax} = 0.8$ μA $V_{GS} = 20$ V $V_{DS} = 10$ V
6.	D_5 [Proposed]	Gate: Al, OSC: PTCDI C-8 Source/Drain: Gold	$I_{Dmax} = 81.08$ mA $I_{on}/I_{off} = 3$ $V_{GS} = -5$ V

Table 9. (Continued.)

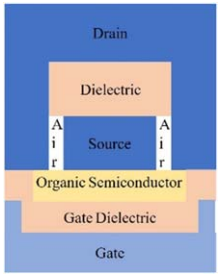
Sr no.	Real existing device structures	Fabricated results along with the materials	
		Materials	Parameters
		Gate: Al	$V_{DS} = -5$ V
		OSC: C8-BTBT Gate Dielectric: pC1B5	$I_{Dmax} = 528\ \mu$A $\mu_{sat} = 80.8\ \text{cm}^2/\text{V.s}$ $I_{on}/I_{off} = 1.1\times10^9$ $V_t = -1.5$

Table 10. Comparison of the proposed device with real devices (simulated results at common platform).

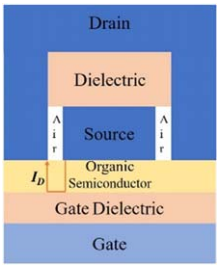
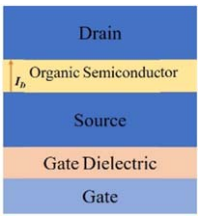
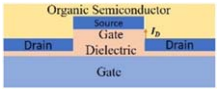
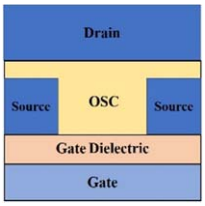
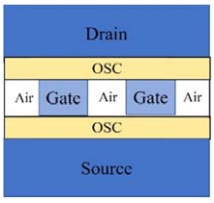
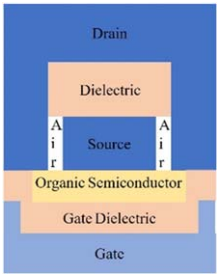
Sr no	Real existing device structures	Simulated results at common platform			
		Materials- (Source/Drain: Gold, Gate: Al, OSC: C8-BTBT, Gate Dielectric: pC1B5)			
		Performance parameters at $V_{GS}=-5$ V and $V_{DS}=-5$ V			
		I_{Dmax} (μA)	V_t (V)	μ_{sat} (cm^2/V.s)	I_{on}/I_{off}
1.	D_2 [20]	221	−0.5	30.2	2.3×10^{10}
					
2.	D_3 [25]	82.5	−1.5	9.7	0.8×10^{10}
					
3.	D_4 [26]	120	−1.2	15.5	0.1×10^{11}
					
4.	D_6 [27]	12	−2.1	1.1	4.1×10^{8}
					
5.	D_7 [28]	147	−1.6	22.4	3.4×10^{7}
					
6.	D_5 [Proposed]	528	−1.5	80.8	1.1×10^{9}

Table 10. (Continued.)

Sr no	Real existing device structures	Simulated results at common platform			
		Materials- (Source/Drain: Gold, Gate: Al, OSC: C8-BTBT, Gate Dielectric: pC1B5)			
		Performance parameters at $V_{GS}=-5$ V and $V_{DS}=-5$ V			
		I_{Dmax} (μA)	V_t (V)	μ_{sat} (cm^2/V.s)	I_{on}/I_{off}
					

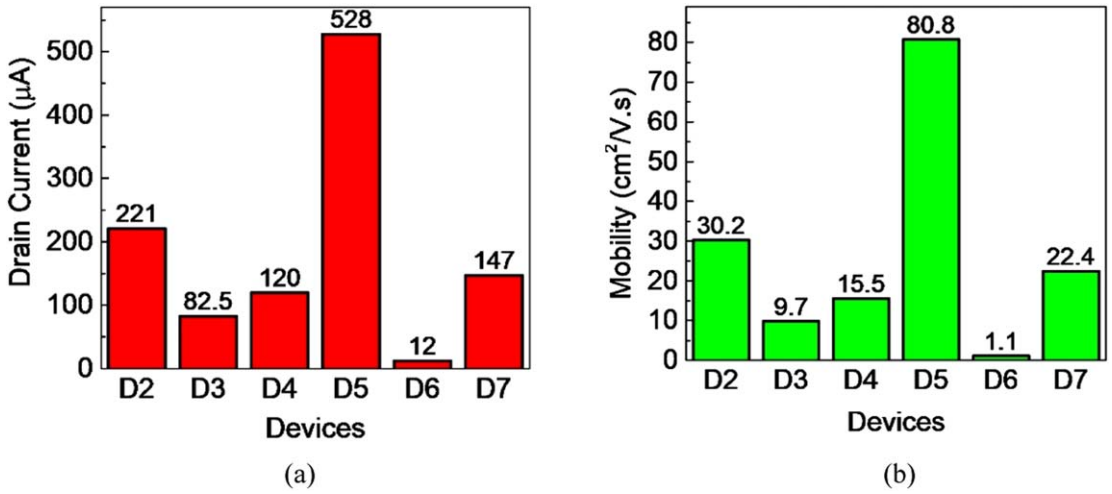


Figure 15. Comparison of various vertical TFTs in terms of (a) drain current and (b) Mobility.

correspondingly as depicted in figure 15(a). Addition to this, the saturation mobility is 2.67, 8.32, 5.21, 448.8 and 3.60 times better as compared with D_2, D_3, D_4, D_6 and D_7, respectively as outlined in figure 15(b).

Realization of vertical TFT [20]: In this sub-section, the complete fabrication steps are discussed of the vertical channel device (D_2). First, to establish a gate layer PVD (physical vapour deposition) is utilized. Thereafter, a thin layer of gate dielectric layer is prepared using ALD (atomic layer deposition). Now, to deposit an organic semiconductor (OSC) spin-coating method is incorporated under nitrogen atmosphere. Then, source electrode is deposited using PVD technique. Here, lithography method is also included to structure the source electrode under ambient conditions. Also, to build an insulator above source photoresist steps are incorporated. Afterwards, drain electrode is also formed similarly as source electrode. For the prevention of the OSC or the source electrode fluoropolymer-based photoresist OSCoR 5001 is involved. At the end, the photoresist is spin coated onto the drain electrode, then pre-baked on a hot plate, exposed to UV light and eventually post-baked again [20].

5. Conclusion

The performance of a proposed VOTFT is analysed and compared. The efforts have been made in the direction to achieve high performance by incorporating some structural variation in an existing vertical structure. The proposed structure demonstrates remarkable performance in terms of V_t, I_{Dmax} and μ_{sat} as 1.5 V, 528 μA and

80.8 cm^2/V.s, correspondingly. Moreover, different vertical structures are compared where D_2 device reveals better results as compared with D_3, D_4, D_6 and D_7. The performance parameters of D_2 on the basis of threshold voltage, maximum drain current and saturation mobility are 0.6, 2.6 and 3.1 times better as compared to D_3 and 0.75, 1.8 and 1.9 times as compared to D_4. Additionally, for better understating horizontal and vertical cutline analysis of proposed device is also incorporated.

Data availability statement

The data cannot be made publicly available upon publication because no suitable repository exists for hosting data in this field of study. The data that support the findings of this study are available upon reasonable request from the authors.

Declarations

Ethics approval

The manuscript is not submitted to anywhere else for the publication. The submitted work is an original work and have not been published elsewhere in any form or language. The authors do not have any conflict of interest. The research does not involve any human participant and/or animal thus, informed consent in not required.

Consent to participate

Not applicable.

Consent for publication

All the authors understand and give their consent for the publication of manuscript 'High-k dielectric Based High Performance Vertical Organic Thin Film Transistor for Flexible Low Power Applications' in 'Physica Scripta' Journal.

Availability of data and materials

Not applicable.

Competing interests

No, all the authors declare that they have no competing interests as defined by IOP, or other interests that might be perceived to influence the results and/or discussion reported in this paper. The authors have no conflicts of interest to declare that are relevant to the content of this article.

Funding

Not applicable.

ORCID iDs

Poornima Mittal https://orcid.org/0000-0002-9479-8628

References

[1] Mittal P, Negi Y S and Singh R K 2016 A depth analysis for different structures of organic thin film transistors: modeling of performance limiting issues *Microelectron. Eng.* **150** 7
[2] Mittal P, Kumar B, Negi Y S, Kaushik B K and Singh R K 2012 Channel length variation effect on performance parameters of organic field effect transistors *Microelectronics J.* **43** 985

[3] Kleemann H, Günther A A, Leo K and Lüssem B 2013 High-performance vertical organic transistors *Small* **9** 3670
[4] Mittal P, Yadav S and Negi S 2021 Advancements for organic thin film transistors: structures, materials, performance parameters, influencing factors, models, fabrication, reliability and applications *Mater. Sci. Semicond. Process.* **133** 105975
[5] Qashou S I 2022 Effect of UV irradiation on the linear and nonlinear optical properties of erbium (III)-Tris (8-hydroxyquinolinato) thin films: optoelectronic performance *Phys. Scr.* **97** 055803
[6] Mahmood A, Nadeem A, Raza Q, Khan T M, Mehmood M, Hassan M M and Mahmood N 2010 'Effect of thermal annealing on the structural and optical properties of ZnO thin films deposited by the reactive e-beam evaporation technique *Phys. Scr.* **82** 065801
[7] Zaidia E F M, Darwish A A A, Yahia I S and Rashad M 2020 'Noncrystalline films of gallium (III) phthalocyanine chloride evaporated on a flexible polymer substrate for flexible organic technology: optical spectroscopy and optical limiting *Phys. Scr.* **95** 115802
[8] Emanetoglu N W, Gorla C, Liu Y, Liang S and Lu Y 1992 Epitaxial ZnO piezoelectric thin films for saw filters *Mater. Sci. Semicond.* **2** 247
[9] Negi S, Rana A, Baliga A K, Mittal P and Kumar B 2015 Performance analysis of dual gate organic thin film transistor and organic SR latch application *In Int. Conf. on Computing, Communication & Automation* 1427
[10] Mittal P 2016 'Low cost dual and single gate organic thin film transistor and their performance parameter analysis *SRM International Journal of Engineering Science* **4** 15
[11] Pal S, Kumar B and Mittal P 2021 Impact of different gate dielectrics on OTFT driven active-matrix OLED pixel circuits *Semiconductor* **55** 618
[12] Klauk H 2018 Will we see gigahertz organic transistors? *Adv. Electron. Mater.* **4** 1700474
[13] Lenz J, Del Giudice F, Geisenhof F R, Winterer F and Weitz R T 2019 Vertical, electrolyte-gated organic transistors show continuous operation in the MA cm− 2 regime and artificial synaptic behaviour *Nat. Nanotechnol.* **14** 579
[14] Kleemann H, Krechan K, Fischer A and Leo K 2020 A review of vertical organic transistors *Adv. Funct. Mater.* **30** 1907113
[15] Chen Y and Shih I 2007 Fabrication of vertical channel top contact organic thin film transistors *Org. Electron.* **8** 655
[16] Yang C Y, Cheng S S, Ou T M, Wu M C, Wu C H, Chao C H, Lin S Y and Chan Y J 2007 Pentacene-based planar-and vertical-type organic thin-film transistor *IEEE Trans. Electron Devices* **54** 1633
[17] Kim Y D, Park J W, Kang I N and Oh S Y 2008 Effects of morphological control on the characteristics of vertical-type OTFTs using Alq3 *Ultramicroscopy* **108** 1237
[18] Rathi R, Ahmad R, Negi S and Panwar V 2018 *In 2018 5th IEEE Uttar Pradesh Section Int. Conf. on Electrical, Electronics and Computer Engineering (UPCON)* p 1
[19] Chen Q, Yan Y, Wu X, Lan S, Hu D, Fang Y, Lv D, Zhong J, Chen H and Guo T 2019 High-performance quantum-dot light-emitting transistors based on vertical organic thin-film transistors *ACS Appl. Mater. Interfaces* **11** 35888
[20] Kneppe D, Talnack F, Boroujeni B K, da Rocha C T, Höppner M, Tahn A, Mannsfeld S C, Ellinger F, Leo K and Kleemann H 2021 Solution-processed pseudo-vertical organic transistors based on TIPS-pentacene *Materials Today Energy* **21** 100697
[21] Choi J, Kang J, Lee C, Jeong K and Im S G 2020 Heavily crosslinked, high-k ultrathin polymer dielectrics for flexible, low-power organic thin-film transistors (OTFTs) *Adv. Electron. Mater.* **6** 2000314
[22] Bai Y, Liu X, Chen L, Khan M A, Zhu W Q, Jiang X Y and Zhang Z L 2007 Organic thin-film field-effect transistors with MoO3/Al electrode and OTS/SiO2 bilayer gate insulator *Microelectron. J.* **38** 1185
[23] Han Y C, Lim M S, Park J H and Choi K C 2013 ITO-free flexible organic light-emitting diode using ZnS/Ag/MoO3 anode incorporating a quasi-perfect Ag thin film *Org. Electron.* **14** 3437
[24] Alam M W, Wang Z, Naka S and Okada H 2013 Temperature dependence of barrier height and performance enhancement of Pentacene based organic thin film transistor with bi-layer MoO3/au electrodes *Current Nanoscience* **9** 407
[25] Roslan N A, Abdullah S M, Halizan M Z M, Bawazeer T M, Alsenany N, Alsoufi M S, Majid W H A and Supangat A 2018 VTP as an active layer in a vertical organic field effect transistor *J. Electron. Mater.* **47** 2184
[26] Naruse H, Naka S and Okada H 2007 Dual self-aligned vertical multichannel organic transistors *Appl. Phys. Express* **1** 011801
[27] Zan H W and Yen K H 2007 Vertical-channel organic thin-film transistors with meshed electrode and low leakage current *Jpn. J. Appl. Phys.* **46** 3315
[28] Oh S Y and Lee J Y 2006 Characteristics of vertical type organic transistor using n-type material and its application for OLED *Mol. Cryst. Liq. Cryst.* **444** 211

Environmental Science and Pollution Research
https://doi.org/10.1007/s11356-024-32049-y

ADVANCES IN ENERGY, ENVIRONMENT AND GREEN TECHNOLOGIES FOR SUSTAINABILITY

Impact of tumbling on production of biomethane from household waste

Pradeep Kumar Meena[1] · **Amit Pal**[1] · **Samsher Gautam**[2]

Received: 21 August 2023 / Accepted: 14 January 2024
© The Author(s), under exclusive licence to Springer-Verlag GmbH Germany, part of Springer Nature 2024

Abstract
This study utilized nine anaerobic digesters (ADs) with individual capacities of 10 l to investigate methane (CH_4) gas generation from various waste combinations and operating conditions, employing both non-tumbling and tumbling processes with the aid of the Taguchi method. The experimentation encompassed different varieties of fruit waste (FW), raw vegetable waste (RVW), and mixed cooked waste (MCW) at varying proportions (1:1, 1:1.5, and 1:2) and temperatures (35 °C, 40 °C, and 45 °C), along with multiple feed inputs. Additionally, the study assessed the impact of tumbling, examining durations of 0, 10, and 20 min at a speed of 15 rpm. The results yielded substantial insights, revealing coefficient of determination (R^2) values of 94.76% and 98.48% for non-tumbling and tumbling processes, respectively. Under the conditions of 40 °C and a 1:1.5 ratio, the average optimal methane (CH_4) gas generation in FW without tumbling was determined to be 37.12%. For RVW and MCW at ratios of 1:1.5 and 1:2, respectively, the estimated CH_4 values were 26.7% and 26.68% at a temperature of 35 °C. Comparison between tumbling and non-tumbling conditions demonstrated noteworthy improvements in CH_4 gas production. For FW, tumbling for 10 and 20 min resulted in 11% and 6% increases in CH_4 gas production, respectively. Tumbling also led to substantial boosts in CH_4 gas production for RVW, with 31.1% and 47.9% increases after 10 and 20 min, and for MCW, with 25.7% and 12.2% increases after 10 and 20 min, respectively. Tumbling enhances CH_4 gas production in anaerobic digesters, promising for waste-to-energy conversion.

Keywords Biogas · Taguchi method · Anaerobic digesters · Waste combinations · Temperature effects · Waste-to-energy conversion

Introduction

The generation of municipal solid waste (MSW) has been steadily increasing due to urbanization and higher consumption levels. The global production of MSW, which was over 1.3 billion metric tons in 2010, is projected to reach 2.2 billion metric tons by 2025 (Bhada-Tata 2012). Wealthy nations are dealing with significant environmental problems due to the excessive production and insufficient handling of organic waste. The Food and Agriculture Organization of the United Nations (FAO) estimates that approximately one-third of all food produced globally, amounting to 1.3 gigatons annually, goes to waste (Megido et al. 2021). The growth of MSW generation is particularly pronounced in developed and developing countries, driven by economic expansion and population growth (Babaee and Shayegan 2011; Plai et al. 2014).

In India, MSW generation is expected to reach 440,460 tons per day by 2026, with nearly 90% of waste being improperly disposed of (Hoornweg and Otten 1999;Begum et al. 2016). Reports indicate that organic materials such as vegetables, fruits, and cooked food waste comprise 51% of MSW (Annepu 2012; Elango et al. 2007). India, the second-largest producer of fruits and vegetables, faces significant challenges in managing the substantial waste generated from residential and commercial activities, including peeling and slicing fresh produce (Lim et al. 2012). Inadequate

Responsible Editor: Ta Yeong Wu

✉ Pradeep Kumar Meena
pradeep_2k18phdme08@dtu.ac.in

[1] Department of Mechanical Engineering, Delhi Technological University, Delhi, India

[2] Harcourt Butler Technical University, Kanpur, India

Published online: 23 January 2024

solid waste disposal exacerbates environmental and health hazards (Das and Mondal 2013). Restaurants, motels, and cafeterias are prominent sources of food waste (FW), and the high biodegradability of fruit and vegetable waste from markets contributes to putrefaction in landfills (Misi and Forster 2002; Viturtia et al. 1995).

Anaerobic digestion is suitable for utilizing FW's great organic content and high moisture levels. It can produce significant amounts of methane, a viable alternative energy source (Latha et al. 2019). The anaerobic digestion of organic waste offers promising results in reducing landfill usage and carbon dioxide emissions. Through anaerobic digestion, discarded food can be repurposed into valuable resources, including energy and liquid fertilizers like biogas, improving soil fertility. This approach helps incorporate organic waste management to mitigate adverse environmental impacts (Kazimierowicz 2017). Anaerobic digestion of various organic wastes, including manure, sewage sludge, the organic fraction of MSW, and fruit and vegetable waste, provides a dual advantage by producing biogas while treating residues, thus reducing their disposal in landfills (Lin et al. 2011; Appels et al. 2011;Di Maria et al. 2015). AD is an alternative approach to addressing organic waste and offers opportunities to reduce environmental contamination. It is a low-technology, cost-effective system that can provide biogas as a clean energy source. At the same time, the nutrient-rich digestate can be utilized as organic fertilizer or a carrier material for agricultural bio-fertilizers (Khalid et al. 2011; Meena et al. 2020; Rehl and Müller 2011; Tambone et al. 2009). In anaerobic digestion, bacteria employ hydrolysis, acidogenesis, acetogenesis, and methanogenesis to convert organic materials into biogas under anoxic conditions.

Microbial activity in anaerobic digestion is notably influenced by both the composition of the substrate and the surrounding environment, ultimately resulting in heightened biogas production (Kadam and Panwar 2017). Fruit and vegetable waste (FVW) and kitchen waste (KW) share a high volatile solids content, which accelerates hydrolysis during digestion but can lead to excessive acidity when digested separately, hindering methanogenesis (Jiang et al. 2012; Ward et al. 2008). Moreover, these wastes' high moisture content and easy biodegradability contribute to issues in MSW landfills and incineration systems, such as unpleasant odors, leachate formation, and unstable combustion (Cheng and Hu 2010; El-Fadel et al. 2002). The microbiological aspects of biogas production are influenced by factors such as temperature, pH, volatile fatty acids, and microbial population (Deressa et al. 2015). Temperature plays a crucial role as it affects reaction rates, stability, and microbial activity, and any sudden or rapid temperature shift can disrupt biogas production (Li et al. 2017).

The C/N ratio and pH are also vital factors in AD, affecting biogas production. Fruit, vegetable, and meat wastes with C/N ratios ranging from 17 to 26 and 30 show increased methane composition (Ghazi et al. 2014). The ratio of cafeteria waste, vegetable waste, and fruit waste at 1:1:1 has been found to yield better results compared to other ratios, indicating its impact on biogas production (Al Mamun and Torii 2014). The size of the anaerobic digester also influences biogas production. Studies have shown that the tri-digestion of FW, KW, and FVW at a ratio of 5:2:3 yields higher biogas and methane yields compared to mono digestion (Li et al. 2020).

Previous research has demonstrated that using an impeller mixer or stirring at specific speeds can increase biogas production (Chol et al. 2021; Sinaga et al. 2018). However, traditional stirring methods may not thoroughly mix the feed inside the biogas digester. In contrast, tumbling techniques ensure thorough mixing, potentially leading to higher biogas production. Despite extensive studies on biogas production, there is limited research on the specific effects of tumbling, precise temperature control, and feed ratios. This study utilized Taguchi analysis to investigate how tumbling, different types and quantities of waste, and temperature influence biogas production. The aim was to systematically assess the combined impact of these factors on biogas generation in anaerobic digesters. This statistical approach could identify optimal conditions for enhancing biogas production, contributing to more effective waste-to-energy conversion processes.

Materials and methods

Biogas digester

A biogas digester is a cylindrical container used for anaerobic digestion, decomposing organic materials without oxygen. This digester has a height and diameter of 381 mm, providing a total capacity of 10 l. A thin MS sheet is used to manufacture a cylindrical container; the top is covered with another thin sheet. A black-color coating is done to maximize the heat absorption capacity of the MS container. The lid at one end can be sealed or opened for feedstock addition, and an outlet valve extracts the produced biogas.

Inside the digester, a thermocouple acts as a sensor, monitoring temperature variations. It displays this information outside, allowing the operator to observe and control the temperature for efficient digestion. The specially coated MS sheet enhances heat retention, facilitating the fermentation and conversion of organic waste into biogas. Higher temperatures optimize the digestion process, increasing biogas production. The feeding capacity is 7.5 l, accommodating enough organic waste to generate a decent amount of biogas daily. Mixed cooked vegetable and fruit waste undergo anaerobic digestion, producing biogas. The thermocouple monitors the digester's temperature and

provides real-time readings. Thus, the operator maintains an optimal temperature range (35–45 °C) necessary for efficient digestion, as high temperatures are essential for the process.

Heating container

It is designed to withstand the corrosive nature of biogas and provides a controlled environment for the efficient decomposition of organic materials. The container, constructed from stainless steel, measures 1220 × 762 mm and accommodates three biogas digesters, totaling nine digesters.

Water is used as a medium to transfer heat to the biogas digesters. The containers are filled with water; a heating element connected to a power source heats this water. The heated water circulates through convection within the containers and transfers heat to the biogas digesters. This elevated temperature enhances the activity of microorganisms responsible for anaerobic digestion, increasing biogas production. Using three containers offers several advantages. It optimizes space and resource utilization, allows for better control and monitoring of the heating process, and ensures even heat distribution among the digesters. Water is an efficient heat transfer medium due to its excellent thermal properties, enabling effective heat transfer to the digesters. This heating container system provides a simple and effective method for generating biogas. It improves the efficiency of the anaerobic digestion process, resulting in a higher biogas yield. Optimizing heat distribution and control, it offers a sustainable solution for converting organic waste into valuable biogas, utilizing space and resources efficiently.

Tumbling setup

The tumbling effect is used by revolving the digester at a set speed, enabling the thorough mixing of organic components to ensure efficient biogas production. A specially designed tumbling set with a capacity of 10 l is used in this case. It is connected by a belt and positioned horizontally at a tilt angle of 30–45°.

The belt rotates the set at 15 rpm, effectively mixing the organic materials and preventing settling at the bottom of the digester. After feedstock addition, the tumbling process typically lasts 10 to 20 min. The tumbling effect is vital for biogas production as it ensures well-mixed organic materials, essential for efficient breakdown and biogas generation. Insufficient mixing can lead to anaerobic dead zones within the digester, producing harmful toxic gases. Additionally, the tumbling action facilitates the analysis of large clumps of organic matter, enabling easier access for bacteria to convert into biogas. Moreover, the uniform distribution of bacteria throughout the digester is achieved through the tumbling effect, ensuring efficient decomposition of the organic matter. In summary, the tumbling effect, achieved through rotation, is a critical process in biogas production. It promotes the thorough mixing of organic materials, prevents the formation of anaerobic dead zones, aids in the breakdown of large clumps, and ensures even distribution of bacteria, all contributing to optimal biogas production.

Feed stock

The feedstock for the experiment mainly consisted of fruit, raw vegetable, and mixed cooked waste. The fruit waste from the juice shop was collected inside the cafeteria. Most fruit wastes were a banana, sweet lemon, mango, and sugarcane. Raw vegetables and cooked kitchen waste were collected from the university's canteens and messes. Their properties are summarized in Table 1.

A crucible with a capacity of 50 ml was taken for TS calculation. First, the weight of the empty crucible was calculated using the weighing machine; then, a 20-ml sample was placed in a crucible and heated to 105 °C in an oven. Due to this, the sample moisture evaporates. After evaporation, the sample can cool in a desiccator, and the final weight is recorded:

$$\text{The initial weight of the empty crucible} = \text{W1 g} \tag{1}$$

$$\text{Final weigh of the crucible} = \text{W2 g} \tag{2}$$

$$\text{Total solids present in the sample (\%)} = \frac{\textit{Final weight}(W2)}{\textit{Intial weight}(W1)} \times 100 \tag{3}$$

A further processor has to be done to calculate VS. After cooling the sample in the desiccator, its weight was calculated. And again, that sample is kept in a muffle furnace at 600-degree temperature for 10 min, and the final weight (W3) is taken.

$$\text{Volatile content (\%)} = \frac{\textit{Intial weight}(W1) - \textit{Final weight}(W3)}{\textit{Intial weight}(W1)} \times 100 \tag{4}$$

Taguchi analysis

Taguchi analysis can be applied to optimize biogas production, a renewable energy source derived from organic waste. By utilizing this statistical method, various

Table 1 Characteristics of substrates

Types of wastes	Total solid (TS) (%)	Volatile solid (VS) (%)	VS/TS (%)	pH
Fruit waste	27.5	25.3	92	5.9
Raw vegetable waste	10.55	9.25	87.67	5.7
Mixed cooked waste	12.15	10.45	86	6.5

factors affecting biogas production, such as temperature, types of feedstocks, ratio, pH, and retention time, can be systematically studied. Taguchi analysis helps identify the optimal combination of factors and levels to maximize biogas yield while minimizing variations caused by uncontrollable factors. This approach enables efficient and cost-effective biogas production processes.

Analysis (Experimental investigation)

Table 2 exhibits that without the tumbling effect, ADs D1, D2, and D3 are placed together in a container whose temperature is maintained at 35 °C. In all three ADs, FW, RVW, and MCW are fed in the 1: 1, 1:1.5, and 1: 2. The feed counts have been kept in 1:1, 1:1.5, and 1:2 throughout the experiment. 1:1 means 0.375 kg of waste and 0.375 l of water, 1:1.5 means 0.3 kg of waste and 0.45 l of water, and 1:2 means 0.25 kg of waste and 0.5 l of water have been used. Similarly, ADs, D4, D5, and D6 are fed into container 2 at a temperature of 40 °C and provided to MCW, FW, and RVW in 1:1, 1:1.5, and 1:2. ADs, D7, D8, and D9 were fed in container 3 at a temperature of 45 °C, and RVW, MCW, and FW were provided 1:1, 1:1.5, and 1:2. As can be seen in Table 3, D3, D9, and D2 are placed in container 1 at a temperature of 35 °C, and FW, MCW, and RVW are fed in the ratio of 1:1:5. Each time after feeding, D3 is tumbled for 0 min, D9 for 10 min, and D2 for 20 min. Each digester will have a 1:1.5 feed ratio, i.e., 0.3 kg of waste and 0.45 l of water. This way, a total waste of 0.75 kg is fed into the digester. And tumbling for 0, 10, and 20 minutes is done on the day the waste is treated in the top-up digester.

Similarly, D7, D1, and D6 are maintained in container 2 at a temperature of 40 °C, followed by a 1:1.5 feed, and tumbled for 10, 20, and 0 min each time. D5, D4, and D8 are tumbled for 20, 0, and 10 minutes each by adding a 1:1.5 feed, maintained at 40 °C in container 3.

Table 2 Design of experiment (DOE) of set up 1 without tumbling effect

Anaerobic digester (AD) no.	Ratio	Types of feed	Temperature (°C)
D1	R1	F1	T1
D2	R2	F2	T1
D3	R3	F3	T1
D4	R1	F3	T2
D5	R2	F1	T2
D6	R3	F2	T2
D7	R1	F2	T3
D8	R2	F3	T3
D9	R3	F1	T3

Table 3 Design of experiment (DOE) of set up 2 with tumbling effect

Anaerobic digester (AD) no.	Temperature (°C)	Ration time (Min.)	Types of feed
D3	T1	N1	F1
D9	T1	N2	F3
D2	T1	N3	F2
D7	T2	N2	F1
D1	T2	N3	F3
D6	T2	N1	F2
D5	T3	N3	F1
D4	T3	N1	F3
D8	T3	N2	F2

T1 = 35 °C, T2 = 40 °C, T3 = 45 °C, and F1 = FW, F2 = RVW, F3 = MCW, R1 = 1:1, R2 = 1:1.5, R3 = 1:2, N1 = 0 min, N2 = 10 min, N3 = 20 min, and no. of anaerobic digester = D1 to D9

Experimental setup

First, small anaerobic digesters (ADs) were fabricated from mild steel sheets, with a waste feed inlet, a biogas outlet, and a thermocouple mounted on the top surface. So, in this way, a total of nine ADs were fabricated (Fig. 1).

The volume of all ADs was 10 l; first, a slurry sample of 7.5 kg (3.75 kg cow dung + 3.75 l of water) was mixed and poured into the biogas digester. Each time, 0.75 kg of FW, RVW, and MCW was added by mixing the solution with the feed water after forming methanogenic bacteria. The experiment design has been made from Taguchi analysis as in experiments 1 and 2; this way, three biogas digesters are placed in each container. Thus, a total of nine ADs are kept in three containers. Water was poured into each container to the height of the digester. The water in the container was heated through a heater to provide heat to the AD. Auto-cut was set through the temperature control panel. This way, the temperature inside the biogas digester in each container was maintained.

The biogas digester has a black coating on its surface to absorb the heat quickly from the water in the container. And secondly, the digester surface should not rust. A feed waste inlet is fitted on the top surface of the biogas digester, from which the feed is topped up every 5 days. An outlet on the side surface adds as much feed waste as the top-up is removed from the digester. A thermocouple was also installed on the surface to check the digester's temperature. The biogas balloon is connected to the biogas inlet valve so that whatever biogas is generated is stored in the biogas balloon. And with the help of a biogas analyzer, the composition of biogas is checked. There is always a difference of 2–3 °C due to heat convection between the temperature of the AD and the water temperature of the container. Therefore, to maintain the temperature of the digester, the water temperature of the container is increased by 2 to 3 °C auto-set. A 200

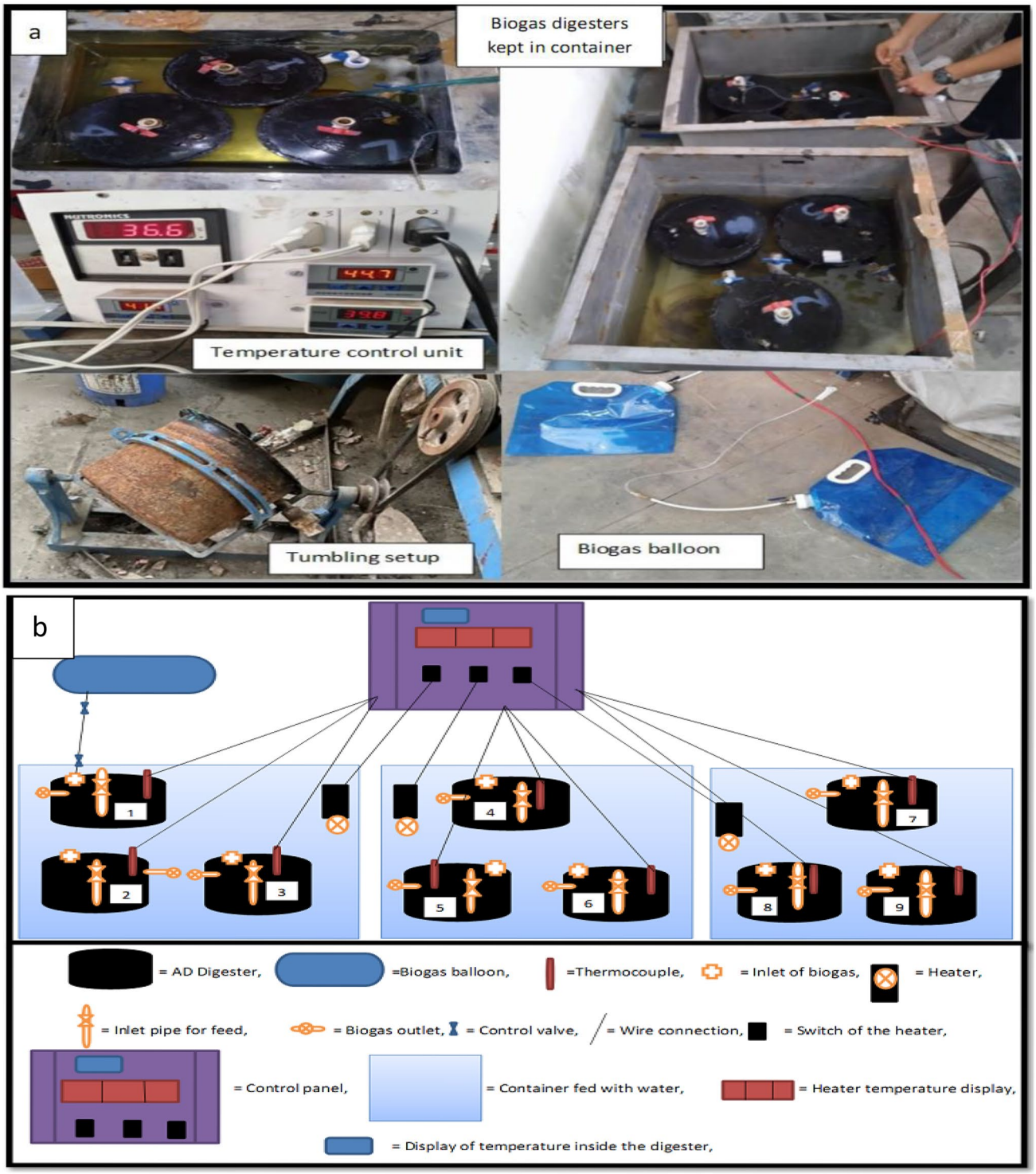


Fig. 1 **a** Experimental setup of anaerobic digester with TCU and tumbling setup. **b** Schematic diagram of the experimental setup and its parts

W heater is used to heat the water in the container. Water is added to the container daily to maintain the container's water level. The tumbling setup is connected via a belt to a 12V DC motor shaft set at 15 rpm.

Results and discussion

Experimental biogas production without tumbling

In container 1, the ADs (D1, D2, and D3) were maintained at 35 °C; among them, the fruit waste was added to D1 in a ratio of 1:1. During the initial days, no gas was generated; in this ratio, the four stages of biogas formation, hydrolysis, acidogenesis, acetogenesis, and methanogenesis, take time to complete. It explains why D1 did not release gas within 5 days of the experiment's beginning. Throughout the 55-day investigation, D1 obtained a maximum of 44.1%, a minimum of 13.7%, and an average of 26.1% methane, a maximum of 81.3% and a minimum of 47.9% CO_2, and a maximum of 10.1% and a minimum of 5% O_2. As the amount of O_2 and CO_2 in a digester increases, the methane-producing bacteria die, reducing CH_4 gas formation. RVW in D2 was estimated to be 1:1.5; at this ratio, biogas mixtures were produced more rapidly than in D1 (Fig. 2).

The maximum, minimum, and average amount of CH_4 were determined to be 36.2%, 7.9%, and 26.7%, respectively; the maximum value of CO_2 was 86.1%, the minimum value was 58.1%, and the maximum value of O_2 was 9.6%, and the minimum value was 4.4%. MCW in D3 was taken in the ratio of 1:2. The average amount of CH_4 in this digester was obtained at 26.68% throughout the experimental window. Maximum amounts of CH_4, CO_2, and O_2 were 46.4%, 81.5%, and 13.6%, respectively, while the minimum quantities were 7.9%, 49%, and 4.2%, respectively. This data demonstrates that when MCW is fed daily at a ratio of 1:2 and a temperature of 35 °C in a biogas digester, CH_4 will be produced rapidly and in more significant quantities. The MCW was taken in a 1:1 ratio by maintaining the digester D4 at a 40 °C temperature; no gas was produced for the first 10 days. The maximum, minimum, and average quantities of CH_4 were obtained at 21.7%, 5.6%, and 12.67%. The maximum amounts of CO_2 and O_2 were 86.3% and 11.3%, and the minimum quantities were 70.6% and 3.2%.

In D5, the FW was maintained at a ratio of 1:1.5, resulting in increased CH_4 production and a higher rate of gas production than in D4. The maximum, minimum, and average amounts of CH_4 were achieved at 45%, 19.1%, and 37.12%, respectively. The maximum amounts of CO_2 and O_2 were obtained at 74.8% and 10%, while their minimum quantities were obtained at 46.3% and 3.8%. In D6, the RVW was placed at 1:2. In this ratio, the average amount of CH_4 gas obtained was 18.87%, which was better than that of D4 and less than that of D5 (Tables 4 and 5).

The maximum amounts of CH_4, CO_2, and O_2 were 32%, 84.7%, and 10.1%, respectively, while the minimum quantities were 7.9%, 62.9%, and 4.3%. At 40 °C, the digester D5 with a feedstock FW and a ratio of 1:1.5 produces the fastest and highest amount of CH_4 gas. Digester D7 is maintained at 45 °C with feedstock RVW in a 1:1 ratio. The biogas composition was formed quickly at this temperature, but the quantity was less. The maximum, minimum, and average amounts of CH_4 were achieved by 26.2%, 9.7%, and 16.23%, respectively. And the maximum quantities of CO_2 and O_2 were obtained at 83.5% and 11.3%, respectively, while the minimum amounts of 70.2% and 3.6% were obtained. At D8, the feedstock MCW was taken as 1:1.5, with an average value of CH_4 of 15.12% during the experiment. A maximum quantity of CH_4, CO_2, and O_2 was obtained at 23.9%, 82.1%, and 10.6%, respectively, while the minimum amount was 7.8%, 69.8%, and 3.7%, respectively.

The feedstock FW in D9 is taken as 1:2 and has better CH_4 gas than in D7 and D8. The maximum, minimum, and average amounts of CH_4 were obtained at 49.6%, 6.4%, and 29.02%. The maximum amount of CO_2 and O_2 was 80.4% and 13.2%, while the minimum was 44.8% and 2.2%. FW produces more CH_4 gas at various temperatures and ratios than other wastes such as RVW and MCW.

Outcome

- The maximum, minimum, and average values of CH_4 obtained at 35 °C in FW (1:1) were 44.1%, 13.7%, and 26.1%. Forty-five percent, 19.1%, and 37.12% in FW (1:1.5) were obtained at 40 °C, and 49.6%, 6.4%, and 29.02% in FW (1:2) at 45 °C. The best average CH_4 gas is produced when the temperature inside the digester is maintained at 40 °C and fed into the feed FW (1:1.5).
- In RVW (1:1.5), the maximum, minimum, and average values of CH_4 obtained at 35 °C are 36.2%, 7.2%, and 26.7%. The RVW (1:2) at 40 °C was 32%, 7.9%, and 18.87%. A total of 26.2%, 9.7%, and 16.23% were obtained at RVW (1:1) at 45 °C. In the case of RVW, the best average production of CH_4 can be achieved when the feed rate is in the ratio of RVW (1:1.5) and the digester temperature is maintained at 35 °C.
- In the case of MCW (1:2), the maximum, minimum, and average values of CH_4 at 35 °C are found to be 46.4%, 7.9%, and 26.68%. A total of 21.7%, 5.6%, and 12.67% were obtained on MCW (1:1) at 40 °C. On MCW (1:1.5) at 45 °C, 23.9%, 7.8%, and 15.12% were obtained. In the case of MCW, the best CH_4 gas can be produced by keeping the feed of MCW (1:2) at a temperature of 35 °C digesters.
- In some digesters, biogas composition starts forming after 10–15 days. This happens because biogas produc-

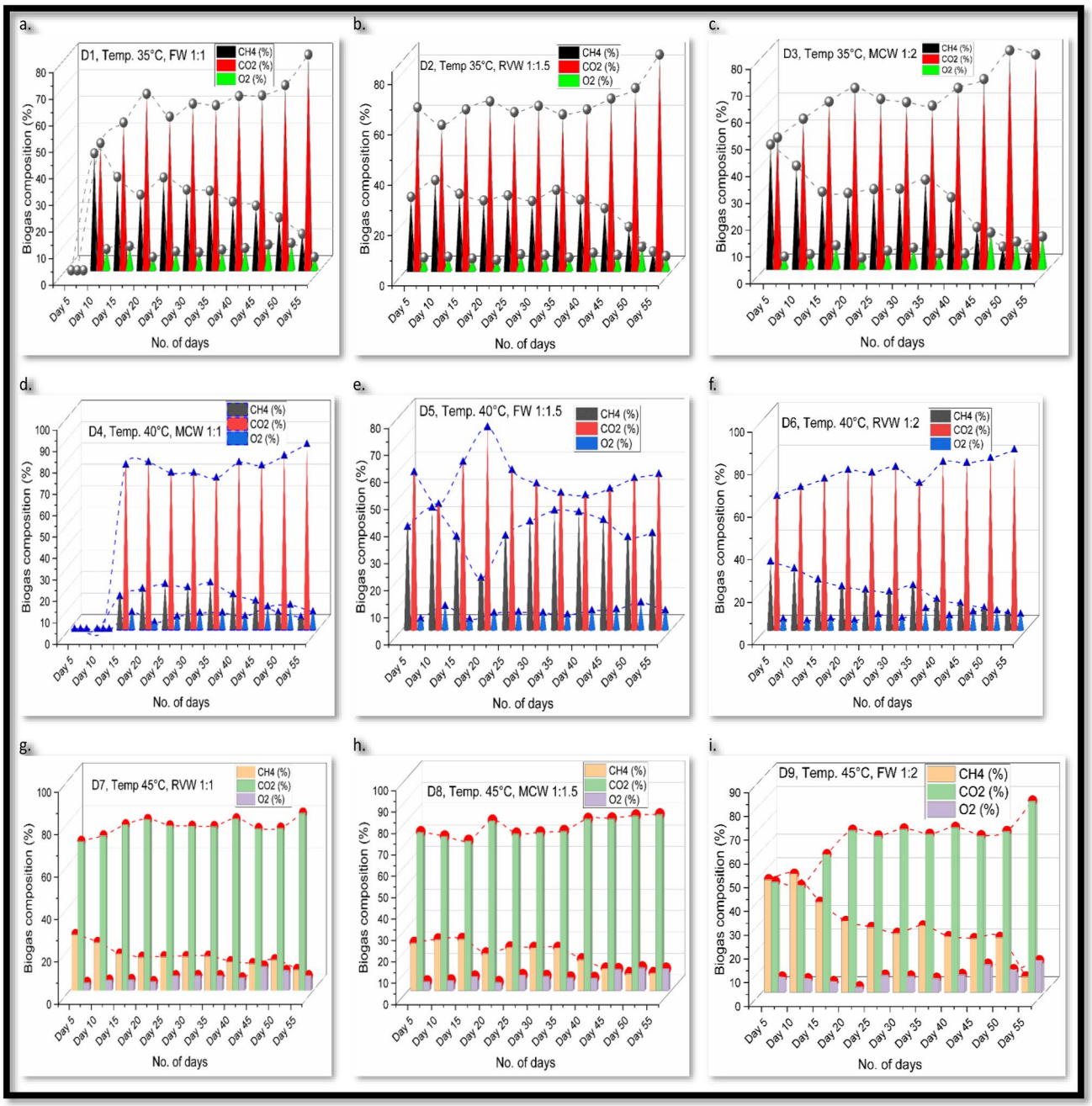


Fig. 2 Composition of biogas at different temperatures and ratios of FW, RVW, and MCW

tion depends on the quality of feedstock, feed ratio, C/N, pH, and temperature.

- Setting a retention time of 10–20 days ensures the microorganisms can decompose the organic waste and produce biogas. Adding feedstock once a week provides a steady supply of organic waste and helps maintain a consistent biogas production rate. After the retention time, the biogas produced was measured and analyzed for composition. Each digester's experimental time to produce biogas was set to 55 days. It provided enough time for the microorganisms to digest the organic waste and produce biogas. The feedstock was stopped in each digester after 40–45 days, allowing for a stable and sustainable biogas production rate.

Temperature is a vital parameter that influences biogas production because it directly affects the activity of microorganisms responsible for digestion. The optimum temperature range

Table 4 Biogas composition (CH_4, CO_2, O_2) obtained without tumbling effect

Anaerobic digester (AD) no.	Ratio	Types of feed	Temperature (°C)	CH_4 (%) (maximum, minimum)	CO_2 (%) (maximum, minimum)	O_2 (%) (maximum, minimum)
D1	1:1	FW	35	(44.1, 13.7)	(81.3, 47.9)	(10.1, 5)
D2	1:1.5	RVW	35	(36.2, 7.2)	(86.1, 58.1)	(9.6, 4.4)
D3	1:2	MCW	35	(46.4, 7.9)	(81.5, 49)	(13.6, 4.2)
D4	1:1	MCW	40	(21.7, 5.6)	(86.3, 70.6)	(11.3, 3.2)
D5	1:1.5	FW	40	(45, 19.1)	(74.8, 46.3)	(10, 3.8)
D6	1:2	RVW	40	(32, 7.9)	(84.7, 62.9)	(10.1, 4.3)
D7	1:1	RVW	45	(26.2, 9.7)	(83.5, 70.2)	(11.3, 3.6)
D8	1:1.5	MCW	45	(23.9, 7.8)	(82.1, 69.8)	(10.6, 3.7)
D9	1:2	FW	45	(49.6, 6.4)	(80.4, 44.8)	(13.2, 2.2)

Table 5 The biogas composition (CH_4, CO_2, O_2) is derived from the tumbling effect

Anaerobic digester (AD) no.	Temperature (°C)	Rotation time (min.)	Types of feed	CH_4 (%) (maximum, minimum)	CO_2 (%) (maximum, minimum)	O_2 (%) (maximum, minimum)
D3	35	0	FW	(56.4, 41.5)	(50.9, 35.1)	(10.8, 6.5)
D9	35	10	MCW	(69, 19.3)	(68.3, 22.1)	(17.1, 7.5)
D2	35	20	RVW	(61, 48)	(42.8, 30.2)	(10.7, 7.9)
D7	40	10	FW	(62, 46.4)	(46.2, 29.4)	(9.1, 7.4)
D1	40	20	MCW	(62.5, 36.9)	(52.8, 27.8)	(10.9, 9)
D6	40	0	RVW	(56.5, 32.5)	(57.8, 35)	(19.6, 7.9)
D5	45	20	FW	(65.4, 30.5)	(60.3, 26.5)	(9.6, 6.7)
D4	45	0	MCW	(50.2, 20.9)	(70.3, 41.1)	(9.5, 6.1)
D8	45	10	RVW	68.5, 22.1	(70, 22.6)	(10.2, 6.9)

for biogas production is between 35 and 45 °C (Pawlita-Posmyk et al. 2018). At this temperature, the anaerobic bacteria that break down the organic matter in the feedstock are most active, resulting in a higher yield of biogas. However, if the temperature is too high or too low, the activity of the microorganisms slows down, and the biogas production rate decreases (Ramatsa et al. 2014). Fruit waste, such as leftover fruits and eels, is a valuable feedstock for biogas production because it contains many easily digestible carbohydrates, such as sugars and starches. The high sugar content of fruit waste results in a high yield of biogas, which includes a high proportion of methane, the primary component of biomethane. The use of fruit waste as a feedstock has been found to increase the yield of biomethane by up to 40% compared to other feedstocks.

Raw vegetable waste, such as peels and trimmings, is another valuable feedstock for biogas production. Vegetables contain a high amount of cellulose and other complex carbohydrates that are more challenging to break down than the sugars found in fruit waste. However, using raw vegetable waste as a feedstock has resulted in a more balanced nutrient composition in the biogas digestate, the leftover material after digestion. The balanced nutrient composition of the digestate can make it an excellent fertilizer for plants and crops. Mixed cooked waste, which includes food waste from households, restaurants, and commercial kitchens, is a feedstock that can be challenging to handle because of its variable composition and high fat and protein content. However, mixed cooked waste has been found to produce good biomethane composition due to its high calorific value and nutrient content. The anaerobic bacteria can break down mixed cooked waste's high fat and protein content during digestion, resulting in a high biomethane yield.

Discussions

Food waste is the primary source for the generation of biogas. Biogas production can be boosted by mixing food waste, kitchen garbage, and fruit waste in varying proportions and temperatures. Some studies support our results. For 40 days, a digester with a capacity of 200 L was used to produce biogas. In this study, the components for the biogas process were combined in five different ratios of food waste with vegetable waste, using chicken dung in the following ways: 1:1 (digester D3), 2:1 (digester D4), 3:1 (digester D5), 1:0 (digester D1), and 0:1 (digester D2). The maximum amount of biogas, 18.83 kg, and the highest percentage of methane gas, 72%, were produced when the ratio of food

waste to chicken dung was 1:1 (digester D3) (Hussaro et al. 2017). The production of biogas from grass (GR) combined with the co-substrate food waste (FW) was then assessed under anaerobic conditions (methane).

Five laboratory-scale reactors were set up with varying amounts of grass and food waste that had an 8% total solid concentration: R1 (100% FW, 0% GR), R2 (75% FW, 25% GR), R3, (50% FW, 50% GR), R4 (25% FW, 75% GR), and R5 (0% FW, 100% GR). Twenty (20) days of digestion at room temperature (35 °C) were conducted. The R1, R2, R3, R4, and R5 produced 805, 840, 485, 243, and 418 mL of biogas. Only 805 mL of biogas was made from food waste, while 418 mL was produced from grass. Biogas from food waste only outperformed grass by 50%. However, 6% more biogas was produced by co-digestion (75% food waste, 25%) than by using solely food waste (Darimani and Pant 2020). Three other food waste (FW) to bovine manure (BM) ratios: 0:1, 1:2, and 3:1 (corresponding to 0, 33, and 75% of food waste in the digester substrate, respectively) were tested in the laboratory experiment using batch feed systems. The continuous feed mechanism for the pilot-scale biodigester delivered a 1:2 FW/BM mixture. The treatment with the 1:2 FW/BM ratio had the largest cumulative biogas generation in the lab, producing 273 mL g^{-1} of volatile solids (VS) (de Morais Andrade et al. 2022). The digester setups were tested for 24 days at room temperature (28 °C) and mesophilic temperature (37 °C) while being fed kitchen waste (KW) and poultry manure (PM) in ratios of 1:0 (D1), 1:1 (D2), 2:1 (D3), and 3:1 (D4) at a constant loading rate of 300 mg/L.

The production of CBG and the amount of methane in D2 above D1 increased by 16% and 74%, respectively, due to the co-digestion of KW and PM. At ambient temperature, the D3 with 66.7% KW and 33.3% PM produced the most CBG and methane (396 8 mL and 36%). All the digesters performed better in mesophilic conditions, although D3 had the greatest CBG (920±11 mL) and methane concentration (48%) levels (Rahman et al. 2021). This study examined the performance and microbial structure of two digesting processes—one including solely food waste and the other involving cow manure—at mesophilic (37 °C) and thermophilic (55 °C) temperatures. The mesophilic digester only fed food waste and showed maximum methane yield (480mL/g VS). Compared to the sum of the individual digestions of manure and food waste, the mesophilic co-digestion of food waste and manure produced 26% more methane (Zamanzadeh et al. 2017).

Experimental Biogas production with a tumbling effect

As shown in Fig. 3, in the tumbling effect, digesters D3, D9, and D2 were maintained at 35 °C FW, MCW, and RVW, respectively. The rotation times for D3, D9, and D2 were kept at 0, 10, and 20 min, respectively.

In D3, the maximum and minimum CH_4 in FW were obtained at 56.4% and 41.5%. The average amount of CH_4 during the entire experiment was 47.2%. The maximum amount of CO_2 and O_2 was 50.9% and 10.8%, and the minimum was 35.1% and 6.5%, respectively. A maximum and minimum amount of CH_4 gas in D9 is achieved by 69% and 19.3%. And the average amount of CH_4 is 45% throughout the experiment. The maximum CO_2 and O_2 were 68.3% and 17.1%, and the minimum values were up to 22.1% and 7.5%. In RVW in D2, the maximum CH_4 content is 61%, the minimum is 48% in 20-min rotations, and the average CH_4 content is 56.3% achieved throughout the experiment. During this period, the maximum quantity of CO_2 and O_2 was obtained at 42.8% and 10.7%, and the minimum amount at 30.2% and 7.9%.

Digesters D7, D1, and D6 are maintained at 40-degree temperatures. The rotation time for FW in the D7 was kept at 10 min. The maximum amount of CH_4 was achieved by 62%, while the minimum amount was 46.4%, and the average amount of CH_4 during the whole duration of the experiment was 52.4%. The maximum values of CO_2 and O_2 were found to be 46.2% and 9.1%, respectively, while the minimum values were 29.4% and 7.4%. The rotation time of MCW in D1 was kept at 20 min. The maximum value of CH_4 was obtained at 62.5%, the minimum was 36.9%, and the average value was 50.9%. The maximum CO_2 and O_2 were obtained at 52.8% and 10.9%, while the minimum values were obtained at 27.8% and 9%.

The RVW's feed was inserted in the D6 digester, which was given a 0-min rotation time. During the entire experiment period, the maximum value of CH_4 was obtained at 56.5%, the minimum was 32.5%, and the average value was 44.8%. The maximum CO_2 and O_2 were obtained at 57.8% and 19.6%, respectively, while the minimum values were 35% and 7.9%. In digester D7, the average CH_4 value was highest when FW was kept at a 40-degree temperature and rotation time of 10 min. The D5, D4, and D8 digesters are maintained at 45°. D5 has FW, whose rotation time is 20 min; D4 has MCW, whose rotation time is 0 min; and D8 has RVW, whose rotation time is 10 min. In D5, the maximum value of CH_4 was 65.4%, the minimum value was 30.5%, and the average value was 50.04% during the entire experiment. The maximum CO_2 and O_2 were 60.3% and 9.6%, while the minimum values were 26.5% and 6.7%. Maximum, minimum, and average values of CH_4 in D4 were obtained at 50.2%, 20.9%, and 34.4%. The highest and lowest values of CO_2 were found to be 70.3% and 41.1%, and the maximum and minimum values of O_2 were 9.5% and 6.1%. The maximum, minimum, and average values of CH_4 in D8 were obtained at 68.5%, 22.1%, and 50.3%, respectively.

The maximum CO_2 and O_2 were obtained at 70% and 10.2%, while the minimum values were 22.6% and 6.9%. Digester D2 with feed RVW and rotation time of 10 min

was the maximum and average value of CH_4 obtained in this digester throughout the experiment. An anaerobic digester with enhanced agitation rates and tumbling can produce increased biogas. As a result, methane bacteria proliferate. During tumbling, the anaerobic digester is rotated as the feed from the stirrer to the digester is mixed using either a pump or a ratchet.

Discussion

The findings underscore the tumbling effect's substantial influence on biogas production efficiency. Tumbling, also called agitation or digester rotation, is a technique that markedly improves biogas production. Rotating the digester after adding the feedstock method increases biogas production and shorter production times than non-tumbling systems. It ensures even distribution and thorough feedstock mixing with the microbial population, resulting in higher digestion rates and increased biogas production. Additionally, it prevents the formation of scum and floating layers on the surface of the digester, which can inhibit digestion and reduce biogas production. The tumbling effect also reduces the retention time required for biogas production, resulting in shorter production times. This means that more biogas can be produced in a shorter time, ultimately enhancing the overall efficiency and productivity of the biogas production system.

Furthermore, the tumbling effect positively impacts the quality and composition of the biogas. The enhanced mixing and digestion rates produce a more homogeneous biogas composition with higher methane content. This improvement is significant because methane is the primary component of biogas and is the most valuable product of the biogas

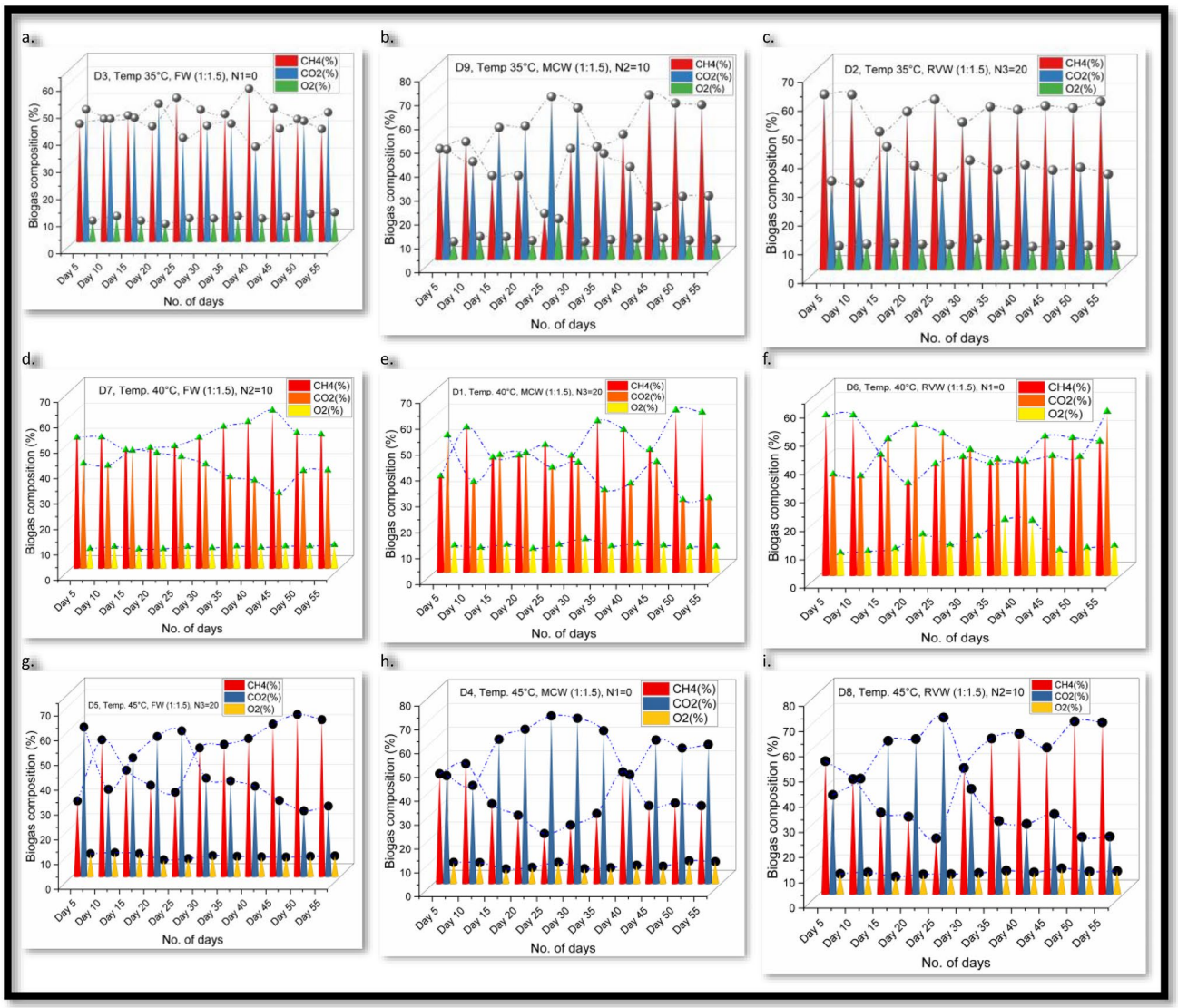


Fig. 3 Composition of biogas with different periods of the tumbling effect

Table 6 Linear model analysis: SN ratios versus feed ratio, types of feed, temperature

Estimated model coefficients for SN ratios					
Term	Coef	SE Coef	*T*	*P*	
Constant	30.7926	0.4150	74.191	0.000	
Ratio 1:1	− 1.4646	0.5870	− 2.495	0.130	
Ratio1:1.5	− 0.1905	0.5870	− 0.324	0.776	
Feed FW	2.4950	0.5870	4.251	0.049	
Feed RVW	− 0.9115	0.5870	− 1.553	0.261	
Temp. 35	1.6718	0.5870	2.848	0.104	
Temp. 40	− 0.8271	0.5870	− 1.409	0.294	
Analysis of variance for SN ratios					
Source	DF	Seq SS	Adj MS	F	P
Ratio	2	14.762	7.381	4.76	0.174
Feed	2	28.689	14.344	9.25	0.098
Temp.	2	12.578	6.289	4.06	0.198
Residual error	2	3.101	1.550		
Total	8	59.129			
Model summary					
S	*R-Sq*	*R-Sq* (adj)			
1.2451	94.76%	79.02%			
Response table for signal-to-noise ratios					
Larger is better					
Level	Ratio	Feed	Temp.		
1	29.33	33.29	32.46		
2	30.60	29.88	29.97		
3	32.45	29.21	29.95		
Delta	3.12	4.08	2.52		
Rank	2	1	3		

Table 7 Linear model analysis: means versus feed ratio, types of feed, temperature

Estimated model coefficients for means					
Term	Coef	SE Coef	*T*	*P*	
Constant	36.122	1.700	21.252	0.002	
Ratio 1:1	− 5.456	2.404	− 2.270	0.151	
Ratio1:1.5	− 1.089	2.404	− 0.453	0.695	
Feed FW	10.111	2.404	4.206	0.048	
Feed RVW	− 4.656	2.404	− 1.937	0.192	
Temp. 35	6.111	2.404	2.542	0.126	
Temp. 40	− 3.222	2.404	− 1.340	0.312	
Analysis of variance for means					
Source	DF	Seq SS	Adj MS	*F*	*P*
Ratio	2	221.34	110.67	4.26	0.190
Feed	2	461.02	230.51	8.87	0.101
Temp.	2	168.22	84.11	3.23	0.236
Residual error	2	52.00	26.00		
Total	8	902.58			
Model summary					
S	*R-Sq*	*R-Sq* (adj)			
5.099	94.24%	76.95%			
Response table for means					
Larger is better					
Level	Ratio	Feed	Temp.		
1	30.67	46.23	42.23		
2	35.03	31.47	32.90		
3	42.67	30.67	33.23		
Delta	12.00	15.57	9.33		
Rank	2	1	3		

production process. The tumbling effect can result in a biogas composition with methane content of up to 70%, as opposed to the 40–50% observed in non-tumbling systems. Another noteworthy advantage of the tumbling effect is its ability to reduce the residual organic material in the digestate, which is the leftover material after digestion. This residual organic material can be a valuable fertilizer for plants and crops. By reducing its quantity, the efficiency and sustainability of the biogas production system are further improved.

The discussions presented in this section align with the findings, emphasizing the critical role of agitation or stirring in biogas production. Studies examining mixer speed and stirring intervals corroborate the importance of mechanical agitation in influencing biogas production rates. Understanding the optimal parameters for stirring, including speed and duration, is essential for maximizing biogas yield.

Without any tumbling (Taguchi analysis)

The study aimed to determine the most efficient feedstock values for the three inputs, namely, ratio, feed, and temperature, to optimize CH_4 gas production. The results show that the feedstock was the primary factor affecting CH_4 gas production, while the feed ratio and temperature were secondary parameters. The study used Taguchi analysis, which is a statistical method for designing experiments to optimize the performance of a system or process. The optimal CH_4 gas production was obtained from fruit feedstock under non-tumbling effect conditions. This finding is consistent with Taguchi's study on the non-tumbling effect.

The method involves identifying the key parameters affecting the system's performance and determining the optimal values to achieve the desired output. Using a linear model analysis, the study analyzed the signal to noise ratio (SN ratio) and means of CH_4 gas production. The analysis results are presented in Tables 6 and 7, respectively. The linear model analysis of SN ratios versus feed ratio, types of feed, and temperature aims to determine the combination of these factors that maximizes the signal-to-noise ratio, representing the desired outcome or quality of the biogas production process. The SN ratio can be defined based on the specific objectives of the experiment, such as

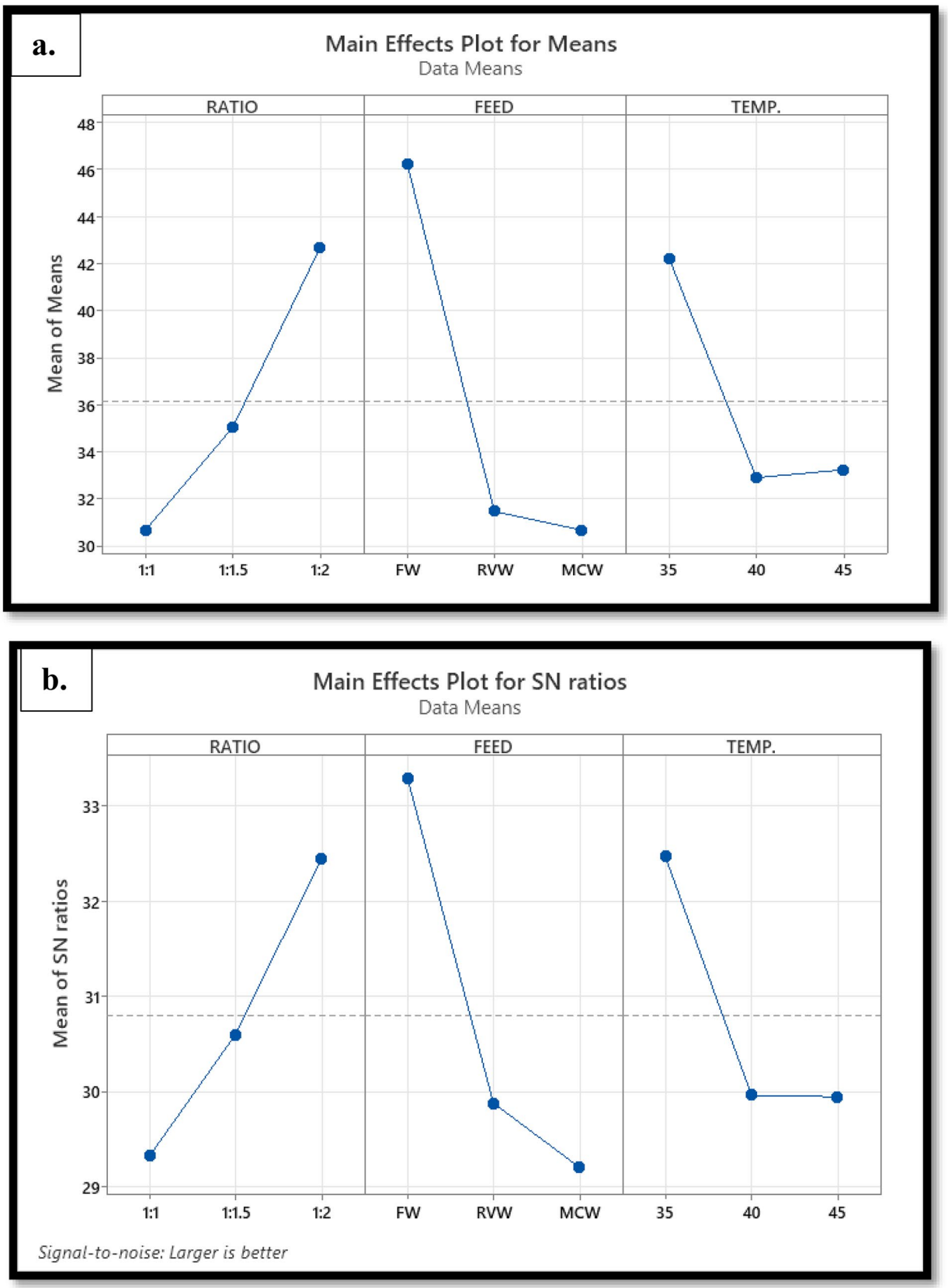


Fig. 4 **a** Mean of means w.r.t feed ratio, types of feed and temperature. **b** Mean of SN ratios w.r.t feed ratio, types of feed and temperature

Table 8 Linear model analysis: SN ratios versus rotation time, types of feed, temperature

Estimated model coefficients for SN ratios					
Term	Coef	SE Coef	*T*	*P*	
Constant	35.7061	0.07328	487.275	0.000	
Rot. time 0	− 1.0126	0.10363	− 9.771	0.010	
Rot. time 10	0.7401	0.10363	7.142	0.019	
Feed FW	0.1796	0.10363	1.733	0.225	
Feed MCW	− 0.5166	0.10363	− 4.985	0.038	
Temp 35	0.1303	0.10363	1.257	0.336	
Temp 40	− 0.1040	0.10363	− 1.003	0.421	
Analysis of variance for SN ratios					
Source	DF	Seq SS	Adj MS	F	P
Rot. Time	2	4.94185	2.47092	51.13	0.019
Feed	2	1.23820	0.61910	12.81	0.072
Temp	2	0.08542	0.04271	0.88	0.531
Residual error	2	0.09665	0.04833		
Total	8	6.36212			
Model summary					
S	*R-Sq*	*R-Sq* (adj)			
0.2198	98.48%	93.92%			
Response table for signal-to-noise ratios					
Larger is better					
Level	Rot. Time	Feed	Temp.		
1	34.69	35.89	35.84		
2	36.45	35.19	35.60		
3	35.98	36.04	35.68		
Delta	1.75	0.85	0.23		
Rank	1	2	3		

Table 9 Linear model analysis: means versus rotation time, types of feed, temperature

Estimated model coefficients for means					
Term	Coef	SE Coef	*T*	*P*	
Constant	61.2778	0.4138	148.084	0.000	
Rot. Time 0	− 6.9111	0.5852	− 11.810	0.007	
Rot. Time10	5.2222	0.5852	8.924	0.012	
Feed FW	1.1889	0.5852	2.032	0.179	
Feed MCW	− 3.5444	0.5852	− 6.057	0.026	
Temp 35	0.8556	0.5852	1.462	0.281	
Temp 40	− 0.9444	0.5852	− 1.614	0.248	
Analysis of variance for means					
Source	DF	Seq SS	Adj MS	*F*	*P*
Rot. time	2	233.662	116.831	75.81	0.013
Feed	2	58.576	29.288	19.00	0.050
Temp.	2	4.896	2.448	1.59	0.386
Residual error	2	3.082	1.541		
Total	8	300.216			
Model summary					
S	*R-Sq*	*R-Sq* (adj)			
1.2414	98.97%	95.89%			
Response table for means					
Larger is better					
Level	Rot. Time	Feed	Temp.		
1	54.37	62.47	62.13		
2	66.50	57.73	60.33		
3	62.97	63.63	61.37		
Delta	12.13	5.90	1.80		
Rank	1	2	3		

maximizing biogas yield or minimizing variations in the gas composition.

By analyzing the SN ratios, researchers can identify the optimal levels of each factor that lead to the desired outcome. Similarly, the linear model analysis of means versus feed ratio, types of feed, and temperature focus on the mean values of the response variable, which could be parameters like biogas production rate or methane content. The tables show that the three inputs' most efficient FW feedstock values were significant at $p < 0.05$. The value of R^2, a measure of the model's goodness of fit, was found to be 94.76% in the SN ratio analysis and 94.24% in the means analysis. This analysis aims to identify the factor levels that yield the highest mean values, indicating the optimal performance of the biogas production process. In both cases, Taguchi analysis employs statistical techniques to analyze the data collected from experimental trials with different factor combinations.

The objective is to determine the most influential factors and their respective levels for achieving the desired outcome. It indicates that the design of the experiment (DOE) approach's experimental process produced more than 94% perfect results. The study also presented the results in Fig. 4a, b. The statistics show that in the mean of SN ratio and mean of means analysis, and the optimal CH_4 value was obtained at FW feed and temperature of 35 °C in level 1. In level 3, the best average CH_4 value was obtained at a ratio of 1:2.

Tumbling effect (Taguchi analysis)

The study aimed to determine the most influential parameters influencing CH_4 gas production: rotation time, feed types, and temperature. The technique involves identifying the key parameters affecting the system's performance and determining the optimal values to achieve the desired output. The analysis results are presented in Tables 6 and 7, and the tables show that the tumbling time (rotation time) is less than $p < 0.05$, indicating that it is the most influential parameter in the production of CH_4 gas in the tumbling process. The coefficient of determination (R^2) obtained in the analysis of variance for SN ratio and analysis of variance for means was found to be 98.48% and 98.97%, respectively. This indicates that the result obtained from the DOE approach was up to 98% accurate (Tables 8 and 9).

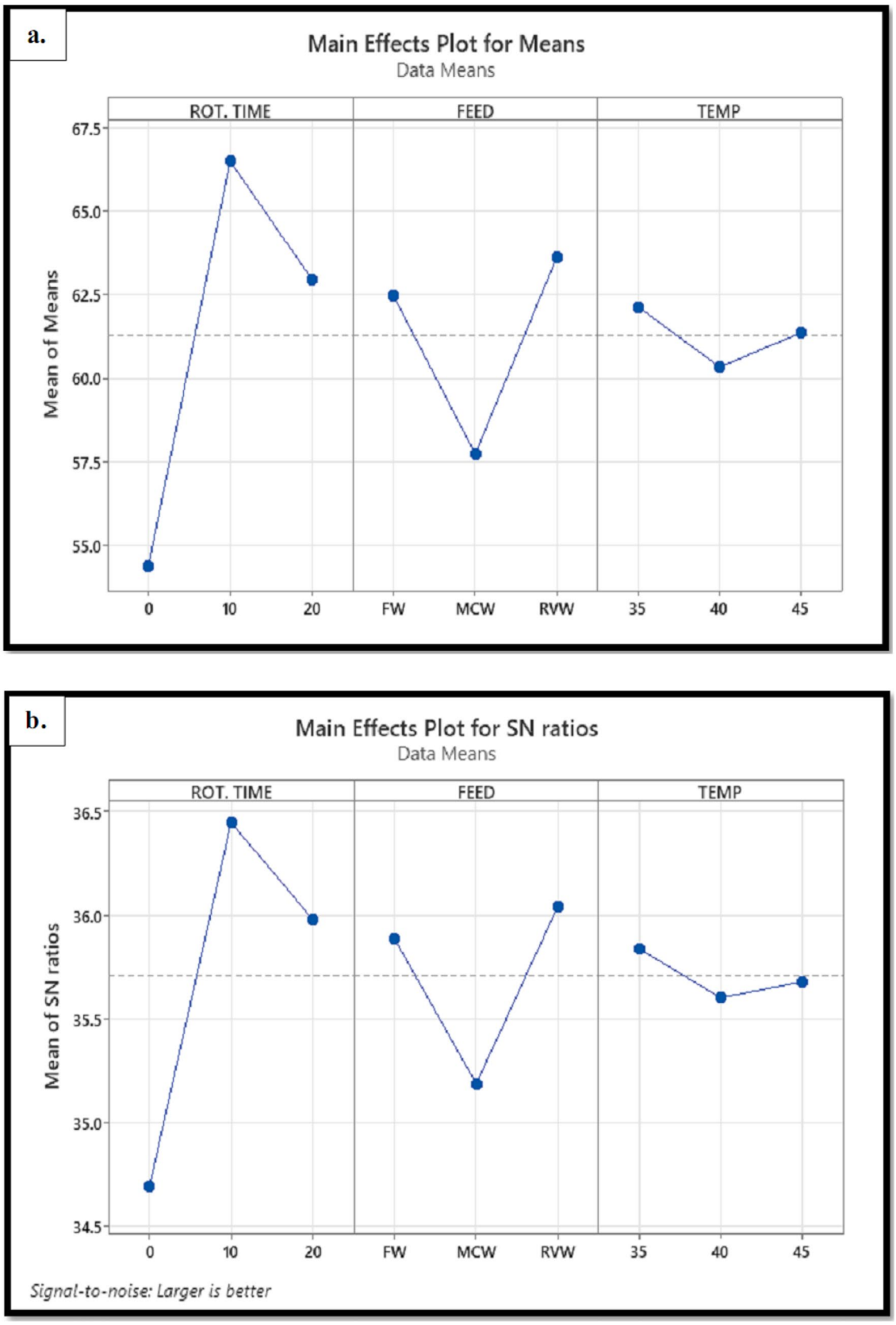


Fig. 5 **a** Mean of means w.r.t rotation time, types of feed, and temperature. **b** Mean of SN ratios w.r.t rotation time, types of feed and temperature

The study found that the optimum CH_4 output was achieved on the FW feed and rotation time of 10 min in level 1 and level 2. In level 3, the tumbling process was performed on the RVW feed. According to the rank of the tumbling effect, the most significant value was the rotation time, which had a position of 1, meaning that the tumbling process produced more CH_4 (Fig. 5).

The second and third affecting parameters were found to be feedstock and temperature. The study also highlighted the importance of the tumbling effect on the production of CH_4 gas. The tumbling development refers to the effect of rotating the feedstock during the process, which enhances the mixing of the feedstock and increases the surface area available for the anaerobic digestion process. The study found that the tumbling effect significantly improved CH_4 gas production.

Conclusion

The study highlights the significant impact of optimizing feed types and incorporating a tumbling effect on enhancing biogas production. This optimization strategy demonstrated substantial improvements in the biogas production process. Utilizing the Taguchi method effectively achieved consistent and higher biogas production rates with reduced variability. Optimal biomethane (CH_4) generation was observed at 40 °C for FW (1:1.5) feed and at 35 °C for both RVW (1:1.5) and MCW (1:2) feeds. The study emphasized the pivotal role of the tumbling effect, particularly in the case of MCW feed, where it led to a remarkable 47.9% increase in CH_4 generation. Tumbling also accelerated the CH_4 gas production process. These findings hold significant implications for refining and improving biogas production methods, ultimately contributing to a greener and more sustainable future.

Supplementary Information The online version contains supplementary material available at https://doi.org/10.1007/s11356-024-32049-y.

Acknowledgements The authors thank Dr. Avtar Singh Meena and Neeraj Budhraja for their support in editing this research and the Delhi Technical University Administration's valuable support.

Author contribution All authors contributed to the study conception and design. Material preparation, data collection and analysis were performed by Pradeep Kumar Meena, Amit Pal and Samsher Gautam. The first draft of the manuscript was written by Pradeep Kumar Meena and all authors commented on previous versions of the manuscript. All authors read and approved the final manuscript.

Data availability All data generated or analyzed during this study are included in this published article and its supplementary information files.

Declarations

Ethical approval and consent to participate Not applicable.

Consent for publication Not applicable.

Competing interests The authors declare no competing interests.

References

Al Mamun MR, Torii S (2014) Production of biomethane from cafeteria, vegetable and fruit wastes by anaerobic co-digestion process. J Adv Agric Technol 1:94–99. https://doi.org/10.12720/joaat.1.2.94-99

Annepu RK (2012) Sustainable solid waste management in India. MS Dissertation. https://doi.org/10.1007/978-981-4451-73-4

Appels L, Lauwers J, Degrve J et al (2011) Anaerobic digestion in global bio-energy production: Potential and research challenges. Renew Sust Energ Rev 15:4295–4301. https://doi.org/10.1016/j.rser.2011.07.121

Babaee A, Shayegan J (2011) Effect of organic loading rates (OLR) on production of methane from anaerobic digestion of vegetables waste. Proceedings of the World Renewable Energy Congress – Sweden, 8–13 May, 2011, Linköping, Sweden 57:411–417. https://doi.org/10.3384/ecp11057411

Begum S, Golluri K, Anupoju GR et al (2016) Cooked and uncooked food waste: a viable feedstock for generation of value added products through biorefinery approach. Chem Eng Res Des 107:43–51. https://doi.org/10.1016/j.cherd.2015.10.032

Bhada-Tata DH and P (2012) What a waste A global review of solid waste management

Cheng H, Hu Y (2010) Municipal solid waste (MSW) as a renewable source of energy: current and future practices in China. Bioresour Technol 101:3816–3824. https://doi.org/10.1016/j.biortech.2010.01.040

Chol MMY, Muchuka NM, Nyaanga DM (2021) Effect of stirring intervals on biogas production from cow dung and maize silage mix ratio. Int J Power Energy Res 5. https://doi.org/10.22606/ijper.2021.51001

Darimani HS, Pant DC (2020) Biogas production from co-digestion of grass with food waste. J Agric Chem Environ 09:27–36. https://doi.org/10.4236/jacen.2020.91003

Das A, Mondal C (2013) Studies on the utilization of fruit and vegetable waste for generation of biogas. Res Invent: Int J Eng Sci Issn WwwResearchinventyCom 3:24–32

de Morais Andrade MM, Alencar BRA, Leite NP et al (2022) Biogas production from co-digestion of different proportions of food waste and fresh bovine manure. Biomass Convers Biorefin 12:2697–2704. https://doi.org/10.1007/s13399-020-00833-8

Deressa L, Libsu S, Chavan RB et al (2015) Production of biogas from fruit and vegetable wastes mixed with different wastes. Environ Ecol Res 3:65–71. https://doi.org/10.13189/eer.2015.030303

Di Maria F, Sordi A, Cirulli G, Micale C (2015) Amount of energy recoverable from an existing sludge digester with the co-digestion with fruit and vegetable waste at reduced retention time. Appl Energy 150:9–14. https://doi.org/10.1016/j.apenergy.2015.01.146

Elango D, Pulikesi M, Baskaralingam P et al (2007) Production of biogas from municipal solid waste with domestic sewage. J Hazard Mater 141:301–304. https://doi.org/10.1016/j.jhazmat.2006.07.003

El-Fadel M, Bou-Zeid E, Chahine W, Alayli B (2002) Temporal variation of leachate quality from pre-sorted and baled municipal solid waste with high organic and moisture content

Ghazi TM, Razif M, Harun B et al (2014) Effect of carbon to nitrogen ratio of food waste on biogas methane production in a batch mesophilic anaerobic di ... effect of carbon to nitrogen ratio of food waste on biogas methane production in a batch mesophilic anaerobic digester. Int J Innov Manag Technol 5. https://doi.org/10.7763/IJIMT.2014.V5.497

Hoornweg D, Otten L (1999) Composting and its applicability in developing countries. World 6:2010–2010

Hussaro K, Intanin J, Teekasap S (2017) Biogas production from food waste and vegetable waste for the Sakaew Temple Community Angthong Province Thailand. GMSARN Int J 11:82–89

Jiang Y, Heaven S, Banks CJ (2012) Strategies for stable anaerobic digestion of vegetable waste. Renew Energy 44:206–214. https://doi.org/10.1016/j.renene.2012.01.012

Kadam R, Panwar NL (2017) Recent advancement in biogas enrichment and its applications. Renew Sust Energ Rev 73:892–903. https://doi.org/10.1016/j.rser.2017.01.167

Kazimierowicz J (2017) Biogas acquisition from selected mixtures of expired food products. J Ecol Eng 18:118–122. https://doi.org/10.12911/22998993/74283

Khalid A, Arshad M, Anjum M et al (2011) The anaerobic digestion of solid organic waste. Waste Manag 31:1737–1744. https://doi.org/10.1016/j.wasman.2011.03.021

Latha K, Velraj R, Shanmugam P, Sivanesan S (2019) Mixing strategies of high solids anaerobic co-digestion using food waste with sewage sludge for enhanced biogas production. J Clean Prod 210:388–400. https://doi.org/10.1016/j.jclepro.2018.10.219

Li P, Liu Z, Zhao M et al (2020) Evaluation of biogas performance and process stability from food, kitchen, and fruit/vegetable waste by mono-, co-, and tridigestion. Energy Fuel 34:12734–12742. https://doi.org/10.1021/acs.energyfuels.0c02598

Li Q, Li H, Wang G, Wang X (2017) Effects of loading rate and temperature on anaerobic co-digestion of food waste and waste activated sludge in a high frequency feeding system, looking in particular at stability and efficiency. Bioresour Technol 237:231–239. https://doi.org/10.1016/j.biortech.2017.02.045

Lim BS, Kim B, Chung I (2012) Anaerobic treatment of food waste leachate for biogas production using a novel digestion system. Environ Eng Res 17:41–46. https://doi.org/10.4491/eer.2012.17.1.041

Lin J, Zuo J, Gan L et al (2011) Effects of mixture ratio on anaerobic co-digestion with fruit and vegetable waste and food waste of China. J Environ Sci 23:1403–1408. https://doi.org/10.1016/S1001-0742(10)60572-4

Meena PK, Pal A, Samsher (2020) Experimental analysis of four-stroke single-cylinder diesel engine using biogas as a dual fuel. In: Recent Advances in Mechanical Engineering. Springer, pp 395–406

Megido L, Negral L, Fernández-Nava Y et al (2021) Impact of organic loading rate and reactor design on thermophilic anaerobic digestion of mixed supermarket waste. Waste Manag 123:52–59. https://doi.org/10.1016/j.wasman.2021.01.012

Misi SN, Forster CF (2002) Semi-continuous anaerobic co-digestion of agro-wastes. Environ Technol 23:445–451. https://doi.org/10.1080/09593332508618405

Pawlita-Posmyk M, Wzorek M, Płaczek M (2018) The influence of temperature on algal biomass growth for biogas production. MATEC Web of Conf 240:4–10. https://doi.org/10.1051/matecconf/201824004008

Plai RR, Roodrigues LLR, Mathew AO, Hebbar S (2014) Impact of urbanization on municipal solid waste management : a system dynamics approach. Int J Renew Energy Environ Eng 02:31–37

Rahman MA, Shahazi R, Nova SNB et al (2021) Biogas production from anaerobic co-digestion using kitchen waste and poultry manure as substrate—part 1: substrate ratio and effect of temperature. Biomass Convers Biorefin. https://doi.org/10.1007/s13399-021-01604-9

Ramatsa IM, Akinlabi ET, Madyira DM, Huberts R (2014) Design of the bio-digester for biogas production: a review. Lect Notes Eng Comput Sci 2:628–631

Rehl T, Müller J (2011) Life cycle assessment of biogas digestate processing technologies. Resour Conserv Recycl 56:92–104. https://doi.org/10.1016/j.resconrec.2011.08.007

Sinaga N, Hatta K, Ahmad NE, Mel M (2018) Effect of Rushton impeller speed on biogas production in anaerobic digestion of continuous stirred bioreactor. J Adv Res Biofuel Bioenergy J 3:9–18

Tambone F, Genevini P, D'Imporzano G, Adani F (2009) Assessing amendment properties of digestate by studying the organic matter composition and the degree of biological stability during the anaerobic digestion of the organic fraction of MSW. Bioresour Technol 100:3140–3142. https://doi.org/10.1016/j.biortech.2009.02.012

Viturtia AM, Mata-Alvarez J, Cecchi F (1995) Two-phase continuous anaerobic digestion of fruit and vegetable wastes. Resour Conserv Recycl 13:257–267. https://doi.org/10.1016/0921-3449(94)00048-A

Ward AJ, Hobbs PJ, Holliman PJ, Jones DL (2008) Optimisation of the anaerobic digestion of agricultural resources. Bioresour Technol 99:7928–7940. https://doi.org/10.1016/j.biortech.2008.02.044

Zamanzadeh M, Hagen LH, Svensson K et al (2017) Biogas production from food waste via co-digestion and digestion- effects on performance and microbial ecology. Sci Rep 7:1–12. https://doi.org/10.1038/s41598-017-15784-w

Publisher's Note Springer Nature remains neutral with regard to jurisdictional claims in published maps and institutional affiliations.

Springer Nature or its licensor (e.g. a society or other partner) holds exclusive rights to this article under a publishing agreement with the author(s) or other rightsholder(s); author self-archiving of the accepted manuscript version of this article is solely governed by the terms of such publishing agreement and applicable law.

AQUA
Water Infrastructure, Ecosystems and Society

Uncorrected Proof

Check for updates

IWA PUBLISHING

© 2024 The Authors

AQUA — Water Infrastructure, Ecosystems and Society Vol 00 No 0, 1 doi: 10.2166/aqua.2024.290

Impact of various design parameters on solar still systems performance: a review

Maneesh Kumar Shivhare[a,*], Samsher[a,b] and Anil Kumar[a,c]

[a] Department of Mechanical Engineering, Delhi Technological University, Delhi 110042, India
[b] Harcourt Butler Technical University, Kanpur 208002, India
[c] Centre for Energy and Environment, Delhi Technological University, Delhi 110042, India
*Corresponding author. E-mail: manishkrshivhare@gmail.com

ABSTRACT

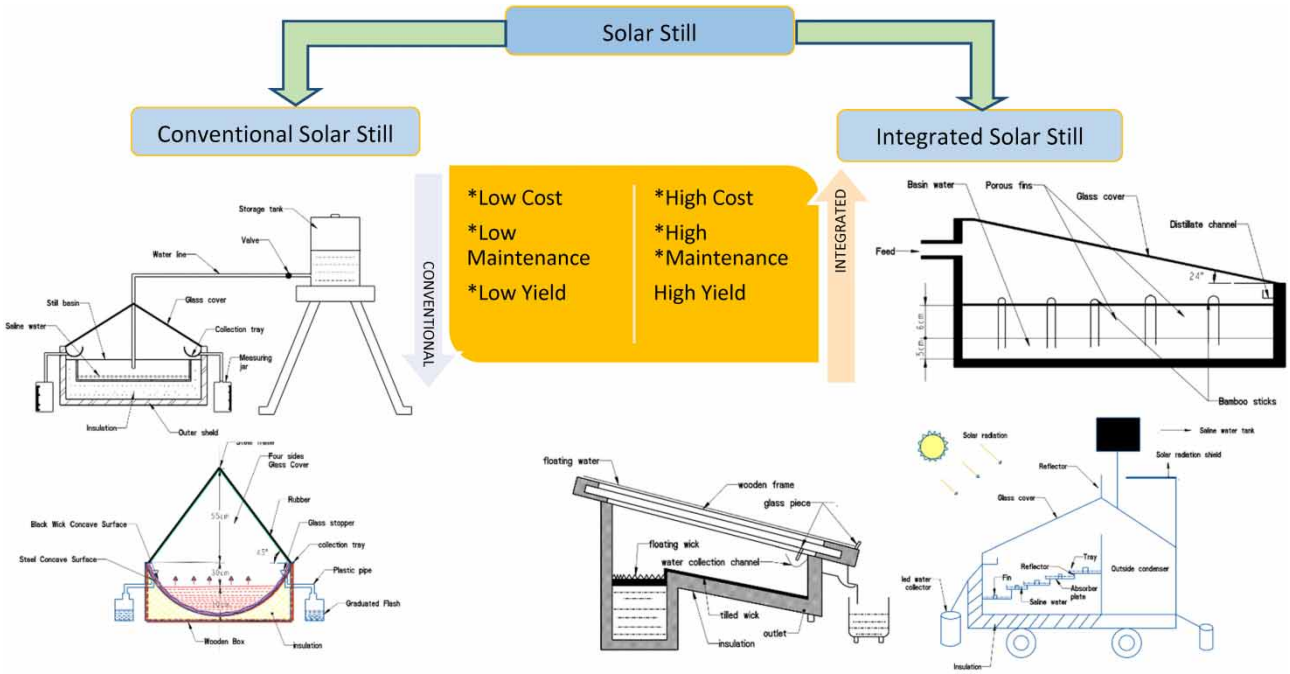
The objective of the current study is to evaluate and appreciate, various design parameters for simple solar stills impact yielding rate and heat transmission characteristics. For improved utility, indicators and performance comparisons of several solar stills have also been created. In the case of the enhanced wick, most of the researchers use wick on water surfaces to enhance the evaporation rate. It has been observed that the solar stills with wet wick on the side walls provide high porosity with thin film evaporation thus improving distillation. Also, the solar stills with wick integration were superior to other types of solar desalination system that utilizes wicking materials to enhance the evaporation and condensation processes. The interpretations were significantly carried out, and numerous recommendations for future improvement and the generation of novel concepts to work around practical constraints were also made in the present study.

Key words: collector, distillation, solar still, wick, yield

HIGHLIGHTS

- Highlights wet wick on the side wall provide high porosity.
- Wick-supported thin film evaporation improves distillation.
- Enhanced vaporization surface along with condensation area is a good suggestion for a significant solar still system.

GRAPHICAL ABSTRACT



This is an Open Access article distributed under the terms of the Creative Commons Attribution Licence (CC BY 4.0), which permits copying, adaptation and redistribution, provided the original work is properly cited (http://creativecommons.org/licenses/by/4.0/).

Downloaded from http://iwaponline.com/aqua/article-pdf/doi/10.2166/aqua.2024.290/1355810/jws2024290.pdf
by DELHI TECHNOLOGICAL UNIVERSITY (DTU) user

Uncorrected Proof

1. INTRODUCTION

Water is the most important substance on earth for living species and day by day the need for freshwater increasing with the development of society, industries, and agriculture. Only 1.6% is accessible as freshwater in lakes, rivers, etc. while 98% is available as groundwater (Arunkumar *et al.* 2019; Chauhan *et al.* 2020). The United Nations (UN) identified a relationship between climate change and water and pointed out the critical situation in the consumption of Earth's water six times in the last 100 years (Mekonnen & Hoekstra 2016). Several processes are producing fresh water but are neither eco-friendly nor economical. Desalination is indeed a promising technology to convert seawater into potable water, and utilizing renewable energy sources like solar power makes the process more sustainable against the global challenge of water scarcity (Suraparaju *et al.* 2021a). As per the International Desalination Association (IDA) report, world's largest desalination plant runs on the RO technique and is based on fossil fuel (Largest Water Desalination Plant, Guinness World Records). Most of the development in the desalination process is done in African Nations, Middle East Arab Nations, India, China, and Australia where fresh water is not available sufficiently (Esfahani *et al.* 2016). Research and modification focused on moving toward sustainable and renewable resources like wind energy, solar energy, biomass energy, and geothermal energy. The solar desalination technique was observed as the most reliable cause of environment-friendly and economical way to produce fresh water from saline or brackish water (Arunkumar *et al.* 2019). As compared to the use of other renewable energy in desalination, the solar still system has the lowest maintenance, low running cost, and negligible effect on the environment (Alsehli *et al.* 2017). Solar energy is completely available at zero cost which can be used to produce fresh water in solar desalination. The major part of receiving solar energy from the sun is wastage throughout the year which is about 1 kW/m^2 (NPTEL: Electrical Engineering-Energy Resources & Technology). Solar desalination is based on the greenhouse effect. When solar radiation falls on the cover surface of solar desalination, some of the incident radiation is transmitted to the inside of the basin while some of them are absorbed and reflected. Some of the transmitted radiation again reflects from the water surface and some of it is absorbed by water and transmitted through water which again reflects from the wall, hence water gets heated and evaporation occurs. Generated steam flows upwards with a buoyancy effect and condenses at the cover surface of the basin causing of lower temperature than saturation temperature corresponding to the partial pressure of water vapor within the basin (Singh *et al.* 2020). Solar desalination is classified as direct and indirect techniques as per management of storage and utilization of solar energy. Direct solar desalination techniques require a huge surface area to receive more solar energy to operate and produce fresh water while indirect solar desalination requires different space to produce potable water, for example, multi-effect desalination (Sharaf *et al.* 2011), reverse osmosis (Freire-Gormaly & Bilton 2019) with a large concentration of solar radiation, therefore indirect solar desalination required huge size of photovoltaic (PV) panel and installation of such arrangement have high initial cost as well maintenance cause of complex structure (Qiblawey & Banat 2008). Solar desalination with humidification and dehumidification methods are also popular nowadays because of its simple installation with enhanced production rate. The studies observed that the heat storage utility of evacuated tube collectors yields solar desalination (Verma *et al.* 2019). Stepped solar still with MgO in water is more effective than TiO_2 in water (Panchal *et al.* 2019). Water pollution and its effects on human health, such as nutrients, thermal pollution, sewage, etc., are also strict reasons to require fresh water. Many technologies are in use to produce fresh water. Solar desalination is mainly classified as direct and indirect as per using of solar energy. Direct solar desalination consumes solar radiation to produce yield while indirect solar desalination collects solar radiation then utilized to produce fresh water. Many technologies are there for solar desalination and are classified in Figure 1 (Ashmad & Hameed 1997; Tiwari & Sahota 2017).

Several researchers have experimented with various design parameters on solar stills to optimize the distillate. It has been observed that various design/operating parameters affect productivity and efficiency such as angle of solar radiation, angle of inclination, cover plate transmissivity, depth of water, wind velocity, basin surface absorptivity, flow rate, convective heat transfer coefficient, insulation of wall of basin, and so on. These parameters help to modify and design solar desalination to be more productive. The present study refers to the evaluation of various design parameters for simple solar stills impact yielding rate and heat transmission characteristics. The observations for the utility indicators and performance comparisons of several solar stills have been mentioned along with the significant interpretations, and finally, recommendations for future improvement of the novel concepts were also made in the proposed work.

Downloaded from http://iwaponline.com/aqua/article-pdf/doi/10.2166/aqua.2024.290/1355810/jws2024290.pdf
by DELHI TECHNOLOGICAL UNIVERSITY (DTU) user

Uncorrected Proof

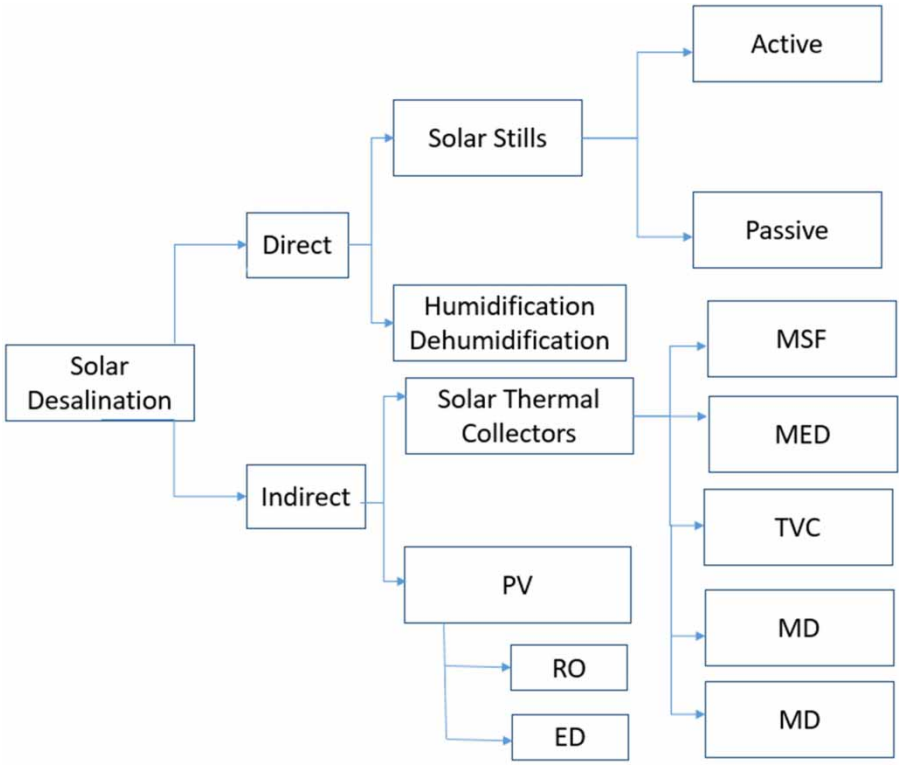


Figure 1 | Classification of solar still technologies (Panchal *et al.* 2019).

1.1. Observation of enhanced parameters for conventional solar still

1.1.1. Single- and double-slope collector solar still

Although it operates similarly to single-slope solar stills (SSSS), a double-slope solar still (DSSS) has two glasses to cover the top that increase the condensation surface area for condensation of the rising vapor inside the still. The DSCSS has a more productive rate of fresh water with effective condensation, as shown in Figure 2 (Kumar & Prakash 2019). Singh (2021), the double slope of the cover plate explores more surface area on a specific inclination to be more efficient of a global warming effect. Condensation on the cover surface is enhanced with a large surface area.

Murugavel *et al.* (2010) designed a double-slope solar still with an outer surface of mild steel and observed the performance of the system with a level of water and various heat-sensible storage materials, including quartzite rock, concrete cement pieces, red brick-washed stones, and iron scraps. They concluded that the basin material was quartzite rock that was still only an inch thick. Additionally, the temperature of the glass and water as well as the production rate was negatively impacted by the still's capacity and materials. In Ghaziabad, India (2840° N, 7725° E), Tiwari (Ashmad & Hameed 1997) performed thermal modeling for a double-slope solar still with 30 cm of water depth operating in the natural circulation mode. They concluded that, despite the double-slope active solar still providing a yield that was 51% larger than that of the double-slope passive solar, the passive system had a higher efficiency than the active system did. Furthermore, the double-slope active solar system still had greater energy efficiency than the passive system.

Rajaseenivasan & Murugavel (2013) used the Microsoft Excel program to research the effectiveness, productivity, and dependent variables of a double-slope solar still and a double-basin solar still under the meteorological conditions of Tamil Nadu, India. In contrast to the single basin system, they concluded that adding an extra basin increased productivity by 85%, reaching 2.99 l/m^2/day. Although the lower basin had higher productivity, the rate of yield was reduced when the water mass in both the upper and lower basins increased. To determine the best parameters of design for both types of systems under the meteorological conditions of Constantine, Algeria (latitude 36° 22′ N, longitude 6°37′ E), Abderachid & Abdenacer (2013) investigated the effect of both orientations (east–west and south–north) on the performance of productivity of a symmetrical double-slope solar still compared with an asymmetric solar still with a double effect. According to their research,

Downloaded from http://iwaponline.com/aqua/article-pdf/doi/10.2166/aqua.2024.290/1355810/jws2024290.pdf
by DELHI TECHNOLOGICAL UNIVERSITY (DTU) user

Uncorrected Proof

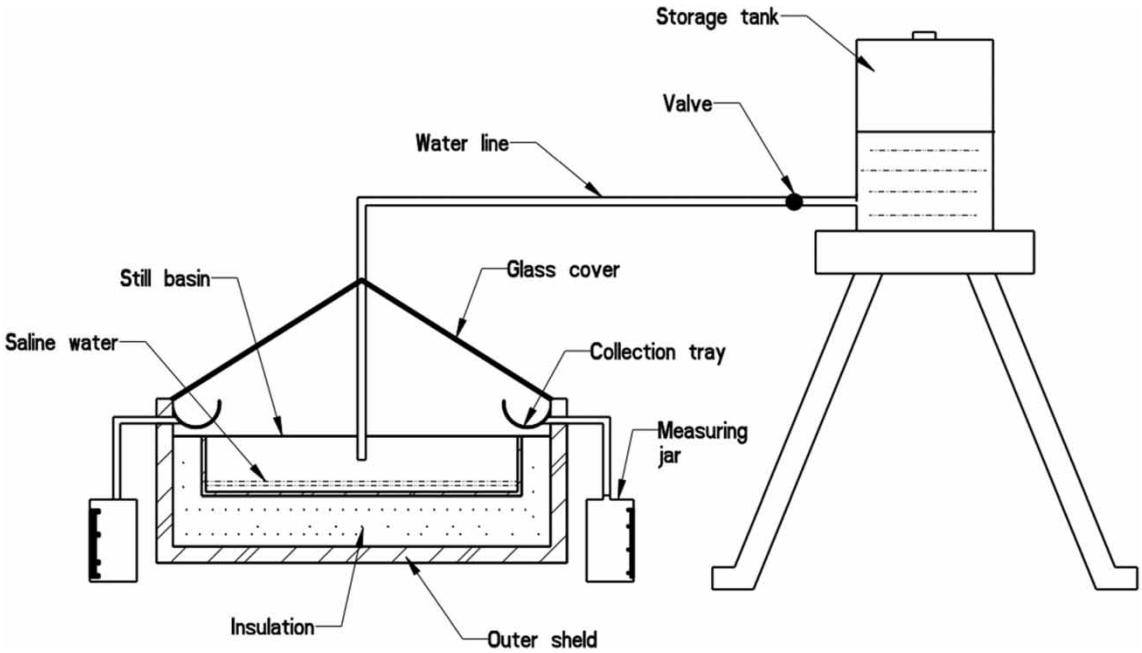


Figure 2 | Double-slope collector solar still (Tiwari & Sahota 2017).

both stills should be inclined at an angle of 10° for maximum solar light absorption and higher productivity. Higher daily production was shown to be associated with a 20 cm depth of water and a south–north (S-N) orientation, particularly in asymmetric solar stills with a double effect (22.57%) as opposed to symmetric solar stills with a double slope (16.23%).

The performance and output of a double-slope solar still with a capillary film-type condenser were examined by Belhadj *et al.* (2015) using FORTRAN 90 under the climate conditions of Adrar, Algeria (longitude of 0.17°W, an altitude of 264 m, and a latitude of 27.53°). Their findings indicated that an increase in the flow of saline water feeding the condensing chamber and the space between its two plates has an adverse effect on productivity. The double-slope solar still with capillary film type condenser, however, produced 7.15 kg/m^2/day while the typical sun still produced just 4.52 kg/m^2/day. Results present the algorithm they employed to compute the temperatures and distill freshwater.

The research was done by Tiwari *et al.* (Singh 2023) on the exergo-economic and environmental economics of a partially covered PVT-FPC active solar distillation system. They discovered that the use of DSSS was incredibly cost-effective for the production of drinkable water. Additionally, the commercialization of PVT active solar was still viable and affordable in outlying places.

1.1.2. Pyramid collector solar still

A solar desalination system with a basin top cover in the shape of a pyramid is referred to as pyramid collector solar water still. In comparison to classic type stills, it still has a larger evaporation surface for the same basin area, increasing the productivity of the particular still. Pyramid collector solar still (PCSS) may be improved by altering the height, orientation angle, and other particulars of the pyramid still's top cover. As seen in Figure 3, Kabeel (2009) carried out an experiment using a PCSS concave simply wick still. It can collect more solar thermal energy and produce more reflections since it has a larger surface area. The still basin had a basin area of 1.2×1.2 m^2, a water depth of 10 cm, and a top glass cover that was angled at a 45° angle. Because it produces a thin layer of water for evaporation, which results in more evaporation and better yielding condensation, concave jute wick achieved better results than simple PCSS. Figure 4 depicts data from Singh (2021) that are pertinent to the system under consideration. They were able to identify the elements that have an impact on triangular PCSS effectiveness thanks to Sathyamurthy *et al.* (2014) experimental investigation. For the most advantageous manipulative design of solar still units, these variables included the heat transfer coefficient, temperature differential at various still segments, cover areas, varied water depths in basins, and fluctuations in wind speed. A greater yield of up to 4.701 l/m^2/day was discovered with a 15.5% enhanced outcome at 4.5 m/s wind speed. This experimental examination was

Downloaded from http://iwaponline.com/aqua/article-pdf/doi/10.2166/aqua.2024.290/1355810/jws2024290.pdf
by DELHI TECHNOLOGICAL UNIVERSITY (DTU) user

Uncorrected Proof

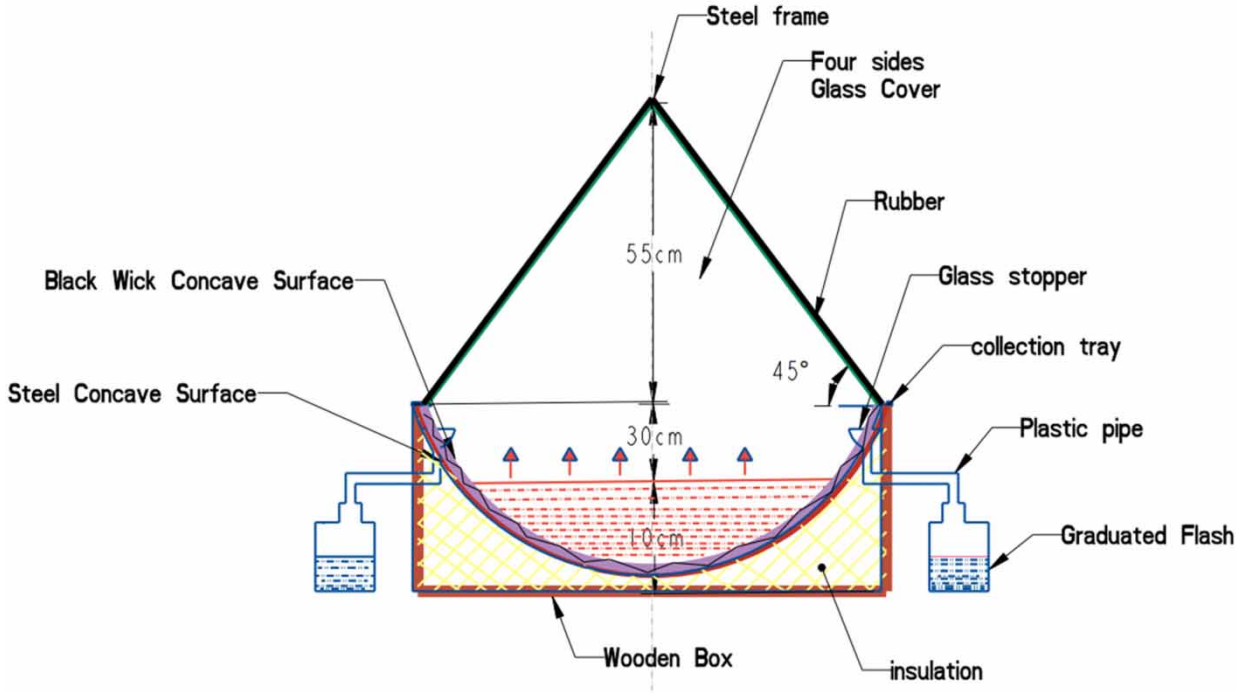


Figure 3 | Concave wick type PSDS (Singh 2023).

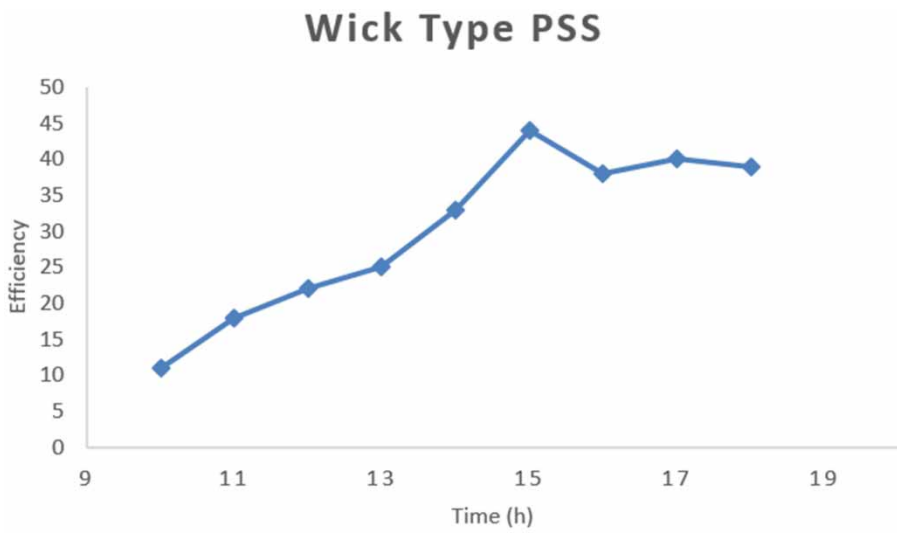


Figure 4 | Efficiency variation with respect to time of concave wick type pyramid solar still (Kumar & Prakash 2019).

carried out in Chennai with a 30° inclination angle and those specific meteorological conditions. Additionally, Tiwari & Tiwari (2008) and El-Sebaii (2000a, 2000b, 2004) examined how various types of solar still units were impacted by various water depths and wind speeds.

1.1.3. Black painted inside wall solar still

The theory of radiation heat transfer justifies that black surfaces have maximum absorptivity for any incoming irradiation (Kabeel *et al.* (Sathyamurthy *et al.* 2020)). Used this concept with the inner side wall of the chamber so that the maximum

Downloaded from http://iwaponline.com/aqua/article-pdf/doi/10.2166/aqua.2024.290/1355810/jws2024290.pdf
by DELHI TECHNOLOGICAL UNIVERSITY (DTU) user

Uncorrected Proof

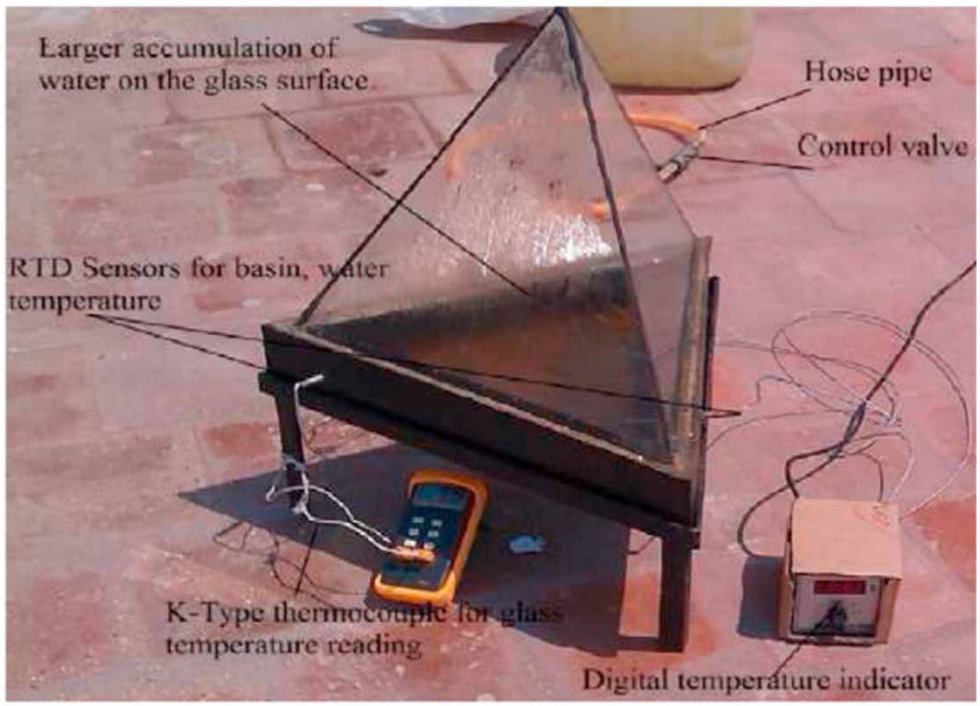


Figure 5 | Experimental setup of triangular PCSS (Kumar & Prakash 2019).

part of incident solar radiation is absorbed by black, and hence the temperature of water and cabin both increases. Hence, the rate of evaporation of water increases, and the performance of solar still enhanced. With a 20% concentration of nanoparticles in black paint, the average temperature of the water, basin, and glass was raised by 10.4, 12.2, and 12.3%, respectively. Beyond 20% of nanoparticle concentration, there is no discernible improvement in water, glass, or basin temperature. When utilizing 10 and 20% nanoparticles in black paint, the yield from solar stills is increased by 27.2 and 34.3%, respectively, and is higher than the output from solar stills using regular black paint.

1.1.4. Spherical solar still

Dhiman (1988) discussed a spherical solar still system and studied it using mathematical modeling. Spherical solar still has a combination of spherical top cover and liner basin. He also compared it to SSSS, and the offered system reported 30% more yield than SSSS because it does not require any solar tracking equipment but instead absorbs solar radiation. Basel later conducted an experimental investigation for the mutable hemispherical solar still (HSSS) and discovered up to 5.7 l/m^2/day with 33% efficiency. With the exception of the second system's portability advantage, both systems are free from solar tracking.

1.1.5. Hemispherical solar still

This is still suited for design and setup with improved approachability of solar radiant energy because it does not require tracking of sun irradiation. Basel (Ismail 2009) found in the experimental observation that the daily average efficiency of the system reached up to 33%. This system is known as a hemispherical solar desalting system because it still has a high water depth in the center of the basin but has superior and identical sun energy inclusion through its hemispherical-shaped upper cove. Figure 6 depicts the results of an experiment conducted on HSSS with or without top cover cooling by flowing water by Arunkumar *et al.* (2012). It has a basin area of 0.71 m^2, a water depth of 50 cm, and a water mass flow rate of 10 ml/min. When compared to HSSS with no water cooling at the top glass surface, which had 34% efficiency, the result was determined to be better with a 42% efficiency water-cooled glass cover. As the water cooled, the top cover increased the rate of condensation, which eventually improved the yield.

Downloaded from http://iwaponline.com/aqua/article-pdf/doi/10.2166/aqua.2024.290/1355810/jws2024290.pdf
by DELHI TECHNOLOGICAL UNIVERSITY (DTU) user

Uncorrected Proof

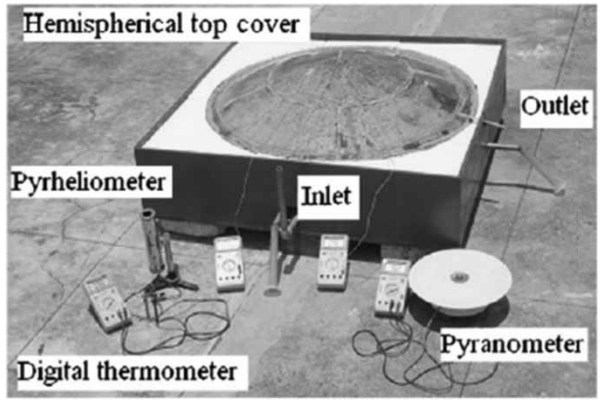


Figure 6 | Experimental setup off hemispherical solar still (HSS) (Ismail 2009).

1.1.6. 'V' type solar still

Singh (2021) observed in solar stills, only half of the top cover is effective when aligned with the solar latitude angle, while the other half is less effective when aligned with the solar latitude side. The still's side of the system from which the water basin can receive more solar energy effectively and glazing effects. A second kind of solar desalination system was used by Selva Kumar *et al.* (2008); it included a 'V'-shaped top glass covering, and the solar still was supported in four different ways, including with or without charcoal, boosting mirror or charcoal, or both. As shown in Figure 7, these combinations produce yields of 2.516, 3.226, 2.7, and 3.526 l/m^2/day, respectively, with efficiency values of 24.47, 30.05, 11.92, and 14.11% in such a system.

1.1.7. Painted inside surface with mixed TiO_2

Kabeel *et al.* (2019a) exposed, till the research in solar still from the economic angle, nanoparticles of TiO_2 arean economical way to mix with paint and paint on the inner surfaces of the basin. The availability of nanoparticles enhances the heat flow rate because of the enhanced thermal conductivity of the mixture as compared to without it. Such painted surface enhanced their absorbing capacity of solar and thermal energy. Such kind of concept enhances the evaporation rate of water and yields solar still. Nanoparticles can indeed enhance the heat flow rate and improve thermal conductivity when incorporated into a mixture or material. This phenomenon is commonly observed in nanofluids, which are liquids containing suspended

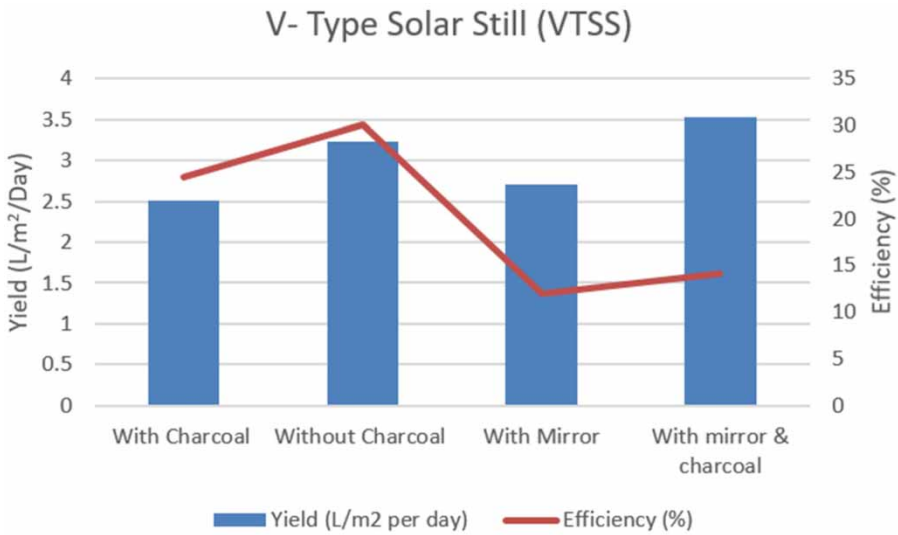


Figure 7 | Efficiency and daily yield variation with 'V' top (VTSS) system (Arunkumar *et al.* 2012).

Downloaded from http://iwaponline.com/aqua/article-pdf/doi/10.2166/aqua.2024.290/1355810/jws2024290.pdf
by DELHI TECHNOLOGICAL UNIVERSITY (DTU) user

Uncorrected Proof

nanoparticles. By adding nanoparticles to a mixture, such as a paint or coating, the thermal conductivity of the material can be significantly increased. This enhanced thermal conductivity allows for better heat transfer within the material, resulting in a higher heat flow rate. As a result, the material can absorb and distribute thermal energy more efficiently. When applied to the inner surfaces of solar still, these nanoparticle-enhanced coatings can enhance their absorbing capacity for both solar and thermal energy. The nanoparticles can help capture a greater amount of incoming solar radiation, converting it into thermal energy that can be utilized or stored. This makes the painted surface more effective at harnessing both types of energy.

1.1.8. Thermal conductivity of glass cover

Enhanced productivity of fresh water is a need of society and hence day by day research is happening. Condensation at the cover surface has an important role in this phenomenon. Condensation is based on the combination of convection and conduction heat transfer. Dimri *et al.* (2008) observed that the productivity of solar still enhanced with a higher value of thermal conductivity of the cover surface. When the cover surface of a solar panel or solar thermal collector has higher thermal conductivity, it facilitates better heat transfer from the surface to the underlying components, such as the absorber or heat transfer fluid. To achieve higher thermal conductivity in the cover surface, various techniques can be employed but it's also important to consider other factors as well, such as cost, durability, and compatibility with the specific application, when selecting or designing the cover surface material.

1.1.9. Depth of water in single slope solar still

The thermal study is performed at two distinct water levels of 3 and 12 cm at an inclination of 23°, according to Prakash *et al.*'s (2021) analysis. When the water depth increases for the active mode of operation, the daily yield production rises. The daily output yield falls with increasing water depth and increases with increasing h_{ew} and h_{cw}. When the evaporative surface temperature is higher and the condensing surface temperature is lower, the output of the solar still distillate increases. The optimal yield output is 0.23885 kg/h at 12 cm of water depth, while it is 0.13 kg/h at 3 cm.

1.1.10. Single solar still with porous structures

Shoeibi *et al.* (2022) observed the temperature gradient between the cover surface and water can be enhanced by water temperature in the basin with porous material which directly enhanced the productivity of the system. The effect of porous material on the performance of pyramid solar still was assessed by Saravanavel *et al.* (2020) which shows enhanced results. The experiments were done with several pieces of clay pot and chalk as porous material at several hours of the day with a fixed depth (0.01 m) of saline water. To reduce the heat losses from the vertical side surfaces, they are covered with insulated glass walls. With the same climate condition, two different conventional and modified solar still were compared. Their results show that the productivity of considering solar still with porous material was enhanced by 36% as compared with a traditional system. Srivastava & Agrawal (2013) experiment enhanced solar still with porous fins. The experiments were done on single slope solar still with old blackened cotton rags as a porous fin, which was located on the basin, as shown in Figure 8. In the experiment, the inclination of the glass cover is taken as 24°, which was equal to the latitude angle. As per the results of the experiment, it is shown that most of the solar radiation is received by porous fins due to which the evaporation rate increased. Besides, they observed that the productivity of water can be increased by a decrement in the depth of water in the still. The maximum productivity of freshwater of the same experimented system with porous fins is recorded as 7.5 kg/m^2 in May.

1.2. Performance evaluation of an integrated solar still system: exploring design parameters

1.2.1. Solar still with fins for condensation

Potable water is collected after condensing generated steam on the cover surface through both convective and conductive heat transfer. Solar stills with fins for condensation are a type of solar desalination system that utilizes fins to enhance the condensation process. Solar stills are devices that use solar energy to evaporate water and then collect and condense the vapor to produce fresh water. Velmurugan & Srithar (2011) observed fins increase the surface area available for condensation, allowing for more efficient heat transfer, water vapor condensation in a single solar still, and efficiency enhancement by 45.5%. The extended surface area helps in maximizing the contact between the warm vapor and the cooler condensing surface, facilitating faster condensation and higher water production rates. The fins used in solar stills can be made from materials with good thermal conductivity to aid in the transfer of heat from the vapor to the condensing surface.

Downloaded from http://iwaponline.com/aqua/article-pdf/doi/10.2166/aqua.2024.290/1355810/jws2024290.pdf
by DELHI TECHNOLOGICAL UNIVERSITY (DTU) user

Uncorrected Proof

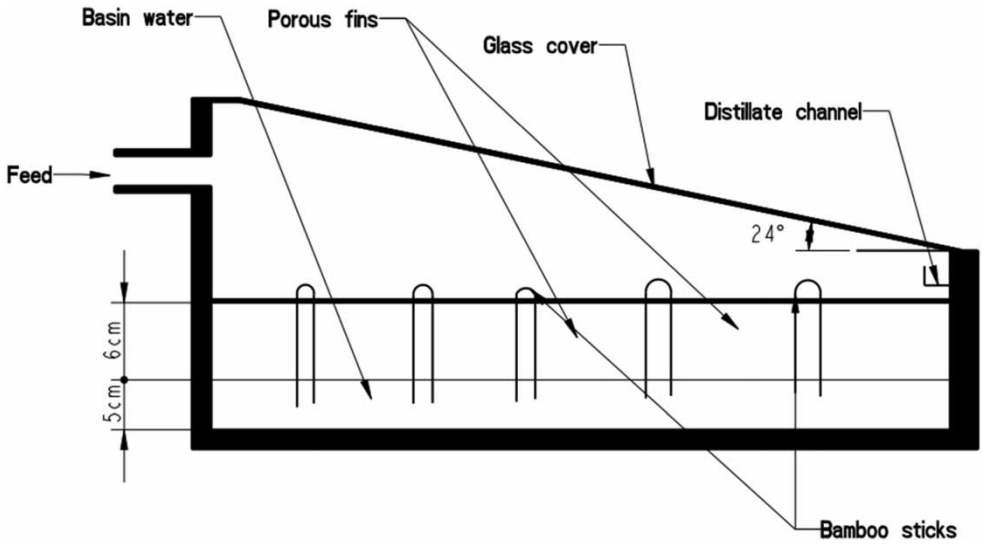


Figure 8 | Modified still using porous absorber (Shoeibi *et al.* 2022).

By introducing a pin fin into a paraffin wax bed of single slope solar still performed more productively. Such experiments are observed with several depths of water from 2 to 4 cm in modified solar still that productivity is higher at 2 cm and also achieve yield 3,750 ml/m^2 for modified solar still while for the same depth, the yield for conventional solar still was 3,017 ml/m^2 (Suraparaju & Natarajan 2021a).

By incorporating fins, solar stills can enhance the condensation rate and improve the overall efficiency of the system. This can result in increased freshwater production, making it a beneficial approach for solar desalination in areas with limited access to freshwater resources. Fins are introduced to increase the heat transfer rate through convection, increasing condensing surface area and enhancing heat rejection to the surroundings. In solar still, vapor loses its latent heat to the inclined cover surface. With the gravitational effect, it collects as freshwater found in comparative research between those with attached fins on a tray, as shown in Figure 9, and without fins with the maximum yield of 1.12 and 0.914 kg/m^2, respectively (Velmurugan *et al.* 2008; Panchal & Mohan 2017).

1.2.2. Solar still with fan for condensation

A solar still with a fan is a type of solar desalination system that incorporates a fan or blower to enhance the evaporation and condensation processes. In a solar still with a fan, the fan is used to increase the airflow within the system. Suraparaju & Natarajan (2022a) investigate that the lower temperature of the cover glass surface of solar still can enhance the condensation rate. After research on enhancing water evaporation, condensation also has an important role in producing fresh water. An *et al.* (2018) vapor condenses on the cover surface as film-wise condensation or drop-wise condensation. The rate of condensation depends upon the heat transfer coefficient (h) of vapor over the surface. Increasing the value of h as the heat transfer coefficient of forced convection with of fan is a fruitful development, as shown in Figure 10. Solar stills with fans can be particularly useful in areas with low humidity or limited solar exposure, as they help overcome these challenges and improve the water production rates of the system.

1.2.3. Solar still with several types of wicks

Psychometry also has an important role in the evaporation of water into a chamber caused by the global warming effect of solar radiation. Both condensation and evaporation occur at saturation temperature, directly linked to the pressure inside. The evaporation rate mainly depends upon the heating effect and partial pressure difference. A solar still with wicks is a type of solar desalination system that utilizes wicking materials to enhance the evaporation and condensation processes. In a solar still with wicks, the wicking materials are placed in contact with the saline or contaminated water source. These materials can be porous and have capillary action, allowing them to absorb and transport the water through the wick structure. As the water is drawn up the wicks, it is exposed to the surrounding air, promoting evaporation. The wicking

Downloaded from http://iwaponline.com/aqua/article-pdf/doi/10.2166/aqua.2024.290/1355810/jws2024290.pdf
by DELHI TECHNOLOGICAL UNIVERSITY (DTU) user

Uncorrected Proof

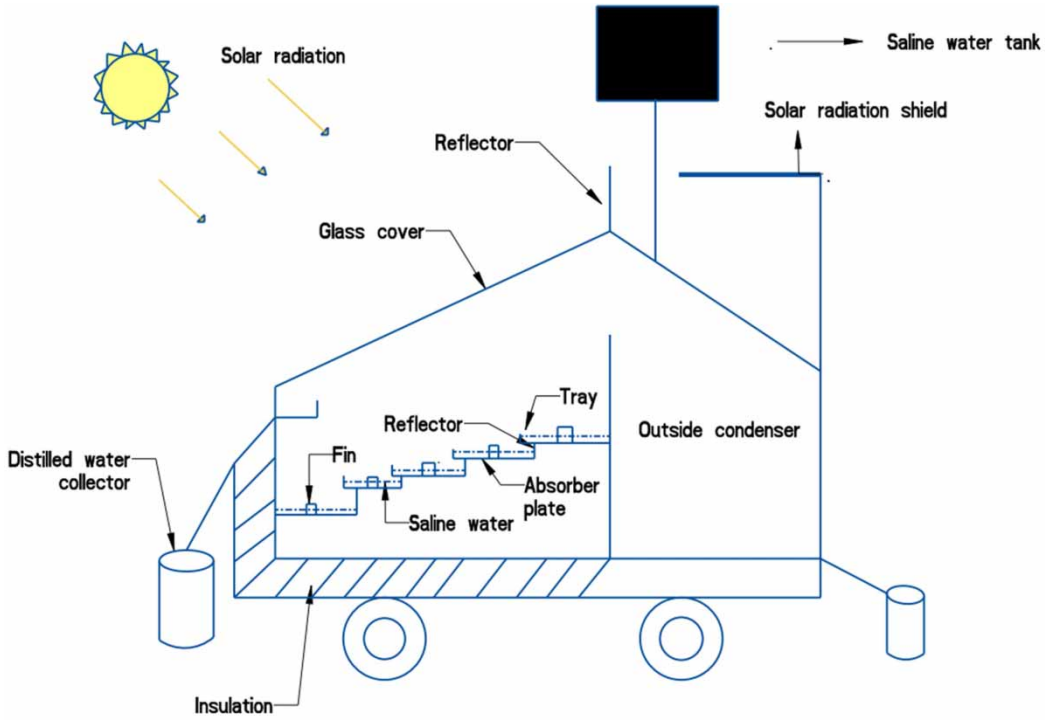


Figure 9 | Solar still with fins (Velmurugan & Srithar 2011).

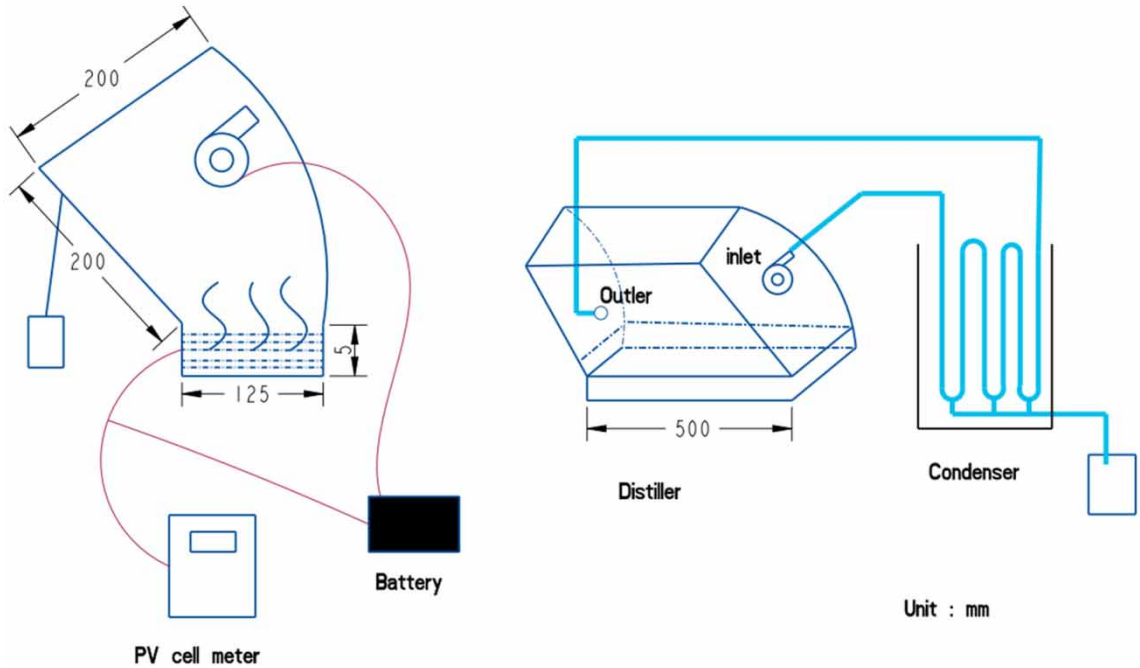


Figure 10 | Experimental setup with fan for condensation (Panchal & Mohan 2017).

action helps to increase surface area, heat transfer, facilitated condensation, etc. Wick floats on the water's surface, as shown in Figure 11, and increases partial pressure differently. Therefore, wick enhanced fresh water's evaporation rate and productivity (Suresh & Shanmugan 2019). Suraparaju *et al.* (2021b) analyzed on experimental work of single slope solar still

Downloaded from http://iwaponline.com/aqua/article-pdf/doi/10.2166/aqua.2024.290/1355810/jws2024290.pdf
by DELHI TECHNOLOGICAL UNIVERSITY (DTU) user

Uncorrected Proof

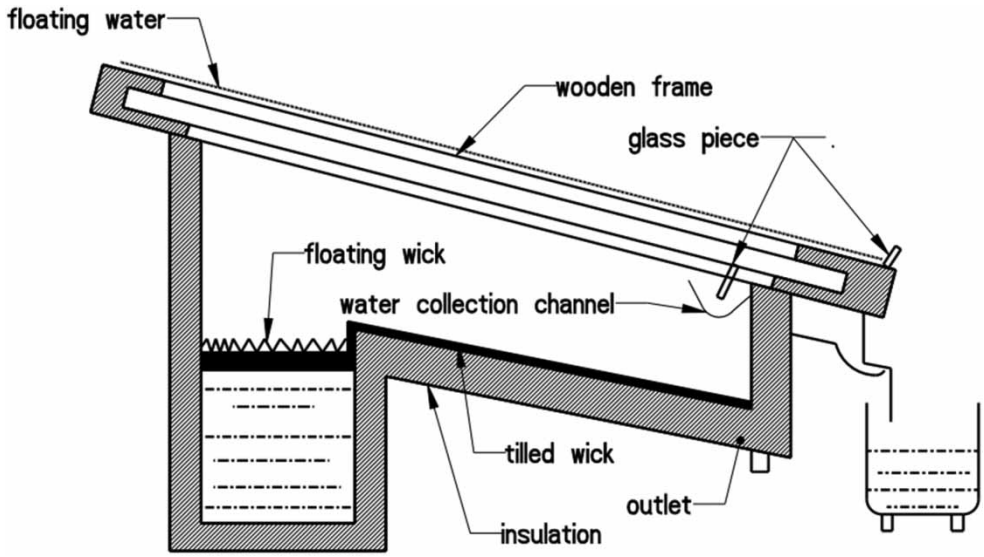


Figure 11 | Wick Type solar still with different thermal conductivity of cover (Velmurugan *et al.* 2008).

with multiple floated fibers of better porosity over the surface seawater to increase the evaporation rate of water. The selection of the number of fibers is based on the percentage occupied surface area of the basin. The result of experimental work is optimized with 5 pond floated fiber and observed enhanced yield of solar still by 29.67% than without floated fiber while with the use of 15 Luffaacutangula fibers (LAF), the productivity of fresh water is increased by 28.35% (Suraparaju & Natarajan 2021b).

Suraparaju *et al.* research better productivity of still with the use of ridge gourd natural fiber in the single slope solar still. Two identical SSSS are used to compare the impact of modification on productivity and the result found that such kind of modification has no impact on the productivity of solar stills (Suraparaju & Natarajan 2020).

1.2.4. Multi-basin solar still

In a study, Kaviti *et al.* (2016) discovered that multi-basin solar stills produced more fresh water than traditional sun stills. The fact that the multi-basin solar still collects and reuses the heat inside the still effectively served as strong evidence in favor of this. These stills feature multiple glazing layers covering the water's surface thus the upper basin's evaporative heat is generated by the lower basin's convective heat. Numerous researchers are conducting extensive research in this field and changing still designs to increase their effectiveness. The MBSS for passive-type solar still is designed as shown in Figure 12 (Bapeshwararao *et al.* 1983).

1.2.5. Tubular solar still

Singh (2021) observed that in comparison to SSSS, Tiwari and Kumar (Tiwari & Selim 1984) showed that the tubular solar still (TSS) performs better over a longer period of time when there are no nighttime conditions because it allows for a bigger basin area and better evaporation. A TSS consists of a rectangular tray as a still basin in a tube that is covered. A model of TSSS with several wicks in place of a rectangular basin was provided by Kumar & Anand (1992). This desalting technology thus provides more space for condensation and superior results to SSSS. Then, Amimul *et al.* (2012) enhanced and provided TSSS in new design parameters with a basin of metal material covered by a thin film of vinyl chloride. The straightforward or traditional TSSS was performed after desalination. Due to the greater temperature difference between the basin water and the thin film tubular covering in this setup, the yield was improved. Then, Arunkumar *et al.* (2016) tested with TSSS undercooled or uncooled settings, together with PSS and CPC, and the successful findings were 7.77 l/m^2/day yield. They also concluded that the system's heavy initial setup cost is offset by its overall enhanced efficiency and the distillate that results from it. Later, Arunkumar & Kabeel (2017) introduce PCM with TSS-CPC and analyze TSS-CPC with PCM, and compare for without PCM; the results show that TSS-CPC with PCM performs better, with a daily yield of 5.78 l/m^2 compared to 5.33 l/m^2 for TSS-CPC alone. The use of PCM, which provides continuous heat as supplemental thermal energy by altering its phase, allowed the

Downloaded from http://iwaponline.com/aqua/article-pdf/doi/10.2166/aqua.2024.290/1355810/jws2024290.pdf
by DELHI TECHNOLOGICAL UNIVERSITY (DTU) user

Uncorrected Proof

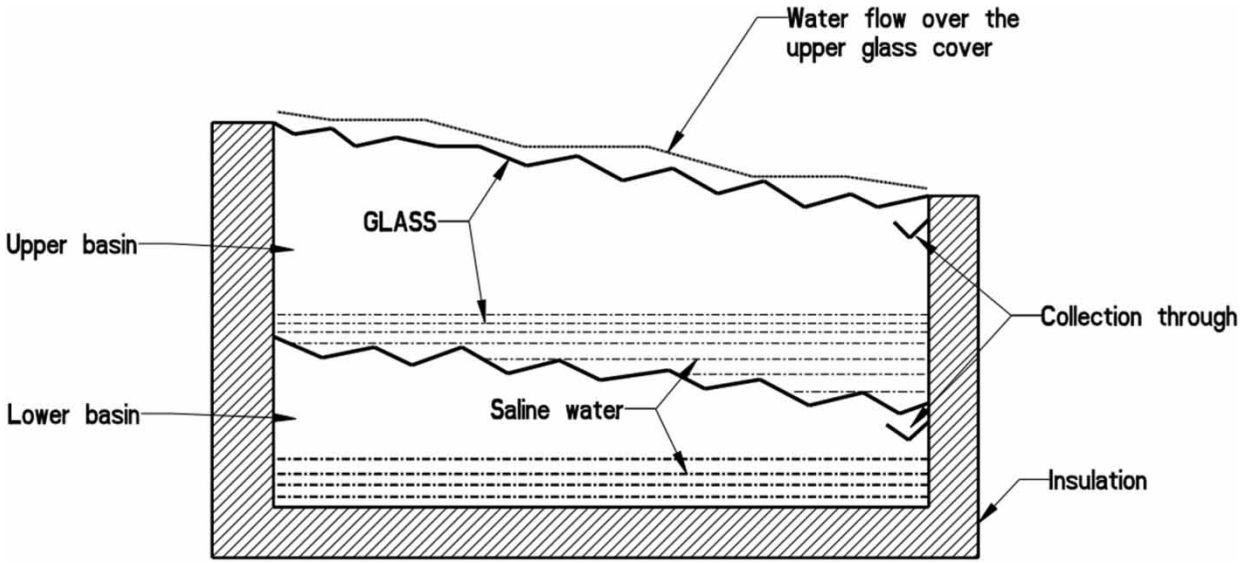


Figure 12 | Schematic diagram of a multi-effect passive-type solar still (An *et al.* 2018).

system to operate more efficiently. As a result, latent heat from PCM was transferred to the basin liner between periods of cooling. In a recent study, Jing et al. examined concentric TSS, which consists of two layers, the outer of which has a wet wick and the inner of which is normal. As distillate output, the outcome was superior to the earlier TSS system. In comparison to other systems, TSS has superior solar radiation usability due to a smaller layer of basin water mass, and the usage of PCM expands its capability. Thus, superior output outcomes are obtained with appropriate PCM for TSS-CPC systems.

1.2.6. Multi-wick solar still

Tiwari & Selim (1984) provided one of the first analyses on the dual-slope multi-wick solar still (MWSS), which revealed higher yields but also higher investment values due to the system's more expensive use of components. Additionally, Singh & Tiwari (1992) provided a multi-effect MWSS with improved efficiency as a result of the use of a wick, which preserves a thin layer of water mass. In addition to using charcoal cloth as a thermal energy-storing medium, Mahdi *et al.* (2011) experiment on tilted WSS also published the results with a deeper understanding. Additionally, the work of Pal *et al.* (2015) was also favorably acknowledged in the field of MWSS, which was presented with minor modifications to traditional solar desalting units and stated to have extremely high performance. Then, Pal & Dev (2016) provided some adjustments to the double-slope traditional solar desalting system, which was successfully transformed into MWSS and exhibits noticeably higher efficiency and distillate output than straight distillers. Multiple wicks are used in these systems, but the effective system performs better for the same basin area because it uses better wick material and better heat storage materials. This system makes use of a variety of materials with qualities like porosity, non-reactivity with filthy water, elevated temperature sustainability, etc. The materials should be long-lasting, cost-effective, and appropriate for the system. Wick offers a very thin water film and promotes effective evaporation when exposed to direct or indirect sunlight. Wick can be positioned in a variety of directions or several configurations. Pal *et al.* (2017) modification to the double-slope solar desalting system includes the addition of transparent walls and multi-wicks (MW) in the basin. The experiment was carried out in the climate of Allahabad, as depicted in Figure 13(a). This still has a 2 m^2 basin with a 2 cm level of water and a top cover that is oriented at a 15° angle. The updated design using jute and black cotton wick produced better outcomes, it was revealed. The yield production response and thermal efficiency for the two tests were, respectively, 9.012 and 7.040 l/m^2/day, and 23.03 and 20.94%. Suraparaju & Natarajan 2022b) explore the impact of evaporation rate and condensation rate with an experimental setup where the evaporation rate is increased by using a novel pond fiber at the surface of the water at basin and a hollow finned absorber while the condensation is enhanced by decreasing the temperature of cover glass with a dripping arrangement of water. The results of the experiment analyzed that the water temperature of modified solar still enhanced by 12%, the glass cover temperature was decreased by 30% and the yield of solar still is enhanced by 126%. According to Ni *et al.*

Downloaded from http://iwaponline.com/aqua/article-pdf/doi/10.2166/aqua.2024.290/1355810/jws2024290.pdf
by DELHI TECHNOLOGICAL UNIVERSITY (DTU) user

Uncorrected Proof

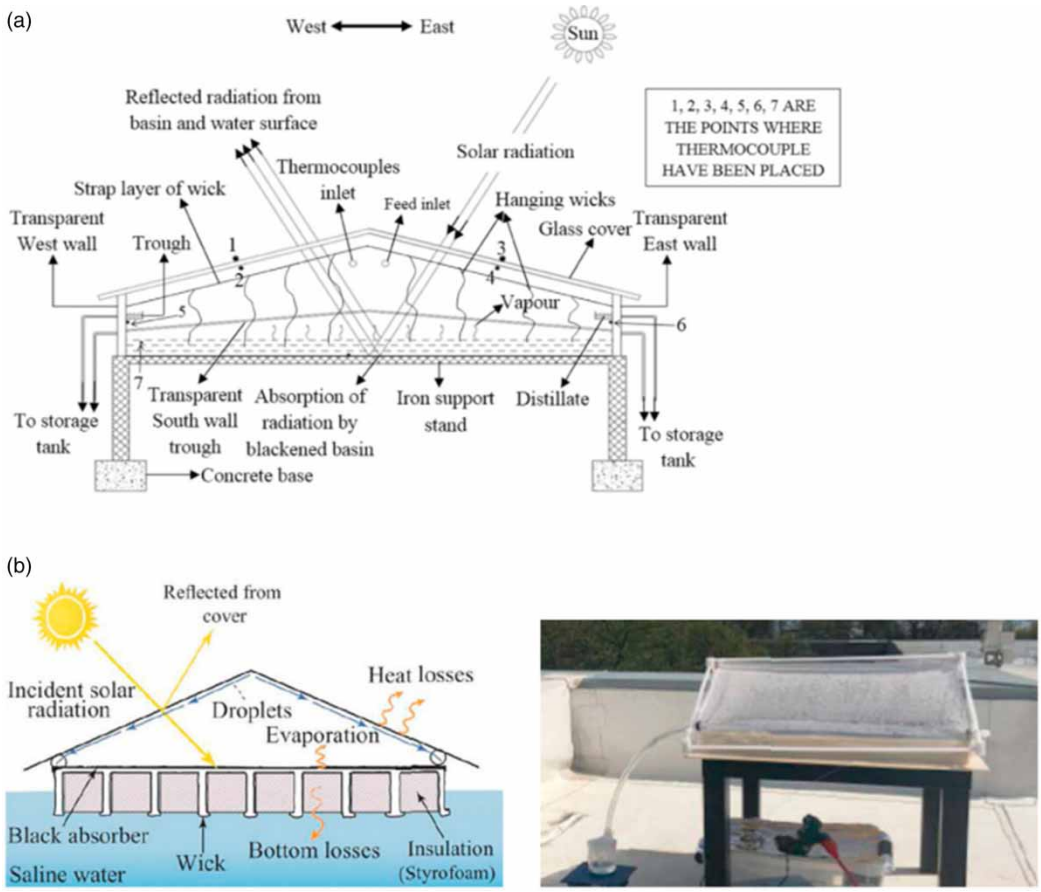


Figure 13 | (a) Multiple wick solar desalination system (b) Floating wick solar desalination system (Jing *et al.* ; Tiwari & Selim 1984).

(2018), a low-cost solar distillation system and process that uses a floating wick (fabric wick) with the ability to reject salt because of its unique design, operating principle, and system mechanism, as illustrated in Figure 13(b). The pores of the filtration medium can become clogged by seawater's 3–3.5 wt% total dissolved solids, which include NaCl, $CaCO_3$, etc. These holes are minimized here by corrugating the filtration medium and floating it over foam. Under one sun solar intensity circumstances, the system has an evaporation area of 21×20 cm^2 and a condensation area of 55×55 cm^2, respectively, with a 57% evaporation efficiency. Additionally, CFD modeling is used to demonstrate the desalting procedure and its results.

1.2.7. Contactless solar steam generation and solar still

Cooper *et al.* (2018) novel idea for superheated steam is provided. In this experiment, the solar absorber does not come into direct touch with the water; instead, it is filled with solar radiation energy, which is then used to superheat the steam with 38% efficiency (under laboratory conditions) and distill water up to 2.5 l/m^2 each day.

As opposed to this, Kashyap *et al.* (2019) demonstrated the circulating CO_2 capture into a grapheme aerogel material for corresponding conversion into water and $CaCO_3$ with the aid of solar localized heating for 1,000 W/m^2 (one sun) solar intensity in a laboratory setting. Diffusion solar stills and weir-type solar stills function well in the various solar desalting systems represented by the body of work. It has a greater effective condensation and evaporation surface area with the lowest water mass at the basin liner or at the diffusion surface which directly dedicates to the corresponding result. Stills with CPC, FPCs, PCM, or additional condenser, etc. directly dedicated to the freshwater production under the same surface area of the basin (Singh & Gautam 2022).

1.2.8. Diffusion solar still

Much research has previously investigated different forms of diffusion solar still (DSS), primarily multi-effect horizontal, vertical, or inclined type DSS (Toyama *et al.* 1983, 1987; Elsayed 1986; Ouahes *et al.* 1987; Ohshiro *et al.* 1996; Bouchekima

Downloaded from http://iwaponline.com/aqua/article-pdf/doi/10.2166/aqua.2024.290/1355810/jws2024290.pdf
by DELHI TECHNOLOGICAL UNIVERSITY (DTU) user

Uncorrected Proof

et al. 1998; Fukui *et al.* 2004). As a result of several flaws in past works that were discovered by researchers' ongoing examination, new concepts for designs are continually being developed nowadays. Hiroshi (Tanaka 2009) explored multi-DSS paired with FPC and provided the extension in earlier work. In his investigation of the specific type of DSS under conditions of maximum solar intensity, it was deemed an excellent result with a yield of 13.3 l/m^2/day. Multi-DSS was described by Chong *et al.* (2014) together with a heat exchanger and connected to a vacuum-type solar spiral collector. In it, water absorbs extra heat; as a result, water temperature increases. This leads to increased evaporation, higher condensation, and higher production of up to 23.9 l/m^2/day. In addition, Huang *et al.* (2015) introduced an improved spiral-type multi-effect DSS with specifications similar to those used in Chong *et al.* (2014) and reported improved highest distillate production of 40.6 l/m^2/day based solely on solar absorber surface under standard test conditions as it simultaneously used directional as well as lateral diffusion to improve overall performance in terms of yield. The productivity of fresh water was captured as a 15.9 l/m^2/day yield by Tanaka (2016) who took into account the multi-effects with vertical type DSS coupled with a slanted wick that produced good in earlier studies (Chong *et al.* 2014). Tanaka (2017) presented a study based on different characteristics, such as dimensional parameters, and optimized it to produce better results. Tanaka & Iishi (2017) then rechecked this model through trials and recorded a sizable yield. Due to their diffusion channels (vertical, horizontal slanted, spiral multi-effect, etc.), DSS systems are quite effective. The efficiency of spiral solar collectors is higher and spiral multi-effect DSS with greater condensation and evaporation in the longitudinal and lateral orientations would raise the efficiency to a higher level. In contrast to conventional distillation procedures, the unique approach of DSS is used to create more distillates. The kind of DSS, such as a vertical, horizontal, or inclined type multi-effect DSS system, is determined by the orientation of the diffuser plate. In it, multiple plates are positioned so that there is an air gap between them, and the plates each have a wick that has been moistened either directly or by capillary action. Diffusion decontamination is the term used to describe how this distillation system operates: initially, heat from solar radiation enters the air opening, causing water to evaporate, diffuse, and condense into the space on its subsequent cold condensing plate (Rajaseenivasan *et al.* 2013). This technology produces more potable water because it uses greater surface surfaces for evaporation and condensation. In their research, Kaushal *et al.* (2017a) used vertical floating wick DSS. Figure 14 illustrates how well the concentrated salty water from the washbasin output was employed in this experiment to reheat the salty water at the input. Due to enhanced design and regular heat recovery, simple vertical multi-effect type DSS and proposed DSS with some alteration (floating wick) were compared with 21% more essence. Additionally, they discussed the economic analysis and correlation component, as well as the short payback period for the suggested approach (Kaushal *et al.* 2017b). The proposed technique uses thermal coal as the cotton wick's floating medium. The suggested system comprises a 1.5×0.77 m^2 basin area, 1.52×0.68 m^2 diffusion plate regions, spaced 10 mm apart, and a 2 cm water level maintained inside. Due to greater heat resurrection through the heat exchanger continuously, as illustrated in Figure 15, it was claimed that the yield was also better at night, measuring 0.98 l/m^2/day from the traditional model and 1.34 l/m^2/day from the experimental model.

1.2.9. Weir-type solar still

Sadineni *et al.* (2008) conducted an experimental and theoretical analysis of the solar desalting weir-type system and found that it performed 20% better than conventional distillers and had a good correlation coefficient. This is because the system has a greater area for evaporation with less glazing, a lower depth of water in the basin, and a continuous flow of water that recovers more and more heat. Following that, Tabrizi *et al.* (2010) introduced a PCM-assisted solar desalination weir cascade-type system. Observation showed low mass flow rates with and without PCM on clear and hazy days, with the clear day without PCM producing higher distillate as the preferred outcome. The study by Zoori *et al.* (2013) included a comparison using the same model as in Figure 16 but without a PCM. This study was replicated, validated by an experimental investigation as well, and was found to be well-aligned. Better output is attributed to weir solar stills, which operate on a thin water layer maintained at the basin liner, as opposed to weir stills supplemented with PCM and water loop, which reduce heat loss and ultimately produce a significantly higher yield. Sarhadi *et al.* (2017) examined various parameters in various air conditions and took into consideration the cascade-type weir solar still system depicted with phase change material and compared it to the identical model without phase change material. A good agreement was used to validate the findings. It was determined that cascade WSDS with PCM performs better in semi-hazy conditions because PCM adds additional heat to the basin water, which is what causes a higher yield. Additionally, a PCM-free system operates better on a clear day. As indicated in Figure 17, the equivalent findings were 76.69% maximum efficiency and 7.05 l/m^2 of potable water per day. Natarajan *et al.* (2022)

Downloaded from http://iwaponline.com/aqua/article-pdf/doi/10.2166/aqua.2024.290/1355810/jws2024290.pdf
by DELHI TECHNOLOGICAL UNIVERSITY (DTU) user

Uncorrected Proof

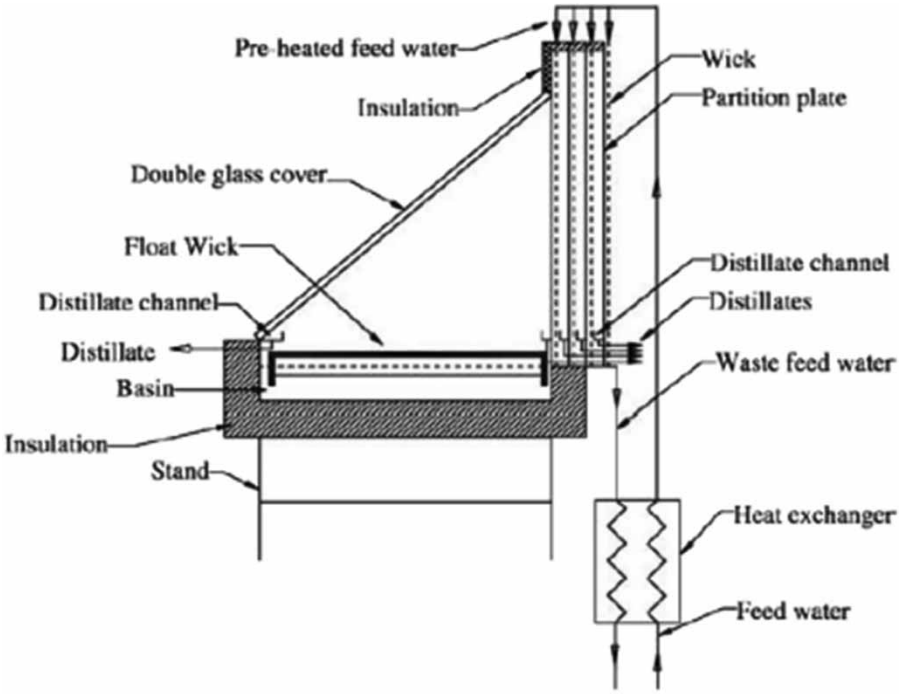


Figure 14 | Diffusion solar still (DSS) with floating wick (Tanaka 2009).

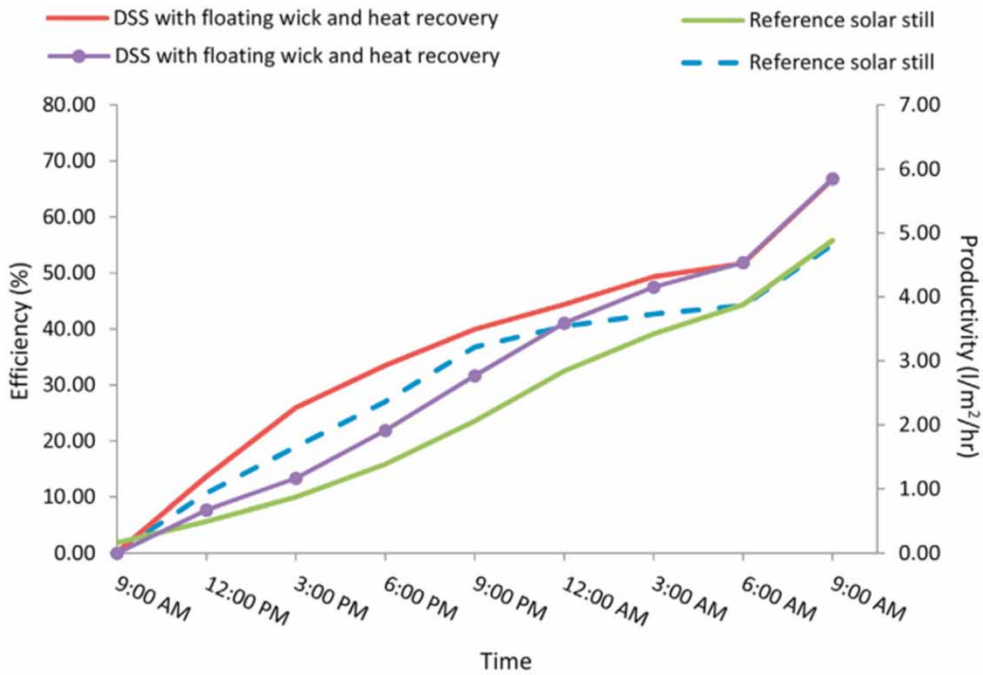


Figure 15 | Variation of efficiency and productivity with respect to time of diffusion solar still (Chong *et al.* 2014).

proposed enhanced solar still by considering nature-friendly and low-cost materials such as sawdust, rice husk, molasses, and so on. with higher yield and enhanced rate of evaporation. Such enhanced solar still performs with 34.81% higher evaporation rate than conventional solar still.

Downloaded from http://iwaponline.com/aqua/article-pdf/doi/10.2166/aqua.2024.290/1355810/jws2024290.pdf
by DELHI TECHNOLOGICAL UNIVERSITY (DTU) user

Uncorrected Proof

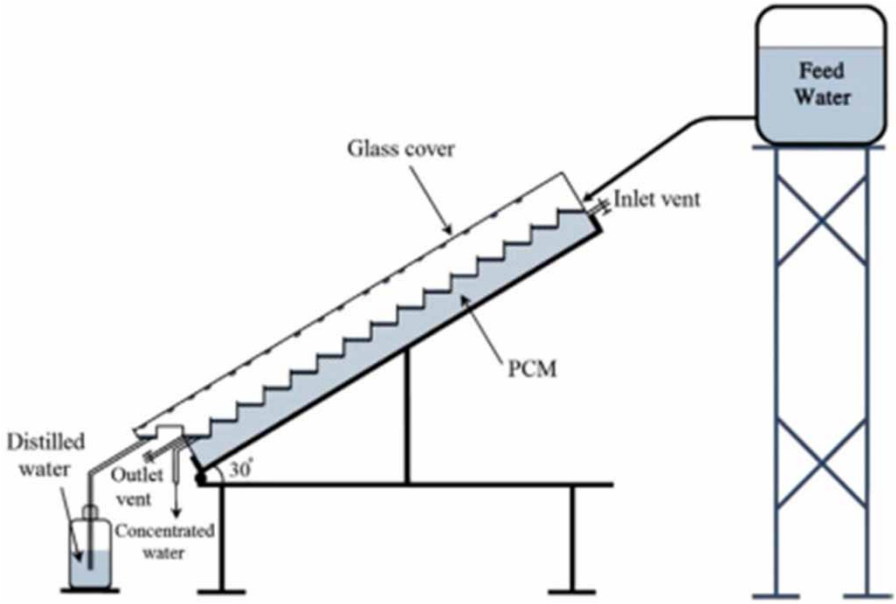


Figure 16 | Weir solar desalination system cascade type with PCM (Tanaka 2017).

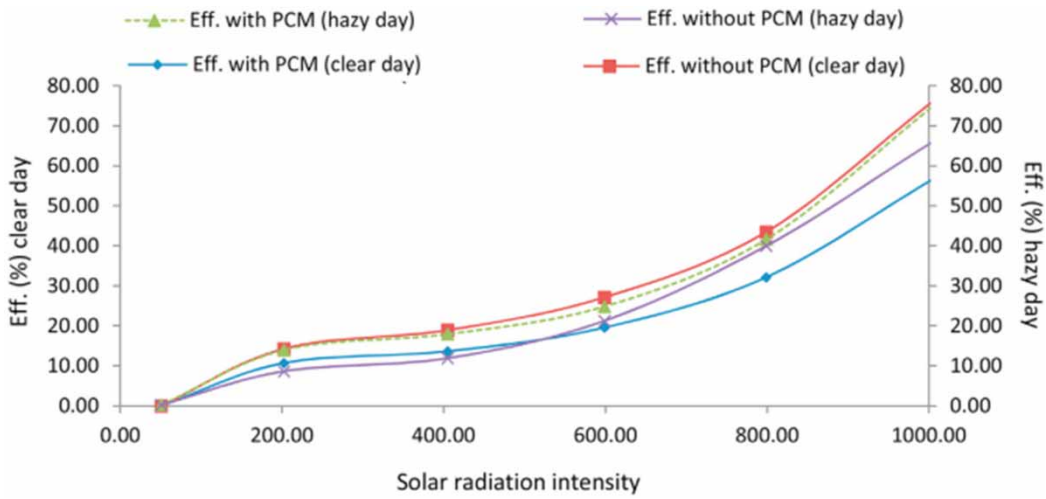


Figure 17 | Efficiency variation with and without PCM for weir solar still cascade type in clear and hazy day (Tanaka & Iishi 2017).

1.2.10. Tubular solar still

Distillation takes place in a long tube that has a rectangular tray filled with water mass in this solar desalination system. This technique does not require separate sun tracking equipment, though optional components like a parabolic concentrator can enhance the outcomes. Arunkumar *et al.* (2013) experimented on a TSS with a concentrator and two 0.03 m^2 basin areas, and they discovered noteworthy outcomes for three conditions: (i) yield with no cooling, (ii) yield with air cooling, and (iii) yield with water cooling, all of which were carried out in the Coimbatore climate, as shown in Figure 18. The observed results for items (i), (ii), and (iii) were, respectively, 2.05, 3.05, and 5.0 l/m^2/day. Following that, Elashmawy (2017) investigated TSS using three different combinations, including TSS filled with salty water and a black cloth wick in the first, TSS without a wick in the second, and TSS with CPC and a solar tracking device in the third. It had daily yields of 4.71, 3.60, and 3.35 l/m^2 with per day efficiencies of 36.5, 30.5, and 28.5% for basin surfaces of 0.59 m^2. As more solar thermal energy is

Downloaded from http://iwaponline.com/aqua/article-pdf/doi/10.2166/aqua.2024.290/1355810/jws2024290.pdf
by DELHI TECHNOLOGICAL UNIVERSITY (DTU) user

Uncorrected Proof

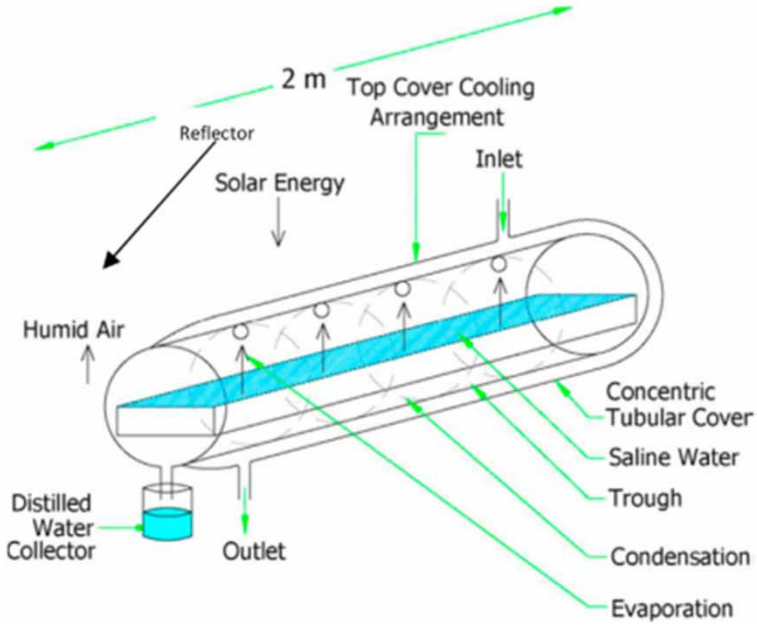


Figure 18 | Tubular solar still (TSS) (Rajaseenivasan *et al.* 2013).

absorbed by the black wick, higher condensation and evaporation occur, producing more fresh water, making the first combination perform better.

1.2.11. Stepped-type inclined solar still

The analysis of several solar still designs discovered that used a storage tank for continuous water circulation in Stepped Solar Stills (STSS) to extend production many times (El-Agouz 2014; Kabeel *et al.* 2019b). The STSS absorber plate has a surface area of 1 m^2, which is separated into 10 equal steps. The feed water (i) seawater and (ii) salt water, and the basin conditions (i) black absorber basin and (ii) cotton absorber basin were changed during the experiments. Black absorber STSS is experimentally explored in the first case of basin circumstances, and the outcomes were compared with Simple solar still (SSS). It has been determined that the STSS and SSS black absorbers' daily efficacy for desalinating seawater is 61 and 42%, respectively, and for desalinating saltwater is 55 and 37%. In the second instance, a cotton absorber is used in place of the black absorber. According to the experimental findings, the STSS and SSS cotton absorbers' daily efficacy for desalinating seawater is 61 and 40%, respectively, and for desalinating saltwater, it is 70 and 48%. For seawater desalination and saltwater desalination, respectively, the black absorber STSS enhances the freshwater production rate by up to 43 and 48% more than that of SSS. For seawater and saltwater desalination, respectively, cotton absorber STSS enhances the freshwater production rate by up to 53 and 47% more than that of SSS. STSS using seawater as the intake yielded 6.1 and 6.3 kg/m^2/day in yield.

2. DISCUSSION

Various types of single slope simple solar stills (SSSS) have been discussed along with SSSS and the overall performances of SSSS. The variations between productivity and efficiency show the effective performance of solar water still, that's why it is recognized easily, the worth of full solar desalination among all the respective parameters under conditions for simple and integrated solar still. The summarized observed data show that cascade-type weir solar desalination systems with and without PCM, multi-step solar still with multiple absorbers are better while weir solar still system without PCM performs more effectively with 3.05% yield and 5.96% efficiency due to the effective utilization of collected solar energy to evaporate saline water at the same time. SSSS performs effectively with 24% more productivity per unit area of basin per day while most of the part is at a mid-time. PSS performs efficiently because PSS does not require any solar tracking machine for solar energy because of its design. This has a per day average efficiency of 45% with distillate as 4.01 l/m^2/day at $ 0.065/l rate. Variations in the performance of various NSDSs based on its novelty, working principle, different physical parameters, utilized material

Downloaded from http://iwaponline.com/aqua/article-pdf/doi/10.2166/aqua.2024.290/1355810/jws2024290.pdf
by DELHI TECHNOLOGICAL UNIVERSITY (DTU) user

Table 1 | Performance observations of various solar still systems

Solar still systems	Enhanced parameter	Maximum solar radiation (W/m^2)	Efficiency (%)	Productivity ($L/m^2/day$)	Concluding remarks	Advantages	Limitations
Double slope (Murugavel *et al.* 2010)	Single basin double-slope solar still with minimum depth, energy-storing material	740	6.2	–	The production rate of potable water depends on the cover glass, water, and surrounding temperatures, temperature difference between water and glass, and temperature difference between glass – surrounding and stored energy.	Yield can be enhanced with economical additional expenses.	Regular maintenance required of energy-stored material due to the salinity of water.
Double slope and double basin (Rajaseenivasan & Murugavel 2013)	Experimental analysis of double-slope solar still with single basin and double basin	900	85	4.75	The productive rate of double basin solar still is greater than that of single basin still by approximately. 85% for the same basin condition.	The productivity of modern still enhanced with small changes in design.	Cleaning is required on daily basis.
Double-slope solar (Belhadj *et al.* 2015)	Coupled with capillary film condenser	900	58	7.15	Productive rate of freshwater increases with the decreasing flow feeding of saline water in still. Productive rate of fresh water varies conversely with the gap between those two condensing plates.	Yield of solar still increases and can be regulated	Need to monitor the flow rate of water.
Pyramid collector solar still (Sathyamurthy *et al.* 2014)	Analysis of factors affecting triangular pyramid solar still	830	15.5	4.701	Water depth in the basin, heat transfer coefficient of convection and evaporation, temperature difference between the convective and evaporative surface, etc. Effects are important for productivity.	Productivity of solar still can be regulated with economical changes	There is a limitation in the enhancement of solar still.
Black paint (Kabeel (Sathyamurthy *et al.* 2020))	With 10% of nanoparticles With 20% of nanoparticles	1,030	27.2 34.3	–	Evaporation rate of water in the solar still majorly influenced by the absorber plate, with an enhanced heat rate.	Enhanced rate of evaporation of water has an important role in the productivity of fresh water.	Impact of paint on the surface has a limited life. Economically, it is optimized because of nanoparticles.

Uncorrected Proof

Downloaded from http://iwaponline.com/aqua/article-pdf/doi/10.2166/aqua.2024.290/1355810/jws2024290.pdf
by DELHI TECHNOLOGICAL UNIVERSITY (DTU) user

Spherical solar (Dhiman 1988)	With spherical cover glass and blackened metallic horizontal basin plate	730	33	5.7	Spherical solar still has more efficiency than conventional during sunshine while after sunshine both stills have equal efficiency. Due to the effect of cooling water only, the productivity was increased by 25% with enhanced condensation (Suraparaju & Natarajan 2022a)	For sunshine duration and per day productivity, both are higher for spherical solar still than convention solar still	Fabrication cost is high.
Hemi spherical solar still (Arunkumar *et al.* 2012)	Without water cooling at the top With water cooling at the top	748	34 42	–	The productivity rate depends upon the temperature of the top cover, water, and atmospheric conditions	During a high sunshine period, productivity is also high due to the enhanced convection rate of cooling.	Additional cost and maintenance are limitations.
'V' type solar still (Selva Kumar *et al.* 2008)	Eff without charcoal Eff with Charcoal Eff with mirror Eff with mirror and charcoal	970	24.47 30.05 11.92 14.11	2.516 3.226 2.7 3.526	Enhanced still receives more solar energy effectively and more glazing effect	Yield enhanced with economic enhancement.	Regular monitoring is required
Single solar still with different depths of water in the basin (Prakash *et al.* 2021)	A 23° inclination is used for the thermal investigation, which is done at two different water levels of 3 and 12 cm.	1,000	81.53	–	The daily output yield falls with increasing water depth and increases with increasing h_{ew} and h_{cw}	Economically, it is the better way to enhance the productivity of solar still.	It is hard to maintain a small depth of water in basin.
Single solar still with porous (Saravanavel *et al.* 2020)	Saravanavel *et al.* (Huang *et al.* 2015) use porous material to increase efficiency.		36	7.5	According to Shoeibi *et al.* (Kaushal *et al.* 2017b), porous materials raise the temperature of the water in the basin which increases the temperature differential between the cover and the water and boosts the system's productivity.	Economically, porous material is good for enhancing evaporation rate of water.	Need to regular cleaning of porous material due to the salinity of water.
Solar still with fins (Velmurugan & Srithar 2011)	Single basin solar still with attached fins (Kaushal *et al.* 2017b)	1,130	45.5	–	Solar still with PCM, without PCM, and nanoparticles in the liner basin helps to increase the temperatures of the fins with cotton wick (FWCW)/fin with jute wick (FWJW)	Enhanced the yield of solar still with high impact	To be more effective, mixture of PCM and water should be stirred on a regular basis
Solar still with fin and wick (Suresh & Shanmugan 2019)	Effective productivity with fin and cotton wick with flowing of water	1,130	13.37	9.429	Observation on experimental setup with fin and cotton wick, fin and jute wick, and PCM	Productivity rate of solar still enhanced	Fabrication and design impact on cost. Required cleaning due to the salinity of water.

(*Continued.*)

Downloaded from http://iwaponline.com/aqua/article-pdf/doi/10.2166/aqua.2024.290/1355810/jws2024290.pdf
by DELHI TECHNOLOGICAL UNIVERSITY (DTU) user

Table 1 | Continued

Solar still systems	Enhanced parameter	Maximum solar radiation (W/m^2)	Efficiency (%)	Productivity ($L/m^2/day$)	Concluding remarks	Advantages	Limitations
Single slope solar still with pin fin into a paraffin wax bed (Suraparaju & Natarajan 2021a)	Enhanced yield of single-slope solar still with fins at several depth of water in basin	–	24.3	3750	Attached pin fin at the wax surface and small depth of water in basin enhanced the evaporation rate and yield of solar sill	Productivity enhanced with small and easy modification	Wax surface needs cleaning due to salinity and impurities of water in basin
Multi-basin solar still (MBSS) (Kaviti *et al.* 2016; Bapeshwararao *et al.* 1983)	Double basin carries water at different temperatures	800	–	–	The lower basin water temperature shows more effect than that of the upper basin.	Yield of solar still enhanced.	Required regular cleaning of basins.
Tubular solar still (TSS) (Singh (2021))	Distillation occurs in a long tube with a rectangular water tray TSS-CPC with PCM TSS-CPC without PCM	1,159 800 800	More than SSSS	2.05 3.05 5.00 5.78 5.33	Yield without cooling Yield with air cooling Yield with water cooling TSS has outer and inner layers where the outer layer contains wet wick while the inner is usual.	Yield of solar sill is much better for commercial purposes.	Economically, design and manufacturing costs do not support this.
Multi-wick solar still (MWSS) (Sathyamurthy *et al.* 2014; Suraparaju & Natarajan 2021b; Suraparaju & Natarajan 2020)	With Jute wick With cotton With floated fiber (Suraparaju & Natarajan 2021b)	1198	23. 20.94 29.67	9.012 7.040	A range of materials with properties like porosity, resistance to corrosive water, high-temperature, covered area by fiber, sustainability, etc., are used in this system. The materials ought to be durable, economical, and suitable for the system. When exposed to either direct or indirect sunlight, the wick offers an extremely thin water coating and facilitates efficient evaporation.	Economically solar still enhanced and required less maintenance	Regular cleaning of jute and cotton is necessary due to the salinity of water.
CSSGSS (Cooper *et al.* 2018)	Solar radiation is used to preheat the steam instead of heating water (Cooper *et al.* 2018)	485		2.5	The efficiency of performance of the solar still structure is achieved as 24.6% at 01 Sun and 38.8% at 1.5 Suns.	Such solar still has better yield.	Need for more safety because of fragile setup

Uncorrected Proof

Downloaded from http://iwaponline.com/aqua/article-pdf/doi/10.2166/aqua.2024.290/1355810/jws2024290.pdf
by DELHI TECHNOLOGICAL UNIVERSITY (DTU) user

Diffusion solar still (DSS) (Tanaka 2009; Chong *et al.* 2014; Huang *et al.* 2015; Tanaka 2016)	A vertical multiple effect diffusion solar still (Tanaka 2009)	890	13.3		Consisting of closely spaced vertical and parallel partitions in contact with saline-soaked wick	Less space is required comparatively. Enhanced both evaporation and condensation of water.	Complex design and manufacturing impact on cost optimization. Maintenance and precaution required on necessary action.
	Multiple effect diffusion solar still with vacuum tube collector and heat pipe (Chong *et al.* 2014)	900	23.9		Another aspect that contributes to great productivity is the MDU's symmetrical design, which reduces heat loss. The bended-plate design of MDU prevents wick peel-off and pollution of clean water. In the continuous operation for 6 months, no decline in performance was seen.		
	Spiral multiple effect diffusion solar still coupled with vacuum tube collector and heat pipe (Huang *et al.* 2015)	1,010	40.6		Greater heat and mass transfer may occur in the outer cell because of the bigger evaporating and condensing area there.		
	Vertical multiple effect diffusion solar still coupled with a titled wick still (Tanaka 2016)	900		15.9	Analysis of three different types of days the spring equinox, summer, and winter solstices at 33° N latitude.		
Weir-type solar still (WTSS)	This type of solar water still is proposed to regenerate rejected water from the water purifier systems for solar hydrogen production (Sadineni *et al.* 2008).	1,000	20	–	The industrial production of distilled water is proposed to use weir-type regenerative solar still. The solar hydrogen projects can utilize the suggested still. In a still of this kind, a sizable portion of the de-ionized water that was rejected may be distilled and recovered.	Required less observation with enhanced yield of solar still. It can be established from industrial point of view.	Such kinds of solar still are not designed for low sunshine.
	A cascade-type weir solar water still with built-in latent heat thermal energy storage system (Tabrizi *et al.* 2010)	610		3.4	On sunny days, the overall production of the still without LHTESS is marginally greater than the still with LHTESS.		
	A cascade WSDS with PCM was observed in semi-hazy conditions (Sarhadi *et al.* 2017).	815		7.05	The evaluated efficiency is 76.69%. A useful parameter for solar still design and optimization is energy efficiency. Exergy analysis reduces internal irreversibility rates, which is more significant than other optimization techniques.		

(*Continued.*)

Uncorrected Proof

Downloaded from http://iwaponline.com/aqua/article-pdf/doi/10.2166/aqua.2024.290/1355810/jws2024290.pdf
by DELHI TECHNOLOGICAL UNIVERSITY (DTU) user

Table 1 | Continued

Solar still systems	Enhanced parameter	Maximum solar radiation (W/m^2)	Efficiency (%)	Productivity (L/m^2/day)	Concluding remarks	Advantages	Limitations
	A solar still is proposed with nature friendly and low-cost material (Natarajan *et al.* 2022)		34.81		Eco-friendly and economical materials are introduced to the enhanced yield of solar still such as saw dust, molasses, rice husk, etc.		
Tubular solar still (TSS)	TSS with no cooling (Arunkumar *et al.* 2013) TSS with air cooling TSS with water cooling	1,159		2.05 3.05 5.00	A unique design for a tubular solar still that uses a rectangular basin to desalinate water as air and water flow over the cover. The concentric tubular solar still with cold water flow, which is 144% more productive than the regular CPC-CTSS without air or water flow, has the highest production.	Yield of solar still is enhanced by 144%. As on requirement productivity can be regulated also.	Due to the complex design of setup, maintenance and manufacturing are not economically fine.
	TSS Black cloth wick (Elashmawy 2017) TSS without wick TSS with CPC	1,010	36.5 30.5 28.5	4.71 3.60 3.35	The first setup works more effectively because the black wick absorbs more solar thermal energy, which increases the rate of evaporation, condensation, and yields large distillate.		
Stepped-type inclined solar still (STSS) [96]	Black absorber STSS For seawater For saltwater	910	43 48		Per day efficiency for modified stepped solar still is more than that for conventional solar still approximately by 20%. The efficiency of all kinds of solar still is greater for seawater as compared to salt water.	Simple and smooth modification in setup to improve the productivity of solar still.	Regular cleaning is required for better yield.
	Cotton absorber STSS For seawater For saltwater	910	53 47	6.126 6.285			

Uncorrected Proof

Downloaded from http://iwaponline.com/aqua/article-pdf/doi/10.2166/aqua.2024.290/1355810/jws2024290.pdf
by DELHI TECHNOLOGICAL UNIVERSITY (DTU) user

Uncorrected Proof

(smart materials, nanoparticles, etc.), designing concepts, and intensity of solar radiation per confined laboratory conditions and open atmospheric conditions. Singh (2021) analyzed new conceptual designs with enhanced techniques with creative novelty represented better performance, as nanoporous aluminum oxide membrane with Au nanoparticles solar distillations system gives better performance by 11.4 l/m^2/day for one solar intensity due to wide band of absorption of solar radiation delivered huge heat to evaporated and regularly more distillation. On the same side, a self-assembled plasmatic absorber (restricted porous substance filled Au/NPs) solar still system and affordable narrow gap solar evaporation and still system

Table 2 | Wick specified solar stills with performance enhancement observations

Solar stills	Enhancement	Concluding observation	Focused objectives
Double-slope solar still (Murugavel *et al.* 2010)	Efficiency increased by 6.2%	The amount of potable water produced is influenced by the temperature of the water, glass cover, and the atmosphere, as well as the temperature difference between the glass and the water and the atmosphere.	To improve the rate of evaporation of water on the fixed-size bottom surface area of the basin.
Pyramid collector solar still (Sathyamurthy *et al.* 2014)	Efficiency increased by 15.5%	Productivity factors include water depth in the basin, the heat transfer coefficient between convection and evaporation, the temperature difference between the convection and evaporation surface, and others.	To improve the rate of evaporation of water on the fixed-size bottom surface area of the basin.
Spherical solar (Dhiman 1988)	Efficiency increased by 33%	When it is sunny, spherical solar panels are still more efficient than traditional ones, but when the sun sets, both systems are still equally efficient. Only the cooling water's effect led to a 25% boost in output.	To improve the rate of evaporation of water on the fixed-size bottom surface area of the basin.
SSSS with different water depths in the basin (Kabeel *et al.* 2019a)	Efficiency increased by 81.53%	The daily output yield increases with increasing water depth and with increasing h_{ew} and h_{cw}.	Required less observation regarding maintenance during running conditions as compared to using nanoparticles.
Multi-wick solar still (MWSS) (Sathyamurthy *et al.* 2014)	Efficiency increased by 23.03% with jute wick and 20.94% with cotton wick	This system uses a variety of materials with properties including porosity, resistance to corrosive water, high-temperature durability, etc. Long-lasting, economical, and system-appropriate materials are required. When exposed to direct or indirect sunlight, the wick provides a very thin water coating and encourages effective evaporation.	To improve the rate of evaporation of water as well as condensation appeared as distilled water with analysis on psychometric terms.
Single solar still with porous (Saravanavel *et al.* 2020)	Efficiency increased by 36%	Porous materials, according to Shoeibi *et al.* (Kaushal *et al.* 2017b), increase the temperature of the water, which raises the temperature differential between the cover and the water and improves the efficiency of the system.	To design a more economically efficient system than contemporary nanoparticles-based solar distillation units.
Single solar still with floated fiber (Suraparaju & Natarajan 2021b)	Efficiency increased by 29.67%	Suraparaju *et al.* (2021b) and Suraparaju & Natarajan (2021b) introduced modern solar still with floated fibers with high porosity and observed efficiency at several numbers of fiber and optimized five-floated fiber-enhanced maximum efficiency.	To improve the rate of evaporation of water on the fixed-size bottom surface area of the basin and design a more economically efficient system.

Downloaded from http://iwaponline.com/aqua/article-pdf/doi/10.2166/aqua.2024.290/1355810/jws2024290.pdf
by DELHI TECHNOLOGICAL UNIVERSITY (DTU) user

Uncorrected Proof

perform efficiently with more efficiency by 90% because of its restricted specialty, i.e. initial system has tightly packed NPs in the membrane which design a porous structure suitable for taking all spectral of solar intensities and for another case, still was concentrated via parabolic concentrator and this concentrated solar radiation heat is received by smart material which is further consumed to evaporate water via a narrow void under the affected of localized heat that helps in performed improved system. It is observed that improved heat transfer through various parameters helps in several ways as also mentioned in Tables 1 and 2.

Enhanced absorption: A covered surface with higher thermal conductivity can more effectively transfer absorbed solar energy to the underlying absorber material. This allows for better utilization of the incident sunlight, resulting in increased energy absorption and overall productivity of the solar system.

Reduced temperature gradients: Efficient heat transfer helps in reducing temperature gradients across the cover surface. This is particularly important for solar panels or collectors because high-temperature gradients can lead to thermal stress, which can degrade the performance and lifespan of the system. By minimizing temperature differentials, a cover surface with higher thermal conductivity promotes more uniform heating and reduces the risk of localized hotspots.

Faster heat dissipation: In solar thermal systems, faster heat dissipation from the cover surface improves thermal management and prevents overheating. When the cover surface can efficiently transfer heat to the surroundings, it helps maintain optimal operating temperatures, which leads to improved overall system performance. Increased Surface Area: By spreading the water across a larger surface area through the wicks, the solar still increases the exposure to the surrounding air. This enables a greater surface area for evaporation, leading to enhanced water vapor production.

Improved heat transfer: The wicking materials can help in efficient heat transfer within the system. As the water evaporates from the wicks, it absorbs heat from the surrounding environment, including solar energy. The wicks facilitate the movement of water and heat, ensuring a continuous supply of water for evaporation.

Facilitated Condensation: Once the water vapor is generated, it needs to be condensed to produce fresh water. The wicking materials can also play a role in the condensation process. They can act as condensation surfaces or provide a structure on which the condensed water droplets can accumulate and flow down into a collection area.

3. CONCLUSION

Based on the above study, a frame of conclusion has been made accordingly:

i. Conventional single-slope stills are effective in summer weather conditions and vice versa for double-slope solar stills.
ii. The modified solar stills perform better according to the augmentation of active components and effective design considerations under suitable meteorological conditions.
iii. A solar still with a wet cloth on the side walls provides high porosity with thin film evaporation thus improving distillation. A solar still with wicks is a type of solar desalination system that utilizes wicking materials to enhance the evaporation and condensation processes.
iv. Solar stills with wicks are particularly useful in situations where there is limited access to freshwater sources or in areas with high salinity levels.

4. SUGGESTION FOR FUTURE SCOPE

The selection of appropriate wicking materials is important to optimize the performance of the solar still. Materials with good capillary action and high evaporation rates are typically chosen. Factors such as porosity, surface area, and durability should be considered when selecting the wicking materials for a specific application. It's worth noting that the design and configuration of the solar still with wicks should be carefully considered to achieve optimal performance. Factors such as wick spacing, thickness, and arrangement can affect water distribution, evaporation rates, and condensation efficiency. Additionally, environmental conditions such as solar radiation, temperature, and humidity levels also impact the overall effectiveness of the system.

ACKNOWLEDGEMENTS

The first author sincerely acknowledges Dr Ashok Kumar Singh, Associate Professor, Galgotias College of Engineering and Technology, Greater Noida for his appreciable help while completing this article and is also grateful to Centre for Energy and Environment, Delhi Technological University, Delhi (India) for providing basic facility in compiling this manuscript.

Downloaded from http://iwaponline.com/aqua/article-pdf/doi/10.2166/aqua.2024.290/1355810/jws2024290.pdf
by DELHI TECHNOLOGICAL UNIVERSITY (DTU) user

Uncorrected Proof

DATA AVAILABILITY STATEMENT

Data cannot be made publicly available; readers should contact the corresponding author for details.

CONFLICT OF INTEREST

The authors declare there is no conflict.

REFERENCES

Abderachid, T. & Abdenacer, K. 2013 Effect of orientation on the performance of a symmetric solar still with a double effect solar still (comparison study). *Desalination* **329**, 68–77.

Alsehli, M., Choi, J. K. & Aljuhan, M. 2017 A novel design for a solar powered multistage flash desalination. *Solar Energy* **153**, 348–359.

Amimul, A., Monzur, I., Ataur, R., Yusuf, B. & Fukuhara, T. 2012 Design, fabrication and performance analysis of an improved solar still. *Desalination* **292**, 105–112.

An, W., Chen, L., Liu, T. & Qin, Y. 2018 Enhanced solar distillation by nanofluid-based spectral splitting PV/T technique: Preliminary experiment. *Solar Energy* **176**, 146–156.

Arunkumar, T. & Kabeel, A. E. 2017 Effect of phase change material on concentric tubular solar still-Integration meets enhancement. *Desalination* **414**, 46–50.

Arunkumar, T., Jayaprakash, R., Denkenberger, D., Ahsan, A., Okundamiya, M. S., Kumar, S., Tanaka, H. & Aybar, H. S. 2012 An experimental study on a hemispherical solar still. *Desalination* **286**, 342–348.

Arunkumar, T., Jayaprakash, R., Ahsan, A., Denkenberger, D. & Okundamiya, M. S. 2013 Effect of water and air flow on concentric and tubular flow water desalting system. *Applied Energy* **103**, 109–115.

Arunkumar, T., Velraj, R., Denkenberger, D. C., Sathyamurthy, R., Vinoth Kumar, K. & Ahsan, A. 2016 Productivity enhancements of compound parabolic concentrator tubular solar stills. *Renewable Energy* **88**, 391–400.

Arunkumar, T., Raj, K., Dsilva Winfred Rufuss, D., Denkenberger, D., Tingting, G. & Xuan, L. 2019 A review of efficient high productivity solar stills. *Renewable and Sustainable Energy Reviews* **101**, 197–220.

Ashmad, I. & Hameed, S. M. K. 1997 Solar sterilization of water. *Renewable Energy* **12**, 321.

Bapeshwararao, V. S. V., Singh, U. & Tiwari, G. N. 1983 Transient analysis of double basin solar still. *Energy Conversion and Management* **23** (2), 83–90.

Belhadj, M. M., Bouguettaia, H., Marif, Y. & Zerrouki, M. 2015 Numerical study of a double-slope solar still coupled with capillary film condenser in South Algeria. *Energy Conversion and Management* **94**, 245–252.

Bouchekima, B., Gros, B., Ouahes, R. & Diboun, M. 1998 Performance study of the capillary film solar distiller. *Desalination* **116**, 185–192.

Chauhan, V. K., Shukla, S. K., Tirkey, J. V. & Rathore, P. K. S. 2020 A comprehensive review of direct solar desalination techniques and its advancements. *Journal of Cleaner Production* 124719.

Chong, T.-L., Huang, B.-J., Wu, P.-H. & Kao, Y.-C. 2014 Multiple effect diffusion solar still coupled with a vacuum-tube collector and heat pipe. *Desalination* **347**, 66–76.

Cooper, T. A., Zandavi, S. H., Ni, G. W., Tsurimaki, Y., Huang, Y., Boriskina, S. V. & Chen, G. 2018 Contactless steam generation and superheating under one sun illumination. *Nature Communications* **9**, 5086.

Dhiman, N. K. 1988 Transient analysis of a spherical solar still. *Desalination* **69**, 47–55.

Dimri, V., Sarkar, B., Singh, U. & Tiwari, G. N. 2008 Effect of condensing cover material on yield of an active solar still: An experimental validation. *Desalination* **227** (1–3), 178–189.

El-Agouz, S. A. 2014 Experimental investigation of stepped solar still with continuous water circulation. *Energy Conversion and Management* **86**, 186–193.

Elashmawy, M. 2017 An experimental investigation of a parabolic concentrator solar tracking system integrated with a tubular solar still. *Desalination* **411**, 1–8.

Elsayed, M. M. 1986 Parametric study of a direct solar-operated, multiple-effect, diffusion still. *Solar & Wind Technology* **3**, 95–101.

El-Sebaii, A. A. 2000a Effect of wind speed on some designs of solar stills. *Energy Conversion and Management* **41**, 523–538.

El-Sebaii, A. A. 2000b Effect of wind speed on active and passive solar stills. *Energy Conversion and Management* **45**, 1187–1204.

El-Sebaii, A. A. 2004 Effect of wind speed on passive solar still performance based on inner/outer surface temperatures of the glass cover. *Energy* **36**, 4943–4949.

Esfahani, I. J., Rashidi, J., Ifaei, P. & Yoo, C. K. 2016 Efficient thermal desalination technologies with renewable energy systems: A state-of-the-art review. *Korean Journal of Chemical Engineering Springer New York LLC* **33**, 351–387.

Freire-Gormaly, M. & Bilton, A. M. 2019 Design of photovoltaic powered reverse osmosis desalination systems considering membrane fouling caused by intermittent operation. *Renewable Energy* **135**, 108–121.

Fukui, K., Nosoko, T., Tanaka, H. & Nagata, T. 2004 A new maritime life saving multistage effect solar still design. *Desalination* **160**, 271–283.

Downloaded from http://iwaponline.com/aqua/article-pdf/doi/10.2166/aqua.2024.290/1355810/jws2024290.pdf
by DELHI TECHNOLOGICAL UNIVERSITY (DTU) user

Uncorrected Proof

Huang, B.-J., Chong, T.-L., Wu, P.-H., Dai, H.-Y. & Kao, Y.-C. 2015 Spiral multiple-effect diffusion solar still coupled with vacuum-tube collector and heat pipe. *Desalination* **362**, 74–83.

Ismail, B. I. 2009 Design and performance of a transportable hemispherical solar still. *Renewable Energy* **34**, 145–150.

Jing, H., Ju-Cai, Y., Ze-Hui, C., Hong-Fei, Z. & Yue-Hong, S. The mass transfer coefficient assessment and productivity enhancement of a vertical tubular solar brackish water still. *Applied Thermal Engineering*

Kabeel, A. E. 2009 Performance of solar still with a concave wick evaporation surface. *Energy* **34** (10), 1504–1509.

Kabeel, A. E., Sathyamurthy, R., Sharshir, S. W., Muthumanokar, A., Panchal, H., Prakash, N. & El Kady, M. S. 2019a Effect of water depth on a novel absorber plate of pyramid solar still coated with TiO_2 nano black paint. *Journal of Cleaner Production* **213**, 185–191.

Kabeel, A. E., Muthu Manokar, A., Sathyamurthy, R., Prince Winston, D., El-Agouz, S. A. & Chamkha, A. J. 2019b A review on different design modifications employed in inclined solar still for enhancing the productivity. *Journal of Solar Energy Engineering* **141** (3), 031007.

Kashyap, V., Medhi, R., Irajizad, P., Jafari, P., Nazari, M., Ali, M., Marquez, M. D., Lee, T. R. & Ghasemi, H. 2019 Capture and conversion of carbon dioxide by solar heat localization, *Sustainable Energy & Fuels* **3**, 272–279.

Kaushal, A. K., Mittal, M. K. & Gangacharyulu, D. 2017a An experimental study of floating wick basin type vertical multiple effect diffusion solar still with waste heat recovery. *Desalination* **414**, 35–45.

Kaushal, A. K., Mittal, M. K. & Gangacharyulu, D. 2017b Productivity correlation and economic analysis of floating wick basin type vertical multiple effect diffusion solar still with waste heat recovery. *Desalination* **423**, 95–103.

Kaviti, A. K., Yadav, A. & Shukla, A. 2016 Inclined solar still designs: A review. *Renewable and Sustainable Energy Reviews* **54**, 429–451.

Kumar, A. & Anand, J. D. 1992 Modeling and performance of a tubular multiwick solar still. *Energy* **17**, 1067–1071.

Kumar, A. & Prakash, O. 2019 *Solar Desalination Technology*. Springer Nature Singapore Pte Ltd.

Largest Water Desalination Plant, Guinness World Records. [Cited June 6, 2023]. https://www.guinnessworldrecords.com/world-records/425709-largestwater-desalination-plant.

Mahdi, J. T., Smith, B. E. & Sharif, A. O. 2011 An experimental wick-type solar still system: Design and construction. *Desalination* **267**, 233–238.

Mekonnen, M. M. & Hoekstra, A. Y. 2016 Sustainability: Four billion people facing severe water scarcity. *Science Advances* **2** (2), e1500323.

Murugavel, K. K., Sivakumar, S., Riaz Ahmed, J., Chockalingam, K. K. S. K. & Srithar, K. 2010 Single basin double slope solar still with minimum basin depth and energy storing materials. *Applied Energy* **87**, 514–523.

Natarajan, S. K., Suraparaju, S. K., Elavarasan, R. M., Pugazhendhi, R. & Hossain, E. 2022 An experimental study on eco-friendly and cost-effective natural materials for productivity enhancement of single slope solar still. *Environmental Science and Pollution Research* **29** (2), 1917–1936.

Ni, G., Zandavi, S. H., Javid, S. M., Boriskina, S. V., Cooper, T. A. & Chen, G. 2018 A salt-rejecting floating solar still for low-cost desalination. *Energy & Environmental Science*.

NPTEL: Electrical Engineering-Energy Resources & Technology. [Cited 6 June 2023]. Available from: https://nptel.ac.in/courses/108/105/108105058/

Ohshiro, K., Nosoko, T. & Nagata, T. 1996 A compact solar still utilizing hydrophobic poly (tetrafluoroethylene) nets for separating neighboring wicks. *Desalination* **105**, 207–217.

Ouahes, R., Ouahes, C. & Le Goff, P. 1987 A. hardy, high-yield solar distiller of brackish water. *Desalination* **67**, 43–52.

Pal, P. & Dev, R. 2016 Experimental study on modified double slope solar still and modified basin type double slope multi-wick solar still. *International Journal of Civil and Environmental Engineering* **10**, 70–75.

Pal, P., Yadav, P. & Dev, R. 2015 Design of modified basin type double slope multi-wick solar still, BLB-Int. *Journal of Science and Technology* 304–309.

Pal, P., Yadav, P., Dev, R. & Singh, D. 2017 Performance analysis of modified basin type double slope multi-wick solar still. *Desalination* **422**, 68–82.

Panchal, H. & Mohan, I. 2017 Various methods applied to solar still for enhancement of distillate output. *Desalination* **415**, 76–89.

Panchal, H., Sathyamurthy, R., Kabeel, A. E., El-Agouz, S. A., Rufus, D. S. & Arunkumar, T. 2019 Annual performance analysis of adding different nanofluids in stepped solar still. *Journal of Thermal Analysis and Calorimetry* **138** (5), 3175–3182.

Prakash, O., Bhushan, B., Kumar, A. & Ahmed, A. 2021 Thermal analysis of domestic type single slope–basin solar still under two different water depths. *Materials Today: Proceedings* **46**, 5482–5489.

Qiblawey, H. M. & Banat, F. 2008 Solar thermal desalination technologies. **220**, 633–644.

Rajaseenivasan, T. & Murugavel, K. K. 2013 Theoretical and experimental investigation on double basin double slope solar still. *Desalination* **319**, 25–32.

Rajaseenivasan, T., KalidasaMurugavel, K., Elango, T. & Samuel Hansen, R. 2013 A review of different methods to enhance the productivity of the multi-effect solar still. *Renewable and Sustainable Energy Reviews* **17**, 248–259.

Sadineni, S. B., Hurt, R., Halford, C. K. & Boehm, R. F. 2008 Theory and experimental investigation of a weir-type inclined solar still. *Energy* **33**, 71–80.

Saravanavel, S., Vijayakumar, K., SathishKumar, G., Meignanamoorthy, M. & Ravichandran, M. 2020 Performance on single basin square pyramid solar still. *Materials Today Proceedings*. https://doi.org/10.1016/j.matpr.2020.10.943

Downloaded from http://iwaponline.com/aqua/article-pdf/doi/10.2166/aqua.2024.290/1355810/jws2024290.pdf
by DELHI TECHNOLOGICAL UNIVERSITY (DTU) user

Uncorrected Proof

Sarhadi, F., Tabrizi, F. F. & Zoori, H. A. 2017 Comparative study of two weir type cascade solar stills with and without PCM storage using energy and exergy analysis. *Energy Conversion and Management* **133**, 97–109.

Sathyamurthy, R., Kennady, H. J., Nagarajan, P. K. & Ahsan, A. 2014 Factors affecting the performance of triangular pyramid solar still. *Desalination* **344**, 383–390.

Sathyamurthy, R., Kabeel, A. E., Balasubramanian, M., Devarajan, M., Sharshir, S. W. & Manokar, A. M. 2020 Experimental study on enhancing the yield from stepped solar still coated using fumed silica nanoparticle in black paint. *Materials Letters* **272**, 127873.

Selva Kumar, B., Kumar, S. & Jayaprakash, R. 2008 Performance analysis of a 'V' type solar still using a charcoal absorber and a boosting mirror. *Desalination* **229**, 217–230.

Sharaf, M. A., Nafey, A. S. & García-Rodríguez, L. 2011 Exergy and thermo-economic analyses of a combined solar organic cycle with multi effect distillation (MED) desalination process. *Desalination* **272** (1–3), 135–147.

Shoeibi, S., Saemian, M., Kargarsharifabad, H., Hosseinzade, S., Rahbar, N., Khiadani, M. & Rashidi, M. M. 2022 A review on evaporation improvement of solar still desalination using porous material. *International Communications in Heat and Mass Transfer* **138**, 106387.

Singh, A. K. 2021 An inclusive study on new conceptual designs of passive solar desalting systems. *Heliyon* **7** (2), e05793.

Singh, A. K. 2023 Mathematical analysis of optimized requisites for novel combination of solar distillers. *Journal of Engineering Research*. https://doi.org/10.1016/j.jer.2023.100121

Singh, A. K. & Gautam, S. 2022 Optimum techno-eco performance requisites for vacuum annulus tube collector–assisted double-slope solar desaltification unit integrated modified parabolic concentrator. *Environmental Science and Pollution Research* **29**, 34379–34405.

Singh, A. K. & Tiwari, G. N. 1992 Performance study of double effect distillation in a multiwick solar still. *Energy Conversion and Management* **33** (3), 207–214.

Singh, A. K., Yadav, R. K., Mishra, D., Prasad, R., Gupta, L. K. & Kumar, P. 2020 Active solar distillation technology: A wide overview. *Desalination* **493**, 114652.

Srivastava, P. K. & Agrawal, S. 2013 Winter and summer performance of single sloped basin type solar still integrated with extended porous fins. *Desalination* **319**, 73–78.

Suraparaju, S. K. & Natarajan, S. K. 2020 Performance analysis of single slope solar desalination setup with natural fiber. *Desalination and Water Treatment* **193** (February), 64–71.

Suraparaju, S. K. & Natarajan, S. K. 2021a Experimental investigation of single-basin solar still using solid staggered fins inserted in paraffin wax PCM bed for enhancing productivity. *Environmental Science and Pollution Research* **28** (16), 20330–20343.

Suraparaju, S. K. & Natarajan, S. K. 2021b Augmentation of freshwater productivity in single slope solar still using Luffaacutangula fibres. *Water Science and Technology* **84** (10–11), 2943–2957.

Suraparaju, S. K. & Natarajan, S. K. 2022a Sustainability assessment of single slope solar still with glass cover cooling using naturally available fibers. *Environmental Progress & Sustainable Energy* **41** (4), e13840.

Suraparaju, S. K. & Natarajan, S. K. 2022b Combined enhancement of evaporation and condensation rates in the solar still for augmenting the freshwater productivity using energy storage and natural fibres. AQUA – water infrastructure. *Ecosystems and Society* **71** (5), 628–641.

Suraparaju, S. K., Sampathkumar, A. & Natarajan, S. K. 2021a Experimental and economic analysis of energy storage-based single-slope solar still with hollow-finned absorber basin. *Heat Transfer* **50** (6), 5516–5537.

Suraparaju, S. K., Dhanusuraman, R. & Natarajan, S. K. 2021b Performance evaluation of single slope solar still with novel pond fibres. *Process Safety and Environmental Protection* **154**, 142–154.

Suresh, C. & Shanmugan, S. 2019 Effect of water flow in solar still using novel materials. *Journal of Thermal Analysis and Calorimetry* 1–14.

Tabrizi, F. F., Dashtban, M. & Moghaddam, H. 2010 Experimental investigation of a weir-type cascade solar still with built-in latent heat thermal energy storage system. *Desalination* **260**, 248–253.

Tanaka, H. 2009 Experimental study of vertical multiple-effect diffusion solar still coupled with a flat plate reflector. *Desalination* **249**, 34–40.

Tanaka, H. 2016 Theoretical analysis of a vertical multiple-effect diffusion solar still coupled with a tilted wick still. *Desalination* **377**, 65–72.

Tanaka, H. 2017 Parametric investigation of a vertical multiple-effect diffusion solar still coupled with a tilted wick still. *Desalination* **408**, 119–126.

Tanaka, H. & Iishi, K. 2017 Experimental study of a vertical single-effect diffusion solar still coupled with a tilted wick still. *Desalination* **402**, 19–24.

Tiwari, G. N. & Sahota, L. 2017 Advanced solar-distillation systems basic principles. thermal modeling and its application. *Green Energy and Technology* **2017**.

Tiwari, G. N. & Selim, G. A. M. 1984 Double slope fiber reinforced plastic (FRP) multiwick solar still. *Solar & Wind Technology* **1** (4), 229–235.

Tiwari, A. K. & Tiwari, G. N. 2008 Effect of cover inclination and water depth on performance of a solar still for Indian climatic conditions. *Journal of Solar Energy Engineering* **130**, 024502–1.

Toyama, S., Aragaki, T., Murase, K. & Tsumura, K. 1983 Simulation of the multieffect solar distillator. *Desalination* **45**, 101–108.

Toyama, S., Aragaki, T., Salah, H. M. & Murase, K. 1987 Dynamic characteristics of a multistage thermal diffusion type solar distillator. *Desalination* **67**, 21–32.

Velmurugan, V. & Srithar, K. 2011 Performance analysis of solar stills based on various factors affecting the productivity – a review. *Renewable and Sustainable Energy Reviews* **15**, 1294–1304.

Downloaded from http://iwaponline.com/aqua/article-pdf/doi/10.2166/aqua.2024.290/1355810/jws2024290.pdf
by DELHI TECHNOLOGICAL UNIVERSITY (DTU) user

Uncorrected Proof

Velmurugan, V., Gopalakrishnan, M., Raghu, R. & Srithar, K. 2008 Single basin solar still with fin for enhancing productivity. *Energy Conversion and Management* **49** (10), 2602–2608.

Verma, S. K., Singhal, P. & Chauhan, D. S. 2019 A synergistic evaluation on application of solar-thermal energy in water purification: Current scenario and future prospects. *Energy Conversion and Management* **180**, 372–390.

Zoori, H. A., Tabrizi, F. F., Sarhaddi, F. & Heshmatnezhad, F. 2013 Comparison between energy and exergy efficiencies in a weir type cascade solar still. *Desalination* **325**, 113–121.

First received 10 November 2023; accepted in revised form 26 December 2023. Available online 24 January 2024

Downloaded from http://iwaponline.com/aqua/article-pdf/doi/10.2166/aqua.2024.290/1355810/jws2024290.pdf
by DELHI TECHNOLOGICAL UNIVERSITY (DTU) user

electronics

MDPI

Article

Innovative Approach to Android Malware Detection: Prioritizing Critical Features Using Rough Set Theory

Rahul Gupta [1,*], Kapil Sharma [1,†] and Ramesh Kumar Garg [2,†]

[1] Department of Information Technology, Delhi Technological University, New Delhi 110042, India; kapil@ieee.org
[2] Department of Mechanical Engineering, Deenbandhu Chhotu Ram University of Science and Technology, Murthal 131039, India
* Correspondence: rahulgupta100689@gmail.com
† These authors contributed equally to this work.

Abstract: The widespread integration of smartphones into modern society has profoundly impacted various aspects of our lives, revolutionizing communication, work, entertainment, and access to information. Among the diverse range of smartphones available, those operating on the Android platform dominate the market as the most widely adopted type. With a commanding 70% share in the global mobile operating systems market, the Android OS has played a pivotal role in the surge of malware attacks targeting the Android ecosystem in recent years. This underscores the pressing need for innovative methods to detect Android malware. In this context, our study pioneers the application of rough set theory in Android malware detection. Adopting rough set theory offers distinct advantages, including its ability to effectively select attributes and handle qualitative and quantitative features. We utilize permissions, API calls, system commands, and opcodes in conjunction with rough set theory concepts to facilitate the identification of Android malware. By leveraging a Discernibility Matrix, we assign ranks to these diverse features and subsequently calculate their reducts–streamlined subsets of attributes that enhance overall detection effectiveness while minimizing complexity. Our approach encompasses deploying various Machine Learning (ML) algorithms, such as Support Vector Machines (SVM), K-Nearest Neighbor, Random Forest, and Logistic Regression, for malware detection. The results of our experiments demonstrate an impressive overall accuracy of 97%, surpassing numerous state-of-the-art detection techniques proposed in existing literature.

Keywords: android; malware; ranking; reduct; rough sets; prediction

check for updates

Citation: Gupta, R.; Sharma, K.; Garg, R.K. Innovative Approach to Android Malware Detection: Prioritizing Critical Features Using Rough Set Theory. *Electronics* **2024**, *13*, 482. https://doi.org/10.3390/electronics13030482

Academic Editors: Zbigniew Kotulski and Juan M. Corchado

Received: 5 October 2023
Revised: 11 January 2024
Accepted: 11 January 2024
Published: 23 January 2024

Copyright: © 2024 by the authors. Licensee MDPI, Basel, Switzerland. This article is an open access article distributed under the terms and conditions of the Creative Commons Attribution (CC BY) license (https://creativecommons.org/licenses/by/4.0/).

1. Introduction

Smartphones, in reality, are the personal desktop computers of today's world. With smartphones, we can do almost anything we intend to do with personal desktop computers. Smartphones have become integral to modern society, impacting various aspects of our lives. Their versatility and functionality have revolutionized how we communicate, work, entertain ourselves, and access information. In addition to being a communication device to place calls and send SMSs, smartphones are used for internet browsing, social media, emails, photography and videography, navigation, online shopping, banking, health and fitness, education and learning, personal organization, and intelligent home control. The current mobile market share is 20% higher than desktops, meaning smartphones are leading the way ahead of desktops in terms of usage [1].

Among all the types of smartphones available in the market, smartphones with the Android operating system are the most popular. The reason for the popularity is that Android is an open-source platform many manufacturers adopt. As per the report of Statcounter [2], the global market share of mobile operating systems is entirely dominated by the Android operating system with a 70% share. The high market share of the Android

operating system is one of the primary reasons for many malware attacks on the Android platform over the past few years. As per the report [3], several mobile trojan subscribers were found on Google's official app marketplace in 2022. As per the blog post by renowned antivirus firm McAfee [4], 60 Android apps with 100 million downloads were found to be spreading a new malware strain to unsuspecting users. According to the news article on TechRadar [5], a new ransomware, "Daam", capable of hiding from antivirus software, was detected. The report on the development of new Android malware shared by Statistica [6] shows that 5.6 million Android malware samples were seen in 2020. Moreover, millions of Android malware have been detected yearly from 2016 to 2020. Hence, there is a dire need to develop Android malware detection mechanisms to see malicious applications.

Malware analysis is a technique by which we can analyze the functionality and source of malware. Malware analysis can be broadly classified into three types [7]: static analysis, dynamic analysis, and hybrid analysis. These different analysis techniques can form a detection model to classify an Android application as malicious or benign. Three types of detection models could be possible: static, dynamic, and hybrid. In static detection, features are extracted using static analysis, which is the art of malware analysis that extracts features from the application without installing or executing the application. In dynamic detection, features are extracted using dynamic analysis, performed by executing or running the application and capturing the features at run time. The hybrid detection model is based upon hybrid analysis, which extracts both static and dynamic features from the application.

In static detection methods, the standard static techniques employed for extracting static features are manifest file-based detection, API calls-based detection, and Java code-based detection methods. In the manifest file-based detection technique, features are extracted from the manifest file of the Android application. Li et al. [8] used permissions from the manifest file and achieved an accuracy of 90%. Arora et al. [9] used permissions pairs from the manifest file and achieved an overall accuracy of 95.44%. IPDroid [10] used both permissions and intents from the manifest file and achieved an accuracy of 94.73% with a Random Forest classifier.

API calls-based feature detection is based on extracting APIs to be called by Android applications. Droidmat [11] used API calls along with manifest file components to detect malicious applications with an accuracy of 97.87%. Elish et al. [12] extracted sensitive API calls invocation by the user to build a detection model. Zhang et al. [13] created association rules between API calls and achieved an accuracy of 96%.

The Java code-based detection methods use Dex files that contain Java code in Android applications for extracting features. Zhu et al. [14] converted the vital parts of Dalvik byte code into RGB images and trained the Convolution neural network to devise the malware detection system with an accuracy of 96.9%. Fang et al. [15] also converted Dex files to RGB images to do malware familial classification with a precision of 96%. The work [16] is based on eliminating code confusion and achieves an overall accuracy of 92.67%.

Contributions

In the current work, we have used permissions, API calls, system commands, and op-codes with rough set theory for Android malware detection. To the best of our knowledge, we are the first to apply rough set theory to the static features mentioned above. The rough set theory has several advantages, such as attribute selection and its ability to work with qualitative and quantitative attributes. We used a Discernibility Matrix to rank and further calculate the reduct of the above features. Ranking of features is done to highlight essential features. Reduct, a reduced feature set, is estimated to improve the overall detection rate with the most minor features. We applied several Machine Learning (ML) algorithms such as Support Vector Machines (SVM), K-Nearest Neighbor, Random Forest, and Logistic Regression for malware detection. Our results demonstrate an overall accuracy of 97%, better than many state-of-the-art detection techniques proposed in the literature. The main contributions of this paper are summarized below.

- Firstly, we performed data pre-processing, in which we eliminated co-related features and features not dependent on the class variable.
- We calculated the ranking score with the help of the discernibility concept of rough set theory to rank the features according to their importance.
- We applied an algorithm for rough set reduct computation to reduce the number of features in each category using the ranking score and discernibility concept of rough set theory.
- We further applied machine learning algorithms to evaluate the detection accuracy with the reduct calculated in the previous step.
- We compared the results of our proposed model with other state-of-the-art detection techniques, and our results highlight that the proposed model outperforms similar state-of-the-art models.

The rest of the paper is organized as follows. We discuss related work in Section 2. The detailed methodology is discussed in Section 3. Section 4 is dedicated for results and discussions, and we conclude the paper with future directions in Section 5.

2. Related Work

This section describes the work on static malware detection methods based on manifest file-based detection, API calls-based detection, and Java code-based detection. Therefore, this section is divided into three subsections: manifest file-based detection, API calls-based detection, and Java code-based detection.

2.1. Manifest File-Based Detection

In this sub-section, we review the works that have analyzed features from manifest files for Android malware detection. Grace et al. [17] established the relationship between embedded ad libraries and host apps as a significant risk factor for Android-based smart devices. Enck et al. [18] developed a lightweight certification model based on security configuration within an application to identify risky applications. A malware detection system, SIGPID, was proposed by Li et al. [8], in which three-level pruning is applied to filter out a minimal permission set that can be used for malicious app identification. Talha et al. [19] developed a client–server-based tool known as APK-auditor to detect malicious applications that maintain the Android profile database based on permission analysis.

The authors in [20] developed context category ontology based on permissions to detect the potential risk of information leakage with the help of a malicious activity. A prototype ASE was developed by Song et al. [21], which applied four levels of filtering based on static analysis to detect an application as benign or malicious. DroidChain [22] is another malware detection approach that applies static analysis and a behavior chain model to detect four types of malicious behaviors, i.e., privacy leakage, SMS financial charges, malware installation, and privilege escalation. ProDroid [23] is another behavior-based malware detection model that uses the biological sequence technique and Markov chain model to match the classes and API of decompiled applications to the stored malicious behavior models. Moonsamy et al. [24] used both requested and used permissions to mine contrasting permission sets, which were further used to detect an application as benign or malware.

Idrees et al. [25] used intent filters and permissions to identify an application as benign and malicious. Wang et al.'s [26] work is based on rankings of requested permissions based on risk, and the selection of risky permission subset is made to train machine learning models. DroidRanger was developed by the authors in [27] as a malicious application detection tool using permission behavior and heuristic filtering, which also successfully discovered zero-day malware. Qiu et al. [28] did a unique work of annotating the capabilities of detected malware regarding security and privacy concerns. APIs, intents, and permissions were used in [29] to perform similarity associations with malware samples and detect malicious applications using hamming distance.

Bai et al. [30] tried to develop a fast malware detection model using multiple features such as permissions and opcode sequences. Drebin [31] is a lightweight malware detection technique that can be deployed on the smartphone. The developed method can detect malicious applications on the smartphone within ten seconds of download. Varsha et al.'s [32] work is based on selecting prominent features from various sets of static features. Mahindru et al. [33] used ten different feature selection techniques to find the best possible combination of features to detect malicious applications effectively. Firdaus et al. [34] is a genetic search-based technique, in which a genetic algorithm minimizes the number of features.

Khariwal et al. [10] proposed a novel method to find the best permissions and intents combined to detect malicious applications. PermPair [9] is another malicious application detection technique that creates permission pairs from each application and further constructed malicious and normal permissions pair graphs used for the detection mechanism. The work in [35] uniquely compared the dynamics between requested permissions and intent filters. In manilyzer [36], stress was given on using different manifest components along with requested permissions. Sanz et al. [37] developed a malware detection model based on used permissions. Li et al. [38] developed a malware detection model using multiple features both from the manifest file as well as from the source file, whereas Sato et al. [39] used multiple features from the manifest file only.

2.2. API Calls-Based Detection

Several researchers have utilized static API calls to identify Android malware. The Droidmat model [11] employed a combination of manifest file features and API calls and applied K-means and KNN algorithms for malware detection. Another study [12] examined user-triggered dependencies and sensitive APIs in malicious apps, while Zhang et al. [40] constructed dependency graphs of API calls to categorize malicious apps into Android malware families using similarity metrics. The authors of [41] introduced a model called Apposcopy, which examined control-flow and dataflow properties derived from API calls to detect malware. Wang et al. [42] focused on analyzing string features like permissions and intents, as well as structural features such as API calls and function call graphs, on detecting malicious behaviour in Android apps. Similarly, the work described in [13] involved the analysis of API calls and their call graphs for malware detection.

2.3. Java Code-Based Detection

Zhu et al. in [14] developed an image-based malware detection method that extracts important parts of Dalvik code and converts it to RGB images. Fang et al. [15] also used RGB images generated from Dex files but, apart from classifying an application as benign or malicious, did malware familial classification. The work [16] eliminated code confusion and calculated scores for every code word based on their importance, which deep learning models then used to detect malicious applications. CDGDroid [43] is another technique to detect Android malware based on control flow graphs and data flow graphs that are constructed from the code of the application with the help of program analysis techniques and later on used as features for the CNN model. Xiao et al. [44] developed a method that captures the system call sequence from the code of the application, and the captured system call sequence is used to train LSTM to detect malicious applications. To form the malware detection model, MSNDroid [45] incorporated native-layer code features and combined them with permissions and Java layer components.

To the best of our knowledge, no other work has used rough set theory to form reducts of multiple features in the area of Android malware detection.

3. The Proposed Methodology

This section describes the overall approach to classifying Android applications as malware or benign. The process is divided into four phases, as depicted in Figure 1. The first phase of the approach is the pre-processing phase, the second phase is feature ranking,

the third phase is the Rough Set Reduct Computation Phase, and the fourth phase is the detection phase.

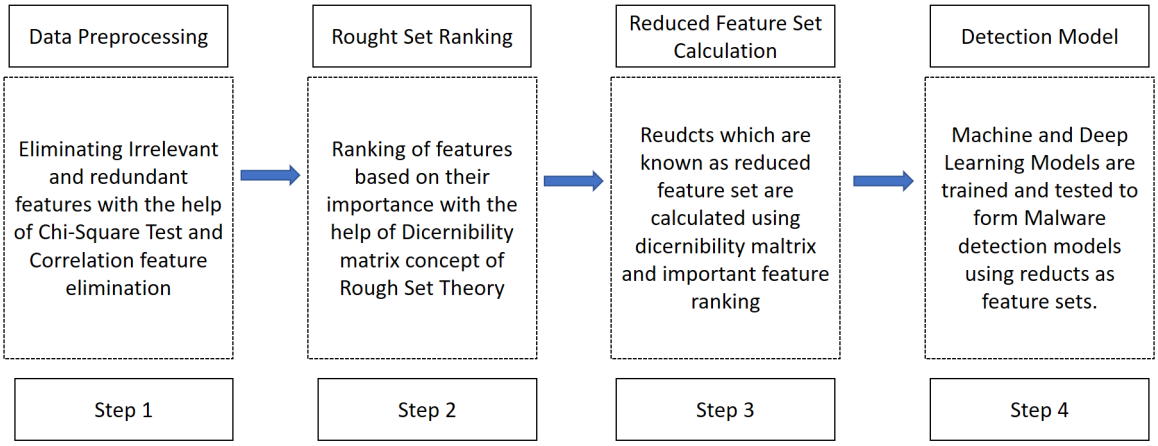


Figure 1. Proposed Methodology.

3.1. Data Pre-Processing Phase

These data pre-processing phase is more focused on the primary feature selection phase. The whole process of this phase is depicted in Figure 2.

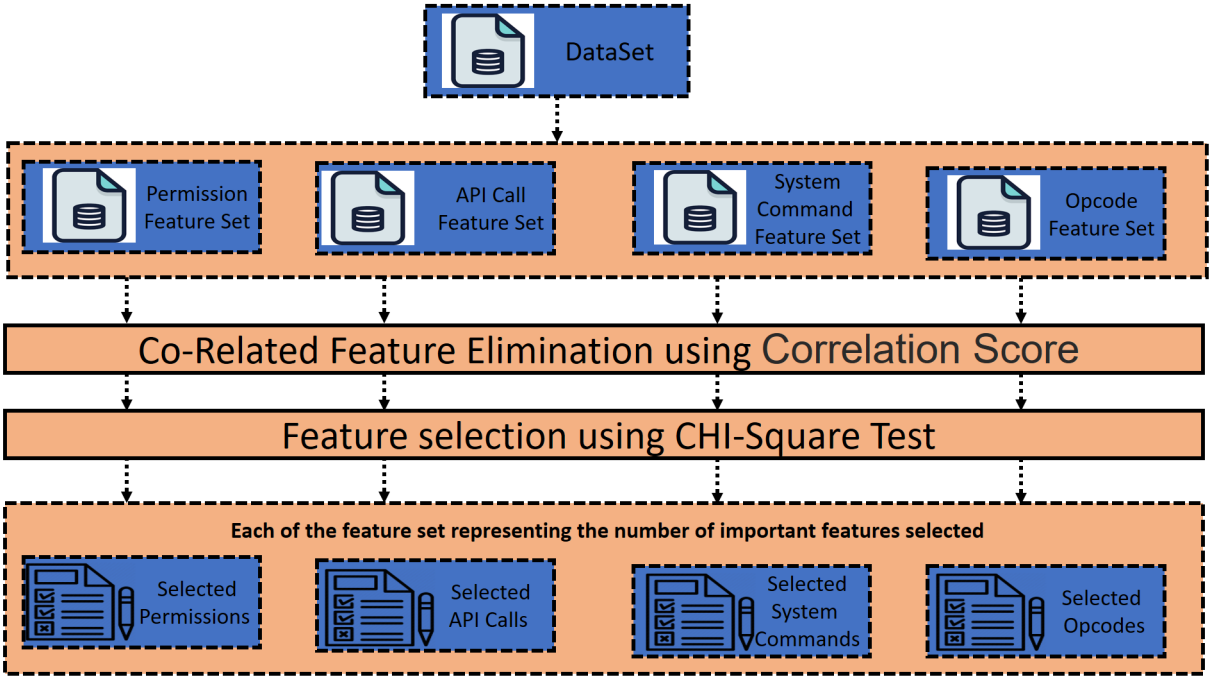


Figure 2. Data Pre-Processing.

The figure referred to here summarizes the whole process of phase 1. The proposed technique first considers the OmniDroid Dataset [46] and Androzoo Dataset [47]. The OmniDroid dataset is the data set in which various features are extracted from an extensive collection of 22,000 APKs. The dataset consists of an equal number of benign and malicious applications, i.e., 11,000 each. An additional 8000 applications are taken from the Androzoo Data set, spreading from 2015 to 2023, making it more diverse. These 8000 apps consist of an equal number of benign and malicious applications, i.e., 4000 each. The features from these 30,000 apps were extracted with the AndroPytool [48]. The AndroPyTool extracts

features from the Android application supplied as input to the tool. Specifically, the AndroPyTool extracts three types of features: pre-static features, static features, and dynamic features. This paper focuses on static features, i.e., permissions, API calls, system commands, and opcodes. The following is the description of each static feature considered in this paper.

1. Permissions: Every Android application requests and requires a particular set of permissions for its functioning. The apps need these permissions to access some data or specific resources. These permissions are listed in the Android Manifest file. The OmniDroid dataset consists of 5501 unique permissions.
2. API Calls: The Application Programming Interface (API) is a set of code snippets that the underlying systems use for communicating. API calls are the calls to such code snippets with some functionality that must be invoked to perform specific tasks. The dataset in consideration consists of 2128 API Calls.
3. System commands: Android applications must access the kernel to perform specific tasks and services. So, the services that need to be accessed by the app are done by calling the OS routines. The calls to such kinds of OS routines are known as system commands. The OmniDroid dataset consists of 103 system commands.
4. Opcodes: The Dalvik Bytecode generated by compiling the Android apps consists of instructions that need to be executed in terms of opcodes. The data set consists of 224 opcodes.

First, each of the features mentioned above are considered individually to be preprocessed. The feature correlation score is calculated for each of the separate features, i.e., permissions, API calls, system commands, and opcodes. This feature correlation score is the basis for eliminating such features that are highly correlated with the existing features. The elimination of closely interconnected attributes occurs due to their strong correlation, resulting in a high degree of linear dependence. As a result, they exert nearly identical influences on the dependent variable. Thus, in cases where two attributes exhibit significant correlation, it is feasible to omit one of them. A correlation score of 90 per cent or more is used to select one feature out of two and eliminate the other. After this round, we received 4428 permissions out of 5501 permissions, 1589 API calls out of 2128 API calls, 93 System commands out of 103 System calls, and 159 Opcodes out of 224 Opcodes.

Further, the Chi-Square test is executed to select a subset of features for each feature set. The Chi-square test is a statistical test used to determine whether there is a significant association between two categorical variables. The chi-square test works based on the following equation:

$$\chi^2 = \sum_{i=1}^{n} \frac{(O_i - E_i)^2}{E_i} \tag{1}$$

The formula for the Chi-square test involves several key terms and calculations, as shown in Equation (1), where χ^2 is the Chi-square test statistic, n is the number of categories in the contingency table, O_i is the observed frequency of category i, and E_i is the expected frequency of category i under the null hypothesis. The sum is taken over all categories in the contingency table.

Initially, the null hypothesis assumes that the two variables, i.e., the feature variable and the class variable, do not have any association. Then, the Chi-square test is applied to those variables using Equation (1) to calculate the Chi-square test statistic value. The Chi-square distribution table maps the estimated chi-square test statistic value to the corresponding p-value. The p-value less than 0.05 means that the null hypothesis assumed is false, and the alternate hypothesis that the class variable and the feature variable are associated with each other is true. All those features in each feature set that fall in the rejection region whose p-value is less than 0.05 are selected as a new feature subset for each feature set. Choosing a p-value of less than 0.05 means the features falling in this rejection region have 95% confidence of dependency on the class variable. Hence, in the end, we got

a subset of each feature space with the minimized feature set from each feature space, i.e., permissions, API calls, system commands, and opcodes' feature space.

For the permission feature set, we achieved 206 permissions selected as a subset of permission out of 4428 permissions. For the API calls feature set, we achieved 1264 API calls selected as a subset of API calls out of 1589 API calls. For system command feature space, out of 94 system commands obtained in the previous step, we achieved a minimized feature space of 52. Similarly, for the opcodes-based feature set, which consisted of 204 opcodes from the previous step, we achieved 158 opcodes. The entire process is also summarized in the Algorithm 1.

Algorithm 1 Data Pre-Processing

Input: A feature set of 22,000 APK regarding four types of features, i.e., Permissions (f_p), API Calls (f_a), System commands (f_s), and Opcodes (f_o).
Output: For each of the feature set f_p, f_a, f_s, and f_o, a minimal feature space of important features is obtained as min_f_p, min_f_a, min_f_s, and min_f_o, respectively.
for each of features set f_i in feature spaces f_p, f_a, f_s, f_o **do**
    set $|f_i| = N$
    for each of the feature x_i in feature set f_i **do**
        set $Truth_val(x_i) = True$
    end for
    for each of the feature x_i in feature set f_i **do**
        if $Truth_val(x_i) == True$ **then**
            for each of the feature x_j in feature set f_i where $j : i + 1 \rightarrow N$ **do**
                if $(correl[x_i, x_j] > 0.9)$ **then**
                    $Select(x_i)$
                    $Reject(x_j)$ and set $Truth_val(x_j) = False$
                end if
            end for
        end if
    end for
end for
for each of the features set f_i in the new feature space f_p, f_a, f_s, and f_o obtained **do**
    for each of the feature x_i in feature set f_i **do**
        Apply Chi-Square Test (x_i)
        if $p_value[x_i] < 0.05$ **then**
            $Select(x_i)$
        else
            $Reject(x_i)$
        end if
    end for
end for

3.2. Feature Ranking Phase

In this phase, the ranking of minimal feature sets obtained in the previous step is performed to rank the features of each type according to their importance. Feature ranking is performed through the Discernibility Matrix concept of rough set theory. The whole process flow of this phase is depicted in Figure 3.

Rough set theory is a mathematical approach to data analysis and data mining. This mathematical tool is powerful in dealing with improper, imprecise, inconsistent, incomplete information, and knowledge [49,50]. The rough set theory has several advantages, such as attribute selection and its ability to work with qualitative and quantitative attributes. The critical concepts of the rough set theory used in this paper are explained below.

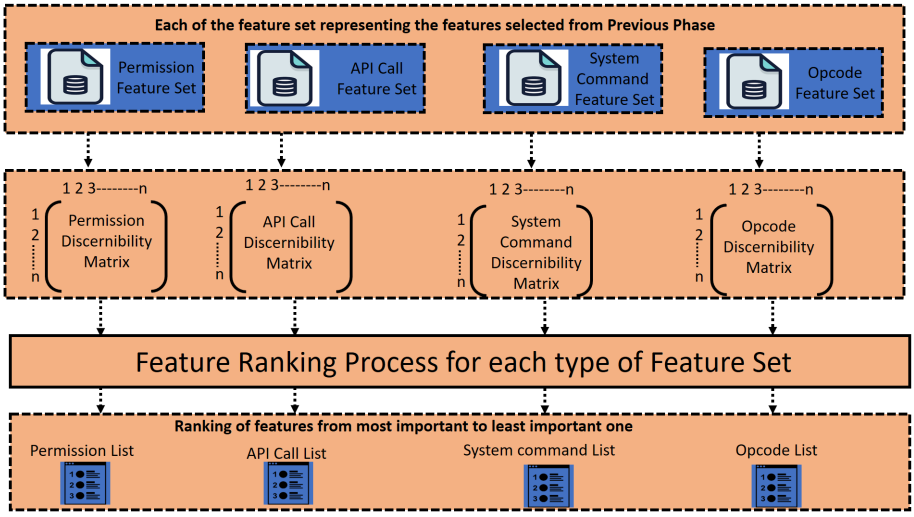


Figure 3. Feature Ranking Phase.

3.2.1. Information System

It is defined as an ordered pair, in which the first element of this ordered pair is called the universe. In our case, the universe is the set of both malicious and benign applications that are considered. We represent the ordered pair as $D = (A, F \cup \{l\})$, where D is the data set under consideration, and A is the non-empty finite set called the universe of Android application, consisting of both the malicious and benign types. F is the non-empty set of features in the data set. In our case, these features are in terms of permissions, API calls, system commands, and opcodes. Here, l is the special attribute known as the label attribute, which stores the type of label corresponding to each application in set A. This label attribute stores whether a particular application in set A is malicious or benign. Table 1 shows an instance of the permission information system for five applications assumed as A_1, A_2, A_3, A_4, and A_5. Here, feature attributes are the Content Provider Access, Settings App widget Provider, and JPUSH Message. These are permissions, with corresponding values such as 0 or 1 for each application A_i. The value 0 signifies that particular permission is not present in application A_i, whereas the value 1 signifies otherwise. The label column has the value BW, signifying that the particular A_i is Benignware, whereas the label value MW signifies that application A_i is malware, i.e., a malicious one.

Table 1. Instance of permission information system.

Application	P_1 = CONTENT PROVIDER ACCESS	P_2 = Settings App Widget Provider	P_3 = JPUSH MESSAGE	Label
A_1	0	1	0	BW
A_2	1	1	0	MW
A_3	0	1	1	BW
A_4	0	0	1	BW
A_5	1	1	1	MW

Similarly, the information systems for API calls, system commands, and opcodes are shown in Tables 2–4, respectively. From these information systems, a Discernibility Matrix is formed. The concept of Discernibility is explained in the following section.

Table 2. Instance of API calls information system.

Application	AP_1 = APICALL-android.view.SubMenu	AP_2 = APICALL-android.net.RouteInfo	AP_3 = APICALL-android.app.Activity	Label
A_1	0	0	0	BW
A_2	1	1	0	MW
A_3	1	1	1	MW
A_4	1	0	1	BW
A_5	1	1	1	MW

Table 3. Instance of system command information system.

Application	S_1 = SYSTEMCOMMAND-svc	S_2 = SYSTEMCOMMAND-stagefright	S_3 = SYSTEMCOMMAND-nandread	Label
A_1	0	1	0	MW
A_2	1	1	0	MW
A_3	0	1	1	BW
A_4	0	0	1	BW
A_5	1	1	1	MW

Table 4. Instance of opcode information system.

Application	O_1 = OPCODE-rem-float/2addr	O_2 = OPCODE-div-int/lit8	O_3 = JOPCODE-sparse-switch	Label
A_1	1	1	0	BW
A_2	0	1	0	MW
A_3	1	0	1	MW
A_4	0	0	1	BW
A_5	0	1	1	BW

3.2.2. Discernibility Matrix

This matrix is created from the information system. The Discernibility Matrix is a symmetric $|A|X|A|$ matrix corresponding to each information system. Each entry C_{ij} is defined as $\{f \in F | f(A_i) \neq f(A_j)\}$ if $l(A_i) \neq l(A_j)$, Φ otherwise. Tables 5–8 show the instances of Discernibility Matrices corresponding to information system shown in Tables 1–4, respectively.

Table 5. Instance of permission discernibility.

	A_1	A_2	A_3	A_4	A_5
A_1					
A_2	P_1				
A_3		P_1, P_3			
A_4		P_1, P_2, P_3			
A_5	P_1, P_3		P_1	P_1, P_2	

Table 6. Instance of API calls discernibility.

	A_1	A_2	A_3	A_4	A_5
A_1					
A_2	AP_1, AP_2				
A_3	AP_1, AP_2, AP_3				
A_4		AP_2, AP_3	AP_2		
A_5	AP_1, AP_2, AP_3			AP_2	

Table 7. Instance of system call discernibility.

	A_1	A_2	A_3	A_4	A_5
A_1					
A_2					
A_3	S_3	S_1, S_3			
A_4	S_2, S_3	S_1, S_2, S_3			
A_5			S_1	S_1, S_2	

Table 8. Instance of opcode discernibility.

	A_1	A_2	A_3	A_4	A_5
A_1					
A_2	O_1				
A_3	O_2, O_3				
A_4		O_2, O_3	O_1		
A_5		O_3	O_1, O_2		

For each of the selected minimal permission set, API call feature set, system command feature set, and opcode feature set, we create the Permission Discernibility Matrix, API Call Discernibility Matrix, System Call Discernibility Matrix, and Opcode Discernibility Matrix, respectively. Algorithm 2 depicts the whole process. The algorithm creates a Discernibility Matrix for each minimal feature set obtained in the previous step and further calls the rough set ranking algorithm described in the next section.

Algorithm 2 Feature Ranking

1: **Input:** Minimal feature space, i.e., $min_f_p, min_f_a, min_f_s$, and min_f_o obtained as output of Algorithm 1.
2: **Output:** For each of the minimal feature space, ranked minimal feature list L_p, L_a, L_s, and L_o, respectively, sorted in decreasing order as per the importance of the features.
3: **for each** of the minimized feature space min_f_i in $min_f_p, min_f_a, min_f_s$, and min_f_o **do**
4: create Discernibilty Matrix for min_f_i.
5: **end for**
6: Let D_p, D_a, D_s, and D_o be Discernibility Matrix corresponding to min_f_i in $min_f_p, min_f_a, min_f_s$, and min_f_o, respectively.
7: **for each** of Discernibility Matrix D_i in D_p, D_a, D_s, and D_o **do**
8: call Algorithm 3 for each D_i in order to perform rough set ranking of each of the features in D_i
9: Let L_p, L_a, L_s, and L_o be be the sorted list of important features for each of min_f_i in $min_f_p, min_f_a, min_f_s$, and min_f_o, respectively
10: **end for**

3.2.3. Rough Set-Based Feature Ranking

After creating each of these Discernibility Matrices, a rough set-based feature ranking methodology, summarized in Algorithm 3, is applied on each matrix to rank each of the Permission, API Call, System Command, and Opcode features separately. The algorithm takes the Discernibility Matrix as an input and initializes the weight of each feature in the corresponding minimal feature set to zero. Then, the Discernibility Matrix is traversed, and each entry in the Discernibility Matrix, which consists of one or more features, receives the updated weight of the features as per Equation (2).

$$w(x_k) = w(x_k) + |min_f_i|/|C_{ij}| \tag{2}$$

In the above equation, C_{ij} is the entry in the Discernibility Matrix corresponding to applications A_i and A_j, and the entry C_{ij} may contain one or more features. Hence, $|C_{ij}|$

represents the count of features in the entry. min_f_i is the minimal feature set corresponding to the Discernibility Matrix, and $|min_f_i|$ is the count of features in the minimal feature set. $w(x_k)$ is the weight of k^{th} feature in the entry C_{ij}, which may contain $x_1, x_2, x_3, \ldots$ and x_n as the features in the entry.

Algorithm 3 Rough Set Ranking

Input: Discernibility Matrix D_i with dimensions nXn.
Output: Ranked feature list L_i w.r.t D_i.
for each x_i in the minimal feature space min_f_i corresponding to D_i **do**
    Let $w(x_i)$ denote the weight of the feature x_i and let $w(x_i) = 0$.
end for
for each $i : 1 \rightarrow N$ **do**
    for each $j : 1 \rightarrow i$ **do**
        Let C_{ij} be the entry in Discernibility Matrix D_i containing features $x_1, x_2, x_3, \ldots and\ x_n$.
        for each x_k in $x_1, x_2, x_3, \ldots and\ x_n$ corresponding to entry C_{ij} **do**
            update weight of every feature $x_k \in C_{ij}$ as
            $w(x_k) = w(x_k) + |min_f_i|/|C_{ij}|$
        end for
    end for
end for
Sort every x_i in the minimal feature space min_f_i w.r.t $w(x_i)$ in decreasing order of $w(x_i)$

This ranking is obtained by arranging each of these features in descending order in terms of their importance.

The Rough Set-based feature ranking embodies the following idea [49].

(1) The more times an attribute appears in the discernibility, the more important is the attribute.
(2) The shorter the entry is, the more important the attributes is in the entry.

3.3. Rough Set Reduct Computation Phase

This phase focuses on reducing the feature space so that, with as few features as possible, i.e., a reduced feature space, the classification algorithms could be applied to detect an application as benign or malicious. The reduced feature space obtained using the underlying principles of rough set theory is called reduct in rough set theory. The Discernibility Matrix and rough set feature ranking obtained in the previous phase are used to attain reducts for each of the permission, API call, system command, and opcode feature spaces. Hence, after this phase, for each feature space, i.e., permission, API call, system command, and opcode, we get a reduced feature space, which we call a reduct in rough set theory. Figure 4 depicts the current phase under discussion. Algorithm 4 describes the whole process in pseudo-code form. The algorithm first calculates the net weight $w(net_{ij})$ of each of the entry C_{ij} in the Discernibility Matrix D_i, containing features $x_1, x_2, x_3, \ldots$ and x_n by summing their individual weights $w(x_1), w(x_2), w(x_3), \ldots\ldots$ and $w(x_n)$, respectively. Then, all the entries C_{ij} in the Discernibility Matrix D_i are copied in the list LD_i, and then LD_i is sorted as per the net weight calculated in the previous step. Initially, Red_i is assumed to be an empty set. For each entry C_z of the sorted list LD_i containing features $x_1, x_2, x_3, \ldots\ldots$ and x_n, we check weather the Red_i contains any common feature in C_z. If no common feature exists, we select the feature x_i with maximal $w(x_i)$ in C_z; otherwise, we skip the entry C_z. The set Red_i is the reduct computed for min_f_i.

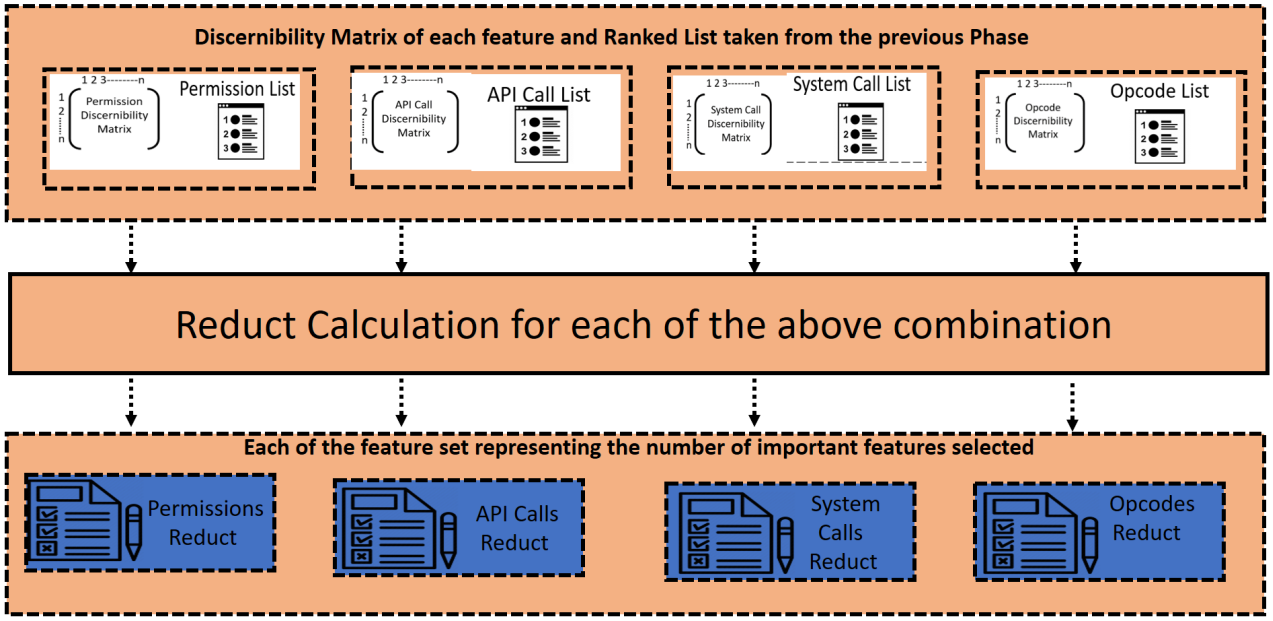


Figure 4. Rough Set Reduct Computation Phase.

Algorithm 4 Rough Set Reduct Computation

Input: Discernibility Matrix D_i with dimensions nXn and weight $w(x_i)$ of every feature x_i in the minimal feature space min_f_i in $min_f_p, min_f_a, min_f_s$, and min_f_o corresponding to D_i in D_p, D_a, D_s and D_o .
Output: Red_i as the reduct of minimal feature space min_f_i corresponding to D_i
Let LD_p, LD_a, LD_s, and LD_o be the empty list corresponding to permission, API call, system command and opcode feature space.
for each D_i in D_p, D_a, D_s, and D_o **do**
    Let $Red_i = \Phi$ denote the empty reduct set corresponding to minimal feature space min_f_i.
    for each $i : 1 \rightarrow N$ **do**
        for each $j : 1 \rightarrow i$ **do**
            Let C_{ij} be the entry in Discernibility Matrix D_i containing features $x_1, x_2, x_3, \ldots$ and x_n .
            Let $w(net_{ij})$ be the cumulative weight of entry C_{ij} having features as $x_1, x_2, x_3, \ldots$ and x_n .
            $w(net_{ij}) = w(x_1) + w(x_2) + w(x_3) \ldots\ldots\ldots + w(x_n)$
            $LD_i = append(C_{ij})$
        end for
    end for
    $Sort(LD_i)$ based on $w(net)$ calculated previously.
    for each $z : 1 \rightarrow |LD_i|$ **do**
        Let C_z be the entry in List LD_i containing features $x_1, x_2, x_3, \ldots$ and x_n .
        if $C_z \cap Red_i = \Phi$ **then**
            Select attribute x_i with maximal $w(x_i)$ in C_z
            $Red_i = Red_i \cup x_i$
        end if
    end for
end for

3.4. Detection Phase

For building our Android Malware detection system, we experimented with four machine learning algorithms, i.e., the Support Vector Machine (SVM), Random Forest, Logistic Regression, and K-nearest neighbour algorithms, to train and test the dataset. We also performed training and testing on two deep learning models, i.e., Artificial neural network (ANN) and Convolution Neural Network (CNN). Figure 5 portrays the overall purpose of the current phase, i.e., with the help of the machine learning models mentioned above and the different reducts, i.e., permission reduct, API call reduct, system call reduct, and opcode reduct calculated in the previous phase; the machine learning models are trained to build the system capable of detecting an Android application as benign or malware.

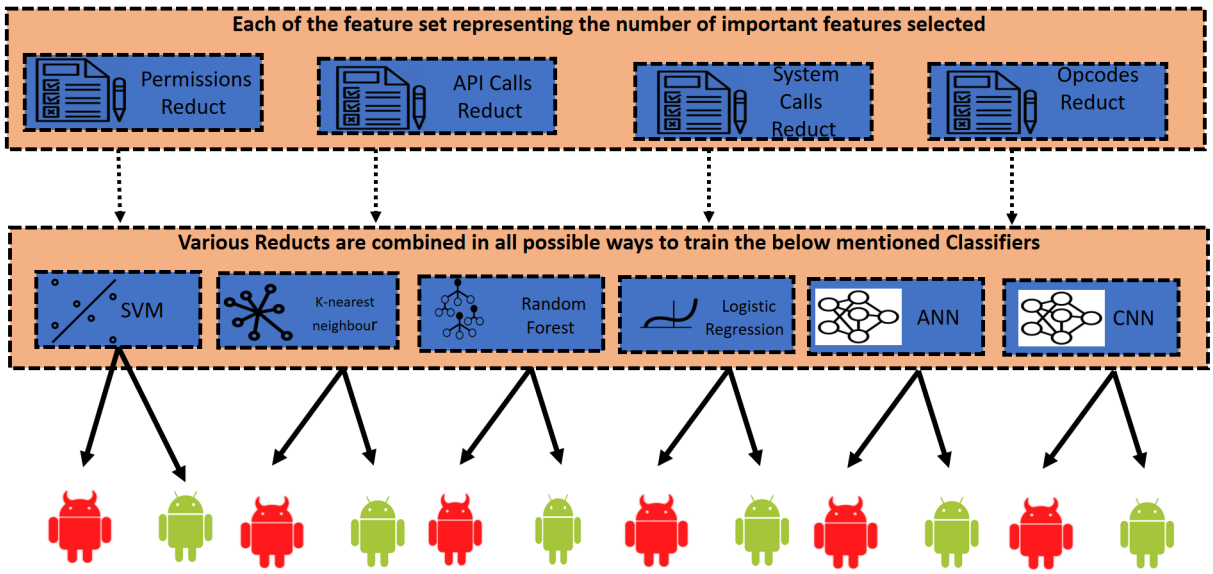


Figure 5. Detection Phase.

4. Results and Discussion

In the current section, we present the results of the evaluation carried out on the proposed malware detection approach. The code and details about data set are available at https://github.com/rahulgupta100689/Rough-Set.git, accessed on 10 January 2024.

4.1. Results of Ranking Phase

Table 9 shows the top 10 important permissions for malware detection. Similarly, the Tables 10–12 represent the top 10 important opcodes, API calls, and system calls, respectively.

Table 9. Top ten important permissions.

Rank	Permission Name	Score
1	*READ_PHONE_STATE*	1.56E9
2	*ACCESS_WIFI_STATE*	1.33E9
3	*WRITE_EXTERNAL_STORAGE*	1.26E9
4	*WAKE_LOCK*	1.2E9
5	*ACCESS_COARSE_LOCATION*	1.03E9
6	*ACCESS_NETWORK_STATE*	1.02E9
7	*ACCESS_FINE_LOCATION*	1.01E9
8	*GET_TASKS*	9.52E8
9	*RECEIVE_BOOT_COMPLETED*	8.82E8
10	*GET_ACCOUNTS*	8.4E8

Table 10. Top ten important opcodes.

Rank	Opcode	Score
1	$OPCODE - xor - int$	3.09E8
2	$OPCODE - rem - float$	3.07E8
3	$OPCODE - rem - float/2addr$	2.98E8
4	$OPCODE - float - to - long$	2.82E8
5	$OPCODE - and - long$	2.78E8
6	$OPCODE - aget - short$	2.7E8
7	$OPCODE - iget - byte$	2.67E8
8	$OPCODE - aput - short$	2.66E8
9	$OPCODE - iget - short$	2.65E8
10	$OPCODE - rem - double/2addr$	2.65E8

Table 11. Top ten important API calls.

Rank	API Call	Score
1	$APICALL - android.app.ActionBar$	2.2E8
2	$APICALL - android.widget.PopupWindow$	2.2E8
3	$APICALL - android.widget.BaseAdapter$	2.17E8
4	$APICALL - android.view.ScaleGestureDetector$	2.15E8
5	$APICALL - android.widget.CheckBox$	2.12E8
6	$APICALL - android.widget.AbsListView$	2.1E8
7	$APICALL - android.widget.ListPopupWindow$	2.1E8
8	$APICALL - android.content.res.XmlResourceParser$	2.1E8
9	$APICALL - android.graphics.Path$	2.09E8
10	$APICALL - android.webkit.MimeTypeMap$	2.09E8

Table 12. Top ten important system commands.

Rank	System Command	Score
1	$SYSTEMCOMMAND - top$	4.27E8
2	$SYSTEMCOMMAND - id$	3.75E8
3	$SYSTEMCOMMAND - start$	3.7E8
4	$SYSTEMCOMMAND - service$	3.58E8
5	$SYSTEMCOMMAND - gzip$	3.54E8
6	$SYSTEMCOMMAND - date$	3.44E8
7	$SYSTEMCOMMAND - log$	3.17E8
8	$SYSTEMCOMMAND - stop$	3.1E8
9	$SYSTEMCOMMAND - mv$	3.06E8
10	$SYSTEMCOMMAND - input$	3.02E8

4.2. Detection Results with Individual Features

Table 13 shows the results of four sets of permissions, i.e., all permissions in the data set, reduced permissions obtained after applying correlation feature elimination as permission correlation, permission chi as a set of permissions obtained after applying chi-square test on permission correlation, and finally permission reduct as the reduced permission feature set obtained after applying rough set reduct on permission chi. All four permission sets are used to train all six classifiers, i.e., Support Vector Machines (SVM), K-nearest neighbours, Random Forest, Logistic regression, ANN, and CNN. The results indicate that, for each type of classifier, as the feature set is changed from all permissions to permission correlation then to permission chi and finally to permission reduct, the

accuracy increases. This means that reduct feature sets are the best for building malware detection systems.

Table 13. Detection results based on permission.

Classifier	Feature Set Used	Accuracy (%)	Precision (%)	Recall (%)	F1-Score (%)
SVM	All Permissions	78	78	79	78
	Permissions Correlation	79	78	79	78
	Permissions Chi	79	79	79	79
	Permissions Reduct	80	79	79	80
K-Nearest Neighbor	All Permissions	77	77	79	78
	Permission Correlation	78	78	79	78
	Permissions Chi	80	81	78	80
	Permissions Reduct	82	81	82	79
Random Forest	All Permissions	82	84	80	82
	Permissions Correlation	82	84	80	82
	Permissions Chi	83	82	80	81
	Permissions Reduct	83	84	80	81
ANN	All Permissions	76	76	76	77
	Permission Correlation	78	78	79	78
	Permissions Chi	79	79	78	79
	Permissions Reduct	80	80	80	79
CNN	All Permissions	77	77	79	78
	Permission Correlation	78	78	79	78
	Permissions Chi	79	80	79	79
	Permissions Reduct	81	80	81	79
Logistic Regression	All Permissions	79	79	77	78
	Permissions Correlation	79	79	77	78
	Permissions Chi	79	80	78	79
	Permissions Reduct	80	80	77	79

Likewise, Tables 14–16 summarize the results for the three types of features, i.e., opcode feature, API call feature, and system command feature, respectively. The same phenomenon is observed in these three tables as was observed in Table 13, i.e., for each type of classifier, as the feature set is changed from all feature to feature correlation then to feature chi and finally to feature reduct, the accuracy increases, and training and testing time gets reduced drastically.

Table 14. Detection results based on opcode.

Classifier	Feature Set Used	Accuracy (%)	Precision (%)	Recall (%)	F1-Score (%)
SVM	All Opcodes	80	88	82	82
	Opcodes Correlation	80	75	87	82
	Opcodes Chi	81	75	87	81
	Opcodes Reduct	81	79	89	81
K-Nearest Neighbor	All Opcodes	84.50	86	83	84
	Opcodes Correlation	85	86	83	84
	Opcodes Chi	85	85	83	84
	Opcodes Reduct	85	85	83	84
Random Forest	All Opcodes	86	88	85	87
	Opcodes Correlation	86.80	88	86	87
	Opcode Chi	87	88	86	87
	Opcode Reduct	87	88	86	87
ANN	All Opcodes	78	77	86	81
	Opcodes Correlation	79	77	85	82
	Opcodes Chi	80	73	82	80
	Opcodes Reduct	79	73	83	78
CNN	All Opcodes	79	75	83	82
	Opcodes Correlation	80	74	85	80
	Opcodes Chi	80	74	84	78
	Opcodes Reduct	79	74	84	78
Logistic Regression	All Opcodes	79	76	86	81
	Opcodes Correlation	80	76	86	81
	Opcodes Chi	80	75	84	79
	Opcodes Reduct	80	74	85	79

Table 13 shows that the Random Forest classifier with the permission reduct feature attains a maximum accuracy of 83% and emerges as the best performing model. Similarly, for Tables 14–16, the best models are Random Forest with opcode reduct having an accuracy of 87%, Random Forest with API calls reduct having an accuracy of 90%, and Random Forest with system command reduct having an accuracy of 83%. Among all the models mentioned in the above four tables, Random Forest with API calls reduct emerges as the best model.

Table 15. Detection results based on API calls.

Classifier	Feature Set Used	Accuracy (%)	Precision (%)	Recall (%)	F1-Score (%)
SVM	All API calls	84	83	88	85
	API calls Correlation	85	83	88	85
	API calls Chi	85	83	88	86
	API calls Reduct	86	85	89	83
K-Nearest Neighbor	All API calls	85	86	85	85
	API Calls Correlation	85.70	87	85	86
	API Calls Chi	86	87	85	86
	API Calls Reduct	86	87	84	86
Random Forest	All API Calls	88	90	88	90
	API Calls Correlation	89	88	90	88
	API Calls Chi	89	90	88	89
	API Calls Reduct	90	90	88	89
ANN	All API Calls	83	82	86	83
	API Calls Correlation	83	82	86	83
	API Calls Chi	83	82	86	83
	API Calls Reduct	84	81	86	83
CNN	All API Calls	84	82	87	84
	API Calls Correlation	84	82	87	84
	API Calls Chi	84	82	87	84
	API Calls Reduct	85	82	87	84
Logistic Regression	All API Calls	85	83	88	85
	API Calls Correlation	85	83	88	85
	API Calls Chi	85	83	88	85
	API Calls Reduct	86	83	88	85

Table 16. Detection results based on system commands.

Classifier	Feature Set Used	Accuracy (%)	Precision (%)	Recall (%)	F1-Score (%)
SVM	All Sys cmd	62	59	86	70
	Sys cmd Correlation	62.50	59	86	70
	Sys cmd Chi	62.80	59	86	70
	Sys cmd Reduct	63	59	86	70
K-Nearest Neighbor	All Sys cmd	79	77	82	80
	Sys cmd Correlation	79	77	82	80
	Sys cmd Chi	79	77	83	80
	Sys cmd Reduct	79	77	83	80

Table 16. *Cont.*

Classifier	Feature Set Used	Accuracy (%)	Precision (%)	Recall (%)	F1-Score (%)
Random Forest	All Sys cmd	82	81	85	83
	Sys cmd Correlation	82	81	86	83
	Sys cmd Chi	83	82	86	83
	Sys cmd Reduct	83	82	86	83
ANN	All Sys cmd	63	59	80	68
	Sys cmd Correlation	63	60	80	68
	Sys cmd Chi	64	60	81	70
	Sys cmd Reduct	64	60	81	71
CNN	All Sys cmd	64	60	81	70
	Sys Cmd Correlation	65	60	81	70
	Sys cmd Chi	65	62	82	70
	Sys cmd Reduct	65	61	82	71
Logistic Regression	All Sys cmd	65	61	82	70
	Sys cmd Correlation	65.13	61	82	70
	Sys cmd Chi	65.98	62	83	71
	Sys cmd Reduct	66	62	83	71

4.3. Detection Results with Combinations of Two Features

Table 17 shows that Random Forest emerges as the best algorithm in terms of accuracy, precision, recall, and F1-score for permissions and opcodes reduct as the feature set.

Table 17. Detection results based on permissions and opcodes.

Classifier	Feature Set Used	Accuracy (%)	Precision (%)	Recall (%)	F1-Score (%)
SVM	Permission + Opcode Reduct	85	86	83	84
K-Nearest Neighbor	Permission + Opcode Reduct	87	88	86	86
Random Forest	Permission + Opcode Reduct	90	92	88	90
ANN	Permission + Opcode Reduct	82	83	82	82
CNN	Permission + Opcode Reduct	83	84	82	83
Logistic Regression	Permission + Opcode Reduct	84	85	83	84

Table 18 shows results of permission and API calls reduct as feature set used by SVM, K-nearest neighbour, Random Forest, and Logistic regression. Random Forest emerges as the best, with an accuracy of 92%.

Table 18. Detection results based on permissions and API calls.

Classifier	Feature Set Used	Accuracy (%)	Precision (%)	Recall (%)	F1-Score (%)
SVM	Permission + API calls Reduct	87	87	85	87
K-Nearest Neighbor	Permission + API calls Reduct	88	88	87	88
Random Forest	Permission + API calls Reduct	92	92	90	91
ANN	Permission + API calls Reduct	85	84	84	84
CNN	Permission + API calls Reduct	86	85	85	85
Logistic Regression	Permission + API calls Reduct	87	86	86	86

Table 19 shows that Random Forest with an accuracy of 88% is proved to be the best detection model among all the other three detection models using permissions and system command reduct as the feature set.

Table 19. Detection results based on permissions and system commands.

Classifier	Feature Set Used	Accuracy (%)	Precision (%)	Recall (%)	F1-Score (%)
SVM	Permission + Sys Cmd Reduct	83	84	81	83
K-Nearest Neighbor	Permission + Sys Cmd Reduct	84	84	84	84
Random Forest	Permission + Sys Cmd Reduct	88	91	85	88
ANN	Permissions+ Sys Cmd Reduct	80	82	79	81
CNN	Permissions + Sys Cmd Reduct	81	83	80	82
Logistic Regression	Permission + Sys Cmd Reduct	82	84	81	83

Table 20 shows that the detection model with classifier as Random Forest and feature set as a combination of opcodes reduct and API calls reduct outperforms the other three detection models with an accuracy of 93%.

Table 20. Detection results based on opcodes and API calls.

Classifier	Feature Set Used	Accuracy (%)	Precision (%)	Recall (%)	F1-Score (%)
SVM	Opcode + API call Reduct	88	88	86	88
K-Nearest Neighbor	Opcode + API call Reduct	90	89	88	89
Random Forest	Opcode + API call Reduct	93	93	92	93
ANN	Opcode + API call Reduct	86	85	85	86
CNN	Opcode + API call Reduct	87	86	86	87
Logistic Regression	Opcode + API call Reduct	88	87	87	88

Table 21 shows the detection results of the models that used opcode reduct and system command reduct as the feature set. The Random Forest classifier performed best with an accuracy of 90%.

Table 21. Detection results based on opcodes and system commands.

Classifier	Feature Set Used	Accuracy (%)	Precision (%)	Recall (%)	F1-Score (%)
SVM	Opcode + Sys Cmd Reduct	84	85	82	84
K-Nearest Neighbor	Opcode + Sys Cmd Reduct	85	87	85	86
Random Forest	Opcode + Sys Cmd Reduct	90	90	88	89
ANN	Opcode + Sys Cmd Reduct	81	83	84	83
CNN	Opcode + Sys Cmd Reduct	82	84	85	84
Logistic Regression	Opcode + Sys Cmd Reduct	83	85	86	85

Table 22 shows that the detection model formed with the help of Random Forest as the classifier and API calls reduct and system command reduct as the feature set attains an accuracy of 91%, which is best among all the models in the table.

Table 22. Detection results based on API calls and system commands.

Classifier	Feature Set Used	Accuracy (%)	Precision (%)	Recall (%)	F1-Score (%)
SVM	API Call + Sys Cmd Reduct	85	86	84	86
K-Nearest Neighbor	API Call + Sys Cmd Reduct	86	88	86	87
Random Forest	API Call + Sys Cmd Reduct	91	91	88	90
ANN	API Call + Sys Cmd Reduct	82	84	86	83
CNN	API Call + Sys Cmd Reduct	83	85	87	84
Logistic Regression	API Call + Sys Cmd Reduct	84	86	88	85

4.4. Detection Results with Combinations of Three Features

Table 23 shows that when permission reduct, opcode reduct, and system command reduct are combined to form a single feature set, that feature set, when used with Random Forest, gives the highest accuracy of 95%.

Table 23. Detection results based on permissions, API calls, and opcodes.

Classifier	Feature Set Used	Accuracy (%)	Precision (%)	Recall (%)	F1-Score (%)
SVM	permissions + API Call + opcode + Reduct	90	90	88	89
K-Nearest Neighbor	permissions + API Call + opcode + Reduct	92	91	90	91
Random Forest	permissions + API Call + opcode + Reduct	95	94	93	95
ANN	permissions + API Call + opcode + Reduct	88	89	89	88
CNN	permissions + API Call + opcode + Reduct	90	91	90	91
Logistic Regression	permissions + API Call + opcode + Reduct	90	89	89	90

Table 24 shows that when permission reduct, opcode reduct, and system command reduct are combined to form a single feature set, that feature set, when used with Random Forest, gives the highest accuracy of 93%.

Table 24. Detection results based on permissions, API calls, and system commands.

Classifier	Feature Set Used	Accuracy (%)	Precision (%)	Recall (%)	F1-Score (%)
SVM	Permissions + API Call + Sys Cmd + Reduct	86	87	85	87
K-Nearest Neighbor	Permissions + API Call + Sys Cmd + Reduct	87	89	87	88
Random Forest	Permissions + API Call + Sys Cmd + Reduct	93	92	90	92
ANN	Permissions + API Call + Sys Cmd + Reduct	84	85	84	84
CNN	Permissions + API Call + Sys Cmd + Reduct	85	87	87	85
Logistic Regression	Permissions + API Call + Sys Cmd + Reduct	85	87	88	86

Table 25 shows that when permission reduct, opcode reduct, and system command reduct are combined to form a single feature set, that feature set, when used with Random Forest, gives the highest accuracy of 93%.

Table 25. Detection results based on permissions, opcodes, and system commands.

Classifier	Feature Set Used	Accuracy (%)	Precision (%)	Recall (%)	F1-Score (%)
SVM	Permission + Opcode + Sys Cmd + Reduct	86	87	83	85
K-Nearest Neighbor	Permission + Opcode + Sys Cmd + Reduct	87	87	86	87
Random Forest	Permission + Opcode + Sys Cmd + Reduct	93	92	89	91
ANN	Permission + Opcode + Sys Cmd + Reduct	84	86	86	86
CNN	Permission + Opcode + Sys Cmd + Reduct	84	86	86	86
Logistic Regression	Permission + Opcode + Sys Cmd + Reduct	84	86	86	86

Table 26 shows combining the opcodes, API calls, and system command reducts and applying all four classifiers the detection model with the Random Forest as the classifier is best among all, with an accuracy of 94%.

Table 26. Detection results based on opcodes, API calls, and system commands.

Classifier	Feature Set Used	Accuracy (%)	Precision (%)	Recall (%)	F1-Score (%)
SVM	Opcode + API Call + Sys Cmd Reduct	90	91	88	90
K-Nearest Neighbor	Opcode + API Call + Sys Cmd Reduct	92	90	90	91
Random Forest	Opcode + API Call + Sys Cmd Reduct	94	94	93	94
ANN	Opcode + API Call + Sys Cmd Reduct	87	87	86	87
CNN	Opcode + API Call + Sys Cmd Reduct	88	88	87	88
Logistic Regression	Opcode + API Call + Sys Cmd Reduct	89	88	88	89

4.5. Detection Results with Combinations of all Four Features

Table 27 shows that all the feature set reducts, i.e., permissions, opcodes, API calls, and system commands reducts, used together with Random Forest emerge as the best classifier, with an accuracy of 97%.

Table 27. Detection results based on permissions, opcodes, API calls, and system commands.

Classifier	Feature Set Used	Accuracy (%)	Precision (%)	Recall (%)	F1-Score (%)
SVM	Permissions + Opcode + API Call + Sys Cmd Reduct	92	91	90	91
K-Nearest Neighbor	Permissions + Opcode + API Call + Sys Cmd Reduct	93	93	92	92
Random Forest	Permissions + Opcode + API Call + Sys Cmd Reduct	97	95	95	95
ANN	Permissions + Opcode + API Call + Sys Cmd Reduct	89	88	87	89
CNN	Permissions + Opcode + API Call + Sys Cmd Reduct	90	89	88	89
Logistic Regression	Permissions + Opcode + API Call + Sys Cmd Reduct	91	90	89	91

4.6. Discussion and Findings

In this subsection, we summarize the reasoning behind the detection results achieved from the proposed model. The proposed model gives us the highest accuracy of 97% with all four features. We observe that the detection accuracy significantly improves when we combine all four types of features for detection. The reason behind this observation is that different categories of features capture different behavioral aspect of malicious application. Hence, combining different types of features gives us wholesome characteristics of a malicious application under consideration. Therefore, increasing the number of features in combinations helps to improve the overall accuracy.

Secondly, we observed that API calls give us better results as compared to other features individually. Malicious software developers might try to avoid being detected by

obscuring their code. Nevertheless, concealing the need for specific API calls is challenging. Identifying these calls can aid in the identification of malware that is intentionally concealed. Hence, results with API calls are better when compared to other features.

Thirdly, Random Forest gives us the better results when compared to other classifiers. The reason lies in the fact that Random Forest is a technique that employs a collection of decision trees to formulate predictions. This method of ensembling is beneficial for mitigating the variance and overfitting risks inherent in individual decision trees. Through the consolidation of predictions from numerous trees, there is a consistent enhancement in overall performance.

Fourthly, we can combine two types of feature sets out of permissions, opcodes, API calls, and system commands in six ways. We experimented on all these six combinations and observed that opcodes and API calls combinations give the highest accuracy among all the six types of combinations. The reason seems to be obvious from the fact that opcodes constitute low-level instructions executed by a processor. In the realm of Android malware detection, scrutinizing the sequence of opcodes within an app's code can unveil discernible patterns suggestive of malicious behavior. Simultaneously, examining the app's API calls offers insights into its conduct. Specific API calls may serve as markers for malicious activities, and analyzing their patterns can assist in identifying malware. Consequently, the amalgamation of opcodes and API examines a more detailed perspective on an app's behavior at the code level. This approach proves advantageous for pinpointing nuanced and sophisticated malware that may employ obfuscation techniques. In contrast, permissions offer a higher-level overview based on declared capabilities, potentially offering less specificity.

Similarly, we combined all these four features in the group of three. The total number of combinations possible are four. Experimenting with all these four combination establishes that combining permissions, opcodes, and API calls is best among them. The reason seem to be that permissions offer insights into an app's officially declared capabilities. Integrating permissions with opcodes and API calls enhances our comprehension of an app's intended functionality and the possibility of misuse. Specific combinations of permissions can act as early indicators of potential issues, even before delving into the details of code execution. While opcodes and API calls provide a granular view of an app's behavior at the code level, incorporating permissions into the analysis contributes to a broader context, fostering a more comprehensive understanding of an app's intentions and the associated risks.

4.7. Comparison with Other Related Work

We conducted a thorough comparison between the detection outcomes achieved by our suggested approach and those of other studies found in the existing literature regarding the detection of Android malware. We implemented several other state-of-the-art techniques on our data sets and to facilitate this comparison; we present a concise summary of the findings in Table 28, which encompasses the results obtained by various works that have utilized certain or all components of the manifest file for detection purposes. By examining these results, it becomes evident that our proposed methodology surpasses all of the aforementioned related works in terms of detection accuracy, signifying its superior performance in comparison to existing approaches.

Table 28. Comparison of proposed model with related works.

Detection Technique	**Feature Set Used**	**Detection Accuracy**	**No. of Applications**	**Feature Ranking Method**	**Feature Selection Method** (%)
SIGPID [8]	Permissions	92	5494 malicious & 310,926 benign apps	Negative rate & support	Sequential Forward Selection (SFS) & Principal Component Analysis (PCA).
PermPair [9]	Permissions	94.60	5993 benign & 7533 malicious applications	Ranked Permission-pairs	Not Used
Alazab et al. [51]	Permissions and API Calls	94.22	14,172 Benign & 13,719 Malicious Application	No ranking done	Not used
Urooj et al. [52]	Permissions, API Calls and other manifest components	96.40	50,000 Benign & 50,000 Malicious Applications	No ranking done	Not used
Zhu et al. [53]	Permissions, API Calls and hardware components	96	1061 Benign & 2126 Malicious Applications	No ranking done	Not used
Firdaus et al. [34]	Java Code and Permissions	94.20	5555 Malicious & 550 Begin	No Ranking Done	Genetic Search
DREBIN [31]	Manifest File Components & Dis ambled Java code	95	123,452 benign & 5560 malicious applications	no ranking done	Not used
Proposed Approach	Permissions, Opcode, API Calls, and System Calls	97	15,000 benign & 15,000 malicious	Rough Set based Ranking	Rough Set Reduct

4.8. Limitations

The work performed in this research paper is based on static analysis. Static Android malware analysis has shortcomings, such as not capturing the run time behavior of applications like data leakage and network communications. Due to obfuscation techniques employed by malware writers, static analysis may not be able to capture the true intention of the code. With these limitations in the picture, static analysis may miss the malicious behaviour of Android applications, which may show its actual hostile conduct at run time.

Additionally, the current proposed model is an off-device model, and hence it can not be installed on smartphones for real-time detection.

5. Conclusions and Future Scope

In this work, we have proposed a novel Android malware detection model based on rough set theory. We have considered the combination of four static features, namely, permissions, opcodes, API calls, and system commands. Initially, a data pre-processing stage was executed, during which correlated features, as well as features that exhibited no dependence on the class variable, were eliminated. A ranking score was computed to establish the significance of each feature by employing the concept of Discernibility Matrices from rough set theory. Subsequently, an algorithm for computing rough set reducts was employed to reduce the number of features within each category based on the ranking score and the Discernibility Matrix concept of rough set theory. Following this reduction step, machine learning algorithms were applied to assess the detection accuracy using the calculated reducts. To gauge the effectiveness of the proposed model, a comparison was drawn against other advanced detection techniques. The results of this comparison underscored the superior performance of the proposed model over other state-of-the-art models in the field.

In our future work, we will try to work on the limitations of static analysis, i.e, we will be using dynamic analysis techniques along with static analysis techniques to build hybrid malware detection methods. Currently, the proposed model is an off-device model, and hence it can not be installed on smartphones for real-time detection. In future, we will propose a client–server-based model to integrate in smartphones.

Author Contributions: R.G. contributed to the conception of design of algorithms. R.G. and K.S. contributed to the implementation of the algorithms. R.G., K.S. and R.K.G. contributed in the acquisition, analysis, and interpretation of data. Each author approved the version of the research paper to be published. Each author verified the integrity of the results and all other details related to the paper. All authors have read and agreed to the published version of the manuscript.

Funding: This research received no external funding.

Data Availability Statement: Data are contained within the article.

Conflicts of Interest: The authors declare that they have no conflicts of interest.

References

1. Petrov, C. 51 Mobile vs. Desktop Usage Statistics for 2023; Technical Report. Available online: https://techjury.net/blog/mobile-vs-desktop-usage/ (accessed on 27 July 2023).
2. Statcounter: Mobile Operating System Market Share Worldwide. 2023. Statcounter. Available online: https://gs.statcounter.com/os-market-share/mobile/worldwide (accessed on 27 July 2023).
3. SHISHKOVA, T. The Mobile Malware Threat Landscape in 2022. Technical Report. SECURELIST by Kaspersky (February 2023). Available online: https://securelist.com/mobile-threat-report-2022/108844/ (accessed on 27 July 2023).
4. McAfee. Goldoson: Privacy-Invasive and Clicker Android Adware Found in Popular Apps in South Korea. 2023. McAfee. Available online: https://www.mcafee.com/blogs/other-blogs/mcafee-labs/goldoson-privacy-invasive-and-clicker-android-adware-found-in-popular-apps-in-south-korea/?AID=11552066&PID=9129747&SID=tomsguide-in-8524612056782596000 (accessed on 27 July 2023).
5. Fadilpašić, S. This Dangerous New Malware Also Has Ransomware Capabilities. Techradar, 2023. Available online: https://www.techradar.com/news/this-dangerous-new-malware-also-has-ransomware-capabilities (accessed on 27 July 2023).

6. Petrosyan, A. Development of Android Malware Worldwide 2016–2020. Statista, 2020. Available online: https://www.statista.com/statistics/680705/global-android-malware-volume/ (accessed on 27 July 2023).
7. Tam, K.; Feizollah, A.; Anuar, N.B.; Salleh, R.; Cavallaro, L. The evolution of android malware and android analysis techniques. *ACM Comput. Surv. (CSUR)* **2017**, *49*, 1–41. [CrossRef]
8. Li, J.; Sun, L.; Yan, Q.; Li, Z.; Srisa-An, W.; Ye, H. Significant permission identification for machine-learning-based android malware detection. *IEEE Trans. Ind. Inf.* **2018**, *14*, 3216–3225. [CrossRef]
9. Arora, A.; Peddoju, S.K.; Conti, M. Permpair: Android malware detection using permission pairs. *IEEE Trans. Inf. Forensics Secur.* **2019**, *15*, 1968–1982. [CrossRef]
10. Khariwal, K.; Singh, J.; Arora, A. Ipdroid: Android malware detection using intents and permissions. In Proceedings of the 2020 Fourth World Conference on Smart Trends in Systems, Security, and Sustainability (WorldS4), London, UK, 27–28 July 2020; pp. 197–202.
11. Wu, D.-J.; Mao, C.-H.; Wei, T.-E.; Lee, H.-M.; Wu, K.-P. Droidmat: Android malware detection through manifest and api calls tracing. In Proceedings of the 2012 Seventh Asia Joint Conference on Information Security, Tokyo, Japan, 9–10 August 2012; pp. 62–69.
12. Elish, K.O.; Shu, X.; Yao, D.D.; Ryder, B.G.; Jiang, X. Profiling user-trigger dependence for android malware detection. *Comput. Secur.* **2015**, *49*, 255–273. [CrossRef]
13. Zhang, H.; Luo, S.; Zhang, Y.; Pan, L. An efficient android malware detection system based on method-level behavioral semantic analysis. *IEEE Access* **2019**, *7*, 69246–69256. [CrossRef]
14. Zhu, H.; Wei, H.; Wang, L.; Xu, Z.; Sheng, V.S. An effective end-to-end android malware detection method. *Expert Syst. Appl.* **2023**, *218*, 119593. [CrossRef]
15. Fang, Y.; Gao, Y.; Jing, F.; Zhang, L. Android malware familial classification based on dex file section features. *IEEE Access* **2020**, *8*, 10614–10627. [CrossRef]
16. Yen, Y.-S.; Sun, H.-M. An android mutation malware detection based on deep learning using visualization of importance from codes. *Microelectron. Reliab.* **2019**, *93*, 109–114. [CrossRef]
17. Grace, M.C.; Zhou, W.; Jiang, X.; Sadeghi, A.-R. Unsafe exposure analysis of mobile in-app advertisements. In Proceedings of the Fifth ACM Conference on Security and Privacy in Wireless and Mobile Networks, Tucson, AZ, USA, 16–18 April 2012; pp. 101–112.
18. Enck, W.; Ongtang, M.; McDaniel, P. On lightweight mobile phone application certification. In Proceedings of the 16th ACM Conference on Computer and Communications Security, Vienna, Austria, 24–28 October 2016; pp. 235–245.
19. Talha, K.A.; Alper, D.I.; Aydin, C. Apk auditor: Permission-based android malware detection system. *Digit. Investig.* **2015**, *13*, 1–14. [CrossRef]
20. Choi, J.; Sung, W.; Choi, C.; Kim, P. Personal information leakage detection method using the inference-based access control model on the android platform. *Pervasive Mob. Comput.* **2015**, *24*, 138–149. [CrossRef]
21. Song, J.; Han, C.; Wang, K.; Zhao, J.; Ranjan, R.; Wang, L. An integrated static detection and analysis framework for android. *Pervasive Mob. Comput.* **2016**, *32*, 15–25. [CrossRef]
22. Wang, Z.; Li, C.; Yuan, Z.; Guan, Y.; Xue, Y. Droidchain: A novel android malware detection method based on behavior chains. *Pervasive Mob. Comput.* **2016**, *32*, 3–14. [CrossRef]
23. Sasidharan, S.K.; Thomas, C. Prodroid—An android malware detection framework based on profile hidden markov model. *Pervasive Mob. Comput.* **2021**, *72*, 101336. [CrossRef]
24. Moonsamy, V.; Rong, J.; Liu, S. Mining permission patterns for contrasting clean and malicious android applications. *Future Gener. Comput. Syst.* **2014**, *36*, 122–132. [CrossRef]
25. Idrees, F.; Rajarajan, M. Investigating the android intents and permissions for malware detection. In Proceedings of the 2014 IEEE 10th International Conference on Wireless and Mobile Computing, Networking and Communications (WiMob), Larnaca, Cyprus, 8–10 October 2014; pp. 354–358.
26. Wang, W.; Wang, X.; Feng, D.; Liu, J.; Han, Z.; Zhang, X. Exploring permission-induced risk in android applications for malicious application detection. *IEEE Trans. Inf. Forensics Secur.* **2014**, *9*, 1869–1882. [CrossRef]
27. Zhou, Y.; Wang, Z.; Zhou, W.; Jiang, X. Hey, you, get off of my market: Detecting malicious apps in official and alternative android markets. *NDSS* **2012**, 25, 50–52.
28. Qiu, J.; Zhang, J.; Luo, W.; Pan, L.; Nepal, S.; Wang, Y.; Xiang, Y. A3cm: Automatic capability annotation for android malware. *IEEE Access* **2019**, *7*, 147156–147168. [CrossRef]
29. Taheri, R.; Ghahramani, M.; Javidan, R.; Shojafar, M.; Pooranian, Z.; Conti, M. Similarity-based android malware detection using hamming distance of static binary features. *Future Gener. Comput. Syst.* **2020**, *105*, 230–247. [CrossRef]
30. Bai, H.; Xie, N.; Di, X.; Ye, Q. Famd: A fast multifeature android malware detection framework, design, and implementation. *IEEE Access* **2020**, *8*, 194729–194740. [CrossRef]
31. Arp, D.; Spreitzenbarth, M.; Hubner, M.; Gascon, H.; Rieck, K.; Siemens, C. Drebin: Effective and explainable detection of android malware in your pocket. *NDSS* **2014**, 14, 23–26.
32. Varsha, M.; Vinod, P.; Dhanya, K. Identification of malicious android app using manifest and opcode features. *J. Comput. Virol. Hacking Tech.* **2017**, *13*, 125–138. [CrossRef]

33. Mahindru, A.; Sangal, A. Fsdroid:-a feature selection technique to detect malware from android using machine learning techniques: Fsdroid. *Multimed. Tools Appl.* **2021**, *80*, 13271–13323. [CrossRef] [PubMed]
34. Firdaus, A.; Anuar, N.B.; Karim, A.; Razak, M.F.A. Discovering optimal features using static analysis and a genetic search based method for android malware detection. *Front. Inf. Technol. Electron. Eng.* **2018**, *19*, 712–736. [CrossRef]
35. Kumaran, M.; Li, W. Lightweight malware detection based on machine learning algorithms and the android manifest file. In Proceedings of the 2016 IEEE MIT Undergraduate Research Technology Conference (URTC), Cambridge, MA, USA, 4–6 November 2016; pp. 1–3.
36. Feldman, S.; Stadther, D.; Wang, B. Manilyzer: Automated android malware detection through manifest analysis. In Proceedings of the 2014 IEEE 11th International Conference on Mobile Ad Hoc and Sensor Systems, Philadelphia, PA, USA, 28–30 October 2014; pp. 767–772.
37. Sanz, B.; Santos, I.; Laorden, C.; Ugarte-Pedrero, X.; Nieves, J.; Bringas, P.G.; Álvarez Marañón, G. Mama: Manifest analysis for malware detection in android. *Cybern. Syst.* **2013**, *44*, 469–488. [CrossRef]
38. Li, C.; Mills, K.; Niu, D.; Zhu, R.; Zhang, H.; Kinawi, H. Android malware detection based on factorization machine. *IEEE Access* **2019**, *7*, 184008–184019. [CrossRef]
39. Sato, R.; Chiba, D.; Goto, S. Detecting android malware by analyzing manifest files. *Proc. Asia-Pac. Adv. Netw.* **2013**, *36*, 17. [CrossRef]
40. Zhang, M.; Duan, Y.; Yin, H.; Zhao, Z. Semantics-aware android malware classification using weighted contextual api dependency graphs. In Proceedings of the 2014 ACM SIGSAC Conference on Computer and Communications Security, Scottsdale, AZ, USA, 3–7 November 2014; pp. 1105–1116.
41. Feng, Y.; Anand, S.; Dillig, I.; Aiken, A. Apposcopy: Semantics-based detection of android malware through static analysis. In Proceedings of the 22nd ACM SIGSOFT International Symposium on Foundations of Software Engineering, Hong Kong, China, 16–21 November 2014; pp. 576–587.
42. Wang, W.; Gao, Z.; Zhao, M.; Li, Y.; Liu, J.; Zhang, X. Droidensemble: Detecting android malicious applications with ensemble of string and structural static features. *IEEE Access* **2018**, *6*, 31798–31807. [CrossRef]
43. Xu, Z.; Ren, K.; Qin, S.; Craciun, F. Cdgdroid: Android malware detection based on deep learning using cfg and dfg. In Proceedings of the Formal Methods and Software Engineering: 20th International Conference on Formal Engineering Methods, ICFEM 2018, Gold Coast, QLD, Australia, 12–16 November 2018; Proceedings 20; pp. 177–193.
44. Xiao, X.; Zhang, S.; Mercaldo, F.; Hu, G.; Sangaiah, A.K. Android malware detection based on system call sequences and lstm. *Multimed. Tools Appl.* **2019**, *78*, 3979–3999. [CrossRef]
45. Qin, X.; Zeng, F.; Zhang, Y. Msndroid: The android malware detector based on multi-class features and deep belief network. In Proceedings of the ACM Turing Celebration Conference, Chengdu, China, 17–19 May 2019; pp. 1–5.
46. Martín, A.; Lara-Cabrera, R.; Camacho, D. Android malware detection through hybrid features fusion and ensemble classifiers: The AndroPyTool framework and the OmniDroid dataset. *Inf. Fusion* **2019**, *52*, 128–142. [CrossRef]
47. Allix, K.; Bissyandé, T.F.; Klein, J.; Le Traon, Y. AndroZoo: Collecting Millions of Android Apps for the Research Community. In Proceedings of the 13th International Conference on Mining Software Repositories, MSR '16, Austin, TX, USA, 14–15 May 2016; pp. 468–471. [CrossRef]
48. Martín, A.; Lara-Cabrera, R.; Camacho, D. A new tool for static and dynamic Android malware analysis. In Data Science and Knowledge Engineering for Sensing Decision Support. In Proceedings of the 13th International FLINS Conference (FLINS 2018), River Edge, NJ, USA, 21–24 August 2018; World Scientific: Singapore, 2018; pp. 509–516.
49. Pawlak, Z. Rough Set Theory and its Applications to Data Analysis. *Cybern. Syst.* **1998**, *29*, 661–688. [CrossRef]
50. Zhang, Q.; Xie, Q.; Wang, G. A survey on rough set theory and its applications. *CAAi Trans. Intell. Technol.* **2016**, *1*, 323–333. [CrossRef]
51. Alazab, M.; Alazab, M.; Shalaginov, A.; Mesleh, A.; Awajan, A. Intelligent mobile malware detection using permission requests and API calls. *Future Gener. Comput. Syst.* **2020**, *107*, 509–521. [CrossRef]
52. Urooj, B.; Shah, M.A.; Maple, C.; Abbasi, M.k.; Riasat, S. Malware detection: A framework for reverse engineered android applications through machine learning algorithms. *IEEE Access* **2022**, *10*, 89031–89050. [CrossRef]
53. Zhu, H.J.; Gu, W.; Wang, L.M.; Xu, Z.C.; Sheng, V.S. Android malware detection based on multi-head squeeze-and-excitation residual network. *Expert Syst. Appl.* **2023**, *212*, 118705–118713. [CrossRef]

Disclaimer/Publisher's Note: The statements, opinions and data contained in all publications are solely those of the individual author(s) and contributor(s) and not of MDPI and/or the editor(s). MDPI and/or the editor(s) disclaim responsibility for any injury to people or property resulting from any ideas, methods, instructions or products referred to in the content.

Intelligent Traffic Light Controller using Verilog and Xilinx Spartan-3e

Apoorva Banerjee

[1]*Student, Department of Electronics and Communication, Delhi Technological University, Delhi*
apoorvabanerjee_me21b17_b17@dtu.ac.in

----------***----------

Abstract - *Traffic lights also known as 'stop-lights' are signaling devices placed at road crossings which control the competing flow of traffic and avoid collisions. The traffic light controller uses a worldwide color code (red, yellow and green). A traffic light controller can be implemented by using a microcontroller, Field Programmable Gate Array or Application Specific Integrated Circuits. Use of Field Programmable Gate Array is beneficial for a number of reasons viz number of Input/Output ports, performance compared to that of a microcontroller and also it is less expensive as compared to Application Specific Integrated Circuits.*

In this paper, an efficient Traffic Light controller is designed using Moore finite state machine. The circuit description is done in Verilog and the design is tested and simulated on FPGA board Spartan-3e. [1]

***Key Words*: Field Programmable Gate Array, Spartan-3e, Verilog**

1.INTRODUCTION

As noticed in any conventional Traffic light controller, they do not have the option of adjustability in timings of traffic signals i.e., being able to change the timing of the traffic signals according to the density of vehicles on the road.

So, there is a need to develop a fast yet secure traffic control system capable of controlling the vehicular traffic in rush hours without a need of traffic sergeant. The main objective of this paper is to design an intelligent traffic controller with the help of timing mechanism and a sensor.

In this paper, I have designed and simulated a real traffic light controller using Moore finite state machine coded in Verilog and designed and implemented the same on FPGA board Spartan-3e. [2]

1.1 Field Programmable Gate Array (FPGA)

Field Programmable Gate Array or FPGA is an Integrated Circuit consisting of arrays which are groups of programmable logic blocks. One of the major advantages is that the user can configure it and later reconfigure it as per need. Both an FPGA and a microcontroller are quite similar i.e., they are built in such a way that allows the manufacturer or the end user to determine their function; however, use of FPGA is more advantageous over a microcontroller in terms of the number of IO (input and Output) ports and performance. On the other hand, even when compared to an Application Specific Integrated Circuit (ASIC), FPGA is preferred as it is less expensive in terms of cost of production.

The design flow of FPGA shown in *Fig 1* is used to implement the TLC using FPGA. The circuit synthesis is done using Verilog- a hardware description language, followed by the functional simulation and synthesis. The design flow is followed till the timing simulation and then the Generated Bit file is downloaded into the 'Target Device' (FPGA board Spartan-3e).

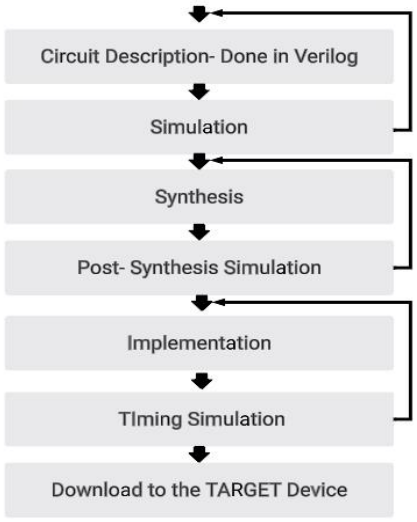


Fig 1

Xilinx Spartan-3e is considered ideal for low-cost and high-volume applications, moreover but it integrates many architectural features associated with high-end programmable logic. This combination of low cost and integrated features has made it an ideal replacement for ASICs (Application Specific

Integrated Circuits). *Fig 2* shows the Spartan-3e FPGA board.[3][6]



Fig 2 Xilinx Spartan-3e

1.2 Finite State Machine (FSM)

An FSM is a mathematical model of computation. There are two types of state machines Moore machines and Mealy machines. In a Mealy machine the output depends on both the input and present state whereas in a Moore machine the output depends only on the present state. A state machine can be divided into three parts: State register, Next-State Logic and Outputs. It is necessary to model each part of the state machine in Verilog [3].

1.2 RELATED WORK

Paper [4] have successfully implemented the TLC (Traffic Light Controller) but the paper shows only Design of an FPGA Based Intelligence Traffic Light Controller with VHDL 93 behavioral simulation. The truth-table however should have been displayed with which a designer can compare with the simulation results. Paper [3] have also successfully implemented the TLC using ChipScope Pro and Virtual Input Output; they however have used the concept that each side i.e., North-South and East-West would be allowed to be turned Green sequentially (giving the Main Road/Highway a longer period of 'Green' light); however turning on the Traffic lights when no vehicular movement is detected often leads to a lot of power consumption. In my paper, keeping in mind the fact that traffic flow is negligible/ absent in the side roads, I have installed a sensor along with the traffic lights present on the side roads to detect any vehicular movements such that little power wastage is minimized by limiting the 'ON/OFF' of the green lights of the side road.

2. SYSTEM IMPLEMENTATION

2.1 Finite State Machine (FSM)

A conventional traffic light has three lights viz green, yellow and red. Green indicating a 'go' signal; yellow indicating 'slow down to stop'; red means to 'stop'. However, a smart and an advanced traffic light controller, senses the presence or absence of vehicles and reacts accordingly. The main objective behind designing a smart TLC system is that the driver doesn't have to spend an unnecessary amount of time waiting for the traffic light to change. In this paper I have assumed a crossroad; a busy main stretched out in the East-West direction and a side road which intersects it in a North-South direction shown in *Fig 3*. On both the sides i.e. North facing as well as South facing, a Sensor has been placed. When no car is on the side road, the main lights remain 'Green', allowing the traffic to flow on the main; giving traffic flow on the main a higher priority. If a vehicle is sensed on the side road by the sensor, the main lights go from 'Green' to 'Yellow' and then finally 'Red'; allowing the side road lights to turn 'Green'. The side road light remains 'Green' as long as there is a vehicle on the side road however it is never longer than the set interval. Keeping in mind the above-mentioned conditions, side road lights then transition from 'Green' to 'Yellow' and then finally 'Red'.

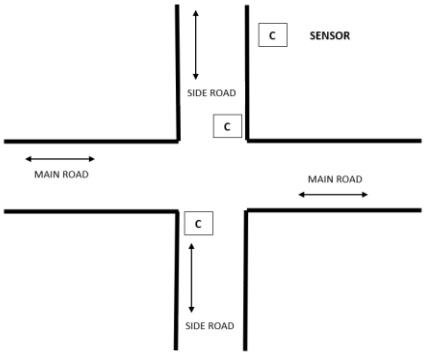


Fig 3

2.2 Working Principle

In this paper, I have an interval timer that generates a short time pulse (TS) and a long time pulse (TL) in response to a start timer (ST) signal. TS is used for the timing of the 'Yellow' lights and 'TL' is used for 'Green' lights. Table 1 and 2 shows the list of input and output signals defined in the Verilog code

Input signal	Description
Reset	Places the FSM back to the initial state
C	Sensor- detects the vehicles, if any, on the side road

TS	Short-time interval expired
TL	Long-time interval expired

Table 1

Output Signal	Description
MG, MY, MR	Assert green/yellow/red main road lights
SG, SY, SR	Asser green/yellow/red side road lights
ST	Start timing a short or long interval

Table 2

2.3 State Diagram

According to Moore finite state machine, the output is associated only with the present state; thus, for the TLC system discussed in this paper, we have four possible scenarios each depicting a unique state of the FSM model. Table 3 depicts the list of the following states along with its description.

States	Description
S0	Main Green and Side road Red
S1	Main Yellow and Side road Red
S2	Side road Green and Main Red
S3	Side road Yellow and Main Red

Table 3

1)S0 is assumed to the default state and 'resetting' the FSM model brings back to state S0. Moreover, 'Reset' also starts the timer. Some lighting configurations imply others i.e., if either of the side road or the main is 'Green' the other road is by default 'Red'.

2)S0, assumed to be the default state or the state when the model is reset. S0 is defined as the state when main road light is 'Green' and the side road light is 'Red'. The FSM stays in the S0 state if TL has not expired yet or no vehicle is detected on the side road.

3)While being in the S0 state, if both, TL has expired and a vehicle is also detected on the side road, we make a transition from S0 to S1. S1, as previously defined, is the state where the main light is 'Yellow' and the side road light is 'Red'. The timer ST is also made to restart both the timers i.e., TL and TS.

4)The FSM stays in the S1 state until the TS expires. If the TS has expired the FSM makes a transition from S1 to S2: the state where the main light is 'Red' and the side road is 'Green'. The timer ST is also made to restart both the timers i.e., TL and TS.

5)While being in the state S2, the FSM stays in that state until TL expires and there is still a vehicle on the side road. However, if the TL has expired or the there aren't any more vehicles on the side road, the FSM makes a transition from S2 to S3 making the timer ST to also restart.

6)Once in the state S3, the side road lights are 'Yellow' and the main road lights are 'Red'. The FSM stays in the state S3 as long as the TS hasn't expired however if the TS expired, a transition is made from S3 and back to the initial state S0.

Fig 4 shows the state diagram of the Smart TLC System.

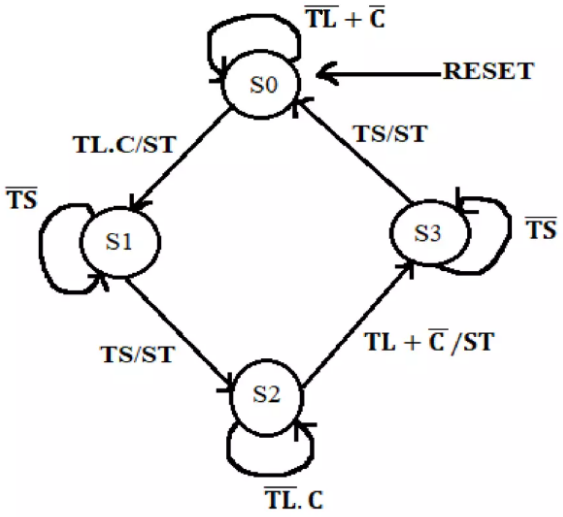


Fig 4

State Diagram

3. SIMULATION RESULT

Fig 5 shows the RTL(Register Transfer Level) schematic of the intelligent TLC system. The RTL

schematic shows the logic implementation, i.e. shows the data flow within the circuit.

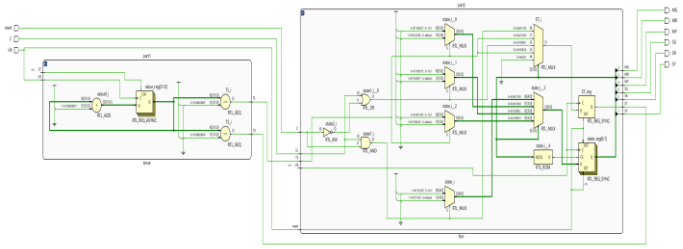


Fig 5 RTL Schematic

Fig 6 shows the behavioral simulation at t=29.5ns. It represents the state S0 with MG=1, SR=1 and no car detected i.e., sensor C=0 and neither of the light i.e., TL and TS have expired i.e. TL, TS=0.

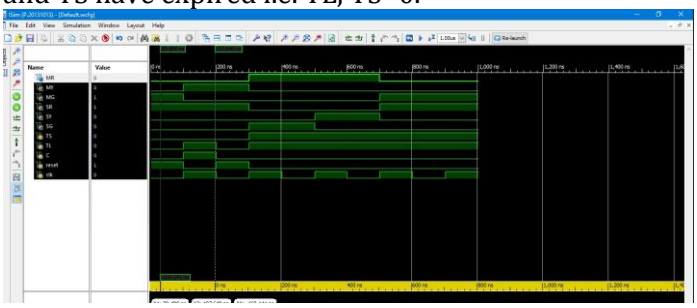


Fig 6

Fig 7 shows the behavioral simulation at time t=144.5ns. It represents the state S1 i.e. MY=1, SR=1 and the sensor detects a car on the side road, thus C=1 and the long timer Tl has also expired: TL=1.

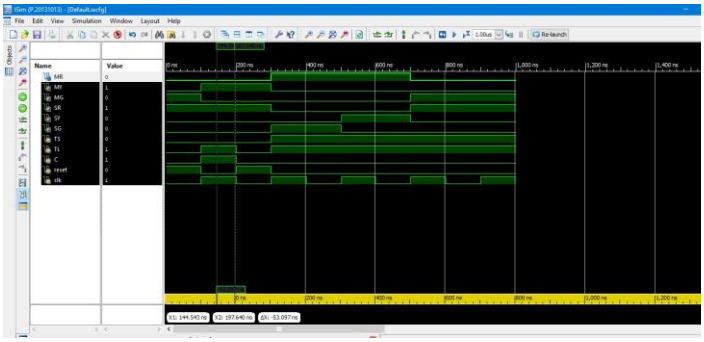


Fig 7

Fig 8 shows the behavioral simulation at time t=374.631 ns. It represents the state S2 with MR=1 and SG=1. No vehicular movement is detected on the side road, therefore C=0 and the short timer has also expired, making TS=1.

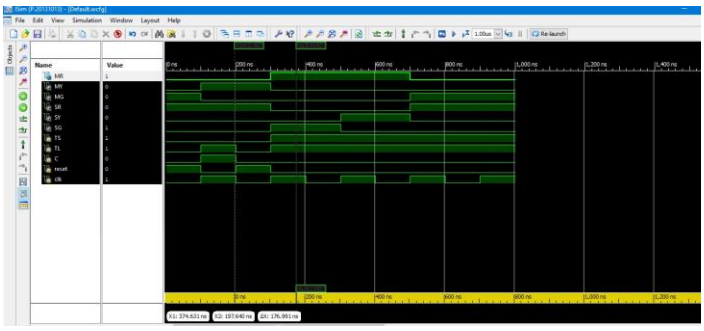


Fig 8

Fig 9 shows the behavioral simulation at time t=566.3ns, representing the state S3 with MR=1, SY=1 and both TS, TL=1.

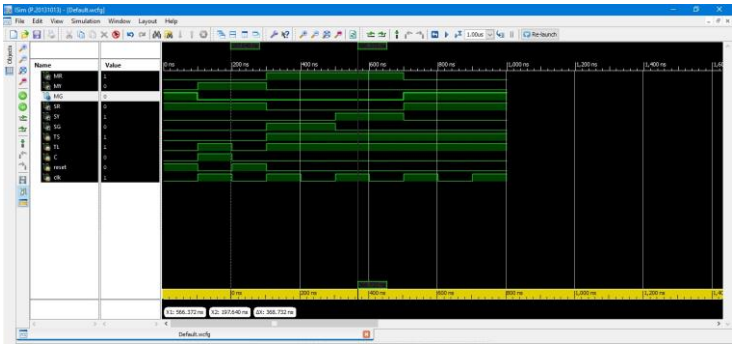


Fig 9

3. CONCLUSION

An intelligent Traffic Light Controller system is designed using FPGA for four roads intersection with sensors. The system has been simulated using Verilog and FSM for efficient T.L.C. with ability to change its timing parameters based on the sensor data. Each subcomponent is constructed and tested thoroughly before moving onto the next one. The design is robust; all the design decisions were inspected comprehensively before employment. Overall, the design and implementation of the traffic light controller is respectable to design more complex system. The system is verified on FPGA Spartan 3E

REFERENCES

[1] Nour T. Gadawe, Sahar L. Qaddoori, "Design and implementation of smart traffic light controller using VHDL language", International Journal of Engineering &Technology, 8 (4) (2019) 596-602, https://www.researchgate.net/profile/Noor-Gadawe/publication/338458961_Design_and_implementation_of_smart_traffic_light_controller_using_VHDL_language/links/5e1f66ba299bf1e1fab4c7c5/Design-and-implementation-of-smart-traffic-light-controller-using-VHDL-language.pdf

[2] A. Raza, A. Kumar, E. Chaudhary, "Traffic Light Controller Using VHDL", International Journal of Modern Trends in Engineering and Research (IJMTER), Vol. 04, Issue 4, PP. 57-62, April 2017. https://doi.org/10.21884/IJMTER.2017.4118.C529F.

[3] Sourav Nath, Chandrajit Pal, Suman Sau, Sreyanka Mukherjee, Abhishek Roy,
Arghya Guchhait and Debdatta Kandar, "Design of an FPGA Based Intelligence Traffic Light Controller with VHDL", 2012 International Conference on Radar, Communication and Computing (ICRCC),

SKP Engineering College, Tiruvannamalai, TN., India. 21 - 22 December, 2012. pp.92-97. https://d1wqtxts1xzle7.cloudfront.net/31707817/traffic-libre.pdf?1392440734=&response-content-disposition=inline%3B+filename%3DDesign_of_an_FPGA_based_Intelligence_Tra.pdf&Expires=1697777138&Signature=TEsGUsDwysZTEeApOWtE-z1JEJ~~Xp3vuw1DNF63Lqs4xDlbRaH8N7k1QmZZfKWKdMi0DWOdn9Bjv6ERJJhXDtN8ArhUKlUdXyumSqW3FXMVbxFko3L-NJi3semVCk7XwgsTHqBXlxa2CvpKnmq~ba9-~KOdUDa3pUwwg1Z3fijIAHtLwMeI-SrNzjdm0zoF7jDlHstYJaKltyhYuHvK9WPjljzc27qO0ff6nElIcuXGj8C-rNiPy470TgaVjonQxUwXsJWcA9BnXcYkuintSIdFMOLa~5qbuhzBRfI76y5UBumerxyciZDMDJua542dCswusjooTBvkv21nLaOfrw__&Key-Pair-Id=APKAJLOHF5GGSLRBV4ZA .

[4] B. Dilip, Y. Alekhya, P. Divya Bharathi, " FPGA Implementation of an Advanced Traffic Light Controller using Verilog HDL", International Journal of Advanced Research in Computer Engineering & Technology (IJARCET) Volume 1, Issue 7, September 2012,https://citeseerx.ist.psu.edu/document?repid=rep1&type=pdf&doi=4a54bc496f4b0788889cca7636a644419ffd95af .

[6] P.G. Prasad, S.V. Krishna, "Design and Implementation of ITLC System Using FPGA", Journal of Electronics and Communication Engineering (IOSR-JECE), Vol. 12, Issue 5, Ver. II, PP. 07-13, Sep.-Oct. 2017, Website: www.iosrjournals.org.

[7] V. V. Dabahde, R. V. Kshirsagar, "FPGA-Based Intelligent Traffic Light Controller System Design", IJISET - International Journal of Innovative Science, Engineering & Technology, Vol. 2, Issue 4, PP. 1268-1271, April 2015, Website: www.ijiset.com.

[8] S. S. GAOPANDE, A. D. BHARADE, "Structural Modeling of Intelligent Traffic Light Controller on FPGA", International Journal of Electrical, Electronics and Data Communication, Vol. 2, Issue 9, PP. 63-66, Sep. 2014.

[9] S. Nath, Ch. Pal, S. Sau, S. Mukherjee, A. Roy, A. Guchhait, D. Kandar, "Design of an FPGA Based Intelligence Traffic Light Controller with VHDL", International Conference on Radar, Communication and Computing (ICRCC), PP. 92-97, 21 - 22 Dec. 2012. https://doi.org/10.1109/ICRCC.2012.6450554.

[10] B. Dilip, Y. Alekhya, P. Divya Bharathi, "FPGA Implementation of an Advanced Traffic Light Controller using Verilog HDL", International Jour-nal of Advanced Research in Computer Engineering & Technology (IJARCET), Vol. 1, Issue 7, PP. 1-6, Sep. 2012.

corrected Proof

Water Practice & Technology

© 2024 The Authors

Water Practice & Technology Vol 00 No 0, 1 doi: 10.2166/wpt.2024.005

Interceptor sewer for abatement of pollution in surface water

Radhey Shyam Tyagi[a,*], S. K. Singh[a] and P. K. Goyal[b]

[a] Department of Environmental Engineering, Delhi Technological University, New Delhi 110042, India
[b] Department of Civil Engineering, Delhi Technological University, New Delhi 110042, India
*Corresponding author. E-mail: radheyshyam_2k20phden501@dtu.ac.in

ABSTRACT

Unplanned population growth in urban cities has largely caused unplanned habitations called slums. Due to various complexities, service providers are unable to provide basic amenities, i.e., water, roads, sanitation, and sewerage in these slums. Water, being the basic need for human survival, is either managed by these residents by extracting groundwater or the minimum required water is provided by the government through water tankers or tube wells. In the absence of sewerage facilities, sewage is discharged directly into stormwater drains, rivers, ponds, lakes, etc. It contaminates the freshwater of these water bodies. The Yamuna River (22 km stretch) from the Wazirabad Barrage to the Okhla Barrage, and about 600 lakes in Delhi, India, are highly polluted. To avoid such severe events of contamination of water resources, it is necessary to develop a system to intercept wastewater at the source, transfer it to the nearest sewage treatment plant, and treat it to the required discharge standard, called the interceptor sewer. This case study is an outcome of a successful mega project of an interceptor sewer along three major drains (Najafgarh, Supplementary, and Shahadra) for the abatement of pollution in river Yamuna, Delhi.

Key words: Delhi, pollution abatement, sewer interception, water bodies, Yamuna River

HIGHLIGHTS

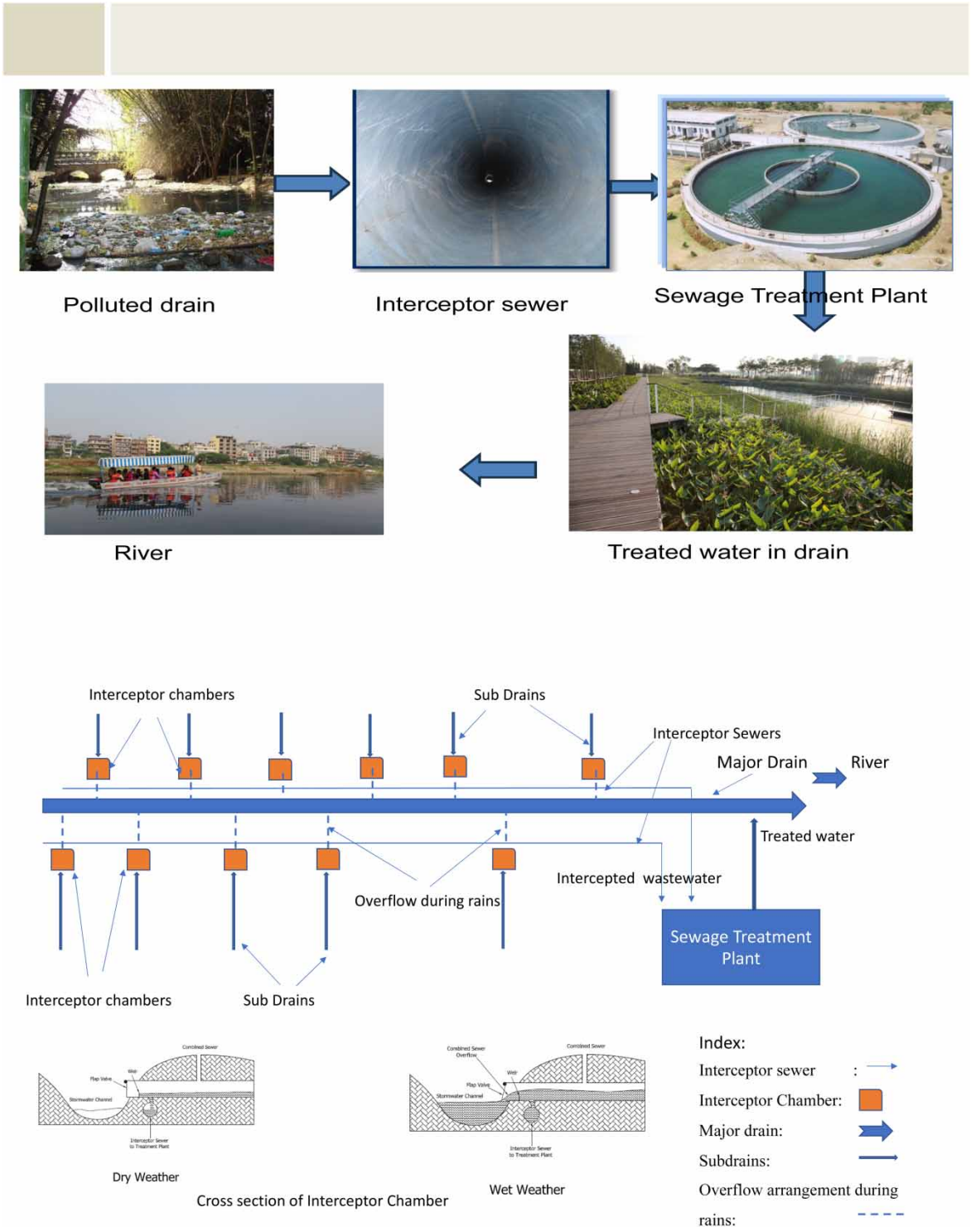
- The interceptor sewer project will reduce the organic and pathogenic pollution in river Yamuna.
- An interceptor sewer will trap wastewater at the source and convey it to STPs.
- Success of an interceptor sewer depends on the lateral coordination and cooperation of various stakeholders.
- CPCB and DPCC must monitor river water quality regularly and instruct the concerned authorities.

This is an Open Access article distributed under the terms of the Creative Commons Attribution Licence (CC BY 4.0), which permits copying, adaptation and redistribution, provided the original work is properly cited (http://creativecommons.org/licenses/by/4.0/).

Downloaded from http://iwaponline.com/wpt/article-pdf/doi/10.2166/wpt.2024.005/1356305/wpt2024005.pdf
by DELHI TECHNOLOGICAL UNIVERSITY (DTU) user

corrected Proof

GRAPHICAL ABSTRACT



1. INTRODUCTION

River Yamuna starts from the Yamunotri Glacier, at an elevation of 6,320 m above the mean sea level, and after flowing 200 km, it is barraged at Tajewala. Around one-third of stored water is diverted into the Eastern Yamuna Canal for the water supply demand of U.P. and two-thirds of water into the Western Yamuna Canals for the water demands of Haryana and Delhi (Figure 1). After traversing around 1,376 km through the states of Himachal Pradesh, Haryana, Uttar Pradesh (U.P.), Uttarakhand, Delhi, Rajasthan, and Madhya Pradesh, it confluences with

Downloaded from http://iwaponline.com/wpt/article-pdf/doi/10.2166/wpt.2024.005/1356305/wpt2024005.pdf
by DELHI TECHNOLOGICAL UNIVERSITY (DTU) user

corrected Proof



- Total length of Yamuna river: 1376 Km)
- Yamuna river enters Delhi near Palla, traverses about 48 kms.
- **22 Km stretch** from Wazirabad to Okhla 2% OF RIVER LENGTH in Delhi
- 70 % of total pollution loaded in Yamuna in DELHI

(BOD:>40; Coliform: 24Millions)

Figure 1 | Diagrammatic presentation of the segments of the Yamuna River.

River Ganga at Allahabad called the Triveni Sangam. River Yamuna enters Delhi on the upstream side of Palla village, and after traveling through Delhi for around 48 km, it enters U.P. near the Okhla Barrage. River water quality in the stretch between Wazirabad and Okhla Barrages is horrible because of receiving massive wastewater discharge from 23 drains (Table 1) in the Delhi National Capital Region (NCR). These 23 stormwater drains carry untreated wastewater from unsewered colonies and discharge it into the river. The Najafgarh drain and supplementary drains confluence at the downstream side of the Wazirabad Barrage, and finally, release wastewater into the river. These two drains are the main polluting contributors that have wastewater discharge varying from 1,360 to 1,800 million liters per day (MLD) and 60% of the total pollution load. The total biological oxygen demand (BOD) load from these drains in the year 2004 was 240.37 tons per day (TPD), and the total average coliform count was 2.4×10^7 coliforms/100 ml (CPCB 2004). Septic conditions and sewage input enhance coliform growth and make water highly harmful for human consumption (Upadhyay *et al.* 2011). Due to the mixing of a considerable amount of solid waste and municipal and industrial effluents with river water, the microbial activity of the aquatic system results in the substantial depletion of dissolved oxygen (DO). At the downstream of Jaitpur (Delhi), the river also receives the discharge of Hindon cut river that carries wastewater from U.P. Hence, the river looks like a sewage canal between the Wazirabad Barrage and the Okhla Barrage, especially during dry weather. Nonavailability of fresh water on the downstream of the Wazirabad Barrage for dilution is also one of the major reasons for the poor water quality in river Yamuna (Paliwal *et al.* 2007; Sharma & Singh 2009). In the year 1994, the Hon'ble Supreme Court took Suo moto on an article 'Quiet Flows Maily Yamuna' published in the newspaper 'The Hindustan Times' about the pathetic/unhealthy condition of the river Yamuna, and issued notices to the Union of India and CPCB. This case became famous with the name 'Maily Yamuna Case' vide WP(C)/725/1994 and continued to be heard by the Apex Court of a five-judge Bench chaired by the Hon'ble Chief Justice of India. Other related central and state government departments became the party, such as the Ministry of Environment and Forest, GOI; Ministry of Urban Development, Government Of India

Downloaded from http://iwaponline.com/wpt/article-pdf/doi/10.2166/wpt.2024.005/1356305/wpt2024005.pdf
by DELHI TECHNOLOGICAL UNIVERSITY (DTU) user

corrected Proof

Table 1 | List of stormwater drains, their discharge, and current status of trapping of discharge

S. no.	Name of drain (2)	Discharge of wastewater (3)			% Contribution of pollution (4)	Current status of trapping of discharge (5)
		m^3/s	Cusecs	MLD		
1.	Najafgarh i/c Supplementary Drain	23.6375	834.7504	2,042.28	52.22	Interceptor sewer Line laid along Najafgarh and Supplementary drain
2.	Shahadra Drain	5.948	210.0634	513.93	13.14	——do——
3.	Old Agra Canal near Kalindi Kunj	5.559	196.317	480.31	12.28	Discharging into River Yamuna
4.	Old Agra Canal at Okhla	2.788	98.463	240.90	6.16	——do——
5.	Barapulla drain	1.577	55.708	136.30	3.49	Partially trapped
6.	Tuglakabad Drain	1.028	36.315	88.85	2.27	Trapped into existing sewer
7.	Powerhouse Drain	0.981	34.667	84.82	2.17	Two S.T.Ps of total capacity 78 MLD are operational at the mouth of drain
8.	Dr Sen Nursing Home	0.748	26.338	64.44	1.65	Partially trapped at STP
9.	AbuFazal Drain	0.589	20.806	50.90	1.30	Discharging into River Yamuna
10.	ISBT/Morigate/ Quadia Drains	0.523	18.481	45.22	1.16	Discharging into River Yamuna
11.	Saritavihar Drain	0.472	16.686	40.82	1.04	Partially trapped
12.	Maharani Bagh Drain	0.306	10.829	26.50	0.68	Partially trapped
13.	Jaitpur Drain	0.192	6.768	16.56	0.42	Partially trapped
14.	Molahad Band Drain	0.162	5.709	13.97	0.36	Discharging into River Yamuna
15.	Kailashnagar Drain	0.137	4.847	11.86	0.30	Partially trapped
16.	Tonga Stand Drain	0.132	4.655	11.39	0.29	Partially trapped
17.	Shastri Park Drain	0.088	3.119	7.63	0.20	Discharging into River Yamuna
18.	Drain No.14	0.085	3.002	7.34	0.19	Trapped in Ring Road T/Sewer
19.	Metcalf House Drain	0.070	2.472	6.05	0.15	Discharge being pumped into Bela Road T/Sewer
20.	Civil Mill Drain	0.072	2.560	6.26	0.16	Trapped into Ring Road T/Sewer
21.	Magazine Road Drain	0.081	2.884	7.06	0.18	All three drains are trapped in the Interceptor sewer and are being pumped to Bela Road Trunk Sewer.
22.	Sweepers Colony Drain	0.069	2.442	5.98	0.15	
23.	Khyberpass Drain	0.015	0.530	1.30	0.03	
	Total Flow MLD			**3,910.68**		

Source: CPCB and Delhi Jal Board, March 2023.

(GOI), CPCB, Delhi Pollution Control Committee (DPCC), Department of Irrigation and Flood Control, GNCTD, Delhi Jal Board (Formerly Delhi Water Supply and Sewage Disposal Undertaking under Municipal Corporation of Delhi); Delhi Development Authority, Haryana and U.P. Govt.; MCD and Central Water Commission, etc.; responsible for the ecological flow in Yamuna, prevention of solid waste dumping, collection and treatment of 100% sewage generated in the city, river front development, quality monitoring of river water, treatment of industrial waste flowing into the river and regulations related to maintaining river water quality.

2. STUDY OF MAJOR SOURCES OF WATER POLLUTION

2.1. Rapid urbanization, unsewered areas, and slum settlements along water bodies

Due to rapid urbanization and the inflow of migrants to the urban areas for earning their livelihood, environmental problems are increasingly severe across Asia, especially in India. It is attributed to the rising human

Downloaded from http://iwaponline.com/wpt/article-pdf/doi/10.2166/wpt.2024.005/1356305/wpt2024005.pdf
by DELHI TECHNOLOGICAL UNIVERSITY (DTU) user

corrected Proof

population, urbanization, and economic activities. Unplanned population growth and poor wastewater management resulted in reduced water resources in a country like India ((Nallathiga 2008) and completely outpaced the augmentation of civic infrastructure. Physical and financial constraints in providing civic infrastructure like water, power supply sanitation, sewage treatment, housing, etc., at the same pace at which growth and in-migration occur, resulted in the discharge of wastewater in the nearby water bodies, i.e., ponds, drains, rivers, etc.

One of the major factors contributing to the pollution in water bodies and low capacity utilization of sewerage treatment plants is the absence of a sewerage network in large unplanned colonies of cities. For example, in Delhi, around 55% population lives in slum areas and is deprived of sewerage facilities. Providing sewerage infrastructures in these congested areas, which have developed in an unplanned manner over a period of time, is also highly complicated and difficult in terms of feasibility, legality, and time-consuming. Hence, wastewater generated in these colonies is discharged untreated into nearby waterbodies through drains.

The population of Yamuna basins' towns and cities was estimated to be 118.34 million in the year 2018. It resulted in huge concretization, reduction in green areas, size and the number of water bodies, which were the source of water to meet the demand of the urban population (Chandramouli & GR 2011; Kumar *et al.* 2020) Along the banks of rivers, there are many illegal colonies within floodplains that discharge untreated waste and fecal residues causing pollution in river water (Supplementary material, Figure S1a, b). The embankments of all smaller and major drains have also been encroached upon, wherein habitats discharge their domestic waste directly into drains. Most of the households have constructed their toilets on the banks of these drains and are directly discharging their soil wastes into the drain, thus increasing fecal coliform in drain water.

2.2. Synchronization of sewage treatment capacity, aging of sewerage system, and poor functioning of STPs

In an ideal situation, sewage treatment capacity has to synchronize with sewage generation in a city to ensure 100% sewage treatment, prevent contamination in water bodies, and maintain a better environment. Like in Delhi, sewage generation is around 4,000 MLD, against which, the total treatment capacity in Delhi is hardly 2,815 MLD. But, only 1,937 MLD of sewage is being treated (CPCB 2021). Hence, around 878.67 MLD of wastewater is discharged into waterbodies untreated (Hima Jwala *et al.* 2020). This is the same conditions in other metro and urban cities. In many cities, the sewer pipe material is reinforced cement concrete which is more than 40–50 years old against its intended life of 30 years. Due to the aging factor and formation of hydrogen sulfide gas inside the sewer pipe line, the material, especially reinforcement, gets rusted and sewer pipes come to highly dilapidated conditions. In many places, the crown of pipes is broken due to rusting and it falls inside the sewer pipe resulting in settlement and chocking of the sewer which blocks the flow of sewage. Over the period, the silt deposited in the sewers becomes hard, which makes it difficult to clean the sewer (Supplementary material, Figure S2). The problem is aggravated during desilting, which further damages the sewer due to abrasion caused by silt removal equipment (Kumar & McMasters 2017). Refurbishment, rehabilitation, and upgrading old sewer lines are challenging and time-consuming in congested areas. Thus, without a proper and inadequate carriage system, sewage is not conveyed to the respective sewage treatment plants (STPs) and these plants are underutilized. The authorities responsible for sewerage management in cities are required to treat sewage as per the standard published vide notification no. GRS 1265 (E): Environment (Protection) Amendment Rules, 2017 (Supplementary material, Table S1). However, they have failed to maintain those quality standards due to many reasons**.** As per the CPCB report 2013, only 51% of sewage in metro cities, 32% in class-I cites, and 8% in class-II cities is being treated. Whereas, 10% STPs are functioning good, 36% satisfactory, 33% poor, and 21% very poor (Figure 2) (CPCB 2013).

2.3. Direct disposal of wastewater into water bodies

Storm water drains are meant for carrying rainwater only. But, in the absence of sewerage facilities in slums, wastewater is discharged into these drains that ultimately outfalls into waterbodies and contaminates the available fresh water, reducing the water resources. In Delhi, 23 drains carrying wastewater of planned and unplanned colonies discharge into river Yamuna. According to CPCB, the river water quality standard of river Yamuna in the Delhi stretch has become class C. This classification is done according to the best use designated to the surface water (Sharma & Singh 2009). River water must have acceptable quality for the survival of aquatic life, flora, and fauna. As water for processing and drinking is available in abundance, there are substantial industrial activities in those cities situated along the banks of rivers, i.e., manufacture of sugar, distilleries, textile,

Downloaded from http://iwaponline.com/wpt/article-pdf/doi/10.2166/wpt.2024.005/1356305/wpt2024005.pdf
by DELHI TECHNOLOGICAL UNIVERSITY (DTU) user

corrected Proof

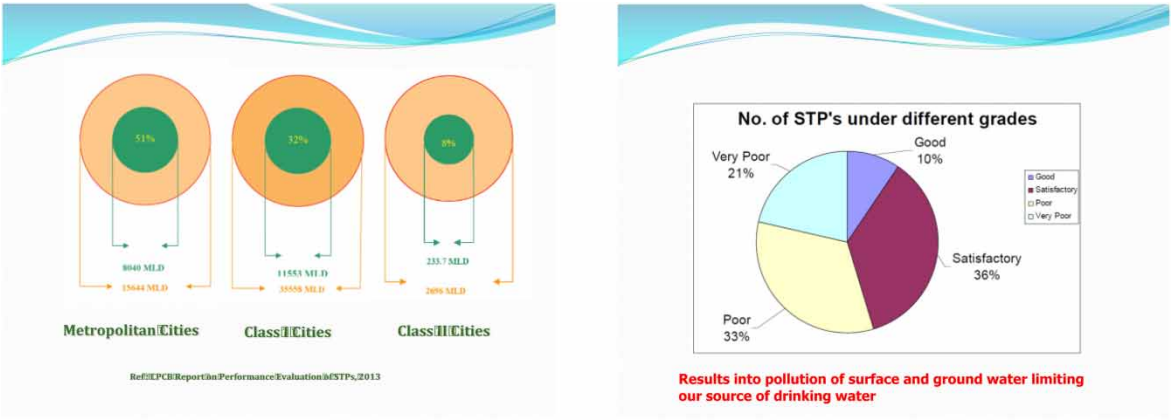


Figure 2 | Status of sewage generation, treatment, and functioning of STPs in India.

leader, pulp and paper, food processing, chemicals, pharmaceuticals, oil refineries, thermal power, etc. resulting into the massive discharge of industrial waste (Sharma *et al.* 2020). The statewise list of industrial cities, their percentage contribution of pollution, and the total industrial discharge generated (Table 2). Despite government regulations for setting up effluent treatment plants at the outlets of such industries, the industrial effluent is bypassed and discharged into nearby drains untreated, which ultimately contaminates river water and further ground water, when it percolates into the ground.

Table 2 | State-wise industrial estates along the Yamuna Riverbank, percentage contribution, and the total industrial discharge generated

S. No.	Name of state/Cities along bank	No. of industries	% Contribution of industrial waste	Total industrial discharge (MLD)
1.	Uttar Pradesh/Yamuna Nagar, Panipat, Sonipat, Bagpat, Delhi, Gautambudh Nagar, Ghaziabad, Mathura, Agra	17	55	1,229.50
2.	NCT of Delhi	42	18	
3.	Haryana	22	13	
4.	Madhya Pradesh		14	

A large amount of solid waste is thrown by the residents into and on the banks of drains, rivers, and ponds. In Delhi, solid waste generation was estimated to be 17,000–25,000 TPD for an anticipated pollution of 22.4 million by 2021. Despite efforts to decompose the waste by composting, incineration, etc., a minimum residue of 4,000–5,000 TPD, i.e., 20%, will require a large area of landfills (MoEF GOI 2001). Hence, there will be a lot of pressure on the municipal bodies to manage even the residue of municipal waste in the future. Without an adequate solid waste management infrastructure in Delhi and less awareness programs, the residents throw their domestic waste in nearby water bodies, i.e., drains and rivers, ultimately increasing the pollution in water bodies.

2.4. Lack of dilution in rivers

Since the entire quantity of raw water of river Yamuna is divided into Eastern and Western Yamuna Canals on the upstream side of the Tajewala Barrage, there is hardly any release of fresh water for ecological flow and dilution of pollutants in river Yamuna, on the downstream side of the Tajewala Barrage. On the intervention of the Hon'ble Supreme Court, and later NGT in 2017, the Haryana Government was directed to release 10 Cumec freshwater from the Tajewala Barrage as the ecological flow for the river. However, this quantity of water was so low that it percolated into the ground after traveling some distance, and no adequate freshwater was left to maintain the ecological flow up to the Delhi stretch. The surface and groundwater quality in the river basin has deteriorated alarmingly (Kumar *et al.* 2020). Whatever freshwater is seen in the Delhi stretch from Palla to Wazirabad Barrage is the quantity of fresh water released by Haryana for the drinking needs of Delhi, as per the memorandum of understanding signed among the basin states of river Yamuna, which is

Downloaded from http://iwaponline.com/wpt/article-pdf/doi/10.2166/wpt.2024.005/1356305/wpt2024005.pdf
by DELHI TECHNOLOGICAL UNIVERSITY (DTU) user

corrected Proof

lifted at the Wazirabad Barrage for treatment at Chandrawal, Wazirabad, and Okhla water treatment plants. Hence, there is no freshwater left to be released downstream of the Wazirabad Barrage for further dilution of polluted river water. In the absence of adequate freshwater on the downstream of the Wazirabad Barrage, the quality of river water cannot be improved to the bathing standard quality (Supplementary material, Table S2), despite making all efforts to reduce pollution in the river Yamuna. This is the condition of most of the river basins in India.

3. ACTION PLAN FOR IMPROVEMENT OF WATER QUALITY IN WATER BODIES AND GROUNDWATER IN DELHI

On the recommendation of the High-Power Technical Committee in the year 2006, constituted by the Hon'ble Supreme Court comprising of the senior representatives of the Central Water Commission, Central Pollution Control Board, Central Ground Water Board, CPHEEO under the Ministry of Urban Development, GOI, and CEO, Delhi Jal Board being the Convener, the Hon'ble Supreme Court considered the concept of 'Laying of interceptor sewers along the three major drains, i.e., Najafgarh, Supplementary, and Shahdara, for the abatement of pollution in river Yamuna'. The objective of this concept was to intercept sewage flowing in small subsidiary drains before it enters the major drain and the intercepted sewage to be conveyed to the nearest STPs for proper treatment to ensure that only treated sewage is discharged into these drains and ultimately into rivers. The overall concept was to lay deep and large sized diameter sewer pipes along the major drains (Najafgarh, Supplementary, and Shahdara) to trap wastewater of sub drains at sources; augmentation of the existing capacity of 10-MLD STP at the mouth of the Delhi Gate drain (constructed as a pilot project under the Yamuna Action Plan (YAP)-I) up to 77 MLD; interception of remaining drains into Bela Road, Ring Road, and other nearby trunk sewers which were rehabilitated under the YAP-II, collected wastewater to be pumped to the Okhla STP. If required, additional STPs will be constructed after utilization of the full capacity of the existing plants. Interceptor sewer system concepts were conceived to reduce the environmental impacts on receiving waters by diverting the combined sewer flow from the original sewer outfalls to Wastewater Treatment Works (WwTWs). Interceptor sewer systems comprised large pipes, and pumping stations to pump wastewater into STPs. This concept was earlier tried in the Liverpool area as part of the Mersey Estuary Pollution Alleviation Scheme (MEPAS), which significantly improved the quality of River Mersey, resulting in the comeback of flora and fauna (Thomas *et al.* 2000, 2004).

4. SALIENT FEATURES OF INTERCEPTOR SEWER CONCEPT

The key features of the interceptor sewer concept include trapping untreated sewage from around 190 sub drains of three major drains (Najafgarh, Supplementary, and Shahadra) into a 59 km long interceptor sewer to be laid along these three major drains through the micro tunneling method for the ease of construction, less inconvenience to the nearby people, and no damage to adjacent properties.

The interceptor chambers will be constructed in such a manner that during dry weather flow, the entire wastewater is trapped in the interceptor sewer. But during rain, excess wastewater beyond the capacity of the interceptor sewer is overflown into the major drains directly. It also involves the construction of trash racks to trap floating materials and screens at the intercepting chambers.

Seven lift stations are proposed to collect and pump the trapped sewage to the nearest STPs so that only treated effluent will be allowed to flow in the major drains (Figure 3). The capacity of the existing STPs at Pappankalan and Nilothi needs to be augmented. The entire unsewered area, predominantly the unauthorized colonies, will be provided a sewerage system as per the Delhi Sewerage Master Plan (DSMP) 2031 (Delhi Jal Board 2015). The diameter and the depth of the interceptor sewer have been selected in such a manner that the interceptor sewer will act as a trunk sewer in the ultimate setup of the sewerage system and will be able to cater to the sewage discharge of the entire unsewered colonies in their command as per the proposed DSMP-2031 (Delhi Jal Board 2015). Hence, interceptor sewers would be completely independent and neutral to the time frame within which unauthorized colonies will be provided sewerage.

The optimization of the design of interceptor sewer systems was adopted as per the design mentioned in (Karovic & Mays 2014). Being a combined sewer system, which carries wastewater and some rainwater from drains, the overflow chamber and its modeling is followed from (Xue *et al.* 2013). Details on the effectiveness of the best management practices are being followed as given in the study by Kaini *et al.* (2012). The best

Downloaded from http://iwaponline.com/wpt/article-pdf/doi/10.2166/wpt.2024.005/1356305/wpt2024005.pdf
by DELHI TECHNOLOGICAL UNIVERSITY (DTU) user

corrected Proof

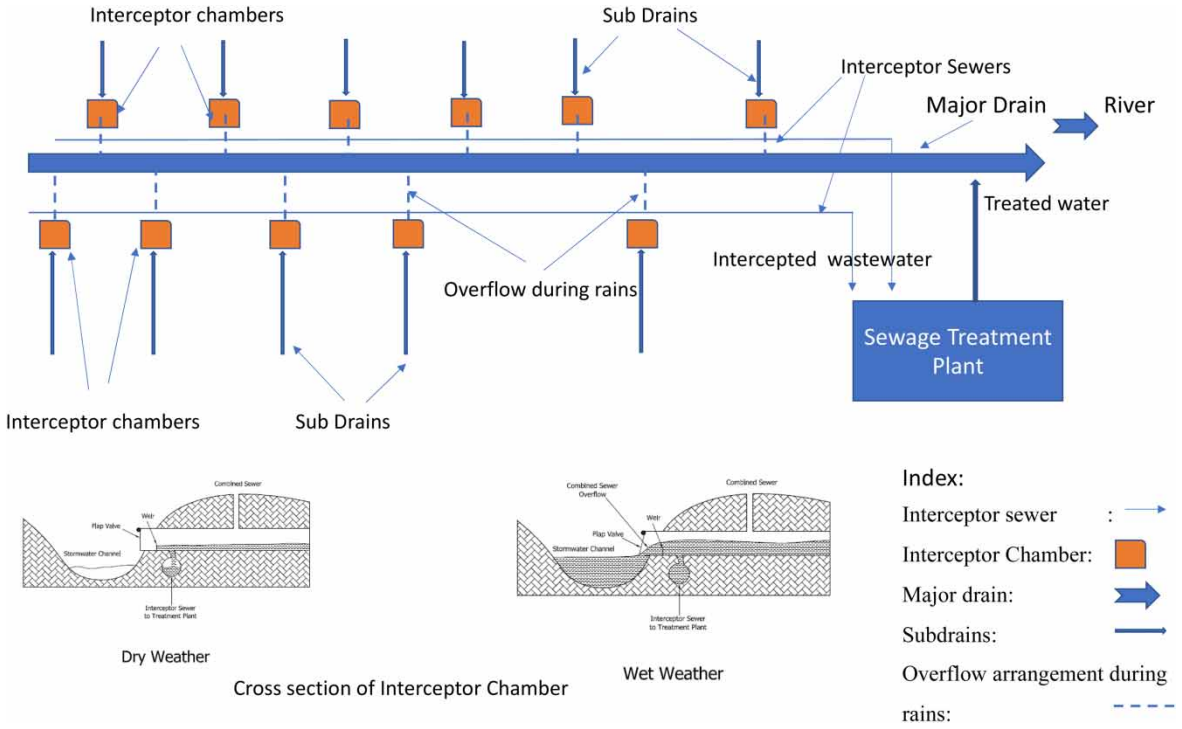


Figure 3 | Wastewater flow arrangement of the interceptor sewer.

management practices are measures that contribute to improve or safeguard the condition of the receiving sub drains (Rathnayake & Tanyimboh 2015). In addition, simplified hydraulic models as in other studies (Meirlaen *et al.* 2002; Gernaey *et al.* 2006) are used, which are accurate and are computationally very demanding (Tavakol-Davani *et al.* 2016).

4.1. Pre-feasibility report

The Delhi Jal Board conducted the pre-feasibility report before the preparation of a detailed project report (DPR) (EIL 2008) including demarcation of the alignment of the interceptor sewer (IS) along the portion of the major drains to intercept the sub drains and to convey trapped sewage into the nearest STP; A topographical survey along the proposed alignment of the interceptor sewer and up to 1 km of each sub drain; Soil investigation to find the water table, soil profile, and bearing capacities up to 50 m depth of the average ground level; proposed L-section of the interceptor sewer alongside drains; Locations of intercepting chambers and manholes; Measurement of dry weather flow in all the sub drains proposed to be trapped into the interceptor sewer; Collection of wastewater samples from the sub drains and major drains to find out the water quality, and subsequently, decide the best sewage treatment technologies; Encroachment observation, if any, along and across the alignment of the entire interceptor sewer; and Title and ownership of the land coming across the proposed alignment of the interceptor sewer along the major drains.

4.2. Methodology of construction and monitoring mechanism

The methodology adopted in the construction of this entire project was the state-of-art. Modern technology, i.e., micro tunneling has been adopted in laying the sewer line and in the construction of lift stations and interceptor sewer chambers (Supplementary material, Figure S3). The entire length of the interceptor sewer has been laid through the micro tunneling method, causing minimum nuisance to the public and nearby structures. In fact, the micro tunneling method is costlier, but it is a better option in terms of social and environmental conditions, which cannot be worked out in terms of money, as it does not obstruct the movement of traffic and prevent environmental pollution. It also saves the cost of cutting of roads and their restoration. All the lift stations were constructed from top to bottom, which eliminated wider excavation and collapse of trenches. The big interception chamber has been provided with mechanical screening and scrapers to remove the floating material to

Downloaded from http://iwaponline.com/wpt/article-pdf/doi/10.2166/wpt.2024.005/1356305/wpt2024005.pdf
by DELHI TECHNOLOGICAL UNIVERSITY (DTU) user

corrected Proof

avoid the chocking of sewer lines. Since most of the construction work of the interception chambers was carried out within the bed of drains, balloon types of cofferdams were used for the diversion of the flow of drains.

To ascertain the timely construction of this project, there was a three-tier monitoring mechanism, i.e., Project Monitoring Committee headed by a member (technical) to monitor the monthly progress as per the bar chart and coordination among various departments, the Project Monitoring Unit headed by the Chief Executive Officer, Delhi Jal Board to ascertain the smooth flow of funds as required, to complete the project in time, and the Apex Committee headed by the Chief Secretary, Delhi, once in 3 months, to monitor the progress and resolve the issues pending with other departments of Delhi.

4.3. Works awards in six packages for fast completion of work

The entire work was divided into six packages with the following scope of work as summarized in Table 3. Thus, the work on all the segments could be started simultaneously and completed as early as possible in a time-bound manner. The packages were divided in such a manner that every package was linked with a particular sewage treatment plant (Supplementary material, Figure S4).

Table 3 | Package-wise length of interceptor sewer, number of intercepting chambers, and names of the associated STPs

Pack No.	Package description STP	Intercepting chamber no.	Interceptor sewers Dia, mm	Total interceptor sewers, Approx. meters
1	Dwarka	3	900–1,600	2,252
2	Nilothi/Keshopur	40	900–1,600–2,000–2,400	23,400
3	Coronation Pillar	35	900–1,600–2,000–2,400	11,865
4	Rohini/Rithala	19	900–1,600	4,880
5	Yamuna Vihar	16	900–1,600–2,000	6,028
6	Kondli	19	900–1,600–2,000–2,400	11,790

4.3.1. Interception of remaining drains

Apart from the above three major drains, the Delhi Jal Board took the initiative to trap the following drains into the nearby sewerage systems or set up STP at the mouth of drains: Magazine Road Drain, Sweepers Colony Drain, and Khyber Pass drains. These three drains have been trapped at the Arunanagar sewage pumping station, and sewage is pumped to the Oklha STP through the Nigam Bodh SPS and the Ring Road Trunk sewer. Metcalf House Drain: The connection of the drain to the Bela Road Sewer was not technically feasible. Hence, a small pump house near the drain has been constructed and is being pumped to the Bela Road Trunk sewer. Qudesia Bagh Drain: Not much discharge in the drain, as Masonic Club has shifted its connection to the Bela Road sewer. Mori Gate Drain: The Delhi Jal Board has proposed an STP of 45 MLD capacity at the outfall point and asked the Delhi Development Authority to allot the land. Tonga Stand Drain: Partially trapped into the Nigam Bodh pumping station. Civil Mill Drain: Very low discharge, and the drain has been connected to the Ring Road sewer. Delhi Gate Drain: An additional STP of 68 MLD was constructed and commissioned in 2015, in addition to the existing 10-MLD capacity STP to treat the entire discharge of the drain. The Sen Nursing Home Nalah + Nalab 12A: 10 MLD is being treated at STP at its mouth and remaining trapped in the Ring Road sewer. Drain No. 14: The drain has been trapped in the Ring Road sewer. Barapula Drain: Barapula Drain is also one of the big drains which starts from Meharoli Badarpur road and, after traversing the entire south Delhi and receiving the discharge of hundreds of sewered and unsewered colonies, meets with Yamuna near Sarai Kalekhan. The Delhi Jal Board ultimately has proposed setting up 180 MLD STP at the mouth of this drain to treat wastewater of the Barapula Drain. Maharani Bagh Drain: Partially trapped in the existing sewer. Kalkaji Drain: Trapped in the existing sewer. Tehkhand Nalah: Not feasible for trapping. Tughlakabad Drain: Trapped.

4.3. Advantages and anticipated outcome of interceptor sewer concept

After completion of this project, no untreated wastewater will enter the waterbodies, i.e., drains and rivers. The sewage coming from unsewered colonies, slums, etc., will be trapped at the source and diverted to the nearest STPs. Hence, only treated effluent will be allowed to flow into the drains that are out falling into the river at present; thus there is a reduction in the pollution of river water. New STPs would be constructed only after utilizing

Downloaded from http://iwaponline.com/wpt/article-pdf/doi/10.2166/wpt.2024.005/1356305/wpt2024005.pdf
by DELHI TECHNOLOGICAL UNIVERSITY (DTU) user

corrected Proof

the existing unutilized STPs, which will reduce the project costs. It was anticipated that hardly new STPs of 318 MLD capacities would be required after successfully commissioning the interceptor sewer. The interceptor sewer has been designed to cater to the dry weather flow of the sub drains and a maximum of up to 80% of water supplied at 272 LPCD (sewage generation as per CPHEEO norms) of the total population under the catchment of the drain. The provisions of overflow structure of surplus discharge during rains shall be made in such a manner that excess water during rains will flow directly into the major drains instead of going to the interceptor sewer. It will avoid the overburden of sewage at all respective STPs during rains. During the conceptualization of the interceptor sewer project and allied works, river quality modeling was conducted, and it predicted the improvement in the quality of river water as in Figure 4.

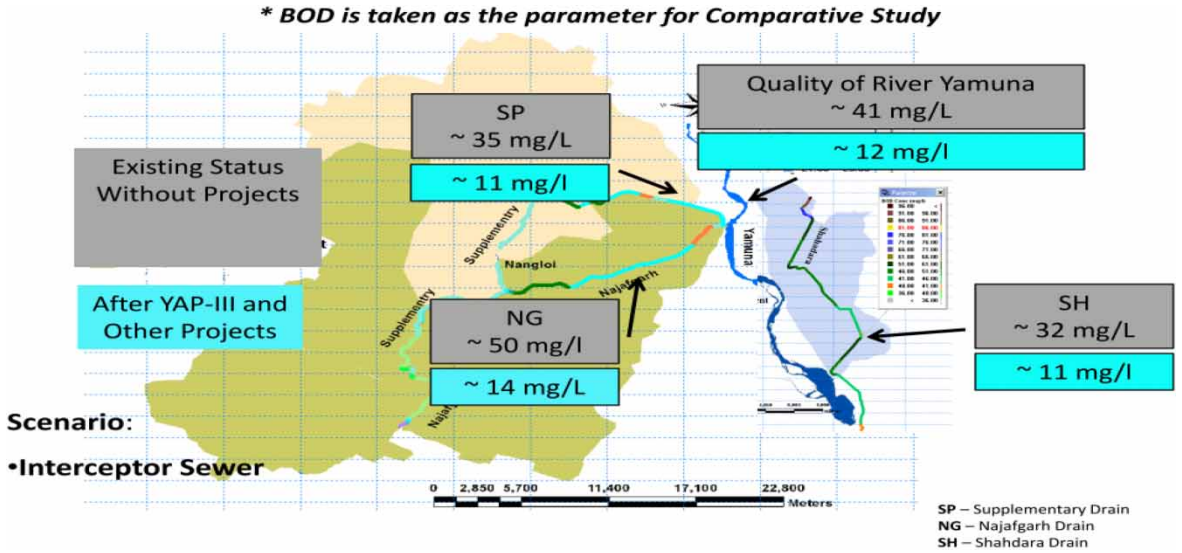


Figure 4 | Anticipated quality of river Yamuna after the implementation of the interceptor project.

Since the interceptor sewer has been completed to the extent of 99%, the quality of water in river Yamuna has been improved as per the CPCB report 2020–21(CPCB 2021) (Table 4). River water quality at the Nizamuddin bridge was most critical from 2008 onward, i.e., more than 40 ppm, which was found to be 26 ppm (Average) in September 2021, after the completion of the interceptor sewer. Near the Okhla Bridge, the BOD was reduced from 32 ppm (In 2008) to 11 PPM in 2021 which is close to the forecast in 2008. River water quality could be

Table 4 | Quality of river water in September 2021, after commissioning of the interceptor sewer

Location parameters	Wazirabad (u/s)	ITO	Nizamuddin bridge	Okhla barrage (d/s)
pH	7.7	7.2	7.2	7.4
Dissolved oxygen (mg/l)	8.0	Nil	Nil	5.6
Conductivity (μohm/cm)	483	1,070	1,069	967
Chemical oxygen demand (mg/l)	27	45	52	37
Biological oxygen demand (mg/l)	4.9	12	15	11
Chloride (mg/l)	53	155	157	132
PO_4-P (mg/l)	BDL	0.4	0.4	0.8
Anionic surfactant-MBA (mg/l)	BDL	1.28	1.23	1.37
Ammonical nitrogen-N (mg/l) (mg/l)	2.6	4.6	9.7	9.8
Total coliform (MPN/100 ml)	13×10^2	54×10^5	24×10^5	14×10^5
Fecal coliform (MPN/100 ml)	45	33×10^4	41×10^4	26×10^4

Downloaded from http://iwaponline.com/wpt/article-pdf/doi/10.2166/wpt.2024.005/1356305/wpt2024005.pdf
by DELHI TECHNOLOGICAL UNIVERSITY (DTU) user

corrected Proof

much improved with the release of adequate freshwater from the Wazirabad Barrage for dilution. These efforts are not adequate until various stakeholders continue to work jointly together to prevent pollution in the Yamuna River by treating sewage and industrial waste as per the new quality standards, proper solid waste management, and discharge of ecological flow in the river round the year (Figure 5).

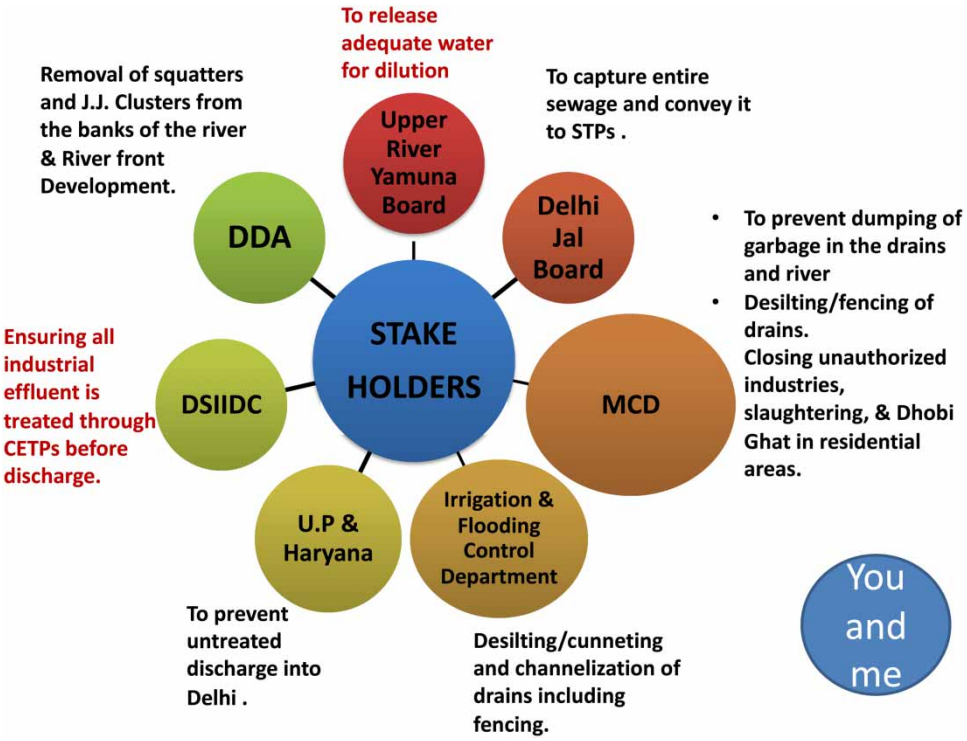


Figure 5 | Stakeholders responsible for improvement in water quality of the Yamuna River.

5. DISCUSSION

DO is necessary for aquatic life which is largely sensitive to changes in the BOD load. The larger the BOD, the lower will be the DO, which results in an anaerobic reaction and production of obnoxious gases. The data of CPCB shows that a higher BOD and a lower DO are present between Wazirabad and Okhla Barrages. Even if Delhi has 100% treatment capacity with treatment standards of BOD < 30 PPM at all STPs, the BOD in the above stretch is more than 12 PPM (Singh *et al.* 2019). The trend of river water quality for the last 12 years shows that the river water quality in terms of BOD reduced in 2012–13, but it started to rise again thereafter till 2018, and reached up to 60 ppm, but the minimum BOD remained constant. The BOD in river water again reduced for one year in 2019, but it started rising again. From 2020 onward, the interceptor sewer was commissioned in phases. Consequently, the maximum BOD in river water started to reduce and reached up to 26 PPM (Figure 6). However, bathing quality in rivers requiring BOD < 3 mg/L and DO > 4 mg/L can only be achieved after dilution with adequate fresh water if released from upper storage dams of river Yamuna and upgradation of all STPs as per the standard prescribed by CPCB for sewage treatment standards. The quantity of freshwater to be released into the downstream of the Wazirabad Barrage to attain the bathing water quality in river Yamuna is still to be worked out. It is also not clear whether all the basin states will agree to spare their shared water to be released into the river compromising their drinking, agricultural, and industrial water demands. The Hon'ble National Green Tribunal (NGT) has ordered the release of only 10 m^3 per second of freshwater at the downstream of the Tajewala Barrage, which is insufficient even for the ecological flow of the river.

The interceptor sewer has been designed to take care of the wastewater of the drains within the territory of NCT Delhi. But a huge quantity of wastewater is also coming from the neighboring states, i.e., Haryana and U.P. The Badshapur Drain from Gurugram carries around 400–450 MLD of wastewater and discharges into the Najafgarh drain. Similarly, drain No. 6 coming from the industrial areas of Samalkhan, Haryana also carries

Downloaded from http://iwaponline.com/wpt/article-pdf/doi/10.2166/wpt.2024.005/1356305/wpt2024005.pdf
by DELHI TECHNOLOGICAL UNIVERSITY (DTU) user

corrected Proof



Figure 6 | Trend of BOD for the last 12 years in the Yamuna River near the Nizamuddin bridge, Delhi.

around 45–50 MLD of wastewater and discharges into the supplementary drain in Delhi. Khureji Khas, Loni Road, and Sahibabad drains carry approximately 270–320 MLD of wastewater from U.P. and discharge into the Shahdara Drain. The respective states must treat the wastewater from these drains before discharging it into Delhi's drains to further improve the quality of river water.

Interceptor sewers will take care of only 75% of the total pollution load in river Yamuna, i.e., North, West, and East Delhi's drains. Delhi must prepare a separate plan for trapping wastewater discharges from the remaining drains and finally implement the DSMP 2031, which is the ultimate solution to prevent sewage flow into water bodies.

It is also observed that the interceptor sewer project has been completed to the extent of 99%. Around 1,080 MLD of wastewater has been intercepted and around 500 MLD of greywater still flow into rivers through drains due to unsewered areas in South Delhi. Besides, the residents have not connected their greywater disposal arrangement with the Delhi Jal Board sewer. Hence, greywater also flow into the drains and finally into rivers. Three STPs, i.e., Kondli (205 MLD), Rithala (182 MLD), and Okhla (563 MLD) are being rehabilitated and ungraded. By the time these STPs are commissioned, the sewage trapped in these plants cannot be treated. After commissioning of these plants, the quality of river water will further improve. Delhi must upgrade all remaining STPs to the treatment standard as prescribed by CPCB to achieve the desired river water quality standards.

Sewage reaching STPs is not purely domestic sewage. It is mixed with industrial waste coming from non-conforming industries illegally set up in residential areas. Hence, many times, the treatment process of sewage is affected, and the results do not meet the desired/designed standards. The disposal of sludge from STPs is also a major challenge. The Delhi Municipal Corporation does not allow sludge at their Sanitary Land Fills (SLFs), as they have exhausted their capacities at all SLFs. Hence, digested sludge is stacked either at STPs itself or disposed of as per the goodwill of the contractors engaged in disposing of silt/sludge, which also affects the treatment process.

6. CONCLUSION

The interceptor sewer project is one of the robust solutions to reduce the organic (BOD) and pathogenic (coliforms) pollution in the river Yamuna. Around 1,080 MLD of wastewater has been trapped from interceptor sewers against the targeted 1,100 MLD and is being treated at the respective STPs, which has improved the quality of river water to some extent, as anticipated. If dilution is not possible, the quality of the treated effluent will have to be of tertiary standards. Thereafter, the quality of river water will further improve by a natural self-cleaning process while traveling in the drains and rivers for miles together. After improvement of water flowing in the

Downloaded from http://iwaponline.com/wpt/article-pdf/doi/10.2166/wpt.2024.005/1356305/wpt2024005.pdf
by DELHI TECHNOLOGICAL UNIVERSITY (DTU) user

corrected Proof

drains and rivers, groundwater quality will also improve, thus adding a source of groundwater in the future. However, the success of the interceptor sewer depends on the lateral coordination and cooperation of various stakeholders. All the above departments, being under different authorities and governments must come under one umbrella to monitor the progress of the projects undertaken by the respective departments and to direct the respective authorities appropriately. The regulating authorities, i.e., CPCB and DPCC, must monitor river water quality at regular intervals and pass the instructions to the concerned authorities appropriately. Thus, this concept can be replicated anywhere globally. However, the quantity of freshwater availability for dilution will ensure whether the bathing quality of river water can be achieved or not. After cleaning river water to bathing quality, the same can be utilized as raw water at water treatment plants. This study is not limited to the NCT of Delhi, but can be replicated elsewhere in India and abroad, for the abatement of pollution in surface water. The concept and methodology may little bit differ for different towns or cities, depending on their geographical and hydrological conditions.

DATA AVAILABILITY STATEMENT

All relevant data are included in the paper or its Supplementary Information.

CONFLICT OF INTEREST

The authors declare there is no conflict.

REFERENCES

Chandramouli & GR 2011 *Census of India 2011. Provisional population totals*. New Delhi; Govt. of India.

CPCB 2004 *Annual Report_9, 2004–2005*. CPCB Report.

CPCB 2013 *Performance Evaluation Report of STPs*.

CPCB 2021 *Study Group Report on Increase of Pollution in River Yamuna*. Central Pollution Control Board, CPCB.

Delhi Jal Board 2015 *Delhi Sewerage Master Plan 2031*. Delhi.

EIL 2008 *Detail Project Report Interceptor Sewer*. Delhi.

Gernaey, K. V., Rosen, C. & Jeppsson, U. 2006 WWTP dynamic disturbance modelling – an essential module for long-term benchmarking development. *Water Sci. Technol.* **53**, 225–234. doi:10.2166/wst.2006.127.

Hima Jwala, V., Rao, P. B. & Agrawal, S. 2020 Performance study on sewage treatment plants in Delhi based on adopted advanced technologies. *Pollution Res.* **39**, 1017–1025.

Kaini, P., Artita, K. & Nicklow, J. W. 2012 Optimizing structural best management practices using SWAT and genetic algorithm to improve water quality goals. *Water Resources Management* **26**, 1827–1845. https://doi.org/10.1007/s11269-012-9989-0.

Karovic, O. & Mays, L. W. 2014 Sewer system design using simulated annealing in excel. *Water Resources Management* **28**, 4551–4565. https://doi.org/10.1007/s11269-014-0750-8.

Kumar, R. & McMasters, F. 2017 Planning and design of sewerage infrastructure for a congested area in Delhi: A case study towards pollution abatement in River Yamuna. *Pipeline* **2017**, 249–260.

Kumar, M., Sharif, M. & Ahmed, S. 2020 Impact of urbanization on the river Yamuna basin. *International Journal of River Basin Management* **18**, 461–475. https://doi.org/10.1080/15715124.2019.1613412.

Meirlaen, J., Van Assel, J. & Vanrolleghem, P. A. 2002 Real time control of the integrated urban wastewater system using simultaneously simulating surrogate models. *Water Sci Technol.* **45**(3), 109–116.

Ministry of Environment and forest GOI 2001 *Delhi Urban Environment and Infrastructure Improvement Project (DUEIIP) 'DELHI 21'*. MoEF.

Nallathiga, R. 2008 *River Water Conservation Through Management Interventions: A Case Study of Yamuna Action Plan in India*. Integrated environmental and economic accounting in NCT-Delhi View project Land use regulation impacts on cities and land markets View project. https://www.researchgate.net/publication/263363809.

Paliwal, R., Sharma, P. & Kansal, A. 2007 Water quality modelling of the river Yamuna (India) using QUAL2E-UNCAS. *J Environ Manage* **83**, 131–144. https://doi.org/10.1016/j.jenvman.2006.02.003.

Rathnayake, U. S. & Tanyimboh, T. T. 2015 Evolutionary multi-objective optimal control of combined sewer overflows. *Water Resources Management* **29**, 2715–2731. https://doi.org/10.1007/s11269-015-0965-3.

Sharma, D. & Singh, R. K. 2009 DO-BOD modeling of River Yamuna for national capital territory, India using STREAM II, a 2D water quality model. *Environ Monit. Assess.* **159**, 231–240. https://doi.org/10.1007/s10661-008-0625-7.

Sharma, R., Kumar, R., Satapathy, S. C., Al Ansari, N., Singh, K. K., Mahapatra, R. P., Agarwal, A. K., Van Le, H. & Pham, B. T. 2020 Analysis of water pollution using different physicochemical parameters: A study of Yamuna River. *Front Environ Sci* **8**, 581591. https://doi.org/10.3389/fenvs.2020.581591.

Singh, A. P., Dhadse, K. & Ahalawat, J. 2019 Managing water quality of a river using an integrated geographically weighted regression technique with fuzzy decision-making model. *Environ Monit Assess* **191**, 378. https://doi.org/10.1007/s10661-019-7487-z.

Downloaded from http://iwaponline.com/wpt/article-pdf/doi/10.2166/wpt.2024.005/1356305/wpt2024005.pdf
by DELHI TECHNOLOGICAL UNIVERSITY (DTU) user

corrected Proof

Tavakol-Davani, H., Burian, S. J., Devkota, J. & Apul, D. 2016 Performance and cost-based comparison of green and gray infrastructure to control combined sewer overflows. *J Sustain Water Built Environ* **2**, 04015009. https://doi.org/10.1061/jswbay.0000805.

Thomas, N. S., Templeman, A. B. & Burrows, R. 2000 Pollutant load overspill minimization of interceptor sewer systems. *Engineering Optimization* **32**, 393–416. https://doi.org/10.1080/03052150008941306.

Thomas, N., Burrows, R., Templeman, A. & Najafian, G. 2004 Optimal pollution control for management of large interceptor sewer systems. *Urban Water J* **1**, 235–250. https://doi.org/10.1080/15730620410001732008.

Upadhyay, R., Dasgupta, N., Hasan, A. & Upadhyay, S. K. 2011 Managing water quality of River Yamuna in NCR Delhi. *Physics and Chemistry of the Earth* **36**, 372–378. https://doi.org/10.1016/j.pce.2010.03.018.

Xue, X., Hong, Y., Limaye, A. S., Gourley, J. J., Huffman, G. J., Khan, S. I., Dorji, C. & Chen, S. 2013 Statistical and hydrological evaluation of TRMM-based multi-satellite precipitation analysis over the Wangchu Basin of Bhutan: Are the latest satellite precipitation products 3b42v7 ready for use in ungauged basins? *J Hydrol.* **499**, 91–99. https://doi.org/10.1016/j.jhydrol.2013.06.042.

First received 12 October 2023; accepted in revised form 13 December 2023. Available online 16 January 2024

Downloaded from http://iwaponline.com/wpt/article-pdf/doi/10.2166/wpt.2024.005/1356305/wpt2024005.pdf
by DELHI TECHNOLOGICAL UNIVERSITY (DTU) user

IOT BASED SANITIZATION ROBOT USING RASPBERRY PI ZERO W AND UV LAMP

B Revanth Raj, Abhishek Sahani, Ravi Yadav
Mechanical Engineering with Specialization in Automobile Engineering
Delhi Technological University
Corresponded author: revanthraj3206@gmail.com

Abstract
As that's not simple to sanitise treatment room simply physical endeavour. It raises increasing risk of disease, allowing hazardous bacteria to propagate even deeper. Ultraviolet beams are being used by Ultraviolet sterilisation robotic to eliminate microbes. The live stream broadcast of the creature's environment is indeed possible. They may operate these robots through Internet, but also its Interface enables everyone to operate inside a waiting area while having to really be actually present. Most of this allows us both to sterilise the maternity ward to their specifications. Ultraviolet light kills bacteria, preventing them from multiplying by disrupting its fertility.

I. INTRODUCTION
Another purpose of green hygiene inside a surgical procedure or a client bed is really to limit germs, especially substance germs, to that of a bare max in establishing as maintaining a safe workplace for both service user and service professional.
People’s future effectively have changed dramatically as a result of something like the COVID-19 virus, but the only method to avoid this diseases from spreading further is to keep good distance as well as obey the standards set out by our individual governments. Sanitation hygiene sterilization, in particular, was becoming unrecognizable part of people's daily lives. When it comes to proper cleaning but instead sterilization, there is indeed a concern: we didn't effectively participate in the filtration even though we risk contracting a fatal disease first from polluted site. However, we could really mitigate this issue by creating a robust, productive, as well as fully independent automaton which could sterilize an area quickly often without uncovering ourself. Computers would be used in a variety of situations whereby people may be exposed. This, in just this article, we'll create an optical sterilization robot which can destroy viral coronavirus inside a facility and residential complex, but we'll use a Nintendo, several Ultraviolet light Lights, plus laser scanners to use it.

II. BACKGROUND
Currently, surgical room viruses account for 14-17% of all pathogens, whilst hospitalized diseases account for 38% of all pathogens.
As a result, regular procedural as well as postoperative scrubbing of an OR atmosphere are among the most efficient aseptic techniques for reducing the number of germs, pollen, as well as green matter in the area.

Nonetheless, because there are numerous blind spots especially unattainable regions including the interior surfaces, typical wiping routine using clean supplies for humans alone will not been capable of minimizing the quantity of these germs. A form of uv – is (uv light) has just been discovered that might help physicians in their continuing struggle to prevent bacteria in remaining in health care facilities as well as creating additional diseases.

This is a worldwide problem. Humankind has really been delayed by the influenza epidemic and quarantine. That concern of contagion from not just immediate communication but then also items believed to already be encountered by sick people had contributed to its use of anionic surfactants to disinfect packs, vessels, or even veggies. It's worth noting that ingesting dishwashing plus related compounds might cause issues for the female organism. As a result, programmed cleaning machines are needed to transport the envelopes to be sterilised on just a production line from the entering endpoint, keep those underneath Ultraviolet light for a defined amount of time, and thereafter transport out towards the output close. This mechanism will prevent washing up liquid and some other similar chemicals from accessing your female beings. The conveyor belt movement will be controlled by sensing at the entering endpoint, its storage point (within the cage), and the discharge end. During sterilization of items encased in packaging, comparable technologies will also be required in massive amount in multiple kinds of production modules, markets, and supermarkets. To just that aim, proper regulations will just be designed to incorporate conveying belts movements, Ultraviolet light bulb operation, and programmed packet/goods retention duration via device.

III. METHODOLOGY

In this chapter the block diagram of the project and design aspect of independent modules are considered. Block diagram is shown in fig.1.

Arrange all or most of the equipment on the quad rotor (UV LED, Raspberry Pi zero W, a wind turbine with batteries, Pi camera, Motor Driver) but then place your Ultraviolet rays on top of the machine. Place the Micro - controller on ahead of robotic so that the video can see why this’s next to it effectively. Later, utilizing VNC, access its window on either a faraway Computer or cell phone, and execute your Interface. The Microcontroller Board is connected to an Electric Controller in the usual sequence.

The project aims in designing a robot which is capable of monitoring and controlling from remote place. It switches on the UV lamp through which UV rays are emitted and also sanitize the surroundings. **Ultraviolet-C** Radiation, Disinfection, and Corona virus has given the current outbreak of Corona virus Disease. As there is no vaccination on the marketplace, the first and only way to survive is to take the necessary measures. It is recommended to sterilise the environment to assist slow the transmission of infection because the virus is communicated mostly by particles that arise from an affected user's nasal passage while sneeze or cough. To address these issues, we created a sanitization robot powered by a Raspberry Pi and equipped with a UV lamp. This is the internet of things (IOT) based project, where we are particularly uses the Raspberry Pi, pi camera, sanitizer ,UV lamp along with relay driver and two DC motor along with l293d motor driver with Robot chassis to build this Robotic car setup. It has a pi camera mounted over it, through which we will get live video feed and the interesting part here

is that we can control and move this robot from a web browser over the internet. The Pi cam will capture live data with regards to its surroundings and then send it to a particular IP address through internet. The user will be observing this live streaming on the mobile and according to that the user will control the robotic vehicle through the webpage and as well as control the sanitizer and UV lamp from the web page .Here relay likes as a switch to on and off the sanitizer and UV lamp.12v, 2ah battery and power bank are used to give the power supply of the robot and raspberry pi. The main controlling device of the project is raspberry pi.

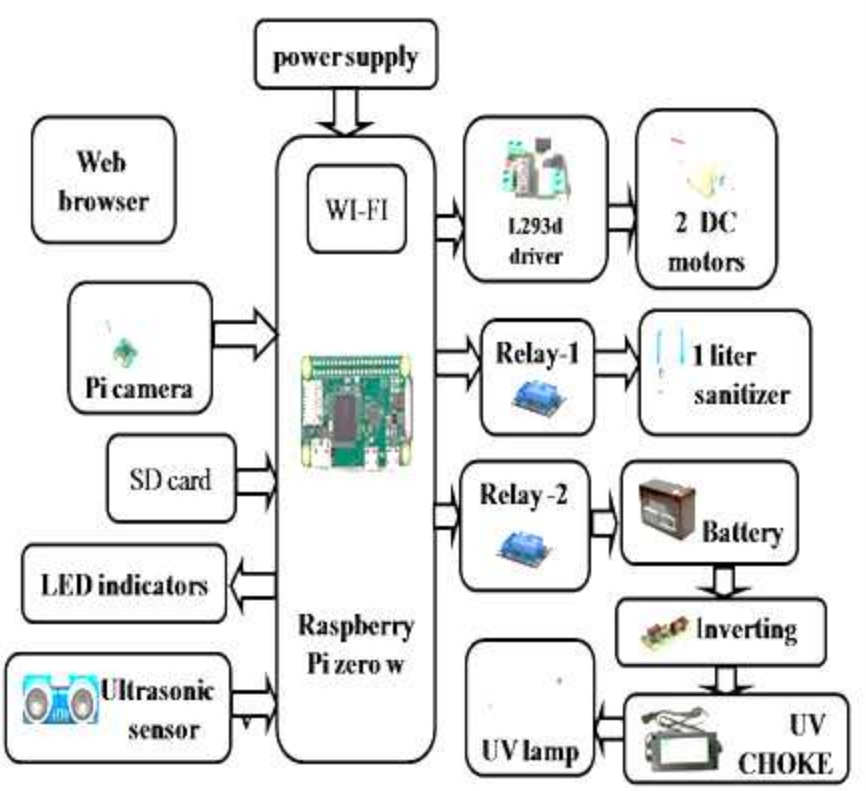


Fig 3.1: Block diagram of IOT based sanitization robot using Raspberry pi zero w and UV lamp

Hardware description

ARM processor

The Raspberry Pi Zero features a **BCM2835 chipset**, overclocked to 1 GHz with **512MB RAM**, and the same **1080p video output,** so there's plenty of oomph in that little board. It also features the same 40 pin GPIO layout as the Raspberry Pi 2/B+/A+, which you'll need to solder your own headers too. With its small form factor and reduction in connectors, the Raspberry Pi Zero **only uses ~ 140mA at 5V.**

Power supply

An AC adapter, also known as an AC/DC adapter or an AC/DC converter, is a form of external power source that is usually housed in a case that looks like an AC socket. Electrical equipment that run on electricity but doesn't have internal parts to extract the appropriate electrical power

and voltage from main grid are connected to AC adapters. An auxiliary power supply's internal circuitry is remarkably similar to the architecture of an internal power source.
External power sources should be used with technology and has no other power source as well as rechargeable batteries device, where the source could sometimes charge batteries as well as power the device when plugged in.
The need for an external power source permits battery-powered technology to be portable without any of the additional size of internal elements, and it eliminates the need to design electronics for utilization with a particular propulsion system.

UV LEDS

LEDS (Light Emitting Diode) that generates uv rays is a kind of infrared energy with wavelengths ranging from 10 (with just a velocity of roughly 30 PHz) to 400 nm (750 THz), which is longer than visible region. UV For high antimicrobial treatment, an uv - b spectrum with in spectrum of 100-400 nanometers is used. Radiation from the sun (200–280 nm), which itself is deemed the much more high antimicrobial wavelengths region based on its ability to inhibit the growth bacteria, is perhaps the most high antimicrobial wavelengths spectrum.

DC motor

The DC motor has two basic parts: the rotating part that is called the armature and the stationary part that includes coils of wire called the field coils. The stationary part is also called the stator. Figure shows a picture of a typical DC motor, Figure shows a picture of a DC armature, and Fig shows a picture of a typical stator. From the picture you can see the armature is made of coils of wire wrapped around the core, and the core has an extended shaft that rotates on bearings. You should also notice that the ends of each coil of wire on the armature are terminated at one end of the armature. The termination points are called the commutator, and this is where the brushes make electrical contact to bring electrical current from the stationary part to the rotating part of the machine.
The DC motor you will find in modem industrial applications operates very similarly to the simple DC motor described earlier in this chapter. Figure 12-9 shows an electrical diagram of a simple DC motor. Notice that the DC voltage is applied directly to the field winding and the brushes. The armature and the field are both shown as a coil of wire. In later diagrams, a field resistor will be added in series with the field to control the motor speed.
When voltage is applied to the motor, current begins to flow through the field coil from the negative terminal to the positive terminal. This sets up a strong magnetic field in the field winding. Current also begins to flow through the brushes into a commutator segment and then through an armature coil. The current continues to flow through the coil back to the brush that is attached to other end of the coil and returns to the DC power source. The current flowing in the armature coil sets up a strong magnetic field in the armature.

Motor driver

It's an embedded system semiconductor that's utilized in humanoid systems as well as embedding electronics to regulate motors. A motor driver is unquestionably anything that causes the machine to operate in accordance with the provided commands or impulses (high

and low). It takes its low power first from gamepad as well as uses that to operate a real engine that possesses a minimum power factor.

Pi camera

The Camera Unit can record high-definition videos along with taking still photos. It has video modes of 1080p30, 720p60, and VGA90, as well as always capturing. It connects to the Raspberry Pi's CSI port via a 15cm ribbon wire.

The camera is made up of a compact circuit board (25mm by 20mm by 9mm) that uses an adaptable ribbon connection to interface to the Raspberry Pi's Camera Serial Interface (CSI) bus socket. The camera's image detector is a fixed focus aperture with a native sensitivity of five megapixels. The camera's software allows still photographs up to 2592x1944 pixels and video resolutions of 1080p30, 720p60, and 640x480p60/90 pixels.

Desired specifications of the project

- The tank capacity of the Sanitizer that can be loaded is 150ml.
- The tube length of UV light designed is about 25cm.
- The Sanitizer Density is measured to be 0.90g/mL.
- The Speed obtained is 5meter/ Sec.

The brightness and time of the UV light is expressed as follows,

Brightness = Luminosity / (4Π * Distance^2)

Time = UV dose / Brightness

UV dose - $\mu Ws / cm^2$

Brightness – W / cm^2

Brightness = 15 * 4W / (4Π * 25^2) = 6W / 7853.98 cm^2

= 76.3 $\mu W / cm^2$

Thus the brightness produced by the desired project is also obtained.

Viscosity affecting the flow rate

The viscosity of a substance can alter due to a variety of circumstances, including temperature, humidity, and conditioning. A substance that performs properly in the lab could have a completely different viscosity when it exits an extreme temperature manufacturing process. If Carbopol is replaced with a green environmentally substitute, a Carbopol-based product that thins when it comes into touch with salt on the skin may lose this property.

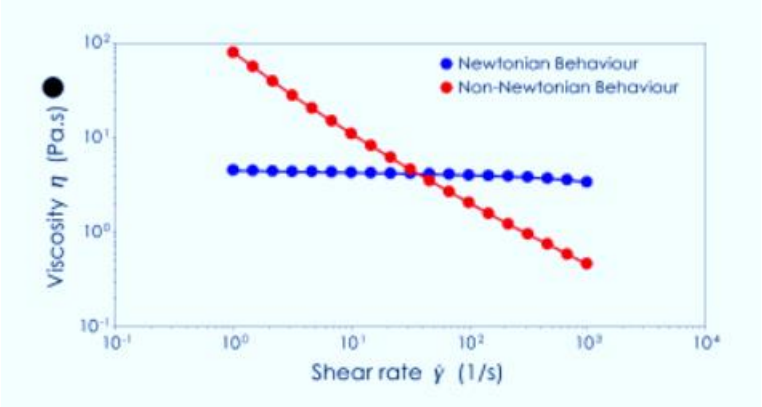


Fig.1.Viscosity of the sanitizer

The sanitizer exhibits a non - newtonian behavior, when the viscosity increases the shear rate decreases. When the viscosity increases the flow rate decreases. Thus the pressure or the force applied has to compensate to proceed with the appropriate flow rate.

IV. RESULT

This robotic can prevent injury as well as navigate about the environment unique combination of either a webcams video as well as lidar. This Ultraviolet robot has airspeed of 5 metres per second and therefore can run for 30-45 minutes on a charge without connected to with a plug socket. Hand wash Machine's Light source disinfected the majority of bacteria inside the environment, if not all. In the specified region, while there were some innocuous, quasi bacteria.

V. CONCLUSION

The above research provides a detailed assessment of robots' possibilities in biology as well as related fields, with either a focus on COVID-19 catastrophe containment. As seen in the epidemic, competent COVID-19 care can drastically limit the amount of people with the disease and casualties. Because it has now become a worldwide problem, technology driven governments may help others by giving weapon systems including automated infrastructures to ensure a successful management of the illness. Cost of health care digitalization, this analysis justifies that the adoption of medical robots had considerably improved both health of the patient’s security solutions due to manual methods. Surgical drones typically solely classified employing implementation subcategories to accommodate everything part of inpatient services, including load balanced supervision but also stable infrastructures for consistent as well as took place in order inside medical institutions.

VI. FUTURE WORK

To create the robotic smart sufficiently to prevent collisions and some other costly healthcare apparatus while efficiently disinfecting everything and every part of something like the facilities, remote sensing techniques were added to that same robotic as well as excellent charting was used with the assistance of Learning Algorithms. This will also assist in instantaneous going to charge and destination via a Photovoltaic Solar Car Charger. A autumn

technology, comprised of a camcorder and a 3D Digitizer, is included in the creature's primary functionality to recognise people who already have fallen asleep. The robot can alert health workers in the case of a serious situation involving a client recognised by the wearable sensors as well as continuous examined closely modules.

REFERENCE

1. *Gabriele Ferri, Alessandro Manzi, Pericle Salvini,Barbara Mazzolai, Cecilia Laschi, and Paolo Dario, "DustCart, an autonomous robot for door-to-door garbage collection: from DustBot project to the experimentation in the small town of Peccioli, 2011 IEEE International Conference on Robotics and Automation, Shanghai International Conference Center, May 9-13, 2011, Shanghai, China.*
2. *Hiroo Takahashi, Kojiro Iizuka, "Analysis on Weight Arrangement Scheme to Reduce theWeight of Multi-Legged Robot Takashi Kubota",Proceedings of the 2005 IEEE International Conference on Robotics and Automation, Barcelona, Spain, April 2005.*
3. *Mahmoud Tarokh and Malrey Lee,"Kinematics Modeling of Multi-legged Robots Walking on Rough Terrain" 2008 Second International Conference on Future Generation Communication and Networking Symposia.*
4. *Himadri Nath Saha, Sourav Gon, Annesha Nayak, Samabrita kundu, Sumandrita Moitra , "IoT Based Garbage Monitoring and Clearance Alert System" 2018 IEEE 9th Annual Information Technology, Electronics and Mobile Communication Conference (IEMCON) Pages: 204 – 208.*
5. *Bharadwaj, Alok & Yadav, Divyanshu & Varshney, Shreyshi. (2015). NON-BIODEGRADABLE WASTE – ITS IMPACT & SAFE DISPOSAL. International Journal of Advanced Technology in Engineering and Science. 3. 184- 191.*
6. *Chanprakon, P., Sae-Oung, T., Treebupachatsakul, T., Hannanta-Anan, P., & Piyawattanametha, W. (2019). An Ultra-violet sterilization robot for disinfection. 2019 5th International Conference on Engineering, Applied Sciences and Technology (ICEAST). doi:10.1109/iceast.2019.8802528*

arXiv:2312.16224v1 [gr-qc] 24 Dec 2023

Joule-Thomson expansion and tidal force effects of AdS black holes surrounded by Chaplygin dark fluid

Dhruv Arora,[1,*] Muhammad Yasir,[2,†] Himanshu Chaudhary,[3,1,4,‡] Faisal Javed,[5,§] G. Mustafa,[6,7,¶] Xia Tiecheng,[8,**] and Farruh Atamurotov[9,10,11,12,††]

[1]*Pacif Institute of Cosmology and Selfology (PICS), Sagara, Sambalpur 768224, Odisha, India*
[2]*Department of Mathematics, Shanghai University, Shanghai, 200444, Shanghai, People's Republic of China*
[3]*Department of Applied Mathematics, Delhi Technological University, Delhi-110042, India*
[4]*Department of Mathematics, Shyamlal College, University of Delhi, Delhi-110032, India.*
[5]*Department of Physics, Zhejiang Normal University, Jinhua 321004, People's Republic of China*
[6]*Department of Physics, Zhejiang Normal University, Jinhua 321004, People's Republic of China*
[7]*Zhejiang Institute of Photoelectronics and Zhejiang Institute for Advanced Light Source, Zhejiang Normal University, Jinhua, Zhejiang 321004, China*
[8]*Department of Mathematics, Shanghai University and Newtouch Center for Mathematics of Shanghai University, Shanghai ,200444, P.R.China*
[9]*New Uzbekistan University, Movarounnahr street 1, Tashkent 100000, Uzbekistan*
[10]*Central Asian University, Milliy Bog' Street 264, Tashkent 111221, Uzbekistan*
[11]*University of Tashkent for Applied Sciences, Str. Gavhar 1, Tashkent 100149, Uzbekistan*
[12]*Institute of Theoretical Physics, National University of Uzbekistan, Tashkent 100174, Uzbekistan*

This study examines a recently hypothesized black hole. We study the Joule-Thomson coefficient, the inversion temperature and also the isenthalpic curves in the $T_i - P_i$ plane. A comparison is made between the Van der Waals fluid and the black hole to study their similarities and differences. The Joule-Thomson coefficient, the inversion curves and the isenthalpic curves are discussed inAdS black holes surrounded by Chaplygin dark fluid. In $T - P$ plane, the inversion temperature curves and isenthalpic curves are obtained with different parameters. Next, we explore the radial timelike geodesics that leads us to explore the tidal force effects for a radially in-falling particle in such black hole spacetime. We also numerically solve the geodesic deviation equation for two nearby radial geodesics for a freely falling particle. Our analysis shows that contrary to the Schwarzschild spacetime, the tidal forces don't become zero at spatial infinity due to the lack of asymptotic flatness because of the presence of a non-zero cosmological constant. The geodesic separation profile shows an oscillating trend and depends on the dynamic spacetime parameters q, B and Λ.

Keywords: Black Hole; Tidal Force; Thermodynamics; Joule-Thomson Expansion.

I. INTRODUCTION

The theory of general relativity has also played a crucial role in explaining the behavior of massive objects, such as black holes (BHs) and the expansion of the universe. Its predictions have been confirmed by numerous experiments and observations, solidifying its status as a cornerstone of modern physics. The physical interpretations of Einstein's gravitational field equation solutions are crucial to the development of general relativity. Therefore, the solutions to these equations and the examination of their properties are essential components of the theory of gravity. Every gravitational solution contributes significantly to our understanding of spacetime and gravity. Furthermore, the investigation of high-dimensional gravitational solutions advances our knowledge of the dimensional dependence and stability of gravitational characteristics in spacetime. The exact solution of Einstein field equations referred as BH is a direct outcome of the theory of general relativity. The event horizon of BH behaves as a barrier that distinguishes between the interior and exterior regions of a BH. Once particles traverse this barrier, their escape becomes impossible. In the last several decades, a significant body of research [1–3] has demonstrated a fundamental and crucial correlation between BHs and general thermodynamic systems. Additionally, BHs may be seen as thermodynamic systems with measurable temperature and entropy. Consequently, the existence of BHs has a profound

* arora09dhruv@gmail.com
† yasirciitsahiwal@gmail.com
‡ himanshuch1729@gmail.com
§ faisaljaved.math@gmail.com
¶ gmustafa3828@gmail.com
** xiatc@shu.edu.cn
†† atamurotov@yahoo.com

influence on our comprehension of quantum gravity, as evidenced by scholarly works [4–7].

Enormous scholarly attention has been dedicated to investigating the thermodynamic characteristics of BHs following a substantial period of scientific advancement. This encompasses inquiries into the impact of quantum phenomena on the thermodynamics of BHs [8–11], the concept of entropy [12, 13], transitions between different thermodynamic phases [14–16], the emission of both thermal and non-thermal radiations [17–19], and other critical phenomena [20–26]. In the context of the extended phase space, the negative cosmological constant is seen as a variable thermodynamic pressure within a system of BHs. Its corresponding conjugate quantity is readily interpreted as the volume of the BH in the mechanics of Anti-de Sitter (AdS) BHs. The mass of a BH is commonly understood to represent the enthalpy of spacetime rather than its intrinsic energy [27]. The aforementioned notions have been widely extended and used in the context of BHs within the framework of the Lovelock theory [28]. Moreover, a scholarly investigation of dilaton-AdS black holes has demonstrated that the mass of a BH is indicative of its enthalpy [28],[30]. The aforementioned investigations have yielded significant outcomes in the field of thermodynamics study pertaining to AdS BHs inside the extended phase space.

It is possible to deduce thermodynamic aspects of certain classical systems by the utilization of similarities between the behavior of BHs [31, 32] and the characteristics exhibited by van der Waals fluids [33–35]. The presence of commonalities across BHs in AdS space implies a substantial correlation between AdS and CFT [36]. Furthermore, there has been much expansion of other ideas, such as those pertaining to revolving and hairy BHs [37, 38], as well as m-theory [39, 40]. In order to accentuate the similarities with van der Waals fluids, researchers have achieved further noteworthy findings, including the examination of quasi-normal modes [41, 42], the investigation of holographic heat engines [43], and the exploration of chaotic structures [44]. Recently, the study of thermal analysis with quantum corrections and emission energy of charged BH with nonlinear electrodynamics are explored in [45]. The study various BHs thermodynamics and phase transitions are discussion in [46–49].

The phenomenon of gas flow from a region of higher pressure to a region of lower pressure at an equivalent rate, as seen in classical thermodynamics, is often known as Joule-Thomson (J-T) expansion. In previous research, Ökcü and E. Aydiner [50] conducted an investigation on the charged AdS BHs, specifically focusing on the J-T effect. Numerous comprehensive research have provided empirical evidence supporting the precise identification of heating and cooling areas through the utilization of the temperature-pressure (T-P) diagram. The point at which the inversion and enthalpic curves overlap provides a means of distinguishing between the zones of heating and cooling within the BH. When the J-T coefficient μ is positive, it corresponds to the cooling zone, whereas a negative value of μ indicates the heating region. Furthermore, the relationship between the minimum temperature (T_{min}) and the critical temperature (T_c) is of importance in the Joule-Thomson expansion. Specifically, for a Reissner-Nordström (RN) AdS, this ratio is determined to be $1/2$ according to reference [50]. Prior research has examined this proportion for additional prominent BHs [51, 52, 54]. This study has restored the ratio to one-half in specified cases. Following this, the research of J-T growth gained prominence and received considerable attention, encompassing the examination of several categories of BHs [51–58].

It is widely acknowledged that within the framework of Schwarzschild spacetime, the motion of a falling object towards the event horizon is subject to radial tidal forces that cause stretching, while compression occurs in the angular directions [59, 60]. Recent research has focused on analyzing tidal forces in different types of BHs, including RN BH [61], Kiselev [62], and other regular BHs [63]. Tidal forces in Kerr spacetime have also been investigated, as evidenced by references [64]-[69]. These forces play a critical role in astrophysics, as they can result in the disruption of a star due to the tidal forces exerted by a BH [64]-[69], leading to the occurrence of a tidal disruption event (TDE). TDEs can produce luminous flares in the form of x-ray [70], ultraviolet [71], and optical [72] radiation.

In this paper, we are interested to generalize the current research on the Joule-Thomson expansion for AdS BHs surrounded by Chaplygin dark fluid and brief study on tidal forces. The formation of the current paper is as written. In Sec. II, we study a brief review of AdS BHs surrounded by Chaplygin dark fluid. Then, we explore the J-T expansion in Sec. III. Sec. IV and V is related to the radial geodesics and tidal forces, respectively. Sec. VI and VII present the radial as well as angular tidal force and geodesic deviation, respectively. Finally, we present a few closing remarks

in the last section.

II. ADS BLACK HOLE SURROUNDED BY DARK FLUID WITH CHAPLYGIN-LIKE EQUATION OF STATE

Exploring the interaction between a BH and the surrounding field involves solving gravitational field equations alongside the equation of motion for the relevant field. This is particularly practical when dealing with a static spherically symmetric BH and its atmosphere composed of a field with a specific Lagrangian. Understanding the nature of the matter near BH solutions becomes challenging, especially in the presence of quintessence dark energy and Chaplygin gas. In such cases, it becomes essential to explore the relationship between matter and spacetime curvature solely based on the equation of state for the fluid matter. In our current investigation, we adopt a specific metric form to characterize the static spherically symmetric spacetime.

$$ds^2 = -f(r)dt^2 + \frac{1}{f(r)}dr^2 + r^2(d\theta^2 + \sin^2\theta d\phi^2). \quad (1)$$

To describe the matter source, we initiate with a perfect fluid, which is given as

$$T_{ab} = pg_{ab} + (\rho + p)u_a u_b, \quad (2)$$

In the field Semiz [73] made significant contributions by investigating the equation of state (EOS) $p = \omega\rho$ (ω being a constant) for ideal fluid sources like dust, phantom energy, radiation, or dark energy, employing Einstein's equations as the foundational framework. Another notable contribution came from Kiselev [74], who derived a novel BH spacetime by considering ambient quintessence matter as an anisotropic fluid, a model that gained widespread popularity. The understanding of the background processes leading to the Chaplygin dark fluid (CDF) remains uncertain from a field theoretical standpoint [75, 76], although some potential explanations exist within the framework of string theory [77, 78]. The CDF is often described by introducing a self-interacting potential and a scalar field φ with the Lagrangian $L_\varphi = -\frac{1}{2}\partial_a\varphi\partial^a\varphi - U(\varphi)$ [79, 80]. This study assumes that the CDF possesses anisotropic properties, and its stress-energy tensor can be expressed covariantly [81].

$$T_{ab} = \rho u_a u_b + p_r k_a k_b + p_t \Pi_{ab}, \quad (3)$$

The radial and tangential pressure components are represented by p_r and p_t, respectively. The four-velocity of the fluid is denoted by u_a, and k_a represents a unit spacelike vector that is orthogonal to u_a. It is worth noting that u_a and k_a satisfy the conditions $u_a u^a = -1$, $k_a k^a = 1$, and $u^a k_a = 0$. The tensor $\Pi_{ab} = g_{ab} + u_a u_b - k_a k_b$ serves as a projection onto the two orthogonal surfaces defined by u^a and k^a. When working in the fluid's comoving frame, specific values can be assigned, such as $u_a = (-\sqrt{f}, 0, 0, 0)$ and $k_a = (0, 1/\sqrt{g}, 0, 0)$. Finally, the stress-energy tensor, as derived from Eq. (3), is expressed as follows.

$$T_a{}^b = -(\rho + p_t)\delta_a{}^0\delta^b{}_0 + p_t\delta_a{}^b + (p_r - p_t)\delta_a{}^1\delta^b{}_1. \quad (4)$$

The anisotropic factor is expressed as the disparity between radial and tangential pressures, denoted as $p_r - p_t$. In situations where $p_r = p_t$, the stress-energy tensor simplifies to the standard isotropic form. Even if a cosmological fluid exhibits anisotropy in the gravitational field produced by a black hole, its equation of state should manifest as $p = p(\rho)$ on a cosmological scale. This allows for the imposition of constraints on the tangential pressure (p_t) by performing an isotropic averaging over angles and incorporating additional conditions. $\langle T_i{}^j \rangle = p(\rho)\delta_i{}^j$, An individual can obtain the following relationship

$$p(\rho) = p_t + \frac{1}{3}(p_r - p_t), \quad (5)$$

The relation $\frac{1}{3} = \langle \delta_i{}^1\delta^j{}_1 \rangle$ is utilized, and considering the equation of state (EOS) $p = \omega\rho$ with $-1 < \omega < -\frac{1}{3}$ for quintessence matter, the expression $p_t = \frac{1}{2}(1 + 3\omega)\rho$ is derived from Eq. (5). This relationship is consistent with the radial pressure $p_r = -\rho$ as discussed in [74]. In our scenario, the non-linear EOS for the Chaplygin Dark Fluid (CDF) is given by $p = -\frac{B}{\rho}$, where B is a positive constant. This leads to the tangential pressure $p_t = \frac{1}{2}\rho - \frac{3B}{2\rho}$ with $p_r = -\rho$. Consequently, the stress-energy tensor of the CDF can be expressed as.

$$-\rho = T_t{}^t = T_r{}^r, \quad (6)$$

$$\tfrac{1}{2}\rho - \tfrac{3B}{2\rho} = T_\theta{}^\theta = T_\phi{}^\phi. \quad (7)$$

On the cosmological scale, the anisotropy of the Cosmic Dust Fluid (CDF) diminishes, leading to an equation of state (EOS) where pressure (p) is expressed as $-B/\rho$. Additionally, a crucial condition, $T_t^t = T_r^r$, must be satisfied, ensuring that the metric components $g(r)$ and $f(r)$ are related through an appropriate time re-scaling, preserving generality. The calculation of the Einstein tensor components is subsequently performed as

$$G_r{}^r = \tfrac{1}{r^2}(f + rf' - 1) = G_t{}^t, \quad (8)$$

$$\tfrac{1}{2r}(2f' + rf'') = G_\theta{}^\theta = G_\phi{}^\phi. \quad (9)$$

Now, by using the Eqs. (6)-(7) and Eqs. (8)–(9), one can get the following relation

$$-\rho = \tfrac{1}{r^2}(f + rf' - 1) + \Lambda, \tag{10}$$

$$\tfrac{1}{2}\rho - \tfrac{3B}{2\rho} = \tfrac{1}{2r}(2f' + rf'') + \Lambda. \tag{11}$$

We now examine the existence of the cosmological constant. The two above differential equations allow us to calculate the two unknown functions, i.e., $f(r)$ and $\rho(r)$, analytically. Now, one can simply the energy density of CDF by solving the above set of differential Eqs. (10)–(11) as:

$$\rho(r) = \sqrt{B + \frac{q^2}{r^6}}, \tag{12}$$

where a normalization factor $q > 0$ denotes the CDF's intensity. Additionally, the conservation law for the stress-energy tensor $\nabla_b T^{ab} = 0$ directly yields Eq. (12). It is evident that the CDF energy density can be approximated by $r^6 \ll q^2/B$ as

$$\rho(r) \approx \frac{q}{r^3}, \tag{13}$$

demonstrating that the CDF behaves as though its energy density were dependent on r^{-3} for matter content. Now, by using Eq. (12) into Eq. (10), we have the final analytical solution for $f(r)$ [82, 83] as

$$f(r) = 1 - \frac{2M}{r} + \frac{q}{3r}\text{ArcSinh}\frac{q}{\sqrt{B}r^3} - \frac{r^2}{3}\sqrt{B + \frac{q^2}{r^6}} - \frac{r^2}{3}\Lambda, \tag{14}$$

where M is the BH mass, however in the current case, the BH mass is regarded as a point mass BH.

From the equation of horizon $f(r) = 0$ and pressure $P = -\frac{\Lambda}{8\pi}$ [50–52], we can deduce the relation between the BH mass M and its event horizon radius r_h, expression as follows

$$M = \frac{1}{6}\left(r^3\left(-\sqrt{B + \frac{q^2}{r^6}}\right) + q\sinh^{-1}\left(\frac{q}{\sqrt{B}r^3}\right) - 8\pi P r^3 + 3r\right) \tag{15}$$

The Hawking temperature of BH related to surface gravity can be obtained as

$$T = -\left\{\frac{2r^6\sqrt{B + \frac{q^2}{r^6}} - \frac{3q^2}{\sqrt{B + \frac{q^2}{r^6}}} + \frac{3q^2}{\sqrt{B}\sqrt{\frac{q^2}{Br^6}+1}}}{12\pi r^5} + \frac{\frac{3q^2}{\sqrt{B}\sqrt{\frac{q^2}{Br^6}+1}} + qr^3\sinh^{-1}\left(\frac{q}{\sqrt{B}r^3}\right) - 6Mr^3 + 16\pi P r^6}{12\pi r^5}\right\} \tag{16}$$

The BH entropy with the help of area law is defined as [52–54]

$$S = \pi r^2. \tag{17}$$

The volume parameter is defined as

$$V = \left(\frac{\partial M}{\partial P}\right)_{S,q_m}, \tag{18}$$

calculated as

$$V = \frac{r^3}{6} \tag{19}$$

To find more data about a phase transition, we study thermodynamic a quantity such as heat capacity. By applying the standard definition of heat capacity follows as

$$\text{Cp} = \frac{\partial S}{\partial T} = -\frac{8\pi^2 r}{\frac{\left(Br^6 - 2q^2\right)\sqrt{B + \frac{q^2}{r^6}}}{Br^6 + q^2} + 8\pi P + \frac{1}{r^2}}. \tag{20}$$

The coordinate location of the horizons in this spacetime when using Schwarzschild coordinates (t,r,θ,ϕ) is given by imposing $g^{rr} = 0$. Since the analytical expression of the lapse function Eq. (14) is a function of multiple variables, it can be plotted against the radial coordinate to find the locations of horizons in the spacetime geometry. Such a curve can be seen in Fig. (1). The coordinate location of the horizons for different values of q, B and Λ is provided in Tab. (I). It can be seen from Fig. (1) that the lapse function curve crosses the horizontal axis at two points suggesting the presence of two horizons i.e. Cauchy (inner horizon) and the event horizon. Also, by studying the radial null curves in this geometry i.e. setting $ds^2 = 0$, $d\theta = d\phi = 0$ we get:

$$\frac{dr}{dt} = \pm\left(1 - \frac{1}{3}r^2\sqrt{B + \frac{q^2}{r^6}} + \frac{q\sinh^{-1}\left(\frac{q}{\sqrt{B}r^3}\right)}{3r} - \frac{2M}{r} - \frac{\Lambda r^2}{3}\right). \tag{21}$$

This equation also defines the coordinate speed of light in this metric. As the radial coordinate approaches the values provided in Tab. (I), $\frac{dr}{dt} \to 0$.

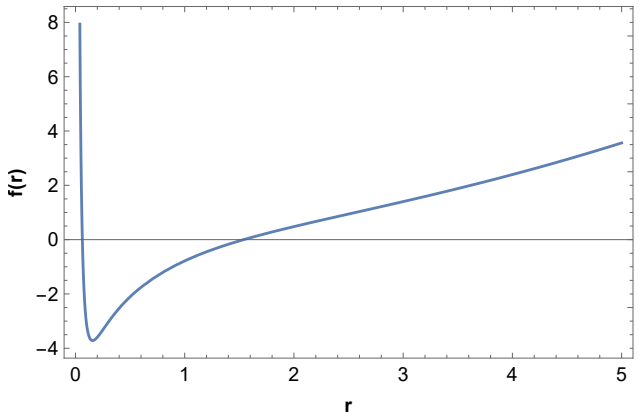


FIG. 1: Plot of the lapse function w.r.t the radial coordinate r depicting the location of horizons for $q = 0.743$, $B = 0.772$ and $\Lambda = -1.234$

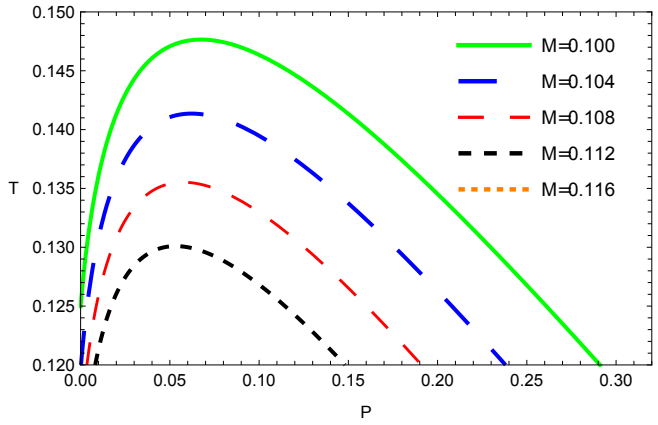


FIG. 2: Plot of inversion curves in $T - P$ plane with fixed values of $B = 0.001$ and $q = 0.04$.

Location of horizons for AdS black hole spacetime		
Spacetime parameters	Cauchy horizon	Event horizon
$q = 0.8$, $B = 0.4$, $\Lambda = -0.70$	0.089	1.833
$q = 0.8$, $B = 0.7$, $\Lambda = -0.90$	0.080	1.846
$q = 0.8$, $B = 0.9$, $\Lambda = -1$	0.077	1.870

TABLE I: Location of event and Cauchy horizons for AdS black hole spacetime. We take $M = 1$ for our analysis

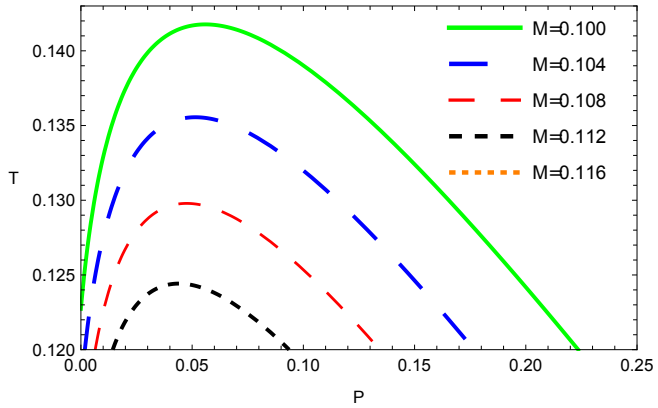


FIG. 3: Plot of inversion curves in $T - P$ plane with fixed values of $B = 0.001$ and $q = 0.05$.

III. JOULE-THOMSON EXPANSION

One of the most well-known and classical physical processes to explain the change in the temperature of gas from a high-pressure section to reduced pressure through a porous plug is called Joule-Thomson expansion. The main focus is on the gas expansion process, which expresses the cold effect (when the temperature drops) and the heat effect (when the temperature increases), with the enthalpy remaining constant throughout the process. This change depends upon the coefficient of Joule-Thomson as [50–55]

$$\mu_{JT} = \left(\frac{\partial T}{\partial P}\right)_H = \frac{1}{C_p}\left[T\left(\frac{\partial V}{\partial T}\right)_p - V\right]. \tag{22}$$

Putting the basic quantities in Eq. (22) coefficient calculated as

$$\mu_{JT} = \left\{\frac{q^2\left(-5r^2\sqrt{B+\frac{q^2}{r^6}} - 16\pi Pr^2 + 4\right)}{48\pi^2\left(Br^6+q^2\right)} \right. \\ \left. \frac{-2Br^6\left(r^2\sqrt{B+\frac{q^2}{r^6}} + 8\pi Pr^2 - 2\right)}{48\pi^2\left(Br^6+q^2\right)}\right\} \tag{23}$$

It is clear from a comparison of these figures that the zero point of the Hawking temperature and the divergence point of the coefficient of Joule-Thomson is the same. This point of divergence gives information on the Hawking temperature and corresponds to the most extreme BHs. From Eq. (23) utilizing the well known condition $\mu_{JT} = 0$, the temperature inversion occurs as

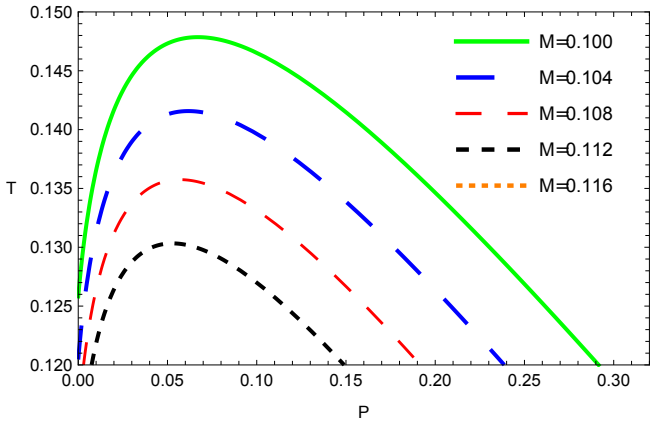


FIG. 4: Plot of inversion curves in $T-P$ plane with fixed values of $B=0.05$ and $q=0.04$.

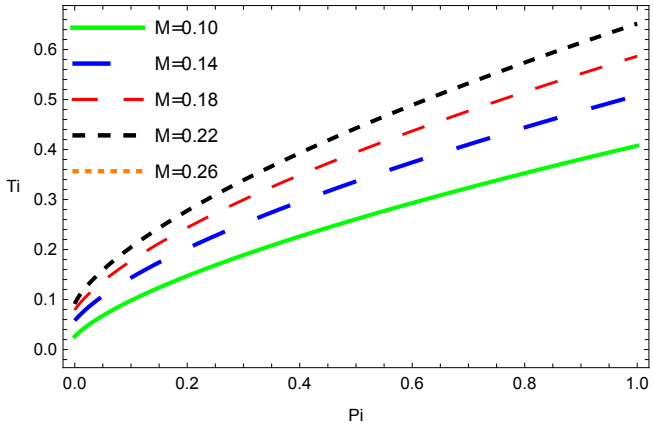


FIG. 5: Plot of isenthalpic curves in $Ti-Pi$ plane with fixed values of $B=0.03$ and $q=0.04$.

$$T_i=\left\{\frac{q^2\left(2r^2\sqrt{B+\frac{q^2}{r^6}}-8\pi Pr^2-1\right)}{12\pi r\left(Br^6+q^2\right)}\right.$$
$$\left.\frac{-Br^6\left(r^2\sqrt{B+\frac{q^2}{r^6}}+8\pi Pr^2+1\right)}{12\pi r\left(Br^6+q^2\right)}\right\} \tag{24}$$

From Figs. (2)-(4), the inversion temperature increases with variations of important parameters respectively. Compared with the van der Waals fluids, the above results in $Ti-Pi$-plan at low pressure, the inversion temperature T_i decreases with the increase of P, which shows the opposite behavior for higher pressure. It is also clear that, unlike the case with van der Waals fluids. We show the constant mass curves for various values of the nonlinear parameter k and the massive gravity couplings From this figure, we observe that with the same

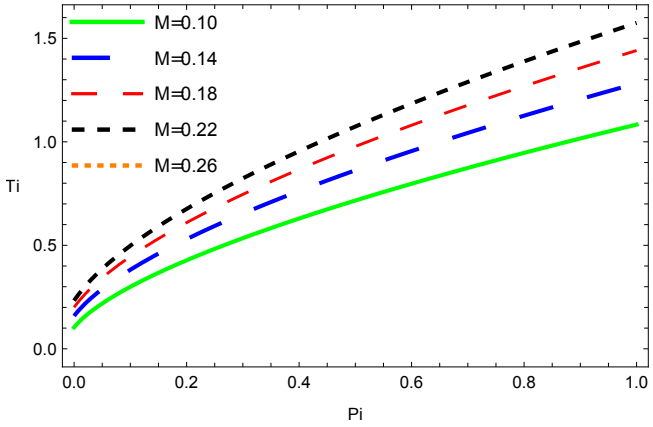


FIG. 6: Plot of isenthalpic curves in $Ti-Pi$ plane with fixed values of $B=0.03$ and $q=0.08$.

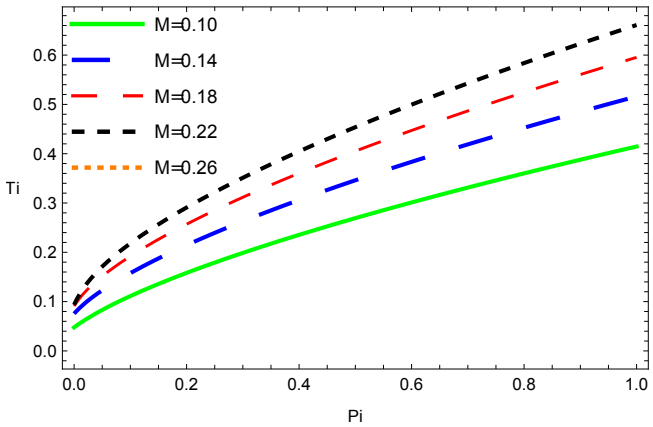


FIG. 7: Plot of isenthalpic curves in $Ti-Pi$ plane with fixed values of $B=0.06$ and $q=0.04$.

mass, as the nonlinear parameter and the massive gravity couplings c1,2 increase, the constant mass curves tend to shrink towards the lower pressure and temperature. In Figs. (5)-(7), we study isenthalpic curves ($Ti-P_i$- plane) by assuming different values of BH mass which are investigated in Eq. (24) with a larger root of r_h. We show the isenthalpic curves and the inversion curves of BH and this result is consistent [54, 55]. Heating and cooling zones are characterized by the inversion curve, and isenthalpic curves possess positive slopes above the inversion curve. In contrast, the pressure always falls in a Joule-Thomson expansion and the slope changes sign when heating happens below the inversion curve. The heating process appears at higher temperatures, as indicated by the negative slope of the constant mass curves in the Joule-Thomson expansion.

IV. RADIAL GEODESICS

In this section we will study about the radial geodesics in AdS black hole spacetime exhibiting dark fluid with Chaplygin like equation of state. Radial geodesics are such that $\dot{\theta}$ and $\dot{\phi} = 0$. For our analysis, we take the geodesics to be in the equatorial plane s.t. $\theta = \frac{\pi}{2}$. Any general spherically symmetric static spacetime can be written as:

$$ds^2 = -g_{tt}dt^2 + g_{rr}dr^2 + r^2(d\theta^2 + \sin^2\theta d\phi^2) \tag{25}$$

where g_{tt} and g_{rr} are the components of the metric tensor, and the azimuthal part shows the spherical symmetry of the spacetime. For any freely falling particle in this spacetime the energy (E) and the angular momentum (L) per unit rest mass is always conserved. It is a direct consequence of the spherical and temporal symmetry of the spacetime [84]. The conserved quantities can be written as:

$$E = g_{tt}\frac{dt}{d\tau}; \quad L = r^2\sin^2\theta\frac{d\phi}{d\tau} \tag{26}$$

where τ is the proper time of the particle. A freely falling particle always follow a timelike geodesic s.t the $u^\mu u_\mu = -1$, where u^μ is the particle's four velocity. From this normalization of four velocity, we can obtain the radial equation of motion for a freely falling particle in the equatorial plane, which can be written as:

$$\frac{\dot{r}^2}{2} = \frac{E^2 - f(r)}{2} \tag{27}$$

For a radially in-falling particle from rest at a point $r = b$, the energy of the particle can be given as $E = \sqrt{f(r=b)}$, since $\frac{dr}{d\tau} = 0$ at $r = b$. We can also define the Newtonian radial acceleration by differentiating Eq. (27). w.r.t proper time. This gives us the expression:

$$A^r = \frac{-f'(r)}{2} \tag{28}$$

For the purpose of this study, inserting the derivative of lapse function in Eq. (28), we get the Newtonian acceleration as:

$$A^r = \left\{ \frac{2\sqrt{\frac{q^2}{r^6} + B}\,r}{3} + \frac{2\Lambda r}{3} + \frac{q\,\mathrm{arcsinh}\left(\frac{q}{\sqrt{B}\,r^3}\right)}{3r^2} \right. \\ \left. \frac{-\frac{2M}{r^2} + \frac{q^2}{\sqrt{B}\sqrt{\frac{q^2}{Br^6} + 1}\,r^5} - \frac{q^2}{\sqrt{\frac{q^2}{r^6} + B}\,r^5}}{2} \right\} \tag{29}$$

Since, in this spacetime the value of $\Lambda < 0$, we can infer that negative values of the cosmological constant provides increased attraction to the black hole. Also, any test particle falling freely from rest from a point $r = b > R_{eh}$ can turn back after reaching a point R^{stop}. This point can be calculated as the root of the equation $E^2 = f(r)$.

V. TIDAL FORCE ANALYSIS

We shall dig into the intricacies of the equations regarding tidal forces in our spacetime in this part. We utilise the following equation for the spacelike components of the geodesic deviation vector η^μ, to analyse the equation for the distance between two infinitesimally close and free falling particles.

$$\frac{D^2\eta^\mu}{D\tau^2} = R^\mu_{\alpha\beta\gamma}v^\alpha v^\beta\eta^\gamma, \tag{30}$$

where $R^\mu_{\alpha\beta\gamma}$ is the Riemann curvature tensor and v^μ is the unit tangent vector to the geodesic. A test body travelling in space alone under the influence of gravity is known to follow a geodesic [85]. since of the variation in curvature at each point on the geodesic, and since each location on the test body tends to follow a different geodesic, the body experiences a change in acceleration, resulting in a stretching and squeezing action known as tidal forces. This is why the Riemann curvature tensor is employed to examine gravity-induced tidal interactions.

We utilise the tetrad formalism to compute the tidal forces in the falling body's frame [86]. Tetrads or vierbien are geometric objects that create a set of local coordinate bases, i.e. a locally defined collection of four linearly independent vector fields. A tetrad frame establishes a local inertial reference frame at each point on a geodesic, where the equations of special relativity apply. Lorentz transformations cannot provide adequate information on the metric link because they can connect an endless number of orthonormal bases at a particular place. To fix this, we apply the orthonormal basis to coordinate basis transformation:

$$\overrightarrow{e}_\mu = \hat{e}^{\hat{i}}_\mu \overrightarrow{e}_{\hat{i}}, \tag{31}$$

where $\overrightarrow{e}_\mu$ represents the coordinate basis, $\overrightarrow{e}_{\hat{i}}$ represents the orthonormal basis and $\hat{e}^{\hat{i}}_\mu$ are the tetrad components. The metric tensor components in the tetrad basis are given as [87]:

$$g_{\mu\nu} = \eta_{\hat{i}\hat{j}}\hat{e}^{\hat{i}}_\mu\hat{e}^{\hat{j}}_\nu. \tag{32}$$

This is the crucial equation for using orthonormal basis in curved spacetime. Tetrad components for freely falling frames are available from Eq. (31) and Eq. (32).

$$\hat{e}^{\mu}_{\hat{0}} = \left\{ \frac{E}{f(r)}, -\sqrt{E^2 - f(r)}, 0, 0 \right\}, \tag{33}$$

$$\hat{e}^{\mu}_{\hat{1}} = \left\{ \frac{-\sqrt{E^2 - f(r)}}{f(r)}, E, 0, 0 \right\}, \tag{34}$$

$$\hat{e}^{\mu}_{\hat{2}} = \left\{ 0, 0, \frac{1}{r}, 0 \right\}, \tag{35}$$

$$\hat{e}^{\mu}_{\hat{3}} = \left\{ 0, 0, 0, \frac{1}{r\sin\theta} \right\}, \tag{36}$$

where the tetrad components follow the following rule:

$$\hat{e}^{\mu}_{\hat{i}} \hat{e}^{\hat{j}}_{\mu} = \delta^{\hat{j}}_{\hat{i}}. \tag{37}$$

We can see that the component $\hat{e}^{\mu}_{\hat{0}} = v^{\mu}$ is the tangent vector to the geodesic, i.e. the particle's four velocity. Furthermore, the geodesic deviation vector adheres to the transformation rule from global to local orthonormal coordinates.

$$\eta^{\mu} = \hat{e}^{\mu}_{\hat{i}} \eta^{\hat{i}}. \tag{38}$$

For spherically symmetric spacetimes, including EBR black hole spacetime, the non-vanishing independent components of the Riemann tensor are given by [88]:

$$R^{1}_{212} = \frac{-rf'(r)}{2}, \tag{39}$$

$$R^{1}_{010} = \frac{f(r)f''(r)}{2}, \tag{40}$$

$$R^{1}_{313} = \frac{-rf'(r)\sin^2\theta}{2}, \tag{41}$$

$$R^{2}_{020} = R^{3}_{030} = \frac{f(r)f'(r)}{2r}, \tag{42}$$

$$R^{2}_{323} = \sin^2\theta \left(1 - r^2 f(r) \right) \tag{43}$$

We utilise the tetrad formalism to compute the Riemann curvature tensor components in tetrad basis as follows:

$$R^{\hat{i}}_{\hat{j}\hat{k}\hat{l}} = R^{\mu}_{\alpha\beta\gamma} e^{\hat{i}}_{\mu} e^{\alpha}_{\hat{j}} e^{\beta}_{\hat{k}} e^{\gamma}_{\hat{l}}. \tag{44}$$

Following the Eq. (44), the tidal tensor components are given by:

$$R^{\hat{1}}_{\hat{0}\hat{1}\hat{0}} = \frac{f''(r)}{2}, \tag{45}$$

$$R^{\hat{2}}_{\hat{0}\hat{2}\hat{0}} = R^{\hat{3}}_{\hat{0}\hat{3}\hat{0}} = \frac{f'(r)}{2r}, \tag{46}$$

A. TIDAL FORCE EQUATIONS

Upon obtaining the expressions from Eq. (45-46), we can obtain the relative acceleration between two nearby particles as:

$$\frac{D^2\eta^{\hat{r}}}{D\tau^2} = \frac{-f''(r)}{2}\eta^{\hat{r}}, \tag{47}$$

$$\frac{D^2\eta^{\hat{\theta}}}{D\tau^2} = -\frac{f'(r)}{2r}\eta^{\hat{\theta}}, \tag{48}$$

$$\frac{D^2\eta^{\hat{\phi}}}{D\tau^2} = -\frac{f'(r)}{2r}\eta^{\hat{\phi}}. \tag{49}$$

By substituting the values of $f(r)$ and its higher derivatives in Eq. (47-49) we get:

$$\frac{D^2\eta^{\hat{r}}}{D\tau^2} = \Bigg\{ \frac{\frac{-2q\,\mathrm{arcsinh}\left(\frac{q}{\sqrt{B}\,r^3}\right)}{3r^3} + \frac{4M}{r^3} - \frac{6q^2}{\sqrt{B}\sqrt{\frac{q^2}{Br^6}+1}\,r^6} + \frac{3q^2}{\sqrt{\frac{q^2}{r^6}+B}\,r^6} + \frac{3q^4}{B^{\frac{3}{2}}\cdot\left(\frac{q^2}{Br^6}+1\right)^{\frac{3}{2}} r^{12}}}{2} - \frac{\frac{3q^4}{\left(\frac{q^2}{r^6}+B\right)^{\frac{3}{2}} r^{12}} + \frac{2\sqrt{\frac{q^2}{r^6}+B}}{3} + \frac{2\Lambda}{3}}{2} \Bigg\}\eta^{\hat{r}}, \tag{50}$$

$$\frac{D^2\eta^{\hat{\theta}}}{D\tau^2} = \frac{\frac{2\sqrt{\frac{q^2}{r^6}+B}\,r}{3} + \frac{2\Lambda r}{3} + \frac{q\,\mathrm{arcsinh}\left(\frac{q}{\sqrt{B}\,r^3}\right)}{3r^2} - \frac{2M}{r^2} + \frac{q^2}{\sqrt{B}\sqrt{\frac{q^2}{Br^6}+1}\,r^5} - \frac{q^2}{\sqrt{\frac{q^2}{r^6}+B}\,r^5}}{2r}\eta^{\hat{\theta}}, \tag{51}$$

$$\frac{D^2\eta^{\hat{\phi}}}{D\tau^2} = \frac{\frac{2\sqrt{\frac{q^2}{r^6}+B}\,r}{3} + \frac{2\Lambda r}{3} + \frac{q\,\mathrm{arcsinh}\left(\frac{q}{\sqrt{B}\,r^3}\right)}{3r^2} - \frac{2M}{r^2} + \frac{q^2}{\sqrt{B}\sqrt{\frac{q^2}{Br^6}+1}\,r^5} - \frac{q^2}{\sqrt{\frac{q^2}{r^6}+B}\,r^5}}{2r}\eta^{\hat{\phi}}. \tag{52}$$

VI. RADIAL TIDAL FORCE

In Fig. (8), we plot the radial tidal force for AdS black hole for fixed value of q and changing values of B and Λ. It can be seen that the presence of non-zero values of q changes the monotonicity of the dependency of the radial tidal force on the radial coordinate r. Fig. (9) shows the radial force profile when the value of q is varied, and the values of B and Λ are fixed. Fig. (9) also takes into account different values for q,B and Λ respectively. It can be seen that in all the three cases, the asymptotic value of radial tidal force is non-zero. At infinitely large distances where the energy density of the cold dark fluid can be approximated by $\rho(r) = \sqrt{B}$, the radial tidal force can be given by the equation:

$$\lim_{r\to\infty} \frac{D^2\eta^{\hat{r}}}{D\tau^2} = \frac{1(\sqrt{B}+\Lambda)}{3}\eta^{\hat{r}} \tag{53}$$

This proves that the radial tidal force at $r \to \infty$ is solely governed by the presence of an effective non-zero cosmological constant. In all the three cases, the radial tidal forces increase drastically at short distances i.e. when the in-falling particle approaches the central singularity. The monotonically increasing trend or the radial stretching switches its behavior at a certain value of radial coordinate, after which it falls rapidly to become compressive. The transition from radial stretching to compression happens at a crossover radial coordinate, where the tidal force is momentarily zero, after which it approaches infinity as $r \to 0$. The analytic expression for it can be computed by equating the RHS of Eq. (47) to zero:

$$R_0^{rtf} = \frac{\frac{4M}{r^3} - g''(r)}{2} = 0 \tag{54}$$

where the function $g(r)$ is taken for simplicity in calculation and representation, and is given by:

$$g(r) = -\frac{1}{3}r^2\sqrt{B+\frac{q^2}{r^6}} + \frac{q\sinh^{-1}\left(\frac{q}{\sqrt{B}r^3}\right)}{3r} - \frac{\Lambda r^2}{3}. \tag{55}$$

In all the cases, the radial tidal force profile peaks at a certain value of the radial coordinate r. The peak behavior is different for changing values of B and Λ. From Fig. (8) it can be seen that for $q = 0.8$, the maximum value of radial stretching is attained for $B = 0.9$ and $\Lambda = -1$. The peak value declines as the value of B is reduced or as the value of Λ is increased. An opposite trend can be seen from Fig. (9). It can be inferred that for fixed values of B and Λ, the peak value of radial stretching drops as the value of q is increased. It can also be seen that the peak value is achieved inside the event horizon and before the Cauchy horizon of the black hole i.e. $R_{ch} < R^{rtf}_{peak} < R_{eh}$ where the R_{ch} and R_{eh} denotes the Cauchy horizon and event horizon respectively. For eg. for the parameters $q = 0.8$, $B = 0.4$, $\Lambda = -0.70$, the peak

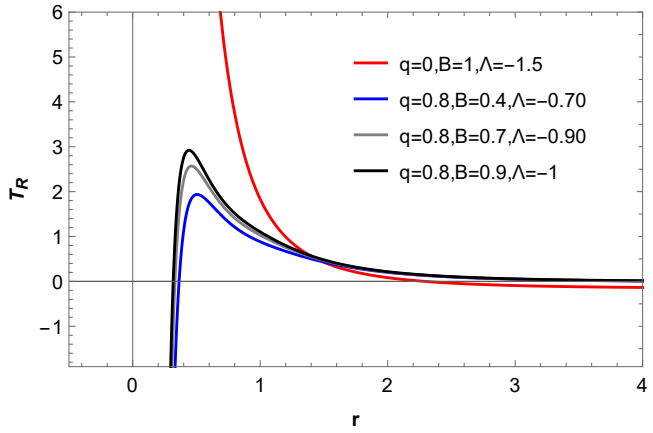


FIG. 8: Radial tidal force as a function of the radial coordinate for fixed value of $q = 0.8$. It can be observed that the force changes monotonicity and vanishes at a particular radial coordinate which lies between the Cauchy horizon and the event horizon of the black hole for non-zero values of q.We take $M = 1$

value is attained at approximately $r = 0.50$ which lies inside the event horizon located at $r = 1.833$ and outside the Cauchy horizon located at $r = 0.089$. The analytic expression for peak value can be given by equating the first derivative of Eq. (47) to zero. Since the tidal force expressions involve the use of higher order polynomials, a more general expression for peak value can be written as:

$$R^{rtf}_{peak} = \frac{d}{dr}\left(\frac{\frac{4M}{r^3} - g''(r)}{2}\right) = 0. \tag{56}$$

The graphs for different values of the spacetime parameters are shown below:

A. ANGULAR TIDAL FORCE

The angular tidal forces exhibit compressive nature unlike the radial tidal forces as a radially in-falling body approaches the central singularity. But, similar to the radial case, angular tidal forces also reach a peak compressive value and then rapidly fall to become momentarily zero at a particular value of radial coordinate r and switching their behavior from compressive to radial stretching. Fig. (10) portray the angular force profile w.r.t the radial coordinate r, keeping the value of q fixed and varying the values of B and Λ. We use $q = 0.8$ for the analysis.

It can be seen that for non-zero values of q, the monotonicity of the force profile changes. Fig. (11) show the trend for different values of q and also displays the trend for different values of q, B and Λ. In all the cases the asymptotic value of the angular tidal force is non-zero, and is given in the limit of $r \to \infty$ by the expression

$$\lim_{r\to\infty} \frac{D^2\eta^{\hat{i}}}{D\tau^2} = \frac{1(\sqrt{B}+\Lambda)}{3}\eta^{\hat{i}} \tag{57}$$

where $i = \{\theta, \phi\}$. Similar to the case of radial tidal forces, the values of angular tidal forces at infinitely large distances is solely governed by the presence of a non-zero effective cosmological constant. The crossing radial coordinate at which the angular tidal force is zero is given by equating the R.H.S of Eq. (48) to zero as:

$$R^{atf}_0 = \frac{\frac{2M}{r^2} + g'(r)}{2r} = 0. \tag{58}$$

where the term $g(r)$ is given by Eq. (55). After becoming radially stretching in nature, the angular tidal forces continue to grow till infinity in the limit $r \to 0$. Following the convention in Eq. (55), the peak value of angular tidal force can be calculated by equating the first derivative of the expression in Eq. (48) to zero.

$$R^{atf}_{peak} = \frac{d}{dr}\left(\frac{\frac{-2M}{r^2} - g'(r)}{2r}\right) = 0. \tag{59}$$

From Fig. (10), it can be seen that for a fixed value of $q = 0.8$, the peak value of angular tidal force goes on decreasing as the value of B is increased. For instance the black curve shows minimum compression for the values of $B = 0.9, \Lambda = -1$ in contrast to the blue curve which shows maximum compression for values of $B = 0.4, \Lambda = -0.70$. An opposite behavior can be seen from Fig. (11), where as the value of q is increased while keeping B and Λ fixed, the angular compression also increases. Similar to the radial case, the peak value is achieved inside the event horizon but before the Cauchy horizon i.e. $R_{ch} < R^{atf}_{peak} < R_{eh}$. For eg. when $q = 0.5, B = 0.7, \Lambda = -0.90$, the Cauchy horizon and the event horizon lies at $r = 0.0143$ and $r = 1.8570$ respectively. The peak value as observed from Fig. (10) is approximately at $r = 0.19$ which lies inside the two horizons. The graphs for angular tidal force profiles for different values of the spacetime parameters are shown below.

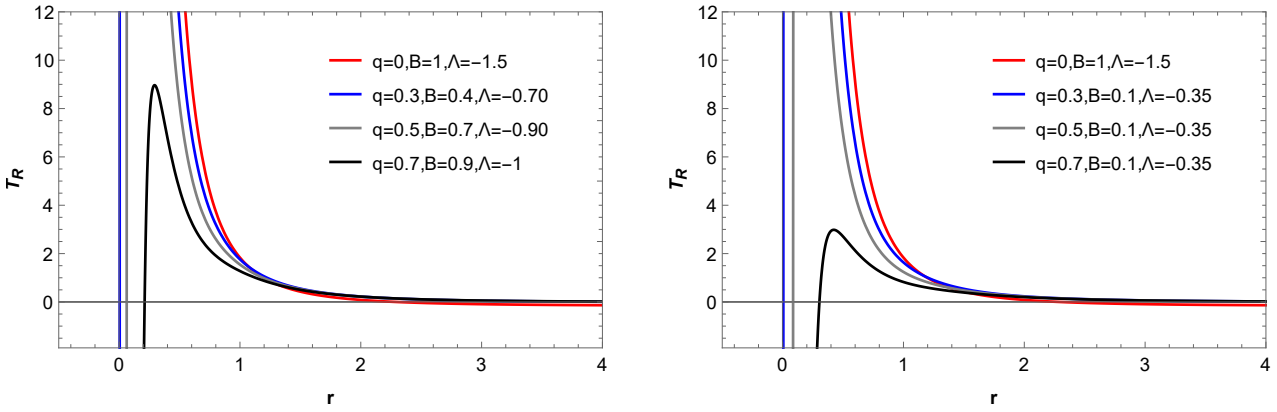


FIG. 9: On left, we plot the radial tidal force profile for varying values of q, B, Λ. On right, we plot the force profile for different values of q while keeping B and Λ fixed. It can be observed that a small drop in the value of q causes a sharp increase in the peak value of the force. We use $M = 1$.

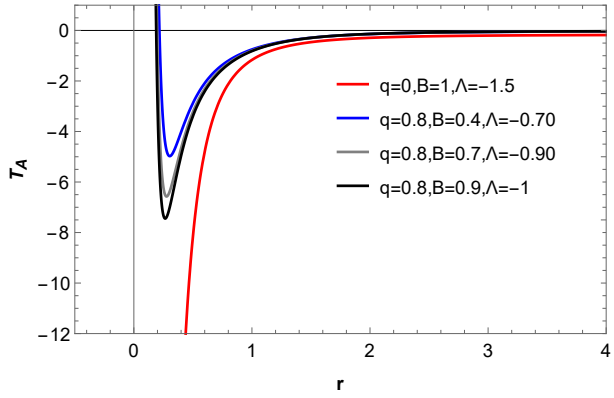


FIG. 10: Angular tidal force as a function of the radial coordinate for fixed value of $q = 0.8$. It can be observed that the force changes monotonicity and vanishes at a particular radial coordinate which lies between the Cauchy horizon and the event horizon of the black hole for non-zero values of q.We take $M = 1$

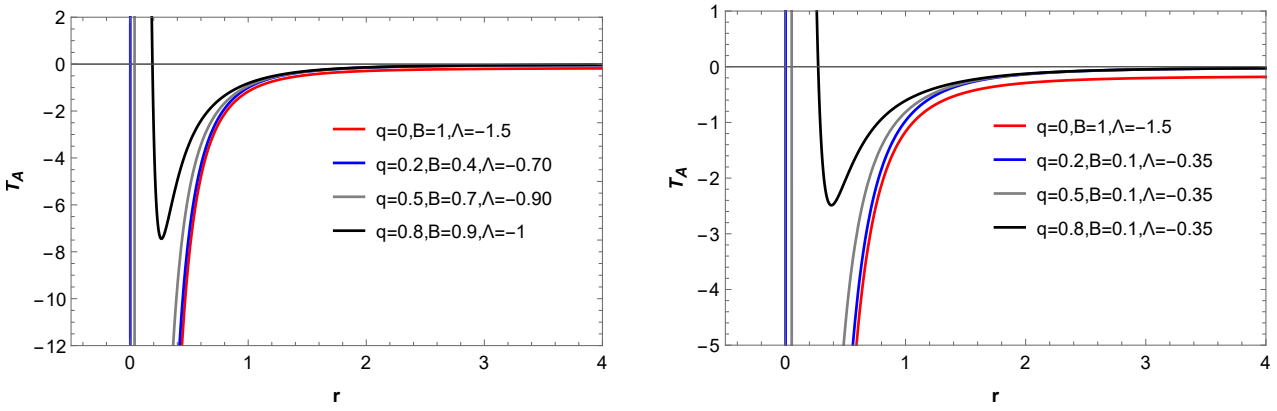


FIG. 11: On left, we plot the angular tidal force profile for varying values of q, B, Λ. On right, we plot the force profile for different values of q while keeping B and Λ fixed. It can be observed that a small drop in the value of q causes a drastic decrease in the compressiveness of the tidal force. We use $M = 1$.

VII. GEODESIC DEVIATION

In this section we discuss the variation of geodesic deviation vector with the radial coordinate in SBR black hole spacetime. The deviation vector measures the deformation of a body falling radially in any spacetime geometry. We can convert Eq. (47) and (48) in second derivatives w.r.t. r by substituting $dr/d\tau = -\sqrt{E^2 - f(r)}$ which results from Eq. (33). This gives us the following second order differential equations in r:

$$(E^2 - f(r))\frac{D^2\eta^{\hat{r}}}{Dr^2} - \frac{f'(r)}{2}\frac{D\eta^{\hat{r}}}{dr} + \frac{f''(r)}{2}\eta^{\hat{r}} = 0, \quad (60)$$

$$(E^2 - f(r))\frac{D^2\eta^{\hat{i}}}{Dr^2} - \frac{f'(r)}{2}\frac{D\eta^{\hat{i}}}{dr} + \frac{f'(r)}{2r}\eta^{\hat{i}} = 0. \quad (61)$$

where $i = \{\theta, \phi\}$. The analytic solution for Eq. (60) and (61) as pointed out in [**?**] can be given as:

$$\eta^{\hat{r}}(r) = \sqrt{E^2 - f(r)}\left[C_1 + C_2 \int \frac{dr}{(E^2 - f(r))^{3/2}}\right], \quad (62)$$

$$\eta^{\hat{i}}(r) = \left[C_3 + C_4 \int \frac{dr}{r^2\sqrt{(E^2 - f(r))}}\right] r. \quad (63)$$

where C_1, C_2, C_3, C_4 are constants of integration. In order to find their value, we numerically solve the differential equations by imposing some initial conditions. For the purpose of this study we take the following initial conditions.

$$\eta^{\hat{\beta}}(b) > 0, \dot{\eta}^{\hat{\beta}}(b) = 0. \quad (64)$$

where $\beta = \{r, \theta, \phi\}$. $\eta^{\hat{\beta}}(b)$ represents the separation between two nearby geodesics at $r = b$ in the radial and angular directions. The initial condition in Eq. (64) represents a mass released from rest at $r = b$. In the next sections we will discuss the components of radial and the angular deviation vectors in detail.

A. RADIAL COMPONENT

In Fig.(12) we have shown the radial component of the geodesic deviation vector after solving Eq. (60) with initial condition. It can be observed that for a fixed value of q and varying values of B and Λ, the geodesic separation increases as a test particle is released from a point $r = b$. The separation reaches a peak positive value at a particular radial coordinate that lies between the event horizon and the Cauchy horizon. After that, the separation vector starts to decrease rapidly and approaches infinity as $r \to 0$. It can be observed that increasing the value of B makes the peak value of deviation higher. Fig. (12) also shows the deviation trend for different values of q, keeping B and Λ constant. An opposite behavior is noticed when compared with the case having fixed values of q. Here, as the value of q is increased, the peak value of deviation decreases.

B. ANGULAR COMPONENT

Fig. (13) shows the angular deviation trend for a radially in-falling particle in AdS black hole using the initial condition in Eq. (64). Here, we fix the value of $q = 0.8$ and vary the values of B and Λ. It can be seen that the separation vector decreases monotonically up to a certain peak value as the particle approaches the spacetime singularity. It reverses its trend and starts growing rapidly and then fall to zero as $r \to 0$. Similar to the case of radial deviation, the angular separation vector also attains the peak value between the Cauchy and the event horizon. It can be noticed that increasing the value of B or equivalently the cosmological constant becomes more negative, the peak value of the separation vector increases as the particle approaches the central spacetime singularity. Fig (13) also shows the trend for changing values of q, keeping B and Λ fixed. Here we can see that increasing the value of q also increases the peak value of deviation attained.

VIII. CONCLUSION

In this paper, we have considered a black hole surrounded by Chaplygin dark fluid and studied thermodynamics in the presence of Bekenstien entropy, and examined the Joule-Thomson expansion. We studied the Joule-Thomson coefficient, the inversion temperature and we also graphed the isenthalpic curves in the $T_i - P_i$ plane. The Joule-Thomson coefficient is computed, and the inversion curves and the isenthalpic curves are discussed in AdS black holes surrounded by Chaplygin dark fluid. In the $T - P$ plane, the inversion temperature curves and isenthalpic curves are investigated with different parameters. In addition, we obtained the results of behaviors like Van der Waals fluid and the black hole to study their similarities and differences. We have compared our results with recent published papers [53–55].

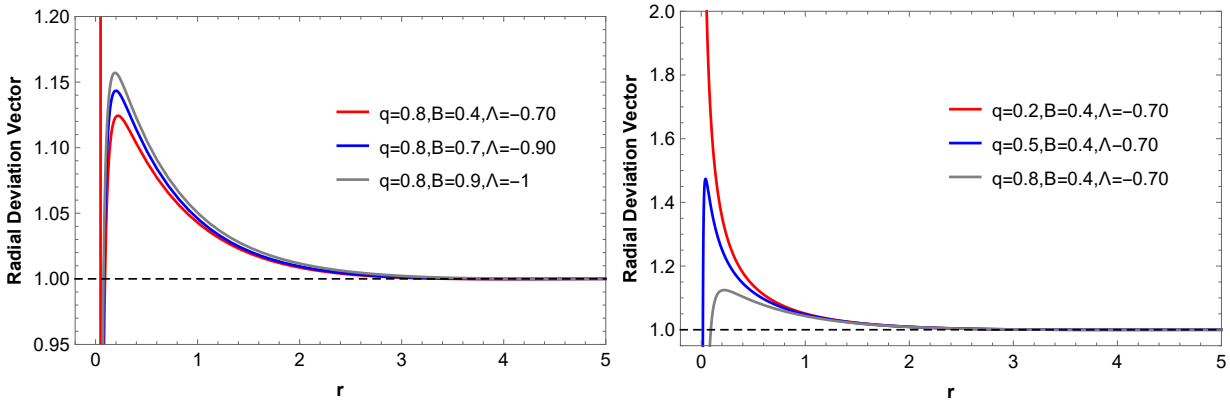


FIG. 12: Radial geodesic deviation profile for a radially in-falling particle in AdS black hole spacetime. We use $M = 1$ to show the trend for different values of the spacetime parameters q, B, Λ. We take $b = 5M$ as the starting position of the particle and $E = 3$ as the energy of the particle at the starting position.

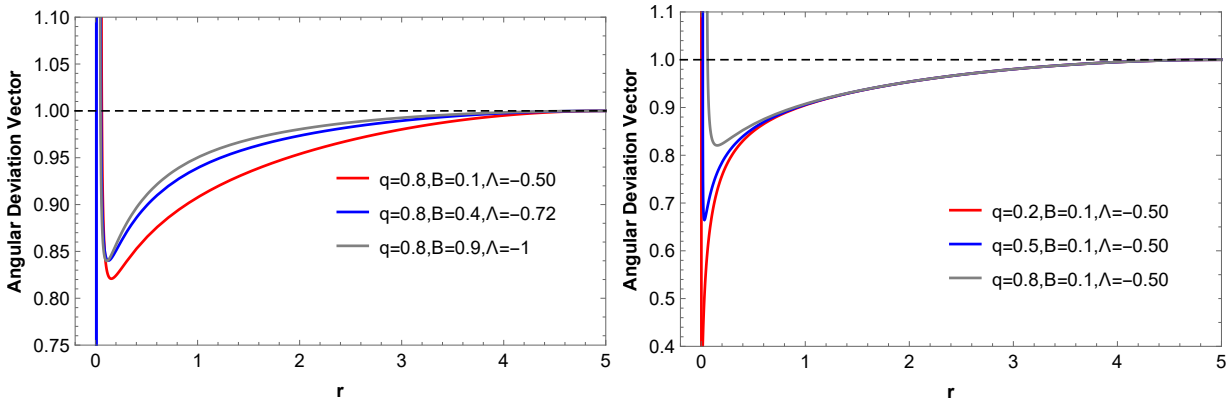


FIG. 13: Angular geodesic deviation profile for a radially in-falling particle in AdS black hole spacetime. We use $M = 1$ to show the trend for different values of the spacetime parameters q, B, Λ. We take $b = 5M$ as the starting position of the particle and $E = 3$ as the energy of the particle at the starting position.

We have also studied tidal force effects and geodesic deviation for a radially in-falling particle in AdS black hole surrounded by Chaplygin dark fluid. This work extends the pre existing literature on thermodynamics and observational techniques to test various theories of gravity, and aims to distinguish different classes of compact objects theorized in such literature. We have explored the radial and angular tidal forces acting on a particle freely falling towards the AdS black hole. It is noticed that both the tidal force profiles have some finite value as $r \to \infty$. This behaviour is solely governed by the presence of an effective non-zero cosmological constant. A peak value is attained for both the force profiles after which the tidal force rapidly falls to switch its behaviour i.e radial stretching gets converted into radial compression and vice versa. The peak value is attained between the Cauchy and the event horizon of the black hole. The radial tidal force is seen to become more of stretching nature as the value of B is increased or when the value of q is reduced. Similarly, as the value of B is increased or when q is reduced, the angular tidal force becomes more compressive

In addition to this, we have also examined the variation of geodesic separation vector with the radial coordinate for two nearby radial geodesics. To numerically solve the geodesic deviation equation we consider the initial condition where the particle is released from rest. We have studied two cases where in the first the value of q is kept as constant and in the second one, the value of B and Λ is kept constant. The separation between two adjacent geodesics for both the radial and angular profiles increases for increasing values of B or when the value of the cosmological constant becomes more negative. Similarly, the radial separation vector also increases when the value of q is decreased. The angular

separation vector shows opposite trend for changing values of q since it increases for higher values of q.

ACKNOWLEDGEMENT

This project was supported by the natural sciences foundation of China (Grant No. 11975145). The authors thank the reviewers for their comments on this paper.

DECLARATION OF COMPETING INTEREST

The authors declare that they have no known competing financial interests or personal relationships that could have appeared to influence the work reported in this paper.

DATA AVAILABILITY STATEMENT

This manuscript has no associated data, or the data will not be deposited. (There is no observational data related to this article. The necessary calculations and graphic discussion can be made available on request.)

[1] J. D. Bekenstein, Phys. Rev. D 7 (1973) 2333.
[2] J. M. Bardeen, B. Carter, and S. W. Hawking, Commun. Math. Phys. 31 (1973) 161.
[3] S. W. Hawking, Commun. Math. Phys. 43 (1975) 199.
[4] R. M. Wald, Living. Rev. Relativ. 4 (2001) 6.
[5] D. N. Page, New. J. Phys. 7 (2005) 203.
[6] S. W. Hawking and D. N. Page, Commun. Math. Phys. 87 (1983) 577.
[7] J. D. Bekenstein, Phys. Rev. D 9 (1974) 3292.
[8] W. S. Chung and H. Hassanabadi, Phys. Lett. B 793 (2019) 451.
[9] H. Hassanabadi, E. Maghsoodi and W. S. Chung, Eur. Phys. J. C 79 (2019) 358.
[10] H. Chen, B. C. Lütfüoglu, H. Hassanabadi and Z. W. Long, Phys. Lett. B 827 (2022) 136994.
[11] Y. Kumaran and A. Övgün, Chin. Phys. C 44 (2020) 025101.
[12] G. t Hooft, Nucl. Phys. B 256 (1985) 727.
[13] J. L. Cardy, Nucl. Phys. B 270 (1986) 186.
[14] S. W. Wei and Y. X. Liu, Phys. Rev. D 90 (2014) 044057.
[15] P. Chen and R. J. Adler, Nucl. Phys. B 124 (2003) 103.
[16] D. W. Yan, Z. R. Huang, N. Li, Chin. Phys. C 45 (2021) 015104.
[17] J. Y. Zhang and J. H. Fan, Phys. Lett. B 648 (2007) 133.
[18] X. X. Zeng and S. Z. Yang, Gen. Rel. Grav. 40 (2008) 2107.
[19] X. X. Zeng, J. S. Hou and S. Z. Yang, Pramana 70 (2008) 409.
[20] S. H. Hendi, Z. Armanfard, Gen. Relat. Gravit. 47 (2015) 125.
[21] S. H. Hendi, K. Jafarzade, Phys. Rev. D 103 (2021) 104011.
[22] E. Spallucci, A. Smailagic, Phys. Lett. B 723 (2013) 436.
[23] S. W. Wei and Y. X. Liu, Phys. Rev. D 87 (2013) 044014.
[24] D. C. Zou, S. J. Zhang, B. Wang, Phys. Rev. D 89 (2014) 044002.
[25] Y. B. Ma, R. Zhao, S. Cao, Eur. Phys. J. C 76 (2016) 1.
[26] A. Dehyadegari, A.Sheykhi, A. Montakhab, Phys. Lett. B 768 (2017) 235.
[27] D. Kastor, S. Ray, J. Traschen, Class. Quant. Grav. 26 (2009) 195011.
[28] D. Kastor, S. Ray, J. Traschen, Class. Quant. Grav. 27 (2010) 235014.
[29] D. Kastor, S. Ray, J. Traschen, Class. Quant. Grav. 28 (2011) 195022.
[30] D. Kastor, S. Ray, J. Traschen, Class. Quant. Grav. 36 (2018) 024002.
[31] S. H. Hendi and M. Vahidinia, Phys. Rev. D 88 (2013) 084045.
[32] A. M. Frassino, D. Kubizňák, R. B. Mann and F. Simovic, JHEP. 80 (2014) 2014.
[33] D. Kubiznak and B. R. Mann, JHEP. 07 (2012) 033.
[34] A. Belhaj, M. Chabab, H. El Moumni, and M. B. Sedra, Chin. Phys. Lett. 29 (2012) 100401.
[35] S. H. Hendi, B. Eslam Panah, and S. Panahiyan, Phys. Lett. B 769 (2017) 191.
[36] J. Maldacena, Int. J. Theor. Phys. 38 (1999) 1113.
[37] A. Belhaj, M. Chabab, H. El Moumni, L. Medari, and M. B. Sedra, Chin. Phys. Lett. 30 (2013) 090402.
[38] A. Belhaj, M. Chabab, H. El Moumni, K. Masmar, and M. B. Sedra, Int. J. Geom. Meth. Mod. Phys. 12 (2014) 1550017.
[39] A. Belhaj, M. Chabab, H. El Moumni, K. Masmar, and M. B. Sedra, Eur. Phys. J. C 76 (2016) 73.
[40] M. Chabab, H. El Moumni, and K. Masmar, Eur. Phys. J. C 76 (2016) 304.
[41] M. Chabab, H. El Moumni, S. Iraoui, and K. Masmar, Eur. Phys. J. C 76 (2016) 676.
[42] M. Chabab, H. El Moumni, S. Iraoui, and K. Masmar, Astrophys. Space Sci. 362 (2017) 192.
[43] A. Belhaj, M. Chabab, H. El Moumni, K. Masmar, M. B. Sedra, and A. Segui, JHEP. 05 (2015) 149.
[44] M. Chabab, H. El Moumni, S. Iraoui, K. Masmar, and S. Zhizeh, Phys. Lett. B 781 (2018) 316.
[45] Javed, F., Basit, A., Caliskan, A. and Gudekli, E.: Frontiers in Astronomy and Space Sciences, 10, p.1174029.

[46] Javed, F., Mustafa, G., Mumtaz, S., Atamurotov, F.: Nuclear Physics B, 990(2023)116180.

[47] Javed F, Fatima G, Sadiq S, Mustafa G.: Fortschritte der Physik. 5(2023)2200214.

[48] Ditta, Allah, et al.: Physics of the Dark Universe (2023): 101345.

[49] Rakhimova, Gulzoda, et al.: Nuclear Physics B 996(2023)116363.

[50] Ö. Ökcü and E. Aydiner, Eur. Phys. J. C 77 (2017) 24.

[51] Ö. Ökcü and E. Aydiner, Eur. Phys. J. C 78 (2018) 123.

[52] J. X. Mo, G. Q. Li, S.Q. Lan, X.B. Xu, Phys. Rev. D 98 (2018) 124032.

[53] J. X. Mo, G. Q. Li, Class. Quantum. Grav. 37 (2020) 045009.

[54] S. Q. Lan, Phys. Rev. D 98 (2018) 084014.

[55] J. T. Xing, Y. Meng, X. M. Kuang, Phys. Lett. B 820 (2021) 136604.

[56] J. Liang, B. Mu, P. Wang, Phys. Rev. D 104 (2021) 124003.

[57] Yasir M, Cheng XT, Javed F, Mustafa G.: Thermal analysis and Joule-Thomson expansion of black hole exhibiting metric-affine gravity. Chinese Physics C. 2023 May 23.

[58] A. Ditta, X. Tiecheng, G. Mustafa, et al. Eur. Phys. J. C 82 (2022) 1.

[59] R. D'Inverno, Introducing Einstein's Relativity (Clarendon Press, Oxford, 1992).

[60] M. P. Hobson, G. P. Efstathiou and A. N. Lasenby, General Relativity: an Introduction for Physicists(Cambridge University Press, New York, 2006).

[61] L. C. B. Crispino, A. Higuchi, L. A. Oliveira and E. S. de Oliveira. Eur. Phys. J. C 76, 168 (2016).

[62] M. U. Shahzad and A. Jawad. Eur. Phys. J. C 77, 372 (2017).

[63] M. Sharif and S. Sadiq. J. Exp. Theor. Phys. 153, 232 (2018).

[64] J. A. Marck. Proc. R. Soc. Lond. A 385, 431 (1983).

[65] D. Tsoubelis and A. Economou. Gen. Rel. Gravit. 20, 37 (1988).

[66] C. Chicone, B. Mashhoon and B. Punsly. Int. J. Mod. Phys. D 13, 945 (2004).

[67] C. Chicone and B. Mashhoon. Class. Quant. Grav. 22, 195 (2005).

[68] C. Chicone and B. Mashhoon. Annalen Phys. 14, 290 (2005).

[69] H. C. D. L. Junior, L. C. B. Crispino and A. Higuchi. Eur. Phys. J Plus 135, 334 (2020).

[70] N. Bade, S. Komossa and M. Dahlem. Astron. Astrophys. 309, L35 (1996).

[71] S. Gezari, D. C. Martin, B. Milliard, S. Basa, J. P. Halpern, K. Forster, P. G. Friedman, P. Morrisseyet, S. G. Neff and D. Schiminovich. Astrophys. J. Lett. 653, L25 (2006).

[72] S. V. Velzen, G. R. Farrar, S. Gezari, N. Morrell, D. Zaritsky, L. Ostman, M. Smith, J. Gelfand and A. J. Drake. Astrophys. J. 741, 73 (2011).

[73] Semiz, I., Rev. Math. Phys. **23** (2011) 865.

[74] Kiselev, V.V., Class. Quant. Grav. **20** (2003) 1187.

[75] Hulke, N., Singh, G.P., Bishi, B.K., Singh, A., New Astron. **77** (2020) 101357.

[76] Ray, S., Tripathy, S.K., Sengupta, R., Bal, B., Rout, S.M., Universe **8** (2023) 581.

[77] Nozari, K., Azizi, T., Alipour, N., Mon. Not. R. Astron. Soc. **412** (2011) 2125.

[78] Benaoum, H.B., Adv. High Energy Phys. **2012** (2012) 357802.

[79] Debnath, U., Banerjee, A., Chakraborty, S., Class. Quant. Grav. **21** (2004) 5609.

[80] Mak, M.K., Harko, T., Phys. Rev. D **71** (2005), 104022.

[81] Raposo, G., Pani, P., Bezares, M., Palenzuela, C., Cardoso, V., Phys. Rev. D **99** (2019) 104072.

[82] G. Mustafa, S. K. Maurya, A. Ditta, Saibal Ray, Farruh Atamurotov, arXiv:2311.13839 .

[83] Li, X.Q., Yan, H.P., Xing, L.L., Zhou, S.W., Phys. Rev. D **107** (2023) 104055.

[84] T. P. Singh and P. S. Joshi, Classical and Quantum Gravity, 13(3):559, 1996.

[85] E. Falcon-Gomez et al., Eur. Phys. J. C, 82(12):1175, 2022. [Erratum: Eur.Phys.J.C 83, 234 (2023)].

[86] E. Mitsou and J. Yoo, Springer Briefs in Physics. Springer, 6 2020.

[87] R. M. Wald, University of Chicago press, 2010.

[88] L. C. B. Crispino et al.,The European Physical Journal C, 76:1–7, 2016.

Hindawi
Wireless Communications and Mobile Computing
Volume 2023, Article ID 2744706, 29 pages
https://doi.org/10.1155/2023/2744706

Research Article

Localization and Detection of Multiple Attacks in Wireless Sensor Networks Using Artificial Neural Network

Gebrekiros Gebreyesus Gebremariam,[1,2] **J. Panda**,[2] **and S. Indu**[2]

[1]*Department of Electronics and Communication Engineering, Raya University, Maychew, 7020 Tigray, Ethiopia*
[2]*Department of Electronics and Communication Engineering, Delhi Technological University, Shahbad Daulatpur, Main Bwana Road, Delhi 110042, India*

Correspondence should be addressed to Gebrekiros Gebreyesus Gebremariam; kiros2004comp@gmail.com

Received 11 June 2022; Revised 30 November 2022; Accepted 19 December 2022; Published 10 January 2023

Academic Editor: Javier Prieto

Copyright © 2023 Gebrekiros Gebreyesus Gebremariam et al. This is an open access article distributed under the Creative Commons Attribution License, which permits unrestricted use, distribution, and reproduction in any medium, provided the original work is properly cited.

Security enhancement in wireless sensor networks (WSNs) is significant in different applications. The advancement of routing attack localization is a crucial security research scenario. Various routing attacks degrade the network performance by injecting malicious nodes into wireless sensor networks. Sybil attacks are the most prominent ones generating false nodes similar to the station node. This paper proposed detection and localization against multiple attacks using security localization based on an optimized multilayer perceptron artificial neural network (MLPANN). The proposed scheme has two major part localization techniques and machine learning techniques for detection and localization WSN DoS attacks. The proposed system is implemented using MATLAB simulation and processed with the IBM SPSS toolbox and Python. The dataset is classified into training and testing using the multilayer perceptron artificial neural network to detect ten classes of attacks, including denial-of-service (DoS) attacks. Using the UNSW-NB, WSN-DS, NSL-KDD, and CICIDS2018 benchmark datasets, the results reveal that the suggested system improved with an average detection accuracy of 100%, 99.65%, 98.95%, and 99.83% for various DoS attacks. In terms of localization precision, recall, accuracy, and f-score, the suggested system outperforms state-of-the-art alternatives. Finally, simulations are done to assess how well the suggested method for detecting and localizing harmful nodes performs in terms of security. This method provides a close approximation of the unknown node position with low localization error. The simulation findings show that the proposed system is effective for the detection and secure localization of malicious attacks for scalable and hierarchically distributed wireless sensor networks. This achieved a maximum localization error of 0.49% and average localization accuracy of 99.51% using a secure and scalable design and planning approach.

1. Introduction

Hierarchically distributed microsensor nodes in the field are linked together with multihop wireless communication technologies to form a wireless sensor networks (WSNs) [1]. The sensor nodes have sensing and wireless communication modules, storage, and processing units. Wireless sensor networks (WSNs) monitor and collect network information, including network state and data transmission. They also monitor object positioning and tracking [2]. WSNs are vulnerable to multiple, including Sybil attacks, wormhole attacks and eavesdropping [3]. The Sybil attack is the most harmful routing attack that fabricates and depreciates multiple fake identities launching a malicious attack on the legitimate node to lower service quality [4, 5]. It is the key research challenge in wireless sensor networks like the other applications, including architecture, healthcare, disaster management, deployment quality of service, calibration [6], and synchronization. Wireless sensor nodes sense and record data from the environment and send the data to the cluster head for the aggregation process. An intelligent sensing and computing framework is essential for the security localization and detection of attacks using an artificial neural network (ANN). This scheme is gaining attention due to its low computational cost and faster convergence. In this paper we proposed an optimized multilayer perceptron artificial

neural network for detection and localization of routing attacks in WSNs.

Emerging applications of wireless sensor networks (WSNs) include traffic management and object tracking, both of which require localization of sensor nodes [7]. For efficient routing and location-aware services, it is crucial to have an accurate estimation of the sensor node location. Without knowing where the sensor is located, the data collected by WSN is often useless. As a result of their potential utility in a wide range of WSN applications, the localization techniques are garnering a rising amount of attention from researchers. Based on the information required, localization techniques can be divided into two broad categories: range-based techniques, which rely on the known distances or angles between nodes to make location estimates, and range-free techniques, which instead make location estimates based on the closeness of a number of reference nodes. Range-free approaches are replacing range-based methods in WSN localization due to their lower hardware and computational requirements. The clustering and localization algorithm is a well-known example of a range-free technique since it uses adjacent reference nodes' positions to estimate the node's own location. During the setup phase, the starting positions of the reference nodes are either hard-coded or computed.

1.1. MLPANN Applications in WSNs. Network traffic identification is becoming increasingly popular as a field of study in the field of network administration, drawing researchers from all over the world [8]. The growth in network capacity is closely proportional to this rise. New forms of network applications, such as peer-to-peer (P2P) file sharing, have rendered some of the more traditional methods of traffic identification, including port-based or deep packet inspection, ineffective. Selecting an appropriate feature selection method, which can select the best features according to the impact of the great traffic behaviour characteristics, is essential for achieving higher recognition efficiency and greater identification accuracy when performing traffic identification based on ML (Machine Learning). The MLP (Multilayer Perceptron) approach is superior to other identification algorithms in terms of identification accuracy. It has been shown that as the number of training samples grows, the identification rate also rises. But MLP is not without its own value and drawbacks that mean it needs to be enhanced.

There is now a great deal of academic focus on creating fingerprint localization algorithms that make use of artificial neural networks (ANNs). Despite noisy RSSI measurements, the ANN can still give accurate recognition of the node's position, which is a major advantage. Using ANNs eliminate the need for detailed knowledge of the indoor environment or the locations of reference nodes. In order to approximate a mapping between the multidimensional fingerprint space and the coordinates of nodes, ANN interpolates the acquired data in the fingerprint database. During the ANN's training process, the collected RSSI vectors are used to fine-tune the weights of connections between neurons. Although training may take a while, the localization process is far faster than any analytical estimates of the node's position.

Multilayer perceptron (MLP) is the most widely utilized ANN architecture in modern range-free wireless sensor node localization applications. In WSN, fingerprint-based localization was accomplished using the MLPANN. For this evaluation, we evaluated 43 distinct backpropagation training algorithms to determine the method's accuracy. Something very close to that was proposed as a tactic. The ANN training has been kept up-to-date at regular intervals so it can adjust to changing conditions on the wireless channel. Four MLPANNs, each with a different amount of inputs, formed an ensemble that was shown to the audience. This tactic specifies that, if the localization operation must be executed, an ANN with the same number of inputs as the currently connected reference nodes is selected and issued. Given the poor scalability of this approach, we settled on a cap of four connections between reference nodes. When compared to methods based on fuzzy learning systems or genetic algorithms, the localization results generated by the ANNs ensemble were shown to be more reliable. Here we propose a cooperatively optimized and secure multilayer perceptron artificial neural network (MLPANN) for scalable and broad area networks that combines range-based and range-free localization technique approaches from the realm of artificial intelligence (AI) to problems inherent to wireless sensor networks (WSNs) [9], such as data aggregation and fusion, routing, task scheduling, optimal deployment, and localization as shown in Figure 1. In this context, the term "computational intelligence" refers to a subfield of machine learning that combines techniques with roots in biology, such as neural networks, fuzzy systems, and evolutionary algorithms, to develop forecasting models. This algorithm for learning could be built using cascading decision chains for recognizing nonlinear and complex functions. However, the high-computational requirements for learning the network weights and the substantial administrative overhead mean that distributed neural networks are not yet widely used in WSNs. Neural networks, on the other hand, are well-suited for handling many network difficulties with a single model because of their ability to simultaneously learn multiple outputs and decision boundaries in centralized solutions.

1.2. WSN Routing Attacks. Attacks on the wireless sensor network's network layer can hinder performance by rendering a genuine node unreachable to the service. The following section will go through some of the more common types of attacks seen in WSNs. With these kinds of attacks, sensitive data is compromised before it even reaches the target node. The attacks in wireless sensor networks operate in all layers of the network exploiting resources and degrading the service quality of the network.

1.2.1. Wormhole Attack. The wormhole attack is created by two malicious nodes having a tunnel path in the two locations and misapprehension. Wormhole attack attracts and manipulates significant network data traffic launching various attacks. It advertises its packets using the intermediate nodes to sniff, modify, and drop from reaching the destination [10]. Figure 2 cluster A shows a wormhole attack scenario depicting when source node S sends the packet to the sink node. A

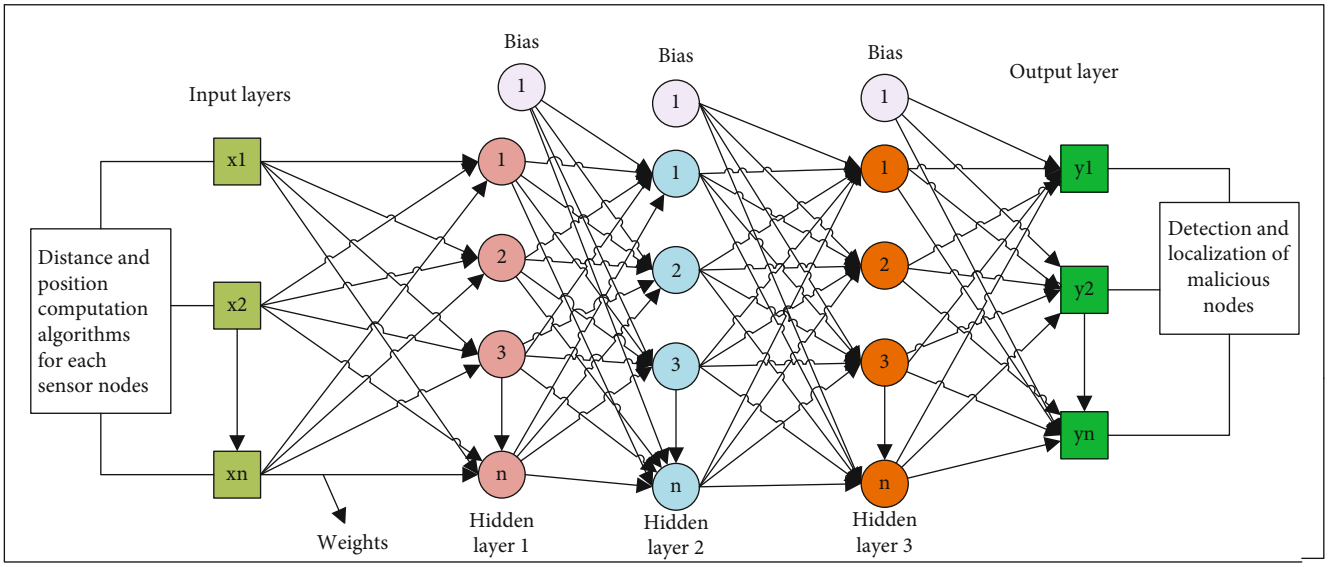


Figure 1: Illustration of MLPANN for detection and localization of WSN attacks based on localization algorithms.

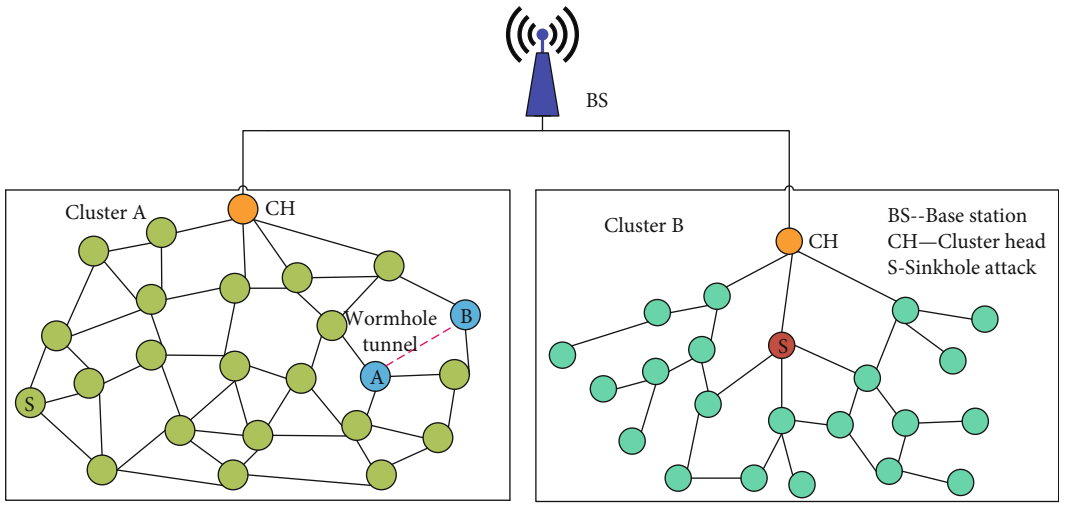


Figure 2: Illustration of wormhole and sinkhole attacks in WSNs in cluster A and B, respectively.

wormhole tunnel is created between malicious nodes A and B. The packet is dropped and modified by the tunnel before reaching the base station. At least the two hostile nodes employing a secure communication channel known as a tunnel can detect a wormhole assault [11]. It is at this point that the wormhole tunnel will begin to collect the data packets and forward them on. The malicious node on the other end of the tunnel receives a control packet. At the other end, it uses a private channel to relay the packet to another node that has caught its attention. For enhanced metrics, such as fewer hops or less time, the private channel is selected as the conduit for communication between the source and the destination. The attack usually consists of two phases. Multiple initial directions are of relevance to the wormhole nodes. The second stage is when the packets begin to make use of the malicious nodes. It is possible for these nodes to hinder the network's performance in a number of ways. Wormhole nodes can be used to steal information or communicate it to a third party if they delete, tamper with, or send it.

1.2.2. Sinkhole Attack. Sinkhole attack advertises routing paths to the base stations, making itself a normal node misguiding the neighbor nodes that cause threats to the network. The malicious nodes create a hole in the routing path that can damage the regular operations of the network. The sinkhole attack uses a compromised node with fewer hops to advertise the route to the destination. This misuse of routing information misguides the legitimate node and attracts the node closer. Figure 2 cluster B illustrates the scenario of a sinkhole attack for attracting and capturing packets from the neighbor nodes. The sinkhole attack utilizes a secret tunnel for attracting nodes and capturing packets. The malicious node then deceived and sent packets to the base station.

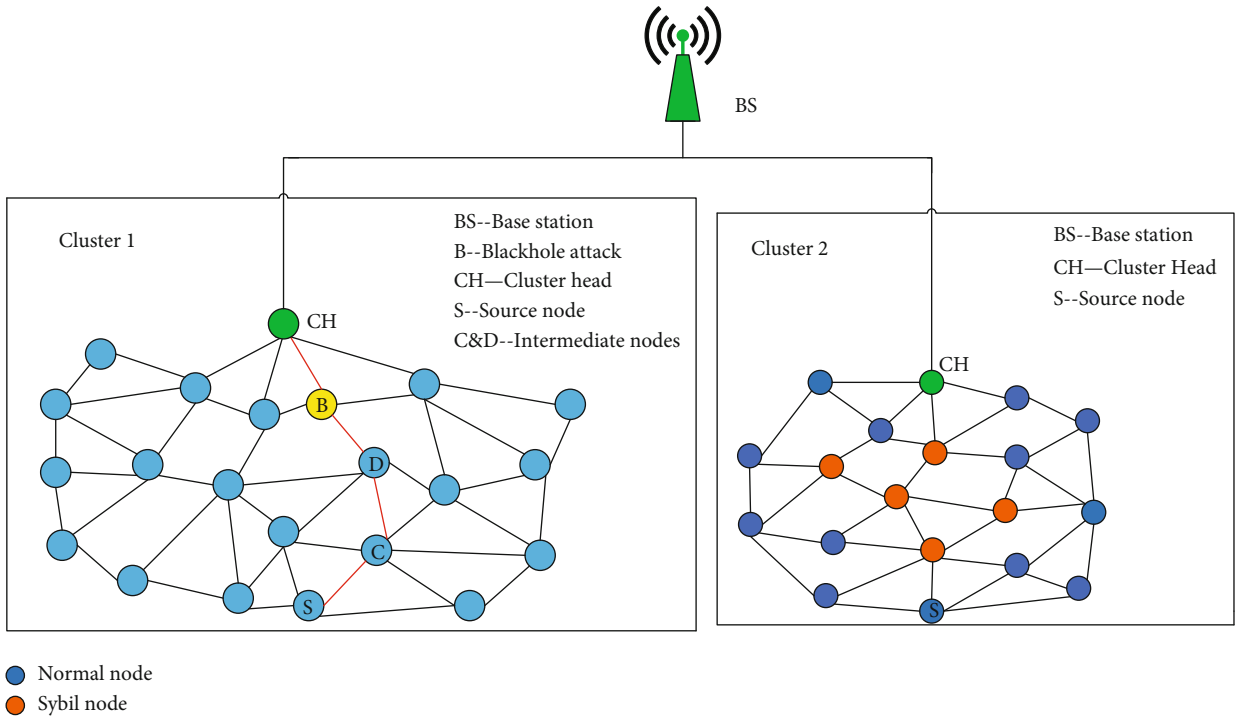


Figure 3: Illustration of blackhole and Sybil attack scenario in WSNs for cluster 1 and cluster 2, respectively.

1.2.3. Blackhole Attack. Blackhole attacks capture and reprogram sensor nodes to block packets instead of receiving and forward to the base station [10]. The blackhole attack compromises the information with the malicious node that enters the blackhole region. The blackhole attack undermines the network performance by using the network partitioning so the essential updates cannot reach the base station. It degrades the network performance metrics and consumes large network traffic. The source node S sends a packet to the base station using the intermediate C and D nodes, as shown in Figure 3 of cluster 1. The blackhole node consumes the entire traffic and is not forwarded to the destination node.

The blackhole attack performs suspicious activity using loopholes for discovering the routing [12]. The blackhole attack compromises the legitimate node with a malicious node so that the packets are dropped and unable to reach the destination nodes. The suspicious node cause packet is dropping for targeted nodes and customizing set of nodes for packet dropping. The information that comes to the blackhole is dropped and sent fake packets to the base station. The routing requests and routing response messages by the blackhole attacks have higher order number which is greater than the normal node request and response so that the normal node will not respond to the routing request with higher order number which causes deletion of routine from the networks [13].

1.2.4. Sybil Attack. Sybil attack forges and spoofs the identity of the legitimate node in wireless sensor networks [14]. Sybil attack interrupts the routing table and the trust value of the node of the legitimate node. Sybil attack duplicates multiple identities for confusing the neighbor nodes [15]. This attack uses geographic routing protocols for targeting authorized nodes. Sybil attack takes numerous identities to disguise the storage entities of the legitimate node [16], as shown in Figure 3 of cluster 2. The malicious node transmits data with imaginary events multiple times. This type of attack creates illusion that makes it difficult to detect the whole network.

1.3. Problem Formulation. Most of the existing literature review papers dealt with single attacks with low localization and detection accuracy in WSNs. Thus the deployment of wireless sensor nodes seeks optimal and intelligent localization methods for accurate node position and attack identification. To overcome this problem, it is essential to design and implement a new effective technique. This paper proposes a security localization and detection scheme employing optimized multilayer perceptron artificial neural network for various classes of attacks against wireless sensor networks, which are vulnerable to a wide variety of denial-of-service (DoS) attacks that exploit the network's resources. The proposed method is designed for multiple attack detection and classification, representing the input and output relationships using the ANN technique. The design and planning of distributed hierarchical clustered topology are also discussed that consists of sink node, cluster head, malicious and sensor nodes as shown in Figure 4. Also, we discuss the effectiveness of the proposed system using the benchmark datasets including CICIDS2018, UNSW-NB 15, WSN-DS and NSL-KDD with different evaluation metrics using training and testing samples as a benchmark for performance evaluation. The dataset is processed using batch mode.

1.4. Research Contribution. The proposed attack localization and detection scheme is based on an optimization multilayer

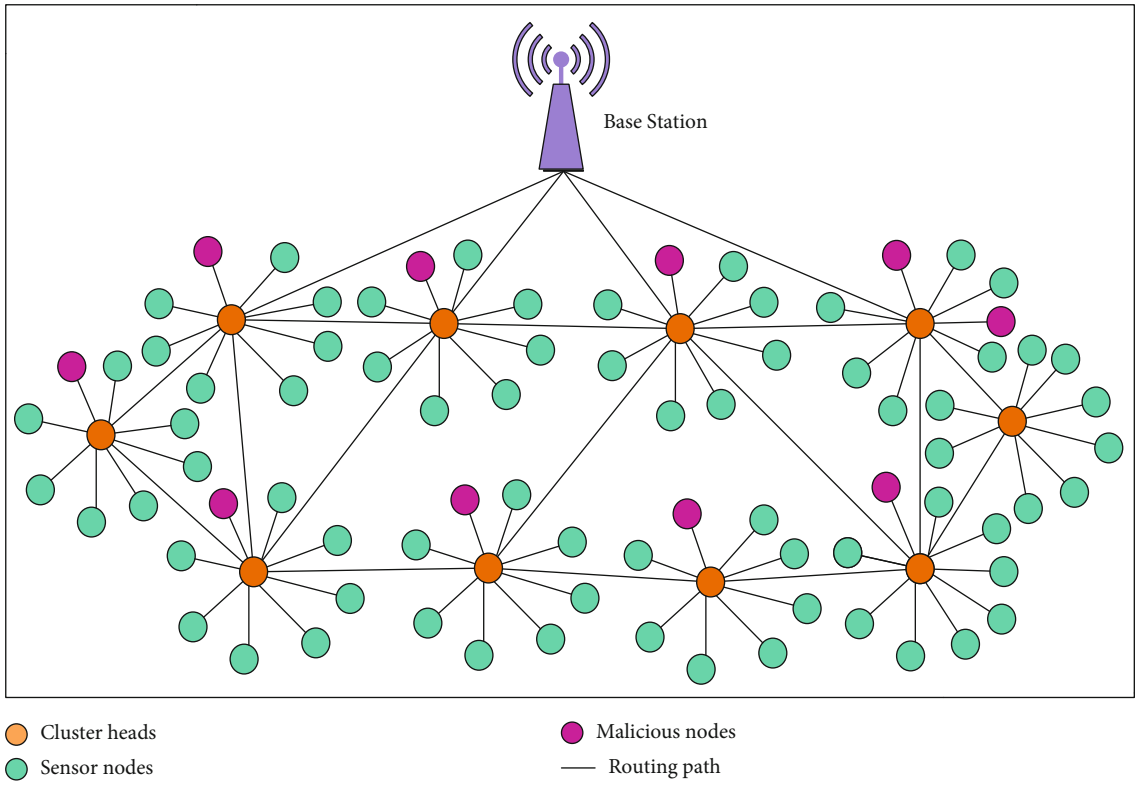


Figure 4: Clustering in hierarchically distributed wireless sensor network model.

perceptron neural network [17]. The proposed system possesses different phases with the proper network planning and node configuration. These include network data processing and feature extraction, training, and testing for attack detection and classification. Some of the novel contributions of this work are as follows:

(1) To design and simulate wireless sensor network topology with attack detection and localization features

(2) To explore the various routing attacks and techniques simulating these attacks using clustering and routing protocols

(3) Evaluate the network performance using a sample public dataset as a benchmark with attack detection localization metrics

(4) Explore machine learning techniques secure localization and detection of routing in wireless sensor networks in all layers of the network

(5) A multilayer perceptron neural network technique enables the detection and classification of malicious nodes using network traffic data and feature extraction. It maximizes the location and position accuracy of the suspicious node

(6) To detect and localize multiple attacks with greater classification accuracy for clustered and hierarchical network architecture

(7) Measure the security performance of the scheme using comparison performance for effective validation and confirmation with similar previous works

(8) Explore hybrid range-based and range-free localization techniques for unknown and malicious nodes that affect quality of service in WSN using collaborative approach

The rest contents of this paper are organized into different sections and structures. Section 2 encompasses the previous literature works. Section 3 describes the network and attack models depicting graphically in detail using clustering and routing protocols. The next part is Section 4, which discusses the proposed attack localization and detection technique in WSNs using MLPANN approach. The next Section 5 details the simulation and experimental analysis using a benchmark dataset for different classes of routing attacks. The last section is Conclusion and remarking for future works.

2. Related Works

Messous and Liouane [1] presented an online successive distance vector hop scheme for node localization accuracy in WSNs. They also discussed the variation of anchor nodes with optimized distance between nodes in the network. Dong et al. [2] examined the distance vector hop algorithm against Sybil attacks for effective node localization and

accuracy for improved security in WSN. The scheme also reduces the average error localization by 3%, setting the beacon nodes 50 in the simulation that is 78%. Chelouah et al. [18] addressed localization algorithm in mobile WSNs. They also presented the mobility of nodes for coverage optimization, connectivity, and analysis. Hadir et al. [19] presented a localization technique in WSNs using an effective distance vector hop scheme. They also discuss the average hop size and localization accuracy by exploiting the information. Almomani et al. [20] designed a low cost and efficient, intelligent DoS attack detection and prevention technique. They also discuss different DoS attack classifications using a specialized dataset for WSN. Patel and Mistry [21] presented Sybil node detection [22] using various schemes. They also discussed and analyzed the protocols used in WSNs. Yavuz et al. [23] proposed detecting IoT-routing attacks using a deep learning machine learning technique. The Cooja simulator generates high-fidelity attack data in the IoT network with 1000 sensors. Sujatha and Anita [24] examined the detection of Sybil attack detection using hybrid fuzzy and powerful extreme learning machines. They also discussed ARM as the main CPU with LEACH environment and ZigBee transceivers on real-time testbeds. Qi et al. [25] researched a localization algorithm to improve the node position accuracy and reducing localization error in WSNs using MA-MDS. They also use the Prussian analysis algorithm for accurate coordinate transformation. Li et al. [26] presented a localization trust valuation scheme to detect spoofing and Sybil attacks. This scheme is obtained by selecting localization performance, estimated distance, and transmission with the threshold property set in WSNs. Song et al. [27] proposed a chaotic hybrid mutation and chaotic inertial weight-updating technique with a glowworm swarm optimization approach. The scheme also avoids premature convergence with better convergence and higher accuracy. Saud Khan and Khan [28] presented Sybil attack detection using signed response authentication techniques for global mobile communication systems. They also discussed the probabilistic model to analyze Sybil attack detection performance.

Abbreviations, acronyms, and shorter variants of terms and phrases used as resources in this paper are included as shown in Table 1

3. Network Model

Sink, cluster head, sensor, and attacker nodes are all represented in the simulated network. The sensor nodes tend to group together throughout the system. When sending information to the beacon nodes and the base station, each cluster chooses its own cluster head node to act as the central hub for that cluster. The beacon nodes decide on the optimal routing path by employing an optimization strategy based on a fitness function. In this context, the terms beacon nodes and anchor nodes are synonymous. Sybil attacks and wormhole assaults are the types of attacks that can be used against this network paradigm. The positioning and placement of anchor nodes are dependent on their relationship to other nodes. Once an anchor node has been put in a network, it will remain in the same location permanently. The sensor nodes have claimed their territory. The localization scheme is used for providing accurate position and location of the sensor nodes by making clustering of the nodes having one cluster head for each group [29, 30]. Unknown nodes locate their positions using the anchor node assistance. Sensor nodes update their locations periodically by the system. Malicious nodes broadcast their positions by creating multiple fake identities and advertising themselves as the beacon nodes. The malicious node also creates tunnels for dropping packets before reaching the destination. The hierarchical clustering of the sensor deployments enables less energy consumption and enhances the network life time as shown in Figure 4.

The legitimate nodes are assumed to be homogenous in computational processing, storage capacity, communication level, and activation energy in the model [31]. Malicious nodes are considered more effective than the legitimate node for the activity in capturing the security key of the base station and clusters. The attacker disrupts the normal functioning of the network by cloning the authorized node.

3.1. Cluster Formation and Data Aggregation. Clustering is a method of organizing a set of sensors to increase the durability of the network and decrease its power consumption [32]. The network's sensor nodes are organized into groups of similar devices. Collectively, the sensor nodes that make up the cluster gather data and send it on to the cluster coordinator. The data is aggregated and filtered by the cluster head before being sent to the hub. The sensor's stable functioning and neighbor evaluation are aided by the clustering method. Cluster heads (CHs) are the most important nodes in the cluster since they serve as the hub for monitoring. The three selection criteria are used to determine which of the sensor nodes will become the cluster head.

(i) The number of nearby neighbor nodes

(ii) The quality of the received signal from the sensor node

(iii) The node's remaining energy before it is activated

(iv) The minimum distance to the base station as calculated by the distance vector protocol. The distance D between any two sensor nodes is computed using the distance vector technique as shown below

$$D = \sqrt{\left(u_i - u_j\right)^2 + \left(v_i - v_j\right)^2}. \quad (1)$$

The u and v coordinate for nodes i and j, respectively. Computing the distance between the base stations to any node with a small distance is likely the cluster head. The energy employed for the communication and activation of the network model is evaluated by setting the threshold parameters with the multipath model approach. The amount of energy E_{TX} for k-bits of data transmission over D distance and D_o threshold distance is given as in

Table 1: List of abbreviations and acronyms used in this paper.

Abbreviations	Descriptions
BS	Base station
WSNs	Wireless sensor networks
CH	Cluster head
D	Distance
E	Energy of the sensor node
RSSI	Received signal strength indicator
DV-H	Distance vector hop
IoT	Internet of Things
ANN-IDS	Artificial neural network-based intrusion detection system
FEMs	Fuzzy extreme machines
MK-ELM	Multikernel extreme learning machine
LEACH-ANN	Low-energy adaptive clustering hierarchy based on ANN
CNN-MCL	Convolutional neural network and mean convolutional layer
HTM-LSTM	Hierarchical temporal memory and long short-term memory
MLPANN	Multilayer perceptron artificial neural network
RL-IDS	Reinforcement learning-based IDS
GBFS-IDS	Gradient boosting feature selection for IDS
ML-ID	Machine learning-based intrusion detection
UWB	Ultrawide band
DI-ADS	Deep intelligent attack detection scheme
PO-CFNN-	Political optimizer based on cascade forward neural network
RNN	Recurrent neural network
ECGAL	Energy-efficient clustering and localization centered on genetic algorithm
LSTM-FFNN	Long short-term memory and feed-forward neural network
DNN-CSO	Deep neural networks with chicken swarm optimization

$$E_{TX} = \begin{cases} k \times E_e + k \times E_f \times D^2, & \text{if } D \le D_o, \\ k \times E_e + k \times E_m \times D^4, & \text{if } D > D_o, \end{cases} \quad (2)$$

where E_{TX} is the transmitted energy, E_f is the reception energy, and E_e is the power dissipated in the transmitter or receiver for single-bit data transmission. The dissipated energy depends on signal spreading, filtering, modulation, and channel-coding factors. The threshold transmission distance D_o with k-length of data transmission is given by

$$D_o = \sqrt{\frac{E_f}{E_m}}. \quad (3)$$

For k-bits of message reception, the energy consumed by the receiver node is

$$E_{\mathrm{RX}(k)} = k \times E_e. \quad (4)$$

3.2. Localization Techniques. Numerous wireless sensor network (WSN) applications rely on localization to locate a target by comparing the signal strengths of transmitters and receivers already set up in the region of interest [33, 34]. Some algorithms are essential for finding and assessing the location and position of the nodes and security enhancement for precise location of the target. The scheme is divided into range-based and range-free localization techniques. The latter one is cost-effective with special hardware requirements. The received signal strength indicator (RSSI) and distance vector hop localization algorithms evaluate wireless sensor node accurate position and location. The distance vector localization procedure is essential to compute the coordinates of the sensor nodes and cluster heads using the beacon nodes [1]. The scheme calculates and manipulates the position and distance of the unidentified nodes. The distance vector hop procedure helps to find the spaces among the beacon nodes in WSN. The calculated minimum distance is the average hop size using the distance vector approach. This algorithm was first identified by [2]. The distance vector localization scheme is a range-free strategy [19] with a series of steps in Table 2.

The average distance hop for the anchor node is computed and obtained relative to another beacon with the minimum hop count given by

$$\mathrm{HS}_i = \frac{\sum_{i \ne j} \sqrt{(ui - uj)^2 + (vi - vj)^2}}{\sum_{i \ne j} hij}. \quad (5)$$

The interpretation of the variables is shown in Table 3.

Table 2: Steps in distance vector technique for computing the position of unknown nodes.

Steps	Description of steps
Routing initialization	Beacon node broadcasts to all nodes and the hop count of its location information with 0 value initialized in the network [19].
Calculating distance	The average size of the hop and the unknown node distance is calculated with the assistance of the beacon node.
Position estimation	Unknown nodes estimate their position by the triangulation algorithm or maximum likelihood estimators or polygon method with the help of the anchor node.

Table 3: Equation (1) variable description and interpretation.

Variable	Description of the variable
i, j	True anchor nodes
$(ui, vi), (uj, vj)$	The known and true coordinates for i and j
Hij	Hop counts of the anchor nodes
HSi	Average hop distance

Anchor node transmits its information [2] followed by hop-size calculation. The distance between sensor node and anchor computed with hop-size details is given by

$$D_{pk} = HpSi_{i\times} hp_{pk}. \tag{6}$$

The polygon technique enables the estimation of the position (P) of each anonymous node. P is the spot of the unidentified node denoted as (u, v) and di, the space among anchor and indefinite nodes. The position of the strange node p assuming n beacon nodes involved is estimated by [2].

$$\begin{aligned}
(u-u_1)^2 + (v-v)^2 &= {D_1}^2,\\
(u-u)^2 + (v-v)^2 &= {D_2}^2,\\
&\vdots\\
(u-u_n)^2 + (v-v_n)^2 &= {D_n}^2.
\end{aligned} \tag{7}$$

We can get a set $(n-1)$ of expressions subtracting from the first equations to make the system linear, given as depicted in

$$\begin{aligned}
{u_1}^2 + v^2 - {u_n}^2 - {v_n}^2 - 2(u-v_n)u - 2(v_1-v_n)v &= {D_1}^2 - {D_n}^2,\\
{u_2}^2 + {v_2}^2 - {u_n}^2 - {v_n}^2 - 2(u_2-u_n)u - 2(v_2-v_n)v &= {D_2}^2 - {D_n}^2,\\
&\vdots\\
{u_{n-1}}^2 + {v_{n-1}}^2 - {u_n}^2 - {v_n}^2 - 2(u_{n-1}-u_n)u - 2(v_{n-1}-v_n)v &= {D_{n-1}}^2 - {D_n}^2.
\end{aligned} \tag{8}$$

Rearranging the previous equations into the formula of ui $= \mathrm{BA}^{-1}$, where A, ui, and B are expressed as in

$$A = \begin{cases} 2(u-u_n)2(v_1-v_n), \\ 2(u_2-u_n)2(v_2-v_n), \\ \vdots \\ 2(y_{n-1}-u_n)2(v_{n-1}-v_n), \end{cases} \tag{9}$$

$$B = \begin{cases} {u_1}^2 + v^2 - {u_n}^2 - v^2 + {D_n}^2 - {D_1}^2 \\ {u_2}^2 + v^2 - {u_n}^2 - {v_n}^2 + {D_n}^2 - {D_2}^2 \\ \vdots \\ {u_{n-1}}^2 + {v_{n-1}}^2 - {u_n}^2 - {v_n}^2 + {D_n}^2 - {D_{n-1}}^2 \end{cases}, \tag{10}$$

$$U_i = \left(\frac{u}{v}\right). \tag{11}$$

The location of the node is computed solving the least square method stated as in

$$U = \left(A'A\right)^{-1} A'B. \tag{12}$$

The clustering and distance vector-routing protocols are used in the proposed scheme for effective wireless sensor network deployment.

In contrast to its range-based equivalents, RSSI-based localization algorithms have gained a lot of traction in the academic community for a variety of compelling reasons [35]. Today's wireless sensor nodes typically include features like RSSI measurement and data transmission to higher stack layers. For RSSI-based localization, no time-synchronization between nodes, ultrawide band (UWB) radios for more precise time of arrival calculations, or antenna arrays are needed. In terms of both software and hardware, it is a straightforward and inexpensive approach to achieving node localization. However, the DV-hop algorithm completely skips measuring the real distances between the one-hop neighbor nodes and leveraging these distances for more precise localization in massive-scale wireless sensor networks.

To localize wireless nodes using the DV-hop technique, the hybrid approach takes two extra steps, as indicated above for improvement of the localization accuracy and malicious

node detection. Instead of relying on the average hop distance like the original DV-hop algorithm did, we first use the RSSI data to estimate the distances between the anchor nodes and their one-hop surrounding sensor nodes. Using the RSSI value does not necessitate any specialized hardware or additional expenditures because the MAC sublayer in most modern wireless sensor nodes computes RSSI value for every received packet and sends that value to higher layers. Second, after a sensor node N has been located, it is elevated to the role of anchor, which is utilized to localize other sensor nodes. With more (repurposed) anchor nodes to work with, the remaining sensor nodes can be localized with greater precision. That is especially useful in wireless networks when there are fewer anchor nodes. Third, differential evolution (DE) is a technique used in evolutionary computation to find the optimal solution to a problem by iteratively trying to enhance a candidate solution with respect to some quality metric. Metaheuristics are approaches that search enormous spaces of possible solutions while making few or no assumptions about the underlying problem. Unfortunately, metaheuristics like DE cannot promise you will get the best possible result every time.

Since DE does not rely on the gradient of the optimization problem, DE can be applied to optimization problems involving multidimensional real-valued functions even if the problem cannot be differentiated, as is the case with traditional optimization techniques like gradient descent and quasi-newton methods. For this reason, DE can be applied to optimization problems that are inherently noncontinuous, noisy, dynamic, etc. Using its basic equations, DE optimizes a problem by keeping a population of candidate solutions, generating new candidate solutions by merging old ones, and finally keeping the candidate solution with the highest score or fitness on the optimization task at hand. As a result, the gradient is unnecessary because the optimization issue is viewed as a black box that only delivers a measure of quality given a candidate solution.

The problem of the localization of techniques is transformed into multilayer perceptron artificial neural network by computing the distance and position of each type of nodes with unique identity for detection and localization of the malicious nodes as shown in Figure 5. The sensor nodes in our purpose are assumed to both homogenous and heterogeneous wireless sensor networks. The beacon nodes have high-computational data processing and have their own localization that helps for other nodes to estimate and compute their location and positon of the ordinary sensor nodes in the network. Adding machine learning to WSN localization helps increase the precision of range-free node positioning [36]. In particular, the use of artificial neural networks (ANNs) in range-free localization algorithms has significantly improved their accuracy and performance compared to more conventional methods. The MLPANN learning strategy is needed that starts with a labelled dataset in order to construct a model that can appropriately generalize to data that was not included in the training set before we can make any adjustments to the weights [37].

3.3. Attack Model. One hundred nodes are distributed randomly in 1000×1000 m square areas with sensor, cluster head, and malicious nodes. The proposed scheme aims to enhance the detection accuracy of security localization [2] to routing attack using the distance vector hop procedure and clustering protocols in WSN using an artificial neural network approach. Figure 6 is the Sybil attack model with three sets of wireless nodes. A Sybil attack is a type of network assault in which a malicious node purposely and illegally displays a large number of forging or false identities to other sensor nodes [38]. This is accomplished by either independently generating new identities or illegally assuming the identities of other sensor nodes. By creating an unpredictable number of fake node identities, a Sybil node might interfere with WSN operations like multipath routing, which uses a variety of routes to find the best one between a source and a destination. The attack model shows how malicious nodes launch fake behaviors creating multiple identities against the position and location of the legitimate node with various routing paths. This degrades the lifetime of the network by reducing the computational performance of the authorized nodes.

The other routing attacks including scheduling, blackhole, grayhole and flooding attacks are used in for simulating and implementation of the proposed scheme using the WSN-DS dataset as a benchmark for evaluating for localization and detection.

3.4. Benchmark Datasets. In this section, three benchmark datasets including UNSW-NB 15, WSN-DS, and NSL-KDD are utilized to measure the effectiveness attack detection and localization accuracy. The raw network packets of the UNSW-NB 15 dataset were generated by cyber LAB using the IXIA PerfectStorm tool for cyber security for generating attack behaviors [39]. The cyber security dataset [40] is structured into training and testing samples using the batch mode for updating the total error for each weight, as shown below in Table 4. The dataset contains ten classes of attacks with different statistical frequency distribution in the network.

There are various attack activities in the dataset for processing and classification of the proposed system. The attacks are classified as normal, shellcode, analysis, backdoor, backdoors, DoS, exploits, fuzzers, reconnaissance, generic, and worms [39, 42–46].

The frequency distribution of the four types of routing attacks found in the WSN-DS dataset is provided in Table 5 and is utilized as a benchmark against which the performance of the proposed can be measured. There are a total of 84556 data points and 23 features available to use in creating a predictive model, eighty percent are utilized for training, while twenty percent are used for testing.

The other benchmark dataset for evaluating the proposed technique is the NSL-KDD containing 100069 samples and with classes of attacks including denial-of-service (DoS), probes, user to root (U2R), root to local (R2L), and normal as shown in Table 5. The dataset has 41 features with 38 numerical and 3 categorical features.

4. Proposed System

The proposed system consists of a series of phases: design and planning, deployment and routing, data processing, training and testing, attack classification, attack detection,

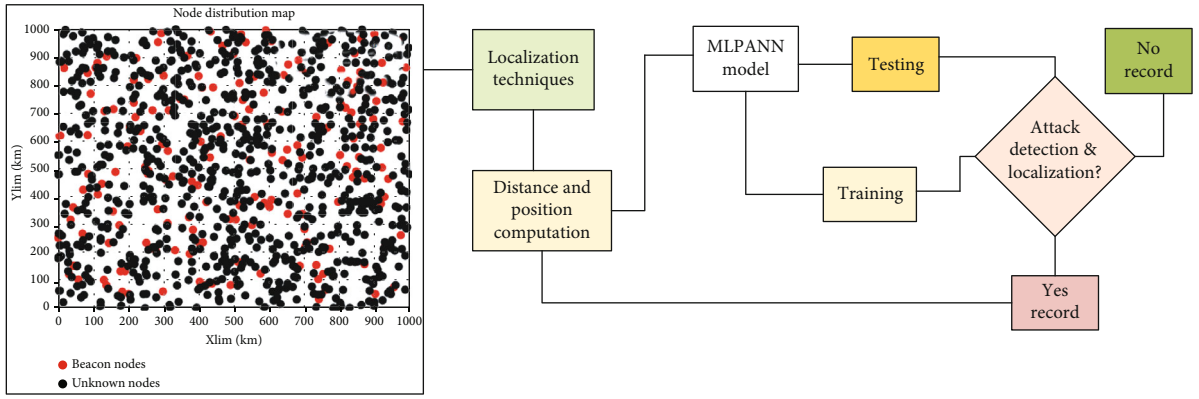


Figure 5: Secure localization techniques for detection and localization of malicious attacks using MLPANN in WSNs [36].

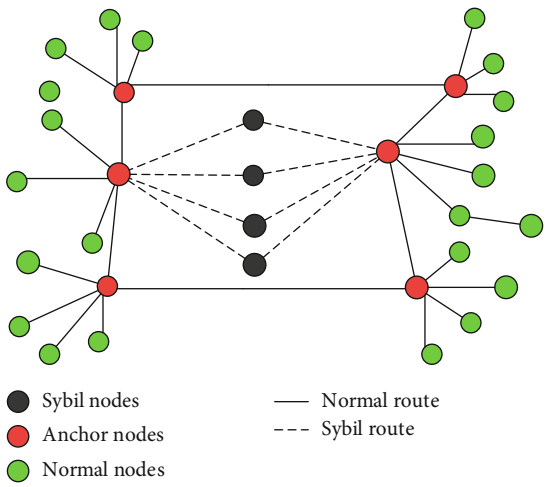


Figure 6: Illustration of routing Sybil attack in wireless sensor networks [2].

and localization. The data processing phase includes feature selection and normalization of the network traffic security dataset. The proposed system shown in Figure 7 is designed using optimized multilayer perceptron artificial neural network (MLPANN). The MLP is a feed-forward ANN with backpropagation to calculate the gradient used for weight calculation [48]. The ANN technique is a stochastic learning model for decision-making using interconnected information processing units [49]. ANN can estimate the nonlinear relationship between inputs and outputs and map the exchange of information among the nodes. The multilayer perceptron (MLP), as shown in Figure 8, configured with input layers, three hidden layers, and output layers. The proposed system used a gradient descent optimization for speeding and enhancing accuracy for detection and localization of attacks. This approach also uses a statically driven technique for training and testing using multilayer perceptron.

Several procedures are included in the proposed framework to identify malicious or unexpected routing. The method begins with a network data collection and preprocessing stage [50]. Next, it must find any missing values in the system and then fill in those blanks with appropriate values that were not present before processing began. We use the mean as our default. Subsequently, the dataset is cleaned up by removing any occurrences of duplicate values. After that, data encoding and normalization are carried out. In order to facilitate data handling, the encoded data undergoes a dimension's reduction procedure. To aid with anomaly detection, it is necessary to do feature optimization in order to extract the most useful characteristics from the data. In order to spot outliers in the dataset, optimal feature selection is crucial. For the same information, it aids in lowering the computational cost required to process it. Below is an equation that can be used to determine the entropy

$$E = -\sum_{i}^{L} P_i \log_2 P_i, \tag{13}$$

where p is the chance of finding a particular class label in the dataset. In this study, a hybrid machine learning approach is recommended for intrusion detection in a wireless sensor network after the optimal selection of features for anomaly detection.

4.1. Artificial Neural Networks. The multilayer perceptron artificial neural network (MLPANN) is a supervised machine learning approach using a human neuron model for data classification [47]. ANN processes and produces accurate information using a massive number of neurons and classify data-based neuron model that digests data and deliver correct output having layers and connecting nodes and active duty [51]. The layers of ANN are connected with nodes with the activation function. The configuration of typical ANN is depicted in Figure 9 with nodes and hidden layers varying from to three of the network using trainable parameters. ANN has wide applications in improving the efficiency of various schemes, including detection and localization of sensor nodes, routing and congestion control, and data aggregation in WSN. Artificial Neural Networks are data-driven tools for demonstrating nonlinear dynamic systems. They are efficient for the identification and modeling of nonlinear systems. They have standard approximation abilities and flexible structures to capture nonlinear

Table 4: Frequency distribution of DoS attacks for training and testing in the dataset [41].

Attack class	Frequency	Percent	Attack class	Frequency	Percent
Analysis	29	0.3	Generic	147	1.5
Normal	8632	86.0	Exploits	538	5.4
DoS	382	3.8	Reconnaissance	97	1.0
Backdoor	21	0.2	Shellcode	48	0.5
Fuzzers	122	1.2	Worms	17	0.2
Total	9186	91.5	Total	847	8.6

Table 5: Frequency distribution of DoS attack in WSN-DS and NSL-KDD dataset.

	WSN-DS dataset			NSL-KDD dataset	
Attack type	Frequency	Percent	Attack type	Frequency	Percent
Blackhole	2607	3.1	DoS	37403	33.7
Flooding	1019	1.2	Normal	61355	55.2
Grayhole	3287	3.9	Probes	10600	9.5
Normal	75300	89.1	R2L	913	.8
Scheduling	2343	2.8	U2R	839	.8
Total	84556	100.0	Total	111110	100.0

characteristics [52]. The input data $x1, x2, \cdots, xn$ denotes the input parameters of the dataset containing various protocols, services and the identity of the nodes, and $y1, y2, \cdots, yn$ represents the classified DoS attacks depending on the benchmark dataset. The ANN addresses the localization of sensor nodes and detection of the malicious nodes [18]. The proposed scheme has multiple trainable parameters for accurate attack localization and detection including the input nodes, hidden layers, bias and output nodes and also the connecting neurons. The ANN technique in WSNs improves the computational intelligence for scalable and adaptable features [30]. The ANN scheme was also used to obtain the accurate position of the sensor node using multilayer perceptron. It is also effective for prediction and clustering to get the location and position accuracy of nodes in WSNs.

The activation functions used for the artificial neural network multilayer perceptron are sigmoid and softmax, respectively. They are activation functions for the hidden layers and output layer, respectively. The sigmoid and softmax functions are stated below as in

$$Y = \frac{1}{1 + e^{-x}}, \tag{14}$$

$$z = \frac{e^{x}}{\sum_{k=1}^{n} e^{x}}, \tag{15}$$

where x is the vector of input to the output layer and y is the network's response with k index and n elements for the multilayer perceptron. The softmax function z is applied for activating for the classifier in the output layer. The number of hidden layers varies from one to three in our case for conducting the performance evaluation. The next step is to shrink the sampling dataset in order to better localize the feature that has to be extracted [53]. The pooling techniques are used to achieve this. In order to reduce the size of the image and the number of computations necessary, pooling is used. The max pooling approach was employed. Max pooling generates a new map after determining the feature maps' maximum value. A node's output in response to an input or combination of inputs is determined by the activation function of that node.

4.2. Optimization and Tuning Techniques. The goal of an ANN's optimization phase is to identify the optimal weighting scheme that leads to optimal performance. This is a tough optimization issue since it is categorized as a continuing nonlinear optimization problem. There are a lot of algorithms in books. Backpropagation is one of the most popular algorithms. This last one achieves excellent results, although it may run into a local minimum difficulty. To circumvent this issue and improve the likelihood of rapid convergence, we incorporate a local search method with a differential evolution algorithm. When training a neural network model, we utilize Adam optimizer to update the weights of the network based on the model's learned parameters with the greatest possible efficiency. Authors claim that Adam is a combination of the best features of two existing extensions of stochastic gradient descent: the Adaptive Gradient (AdaGrad) algorithm and the Root Mean Squared Propagation (RMSProp) algorithm. These two algorithms have a common characteristic: they both maintain a constant learning rate across all parameters. Adam sees the value in AdaGrad and RMSProp [53]. To fine-tune the weights of the neurons, we compute the gradient of the loss function and apply gradient descent optimization. The networks are trained via a gradient-based algorithm and the gradient descent nonlinear optimization method [29]. The gradient descent algorithm

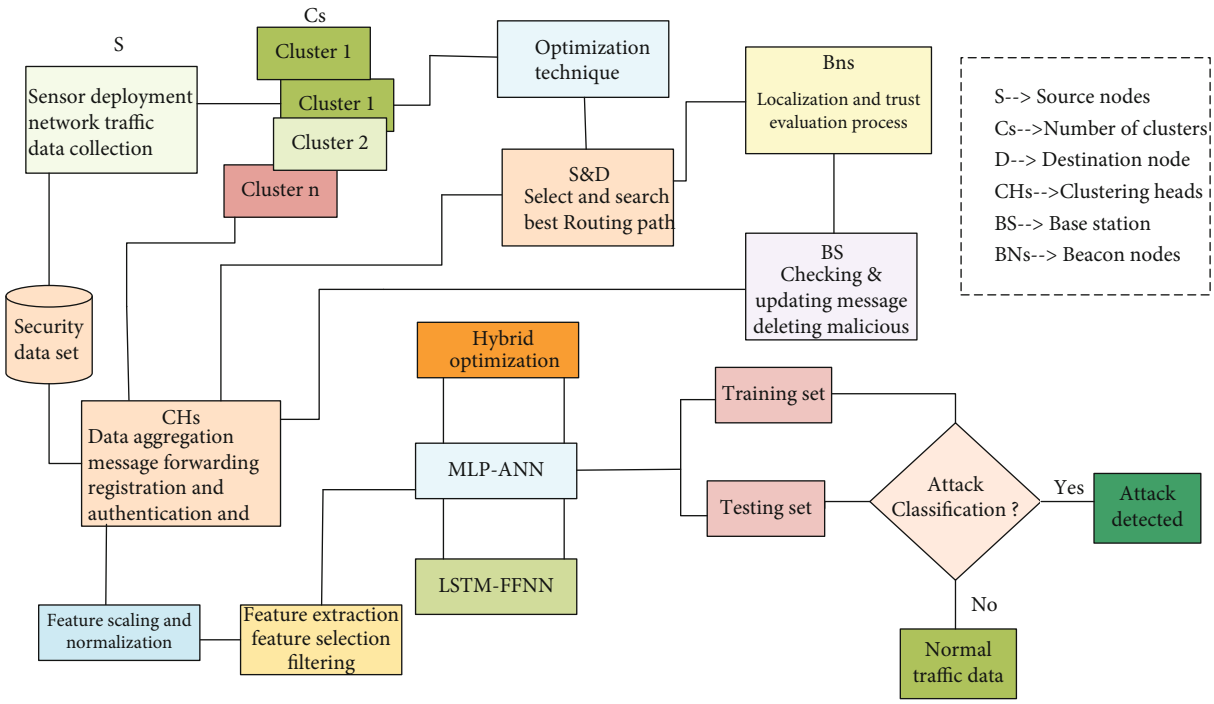


Figure 7: The proposed block diagram for attack localization and detection scheme in WSNs.

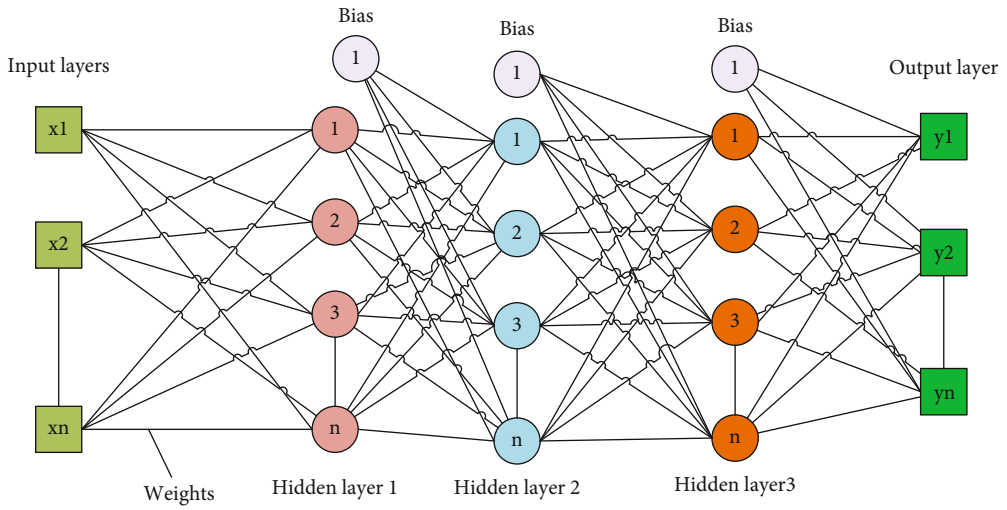
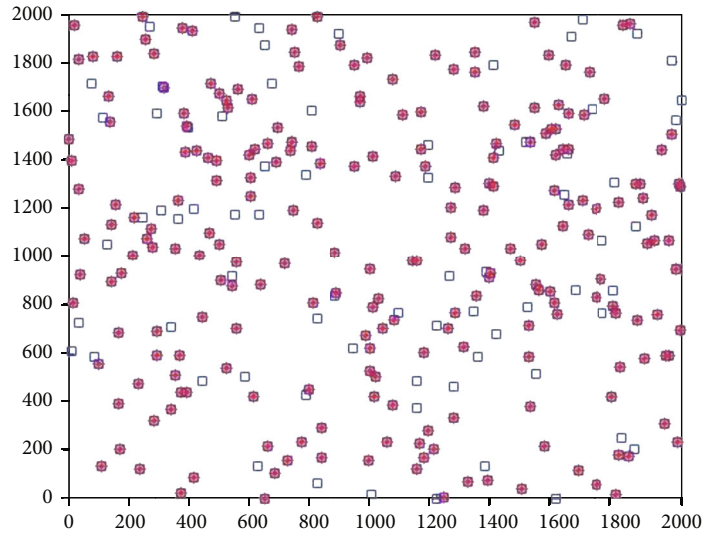


Figure 8: Structure of the proposed MLPANN architecture with three hidden layers [47].

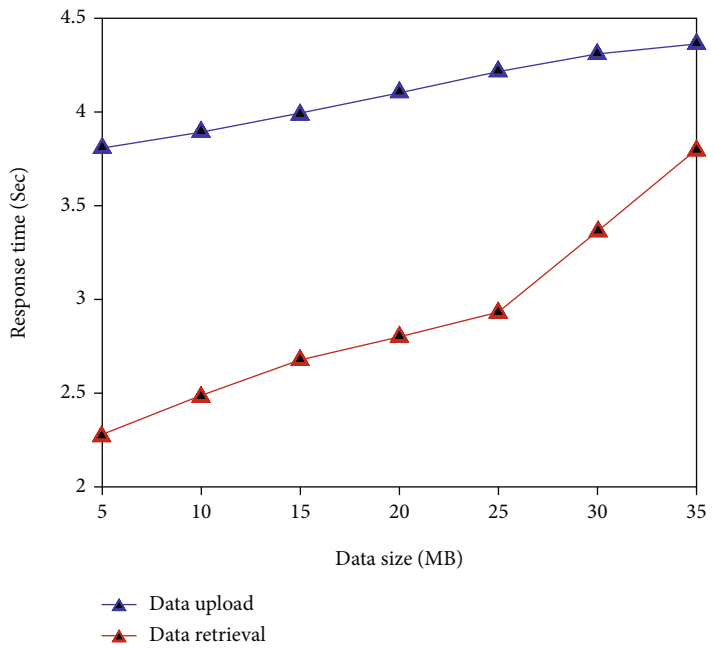
speeds up the training phase on the artificial neural network multilayer perceptron. The algorithm also helps to converge the weight iterations of the network.

Optimal weights, the optimal number of hidden layers and hidden nodes, and the optimal set of relevant characteristics are all necessary for building a multilayer perceptron [54]. The layer-by-layer weighted output data are collected at a secret node. The value of a bias node's weight is also given to it. One uses a nonlinear activation function on the aggregate of the weighted input values. The only restrictions are that the nonlinear function be differentiable and that the function's output values lie inside some interval. Finding an optimal set of weights that approximates both actual and estimated outputs is the goal of the MLP optimization issue. Continuous optimization is used to model this issue, invoking the problem classification of optimization techniques.

4.3. LSTM-FFNN. Using long short-term memory and feed-forward neural networks (LSTM-FFNNs), the suggested optimized multilayer perceptron artificial neural network achieved better results. Within the realm of DL, the long short-term memory (LSTM) RNN is analogous to a recursive function that repeatedly calls itself. With a recurrent neural network, the same computation is performed repeatedly on each data point in a recursive fashion, giving rise to the term "recurrent." The RNN suffers from the gradient vanishing and explosion issues. In contrast to other DL

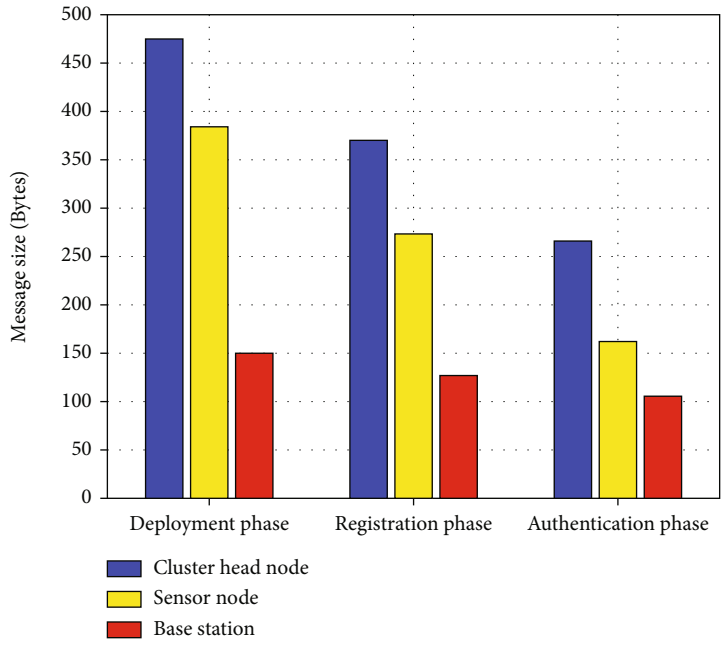


(a) Beacon node distribution phases

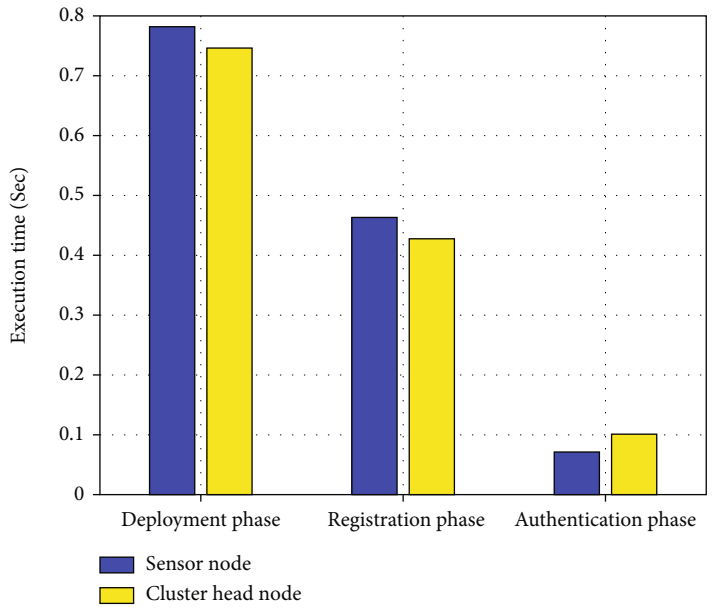


(b) Data uploading and retrieval phases

Figure 9: Continued.



(c) Authentication and registration phases in SN, CH, and BS



(d) Authentication and registration phases in SN and CH

Figure 9: The various phases of authentication and registration in the network model for secure data aggregation and transmission in WSNs.

techniques like deep NNs, the LSTM can recognize interdependencies in a time series and remember important data from earlier iterations to use in future predictions. We suppose that the model's inputs consist of the three preceding time steps. The data from the first unit flows into the second, as seen in the unfolded version [55, 56].

In contrast to the RNN-like LSTM, NNs like the fast forward neural network (FFNN) derive their predictions without looking back at prior time steps. They make their predictions based solely on data from the present lag. Inputs plus an n-node hidden layer make up the FFNN. Each node's output is a function of its inputs and the weights of the connections between them. Our model consists of five distinct layers: a vector input layer, three hidden layers, and a single-node output layer that returns a 1 or 0 depending on the type of classification being performed.

In this paper, we applied various activation functions considering the threshold value. The ReLU activation function is being used. It is an acronym for a nonlinear operation's rectified linear unit. Since the real world is typically highly nonlinear, the goal of adding nonlinearity to the network is achieved. It can be defined as mathematically as in

$$\text{Re Lu}(x) = \begin{cases} x & \text{if } x \geq 0, \\ 0 & \text{if } x < 0. \end{cases} \tag{16}$$

The sigmoid (or logistic) activation function (δ) was used to input the z value into the logistic function and generate values between 0 and 1 using a threshold of 0.5 as the reference value. This can be defined as mathematically

$$\delta(z) = \frac{1}{1 + e^{-x}}. \tag{17}$$

The choice of activation function is motivated by the presence of two classes of labels (outputs) for this method. Therefore, the method of binary classification technique should be used. Cross-entropy, a well-known loss function for ANNs, was the one we employed. Specifically, [47] defines cross-entropy (C) as

$$\begin{aligned} C &= -\frac{1}{n}\sum_{x}^{n}[\text{ylna} + (1-y)\ \ln\ (1-a)], \\ a &= \delta(z) = \delta\left(\sum_{j} w_j x_j + b\right), \end{aligned} \tag{18}$$

where Adam, the hybrid optimizer, will iteratively adjust the weights w and biases b. Adam is an improved version of the Stochastic Gradient Descent (SGD) algorithm. According to the scikit-learn documentation, Adam performs reasonably well on huge datasets. There are four variables you can adjust in Adam: the rate at which one is learning, the exponential decay rate for first-moment estimates, the rate at which one's second-moment estimates decay, and a very small amount to avoid a division by zero. Also, Adam is superior to SGD in noisy environments because it combines the advantages of two other popular optimizers (the adaptive gradient algorithm and root mean square propagation). We get things off with an early architecture for hyperparameter optimization that seeks optimal performance with as little computational complexity as possible.

5. Simulation and Result Discussion

The simulation setting configuration and evaluation metrics will be discussed in this section. Wireless sensors are distributed randomly forming clustering with cluster heads in the target field with an area of $1000 \times 1000\ \text{m}^2$. The routing protocols are used for making clustering and selection of the cluster head in each round of the simulation and localization of the unknown nodes with help of the beacon nodes and sink nodes. The cluster head achieves more computational data processing from the sensor nodes and communication with base station. The simulation parameter configuration is shown in Table 6. Intel (R) Xeon (R) Silver 4214 CPU @ 2.20GHz 2.19GHz (2 processors) with 128 GB (128 GB useable), x64-based processor, and 64-bit operating system running Windows using MATLAB R2021a is used for network planning and simulation.

Table 6: Simulation setup for the proposed network model.

Parameter	Values
Number of sensors	300-1000
Beacon nodes	60-120
Unknown nodes	240-840
Protocol type	Clustering and routing
Deployment area	$1000 \times 1000\ \text{m}^2$
Mobility	Random
Number of clusters	10
Sink position	500, 1000
Number of attacks	5-60
Data size	4000 kb
Attacks	Routing
Transmission radius	400 m

Our primary effort is devoted to determining how well various hybrid-based improvements to the original DV-hop algorithm perform in detecting and pinpointing hostile nodes that have hijacked the beacon node and are supplying false routing information [57]. All of our proposed algorithms have been implemented in the MATLAB simulator for thorough testing and analysis of their localization faults and precision. Numerous researchers rely on MATLAB, a simulation programed and numerical computing environment, to test out new ideas, conduct research, and build models. In our tests, we have examined the localization accuracy and the localization error per node by changing the percentage of anchor nodes, the total number of sensor nodes, and the nodes' communication range across four different topologies. One way to measure an algorithm's efficacy in localization is by looking at how it performs on average with regard to localization errors. We employ IBM SPSS, Python, and the WEKA Java toolboxes for data processing and analysis to gauge the effectiveness of the suggested strategy against the dataset [58]. The average error of localization to all the nodes is calculated using Equation (15). The clustering and routing protocols are used for clustering and selection of the cluster head selection and maximizing the network lifetime and improving the network performance. The routing attacks including the sinkhole attacks, blackhole attacks, and Sybil attacks are used in the simulation scenario for evaluating the localization and detection accuracy.

The simulation results depict that the data processed from the environment is authenticated and registered. Figure 9 shows data processing and aggregation by the cluster head sent to the base station (BS). Figures 9(a) and 9 show the dynamic clustering and data retrieval of the sensors by the beacon nodes. The cluster head (CH) aggregates huge message size as in Figures 9(c) and 2(d); the sensor nodes (SNs) consume greater time form data execution.

Registration phases are utilized to identify sensor nodes, aggregation nodes, and base stations using smart contact of the public blockchain [59]. The intelligent communications verify the existence of the aggregation node validated by its MAC address and its identity checked by the base station.

The public blockchain records of validated aggregated nodes and stored data of the aggregated node provide reliable authentication techniques in WSNs. The sensor nodes are allowed to join the blockchain after the completion of the registration process to reduce external attacks on WSNs. The sensor nodes have aggregation nodes after random deployment in the target field. The aggregation nodes authenticate the identities of the sensor nodes using a private for communicating with them, and the base station also authenticates the aggregation node for communicating with it using a public key. The aggregation nodes communicate with each other using mutual authentication process.

Figure 10 shows the distribution and the experimental simulation of the nodes. Moreover, this work introduces the average localization error and coverage, localization, and detection accuracy as evaluation metrics. The average localization error (ALE), average localization accuracy (ALA), accuracy, detection rate precision, and recall are used as evaluation metrics. The average error localization, shortened as ALE [2], is computed as follows in Equation (19). The ALE is the summation of the LE of all the unknown nodes to the total number of unknown nodes. The LE is the difference between estimated and actual position of unknown nodes.

$$\begin{aligned}
\text{Localization Error (LE)} &= \sqrt{\left(u_i' - u_i\right)^2 + (v_i' - v_i)^2}, \\
\text{Average Localization Error (ALE)} &= \sum_{i=1}^{n} \frac{\sqrt{\left(u_i' - u_i\right)^2 + (v_i' - v_i)^2}}{\text{nR}}, \\
\text{Average Localization Accuracy (ALA)} &= \left(1 - \left(\sum_{i=1}^{n} \frac{\sqrt{\left(u_i' - u_i\right)^2 + (v_i' - v_i)^2}}{\text{nR}}\right)\right) \times 100\%,
\end{aligned} \tag{19}$$

where (u_i' and v_i') are the real coordinates of the anonymous node i and (ui, vi) are the computed coordinates, n denotes unknown nodes, and R is radius of communication in the network. Wireless sensor nodes are deployed and simulated using localization process using the beacon nodes as in Figure 10(a). The error for the anonymous sensor nodes is displayed in Figure 10(b). The position and error for each node are computed using the localization scheme. The computation of the localization accuracy for each node enables for effective identification and localization of the malicious nodes with help of the beacon nodes and the base station.

The effectiveness of the distance vector hop algorithm is measured by malicious node detection, localization accuracy, and localization efficiency [60]. The practical localization estimation of the unknown and malicious nodes is determined by the number of the anchor nodes for its evaluation metrics, as shown in Figure 11. The relative error defines between the computed position of the node and the actual location of the node. Malicious nodes affect nodes' distribution and localization accuracy by creating the wrong position and location of the unknown sensor nodes in WSNs. Malicious nodes mislead the sensor nodes' routing path and information, making the network service and performance degrade.

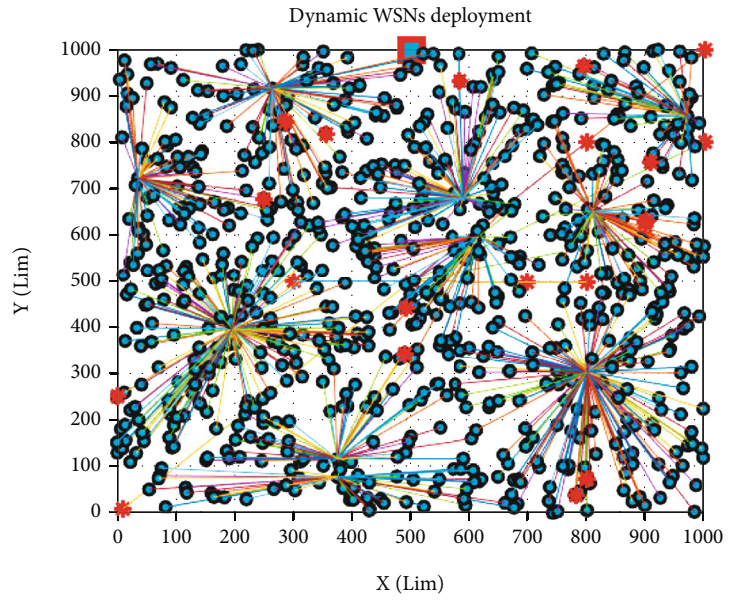
The average localization accuracy and detection accuracy of the proposed system are 99.51% and 99.83% with 840 unknown nodes and 160 beacon nodes for accurate computation of malicious nodes, respectively, as shown in Figures 11(a) and 11(b).

According to the findings of the simulation, anchor nodes have a greater number of neighbors and a higher degree of connectedness than regular sensor nodes, as can be seen in Figure 12(a). If we use the regular model, we can determine that the average connectivity of the network is 404, and the average number of neighbor nodes that each anchor node has is 63. As can be seen in Figure 12(b), the overall network's average localization error was reduced to 0.0049 thanks to the simulation's efforts, and this was achieved across all nodes. This would imply that all sensor nodes are precisely located and have a unique identity thanks to the beacon nodes, which help in the identification and localization of malicious nodes.

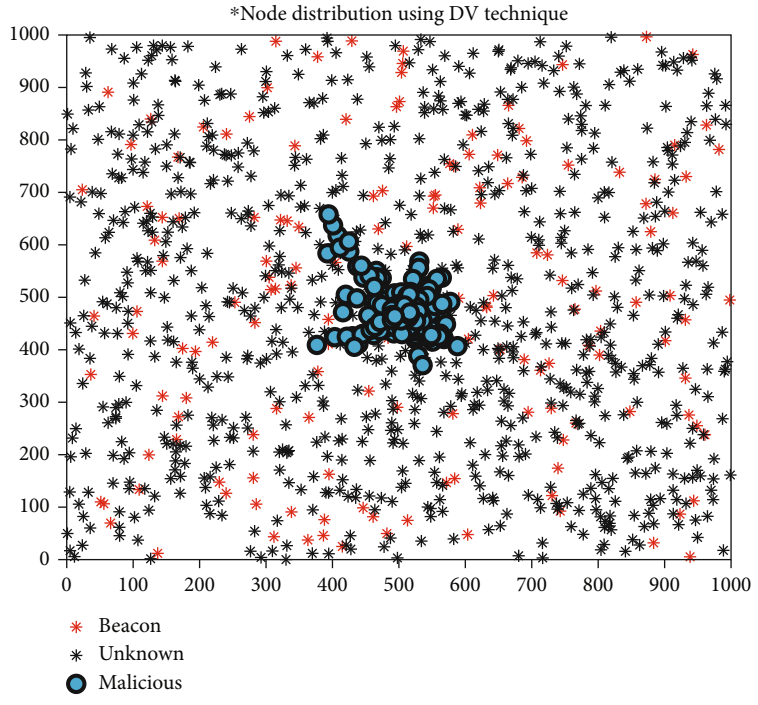
The simulation results demonstrate that the suggested method utilizes hybrid localization techniques utilizing both range-free and range-based approaches to accurately determine the position and location of each unknown node while minimizing energy consumption. As twenty mobile anchor nodes are utilized in the proposed method, the price is kept low while the accuracy of pinpointing malicious nodes in WSNs is much enhanced. Figures 13(a) and 13(b) for the beacon nodes and the unknown nodes, respectively, illustrate how the hybrid strategy combining the DV-hop technique with other approaches such as RSSI and DE improves the average localization accuracy of the proposed scheme.

The experimental findings for calculating the location error against changing numbers of beacon nodes are displayed in Figures 14(a) and 14(b). In addition, the localization error for all the algorithms gradually decreases as the number of the activated sensor nodes grows [34]. The proposed hybrid method has the lowest localization error score of all the methods we have tested. With 200 beacon nodes, more reference points are detected, reducing the margin of error for localization. Figure 14 shows conclusive proof that the new method outperforms conventional location-based algorithms when it comes to pinpointing the origin of an error. In the same setup, nearly all of the methods that have been tried and tested have been effective. As a result of having more points of reference for the target nodes, the suggested method allows for a gradual decline. In contrast, the network is strengthened by an adequate number of anchor nodes, as the distance between the unknown nodes and the anchor nodes decreases.

As may be shown in Figures 14(a) and 14(b), the ALE of four different localization techniques decreases as the number of beacon nodes increases. Since there are more anchor nodes now, the average distance travelled in one hop can be calculated with more precision. The distances predicted by the anchor nodes from the unknown nodes are more accurate [61, 62]. This shows that the proposed approach is effective to estimate the placement of unknown nodes as the number of anchors grows because it has more



(a) Clustering and localization of WSNs

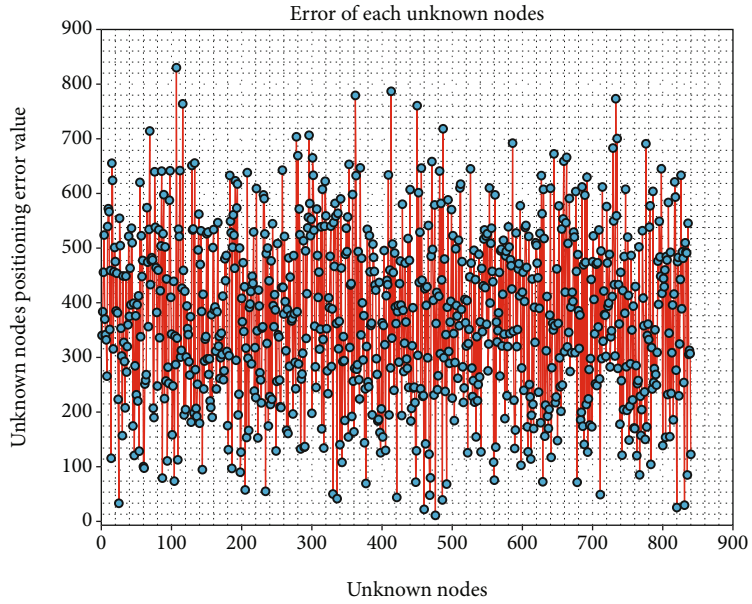


(b) Malicious node localization in WSNs

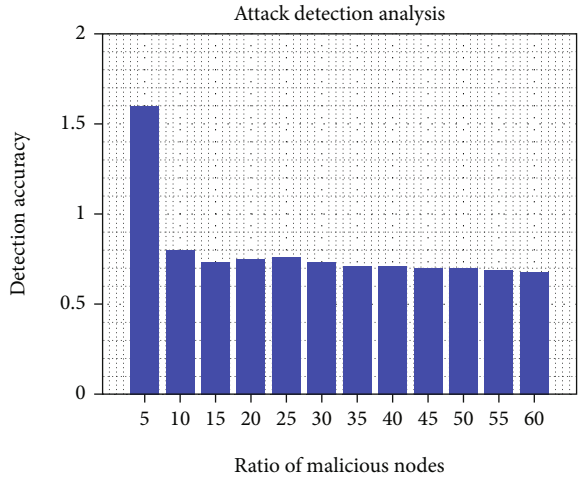
Figure 10: Sensor node deployment using distance vector protocol and triangulation process in WSNs.

circumstances to work with. Given that some fraction of the nodes can serve as anchor nodes for node localization, the suggested methodology exhibits lower error compared to the previous methods.

5.1. Performance Metrics. In this section, a cybersecurity dataset is applied with different types of attack categories. The benchmark datasets are utilized for analyzing and processing using the optimized artificial neural network technique to detect and localize multiple attacks to evaluate the proposed system about the Sybil attacks. The dataset is used as a benchmark for the security localization and detection of accuracy of various classes of routing attacks in the network. The Python programming language, SPSS, and WEKA toolboxes are used for data processing and classification to detect the different classes of attacks in WSNs [20]. There are different types of performance metrics for measuring the effectiveness of the proposed scheme. Table 7 shows the measurement entities of the system with mathematical equations.



(a) Positioning error of unknown nodes

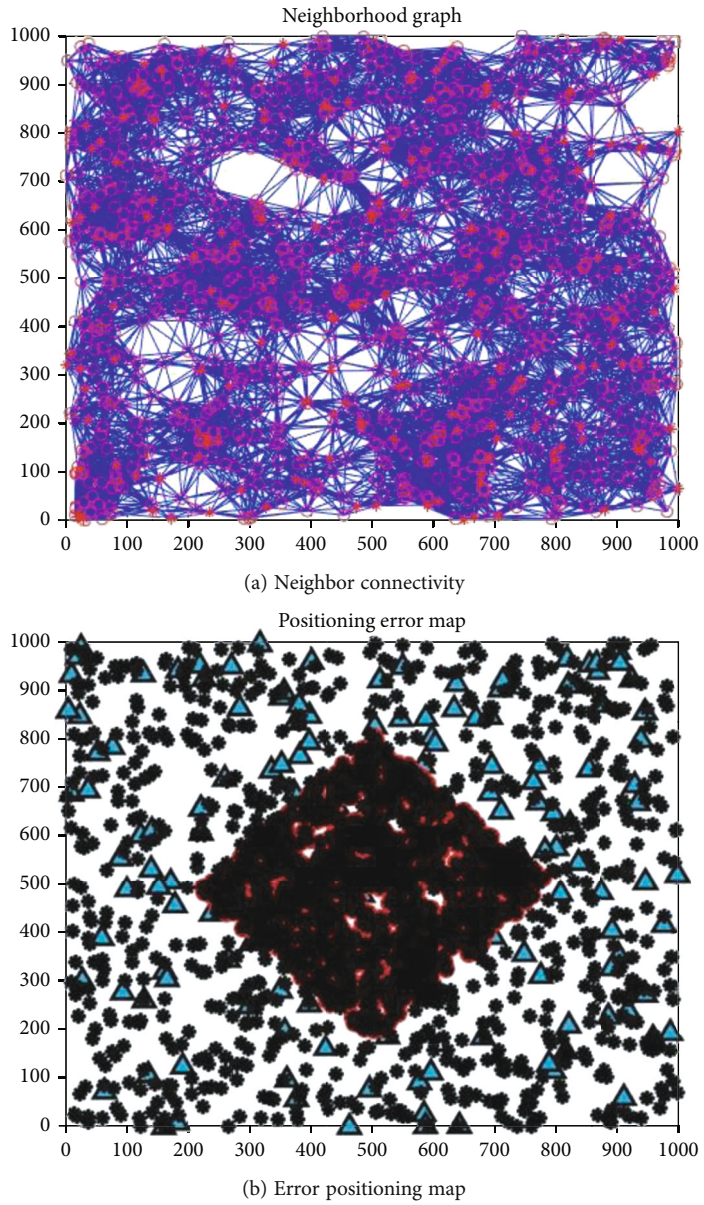


(b) Detection of accuracy of malicious nodes

Figure 11: Computing localization and position of unknown node errors and detection accuracy of malicious nodes using distance vector hop algorithm and trilateration process.

The parameters are false negatives = F_n [47], true positives = T_p, true negatives = T_n, and false positives = F_p [63]. Accuracy is the parameter for evaluating the performance of proposed classification model [64]. Informally, it is the section of predictions the model achieved successfully. Formally, it can be computed [20] as shown in Table 7. The F-measure [65] is a combination of recall and precision [63] computed as in Table 7. The Matthews correlation coefficient (MCC) is also the measure of the performance for scoring prediction of the model. The proposed system has training and testing phases using the cybersecurity dataset as benchmark with different classes of attacks. The system is based on the ANN approach achieves an accuracy of 99.84% and error of 0.16% using three hidden layers with 10-fold cross-validation using CICIDS2018 a benchmark dataset. The different attacks are correctly detected and localized, greater than 78% proposed by Dong et al. [2] using the distance vector hop scheme with an error of 22% malicious node localization.

Receiver operating characteristic analysis is useful to assess the model's accuracy using the ANN technique [66]. The total area under the ROC represents the statistical probability prediction of the classification of the proposed model for different types of attacks using a threshold cutting point $C\epsilon(0, 1)$ as shown in Table 7. This ROC analysis supports the inference area under the curve and Precision-recall curves. The ROC is a plot of the sensitivity versus 1-specificity, as shown above in Figure 15(a). Sensitivity is the number of attacks correctly identified in the network. 1-specificity is the attack classes wrongly rejected. The cumulative chart gain in Figure 15(b) shows the overall percentage of the total observations for the given class of attacks in the network. The target category is the percentage of the overall amount



(a) Neighbor connectivity

(b) Error positioning map

Figure 12: Simulated results of sensor deployment (a) and neighbor relationship diagram (b).

of samples in the dataset. The diagonal line is the baseline for the classification of the target samples. The cumulative gain chart is a cutoff choosing the attack classification and mapping the appropriate cutoff values. Table 8 depicts the area under the curve detection rate performance for each type of attack.

The area under curve is visualized in Figure 16 for each attack category of the dataset. The area under the curve is more significant for the standard class in the proposed network traffic analysis. The ROC analysis shows that the MLPANN approach is practical for multiclass attack localization and detecting DoS attacks. The ROC shows that the proposed scheme is effective for DoS attack classification using a benchmark dataset.

The area under the curve is a statistical summary of the ROC curve, and the values represent each attack category. The area under the curve also indicates the probability of the classification model. The standard class of the attack has a greater extent, which is effectively detected. The pseudopredictive probability in Figure 17 describes each attack class's scaling by dividing their sum of classification accuracy. The effectiveness of the scheme can be proved using other attacks types and datasets as threshold measurements.

The average classification of the proposed system is 96% using the predictive probability model. Figure 17 shows the effectiveness of the various attack classification model. The classification model is trained 80% of the dataset, and 20% tested samples using the batch mode with the activation function using gradient descent algorithm with three hidden layers and trainable parameters.

5.2. Performance Comparison. The performance of the proposed methodology is validated and confirmed by comparing and testing with other previous works using various

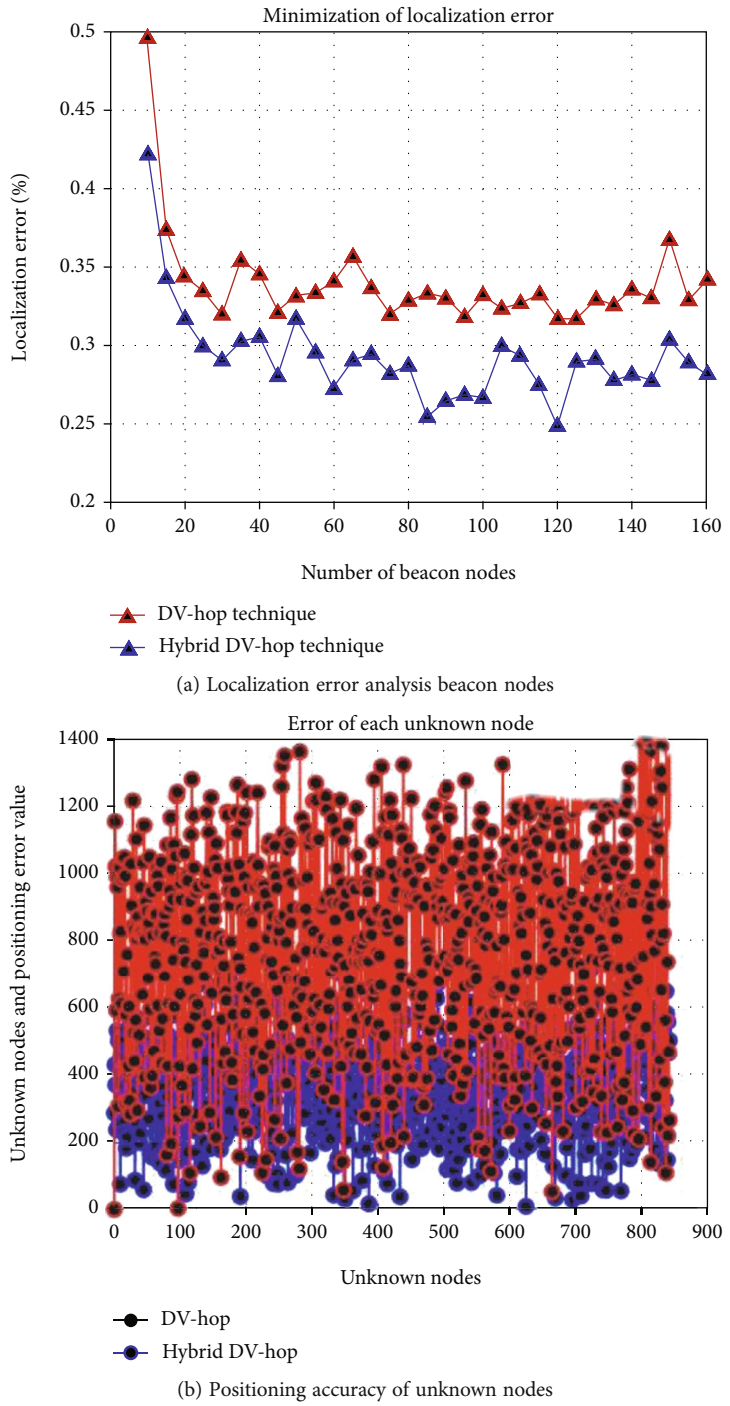
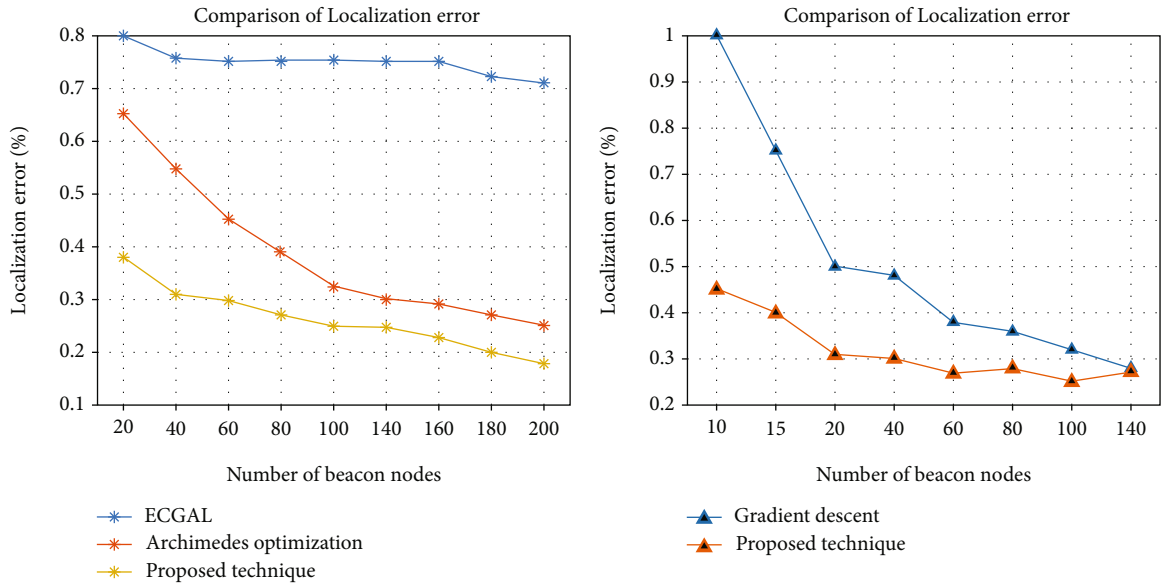


Figure 13: Improving the localization and position accuracy of wireless sensor nodes using hybrid scheme.

benchmark datasets. The comparison performance of recent works as shown in Table 9 suggests the optimized MLPANN technique is effective for detection and localization of attacks in WSNs.

Figures 18(a) and 18(b) show the performance comparison of the proposed system using four benchmark datasets and different attack detection models using the accuracy, precision, recall, and F1-measure. This suggests that the proposed scheme is effective for detecting and localization attacks in WSNs.

This suggests that the proposed system is more effective than the previous work by Almomani et al. [20] artificial neural network-based intrusion detection system (ANN-IDS) for routing attack detection and classification, as shown in Figure 18(b) with an average detection accuracy of 97.2% using sample WSN-dataset using ten-fold cross-validation with three hidden layers. Dong et al. [2] used the distance vector hop algorithm to detect Sybil attacks with a localization accuracy of 78%, which is less than the proposed scheme. The proposed work is also



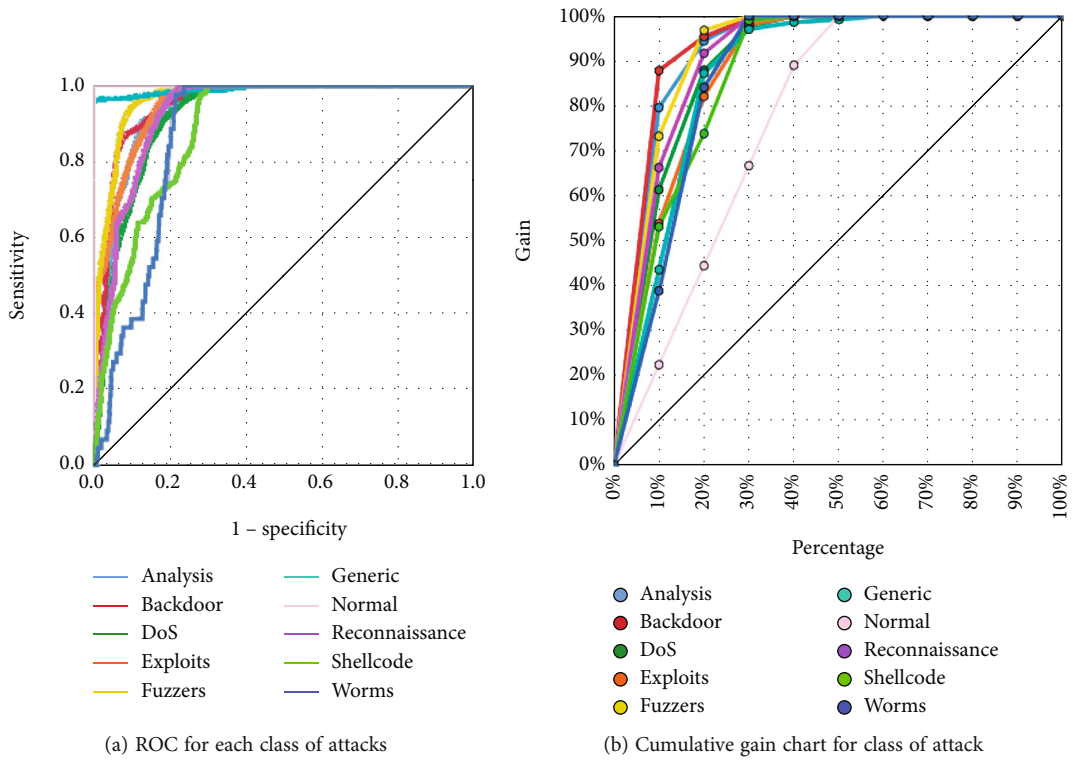
(a) Comparison of localization schemes

(b) Comparison with gradient descent

FIGURE 14: Comparison of the localization error of the proposed scheme with other modes by varying the number of nodes.

TABLE 7: Performances metrics of the proposed system with their technical and mathematical expressions.

Metrics	Technical description	Mathematical equations
Sensitivity	The positive prediction of the model	$\text{Sensitivity} = \frac{T_p}{T_p + F_n}$
Specificity	The negative prediction of the model	$\text{Specificity} = \frac{T_n}{F_n + T_p}$
Precision	Truly identified instances of samples	$\text{Precision}(p) = \frac{T_p}{F_p + T_p}$
ROC	Classifier performances of the model	$\text{ROC}(.) = \{\text{FPR}(C), \text{TPR}(C), C\epsilon(0,1)\}$
Recall	Equivalent to TP rate	$\text{Recall} = \frac{T_p}{T_p + F_n}$
F-measure	Combination of precision and recall	$\text{F} - \text{measure} = \frac{2 \times T_p}{2 \times T_p + F_p + F_n}$
Accuracy	Classification prediction of the model	$\text{Acc.} = \frac{T_n + T_p}{T_n + T_p + F_n + F_p}$
FP rate	Wrongly classified events	$\text{FPR} = \frac{F_p}{F_p + T_n}$
Energy	Energy consumption analysis	$E_c = E_t - E_l$
Lifetime	Over all alive nodes (N)	$\text{Aliv}(N) = \text{Total}(N) - \text{Dead}(N)$
MCC	Binary classification	$\text{Mcc} = \frac{T_p.T_n - F_p.F_n}{\sqrt{(T_p + F_p).(T_p + F_n).(T_n + F_p).(T_n + F_n)}}$
ALE	Average localization error	$\text{ALE} = \sum_{i=1}^{n} \frac{\sqrt{\left(u_i' - u_i\right)^2 + (v_i' - v_i)^2}}{nR}$



(a) ROC for each class of attacks

(b) Cumulative gain chart for class of attack

Figure 15: Receiver operating characteristics (ROCs) and cumulative chart of the proposed system.

Table 8: Area under the curve for each class of attack.

Class	Analysis	DoS	Backdoor	Exploits	Fuzzers	Generic	Normal	Reconnaissance	Shellcode	Worms
Area	99.8%	98.8%	97.2%	99.1%	99.9%	96.7%	100%	99.2%	97.8%	94.9%

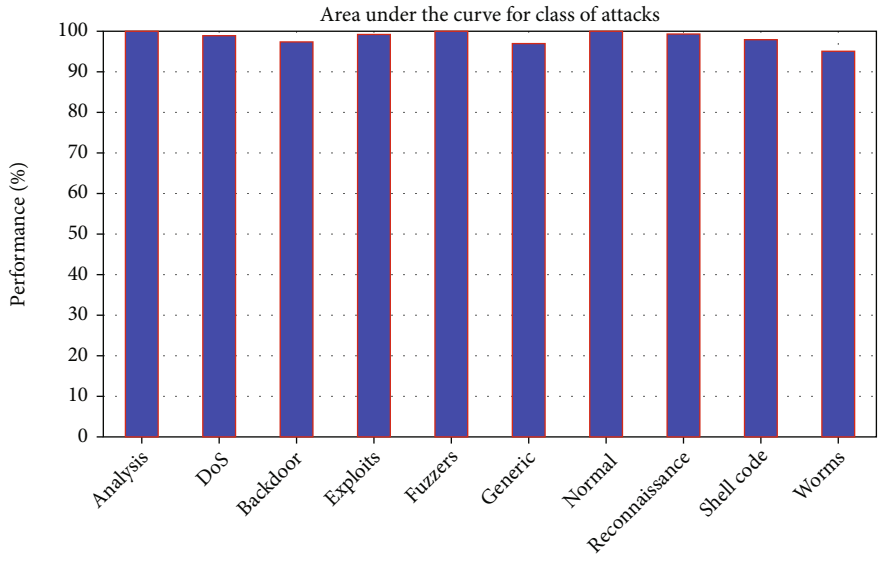


Figure 16: Area of under the curve for each class of attack using UNSW-NB 15 benchmark dataset.

practical compared to the MK-ELM model [67], which has an accuracy of 92.10% using UNSW-NB 15 dataset. Figure 18 shows the detection and localization for the proposed ANN approach compared with other works for Sybil attack detection. The comparison performance is using sample experimental dataset examined by Sujatha and Anita [24] with an average detection rate of 97% using fuzzy extreme machines (FEMs).

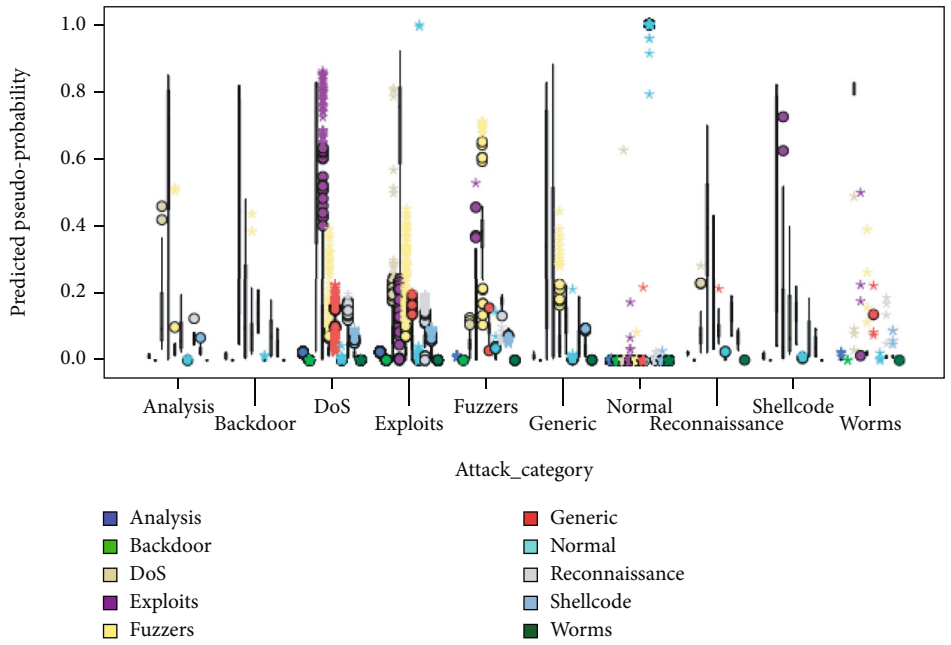


Figure 17: Attack classification prediction probability of the model.

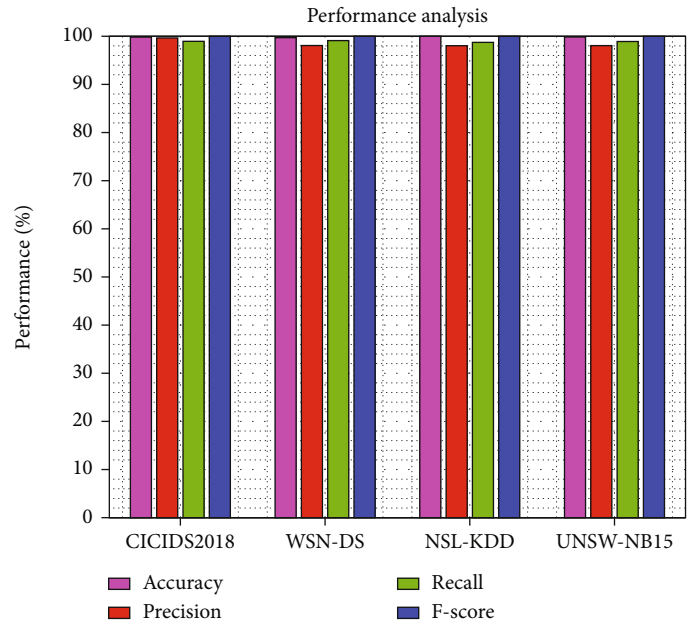
Table 9: Comparative analysis of the proposed technique with recent attack detection models using CICIDS2018 dataset.

	Methods	Accuracy	Precision	Recall	F1-score
Zhou et al. [8]	MLP	97.56	99.12	98.79	98.23
Almomani et al. [20]	ANN-IDS	97.18	97.8	97.5	97.69
Sujatha and Anita [24]	FEM	99	98	98	98.98
Zhang et al. [67]	MK-ELM	98.34	98.03	97.63	97.64
Khan et al. [68]	LEACH++-ANN	97	96.8	96	96.4
Mohammadpour et al. [69]	CNN-MCL	99.46	99.76	99.15	99.46
Xinlong and Zhibin [70]	HTM-LSTM	97.74	97.20	97.92	97.72
Proposed system	MLPANN	99.83	99.71	100.00	99.85

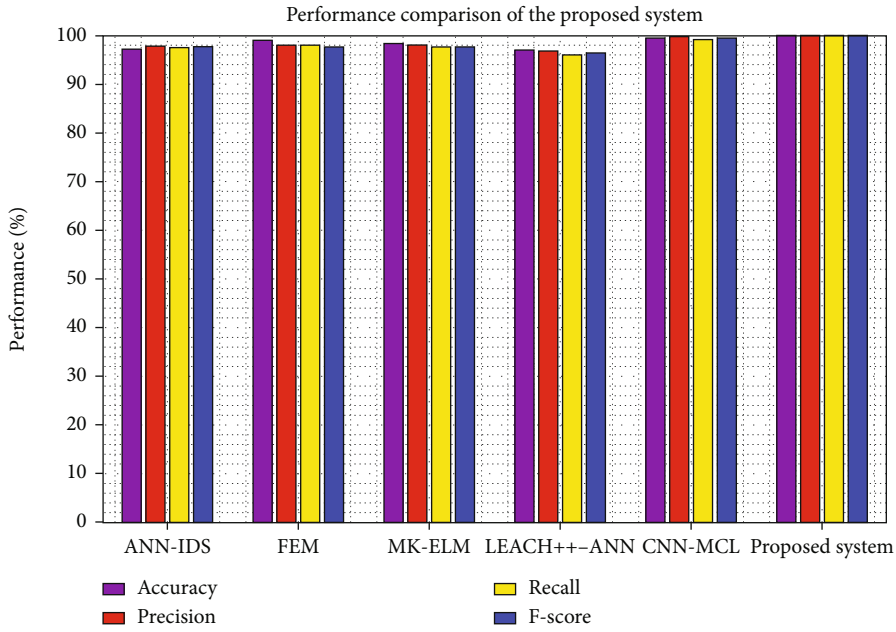
The proposed attack detection and localization scheme achieve 100% using the same dataset. Hasan et al. [71] determined the detection accuracy of 91.66% of the malicious node using an optimized artificial neural network using the packet delivery and energy consumption evaluation metrics. The various comparison performances conclude our proposed scheme is effective for the detection localization of attacks in WSNs. Khan et al. [68] analyzed the detection of routing attacks using the LEACH++ protocol based on an artificial neural network (LEACH++-ANN) and achieved a detection accuracy of 98%. This proves the proposed scheme is more effective for detecting routing attacks, with an average detection accuracy of 99.62%. The proposed system also achieves average detection accuracy of 98.4% using the benchmark dataset NSL-KDD as shown in Figure 18(b) for each class of attack. The proposed approach is practical for detecting and localization DoS attacks in WSNs compared to the convolutional neural network and mean convolutional layer (CNN-MCL) model proposed by Mohammadpour et al. [69] with an average detection accuracy of 99.46%. Zhang et al. [67] proposed an hierarchical intrusion detection model (HIDM) for WSNs using a multikernel-based extreme learning machine (MK-ELM) classification technique using UNSW-NB and NSL-KDD benchmark datasets.

The proposed system's average localization and detection rate are validated by comparing previous works with different classes of attacks. Table 10 shows that when applied the UNSW-NB 15 dataset, which serves as a benchmark for identifying and classifying routing assaults, the proposed approach improves detection accuracy by class using 80% of training and 20% of testing of samples with five hidden layers. The demonstration further shows that the verification of the suggested performance parameters and metrics (accuracy, precision, F1-score, and recall) against those of recently published attack detection models.

The performance of the proposed system is effective for detection and localization of DoS attacks in WSNs using benchmark datasets in terms of the evaluation metrics such as accuracy, precision, recall and F1-score as shown in



(a) Comparison using benchmark datasets

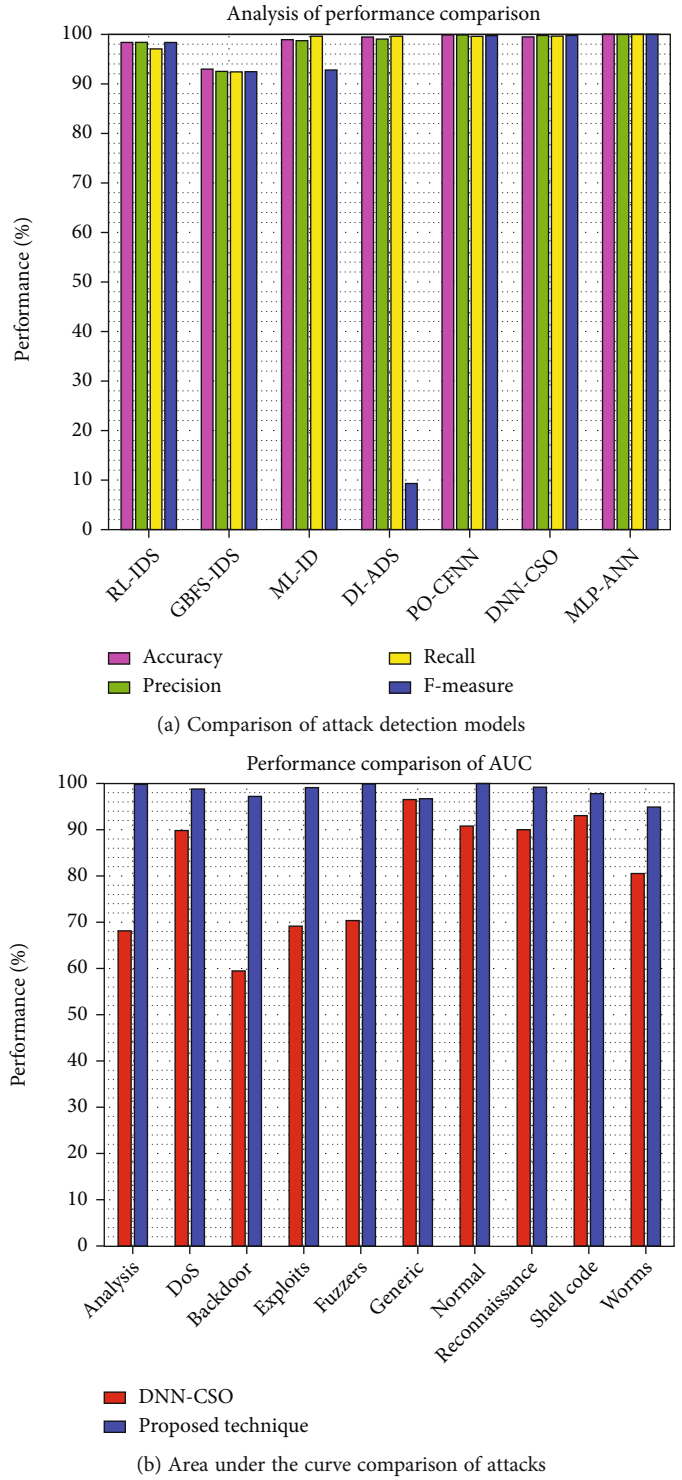


(b) Comparison of various attack detection models

Figure 18: Performance comparison of the proposed system using benchmark datasets for attack detection and classification.

Table 10: Comparative analysis of the proposed technique with recent attack detection models using UNSW-NB 15 dataset.

Author	Method	Accuracy	Precision	Recall	F1-score
Pasikhani,et al. [72]	RL-IDS	98.35	98.36	97.04	98.34
Upadhyay et al. [73]	GBFS-IDS	92.96	92.50	92.40	92.44
Abdan and H. Seno [11]	ML-ID	98.9	87.7	99.6	92.78
Gudla et al. [74]	DI-ADS	99.44	99.02	99.60	99.30
Alghamdi [75]	PO-CFNN	99.86	99.89	99.58	99.72
Khilar et al. [76]	DNN-CSO	99.46	99.75	99.62	99.76
Proposed system	MLPANN	100.00	100.00	100.00	100.00



(a) Comparison of attack detection models

(b) Area under the curve comparison of attacks

Figure 19: Performance comparison of the proposed system with recent works using benchmark datasets.

Figure 19(a). The area under the curve (AUC) is also used for evaluating the performance of the system as show in Figure 19(b). This confirms that the optimized MLPANN approach is effective in attack detection and localization of WSNs attacks.

The proposed multilayer perception artificial neural network (MLPANN) technique is further compared with MK-ELM using the NSL-KDD benchmark dataset, taking a section of 14,000 sample records with three hidden layers, as shown below in Table 11. The average detection accuracy of the proposed technique is 98.4% using 111,110 samples which is more effective than MK-ELM with 14,000 samples with an average detection accuracy of 98.34%.

Table 11: Comparison of performance of the proposed MLPANN with MK-ELM using the section of the NSL-KDD dataset with hidden layers.

Class of attacks	TP rate (%)		FP rate (%)		FN rate (%)		TN rate (%)	
	MK-ELM	Proposed scheme	MK-ELM	Proposed scheme	MK-ELM	Proposed scheme	MK-ELM	Proposed scheme
DoS	98.04	99.00	0.49	0.001	1.96	1.00	99.51	99.90
Probes	95.67	97.20	0.47	0.001	4.33	2.80	99.53	99.90
R2L	76.12	96.80	0.11	0.015	23.88	3.20	99.89	99.98
U2R	50.00	90.04	0.00	0.003	50.00	9.96	100.00	99.99

Table 12: Comparison performance of machine learning models using the CICIDS2017 benchmark dataset.

Classifier	ML models results				Hybrid PTE-BO ML model results			
	Accuracy	Precision	Recall	F1-score	Accuracy	Precision	Recall	F1-score
XGBoost	99.82	99.82	99.82	99.80	99.82	99.86	99.82	99.83
Ensemble stacking	99.82	99.91	99.82	99.85	99.82	99.91	99.82	99.85
Random forest	99.77	99.77	99.77	99.75	99.82	99.82	99.82	99.80
Decision tree	99.77	99.77	99.77	99.75	99.82	99.91	99.82	99.85
Extra tree	99.82	99.82	99.82	99.80	99.82	99.80	99.82	99.80

The validation of the result can also be confirmed by comparing the previous works as stated theoretically and graphically. The multilayer perception artificial neural network (MLPANN) effectively detects and classifies multiple attacks using public datasets, including UNSW-NB, WSN-DS, and NSL-KDD, as a benchmark for performance evaluation. By combining a tree based on the Parzen estimation (PTE) with hyperparameter and Bayesian optimization (BO) techniques, we are able to better classify the machine learning models for the proposed scheme on the benchmark dataset as shown in Table 12. Every single machine learning task uses hyperparameters to fine-tune the aforementioned parameters and get optimal results. Hyperparameter optimization (HPO) accomplishes both of these goals with less manual labor and better results from machine learning [77].

The MLPANN technique also achieves better detection accuracy of 99.62% using the WSN-DS benchmark dataset. The proposed scheme is effective for the localization and detection of different classes of attacks, approving that the proposed system has optimal average detection for multiple suspicious nodes. The novelty of this work is that it is effective in the detection and localization of various attacks. The proposed scheme is innovative for its ability to scale in both security and performance for optimal area coverage in wireless sensor networks with a hierarchical architecture and both heterogeneous and homogeneous sensor nodes.

6. Conclusion and Remarks

In this work, we proposed a multilayer perceptron artificial neural network (MLPANN) for detecting and localizing multiple attacks in WSNs. The proposed scheme achieved an average detection accuracy of 100%, 99.65%, 98.95%, and 99.83% for the various malicious nodes using UNSW-NB, WSN-DS, NSL-KDD, and CICIDS2018 benchmark datasets, respectively. The optimized localization approach is more effective and performs more significantly by 20% than the distance vector hop technique, with average localization accuracy of 99.12% using 160 beacon nodes. The validation of the proposed method is confirmed with the previous studies using the ANN classification technique using Python, IBM SPSS, and WEKA toolboxes for data processing and MATLAB R2021a for network planning and simulation. The datasets are used to evaluate the proposed system for detecting and localization accuracy of different attacks. The effectiveness of the proposed scheme is assessed using detection rate, ROC, false-positive rate, a lifetime of the network, residual energy, and the area under the curve metrics. The beacon, sensor, and malicious nodes were used hierarchically to simulate the target field. It is recommended to enhance further the detection and localization of accuracy of malicious nodes using different approaches in WSNs. We will extend this work with various attack classes and methods. The results show that performance and security of the proposed scheme are applicable for scalable and large network coverage in wireless sensor networks with heterogeneous and homogenous sensors for ensuring quality of services and availably. The proposed scheme will be examined in the future using other network planning and tools with different public datasets as benchmarks for detecting and localization attacks in WSNs.

Data Availability

The underlying dataset used to generate the results presented in this article is available upon request to the corresponding author.

Conflicts of Interest

The authors declare that there is no competing interest in this work.

References

[1] S. Messous and H. Liouane, "Online sequential DV-hop localization algorithm for wireless sensor networks," *Mobile Information Systems*, vol. 2020, Article ID 8195309, 14 pages, 2020.

[2] S. Dong, X. G. Zhang, and W. G. Zhou, "A security localization algorithm based on DV-hop against Sybil attack in wireless sensor networks," *Journal of Electrical Engineering and Technology*, vol. 15, no. 2, pp. 919–926, 2020.

[3] G. Farjamnia, Y. Gasimov, and C. Kazimov, "An improved DV-hop for detecting wormhole attacks in wireless sensor networks," *Journal of Communication Engineering*, vol. 9, no. 1, pp. 1–24, 2020.

[4] S. T. Patel and N. H. Ministry, "A Review: Sybil Attack Detection Techniques in WSN," in *4th International Conference on Electronics and Communication Systems (ICECs)*, pp. 4–8.

[5] J. Jiang, G. Han, C. Zhu, Y. Dong, and N. Zhang, "Secure localization in wireless sensor networks: a survey (invited paper)," *The Journal of Communication*, vol. 6, no. 6, pp. 460–470, 2011.

[6] B. Madagouda and R. Sumathi, "Artificial neural network approach using mobile agent for localization in wireless sensor networks," *Advances in Science, Technology and Engineering Systems Journal*, vol. 6, no. 1, pp. 1137–1144, 2021.

[7] M. Bernas and B. Płaczek, "Fully connected neural networks ensemble with signal strength clustering for indoor localization in wireless sensor networks," *International Journal of Distributed Sensor Networks*, vol. 11, no. 12, Article ID 403242, 2015.

[8] D. Zhou, W. Liu, W. Zhou, and S. Dong, "Research on network traffic identification based on multi layer perceptron," *Telkomnika (Telecommunication Computing Electronics and Control)*, vol. 12, no. 1, pp. 201–208, 2014.

[9] M. A. Alsheikh, S. Lin, D. Niyato, and H. P. Tan, "Machine learning in wireless sensor networks: algorithms, strategies, and applications," *IEEE Communication Surveys and Tutorials*, vol. 16, no. 4, pp. 1996–2018, 2014.

[10] M. Wazid and A. K. Das, "An efficient hybrid anomaly detection scheme using K-means clustering for wireless sensor networks," *Wireless Personal Communications*, vol. 90, no. 4, pp. 1971–2000, 2016.

[11] M. Abdan and S. A. H. Seno, "Machine learning methods for intrusive detection of wormhole attack in mobile ad hoc network (MANET)," *Wireless Communications and Mobile Computing*, vol. 2022, Article ID 2375702, 12 pages, 2022.

[12] B. Ahmad, W. Jian, Z. A. Ali, S. Tanvir, and M. S. A. Khan, "Hybrid anomaly detection by using clustering for wireless sensor network," *Wireless Personal Communications*, vol. 106, no. 4, pp. 1841–1853, 2019.

[13] G. Farjamnia, Y. Gasimov, and C. Kazimov, "Review of the techniques against the wormhole attacks on wireless sensor networks," *Wireless Personal Communications*, vol. 105, no. 4, pp. 1561–1584, 2019.

[14] R. Singh, J. Singh, and R. Singh, "Fuzzy based advanced hybrid intrusion detection system to detect malicious nodes in wireless sensor networks," *Wireless Communications and Mobile Computing*, vol. 2017, Article ID 3548607, 14 pages, 2017.

[15] M. Mahajan, K. T. V. Reddy, and M. Rajput, "Design and simulation of a blacklisting technique for detection of hello flood attack on LEACH protocol," *Procedia Computer Science*, vol. 79, pp. 675–682, 2016.

[16] U. Jain and M. Hussain, "Securing wireless sensors in military applications through resilient authentication mechanism," *Procedia Computer Science*, vol. 171, no. 2019, pp. 719–728, 2020.

[17] S. Z. Wang, Y. Li, and W. Cheng, "Distributed classification of localization attacks in sensor networks using exchange-based feature extraction and classifier," *Journal of Sensors*, vol. 2016, Article ID 8672305, 18 pages, 2016.

[18] L. Chelouah, F. Semchedine, and L. Bouallouche-Medjkoune, "Localization protocols for mobile wireless sensor networks: a survey," *Computers and Electrical Engineering*, vol. 71, pp. 733–751, 2018.

[19] A. Hadir, K. Zine-Dine, M. Bakhouya, and J. El Kafi, "An improved DV-hop localization algorithm for wireless sensor networks," in *2018 13th IEEE conference on industrial electronics and applications (ICIEA)*, pp. 330–334, Wuhan, China, June 2014.

[20] I. Almomani, B. Al-Kasasbeh, and M. Al-Akhras, "WSN-DS: a dataset for intrusion detection systems in wireless sensor networks," *Journal of Sensors*, vol. 2016, Article ID 4731953, 16 pages, 2016.

[21] S. T. Patel and N. H. Mistry, "A review: Sybil attack detection techniques in WSN," in *2017 4th International conference on electronics and communication systems (ICECS)*, vol. 17, pp. 184–188, Coimbatore, India, February 2017.

[22] O. Cheikhrouhou and A. Koubaa, "BlockLoc: secure localization in the internet of things using blockchain," in *2019 15th International Wireless Communications & Mobile Computing Conference (IWCMC)*, pp. 629–634, Tangier, Morocco, June 2019.

[23] F. Y. Yavuz, D. Ünal, and E. Gül, "Deep learning for detection of routing attacks in the internet of things," *International Journal of Computational Intelligence Systems*, vol. 12, no. 1, pp. 39–58, 2018.

[24] V. Sujatha and E. A. M. Anita, "FEM-hybrid machine learning approach for the detection of sybil attacks in the wireless sensor networks," *International Journal of Innovative Technology and Exploring Engineering*, vol. 8, no. 7, pp. 1171–1179, 2019.

[25] X. Qi, X. Liu, and L. Liu, "A combined localization algorithm for wireless sensor networks," *Mathematical Problems in Engineering*, vol. 2018, Article ID 4648109, 10 pages, 2018.

[26] P. Li, X. Yu, H. Xu, J. Qian, L. Dong, and H. Nie, "Research on secure localization model based on trust valuation in wireless sensor networks," *Security and Communication Networks*, vol. 2017, Article ID 6102780, 12 pages, 2017.

[27] L. Song, L. Zhao, and J. Ye, "DV-hop node location algorithm based on GSO in wireless sensor networks," *Journal of Sensors*, vol. 2019, Article ID 2986954, 9 pages, 2019.

[28] M. Saud Khan and N. M. Khan, "Low complexity signed response based Sybil attack detection mechanism in wireless sensor networks," *Journal of Sensors*, vol. 2016, Article ID 9783072, 9 pages, 2016.

[29] A. Payal, C. S. Rai, and B. V. R. Reddy, "Artificial neural networks for developing localization framework in wireless sensor networks," in *2014 international conference on data mining and intelligent computing (ICDMIC)*, p. 5, Delhi, India, September 2014.

[30] R. Dela Cruz, "Artificial neural network-based localization in wireless sensor networks artificial neural network-based localization in wireless sensor networks," p. 14, 2019.

[31] J. Jiang, G. Han, H. Wang, and M. Guizani, "A survey on location privacy protection in wireless sensor networks," *Journal of*

Network and Computer Applications, vol. 125, pp. 93–114, 2019.

[32] R. Rastogi, S. Srivastava, M. S. Tarun, V. Manshahia, and N. Kumar, "A withdrawn: a hybrid optimization approach using PSO and ant colony in wireless sensor network," *Materials Today: Proceedings*, vol. 2021, 2021.

[33] Z. Han, L. Lin, Z. Wang et al., "CNN-based attack defense for device-free localization," *Mobile Information Systems*, vol. 2022, Article ID 2323293, 7 pages, 2022.

[34] J. Chen, S. H. Sackey, J. H. Anajemba, X. Zhang, and Y. He, "Energy-efficient clustering and localization technique using genetic algorithm in wireless sensor networks," *Complexity*, vol. 2021, Article ID 5541449, 12 pages, 2021.

[35] O. Cheikhrouhou, G. M. Bhatti, and R. Alroobaea, "A hybrid DV-hop algorithm using RSSI for localization in large-scale wireless sensor networks," *Sensors*, vol. 18, no. 5, pp. 1–14, 2018.

[36] W. He, F. Lu, J. Chen, Y. Ruan, T. Lu, and Y. Zhang, "A kernel-based node localization in anisotropic wireless sensor network," *Scientific Programming*, vol. 2021, Article ID 9944358, 8 pages, 2021.

[37] B. K. Madagouda and R. Sumathi, "Analysis of localization using ANN models in wireless sensor networks," in *2019 IEEE Pune Section International Conference (PuneCon)*, pp. 18–21, Pune, India, December 2019.

[38] R. Singh, J. Singh, and R. Singh, "Detection of Sybil Nodes in wireless sensor networks," *Journal of Advanced Computer Science & Technology*, vol. 10, no. 3, pp. 185–202, 2017.

[39] N. Moustafa, G. Creech, and J. Slay, "Anomaly detection system using beta mixture models and outlier detection," in *Progress in Computing, Analytics and Networking. Advances in Intelligent Systems and Computing*, P. Pattnaik, S. Rautaray, H. Das, and J. Nayak, Eds., vol. 710, Springer, Singapore, 2018.

[40] "Cybersecurity_attacks|Kaggle," 2021, https://www.kaggle.com/iamranjann/cybersecurity-attacks.

[41] Z. Zoghi, G. Serpen, and C. Science, "UNSW-NB15 computer security dataset: analysis through visualization".

[42] N. Moustafa, G. Creech, and J. Slay, "Flow aggregator module for analysing network traffic," in *Progress in Computing, Analytics and Networking. Advances in Intelligent Systems and Computing*, P. Pattnaik, S. Rautaray, H. Das, and J. Nayak, Eds., vol. 710, Springer, Singapore, 2018.

[43] "The UNSW-NB15 data set description," 2021, https://www.unsw.adfa.edu.au/unsw-canberra-cyber/cybersecurity/ADFA-NB15-Datasets/.

[44] N. Moustafa and J. Slay, "A network forensic scheme using correntropy-variation for attack detection," *IFIP Advances in Information and Communication Technology*, vol. 532, pp. 225–239, 2018.

[45] N. Moustafa, G. Creech, and J. Slay, "Big data analytics for intrusion detection system: statistical decision-making using finite Dirichlet mixture models," in *Data Analytics and Decision Support for Cybersecurity*, pp. 127–156, Springer, 2017.

[46] N. Moustafa and J. Slay, "The evaluation of network anomaly detection systems: statistical analysis of the UNSW-NB15 data set and the comparison with the KDD99 data set," *Information Security Journal: A Global Perspective*, vol. 25, no. 1–3, pp. 18–31, 2016.

[47] D. Praveen Kumar, T. Amgoth, and C. S. R. Annavarapu, "Machine learning algorithms for wireless sensor networks: a survey," *Information Fusion*, vol. 49, pp. 1–25, 2019.

[48] C. R. Panigrahi, "Advanced computing and intelligent engineering," *Proceedings of ICACIE*, vol. 1, 2018.

[49] M. N. A. Shaon and K. Ferens, "A computationally intelligent approach to the detection of wormhole attacks in wireless sensor networks," *Advances in Science, Technology and Engineering Systems*, vol. 2, no. 3, pp. 302–320, 2017.

[50] M. Mittal, R. P. de Prado, Y. Kawai, S. Nakajima, and J. E. Muñoz-Expósito, "Machine learning techniques for energy efficiency and anomaly detection in hybrid wireless sensor networks," *Energies*, vol. 14, no. 11, 2021.

[51] R. Ahmad, R. Wazirali, and T. Abu-Ain, "Machine learning for wireless sensor networks security: an overview of challenges and issues," *Sensors*, vol. 22, no. 13, p. 4730, 2022.

[52] "Artificial neural network - an overview | ScienceDirect Topics," 2021, https://www.sciencedirect.com/topics/engineering/artificial-neural-network.

[53] V. Hassija, S. Batra, V. Chamola et al., "A blockchain and deep neural networks-based secure framework for enhanced crop protection," *Ad Hoc Networks*, vol. 119, article 102537, 2021.

[54] K. Ncibi, T. Sadraoui, M. Faycel, and A. Djenina, "A multilayer perceptron artificial neural networks based a preprocessing and hybrid optimization task for data mining and classification," *International Journal of Economics, Finance and Management Sciences*, vol. 5, no. 1, pp. 12–21, 2017.

[55] M. Al-Imran and S. H. Ripon, "Network intrusion detection: an analytical assessment using deep learning and state-of-the-art machine learning models," *International Journal of Computational Intelligence Systems*, vol. 14, no. 1, pp. 1–20, 2021.

[56] D. Kothona, I. P. Panapakidis, and G. C. Christoforidis, "A novel hybrid ensemble LSTM-FFNN forecasting model for very short-term and short-term PV generation forecasting," *IET Renewable Power Generation*, vol. 16, no. 1, pp. 3–18, 2022.

[57] A. Hadir, Y. Regragui, and N. M. Garcia, "Accurate range-free localization algorithms based on PSO for wireless sensor networks," *IEEE Access*, vol. 9, pp. 149906–149924, 2021.

[58] H. Chen, W. Lou, Z. Wang, J. Wu, Z. Wang, and A. Xi, "Securing DV-Hop localization against wormhole attacks in wireless sensor networks," *Pervasive and Mobile Computing*, vol. 16, pp. 22–35, 2015.

[59] S. Awan, N. Javaid, S. Ullah, A. U. Khan, A. M. Qamar, and J. G. Choi, "Blockchain based secure routing and trust management in wireless sensor networks," *Sensors*, vol. 22, no. 2, pp. 1–24, 2022.

[60] G. Kumar, M. K. Rai, H. J. Kim, and R. Saha, "A secure localization approach using mutual authentication and insider node validation in wireless sensor networks," *Mobile Information Systems*, vol. 2017, Article ID 3243570, 12 pages, 2017.

[61] M. Cheng, T. Qin, and J. Yang, "Node localization algorithm based on modified Archimedes optimization algorithm in wireless sensor networks," *Journal of Sensors*, vol. 2022, Article ID 7026728, 18 pages, 2022.

[62] Z. Ansari, R. Ghazizadeh, and Z. Shokhmzan, "Gradient descent approach to secure localization for underwater wireless sensor networks," in *2016 24th Iranian Conference on Electrical Engineering (ICEE)*, pp. 103–107, Shiraz, Iran, May 2016.

[63] "Classification: accuracy|Machine Learning Crash Course," 2021, https://developers.google.com/machine-learning/crash-course/classification/accuracy.

[64] D. Parikh and V. Menon, "Machine learning applied to cervical cancer data," *International Journal of Mathematics and Computer Science*, vol. 5, no. 1, pp. 53–64, 2019.

[65] "What are TP rate, FP rate, precision, recall, F measure, MCC, ROC area and PRC areas in the Weka tool?- Quora," 2020, https://www.quora.com/What-are-TP-rate-FP-rate-precision-recall-F-measure-MCC-ROC-area-and-PRC-areas-in-the-Weka-tool.

[66] "ROC analysis," 2021, https://www.ibm.com/support/knowledgecenter/SSLVMB_sub/statistics_mainhelp_ddita/spss/base/idh_roc.html.

[67] W. Zhang, D. Han, K. C. Li, and F. I. Massetto, "Wireless sensor network intrusion detection system based on MK-ELM," *Soft Computing*, vol. 24, no. 16, pp. 12361–12374, 2020.

[68] F. A. Khan, A. H. Farooqi, and A. Derhab, "A comprehensive security analysis of LEACH++ clustering protocol for wireless sensor networks," *The Journal of Supercomputing*, vol. 75, no. 4, pp. 2221–2242, 2019.

[69] L. Mohammadpour, T. C. Ling, C. S. Liew, and A. Aryanfar, "A mean convolutional layer for intrusion detection system," *Security and Communication Networks*, vol. 2020, Article ID 8891185, 16 pages, 2020.

[70] L. Xinlong and C. Zhibin, "DDoS attack detection by hybrid deep learning methodologies," *Security and Communication Networks*, vol. 2022, Article ID 7866096, 7 pages, 2022.

[71] B. Hasan, S. Alani, and M. A. Saad, "Secured node detection technique based on artificial neural network for wireless sensor network," *International Journal of Electrical & Computer Engineering*, vol. 11, no. 1, pp. 536–544, 2021.

[72] A. M. Pasikhani, J. A. Clark, and P. Gope, "Reinforcement-learning-based IDS for 6LoWPAN," in *2021 IEEE 20th International Conference on Trust, Security and Privacy in Computing and Communications (TrustCom)*, pp. 1049–1060, Shenyang, China, 2022.

[73] D. Upadhyay, J. Manero, M. Zaman, and S. Sampalli, "Gradient boosting feature selection with machine learning classifiers for intrusion detection on power grids," *IEEE Transactions on Network and Service Management*, vol. 18, no. 1, pp. 1104–1116, 2021.

[74] S. P. K. Gudla, S. K. Bhoi, S. R. Nayak, and A. Verma, "DI-ADS: a deep intelligent distributed denial of service attack detection scheme for fog-based IoT applications," *Mathematical Problems in Engineering*, vol. 2022, Article ID 3747302, 17 pages, 2022.

[75] M. I. Alghamdi, "A hybrid model for intrusion detection in IoT applications," *Wireless Communications and Mobile Computing*, vol. 2022, Article ID 4553502, 9 pages, 2022.

[76] R. Khilar, K. Mariyappan, M. S. Christo et al., "Artificial intelligence-based security protocols to resist attacks in Internet of Things," *Wireless Communications and Mobile Computing*, vol. 2022, Article ID 1440538, 10 pages, 2022.

[77] M. Feurer and F. Hutter, "Hyperparameter optimization," in *Automated Machine Learning. The Springer Series on Challenges in Machine Learning*, F. Hutter, L. Kotthoff, and J. Vanschoren, Eds., Springer, Cham, Switzerland, 2019.

Astrophysics and Space Science (2024) 369:2
https://doi.org/10.1007/s10509-024-04267-w

RESEARCH

Matter creation cosmology with generalized Chaplygin gas

Yogesh Bhardwaj[1] · **C.P. Singh**[1]

Received: 27 September 2023 / Accepted: 3 January 2024 / Published online: 12 January 2024
© The Author(s), under exclusive licence to Springer Nature B.V. 2024

Abstract
In this work, we discuss the dynamics of a spatially homogeneous and isotropic flat Friedmann-Lemaître-Robertson-Walker (FLRW) model of the Universe powered by the gravitationally induced 'adiabatic' matter creation with generalized Chaplygin gas (GCG) equation of state. In recent years, the CGC has been proposed successfully to unify the dark matter and dark energy by using an exotic equation of state $p = -A/\rho^{\alpha}$. Considering adiabatic matter creation cosmology, as developed by Prigogine et al, we examine the effect of matter creation in describing the unification with GCG by assuming the natural phenomenological matter creation rate $\Gamma = 3\beta H$, where β is a constant and H is the Hubble parameter. We constrain the proposed model using a joint observational dataset of Type Ia supernovae Pantheon, $H(z)$ and BAO with Markov-Chain Monte-Carlo (MCMC) method. In addition, we discuss the selection criterion (AIC and BIC) and stability criteria to analyze the dynamics and differences with the standard ΛCDM model.

Keywords FLRW model · Matter creation cosmology · Chaplygin gas model · Dark energy

1 Introduction

The cosmological observations from Type Ia supernovae (Riess et al. 1998, 1999; Perlmutter et al. 1999), baryonic acoustic oscillations (Weinberg et al. 2013) and cosmic microwave background anisotropies (Bennett et al. 2013; Ade et al. 2014) provide strong evidence for an accelerated expansion of the Universe. In relativistic cosmology, such a phenomenon is usually explained by the existence of some unknown component(s), named as dark energy (DE), which contributes approximately 68% of the Universe and has a negative pressure. Many theoretical ideas have been suggested to explore the nature and origin of the DE, such as the cosmological constant (Weinberg 1989; Padmanabhan 2003; Peebles and Ratra 2003), quintessence (Caldwell et al. 1998), Phantom (Caldwell et al. 2003) and quintom (Guo et al. 2005; Copeland et al. 2006). The most obvious candidate is the cosmological constant, Λ which is associated with the vacuum energy in empty space and has negative pressure, $p = -c^2\rho$.

The Lambda-cold dark matter (abbreviated as ΛCDM) model is the simplest model which provides a reasonably good explanation of cosmological phenomena like the formation of large-scale structures and accelerating expansion of the Universe. However, the ΛCDM model has two major problems: cosmological constant problem and cosmic coincidence problem. To alleviate these problems, modified theories of gravity, namely, $f(R)$ gravity (Felice and Tsujikawa 2010), $f(G)$ or $f(R, G)$ gravity (Nojiri and Odintsov 2005, 2007), $f(R, T)$ gravity (Harko et al. 2011), $f(Q)$ gravity (Jimenez et al. 2018), $f(Q, T)$ gravity (Xu et al. 2019) have also been proposed.

In recent years, another interesting proposal has been presented by a change in the equation of state of the background cosmic fluid, so-called exotic equation of state which has negative pressure. One such example is the Chaplygin gas (CG) whose equation of state is given by $p_{cg} = -A/\rho_{cg}$, and was originally suggested by Kamenshchik et al. (2001). It is worthy to mention that the initial idea of CG was originated in aerodynamics by Chaplygin (1904) to describe the lifting force on the wing of aeroplane. Nowadays, it is used as an exotic equation of state in perfect fluid to describe the accelerating expansion of the Universe. The CG has been extended to other more flexible models keeping the view of observations. The CG model is a viable alternative to

✉ C.P. Singh
cpsingh@dce.ac.in

Y. Bhardwaj
yogeshbhardwaj1597@gmail.com

[1] Department of Applied Mathematics, Delhi Technological University, Bawana Road, Delhi-110 042, India

quintessence (Kamenshchik et al. 2001), which gives a unify picture of DE and DM. It behaves like a pressure-less DM in the early Universe and like the cosmological constant in late-time. However, it is ruled out in cosmology due to non-consistence with the observational data namely, supernova, baryoinc acoustic oscillations and cosmic microwave background (Bento et al. 2003a).

To resolve this problem, Bento et al. (2002) and Bilić et al. (2002) have proposed the generalized form of CG, so-called the "generalized Chaplygin gas (GCG)", which smoothly interpolates between dust matter and DE dominated era. The equation of state for GCG is given by $p_{gcg} = -A/\rho^{\alpha}_{gcg}$, where A and $0 < \alpha \leq 1$ are constants to be determined. The important feature of GCG model is that it unifies the dark matter and dark energy components. Thus, keeping in view of its potentiality, the GCG model has been the subject of great interest to study the evolution of early and late-time Universe. Many authors (Makler et al. 2003a,b; Silva and Bertolami 2003; Bento et al. 2003b; Chen 2003; Amendola et al. 2003; Alcaniz et al. 2003) have constrained the GCG model using various observational data to present the unified model of the Universe. Choudhury and Padmanabhan (2005) analyzed the GCG model with 194 data points of supernova and found that the GCG model provides relevant constraints on some cosmological parameters. The results show that the model rules out the decelerating model by considering the full supernova data set with significant confidence level.

However, besides these distinct approaches, very recently, matter creation cosmology has been studied to explain the current cosmic acceleration of the Universe. The microscopic description of this process was pioneered by Schrödinger (1939), and developed by (Parker 1968, 1969) based on the quantum field theory (QFT) in curved spacetimes. Later on, Prigogine et al. (1989) studied the macroscopic description of particle production mechanism based on the non-equilibrium thermodynamics of open systems and formulated the background equations how to insert this creation mechanism into the Einstein field equation to describe the evolution of the Universe.

Calvão et al. (1992) studied this macroscopic approach by formulating a covariant approach allowing specific entropy variation as usually expected for non-equilibrium processes in fluids. There may be a question what kind of particles are created by the gravitational field. Since, at present-day Universe there is no effect of radiation on late-time accelerated expansion of the Universe and dark matter is one of the dominant sources after dark energy component. Therefore, it is assumed that the produced particles are simply the CDM particles. It has been observed that the model with matter creation can mimic ΛCDM cosmology. It has been pointed out that the matter creation can play the role of dark energy component and leads to drive the accelerating expansion of the Universe (Steigman et al. 2009; Lima et al. 2010; Basilakos and Lima 2010; Lima et al. 2012; Fabris et al. 2014; Lima et al. 2014; Chakraborty et al. 2014; Nunes and Pavón 2015; Harko et al. 2015; Haro and Pan 2016; Nunes 2016). Some more literature on matter creation may be found in Refs. (Pan et al. 2016; Salo and Haro 2017; Pan et al. 2018; Singh and Kaur 2019; Singh and Kumar 2020a,b; Peracaula and Yu 2020; Kaur and Singh 2021; Harko et al. 2021; Kaur and Singh 2022; Hulke et al. 2020; Singh et al. 2020; Singh 2020a), which explain the late-time evolution of the Universe. The matter creation cosmology is very interesting topic because many important observations are investigated during the past few years which successfully explains the current accelerated expansion of the Universe. The key point in such models is to consider the choices for the rate of particle production, which, in general, are assumed to be the functions of the Hubble parameter H.

In this paper, we present a hybrid model which consists of matter creation cosmology and the features of Chaplygin gas to discuss the late-time accelerated expansion of the Universe. A similar kind of model was discussed in Ref. (Gangopadhyay et al. 2016) in explaining the emergent Universe scenario. Firstly, we present the analytical solution of the field equation and then constrain the parameter space of hybrid model in the light of the latest supernova (Pantheon) data, Hubble data and baryon acoustic oscillations data by performing the Bayesian analysis. Our analysis shows that the flat GCG model with and without matter creation and CG with matter creation are consistent with the used data sets. We have also analyzed the selection information criterion (AIC and BIC) and the stability of sound speed to find the degeneracy between the GCG models and ΛCDM model.

The paper is organized as follows: Section 2 presents the basic field equations of a hybrid model consisting of matter creation cosmology and GCG equation of state and give the general expressions of different cosmological parameters. In Section 3, we present solution of field equations using GCG equation of state. Section 4 is devoted to a particular case of Section 3 for matter creation with CG equation of state. In Section 5, the observational data like, Hubble data, Type Ia supernova (Panthoen) and baryon Acoustic Oscillations are discussed. Section 6 gives the methodology to perform the observation. Section 7 contains the results and discussion of the finding through observation. Finally, the conclusion of the work is summarized in Section 8.

2 Basic field equations

We start with the line element which is homogeneous and isotropic at large scale and described by the flat Friedmann-Lemaître-Robertson-Walker (FLRW) metric

$$ds^2 = -dt^2 + a^2(t)\left[dr^2 + r^2(d\theta^2 + sin^2\theta d\phi^2)\right], \qquad (1)$$

where $a(t)$ is the scale factor of the Universe and (t, r, θ, ϕ) are the co-moving coordinates. Throughout we use the units such that the speed of light $c = 1$. For comoving observer, $u^\mu = \delta^\mu_\nu$, where $u^\mu u_\mu = -1$, and the line element (1), the expansion scalar becomes $\Theta = 3H$, where $H = \dot{a}/a$ is the Hubble parameter. A dot denotes derivative with respect to cosmic time t.

In matter creation cosmology as proposed in Ref. (Prigogine et al. 1989), it is considered the Universe as an open adiabatic system with N particles. It is assumed that the particle number is not conserved $N^\mu_{;\mu} \neq 0$, which provides a modification of the energy conservation equation. The particle flux vector is assumed to be $N^\mu = nu^\mu$, where $n = N/V$ is the particle number density, and u^μ is the four-velocity of the fluid. Now, the particle flux vector, N^μ satisfies the balance equation

$$\nabla_\mu N^\mu \equiv n_{,\mu} u^\mu + 3Hn = n\Gamma, \tag{2}$$

where $V = a^3$ is the comoving volume and Γ is a particle creation rate. Equation (2) shows that $\Gamma > 0$ gives the creation of particle while $\Gamma < 0$ for particle annihilation and $\Gamma = 0$ means there is no creation of matter, i.e., particle number is conserved.

The entropy flux vector is defined by $s^\mu = n\sigma u^\mu$, where σ is the entropy per particle. It is to be noted that the entropy must fulfill the second law of thermodynamics $s^\mu_{;\mu} \geq 0$. It is also to be noted that we consider adiabatic matter creation, i.e., the system in which σ is constant. Assuming N as variable, the first law of thermodynamics modifies as

$$d(\rho V) + pdV - (h/n)d(nV) = 0, \tag{3}$$

where $h = (\rho + p)$ is the enthalpy (per unit volume), ρ and p are the energy density and the equilibrium thermostatic pressure of the usual cosmic fluids (baryons and dark matter). The extra contribution in (3) can be interpreted as a non-thermal pressure, known as creation pressure which is related to Γ by

$$P_c = -\frac{h}{n}\frac{d(nV)}{dV}. \tag{4}$$

Using (2) into (4), we get the following form of creation pressure (Prigogine et al. 1989; Calvão et al. 1992)

$$P_c = -\frac{(\rho + p)}{3H}\Gamma. \tag{5}$$

It can be observed from Eq. (5) that the creation of matter results to a negative supplementary pressure P_c. This pressure must be considered as part of the cosmological pressure $\bar{p} = p + P_c$ which modified the energy-momentum tensor into Einstein field equations

$$R_{\mu\nu} - \frac{1}{2}Rg_{\mu\nu} = \kappa T^{(eff)}_{\mu\nu}, \tag{6}$$

where $\kappa = 8\pi G$ and $T^{eff}_{\mu\nu}$ is the total energy-momentum tensor $T^{(eff)}_{\mu\nu} = T^{(g)}_{\mu\nu} + T^{(c)}_{\mu\nu}$, where $T^{(g)}_{\mu\nu}$ is the energy-momentum tensor corresponding to the cosmic fluid and generalized Chaplygin gas, that is,

$$T^{(g)}_{\mu\nu} = (\rho + p)u_\mu u_\nu + pg_{\mu\nu}, \tag{7}$$

and $T^{(c)}_{\mu\nu}$ is the energy-momentum tensor corresponding to the matter creation which is given by

$$T^{(c)}_{\mu\nu} = P_c(g_{\mu\nu} + u_\mu u_\nu), \tag{8}$$

where P_c is the matter creation pressure given by Eq. (5). The Bianchi identities $\nabla^\nu T^{(eff)}_{\mu\nu} = 0$ gives

$$d(\rho V) + (p + P_c)dV = 0. \tag{9}$$

In this paper, we consider a flat Universe that contains the baryon component with equation of state $w_b = p_b/\rho_b = 0$ and a perfect fluid following the generalized Chaplygin gas (GCG)equation of state (EoS). Thus, we assume a perfect fluid structure for the cosmic medium as a whole, and both the baryonic matter and the GCG components satisfy energy conservation equations separately. From Eq. (6) for line element (1), the Friedmann and conservation equations are given by

$$3H^2 = \kappa\rho, \tag{10}$$

$$\dot{\rho_b} + 3H\rho_b = 0 \tag{11}$$

$$\dot{\rho}_{gcg} + 3H(\rho_{gcg} + p_{gcg} + P_c) = 0. \tag{12}$$

where $\rho = \rho_{gcg} + \rho_b$ is the total energy density and p_{gcg} being the pressure of the GCG assumed as perfect fluid. By integrating the conservation equation (11), we have $\rho_b = \rho_{b,0}a^{-3}$, where $\rho_{b,0}$ is the energy density at present.

The solution of the field equations are found by the choice for the particle creation rate Γ. The simplest possible case, and probably the most physically choice would be the function of Hubble parameter. Phenomenologically, this is equivalent to (Lima et al. 1996; Lima and Alcaniz 1999)

$$\Gamma = 3\beta H, \tag{13}$$

where β is a positive constant. Using (13) into (5), the creation pressure can be expressed as

$$P_c = -\beta(\rho_{gcg} + p_{gcg}). \tag{14}$$

Models with non-linear equations of state have raised a substantial interest recently, mainly due to the possibility of DE and DM unification (Bilić et al. 2002). This non-linear equation of state (EoS) leads to a positive (adiabatic) squared sound speed ($\mathcal{C}_S^2 = \partial p_{cg}/\partial\rho_{cg}$), even for negative pressure.

An example of an equation of state exhibiting these properties is given by Chaplygin gas (CG) equation of state $p_{cg} = -A/\rho_{cg}$ (Kamenshchik et al. 2001), where A is a positive constant. The Chaplygin gas may be considered as viable alternative to quintessence. However, this was ruled out in cosmology as cosmological models were not consistent with the observational data. Subsequently, a more generalized model of the Chaplygin gas is characterized by an equation of state $p_{gcg} = -A/\rho^{\alpha}_{gcg}$ (Bilić et al. 2002) which is known as 'generalized Chaplygin gas' (GCG). The GCG model is consistent with a number of observational data involving background evolution of the Universe for $-1/2 \leq \alpha \leq 1/2$ (Makler et al. 2003a). It has been shown that this models can be accommodated within the standard structure formation scenarios (Bento et al. 2002; Bilić et al. 2002; Fabris et al. 2014). Therefore, Chaplygin gas models look to be good alternative to describe the accelerated expansion of the Universe. In what follows, we find the solutions of GCG and CG models with matter creation cosmology to observe the dynamics of the evolution of the Universe.

3 GCG model with matter creation

To solve the field equations, let us consider a generalized Chaplygin gas (GCG) whose equation of state (EoS) is given by (Bento et al. 2002; Bilić et al. 2002)

$$p_{gcg} = -\frac{A}{\rho^{\alpha}_{gcg}}, \tag{15}$$

where A and $0 < \alpha \leq 1$ are positive parameters to be determined. For the particular case $\alpha = 1$, the EoS is reduced to the so-called Chaplygin gas which was first studied by Kamenshchik et al. (2001).

Using (14) and (15) into the conservation equation (12), the energy density ρ_{gcg} as a function of the scale factor a is given as

$$\rho_{gcg}(a) = \left(A + Ca^{-3(1-\beta)(1+\alpha)}\right)^{\frac{1}{1+\alpha}}, \tag{16}$$

where C is the constant of integration. Considering $\rho_{gcg} = \rho_{gcg,0}$ at $a = a_0 = 1$ at present, the above equation can be re-written as

$$\rho_{gcg} = \rho_{gcg,0}\left[A_s + (1 - A_s)(1+z)^{3(1-\beta)(1+\alpha)}\right]^{\frac{1}{1+\alpha}}, \tag{17}$$

where $z = a^{-1} - 1$ is the redshift and $A_s = A/\rho^{(1+\alpha)}_{gcg,0} > 0$ is the scaled parameter. In the absence of matter creation ($\beta = 0$), Eq. (17) reduces to the result obtained in Ref. Bento et al. (2002). For $A_s = 0$, the GCG model behaves always as matter where it behaves like cosmological constant for $A_s = 1$. Thus, to describe the unified model, we have to assume the range for A_s as $0 < A_s < 1$.

From Friedman equation (10), we get the Hubble parameter as

$$H^2(z) = H_0^2\Big[\Omega_{gcg,0}\,(A_s + (1 - A_s)(1+z)^{3(1-\beta)(1+\alpha)}\Big)^{\frac{1}{(1+\alpha)}} + \Omega_{b,0}(1+z)^3\Big] \tag{18}$$

where $H(z=0) = H_0 = 100h\ kms^{-1}Mpc^{-1}$ is the present Hubble parameter, and $\Omega_{b,0} = \rho_{b,0}/(3H_0^2)$ and $\Omega_{gcg,0} = \rho_{gcg,0}/(3H_0^2)$ are the density parameters of the baryonic matter and Chaplygin gas components, respectively such that $\Omega_{b,0} + \Omega_{gcg,0} = 1$. The observed abundances of light elements together with primordial nucleosynthesis gives $\Omega_{b,0}h^2 = 0.0224 \pm 0.0001$ (Aghanim et al. 2020).

Let us explore the cosmological parameters, mainly the Hubble parameter, deceleration, jerk parameter and EoS parameter, to distinguish the effect of creation pressure included in the different Chaplygin gas models and also compare these models with ΛCDM.

In cosmology, the Hubble parameter $H(z)$, deceleration parameter $q(z)$ and jerk Parameter $j(z)$ are purely kinematical as they are independent of any gravity theories. The deceleration parameter measures the transition from deceleration to acceleration. In terms of redshift, it is defined as

$$q(z) = -1 + (1+z)E(z)^{-1}\frac{dE(z)}{dz}, \tag{19}$$

where $E(z) \equiv H(z)/H_0$ is the dimensionless Hubble parameter.

For this model the deceleration parameter can be written as

$$q(z) = -1 + \frac{3}{2E^2(z)}\left[\Omega_{b,0}(1+z)^3 + \frac{\Omega_{gcg,0}(1-A_s)(1-\beta)(1+z)^{3(1-\beta)(1+\alpha)}}{\{A_s + (1-A_s)(1+z)^{3(1-\beta)(1+\alpha)}\}^{\frac{\alpha}{1+\alpha}}}\right] \tag{20}$$

It is to be noted that the solutions (16), (17) and (18) reduce to GCG solutions obtained in Refs. (Makler et al. 2003a; Zhu 2004; Fabris et al. 2010) in the absence of matter creation, i.e., for $\beta = 0$.

The jerk parameter is another kinematics diagnostic parameter that provides us the simplest approach to observe the departure from the ΛCDM model. It is defined as a dimensionless third order derivative of the scale factor a with respect to the cosmic time t, i.e., $j = \dddot{a}/aH^3$ (Visser 2004; Blandford et al. 2004). For ΛCDM model in flat FLRW metric, jerk parameter is a constant with the value $j = 1$.

It should be noted here that Sahni et al. (2003) drew attention to the importance of j for discriminating different dark energy models. Any deviation from the value $j = 1$ would favor a non-ΛCDM model.

In terms of deceleration parameter q, the jerk parameter j can be written as (Rapetti et al. 2007)

$$j(z) = q(2q+1) + (1+z)\frac{dq}{dz}. \tag{21}$$

Equation (21) enables us to constrain the departure from the ΛCDM value in an effective manner.

The equation of state (EoS) parameter for the GCG fluid is

$$w_{gcg}(z) = -\frac{A_s}{A_s + (1-A_s)(1+z)^{3(1-\beta)(1+\alpha)}}. \tag{22}$$

The present-day value of EoS parameter, $w_{gcg,0}$ for GCG at $z = 0$ is obtained as

$$w_{gcg,0} = -A_s, \tag{23}$$

It can be observed that Eq. (23) gives the physical significant of A_s. The behavior of GCG depends on the values of A_s, α and β. For $A_s = 1$, we get a trivial solution $w_{gcg} = -1$ which shows that GCG model behaves exactly as ΛCDM at all times for all values of α and β. For $A_s = 0$, we have $w_{gcg} = 0$ and hence GCG model behaves as pressureless dust fluid all the times for all values of α and β.

4 Particular case: CG model with matter creation

In this section, we consider a particular case for $\alpha = 1$ in Eq. (15), i.e., equation of state $p_{cg} = -A/\rho_{cg}$ (Kamenshchik et al. 2001), the so-called Chaplygin gas with matter creation. Using the continuity equation (12), the energy density is given by

$$\rho_{cg} = \rho_{cg,0}\sqrt{\left[A_s + (1-A_s)(1+z)^{6(1-\beta)}\right]}, \tag{24}$$

where $A_s = A/\rho_{cg,0}^2$ is the scaled parameter. The corresponding Hubble function is given by

$$E^2(z) = \left[\Omega_{cg,0}\left\{A_s + (1-A_s)(1+z)^{6(1-\beta)}\right\} + \Omega_{b,0}(1+z)^3\right]. \tag{25}$$

Using (25) into (19), we get

$$q(z) = -1 + \frac{3}{2E^2(z)}\left[\Omega_{b,0}(1+z)^3 + \frac{\Omega_{cg,0}(1-A_s)(1-\beta)(1+z)^{6(1-\beta)}}{\sqrt{\{A_s + (1-A_s)(1+z)^{6(1-\beta)}\}}}\right] \tag{26}$$

We can recover the solutions obtained in Ref. (Kamenshchik et al. 2001) in the absence of matter creation, i.e., for $\beta = 0$.

The equation of state (EoS) parameter for the CG fluid is

$$w_{cg}(z) = -\frac{A_s}{A_s + (1-A_s)(1+z)^{6(1-\beta)}}. \tag{27}$$

5 Observational data

In this section, we perform the global constraints on our two models: GCG and CG with matter creation along with ΛCDM by using the recent and relevant observational data, which are exhibited as follows:

5.1 Hubble data

The Hubble data $H(z)$ can be classify into two category: Baryonic Acoustic Oscillations (BAO) surveys and cosmic chronometer (CC) data. In general, $H(z)$ data obtained from BAO survey data is model-dependent which can not be utilized to constraint a cosmological model. On the other hand, the cosmic chronometer (CC) data determined by using the most massive and passively evolving galaxies based on the "galaxy differential age" method are model-independent (Moresco et al. 2016; Wang and Meng 2017). Therefore, we use 32 CC data points in our analysis covering the range $0.07 \le z \le 1.965$ (Moresco et al. 2022).

The χ^2 function is defined

$$\chi^2_{H(z)} = \sum_{i=1}^{32}\frac{[H_{obs}(z_i) - H(\mathbf{p}, z_i)]^2}{\sigma(z_i)^2}, \tag{28}$$

where $H(\mathbf{p}, z_i)$ denotes the theoretical value of $H(z)$ at redshift z_i for a given set of cosmological parameters $\mathbf{p} = (H_0, \Omega_{b,0}, A_s, \beta, \alpha)$, $H_{obs}(z_i)$ denotes the observed values of $H(z)$ at redshift z_i, and $\sigma(z_i)$ is the uncertainty in the measurement of H_i.

5.2 Type Ia supernovae

We use the Pantheon sample, a recent Type Ia supernovae (SNe) dataset with 1048 points of distance moduli at various redshift in the range $0.01 \le z \le 2.26$. Pantheon sample is collected from the DE Survey and the Supernova Legacy Survey and has been extensively calibrated to eliminate systematic errors and increase the accuracy of distance estimations (Scolnic et al. 2018; Chang et al. 2019).

We employ the χ^2 statistics,

$$\chi^2_{SNe} = \sum_{i,j=1}^{1048}\Delta\mu_i\left(C^{-1}_{SNe}\right)_{ij}\Delta\mu_j, \tag{29}$$

Table 1 Clustering measurements for the BAO samples (Alam et al. 2021)

Parameter	Redshift range	z_{eff}	$D_H(z)/r_d$
Boss galaxy	$0.2 < z < 0.5$	0.38	25.00 ± 0.76
Boss galaxy	$0.4 < z < 0.6$	0.51	22.33 ± 0.58
eBoss LRG	$0.6 < z < 1.0$	0.70	19.33 ± 0.53
eBoss quasars	$0.8 < z < 2.2$	1.48	13.26 ± 0.55
$Ly\alpha - Ly\alpha$	$z > 2.1$	2.33	8.93 ± 0.28
$Ly\alpha - Quasars$	$z > 1.77$	2.33	9.08 ± 0.34

where $\Delta\mu_i = \mu_{th} - \mu_{obs}$ represents the difference between the theoretical and observational distance modulus, and C_{SNe}^{-1} denotes the data's inverse covariance matrix. In addition, we define $\mu = m_B - \mathcal{M}_B$, where m_B and $\mathcal{M}_B$ represent the measured apparent magnitude and absolute magnitude at a certain redshift, respectively. The theoretical value is calculated as,

$$\mu_{th}(z) = 5log_{10}\frac{d_L(z)}{1Mpc} + 25, \tag{30}$$

where $d_L(z)$ is the luminosity distance and is defined as

$$d_L(z) = (1+z)\int_0^z \frac{dz'}{H(z', \mathbf{p})}. \tag{31}$$

5.3 Baryon acoustic oscillations ($BAOs$)

Baryon Acoustic Oscillations (BAO) are also excellent geometrical probes and largely unaffected by errors in the non linear evolution of the matter density field and other systematic uncertainties. It is a feature of the large-scale structure of the Universe that emerge from primordial density perturbations in the baryon-photon plasma in the early Universe. In this paper, we use BAO data from several surveys, including Lyman-α(Lyα) and quasars. These experiments include the samples from SDSS, BOSS and eBOSS. To break the parameter degeneracies from other measurements, we employ six points of BAO datasets as shown in Table 1 (for detail, refer to Table 3 of Ref. Alam et al. 2021).

In a spectroscopic survey, the BAO feature along the line-of-sight direction measures the Hubble distance at redshift z,

$$D_H(z) = \frac{c}{H(z)}. \tag{32}$$

When considering the dependence of r_d, the BAO measurements constrain the quantities $D_H(z)/r_d$. The cosmological parameters used to calibrate the characteristic BAO scale r_d are typically derived from CMB observations. This BAO feature has a comoving scale set by the distance r_d traveled by sound waves between the end of inflation and decoupling of baryons from photons after recombination. The χ^2 function for BAO data set is defined as

$$\chi^2_{BAO} = \sum_{i=1}^{6}\left(\frac{[d_{obs}(z_i) - d_{th}(z_i)]}{\sigma(d_{obs}(z_i)}\right)^2, \tag{33}$$

where d denotes for $D_H(z)/r_d$ and d_{obs} is the observed distance value as given in Table 1 and d_{th} is the theoretical value calculated for the models under consideration.

6 Methodology

Using the above dataset, we proceed to analyze whether the two extensions of Chaplygin gas being considered in this work, namely, the GCG with matter creation and CG with matter creation models capable to fit the observations in a comparable way to ΛCDM model. In this respect, we employ the total likelihood function to establish the joint constraints on the model parameter space (H_0, Ω_b, A_s, α, β) from the aforementioned observational data. The best-fit of the parameters are maximized by using the following total χ^2-function.

$$\chi^2_{tot} = \chi^2_{H(z)} + \chi^2_{SNe} + \chi^2_{BAO}, \tag{34}$$

where $\chi^2_{H(z)}$, χ^2_{SNe} and χ^2_{BAO} are given by Eqs. (28), (29) and (33), respectively. It is noted that the current observational constraints on baryon density $\Omega_{b,0}$ are stringent.[1] We follow the Markov Chain Monte Carlo (MCMC) sample from the python package *emcee* to minimize the likelihood. We have chosen 2000 iterations with 120 walkers to explore the confidence region taking into account a Gaussian priors on the Hubble constant H_0 and on the baryon density $\Omega_{b,0}$. Additionally, we select priors for A_s, α and β. Table 2 summarizes the priors used in the Bayesian analysis.

We also utilize two selection criteria, like the Akaike information criteria (AIC) (Akaike 1974) and the Baysian information criteria (BIC) (Schwarz 1978) to determine which of the models is performing better. The AIC is defined as

$$AIC = \chi^2_{min} + \frac{2nN}{N-n-1}, \tag{35}$$

where χ^2_{min} is the minimum value of the χ^2-function, n ($n = 3$, 5, 4 and 4 for ΛCDM, GCG with β, GCG without β and CG with β, respectively) is the number of independent parameters and $N = 1086$ (H(z) = 32, SNe = 1048 and BAO = 6) is the total number of data points.

The BIC value is computed from

$$BIC = \chi^2_{min} + n\ln N. \tag{36}$$

We define the AIC and BIC differences by considering ΛCDM as the reference model: $\Delta AIC = AIC_x -$

[1] For example, $\Omega_{b,0}h^2 = 0.0224 \pm 0.0001$ from Planck 2018 results (Aghanim et al. 2020).

Table 2 The priors ranges and the best-fit values and 1σ marginalized uncertainties of parameters obtained from the $SNe + H(z) + BAO$ fitting analysis for ΛCDM, GCG with β, GCG without β and CG with β

Parameters	Priors	ΛCDM	GCG with β	GCG without β	CG with β
H_0	[50, 80]	$68.595^{+1.803}_{-1.680}$	$68.804^{+1.066}_{-1.062}$	$69.432^{+0.034}_{-0.062}$	$68.778^{+0.123}_{-0.128}$
Ω_m	–	$0.307^{+0.026}_{-0.022}$	–	–	–
Ω_Λ	–	$0.701^{+0.032}_{-0.032}$	–	–	–
Ω_b	[0.02, 0.04]	–	$0.029^{+0.006}_{-0.005}$	$0.029^{+0.001}_{-0.004}$	$0.030^{+0.003}_{-0.002}$
A_s	[0.5, 1.5]	–	$0.713^{+0.043}_{-0.035}$	$0.777^{+0.011}_{-0.021}$	$0.705^{+0.032}_{-0.044}$
α	[0, 1]	–	$0.995^{+0.078}_{-0.022}$	$0.350^{+0.024}_{-0.033}$	1
β	[0, 1]	–	$0.140^{+0.022}_{-0.042}$	–	$0.498^{+0.009}_{-0.013}$

Table 3 The present values of q, j, w, $\mathcal{C}_S^2$ and age of the Universe corresponding to ΛCDM, GCG with β, GCG without β and CG with β models.

Model	q_0	j_0	w_0	$\mathcal{C}_S^2$	t_0 (Gyr)
ΛCDM	$-0.551^{+0.020}_{-0.020}$	1	$-0.701^{+0.013}_{-0.015}$	≤ 1	13.8 ± 0.14
GCG with β	$-0.597^{+0.016}_{-0.013}$	$1.440^{+0.023}_{-0.022}$	$-0.713^{+0.044}_{-0.012}$	0.638	13.8 ± 0.16
GCG without β	$0.271^{+0.033}_{-0.031}$	$1.264^{+0.034}_{-0.023}$	$-0.777^{+0.055}_{-0.012}$	0.271	13.6 ± 0.11
CG with β	$-0.523^{+0.011}_{-0.022}$	$1.006^{+0.031}_{-0.027}$	$-0.705^{+0.013}_{-0.022}$	0.705	13.6 ± 0.13

$AIC_{\Lambda CDM}$ and $\Delta BIC = BIC_x - BIC_{\Lambda CDM}$, where x represents either of GCG with β, GCG without β and CG with β models.

In case of AIC, if $\Delta AIC < 2$, both the models are equally supported by data. If $2 < \Delta AIC < 4$, there is average support. The range $4 < \Delta AIC < 10$ still supports the considered model but less than the preferred one. For the value of $\Delta AIC > 10$, the model is not supported by the observational data.

Similarly, in case of BIC, $\Delta BIC < 2$ indicates no evidence against the model. If $2 < \Delta BIC < 6$, there is modest evidence against the considered model. We get a strong evidence against the considered model for a value in the range $6 < \Delta BIC < 10$ suggests and a stronger evidence against the model if $\Delta BIC > 10$. For BIC, models with more number of parameters, compared to ΛCDM, penalised further due to the $\ln N$ factor.

We are also interested to discuss the stability of the models using the method of squared sound speed, $\mathcal{C}_S^2$. The equation describing the evolution of linear perturbations of the background energy density define the squared sound speed. Therefore, it is a background quantity which is essentially a perturbative in nature. The bound $\mathcal{C}_S^2 > 0$ is required to have small perturbations of the background energy density, otherwise, the energy density perturbations will grow and there will be a classical instability. Thus, stability or instability of a given perturbation in the background, can be specified by determining the sign of $\mathcal{C}_S^2$. The model is stable if $\mathcal{C}_S^2 > 0$ and for $\mathcal{C}_S^2 < 0$, the model approaches to instability.

The squared sound speed is defined as (DeDeo et al. 2003; Hannestad 2005)

$$\mathcal{C}_S^2 = \partial p / \partial \rho. \tag{37}$$

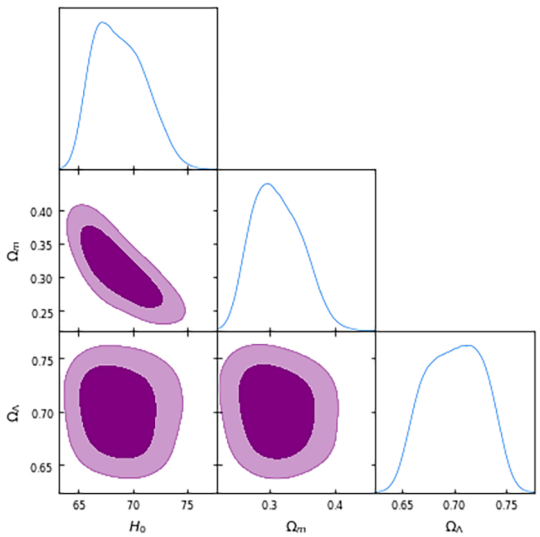


Fig. 1 2D contour at 68.3% and 95.4% confidence levels for ΛCDM model using $H(z) + SNe + BAO$ data-set.

Using (17) in the above equation, the squared sound speed for GCG model with matter creation is calculated as

$$\mathcal{C}_S^2 = \frac{\alpha\, A_s}{A_s + (1 - A_s)(1+z)^{3(1-\beta)(1+\alpha)}}. \tag{38}$$

In terms of EoS parameter, it gives

$$\mathcal{C}_S^2 = -\alpha\, w_{gcg}(z). \tag{39}$$

Using above equation, we can obtain the present value as $\mathcal{C}_S^2(z=0) = \alpha A_s = -\alpha w_{gcg,0}$. The positive value of A_s restricts the value $\alpha > 0$. It is to be noted that for causality and stability under perturbation, it is required to satisfy the inequality condition $0 \leq \mathcal{C}_S^2 \leq 1$ (Lixin et al. 2012).

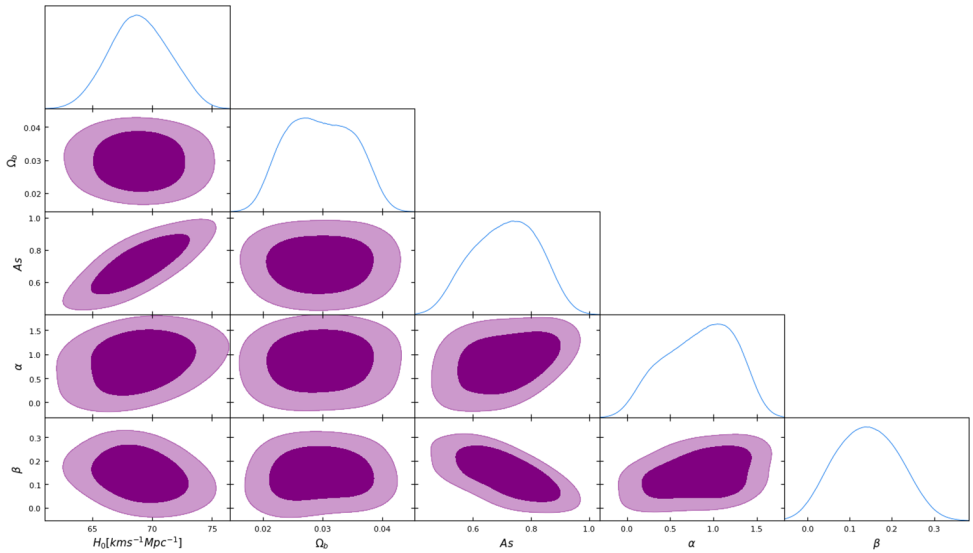


Fig. 2 2D contour at 68.3% and 95.4% confidence levels for GCG model with matter creation using $H(z) + SNe + BAO$ data-set.

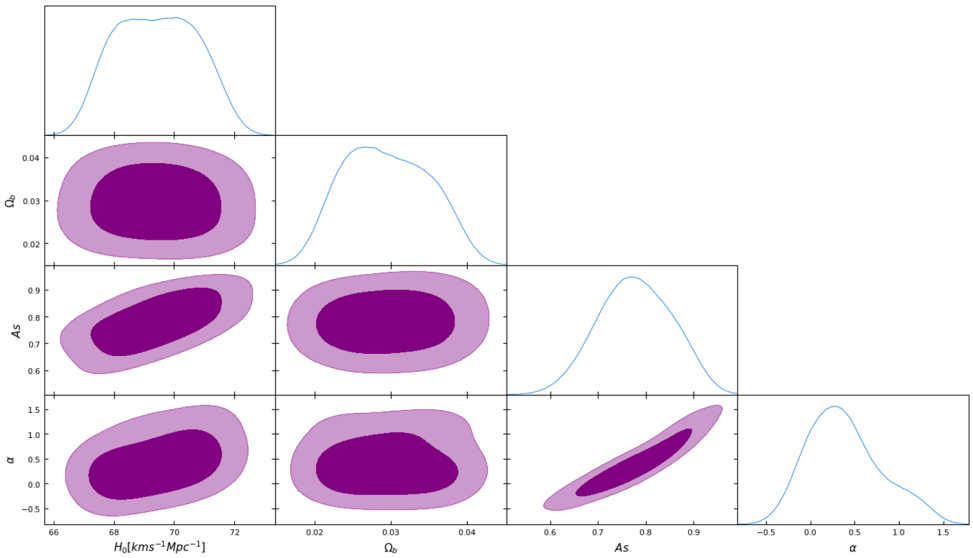


Fig. 3 2D contour at 68.3% and 95.4% confidence levels for GCG model without matter creation using $H(z) + SNe + BAO$ data-set.

7 Results and discussion

The best-fit values of model parameters are displayed in tables and figures. In Table 2 we present the values of various model parameters under consideration, namely ΛCDM, GCG with β, GCG without β and CG with β. In Table 3 we provide the present values of $q(z)$, $j(z)$, $w(z)$, $\mathcal{C}_S^2$ and t_0 using the best-fit values of the models. The 1-dimensional marginalized posterior distributions and two-dimensional contours correspond to 68.3% and 95.4% confidence levels for the parameters space of these models are shown in Figs. 1-4. Finally, in Figs. 5-9 we plot the evolution of the cosmological parameters, namely $H(z)$, $q(z)$, $j(z)$, $w(z)$ and $\mathcal{C}_S^2$ of these considered models. In what follows, we discuss our results with some more detail.

Analysing the constraints of the parameters of the various versions of the models listed in Table 2, we find that the ΛCDM model gives $H_0 = 68.595^{+1.803}_{-1.680}$ km/s/Mpc, the GCG with β gives $H_0 = 68.804^{+1.066}_{-1.062}$ km/s/Mpc, the GCG without β yields $H_0 = 69.432^{+0.034}_{-0.062}$ km/s/Mpc, and finally, the CG with β gives $H_0 = 68.778^{+0.123}_{-0.128}$ km/s/Mpc. We observe that these results are very competitive with the other current estimates performed by assuming ΛCDM cosmology (Ade et al. 2016; Aghanim et al. 2020; Schöneberg et al. 2022). The evolution of $H(z)$ with redshift for different models are plotted in Fig. 5.

Also, the deceleration parameters are constrained to $q_0 = -0.597^{+0.016}_{-0.013}$ for GCG with β, $q_0 = -0.271^{+0.033}_{-0.031}$ for GCG without β, $q_0 = -0.523^{+0.011}_{-0.022}$ for CG with β (c.f. Table 3) which suggest the current accelerating expansion of the Universe at high statistical significance evidence. The evolutions of the deceleration parameter for different models are plotted in Fig. 6. The parameter $q(z)$ transits from posi-

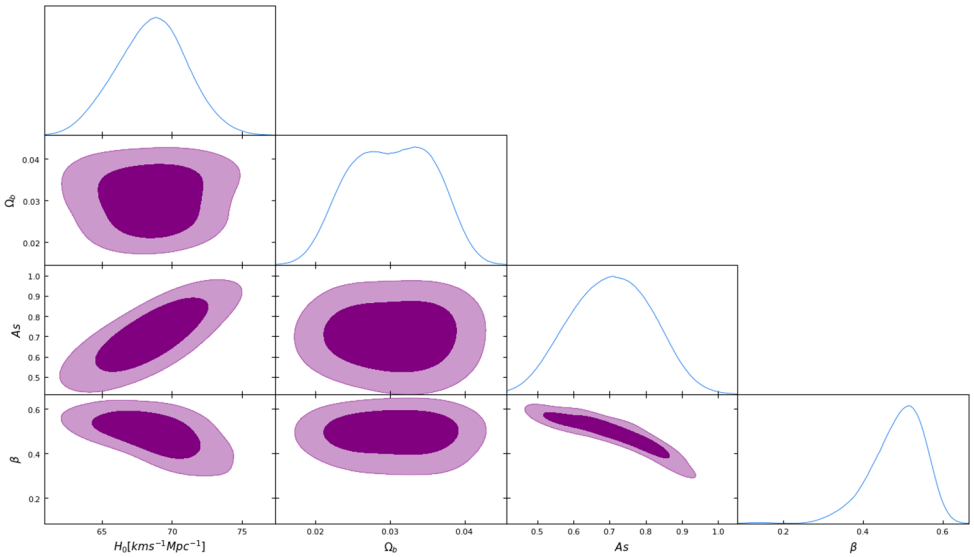


Fig. 4 2D contour at 68.3% and 95.4% confidence levels for CG model with matter creation using $H(z) + SNe + BAO$ data-set.

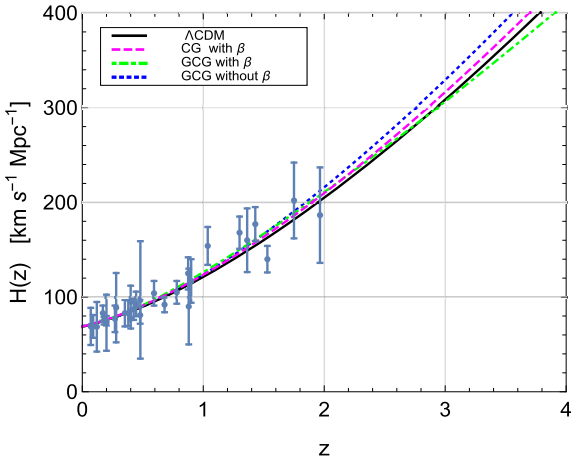


Fig. 5 Best fits over $H(Z)$ data for ΛCDM (black solid line), and GCG with β (green dot-dashed line), GCG without β (blue dotted line) and CG with β (magenta dashed line) models are shown. The grey points with uncertainty bars correspond to the 32 $H(z)$ sample.

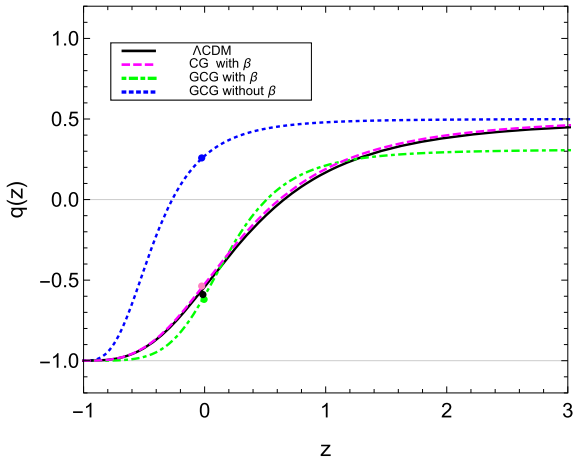


Fig. 6 Evolution of the deceleration parameter, $q(z)$ with redshift for GCG and CG models with and without matter creation. The trajectory of $q(z)$ for ΛCDM model is also shown in bold line. The dot represents the present value of $q(z)$ (hence q_0).

tive ($q > 0$, deceleration) to negative ($q < 0$, acceleration) in each model which shows that the Universe decelerates at early time followed by acceleration in late time. The GCG with β model starts late acceleration than CG with β and ΛCDM models. We observe that the all Chaplygin gas models (GCG and CG) have characteristics of quintessence DE.

The present value of EoS parameter of Chaplygin gas models are displayed in Table 3. Figure 8 shows the evolution of the EoS parameter for different models. It is observed that the EoS parameter of all the models tend to -1 in late-time. In Fig. 7, we show the jerk parameter, $j(z)$ of our models in comparison to ΛCDM model. In late-time all the Chaplygin gas with or without matter creation converge to ΛCDM state. Based on the joint analysis, the present values of $j(z)$ are $j_0 = 1.440^{+0.023}_{-0.022}$, $1.264^{+0.034}_{-0.023}$ and $1.006^{+0.031}_{-0.027}$ for GCG with β, GCG without β and CG with β, respectively.

Following the selection criteria of AIC and BIC as discussed in Section 5, the values of ΔAIC and ΔBIC are listed in Table 4. According to ΔAIC values of Chaplygin gas models, we find that GCG with β, GCG without β and CG with β models have $\Delta AIC < 2$ which show that the joint observational data strongly support these models. In BIC, we have $2 < \Delta BIC < 6$ for GCG without β and CG with β, and thus there is positive evidence against the model. The GCG with β model has $\Delta BIC > 10$ which tells us that there is a very strong evidence against this model. This may happen due to the large number of free parameters for which BIC penalizes.

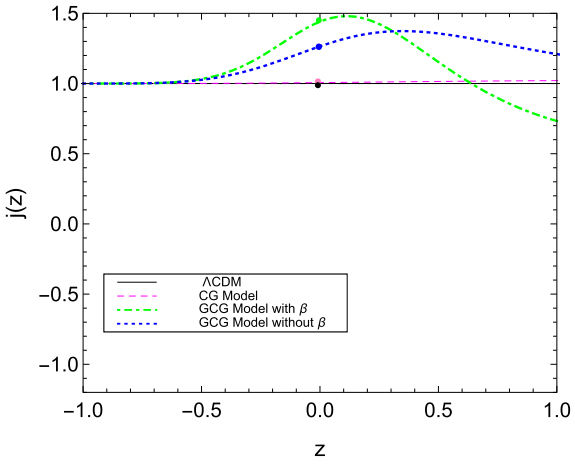


Fig. 7 Evolution of the jerk parameter, $j(z)$ for GCG and CG models with and without matter creation. The horizontal bold line represents the value of $j(z)$ for ΛCDM. The dot represents the present value of $j(z)$ (hence j_0).

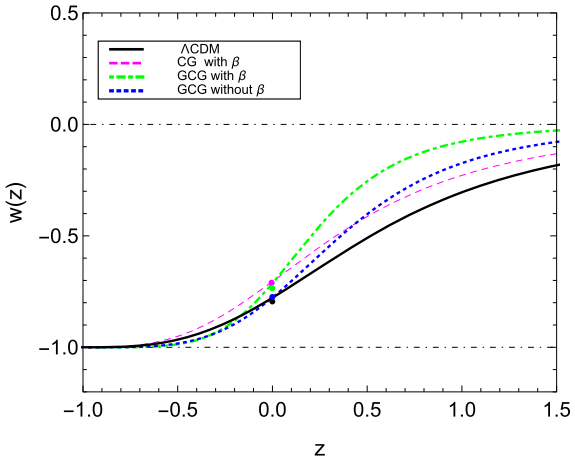


Fig. 8 Evolution of the state parameter, $w(z)$ for GCG and CG models with and without matter creation. The dot represents the present value of $w(z)$ (hence w_0).

The evolution of $\mathcal{C}_S^2$ with respect to redshift for different models is shown in Fig. 9. Using the best-fit values of α and A_s, we find that $\mathcal{C}_S^2 = 0.638$ for GCG model with β, $\mathcal{C}_S^2 = 0.271$ for GCG model without matter creation and $\mathcal{C}_S^2 = 0.705$ for CG with β [c.f. Table 3]. It is obvious that the squared sound speed of these models are in the range of $0 < \mathcal{C}_S^2 < 1$, which is not exceeding the speed of light (unity), and hence the models are stable. We have computed the present age of the Universe in different models which are summarized in Table 3.

8 Conclusion

In this work, we have studied the gravitationally- induced matter creation cosmology with a generalization of the

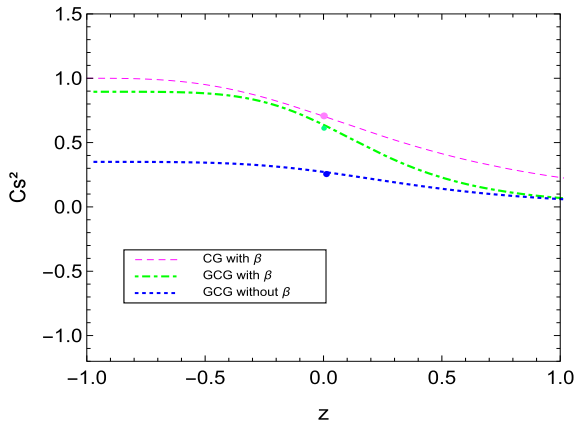


Fig. 9 Evolution of speed of sound, $\mathcal{C}_S^2$ for GCG and CG models with and without matter creation. The dot represents the present value $\mathcal{C}_S^2(z=0)$.

Chaplygin gas equation of state, $p = -A/\rho^\alpha$, with $0 < \alpha \leq 1$ to observe the late-time cosmic acceleration in the framework of flat FLRW spacetime. We have also considered a particular case of $\alpha = 1$, i.e. the Chaplygin gas EoS, $p = -A/\rho$ with matter creation. The cosmological relevance of pure CG model has been pointed out in Ref. Kamenshchik et al. (2001) and it has been found that the SNe data rules out the CG model.

As discussed in the introductory part, gravitationally- induced matter creation can be treated as an irreversible scalar process which provides an additional decay (creation) pressure in the energy-momentum tensor of the cosmological mixture. This extra creation pressure is defined in terms of matter creation rate, Γ and other physical quantities describing the fluid. It has been demonstrated that considering the Universe as a open systems with matter creation, one can understand the current accelerated expansion of the Universe. Since the rate of matter creation, Γ, is still unknown, we have assumed phenomenological ansätze of the matter creation rate evolving as $\Gamma = 3\beta H$, where β is a constant. Many authors (Lima et al. 1996; Lima and Alcaniz 1999; Cárdenas 2012) have studied some properties of adiabatic matter creation models with this form of matter creation rate. It has been found that this kind of models are always decelerating or accelerating, that is, there is no transition from decelerated to accelerated expansion phase as required by the SNe observations. However, we have found that considering the GCG and CG EoS in matter creation model there is a transition from one phase to other phase with the same form of matter creation rate. In what follows, we have summarized the result of our findings in more detail.

In the first part of the paper, we have presented the analytical solution of matter creation models with GCG and CG equation of states. We have obtained the solutions of cosmological parameters, like energy density, Hubble parameter, deceleration parameter, EoS parameter and jerk parameter

Table 4 The AIC and BIC obtained for the ΛCDM, GCG with β, GCG without β and CG with β models. We assume ΛCDM model as reference model.

Model	χ^2_{min}	n	N	AIC	BIC	ΔAIC	ΔBIC
ΛCDM	1088.121	3	1086	1094.02	1108.97	–	–
GCG with β	1087.334	5	1086	1095.03	1119.95	1.00	10.54
GCG without β	1087.223	4	1086	1095.09	1114.96	1.06	5.99
CG with β	1086.336	4	1086	1096.01	1113.96	1.988	4.99

as function of the redshift. In the second part of the paper, we have performed a joint observation to constrain the model's parameters by using the latest observational data such as Type Ia supernovae (Pantheon data), Hubble data and BAO data. The best-fit values of model parameters are listed in Table 2. The present values of $q(z)$, $j(z)$, $w(z)$, $\mathcal{C}_S^2$ and age of Universe are presented in Table 3. We have shown the evolution of the cosmological parameters, $H(z)$, $q(z)$, $w(z)$, $j(z)$ and $\mathcal{C}_S^2$ in Figs. 5-9, respectively. We have observed a deviation of GCG and CG with β with respect to the ΛCDM and GCG models in the deceleration phase. The plot of these cosmological parameters clearly show that the models successfully generate late-time cosmic acceleration along with a decelerated expansion in the past. The evolutions of $j(z)$ show that the GCG without β and CG with β do not deviate very far from the ΛCDM model. However, the GCG with β show much deviation from ΛCDM during early Universe. But $j(z)$ of all the models tends to 1 as $z \to -1$. The plot of data points of $H(z)$ with 1σ error bars show that our models are well consistent with these data against the redshift parameter.

We have compared the present model with those obtained from the standard ΛCDM. The evolution of different cosmological parameters show that the matter creation model with GCG EoS mimics exactly the ΛCDM model. The present value q_0, w_0 and t_0 are very close to the present value of ΛCDM. Similarly, the other value, like H_0 and Ω_b are very competitive with ΛCDM obtained in Ref. (Ade et al. 2016; Aghanim et al. 2020; Cárdenas 2012). All the models transit from early deceleration phase to late-time acceleration phase. We have explored through the joint observational analysis that the models favor the EoS for DE greater than -1, that is, quintessence region. Thus, the results of the models are fully consistent with respect to the expected ΛCDM value.

Makler et al. (2003a) have derived the constraints from SNe on flat cosmological models with GCG EoS and found that the GCG model is a promising model for unifying the dark components. Bertolami et al. (2004) analyzed the GCG EoS for flat and non-flat models with the SNe data. Considering all mater and energy components for the flat case, they found the best-fit values for (A_s, α) as $(0.79, 0.999)$ and $(0.936, 3.75)$ with and without the constraint $\alpha \geq 1$, respectively. Bento et al. (2003b) constrained the GCG model and obtained $0.74 \leq A_s \leq 0.85$ and $\alpha \leq 0.6$. Choudhury and Padmanabhan (2005) obtained the best-fit values for (A_s, α) as (0.79, 0.999) with the restriction of $\alpha \leq 1$. However, for wider range the best-fit value are (0.936, 3.75). Zhu (2004) obtained the best-fit at $A_s = 0.74$ and $\alpha = 0.32$ from the dimensionless coordinate distance data. However, the author constrained the best-fit at $A_s = 0.70$ and $\alpha = -0.09$ from the X-ray gas mass fractions of galaxy clusters and dimensionless coordinate distances to SNe and FRIIb radio galaxies. Wu and Yu (2007) examined the observational constraints on the GCG model for DE from the 9 $H(z)$ data points. They found that the best-fit happens at $A_s = 0.82$ and $\alpha = 0.71$. Further, the authors used joint observational data of $H(z)$, BAO and supernovae Legency Survey (SNeLS) and obtained the best-fit at $A_s = 0.75$ and $\alpha = 0.05$.

In our investigations, we have observed that the best-fit values of our GCG and CG models with matter creation are comparable with results discussed above which are within the expected parameters ranges of the GCG to describe the unified model. It is also noted that the pure CG model ($\alpha = 1$) is ruled out by the used observational data sets. However, CG with matter creation is consistent with these data sets. Makler et al. (2003a,b) pointed out that the GCG model can be explored further, both from the particle physics as well as observational side. It is expected that the negative pressure of both the matter creation and GCG EoS might be jointly guide us to unveil the nature of the Universe.

The AIC and BIC analysis show that GCG with β, GCG without β and CG with β models have $\Delta AIC < 2$ which means that the joint observational data strongly support these models. In BIC, we have $2 < \Delta BIC < 6$ for GCG without β and CG with β, and thus there is positive evidence against the model. The GCG with β model has $\Delta BIC > 10$ which tells us that there is a very strong evidence against this model. This may happen due to the large number of free parameters for which BIC penalizes. It has been found that the squared sound speed of these models are in the range of $0 < \mathcal{C}_S^2 < 1$, which is not exceeding the speed of light (unity), and hence the models are stable. Therefore, we conclude that the presented models in this paper provide well constrained values of cosmological parameters from the joint observational data of SNe, $H(z)$ and BAO and the models remain at very close proximity of the ΛCDM model.

Acknowledgements The authors express their thanks to the potential reviewers for the useful comments and suggestions to improve the

quality of the work in this paper. One of the authors, YB is thankful to Delhi Technological University, New Delhi for providing Research Fellowship to carry out this work.

Author contributions The conceptualization of this paper is mainly due to C. P. Observations and figures are due to Y.S. Investigation and methodology carried out by several common discussions on the topics. Both the authors have contributed to writing and reviewed the manuscript for final submission.

Data Availability The manuscript has no associated data. The datasets used in this paper are openly available on https://doi.org/10.17909/T95Q4X.

Declarations

Competing interests The authors declare no competing interests.

References

Ade, P.A.R., et al.: Astron. Astrophys. **571**, A16 (2014)
Ade, P.A.R., et al.: Planck collaboration: "Planck 2015 results. XIII. Cosmological parameters". Astron. Astrophys. **594**(13), A13 (2016)
Aghanim, N., et al. (Planck Collaboration): Planck 2018 results. VI. Cosmological parameters. Astron. Astrophys. **641**, A6 (2020)
Akaike, H.: IEEE Trans. Autom. Control **19**, 716 (1974)
Alam, S., et al.: Phys. Rev. D **103**, 083533 (2021). arXiv:2007.08991 [astro-ph.Co]
Alcaniz, J.S., Jain, D., Dev, A.: Phys. Rev. D **67**, 043514 (2003)
Amendola, L., et al.: J. Cosmol. Astropart. Phys. **307**, 005 (2003)
Basilakos, S., Lima, J.A.S.: Phys. Rev. D **82**, 023504 (2010)
Bennett, C.L., et al.: Astrophys. J. Suppl. Ser. **208**, 20 (2013)
Bento, M.C., Bertolami, O., Sen, A.A.: Phys. Rev. D **66**, 043507 (2002)
Bento, M.C., Bertolami, O., Sen, A.A.: Phys. Lett. B **575**, 172 (2003a)
Bento, M.C., Bertolami, O., Sen, A.A.: Phys. Rev. D **67**, 063003 (2003b)
Bertolami, O., Sen, A.A., Sen, S., Silva, P.T.: Mon. Not. R. Soc. **353**, 329 (2004). arXiv:astro-ph/0402387
Bilić, N., Tupper, G.B., Viollier, R.D.: Phys. Lett. B **535**, 17 (2002)
Blandford, R.D., et al.: ASP Conf. Ser. **339**, 27 (2004). arXiv:astro-ph/0408279
Caldwell, R.R., Dave, R., Steinhardt, P.J.: Phys. Rev. Lett. **80**, 1582 (1998)
Caldwell, R.R., Kamionkowski, M., Weinberg, N.N.: Phys. Rev. Lett. **91**, 071301 (2003)
Calvão, M.O., Lima, J.A.S., Waga, I.: Phys. Lett. A **162**, 223 (1992)
Cárdenas, V.H.: Eur. Phys. J. C **72**, 2149 (2012)
Chakraborty, S., Pan, S., Saha, S.: Phys. Lett. B **738**, 424 (2014)
Chang, Z., et al.: Chin. Phys. C **43**, 125102 (2019)
Chaplygin, S.: Sci. Moscow Univ. Math. Phys. **21**, 1 (1904)
Chen, D.M.: Astrophys. J. **587**, L55 (2003)
Choudhury, T.R., Padmanabhan, T.: Astron. Astrophys. **429**, 807 (2005)
Copeland, E., Sami, M., Tsujikawa, S.: Int. J. Mod. Phys. D **15**, 1753 (2006)
Felice, A. De, Tsujikawa, S.: Living Rev. Relativ. **13**, 3 (2010)
DeDeo, S., Caldwell, R.R., Steinhardt, P.J.: Phys. Rev. D **67**, 103509 (2003)
Fabris, J.C., Velten, H.E.S., Zimdahl, W.: Phys. Rev. D **81**, 087303 (2010)
Fabris, J.C., Pacheco, J.A.F., Piattella, O.F.: J. Cosmol. Astropart. Phys. **06**, 038 (2014)
Gangopadhyay, S., Saha, A., Mukherjee, S.: Int. J. Theor. Phys. **55**, 4445 (2016)
Guo, Z.K., Piao, Y.S., Zhang, X., Zhang, Y.Z.: Phys. Lett. B **608**, 177 (2005)
Hannestad, S.: Phys. Rev. D **71**, 103519 (2005)
Harko, T., Lobo, F.S.N., Nojiri, S., Odintsov, S.D.: Phys. Rev. D **84**, 024020 (2011)
Harko, T., Lobo, F.S.N., Mimeso, J.P., Pavón, D.: Eur. Phys. J. C **75**, 386 (2015)
Harko, T., Lobo, F.S.N., Saridakis, E.N.: Universe **7**, 227 (2021)
Haro, J., Pan, S.: Class. Quantum Gravity **33**, 165007 (2016)
Hulke, N., Singh, G.P., Bishi, A., Singh, A.: New Astron. **77**, 101357 (2020)
Jimenez, J.B., et al.: Phys. Rev. D **98**, 044048 (2018)
Kamenshchik, A.Y., Moschella, U., Pasquir, V.: Phys. Lett. B **511**, 265 (2001)
Kaur, S., Singh, C.P.: Phys. Dark Universe **33**, 100869 (2021)
Kaur, S., Singh, C.P.: Mod. Phys. Lett. A **37**, 2250161 (2022)
Lima, J.A.S., Alcaniz, J.S.: Astron. Astrophys. **348**, 1 (1999)
Lima, J.A.S., Germano, A.S.M., Abramo, L.R.W.: Phys. Rev. D **53**, 4287 (1996)
Lima, J.A.S., Jesus, J.F., Oliveira, F.A.: J. Cosmol. Astropart. Phys. **11**, 027 (2010)
Lima, J.A.S., Basilakos, S., Costa, F.E.M.: Phys. Rev. D **86**, 103534 (2012)
Lima, J.A.S., Graef, L.L., Pavón, D., Basilakos, S.: J. Cosmol. Astropart. Phys. **10**, 042 (2014)
Lixin, X., Yuting, W., Hyerim, N.: Eur. Phys. J. C **72**, 1931 (2012)
Makler, M., Oliveira, S.Q., Waga, I.: Phys. Lett. B **555**, 1 (2003a)
Makler, M., Oliveira, S.Q., Waga, I.: Phys. Rev. D **68**, 123521 (2003b)
Moresco, M., et al.: J. Cosmol. Astropart. Phys. **05**, 014 (2016)
Moresco, M., et al.: Living Rev. Relativ. **25**, 6 (2022)
Nojiri, S., Odintsov, S.D.: Phys. Lett. B **631**, 1 (2005)
Nojiri, S., Odintsov, S.D.: Int. J. Geom. Methods Mod. Phys. **4**, 115 (2007)
Nunes, R.C.: Int. J. Mod. Phys. D **25**, 1650067 (2016)
Nunes, R.C., Pavón, D.: Phys. Rev. D **91**, 063526 (2015)
Padmanabhan, T.: Phys. Rep. **380**, 235 (2003)
Pan, S., Haro, J.D., Paliathanasis, A., Slagter, R.J.: Mon. Not. R. Astron. Soc. **460**, 1445 (2016)
Pan, S., et al.: Int. J. Geom. Methods Mod. Phys. **15**, 1850042 (2018)
Parker, L.: Phys. Rev. Lett. **21**, 562 (1968)
Parker, L.: Phys. Rev. **183**, 1057 (1969)
Peebles, P.J.E., Ratra, B.: Rev. Mod. Phys. **75**, 559 (2003)
Peracaula, J.S., Yu, H.: Gen. Relativ. Gravit. **52**, 17 (2020)
Perlmutter, S., et al.: Astrophys. J. **517**, 565 (1999)
Prigogine, I., et al.: Gen. Relativ. Gravit. **21**, 767 (1989)
Rapetti, D., et al.: Mon. Not. R. Astron. Soc. **375**, 1510 (2007)
Riess, A.G., et al.: Astron. J. **116**, 1009 (1998)
Riess, A.G., et al.: Astron. J. **117**, 707 (1999)
Sahni, V., Saini, T.D., Starobinsky, A.A., Alam, U.: JETP Lett. **77**, 201 (2003)
Salo, L.A., Haro, J. de: Class. Quantum Gravity **34**, 065001 (2017)
Schöneberg, N., et al.: J. Cosmol. Astropart. Phys. **11**, 039 (2022). arXiv:2209.14330 [astro-ph.CO]
Schrödinger, E.: Physica **6**, 899 (1939)
Schwarz, G.: Ann. Stat. **6**, 461 (1978)
Scolnic, D.M., et al.: Astrophys. J. **859**, 101 (2018)
Silva, P.T., Bertolami, O.: Astrophys. J. **599**, 829 (2003)
Singh, A.: Astrophys. Space Sci. **365**, 54 (2020a)
Singh, C.P., Kaur, S.: Phys. Rev. D **100**, 084057 (2019)
Singh, C.P., Kumar, A.: Eur. Phys. J. C **80**, 106 (2020a)
Singh, C.P., Kumar, A.: Phys. Rev. D **102**, 123537 (2020b)
Singh, G.P., Hulke, N., Singh, A.: Indian J. Phys. **94**, 127 (2020)
Steigman, G., Santos, R.C., Lima, J.A.S.: J. Cosmol. Astropart. Phys. **06**, 033 (2009)

Visser, M.: Class. Quantum Gravity **21**, 2603 (2004)
Wang, D., Meng, X.: Phys. Rev. D **95**, 023508 (2017)
Weinberg, S.: Rev. Mod. Phys. **61**, 1 (1989)
Weinberg, D.H., et al.: Phys. Rep. **530**, 87 (2013)
Wu, P., Yu, H.: Phys. Lett. B **644**, 16 (2007)
Xu, Y., et al.: Eur. Phys. J. C **79**, 708 (2019)
Zhu, Z.H.: Astron. Astrophys. **423**, 421 (2004)

Publisher's Note Springer Nature remains neutral with regard to jurisdictional claims in published maps and institutional affiliations.

Springer Nature or its licensor (e.g. a society or other partner) holds exclusive rights to this article under a publishing agreement with the author(s) or other rightsholder(s); author self-archiving of the accepted manuscript version of this article is solely governed by the terms of such publishing agreement and applicable law.

Environmental Science and Pollution Research (2024) 31:8354–8368
https://doi.org/10.1007/s11356-023-31680-5

REVIEW ARTICLE

Mechanistic understanding on the uptake of micro-nano plastics by plants and its phytoremediation

Megha Bansal[1] · **Deenan Santhiya**[2] · **Jai Gopal Sharma**[1]

Received: 25 October 2022 / Accepted: 19 December 2023 / Published online: 3 January 2024
© The Author(s), under exclusive licence to Springer-Verlag GmbH Germany, part of Springer Nature 2024

Abstract

Contaminated soil is one of today's most difficult environmental issues, posing serious hazards to human health and the environment. Contaminants, particularly micro-nano plastics, have become more prevalent around the world, eventually ending up in the soil. Numerous studies have been conducted to investigate the interactions of micro-nano plastics in plants and agroecosystems. However, viable remediation of micro-nano plastics in soil remains limited. In this review, a powerful in situ soil remediation technology known as phytoremediation is emphasized for addressing micro-nano-plastic contamination in soil and plants. It is based on the synergistic effects of plants and the microorganisms that live in their rhizosphere. As a result, the purpose of this review is to investigate the mechanism of micro-nano plastic (MNP) uptake by plants as well as the limitations of existing MNP removal methods. Different phytoremediation options for removing micro-nano plastics from soil are also described. Phytoremediation improvements (endophytic-bacteria, hyperaccumulator species, omics investigations, and CRISPR-Cas9) have been proposed to enhance MNP degradation in agroecosystems. Finally, the limitations and future prospects of phytoremediation strategies have been highlighted in order to provide a better understanding for effective MNP decontamination from soil.

Keywords Soil remediation · Contaminants · Omics-based · Hyperaccumulator · CRISPR-Cas9

Responsible Editor: Elena Maestri

Highlights
- Micro-nano plastics (MNPs) pose detrimental effects on agroecosystem.
- Mechanism of uptake of MNPs by plants is highlighted.
- Phytoremediation offers great insight to remediate MNPs from soil and plants.
- Advanced phytoremediation approaches (Omics and CRISPR-Cas9) are essential.
- Bioaugmentation and system science can enhance phytoremediation of MNPs.

✉ Deenan Santhiya
deenan.santhiya@dce.ac.in

Megha Bansal
megha_2k21phdbt01@dtu.ac.in

Jai Gopal Sharma
sharmajaigopal@dce.ac.in

[1] Department of Biotechnology, Delhi Technological University, Delhi, India

[2] Department of Applied Chemistry, Delhi Technological University, Main Bawana Road, Delhi 110042, India

Introduction

The most influential attribute of man-made activities is the discharge of plastic (Galloway et al. 2017), a polymer used in everyday life. According to reports from the Centre for Science and Environment (CSE) of India, 79% of the total plastic produced enters the environment in the form of waste, of which only around 9% is recycled ("Managing Plastic Waste in India," 2020). Various reports have claimed that most plastic materials are more integrated towards breakdown compared to degradation (Bansal et al. 2021). These large plastics generate smaller fragments of size less than 5 mm, referred to as microplastics (Mammo et al. 2020). Further deterioration of these microplastic fragments results in the formation of eventually smaller particles of size less than 0.1 µm, commonly called nanoplastics (Ng et al. 2018). Significant efforts have recently been made in the detection and analysis of micro-nano plastics (MNPs) (Tian et al. 2022; Pfohl et al. 2022), the current pollution study (Gong et al. 2023), and biological toxicity evaluation (Teng et al. 2022). Although many studies have focused on understanding the impacts of metal nanoparticles on plants

and soil, very little evidence exists on understanding the uptake and effect of MNPs on plants (Yadav et al. 2022; Kumar et al. 2023; Bansal et al. 2023). For example, the alleviation of lead toxicity in *Brassica juncea* by salicylic acid helped to minimize oxidative damage to the plant (Agnihotri et al. 2018). Another study showed antioxidant defense mechanisms in *Brassica juncea* L. by alleviating salinity stress through 24-Epibrassinolide (Gupta and Seth 2023). Although source control, such as cutting down on plastic consumption and developing alternative materials, is advocated, such processes may not be effective in a short time. Thus, it is imperative to seek efficient pathways to deal with the existing MNP pollution. A growing concern about the ingestion of microplastics and nanoplastics by aquatic species, some migration to microbial guts and trophic level transfers, has been reviewed since a long time (Galloway et al. 2017). However, the terrestrial landmasses are majorly empty for mapping global plastic distribution and its detrimental effects on agro-ecosystems. In the current context, the global expansion of a small fraction of plastics, namely, micro-nano plastics (MNPs), is gaining significant consideration from researchers around the globe because of their critical environmental effects (Wright et al. 2013).

MNPs and their sources

MNPs are divided into fiber, film, pellet, powder, and fragments based on their morphology. MNPs are composed of polypropylene (PP), polyethylene (PE), polystyrene (PS), polyvinyl chloride (PVC), and polyamide (PA) as chemical ingredients. MNPs are widely classified into primary and secondary classes based on their commercial applications. Primary MNPs are manufactured for specialized uses such as cosmetics, medicine delivery carriers, industrial use, and military aids. Furthermore, synthetic textiles account for roughly 35% of total primary MNPs emitted in bodies of water (Boucher and Friot 2017). Secondary MNPs are formed by the breakdown of large plastics through physical, chemical, and biological approaches. Mechanical forces, chemical breakdown, or microbial degradation of large plastic fragments result in the formation of secondary MNPs. Also, fishing, travelling, and catering contribute a significant proportion of secondary MNPs (Guo et al. 2020). Vehicular transport, including tyre wear, brakes, markings, is also a major source of microplastics in the ecosystem (Luo et al. 2021). Apart from major sources of MNPs in the environment, agricultural practices, recreational activities, sewage sludge application, and organic fertilizers can also contribute to MNP pollution (Guo et al. 2020). So, better knowledge of the potentially detrimental or deleterious consequences of these contaminants on agroecosystems is critical.

Impacts of MNPs to terrestrial and aquatic plants

Size, thickness, shape, and shade of MNPs control their bioavailability, and, subsequently, their toxicological impact (Haegerbaeumer et al. 2019). MNPs get adsorbed by plants, the soil rhizosphere, and soil organism thereby affecting soil physiochemical properties (Junhao et al. 2021). Likewise, the impacts of MNPs on aquatic plants are crucial to the well-being of flora and fauna (Fig. 1). Recently, airborne MNPs have also gained attention, suggesting that they are present both in indoor and outdoor air (Enyoh et al. 2019). Effluent discharge and surface runoff from rivers, lakes, and sediments have a direct impact on aquatic water bodies and related coastlines (Jeyavani et al. 2021). Also, MNPs aggregate and get ingested by marine species, thereby affecting the food chain (Prata et al. 2020). Apart from this, agricultural practices, road, and tyre wear discharge also emit MNPs on land and in the air (Luo et al. 2021). These sediments

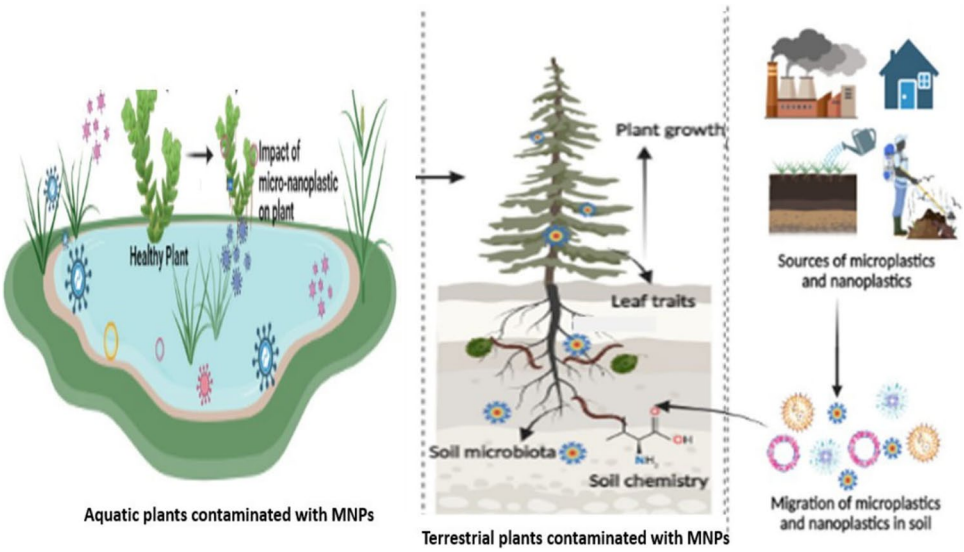


Fig. 1 Sources of MNPs, their migration, impact, and structural changes on terrestrial and aquatic plants

get infiltrated within the soil or discharge into water bodies, thereby affecting the ecosystem.

Toxicity to terrestrial plants and soil

MNPs can physically block or clog plant tissues, such as stomata or root hairs, limiting their ability to carry out essential functions like gas exchange and nutrient uptake (Banerjee et al. 2019). MNPs contain various additives, such as plasticizers and flame retardants, which can leach out and affect plants. These chemicals may have toxic effects on plants, disrupting their metabolism, photosynthesis, and hormonal balance (Tun et al. 2022). MNPs can adsorb nutrients such as nitrogen and phosphorus, reducing their bioavailability to plants. This can lead to nutrient deficiencies and affect plant growth and productivity (Dovidat et al. 2020). MNPs can provide a surface for microbial colonization, forming biofilms. These biofilms can alter the composition and activity of soil and water microbial communities, potentially affecting the plant–microbe interactions that are crucial for nutrient uptake and disease resistance (He et al. 2022). Despite having lower MNP emphasis than soil, air has a higher liquidity that allows for more accumulation of MNPs on leaf surfaces by means of fluid-elevated openings (de Souza Machado et al. 2019). MNPs appended to leaf surfaces might obstruct daylight and hamper photosynthesis, with comparable outcomes found in green growth (Wu et al. 2019). Due to the presence of MNPs in soil, a reduction in water-holding capacity occurs, which negatively causes a decrease in oxygen in soil aggregates (Liu et al. 2014). Similarly, micrometer-sized polystyrene (PS) microparticles may also penetrate inside the crop plants at the site of lateral root emergence, thereby contaminating the crops (Li et al. 2020a). Seeds may be harmed as a result of plastic leachate mixed with water, which seeds absorb during germination, or as a consequence of smaller MNPs altering soil structure (Pflugmacher et al. 2020).

Toxicity to aquatic plants

Not only do MNPs have impacts on terrestrial plants, but recent research has found their potential to deteriorate aquatic flora. The formation of phytoplankton on the surface of water could encapsulate and entrap MNPs (Prokin et al. 2015). This sorption of MNPs may result in decreased length of principle outgrowths of established plants, repress root development, photosynthetic action, and suitability of freshwater phytoplankton. Considering past works, microplastics can influence the photosynthesis of green plants through attachment to the outer layer of xylem and phloem tissues and consequently assemble to repress their photosynthesis (Dovidat et al. 2020). PS nanoplastic adsorption also slows down green plant photosynthetic movement while speeding up the formation of responsive oxygen, which is dependent on the physiochemical qualities of plastics as well as the morphology and biochemical properties of green plants (Bhattacharya et al. 2010). Light is crucial for the photosynthetic process, and decreased light availability can impede plant growth and productivity (Mateos-Cárdenas et al. 2021). MNPs can induce oxidative stress in aquatic plants. These particles can generate reactive oxygen species (ROS) when interacting with plant tissues. ROS can cause cellular damage by oxidizing biomolecules, disrupting cellular processes, and impairing plant growth (van Weert et al. 2019). As higher trophic levels feed on these plants, the MNPs can be transferred up the food chain through a process called biomagnification, potentially affecting other organisms as well. The debilitating or even loss of porousness influences ordinary development and digestion cycle like the migration of compounds within and outside the cell walls of aquatic plants (Xia et al. 2015).

Keeping in view the above-stated facts and examples, most of the investigations have intensified on determining the effects of MNPs on terrestrial and aquatic plant species. The necessity of phytoremediation of micro-nano plastics results from the pressing need to address the negative environmental effects of plastic pollution, the shortcomings of current cleanup techniques, and the potential of plants to provide a viable and efficient response to this new environmental problem. The significance of phytoremediation stems from its capacity to offer environmentally sound, economically viable, and long-lasting solutions for waste management. Many advantages it provides include safeguarding human health, promote long-term environmental sustainability, and improve the general health of ecosystems. In light of this, this review is divided into five major objectives aimed at (i) exploring the importance of phytoremediation and highlighting the drawbacks associated with conventional methodologies to eliminate MNPs; (ii) examining the size of MNPs absorbed by plants, the mechanism of MNPs uptake, and the approaches involved in phytoremediation of MNPs; (iii) exploring the factors influencing phytoremediation of MNPs; (iv) proposing strategies for phytoremediation of MNPs in agroecosystems; and (v) policies and future directions to address the knowledge gaps and provide substantial inputs on combating MNPs in agroecosystems.

Objectives

Objective: importance of phytoremediation highlighting the drawbacks associated with conventional methodologies to eliminate MNPs

The aforementioned impact of MNPs on ecosystems necessitates the utilization of various methodologies to

tackle and reduce plastic contamination. Different conventional methods of eliminating plastic contaminants and their drawbacks are explained below:

1. Adsorption: In this technique, physical, chemical, or biological adsorbents such as carbon materials, zeolites, metal organic frameworks, and mesoporous materials are used to eliminate micro-nano plastic pollutants (Reineccius et al. 2021). MNPs can adhere to the surface of certain materials through physical interactions such as van der Waals forces, electrostatic interactions, and hydrophobic interactions. For example, a covalent organic framework like Tpa-H showed high adsorption energy for polyethylene, polyethylene terephthalate, and nylon-6 via molecular dynamics (Shang et al. 2022). MNPs can chemically bind to specific functional groups on the surface of adsorbent materials through covalent or coordinate bonding (Song et al. 2023). This mechanism is often employed using modified materials with functional groups such as amino groups, carboxyl groups, or sulfonic acid groups. For example, sulfate groups of polystyrene nanoplastics were degraded under UV radiation, thereby decreasing their electrostatic potential (Wang et al. 2020). The major disadvantage of using this technique is the generation of additional toxic wastes, and the cost of commercial adsorbents used for the treatment of MNPs is still high (De Gisi et al. 2016).
2. Coagulation: Different types of organic and inorganic coagulants are used for MNP removal, including ferric chloride, polyaluminum chloride, ferrous chloride, and polyamine (Zhou et al. 2021). These coagulants bind to microplastic particles by an uptake-complexation mechanism, thereby forming strong bonds with pollutants (Xu et al. 2021). For example, iron and aluminum coagulants were used for the removal of polyethylene microplastics under high polyacrylamide concentrations (Ariza-Tarazona et al. 2019). Also, metal hydroxide coagulants like iron and aluminum could help stabilize microplastics suspended in wastewater, thereby interacting via van der Waals forces to form sludge blankets (Perren et al. 2018). The major drawback of this method is its low selectivity; adsorbents are sensitive to pH, and competing ions tend to reduce the efficacy of adsorbents.
3. Membrane filtration: Dynamic membranes are utilized for influent flux and concentration of respective MNPs on the membrane during the process of filtration to enhance the removal of contaminants (Liu et al. 2021). For example, wastewater treatment plants were studied for their efficiency in removing microplastics in terms of shape, color, and dimensions using filtration processes. The microplastic removal efficiency reached approximately 90% (Ma et al. 2019). Another study showed that membrane bioreactors in combination with sand filters or disk filters, showed higher removal efficiency of microplastics when analyzed by Fourier transform infrared spectroscopy (FTIR) (Talvitie et al. 2017). The results revealed an abundance of polymers in the influent, with a high concentration of polyethylene terephthalate and polyester. The drawback of this technique is that the initial operational cost is high, and there is a need for post-treatment mineralization.
4. Microbial remediation: The technique of microbial remediation uses microorganisms to eliminate toxic MNPs from the environment (2018). Microbes produce enzymes, such as esterase, lipases, and proteases, which can break down the polymer chains of microplastics. These enzymes target specific chemical bonds present in plastics and initiate the process of degradation (Othman et al. 2021). Through enzymatic activity, microbes can gradually break down microplastics into smaller fragments. For example, *Phanerochaete chrysosporium* produces an enzyme, manganese peroxidase, which could help in the degradation of polyethylene (Kang et al. 2019). Also, *Ideonella sakaiensis 201-F6* was able to degrade polyethylene terephthalate by an enzyme called polyethylene terephthalate-ase (Yoshida et al. 2016). The method of microbial remediation is restricted to compounds that can easily biodegrade and is also time-consuming.

Importance of phytoremediation

The above-mentioned techniques are associated with drawbacks that facilitate the use of phytoremediation approaches which are considered eco-friendly and effective for elimination of pollutants from environment. Conventional methods used for exclusion of plastic pollutants are energy-dependent, time consuming, expensive, environmentally destructive and have adverse impact on ecosystem (Lourenço et al. 2019). Ability of various plants for phytoremediation is explored by numerous scientists (Rahbar et al. 2016; Rezania et al. 2016). Therefore, excessive interest is shown by researchers for improving the efficacy of conventionally used methods by an environmentally sound technique called phytoremediation. It refers to efficient green technology to dispose contaminants existing in air, water, and soil (Sarwar et al. 2017). Various plants act as efficient phytoremediators owing to their characteristic property of intake of pollutants and degradation by various bacteria and enzymes secreted by plant tissues (Chirakkara et al. 2016).

Objective: size of MNPs absorbed, mechanism of uptake and different approaches of phytoremediation for MNPs by plants

Size of MNPs absorbed by plants Plants can accumulate different sizes of MNP pollutants, thus acting as a potential source for remediation (Ebere et al. 2019). A study reported that nanoplastics ranging between 0 and 200 nm can be absorbed by plants internally and externally (Mateos-Cárdenas et al. 2021). Also, plants can uptake small microplastics (< 1000 µm) internally from xylem to phloem. Similarly, microplastics ranging in size from 1 to 5 mm can also be absorbed and transported to the aerial parts of plants from soil (Mateos-Cárdenas et al. 2021). Polystyrene microbeads (4.8 mm), for instance, were shown to be obstructing pores on the leaves, especially the root Garden cress (*Lepidium sativum* L.) hairs (Bosker et al. 2019). Additionally, there were microplastics of diameters 1–100 µm and 20 µm on the bladder wrack *Fucus vesiculosus* L., forming on its surface (Gutow et al. 2016), and the top layer of mucus (Sundbæk et al. 2018). Moreover, it has been observed that freshwater plants like *Lemna minor* L. may absorb < 600 µm polyethylene microbeads on the foliage of plants (Kalčíková et al. 2020). Wheat and lettuce are examples of agricultural plants that can internalize 200-nm polystyrene nanobeads and 2.0-µm polymethylmethacrylate microbeads (Li et al. 2020b). Plastic internalization appears to be influenced by particle charge. As demonstrated most recently by Wu et al. (2021a, b), *Arabidopsis thaliana* L. is capable of internalizing both positively and negatively charged 200-nm polystyrene beads in the stele of the root maturation zone. Micro-nanoplastics' (MNPs) absorption and internalization might have a significant impact on the environment.

Mechanisms of MNP uptake by plants The uptake of MNPs by plants is dependent on their physiological characteristics, demonstrating diverse absorption and accumulation inside plants and soil. Although very few studies have discussed the uptake mechanism of MNPs in plants, some evidence can be put forward through them. For example, one study observed the extracellular entrapment of polystyrene microbeads in the root caps of plant tissues. Furthermore, microbeads traversed from root to leaf parts through intercellular spaces via the vascular system following the transpiration stream (Li et al. 2019). Another study showed the absorption of microplastics within the endodermis of plant tissues through damaged root gaps and their transport to the aerial parts of the plant by transpiration (Sun et al. 2023). The apoplast and symplast are two pathways for MNPs to go through tissues once they have entered the plant. In contrast to symplastic transport, which involves movement of water and other substances between the cytoplasm of adjacent cells through specialized structures called plasmodesmata and sieve plates, apoplastic transport occurs outside the plasma membrane through extracellular spaces, the cell walls of adjacent cells, and xylem vessels (Pérez-de-Luque 2017). The apoplastic route is crucial for radial movement inside plant tissues and enables the passage of MNPs to vascular tissues and root central cylinder for further movement to the aerial portion (Li et al. 2020a). However, getting to the xylem through the root requires getting past a barrier to apoplastic pathway, the Casparian strip, which must be done by taking a symplastic route via endodermal cells. Using sieve tube components in the phloem, another significant symplastic transport is also conceivable, allowing distribution to non-photosynthetic tissues and organs (Liu et al. 2022b). Sieve tubes in phloem also provide a passage for MNP entry into the aerial parts of plants, as they have a thickness of approximately 0.77 to 1 µm, allowing small microplastics to traverse inside the plant tissues (Bussières 2014) (Fig. 2).

The uptake mechanisms of micro- and nanoplastics (MNPs) by plants can share similarities with the uptake mechanisms of other nanoparticles. While research on the specific uptake mechanisms of MNPs by plants is still emerging, studies on other nanoparticles provide insights into potential similarities. Here are a few examples of how the uptake mechanisms of MNPs may share similarities with the uptake mechanisms of other nanoparticles:

a. Size-dependent uptake: Plants can take up nanoparticles through various pathways, including root uptake, foliar uptake, and uptake through plant cell walls (Ali et al. 2021). This size-dependent uptake has been reported for a range of nanoparticles, including metal-based nanoparticles and carbon-based nanoparticles (Khan et al. 2022), and it may also apply to MNPs as postulated in different studies (Sun et al. 2021; Liu et al. 2022b; Huang et al. 2022).
b. Endocytosis: Some nanoparticles can be taken up by plants through endocytosis, which involves the internalization of particles by plasma membrane (Palocci et al. 2017). This mechanism has been reported for various nanoparticles, such as metal-based nanoparticles and quantum dots (Raven 2022). It is possible that MNPs can also be internalized by plants through endocytosis, for example, in rice seedlings exposed to polystyrene microplastics. The study observed accumulation of polystyrene microplastics in the roots of rice due to endocytosis (Wu et al. 2021a).
c. Passive diffusion: Nanoparticles can also passively diffuse across plant cell membranes. This process depends on the physicochemical properties of the particles, such as their size, surface charge, and hydrophobicity (Geisler-Lee et al. 2013). MNPs may exhibit similar passive diffusion mechanisms as other nanoparticles when entering plant cells (Xu et al. 2022).

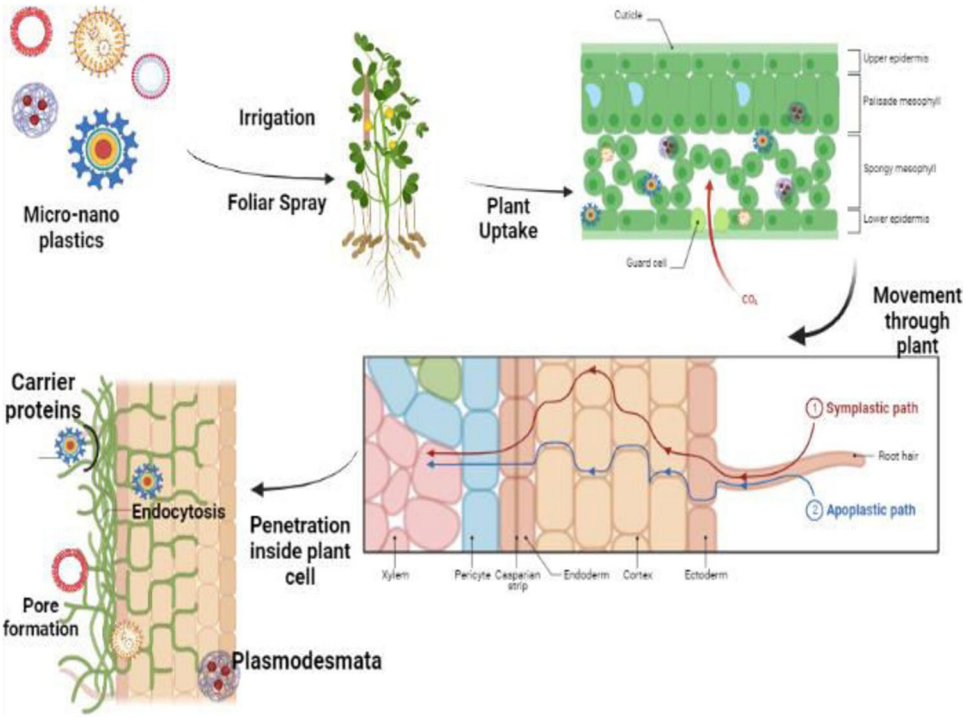


Fig. 2 Mechanism showing uptake of MNPs by plants from root hairs to plant cells and finally to inside parts of leaf through processes of endocytosis, intercellular spaces, plasmodesmata, carrier proteins, and pore formation

It is important to note that the uptake mechanisms of MNPs by plants are still an active area of research, and more studies are needed to understand the specific pathways and processes involved. Hence, the migration of MNPs inside plants is really important, as it gives an indication of the accumulation and absorption of MNPs on plant parts. Also, after the accumulation and absorption of MNPs, the phytoremediation potential can be determined to provide a sustainable solution for environmental cleanup.

Approaches of phytoremediation for MNPs Different approaches, including phytoextraction, phytostabilization, phytodegradation, phytovolatilization, and rhizosphere bioremediation, are employed by plants to facilitate the uptake of organic and inorganic pollutants from soil, thus forming the basis for phytoremediation technology. The major plants that are utilized for phytoremediation of MNPs are described in Table 1.

Phytoextraction Phytoextraction is a method to clean up contaminants from soil by absorption, accretion, and transfer of contaminants from soil to plant shoots, also referred to as phytomining (Tangahu et al. 2011). Plants act as hyper accumulators to absorb various pollutants in their shoots without any toxic effects on soil (Bian et al. 2020). An ideal hyper accumulator plant possesses the characteristic property of gathering large concentrations of MNPs within its shoots (Yu et al. 2021). For example, polystyrene microplastics and bisphenol-S showed no effect on *Pistis stratiotes* L. due to the accumulation of contaminants within the roots of plant and less translocation to other parts (Zhang et al. 2022). Another study showed accumulation of polystyrene

Table 1 Examples of different plants acting as potential sources for phytoremediation of various contaminants

Plant species	Accumulation part	Contaminant for remediation	Reference
Festuca arundinacea S	Shoots or roots	Petroleum hydrocarbon	Steliga and Kluk (2020)
Zea mays L	Roots	Phenanthrene	Baoune et al. (2019)
Chrysocoma Ciliate L	Roots	Petroleum aromatic hydrocarbons	Anyasi and Atagana (2018)
Lolium multiflorum L	Rhizosphere	Crude oil	Hussain et al. (2018)
Lolium perenne L	Rhizosphere microbes	Petroleum hydrocarbon	Iqbal et al. (2019)
Suaeda glauca L	Rhizosphere	Polycyclic aromatic hydrocarbons	Chaudhary et al. (2021a)
Iris dichotoma P	Roots	Petroleum hydrocarbon	Cheng et al. (2017)

microplastics within *Vicia faba* L. roots merely for around 48 h after being exposed to microplastics (Jiang et al. 2019).

Phytostabilization Phytostabilization, also referred to as phytoimmobilization, is a process of immobilizing contaminants in soil, roots, or shoots of plants thereby reducing their bioavailability in the environment (Tangahu et al. 2011). For example, polyethylene microplastics were able to adhere to aquatic macrophyte *L. minor*, due to surface stickiness and electrostatic interaction between MNPs and plant biomass (Rozman et al. 2022). Another study observed the immobilization of polystyrene microplastics in *F. vesiculosus* due to release of anionic polysaccharide on plant surface (Sundbæk et al. 2018). Also, microplastics captured within roots can reduce mobility and interaction with soil microorganisms and act as a potential source of phytostabilization. In a study by Gao et al. (2021), polyethylene microplastics adhered to root surface of *Lactuca sativa* L. without entering inside root hairs or other parts of the plant (Gao et al. 2021).

Phytovolatilization Phytovolatilization is a method that uses metabolic ability of plants and soil microorganism to change toxic plastic contaminants into volatile and less toxic forms, thereby releasing them into the atmosphere (Tangahu et al. 2011). While phytovolatilization is commonly associated with the uptake and release of organic compounds, such as volatile organic compounds (VOCs), there is limited research on its applicability to microplastics. Very few studies have investigated the potential for microplastic phytovolatilization by examining their uptake by plants as well as the subsequent release of volatile microplastic-associated compounds into the atmosphere. For example, laser confocal scanning microscopy and scanning electron microscopy provided evidence for the translocation of polystyrene nanoplastics from roots to shoots of *Triticum aestivum* L. without any effect on seed germination (Lian et al. 2020). Another study by Li et al. (2020a) observed transport of polystyrene and polymethylmethacrylate microplastics from roots to shoots of *T. aestivum* through crack-entry pathway and transpirational pull (Li et al. 2020a).

Phytodegradation Phytodegradation, also known as phytotransformation, is a method to decompose inorganic pollutants in soil by the application of enzymes such as oxygenases, nitroreductases, and dehydrogenases (Ali et al. 2013). The phytodegradation process occurs through the uptake of plastic contaminants within metabolic compartment of plants or microbes and their disintegration in soil. Degradation of pollutants occurs through two mechanisms: internal and external. In internal degradation mechanism, the MNPs are absorbed by plants that decompose through catalytic reactions by enzyme molecules, resulting in metabolic products utilized for plant growth and nutrition (Jeevanantham et al. 2019). In external degradation process, the plastic contaminants get absorbed by plant metabolic processes and hydrolyzed into smaller units (Jeevanantham et al. 2019). Formed monomer units are introduced into plant tissues for their growth and survival. For example, laccase and alkane hydrolase produced by *Staphylococcus epidermis* facilitated the depolymerization of polyethylene, forming monomer and oligomer units (Montazer et al. 2020). Also, the oxidase enzyme produced from *Pseudomonas vesicularis* PD could help in the degradation of polyvinyl chloride by oxidation of serine hydrolase active site present in polyvinyl chloride (Wilkes and Aristilde 2017).

Rhizosphere bioremediation Rhizosphere bioremediation is a process for eliminating MNPs from soil through their degradation and breakdown under the action of plant microorganisms (Jeevanantham et al. 2019). Besides, it is also referred to phytostimulation, rhizosphere degradation, and plant-assisted bioremediation (Kumar et al. 2018). The growth and proliferation of soil microorganisms occur due to the presence of carbohydrates in the soil. The different microorganisms employed for remediation of contaminants in soil are listed in Table 2. Various soil microorganisms can facilitate degradation of MNPs in soil. For example, *Bacillus cereus* and *Bacillus gottheilii* could change the structural properties of polyethylene microplastics (Auta et al. 2018). Also, *Pseudomonas capeferrum* TDA1 helped in the formation of a hydrolase enzyme that played an important role in the degradation of polyurethane (Puiggené et al. 2022). Root exudates also perform as excellent contributors to improving the degradation of pollutants by increasing their activity in rhizosphere. For example, MNPs induce stress with a negative influence on the growth of *T. aestivum* and genotoxic effects on *V. faba* (Jiang et al. 2019; Qi et al. 2020). Root exudates could alleviate the stress response in plants, thereby facilitating phytoremediation of MNPs.

Objective: factors influencing phytoremediation of MNPs

Phytoremediation, the use of plants to remediate pollutants from the environment, has gained attention as a potential method for addressing microplastic pollution. While research on phytoremediation of microplastics is still in its early stages, several factors are thought to influence the effectiveness of this approach like:

1. Plant species: Different plant species possess varying abilities to take up and accumulate microplastics (Colzi et al. 2022). Some plants may have higher affinity for microplastics due to their root structures or physiological characteristics. For example, certain aquatic plants

Table 2 Different microorganisms employed for remediation of various contaminants that are present in the soil

Microorganisms	Contaminant Remediation	Reference
Penicillium sp.	Low-density polyethylene (LDPE)	Rodrigo et al. (2021)
Klebsiella pneumoniae	High-density polyethylene (HDPE)	Awasthi et al. (2017)
Pseudomonas sp.	Polypropylene	Habib et al. (2020)
Penicillium sp.	Polyurethane	Magnin et al. (2019)
Vibrio sp.	Polyvinyl chloride	Khandare et al. (2021a)
Ideonella sakaiensis	Polyethylene terephthalate	Azubuike et al. (2016)
Lysinibacillus sp.	Polyethylene	Jeon et al. (2021)
Halomonas sp.	Low-density polyethylene (LDPE)	Khandare et al. (2021b)
Cephalosporium sp.	UV-treated polystyrene	Chaudhary et al. (2021b)

like water hyacinth (*Eichhornia crassipes* L.) and duckweed (*Lemna* spp.) have been found to effectively accumulate microplastics in water bodies (Christian and Beniah 2019; Rozman et al. 2022).

2. Root characteristics: The morphology and structure of plant roots can influence their ability to uptake microplastics. Plants with extensive root systems, such as those with fibrous or adventitious roots, have a larger surface area for interaction with microplastics. Plants with root exudates rich in enzymes and organic compounds may also enhance microbial activity around the roots, potentially facilitating microplastic degradation (Bosker et al. 2019). For instance, maize (*Zea mays* L.) and ryegrass (*Lolium perenne* L.) have shown promise in terms of their root characteristics for microplastic phytoremediation (Wang et al. 2012; Ullah et al. 2021).
3. Microplastic characteristics: The properties of microplastics, such as size, shape, and surface charge, can affect their interaction with plants. Smaller microplastics tend to have a larger surface area and may be more readily taken up by plants. Furthermore, the surface properties of microplastics can influence their adsorption to root surfaces and subsequent translocation within the plant (Wang et al. 2020; Xu et al. 2022).
4. Environmental conditions: Factors such as temperature, light intensity, and nutrient availability can impact the growth and metabolism of plants, which in turn may influence their ability to remediate microplastics (Gong et al. 2023). Certain environmental conditions may enhance plant-microplastic interactions or promote the activity of microorganisms involved in microplastic degradation (Ebere et al. 2019).

Hence, future research is necessitated to focus on phytoremediation techniques that are easy, inexpensive, and sustainable to environment. The merits and demerits of phytoremediation approaches are broadly listed in Table 3. Also, advanced strategies must be framed for effective phytoremediation of MNP contaminants.

Objective: proposed strategies for progressive phytoremediation of MNPs

Phytoremediation mechanisms offer great potential for the removal of MNPs. However, advanced strategies can

Table 3 Various approaches of phytoremediation highlighting their merits and demerits

Phytoremediation approach	Merits	Demerits
Phytoextraction	i. Cost-effective method compared to other strategies ii. Contaminant can be reused iii. Removal efficiency up to 95%	i. Enhanced uptake of plastic by roots ii. Leaches into groundwater iii. Phyto mass disposal is difficult
Phytovolatilization	i. Economically efficient method ii. Contaminant is less toxic	i. Redeposition of the contaminant back in the soil by precipitation
Phytostabilization	i. Low cost and efficient system ii. Reduction in soil erosion iii. Tolerates high concentration of pollutants	i. Soil not rendered suitable for plant growth ii. Obligatory checks necessary for effective remediation
Phytodegradation	i. Financially and economically stable system ii. Enzymatic breakdown of pollutants feasible	i. Dependent on soil abiotic conditions and plant species ii. Contaminants may re-emerge by soil microorganisms
Rhizosphere bioremediation	i. Microbial activity increases ii. Self-sustaining method for removal of pollutants iii. Environment friendly with low cost	i. Continuous monitoring of pH to uptake pollutants ii. Laboratory scale studies not stabilized for commercial and field purposes

deliver greater potential for phytoremediation to be effective (Fig. 3). Thus, various strategies have been proposed for efficient phytoremediation.

Selection of hyper accumulator plant species Exploration of various hyper accumulator plant species can revolutionize the technique of phytoremediation because of their ability to absorb contaminants 100 times more as compared to natural plants (Kumar Yadav et al. 2018). For example, *L. minor* is commonly used for phytoremediation of wastewater facilities, experimented with polystyrene nanoplastics to observe the impacts on accumulation and tolerance in plants. The results could provide direct evidence of no oxidative damage, unaltered chlorophyll contents, increased lipid peroxidation, and no growth suppression (Arikan et al. 2022). The polystyrene nanoplastics could only accumulate to some extent in the leaves of plants but not be translocated to other parts, thereby showing hyperaccumulation within specific plant parts (Arikan et al. 2022). Another study showed the accumulation of polystyrene nano- and microplastics within the root surface and cap cells of *A. thaliana* and *T. aestivum*. Laser confocal scanning microscopy and pyrolysis gas chromatography–mass spectrometry confirmed that polystyrene spheres accumulated only at root surface of each plant, without any evidence for internal uptake or accumulation (Taylor et al. 2020).

Utilization of plant growth–promoting bacteria for removal of MNPs Plants contain diverse microbial communities residing in the rhizosphere, phyllosphere, and endosphere (Feng et al. 2017). These microorganisms participate in essential roles for plant growth, nutrition, and degradation of contaminants (Kumar Yadav et al. 2018). For example, endophytic bacteria obtained from *Oryza meridionalis* L. were found to degrade phthalates, thereby reducing their accumulation in plants and increasing yield efficiency. A culture experiment containing various endophytic strains showed that the highest degradation of di-*n*-butyl-phthalate occurred using *Bacillus amyloliquefaciens*. The results confirmed the ability of endophytic bacterial strain to remove phthalates and promote plant growth and development (Liu et al. 2022a). Another study showed the isolation of *Achromobacter xylosoxidans* from soil that could degrade high-density polyethylene. Attenuated total reflectance Fourier transform infrared spectroscopy and scanning electron microscopy revealed degradation of microplastics by approximately 9% (Kowalczyk et al. 2016). Also, *Bacillus* spp. and *Rhodococcus* spp. strains isolated from mangrove sediments could help in degradation of polypropylene. Around 6% and 4% weight loss could be observed after 40 days of incubation in bacterial strains, which was confirmed by Fourier transform infrared spectroscopy and scanning electron microscopy

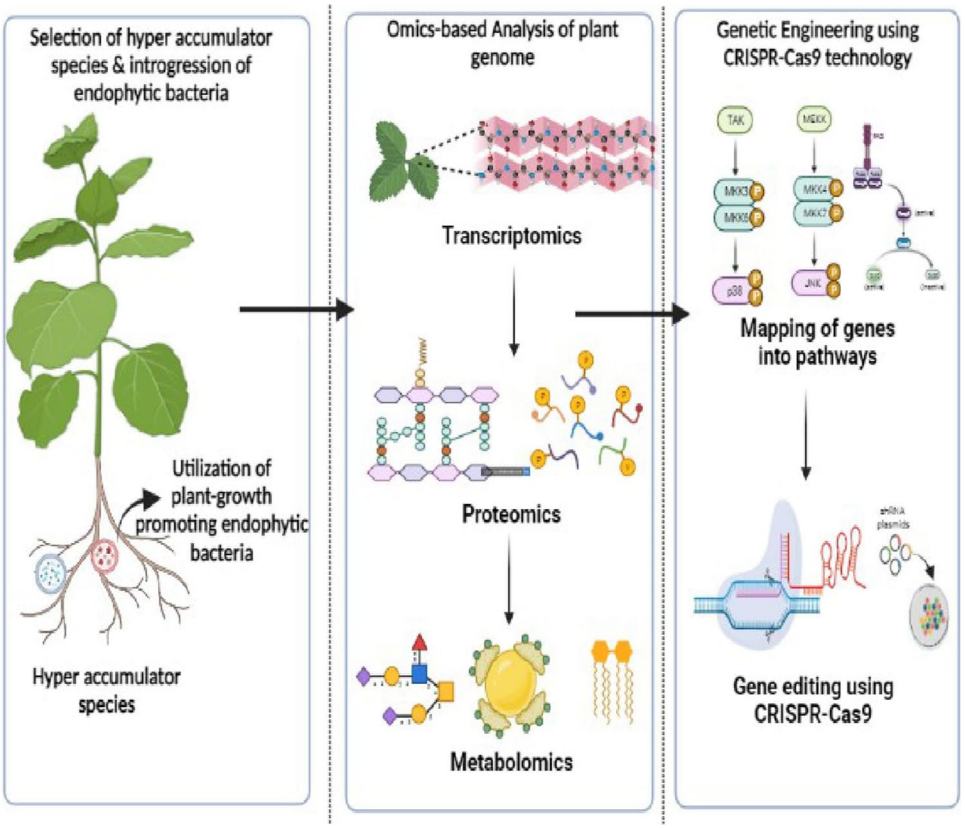


Fig. 3 Advanced strategies for phytoremediation of MNPs: selection of hyperaccumulator species, Omics-based analysis of plant genome, genetic engineering using Crispr-Cas9 technology

analysis (Auta et al. 2018). Thus, various bacterial strains could help in degradation of MNPs and increase plant growth yield.

Omics-based approaches to study MNPs degradation Plants respond differently to environmental conditions involving a range of routes, starting with changes in gene expression (transcriptomics), accumulation of protein products that help in degradation (proteomics), and formation of metabolites (metabolomics) (Forde and O'Toole, 2013). Metagenomics analysis could help in the identification of MNPs that degrade microbes and enzymes that could facilitate degradation (Staley and Sadowsky 2016). For example, cytochrome P450, esterase, and lipase enzymes were isolated from *Nocardioides* spp. and capable of degrading monoalkyl and dialkyl phthalate esters (Qiu et al. 2020). Apart from the identification of microbes for degradation, metabolic processes, gene identification, and expression are also essential for MNP degradation. For example, transcriptomics was applied to identify the mechanism of degradation of polyethylene by *Rhodococcus ruber* C20 strain (Gravouil et al. 2017). Another study showed the expression of pht and pca genes isolated from *Arthrobacter* sp. ZJUTW capable of degrading dibutyl phthalate. This study revealed a combination of metagenomic and metatranscriptomic studies to ascertain the degradation of phthalate (Liu et al. 2020). Besides transcriptomics and metagenomics, metaproteomics could also facilitate the mechanisms of protein synthesis that control metabolism and obtain metabolites (Medić et al. 2019). For example, proteomic profiling of *Pseudomonas pseudoalcaligenes* helped in the identification of a PpEst enzyme that could hydrolyze polybutylene adipate terephthalate (Wallace et al. 2017).

Gene Editing tools to increase MNP degradation Phytoremediation efficiency of plants can be increased by introducing plastic accumulating genetic determinants into the genomes of hyper accumulating species (DalCorso et al. 2019). Thus, genetic engineering tools can be explored to increase MNP accumulation by genes accountable for plastic uptake and their decontamination (Fasani et al. 2018). For example, *Ideonella sakaiensis* 201-F6 produces a polyethylene terephthalate-degrading enzyme. The genes of this bacterial strain can be genetically encoded in other bacterial strains to promote polyethylene terephthalate degradation (Anand et al. 2023). In a study by Moog et al. (2019), polyethylene terephthalate hydrolyzing enzymes were introduced into *Phaeodactylum tricornutum*, thereby showing efficient degradation (Moog et al. 2019). Apart from these genetic modifications, gene editing tools like clustered regularly interspaced palindromic repeats (CRISPR)/Cas9 could also promote manipulation of microbial species for faster degradation of MNPs. For example, *Streptomyces albogriseolus* LBX-2 could produce three different types of CRISPR sequences in which the main enzyme that helped in polyethylene degradation was oxygenase (Shao et al. 2019). Thus, genome editing could help in incorporating genes encoding MNP-degrading enzymes.

Objective: policies and future directions to address the knowledge gaps and provide substantial inputs on combating MNPs

Despite the cost-effective and eco-friendly approach to phytoremediation, challenges still continue in its implementation by the government and commercial sector (Saxena et al. 2020). Application of phytoremediation towards biotic or climatic factors, food-chain adulteration, and utilization of MNPs pollutants are some constraints in utilizing phytoremediation technology (Gunarathne and Lee 2019). Furthermore, low budgets by small-scale industries and short-term funds by government agencies limit the application of phytoremediation approaches on a wide scale. Furthermore, the molecular techniques of hyper accumulator species are not evidently described and may take a longer time span to degrade and remove MNP pollutants. Hence, establishing effective management strategies and low-cost processing technology for decontamination of MNPs pollutants is essential for efficient phytoremediation (Anand et al. 2023).

Policies to eliminate MNPs from the environment Soil inhabits various microorganisms that have proven to degrade MNPs. Bacterial strains are equipped for biodegrading plastics; however, bacterial consortia or biofilm offer less proficiency in the biodegradation processes, where a few strains are engaged with the disintegration and others are responsible for killing harmful metabolites discharged by the counterparts (Kumar et al. 2018). In spite of the fact that biodegradation by microorganisms appears to offer minimal expense and an eco-accommodating remediation approach, it remains a sluggish cycle for all intents and purposes profoundly reliant upon a few factors (biotic and abiotic).

1. One way to deal with advanced in situ plastic bioremediation is through bio stimulation (with the use of development supplements, manures, normal surfactants, and nanoparticles, alongside the improvement of ecological prerequisites) or potentially bioaugmentation (Fomina and Gadd 2014).
2. Another methodology incorporates applying current biotechnological procedures, for example, protein or chemical design. The advancement of enhanced microbial consortium, the use of hereditary design, systems science, and the use of hereditarily changed living beings are likely answers for further developing plastic biodegradation processes (Liu et al. 2020).

Notwithstanding, these creative remediation approaches do not tackle plastic contamination and should be joined by viable moderation methodologies that focus on source reduction. This could be accomplished by (I) fixing plastic decrease strategies underscoring a diminishing use furthermore; (ii) streamlining waste executive frameworks; (iii) looking for economical plastics to guarantee their environmental amicability; and (iv) expanding public awareness on plastic contamination alongside a social shift.

Conclusion

Micro-nano plastic pollution has increased dramatically in recent years, posing a threat to ecosystem diversity. Phytoremediation is a completely natural method for removing MNPs from agricultural ecosystems and restoring soil productivity and plant health. To determine the best use of phytoremediation technologies, it is required to investigate the fate of MNPs, their absorption and migration inside plant parts, trafficking along membranes, tolerance, and behavior in the rhizosphere under various environmental conditions. Plant species, root properties, MNP size, and environmental variables all influence MNP uptake and phytoremediation. Furthermore, advanced phytoremediation tactics concentrating on the use of hyperaccumulator plant species, the use of plant-growth boosting bacteria, omics-based investigations, and genetic engineering CRISPR-Cas9 technology are effective methodologies for MNP ecosystem restoration. The use of microbial and enzymatic substances in the breakdown of MNP has the potential to solve this problem on a broad scale. As a result, a thorough understanding of these mechanisms is required for MNP-contaminated soil. Furthermore, the review's restrictions and future possibilities could be critical in creating cost-effective and environmentally acceptable ways for comprehensive MNP degradation in terrestrial ecosystems. More research on the impact of MNPs on soil and developing an integrated approach to plant-based technologies for monitoring, assessment, and remediation of MNPs in terrestrial agroecosystems is needed.

Acknowledgements The authors like to thank Delhi Technological University for providing infrastructure and facility.

Author contribution Megha Bansal: investigation, methodology, writing—original draft. Deenan Santhiya: conceptualization, methodology, writing—review and editing, supervision, Jai Gopal Sharma: funding acquisition, resources, supervision.

Data availability Not applicable.

Declarations

Ethics approval Not applicable.

Consent to participate Not applicable.

Consent for publication Not applicable.

Competing interests The authors declare no competing interests.

References

(2018) Advantages and disadvantages of bioremediation. https://agriculturistmusa.com/advantages-and-disadvantages-of-bioremediation/. Accessed 20 Jun 2022

Agnihotri A, Gupta P, Dwivedi A, Seth CS (2018) Counteractive mechanism (s) of salicylic acid in response to lead toxicity in Brassica juncea (L.) Czern. cv. Varuna Planta 248:49–68. https://doi.org/10.1007/s00425-018-2867-0

Ali H, Khan E, Sajad MA (2013) Phytoremediation of heavy metals—concepts and applications. Chemosphere 91:869–881. https://doi.org/10.1016/j.chemosphere.2013.01.075

Ali S, Mehmood A, Khan N (2021) Uptake, Translocation, and consequences of nanomaterials on plant growth and stress adaptation. J Nanomater 2021:e6677616. https://doi.org/10.1155/2021/6677616

Anand U, Dey S, Bontempi E et al (2023) Biotechnological methods to remove microplastics: a review. Environ Chem Lett 21:1787–1810. https://doi.org/10.1007/s10311-022-01552-4

Anyasi RO, Atagana HI (2018) Profiling of plants at petroleum contaminated site for phytoremediation. Int J Phytoremediation 20:352–361. https://doi.org/10.1080/15226514.2017.1393386

Arikan B, Alp FN, Ozfidan-Konakci C et al (2022) The impacts of nanoplastic toxicity on the accumulation, hormonal regulation and tolerance mechanisms in a potential hyperaccumulator - Lemna minor L. J Hazard Mater 440:129692. https://doi.org/10.1016/j.jhazmat.2022.129692

Ariza-Tarazona MC, Villarreal-Chiu JF, Barbieri V et al (2019) New strategy for microplastic degradation: green photocatalysis using a protein-based porous N-TiO2 semiconductor. Ceram Int 45:9618–9624. https://doi.org/10.1016/j.ceramint.2018.10.208

Auta HS, Emenike CU, Jayanthi B, Fauziah SH (2018) Growth kinetics and biodeterioration of polypropylene microplastics by Bacillus sp. and Rhodococcus sp. isolated from mangrove sediment. Mar Pollut Bull 127:15–21. https://doi.org/10.1016/j.marpolbul.2017.11.036

Awasthi S, Srivastava P, Singh P et al (2017) Biodegradation of thermally treated high-density polyethylene (HDPE) by Klebsiella pneumoniae CH001. 3 Biotech 7:332. https://doi.org/10.1007/s13205-017-0959-3

Azubuike CC, Chikere CB, Okpokwasili GC (2016) Bioremediation techniques–classification based on site of application: principles, advantages, limitations and prospects. World J Microbiol Biotechnol 32:180. https://doi.org/10.1007/s11274-016-2137-x

Banerjee K, Pramanik P, Maity A et al (2019) Chapter 4 - methods of using nanomaterials to plant systems and their delivery to plants (mode of entry, uptake, translocation, accumulation, biotransformation and barriers). In: Ghorbanpour M, Wani SH (eds) Advances in Phytonanotechnology. Academic Press, pp 123–152

Bansal M, Santhiya D, Sharma JG (2021) Behavioural mechanisms of microplastic pollutants in marine ecosystem: challenges and remediation measurements. Water Air Soil Pollut 232:372. https://doi.org/10.1007/s11270-021-05301-1

Bansal M, Santhiya D, Sharma JG (2023) Exploring the impacts of HDPE microplastics on growth and physiological behavior of Brassica juncea (Mustard Plant). Water Air Soil Pollut 234:520. https://doi.org/10.1007/s11270-023-06548-6

Baoune H, Aparicio JD, Acuña A et al (2019) Effectiveness of the Zea mays-Streptomyces association for the phytoremediation of petroleum hydrocarbons impacted soils. Ecotoxicol Environ Saf 184:109591. https://doi.org/10.1016/j.ecoenv.2019.109591

Bhattacharya P, Lin S, Turner JP, Ke PC (2010) Physical adsorption of charged plastic nanoparticles affects algal photosynthesis. J Phys Chem C 114:16556–16561. https://doi.org/10.1021/jp1054759

Bian F, Zhong Z, Zhang X et al (2020) Bamboo – an untapped plant resource for the phytoremediation of heavy metal contaminated soils. Chemosphere 246:125750. https://doi.org/10.1016/j.chemosphere.2019.125750

Bosker T, Bouwman LJ, Brun NR et al (2019) Microplastics accumulate on pores in seed capsule and delay germination and root growth of the terrestrial vascular plant Lepidium sativum. Chemosphere 226:774–781. https://doi.org/10.1016/j.chemosphere.2019.03.163

Boucher J, Friot D (2017) Primary microplastics in the oceans: a global evaluation of sources. IUCN International Union for Conservation of Nature

Burstein D, Harrington LB, Strutt SC et al (2017) New CRISPR–Cas systems from uncultivated microbes. Nature 542:237–241. https://doi.org/10.1038/nature21059

Bussières P (2014) Estimating the number and size of phloem sieve plate pores using longitudinal views and geometric reconstruction. Sci Rep 4:4929. https://doi.org/10.1038/srep04929

Chaudhary AK, Chaitanya K, Vijayakumar RP (2021a) Synergistic effect of UV and chemical treatment on biological degradation of Polystyrene by Cephalosporium strain NCIM 1251. Arch Microbiol 203:2183–2191. https://doi.org/10.1007/s00203-021-02228-3

Chaudhary AK, Chaitanya K, Vijayakumar RP (2021b) Synergistic effect of UV and chemical treatment on biological degradation of Polystyrene by Cephalosporium strain NCIM 1251. Arch Microbiol 203:2183–2191. https://doi.org/10.1007/s00203-021-02228-3

Cheng L, Wang Y, Cai Z et al (2017) Phytoremediation of petroleum hydrocarbon-contaminated saline-alkali soil by wild ornamental Iridaceae species. Int J Phytoremediation 19:300–308. https://doi.org/10.1080/15226514.2016.1225282

Chirakkara RA, Cameselle C, Reddy KR (2016) Assessing the applicability of phytoremediation of soils with mixed organic and heavy metal contaminants. Rev Environ Sci Biotechnol 15:299–326. https://doi.org/10.1007/s11157-016-9391-0

Christian E, Beniah I (2019) Phytoremediation of polluted waterbodies with aquatic plants: recent progress on heavy metal and organic pollutants. https://doi.org/10.20944/preprints201909.0020.v1

Colzi I, Renna L, Bianchi E et al (2022) Impact of microplastics on growth, photosynthesis and essential elements in Cucurbita pepo L. J Hazard Mater 423:127238. https://doi.org/10.1016/j.jhazmat.2021.127238

DalCorso G, Fasani E, Manara A et al (2019) Heavy metal pollutions: state of the art and innovation in phytoremediation. Int J Mol Sci 20:3412. https://doi.org/10.3390/ijms20143412

De Gisi S, Lofrano G, Grassi M, Notarnicola M (2016) Characteristics and adsorption capacities of low-cost sorbents for wastewater treatment: a review. Sustain Mater Technol 9:10–40. https://doi.org/10.1016/j.susmat.2016.06.002

de Souza Machado AA, Lau CW, Kloas W et al (2019) Microplastics can change soil properties and affect plant performance. Environ Sci Technol 53:6044–6052. https://doi.org/10.1021/acs.est.9b01339

Dovidat LC, Brinkmann BW, Vijver MG, Bosker T (2020) Plastic particles adsorb to the roots of freshwater vascular plant Spirodela polyrhiza but do not impair growth. Limnol Oceanogr Lett 5:37–45. https://doi.org/10.1002/lol2.10118

Ebere EC, Wirnkor VA, Ngozi VE (2019) Uptake of microplastics by plant: a reason to worry or to be happy? 12

Enyoh CE, Verla AW, Verla EN et al (2019) Airborne microplastics: a review study on method for analysis, occurrence, movement and risks. Environ Monit Assess 191:668. https://doi.org/10.1007/s10661-019-7842-0

Fasani E, Manara A, Martini F et al (2018) The potential of genetic engineering of plants for the remediation of soils contaminated with heavy metals. Plant Cell Environ 41:1201–1232. https://doi.org/10.1111/pce.12963

Feng N-X, Yu J, Zhao H-M et al (2017) Efficient phytoremediation of organic contaminants in soils using plant–endophyte partnerships. Sci Total Environ 583:352–368. https://doi.org/10.1016/j.scitotenv.2017.01.075

Fomina M, Gadd GM (2014) Biosorption: current perspectives on concept, definition and application. Biores Technol 160:3–14. https://doi.org/10.1016/j.biortech.2013.12.102

Forde BM, O'Toole PW (2013) Next-generation sequencing technologies and their impact on microbial genomics. Brief Funct Genomics 12(5):440–453. https://doi.org/10.1093/bfgp/els062

Galloway TS, Cole M, Lewis C (2017) Interactions of microplastic debris throughout the marine ecosystem. Nat Ecol Evol 1:1–8. https://doi.org/10.1038/s41559-017-0116

Gao M, Liu Y, Dong Y, Song Z (2021) Effect of polyethylene particles on dibutyl phthalate toxicity in lettuce (Lactuca sativa L.). J Hazard Mater 401:123422. https://doi.org/10.1016/j.jhazmat.2020.123422

Geisler-Lee J, Wang Q, Yao Y et al (2013) Phytotoxicity, accumulation and transport of silver nanoparticles by Arabidopsis thaliana. Nanotoxicology 7:323–337. https://doi.org/10.3109/17435390.2012.658094

Gong X, Shi G, Zou D et al (2023) Micro- and nano-plastics pollution and its potential remediation pathway by phytoremediation. Planta 257:35. https://doi.org/10.1007/s00425-023-04069-4

Gravouil K, Ferru-Clément R, Colas S et al (2017) Transcriptomics and lipidomics of the environmental strain rhodococcus ruber point out consumption pathways and potential metabolic bottlenecks for polyethylene degradation. Environ Sci Technol 51:5172–5181. https://doi.org/10.1021/acs.est.7b00846

Gunarathne ADN, Lee K-H (2019) Environmental and managerial information for cleaner production strategies: an environmental management development perspective. J Clean Prod 237:117849. https://doi.org/10.1016/j.jclepro.2019.117849

Guo J-J, Huang X-P, Xiang L et al (2020) Source, migration and toxicology of microplastics in soil. Environ Int 137:105263. https://doi.org/10.1016/j.envint.2019.105263

Gupta P, Seth CS (2023) 24-epibrassinolide regulates functional components of nitric oxide signalling and antioxidant defense pathways to alleviate salinity stress in Brassica juncea L. cv. Varuna J Plant Growth Regul 42:4207–4222. https://doi.org/10.1007/s00344-022-10884-y

Gutow L, Eckerlebe A, Giménez L, Saborowski R (2016) Experimental evaluation of seaweeds as a vector for microplastics into marine food webs. Environ Sci Technol 50:915–923. https://doi.org/10.1021/acs.est.5b02431

Habib S, Iruthayam A, Abd Shukor MY et al (2020) Biodeterioration of untreated polypropylene microplastic particles by antarctic bacteria. Polymers 12:2616. https://doi.org/10.3390/polym12112616

Haegerbaeumer A, Mueller M-T, Fueser H, Traunspurger W (2019) Impacts of micro- and nano-sized plastic particles on benthic invertebrates: a literature review and gap analysis. Front Environ Sci 7

He S, Jia M, Xiang Y et al (2022) Biofilm on microplastics in aqueous environment: physicochemical properties and environmental implications. J Hazard Mater 424:127286. https://doi.org/10.1016/j.jhazmat.2021.127286

Huang D, Chen H, Shen M et al (2022) Recent advances on the transport of microplastics/nanoplastics in abiotic and biotic compartments. J Hazard Mater 438:129515. https://doi.org/10.1016/j.jhazmat.2022.129515

Hussain F, Hussain I, Khan AHA et al (2018) Combined application of biochar, compost, and bacterial consortia with Italian ryegrass enhanced phytoremediation of petroleum hydrocarbon contaminated soil. Environ Exp Bot 153:80–88. https://doi.org/10.1016/j.envexpbot.2018.05.012

Iqbal A, Mukherjee M, Rashid J et al (2019) Development of plant-microbe phytoremediation system for petroleum hydrocarbon degradation: An insight from alkb gene expression and phytotoxicity analysis. Sci Total Environ 671:696–704. https://doi.org/10.1016/j.scitotenv.2019.03.331

Jeevanantham S, Saravanan A, Hemavathy RV et al (2019) Removal of toxic pollutants from water environment by phytoremediation: a survey on application and future prospects. Environ Technol Innov 13:264–276. https://doi.org/10.1016/j.eti.2018.12.007

Jeon J-M, Park S-J, Choi T-R et al (2021) Biodegradation of polyethylene and polypropylene by Lysinibacillus species JJY0216 isolated from soil grove. Polym Degrad Stab 191:109662. https://doi.org/10.1016/j.polymdegradstab.2021.109662

Jeyavani J, Sibiya A, Shanthini S et al (2021) A review on aquatic impacts of microplastics and its bioremediation aspects. Curr Pollution Rep 7:286–299. https://doi.org/10.1007/s40726-021-00188-2

Jiang X, Chen H, Liao Y et al (2019) Ecotoxicity and genotoxicity of polystyrene microplastics on higher plant Vicia faba. Environ Pollut 250:831–838. https://doi.org/10.1016/j.envpol.2019.04.055

Junhao C, Xining Z, Xiaodong G et al (2021) Extraction and identification methods of microplastics and nanoplastics in agricultural soil: a review. J Environ Manage 294:112997. https://doi.org/10.1016/j.jenvman.2021.112997

Kalčíková G, Skalar T, Marolt G, Jemec Kokalj A (2020) An environmental concentration of aged microplastics with adsorbed silver significantly affects aquatic organisms. Water Res 175:115644. https://doi.org/10.1016/j.watres.2020.115644

Kang BR, Kim SB, Song HA, Lee TK (2019) Accelerating the biodegradation of high-density polyethylene (HDPE) using Bjerkandera adusta TBB-03 and lignocellulose substrates. Microorganisms 7:304. https://doi.org/10.3390/microorganisms7090304

Khan I, Awan SA, Rizwan M et al (2022) Nanoparticle's uptake and translocation mechanisms in plants via seed priming, foliar treatment, and root exposure: a review. Environ Sci Pollut Res 29:89823–89833. https://doi.org/10.1007/s11356-022-23945-2

Khandare SD, Chaudhary DR, Jha B (2021a) Bioremediation of polyvinyl chloride (PVC) films by marine bacteria. Mar Pollut Bull 169:112566. https://doi.org/10.1016/j.marpolbul.2021.112566

Khandare SD, Chaudhary DR, Jha B (2021b) Marine bacterial biodegradation of low-density polyethylene (LDPE) plastic. Biodegradation 32:127–143. https://doi.org/10.1007/s10532-021-09927-0

Kowalczyk A, Chyc M, Ryszka P, Latowski D (2016) Achromobacter xylosoxidans as a new microorganism strain colonizing high-density polyethylene as a key step to its biodegradation. Environ Sci Pollut Res 23:11349–11356. https://doi.org/10.1007/s11356-016-6563-y

Kumar V, Shahi SK, Singh S (2018) Bioremediation: an eco-sustainable approach for restoration of contaminated sites. In: Singh J, Sharma D, Kumar G, Sharma NR (eds) Microbial Bioprospecting for Sustainable Development. Springer, Singapore, pp 115–136

Kumar D, Dhankher OP, Tripathi RD, Seth CS (2023) Titanium dioxide nanoparticles potentially regulate the mechanism(s) for photosynthetic attributes, genotoxicity, antioxidants defense machinery, and phytochelatins synthesis in relation to hexavalent chromium toxicity in Helianthus annuus L. J Hazard Mater 454:131418. https://doi.org/10.1016/j.jhazmat.2023.131418

Kumar Yadav K, Gupta N, Kumar A et al (2018) Mechanistic understanding and holistic approach of phytoremediation: a review on application and future prospects. Ecol Eng 120:274–298. https://doi.org/10.1016/j.ecoleng.2018.05.039

Li L, Zhou Q, Yin N et al (2019) Uptake and accumulation of microplastics in an edible plant. Kexue Tongbao/chinese Sci Bull 64:928–934. https://doi.org/10.1360/N972018-00845

Li L, Luo Y, Li R et al (2020) Effective uptake of submicrometre plastics by crop plants via a crack-entry mode. Nat Sustain 3:929–937. https://doi.org/10.1038/s41893-020-0567-9

Li Q, Feng Z, Zhang T et al (2020) Microplastics in the commercial seaweed nori. J Hazard Mater 388:122060. https://doi.org/10.1016/j.jhazmat.2020.122060

Lian J, Wu J, Xiong H et al (2020) Impact of polystyrene nanoplastics (PSNPs) on seed germination and seedling growth of wheat (Triticum aestivum L.). J Hazard Mater 385:121620. https://doi.org/10.1016/j.jhazmat.2019.121620

Liu J, Zhu L, Luo S et al (2014) Response of nitrous oxide emission to soil mulching and nitrogen fertilization in semi-arid farmland. Agr Ecosyst Environ 188:20–28. https://doi.org/10.1016/j.agee.2014.02.010

Liu T, Li J, Qiu L et al (2020) Combined genomic and transcriptomic analysis of the dibutyl phthalate metabolic pathway in Arthrobacter sp. ZJUTW Biotechnol Bioeng 117:3712–3726. https://doi.org/10.1002/bit.27524

Liu W, Zhang J, Liu H et al (2021) A review of the removal of microplastics in global wastewater treatment plants: characteristics and mechanisms. Environ Int 146:106277. https://doi.org/10.1016/j.envint.2020.106277

Liu L-H, Yuan T, Zhang J-Y et al (2022) Diversity of endophytic bacteria in wild rice (Oryza meridionalis) and potential for promoting plant growth and degrading phthalates. Sci Total Environ 806:150310. https://doi.org/10.1016/j.scitotenv.2021.150310

Liu Y, Guo R, Zhang S et al (2022) Uptake and translocation of nano/microplastics by rice seedlings: evidence from a hydroponic experiment. J Hazard Mater 421:126700. https://doi.org/10.1016/j.jhazmat.2021.126700

Lourenço J, Mendo S, Pereira R (2019) Rehabilitation of radioactively contaminated soil: use of bioremediation/phytoremediation techniques. In: Gupta DK, Voronina A (eds) Remediation Measures for Radioactively Contaminated Areas. Springer International Publishing, Cham, pp 163–200

Luo Z, Zhou X, Su Y et al (2021) Environmental occurrence, fate, impact, and potential solution of tire microplastics: similarities and differences with tire wear particles. Sci Total Environ 795:148902. https://doi.org/10.1016/j.scitotenv.2021.148902

Ma B, Xue W, Ding Y et al (2019) Removal characteristics of microplastics by Fe-based coagulants during drinking water treatment. J Environ Sci 78:267–275. https://doi.org/10.1016/j.jes.2018.10.006

Magnin A, Hoornaert L, Pollet E et al (2019) Isolation and characterization of different promising fungi for biological waste management of polyurethanes. Microb Biotechnol 12:544–555. https://doi.org/10.1111/1751-7915.13346

Mammo FK, Amoah ID, Gani KM et al (2020) Microplastics in the environment: interactions with microbes and chemical contaminants. Sci Total Environ 743:140518. https://doi.org/10.1016/j.scitotenv.2020.140518

Managing plastic waste in India. https://www.cseindia.org/managing-plastic-waste-in-india-10352. Accessed 8 Jul 2021

Mateos-Cárdenas A, van Pelt FNAM, O'Halloran J, Jansen MAK (2021) Adsorption, uptake and toxicity of micro- and nanoplastics: effects on terrestrial plants and aquatic macrophytes.

Environ Pollut 284:117183. https://doi.org/10.1016/j.envpol.2021.117183
Medić A, Stojanović K, Izrael-Živković L et al (2019) A comprehensive study of conditions of the biodegradation of a plastic additive 2,6-di- tert -butylphenol and proteomic changes in the degrader Pseudomonas aeruginosa san ai. RSC Adv 9:23696–23710. https://doi.org/10.1039/C9RA04298A
Montazer Z, Habibi Najafi MB, Levin DB (2020) Challenges with verifying microbial degradation of polyethylene. Polymers 12:123. https://doi.org/10.3390/polym12010123
Moog D, Schmitt J, Senger J et al (2019) Using a marine microalga as a chassis for polyethylene terephthalate (PET) degradation. Microb Cell Fact 18:171. https://doi.org/10.1186/s12934-019-1220-z
Ng E-L, Huerta Lwanga E, Eldridge SM et al (2018) An overview of microplastic and nanoplastic pollution in agroecosystems. Sci Total Environ 627:1377–1388. https://doi.org/10.1016/j.scitotenv.2018.01.341
Othman AR, Hasan HA, Muhamad MH et al (2021) Microbial degradation of microplastics by enzymatic processes: a review. Environ Chem Lett 19:3057–3073. https://doi.org/10.1007/s10311-021-01197-9
Palocci C, Valletta A, Chronopoulou L et al (2017) Endocytic pathways involved in PLGA nanoparticle uptake by grapevine cells and role of cell wall and membrane in size selection. Plant Cell Rep 36:1917–1928. https://doi.org/10.1007/s00299-017-2206-0
Pérez-de-Luque A (2017) Interaction of nanomaterials with plants: what do we need for real applications in agriculture? Front Environ Sci 5:12. https://doi.org/10.3389/fenvs.2017.00012
Perren W, Wojtasik A, Cai Q (2018) Removal of microbeads from wastewater using electrocoagulation. ACS Omega 3:3357–3364. https://doi.org/10.1021/acsomega.7b02037
Pflugmacher S, Sulek A, Mader H et al (2020) The influence of new and artificial aged microplastic and leachates on the germination of Lepidium sativum L. Plants 9:339. https://doi.org/10.3390/plants9030339
Pfohl P, Wagner M, Meyer L et al (2022) Environmental degradation of microplastics: how to measure fragmentation rates to secondary micro- and nanoplastic fragments and dissociation into dissolved organics. Environ Sci Technol 56:11323–11334. https://doi.org/10.1021/acs.est.2c01228
Prata JC, da Costa JP, Lopes I et al (2020) Environmental exposure to microplastics: an overview on possible human health effects. Sci Total Environ 702:134455. https://doi.org/10.1016/j.scitotenv.2019.134455
Prokin AA, Dubov PG, Bolotov SE (2015) Formation of macroinvertebrates communities in duckweed (Lemnaceae) and artificial surface-floating substrate: results of the experiment under natural conditions. Inland Water Biol 8:373–383. https://doi.org/10.1134/S1995082915040136
Puiggené Ò, Espinosa MJC, Schlosser D et al (2022) Extracellular degradation of a polyurethane oligomer involving outer membrane vesicles and further insights on the degradation of 2,4-diaminotoluene in Pseudomonas capeferrum TDA1. Sci Rep 12:2666. https://doi.org/10.1038/s41598-022-06558-0
Qi Y, Ossowicki A, Yang X et al (2020) Effects of plastic mulch film residues on wheat rhizosphere and soil properties. J Hazard Mater 387:121711. https://doi.org/10.1016/j.jhazmat.2019.121711
Qiu J, Zhang Y, Shi Y et al (2020) Identification and characterization of a novel phthalate-degrading hydrolase from a soil metagenomic library. Ecotoxicol Environ Saf 190:110148. https://doi.org/10.1016/j.ecoenv.2019.110148
Rahbar A, Farjadfard S, Leili M et al (2016) Experimental data of biomaterial derived from Malva sylvestris and charcoal tablet powder for Hg2+ removal from aqueous solutions. Data Brief 8:132–135. https://doi.org/10.1016/j.dib.2016.05.032
Raven JA (2022) Commentary on the use of nutrient-coated quantum dots as a means of tracking nutrient uptake by and movement within plants. Plant Soil 476:535–548. https://doi.org/10.1007/s11104-022-05507-0
Reineccius J, Bresien J, Waniek JJ (2021) Separation of microplastics from mass-limited samples by an effective adsorption technique. Sci Total Environ 788:147881. https://doi.org/10.1016/j.scitotenv.2021.147881
Rezania S, Taib SM, Md Din MF et al (2016) Comprehensive review on phytotechnology: heavy metals removal by diverse aquatic plants species from wastewater. J Hazard Mater 318:587–599. https://doi.org/10.1016/j.jhazmat.2016.07.053
Rodrigo O-A, del Castillo Daynet S, Jaime N-M et al (2021) Analysis of the degradation of polyethylene, polystyrene and polyurethane mediated by three filamentous fungi isolated from the Antarctica. Afr J Biotechnol 20:66–76. https://doi.org/10.5897/AJB2020.17200
Rozman U, Jemec Kokalj A, Dolar A et al (2022) Long-term interactions between microplastics and floating macrophyte Lemna minor: the potential for phytoremediation of microplastics in the aquatic environment. Sci Total Environ 831:154866. https://doi.org/10.1016/j.scitotenv.2022.154866
Sarwar N, Imran M, Shaheen MR et al (2017) Phytoremediation strategies for soils contaminated with heavy metals: modifications and future perspectives. Chemosphere 171:710–721. https://doi.org/10.1016/j.chemosphere.2016.12.116
Saxena G, Purchase D, Mulla SI et al (2020) Phytoremediation of heavy metal-contaminated sites: eco-environmental concerns, field studies, sustainability issues, and future prospects. In: de Voogt P (ed) Reviews of Environmental Contamination and Toxicology, vol 249. Springer International Publishing, Cham, pp 71–131
Shang S, Liu Y, Liu M et al (2022) Studying the adsorption mechanisms of nanoplastics on covalent organic frameworks via molecular dynamics simulations. J Hazard Mater 421:126796. https://doi.org/10.1016/j.jhazmat.2021.126796
Shao H, Chen M, Fei X et al (2019) Complete genome sequence and characterization of a polyethylene biodegradation strain, Streptomyces Albogriseolus LBX-2. Microorganisms 7:379. https://doi.org/10.3390/microorganisms7100379
Song Z, Zhao X, Dong Y et al (2023) Effects of polystyrene nanoplastics with different functional groups on the accumulation and toxicity of Pb on dandelion. Chemosphere 310:136874. https://doi.org/10.1016/j.chemosphere.2022.136874
Staley C, Sadowsky MJ (2016) Application of metagenomics to assess microbial communities in water and other environmental matrices. J Mar Biol Assoc UK 96:121–129. https://doi.org/10.1017/S0025315415001496
Steliga T, Kluk D (2020) Application of Festuca arundinacea in phytoremediation of soils contaminated with Pb, Ni, Cd and petroleum hydrocarbons. Ecotoxicol Environ Saf 194:110409. https://doi.org/10.1016/j.ecoenv.2020.110409
Sun H, Lei C, Xu J, Li R (2021) Foliar uptake and leaf-to-root translocation of nanoplastics with different coating charge in maize plants. J Hazard Mater 416:125854. https://doi.org/10.1016/j.jhazmat.2021.125854
Sun L, Wang X, Zhao H et al (2023) Micro/nanoplastics: a potential threat to crops. V 3. https://doi.org/10.48130/VR-2023-0018
Sundbæk KB, Koch IDW, Villaro CG et al (2018) Sorption of fluorescent polystyrene microplastic particles to edible seaweed Fucus vesiculosus. J Appl Phycol 30:2923–2927. https://doi.org/10.1007/s10811-018-1472-8

Talvitie J, Mikola A, Koistinen A, Setälä O (2017) Solutions to microplastic pollution – removal of microplastics from wastewater effluent with advanced wastewater treatment technologies. Water Res 123:401–407. https://doi.org/10.1016/j.watres.2017.07.005

Tangahu BV, Sheikh Abdullah SR, Basri H et al (2011) A review on heavy metals (As, Pb, and Hg) uptake by plants through phytoremediation. Int J Chem Eng 2011:e939161. https://doi.org/10.1155/2011/939161

Taylor SE, Pearce CI, Sanguinet KA et al (2020) Polystyrene nano- and microplastic accumulation at Arabidopsis and wheat root cap cells, but no evidence for uptake into roots. Environ Sci Nano 7:1942–1953. https://doi.org/10.1039/D0EN00309C

Teng M, Zhao X, Wang C et al (2022) Polystyrene nanoplastics toxicity to zebrafish: dysregulation of the brain–intestine–microbiota axis. ACS Nano 16:8190–8204. https://doi.org/10.1021/acsnano.2c01872

Tian C, Lv J, Zhang W et al (2022) Accelerated degradation of microplastics at the liquid interface of ice crystals in frozen aqueous solutions. Angew Chem Int Ed 61:e202206947. https://doi.org/10.1002/anie.202206947

Tun TZ, Kunisue T, Tanabe S et al (2022) Microplastics in dumping site soils from six Asian countries as a source of plastic additives. Sci Total Environ 806:150912. https://doi.org/10.1016/j.scitotenv.2021.150912

Ullah R, Tsui MT-K, Chen H et al (2021) Microplastics interaction with terrestrial plants and their impacts on agriculture. J Environ Qual 50:1024–1041. https://doi.org/10.1002/jeq2.20264

van Weert S, Redondo-Hasselerharm PE, Diepens NJ, Koelmans AA (2019) Effects of nanoplastics and microplastics on the growth of sediment-rooted macrophytes. Sci Total Environ 654:1040–1047. https://doi.org/10.1016/j.scitotenv.2018.11.183

Wallace PW, Haernvall K, Ribitsch D et al (2017) PpEst is a novel PBAT degrading polyesterase identified by proteomic screening of Pseudomonas pseudoalcaligenes. Appl Microbiol Biotechnol 101:2291–2303. https://doi.org/10.1007/s00253-016-7992-8

Wang Z, Xie X, Zhao J et al (2012) Xylem- and phloem-based transport of CuO nanoparticles in maize (Zea mays L.). Environ Sci Technol 46:4434–4441. https://doi.org/10.1021/es204212z

Wang X, Li Y, Zhao J et al (2020) UV-induced aggregation of polystyrene nanoplastics: effects of radicals, surface functional groups and electrolyte. Environ Sci Nano 7:3914–3926. https://doi.org/10.1039/D0EN00518E

Wei Z, Van Le Q, Peng W et al (2021) A review on phytoremediation of contaminants in air, water and soil. J Hazard Mater 403:123658. https://doi.org/10.1016/j.jhazmat.2020.123658

Wilkes RA, Aristilde L (2017) Degradation and metabolism of synthetic plastics and associated products by Pseudomonas sp.: capabilities and challenges. J Appl Microbiol 123:582–593. https://doi.org/10.1111/jam.13472

Wright SL, Thompson RC, Galloway TS (2013) The physical impacts of microplastics on marine organisms: a review. Environ Pollut 178:483–492. https://doi.org/10.1016/j.envpol.2013.02.031

Wu Y, Guo P, Zhang X et al (2019) Effect of microplastics exposure on the photosynthesis system of freshwater algae. J Hazard Mater 374:219–227. https://doi.org/10.1016/j.jhazmat.2019.04.039

Wu J, Liu W, Zeb A et al (2021) Polystyrene microplastic interaction with Oryza sativa: toxicity and metabolic mechanism. Environ Sci: Nano 8:3699–3710. https://doi.org/10.1039/D1EN00636C

Wu X, Lu J, Du M et al (2021) Particulate plastics-plant interaction in soil and its implications: a review. Sci Total Environ 792:148337. https://doi.org/10.1016/j.scitotenv.2021.148337

Xia B, Chen B, Sun X et al (2015) Interaction of TiO2 nanoparticles with the marine microalga Nitzschia closterium: growth inhibition, oxidative stress and internalization. Sci Total Environ 508:525–533. https://doi.org/10.1016/j.scitotenv.2014.11.066

Xu Q, Huang Q-S, Luo T-Y et al (2021) Coagulation removal and photocatalytic degradation of microplastics in urban waters. Chem Eng J 416:129123. https://doi.org/10.1016/j.cej.2021.129123

Xu Z, Zhang Y, Lin L et al (2022) Toxic effects of microplastics in plants depend more by their surface functional groups than just accumulation contents. Sci Total Environ 833:155097. https://doi.org/10.1016/j.scitotenv.2022.155097

Yadav M, Gupta P, Seth CS (2022) Foliar application of α-lipoic acid attenuates cadmium toxicity on photosynthetic pigments and nitrogen metabolism in Solanum lycopersicum L. Acta Physiol Plant 44:112. https://doi.org/10.1007/s11738-022-03445-z

Yoshida S, Hiraga K, Takehana T et al (2016) A bacterium that degrades and assimilates poly(ethylene terephthalate). Science 351:1196–1199. https://doi.org/10.1126/science.aad6359

Yu B, Peng Y, Xu J et al (2021) Phytoremediation potential of Youngia japonica (L.) DC: a newly discovered cadmium hyperaccumulator. Environ Sci Pollut Res 28:6044–6057. https://doi.org/10.1007/s11356-020-10853-6

Zhang L, Cheng Y, Qian Y et al (2022) Phytotoxicity and accumulation of BPS to Pistia stratiotes under the influence of microplastics. Chemosphere 307:135854. https://doi.org/10.1016/j.chemosphere.2022.135854

Zhou G, Wang Q, Li J et al (2021) Removal of polystyrene and polyethylene microplastics using PAC and FeCl3 coagulation: performance and mechanism. Sci Total Environ 752:141837. https://doi.org/10.1016/j.scitotenv.2020.141837

Publisher's Note Springer Nature remains neutral with regard to jurisdictional claims in published maps and institutional affiliations.

Springer Nature or its licensor (e.g. a society or other partner) holds exclusive rights to this article under a publishing agreement with the author(s) or other rightsholder(s); author self-archiving of the accepted manuscript version of this article is solely governed by the terms of such publishing agreement and applicable law.

MF^{2}ShrT: Multi-Modal Feature Fusion Using Shared Layered Transformer for Face Anti-Spoofing

AASHANIA ANTIL

Department of Electronics and Communication Engineering, Delhi Technological University, New Delhi, Delhi, India

CHHAVI DHIMAN

Department of Electronics and Communication Engineering, Delhi Technological University, New Delhi, Delhi, India

In recent times, Face Anti-spoofing (FAS) has gained significant attention in both academic and industrial domains. Although various CNN-based solutions have emerged, multi-modal approaches incorporating RGB, depth, and IR have exhibited better performance than unimodal classifiers. The increasing veracity of modern presentation attack instruments results in a persistent need to enhance the performance of such models. Recently, self-attention-based vision transformers (ViT) have become a popular choice in this field. Their fundamental aspects for multimodal FAS have not been thoroughly explored yet. Therefore, we propose a novel framework for FAS called MF^{2}ShrT, which is based on a pre-trained vision transformer. The proposed framework uses overlap patches and parameter sharing in the ViT network, allowing it to utilize multiple modalities in a computationally efficient manner. Furthermore, to effectively fuse intermediate features from different encoders of each ViT, we explore a T-encoder-based hybrid feature block enabling the system to identify correlations and dependencies across different modalities. MF^{2}ShrT outperforms conventional vision transformers and achieves state-of-the-art performance on benchmarks CASIA-SURF and WMCA, demonstrating the efficiency of transformer-based models for PAD.

CCS Concepts: • Computing methodologies → Biometrics;

Additional Key Words and Phrases: Face anti-spoofing, presentation attack detection, multi-modal, vision transformer

1 INTRODUCTION

Facial recognition technology has become a ubiquitous aspect of modern-day interactive AI systems. Various stakeholders in public and private industries (e.g., Airports, banks, etc.) employ it in a wide-ranging and ever-growing array of applications, such as electronic payments, security, access control, and surveillance. Despite the advancements in authentication systems, facial recognition technology remains susceptible to presentation attacks (PAs) [1]such as print photos [2], replay videos [3], face forgery [4] and 2D/3D masks [5]. Developing reliable and efficient face anti-spoofing (FAS) detection algorithms is necessary to address the significant compromise in the reliability and accuracy of facial recognition systems.

In literature, experts have broadly categorized the existing presentation attack detection (PAD) methods into two main categories: Traditional approaches [3] [6] [7] and deep learning-based approaches [8] [9] [10] [11]. Both have shown effective performance in distinguishing real from fake faces and have often formalized FAS as a binary task [12] [13]. However, these approaches often lack in exploring the nature of spoof patterns [10] [14]. Furthermore, most FAS works [13] are supervised under predefined scenarios and presentation attacks, leading to overfitting and reduced generalization capabilities. Owing to rapidly advancing technologies, there has been an increase in the quality and quantity of Presentation attack instruments (PAIs), making it difficult to detect presentation attacks (PAs)

Permission to make digital or hard copies of all or part of this work for personal or classroom use is granted without fee provided that copies are not made or distributed for profit or commercial advantage and that copies bear this notice and the full citation on the first page. Copyrights for components of this work owned by others than the author(s) must be honored. Abstracting with credit is permitted. To copy otherwise, or republish, to post on servers or to redistribute to lists, requires prior specific permission and/or a fee. Request permissions from permissions@acm.org.
© 2024 Copyright held by the owner/author(s). Publication rights licensed to ACM.
ACM 1551-6857/2024/01-ART
http://dx.doi.org/10.1145/3640817

Just Accepted

using only a single modality. Therefore, researchers have explored the feasibility of other modalities like IR, depth, and thermal images to detect PAs. Multi-stream architectures [15] [16] [17] have been employed to extract features from various modalities for fusion. Though these approaches have shown superior performance, they often lack interaction between modalities which limits their ability to extract complementary details. Additionally, such multi-modal methods often capture redundant features that are shared across all modalities, such as eye orientation. Designing and implementing deep model-based systems is a complex task, requiring significant computational resources as well as data for training. Thus, creating a framework that can effectively combine relevant details from different modalities without significantly increasing parameter count to enhance performance beyond using a single modality remains a significant challenge.

The recent emergence of vision transformers (ViT) [18] in general-purpose computer vision tasks has motivated researchers to rethink feature extraction with methods beyond CNN. ViT utilizes a self-attention mechanism to capture long-range dependencies and global context in images, leading to significant improvements in visual recognition [19]. Previous efforts to integrate self-attention into CNNs faced limitations in fully realizing its potential. In contrast, ViT takes a novel approach by constructing its entire backbone with transformer blocks, thus enhancing the overall performance. By leveraging its robust long-range and cross-modal representation capabilities, expert have proposed ViT-based methods [19] [20] [21] to enhance the robustness of FAS systems. However, these approaches primarily involve direct finetuning of ViT [19] or the incorporation of complex and powerful modules into ViT [22]. Most of these works rely solely on RGB as input, overlooking essential aspects like incorporating inputs from diverse modalities, appropriate multimodal pre-training, and efficient ViT-specific fine-tuning for FAS. Therefore, developing a more efficient ViT-based transfer learning framework for FAS that can effectively handle diverse modalities (i.e., RGB, Depth, IR, or a combination) with sophisticated face spoofing attacks, is an important area for future research.

Motivated by the above discussion, we propose a novel and efficient framework for frame-level FAS called MF^{2}ShrT. It captures a comprehensive representation across diverse modalities. While it is common practice to use a multi-stream architecture [15] [16] to independently learn the characteristics of different modalities, these methods lack interaction and thus limit the ability to extract complementary information from multiple modalities. Therefore, this paper adopts a two-branch parameter-sharing transformer-based framework that integrates RGB, depth and IR modalities to extract complementary features. Vision transformers [23] outperform ConvNet-based frameworks by not only capturing local spoofing traces and establishing their long-term dependence on patch tokens, it even fuses multimodal information directly without prior alignment of modal features. The proposed work highlights that strategically using overlapping patches in ViT provides a distinct advantage over non-overlapping patches, offering a more comprehensive and contextually rich representation of face images**.** This ensures that each facial feature is covered by multiple patches, significantly enhancing the framework's capacity to capture fine-grained details—a crucial aspect in FAS, where spoofing attacks often involve subtle changes in facial features. Despite the transformative capabilities of transformers, their numerous encoders block can lead to a high parameter count, increasing the memory and computation requirements of the framework. To mitigate this issue, our framework employs parameter sharing in the ViT, thereby reducing the overall parameters, and enhancing computational efficiency. Further, a T-encoder-based hybrid feature block is designed to mine complementary relation among patches of different layers. This is followed by an adaptive weighted fusion mechanism to

Just Accepted

ensure rich coalescence among diverse modality inputs, thereby further optimizing the performance of the framework.

To conclude, the primary contributions of this paper are outlined as follows:

1. A simple yet efficient Multi-modal Feature Fusion framework, MF^{2}ShrT, is proposed which utilizes overlapping patches and shared layered ViT. Overlap patches highlights local contextual information in feature extraction phase.
2. Proposed parameter-sharing mechanism in the base ViT, named as SharLViT, that enhances the feature representation ability of the ViT while considerable reduction of number of parameters and hence computation complexity.
3. Introduced a novel T-Encoder-based Hybrid Feature Block to mine the inter-modal correlations and dependencies for richer feature representation.
4. An adaptive fusion mechanism is defined to adaptively fuse three branches {RGB, Hybrid, RID} in the Adaptive Weighted Fusion and Classification Block (AWFCB). It enhances the flexibility and responsiveness of the fusion process by learning the weightage to be given to salient multi-modal features adaptively, giving less attention to redundant information across the modalities.
5. Extensive experiments are carried out on two challenging datasets, namely CASIA-SURF and WMCA dataset using intra and cross-dataset evaluation protocols to showcase the competitive performance of the proposed MF^{2}ShrT framework when compared to state-of-the-art in terms of both computational efficiency and accuracy.

The paper is structured is as follows: Section II provides an overview of the current state-of-the-art and related works, giving context to the proposed framework; Section III delves into the details of the proposed face anti-spoofing framework, describing comprehensive representation of spoof faces across different modalities; Section IV presents a thorough experimental analysis of the proposed framework, highlighting its performance in comparison to existing methods and demonstrating its effectiveness in face anti-spoofing task. Finally, Section V concludes the paper by summarizing the significant contributions of the proposed work and outlining its potential for future research and development.

2 RELATED WORK

Multi-Modal FAS: With the emergence of multi-spectral cameras, modality-based approaches to learning complementary characteristics have recently received attention to enhance the FAS problem. These approaches leverage complementary information from different modalities to provide more robust performance on FAS tasks. For instance, Atoum et al. [24] capture characteristics from both depth and RGB images using a two-stream architecture. By using pixel-wise detailed information and facial geometry, this approach uses facial depth estimation to attempt to capture spoofing cues. In [10], Liu et al. deployed rPPG signals and estimated depth as auxiliary signals to train the model. The issue of accurately estimating depth from RGB still remains, as depth estimation errors can affect feature representation and cause classification errors. To solve this problem, Zhang et al. [25] published a large-scale multi-modal FAS dataset CASIA-SURF containing all three modalities (i.e., RGB, Depth, and IR). Liu et al. [26] released CeFA, the largest face anti-spoofing dataset to date, featuring unmatched diversity in ethnicities, modalities, subjects, and attack types. In [27], Parkin and Grinchuk presented a multilayer feature aggregation model that accomplishes feature fusion of distinct modality at both coarse and fine levels. Similarly, Zhang et al. [28] used ResNet18 as the backbone and gave RGB, Depth, and IR face photos as the inputs for each stream. Later, the output traits are concatenated and made

Just Accepted

to pass from the final two remaining blocks. FaceBagNet [29] made from multi-stream CNN architecture used patch-level images as input to enhance the capability of local detailed representation. Also, the introduction of the modality features erasing part prevented overfitting and made the model more robust. Most previous work [15] [27] [28] are based on standard backbone ResNet for triple modalities that might be inadequate in representing the inherent features between actual and spoof faces. Besides modality-specific branch architecture, few works [22] have attempted explicitly to find a correlation among various modalities. For instance, MA-Net [22] mapped

RGB to IR modality using a generative model to bridge the domain gap across modalities. The discriminative face anti-spoofing model is trained using both the source RGB and the produced IR modalities. In addition to multi-model inputs (i.e., RGB, Depth, and IR), some works have also explored different types of fusion techniques such as input-level [30] [17] [31], feature-level fusion [22] [32] [33] [34] [35]and decision-level[36]. Direct feature concatenation [37]produces high-dimensional features and overfitting readily since multi-modal features have redundancy. Therefore, works like [25] [28] [29] [38] introduced different approaches to prevent overfitting. Under restricted conditions, deep learning-based algorithms though outperform traditional approaches. However, these approaches show unsatisfactory generalization capability due to the limited subject number and data modalities.

Vision Transformer: Transformers [39] are widely employed in natural language processing (NLP) and have demonstrated immense potential in computer vision [40] [41] [42]. A hierarchical transformer-based architecture achieved great results on numerous computer vision tasks with shifted windows. The transformer's efficacy extends beyond traditional vision applications, excelling in image captioning [43] and image ranking [44], highlighting its adaptability across various implementations. Therefore, there have been several attempts to use the ViT framework for FAS tasks. Vision transformers [23] consider the image as a series of patches that achieves superiority in image classification. For example, to extract features from all patches for Zero-shot FAS, a pure vision transformer was first presented [19]. The self-attention mechanism is useful for exploring the global relationships between several patches. Due to insufficient data, the backbone's weights and structure are frozen which allows further improvements. Further, works [19] [20] [21][32] [45] have also explored ViT in the FAS field. ViT have been used in the spatial domain [19] [20] [21]to detect live and spoof relations between local patches. Some works [46] [47] used ViT in the temporal domain extracting global features. By combining a transformer with a CNN, a detection transformer suggested in [41] that directly makes the predictions. For multi-modal FAS, Liu and Liang [32] proposed modality-agnostic transformer blocks. Despite a good performance by modified ViT with complex customized modal-disentangled and cross-modal [32] attention modules, there are no works exploring the fundamental characteristics of vanilla ViT for multi-modal FAS. Thus, it is worth exploring ViT based multi-modal FAS.

3 PROPOSED METHODOLOGY

In this section, we describe the proposed MF^{2}ShrT framework for face anti-spoofing based on a pre-trained vision transformer, as shown in Figure 1. MF^{2}ShrT is a bi-branch bi-stage network that utilizes overlapped patches and parameter sharing in the ViT network. The former stage consists of the input adaptor and the multi-modal feature extractor. The latter stage employs the proposed T-encoder-based hybrid feature block and adaptive weighted fusion followed by classification block. The pre-trained ViT expects a tri-channel input. Simply using multiple modalities independently may not fully utilize the potential of the discriminative features present in different modalities. One branch uses the RGB images

Just Accepted

directly, whereas all three modalities are fed as a composite input to the second branch. This input augmentation is computationally efficient compared to using one transformer per modality. It also ensures a comprehensive representation of the input images in which the independent modalities (RGB, Depth, and IR) complement each other during feature extraction. Therefore, the three-channel RGB image is projected into a single channel via a single filter convolution, resulting in a single-channel representation distinct from the typical grayscale representation. Next, we stack this single channel with the Depth and IR image to form a proper 3-channel input for the other transformer. The output of each transformer passes to the fully connected dense layer individually. The second stage of the framework is a T-encoder-based hybrid feature block. A feature aggregator collects the intermediate features from different encoders of each ViT and passes them to T-encoder feature projector. This enables the system to learn inter-modal correlations and dependencies that are not directly evident in frameworks [27] [28] with a discrete modality feature extraction schema. The generated hybrid features are then fused with the output features of each branch and used for classification, providing a robust solution.

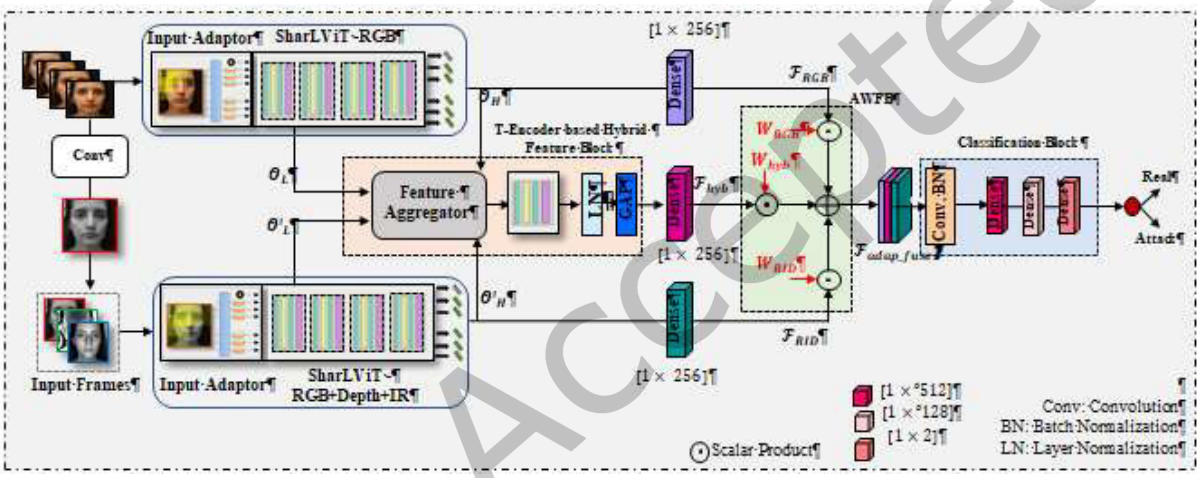


Figure 1: The Proposed framework MF^{2}ShrT for Face Anti-Spoofing; AWFB: Adaptive Weighted Fusion Block

3.1 Input Adaptor

The standard ViT first segments an input image into non-overlapping patches, which may ignore inter-patch information [48]. This often leads to loss of important facial features and local contextual information due to partitioning into different tokens. Therefore, we define the ViT token generation technique using sliding patches with overlapping regions. This enables us to better describe the inter-patch information and retain local contextual information. To implement this technique, we first extract sliding patches from the input image size $Z \in \mathbb{R}^{H\times H\times C}$ with stride S and patch size P ($S = P \times (1 - overlap\%)$), resulting in a sequence of flattened $2D$ patches $Z_P \in \mathbb{R}^{N\times(P^2\times C)}$. The resolution of the input image is (H, H), and each
image patch resolution is (P, P). The sequence of effective length is the number of patches

$$N = [\frac{H+2\times\rho-(P-1)}{S} + 1], \qquad (1)$$

where ρ denotes the amount of zero-padding.

The flattened patches Z_P are mapped to the model dimension D using a trainable linear project by the ViT and produces the patch embeddings $Z_P E$. Then a learnable embedding, the class token ($Z_{CLS} = X_0^0$) is also concatenated to the patch embeddings, followed by the addition of position embeddings to retain positional information.

Just Accepted

The final face image embedding is obtained as the state of the token at the output of transformer encoder (X_L^0), as equation 2.

$$X_0 = [Z_{CLS}; Z_P^1 E; Z_P^2 E; \ldots\ldots\ldots\ldots; Z_P^N E] + E_{Position}, \quad (2)$$

The embeddings are combined to form X_0, that serves as input to the subsequent Transformer encoders, L. Figure 2 illustrates the varying levels of overlapping rates. Here, we have employed a ½ overlap rate between the consecutive patches. Section IV outlines a thorough ablation study conducted to identify the optimal overlap rate for detecting effective results.

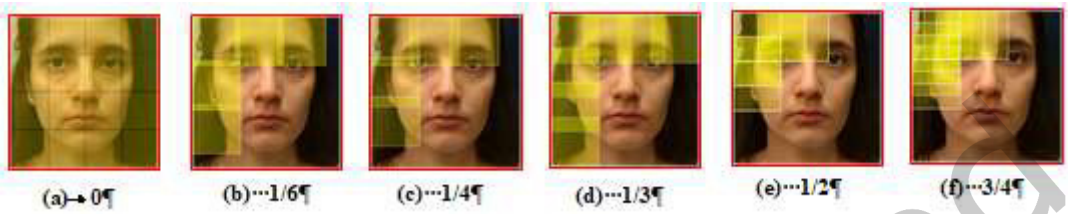


Figure 2: Illustration of Overlapping Patch Rate for different values

3.2 SharLViT: Parameter Sharing in ViT

ViT is well-suited for handling images with extensive data, including high-resolution images, and can extract features that capture both local and global dependencies among different modalities [25]. The architecture of ViT includes several encoder layers that receive combined embeddings. Each layer consists of Multi-Head Self-Attention (MSA) and multilayer perceptron (MLP) blocks, enabling the step-by-step calculation of the relation between patch and classification embeddings across the layers. The resulting feature embeddings can be expressed as:

$$y_l = MSA\big(LN(X_{l-1})\big) + X_{l-1}, l \in= 1, \ldots, L, \quad (3)$$

$$X_l = MLP\big(LN(y_l)\big) + y_l, l = 1, \ldots, L, \quad (4)$$

$$X_{out} = LN(X_L) \quad (5)$$

Where $X_{l-1} \in R^{(L+1)\times C}$ is the output of $(l-1)_{th}$ encoder and X_l will serve as input to the $(l+1)_{th}$ encoder and LN denotes the layer normalization operation. The final output X_{out} is obtained after normalizing the output of last encoder. For the given input, ViT encoder block backbone equipped with self-attention mechanism allow the framework to capture inconsistencies among the artifacts localized in the masked patches for any face spoof attempt.

In the proposed framework, one transformer extracts spoofing cues using RGB input. While the composite tri-modal input given to the other transformer enables the MSA and MLP modules to act simultaneously on all three modalities, effectively filtering out redundant features and reinforcing the in-branch cross-modal discriminatory cues.

According to Brown et al. [49], a larger number of parameters typically results in improved performance. However, using a model with too many parameters can consume a significant GPU memory. To address this issue, we opted to utilize the ViT-B_16 [23] architecture as a backbone with 86M trainable parameters, which consists of 12 layers. It is lighter in terms of the number of trainable parameters compared to other pre-trained computationally intensive transformer architectures like ViT-L_16 [23], ViT-L_32 [23], or ViT-H [23]. To further reduce the number of parameters, the ViT-B_16 [23] is employed

Just Accepted

with an efficient parameter-sharing technique leading to the development of the SharLViT architecture (see Figure3). As reported in [50], there are different ways to share transformer parameters across its layer. It involves creating N layers with an M set of parameters, which are shared between encoding blocks in sequential, cyclical, or reverse cyclical order (see Fig. 6). We adopted a sequential sharing strategy to optimize transformer parameters, resulting in a significant reduction in the number of learnable parameters. This approach assigns the same parameters to sequential $[N/M]$ layers and is considered the simplest among the three strategies. Let the total number of blocks be N and M represents the number of blocks among which a specific set of parameters is shared, then the number of distinct parameters will be $J = \left[\frac{N}{M}\right]$.

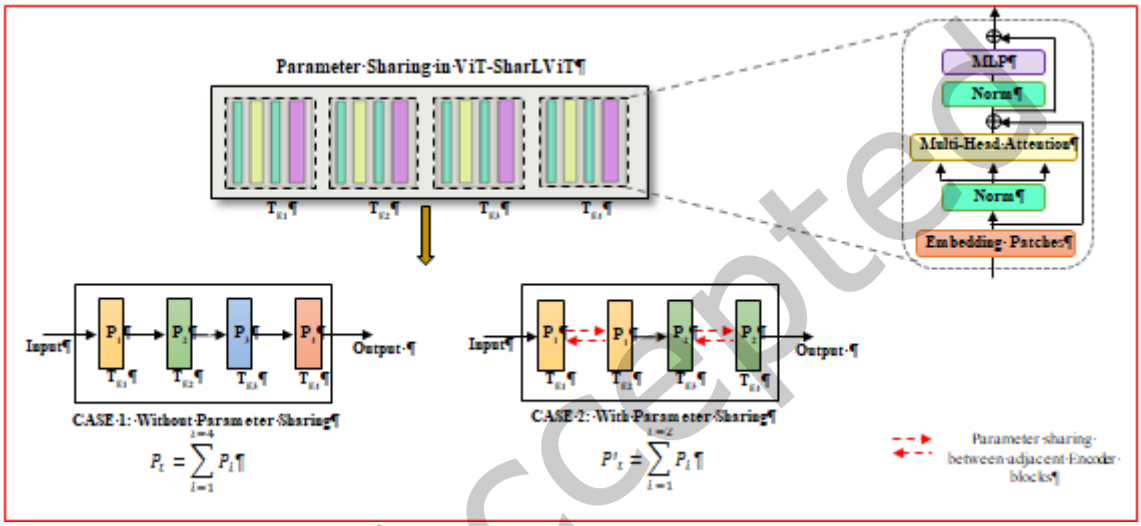


Figure 3: SharLViT- Sequential Parameter Sharing in Vision Transformer Encoder Blocks. T_{E1}, T_{E2}, T_{E3} and T_{E4} denotes 4 encoder blocks within a Transformer. Case 1: Without Parameter Sharing- Each encoder block has parameters P_1, P_2, P_3 and P_4 respectively. Case 2: With Parameter Sharing: P_1 parameter is shared between encoders T_{E1} and T_{E2}, while the P_2 parameter is shared between encoders T_{E3} and T_{E4}.

Let us consider a random block in the set of M shared blocks, the input will be z_i and output to subsequent block will be z_{i+1}, defined as:

$$y_i = MSA_j\big(LN(z_i)\big) + z_i, \quad i \in [1, M] \tag{6}$$

$$z_{i+1} = MLP_j\big(LN(y_i)\big) + y_i, \quad j \in [1, J] \tag{7}$$

where MSA_j, MLP_j denote the internal blocks using shared parameters. This effectively reduces the parameter count by a factor of J.

Figure 3 illustrate SharLViT with Sequential Parameter Sharing in vision transformer Encoder Blocks. As shown in case 1, in a standard transformer, each encoder block (T_{E1}, T_{E2}, T_{E3} and T_{E4}) typically has its own set of parameters (P_1, P_2, P_3 and P_4). The total number of parameters P_t for n encoder blocks transformer is expressed as:

$$P_t = \sum_{i=1}^{i=n} P_i \tag{8}$$

In Case 2, parameter sharing optimizes the framework with P_1 shared between T_{E1} and T_{E2}, and P_2 shared between T_{E3} and T_{E4}, enhancing efficiency and collaborative learning. This visually illustrate how specific parameters are selectively shared between adjacent encoder blocks, reducing the total number of parameters P'_t to:

Just Accepted

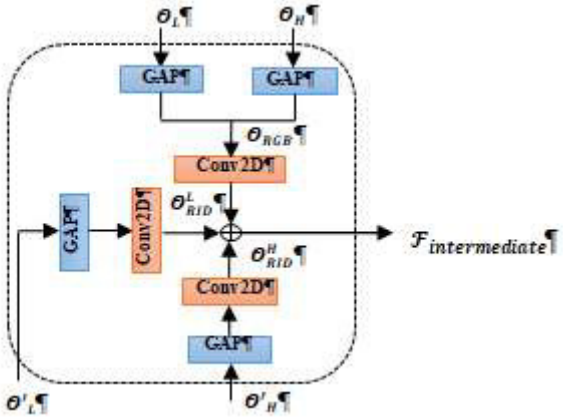


Figure 4: Detailed structure of feature aggregator

$$P'_t = \sum_{i=1}^{i=n/2} P_i \quad (9)$$

The proposed MF^{2}ShrT employes four encoder blocks $T_{E1:4}$ with $M = 2$ and $N = 4$ per branch. This approach efficiently learns feature representation with eight encoder blocks (4 per branch) while utilizing only half of the parameters. Our ablation studies presented in experimental section IV further confirms the effectiveness of the parameter sharing technique in achieving optimized performance while utilizing fewer parameters.

3.3 T-Encoder-based Hybrid Feature Block

Current research [15] [29] typically uses network layer stacking to capture semantic characteristics. However, as the depth of the network increases, low-level features become less prominent. Capturing the relationship between extracted multi-modal features at different levels is expected to improve the performance. Therefore, in the proposed work, a novel T-encoder based hybrid feature block is defined. The T-encoder based hybrid feature block extracts intermediate features, $\mathcal{F}_{intermediate}$ across two branches using a feature aggregator. This is followed by a T-encoder feature projector that translates these $\mathcal{F}_{intermediate}$ features into a hybrid feature space. This provides an effective way to introduce additional global context to the feature representation bridging the modality gap typically observed in CNN-based models [15] [27] [28]. As a result, this method enables a more comprehensive representation of input data and enhances our understanding of the relationships between different modalities, ultimately leading to improved performance.

Feature Aggregator: To accomplish this, we design a feature aggregator, as shown in Figure 4, that captures feature maps generated by the T_{E2} and T_{E4} encoders from both branches. The feature aggregator operates by taking the encoded feature maps from one branch and combining them with their corresponding counterparts from the other branch. For the RGB branch encoder outputs ($RGB - \Theta_L \; and \; \Theta_H$), the process involves stacking the outputs, followed by a convolution ($conv$) operation and subsequent Global Average Pooling (GAP). Meanwhile, the RID branch features ($RID - \Theta'_L \; and \; \Theta'_H$) undergo individual convolution filtering, followed by their own GAP. This difference in dimensionality reduction approach assumes that the RID branch features have more robust discriminatory information than the RGB branch due to the three constituent independent modalities. To preserve this information, the individual outputs of the RID branch are kept separate before the hybrid fusion. Finally, the three convolution outputs are concatenated ($conc$) to form the resulting feature aggregator output, $\mathcal{F}_{intermediate}$. This can be formulated as:

Just Accepted

$$\mathcal{F}_{intermediate} = conc(\Theta_{RGB}, \Theta^{L}_{RID}, \Theta^{H}_{RID}) \quad (10)$$

where,

$$\Theta_{RGB} = conv(conc(GAP(\Theta_L), GAP(\Theta_H))) \quad (11)$$

$$\Theta^{L}_{RID} = conv(GAP(\Theta'_L)) \quad (12)$$

$$\Theta^{H}_{RID} = conv(GAP(\Theta'_H)) \quad (13)$$

T-Encoder Feature Projector: T-Encoder Feature Projector translates aggregated features, $\mathcal{F}_{intermediate}$ in a hybrid feature space. This is achieved by passing $\mathcal{F}_{intermediate}$ through a uni-encoder transformer, followed by layer normalization (LN) and Global Average Pooling (GAP) operation. This block plays a pivotal role in refining the multimodal features and discerning the importance of different tokens. It effectively captures intricate dependencies within and across modalities. The size of $\mathcal{F}_{intermediate}$ is reshaped to fed into a uni-encoder transformer (T_{E5}). The hierarchical structure of the T_{E5} facilitates the extraction of high-level abstract representations and fine-grained cross-modal discriminatory features from both the branches. Subsequently, it is processed through a fully connected dense layer (D) with dimension $[1 \times 256]$ as hybrid feature map, $\mathcal{F}_{hyb}$ to adaptively fuse with RGB and RID branch features. Mathematically, $\mathcal{F}_{hyb}$ is defined as follows:

$$\mathcal{F}_{hyb} = D\left(GAP\left(LN\left(T_{E5}\left(Conv(\mathcal{F}_{intermediate})\right)\right)\right)\right) \quad (14)$$

3.4 Adaptive Weighted Fusion and Classification block

As discussed above, we obtained three different feature representation $\mathcal{F}_{RGB}$, $\mathcal{F}_{hyb}$ and $\mathcal{F}_{RID}$ from the input feed. The explicit concatenation [37] of features from each sub-network does not allow for full utilization of the traits. Therefore, to enhance feature learning for classification, we introduce an adaptive weighted fusion block. This block dynamically assigns weights to each branch based on their significance, denoted as w_{RGB} for $\mathcal{F}_{RGB}$, w_{hyb} for $\mathcal{F}_{hyb}$and w_{RID} for $\mathcal{F}_{RID}$. The resulting adaptively fused features, $\mathcal{F}_{adap_fuse}$ are mathematically defined as follows:

$$\mathcal{F}_{adap_fuse} = \left(conc\left((w_{RGB} * \mathcal{F}_{RGB}), (w_{hyb} * \mathcal{F}_{hyb}), (w_{RID} * \mathcal{F}_{RID})\right)\right) \quad (15)$$

here, $conc$ represents concatenation operation.

The obtained $\mathcal{F}_{adap_fuse}$ is processed through a set of classification layers, including convolution ($conv$), Batch Normalization (BN), and three dense layers with dimensions $[1 \times 512]$, $[1 \times 128]$ and $[1 \times 2]$ respectively, to capture the non-linearity of the $\mathcal{F}_{adap_fuse}$ features. In first two dense layers, Rectified Linear Unit (ReLU) [51] is used as the non-linear activation function, and in last dense layer, a SigmoidFocalCrossEntropy is applied to determine the probability of an input being real or fake.

4 EXPERIMENTAL EVALUATION

The preliminary work will initially discuss the dataset used, the evaluation metrics and the implementation details of the proposed work. Secondly, the evaluation performance of the proposed work will be shown along with the comparative analyses. Finally, the effectiveness of the designed framework is verified by ablation experiments.

4.1 Datasets and Metrics

Dataset: We perform our experimental evaluation on two challenging dataset CASIA-SURF (CS) [25] and WMCA [52] dataset. *CS* consists of 21000 videos for 1000 subjects. For each of these 1000 subjects, one live video clip and six false video clips are provided. Intel

Just Accepted

RealSense SR300 captures RGB, depth, and infrared (IR) videos simultaneously. A4-sized color prints of the collector's photos are used as attack samples. The eyes, nose, mouth areas, or combination are cut to feature six different styles of attack faces. After sampling every tenth frame from videos the dataset is split into training, validation, and testing sets. Each set contains around 148K, 48K, and 295K frames of 300, 100, and 600 subjects respectively. Here, live and attack numbers 4,5,6 are used as the training and validation data, while live and attack samples 1,2,3 as test data for the final evaluation. WMCA comprises a wide range of 2D and 3D PAs with four modalities. Further, it includes two protocols: the "seen" protocol replicates a scenario of a visible attack, and the "unseen" attack protocol evaluates the generalization of an unseen attack.

Evaluation Metrics: To perform the comparison of works, we follow the standard metrics: APCER, BPCER, and ACER. The following defines these metrics:

$$APCER = \frac{FP}{FP+TN} \tag{16}$$

$$BPCER = \frac{FN}{FN+TP} \tag{17}$$

$$ACER = \frac{APCER+BPCER}{2} \tag{18}$$

where FP, TN, FN, and TP denote false positive, true negative, false negative, and true positive respectively. According to the convention in [53], Half Total Error Rate (HTER), which calculates the average of the False Rejection Rate (FRR) and the False Acceptance Rate, is adopted for cross-database testing (FAR). The area under the ROC curve (AUC), is also observed.

4.2 Implementation Details

Using the open-source implementation, we adopted the ViT-B_16 [23]vision transformer as the backbone for our framework and initialized it with pre-trained ImageNet weights. The newly added fully connected dense layers in the framework are initialized using the HeUniform initializer and ReLU [51] activation. We used $[224 \times 224]$ and $[128 \times 128]$ as the input image size for SharLViT-RGB and SharLViT-RGB+Depth+IR transformers respectively. The experiment is implemented with Keras on single NVIDIA P100 GPUs with 16GB RAM using google Colab Pro. Various data augmentation techniques are employed, including rotation and random flips, alongside random shuffling. The framework is trained for 30 epochs with a batch size of 32 using the ADAM optimizer and a learning rate of 0.0001 to minimize SigmoidFocalCrossEntropy loss. The best model is selected corresponding to minimum validation loss.

4.3 Comparative analysis with other state-of-arts

To validate the performance of the proposed framework, we compared the results with some of the most representative state-of-the-arts. Tables 1-3 depict the performance comparison on WMCA and CASIA-SURF datasets for both intra-dataset and cross-dataset testing. The bold values in the tables show the best-reported results.

Table 1: Performance on the WMCA dataset during Intra-dataset Testing (%).

Methods	APCER	BPCER	ACER
DeepPixBis **[54]**	8.2	3.7	6.0
MA-Net **[22]**	11.1	2.6	6.8
ResNet **[55]**	3.5	1.6	2.6
LBP-SVM **[3]**	8.5	0.6	4.6
MLP-Mixer **[56]**	1.7	2.3	2.0
Conv-MLP **[34]**	0.8	1.0	0.9
MF^{2}ShrT without T-Encoder branch (ours)	2.3	2.1	2.2
MF^{2}ShrT with T-Encoder branch (ours)	**0.11**	**0.13**	**0.12**

Just Accepted

Table 2: Performance on the CASIA-SURF dataset during Intra-dataset Testing (%).

Methods	APCER	BPCER	ACER
Halfway Fusion **[28]**	5.6	3.8	4.7
SE Fusion **[28]**	3.8	1.0	2.4
Zhang et al. **[25]**	2.8	0.3	1.5
MA-Net **[22]**	2.4	1.7	2.0
Conv-MLP **[34]**	1.5	1.8	1.6
ViT+AMA+M^{2}A^{2}E **[57]**	**0.81**	**0.42**	**0.62**
MF^{2}ShrT without T-Encoder branch (ours)	4.1	2.9	3.5
MF^{2}ShrT with T-Encoder branch (ours)	**1.6**	**1.2**	**1.4**

***Intra-testing Results*.** In Table 1, the performance of the proposed framework is compared for WMCA dataset with other similar approaches [3] [22] [54]. Our proposed framework, MF^{2}ShrT stands out for its ability to significantly reduce error rates. With an ACER of 0.12%, our framework achieved the best result among all the approaches. It is observed that all the methods compared in Table 1 utilize only CNN-based backbones for feature extraction, whereas our proposed framework, MF^{2}ShrT, is one of the few methods to use a ViT for FAS task, showcasing its exceptional ability. In addition, we also evaluate the performance of MF^{2}ShrT on the CASIA-SURF dataset, as shown in Table 2. We compare it with five famous multi-modal methods [22] [25] [28] [34] [57]. From Table 2, it is observed that MF^{2}ShrT delivers competitive performance, with almost lower ACER of 1.4%, indicating its efficiency in handling previously unseen presentation attack scenarios. As observed from Table 2, our framework exhibits a remarkable performance surpassing various methods [25] [28] [22] [34] except for the ViT+AMA+M^{2}A^{2}E [57] approach. Notably, ViT+AMA+M^{2}A^{2}E [57] adopted a modality asymmetric masked autoencoders based self-supervised learning mechanism with ViT. The experimental results affirm that our performance aligns with other state-of-the-art benchmarks. This observation provides further evidence that Vision Transformer-based frameworks are suitable for FAS tasks and have the potential to provide more robust and accurate frameworks.

Cross-Dataset Testing. To evaluate the generalization ability of the proposed framework MF^{2}ShrT, we also conducted cross-dataset testing experiments between frameworks trained on WMCA and CASIA-SURF datasets. In our literature survey, we observed that relatively few works on multi-modal FAS have reported cross-dataset testing results as compared to intra-dataset performance results. Therefore, we followed the convention in [57] and evaluated the cross-dataset testing results in terms of HTER to check the robustness of our proposed framework. In Table 3, we have tabulated all methods trained on one dataset and tested on another. In cross-dataset testing, where CASIA-SURF is employed for training and WMCA for testing, an HTER of 19.43% is obtained. The comparison of the results shows that our approach MF^{2}ShrT have the second highest performance. When the framework is trained on WMCA and tested on the CASIA-SURF dataset, it attains an impressive HTER of 13.84%, securing a commendable fourth position. While further improvements in HTER may be challenging due to the inherent variations in sample quality between the WMCA and CASIA-SURF dataset. Therefore, this result is noteworthy because cross-testing is known to be more challenging than intra-testing. Despite the steep increase in difficulty from intra dataset to inter-dataset protocol, our cross-testing performance is on par with the highest intra-testing performance, demonstrating the generalization ability of our proposed framework. The results are also presented in ROC curves, Figure 5, to show the performance more comprehensively for both intra-dataset and cross-dataset testing.

Just Accepted

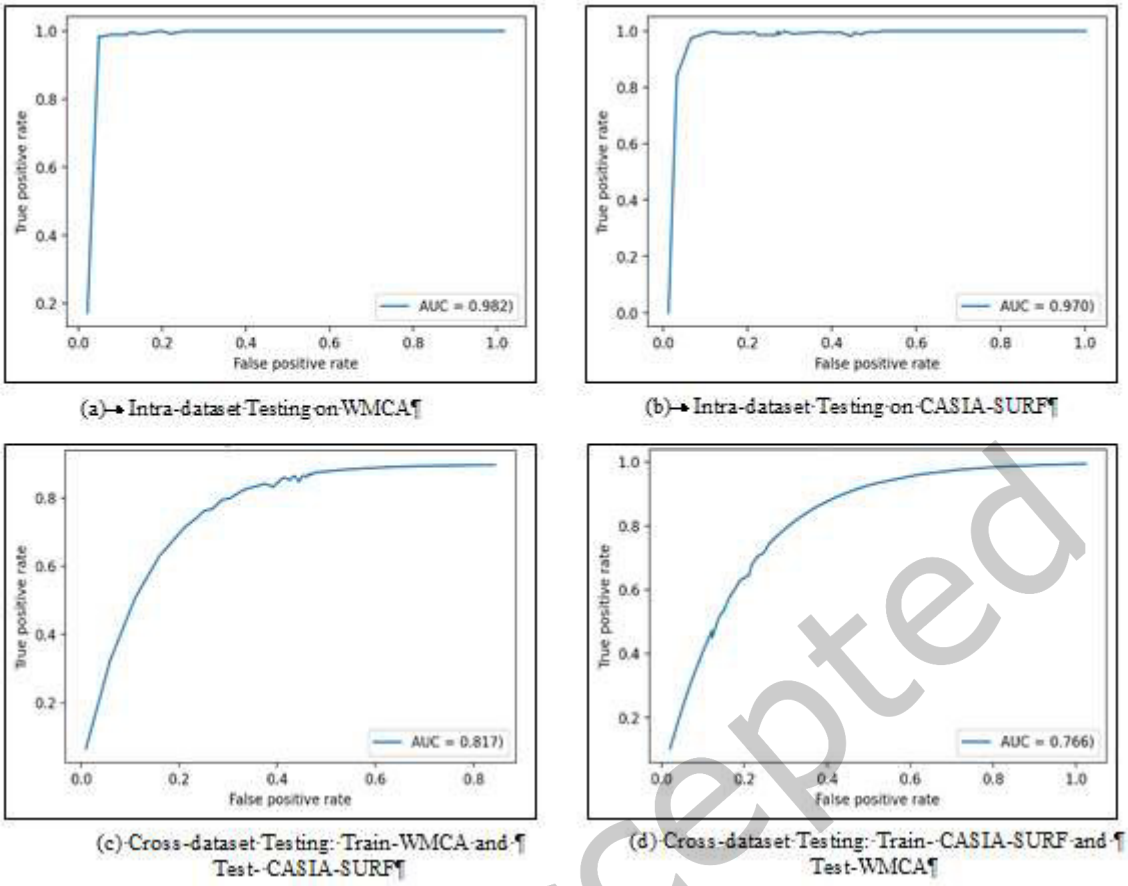


Figure 5: ROC curves for both Intra-dataset and Cross-dataset Testing on WMCA and CASIA-SURF

Table 3: Performance Evaluation for Cross-dataset Testing in terms of HTER (%)

Methods	Train: CASIA-SURF Test: WMCA	Train: WMCA Test: CASIA-SURF
Aux. (Depth) **[10]**	24.54	12.35
MM-CDCN **[37]**	21.83	21.25
MA-ViT **[22]**	20.63	10.41
ViT **[23]**	23.21	19.19
ViT+AMA+M^{2}A^{2}E **[57]**	**18.83**	**8.60**
MF^{2}ShrT without T-Encoder branch (ours)	20.21	14.13
MF^{2}ShrT with T-Encoder branch (ours)	**19.43**	**13.84**

Statistical Significance Test. To exhibit the significance of the classification results, we conducted a statistical test employing the Friedman statistic for Intra-dataset testing and Mann-Whitney U Test for Cross-dataset testing.

Defining NULL (H_0) and Alternate Hypothesis (H_0)

H_0: Reject the null hypothesis: There is a significant gap between the proposed approach and the previous methods.

Just Accepted

Table 4: Results of the Statistical Significance Test *(*significance condition:* if p>0.05: H_0 is true else H_a is true)

Test	Test Parameter	Intra-dataset Testing on WMCA	Intra-dataset Testing on CASIA-SURF	Cross-dataset Testing
Friedman Statistic	Chi-square statistics	16.88	16.77	-
	p-value*	**0.01812**	**0.0188**	-
Mann-Whitney U Test	U-statistic	-	-	44.0
	p-value*	-	-	**0.01**

Table 5: Ablation study of the effect of overlapping rate on the performance of WMCA dataset (%)

Overlapping Rate	ACER	Accuracy
0	7.45	92.86
1/6	10.85	89.21
1/4	3.55	96.60
1/3	1.5	97.97
1/2	**1.3**	**98.48**
3/4	**1**	**98.97**

H_a: Fail to reject the null hypothesis: No significant gap between the proposed approach and the previous methods.

As indicated in Table 4, the Chi-square statistic is notably high with p-values consistently below 0.05 across both cases i.e., Intra-dataset Testing on WMCA and Intra-dataset Testing on CASIA-SURF. Similarly, for Inter-dataset Testing, we obtain high U-Statistic and low p-value. This shows that our result is statistically significant and we can trust that the difference is not due to chance alone.

4.4 Ablation Study

In this section, we demonstrate the contribution of each associated strategy in the proposed approach by performing a series of ablation experiments on the WMCA dataset. The evaluation metrics are ACER (%).

Analysis of Overlapping Rate: Table 5 demonstrates the influence of the overlapping rate on the classification performance under the WMCA dataset. Intuitively, classification performance should improve with a higher overlapping rate. The table shows the poor ACER obtained for no overlap between patches. The value of ACER increases for $1/6$ overlap rate. However, the ACER starts decreasing as the overlapping rate among patches increases further. The lowest ACER (1.13%) is achieved for the model when the overlapping rate across patches is $3/4$. It is noteworthy that the increase in number of patches generated with increase in overlap is significant, also an increase in overlap does not necessarily guarantee a steep increase in accuracy. Hence it is desirable to select an optimum overlap rate. Since, the performance of $1/2$ and $3/4$ is almost similar in terms of ACER and accuracy. Therefore, we use $1/2$ as the final overlapping rate in our proposed framework.

Just Accepted

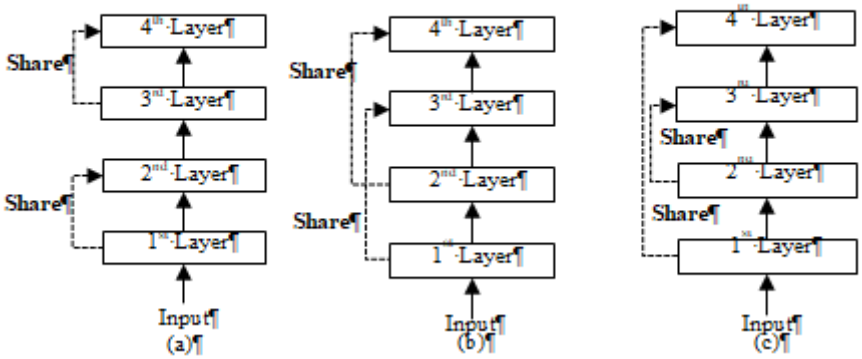


Figure 6: Types Parameter Sharing Strategies (a) Sequence Sharing (b) Cyclic Sharing (c) Reverse Cyclic Sharing

Table 6: Ablation study of baseline model and the effect of parameter sharing in ViT model of WMCA dataset(%).

Model	APCER	BPCER	ACER
Vit-base	5.11	4.35	4.77
Sequence Sharing	**0.1**	**2.5**	**1.3**
Cycle Sharing	1.92	1.64	1.78
Reverse Cycle Sharing	3.19	2.51	2.88

Table 7: Ablation study of effect of different Adaptively Weighted Fusion techniques on the performance of WMCA dataset

Fusion Technique	Initial Weights			Final Weights			ACER (%)
	w_{RGB}	w_{hyb}	w_{RID}	w_{RGB}	w_{hyb}	w_{RID}	
With Direct Concatenation	-	-	-	-	-	-	3.57
Adaptively weighted fusion & Classification Block- BCE	0.66	0.22	0.12	0.14	0.55	0.31	1.7
	0.12	0.66	0.22	0.16	0.51	0.33	2.1
	0.22	0.12	0.66	**0.15**	**0.49**	**0.36**	**1.3**
	0.33	0.33	0.33	0.11	0.58	0.31	1.9
Adaptively weighted fusion & Classification Block - SigmoidFocalCrossEntropy	0.66	0.22	0.12	0.14	0.5	0.36	0.6
	0.12	0.66	0.22	0.13	0.52	0.35	0.9
	0.22	0.12	0.66	0.15	0.55	0.3	0.15
	0.33	0.33	0.33	**0.18**	**0.55**	**0.37**	**0.12**

Effectiveness of parameter sharing in ViT model: We tested three different parameter-sharing techniques for internal layers in ViT, namely sequence, cycle, and Reverse cycle shown in Figure 6. Under sequence sharing scheme, sequential $[N/M]$ layers are assigned the same parameters. The Cyclical sharing method involves stacking M layers with independent parameters and then repeating the process by stacking the same M layers in the exact order as the first M layers until a total of N layers is achieved. With the Reverse Cycle parameter-sharing method, we repeat stacking M layers in the same order as Cycle until $M * ([N/M] - 1)$ layers have been stacked. For the remaining layers, we stack M layers in reverse order. By sharing parameters, we can significantly optimize parameter size and computational time, reducing it by a factor of $[N/M]$. After conducting experiments, we found that sequence parameter sharing led to lower ACER than both the pure transformer and the other two parameter-sharing techniques, as illustrated in Table 6. In Figure 7(a) ROC curves are reported exhibiting the effect of different parameter sharing strategies, discussed in Figure 6. It shows the effectiveness of incorporating a sequence parameter-sharing approach in ViT for face PAD, and suggests that parameter-sharing techniques can be useful in situations where multiple parameters require training with a significant amount of data.

Just Accepted

Analysis of different types of Fusion techniques: Table 7 presents the results of a comparative analysis conducted to assess the effectiveness of the weighted fusion classification block. The ROC Curve visualization for different fusion techniques is shown in Figure 7(b). The findings indicate that the addition of this block significantly enhances the framework's performance. We observed that the importance of the outputs from the three branches varies, and therefore, we included an adaptive fusion block during our ablation testing to determine a set of optimized weights for fusion. As shown in Table 7, the final adaptively learnt weights

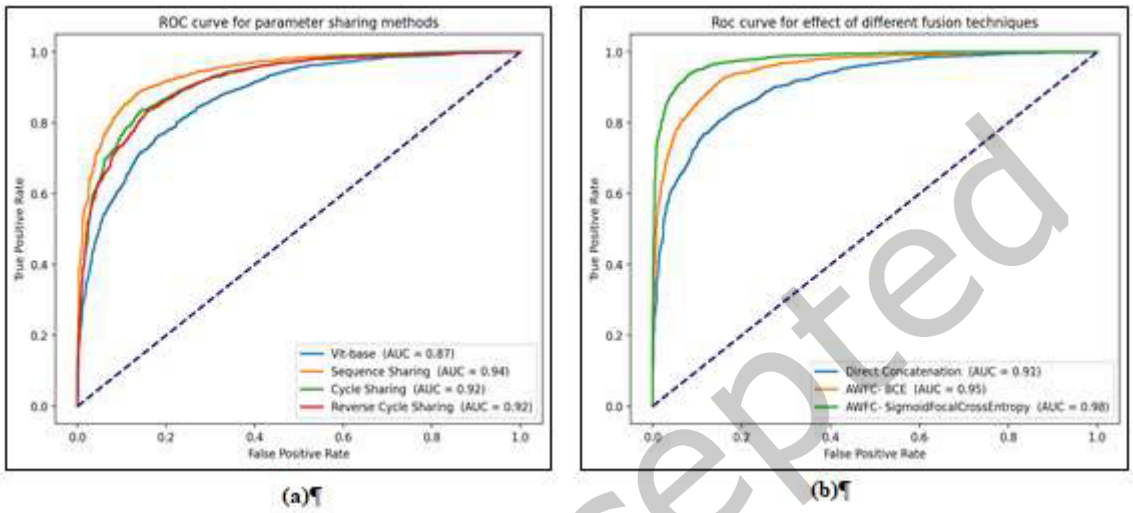


Figure 7: ROC curve for (a) parameter sharing methods, (b) Effect of Adaptively Weighted Fusion & Classification (AWFC) block

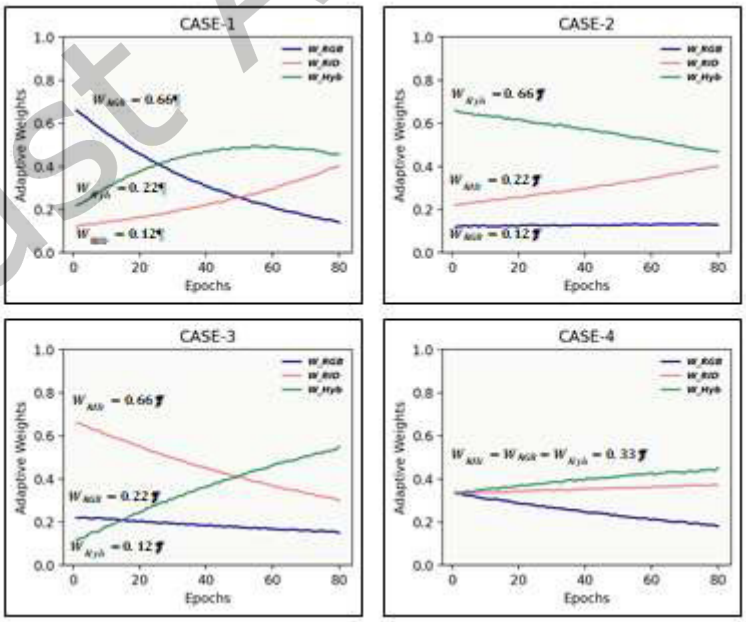


Figure 8: Curve Analysis of the Adaptively assigned weighted over epochs; initial values of W_{RID} , W_{RGB}, W_{Hyb} are indicated in each case, that converge adaptively to different values representing different contribution of RID, RGB and hybrid features respectively.

Just Accepted

$\{W_{RGB}, W_{hyb}, W_{RID}\}$ are $\{0.18, 0.51 \text{ and } 0.31\}$ to adaptively fuse $\mathcal{F}_{RGB}$, $\mathcal{F}_{hyb}$ and $\mathcal{F}_{RID}$ branch features respectively. It ensures that the branch with more discriminative features get prioritize as compared to the branch with relatively redundant feature. In Figure 8, a comprehensive view of the analysis of adaptively assigned weights over epochs is presented. This analysis evaluates the performance of the AWFC block, utilizing SigmoidFocalCrossEntropy as the activation function, by examining their behavior across all four cases with respect to the number of training epochs. It shows that despite of any random distribution of weights given to RGB, RID and hybrid features, the framework performs best for adaptively assigning more weightage to hybrid branch, followed by RID and lowest RGB branch features.

Analysis of Losses: We examine two types of losses that are appropriate for binary tasks: BCE and Sigmoidal Focal Cross Entropy. The Focal loss was first introduced in RetinaNet [60], and is particularly effective in situations where there is class imbalance. Cross entropy loss is defined as:

$$CE(p, y) = \begin{cases} -log(p) & y = 1 \\ -lg(1-p) & otherwise \end{cases} \quad (19)$$

where $y \in [0,1]$ represents the ground truth and $p \in [0,1]$ is be the model's predicted probability. By using a weighting parameter $\alpha \in [0,1]$ for class 1 and $1 - \alpha$ for class 0, this loss function can address the issue of class imbalance in input classes. The resulting class weighted CE can be expressed as:

$$CE(p, y) = \begin{cases} -\alpha * log(p) & y = 1 \\ -(1-\alpha) * log(1-p) & otherwise \end{cases} \quad (20)$$

The parameter α is not tunable in runtime for dynamic set of data present across different datasets. As reported in [60], this can be improved by adding a modulating factor such that the Focal loss is defined as follows:

$$FL(p, y) = \begin{cases} -(1-p)^{\theta} * log(p) & y = 1 \\ -(p)^{\theta} * log(1-p) & otherwise \end{cases} \quad (21)$$

The parameter θ is called as smoothing parameter and can be adopted as learnable parameter for online dynamic weighed loss adjustments. We have observed that employing sigmoidal focal cross entropy loss in this manner leads to an improvement in the model's performance, as reported in the accompanying Table 8.

Just Accepted

Table 8: Comparison the performance of the WMCA dataset using different losses (%)

Loss	APCER	BPCER	ACER
BCE	0.1	2.5	1.3
SigmoidFocalCrossEntropy	**0.11**	**0.13**	**0.12**

Table 9: Comparison of computation efficiency for various models on the WMCA dataset

Method	Backbone model	Modality	No. of branches	Parameters	ACER (%)
ViTFAS **[19]**	Transformer	RGB	1	85.8 M	7.56 ± 5.36
CDCN **[58]**	CNN	RGB	1	6.9 M	7.99 ± 5.51
MCCNN **[52]**	CNN	RGB, IR, Depth	4	37.7 M	22.74 ± 15.33
ResNet **[55]**	CNN	RGB	1	42.5 M	19.56 ± 16.09
DenseNet **[59]**	CNN	RGB	1	26.4 M	21.02 ± 15.67
MLP-Mixer **[56]**	MLP	RGB	1	64.0 M	10.11 ± 12.05
FaceBagNet **[29]**	CNN	RGB, IR, Depth	3	14.5 M	9.20 ± 9.99
Conv-MLP **[34]**	CNN+MLP	RGB, IR, Depth	1	17.4 M	7.05 ± 11.16
MF^{2}ShrT (Ours)	Transformer	RGB, IR, Depth	**2**	**37.9 M**	**6.81±14.67**

Computational complexity: Based on the analysis conducted in [34], we have compared the computational efficiency of our proposed framework with other state-of-the-arts. Table 9 comprehensively outlines the backbone model, number of modalities utilized, branches employed, trainable parameters, and ACER for each method. Notably, the base ViT model [19] and MLP-Mixer [56] exhibit the highest computational requirements in terms of parameters and processing when using a single modality. Despite CDCN [58] employing single branch with RGB modality input, it incurs significant computational complexity due to computation of the gradient of the feature map. Additionally, the convolutional filter in [52] [55] [59] traverses the entire image, resulting in a considerable computational burden on the system. In contrast, FaceBagNet [29] benefits from patch-based shared convolution, leading to lower model parameters and reduced computational load, albeit with a comparatively higher ACER with three branches. Conv-MLP [34] demonstrates a moderate computing cost. Notably, all methods except ViTFAS are CNN-based methods. Our proposed framework has significantly fewer parameters than ViTFAS. When compared to CNN-based methods, our proposed framework achieves the lowest ACER with a reasonable set of parameters and moderate computational cost. The lightweight and efficient nature of the proposed framework makes it adaptable and scalable for applications.

Just Accepted

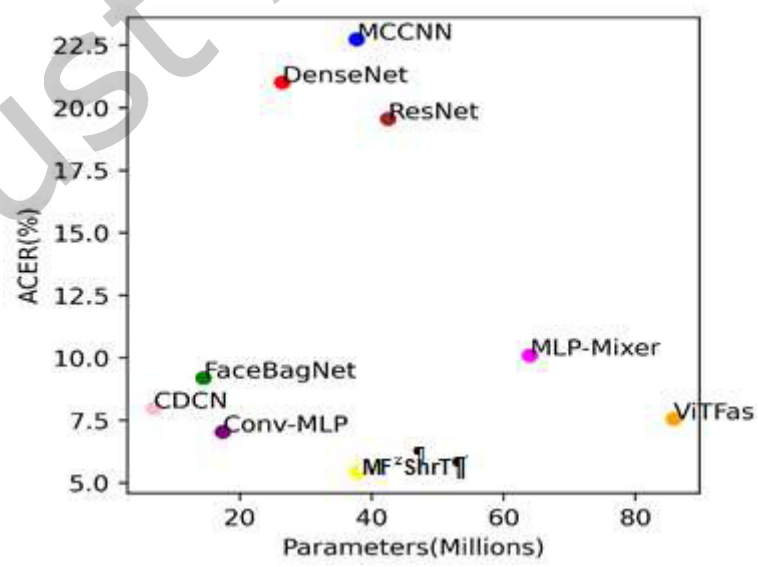


Figure 9: Trade-off between ACER and computational efficiency for various models under LOO protocol of WMCA dataset

Figure 9 depicts ACER versus computational efficiency for the methods discussed above, recorded in accordance with the Leave-One-Out (LOO) protocol of the WMCA dataset. The

yellow color in the Figure 9 represents our proposed framework, which performs competitively in terms of classification accuracy and processing efficiency. Overall, our proposed framework outperforms the standard approaches in terms of computational efficiency while maintaining a balance between complexity and performance. The model achieves and predicts throughput of ~375 images per second (one per modality) for an effective throughput of 125 samples per second. The throughput is about 4-5 times the general framerate of consumer-grade cameras used in FA applications. Which gives a sufficient overhead for possible deployment in real-time implementations.

5 CONCLUSION

This paper proposed a simple and effective framework called MF^{2}ShrT based on a pre-trained ViT network for FAS. MF^{2}ShrT incorporates overlap patches and ViT encoder blocks to build relations upon comprehensive local patches and extract several types of features from multi-modal input, including local, global, multi-modal, and relation features. By capturing interactions between different modalities, the ViT encoder block was able to identify inconsistencies among the artifacts localized in the masked patches, which improved the accuracy of our face anti-spoofing model. To further optimize the performance of our framework, we also employed parameter-sharing techniques that significantly reduced the complexity and number of parameters required for the implementation. We also extract the intermediate features across different modalities using a T-encoder-based hybrid feature block. Subsequently, the framework leverages an adaptive weighted fusion mechanism to ensure a robust integration of diverse modality inputs, thereby enhancing the overall optimization of the framework's performance. Experimental results demonstrated that our approach achieved optimized performance with fewer parameters, making it a more efficient and effective solution for face anti-spoofing.

Under Accepted

REFERENCES

[1] R. Ramachandra and C. Busch, "Presentation Attack Detection Methods for Face Recognition Systems: A Comprehensive Survey," *ACM Computing Surveys (CSUR),* vol. 50, no. 1, pp. 1-37, 2017.

[2] Z. Zhang, J. Yan, S. Liu, Z. Lei, D. Yi and S. Z. Li, "A face antispoofing database with diverse attacks," in *5th IAPR International Conference on Biometrics (ICB)*, New Delhi, India , 2012 .

[3] I. Chingovska, A. Anjos and S. Marcel, "On the effectiveness of local binary patterns in face anti-spoofing," in *BIOSIG - Proceedings of the International Conference of Biometrics Special Interest Group (BIOSIG)*, Darmstadt, Germany, 2012.

[4] Y. Li , W. Liu, . Y. Jin and Y. Cao, "SPGAN: Face Forgery Using Spoofing Generative Adversarial Networks.," *ACM transactions on Multimedia Computing, Communications, and Applications,* vol. 17, pp. 1-20, 2021.

[5] A. Liu, C. Zhao, Z. Yu, J. Wan, A. Su, X. Liu, Z. Tan, S. Escalera, J. Xing, Y. Liang, G. Guo, Z. Lei, S. Z. Li, and D. Zhang, "Contrastive Context-Aware Learning for 3D High-Fidelity Mask Face Presentation Attack Detection," *IEEE Transactions on Information Forensics and Security,* vol. 17, pp. 2497 - 2507, 2021.

[6] P. N. Belhumeur, J. P. Hespanha and D. J. Kriegman, "Eigenfaces vs. Fisherfaces: recognition using class specific linear projection," *IEEE Transactions on Pattern Analysis and Machine Intelligence ,* vol. 19, no. 7, July, pp. 711 - 720, 1997.

[7] B. Zhang, S. Shan, X. Chen and W. Gao, "Histogram of Gabor Phase Patterns (HGPP): A Novel Object Representation Approach for Face Recognition," *IEEE Transactions on Image Processing,* vol. 16, no. 1, January, pp. 57 - 68, 2007.

[8] H. Chen, G. Hu, Z. Lei, Y. Chen, N. M. Robertson and S. Z. Li, "Attention-based two-stream convolutional networks for Face Spoofing Detection," *IEEE Transactions on Information Forensics and Security,* vol. 15, pp. 578 - 593, 2019.

[9] W. R. Almeida, F. A. Andaló, R. Padilha, G. Bertocco, W. Dias, R. d. S. Torres, J. Wainer and A. Rocha, "Detecting face presentation attacks in mobile devices with a patch-based CNN and a sensor-aware loss function," *PLos one,* vol. 15, no. 9, 2020.

[10] Y. Liu, A. Jourabloo and X. Liu, "Learning Deep Models for Face Anti-Spoofing: Binary or Auxiliary Supervision," in *IEEE/CVF Conference on Computer Vision and Pattern Recognition*, Salt Lake City, UT, USA, 2018.

[11] Z. Wang, Y. Xu, L. Wu, H. Han, Y. Ma and Z. Li, "Improving Face Anti-spoofing via Advanced Multi-perspective Feature Learning," *ACM Transactions on Multimedia Computing, Communications, and Applications,* vol. 19, no. 6, p. 1–18, 2023.

[12] L. Feng, L.-M. Po, Y. Li, X. Xu, F. Yuan, T. C.-H. Cheung and K.-W. Cheung, "Integration of image quality and motion cues for face anti-spoofing: A neural network approach," *Journal of Visual Communication and Image Representation,* vol. 38, pp. 451-460, 2016.

[13] A. Antil and C. Dhiman, "A two stream face anti-spoofing framework using multi-level deep features and ELBP features," *Multimedia Systems,* 2023.

[14] Z. Yu, X. Li, J. Shi, Z. Xia and G. Zhao, "Revisiting Pixel-Wise Supervision for Face Anti-Spoofing," *IEEE Transactions on Biometrics, Behavior and Identity Science,* 2021.

[15] G. Wang, C. Lan, H. Han, S. Shan, and X. Chen, "Multi-Modal Face Presentation Attack Detection via Spatial and Channel Attentions," in *CVPRW*, 2019.

[16] Q. Yang, X. Zhu, J.-K. Fwu, Y. Ye, G. You and Y. Zhu, "PipeNet: Selective Modal Pipeline of Fusion Network for Multi-Modal Face Anti-Spoofing," *arXiv:2004.11744 [cs.CV],* 2020.

[17] W. Liu, X. Wei, T. Lei, X. Wang, H. Meng and A. K. Nandi, "Data Fusion based Two-stage Cascade Framework for Multi-Modality Face Anti-Spoofing," *IEEE Transactions on Cognitive and Developmental Systems,* pp. 1 - 1, 2021.

[18] K. Han, Y. Wang, H. Chen, X. Chen, J. Guo, Z. Liu, Y. Tang, A. Xiao, C. Xu, Y. Xu, Z. Yang, Y. Zhang and D. Tao, "A Survey on Vision Transformer," *IEEE Transactions on Pattern analysis and Machine Intelligence,* vol. 45, pp. 87-110, 2023.

[19] A. George and S. Marcel, "On the Effectiveness of Vision Transformers for Zero-shot Face Anti-Spoofing," *arXiv:2011.08019 [cs.CV].*

[20] Z. Ming, Z. Yu, M. A.-. Ghadi, M. Visani, M. MuzzamilLuqman and J.-. C. Burie, "ViTransPAD: Video Transformer using convolution and self-attention for Face Presentation Attack Detection," *arXiv:2203.01562 [cs.CV].*

[21] Z. Wang, Q. Wang, W. Deng and G. Guo, "Face Anti-Spoofing Using Transformers With Relation-Aware Mechanism," *IEEE Transactions on Biometrics, Behavior, and Identity Science ,* vol. 4, no. 3, pp. 439 - 450, 2022.

[22] A. Liu, Z. Tan, J. Wan, Y. Liang, Z. Lei, G. Guo and S. Z. Li, "Face Anti-Spoofing via Adversarial Cross-Modality Translation," *IEEE Transactions on Information Forensics and Security ,* vol. 16, pp. 2759 - 2772, 2021.

[23] A. Dosovitskiy, L. Beyer, A. Kolesnikov, D. Weissenborn, X. Zhai, T. Unterthiner, M. Dehghani, M. Minderer, G. Heigold, S. Gelly, J. Uszkoreit and N. Houlsby, "An Image Is Worth 16x16 Words:Transformers For Image Recognition At Scale," in *ICLR*, Vienna, Austria, 2021.

[24] Y. Atoum, Y. Liu, A. Jourabloo and X. Liu, "Face anti-spoofing using patch and depth-based CNNs," in *IEEE International Joint Conference on Biometrics (IJCB)*, Denver, CO, USA, 2017.

[25] S. Zhang, A. Liu, J. Wan, Y. Liang, G. Guo, S. Escalera, H. J. Escalante and S. Z. Li, "CASIA-SURF: A Large-Scale Multi-Modal Benchmark for Face Anti-Spoofing," *IEEE Transactions on Biometrics, Behavior, and Identity Science,* vol. 2, no. 2, April 2020, pp. 182 - 193, 2020.

[26] A. Liu, Z. Tan, J. Wan, S. Escalera, G. Guo and S. Z. Li, "CASIA-SURF CeFA: A Benchmark for Multi-Modal Cross-Ethnicity Face Anti-Spoofing," in *IEEE/CVF Winter Conference on Applications of Computer Vision (WACV)*, 2021.

[27] A. Parkin and O. Grinchuk, "Recognizing Multi-Modal Face Spoofing With Face Recognition Networks," in *IEEE/CVF Conference on Computer Vision and Pattern Recognition Workshops (CVPRW)*, Long Beach, CA, USA, 2019.

[28] S. Zhang, X. Wang, A. Liu, C. Zhao, J. Wan, S. Escalera, H. Shi, Z. Wang and S. Z. Li, "A Dataset and Benchmark for Large-scale Multi-modal Face Anti-spoofing," in *IEEE Conference on Computer Vision and Pattern Recognition (CVPR)*, Long Beach, 2019.

[29] T. Shen, Y. Huang and Z. Tong, "FaceBagNet: Bag-of-local-features Model for Multi-modal Face Anti-spoofing," in *IEEE/CVF Conference on Computer Vision and Pattern Recognition Workshops (CVPRW)*, Long Beach, CA, USA, 2019.

[30] A. George and S. Marcel, "Learning One Class Representations for Face Presentation Attack Detection Using Multi-Channel Convolutional Neural Networks," *IEEE Transactions on Information Forensics and Security,* vol. 16, pp. 361 - 375, 2020.

[31] O. Nikisins, A. George and S. Marcel, "Domain Adaptation in Multi-Channel Autoencoder based Features for Robust Face Anti-Spoofing," in *International Conference on Biometrics (ICB)*, Crete, Greece, 2019.

[32] A. Liu and Y. Liang, "MA-ViT: Modality-Agnostic Vision Transformers for Face Anti-Spoofing," in *Proceedings of the Thirty-First International Joint Conference on Artificial Intelligence (IJCAI-22)*, Vienna, Austria, 2022.

[33] Z. Li, H. Li, X. Luo, Y. Hu, K.-Y. Lam and A. C. Kot, "Asymmetric Modality Translation For Face Presentation Attack Detection," *arXiv:2110.09108 [cs.CV].*

[34] W. Wang, F. Wen, H. Zheng, R. Ying and P. Liu, "Conv-MLP: A Convolution and MLP Mixed Model for Multimodal Face Anti-Spoofing," *IEEE Transactions on Information Forensics and Security,* vol. 17, pp. 2284 - 2297, 2022.

[35] Q. Liu and L. Zhang, "Face anti-spoofing by using Feature Fusion," in Proceedings of the 2021 International Conference on Pattern Recognition and Intelligent Systems, Bangkok, 2021.

[36] P. Zhang, F. Zou, Z. Wu, N. Dai, S. Mark, M. Fu, J. Zhao and K. Li, "FeatherNets: Convolutional Neural Networks as Light as Feather for Face Anti-spoofing," in *CVPRW*, 2019.

[37] Z. Yu, Y. Qin, X. Li, Z. Wang, C. Zhao, Z. Lei and G. Zhao, "Multi-Modal Face Anti-Spoofing Based on Central Difference Networks," *arXiv:2004.08388 [cs.CV],* 2020.

[38] A. George and S. Marcel, "Cross Modal Focal Loss for RGBD Face Anti-Spoofing," *arXiv:2103.00948 [cs.CV],* 2021.

[39] A. Vaswani, N. Shazeer, N. Parmar, J. Uszkoreit, L. Jones, A. N. Gomez, L. Kaiser and I. Polosukhin, "Attention Is All You Need," *arXiv:1706.03762 [cs.CL].*

[40] Z. Liu, Y. Lin, Y. Cao, H. Hu, Y. Wei, Z. Zhang, S. Lin and B. Guo, "Swin Transformer: Hierarchical Vision Transformer using Shifted Windows," in *IEEE/CVF International Conference on Computer Vision (ICCV)*, 2021.

[41] N. Carion, F. Massa, G. Synnaeve, N. Usunier, A. Kirillov and S. Zagoruyko, "End-to-end object detection with transformers," *arXiv:2005.12872 [cs.CV].*

[42] S. Zheng, J. Lu, H. Zhao, X. Zhu, Z. Luo, Y. Wang, Y. Fu, J. Feng, T. Xiang, P. H. Torr and L. Zhang, "Rethinking Semantic Segmentation from a Sequence-to-Sequence Perspective with Transformers," *arXiv:2012.15840 [cs.CV].*

[43] J. Yu, J. Li, Z. Yu and Q. Huang, "Multimodal Transformer With Multi-View Visual Representation for Image Captioning," *IEEE Transactions on Circuits and Systems for Video Technology,* vol. 30, no. 12, 2020.

[44] J. Yu, X. Yang, F. Gao and D. Tao, "Deep Multimodal Distance Metric Learning Using Click Constraints for Image Ranking," *IEEE Transactions on Cybernetics,* vol. 47, no. 12, pp. 4014 - 4024, December 2017.

[45] A. Liu, Z. Tan, Z. Yu, C. Zhao, J. Wan, Y. Liang, D. Zhang, S. Z. Li and G. Guo, "FM-ViT: Flexible Modal Vision Transformers for Face Anti-Spoofing," *arXiv:2305.03277v1 [cs.CV] ,* 2023.

[46] Z. Wang, Q. Wang, W. Deng and G. Guo, "Learning Multi-Granularity Temporal Characteristics for Face Anti-Spoofing," *IEEE Transactions on Information Forensics and Security,* vol. 17, pp. 1254 - 1269, 2022.

Just Accepted

[47] Z. Yu, X. Li, P. Wang and G. Zhao, "Transrppg: Remote photoplethysmography transformer for 3D Mask Face Presentation Attack Detection," *arXiv:2104.07419 [cs.CV].*

[48] Y. Zhong and W. Deng, "Face Transformer for Recognition," *arXiv:2103.14803 [cs.CV].*

[49] T. B. Brown, B. Mann, N. Ryder, M. Subbiah, J. Kaplan, P. Dhariwal, A. Neelakanta, P. Shyam, G. Sastry, A. Askell, S. Agarwal, A. H.-. Voss, G. Krueger, T. Henighan, R. Child, A. Ramesh, D. M. Ziegler, J. Wu, C. Winter, C. Hesse, M. Chen, E. Sigler, M. Litwin, S. Gray, B. Chess, J. Clark, C. Berner, S. McCandlish, A. Radford, I. Sutskever and D. Amodei, "Language Models are Few-Shot Learners," *arXiv:2005.14165 [cs.CL].*

[50] S. Takase and S. Kiyono, "Lessons on Parameter Sharing across Layers in Transformers," *arXiv:2104.06022 [cs.CL].*

[51] V. Nair and G. E. Hinton, ""Rectified linear units improve restricted boltzmann machines," in *ICML*, Haifa, Israel, 2010.

[52] A. George, Z. Mostaani, D. Geissenbuhler, O. Nikisins, A. Anjos and S. Marcel, "Biometric Face Presentation Attack Detection With Multi-Channel Convolutional Neural Network," *IEEE Transactions on Information Forensics and Security,* vol. 15, pp. 42 - 55, 2019.

[53] A. Anjos and S. Marcel, "Counter-measures to photo attacks in face recognition: A public database and a baseline," in *International Joint Conference on Biometrics (IJCB)*, Washington, DC, USA, 2011.

[54] A. George and S. Marcel, "Deep Pixel-wise Binary Supervision for Face Presentation Attack Detection," in *International Conference on Biometrics, ICB 2019*, Crete, Greece, 2019.

[55] K. He, X. Zhang, S. Ren and J. Sun, "Deep Residual Learning for Image Recognition," *arXiv:1512.03385 [cs.CV],* 2015.

[56] I. Tolstikhin, N. Houlsby, A. Kolesniko, L. Beyer, X. Zhai, T. Unterthiner, J. Yung, A. Steiner, D. Keysers, J. Uszkoreit, M. Lucic and A. Dosovitskiy, "MLP-Mixer: An all-MLP architecture for vision," *arXiv:2105.01601 [cs.CV].*

[57] Z. Yu, R. Cai, Y. Cui, X. Liu, Y. Hu and A. Kot, "Rethinking Vision Transformer and Masked Autoencoder in Multimodal Face Anti-Spoofing," *arXiv:2302.05744 [cs.CV].*

[58] T.-Y. Lin , P. Goyal, R. Girshick , K. He and P. Dollar, "Focal Loss for Dense Object Detection," *arXiv:1708.02002v2 [cs.CV].*

[59] Z. Yu, C. Zhao, Z. Wang, Y. Qin, Z. Su, X. Li, F. Zhou and G. Zhao, "Searching Central Difference Convolutional Networks for Face Anti-Spoofing," in *CVPR*, Seattle, Washington, 2020.

[60] G. Huang, Z. Liu, L. v. d. Maaten and K. Q. Weinberger, "Densely Connected Convolutional Networks," *arXiv:1608.06993 [cs.CV].*

[61] A. Liu, Z. Tan, X. Li, J. Wan, S. Escalera, G. Guo and S. Z. Li, "Static and Dynamic Fusion for Multi-modal Cross-ethnicity Face Anti-spoofing," *arXiv:1912.02340v2 [cs.CV] .*

Just Accepted

frontiers | Frontiers in Ecology and Evolution

TYPE Original Research
PUBLISHED 05 February 2024
DOI 10.3389/fevo.2024.1277332

Check for updates

OPEN ACCESS

EDITED BY
Jiang-Shiou Hwang,
National Taiwan Ocean University, Taiwan

REVIEWED BY
Devesh Kumar Yadav,
Central University of South Bihar, India
Ahmet Erkan Kideys,
Middle East Technical University, Türkiye

*CORRESPONDENCE
Jaigopal Sharma
sharmajaigopal@dce.ac.in

†PRESENT ADDRESS
Malayaj Rai,
Department of Microbiology, University of Hawai'i at Mānoa, Honolulu, HI, United States

‡These authors have contributed equally to this work

RECEIVED 14 August 2023
ACCEPTED 08 January 2024
PUBLISHED 05 February 2024

CITATION
Sharma J, Rai M and Guino-o RS II (2024) Microplastics influence the functional responses of a tropical estuarine calanoid *Pseudodiaptomus annandalei*. *Front. Ecol. Evol.* 12:1277332. doi: 10.3389/fevo.2024.1277332

COPYRIGHT
© 2024 Sharma, Rai and Guino-o. This is an open-access article distributed under the terms of the Creative Commons Attribution License (CC BY). The use, distribution or reproduction in other forums is permitted, provided the original author(s) and the copyright owner(s) are credited and that the original publication in this journal is cited, in accordance with accepted academic practice. No use, distribution or reproduction is permitted which does not comply with these terms.

Microplastics influence the functional responses of a tropical estuarine calanoid *Pseudodiaptomus annandalei*

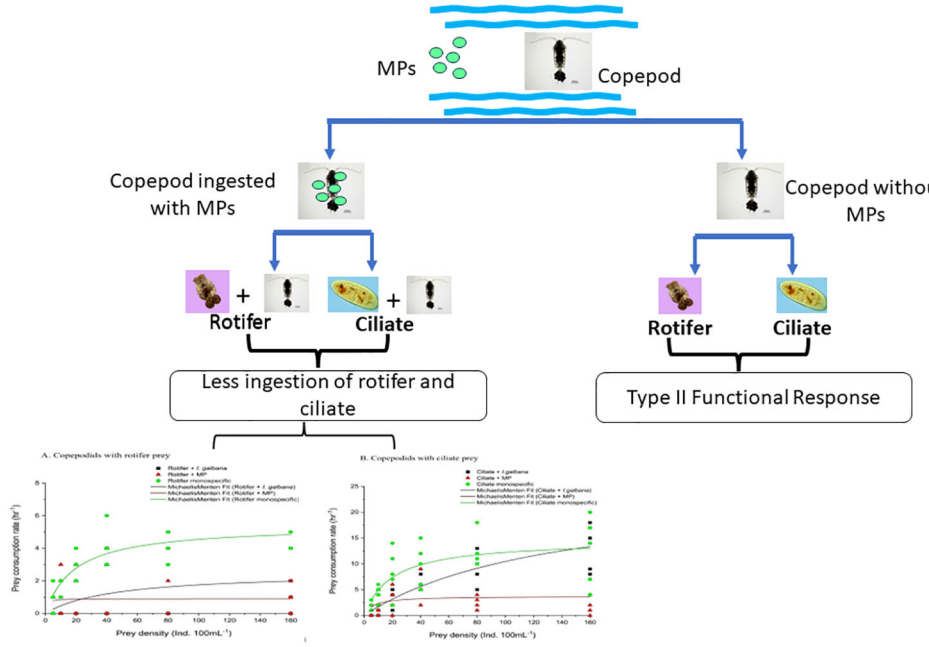
Jaigopal Sharma[1*‡], Malayaj Rai[2†‡] and Robert S. Guino-o II[2]

[1]Department of Biotechnology, Delhi Technological University, Delhi, India, [2]Biology Department, Silliman University, Dumaguete, Philippines

Being chemically inert and morphologically similar (<5 mm in size) to the natural prey of copepods, microplastics (MPs) affect them through entanglement, ingestion, and interference with their natural prey selection. The effects of external factors, such as MP, can be observed in the form of alterations in the functional and numerical responses of copepods. Functional response is explained as the relationship between the intake rate of a consumer and the amount of food available in a particular ecotope. Considered three types of functional response: (i) with increasing food density, when intake rate increases linearly until asymptote, called Type-I functional response; (ii) when the proportion of prey ingested by the consumer decreases monotonically with prey density, considered as a Type-II functional response; and (iii) when ingestion rate and food density show a sigmoid relationship, is considered as Type-III functional response. In the present study, we attempted to elucidate the effects of MP on the functional responses of brackish water, demersal, calanoid copepod, *Pseudodiaptomus annandalei*, feeding on the rotifer *Brachionus rotundiformis*, and the ciliate *Frontonia microstoma*. The ability of *P. annandalei* to survive environmental fluctuations and its nutritional value make it an ecologically important organism in estuarine ecosystems. The experiment for estimation of functional response included four setups with adult and copepodite stages of *P. annandalei*, each with six replicates at six different prey densities, in the presence and absence of MP particles. Without MPs, *P. annandalei* showed a typical Type-II functional response, where the proportion of prey consumed significantly declined with increasing prey density. In the MP-applied medium, the proportion of prey consumed did not exhibit a significant relationship with the initial prey density. The number of ciliates and rotifers ingested by copepodites and adults was significantly lower in MP-contaminated medium than in prey either monospecific or in combination with microalgae. Because of the comparable size of MP to the prey species and unspecialized feeding of *P. annandalei* in natural waters, we hypothesized reduced predation rates as a result of pseudo-satiation resulting from MP ingestion leading to malnutrition and MP storage in copepod biomass.

KEYWORDS

copepods, microplastics, functional response, foraging, ecosystem



GRAPHICAL ABSTRACT

Highlights

- Microplastic (MP) has negative effects on prey consumption rates of *Pseudodiaptomus annandalei*
- *P. annandalei* exhibited *type*-II functional response to monospecific prey and in the presence of microalgae
- MPs *per se* caused deviation from Type-II functional response
- MP contamination caused a ~20%–95% reduction in prey consumption by *P. annandalei* copepodites and adults.
- MP imposed alterations in the functional response type and prey ingestion can be used as sensitive endpoints to establish the impact of MP pollution.

Introduction

Microplastic (MP) particles have been reported from surface waters to the deepest trenches in every ocean (Auta et al., 2017; Richon et al., 2022). The rise in oceanic contamination by these small (<5 mm) and sometimes down to the micro- to nanometer scale (Barnes et al., 2009; Ter Halle et al., 2017) anthropogenic debris may lead to widespread contamination of oceanic food webs. MP particles or fibers have become emergent pllutants in estuarine and marine ecosystems. Food-web contamination by MP has been observed in fish and other higher trophic levels (Neves et al., 2015; Ugwu et al., 2021; Nair and Perumal, 2022; Avignon et al., 2023).

Recent studies have found MPs in wild-caught and commercial fish stomachs and guts (Jabeen et al., 2017; Baalkhuyur et al., 2018; Halstead et al., 2018; Kumari et al., 2023b), indicating large-scale MP contamination of the oceanic food web caused by direct MP ingestion (Roch et al., 2020), indirect MP ingestion, such as consumption of contaminated prey, or MP entanglements (Setälä et al., 2014; Nelms et al., 2018; Zhang et al., 2019). The ubiquitous nature of MP pollution in air, water, and soil has become a major concern among environmental activists, scientists, and citizens alike (Cunningham et al., 2020). In estuarine and brackish water ecosystems, copepods and rotifers play an important role in linking nano-and microplankton to higher trophic levels (Beaugrand et al., 2003; Tseng et al., 2011). Food-web contamination may begin with MP ingestion by zooplankton, which is the primary consumer and constitutes the lowest heterotrophic trophic level of aquatic ecosystems (Kumar, 2005; Amélineau et al., 2016; Richon et al., 2022). Zooplankton contamination with MPs may also have several biological implications, such as decreased growth, reproduction, and lower survival rates (Cole et al., 2019; Isinibilir et al., 2023). Their position in the food web is at the interface between the primary producers and higher trophic levels (Kumar, 2005; Kerfoot and DeMott, 2019). Thus, MP ingestion by zooplankton may act as an entry point for MPs into the marine food web (Gunaalan et al., 2023).

The ingestion of inert particles such as plastic beads by calanoid copepods has been frequently documented (Bundy and Vanderploeg, 2002; Ferrao Filho et al., 2005). With the help of mechanoreception ability, calanoid copepods can detect boundary layer disturbances and ingest non-motile inert particles in proximity to the first antennae of copepods (Bundy et al., 1998; Ayukai, 2020). These copepods redirect and ingest large inert particles entrained in their feeding currents (Vanderploeg et al., 1990). MPs are chemically inert and morphologically similar to the

natural food of copepods, and may affect them through entanglement, ingestion, and interference with other natural food organisms (Bhuyan, 2022). The smaller size and higher availability of MPs increases the probability of ingestion by marine organisms (Woods et al., 2020). The patchy heterogeneous distribution of MPs in estuaries (Akdogan et al., 2023; Rajan et al., 2023) and oceans (Pan et al., 2021) may also lead to zooplankton in some parts of the ocean being much more vulnerable to MPs than the rest. The extent of spread is also on the rise at an alarming rate, with more recent studies such as Kanhai et al. (2020) showing the presence of MPs even in the sea ice cores of the Arctic central basin. A range of zooplankton taxa have been shown to be able to ingest MPs of similar size to algal prey (7 µm–30 µm; 650 MP mL^{-1}–3,000 MP mL^{-1}), while smaller microplastics (3.8 µm; 40 MP $mL^{-1} \times 10^3$ MP mL^{-1}) can externally adhere to a copepod's functional appendages (Cole et al., 2015). Ingestion of plastic or latex beads, used as mimics or tracers of prey, by copepods has been reported by Frost (1977); Paffenhöfer and Van Sant (1985), and Cole et al. (2015). The feeding capacity and metabolic rates of calanoids, *Centropages typicus* and *Calanus helgolandicus* were significantly reduced in the presence of 6 µm–12 µm polystyrene beads (>4,000 MPs mL^{-1}) (Cole et al., 2013; Isinibilir et al., 2020). However, another recent study by Svetlichny et al. (2021) showed an increase in the consumption rate of pure microplastics in a mixture of microplastic beads (6µm diameter) and algae *Rhodomonas salina* (5 µm–10 µm size range) with equal concentrations of approximately 5,000 cells/beads mL^{-1}. The presence of micro- and nano-sized polystyrene in the environment has been observed to alter the feeding behavior of diving beetle (*Cybister japonicas*) and crucian carp (*Carassius carassius*) (Kim et al., 2018). The negative effects of MPs on physiology, organ damage, and even mortality have been shown in the laboratory (Franzellitti et al., 2019; Isinibilir et al., 2023), but only limited information is available on the behavioral impacts, feeding response, and functional and numerical responses of brackish water copepods commonly occurring in regions with higher MP pollution (Franzellitti et al., 2019; Cunningham et al., 2021; Rajan et al., 2023).

The ingestion of MP by zooplankton not only affects the aquatic food web, but also the entire ecosystem (Alava et al., 2023). Isinibilir et al. (2020) highlighted the negative effects of microplastic intake on the energy metabolism and swimming frequency of the calanoid copepod *C. helgolandicus*. As feeding is fundamental to the energetic requirements of an organism, MPs are likely to negatively affect zooplankton health by inducing a false sense of satiety, bioaccumulation in organisms, and blocking gut passage. Since copepods are an important component of the fish diet (Kerfoot and DeMott, 2019), they can also lead to trophic transfer of MPs to higher trophic levels, thereby posing a threat to the ecological functioning of the entire aquatic ecosystem.

Most feeding studies related to food selection have shown that copepods can distinguish between algal-flavored and unflavored artificial particles (DeMott, 1986), algae and polystyrene microspheres of similar size (DeMott, 1988), live and dead prey of the same species (Paffenhöfer and Van Sant, 1985; DeMott, 1988), toxic and non-toxic algae (Fulton and Paerl, 1987; DeMott and Moxter, 1991; Kumar, 2003), nitrogen-sufficient and nitrogen-limited algae of the same species (Cowles et al., 1998), algae and ciliates (Hartmann et al., 1993), ciliates and rotifers (Rao and Kumar, 2002), and larger and smaller rotifers (Dhanker et al., 2012). In contrast, some studies have reported that calanoid copepods are unable to exercise selection in regions with higher levels of suspended solids (Arendt et al., 2011) and tidally influenced estuaries with high sediment concentrations.

Previous studies have shown the effect of algae on animal prey consumption rate and alterations in the functional response of copepods (Kumar and Rao, 1999; Enríquez-García et al., 2013). Being numerically dominant and a preferred live food for fish larvae, *Psudodiaptomus annadalei* exerts a significant impact on the estuarine food web in the Indo-Pacific. Recent studies have demonstrated the predation efficiency of *P. annandalei* in natural setups, and ciliates and rotifers are important food items in their diet (Dhanker et al., 2012). *P. annandalei* is a generalist species with a large dietary niche breadth ranging from algal size, i.e., 7 µm–20 µm (Lee et al., 2010; Beyrend-Dur et al., 2011; Dhanker et al., 2015), to the size (150 µm–220 µm) of a rotifer (Dhanker et al., 2012). *P. annandalei* is able to select similarly sized rotifer over ciliate diet and show prey switching behavior on the basis of relative abundance of prey species. Dhanker et al. (2012) determined that the predatory success of *P. annandalei* on rotifers and ciliates followed an inverse size function, as observed for other invertebrate predators (Rao and Kumar, 2002; Hwang et al., 2009). However, there is limited knowledge regarding its ecology and functional feeding response. These organisms are currently facing potential threats from rapidly increasing MP concentrations in their immediate surroundings. MPs have been recorded in various domains of marine and estuarine environments (Li et al., 2019), which are supposed to be the habitat of the calanoid copepod *P. annandalei*, in the tropical and subtropical Indo-Pacific region. Another calanoid copepod, *C. helgolandicus*, showed a gradual decrease in food consumption rate during the 6-day experiment, feeding on a mixture of the microalgae *R. salina* and MP (Isinibilir et al., 2020). In a short-term experiment to evaluate the effect of initial MP concentration on consumption rate, Isinibilir et al. (2020) recorded a linear increase in MP consumption rates in *C. helgolandicus* with increasing concentration of MP in the medium, showing a Type-I functional response. Recent studies have shown the ability of copepods to distinguish between the chemical properties of MPs with the help of their mouthparts (Xu et al., 2022); however, despite the study showing the preference of zooplankton for its natural prey when both MP and natural prey are present, they do not shed light on the effect of MPs on the overall functional response of zooplankton. However, it is worth noting that the functional response can be best assessed in the presence of alternative prey (Iyer and Rao, 1996; Chan et al., 2017) as the functional response elucidates predator feeding rates with varying food densities (Solomon, 1949; Smith and Smith, 2020), thus, providing an estimation of energy transfer across trophic levels, understanding the stability and mechanism of coexistence of prey and predators (Oaten and Murdoch., 1975; Kumar and Rao, 2001). Xu et al. (2022) compares the ingestion of natural prey to MPs, it does not attempt to address and compare the number of natural prey consumed in presence and absence of MP.

Current knowledge of MP-imposed impacts on zooplankton largely focuses on the potential of zooplankton to engulf plastics. Most studies have used ingestion rates of MP as a parameter to describe the effects of MP on copepods (Jeong et al., 2017; Li et al., 2019).

Scientific knowledge of the functional response to a gradient of food density in MP-contaminated environment is essential to elucidate the adaptability of *P. annandalei* in an MP-contaminated environment and its response to the differential density of natural food. To date, no information is available on the estuarine calanoid, *P. annandalei*, whose natural habitats are contaminated by MP. A thorough understanding of the effects of MPs on the feeding ecology and foraging strategy of micro-meso-sized organisms is relevant to understand the effects of MPs on ecosystem functioning. To elucidate the impact of MPs on ecosystem functioning and feeding ecology, it is important to address the effects on the functional and numerical responses of an organism at the base of the food chain. Herein, we demonstrated the effects of MPs falling within the dietary niche size of the copepod *P. annandalei*. We also compared the effects of microalgae as an alternative food type in the medium to determine whether MP-imposed effects are similar to, or different from, alternative natural diets.

Thus, in the present study, we investigated the effects of MPs on the functional responses of *P. annandalei* (adult and copepodid stages, C2–C3) feeding on the rotifer *B. rotundiformis* and ciliate *F. microstoma*. We hypothesized that the presence of MPs along with the rotifer or ciliate would negatively influence prey ingestion rates in the copepod, *P. annandalei*, by inducing a false sense of satiety upon uptake of MPs, which would be reflected as an alteration in its functional response.

Materials and methods

Culture of experimental organisms

All experimental organisms were cultured in the laboratory three months prior to the start of the experiment. The starter cultures of the copepod *P. annandalei* (Sewell, 1919) and the rotifer *B. rotundiformis* (Tshugunoff 1921) were originally obtained from a coastal brackish water pond (salinity ~18 psu–20 psu) by filtering water through a 70 µm mesh plankton net. Field-collected animals were acclimatized to laboratory culture conditions. Pure cultures of the rotifer *B. rotundiformis* were performed in a 2-L beaker at 18 psu-20 psu salinity and 28°C ± 1.5°C using food from the microalgae *Isochrysis galbana* Parke (length: 5 µm–8 µm; width: 2.5 µm–4 µm). The copepod cultures were expanded to 20 L round cylindrical plastic tanks. A mixture of *I. galbana* (6–10 × 10^4 cells mL^{-1}) and rotifer *B. rotundiformis* was used as food for the copepods. The copepod culture was mildly aerated continuously to mix and maintain the food uniformly distributed in the culture tank. The culture medium was renewed with a mixture of filtered seawater (0.45 µm Millipore filters) and autoclaved freshwater twice a week. All cultures were maintained at ambient temperature (annual range: 20°C–30°C) under a 12L:12D. Mass cultures of the algae, *I. galbana*, were established in the laboratory. The algal culture was maintained in a 2 L borosilicate glass flask in Walne medium (Walne, 1970). Cultures of algae were maintained at 20–22 salinity at 25°C –32°C at 1,000 lx–20,000 lx under 12 h light:12 h dark photoperiodic conditions. The algae were harvested in the log phase of growth, sedimented by centrifugation, and resuspended in experimental medium. The ciliated protist *Frontonia microstoma* was continuously cultured at 20–22 salinity and 25°C using the algae *I. galbana* and adding Hay infusions (10%) to the culture medium. Table 1 lists the attributes of the grazer, prey type, and prey density used in the experiment.

MP preparation

Commercial polystyrene and polyethylene spheres were used in the experiment. The bead sizes (15 µm–30 µm) used in each experiment were selected to be comparable to the algal-food size range of *P. annandalei*. The encounter rate depends on the ratio of MP to zooplankton; therefore, our experimental protocol represented different ratios of ciliate and rotifer diets. In one set of treatments (i.e., prey ingestion in the presence of MP) with six replicates, MP particles were carefully counted and added to each treatment medium at a concentration of 100 particles mL^{-1} in each experimental vessel.

Experimental design

To understand the effect of MP on functional response of *P. annandalei* adult (females) and copepodites, following experiments were conducted (i) Feeding rates of copepodites (C3–C4 stage) on

TABLE 1 Taxonomic group, body length (Mean ± SE) and density of experimental organisms, and experimental protocol followed of the functional response experiment.

Group	Species	Body Length (µm)	Experimental protocol: No. of replicate-06 Density used (ind. 100 ml^{-1})					
Copepoda: Calanoida	*Pseudodiaptomus annandalei* (Adults)	1,128 ± 63 (n = 18)	3	3	3	3	3	3
Copepoda: Calanoida	*P. annandalei* (Copepodites)	643 ± 75 (n = 18)	3	3	3	3	3	3
Protista: Cilaiata	*Frontonia microstoma*	218 ± 39 (n = 20)	5	10	20	40	80	160
Rotifera: Monogononta	*Brachionus rotundiformis*	156 ± 18 (n = 20)	5	10	20	40	80	160

ciliate *F. microstoma* (ii) feeding rates of copepodites (C3–C4 stage) on rotifer *B. rotundiformis*, (iii) feeding rates of adult *P. annandalei* on ciliate *F. microstoma*, and (iv) feeding rates of adult *P. annandalei* on rotifer *B. rotundiformis.*

A batch of copepods (n = 180) of the same age group and previously exposed to the prey species to be used in the experiments were removed and kept in filtered water for 3 **h** for starvation and acclimation to the experimental volume to ensure uniform acclimation and hunger levels. Prior to the functional response experiment, the optimal feeding duration was standardized using a satiation time experiment. Based on the results obtained from the preliminary satiation time experiment, a 120-minute duration of feeding was followed for all the feeding trial experiments.

Functional response estimation

For both ciliate and rotifer prey types, six selected prey densities (Table 1) were offered to 3 h prestarved *P. annandalei* to elucidate the effects of MP on the functional response (response to changing prey density in the environment) of *P. annandalei*. Two sets of experiments were conducted in phases, consisting of (i) adult and (ii) copepodite stages of *P. annandalei*, each with three diet combinations (monospecific prey, presence of algae, and presence of MP), making a total of 108 (three prey combinations × six prey concentrations × six replicates) test jars of 150 ml capacity, containing 100 ml medium. For functional response studies involving copepodites, the experimental design was similar and copepodites at stages C3–C4 were used for the experiment. Prey concentrations set up in the geometric series (Table 1) were chosen based on preliminary experiments to cover the steeply rising and satiated portions of the functional response. All prey species were individually counted and introduced into the test jars at the desired density using a stereomicroscope. The experimental vessels were placed on black paper to provide contrast and minimize the prey stratification caused by uneven illumination. The copepods (three individuals per vessel) were then gently introduced into the experimental vessels and allowed to feed for 120 min. All the experimental vessels were covered with Perspex sheets, and light was provided by overhead fluorescent illumination. The number of prey eaten was estimated as the difference between the initial and final prey numbers after allowing copepods to feed for 120 min in the test jars. At the end of the experiment, copepods were anesthetized with 2-phenoxy ethanol and then preserved in buffered formalin for later gut content analysis and validation of the estimated number of prey eaten during the experimental period. The ciliate *F. microstoma* was kept in separate experimental vessels at the same density as that used for the experiment in quadruplicate to monitor any multiplication during the experimental period. Prey consumption by the predator was expressed as the number of prey items (rotifers and ciliates) consumed per 120 min.

Statistical analyses

The data on functional response were analyzed in two steps. First, to discriminate the type of functional response (Holling, 1959), the positive or negative sign of the linear coefficient was determined by logistic regression of the proportion of prey consumed (N_a/N_t) as a function of prey density (N_t):

$$\frac{N_a}{N_t} = \frac{\exp\left(P_0 + P_1 N_t + P_2 N_t^2 + P_3 N_t^3\right)}{1 + \exp\left(P_0 + P_1 N_t + P_2 N_t^2 + P_3 N_t^3\right)}$$

where N_t is the initial prey density, N_a is the number of preys consumed, and N_a/N_t is the probability of being eaten. P_0, P_1, P_2, and P_3 are the intercept, linear, quadratic, and cubic coefficients, respectively, estimated using the maximum likelihood method. Type-II functional response is described by $P_1 < 0$, as the proportion of prey consumed, declines gradually with increasing the initial prey density offered. If $P_1 > 0$ and $P_2 < 0$, the proportion of prey consumed is positively density-dependent, i.e., prey consumption increases with an increase in prey density, which indicates a Type-III functional response (Juliano, 2001).

The data were then transformed using the Michaelis–Menten equation as shown below (Lampert and Sommer, 1997; Sarma and Nandini, 2002)

$$V = Vmax \times S(S + Kt)$$

Where, V = prey consumption rate, V_{max} = saturation value of consumption rate, S = density of prey offered k_t = the half saturation constant, the prey concentration at which $^{V_{max}}/_{2}$ is reached. Functional response curves were plotted using Excel. A Shapiro–Wilk test was used to assess the normal distribution.

Results

The presence of MPs significantly affected the functional response curves of adult *P. annandalei* feeding on either exclusive ciliate or exclusive rotifer diets. In general, *P. annandalei* adults exhibited a classical Type-II functional response to ciliates or rotifers when offered as monospecific or in combination with algae (Figure 1). Where no clear asymptote was observed, the proportion of prey consumed in relation to initial prey density declined significantly in the MP-contaminated medium (Figure 2). The prey ingestion rate initially increased with increasing prey density but reached a plateau, after which the prey ingestion rates slightly declined (Figures 1A, B). The maximum number of rotifers consumed at the highest prey density (160 ind. 100 mL^{-1}) in medium without MP was ~89.2 ± 5.51, while the maximum number of rotifers consumed by three adults *P. annandalei* at the highest prey density was (~40.4 ± 4.26) in the MP contaminated medium. The same prey species and density when offered in combination with MP showed a deviation from the Type-II functional response for copepodites (Figure 2), as the gradual decrease in the proportion of prey consumed was not significant (Pearson's correlation; $R^2 = 0.018$; $P = 0.086$) with increasing prey concentration (Figure 3) for copepodites (C3–C4).

The copepodites (C3–C4) of *P. annandalei* exhibited different responses to the prey type and density. The functional response curve for copepodites with ciliate diet showed a Type-II curve, where the rate of prey consumption increased with an increase in prey density but eventually levelled off and declined thereafter. Type-II functional

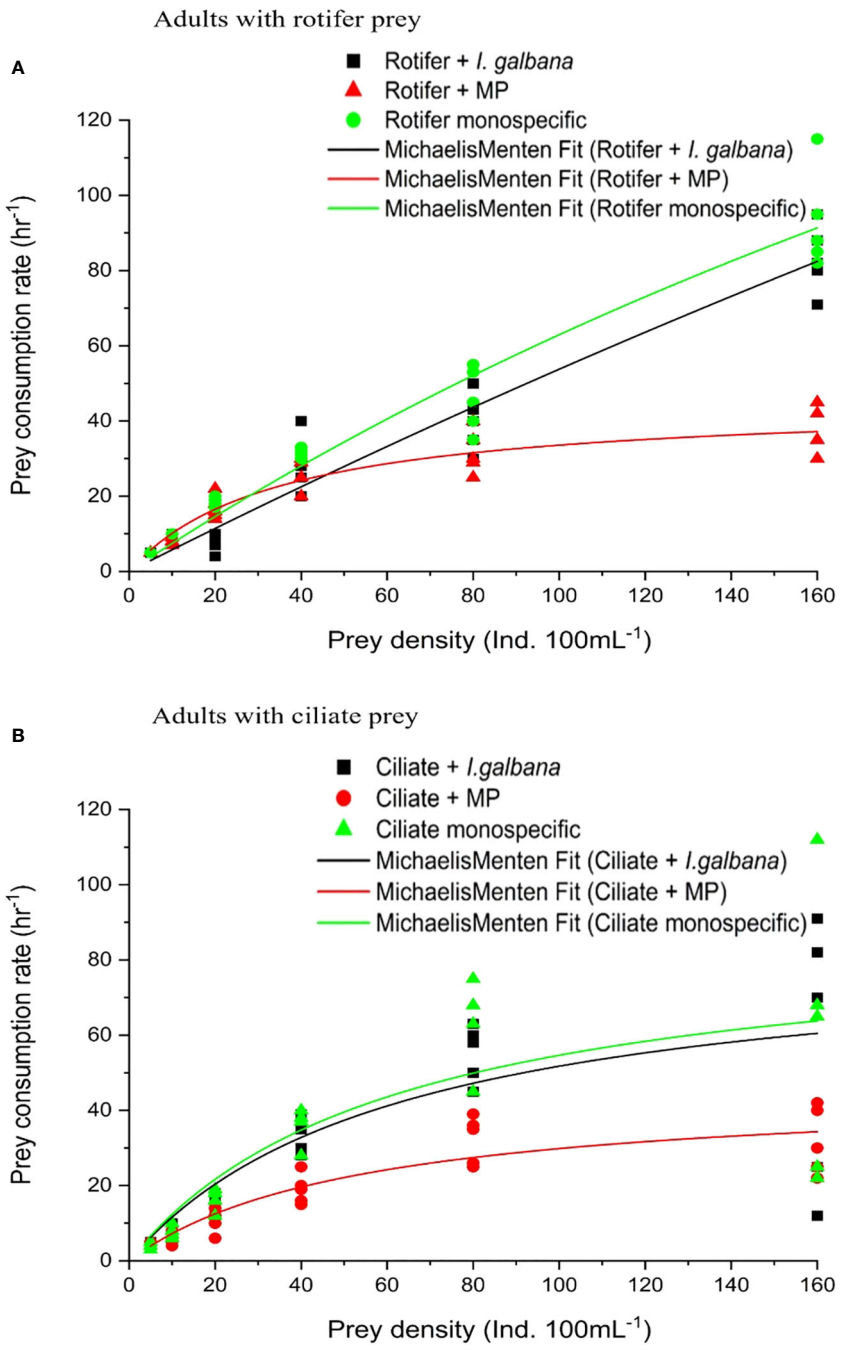


FIGURE 1
Functional response of *P. annandalei* adults offered monospecific prey, in the presence of microalgae *I. galbana*, and in the presence of Microplastic particles; **(A)** Rotifer prey *B. rotundiformis*, **(B)** Ciliate prey *Frontonia microstoma*. Shown are the actual prey consumption and the transformation of the curve using the Michaelis–Menten equation.

responses of copepodites were recorded with monospecific rotifer and ciliate prey types (Figure 3). In the presence of microalgae, copepodites showed a stronger response to ciliate density (R^2 = 0.77; P <0.001), exhibiting a Type-II functional response (Figure 3). The presence of MPs along with natural prey affected prey consumption in both adults and copepodites. The functional response curve of copepodites showed a Type-II functional response with rotifers both with a monospecific diet and with algae (Figure 2A), but the functional response curve in the presence of MPs showed linear regression with a negative slope (Figure 3A). The gradual decline in the proportion of prey consumed showed a highly significant correlation with the increasing initial prey density (Figure 4). Copepodites did not exhibit any response with rotifers or ciliates to the changed initial prey availability in the medium treated with MP (Figure 3). In the MP medium, the proportion of initial prey consumed by the copepodites did not correlate significantly (R^2 = 0.02, MP-rotifer; R^2 = 0.2, MP-ciliate) with increasing initial prey density (Figure 4).

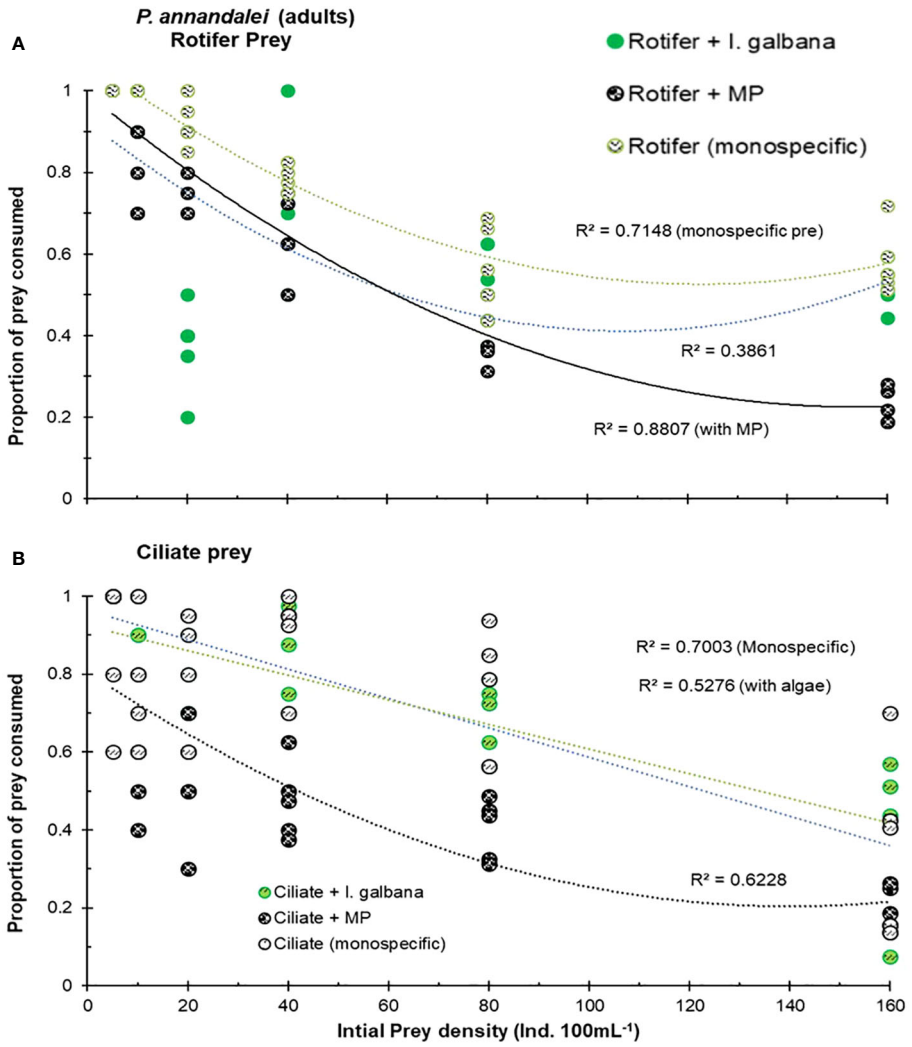


FIGURE 2
Proportion of initial prey consumed by the copepod *P. annandalei* adults, in the medium with monospecific prey, in the presence of microalgae *I. galbana*, and in the presence of MP particles **(A)** Rotifer prey *B. rotundiformis*, **(B)** Ciliate prey *Frontonia microstoma*.

In the present study, adults in all cases ingested natural rotifer and ciliate prey, but the presence of MPs differentially affected ingestion depending on food type. Regardless of prey density, the prey ingestion rates were significantly lower (Figure 5; $p < 0.01$; one-way ANOVA) for rotifer prey than for ciliate prey. The ingestion of natural prey by *P. annandalei* adults and copepodites varied significantly with prey density, MPs concentration, and their interaction (Figure 5; $p < 0.001$; two-factor ANOVA). MP contamination did not affect prey ingestion in adults or copepodites at lower prey densities. The number of preys consumed in case of rotifer diet was maximum at the maximum prey density (160 ind. 100 mL^{-1}) ~80.4 ± 2.7 which reduced by ~60% in presence of MPs. A similar decrease in prey consumption at maximum density was observed in the case of ciliate *F. microstoma* (maximum prey consumed with only ciliate prey was ~117 ± 4.55, while in the presence of MPs, ciliate consumption was reduced to ~39.8 ± 2.305 (Figure 5). At medium and high prey densities, we recorded a 40%–66% reduction in ciliate ingestion and 20%–60% reduction in rotifer ingestion by *P. annandalei* adults (Figure 5; Table 2). In the case of copepodites, we recorded a 40% to 98% reduction in ciliate consumption and a 50% to 91% reduction in rotifer consumption due to the presence of MP in the medium (Figure 5; Table 2).

Discussion

The main aim of this study was to obtain definitive information on the impact of MP contamination on feeding rates in *P. annandalei*, a common brackish water copepod species, with natural prey. In the natural setup, the distribution of prey species and MP (Rajan et al., 2023) are patchy, where copepods encounter an array of prey concentrations (Hwang et al., 2010). Various types of MP, similar to the size range of microzooplankton, are abundant in coastal and estuarine ecosystems (Cole et al., 2019; Rajan et al., 2023).

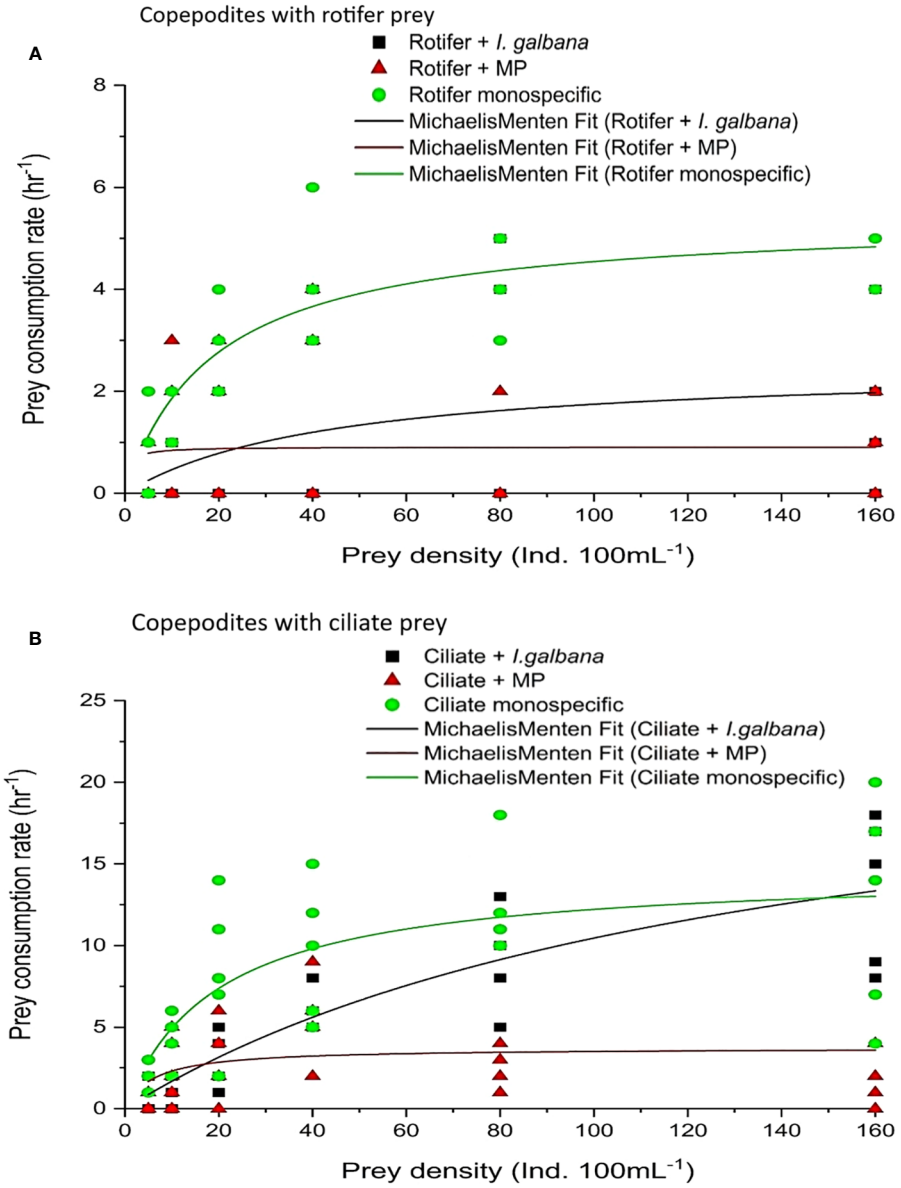


FIGURE 3
Functional response of *P. annandalei* copepodites (C3–C4) offered monospecific prey, in the presence of microalgae *I. galbana*, and in the presence of Microplastic particles; **(A)** Rotifer prey *B. rotundiformis*, **(B)** Ciliate prey *Frontonia microstoma*. Shown are the actual prey consumption and the transformation of the curve using the Michaelis–Menten equation.

Evaluation of MP imposed alterations in consumer behavior is complex because of (i) patchy distribution and natural concentrations of MP, (ii) limited information on MP concentration-specific ingestion of natural diet, and (iii) lack of quantitative data on behavioral responses of zooplankton at varying MP concentrations. Unless colonized by biota or affected by external pollutants, MP are inert particles, and the main mode of effects on consumers is food dilution and behavioral responses, such as functional and numerical responses of consumers to MP, as the polymer structure and chemical properties of particles are less important (Mehinto et al., 2022). While food dilution outweighs other effects, the major response of organisms with a dietary niche size overlapping with MP would be the adjustment of feeding rates, i.e., functional response.

Our results on prey ingestion by *P. annandalei* adults and copepodites were within the ranges reported for related taxa (Hwang et al., 2009; Dhanker et al., 2012; He et al., 2020). Recent studies have also confirmed ingestion of MP by copepods (Desforges et al., 2015; Cheng et al., 2020; Bai et al., 2021); however, this is the first study to understand the effect of MP on natural prey ingestion in *P. annandalei*. Contributing to the size range, sorption potential, hydrophobicity, wide occurrence in the global ocean (Foekema et al., 2013; Mathalon and Hill, 2014; Ugwu et al., 2021), and bioavailability to zooplankton (Cole et al., 2013; Setälä et al., 2014), ichthyoplankton (Rochman et al., 2013; Batel et al., 2016), and other meso-macro-sized invertebrates (Browne et al., 2008; Graham and Thompson, 2009; Gray and Weinstein, 2017; Kumari et al., 2023a), MPs are likely to have large-scale effects

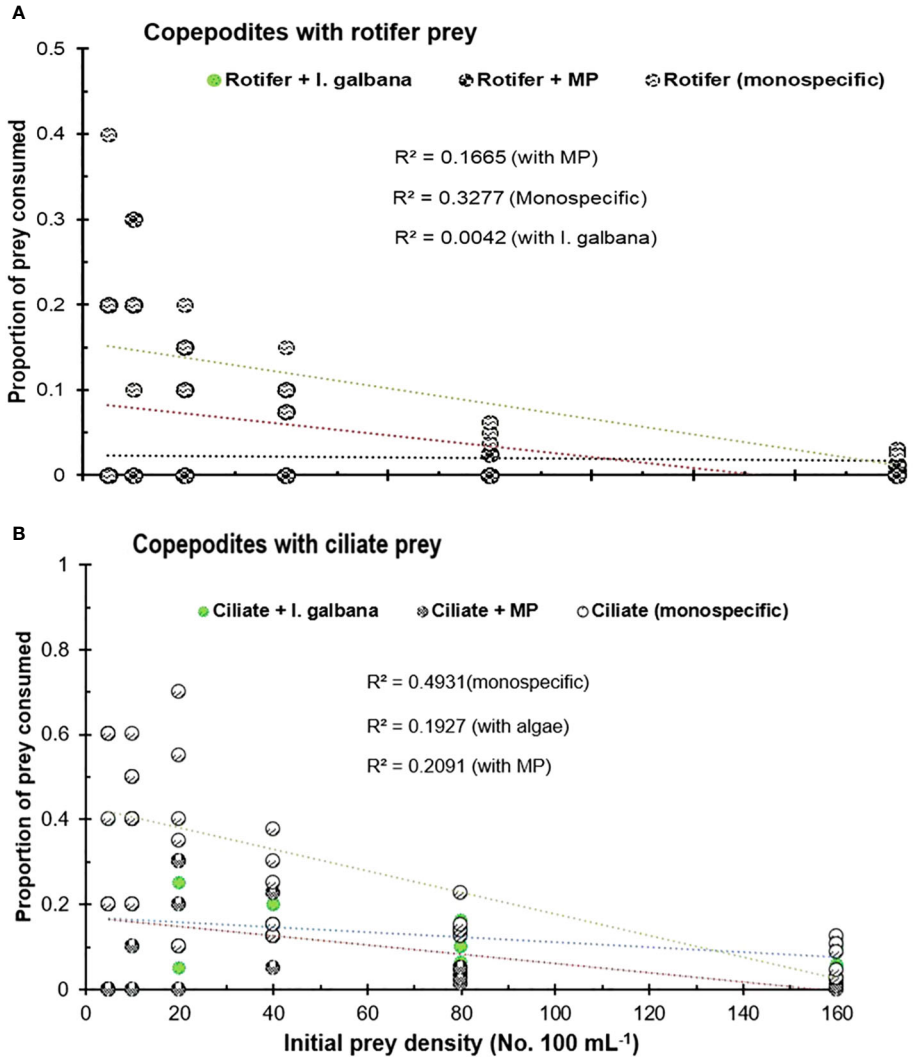


FIGURE 4
Proportion of initial prey consumed by the copepodid (C3–C4) stage of P. *annandalei* in the medium with monospecific prey, in the presence of microalgae *I. galbana*, and in the presence of MP particles. **(A)** Rotifer prey *B. rotundiformis*. **(B)** Ciliate prey *Frontonia microstoma*.

on marine ecosystem functioning. Various experimental results have revealed lethal and sublethal effects on different organisms (von Moos et al., 2012; Rochman et al., 2013; Au et al., 2015; Gray and Weinstein, 2017).

P. annandalei showed a direct functional response to varying concentration of prey in the medium. Thus, the presence of MPs (size range 15 µm–30 µm diameter) in the environment of *P. annandalei* directly affects the functional response and feeding behavior of both adults and the developmental stages of copepods. The prey ingestion rate showed a decline in the presence of MPs in all cases, suggesting interference of MPs in the feeding behavior and feeding efficiency of *P. annandalei*. Copepods can ingest plastics by either selective grazing or by indiscriminately ingesting particles with natural prey (Traboni et al., 2023). Copepods can also actively refuse MPs or passively reduce MP intake by physical impacts/interference or chemical toxicity associated with plastics (leachates or sorbed pollutants) (Cássio et al., 2022). Similarly, the presence of plastics in the environment, along with natural prey, may obstruct predator–prey interactions, leading to a reduced prey ingestion rate (Turner and Tester, 1989). The linear increase in prey ingestion by copepods with increasing prey density suggests a Type-I functional response, which assumes a linear increase in food ingestion rate with food concentration, either for all initial food concentrations or only for the particular maximum concentration, beyond which the feeding rate is constant. This could be attributed to the adaptive feeding response of *P. annandalei*, as has also been reported for other copepods (Abrams, 1990; Kumar and Rao, 1999; Kerfoot and DeMott, 2019). The MP incurred reduction in ciliate and rotifer prey ingestion, recorded in this study, indicating the adaptive feeding strategy, as adults of *P. annandalei* did not exhibit any discernible reduction in prey consumption at lower concentrations; however, at higher concentrations, it showed a 20% to 60% reduction in rotifer ingestion and a 40% to 66% reduction in ciliate ingestion. Thus, the presence of a more satiating prey has the potential to reduce MP uptake by copepods. *P. annandalie* is

10.3389/fevo.2024.1277332

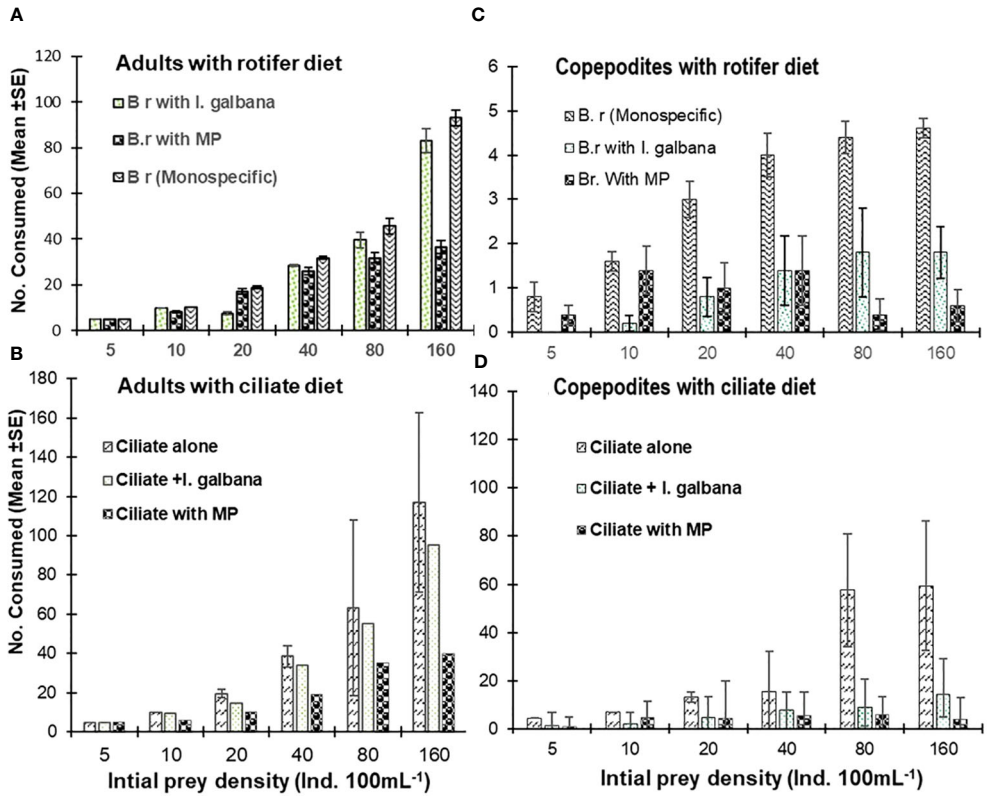


FIGURE 5
No. of prey consumed (mean ± SD) by the adults **(A, B)**, and copepodites **(C, D)** of *Pseudodiaptomus annandalei* when offered as prey the rotifer *Brachionus rotundiformis* **(A, C)** and the ciliate *Frontonia microstoma* **(B, D)** as monospecific prey, in the medium containing either microalgae *I. galbana* or MP particle.

mainly a suspension feeder copepod, though occasionally capture a food item through a surprise jerky movement of appendages. A previous study recorded different feeding modes for *P. annandalei* when dealing with different prey sizes and mobilities (Dhanker et al., 2013). MP-driven alterations in the behavioral and physiological responses of the calanoid copepods *Acartia clausi* and *C. typicus* have been attributed to differences in the feeding strategies of the two species (Svetlichny et al., 2021). Further comparative studies are required to understand the role of different feeding strategies in the uptake of MP by *P. annandalei*.

In the present study, copepods showed neither linear nor curvilinear relationships with the initial prey concentrations in the medium with MP. Conclusively *P. annandalei* was much less efficient in feeding *B. rotundiformis* or *F. microstoma* when MP was present, indicating a negative impact of MPs contamination. The ability of copepods, such as *Temora longicornis*, to selectively refuse MPs and their preference for natural prey has been previously demonstrated (Xu et al., 2022). Overall, copepods have been shown to be equipped with diverse sensors on their antennae, feeding appendages or body surfaces for detecting either hydromechanical or chemical signals emitted by their prey (Turner and Tester, 1989; Vanderploeg et al., 1990; DeMott, 1995). The reduced frequency of prey predator encounters in the presence of MPs may be a factor in changes in the functional response. In addition, accidental or

TABLE 2 MP induced changes in prey ingestion rates on natural prey (*F. microstoma* and *B. rotundiformis*) by adult and copepodid stages of *P. annandalei* at different food density levels.

Alternative in the medium	Copepod stages used	% change in ciliate ingestion			% change in rotifer ingestion		
		Food density			Food density		
		Low	Medium	High	Low	Medium	High
Microalgae	Adults	_−2.00	−18.20	−15.70	−2.00	−5.34	−11.85
	Copepodites	−69.81	−56.93	−80.41	−93.75	−69.17	−60.00
Microplastic	Adults	−21.00	−48.56	−55.30	−10.00	−14.22	−45.56
	Copepodites	−40.80	−66.03	−91.77	−31.25	−65.83	−88.93

voluntary intake of MPs by *P. annandalei* could induce false feelings of satiety that may reduce the hunger level of copepods (Gommer et al., 2018; Botterell et al., 2019). MPs acceptance and rejection by copepods create a challenging environment for copepods to extract natural food particles from the environment because of the morphological similarity of MPs with the natural diet (Nielsen et al., 2020) and microbial coating on MP surfaces as biofilms (Zimmermann et al., 2019). The purpose of this study was to evaluate the effect of MP on the functional response (prey consumption rate) of *P. annandalei*. The complete life cycle of this species has been studied on an exclusive algal diet (Beyrend-Dur et al., 2011; Nielsen et al., 2020), and lower availability of microalgae showed an increase in MP ingestion and retention in *P. annandalei* (Cheng et al., 2020); therefore, it is also relevant to study the effect of MP on the clearance rate.

Earlier reports suggest ingestion of inorganic particles of low nutritional value (Arendt et al., 2011) resulting in pseudo-satiation (Turner and Tester, 1989). However, a lack of nutrients adversely affects an organism's reproductive potential and inclusive fitness (White and Dagg, 1989; Kang, 2012).

The brackish water, egg-carrying euryhaline copepod, *P. annandalei*, is distributed widely in tropical and subtropical Indo-Pacific with an ability to survive in altered marine and brackish waters (Beyrend-Dur et al., 2011; Beyrend-Dur et al., 2013; Blanda et al., 2015). This species is widely used as a live feed in the aquaculture industry; however, the harvest of *P. annandalei* in aquaculture ponds has declined in recent years (Blanda et al., 2015). The present results emphasize the need to assess MP contamination in aquaculture ponds and further large-scale studies of the numerical response of *P. annandalei* in the presence and absence of MP. The impact of MPs on the functional responses of *P. annandalei* is of particular concern because they have the potential for trophic transfer to fish and humans (Lee et al., 2010; Nelms et al., 2018; Ugwu et al., 2021). Furthermore, *P. annandalei* which is a filter-feeder, is more vulnerable to MPs ingestion. It is important to consider that a cocktail of various additives and chemical contaminants (Rochman et al., 2019; Zimmermann et al., 2019) are adsorbed by plastic surfaces and ingested along with microplastics, which further adds to toxicity and oxidative stress (Jeong et al., 2017; Qiao et al., 2019). Although the present study does not suggest any toxic effects of MPs, the effects on functional responses are suggestive of chronic effects on ecosystem functioning of planktonic organisms, particularly at the base of the pelagic food webs, hints at the knock-on alterations in ecosystem functioning, resulting in trophic cascades (Galloway et al., 2017; Botterell et al., 2019; Nair and Perumal, 2022). MPs are expected to become more prevalent in aquatic environments because of their extensive use and dumping in aquatic ecosystems (Zeynep et al., 2023). Their potential to transport and adsorb toxic materials, as well as their absorbance by living cells, tissues, and organs of aquatic organisms, and interfere with physiological functions, all cause significant health risks. Could the observed MP imposed alterations in functional responses have implications for the numerical responses of copepods? The predator's functional response is hypothesized to be an important determinant of the population structure and numerical responses (Dhanker et al., 2012; Dhanker et al., 2015).

To support the generalizability of the present results, we recommend studying a range of brackish water zooplankton species used as live feed in the aquaculture industry, by applying different types of MP particles.

Conclusions

This paper reports significant changes in the functional response curve of the adult and copepodid stages of *P. annandalei* when MPs are present along with natural prey. These results clearly suggest that MP contamination adversely affects the feeding rates of *P. annandalei* adults and juveniles fed on their natural diets. The impact of MPs on the functional responses of *P. annandalei* and prey ingestion rates is of particular concern because they have the potential for trophic transfer to fish and humans. Ingestion of inert particles, such as MP, gives a sense of false satiety, which in turn results in an altered prey selection pattern (Gommer et al., 2018) and reduced saturation level prey intake. Further research is needed to fully understand the feeding modes in zooplankton species, prey behavior, prey selection patterns, and trophic transfer to fish in MP-contaminated environments.

Data availability statement

The original contributions presented in the study are included in the article/Supplementary Material. Further inquiries can be directed to the corresponding author.

Ethics statement

The manuscript presents research on animals that do not require ethical approval for their study.

Author contributions

JS: Conceptualization, Writing - review & editing. MR: Writing – original draft, Writing – review & editing. RG-o: Writing – original draft, Writing – review & editing.

Funding

The author(s) declare that no financial support was received for the research, authorship, and/or publication of this article.

Acknowledgments

The authors thank the guest editor for inviting us to submit this special issue. We thank Silliman University for providing the facility for conducting this research. MR thanks Delhi Technological University for the internship.

Conflict of interest

The authors declare that the research was conducted in the absence of any commercial or financial relationships that could be construed as a potential conflict of interest.

Publisher's note

All claims expressed in this article are solely those of the authors and do not necessarily represent those of their affiliated organizations, or those of the publisher, the editors and the reviewers. Any product that may be evaluated in this article, or claim that may be made by its manufacturer, is not guaranteed or endorsed by the publisher.

Supplementary material

The Supplementary Material for this article can be found online at: https://www.frontiersin.org/articles/10.3389/fevo.2024.1277332/full#supplementary-material

References

Abrams, P. A. (1990). The effects of adaptive behavior on the type-2 functional response. *Ecology* 71, 877–8 85. doi: 10.2307/1937359

Akdogan, Z., Guven, B., and Kideys, A. E. (2023). Microplastic distribution in the surface water and sediment of the Ergene River. *Environ. Res.* 234, 116500. doi: 10.1016/j.envres.2023.116500. ISSN 0013-9351.

Alava, J. J., Báez, M. M., McMullen, K., Tekman, M. B., Barrows, A. P. W., Bergmann, M., et al. (2023). *Ecological Impacts of Marine Plastic Pollution, Microplastics' Food web Bioaccumulation Modelling and Global Ocean Footprint: Insights into the Problems, the Management Implications and Coastal Communities Inequities. The Nippon Foundation-Ocean Litter Project, (2019-2023)* (Main Mall, Vancouver, BC, V6T 1Z4, Canada: Institute for the Oceans and Fisheries, University of British Columbia). *Working Paper* 2023 – 01.

Amélineau, F., Bonnet, D., Heitz, O., Mortreux, V., Harding, A. M. A., Karnovsky., N., et al. (2016). MP pollution in the Greenland Sea: Background levels and selective contamination of planktivorous diving seabirds. *Environ. pollut.* 219, 1131–1139. doi: 10.1016/j.envpol.2016.09.017

Arendt, K. E., Dutz, J., Jónasdóttir, S. H., Jung-Madsen, S., Mortensen, J., Møller., E. F., et al. (2011). Effects of suspended sediments on copepods feeding in a glacial influenced sub-Arctic fjord. *J. Plankton Res.* 33, 10, 1526–1537. doi: 10.1093/plankt/fbr054

Au, S. Y., Bruce, T. F., Bridges, W. C., and Klaine, S. J. (2015). Responses of *Hyalella azteca* to acute and chronic microplastic exposures. *Environ. Toxicol. Chem.* 34, 2564–2572. doi: 10.1002/etc.3093

Auta, H. S., Emenike, C. U., and Fauziah, S. H. (2017). Distribution and importance of MPs in the marine environment: A Review of the Sources, Fate, Effects, and Potential Solutions. *Environ. Int.* 2017, 165–176. doi: 10.1016/j.envint.2017.02.013

Avignon, G. D., Hsu, S. S. H., Gregory-Eaves, I., and Ricciardi, A. (2023). Feeding behavior and species interactions increase the bioavailability of microplastics to benthic food webs. *Sci. Total Environ.* 896, 165261. doi: 10.1016/j.scitotenv.2023.165261

Ayukai, T. (1987). Discriminate feeding of the calanoid copepod *Acartia clausi* in mixtures of phytoplankton and inert particles. *Mar. Biol.* 94, 579–587. doi: 10.1007/BF00431404

Baalkhuyur, F. M., Dohaish, E.-J. A., Elhalwagy, M. E. A., Alikunhi, N. M., Suwailem, A. M., Røstad, A., et al. (2018). MP in the gastrointestinal tract of fishes along the Saudi Arabian Red Sea coast. *Mar. pollut. Bull.* 131, 407–415. doi: 10.1016/j.marpolbul.2018.04.040

Bai, Z., Wang, N., and Wang, M. (2021). Effects of microplastics on marine copepods. *Ecotoxicol Environ. Saf.* 217, 112243. doi: 10.1016/j.ecoenv.2021.112243

Barnes, D. K. A., Galgani, F., Thompson, R. C., and Barlaz, M. (2009). Accumulation and fragmentation of plastic debris in global environments. *Phil. Trans. R. Soc B* 364, 1526. doi: 10.1098/rstb.2008.0205

Batel, A., Linti, F., Scherer, M., Erdinger, L., and Braunbeck, T. (2016). Transfer of benzo[a]pyrene from microplastics to Artemia nauplii and further to zebrafish via a trophic food web experiment: CYP1A induction and visual tracking of persistent organic pollutants. *Environ. Toxicol. Chem.* 35 (7), 1656–1666. doi: 10.1002/etc.3361

Beaugrand, G., Brander, K. M., Alistair, J. A., Souissi, S., and Reid, P. C. (2003). Plankton effect on cod recruitment in the North Sea. *Nature* 426, 661–664. doi: 10.1038/nature02164

Beyrend-Dur, D., Kumar, R., Rao, T. R., Souissi, S., Cheng, S. H., and Hwang, J. S. (2011). Demographic parameters of adults of *Pseudodiaptomus annandalei* (Copepoda: Calanoida): Temperature–salinity and generation effects. *J. Exp. Mar. Biol. Ecol.* 404 (1–2), 1–14. doi: 10.1016/j.jembe.2011.04.012

Beyrend-Dur, D., Souissi, S., and Hwang, J. S. (2013). Population dynamics of calanoid copepods in the subtropical mesohaline Danshuei Estuary (Taiwan) and typhoon effects. *Ecol. Res.* 28, 771–780. doi: 10.1007/s11284-013-1052-y

Bhuyan, M. (2022). Effects of MPs on fish and in human health. *Front. Environ. Sci.* 10, 827289. doi: 10.3389/fenvs.2022.827289

Blanda, E., Drillet, G., Huang, C.-C., Hwang, J.-S., Jakobsen, H. H., Rayner, T. A., et al. (2015). Trophic interactions and productivity of copepods as live feed from tropical Taiwanese outdoor aquaculture ponds. *Aquaculture* 445, 11–21. doi: 10.1016/j.aquaculture.2015.04.003

Botterell, Z. L. R., Beaumont, N., Dorrington, T., Steinke, M., Thompson, R. C., and Lindeque, P. K. (2019). Bioavailability and effects of microplastics on marine zooplankton: A review. *Environ. pollut.* 245, 98–110. doi: 10.1016/j.envpol.2018.10.065

Browne, M. A., Dissanayake, A., Galloway, T. S., Lowe, D. M., and Thompson, R. C. (2008). Ingested microscopic plastic translocates to the circulatory system of the mussel, Mytilus edulis (L). *Environ. Sci. Technol.* 42 (13), 5026–5031. doi: 10.1021/es800249a

Bundy, M. H., Gross, T. F., Vanderploeg, H. A., and Strickler, J. R. (1998). Perception of inert particles by calanoid copepods: Behavioral observations and a numerical model. *J. Plankton Res.* 20, 2129–2152. doi: 10.1093/plankt/20.11.2129

Bundy, M. H., and Vanderploeg, H. A. (2002). Detection and capture of inert particles by calanoid copepods: the role of the feeding current. *J. Plankton Res.* 24, 3, 215–223. doi: 10.1093/plankt/24.3.215

Cássio, F., Batista, D., and Pradhan, A. (2022). Plastic interactions with pollutants and consequences to aquatic ecosystems: what we know and what we do not know. *Biomolecules* 12 (6), 798. doi: 10.3390/biom1206079898

Chan, K., Boutin, S., Hossie, T. J., Krebs, C. J., O'Donoghue, M., and Murray, D. L. (2017). Improving the assessment of predator functional responses by considering alternate prey and predator interactions. *Ecology* 98, 1787–17 96. doi: 10.1002/ecy.1828

Cheng, Y., Wang, J., Yi, X., Li, L., Liu, X., and Ru, S. (2020). Low microalgae availability increases the ingestion rates and potential effects of microplastics on marine copepod *Pseudodiaptomus annandalei*. *Mar. Poll. Bul.* 152, 110919. doi: 10.1016/j.marpolbul.2020.110919

Cole, M., Coppock, R., Lindeque, P. K., Altin, D., Reed, S., Pond, D. W., et al. (2019). Effects of nylon MP on feeding, lipid accumulation, and moulting in a coldwater copepod. *Environ. Sci. Technol.* 53, 7075–7082. doi: 10.1021/acs.est.9b01853

Cole, M., Lindeque, P., Fileman, E., Halsband, C., and Galloway, T. S. (2015). The impact of polystyrene MPs on feeding, function and fecundity in the marine copepod *Calanus helgolandicus*. *Environ. Sci. Technol.* 49 (2), 1130–1137. doi: 10.1021/es504525u

Cole, M., Lindeque, P., Fileman, E., Halsband, C., Goodhead, R., Moger, J., et al. (2013). Microplastic ingestion by zooplankton. *Environ. Sci. Technol.* 47 (12), 6646–6655. doi: 10.1021/es400663f

Cowles, T. J., Desiderio, R. A., and Carr, M.-E. (1998). Small-scale planktonic structure: persistence and trophic consequences. *Oceanography* 11 (1), 4–9. doi: 10.5670/oceanog.1998.08

Cunningham, E. M., Cuthbert, R. N., Coughlan, N. E., Kregting, L., Cairnduff, V., and Dick, J. T. A. (2021). Microplastics do not affect the feeding rates of a marine predator'. *Sci. Total Environ.* 779, 146487. doi: 10.1016/j.scitotenv.2021.146487

Cunningham, E. M., Kiriakoulakis, K., Dick, J. T. A., Kregting, L., Schuchert, P., and Sigwart, J. D. (2020). Driven by speculation, not by impact - the effects of plastic on fish species. *J. Fish Biol.* 96 (6), 1294–1297. doi: 10.1111/jfb.14303

DeMott, W. R. (1986). The role of taste in food selection by freshwater zooplankton. *Oecologia* 69, 334–340. doi: 10.1007/BF00377053

DeMott, W. R. (1988). Discrimination between algae and artificial particles by freshwater and marine copepods. *Limnol. Oceanogr.* 33, 397–408. doi: 10.4319/lo.1988.33.3.0397

DeMott, W. R. (1995). Optimal foraging by a suspension-feeding copepod: responses to short-term and seasonal variation in food resources. *Oecologia* 103 (2), 230–240. doi: 10.1007/BF00329085

DeMott, W. R., and Moxter, F. (1991). Foraging cyanobacteria by copepods: responses to chemical defense and resource abundance. *Ecology* 72 (5), 1820–1834. doi: 10.2307/1940981

Desforges, J. P., Galbraith, M., and Ross, P. S. (2015). Ingestion of microplastics by zooplankton in the Northeast Pacific Ocean. *Arch. Environ. Contam Toxicol.* 69 (3), 320–330. doi: 10.1007/s00244-015-0172-5

Dhanker, R., Kumar, R., and Hwang, J. S. (2012). Predation by *Pseudodiaptomus annandalei* (Copepoda: Calanoida) on rotifer prey: size selection, egg predation and effect of algal diet. *J. Exp. Mar. Biol. Ecol.* 414–415, 44–53. doi: 10.1016/j.jembe.2012.01.011

Dhanker, R., Kumar, R., Tseng, L. C., and Hwang, J. S. (2013). Ciliate (*Euplotes* sp.) predation by *Pseudodiaptomus annandalei* (Copepoda: Calanoida) and the effects of mono-algal and pluri-algal diets. *Zool. Stud.* 52, 34. doi: 10.1186/1810-522X-52-34

Dhanker, R., Molinero, J. C., Kumar, R., Tseng, L. C., Ianora, A., and Hwang, J. S. (2015). Responses of the estuarine copepod *Pseudodiaptomus annandalei* to diatom polyunsaturated aldehydes: Reproduction, survival and postembryonic development. *Harmful Algae* 43, 74–81. doi: 10.1016/j.hal.2015.02.002

Enríquez-García, C., Nandini, S., and Sarma, S. S. S. (2013). Feeding behaviour of Acanthocyclops americanus (Marsh)(Copepoda: Cyclopoida). *J. Nat. Hist.* 47 (5-12), 853–862. doi: 10.1080/00222933.2012.747637

Ferrao Filho, A. D. S., Demott, W. R., and Tessier, A. J. (2005). Responses of tropical cladocerans to a gradient of resource quality. *Freshwater Biol.* 50 (6), 954–964.

Foekema, E. M., De Gruijter, C., Mergia, M. T., van Franeker, J. A., Murk, A. J., and Koelmans, A. A. (2013). Plastic in North Sea fish. *Environ. Sci. Technol.* 47 (15), 8818–8824. doi: 10.1021/es400931b

Franzellitti, S., Canesi, L., Auguste, M., Wathsala, R. H., and Fabbri, E. (2019). Microplastic exposure and effects in aquatic organisms: A physiological perspective. *Environ. Toxicol. Pharmacol.* 68, 37–51. doi: 10.1016/j.etap.2019.03.009

Frost, W. E. (1977). The food of Charr *Salvelinus willughbii* (Gunther) in Windermere. *J. Fish Biol.* 11, 531–547. doi: 10.1111/j.1095-8649.1977.tb05710.x

Fulton, R. S., and Paerl, H. W. (1987). Toxic and inhibitory effects of the blue-green alga *Microcystis aeruginosa* in herbivorous zooplankton. *J. Plankton Res.* 9, 837–855. doi: 10.1093/plankt/9.5.837

Galloway, T., Cole, M., and Lewis, C. (2017). Interactions of microplastic debris throughout the marine ecosystem. *Nat. Ecol. Evol.* 1, 116. doi: 10.1038/s41559-017-0116

Gommer, R., Bom, R. A., Fijen, T. P. M., and van Gils, J. A. (2018). Stomach fullness shapes prey choice decisions in crab plovers (*Dromas ardeola*). *PloS One* 13 (4), e0194824. doi: 10.1371/journal.pone.0194824

Graham, E. R., and Thompson, J. T. (2009). Deposit and suspension- feeding sea cucumbers (Echinodermata) ingest plastic fragments. *J. Exp. Mar. Biol. Ecol.* 368, 22–29. doi: 10.1016/j.jembe.2008.09.007

Gray, A. D., and Weinstein, J. E. (2017). Size- and shape-dependent effects of microplastic particles on adult daggerblade grass shrimp (Palaemonetes pugio). *Environ. Toxicol. Chem.* 36 (11), 3074–3080. doi: 10.1002/etc.3881

Gunaalan, K., Almeda, R., Lorenz, C., Vianello, A., Iordachescu, L., Papacharalampos, K., et al. (2023). Abundance and distribution of microplastics in surface waters of the Kattegat/ Skagerrak (Denmark). *Environ. pollut.* 318, 120853. doi: 10.1016/j.envpol.2022.120853

Halstead, J. E., Smith, J. A., Carter, E. A., Lay, P. A., and Johnston, E. L. (2018). Assessment tools for MPs and natural fibres ingested by fish in an urbanised estuary. *Environ. pollut.* 234, 552–561. doi: 10.1016/j.envpol.2017.11.085

Hartmann, H. J., Taleb, H., Aleya, L., and Lair, N. (1993). Predation on ciliates by the suspension-feeding calanoid copepod *Acanthodiaptomus denticornis*. *Can. J. Fish. Aquat. Sci.* 50, 1382–1393. doi: 10.1139/f93-158

He, X., Cheng, F., and Chen, W. (2020). Effects of maternal phosphorus deficiency on reproductive allocation of the copepod *Pseudodiaptomus annandalei* Sewel. *Hydrobiologia* 847, 2035–2048. doi: 10.1007/s10750-020-04229-7

Holling, C. S. (1959). The components of predation as revealed by a study of small-mammal predation of the European pine sawfly. *Can. Entomologist.* 91 (5), 293–320. doi: 10.4039/Ent91293-5

Hwang, J. S., Kumar, R., Hsieh, C. W., Kuo, A. Y., Souissi, S., Hsu, M. H., et al. (2010). Patterns of zooplankton distribution along the marine, estuarine and riverine portions of the Danshuei ecosystem in northern Taiwan. *Zoological Studies* 49 (3), 335–352.

Hwang, J. S., Kumar, R., and Kuo, C.-S. (2009). Impacts of predation by the copepod, mesocyclops pehpeiensis, on life table demographics and population dynamics of four cladoceran species: A comparative laboratory study. *Zoological Stud.* 48 (6), 738–752.

Isinibilir, M., Eryalçın, K. M., and Kideys, A. E. (2023). Effect of Polystyrene Microplastics in Different Diet Combinations on Survival, Growth and Reproduction Rates of theWater Flea (*Daphnia magna*). *Microplastics* 2, 27–38. doi: 10.3390/microplastics2010002

Isinibilir, M., Svetlichny, L., Mykitchak, T., Türkeri, E. E., Eryalçın, K. M., Doğan, O., et al. (2020). Microplastic consumption and its effect on respiration rate and motility of *calanus helgolandicus* from the Marmara Sea. *Front. Mar. Science.* 7. doi: 10.3389/fmars.2020.603321

Iyer, N., and Rao, T. R. (1996). Responses of the predatory rotifer *Asplanchna intermedia* to prey species differing in vulnerability: laboratory and field studies. *Freshw. Biol.* 36 (3), 521–533. doi: 10.1046/j.1365-2427.1996.d01-510.x

Jabeen, K., Su, L., Li, J., Yang, D., Tong, C., and Mu, J. (2017). MPs and mesoplastics in fish from coastal and fresh waters of China. *Environ. pollut.* 221, 141–149. doi: 10.1016/j.envpol.2016.11.055

Jeong, C. B., Kang, H. M., Lee, M. C., Kim, D. G., Han, J., Hwang, D. S., et al. (2017). Adverse effects of microplastics and oxidative stress-induced MAPK/Nrf2 pathway-mediated defense mechanisms in the marine copepod. *Paracyclopina nana*. *Sci. Rep.* 2017, 7. doi: 10.1038/srep41323

Juliano, S. A. (2001). Nonlinear curve fitting: predation and functional response curves. *Design Anal. Ecol. Experiments* 2, 178–96. doi: 10.1093/oso/9780195131871.003.0010

Kang, H. K. (2012). Effects of suspended sediments on reproductive responses of Paracalanus sp. (Copepoda: Calanoida) in the laboratory. *J. Plankton Res.* 34, 7, 626–635. doi: 10.1093/plankt/fbs033

Kanhai, L. D. K., Gardfeldt, K., Krumpen, T., Thompson, R. C., and O'Connor, I. (2020). MPs in sea ice and seawater beneath ice floes from the Arctic Ocean. *Sci. Rep.* 10 (1), 5004. doi: 10.1038/s41598-020-61948-6

Kerfoot, C. W., and DeMott, W. R. (2019). Food web dynamics: dependent chains and vaulting. In *Trophic interactions within aquatic ecosystems* (pp. 347–382). Routledge.

Kim, S. W., Kim, D., Chae, Y., and An, Y.–J. (2018). Dietary uptake, biodistribution, and depuration of microplastics in the freshwater diving beetle *Cybister japonicus:* Effects on predacious behavior. *Environ. Poll* 242, 839e844. doi: 10.1016/j.envpol.2018.07.071

Kumar, R. (2003). Effects of *mesocyclops thermocyclopoides* (Copepoda: cyclopoida) predation on the population growth patterns of different prey species. *J. Freshwat. Ecol.* 18 (3), 383–393. doi: 10.1080/02705060.2003.9663974

Kumar, R. (2005). Feeding modes and associated mechanisms in zooplankton, (In *ecology of plankton* ed: kumar, A). *Daya Publ.*, 241–265.

Kumar, R., and Rao, T. R. (1999). Effect of algal food on animal prey consumption rates in the omnivorous copepod, *mesocyclops thermocyclopoides*. *Internat. Rev. der gesamten Hydrobiologie und Hydrographie* 84 (5), 419–426. doi: 10.1002/iroh.199900035

Kumar, R., and Rao, T. R. (2001). Effect of the cyclopoid copepod *Mesocyclops thermocyclopoides* on the interactions between the predatory rotifer *Asplanchna intermedia* and its prey *Brachionus calyciflorus* and *B. angularis*. *Hydrobiologia* 453, 261–268. doi: 10.1023/A:1013105125857

Kumari, N., Samantaray, B. P., Patel, A., and Kumar, R. (2023a). Microplastics affect rates of locomotion and reproduction via dietary uptake in globally invasive snail. *Physa acuta. Water* 15 (5), 928. doi: 10.3390/w15050928

Kumari, N., Yadav, D. K., Khan, P. K., and Kumar, R. (2023b). Occurrence of plastics and their characterization in wild-caught fish species (Labeo rohita, Wallago attu, and Mystus tengara) of River Ganga (India) compared to a commercially cultured species (L. rohita). *Environ. pollut.* 334, 122141. doi: 10.1016/j.envpol.2023.122141

Lampert, W., and Sommer, U. (1997). *Limnoloecology: the ecology of lakes and streams* (Oxford: Oxford University Press).

Lee, C.-H., Dahms, H.-U., Cheng, S.-H., Souissi, S., Schmitt, F. G., Kumar, R., et al. (2010). Predation of *Pseudodiaptomus annandalei* (Copepoda: Calanoida) by the grouper fish fry *Epinephelus coioides* under different hydrodynamic conditions. *J. Exp. Mar. Bio. Ecol.* 393 (1-2), 17–22. doi: 10.1016/j

Li, D., Peng, G., and Lixin, Z. (2019). Progress and prospects of marine microplastic research in China. *Anthropocene Coasts.* 2 (1), 330–339. doi: 10.1139/anc-2018-0014

Mathalon, A., and Hill, P. (2014). Microplastic fibers in the intertidal ecosystem surrounding Halifax Harbor, Nova Scotia. *Mar. pollut. Bull.* 81 (1), 69–79. doi: 10.1016/j.marpolbul.2014.02.018

Mehinto, A. C., Coffin, S., Koelmans, A. A., Brander, S. M., Wagner, M., Thornton Hampton, L. M., et al. (2022). Risk-based management framework for microplastics in aquatic ecosystems. *Micro Nanoplastics* 2, 17. doi: 10.1186/s43591-022-00033-3

Nair, H. T., and Perumal, S. (2022). Trophic transfer and accumulation of microplastics in freshwater ecosystem: risk to food security and human health. *Internat. J. Ecol.* 2022, 1234078. doi: 10.1155/2022/1234078

Nelms, S. E., Galloway, T. S., Godley, B. J., Jarvis, D. S., and Lindeque, P. K. (2018). Investigating MP trophic transfer in marine top predators. *Environ. pollut.* 238, 999–1007. doi: 10.1016/j.envpol.2018.02.016

Neves, D., Sobral, P., Ferreira, J. L., and Pereira, T. (2015). Ingestion of MPs by commercial fish off the Portuguese coast. *Mar. pollut. Bull.* 101 (1), 119–126. doi: 10.1016/j.marpolbul.2015.11.008

Nielsen, B. L. H., Gréve, H. V. S., and Hansen, B. W. (2020). Cultivation success and fatty acid composition of the tropical copepods *Apocyclops royi* and *Pseudodiaptomus annandalei* fed on monospecific diets with varying PUFA profiles. *Aquaculture Res.* 52 (3), 1127–1138. doi: 10.1111/are.14970

Oaten, A., and Murdoch., W. W. (1975). Functional response and stability in predator-prey systems. *Am. Nat.* 109, 289–298. Available at: http://www.jstor.org/stable/2459696.

Paffenhöfer, G.-A., and Van Sant, K. B. (1985). The feeding response of a marine planktonic copepod to quantity and quality of particles. *Mar. Ecol. Prog. Ser.* 27, 55–65. doi: 10.3354/meps027055

Pan, D., Su, F., Liu, H., Liu, C., Umar, A., Castañeda, L., et al. (2021). Research progress on catalytic pyrolysis and reuse of waste plastics and petroleum sludge. *ES Mat Manuf* 11, 3–15. doi: 10.30919/esmm5f415

Qiao, R., Lu, K., Deng., Y., Ren, H., and Zhang, Y. (2019). Combined effects of polystyrene microplastics and natural organic matter on the accumulation and toxicity of copper in zebrafish. *Sci. Total Environ.* .682, 128–137. doi: 10.1016/j.scitotenv.2019.05.163

Rajan, K., Khudsar, F. A., and Kumar, R. (2023). Spatio-temporal patterns of microplastic contamination in surface waters of Hooghly River Estuary: Causes and consequences. *Regional Stud. Mar. Sci.* 65, 103111. doi: 10.1016/j.rsma.2023.103111

Rao, T. R., and Kumar, R. (2002). Patterns of prey selectivity in the cyclopoid copepod *Mesocyclops thermocyclopoides*. *Aquat. Ecol.* 36, 411–424. doi: 10.1023/A:1016509016852

Richon, C., Gorgues, T., Paul-Pont, I., and Maes, C. (2022). Zooplankton exposure to MPs at global scale: Influence of vertical distribution and seasonality. *Front. Mar. Sci.* 9. doi: 10.3389/fmars.2022.947309

Roch, S., Friedrich, C., and Brinker, A. (2020). Uptake routes of MPs in fishes: Practical and theoretical approaches to test existing theories. *Sci. Rep.* 10, 3896. doi: 10.1038/s41598-020-60630-1

Rochman, C. M., Brookson, C., Bikker, J., Djuric, N., Earn, A., Bucci, K., et al. (2019). Rethinking microplastics as a diverse contaminant suite. *Environ. Toxicol. Chem.* 38, 703–711. doi: 10.1002/etc.4371

Rochman, C., Hoh, E., Kurobe, T., and Teh, S. J. (2013). Ingested plastic transfers hazardous chemicals to fish and induces hepatic stress. *Sci. Rep.* 3, 3263. doi: 10.1038/srep03263

Sarma, S. S. S., and Nandini, S. (2002). Studies on functional response and prey selection using zooplankton in the anostracan *Chirocephalus diaphanus* Prevos. *Hydrobiologia* 486, 169–174. doi: 10.1023/A:1021398718074

Setälä, O., Fleming-Lehtinen, V., and Lehtiniemi, M. (2014). Ingestion and transfer of MPs in the planktonic food web. *Environ. pollut.* 185, 77–83. doi: 10.1016/j.envpol.2013.10.013

Smith, B. E., and Smith, L. A. (2020). Multispecies functional responses reveal reduced predation at high prey densities and varied responses among and within trophic groups. *Fish Fisheries* 21, 891–905. doi: 10.1111/faf.12468

Solomon, M. E. (1949). The natural control of animal populations. *J. Anim. Ecol.* 18, 1–35. doi: 10.2307/1578

Svetlichny, L., İşinibilir, M., Mykitchak, T., Eryalçın, K. M., Türkeri, E. E., and Yüksel, E. (2021). Microplastic consumption and physiological response in *Acartia clausi* and *Centropages typicus*: possible roles of feeding mechanisms. *Regional Stud. Mar. Sci.* 43, 101650. doi: 10.1016/j.rsma.2021.101650

Ter Halle, A., Ladirat, L., Martignac., M., Mingotaud, A. F., Boyron, O., and Perez, E. (2017). To what extent are MPs from the open ocean weathered? *Environ. pollut.* 227, 167–174. doi: 10.1016/j.envpol.2017.04.051

Traboni, C., Sarno, D., Ribera d'Alcalà, M., and Mazzocchi, M. G. (2023). Microplastics in the menu of Mediterranean zooplankton: Insights from the feeding response of the calanoid copepod *Centropages typicus*. *Mar. Ecol.* 00, e12760. doi: 10.1111/maec.12760

Tseng, L. C., Kumar, R., Chen, Q. C., and Hwang, J. S. (2011). Summer distribution of *noctiluca scintillans* and mesozooplankton in the Western and Southern East China Sea prior to the three gorges dam operation. *Hydrobiologia* 666 (1), 239–256. doi: 10.1007/s10750-010-0587-y

Turner, J., and Tester, P. (1989). Zooplankton feeding ecology: copepod grazing during an expatriate red tide. 359–374. doi: 10.1007/978-3-642-75280-3_21

Ugwu, K., Herrera, A., and Gomez, M. (2021). Microplastics in marine biota: A review. *Mari Pol. Bul.* 169, 112540. doi: 10.1016/j.marpolbul.2021.112540

Vanderploeg, H. A., Paffenhöfer, G. A., and Liebig, J. R. (1990). Concentration-variable interactions between calanoid copepods and particles of different food quality: observations and hypotheses. *Behav. Mech. Food Selection* 20, 595–613. ISBN: 978-3-642-75120-2.

von Moos, N., Burkhardt-Holm, P., and Köhler, A. (2012). Uptake and effects of microplastics on cells and tissue of the blue mussel *Mytilus edulis* L. after an experimental exposure. *Environ. Sci. Technol.* 46 (20), 11327–11335. doi: 10.1021/es302332w

Walne, P. R. (1970). Studies on the food value of nineteen genera ofalgae to juvenile bivalves of the genera Ostrea, Crassostrea, Mercenaria,and Mytilis. *Fishery Investigations* 26, 1–62.

White, J. R., and Dagg, M. J. (1989). Effects of suspended sediments on egg production of the calanoid copepod Acartia tonsa. *Mar. Biol.* 102, 315–319. doi: 10.1007/BF00428483

Woods, M. N., Hong, T. J., Baughman, D., Andrews, G., Fields, D. M., and Matrai, P. A. (2020). Accumulation and effects of microplastic fibers in American lobster larvae (*Homarus americanus*). *Marine Pollu. Bulletin* 157, 111280.

Xu, J., Rodríguez-Torres, R., Rist, S., Nielsen, T. G., Hartmann, N. B., Brun, P., et al. (2022). Unpalatable plastic: efficient taste discrimination of MPs in planktonic copepods. *Environ. Sci. Technol.* 56 (10), 6455–6465. doi: 10.1021/acs.est.2c00322

Zhang, F., Wang, X., Xu, J., Zhu, L., Peng, G., Xu, P., et al. (2019). Food-web transfer of MPs between wild caught fish and crustaceans in East China Sea. *Mar. pollut. Bull.* 146, 173–182. doi: 10.1016/j.marpolbul.2019.05.061

Zimmermann, L., Dierkes, G., Ternes, T. A., and Völker, C. (2019). Wagner M. Benchmarking the in *vitro* toxicity and chemical composition of plastic consumer products. *Environ. Sci. Technol.* 53 (19), 11467–11477. doi: 10.1021/acs.est.9b02293

The Journal of Supercomputing
https://doi.org/10.1007/s11227-023-05875-z

Multi-level trust-based secure and optimal IoT-WSN routing for environmental monitoring applications

Vishal Sharma[1] · Rohit Beniwal[1] · Vinod Kumar[1]

Accepted: 22 December 2023
© The Author(s), under exclusive licence to Springer Science+Business Media, LLC, part of Springer Nature 2024

Abstract

Wireless sensor networks (WSNs) are a critical component of the Internet of Things (IoT) which can be used in various fields, including environmental monitoring, smart agriculture, etc. However, WSNs used in environmental monitoring particularly in border areas are vulnerable to various security threats caused by illegal intruders who perform eavesdropping, garnishing, gray-hole attacks, etc. to compromise the network and forge the sensitive data. A multi-level hierarchical secure and optimal routing (ML-HSOR) protocol is proposed to overcome these issues. The proposed ML-HSOR protocol has four stages: registration, clustering, authentication, and optimal routing. In the registration step, the new sensor nodes are registered with the base station (BS) using unique identities. In the clustering stage, a Markov model with adaptive weighting mechanism is used to choose the most suitable node as the cluster head (CH), enhancing network lifespan and performance. The authentication stage involves a multi-level trust evaluation to detect malicious nodes. The aggregated message and timestamp are encrypted, and finally, the optimal data transmission path is chosen based on the polarity learning-based chimp optimization algorithm (PL-COA). This approach computes node fitness based on residual energy, distance, link quality, delay, and trust, ensuring high packet delivery ratio (PDR) (99.8% for 500 nodes), high throughput (48,000 bits per second for 500 nodes), less delay (0.058s for 500 nodes), high detection rate (95%), and less energy consumption (0.39 J for 500 nodes).

Keywords Environmental monitoring · Internet of Things · Optimization · Routing · Security · Trust

✉ Rohit Beniwal
dr.rohitbeniwal@gmail.com

Vishal Sharma
vishalmtr@gmail.com

Vinod Kumar
vinod_k@dtu.ac.in

[1] Department of Computer Science and Engineering, Delhi Technological University, Main Bawana Road, New Delhi, Delhi 110042, India

Published online: 23 January 2024

1 Introduction

The IoT is an expanding network of devices that are connected to gather and share data in real time. With the evolution of unified communication, there has been a significant rise in the use of devices connected to the IoT [1–3]. Wireless sensor networks (WSNs) use low-cost, smart sensors to improve data collection capabilities as the Internet of Things (IoT) expands. In an IoT system, sensors broadcast their data directly to the internet, but in WSNs, sensors are connected to a central node or a router [4]. To obtain data from WSN, an IoT system can establish a connection with the WSN's router. The gateway offers LoRaWAN wireless connectivity to the sensor network over a range of up to 15 km. Low-power, short-distance radios that comply with IEEE 802.15.4 are often utilized in several IoT applications [5]. IoT applications are being developed for a wide range of fields, like the transportation sectors, smart cities, the energy and medical sectors, military, and agricultural monitoring, forest monitoring, etc. [6, 7].

The collaboration between IoT and WSNs has brought about transformative advancements in various sectors. By connecting IoT systems to a WSN, farmers gain access to real-time data regarding soil moisture, weather conditions, and crop health, thus enabling precision irrigation and enhancing crop yields [8]. Similarly, in the healthcare sector, IoT devices integrated with WSN technology offer continuous monitoring of patients' vital signs, transmitting crucial data to healthcare providers for remote patient care, and timely medical interventions. In the medical sector, IoT-WSN integration is a game changer, with wearable devices collecting patient health data, transmitting it to healthcare providers, and enhancing remote patient care and early disease detection [9]. Moreover, the energy sector benefits from IoT-WSN applications for smart grid management, facilitating the monitoring and optimization of energy distribution [10]. These concrete examples illustrate how the fusion of IoT and WSN technologies drives efficiencies, optimizes resource utilization.

However, it is essential to acknowledge that this synergy between IoT and WSNs brings about new challenges, particularly in terms of security. The security of IoT-based WSNs is critical to ensure the integrity and reliability of data, as well as the proper functioning of applications. These security challenges encompass various threats, such as unauthorized access, data breaches, and network disruptions [6]. In precision agriculture, for instance, unauthorized access to IoT-WSN systems can lead to inaccurate data collection, potentially resulting in suboptimal crop yields or even crop losses. Furthermore, in health care, the compromise of patient health data transmitted through IoT-WSN technology poses a significant risk to patient care and privacy. These specific examples underscore the gravity of security risks in IoT-based WSN applications, emphasizing the need for robust security measures.

Rosewood, pine, teak wood, and sandalwood are a few of the precious trees that have seen a dramatic rise in poaching as a result of man's excessive desire to satisfy his desires [11]. Moreover, Rhino poaching is a serious problem in India. The horn may range in length from around 20 cm to about 60 cm; it can cost as

much as $300,000 due to its high demand in the treatment of diseases, including cancer and hangovers. Most of the world's population of the Indian one-horned rhinoceros reside in the protected areas of Assam, particularly in Kaziranga National Park, Orang National Park, etc. The nails, skin, and horns of rhinos are all highly prized because of its usage in traditional Vietnamese and Chinese medicine [12]. Moreover, international boundaries may not have nearby settlements, patrolling troops, or barriers in challenging terrain such as forests [13, 14]. Therefore, IoT-based WSNs provide a solution for real-time environmental monitoring. However, these networks are prone to various security threats by illegal intruders that may affect the national security [15].

Wireless sensor nodes, constrained by factors such as limited processing power, storage space, and battery life, encounter challenges in network lifetime due to inefficient clustering and routing techniques. Addressing these constraints is crucial for sustaining network performance. Additionally, securing data in potentially hostile environments against malicious attacks poses a significant challenge for IoT-based wireless sensor networks (WSNs). These attacks aim to deplete node energy, disrupt services, or extract sensitive data. They provide further challenges, encompassing deceptive behaviors like garnishing and bad mouthing attacks, covert tactics such as gray-hole attacks, disruptive strategies like denial of service attacks, and identity manipulation in whitewashing attacks. Furthermore, the network faces threats from data replay methods and information interception through eavesdropping attacks. Combating these security risks is essential for ensuring the reliable and secure operation of WSNs in IoT applications.

Recently, intrusion detection system (IDS)-based methods [16], machine learning methods (ML) [17], trust-based methods [18], and cryptographic techniques [19] have been proposed to minimize the routing attacks. However, cryptographic methods cannot guarantee complete network security for sensor nodes. By comparing nodes' behaviors against a set of criteria, trust may be established between them. In recent years, researchers focus toward trust-based methods because of its easy implementation and less complexity [20]. Several trust formation systems have been suggested in different industries, including web-based services, e-commerce, and WSNs. In WSNs, trust is calculated regularly depending upon the number of occurrences of good and bad conduct measured within a certain span of time and using a specific mechanism [21]. Therefore, this work proposes a multi-level trust-based optimal routing technique for IoT-based WSN applications. The following are our main contributions:

- The proposed ML-HSOR methodology employs an adaptive clustering approach based on the Markov model for CH selection and distinguishes itself by introducing a dynamic feature that allows real-time adjustment of attribute weighting based on current network conditions. This adaptive mechanism continuously evaluates sensor nodes and their attributes, ensuring that the most suitable nodes are appointed as CHs. This adaptability enhances network lifespan, performance, and CH selection, making the methodology more resilient and dynamic compared to traditional Markov models.

- ML-HSOR addresses the problem of malicious nodes that cause various attacks, such as garnishing and bad mouthing, by introducing a multi-level hierarchical trust evaluation approach. Trust is evaluated at both intra-cluster and inter-cluster levels, considering factors such as interaction trust, data trust, validation trust, transmission trust, and identity trust. This approach significantly enhances security and reliability, a novel contribution that safeguards environmental monitoring systems.
- In the context of garnishing attacks, a time-window mechanism is introduced to observe the behavior of nodes over specific periods. This approach monitors the number of successful and unsuccessful interactions between nodes and uses this information to assess trustworthiness. The time-window mechanism contributes to effectively countering dynamic threats and maintaining system integrity, a novel feature not typically found in existing methodologies.
- To prevent replay attacks and eavesdropping, timestamps are added to each message, and data are encrypted using the improved blowfish algorithm (IBFA). This ensures data integrity and confidentiality, particularly in forest areas where sensitive information needs protection.
- The congestion is reduced and the optimal path is determined using PL-COA. The performance of COA is improved by introducing polarity learning and Levy flight strategy.
- Polarity-based learning enables solutions to be found efficiently by examining opposite search spaces. This novel feature helps prevent local optima entrapment and enhances the algorithm's exploration capabilities, a unique contribution that is not commonly found in traditional metaheuristic algorithms.
- Levy flights facilitating comprehensive data surveying and navigation in complex and high-dimensional environmental data spaces. This feature enables the algorithm to avoid local optima and discover better solutions, contributing to more robust environmental monitoring in dynamic and evolving conditions.

The remaining sections of the paper are organized as follows: Sect. 2 presents the related works, Sect. 3 introduces the proposed ML-HSOR protocol, Sect. 4, provides the comparative result analysis, and finally, Sect. 5 gives the conclusions and future scope.

2 Related works

This section provides an overview of relevant research conducted in the field of IoT, specifically focusing on clustering, routing, and security. Clustering specifies the grouping of nodes into clusters to increase network efficiency and reduce energy consumption. Security is another critical aspect of IoT systems, and the reviewed literature delves into the different security mechanisms deployed in IoT networks to ensure confidentiality, integrity, and availability of data.

Bany et al. [22] introduced a unique clustering technique with the goal of increasing network lifespan by load balancing. The suggested technique is divided into two stages: CH allocation and relay node allocation. The energy level of the CH and its

distance from other cluster nodes are the two criteria used to determine which CH is chosen. The choice of a relay node is based on how close it is to the sink, providing the shortest path and facilitating in energy conservation. Also, the amount of remaining energy in a relay node has an impact on the choice of that node.

Salim et al. [23] presented a strategy for the safe and efficient collection of IoT data. Their approach is divided into three stages: setup stage, secure data collection, and data reconstruction. The compressive sensing-based technique is employed during the safe intra-communication operation for encryption and data compression. The security is enhanced by integrating public and private key algorithms.

Kaur et al. [24] introduced a routing approach for IoT-WSNs that utilizes deep reinforcement learning (DRL). Their work is separated into two stages: uneven cluster construction and smart data routing. This approach splits the network into multiple clusters on the basis of data load. Multi-objective DRL is presented for inter- and intra-cluster routing during the data routing phase to greatly boost network performance and minimize communication time. This method dramatically reduces latency and increases the lifetime of the network.

Abasıkele¸s-Turgut et al. [25] presented a technique for cluster communication. The separation between the BS and the cluster heads determines the size of the coverage region. The self-organized nodes identify the cluster heads, clusters, and clustering ranges, without the need for a central control mechanism. Furthermore, static clustering reduces the number of control messages created by the system. Their technique reduced the rate of CH change and prevented the network's head nodes from dying prematurely.

Mahajan et al. [26] introduced a nature-inspired algorithm-based cross-layer clustering (NICC) technique to significantly increase the lifespan of WSN in a smart farming application. This technique is used for constant monitoring of the agricultural field. As a WSN protocol designed for IoT applications, NICC operates in clusters. Bacterial Foraging Optimization determined the ideal sensor for routing and clustering issues. The energy balancing is achieved, and the jitter, delay, and overhead are reduced. However, data privacy and security were poor.

Alotaibi [27] developed a novel secure routing technique by selecting the most efficient route possible and encrypting the data. In the beginning, optimum link-state multipath routing is executed, during which optimal nodes are chosen for the purpose of ensuring secure transmission. Following this, encryption takes place, which makes communication completely safe. For the purpose of providing safe authentication, an Improved Blowfish algorithm is presented in this study. This method is secure against several attacks. However, the energy efficiency was low.

In order to lessen the amount of power that is used by WSNs, an energy-efficient two-stage routing protocol known as EETSP was developed by Dwivedi et al. [28]. The EETSP is segmented into two distinct phases. The key step involves the selection of CH and secondary CH. The secondary CH serves as a backup for the initial CH. The second stage performs intra- and inter-cluster routing. The number of packets transmitted to the BS experiences a substantial surge, while the CHs strive to diminish the network's overall energy consumption.

Subramani et al. [29] introduced mobile sink-based energy aware clustering for routing in IoT-enabled WSNs. This approach efficiently minimizes energy

consumption. In addition, the type-II fuzzy logic approach is employed to optimize the selected routes. However, this method has a high delay, less reliability, and less security.

Arya et al. [30] proposed a deep belief network to enable improved data transfer along the selected path. In this architecture, the nodes in the whole network were first clustered using a reinforcement learning method. A manta ray foraging optimization (MRFO) method was then used to choose the CH necessary for effective data transfer. Through the implementation of a proficient deep-learning approach, the packet is directed to the BS node via the selected CH. Consequently, there was an improvement in the packet delivery ratio (PDR). Nevertheless, this method does not provide safeguards against various forms of attacks in WSNs.

By leveraging controller discovery, virtual routing, and topology available in novel virtualization and load-balancing routing (VLBR), Hajian et al. [31] proposed architecture resulted in an extended lifespan and decreased load. This solution minimized the interchange of network status and other pertinent data. Network load distribution reduced network energy usage and increased network lifetime.

Seyyedabbasi et al. [32] proposed two metaheuristic algorithms: improved gray wolf optimization (I-GWO) and extended (Ex-GWO) to optimize the pathfinding and data transmission processes in WSN and decentralized IoT systems. The energy-efficient routing based on the I-GWO algorithm (EERI-GWO) was used to optimize the pathfinding process by finding the optimal path for data transmission between the source and destination nodes. The Ex-GWO algorithm was created to enhance the data transmission process by minimizing both delay and energy consumption that occurs during the transmission of data.

Benelhouri et al. [33] suggested an evolutionary gateway-based load-balanced routing (E-GLBR) protocol that focuses on balancing the load between nodes and improving the quality of service (QoS) by optimizing the path selection process. This protocol used Genetic Algorithm to optimize the routing paths and improve the QoS in WSNs. The primary goals of this algorithm are to improve the selection process for CHs, reduce the range of energy transmission, enhance stability, and extend the lifespan of the network with the increase in the coverage of WSN.

Preeti et al. [34] presents a focus on addressing energy constraint issues in WSNs through the development of the Improved Chimp Optimizer Algorithm (IChoA). While this approach integrates the chimp optimizer with the dimension learning-based hunting (DLH) search technique, aiming to strike a balance between exploitation and exploration, it's essential to highlight some limitations in their method. Notably, this work lacks a comprehensive discussion of the practical implications and real-world applications of their proposed approach. Also, the absence of polarity learning and Levy flight-based algorithms in this approach can result in suboptimal path selection, limiting the network's ability to efficiently adapt to dynamic conditions, resulting in reduced throughput and less effective energy management in wireless sensor networks.

Hosseinzadeh et al. [35] primarily focuses on enhancing security within wireless sensor networks (WSNs) by employing the Fire Hawk Optimizer (FHO) for trusted routing. They introduce a weighted trust mechanism (WTM) that dynamically adjusts trust levels based on interactions between sensor nodes, considering

aspects like the weighted reception rate, weighted redundancy rate, and energy state. Furthermore, their approach utilizes a FHO-based clustering method for selecting cluster heads from a candidate set, comprising nodes with energy and trust levels above network averages. However, it exhibits suboptimal path selection, reduced throughput, and inefficient energy management, which limits its suitability for dynamic and resource-constrained WSN environments.

Khan et al. [36] proposed a novel and comprehensive trust estimation approach (LTS) for large-scale WSNs, leveraging clustering to enhance cooperation, trust, and security by identifying malicious nodes with reduced power consumption. The approach operates at both intra and inter levels to facilitate accurate trust decisions with minimal overhead. To address malicious nodes, it introduces unique features, including a robust trust estimation function, resistance to attacks, and efficient trust aggregation at the cluster head for obtaining a global feedback trust value. These features aid in eliminating dishonest recommendations, incorporating punishment mechanisms, and introducing a trust severity feature for finer network tuning. However, the method does not account for the weight and frequency of misbehavior, making it susceptible to on–off and collusion attacks. Additionally, it is not optimized for homogeneous WSNs.

In a work conducted by Kalidoss et al. [37], they proposed a wireless sensor network (WSN) with a Quality of Service (QoS)-aware, trust-based routing algorithm designed to provide accurate trust scores. The algorithm calculates three different trust scores to enhance communication security. Additionally, they suggested a cluster-based secure routing algorithm tailored for secure routing within clusters. The final path selection is determined through a consideration of path-trust, energy, and hop count for routing purposes. The study was simulated using the NS2 simulator. However, it did not address the issue of handling uncertainty.

Arulanantham and Palanisamy [38] proposed a trusted cognitive sensor-based dual-routing network (TCSRN) for IoT to handle different types of attacks. Building upon this, the communication system achieves the highest packet delivery ratio and minimal delay toward the conclusion. This outcome results from the utilization of a reliable path selection approach employing the dual-path selection method. The method relies on one-hop reports and endorsement reports for reliability assessment, as well as global cumulative reliability, establishing connections between sensors. However, they were unable to reduce the complexity by minimizing parameters such as congestion, channel selection, and interruption.

Bangotra et al. [39] proposed a trust-based secure intelligent opportunistic routing protocol (TBSIOP) designed to identify malicious nodes based on three distinct characteristics, which are also employed in trust computation. The relay selection algorithm removes malicious nodes before they can be chosen as relay nodes. The proposed protocol is applied to the forwarder node list generated by the intelligent opportunistic routing protocol. The protocol is then simulated and compared with existing trust-based routing protocols from the literature. However, the utilization of only three wireless sensor network (WSN) attributes may pose disadvantages, particularly in terms of scalability within large networks. Table 1 provides comparison of the proposed and the existing WSN.

Table 1 Comparison of the proposed and existing WSN

Author	Technique	Advantage	Limitation
Bany et al. [22]	2-level clustering	Improves the network's longevity by minimizing the total energy usage through load balancing	Do not provide comprehensive trust evaluation mechanisms, leaving WSNs vulnerable to different attacks, including malicious nodes
Salim et al. [23]	Data Gathering with Secure Transmission and Reconstruction	Minimized power consumption during data transmission, extending device lifespan and energy efficiency Improved security through Private and Public key algorithms, considering IoT device power constraints	Have not accounted for potential scalability issues when applied to larger networks or complex scenarios
Kaur et al. [24]	DRL	Significantly reduces latency and extends network lifetime	No data security and privacy aspects
Abasıkeleş-Turgut and Altan [25]	FDEAM	Reduces control message overhead through static clustering Prevents the premature death of cluster heads	Lack dynamic CH selection mechanisms, which can lead to suboptimal performance in dynamic WSN environments
Mahajan and Badarla [26]	NICC	Offers improved network performance and reliability	Lack comprehensive security measures, leaving the network vulnerable to various security threats
Alotaibi [27]	CM-MH	Secure routing with efficient route selection and data encryption	Relatively low energy efficiency
Dwivedi et al. [28]	EETSP	Employs cluster heads and secondary cluster heads for energy efficiency	Not adequately considering trust metrics and multi-objective optimization, may lead to suboptimal paths and reduced network efficiency
Subramani et al. [29]	EACMRP-MS	Minimizes energy consumption with energy-aware clustering and mobile sink	High delay, reduced reliability, and limited security

Table 1 (continued)

Author	Technique	Advantage	Limitation
Arya et al. [30]	DBN	Increases the likelihood of successful packet delivery, reduces data loss and improving the overall data transmission reliability by optimizing the path for data transfer	Not accounting for the temporal behavior of nodes makes them susceptible to attacks that vary over time
Hajian et al. [31]	VLBR	Load-balancing routing reduces the need for frequent exchange of network status and information	Face challenges in providing robust security measures, leaving the network exposed to various security threats
Seyyedabbasi et al. [32]	EERI-GWO	By optimizing path selection and parameters, network reliability is enhanced	Limited exploration capabilities in complex and high-dimensional environmental data spaces
Benelhouri et al. [33]	E-GLBR	By improving CH selection and reducing energy wastage, the approach expands the network coverage area	Do not offer a comprehensive approach to secure path establishment and validation in WSN's
Preeti et al. [34]	IChoA	Provides a balance between exploitation and exploration	Suboptimal energy management, reduced throughput, and less efficient data transfer due to the absence of polarity learning and Levy flight-based algorithms
Hosseinzadeh et al. [35]	FHO	Dynamically adjust trust levels	Suboptimal path selection, reduced throughput, and Inefficient energy management
Khan et al. [36]	Comprehensive trust estimation approach (LTS)	Leveraging clustering to enhance cooperation, trust, and security by identifying malicious nodes with reduced power consumption. The approach operates at both intra and inter levels to facilitate accurate trust decisions with minimal overhead	Susceptible to on–off and collusion attacks. Additionally, it is not optimized for homogeneous WSN's

Table 1 (continued)

Author	Technique	Advantage	Limitation
Kalidoss et al. [37]	WSN with a quality of service (QoS)-aware, trust-based routing algorithm	Accurate trusts scores along with enhanced computational security. Secure routing within clusters	No uncertainty handling estimation
Arulanantham and Palanisamy [38]	TCSRN	To handle different types of attacks and reliable path selection approach	Not reducing the complexity by minimizing parameters such as congestion, channel selection, and interruption
Bangotra et al. [39]	TBSIOP	Removal of malicious nodes and providing a forward node list	Difficulty in scalability within large networks
Proposed method	ML-HSOR	It offers dynamic, real-time attribute weighting for CH selection, multi-level trust assessment for data reliability, robust countermeasures against evolving threats, data security through timestamps and encryption, congestion reduction and optimal pathfinding using PL-COA, and advanced solution discovery via polarity-based learning and Levy flights in complex environmental data spaces	Increased complexity and resource demands associated with addressing a wider range of threats and ensuring scalability for larger networks

Traditional clustering algorithms, such as Markov models [40], may get trapped in local optima, leading to suboptimal solutions. The proposed method overcomes this by introducing Levy flights for exploration, which allows it to escape local optima and discover better solutions. Also, environmental conditions can change rapidly, affecting the performance of WSNs. The proposed methodology adapts to real-time environmental changes and varying network conditions, ensuring its robustness and effectiveness in dynamic and evolving environments. WSNs are vulnerable to various security threats, including malicious nodes and attacks like garnishing and bad mouthing. The proposed multi-level hierarchical trust evaluation approach enhances security and reliability by identifying and mitigating these threats. Replay attacks, where intercepted messages are retransmitted, and eavesdropping on sensitive data can compromise network integrity. The use of timestamps and encryption in the proposed method safeguards against these security threats. Network congestion can lead to delays in detecting environmental activities and anomalies. The PL-COA algorithm reduces congestion and optimizes the network's data transmission, ensuring timely and efficient monitoring. Many traditional metaheuristic algorithms have limited exploration capabilities in complex and high-dimensional environmental data spaces. The incorporation of Levy flights in the proposed method facilitates comprehensive data surveying and navigation, enabling it to discover better solutions effectively. Static clustering approaches like traditional Markov models lack the ability to dynamically adjust attribute weighting in real time based on network conditions. The proposed methodology introduces dynamic attribute weighting, improving CH selection and network performance.

3 Proposed ML-HSOR methodology

In our proposed ML-HSOR methodology, we assume that the Base Station (BS) does not face resource limitations and remains secure from potential attackers. As the central command authority, the BS has the ability to eliminate malicious nodes and replace them with trustworthy ones to ensure stable operation. This assumption is grounded in practical considerations where the BS typically possesses greater computational resources and security measures compared to individual sensor nodes in WSNs. This distinction allows the BS to perform resource-intensive tasks and security functions. In practice, the BS often serves as the network's control center, enabling measures such as physical isolation, security protocols, and secure communication channels. These safeguards protect the BS and align with real-world practices to ensure its resource adequacy and security, thereby empowering it as the central command authority within our methodology to enhance network stability and security. Figure 1 illustrates the architecture of the proposed ML-HSOR methodology. It consists of perception, networking, and application layer. First, all the nodes in the network are registered, and then clustering is performed using the Markov model. The aggregated data are encrypted and transmitted via a secure and optimal path using the PL-COA algorithm.

Furthermore, the assumption of the BS's security extends to its resilience against sophisticated attacks, requiring the implementation of anomaly detection systems,

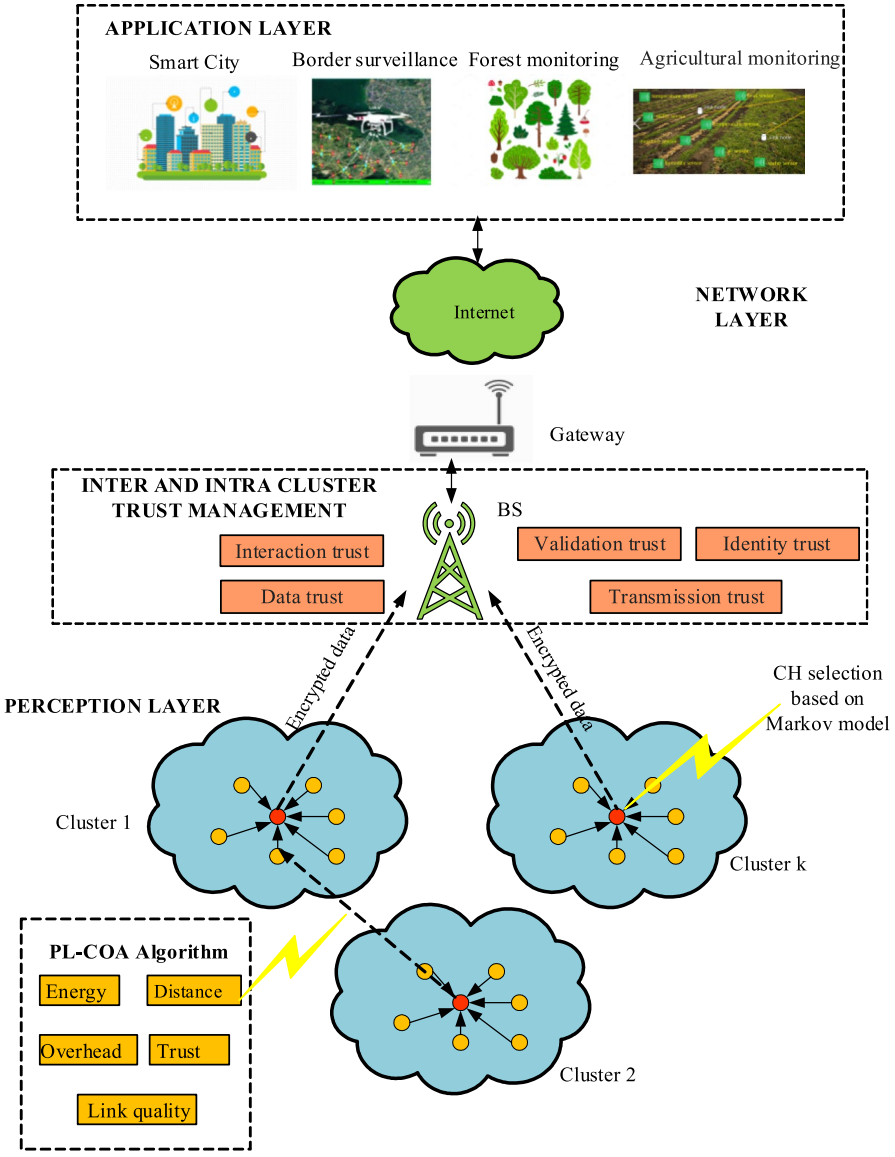


Fig. 1 The architecture of the proposed ML-HSOR methodology

intrusion prevention measures, and constant vigilance. The complexity is heightened by the need for the BS to dynamically adjust its security protocols based on evolving threat landscapes, ensuring a proactive defense mechanism against emerging vulnerabilities.

The proposed algorithm's complexity is further compounded by the interplay between the perception, networking, and application layers. The registration and

clustering of nodes, encryption of aggregated data, and transmission through a secure path using the PL-COA algorithm demand meticulous coordination and synchronization. Achieving optimal performance while maintaining security adds layers of intricacy, necessitating a carefully crafted algorithmic framework. The BS dynamically allocates resources that perfectly complements the adaptability built into our algorithm. The ML-HSOR model excels in real-time resource optimization, intelligently responding to changing network conditions. This synergy between the assumed resource allocation capabilities of the BS and our algorithm's adaptability enhances the overall responsiveness and efficiency of the WSN.

Real-time decision-making stands as a core strength of our proposed model. The BS, as the central command authority, capitalizes on the strengths of our algorithm to make instantaneous decisions. The energy efficiency for the BS mirrors the energy-saving strategies embedded in our algorithm. The ML-HSOR model optimizes communication protocols, manages power consumption, and employs sleep–wake strategies for sensor nodes, all contributing to the sustainable operation of the network. Scalability is a prominent strength of our algorithm, and the assumption that the BS accommodates network growth seamlessly reinforces this. The ML-HSOR model scales effectively with an increasing number of nodes, maintaining optimal performance.

3.1 Registration

The new sensor node that is added to the network is first registered with the BS using a unique identity. To enhance the security of the system, each node is assigned a distinct identity such as labels or hash values using a modified SHA-1 and SHA-2 algorithm [41]. The unique identities of the sensor nodes (SN) are generated by using Eq. (1).

$$U_{\mathrm{ID}} = \left((\mathrm{Ky}+1) \oplus N_{\mathrm{Rd}} \| H(\mathrm{Ky}+1) \oplus \mathrm{ID} \| N_{\mathrm{Rd}}\right) \tag{1}$$

where, Ky represents the key needed for the hash function, N_{Rd} denotes the random number generated by the BS, and ID denote the serial number. By using this labeling approach, communication becomes more efficient, and the system is protected against various external attacks, such as the spoofing and whitewashing attacks.

3.2 Clustering

In our clustering approach, we uphold the core principles of the Markov model [40] for CH selection. This model is the fundamental of our methodology, enabling the meticulous selection of secure and energy-efficient CHs. However, what sets our approach apart is the introduction of a pioneering feature: the ability to adaptively adjust the weighting of attributes in real time, based on the network's current conditions. This adaptive weighting mechanism performs a continuous evaluation of sensor nodes and their attributes, ensuring that the most suitable nodes are appointed as CHs. This adaptability grants us a unique advantage. For instance, if particular nodes consistently demonstrate exceptional energy efficiency, our model may assign a higher weight to

energy-related attributes for CH selection. This dynamic responsiveness allows our network to swiftly adapt to variations in energy levels and node behavior, ultimately leading to more precise CH selection. The innovative essence of our method lies in this adaptability, transforming it from a static model into a dynamic and resilient solution, capable of maintaining optimal performance throughout its operational lifetime. This dynamic and adaptive CH selection mechanism significantly boosts network lifespan and performance, all while optimizing the distribution of responsibilities among CHs. By integrating this novel feature, our methodology ensures efficient operation and longevity, rendering it a robust choice for WSNs in evolving environments. While the Markov model naturally adapts to changes in energy levels and node behavior over discrete time slots, the adaptive adjustment we introduce serves to fine-tune the model's parameters continuously in real time. This means the Markov model operates in a step-wise fashion, periodically reassessing and reselecting CHs based on discrete time slots. In contrast, our adaptive adjustment is more continuous and responsive, enabling real-time fine-tuning of model parameters to accurately mirror the immediate state of the network. The goal of introducing adaptive adjustment is to enhance CH selection responsiveness to the network's real-time condition. It accomplishes this by continually monitoring and adjusting parameters, a capability not captured by the Markov models discrete time slots. This added adaptability further optimizes CH selection and elevates overall network performance.

For example, consider a network with 100 sensor nodes. Our methodology employs the Markov model, a dynamic and adaptive approach, to continuously monitor the energy levels and behaviors of these sensor nodes in real time. This model updates the network state as it evaluates each node for the role of CH. For instance, at the beginning of the observation period, in time slot 1, node 50 exhibits the highest energy level. The Markov model, recognizing this, selects node 50 as the CH for that specific time slot. However, as time progresses and the network's state evolves, the energy levels of the nodes are subject to change. In the next time slot, it may turn out that node 20 now has the highest energy level, surpassing node 50. In response to this shift in energy levels, the Markov model dynamically adjusts and selects node 20 as the new CH. This process of continually updating the CH selection carries on, with the Markov model making real-time decisions based on changing energy levels and other relevant network conditions. The ability to select CHs dynamically and adapt to the network's immediate state ensures the efficient operation and longevity of the network, making our methodology a robust choice for WSNs in dynamic and evolving environments.

Every CH is responsible for managing the Member Nodes (MN) within its cluster and maintaining a record of their IDs and locations. The CH also maintains and updates the energy values of each node with the arrival of each message in a matrix, as given in Eq. (2).

$$\mathrm{Mat}_{\mathrm{MN}} = \begin{bmatrix} \mathrm{ID}_1 & \mathrm{PO}_1 & \mathrm{En}_1 \\ \mathrm{ID}_2 & \mathrm{PO}_2 & \mathrm{En}_2 \\ \vdots & \vdots & \vdots \\ \mathrm{ID}_{k-1} & \mathrm{PO}_{k-1} & \mathrm{En}_{k-1} \end{bmatrix} \tag{2}$$

where, ID, PO, and En denotes the identity, position, and energy of the MNs respectively. Similarly, the BS keeps a record of IDs, positions, and energy of the CHs as given in Eq. (3).

$$\mathrm{Mat}_{\mathrm{CH}} = \begin{bmatrix} \mathrm{ID}'_1 & \mathrm{PO}'_1 & \mathrm{En}'_1 \\ \mathrm{ID}'_2 & \mathrm{PO}'_2 & \mathrm{En}'_2 \\ \vdots & \vdots & \vdots \\ \mathrm{ID}'_{l-1} & PO'_{l-1} & \mathrm{En}'_{l-1} \end{bmatrix} \tag{3}$$

where, ID′, PO′, and En′ denotes the identity, position, and energy of the CHs respectively.

3.3 Authentication by multi-level hierarchical trust evaluation

Wireless sensors used in environmental monitoring applications can play a role in detecting illegal poaching in wildlife reserves and protected areas. For example, the sensors can detect any movement and trigger an alert, while infrared cameras can provide real-time images of the poacher, and sound recorders can pick up any sounds of vehicles or weapons. When a poacher enters the protected area, the wireless sensors are activated and send an alert to the park rangers. With this information, park rangers can quickly respond to the situation and prevent the illegal activity from taking place. This helps to protect wildlife and their habitats and supports conservation efforts. However, if the sensor network is disabled or otherwise compromised by the attackers, it becomes much easier for poachers to engage in illegal activities.

To overcome these issues, the proposed method detects the malicious nodes that cause various attacks such as garnishing, bad mouthing, gray-hole etc., using a multi-level hierarchical trust evaluation approach as provided in Fig. 2. The trust of

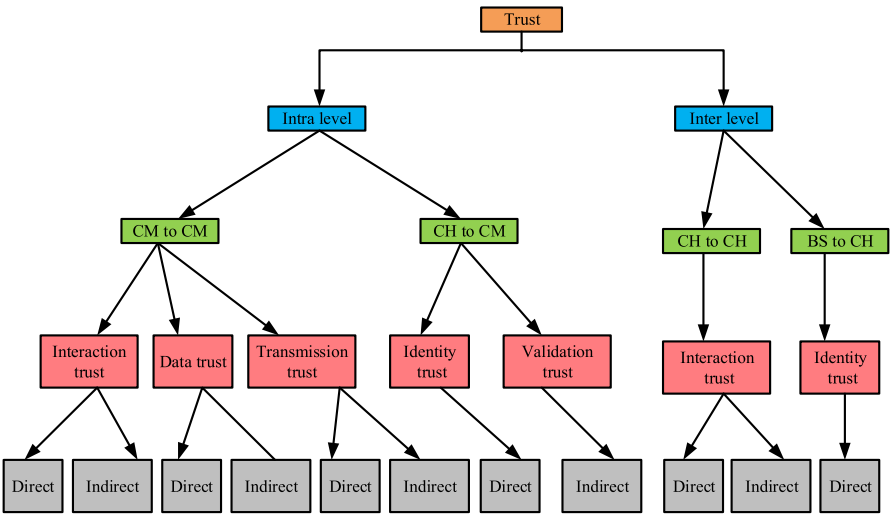


Fig. 2 Multi-level hierarchical trust evaluation

the nodes is determined at inter as well as intra cluster level. Intra-cluster trust refers to the level of trust evaluated between Cluster Members (CM) and between CH and CM, while inter-cluster trust pertains to the trust evaluated between CH and CH, as well as between BS and CH. The proposed method computes the interaction trust, data trust, validation trust, transmission trust, and identity trust of a node directly or based on the feedback (indirect) trust obtained from the neighboring nodes.

The process depicted in Fig. 3 involves the interaction between CM-CM and CM-CH for cluster head selection and information transfer to the BS. In this process, the trust level of CMs is assessed using three distinct types: interaction trust, data trust, and transmission trust. Subsequently, the most secure CMs undergo identity and validation trust to pinpoint the CM with a high trust level, who then transmits information to the CH. This process involves both direct and indirect nodes. Additionally, the information gathered from various cluster heads undergoes identity trust once again to identify the reliable cluster head in the network. Once the secure CH is determined, the information is sent to the BS, which encrypts the data before forwarding it. In a garnishing attack, the malicious nodes alternate their behavior between trustworthy and malicious, which aims to harm

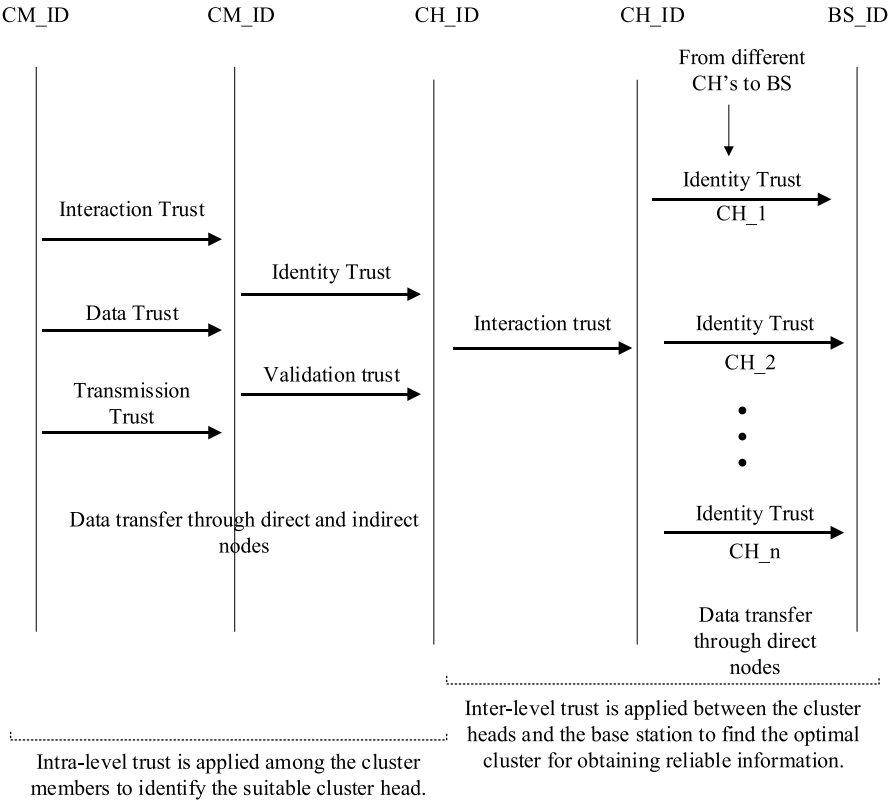


Fig. 3 Interactions between the different nodes in the Trust evaluation

the network while remaining undetected. To address this issue, trust is computed in which, a time-window mechanism, as illustrated in Fig. 4, is used to observe the behavior of nodes over a certain time frame.

(i) Time window

Trust computation takes advantage of a time-window mechanism each lasting a fixed amount of time interval. Interactions between nodes are periodically tracked and recorded for successful and unsuccessful outcomes. The time window then moves to the right and includes new interactions while discarding the oldest ones. This way, the time window provides an overview of a node's behavior over a certain period, taking into account both past and current actions.

For instance, if node A transmitted 5 successful readings and 2 unsuccessful readings in the first interval, this information is recorded. After each 5-min interval, the time-window slides to the right and includes new interactions while discarding the oldest ones. If the BS notices that a particular node has a high rate of unsuccessful transmissions during this time interval, the BS gives a penalty to reduce trust or replaces the node to ensure the reliability and security of the environmental monitoring system.

(ii) Time stamp

A replay attack in WSNs can occur when an attacker intercepts a message and later retransmits it. This kind of attack has the potential to interfere with the WSN's regular operations or grant the attacker unauthorized access. To prevent this, a timestamp is added to each message before transmission. The recipient can check whether the message is new and hasn't been replayed by looking at the timestamp, which shows the date and time the message was sent. The receiver has the option to delete messages that are too old. By discarding a message with an outdated timestamp, the receiver prevents an attacker from intercepting and later retransmitting it. Nevertheless, an attacker could alter the timestamp to an earlier time, deceiving the recipient into believing that the message was transmitted earlier than it actually was.

Moreover, eavesdropping attacks in forest areas can have various motives for attackers. They may aim to access sensitive or confidential information about environmental or conservation activities in the forest. By eavesdropping on the

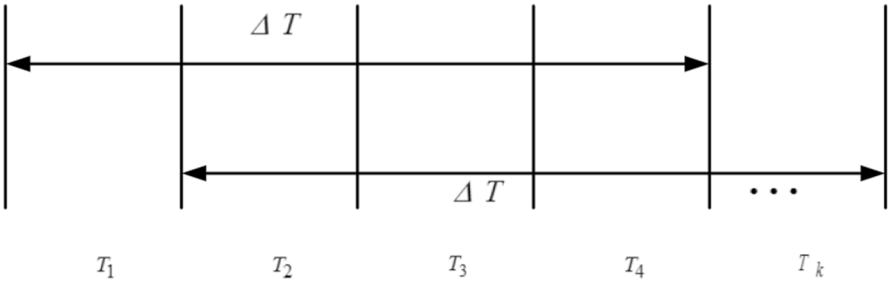


Fig. 4 Illustration of time window

communication signals, they can obtain sensitive details regarding the location of valuable resources such as timber or minerals and execute their theft more efficiently.

To address this issue, the aggregated data and the timestamp are encrypted before transmitting them to the receiving node using the Improved Blowfish Algorithm (IBFA) [27]. Upon reception, the recipient can decode the message and timestamp. Since the attacker does not possess the decryption key, an attacker who intercepts the communication cannot read or alter the message or timestamp. Encryption helps secure the integrity of the timestamp and aggregated data.

3.3.1 Intra-cluster trust

The intra-cluster trust is computed in two levels: CM-CM and CH-CM.

3.3.1.1 CM-CM level The trust between CM-CM relies on factors such as interaction trust, data trust, and transmission trust.

(i) Interaction trust (IT)

The direct interaction trust of node A on node B is computed using Eq. (4).

$$I_{\mathrm{A,B}}(\Delta T) = \left[N_{\mathrm{TW}} \times \left(\frac{S_{\mathrm{A,B}}(\Delta T)}{S_{\mathrm{A,B}}(\Delta T) + F_{\mathrm{A,B}}(\Delta T)} * \frac{1}{\varphi} \left(\frac{S_{\mathrm{A,B}}(\Delta T)}{S_{\mathrm{A,B}}(\Delta T) + 1} \right)^{\beta} \right) \right] \tag{4}$$

where, N_{TW} denotes the number of units in the time window, $S_{\mathrm{A,B}}(\Delta T)$ denotes the sum of successful interaction of node A with node B during the time window ΔT, $F_{\mathrm{A,B}}(\Delta T)$ represents the sum of failed interaction of node A with node B, φ and β signifies the penalty and pay factor that changes the trust value. The values of φ and β are tuned based on the application requirement.

Consider the case of node A which has never communicated with node B before but wants to determine whether node B can be trusted to forward a packet. In this case, the IT of node B is computed on the basis of scores given by other neighboring nodes (indirect trust) of the node B. The trust estimation accuracy is improved by utilizing feedback from neighboring nodes to determine the node B trust level. Thus, the indirect interaction trust is computed using Eq. (5).

$$I'_{\mathrm{A,B}}(\Delta T) = \frac{1}{n} \sum_{k=1}^{n} I_{\mathrm{N,B}}(\Delta T) \tag{5}$$

where, n denotes total number of neighbors of node B, $I_{N,\mathrm{B}}(\Delta T)$ represents the trust calculated directly by neighboring node N on node B which can be computed similar to Eq. (4).

(ii) Data trust (DT)

The concept of data trust is utilized to detect the presence of malicious nodes that cause gray-hole attacks, in which the intruder drops only certain kinds of data packets to stay as hidden as possible. An example to illustrate a gray-hole attack in

a WSN could be monitoring the temperature in a forest for early fire detection. A malicious node, acting as a gray-hole attacker, might drop data indicating high temperatures, making it appear as if the forest is not in danger even if there is an active fire. Failure to detect the fire promptly could result in significant damage.

Direct DT of node B is computed using Eq. (6).

$$D_{\mathrm{A,B}}(\Delta T) = \frac{\mathrm{DP_B}(\Delta T)}{\mathrm{ST_A}(\Delta T)} \tag{6}$$

where, $\mathrm{ST_A}$ denotes the sum of data packets sent by node A, $\mathrm{DP_B}$ represents the sum of packets dropped by node B.

Similarly, the indirect data trust of node B is computed using Eq. (7).

$$D'_{\mathrm{A,B}}(\Delta T) = \frac{1}{n}\sum_{k=1}^{n} D_{\mathrm{N,B}}(\Delta T) \tag{7}$$

where, n denotes total number of neighbors of node B, $D_{\mathrm{N,B}}(\Delta T)$ represents the trust calculated directly by neighboring node N on node B which can be computed similar to Eq. (6).

(iii) Transmission trust

A DoS attack can cause a node to become overloaded and reduce the responsiveness of the system. This causes delays in detecting environmental activities or anomalies, which can be critical in real-time monitoring applications. To prevent this, the transmission trust of a node is computed using Eq. (8).

$$\mathrm{TT_{A,B}}(\Delta T) = \frac{\mathrm{Pt(A,B)}}{t} \tag{8}$$

where, Pt(A,B) denotes the sum of packets transmitted from node A to node B at time t.

The indirect transmission trust is computed using Eq. (9).

$$\mathrm{TT'_{A,B}}(\Delta T) = \frac{1}{n}\sum_{k=1}^{n} \mathrm{TT_{N,B}}(\Delta T) \tag{9}$$

where, n denotes total number of neighbors of node B, $\mathrm{TT_{N,B}}(\Delta T)$ denotes the direct transmission trust calculated by neighboring node N on node B.

3.3.1.2 CH-CM level Trust between CH-CM is determined as follows:

(i) Identity trust

A whitewashing attack is a security threat that occurs when the system detects the malicious node and disconnects it from the network, and the malicious node then attempts to reenter the network under a different identity in order to trick the system into assigning it a new reputation score. To prevent this threat, identity trust is computed, in which each CM sends its data to its corresponding CH along with its ID

for trust evaluation. During trust evaluation, the identity trust of node A is computed directly by using Eq. (10).

$$ID_A = \begin{cases} 1 \text{ IF } \mathrm{ID_A} = \mathrm{ID}\left(\mathrm{Mat_{MN}}\right) \\ 0 \text{ otherwise} \end{cases} \tag{10}$$

where, $\mathrm{ID_A}$ represents the identity of node A, $\mathrm{ID}\left(\mathrm{Mat_{MN}}\right)$ represents the MN identities registered in matrix $\mathrm{Mat_{MN}}$ by the base station. The data are forwarded to the base station by the CH after undergoing trust verification and aggregation.

(ii) Validation trust

The CH gathers data from the MNs and makes decisions based on the information. During these processes, the CH obtains the reputation score of the target node from other nodes in the cluster. However, a malicious node can affect the reputation of legitimate nodes by giving them a low reputation score (bad mouthing attack). To determine if the information received is accurate, it is crucial to evaluate the reliability of the recommender. To counteract such attacks, the validity of the reputation score computed by node A is determined indirectly from other nodes using Eq. (11).

$$\mathrm{VT_{CH,A}}(\Delta T) = \left| R_{\mathrm{score(A,B)}} - R_{\mathrm{avg(B)}} \right| \tag{11}$$

where, $\mathrm{VT_{CH,A}}(\Delta T)$ denotes the validation trust score of node A computed by the CH at the time interval $\Delta T \cdot R_{\mathrm{score(A,B)}}$ represents the reputation score of node A given to node B. $R_{\mathrm{score(A,B)}}$ is obtained based on other trust measures such as interaction trust, data trust, transmission trust, and identity trust. The average of all the trust measures gives the reputation score and $\mathrm{RS_{avg(b)}}$ represents the average reputation score of node B obtained from other neighboring MNs (indirect) in the cluster.

3.3.2 Inter cluster trust

The degree of trust built between several clusters in a WSN is referred to as inter-cluster trust. The inter-cluster trust is computed in two levels: CH-CH and BS-CH.

3.3.2.1 CH-CH level It demonstrates how much a CH trusts the information provided by other CHs in the network. The ability of the CHs in various clusters to acquire and convey data accurately and reliably is indicated by the amount of inter-cluster trust between them.

The direct interaction trust of CH 'Q' is computed using Eq. (12). Formula 12 calculates the direct interaction trust of CH 'Q' in CH 'P'. This trust value represents how much CH 'Q' relies on the information provided by CH 'P'. The formula considers the accuracy and reliability of data shared by CH 'P' and CH 'Q's assessment of CH 'P's overall network activity.

$$I_{\mathrm{P,Q}}(\Delta T) = \left[N_{TW} \times \left(\frac{S_{\mathrm{P,Q}}(\Delta T)}{S_{\mathrm{P,Q}}(\Delta T) + F_{\mathrm{P,Q}}(\Delta T)} * \frac{1}{\varphi} \left(\frac{S_{\mathrm{P,Q}}(\Delta T)}{S_{\mathrm{P,Q}}(\Delta T) + 1} \right)^{\beta} \right) \right] \tag{12}$$

where, $S_{P,Q}(\Delta T)$ denotes the number of successful interaction of CH 'P' with CH 'Q' during the time window ΔT, $F_{P,Q}(\Delta T)$ represents the number of failed interaction of CH 'P' with CH 'Q', φ and β signifies the penalty and pay factor that changes the trust value depending on the CH behavior.

The indirect interaction trust of CH 'Q' is computed using Eq. (13).

$$I'_{P,Q}(\Delta T) = \frac{1}{n}\sum_{k=1}^{n} I_{M,Q}(\Delta T) \tag{13}$$

where, n denotes total number of neighbors of CH 'A', $I_{M,Q}(\Delta T)$ represents the direct interaction trust calculated by neighboring CH 'M' on node CH 'Q'.

3.3.2.2 BS-CH level It is essential for the BS to trust the data sent by CHs since it uses this data to make critical decisions. Therefore, the identity trust of CH 'P' is computed by using Eq. (14).

$$\mathrm{ID}_P(\Delta T) = \begin{cases} 1 \ \text{IF}\, \mathrm{ID}_P = \mathrm{ID}\left(\mathrm{Mat}_{\mathrm{CH}}\right) \\ 0 \ \text{otherwise} \end{cases} \tag{14}$$

where, ID_P represents the identity of CH 'P', $\mathrm{ID}\left(\mathrm{Mat}_{\mathrm{CH}}\right)$ represents the CH identities registered in matrix $\mathrm{Mat}_{\mathrm{CH}}$ by the BS.

3.4 Optimal route selection

The encrypted data are then sent to the destination node via a secure and optimal path using the PL-COA algorithm. Algorithm 1 outlines the Optimal Route Selection process using the PL-COA. This algorithm is designed to efficiently find the best route for secure data transmission in a network of nodes. The process involves population initialization, dynamic location updates, fitness evaluation, and the utilization of Levy flights for exploration. The ultimate goal is to identify the optimal path for data transmission while considering factors like residual energy, distance, link quality, overhead, and trust.

There are four categories of chimpanzees in a group named driver chimp, barrier chimp, chaser chimp, and attacker chimp. The drivers (source node) pursue the preys (destination node) but don't try to catch them. Barriers put themselves in trees to block the way of the prey's escape route (block the malicious nodes). Chasers (intermediate nodes) move quickly to catch their prey. When the target stops moving, the attackers (node closest to the destination) attack the prey and end the hunt. The paper uses this approach to identify the most efficient route to reach the destination node. Here, the prey is considered the destination node.

In the context of environmental monitoring, our approach introduces two significant innovations. Firstly, the utilization of Levy flights for exploration enhances the algorithm's ability to comprehensively survey the environmental parameters, making it adept at navigating intricate and multidimensional data spaces. This novel feature enables the algorithm to effectively avoid local optima and discover more optimal solutions in dynamic and complex environmental conditions. Secondly, our algorithm

incorporates polarity-based learning, which empowers it to dynamically adjust its monitoring strategy based on the evolving environmental conditions and the presence of critical data patterns. By preventing the algorithm from becoming trapped in local data minima and allowing it to adapt to real-time environmental changes, these innovations significantly improve its performance in environmental monitoring applications, addressing a limitation in existing algorithms that often fail to consider these aspects and, as a result, struggle to adapt to changing environmental conditions effectively.

This algorithm computes the fitness of the solution based on trust, delay, link quality, residual energy, and distance. The residual energy, distance, and link quality metrics improve the network lifetime and QoS. The trust metric helps to protect the network against various malicious attacks, while the delay metric reduces congestion. The chimp population y_i^0 is randomly initialized at the beginning.

3.4.1 Fitness evaluation

The optimal path is chosen based on the nodes with maximum residual energy, minimum distance, maximum link quality, maximum residual energy, and, minimum overhead. The objective is to maximize the fitness. The objective is to maximize fitness. To optimize the system, the objective is to increase the fitness value F in Eq. (15).

$$F = wt_1 E_{res} + wt_2 D(A,S) + wt_3 L_{qty} + wt_4 O_{hd} + wt_5 T \tag{15}$$

The weights wt_1, wt_2, wt_3, wt_4, and wt_5 are used to balance the importance of each objective function, where higher weights indicate higher priority. The values $wt_1 = 0.3$, $wt_2 = 0.1$, $wt_3 = 0.2$, $wt_4 = 0.1$, and $wt_5 = 0.3$ adjusted such that $wt_1 + wt_2 + wt_3 + wt_4 + wt_5 = 1$. E_{res}, $D(A,S)$, L_{qty}, O_{hd}, and T are the residual energy, distance, link quality, overhead, and trust.

(i) Residual energy

The residual energy of a SN is computed using Eq. (16).

$$E_{res} = E_{ini} - E_{T_con} \tag{16}$$

where, E_{ini} is the initial energy of a node and E_{T_con} denotes the total energy consumed which can be determined using Eq. (17).

$$E_{T_con} = E_{tx} + E_{rx} \tag{17}$$

where, E_{tx} and E_{rx} represents the energy consumed during data transmission and data reception which can be determined using Eq. (55) and Eq. (54).

(ii) Distance

The distance between node A and sink S is computed by Eq. (18).

$$D(\mathrm{A,S}) = \sqrt{\left(X'_{\mathrm{A}} - X'_{\mathrm{S}}\right)^2 + \left(Y'_{\mathrm{A}} - Y'_{\mathrm{S}}\right)^2} \tag{18}$$

where, $\left(X'_{\mathrm{A}}, X'_{\mathrm{S}}\right)$ and $\left(Y'_{\mathrm{A}}, Y'_{\mathrm{S}}\right)$ are the coordinates of the node A and sink S respectively.

(iii) Link quality

The link quality of two nodes A and B is computed using Eq. (19).

$$L_{\text{qty}} = \begin{cases} 1 \text{ if dist(A,B)} \le R_{\text{com}} \\ 0 \text{ otherwise} \end{cases} \tag{19}$$

where, $dist(A, B)$ represents the distance between node A and B, R_{com} represents the node's communication range.

(iv) Overhead

The overhead of a node A is computed by using Eq. (20)

$$O_{hd} = \begin{cases} 1, \text{ if } L_{\text{queue}}(\text{A}) \le L_{\min} \\ 0, \text{ otherwise} \end{cases} \tag{20}$$

where, $L_{\text{queue}}(\text{A})$ denotes the queue length of node A and $L_{\min}$ denotes the minimum queue length.

(v) Trust

During data transmission, the trust T of a node or CH is determined based on the multi-level hierarchical trust evaluation approach provided in Sect. 3.3.

3.4.2 Driving and chasing the prey

The current location of the chimp is denoted as given in Eq. (21).

$$Z_{\text{chimp}}(t+1) = Z_{\text{prey}}(t) - d \cdot C \tag{21}$$

where, $Z_{\text{prey}}(t)$ denotes the location of the prey, the parameters d and C are computed using Eqs. (22) and (23).

$$d = 2 \cdot h \cdot s_1 - h \tag{22}$$

$$C = \left| m \cdot Z_{\text{prey}}(t) - n \cdot Z_{\text{chimp}}(t) \right| \tag{23}$$

where, s_1 and s_2 represents the random number in the range [0, 1], n represents chaotic map vector, and the coefficient h is decreased from 2.5 to 0 nonlinearly, $m = 2s_2$.

3.4.3 Exploration

Exploration involves searching the entire search space to find new solutions. It is assumed that the attacker is in the same location as the prey. The attacker's location could then be used to change the location of the driver, barrier, and chaser. The other chimp's locations are updated to the best chimp's locations as given in Eqs. (24) to (28).

$$Z_1 = Z_A(t) - d_1 \cdot C_A \tag{24}$$

$$Z_2 = Z_B(t) - d_2 \cdot C_B \tag{25}$$

$$Z_3 = Z_C(t) - d_3 \cdot C_C \tag{26}$$

$$Z_4 = Z_D(t) - d_4 \cdot C_D \tag{27}$$

$$Z(t+1) = \frac{Z_1 + Z_2 + Z_3 + Z_4}{4} \tag{28}$$

where, t represents the present iteration, $Z_A(t)$, $Z_B(t)$, $Z_C(t)$, and $Z_D(t)$ represents the attacker chimp, barrier chimp, chaser chimp, and driver chimp's location respectively. The value of d for various chimps can be computed similar to Eq. (22) and C can be computed using Eqs. (29) to (32).

$$C_A = \left| m_1 \cdot Z_A(t) - n_1 \cdot Z(t) \right| \tag{29}$$

$$C_B = \left| m_2 \cdot Z_B(t) - n_2 \cdot Z(t) \right| \tag{30}$$

$$C_C = \left| m_3 \cdot Z_C(t) - n_3 \cdot Z(t) \right| \tag{31}$$

$$C_D = \left| m_4 \cdot Z_D(t) - n_4 \cdot Z(t) \right| \tag{32}$$

3.4.4 Exploitation

Utilizing information from past iterations, exploitation improves the exploration of potential solutions. In addition to the d and m parameters specified in the exploration phase, an additional parameter introduced in the exploitation phase determines how to prevent local minima trapping. If $|d|$ is higher than one, the chimpanzees are pushed to depart from the prey (preventing local optima entrapment), but if $|d|$ is less than one, the chimps are driven to converge at global optima. The following Eq. (33) models the updating process in this technique.

$$Z_{\text{chimp}}(t+1) = \begin{cases} Z_{\text{prey}}(t) - d \cdot C & \mu < 0.5 \\ \text{choatic value} & \mu > 0.5 \end{cases} \tag{33}$$

where, μ denotes random number in [0, 1].

3.4.5 Polarity-based learning

In general, when the initial solutions in metaheuristic algorithms are closer to the optimal location, convergence occurs quickly; else, slow convergence occurs. Polarity

learning finds the optimal solution by looking at the opposite search space. The polarity learning then selects the best path among all possible paths.

(i) Polarity Number

The following can be used to identify a polarity-based number. Let's say y_0 is a real number that falls within an interval $y_0 \in [p, q]$, the opposite number of y_0 is determined by Eq. (34).

$$\overline{y}_0 \in p + q - y_0 \tag{34}$$

Similarly, the opposite point is given by Eqs. (35) and (36).

$$y = y_1, y_2, \ldots, y_D \tag{35}$$

$$\overline{y} = \overline{y}_1, \overline{y}_2, \ldots, \overline{y}_D \tag{36}$$

Equation (37) is used to calculate the values of each item in $\overline{y}$.

$$\overline{y}_l = p_l + q_l - y_l \tag{37}$$

where, $l = 1, 2, 3, \ldots, D$. If $f(y_0)$ is greater than $f(\overline{y}_0)$, then y_0 remains unchanged; else, $y_0 = \overline{y}_0$; thus, population solutions are updated depending upon the better value of y_0 and $\overline{y}_0$.

(ii) Levy flights (LF)

LF is focused on a heavy-tailed probability distribution for random walks to explore the search space efficiently using step length and potentially find better solutions. Traditional random walks tend to get trapped in local optima, but Levy flight can make larger jumps and explore farther away regions of the search space, increasing the chance of finding better solutions. The Levy distribution computed using Eq. (38) is used to identify a probability function, from which the step sizes of LF are calculated.

$$L(y_i) = |y_i|^{1-\gamma} \tag{38}$$

where, y_i denotes the flight length, $1 < \gamma \leq 2$ signifies the power law exponent. The Levy probability density in integral form is determined using Eq. (39).

$$f_L(y;\gamma,\alpha) = \frac{1}{\pi}\int_0^{\infty} \exp(-\alpha q^{\gamma})\cos(qy)\mathrm{d}q \tag{39}$$

where, α denotes the scale unit, γ signifies the distribution index. When y has a large value, Eq. (39) typically require series expansion as given in Eq. (40).

$$f_L(y;\gamma,\alpha) \approx \frac{\alpha\Gamma(1+\gamma)\sin\left(\frac{\pi\gamma}{2}\right)}{\pi y^{(1+\gamma)}}, y \to \infty \tag{40}$$

where, Γ signifies gamma function. Random numbers are produced using the Mageta technique based on the Levy distribution as given in Eq. (41).

$$levy(\gamma) = 0.05 \times \frac{y}{|z|^{1/\gamma}} \tag{41}$$

where, y and z represents two normal distribution variables computed using Eq. (42) and Eq. (43) σ_y and σ_z represents the standard deviation of y and z.

$$y = \text{Normal}\left(0, \sigma_y^2\right) \tag{42}$$

$$z = \text{Normal}\left(0, \sigma_z^2\right) \tag{43}$$

$$\sigma_y = \left[\frac{\Gamma(1+\gamma)\sin\left(\frac{\pi\gamma}{2}\right)}{\Gamma\frac{(1+\gamma)}{2}\gamma 2^{\frac{(\gamma-1)}{2}}}\right]^{1/\gamma}, \sigma_z = 1, \gamma = 1.5 \tag{44}$$

The new location after applying LF becomes,

$$\overline{C}_A = levy(\gamma) \otimes \left|m_1 \cdot Z_A(t) - n_1 \cdot Z(t)\right| \tag{45}$$

$$\overline{C}_B = levy(\gamma) \otimes \left|m_2 \cdot Z_B(t) - n_2 \cdot Z(t)\right| \tag{46}$$

$$\overline{C}_C = levy(\gamma) \otimes \left|m_3 \cdot Z_C(t) - n_3 \cdot Z(t)\right| \tag{47}$$

$$\overline{C}_D = levy(\gamma) \otimes \left|m_4 \cdot Z_D(t) - n_4 \cdot Z(t)\right| \tag{48}$$

$$\overline{Z}_1 = Z_A(t) - d_1 \cdot \overline{C}_A \tag{49}$$

$$\overline{Z}_2 = Z_B(t) - d_2 \cdot \overline{C}_B \tag{50}$$

$$\overline{Z}_3 = Z_C(t) - d_3 \cdot \overline{C}_C \tag{51}$$

$$\overline{Z}_4 = Z_D(t) - d_4 \cdot \overline{C}_D \tag{52}$$

The algorithm 1 stops the process when the optimal path is found out or when $I_{\max}$ is reached.

Pseudo-code of PL-COA

Input: Population size P, I_{max} , upper and lower bound, dimension
Output: Optimal path

1. Initialize the population y_i^0 randomly with dimension Dim
2. Compute the location of each chimp
3. Categorize the chimps randomly into Z_A, Z_B , Z_C , and Z_D
4. Apply polarity learning on y_i^0 and store the result as OL_i
5. **while** $I \le I_{max}$ **do**
6. **for** $I \le P$ **do**
7. Evaluate y_i using Eqn. (15) and store the outcome as F_i
8. Compute the fitness of the solution OL_i using Eqn. (15) and store the result in FOL_i
9. **if** $F_i < FOL_i$ **then**
10. $y_i = OL_i$
11. **end if**
12. **end for**
13. Initialize h, n , d , and m
14. **for** each chimp **do**
15. Extract the group of the chimp
16. Update h, n , and m
17. Compute d and c
18. **end for**
19. **for** each search chimp **do**
20. **if** $\mu < 0.5$ **then**
21. **if** $|d| < 1$ **then**
22. Update search agent's location by Eqn. (24-27)
23. **else if** $|d| > 1$ **then**
24. Choose a search agent randomly
25. **else if** $\mu < 0.5$ **then**
26. Apply LF using Eqn. (45) to Eqn. (48)
27. Update present search agent's location by Eqn. (49-52)
28. **end if**
29. **end for**
30. Update h, n, d , and m
31. Update $Z_A(t)$, $Z_B(t)$, $Z_C(t)$, and $Z_D(t)$
32. $T = t + 1$
33. **end while**
34. Return the optimal path

4 Simulation results and analysis

The proposed ML-HSOR protocol is implemented in Python 3.9 and the obtained results are compared with the recent existing techniques such as EACMRP-MS [29], DBN [30], VLBR [31], EERI-GWO [32], and E-GLBR [33] in terms of energy consumption, delay, detection rate, throughput, etc. Table 2 gives the parameter settings used for implementing the proposed ML-HSOR method.

4.1 Simulation setup

The proposed ML-HSOR protocol is implemented in Python 3.9. The implementation relies on NumPy for efficient numerical operations and array manipulations, Matplotlib and Seaborn for compelling data visualization, and scikit-learn's StandardScaler module to standardize input data. The Cryptography library's Fernet module is employed for secure encryption processes, while SymPy enhances the simulation's mathematical modeling capabilities. Additionally, Python's built-in libraries, such as 'uuid' for universal identifier generation and 'random' for random number generation, contribute to the robustness of the simulation setup.

The simulation also utilizes the LT-FS-ID intrusion detection dataset [42], which includes information such as area, sensing range, transmission range, and the number of sensor nodes. The dataset's target variable is the "Number of barriers", which is predicted during the simulation. It is important to note that this dataset is synthetically generated through Monte Carlo simulations.

Table 2 Parameter setup

Parameters	Value
Sensing area	800 m × 800 m
Number of sensors	100–500
BS location	(500,800)
Malicious nodes	5–25
Initial energy of a node	1 J
Size of data packet	512 bytes
Node's communication range	30 m
Receiving and Transmission energy	0.01 J
ϵ_{fs}	10 pJ/bit/m^2
E_{elec}	100 nJ/bit
ϵ_{mp}	0.0013 pJ/bit/m^2
Population	50
Maximum iteration	100
Simulation time	1000 s
Number of units in the time window	4

4.2 Evaluation metrics

The metrics used for evaluating the proposed ML-HSOR method are defined in this section.

(i) Energy Consumption

The energy consumed in the network can be computed by using Eq. (53).

$$E_{con} = (E_{rx} \times N_T) + E_{tx} \tag{53}$$

where, N_T denotes the total number of nodes, E_{rx} and E_{tx} represents the energy consumed during reception and transmission respectively.

$$E_{rx} = M_{bits} E_{elec} \tag{54}$$

where, M_{bits} signifies the number of bits in the message, the energy needed to activate electronic circuits during reception is expressed as E_{elec}.

The required energy to run the transmitter is given by Eq. (55).

$$E_{tx} = \begin{cases} M_{bits} E_{elec} + M_{bits} \varepsilon_{fs} d^2, & d < d_0 \\ M_{bits} E_{elec} + M_{bits} \varepsilon_{amp} d^4, & d \geq d_0 \end{cases} \tag{55}$$

where $d_0 = \sqrt{\frac{\varepsilon_{fs}}{\varepsilon_{amp}}}$, d indicates the distance between the source and the destination node, ε_{amp} and ε_{fs} indicates the dissipated energy in the transmit amplifier and the energy lost in free space respectively.

(ii) Delay

It refers to the time it takes for data to be transmitted from one node to another. It can be computed using Eq. (56).

$$\text{Dly} = \sum_{i,j=1}^{n} \frac{At_j - St_i}{N_{\text{con}}} \tag{56}$$

where, St_i is the time at which the packet is sent from node i, At_j is the time at which the packet is received at node j, N_{con} indicates number of connections that is made between the source and destination.

(iii) PDR

It is a metric used to measure the percentage of data packets transmitted by a sender that are successfully received by the intended recipient. It is computed by using Eq. (57).

$$\text{PDR} = \frac{P_{\text{DN}}}{P_{\text{SN}}} \times 100 \tag{57}$$

where, P_{DN} denotes the data packets received by the destination node (DN) and P_{SN} denotes the data packets sent by the sender node.

(iv) Throughput

It is the volume of data that can be sent across a communication link in a specific amount of time. Typically, it is expressed in bits per second (bps) and can be estimated using Eq. (58).

$$\text{Throughput} = \frac{P_{d(\text{DN})}}{T_{\text{sim}}} \times 100 \tag{58}$$

where, T_{sim} indicates the simulation time and $P_{d(DN)}$ represents the packets delivered to the destination.

(v) Detection Rate

It is used to calculate the proportion of events or occurrences observed by the network's sensor nodes like environmental tracking, spying, etc. Detection rate is computed using Eq. (59).

$$D_r = \frac{T_{\text{det}}}{T_{\text{act}}} \times 100 \tag{59}$$

where, T_{det} signifies the sum of malicious nodes that are detected and T_{act} denotes the actual number of malicious nodes.

(vi) Network Lifetime

It the amount of time the network can operate effectively before the batteries of the sensor nodes run out or the nodes begin to fail or malfunction.

4.3 Comparative analysis

The reduction in energy consumption and delay holds paramount importance in the context of Quality of Service (QoS) for IoT wireless sensor networks (WSNs), particularly in applications like environmental monitoring. It directly affects the network's efficiency, reliability, and overall performance. IoT WSNs are often deployed in remote or inaccessible areas, where replacing sensor node batteries is impractical. Minimizing energy consumption is essential for prolonging network lifetime. This extended network lifespan, as demonstrated by the ML-HSOR protocol, reduces maintenance and operational costs, making it highly practical for long-term deployments. Real-time monitoring applications, such as environmental sensing, surveillance, and industrial control, rely on low-latency data transmission. High end-to-end delays can result in missed critical events, affecting the timeliness and effectiveness of decision-making processes. ML-HSOR's reduced delay ensures that data reaches the application layer promptly, making it suitable for time-sensitive applications.

In addition to energy consumption and delay, other performance indicators also play pivotal roles in evaluating the effectiveness of the ML-HSOR protocol. High throughput, as achieved by the ML-HSOR protocol, is essential for IoT applications requiring real-time data transmission. In environmental monitoring, for example, rapid data transfer ensures that environmental changes are reported promptly,

enabling timely response to critical events. The high throughput of ML-HSOR enhances its practicality in these applications. Maintaining a high PDR is crucial in IoT WSNs, especially in applications like surveillance and environmental monitoring, where data accuracy is paramount. By enhancing PDR through the prevention of gray-hole attacks, ML-HSOR ensures that the collected data are dependable, making it highly suitable for applications demanding data integrity and trustworthiness. A longer network lifetime, as demonstrated by ML-HSOR, is of immense practical value in remote and challenging deployment scenarios. Reduced maintenance and prolonged operational lifespans reduce the costs and logistical challenges associated with battery replacement, making it a cost-effective solution for applications in remote or hostile environments. High detection rates are essential for ensuring the security of IoT WSNs. By improving the detection rate of malicious nodes, the ML-HSOR protocol enhances network security and reliability. This is of paramount importance in critical infrastructure protection and surveillance applications, where the detection of malicious events is imperative.

The proposed ML-HSOR protocol is evaluated by comparing its performance to established techniques, such as EACMRP-MS [29], DBN [30], VLBR [31], EERI-GWO [32], and E-GLBR [33].

By altering the number of nodes, Fig. 5 provides an analysis of energy consumption across different methods. It is observed that the proposed ML-HSOR method has consumed less energy compared to the existing methods such as EACMRP-MS

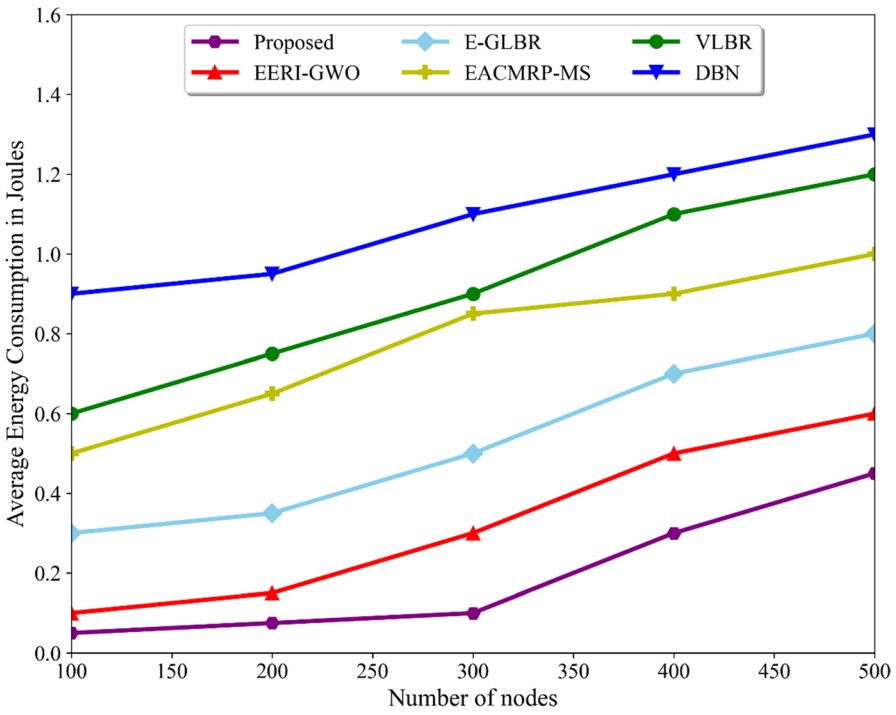


Fig. 5 Energy consumption analysis

[29], DBN [30], VLBR [31], EERI-GWO [32], and E-GLBR [33]. The consumption of energy by the existing EACMRP-MS [29], DBN [30], VLBR [31], EERI-GWO [32], and E-GLBR [33] methods are 1.0 J, 1.2 J, 1.1 J, 0.5 J, and 0.7 J when the number of nodes is raised to 500 whereas ML-HSOR has the lowest energy consumption, at 0.39 J. Energy-efficient CH selection and routing contribute to minimizing the energy consumption of the proposed ML-HSOR protocol.

ML-HSOR exhibits dynamic adaptability by adjusting energy consumption strategies based on real-time variations in network conditions and node characteristics. The comparative analysis explores the protocol's effective handling of varying traffic levels, showcasing its prowess in optimizing energy consumption under fluctuating communication demands. Additionally, the theoretical framework of ML-HSOR is scrutinized for resilience to changes in network topology, emphasizing its capacity to maintain energy efficiency even in dynamic Wireless Sensor Network (WSN) environments. The protocol's robustness extends to fault tolerance, with an in-depth exploration of its capabilities for fault recovery and energy optimization in the face of node failures or network disturbances.

ML-HSOR's scalability is a notable feature, ensuring sustained energy efficiency as the network scales, making it applicable across both small and large-scale deployments. The protocol's adaptability to varying transmission ranges is investigated theoretically, shedding light on its effectiveness in optimizing energy consumption for different communication distances. Furthermore, the analysis delves into latency considerations, investigating how ML-HSOR minimizes delays, contributing to its overall energy-efficient operation. A nuanced understanding of trade-offs within ML-HSOR, striking a balance between energy efficiency and communication reliability, adds depth to the assessment of its performance characteristics.

The ML-HSOR protocol significantly minimizes energy consumption, making it well-suited for long-term, remote deployments common in environmental monitoring. This is achieved through a dynamic Markov model for CH selection, which intelligently considers real-time energy levels and network conditions. By ensuring judicious selection of CHs and employing energy-efficient routing mechanisms, the protocol optimizes energy consumption. Techniques such as data aggregation and intelligent path selection play a vital role in reducing the energy footprint of the protocol. This reduction in energy consumption has direct practical implications in environmental monitoring. IoT sensors deployed in remote areas, such as rainforests, wildlife reserves, or Arctic ecosystems, can operate for extended periods without the need for frequent battery replacements. The cost savings and logistical benefits of this approach are particularly relevant in environmental conservation and biodiversity studies.

One of the key factors that have a significant impact on the quality of service (QoS) of IoT-based wireless sensor networks is a delay. For real-time monitoring applications, it is required to maintain less delay. High delays occur due to factors such as network congestion or high processing time. When the network has 500 nodes, the delay for the existing methods such as EACMRP-MS [29], DBN [30], VLBR [31], EERI-GWO [32], and E-GLBR [33] are 0.08 s, 0.09 s, 0.084 s, 0.065 s, and 0.078 s. The outcomes from Fig. 6 show that the ML-HSOR protocol has less delay of 0.058s compared to the existing methods such

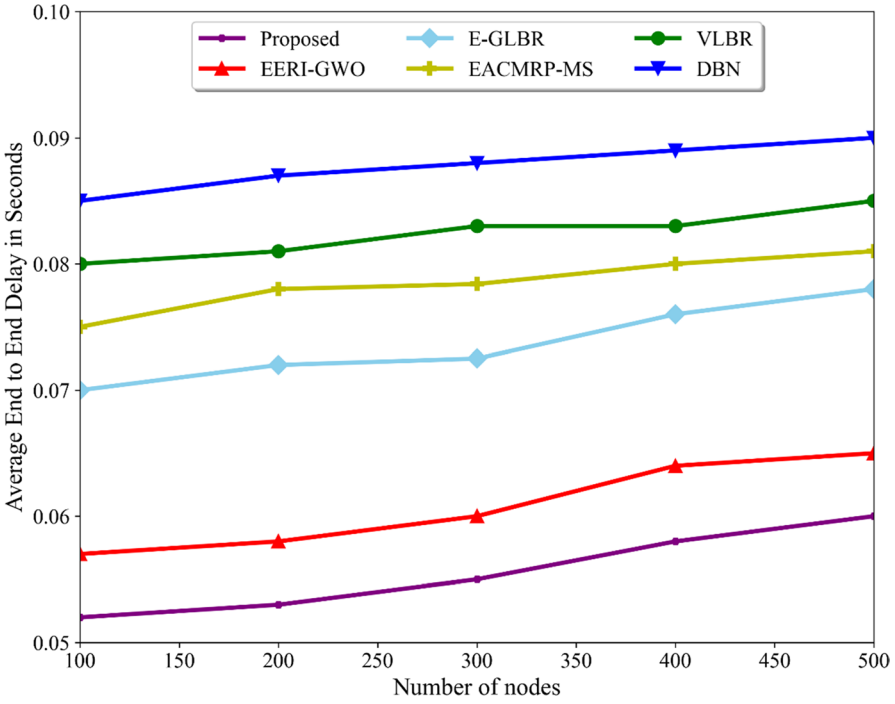


Fig. 6 End-to end delay analysis

as EACMRP-MS [29], DBN [30], VLBR [31], EERI-GWO [32], and E-GLBR [33]. The delay is minimized by transmitting the packet via the path that has less overload/congestion.

Low-latency data transmission, as demonstrated by the ML-HSOR protocol, is essential for real-time environmental monitoring. Environmental changes and critical events can occur at any time, and minimizing end-to-end delay is crucial for timely response. By dynamically evaluating network conditions and selecting paths with minimal congestion, the protocol reduces delay. This is particularly important in applications like wildfire detection, where timely data transmission can help mitigate ecological damage and protect human lives. The ML-HSOR protocol's ability to minimize delays directly enhances its practicality in environmental monitoring scenarios.

Throughput is a crucial metric in WSNs because it shows how well the network can transmit data. It depends on a number of variables, including the size of the network, the type of transmission medium, and the data-transfer routing protocol. High throughput is preferred because it guarantees that data can be transmitted quickly and effectively, allowing applications to receive data on time. For instance, high throughput is crucial in applications like environmental monitoring to ensure that the data are transmitted in real time and can be analyzed quickly to make informed decisions. From Fig. 7, it can be observed that the proposed ML-HSOR protocol has a high throughput of 48,000 bps compared to the existing methods such as

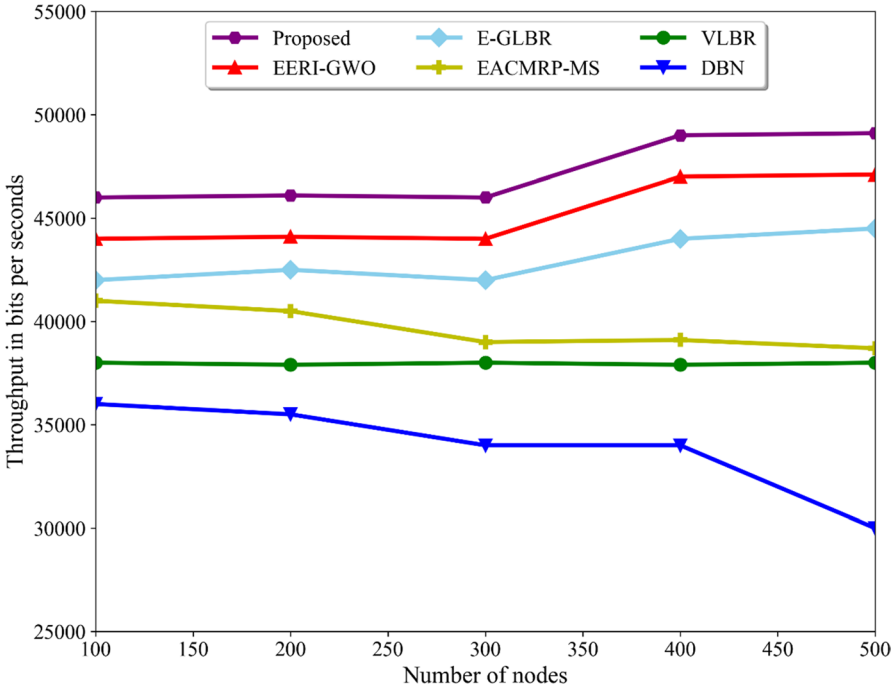


Fig. 7 Throughput analysis

EACMRP-MS [29], DBN [30], VLBR [31], EERI-GWO [32], and E-GLBR [33]. Based on the analysis, DBN has the least throughput of 30,000 bps followed by VLBR (38,000 bps), EACMRP-MS (39,000 bps), E-GLBR (45,000 bps), and EERI-GWO (47,000 bps). Since the PL-COA algorithm converges quickly by using polarity learning and levy flight, the throughput is increased.

The PL-COA algorithm, incorporating polarity learning and Levy flight, enhances the protocol's search for optimal data transmission paths. This results in faster and more efficient data transfer, crucial for applications like environmental monitoring that require real-time data analysis. High throughput, which the ML-HSOR protocol excels at, is indispensable in applications like environmental monitoring. The ability to transfer data quickly is essential for real-time data analysis. For example, in the context of tracking climate parameters in rapidly changing environments, high throughput is crucial for ensuring that data reaches the application layer promptly. The protocol's enhanced throughput is particularly relevant for applications where timely decision-making is imperative.

PDR measures the dependability of the communication link between a sender and a receiver in a WSN. A high PDR indicates that the majority of packets are received successfully, whereas a low PDR indicates that a significant number of packets are lost during transmission. PDR is especially important for applications requiring reliable data delivery, such as surveillance and environmental monitoring, because a high PDR ensures that the collected data are accurate and complete. From Fig. 8, it

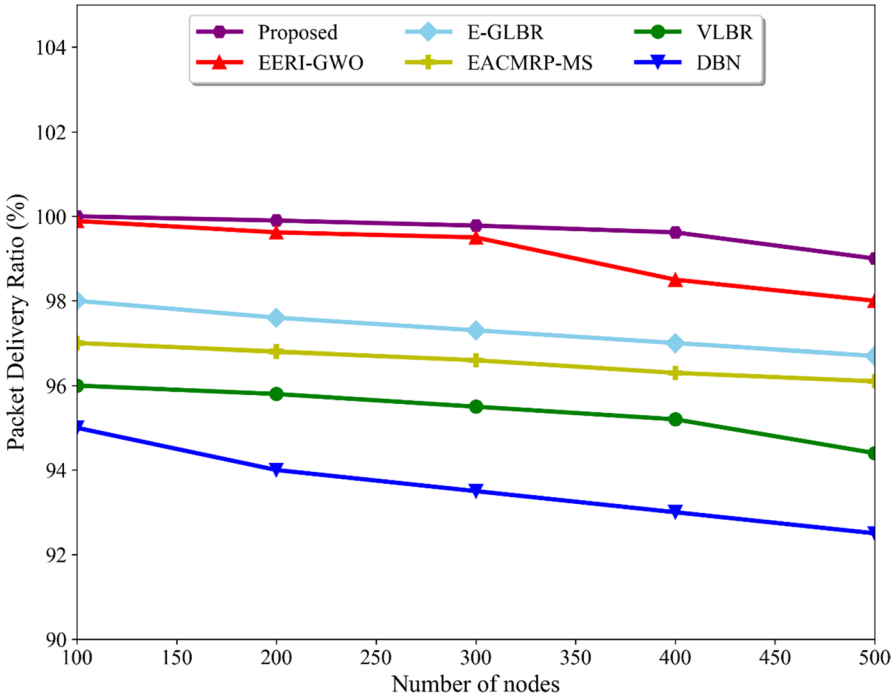


Fig. 8 PDR analysis

can be seen that the PDR of the proposed ML-HSOR protocol is higher (99.8% for 500 nodes) than the existing methods such as EACMRP-MS (96.5%), DBN (93.0%), VLBR (95.0%), EERIGWO (98.9%), and E-GLBR (97.5%). The PDR is increased by preventing gray-hole attacks using the data trust metric.

ML-HSOR employs a data trust metric and a multi-level hierarchical trust evaluation, which significantly enhance the PDR. These measures efficiently detect and mitigate gray-hole attacks, ensuring reliable data delivery. A high PDR, as achieved by the ML-HSOR protocol, is vital for applications like environmental sensing and surveillance. In these scenarios, data accuracy and completeness are critical. By efficiently detecting and preventing gray-hole attacks, the protocol ensures that data collected for environmental analysis is reliable and trustworthy. This trustworthiness is vital for making informed decisions based on sensor data, such as those required for pollution control or wildlife conservation.

Network lifetime refers to the time duration for which the network can operate effectively before the batteries of the sensor nodes are depleted or the nodes start to malfunction or fail. The network lifetime is a crucial metric in WSNs, especially in applications where the nodes are deployed in remote locations, and battery replacement or maintenance is difficult or impossible. A longer network lifetime is needed in such applications to minimize the cost required to operate the network. From Fig. 9, it is observed that the proposed ML-HSOR method has 250 alive sensors at the end of 36,000 rounds and EERI-GWO method has 200 alive sensors at the

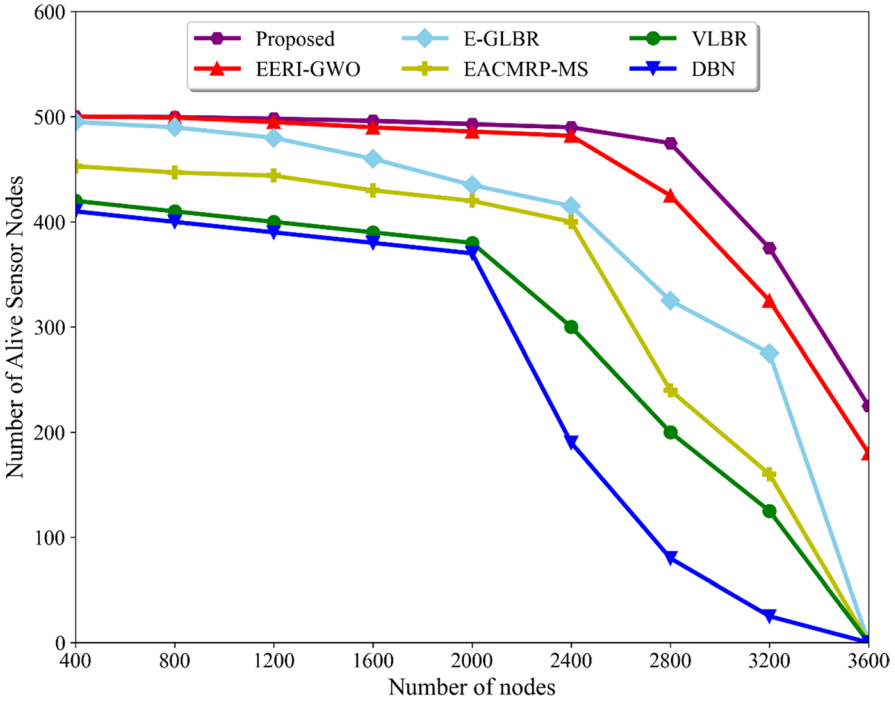


Fig. 9 Network lifetime analysis

end of 36,000 rounds. On the other hand, all the other existing methods such as EACMRP-MS [29], DBN [30], VLBR [31], and E-GLBR [33] have no alive sensors at the end of 36,000 rounds. The analysis from Fig. 9 shows that the network lifetime of the proposed ML-HSOR method is high compared to the existing methods such as EACMRP-MS [29], DBN [30], VLBR [31], EERI-GWO [32], and E-GLBR [33]. The dynamic change in CH by the Markov model helps to increase the network lifetime.

The extended network lifetime achieved by ML-HSOR is crucial for remote and challenging deployment scenarios. The dynamic change in CHs, guided by the Markov model, effectively optimizes energy usage and node lifespan. This is particularly vital in remote locations where battery replacement or maintenance is challenging. Deployments in remote or hostile environments, such as ocean monitoring or desert climate studies, benefit from prolonged network lifespans. Reduced maintenance requirements and operational longevity are cost-effective and logistical advantages in scenarios where sensor nodes are challenging to access.

In an IoT-based WSN, high detection rate relies on the security level of the protocol used. A high detection rate indicates that the sensor nodes are efficient at detecting malicious events, whereas a low detection rate suggests that some malicious events are missed or not noticed by the nodes. When 25 malicious nodes are deployed in the network, the proposed ML-HSOR protocol has the highest detection rate of 95% and DBN has the lowest detection rate of 45%. The outcomes obtained

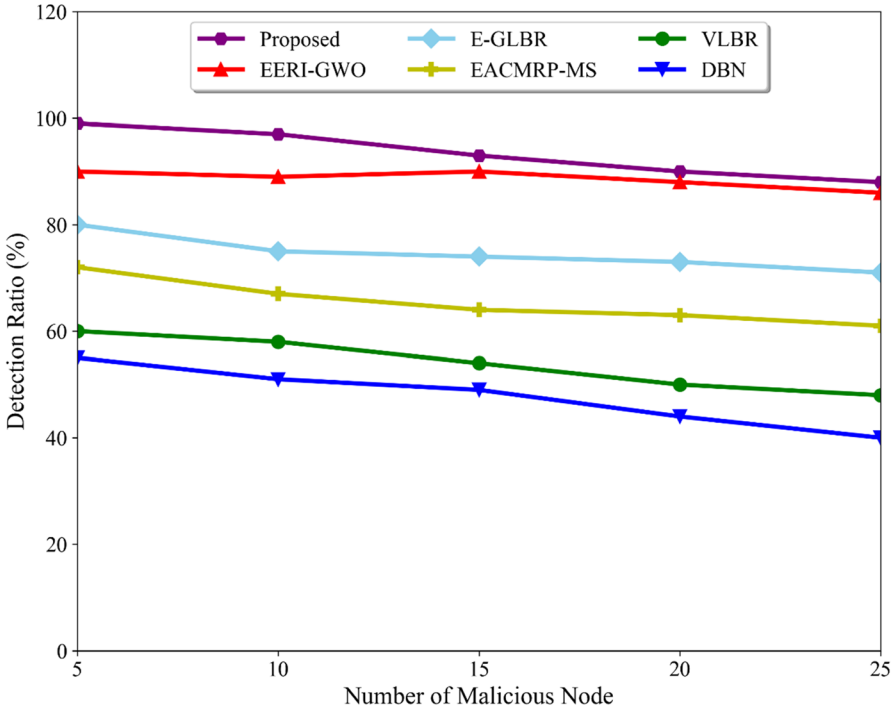


Fig. 10 Detection rate analysis

from Fig. 10 show that, compared to existing methods, the proposed ML-HSOR protocol demonstrates a high detection rate. This is because the multi-level hierarchical trust evaluation in the proposed ML-HSOR protocol increased the detection rate of the malicious nodes.

ML-HSOR implements a multi-level hierarchical trust evaluation that elevates the detection rate of malicious nodes. This trust-based approach ensures enhanced security and reliability in IoT-based WSNs. In environmental monitoring, maintaining a high detection rate is critical. Malicious events or sensor malfunctions can have adverse ecological consequences. By employing a multi-level hierarchical trust evaluation, the ML-HSOR protocol enhances the detection rate of malicious nodes, ensuring the security and reliability of the monitoring network. This is invaluable in applications like forest fire detection and pollution tracking, where the identification of anomalies is imperative for environmental protection.

The ML-HSOR model distinguishes itself through a myriad of distinctive features, setting it apart from the other models under comparison. A key highlight is its adaptive clustering approach, dynamically adjusting attribute weighting in real time during cluster head (CH) selection—an aspect that optimizes network lifespan and performance. Furthermore, ML-HSOR confronts the challenge posed by malicious nodes by introducing a unique multi-level hierarchical trust evaluation approach. Factors like interaction trust and identity trust are considered, significantly bolstering network security.

To counteract garnishing attacks, ML-HSOR introduces an innovative time-window mechanism, systematically observing node behavior over specific periods to conduct effective trustworthiness assessments. Security enhancements in ML-HSOR extend to the use of timestamps and the application of the improved blowfish algorithm (IBFA) for encryption. These advanced security measures ensure data integrity and confidentiality, providing an additional layer of protection. Noteworthy are ML-HSOR's optimization strategies involving the PL-COA algorithm, polarity-based learning, and Levy flights. This combination presents a unique approach for efficient exploration and data surveying in complex environmental spaces, demonstrating greater superiority when compared to other models. Thus, ML-HSOR emerges as a comprehensive and advanced solution, adeptly addressing specific challenges in wireless sensor networks through its dynamic adaptability, enhanced security measures, and unique optimization techniques.

In conclusion, the ML-HSOR protocol's superior performance in energy consumption, delay reduction, and other evaluation metrics carries substantial practical implications for environmental monitoring. The reduction in energy consumption enhances the protocol's suitability for long-term deployments in remote areas, reducing operational costs and logistical challenges. Its low-latency data transmission capabilities make it suitable for real-time monitoring, ensuring timely response to critical environmental events. These features position the protocol for applications such as air quality monitoring, wildlife conservation, climate change research, and natural disaster monitoring. The high PDR, throughput, network lifetime, and detection rate further enhance its applicability in environmental monitoring, providing reliable, timely, and cost-effective data collection and analysis. Overall, the ML-HSOR protocol's remarkable performance metrics directly translate into its relevance and significance in real-world scenarios across various industries and applications, with a strong emphasis on environmental monitoring.

4.4 Simulation on LT-FS-ID dataset

The proposed model is simulated using the LT-FS-ID intrusion detection dataset and compared with other standard models, including EACMRP-MS [29], DBN [30], VLBR [31], EERIGWO [32], and E-GLBR [33], across five evaluation metrics: correlation coefficient (R), root-mean-square error (RMSE), mean squared error (MSE), bias, and computational time. The corresponding values are presented in Table 3.

The ML-HSOR model presents a holistic and advanced solution for wireless sensor networks, particularly evident in its superior performance compared to other models as given in Table 3. In terms of the trust process, ML-HSOR exhibits exceptional adaptability through its adaptive clustering and Cluster Head (CH) selection, as demonstrated by its significantly higher correlation coefficient (R: 0.95) compared to EACMRP-MS (0.89), DBN (0.92), VLBR (0.88), EERI-GWO (0.91), and E-GLBR (0.87). This signifies ML-HSOR's ability to dynamically adjust attributes in real time, ensuring precise CH selection.

Table 3 Simulated results for different models in LT-FS-ID dataset

Model	R	RMSE	MSE	Bias	Computational time
Proposed ML-HSOR	0.95	2.1	4.41	0.2	20 ms
EACMRP-MS[29]	0.89	3.0	9.0	− 1.5	25 ms
DBN[30]	0.92	2.5	6.25	− 0.5	30 ms
VLBR[31]	0.88	3.2	10.24	− 2.0	22 ms
EERI-GWO[32]	0.91	2.8	7.84	− 1.0	28 ms
E-GLBR[33]	0.87	3.5	12.25	− 2.5	32 ms

In the routing process, ML-HSOR excels in optimized path determination, achieving the lowest root-mean-square error (RMSE: 2.1) and Mean Squared Error (MSE: 4.41) among all models. This showcases its proficiency in selecting optimal paths for data transfer, contributing to enhanced network stability and lifetime. Furthermore, ML-HSOR's security assessments exhibit a remarkable level of precision, reflected in its high correlation coefficient (R: 0.95) and low RMSE and MSE values (2.1 and 4.41, respectively). This precision reinforces its seamless integration of trust considerations into the network, ensuring reliable security assessments. The model also demonstrates a strong correlation between security and energy consumption, guiding accurate and energy-efficient decisions. Its low RMSE and MSE values (2.1 and 4.41) in the context of energy consumption emphasize its effectiveness in predicting and optimizing energy usage based on trust information. Additionally, ML-HSOR's efficient computational time (20 ms) positions it as a practical and effective choice for real-time applications, ensuring timely security and energy-related decisions. Therefore, ML-HSOR emerges as a comprehensive and advanced solution, adeptly addressing specific challenges in wireless sensor networks through its dynamic adaptability, enhanced security measures, and unique optimization techniques. The visual representation of the performance metrics of different models in the given dataset is given in Fig. 11.

5 Conclusion

In conclusion, the secure and optimal routing method in IoT-based environmental monitoring WSN that employs the improved chimp optimization algorithm is a promising approach for achieving high performance and reliability in WSNs. By computing the fitness of the nodes based on residual energy, distance to the destination, link quality, delay, and trust, this method ensures a high packet delivery ratio (PDR), high throughput, low delay, a high detection rate, and low energy consumption. Moreover, the multi-level trust evaluation approach helps to detect and avoid malicious nodes, making the network more secure and reliable. The improved chimp optimization algorithm and the trust evaluation approach provide an effective solution for addressing the challenges of routing in WSNs, making it suitable for applications like environmental monitoring, smart agriculture,

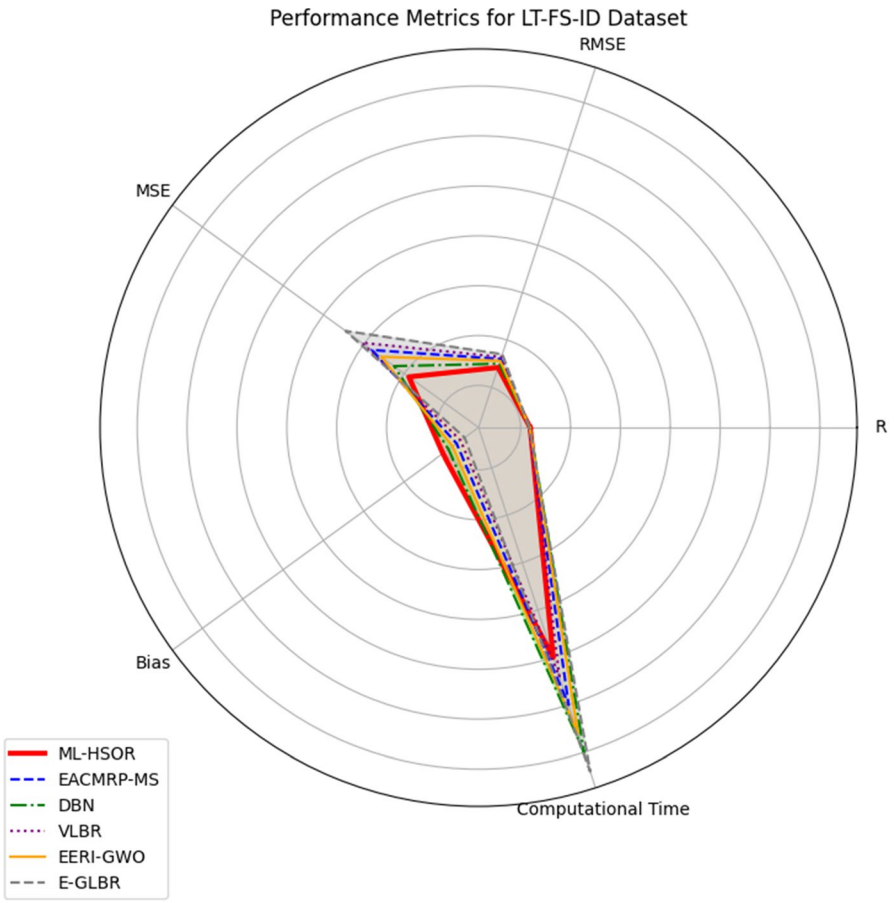


Fig. 11 Visual representation of performance metrics of simulated results on LT-FS-ID dataset

and industrial automation. ML-HSOR significantly reduces energy consumption through intelligent CH selection, energy-efficient routing, data aggregation, and path optimization. This translates into extended network lifespans, making it an ideal choice for long-term deployments in remote and inaccessible areas where frequent battery replacements are impractical. ML-HSOR's ability to minimize end-to-end delay ensures that data reach the application layer promptly. This is critical for real-time environmental monitoring, enabling timely responses to crucial events like wildfire detection. The protocol's high throughput, achieved through the PL-COA algorithm, ensures that data can be transmitted quickly and efficiently. This is particularly relevant for applications like environmental monitoring, where real-time data analysis is essential for informed decision-making. Also, ML-HSOR excels in PDR by employing data trust metrics and multi-level hierarchical trust evaluations. This enhances data accuracy and completeness,

vital for applications requiring reliable data delivery, such as surveillance and environmental monitoring. The protocol effectively prolongs network lifespans by optimizing energy usage and node lifespan through dynamic CH selection guided by the Markov model. This is a crucial benefit in remote or challenging deployment scenarios. ML-HSOR's high detection rate of malicious nodes, achieved through a multi-level hierarchical trust evaluation, ensures the security and reliability of environmental monitoring networks. This is indispensable for identifying anomalies that could have adverse ecological consequences. Overall, this method is a promising approach for achieving efficient and secure routing in IoT-WSNs. Future works will focus on enhancing the security against other attacks and testing the scalability. Specifically, we aim to fortify security by addressing a broader spectrum of threats, including advanced intrusion techniques, emerging AI-driven attacks, and quantum computing-based vulnerabilities. Simultaneously, we will focus on ensuring the scalability of the methodology for larger networks, possibly encompassing thousands or even millions of devices, through optimized network protocols, resource management, and energy-efficient strategies. Further advancements in machine learning algorithms will be a focal point to enhance predictive capabilities. The methodology will be rigorously validated in diverse real-world environments and industry settings, ensuring its adaptability and robustness across various use cases. This comprehensive approach aligns with the evolving demands of secure and efficient data transmission in modern sensor networks and the dynamic landscape of emerging security threats and network scales.

Author contributions VS, RB, and VK contributed to the design, implementation of the research, analysis of the results, and writing of the manuscript. All authors reviewed the results and approved the final version of the manuscript.

Funding No funding was received for conducting this study.

Data availability Data sharing is not applicable.

Declarations

Conflict of interest The authors have no competing interests to declare that are relevant to the content of this article.

Ethical approval This article does not contain any studies with human participants or animals performed by any of the authors.

References

1. Behera TM, Mohapatra SK, Samal UC, Khan MS, Daneshmand M, Gandomi AH (2020) I-SEP: an improved routing protocol for heterogeneous WSN for IoT-based environmental monitoring. IEEE Internet Things J 7(1):710–717. https://doi.org/10.1109/JIOT.2019.2940988

2. Haseeb K, Islam N, Almogren A, Ud Din I, Almajed HN, Guizani N (2019) Secret sharing-based energy-aware and multi-hop routing protocol for IoT based WSNs. IEEE Access 7:79980–79988. https://doi.org/10.1109/ACCESS.2019.2922971
3. Gopika D, Panjanathan R (2020) Withdrawn: energy efficient routing protocols for WSN based IoT applications: a review. Mater Today Proceed. https://doi.org/10.1016/j.matpr.2020.10.137
4. Manchanda R, Sharma K (2020) Energy efficient compression sensing-based clustering framework for IoT-based heterogeneous WSN. Telecommun Syst 74(3):311–330. https://doi.org/10.1007/s11235-020-00652-2
5. Kala I, Karthik S, Srihari K (2021) Advanced hybrid secure multipath optimized routing in Internet of Things (IoT)-based WSN. Int J Commun Syst 34:1–14. https://doi.org/10.1002/dac.4782
6. Bd D, Al-Turjman F (2020) A hybrid secure routing and monitoring mechanism in IoT-based wireless sensor networks. Ad Hoc Networks. 97:102022. https://doi.org/10.1016/j.adhoc.2019.102022
7. Banerjee A, Mitra A, Biswas A. An Integrated Application of IoT-Based WSN in the Field of Indian Agriculture System Using Hybrid Optimization Technique and Machine Learning. Agricultural Informatics: Automation Using the IoT and Machine Learning. Published online 2021:171–187. https://doi.org/10.1002/9781119769231.ch9
8. Keswani B et al (2019) Adapting weather conditions based iot enabled smart irrigation technique in precision agriculture mechanisms. Neural Comput Appl 31(1):277–292. https://doi.org/10.1007/s00521-018-3737-1
9. Chanak P, Banerjee I (2020) Congestion free routing mechanism for IoT-enabled wireless sensor networks for smart healthcare applications. IEEE Trans Consum Electron 66(8):223–232. https://doi.org/10.1109/TCE.2020.2987433
10. Bagdadee AH et al (2020) IoT based wireless sensor network for power quality control in smart grid. Procedia Comput Sci 167:1148–1160. https://doi.org/10.1016/j.procs.2020.03.417
11. Salunkhe PPG, Chaudhari PU (2018) Against poaching based MSP430. In: 2018 International Conference on Advances in Communication and Computing Technology (ICACCT). Published online 03:520–523
12. Nath T, Azharuddin M (2019) Application of wireless sensor networks for Rhino protection against poachers in Kaziranga National Park. AEU-Int J Electron C 111:152882. https://doi.org/10.1016/j.aeue.2019.152882
13. Ghosh K, Neogy S, Das PK, Mehta M (2018) Intrusion detection at international borders and large military barracks with multi-sink wireless sensor networks: an energy efficient solution. Wireless Pers Commun 98(1):1083–1101. https://doi.org/10.1007/s11277-017-4909-5
14. Ali A, Jadoon YK, Changazi SA, Qasim M (2020) Military operations: wireless sensor networks based applications to reinforce future battlefield command system. In: Proceedings—2020 23rd IEEE International Multi-topic Conference, INMIC 2020. Published online 2020. https://doi.org/10.1109/INMIC50486.2020.9318168
15. Huanan Z, Suping X, Jiannan W (2021) Security and application of wireless sensor network. Procedia Comput Sci 183:486–492
16. Selvakumar K, Karuppiah M, SaiRamesh L et al (2019) Intelligent temporal classification and fuzzy rough set-based feature selection algorithm for intrusion detection system in WSNs. Inf Sci 497:77–90. https://doi.org/10.1016/j.ins.2019.05.040
17. Puri D, Bhushan B (2019) Enhancement of security and energy efficiency in WSNs: Machine Learning to the rescue. In: Proceedings—2019 International Conference on Computing, Communication, and Intelligent Systems, ICCCIS 2019. 120–125. https://doi.org/10.1109/ICCCIS48478.2019.8974465
18. Abdalzaher MS, Samy L, Muta O (2019) Non-zero-sum game-based trust model to enhance wireless sensor networks security for IoT applications. IET Wirel Sens Syst 9(4):218–226
19. Shah A, Engineer M (2019) A survsey of lightweight cryptographic algorithms for IoT-based applications. vol 851. Springer Singapore; pp 283–293. https://doi.org/10.1007/978-981-13-2414-7_27
20. Gaber T, Abdelwahab S, Elhoseny M, Hassanien AE (2018) Trust-based secure clustering in WSN-based intelligent transportation systems. Comput Netw 146:151–158. https://doi.org/10.1016/j.comnet.2018.09.015
21. Ali BA, Abdulsalam HM, AlGhemlas A (2018) Trust based scheme for IoT enabled wireless sensor networks. Wireless Pers Commun 99(2):1061–1080. https://doi.org/10.1007/s11277-017-5166-3

22. Bany Salameh H, Obaidat H, Al-Shamali A, Jararweh Y (2021) A two-level clustering mechanism for energy enhancement in Internet-of-Things-based wireless sensor networks. Int J Commun Syst 34(13):1–10. https://doi.org/10.1002/dac.4913
23. Salim A, Osamy W, Khedr AM, Aziz A, Abdel-Mageed M (2021) A secure data gathering scheme based on properties of primes and compressive sensing for IoT-Based WSNs. IEEE Sens J 21(4):5553–5571. https://doi.org/10.1109/JSEN.2020.3032585
24. Kaur G, Chanak P, Bhattacharya M (2021) Energy-efficient intelligent routing scheme for IoT-enabled WSNs. IEEE Internet Things J 8(14):11440–11449. https://doi.org/10.1109/JIOT.2021.3051768
25. Abasıkeleş-Turgut İ, Altan G (2021) A fully distributed energy-aware multi-level clustering and routing for WSN-based IoT. Trans Emerg Telecommun Technol 32(12):1–16. https://doi.org/10.1002/ett.4355
26. Mahajan HB, Badarla A (2021) Cross-layer protocol for WSN-assisted IoT smart farming applications using nature inspired algorithm. Wireless Pers Commun 121(4):3125–3149. https://doi.org/10.1007/s11277-021-08866-6
27. Alotaibi M (2021) Improved blowfish algorithm-based secure routing technique in IoT-based WSN. IEEE Access 9:159187–159197. https://doi.org/10.1109/ACCESS.2021.3130005
28. Dwivedi AK, Mehra PS, Pal O, Doja MN, Alam B (2021) EETSP: energy-efficient two-stage routing protocol for wireless sensor network-assisted Internet of Things. Int J Commun Syst 34(17):1–19. https://doi.org/10.1002/dac.4965
29. Subramani N, Perumal SK, Kallimani JS, Ulaganathan S, Bhargava S, Meckanizi S (2022) Controlling energy aware clustering and multihop routing protocol for IoT assisted wireless sensor networks. Concurr Comput Pract Exper. https://doi.org/10.1002/cpe.7106
30. Arya G, Bagwari A, Chauhan DS (2022) Performance analysis of deep learning-based routing protocol for an efficient data transmission in 5G WSN communication. IEEE Access 10:9340–9356. https://doi.org/10.1109/ACCESS.2022.3142082
31. Hajian E, Khayyambashi MR, Movahhedinia N (2022) A mechanism for load balancing routing and virtualization based on SDWSN for IoT applications. IEEE Access 10:37457–37476. https://doi.org/10.1109/ACCESS.2022.3164693
32. Seyyedabbasi A, Kiani F, Allahviranloo T, Fernandez-Gamiz U, Noeiaghdam S (2023) Optimal data transmission and pathfinding for WSN and decentralized IoT systems using I-GWO and Ex-GWO algorithms. Alex Eng J 63:339–357. https://doi.org/10.1016/j.aej.2022.08.009
33. Benelhouri A, Idrissi-Saba H, Antari J (2022) An evolutionary routing protocol for load balancing and QoS enhancement in IoT enabled heterogeneous WSNs. SSRN Electron J 124(February):102729. https://doi.org/10.2139/ssrn.4135169
34. Preeti KR, Singh D (2022) Dimension learning based chimp optimizer for energy efficient wireless sensor networks. Sci Rep 12(1):14968. https://doi.org/10.1038/s41598-022-18001-5
35. Hosseinzadeh M, Yoo J, Ali S et al (2023) A cluster-based trusted routing method using fire hawk optimizer (FHO) in wireless sensor networks (WSNs). Sci Rep 13(1):13046. https://doi.org/10.1038/s41598-023-40273-8
36. Khan T, Singh K, Abdel-Basset M, Long HV, Singh SP, Manjul M (2019) A novel and comprehensive trust estimation clustering based approach for large scale wireless sensor networks. IEEE Access 7:58221–58240. https://doi.org/10.1109/ACCESS.2019.2914769
37. Kalidoss T, Rajasekaran L, Kanagasabai K, Sannasi G, Kannan A (2020) QoS aware trust based routing algorithm for wireless sensor networks. Wireless Pers Commun 110:1637–1658. https://doi.org/10.1007/s11277-019-06788-y
38. Arulanantham D, Palanisamy C (2021) Trusted cognitive sensor based dual routing network on Internet of Things. Int J Commun Syst 34(10):e4836. https://doi.org/10.1002/dac.4836
39. Bangotra DK, Singh Y, Selwal A, Kumar N, Singh PK (2022) A trust based secure intelligent opportunistic routing protocol for wireless sensor networks. Wireless Pers Commun 127(2):1045–1066. https://doi.org/10.1007/s11277-021-08564-3
40. Al-Odat ZA, Khan SU, Al-Qtiemat E (2022) A modified secure hash design to circumvent collision and length extension attacks. J Inf Secur Appl 71:1–25. https://doi.org/10.1016/j.jisa.2022.103376
41. Amuthan A, Arulmurugan A (2021) Semi-Markov inspired hybrid trust prediction scheme for prolonging lifetime through reliable cluster head selection in WSNs. J King Saud Univ Comput Inf Sci 33(8):936–946. https://doi.org/10.1016/j.jksuci.2018.07.006

42. Singh A, Amutha J, Nagar J, Sharma S, Lee CC (2022) Lt-fs-id: Log-transformed feature learning and feature-scaling-based machine learning algorithms to predict the k-barriers for intrusion detection using wireless sensor network. Sensors 22(3):1070. https://doi.org/10.3390/s22031070

Publisher's Note Springer Nature remains neutral with regard to jurisdictional claims in published maps and institutional affiliations.

Springer Nature or its licensor (e.g. a society or other partner) holds exclusive rights to this article under a publishing agreement with the author(s) or other rightsholder(s); author self-archiving of the accepted manuscript version of this article is solely governed by the terms of such publishing agreement and applicable law.

NLP-enabled Recommendation of Hashtags for Covid Based Tweets Using Hybrid BERT-LSTM Model

KIRTI JAIN

Department of Computer Science and Engineering, Delhi Technological University, Delhi, India, kj.kirtijain25@gmail.com

RAJNI JINDAL

Department of Computer Science and Engineering, Delhi Technological University, Delhi, India, 2rajnijindal@dce.ac.in

Hashtags have become a new trend to summarize the feelings, sentiments, emotions, swinging moods, food tastes and much more. It also represents various entities like places, families and friends. It is a way to search and categorize various stuff on social media sites. With the increase in the hashtagging, there is a need to automate it, leading to the term "Hashtag Recommendation". Also, there are plenty of posts on social media sites which remain untagged. These untagged posts get filtered out while searching and categorizing the data using a label. Such posts do not make any contribution to any helpful insight and remain abandoned. But, if the user of such posts is recommended by labels according to his post, then he may choose one or more of them, thus making the posts labelled. For such cases Hashtag recommendation comes into the picture. Although much research work has been done on Hashtag Recommendation using traditional Deep Learning approaches, not much work has been done using NLP based Bert Embedding. In this paper, we have proposed a model, BELHASH, Bert Embedding based LSTM for Hashtag Recommendation. This task is considered as a Multilabel Classification task as the hashtags are one-hot encoded into multiple binary vectors of zeros and ones using MultiLabelBinarizer. This model has been evaluated on Covid 19 tweets. We have achieved 0.72 accuracy, 0.7 Precision, 0.66 Recall and 0.67 F1-Score. This is the first paper of hashtag recommendation to the best of our knowledge combining Bert embedding with LSTM model and achieving the state of the arts results.

Keywords: Hashtag Recommendation, BERT Embedding, Deep Learning, Social Media, Covid-19

1 INTRODUCTION

Recommendation systems (RS) are of much help to the users. Sometimes, in the case of online shopping sites, users are not aware of the similar products that can go with their choice. Here, RS provides the users the relevant products [1]. Sometimes, users want to listen to the music or watch a movie but he doesn't know which song / movie to play. In such cases, recommendations are made according to the users' past choices [2,3]. Also, RS are quite helpful in case of marketing and sales [4] by analyzing the past patterns and then suggesting the next steps to be taken in order to increase the sales. They also help the developers in a variety of tasks like reusing code, writing bug reports etc. [5]. A review of recommendation systems using deep learning approaches is provided in detail in [49].

Despite being such a helpful tool for our daily lives, RS comes with certain challenges as well:

- Investment - Significant investment is required to make a robust and efficient RS.
- Selection of the Best Choice - There are many options available in the market. To choose the best RS is a challenging task.
- Cold start problem - Whenever a new user enters a system or a new item is added to the catalogue, then it becomes difficult for the RS to predict that user's choice or the rating of that item.
- User behavior - As the behavior of the user changes dynamically, it is difficult to capture that dynamic change in the behavior and recommend items according to this change.

Natural Language Processing (NLP) has emerged as a trending approach to be applied on language related domains [57,58]. NLP-powered algorithms can detect trends, sentiment, and emerging issues in real-time, providing a deeper understanding of online conversations. Furthermore, they contribute to the development of recommendation systems and content curation, shaping our social media interactions and experiences. Social media has become an important part of our daily life. Plenty of data is available on social media sites which can be used for mining patterns indicating various implications related to health [6], understanding and assessing the disasters and thus helping in disaster management [7], analyzing customer feedback [8], developing marketing strategies [9], brand communication and monitoring [10], analyzing social media reviews for various purposes such as election candidate approval ratings [11], hotel and restaurant ratings

Permission to make digital or hard copies of all or part of this work for personal or classroom use is granted without fee provided that copies are not made or distributed for profit or commercial advantage and that copies bear this notice and the full citation on the first page. Copyrights for components of this work owned by others than the author(s) must be honored. Abstracting with credit is permitted. To copy otherwise, or republish, to post on servers or to redistribute to lists, requires prior specific permission and/or a fee. Request permissions from permissions@acm.org.
© 2024 Copyright held by the owner/author(s). Publication rights licensed to ACM.
ACM 2375-4699/2024/01-ART
http://dx.doi.org/10.1145/3640812

Just Accepted

[12,13]. As the number of Internet users is increasing day by day, the number of posts on social media sites has also increased. Users keep posting their day-to-day life on social media. Among many social media sites, Twitter has become a popular microblogging social site where users interact by posting tweets. Tweets not only describe one's thoughts or life, but also represent the various trends going around in the world at that moment. Twitter data has been used for different purposes such as sentiment analysis [14], healthcare field [15], educational sector [16], predicting elections [17], and few more [18-20].

With the increase in the number of posts on Twitter, there is a need to label these posts. Many users are not aware or have little knowledge of the concept of hashtagging. For such users, recommendation is provided so that they can select the hashtags according to their needs from among the recommended ones. This hashtag recommendation makes the posts labelled from being unlabelled.

A few years back, Covid-19 pandemic shook the entire world. Almost all the countries were affected economically as well as medically by this infectious virus. Twitter was filled with tweets related to coronavirus and its impact on health. Although many of these tweets are accompanied by hashtags, still many tweets remain untagged. Such untagged tweets get filtered out while searching and categorizing tweets using a label. A hashtag is a label which summarizes the entire text. As the hashtags are being posted along with the tweets, there is a need to automate this system. Automating means recommending the hashtags based on the tweets as posted by the user. Such recommendation will help the untagged tweets to get a tag from the recommended hashtags. Also, it will help the users of tagged tweets to get the appropriate tags. Thus, a need is felt to make a model which recommends hashtags by taking tweets as input and generating hashtags as output.

As mentioned in [50], recommendation systems are mainly of two types: Content based RS and Collaborative Filtering RS. Content based RS mainly focus on the users' content and then recommending the tags according to that content. Whereas, Collaborative Filtering RS makes use of other users' tagging history with the similar interests of posts as the current user is having. For example, Alice and Bob are two online social media users having similar interests. Now, RS will have a look at the labeling trend of Alice and then recommend hashtags to Bob. In this work, we will be focussing on Content Based RS. This task is considered as a Multilabel Classification task. In the context of multilabel classification, the hashtag recommendation task can be seen as predicting a set of relevant hashtags for a given text input. Each hashtag acts as a distinct label, and the goal is to determine which hashtags are most suitable for describing or categorizing the content of the text. Hashtags are one-hot encoded into multiple binary vectors, where multiple tags can be set to 1 for a given tweet.

In this paper, we have proposed a model, BELHASH, Bert Embedding based LSTM for Hashtag Recommendation. This is the first work to the best of our knowledge to use LSTM based on Bert embedding in the field of Hashtag recommendation. This model has been evaluated on 100K Covid-19 tweets. The process flow diagram is shown in Figure 1. Combining LSTM with BERT in the hashtag recommendation task serves a unique purpose. The integration of these two powerful architectures offers complementary advantages, enhancing the model's ability to capture both local context and global semantics i.e. BERT's global understanding of the text and LSTM's ability to capture sequential information. This fusion allows the model to capture both short-term and long-term dependencies effectively.

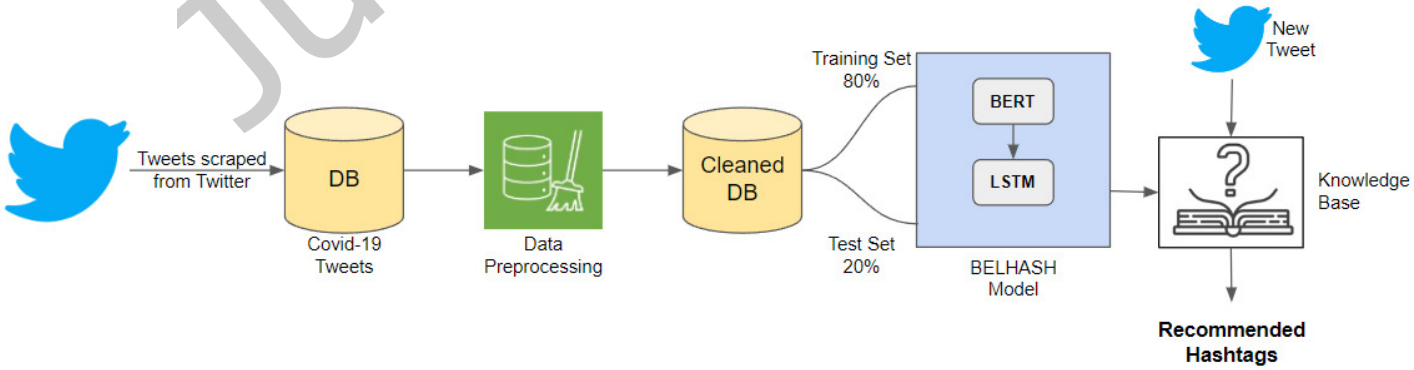


Figure 1: Flow diagram of Data Preprocessing leading to Recommended Hashtags

The main contributions of this paper are:

- We have proposed a model named BELHASH to recommend Hashtags of Covid-19 Tweets.

Just Accepted

- Proposed model is composed of a cascading of BERT-LSTM for relevant text feature extraction. This is the first paper of hashtag recommendation to the best of our knowledge combining Bert embedding with LSTM model and achieving the state of the arts results.
- Proposed model is experimented with 100K Covid-19 related tweets.
- The model's comparison is presented with the state-of-art models to validate results.

The remainder of the paper is organized as follows: Section 2 describes the related work in the field of hashtag recommendation. Section 3 explains the methodology of the proposed model. Dataset preprocessing, implementation details and evaluated results are given in Section 4. Section 5 finally concludes the paper.

2 RELATED WORK

Many researchers have proposed a variety of hashtag recommendation systems based on different perspectives. A survey paper [21] has discussed many related works in detail and concludes that hashtag recommendation can be applied to images and multimodal blogs as well. The authors of [22] propose a novel method, 5WTAG, which relates each word of the microblog to one of the 5 Ws (Why, What, When, Where and hoW) and then recommends hashtags in Chinese microblogs. It also combines the syntax and semantic analysis of the topic hashtags. The Deep Learning framework proposed in [23] for the dataset of Stackoverflow uses the content of questions (title and body) and also heterogeneous network of user-tag relationships for hashtag recommendation. Another approach named TOAST, senTiment enhanced multi-mOdal Attentive haShtag recommendaTion, is proposed in [24]. It works on multimodal data and uses both content and sentiment features for visual, audio and text modalities. The content and sentiment features are captured by an attention neural network. Results reveal that TOAST performs better than other state of the art methods. DemoHash [25] uses demographic information of users along with textual and visual information, to recommend hashtags. VGG-16 is used to extract features from users' selfie images and LSTM is used to extract text features along with demographic features such as users' age, gender and race. DemoHash is evaluated on Instagram posts and reveals good results by combining content based as well as user demographic details for personalized hashtag recommendation. A recent work proposed in [55] uses a deep learning hybrid approach for automatic image description extraction. The authors use U-Net for removing the main objects from the image in order to add more elements from the background for additional classification. This is done to find the probability of belonging to each class through the Skip-Gram module.

Twitter has become one of the most emerging social media sites. There have been a number of proposed methods to recommend hashtags for tweets. [26,27] propose a learning to rank method for streaming news articles to increase the interest of users for a particular tweet. Streaming content is also used to learn the dynamic interests of users in [28] to discover latent topics to recommend hashtags. [29] explains how multimodal features extracted from Twitter containing both text and images improve the hashtag recommending process. It uses VGG to extract image features and LSTM to extract text content and both are combined using co-attention for recommending hashtags. Another approach, PM-HRec (Pattern Mining for Hashtag Recommendation) is proposed in [30] to find the high average utility patterns of hashtags. Zero Shot Learning approach is used in [31] to recommend twitter hashtags. Twitter hashtag recommendation is also done by making use of user profiles [32]. Another model proposed for including hyperlinked tweets for hashtag recommendation reveals good results [33]. Semantic features of tweets are incorporated in [34] using word-embeddings which also resolves the problem of data sparsity using external knowledge sources. Another work [35] proposed a model, SCPO, Sine Cosine Political Optimization, which is based on Deep Residual Network for hashtag Recommendation. This model is composed by integration of Sine Cosine algorithm and Political Optimization algorithm. Experiments of SCPO are conducted on Apple Twitter Sentiment and Twitter datasets. Results reveal that SCPO performs better than other works. Recent work proposed in [56] enhances the popularity of social media posts by recommending hashtags. In this approach, hashtags are recommended by analyzing the post keywords and the popularity of the users and the posts to learn about the current trends on social media sites.

As microblogs contain images and text data, many models have been proposed taking both into account and then combining the features of both through attention mechanisms. [36] proposes a model using attention networks to combine user profile and historical hashtags to recommend hashtags. A model MACON (Memory Augmented Co-Attention model) is proposed in [37] for similar work combining both text and images, which learns users' past hashtag posts. Another approach proposed in [38] makes use of Graph Convolution Network (GCN) to analyze the relationships amongst the user, hashtag and micro-videos. It also makes use of an attention mechanism to remove the redundant messages passed by microvideos to users and hashtags. The authors of [39] map the user profiles' on graph data and incorporate it with the recommendation process. Another work proposed (SANN) in [40] represents a word of microblog post using self attention mechanism. Then,

Just Accepted

the microblog post representation is calculated by weighted sum of all the words. Finally, Multilayer Perceptron is used to recommend hashtags of microblog posts. Another work described in [53] proposes a TCAN (Topical Co-Attention network) model which uses both content and topic attention mechanisms. Both the parts guide each other simultaneously. Attention mechanisms also incorporate temporal information to remove noise for hashtag recommendation. Authors of [54] develop a novel approach using LSTM which incorporates selective sentence-level attention for reducing noise factor. Selective sentence-level attention is used to assign weights to each sentence and then remove the noisy data. Temporal information is then introduced to recommend hashtags using a Softmax pooling layer.

NLP has a wide variety of applications, such as dynamic question generation [59], sentiment analysis for online product reviews [60], fake news classification [61]. Within the domain of Natural Language Processing (NLP), models like BERT have emerged as powerful tools for recommendation systems, effectively understanding the nuances of user preferences and content to provide more personalized and context-aware suggestions. Bert Embedding is used for hashtag recommendation in few proposed works. The authors of EmHash model [41] have applied BERT embedding to recommend hashtags. They recommend hashtags in two granularity levels: Coarse Grain which recommends the cluster of hashtags for a tweet and Fine Grain which recommends the hashtags from that cluster. A recent work proposed in [42] uses RoBert's tokenizer to capture the discontinuous semantics of the text. They propose a Semantics Selection Mechanism (SSM) model based on the transformer, to perform the 3 tasks: encoding, segment selection and decoding. This model captures the discontinuous semantic segments and transforms the text to hashtags. Another proposed model, HASHET (HAshtag recommendation using Sentence-to-Hashtag Embedding Translation) [43], is based on two latent spaces, one for embeddings of text and other for embeddings of hashtags. This embedding is performed using BERT. Then Multi-layer Perceptron (MLP) is applied to transform semantic features of text embeddings to hashtags embeddings. The authors of proposed work [44] recommend hashtags in Brazilian Portuguese for Ecommerce websites. They recommend hashtags by making models using Bert and BiLSTM separately on Ecommerce websites. Their work is evaluated using 4 metrics: NIST, BLUE, METEOR and a crowdsourced score. While the first three metrics indicated a bad score, the crowdsourced score achieved good results.

There are other proposed works of hashtag recommendation using embeddings other than the Bert Embedding. EmTaggeR [45] is based on learning word embedding for a hashtag and then deriving a word vector for a given hashtag. Here, training is done by 2 procedures. In one procedure, each hashtag is trained by a separate word embedding model and another procedure comprises obtaining the embeddings of a hashtag in a global context. In the testing phase, average word embedding is taken for recommending hashtags. More proposed works encode vector representation of a tweet by LSTM [46,47]. Skip gram model is used to learn vector representation of tweets, and then DBSCAN is applied to cluster similar tweets in a homogenous cluster. Then top-k recommendations are made by calculating co-occurrence or similarity between the given tweet and nearest cluster centers.

3 METHODOLOGY

In this section, we describe our proposed model, BELHASH (Bert Embedding based LSTM for Hashtag Recommendation), in detail followed by the various terminologies used for our work.

3.1 Proposed Work -

BELHASH is a Bert Embedding based LSTM for Hashtag Recommendation. The architecture of the proposed model is shown in Figure 2. This model has mainly five components. The first component is hashtag encoding where hashtags are one-hot encoded into a binary vector of 0s and 1s. 0 represents the absence of a hashtag for that tweet whereas 1 represents the presence of a hashtag for that tweet. The second component is word tokenization where tweets are tokenized into multi-dimensional vectors using BERT tokenizer. The third component comprises feature extraction by LSTM. The fourth component is Part-of-speech (POS) tagging where tags are given a probability of being associated with a tweet. The last component is hashtag recommendation where cosine similarity is applied between all tags and encoded vector representation of a new tweet. Those tags having high similarity are given a ranking according to the probability distribution of cosine similarity function. Then these hashtags are sorted in the descending order according to their probabilities. Then top-k recommendations are made. Now, each of these components are described below in detail.

Just Accepted

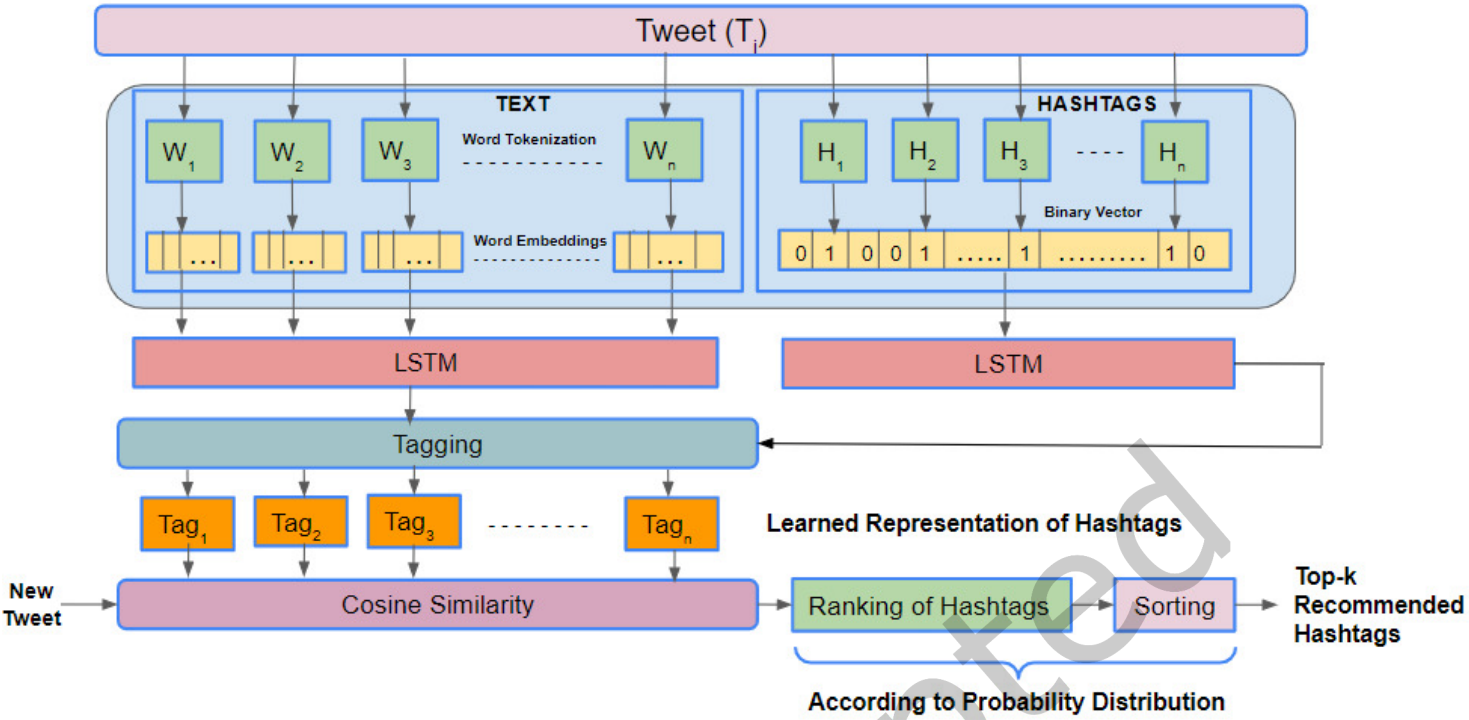


Figure 2: Workflow of the proposed BELHASH model

Just Accepted

A. Hashtag Encoding

The Covid-19 tweets dataset has 25000 unique hashtags. Out of these, we have filtered out 1350 hashtags having frequency of occurrence greater than or equal to 10. These hashtags are encoded using Multi Label Binarizer (MLB). MLB is used to encode the presence or absence of each hashtag for a given tweet. It creates a binary vector where each element corresponds to whether a specific hashtag is present in the tweet or not. This vector is often referred to as a "binary label vector." Thus, through MLB, a binary vector is created for a given tweet containing zeros and ones. If a hashtag is present in the tweet, the corresponding element in the binary vector is set to 1; otherwise, it's set to 0. Let's take an example:

total_hashtags: ['covid19', 'home', 'health', 'staysafe', ...]

tweet_hashtags: ['covid19', 'health']

binary vector: [1, 0, 1, 0, ...]

Here, for the given tweet, the element at index 0 represents the presence of 'covid19', the element at index 1 represents the absence of 'home', the element at index 2 represents the presence of 'health', the element at index 3 represents the absence of 'staysafe' and so on. During training, the binary label vectors are used as target values, and during inference, the predicted binary vectors are decoded to obtain the recommended hashtags for a given tweet.

B. Word Tokenization and Embedding

Word tokenization is the second step of text processing tasks. In this step, each tweet goes through the process of word tokenization. It is a method to split the words in the form of tokens or unbreakable units. Each word is then given a unique number which is represented by a multi dimensional vector. We have used Bert tokenizer for this purpose. Bert tokenizer captures the context of the same words according to the sentences in which they are appearing. If a word is appearing with two different semantics, then that word will be represented by two different vectors. In contrast, other embedding techniques like Word2Vec, Glove, generate the same vector representation for the same word, even if it is appearing in two different contexts. This is because other embedding techniques do not capture the semantics of the words according to their occurrences.

C. Feature Extraction by LSTM

Long Short Term Memory (LSTM) is a variation of Recurrent Neural Networks (RNN). LSTM resolves the vanishing gradient problem of RNN by retaining the previous words in the memory to generate the next outputs in the sequences. In the context of hashtag recommendation, the LSTM neural network plays a crucial role in extracting meaningful features from the input text. These features are essential for capturing the underlying semantics and context of the text, which in turn aids in making accurate hashtag predictions. Simultaneously, the hashtags associated with each tweet are one-hot encoded and processed through a separate LSTM layer.

The LSTM learns to associate specific patterns, phrases, and contextual cues with relevant hashtags. For instance, consider the sentence "Stay safe and wash your hands regularly. #COVID19 #health." The LSTM can learn that the presence of phrases like "wash your hands" and "#health" are indicative of the hashtags "#COVID19" and "#health." These associations are learned over time through the iterative process of training. Thus, LSTM extract the features in a text processing task effectively.

D. POS Tagging

The textual features of input tweets are extracted through LSTM networks, capturing the contextual nuances and sequential dependencies within the text. Simultaneously, the hashtags associated with each tweet are one-hot encoded and processed through a separate LSTM layer. The outputs from these two distinct LSTM pathways are then fused in a tagging layer, where the model learns to generate relevant part-of-speech (POS) tags based on the intricate interplay between the textual content and the hashtag information. The tagging layer serves as a bridge between the textual and hashtag domains, synthesizing meaningful representations that encapsulate the essence of the input tweet.

E. Hashtag Recommendation

At last, Cosine Similarity is applied between all POS tags and encoded vector representation of a new tweet. Those tags having high similarity are given a ranking according to the probability distribution of cosine similarity function. Then these hashtags are sorted in the descending order according to their probabilities. Then top-k recommendations are made.

3.2 Terminologies Used

The various terminologies used are given below followed by two algorithms of BELHASH. Algorithms 1 and 2 describe the hashtag and text processing parts of the tweet respectively.

$T = \{T_1, T_2, \ldots. T_i \ldots T_n\}$: Set of Cleaned Tweets, where T_i is the tweet at the i^{th} location and n is the total number of tweets.

$H = \{H_1, H_2, \ldots. H_i \ldots H_n\}$: Set of hashtags for a Tweet T, where H_i is the hashtag at the i^{th} location and n is the total number of hashtags.

$H_R = \{H_{R1}, H_{R2}, \ldots. H_{Ri} \ldots H_{Rk}\}$: Set of recommended hashtags for a Tweet T, where H_{Ri} is the hashtag at the i^{th} location according to the rank probability and k is the number of recommended hashtags.

$T_i(w)$: Word Tokenization of tweet T_i

$T_i(E)$: Encoded vector representation of tokenized words of tweet T_i

$T_i(F)$: Features extracted for tweet T_i

$P = \{H_{P1}, H_{P2}, \ldots. H_{Pi} \ldots H_{Pn}\}$: H_{Pi} is the Probability distribution (Ranking) of the hashtag H_i for a given tweet T.

$S = \{H_{P1}, H_{P2}, \ldots. H_{Pi} \ldots H_{Pn}\}$: Set of hashtags of tweet T_i sorted according to their probability distributions. H_{P1} is the hashtag with the highest probability. H_{P2} is the hashtag with the second highest probability and so on.

$FH = \{FH_1, FH_2, \ldots. FH_i \ldots FH_n\}$: Set of all 1350 filtered hashtags where FH_i is the hashtag at the i^{th} location.

V: Binary vector of all Hashtags(H) for a tweet T_i

V(F): Features extracted for Binary Vector V of all Hashtags(H) for a tweet T_i

Just Accepted

Algorithm 1: HASHTAG_PROCESSING(FH, H)

Input: Set of hashtags (H) for a tweet T_i and all filtered hashtags (FH)
Output: Extracted features of Binary Vector (V(F))
1. **Procedure** HASHTAG_PROCESSING(FH, H)
2. Transformed_labels (TL) ← MLB(FH)
3. **for** each FH_i in TL do
4. **for** each $H_i \in H$ do
5. **if** $FH_i == H_i$, then
6. Set $V[FH_i] = 1$
7. **else**
8. Set $V[FH_i] = 0$
9. **end if**
10. **end**
11. **end**
12. Extracted_features (V(F)) ← LSTM (V)
13. Return V(F)

Algorithm 2: TEXT_PROCESSING(T, H)

Input: Set of Tweets (T) and its hashtags (H)
Output: Top-k recommended hashtags (H_R)
1. **Procedure** TEXT_PROCESSING(T, H)
2. **for** each tweet T_i do
3. $T_i(w)$ ← bert-based-uncased-tokenizer (T_i)
4. $T_i(E)$ ← bert-based-uncased-model-encoder ($T_i(w)$)
5. Extracted_features ($T_i(F)$) ← LSTM ($T_i(E)$)
6. Part-of-speech Tags (POST) ← Tagging ($T_i(F)$ + V(F))
7. Probability distribution (P) ← Cosine_Similarity (POST)
8. Sorted probabilities (S) ← Sorting (P)
9. H_R ← Pick Top-k recommendations from S
10. **end**
11. return H_R

4. EVALUATION AND RESULTS

In this section, we provide the details to the dataset and its preprocessing, implementation details and comparison with base papers.

4.1 Dataset

We have evaluated our proposed model on the Covid-19 dataset, which is scraped using Twitter API. A sample of collected tweets is shown in Figure 3.

Just Accepted

text	hashtags
If I smelled the scent of hand sanitizers today on someone in the past, I would think they were so intoxicated thatâ€¦ https://t.co/QZvYbrOgb0	
Hey @Yankees @YankeesPR and @MLB - wouldn't it have made more sense to have the players pay their respects to the Aâ€¦ https://t.co/1QvW0zgyPu	
@diane3443 @wdunlap @realDonaldTrump Trump never once claimed #COVID19 was a hoax. We all claim that this effort toâ€¦ https://t.co/Jkk8vHWHb3	['COVID19']
@brookbanktv The one gift #COVID19 has give me is an appreciation for the simple things that were always around meâ€¦ https://t.co/Z0pOAlFXcW	['COVID19']
25 July : Media Bulletin on Novel #CoronaVirusUpdates #COVID19 @kansalrohit69 @DrSyedSehrish @airnewsalerts @ANIâ€¦ https://t.co/MN0EEcsJHh	['CoronaVirusUpdates', 'COVID19']
#coronavirus #covid19 deaths continue to rise. It's almost as bad as it ever was. Politicians and businesses wantâ€¦ https://t.co/hXMHooXX2C	['coronavirus', 'covid19']
How #COVID19 Will Change Work in General (and recruiting, specifically) via/ @ProactiveTalent #Recruitingâ€¦ https://t.co/bjZxzGPMbK	['COVID19', 'Recruiting']

Figure 3: A sample of raw/ unprocessed Covid-19 tweets

We performed data preprocessing so as to remove noisy data. Several steps of data preprocessing are described below:

1. Non-Hashtags Tweets Removal - We removed the tweets containing no hashtags and kept the tweets containing at least one hashtag for a given tweet.
2. Non-English Tweets and Unicode Characters Removal - We removed non-english characters from tweets and non-english hashtags. We also removed tweets and hashtags containing unicode characters.
3. URL, HTML and Punctuations Removal - In this step we removed tweets containing URL patterns starting from http(s), email IDs and punctuation marks.
4. Emojis Removal - This step is concentrated on removing emoticons, symbols & pictographs, transport & map symbols, and flags.
5. Conversion to Lowercase - In this step, we convert all the tweets and their associated hashtags to lowercase so that the same hashtags but in uppercase can be treated as one.
6. Hashtag Removal - In this step, we removed all the hashtags appearing at the end of the tweets but retained the ones appearing in between the tweets.
7. Lemmatization - We lemmatized all tweets and hashtags so that the variant forms of one word can be treated as a single word.
8. Filter Candidate Tweets - In this step, tweets with very short length compared to its numbers of hashtags, are filtered out based on a threshold.

   If length(tweets) / Number of Hashtags < Threshold
   => drop that tweet

9. Drop Duplicate Tweets - For duplicate tweets, we have kept only the first tweet and removed the duplicates.
10. Hashtag Filtration - Hashtags having frequency of occurrence greater than or equal to 10 in the entire dataset are kept. So, out of 25K tags, 1350 tags are kept.

After preprocessing, we split our dataset into 80% and 20% for the training and testing respectively. A sample of the cleaned dataset is shown in Figure 4. Table 1 shows the dataset details.

	text	hashtags
0	diane3443 wdunlap realdonaldtrump trump never once claim covid19 be a hoax . we all claim that this effort to	['covid19']
1	brookbanktv the one gift covid19 have give me be an appreciation for the simple thing that be always around me	['covid19']
2	25 july : medium bulletin on novel coronavirusupdates covid19 kansalrohit69 drsyedsehrish airnewsalerts ani	['coronavirusupdates', 'covid19']
3	coronavirus covid19 death continue to rise . it s almost as bad a it ever be . politician and business want	['coronavirus', 'covid19']
4	how covid19 will change work in general and recruiting , specifically via proactivetalent	['covid19', 'recruiting']
5	pray for good health and recovery of chouhanshivraj .	['covid19', 'covidpositive']
6	pope a god prophet sadhu sundar selvaraj . watch here at	['hurricanehanna', 'covid19']

Figure 4: A sample of pre-processed Covid-19 tweets

Just Accepted

Table 1: Dataset Values before and after pre-processing the tweets

Dataset Parameters	Values
Total fetched Tweets	1.65 Lakhs
Pre-processed Tweets	1 Lakh
Unique hashtags before preprocessing	25000
Unique hashtags after preprocessing	1350
Training Dataset	80K Tweets
Test Dataset	20K Tweets

4.2 Implementation Details

Pytorch library of Python is used to perform the experiments. The dataset is divided into 80% training set and 20% test set. All the tweets are padded to the maximum length of tweets i.e. 280 characters. Both the training set and test set are divided into batches each of 32 size. For the training set, we shuffle the tweets but not for the test set. We have used 0.05 as the Learning Rate and Adam as the optimizer. The hyperparameters and their values are given in Table 2.

A. Model Training

The Bert-based-uncased Pretrained model is used to tokenize the tweets. Then this tokenized form is encoded into a vector representation capturing the semantics of the words. LSTM layer is applied over this vector representation of tweets to extract the features. After this, a Dropout of value 0.3 is used to regularize the weights in the backpropagation process. Then the last layer of Softmax is applied to get the learned representation of hashtags of a given tweet.

B. Model Testing

For a new tweet, Bert embedding and LSTM layers are applied to have features extracted from encoded vector representation for that tweet. Then, Cosine Similarity is applied for that encoded representation of the new tweet and the learned representation of hashtags obtained in the training step. Cosine similarity gives a probability distribution (rank) of hashtags to be recommended for the new tweet. Then, sorting is applied over the rank of the hashtags, arranging them in a descending sequence in order to recommend top-k hashtags.

Table 2: Hyperparameters names and their values used in BELHASH

Parameter Name	Parameter Value
Tokenizer	'bert-base-uncased'
Max_Padding	280
Batch Size	32
Epochs	50
Dropout	0.3
Learning Rate	0.05
Optimizer	Adam
Loss function	BCEWithLogitsLoss

Just Accepted

4.3 Evaluation Metrics

To evaluate the performance of our model, Precision, Recall, F1 Score and Support are taken as evaluation metrics. These metrics are defined below.

A. Precision - It is defined as the fraction of relevant recommended hashtags over all recommended hashtags.

$$Precision = \frac{TP}{TP + FP} \quad (1)$$

B. Recall - It is defined as the fraction of relevant recommended hashtags over all hashtags.

$$Recall = \frac{TP}{TP + FN} \quad (2)$$

C. F1 Score - It is defined as the Harmonic Mean of Precision and Recall.

$$F1 = \frac{2 * Precision * Recall}{Precision + Recall} \quad (3)$$

*D. Suppor*t - It is defined as the percentage of occurrences of a specific hashtag within the dataset of social media posts.

$$Support = \frac{Number\ of\ tweets\ containing\ the\ hashtag}{Total\ number\ of\ tweets} \quad (4)$$

4.4 Baseline models

To compare our model with other models, following baseline models are considered:

- LDA: Latent Dirichlet Allocation method extracts latent topics from social media content and associates hashtags with these topics [48].
- SVM: The method proposed in [51] converts the tag recommendation problem into classification task and uses SVM to model it.
- TTM: Topical Translation Model is proposed in [52] for tag recommendation.
- DemoHash: Hashtag recommendation model based on user demographic information [25].
- SANN: A neural network based on Self-Attention mechanism [40].
- EmHash: Bert Embedding based model forming clusters of hashtags and then recommending hashtags by predicting the desired cluster [41].

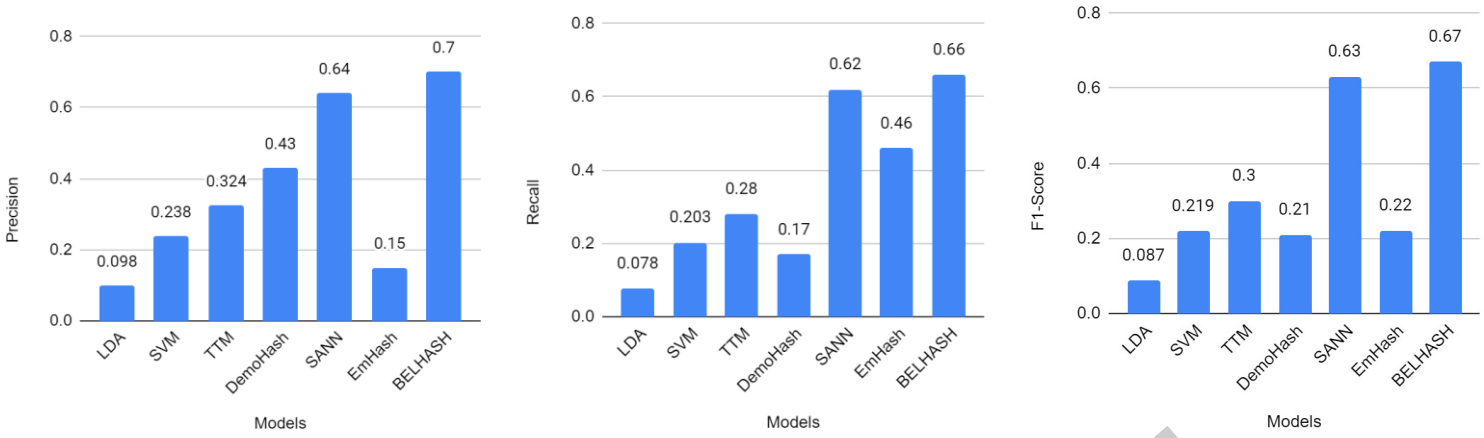
4.5 Evaluation Results

The results obtained after training and evaluating the BELHASH model over the scraped tweets are given in Table 3. It achieved an accuracy of 72.31%. The graphs of various benchmark models compared with our model are given in Figure 5. Precision, Recall and F1-Scores for top-k (k=6) recommendations are given in table 4 and its graph is shown in figure 6. The results show that BELHASH performs better than other state-of-the-art models.

Table 3: Comparative analysis of evaluation results of different methods for hashtag recommendation

Models	Precision	Recall	F1-Score
LDA	0.098	0.078	0.087
SVM	0.238	0.203	0.219
TTM	0.324	0.280	0.300
DemoHash	0.43	0.17	0.21
SANN	0.64	0.62	0.63
EmHash	0.15	0.46	0.22
BELHASH	**0.70**	**0.66**	**0.67**

Just Accepted



a) Precision of various models b) Recall of various models c) F1-Score of various models

Figure 5: Comparison of our model with other models with respect to Precision (a), Recall (b) and F1-Score (c)

Table 4: Precision, Recall, F1-Scores and Support Values for top-k (k=6) recommendations

	k=1	**k=2**	**k=3**	**k=4**	**k=5**	**k=6**
Precision	0.66	0.4	0.5	0.71	1	0.92
Recall	0.7	0.4	0.5	0.92	0.63	0.8
F1-Score	0.69	0.4	0.5	0.8	0.77	0.86
Support	20	5	4	13	8	15

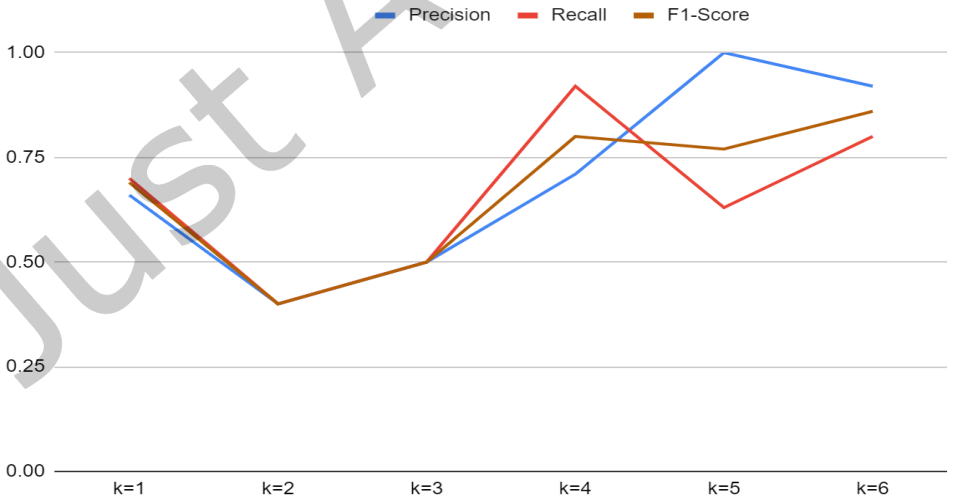


Figure 6: Evaluation Metrics used for BELHASH model for top-k (k=6) recommendations

5. CONCLUSION

In this paper, we have proposed a novel model named BELHASH, which stands for Bert Embedding based LSTM for Hashtag Recommendation. This model is evaluated on 100K covid-19 tweets, scraped using Twitter API. Existing works related to Hashtag recommendation comprises other embeddings like Word2Vec, GLOVE etc. But these embeddings do not capture the semantics or the context of the words and thus generate the same embeddings for different appearances of a word even if the word is used for different contexts in different

Just Accepted

appearances. Bert Embedding, on the other hand, captures the context of the same word in different perspectives and thus generates different embeddings. Bert combined with LSTM works effectively and generates good results. To the best of our knowledge, this is the first work in the field of hashtag Recommendation to use LSTM over Bert embedding. In experimentation, we achieved the best performance metrics as precision 100% on top-5, recall as 92% on top-4 and F1-score as 86% on top-6 recommendations. The average of these values are Precision-70%, Recall-66% and F1-Score-67%. The overall accuracy of the proposed methodology is 72%. The results show that BELHASH performs better than other state-of-the-art models. In the future work, we can improve our results by changing the number of layers or fine tuning the different parameters.

REFERENCES

[1] Dabrowski, M., & Acton, T. (2013). The performance of recommender systems in online shopping: A user-centric study. *Expert Systems with Applications*, *40*(14), 5551-5562.

[2] Schedl, M. (2019). Deep learning in music recommendation systems. *Frontiers in Applied Mathematics and Statistics*, 44.

[3] Khadse, V. P., Basha, S. M., Iyengar, N., & Caytiles, R. (2018). Recommendation Engine for Predicting Best Rated Movies. *International Journal of Advanced Science and Technology*, *110*(2), 65-76.

[4] Pathak, B., Garfinkel, R., Gopal, R. D., Venkatesan, R., & Yin, F. (2010). Empirical analysis of the impact of recommender systems on sales. Journal of Management Information Systems, 27(2), 159-188.

[5] Robillard, M., Walker, R., & Zimmermann, T. (2009). Recommendation systems for software engineering. IEEE software, 27(4), 80-86.

[6] Antheunis, M. L., Tates, K., & Nieboer, T. E. (2013). Patients' and health professionals' use of social media in health care: motives, barriers and expectations. *Patient education and counseling*, *92*(3), 426-431.

[7] De Albuquerque, J. P., Herfort, B., Brenning, A., & Zipf, A. (2015). A geographic approach for combining social media and authoritative data towards identifying useful information for disaster management. *International journal of geographical information science*, *29*(4), 667-689.

[8] Ordenes, F. V., Theodoulidis, B., Burton, J., Gruber, T., & Zaki, M. (2014). Analyzing customer experience feedback using text mining: A linguistics-based approach. *Journal of Service Research*, *17*(3), 278-295.

[9] Appel, G., Grewal, L., Hadi, R., & Stephen, A. T. (2020). The future of social media in marketing. *Journal of the Academy of Marketing Science*, *48*(1), 79-95.

[10] Tedeschi, A., & Benedetto, F. (2015, September). A cloud-based big data sentiment analysis application for enterprises' brand monitoring in social media streams. In *2015 IEEE 1st International Forum on Research and Technologies for Society and Industry Leveraging a better tomorrow (RTSI)* (pp. 186-191). IEEE.

[11] Contractor, D., & Faruquie, T. A. (2013, May). Understanding election candidate approval ratings using social media data. In *Proceedings of the 22nd International Conference on World Wide Web* (pp. 189-190).

[12] Chang, Y. C., Ku, C. H., & Chen, C. H. (2019). Social media analytics: Extracting and visualizing Hilton hotel ratings and reviews from TripAdvisor. *International Journal of Information Management*, *48*, 263-279.

[33] Khan, M. U., Javed, A. R., Ihsan, M., & Tariq, U. (2020). A novel category detection of social media reviews in the restaurant industry. *Multimedia Systems*, 1-14.

[14] Gautam, G., & Yadav, D. (2014, August). Sentiment analysis of twitter data using machine learning approaches and semantic analysis. In *2014 Seventh international conference on contemporary computing (IC3)* (pp. 437-442). IEEE.

[15] Lee, K., Agrawal, A., & Choudhary, A. (2013, August). Real-time disease surveillance using twitter data: demonstration on flu and cancer. In *Proceedings of the 19th ACM SIGKDD international conference on Knowledge discovery and data mining* (pp. 1474-1477).

[16] Jalali, A., Sherbino, J., Frank, J., & Sutherland, S. (2015). Social media and medical education: exploring the potential of Twitter as a learning tool. *International Review of Psychiatry*, *27*(2), 140-146.

[17] Soler, J. M., Cuartero, F., & Roblizo, M. (2012, August). Twitter as a tool for predicting elections results. In *2012 IEEE/ACM International Conference on Advances in Social Networks Analysis and Mining* (pp. 1194-1200). IEEE.

[18] Chae, B. K. (2015). Insights from hashtag# supplychain and Twitter Analytics: Considering Twitter and Twitter data for supply chain practice and research. *International Journal of Production Economics*, *165*, 247-259.

[19] Arias, M., Arratia, A., & Xuriguera, R. (2014). Forecasting with twitter data. *ACM Transactions on Intelligent Systems and Technology (TIST)*, *5*(1), 1-24.

[20 Mishra, N., & Singh, A. (2018). Use of twitter data for waste minimisation in beef supply chain. *Annals of Operations Research*, *270*(1), 337-359.

[21] Jain, K., & Jindal, R. (2020). A survey on hashtag recommendations. In *Conference of open innovations association, FRUCT* (No. 27, pp. 323-327). FRUCT Oy.

[22] Zhao, Z., Sun, J., Yao, L., Wang, X., Chu, J., Liu, H., & Yu, G. (2017). Modeling Chinese microblogs with five Ws for topic hashtags extraction. *Tsinghua Science and Technology*, *22*(2), 135-148.

[23] Maity, S. K., Panigrahi, A., Ghosh, S., Banerjee, A., Goyal, P., & Mukherjee, A. (2019, April). DeepTagRec: A content-cum-user based tag recommendation framework for stack overflow. In *European Conference on Information Retrieval* (pp. 125-131). Springer, Cham.

[24] Yang, C., Wang, X., & Jiang, B. (2020). Sentiment enhanced multi-modal hashtag recommendation for micro-videos. *IEEE Access*, *8*, 78252-78264.

[25] Jeong, D., Oh, S., & Park, E. (2022). DemoHash: Hashtag recommendation based on user demographic information. *Expert Systems with Applications*, *210*, 118375.

[26] Shi, B., Ifrim, G., & Hurley, N. (2016, April). Learning-to-rank for real-time high-precision hashtag recommendation for streaming news. In *proceedings of the 25th international conference on World Wide Web* (pp. 1191-1202).

[27] Shi, B., Poghosyan, G., Ifrim, G., & Hurley, N. (2017). Hashtagger+: Efficient high-coverage social tagging of streaming news. *IEEE Transactions on Knowledge and Data Engineering*, *30*(1), 43-58.

[28] Li, J., & Xu, H. (2016). Suggest what to tag: Recommending more precise hashtags based on users' dynamic interests and streaming tweet content. *Knowledge-based systems*, *106*, 196-205.

[29] Zhang, Q., Wang, J., Huang, H., Huang, X., & Gong, Y. (2017, August). Hashtag Recommendation for Multimodal Microblog Using Co-Attention Network. In *IJCAI* (pp. 3420-3426).

[30] Belhadi, A., Djenouri, Y., Lin, J. C. W., & Cano, A. (2020). A data-driven approach for Twitter hashtag recommendation. *IEEE Access*, *8*, 79182-79191.

[31] Kumar, A., Jain, N., Tripathi, S., & Singh, C. (2019). From fully supervised to zero shot settings for twitter hashtag recommendation. *arXiv preprint*

Just Accepted

arXiv:1906.04914.

[32] Tran, V. C., Hwang, D., & Nguyen, N. T. (2018). Hashtag recommendation approach based on content and user characteristics. *Cybernetics and Systems*, *49*(5-6), 368-383.

[33] Sedhai, S., & Sun, A. (2014, July). Hashtag recommendation for hyperlinked tweets. In *Proceedings of the 37th international ACM SIGIR conference on Research & development in information retrieval* (pp. 831-834).

[34] Kumar, N., Baskaran, E., Konjengbam, A., & Singh, M. (2021). Hashtag recommendation for short social media texts using word-embeddings and external knowledge. *Knowledge and Information Systems*, *63*(1), 175-198.

[35] Banbhrani, S. K., Xu, B., Liu, H., & Lin, H. (2021). SC-political ResNet: hashtag recommendation from Tweets using hybrid optimization-based deep residual network. *Information*, *12*(10), 389.

[36] Liu, S., Xie, J., Zou, C., & Chen, Z. (2020, July). User conditional hashtag recommendation for micro-videos. In *2020 IEEE International Conference on Multimedia and Expo (ICME)* (pp. 1-6). IEEE.

[37] Zhang, S., Yao, Y., Xu, F., Tong, H., Yan, X., & Lu, J. (2019, July). Hashtag recommendation for photo sharing services. In *Proceedings of the AAAI Conference on Artificial Intelligence* (Vol. 33, No. 01, pp. 5805-5812).

[38] Wei, Y., Cheng, Z., Yu, X., Zhao, Z., Zhu, L., & Nie, L. (2019, October). Personalized hashtag recommendation for micro-videos. In *Proceedings of the 27th ACM International Conference on Multimedia* (pp. 1446-1454).

[39] Javari, A., He, Z., Huang, Z., Jeetu, R., & Chen-Chuan Chang, K. (2020, April). Weakly supervised attention for hashtag recommendation using graph data. In *Proceedings of The Web Conference 2020* (pp. 1038-1048).

[40] Yang, D., Zhu, R., & Li, Y. (2019). Self-Attentive Neural Network for Hashtag Recommendation. *Journal of Engineering Science & Technology Review*, *12*(2).

[41] Kaviani, M., & Rahmani, H. (2020, April). Emhash: Hashtag recommendation using neural network based on bert embedding. In *2020 6th International Conference on Web Research (ICWR)* (pp. 113-118). IEEE.

[42] Mao, Q., Li, X., Peng, H., Liu, B., Guo, S., Li, J., ... & Yu, P. S. (2021). Attend and Select: A Segment Attention based Selection Mechanism for Microblog Hashtag Generation. arXiv preprint arXiv:2106.03151.

[43] Cantini, R., Marozzo, F., Bruno, G., & Trunfio, P. (2021). Learning sentence-to-hashtags semantic mapping for hashtag recommendation on microblogs. *ACM Transactions on Knowledge Discovery from Data (TKDD)*, *16*(2), 1-26.

[44] Camargo, A., Carvalho, W., Peressim, F., Barzilay, A., & Finger, M. (2021). Text-to-hashtag Generation using Seq2Seq Learning. *arXiv preprint arXiv:2102.00904*.

[45] Dey, K., Shrivastava, R., Kaushik, S., & Subramaniam, L. V. (2017, November). Emtagger: a word embedding based novel method for hashtag recommendation on twitter. In *2017 IEEE International Conference on Data Mining Workshops (ICDMW)* (pp. 1025-1032). IEEE.

[46] Ben-Lhachemi, N., & Boumhidi, J. (2019, October). Hashtag recommender system based on LSTM neural reccurent network. In *2019 Third International Conference on Intelligent Computing in Data Sciences (ICDS)* (pp. 1-6). IEEE.

[47] Ben-Lhachemi, N. (2018). Using tweets embeddings for hashtag recommendation in Twitter. *Procedia Computer Science*, *127*, 7-15.

[48] Krestel, R., Fankhauser, P., & Nejdl, W. (2009, October). Latent dirichlet allocation for tag recommendation. In *Proceedings of the third ACM conference on Recommender systems* (pp. 61-68).

[49] Rajni Jindal, Kirti Jain, A Review on Recommendation Systems Using Deep Learning, International Journal of Scientific & Technology Research (IJSTR), ISSN: 2277-8616, Volume 8, Issue 10, October 2019.

[50] Jain, K., & Jindal, R. (2023). Sampling and noise filtering methods for recommender systems: A literature review. *Engineering Applications of Artificial Intelligence*, *122*, 106129.

[51] Chen, H. M., Chang, M. H., Chang, P. C., Tien, M. C., Hsu, W. H., & Wu, J. L. (2008, October). Sheepdog: group and tag recommendation for flickr photos by automatic search-based learning. In *Proceedings of the 16th ACM international conference on Multimedia* (pp. 737-740).

[52] Ding, Z., Qiu, X., Zhang, Q., & Huang, X. (2013, June). Learning topical translation model for microblog hashtag suggestion. In *Twenty-third international joint conference on artificial intelligence*.

[53] Li, Y., Liu, T., Hu, J., & Jiang, J. (2019). Topical co-attention networks for hashtag recommendation on microblogs. *Neurocomputing*, *331*, 356-365.

[54] Ma, J., Feng, C., Shi, G., Shi, X., & Huang, H. (2018). Temporal enhanced sentence-level attention model for hashtag recommendation. *CAAI Transactions on Intelligence Technology*, *3*(2), 95-100.

[55] Połap, D. (2023). Hybrid image analysis model for hashtag recommendation through the use of deep learning methods. *Expert Systems with Applications*, 120566.

[56] Chakrabarti, P., Malvi, E., Bansal, S., & Kumar, N. (2023). Hashtag recommendation for enhancing the popularity of social media posts. *Social Network Analysis and Mining*, *13*(1), 21.

[57] Sharma, V. K., Mittal, N., Vidyarthi, A., & Gupta, D. (2022). Exploring Web-based Translation Resources Applied to Hindi-English Cross-Lingual Information Retrieval. *ACM Transactions on Asian and Low-Resource Language Information Processing*.

[58] Sharma, V. K., Mittal, N., & Vidyarthi, A. (2022). Context-based translation for the out of vocabulary words applied to hindi-english cross-lingual information retrieval. *IETE Technical Review*, *39*(2), 276-285.

[59] Dara, S., Srinivasulu, C. H., Babu, C. M., Ravuri, A., Paruchuri, T., Kilak, A. S., & Vidyarthi, A. (2023). Context-Aware Auto-Encoded Graph Neural Model for Dynamic Question Generation using NLP. *ACM Transactions on Asian and Low-Resource Language Information Processing*.

[60] Perti, A., Sinha, A., & Vidyarthi, A. (2023). Cognitive Hybrid Deep Learning-based Multi-modal Sentiment Analysis for Online Product Reviews. *ACM Transactions on Asian and Low-Resource Language Information Processing*.

[61] Mundra, S., Reddy, J., Mundra, A., Mittal, N., Vidyarthi, A., & Gupta, D. (2023). An Automated Data-driven Machine Intelligence Framework for Mining Knowledge To Classify Fake News Using NLP. *ACM Transactions on Asian and Low-Resource Language Information Processing*.

Just Accepted

Taylor & Francis
Taylor & Francis Group

Preparative Biochemistry & Biotechnology

ISSN: (Print) (Online) Journal homepage: https://www.tandfonline.com/loi/lpbb20

Optimization of phytase production by *Penicillium oxalicum* in solid-state fermentation for potential as a feed additive

Priya, Bijender Singh, Jai Gopal Sharma & Bhoopander Giri

To cite this article: Priya, Bijender Singh, Jai Gopal Sharma & Bhoopander Giri (28 Dec 2023): Optimization of phytase production by *Penicillium oxalicum* in solid-state fermentation for potential as a feed additive, Preparative Biochemistry & Biotechnology, DOI: 10.1080/10826068.2023.2297688

To link to this article: https://doi.org/10.1080/10826068.2023.2297688


Published online: 28 Dec 2023.


Submit your article to this journal


Article views: 45


View related articles


View Crossmark data

Full Terms & Conditions of access and use can be found at
https://www.tandfonline.com/action/journalInformation?journalCode=lpbb20

PREPARATIVE BIOCHEMISTRY & BIOTECHNOLOGY
https://doi.org/10.1080/10826068.2023.2297688

Taylor & Francis
Taylor & Francis Group

Check for updates

Optimization of phytase production by *Penicillium oxalicum* in solid-state fermentation for potential as a feed additive

Priya[a], Bijender Singh[b,c], Jai Gopal Sharma[a], and Bhoopander Giri[d]

[a]Environmental and Industrial Biotechnology Laboratory, Department of Biotechnology, Delhi Technological University, Delhi; [b]Laboratory of Bioprocess Technology, Department of Microbiology, Maharshi Dayanand University, Rohtak, Haryana; [c]Department of Biotechnology, Central University of Haryana, Mahendargarh, Haryana; [d]Department of Botany, Swami Shraddhanand College, University of Delhi, Delhi

ABSTRACT

The study aims to statistically optimize the phytase production by *Penicillium oxalicum* PBG30 in solid-state fermentation using wheat bran as substrate. Variables viz. pH, incubation days, $MgSO_4$, and Tween-80 were the significant parameters identified through the Plackett-Burman design (PBD) that majorly influenced the phytase production. Further, central composite design (CCD) method of response surface methodology (RSM) defined the optimum values for these factors i.e., pH 7.0, 5 days of incubation, 0.75% of $MgSO_4$, and 3.5% of Tween-80 that leads to maximum phytase production of 475.42 U/g DMR. Phytase production was also sustainable in flasks and trays of different sizes with phytase levels ranging from 394.95 to 475.42 U/g DMR. Enhancement in phytase production is 5.6-fold as compared to unoptimized conditions. The *in-vitro* dephytinization of feed showed an amelioration in the nutritive value by releasing inorganic phosphate and other nutrients in a time-dependent manner. The highest amount of inorganic phosphate (33.986 mg/g feed), reducing sugar (134.4 mg/g feed), and soluble protein (115.52 mg/g feed) was achieved at 37 °C with 200 U of phytase in 0.5 g feed for 48 h. This study reports the economical and large-scale production of phytase with applicability in enhancing feed nutrition.

KEYWORDS

Dephytinization; fish feed; large-scale; *P. oxalicum*; phytase; statistical optimization; wheat bran

Introduction

Phytic acid (myo-inositol hexakis dihydrogen phosphate) is a reserve of organic phosphorus and exists as phytate, i.e., the more complex form of phytic acid. Phytate binds cations and other essential biomolecules like amino acids, lipids, proteins, digestive enzymes, and carbohydrates and acts as an anti-nutritional factor for monogastric animals.[35] Besides, it causes severe phosphorus pollution due to the enrichment of nutrients and algal bloom formation in water bodies leading to hypoxia and the death of aquatic animals.[29]

Phytase (myo-inositol hexakisphosphate phosphohydrolases) is a significant enzyme in the food and feed industry that makes phytate-restricted nutrients accessible for utilization. It catalyzes the hydrolysis of phytic acid sequentially and liberates inorganic phosphate and lower esters of myo-inositol. It also removes metal ions, proteins, enzymes, and other biomolecules associated with the phytate complex. Plants, animals, and microbes produce phytases in intracellular and extracellular forms. Microbial phytases are preferable over other phytase sources because of their thermostability, wide pH range, and resistance toward proteases.[16] It has applications in animal nutrition, human nutrition, pharmaceutical, plant growth, bioethanol production, environmental issues, and transgenic plant formation.[29]

Both solid-state (SSF) and submerged fermentation (SmF) are applicable for phytase production, but acceptance of SSF over SmF is more due to its simple process, low cost, and yield of more end product.[36] In SSF, microbes are grown on solid material in the absence of oxygen and require adequate moisture for the growth,[20] and agricultural residues are used as a substrate for the fermentation process because being lignocellulosic, they stimulate the growth of microorganisms and are less costly.[12] One variable at a time (OVAT) approach analyses the factors one by one, which is more time-consuming, laborious, and costly. At the same time, the statistical methods (PBD and RSM via CCD) involve an experimental design that examines various parameters in a single duration and their relation with the help of mathematics and statistics. Furthermore, it creates two- and three-dimensional contour plots to demonstrate the optimization of parameters and interaction among them.[16] Previous literature also supported the use of statistical methods in enhancing phytase production via SSF using *Aspergillus niger*,[2] *A. oryzae* SBS50,[36] *Sporotrichum thermophile*,[17] *Rhizopus oligosporus*,[40] *Pholiota adiposa*,[12] *A. niger* NT7,[16] *A. tubingensis*,[20] *A. niger*.[22]

The plant-based feed contains anti-nutritional factors (ANFs) like phytic acid, oxalates, saponins, and tannins which deprive the nutrients in the feed. Up to 80% of phosphorus in the plant feed exists as phytate-phosphorus (P).

CONTACT Bhoopander Giri bhoopg@yahoo.com Department of Botany, Swami Shraddhanand College, University of Delhi, Delhi.
© 2023 Taylor & Francis Group, LLC

Due to the lack of phytase in monogastric animals, phytate-P remains undigestible; thus, additional inorganic phosphate (Pi) is requisite in the diet to fulfill the demand of P, which affects the finite P reserve stock. Also, unutilized phosphorus in the form of phytate-P and Pi excreted in feces causes P pollution in aquatic bodies.[16] Moreover, the phytate-metal complex inhibits the activity of digestive enzymes in the gastrointestinal region, thus regulating the digestibility of protein, lipids, and starch. Supplementation of phytase is the practical approach that degrades phytic acid, makes nutrients available for utilization, improves the quality of feed, and reduces P pollution.[29]

The phytases involved in the fish feeding are mostly commercial and obtained by SmF while, this work is utilizing SSF for phytase production from a new fungal isolate, *P. oxalicum*. SSF is economical cheaper method than SmF and makes a cost-effective process for phytase production. The phytase is useful in removing ANFs, mainly phytate and makes the feed healthy and nutritious. Initial degradation of phytate is started in the formulated feed. The determination of phytate hydrolysis is necessary to understand the impact of phytase in the feed before fish feeding. Therefore, *in-vitro* analysis of plant-based feed is requisite. Most of the investigation is done on the fish growth and its performance (*in-vivo*) by adding phytase to their diet.[9,29] But limited research is available on the dephytinization of fish feed at *in-vitro* level. Dephytinization is a process of phytic acid degradation and liberation of inorganic phosphorus on the addition of phytase in the diet. Besides, it also releases reducing sugars and soluble protein. These products enhance the nutritional value of diet.

The study investigates the extracellular phytase production from *Penicillium oxalicum* in SSF using wheat bran as a substrate and its enhancement through statistical optimization. Here, the study also evaluates the production of cost-effective phytase on large scale. The *in-vitro* effect of partially purified phytase in dephytinizing plant-based fish feed and ameliorating its nutritional value was analyzed. Optimization of various factors (temperature, dose, amount of feed, incubation time) were performed to know the best conditions for the operation of phytase in fish feeding. This research indicates the potential of *P. oxalicum* phytase as a supplement in feed industry.

Materials and methods

Microorganism and culture conditions

The fungus was isolated from the rotten orange peel collected from the local market of Delhi. The mold was identified as *Penicillium oxalicum* PBG30 on the basis of morphological features as well as ITS sequencing (data not shown). The mold was cultured on the potato dextrose agar media at 30 °C and stored at 4 °C and at −20 °C in glycerol stock.[33]

The fungal spores were scrapped from 3-day-old culture via a sterile loop by adding 25 ml normal saline solution containing 0.1% Tween 80. The spore suspension was filtered through a sterile filter assembly, and the spore count was measured by a hemocytometer.[36]

Phytase production in solid-state fermentation

Phytase production was carried out using four different moistening media (pH 5.0) in 250 ml Erlenmeyer flasks (Table 1). Wheat bran is used as a substrate (5 g) with 10 ml moistening media (1:2), and autoclaved at 121 °C for 20 min. After cooling at room temperature, inoculated with 1 ml of spore suspension (7.7×10^7 CFU/ml) and kept in the incubator for 3 days at 30 °C. After 3 days of incubation, the enzyme extraction was done by adding the 50 ml normal saline solution with 0.1% Tween 80 in the flask and shaking at 30 °C with 200 rpm for 1 h. The extract was filtered by double-layered muslin cloth and centrifuged the filtrate at 10,000 rpm for 10 min at 4 °C. The supernatant was used to test the phytase activity, and the residual substrate was dried at 60 °C for 24 h.[36]

Phytase assay

Phytase activity was determined by measuring the release of inorganic phosphate from the calcium phytate substrate at 70 °C with 0.1 M sodium acetate buffer (pH 3.0) through[8] method. Blank and control (substrate and enzyme) were also set during the experiment, and all were performed in triplicate. Phytase activity was calculated using the regression equation of the standard graph of inorganic phosphate (KH_2PO_4). The phytase activity is expressed as unit per gram dry moldy residue (U/g DMR).[36] One unit of phytase is defined as the amount of enzyme used to liberate 1 nmol of inorganic phosphorus per sec under assay conditions.[33]

Optimization of phytase production by statistical approach

Plackett-Burman design

The optimization of phytase production from *P. oxalicum* includes two steps. In the first step, the Plackett-Burman method helps to identify the significant factors useful for production.[28] In this design, a selection of 11 variables (n) with their high (+) and low (-) concentration values and 12 runs of the experiment (n + 1) was set in an equal manner

Table 1. Different moistening media used for the phytase production.

S. No.	Composition of moistening media	Reference
Medium I	Distilled water	[37]
Medium II	Starch – 1.5% (w/v), Beef extract – 0.6% (w/v), $FeSO_4.7H_2O$ – 0.01% (w/v), KCl – 0.05% (w/v)	[37]
Medium III	$(NH_4)_2SO_4$ – 0.5% (w/v), $MgSO_4.7H_2O$ – 0.5% (w/v), $FeSO_4.7H_2O$ – 0.03% (w/v), NaCl – 0.1% (w/v)	[37]
Medium IV	Urea – 0.5% (w/v), $MgSO_4.7H_2O$ – 0.1% (w/v), KCl – 0.1% (w/v), $FeSO_4.7H_2O$ – 0.1% (w/v)	[21]

Table 2. Factors studied during Plackett Burman experiment.

Run No	A	B	C	D	E	F	G	H	I	J	K	Phytase Activity (U/g DMR ± S.E)
1	5	5	5	1	2	0	1	0.05	0.0	0.5	0	108.56 ± 10.01
2	10	5	3	0	2	2	1	0.00	0.2	0.5	0	24.01 ± 15.51
3	10	8	3	1	2	0	1	0.00	0.0	0.1	1	150.5 ± 31.80
4	5	8	3	0	0	2	1	0.05	0.0	0.5	1	239.81 ± 0.08
5	5	8	5	1	0	2	1	0.00	0.2	0.1	0	97.24 ± 8.84
6	10	5	5	0	0	0	1	0.05	0.2	0.1	1	102.29 ± 3.93
7	10	8	3	1	0	0	0	0.05	0.2	0.5	0	59.36 ± 18.96
8	5	5	3	1	2	2	0	0.05	0.2	0.1	1	97.54 ± 14.40
9	5	8	5	0	2	0	0	0.00	0.2	0.5	1	268.77 ± 0.03
10	5	5	3	0	0	0	0	0.00	0.0	0.1	0	5.75 ± 1.94
11	10	5	5	1	0	2	0	0.00	0.0	0.5	1	102.06 ± 39.92
12	10	8	5	0	2	2	0	0.05	0.0	0.1	0	137.578 ± 1.47

A – Wheat bran (g), B – pH, C – Incubation period (days), D – Urea (% w/v), E – Starch (% w/v), F – Glucose (% w/v), G -Ammonium sulfate (% w/v), H – Ferrous sulfate (% w/v), I – Calcium chloride (% w/v), J – Magnesium sulfate (% w/v), K – Tween 80 (% v/v).

(Table 2). The selected independent factors were A) wheat bran, B) pH, C) incubation days, D) ammonium sulfate, E) urea, F) starch, G) glucose, H) ferrous sulfate I) calcium chloride, J) magnesium sulfate, and H) Tween 80. The difference between the average of one variable at its high and low levels provides the impact of that variable on the production, which was calculated by

$$E(Xi) = \frac{2(\Sigma Pi+ \; - \; \Sigma Pi-)}{N}$$

Here, E(Xi) denotes the effect of each variable, Pi+, and Pi- means high and low values, and N means the total number of runs performed in the experiment.[36] All the runs were performed in triplicates, phytase activity was calculated, and the critical factors were determined by a pareto chart.[42]

Response surface methodology

In the second step, four independent factors, pH (A), incubation time (B), $MgSO_4$ (C), and Tween 80 (D) obtained from PBD, were evaluated further by the RSM experiment. The optimal level and interaction effect of these parameters on phytase production is determined using central composite design (CCD Version 6.0.7, Stat-Ease, and Minneapolis, MN). In addition, 0.5% ammonium sulfate and 0.01% $FeSO_4$ supplied as a supplement. Five levels (-α, −1, 0, +1, +α) were assigned to each parameter, and 30 experimental runs were designed as shown in Tables 3 and 4 respectively.

Production of phytase is measured by the following equation:

$$\begin{aligned} Y = \; & ß_0 + ß_1A + ß_2B + ß_3C + ß_4D + ß_{11}A^2 \\ & + ß_{22}B^2 + ß_{33}C^2 + ß_{44}D^2 + ß_1ß_2AB + ß_1ß_3AC \\ & + ß_1ß_4AD + ß_2ß_3BC + ß_2ß_4BD + ß_3ß_4CD \end{aligned}$$

(Y- predicted phytase production, $ß_0$ - intercept, $ß_1$, $ß_2$, $ß_3$, $ß_4$ - linear coefficients, $ß_{11}$, $ß_{22}$, $ß_{33}$, $ß_{44}$ - squared coefficients, $ß_1ß_2$, $ß_1ß_3$, $ß_1ß_4$, $ß_2ß_3$, $ß_2ß_4$, $ß_3ß_4$ - interaction coefficients, A, B, C, D, AB, AC, AD, BC, BD, CD – variables and their interaction.[33] Statistical software was used to set up the experiment and created 3-D contour plots.[11] In this method, predicted and experimental values were compared, and statistical analysis was done by analysis of variance (ANOVA).[42]

Table 3. Parameters with their assigned level in CCD method of RSM for phytase production.

S. No.	Parameters	Level of parameters				
		-α	−1	0	+1	+α
1.	pH	5	6	7	8	9
2.	Incubation period	3	4	5	6	7
3.	Tween 80 (%)	0.5	1	2	3	3.5
4.	$MgSO_4$ (%)	0.25	0.50	0.75	1.00	1.25

Phytase production in flasks and trays

Phytase production was carried out in flasks (250-1000 ml) and enamel-coated metallic trays (27 cm × 22 cm × 5 cm, 35 cm × 32 cm × 5 cm) containing wheat bran moistened with medium (5, 10, 20, 100, 150) in a 1:2 ratio. The flasks were autoclaved at 121 °C for 20 min and cooled down.[36] Inoculated with a spore suspension of *P. oxalicum*, mixed with a sterile spatula, covered with a clean wrap for trays, and incubated for 5 days at 30 °C. Samples were collected from different sections of the tray, and extraction was performed, as mentioned earlier.[17]

Dephytinization of feed by P. oxalicum phytase

In-vitro hydrolysis of phytate was performed by adding partially purified phytase to the feed and analyzing the quantity of released inorganic phosphate, reducing sugar and protein content. Partial purification of phytase is done by salt precipitation and dialysis method. One gram of commercial fish feed was dissolved in 20 ml sodium acetate buffer (0.1 M, pH 3.0) and autoclaved at 121 °C for 20 min. Phytase from *P. oxalicum* (80 U/g) was mixed and incubated at 37 °C, 50 °C, and 70 °C with shaking at 100 rpm. Samples were taken at different time intervals, kept at 4 °C, and centrifuged at 10,000 rpm for 10 min. The supernatant was used to detect inorganic phosphate, reducing sugars and soluble protein content by the[8,19,23] respectively. Further experiments with different doses of phytase (25-200 U/g), feed amount (0.5-2 g), and incubation time (2-48 h) were performed at 37 °C.[38] All the experiments were conducted in triplicates and statistical analysis was done by showing

Table 4. Phytase activity of RSM experimental runs designed by CCD method.

Run No	pH	Incubation Period (days)	Tween 80 (%)	Magnesium sulphate (%)	Phytase activity (U/g DMR ± S.E)	
					Experimental value	Predicted value
1	7	5	2.0	0.75	114.74 ± 14.70	117.85
2	6	4	3.0	0.50	278.39 ± 17.17	297.11
3	7	5	2.0	1.25	64.48 ± 6.39	62.82
4	6	6	1.0	0.50	12.27 ± 1.85	18.60
5	8	6	3.0	1.00	120.42 ± 7.47	124.90
6	6	3	1.0	0.50	51.28 ± 6.91	50.25
7	8	6	3.0	0.50	177.51 ± 12.47	188.98
8	9	5	2.0	0.75	13.28 ± 1.74	4.82
9	7	5	0.5	0.75	109.57 ± 6.68	108.87
10	6	4	1.0	1.00	60.27 ± 8.02	62.80
11	6	6	3.0	1.00	141.69 ± 6.17	154.13
12	6	6	1.0	1.00	76.52 ± 6.48	73.58
13	7	4	2.0	0.75	144.09 ± 7.34	138.52
14	7	4	2.0	0.75	145.74 ± 8.06	138.52
15	8	4	1.0	0.50	44.36 ± 4.56	45.92
16	7	5	2.0	0.75	114.74 ± 14.70	117.85
17	6	4	3.0	1.00	264.27 ± 18.60	260.82
18	7	5	3.5	0.75	373.32 ± 3.28	346.66
19	8	4	3.0	0.50	278.09 ± 1.28	282.42
20	8	4	1.0	1.00	25.71 ± 8.49	30.45
21	8	6	1.0	0.50	65.12 ± 5.90	69.95
22	6	6	3.0	0.50	172.45 ± 15.59	169.09
23	7	5	2.0	0.75	114.74 ± 20.79	117.85
24	7	7	2.0	0.75	82.73 ± 7.41	76.52
25	8	4	3.0	1.00	191.39 ± 14.52	197.01
26	8	6	1.0	1.00	80.52 ± 9.68	75.81
27	5	5	2.0	0.75	24.21 ± 5.56	17.28
28	7	5	2.0	0.75	114.74 ± 14.70	117.85
29	7	5	2.0	0.25	106.99 ± 7.15	93.25
30	7	5	2.0	0.75	114.74 ± 14.70	117.85

significant differences ($p < 0.05$) via using one-way ANOVA and Tukey's post hoc tests. GraphPad Prism software version 10.0 (GraphPad Software, San Diego, CA, USA) is used for the statistical analysis. Sigma plot (version 10.0) is used for the creating the graphs.[34]

Results and discussion

Phytase production in SSF

Among the different production media for SSF, media IV (84.60 ± 2.54 U/g DMR) supports the maximum phytase production, as shown in Figure 1. Different fungi were studied for producing phytase through SSF by using wheat bran as substrate.[15,20,30,32,36] Wheat bran is commonly used for SSF because it is rich in carbon, nitrogen, and amino acids and high amount of phytic acid. Due to presence of phytate, it acts as inducer for the production of phytase.[3] It also provides support for the growth of fungi, easily available, and low cost.[15] The production of phytase via wheat bran as substrate has been reported in *A. oryzae* SBS50 (5.05 U/g DMR) using 10 g substrate in 1:2 ratio of moistening media incubated at 30 °C for 4 days.[36] Similarly, *R. oligosporus* MTCC 556 produced 15.8 U/gds,[39] 208.30 U/gds by *A. niger* NT7[15] and 225.6 U/g by *A. tubingensis*[20] using wheat bran as substrate. [7] studied the phytase production with different fungal strains on wheat bran and reported that *A. oryzae* F-923, *A. oryzae* F-937, *A. niger* F-258, *A. awamori* NRC- F18, *A. fumigatus* NRCF-113, *Trichoderma viride* NRCF-107 and *Saccharomyces cerevisiae* F-307

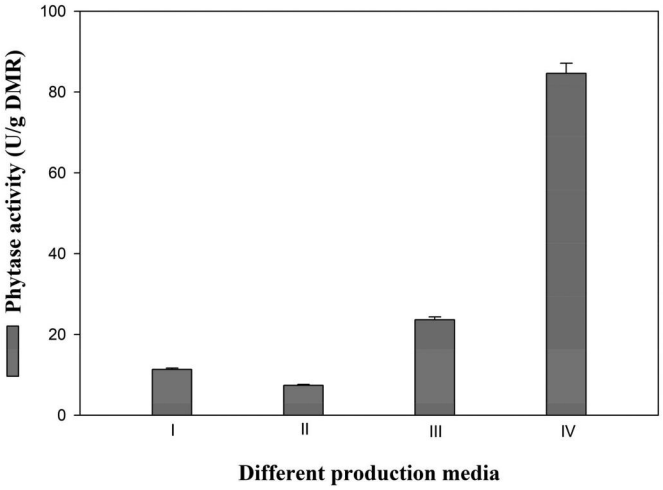


Figure 1. The graph shown the involvement of different media in the production of phytase.

secreted phytase as 66.56, 58.19, 110.62, 143.67, 60.24, 54.41 and 64.86 IU/g, respectively.

Screening of critical components through PB design

Plackett-Burman is a majorly adopted statistical method used for studying several factors together, which consumes less time and provides significant factors that influence the production of phytases. The factors showing a high impact on phytase production are considered critical or essential parameters. A PB design was performed with 11 variables and 12 experimental runs with their high (+) and low (-)

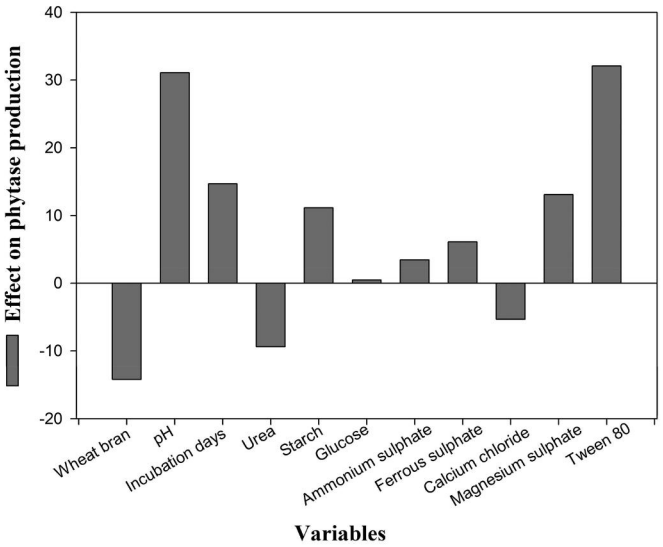


Figure 2. Pareto chart showing the effect of different variables on phytase production.

Table 5. ANOVA for response surface reduced quadratic model.

Source	Sum of Squares	dF	Mean square	F value	Prob > F	
Model	2.121E + 005	13	16315.40	127.35	<0.0001	significant
A	226.28	1	226.28	1.77	0.2025	
B	11156.38	1	11156.38	87.08	<0.0001	
C	1.245E + 005	1	1.245E + 005	971.51	<0.0001	
D	1349.22	1	1349.22	10.53	0.0051	
A^2	20241.05	1	20241.05	157.99	<0.0001	
C^2	28704.97	1	28704.97	224.05	<0.0001	
D^2	2813.01	1	2813.01	21.96	0.0002	
AB	1527.12	1	1527.12	11.92	0.0033	
AC	947.85	1	947.85	7.40	0.0151	
AD	2310.40	1	2310.40	18.03	0.0006	
BC	17622.46	1	17622.46	137.55	<0.0001	
BD	580.75	1	580.75	4.53	0.0491	
CD	4683.10	1	4683.10	36.55	<0.0001	

Table 6. ANOVA regression analysis.

Std. Dev.	11.32	R^2	0.9904
Mean	122.61	Adj R^2	0.9827
C.V.	9.23	Pred R^2	0.9571
PRESS	9188.99	Adeq Precision	44.209

level. Table 2 shows the phytase production of 12 experimental runs. A pareto chart was created to determine the impact of variables on phytase production (Figure 2). The positive and negative values in the pareto graph showed the importance of individual components in phytase production. Run no. 9 showed the maximum output in term of phytase production. This experiment concluded that among the 11 factors, pH, incubation time, $MgSO_4$, and Tween 80 are the critical variables that contribute more to the production of *P. oxalicum* phytase, and others have low contributions and thus are less significant. Surfactants like Tweens and Triton X-100 seem to affect the fungus growth and enzyme production and hence, involved in the enhancement of enzyme yield. Surfactants solubilize proteins on the membrane that increases cell permeability and more liberation of enzymes.[17] Tween-80 has been reported for enhancing the phytase production by *S. thermophile*[17] and *A. oryzae* SBS50.[33] Triton X-100 enhanced phytase production by *A. oryzae* SBS50[36] and Tween-40 by *A. niger*[22] in SSF.

Moisture content is also one of the factors that affect the phytase production. At low moisture content, substrate becomes dry and at high level, the substrate air content is decreased. So, an optimum moisture is required for the growth.[33] It has been mentioned as important component in the production of phytase from *A. oryzae* SBS50,[36] *A. niger,*[2] *P. adiposa*[12] and *A. oryzae* SBS50.[33] Metal ions like $MgSO_4$, are necessary for the growth of fungi but have no influence on phytase activity.[33] Many studies showed the importance of $MgSO_4$ in phytase production from *A. oryzae* SBS50,[36] *A. niger*[2] and *A. oryzae.*[33]

The impact of incubation period and pH occurs on the metabolic process during the fungal growth and they also help in stabilizing the enzymes.[15] Incubation period is shown as a major component for production of phytase in *A. oryzae* SBS50,[36] *S. thermophile,*[17] *A. niger* NT7[16] and *A. niger.*[22] Similarly, pH is found necessary in the phytase production from *Williopsis saturnus* NCIM 3298,[27] *A. niger* NT7[16] and *A. niger.*[22] Other useful factors involved in the production of phytase were selected through PBD like glucose and dextrin for *A. niger,*[2] yeast extract for *S. thermophile,*[17] glucose, $FeSO_4$, citric acid for *W. saturnus,*[27] water hyacinth for *P. adiposa,*[12] amount of wheat bran, temperature, mannitol and ammonium sulfate for *A. niger* NT7,[16] temperature and NH_4NO_3 for *A. niger,*[22] glucose for *A. oryzae.*[33]

Optimization by response surface methodology

A total of 30 experiments were designed via CCD using 5 g wheat bran, 0.5% ammonium sulfate, and 0.01% ferrous sulfate as fixed parameters and pH, incubation period, magnesium sulfate, and Tween 80 as varying parameters. The best result of phytase activity (373.32 U/g DMR) was found in the flask containing 5 g of wheat bran moistened with 10 ml of media including 0.5% ammonium sulfate, 0.01% $FeSO_4$, 3.5% Tween 80 and 0.75% $MgSO_4$ with pH 7.0 and 5 days of incubation. The phytase production was elucidated by following model equation:

$$\begin{aligned} Y\ (\mathrm{U/g\ DMR}) = {} & 117.85 - 3.12\ A - 20.67\ B \\ & + 79.26\ C - 7.61\ D - 26.70\ A^2 + 48.85\ C^2 - 9.95\ D^2 \\ & + 8.64\ AB - 7.87\ AC - 12.28\ AD - 29.37\ BC \\ & + 5.33\ BD - 17.49CD \end{aligned}$$

ANOVA is used for evaluating the data designed by the RSM experiment as shown in Tables 5 and 6 The Pred R^2 value is 0.9571 depicting the correlation between the predicted and experimental values. R^2 value, i.e., the coefficient of determination, is found to be 0.99, indicating 99% variability within the model's parameters. Adequate precision gives us a signal-to-noise ratio that should be > 4 for better results.[13] The ratio in this model comes out to 44.209, delivering more than a sufficient signal to navigate the design space. The significance of the model is determined by the F value, which is 127.35 in our experiment, indicating

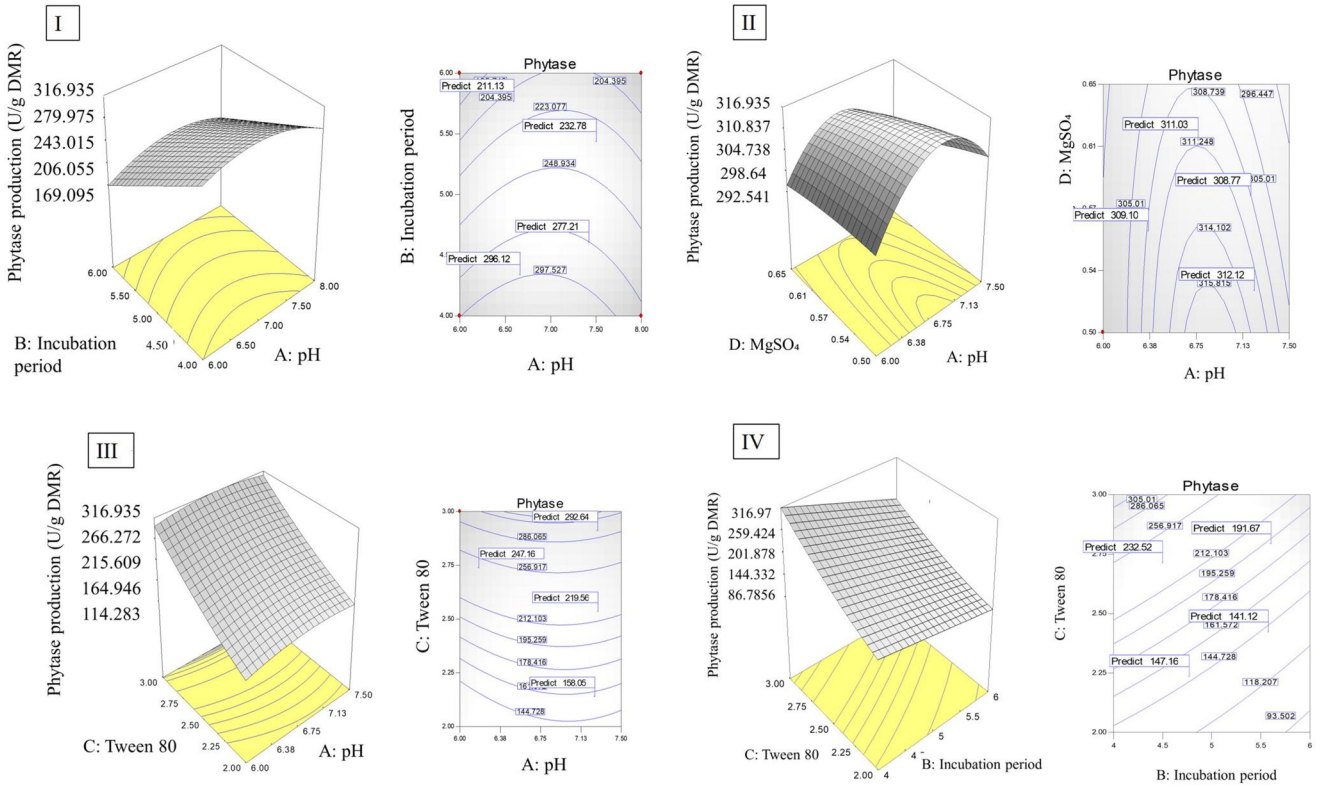


Figure 3. 3D response surface plot showing interaction between I) pH and incubation period II) pH and $MgSO_4$ III) pH and Tween 80 IV) incubation period and Tween 80.

that the model is significant and Prob > F was less than 0.05, which implies that there is only a 0.01% chance that the occurrence of the F value is due to noise.[33] Significant model terms were B, C, D, A^2, C^2, D^2, AB, AC, AD, BC, BD, and CD that significantly affected phytase production in SSF.

Response surface graphs showed the optimum level of parameters and interaction among them on which phytase activity is demonstrated on the y-axis and influencing parameters on the x-axis and z-axis.[16] The peak denotes the phytase production with the optimal value of each variable.[22] Figure 3(I) shows the relation between pH and the incubation period. At pH 7.0 and 5 days of incubation, production is higher than below or above the values of both factors. The trial showing maximum phytase titer was repeated further to validate the experiment and found to be 339.94 U/g DMR which was closer to the estimated value of 346.66 U/g DMR.

Optimization is requisite for the identification of essential components and culture conditions necessary for the fungal growth and production of enzymes. Incubation time is a significant influencing variable in enzyme production. In the logarithmic phase, most of the enzymes are produced. A long time period decreases the production level due to a deficiency of nutrients and cell lysis.[36] The results showed maximum production within 5 days of incubation; after that, phytase yield decreases due to a deficiency of nutrients for the growth of fungi. Likewise, the incubation period was also found 5 days for *A. niger* NT7[16] and *R. oligosporus.*[40] In contrast, 2 days were reported for *A. oryzae* SBS50[36] and *S. thermophile*[17] and 6 days for *A. niger.*[22]

Medium pH is crucial for all metabolic processes and strongly affects phytase production. The optimum pH for *P. oxalicum* is 7.0, i.e., neutral pH. Opposite to this, *A. niger* NT7 requires pH 5.0,[16] and *A. niger* requires pH 6.0[22] for high phytase production. Tween-80 is one of the surfactants that significantly affects the production level as it permeabilizes the cell membrane and releases more proteins/enzymes in the medium.[36] At 3.5% concentration, Tween-80 depicts its highest effect. Tween-80 (2.5%) was found optimum for phytase production from *S. thermophile*[17] and *A. oryzae* SBS50.[33] Metal ions such as magnesium are requisite for the fungus growth but barely affect the phytase production.[33] In our results, 0.75% $MgSO_4$ was involved in increasing the production of phytase, while 0.4% $MgSO_4$ is found for *A. oryzae* SBS50[36] and 1.5% for *A. niger.*[2]

Optimization through statistical methods enhanced phytase production significantly. In our results, the phytase activity showed 4.4-fold enhancement after statistical optimization compared to unoptimized conditions. Similarly, 3.35-fold enhancement has been mentioned in the phytase production from *A. oryzae* SBS50,[36] 36.67-fold in *A. niger,*[2] 11.6-fold in *S. thermophile,*[17] 2.73-fold in *R. oligosporus,*[40] 3.15-fold in *P. adiposa,*[12] 6.8-fold in *A. niger,*[16] 1.37-fold by *A. niger*[22] and 2.29-fold in *A. oryzae* SBS50[33] through statistical approaches.

Optimization of phytase on large scale production

The RSM model was validated by performing phytase production in Erlenmeyer flasks and trays on a large scale using 5-150 g of wheat bran, as shown in Table 7. The amount of substrate was enhanced from 5 g wheat bran in a 250 ml flask to 150 g wheat bran in the enamel-coated metallic tray. The phytase production was found sustainable in the range of 394.95 – 475.42 U/g DMR and validated the model at large scale. These results uplift the optimization of *P. oxalicum* phytase via SSF under pilot scale. On a large scale, trays production is influenced by substrate amount, presence of oxygen and unevenly allocation of inoculum and bed height.[1] If the amount of substrate is more than sufficient level, oxygen becomes unavailable to fungus, and production decreases.[39] A 1.5-2 cm bed height is considerable for the production, but it is not compulsory. It may varies depending upon the production system, kinetic parameters and operating conditions Above than 2 cm, cell biomass and production are affected due to high level of substrate and less availability of moisture and oxygen.[1] Similarly, sustainable production of phytase in flasks and trays on a large scale was studied in *A. oryzae* SBS50,[38] *R. oligosporus* MTCC 556,[39] *S. thermophile,*[17] *R. oryzae*[1] and *A. niger* 7 A-1.[25]

Table 7. Phytase production on large scale in flasks and trays.

S.No.	Flasks/Trays	Amount of substrate used (g)	Phytase production (U/g DMR) ± S.E
1.	250ml	5	394.95 ± 34.63
2.	500ml	10	431.25 ± 48.33
3.	1000ml	20	432.81 ± 15.99
4.	Tray (27cm x 22cm x 5cm)	100	475.42 ± 77.31
5.	Tray (35cm x 32cm x 5cm)	150	463.42 ± 92.16

Moreover, phytase production showing overall 5.6-fold enhancement makes the fermentation process less costly. The approach of fermentation in trays can be upgraded by using bioreactors for the production of phytase which provides constant temperature and moisture.[39]

Application of phytase in dephytinization of feed

Agricultural feed additives contain phytic acid that binds minerals, proteins, and other biomolecules and makes phytate complex which restricts the availability of nutritional components and lowers downs the nutritive value of feed. Phytase is effective in phytate hydrolysis and releases inorganic phosphate, soluble protein, and reducing sugar. Monogastric animals like humans, poultry, birds, and fishes lack phytase enzyme in their gastrointestinal region. Due to this, phytate accumulates in the body and remains undigested and excreted out in manure, runs off through erosion reaches water bodies, and pollutes the environment. Dephytinization is the best-selected approach to hydrolyze the phytate and release the P and other essential components by supplementing the phytase exogenously. The addition of phytase as a feed additive not only ameliorates the feed's nutritive value but also reduces phosphorus pollution.[29] The study demonstrated the impact of *P. oxalicum* phytase on hydrolyzing phytate present in the feed. With time, the liberation of inorganic phosphate, reducing sugar, and soluble protein is enhanced due to the supplementation of phytase in the diet.[10]

In this experiment, the effect of *P. oxalicum* phytase in dephytinizing fish feed is performed at different temperatures (37 °C, 50 °C, and 70 °C). The liberation of inorganic

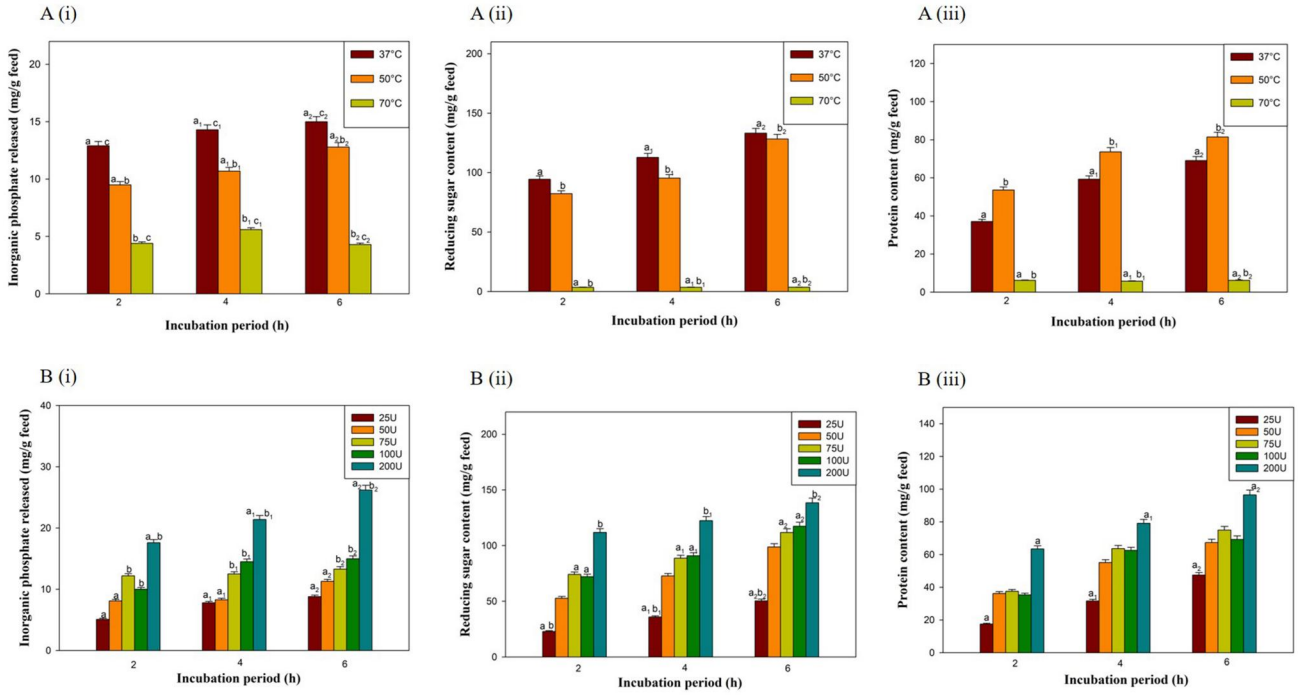


Figure 4. Dephytinization of feed by phytase from *P. oxalicum* A) at different temperature (37 °C, 50 °C, 70 °C), B) with different dose (25 U, 50 U, 75 U, 100 U, 200 U): i) inorganic phosphate ii) reducing sugar iii) protein content. The data showed as means ± standard deviation. Samples were studied in triplicates. Means with different letters represent values significantly different ($p < 0.05$).

phosphorus from the fish feed is observed at 37 °C, 50 °C, and 70 °C with 2, 4, and 6 h by using *P. oxalicum* phytase. A high release of inorganic phosphorus (14.993 mg/g feed) is seen at 37 °C (Figure 4A). Less difference is found in the amount of inorganic phosphorus between 37 °C and 50 °C showing the activeness of phytase enzyme at both temperatures. But, at 70 °C, there is almost a low secretion of inorganic phosphorus might be due to the denaturation of enzyme for a long period of incubation or disruption of nutritional components of feed. Also, nutritional by-products, soluble protein (69.08 mg/g feed), and reducing sugars (133.2) are liberated from the feed treated with phytase due to the presence of other hydrolytic enzymes in *P. oxalicum*. The amount of soluble protein is found more at 50 °C (81.48 mg/g feed). A significant variation ($p < 0.05$) was observed between feed sample treated at 37 °C and 70 °C after the supplementation of phytase.

Likewise, the reduction of phytic acid in flours was studied at 50 °C and 37 °C by adding phytase isolated from *A. oryzae* and exhibited maximum secretion of inorganic phosphate, soluble proteins and reducing sugars at 50 °C.[34] Dephytinization of feed samples was analyzed at 50 °C with *A. oryzae* phytase,[38] and at 55 °C with *R. oligosporus* phytase[39] and poultry feed at 37 °C by *A. niger* phytase[2] showed maximum liberation of nutritional components. Similarly, the release of inorganic phosphorus after the addition of phytase is studied in poultry feed by rPPHY at 40 °C,[13] animal feed by *P. griseoroseum* T73 at 37 °C,[4] pig feed by *A. niger* UFV-1 at 50 °C,[24] feedstuffs by *P. oxalicum* at 55 °C,[14] fish feed by *Morchella importuna* at 25 °C.[41]

Also, different phytase doses (25-200 U/g) were supplied to the feed and evaluated their impact on phytate degradation (Figure 4B). Phytase exhibits a dose-response relationship. The secretion of inorganic phosphorus is enhanced as the amount of phytase doses increases as the phytase removes an organically bound phosphate associated with the phytate molecule and reaches a plateau when the phytate becomes deficient.[43] The results showed that the liberation of inorganic phosphate enhances as the amount of dose increases. At 25 U/g (8.79 mg/g feed), 50 U/g (11.29 mg/g feed), 75 U/g (13.29 mg/g feed), 100 U/g (14.99 mg/g feed), and 200 U/g (26.19 mg/g feed) of inorganic phosphate released. Inorganic phosphate is found at maximum with

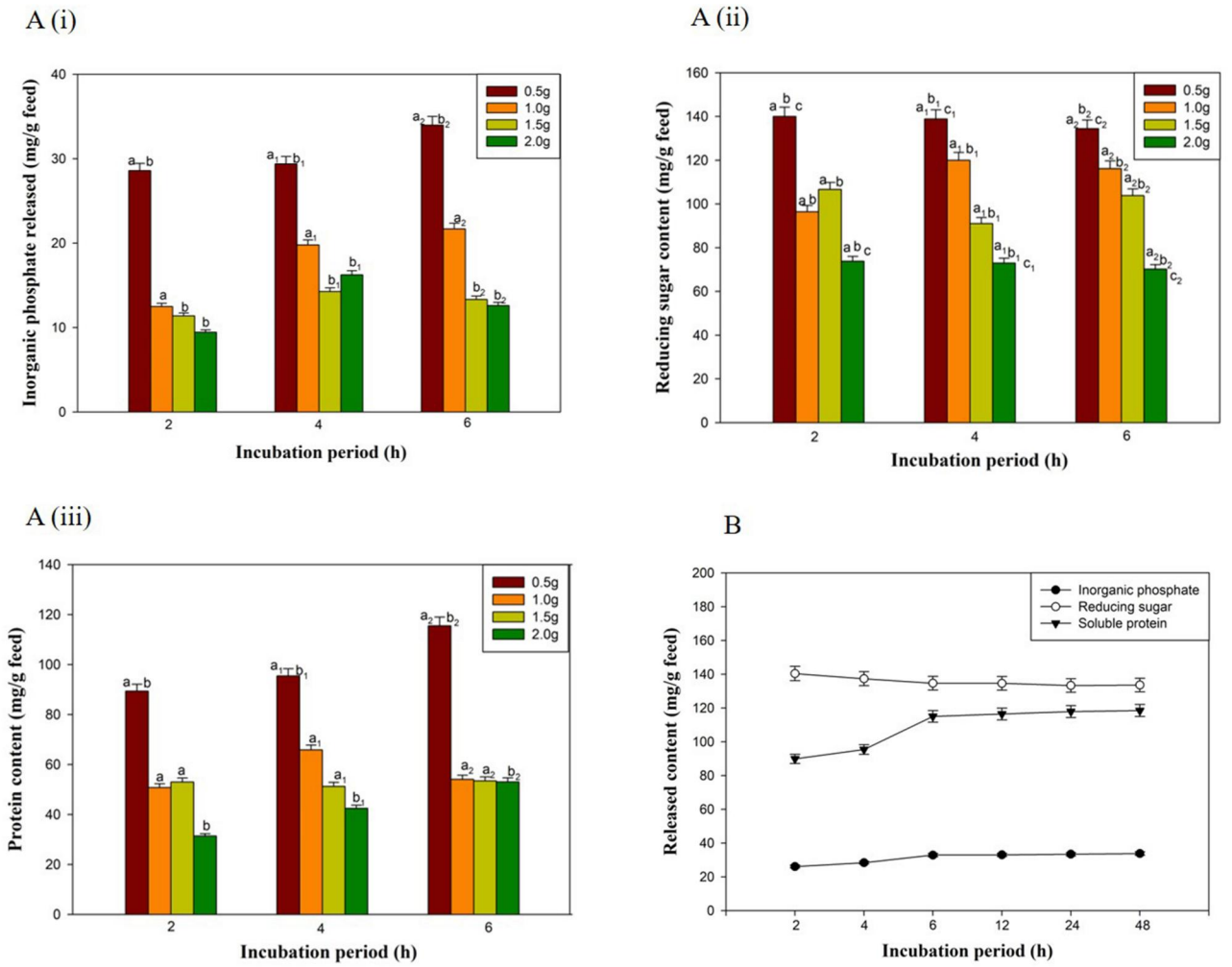


Figure 5. Dephytinization of feed by phytase from *P. oxalicum* A) with varied amount of feed (0.5 g, 1.0 g, 1.5 g, 2.0 g): i) inorganic phosphate ii) reducing sugar iii) protein content, B) with different incubation period. The data showed as means ± standard deviation. Samples were studied in triplicates. Means with different letters represent values significantly different ($p < 0.05$).

200 U/g (26.193 mg/g feed). Along with this, 138.48 mg/g feed and 96.5 mg/g feed amount of reducing sugar and protein content are obtained respectively. Reducing sugar is not much affected by increasing the phytase dosage, whereas soluble protein is enhanced. In contrast, poultry feed treated with different doses of *S. thermophile* showed equivalent nutritional amounts at 50 and 100 U,[17] while in flours it was observed that increment of these released components is gradually increased with phytase dose and declined after a certain level.[34]

The effect of phytase on varied amounts of feed (0.5-2 g) concluded that 0.5 g feed releases inorganic phosphate (33.986 mg/g feed) at the most (Figure 5A). This might be due to highest binding between active sites of substrate and enzyme in 0.5 g feed. As the amount of feed increases, no more enhancement is observed due to the possibility of no more binding sites availability or presence of substrate in insoluble form. Reduction in liberation of inorganic P might be due to negative feedback inhibition of inorganic P (the hydrolytic end product) on the phytase. Similarly, reducing sugar is found unaffected (134.4 mg/g feed) and protein is enhanced (115.52 mg/g feed).

Further, the dephytinization was performed for up to 48 h. Degradation of phytic acid with phytase shows the highest liberation of inorganic phosphate, soluble protein, and reducing sugars at 6 h and maintained up to 48 h, as shown in Figure 5B. Likewise, the release of inorganic phosphorus in poultry feed by rSt-Phy was evaluated on 25 min, 50 min and 75 min, with 50 min exhibited highest secretion.[31] At 2.5 h, pig feed represented the maximum release from *A. niger* UFV-1 phytase.[24] Supplementation of *A. niger* NT7 phytase in cattle feed secretes the highest inorganic phosphate up to 72 h.[15]

Maximum hydrolysis was observed with 200 U of *P. oxalicum* phytase added in 0.5 g of feed dissolved in 20 ml buffer and incubated at 37 °C for 6 h. The highest inorganic phosphorus (33.986 mg/g of feed), reducing sugars (134.4 mg/g of feed), and soluble protein (115.52 mg/g of feed) were found during the experiment.

Also, the application of immobilized phytase on feed and flours has been studied showing the release of inorganic phosphorus, reducing sugars and soluble proteins with time.[18] The comparison effect of free and immobilized phytase was evaluated on the hydrolysis of a legumes-based diet and concluded that immobilized phytase hydrolyzed more efficiently[26] while the efficiency of free and immobilized phytase is observed similar.[5] [6] performed the dephytinization of flours by supplementing both phytase and xylanase and showed the highest liberation due to the synergistic action of both enzymes.

Conclusion

In the present study, phytase production was enhanced by 5.6-fold by *Penicillum oxalicum* PBG30 as a result of statistical optimization in SSF using wheat bran as substrate. The maximum phytase production (475.42 U/g DMR) was obtained with 5 g wheat bran mixed with moistening media in a 1:2 ratio at 30 °C, pH 7.0, and 5 days of incubation. pH, incubation period, $MgSO_4$, and Tween 80 are essential components that majorly influence phytase production. Phytase production was sustainable in shake flasks and trays of different sizes. In addition, partially purified phytase is applied in the feed to determine the hydrolysis of phytate. It effectively degrades phytate and liberates inorganic phosphate from the fish feed. Also, it lessens the requirement for additional dietary inorganic phosphate in the feed. Therefore, cost-effective phytase from *P. oxalicum* can be produced at industrial scale and can be considered an excellent additive for fish feed in aquaculture and other industries.

Acknowledgement

The author acknowledges the Department of Biotechnology, Delhi Technological University, Delhi and Department of Microbiology, Maharshi Dayanand University, Rohtak for supporting this research work.

Authors contributions

The original draft was prepared and edited by Ms. Priya and all the experiments were performed by her. Data were analyzed by Priya, Dr. Bijender Singh, Dr. Bhoopander Giri and Dr. Jai Gopal Sharma. The draft was critically revised and improved under the supervision of Dr. Bijender Singh, Dr. Bhoopander Giri and Dr. Jai Gopal Sharma. All authors read and approved the final manuscript.

Disclosure statement

The authors declare no conflicts of result.

Financial support

The author (Ms. Priya) gratefully acknowledges the financial assistance as Junior/Senior research fellowship from the University Grants Commission (UGC), New Delhi, India.

ORCID

Bijender Singh http://orcid.org/0000-0002-2193-2910
Bhoopander Giri http://orcid.org/0000-0002-5510-4021

Data availability statement

Data will be made available on request.

References

[1] Arora, S.; Dubey, M.; Singh, P.; Rani, R.; Ghosh, S. Effect of Mixing Events on the Production of a Thermo-Tolerant and Acid-Stable Phytase in a Novel Solid-State Fermentation Bioreactor. *Process. Biochem.* **2017**, *61*, 12–23. DOI: 10.1016/j.procbio.2017.06.009.

[2] Buddhiwant, P.; Bhavsar, K.; Kumar, V. R.; Khire, J. M. Phytase Production by Solid-State Fermentation of Groundnut Oil Cake by *Aspergillus niger*: A Bioprocess Optimization Study for Animal Feedstock Applications. *Prep. Biochem. Biotechnol.* **2016**, *46*, 531–538. DOI: 10.1080/10826068.2015.1045606.

[3] Chanderman, A.; Puri, A. K.; Permaul, K.; Singh, S. Production, Characteristics and Applications of Phytase from a Rhizosphere

Isolated *Enterobacter* sp. ACSS. *Bioprocess Biosyst. Eng.* **2016**, *39*, 1577–1587. DOI: 10.1007/s00449-016-1632-7.

[4] Corrêa, T. L. R.; de Queiroz, M. V.; de Araújo, E. F. Cloning, Recombinant Expression and Characterization of a New Phytase from *Penicillium chrysogenum*. *Microbiol. Res.* **2015**, *170*, 205–212. DOI: 10.1016/j.micres.2014.06.005.

[5] Coutinho, T. C.; Tardioli, P. W.; Farinas, C. S. Phytase Immobilization on Hydroxyapatite Nanoparticles Improves Its Properties for Use in Animal Feed. *Appl. Biochem. Biotechnol.* **2020**, *190*, 270–292. DOI: 10.1007/s12010-019-03116-9.

[6] Dahiya, S.; Kumar, A.; Singh, B. Enhanced Endoxylanase Production by *Myceliophthora thermophila* Using Rice Straw and Its Synergism with Phytase in Improving Nutrition. *Process. Biochem.* **2020**, *94*, 235–242. DOI: 10.1016/j.procbio.2020.04.032.

[7] Elkhateeb, Y. A.; Fadel, M. Bioinformatic Studies, Experimental Validation of Phytase Production and Optimization of Fermentation Conditions for Enhancing Phytase Enzyme Production by Different Microorganisms under Solid-State Fermentation. *TOMICROJ.* **2022**, *16*, 1–11. DOI: 10.2174/18742858-v16-e2202160.

[8] Fiske, C. H.; Subbarow, Y. The Colorimetric Determination of Phosphorus. *J. Biol. Chem.* **1925**, *66*, 375–400. DOI: 10.1016/S0021-9258(18)84756-1.

[9] Hussain, S. M.; Hanif, S.; Sharif, A.; Bashir, F.; Iqbal, H. M. N. Unrevealing the Sources and Catalytic Functions of Phytase with Multipurpose Characteristics. *Catal. Lett.* **2021**, *152*, 1358–1371. DOI: 10.1007/s10562-021-03752-z.

[10] Jain, J.; Kumar, A.; Singh, D.; Singh, B. Purification and Kinetics of a Protease-Resistant, Neutral, and Thermostable Phytase from *Bacillus subtilis* Subsp. subtilis JJBS250 Ameliorating Food Nutrition. *Prep. Biochem. Biotechnol.* **2018**, *48*, 718–724. DOI: 10.1080/10826068.2018.1487848.

[11] Jain, J.; Singh, B. Phytase Production and Development of an Ideal Dephytinization Process for Amelioration of Food Nutrition Using Microbial Phytases. *Appl. Biochem. Biotechnol.* **2017**, *181*, 1485–1495. DOI: 10.1007/s12010-016-2297-z.

[12] Jatuwong, K.; Kumla, J.; Suwannarach, N.; Matsui, K.; Lumyong, S. Bioprocessing of Agricultural Residues as Substrates and Optimal Conditions for Phytase Production of Chestnut Mushroom, *Pholiota adiposa*, in Solid State Fermentation. *J. Fungi (Basel)* **2020**, *6*, 384. DOI: 10.3390/jof6040384.

[13] Joshi, S.; Satyanarayana, T. Bioprocess for Efficient Production of Recombinant *Pichia anomala* Phytase and Its Applicability in Dephytinizing Chick Feed and Whole Wheat Flat Indian Breads. *J. Ind. Microbiol. Biotechnol.* **2015**, *42*, 1389–1400. DOI: 10.1007/s10295-015-1670-1.

[14] Kim, B. H.; Lee, J. Y.; Lee, P. C. Purification, Sequencing and Evaluation of a Divergent Phytase from *Penicillium oxalicum* KCTC6440. *J. Gen. Appl. Microbiol.* **2015**, *61*, 117–123. DOI: 10.2323/jgam.61.117.

[15] Kumari, N.; Bansal, S. Production and Characterization of a Novel, Thermotolerant Fungal Phytase from Agro-Industrial Byproducts for Cattle Feed. *Biotechnol. Lett.* **2021**, *43*, 865–879. DOI: 10.1007/s10529-020-03069-8.

[16] Kumari, N.; Bansal, S. Statistical Modeling and Optimization of Microbial Phytase Production towards Utilization as a Feed Supplement. *Biomass Conv. Bioref.* **2021**, *13*, 8339–8349. DOI: 10.1007/s13399-021-01672-x.

[17] Kumari, A.; Satyanarayana, T.; Singh, B. Mixed Substrate Fermentation for Enhanced Phytase Production by Thermophilic Mould *Sporotrichum thermophile* and Its Application in Beneficiation of Poultry Feed. *Appl. Biochem. Biotechnol.* **2016**, *178*, 197–210. DOI: 10.1007/s12010-015-1868-8.

[18] Lopes, M. M.; Coutinho, T. C.; Malafatti, J. O. D.; Paris, E. C.; de Sousa, C. P.; Farinas, C. S. Immobilization of Phytase on Zeolite Modified with Iron (II) for Use in the Animal Feed and Food Industry Sectors. *Process. Biochem.* **2021**, *100*, 260–271. DOI: 10.1016/j.procbio.2020.10.017.

[19] Lowry, O.; Rosebrough, N.; Farr, A.; Randall, R. J. Protein Measurement with the Folin Phenol Reagent. *J. Biol. Chem.* **1951**, *193*, 265–275. DOI: 10.1016/S0021-9258(19)52451-6.

[20] Mahendran, S.; Sankaralingam, S.; Maheswari, P.; Dhivya, R. R.; Kathiresan, D.; Karthikeyan, S.; Ramya, S. S.; Seethapathy, P.; Harinathan, B.; Palpperumal, S. Production, Characterization, and Feed Supplement Applications of Phytase Enzyme from *Aspergillus tubingensis* Isolated from Western Ghats Soil. *Biomass Convers. Biorefinery.* **2022**, 1–11. DOI: 10.1007/s13399-022-02894-3.

[21] Mahmood, S.; Shahid, M. G.; Nadeem, M. Screening of Phytate Degrading Fungi and Optimization of Culture Conditions for Phytase Synthesis Using Agro-Industrial by-Products. *Pak. J. Bot.* **2021**, *53*, 763–770. DOI: 10.30848/PJB2021-2(12).

[22] Mahmood, S.; Shahid, M. G.; Nadeem, M.; Nelofer, R.; Irfan, M. Application of Statistical Design for the Economical Production of Phytase by *Aspergillus niger* Using Solid State Fermentation. *J. Anim. Plant Sci.* **2022**, *32*, 238–246. DOI: 10.36899/JAPS.2022.1.0419.

[23] Miller, G. L. Use of Dinitrosalicylic Acid Reagent for Determination of Reducing Sugar. *Anal. Chem.* **1959**, *31*, 426–428. DOI: 10.1021/ac60147a030.

[24] Monteiro, P. S.; Guimarães, V. M.; Melo, R. R. D.; Rezende, S. T. D. Isolation of a Thermostable Acid Phytase from *Aspergillus Niger* UFV-1 with Strong Proteolysis Resistance. *Braz. J. Microbiol.* **2015**, *46*, 251–260. DOI: 10.1590/S1517-838220120037.

[25] Neira-Vielma, A. A.; Aguilar, C. N.; Ilyina, A.; Contreras-Esquivel, J. C.; Carneiro-da-Cunha, M. D. G.; Michelena-Álvarez, G.; MartÃnez-Hernandez, J. L. Optimized Production of Phytase by Solid-State Fermentation Using Triticale as Substrate and Source of Inducer. *Afr. J. Biotechnol.* **2018**, *17*, 81–90. DOI: 10.5897/AJB2017.16267.

[26] Onem, H.; Cicek, S.; Nadaroglu, H. Immobilization of a Thermostable Phytase from Pinar Melkior (*Lactarius piperatus*) onto Magnetite Chitosan Nanoparticles. *CYTA J. Food.* **2016**, *14*, 74–83. DOI: 10.1080/19476337.2015.1045942.

[27] Pable, A. A.; Shah, S.; Ravi Kumar, V.; Khire, J. M. Use of Plackett–Burman Design for Enhanced Phytase Production by *Williopsis saturnus* NCIM 3298 for Applications in Animal Feed and Ethanol Production. *3 Biotech.* **2019**, *9*, 237. DOI: 10.1007/s13205-019-1764-y.

[28] Plackett, R. L.; Burman, J. P. The Design of Optimum Multi-Factor Experiments. *Biometrika*. **1946**, *33*, 305–325. DOI: 10.1093/biomet/33.4.305.

[29] Priya; Virmani, I.; Pragya; Goswami, R. K.; Singh, B.; Sharma, J. G.; Giri, B. Role of Microbial Phytases in Improving Fish Health. *Rev Aquac* **2023**, *15*, 1480–1500. DOI: 10.1111/raq.12790.

[30] Qasim, S. S.; Shakir, K. A.; Al-Shaibani, A. B. Isolation, Screening and Production of Phytate Degrading Enzyme (Phytase) from Local Fungi Isolate. *Iraqi J. Agric. Sci.* **2016**, *47*, 121–128.

[31] Ranjan, B.; Satyanarayana, T. Recombinant HAP Phytase of the Thermophilic Mold *Sporotrichum thermophile*: expression of the Codon-Optimized Phytase Gene in *Pichia pastoris* and Applications. *Mol. Biotechnol.* **2016**, *58*, 137–147. DOI: 10.1007/s12033-015-9909-7.

[32] Saxena, A.; Verma, M.; Singh, B.; Sangwan, P.; Yadav, A. N.; Dhaliwal, H. S.; Kumar, V. Characteristics of an Acidic Phytase from *Aspergillus aculeatus* APF1 for Dephytinization of Biofortified Wheat Genotypes. *Appl. Biochem. Biotechnol.* **2020**, *191*, 679–694. DOI: 10.1007/s12010-019-03205-9.

[33] Sharma, Krishna Kant; Kumar, Sandeep; Singh, Davender; Kumar, Vijay; Singh, Bijender; Pragya; Manisha. Enhanced Production and Immobilization of Phytase from *Aspergillus oryzae*: A Safe and Ideal Food Supplement for Improving

Nutrition. *Lett. Appl. Microbiol.* **2023**, *76*(2), ovac077. DOI: 10.1093/lambio/ovac077.

[34] Sharma, Krishna Kant; Singh, Bijender; Pragya. Phytase from *Aspergillus oryzae* SBS50: Biocatalytic Reduction of Anti-Nutritional Factor and Exhibiting Vanadium-Dependent Haloperoxidase Activity. *Biocatal. Agric. Biotechnol.* **2023**, *52*, 102840. DOI: 10.1016/j.bcab.2023.102840.

[35] Singh, Bijender; Boukhris, Ines; Kumar, Vinod; Yadav, Ajar Nath; Farhat-Khemakhem, Ameny; Kumar, Anil; Singh, Davender; Blibech, Monia; Chouayekh, Hichem; Alghamdi, Othman A.; Pragya. Contribution of Microbial Phytases to the Improvement of Plant Growth and Nutrition: A Review. *Pedosphere*. **2020**, *30*(3), 295–313. DOI: 10.1016/S1002-0160(20)60010-8.

[36] Singh, Bijender; Sapna. Biocatalytic Potential of Protease-Resistant Phytase of *Aspergillus oryzae* SBS50 in Ameliorating Food Nutrition. *Biocatal. Biotransform*. **2015**, *33*(3), 167–174. DOI: 10.3109/10242422.2015.1076215.

[37] Singh, Bijender; Sapna. Phytase Production by *Aspergillus oryzae* in Solid-State Fermentation and Its Applicability in Dephytinization of Wheat Bran. *Appl. Biochem. Biotechnol.* **2014**, *173*, 1885–1895. DOI: 10.1007/s12010-014-0974-3.

[38] Singh, Bijender; Sapna. Purification and Characterization of a Protease-Resistant Phytase of *Aspergillus oryzae* SBS50 Whose Properties Make It Exceptionally Useful as a Feed Supplement. *Int. J. Biol. Macromol.* **2017**, *103*, 458–466. DOI: 10.1016/j.ijbiomac.2017.05.077.

[39] Suresh, S.; Radha, K. V. Effect of a Mixed Substrate on Phytase Production by *Rhizopus oligosporus* MTCC 556 Using Solid State Fermentation and Determination of Dephytinization Activities in Food Grains. *Food Sci. Biotechnol.* **2015**, *24*, 551–559. DOI: 10.1007/s10068-015-0072-5.

[40] Suresh, S.; Radha, K. V. Statistical Optimization and Mutagenesis for High Level of Phytase Production by *Rhizopus oligosporus* MTCC 556 under Solid State Fermentation. *J. Environ. Biol.* **2016**, *37*, 253.

[41] Tan, H.; Tang, J.; Li, X.; Liu, T.; Miao, R.; Huang, Z.; Wang, Y.; Gan, B.; Peng, W. Biochemical Characterization of a Psychrophilic Phytase from an Artificially Cultivable Morel *Morchella importuna*. *J. Microbiol. Biotechnol.* **2017**, *27*, 2180–2189. DOI: 10.4014/jmb.1708.08007.

[42] Thakur, N.; Patel, S. K.; Kumar, P.; Singh, A.; Devi, N.; Sandeep, K.; Pandey, D.; Chand, D. Bioprocess for Hyperactive Thermotolerant *Aspergillus fumigatus* Phytase and Its Application in Dephytinization of Wheat Flour. *Catal. Lett.* **2022**, *152*, 3220–3232. DOI: 10.1007/s10562-021-03886-0.

[43] Thorsen, M.; Nielsen, L. A.; Zhai, H. X.; Zhang, Q.; Wulf-Andersen, L.; Skov, L. K. Safety and Efficacy Profile of a Phytase Produced by Fermentation and Used as a Feed Additive. *Heliyon.* **2021**, *7*, e07237. DOI: 10.1016/j.heliyon.2021.e07237.

International Journal of Engineering Technology and Management Sciences
Website: ijetms.in Issue: 5 Volume No.7 September - October – 2023
DOI:10.46647/ijetms.2023.v07i05.043 ISSN: 2581-4621

Optimizing Reservoir Operation with Artificial Intelligence: A State-of-the-Art Review

Astha Yadav[1], Prof. Vijay K. Minocha[2], Prof. Rakesh Kumar[3]
[1]Ph.D. Scholar, Hydraulics and Water Resources Engineering, Civil Engineering Department, Delhi Technological University, 110042, Delhi, India
[2]Professor, Department of Civil Engineering, Delhi Technological University,110042, India
[3] Professor, Department of Civil Engineering, Delhi Technological University,110042, India
Corresponding author ORCID ID: 0000-0002-2602-8154

ABSTRACT
Reservoir operation is an important aspect of water resource management since it involves the prudent distribution of water for a variety of reasons such as water supply, irrigation, hydropower generation, flood control, and environmental preservation. Historically, reservoir operation has depended on heuristic and rule-based approaches, which frequently struggle to adapt to the dynamic and variable character of water arrangements. Artificial intelligence (AI) technologies have grown in popularity in recent years to increase reservoir operation efficiency and adaptability. This cutting-edge review investigates the use of AI in reservoir optimization. We offer a complete overview of several AI methods used in reservoir operations, such as machine learning (ML), reinforcement learning (RL), artificial neural networks (ANNs), fuzzy logic (FL), evolutionary algorithms (EA), optimization algorithms (OA), and hybrid models (HM). We analyze the advantages and limits of AI-driven reservoir operating models on their potential to optimize water resource management, alleviate climate change impacts, and improve reservoir system sustainability using a comprehensive review of the literature. This review paper aims to provide an overview of the current level of reservoir operation optimization with AI as well as insights into future approaches. As the globe faces increasing difficulties related to water scarcity, climate unpredictability, and environmental protection, utilizing the potential of artificial intelligence in reservoir operation becomes critical for building efficient, adaptive, and sustainable water management approaches.
Keywords: Reservoir Operations, Optimization Techniques, Artificial Intelligence

1. INTRODUCTION

Managing water resources is critical as you respond to a growing population, changing climate patterns, and the need for sustainable environmental practices. As integral parts of water supply, flood control, and hydropower production systems, reservoirs play a key role in addressing these challenges. Optimal operation of reservoirs is crucial in balancing the conflicting goals of ensuring a reliable water supply, reducing flood risks, and preserving aquatic ecosystems. Reservoir operation has traditionally been based on heuristics and deterministic models, which often struggle to cope with the dynamics and uncertainties of hydrological systems. However, in recent years there has been a paradigm shift due to the integration of artificial intelligence (AI) technologies, which has changed the way reservoirs are managed.

Artificial intelligence has emerged as a powerful toolset for optimizing reservoir operations, encompassing a wide range of methods such as machine learning (ML), reinforcement learning (RL), artificial neural networks (ANNs), fuzzy logic (FL), evolutionary algorithms (EA), optimization algorithms (OA), and hybrid models (HM). These AI approaches can learn from historical data, forecast future conditions, and make intelligent judgments in real-time. As a result,

International Journal of Engineering Technology and Management Sciences
Website: ijetms.in Issue: 5 Volume No.7 September - October – 2023
DOI:10.46647/ijetms.2023.v07i05.043 ISSN: 2581-4621

AI has the potential to improve reservoir operations' efficiency, adaptability, and sustainability in an era of tremendous environmental difficulties.

The goal of this comprehensive research is to investigate the numerous uses of AI in reservoir operation optimizations. As the globe faces rising difficulties connected to water scarcity, catastrophic weather events, and the need for responsible water allocation, utilizing the capabilities of Artificial Intelligence in reservoir operations has never been more vital. This review acts as a compass for researchers, practitioners, and policymakers, guiding them towards harnessing AI to enhance reservoir management, ensuring a sustainable and resilient water future for years to come.

2. METHODS

The simulation of human intellect in computers and other technologies is referred to as artificial intelligence (AI). It entails the creation of algorithms and software that allow computers to execute activities that would normally need human intellect.

Artificial intelligence approaches play a crucial role in optimizing reservoir operations and delivering improved decision-making capabilities and resource allocation. Commonly used AI methods in reservoir operations are shown in Figure 1.

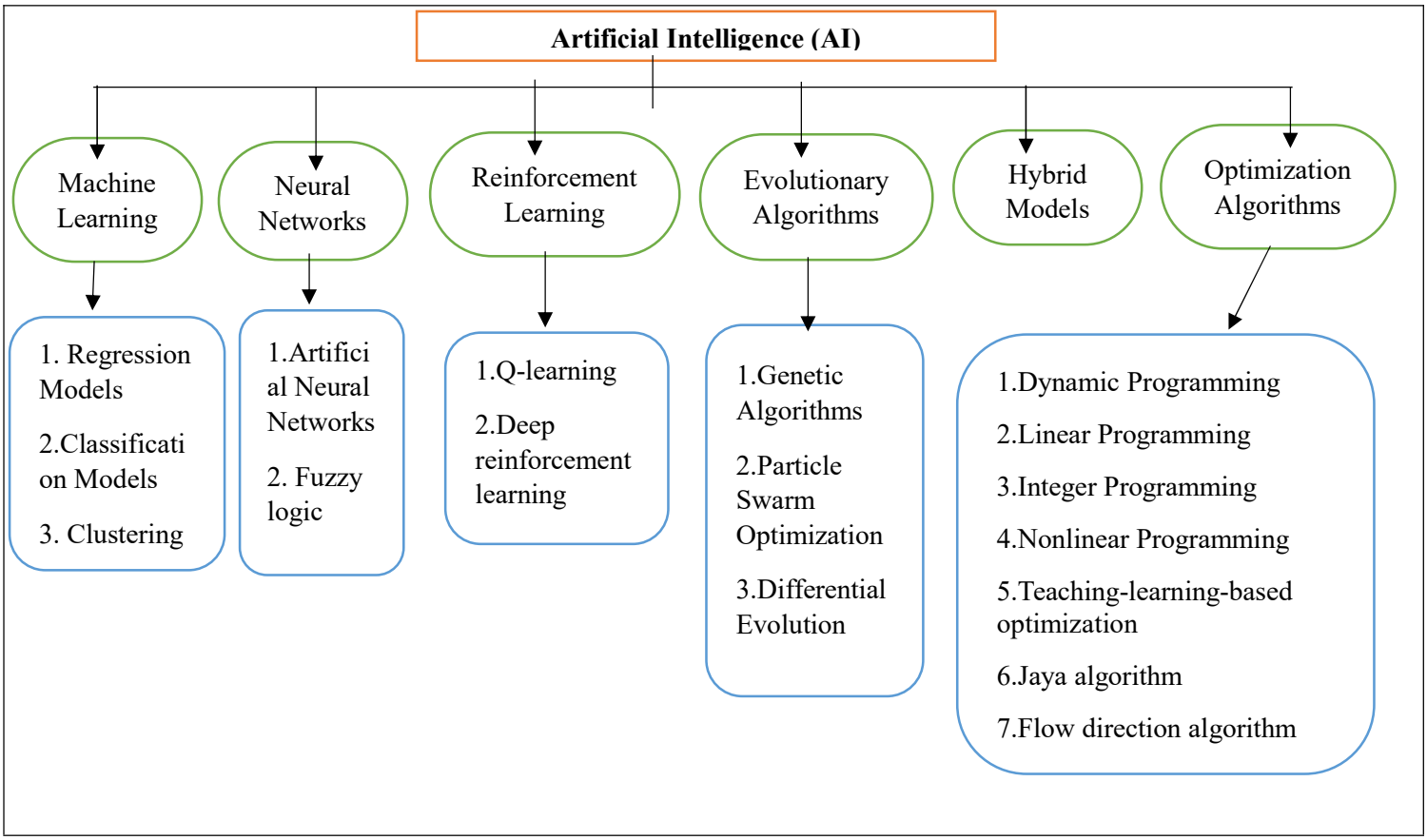


Figure 1: Artificial Intelligence Methods in Reservoir Operations

➢ **Machine Learning (ML):**

i. **Regression model:** They can be used to predict factors such as supply, demand, and water levels, which can help with reservoir design and operations. Two examples of these models are linear regression and support vector machines.

ii. **Classification models:** Machine learning models for classification help classify situations, for example, by identifying possible flood conditions to trigger necessary actions.

DOI:10.46647/ijetms.2023.v07i05.043 ISSN: 2581-4621

iii. **Clustering:** Clustering such as K-means can combine linked historical data to reveal patterns and trends, allowing us to better understand the behavior of reservoir systems.

➢ **Neural Networks**

i. **Artificial Neural Networks (ANNs):** ANNs are used in complex applications such as hydrological forecasting to capture nonlinear correlations between input parameters and reservoir conditions.

ii. **Fuzzy logic (FL):** It is a mathematical model used to manage uncertainty and imprecision. Fuzzy logic is well suited to reservoir modeling and regulation because they are complex systems subject to many different uncertainties, including flow changes, weather conditions, and demand fluctuations.

➢ **Reinforcement Learning (RL):**

Deep reinforcement learning (DRL) and Q-learning are two examples of RL algorithms used to develop control strategies to improve reservoir performance over time.

➢ **Evolutionary Algorithms (EA):**

Differential evolution, genetic algorithms, and particle swarm optimization are examples of EAs applied to address reservoir operation optimization challenges.

i. **Genetic Algorithms (GA):** Inspired by the idea of natural selection, genetic algorithms are heuristic search algorithms.

ii. **Particle Swarm Optimization (PSO):** It is a population-based optimization approach inspired by the social behavior of birds and fish. It may be used to enhance reservoir performance by constantly changing the release rules.

iii. **Differential Evolution (DE):** To optimize reservoir operations, one may use Differential Evolution (DE), a well-known and effective optimization technique. DE, a population-based stochastic optimization method, excels at solving challenging optimization problems including continuous and/or discrete variables.

➢ **Hybrid Models:**

Hybrid models that combine several AI techniques, such as employing RL to optimize releases and neural networks to anticipate inflow, can outperform conventional reservoir models.

➢ **Optimization Algorithms:**

They are a class of algorithms that are used to find the best possible solution to a given problem. Some OA are given below,

i. **Dynamic programming (DP):** it is a well-known technique for addressing reservoir operational issues. By breaking the problem into smaller subproblems, it is resolved recursively.

ii. **Linear Programming (LP):** Linear programming is suitable for reservoir operation problems with linear constraints and objectives.

iii. **Integer Programming (IP):** IP extends linear programming by enabling variables to accept integer values. It is useful when decisions like release volumes need to be made in discrete units, such as for flood control gates.

iv. **Nonlinear Programming (NLP):** Nonlinear programming can handle more complex and nonlinear objective functions and constraints.

v. **Teaching-learning-based optimization (TLBO):** TLBO is a nature-inspired optimization algorithm that simulates the teaching and learning processes that occur in a classroom. It was developed by Rao et al. in 2011 as a population-based optimization technique. When using TLBO for reservoir operation, you aim to find the optimal release policies and operational strategies that maximize the benefits of the reservoir system while meeting various constraints and objectives, such as water supply, flood control, hydropower generation, and environmental conservation.

International Journal of Engineering Technology and Management Sciences
Website: ijetms.in Issue: 5 Volume No.7 September - October – 2023
DOI:10.46647/ijetms.2023.v07i05.043 ISSN: 2581-4621

vi. **Jaya algorithm (JA):** JA is an optimization algorithm inspired by the social behavior of individuals striving to improve their fitness. It was introduced by Rao and Savsani in 2012 and is designed for solving optimization problems, including reservoir operation optimization. JA operates on a population of potential solutions, and it iteratively updates these solutions to find the optimal or near-optimal solution to the problem.

vii. **Flow direction algorithm (FDA):** FDA is a concept commonly used in the field of hydrology and hydraulic modeling for determining the direction in which water flows across a digital elevation model (DEM) or terrain.

The use of AI approaches in reservoir operations improves the ability to make educated decisions in real-time, adapt to changing conditions, and optimize water resource management, assuring reservoir system sustainability and efficiency. Table 1 contains some case studies.

Table 1: several case studies of artificial intelligence-based reservoir operations

Author (Year)	Optimization Technique	Problem / Case Studies	Findings
Manizhe Zarei (2021)	Machine Learning (ML)	Dez and Karkheh reservoir	Using a Regression Tree and Support Vector Machine, the suggested technique forecasts inflows accurately.
Ali Thaeer Hammid (2016)	Artificial Neural Networks (ANNs)	Himreen lake dam	According to the findings, the ANN can forecast plant performance if the correlation coefficient (R) between predicted and observed output variables is more than 0.96.
D. P. Panigrahi (2000)	Fuzzy Logic	Malaprabha reservoir	As a result, the operators may feel more comfortable in using such models.
Mariwan R. Faris (2021)	Fuzzy Logic	Darbandikhan Reservoir	The results show that the FLC model outperformed the NLP and LP models in terms of producing hydropower.
Zhong-Zheng Wang (2022)	Deep Reinforcement Learning (RL)	waterflooding reservoir models	In contrast to previous techniques that only optimized a solution for a certain case, the proposed method teaches a policy that can adapt to unknown situations and make real-time judgments to deal with unforeseen changes.
Jatin Anand (2018)	Genetic Algorithm (GA)	Rihand Dam and Tehri Dam	This research suggests a limited evolutionary algorithm for multi-objective watershed planning and management, which includes fulfilling human and hydropower demands.
Yousif H. Al-Aqeeli (2020)	Particle Swarm Optimization (PSO)	Mosul Reservoir	The results show that the PSO model may be utilized to calculate the best operating parameters for any reservoir.
Mahdi Sedighkiaa (2022)	Particle Swarm Optimization (PSO)	Garan dam	The result shows that the PSO method can optimize reservoir operation based on the objectives defined in the objective function.
K. Srinivasa Raju (2012)	Differential Evolution (DE)	Mahi Bajaj Sagar Project	The outcome reveals that adequate parameter selection is required to make the DE algorithm satisfactory.
B. C. Kumar	Linear	Hemavathy	The results show that the linear programming

DOI:10.46647/ijetms.2023.v07i05.043 ISSN: 2581-4621

Raju (2020)	Programming (LP)	Reservoir	optimization method significantly enhances the reservoir performance.
V. Jothi Prakash (2013)	Non-linear Programming (NLP)	Koyna hydroelectric project	The result indicates that the NLP algorithm gives better results for hydropower production.
Vartika Paliwal (2019)	Jaya Algorithm (JA)	Mula reservoir	It can be concluded that JA has successfully achieved optimum performance for the Mula reservoir.
S. M. Yadav (2019)	Elitist-JA and Elitist-TLBO	Karjan irrigation project of Gujarat	The result shows that EJA gives the best optimal solution compared to ETLBO, JA, and LP
Vijendra Kumar (2020)	Jaya Algorithm (JA)	Ukai dam	The results show that JA gives better optimal results, so it can be used to solve reservoir operation problem
Vijendra Kumar (2021)	Self-Adaptive multi-population (SAMP-JA)	Ukai reservoir	SAMP-JA outperforms JA, PSO, and IWO in terms of convergence.
Abbas Moghani (2022)	Flow Direction Algorithm (FDA)	Karun-4 reservoir	FDA outperformed PSO, WA, and GA, with hydropower generating in the reservoir running in less time and to a higher standard.

3. CONCLUSION

Artificial intelligence (AI)-powered reservoir operations present a viable strategy for enhancing the effectiveness, dependability, and sustainability of managing water resources. Here are some crucial considerations in conclusion:

- **Enhanced Decision Making:** AI approaches, like as machine learning and neural networks, may analyze large datasets and historical data to make more educated and timely reservoir operations choices. This involves water release, flood control, and drought management.
- **Real-time Adaptability:** Artificial intelligence can monitor and run reservoirs in real time, allowing for fast changes in response to changing weather patterns, inflow variances, and other dynamic elements. This contributes to increased water storage and waste reduction.
- **Risk mitigation:** AI models may evaluate the risk related to different operational actions, considering the ambiguity of inflow estimates as well as environmental constraints.
- **Enhancing environmental conservation:** it requires balancing the requirements of multiple stakeholders, such as preserving aquatic ecosystems and satisfying water supply demands. In order to minimize detrimental environmental effects, reservoir operation can be optimized.
- **Data Integration:** AI may combine data from several sources, like remote sensing, weather predictions, and water quality monitoring, to provide a complete picture of the reservoir system.
- **Energy Efficient:** AI can optimize the use of hydropower generation in conjunction with reservoir operations, aiding in the efficient management of energy production and consumption.

In conclusion, reservoir operations using artificial intelligence hold great potential for optimizing water management in an era of increasing climate variability and water scarcity. By harnessing the power of AI, reservoir managers can make more informed decisions, mitigate risks, and contribute to sustainable water resource management. However, careful planning, integration with existing

DOI:10.46647/ijetms.2023.v07i05.043 ISSN: 2581-4621

infrastructure, and ongoing validation are essential for the successful implementation of AI in this context.

References

1. Abbas Moghani, Hojat Karami. "The Implementation Of A New Optimization Method For Multi-Reservoir And Single Reservoir systems." *Research Square* (2022): pp 1-28.
2. Agha1, Yousif H. Al-Aqeeli1 & Omar M. A Mahmood. "Optimal Operation of Multi-reservoir System for Hydropower Production Using Particle Swarm Optimization Algorithm." *Water Resources Management* (2020): pp 3099–3112.
3. Ali Thaeer Hammid a, b,*, Mohd Herwan Bin Sulaiman a, Ahmed N. Abdalla. "Prediction of small hydropower plant power production in Himreen Lake dam (HLD) using artificial neural network." *Alexandria Engineering Journal* (2016): pp 1-11.
4. Arunkumar, V. Jothiprakash and R. "Multi-reservoir Optimization for Hydropower Production using NLP Technique." *KSCE Journal of Civil Engineering* (2013): pp 344-354.
5. B. C. Kumar Raju, Chandre Gowda C., Karthika B. S. "Optimization of Reservoir Operation using Linear Programming ." *International Journal of Recent Technology and Engineering* (2020): pp 1028-1032.
6. Jatin Anand, Ashvani Kumar Gosain and Rakesh Khosa. "Optimisation of Multipurpose Reservoir Operation by Coupling Soil andWater Assessment Tool (SWAT) and Genetic Algorithm for Optimal Operating Policy (Case Study: Ganga River Basin)." *Sustainability* (2018): pp 1-20.
7. K. Srinivasa Raju a, A. Vasan a , Piyush Gupta b , Karthik Ganesan b & Hitesh Mathur. "Multi-objective differential evolution application to irrigation planning." *ISH Journal of Hydraulic Engineering* (2012): pp 54-64.
8. Mahdi Sedighkiaa, Bithin Dattaa and Zeynab Fathib. "Linking ecohydraulic simulation and optimization system for mitigating economic and environmental losses of reservoirs." *AQUA — Water Infrastructure, Ecosystems and Society* (2022): pp 229-247.
9. Manizhe Zarei, Omid Bozorg-Haddad, Sahar Baghban, Mohammad Delpasand. "Machine-learning algorithms for forecast-informed reservoir operation (FIRO) to reduce flood damages." Scientific Reports. 2021.
10. Mariwan R. Faris, Hekmat M. Ibrahim, Kawa Z. Abdulrahman, Luqman S. Othman3, Kilgour D. Marc4. "Fuzzy Logic Model for Optimal Operation of Darbandikhan Reservoir, Iraq." *International Journal of Design & Nature and Ecodynamics* (2021): pp 335-343.
11. MUJUMDAR, D. P. PANIGRAHI. "Reservoir Operation Modelling with Fuzzy Logic." *Water Resources Management* (2000): pp 89–109.
12. Vartika Paliwal, Aniruddha D. Ghare , Ashwini B. Mirajkar. "Computer Modeling for the Operation Optimization of Mula Reservoir, Upper Godavari Basin, India Using the Jaya Algorithm." *Sustainability* (2019): pp 2-21.
13. Yadav, Vijendra Kumar & S. M. "Optimization of Cropping Patterns Using Elitist-Jaya and Elitist-TLBO Algorithms." *Water Resources Management* (2019): pp 1817–1833.
14. yadav, Vijendra Kumar and S. M. "Multi-objective reservoir operation of the Ukai reservoir system using an improved Jaya algorithm." *Water Supply* (2021): pp 2287-2309.
15. Yadav, Vijendra Kumar and S. M. "Optimal Monthly Reservoir Operation to Maximize the Hydropower Generation." *Roorkee Water Conclave*. 2020. pp 1-8.
16. Zhong-Zheng Wang, Kai Zhang , Guo-Dong Chen , Jin-Ding Zhang. "Evolutionary-assisted reinforcement learning for reservoir real-time production optimization under uncertainty." *Petroleum Science* (2022): pp 261-276.

Performance Evaluation of Dual-Slope Digitizer for Self-Heating Compensation in Resistive Sensor

Gopal Singh, *Graduate Student Member, IEEE*, Shiraz Sohail, *Senior Member, IEEE*, Ashish Dineshkumar Joshi, and Tarikul Islam, *Senior Member, IEEE*

***Abstract*— This study addresses the prevalent issue of self-heating (S-H) error observed in resistive sensors (R_X) when integrated with electronic circuits to produce output signals. An efficient digitizer circuit is proposed to interface R_X and compensate for the S-H error. The circuit employs a dual-slope integrator and a comparator to generate a time sequence output signal. The input current through R_X is maintained in the microampere range to minimize the S-H error. Additionally, a T-network is connected to the integrating capacitor to amplify the feedback path's incoming current. The digitizer is tested for measuring in a wide range of R_X 3.63–488.2 kΩ, with corresponding power dissipation of 0.273 mW–2.05 μW, respectively. The current through R_X ranges from 274.59 to 2.05 μA, and with the current boosting technique (gain ranging from 21.68 to 50.22), it requires a measurement time of 4.73–382.39 ms. This scheme reduces power dissipation by 472.6–1294.94 times compared to existing techniques, signifying a noteworthy improvement. The proposed digitizer produces accurate results with an average error of ±0.56% in experiments where negligible S-H is observed in testing.**

***Index Terms*— Dual-slope integrator, resistance to digital converter (RDC), resistive sensor, self-heating (S-H) error, time sequence signal, T-network.**

I. Introduction

RESISTIVE sensors find extensive application in the industrial setting for measuring parameters like temperature, pressure, strain, force, gas flow, displacement, and humidity [1]. These sensors work by exhibiting a change in resistance that corresponds to the change in the measurement parameter. The sensor (R_X) is connected to an electronic circuit to measure the resistance facilitating its calibration with the measurement parameter. Nonetheless, the connection of R_X within the circuit introduces various errors in the measurement process. Among these, the self-heating (S-H) error is inherent in nature and an old classical problem of significant importance [2]. In this context, when a current I_X passes through R_X, it results in power dissipation ($I_X^2 R_X$) and heat generation. This decreases the resistance of a negative temperature coefficient (NTC) sensor, which leads to a subsequent increase in the sensor's current, further contributing to the temperature rise. This sequence of events compounds over time, leading to a significant temperature increase, which in turn generates a notable measurement error. The positive temperature coefficient (PTC) resistive sensor naturally mitigates the S-H error due to the absence of compounding heating effects, since I_X decreases (as resistance increases) with the temperature rise. So, if the value of R_X is high (greater than 10 kΩ), the S-H error will be less. However, for PTC low R_X values (less than 100 Ω), the S-H error becomes significantly high and requires careful consideration [3]. In industry, several popular PTC-type resistive sensors, such as Pt100, and strain gauges are used, whose resistance lies in the range of $R_X \approx 100$ Ω. Thus, it can be concluded that S-H error is more prominent in NTC sensors and low-resistance PTC sensors.

Employing a low-current excitation reduces the impact of S-H error, given that it minimizes heat dissipation and therefore enhances measurement accuracy. It is advisable to restrict the current passing through R_X to a level where the temperature increase resulting from heat dissipation remains below the desired accuracy. As an illustration, consider R_X as a thermistor (TCS651 Bead Head) whose resistance varies from 3.63 to 488.2 kΩ for a temperature span of −6 °C–114 °C [4]. Assume that the thermistor possesses a dissipation factor (P) of 1 mW/°C above the surrounding temperature and aims for a temperature accuracy of 0.5 °C. Therefore, the dissipated power across R_X must be restricted to less than 0.5 mW [3]. This constraint establishes that the permissible current ($=(P/R_X)^{1/2}$) through R_X should span from 371 to 32 μA.

However, employing an exceedingly small I_X decreases the sensitivity of the interfacing circuit, as well as the resolution of the entire sensor system. Additionally, the weak sensor signal becomes more vulnerable to transmission noises, thermal noises, loading effects, and other similar influences. A notable consideration is that, in the literature, several sensors show an exceedingly small resistance change in response to the measurement parameter. Such sensors require a highly sensitive interfacing circuit. Consequently, the conventional approach involves negotiating a balance between accuracy and sensitivity. In recent times, sensor interfacing digitizers (or digital converters) have gained significant prominence due to their ability to produce a time sequence output signal [5], [6], [7], [8], [9], [10], [11], [12], [13], [14], [15], [16], [17]. These

Manuscript received 30 August 2023; revised 23 November 2023; accepted 11 December 2023. Date of publication 1 January 2024; date of current version 12 January 2024. This work was supported by the Seed Grant of the National Institute of Technology Tiruchirappalli (NIT Tiruchirappalli) under Grant NITT/R&C/SEED GRANT/2021-22/PROJ.NO.29. The Associate Editor coordinating the review process was Dr. Ada Fort. *(Corresponding author: Shiraz Sohail.)*

Gopal Singh and Shiraz Sohail are with the Department of Instrumentation and Control Engineering, National Institute of Technology Tiruchirappalli, Tiruchirappalli, Tamil Nadu 620015, India (e-mail: ssohail@nitt.edu).

Ashish Dineshkumar Joshi is with the Department of Chemical Engineering, National Institute of Technology Tiruchirappalli, Tiruchirappalli, Tamil Nadu 620015, India.

Tarikul Islam is with the Department of Electrical Engineering, Jamia Millia Islamia (A Central University), New Delhi 110025, India.

Digital Object Identifier 10.1109/TIM.2023.3348896

1557-9662 © 2024 IEEE. Personal use is permitted, but republication/redistribution requires IEEE permission.
See https://www.ieee.org/publications/rights/index.html for more information.

Authorized licensed use limited to: DELHI TECHNICAL UNIV. Downloaded on February 07,2024 at 07:19:10 UTC from IEEE Xplore. Restrictions apply.

digital interfacing circuits can be broadly classified based on their working principles as: 1) a dual-slope integrator [5], [6], [8], [9], [12], [13]; 2) sigma-delta [7], [11]; 3) a relaxation oscillator [10]; and 4) a direct interface circuit (DIC) [14], [15], [16], [17].

In [5], a resistance to digital converter (RDC) using a dual-slope integrator and an instrumentation amplifier is designed for a full bridge load cell, but it requires a high measurement time. In [6], a circuit for both, single element as well as the differential resistive sensor is presented for a small range (100 Ω–5 kΩ) due to gain and offset errors. The circuit in [8] connects a remotely located sensor bridge, but uses six wires, hence costly. In [9], two wires are used for the remote sensor, via the diode-controlled switch to eliminate the effect of lead resistance. Another circuit using T-Network in the integrator to measure low resistance is presented in [12]. In [13], a circuit is presented for the π-network sensor which requires a single supply, but extra power dissipation occurs in the side arm of the π-network.

The sigma-delta-based circuit for resistive sensors is reported in [7], which has high component counts and uses costly digital filter and decimation (DFD) IC. Moreover, the lead resistance compensation feature is not found. In [11], the circuit is designed for a magnetoresistive sensor for a small span. The circuit uses a complex algorithm, hence requiring a high-end digital signal processor. The circuit based on a relaxation oscillator for the three-wire resistive sensor is presented in [10] for a wide range of measurements using a programmable gain array (PGA), but both power dissipation and measurement time are high.

In DICs, R_X is connected to a programmable digital device (PDD; e.g., microcontroller, FPGA, etc.) along with some calibration resistors, capacitors, and diodes to convert the resistance into time pulses for measurement. However, the DIC has inherent issues related to pin resistance of the PDD and exponential capacitor voltage accuracy, uncertainty, resolution, acquisition time, and power consumption, which are studied extensively. Among them, two problems are of prime importance: 1) quantization errors in the measurement of times, which creates large errors for low resistance values and 2) uncertainty in the time measurements for high resistance values, due to the presence of noise in the circuit. Recent works on DIC address these two important issues separately [14] as well as together [15]. Moreover, the latest work also incorporates the lead resistance compensation feature [16] and also uses the well-known sigma-delta technique [17] to improve figures of merits over the existing techniques.

It is noteworthy that none of the digitizers previously documented in the literature [5], [6], [7], [8], [9], [10], [11], [12], [13], [14], [15], [16], [17] have addressed the issue of the S-H error. The assessment of power dissipation across R_X has been conducted for these digitizers and outlined in Table I. It is evident that the power dissipation is notably high in the majority of the cases,[1] which has the potential to result in a significant S-H error.

[1]Power dissipations for [7], [10], and [11] are 2.37, 1.44, and 2 mW, respectively, which is higher than this work, and also these schemes require longer measurement time.

TABLE I
POWER DISSIPATION ACROSS THE SENSOR IN LITERATURE

Ref.	Sensor Resistance (R_X)	Power Dissipation (I^2R_X) (mW)	•Meas. Time (ms)	•Meas. Time (max.)/R_X (max.) ($ms/k\Omega$)
[5]	290.88 Ω	21.51	251.5	862.92
[6]	140 Ω	87.5	10	50
[6]	1.25 kΩ	7.8125	11.25	9
[7]	606 Ω	2.37	40	44.44
[7]	0.9 kΩ	1.6	40	44.44
[8]	100 Ω	15.625	10	71.43
[8]	5 kΩ	0.3125	10	2
[9]	100 Ω	4.45	2.09	11.9
[10]	1 kΩ	1.44	55	0.55
[11]	4.5 kΩ	2	2	0.4
[12]	0.9 Ω	0.252⋆	286	317.78*
[13]	10 kΩ	25	0.5	0.055
This Paper	488.2 kΩ	2.05⋆	382.39	0.783
	3.63 kΩ	0.275	4.73	1.303
	100 Ω	23.96⋆	2.59	25.9

* in ms/ Ω, ⋆ in μW, •Measurement

To resolve this important concern, [18] introduces a simulation and initial investigation of a digitizer for resistive sensors in which the S-H effect is negligible. This study offers an intricate examination of this circuit, which relies on a dual-slope integrator and a comparator to directly give a time sequence output signal. Furthermore, the circuit's hardware implementation is realized and subjected to testing for an NTC thermistor (TCS651 Bead Head) and Pt100 RTD sensors.

The proposed circuit has the following key parameters: 1) power dissipation varies from 0.273 mW to 2.05 μW for a wide range of R_X −3.63 to 488.2 kΩ measurement; 2) measurement time varies from 4.73 to 382.39 ms; 3) current through R_X ranges from 274.59 to 2.05 μA; and 4) compared to the state-of-the-art, power dissipation decreases by 472.6–1294.94 times. In summary, the circuit has the following novelty and features over prior state-of-the-art: 1) power dissipation is very low; 2) measurement time is less; 3) a new parameter, current gain, due to the T-network in feedback is introduced to make a balance between power dissipation and measurement time; 4) provides time sequence digital output signal; 5) minimum error (±0.56%) due to circuit imperfection and exhibit good linearity (0.49% NL); and 6) does not require costly components such as a waveform generator.

II. PROPOSED TECHNIQUE

The schematic of the proposed circuit is shown in Fig. 1 which consists of an integrator (OA_1), a comparator (OC_1), and three switches (S_1, S_2, and S_3). The integrator has a T-network in the feedback path, which consists of two fixed resistors (R_2 and R_3) in the opposite arms and a capacitor (C_1) in the middle arm. The sensor (R_X) is placed at the inverting terminal of OA_1. Assuming S_2 and S_3 are at position 0, and S_1 is open, first negative input ($-V_S$) is connected to R_X, and the feedback current (I_2) passes through R_X (I_X, μA range), and sinks to $-V_S$. Because of the T-network, the capacitor current $I_C^{T_1}$ is $(1 + R_2/R_3)I_X$ and charges C_1. During this time, the threshold voltage of OC_1 is V_T, and the integrator output (V_O) ramp-up and the comparator output (V_C) remain

Authorized licensed use limited to: DELHI TECHNICAL UNIV. Downloaded on February 07,2024 at 07:19:10 UTC from IEEE Xplore. Restrictions apply.

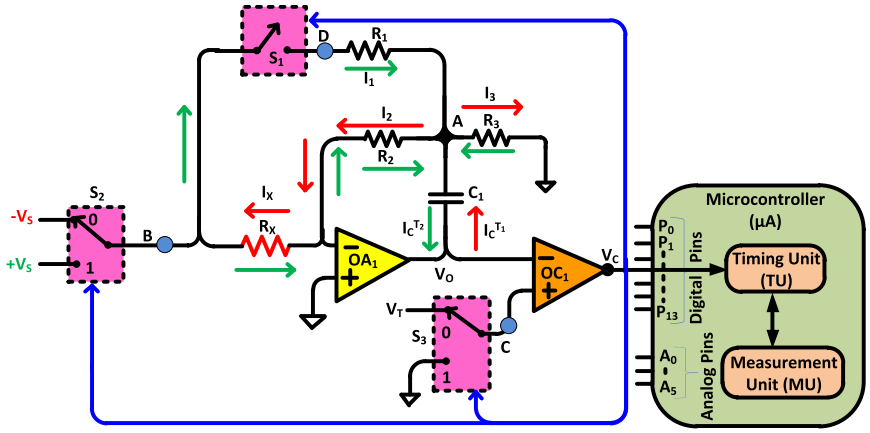


Fig. 1. Circuit diagram of the proposed RDC with S-H compensation.

HIGH. This mode of operation corresponds to the T_1 period of the charging–discharging cycle. It is to be noted that the $I_C^{T_1}$ current is bifurcated into two components—I_2 and I_3 as shown in Fig. 1. The, I_3 is bypassed to ground through R_3 and the remaining current I_2 passes through R_2. The directions of currents (I_2, I_3, and $I_C^{T_1}$) are shown in red color in Fig. 1 and the expressions are as follows:

$$I_X = I_X^{\text{RMS}} = \frac{|V_S|}{R_X} \tag{1}$$

$$I_C^{T_1} = I_2 + I_3 \tag{2}$$

$$I_2 = \frac{R_3}{R_2 + R_3} I_C^{T_1} = I_X \tag{3}$$

$$I_3 = \frac{R_2}{R_2 + R_3} I_C^{T_1} = \frac{R_2}{R_3} I_2 = \frac{R_2}{R_3} I_X. \tag{4}$$

The expression of V_O during T_1 period is as follows:

$$V_O = \left(I_2 R_2 + \frac{I_C^{T_1}}{C_1} t \right). \tag{5}$$

Once V_O rises to the threshold voltage (V_T) of OC_1, the V_C from the HIGH state goes to the LOW state, and this marks the end of the T_1 interval. Thus, the change in the integrator output (ΔV_O) is as follows:

$$\Delta V_O = \left(I_2 R_2 + \frac{I_C^{T_1}}{C_1} T_1 \right) = V_T. \tag{6}$$

The expression for T_1 is given as

$$T_1 = \frac{C_1 (V_T - I_2 R_2)}{I_C^{T_1}}. \tag{7}$$

After the T_1 interval, all switches change their position. The, S_2 and S_3 go to position 1, and S_1 is closed. Now the R_X is connected to positive input ($+V_S$) and the reference voltage of OC_1 is ground. Three currents (I_1, I_2, and I_3) enter the $I_C^{T_2}$ and discharges it. Due to the additional current I_1, which is not found in T_1 interval, V_O ramp-down fast. This helps to decrease the measurement time and corresponds to the T_2 interval of the charging–discharging cycle. During this time, V_C remained LOW. Again, once V_O decreases to ground, V_C goes HIGH, S_2 and S_3 are returned to position 0, and S_1 is open. The directions of currents (I_1, I_2, I_3, and $I_C^{T_2}$) are shown in green color in Fig. 1. The expressions for I_X, I_2, and I_3 are the same as in the T_1 interval given by (1), (3), and (4), respectively. The expressions for $I_C^{T_2}$ and I_1 are given as follows:

$$I_1 = \frac{V_S + R_2 I_X}{R_1} \tag{8}$$

$$I_C^{T_2} = I_1 + I_2 + I_3. \tag{9}$$

The expression of V_O during T_2 period is as follows:

$$V_O = V_T - \left(I_2 R_2 + \frac{I_C^{T_2}}{C_1} t \right). \tag{10}$$

Once V_O decreases to the ground, the V_C from the LOW state goes to the HIGH state, and this marks the end of the T_2 interval. Thus, the change in the integrator output (ΔV_O) is as follows:

$$\Delta V_O = \left(I_2 R_2 + \frac{I_C^{T_2}}{C_1} T_2 \right) = V_T. \tag{11}$$

The expression for T_2 is given as

$$T_2 = \frac{C_1 (V_T - I_2 R_2)}{I_C^{T_2}}. \tag{12}$$

The net charge in the C_1 capacitor will be zero at the end of the T_2 interval, and (6) and (11) can be equated as follows:

$$\left(I_2 R_2 + \frac{I_C^{T_1}}{C_1} T_1 \right) = \left(I_2 R_2 + \frac{I_C^{T_2}}{C_1} T_2 \right). \tag{13}$$

Finally, the unknown resistance R_X obtained from (1), (2), (3), (4), (8), (9), and (13) is as follows:

$$R_X = K R_1 \left(\frac{T_1}{T_2} - 1 \right) - R_2 \tag{14}$$

where $K = (1 + (R_2/R_3))$ is a constant.

III. Analysis

A. Effect of On Resistance of the SPST Switches

The expression of R_X in (14) is derived with the assumption that ON resistances (r_1 and r_2) of the switches (S_1 and S_2) are negligible compared to sensor resistance. This is typically true when R_X is in the range of kΩ. However, for the measurement

Authorized licensed use limited to: DELHI TECHNICAL UNIV. Downloaded on February 07,2024 at 07:19:10 UTC from IEEE Xplore. Restrictions apply.

of R_X in the range of 100 Ω (typical value of strain gauge, Pt100, etc.), ignoring r_1 and r_2 may lead to measurement error. Consequently, for a more realistic representation, the generalized form of (13) is

$$\begin{aligned} V_T &= V_S\left(\frac{R_2}{R_X'+r_2}+\frac{R_2T_1'}{R_3(R_X'+r_2)C_1}+\frac{T_1'}{(R_X'+r_2)C_1}\right) \\ &= V_S\left(\frac{R_2}{R_X'+r_2}+\frac{T_2'}{(R_1+r_1)C_1}+\frac{T_2'R_2}{(R_1+r_1)(R_X'+r_2)C_1}\right) \\ &\quad + V_SK\left(\frac{T_2'}{(R_X'+r_2)C_1}\right). \end{aligned} \tag{15}$$

Hence, the generalized form of T_1' and T_2' can be written as

$$\begin{aligned} T_1' &= C_1R_3\left(\frac{V_T(R_X'+r_2)-R_2V_S}{V_S(R_2+R_3)}\right) \\ T_2' &= \left(\frac{C_1R_3(R_1+r_1)[V_T(R_X'+r_2)-R_2V_S]}{V_S[R_3(R_2+(R_X'+r_2))+(R_1+r_1)(R_3+R_2)]}\right). \end{aligned} \tag{16}$$

Using (15) and assuming $r_1 = r_2 = r$, we get

$$R_X' = KR_1\left(\frac{T_1'}{T_2'}-1\right)-R_2+N \tag{17}$$

where $N = Kr((T_1'/T_2')-1)-r$. R_X' in (17) is same as in (14) with extra term N. Hence, (17) can be rewritten as

$$R_X' = R_X^{14}+N \tag{18}$$

where $R_X^{14} = KR_1((T_1'/T_2')-1)-R_2$ as taken from (14). In the expression of N, all parameters are either known or measured except r. The typical value of r for the CMOS switch used in the present work is 1.25 Ω as stated in the datasheet [19]. Thus, the value of N can be evaluated and used in (18) to find more accurate R_X. However, to simplify the expression to (14), if N is ignored, for the full span of R_X, the error introduced ranges from ±0.009% to ±0.024% which is almost negligible.

B. Effect of Deviation of Fixed Resistance (R_1, R_2, and R_3) and Capacitance (C_1)

The change in C_1 value does not affect the measurement of R_X as per (14). The changes in the fixed resistance (R_1, R_2, and R_3) values affect measurement negligibly and can be ignored. This observation is obtained in the following analytical analysis.

Let us assume that the fixed resistors are changed to R_1', R_2', and R_3'. These are defined as follows:

$$\begin{aligned} R_1' &= R_1(1+\alpha) \\ R_2' &= R_2(1+\beta) \\ R_3' &= R_3(1+\gamma) \end{aligned}$$

where α, β, and γ are percentage change in R_1, R_2, and R_3, respectively, due to aging. Then, (14) can be rewritten as

$$R_X' = K'R_1'\left(\frac{T_1}{T_2}-1\right)-R_2' \tag{19}$$

where $K' = (1+(R_2'/R_3'))$. Substituting R_1', R_2', and R_3' in (19)

$$R_X' = \left(1+\frac{R_2(1+\beta)}{R_3(1+\gamma)}\right)R_1(1+\alpha)\left(\frac{T_1}{T_2}-1\right)-R_2(1+\beta). \tag{20}$$

Since the changes in resistance are due to aging, it can be assumed that $\alpha = \beta = \gamma$. Hence, (20) can be written as

$$\begin{aligned} R_X' &= (1+\alpha)\left[KR_1\left(\frac{T_1}{T_2}-1\right)-R_2\right] \\ &= (1+\alpha)R_X. \end{aligned} \tag{21}$$

Hence, the change in R_X is given as

$$\Delta R_X = R_X'-R_X = R_X\alpha. \tag{22}$$

Therefore, (22) concurs with our previously stated observation that variations in fixed resistances have a negligible impact on the measurement of R_X.

C. Effect of Deviation of V_S

The circuit output will not be affected by the change in the $\pm V_S$ value. However, if there is a mismatch between $+V_S$ and $-V_S$, the following analysis discusses how much the measurement of R_X will be affected by this mismatch.

Let us assume that the input negative ($-V_S$) and positive ($+V_S$) voltages are changed to V_{S1} and V_{S2}, respectively, and are defined as follows:

$$\begin{aligned} V_{S1} &= -V_S(1+\delta) \\ V_{S2} &= +V_S(1+\sigma). \end{aligned}$$

Here, δ and σ are the percentage change in $-V_S$ and $+V_S$, respectively. Hence, the charge balance in (13) can be written in the form of node voltage as

$$\begin{aligned} &V_{S1}\left(\frac{R_2}{R_X}+\frac{R_2T_1}{R_3R_XC_1}+\frac{T_1}{R_XC_1}\right) \\ &\quad = V_{S2}\left(\frac{R_2}{R_X}+\frac{T_2}{R_1C_1}+\frac{T_2R_2}{R_1R_XC_1}+\frac{T_2}{R_XC_1}+\frac{R_2T_2}{R_XR_3C_1}\right). \end{aligned} \tag{23}$$

On substitution of V_{S1} and V_{S2} values in (23), we get the simplified expression as

$$\begin{aligned} R_X' &= \left(\frac{\delta-\sigma}{1+\sigma}\right)\left(\frac{R_2R_1C_1}{T_2}\right) \\ &\quad +\left[\left(\frac{1+\delta}{1+\sigma}\right)\left(\frac{T_1}{T_2}\right)-1\right]KR_1-R_2. \end{aligned} \tag{24}$$

An important observation is that when δ and σ hold equal numerical values, then (24) can be reduced to the simpler form as in (14). Additionally, since the influences of δ and σ oppose each other, their combined effect on the measurement of R_X becomes negligible.

Authorized licensed use limited to: DELHI TECHNICAL UNIV. Downloaded on February 07,2024 at 07:19:10 UTC from IEEE Xplore. Restrictions apply.

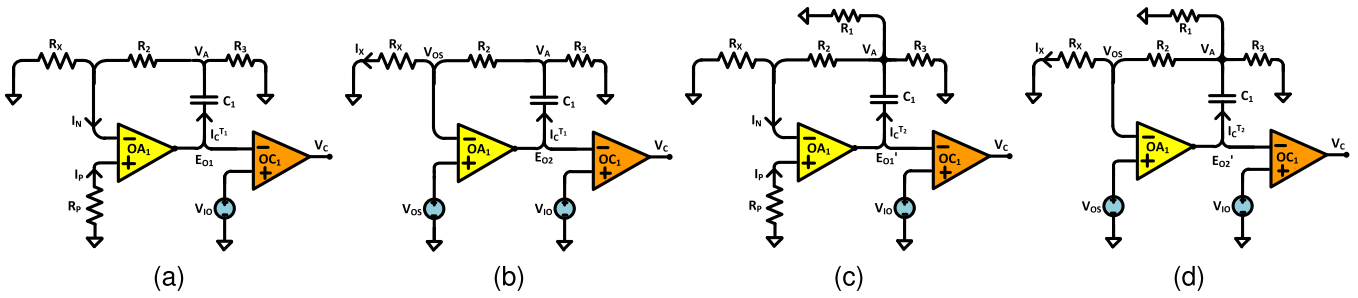


Fig. 2. Equivalent circuit during charging (T_1) and discharging (T_2) considering offset noises. (a) Error due to I_{OS} and V_{IO} in T_1. (b) Error due to V_{OS} and V_{IO} in T_1. (c) Error due to I_{OS} and V_{IO} in T_2. (d) Error due to V_{OS} and V_{IO} in T_2.

D. Effect of Opamp and Comparator Offset Noise

The integrator (OA_1) has inherent input offset voltage (V_{OS}) and input offset current (I_{OS}), resulting in an output offset error (E_O). The proposed scheme equivalent circuit is shown in Fig. 2(a) and (b), once V_S is set to zero. This circuit is used to evaluate the error caused by I_{OS} and V_{OS} in the measurement. OC_1 has also inherent input offset error V_{IO}. Both OA_1 and OC_1 are only connected to the supply voltage (i.e., VCC and VEE).

A compensation resistor (R_P) is connected at the noninverting terminal of OA_1 to minimize the error. The appropriate R_P value should be selected, as discussed in the following section. The error in the integrator output due to I_{OS} at the end of T_1 is as follows:

$$E_{01}(t) = \frac{1}{R_X C_1}\int_0^t \left(cI_B - d\frac{I_{OS}}{2}\right)dt \tag{25}$$

where $a = 1 + (R_2/R_3)$, $b = 1 + (R_2/R_3) + (R_X/R_3)$, $c = R_X a - R_P b$, and $d = R_X a + R_P b$.

Substituting $R_P = (R_X a/b)$ in (25), we get

$$E_{01}(t) = \frac{1}{R_X C_1}\int_0^t (-R_X a I_{OS})dt = -\frac{a I_{OS} t}{C_1} \tag{26}$$

where I_P and I_N are the input bias currents at noninverting and inverting terminals of OA_1. The, I_{OS} is $(I_P - I_N)$ and I_B (input bias current) is $(I_P + I_N)/2$.

Error in the integrator output due to V_{OS} during T_1 is as follows:

$$E_{02}(t) = \frac{1}{R_X C_1}\int_0^t (bV_{OS})dt = \frac{bV_{OS}}{R_X C_1}t. \tag{27}$$

Thus, the total error in the integrator output during T_1 is

$$|E_0(t)| = |E_{01}(t)| + |E_{02}(t)| = \left[aI_{OS} + \frac{bV_{OS}}{R_X}\right]\frac{t}{C_1}. \tag{28}$$

Substituting $t = T_1$ will give the integrator output at the end of T_1

$$|E_0(T_1)| = \left[aI_{OS} + \frac{bV_{OS}}{R_X}\right]\frac{T_1}{C_1}. \tag{29}$$

Now, the effect of V_{IO} in the OC_1 output is being analyzed. The threshold voltage (V_T) of the comparator is shifted to $V_T + V_{IO}$. When the integrator output (including the offset voltage) increases to $V_T + V_{IO}$, then V_C swings from $+V_{SAT}$ to $-V_{SAT}$. Thus, the voltage balance equation for finding T_1 is

$$\begin{aligned} V_T + V_{IO} &= V_0(T_1) + |E_0(T_1)| \\ &= V_S\left[\frac{R_2}{R_X} + \frac{T_1 a}{C_1 R_X}\right] + |E_0(T_1)|. \end{aligned} \tag{30}$$

$V_O(T_1)$ expression is substituted from (5), and finally, T_1 is calculated as

$$T_1 = \frac{[(V_T + V_{IO})R_X - V_S R_2]R_3 C_1}{(R_2 + R_3)[V_S + I_{OS}R_X] + V_{OS}(R_X + R_2 + R_3)}. \tag{31}$$

Then, I_{OS} is neglected since its typical value is 1 pA (for OP482, [20]). $V_T + V_{IO}$ is considered as V_T since V_{IO} is 0.2 mV (for OP482 [20]) which is very small compared to $V_T = 3$ V. $V_S + V_{OS}$ is considered as V_S. Thus, we can rewrite T_1 as

$$T_1 = \frac{[V_T R_X - V_S R_2]R_3 C_1}{(R_2 + R_3)V_S + V_{OS}R_X}. \tag{32}$$

After T_1 time, all switches change position, and the integrator discharges leading to a decrease in V_O. At the same time, I_{OS} and V_{OS} charge the integrator very slowly, but the net effect decreases V_O. This results in measurement error, and also V_{IO} is found at the noninverting terminal of OC_1. Thus, both sources of error should be accounted for in the analytical model. The complete equivalent circuit is shown in Fig. 2(c) and (d) during the discharging of the integrator when V_S is set to zero.

Error in the integrator output due to I_{OS} during T_2 is

$$E'_{01}(t) = \frac{1}{R_X C_1}\int_0^t \left(gI_B - h\frac{I_{OS}}{2}\right)dt \tag{33}$$

where $e = 1 + (R_2/R_3) + (R_2/R_1)$, $f = 1 + (R_2/R_3) + (R_X/R_3) + (R_X/R_1) + (R_2/R_1)$, $g = R_X e - R_P f$, and $h = R_X e + R_P f$.

Substituting $R_P = (R_X e/f)$ in (33)

$$E'_{01}(t) = \frac{1}{R_X C_1}\int_0^t (-R_X e I_{OS})dt = -\frac{e I_{OS} t}{C_1}. \tag{34}$$

Error in the integrator output due to V_{OS} during T_2 is

$$E'_{02}(t) = \frac{1}{R_X C_1}\int_0^t (V_{OS} f)dt = \frac{f V_{OS} t}{R_X C_1}. \tag{35}$$

Thus, the total error in the integrator output is

$$\left|E'_0(t)\right| = \left|E'_{01}(t)\right| + \left|E'_{02}(t)\right| = \left[eI_{OS} + \frac{fV_{OS}}{R_X}\right]\frac{t}{C_1}. \tag{36}$$

Authorized licensed use limited to: DELHI TECHNICAL UNIV. Downloaded on February 07,2024 at 07:19:10 UTC from IEEE Xplore. Restrictions apply.

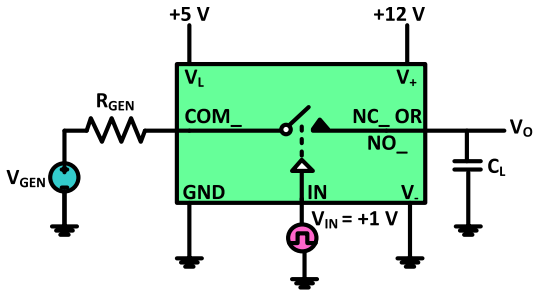


Fig. 3. Switch model to minimize ΔV caused by Q_{INJ} by connecting C_L.

Substituting $t = T_2$ will give the integrator output at the end of T_2

$$\left|E_0'(T_2)\right| = \left[eI_{\text{OS}} + \frac{fV_{\text{OS}}}{R_X}\right]\frac{T_2}{C_1}. \tag{37}$$

During discharge mode (T_2), integrator output decreases from ($V_T + V_{\text{IO}}$) to V_{IO}, and at $t = T_2$, V_C swings from $-V_{\text{SAT}}$ to $+V_{\text{SAT}}$. Thus, for finding T_2, the voltage balance equation is

$$V_0(T_2) - \left|E_0'(T_2)\right| = V_S\left[\frac{R_2}{R_X} + \frac{T_2}{C_1}\left(\frac{1}{R_1} + \frac{e}{R_X}\right)\right] - \left|E_0'(T_2)\right| = V_T. \tag{38}$$

$V_O(T_2)$ expression is substituted from (10), and finally T_2 is calculated as

$$T_2 = \frac{[V_T R_X - V_S R_2]R_1 R_3 C_1}{V_S[R_2(n) + R_1 R_3] + R_X[V_S R_3 - V_{\text{OS}}(n)]} \tag{39}$$

where $n = R_1 + R_3$. From (32) and (39), R_X is obtained as

$$R_X = \frac{KR_1\left(\frac{T_1}{T_2} - 1\right)}{q} - \frac{R_2}{q} \tag{40}$$

where $q = V_S - V_{\text{OS}}[1 + (R_1/R_3)(T_1/T_2 + 1)]$. Thus, if we compare (40) with (14), it can be concluded that OA_1 should be selected such that V_{OS} should be as small as possible to obtain an accurate measurement. It is to be noted that R_P has two different values (($R_X a/b$) and ($R_X e/f$)) to minimize the error due to input bias currents. On analyzing, analytically and numerically with practical assumptions ((R_2/R_1) $\ll a$, ($1/R_3$) $\gg$ ($1/R_1$), and (R_X/R_3) $\gg a$), both the values are approximately equal to aR_3.

E. Effect of Charge Injection (Q_{INJ}) of Switch On Measurement

We have used a CMOS MAX 4690 switch and operated it with a single supply (+12 V). In this setting, the charge injection (Q_{INJ}) in the switch is −60 pC as given in the datasheet [19], which may change the voltage by ΔV at nodes B, C, and D as shown in Fig. 1. ΔV is minimized by connecting a load capacitor (C_L) as recommended in the datasheet following the below equation:

$$\Delta V = \frac{Q_{\text{INJ}}}{C_L}. \tag{41}$$

To minimize ΔV below 1 mV, a C_L of 60 nF is connected in every switch as shown in Fig. 3. Now, the circuit is analyzed for error calculation due to Q_{INJ}. The voltage at node B during charging and discharging will be $-V_S + \Delta V$ and $+V_S - \Delta V$, respectively. Similarly, the voltage at node C during charging and discharging will be $V_T - \Delta V$ and $-\Delta V$, respectively. Lastly, node D exists during discharging only and its voltage will be $+V_S - 2\Delta V$. Substituting the value of $I_C^{T_1}$ and $I_C^{T_2}$ from (2) and (9) in (13), we obtain

$$\frac{T_1}{T_2} = \frac{I_C^{T_2}}{I_C^{T_1}} = \frac{I_1 + I_2 + I_3}{I_2 + I_3}$$
$$\frac{T_1}{T_2} - 1 = \frac{I_1}{I_2 + I_3} = \frac{I_1}{I_2 K}. \tag{42}$$

Now I_1 and I_2 are changed due to Q_{INJ} and can be written as

$$I_1 = \frac{V_S - 2\Delta V + V_A}{R_1}$$
$$I_2 = \frac{V_S - \Delta V}{R_X}. \tag{43}$$

Putting the value of I_1 and I_2, (42) can be written as

$$\frac{T_1}{T_2} - 1 = \frac{R_X}{R_1 K} + \frac{R_2}{R_1 K} + \frac{\Delta V}{R_1 I_2 K}$$
$$R_1 K\left(\frac{T_1}{T_2} - 1\right) - R_2 = R_X - \frac{\Delta V}{I_2}$$
$$R_1 K\left(\frac{T_1}{T_2} - 1\right) - R_2 = R_X\left(1 - \frac{\Delta V}{V_S - \Delta V}\right). \tag{44}$$

Finally, R_X can be rewritten as

$$R_X = \frac{R_X^{14}}{\varepsilon} \tag{45}$$

where $R_X^{14} = R_1 K((T_1/T_2) - 1) - R_2$ and $\varepsilon = (1 - (\Delta V/V_S - \Delta V))$. Thus, to minimize the error in the R_X measurement, ε should be close to 1. For this, ΔV should be as small as possible by connecting a suitable C_L.

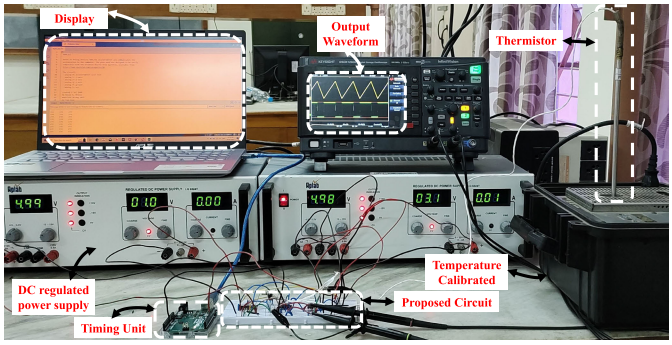


Fig. 4. Experimental setup used for testing the proposed RDC.

IV. Experimental Setup

The hardware prototype of the proposed dual-slope digitizer is realized on the breadboard for testing as shown in Fig. 4. The opamp (OA_1) and the comparator (OC_1) are implemented using OP482 [20] and LM311 ICs, respectively. The switches S_1, S_2, and S_3 are realized using SPST CMOS MAX 4690 [19] IC. V_C is inverted using SN7404 IC so that switches S_1, S_2, and S_3 can change their positions between 0 and 1. R_1, R_2, and R_3 are fixed resistors of value 5 kΩ, 100 Ω, and 5 Ω, respectively, while R_X is an NTC-type thermistor

Authorized licensed use limited to: DELHI TECHNICAL UNIV. Downloaded on February 07,2024 at 07:19:10 UTC from IEEE Xplore. Restrictions apply.

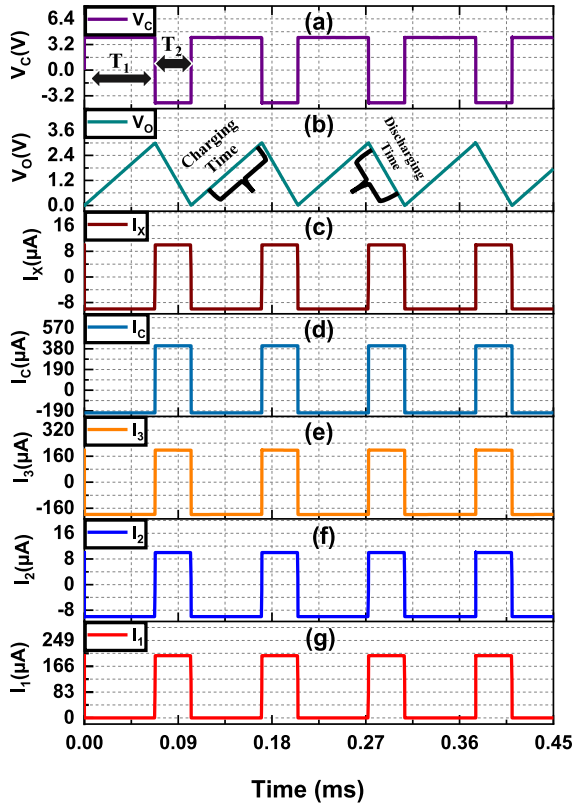


Fig. 5. Plot of different node voltages and branch currents for $R_X = 100$ kΩ. (a) V_C. (b) V_0. (c) I_X. (d) I_C. (e) I_3. (f) I_2. (g) I_1.

(TCS651 Bead Head) whose resistance varies from 3.6 to 488.2 kΩ corresponding to temperature 114 °C to −6 °C [4]. The feedback capacitor C_1 is 4.7 μF. The input voltage (V_S) is ±1 V, and the V_T of OC_1 is kept constant at 3 V. The circuit is tested by dipping the thermistor (R_X) in a temperature calibrator (Fluke Calibration 9009 Dual-Well Dry-Well). R_X is measured at different temperatures using a handheld LCR meter (U1733C, Keysight). The sensor current I_X is measured using a source measurement unit (SMU, B2910BL, Keysight), and the capacitor current I_C is measured using a 6 1/2 Digit Table-top multimeter (DM3068, Rigol). For measuring T_1 and T_2 intervals, the timing unit (TU) is realized in Arduino Uno ATMEGA328P using PulseIn() function as described in [9].

V. Results and Discussion

The proposed digitizer is simulated into LTspice and Proteus software. V_S is kept at 1 V so that the amplified current (I_C) due to the T-network remains small which enters the OA_1 and keeps it in the linear region. It is to be noted that if higher V_S is used, high I_C may cause OA_1 to saturate. The comparator output signal (V_C) can be approximated as a quasi-square waveform whose duty cycle varies depending on the amplitudes of integrator output (V_O) and threshold voltage (V_T). As V_T is a constant, the T_1 and T_2 intervals mainly depend on V_O, which takes the form of a triangular waveform. V_C is HIGH during the rising of V_O and vice versa. As predicted in (7) and (12), both T_1 and T_2 vary with R_X.

Fig. 5(a) and (b) shows the simulation plot of V_O and V_C for $R_X = 100$ kΩ which corresponds to the thermistor's resistance (TCS651 Bead Head) at 25 °C [4]. Fig. 6 shows

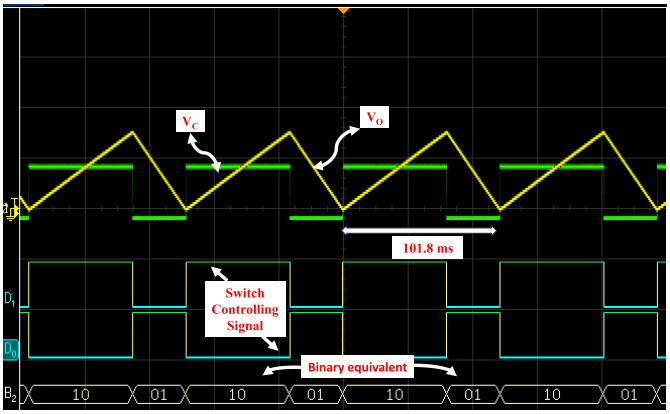


Fig. 6. Experimental waveform of the integrator (V_O) and the comparator (V_C) on the mixed-signal oscilloscope for $R_X = 100$ kΩ. Control signals for switch operation are also shown.

the experimental waveforms of V_O, V_C, and control signals in the mixed signal oscilloscope (MSOX3014G, Keysight) for $R_X = 100$ kΩ. T_1 and T_2 in the simulation are 68.01 and 34.71 ms, respectively, while in the experiment it is 67.46 and 34.38 ms. Thus, the experimental waveforms closely match the simulation.

Fig. 5(c)–(g) also shows simulation waveform of different branch currents—I_X, I_C, I_3, I_2, and I_1 for $R_X = 100$ kΩ in the proposed digitizer, respectively. I_X and I_2 are the same currents because of the virtual ground of OA_1 [2]. The I_2 and I_3 currents are bipolar square waveforms with equal amplitude in both polarities. I_1 is a unipolar square waveform (201.45 μA) because S_1 is closed during discharging (T_2 interval) only. I_C is the summation of I_1, I_2, and I_3 currents and is a bipolar square waveform with unequal amplitude. The duty cycles of all current waveforms are the same.

Due to the quasi-square nature of the current waveforms, the root mean square (RMS) value of equal-value bipolar currents such as I_X, I_2, and I_3 are the modulus of the peak current. But, I_C is an unequal quasi-square waveform with amplitude given by (2) and (9) in T_1 and T_2 intervals, respectively, as shown in Fig. 5(d). The unequal current is due to the I_1 current found only during T_2 not in T_1. The RMS value I_C^{RMS} is calculated using the following equation:

$$I_C^{\text{RMS}} = \sqrt{\frac{1}{T}\left(\int_0^{T_1} {I_C^{T_1}}^2\, dt + \int_{T_1}^{T} {I_C^{T_2}}^2\, dt\right)} \tag{46}$$

where $T = T_1 + T_2$.

R_X is varied over the full span (3.6–488.2 kΩ), correspondingly I_X through R_X varies from 275.2 to 2.04 μA, respectively, in simulation. In the experiment, I_X varies from 274.59 to 2.05 μA. I_C also varies from 5800 to 101.19 μA, respectively, in simulation, while in the experiment, it varies from 5955.16 to 103.18 μA. The other branch current such as I_2 and I_3 varies in the range of 274.59–2.05 μA and 5491.8–41 μA, respectively.

Fig. 7(a) shows the simulation and experimental plot of I_X^{RMS} with $\log(R_X)$. The percentage deviation (%) is calculated by comparing simulation and experimental results with analytical values obtained from (1). The % relative error is calculated using formula $((|\, I_X^{\text{RMS}} - I_X^{\text{RMS}*}\, |)/I_X^{\text{RMS}}) \times 100$,

Authorized licensed use limited to: DELHI TECHNICAL UNIV. Downloaded on February 07,2024 at 07:19:10 UTC from IEEE Xplore. Restrictions apply.

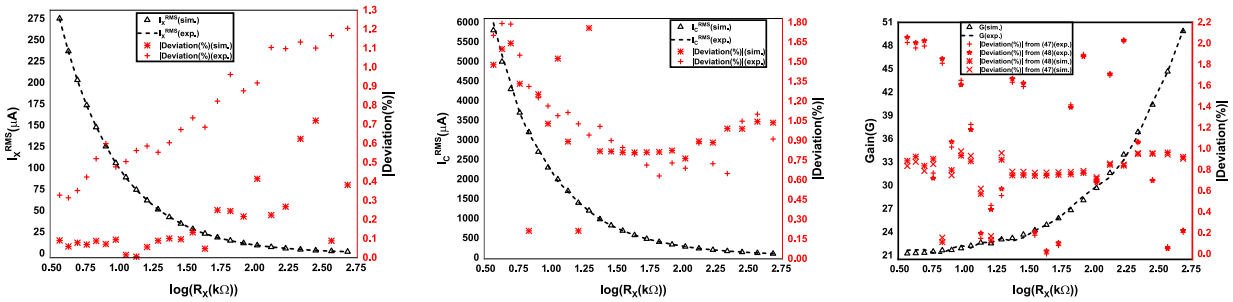


Fig. 7. Plot of branch currents and variable with $\log(R_X)$ for full span (3.6–488.2 kΩ). (a) Sensor current (I_X^{RMS}). (b) Capacitor current (I_C^{RMS}). (c) Current gain (G).

where $I_X^{\mathrm{RMS}*}$ is the measured sensor current. The maximum and average deviations in the simulation are 0.72% and 0.18%, while in the hardware it is 1.10% and 0.42%, respectively. The simulation and experimental plot of I_C^{RMS} versus $\log(R_X)$ is shown in Fig. 7(b), and the average deviation is found using the analytical model in (20). The deviation of simulation and experimental results are 1.06% and 0.96%, respectively. Therefore, values of I_X^{RMS} and I_C^{RMS} are in close proximity to analytically predicted values.

The novelty of this work is that I_C is equal to I_X multiplied by the gain (G). As a result, the plot of I_C shares similar characteristics with that of I_X. The expression for G is found using RMS values of I_X and I_C and given by the following equation:

$$G = \frac{I_C^{\mathrm{RMS}}}{I_X^{\mathrm{RMS}}} = \frac{\sqrt{\frac{1}{T}\left(\int_0^{T_1} {I_C^{T_1}}^2\,dt + \int_{T_1}^{T} {I_C^{T_2}}^2\,dt\right)}}{I_X^{\mathrm{RMS}}} = \sqrt{p^2 + kx^2 + 2kxp} \tag{47}$$

where $p = (1 + (R_2/R_3))$, $x = ((R_X + R_2)/R_1)$, and $k = (p/(x + 2p))$. Neglecting the negligible terms (R_2/R_1) and $((2P^2(R_2/R_1))/(y + 2p))$, (47) can be rewritten as

$$G = \sqrt{p(p + y)} \tag{48}$$

where $y = (R_X/R_1)$.

As predicted from (47) and (48), G is dependent on R_X. Fig. 7(c) shows the plot of G with $\log(R_X)$ in simulation as well as experiment. The value of G in simulation varies from 21.07 to 49.41 when R_X varies over the full span (3.63–488.2 kΩ). In the experiment, the value of G varies from 21.68 to 50.22. The percentage deviation in G is obtained from the analytical model in (47). The maximum deviation[2] for the full span in simulation is 1.89% and the average deviation is 1.01%. However, in the experiment, the maximum deviation is 1.92% and the average deviation is 1.02%. Hence, the experimental value of G exhibits a close resemblance to the simulated ones.

The simulation and experimental results of T_1 and T_2 for $\log(R_X)$ in the full span are shown in Fig. 8(a) and (b), respectively. It should be noted that despite its apparent linearity, the plot is not actually linear. This outcome aligns with the prediction in the analytical model in (7) and (12) which are also used for comparison and finding deviations. The simulation and experimental results are in close proximity to the predicted values from the analytical model. In the simulation, the maximum deviation for T_1 is 0.95% and the average deviation is 0.78% for the full span. The experiment shows a maximum deviation of 1.24% and the average deviation is 0.81%. Thus, the simulation outcomes for T_2 also closely match, with an average deviation of 0.72%. The experiment shows an average deviation of 0.69%. Thus, it can be said that different node voltages and branch currents in the proposed circuit follow the analytical models presented in (1)–(14).

Fig. 8(c) shows the plot of known $\log(R_X)$ with measured $\log(R_X)$ in simulation and experiment. The simulation curve shows a maximum nonlinearity (NL) of 0.07%. The maximum % error is found to be 0.62% and the average% error for the full span is ±0.28%. In the experiment, the maximum NL is 0.49%, and the average% relative error is ±0.56%. In Monte Carlo simulation, the proposed circuit with component tolerances (R_1, R_2, and R_3—0.1%, C_1—1%) is tested for 100 runs. Fig. 9(a) shows the histogram plot for the measurement of R_X at 100 kΩ. The maximum, minimum, and mean values of R_X are 100.25 kΩ, 99.749 kΩ, and 100.013 kΩ, respectively. The standard deviation (σ) is 0.124 which is an acceptable value for obtaining a reasonable accuracy. It is to be noted that circuits intended for measurement should use components with low tolerance values because these measurements are used to control a system that can otherwise (if high-tolerance components are employed) malfunction. The above-discussed results indicate good agreement between the simulation, experiment, and the analytical model.

Fig. 9(b) shows the plot of power dissipation [$P = (I_X^{\mathrm{RMS}})^2 R_X$] with $\log(R_X)$ varies over the full span in simulation and experiment. P decreases from 0.275 mW to 2.03 μW, respectively, in simulation. However, in the experiment, P decreases from 0.273 mW to 2.05 μW, respectively. The average value of measurement uncertainty (standard deviation, σ) for five trials in the full span is 0.514 μW. In conventional dual-slope RDC, integrating the feedback capacitor with incoming current (274.59–2.05 μA range)[3] results in a longer measurement time (103.28 ms–13.70 s). To decrease the measurement time, a high current is required, which increases the S-H error. However, since in the proposed digitizer, the current boosting approach is

[2]If the deviation is obtained from the analytical model in (48), the maximum deviation is 0.95% and the average deviation is 0.77%.

[3]The current through R_X when it varies from 3.63 to 488.2 kΩ in a typical dual-slope RDC with same circuit parameters.

Authorized licensed use limited to: DELHI TECHNICAL UNIV. Downloaded on February 07,2024 at 07:19:10 UTC from IEEE Xplore. Restrictions apply.

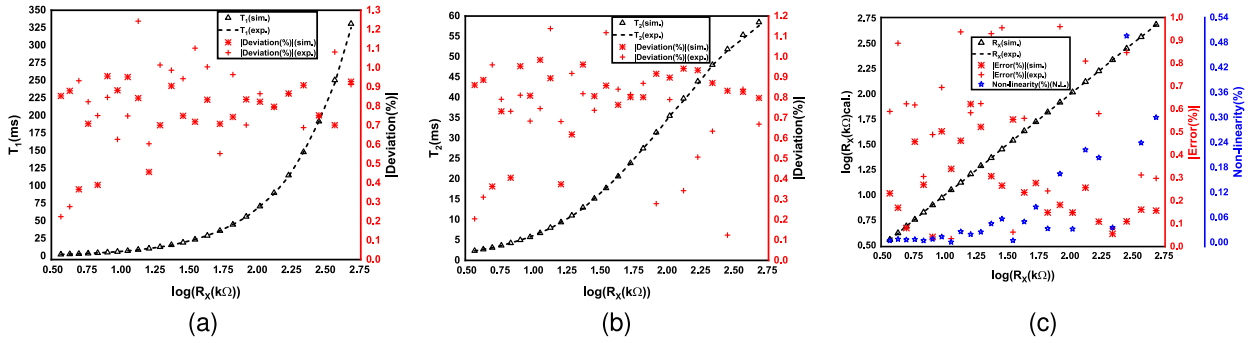


Fig. 8. Plot of different variables of the circuit with known $\log(R_X)$ for full span (3.6–488.2 kΩ). (a) Charging interval (T_1). (b) Discharging interval (T_2). (c) Measured sensor resistance $\log(R_X)$. For each plot, deviation (%) is calculated from the analytical model equations (7), (12), and (14), respectively.

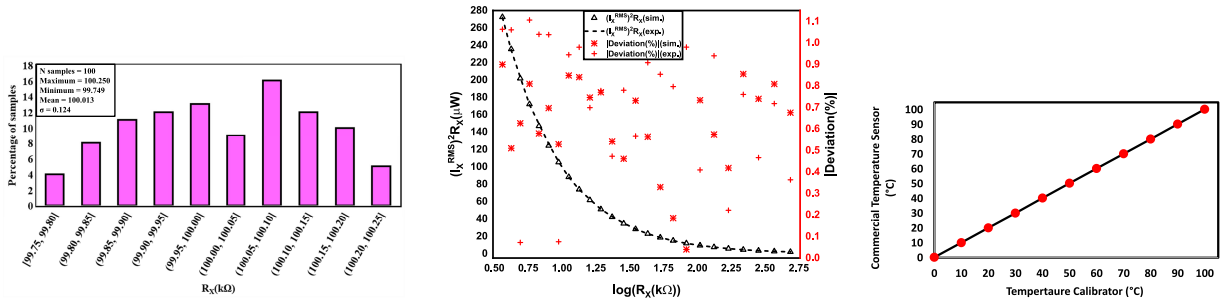


Fig. 9. (a) Histograms plot of Monte-Carlo simulations for $R_X = 100$ kΩ. (b) Plot of power dissipation ($I_X^2 R_X$) with known $\log(R_X)$ for full span (3.6–488.2 kΩ) in experiment and simulation. (c) Sensor surface temperature from the commercial meter is plotted with respect to the temperature meter of the calibrator to verify experimentally that S-H is negligible.

employed (ranging from 21.68 to 50.22 times in the experiment), the measurement time decreases in the range of 4.73–382.39 ms. It is to be noted that the conventional digitizer with a measurement time of 4.73–382.39 ms would require 5961.94–73.74 μA to pass through R_X which would dissipate 29.02 mW–2654.63 μW. Thus, this scheme decreases power dissipation by 472.6–1294.94 times. This represents a significant improvement in the performance of the proposed digitizer.

To check S-H experimentally, first, a commercial temperature sensor (Hanna Instruments HI98509) is calibrated to the temperature meter of the Fluke Calibration 9009 Dual-Well Dry-Well, so that both show the same reading for a specific temperature. Now, the NTC thermistor (TCS651) is connected to the proposed circuit. On the surface of the thermistor, the commercial sensor is placed. Now power is supplied to the proposed circuit. The temperature readings of the calibrator and commercial sensor are noted down for different sets of temperatures. The temperature is measured in the range of 0 °C–100 °C with a step size of 10 °C which is plotted in Fig. 9(c). It is found that both the calibrator and the commercial sensor show almost the same reading (±0.2 °C difference), which may be attributed to the measurement error of both meters as specified in the datasheet. Thus, there is no significant S-H in R_X.

A. Proposed Circuit Interfaced With Low-Resistance Sensor ($R_X = 100$ Ω)

The proposed digitizer is tested with a Pt100 temperature sensor. For this, V_S is set to 50 mV by a programmable DC power supply (EDU36311A, Keysight). Other circuit parameters are the same as mentioned in Section IV. The Pt100 temperature sensor is tested in the range of 0 °C–200 °C where its resistance changes from 100 to 175.84 Ω [21]. The step change of 10 °C is considered for testing. The average error is found to be ±0.78%. The power dissipation is 23.96 μW for $R_X = 100$ Ω. Hence, the proposed digitizer circuit can be used for low-resistance sensors. Apart from changing the V_S value, if other parameters are also optimized, the circuit error can further be reduced.

VI. Conclusion

An interfacing circuit for resistive sensors is proposed, aiming to reduce S-H errors. This circuit utilizes a dual-slope integrator to generate a time sequence output signal. The circuit is tested for a wide range of sensor resistance of 3.63–488.2 kΩ. To minimize the S-H error, microampere current (274.59–2.05 μA) is allowed to pass through R_X which corresponds to the power dissipation of 0.273 mW–2.05 μW, respectively. By implementing the current amplification technique (gain varying from 21.68 to 50.22 times) through a T-network within this digitizer, the measurement time is small in the range of 4.73–382.39 ms. Compared to the state-of-the-art, this circuit reduces power dissipation by a factor ranging from 472.6 to 1294.94. The proposed digitizer produces accurate outcomes, exhibiting an average error of ±0.56%, and a negligible S-H is evident during testing.

Acknowledgment

The authors would like to acknowledge the Advanced Instrumentation and Measurement (I&M) Laboratory, Department of Instrumentation and Control Engineering, NIT

Authorized licensed use limited to: DELHI TECHNICAL UNIV. Downloaded on February 07,2024 at 07:19:10 UTC from IEEE Xplore. Restrictions apply.

Tiruchirappalli, Tiruchirappalli, India, for carrying out the research work.

REFERENCES

[1] J. P. Bentley, *Principles of Measurement Systems*. London, U.K.: Pearson, 2005.

[2] R. Pallas-Areny and J. G. Webster, *Sensors Signal Conditioning*. Wiley & Sons, 2012.

[3] A. Barua, *Fundamentals of Industrial Instrumentation*. Hoboken, NJ, USA: Wiley, 2011.

[4] *TCS Series Thermistors*. Accessed: Aug. 20, 2023. [Online]. Available: https://www.teamwavelength.com/download/Datasheets/tcs-series-thermistors.pdf

[5] P. R. Nagarajan, B. George, and V. J. Kumar, "An improved direct digital converter for bridge-connected resistive sensors," *IEEE Sensors J.*, vol. 16, no. 10, pp. 3679–3688, May 2016.

[6] K. Elangovan, S. Dutta, A. Antony, and A. C. Sreekantan, "Performance verification of a digital interface suitable for a broad class of resistive sensors," *IEEE Sensors J.*, vol. 20, no. 23, pp. 13901–13909, Dec. 2020.

[7] N. M. Mohan, B. George, and V. J. Kumar, "Analysis of a sigma–delta resistance-to-digital converter for differential resistive sensors," *IEEE Trans. Instrum. Meas.*, vol. 58, no. 5, pp. 1617–1622, May 2009.

[8] K. Elangovan and A. C. Sreekantan, "An efficient universal digitizer with linear transfer characteristic for resistive sensor bridges," *IEEE Trans. Instrum. Meas.*, vol. 70, pp. 1–4, 2021.

[9] G. Singh, S. Sohail, U. Mangalanathan, U. Gandhi, and T. Islam, "A novel dual-slope resistance to digital converter with lead resistance compensation," *IEEE Trans. Instrum. Meas.*, vol. 72, pp. 1–10, 2023.

[10] K. Elangovan and A. C. Sreekantan, "Evaluation of new digital signal conditioning techniques for resistive sensors in some practically relevant scenarios," *IEEE Trans. Instrum. Meas.*, vol. 70, pp. 1–9, 2021.

[11] T. Sen, A. C. Sreekantan, and S. Sen, "Linearized sigma-delta-based direct digital converter for GMR sensors," *IEEE Trans. Instrum. Meas.*, vol. 70, pp. 1–10, 2021.

[12] G. Singh, S. Sohail, and T. Islam, "A dual-slope RDC using T-network for low resistance measurement," in *Proc. IEEE Appl. Sens. Conf. (APSCON)*, Jan. 2023, pp. 1–3.

[13] K. Elangovan and A. C. Sreekantan, "Simple digitizing circuit for resistive sensors in p-network form," *IEEE Trans. Instrum. Meas.*, vol. 72, pp. 1–3, 2023.

[14] J. A. Hidalgo-López, J. A. Sánchez-Durán, and Ó. Oballe-Peinado, "Method to reduce quantization error in direct interface circuits for resistive sensors," *IEEE Sensors J.*, vol. 20, no. 23, pp. 13910–13918, Dec. 2020.

[15] J. A. Hidalgo-López, Ó. Oballe-Peinado, J. Castellanos-Ramos, J. C. Tejero-Calado, and F. Vidal-Verdú, "Wide range calibration method for direct interface circuits and application to resistive force sensors," *IEEE Sensors J.*, vol. 21, no. 20, pp. 22956–22966, Oct. 2021.

[16] J. A. Hidalgo-López, "Direct interface circuits for resistive sensors affected by lead wire resistances," *Measurement*, vol. 218, Aug. 2023, Art. no. 113250.

[17] J. A. Hidalgo-López, "Sigma-delta approach in direct interface circuits for readout of resistive sensors," *IEEE Trans. Instrum. Meas.*, vol. 71, pp. 1–8, 2022.

[18] A. D. Joshi, S. Sohail, G. Singh, N. P. Kumar, and T. Islam, "An efficient digitizer for self-heating compensation in resistive sensor," in *Proc. Int. Conf. Recent Adv. Electr., Electron. Digit. Healthcare Technol. (REEDCON)*, May 2023, pp. 454–459.

[19] *Data Sheet-Max4690*, 1.25 Ohm, Dual SPST, CMOS Analog Switches, Maxim Corp. Accessed: Aug. 20, 2023. [Online]. Available: https://www.analog.com/media/en/technical-documentation/data-sheets/MAX4680-MAX4700.pdf

[20] *Data Sheet-Op482*. dual/Quad, JFET Operational Amplifiers, Analog Devices. Accessed: Aug. 20, 2023. [Online]. Available: https://www.analog.com/media/en/technical-documentation/data-sheets/OP282_482.pdf

[21] *Sterling Sensors UK Ltd. RTD Sensors Including Pt100 and Pt1000 Elements (PRT)*. Accessed: 20 Aug. 2023. [Online]. Available: https://www.sterlingsensors.co.uk/rtds



Gopal Singh (Graduate Student Member, IEEE) received the bachelor's degree in instrumentation and control engineering from the Institute of Engineering and Rural Technology (IERT) Prayagraj, Prayagraj, India, in 2017, and the master's degree in control and instrumentation from Delhi Technological University (DTU), New Delhi, India, in 2020.

He is currently a Research Scholar with the Department of Instrumentation and Control Engineering, National Institute of Technology (NIT) Tiruchirappalli, Tiruchirappalli, India. His research interests include sensors, measurements, and electronic instrumentation.



Shiraz Sohail (Senior Member, IEEE) received the M.Tech. and Ph.D. degrees in electrical engineering from IIT Kharagpur, Kharagpur, India, in 2010 and 2016, respectively.

He joined the Department of Instrumentation and Control Engineering, National Institute of Technology (NIT) Tiruchirappalli, Tiruchirappalli, India, in 2020, where he is currently an Assistant Professor. His research interests include sensors, measurements, and electronic instrumentation.

Dr. Sohail is serving as one of the Associate Editors for IEEE TRANSACTIONS ON INSTRUMENTATION AND MEASUREMENT (TIM) and the *IET Science, Measurement and Technology*. He was selected as the 2021 IEEE TIM Outstanding Reviewer and also served as one of the Associate TPCs for the International Instrumentation and Measurement Technology Conference (I^2MTC) in 2021 in Ottawa, Canada, and in 2024 in Glasgow, Scotland.



Ashish Dineshkumar Joshi received the bachelor's degree in instrumentation and control engineering from the Dr. D. Y. Patil College of Engineering and Technology, Pune, India, in 2018, and the master's degree in process control and instrumentation from the National Institute of Technology (NIT) Tiruchirappalli, Tiruchirappalli, India, in 2023.

He is currently a Post-Graduate Engineer Trainee (PGET) with Mercedes-Benz Research and Development India, Bengaluru, India. His research interests include electronic instrumentation.



Tarikul Islam (Senior Member, IEEE) received the M.Sc. (Eng.) degree in instrumentation and control systems from Aligarh Muslim University (AMU), Aligarh, India, in 1997, and the Ph.D. (Eng.) degree from Jadavpur University, Kolkata, India, in 2007.

He joined the Electrical Engineering Department, Jamia Millia Islamia (A Central University), New Delhi, India, in 1997, where he is currently a Professor. His research interests include sensors and sensing technologies and electronic instrumentation.

Dr. Islam is a Life Member of the Institute of Electronics and Telecommunication Engineers (IETE), India, and the Indian Society for Technical Education (ISTE), India. He is also serving as one of the Topical Editors for IEEE SENSORS JOURNAL and an Associate Editor for IEEE TRANSACTIONS ON INSTRUMENTATION AND MEASUREMENT (TIM) and the *International Journal on Smart Sensing and Intelligent Systems*.

Authorized licensed use limited to: DELHI TECHNICAL UNIV. Downloaded on February 07,2024 at 07:19:10 UTC from IEEE Xplore. Restrictions apply.

This article has been accepted for publication in IEEE Wireless Communications Letters. This is the author's version which has not been fully edited and content may change prior to final publication. Citation information: DOI 10.1109/LWC.2024.3353218

Performance of an Intelligent Reflecting Mirror Aided Uplink Lightwave Communication System

Vishal Kumar*, Rohit Kumar*, Shankar Prakriya†
*Delhi Technological University, New Delhi, India ,† Indian Institute of Technology, New Delhi, India
Email-id: {vishalkumar_2k21phdec07, rohit.kumar}@dtu.ac.in, shankar@ee.iitd.ac.in

***Abstract*—In this paper, the performance of an uplink visible light communication (VLC) system with intelligent reflecting mirror (IRM) is analyzed. It is shown for the first time in literature that the high uplink data rates in VLC can be ensured without the unpleasant eye irradiance problem with the application of IRM. When compared with a counterpart system without IRM, numerical and synthetic results for the proposed IRM-aided VLC system indicate that the required transmit power is lowered to such an extent that reliable communication is possible without the eye irradiance problem. In addition, the IRM significantly improves the coverage area of the uplink transmitter. Extensive numerical results indicate that uplink VLC is feasible when an IRM is used.**

***Index Terms*—Visible light communication, Uplink, Intelligent reflecting mirror, Energy Efficiency, Achievable data rate.**

I. Introduction

In the recent years, an enormous growth has been observed in the data demand due to rise in online gaming, industry 4.0, Internet-of-Things, and increased media consumption. This has led to an acute shortage of RF spectrum. Recently, there has been a lot of research efforts to utilize the RF spectrum and its alternatives efficiently. Of these, visible light communication (VLC) and infrared communication (IRC) are commonly acknowledged to have the greatest potential to deal with RF spectrum scarcity [1].

Uplink VLC communication system presents many challenges. The optical power needs to be limited to ensure that the irradiance does not harm the human eye [2]. In the downlink VLC, LED source is deployed at the ceiling of the room and it is far away from human eye and irradiance generated will not affect the eye significantly. Whereas, in the uplink VLC, optical source may be much nearer to human eye and hence irradiance problem is more prevalent. Although, the VLC has the capacity to provide moderate data rates but attaining elevated data rates for uplink communication is challenging. This is due to the constraints posed by the restricted transmission power and the sensitivity of photodetectors. Restricted transmit power results in weaker signals reaching the receiver, which may lead to a reduced signal-to-noise ratio. To eradicate the irradiance problem and improve the data rate, several authors have considered a bidirectional system with VLC downlink and RF uplink [3]. However, there are certain scenarios where RF is prohibited (for example in hospitals or in aircraft). Thus, these types of hybrid VLC/RF systems cannot be deployed. IRC is another alternate potential solution [4], but it is equally compelling to explore the concept of crafting a low powered uplink system based on VLC. This approach capitalizes the utilization of pre-existing LEDs and maximizes the benefits offered by VLC technology.

In [5], an uplink VLC system has been proposed where Decode-and-forward (DF) relay has been incorporated. However, in such systems, the relay nodes are active and require energy for operation. Therefore, such a system is not significantly energy efficient. From [6], it can clearly be inferred that intelligent reflecting surfaces (IRS) can outperform DF type of relaying system. Generally, in VLC, non line of sight (NLOS) signals loose their strength due to reflection and diffraction from the surfaces and obstacles present in the indoor environment. Thus, the signal received from NLOS path is quite low and negligible. Here, IRS plays a significant role in focusing the NLOS signal at the receiver to improve the received signal strength. Motivating with the advantages of IRS, we study the use of IRS for uplink lightwave communication. Although the analysis and results presented here pertain to visual light communications, the ideas can readily be extended to infrared using 'hot' mirrors [7] and a large increase in data rates can be attained. In this paper, we restrict our attention to VLC and demonstrate that high data rates can be attained when IRS is used, without harmful effects on the eyes due to irradiance.

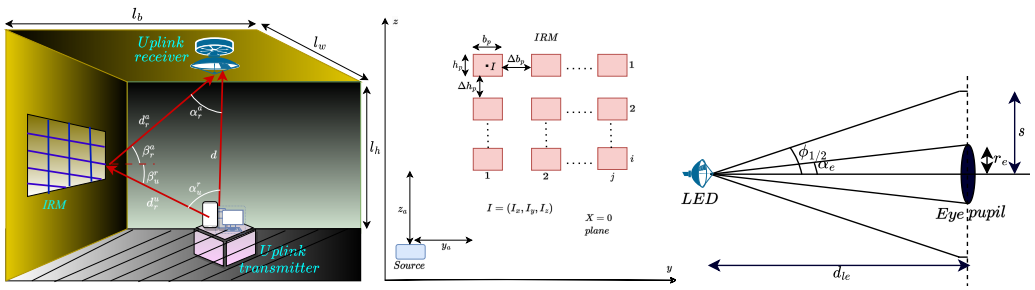
Performance with two different types of IRS elements - meta surfaces and reflecting mirrors - have been compared in [8]. [8] shows that intelligent reflecting mirror (IRM) type IRS elements outperform the meta surface type IRS elements in the VLC system. Meta surface type IRS requires more power in order to change the phase gradient. In reflecting mirrors type IRS, the mirrors are simply rotated to beamform the signal.

Our focus in this work is to utilize reflecting mirror type IRS elements to study and analyse the IRM-aided uplink VLC system. To the best of our knowledge, this is the first attempt to show that IRM can make uplink data communication possible at optical frequencies. The major contributions of our work are as follows:

- We develop an uplink VLC system model with intelligent reflecting mirror which help in focusing the reflected rays of light to the receiver. The transmit power analysis shows that the use of IRM makes uplink transmission at high data rates possible while meeting safety considerations.
- The achievable data rate performances are analyzed with a transmit power constraint.
- The analytical and simulation results show that the IRM elements influence the coverage area of uplink transmission assuming fixed Ergodic capacity (EC) requirements.
- It is demonstrated that our proposed system with IRM outperforms the DF relay-based VLC system.

Authorized licensed use limited to: DELHI TECHNICAL UNIV. Downloaded on February 07,2024 at 06:53:45 UTC from IEEE Xplore. Restrictions apply.
© 2024 IEEE. Personal use is permitted, but republication/redistribution requires IEEE permission. See https://www.ieee.org/publications/rights/index.html for more information.

This article has been accepted for publication in IEEE Wireless Communications Letters. This is the author's version which has not been fully edited and content may change prior to final publication. Citation information: DOI 10.1109/LWC.2024.3353218



(a) (b) (c)

Fig. 1: (a) System model, (b) Orientation of IRM, (c) LED-Eye configuration

II. System Model

We consider an uplink VLC system in a room of dimensions $l_w \times l_b \times l_h$ as depicted in Fig. 1 (a). The (X, Y, Z) coordinates of the transmitter and receiver in the room are denoted by (x_a, y_a, z_a) and (x_u, y_u, z_u), respectively. The uplink receiver is embedded on the ceiling, and the IRM is mounted on the wall in the $X = 0$ plane. The IRM consists of 'N' number of IRM elements of size $h_p \times b_p$ as depicted in Fig. 1 (b). The vertical and horizontal spacing between the elements is denoted by Δh_p and Δb_p, respectively.

A. VLC LOS link

The channel gain of the LOS VLC link is given by [9],

$$H_{LOS} = \frac{A(m+1)R_p}{2\pi d^2}\cos^m(\alpha)U(\beta)G(\beta)\cos(\beta) \quad (1)$$

where, $U(\beta)$ is optical filter gain, $G(\beta)$ is optical concentrator gain, 'A' is the physical area of the photodetector (PD), R_p is responsivity of the PD, 'd' is the euclidean distance between transmitter and receiver, 'α' is the angle of irradiance of the VLC system, and β is the angle of incidence (with $H_{LOS} = 0$ for $\beta > \psi_c$). Here, ψ_c is a field of view (FOV) at the semi-angle of the concentrator. $\phi_{1/2}$ denotes the LED's semi-angle at half power and m is Lambertian order of emission and is calculated as, $m = \frac{-\ln 2}{\ln(\cos(\phi_{1/2}))}$. Optical concentrator gain $G(\beta)$ is given by [9] as, $G(\beta) = \frac{f^2}{\sin^2(\psi_c)}$ for $0 \le \beta \le \psi_c$ and $G(\beta) = 0$ for $\beta > \psi_c$ where f is an internal refractive index. Here, distance d is given as $d = \sqrt{(x_a - x_u)^2 + (y_a - y_u)^2 + (z_a - z_u)^2}$.

With a change in the orientation of the transmitter, α does not vary, but β is highly affected. Thus, β can be defined using the device's polar and azimuth angle as γ and ω respectively [10]. Thus, $cos(\beta) = \frac{x_a - x_u}{d}\sin(\gamma)\cos(\omega) + \frac{y_a - y_u}{d}\sin(\gamma)\sin(\omega) + \frac{z_a - z_u}{d}\cos(\gamma)$. Based on results obtained experimentally in [10], the Laplace distribution can be used to model γ with mean as 41^o and 9^o as the standard deviation. The range of γ can be typically defined in $\left[0, \frac{\pi}{2}\right]$. The uniform distribution between $[-\pi, \pi]$ is followed by ω [10].

B. IRM Aided Link

When a signal strikes on IRM, each IRM element intelligently reconfigures its surface orientations independently to focus the transmitted signal to the receiver which enhances the strength of the received signal. Here, it is considered that the IRM knows the position of the receiver. Position vector (x_r, y_r, z_r) can be used to locate the position of IRM element. The IRM elements are rotated with vertical and horizontal angles denoted by ϕ and ξ respectively in $[\frac{-\pi}{2}, \frac{\pi}{2}]$. The channel gain of the signal reflected from the n-th mirror [8]

$$H_{IRM}(\phi,\xi) = \frac{A(m+1)R_p}{2\pi^2 (d_r^a)^2 (d_r^u)^2}\rho_{irm} dA_w \cos^m(\alpha_r^a) \times U(\beta)G(\beta)\cos(\beta_r^a)\cos(\beta_u^r)\cos(\alpha_u^r) \quad (2)$$

Here, ρ_{irm} is the reflection coefficient of IRM, d_r^a and d_r^u is the distance of receiver and transmitter respectively from IRM reflection spot, dA_w is the small reflection area of n-th IRM element. The channel gain $H_{IRM}(\phi,\xi) = 0$ for $\beta > \psi_c$. $cos(\alpha_u^r) = \frac{x_r - x_u}{d_r^u}\sin(\phi)\cos(\xi) + \frac{y_r - y_u}{d_r^u}\cos(\phi)\cos(\xi) + \frac{z_r - z_u}{d_r^u}\sin(\xi)$ and $cos(\beta_u^r) = \frac{x_r - x_u}{d_r^u}\sin(\gamma)\cos(\omega) + \frac{y_r - y_u}{d_r^u}\sin(\gamma)\sin(\omega) + \frac{z_r - z_u}{d_r^u}\cos(\gamma)$. Here, $d_r^a = \sqrt{(x_a - I_x)^2 + (y_a - I_y)^2 + (z_a - I_z)^2}$ and $d_r^u = \sqrt{(I_x - x_u)^2 + (I_y - y_u)^2 + (I_z - z_u)^2}$. If a perfect reflecting surface is considered, then $\beta_r^a = \beta_u^r$ and $\alpha_r^a = \alpha_u^r$. IRM element reflecting spot position is denoted by $I = (I_x, I_y, I_z)$ and can be obtained using position vector

$$I = \begin{bmatrix} I_x \\ I_y \\ I_z \end{bmatrix} = \begin{bmatrix} 0 \\ y_a + \frac{b_p}{2} + (i-1)(b_p + \Delta b_p) \\ z_a + \frac{h_p}{2} + (j-1)(h_p + \Delta h_p) \end{bmatrix} \quad (3)$$

III. Theoretical Analysis

The received signal at the receiver is $y = hx + w$ where, x is the transmitted signal, $w = w_0 + w_1$ and $w_0 \sim (0, \sigma^2)$ is the thermal and amplifier noise which consists of independent additive white Gaussian noise (AWGN) samples, and $w_1 \sim (0, \varsigma^2\sigma^2)$ is the input dependent AWGN noise with scaling factor ς. Shot noise is regarded as input-dependent noise. Further, w_0 and w_1 are independent to each other, $h = H_{LOS}$ for VLC system without IRM and $h = \Xi(\phi,\xi)$ for IRM-aided VLC system and $\Xi(\phi,\xi) = \left(H_{LOS} + \sum_{n=1}^{N} H_{IRM_n}(\phi,\xi)\right)$.

A. Achievable Data Rate and Transmit Power

The achievable data rate (ADR) of the IRM-aided VLC system can be characterized by the lower bound [11]

$$R_{VLC}^{IRM}(\phi,\xi) = B\log_2\left[1 + \frac{e}{2\pi}\frac{p\left(\Xi(\phi,\xi)\right)^2}{q\eta B}\right] \quad (4)$$

Authorized licensed use limited to: DELHI TECHNICAL UNIV. Downloaded on February 07,2024 at 06:53:45 UTC from IEEE Xplore. Restrictions apply.
© 2024 IEEE. Personal use is permitted, but republication/redistribution requires IEEE permission. See https://www.ieee.org/publications/rights/index.html for more information.

This article has been accepted for publication in IEEE Wireless Communications Letters. This is the author's version which has not been fully edited and content may change prior to final publication. Citation information: DOI 10.1109/LWC.2024.3353218

where p is the transmitted power of the optical source, q is the ratio of transmitted optical power to electrical power, B is the bandwidth, and the power spectral density of the noise is η. Typically, the value of q is 3 [6]. Similarly, the achievable data rate for a system without IRM can be given as

$$R_{VLC} = B\log_2\left[1+\frac{e}{2\pi}\frac{p\left(H_{LOS}\right)^2}{q\eta B}\right] \tag{5}$$

By using (4) and (5), transmit power for an IRM-aided system and system without IRM can be obtained as $p(\phi,\xi) = \frac{2\pi}{e}\frac{q\eta B}{(\Xi(\phi,\xi))^2}\left(2^{\frac{R_{VLC}^{IRM}(\phi,\xi)}{B}}-1\right)$ and $p = \frac{2\pi}{e}\frac{q\eta B}{(H_{LOS})^2}\left(2^{\frac{R_{VLC}}{B}}-1\right)$ respectively.

B. Coverage Area and Ergodic Capacity

In this subsection, the effect of IRM on coverage area by keeping EC as a constraint has been discussed. In order to derive the expression for EC, the position of the receiver can be modeled using random variable r_i which is uniformly distributed inside the circular area with a maximum radius of r_{max}. The probability density function (PDF) of r_i is expressed as $f_{r_i}(r_i) = \frac{2r_i}{r_{max}^2}$. Based on geometry, $cos(\alpha) = cos(\beta) = \frac{l_h}{d}$ and $d = \sqrt{r_i^2+l_h^2}$. Thus, (1) can be rewritten by taking $\mathcal{P} = \frac{AR_pU(\beta)G(\beta)}{2\pi}$ as

$$H_{LOS} = \mathcal{P}\frac{(m+1)l_h^{m+1}}{(r_i^2+l_h^2)^{\frac{m+3}{2}}} \tag{6}$$

Similarly, by considering $\tilde{\mathcal{P}} = \frac{(m+1)\rho_{irs}dA_w\cos(\beta_u^r)\cos(\alpha_u^r)}{\pi(d_r^u)^2}$, (2) can be rewritten as

$$H_{IRM} = \mathcal{P}\tilde{\mathcal{P}}\frac{(m+1)l_r^{m+1}}{\left(\sqrt{l_r^2+r_i^2}\right)^{m+1}} \tag{7}$$

Using the transformation of random variables, PDF of the channel gain H_{LOS} and H_{IRM} can be obtained as

$$f_{H_{LOS}}(h) = \frac{2\left[\mathcal{P}(m+1)l_h^{m+1}\right]^{\frac{2}{m+3}}}{r_{max}^2(m+3)}h^{\frac{-2}{m+3}-1} \tag{8}$$

$$f_{H_{IRM}}(h_{IRM}) = \frac{2l_r^2(\mathcal{P}\tilde{\mathcal{P}})^{2/(m+1)}}{r_{max}^2(m+1)^{(m-1)/(m+1)}}h_{IRM}^{-\frac{m+3}{m+1}} \tag{9}$$

The signal to noise ratio (SNR) is $\gamma_v = \gamma_1+\gamma_2$. γ_1 is the SNR of direct LOS link and is given by $\gamma_1 = \bar{\gamma}H_{LOS}^2$ and γ_2 is the SNR contributed by the IRM paths and it is given as $\gamma_2 = \bar{\gamma}\sum_{n=1}^{N}(H_{IRM_n})^2$. Considering all the paths from IRM to be identical and independently distributed (i.i.d), thus, γ_2 is modified as $\gamma_2 = \bar{\gamma}NH_{IRM}^2$, where $\bar{\gamma} = \frac{\mu^2p^2}{\sigma^2}$. And, here, μ is electrical to optical conversion efficiency.

The PDF of γ_1 and γ_2 are obtained respectively in (10) and (11) as

$$f_{\gamma_1}(\gamma_1) = \mathcal{H}\left(\gamma_1\right)^{-\frac{m+4}{m+3}} \tag{10}$$

$$f_{\gamma_2}(\gamma_2) = \tilde{\mathcal{H}}\left(\gamma_2\right)^{\frac{-(m+2)}{(m+1)}} \tag{11}$$

Here, $\mathcal{H}$ and $\tilde{\mathcal{H}}$ are respectively defined as

$$\mathcal{H} = \frac{\bar{\gamma}^{1/m+3}\left[\mathcal{P}(m+1)l_h^{m+1}\right]^{\frac{2}{m+3}}}{r_{max}^2(m+3)} \tag{12}$$

$$\tilde{\mathcal{H}} = \frac{l_r^2(\mathcal{P}\tilde{\mathcal{P}})^{2/(m+1)}}{r_{max}^2(m+1)^{(m-1)/(m+1)}}\left(\sqrt{\bar{\gamma}N}\right)^{\frac{(m+5)}{(m+1)}} \tag{13}$$

The Ergodic capacity is given as $EC = \mathbb{E}\left[\log_2(1+\gamma_v)\right]$, where $\mathbb{E}[.]$ is Expectation operator.

Lemma 1. *The EC without IRM and with IRM are respectively denoted as EC_{VLC} and EC_{VLC}^{IRM} and given by* (14) *and* (15) *respectively where, $G_{p,q}^{m,n}(\cdot)$ denotes the Meijer-G function [12].*

$$\begin{aligned}EC_{VLC} =& -\frac{m+4}{m+3}\mathcal{H}\log_2(1+\gamma_1)\gamma_1^{-\frac{m+4}{m+3}-1}\\ &-\frac{\mathcal{H}}{\ln 2}G_{2,2}^{1,2}\left(\gamma_1|_{-\frac{1}{m+3},0}^{1,-\frac{1}{m+3}}\right)\end{aligned} \tag{14}$$

$$\begin{aligned}EC_{VLC}^{IRM} =& \frac{-2\mathcal{H}\tilde{\mathcal{H}}(m+2)\log_2(1+\gamma_v)}{m(m^2+6m+7)^{-1}(m+3)^2}\gamma_v^{\frac{-(6m+4)}{(m+3)(m+1)}}\\ &-\frac{2\mathcal{H}\tilde{\mathcal{H}}(m+1)(m+2)}{m(m+3)\ln 2}G_{2,2}^{1,2}\left(\gamma_v|_{\frac{-2(m+2)}{(m+1)(m+3)},0}^{1,\frac{-2(m+2)}{(m+1)(m+3)}}\right)\end{aligned} \tag{15}$$

Proof. For a system without IRM, $N=0$ is substituted in (13) and hence, γ_v becomes $\gamma_v = \gamma_1$. Thus, (10) can be used in order to derive the EC for system without IRM. Hence, it can be written as

$$EC_{VLC} = \int_0^\infty \log_2(1+\gamma_1)f_{\gamma_1}(\gamma_1)d\gamma_1 \tag{16}$$

By plugging (10) in (16), and as $\gamma_v = \gamma_1$, the obtained expression

$$\begin{aligned}EC_{VLC} =& -\frac{m+4}{m+3}\mathcal{H}\log_2(1+\gamma_1)\gamma_1^{-\frac{m+4}{m+3}-1}\\ &-\frac{\mathcal{H}}{\ln 2}\int(1+\gamma_1)^{-1}\gamma_1^{-\frac{1}{m+3}-1}d\gamma_1\end{aligned} \tag{17}$$

Based on identity [[12], Eq. (8.4.2.5)]

$$\begin{aligned}EC_{VLC} =& -\frac{m+4}{m+3}\mathcal{H}\log_2(1+\gamma_1)\gamma_1^{-\frac{m+4}{m+3}-1}\\ &-\frac{\mathcal{H}}{\ln 2}\int\gamma_1^{-\frac{1}{m+3}-1}G_{1,1}^{1,1}\left(\gamma_1|_0^0\right)d\gamma_1\end{aligned} \tag{18}$$

Next, by using the identity in [12], derivation of (14) is completed.

For a system with IRM, $\gamma_v = \gamma_1+\gamma_2$. Here, γ_1 and γ_2 are independent. With the use of (10) and (11) and applying random variable transformation, the PDF of γ_v is obtained as

$$f_{\gamma_v}(\gamma_v) = \frac{2\mathcal{H}\tilde{\mathcal{H}}(m+1)(m+2)}{m(m+3)}\left(\gamma_v\right)^{\frac{-(m^2+6m+7)}{(m+3)(m+1)}} \tag{19}$$

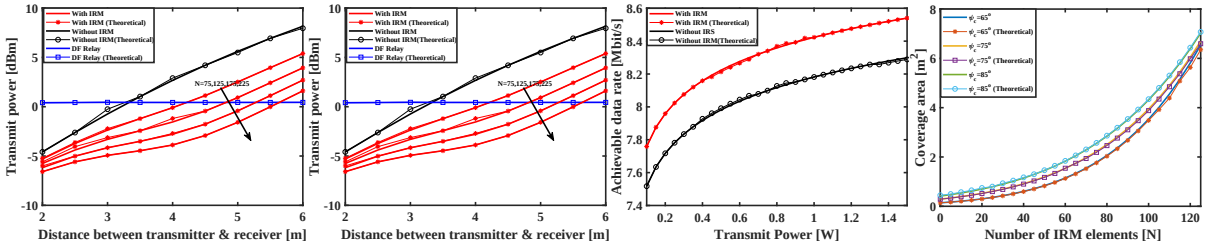
EC for a system with IRM is derived using

$$EC_{VLC}^{IRM} = \int_0^\infty \log_2(1+\gamma_v)f_{\gamma_v}(\gamma_v)d\gamma_v \tag{20}$$

By substituting (19) in (20), and based on the series expansion of $(1+z)^{-1}$ and neglecting higher order terms as they are

Authorized licensed use limited to: DELHI TECHNICAL UNIV. Downloaded on February 07,2024 at 06:53:45 UTC from IEEE Xplore. Restrictions apply.
© 2024 IEEE. Personal use is permitted, but republication/redistribution requires IEEE permission. See https://www.ieee.org/publications/rights/index.html for more information.

This article has been accepted for publication in IEEE Wireless Communications Letters. This is the author's version which has not been fully edited and content may change prior to final publication. Citation information: DOI 10.1109/LWC.2024.3353218



(a) (b) (c) (d)

Fig. 2: The performance metric: (a) Power transmit needed to achieve the data rate of 8 Mb/s, and for the peak transmit power of 1.5 W: (b) EE characteristic (c) ADR versus transmit power (d) Impact of IRM elements on coverage area.

insignificant [13]. And, further using Eq. (8.4.2.5) of identity [12], the obtained expression is

$$EC_{VLC}^{IRM} = \frac{-2\mathcal{H}\tilde{\mathcal{H}}(m+2)\log_2(1+\gamma_v)}{m(m^2+6m+7)^{-1}(m+3)^2}\gamma_v^{\frac{-(6m+4)}{(m+3)(m+1)}} - \frac{2\mathcal{H}\tilde{\mathcal{H}}(m+1)(m+2)}{m(m+3)\ln 2} \times \int (\gamma_v)^{\frac{-(m^2+6m+7)}{(m+3)(m+1)}} G_{1,1}^{1,1}\left(\gamma_v|_0^0\right) d\gamma_v \quad (21)$$

With the use of identity in [12], the final expression (15) is derived and hence proof of Lemma 1 is completed. ■

Remark. *Ergodic capacity with IRM, N, and r_{max} are related and can be inferred from* (15)*. Keeping EC constant, the number of IRM elements (N) can be varied and it is observed that there is a drastic improvement in the coverage area.*

C. Energy Efficiency

Energy efficiency (EE) is always a vital parameter while designing and proposing any system. Therefore, in this sub-section energy aspect is considered, and it is shown that IRM can be very effective in improving the EE of the system. It was shown in [14] that EE can be calculated by using (22) and (23) for systems without IRM and with IRM respectively.

$$EE_{VLC} = \frac{R_{VLC}B}{p + P_T + P_R} \quad (22)$$

$$EE_{VLC}^{IRM} = \frac{R_{VLC}^{IRM}B}{p + P_T + P_R + NP_I} \quad (23)$$

Here, power dissipation due to hardware components at the transmitter and receiver are denoted by P_T & P_R, respectively and P_I is the power dissipation of individual IRM elements.

D. Eye Safety

Eye safety is an important consideration and a major challenge while designing an uplink VLC system. Thus, in this section with the help of analysis, sufficient evidence is presented to guarantee eye safety based on the practical parameter values. A mathematical expression of irradiance for the human eye is obtained.

In Fig. 1 (c), d_{le} is the distance between LED and the eye, α_e is the angle formed by the eye pupil and the origin, the eye pupil's radius is r_e and s is the distance made by the angle $\phi_{1/2}$ and given as, $s = d_{le}\tan(\phi_{1/2})$. The portion of the optical power emitted by the LED source that actually falls onto the eye pupil is calculated in order to show eye safety in our proposed work. Radiation pattern $\mathcal{R}_{LED}$ of a generalized lambertian source is given as, $\mathcal{R}_{LED} = \frac{m+1}{2\pi}\cos^m(\alpha)p$, where $\frac{-\pi}{2} \leq \alpha \leq \frac{\pi}{2}$ is zenith angle. The amount of the emitted power I_{rad} irradiating the eye pupil is

$$I_{rad} = \int_0^{2\pi}\int_0^{\alpha_e} \mathcal{R}_{LED}\sin(\alpha)d\alpha d\phi_l \quad (24)$$

Substituting $\mathcal{R}_{LED}$ expression in (24), I_{rad} is obtained as

$$I_{rad} = \left[1 - cos^{m+1}(\alpha_e)\right]p(\phi,\xi) \quad (25)$$

where, $\alpha_e = \arctan\left(\frac{r_e}{d_{le}}\right)$. The irradiance of the human eye, E_{eye} is expressed as

$$E_{eye} = \frac{I_{rad}}{\pi r_e^2} \quad (26)$$

The eye safety specified standards show that E_{eye} must be less than $100W/m^2$ [2]. In the next section, extensive computer simulations are presented to demonstrate the efficacy of IRM in overcoming the eye irradiance problem.

Remark. *E_{eye} is related to I_{rad} and it can be clearly observed from* (25) *that I_{rad} depends on $p(\phi,\xi)$. Further, based on $\Xi(\phi,\xi)$ and transmit power of the IRM-aided system it can be depicted that E_{eye} depends on IRM channel gain and the number of IRM elements. Thus, with the application of the IRM, the E_{eye} value reduces which ensures eye safety.*

IV. Results and Analysis

The dimensions of the room is considered to be $(5m \times 5m \times 3m)$ with a single uplink transmitter and receiver. The plane of uplink transmitter is $0.5m$ above the floor of the room and can be located anywhere on that plane. The dimensions of each IRM element is $(0.6cm \times 1cm)$ and there is 15×15 i.e., 225 IRM elements. The horizontal and vertical separation between each IRM element is considered to be 0. All other simulation parameters [6] are summarized in Table I.

Table I: Simulation Parameters

Parameter	Value	Parameter	Value
R_p	0.53 A/m	ρ_{irm}	0.95
A	1 cm^2	B	200 MHz
$U(\beta)$	1	f	1.5
ψ_c	85^o	$\phi_{1/2}$	70^o
η	10^{-21} A^2/Hz	r_e	2 mm

Fig. 2 (a) shows that the transmit power required to attain a required data rate (of 8 Mbps) can decrease significantly

Authorized licensed use limited to: DELHI TECHNICAL UNIV. Downloaded on February 07,2024 at 06:53:45 UTC from IEEE Xplore. Restrictions apply.
© 2024 IEEE. Personal use is permitted, but republication/redistribution requires IEEE permission. See https://www.ieee.org/publications/rights/index.html for more information.

This article has been accepted for publication in IEEE Wireless Communications Letters. This is the author's version which has not been fully edited and content may change prior to final publication. Citation information: DOI 10.1109/LWC.2024.3353218

when IRM is used. This fact has been verified by extensive simulation for different required uplink VLC data rates. In Fig. 2 (a), it can be clearly deduced that with the application of IRM, the transmit power requirements of the source reduces. Fig. 2 (a) also shows that an increase in the number of IRM elements results in more reduction in the required transmit power and can also overpower the DF relay assisted system.

One of the major issues with the uplink VLC transmitter is that the practical transmit power which is required to send information to the receiver is significant enough to cause irradiance to the human eye. However, this problem is tackled with the deployment of IRM as it reduces the transmit power requirements. The lower required transmit power makes the irradiance value much lower, even below the limit specified by the standard for eye safety [2]. Transmitted power is taken to be 1.5 W and distance between LED source and human eye, d_{le} is 200 mm and remaining parameter values are mentioned in the Table I. In order to calculate the irradiance of eye, (26) is used. According to the eye safety standard [2], specified E_{eye} must be less than 100 W/m^2. However, our obtained value of E_{eye} is 9.833 W/m^2 which is much lower than the specified standard limit.

For an ADR of 8 Mb/s, EE_{VLC}^{IRM} is 136.8 $Mb/Joule$, EE_{VLC} is 36.09 $Mb/Joule$ and EE in case of DF relay is 51.15 $Mb/Joule$ which shows that IRM-aided uplink VLC transmitter is much more energy efficient. This can also be clearly deduced from Fig. 2 (b) that the energy efficiency performance of the system with IRM is superior to that of the VLC system without IRM and DF relay assisted system. In this simulation, the values of P_T, P_R and P_I are taken to be $100mW$, $100mW$ and $5mW$ respectively.

It is clearly evident from Fig. 2 (b) that with $N = 225$, IRM aided uplink VLC system outperforms the DF relay-aided VLC system. The reason for this is that the DF relay node requires extra power to first receive the signal and thereafter decode and forward the data. On the other hand, IRM requires very low power to control and intelligently vary the rotations of IRM elements to improve the channel gain.

While designing an uplink transmitter, the transmitted power must satisfy two constraints. First, it should be enough to attain a certain required value of the data rate. Secondly (at the same time), this power should be within a limit to eradicate the irradiance problem.

Fig. 2 (c) indicates that the ADR of the system with IRM is superior to that without IRM for any transmit power within the transmit power limit of $p = 1.5W$ which is used in our work in order to eradicate the irradiance problem. The difference can be more significant if the value of N is further increased.

Expanding coverage area relies on a reliable signal over a wider area. Fixing peak transmit power to address irradiance issues means transmit power can not be increased to enhance the coverage. In VLC, NLOS signals are weak due to widespread dispersion. IRM concentrates these signals toward the receiver, boosting channel gain and extending signal reach compared to systems without IRM. As the quantity of IRM elements increases, an increasing number of dispersed rays are channeled toward the receiver, resulting in a substantial improvement in coverage area. With a fixed EC value of 4.5 nats, the coverage area of the proposed system is analysed by varying the number of IRM elements. In Fig. 2 (d), the impact of IRM on coverage area is shown with $EC = 4.5$ nats and for different values of ψ_c i.e, $65^o, 75^o$ and 85^o. A coverage area of 0.5 m^2 is achieved if $N = 0$ (without IRM) which is significantly low. Note that in order to eradicate the eye irradiance problem, we have considered a lower value of transmit power. As we increase the value of N, a much better coverage area is achieved even with this low transmit power. In this work with $N = 125$ and with $\psi_c = 85^o$ approximately $7m^2$ of the area is covered.

V. Conclusion

In this paper, a novel VLC uplink transmitter with IRM has been considered to combat the irradiance problem associated with the uplink VLC system. Further, the study has been carried out to show that IRM makes the uplink VLC system practical even with lower transmit power. All the analytical and simulation results clearly show that IRM helps in reducing the required transmit power and makes the system more energy efficient. By utilizing the reduced transmitted power, on one hand system achieves practical data rate and on the other hand outperforms the system without IRM. Additionally, IRM also helps in improving the coverage area of the uplink transmitter.

References

[1] L. Hanzo, H. Haas, S. Imre, D. O'Brien, M. Rupp, and L. Gyongyosi, "Wireless myths, realities, and futures: from 3g/4g to optical and quantum wireless," *Proceedings of the IEEE*, vol. 100, no. Special Centennial Issue, pp. 1853–1888, 2012.

[2] *BS EN 62471:2008, Photobiological Safety of Lamps and Lamp Systems, BSI British Standards Std., Sep.*, 2008.

[3] A. Jovicic, J. Li, and T. Richardson, "Visible light communication: opportunities, challenges and the path to market," *IEEE communications magazine*, vol. 51, no. 12, pp. 26–32, 2013.

[4] A. Burton, E. Bentley, H. Le Minh, Z. Ghassemlooy, N. Aslam, and S.-K. Liaw, "Experimental demonstration of a 10base-t ethernet visible light communications system using white phosphor light-emitting diodes," *IET Circuits, Devices & Systems*, vol. 8, no. 4, pp. 322–330, 2014.

[5] Y. Yang, Z. Zeng, J. Cheng, C. Guo, and C. Feng, "A relay-assisted ofdm system for vlc uplink transmission," *IEEE Transactions on Communications*, vol. 67, no. 9, pp. 6268–6281, 2019.

[6] S. Aboagye, T. M. Ngatched, O. A. Dobre, and A. R. Ndjiongue, "Intelligent reflecting surface-aided indoor visible light communication systems," *IEEE Comm. Letters*, vol. 25, no. 12, pp. 3913–3917, 2021.

[7] A. Thelen, "Design of a hot mirror: contest results," *Applied optics*, vol. 35, no. 25, pp. 4966–4977, 1996.

[8] A. M. Abdelhady, O. Amin, A. K. S. Salem, M.-S. Alouini, and B. Shihada, "Channel characterization of irs-based visible light communication systems," *IEEE Tran. on Comm.*, vol. 70, no. 3, pp. 1913–1926, 2022.

[9] X. Deng, K. Arulandu, Y. Wu, S. Mardanikorani, G. Zhou, and J.-P. M. Linnartz, "Modeling and analysis of transmitter performance in visible light communications," *IEEE Tran. on Vehicular Tech.*, vol. 68, no. 3, pp. 2316–2331, 2019.

[10] M. D. Soltani, A. A. Purwita, Z. Zeng, H. Haas, and M. Safari, "Modeling the random orientation of mobile devices: Measurement, analysis and lifi use case," *IEEE Transactions on Communications*, vol. 67, no. 3, pp. 2157–2172, 2018.

[11] J.-B. Wang, Q.-S. Hu, J. Wang, M. Chen, and J.-Y. Wang, "Tight bounds on channel capacity for dimmable visible light communications," *Journal of Lightwave Technology*, vol. 31, no. 23, pp. 3771–3779, 2013.

[12] A. Prudnikov, Y. Brychkov, and O. Marichev, *Integrals and Series. Vol.3: More Special Functions. Boca Raton, FL, USA: CRC Press*, 1999.

[13] I. S. Gradshteyn and I. M. Ryzhik, *Table of integrals, series, and products*. Academic press, 2014.

[14] C. Huang, A. Zappone, G. C. Alexandropoulos, M. Debbah, and C. Yuen, "Reconfigurable intelligent surfaces for energy efficiency in wireless communication," *IEEE transactions on wireless communications*, vol. 18, no. 8, pp. 4157–4170, 2019.

Authorized licensed use limited to: DELHI TECHNICAL UNIV. Downloaded on February 07,2024 at 06:53:45 UTC from IEEE Xplore. Restrictions apply.
© 2024 IEEE. Personal use is permitted, but republication/redistribution requires IEEE permission. See https://www.ieee.org/publications/rights/index.html for more information.

Potential and Achievement of Floating Solar Photo Voltage in India

Yash Dalal, Saksham Rana and Dr J P Kesari*

Mechanical Engineering Department, Delhi Technological University, Delhi, India
*Corresponding author: drjpkesari@gmail.com

Abstract. India's contributions to the development of alternative energy sources are substantial. India has almost tripled the capacity of its renewable energy installations over the last five to six years, with coastal wind and solar photovoltaic (PV) installations accounting for the vast bulk of this growth. Since land scarcity is a big challenge nowadays, it is an excellent idea to construct solar plants on rivers, lakes, and dams, which are otherwise idle water bodies. The progressive depletion of fossil resources and the ever-increasing need for electricity both pose serious obstacles to progress. The electricity generated by floating solar photovoltaic systems is significant. India has completed a number of large-scale projects, including the 100MW Ramagundam, Telangana project and the NTPC Simhadri Solar Plant. This investigation highlights the potential benefits and challenges of these plants. Feasibility analysis of 5MW FSPV at Somasila Dam, Andhra Pradesh is also done in this paper. Additional to this, the article gave the economic and technological analysis of floating solar photovoltaics, in addition to discussing several case studies.

Keywords: energy sources, photovoltaic, solar plants, solar photovoltaies

1 Introduction

Present day issues with electricity use and fossil fuel depletion are progressing quickly. Renewable energy comes mostly from the sun. Numerous large-scale projects have been constructed or are now in process in order to meet the growing demand for solar power in key markets including India, China, Japan, Singapore, and the United Kingdom.Since the availability of land is a key issue when it comes to setting up solar panels, unused water resources like lakes, dams, reservoirs, saltwater lakes and rivers may be utilised instead. The water won't evaporate, the blue-green algae won't multiply, the solar panels will cool down quickly, which will boost their efficiency, and the installation costs will go down. In addition, there are obstacles that arise during the establishment of floating solar PV, such as securing permission for the plant, determining who owns the water bodies, and dealing with the fact that strong winds may cause PV modules to shift in their optimal orientation.

China: When it comes to solar power, China is far and away the frontrunner. About 960 MWp of the world's total 1314 MWp comes from this nation. Huainan, in the south of Anhui province, is home to the world's biggest floating solar photovoltaic plant, with a capacity of 150 MW, providing electricity for 21,000 residences.

© The Authors, published by EDP Sciences. This is an open access article distributed under the terms of the Creative Commons Attribution License 4.0 (https://creativecommons.org/licenses/by/4.0/).

India. The solar energy industry in India is also booming. Ramagundam, Telangana is home to the world's biggest floating solar facility. It can produce 100MW at full capacity. In addition to the 450 GW NTPC Simhadri Floating Solar Project and the 10 kW West Bengal Floating Solar Power Plant, there are a number of other completed projects across the world. There are projects under process with a capacity of more than 1700 MW.

Japan. Japan created the first floating solar facility. Japan has several lakes and reservoirs and 73 of the 100 biggest floating solar plants (246MW) are in Japan. Yamakura Dam, Chiba, has the biggest solar facility. Saving 8000 tonnes of CO2 and powering roughly 5000 houses.

In this paper the potential and achievements of floating solar photovoltaics in India are covered in this article. In the II segment, we will go through the efforts and studies done in the past. Section III includes a comprehensive description of the various components of a floating solar PV system, as well as a technical analysis and an economic analysis. In section IV, we will explore both the advantages and the limitations of using solar PV on floating platforms. Feasibility analysis of Floating Solar PV 5MW project at Somasila Dam, Andhra Pradesh is carried out in section V. In section VI, we also talk about a variety of initiatives happening all around India. This work comes to a close with Section VII. Review of literature

Both integrated renewable energy systems and renewable energy systems are required in order to make use of the renewable supply that is now available [1,2]. Due to its capability of reducing dependency on nonrenewable resources, renewable energy sources play a significant role in the generation of electrical energy [3-6]. Renewable sources of energy are the most viable solution to the problem of meeting the growing demand for electricity (RE) [7,8]. The primary generators are from solar photovoltaic systems, wind power producing systems, fuel cells (FC), micro-turbines, and other renewable energy-based systems.

Renewable energy sources are being used in homes and businesses because to their reliability, availability, and environmental friendliness. Solar energy is steady, affordable, and promising. Its longevity, minimal maintenance, and pollution-free nature are advantages [9].

The Solar energy is the most common form of energy that can meet the demands of a community as a consequence of sustainable economic growth [10-17]. Increased demand for PV energy may be traced back to the enhanced efficiency of solar cells and the development of more reliable solar panel production methods [18-21].

Desalination plants that employ nonrenewable energy sources often power their solar generators on fossil fuels, adding to their impact on climate change and environmental damage [22].

2 Methodology

Components of Floating Solar PV System

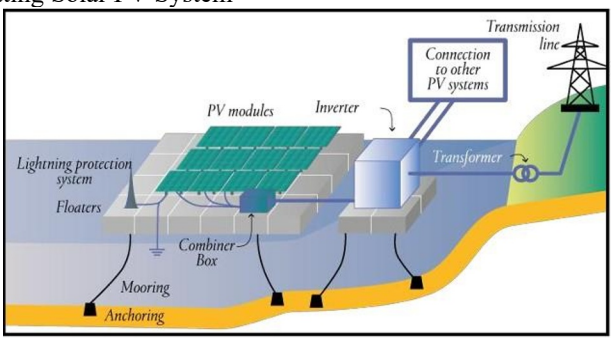


Fig. 1. Solar Floating PV[3]

2.1 Solar Module

Solar module is a collection of solar cells that converts sunlight into electricity. Monocrystalline solar modules and polycrystalline solar modules are two of the most common forms of solar panels. The solar panels powering the floating system are located at its peak.

2.2 Pontoon / Floating Structure

The floating pontoons are constructed from a polystyrene void, a concrete deck, and an aluminum gangway. The pontoon is sufficiently buoyant to float on the water and bear a significant weight. To put PV modules on, they are the most crucial part of any floating solar plant.

2.3 Underwater Cable

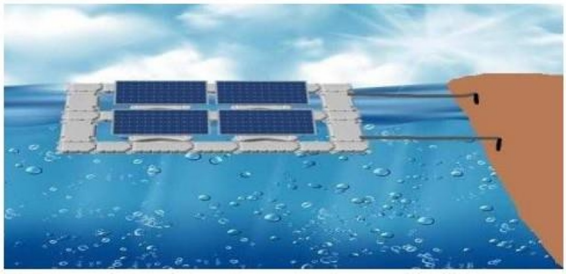
Electricity produced is transmitted through these lines to distribution substations. Cables can withstand intense heat and UV radiation because to their advanced construction. Also, these wires are often not harmed by the elements.

2.4 Inverter

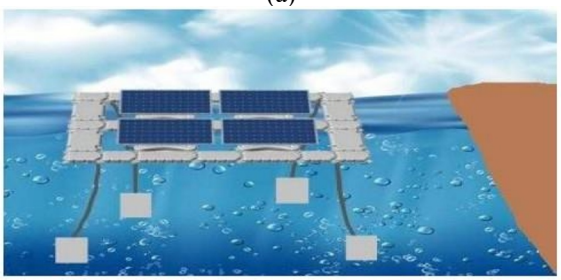
The energy produced by solar PV modules is direct current (DC), and it is transformed into alternating current (AC) by the inverters after being routed via a series of combiner boxes. Produced electricity can be used for common uses such as homes, farms, and businesses.

2.5 Mooring Structure

The mooring system prevents the floating structure from moving independently on the water. Mooring a floating building to an anchor fixes its position in reference to a point on the water's bottom and does not need any kind of connection to the land.



(a)



(b)

Fig. 2. (a) Bank Anchoring & (b) Bottom Anchoring[3]

2.6 Parameters to Analyse Technical Performance

2.6.1 Weather Forecast

Analysis of annual, monthly, and daily weather data from NASA's website or other reliable weather information sources is required. When selecting a place, it's important to take local climate conditions into account.

2.6.2 Cell Temperature

When exposed to sunlight, the internal temperature of a cell rises above that of its surrounding environment. Even at night, the temperature inside the cell is the same as the outside air.
By Duffle and Beckman equation,

$$\tau\alpha G_T = \eta_c G_T + U_T(T_c - T_a) \quad (1)$$

Where,
τ is the solar transmittance of PV array (%), α is the PV solar absorption (%), G_T is insolation striking on the solar panel (kWh/m^2), $\eta_c$is the efficiency (%), U_T is heat transfer coefficient (kWh/m^2 ^{0}C), T_c& T_a are cell and ambient temperatures (^{0}C).

2.6.3 Performance Ratio (PR)

Simply said, it is the ratio of the total power produced by the modules to the power provided by the direct solar radiations. The National Renewable Energy Laboratory (NREL) recommends a PR value between 0.6 and 0.9.

$$\text{Performance Ratio (PR)} = E_{FPV} / GA\eta \quad (2)$$

Where E_{FPV} is the total power by modules (kWh), G is the incident solar radiation (kWh/m^2), A is module area (m^2) and η is efficiency (%)

2.6.4 Capacity Utilisation Factor (CUF)

It is the ratio of PV module production in a year to maximum output under perfect circumstances.

$$\text{CUF= Actual Output/ (8760 * installed capacity of plant)} \quad (3)$$

2.6.5 Energy Demand

Multiplying time and quantity of electrical devices yields total energy consumption.

$$E = P * n * t \text{ (kWh/day)} \quad (4)$$

Where,
E is the energy demand, P is the power (watt), t is the time (hr), n is no. of items

2.7 Parameters to Analyse Economic Performance

2.7.1 LevelisedCost of Electricity (LCOE)

This his variable is used to determine the lifetime cost of electricity produced by the PV installation. This criterion is frequently used to cost comparisons with other plant types and capacities.

$$LCOE = \frac{CAPEX + \sum_{i=1}^{N} \frac{OPEX}{(1+r)^i}}{\sum_{i=1}^{N} \frac{E_{FPV,i}}{(1+r)^i}(1-k)^i} \quad (5)$$

Where,
CAPEX is the total investment, OPEX is the variable investment with operating and maintenance cost, E_{FPV} is the total energy output, k is constant of degradation.

2.7.2 Internal Rate of Return (IRR)

By setting the Net Present Value (NPV) equal to zero, the internal rate of return may be determined. It is a crucial indicator of the project's potential for success. The greater the internal rate of return, the more money you will make.

2.7.3 Net Present Value (NPV)

The Net Present Value (NPV) of a project is calculated by subtracting its cash outflows from its cash inflows over the course of its lifetime.

$$\text{NPV}=\sum_{i=1}^{N}\frac{C_T}{(1+d)^i}-C_o \qquad (6)$$

Where, $C_O$is the total investment, d is discount and C_T is cash flow for a year.

2.7.4 Return On Investment(ROI)

The ROI measures how much money was made in comparison to how much was put into the venture. If the return on investment (ROI) for a project is more than 1, then the project is cost-effective.

$$\text{ROI} = (\text{Total Profit} / \text{Total Investment}) * 100 \qquad (7)$$

2.7.5 Payback Period

Payback Period refers to the time frame after which a project begins to generate a profit. Calculated as the percentage of the project's total cost that will be recouped within a year.

3 Benefits And Challenges of Floating Solar Photovoltage

- Increased plant production and decreased running expenses are additional benefits for farm developers, hastening the return on investment. This new source of revenue generated by these plants is a boon for water body owners. Large transmission losses are mitigated since the produced energy is mostly used by neighboring communities. The local community would benefit from these plants because they would increase the standard of living by making reliable energy for irrigation requirements more accessible.
- Direct sunlight prevents water from evaporating, coal is used less often to produce electricity, fewer greenhouse gases are released, land scarcity is a major issue that can be mitigated by installing solar plants on bodies of water, and the efficiency of the solar modules is improved because they cool off more quickly when submerged in water than when placed on land.
- Installation, operation and maintenance challenges include issues with water body ownership, authorization for floating solar PV plants, and increased expenditures for moving floating platforms. Anchoring and mooring systems must be carefully coordinated in floating solar PV since PV module orientation might change due to high wind loads. The location of these facilities on water bodies makes maintenance and operation relatively challenging.
- Long-term floating solar PV plants may affect water ecosystems and harm aquatic habitats. These plants shade water bodies, lowering dissolved oxygen. This may affect local marine farmed food chains. Algae cannot develop without sunshine because surface warmth is reduced. Algal toxin in excess may harm humans and animals.

4 Feasibility analysis Of FSPV at Somasila Dam, Andhra Pradesh

The feasibility of 5MW floating solar plant is proposed in this section at Somasila Dam located at Penna River, Nellore District Andhra Pradesh, India (Latitude: 14.4893^{0}N and Longitude: 79.3037^{0}E). The reservoir area is 212.28 km^2.



Fig. 3. Somasila Dam Satellite View, Andhra Pradesh[21]

Table 1: Meteorological Parameters of SomasilaDam[20]

Month	Solar Irradiation kWh/m^2	T-Amb ^{o}C	Wind Velocity m/s
January	146.5	24.9	0.80
February	154.5	26.6	0.90
March	189.5	29.1	1.20
April	189.9	30.9	1.40
May	186.6	33.6	1.50
June	156.7	32.1	1.70
July	139.7	31.3	1.69
August	141.2	30.6	1.59
September	139.6	29.7	1.20
October	132.2	28.8	0.90
November	110.1	26.3	0.90
December	116.8	25.2	0.99
Year	1803.3	29.1	1.2

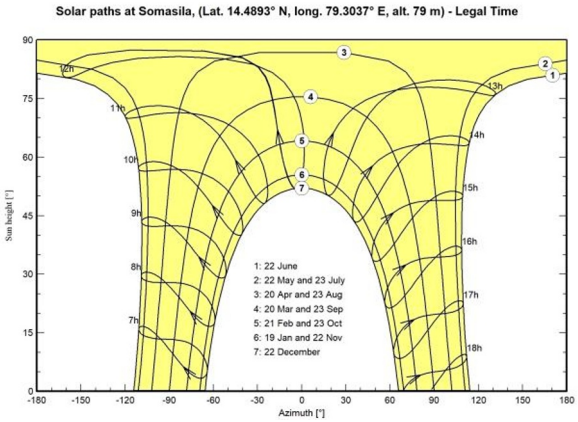


Fig. 4. Solar Pathsat Somasila Dam[20]

Table 2: Monocrystalline Solar Module Specifications

Rated Power	400 W
Voltage across open circuit	37.06 V
Cells connected in parallel (N_P)	2
Cells connected in series (Ns)	54
Maximum Current	12.8 A
Maximum Voltage	26.8 V
Temperature Coefficient	-0.35% / ^{0}C
Short Circuit Current	13.71 A
Module Area	1.96 m^2

Table 3: 5MW Plant Specifications

Inverters	34
DC Power	5000 kWp
AC Power	4250 kWac
Inverter Capacity	125 kW
PV Module	400 W
No. of Modules	12500
Modules in string	34
No. of strings	500

By MATLAB(coding) the proposed floating solar plant is analysed with the specifications in Table 2 and Table 3.

P-V graphs are drawn, it is observed that the minimum output power of the PV module is 177.3W in the month of November and the maximum PV output power is 300.42W in month of April. It is also observed that power is increased from month of January to May and then decreased due to winter season as observed in September to December.

The output power depends on both temperature and irradiations. The performance ratio is varies in between 0.832-0.861.A grid output of 8349.3 MWh and a total array output of 8574.2 MWh are produced yearly by the proposed 5 MW FSPVproject[19].

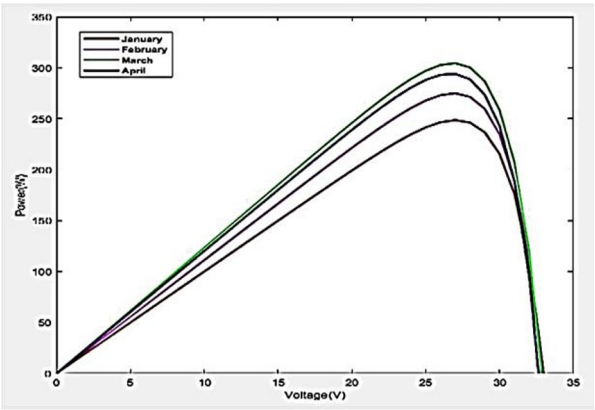


Fig. 5. P-V graph (January-April)

CASE STUDIES

4.1 100MW Floating Solar Power Plant – Ramagundam, Telangana

The 100 MW capacity of this project makes it the biggest floating solar power installation in India. There are a total of 11,200 solar panels spread over 40 sections. Each section is of 2.5 MW. The HT breaker, Inverter, and Transformer may all be found on the floating platform.

- Location – Ramagundam, Telangana
- Project Budget – 423 Crores through BHEL
- Area – 500 Acres
- CO_2Emission Avoided – 2,10,000 tons / year
- H_2O Saving –32.5 lakh cubic meters / year
- Coal Consumption Avoided – 1,65,000 tons / year

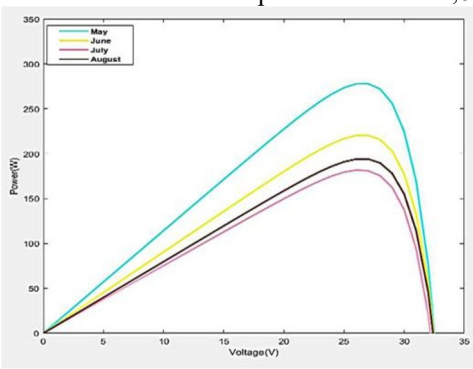


Fig. 6. P-V graph (May-August)

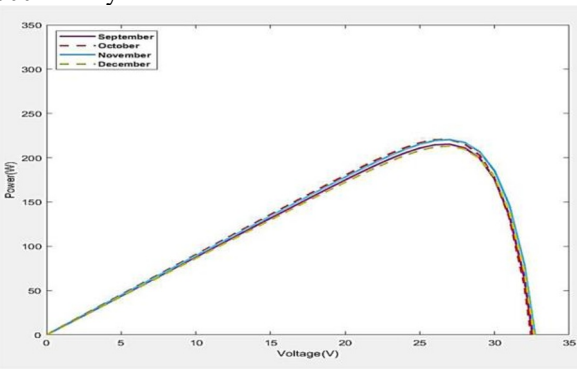


Fig. 7. P-V graph (September-December)



Fig. 8. 100MW Solar Power Plant[12]

4.2 10kW Floating Solar Power Plant – West Bengal



Fig. 9. 10kW Solar Power Plant[15]

The solar power facility is the first of its kind in India. The facility uses 1 kW fibreglass modules to generate around 14 MWh of solar energy each year. In this endeavour, polycrystalline modules are utilised.

- Location – New Town, West Bengal
- Annual Energy Yield – 1765 kWh
- No. Of Modules – 40
- CO_2 Savings –2942 kgs / year
- Installer – Vikram Solar Limited

4.3 NTPC Simhadri Floating Solar Project



Fig. 10. NTPC Simhadri Solar Plant[14]

The 15MW capacity of the NTPC Simhadri facility generates over 450 GW of electricity. Its 109,800 modules are enough to power almost 7,000 average American households for a whole year.

- Location –Simhadri Reservoir, Andhra Pradesh
- CO_2 Savings – 46000 tons

- H_2O Savings –1364 million litres
- Area – 75 Acres
- Budget – 114 Crores

An innovative floating solar power plant is in the works for Khandwa, Madhya Pradesh. It will become the world's biggest floating solar plant once it reaches full capacity in 2022–2023. The estimated cost of the project is about Rs. 3000 Cr.

5 Conclusion

India has an abundance of renewable energy from the sun. Since fossil fuels will eventually become extinct, it will be vital to find novel ways to meet the growing need for electricity, and here is where floating solar photovoltaic plants come in. The benefits of floating solar PV power plants over land-mounted photovoltaic systems, such as less water evaporation, greater efficiency, and reduced CO_2 emissions, have led to their widespread adoption in many countries. Countries with semiarid and arid regions have a severe water scarcity problem; one approach is to install FPV modules to reduce water loss via evaporation. The cost of solar energy is often lower in these countries. India's most significant accomplishment is the Telangana state's Ramagundam floating solar plant. As India's biggest floating solar installation, the facility can produce 100 megawatts of electricity.Analysis of proposed 5MW plant at Somasila Dam, Andhra Pradesh shows thatthe plant generates the grid output of 8349.3 MWh and a total array output of 8574.2 MWh are produced yearly by the proposed 5MW FSPV project. It is feasible to built 5MW FSPV at Somasila Dam.
In addition, in 2023, India plans to build a 600-megawatt (MW) floating solar plant in Khandwa, Madhya Pradesh. The project's estimated cost of Rs. 3,000 crores suggests that solar power in India has a promising future.

6 Acknowledgment

The authors would like to express their gratitude to the Mechanical Engineering Department and Associate Prof. Dr J P Kesari at Delhi Technological University, India.

References

1. R. Giri, A. Kumar et al, Floating Solar Collector for Hybrid Hydro-Solor Power Plant, 2018 International Conference of Smart City and Emerging Technology (ICSCET), Mumbai, pp1-5, doi: 10.1109/ICSCET.2018.8537271
2. Yoshikawa, K., et al., Silicon heterojunction solar cell with interdigitated back contacts for a photoconversion efficiency over 26%. 2017. 2(5): p. 1-8.
3. Vijay Kumar, et al, SOLAR PHOTOVOLTAIC ON WATER BODIES IN RAJASTHAN DOI: 10.1109/ICPS52420.2021.9670248
4. Sahu, A., et al., Floating photovoltaic power plant: A review. 2016. 66: p. 815-824.
5. Ayna Banik, Anubrata Sengupta, Scope, Challenges,Opprtunities and Future Goal Assesment of Floating Solar Park, 2021 Innovations in Energy Management and Renewable Sources (IEMRE), DOI: 10.1109/IEMRE52042.2021.9386735
6. Slimani, K., Khoulji, S., & Kerkeb, M. L. (2023). Advancements and challenges in energy-efficient 6G mobile communication network. In E3S Web of Conferences (Vol. 412, p. 01036). EDP Sciences.

7. G Mamatha, P S Kulkarni, Feasibility analysis of Floating Solar Photovoltaic Plant at Srisailam in Andhra Pradesh: India 2021 IEEE 2nd International Conference on Smart Technologies for Power, Energy and Control (STPEC) doi: 10.1109/STPEC52385.2021.9718627
8. Ayush Goel et al, FLOATING SOLAR PHOTOVOLTAIC SYSTEM 2022 pg 2230-2239
9. Swati S Gurfude, Chappidi Bhavitha, Deshetty Tanusha, Dhayapule Mounika, Suma Pyate Gouda Kake, Myadam Sai Sudha, and P S Kulkarni," Techno-economic analysis of 1MWp Floating Solar PV Plant", Smart Technologies for Power, Energy and Control (STPEC), VNIT Nagpur, India 2020.
10. Sahu, A., et al., Floating photovoltaic power plant: A review. 2016. 66: p. 815-824.
11. Current status, Solar Energy, Ministry of New and Renewable Energy (MNRE), Government of India, Accessed on: July 5th, 2021. [Online]. Available: https://mnre.gov.in/solar/current-status
12. A. Goswami and P. K. Sadhu, "Degradation analysis and the impacts on feasibility study of floating solar photovoltaic systems," Sustainable Energy, Grids and Networks, vol. 26, p. 100425, 2021.
13. India's largest floating solar power project commissioned. (https://pib.gov.in/PressReleasePage.aspx?PRID=1838489)
14. Eshaan Gupta et al, ANALYSIS ON FLOATING SOLAR POWER PLANT pg 518-522
15. NTPC Simhadri Floating Solar Project, India. (https://www.power-technology.com/marketdata/ntpc-simhadri-floating-solar-project-india/)
16. Floating solar power plant in West Bengal, India (https://www.vikramsolar.com/case-studies/floating-solar-power-plant-in-west-bengal-india/)
17. Akash Kumar Shukla, Sudhakar K, Prashant Baredar, et al. BIPV in Southeast Asian countries – opportunities and challenges. Renewable Energy Focus. 21;25−32.
18. Deepak Bishoyi, Sudhakar K. Modeling and performance simulation of 100 MW LFR based solar thermal power plant in Udaipur India. Resource-Efficient Technologies. 2017;10:216−226.
19. Hyder Farhan, Sudhakar K, Rizalman Mamat. Solar PV tree design: A review. Renewable and Sustainable Energy Reviews. 2018;82(2018):1079−1096.
20. Vijay Kumar, et al, SOLAR PHOTOVOLTAIC ON WATER BODIES IN RAJASTHAN
21. PVsyst(Version 7.3) Software used to calculate meteorological data.
22. Google Earth (https://earth.google.com/) for statellite view.

J. Inst. Eng. India Ser. B
https://doi.org/10.1007/s40031-023-00975-z

ORIGINAL CONTRIBUTION

PV-Fed Single-Phase Induction Motor for Irrigation Application

Dawda Bojang[1] · Eleyde Nhantumbo[1] · Monika Verma[1] · Ashish Kulkarni[1]

Received: 11 May 2023 / Accepted: 13 December 2023
© The Institution of Engineers (India) 2024

Abstract This research paper examines the feasibility of using solar energy as an alternative power source for a water pump motor in rural areas that have limited access to electricity and conventional fuels. The proposed system comprises solar cells or photovoltaic (PV) modules, a boost converter, a single-phase inverter, and an electric motor connected to a pump. The problems associated with the primary source of energy, i.e., solar radiation, are changing dynamics, nonlinearities, and uncertainties due to the occurrence of daily or seasonal variations. To manage these, the proposed research employs advanced control strategies and industrial electronics in the system. The technique of maximum power point tracking (MPPT) is implemented in order to optimize the system's efficiency. The simulation environment used to study the proposed system is designed via MATLAB/Simulink 2022a software. The experimental study suggests that the system has the potential to conserve energy and offer an effective irrigation solution in rural areas.

Keywords Water pump motor · Photovoltaic cell · Boost converter · Inverter · Maximum power point tracking (MPPT)

Introduction

For reducing the degrading environmental impact of fossil fuels, it becomes extremely essential for researchers to overview the merits of renewable energy sources, particularly solar energy. Despite its promising abundance and sustainability, solar radiation has two main drawbacks: high costs and its unavailability, as the need arises [1, 2]. The control of solar photovoltaic (PV) systems has two primary objectives: to obtain the maximum available PV power through maximum power point tracking (MPPT) control and to utilize the PV power for different applications [3]. A few examples of areas of application where maximum power point tracking (MPPT) is utilized are solar water pumping systems [4], hybrid renewable energy systems [5], and solar-powered electric vehicles [6]. In the literature, the till-date implemented techniques in order to feed the irrigation system are shown in Table 1.

Our system relies on solar energy to power the irrigation process, making it environmentally friendly and cost-effective. Furthermore, our irrigation system can operate in remote locations, like Boane Village in Maputo Mozambique where access to electricity is limited or nonexistent, providing a sustainable solution for agriculture and water management in this area.

The aspiration of this study is to create a PV-fed single-phase induction motor for an irrigation system. In the system, the electrical energy obtained from PV panels is fed to the boost converter integrated inverter system. The MPPT methodologies are utilized for maximizing the power output. Thus, an integrated DC–AC converter is used to power the induction motor. Once various components of the system are installed, it can generate efficient power and easily supply it to the load.

This paper is organized into a total of four sections. The motivation and historical background are described in "Introduction" section. The system characteristics and its configuration are explained in "The System Illustration and Working Configuration" section. Next, "Designed Model, Working Conditions and Corresponding Results" section

✉ Monika Verma
monikaverma.evrt@dtu.ac.in

[1] Department of Electrical Engineering, Delhi Technological University, Shahbad Extenion, Delhi, Delhi 110042, India

Published online: 10 January 2024

Table 1 Historical background of strategies implemented for irrigation application

References	Strategy used	Remarks
Jia et al. [7]	Micro-irrigation system	Improved crop yield and water use efficiency in arid areas
Gheysari et al. [8]	Mulching	Reduced soil moisture loss and increased crop yield
Wang et al. [9]	Fertigation	Simultaneous application of fertilizers and water increased crop growth and yield
Thabet et al. [10]	Aquaponics	Combined aquaculture and hydroponic farming to increase water use efficiency and nutrient recycling
Mirzaei et al. [11]	Deficit irrigation	Reduced water use without significantly reducing crop yield
Eldeiry et al. [12]	Variable rate irrigation	Uses satellite or aerial imagery to monitor crop water use and guide irrigation decisions
Chen et al. [13]	Remote sensing	Adjusts water application rates based on soil and crop conditions to optimize water use

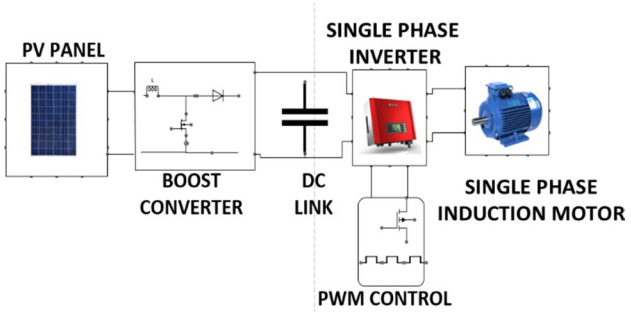


Fig. 1 Representation of the overall studied system

presents the designed MATLAB model for the system and the corresponding results. The concluding statements and future scopes are presented in "Conclusions" section.

The System Illustration and Working Configuration

This section confers the technical configuration of the proposed system. This research focuses on the incremental conductance (IC) technique as well as the perturb-and-observe (P&O) method for MPPT control [14]. The overall system is represented in the form of block diagram in Fig. 1.

Design of PV Array

The proposed system employs a 2.2 kW single-phase induction motor to drive a hydraulic pump. Neglecting motor losses, the PV array capacity should be correspondent to the capacity of motor. Here, a PV array is chosen to be of 6 kW as it is a common rule of thumb used in the design and sizing of standalone PV systems that the system needs to be 2 or 2.5 times higher than the required output voltage [15, 28].

The PV output power, P, is computed by Eq. (1). Here, N_p represents number of parallel connected PV modules, I_{mp} is the current produced by a single PV module working at its peak power point, N_s represents number of series connected

Table 2 Specifications of PV panels

S. No.	Parameter	Value
1.	Peak power point (P_{Max})	250 W
2.	Peak power voltage (V_{MP})	31 V
3.	Peak power current (I_{MP})	8.06 A
4.	Short-circuit current (I_{SC})	8.55 A
5.	Open-circuit volts (V_{OC})	37.6 V

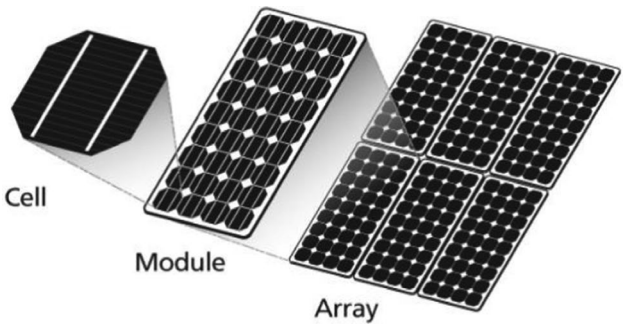


Fig. 2 Representation of the PV array used in the proposed system

PV modules, and V_{mp} represents the voltage produced by a single PV module running at its peak power point.

$$P = \left(N_p \times I_{mp}\right)\left(N_s \times V_{mp}\right) = 6\ \text{kW} \tag{1}$$

Thus, the characteristics of the PV panels are shown in Table 2. The representation of PV array utilized for this study is shown in Fig. 2. Assuming V_{OC}, open-circuit voltage from the panel nearby DC-link voltage, series and parallel connected modules are chosen as 14 and 2. This selection has been made based on the availability of modules in the research area. The importance of finding out V_{OC} of PV module is that it indicates the highest possible voltage producible by the module, to ensure maximum power transfer efficiency. Hence, the computed V_{oc} is found to be 460 V.

Computation of DC-Link Voltage

The calculation of DC-link voltage is important in power electronics because it affects the overall size, cost, and efficiency of the conversion system, and the selection of components and their operating characteristics.

In a single-phase voltage–source–inverter system, the DC-link voltage, V_{DC}^{*}, is estimated using Eq. (2). Where V_{LL} is the line-to-line voltage.

$$V_{DC}^{*} = \frac{2\sqrt{2}V_{LL}}{\sqrt{3}} = \frac{2\sqrt{2}\times 230}{\sqrt{3}} = 375\ \text{V} \tag{2}$$

Hence, V_{DC} is the chosen DC-link voltage, which is taken as 400 V. Choosing a large value for chosen DC-link voltage in a power electronic system provides a safety margin against voltage drops and transient events, and can be helpful in refining the system performance.

Design of DC-Link Capacitor

The DC-link capacitor performs the duty of providing appropriate energy at the transition times, for example, instant of fall in radiation or instant of load increment. Therefore, the DC-link capacitor, C_{DC}, is calculated using Eq. (3).

$$\frac{1}{2}C_{DC}\left[V_{DC}^{*2} - V_{DC}^{2}\right] = 3\alpha VIt \tag{3}$$

where C_{DC} = capacitance, V_{DC}^{*} is calculated DC-link voltage, V_{DC} is chosen DC-link voltage, α = efficiency factor, V is motor output voltage, I is motor output current, and t = time. Hence, the computed value of C_{DC} is found out to be 2026 µF.

Design of DC–DC Boost Converter

The presence of DC–DC boost converter has its importance in a power electronic system because it enables the step-up of a low voltage to a higher voltage, which is essential in many applications. The boost converter's duty cycle is a key parameter that is required to be designed attentively to ensure the desired output voltage and efficiency of the converter.

The desired duty cycle is thus computed using Eq. (4), where D = duty cycle, V_{DC} = input voltage of converter, and V_{mp} = voltage at which PV module works at its peak power point. The inductor is designed using Eq. (5), where ΔI_1 is ripple current and f_s is switching frequency.

$$D = \frac{V_{DC} - V_{mp}}{V_{DC}} \tag{4}$$

$$L_m = \frac{V_{mp}D}{\Delta I_L f_s} \tag{5}$$

The duty ratio is found to be 0.0675 and the inductor value is 1.875 mH. Hence, we have chosen 3 mH, since a higher value for the inductor in a DC–DC boost converter can help reduce output ripple, improve efficiency, and provide a safety margin against unexpected load conditions.

Computation of the Pump Parameters

For the chosen hydraulic pump, K_{pump}, the constant of proportionality, is computed using Eq. (6):

$$K_{pump} = \frac{T_L}{\omega_r^2} \tag{6}$$

where T_L indicates load torque to hydraulic pump, which is equivalent to the torque produced by the induction motor during steady-state condition; and ω_r indicates motor's rotational speed. At rated operating conditions of 14.69 Nm of torque and 1430 rpm of speed, the value of K_{pump} is calculated as 6.55×10^{-4} Nm/rps^2.

Implementation of MPPT

The MPPT algorithms continuously track the point of operation and adjust the load to retain the module operation at its peak value point, regardless of the changes in solar irradiance levels or temperature [16]. The irradiance levels of Boane, Maputo City, in Mozambique are studied and implemented in this paper. Boane is situated close to the equator. As a result, it experiences high levels of solar irradiation throughout the year, with relatively consistent levels of sunlight and daylight hours [17].

The daily irradiation levels at Boane Maputo depend on factors such as the particular time of day, season, and weather conditions [18]. On a clear day, the daily irradiation levels at Boane Maputo is relatively high, with peak levels occurring in the afternoon time. The yearly irradiation levels at Boane Maputo are also generally high, with an average annual irradiation level of around 5.5 kWh/m^2/day. This makes it a potentially suitable location for the installation of solar power systems, with the potential for high energy output throughout the year [19]. The variation in irradiation levels at Mozambique is shown in Fig. 3.

Perturb-and-Observe Technique

The basic idea behind the P&O algorithm is to, first, disturb the PV operating point by a small amount and then observe

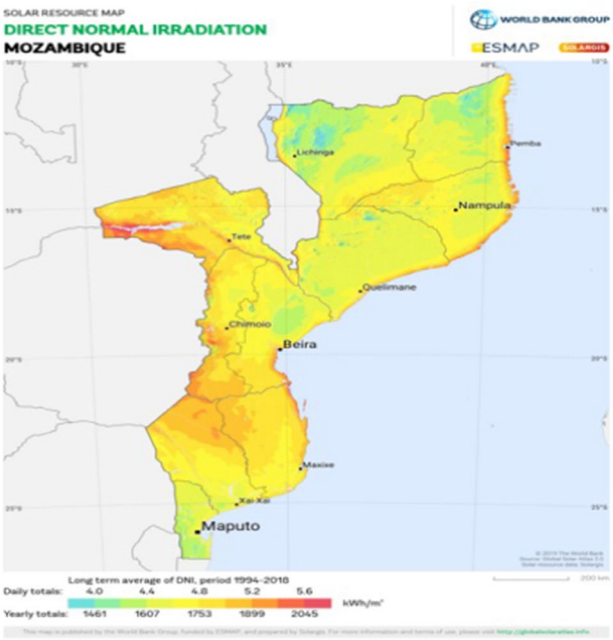


Fig. 3 Irradiation levels at Mozambique per city

its effect on the power output. This algorithm then shifts the functional point in increasing power direction until the peak power point is attained. The process flow for P&O technique is presented in Fig. 4.

This technique is relatively simpler to implement and works effectively under steady-state conditions [20]. However, the algorithm can cause the PV system to oscillate around the MPP when irradiance and temperature change rapidly. These oscillations can decrease the system efficiency and cause additional wear and tear on the PV module [20, 21]. Although P&O works effectively under steady-state conditions and Boane, Maputo City, has stable conditions, we cannot fully rely on it [22]. It is because weather conditions can change suddenly due to global warming. So, using IC will ensure our system has the best performance in case of any change in the irradiance and temperature.

Incremental Conductance Method

The IC method includes the measurement and comparison of the instantaneous and incremental conductance of the module to study its terminal voltage [23]. When the value of instantaneous conductance is found to be equal to value of incremental conductance, it indicates that the attainment of peak power point. The module output power increases with a rise in the terminal voltage within the operating limits [24]. After the peak power point, the output power declines. At the peak power point, the power curve is found to be having zero value of slope. The process flow for IC methodology is presented in Fig. 5.

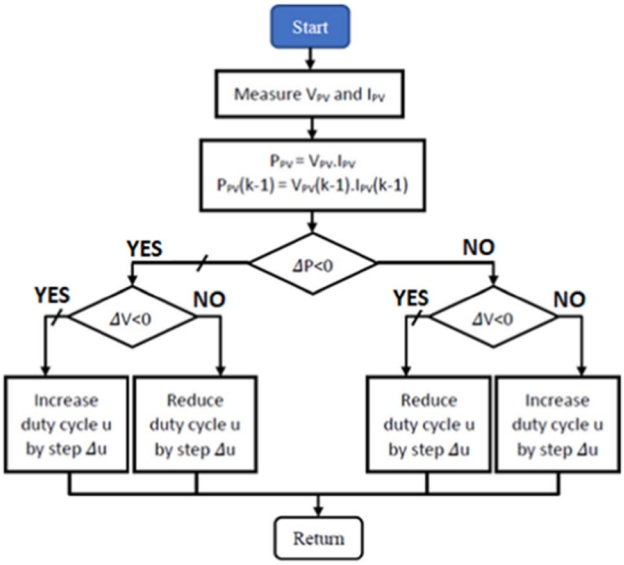


Fig. 4 Process flow of P&O technique; V_{PV} = PV on-load voltage, I_{PV} = current generated by PV array, P_{PV} = power delivered by PV module, k = instant at which power consumed is being studied, Δ = change in particular quantity, u = duty cycle of the controller, 'Return' block indicates the process has to return to the start point to measure PV quantities again until MPP is reached

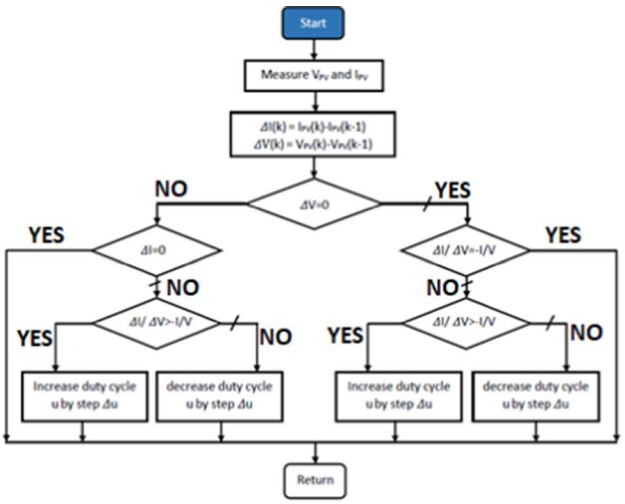


Fig. 5 Process flow of IC method; V_{PV} = PV on-load voltage, I_{PV} = current generated by PV array, P_{PV} = power delivered by PV module, k = instant at which power consumed is being studied, Δ = change in particular quantity, u = duty cycle of the controller, 'Return' block indicates the process has to return to the start point to measure PV quantities again until MPP is reached

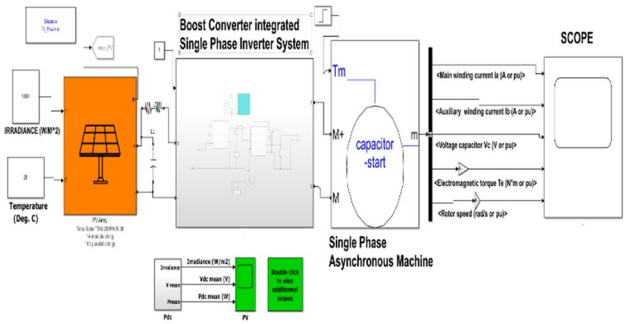


Fig. 6 Designed model of the overall system in MATLAB/Simulink

Designed Model, Working Conditions and Corresponding Results

This section presents the designed model, working of the system and the tools/techniques used in the model along with the analyzed conditions.

Tools and Techniques Used in the Proposed System

The proposed system model is designed via MATLAB/Simulink R2022a tool. This designed model is shown in Fig. 6. The pulse width modulation (or PWM) technique is utilized to operate the VSI system [25, 26]. The assumption of zero initial conditions is considered for all parameters to ensure exact monitoring of system performance [27].

The system is composed by a PV array connected to a boost converter then to an DC–AC inverter, which feeds the motor.

Working of the System

The proposed system is implemented by considering the reference temperature of 25 °C and the irradiance of Boane, Maputo City. The output parameters of single-phase asynchronous induction motor namely: main winding current, auxiliary winding current, stator voltage capacitor, electromagnetic torque, and motor speed at different irradiance levels (0.2 kW/m^2, 1 kW/m^2, and 5 kW/m^2), maintaining constant temperature of 25 °C, are analyzed.

Condition 1 For 5 kW/m^2, i.e., Boane, Maputo City, irradiance, the system response is presented in Fig. 7.

- It is observed from the response that the main winding current is higher than auxiliary winding current due to the presence of the capacitor in the circuit, which is used to create a phase shift between the main winding and the auxiliary winding.

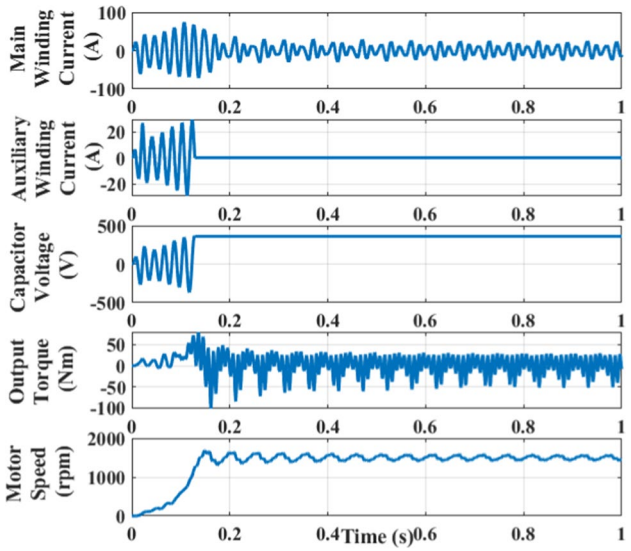


Fig. 7 Response of designed model for Boane, Maputo City, Mozambique

- This phase shift creates a rotating magnetic field that starts the motor.
- During the starting process, the capacitor is used to provide an initial boost to the starting torque of the motor.
- As the motor starts to rotate, the capacitor is no longer needed and its effect on the circuit diminishes.
- At this point, the current in the main winding becomes dominant, and the current in the auxiliary winding decreases. This is why the main current is lower than the auxiliary current during normal operation.
- The voltage across capacitor, at start, is fluctuating. After 0.2 s, it stabilizes, because the stator voltage capacitor, in a single-phase asynchronous induction motor, is utilized to create a phase shift between main and auxiliary winding. This creates a rotating magnetic field that starts the motor and provides an initial boost to the starting torque.
- The motor has a high starting torque and low speed.
- The starting torque is produced by the interaction of two magnetic fields, one produced by the stator winding and the other by the rotor bars.
- During running period, the motor has a lower torque compared to the starting period.
- The torque is maximum at zero speed and gradually decreases as the speed increases.
- The motor reaches its maximum torque at the starting point and then operates at a lower torque during the running period.

The torque required for the single-phase induction motor to drive the pump with a power of 2.2 kW would be between around 5.2 Nm and 8.4 Nm. The motor is operating within

an acceptable range of the rated speed of 1500 rpm (4 poles) (Fig. 7).

Condition 2 Similarly, after performing the simulation with difference irradiance levels (0.2 kW/m^2 and 1 kW/m^2), the results show that at lower irradiance levels, main and auxiliary winding currents, voltage of capacitor, torque and speed value decreases. This is due to the reduction in the motor's output power (see Figs. 8 and 9, respectively). The following observations were drawn:

- Using the P&O method, the ripple factor obtained in the output voltage was 0.48%.
- Using the IC method, the ripple factor obtained in the output voltage was 0.21%.
- The ripple present is the fluctuating AC component present in the output after rectification, and a lower ripple factor leads to higher efficiency in the output [28].
- The output current from the boost converter value is 0.8037 A for IC method and 0.4947 A for the P&O method.
- Specifically, with the same initial voltage from panels of 108.9 V, the IC method yields an output voltage from the boost converter of 284.9 V, while the P&O technique only yields an output voltage from boost converter of 259.9 V.
- The two methods are categorically compared and presented in Table 3.

Conclusions

The primary goal of this work is to develop a power electronics-controlled PV system that feeds a single-phase induction motor and a water pump for irrigation purposes at Boane, Maputo City. In this city, the irradiance per day is 5.5 kWh/m^2 for an average of 5 h. This aspect of city climate has been utilized in this study to realize the overall system.

Here, a controlled solar array system was developed to convert the available sunlight into electrical energy. The voltage energy levels were enhanced by a boost converter, which is integrated with an inverter. Thereafter, two types of MPPT techniques, the P&O method, and IC method, are employed to track the power output from the motor. Furthermore, we have performed calculations to determine the parameter values to be used on the system.

After performing the simulations, we have concluded that the IC method is better than the perturb-and-observe method as it gives higher output voltage and current values. Similarly, after performing the simulation, we successfully ran our single-phase induction motor aiming to connect a water pump [29].

In the future, the aim is to improve the system by developing hardware smaller in size compared to the one proposed in this paper. The future system is to be composed of 2 solar panels of 100 W each, a battery 100 Ah, a boost converter coupled with an inverter of at least 1000 W, and a Motor coupled with a pump of 746 W.

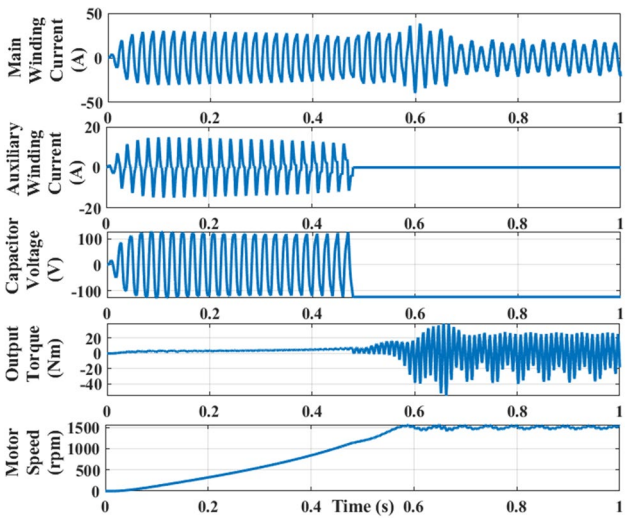


Fig. 8 Response of designed model for irradiance level of 0.2 kW/m^2

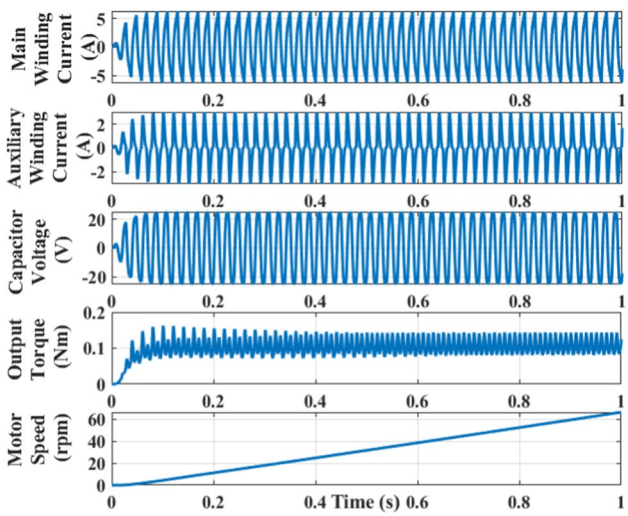


Fig. 9 Response of designed model for irradiance level of 1 kW/m^2

Table 3 Comparisons between P&O and IC method

Parameter	P&O method	IC method
Ripple in terminal voltage	More	Less
Response speed	Slow	Fast
Values of output voltage	Low	High

Acknowledgements This work is supported by the Centre of Excellence for Electric Vehicle and Related Technologies, Electrical Engineering Department, Delhi Technological University, Delhi.

Funding Not applicable.

Declarations

Competing Interests There are no competing interests.

References

1. M.A. Green, Solar cells: operating principles, technology, and system applications. IEEE J. Sel. Topics Quantum Electron. **6**(6), 1354–1360 (2000)
2. H. Wang, Y. Li, X. Wu, Challenges and solutions in autonomous vehicle control systems. IEEE Trans. Intell. Transp. Syst. **19**(12), 3929–3939 (2018)
3. A.M. Eltamaly, A review of maximum power point tracking algorithms for wind and solar photovoltaic systems. Renew. Sustain. Energy Rev. **76**, 839–854 (2017)
4. P. Kumar, P. Kumar, A. Sharma, An optimized MPPT technique for solar water pumping system, in *2016 IEEE International Conference on Advances in Electrical, Electronic and Systems Engineering (ICAEES), Putrajaya, Malaysia* (2016), pp. 250–253
5. A.R. Chilipi, R.M. Kamat, Performance analysis of solar water pumping system with maximum power point tracking, in *2018 International Conference on Sustainable Energy and Future Electric Transportation (SEFET), Pune, India* (2018), pp. 1–6
6. A.M. Alsharif, A.I. Alolah, A.A. Abdelsalam, Analysis of maximum power point tracking (MPPT) techniques for hybrid renewable energy systems, in *2018 2nd International Conference on Power and Embedded Drive Control (ICPEDC), Tlemcen, Algeria* (2018), pp. 1–6
7. W. Jia et al., A survey of machine learning for big data processing. IEEE Access **8**, 205161–205191 (2020). https://doi.org/10.1109/ACCESS.2020.3030297
8. K. Gheysari, M.R. Gholamian, M. Keshavarz-Ghorabaee, A fuzzy decision-making model for green supplier selection: a case study of the oil industry. IEEE Access **8**, 173026–173034 (2020). https://doi.org/10.1109/ACCESS.2020.3020584
9. X. Wang, Y. Li, Z. Li, Y. Zhang, Machine learning for energy consumption prediction: a review. IEEE Access **7**, 88393–88404 (2019). https://doi.org/10.1109/ACCESS.2019.2921129
10. M. Thabet, T.Y. Al-Naffouri, M.S. Alouini, Reinforcement learning for wireless networks: a comprehensive survey. IEEE Commun. Surv. Tutor. **23**(1), 568–612 (2021). https://doi.org/10.1109/COMST.2020.3007624
11. M.A. Mirzaei, M. Abedi, P. Ahmadi, IoT-based intelligent transportation systems: a comprehensive review. IEEE Internet Things J. **7**(5), 3875–3899 (2020). https://doi.org/10.1109/JIOT.2019.2956005
12. A.A. Eldeiry, A. Abou-Elnour, A. Elsaid, A.M. Alsumaiti, A novel method for multi-objective optimal sizing of renewable energy systems for residential applications. IEEE Access **8**, 160876–160889 (2020). https://doi.org/10.1109/ACCESS.2020.3024002
13. K. Chen, K. Xu, H. Wang, Z. Zhang, A survey on machine learning for intelligent transportation systems: applications, challenges, and opportunities. IEEE Trans. Intell. Transp. Syst. **22**(2), 760–780 (2021). https://doi.org/10.1109/TITS.2020.2994271
14. S.J. Alam, A.H.M. Zahirul Alam, M.A. Hannan, A. Mohamed, A comparative study of incremental conductance and perturb and observe MPPT algorithms for PV systems, in *2016 IEEE Region 10 Conference (TENCON), Singapore* (2016), pp. 2889–2892
15. K.H. Hussein, I. Muta, T. Hoshino, Maximum photovoltaic power tracking: an algorithm for rapidly changing atmospheric conditions. IEE Proc. Gener. Transm. Distrib. **142**(1), 59–64 (1995)
16. U. Sharma, S. Kumar, B. Singh, Solar array fed water pumping system using induction motor drive, in *2016 IEEE 1st International Conference on Power Electronics, Intelligent Control and Energy Systems (ICPEICES), Delhi, India* (2016)
17. J. Kulkarni, N. Kumar, B. Singh, Design and control of medium-voltage multilevel converter for direct grid integration of photovoltaic system. J. Inst. Eng. India Ser. B **102**, 203–212 (2021)
18. M.H. Krishna, S. Manmadharao, Grid integrated solar irrigation system by using BLDC motor pump set, in *2018 International Conference on Inventive Research in Computing Applications (ICIRCA)* (2018)
19. A. Bhowmik, et al., *Renewable Energy for Sustainable Development in India, Review on Status, Potential and Policies* (2012)
20. I. Dincer, Renewable energy and sustainable development: a crucial review. Renew. Sustain. Energy Rev. **4**, 157–175 (2000)
21. J. Chang et al., A review on the energy production, consumption, and prospect of renewable energy in China. Renew. Sustain. Energy Rev. **7**, 453–468 (2003)
22. D. Kraemer et al., High-performance flat-panel solar thermoelectric generators with high thermal concentration. Nat. Mater. **10**, 532–538 (2011)
23. A. Kay, M. Grätzel, Low cost photovoltaic modules based on dye sensitized nanocrystalline titanium dioxide and carbon powder. Sol. Energy Mater. Sol. Cells **44**, 99–117 (1996)
24. M.A. Green et al., Solar cell efficiency tables (version 39). Prog. Photovolt. Res. Appl. **20**, 12–20 (2011)
25. T. Chow, A review on photovoltaic/thermal hybrid solar technology. Appl. Energy **87**, 365–379 (2010)
26. M. Huang et al., Microencapsulated phase change slurries for thermal energy storage in a residential solar energy system. Renew. Energy **36**, 2932–2939 (2011)
27. J.W. Kimball et al., A system design approach for unattended solar energy harvesting supply. IEEE Trans. Power Electron. **24**, 952–962 (2009)
28. H. Mousazadeh, A. Keyhani, Optimum sizing of stand-alone photovoltaic systems considering reliability and uncertainty in load demand and renewable energy resources. IEEE Trans. Sustain. Energy **4**(2), 427–435 (2013). https://doi.org/10.1109/TSTE.2012.2227795
29. J. Kulkarni, N. Kumar, B. Singh, Control and design of seven-level cascaded multilevel converter for transformer-less large-scale photovoltaic integration. J. Inst. Eng. India Ser. B **102**, 203–212 (2020)

Publisher's Note Springer Nature remains neutral with regard to jurisdictional claims in published maps and institutional affiliations.

Springer Nature or its licensor (e.g. a society or other partner) holds exclusive rights to this article under a publishing agreement with the author(s) or other rightsholder(s); author self-archiving of the accepted manuscript version of this article is solely governed by the terms of such publishing agreement and applicable law.



Dawda Bojang



Ashish Kulkarni



Eleyde Nhantumbo



Monika Verma

Materials Advances

ROYAL SOCIETY OF CHEMISTRY

REVIEW

View Article Online
View Journal | View Issue

Check for updates

Cite this: *Mater. Adv.*, 2024, 5, 475

Recent advancement in the detection of potential cancer biomarkers using the nanomaterial integrated electrochemical sensing technique: a detailed review

Hema Bhardwaj,[a] Archana,[a] Ashab Noumani,[a] Jayendra Kumar Himanshu,[ab] Shreeti Chakravorty[a] and Pratima R. Solanki *[a]

Cancer is a leading cause of morbidity and mortality worldwide but early diagnosis, management or screening and treatment of cancer can significantly improve the survival rate of cancer patients. Oral cancer is the sixth most common cancer leading to approx. one-third of deaths worldwide. Oral cancer poses a serious threat due to its soaring case-fatality rate and metastatic characteristics and it is a type of head and neck cancer where cancerous tissue growth is located in the oral cavity. Also, lung cancer is the second most common cancer in the world with a five-year survival rate of only 15%. However, conventional techniques are available for cancer detection but these techniques are time consuming and involve a pretreatment process and sophisticated instruments. Therefore, technological advancement in the area of electrochemical sensors with miniaturization of point-of-care devices including nanomaterials has shown significant enhancement in overall sensing performance for cancer detection. Non-invasive diagnosis of cancer reduces the death risk of the disease or increases survival rate. Therefore, in this review article, the background of cancer, definition of the problem related to cancer, available conventional techniques for diagnosis and recent progress in the development of electrochemical sensors for cancer detection using nanomaterials are summarized. This review emphasizes on the use of an electrochemical sensing technique that can provide simpler, faster, non-invasive and ultraprecise detection of cancer biomarkers. Additionally, this review focuses on the recent literature on cancer detection and advancement in the diagnosis and treatment together with future perspectives on further advancements.

Received 30th August 2023,
Accepted 16th November 2023

DOI: 10.1039/d3ma00621b

rsc.li/materials-advances

Open Access Article. Published on 04 January 2024. Downloaded on 2/7/2024 7:04:31 AM.
This article is licensed under a Creative Commons Attribution 3.0 Unported Licence.

1. Introduction

According to the National Cancer Institute, cancer refers to a complex group of diseases characterized by the uncontrolled growth and division of abnormal cells.[1] These abnormal cells have the potential to invade and infiltrate nearby tissues and organs, interfering with their normal functioning, and can affect any organ or part of the body, and lead to cancer.[2] The development of cancer typically begins with genetic mutations or changes in the DNA of cells. When cancer cells divide and multiply, they form a mass of tissue called a tumor. Tumors can be classified as benign or malignant. Benign tumors are non-cancerous and generally do not spread to other parts of the body. They are usually localized and can often be surgically removed without causing significant harm. On the other hand, malignant tumors are cancerous and have the ability to invade the surrounding tissues and spread to distant sites in the body through the lymphatic system or bloodstream.[3] This process is known as metastasis. There are over 100 types of cancer that have been identified, each with its own unique characteristics, treatment approaches, and prognosis. Some common types of cancer include breast cancer, lung cancer, colorectal cancer, prostate cancer, skin cancer, and ovarian cancer, among many others.[4] Diagnosing cancer involves various methods such as imaging tests (*e.g.*, X-rays, CT scans, MRI), laboratory tests (*e.g.*, blood tests, tumor marker tests), and invasive procedures (*e.g.*, biopsies) to analyze tissue samples for the presence of cancer cells.[5–9] Common treatment modalities include surgery, radiation therapy, chemotherapy, targeted therapy, immunotherapy, and hormone therapy. In many cases, a combination of these treatments may be used to achieve the best possible outcome.[10]

[a] *Nano-Bio Laboratory, Special Centre for Nano Science (SCNS), Jawaharlal Nehru University, Delhi 110067, India. E-mail: pratimarsolanki@gmail.com, partima@mail.jnu.ac.in*
[b] *Department of Biotechnology, School of Life Sciences, Mahatma Gandhi Central University, Motihari, Bihar 845401, India*

© 2024 The Author(s). Published by the Royal Society of Chemistry

Open Access Article. Published on 04 January 2024. Downloaded on 2/7/2024 7:04:31 AM. This article is licensed under a Creative Commons Attribution 3.0 Unported Licence.

It is important to note that significant advancements have been made in cancer research and treatment over the years, leading to improved outcomes and increased survival rates for many types of cancer. Early detection, timely intervention, and access to quality healthcare services play crucial roles in improving prognosis and quality of life for individuals diagnosed with cancer.[11] The recent worldwide incidence of major types of cancer with new cancer cases as well as deaths is depicted in Fig. 1. In 2020, there were an estimated approximately 18 million new cancer cases and around 10 million cancer deaths worldwide.

The second-leading cause of mortality in India and the United States is cancer, which represents a serious global public health concern. Sadly, the 2019 coronavirus disease (COVID-19) pandemic has had a negative impact on cancer diagnosis and therapy. Cancer care has been delayed as a result of a number of issues, such as temporary closure of healthcare institutions, changes in employment and health insurance, and worries about COVID-19 exposure. The COVID-19 outbreak's peak in the middle of 2020 had the most effect, and the healthcare system has not yet fully recovered.[1,12] The Massachusetts General Hospital's surgical oncology operations provide an illustration of the scope of the



Hema Bhardwaj

Hema Bhardwaj is a post-doctoral fellow as a DBT-Research Associate at the Special Centre for Nanosciences, Jawaharlal Nehru University, Delhi, India. She received her PhD degree in chemical sciences from CSIR-National Physical Laboratory, Delhi, in December 2020. She worked as a guest lecturer at Delhi Technological University, Delhi. During her PhD, she received the prestigious Raman-Charpak Fellowship (RCF) awarded by CEFIPRA, Department of Science and Technology, India. She has worked as a RCF at ICBMS Department, Claude Bernard University Lyon1, France. She has published many research articles in peer-reviewed journals. Her research area involves nanomaterial based development of sensors/biosensors for cancer detection and developing microfluidic based multiplex detection system on a single platform.



Archana

Archana is a doctoral student at Special Centre for Nanoscience, Jawaharlal Nehru University. She completed her BSc (hons.) Microbiology from the University of Delhi in 2019 followed by her MSc in Biotechnology from the University of Mysore in 2021. At present she is working as a research scholar supported by DBT-JRF at Nanobio-Laboratory, Special Centre for Nanoscience, JNU, under the supervision of Dr. Pratima R Solanki. Her research area involves fabrication of electrochemical sensors for non-invasive diagnostic purpose. She has published a research article, a review paper, and two book chapters in internationally recognised journals and books.



Ashab Noumani

Ashab Noumani currently holds the position of a project associate at the Special Center for Nanoscience, Nano-Bio Laboratory, Jawaharlal Nehru University, New Delhi. His educational background includes BSc in Biotechnology, MSc in Biotechnology, and MTech in Nanoscience obtained from Jawaharlal Nehru University in 2023. He is presently working as a project associate under the guidance of Dr. Pratima R. Solanki. His primary research focuses on the development of nanomaterial based point-of-care devices for the identification of cancer biomarkers. He has contributed significantly in a review article in an internationally recognized journal.



Jayendra Kumar Himanshu

Jayendra Kumar Himanshu is a doctoral student at Mahatma Gandhi Central University. He completed his BSc Biotechnology from Jiwaji University in 2010 and MSc in Applied Microbiology from Vellore Institute of Technology in 2012. He also completed his MPhil in Life Sciences from Central University of Gujarat in 2015. Currently he is working as a research scholar at the Nanobio-Laboratory, Special Centre for Nanoscience, Jawaharlal Nehru University, under the co-supervision of Dr. Pratima R. Solanki. His research area involves fabrication of nanomaterial based electrochemical sensors for the detection of food contaminants. He has published a research article in an internationally recognised journal.

© 2024 The Author(s). Published by the Royal Society of Chemistry

Open Access Article. Published on 04 January 2024. Downloaded on 2/7/2024 7:04:31 AM.
This article is licensed under a Creative Commons Attribution 3.0 Unported Licence.

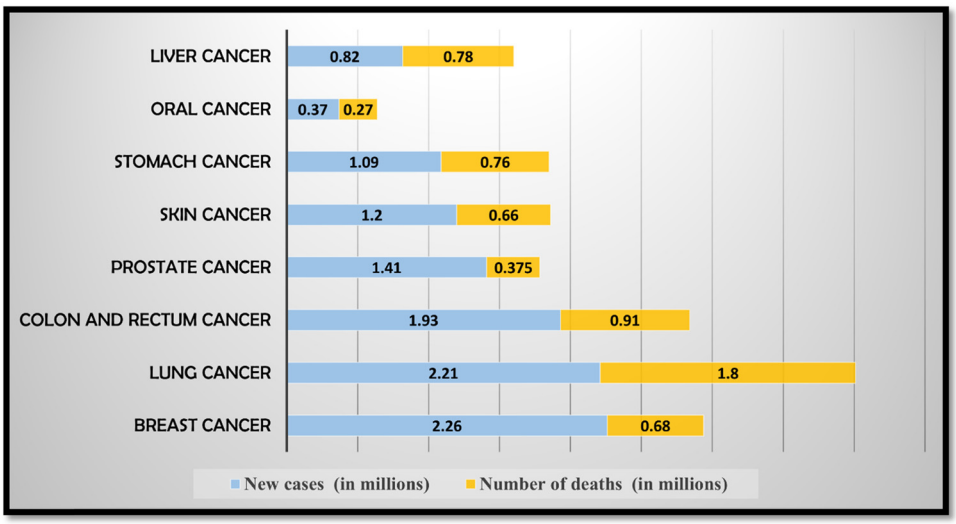


Fig. 1 The recent worldwide incidence of major types of cancer with new cases and deaths. There were an estimated approximately 18 million new cancer cases and around 10 million cancer deaths in 2020.

problem. These operations were only at 72% of the levels recorded in 2019 in the second half of 2020. Additionally, they only got to 84% in 2021, which was the slowest recovery rate among all surgical specialties. Potential effects of the delay in cancer detection and treatment include a rise in advanced-stage disease and fatality rates. Due to the delay in gathering complete data on cancer incidence and mortality, which normally takes two to three years, these harmful consequences may manifest gradually over time and will take several years to accurately assess at the population level. The pandemic disproportionate effect on communities of color is one factor that has received considerable attention. This inequality is a consequence of both direct and indirect effects of a number of things, including uneven socioeconomic situations, systemic inequalities, and restricted access to healthcare services. The detrimental consequences in these areas emphasize the urgent need for targeted measures and assistance to lessen the uneven impact of the epidemic on cancer treatment.[13–15]

According to a cancer survey, in 2018, 18.1 million cancer cases were diagnosed and 9.6 million cancer related mortalities were reported. Of all cancers, lung cancer has the highest mortality rate, followed by oral cancer, stomach cancer, liver



Shreeti Chakravorty

Shreeti Chakravorty recently completed her MSc in Biotechnology from the School of Biotechnology, Gautam Buddha University. She completed her BSc (Hons) Biotechnology from Vinoba Bhave University in the year 2020. After completing her MSc, she joined as a project assistant in 3K Nano LLP led by Dr. Pratima R Solanki. Her research area involves the development of sensors for the determination of sea food freshness.



Pratima R. Solanki

Dr. Pratima R. Solanki is working as an Assistant Professor at Special Centre for Nanoscience, Jawaharlal Nehru University, Delhi, India. Dr. Solanki received her PhD degree in biological sciences from Maharishi Dayanand University, Haryana, India. She worked as a postdoctoral fellow at National Physical Laboratory, Delhi, Institute of Genomics and Integrative Biology, Delhi, and Tokyo Institute of Technology (TIT), Japan. She has received the prestigious Fast Track Young Scientist Award from the Department of Science and Technology, Delhi, India. She is the co-author of more than 200 research papers published in peer-reviewed Journals and >25 international book chapters with 10867 citations and with an H-index of 56 (according to Google Scholar). She is actively engaged in the research and development of biosensors utilizing nanostructured materials for healthcare and environmental monitoring. She has received Visitor Award 2019 from the Hon'ble President of India.

Open Access Article. Published on 04 January 2024. Downloaded on 2/7/2024 7:04:31 AM. This article is licensed under a Creative Commons Attribution 3.0 Unported Licence.

Table 1 Type of cancer with estimated new cancer cases and estimated death across the globe and specifically in India

Cancer site	Cancer type	Estimated new cases in India	Estimated death in India	Estimated new cases in the world	Estimated death in the world
Oral cavity and pharynx	Tongue	42 220	19 350	120 140	54 680
	Mouth	114 600	50 230	422 440	50 230
	Pharynx	18 200	8500	95 000	45 000
	Other oral cavity	13 800	6300	54 000	24 000
Respiratory system	Larynx	11 000	5500	166 000	93 000
	Lung and bronchus	1 067 000	669 000	2 210 000	1 376 000
	Other respiratory organs	5000	2500	34 000	17 000

cancer and colorectal cancer.[16] One of the major issues leading to cancer fatalities is late and incorrect diagnosis of cancer cell and improper treatment.[17] According to analysis and research conducted by the World Health Organization, 80% or more of cancer patients can be successfully treated if they are diagnosed when the disease is still in its early stages.[18] Therefore, in view of the highest cancer cases and deaths of lung and oral cancer, this review article is focused on these two types of cancer, *i.e.* oral and lung cancer. Table 1 provides a brief summary of the type of cancer, and estimated new cancer cases and deaths that occurred worldwide as well as in India due to oral and lung cancer.

In the following sections, detailed information about oral and lung cancer including biology of cancer development, conventional techniques for diagnosis and the recent progress in the detection of oral and lung cancer using electrochemical sensors as well as future perspectives related to the monitoring or prognosis of oral or lung cancer is provided.

Oral cancer

Head and neck squamous cell carcinoma (HNSCC) is a type of cancer that arises from the squamous cells lining the mucosal surfaces of the head and neck region. It is a significant health concern worldwide, with a substantial impact on morbidity and mortality. Squamous cell carcinoma accounted for 85% of cases in the current study, and confirmation of the diagnosis is typically made at an advanced stage of the tumor, which lowers patient survival. The head and neck region includes the oral cavity (mouth), oropharynx (tonsils, base of the tongue), larynx (voice box), and hypopharynx (lower part of the throat).[19] Oral cancer is a significant malignancy that ranks sixth as the most common cancer globally.[20] Oral cancer poses a serious health challenge to the nations undergoing economic transition. In India, around 77 000 new cases and 52 000 deaths are reported annually, which is approximately one-fourth of global incidences.[21] The increasing cases of oral cancer are the most important concern for community health as it oral cancer is one of the common types of cancer in India. In the year 2012, the incidence of cancer of the oral cavity and lip reached approximately 300 000 cases, representing 2.1% of the total cancer burden; on the other hand, the reported cancer incidence in India 2023 was estimated to be 1.9 to 2.0 million, whereas the real incidence is 1.5 to 3 times higher than the reported cases.[22] Regrettably, the mortality rate associated with this disease is equally alarming, resulting in the loss of 145 000 lives. Pharyngeal and laryngeal tumors may be treated with radiation and CRT, but oral cavity cancers are often treated with surgery. Understanding the scientific aspects and implications of oral cancer is crucial for addressing this public health issue effectively.[23] Cancer of the oral cavity and lip primarily encompasses tumors that arise from the epithelial lining of the mouth, including the lips, tongue, gums, and oral mucosa. The development of oral cancer is influenced by various risk factors, including tobacco and alcohol use, betel quid chewing, poor oral hygiene, viral infections such as human papillomavirus (HPV) infection, and genetic predisposition. These risk factors contribute to the accumulation of genetic mutations and alterations in key cellular signaling pathways, leading to uncontrolled cell growth and tumor formation. The scientific community has made significant progress in understanding the molecular mechanisms underlying oral cancer. Studies have identified specific genetic mutations, such as alterations in tumor suppressor genes (*e.g.*, TP53, CDKN2A) and oncogenes (*e.g.*, EGFR, KRAS), which play critical roles in the initiation and progression of oral cancer. Nowadays there are a lot of studies that have been done and some of the recent research is briefly discussed in this review article. One example is a 2023 study in which Balakittnen *et al.* introduced noncoding RNAs in an oral cancer. Due to their participation in almost all biological processes, it can be said that this group of biomarkers is among the most promising ones.[24] With regard to early detection of cancer, scientists have developed a deep learning concept. In 2023, Huang *et al.* were the first to use preprocessing techniques such as data augmentation, gamma correction, and noise reduction to improve the raw image quality and boost their quantity to supply enough data for convolutional neural network training. They used ISSA (an improved version of the squirrel search algorithm) to select the network weights optimally and deliver greater accuracy.[25] By utilizing artificial intelligence, Rawi *et al.* offered a cutting-edge technological advancement in the management of oral cancer in the year 2022.[26]

Lung cancer

Throughout the world, lung cancer is one of the leading causes of death.[27] Surgery, radiation therapy, chemotherapy, and targeted medication therapy are therapeutic options for treating lung cancer.[28] Medical management is frequently linked to the emergence of treatment resistance that results in relapse. Due to its manageable safety profile, persistent therapeutic

 © 2024 The Author(s). Published by the Royal Society of Chemistry

Open Access Article. Published on 04 January 2024. Downloaded on 2/7/2024 7:04:31 AM.
This article is licensed under a Creative Commons Attribution 3.0 Unported Licence.

response due to immunological memory development, and effectiveness across a wide patient population, immunotherapy is significantly changing how cancer is treated.[29] Different tumor-specific vaccination strategies are gaining ground in the treatment of lung cancer.[28] This review discusses the recent developments in the clinical studies of lung cancer and the related challenges.

Globally, cancer incidence and death are rising, with lung cancer being the most commonly diagnosed form of cancer (11.6% of the total cases).[30] Also, it is found that there was a roughly 110 000 and 236 740 and 2.2 million cases and new cases of lung cancer along with 60 000, 130 180 and 1.8 million fatalities, respectively were observed. With a share of 18.4% of all cancer-related fatalities worldwide, this malignancy maintains its position as the main cause of cancer-related deaths.[31] As a result, it places heavy societal and economic burden. Approximately 80% of lung cancer fatalities are primarily caused by tobacco use. Exposure to substances like radon and asbestos, and continuous and cumulative contact with airborne contaminants, particularly emissions containing polycyclic aromatic hydrocarbons (PAH), are additional risk factors for lung cancer. Lung cancer history, either personal or familial, is also acknowledged as a risk factor.[32]

While both non-small cell lung cancer (NSCLC) and small cell lung cancer (SCLC) are treated using a variety of therapeutic modalities, including surgery, chemotherapy, and radiation, there is an urgent need for the development of effective methods to either cure or effectively manage lung cancer, particularly at advanced stages. Due to the lack of a reliable platform for early-stage identification and the delayed onset of symptoms during disease development, which restricts therapy options and overall survival, the prognosis of NSCLC is particularly difficult. Low-dose computed tomography (LDCT), the current gold standard for lung cancer screening in patients, is used. However, LDCT has issues like false-positive identification, radiation risk, early detection sensitivity, and the lack of funding for effective CT-based screening programs. Only 5% of the recommended 15 million high-risk persons in the United States have received LDCT screening. Despite the potential benefits of early detection in facilitating tumor removal, treatment effectiveness, and favourable outcomes, the refractory nature of lung cancer is largely due to the lack of a suitable screening platform, as well as the disease's metastatic nature, genetic diversity, and limited responsiveness to late-stage chemotherapy.[28]

However, for locally advanced and metastatic lung malignancies, chemotherapy and radiation therapy regimens, including neoadjuvant and/or adjuvant methods, are advised. These therapies, however, have limited overall survival rates and frequently have negative side effects. Notably, targeted treatments in combination with chemotherapy have become standard procedures for NSCLC patients carrying actionable oncogenic changes such as driver mutations and fusions/rearrangements. In some circumstances, these targeted medicines have shown promise in improving progression-free survival (PFS) and overall survival. It is vital to understand that targeted therapies have different side effect profiles from standard chemotherapy and might not always produce long-lasting therapeutic results.[28]

2. Development of cancer and problem definition

Tumorigenesis is a multifaceted process, and the metastatic behavior of malignant neoplasms represents both hallmark and a significant challenge in oncology. As neoplastic progression occurs, cells from the primary neoplasm infiltrate the

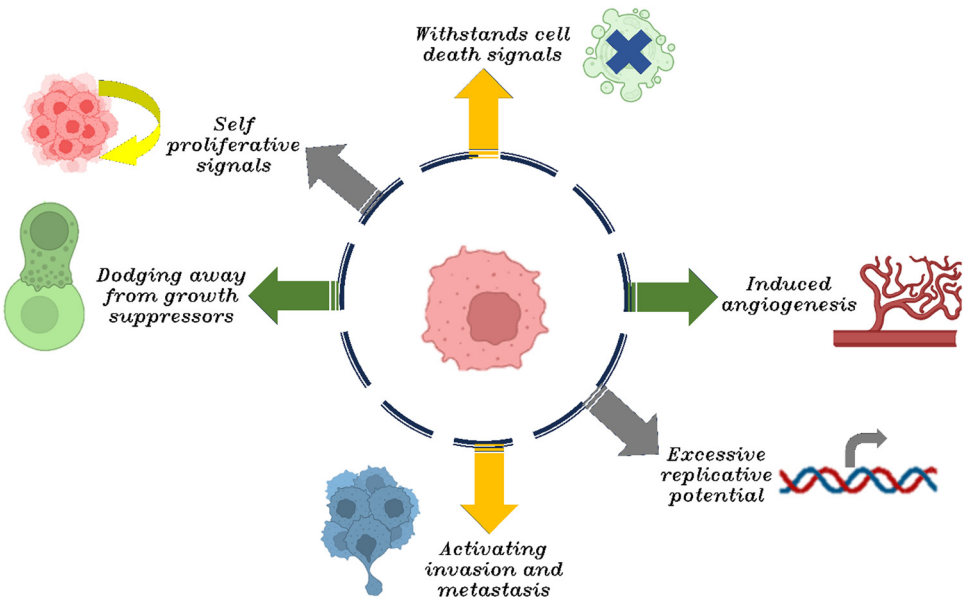


Fig. 2 Six hallmarks of cancer cell development.

Open Access Article. Published on 04 January 2024. Downloaded on 2/7/2024 7:04:31 AM. This article is licensed under a Creative Commons Attribution 3.0 Unported Licence.

surrounding healthy tissues, migrate to distal sites, and establish secondary colonies. It is estimated that metastatic events account for approximately 90% of cancer-related fatalities.[33,34] Also, the neoplastic cells demonstrate a dynamic shift between epithelial and mesenchymal phenotypes.[35,36] As cancer predominantly originates in epithelial tissue, with roughly account 80 to 90% of all cancer cases that being characterized as carcinomas. In 2000, Hanahan and Weinberg delineated six hallmark capabilities that typify the majority of cancers, if not all. Fig. 2 illustrates the six characteristic features commonly exhibited by cancer cells. These hallmarks encompass sustaining self-proliferative signals, dodging away from growth suppressors, withstanding cell death signals, inducing angiogenesis, excessive replicative potential, and activating invasion and metastasis.[37]

During tumorigenesis, cancer cells are subjected to an array of stresses, stemming from dysregulated proliferative signals driven by oncogenes and a substantial mutational load. While these signals would typically initiate apoptosis in normal cells, malignancies have evolved ways to bypass these death cues, facilitating progression to more advanced and aggressive cancer stages.

3. Conventional techniques used for cancer biomarker detection

3.1 Histopathology

Cancer incidence and mortality have dramatically increased and cancer is a notable cause of death worldwide in recent decades.[38,39] Unfortunate incidents of cancer are a result of changes in lifestyle as there is a dynamic global change in geographical and economic factors. The factors which are responsible for cancer include obesity, alcohol intake, lack of physical activity, hormonal imbalance, and smoking. Also, there is a strong relationship between enhanced risk of cancer and mental health ailments. Therefore, change in the modern lifestyle adversely impacts the human health that lead to cause several health issues including cancer. Also, in the view of elevation of cancer cases, recent progressive advancement also being achieved towards the diagnosis of diseases and monitoring of human health. Thereby, advanced screening facilities also increased for rapid diagnoses of cancer cases and these facilities are available not only in the urban areas but also in the rural region. Since 2020, awareness about the cancer prevention steps and advanced treatment strategies have assisted the people to increase the likelihood of fighting against the diseases.[40,41] As a result, cancer diagnosis is absolutely essential. Cancer can be diagnosed using a variety of techniques, such as biochemical analysis, surgery, diagnostic medical imaging (DMI), clinical tests, *etc.* The most popular diagnostic method used by experts is image diagnosis such as ultrasound, magnetic resonance imaging, nuclide, X-ray computed tomography (CT), X-ray, differential contrast, and histopathology image analysis. Histopathology image analysis involves examining the biopsy tissue under a microscope to enable specialists to clearly see the details of the cell characteristics in tissue.[42,43]

Histopathological detection techniques are considered to be the best for determining the type of cancer.[44] Histopathology, which derives from the Greek terms *histos* (tissue), *pathos* (sickness/suffering), and log *y* (−log *ia*), is the study of changes in any tissue, whether it be human, animal, or plant, connected with a disease or disorder. In a medical setting, sampling occurs either during surgery or during an autopsy, and the tissue is then processed for microscopic study.[45] The examination of a slide for research and diagnostic purpose is known as histopathology. It is a field of study that only relies on microscopic interpretation and analysis. For an accurate diagnosis to be made, processing procedures, suitable fixation and suitable biopsy technique, staining, and sufficient sectioning are crucial. It is crucial to distinguish the structural and morphological characteristics of tissue components for a complete diagnosis.[46] The majority of tissue-based diagnostics require staining. Haematoxylin and eosin (H&E) staining is a staining technique that is often used in histology labs.[47] In this procedure, different tissue components are colored by a staining component; after being suitably colored, different types of cells, structures of cells, and other foreign substances are clearly noticeable under high resolution.[48,49] Because all structures appear the same dark grey when the tissue is examined under a microscope, it is impossible to distinguish the structural details, and hence must be colored.[47] Following this, pathologists examine the stained tissue slide under a microscope or with the help of high-resolution images taken by the camera. To find tumors, a histopathology test is required. It is a time-and-tested method for predicting the presence of invasive cancer cells in tissues that are stained with H&E. In H&E staining, the chromatin in the nucleus and the nucleic acid in the cytoplasm turn pink, while the components in the cytoplasm and extracellular matrix turn purple-blue. The benefit of free scaling in histopathological images is that they may accurately display the minute features in tissue images and increase the precision of detection. Pathologists directly examine, evaluate, and grade these tissues under a microscope as part of conventional cancer testing, which is a well-established practice for identifying cancer cells. But while working under a microscope, pathologists are prone to feeling dizzy and neck strain. It takes time for the pathologist to make notes and write out their ultimate judgment in the interim.[48] It takes a lot of time and effort for pathologists to manually analyze many sections because of the continually rising number of cancer patients. A lack of traceability between observers, internal alterations, and inconsistent results can also result from manual diagnosis. Cancer diagnosis accuracy varies by 20% between pathologists with expertise and those with less experience. Individual diagnoses and expert diagnoses differed by 75.3%, according to recent research.[47,48] The objective is to determine if a tumor is benign or malignant since cancerous tumors need to be treated right away to lessen and avoid subsequent consequences. Numerous problems with this approach include intra-observer variability, the potential for recurrence in tissues and cancer cells, and the identification difficulty caused by the fact that numerous additional

© 2024 The Author(s). Published by the Royal Society of Chemistry

Open Access Article. Published on 04 January 2024. Downloaded on 2/7/2024 7:04:31 AM. This article is licensed under a Creative Commons Attribution 3.0 Unported Licence.

structures in cells have the same hyperchromatic properties. Due to the fact that the surgery only impacts a small amount of tissue, the site must be carefully considered. It is best to choose a region around the borders of the tumor.

Consequently, a detection strategy based on machine vision is necessary. It is able to carry out accurate, reliable, and efficient quantitative analysis. So, to improve the consistency of cancer detection and accuracy, therapy machine vision technology eliminates differences between internal and external observers.

3.2 Bioimaging

Bioimaging plays a crucial role in documenting the information details about biological substances for diagnosis, staging, and treatment using a variety of imaging devices to treat various diseases including cancer. Bioimaging also helps in the evaluation of the cellular process (ion or metabolite level) in cell biology. These imaging methods can be employed for non-invasive recognition or for the purpose of recording and extracting information from biological samples externally, without any physical intervention. Bioimaging is a powerful tool which is also used in cancer for visualizing the abnormal state at the target site.[50] This technique helps healthcare professionals to visualize internal structures and identify abnormalities such as tumor, by providing a more detailed image to help in early detection and plan a course of action.[51] The rapid growth and significant advancement in bioimaging technology have led to wide application based on different principles and instruments with various types of biological techniques developed such as X-ray, X-ray computed tomography (CT), hyperspectral imaging, magnetic resonance imaging (MRI), optical imaging and thermal imaging which required a large setup of instruments.[52] The basic components of an imaging system are an illumination system, camera, frame grabber and image processing software and hardware.[53] Camera is used for capturing the biological image of the object but for the evaluation of the external morphology including size, color, shape and surface structure there is the need of a sensor such as X-ray, ultrasound, MRI, X-ray CT and charge-coupled device (CCD) camera. Mostly a charge-coupled device (CCD) camera is used for this purpose. After that, the analog video signal is converted into digital signal, and the process of conversion is known as digitization. A digitizer (also known as a frame grabber) is utilized to transform visual images into a digital format. Processing of the digital image is done by hardware and software to analyze the obtained images. Image processing involves a number of phases that must be completed, including image capturing, partitioning, initial image processing, augmentation, depiction, and detailing. X-rays, magnetic resonance imaging (MRI), computed tomography (CT), positron emission tomography (PET) and single photon emission CT (SPECT) are among the conventional bioimaging techniques but their practical use is constrained by complicated processes, expensive instruments, time-consuming steps and low resolution of the image. Therefore, alternative bioimaging techniques are required that are less expensive, and more precise technologies are needed to get rapidly fast-growing domain of super-resolution; three new techniques such as two-photon fluorescence excitation microscopy, fluorescence recovery/redistribution after photobleaching (FRAP), and fluorescence resonance energy transfer (FRET) are recently developed. *In vitro* imaging can give important details of the distribution, cytotoxicity, and imaging ability of probes in cells. For clinical imaging applications, there is the requirement of good biocompatibility and minimal cytotoxicity of probes. Conventional quantum dots and similar core–shell nanoparticles were previously employed for optical bioimaging both *in vitro* and *in vivo*. But those containing toxic heavy metals cause problem to health and the environment. Other nanomaterials such as gold and silver nanoparticles are a safe alternative but they are costly and lack photostability. On the other hand, there are interesting alternatives of QDs which contain toxic heavy metals but in the biological system they are exposed to oxidative degradation which makes them slightly toxic. Therefore, there is the need of excellent nanoparticles which have good photoluminescence properties and which are biocompatible, highly photostable and of low toxicity for bioimaging.[54] Nanotechnology can also be used in bioimaging techniques. Nanoparticles are regarded as promising candidates for bioimaging due to their applicability in fluorescence imaging within the second near-infrared spectral region (NIR-II, 1000–1700 nm). Additionally, they can offer the benefits of exceptional spatial resolution and significant penetration depth, facilitated by reduced light scattering.[55] It has been demonstrated that NIR-II quantum dots (QDs) have the potential to be utilized in biomedical and clinical applications for deep tissue imaging application because of their remarkable biocompatibility, photostability, and luminosity.[56] Because of their innovative fluorescent carbon nanomaterial, robust resistance to photobleaching, absence of blinking, biocompatibility, minimal toxicity, and environmentally friendly attributes, carbon dots (CDs) have attracted a lot of interest for use in bioimaging, catalysis, and sensing techniques.[57–61] Small sized carbon dots with strong biocompatibility can easily penetrate cells. Nanoparticles that exhibit multi-imaging characteristics have drawn a lot of interest and can be employed in composite systems. Nanocarriers with cell-targeting drug storage, detection, cancer cell separation and controlled drug release capabilities[62,63] have been designed to enhance the bioimaging capability. Currently, a diverse range of inorganic nanoparticles (NPs) such as biomolecules, CDs, gold and silica nanoparticles, and carbon nanotubes are being utilized for the purpose of drug and gene delivery.[64,65] Due to their outstanding chemical inertness, biocompatibility, and precise sizing for mesopore entry, CDs have emerged as a fitting option for a novel bioimaging agent.[66] Utilization of carbon dot delivery techniques can reduce cytotoxicity, improve clinical results, and offer promising nano-carriers for the advancement of multifunctional nanomedicine in the future,[67] when compared to carbon nanotubes and gold and silica nanoparticles.[68] CDs have been utilized for bioimaging across various normal and cancer cells, as illustrated in Table 2.

Bioimaging applications in cancer disease are diverse and crucial to improve diagnosis, treatment, and monitoring of cancer patients. Fig. 3 illustrates the different types of

Open Access Article. Published on 04 January 2024. Downloaded on 2/7/2024 7:04:31 AM.
This article is licensed under a Creative Commons Attribution 3.0 Unported Licence.

Table 2 Bioimaging techniques used for the detection of lung and oral cancer using CDs

Nanoparticles	Synthesis method	Technique	Target	Limit of detection range	Limit of detection	Quantum yield (%)	Size (nm)	Ref.
N,S-CDs	—	Cell imaging	A549 cells	—	—	80.3	3	69
CD incorporated polymeric hydrogels	—	Fluorescence imaging	A549 cells	—	—	—	—	70
CQDs	Hydro thermal	Bioimaging	A549 cells	—	—	—	1.8	71
AA-CDs	Hydro thermal	Bio-imaging (cancer cells)	HeLa, SMMC-7721 and A549 cells	—	—	56.5	1.6	72
Amino-functionalized fluorescent carbon nanoparticles	—	Bio-imaging (cancer cells)	A549 cells	—	—	7.8	4–7	73
N-P-doped CDs	Hydro thermal	Bio-imaging	HeLa cells, A549 cells	—	—	—	3.8	74
m-Phenylenediamine and L-cysteine	Hydro thermal	Nucleolus imaging	HeLa, A549, HepG2, L02, AT II, RAW264.7	—	—	—	3.8 ± 0.5	75
Spinach	One-step solvo-thermal	Bio-imaging	A549 cells	—	—	15.34	3–11	76
Citric acid (CA) and glutathione (GSH)	Hydro thermal	Cell imaging	A549 cells	—	—	80.3	3	69
Glycerol and dimethyl sulfoxide (DMSO)	Solvo-thermal	Imaging of cancerous cells	A549 cells	0.1–100 μM	16 nM	—	6.1 ± 1.4	77

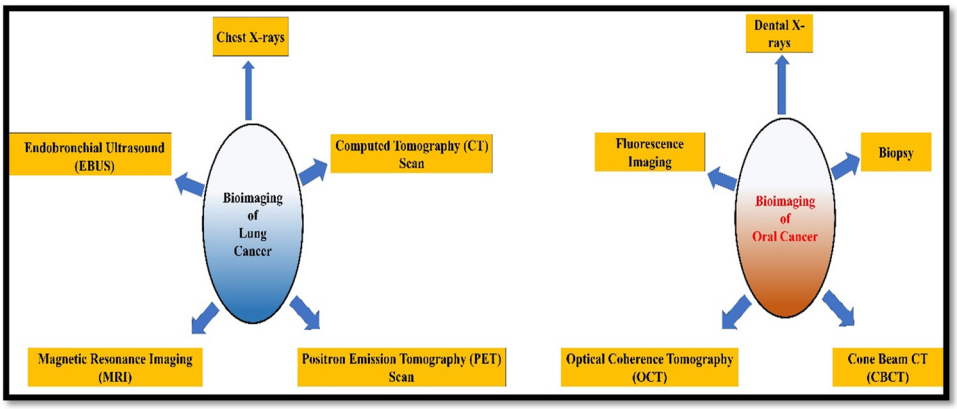


Fig. 3 Different types of bioimaging techniques used in lung and oral cancer.

bioimaging techniques used for oral and lung cancer detection and their applications are depicted in a pictorial form in Fig. 4. These imaging techniques provide valuable information about the tumor's characteristics and location. They provide informational data to healthcare professionals and help in making informed decisions related to the treatment of cancer.

3.3 Enzyme linked immunoassay (ELISA)

Among the conventional diagnostic methodologies, enzyme-linked immunoassay (ELISA) stands out as a predominant technique employed to validate and quantify biomarkers associated with the proliferation of several cancer types, including lung and oral cancer. Recognized as a cornerstone in analytical chemistry, ELISA has been refined into multiple variants to suit varied analytical needs. Mainly four primary types of ELISA are identified: direct ELISA, indirect ELISA, sandwich ELISA, and competitive ELISA.[78] Of these, competitive ELISA, direct ELISA, and sandwich ELISA are the most frequently utilized immunosorbent assays in the context of cancer biomarker detection.

3.3.1 Direct ELISA. In direct and indirect ELISA the antigens are adsorbed onto the wells of the ELISA plate. In direct ELISA, only one antibody is used as the detection probe which is specific towards the target antigen and binds directly to it. Subsequent to this binding, a chromogenic substrate which might be associated with enzymes is introduced to the system. This leads to a discernible color change. The mechanism underlying this color change can be attributed either to the removal of phosphate groups from the substrate by the enzyme or the oxidation of substrates in the presence of HRP. Also, there are several merits of employing direct ELISA. Firstly, by eliminating the need for a secondary antibody, potential cross-reactivity issues are avoided. Additionally, its procedure is more streamlined and faster than indirect ELISA due to the reduced number of steps. However, it does come with drawbacks. For one, direct ELISA is generally less sensitive in comparison to other ELISA variants. Furthermore, the costs associated with the reagents and procedure can be relatively high.

In a study by Danae *et al.*, the direct ELISA technique was harnessed to ascertain elevated levels of ProTα. The study

© 2024 The Author(s). Published by the Royal Society of Chemistry

Open Access Article. Published on 04 January 2024. Downloaded on 2/7/2024 7:04:31 AM.
This article is licensed under a Creative Commons Attribution 3.0 Unported Licence.

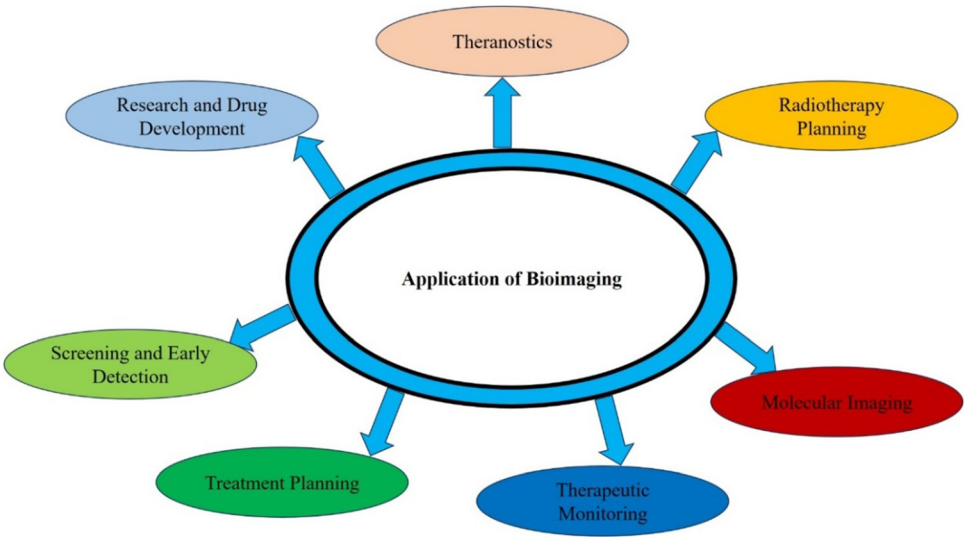


Fig. 4 Application of bioimaging in various fields of diagnosis to improve the quality of human health.

employed antibodies targeted against the C-end peptide sequence 101–109 of ProTα. They compared its presence in breast tumor tissue samples with that in normal breast tissue controls.[79] Furthermore, in another significant study, Neal *et al.* devised a direct ELISA-based assay specifically for detecting bone sialoprotein, a vital biomarker. The presence of bone sialoprotein is especially crucial in the context of several cancers, notably breast, prostate, colon, and lung cancers. The development of such assays is instrumental in the early diagnosis and monitoring of these malignancies, underscoring the critical role of direct ELISA in oncological research and clinical applications.[80]

3.3.2 Sandwich ELISA. In contrast to direct and indirect ELISA methodologies, the sandwich ELISA has a unique setup. It begins with the plate wells being coated with a capture antibody. The technique is aptly named ''sandwich'' ELISA because the target antigen becomes ensconced or ''sandwiched'' between two antibody layers: the capture and the detection antibodies. The procedural steps of the assay are as follows:

- The capture antibody is first added to the plate wells, which are then sealed and incubated overnight at 4 °C.
- After the incubation, the plate is rinsed with phosphate-buffered saline (PBS) to remove any unbound capture antibody.
- The wells are then buffered or blocked using bovine serum albumin (BSA) to prevent non-specific binding. This buffering step is executed at room temperature and spans roughly 1 to 2 hours.
- Another PBS wash follows.
- The antigen sample, containing the molecule of interest, is added. It binds specifically to the capture antibody. This binding phase is maintained for 90 minutes at 37 °C.
- After this, the plate undergoes another wash.
- The primary detection antibody, which recognizes a different epitope or region of the antigen than the capture antibody, is introduced and allowed to bind to the antigen. This incubation lasts for another 1 to 2 hours at ambient temperature, followed by a subsequent wash.
- Next, a secondary antibody, conjugated to an enzyme, is added. This incubation also extends for about 1 to 2 hours.
- A final wash is performed, post which a substrate solution is introduced, which, upon interaction with the enzyme, yields a colorimetric change.

One of the significant merits of sandwich ELISA is its superior sensitivity, arguably the highest among all ELISA variations. However, this method does have its disadvantages, most notably the extended time required, increased costs, and the need for ''matched pair'' antibodies (those that can simultaneously bind different sites on a divalent or multivalent antigen) along with a suitable secondary antibody.

3.3.3 Competitive ELISA. Competitive ELISA serves as a distinctive assay, primarily employed to determine the presence of specific antibodies against antigens in the test serum. This variant of ELISA is characterized by the competitive binding of two distinct antibodies to a single antigen.

Here's a breakdown of the process:

- Two specific antibodies are utilized: one that is enzyme-conjugated and another that may be present in the test serum (if the serum is positive for that particular antibody).
- When both antibodies are introduced into the wells, they compete for binding sites on the antigen.
- If a color change manifests, the test result is negative. This indicates that the enzyme-conjugated antibody has effectively bound to the antigen, signifying the absence of the test serum's specific antibodies.
- Conversely, a lack of color change signifies a positive test, indicative of the presence of antibodies in the test serum.

While competitive ELISA offers various advantages, such as the reduced need of the sample, the ability to assess a vast spectrum of antigens to be detected in a sample, suitability for smaller antigens, and minimized variability, it also has its share of drawbacks. Its specificity is relatively low, and it is less effective in analysing dilute samples. To emphasize the utility of competitive ELISA in oncology, numerous studies have

Open Access Article. Published on 04 January 2024. Downloaded on 2/7/2024 7:04:31 AM. This article is licensed under a Creative Commons Attribution 3.0 Unported Licence.

showcased its effectiveness in detecting biomarkers pertinent to cancer diagnostics and research. Two notable studies highlight the utility of ELISA in detecting specific biomarkers relevant to lung cancer. In the first study, carried out by Yagihashi, Atshuhito, *et al.*, the researchers reported a significant presence of anti-livin antibodies in lung cancer patients using a specific ELISA. They employed recombinant proteins since both survivin and livin are predominantly expressed in cancer and transformed cells but are scarcely present in normal, differentiated tissues.[81] The outcomes of their research revealed the following:

- 19 out of 37 lung cancer patients (51.3%) tested positive for anti-livin antibodies.
- Of 31 samples drawn from these lung cancer patients, 18 (58.1%) exhibited the presence of anti-survivin antibodies.
- When examining sera from 31 lung cancer patients for both anti-survivin and anti-livin antibodies, a striking 71% tested positive for either survivin or livin, or both.
- However, the study also found that the intensity of anti-livin antibody responses did not have any correlation with the intensity of anti-survivin responses.

The second investigation, performed by Yamashita *et al.*, aimed to determine the potential diagnostic value of detecting epidermal growth factor receptor expression on exosomal membranes.[82] The researchers attempted to identify lung cancer by using a targeted ELISA that used an anti-CD81 antibody as the capture antibody. Together, these studies underscore the versatility and importance of ELISA as a diagnostic tool in oncology, especially for detecting and understanding lung cancer. Ruay-Sheng *et al.* designed a study to investigate whether CYFRA2I-1 is a sensitive and specific tumor marker for non-small cell lung cancer (NSCLC) or not. CYFRA 2I-1, a newly developed sandwich ELISA, was used to measure the soluble cytokeratin 19 fragment in serum that is expressed in simple epithelium and its malignant counterpart.[83] As an oncogene and crucial component in the diagnosis of lung cancer, Wang *et al.* described a double-antibody sandwich ELISA kit for the detection of MUC1 in serum from lung cancer patients. Through this work a double-antibody sandwich ELISA kit was successfully constructed and the sensitivity was up to 0.5 μg L^{-1}.[84]

Two distinct studies focused on the applicability and efficacy of ELISA in diagnosing lung cancer through different biomarkers:

CYFRA 21-1 as a biomarker for NSCLC. In one study, the researchers sought to determine the diagnostic efficacy of CYFRA 21-1 as a marker for NSCLC. For this purpose, they employed the CYFRA 21-1 sandwich ELISA technique to measure the levels of the soluble cytokeratin 19 fragment in the serum. Cytokeratin 19 is expressed in simple epithelia and their malignant counterparts. By quantifying this fragment, the researchers aimed to discern its utility as a sensitive and specific tumor marker for NSCLC.

MUC1 as a biomarker for lung cancer. In another study the central focus was the MUC1 oncogene and its significance in diagnosing lung cancer. MUC1 plays a pivotal role in several cancers, including lung cancer. In this investigation, a double-antibody sandwich ELISA kit was devised to detect serum levels of MUC1 in lung cancer patients. This constructed ELISA kit exhibited a high degree of sensitivity, being able to detect MUC1 concentrations as low as 0.5 μg L^{-1}.[84]

Together, these investigations illustrate the power and versatility of the ELISA technique, with different adaptations, in the realm of oncological diagnostics. They highlight the potential of specific biomarkers, when quantified and analyzed accurately, in aiding early detection and understanding of lung cancer.

The study by the cited authors indicates that chemokines play a significant role in inflammation and carcinogenesis. Techniques like enzyme-linked immunosorbent assays (ELISA) have provided reliable methods for their detection in saliva. Based on this, there's a proposition that individuals with oral cancer or precancerous oral lesions might exhibit increased concentrations of specific chemokines in their oral fluids. Such elevations could potentially serve as indicators for early malignant detection or for monitoring progression towards malignancy. In a related study, the utilization of ELISA revealed notably higher levels of CXCL8, CXCL10, and CCL14 in the oral fluids of individuals diagnosed with cancer.[85]

4. Fabrication of electrochemical sensors for cancer detection

From the last decade, progressive exploration has been achieved for the fabrication of sensors for cancer detection using nanobiotechnology and nanomaterial science. The overall performance of the sensor could be improved by the use of nanomaterials such as carbon-based materials, metal oxides, transition metal dichalcogenides, nanoparticles, quantum dots, *etc.* These nanomaterials possess tremendous potential related to optical, electrical and catalytic properties such as wide band gap, excellent conductivity, biocompatibility, improved surface to volume ratio, good permeability, electronic conductivity, *etc.* Therefore, the use of nanomaterials in the fabrication of sensors helps to promote the progress of electroanalytical sensors in various aspects such as enhanced detection range, sensitivity, selectivity, specificity, stability and limit of detection.

Nanomaterials are low dimension materials compared to building units of sub-micron size, and at least one of their dimensions is in the nanometer range. These materials can be nanotubes (carbon nanotubes), nanosheets (graphene oxide, reduced graphene oxide, molybdenum disulfide, tungsten disulphide), nanoparticles (zinc sulphide, gold, silver, platinum), functionalized materials (acid, base, or capping agents/ligands) or their composites which enhance the intriguing properties of the materials, by providing a large surface to volume ratio, biocompatibility, fast electrochemical signal propagation, amplification of the sensing response, *etc.*

The electrochemical sensing technique has been extensively explored for the diagnosis purpose and for monitoring clinical

 © 2024 The Author(s). Published by the Royal Society of Chemistry

Open Access Article. Published on 04 January 2024. Downloaded on 2/7/2024 7:04:31 AM. This article is licensed under a Creative Commons Attribution 3.0 Unported Licence.

as well as non-clinical samples. Electrochemical transduction between the recognition element and the analyte occurs at the electrode surface which can be measured as an electrochemical signal in terms of potential, current, or impedance. Various types of electrochemical sensors have been fabricated such as nucleic acid sensors, aptasensors, enzyme sensors, immunosensors or MIP based sensors for oral or lung cancer biomarker detection in human body fluids. These sensors have been broadly discussed further based on the recent literature articles and analytical sensing responses. The sensitivity, selectivity, specificity, stability, detection range and limit of detection of the fabricated sensor have been discussed for cancer biomarker detection. For the construction of the sensor, the target analyte as a cancer biomarker is used for the specific and selective detection of particular cancer. The sensor matrix surface can be modified by the use of nanomaterials to enhance the surface immobilization of the recognition element, biocompatibility, stability, conductivity and the sensing signal. Therefore, a biorecognition element such as antibodies, enzymes, DNA, and artificial recognition sites as cavities for MIPs is used for the construction of sensors. A few of the oral and lung cancer biomarkers for cancer detection are described in Table 3.

4.1. Types of sensors

4.1.1 Nucleic acid based sensor for cancer detection. The nucleic acid sensor is a DNA based sensor in which probe DNA and complementary DNA act as recognition elements and upon hybridization, the probe DNA gets attached to the complementary DNA resulting in changes in the electrochemical signal. By increasing the concentration of complementary DNA, changes in the electrochemical signal response can be observed.

Nucleic acid based sensor for oral cancer detection. Advanced invasive and metastatic oral cancer can now be diagnosed using cancer cell lines or biopsy samples. The most efficient way to decrease oral cancer-related deaths is by early, non-invasive detection. In current times, there has been an evident rise in the number of cancer-related nucleic acids discovered in oral fluid, making it an ideal diagnostic fluid. Oral fluid offers several clear advantages over blood.[90] Yet, there are still a number of significant difficulties with the diagnostic method used with saliva, including low sensitivity and poor specificity. Therefore, it is crucial to create procedures that are very sensitive and focused for using saliva to diagnose oral cancer.[91]

The ability of catalytic nucleic acid (DNAzyme)-based techniques to catalyse a variety of chemical processes, including DNA self-modification and metal ion-dependent DNA/RNA breakage, has garnered growing interest.[92,93] One of the most intriguing DNAzymes is the G-quadruplex-hemin DNAzyme, which is made up of hemin and a G-rich nucleic acid and can efficiently catalyse the H_2O_2-mediated oxidation. For the creation of diverse DNA biosensors, it has therefore demonstrated tremendous promise as a novel type of catalytic label.

For quick, sensitive, dependable, and affordable DNA detection in clinical diagnostics, DNA electrochemical biosensors have shown considerable promise. The sensitivity and selectivity of electrochemical DNA biosensors have been improved *via* the development of several sensing techniques.[94,95] Conventional biosensors are not able to detect a minute amount present of analyte therefore, nucleic acid based sensor helps to quantify the biomarkers present in saliva as they present in a very low concentration.

Chen *et al.* in 2011 described the fabrication of an electrochemical sensor for the detection of DNA associated with the oral cancer overexpressed 1 gene (ORAOV1) in saliva.[96] Through S–Au bonding, the single probe (Sp) is covalently joined to a gold electrode (GE). Then, 2-mercaptoethanol (MCH) is used to inhibit the Sp-modified GE, resulting in the formation of a mixed monolayer. When a target is precisely matched, Sp attaches with the DNA and forms a double-helical structure with a complete N.BstNB I recognition site. Sp gets detached from the DNA when the affinity between the two decreases. When the target DNA is released, it can combine with a fresh, unnicked Sp to start a new cycle of probe transformation. This enables a single target DNA to permanently change a number of Sps into G-rich nucleic acid sequences.[97,98] After the strand-scission cycle is over, washing is a simple way to get rid of the target recognised Sp fragment. As a result, only G-rich pieces are left on the sensor surface. Therefore, following hemin addition, the G-rich sequences can interact with hemin to produce the G-quadruplex-hemin DNAzyme. 3,3′,5,5′-Tetramethylbenzidine (TMB) is subsequently oxidised by H_2O_2 with the help of this DNAzyme, which results in a modified color in the reaction solution and an increase in the current signal. The nicking endonuclease, however, is unable to cleave the Sp in the absence of the target DNA. Consequently, the steric-hindrance effect prevents Sp from binding hemin to create the G-quadruplex-hemin DNAzyme.

In order to confirm the catalytic nature of the DNAzyme, it was further compared with the CV signals of the TMB substrate and oxidation as well as reduction peaks were observed in the bare electrode when CV was performed and after the DNAzyme was added indicating that the DNAzyme effectively reduced hydrogen peroxide with the aid of TMB (an electroactive co-substrate) and amplified electrochemical current signals. During

Table 3 Type of cancer along with cancer biomarkers for the detection of cancer using the sensing technique

Cancer type	Biomarker		Ref.
Lung	RNA	miR-106a-5p, miR-10b-5p, miR-141-3p	86,87
	Protein	ALK, CEA, KRAS, *EGFR*, *ROS*, *KRAS*, *MET, NTRK1*, *FGFR*A, *HER2*, *BRAF*, *PIK3CA*, *RET, DDR2*, *PTEN*	
Oral	Protein	IL-8, IL-1b, TNF-α, defensin-1, P53, Cyfra 21-1, tissue polypeptide-specific antigen	88
	DNA	Human papillomavirus type 16 and 18	89

Open Access Article. Published on 04 January 2024. Downloaded on 2/7/2024 7:04:31 AM.
This article is licensed under a Creative Commons Attribution 3.0 Unported Licence.

this period, the hue of the solution that could be seen with the naked eye changed progressively from colorless to blue.[99]

Nucleic acid based sensor for lung cancer detection. Lung cancer is the most common cause of death globally. Flexible bronchoscopy (FB), imaging diagnosis and sputum cytology are the three primary traditional methods for diagnosing lung cancer. Sputum cytology is an invasive procedure that has limited sensitivity and relies on exact specimen collection and preservation procedures to provide accurate diagnoses.[100] Similarly, FB can be helpful in the evaluation of a patient who is suspected of having lung cancer, but its sensitivity is constrained by the location and size of the lesion.[101] As the most popular approach for identifying lung cancer, computed tomography (CT) has proven to be far more effective than chest radiography.[102] CT screening, however, has not been regarded as a cost-effective method because there is still room for improvement in terms of performance.[102,103]

Small, non-coding RNAs called microRNAs serve as regulators. Although tiny, these microRNAs may be crucial regulators of a variety of human tumors. Therefore, it is thought that a possible method for early cancer diagnostics that would result in a better treatment for patients is quick and sensitive detection of cancer-related microRNAs. However, because of the short sequence and low abundance of microRNAs, it is incredibly difficult to create a quick, low-cost, and straightforward microRNA detection platform. Numerous studies have been conducted in recent years to develop quick and accurate microRNA detection methods, such as Northern blotting and polymerase chain reaction (PCR). The limitations of Northern blotting are its insensitivity and time-consuming process.[104] For PCR, small primers are used in the microRNA due to which it gives false positive results. Widespread fluidic management, separation, and other engineering detection situations have been combined and hyphenated with electrochemical sensors. Electrochemical biosensors have many benefits including relatively low cost, quick response times, ease of use for continuous on-site analysis, high selectivity and sensitivity, minimal sample preparation, and reliable reproducibility. These advantages make electrochemical biosensors a promising technology for biomolecule detection. The development of electrochemical genosensors as point-of-care diagnostic tools and multiplexing platforms for quick, easy, and affordable nucleic acid detection has shown considerable promise.[105]

Lung cancer-related microRNAs (miRNAs) are evolving. Let-7, miR-141, and miR-21 are frequently used as diagnostic targets. MiR-25, miR-145, and miR-126 are a few recent lung cancer miRNAs that have drawn more and more attention. Although there are several methods for analysing lung cancer miRNAs, electrochemistry has gained popularity for its great sensitivity, low cost, and quick response. Electrochemistry has been praised for its high sensitivity, cheap cost, and quick response despite the fact that there are several methods available for the investigation of lung cancer miRNAs. An electrochemical genosensor's specificity and sensitivity depend heavily on the design of the probes. The typical properties of microRNAs include high sequence similarity, low melting points, and short sequences.[101] Because of this, high sensitivity detection of microRNAs using conventional sandwich structure DNA probes and single strand DNA probes is difficult. On the other side, single-base mismatch nucleic acid detection has been effectively accomplished using DNA probes with a stem-loop structure. A stem-loop DNA probe-based electrochemical sensor has also been proposed in order to detect the complementary sequence and significantly boost the sensitivity of nucleic acid detection.[106] But because it was a signal-off sensor—meaning that its detecting signals were bigger than its baseline—it needed a consistent, steady background level in order to prevent being readily influenced by false positive signals.[107]

Consequently, there is a need for a promising method for early diagnosis of lung cancer which is very sensitive for the detection of particular microRNAs. In this regard, a 3D DNA origami structure was developed that allows for the electrochemical detection of microRNAs associated with lung cancer. The 3D DNA origami structure is composed of a thiolated tetrahedron DNA nanostructure at the bottom and a stem-loop DNA structure with ferrocene tags at the top. The top section hybridised with the microRNA linked to lung cancer, whereas the bottom piece self-assembled on a gold electrode surface that had been treated with gold nanoparticles (Au NPs) and blocked with mercaptoethanol (MCH). Cyclic voltammetry (CV), scanning electron microscopy (SEM), differential pulse voltammetry (DPV) and atomic force microscopy (AFM) were used to characterize the fabrication procedure and the performance of the proposed electrochemical genosensor. The proposed genosensor demonstrated tremendous promise for very sensitive clinical cancer diagnostic application for detecting microRNA at concentrations ranging from 100 pM to 1 M, with a detection limit of 10 pM with outstanding linearity.[104]

4.1.2 Aptamer based sensor for cancer detection. Aptamers, derived from the Latin word "*aptus*" meaning "to fit," are synthetic single-stranded oligonucleotide ligands (either DNA or RNA). They can be chosen from combinatorial collections of artificial nucleic acids and exhibit distinct binding capabilities towards a diverse array of targets, characterized by both high specificity and affinity. By employing the SELEX technique, aptamers can be extracted from large pools of diverse oligonucleotides that are randomly synthesized. This process yields artificial single-stranded oligonucleotides (either DNA or RNA) with exceptional specificity and affinity for a wide range of targets. Nowadays, new modifications of the SELEX technique has generated new aptamers referred to as "chemical antibodies" due to the ability to recognize and bind to various target molecules such as peptides, small organics, whole cell[108,109] and proteins. Moreover, aptamers can be chosen for a broad spectrum of applications due to the simplified process of designing and synthesizing probes (aptamers) or capture molecules. These capture molecules are intended for targets like non-immunogenic and toxic substances, rendering the technique superior in comparison to antibodies. Biosensors utilizing aptamers as the recognition element for their construction are referred to as aptasensors. These aptasensors are designed to convert the signal through an electrochemical process.[110]

© 2024 The Author(s). Published by the Royal Society of Chemistry

Open Access Article. Published on 04 January 2024. Downloaded on 2/7/2024 7:04:31 AM. This article is licensed under a Creative Commons Attribution 3.0 Unported Licence.

A unique biological recognition element as aptamer attached to the binding surface through physical or chemical interactions, that generate the changes in the electrochemical signals. While attachment of the target analyte with the aptamer, conformational changes take place resulted to changed in the electrochemical signal. Also, continuous increased or decreased in the electrochemical signal take place by changes in the target analyte concentration.

Aptamers have gained significant attention in various fields, including sensor fabrication due to their unique properties and potential applications. In sensor fabrication, aptamers can be used as unique recognition elements to develop aptamer-based sensors. These sensors utilize the binding affinity of aptamers to detect and quantify target molecules.

Aptamers are first selected or synthesized to specifically bind to the target molecule of interest. This involves an *in vitro* selection process, where a library of random sequences is iteratively enriched for sequences that bind to the target. The SELEX procedure involves two alternating steps. During the initial stage, the original oligonucleotides are subjected to amplification through a polymerase chain reaction until the desired concentration is achieved. In the subsequent phase, the amplified pool is exposed to specific targets, and the oligonucleotides that interact with these targets are utilized for the initial step of the subsequent SELEX round. Using this method, it is possible to isolate aptamers that exhibit elevated specificity and affinity toward their target molecules from larger collections of diverse oligonucleotides through a profoundly iterative process. Within this scenario, the oligonucleotides that form a bond with a target molecule are extracted and subjected to amplification through a polymerase chain reaction, while the non-bound oligonucleotides are effectively removed through a washing process.

Aptamers are immobilized onto a sensor surface, which could be a solid substrate such as a glass slide, a metal electrode, nanoparticles or carbon nanotubes and polymers.[111–113] Aptamers have the capability to be directly attached to a sensor's surface or indirectly linked through chemical coupling methods. Direct immobilization of aptamers primarily arises from electrostatic interactions, hydrogen bonding, or van der Waals forces. The range of feasible approaches here implies the convenient adaptability of aptamers for modification.[114] The selection of an immobilization method is contingent upon various considerations, including the characteristics of the biological recognition component and the transducer surface, the attributes of the target molecule, and the operational circumstances of the aptasensor.[115] Immobilization methods can include physical adsorption, covalent attachment, or hybridization with complementary sequences on the surface such as biotin/avidin affinity, covalent bonds, complementary nucleic acid chain connections and gold–sulfur self-assembled monolayers. Upon binding of the target molecule to the immobilized aptamer, a conformational alteration occurs within the aptamer structure. This modification can be converted into a quantifiable signal through diverse techniques, including electrochemical, thermal, optical, and piezoelectric methods, or mass-sensitive approaches.[116] The alteration in the signal is directly correlated with the concentration of the target molecule present in the sample. The generated signal is detected and quantified using appropriate instrumentation by correlating the measured signal with known concentrations of the analyte. Calibration curves are constructed to establish a quantitative relationship between signal intensity and analyte concentration. The sensitivity and specificity of aptamer-based sensors can rival or even surpass traditional antibody-based sensors. They have the capability to detect an extensive array of targets, encompassing small molecules as well as large proteins.

Nanomaterials play a crucial role in enhancing the performance and capabilities of aptasensors, which are biosensors that utilize aptamers as the recognition element for target molecule detection. It is important to note that the selection of nanomaterials depends on the specific requirements of the aptasensor and the target molecule to be detected. The choice of nanomaterial, surface functionalization, and sensor architecture can greatly influence the sensor's sensitivity, selectivity, and overall performance. Ongoing research in nanomaterial synthesis, modification, and integration continues to expand the capabilities of aptasensors and their potential applications in various fields. The integration of nanomaterials such as nanoparticles (*e.g.*, gold nanoparticles, quantum dots) and nanowires with aptasensors offers several advantages, such as a high surface area-to-volume ratio, allowing for increased immobilization of aptamers and target binding sites. This leads to improved sensitivity as more target molecules can interact with the aptamer molecules. Nanomaterials can be used to amplify the signal generated upon target binding. For example, gold nanoparticles can serve as labels to enhance the electrochemical or optical signal. When a target molecule binds to the immobilized aptamer–nanoparticle complex, the resulting signal change is magnified due to the presence of multiple nanoparticles. Many nanomaterials exhibit good biocompatibility, making them suitable for bioanalytical applications and potential use in medical diagnostics. Specific nanomaterials, like carbon nanotubes and graphene, exhibit remarkable electrical conductivity. They can be used as transducing elements in electrochemical aptasensors, where the binding event between the aptamer and the target molecule leads to a change in electrical conductivity, which can be easily measured. Nanomaterials can provide stability to the aptamer molecules, preventing their degradation and maintaining their functionality over time. Nanomaterials can be functionalized with multiple aptamers or other biomolecules, allowing for the simultaneous detection of multiple target molecules or the integration of additional functionalities, such as controlled release of captured targets. Nanomaterials facilitate the creation of compact and portable aptasensor devices, well-suited for point-of-care and field-based applications. Tiwari *et al.* in 2016 reported Cys-$La(OH)_3$ nanoparticles electrophoretically deposited onto an ITO glass substrate to immobilize anti-Cyfra-21-1 for the electrochemical detection of Cyfra-21-1 (oral cancer biomarker). This immunosensor demonstrates a wide detection span ranging from 0.001 to 10.2 ng mL^{-1} using artificial saliva, a limit of

Open Access Article. Published on 04 January 2024. Downloaded on 2/7/2024 7:04:31 AM. This article is licensed under a Creative Commons Attribution 3.0 Unported Licence.

detection (LOD) of 0.001 ng mL^{-1}, and notable sensitivity at 12.044 μA (ng per mL $cm^{-2})^{-1}$, accompanied by a response time of 5 minutes.[117] The practical utility of the developed sensor for Cyfra-21-1 was tested in artificial saliva samples and the results indicate good correlation with the relative standard deviation which was within the acceptable range.

Khaksari *et al.* in 2023 reported a novel microfluidic electrochemical aptasensor to identify A549 cancer cells. These cells act as a representation of integrin α6β4-containing cells and stand as a circulating tumor cell (CTC) model for non-small cell lung cancer (NSCLC). This aptasensor relies on a target-triggered structural change in an IDA aptamer's conformation, which has a specific affinity for A549 cells. By observing this conformational change in the aptamer structure, the presence of A549 cancer cells can be accurately and selectively determined. The microfluidic biosensor is composed of a microchip that includes a screen-printed gold electrode. The electrode is modified with SH-IDA aptamers through covalent chemical bonding. The biosensor provides an extensive linear detection span ranging from 50×10^5 cells mL^{-1}, achieving a notable level of detection sensitivity with a limit of detection (LOD) as low as 14 cells mL^{-1} for A549 cancer cells. This microfluidic biosensor has demonstrated successful performance in detecting A549 cells within complex samples like human serum.[118] In another report, Chen *et al.* in 2023 developed an innovative and highly sensitive aptasensor that utilizes surface-modified graphene to detect the lung cancer biomarker CA125. This aptasensor takes advantage of the combined effects of incorporating graphene surfaces and electrodeposited gold nanoparticles (AuNPs), resulting in an exceptional level of sensitivity and specificity for accurate biomarker detection. The introduction of AuNPs through deposition significantly reduces electron transfer resistance, thereby greatly improving the electrochemical performance of the sensor. The findings validate a direct correlation between the sensor response and the concentrations of the lung cancer biomarker CA125, encompassing a range from 0.2 to 15.0 ng mL^{-1}. The results also reveal a limit of detection (LOD) of 0.085 ng mL^{-1}.[119]

Electrochemical aptasensors are based on the detection of electrochemical signals generated by the binding of a target biomarker to an immobilized aptamer. The change in the electrochemical signal can be detected using various techniques, such as cyclic voltammetry, impedance spectroscopy, and amperometry. For example, an aptamer-based electrochemical biosensor was developed for the detection of TNF-α in three serum samples collected from healthy individuals.[120] The aptamer was immobilized onto Ag@Pt core–shell nanoparticles supported on reduced graphene oxide, and showed changes in the electrochemical signal, which were quantified using differential pulse voltammetry and square wave voltammetry. The biosensor showed high sensitivity and specificity, and the results indicate its broad application in bioassay and protein diagnostics.

Conventional techniques such as ELISA, western blot, and PCR can show cross-reactivity with other proteins or molecules in a sample, leading to false-positive results, which can lead to unnecessary treatment and anxiety for patients. Specificity is another crucial factor in cancer biomarker detection with aptasensors. Aptamers can bind to specific biomarkers, allowing for the detection of a particular cancer biomarker without cross-reactivity with other proteins or molecules in a sample. Aptasensors have shown higher specificity than conventional techniques for cancer biomarker detection. An electrochemical aptasensor was developed for the detection of human epidermal growth factor receptor 2 (HER2) in human serum samples with albumin depletion for the diagnosis of early stage breast cancer.[121] Also, clinical application of the developed sensor was tested in patient's blood samples with HER2 positive breast cancer and the results showed good correlation with standard samples. The aptasensor showed high selectivity for HER2, with minimal cross-reactivity with other proteins. Another study developed an aptamer-based biosensor for the detection of carcinoembryonic antigen (CEA) in human serum samples suffering from lung disease and the results showed accurate correlation with standard chemiluminescence immunoassay.[122] The performance of hairpin oligonucleotide aptamer-functionalized gold nanorod labels and the graphene-streptavidin nanomatrix was quantified using DPV. The biosensor showed high selectivity and sensitivity for CEA with a wide dynamic range of 5 pg mL^{-1} and 50 ng mL^{-1} toward CEA standards with a low detection limit of 1.5 pg mL^{-1}. Moreover, a few of the recently published research articles related to aptasensors for cancer biomarker detection using the electrochemical technique and their findings of biosensing parameters are summarized in Table 4.

4.1.3 Enzyme based sensor for cancer detection. Enzymes are an important class of biomacromolecules with a variety of catalytic functions that have been proven to be essential regulators of cellular metabolism and they maintain equilibrium in living organisms. Enzymes play a crucial role in human body's energy metabolism, metabolite production, cellular homeostasis, and metabolic detoxification of numerous drugs and environmental xenobiotics (such as pollutants, carcinogens, and pesticides).[135,136] The complex and intricate nature of enzyme-mediated biochemical cascades *in vivo* highlights their significant involvement in a wide range of pathological pathways, including the development of cancerous tumors, neurodegenerative diseases, cardiovascular anomalies, cerebrovascular diseases, and other cases of organismal impairment. Enzymes are important targets for therapeutic intervention[137] because over 53% of pharmacological drugs used to treat these diseases interact directly with enzymes (including 30% that target kinases). Researchers are ardently working to develop novel approaches that target enzymes, whether for therapeutic applications or for the design of diagnostic methodologies with specific goals. These approaches can take advantage of the rapid advancements observed in high-throughput technologies and structural biology within the realms of life sciences. Enzymes have found extensive use as essential components in the creation of practical biosensors owing to their amazing catalytic activity and notable substrate selectivity.[138,139] These biosensors are used to find or measure

 © 2024 The Author(s). Published by the Royal Society of Chemistry

Open Access Article. Published on 04 January 2024. Downloaded on 2/7/2024 7:04:31 AM. This article is licensed under a Creative Commons Attribution 3.0 Unported Licence.

Table 4 Aptasensor based cancer biomarker detection

S. no	Biomarker	Cancer type	Nanomaterials	Techniques	Linear range	LOD	Year	Ref.
1.	α-Enolase	Lung	SPE/AuNP	Voltammetry	10^{-8}–10^{-12} g mL^{-1}	2.38 pg mL^{-1}	2010	123
2.	CEA	Multiple	Graphene films	Voltammetry	5–60 ng mL^{-1}	5 ng mL^{-1}	2011	124
3.	α-Fetoprotein	Multiple	SPCE/nanogold-enriched carbon nanohorn	Voltammetry	0.1 pg mL^{-1} ng mL^{-1}	0.07 pg mL^{-1}	2013	125
4.	miRNA-24	Multiple	GCE/SWCNT-polyamidoamine dendrimer hybrid	Voltammetry	10 fM–1 nM	0.5 fM	2015	126
5.	CEA	Multiple	GCE/AuNP-thionine-reduced GO nanocomposite	Voltammetry	10–500 pg mL^{-1}	4 pg mL^{-1}	2011	127
6.	Platelet-derived growth factor	Multiple	GCE/SWCNT/platinum NP/AuNP	Voltammetry	0.01–35 nM	8 pM	2012	128
7.	L-lactate	Multiple	SPCE/AuNP anchored-reduced GO	Amperometry	5 mM–10 mM	0.13 mM	2015	129
8.	CEA	Multiple	CPE/TiO_2 and Au nanocomposite + chitosan	Amperometric	0.01–1 ng mL^{-1}	0.01 ng mL^{-1}	2014	130
9.	Let-7b	Multiple	ITO/$Ru(PD)_2Cl_2$ + oxidation of hydrazine	Amperometric	0.50–400 pM	0.20 pM	2007	131
10.	Osteopontin	Multiple	AuE/3D scaffold of mercapto-peptides + AB	Impedimetric	2.27–20.43 nM	0.17 nM	2014	132
11.	Interleukin-6	Multiple	SiO_2/Si-wafer/aligned SWCNT + AuNP	Impedimetric	0.01–100 fg mL^{-1}	0.01 fg mL^{-1}	2013	133
12.	Lysozyme	Multiple	AuE/AuNP	Impedimetric	0.1 pM–500 pM	0.01 pM	2011	134

particular target molecules in complex biological matrices. Significant efforts have been made in recent years by biochemists to develop a wide range of enzyme-based biosensors that exhibit excellent selectivity, increased sensitivity, and practical viability. Enzyme-based biosensors' components have been shown to be effective at detecting dynamic fluctuations of target analytes in real samples and, in some cases, in living systems. The conceptualization and construction of unique and practical enzyme-based biosensors, including both electrochemical and optical biosensing modalities, has simultaneously been accomplished through the amalgamation of a variety of imaginative concepts and diverse technologies. This specialized compendium serves as an academic forum, highlighting recent developments in the field of functional enzyme-based biosensors, greatly advancing efforts in drug discovery, environmental monitoring, food safety assurance, clinical diagnostics, as well as fundamental research in the areas of medical and biological sciences. For the therapeutic care of cancer, a wide range of methods, including radiation therapy, chemotherapy, surgical procedures, and immunotherapy, are now accessible. Finding methods to aid in the early detection of malignancies is a major goal in the field of cancer treatment because doing so would significantly reduce the burden of the disease and save a large number of lives. The patients being assessed frequently experience physical discomfort as a result of commonly used clinical diagnostic procedures. However, the development of non-invasive methods for cancer detection continues to be a significant scientific problem. Keshavarz *et.al.* conducted a study using a microRNA (miRNA) in 2015. It is regarded as one of the finest indicators for the electrochemical sensing method's early cancer diagnosis.[140] In 2020 Meng *et al.* summarized and reported the enzymatic activities of MNCs and explored their applications in different fields, such as molecular diagnostics and pollution removal.[141] They placed particular emphasis on MNCs manufactured with protein as a protective agent. In this article, they have included several references for several samples such as human urine and serum, water samples, food samples, and lake water samples.

4.1.4 Immunosensor for cancer detection. In order to track antibody–antigen responses in real time, immunosensors are crucial analytical tools. Immunosensor technology has recently advanced to the point where systems are now available that enable a quick and continuous examination of the binding event without the need for additional reagents or separation/washing processes. Due to this, the commercialization of immunosensors for use in fields such as clinical, environmental, and food analysis has attracted a lot of attention.[142]

Immunosensors are made to be simple for untrained staff to operate, have quick test times, and have sensitivity similar to ELISA techniques. Antibody–antigen interactions have been used in surface plasmon resonance, resonant mirror, continuous-flow immunosensors, fiber-optic waveguides, and planar waveguides for the detection and measurement of therapeutically relevant analytes[143]

Because antibodies are sensitive and specific, immunoassay tools have become essential in clinical diagnosis. Immunosensors, which are compact, portable devices for the measurement of analytes in complicated fluids, find useful application in the quick and accurate diagnostic examination of clinical samples.[143]

The biosensor class known as electrochemical immunosensors are widely known for their high selectivity, ease of use, point of care, and quickness in providing data.[144] The analyte of choice, the biological recognition component, and an appropriate immobilization matrix are all important in the fabrication of immunosensors. The manufacture of biosensors has utilized a variety of immobilization matrix types, including polymers and nanomaterials, and immobilization techniques.[145,146] The construction of biosensors frequently makes use of electrochemical transducers using platinum, carbon, and gold bases.

As 70% of oral cancers are discovered at advanced stages, it might be difficult to detect OC at an early stage.[142] As a result, OC patients often have a bad prognosis because the overall 5-year survival rate for OCs is less than 40%.[147] In an effort to improve prognosis, a wide variety of OC screening techniques have been developed including visual, toluidine blue (TB) staining, auto-fluorescence spectroscopy,[148] exfoliative cytology, and biopsy/histopathology.

However, these methods have drawbacks such as limited sensitivity, lack of specificity for malignant tissue, time consumption,

Open Access Article. Published on 04 January 2024. Downloaded on 2/7/2024 7:04:31 AM. This article is licensed under a Creative Commons Attribution 3.0 Unported Licence.

high cost, and tedious work-up. Therefore, there is a need for the creation of a quick, inexpensive, and highly sensitive technology that may be employed for early diagnosis of lung cancer. Recent research has concentrated on methods using biosensors for a quicker, less expensive, and early cancer diagnosis.[149,150]

Deepa *et al.* in 2016 fabricated a label-free impedimetric immunosensor that can identify CD 59, an essential and early-stage OC biomarker, and be used to diagnose OC. The self-assembled molecular layer of L-cysteine (Cys) on a gold electrode is used to immobilize CD 59 antibodies (anti-CD 59) in order to create the immunosensor probe. In order to get the highest level of sensitivity, the experimental settings were optimized for antibody concentration, temperature, pH, and incubation duration. The CD 59 is subjectively recognized by EIS, which has a detection limit of 0.38 (0.03) fg mL^{-1} and a linear range of detection from 1 fg mL^{-1} to 1000 fg mL^{-1}. The developed immunosensor successfully detects CD 59 in clinically relevant quantities.[151] Moreover, real application of the oral cancer biosensor was investigated in human saliva samples and the detection limit was found to be 0.84 fg mL^{-1}. This study demonstrates that the developed sensor is highly efficient towards the detection of CD59 in saliva samples, and hence the developed sensor shows precise clinical application.

Verma *et al.* in 2017 found that salivary interleukin-8 (IL8), an oral cancer biomarker, can be used to detect cancer without using labels or other intrusive methods. They fabricated an electrochemical immunosensor using a transducer matrix made of an extremely stable composite material of reduced graphene oxide and gold nanoparticles (AuNPs-rGO). Due to the increased electron transfer abelled of the composite made possible by the synergy between rGO and AuNPs, the immunosensor could now respond quickly and with great sensitivity. The immunosensor had an experimental linear range of detection from 500 fg mL^{-1} to 4 ng mL^{-1} and a LOD of 72.73 $\pm$ 0.18 pg mL^{-1}. It also exhibited great sensitivity and enabled extremely quick detection of IL8 (9 min). The created immunosensor had outstanding specificity for detecting IL8 in samples of human saliva. Additionally, the immunosensor showed reusability and stability for up to three months revealing the commercial potential of this nanoplatform for the detection of other clinically relevant biomarkers.[152]

Malhotra *et al.* in 2010 found another biomarker for oral cancer detection based on the observation that interleukin-6 (IL-6)-mediated angiogenic, immunological, and inflammatory responses are linked to head and neck squamous cell carcinoma (HNSCC). In this the authors fabricated an electrochemical immunosensor for human IL-6 along with proof-of-concept tests on HNSCC cells to demonstrate IL-6 detection. In an electrochemical sandwich immunoassay approach employing enzyme abelled horseradish peroxidase (HRP), single wall carbon nanotube (SWNT) forests with connected capture antibodies (Ab1) for IL-6 were utilized to quantify extremely low ($\leq$30 pg mL^{-1}) and increased amounts of IL-6. A representative panel of HNSCC cells was employed to quantify a wide concentration range of IL-6 using two levels of multienzyme labelling. The best detection limit (DL) for IL-6 in 10 L of calf serum was 0.5 pg mL^{-1} (25 fM) and the maximum sensitivity was 19.3 nA mL (pg IL-6)$^{-1}$ cm^2. This was achieved using secondary antibodies (Ab2) linked to carboxylated multiwall carbon nanotubes with 106 HRP labels per 100 nm. In order to give 14–16 labels for each antigen, biotinylated Ab2 coupled to streptavidin-HRP was used. The excellent correlations between this immunosensor's measurements of secreted IL-6 in a variety of HNSCC cells and the results of standard enzyme-linked immunosorbent assay (ELISA) suggest that SWNT immunosensors in combination with multilabel detection hold great promise for detecting IL-6 in both research and human serum clinical applications.[153]

Also, Pachauri *et al.* fabricated a noninvasive electrochemical immunosensor using silver molybdate nanoparticles for the detection of another oral cancer biomarker interleukin-8 (IL-8). This sensor had a linear range of detection of 1 fg mL^{-1} to 40 ng mL^{-1} and showed an LOD of 90 pg mL^{-1} and a sensitivity of 7.03 $\mu A\ ng^{-1}\ mL\ cm^{-2}$.[154] Also, experiments were conducted for practical utility of the developed immunosensor in human saliva samples by spiking of various concentrations ranging from 400 fg mL^{-1} to 40 ng mL^{-1} and current values were recorded using the DPV technique. It was found that the current values increased with the increasing concentration of the IL-8 antigen revealing the successful binding of the antigen of IL-8 to the antibody of IL-8. This study shows that the developed immunosensor is suitable for real sample sensing applications.

Lung cancer is screened for at an early stage of the disease using a variety of techniques, including a chest radiograph, X-ray, CT scan, tissue biopsy, and sputum cytology. However, due to several restrictions, these techniques are not applicable on all patients. Other therapeutic approaches have also been employed, including chemotherapy, radiation therapy, and surgical procedures.[155,156] The present diagnostic techniques do, however, have several limitations, such as cost, long-term therapy, pricey instruments, and limited sensitivity.

Cytokeratin fragment antigen 21-1 (CYFRA21-1) is a sensitive diagnostic marker for detecting non-small cell lung cancer (NSCLC). CYFRA21-1 is recognized as a protein marker for sensitive and specific diagnosis of NSCLC since lung SCC patients express it more than cancer patients with other types of disease.[157,158] Enzyme-linked immunosorbent assay (ELISA), fluorometric immunoassay,[159,160] and inductively coupled plasma source mass spectrometer (ICP-MS) detection are only a few of the methodologies currently being used for the detection and profiling of CYFRA21-1.[161,162] These techniques can be utilized to detect CYFRA21-1; however they still have limitations, such as low sensitivity, high analytical costs, or high equipment costs.[163] Due to its simplicity, sensitivity, quick reaction, and low cost, the electrochemical biosensor has emerged as a new research hotspot in the detection of protein markers.[160] Over the years, several types of high-performing materials have been created to build more sensitive electrochemical sensors, including graphene, molybdenum disulfide (MoS_2), and others. AuNPs@MoS_2@$Ti_3C_2T_x$ composite materials labelled with secondary antibody (Ab2) and toluidine blue (TB) as the signal probe were integrated with Nafion-AuNPs as

© 2024 The Author(s). Published by the Royal Society of Chemistry

Open Access Article. Published on 04 January 2024. Downloaded on 2/7/2024 7:04:31 AM. This article is licensed under a Creative Commons Attribution 3.0 Unported Licence.

the electrode material to create a sensor for the first time that can detect CYFRA21-1 quantitatively. Nafion-AuNPs may offer a high conductivity interface, and its large surface area can offer a variety of places for the loading of Ab1. In the meanwhile, the Ab2-TB-AuNPs@MoS_2@$Ti_3C_2T_x$ composite materials were employed as signal amplification labels; they have the all-inclusive benefits of $Ti_3C_2T_x$'s large specific surface area, MoS_2's strong catalytic performance, and AuNPs' biocompatibility. The sensor therefore demonstrated excellent electrochemical performance with respect to CYFRA21-1 in real patient serum samples, a strong electrochemical signal, a low detection limit (LOD) of 0.03 pg mL^{-1} (S/N = 3), good selectivity, and sensitivity, indicating that it has a potential application prospect in the early diagnosis of NSCLC.[164]

Along with this approach for detecting CYFRA21-1, an electrochemical immunosensor was fabricated based on a silicon nitride (Si_3N_4)–molybdenum disulfide (MoS_2) composite on multi-walled carbon nanotubes (Si_3N_4/MoS_2–MWCNTs) as an electrochemical sensor platform. First, the capture antibody (Ab1) was immobilized on Si_3N_4/MoS_2-MWCNT modified on a glassy carbon electrode (Si_3N_4/MoS_2-MWCNTs/GCE) through stable electrostatic/ionic contacts between the $-NH_2$ groups of the capture antibody and the polar groups of Si_3N_4/MoS_2. A unique voltammetric CYFRA21-1 immunosensor was then fabricated through specific antibody–antigen interactions between the electrochemical sensor platform and the signal amplifier. For analytical applications, a linearity range of 0.01–1.0 pg mL^{-1} and a low detection limit (LOD) of 2.00 fg mL^{-1} were also attained.[165] Moreover, a validation study of the fabricated immunosensor for CYFRA21-1 detection was performed in four different plasma samples by the voltammetric technique and the percentage recoveries were found to be within the acceptable range (from 99.34 to 99.43%).

Pachauri *et al.* also constructed an electrochemical immunosensor for CYFRA21-1 detection using cubic CeO_2 implanted rGO [Fig. 5].[166] A highly sensitive and selective non-invasive biosensor for oral cancer detection was fabricated using the electrochemical technique. *In situ* reduction of GO to rGO in the presence of CeO_2 materials was performed using hydrazine hydrate as the reducing agent. The synthesized nanocomposite of CeO_2-rGO was decorated onto an ITO substrate and further anti-CYFRA21-1 antibodies were immobilized using EDC:NHS coupling chemistry. This fabricated immunosensor was used to detect CYFRA21-1 in the concentration range from 0.625 pg mL^{-1} to 15 ng mL^{-1} with a LOD of 0.625 pg mL^{-1} and the sensitivity of the sensor was 14.5 μA ng^{-1} mL cm^{-2} and the sensor was highly selective towards the CYFRA21-1 antigen. To check the practical utility of the developed sensor, the authors conducted a spiked human saliva sample study using the DPV technique.% of relative standard deviation was found in the range of 0.18 to 2.10% which was within the acceptable range.

Similarly, other biomarkers of lung cancer are also detected such as enolase (ENO). In addition, an elevated level of ENO2 can be used as an indicative, useful tumor marker for small cell lung cancer (SCLC). Recent research has additionally dealt with the potential for linking ENO1, a cancer marker that is highly expressed, with non-small cell lung cancer (NSCLC).[167,168] Additionally, SCLC tissue frequently contains overexpressed ENO1, and the ratio of ENO2 to ENO1 [ENO1 + ENO2] has been thought to be a useful indicator for SCLC identification.[169] In recent years, it has been shown that the amount of ENO1 strongly influences the migration of cancer cells.[170] Consequently, it is crucial to measure ENO1 in biological samples, which has turned into a significant difficulty. Although several methods for the detection of ENO1 have been described based on two-dimensional differential in-gel electrophoresis, mass spectrometry and immunobioluminescence assays, these methods frequently require the tedious and time-consuming pretreatment of complex samples.[169–172] In order to detect ENO1 at traces of pg mL^{-1}, the author has devised a simple yet creative electrochemical immunosensor that utilizes gold nanoparticle (AuNP) congregates as bioprobes. The altering properties of AuNPs make them flexible materials for the creation of electrochemical sensors when they are dropcast on disposable screen-printed carbon electrodes (SPCE). Their sensors are fabricated by physically adsorbing polyethylene glycol (PEG) onto SPCE. In order to construct 151 nm AuNP congregates sensitized with secondary anti-ENO1 antibody molecules, polyclonal secondary anti-ENO1 and 33.0 nm diameter AuNPs were combined simultaneously to form the signal amplification probes. Following further incubation with the sample ENO1, the secondary anti-ENO1-tagged AuNP congregate bioprobes produced immunocomplexes on the primary monoclonal anti-ENO1-modified SPCE surface. A later research study employing square wave voltammetry revealed that this electrochemical immunosensor was capable of detecting ENO1 levels in the linear dynamic range from 10^{-12} to 10^{-8} g mL^{-1} with a low detection limit of 11.9 fg mL^{-1}.[123]

Choudhary *et.al.* found CD59 is a biomarker with therapeutic value for lung cancer and fabricated an immunosensor. To fabricate the functional immunosensor assembly, anti-CD59 antibodies were immobilized on a pencil-shaped graphite electrode covered with graphene oxide nanoparticles (GrONPs). In order to get the greatest degree of activity, the experimental parameters were changed for pH, incubation time, temperature, and antigen concentration. When the current was measured, CD59 could be found, and this revealed a range of 1 fg mL^{-1} to 10 ng mL^{-1}. The sensor's minimal limit of detection (LOD) was 1 fg mL^{-1}.[173] The presence of CD59 was also validated in human urine samples of lung cancer patients and the results were compared with the healthy adult's samples. It was found that the levels of the CD59 protein range from 3 ± 0.02 to 9 ± 0.04 ng mL^{-1} ($n = 7$) in apparently healthy persons whereas the levels of CD59 were found to be 0.001 ± 0.02 to 0.35 ± 0.01 ng mL^{-1} ($n = 7$) in lung cancer patients. This developed sensor was highly specific, selective, accurate and ultrasensitive towards lung cancer biomarker detection.

4.1.5 MIP-based sensor for cancer detection. Molecularly imprinted polymers (MIPs) have significant potential in the field of biosensors as they demonstrate superior chemical and mechanical stability. These polymers are developed using a basic ''lock–key'' process, in which the polymer is formed

Open Access Article. Published on 04 January 2024. Downloaded on 2/7/2024 7:04:31 AM.
This article is licensed under a Creative Commons Attribution 3.0 Unported Licence.

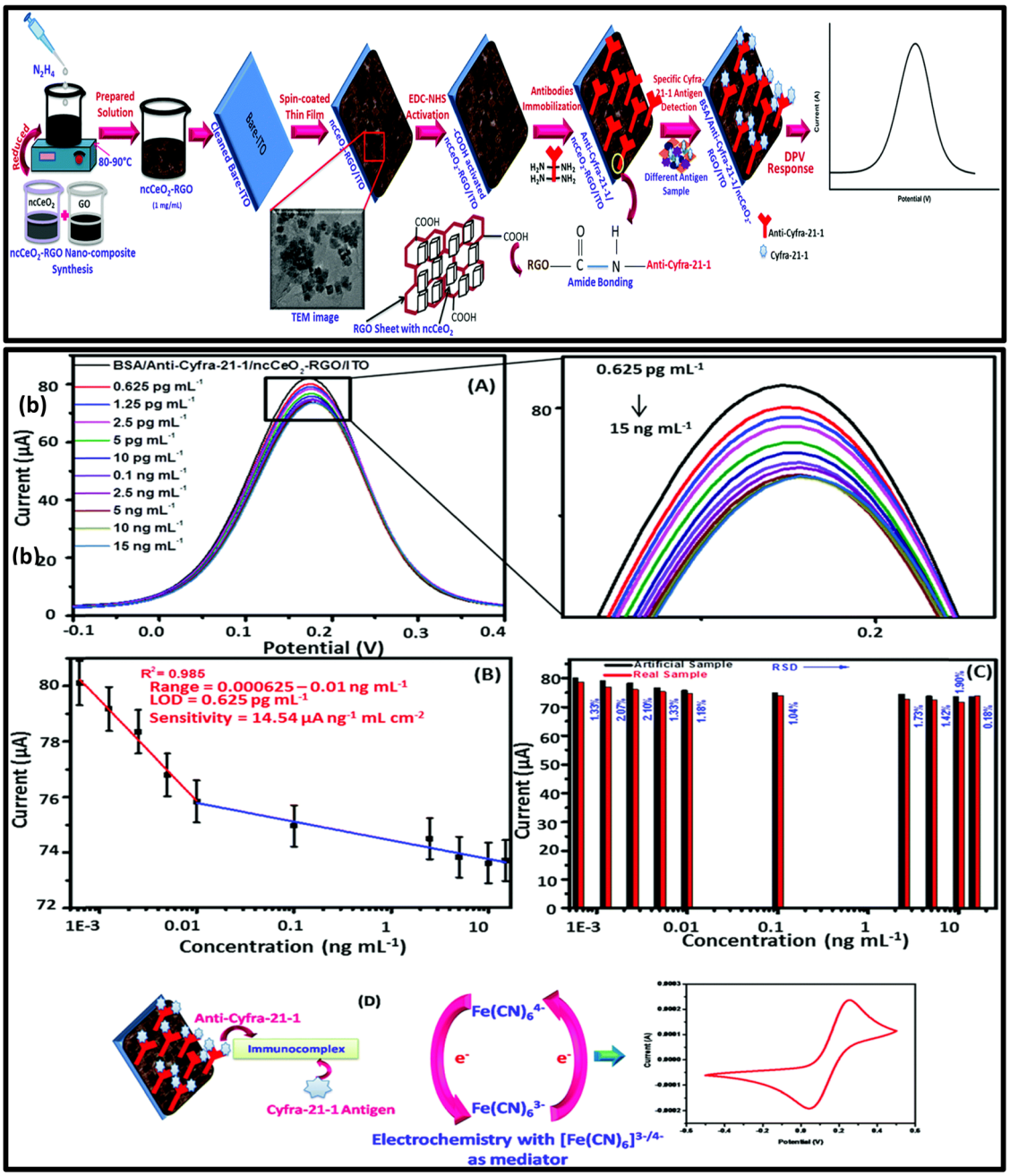


Fig. 5 (a) Fabrication of an electrochemical sensor for CYFRA21-1 detection, (b) the electrochemical sensing results using the immunosensor for CYFRA21-1 detection[166]

around template molecules before the template is removed creating template specific interaction pockets. Three Nobel laureates Cram, Len, and Pedersen in the 1980s introduced the concept of receptor synthesis. This concept explains how molecules are accurately identified, emphasizing the necessity for the molecules to have structural compatibility. Yet, merely matching size and shape often doesn't guarantee precise molecular detection. It is also vital to develop chemical binding sites similar to those found in natural interactions between receptors and their targets. With the right choice of monomers, one can achieve high selectivity and binding to desired compounds. Still, designing these receptors is intricate and time-consuming. It becomes even more complex when dealing with larger molecules, like those spanning several nanometers.

Prominent researchers such as Mosbach, Wolf, Shea, Takeuchi, and others who have made significant contributions in this field have continually refined the process of molecular imprinting over time. Their advancements provide potential solutions to challenges associated with natural biorecognition elements in sensors. Introduced first in 1972, the molecular imprinting technique has since witnessed substantial growth.[174] Here the key to its efficacy is the intricate chemical interactions that take place during the

 © 2024 The Author(s). Published by the Royal Society of Chemistry

Open Access Article. Published on 04 January 2024. Downloaded on 2/7/2024 7:04:31 AM. This article is licensed under a Creative Commons Attribution 3.0 Unported Licence.

polymerization phase during which the shape and size of the target molecule get imprinted in the polymer matrix. The interactions within the pre-polymerized mixture can follow either of the molecular imprinting techniques, namely, "covalent imprinting" and "non-covalent imprinting", based on these interactions.

In the covalent imprinting approach, the template molecule and functional monomers initially form covalent bonds. Subsequently, to remove the template, these bonds are chemically cleaved. The covalent imprinting tends to offer superior host selectivity because the monomer forms a robust bond during polymerization, ensuring precise complementarity. However, a drawback is that the template removal can occasionally be problematic due to the strength of these covalent interactions. In contrast, the non-covalent imprinting method involves the interaction between the template and the functional monomer through non-covalent interactions. Fig. 6 presents the synthesis of an MIP for the targeted analyte. These interactions are readily reversible, allowing for the template's removal simply by washing the polymer in an appropriate solvent. In addition, non-covalent imprinting has the advantage of simplicity. This flexibility means imprinting can be executed across various systems without significant constraints on material selection. The formation of an MIP can be validated using different techniques such as atomic force microscopy (AFM), Fourier transform infrared spectroscopy (FTIR), scanning electron microscopy (SEM), electrochemical techniques, *etc.*[175,176] Some of the relevant studies for the detection of cancer biomarkers are highlighted in further sections.

Moussa *et al.* reported an rGO-AgNPs–Au electrode-MIP based electrochemical sensor for the detection of lactic acid, an important biomarker for cancer cell determination. The confirmation of rGO-AgNPs was performed using X-ray diffraction, SEM, and FTIR. Here $[Fe(CN)_6]^{3-/4-}$ was used as an active redox couple for the cyclic voltammetry study. The fabricated sensor showed a low limit of detection of 0.726 μM. This lactic acid sensor demonstrated superior consistency, selectivity, and durability. Its efficacy remained consistent in varied pH environments. Furthermore, its applicability in real-world scenarios was confirmed through tests on human serum samples, emphasizing its potential for cancer detection and monitoring.[177] Also, Oliveira *et.al.* in 2023 reported a MIP based sensor for the detection of the CA15-3 antigen on a paper based substrate using *o*-phenylenediamine (oPD) as the polymer matrix to synthesis an MIP. The electrodes were printed using carbon-based ink consisting of silver nanoparticles and were further modified using gold nanoparticles. Here, the MIP was synthesized using the electro-polymerization technique and was further validated using AFM and FTIR. Electro-polymerization was conducted at 50 mV s^{-1} from −0.2 V to 1.0 V for 20 cycles in the presence of the analyte and the polymer. Oxalic acid was used as the elution solution to remove the molecules from the polymer matrix and left behind CA15-3 specific cavities in the poly-oPD matrix. The fabricated sensor was further validated by using it for the detection of CA15-3 in serum samples, and it gave satisfactory results.[178]

Moreover, a state-of-the-art electrochemical sensor using Fe_3O_4@graphene oxide (GO)-MIP was fabricated for the quantification of interleukin-8 (IL-8) in saliva samples. It is crucial to highlight that IL-8, having a molecular weight of 8.5 kDa, plays a pivotal role in oral cancer diagnostics. The imprinting surface used here was GO and the implication of super paramagnetic Fe_3O_4 nanoparticles helped in the assembly of Fe_3O_4@(GO)-MIP on a gold film electrode using magnetic forces. The core–shell architecture of these nanoparticles was deciphered through the combined use of SEM and energy dispersive X-ray spectroscopy. Also, cyclic voltammetry was employed to investigate and fine-tune the electrochemical properties of the Fe_3O_4@(GO)-MIP composite. The outcomes revealed that the sensor could selectively bind with IL-8, leading to a measurable decline in the resultant electrical current, a phenomenon that became more pronounced with increasing IL-8 concentrations. The sensor efficacy was marked by its exceptional specificity, a noteworthy detection limit of 0.04 pM, and an extensive linear detection window ranging from 0.1 to 10 pM for IL-8. Moreover, it demonstrated proficiency in quantifying IL-8 levels within saliva samples. Given these attributes, the Fe_3O_4@(GO)-MIP nanoparticle-infused sensor is positioned as a front-runner for the rapid, precise, efficient, and economically viable evaluation of IL-8 and related oral cancer markers.[179]

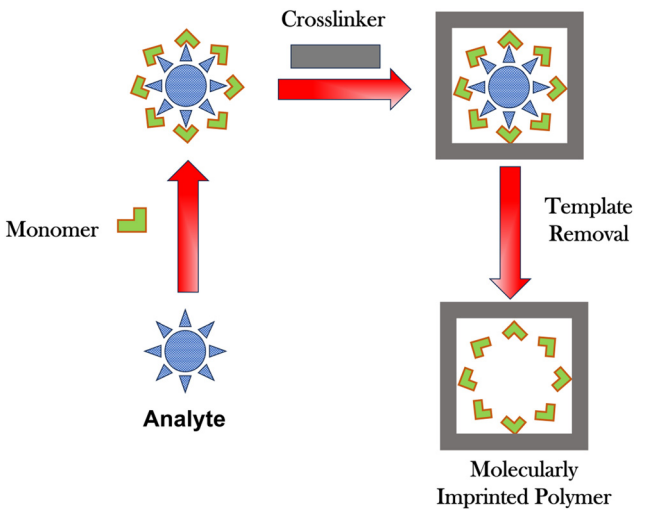


Fig. 6 The synthesis of an MIP for the targeted analyte.

5. Recent advancement in cancer biomarker detection: miniaturization of the electrochemical diagnostic device and multiplex sensing platform

Over the past few years, researchers have been focused on the development of miniaturized point-of-care analytical devices to resolve the diagnosis problem and provide the easiest, easily accessible, portable, ultra-precise and onset detection. The microfluidic based analytical technique is a highly advanced detecting tool which requires minimum sample volume and

Open Access Article. Published on 04 January 2024. Downloaded on 2/7/2024 7:04:31 AM.
This article is licensed under a Creative Commons Attribution 3.0 Unported Licence.

provides a compact and portable platform for on-site detection. Microfluidic devices are micro total analysis systems having 10 to 200 μm microchannels that allow a small amount of fluid to flow in a laminar motion.[180] Microfluidic device-based sensors for cancer biomarker detection have undergone a substantial improvement in the past few years and they can easily detect multiple analytes in a single chip unit system.

The microfluidic system integrated electrochemical detection method is increasingly utilized for the development of sensors and designing of paper based analytical devices. Low fabrication cost, less power consumption and ability to miniaturize the device and portability are the key advantages of paper based electrochemical sensors. Also, paper substrates used in the construction of electrochemical sensors eliminate the disadvantages of non-portable devices. The high availability with a variety of paper as well as excellent mechanical properties such as lightness, specific stiffness, ease of use and stability of the paper, biodegradability, and easy disposal are the uniqueness of paper substrates utilized for the development of electrochemical sensors. Some of the intrinsic properties of fibrous or porous cellulose fiber paper based substrates are high absorption ability for effective storage of aptamers, enzymes, and antibodies, increased sensitivity, faster response time and accuracy of time-dependent measurement, elimination of the air bubble problem, large specific area to improve biomolecule immobilization, reduced need for a pump for transportation of fluid due to their capillary action, better electrochemical detecting ability by the use of conductive ink that can easily be deposited on paper and detection using a low volume of samples.

A microfluidic multiplex immunoarray sensor was developed by Tang *et al.* using an electrochemical analytical device for the multiplex cancer biomarker protein detection such as prostate specific antigen (PSA), prostate specific membrane antigen, interleukin-6, and platelet factor-4 in serum using eight 32-sensor immunoarrays which were connected to an 8-port manifold that allowed 256 measurements in <1 h.[181] Clinically, the relevant detection limit was in the range of 0.05 to 2 pg mL^{-1} and the 5-decade dynamic range was from sub pg mL^{-1} to above ng mL^{-1}. Also, validation of the sensor was conducted by using seven serum samples from prostate cancer patients and one sample from a cancer-free patient and the relative standard deviation in the serum sample study was found to be ±3% to ±10%.

Another biosensor for multiple cancer biomarker detection was developed by Wang *et al.* in 2019. A label-free microfluidic paper based electrochemical aptasensor was constructed for multiplex detection of cancer biomarkers.[182] A highly sensitive and selective, and low-cost disposable simultaneous detecting platform was developed using the paper based microfluidic platform for CEA and neuron-specific enolase (NSE) cancer biomarkers in clinical samples. For the construction of the aptasensor, wax printing and screen-printing techniques were used, which enabled the functions of sample filtration and sample auto-injection [Fig. 7]. Surface functionality of the sensor surface for aptamer immobilization was improved by

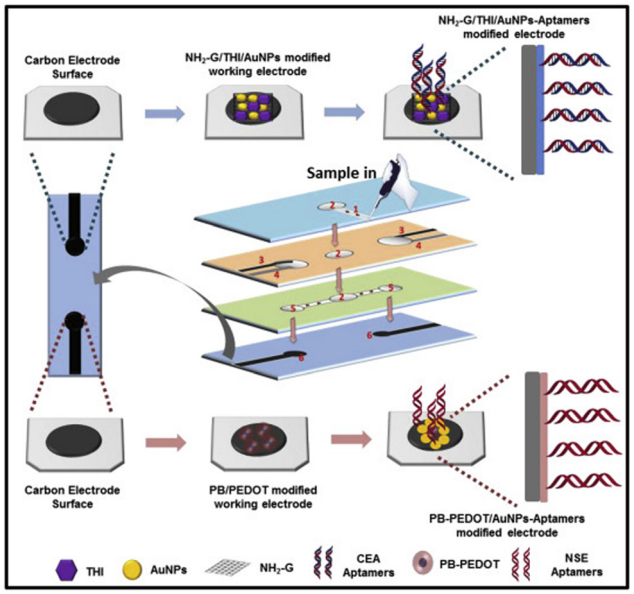


Fig. 7 Schematic illustration of the fabrication of an electrochemical paper based aptasensor for multiplex cancer biomarker detection.[182]

the use of amino functional graphene thionine-gold nanoparticles and Prussian blue-poly(3,4-ethylenedioxythiophene) gold nanocomposite. This nanocomposite was used as a signal transduction element to improve stability as well as intensity of redox signals. The electrochemical sensing results showed that the constructed multiplex aptasensor worked in the linear range from 0.01 to 500 ng mL^{-1} with a LOD of 2 pg mL^{-1} for the CEA cancer biomarker whereas the sensor showed ability to detect NSE cancer biomarkers linearly in the detection range of 0.05 to 500 ng mL^{-1} with a LOD of 10 pg mL^{-1}. In addition to the good linear detection range, the developed aptasensor also worked for the clinical serum samples and the percentage of relative error was found to be 7.81% for CEA and 22.43% for NSE, indicating good accuracy and high sensitivity for the simultaneous detection of CEA and NSE in clinical serum samples.

Recently, Wang *et al.* in 2021 developed a label-free electrochemical impedimetric aptasensor for lung cancer detection based on the CEA cancer biomarker using a Au NP decorated graphene material.[183] For the working electrode surface modification, the graphene electrode was used as the base electrode and gold nanoparticles were decorated using the electrodeposition cyclic voltammetry technique. An optimized concentration of the aptamer was immobilized over the nanoparticle decorated graphene electrode and electrochemical sensing response was evaluated using the EIS technique. A change in the impedance signal was observed upon binding of CEA with the carcinoembryonic antigen aptamer. This developed sensor worked in the range of 0.2 to 15.0 ng mL^{-1} with a LOD of 0.085 ng mL^{-1}. The developed sensor was highly sensitive and selective but the authors did not perform the real sample study for validation of the sensor.

Yang *et al.* in 2021 worked on the electrochemical based simultaneous detection of cancer biomarkers CEA and CYFRA-

© 2024 The Author(s). Published by the Royal Society of Chemistry

Open Access Article. Published on 04 January 2024. Downloaded on 2/7/2024 7:04:31 AM.
This article is licensed under a Creative Commons Attribution 3.0 Unported Licence.

21 using gold doped poly-thionine and poly-*m*-cresol[156] since the use of a single tumor biomarker is not sufficient in terms of sensitivity and specificity for accurate detection of markers in the body fluid. Single antigen detection is prone to false negative or false positive results. Therefore, simultaneous detection of biomarkers instead of a single biomarker is precise to diagnose the accurate level in body fluids. This multiple detection of an analyte is a highly encouraging analytical method for more than one analyte detection of biomarkers. In this work, gold nanoparticles are decorated over the three-dimensional graphene material, poly-thionine, and poly-*m*-cresol which provide a large number of binding sites that helps to amplify the electrochemical sensing signal for better sensitivity performance. This multianalyte sensor worked in the range of 0.5 to 200 ng mL^{-1} with a limit of detection of 0.18 ng mL^{-1} and 0.31 ng mL^{-1} for CYFRA-21 and CEA antigen, respectively. Also, the authors conducted the real spiked serum sample study with different concentrations of CYFRA-21 and CEA. The average recoveries were found to be 92.1–108.4% for CYFRA21-1 and 94.3–107.0% for CEA with RSD less than 4.0% (n = 3). Therefore, the developed sensor showed great potential towards the simultaneous detection of both cancer biomarkers CYFRA-21 and CEA.

Recently, MIP based sensors have gained more attention in the area of biomedical point-of-care device development and diagnosis owing to their low cost, specificity, sensitivity and stability to detect various chemical and biological responses. It has been reported that MIP based sensors are very good alternatives of aptamer- or antibody-based sensors, due to the generation of artificial recognition sites as site-specific cavities for the non-covalent adsorption of the target analyte. Many researchers have worked on the development of electrochemical sensors using MIPs for single analyte detection, but recently, the approach has been focused on the development of sensors for multianalyte detection. Therefore, developing dual template-based MIP sensors for detection of more than one target analyte offers the advantages of low cost, less analysis time, less time needed for the results and less laborious. For the preparation of a MIP, a conductive polymer film is used for the generation of a stable, conductive, sensitive sensor. Polymers such as polypyrrole, polydopamine, poly-methylacrylate, *etc.* are used for imprinting and template preparation.

Taheri *et al.* developed imprinting of dual molecules into a single polymer as a dual template based MIP for the two biomarker detection of CEA and alpha-fetoprotein (AFP) as lung cancer biomarkers.[184] Artificial recognition sites were created in the electropolymerized polypyrrole on the fluorine doped tin oxide electrode surface. Various characterization techniques were used for the analysis of formation and characterization of the sensing layer such as Raman spectroscopy and scanning electron microscopy, and for electrochemical measurements cyclic voltammetry and electrochemical impedance spectroscopy were used. To improve the conductivity of the synthesized polymer of polypyrrole, methyl orange was used as a doping agent and rectangular shaped nanotubes were synthesized. The impedimetric technique was used for the evaluation of the sensing performance of AFP and CEA target analytes. The linear dynamic range was found to vary from 5 to 10^4 pg mL^{-1} with a LOD of 1.6 pg mL^{-1} for the CEA biomarker. Also, the linear detection range was observed for the AFP biomarker, ranging from 10 to 10^4 pg mL^{-1} with a LOD of 3.3 pg mL^{-1}. The dual template-based MIP sensor for AFP and CEA detection was also validated in real serum samples with a satisfactory result. The high sensitivity, selectivity and stability of the dual template-based MIP sensor proved to be promising for AFP and CEA detection in serum samples.

Liu *et al.* in 2022 demonstrated the development of an electrochemical immunosensor for simultaneous detection of dual lung cancer biomarkers using an electro-active probe system.[185] A multiplex electrochemical immunosensor was constructed for CEA and CA-125 detection using electroactive probes of toluidine blue (TB) and Prussian blue (PB) indicators. Copper-tetrakis(4-carboxyphenyl)porphyrin (Cu-TCPP) with a laminar structure was synthesized using a hydrothermal process and was attached to TB and PB indicators to improve electrochemical activity and biocompatibility. The Cu-TCPP-TB complex was labeled with the antibody of CEA and the Cu-TCPP-PB complex was labeled with the antibody of CA-125 for the multiplex sensor. This sensor worked for both analytes of CEA and CA-125. By changing the CEA concentration a linear change in the electrochemical signal was observed in the range of 0.1 to 160 ng mL^{-1} with a LOD of 0.03 ng mL^{-1}, whereas for CA-125, a linear response in the signal was observed from 0.5 to 200 U mL^{-1} with a LOD of 0.05 U mL^{-1}. Furthermore, the fabricated multiplex immunosensor was tested in real human blood serum samples and the obtained results were comparable with those of the ELISA kit. Hence, the constructed electrochemical immunosensor showed simultaneous detection of two lung cancer markers CEA and CA-125 on the same substrate matrix.

Jiang *et al.* in 2023 fabricated an ultrasensitive sandwich type electrochemical aptasensor for dual lung cancer biomarker detection of NSE and epidermal growth factor receptor (EGFR) using the black phosphorus–gold nanocomposite (BP–AuNC).[186] BP–AuNC was synthesized using an *in situ* reduction process without using other reducing agents and the synthesized nanocomposite was decorated onto the working area of an electrode of a cloth substrate matrix and a three electrode system was fabricated by screen printing. This BP–AuNC provides good electrical conductivity and a large number of binding sites to capture the aptamer. Differential pulse voltammetry response was obtained for detection of NSE and EGFR lung cancer biomarkers. Upon changing the concentration of NSE and EGFR analytes, a change in the DPV signal was observed in the linear range of 1 to 400 ng mL^{-1} for NSE and 1 to 600 ng mL^{-1} for the EGFR analyte. The limit of detection for the NSE analyte was found to be 0.1 ng mL^{-1} and for EGFR the LOD was 0.6 ng mL^{-1}. This constructed multiplex aptasensor displayed good selectivity, stability, accuracy and low-cost detection for lung cancer biomarkers but the authors did not perform the real sample study of the developed sensor for further validation.

Open Access Article. Published on 04 January 2024. Downloaded on 2/7/2024 7:04:31 AM.
This article is licensed under a Creative Commons Attribution 3.0 Unported Licence.

6. Conclusions and future perspectives

In summary, this review article discusses literature search on cancer disease which is a leading cause of death worldwide. Cancer is estimated to cause nearly 10 million deaths worldwide due to cancer-causing agents including physical (ultraviolet rays or ionizing radiation), chemical (tobacco, smoke, food or drinking water contaminants) or biological carcinogens (infections, bacteria, viruses, parasites). Moreover, information about the cancer cases of oral or lung cancer is discussed thoroughly. Biology of cancer development and definition of the problem related to cancer, both hallmarks and significant challenges in oncology, and six characteristic features commonly exhibited by cancer cells are described in detail. Also, a brief discussion of conventional techniques such as histopathology, bioimaging, and ELISA for cancer detection and their advantages as well as disadvantages is provided. Further advancements in sensing techniques used for cancer detection that are based on significant cancer biomarkers related to oral or lung cancer using nanomaterials are also summarized.

A detailed overview of the electrochemical sensors mainly focused on nucleic acids, aptamers, immunosensors, enzyme-based sensors or MIP based sensors using nanomaterials for cancer biomarker detection. Various types of nanomaterials like graphene-based materials, metal oxides, polymers, conducting nanoparticles, *etc.* are used to improve the electrochemical or optical properties by enhancing the surface to volume ratio, biocompatibility, electrical conductivity, electron transfer process, and conjugating ability. The integration of nanomaterials into the construction of sensors enhances sensitivity, selectivity, specificity, reproducibility, stability as well as detection range or limit of detection of the device. Therefore, nanomaterials owing to their potential physiochemical properties can provide effective ways to design ultrasensitive biosensors. Therefore, recent research articles mainly on lung and oral cancer detection using the electrochemical sensor have been summarized. Electrochemical sensors which provide a low-cost and convenient solution for variable analyte detection are widely used in biomedical applications. The main key advantages of electrochemical sensors are the ability to detect the analyte over a wide range of concentrations, better sensitivity, good stability, reproducibility, low detection limit, affordability and robustness which have led to their high demand compared to other detecting technologies. Apart from the detection of a single cancer biomarker on the sensing surface, recent research has focused on multiple cancer biomarker detection. The detection of two or more cancer biomarkers on a single sensing platform has various advantages compared to the single detection such as low cost, less analysis time requirement, less time needed for the results and less laborious, less sample volume requirement, less average test time, more informative results and more statically reliable analysis results. Sometimes, it becomes difficult to identify cancer by one cancer biomarker; therefore, multiple biomarker detection gives more clear confirmation about the development of cancer in a particular site, *i.e.*, primary cancer as well as metastasis stage of cancer. Simultaneous detection of biomarkers instead of a single biomarker is precise to diagnose the accurate level in the human body. Additionally, a critical overview of integration of the microfluidic-paper based electrochemical sensor is also discussed for cancer biomarker detection. Low fabrication cost, less power consumption and ability to miniaturize the device and portability are the key advantages of the paper based electrochemical sensor. Also, a paper-based substrate is useful in the construction of an electrochemical sensor that is immensely required for portable devices. Although most electrochemical biosensors perform well under ambient working conditions, changes in the temperature conditions particularly in the case of antigen–antibody based biosensors result in drastic changes in the sensing performance. Also, shorter or limited shelf-life, *i.e.* from 6 months to one year, and sensitivity to humidity conditions are certain limitations of electrochemical sensors. During the past few years, researchers have particularly focused on overcoming these pre-existing limitations for the development of electrochemical sensors using the advanced nanomaterials for particular sensor surface modifications.

In the near future, electrochemical portable designing and construction of sensors for cancer detection will be commercially available for clinical samples' monitoring with early diagnosis of level of biomarkers in the body fluids. Simple, sensitive, and selective detection by electrochemical sensors is an effective alternative approach for early detection of level of cancer biomarkers in real cancer patient samples than the existing conventional techniques. In the far future of nano biosensor integration with artificial intelligence, machine learning could achieve impressive advances in the construction and fabrication of biosensors and impact the commercialization of devices.

Availability of data and material

Available data and material in this work are properly cited.

Author contributions

HB: conceptualization, investigation, writing original draft, review, editing. Archana: conceptualization, writing original draft, review, editing. AN: writing original draft, editing, review. JKH: writing original draft, editing, review. SC: writing original draft, editing, review. PRS: conceptualization, editing, review.

Conflicts of interest

The authors declare that they have no conflict of interest.

Acknowledgements

HB is thankful to DBT for the Research Associate fellowship [DBT-RA/2022/July/N/2383]. PRS is thankful to ICMR for the project [34/13/2019-TF/Nano/BMS]. Archana is thankful to DBT

© 2024 The Author(s). Published by the Royal Society of Chemistry

for the JRF fellowship [DBTHRDPMU/JRF/BET-21/I/2021-22/364]. AN is thankful to DST for the project. JKH is thankful to UGC for the non-NET fellowship.

Open Access Article. Published on 04 January 2024. Downloaded on 2/7/2024 7:04:31 AM. This article is licensed under a Creative Commons Attribution 3.0 Unported Licence.

References

1 S. D. Hohl, K. A. Shoenbill and K. L. Taylor, *et al.*, The Impact of the COVID-19 Pandemic on Tobacco Treatment Program Implementation at National Cancer Institute-Designated Cancer Centers, *Nicotine Tob. Res.*, 2023, **25**, 345–349.

2 N. Y. Spencer and R. C. Stanton, The Warburg effect, lactate, and nearly a century of trying to cure cancer, *Seminars in nephrology*, Elsevier, 2019, pp. 380–393.

3 J. Boutry, S. Tissot and B. Ujvari, *et al.*, The evolution and ecology of benign tumors. Biochim Biophys Acta (BBA)-Reviews, *Cancer*, 2022, **1877**, 188643.

4 R. A. Weinberg, How cancer arises, *Sci. Am.*, 1996, **275**, 62–70.

5 K. P. Gunasekaran, Leveraging object detection for the identification of lung cancer, *arXiv*, arXiv230515813, 2023, Prepr.

6 P.-T. Chen, T. Wu and P. Wang, *et al.*, Pancreatic cancer detection on CT scans with deep learning: a nationwide population-based study, *Radiology*, 2023, **306**, 172–182.

7 M. B. Lawson, S. C. Partridge and D. S. Hippe, *et al.*, Comparative Performance of Contrast-enhanced Mammography, Abbreviated Breast MRI, and Standard Breast MRI for Breast Cancer Screening, *Radiology*, 2023, **308**, e230576.

8 J. M. Rafalko, K. M. Kruglyak and A. L. McCleary-Wheeler, *et al.*, Age at cancer diagnosis by breed, weight, sex, and cancer type in a cohort of more than 3,000 dogs: Determining the optimal age to initiate cancer screening in canine patients, *PLoS One*, 2023, **18**, e0280795.

9 S. Connal, J. M. Cameron and A. Sala, *et al.*, Liquid biopsies: the future of cancer early detection, *J. Transl. Med.*, 2023, **21**, 118.

10 F. Ye, S. Dewanjee and Y. Li, *et al.*, Advancements in clinical aspects of targeted therapy and immunotherapy in breast cancer, *Mol. Cancer*, 2023, **22**, 1–40.

11 M. D. Melisa Hunis and M. D. Adrian Hunis, *MAR Gynecol. Urol.*, 2023, **5**, 4.

12 T. Muka, J. J. X. Li, S. J. Farahani and J. P. A. Ioannidis, An umbrella review of systematic reviews on the impact of the COVID-19 pandemic on cancer prevention and management, and patient needs, *eLife*, 2023, **12**, DOI: 10.7554/eLife.85679.

13 L. A. Hall, S. C. McKay and J. Halle-Smith, *et al.*, The impact of the COVID-19 pandemic upon pancreatic cancer treatment (CONTACT Study): a UK national observational cohort study, *Br. J. Cancer*, 2023, **128**, 1922–1932, DOI: 10.1038/s41416-023-02220-2.

14 T. Li, B. Nickel and P. Ngo, *et al.*, A systematic review of the impact of the COVID-19 pandemic on breast cancer screening and diagnosis, *Breast*, 2023, **67**, 77–88, DOI: 10.1016/j.breast.2023.01.001.

15 I. S. Jabbal, S. Sabbagh and B. Dominguez, *et al.*, Impact of COVID-19 on cancer-related care in the United States: An overview, *Curr. Oncol.*, 2023, **30**, 681–687.

16 Y.-L. Zhang, W.-S. Feng and X.-K. Zheng, *et al.*, Three new ursane-type triterpenes from the leaves of Rehmannia glutinosa, *Fitoterapia*, 2013, **89**, 15–19, DOI: 10.1016/j.fitote.2013.05.013.

17 P. Wang, X. Hu and Y. Li, *et al.*, Automatic cell nuclei segmentation and classification of breast cancer histopathology images, *Signal Process.*, 2016, **122**, 1–13, DOI: 10.1016/j.sigpro.2015.11.011.

18 M. de Bruijne, Machine learning approaches in medical image analysis: From detection to diagnosis, *Med. Image Anal.*, 2016, **33**, 94–97, DOI: 10.1016/j.media.2016.06.032.

19 X. Huang, P. H. G. Duijf and S. Sriram, *et al.*, Circulating tumour DNA alterations: emerging biomarker in head and neck squamous cell carcinoma, *J. Biomed. Sci.*, 2023, **30**, 1–19.

20 J. M. García-Martín, P. Varela-Centelles and M. González, *et al.*, Epidemiology of oral cancer, *Oral cancer detection: novel strategies and clinical impact,* Springer, Cham, 2019, pp. 81–93, DOI: 10.1007/978-3-319-61255-3_3.

21 K. S. Ravi, N. B. Pushpa and S. Kishore, *et al.*, Taxation of micronuclei frequency as a prognostic marker in oral and oropharyngeal carcinoma: A cytogenetic study, *Natl. J. Clin. Anat.*, 2021, **10**, 57–60.

22 R. Sankaranarayanan, K. Ramadas and H. Amarasinghe, *et al.*, Oral cancer: prevention, early detection, and treatment, *Cancer Dis Control priorities*, 3rd edn, vol. 3, 2015.

23 E. E. W. Cohen, J. Baru and D. Huo, *et al.*, Efficacy and safety of treating T4 oral cavity tumors with primary chemoradiotherapy, *Head Neck J. Sci. Spec.*, 2009, **31**, 1013–1021.

24 J. Balakittnen, C. E. Weeramange and D. F. Wallace, *et al.*, Noncoding RNAs in oral cancer, *Wiley Interdiscip. Rev.: RNA*, 2023, **14**, e1754.

25 Q. Huang, H. Ding and N. Razmjooy, Optimal deep learning neural network using ISSA for diagnosing the oral cancer, *Biomed. Signal Process. Control*, 2023, **84**, 104749.

26 N. Al-Rawi, A. Sultan and B. Rajai, *et al.*, The effectiveness of artificial intelligence in detection of oral cancer, *Int. Dent. J.*, 2022, **72**, 436–447.

27 A. Leiter, R. R. Veluswamy and J. P. Wisnivesky, The global burden of lung cancer: current status and future trends, *Nat. Rev. Clin. Oncol.*, 2023, 1–16.

28 A. Lahiri, A. Maji and P. D. Potdar, *et al.*, Lung cancer immunotherapy: progress, pitfalls, and promises, *Mol. Cancer*, 2023, **22**, 1–37.

29 B. Wang, Y. Han and Y. Zhang, *et al.*, Overcoming acquired resistance to cancer immune checkpoint therapy: potential strategies based on molecular mechanisms, *Cell Biosci.*, 2023, **13**, 1–23.

30 A. Nath, K. Sathishkumar and P. Das, *et al.*, A clinicoepidemiological profile of lung cancers in India–Results from the National Cancer Registry Programme, *Indian J. Med. Res.*, 2022, **155**, 264.

Open Access Article. Published on 04 January 2024. Downloaded on 2/7/2024 7:04:31 AM. This article is licensed under a Creative Commons Attribution 3.0 Unported Licence.

31 J. T. Yan, Y. Jin and E. Lo, *et al.*, Real-World Biomarker Test Utilization and Subsequent Treatment in Patients with Early-Stage Non-small Cell Lung Cancer in the United States, 2011–2021, *Oncol. Ther.*, 2023, 1–18.
32 K. Sathishkumar, M. Chaturvedi and P. Das, *et al.*, Cancer incidence estimates for 2022 & projection for 2025: Result from national cancer Registry Programme, India, *Indian J. Med. Res.*, 2022, **156**, 598.
33 C. L. Chaffer and R. A. Weinberg, A Perspective on Cancer Cell Metastasis, *Science*, 2011, **331**, 1559–1564, DOI: 10.1126/science.1203543.
34 A. W. Lambert, D. R. Pattabiraman and R. A. Weinberg, Emerging Biological Principles of Metastasis, *Cell*, 2017, **168**, 670–691, DOI: 10.1016/j.cell.2016.11.037.
35 X. Zheng, J. L. Carstens and J. Kim, *et al.*, Epithelial-to-mesenchymal transition is dispensable for metastasis but induces chemoresistance in pancreatic cancer, *Nature*, 2015, **527**, 525–530, DOI: 10.1038/nature16064.
36 G. Evan and T. Littlewood, A matter of life and cell death, *Science*, 1998, **281**, 1317–1322.
37 D. Hanahan and R. A. Weinberg, Hallmarks of cancer: the next generation, *Cell*, 2011, **144**, 646–674.
38 P. Vineis and C. P. Wild, Global cancer patterns: causes and prevention, *Lancet*, 2014, **383**, 549–557, DOI: 10.1016/S0140-6736(13)62224-2.
39 M. Iranifam, Analytical applications of chemiluminescence methods for cancer detection and therapy, *TrAC, Trends Anal. Chem.*, 2014, **59**, 156–183, DOI: 10.1016/j.trac.2014.03.010.
40 V. A. Katzke, R. Kaaks and T. Kühn, Lifestyle and Cancer Risk, *Cancer J.*, 2015, **21**, 104–110, DOI: 10.1097/PPO.0000000000000101.
41 K. Gilham, A. Gadermann, T. Dummer and R. A. Murphy, Mental health, cancer risk, and the mediating role of lifestyle factors in the CARTaGENE cohort study, *PLoS One*, 2023, **18**, e0281588.
42 M. Narwaria, Does explainable machine learning uncover the black box in vision applications?, *Image Vis. Comput.*, 2022, **118**, 104353, DOI: 10.1016/j.imavis.2021.104353.
43 N. Sharma, R. Sharma and N. Jindal, Machine Learning and Deep Learning Applications-A Vision, *Glob. Transitions Proc.*, 2021, **2**, 24–28, DOI: 10.1016/j.gltp.2021.01.004.
44 M. L. Smith, L. N. Smith and M. F. Hansen, The quiet revolution in machine vision - a state-of-the-art survey paper, including historical review, perspectives, and future directions, *Comput. Ind.*, 2021, **130**, 103472, DOI: 10.1016/j.compind.2021.103472.
45 D. Komura and S. Ishikawa, Machine learning methods for histopathological image analysis, *Comput. Struct. Biotechnol. J.*, 2018, **16**, 34–42.
46 A. Korzynska, L. Roszkowiak, J. Zak and K. Siemion, A review of current systems for annotation of cell and tissue images in digital pathology, *Probl. Biocybern. Biomed. Eng.*, 2021, **41**, 1436–1453, DOI: 10.1016/j.bbe.2021.04.012.
47 O. Kott, D. Linsley and A. Amin, *et al.*, Development of a Deep Learning Algorithm for the Histopathologic Diagnosis and Gleason Grading of Prostate Cancer Biopsies: A Pilot Study, *Eur. Urol. Focus*, 2021, **7**, 347–351, DOI: 10.1016/j.euf.2019.11.003.
48 Y. Zeng and J. Zhang, A machine learning model for detecting invasive ductal carcinoma with Google Cloud AutoML Vision, *Comput. Biol. Med.*, 2020, **122**, 103861, DOI: 10.1016/j.compbiomed.2020.103861.
49 D. G. Vinsard, Y. Mori and M. Misawa, *et al.*, Quality assurance of computer-aided detection and diagnosis in colonoscopy, *Gastrointest. Endosc.*, 2019, **90**, 55–63, DOI: 10.1016/j.gie.2019.03.019.
50 S. Shaikh, F. U. Rehman and T. Du, *et al.*, Real-Time Multimodal Bioimaging of Cancer Cells and Exosomes through Biosynthesized Iridium and Iron Nanoclusters, *ACS Appl. Mater. Interfaces*, 2018, **10**, 26056–26063, DOI: 10.1021/acsami.8b08975.
51 M. S. Ghamsari, in *Introductory Chapter: Nano-bio-imaging—Past, Present, and Future*, ed. M. S. Ghamsari, IntechOpen, Rijeka, ch. 1, 2018.
52 *Biomedical Signals, Imaging, and Informatics*, ed. J. D. Bronzino and D. R. Peterson, 1st edn, 2014.
53 R. Vadivambal and D. S. Jayas, *Bio-Imaging: Principles, Techniques, and Applications*, CRC Press, 1st edn, 2015.
54 J. Wen, Y. Xu and H. Li, *et al.*, Recent applications of carbon nanomaterials in fluorescence biosensing and bioimaging, *Chem. Commun.*, 2015, **51**, 11346–11358, DOI: 10.1039/C5CC02887F.
55 S. Goel, C. G. England, F. Chen and W. Cai, Positron emission tomography and nanotechnology: A dynamic duo for cancer theranostics, *Adv. Drug Delivery Rev.*, 2017, **113**, 157–176, DOI: 10.1016/j.addr.2016.08.001.
56 A. Zebibula, N. Alifu and L. Xia, *et al.*, Ultrastable and Biocompatible NIR-II Quantum Dots for Functional Bioimaging, *Adv. Funct. Mater.*, 2018, **28**, 1–13, DOI: 10.1002/adfm.201703451.
57 R. Liu, D. Wu and S. Liu, *et al.*, An aqueous route to multicolor photoluminescent carbon dots using silica spheres as carriers, *Angew. Chem., Int. Ed.*, 2009, **48**, 4598–4601, DOI: 10.1002/anie.200900652.
58 S. N. Frank and A. J. Bard, Heterogeneous photocatalytic oxidation of cyanide and sulfite in aqueous solutions at semiconductor powders, *J. Phys. Chem.*, 1977, **81**, 1484–1488.
59 X. Cui, L. Zhu and J. Wu, *et al.*, A fluorescent biosensor based on carbon dots-labeled oligodeoxyribonucleotide and graphene oxide for mercury(II) detection, *Biosens. Bioelectron.*, 2015, **63**, 506–512, DOI: 10.1016/j.bios.2014.07.085.
60 Q. Xu, P. Pu and J. Zhao, *et al.*, Preparation of highly photoluminescent sulfur-doped carbon dots for Fe(III) detection, *J. Mater. Chem. A*, 2015, **3**, 542–546, DOI: 10.1039/C4TA05483K.
61 S.-T. Yang, X. Wang and H. Wang, *et al.*, Carbon Dots as Nontoxic and High-Performance Fluorescence Imaging Agents, *J. Phys. Chem. C Nanomater Interfaces*, 2009, **113**, 18110–18114, DOI: 10.1021/jp9085969.

© 2024 The Author(s). Published by the Royal Society of Chemistry

Open Access Article. Published on 04 January 2024. Downloaded on 2/7/2024 7:04:31 AM. This article is licensed under a Creative Commons Attribution 3.0 Unported Licence.

62 Q. Wang, X. Huang and Y. Long, *et al.*, Hollow luminescent carbon dots for drug delivery, *Carbon N Y*, 2013, **59**, 192–199, DOI: 10.1016/j.carbon.2013.03.009.
63 J. Tang, B. Kong and H. Wu, *et al.*, Carbon nanodots featuring efficient FRET for real-time monitoring of drug delivery and two-photon imaging, *Adv. Mater.*, 2013, **25**, 6569–6574, DOI: 10.1002/adma.201303124.
64 T. Atabaev, G. Urmanova and N. Hong, Highly Mesoporous Silica Nanoparticles for Potential Drug Delivery Applications, *Nano LIFE*, 2014, **04**, 1441003, DOI: 10.1142/S1793984414410037.
65 M. Karimi, H. Mirshekari and M. Aliakbari, *et al.*, Smart mesoporous silica nanoparticles for controlled-release drug delivery, *Nanotechnol. Rev.*, 2016, 5, DOI: 10.1515/ntrev-2015-0057.
66 Z. Wang, H. Liao and H. Wu, *et al.*, Fluorescent carbon dots from beer for breast cancer cell imaging and drug delivery, *Anal. Methods*, 2015, **7**, 8911–8917, DOI: 10.1039/C5AY01978H.
67 H. Lee, C. Kim and E. Park, *et al.*, [ACS AMI 2014] Photoluminescent green carbon nanodots from food-waste-derived sources Large-scale synthesis Properties and Biomedical applications, *ACS Appl. Mater. Interfaces*, 2014, **6**, 3365–3370, DOI: 10.1021/am500159p.
68 J.-H. Park, L. Gu and G. von Maltzahn, *et al.*, Biodegradable luminescent porous silicon nanoparticles for in vivo applications, *Nat. Mater.*, 2009, **8**, 331–336, DOI: 10.1038/nmat2398.
69 Y. Zhuo, H. Miao and D. Zhong, *et al.*, One-step synthesis of high quantum-yield and excitation-independent emission carbon dots for cell imaging, *Mater. Lett.*, 2015, **139**, 197–200, DOI: 10.1016/j.matlet.2014.10.048.
70 A. Sachdev, I. Matai and P. Gopinath, Carbon dots incorporated polymeric hydrogels as multifunctional platform for imaging and induction of apoptosis in lung cancer cells, *Colloids Surf., B*, 2016, **141**, 242–252, DOI: 10.1016/j.colsurfb.2016.01.043.
71 F. Du, M. Zhang and X. Li, *et al.*, Economical and green synthesis of bagasse-derived fluorescent carbon dots for biomedical applications, *Nanotechnology*, 2014, **25**, 315702, DOI: 10.1088/0957-4484/25/31/315702.
72 J. Qian, F. Quan and F. Zhao, *et al.*, Aconitic acid derived carbon dots: Conjugated interaction for the detection of folic acid and fluorescence targeted imaging of folate receptor overexpressed cancer cells, *Sens. Actuators, B*, 2018, **262**, 444–451, DOI: 10.1016/j.snb.2018.01.227.
73 Y. Yang, J. Cui and M. Zheng, *et al.*, One-step synthesis of amino-functionalized fluorescent carbon nanoparticles by hydrothermal carbonization of chitosan, *Chem. Commun.*, 2012, **48**, 380–382, DOI: 10.1039/c1cc15678k.
74 M. Zhang, C. Chi and P. Yuan, *et al.*, A hydrothermal route to multicolor luminescent carbon dots from adenosine disodium triphosphate for bioimaging, *Mater. Sci. Eng., C*, 2017, **76**, 1146–1153, DOI: 10.1016/j.msec.2017.03.144.
75 X.-W. Hua, Y.-W. Bao and F.-G. Wu, Fluorescent Carbon Quantum Dots with Intrinsic Nucleolus-Targeting Capability for Nucleolus Imaging and Enhanced Cytosolic and Nuclear Drug Delivery, *ACS Appl. Mater. Interfaces*, 2018, **10**, 10664–10677, DOI: 10.1021/acsami.7b19549.
76 L. Li, R. Zhang and C. Lu, *et al.*, *In situ* synthesis of NIR-light emitting carbon dots derived from spinach for bio-imaging applications, *J. Mater. Chem. B*, 2017, **5**, 7328–7334, DOI: 10.1039/C7TB00634A.
77 G. Gao, Y.-W. Jiang and H.-R. Jia, *et al.*, On-off-on fluorescent nanosensor for Fe^{3+} detection and cancer/normal cell differentiation *via* silicon-doped carbon quantum dots, *Carbon N Y*, 2018, **134**, 232–243, DOI: 10.1016/j.carbon.2018.02.063.
78 M. Alhajj and A. Farhana, Enzyme linked immunosorbent assay, *StatPearls*, StatPearls Publishing, 2023.
79 D. Costopoulou, L. Leondiadis and J. Czarnecki, *et al.*, Direct ELISA method for the specific determination of prothymosin alpha in human specimens, *J. Immunoassay Immunochem.*, 1998, **19**, 295–316.
80 N. S. Fedarko, A. Jain and A. Karadag, *et al.*, Elevated serum bone sialoprotein and osteopontin in colon, breast, prostate, and lung cancer, *Clin. Cancer Res.*, 2001, **7**, 4060–4066.
81 A. Yagihashi, K. Asanuma and D. Kobayashi, *et al.*, Detection of autoantibodies to livin and survivin in Sera from lung cancer patients, *Lung Cancer*, 2005, **48**, 217–221.
82 T. Yamashita, H. Kamada and S. Kanasaki, *et al.*, Epidermal growth factor receptor localized to exosome membranes as a possible biomarker for lung cancer diagnosis, *Int. J. Pharm. Sci.*, 2013, **68**, 969–973.
83 R.-S. Lai, H.-K. Hsu and J.-Y. Lu, *et al.*, CYFRA 21–1 enzyme-linked immunosorbent assay: evaluation as a tumor marker in non-small cell lung cancer, *Chest*, 1996, **109**, 995–1000.
84 J. Wang, S. Zhang and W. Ni, *et al.*, Development and application of a double-antibody sandwich ELISA kit for the detection of serum MUC1 in lung cancer patients, *Cancer Biomarkers*, 2016, **17**, 369–376.
85 G. Prasad and M. McCullough, Chemokines and cytokines as salivary biomarkers for the early diagnosis of oral cancer, *Int. J. Dent.*, 2013, **2013**, 1–7, DOI: 10.1155/2013/813756.
86 S. N. Topkaya, M. Azimzadeh and M. Ozsoz, Electrochemical Biosensors for Cancer Biomarkers Detection: Recent Advances and Challenges, *Electroanalysis*, 2016, **28**, 1402–1419, DOI: 10.1002/elan.201501174.
87 P. Villalobos and I. I. Wistuba, Lung Cancer Biomarkers, *Hematol. Oncol. Clin. North Am.*, 2017, **31**, 13–29, DOI: 10.1016/j.hoc.2016.08.006.
88 Z. Khurshid, M. S. Zafar and R. S. Khan, *et al.*, Role of Salivary Biomarkers in Oral Cancer Detection, *Adv. Clin. Chem.*, 2018, **86**, 23–70, DOI: 10.1016/bs.acc.2018.05.002.
89 S. Yete, W. D'Souza and D. Saranath, High-risk human papillomavirus in oral cancer: clinical implications, *Oncology*, 2018, **94**, 133–141.
90 G. Corso, A. Villa, A. Tarsitano and A. Ghoel, Current trends in oral cancer: a review, *Cancer cell Microenviron.*, 2016, 3, DOI: 10.14800/ccm.1332.

Open Access Article. Published on 04 January 2024. Downloaded on 2/7/2024 7:04:31 AM. This article is licensed under a Creative Commons Attribution 3.0 Unported Licence.

91 S. Balakrishnan, S. Manoharan, L. M. Alias and M. R. Nirmal, Effect of curcumin and ferulic acid on modulation of expression pattern of p53 and bcl-2 proteins in 7, 12-dimethylbenz [] anthracene-induced hamster buccal pouch carcinogenesis, *Indian J. Biochem. Biophys.*, 2010, **47**(1), 7–12.

92 J. Rittscher, R. Machiraju and S. T. C. Wong, *Microscopic image analysis for life science applications*, Artech House, 2008.

93 M. N. Gurcan, L. E. Boucheron and A. Can, *et al.*, Histopathological image analysis: A review, *IEEE Rev. Biomed. Eng.*, 2009, **2**, 147–171.

94 C. D. M. Fletcher, Diagnostic histopathology of tumors: 2-volume set with CD-ROMs. *Elsevier Health Sciences*, 2007.

95 S. Di Cataldo, E. Ficarra and E. Macii, Computer-aided techniques for chromogenic immunohistochemistry: status and directions, *Comput. Biol. Med.*, 2012, **42**, 1012–1025.

96 L. Jiang, X. Zeng and H. Yang, *et al.*, Oral cancer over-expressed 1 (ORAOV1): a regulator for the cell growth and tumor angiogenesis in oral squamous cell carcinoma, *Int. J. Cancer*, 2008, **123**, 1779–1786.

97 K. Hsieh, Y. Xiao and H. Tom Soh, Electrochemical DNA detection *via* exonuclease and target-catalyzed transformation of surface-bound probes, *Langmuir*, 2010, **26**, 10392–10396, DOI: **10.1021/la100227s**.

98 F. Xia, X. Zuo and R. Yang, *et al.*, Label-Free, Dual-Analyte Electrochemical Biosensors: A New Class of Molecular-Electronic Logic Gates, *J. Am. Chem. Soc.*, 2010, **132**, 8557–8559, DOI: **10.1021/ja101379k**.

99 S. Bi, J. Zhang and S. Zhang, Ultrasensitive and selective DNA detection based on nicking endonuclease assisted signal amplification and its application in cancer cell detection, *Chem. Commun.*, 2010, **46**, 5509–5511.

100 M. P. Rivera and A. C. Mehta, Initial Diagnosis of Lung Cancer: ACCP Evidence-Based Clinical Practice Guidelines, 2nd edn, *Chest*, 2007, **132**, 131S–148S, DOI: **10.1378/chest.07-1357**.

101 K. Han, H. Liu and J. Cui, *et al.*, Recent strategies for electrochemical sensing detection of miRNAs in lung cancer, *Anal. Biochem.*, 2023, **661**, 114986, DOI: **10.1016/j.ab.2022.114986**.

102 C. I. Henschke, D. Shaham, D. F. Yankelevitz and N. K. Altorki, CT Screening for Lung Cancer: Past and Ongoing Studies, *Semin. Thorac. Cardiovasc. Surg.*, 2005, **17**, 99–106, DOI: **10.1053/j.semtcvs.2005.05.002**.

103 U. Pastorino, M. Bellomi and C. Landoni, *et al.*, Early lung-cancer detection with spiral CT and positron emission tomography in heavy smokers: 2-year results, *Lancet*, 2003, **362**, 593–597, DOI: **10.1016/S0140-6736(03)14188-8**.

104 S. Liu, W. Su, Z. Li and X. Ding, Electrochemical detection of lung cancer specific microRNAs using 3D DNA origami nanostructures, *Biosens. Bioelectron.*, 2015, **71**, 57–61, DOI: **10.1016/j.bios.2015.04.006**.

105 G. Bonnet, S. Tyagi, A. Libchaber and F. R. Kramer, Thermodynamic basis of the enhanced specificity of structured DNA probes, *Proc. Natl. Acad. Sci. U. S. A.*, 1999, **96**, 6171–6176, DOI: **10.1073/pnas.96.11.6171**.

106 L. V. Sequist, S. Nagrath and M. Toner, *et al.*, The CTC-Chip: An Exciting New Tool to Detect Circulating Tumor Cells in Lung Cancer Patients, *J. Thorac. Oncol.*, 2009, **4**, 281–283, DOI: **10.1097/JTO.0b013e3181989565**.

107 T. Xiao, W. Ying and L. Li, *et al.*, An Approach to Studying Lung Cancer-related Proteins in Human Blood, *Mol. Cell. Proteomics*, 2005, **4**, 1480–1486, DOI: **10.1074/mcp.M500055-MCP200**.

108 D. S. Wilson and J. W. Szostak, In vitro selection of functional nucleic acids, *Annu. Rev. Biochem.*, 1999, **68**, 611–647, DOI: **10.1146/annurev.biochem.68.1.611**.

109 S. M. Shamah, J. M. Healy and S. T. Cload, Complex target SELEX, *Acc. Chem. Res.*, 2008, **41**, 130–138, DOI: **10.1021/ar700142z**.

110 C. K. O'Sullivan, Aptasensors--the future of biosensing?, *Anal. Bioanal. Chem.*, 2002, **372**, 44–48, DOI: **10.1007/s00216-001-1189-3**.

111 C. Zhu, D. Liu and Z. Chen, *et al.*, An ultra-sensitive aptasensor based on carbon nanohorns/gold nanoparticles composites for impedimetric detection of carbendazim at picogram levels, *J. Colloid Interface Sci.*, 2019, **546**, 92–100, DOI: **10.1016/j.jcis.2019.03.035**.

112 M. Adeel, M. M. Rahman and J.-J. Lee, Label-free aptasensor for the detection of cardiac biomarker myoglobin based on gold nanoparticles decorated boron nitride nanosheets, *Biosens. Bioelectron.*, 2019, **126**, 143–150, DOI: **10.1016/j.bios.2018.10.060**.

113 X. Wang, F. Gao and Y. Gong, *et al.*, Electrochemical aptasensor based on conductive supramolecular polymer hydrogels for thrombin detection with high selectivity, *Talanta*, 2019, **205**, 120140, DOI: **10.1016/j.talanta.2019.120140**.

114 S. C. B. Gopinath, K. Awazu and M. Fujimaki, Waveguide-mode sensors as aptasensors, *Sensors*, 2012, **12**, 2136–2151, DOI: **10.3390/s120202136**.

115 S. G. Meirinho, L. G. Dias, A. M. Peres and L. R. Rodrigues, Voltammetric aptasensors for protein disease biomarkers detection: A review, *Biotechnol. Adv.*, 2016, **34**, 941–953, DOI: **10.1016/j.biotechadv.2016.05.006**.

116 I. E. Tothill, Biosensors for cancer markers diagnosis, *Semin. Cell Dev. Biol.*, 2009, **20**, 55–62, DOI: **10.1016/j.semcdb.2009.01.015**.

117 S. Tiwari, P. K. Gupta and Y. Bagbi, *et al.*, L-cysteine capped lanthanum hydroxide nanostructures for non-invasive detection of oral cancer biomarker, *Biosens. Bioelectron.*, 2017, **89**, 1042–1052, DOI: **10.1016/j.bios.2016.10.020**.

118 S. Khaksari, A. R. Ameri and S. M. Taghdisi, *et al.*, A microfluidic electrochemical aptasensor for highly sensitive and selective detection of A549 cells as integrin α6β4-containing cell model *via* IDA aptamers, *Talanta*, 2023, **252**, 123781, DOI: **10.1016/j.talanta.2022.123781**.

119 J. Chen, L. Yu and W. Xu, *et al.*, A graphene-based highly sensitive aptasensor for the detection of lung cancer marker CA125, *Carbon Lett.*, 2023, **33**, 1811–1817, DOI: **10.1007/s42823-023-00560-w**.

© 2024 The Author(s). Published by the Royal Society of Chemistry

Open Access Article. Published on 04 January 2024. Downloaded on 2/7/2024 7:04:31 AM. This article is licensed under a Creative Commons Attribution 3.0 Unported Licence.

120 M. Mazloum-Ardakani, L. Hosseinzadeh and Z. Taleat, Synthesis and electrocatalytic effect of Ag@Pt core–shell nanoparticles supported on reduced graphene oxide for sensitive and simple label-free electrochemical aptasensor, *Biosens. Bioelectron.*, 2015, **74**, 30–36, DOI: 10.1016/j.bios.2015.05.072.

121 G. Bezerra, C. Córdula and D. Campos, *et al.*, Electrochemical aptasensor for the detection of HER2 in human serum to assist in the diagnosis of early stage breast cancer, *Anal. Bioanal. Chem.*, 2019, **411**, 6667–6676, DOI: 10.1007/s00216-019-02040-5.

122 W. Wen, J.-Y. Huang and T. Bao, *et al.*, Increased electrocatalyzed performance through hairpin oligonucleotide aptamer-functionalized gold nanorods labels and graphene-streptavidin nanomatrix: Highly selective and sensitive electrochemical biosensor of carcinoembryonic antigen, *Biosens. Bioelectron.*, 2016, **83**, 142–148, DOI: 10.1016/j.bios.2016.04.039.

123 J. A. Ho, H.-C. Chang and N.-Y. Shih, *et al.*, Diagnostic detection of human lung cancer-associated antigen using a gold nanoparticle-based electrochemical immunosensor, *Anal. Chem.*, 2010, **82**, 5944–5950.

124 S. Gamagedara and Y. Ma, Biomarker analysis for prostate cancer diagnosis using LC–MS and CE–MS, *Bioanalysis*, 2011, **3**, 2129–2142, DOI: 10.4155/bio.11.203.

125 C. Zhao, D. Lin and J. Wu, *et al.*, Nanogold-Enriched Carbon Nanohorn Label for Sensitive Electrochemical Detection of Biomarker on a Disposable Immunosensor, *Electroanalysis*, 2013, **25**, 1044–1049, DOI: 10.1002/elan.201200423.

126 F. Li, J. Peng and Q. Zheng, *et al.*, Carbon Nanotube-Polyamidoamine Dendrimer Hybrid-Modified Electrodes for Highly Sensitive Electrochemical Detection of MicroRNA24, *Anal. Chem.*, 2015, **87**, 4806–4813, DOI: 10.1021/acs.analchem.5b00093.

127 F.-Y. Kong, M.-T. Xu, J.-J. Xu and H.-Y. Chen, A novel lable-free electrochemical immunosensor for carcinoembryonic antigen based on gold nanoparticles–thionine–reduced graphene oxide nanocomposite film modified glassy carbon electrode, *Talanta*, 2011, **85**, 2620–2625, DOI: 10.1016/j.talanta.2011.08.028.

128 L. Bai, R. Yuan and Y. Chai, *et al.*, Simultaneous electrochemical detection of multiple analytes based on dual signal amplification of single-walled carbon nanotubes and multi-labeled graphene sheets, *Biomaterials*, 2012, **33**, 1090–1096, DOI: 10.1016/j.biomaterials.2011.10.012.

129 S. Azzouzi, L. Rotariu and A. M. Benito, *et al.*, A novel amperometric biosensor based on gold nanoparticles anchored on reduced graphene oxide for sensitive detection of L-lactate tumor biomarker, *Biosens. Bioelectron.*, 2015, **69**, 280–286, DOI: 10.1016/j.bios.2015.03.012.

130 S. Aslan and Ü. Anik, Development of TiO2 and Au Nanocomposite Electrode as CEA Immunosensor Transducer, *Electroanalysis*, 2014, **26**, 1373–1381, DOI: 10.1002/elan.201400086.

131 Z. Gao and Y. H. Yu, Direct labeling microRNA with an electrocatalytic moiety and its application in ultrasensitive microRNA assays, *Biosens. Bioelectron.*, 2007, **22**, 933–940, DOI: 10.1016/j.bios.2006.04.020.

132 H. Chen, Q. Mei and S. Jia, *et al.*, High specific detection of osteopontin using a three-dimensional copolymer layer support based on electrochemical impedance spectroscopy, *Analyst*, 2014, **139**, 4476–4481, DOI: 10.1039/C4AN00576G.

133 T. Yang, S. Wang and H. Jin, *et al.*, An electrochemical impedance sensor for the label-free ultrasensitive detection of interleukin-6 antigen, *Sens. Actuators, B*, 2013, **178**, 310–315, DOI: 10.1016/j.snb.2012.12.107.

134 Z. Chen, L. Li and H. Zhao, *et al.*, Electrochemical impedance spectroscopy detection of lysozyme based on electrodeposited gold nanoparticles, *Talanta*, 2011, **83**, 1501–1506, DOI: 10.1016/j.talanta.2010.11.042.

135 J. Sheng, Y. Wu and H. Ding, *et al.*, Multienzyme-like Nanozymes: Regulation, Rational Design, and Application, *Adv. Mater.*, 2023, 2211210, DOI: 10.1002/adma.202211210.

136 R. Miglani, N. Parveen and A. Kumar, *et al.*, Degradation of xenobiotic pollutants: an environmentally sustainable approach, *Metabolites*, 2022, **12**, 818.

137 G. K. Arora, L. Palamiuc and B. M. Emerling, Expanding role of PI5P4Ks in cancer: a promising druggable target, *FEBS Lett.*, 2022, **596**, 3–16.

138 W. Huang, S. Huang, G. Chen and G. Ouyang, Biocatalytic Metal-Organic Frameworks: Promising Materials for Biosensing, *ChemBioChem*, 2022, **23**, e202100567.

139 B. Das, J. Lou Franco and N. Logan, *et al.*, Nanozymes in point-of-care diagnosis: an emerging futuristic approach for biosensing, *Nano-Micro Lett.*, 2021, **13**, 1–51.

140 H. Keshavarz Alikhani, M. Pourhamzeh and H. Seydi, *et al.*, Regulatory non-coding RNAs in familial hypercholesterolemia, theranostic applications, *Front. Cell Dev. Biol.*, 2022, **10**, 894800.

141 X. Meng, I. Zare, X. Yan and K. Fan, Protein-protected metal nanoclusters: An emerging ultra-small nanozyme. Wiley Interdiscip Rev Nanomedicine, *Nanobiotechnology*, 2020, **12**, e1602.

142 R. Sankaranarayanan, R. Swaminathan and H. Brenner, *et al.*, Cancer survival in Africa, Asia, and Central America: a population-based study, *Lancet Oncol.*, 2009, **11**, 165–173, DOI: 10.1016/S1470-2045(09)70335-3.

143 C. A. Rowe, S. B. Scruggs and M. J. Feldstein, *et al.*, An Array Immunosensor for Simultaneous Detection of Clinical Analytes, *Anal. Chem.*, 1999, **71**, 433–439, DOI: 10.1021/ac980798t.

144 C. A. Rowe, J. S. Bolitho and A. Jane, *et al.*, Rapid detection of D-dimer using a fiber optic biosensor, *Thromb. Haemostasis*, 1998, **59**, 94–98.

145 C. A. Rowe, L. M. Tender and M. J. Feldstein, *et al.*, Array Biosensor for Simultaneous Identification of Bacterial, Viral, and Protein Analytes, *Anal. Chem.*, 1999, **71**, 3846–3852, DOI: 10.1021/ac981425v.

146 Z. Liron, L. M. Tender, J. P. Golden and F. S. Ligler, Voltage-induced inhibition of antigen-antibody binding at conducting optical waveguides, *Biosens. Bioelectron.*, 2002, **17**, 489–494.

Open Access Article. Published on 04 January 2024. Downloaded on 2/7/2024 7:04:31 AM. This article is licensed under a Creative Commons Attribution 3.0 Unported Licence.

147 M. W. Lingen, J. R. Kalmar, T. Karrison and P. M. Speight, Critical evaluation of diagnostic aids for the detection of oral cancer, *Oral Oncol.*, 2008, **44**, 10–22, DOI: 10.1016/j.oraloncology.2007.06.011.

148 R. Kortum and E. Sevick, Quantitative Optical Spectroscopy for Tissue Diagnosis, *Annu. Rev. Phys. Chem.*, 1996, **47**, 555–606, DOI: 10.1146/annurev.physchem.47.1.555.

149 D. C. Christian, Computer-assisted analysis of oral brush biopsies at an oral cancer screening program, *J. Am. Dent. Assoc.*, 2002, **133**, 357–362, DOI: 10.14219/jada.archive.2002.0175.

150 A. R. Kerr, D. A. Sirois and J. B. Epstein, Clinical evaluation of chemiluminescent lighting: an adjunct for oral mucosal examinations, *J. Clin. Dent.*, 2006, **17**, 59–63.

151 Deepa, B. Nohwal and C. S. Pundir, An electrochemical CD59 targeted noninvasive immunosensor based on graphene oxide nanoparticles embodied pencil graphite for detection of lung cancer, *Microchem. J.*, 2020, **156**, 104957, DOI: 10.1016/j.microc.2020.104957.

152 S. Verma, A. Singh and A. Shukla, *et al.*, Anti-IL8/AuNPs-rGO/ITO as an Immunosensing Platform for Noninvasive Electrochemical Detection of Oral Cancer, *ACS Appl. Mater. Interfaces*, 2017, **9**, 27462–27474, DOI: 10.1021/acsami.7b06839.

153 R. Malhotra, V. Patel and J. P. Vaqué, *et al.*, Ultrasensitive Electrochemical Immunosensor for Oral Cancer Biomarker IL-6 Using Carbon Nanotube Forest Electrodes and Multilabel Amplification, *Anal. Chem.*, 2010, **82**, 3118–3123, DOI: 10.1021/ac902802b.

154 N. Pachauri, G. B. V. S. Lakshmi and S. Sri, *et al.*, Silver molybdate nanoparticles based immunosensor for the non-invasive detection of Interleukin-8 biomarker, *Mater. Sci. Eng., C*, 2020, **113**, 110911, DOI: 10.1016/j.msec.2020.110911.

155 N. Wang, J. Wang and X. Zhao, *et al.*, Highly sensitive electrochemical immunosensor for the simultaneous detection of multiple tumor markers for signal amplification, *Talanta*, 2021, **226**, 122133, DOI: 10.1016/j.talanta.2021.122133.

156 H. Yang, J. Bao and D. Huo, *et al.*, Au doped poly-thionine and poly-*m*-Cresol purple: Synthesis and their application in simultaneously electrochemical detection of two lung cancer markers CEA and CYFRA21-1, *Talanta*, 2021, **224**, 121816.

157 G. Yang, Z. Xiao and C. Tang, *et al.*, Recent advances in biosensor for detection of lung cancer biomarkers, *Biosens. Bioelectron.*, 2019, **141**, 111416, DOI: 10.1016/j.bios.2019.111416.

158 J. Chen, H.-M. Meng and Y. An, *et al.*, Structure-switching aptamer triggering hybridization displacement reaction for label-free detection of exosomes, *Talanta*, 2020, **209**, 120510, DOI: 10.1016/j.talanta.2019.120510.

159 L. Kashefi-Kheyrabadi, A. Koyappayil and T. Kim, *et al.*, A MoS_2@$Ti_3C_2T_x$ MXene hybrid-based electrochemical aptasensor (MEA) for sensitive and rapid detection of Thyroxine, *Bioelectrochemistry*, 2021, **137**, 107674, DOI: 10.1016/j.bioelechem.2020.107674.

160 F. Hou, X.-B. Hu and S.-H. Ma, *et al.*, Construction of electrochemiluminescence sensing platform with *in situ* generated coreactant strategy for sensitive detection of prostate specific antigen, *J. Electroanal. Chem.*, 2020, **858**, 113817, DOI: 10.1016/j.jelechem.2019.113817.

161 B. Feyzi-barnaji, R. Dinarvand and H. Salehzadeh, *et al.*, Construction of a ternary nano-architecture based graphene oxide sheets, toward electrocatalytic determination of tumor-associated anti-p53 autoantibodies in human serum, *Talanta*, 2021, **230**, 122276, DOI: 10.1016/j.talanta.2021.122276.

162 K. Hu, T. Pang and Y. Shi, *et al.*, Magnetic borate-modified Mxene: A highly affinity material for the extraction of catecholamines, *Anal. Chim. Acta*, 2021, **1176**, 338769, DOI: 10.1016/j.aca.2021.338769.

163 R. A. Soomro, S. Jawaid and Q. Zhu, *et al.*, A mini-review on MXenes as versatile substrate for advanced sensors, *Chin. Chem. Lett.*, 2020, **31**, 922–930, DOI: 10.1016/j.cclet.2019.12.005.

164 K. Hu, J. Cheng and K. Wang, *et al.*, Sensitive electrochemical immunosensor for CYFRA21-1 detection based on AuNPs@MoS_2@$Ti_3C_2T_x$ composites, *Talanta*, 2022, **238**, 122987, DOI: 10.1016/j.talanta.2021.122987.

165 M. L. Yola, N. Atar and N. Özcan, A novel electrochemical lung cancer biomarker cytokeratin 19 fragment antigen 21-1 immunosensor based on Si_3N_4/MoS_2 incorporated MWCNTs and core–shell type magnetic nanoparticles, *Nanoscale*, 2021, **13**, 4660–4669.

166 N. Pachauri, K. Dave, A. Dinda and P. R. Solanki, Cubic CeO_2 implanted reduced graphene oxide-based highly sensitive biosensor for non-invasive oral cancer biomarker detection, *J. Mater. Chem. B*, 2018, **6**, 3000–3012.

167 P. He, T. Naka and S. Serada, *et al.*, Proteomics-based identification of α-enolase as a tumor antigen in non-small lung cancer, *Cancer Sci.*, 2007, **98**, 1234–1240.

168 K.-J. Liu and N.-Y. Shih, The role of enolase in tissue invasion and metastasis of pathogens and tumor cells, *J. Cancer Mol.*, 2007, **3**, 45–48.

169 J. L. Viallard, D. Caillaud and B. Kantelip, *et al.*, Enzymatic determination of serum neuron-specific enolase in small cell lung cancers: utility of the serum neuron-specific enolase/serum nonneuronal enolase ratio, *Chest*, 1988, **93**, 1225–1233.

170 R. A. Wevers, A. A. C. Jacobs and O. R. Hommes, A bioluminescent assay for enolase (EC 4.2. 1.11) activity in human serum and cerebrospinal fluid, *Clin. Chim. Acta*, 1983, **135**, 159–168.

171 M. Katayama, H. Nakano and A. Ishiuchi, *et al.*, Protein pattern difference in the colon cancer cell lines examined by two-dimensional differential in-gel electrophoresis and mass spectrometry, *Surg. Today*, 2006, **36**, 1085–1093.

172 D. B. Wall, M. T. Kachman and S. Gong, *et al.*, Isoelectric focusing nonporous RP HPLC: a two-dimensional liquid-phase separation method for mapping of cellular proteins with identification using MALDI-TOF mass spectrometry, *Anal. Chem.*, 2000, **72**, 1099–1111.

© 2024 The Author(s). Published by the Royal Society of Chemistry

Open Access Article. Published on 04 January 2024. Downloaded on 2/7/2024 7:04:31 AM.
This article is licensed under a Creative Commons Attribution 3.0 Unported Licence.

173 M. Choudhary, P. Yadav and A. Singh, *et al.*, CD 59 Targeted Ultrasensitive Electrochemical Immunosensor for Fast and Noninvasive Diagnosis of Oral Cancer, *Electroanalysis*, 2016, **28**, 2565–2574, DOI: **10.1002/elan.201600238**.

174 J. J. BelBruno, Molecularly Imprinted Polymers, *Chem. Rev.*, 2019, **119**, 94–119, DOI: **10.1021/acs.chemrev.8b00171**.

175 S. Bhakta and P. Mishra, Molecularly imprinted polymer-based sensors for cancer biomarker detection, *Sens. Actuators Rep.*, 2021, **3**, 100061, DOI: **10.1016/j.snr.2021.100061**.

176 Archana, D. Verma and S. Z. H. Hashmi, *et al.*, Electrochemical Sensor based on Polydopamine-Molecularly Imprinted Polymer for Detection of 4-Ethylphenyl Sulfate "a Novel Gut Metabolite": Fabrication, Characterization, and Performance Evaluation in Human Urine, *Microchem. J.*, 2023, **193**, 108964.

177 F. B. Moussa, F. Achi and H. Meskher, *et al.*, Green one-step reduction approach to prepare rGO@ AgNPs coupled with molecularly imprinted polymer for selective electrochemical detection of lactic acid as a cancer biomarker, *Mater. Chem. Phys.*, 2022, **289**, 126456, DOI: **10.1016/j.matchemphys.2022.126456**.

178 A. E. F. Oliveira, A. C. Pereira and L. F. Ferreira, Disposable electropolymerized molecularly imprinted electrochemical sensor for determination of breast cancer biomarker CA 15-3 in human serum samples, *Talanta*, 2023, **252**, 123819.

179 P. Tang, H. Zhang, J. Huo and X. Lin, An electrochemical sensor based on iron (II, III)@ graphene oxide@ molecularly imprinted polymer nanoparticles for interleukin-8 detection in saliva, *Anal. Methods*, 2015, **7**, 7784–7791.

180 K. Ren, J. Zhou and H. Wu, Materials for microfluidic chip fabrication, *Acc. Chem. Res.*, 2013, **46**, 2396–2406.

181 C. K. Tang, A. Vaze, M. Shen and J. F. Rusling, High-throughput electrochemical microfluidic immunoarray for multiplexed detection of cancer biomarker proteins, *ACS Sens.*, 2016, **1**, 1036–1043.

182 Y. Wang, J. Luo and J. Liu, *et al.*, Label-free microfluidic paper-based electrochemical aptasensor for ultrasensitive and simultaneous multiplexed detection of cancer biomarkers, *Biosens. Bioelectron.*, 2019, **136**, 84–90.

183 Y. Wang, L. Chen and T. Xuan, *et al.*, Label-free electrochemical impedance spectroscopy aptasensor for ultrasensitive detection of lung cancer biomarker carcinoembryonic antigen, *Front. Chem.*, 2021, **9**, 721008.

184 N. Taheri, H. Khoshsafar and M. Ghanei, *et al.*, Dual-template rectangular nanotube molecularly imprinted polypyrrole for label-free impedimetric sensing of AFP and CEA as lung cancer biomarkers, *Talanta*, 2022, **239**, 123146.

185 J. Liu, J. Liu and Y. Shang, *et al.*, An electrochemical immunosensor for simultaneous detection of two lung cancer markers based on electroactive probes, *J. Electroanal. Chem.*, 2022, **919**, 116559.

186 H. Jiang, H. Zhang and M. Qin, *et al.*, Ultrasensitive Sandwich-type Electrochemical Aptasensor for Dual Detection of Lung Cancer Biomarkers, *IEEE Sens. J.*, 2023, **23**(17), 18977–18985, DOI: **10.1109/JSEN.2023.3294886**.

© 2024 The Author(s). Published by the Royal Society of Chemistry

Reconfigurable Low Weight Hybrid PUF Design Against Side Channel Attacks

Bhagyalakshmi Narayanapuram
ECE Department
Delhi Technological University
Delhi , India
bhagyalakshminarayanapuram_2k20phdec502@dtu.ac.in

Jeebananda Panda
ECE Department
Delhi Technological University
Delhi , India
jpanda@dce.ac.in

2023 4th International Informatics and Software Engineering Conference (IISEC) | 979-8-3503-1803-6/23/$31.00 ©2023 IEEE | DOI: 10.1109/IISEC59749.2023.10391050

***Abstract*— Silicon based PUF uses manufacturing process variations to generate PUF signature to protect from side channel attacks. In this paper a new hybrid PUF design has been implemented on FPGA with programmable delays with Galois RO and glitch architectures. The proposed PUF is immune to existing side channel vulnerabilities such as EM emissions, modelling attacks etc. To generate unit bit response the designed PUF occupies lower area than literature. The novel architecture has improved uniqueness, uniformity, reliability. The randomness is increased by programmable delays, Galois architectures and glitch circuits. The proposed PUF has uniformity of 49.78%, Bit Error Rate (BER) is 0.35%, uniqueness 49.38% and reliability of PUF is around 99.7%.**

***Index Terms*—Physically Unclonable Functions Attack, ring oscillator PUF, Side Channel Attacks**

I. Introduction

Now a days hardware security is crucial for all industrial ap- plications. Hardware security is nothing but protecting design hardware like FPGA or ASIC from third party side channel attacks. The security to crucial hardware can be provided by various authentication and key generation protocols. For these protocols Physically unclonable functions (PUFs) became a vital building block [1], [2]. In silicon IC manufacturing no two identical ICs will match cent percent because of the intrinsic silicon process variations. These variations are unique and can be used as unique PUF signature [3]. The input of the PUF is known as Challenge and produced output is called as response. Based on these challenges and responses (CRPS), PUFs are classified into Strong and weak PUFs. The PUF which has a greater number of Challenge Response Pair is termed as strong PUF and with no or very less Challenge response pair is termed as weak PUF. The basic topology of strong PUF is shown in Fig.1. In recent years many kinds of PUF architectures are designed on memory, silicon intrinsic delay and oxide breakdown variations [4] etc.

In Application specific Integrated Circuits, implementation of gate level PUF can be done but it is limited by manufacturing cost. Therefore, in recent trends FPGA based PUF designs have become a good research area. In the literature so many FPGA PUF are proposed among them Ring oscillator based (RO PUF) PUFs are used for various intra-key generation and authentication applications [5], [6] etc. The beauty of the RO PUF is it can be configured in both weak and strong PUF modes by controlling CRPS.

The Ring oscillator is designed by connecting odd number of NOT gates (inverters) back-to-back to form a loop. This inverter chain can produce oscillations. The RO PUF is formed by a number of symmetrical RO stages. No two Ring oscillators can produce the same delay because of the process

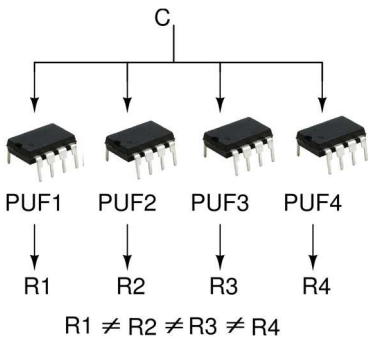


Fig. 1. Strong PUF

variations. This delay variations are converted to frequency which can enhance the differential variations. These variations are captured by counters and multiplexers to produce random Output PUF bit. However, in the literature so many semi-invasive attacks were performed to alter the PUF response.

In this paper side channel attack resistant new PUF design has been implemented. The introduction is discussed in Section-

I. Limitations of conventional PUFs are described in Section.

II. The proposed PUF design is explained in Section.

III. The vulnerability analysis and PUF metrics are discussed in section.

IV. Results obtained are shown in Section V and finally section VI describes the conclusion.

II. Limitations of Delay Based Pufs

In the survey there are many third-party vulnerabilities (attacks) are noticed and has been performed successfully to alter or retrieve the keys. The main vulnerability will be poor metric properties of PUF such as uniqueness, reliability, uniformity etc. [9], [10]. If the challenge response pair data is available with the attacker, he may try to model the PUF with some Algorithms. Among the FPGA PUFs Ring oscillator.

PUF gained attention because of its entropy. However, the RO PUF is also limited because of its huge on chip area consumption. For one bit response generation so many RO stages are required which may increase the power dissipation and on chip area consumption.

In addition to this, semi-invasive (EM) attacks [7], [8] tested successfully on Ring oscillator to identify the exact placement of RO stages with Electromagnetic emanations. The identification of RO inverter stages based on the EM emission is shown in Fig.2. It is easy to perform above mentioned side channel attacks because of the three

979-8-3503-1803-6/23/$31.00 ©2023 IEEE

Authorized licensed use limited to: DELHI TECHNICAL UNIV. Downloaded on February 07,2024 at 06:20:16 UTC from IEEE Xplore. Restrictions apply.

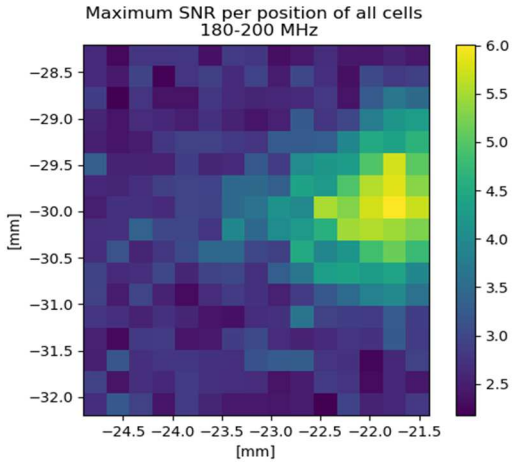


Fig. 2. EM cartography on RO PUF for location identification

vulnerabilities. The first one is a greater number of Ring oscillators stages can produce more Electromagnetic emanations. In the same manner some other delay based PUFs can produce light (photon) emissions. The second one is, if the PUF topology is based on only delays, then it is more prone to third party attacks. The third one is a good PUF should have Strong metrics such as uniformity, reliability etc. The PUF with poor metrics sensitive to third party attacks [11], [12].

III. Proposed Hybrid Puf Design

The above discussed third party vulnerabilities can be eliminated by the proposed Hybrid PUF. The major building blocks for the proposed designs are GARO design with re configurable inverters, glitch capturing architecture. .

Keep your text and graphic files separate until after the text has been formatted and styled. Do not use hard tabs, and limit use of hard returns to only one return at the end of a paragraph. Do not add any kind of pagination anywhere in the paper. Do not number text heads-the template will do that for you.

A. GARO Design

The conventional ring oscillator PUF may not produce sufficient uniqueness in the response to enhance random entropy Galois field function-based ring oscillator (GARO) has used. The random bit generation capability of GARO is

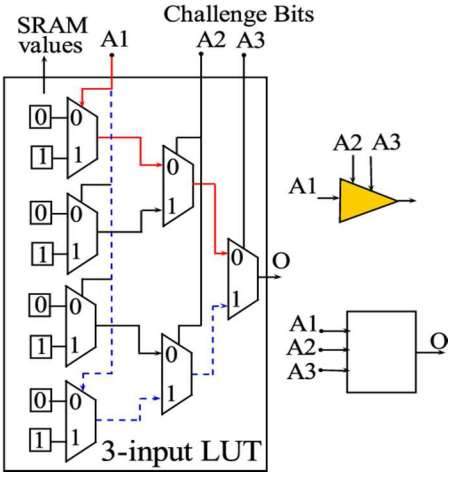


Fig. 3. Reprogrammable injected delay in 3 input LUT

better than conventional RO. As shown in Fig 3 for injecting re- programmable delays into the inverter a three input LUT is used. As mentioned in Fig.3 the A1 input is normal logic input to the inverter. whereas A2, A3 are extra unused inputs cannot change the logic but can help to change the transmission paths from i/p stage to o/p stage. For example, if A2A3=”00” it can generate more delay than ”11”. Hence these don’t care i/p bits are helpful to produce reconfigure path delays. In this paper GARO designed with these reconfigurable delays is shown in Fig.4. As per the Galois field, the second and sixth position of the inverters are ex-ored to produce better random behaviors and glitches.

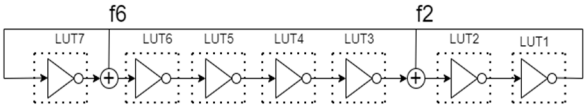


Fig. 4. GARO PUF Architecture

B. PUF Design

The schematic of 1 bit response PUF cell has given in the Fig. 5. The output frequency of GARO cells is completely random, and it is almost difficult to predict it. The response of these cells is connected to similar shift registers. The shift register response is sequence of bits. The shift register response is given to the glitch generation circuit. Whenever glitch is occurred in the bits the D flipflop will preset that means it will produce logic ’1’ response bit otherwise logic ’0’. Similarly, the bottom glitch cell will also generate random bit response. the top (response bit generator 1) and bottom (response bit generator 2) responses are ex-ored to increase the PUF uniqueness. The response bit is almost truly random because of multiple random bit generation stages such as Galois stage, reconfigurable inverters and glitch stage. As the challenges are given externally from PC through UART. From the master challenge sub challenges are derived which are given to programmable inverters. The response from the PUF stages will be given to UART. From the UART, the output will be received by the PC.

IV. Quality Metrics And Vulnerability Analysis of Proposed PUF

The three main third party vulnerabilities are mentioned in section II. The proposed design overcomes all these three limitations. Because the Proposed design has only two RO stages to reduce the Electromagnetic emissions and to reduce the on-chip area. The PUF response is not direct output of delay paths hence mathematical modelling is also not possible. The power analysis side channel attack is not feasible on this PUF because of the less power dissipation of the PUF as there are only two RO stages. The all-test suits of NIST are passed successfully by this design.

A. Uniqueness

Uniqueness: It is the quantitative property of PUF. It is used to differentiate one PUF from other PUF. The Uniqueness will be evaluated based on the Hamming Distance (HD). As shown in the table.1 In that equation i and j (i not equal to j), has n-bit outputs, Ri and Rj respectively for the inputs C, k is number of chips.

Authorized licensed use limited to: DELHI TECHNICAL UNIV. Downloaded on February 07,2024 at 06:20:16 UTC from IEEE Xplore. Restrictions apply.

B. Reliability

It is the property of the PUF to talk about how efficient the PUF is to reproduce its response bits. The measurement of this property can be done by varying Supply Voltages and varying surrounding temperatures.

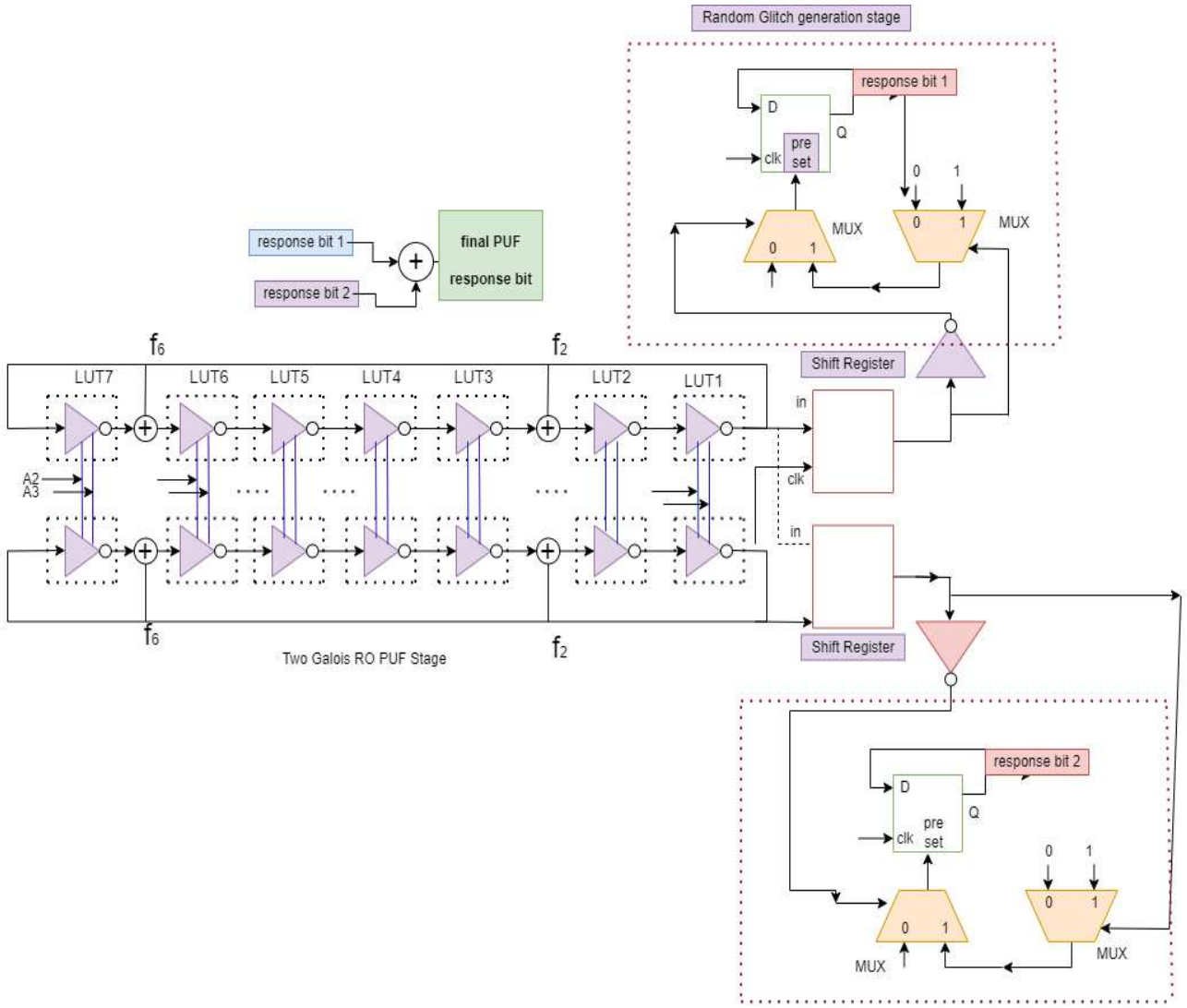


Fig. 5. Proposed PUF

TABLE. 1. PERFORMANCE COMPARISON

Ref	PUF Type	Uniqueness (%)	BER (%)		Mechanism	Reliability (%)	# LUT (1 bit response
CRO PUF [13]	FPGA	47.130	0.860		Delay based	99.14	64
RRO PUF [14]	FPGA	49.970	2.6		Delay based	97.40	30
XOR RO PUF[15]	FPGA	48.430	1.758		Delay based	98.24	16
CHOICE PUF[16]	FPGA	49.17	2.96		Delay based	97.04	NA
CRO PUF[17]	FPGA	NA	0.4		Delay based	99.6	58
THIS WORK	FPGA	49.38	0.35		Delay based	99.7	14

Authorized licensed use limited to: DELHI TECHNICAL UNIV. Downloaded on February 07,2024 at 06:20:16 UTC from IEEE Xplore. Restrictions apply.

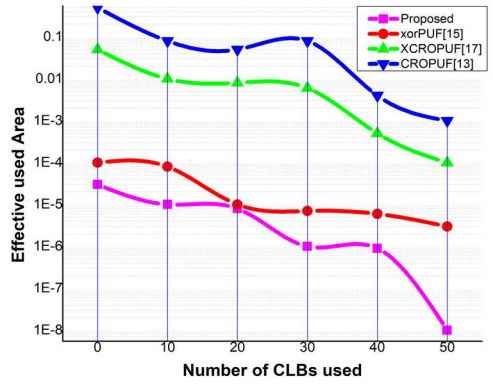


Fig. 6. Area Comparison

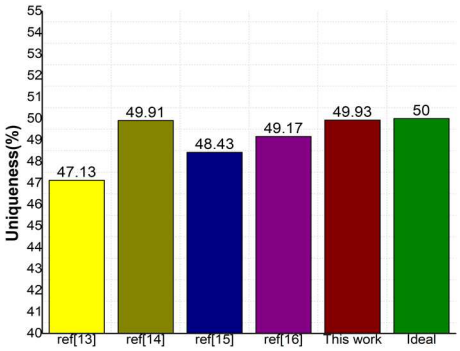


Fig. 7. Uniqueness Comparison

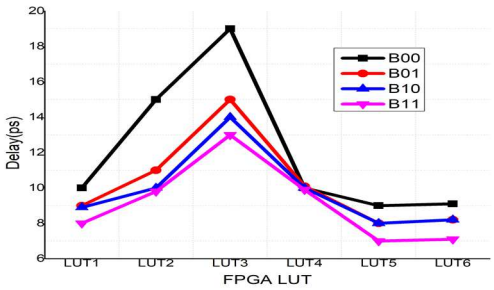


Fig. 8. LUT delay

C. *Uniformity*

It is the property of the PUF to calculate similar proportions of '1's and '0's is in the output of the various chip PUFs.

D. *Bit aliasing*

For ideal PUF the value of this property should be 50%, when this value closes to 50 it indicates better performance of PUF.

V. RESULTS

The new hybrid PUF design mentioned above has been implemented on Xilinx Spartan6 FPGA Device. The re-configured delays produced by LUTs of different slices of FPGA are shown in Fig.8. From the figure it is clear that the LUT delay will be varied by varying unused extra inputs of LUT to increase the randomness in the sequence. These will change according to LUTs position on FPGA board.

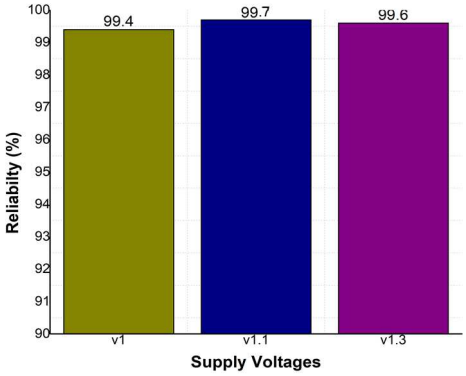


Fig. 11. Reliability with respect to voltage variations

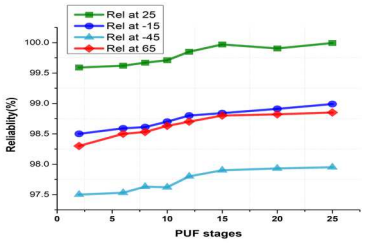


Fig. 9. Reliability with respect to temperature

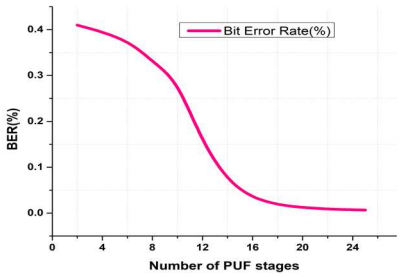


Fig. 10. BER with number of PUF stages

The comparison of various on chip areas of the literature with proposed design shown in Fig.6. From the graph it confirms that the design was built on FPGA with a smaller number of slices and CLBS of FPGA. Similarly, Fig.7 shows the comparison graph of uniqueness with the literature. Fig.9 shows the reliability of proposed PUF. The reliability has been tested with varying temperatures. The variance is least among the existing designs. Fig shows the amount of reproducibility of PUF with varying supply voltages. Fig 10 shows the BER with varying PUF stages. Fig 11 shows the reliability with supply voltage variations. The uniqueness of proposed PUF design is about (49.78%) to ideal PUF uniqueness response i.e. 50%. It is a low weight design. because the number of PUF stages used are less compared to the survey for generating one bit output.

Authorized licensed use limited to: DELHI TECHNICAL UNIV. Downloaded on February 07,2024 at 06:20:16 UTC from IEEE Xplore. Restrictions apply.

VI. Conclusions

In this paper a new glitch and delay-based hybrid PUF is discussed. The hybrid design used in this paper has good performance metrics and it is robust for third party attacks mathematical algorithmic based cloning, which is also difficult to perform. The proposed PUF has uniformity of 49.78%, Bit Error rate is 0.35%, uniqueness 49.38% and reliability is around 99.7%. This design occupies lees on chip area of FPGA.

References

[1] Baek S, Yu GH, Kim J, Ngo CT, Eshraghian JK, Hong JP. A Reconfigurable SRAM Based CMOS PUF With Challenge to Response Pairs. IEEE Access. 2021 May 28.

[2] Nedospasov, Dmitry, Jean-Pierre Seifert, Clemens Helfmeier, and Chris- tian Boit. "Invasive PUF analysis." In 2013 Workshop on Fault Diagnosis and Tolerance in Cryptography, pp. 30-38. IEEE, 2013.

[3] Lohrke, Heiko, Shahin Tajik, Christian Boit, and Jean-Pierre Seifert. "No place to hide: contactless probing of secret data on FPGAs." In Interna- tional Conference on Cryptographic Hardware and Embedded Systems, pp. 147-167. Springer, Berlin, Heidelberg, 2016.

[4] Yu, Meng-Day, Matthias Hiller, Jeroen Delvaux, Richard Sowell, Srinivas Devadas, and Ingrid Verbauwhede. "A lockdown technique to prevent ma- chine learning on PUFs for lightweight authentication." IEEE Transactions on Multi-Scale Computing Systems 2, no. 3 (2016): 146-159.

[5] Cao, Y., Zhao, X., Ye, W., Han, Q. and Pan, X., 2018. A Compact and Low Power RO PUF with High Resilience to the EM Side-Channel Attack and the SVM Modelling Attack of Wireless Sensor Networks. Sensors, 18(2), p.322.

[6] Saidi, S. and Ben Hadj Slama, J., 2013. Analysis and modeling of power mosfet radiation. Progress In Electromagnetics Research, 31, pp.247-262.

[7] Merli, D., Schuster, D., Stumpf, F. and Sigl, G., 2011, October. Semi-invasive EM attack on FPGA RO PUFs and countermeasures. In Proceedings of the Workshop on Embedded Systems Security (p. 2). ACM.

[8] Rahman, M.T., Rahman, F., Forte, D. and Tehranipoor, M., 2015. An aging-resistant RO-PUF for reliable key generation. IEEE Transactions on Emerging Topics in Computing, 4(3), pp.335-348.

[9] Long, J., Liang, W., Li, K.C., Zhang, D., Tang, M. and Luo, H., 2019. PUF-based Anonymous Authentication Scheme for Hardware Devices and IPs in Edge Computing Environment. IEEE Access.

[10] Colp, P., Zhang, J., Gleeson, J., Suneja, S., De Lara, E., Raj, H., Saroiu, S. and Wolman, A., 2015, March. Protecting data on smartphones and tablets from memory attacks. In ACM SIGPLAN Notices (Vol. 50, No. 4, pp. 177-189). ACM.

[11] Kai, Y., Xuecheng, Z., Guoyi, Y. and Weixu, W., 2009. Security strategy of powered-off SRAM for resisting physical attack to data remanence.Journal of Semiconductors, 30(9), p.095010

[12] Che, W., Saqib, F. and Plusquellic, J., 2015, November. PUF-based authentication. In 2015 IEEE/ACM International Conference on Computer-Aided Design (ICCAD) (pp. 337-344). IEEE

[13] Suh, G.E. and Devadas, S., 2007, June. Physical unclonable functions for device authentication and secret key generation. In 2007 44th ACM/IEEE Design Automation Conference (pp. 9-14). IEEE.

[14] Cui, Y., Wang, C., Liu, W., Yu, Y., O'Neill, M. and Lombardi, F., 2016, May. Low-cost configurable ring oscillator PUF with improved uniqueness. In 2016 IEEE International symposium on circuits and systems (ISCAS) (pp. 558-561). IEEE.

[15] Yao, L., Liang, H., Huang, Z., Jiang, C., Yi, M. and Lu, Y., 2021, May. A lightweight configurable XOR RO-PUF design based on Xilinx FPGA. In 2021 IEEE 4th International Conference on Electronics Technology (ICET) (pp. 83-88). IEEE.

[16] Streit, F.J., Kru¨ger, P., Becher, A., Schlumberger, J., Wildermann, S. and Teich, J., 2021, August. Choice–A Tunable PUF-Design for FPGAs. In 2021 31st International Conference on Field-Programmable Logic and Applications (FPL) (pp. 38-44). IEEE.

[17] Amsaad, F., Razaque, A., Baza, M., Kose, S., Bhatia, S. and Srivastava, G., 2021, June. An efficient and reliable lightweight PUF for IoT-based applications. In 2021 IEEE international conference on communications workshops (ICC Workshops) (pp. 1-6). IEEE.

Authorized licensed use limited to: DELHI TECHNICAL UNIV. Downloaded on February 07,2024 at 06:20:16 UTC from IEEE Xplore. Restrictions apply.

Molecular Biotechnology
https://doi.org/10.1007/s12033-023-01006-4

ORIGINAL PAPER

Simulation and Computational Study of RING Domain Mutants of BRCA1 and Ube2k in AD/PD Pathophysiology

Mehar Sahu[1] · Neetu Rani[1] · Pravir Kumar[1]

Received: 9 June 2023 / Accepted: 27 November 2023
© The Author(s), under exclusive licence to Springer Science+Business Media, LLC, part of Springer Nature 2024

Abstract

Lysine-based post-translational modification (PTM) such as acylation, acetylation, deamination, methylation, SUMOylation, and ubiquitination has proven to be a major regulator of gene expression, chromatin structure, protein stability, protein–protein interaction, protein degradation, and cellular localization. However, besides all the PTMs, ubiquitination stands as the second most common PTM after phosphorylation that is involved in the etiology of neurodegenerative diseases (NDDs) namely, Alzheimer's disease (AD) and Parkinson's disease (PD). NDDs are characterized by the accumulation of misfolded protein aggregates in the brain that lead to disease-related gene mutation and irregular protein homeostasis. The ubiquitin–proteasome system (UPS) is in charge of degrading these misfolded proteins, which involve an interplay of E1, E2, E3, and deubiquitinase enzymes. Impaired UPS has been commonly observed in NDDs and E3 ligases are the key members of the UPS, thus, dysfunction of the same can accelerate the neurodegeneration process. Therefore, the aim of this study is firstly, to find E3 ligases that are common in both AD and PD through data mining. Secondly, to study the impact of mutation on its structure and function. The study deciphered 74 E3 ligases that were common in both AD and PD. Later, 10 hub genes were calculated of which protein–protein interaction, pathway enrichment, lysine site prediction, domain, and motif analysis were performed. The results predicted BRCA1, PML, and TRIM33 as the top three putative lysine-modified E3 ligases involved in AD and PD pathogenesis. However, based on structural characterization, BRCA1 was taken further to study RING domain mutation that inferred K32Y, K32L, K32C, K45V, K45Y, and K45G as potential mutants that alter the structural and functional ability of BRCA1 to interact with Ube2k, E2-conjugating enzyme. The most probable mutant observed after molecular dynamics simulation of 50 ns is K32L. Therefore, our study concludes BRCA1, a potential E3 ligase common in AD and PD, and RING domain mutation at sites K32 and K45 possibly disturbs its interaction with its E2, Ube2k.

Mehar Sahu and Neetu Rani have contributed equally to this work and also considered joint first author.

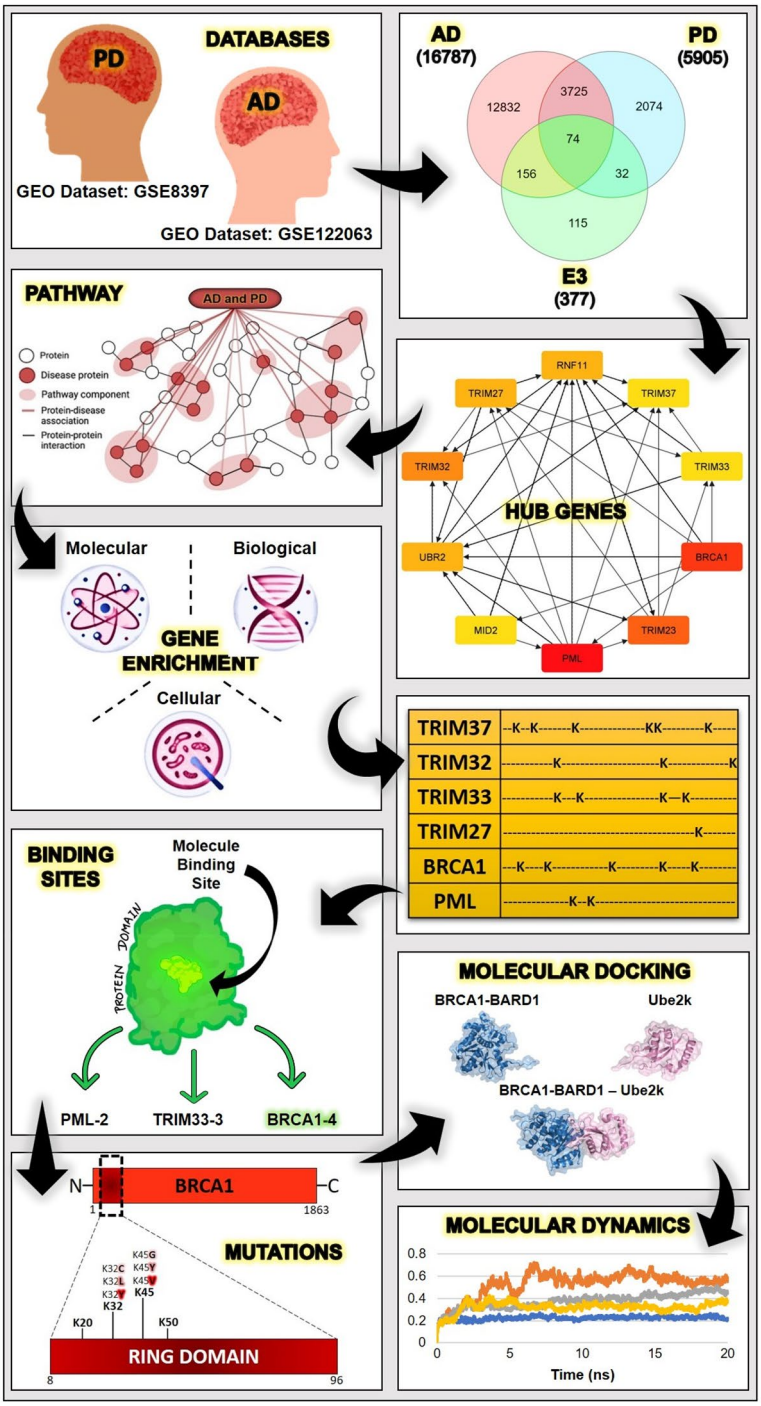
✉ Pravir Kumar
pravirkumar@dtu.ac.in; kpravir@gmail.com

[1] Molecular Neuroscience and Functional Genomics Laboratory, Department of Biotechnology, Delhi Technological University (Formerly Delhi College of Engineering), Shahbad Daulatpur, Bawana Road, Delhi 110042, India

Published online: 03 January 2024

Graphical Abstract

Graphical representation of all the steps involved to study mutation in the RING domain of BRCA1 which is a common E3 ligase observed in Alzheimer's disease and Parkinson's disease.



Keywords BRCA1 · Ubiquitination · Neurodegeneration · RING domain · Mutation · Alzheimer's disease · Parkinson's disease

Introduction

Neurodegenerative diseases (NDDs) such as Alzheimer's disease (AD) and Parkinson's disease (PD) manifest as an aggregation of misfolded proteins causing synaptic dysfunction, cognitive decline, and motor impairment [1]. Post-translational modifications (PTMs) are crucial in the regulation of many biological processes and their alterations disrupt the genetic regulation that hamper the protein quality control [2]. After phosphorylation, ubiquitination is the second most important PTM linked to several NDDs as it regulates virtually all events in cells [3].

Ubiquitination is a multistep ATP-dependent mechanism involving ubiquitin-activating (E1), conjugating (E2), and ligase (E3) enzymes, which ubiquitinate the misfolded proteins [4]. The Ubiquitin tag is attached to the lysine of the target protein under the regulation of these enzymes which is further marked to the ubiquitin–proteasome system (UPS) for its degradation. The aberration in the regulatory mechanism of ubiquitination results in the abnormal accumulation of toxic proteins which is a key characteristic feature of many NDDs.

Evidence suggests that alterations in E3 ligase are associated with the pathophysiology of NDDs, for instance, it has been observed that the implication of mutation in E3 ligases directly affects the ubiquitin signaling cascade [5]. Presently, 2 E1, 35–40 E2, and 600 E3 enzymes have been reported in humans [6]. E3 ubiquitin ligases play a vital role in developmental processes and their maintenance is necessary which involves cell signaling, metabolism, transcriptional control, protein sorting, trafficking, and degradation of cellular components. E3 ligases are broadly classified based on their catalytic activities: homologous with E6 associated protein C terminus (HECT), U-Box, really interesting new gene (RING), and RING between RING (RBR) [7]. HECT- and RBR-type E3 enzymes transfer ubiquitin from the E2-Ub complex to the target, whereas RING and U-Box directly transfer ubiquitin to the substrate [8]. Nedd4, a HECT-type E3 ligase has been observed to be upregulated in AD, PD, and Huntington's disease (HD), which further ubiquitinates several neuronal receptors to enhance their lysosomal degradation mechanism [9]. Contrarily, Parkin is an RBR-type E3 ligase that has been extensively studied in PD; mutation in the same can lead to the accumulation of damaged mitochondria which contributes to the progression of PD [10]. An example of U-Box-type E3 ligase is carboxyl terminus of Hsp70-interacting protein (CHIP) that maintains the protein folding homeostasis by refolding or dephosphorylating the pathological proteins, hence, once CHIP becomes dysfunctional, the degradation process is severely compromised as proteasomal and lysosomal machinery are overburdened [11]. RING-type E3 ligases constitute the largest class of ubiquitin ligases, however, due to the lack of a catalytic center, it becomes difficult to target [12]. Here, we identify the E3 ligase activity of Breast cancer gene 1 (BRCA1) and BRCA-associated ring domain 1 (BARD1), which is a RING-type ubiquitin ligase that is associated with stress-induced senescence which contributes to brain dysfunction and results in neurodegeneration [13].

BRCA1-BARD1 form a heterodimer (Fig. 1); mutation in this heterodimeric complex is associated with breast and ovarian cancer and has a vital role in the regulation of cell cycle, DNA damage repair, and transcriptional regulation [14]. In this study, BRCA1 was found to be a potential E3 ligase whose dysregulation is observed in the pathogenesis of AD and PD. The domain architecture of BRCA1 indicates its multifunctionality, as it contains an N-terminal RING-finger domain which interacts with another RING-containing protein, BARD1 allowing it to behave enzymatically as an E3 ubiquitin ligase. The C-terminal of BRCA1 contains BRCT domain which is a globular domain [15].

E2s have a conserved structure that aids them in binding with E1 enzymes and interacting with the RING domain of BRCA1. Class I E2s such as UbcH5, UbcH7, Ubc13, and Ube2W possess only the ubiquitin-conjugating (UBC) core domain. The C-terminal domain along with UBC core domain is seen in Ube2k, a class II E2, whereas UbcM2, a class III E2, shows N-terminal extension along with the UBC domain. In this study, Ube2k also known as Huntingtin-interacting protein 2 (HIP2) was extensively studied because it has both UBC and ubiquitin-associated (UBA) domains forming a ubiquitin chain that is degradative by nature, moreover, it has a high prevalence in NDD studies [16]. For instance, it acts as a mediator of amyloid β (Aβ) neurotoxicity in AD, increases the accumulation of huntingtin (HTT) aggregates in Huntington's disease (HD), represents motor dysfunction in PD, and Ube2k binding with mutated superoxide dismutase 1 (SOD1) is observed in Amyotrophic lateral sclerosis (ALS) [17–20].

BRCA1 is the major DNA repair protein and its mutation marks 80% of breast cancer (BC) and ovarian cancer (OC) cases in females, however, there are studies that highlight the increasing cases of BC-AD with age in BC patients, therefore, there is a direct association between cancer and neurodegeneration and the potential link behind them is their molecular mechanism [21]. Previous studies demonstrate that as per neuron-specific methylome analysis in AD brains, BRCA1, a major DNA repair protein that once dysfunctional is mislocalized to the cytoplasm of neuronal cells and co-localized with tau proteins [22, 23]. However, this study aims to understand the role of E3 ligase activity of BRCA1 in neurodegeneration, a common E3 ligase in both AD and PD. Also, to assess its binding affinity with its corresponding E2, Ube2k when the key lysine sites are being mutated in its RING domain. Therefore, ubiquitin-related genes were

screened for biomarker through in silico high-throughput analysis. Web-based bioinformatics tools were assessed to perform gene enrichment and domain architecture analysis and to predict the PTM sites in extracted hub genes. Later, BRCA1 was found to be the most significant E3 ligase in both AD and PD. Mutational analysis, structural characterization, molecular docking, and molecular dynamics simulation were performed to determine the probable impact of critical lysine residues on ubiquitination. This would help us decipher the quest to understand the E3 ligase activity of BRCA1.

Materials and Methods

Data Retrieval

The expression profiling of genes was carried out by high-throughput screening. The AD and PD datasets were downloaded from the Gene Expression Omnibus (GEO) of the National Centre For Biotechnology Information (NCBI) (https://www.ncbi.nlm.nih.gov/geo/query/acc.cgi?) [25, 26]. The microarray dataset GSE8397 carries genes from post-mortem brain samples of Parkinson's Disease comprising 47 individual samples from substantia nigra, which was further divided into lateral, medial parts, and the frontal cortex. In this study, 30 diseased samples and 17 control samples were used. The study was based on the platform data Affymetrix HG_U133 array set A for Parkinson's Disease. The 2nd dataset GSE122063 consists of 36 samples of Vascular Dementia, 18 each from frontal and temporal cortex, and 56 samples of Alzheimer's Disease, 28 each from frontal and temporal cortex, i.e., 92 diseased samples, and 44 control samples were selected. The study was based on Agilent-039494 SurePrint G3 Human GE v2 8 × 60 K Microarray 039381.

Data Pre-processing and Screening of Differentially Expressed Genes

GEO2R tool (https://www.ncbi.nlm.nih.gov/geo/geo2r/) is a web-based program using GEOQuery and Limma packages of R from Bioconductor projects. It can be utilized to compare datasets and analyze Differentially Expressed Genes (DEGs) from GEO series datasets. In this study, GEO2R was used to predict the role of DEGs in cellular, molecular, and biological functions [27, 28]. The Benjamini–Hochberg correction method was used to calculate the adjusted P value of the false discovery rate (FDR) [29]. The DEGs were categorized significantly based on the cut-off limit applied on the GEO2R tool which was an adjusted P value < 0.05 and P value < 0.05.

Screening of Common Ubiquitin E3 Ligase and DEGs Through Venn Analysis

The E3 ligase list was collected from the Epithelial Systems Biology Library (ESBL) database (https://esbl.nhlbi.nih.gov/Databases/KSBP2/Targets/Lists/E3-ligases/) consisting of 377 E3 ligases [30]. The DEGs screened based on adjusted P value were significant by nature, these significant DEGs of the above two datasets were analyzed for the ubiquitin E3 ligase list using InteractiVenn analysis (http://www.interactivenn.net/) [31] It is a web-based tool used to generate a Venn diagram illustrating common DEGs of AD and PD that were overlapping with the Ubiquitin E3 ligase list. These significantly common DEGs that are also E3 Ubiquitin ligases were further analyzed to interpret their involvement in the pathogenesis of AD and PD.

Protein–Protein Interaction (PPI) Analysis

Various protein–protein interaction tools were explored, namely, BIOGRID which is a public database that contains curated proteins and their genetic interaction data for model organism species—yeast, nematode, fly, zebrafish, mouse, and human, whereas, STRING is another freely available database that helps assess the physical and functional associations between two proteins [32, 33]. STRING v 11.5 (https://string-db.org/cgi/input?sessionId=bdlLHZYR2FDe&input_page_show_search=on) was used to generate PPI network of the overlapping DEGs. The gene symbol of common DEGs was uploaded on the multiple protein module available on the server and was screened for the PPI in the *Homo sapiens* category with adjusted P value < 0.05 and confidence score of 0.40 [34]. The high-throughput labs experiment and knowledge were used by the STRING database to analyze the PPI network with a score ≥ 0.4 [35, 36]. The PPI STRING network was exported to CytoScape v.3.9.1 [37] to visualize and acquire the PPI network. There are three methods to obtain 10 hub genes, namely, maximal clique centrality (MCC), maximum neighborhood component (MCN), and degree method [38]. Here, 10 hub genes with the highest node degree score were screened out as the degree of the node signifies the number of connections with other nodes.

Pathway Enrichment Analysis of E3 Ubiquitin Ligases

Numerous databases are available for gene information extraction consisting of three major domains (1) Biological Processes (BP), (2) Cellular Processes (CP), and (3) Molecular function (MF). Widely used software for gene set enrichment analysis like g:Profiler that maps genes to know functional information and detect statically significant enriched

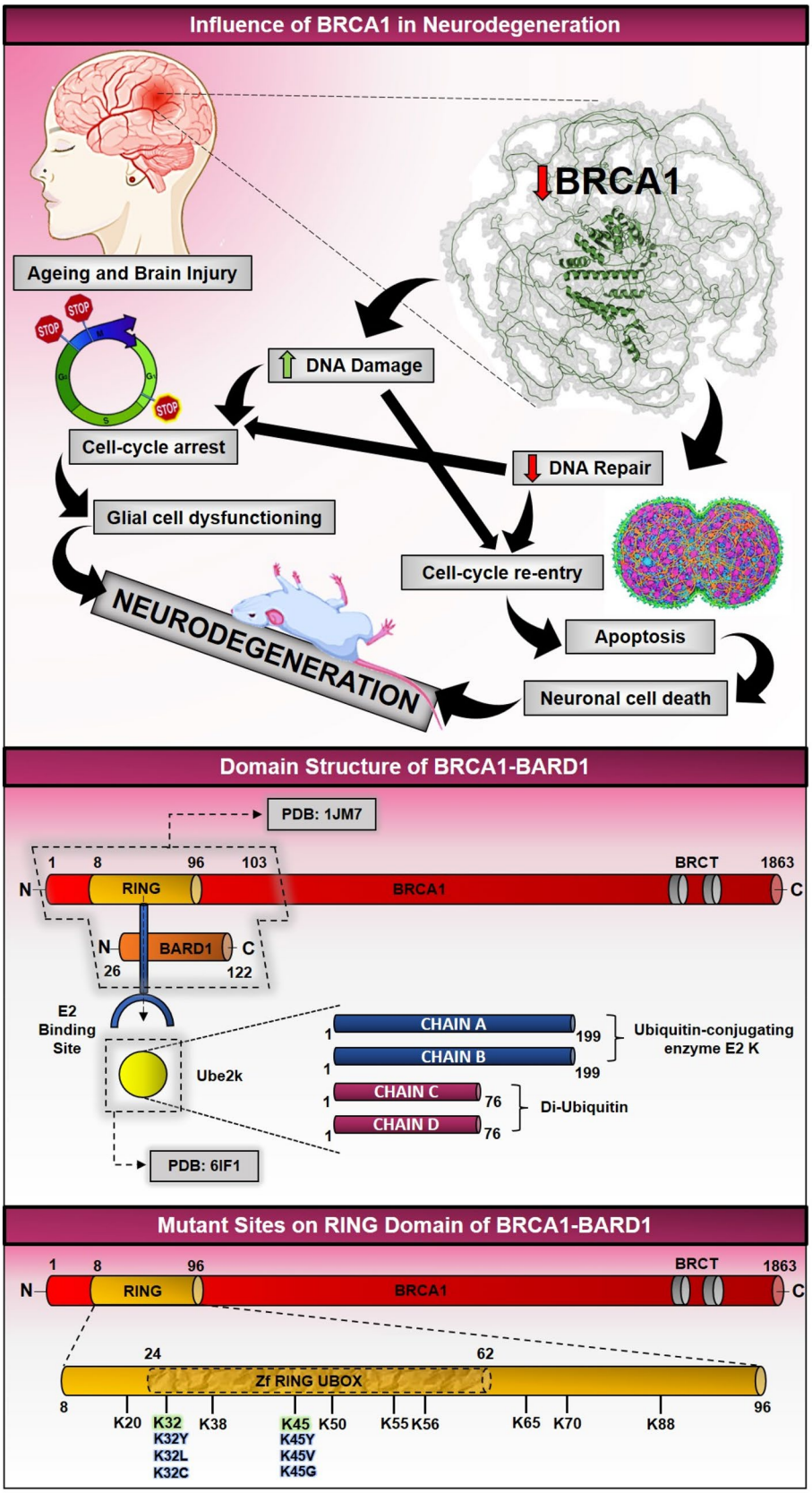


Fig. 1 Schematic representation of BRCA1 illustrating its involvement in neurodegeneration known to affect DNA repair mechanism, disturbing cell cycle leading to apoptosis, and ultimately neuronal death [24]. The second half of the figure explains the domain structure of BRCA1-BARD1 in which the RING domain of BRCA1 projects the binding site for Ube2k, E2-conjugating enzyme to attach with it and aid BRCA1 to carry out its E3 ligase activity in ubiquitination. Ube2k has four chains, the first two are the ubiquitin-conjugating enzyme E2K and the other two are ubiquitin that will be transferred once BRCA1 and E2K binding is complete. The last part of the figure shows all the lysine sites present on the RING domain of BRCA1. Out of all the lysine sites, K32 and K45 were studied in detail. The top three mutants for K32 are tyrosine, leucine, and cysteine, whereas, for K45, it is tyrosine, valine, and glycine

terms [39]; Enricher provides various types of visualization summaries of collective functions of gene lists [40] and ShinyGO 0.77 which is an intuitive graphical web application that aids researchers in gaining actionable insights from gene sets (http://bioinformatics.sdstate.edu/go/) [41] were used for gene set enrichment and pathway analysis. The threshold parameters were set on P value < 0.05 for significantly enriched genes, thereby, the functional enrichment was calculated.

Domain and Motif Analysis

For the Domain architecture and motif analysis, we used several web-based tools such as SMART which uses profile-hidden Markov models built from multiple sequence alignments (MSA) to detect protein domains (http://smart.embl-heidelberg.de/) [42]; MEME Suite allows to identify novel motifs in protein sequences and performs other motif-based analysis (https://meme-suite.org/meme/) [43]; similarly, Scansite 4 uses accession number of protein to identify its motifs (https://scansite4.mit.edu/ webservice/) [44]. We submitted the FASTA sequences of our key proteins on these servers to analyze their domains. For structure analysis of common genes, we used Consurf (https://consurf.tau.ac.il/consurf_index.php) [45].

Prediction of Post-translational Modification Sites

Various datasets were explored for screening PTMs effect on the selected genes. Protein lysine modification database (PLMD) (https://pubmed.ncbi.nlm.nih.gov/28529077/) [46] was used to extract the ubiquitination, acetylation, and sumoylation sites of the selected gene. As the data were deduced, the duplicate PTM sites were removed manually as there are some sites that undergo two different functions when ubiquitinated. Finally, the PTM sites were arranged according to their PTM types happening on the different motifs of genes.

Prediction of Deleterious Mutations and Their Impact on Structural and Functional Stability

We used PredictSNP (https://loschmidt.chemi.muni.cz/predictsnp/) web-based tool to predict the mutation. PredictSNP consists of several other tools such as PhD-SNP, SNAP, SIFT, PolyPhen-1, PolyPhen-2, and PANTHER [47]. We also used another web-based tool MutPred 2 (http://mutpred.mutdb.org/#q) [48] that associates molecular and genetic data to ascertain the pathogenicity by substituting different amino acids. It can also anticipate the molecular origin of pathogenicity. Further, we used the Project HOPE tool (https://www3.cmbi.umcn.nl/hope/input/#) [49] that helped in assessing the effect of mutation on the structure and function of the protein sequence. We submitted the FASTA sequences of our key proteins to this server to analyze the impact of the mutation.

Structure Preparation

We extracted the three-dimensional structure of the BRCA1-BARD1 complex (PDB ID-1JM7) with resolution 0.45 Å to 0.95 Å [50] and Ube2k (PDB ID-6IF1) with resolution 2.47 Å from RCBS protein databank (https://www.rcsb.org/) [51]. The FTSite server was used to predict the active sites on BRCA1 domain (https://ftsite.bu.edu/) [52]. Furthermore, mutation was incorporated in BRCA1 using the mutagenesis built-in wizards in PyMOL software. CPORT tool was used to determine the active–passive sites of selected domain (https://alcazar.science.uu.nl/services/CPORT/) de Vries and Bonvin [53].

Molecular Docking

Protein–protein docking tool was used to analyze the complexity of the BRCA1-BARD1 and Ube2k binding. Wild-type (Control) and mutant (Variable- K32Y, K32L, K32C, K45V, K45Y, and K45G) structures of BRCA1-BARD1 were prepared using PyMOL and were docked with Ube2k using ClusPro (https://cluspro.bu.edu/login.phpand) [54–58] that gave the cluster size and lowest binding energy which does not directly report energy value in kcal/mol or kJ/mol but predicts the most favorable spatial arrangement between two proteins and focuses on the relative ranking of predicted binding structures; HADDOCK (https://wenmr.science.uu.nl/haddock2.4/) [59, 60] was used which is based on z-score parameters; and lastly, in LZerD the models are assessed based on four scores, namely GOAP, DFIRE, ITScore, and Ranksum. GOAP, DFIRE, and ITScore are statistical potentials, whereas Ranksum is used to rank the models and is the sum of all three scores. As Ranksum score is the recommended score for interpreting the result, hence, the Ranksum score for wild-type and mutant structures was studied [61] (Figure S1). The purpose behind using three different docking tools was the specificity behind their functioning, for instance, ClusPro uses the Fast Fourier transforms (FFT)-based program PIPER which generates 1000 lowest energy structures that are clustered using pairwise RMSD and centers of the largest cluster; HADDOCK is a semi-flexible docking algorithm which used experimental data and bioinformatics interface predictions, whereas LZerD uses 3D Zernike descriptors, which depends on mathematical series expansion of protein surface [62].

Molecular Dynamics Simulation

The GROMACS 2022 package [63] was applied for molecular dynamic (MD) simulations with the OPLS-AA/L force field [64]. The OPLS-AA/L force field was selected, as its parameters are public and can be used in wide range of MD simulations. The docked complex structures were prepared in the pdb2gmx format and converted it into the gromacs format i.e., ignh to prepare the clean file after removing the hydrogen atoms from the docked structures. The orthorhombic cubic complex was centered at least 10 A° and filled with the solvent SPCE molecule in the middle of cubic box to perform the process of solvation. The genion file was used to neutralize the system by replacing the solvent ions with 5 sodium molecules. The energy minimization was performed for 50,000 nsteps with a maximum force of 1000.0 kJ/mol/nm to ensure that there are no steric clashes in the system. The next phase was equilibration to avoid the uncontrolled dynamics. The NVT ensemble was the first phase of equilibration where temperature was kept 300 K with 1 ps constant time. In the next phase pressure was equilibrated at 1 atm by NVT. After attaining desired equilibration, the system was ready to run the MD simulation for 20 ns and 50 ns. The frames have been examined using the MD simulation results which helped in determining the root mean square deviation (RMSD), root mean square fluctuation (RMSF), and radius of gyration (RG) of wild-type and mutant structures.

Results

Common E3 Ligase in AD and PD

The list of E3 ubiquitin ligase enzymes from ESBL and all the significant DEGs of AD (GSE122063) and PD (GSE8397) datasets which were screened based on adjusted P value < 0.05 were extracted. All the genes were intersected ($A \cap B \cap C$) using InteractiVenn that gave 74 genes which were common E3 ligase enzymes in both AD and PD datasets (Fig. 2). These genes were further analyzed on the STRING database to predict their protein–protein interactions and understand their direct and indirect functional associations. The network was then shared with CytoScape to run CytoHubba interface to do the topological analysis of these genes. Based on the degree method, the highest degree score was calculated and the top 10 hub genes were given, namely PML, BRCA1, TRIM23, TRIM32, RNF11, TRIM27, UBR2, TRIM37, MID2, and TRIM33. The network of these hub genes was also analyzed on CytoScape plug-in, CentiScaPe for performing the network centrality analysis to identify the most relevant nodes for experimental prioritization [65]. There are six centralities, namely, bottleneck, eccentricity, closeness, radiality, betweenness, and stress [66]. Here, based on betweenness the nodes were identified and were marked red and yellow based on high and low degree scores, respectively (Fig. 2).

Functional Enrichment Analysis of E3 Ligases in AD-PD Crosstalk

To understand the connection between these hub genes and identify the key genes involved, pathway analysis was performed that helped in analyzing the involvement of these hub genes in different pathways. A web-based tool, Enrichr was used to access different pathway databases such as REACTOME 2022, BioPlanet 2019, WikiPathway 2021 Human, KEGG 2021 Human, and Elsevier Pathway Collection (Table S1). Those pathways were selected that were involved in post-translational modifications and cell signaling having a P value < 0.5. Ubiquitin mediated-proteolysis pathway involves maximum number of genes including TRIM37, BRCA1, TRIM32, and PML. The result of pathway analysis showed that BRCA1 was involved in the maximum number of pathways followed by PML, TRIM27, TRIM33, TRIM32, and TRIM37 depicting its biological significance in AD and PD.

Further, to decipher the relationship between biological processes, molecular phenotypes, environmental factors, and adaptive functions among the selected genes, gene ontology study were performed for BRCA1, PML, TRIM27, TRIM33, TRIM32, and TRIM37 using g:Profiler. It was observed that according to GO Biological Process 2021, Protein ubiquitination (GO:0016567) was involved in all the genes with adjusted P value 2.766×10^{-9}. Regarding GO Molecular Function 2021, Ubiquitin-protein transferase activity (GO:0004842) was common in all the genes with adjusted P value 6.381×10^{-11}, whereas as per GO Cellular Component 2021, all genes except TRIM32 and TRIM33 were observed in Nucleoplasm (GO:0005654) and Intracellular non-membrane-bounded organelle (GO:0043232) with adjusted P value 2.0×10^{-3} and 1.8×10^{-2}, respectively. Moreover, as per ShinyGO 0.77, all 6 genes showed Zinc ion binding site that confers ligase functionality (Fig. 3).

Protein Motif Discovery and RING Domain Analysis

The binding site of the motif provides more information about protein function, therefore, we tried to find motifs of our selected genes (BRCA1, PML, TRIM27, TRIM33, TRIM32, and TRIM37) using MotifFinder considering Pfam and NCBI-CDD databases, respectively. We got 15 and 235 motifs for BRCA1, 7 and 115 motifs for PML, 12 and 250 motifs for TRIM27, 8 and 250 motifs for TRIM33, 17 and 228 motifs for TRIM32, 8 and 160 motifs for TRIM37. However, to narrow down our selection process we went

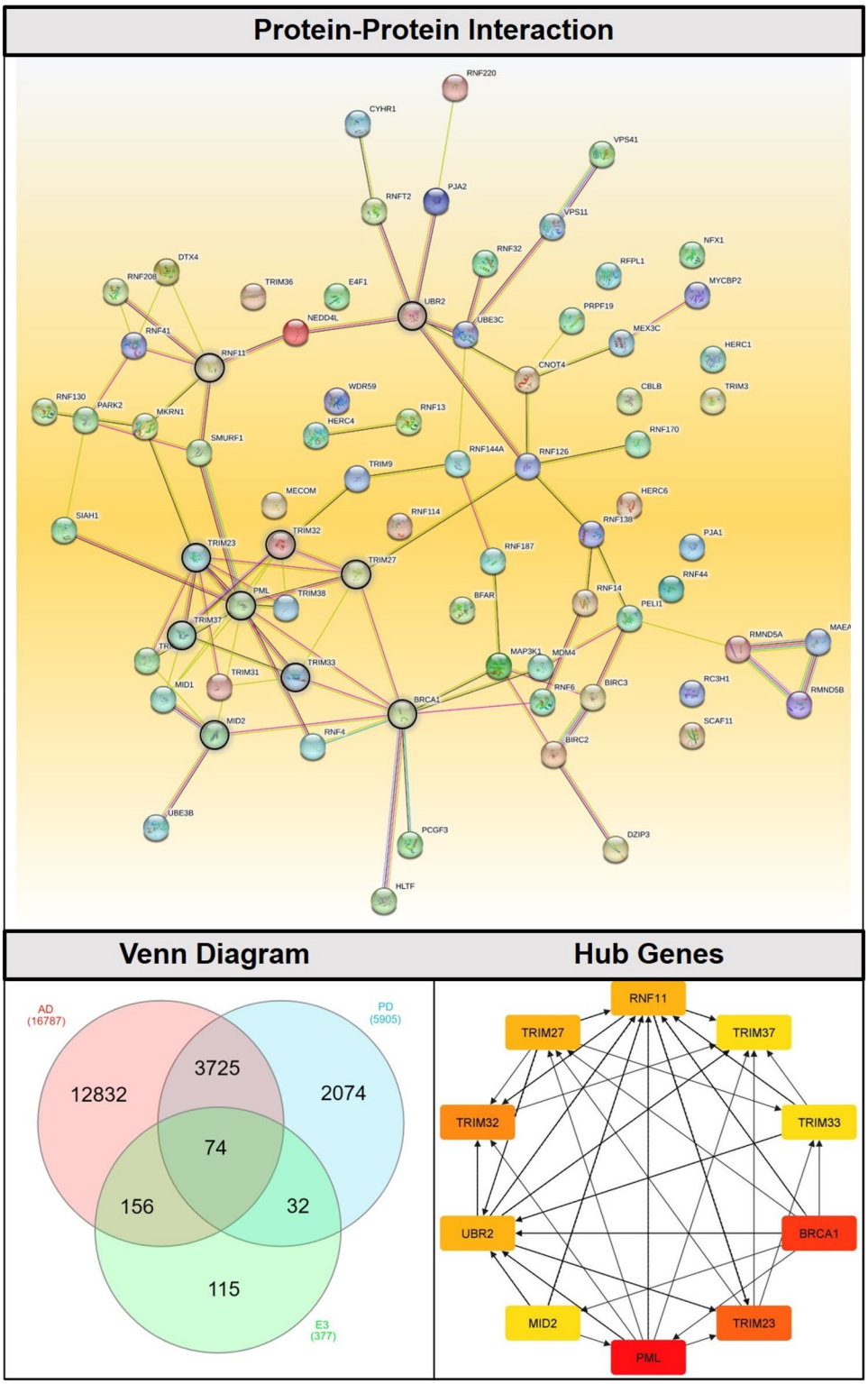


Fig. 2 Protein–protein interaction network of 74 genes that are common E3 ligase enzymes in both AD and PD. Out of the 74 genes, the top 10 hub genes were selected based on degree topological analysis which are also highlighted in protein–protein interaction

forward with motifs from Pfam database. As these selected genes are also E3 ligases thus, E3 ligases can be divided into four types: Homologous to the E6-AP Carboxyl Terminus (HECT) type, U-box type, Really Interesting New Gene (RING-finger) type, and RING Between RING (RBR) type. The motifs of our selected genes were only limited to U-box and RING-finger type. Moreover, E3 ligase activity is intrinsic to RING domains having a RING-finger-containing

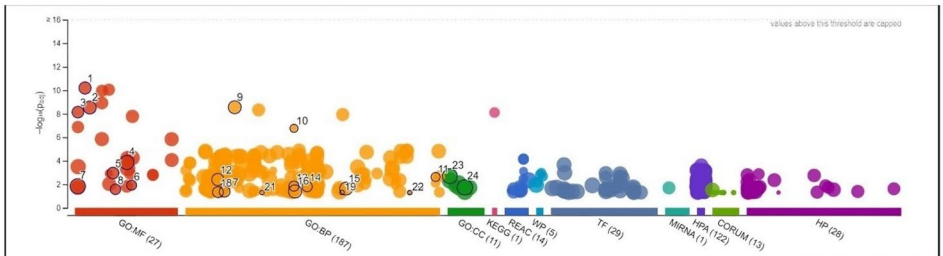
protein (AO7) that attaches with E2 that is necessary for the process of ubiquitination. Perhaps, there are other RING-finger-associated proteins, namely BRCA1, Siah-1, TRC8, NF-X1, kf-1, and Praja1 which also enable E2-dependent ubiquitination [67]. For our selected genes, different RING domain superfamilies were also observed like C3HC4, C3H2C3, C4HC3, and U-box as they display similar protein folding and functional similarity, however, their sequence identity is less than 30% depicting that they are poorly conserved. Hence, such domains were not taken forward for further analysis. Based on this observation, the potential genes having the desired domain were BRCA1, PML, TRIM33, and TRIM32 [68]. To produce an alignment of each significant match we run our query motif on MEME-Suite TOMTOM to get the list of target motifs ranked by P value and total overall matches. For BRCA1, PML, and TRIM33 the overall matches were more than 15, however, this was not the case for TRIM32. The target motif of BRCA1 is Zf RING Ubox (24–62)—CPICLELI**K**EPVST**K**CDHIF-C**K**FCML**K**LLNQ**KK**GPSQCP, target motif of PML is Zf B-box (127–223)—AVCTRC**K**ESADFWCFECEQLL-CA**K**CFEAHQWFL**K**HEARPLAELRNQSVREFLDGTR **K**TNNIFCSNPNHRTPTLTSIYCRGCS**K**PLCCSCALL-DSSHS and target motif of TRIM33 is Zf RING Ubox (125–182)—CAVCQQSLQSRREAEP**K**LLPCLHSFCLR-CLPEPERQLSVPIPGGSNGDIQQVGVIRCP. Once the E2 conjugated ubiquitin is ready, it has four possibilities that it might form a thioester bond with Cys or oxy ester bond through Ser/Thr or form peptide bond on N-terminal or have an isopeptide bond with Lys residue of substrate/E3. Our further study extensively involved Lysine residues (Lys/K), so the total number of lysine residues was counted for the target motifs of BRCA1, PML, and TRIM33 using Scansite 4. 6 K residues were found in the target motif of BRCA1 (K32; K38; K45; K50; K55; K56;), 5 K residues were found for PML (K133; K150; K160; K183; K209), and 1 K site was observed in TRIM33, i.e., (K141). Later, post-translational modification sites were checked for these lysine residues using PLMD and SMART. Results state that in BRCA1, K32 undergoes ubiquitination and sumoylation, K55 undergoes ubiquitination and acetylation, whereas the remaining lysine residues, K38, K45, K50, K56 only undergo ubiquitination. When it comes to PML, ubiquitination takes place on all the residues, namely, K133, K150, K183, K209 except K160 as it undergoes sumoylation and acetylation. However, K141 of TRIM33 only undergoes ubiquitination.

Structure Characterization of BRCA1, PML, and TRIM33

As BRCA1, PML, and TRIM33 were found to be the most potent E3 ligases which were common in both AD and PD, thus, it becomes important to study in depth their structures. To study the functional regions in the protein domain, ConSurf server was used, where the FASTA sequence was uploaded for all three genes simultaneously. ConSurf is a bioinformatics tool that helps to estimate the evolutionary conservation of amino acid positions based on phylogenetic analysis among homologous sequences and then grading them 1 through 9 with a color code cyan-through-purple, where 1 indicates the most rapidly evolving position, 5 stands for intermediate results, and 9 depicts most evolutionarily conserved position [69]. In the domain structure of BRCA1, K32, K50, K55, and K56 are exposed as well as functional, however, K38 and K45 are only exposed, and based on the conservation analysis there is no revelation of whether K38 and K45 are structural or functional. Similarly, in PML, K183 and K209 are exposed and functional, while K133 and K150 are only exposed. Interestingly, in TRIM33, K141 is buried and structural (Fig. 4). Therefore, it becomes evident that a site must be functional in order to bind with E2-conjugating enzyme. Further, we performed the pocket detection using Fpocket suite which helped us to find possible cavities, where E2-conjugating enzyme might fit in E3 ligase enzyme [70]. We performed pocket detection of wild-type full structures as well as domain structure of all three genes, BRCA1, PML, and TRIM33. The observation describes that the pockets of wild-type BRCA1, PML, and TRIM33 are 113, 67, and 83, respectively, although, for their domains, it is 4, 2, and 3 (Fig. 4). Ubiquitination is distinct from sumoylation which happens more commonly in PML as it has four SUMO family proteins, including SUMO1, SUMO2, SUMO3, and SUMO5, which are known to modify PML at different lysine sites [71–73]. Interestingly, it has been found that PIAS1 and PIASxα promote sumoylation in PML, moreover, PIAS1-dependent PML sumoylation further governs PML ubiquitination, contrary to this, PIASxα directs stabilization of PML [74]. Thus, BRCA1 stands as the most potential E3 ligase and is further taken forwards for mutational analysis.

Mutagenesis and Its Stability Analysis on RING Domain of BRCA1

Studies done on the amino acids of BRCA1 have not deciphered much about its function, nonetheless, it is quite evident from the literature that there are two potential motifs in BRCA1, BRCT domain and zinc RING-finger domain [75–77]. The RING domain is necessary for E2 binding, whereas the rest of the complex takes part in substrate binding. Interestingly, in the human proteome, BRCA1 and BARD1 are the only two proteins that have the RING domain at N-terminal, BRCT domain at C-terminal, and flanking α-helices that make BRCA1-BARD1 complex a heterodimer. Though both have RING domains, still only the



ID	SOURCE	TERM ID	TERM NAME	Padj	PML	BRCA1	TRIM32	TRIM27	TRIM37	TRIM33
1	GO:MF	GO:0004842	Ubiquitin-protein transferase activity	6.377×10-11						
2	GO:MF	GO:0008270	Zinc ion binding	2.929×10-9						
3	GO:MF	GO:0003713	Transcription coactivator activity	7.203×10-9						
4	GO:MF	GO:0042802	Identical protein binding	1.392×10-4						
5	GO:MF	GO:0031625	Ubiquitin protein ligase binding	1.087×10-3						
6	GO:MF	GO:0046332	SMAD binding	1.191×10-2						
7	GO:MF	GO:0003676	Nucleic acid binding	1.475×10-2						
8	GO:MF	GO:0032182	Ubiquitin-like protein binding	2.642×10-2						
9	GO:BP	GO:0016567	Protein ubiquitination	2.765×10-9						
10	GO:BP	GO:0044790	Suppression of viral release by host	1.727×10-7						
11	GO:BP	GO:2000758	Positive regulation of peptidyl-lysine acetylation	2.365×10-3						
12	GO:BP	GO:0009314	Response to radiation	3.899×10-3						
13	GO:BP	GO:0044773	Mitotic DNA damage checkpoint signaling	1.416×10-2						
14	GO:BP	GO:0048145	Regulation of fibroblast proliferation	1.553×10-2						
15	GO:BP	GO:0071345	Cellular response to cytokine stimulus	2.309×10-2						
16	GO:BP	GO:0045087	Innate immune response	4.025×10-2						
17	GO:BP	GO:0010508	Positive regulation of autophagy	4.245×10-2						
18	GO:BP	GO:0009411	Response to UV	4.598×10-2						
19	GO:BP	GO:0070512	Positive regulation of histone H4-K20 methylation	4.988×10-2						
20	GO:BP	GO:1903883	Positive regulation of interleukin-17-mediated signaling pathway	4.988×10-2						
21	GO:BP	GO:0032938	Negative regulation of translation in response to oxidative stres	4.988×10-2						
22	GO:BP	GO:1903884	Regulation of chemokine (C-C motif) ligand 20 production	4.988×10-2						
23	GO:CC	GO:0005654	Nucleoplasm	1.999×10-3						
24	GO:CC	GO:0043232	Intracellular non-membrane-bounded organelle	1.803×10-2						

Direct assay [IDA], Mutant phenotype [IMP]
Genetic interaction [IGI], Physical interaction [IPI]
Traceable author [TAS], Non-traceable author [NAS], Inferred by curator [IC]
Expression pattern [IEP], Sequence or structural similarity [ISS], Genomic context [IGC]
Reviewed computational analysis [RCA], Electronic annotation [IEA]

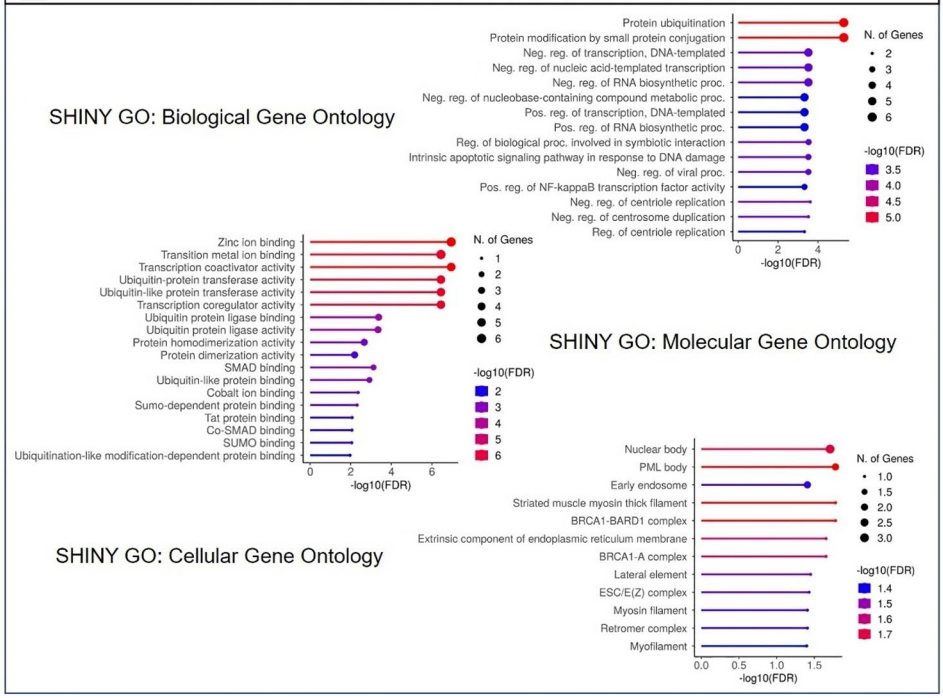


Fig. 3 The first half of the figure displays the results of g:Profiler used to perform gene ontology studies. BRCA1, PML, TRIM27, TRIM33, TRIM32, and TRIM37 genes were uploaded that gave top 24 enriched functions comprising of 8 molecular functions, 14 biological processes, and 2 cellular components. The latter half of the figure represents the results of SHINY GO which was used to validate the results and it suggested that protein ubiquitination and protein modification by small protein conjugation are the two processes in which all 6 genes are highly involved. Whereas all 6 genes showed zinc ion binding sites which is necessary for E2 enzyme to bind successfully and according to the cellular component, all were found in nuclear bodies

BRCA1 RING domain binds with E2 [78]. Yet, how ubiquitination of BRCA1-BARD1 directly affects its ligase activity stands unsolved. Several BRCA1 missense variants occur in the N-terminus and have the potential to disrupt E3 ligase activity. To get to the depth of that, firstly, the structure of BRCA1-BARD1 was retrieved from the PDB database, 1JM7, and active sites was studied for the same using FTSite. Three active sites were visualized using PyMOL, namely, Active Site 1: (**K**ILECP--L--I--------DHIF---…--- L---…---RF) (20-79), Active Site 2: (IC---…---FC--**K**L) (26–51), and Active Site 3: (ELI**K**E---…---C**K**F) (29–46). Moreover, as the growing characterization of BRCA1-dependent ubiquitination is widely studied on lysine residues, thus, we targeted lysine residues from these three active sites. Four lysine residues were observed, namely, K20 from Active Site 1, K50 from Active Site 2, and K32 and K45 from Active Site 3. Later, pathogenic variants of these lysine residues were analyzed using MutPred2, which gave a general score with a threshold of 0.5 suggesting whether the amino acid substitution is pathogenic or not [79]. Intriguingly, K20 and K50 showed no score > 0.5. Moreover, as K20 does not come in the selected motif of BRCA1 as well as ubiquitination does not affect this site, as verified by PLMD and SMART, thus, this residue was dropped for further mutational analysis. Similarly, K50 was also dropped though it undergoes ubiquitination yet no pathogenic variant was observed from its MutPred2 analysis. MutPred2 analysis of K32 showed 8 variants with pathogenicity score > 0.5, where the top three in increasing order were K32C, K32L, and K32Y. Likewise, for K45, 17 mutants were found pathogenic out of which K45G, K45V, and K45Y were the top three in increasing order. The result was validated using other mutational tools including, PredictSNP, PHD-SNP, PolyPhen-1, PolyPhen-2, SIFT, SNAP, and PANTHER (Figure S2). Therefore, Active Site 3 carrying K32 and K45 sites was considered as it displays strong mutagenesis. Lastly, stability analysis was performed for the variants of K32 and K45 using ProjectHOPE that compared mutants with the wild-type based on size, charge, and hydrophobicity. Results suggested that all mutants were variable in size, neutral in charge, and more hydrophobic than the wild-type. The green color represents the wild-type, while the red color represents the mutant (Table S2).

BRCA1-BARD1 Docking with Ube2k

As BRCA1-BARD1 likely acts as E3 ligase in most cellular complexes and leads to ubiquitination of different substrates in each complex, it becomes necessary to identify which all E2-conjugating enzymes are bringing ubiquitin to it. Many studies state that the RING domain of BRCA1 has the ability to bind with the following E2-conjugating enzymes, UbcH6, UbcH7, Ube2e2, UbcM2, Ube2w, Ubc13, Ube2k, and UbcH5 [16, 80, 81]. However, in one study it was further clarified that for BRCA1, Ubc13, and Ube2k are ubiquitin-specific E2s which means that E2 conjugates ubiquitin to another ubiquitin, while UbcH6, Ube2e2, UbcM2, and Ube2w are substrate-specific E2s suggesting that they transfer ubiquitin directly to the substrate [16]. UbcH7, Ube2w, Ubc13, and UbcH5 are class I E2s as they only have ubiquitin-conjugating (UBC) core domain. Ube2k is a class II E2, having a C-terminal extension from UBC core domain containing an ubiquitin-associated (UBA) domain that attaches ubiquitin molecule and helps to dispense its transfer in vitro [82]. UbcH6, Ube2e2, and UbcM2 own an exclusive N-terminal extension from their closely-related UBC core domain [16]. Although, there are different classes of E2s, yet they all share many conserved features along with the same core domains and their ability to bind with E1s. Nonetheless, in our study, we picked Ube2k (PDB:6IF1) to dock with BRCA1-BARD1 because, firstly, Ube2k explicitly shapes a ubiquitin chain that is degradative in function such that whenever it binds with its suitable substrate, it gets degraded. Secondly, Ube2k is the only E2 that has a ubiquitin-binding domain that may lead to an increased local concentration of enzymes, which further encourages to quickly build a ubiquitin chain for degradation [83]. Lastly, pieces of evidence suggest that Ube2k plays a crucial role in different neurodegenerative diseases, for instance, its involvement in Huntington's disease and Polyglutamine diseases [18, 84]. Elevated levels of Ube2k in the whole blood of individuals with schizophrenia show its surge in the brain indicating UPS dysfunction [85]. Moreover, Ube2k response is proapoptotic to the amyloid-β neurotoxicity as it upregulates signal-regulating kinase 1 (ASK1) and c-Jun N-terminal kinase (JNK) signaling pathway, thereby inhibiting proteasome activity [17]. Furthermore, reduced expression of Ube2k contributes to dopaminergic neuronal death and motor deficits in patients with Parkinson's disease [86]. Before docking analysis, the active/attraction and passive/repulsion sites for both BRCA1-BARD1 (PDB:1JM7) and Ube2k (PDB:6IF1) were identified using CPORT. Active and passive sites of BRCA1-BARD1 and Ube2k are given in Supplementary Table 3. Three protein–protein docking tools, HADDOCK, ClusPro, and LZerD were used to understand the binding of Ube2k with the mutants of BRCA1-BARD1 namely, K32Y, K32L, K32C, K45V, K45Y, and K45G. HADDOCK results were compiled based on the top cluster found and its z-score, which signifies the total number of standard deviations from the average, the more negative the better. Contrarily, ClusPro results were evaluated on the basis of highly populated clusters and low energy conformation of balance structures, suggesting that the cluster size should be more positive and energy should be more

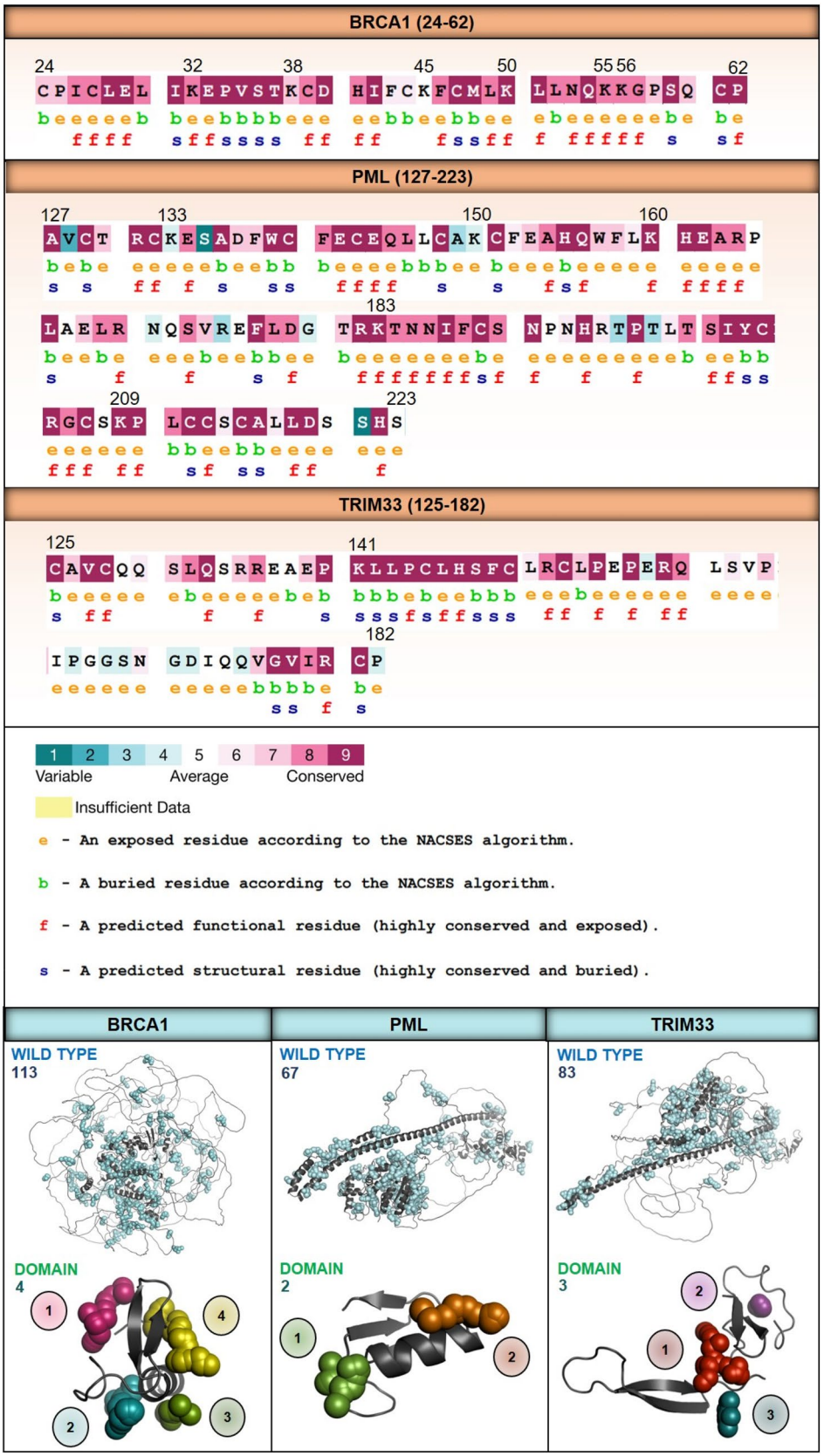


Fig. 4 The top part depicts the motif selected to study E2-E3 binding and the potential lysine sites involved in the process of ubiquitination, sumoylation, and acetylation. It also represents the evolutionary conservation scale demonstrating 1 as the most variable position and 9 as the most conserved position; the score obtained for a position is based on alignment, thus, those positions that have < 6 un-gapped amino acids are taken as unreliable. The second half of the figure illustrates the binding pockets observed in full structure and the selected motif of wild-type genes of BRCA1, PML, and TRIM33

negative. Moreover, LZerD results were assessed on the basis of ranksum score, indicating smaller the ranksum score, better is the result (Fig. 5).

Molecular Dynamics Simulation of Protein–Protein Docked Structure

Molecular dynamics simulation was performed for 20 ns for wild-type and all the mutants using an open-source software, GROMACS, following the steps of lysozyme in water to apprehend the conformational variations in BRCA1 owing to mutations K32Y, K32L, K32C, K45V, K45Y, and K45G (Fig. 6). The top mutants, i.e., K32L and K45Y were further analyzed for 50 ns (Fig. 7).

RMSD, RMSF, and RG have been investigated throughout the simulation trajectory of the protein with time-dependent function. The RMSD value for the backbone residue of wild-type and mutants of BRCA1 was observed for all the atoms from the initial structure (1-103aa) to decipher the impact of mutation on protein stability. It has been observed that the RMSD value of all the mutants is highly unstable compared to the wild-type, however, the maximum deviation showed up in mutant K32L ranging from ~ 0.25 nm (wild-type) to ~ 0.7 nm (mutant), respectively. The second most unstable mutant observed was K45Y with deviation ranging from ~ 0.25 (wild-type) nm to ~ 0.6 nm (mutant) correspondingly (Figs. 6 and 7). Later, RMSF of Cα atom of wild-type and mutants were calculated to assess the fluctuation in each residue after mutation. The result depicted high residue-level fluctuations in mutants compared to wild-type, exclusively for residues located between 40 and 70 positions. However, residue flexibility was not much affected in Ube2k docked with mutants of K45, nonetheless, in the case of mutants of K32, noticeable fluctuations were observed, especially for Ube2k docked with mutant K32L. Lastly, the analysis of RG revealed that only the mutant K32L had least compactness in its structure with ~ 2.38 nm compared to wild-type with compactness ~ 2.28 nm, however, RG of K32C and K32Y had the highest compactness in structure with ~ 2.15 nm and ~ 2.2 nm, respectively. Whereas, in case of mutants of K45, K45Y showed least compactness with ~ 2.36 compared to wild-type with compactness ~ 2.28 nm.

Discussion

The hallmark feature of NDDs is the accumulation of non-functional proteins in the cellular milieu and PTMs playing a very crucial role in regulating these non-functional protein aggregates in the pathogenesis of NDDs [87]. Alzheimer's disease and Parkinson's disease are two such NDDs that are characterized by progressive neuronal cell death that further causes memory and motor impairment. Ubiquitination is a prevalent pathway that degrades or modifies proteins, controls many cellular complexes, and is majorly involved whenever there is growth and development [88, 89]. Therefore, ubiquitination is a more important modification than phosphorylation because of its high involvement in numerous functions. In this modification, E2 plays a vital role in transferring ubiquitin from E1 to E3 to the substrate. One of the ways by which ubiquitin is conjugated to the target protein is by forming an isopeptide bond between its glycine and ε-amino group of a lysine residue. Nonetheless, more observations and analysis are demanded to completely understand the role of E2. In this study, the binding of E2, Ube2k with E3, BRCA1-BARD1 are primarily discussed, with a focus, particularly on Ube2k binding with the mutants of BRCA1-BARD1.

Firstly, Venn analysis of the AD dataset (GSE122063), PD dataset (GSE8397), and E3 dataset (ESBL) gave a list of 74 E3 ligases that were common in both AD and PD from which we computed 10 hub genes namely, PML, BRCA1, TRIM23, TRIM32, RNF11, TRIM27, UBR2, TRIM37, MID2, and TRIM33. Gene enrichment analysis of these 10 genes demonstrated that the majority of the genes took part in the Ubiquitin mediated-proteolysis pathway. Afterward, by using MotifFinder, total number of motifs were observed for the genes: BRCA1-15, PML-7, TRIM27-12, TRIM33-8, TRIM32-17, and TRIM37-8. Later, it was observed that only three genes, i.e., BRCA1, PML, and TRIM33 have more than 15 overlap matches. As aforementioned, lysine is the key amino acid on which the attachment takes place, therefore, for BRCA1, PML, and TRIM33, 6, 5, and 1 lysine hotspot sites were observed, respectively. In BRCA1 and TRIM33, all lysine sites undergo at least ubiquitination, however, in PML, 4/5 lysine sites undergo ubiquitination. Using ConSurf, the role of these lysine residues in the protein was checked and it was found that all these hotspot sites of BRCA1 and PML were exposed and functional, whereas, in TRIM33, it was structural and buried. The binding pockets for BRCA1, PML, and TRIM33 were 4, 3, and 2, respectively. Furthermore, ubiquitination in PML is often dependent on other post-translational modifications like sumoylation, phosphorylation, and prolyl-isomerization indicating that PML ubiquitination is highly complex by nature [90]. Therefore, BRCA1 was further taken forward for mutational analysis.

BRCA1 plays a crucial role in many cellular processes, however, here we target one of its well-established functions as a ubiquitin E3 ligase. Although, BRCA1 has its own RING domain for E2 binding, despite that its E3 ligase activity necessitates both BRCA1 and BARD1 protein. The putative substrates identified so far of BRCA1-BARD1 to carry out its E3 ligase activity are nucleophosmin 1 (NPM1), RNA Polymerase II Subunit A (RPB1), RNA polymerase core subunit (RPB8), progesterone receptor-A (PR-A),

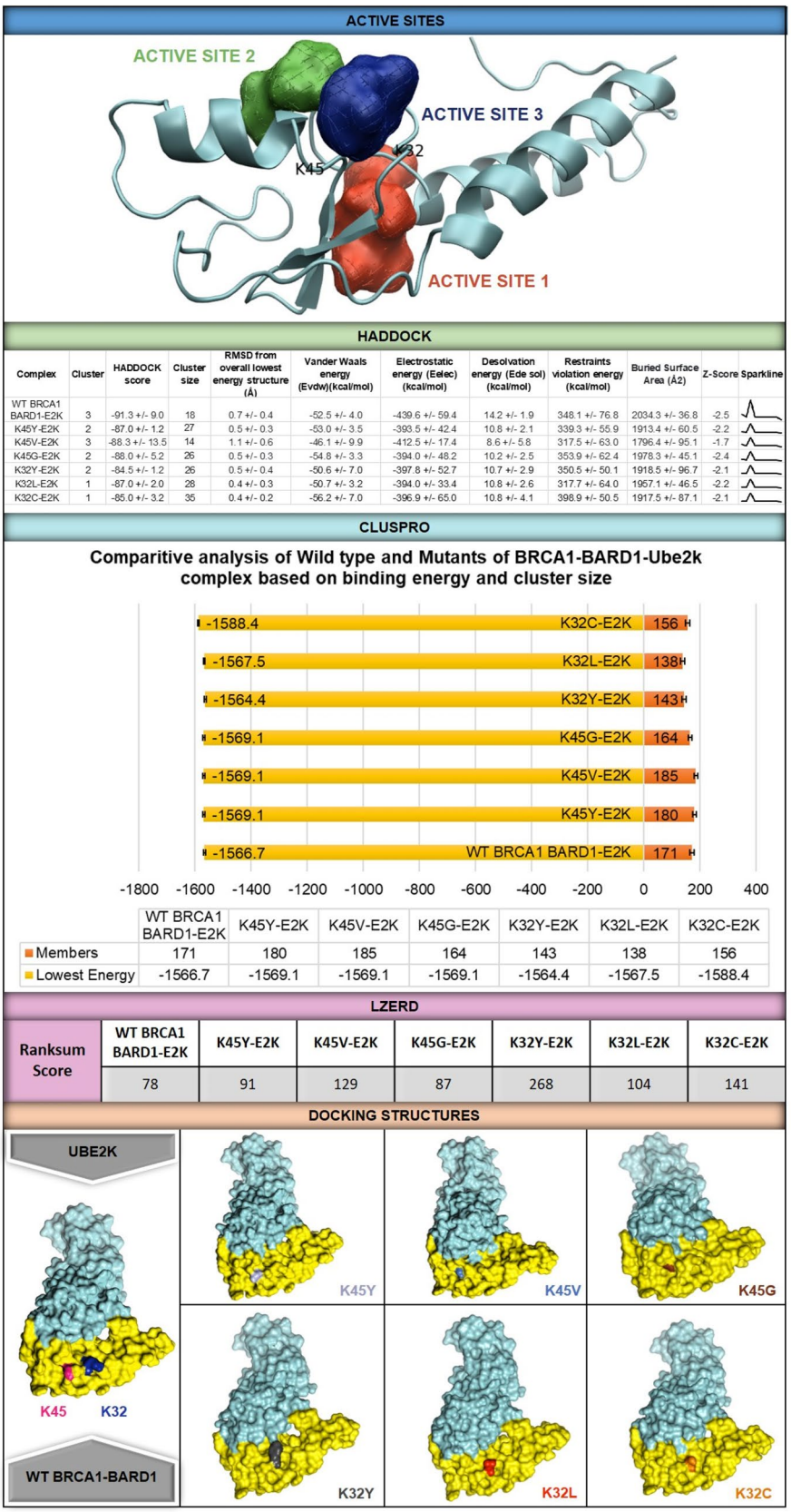


Fig. 5 Diagrammatic view of 3 active sites observed in the RING domain of BRCA1. The 2 potential lysine sites, i.e., K32 and K45 lie in the blue-colored active site. The docking results of HADDOCK suggest that the z-score for all the mutant were less than the wild-type suggesting that the mutants have a significant impact on E2-E3 binding, while the ClusPro results indicate the lowest energy and the cluster size of each mutant (balanced model). LZerD gave a Ranksum for wild-type and each mutant which is calculated as the sum of GOAP, DFIRE, and ITScore, therefore, smaller Ranksum score suggests better result. Lastly, docking structures of BRCA1-BARD1 with Ube2k reveal structural changes detected in each case

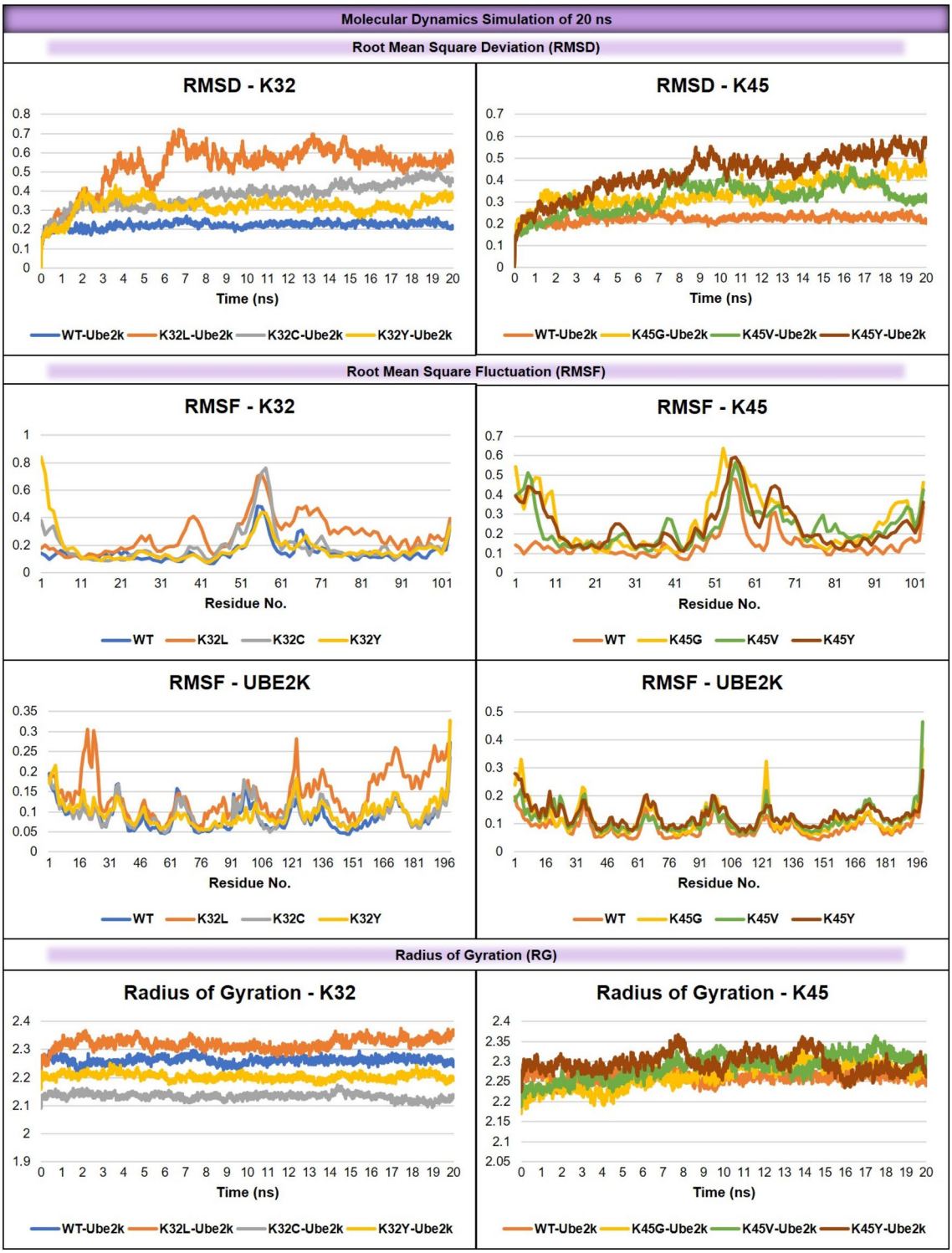


Fig. 6 Molecular dynamics simulation of wild-type and mutants K32Y, K32L, K32C, K45V, K45Y, and K45G at 20 ns, where several parameters were analyzed including root mean square deviation (RMSD), root mean square fluctuation (RMSF), and radius of gyration (RG). The results suggest K32L as the most potential mutant that affects the E2-E3 binding

transcription factor IIE (TFIIE), Topoisomerase IIa, Estrogen receptor alpha (ERα), progesterone receptor, γ-tubulin, histones, H2A, macroH2A1, p50, neurofibromatosis type 2 (NF2), organic cation/carnitine transporter 1 (Oct1), la ribonucleoprotein 7 (LARP7), Claspin, and Aurora Kinase which could possibly have diverse involvement in AD and

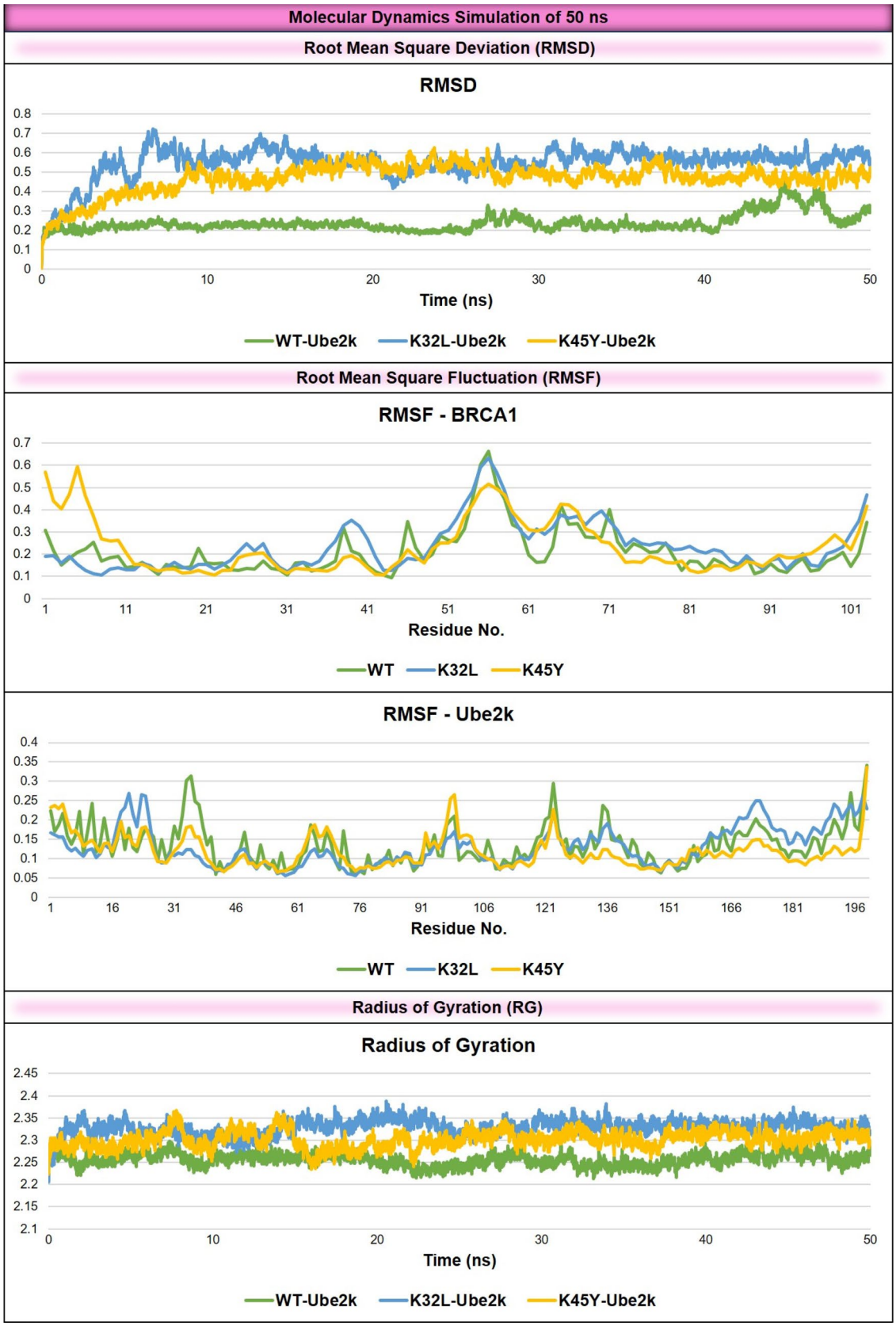


Fig. 7 Molecular dynamics simulation of wild-type and mutants K32L and K45Y at 50 ns, where K32L found to be most probable mutant that could affect the binding of BRCA1-Ube2k

PD. E3 ligase activity of BRCA1 has been extensively studied in cancer, however, in neurodegeneration, BRCA1 acts as a key DNA repair protein which is associated with cell senescence, transcriptional regulation, cell-cycle checkpoint, apoptosis, chromatic remodeling, and centrosome replication [91]. BARD1 forms a heterodimer with BRCA1 through its RING domain and supports its migration into the nucleus. In AD, it has been reported that BRCA1 colocalizes with tau protein in a diseased brain, whereas in PD, BRCA1 does not colocalize with α-synuclein [92].

In BRCA1, it has been observed that all the known missense substitutions due to missense dysfunction either on RING domain or BRCT domain are pathogenic [93]. A study observed that missense mutation in the RING domain alters the region of BRCA1 that is required for interaction with ubiquitin-conjugating enzymes [94]. Although, increased level of BRCA1-BARD1 complex is vital for ubiquitin E3 ligase activity of BRCA1, however, under pathological conditions BRCA1-BARD1 ubiquitin ligase activity results in the ubiquitination of γ-tubulin in the cytosol, a process important for centrosomal complex concentration of proteins involved in cell cycle; this directs towards dysfunctioning of BRCA1 in ubiquitination and results in subcellular mislocalization of a large portion of BRCA1 protein in neurons during neurodegeneration. Therefore, this also suggests that inflection in BRCA1 levels and activity is significant for different brain conditions [95].

The mutagenesis studies were performed on the target motif of BRCA1—Zf RING Ubox, position 24–62. Also, out of the three active sites, Active Site 3 was considered because the lysine residues of Active Site 1 and Active Site 2 did not show pathogenicity on different amino acid substitutions. However, lysine sites K32 and K45 of Active Site 3 showed high pathogenicity on substituting with other amino acids. The top three mutants for both hotspots were K32Y, K32L, K32C, and K45Y, K45V, K45G, respectively. To further decipher the impact of these mutants on the E3 ligase activity of BRCA1-BARD1, protein–protein docking was carried out with one of its potential E2, Ube2k using HADDOCK and ClusPro. According to HADDOCK results, there was a considerable difference observed in the z-score of the wild-type and the other six variants. Moreover, as per ClusPro results, all the mutants of K32, namely K32Y, K32L, and K32C exhibited smaller cluster size compared to the wild-type. Out of the three variants of K45, only K45G displayed a smaller cluster size. However, the lowest binding energies of all the variants did not show any significant changes in their values in comparison to the wild-type. As per the LZerD, all mutants had Ranksum score higher than the wild-type, thereby, suggesting substitution mutation has a significant impact on protein structure.

MD simulation analysis facilitated in investigation of the impact of mutation on the structure of the protein. RMSD data suggested a significant deviation in mutants as compared to wild-type throughout the simulation time, hence it clearly indicates that the mutation has a destabilizing effect on the protein. The results were substantiated by RMSF data which represented high residue-level fluctuations for variant protein thereby directing that mutation affects the flexibility of the protein. RG plot revealed that variant K32L destabilizes the structure resulting in loss of protein compactness.

Conclusion

BRCA1 has been extensively studied in breast and ovarian cancer, however, in neurodegeneration, BRCA1 acts as a key DNA repair protein. BRCA1 acts as an E3 in many cellular complexes that ubiquitinates different substrates. There is a potential link between cellular senescence and neurodegeneration, where a deficient DNA repair mechanism leads to structural and functional impairment of BRCA1 that contributes to the pathogenesis of neurodegeneration. Here, we studied the E3 ligase activity of BRCA1 with its E2-conjugating partner, Ube2k. Results suggest that mutagenesis of K32 and K45 has a significant impact on their binding. Thereby, giving an insight into how Ube2k binding is affected at the RING domain of BRCA1, impacting its ability to do E3 ligase activity and resulting in detrimental ubiquitination events. Molecular dynamics simulation validated K32L as the most potential mutant. However, more in vivo studies and experiments are required for further validation. The broader implication of this work is to elucidate the functional mechanistic insights behind lysine mutation in RING domain of BRCA1 to find therapeutic intervention for NDDs. Future prospects of this study address that mutation in RING domain of BRCA1 could decrease its co-localization with BARD1 and BACH1. Moreover, histidine and cysteine are two key residues involved in many E2–E3 interactions, therefore mutation of these amino acids could be explored in BRCA1 as well.

Supplementary Information The online version contains supplementary material available at https://doi.org/10.1007/s12033-023-01006-4.

Acknowledgements We would like to thank the senior management of Delhi Technological University for their constant support and guidance. The authors would like to thank the University Grant Commission, Government of India, for providing junior research fellowship to NR, NTA ref no 201610125084.

Authors Contribution PK: conceptualized, designed, and supervised this work. MS and NR: drafted the manuscript, analyzed, and interpreted the data, and did the artwork. All authors have read and given consent for submission.

Funding Not applicable.

Data Availability The authors confirm that the data supporting the findings of this study are available within the article.

Declarations

Competing interest The author declared no potential competing interest with respect to the research, authorship, and/or publication of this article.

Ethical Approval and Consent to Participate
Not applicable.

Consent for Publication Not applicable.

References

1. Watanabe, Y., Taguchi, K., & Tanaka, M. (2020). Ubiquitin autophagy and neurodegenerative diseases. *Cells, 9*(9), 2022. https://doi.org/10.3390/CELLS9092022
2. Chen, L., Liu, S., & Tao, Y. (2020). Regulating tumor suppressor genes: Post-translational modifications. *Signal Transduction and Targeted Therapy, 5*(1), 1–25. https://doi.org/10.1038/s41392-020-0196-9
3. Salas-Lloret, D., & González-Prieto, R. (2022). Insights in Post-translational modifications: Ubiquitin and SUMO. *International Journal of Molecular Sciences, 23*(6), 3281. https://doi.org/10.3390/IJMS23063281
4. Kumar, V. S., & Vellaichamy, A. (2019). Sequence and structure-based characterization of ubiquitination sites in human and yeast proteins using Chou's sample formulation. *Proteins: Structure, Function, and Bioinformatics, 87*(8), 646–657. https://doi.org/10.1002/PROT.25689
5. Jaishankar, A., Tang, N. L. S., Jelani, M., Mabb, A. M., George, A. J., Hoffiz, Y. C., & Zhu, Y. (2018). A comprehensive atlas of E3 ubiquitin ligase mutations in neurological disorders. *Frontiers in Genetics, 9*, 29. https://doi.org/10.3389/fgene.2018.00029
6. Upadhyay, A., Joshi, V., Amanullah, A., Mishra, R., Arora, N., Prasad, A., & Mishra, A. (2017). E3 ubiquitin ligases neurobiological mechanisms: Development to degeneration. *Frontiers in Molecular Neuroscience, 10*, 151. https://doi.org/10.3389/FNMOL.2017.00151/BIBTEX
7. LeBlanc, N., Mallette, E., & Zhang, W. (2021). Targeted modulation of E3 ligases using engineered ubiquitin variants. *The FEBS Journal, 288*(7), 2143–2165. https://doi.org/10.1111/FEBS.15536
8. Yang, Q., Zhao, J., Chen, D., & Wang, Y. (2021). E3 ubiquitin ligases: Styles, structures and functions. *Molecular Biomedicine*. https://doi.org/10.1186/S43556-021-00043-2
9. Schmidt, M. F., Gan, Z. Y., Komander, D., & Dewson, G. (2021). Ubiquitin signalling in neurodegeneration: Mechanisms and therapeutic opportunities. *Cell Death & Differentiation, 28*(2), 570–590. https://doi.org/10.1038/s41418-020-00706-7
10. Roverato, N. D., Sailer, C., Catone, N., Aichem, A., Stengel, F., & Groettrup, M. (2021). Parkin is an E3 ligase for the ubiquitin-like modifier FAT10, which inhibits Parkin activation and mitophagy. *Cell reports*. https://doi.org/10.1016/J.CELREP.2021.108857
11. Wang, T., Wang, W., Wang, Q., Xie, R., Landay, A., & Chen, D. (2020). The E3 ubiquitin ligase CHIP in normal cell function and in disease conditions. *Annals of the New York Academy of Sciences, 1460*(1), 3–10. https://doi.org/10.1111/NYAS.14206
12. Metzger, M. B., Pruneda, J. N., Klevit, R. E., & Weissman, A. M. (2014). RING-type E3 ligases: Master manipulators of E2 ubiquitin-conjugating enzymes and ubiquitination. *Biophysica Acta (BBA) - Molecular Cell Research, 1843*(1), 47–60. https://doi.org/10.1016/J.BBAMCR.2013.05.026
13. Leung, E., & Hazrati, L. N. (2021). Breast cancer type 1 and neurodegeneration: Consequences of deficient DNA repair. *Brain Communications*. https://doi.org/10.1093/BRAINCOMMS/FCAB117
14. Gough, C. A., Gojobori, T., & Imanishi, T. (2007). Cancer-related mutations in BRCA1-BRCT cause long-range structural changes in protein–protein binding sites: A molecular dynamics study. *Proteins: Structure, Function, and Bioinformatics, 66*(1), 69–86. https://doi.org/10.1002/PROT.21188
15. Drikos, I., Nounesis, G., & Vorgias, C. E. (2009). Characterization of cancer-linked BRCA1-BRCT missense variants and their interaction with phosphoprotein targets. *Proteins: Structure, Function, and Bioinformatics, 77*(2), 464–476. https://doi.org/10.1002/PROT.22460
16. Christensen, D. E., Brzovic, P. S., & Klevit, R. E. (2007). E2–BRCA1 RING interactions dictate synthesis of mono- or specific polyubiquitin chain linkages. *Nature Structural & Molecular Biology, 14*(10), 941–948. https://doi.org/10.1038/nsmb1295
17. Song, S., Kim, S. Y., Hong, Y. M., Jo, D. G., Lee, J. Y., Shim, S. M., Chung, C. W., Seo, S. J., Yoo, Y. J., Koh, J. Y., Lee, M. C., Yates, A. J., Ichijo, H., & Jung, Y. K. (2003). Essential role of E2–25K/Hip-2 in mediating amyloid-beta neurotoxicity. *Molecular Cell, 12*(3), 553–563. https://doi.org/10.1016/J.MOLCEL.2003.08.005
18. de Pril, R., Fischer, D. F., Roos, R. A. C., & van Leeuwen, F. W. (2007). Ubiquitin-conjugating enzyme E2–25K increases aggregate formation and cell death in polyglutamine diseases. *Molecular and cellular neurosciences, 34*(1), 10–19. https://doi.org/10.1016/J.MCN.2006.09.006
19. Su, J., Huang, P., Qin, M., Lu, Q., Sang, X., Cai, Y., Wang, Y., Liu, F., Wu, R., Wang, X., Jiang, X., Wang, J., Sun, Q., Chen, S., & Xu, J. (2018). Reduction of HIP2 expression causes motor function impairment and increased vulnerability to dopaminergic degeneration in Parkinson's disease models. *Cell Death and Disease*. https://doi.org/10.1038/s41419-018-1066-z
20. Tak, Y. J., & Kang, S. (2022). The E2 ubiquitin-conjugating enzyme HIP2 is a crucial regulator of quality control against mutant SOD1 proteotoxicity. *Biochimica et Biophysica Acta (BBA) - Molecular Basis of Disease, 1868*(2), 166316. https://doi.org/10.1016/J.BBADIS.2021.166316
21. Mezencev, R., & Chernoff, Y. O. (2020). Risk of Alzheimer's disease in cancer patients: Analysis of mortality data from the US SEER population-based registries. *Cancers, 12*(4), 796. https://doi.org/10.3390/CANCERS12040796
22. Mano, T., Iwata, A., Nonaka, T., Tarutani, A., Hashimoto, T., Hasegawa, M., Iwatsubo, T., & Toda, T. (2018). Tau-related dysfunction of BRCA1 leads to reduced neuronal plasticity in Alzheimer's disease. *Alzheimer's & Dementia*. https://doi.org/10.1016/J.JALZ.2018.06.2771
23. Evans, T. A., Raina, A. K., Delacourte, A., Aprelikova, O., Lee, H. G., Zhu, X., Perry, G., & Smith, M. A. (2007). BRCA1 may modulate neuronal cell cycle re-entry in alzheimer disease. *International Journal of Medical Sciences, 4*(3), 140. https://doi.org/10.7150/IJMS.4.140
24. Goodsell, D. S. (2022). JCVI-syn3A minimal cell. *RCSB Protein Data Bank*. https://doi.org/10.2210/RCSB_PDB/GOODSELL-GALLERY-042
25. Barrett, T., Wilhite, S. E., Ledoux, P., Evangelista, C., Kim, I. F., Tomashevsky, M., Marshall, K. A., Phillippy, K. H., Sherman, P. M., Holko, M., Yefanov, A., Lee, H., Zhang, N., Robertson, C.

L., Serova, N., Davis, S., & Soboleva, A. (2013). NCBI GEO: Archive for functional genomics data sets–update. *Nucleic Acids Research*. https://doi.org/10.1093/NAR/GKS1193
26. Edgar, R., Domrachev, M., & Lash, A. E. (2002). Gene expression omnibus: NCBI gene expression and hybridization array data repository. *Nucleic Acids Research, 30*(1), 207–210. https://doi.org/10.1093/NAR/30.1.207
27. Hunt, G. P., Grassi, L., Henkin, R., Smeraldi, F., Spargo, T. P., Kabiljo, R., Koks, S., Ibrahim, Z., Dobson, R. J. B., Al-Chalabi, A., Barnes, M. R., & Iacoangeli, A. (2022). GEOexplorer: a webserver for gene expression analysis and visualisation. *Nucleic Acids Research, 50*(W1), W367–W374. https://doi.org/10.1093/NAR/GKAC364
28. Udhaya Kumar, S., Thirumal Kumar, D., Bithia, R., Sankar, S., Magesh, R., Sidenna, M., George Priya Doss, C., & Zayed, H. (2020). Analysis of differentially expressed genes and molecular pathways in familial hypercholesterolemia involved in atherosclerosis: A systematic and bioinformatics approach. *Frontiers in Genetics, 11*, 1–16. https://doi.org/10.3389/FGENE.2020.00734/BIBTEX
29. Wu, A. T. H., Lawal, B., Wei, L., Wen, Y. T., Tzeng, D. T. W., & Lo, W. C. (2021). Multiomics identification of potential targets for alzheimer disease and antrocin as a therapeutic candidate. *Pharmaceutics, 13*(10), 1555. https://doi.org/10.3390/PHARMACEUTICS13101555
30. Li, W., Bengtson, M. H., Ulbrich, A., Matsuda, A., Reddy, V. A., Orth, A., Chanda, S. K., Batalov, S., & Joazeiro, C. A. (2008). Genome-wide and functional annotation of human E3 ubiquitin ligases identifies MULAN, a mitochondrial e3 that regulates the organelle's dynamics and signaling. *PLOS ONE, 3*(1), e1487. https://doi.org/10.1371/JOURNAL.PONE.0001487
31. Heberle, H., Meirelles, V. G., da Silva, F. R., Telles, G. P., & Minghim, R. (2015). InteractiVenn: A web-based tool for the analysis of sets through Venn diagrams. *BMC Bioinformatics, 16*(1), 1–7. https://doi.org/10.1186/S12859-015-0611-3/FIGURES/4
32. Szklarczyk, D., Franceschini, A., Wyder, S., Forslund, K., Heller, D., Huerta-Cepas, J., Simonovic, M., Roth, A., Santos, A., Tsafou, K. P., Kuhn, M., Bork, P., Jensen, L. J., & von Mering, C. (2015). STRING v10: Protein-protein interaction networks, integrated over the tree of life. *Nucleic Acids Research, 43*(D1), D447–D452. https://doi.org/10.1093/nar/gku1003
33. Oughtred, R., Chatr-aryamontri, A., Breitkreutz, B. J., Chang, C. S., Rust, J. M., Theesfeld, C. L., Heinicke, S., Breitkreutz, A., Chen, D., Hirschman, J., Kolas, N., Livstone, M. S., Nixon, J., O'Donnell, L., Ramage, L., Winter, A., Reguly, T., Sellam, A., Stark, C., … Tyers, M. (2016). BioGRID: A tool for studying biological interactions in yeast. *Cold Spring Harbor protocols, 2016*(1), pdb.top080754. https://doi.org/10.1101/PDB.TOP080754
34. Szklarczyk, D., Gable, A. L., Nastou, K. C., Lyon, D., Kirsch, R., Pyysalo, S., Doncheva, N. T., Legeay, M., Fang, T., Bork, P., Jensen, L. J., & von Mering, C. (2021). The STRING database in 2021: customizable protein–protein networks, and functional characterization of user-uploaded gene/measurement sets. *Nucleic Acids Research, 49*(D1), D605–D612. https://doi.org/10.1093/NAR/GKAA1074
35. Cao, M., Pietras, C. M., Feng, X., Doroschak, K. J., Schaffner, T., Park, J., Zhang, H., Cowen, L. J., & Hescott, B. J. (2014). New directions for diffusion-based network prediction of protein function incorporating pathways with confidenc. *Bioinformatics (Oxford, England)*. https://doi.org/10.1093/BIOINFORMATICS/BTU263
36. Cao, M., Zhang, H., Park, J., Daniels, N. M., Crovella, M. E., Cowen, L. J., & Hescott, B. (2013). Going the distance for protein function prediction: A new distance metric for protein interaction networks. *PLoS ONE*. https://doi.org/10.1371/JOURNAL.PONE.0076339
37. Shannon, P., Markiel, A., Ozier, O., Baliga, N. S., Wang, J. T., Ramage, D., Amin, N., Schwikowski, B., & Ideker, T. (2003). Cytoscape: A software environment for integrated models of biomolecular interaction networks. *Genome Research, 13*(11), 2498. https://doi.org/10.1101/GR.1239303
38. Elbashir, M. K., Mohammed, M., Mwambi, H., & Omolo, B. (2023). Identification of hub genes associated with breast cancer using integrated gene expression data with protein-protein interaction network. *Applied Sciences (Switzerland), 13*(4), 2403. https://doi.org/10.3390/APP13042403/S1
39. Reimand, J., Arak, T., & Vilo, J. (2011). g:Profiler—a web server for functional interpretation of gene lists (2011 update). *Nucleic Acids Research, 39*(2), W307–W315. https://doi.org/10.1093/NAR/GKR378
40. Xie, Z., Bailey, A., Kuleshov, M. V., Clarke, D. J. B., Evangelista, J. E., Jenkins, S. L., Lachmann, A., Wojciechowicz, M. L., Kropiwnicki, E., Jagodnik, K. M., Jeon, M., & Ma'ayan, A. (2021). Gene set knowledge discovery with enrichr. *Current Protocols, 1*(3), e90. https://doi.org/10.1002/CPZ1.90
41. Ge, S. X., Jung, D., Jung, D., & Yao, R. (2020). ShinyGO: A graphical gene-set enrichment tool for animals and plants. *Bioinformatics, 36*(8), 2628–2629. https://doi.org/10.1093/BIOINFORMATICS/BTZ931
42. Letunic, I., & Bork, P. (2018). 20 years of the SMART protein domain annotation resource. *Nucleic Acids Research, 46*(D1), D493–D496. https://doi.org/10.1093/NAR/GKX922
43. Bailey, T. L., Johnson, J., Grant, C. E., & Noble, W. S. (2015). The MEME suite. *Nucleic Acids Research, 43*(W1), W39–W49. https://doi.org/10.1093/NAR/GKV416
44. Obenauer, J. C., Cantley, L. C., & Yaffe, M. B. (2003). Scansite 20: Proteome-wide prediction of cell signaling interactions using short sequence motifs. *Nucleic Acids Research, 31*(13), 3635–3641. https://doi.org/10.1093/NAR/GKG584
45. Ashkenazy, H., Abadi, S., Martz, E., Chay, O., Mayrose, I., Pupko, T., & Ben-Tal, N. (2016). ConSurf 2016: An improved methodology to estimate and visualize evolutionary conservation in macromolecules. *Nucleic Acids Research*. https://doi.org/10.1093/nar/gkw408
46. Xu, H., Zhou, J., Lin, S., Deng, W., Zhang, Y., & Xue, Y. (2017). PLMD: An updated data resource of protein lysine modifications. *Journal of Genetics and Genomics = Yi chuan xue bao, 44*(5), 243–250. https://doi.org/10.1016/J.JGG.2017.03.007
47. Bendl, J., Stourac, J., Salanda, O., Pavelka, A., Wieben, E. D., Zendulka, J., Brezovsky, J., & Damborsky, J. (2014). PredictSNP: Robust and accurate consensus classifier for prediction of disease-related mutations. *PLoS Computational Biology*. https://doi.org/10.1371/JOURNAL.PCBI.1003440
48. Pejaver, V., Urresti, J., Lugo-Martinez, J., Pagel, K. A., Lin, G. N., Nam, H. J., Mort, M., Cooper, D. N., Sebat, J., Iakoucheva, L. M., Mooney, S. D., & Radivojac, P. (2020). Inferring the molecular and phenotypic impact of amino acid variants with MutPred2. *Nature Communications*. https://doi.org/10.1038/S41467-020-19669-X
49. Venselaar, H., te Beek, T. A. H., Kuipers, R. K. P., Hekkelman, M. L., & Vriend, G. (2010). Protein structure analysis of mutations causing inheritable diseases. An e-Science approach with life scientist friendly interfaces. *BMC Bioinformatics, 11*(1), 1–10. https://doi.org/10.1186/1471-2105-11-548/FIGURES/5
50. Brzovic, P. S., Rajagopal, P., Hoyt, D. W., King, M. C., & Klevit, R. E. (2001). Structure of a BRCA1-BARD1 heterodimeric RING-RING complex. *Nature Structural Biology, 8*(10), 833–837. https://doi.org/10.1038/nsb1001-833
51. Burley, S. K., Bhikadiya, C., Bi, C., Bittrich, S., Chao, H., Chen, L., Craig, P. A., Crichlow, G. V., Dalenberg, K., Duarte, J. M.,

Dutta, S., Fayazi, M., Feng, Z., Flatt, J. W., Ganesan, S., Ghosh, S., Goodsell, D. S., Green, R. K., Guranovic, V., … Zardecki, C. (2023). RCSB Protein Data Bank (RCSB.org): delivery of experimentally-determined PDB structures alongside one million computed structure models of proteins from artificial intelligence/machine learning. *Nucleic Acids Research, 51*(D1), D488–D508. https://doi.org/10.1093/NAR/GKAC1077

52. Kozakov, D., Grove, L. E., Hall, D. R., Bohnuud, T., Mottarella, S. E., Luo, L., Xia, B., Beglov, D., & Vajda, S. (2015). The FTMap family of web servers for determining and characterizing ligand-binding hot spots of proteins. *Nature Protocols, 10*(5), 733–755. https://doi.org/10.1038/nprot.2015.043
53. de Vries, S. J., & Bonvin, A. M. J. J. (2011). CPORT: A consensus interface predictor and its performance in prediction-driven docking with HADDOCK. *PLoS ONE*. https://doi.org/10.1371/JOURNAL.PONE.0017695
54. Desta, I. T., Porter, K. A., Xia, B., Kozakov, D., & Vajda, S. (2020). Performance and its limits in rigid body protein-protein docking. *Structure, 28*(9), 1071-1081.e3. https://doi.org/10.1016/j.str.2020.06.006
55. Vajda, S., Yueh, C., Beglov, D., Bohnuud, T., Mottarella, S. E., Xia, B., Hall, D. R., & Kozakov, D. (2017). New additions to the ClusPro server motivated by CAPRI. *Proteins: Structure Function, and Bioinformatics*. https://doi.org/10.1002/prot.25219
56. Kozakov, D., Beglov, D., Bohnuud, T., Mottarella, S. E., Xia, B., Hall, D. R., & Vajda, S. (2013). How good is automated protein docking? *Proteins: Structure Function, and Bioinformatics, 81*(12), 2159–2166. https://doi.org/10.1002/prot.24403
57. Kozakov, D., Hall, D. R., Xia, B., Porter, K. A., Padhorny, D., Yueh, C., Beglov, D., & Vajda, S. (2017). The ClusPro web server for protein–protein docking. *Nature Protocols, 12*(2), 255–278. https://doi.org/10.1038/nprot.2016.169
58. Porter, K. A., Xia, B., Beglov, D., Bohnuud, T., Alam, N., Schueler-Furman, O., & Kozakov, D. (2017). ClusPro peptidock: Efficient global docking of peptide recognition motifs using FFT. *Bioinformatics, 33*(20), 3299–3301. https://doi.org/10.1093/bioinformatics/btx216
59. van Zundert, G. C. P., Rodrigues, J. P. G. L. M., Trellet, M., Schmitz, C., Kastritis, P. L., Karaca, E., Melquiond, A. S. J., van Dijk, M., de Vries, S. J., & Bonvin, A. M. J. J. (2016). The HADDOCK2.2 web server: User-friendly integrative modeling of biomolecular complexes. *Journal of Molecular Biology, 428*(4), 720–725. https://doi.org/10.1016/J.JMB.2015.09.014
60. Dominguez, C., Boelens, R., & Bonvin, A. M. J. J. (2003). HADDOCK: A protein-protein docking approach based on biochemical or biophysical information. *Journal of the American Chemical Society, 125*(7), 1731–1737. https://doi.org/10.1021/JA026939X/SUPPL_FILE/JA026939XSI20021128_085857.TXT
61. Venkatraman, V., Yang, Y. D., Sael, L., & Kihara, D. (2009). Protein-protein docking using region-based 3D Zernike descriptors. *BMC Bioinformatics*. https://doi.org/10.1186/1471-2105-10-407
62. Porter, K. A., Desta, I., Kozakov, D., & Vajda, S. (2019). What method to use for protein–protein docking? *Current Opinion in Structural Biology, 55*, 1–7. https://doi.org/10.1016/j.sbi.2018.12.010
63. Van Der Spoel, D., Lindahl, E., Hess, B., Groenhof, G., Mark, A. E., & Berendsen, H. J. C. (2005). GROMACS: Fast, flexible, and free. *Journal of Computational Chemistry, 26*(16), 1701–1718. https://doi.org/10.1002/JCC.20291
64. Robertson, M. J., Tirado-Rives, J., & Jorgensen, W. L. (2015). Improved peptide and protein torsional energetics with the OPLS-AA force field. *Journal of Chemical Theory and Computation, 11*(7), 3499–3509. https://doi.org/10.1021/acs.jctc.5b00356
65. Scardoni, G., Tosadori, G., Faizan, M., Spoto, F., Fabbri, F., & Laudanna, C. (2014). Biological network analysis with CentiScaPe: Centralities and experimental dataset integration. *F1000Research*. https://doi.org/10.12688/F1000RESEARCH.4477.2
66. Chin, C. H., Chen, S. H., Wu, H. H., Ho, C. W., Ko, M. T., & Lin, C. Y. (2014). cytoHubba: Identifying hub objects and sub-networks from complex interactome. *BMC Systems Biology, 8*(4), 1–7. https://doi.org/10.1186/1752-0509-8-S4-S11/TABLES/4
67. Lorick, K. L., Jensen, J. P., Fang, S., Ong, A. M., Hatakeyama, S., & Weissman, A. M. (1999). RING fingers mediate ubiquitin-conjugating enzyme (E2)-dependent ubiquitination. *Proceedings of the National Academy of Sciences of the United States of America, 96*(20), 11364. https://doi.org/10.1073/PNAS.96.20.11364
68. Ying, M., Huang, X., Zhao, H., Wu, Y., Wan, F., Huang, C., & Jie, K. (2011). Comprehensively surveying structure and function of RING domains from *Drosophila melanogaster*. *PLoS ONE, 6*(9), e23863. https://doi.org/10.1371/JOURNAL.PONE.0023863
69. Ashkenazy, H., Abadi, S., Martz, E., Chay, O., Mayrose, I., Pupko, T., & Ben-Tal, N. (2016). ConSurf 2016: An improved methodology to estimate and visualize evolutionary conservation in macromolecules. *Nucleic Acids Research, 44*, W344. https://doi.org/10.1093/NAR/GKW408
70. Le Guilloux, V., Schmidtke, P., & Tuffery, P. (2009). Fpocket: An open source platform for ligand pocket detection. *BMC Bioinformatics, 10*(1), 1–11. https://doi.org/10.1186/1471-2105-10-168/TABLES/1
71. Hsu, K. S., & Kao, H. Y. (2018). PML: Regulation and multifaceted function beyond tumor suppression. *Cell & Bioscience, 8*(1), 1–21. https://doi.org/10.1186/S13578-018-0204-8
72. Tessier, S., Ferhi, O., Geoffroy, M. C., González-Prieto, R., Canat, A., Quentin, S., Pla, M., Niwa-Kawakita, M., Bercier, P., Rérolle, D., Tirard, M., Therizols, P., Fabre, E., Vertegaal, A. C. O., de Thé, H., & Lallemand-Breitenbach, V. (2022). Exploration of nuclear body-enhanced sumoylation reveals that PML represses 2-cell features of embryonic stem cells. *Nature Communications, 13*(1), 1–15. https://doi.org/10.1038/s41467-022-33147-6
73. Ivanschitz, L., De Thé, H., & Le Bras, M. (2013). PML, SUMOylation, and senescence. *Frontiers in Oncology*. https://doi.org/10.3389/FONC.2013.00171
74. Rabellino, A., & Scaglioni, P. P. (2013). PML degradation: Multiple ways to eliminate PML. *Frontiers in Oncology*. https://doi.org/10.3389/FONC.2013.00060/BIBTEX
75. Clark, S. L., Rodriguez, A. M., Snyder, R. R., Hankins, G. D. V., & Boehning, D. (2012). Structure-function of the tumor suppressor BRCA1. *Computational and Structural Biotechnology Journal, 1*(1), e201204005. https://doi.org/10.5936/CSBJ.201204005
76. Chatterjee, P., Karn, R., Emerson, I. A., & Banerjee, S. (2023). Docking and molecular dynamics simulation revealed the potential inhibitory activity of amygdalin in triple-negative breast cancer therapeutics targeting the brct domain of BARD1 receptor. *Molecular Biotechnology, 2023*, 1–19. https://doi.org/10.1007/S12033-023-00680-8
77. Gouveia, C., Peña-Guerrero, J., Fernández-Rubio, C., García-Sosa, A. T., & Nguewa, P. A. (2023). BRCT domains: Structure, functions, and implications in disease—New therapeutic targets for innovative drug discovery against infections. *Pharmaceutics, 15*(7), 1839. https://doi.org/10.3390/PHARMACEUTICS15071839
78. Witus, S. R., Stewart, M. D., & Klevit, R. E. (2021). The BRCA1/BARD1 ubiquitin ligase and its substrates. *The Biochemical Journal, 478*(18), 3467. https://doi.org/10.1042/BCJ20200864
79. Pejaver, V., Urresti, J., Lugo-Martinez, J., Pagel, K. A., Lin, G. N., Nam, H. J., Mort, M., Cooper, D. N., Sebat, J., Iakoucheva, L. M., Mooney, S. D., & Radivojac, P. (2020). Inferring the molecular and phenotypic impact of amino acid variants with MutPred2. *Nature Communications, 11*(1), 1–13. https://doi.org/10.1038/s41467-020-19669-x

80. Wu, W., Koike, A., Takeshita, T., & Ohta, T. (2008). The ubiquitin E3 ligase activity of BRCA1 and its biological functions. *Cell Division, 3*(1), 1–10. https://doi.org/10.1186/1747-1028-3-1/FIGURES/2
81. (2007). New partners for BRCA1. *Nature Structural & Molecular Biology*, *14*(10), 879–879. https://doi.org/10.1038/nsmb1007-879
82. Merkley, N., & Shaw, G. S. (2004). Solution structure of the flexible class II ubiquitin-conjugating enzyme Ubc1 provides insights for polyubiquitin chain assembly. *The Journal of Biological Chemistry, 279*(45), 47139–47147. https://doi.org/10.1074/JBC.M409576200
83. Middleton, A. J., Teyra, J., Zhu, J., Sidhu, S. S., & Day, C. L. (2021). Identification of ubiquitin variants that inhibit the E2 ubiquitin conjugating enzyme, Ube2k. *ACS Chemical Biology, 16*(9), 1745–1756. https://doi.org/10.1021/ACSCHEMBIO.1C00445/ASSET/IMAGES/LARGE/CB1C00445_0006.JPEG
84. Kalchman, M. A., Graham, R. K., Xia, G., Koide, H. B., Hodgson, J. G., Graham, K. C., Goldberg, Y. P., Gietz, R. D., Pickart, C. M., & Hayden, M. R. (1996). Huntingtin is ubiquitinated and interacts with a specific ubiquitin-conjugating enzyme. *The Journal of Biological Chemistry, 271*(32), 19385–19394. https://doi.org/10.1074/JBC.271.32.19385
85. Meiklejohn, H., Mostaid, M. S., Luza, S., Mancuso, S. G., Kang, D., Atherton, S., Rothmond, D. A., Weickert, C. S., Opazo, C. M., Pantelis, C., Bush, A. I., Everall, I. P., & Bousman, C. A. (2019). Blood and brain protein levels of ubiquitin-conjugating enzyme E2K (UBE2K) are elevated in individuals with schizophrenia. *Journal of Psychiatric Research, 113*, 51–57. https://doi.org/10.1016/J.JPSYCHIRES.2019.03.005
86. Su, J., Huang, P., Qin, M., Lu, Q., Sang, X., Cai, Y., Wang, Y., Liu, F., Wu, R., Wang, X., Jiang, X., Wang, J., Sun, Q., Chen, S., & Xu, J. (2018). Reduction of HIP2 expression causes motor function impairment and increased vulnerability to dopaminergic degeneration in Parkinson's disease models. *Cell Death & Disease*. https://doi.org/10.1038/S41419-018-1066-Z
87. Gupta, R., Sahu, M., Srivastava, D., Tiwari, S., Ambasta, R. K., & Kumar, P. (2021). Post-translational modifications: Regulators of neurodegenerative proteinopathies. *Ageing Research Reviews*. https://doi.org/10.1016/j.arr.2021.101336
88. Liu, W., Tang, X., Qi, X., Fu, X., Ghimire, S., Ma, R., Li, S., Zhang, N., & Si, H. (2020). The ubiquitin conjugating enzyme: An important ubiquitin transfer platform in ubiquitin-proteasome system. *International Journal of Molecular Sciences*. https://doi.org/10.3390/IJMS21082894
89. Radivojac, P., Vacic, V., Haynes, C., Cocklin, R. R., Mohan, A., Heyen, J. W., Goebl, M. G., & Iakoucheva, L. M. (2010). Identification, analysis, and prediction of protein ubiquitination sites. *Proteins: Structure, Function, and Bioinformatics, 78*(2), 365–380. https://doi.org/10.1002/PROT.22555
90. Chen, R. H., Lee, Y. R., & Yuan, W. C. (2012). The role of PML ubiquitination in human malignancies. *Journal of biomedical science, 19*(1), 81. https://doi.org/10.1186/1423-0127-19-81/FIGURES/1
91. Miyahara, K., Takano, N., Yamada, Y., Kazama, H., Tokuhisa, M., Hino, H., Fujita, K., Barroga, E., Hiramoto, M., Handa, H., Kuroda, M., Ishikawa, T., & Miyazawa, K. (2021). BRCA1 degradation in response to mitochondrial damage in breast cancer cells. *Scientific Reports, 11*(1), 1–13. https://doi.org/10.1038/s41598-021-87698-7
92. Kurihara, M., Mano, T., Saito, Y., Murayama, S., Toda, T., & Iwata, A. (2020). Colocalization of BRCA1 with tau aggregates in human tauopathies. *Brain Sciences*. https://doi.org/10.3390/BRAINSCI10010007
93. Clark, K. A., Paquette, A., Tao, K., Bell, R., Boyle, J. L., Rosenthal, J., Snow, A. K., Stark, A. W., Thompson, B. A., Unger, J., Gertz, J., Varley, K. E., Boucher, K. M., Goldgar, D. E., Foulkes, W. D., Thomas, A., & Tavtigian, S. V. (2022). Comprehensive evaluation and efficient classification of BRCA1 RING domain missense substitutions. *American Journal of Human Genetics, 109*(6), 1153. https://doi.org/10.1016/J.AJHG.2022.05.004
94. Brzovic, P. S., Meza, J. E., King, M. C., & Klevit, R. E. (2001). BRCA1 RING domain cancer-predisposing mutations. Structural consequences and effects on protein-protein interactions. *The Journal of Biological Chemistry, 276*(44), 41399–41406. https://doi.org/10.1074/JBC.M106551200
95. Wezyk, M., & Zekanowski, C. (2018). Role of BRCA1 in neuronal death in Alzheimer's disease. *ACS Chemical Neuroscience*. https://doi.org/10.1021/acschemneuro.8b00149

Publisher's Note Springer Nature remains neutral with regard to jurisdictional claims in published maps and institutional affiliations.

Springer Nature or its licensor (e.g. a society or other partner) holds exclusive rights to this article under a publishing agreement with the author(s) or other rightsholder(s); author self-archiving of the accepted manuscript version of this article is solely governed by the terms of such publishing agreement and applicable law.

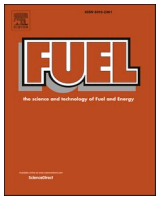
Fuel 362 (2024) 130742



Contents lists available at ScienceDirect

Fuel

journal homepage: www.elsevier.com/locate/fuel



Full Length Article

Simulation modelling of hydrogen production from steam reforming of methane and biogas

Ravindra Kumar [a], Anil Kumar [a,b,*], Amit Pal [a]

[a] Department of Mechanical Engineering, Delhi Technological University, Delhi 110042, India
[b] Centre for Energy and Environment, Delhi Technological University, Delhi 110042, India

ARTICLE INFO

Keywords:
Steam reforming
Hydrogen production
Numerical simulation
Biogas

ABSTRACT

The use of fossil fuels in energy systems has environmental consequences, which are driving investigations into H_2 production. While steam methane reforming is the most well-known method for producing H_2, other thermochemical pathways are becoming more prevalent. Steam-reforming of biogas is also a beneficial procedure for producing eco-friendly hydrogen gas and minimizing the burden on fossil fuels. In this study, a simulation modelling of steam methane reforming (SMR) and steam biogas reforming (SBR) are presented. The model reveals the hydrogen production reaction mechanism and validates its performance through simulation analysis using COMSOL Multiphysics 5.6 software (finite element analysis). The developed model has been validated by available previous experiments and simulation work for biogas reforming with various compositions as well as the methane reforming process. The core aim of this study is to estimate the yield of H_2 for SMR, and H_2 and CO for SBR at steam carbon ratio (S/C) from 1 to 3 with various temperatures, and find the optimum temperature for the reforming process. The yields of hydrogen (mol/mol-CH_4) are achieved higher from SMR as 12% and 22 % for comparison with the experiment and previous simulation study at S/C = 2, at a temperature of 700 °C. The H_2 yields (mol/mol-CH_4) are achieved higher as 30% at 800 °C, 21% at 1000 °C, and 20% at 1200 °C (average percentage of mol for steam carbon ratio from 1 to 3) and compared with previous simulation study at the same operating temperatures, stated by SBR. The findings indicate that the proposed work offers a viable method for utilizing distributed renewable methane resources to fuel cells and generate local electricity.

1. Introduction

Hydrogen is recognized as a highly auspicious energy carrier because its combustion does not generate greenhouse gases or pollutants [1]. However, the majority of hydrogen is currently produced from fossil fuels through the steam reforming of natural gas accounting for nearly half of its overall production [2,3]. As the demand for energy increases, while the fossil fuel reserves continue to diminish, the production of sustainable hydrogen must rely on renewable sources. Biogas is commonly generated through biodegradable substrates made of organic material under anaerobic conditions which provides an attractive renewable alternative for replacing or supplementing fossil fuels in hydrogen production. The composition of biogas primarily depends on the specific substrate utilized in the biogas digester, which may include agro-industrial waste, animal farm manure, sewage sludge, municipal solid waste, energy crops, and other organic waste materials [4,5].

The two main constituents of biogas are CH_4 (40–80%) and CO_2 (20–60%), it also presents small amounts of H_2S, N_2, H_2O, O_2, and siloxanes [6–10]. It has been reported that the presence of H_2S and siloxanes can significantly decrease the catalyst (Ni-based) activity during the reforming of the biogas process. Therefore, it is necessary to eliminate these components before conducting the biogas reforming operation [8–10]. The process of steam reforming of biogas (SRB) incorporates the group of dual reforming reactions, namely the dry reforming of methane (DRM) and the steam reforming of methane (SRM), both of which exhibit significant endothermic characteristics. Table 1 presents a compilation of chemical reactions that typically take place during the steam reforming process of biogas or methane. The primary outcomes of significance in the reforming of biogas are hydrogen and syngas.

To achieve a significant conversion of methane, it is obligatory to operate the steam reformer at high temperatures between 973 and 1273 K. Considering the endothermic nature of the process, it is crucial to have an efficient heat source to provide the necessary energy to drive the reactions [16]. Due to the presence of CH_4 and CO_2 as the primary

* Corresponding author at: Department of Mechanical Engineering, Delhi Technological University, Delhi 110042, India.
E-mail address: anilkumar76@dtu.ac.in (A. Kumar).

https://doi.org/10.1016/j.fuel.2023.130742
Received 28 September 2023; Received in revised form 10 December 2023; Accepted 23 December 2023
Available online 5 January 2024
0016-2361/© 2023 Elsevier Ltd. All rights reserved.

Nomenclature

V_r	Volume of the reactor [m^3]
c_i	Molar flow rate of the species [mol/s]
R_i	Net reaction rate of the species in [mol/ (m^3s)]
C_p	Molar heat capacity of the species [J/(mol·K)]
Q_{ext}	Heat added to the system per unit volume [J/(m^3·s)]
Q	Heat from the chemical reaction [J/(m^3·s)]
H_j	Heat of the reaction [J/mol]
r_j	Reaction rate [mol/ (m^3·s)]
R_i	Reaction rates [kmol/kg.h]
k_i	Reaction rate constants [-]
K_i	Adsorption constants of chemical species [-]
K_{eq}.i	Equilibrium constants [-]
Pi	Partial pressures of chemical species [bar]
F_i^{in}	Molar flow rate of i^{th} component [kmol/hr]
X_{CH_4}	Equilibrium conversion of methane [%]
X_{CO_2}	Equilibrium conversion of carbon dioxide
X_{CO}	Equilibrium conversion to carbon monoxide.
F_j^{in}	Inlet molar flow rates of chemical components j [kmol/h]
$F_{CH_4}^{in}$	Inlet molar flow rate of methane [kmol/h]
R	gas constant (J/kmol K),
$T_{op.}^{in}$	Inlet operating temperature (^oC)
i	Chemical component [-]
j	Reaction [-]
Y_{H_2}	Yield of hydrogen [mol]
Y_{CO}	Yield of carbon monoxide [mol]
S/C	Steam to Carbon ratio [-]

Greek symbols

η_i	Reaction effectiveness factor [-]
σ_{ij}	Stoichiometric coefficients of chemical components [-]
σ	Stated parameter [-]
θ_j	Inlet Molar Flow Ratio of chemical components j to methane [-]

Abbreviations

BG	Biogas
DRM	Dry reforming of methane
SRM	Steam reforming of methane reaction
RWGS	Reverse water gas shift reaction
RM	Reverse methanation reaction
SRB	Steam reforming of biogas

Table 1
Chemical reactions involved in the reforming process of biogas/methane [11–15].

Reaction No.	Name of reaction	Type of reaction	ΔH_{298K} (kJ/mol) at P = 1 atm
R1	SRM	$CH_4 + H_2O \rightarrow CO + 3H_2$	206.2
R2	Gas-shift reaction	$CO + H_2O \rightarrow CO_2 + H_2$	−41.2
R3	Combined reaction or RMR	$CH_4 + 2H_2O \rightarrow CO_2 + 4H_2$	165
R4	DR	$CH_4 + CO_2 \rightarrow 2CO + 2H_2$	247.4
R5	Methane cracking	$CH_4 \rightarrow C_{solid} + 2H_2$	74.9
R6	Reduction of CO	$CO + H_2 \rightarrow C_{solid} + H_2O$	−131.3
R7	Boudouard reaction	$2CO \rightarrow C_{solid} + CO_2$	−172.4
R8	Reduction of CO_2	$CO_2 + 2H_2 \rightarrow C + 2H_2O$	−90.08

constituents of biogas, the Dry Reforming (DR) method is well-suited for the production of hydrogen/syngas. However, the DR process operates under severe conditions characterized by high reaction temperatures and the absence of steam, which can cause catalyst deactivation due to coke deposition and sintering of the metallic phase and support [17].

Hence, there is a further requirement for the successful conversion of methane into hydrogen, particularly in developing catalyst formulations that are both active and stable. SRM is the utmost regularly utilized chemical progression for this purpose. Although the reaction is endothermic and requires an exact ratio of 1:1 (H_2O:CH_4) of steam to methane, excess steam is typically utilized to minimize carbon formation, usually exceeding three times the stoichiometry. Consequently, the use of heterogeneous catalytic reactors for Steam Reforming of biogas is expected to become a viable short-term solution for producing hydrogen/syngas [18,19]. Studies have predominantly focused on Ni-based catalysts for this process, which have the potential for industrial application [9,20,21].

Biogas offers significant advantages as a substitute gas for natural gas in hydrogen production via steam reforming. Its renewable nature, sustainability, and carbon neutrality make it a highly favorable option for this process. However, there is an inadequate modeling study on the subject, typically conducted on laboratory-scale reactors with fixed biogas compositions at low pressure. Currently, no modeling study exists on an industrial scale through steam biogas reforming, which is necessary to evaluate the feasibility of large-scale hydrogen production using biogas with a broad range of compositions.

Steam-reforming of biogas technique is close to achieving equivalent efficiency to natural gas, which currently constitutes 50% of global hydrogen production. Moreover, it offers environmental benefits. Given the similar compositions of biogas and natural gas (CH_4), only minor modifications to steam reforming technology are necessary. The main benefit of using biogas for H_2 production as a sustainable energy source is the reduction of the excessive demand for natural gas and the emission of greenhouse gases. The need for pure H_2 as well as the depletion of fossil fuel supplies and other factors have made renewable H_2 generation more important nowadays. Various application methods for biogas have emerged, including its capacity to generate hydrogen for fuel cells through a reforming process.

There are multiple reports in the literature about simulation and modeling research on utilizing biogas for hydrogen production. For example, Hajjaji et al. [22] conducted a study; they used Aspen Plus software to simulate a hydrogen production plant that utilized steam reforming of biogas. Their study directed that utilizing biogas for hydrogen production through steam reforming offered significant benefits based on a life cycle assessment approach. As part of their research into hydrogen production from mixed reforming of biogas, Rosa et al. [23] utilized Aspen Plus to optimize the process conditions. Based on their thermodynamic simulations, they recommended the most effective operating parameters to be a pressure (1 bar), a temperature range (1008–1063 K), and ratios of O_2/CH_4 ranging from 0 to 0.1, as well as S/C ratio ranging from 2.4 to 3.0. These optimized conditions were determined through their experimental work. In a study by Minutillo et al. [24], two distinct hydrogen production plants from biogas were simulated using Aspen Plus. The simulations focused on steam reforming and auto-thermal reforming methods. The outcomes exposed that the energy efficiency of steam reforming was 19% greater than that of auto-thermal reforming. Hwanglo et al. [25] used a network modeling approach to combine biogas supply with a conventional methane steam reformer to account for variable demand scenarios. The main outcomes

of the study presented a noteworthy decrease of 24% in the overall cost of producing hydrogen.

Recent literature on modeling and simulation research extensively covers the utilization of methane in hydrogen production through the reforming process. For example, Pashchenko et al. [34] conducted an exploration of the steam methane reforming process within a microchannel reformer employing a Ni-based catalyst. The results of the reformer such as temperature and reforming products were obtained through experiments, CFD modeling, and numerical analysis. Initial conditions encompassed a temperature range of 327–727 °C, Reynolds numbers (10, 50, and 100), and heat flux values (500 W/m^2, 1000 W/m^2). It was observed that as inlet temperature, heat flux, and Reynolds number increased, methane conversion in the reformer decreased. Specifically, at 727 °C, Re = 10, and heat flux 1000 W/m^2, methane conversion was 39%, compared to the equilibrium conversion of 63%. Lu et al. [35] developed and validated a 0-D model for the steam methane reforming process. The process employs a Ni-based catalyst with spherical particles having a diameter of 4 mm. This model incorporates six gaseous chemical species such as CH_4, H_2O, CO_2, CO, N_2, and H_2. The new model predicts both internal temperature and species mass fractions within the particle, along with surface-averaged temperature and species mass fractions at the particle level. The validity of the 0-D model has been confirmed by comparison with an extensive 3D-CFD-based model that addresses bulk flow, temperature, and species boundary layers around the particle, and the convection–diffusion processes occurring within the porous catalyst particle. CFD calculations showed that the temperature and species mass fractions within the particle changed significantly when the ambient temperature increased from 527 to 727 °C.

Pashchenko et al. [36] performed the pressure drop in the fixed-bed reactor and examined both experimental and numerical simulation approaches to investigate the flow dynamics within a fixed-bed reactor containing porous particles. The simulation models the flow dynamics, and experimental data are utilized for result validation. Demonstrating the utility of a commercial CFD code, the pressure drop characteristics for fixed-bed reactors with porous particles were determined with less than a 10% average error. This level of error is deemed acceptable for design purposes. The results suggested flow through the fixed-bed reactor porous elements when the pore size is over 0.5 mm. Conversely, if the pore size is less than 0.5 mm, there is no flow through the porous medium, treating the particles as solid bodies in numerical analysis. When the pore size is increased from 0.2 mm to 2 mm, it decreases the pressure drop by more than three times. Pashchenko et al. [37] studied experimental and thermodynamic investigation of carbon deposition during steam methane reformation using a Ni-based catalyst. Experiments tested diverse operating conditions, including temperatures of 600 °C and 800 °C, S/C ratios (0.5, 1.0, and 2.0), and pressure. Thermodynamic analysis determined equilibrium carbon formation zones for these conditions, and experimental results were compared with the analysis outcomes. The results showed that at a residence time of around 5 kg_{cat}.s/molCH_4, methane conversion approaches equilibrium. When the steam-to-carbon (S/C) ratio was 0.5, the methane conversion was significantly reduced. On the other hand, there is very little methane conversion for S/C = 2.0 and S/C = 1.0. The rate of carbon deposition on the stream has an approximately linear relationship on time when the steam-to-methane ratio is larger than 1. The carbon deposition rate is roughly 0.12 g/h for S/C = 2 and T = 800 °C, 0.21 g/h for S/C = 2 and T = 600 °C, 0.29 g/h for S/C = 1 and T = 800 °C, and 1.02 g/h for S/C = 1 and T = 600 °C.

Based on the above considerations, this paper introduces a 0-D mathematical model to explore hydrogen production through steam reforming of methane and biogas with varying compositions. The model was performed by using a batch reactor and incorporated both heat and mass transfer with the chemical reactions occurring in the reactor and calculated product distribution and temperature through the application of energy and mass balances. The model was also presented to explain the reaction mechanism involved in the production of hydrogen, and the reaction performance was validated through a simulation analysis using the finite element analysis software (COMSOL Multiphysics 5.6). The presented reactor model closely predicts outcomes from both the 1-D and 2-D non-isothermal models of methane and biogas steam reforming. Therefore, a zero-dimensional model is favored to simplify this study.

The primary aim of this paper is to analyze the steam reforming of methane and biogas for H_2 production. The numerical model has been validated for both methane and biogas reforming at various compositions as well as the simulation process at various temperatures for both methane (700–900°C) and biogas (800–1200°C). The mathematical model has been validated with current work and previous experimental as well as simulation work. The novelty of this research lies in the methodology developed for examining a chemical reaction system and proposing suggestions for enhancing the operational parameters for mixed reforming of methane and biogas.

2. Computational methodology

2.1. Reactor modeling

To model a wide range of processes occurring in a reactor, transport phenomena are represented using Partial Differential Equations (PDEs) and solved through the application of finite element methods. This comprehensive model effectively combines heat and mass transport with chemical reactions that occur within the reactor. By employing energy and mass balances, it becomes feasible to analyze the temperature and product distributions along the length of the reactor.

The reactor is simplified to a batch-type model with a focus on the transient state. Primary governing equations of model as given as.

Species mass balance [33]:

$$\frac{dc_i}{dt} = R_i \tag{1}$$

Reactor energy balance [33]:

$$V_r C_p \frac{dT}{dt} = Q + Q_{ext} + \frac{dp}{dt} V_r \tag{2}$$

$$Q = -V_r \sum_j H_j r_j \tag{3}$$

The following primary assumptions are considered for the model.

- Consideration is given to the ideal gas law.
- The catalyst particles exhibit uniformity in both shape and size.
- Reformer operation is considered under transient state conditions.
- Chemical components such as CH_4, CO_2, CO, H_2, and H_2O are considered in the present reactor model.
- Carbon formation is not reflected in this study.
- N_2, H_2S, and other traces of gases are neglected.

2.2. Simulation procedure

- The utilization of Chemical Species Transport interfaces involves the computation of the concentration of chemical species fields in solutions, accounting for diverse transport mechanisms including diffusion, convection, and migration. Furthermore, these interfaces also account for chemical reactions occurring in dilute and concentrated solutions. This comprehensive modeling allows for a more accurate understanding of the complex behavior of chemical species in a range of different contexts.
- Reaction engineering interface facilitates the modeling of different types of chemical reactors and the temporal evolution of chemical reactions.

- Mass balance and energy balance equations in these systems assume the presence of ideal or clearly defined mixing within the reactor. The kinetic and thermodynamic expressions of the reaction(s) occurring in a reactor can be distributed to a space-dependent model.
- A time-dependent study is employed to analyze systems where the field variables are time-dependent.
- The technique finds application in a broad array of fields, including calculating the time-dependent chemical composition in chemical species transport or analyzing reaction kinetics and the chemical composition of a system undergoing chemical reactions.

3. Reaction kinetic model

The literature extensively examines various kinetic models for SMR and WGSR reactions. The model presented here can be applied to any suitable kinetic model for the specific catalyst employed. The model expressed by Xu and Froment [26] has experimented on a laboratory scale for SMR using Ni-based catalysts. The expression of kinetic rate for main reactions such as steam methane reforming (SMR-R_1), water gas shift (WGS- R_2) reaction, and reverse methanation reforming (RMR- R_3) have been developed based on Langmuir- Hinshelwood approach, have been extensively used to simulate the kinetics of SMR [27] and also used in the present work.

There are some limitations on intra-particle diffusion for steam methane reforming. For example, Pashchenko [38] studied the limitations of intra-particle diffusion in steam methane reforming using a nickel-based catalyst (Ni/α-Al_2O). Intrinsic and actual reaction rates were determined numerically using a CFD model, and these results were validated against experimental data with good agreement. The diffusion limitations within the porous catalyst particle were expressed by the effectiveness factor. The calculation of the effectiveness factor was conducted for a range of operational parameters, including temperatures between 800 and 1300 K and steam-to-methane ratios between 1 and 5. According to the findings, the effectiveness factor and catalyst particle diameter are inversely correlated, and diffusion limitation increases with increasing reaction temperature and steam-to-methane ratio. It was determined that an increase in the diameter of spherical catalyst particles results in a decrease in the effectiveness factor, described by the function $\eta \approx 0.11/d$.

The kinetic rate expression for the main three reactions R_1, R_2, and R_3 are expressed in Table 2.

The calculated values of the partial pressures (Pi) for chemical constituents including CH_4, H_2O, CO_2, H_2, and CO in the feeding process are offered in Table 3.

Kinetic rates, adsorption, equilibrium constants, and net rate of chemical species are computed by using expressions, given in Table 4.

Table 2
Xu and Froment kinetic equations [27,28].

Name of reaction	Kinetic rate expression
SMR	$R_1 = \frac{\frac{k_1}{P_{H_2}^{2.5}}\left(P_{CH_4}P_{H_2O} - \frac{P_{H_2}^3 P_{CO}}{K_{eq.1}}\right)}{[DEN]^2}$
WGSR	$R_2 = \frac{\frac{k_2}{P_{H_2}}\left(P_{CO}P_{H_2O} - \frac{P_{H_2}P_{CO_2}}{K_{eq.2}}\right)}{[DEN]^2}$
RMR	$R_3 = \frac{\frac{k_3}{P_{H_2}^{3.5}}\left(P_{CH_4}P_{H_2O}^2 - \frac{P_{H_2}^4 P_{CO_2}}{K_{eq.3}}\right)}{[DEN]^2}$
$DEN = 1 + \frac{F_{H_2O}^{in}}{F_{CH_4}^{in}} + \frac{F_{H_2}^{in}}{F_{CH_4}^{in}} + K_{CO}P_{CO} + K_{H_2}P_{H_2} + K_{CH_4}P_{CH_4} + \frac{K_{H_2O}P_{H_2O}}{P_{H_2}}$ Where the parameter DEN represents a dimensionless value, while P represents the partial pressure of the respective component within the catalyst.	

Table 3
Expression for Partial pressure of chemical species.

Type of pressure	Expression
Partial Pressures	$P_{CH_4} = \frac{(1 - X_{CH_4})}{\sigma}$ $P_{H_2O} = \frac{(\theta_{H_2O} - X_{CH_4} - X_{CO_2})}{\sigma}$ $P_{CO} = \frac{(\theta_{CO} + X_{CH_4} - X_{CO_2})}{\sigma}$ $P_{CO_2} = \frac{(\theta_{CO_2} + X_{CO_2})}{\sigma}$ $P_{H_2} = \frac{(\theta_{H_2} + 3X_{CH_4} - X_{CO_2} - \frac{F_{H_2}}{F_{CH_{4,0}}})}{\sigma}$ Where, $\sigma = \frac{1 + \theta_{H_2O} + \theta_{CO} + \theta_{CO_2} + \theta_{H_2}}{P_{op.}}; \theta_j = \frac{F_j^{in}}{F_{CH_4}^{in}}$

4. Results and discussion

4.1. Simulation analysis of steam methane reforming (SRM)

The evaluation of species concentration (mol/m^3) to reach steady levels straightaway after the feed gas is offered as displayed in Fig. 1. Generally, all curves define the distribution of product gas that attains a steady state after running the reactor at a certain temperature. As could be seen after 140 sec. (Fig. 1a), 80 sec. (Fig. 1b and c), and the curves of chemical reaction achieved a constant condition with time along the reactor volume. It is observed that methane amount is consumed with the amount of water in the inlet condition of a gas mixture, also known as the steam methane reforming process during transient periods as well as operation proceeds. The by-product gas as wet basis contains 2.8 of H_2 mol/m^3, 0.9 of CO mol/m^3, CO_2 of 0.05 mol/m^3, CH_4 of 0.1 mol/m^3, and H_2O of 0.1 mol/m^3 under the prescribed condition with temperature 1173 K at S/C are equal to 1, (Fig. 1a). As in a similar way, the by-product gas concentration species at temperature 1173 K for S/C = 2 and 3 as mentioned in Fig. 1(b) and (c).

Fig. 1(d) shows the influence of H_2 yield along with time and various temperatures at steam carbon ratio 1. It is remarked that the optimum temperature is 1173 for S/C = 1 for the yield of hydrogen but there are no more variations in H_2 yield from the initial temperature 973–1373 K. The concentrations of species evaluation are generated by COMSOL multiphysics 5.6 software as similar trends of the curve are also explained by Silva et al. [29].

4.1.1. Temperature effects on chemical equilibrium amounts

The results presented in Fig. 2 illustrate the relationship between temperature and the gaseous products mole fractions as a function of time. As temperature progressively increases, H_2 mole fraction exhibits a gradual rise starting from zero value and eventually stabilizes approximately at temperature 1123 K. On the other hand, CH_4 mole fraction consistently decreases until it reaches zero. This indicates a simultaneous occurrence where H_2 formation and CH_4 consumption take place in parallel at high temperatures.

- *H_2 yield*

Fig. 2 (a) depicts the comparison of H_2 mole with different S/C ratios from 1 to 3 at optimum temperature through the simulation process. Hydrogen amount touches the maximum yield because of the existence of WGSR as well as increasing the S/C ratio from 2:1 to 3:1.

- *CO_2 amount*

The water gas shift (WGS) reaction is accountable to produce CO_2 amount and it is also an assessment of CO_2 amount in Fig. 2 (b). The quantity of CO_2 rises as well as increases the S/C molar ratio at a certain

Table 4
Expression for kinetic rates, adsorption, equilibrium constants, and net rate of chemical species [27–29,38].

Category	Parameters expression
Rate constants: The inlet operating temperature is a determining factor in the value of the kinetic constants of the rate equations, which are represented by Arrhenius-type functions.	$k_1 = 9.490 \times 10^{16} \exp\left(-\frac{240.10}{RT^{in}_{op.}}\right)\left[\frac{kmol(kPa)^{0.5}}{kg_{cat.}h}\right] k_2 = 4.390 \times 10^{4} \exp\left(-\frac{67.13}{RT^{in}_{op.}}\right)\left[\frac{kmol(kPa)^{0.5}}{kg_{cat.}h}\right] k_3 = 2.290 \times 10^{16} \exp\left(-\frac{243.90}{RT^{in}_{op.}}\right)\left[\frac{kmol(kPa)^{0.5}}{kg_{cat.}h}\right]$
Adsorption constants: The constants K_{CH_4}, K_{H_2O}, K_{H_2}, K_{co} are associated with the equilibrium of surface adsorption and their behavior is influenced by the operating temperature at the inlet.	$K_{CH_4} = 6.650 \times 10^{-6} \exp\left(-\frac{38.28}{RT^{in}_{op.}}\right)\left[kP_a^{-1}\right] K_{H_2O} = 1.770 \times 10^{5} \exp\left(-\frac{88.68}{RT^{in}_{op.}}\right)[-] K_{H_2} = 6.120 \times 10^{-11} \exp\left(-\frac{82.90}{RT^{in}_{op.}}\right)\left[kP_a^{-1}\right] K_{co} = 8.230 \times 10^{-7} \exp\left(-\frac{70.65}{RT^{in}_{op.}}\right)[kPa^{-1}]$
Equilibrium constants: Through the calculation of the standard Gibbs energy intended for every reaction at the inlet operating temperature, the equilibrium factors in order to reactions R_1, R_2, and R_3 have been determined. This method involves assessing the thermodynamic behavior of the reactions at specific temperature conditions in order to establish their equilibrium constants.	$K_{eq.1} = 10266.76 \exp\left(-\frac{26830}{RT^{in}_{op.}} + 30.114\right)[kP_a^2] K_{eq.2} = \exp\left(\frac{4400}{RT^{in}_{op.}} - 4.063\right)[-] K_{eq.3} = T^{in}_{op.} K_{eq.1} T^{in}_{op.} K_{eq.2}[kP_a^2]$
Net rates: The formula is utilized to calculate the net rates (r_i) of chemical constituents, including both consumption and formation for reactions like R_1, R_2, and R_3 as indicated in Table 2.	$r_i = \sum_{j=1}^{3} \sum_{i=1}^{5} \eta_i \sigma_{ij} R_j$
Net rates of chemical components: The net rate (consumption and formation) of each i element kmol per kgh was then expressed by using the net rate expression. These net rates ($r_{CH_4}, r_{H_2O}, r_{H_2}, r_{co}, r_{CO_2}$) are obtained by summing the reaction rates of each chemical species across all reactions (R1 to R3). The effectiveness factors ($\eta_i T_{op.}$) are employed to consider the impact of intraparticle transport limitation. These factors take into account the influence of intraparticle transport on the overall reaction rates.	$r_{CH_4} = -[\eta_1(T_{op.})R_1 + \eta_3(T_{op.})R_3] r_{H_2O} = -[\eta_1(T_{op.})R_1 + \eta_2(T_{op.})R_2 + 2\eta_3(T_{op.})R_3] r_{H_2} = [3\eta_1(T_{op.})R_1 + \eta_2(T_{op.})R_2 + 4\eta_3(T_{op.})R_3] r_{co} = [\eta_1(T_{op.})R_1 - \eta_2(T_{op.})R_2 r_{CO_2} = \eta_2(T_{op.})R_2 + \eta_3(T_{op.})R_3]$

temperature and it touches a maximum mole of CO_2 at optimum temperature 1173 K with S/C ratio 1–3.

- *CH_4 conversion*

Fig. 2 (c) presents the effect of methane conversion at various temperatures with steam carbon ratio 1. CH_4 mole fraction steadily decreases when increases the temperature. Meanwhile more consumption of methane mole as well as increase the H_2 moles.

- *CO amount*

The amount of CO attained after 873 K, also increases its amount with a certain temperature as presented in Fig. 2 (d). The amount of CO is slightly affected by the molar ratio of S/C at nearly 1173 K, after that temperature, the increasing molar ratio is favored by WGS and thus starts to reduce the CO amount.

Table 5 shows the relationship between a diverse set of operating temperatures and the equilibrium conversions of reactants, as well as the S/C ratio in the resulting product. Notably, the optimal quantities of H_2, CH_4, CO, CO_2, and H_2O were observed at 1173 K. At a specific temperature, a higher molar ratio of S/C can lead to an enlarged yield of H_2. The equilibrium amounts of these components depend on the stoichiometric ratio. The outcomes presented here exhibit strong concurrence with the previously reported results by Khzouz and Gkanas [30], whose study employed the CAE software program for their calculations.

4.2. Validation of the numerical model

To compare the results of the model with experimental data published by Khzouz and Gkanas [30], similar initial operating parameters were selected as temperatures, mass fraction, and pressure and steam carbon ratio for the current study. The model suggested and discussed in the current study provides the concentration of species and temperature profiles during the chemical reaction. The simulation work has been done on the steam reforming process at various temperatures such as 773, 823, 873,923, and 973 K to validate the proposed mathematical model. The simulation study and mathematical equations were performed by COMSOL Multiphysics 5.6.

Steam carbon ratio (S/C 2 and 3) was considered for calculations to validate the process. The formation of hydrogen yield increases with increased temperatures as depicted in Fig. 3 (a) and (b). The present study of results follows a similar trend of H_2 yields obtained from chemical reactions using COMSOL software and compared with the experiment and chemical equilibrium data (analysis from CAE software) [30]. The system approach is calculated from 500 to 700 °C for steam carbon ratios 2 and 3. Although, hydrogen yield form experimentally at S/C = 2 and 3 are less than the present work and calculated (Equilibrium) results since the water amount is more consumed.

The present study data showed a maximum and minimum yield of hydrogen 3.2 mol/mol-CH_4 at 700 °C and 1.8 mol/mol-CH_4 at 500 °C respectively, at S/C = 2, with a higher value than the experiment data. Similarly, at S/C = 3, maximum and minimum hydrogen yields 3.6 mol/mol-CH_4 at 700 ∘C and 2.5 mol/mol-CH_4 at 500 °C respectively.

Fig. 3 (c) presents the comparative assessment between the present work and the previous study as experiment and simulation work. The results for H_2 yield; experiment and present simulation work as well as previous simulation work (Comsol software) follow an almost similar trend and hydrogen yields are increasing as well as increasing temperature at S/C = 2. The results of the present study for yields of hydrogen are achieved higher as 18% and 33% for comparison with the experiment and previous simulation study at S/C = 2 and temperature 700 °C.

4.3. Simulation analysis of steam biogas reforming (SBR)

The evaluation of species concentration (mol/m^3) to reach steady levels straightaway after the feed gas is offered as shown in Fig. 4. Generally, all curves define the distribution of product gas that attains a steady state after running the reactor at a certain temperature. As it could be seen after 200 sec. (Fig. 4a), 100 sec. (Fig. 4b and c), the curves of chemical reaction achieve a constant condition with time along the reactor volume.

It is observed that methane and CO_2 amounts are consumed with the

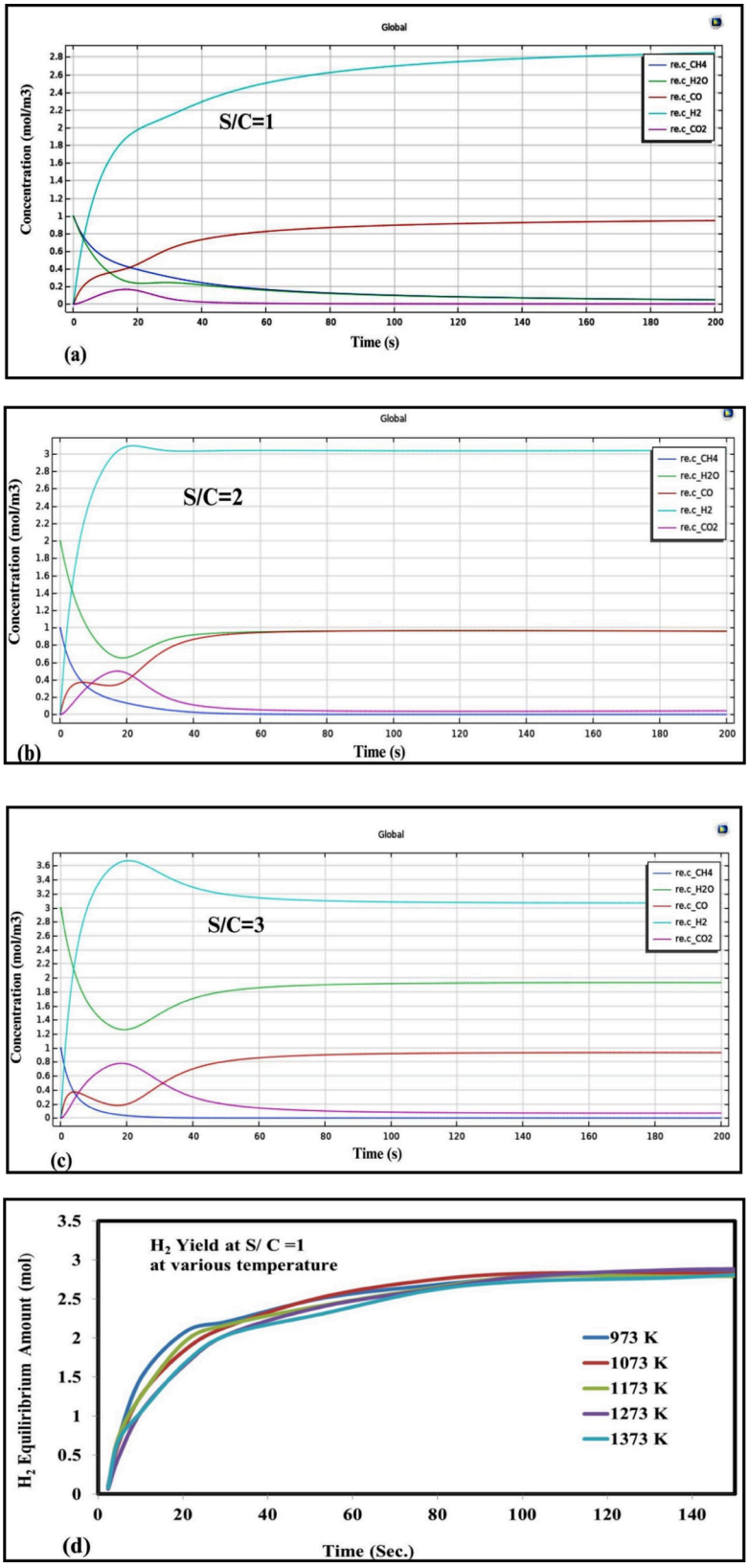


Fig. 1. Simulation analysis of the product gas distribution in the batch reactor at 1 bar and 1173 K (a) S/C = 1, (b) S/C = 2, (c) S/C = 3, and (d) Temperature effects on H_2 yields over time at S/C = 1.

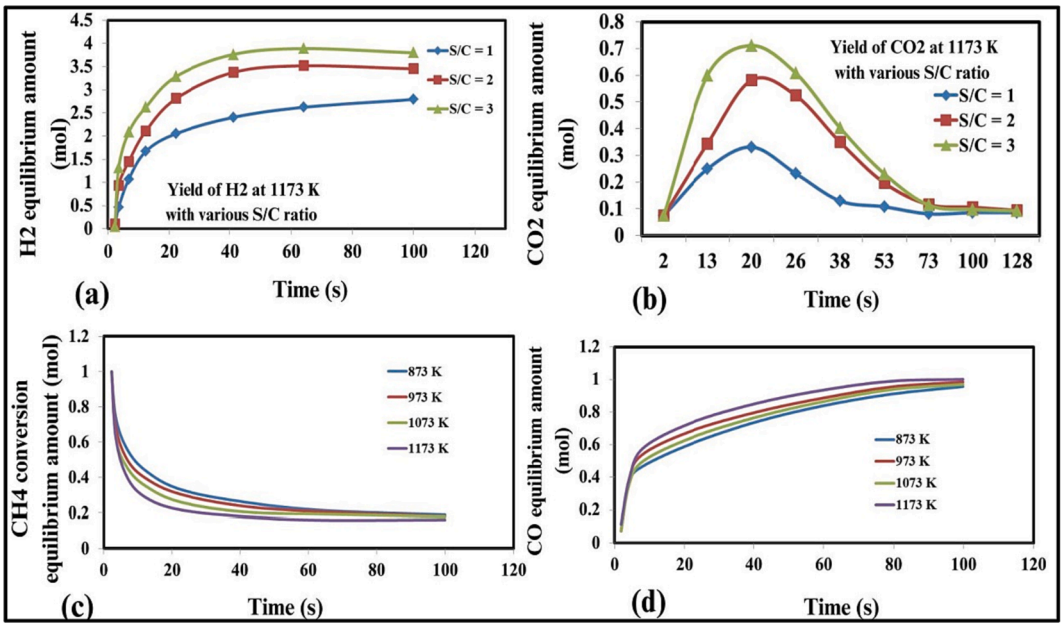


Fig. 2. Simulation results of equilibrium amount of chemical species at various operating temperature and time at atmospheric pressure (a) Compare of H_2 yield (mol) at 1173 K, (b) compare of CO_2 amount at 1173 K, (c) CH_4 conversion with various temperature, (d) CO amount at different temperature.

Table 5
Optimal simulation results for SRM at various temperatures, P = 1 bar, S/C = 1–3.

S/C ratio	Operating Temperature (K)	Equilibrium Amount (mol)			
		H_2	CH_4	CO	H_2O
1	873	2.20	0.19	0.899	0.212
	973	2.52	0.17	0.932	0.183
	1073	2.68	0.153	1.00	0.161
	1173	2.77	0.139	1.02	0.131
2	873	2.27	0.22	0.714	1.04
	973	3.10	0.141	0.98	1.06
	1073	3.25	0.114	1.08	1.10
	1173	3.35	0.081	1.14	1.12
3	873	3.10	0.03	0.977	1.98
	973	3.33	0.011	0.978	2.09
	1073	3.40	0.011	1.00	2.095
	1173	3.42	0.01	0.809	1.78

amount of water in the inlet condition of the gas mixture, also known as the steam biogas reforming process during transient periods as well as operation proceeds. The by-product gas as dry basis contains 2.2 of H_2 mol/m^3, 1.2 of CO mol/m^3, CO_2 of 0.05 mol/m^3, CH_4 of 0.1 mol/m^3, and H_2O of 0.1 mol/m^3 under the prescribed condition with temperature 1000 °C at S/C equal to 1, (Fig. 4a). As in a similar way, the by-product gas concentration species at temperature 1000 °C for S/C = 2 and S/C = 3 as mentioned in Fig. 4(b) and (c).

4.3.1. Effect of temperature on equilibrium conversion

Temperature is the main parameter to produce a mole fraction of hydrogen. As the progression of temperature, H_2 mole fraction starts to produce and stabilize nearly 850–1000 °C. At the same time, the mole fraction of CH_4 steadily decreases until it reaches zero, indicating a simultaneous occurrence of H_2 formation and CH_4 consumption at high temperatures. At temperatures below 600 °C, the mole fraction of CO_2 increases. This observation strongly indicates a preference for the water–gas shift reaction over the reaction of CO_2 reforming at comparatively low temperatures. The reducing H_2O mole fraction further reinforces this conclusion as supporting evidence. As the CO_2 reforming reaction is endothermic in nature, it becomes more favourable as the operating temperatures increase. As a consequence, CO_2 mole fraction shows a gradual rise before displaying a significant reduction as the temperature exceeds 600 °C. With the prevalence of the reaction of CO_2 reforming, there is also an enhancement in the mole fraction of CO.

- *Effect of temperature and steam-carbon (S/C) ratio*

At lower temperatures, an increase in H_2O content leads to a significant decrease in CH_4 conversion. However, as the temperature rises and surpasses an inflection point at relatively higher temperatures, CH_4 conversion shows a transition towards an increasing trend. Impressively, regardless of the H_2O content, CH_4 conversion reaches nearly 100% above 850 °C. An increase in the H_2O content leads to a considerable reduction in CO_2 conversion. In the biogas process, both CO_2 and H_2O are well-known oxidants. However, CH_4 shows a higher tendency to react with H_2O rather than CO_2, mainly since H_2O exhibits higher chemical reactivity compared to CO_2.

- *Effect of CO_2/CH_4 ratio*

The relationship between the CO_2/ CH_4 ratio and temperature is studied to understand its effects. It is perceived that as the ratio of CO_2/ CH_4 and temperature increases, CH_4 conversion also increases. On the other hand, CO_2 conversion shows an inverse relationship with the CO_2/ CH_4 ratio at high temperatures, leading to a decrease as the ratio increases. Unlike the trends observed in the conversion of CH_4 and CO_2, the effect of the ratio of CO_2/ CH_4 on the yield of H_2 and CO amounts appears to be insignificant when varying the CO_2/CH_4 ratios at low temperatures. It is noteworthy that there is a significant decrease in H_2 and CO yields when CO_2 is added at temperatures between 800 and 1200 °C. Due to the endothermic nature of both CO_2 reforming and RWGS, an increase in temperature will promote and favor the existence of these reactions.

Due to the continuous presence of a net positive amount of H_2O as a feedstock throughout the process, RWGS has a greater probability of occurring compared to CO_2 reforming. The CO_2 reforming reaction continuously consumes CH_4 as a reactant, resulting in a net negative

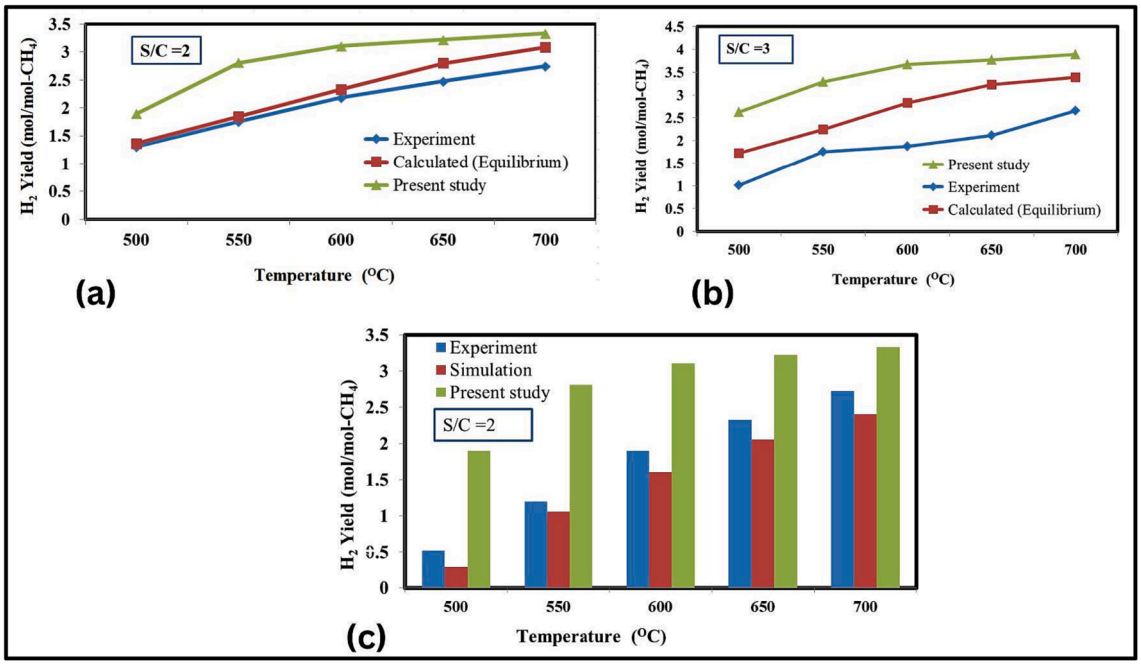


Fig. 3. Validation of experiment work with present simulation work and previous simulation data within temperature between 500 °C and 700 °C at atmospheric pressure using Ni/Al_2O_3 based catalyst; (a) H_2 yield at S/C = 2, (b) H_2 yield at S/C = 3 and (c) H_2 yield at S/C = 2.

amount of CH_4. The superior performance of RWGS over the reaction of CO_2 reforming is evident as it leads to a noticeable reduction in the H_2 yield [31] (see Table 6). An increase in the ratio of CO_2/CH_4 leads to a decrease in the conversion of H_2O amount in higher temperature zones. The presence of an increasing content of CO_2 is the outcome of a minor drop in the ratio of H_2/CO, which can be endorsed to the entire reaction selectivity favoring reverse water–gas shift over CO_2 reforming.

4.4. Validation of the numerical model

To compare the results of the model with simulation data published by Hajjaji et al, [22], the main operating parameters were selected as S/C ratio, mass fraction, pressure, CO_2 composition, and operating temperature in order to present the study. The model suggested and discussed in the present study offers the concentration of species and temperature profiles during the chemical reaction process. The simulation work has been done on the biogas steam reforming process at various temperatures such as 600, 800, 1000, and 1200 °C to validate the proposed mathematical model. The simulation study and mathematical equations were performed by COMSOL, whereas the previous simulation result was performed by Aspen plus™ to the simulation of the reforming process.

Fig. 5 shows the comparative assessment between the present work and the previous study as simulation work. The results for H_2 yield; present simulation work (COMSOL software) as well as previous simulation work (Aspen plus™) are following the almost similar trend and hydrogen yields are increasing as well as increasing temperature at S/C 1–3.

The results of the current study for H_2 yields are achieved higher as 30% at 800 °C, 21% at 1000 °C, and 20% at 1200 °C (average percentage of mol for steam carbon ratio from 1 to 3) and compared with previous simulation study at same operating temperatures.

According to Fig. 5 the yield of H_2 amount as a function of steam/Carbon ratio (S/C) and operating temperature. The amount of H_2 increases as the S/C ratio (1/1 to 3/1) increases for temperature. This trend can be explained by Le Chatelier's Principle, which states that an increase in steam on the reactant side favors the H_2 production on the product side. However, the H_2 productivity gain becomes less significant when the S/C ratio exceeds 3, as the reaction starts to consume excessive amounts of water. As for the effect of temperature, the H_2 yield rises with increasing reforming temperature, reaching a maximum before slightly decreasing. This behavior is attributed to the inhibition of the exothermic WGS reaction. To summarize, increasing the steam-carbon ratio up to a certain point and raising the reforming temperature can enhance H_2 productivity, but the excessive use of water and the inhibition of the WGS reaction can limit this enhancement.

The data presented in Fig. 6 demonstrates a clear correlation between temperature and CO yields. As the temperature increases, there is a noticeable rise in the CO content of the synthesis gas (SG). The observed phenomenon can be attributed to the inhibitory impact of high temperatures on the exothermic WGSR, ultimately leading to a higher concentration of CO in the syngas. It is important to note that achieving high production of H_2 while maintaining a low CO content in the synthesis gas simultaneously is challenging. This is because the reforming temperature needs to be sufficiently high to ensure a reasonable yield of H_2. However, to minimize the CO content, it is preferable to keep the temperature as low as possible. The results obtained from the thermodynamic calculations lead us to recommend a reforming temperature of 800 °C and an S/C ratio of approximately 3 for the biogas reforming system. These optimal conditions will be further employed to simulate the entire process of converting biogas (BG) into hydrogen (H_2).

5. Estimation of simulation analysis results with thermodynamic analysis

The simulation analysis of the SRM has been performed at a fixed pressure of 1 bar, over a temperature range from 500 to 1000 °C, and at various S/C (Steam-to-Carbon) ratios ranging from 1 to 3 as well as biogas has also been performed at the condition of S/C ratio = 1–3, P = 10 bar, temperature ranges from 600 to 1200 °C. According to simulation results, it is observed that the CH_4 mole fraction steadily decreases when increases the temperature for both SRM and BSR processes. Meanwhile more consumption of methane mole as well as increase the H_2 moles. Hydrogen amount touches the maximum yield due to the existence of WGSR as well as increasing S/C ratio from 2:1 to 3:1. The performance of the reformer has been assessed based on several criteria,

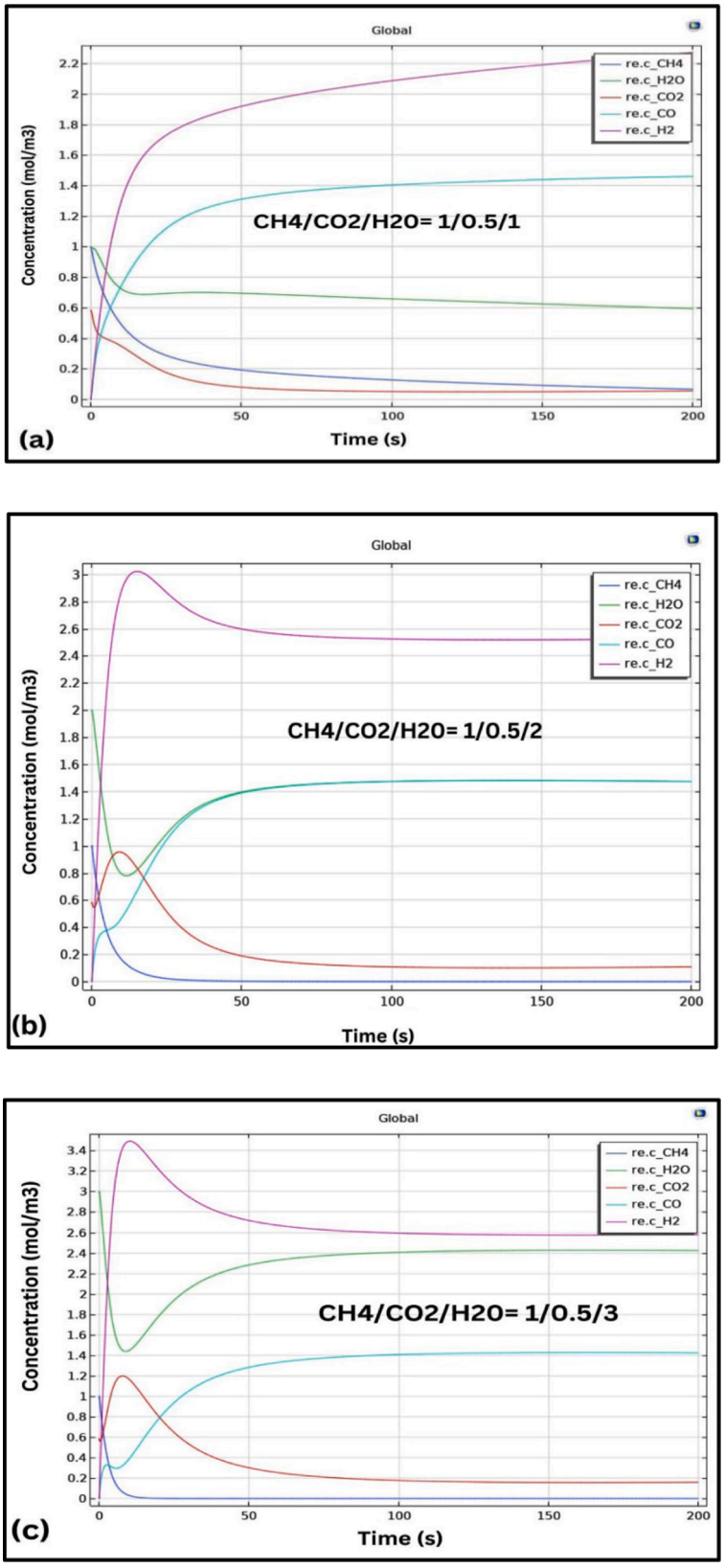


Fig. 4. Simulation analysis of the product gas distribution in the batch reactor at 1 bar and 1173 K along with the time (sec.) at various steam carbon ratios (a) S/C = 1, (b) S/C = 2, and (c) S/C = 3.

Table 6
Optimal simulation results for SRB at varying temperatures and the respective operating conditions: P = 10 bar, CO_2 = 0.583, S/C = 1–3.

S/C ratio	Operating Temperature (°C)	Conversions Amount (mol)				
		H_2	CH_4	CO_2	CO	H_2O
1	600	1.8	0.45	0.82	0.6	0.3
	800	1.9	0.40	0.70	0.8	0.4
	1000	2.2	0.1	0.40	1.45	0.6
	1200	2.3	0.1	0.30	1.45	0.5
2	600	3.45	0.15	0.9	1.30	0.4
	800	3.3	0.14	1.1	0.6	0.8
	1000	2.9	0.06	0.9	1.41	1.4
	1200	2.7	0.07	0.7	1.42	1.45
3	600	3.6	0.11	1.5	0.66	1.1
	800	3.8	0.09	1.3	0.60	1.2
	1000	3.1	0.04	1.2	0.40	1.5
	1200	3.0	0.04	0.7	1.23	2.0

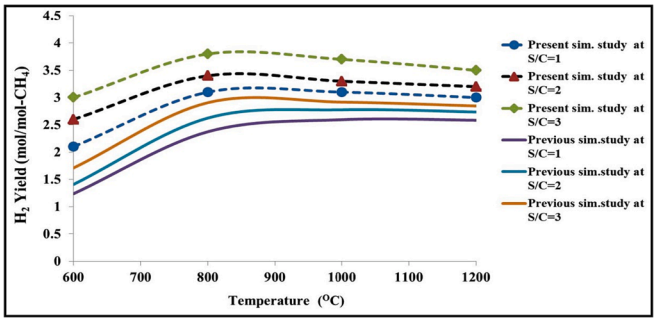


Fig. 5. Comparison assessment of yield of hydrogen between present and previous studies at S/C (1–3) via biogas reforming.

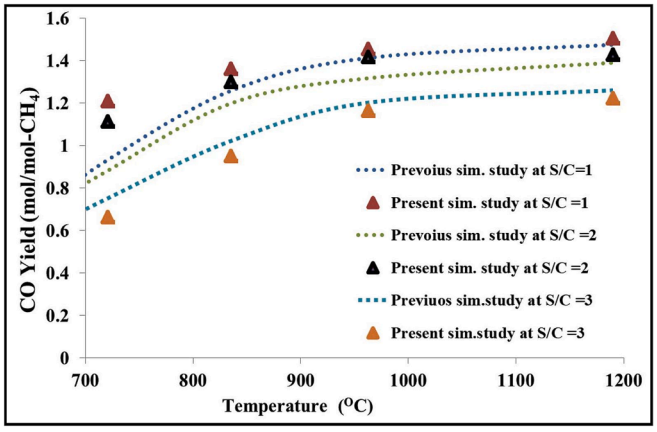


Fig. 6. Comparison assessment of CO yield between present and previous studies at S/C (1–3) from biogas reforming.

including hydrogen yield (Y_{H2}), carbon monoxide yield (Y_{CO}), total methane conversion (X_{CH4}) and the molar compositions of the products.

Furthermore, the simulation results of the reactor were compared with the outcomes of an analysis of thermodynamic equilibrium at exit conditions, which include temperature and pressure. The simulation results of the reactor indicate that methane conversion can be achieved within the range of 96% to 86.10% for S/C ratios ranging from 1 to 3, with varying optimum temperature and pressure conditions. The simulation results closely align with the thermodynamic analysis, as depicted in Table 7.

6. Conclusion

Reducing the excessive demand for natural gas and greenhouse gas emissions is the primary advantage of using biogas for H_2 production as a sustainable energy source. The depletion of fossil fuel supplies, the need for pure H_2, and other factors have increased the importance of renewable H_2 generation in the modern world. In the current study, a 0-D mathematical model to explore hydrogen production through steam reforming of methane and biogas with varying compositions. An examination of the reaction performance was carried out by conducting a parametric analysis that involved changing the main operating conditions, for example, the reagent molar ratio and inlet temperature, etc. The simulation data revealed a significantly positive correlation between the experimental and theoretical results, validating the reliability of the theoretical model. This model has the potential to serve as both a predictive tool for product distribution and reactor performance and as a means of advancing fuel-reforming technology through the optimization of reactor design.

The main outcomes of this study are as:

Simulation analysis of SRM:

- The present study data showed a maximum and minimum yield of hydrogen 3.2 mol/mol-CH_4 at 700 °C and 1.8 mol/mol-CH_4 at 500 °C respectively, at S/C = 2, whereas higher values than the experiment data. Similarly, at S/C = 3, maximum and minimum hydrogen yields 3.6 mol/mol-CH_4 at 700 °C and 2.5 mol/mol-CH_4 at 500 °C respectively.
- The yields of hydrogen are achieved higher as 18% and 33% for comparison with the experiment and previous simulation study at a temperature of 700 °C with S/C = 2.
- At a specific temperature, a higher molar ratio of S/C can lead to an enlarged yield of H_2. The equilibrium amounts of these components depend on the stoichiometric ratio.

Simulation analysis of SRB:

- The H_2 yields are achieved higher as 30% at 800 °C, 21% at 1000 °C, and 20% at 1200 °C (average percentage of mol for steam carbon ratio from 1 to 3) and compared with previous simulation study at the same operating temperatures.
- H_2 productivity gain becomes less significant when the S/C ratio exceeds 3, as the reaction starts to consume excessive amounts of water. As for the effect of temperature, the H_2 yield rises with

Table 7
Evaluation of simulation results of reactor with thermodynamic equilibrium at optimum pressure and temperature.

Gas Composition	S/C ratio	X_{CH_4} (%)		Y_{H_2} (mol)	
$CH_4/CO_2/H_2O$		Simulation	Thermodynamic [32]	Simulation	Thermodynamic[32]
1/0/1	1	86.1	92.06	2.77	2.98
1/0/2	2	91.9	97.05	3.35	3.43
1/0/3	3	96	98.10	3.42	3.65
1/0.58/1	1	92	96.08	2.1	2.30
1/0.58/2	2	93	98.90	2.90	2.70

increasing reforming temperature, reaching a maximum before slightly decreasing.

- It can be observed that increasing the temperature leads to an increase in the CO yields. This outcome is attributed to the high temperature inhibiting the exothermic WGS reaction and resulting in a higher CO content in the SG.
- Higher temperatures result in more CO yields. This can be attributed to the inhibitory effect of high temperatures on the exothermic water–gas shift reaction, leading to an increased concentration of CO in the synthesis gas.
- The results obtained from the thermodynamic calculations lead us to recommend a reforming temperature of 800 °C and an S/C ratio of approximately 3 for the biogas reforming system. These optimal conditions will be further employed to simulate the entire process of converting biogas (BG) into hydrogen (H_2).

CRediT authorship contribution statement

Ravindra Kumar: Writing – original draft, Software, Methodology, Investigation, Formal analysis, Data curation. **Anil Kumar:** Writing – review & editing, Visualization, Supervision, Conceptualization. **Amit Pal:** .

Declaration of competing interest

The authors declare that they have no known competing financial interests or personal relationships that could have appeared to influence the work reported in this paper.

Data availability

Data will be made available on request.

Acknowledgment

The authors are highly grateful to the Department of Mechanical Engineering and the Centre for Energy and Environment, Delhi Technological University Delhi (India) for providing basic facilities to compile this work.

References

[1] Chen B, Xu H, Zhang Y, Dong F, Tan P, Zhao T, et al. Combined methane reforming by carbon dioxide and steam in proton conducting solid oxide fuel cells for syngas/power co-generation. Int J Hydrogen Energy 2019;44(29):15313–21. https://doi.org/10.1016/j.ijhydene.2019.02.244.

[2] Chompupun T, Limtrakul S, Vatanatham T, Kanhari C, Ramachandran PA. Experiments, modeling and scaling-up of membrane reactors for hydrogen production via steam methane reforming. Chem Eng Process-Process Intens 2018;134:124–40. https://doi.org/10.1016/j.cep.2018.10.007.

[3] Antzaras AN, Heracleous E, Lemonidou AA. Sorption enhanced-chemical looping steam methane reforming: optimizing the thermal coupling of regeneration in a fixed bed reactor. Fuel Process Technol 2020;208:106513. https://doi.org/10.1016/j.fuproc.2020.106513.

[4] Osman AI, Abdelkader A, Farrell C, Rooney D, Morgan K. Reusing, recycling and up-cycling of biomass: a review of practical and kinetic modelling approaches. Fuel Process Technol 2019;192:179–202. https://doi.org/10.1016/j.fuproc.2019.04.026.

[5] Dan M, Mihet M, Lazar MD. Hydrogen and/or syngas production by combined steam and dry reforming of methane on nickel catalysts. Int J Hydrogen Energy 2020;45(49):26254–64. https://doi.org/10.1016/j.ijhydene.2019.12.158.

[6] Chouhan K, Sinha S, Kumar S, Kumar S. Utilization of biogas from different substrates for SOFC feed via steam reforming: thermodynamic and exergy analyses. J Environ Chem Eng 2019;7(2):103018. https://doi.org/10.1016/j.jece.2019.103018.

[7] Wasajja H, Lindeboom RE, van Lier JB, Aravind PV. Techno-economic review of biogas cleaning technologies for small scale off-grid solid oxide fuel cell applications. Fuel Process Technol 2020;197:106215. https://doi.org/10.1016/j.fuproc.2019.106215.

[8] Alves HJ, Junior CB, Niklevicz RR, Frigo EP, Frigo MS, Coimbra-Araújo CH. Overview of hydrogen production technologies from biogas and the applications in fuel cells. Int J Hydrogen Energy 2013;38(13):5215–25. https://doi.org/10.1016/j.ijhydene.2013.02.057.

[9] Appari S, Janardhanan VM, Bauri R, Jayanti S. Deactivation and regeneration of Ni catalyst during steam reforming of model biogas: An experimental investigation. Int J Hydrogen Energy 2014;39(1):297–304. https://doi.org/10.1016/j.ijhydene.2013.10.056.

[10] Kadam R, Panwar NL. Recent advancement in biogas enrichment and its applications. Renew Sustain Energy Rev 2017;73:892–903. https://doi.org/10.1016/j.rser.2017.01.167.

[11] Kumar R, Kumar A, Pal A. An overview of conventional and non-conventional hydrogen production methods. Mater Today: Proc 2021;46:5353–9.

[12] Effendi A, Hellgardt K, Zhang ZG, Yoshida T. Optimising H_2 production from model biogas via combined steam reforming and CO shift reactions. Fuel 2005;84(7–8):869–74. https://doi.org/10.1016/j.fuel.2004.12.011.

[13] Larentis AL, de Resende NS, Salim VM, Pinto JC. Modeling and optimization of the combined carbon dioxide reforming and partial oxidation of natural gas. Appl Catal A 2001;215(1–2):211–24. https://doi.org/10.1016/S0926-860X (01)00533-6.

[14] Chouhan K, Sinha S, Kumar S, Kumar S. Simulation of steam reforming of biogas in an industrial reformer for hydrogen production. Int J Hydrogen Energy 2021;46(53):26809–24. https://doi.org/10.1016/j.ijhydene.2021.05.152.

[15] Kumar R, Kumar A, Pal A. Overview of hydrogen production from biogas reforming: technological advancement. Int J Hydrogen Energy 2022;47(82):34831–55. https://doi.org/10.1016/j.ijhydene.2022.08.059.

[16] Pantoleontos G, Kikkinides ES, Georgiadis MC. A heterogeneous dynamic model for the simulation and optimisation of the steam methane reforming reactor. Int J Hydrogen Energy 2012;37(21):16346–58. https://doi.org/10.1016/j.ijhydene.2012.02.125.

[17] Barrai F, Jackson T, Whitmore N, Castaldi MJ. The role of carbon deposition on precious metal catalyst activity during dry reforming of biogas. Catal Today 2007;129(3–4):391–6. https://doi.org/10.1016/j.cattod.2007.07.024.

[18] Kolbitsch P, Pfeifer C, Hofbauer H. Catalytic steam reforming of model biogas. Fuel 2008;87(6):701–6. https://doi.org/10.1016/j.fuel.2007.06.002.

[19] Avraam DG, Halkides TI, Liguras DK, Bereketidou OA, Goula MA. An experimental and theoretical approach for the biogas steam reforming reaction. Int J Hydrogen Energy 2010;35(18):9818–27. https://doi.org/10.1016/j.ijhydene.2010.05.106.

[20] Lin KH, Chang HF, Chang AC. Biogas reforming for hydrogen production over mesoporous $Ni_2xCe1\text{-}xO_2$ catalysts. Int J Hydrogen Energy 2012;37(20):15696–703. https://doi.org/10.1016/j.ijhydene.2012.03.130.

[21] Vita A, Pino L, Cipitì F, Laganà M, Recupero V. Biogas as renewable raw material for syngas production by tri-reforming process over $NiCeO_2$ catalysts: optimal operative condition and effect of nickel content. Fuel Process Technol 2014;127:47–58. https://doi.org/10.1016/j.fuproc.2014.06.014.

[22] Hajjaji N, Martinez S, Trably E, Steyer JP, Helias A. Life cycle assessment of hydrogen production from biogas reforming. Int J Hydrogen Energy 2016;41(14):6064–75. https://doi.org/10.1016/j.ijhydene.2016.03.006.

[23] De Rosa F, Smyth BM, McCullough G, Goguet A. Using multi-criteria and thermodynamic analysis to optimize process parameters for mixed reforming of biogas. Int J Hydrogen Energy 2018;43(41):18801–13. https://doi.org/10.1016/j.ijhydene.2018.08.127.

[24] Minutillo M, Perna A, Sorce A. Green hydrogen production plants via biogas steam and autothermal reforming processes: energy and exergy analyses. Appl Energy 2020;277:115452. https://doi.org/10.1016/j.apenergy.2020.115452.

[25] Hwangbo S, Heo S, Yoo C. Network modeling of future hydrogen production by combining conventional steam methane reforming and a cascade of waste biogas treatment processes under uncertain demand conditions. Energ Conver Manage 2018;165:316–33. https://doi.org/10.1016/j.enconman.2018.03.069.

[26] Xu J, Froment GF. Methane steam reforming, methanation and water-gas shift: I. Intrinsic kinetics. AIChE J 1989;35(1):88–96. https://doi.org/10.1002/aic.690350109.

[27] Akers WW, Camp DP. Kinetics of the methane-steam reaction. AIChE J 1955;1(4):471–5. https://doi.org/10.1002/aic.690010415.

[28] Cruz BM, da Silva JD. A two-dimensional mathematical model for the catalytic steam reforming of methane in both conventional fixed-bed and fixed-bed membrane reactors for the Production of hydrogen. Int J Hydrogen Energy 2017;42(37):23670–90. https://doi.org/10.1016/j.ijhydene.2017.03.019.

[29] Silva JD, de Abreu CA. Modelling and simulation in conventional fixed-bed and fixed-bed membrane reactors for the steam reforming of methane. Int J Hydrogen Energy 2016;41(27):11660–74. https://doi.org/10.1016/j.ijhydene.2016.01.083.

[30] Khzouz M, Gkanas EI. Experimental and numerical study of low temperature methane steam reforming for hydrogen production. Catalysts 2017;8(1):5. https://doi.org/10.3390/catal8010005.

[31] Zhang Y, Zhang S, Gossage JL, Lou HH, Benson TJ. Thermodynamic analyses of tri-reforming reactions to produce syngas. Energy Fuel 2014;28(4):2717–26. https://doi.org/10.1021/ef500084m.

[32] Minh DP, Siang TJ, Vo DV, Phan TS, Ridart C, Nzihou A, et al. Hydrogen production from biogas reforming: an overview of steam reforming, dry reforming, dual reforming, and tri-reforming of methane. Hydrogen Supply Chains 2018:111–66.

[33] Cipitì F, Barbera O, Briguglio N, Giacoppo G, Italiano C, Vita A. Design of a biogas steam reforming reactor: a modelling and experimental approach. Int J Hydrogen Energy 2016;41(27):11577–83.

[34] Pashchenko D, Mustafin R, Mustafina A. Steam methane reforming in a microchannel reformer: experiment. CFD-Model Numer Study Energy 2021;237:121624.

[35] Lu YR, Pashchenko D, Nikrityuk PA. A new semiempirical model for the heat and mass transfer inside a spherical catalyst in a stream of hot CH_4/H_2O gases. Chem Eng Sci 2021;238:116565.

[36] Pashchenko D, Karpilov I, Mustafin R. Numerical calculation with experimental validation of pressure drop in a fixed-bed reactor filled with the porous elements. AIChE J 2020;66(5):16937.

[37] Pashchenko D, Makarov I. Carbon deposition in steam methane reforming over a Ni-based catalyst: experimental and thermodynamic analysis. Energy 2021;222:119993.

[38] Pashchenko D. Intra-particle diffusion limitation for steam methane reforming over a Ni-based catalyst. Fuel 2023;353:129205.

International Research Journal of Engineering and Technology (IRJET) e-ISSN: 2395-0056
Volume: 10 Issue: 05 | May 2023 www.irjet.net p-ISSN: 2395-0072

Stress Analysis Of Connecting Rod For Diesel Engine With Different Materials

Dipanker Meena[1], Kamal Negi[2], Karan Pradhan[3]

[1,2,3] *Dept. of Mechanical Engineering, Delhi Technological University, New Delhi-110042*

Abstract - *The connecting rod is an important component of an engine assembly as it serves the purpose of transferring energy from the piston to the crankshaft. Its primary function is to convert the linear, back-and-forth motion of the piston into the rotary motion of the crankshaft. The connecting rod primarily undergoes tensile and compressive loading under the cyclic engine process. In this project, Static analysis was done on the connecting rod. Different materials are used for the analysis, like structural steel, titanium, and aluminum alloy. The study was done on several research papers, and after that, critical dimension data of the connecting rod was decided upon. A three-dimensional model of the connecting rod and its assembly was created on DS SolidWorks 2019. The model was then imported as a geometry parameter in Ansys 2023 R1 for finding von mises stress, Total Deformation, and safety factor. Then they were compared to choose the best material amongst them for the connecting rod.*

Key Words: Connecting Rod, Structural Analysis, Finite Element Analysis, Titanium, Steel, 42CrMo4.

1. INTRODUCTION

Connecting rods are of utmost importance in the functioning of an internal combustion engine. Their primary role is to convert the reciprocating motion of the piston into rotary motion in the crankshaft, enabling the vehicle's wheels to rotate. Comprising a small end connected to the piston and a big end attached to the crankshaft, the connecting rod experiences various forces during each rotation of the crankshaft. These forces include compression when the piston moves downward and tension when the piston moves upward. Any damage to the connecting rod, such as cracking or buckling, can result in engine immobilization. Such failures lead to substantial financial losses due to material damage and pose significant safety risks, as accidents resulting from these failures can have severe and potentially fatal consequences.

Many materials are used to make connecting rods. Every material has its advantages and disadvantages. They are used depending on the engine requirement, the purpose of the engine (work type), and other factors that matter in the engine's working.

In this research the best material for the connecting rod has been chosen by comparing the von mises stresses, total deformation and factor of safety of different materials on Ansys software. The connecting rod assembly has been shown in Fig –1.

1.1 Parts of the Connecting Rod

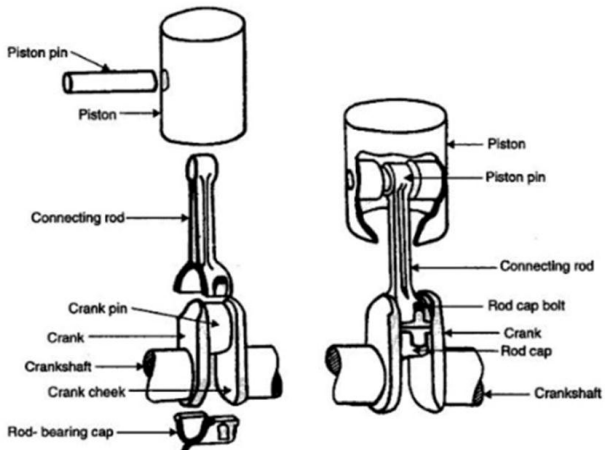


Fig -1: Connecting Rod

1. Small End
2. Big End
3. Bush bearing
4. Bearing Insert
5. Bolt and Nut
6. Shank
7. Crankshaft
8. Piston
9. Bearing cap

2. LITERATURE REVIEW

Comparisons were made between two different aluminum alloys and forged steel regarding von Mises stress, total deformation, and factor of safety [1].

The optimization of IC engine connecting rods involved the selection of forged steel or C-70, with a focus on size optimization and material choice [2][3].

ANSYS software was utilized to assess parameters like von Mises stress, strain, deformation, factor of safety, and weight reduction in two-wheeler pistons, indicating that aluminum alloy exhibited higher factors of safety, reduced stress, decreased weight, and greater stiffness compared to forged steel [4].

An optimization approach to connecting rods was proposed, involving an increase in torque of the bolt assembly to reduce stress amplitude [5].

Load and stress analysis of connecting rods for weight reduction was conducted [6].

Optimal designs for connecting rods were analyzed using ANSYS Workbench and CATIA V5R19, resulting in improved outcomes within permissible limits and safe stresses [7].

The design of a two-wheeler connecting rod was carried out analytically, followed by FEA for stress calculations and thermal analysis, leading to a significant reduction in weight [8].

Simulation studies involving SolidWorks and ANSYS were performed to assess von Mises stresses and frequencies of connecting rod materials, aiding in material selection [9].

The strength simulation analysis of a low-speed diesel engine's connecting rod was conducted using professional simulation software, followed by a static strength test using a servo universal testing machine [10].

3. MATERIALS USED

A variety of materials are utilized in the production of connecting rods which includes different grades of structural steel, aluminum, and titanium. Steel rods are the most commonly produced and employed due to their high strength and durability, making them suitable for both daily driving and endurance racing. However, one downside to using steel rods is their weight, which places added stress on the rotating assembly and consumes more power. This study examines the use of alternative materials for connecting rods and conducts an analysis of their properties. In this work, the below mentioned materials were taken for connecting rod simulation.

Structural Steel,

42CrMo4,

T6-7075 Aluminum,

Ti-6Al-4v,

C-70(SAE-AISI 1070) Carbon steel

4. METHODOLOGY

In this research work, a connecting rod was meticulously crafted employing the aid of DS SolidWorks 2019, a sophisticated computer-aided design (CAD) software application renowned for its prowess in generating intricate three-dimensional models of mechanical components, assemblages, and blueprints. Its pervasive adoption by engineers, designers, and manufacturers spanning a spectrum of industries, ranging from automotive and aerospace to consumer goods and industrial machinery, attests to its indispensable nature. This exceptional software offers an extensive array of utilities for the construction of intricate geometries, assemblages, and simulations, along with the generation of detailed technical drawings and animated representations. Capitalizing on a parametric design methodology, this software empowers users to effortlessly manipulate and revise models by effecting modifications to pertinent parameters or dimensions.

. The dimensions taken were those, which are of common use in the market. Each of the parts of the connecting rod was modeled and was merged together in the assembly.

Another software that was used for conducting Finite Element Analysis was Ansys Workbench 2023 R1. It is a software commonly used for stress/strain analysis and to determine the factor of safety of a proposed prototype.

The assembly of Solidworks is imported into Ansys as a geometry to perform FEA. Forces were applied on the connecting rod based on a number of research texts and

5. MODELING AND ANALYSIS OF CONNECTING ROD

Solidworks is a comprehensive 3D solid modeling software that provides users with the ability to design and analyze models in a virtual environment. It empowers designers, engineers, and professionals to conceptualize ideas and explore different design possibilities by creating accurate and detailed 3D models, assemblies, and drawings. By leveraging the capabilities of Solidworks, users can significantly reduce the time, effort, and expenses associated with physical prototyping. The software offers a streamlined and efficient approach to design, enabling users to visualize and evaluate their designs before moving forward with production.

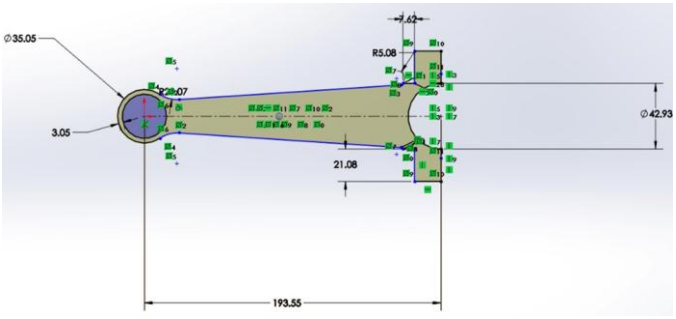


Fig -2: Dimensions of Connecting Rod

In this research, a connecting rod model was designed in SolidWorks 2019 software. The connecting rod was fabricated with a length of 193.55 mm, diameter of the smaller end, 35.05 mm, and the diameter of the bigger end, 42.93mm, shown in Fig -2.

Connecting rod assembly includes piston rod, cap end, nut, and bolt. The 3-Dimensional model of the assembly is shown in Fig -3.

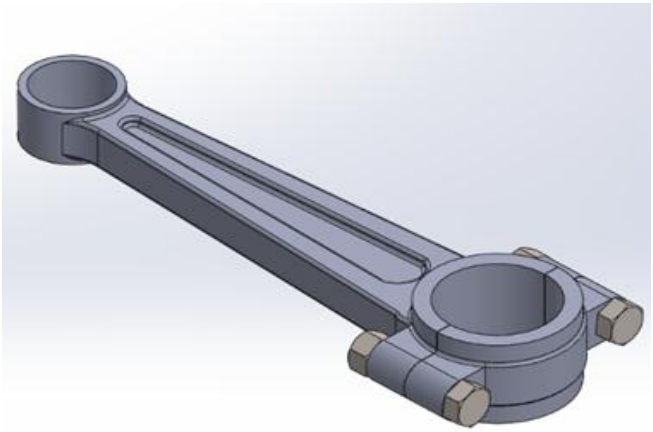


Fig -3: Connecting Rod Assembly

FEA, or Finite Element Analysis, is founded on the concept of dividing a given domain into a finite number of smaller regions called elements. By employing the variational or weighted residual method, FEA constructs a systematic approximate solution for these elements. This approach enables the reduction of the original problem, which involves an infinite number of unknowns, into a finite number of unknowns. The division of the domain into elements allows the representation of the unknown field variable through assumed approximating functions within each element.

ANSYS Workbench serves as the foundation for a comprehensive range of cutting-edge engineering simulation technologies in the industry. Its distinctive project schematic view seamlessly connects the entire simulation process, providing guidance to users at each step. With ANSYS Workbench, even intricate multi-physics analyses can be conducted effortlessly using a drag-and-drop approach. The platform facilitates automatic geometry sharing between fluid and structural analyses, streamlining data storage and enabling easy exploration of the effects of geometry modifications in both analyses. In the research, the Static Structural module of ANSYS was utilized.

5.1 Static Structural Analysis

Static analysis involves the meticulous examination of equilibrium conditions exhibited by objects when subjected to external forces. It encompasses both linear and nonlinear approaches, with the latter accommodating an extensive array of nonlinear phenomena such as significant deformations, plasticity, creep, stress stiffening, and contact elements. The current focus pertains specifically to static analysis, a comprehensive exploration of the effects resulting from sustained loading conditions on a given structure. Notably, this analysis disregards the intricate dynamics introduced by inertia and damping effects inherent in time-varying loads. The primary objective of static analysis lies in the precise determination of essential parameters including displacements, stresses, strains, and forces within structures or components, all of which arise from loads that lack substantial influence from inertia and damping mechanisms. Additionally, the process of meshing, an indispensable aspect of numerical analysis, assumes a significant role. Meshing involves the intricate segmentation of complex geometries or domains into simpler, more manageable elements. This segmentation facilitates enhanced analytical techniques and contributes substantially to the accuracy and efficiency of the overall analysis. To illustrate this concept further, Figure 4 provides a visual representation of intricate mesh details, while Figure 5 demonstrates the process of meshing specifically applied to the connecting rod under investigation.

Defaults	
Physics Preference	Mechanical
Element Order	Program Controlled
Element Size	1.5 mm
Sizing	
Use Adaptive Sizi...	Yes
Resolution	Default (2)
Mesh Defeaturing	Yes
Defeature Size	Default
Transition	Fast
Span Angle Center	Fine
Initial Size Seed	Assembly
Bounding Box Di...	263.97 mm
Average Surface ...	182.23 mm^2
Minimum Edge L...	3.2633e-003 mm

Fig -4: Mesh Details

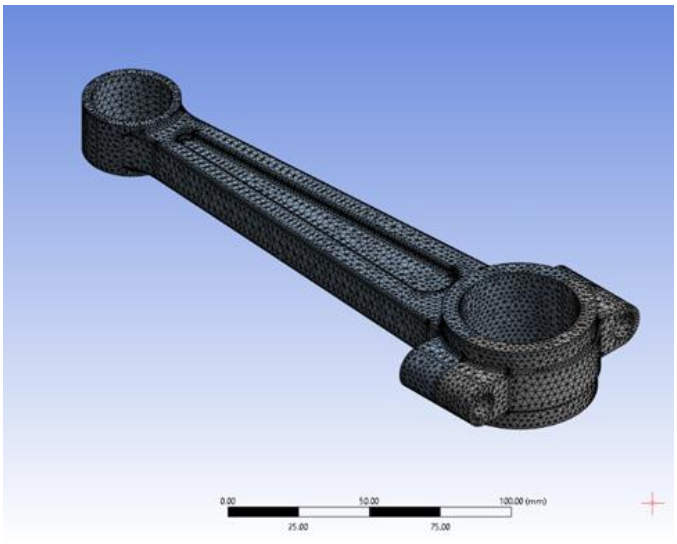


Fig -5: Connecting Rod Mesh Model.

Establishing boundary conditions is an essential and crucial step in Finite Element Analysis (FEA). This process involves defining constraints for the meshed model to simulate real-life scenarios accurately. The boundary conditions encompass fixed support, forces, and pressure that are applied to the model. By specifying these constraints, the analysis can determine the deformation, fatigue, stress, and strain values of the connecting rod while adhering to acceptable design limits. In the analysis of the connecting rod, a fixed support was applied at the bigger end, which is connected to the crankshaft. Additionally, pressure and forces were exerted at the smaller end, connected to the piston, as illustrated in Figure 5.

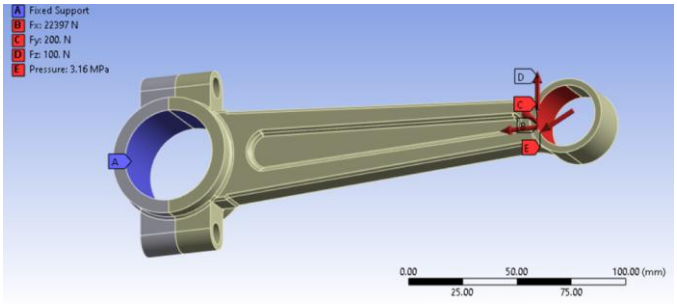


Fig -6: Application of Load/Forces

The Static Structural module of ANSYS has been used to perform the simulation on steel, aluminum and titanium alloys which are used nowadays for the production of connecting rods for vehicles. Following are the materials which were used in the research for simulation: structural steel, 42CrMo4, T6-7075 aluminum, Ti-6Al-4v and C-70.

1) Structural Steel

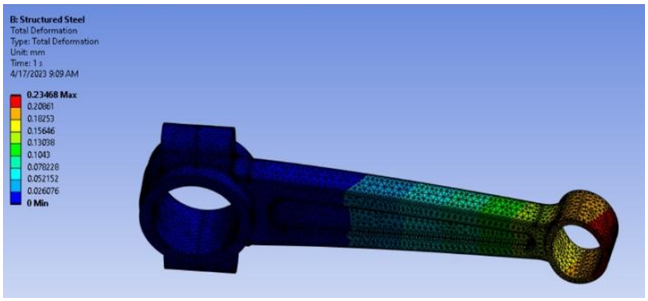


Fig -7: Total Deformation

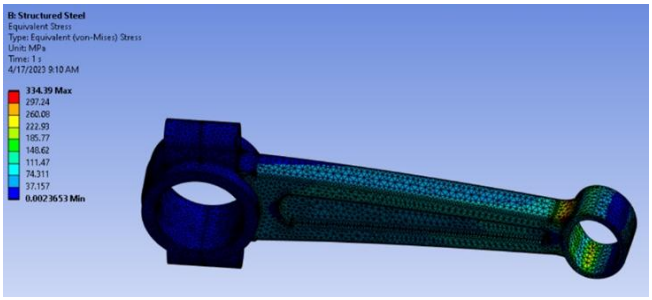


Fig -8: Equivalent Stress

Total Deformation and Equivalent stress of Structural Steel has been shown in Fig -7 and Fig -8 respectively.

2)42CrMo4

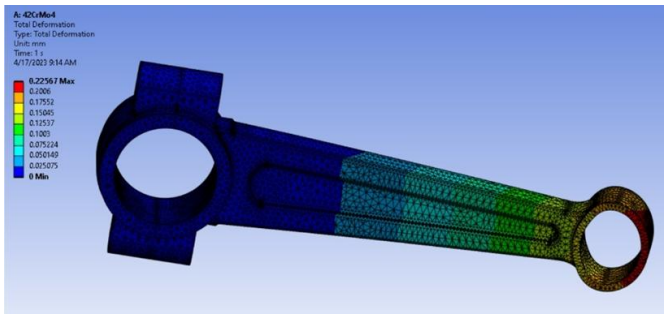


Fig -9: Total Deformation

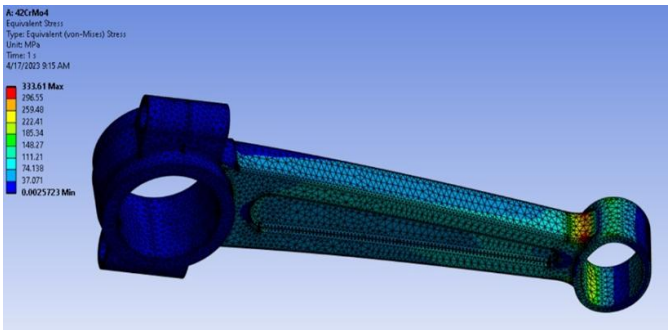


Fig -10: Equivalent Stress

Total Deformation and Equivalent stress of 42CrMo4(an engineering alloy steel containing chromium and molybdenum) has been shown in Fig -9 and Fig -10 respectively.

3) T6-7075 Aluminum

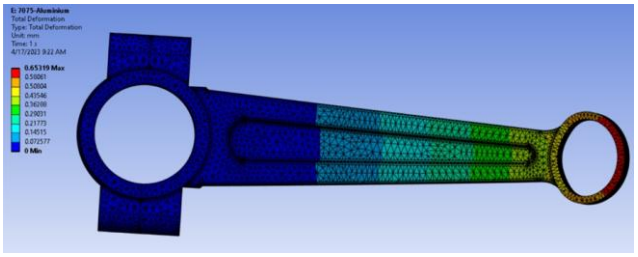


Fig -11: Total Deformation

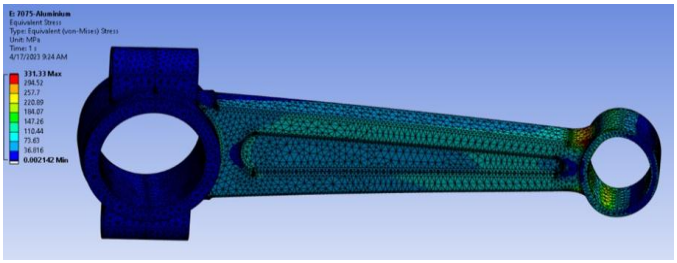


Fig -12: Equivalent Stress

Total Deformation and Equivalent stress of T6-7075 Aluminium(an Aluminium alloy) has been shown in Fig -11 and Fig -12 respectively.

4) Ti-6Al-4v

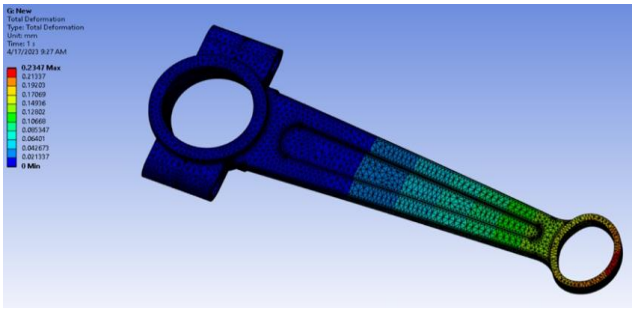


Fig -13: Total Deformation

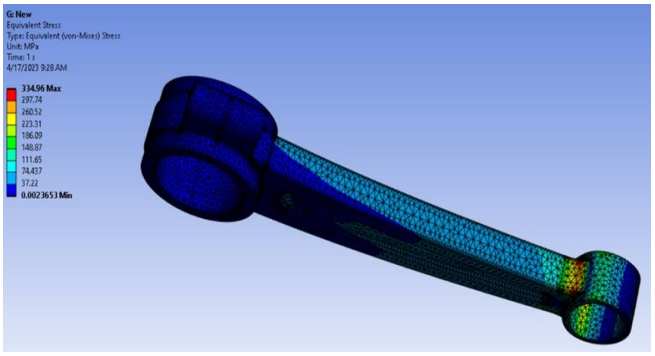


Fig -14: Equivalent Stress

Total Deformation and Equivalent stress of Ti-6Al-4v(a titanium alloy composed of 90% titanium, 6% aluminum and 4% vanadium) has been shown in Fig -13 and Fig -14 respectively.

5) C-70(SAE-AISI 1070) Carbon steel

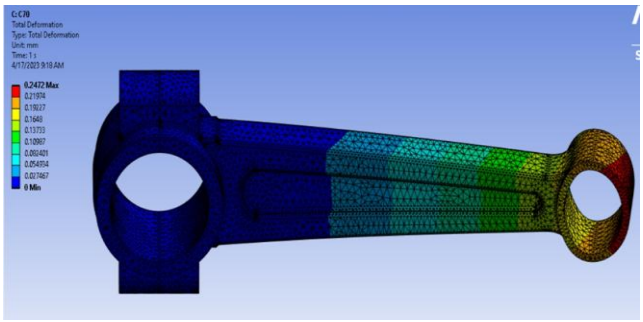


Fig -15: Total Deformation

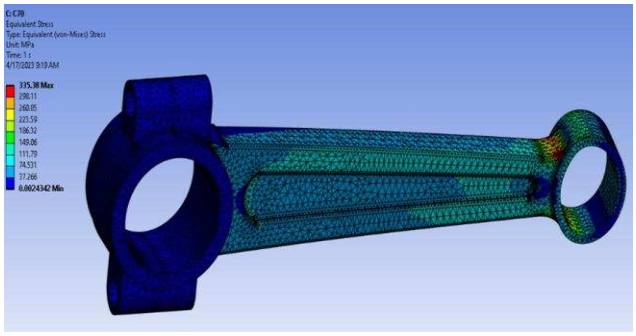


Fig -16: Equivalent Stress

Total Deformation and Equivalent stress of C-70(Carbon Steel) has been shown in Fig -15 and Fig -16 respectively.

6. RESULTS AND DISCUSSIONS

Table -1: Comparison of Values

Materials	Total Deformation (mm)	Equivalent Stress (MPa)	Safety Factor
Structural Steel	0.23468	334.39	0.7476
42CrMo4	0.22567	333.61	2.6977
T6-7075 Aluminum	0.65319	331.33	1.5181
Ti-6Al-4v	0.23410	334.96	3.2840
C-70	0.24720	335.38	1.4312

A comparison of values of total deformation, equivalent stress, and factor of safety for five different materials has been shown in Table 1. From the table it can be concluded that the minimum total deformation has been shown by 42CrMo4(Steel alloy) while the maximum total deformation has been shown by T6-7075 Aluminum.

The minimum equivalent stress has been shown by T6-7075 Aluminum and maximum equivalent stress has been shown by C-70(Carbon steel).

The highest factor of safety has been shown by Ti-6Al-4v (a Titanium alloy) while Structural steel has the lowest factor of safety.

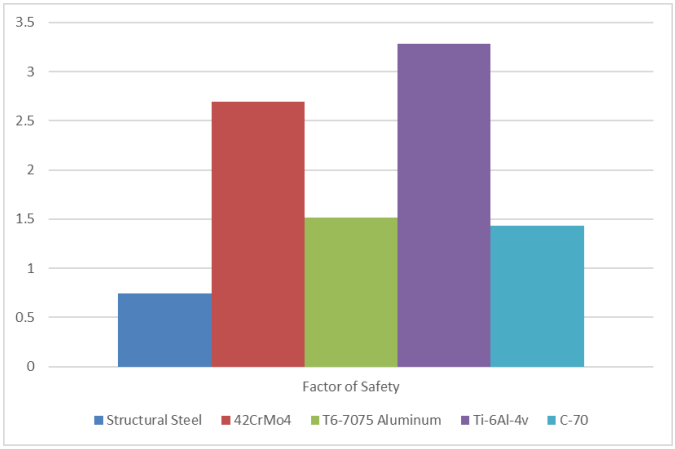


Chart -1: Factor of Safety

7. CONCLUSIONS

From the static analysis the stress is found maximum at the small end of the connecting rod which is connected to the piston.

It has been found that titanium alloy is the best material for manufacturing connecting rods as it has a high factor of safety although it has more weight than aluminum alloy. The only thing that is a barrier to implement Titanium alloy is cost, availability, and its repair.

42CrMo4 is the second choice for production as it has the lowest value of total deformation and has a high factor of safety after Titanium alloy.

Structural steel is not effective regarding mass, and it increases the weight of the connecting rod. It also has the lowest factor of safety among the chosen materials.

ACKNOWLEDGEMENT

This Bachelor of Technology dissertation titled "Static Analysis of Connecting Rod" has been carried out under the guidance and supervision of Prof. R.C Singh and the aegis of the Mechanical Engineering Department, Delhi Technological University.

In this research journey, we came across several people who helped and traveled with us to achieve this ambition of our life. Therefore, for this achievement of ours, we should express our sense of gratitude towards those persons who unconditionally supported, helped, and encouraged us in all situations. We are highly thankful to the Almighty for blessing us and giving us the strength, energy, and patience to overcome all the difficulties and reach this ambition.

Firstly, we would like to thank **Prof. S. K. Garg** (Head of the Department) for giving us the opportunity to work on this project.With our profound gratitude and deep regards, we would also like to thank **Prof. R.C. Singh** for their personal input, enthusiasm, meticulous manuscript checking, constructive comments, and remarks. Except for the vision they set for us, they helped us conceptualize the project and helped in the actual building and procedure to complete it.

We thank **Ms. Yamika Patel** for their continuous support and guidance throughout the project.

We want to thank our professors for their guidance and patience and for imparting in-depth knowledge about the subjects, which helped complete our project.

REFERENCES

[1] R A Savanoor, Abhishek Patil, Rakesh Patil and Amit Rodagi, Int. J. Mech. Eng. & Rob. Res. 2014, ISSN 2278 – 0149 Vol. 3, No. 3.

[2] Kumbha Sambaiah, DR. Rama Rao and DR. M Mahesh "Optimization for thermal analysis connecting rod of internal combustion engine by using two different materials", International Journal of Applied Research 2017; 3(12): 278-282

[3] Ashish Kumar and Er. Shubham Parmar "Analytical Study and Design Analysis of Connecting Rod of Mahindra Pijo by Finite Element Analysis", International Journal of Scientific Development and Research (IJSDR) www.ijsdr.org

[4] Mr. H D. Nitturkar, Mr. S M. Kalshetti and Mr. A R. Nadaf "Design and Analysis of Connecting Rod using Different Materials", International Research Journal of Engineering and Technology (IRJET).

[5] Griza, S.; Bertoni, F.; Zanon, G.; Reguly, A.; Strohaecker, T. Fatigue in engine connecting rod bolts due to forming laps. Eng. Fail. Anal. 2009, 16, 1542–1548.

[6] Ramani et al Int. Journal of Engineering Research and Applications, Vol. 4, Issue 3(Version 1), March 2014, pp.216- 220

[7] DR. B.K.Roy "Design Analysis and Optimization of Various Parameters of Connecting Rod using CAE Softwares" International Journal of New Innovations in Engineering and Technology (IJNIET)

[8] Vivek C. Pathade, Bhumeshwar Patle and Ajay N. Ingale, "Stress analysis of I.C engine connecting rod by FEM", International Journal of Engineering and Innovative Technology, Vol-1, Issue-3, pp. 12-15, March 2014

[9] Chinnari Natraj, Bantu Sandhya, Agatha Naveen, Seera vivek and Seera N. Kumar,"Design, Static and Modal analysis of connecting rod of four stroke Spark Ignition engine", Anil Neerukonda Institute of Technology and Science, India,2022.

[10] W. Gao, G. Wang, J. Zhu, Z. Fan, Xiaobo "Structural Optimization Design and Strength Test Research of Connecting Rod Assembly of High-Power Low-Speed Diesel Engine" College of Power and Energy Engineering, Harbin Engineering University, Harbin 150001, China,2022.

Journal of Fluorescence
https://doi.org/10.1007/s10895-023-03553-0

RESEARCH

Structural Investigation and Optical Properties of Dysprosium (Dy^{3+}) Ions Doped Oxyfluoro Antimony Borate Glasses for Photonics Applications

Ch. Pravallika[1] · K. Swapna[1] · Ib Singh Deo[2] · Sk. Mahamuda[1] · M. Venkateswarulu[1] · A. S. Rao[3] · Vijaya Prakash G.[2]

Received: 4 September 2023 / Accepted: 12 December 2023
© The Author(s), under exclusive licence to Springer Science+Business Media, LLC, part of Springer Nature 2023

Abstract
Dysprosium oxide-doped glasses with a composition of $60B_2O_3$-$10Sb_2O_3$-$10Al_2O_3$-10NaF-(10-x) LiF-xDy_2O_3 (x = 0.1,0.5, 1.0,1.5,2.0,2.5 mol%) were prepared using a conventional melt-quenching technique. The glasses were characterized through various analytical investigations, including X-ray diffraction (XRD), Fourier transform infrared (FTIR) spectroscopy, refractive index, density, optical absorption, excitation, photoluminescence (PL) studies, decay measurements and radiation shielding parameters. The XRD and FT-IR confirms the glassy nature and functional groups present in the titled glass. The absorption spectra were used to determine the oscillator strength of the Dy^{3+} absorption transitions as well as the bond created with the O^{-2} ion in the titled glass network. The degree of the suitability of developed glasses for lasing applications was demonstrated by radiative parameters determined using Judd–Ofelt theory. In the prepared glass samples, the optical bandgap measurements indicate the presence of non-bridging oxygen (NBOs), localization of charges and donor centers in the titled glasses. Due to the de-excitation of $^4F_{9/2}$ to the corresponding $^6H_{15/2}$,$^6H_{13/2}$ and $^6H_{11/2}$ states, the PL emission spectrum shows two main strong emissions at blue(480nm), yellow (575nm) and one less emission at red (663nm). The CIE coordinates determined using PL emission spectra reveal the coordinates that are falling within the white light region. Various shielding parameters such as mass attenuation coefficient, mean free path, effective atomic number were estimated to understand the radiative shielding nature of the titled glasses. Within the addition of Dy_2O_3, it was found that the shielding parameters values of the titled glass samples are increasing. The Mass Attenuation Coefficient, Half Value Layer and Mean Free Path of the as prepared glasses has been compared with different types of concretes to understand the shielding effectiveness of prepared glass.

Keywords Dy^{3+} ions · Absorption · J-O parameters · PL Studies · Radiation shielding parameters

Introduction

The rare-earth (RE) doped materials have gained considerable attention owing to their potential applications in many fields, like medicine, optoelectronics, and telecommunication (optical fibers, lasers, and amplifiers) because RE ions exhibit emission transitions in 4f-4f or 4f-5d, additionally their unique electronic configuration from the ultraviolet region to the infrared region makes them to act as an excellent activator to emit sharp luminescence [1–3]. In particular, glasses doped with RE ions have gained significant attention for the development of Solid-State Lighting devices (SSL). The SSL technology is used in many lighting applications because of its advantages like durability, energy saving and eco-friendly [4]. In SSL, white light-emitting diodes (wLEDs) are an interesting possible substitute for fluorescent lamps because of their advantageous properties such as transparency, thermal stability, and low cost. Currently, blue or near-ultraviolet LED chips are used to excite phosphors (YAG: Ce^{3+}, for example) in epoxy resin to provide white light. To achieve great brightness, however, the output power of the LEDs must be raised, which raises the chip's temperature. The resin can break down as a result of the temperature rise, which would lower the light's quality and intensity. Since they may be made in the form of a lens,

✉ K. Swapna
kswapna80@gmail.com

[1] Department of Physics, Koneru Lakshmaiah Education Foundation, Vaddeswaram, Andhra Pradesh, India

[2] Nanophotonics Lab, Department of Physics, Indian Institute of Technology, Delhi, New Delhi 110016, India

[3] Department of Applied Physics, Delhi Technological University, Bawana Road, New Delhi 110042, India

Published online: 29 December 2023

luminescent materials doped with trivalent RE ions can be utilized to replace the phosphor particles to promote direct encapsulation of the LED chip [5].

On the other hand, the RE ions are using to replace the concretes [6] which are opaque and unclear to visible light, as alternative gamma ray shielding materials for various uses in high energy physics applications and nuclear waste management. The gamma rays which may lead to increase the risks for cancer, damage to human cells, and environmental effects. Therefore, the use of reliable shields is fundamental. Radiation shields are the most widely used materials because of their high density, good structural properties, and cost efficiency. Although lead is a very efficient shielding material but it is highly toxic and harmful to the environment; therefore, the present research is focused on non-toxic alternatives [7]. Numerous studies have been reported to replace the lead-based glass with different types of glass matrices like borates [8], silicates [9], phosphates [10], tellurites [11], etc., borate glasses are well-suited application for the prepared glasses [12–14].Boric acid (B_2O_3) is one of the excellent glass former in oxide materials because it has a high glass-forming trend and exhibits unique advantages, like minimum dielectric constant, ease of formation, low melting point, low cost, high RE ion solubility, and good transparency. Borate glasses are suitable for a variety of applications in fiberglass as they tend to reduce thermal expansion and resist thermal shock at high temperature. However, the main drawback of borate glasses is that, they possess a phonon energy of approximately 1300 cm^{-1}, which is relatively quite high because the presence of lightweight which possess relatively high phonon energy. Such high phonon energies increase nonradiative loss through the multiphonon relaxation process. Heavy metal oxides like bismuth, tellurite, tungsten, and antimony have attracted attention because of their relatively low phonon energies, high polarizabilities, and high refractive indices [15]. In addition to the this, alkali fluorides such as NaF and LiF in the glass minimizes the non-radiative energy loss and decreases the phonon energy. Such alkali fluorides also help to remove the -OH groups present in the borate glasses. In addition, Aluminum Oxide (Al_2O_3), as a glass modifier, provides mechanical strength to glass and improves its optical response. The thermal and chemical properties also enhanced the emission properties of the prepared glass samples [16]. By adding the Al_2O_3 to a borate glass matrix it can form the AlO_4 and AlO_6 units [17].

Among lanthanides, Dysprosium ions (Dy^{3+}), is a promising ion for white-light devices and visible-laser applications. It has distinct emission bands between the visible and near-infrared regions, which lend themselves to a variety of interesting optical properties. Due to electronic transitions at $^4F_{9/2} \rightarrow {}^6H_{15/2}$, $^4F_{9/2} \rightarrow {}^6H_{13/2}$, and $^4F_{9/2} \rightarrow {}^6H_{11/2}$, Dy^{3+} ions primarily exhibit two strong emission bands, which are pure magnetic dipole transition at blue (470–500 nm) and pure electric dipole transition at yellow (570–600 nm) regions, as well as one weak red emission band (660–700 nm). Among these, the hypersensitive transition $^4F_{9/2} \rightarrow {}^6H_{13/2}$ is strongly affected by the environment. Emission of white light at a regulated yellow to blue (Y/B) ratio can be achieved by adjusting the concentration of dysprosium ions in a host matrix and adjusting excitation wavelength. The Y/B ratio also provides information on the Dy^{3+} -O^{2-} ion environment in the nearby regions of the dysprosium ions, such as the degree of covalence. Both visible and near-infrared solids state lasers can be created through glasses doped with Dy^{3+} ions [18, 19].

In the present work, we synthesized the Dy^{3+} ions activated $60B_2O_3$-$10Sb_2O_3$-$10Al_2O_3$-10NaF-(10-x) LiF-xR.E (OFSbB) glass samples were synthesized and characterized them by using XRD, FT-IR and optical properties such as absorption, luminescence spectra and decay time measurements. Evaluation of Judd-Oflet (J-O) intensity parameters and their trends, as well as physical parameters, were investigated with respect to Dy^{3+} concentration. The optical band-gap energy was estimated using Tauc's plot for the indirect and direct transitions from the absorption data. Under excitation at 351 nm, the yellow-blue (Y/B) intensity ratio results in the application of white-light-emitting devices. The PSD software was used to investigate OFSbBDy glasses gamma-ray shielding parameters, including the Effective Atomic Number, Linear Attenuation Coefficient, Half Value Layer, Tenth Value Layer, Mean Free Path, Mass Attenuation Coefficient, and Exposure Buildup Factor.

Experimental Approach

Synthesis

The Melt-quenching method was used to synthesize the Dy^{3+} ions-doped glass with a $60B_2O_3$-$10Sb_2O_3$-$10Al_2O_3$-10NaF-(10-x) LiF-xDy_2O_3 composition (where, x = 0.1, 0.5, 1.0, 1.5, 2.0, 2.5 mol %). The prepared glasses are referred to as OFSbBDy0.1, OFSbBDy0.5, OFSbBDy1.0, OFSbBDy1.5, OFSbBDy2.0, and OFSbBDy2.5, depending on the Dy-ion concentration from 0.1 to 2.5mol% respectively. All the chemicals were weighed using an electrical weighing balance with an appropriate molecular weight. After weighing, the chemical composition was ground into a fine powder using an agate mortar and pestle. The batch materials, which were placed in silica crucibles and heated for ten minutes at 1200 °C in an electric furnace, had a stoichiometric composition of approximately 8 g. The melt was kept homogeneous by being stirred every three minutes. To eliminate the internal thermal stress caused by the quenching process, the melt was quenched in a brass mold and plates that had been preheated and then annealed for two hours at 500 °C. The prepared glasses had a 2 mm thickness and were transparent.

Sample Characterization

Using Cu K (λ = 1.5405Å) radiation, an XRD analysis of the prepared glasses amorphous nature was performed on PANalytical EMPRYREAN diffractometer. The densities and refractive index of the glass samples were measured using Archimedes rule and Brewster's angle method respectively. FT-IR spectra of the glass samples were recorded using a JASCO FT/IR- 4700 spectrometer. A JASCO V-670 UV–vis-NIR spectrometer was utilized for the recording of the absorption spectra. Using a JASCO FP-8300 spectrofluorometer, excitation, PL spectra and PL decay curves of the as prepared glass samples were recorded at room temperature. The characteristics of photon shielding for the OFSbBDy glasses were computed using the PSD/Phy-X software [20].

Results and Discussion

Structural Analysis

X-ray Diffraction

Figure 1 shows the patterns of X-Ray Diffraction at the different concentrations of Dy^{3+} ions-activated OFSbB glass samples recorded in the 2θ range of 20–80° on a PANalytical EMPYREAN diffractometer with Cu Kα (λ = 1.5405Å) radiation. In general, non-crystalline materials do not exhibit sharp peaks because of the nonperiodic arrangement of atoms in these solids, which does not satisfy the diffraction condition [21]. The prepared glass samples exhibited a broad hump at approximately 27°, indicating the presence of the BO_3 group [5].

Fourier Transform Infrared Spectroscopy

FT-IR plays an important role in determining the structural properties of the as prepared glass samples. Figure 2 represents the FT-IR spectra of Dy^{3+} ions-doped and un-doped OFSbB glass samples, which were recorded in the wavelength range from 450 to 3500 cm^{-1}. The BO_3 group is present, as an evidenced by the peak at 512cm^{-1}. The bending vibrations of the BO – O– BO_4 bonds is attributed due to the peak at 688cm^{-1}. The peak at 891 cm-1 corresponds to the stretching vibrations of the tetrahedral BO_4^{-1} units. The peak at 1047 cm^{-1} indicates the pentaborane group. The peaks at 1209 cm^{-1} represent the B-O-B bending vibrations in the tetrahedra corresponding to boron-tetrahedral units. The peak at 1335 cm^{-1} represents the stretch vibration between Boron-Oxygen bonds of the BO_3 unit, which also results about the link between oxygen and different connecting diverse groups like orthoborate, metaborate and pyroborate. The peak at 2345 cm^{-1} indicates the presence of hydrogen bonds in the prepared glasses. The peak at 3057 cm^{-1} indicates the presence of the OH group [22–25].

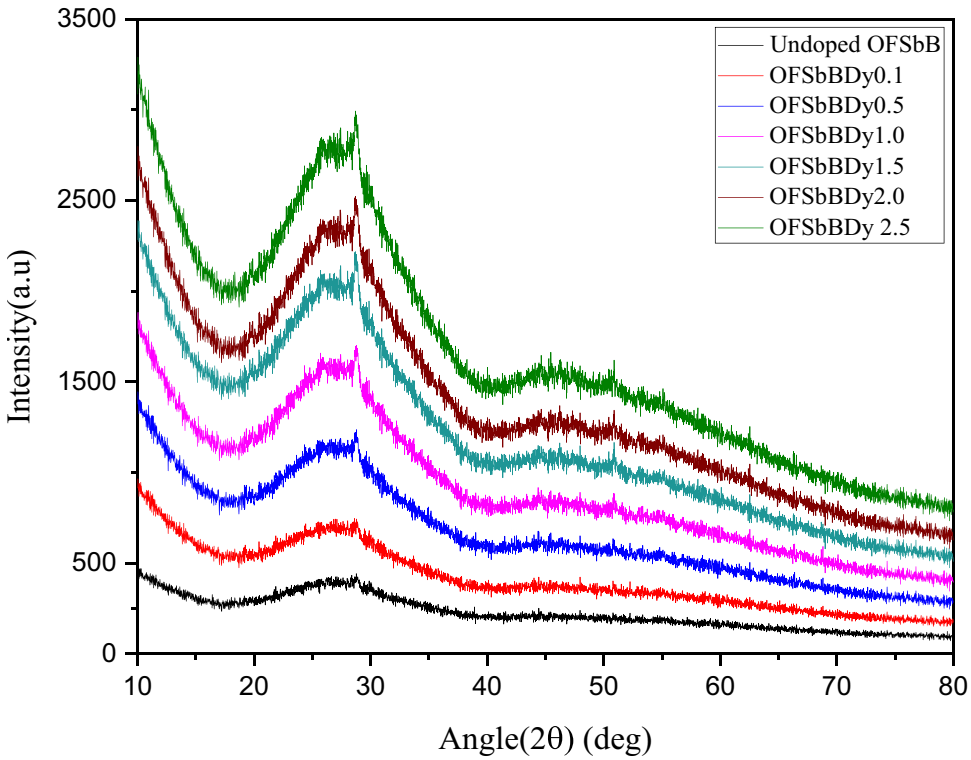


Fig. 1 The X-Ray Diffraction patterns of the undoped and doped OFSbBDy glass samples

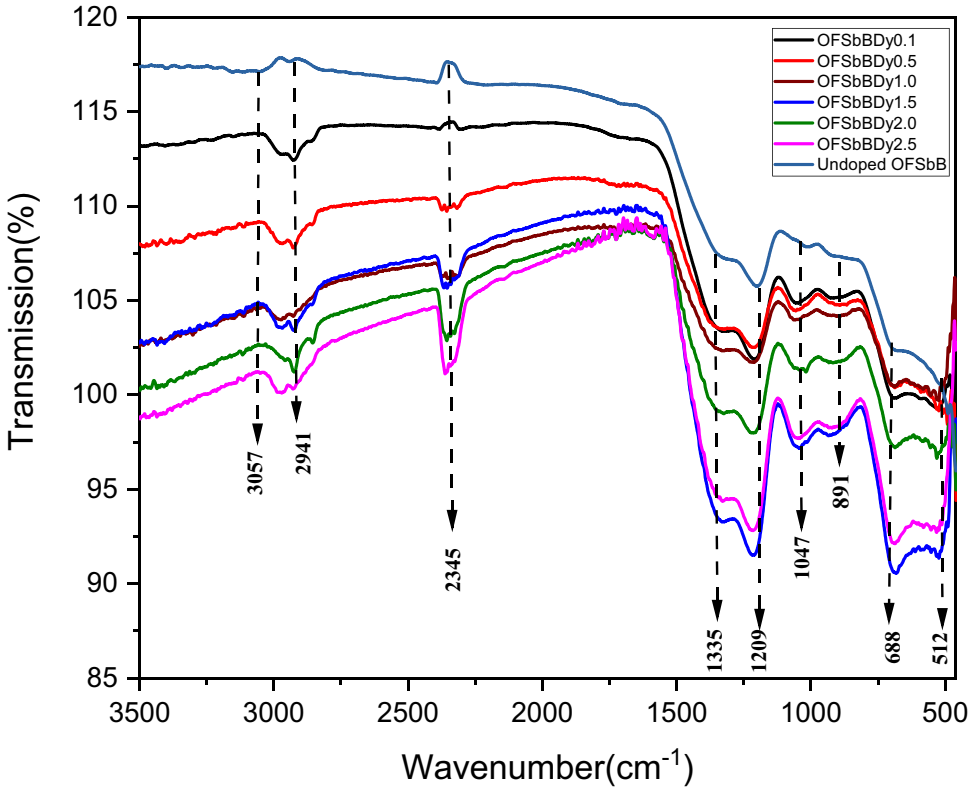


Fig. 2 The Fourier transform infrared (FTIR) spectra of the Dy^{3+} ions doped into the OFSbB glass samples

Physical Parameters

Table 1 describes Physical parameters of Dy^{3+} ions doped OFSbB glasses like refractive index(n), density, RE ion concentration(N), average molecular weight(M), polaron radius(r_p), inter-ionic distance(r_i), and field strength(F) of the prepared glasses. The OFSbB glasses density increased with an increase in Dy^{3+} ions concentration. The density increased because of the increase in the molar mass and modifications of the BO_3 triangles in to BO^{-4} tetrahedra. The density depends on the alkali type and alkali earth modifier, which occupy the interstitial positions in the glass network. The Li^+ ion connects with the glass former cations, that is with B^{3+} ions, and enhances ring-type structures and coordination numbers, which also leads to a increase in density because of the presence of Non-Bridging Oxygen (NBO) atoms

Table 1 Physical parameters of Dy^{3+} ions doped OFSbB glasses

Physical Parameters	OFSbBDy0.1	OFSbBDy0.5	OFSbBDy1.0	OFSbBDy1.5	OFSbBDy2.0	OFSbBDy2.5
Refractive index (n_d)	2.243	2.252	2.256	2.259	2.267	2.271
Density (g/cc)	2.916	2.936	2.962	2.988	3.014	3.04
Average molecular weight (g)	83.586	94.452	96.187	97.922	99.658	101.393
Dy^{3+} ion concentration ($\times 10^{22}$ ions/cm^3)	0.034	0.172	0.341	0.506	0.668	0.826
Mean atomic volume (g/cm^3/atom)	6.901	7.721	7.767	7.867	7.853	14.208
Dielectric constant (Ɛ)	5.031	5.071	5.089	5.103	5.139	5.157
Optical dielectric constant($P\partial t/\partial p$)	4.031	4.071	4.089	4.103	4.139	4.157
Reflection losses (R)	0.146	0.148	0.148	0.149	0.150	0.150
Molar refraction R_m (cm^{-3})	16.435	18.517	18.728	18.928	19.169	19.373
Polaron radius (Å)	5.816	3.413	2.720	2.385	2.175	2.026
Interionic distance (Å)	0.144	8.470	6.750	5.919	5.398	5.029
Molecular electronic polarizability ($\times 10^{-23}$ cm^3)	0.392	7.958	4.032	2.722	2.071	1.677
Field strength ($\times 10^{15}$ cm^2)	0.886	2.574	4.053	5.270	6.338	7.302

in dysprosium oxide. The refractive indices of the glasses increased with increasing Dy^{3+} ions concentration because the polarizability of oxide increase with rare earth ions and also related to the density. The prepared glasses result the low molar electronic polarizability value results the increase in the glass network stability because the molar polarizability connected to macro and micro, physical, chemical properties like UV absorption, chemical stability [14, 26].

Absorption Spectral Analysis

Figure 3 shows the absorption spectral data of the Dy^{3+} ions-doped OFSbB glasses, which were recorded at room temperature from the ultraviolet–visible to near-infrared region. The absorption spectra show twelve peaks that are arising due to f-f transition from the ground energy state $^6H_{15/2}$ to various higher energy states of the doped dysprosium ions. The twelve electronic transitions of the absorption bands from $^6H_{15/2}$ ground state are $^4M_{15/2}$, $^6P_{5/2}$, $^4I_{13/2}$, $^4G_{11/2}$, $^4I_{15/2}$, $^4F_{9/2}$, $^6F_{3/2}$, $^6F_{5/2}$, $^6F_{7/2}$, $^6F_{9/2}$, $^6F_{11/2,}$ $^6H_{11/2}$ with the energies 350, 364, 387, 426, 451, 473, 683,753, 802, 901, 1092, 1275 and 1684 nm respectively. All electronic transitions were identified according to a report available in literature [27]. The resultant band peak intensity exhibiting high energy in the UV region is weak because of less absorption, and the low-energy near-infrared region (NIR) exhibits a strong absorption titled host matrix. The Dy^{3+} ions electronic configuration is $4f^9$, which results in a ground state multiplet (^6H), a high-intensity band at 1275 nm in the near-infrared region, and free ions in the ultraviolet region because of the overlapping of different $^{2S+1}L_J$ levels. The spectra exhibited high intensity because of the

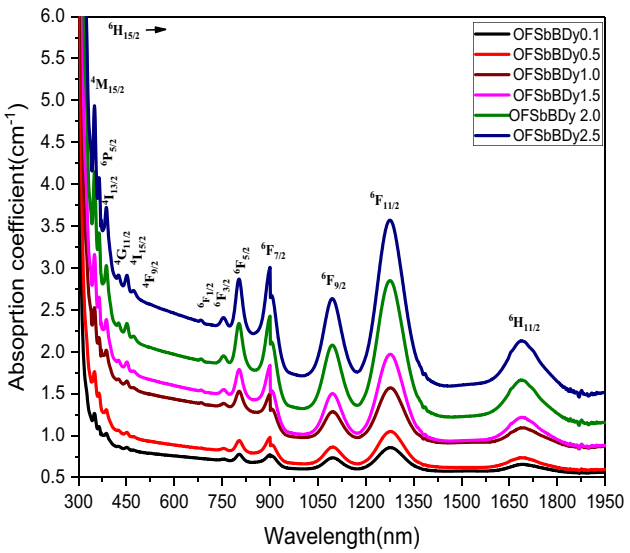


Fig. 3 The absorption spectra Dy^{3+} ions doped OFSbB glass samples

hypersensitive nature of the $^6H_{15/2} \rightarrow {}^6F_{11/2}$ electronic transition, and obeyed the selection rules $|\Delta S|=0$, $|\Delta L| \leq 2$, and $|\Delta J| \leq 2$ [28]. The electronic transition between the ground state ($^6H_{15/2}$) and excited states (^6H, ^6F) exhibited sharp and intense bands, owing to their spin-allowed nature.

Nephelauxetic Effects and Bonding Parameters

From the optical absorption spectra, the bonding nature of Dy-O in the OFSbB glass was determined. The nephelauxetic ratio (β) and the bonding parameter (δ) studies were used to determine the Dysprosium ion ligand's bonding nature. The following equations are used to determine the Nephelauxetic ratio:

$$\beta = \frac{\vartheta_c}{\vartheta_a} \tag{1}$$

where, ϑ_c is the wavenumber (cm^{-1}) of a specific shift of the rare earth ions & ϑ_a stands the wavenumber (cm^{-1}) for the similar shift of an aqua ion. The δ is calculated by the following equation.

$$\delta = \frac{1-\bar{\beta}}{\bar{\beta}} \tag{2}$$

Here, $\bar{\beta}$ is the average of β value. `based upon the environment of δ results either positive or negative which indicates the covalent or ionic nature if bonding. The bonding parameter of the prepared Dy^{3+} ions-doped OFSbB glass was negative, -0.936, -0.932, -0.930, -0.929, -0.924, and -0.923 for 0.1,0.5,1.0,1.5,2.0 and 2.5 mol% indicating ionic bonding. It indicates that when the concentration of RE ions increases, the ligand network surrounding the RE ions changes. The number of NBO's in the glass matrix, which are reason for the large changes in bonding parameter values, is also influenced by the doping concentration. The prepared glass samples, a decrease in ionicity corresponds to a reduction of bonding defects.

Optical Bandgap Analysis

Optical bandgap analysis was used to determine the bandgap between the conduction and valence bands in the oxide glasses. The nature of the glass structure and chemical bonding can be explored by analyzing the optical absorption spectral transitions [27, 29, 30]. By calculating the absorption coefficient α(ν), information about the induced transitions, such as direct and indirect allowed transitions, can be obtained. From the Davis and Mott theory, the following expression is used to evaluate the absorption coefficient [31].

$$\alpha h\nu = B\left(h\nu - E_g\right)^n \quad (3)$$

where B is the band tailing parameter, E_g is the bandgap energy & n = 1/2 or 2, depends upon either indirect allowed transition or direct allowed transition, respectively. By using Tauc plot ($(\alpha h\nu)^{1/n}$ vs. $h\nu$) the E_g values of the OFSbBDy glasses were determined through extrapolating the linear portion of the curve. Figure 4 represents the Tauc plot for indirect (n = 1/2) and direct (n = 2) transitions of the prepared glasses.

Estimation of Oscillator Strengths and Judd–Ofelt Intensity Parameters

The oscillator strengths are determined using the J–O theory, which explains the strength of the absorption peaks of RE ions. This determines the integration of the area under the curve of each observed band. Using the equation given below, the experimental oscillator strength(f_{exp}) was calculated as follows:

$$f_{exp} = 4.318 \times 10^{-9} \int \varepsilon(\nu) d\nu \quad (4)$$

Here, $\varepsilon(\nu)$, ν addresses the molar absorption of the peak(cm^{-1}), frequency of specific band.

Additionally, the following formula can be used to estimate the calculated oscillator strength(f_{cal}) during the primary and final state transitions [32, 33]:

$$f_{cal} = \frac{8\pi^2 mc}{3h} \frac{\left(n^2+2\right)^2}{9n} \frac{\nu}{(2J+1)} \sum_{\lambda=2,4,6} \Omega_\lambda \left(\psi J \| U^\lambda \| \psi' J'\right)^2 \quad (5)$$

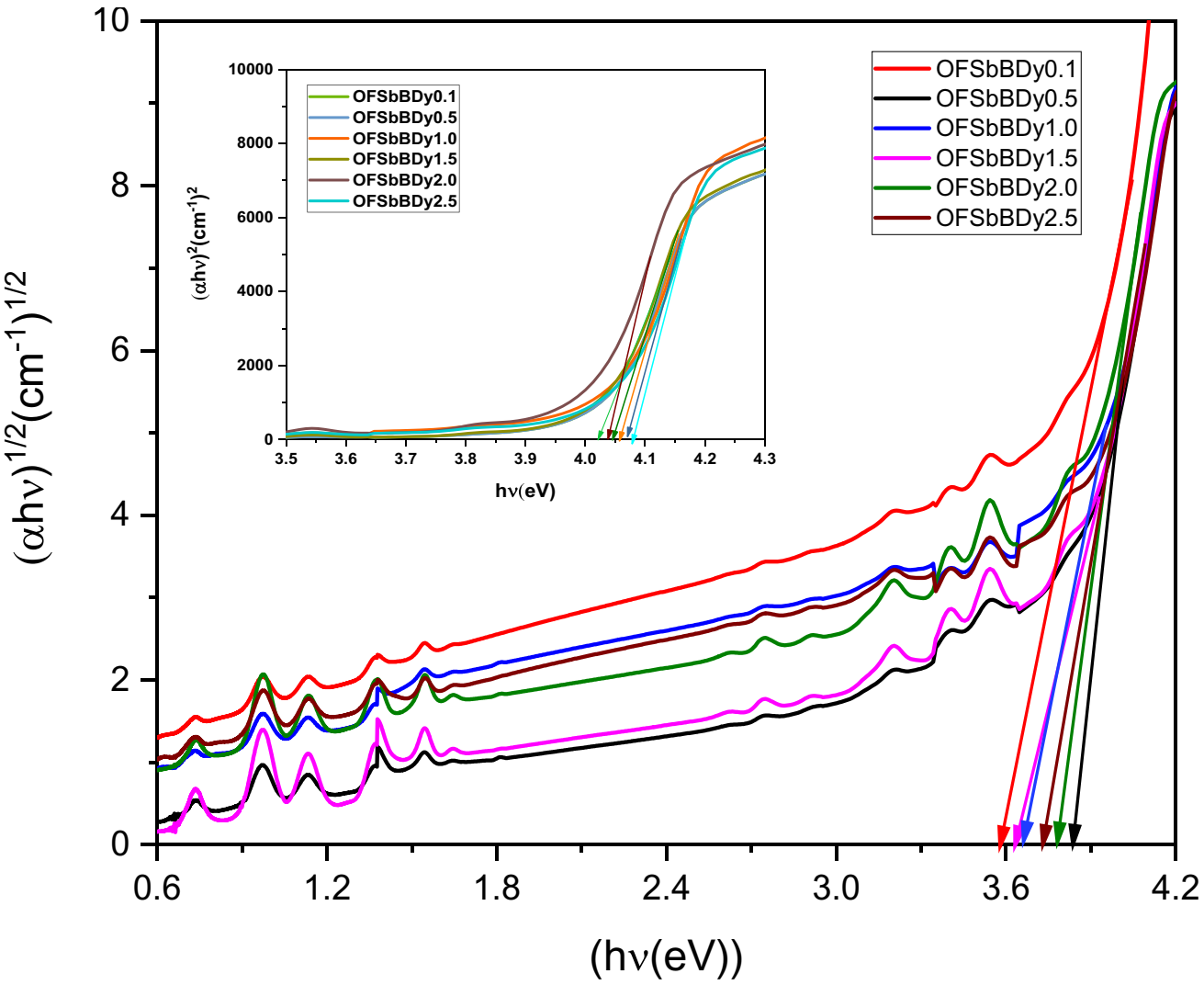


Fig. 4 The indirect band gap of Dy^{3+} ions doped OFSbB glass samples. The inset shows direct band gap of Dy^{3+} ions doped OFSbB glass samples

Table 2 The oscillator strength (f_{exp} and f_{cal} X 10^{-6}), rms deviation ($\delta_{rms} \times 10^{-6}$) of the OFSbBDy glasses for different absorption bands

Transition	OFSbBDy0.1		OFSbBDy0.5		OFSbBDy1.0		OFS-bBDy1.5		OFS-bBDy2.0		OFS-bBDy2.5	
$^6H_{15/2} \rightarrow$	f_{exp}	f_{cal}	f_{exp}	f_{cal}	f_{exp}	f_{cal}	f_{exp}	f_{cal}	f_{exp}	f_{cal}	f_{exp}	f_{cal}
$^4M_{15/2}$	0.154	0.093	0.617	0.106	0.58	0.951	0.389	0.091	0.28	0.073	0.245	0.055
$^6P_{5/2}$	1.714	1.714	2.062	2.085	1.891	1.891	1.757	1.684	1.12	1.142	1.04	0.794
$^4I_{13/2}$	0.814	0.691	1.634	0.826	1.074	0.726	1.201	0.669	0.954	0.472	0.761	0.336
$^4G_{11/2}$	1.525	1.539	1.994	1.861	1.567	1.64	1.464	1.516	1.261	1.055	1.184	0.746
$^4I_{15/2}$	1.027	0.175	1.647	0.134	1.095	0.098	0.924	0.033	0.68	0.039	0.483	0.033
$^4F_{9/2}$	0.841	0.606	1.065	0.715	0.597	0.619	0.52	0.548	0.346	0.376	0.239	0.263
$^6F_{1/2}$	-	-	1.836	0	0.793	0	0.654	0	0.517	0	0.351	0
$^6F_{3/2}$	0.96	0.725	1.096	0.882	0.957	0.773	0.998	0.706	0.64	0.479	0.419	0.333
$^6F_{5/2}$	3.496	3.842	4.709	4.673	3.744	4.103	3.559	3.749	2.752	2.539	1.151	1.764
$^6F_{7/2}$	6.788	7.841	8.591	9.163	6.511	7.989	5.882	7.029	3.147	4.836	2.118	3.39
$^6F_{9/2}$	8.804	8.544	9.217	9.093	7.998	7.635	6.32	6.043	4.74	4.338	3.432	3.106
$^6F_{11/2}$	11.73	11.799	12.324	12.324	10.49	10.583	9.236	9.305	7.68	7.766	5.91	5.999
$^6H_{11/2}$	4.564	4.035	5.05	4.825	4.952	4.237	4.418	3.892	3.39	2.736	2.616	1.944
RMS(δ)	0.45		0.746		0.619		0.511		0.59		0.509	

The plank constant, electron mass, refractive index, and wavenumber (in cm^{-1}) are all represented here by h, m, n and ν respectively. The angular momentum from the ground start to the excited state is represented by J (J = L + S); the absorption band's Lorentz local field correction is $(n^2+2)^2/9n$; the host-dependent J-O intensity parameters and U^{λ} are the host-independent elements of the unit tensor square matrix. The following expression is used to evaluate the quality of fitting between the f_{exp} and f_{cal} data using root mean square deviation(δ_{rms}). The following expression is used to evaluate the quality of fitting between the f_{exp} and f_{cal} data using δ_{rms}.

$$\delta_{rms} = \sqrt{\frac{\sum \left(f_{exp} - f_{cal}\right)^2}{N}} \tag{6}$$

where N represents the level. Table 2 shows the f_{exp}, f_{cal} and δ_{rms} values of the as prepared glass samples. The three calculated J-O intensities $\Omega_{\lambda}(\lambda = 2,4,6)$ parameters are shown in Table 3. The parameters demonstrate nature of the local arrangement and bonding nature of the RE ions. From the Table 3, the evaluated Ω_{λ} values results the same trend ($\Omega_2 > \Omega_6 > \Omega_4$) for all the titled glasses. From Jorgensen and Reisfeld theory [34], the covalent valence of the metal–ligand bond and the asymmetry of the ion sites in the ligand field around the Dy^{3+} ions affect the Ω_2 parameter, while Ω_4 and Ω_6 depend on the viscosity of the medium and rigidity of medium. The Ω_6 specifies the rigidity and a lower polarizability. Moreover, the determined Ω_6 value indicates strong ionic network coupling and also results merging the opposite similarity energy levels. This remains vital increase to emission intensity the Dy^{3+} ions and keeps the thermal stresses low in order to achieve the thermal equilibrium of the quantum efficiency. The large value of Ω_2 comparing with the Ω_6 indicates the large asymmetry around the Dy^{3+} ions and closes the binding of the ligand ions. Moreover, the Ω_2 value highly depends upon the sensitive transitions and

Table 3 Comparison of J-O intensity parameters (Ω_2, Ω_4, $\Omega_6 \times 10^{-22}$ cm^2) between OFSbBDy glasses and different reported Dy^{3+} ions doped glasses

Glass system	Ω_2	Ω_4	Ω_6	Trend	References
OFSbBDy0.1	572.59	299.74	530.97	$\Omega_2 > \Omega_6 > \Omega_4$	Present work
OFSbBDy0.5	672.23	219.89	652.8	$\Omega_2 > \Omega_6 > \Omega_4$	Present work
OFSbBDy1.0	609.98	157.3	575.25	$\Omega_2 > \Omega_6 > \Omega_4$	Present work
OFSbBDy1.5	629.11	36.39	531.38	$\Omega_2 > \Omega_6 > \Omega_4$	Present work
OFSbBDy2.0	531.4	53.85	365.75	$\Omega_2 > \Omega_6 > \Omega_4$	Present work
OFSbBDy2.5	412.76	47.77	255.57	$\Omega_2 > \Omega_6 > \Omega_4$	Present work
LBGS0.5Dy	832	214	275	$\Omega_2 > \Omega_6 > \Omega_4$	[35]
Lead fluorophosphate glass	712	159	220	$\Omega_2 > \Omega_6 > \Omega_4$	[19]
oxyfluoride glass	641	102	225	$\Omega_2 > \Omega_6 > \Omega_4$	[36]
TSWD5	1220.2	264.4	337.5	$\Omega_2 > \Omega_6 > \Omega_4$	[37]
BTLN0.5D	632.9	171.5	114.1	$\Omega_2 > \Omega_6 > \Omega_4$	[38]

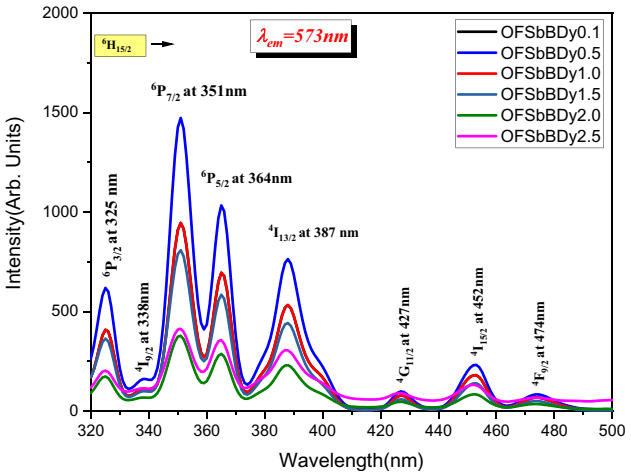


Fig. 5 The excitation spectra of Dy^{3+} ion doped OFSbB glass samples

provides the information on the nature of the Dy-O bonds. Higher oscillator strengths of hypersensitive transitions lead to maximum values of Ω_2. The prepared glasses typically have Ω_2 values that lies between in the range of Ω_6 and Ω_4 for the oxyfluoride glass. As we see that Ω_2 increases until OFSbBDy0.5 glass greater and confirming the high asymmetry ligand field around the Dy^{3+} ions of the prepared glass. The J-O values results are compared with published work which is shown in Table 3 [19, 35–38].

Photoluminescence Spectra

PL spectral studies of the Dy^{3+} ions doped OFSbB glasses were recorded and which are represented in the Figs. 5 and 6. Figure 5 The excitation spectra were in the range of 320 nm to 500 nm, and the emission spectra (Fig. 6) were in the range of 450 nm to 750 nm. At an emission wavelength of 573 nm, the peaks of the excitation bands located at 325, 338, 351, 364, 387, 427, 452, and 474 nm were related to transitions from $^4M_{17/2}$, $^6P_{7/2}$, $^6P_{5/2}$, $^4I_{13/2}$, $^4G_{11/2}$, $^4I_{15/2}$, and $^4F_{9/2}$. Amongst these transitions, the $^6H_{15/2} \rightarrow {}^6P_{7/2}$ band at 351nm was relatively more intense than the other transitions. The results of the two highly intense bands at 480 nm(blue), 575 nm (yellow) and one less intense band at 663nm (red) corresponding to the transitions from the excited level $^4F_{9/2} \rightarrow {}^6H_{15/2}$, $^4F_{9/2} \rightarrow {}^6H_{13/2}$ and $^4F_{9/2} \rightarrow {}^4H_{11/2}$ respectively. The Fig. 7 represents the variation of emission intensities of OFSbBDy0.5 glass excited at different excitation wavelengths. From the emission spectra, it is observed that luminescence intensity increases up to 0.5 mol% of Dy_2O_3 and decreases beyond because of concentration quenching effect. The concentration quenching effect is the result of the Dy-Dy distance, which occurs with increasing Dy_2O_3 concentration. The reduction in Dy-Dy distance shows resonant energy transfer (RET), which is otherwise called "energy migration" and the cross-relaxation (CR) energy transfer process between Dy^{3+}

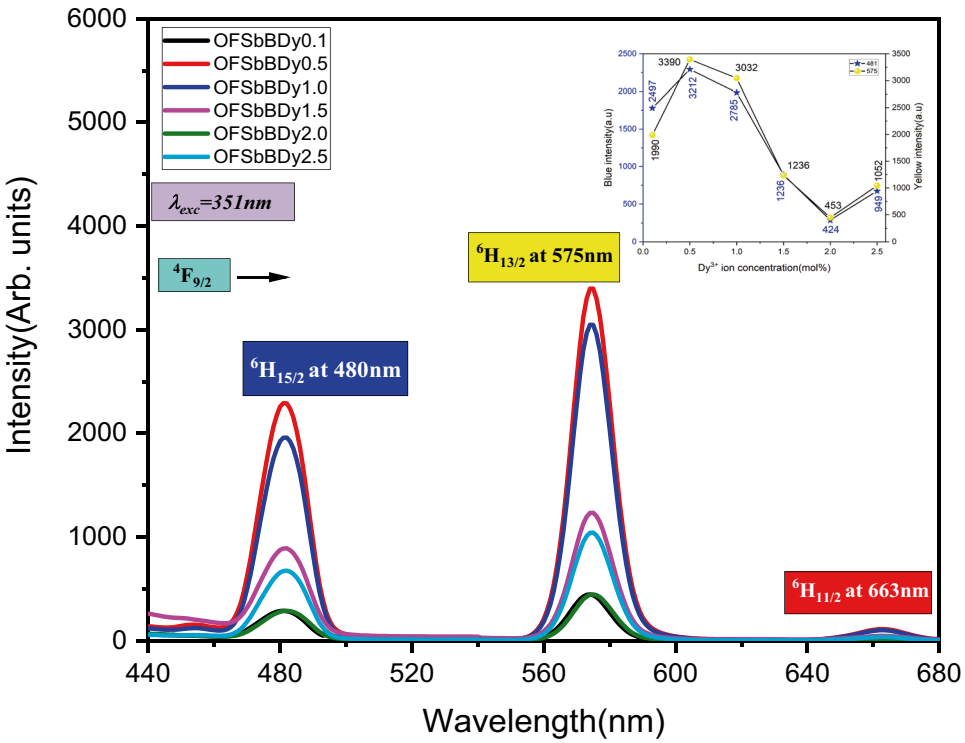


Fig. 6 The emission spectra of Dy^{3+} ion doped OFSbB glass at an excitation wavelength 351 nm. The inset shows the Yellow-blue (Y/B) intensity ratio of Dy^{3+} ions doped OFSbB glasses

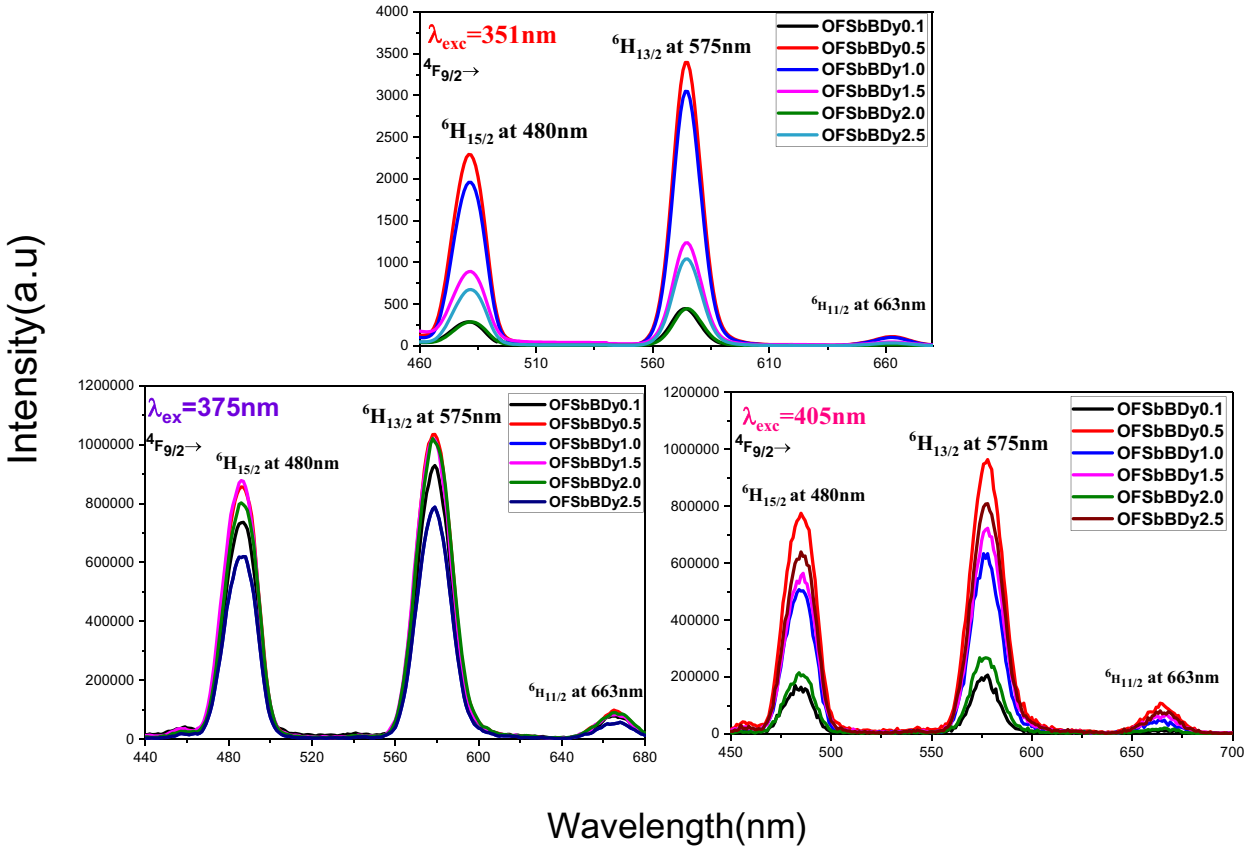


Fig. 7 The emission spectra of Dy^{3+} ion doped OFSbB glass at an excited at 351 nm,375 nm and 405 nm wavelengths

donor ions and acceptor ions. In Fig. 8, the Dy^{3+} ions partial energy level diagram and the RET, which corresponds to the PLE and PL transitions ($^6H_{15/2} \rightarrow {}^6H_{15/2}$: $^4F_{9/2}$) as well as CR ($^6H_{15/2} \rightarrow {}^6F_{5/2}$: $^6F_{9/2}$), ($^4F_{9/2}$: $^6H_{15/2} \rightarrow {}^6F_{3/2}$: $^6F_{11/2}$) [39].

Among all the above-mentioned transitions of the PL spectra, the transition at $^4F_{9/2} \rightarrow {}^6H_{15/2}$ is allowed magnetic dipole and the transition at $^4F_{9/2} \rightarrow {}^6H_{11/2}$ is forced electric dipole in nature [40]. The relationship between these two transitions indicates the nature of the dysprosium-oxygen bond by determining the ratio of yellow to blue, the degree of covalence between Dy-O ions increases with its value. In addition, for studying the symmetry shifts in Dy^{3+} ions, an important parameter is the yellow-to-blue intensity ratio (Y/B) which is shown inset of Fig. 6. The Y/B intensity ratios were 1.11,1.56,1.48,1.38,1.55, and 1.54, corresponding to the OFSbBDy0.1, OFSbBDy0.5, OFSbBDy1.0, OFSbBDy1.5, OFSbBDy2.0 and OFSbBDy2.5 glasses. The increase in the Y/B ratio indicated an increase in the covalent nature of the Dy-O bond. This indicates higher structural disorder around the Dy^{3+} ions [26, 27].

Radiative Properties

Following the expressions reported in the literature [41].The radiative properties have been calculated using J-O Parameters which includes effective bandwidths, radiative lifetimes (τ_R), radiative transition probabilities (A_R), Stimulated emission cross-sections (σ_{se}) and branching ratios (β_{exp}). The A_R values influenced by the J-O intensity parameters and the energy gap between the initial and terminal levels, to determine the radiative relaxation of an excited state to all its lower levels

$$\tau R = \frac{1}{A_\tau(\psi J)} \tag{7}$$

where A_T denotes the total probability of transition which is the summation of transition probability values for a potential transition. The branching ratio (β_R) is the basic parameter for the designing the laser since it portrays the chance of accomplishing the stimulated emission from any specific transition. The value for the potential laser activity must be greater than 0.5. The following expression can be used to determine the value of R from the total transition probability (A_T) that corresponds to the emission and excited level to the lower level

$$\beta_R = \frac{A_R(\psi J, \psi' J')}{A_T(\psi J)} \tag{8}$$

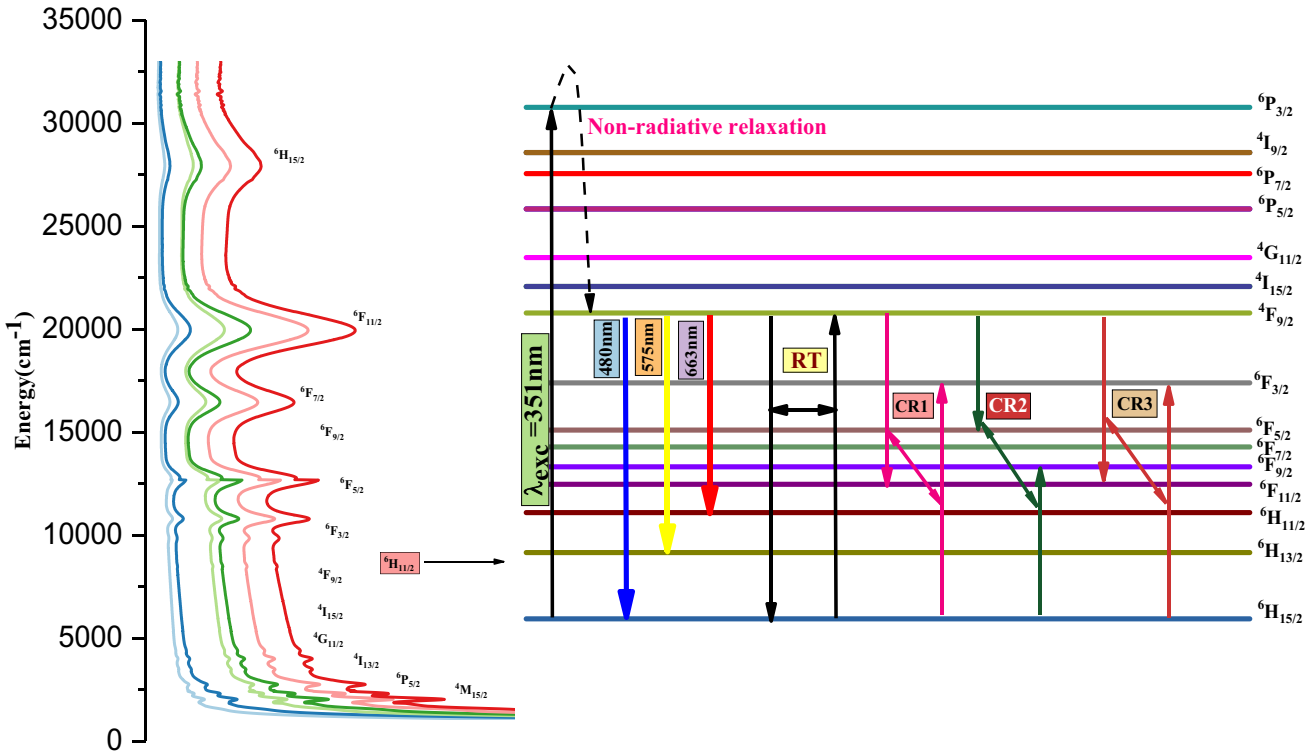


Fig. 8 The partial energy level diagram of Dy^{3+} ions doped OFSbB glass samples

The higher branching ratio of the $^4F_{9/2} \rightarrow {}^6H_{13/2}$ shift among the observed emission shifts indicates that it is suitable for its lasing action. From the Table 5, the observed β_{exp} values for each prepared glasses tend to be $^6H_{13/2} > {}^6H_{15/2} > {}^6H_{11/2}$ which indicates that yellow emission is predominant. As a result, the prepared glasses are promising materials for visible yellow laser applications. Laser execution is highly dependent upon the σ_{se} which lies between the primary level (ΨJ) and the concluding level (Ψ'J') with possibility A_R is calculated as follows

$$\sigma_{se}(\psi J, \psi' J') = \left(\frac{\lambda_p^4}{8\pi c n^2 \Delta\lambda_p}\right) A_R(\psi J, \psi' J') \quad (9)$$

where, λ_P is the emission lines peak wavelength and $\Delta_{\lambda eff}$ is the effective bandwidth of the emission band, The effective bandwidth is determined by integrating the luminescence line's intensity and dividing it by the intensity at the peak wavelength. The outcome for the radiative properties is recorded in Table 4. The optical gain bandwidth ($\sigma_{se} \times \Delta\lambda_p$) and optical gain ($\sigma_{se} \times \tau_R$) values fundamental for manufacturing lasers and optical materials [42]. For the $^4F_{9/2} \rightarrow {}^6H_{13/2}$ transition, OFSbBDy0.5 glass has relatively higher values for gain bandwidth and optical gain parameters than the other prepared glasses which is shown in Table 5, This indicates the suitability of OFSbBDy0.5 glass for the visible laser and fiber amplifiers. [30, 35, 43–49].

Photoluminescence Decay Analysis

With an excitation wavelength of 351nm and an emission wavelength of 575nm, the time decay profile for all the as

Table 4 The Radiative transition probability (A^{s-1}), radiative branching ratios (β_R) and stimulated emission cross-section (σ_{se}) (10^{-22} cm^2) for the emission transitions of Dy^{3+} ions doped OFSbB glasses

Glass system	Transition	A	β_R	σ_{SE}
OFSbBDy0.1	$^4F_{9/2} \rightarrow {}^6H_{11/2}$	288	0.05	0.325
	$^4F_{9/2} \rightarrow {}^6H_{13/2}$	3254	0.573	2.724
	$^4F_{9/2} \rightarrow {}^6H_{15/2}$	1528	0.269	0.886
OFSbBDy0.5	$^4F_{9/2} \rightarrow {}^6H_{11/2}$	321	0.05	0.366
	$^4F_{9/2} \rightarrow {}^6H_{13/2}$	3707	0.577	3.139
	$^4F_{9/2} \rightarrow {}^6H_{15/2}$	1775	0.276	1.041
OFSbBDy1.0	$^4F_{9/2} \rightarrow {}^6H_{11/2}$	287	0.051	0.329
	$^4F_{9/2} \rightarrow {}^6H_{13/2}$	3246	0.578	2.764
	$^4F_{9/2} \rightarrow {}^6H_{15/2}$	1533	0.273	0.904
OFSbBDy1.5	$^4F_{9/2} \rightarrow {}^6H_{11/2}$	275	0.054	0.319
	$^4F_{9/2} \rightarrow {}^6H_{13/2}$	3002	0.589	2.586
	$^4F_{9/2} \rightarrow {}^6H_{15/2}$	1533	0.263	0.8
OFSbBDy2.0	$^4F_{9/2} \rightarrow {}^6H_{11/2}$	223	0.058	0.263
	$^4F_{9/2} \rightarrow {}^6H_{13/2}$	2257	0.595	1.976
	$^4F_{9/2} \rightarrow {}^6H_{15/2}$	905	0.238	0.549
OFSbBDy2.5	$^4F_{9/2} \rightarrow {}^6H_{11/2}$	176	0.062	0.209
	$^4F_{9/2} \rightarrow {}^6H_{13/2}$	1668	0.59	1.467
	$^4F_{9/2} \rightarrow {}^6H_{15/2}$	631	0.223	0.384

Table 5 Emission peak wavelength(λ_p) (nm), effective band width ($\Delta\lambda_p$) (nm), stimulated emission cross-section (σ_{se}) (10^{-22} cm^2), gain band width (σ_{se} x $\Delta\lambda_p$) (10^{-28} cm^3) and optical gain (σ_{se} x τ_R) (10^{-25} cm^2 s) for the emission transitions of Dy^{3+}ions doped OFSbB glasses

Glass code	$^4F_{9/2} \rightarrow {}^6H_{15/2}$ (Blue)					$^4F_{9/2} \rightarrow {}^6H_{13/2}$ (Yellow)						$^4F_{9/2} \rightarrow {}^6H_{11/2}$ (Red)			
	$\Delta\lambda_P$	σ_{SE}	σ_{SE} x $\Delta\lambda_P$	τ_R	σ_{SE} x τ_R	$\Delta\lambda_P$	σ_{SE}	σ_{SE} x $\Delta\lambda_P$	τ_R	σ_{SE} x τ_R	$\Delta\lambda_P$	σ_{SE}	σ_{SE} x $\Delta\lambda_P$	τ_R	σ_{SE} x τ_R
OFSbBDy0.1	3.84	0.886	3.402	176	1.559	5	2.724	13.62	176	4.794	5.25	0.325	1.706	176	0.572
OFSbBDy0.5	5	1.041	5.205	155	1.613	5.55	3.139	17.421	155	4.865	6.25	0.366	2.287	155	0.567
OFSbBDy1.0	5	0.904	4.52	178	1.609	3.84	2.764	10.613	178	4.919	4.17	0.329	1.371	178	0.585
OFSbBDy1.5	5.55	0.8	4.44	196	1.568	5	2.586	12.93	196	5.068	4.55	0.319	1.451	196	0.625
OFSbBDy2.0	5	0.549	2.745	263	1.443	3.57	1.976	7.054	263	5.196	5.55	0.263	1.459	263	0.691
OFSbBDy2.5	5	0.384	1.92	353	1.355	4.54	1.467	6.660	353	5.178	5.55	0.209	1.159	353	0.737

prepared samples that correspond to the $^4F_{9/2}$ state was taken into consideration. As can be seen in Fig. 9, the time decay profile of each Dy^{3+} ions doped glass sample contained only one exponential and the estimated values for the decay time. Due to the concentration quenching effect, it was discovered that the time decay values decreased as Dy^{3+} ions concentration increased [50]. Using the following the expressions reported in the literature [41], the experimental lifetimes of the as prepared glasses are calculated by fitting the decay profiles by using following equation

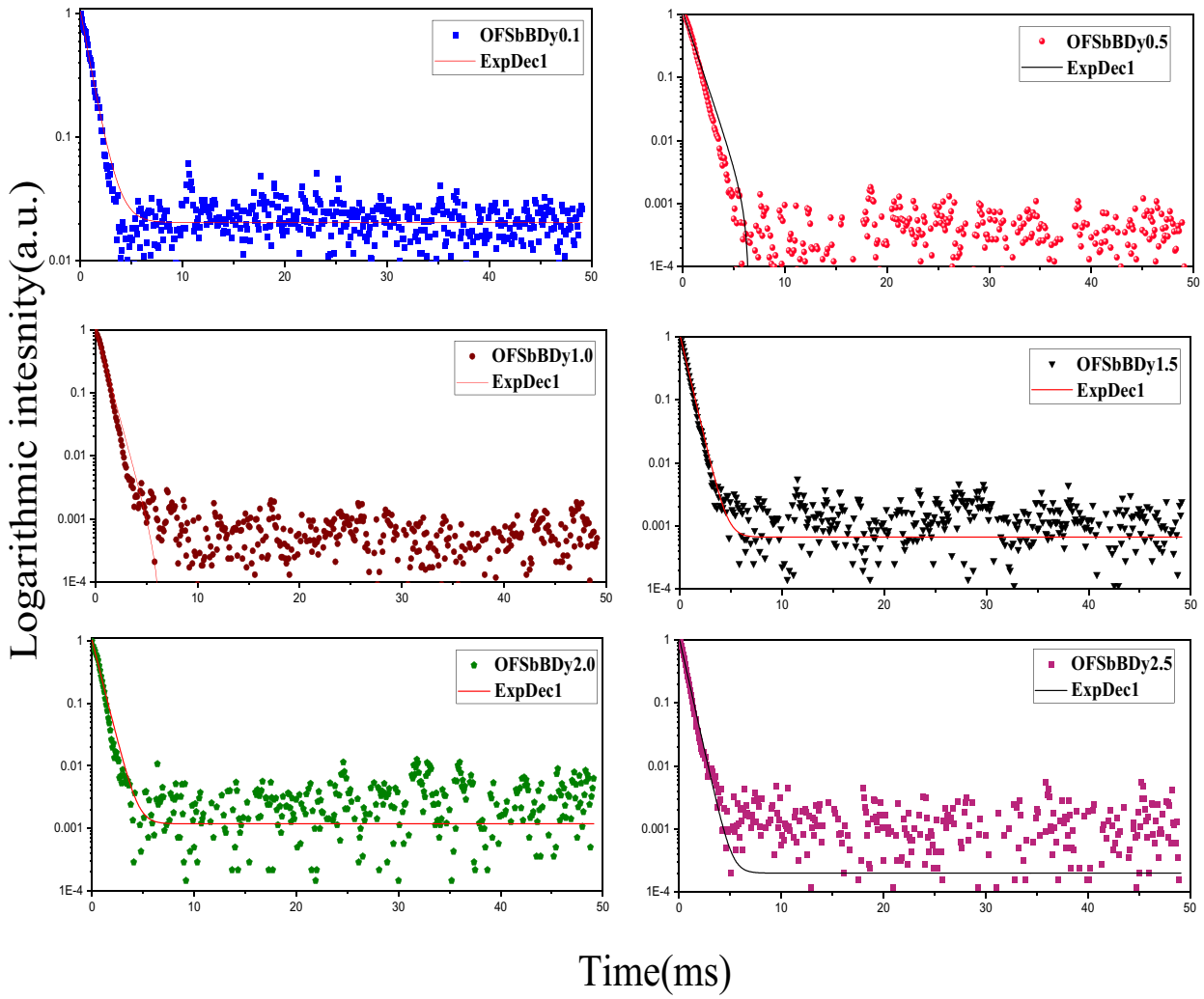


Fig. 9 The decay curves of Dy^{3+} ions doped OFSbB glass samples

$$I_t = I_o e^{\frac{t}{\tau_{exp}}} \tag{10}$$

where I_t and I_o represent the intensities of emission for decay curves at t = 0 and t = t respectively. With an increase in the concentration of the Dy^{3+} ions, the experimental lifetime values of the $^4F_{9/2}$ level are 140, 135, 115, 105, 95 and 84(μs) corresponding to OFSbB0.1, OFSbB0.5, OFSbB1.0, OFSbB1.5, OFSbB2.0, and OFSbB2.5, respectively. The determined radiative lifetimes are opposing more from the experimental lifetimes which is due to non-radiative transition in the glass. The quantum efficiency (η) is the ratio of number photons emitted to the photons observed. For RE ions doped glasses, the quantum efficiency is expressed as

$$\eta = \frac{\tau_{exp}}{\tau_R} x100 \tag{11}$$

The η values are decrease with increase in Dy^{3+} ions concentration due to increase of non-radiative transition rates. These rates can be calculated by difference of inverses of experimental and radiative lifetime value:

$$W_{NR} = \frac{1}{\tau_{exp}} - \frac{1}{\tau_{rad}} \tag{12}$$

The determined values of the quantum efficiency and W_{NR} are of prepared glasses are tabulated in the Table 6 and compared with reported values. The W_{NR} values of OFSbBDy0.5 are minimum which is evidently the OFSbBDy0.5 possess higher stimulated emission cross section and quantum efficiency.

Commission Intermediate de l' Elcairage (CIE) Chromaticity Coordinates.

The combination of two intense emissions (blue and yellow) in the visible region can generate white light, which was analyzed using the Commission Internationale de l'Eclairage (CIE) to obtain color coordinates. Slightly emission color is labeled using color identical function (X, Y, Z) besides the color of the spectral power density P(λ) must match the simulation for each of the three primary colors. The tristimulus values are used to calculate the chromaticity coordinates x and y using the equations.

$$x = \frac{X}{(X+Y+Z)} \cdots ; \cdots = \frac{Y}{(X+Y+Z)} \text{ and } z = \frac{Z}{(X+Y+Z)} \tag{13}$$

As a result, the coordinates for white-light emission are close to the center of the chromaticity diagram. Plots of the CIE chromaticity diagram was made for each prepared glass sample in relation to various excitation wavelengths. Figures 10 and 11 depicts the CIE diagram for the OFSbBDy0.5 sample with various excitations, as well as the CIE diagram for all samples with an excitation wavelength of 351nm. In comparison to the other excitations, the OFSbBDy0.5 sample produce the significant near-white light emission for the 351nm excitation. The emission from Dy^{3+} ions-doped glasses as depicted by the corresponding CIE coordinates (x,y) in Table 7 which suggests their potential use as materials for w-LEDs applications.

McCamy proposed a third-order polynomial equation for calculating CCT from CIE 1931 color coordinates in order to examine the quality of any light source in terms of correlated color temperature. This equation reduces the specification of white color from two dimensions (CIE diagram) to one dimension [51].

Table 6 Experimental lifetimes (τ_{exp}), radiative lifetimes (τ_R), quantum efficiency (η) and non-radiative decay rates (W_{NR}) of $^4F_{9/2} \rightarrow {}^6H_{13/2}$ transition of OFSbBDy glasses along with reported other glasses.

Glass system	τ_{exp}(μs)	τ_R (μs)	η(%)	W_{NR} (s^{-1})	References
OFSbBDy0.1	140	176	79.54	1461	Present work
OFSbBDy0.5	135	155	87.09	955	Present work
OFSbBDy1.0	115	178	64.6	3077	Present work
OFSbBDy1.5	105	196	53.57	4421	Present work
OFSbBDy2.0	95	263	36.12	6724	Present work
OFSbBDy2.5	84	353	23.79	9071	Present work
BTKA0.5D	461	1160	39.4	1310	[47]
TWZDy0.5D	145	-	54	447	[48]
BTLNDy0.5	414	1043	45	1457	[38]
DZCTFB0.5	340	515	66	999	[49]

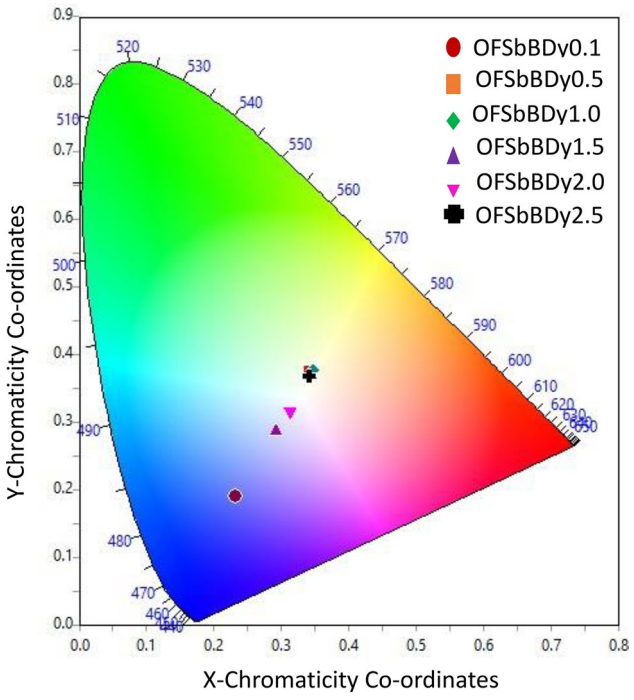


Fig. 10 CIE 1931 chromaticity diagram of Dy^{3+} ions doped OFSbB glass samples

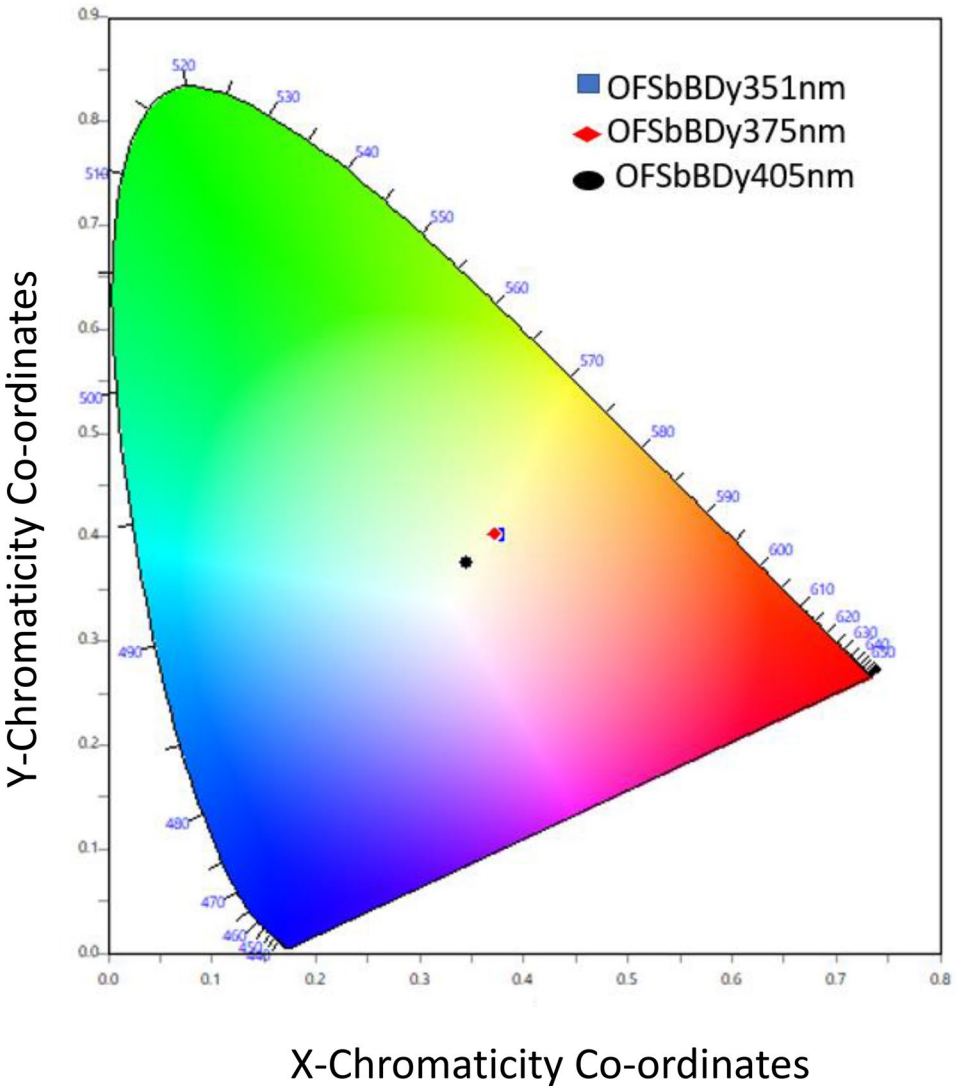


Fig. 11 CIE profile for Dy series at different excitation wavelengths

$$CCT = -49n^2 + 352n^2 - 682n + 5520.33 \quad (14)$$

The reciprocal slope is given by $n = (x - x_e)/(y - y_e)$ and the convergence epicenter is given by $x_e = 0.332$, $y_e = 0.186$ respectively. In most cases, the CCT values can be used to identify white light. If CCT value ≤ 3700 K, it corresponds to emission which represent warm and the emission color is pure for CCT values between 3700 and 5000K, it is considered as pure and below 5000 K, it is considered cooler. Hence, it is noteworthy that the CCT values estimated in Tables 8 and 9 for the OFSbBDy0.5 sample excited at wavelength of 351nm were found to be pure white light.

Gamma Radiation Shielding Properties

Web-based software.

Photon shielding and dosimetry (PSD) software is a user-friendly online software program accessible on https://phy-x.net/PSD, which was established used for to calculate the parameters related to shielding and dosimetry. Depending on the number of calculations, it produces results on a NodeJS platform in a reasonable amount of time. The software generates data on radiation shielding parameters by selecting two energies that have been defined in the software namely 0.0015MeV-15MeV & 1keV to 100GeV. In addition, the software includes a number of well-known radioactive sources (^{22}Na, ^{55}Fe, ^{60}Co, ^{109}Cd, ^{131}I, ^{133}Ba, ^{137}Cs, ^{152}Eu, & ^{241}Am), as well as their energies and some characteristic like K-shell X-ray energies for Rb, Mo, Ag, Cu, Ba & Tb elements, which the user can select. The parameters include the mass attenuation coefficient, linear attenuation coefficient, half-value layer, tenth value layer, effective atomic number, mean free path, effective conductivity, electron density, energy absorption, and exposure buildup factor.

Table 7 CIE Chromaticity coordinates (X and Y) and Y/B ratios of Dy^{3+} ions doped OFSbB glasses excited at 351nm wavelength.

Glass Code	Y/B ratio	Chromaticity co-ordinates		CCT(K)
		x	y	
OFSbBDy0.1	1.11	0.2826	0.2992	9225
OFSbBDy0.5	1.56	0.3434	0.3724	5122
OFSbBDy1.0	1.48	0.3477	0.3769	4989
OFSbBDy1.5	1.38	0.2921	0.2871	8844
OFSbBDy2.0	1.55	0.3131	0.3161	6589
OFSbBDy2.5	1.54	0.3422	0.3674	5152

Table 9 Comparison of CIE Chromaticity coordinates (X and Y) and Y/B ratios of OFSbBDy glasses with other reported Dy^{3+} doped glasses.

Glass code	Y/B	Chromaticity coordinate		CCT(K)	References
		x	y		
OFSbBDy0.5	1.56	0.34	0.37	5122	PW
LBGS0.5Dy	1.66	0.41	0.42	3621	[35]
BTSrZofDy0.5	1.76	0.32	0.35	5841	[46]
BiNFB0.5Dy	-	0.37	0.38	4144	[44]
NbFSDy	0.82	0.33	0.37	5593	[30]

Gamma Ray-radiation Shielding Parameters Fundamental Relations: By following the Beer-Lambert's law, reduces the intensity of the beam when a material with the thickness "x" is placed in the path of a monoenergetic x-ray and gamma ray beam.

$$I = I_0 e^{-\mu x} \tag{15}$$

where I_0 and I are the intensities prior to and following attenuation, respectively; x is the thickness of the sample; and μ is the Linear Attenuation Coefficient cm^{-1} (LAC). LAC is important because it describes the material interaction with radiation and it quantifies how much radiation is absorbed/scattered as it passes through the material.

The mass attenuation coefficient (MAC) is an important parameter for calculating the radiation shielding parameters. Understanding behavior of radiation and developing new applications for radiation-based new technologies require the MAC. It is used to evaluate the probability of interaction of the photons with the glass sample. It is theoretically calculated by using mixture rule [52].

$$MAC_{(\mu_m)} = \mu/\rho = \Sigma_i w_i (\mu/\rho)_i \tag{16}$$

Here, $(\mu/\rho)_i$ and w_i are the photon mass attenuation coefficient and weight fraction of the element and the "i" is obtained from the aforementioned software.

The material's thickness level in cm is referred to as the half-value layer (HVL). which can reduce the incoming radiation to half of its initial value [53, 54]. The low HVL value implies many interactions of gamma rays with the sample; thus, the prepared sample has better gamma ray shielding effectiveness. HVL is likewise to another parameter called the Mean Free Path (MFP), which characterizes the typical distance went by a photon in the medium before the interaction happens. The following equations can be used to determine the HVL and MFP:

$$HVL = \frac{0.693}{\mu} \tag{17}$$

and,

$$MFP = \frac{1}{\mu} \tag{18}$$

where, μ is the Linear Attenuation Coefficient "which is equal to the MAC x density of the prepared sample."

The effective atomic number (Z_{eff}) was used to calculate the shielding characteristics of the materials. Z_{eff} can be calculated using the following equation [55, 56].

$$Z_{eff} = \frac{\sigma_{t,a}}{\sigma_{t,el}} \tag{19}$$

Here,

$$\sigma_{t,a} = \frac{\mu/\rho}{N_A \Sigma_i (\frac{W_i}{A_i})} \cdots ; \cdots \sigma_{t,el} \frac{1}{N_A} \Sigma_i \frac{f_i A_i}{Z_i} (\mu/\rho)$$

Table 8 CIE Chromaticity coordinates (X and Y) and Y/B ratios of OFSbBDy0.5 glasses at different excitation wavelengths.

Glass Code	Excitation(nm)	Y/B ratio	Chromaticity Co-ordinates		CCT(K)
			x	y	
OFSbBDy0.5	351	1.56	0.3434	0.3724	5122
OFSbBDy0.5	375	0.116	0.3746	0.4026	4320
OFSbBDy0.5	405	1.24	0.3717	0.4031	4397

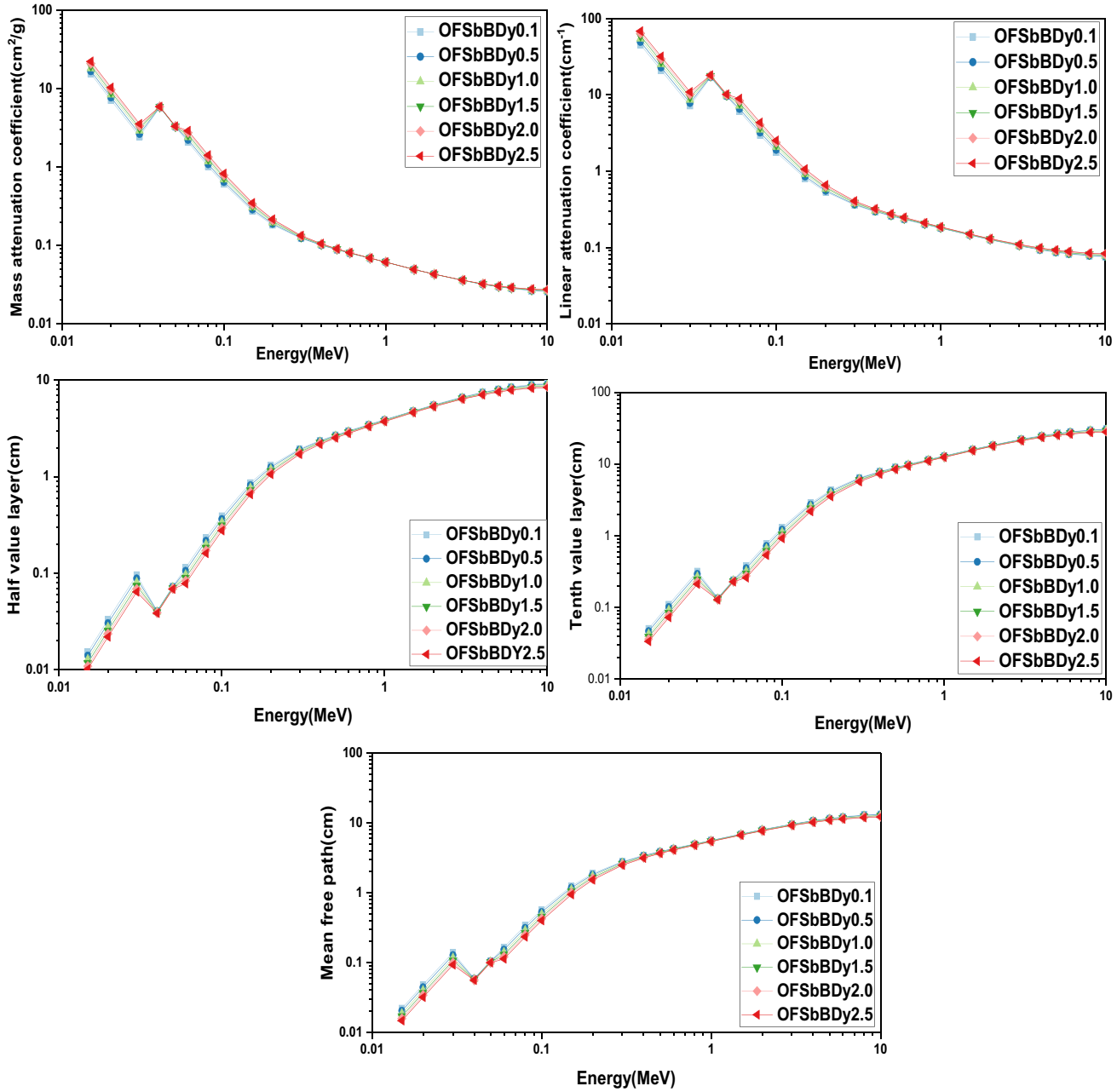


Fig. 12 The variation of mass attenuation coefficient, linear attenuation coefficient, half value layer, tenth value layer, Mean free path of the prepared OFSbBDy glasses

Where, A_i is atomic weight of the i^{th} element, N_A is Avogadro's number, f_i & Z_i are fractional abundance & atomic number respectively of the i^{th} element.

In high-energy radiation fields, where the radiation buildup can be significant, exposure buildup factor (EBF) plays crucial role. Also, the EBF is an essential parameter for estimating the distribution of photons in an illuminated medium [57]. The ability of the EBP is to predict the dose rate at a specific point behind a shield. The EBP was calculated using the following steps:

(a) Finding the equivalent atomic number (Zeq)
(b) Finding the G-P fitting parameters (b,c,a,Xk & d)
(c) Finding the exposure buildup factor EBF.

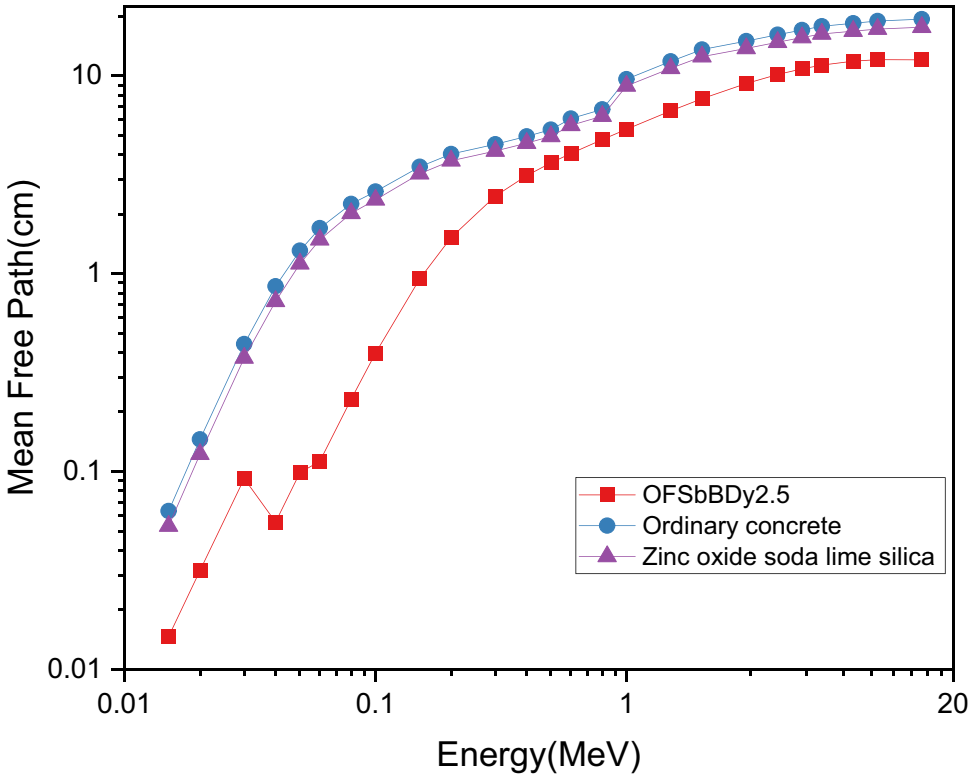


Fig. 13 Mean Free Path for prepared glass in comparison with ordinary concrete and zinc oxide soda lime silica

Results

The gamma-ray shielding parameters of the prepared glasses were measured for incident photon energy 0.015-15MeV

Figure 12. The variation of MAC, LAC, HVL, TVL and MFP of the prepared OFSbBDy glasses. The decrease with increasing photon energy is owing to attenuators deeper penetration of photons. The fact that the change of the

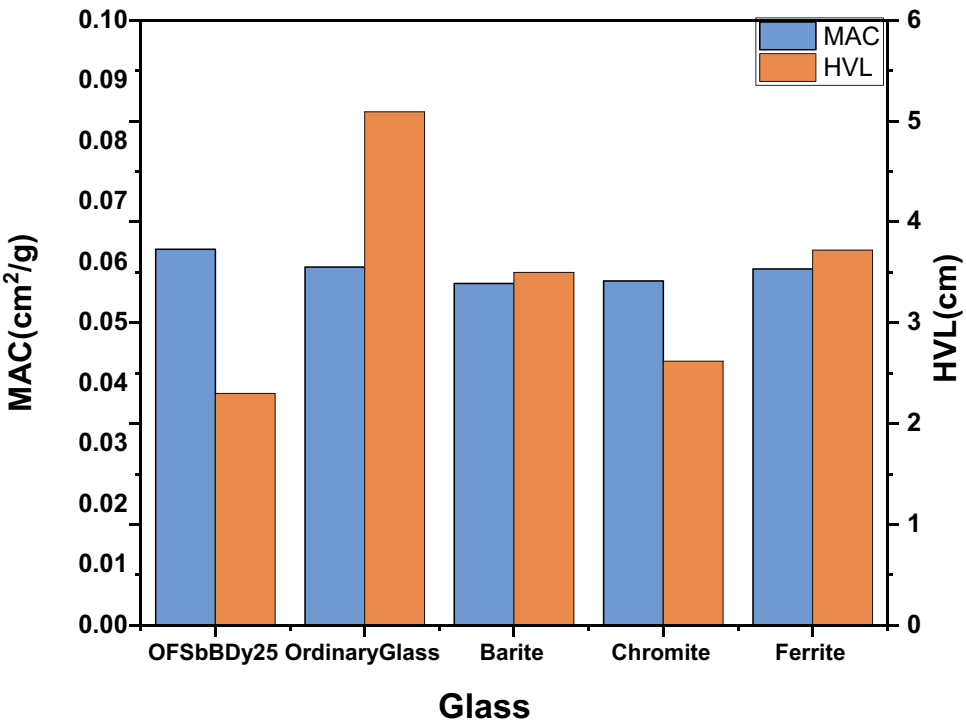


Fig. 14 Comparison of Mass Attenuation Coefficient (MAC) (cm^2/g) and Half Value Layer (HVL) (cm) at 1173 keV of 2.5 mol% doped OFSbB glass with different concretes

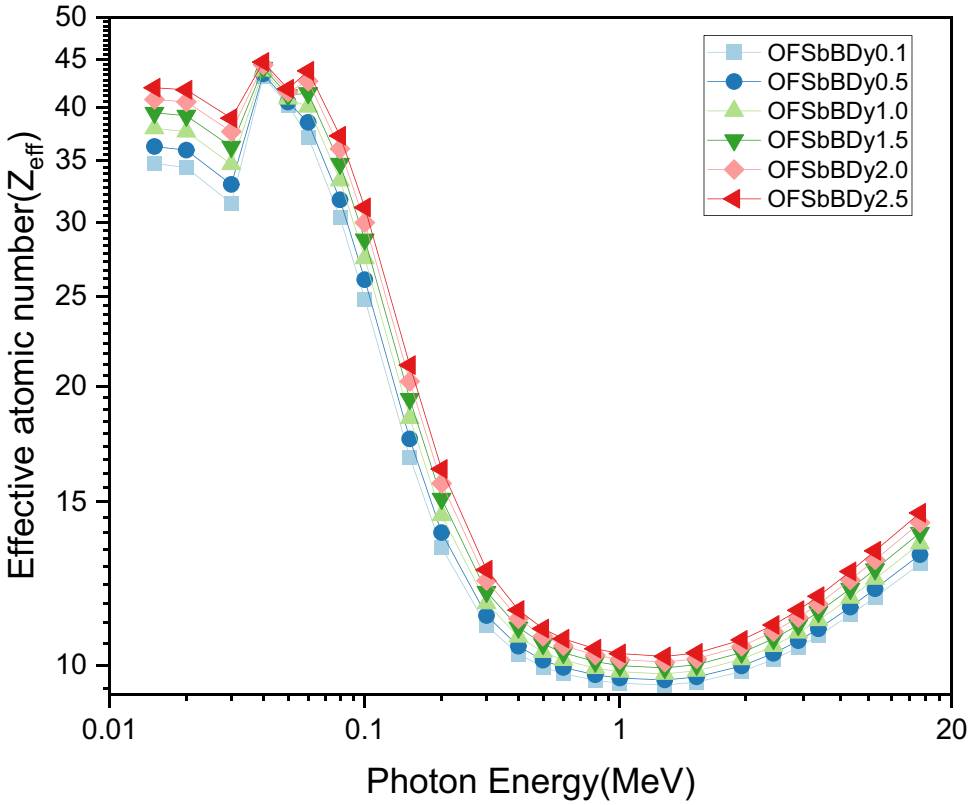


Fig. 15 The variation of the effective atomic number (Z_{eff}) with the photon energy for the OFSbBDy glasses

MAC values seen that the swift decrease at the range of 0.02–0.5MeV is due to photoelectric absorption (PE) which becomes dominant process. After a slight decrease in the range of 0.5-3MeV MeV, Compton scattering (CS) becomes the dominant process. Subsequently, the minor increase in the photon energy range of 4-15MeV was due to the pair production process (PP). The linear attenuation coefficient of the prepared glasses, which has a higher value in the lower-energy region and a lower value in the higher-energy region. The LAC results in a trend similar to of that the MAC. Hence, OFSbBDy2.5 glass had a higher shielding effectiveness than the others.

The HVL in the lower region is the same for all the samples; thereafter, an increase in the value, peak is observed in the range of 0.02–0.5MeV for all glass samples. The TVL results which exhibits the same trend as the HVL. The MFP exhibits a behavior similar to that of the HVL and TVL, which are independent in the lower region (0.01MeV) and dependent in the higher region(15MeV). The Mean Free Path values for the prepared glass samples, ordinary concrete [58], and zinc oxide soda-lime silica glass [59] are compared in Fig. 13. This clearly indicates that the prepared glass samples possessed better shielding properties. Furthermore, the results of MAC and HVL at 1173keV are also compared to those of other radiation shielding concretes (ordinary glass, barite, chromite and Ferrite) in order to provide a more conclusive picture of studied glasses attenuation capacity and the results are shown in Fig. 14 the OFSbBDy2.5 glass has a lower value than concrete, indicating that OFSbBDy glasses are better protection form γ-radiation.

For all prepared glass samples, the high Z_{eff} value is observed in low region and decreased with increases photon energy. Z_{eff} increases with increase in Dy_2O_3 content and it results that OFSbBDy2.5 can absorb high photon energy.

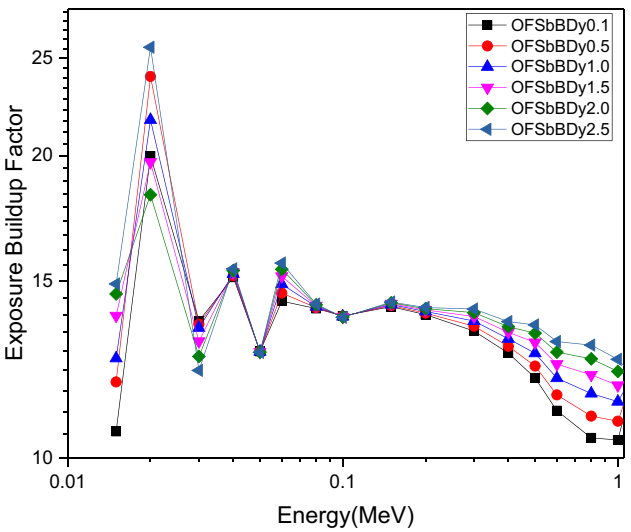


Fig. 16 The variation of the Exposure build factor with the photon energy for the OFSbBDy glasses

Figure 15 shows the variation of the effective atomic number (Z_{eff}) with the photon energy for the OFSbBDy glasses. From the Fig. 15 we can observe that high Z_{eff} was observed at 0.04MeV, where the photoelectric effect and predominant scattering is Compton. The interaction of cross-section, which is directly proportional to the atomic(Z) number, is the Compton scattering process. Consequently, it explains the change of the value in the lower region of Z_{eff}. However, Z_{eff} reaches its minimum value in the range of 1MeV to 5MeV. Finally, it remains constant after increase in photon energy hence the prepared glasses are competent shielding materials.

Figure 16 represents the variation of the Exposure build factor with the photon energy for the OFSbBDy glasses. Figure 17 shows the EBF values in the lower range (0.015–0.3MeV) are most unity for different penetration depths. As we observed that the sharp peak in the EBF values which can be attributed of k-edge absorption of the glass continents. The graph makes it abundantly clear that the prepared glasses' EBF increase with

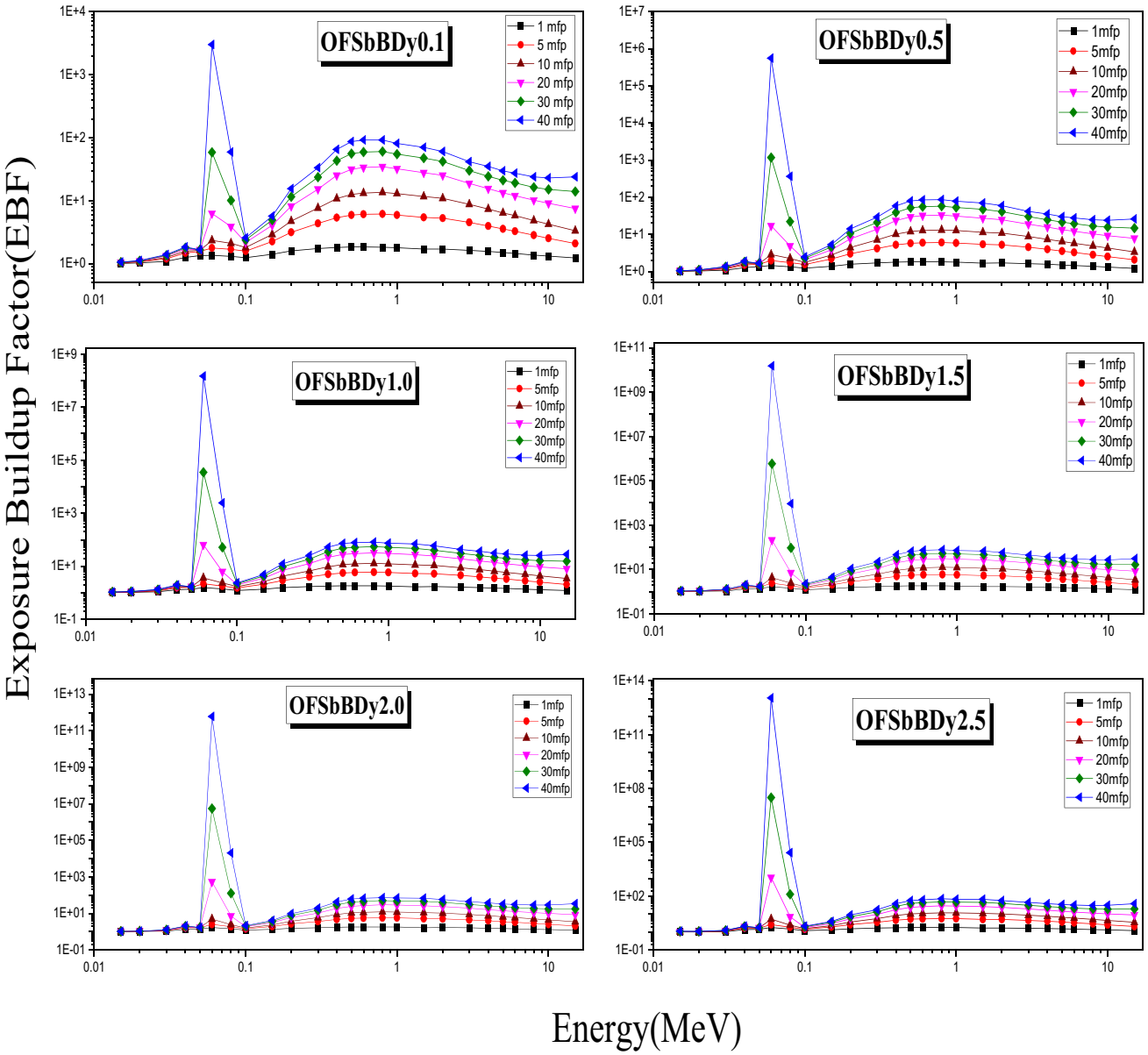


Fig. 17 The variation of the Exposure build factor with the photon energy for the OFSbBDy glasses

the mean free path. This also results increase of scattering events in target medium. Hence it results in large EBF values.

Conclusion

A series of Dy^{3+} ions doped antimony-oxyfluoro-borate glasses with a composition of $60B_2O_3$-$10Sb_2O_3$-$10Al_2O_3$-10NaF-(10-x) LiF-xDy_2O_3(x = 0.1,0.5,1.0,1.5,2.0,2.5mol%) were prepared by using the conventional melt quenching method in this study. Various characterization methods, including UV–Vis-NIR, FTIR, luminescence, time decay. The non-metallic nature of NBO and glasses is the result of significant changes in a number of physical parameters brought about by the incorporation of Dy^{3+} ions into the host. UV–Vis-NIR absorption spectra also reveals the other host-dependent transitions and an intense peak that is associated with a hypersensitive transition. The Judd–Ofelt theoretical calculations were used to determine the radiative parameters and efficiency. From the J-O analysis, it was found that the J-O parameters follow the order($\Omega_2 > \Omega_6 > \Omega_4$). The optical bandgap analysis was estimated using Tauc's method. Emission studies have been analyzed using the excitation wavelengths from 351 to 575nm. The glass containing 0.5mol% of Dy^{3+} ions produced intense light-like emission when excited at 351nm wavelength. In general, Dy^{3+} ions incorporated antimony-oxyfluoroborate glasses are potential candidates for white light emission applications. The radiation shielding parameters of the prepared OFSbBDy glasses were studied at various photon energies (0.015MeV-15MeV) using PSD software. The MAC, LAC, HVL, TVL, MFP of the prepared glasses results same trend. The prepared glass OFSbBDy2.5 sample is capable of better radiation absorption glasses than the ordinary concrete and some other glass systems. Hence the prepared glass samples are good for shielding materials as well as optical applications.

Acknowledgements The authors Dr. K.Swapna , Dr. Sk.Mahamuda, are very thankful for the support of Department of Science and Technology core research grant (DST-CRG), Government of India, New Delhi for the award of project (File number: CRG/2022/003549, DST-SERB), DST-FIST(Fund for Improvement of S&T Infrastructure in Universities) (Level-I), DST-Promotion of University Research and Scientific Excellence (PURSE), SR/PURSE/2023/196) to Department of Physics, and Department of Electronics and Communication Engineering (ECE), Koneru Lakshmaiah Education Foundation (SR/FST/PS-1/2018/35) and also thankful to the management of Koneru Lakshmaiah Education Foundation for the Full-Time Fellowship awarded to the Research Scholar, Ch. Pravallika (Regd. No: 2102520001) for her doctoral work.

Author Contributions All authors contributed to this manuscript, study conception and design. The first draft of the manuscript was written by Ch. Pravallika under the guidance of Dr. K. Swapna and all authors Ib Singh Deo, M. Venkateswarulu, Sk. Mahamuda, A. S. Rao, Vijaya Prakash. G, are worked for the Resources, Writing-Editing-Review of the manuscript. All authors read and approved the final manuscript.

Funding No financial funding.

Data Availability Not Applicable.

Declarations

Competing Interests The authors declare no competing interests.

Ethics Approval Not applicable.

Consent to Participate Not applicable.

Consent for Publication Not applicable.

Conflicts of Interest The authors have no conflict of interest in this research.

References

1. Tanabe S (1999) Optical transitions of rare earth ions for amplifiers: how the local structure works in glass. J Non Cryst Solids 259:1–9. https://doi.org/10.1016/S0022-3093(99)00490-1
2. Himamaheswara Rao V, Syam Prasad P, Mohan Babu M, Venkateswara Rao P, Satyanarayana T, Luís F, Veeraiah N (2018) Spectroscopic studies of Dy^{3+} ion doped tellurite glasses for solid state lasers and white LEDs. Spectrochim Acta A Mol Biomol Spectrosc 188:516–524. https://doi.org/10.1016/J.SAA.2017.07.013.
3. Reddy KS, Swapna K, Mahamuda SK, Venkateswarlu M, Rao AS, Prakash GV (2018) Investigation on structural and luminescence features of Dy^{3+} ions doped alkaline-earth boro tellurite glasses for optoelectronic devices. Opt Mater (Amst) 85:200–210. https://doi.org/10.1016/J.OPTMAT.2018.08.057.
4. Deopa N, Rao AS (2017) Spectroscopic studies of Sm^{3+} ions activated lithium lead alumino borate glasses for visible luminescent device applications. Opt Mater (Amst) 72:31–39. https://doi.org/10.1016/J.OPTMAT.2017.04.067
5. Lodi TA, Dantas NF, Gonçalves TS, de Camargo ASS, Pedrochi F, Steimacher A (2019) Dy^{3+} doped calcium boroaluminate glasses and Blue Led for smart white light generation. J Lumin 207:378–385. https://doi.org/10.1016/J.JLUMIN.2018.11.045
6. Rajesh D, Ratnakaram YC, Seshadri M, Balakrishna A, Krishna TS (2012) Structural and luminescence properties of Dy^{3+} ion in strontium lithium bismuth borate glasses. J Lumin 132:841–849. https://doi.org/10.1016/j.jlumin.2011.08.050.
7. Rashad M, Ali AM, Sayyed MI, Somaily HH, Algarni H, Rammah YS (2020) Radiation attenuation and optical features of lithium borate glasses containing barium: B_2O_3,Li_2O. BaO. Ceram Int 46:21000–21007. https://doi.org/10.1016/J.CERAMINT.2020.05.165.
8. Chanthima N, Kaewkhao J, Limkitjaroenporn P, Tuscharoen S, Kothan S, Tungjai M, Kaewjaeng S, Sarachai S, Limsuwan P (2017) Development of BaO–ZnO–B_2O_3 glasses as a radiation shielding material. Radiat Phys Chem 137:72–77. https://doi.org/10.1016/J.RADPHYSCHEM.2016.03.015
9. Bagheri R, Moghaddam AK, Yousefnia H (2017) Gamma ray shielding study of barium–bismuth–borosilicate glasses as transparent shielding materials using MCNP-4C Code, XCOM program, and available experimental data. Nucl Eng Technol 49:216–223. https://doi.org/10.1016/J.NET.2016.08.013.
10. Mahmoud KA, El-Agawany FI, Tashlykov OL, Ahmed EM, Rammah YS (2021) The influence of BaO on the mechanical and gamma / fast neutron shielding properties of lead phosphate glasses, Nuclear. Eng Technol 53:3816–3823. https://doi.org/10.1016/J.NET.2021.06.005

11. Sayyed MI (2017) half value layer, mean free path and exposure buildup factor for tellurite glasses with different oxide compositions. J Alloys Compd 695:3191–3197. https://doi.org/10.1016/J.JALLCOM.2016.11.318
12. Saleem SA, Jamalaiah BC, Jayasimhadri M, Rao AS, Jang K, Moorthy LR (2011) Luminescent studies of Dy^{3+} ion in alkali lead tellurofluoroborate glasses. J Quant Spectrosc Radiat Transf 112:78–84. https://doi.org/10.1016/J.JQSRT.2010.08.017.
13. Swapna K, Mahamuda S, Rao AS, Jayasimhadri M, Sasikala T, Moorthy LR (2013) Optical absorption and luminescence characteristics of Dy^{3+} doped Zinc Alumino Bismuth Borate glasses for lasing materials and white LEDs. J Lumin 139:119–124. https://doi.org/10.1016/J.JLUMIN.2013.02.035.
14. Mahamuda S, Swapna K, Packiyaraj P, Rao AS, Prakash GV (2014) Lasing potentialities and white light generation capabilities of Dy^{3+} doped oxy-fluoroborate glasses. J Lumin 153:382–392. https://doi.org/10.1016/J.JLUMIN.2014.03.009.
15. Toufik SM, Soltani MT, Djouama T, Boutarfaia A, Poulain M (2009) New heavy metal oxide glasses based on Sb_2O_3 New heavy metal oxide glasses based on Sb_2O_3. J Optoelectron Adv Mater Symp 1:339–342
16. Deopa N, Rao AS (2018) Spectroscopic studies of single near ultraviolet pumped Tb^{3+} doped Lithium Lead Alumino Borate glasses for green lasers and tricolour w-LEDs. J Lumin 194:56–63. https://doi.org/10.1016/J.JLUMIN.2017.09.057
17. Scholze H (2012) Glass: nature, structure, and properties. https://books.google.com/books?hl=en&lr=&id=aNTcBwAAQBAJ&oi=fnd&pg=PR5&ots=Z2rVtkxSIf&sig=fG5VF4R3LQhYr0lypHbXZTi1OWQ
18. Liu R, Chen M, Zhu X, Zhou Y, Zeng F, Su Z (2020) Luminescent properties and structure of Dy^{3+} doped germanosilicate glass. J Lumin 226:117378. https://doi.org/10.1016/J.JLUMIN.2020.117378
19. Kesavulu CR, Jayasankar CK (2011) White light emission in Dy^{3+}-doped lead fluorophosphate glasses. Mater Chem Phys 130:1078–1085. https://doi.org/10.1016/J.MATCHEMPHYS.2011.08.037
20. Şakar E, Özpolat ÖF, Alım B, Sayyed MI, Kurudirek M (2020) Phy-X / PSD: Development of a user-friendly online software for calculation of parameters relevant to radiation shielding and dosimetry. Radiat Phys Chem 166:108496. https://doi.org/10.1016/J.RADPHYSCHEM.2019.108496
21. Dahiya MS, Khasa S, Agarwal A (2015) Optical absorption and heating rate dependent glass transition in vanadyl doped calcium oxy-chloride borate glasses. J Mol Struct 1086:172–178. https://doi.org/10.1016/J.MOLSTRUC.2015.01.023
22. Gautam C, Yadav AK, Singh AK (2012) A Review on Infrared Spectroscopy of Borate Glasses with Effects of Different Additives. ISRN Ceram 2012:1–17. https://doi.org/10.5402/2012/428497
23. Moustafa ES, Saddeek YB, Shaaban ER (2008) Structural and optical properties of lithium borobismuthate glasses. J Phys Chem Solids 69:2281–2287. https://doi.org/10.1016/J.JPCS.2008.04.020
24. Garrett DE (1998) Uses of Borates, Borates. 401–429. https://doi.org/10.1016/B978-012276060-0/50010-3.
25. Doweidar H, Saddeek YB (2009) FTIR and ultrasonic investigations on modified bismuth borate glasses. J Non Cryst Solids 355:348–354. https://doi.org/10.1016/J.JNONCRYSOL.2008.12.008
26. Ahamed SZ, Reddy CM, Raju BD (2013) Structural, thermal and optical investigations of Dy^{3+} ions doped lead containing lithium fluoroborate glasses for simulation of white light. Opt Mater (Amst) 35:1385–1394. https://doi.org/10.1016/J.OPTMAT.2013.02.006.
27. Carnall WT, Fields PR, Rajnak K (2003) Electronic Energy Levels in the Trivalent Lanthanide Aquo Ions. I. Pr^{3+}, Nd^{3+}, Pm^{3+}, Sm^{3+}, Dy^{3+}, Ho^{3+}, Er^{3+}, and Tm^{3+}. J Chem Phys 49:4424. https://doi.org/10.1063/1.1669893.
28. Jørgensen CK, Judd BR (2006) Hypersensitive pseudo quadrupole transitions in lanthanides 8:281–290. https://doi.org/10.1080/00268976400100321
29. Maheshvaran K, Marimuthu K (2011) Structural and optical investigations on Dy^{3+} doped boro tellurite glasses. J Alloys compd 509:7427–7433. https://doi.org/10.1016/J.JALLCOM.2011.04.055
30. Mariyappan M, Arunkumar S, Marimuthu K (2017) White light emission and spectroscopic properties of Dy^{3+} ions doped bismuth sodium fluoroborate glasses for photonic applications. J Alloys Compd 723:100–114. https://doi.org/10.1016/J.JALLCOM.2017.06.244
31. Mott NF, Davis EA (2012) Electronic processes in non-crystalline materials. https://books.google.co.in/books?hl=en&lr=&id=Pl1b_yhKHYC&oi=fnd&pg=PP1&dq=N.F.+Mott,+E.A.+Davis,+Electronic+processes+in+NonCrystalline+Materials,+Second+ed.,+Clarendon+Press,+Oxford,+1979&ots=d7yZhGG4Xe&sig=SjdScfy6fPkFUTVg_NnGrDQTMDQ.
32. Judd BR (1962) Optical Absorption Intensities of Rare-Earth Ions. Phys Rev 127:750. https://doi.org/10.1103/PhysRev.127.750
33. Opelt GS (2004) Intensities of Crystal Spectra of Rare-Earth Ions. J Chem Phys 37:511. https://doi.org/10.1063/1.1701366
34. Jørgensen CK, Reisfeld R (1983) Judd-Ofelt parameters and chemical bonding. J Less Common Met 93:107–112. https://doi.org/10.1016/0022-5088(83)90454-X
35. Khan I, Rooh G, Rajaramakrishna R, Srisittipokakun N, Wongdeeying C, Kiwsakunkran N, Wantana N, Kim HJ, Kaewkhao J, Tuscharoen S (2019) Photoluminescence and white light generation of Dy_2O_3 doped Li_2O-BaO-Gd_2O_3- SiO_2 for white light LED. J Alloys Compd 774:244–254. https://doi.org/10.1016/j.jallcom.2018.09.156
36. Klimesz B, Dominiak-Dzik G, Żelechower M, Ryba-Romanowski W (2008) Optical study of GeO_2–PbO–PbF_2 oxyfluoride glass single doped with lanthanide ions. Opt Mater (Amst) 30:1587–1594. https://doi.org/10.1016/j.optmat.2007.09.011
37. Satyanarayana T, Veeraiah N (2018) Spectroscopic studies of Dy^{3+} ion doped tellurite glasses for solid state lasers and white LEDs. Spectrochim Acta A Mol Biomol Spectrosc 188:516–524. https://doi.org/10.1016/j.saa.2017.07.013.
38. Uma V, Maheshvaran K, Marimuthu K, Muralidharan G (2016) Structural and optical investigations on Dy^{3+} doped lithium tellurofluoroborate glasses for white light applications. J Lumin 176:15–24. https://doi.org/10.1016/j.jlumin.2016.03.016
39. Vijayakumar M, Marimuthu K (2015) Structural and luminescence properties of Dy^{3+} doped oxyfluoro-borophosphate glasses for lasing materials and white LEDs. J Alloys Compd 629:230–241. https://doi.org/10.1016/J.JALLCOM.2014.12.214.
40. Vijayakumar R, Venkataiah G, Marimuthu K (2015) Structural and luminescence studies on Dy^{3+} doped boro-phosphate glasses for white LED's and laser applications. J Alloys Compd 652:234–243. https://doi.org/10.1016/J.JALLCOM.2015.08.219
41. Suresh Kumar J, Pavani K, Mohan Babu A et al (2010) Fluorescence characteristics of Dy3+ ions in calcium fluoroborate glasses. J Lumin 130:1916–1923. https://doi.org/10.1016/j.jlumin.2010.05.006
42. Ravi O, Reddy CM, Reddy BS, Deva Prasad Raju B (2014) Judd-Ofelt analysis and spectral properties of Dy3+ ions doped niobium containing tellurium calcium zinc borate glasses. Opt Commun 312:263–268. https://doi.org/10.1016/j.optcom.2013.09.044
43. Praveena R, Vijaya R, Jayasankar CK (2008) Photoluminescence and energy transfer studies of Dy^{3+}-doped fluorophosphate glasses. Spectrochim Acta A Mol Biomol Spectrosc 70:577–586. https://doi.org/10.1016/J.SAA.2007.08.001
44. Krishnaiah KV, Kumar KU, Jayasankar CK (2013) Spectroscopic properties of Dy^{3+}-doped oxyfluoride glasses for white

light emitting diodes. Mater Express 3:61–70. https://doi.org/10.1166/MEX.2013.1094
45. Karunakaran RT, Marimuthu K, Surendra Babu S, Arumugam S (2010) Dysprosium doped alkali fluoroborate glasses—Thermal, structural and optical investigations. J Lumin 130:1067–1072. https://doi.org/10.1016/J.JLUMIN.2010.01.026.
46. Chandrappa V, Basavapoornima C, Venkatramu V, Depuru SR, Kaewkhao J, Pecharapa W, Jayasankar CK (2022) A critical review and future prospects of Dy^{3+}-doped glasses for white light emission applications. Optik (Stuttg) 266:169583. https://doi.org/10.1016/J.IJLEO.2022.169583
47. Annapoorani K, Karthikeyan P, Basavapoornima Ch, Marimuthu K (2017) Investigations on the optical properties of Dy^{3+} ions doped potassium aluminium telluroborate glasses for white light applications. J Non-Cryst Solids 476:128–136. https://doi.org/10.1016/j.jnoncrysol.2017.09.038
48. Venkataiah G, Jayasankar CK (2015) Dy^{3+}-doped tellurite-based tungsten-zirconium glasses: Spectroscopic study. J Mol Struct 1084:182–189. https://doi.org/10.1016/j.molstruc.2014.11.062
49. Karthikeyan P, Arunkumar S, Annapoorani K, Marimuthu K (2018) Investigations on the spectroscopic properties of Dy^{3+} ions doped Zinc calcium tellurofluoroborate glasses. Spectrochim Acta A Mol Biomol Spectrosc 193:422–431. https://doi.org/10.1016/j.saa.2017.12.049
50. Ye Y, Wang S, An H (2019) White-light emission and chromaticity characterization of Dy3+ doped fluoride glass for standard white light source. J Non-Cryst Solids 526:119697. https://doi.org/10.1016/j.jnoncrysol.2019.119697
51. McCamy CS (1992) Correlated color temperature as an explicit function of chromaticity coordinates. Color Res Appl 17:142–144. https://doi.org/10.1002/COL.5080170211
52. Jackson DF, Hawkes DJ (1981) X-ray attenuation coefficients of elements and mixtures. Phys Rep 70:169–233. https://doi.org/10.1016/0370-1573(81)90014-4
53. Sayyed MI (2016) Bismuth modified shielding properties of zinc boro-tellurite glasses. J Alloys Compd 688:111–117. https://doi.org/10.1016/J.JALLCOM.2016.07.153
54. Tekin HO, Altunsoy EE, Kavaz E, Sayyed MI, Agar O, Kamislioglu M (2019) Photon and neutron shielding performance of boron phosphate glasses for diagnostic radiology facilities. Results Phys 12:1457–1464. https://doi.org/10.1016/J.RINP.2019.01.060
55. Perişanoğlu U, Demir L (2015) A study of K shell X-ray intensity ratios of NixCr1−x alloys in external magnetic field and determination of effective atomic numbers of these alloys. Radiat Phys Chem 110:119–125. https://doi.org/10.1016/J.RADPHYSCHEM.2015.01.032
56. Singh K, Singh H, Sharma G, Gerward L, Khanna A, Kumar R, Nathuram R, Sahota HS (2005) Gamma-ray shielding properties of $CaO–SrO–B_2O_3$ glasses. Radiat Phys Chem 72:225–228. https://doi.org/10.1016/J.RADPYHSCHEM.2003.11.010
57. Harima Y, Sakamoto Y, Tanaka S, Kawai M (2017) Validity of the geometric-progression formula in approximating gamma-ray buildup factors. 24–35. https://doi.org/10.13182/NSE86-A17113.
58. Bashter II (1997) Calculation of radiation attenuation coefficients for shielding concretes. Ann Nucl Energy 24:1389–1401. https://doi.org/10.1016/S0306-4549(97)00003-0
59. Sayyed MI, Elmahroug Y, Elbashir BO, Issa SAM (2017) Gamma-ray shielding properties of zinc oxide soda lime silica glasses. J Mater Sci: Mater Electron 28:4064–4074. https://doi.org/10.1007/S10854-016-6022-Z/TABLES/8

Publisher's Note Springer Nature remains neutral with regard to jurisdictional claims in published maps and institutional affiliations.

Springer Nature or its licensor (e.g. a society or other partner) holds exclusive rights to this article under a publishing agreement with the author(s) or other rightsholder(s); author self-archiving of the accepted manuscript version of this article is solely governed by the terms of such publishing agreement and applicable law.

How to Cite:
Gupta, G., Anand, A., Raj, A., & Robert , B. (2022). Study of traffic volumes. *International Journal of Health Sciences*, *6*(S1), 9997–10012. https://doi.org/10.53730/ijhs.v6nS1.7363

Study of traffic volumes

Gunjit Gupta
Undergraduate Student, Department of Civil Engineering, Delhi Technological University (DTU), Delhi, India

Ayush Anand
Undergraduate Student, Department of Civil Engineering, Delhi Technological University (DTU), Delhi, India

Ayush Raj
Undergraduate Student, Department of Civil Engineering, Delhi Technological University (DTU), Delhi, India

Mr. B.R.G Robert
Assistant Professor, Department of Civil Engineering, Delhi Technological University (DTU), Delhi, India
Corresponding author email: brgrobert@dce.ac.in

***Abstract*---**"The area of transportation planning deals with transportation facilities (usually streets, roads, walkways, bike lanes, and public transit lines)." It is vital to assess the present state of traffic volume and anticipate the future state of traffic volume in this field traffic volume survey. The purpose of traffic volume studies is to determine the number, movement, and categories of highway vehicles in a given region. An attempt was made to grasp traffic patterns throughout various time periods using data collection. The characteristics of the traffic flow at that crossroads also have an impact on traffic control. As a consequence, the study's findings are valuable in controlling traffic at the intersection and giving some corrective measures to improve traffic safety in the region. Based on the findings, corrective actions such as road widening or enhanced public transit may be recommended.

***Keywords*---**Volume Survey, Average Daily Traffic, Green Shield Equation, Traffic Volume, Level of Service.

Introduction

A traffic volume study is often referred to as a traffic flow survey or just a traffic survey. It is described as the technique for determining the volume of traffic flowing on the roadways at a certain stretch at a specific time. It is quantified in

terms of vehicles per minute, hours, and days. The flow of the various vehicle classes must be translated into a common vehicle class known as the passenger car unit in order to show the traffic flow on a route per unit time. The volume of traffic fluctuates throughout the day. The volume of daily traffic varies depending on the day of the week, as well as the months and seasons of the year. Traffic surveys are a means of acquiring traffic statistics. This is a data gathering approach that may be utilised for a range of traffic engineering applications. Traffic surveys are used for a variety of purposes, including traffic monitoring, control and management, enforcement, forecasting, model calibration and validation, and so on [1].

When there is too much traffic on the road, vehicles go at a slower speed. This lengthens travel times and increases queuing. This is also referred to as a traffic gridlock. Congestion can occur as a result of a decrease in capacity, such as accidents on the road or road closures. Inadequate road design might also limit capacity. Congestion can also be produced by increased traffic, such as when a large number of automobiles exit a sports venue at the same time. Several methods are used to alleviate congestion in areas where it is common, such as commuting in large cities. Cars may be prohibited in certain areas or at certain times, or forced to carry passengers or pay a fee, or people may use public transportation, such as rapid transit, which travels independently of car traffic and is not affected by traffic jams [2,3].

Congestion is not the primary issue; rather, it is a solution to our underlying mobility problem, which is that too many people want to travel at the same times every day. Because the successful operation of the economic and educational institutions requires that people work, go to school, and even do errands during about the same hours so that they may connect with one another. That fundamental criterion cannot be changed without wreaking havoc on our economy and society [4]. Every major urban city in the globe has the same issue. Our project's goals include the following:

- Observe the various types of vehicle composition.
- Investigate the traffic flow and its characteristics.
- To calculate the average daily traffic at different periods of the day.
- To ascertain the traffic dispersion's directional distribution.
- Identifying and resolving traffic flow fluctuations

Objectives of traffic volume study

Planning Objectives:
Accurate information on the quantity of traffic on the roads is critical for the design of both road maintenance and enhancement programmes. Analysis of traffic volume networks aids in determining/planning the need for the improvement in terms of expansion of building missing links, by-passes, alternate roads, and so on [5].

Improvement Purpose:
To properly distribute a limited maintenance budget, it is required to evaluate the traffic volume carried by a given highway section in order to estimate the worth of the road and its relative priority. It is critical to understand traffic volume in order to optimise highway operating conditions.

- To assess the current operational/service condition of a highway segment.
- To assess the need for traffic control equipment (warrant).
- Determining the type of improvement measure to be employed.
- To assess the efficacy of a traffic control measure.

The Goals of Dynamic Traffic Management:

- Up to current and continuous flow/congestion information is vital for optimising.
- Improving junction performance through traffic signal design
- By giving information to road users, network productivity may be increased [6,7]

Other Goals:

- To assess the worth of any route or road infrastructure.
- Determining the priority for road renovation and growth and allocating funding appropriately
- Developing and designing existing and new traffic operations facilities.
- Examine traffic patterns and trends along the route.
- To carry out structural pavement design and geometric road design based on a categorised traffic volume research.
- Volume distribution studies will be used to develop one-way streets and other regulatory measures.

Method for volume survey

Method of manual counting

A field crew is used in this approach to record traffic volume on the mandated record sheets. This approach can get data that mechanical counters cannot capture, such as vehicle categorization, turning motions, and counts when the loading condition or number of people are necessary.

However, having a manual count for all 24 hours of the day is impractical. As a result, in order to reduce the manual hours involved in talking complete counts, statically sampling techniques must be used. First, the fluctuation of traffic volume during the hours of day and the daily variations are observed.

The traffic volume analysis is then performed manually by picking a typical brief count period. The peak hourly traffic levels and average daily traffic volumes are then estimated using statistical analysis [8,9].

Simple Method:
Hand tally and manual counters/enumerators are used to count data.

10000

Benefits include the ability to collect traffic volume, vehicle categorization, and turning proportions using this approach. Data can be utilised immediately after it is obtained.
Disadvantages: For long duration counts and high flow rates, this method is unworkable. Error is common, especially when the volume is high. The count cannot be double-checked. In severe weather, the count cannot be completed [10].

Data Collection



Fig: Lala Jagat Narayan Marg Road
(Google image of the road)

Data of NSP to Pitampura Road

TIME	BUS/TRUCK	CAR + VAN	MOTORCYCLE	AUTORICKSHAW	TOTAL
3:30-4:30	72	1304	1068	0	2664
4:30-5:30	68	1160	992	172	2392
5:30-6:30	56	1068	728	144	1996
6:30-7:30	40	888	716	168	1812
TOTAL =	236	4420	3504	704	

Data of Pitampura to NSP Road

TIME	BUS/TRUCK	CAR + VAN	MOTORCYCLE	AUTORICKSHAW	TOTAL
3:30-4:30	60	1200	936	140	2336
4:30-5:30	64	1244	792	100	2200
5:30-6:30	36	1036	532	80	1684
6:30-7:30	24	840	600	144	1608
TOTAL=	176	4320	2860	664	

Vehicle composition of traffic stream from NSP to Pitampura Road

TIME	BUS/TRUCK	CAR + VAN	MOTORCYCLE	AUTO-RICKSHAW
3:30 – 4:30	72	1304	1068	220
4:30 – 5:30	68	1160	992	172
5:30 – 6:30	56	1068	728	144
6:30 – 7:30	40	888	716	168
TOTAL	236	4420	3504	704
%AGE	2.66	49.86	39.53	7.94

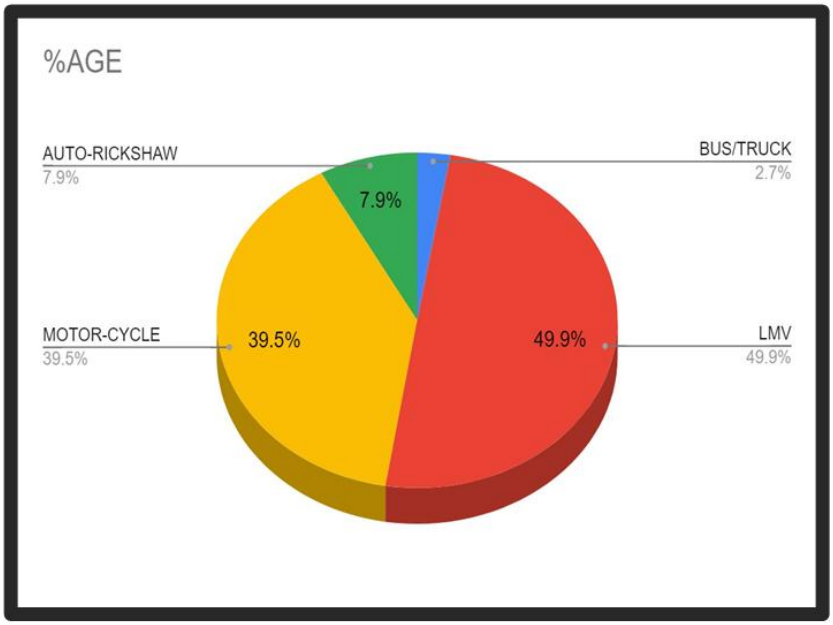


Fig. 4. Percentage vehicle composition of traffic stream from NSP to Pitampura Road

Vehicle composition of traffic stream from Pitampura to NSP Road

TIME	BUS/TRUCK	CAR + VAN	MOTORCYCLE	AUTO-RICKSHAW
3:30-4:30	60	1200	936	140
4:30-5:30	64	1244	792	100
5:30-6:30	36	1036	532	80
6:30-7:30	24	840	600	144
TOTAL	176	4320	2860	664
%AGE	2.25	55.24	36.57	5.93

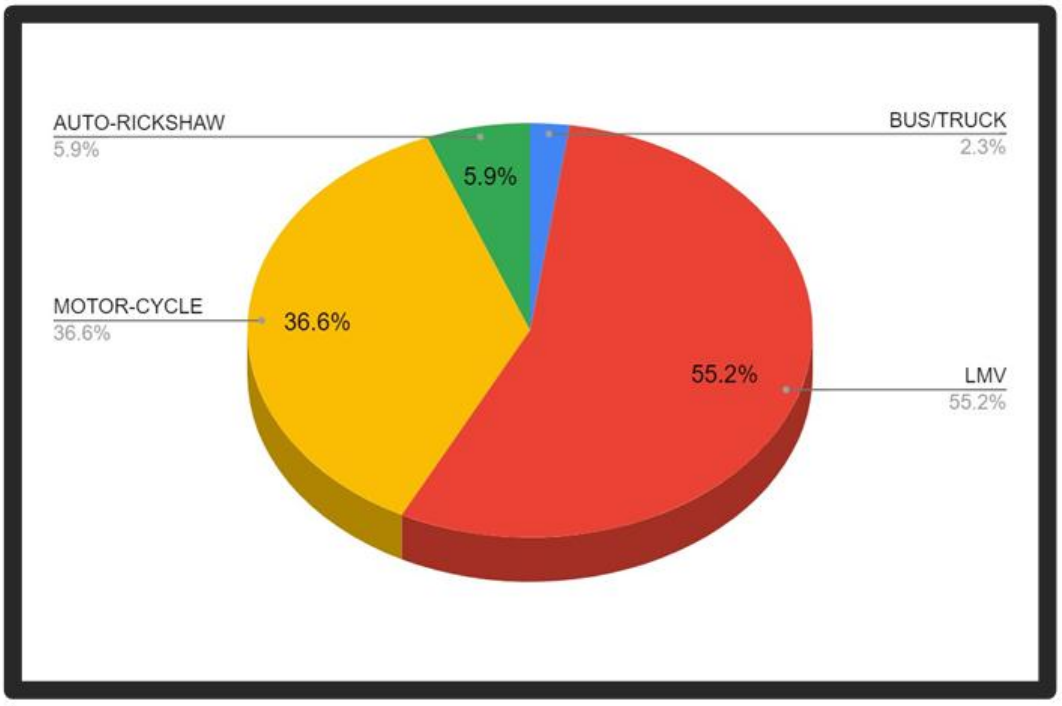


Fig. 5. Percentage vehicle composition of traffic stream from pitampura to nsp road

Table for passenger carrying unit

VEHICLE	VALUE OF PCU
BUS/TRUCK	2.2
CAR+VAN	1
MOTOR-CYCLE	0.5

AUTO-RICKSHAW	1.2

Conversion table of vehicles into PCE and flow rate calculation

NSP to Pitampura

TYPES OF VEHICLES	PCU	TIME SLOT 1	TIME SLOT 2	TIME SLOT 3	TIME SLOT 4
BUS/TRUCK	2.2	72	68	56	40
CAR +VAN	1	1304	1160	1068	888
MOTORCYCLE	0.5	1068	992	728	716
AUTO RICKSHAW	1.2	220	172	144	168
FLOWRATE	(PCU/hr)	2260.4	2012	1728	1536

Pitampura to NSP

TYPE OF VEHICLE	PCU	TIME SLOT 1	TIME SLOT 2	TIME SLOT 3	TIME SLOT 4
BUS/TRUCK	2.2	60	64	36	24
CAR + VAN	1	1200	1244	1036	840
MOTORCYCLE	0.5	936	792	532	600
AUTORICKSHAW	1.2	140	100	80	144
FLOW RATE	(PCU/hr)	1968	1900.8	1477.2	1348

- SERVICE FLOW-RATE IN NSP TO PITAMPURA – 2260.4PCU/hr.
- SERVICE FLOW-RATE IN PITAMPURA TO NSP – 1968.0 PCU/hr.

Percentage of directional distribution

DIRECTION	PCU/hr	TOTAL	DIRECTIONAL DISTRIBUTION
NSP TO	2260.4	4228.4	53.45%

PITAMPURA			
PITAMPURA TO NSP	1968.0	4228.4	46.542%

Time	NSP TO PITAMPURA Flow Rate (PCU/hr)	PITAMPURA TO NSP (PCU/hr)	NSP TO PITAM PURA ADT	PITAMPURA TO NSP ADT	NSP TO PITAMPURA (%ADT)	PITAMPURA TO NSP (%ADT)
3:30 PM-4:30 PM	2260.4	1968	28195	24972	8.01	7.88
4:30 PM – 5:30 PM	2012	1900.8			7.13	7.60
5:30 PM - 6:30 PM	1728	1477.2			6.128	5.91
6:30 PM – 7:30 PM	1535	1348			5.44	5.39

I. Now, ADT in NSP TO PITAMPURA direction: 28195 PCU
AADT in NSP TO PITAMPURA direction: 33440 PCU

II. ADT in PITAMPURA TO NSP direction: 24972 PCU
PCU AADT in PITAMPURA TO NSP direction 29617 PCU

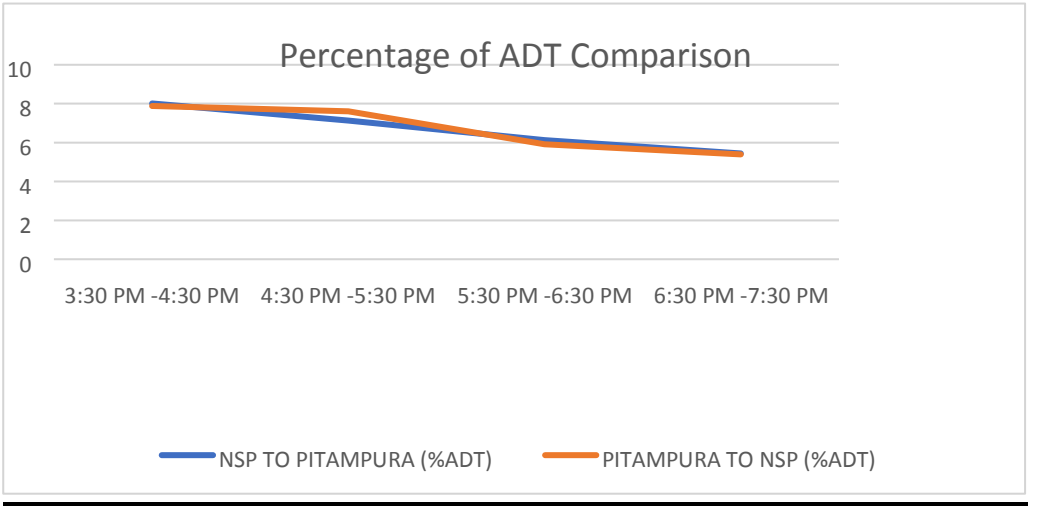


Fig. 6. Comparison between percentage ADT for both road

Theory of green shield equation:

❑ The concept of fluid mechanics inspired traffic flow analysis.

$q = k \; X \; v$

.....[1] Where:

v - average vehicle speed(km/hr) k - traffic density(veh/km) q - traffic flow rate(veh/hr)

✈ Fundamental relationship is given by Greenshields model:

$v = v_f\,(1 - {}_k{}^k j)$ .....[2]

Where:

- maximum speed at zero density.

k_j - Jam traffic density/condition of zero vehicle speed.

✈ substituting the values FROM EQUATION 1 AND 2 and converting it into traffic density quadratic equation; ❑ we get:

$$\boldsymbol{q = -___kvjf\ (k - k2j) + vfk__4j}\ \textbf{....[3]}$$

from the above equation we get two fundamental traffic Flow characteristics [11,12].

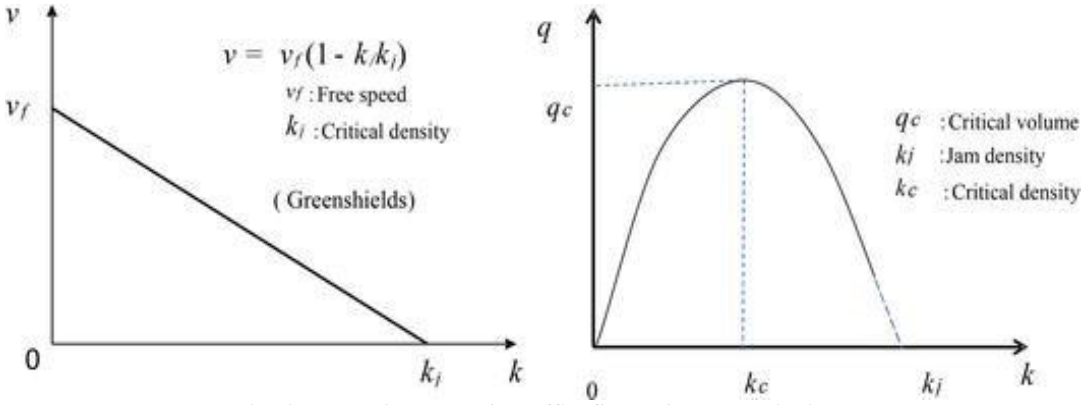


Fig. 7. Fundamental traffic flow characteristics

10006

Data collection and calculation using greenshield equation

DAY 3: OF DATA COLLECTION (18TH FEB 2022)

(1) NSP TO PITAMPURA

TIME	BUS/TRUCK	CAR + VAN	MOTORCYCLE	AUTORICKSHAW	TOTAL(X4)
3:30PM - 4:30PM	60	1364	1032	276	2732
4:30 PM -5:30PM	80	1308	1120	164	2672
5:30PM – 6:30PM	64	1008	628	140	1840
6:30PM-7:30PM	60	732	724	168	1684

(2) PITAMPURA TO NSP

TIME	BUS/TRUCK	CAR + VAN	MOTORCYCLE	AUTO-RICKSHAW	TOTAL(X4)
3:30 PM – 4:30 PM	64	1256	1004	168	2528
4:30PM – 5:30PM	72	1312	868	108	2360
5:30PM-6:30 PM	32	1104	500	100	1736
6:30 PM -7:30 PM	28	932	656	128	1744
TOTAL=	196	4604	3028	504	

DAY 3: OF DATA COLLECTION (18TH FEB 2022)

(1) NSP TO PITAMPURA

TIME	BUS/TRUCK	CAR + VAN	MOTORCYCLE	AUTORICKSHAW	TOTAL(X4)
3:30PM - 4:30PM	60	1364	1032	276	2732
4:30 PM -5:30PM	80	1308	1120	164	2672
5:30PM – 6:30PM	64	1008	628	140	1840
6:30PM-7:30PM	60	732	724	168	1684

(2) PITAMPURA TO NSP

TOTAL =	264	4412	3504	748	

10008

DAY 4: OF DATA COLLECTION (19TH FEB 2022)

(1) NSP TO PITAMPURA

TIME	BUS/TRUCK	CAR + VAN	MOTORCYCLE	AUTORICKSHAW	TOTAL(X4)
3:30PM - 4:30PM	92	1400	1204	128	2824
4:30 PM -5:30PM	44	1332	828	180	2384
5:30PM – 6:30PM	80	1068	516	100	1764

(2) PITAMPURA TO NSP

TIME	BUS/TRUCK	CAR + VAN	MOTORCYCLE	AUTO-RICKSHAW	TOTAL(X4)
3:30 PM – 4:30 PM	56	1420	948	152	2576
4:30PM – 5:30PM	64	1148	684	88	1960
5:30PM-6:30 PM	36	1168	596	128	1928
6:30 PM -7:30 PM	20	1024	760	100	1904
TOTAL=	176	4760	2988	468	
6:30PM-7:30PM	68	644	604	152	1468
TOTAL =	284	4444	3152	560	

DAY 5: OF DATA COLLECTION (20TH FEB 2022)

(1) NSP TO PITAMPURA

TIME	BUS/TRUCK	CAR + VAN	MOTORCYCLE	AUTORICKSHAW	TOTAL(X4)
3:30PM - 4:30PM	104	1084	1392	84	2664
4:30 PM -5:30PM	68	1236	956	168	2428

(2) PITAMPURA TO NSP

TIME	BUS/TRUCK	CAR + VAN	MOTORCYCLE	AUTO-RICKSHAW	TOTAL(X4)
3:30 PM – 4:30 PM	68	1244	768	124	2204
4:30PM – 5:30PM	52	932	732	92	1808
5:30PM-6:30 PM	40	900	660	136	1736
6:30 PM -7:30 PM	28	1060	632	116	1836
TOTAL=	148	4136	2792	468	
5:30PM – 6:30PM	60	936	584	108	1688
6:30PM-7:30PM	40	688	504	124	1356
TOTAL =	272	3984	3436	484	

10010

AVERAGE VELOCITY:

5.2.1 Average velocity from NSP to Pitampura side:

9.

$$= \frac{85 + 9.24 + 9.04 + 7.77 + 6.97}{5}$$

=8.574 m/hr.

5.2.2 Average velocity from Pitampura to NSP side:

8.

$$= \frac{51 + 9.40 + 10.48 + 9.34 + 8.51}{5}$$

= 9.248 km/hr.

Conclusion and Recommendations

This report summarises the analysis's findings and their significance. This report included all feasible analyses based on field survey data.
Discussion on Vehicle Composition (BASED ON DATA OF DAY1):

- Lights vehicle (car, jeep, etc.) occupied about 49.9% of total vehicle.
- Percentage of bus/truck is very low which is about 2.7%.
- Percentage of utility auto-rickshaw is in between 7.9%.

Discussion on Directional Distribution
Approximately 46.542 percent of traffic flow was towards NSP. It was evening rush hour.

Discussion on level of service:

- According to the value of average velocity determined from Greenshields model(9.248 and 8.574 km/hr); our urban street falls under the category "F" of LOS.
- This leaves us to a conclusion that:
- There is breakdown in flow.
- Every car follows the vehicle in front of it in lockstep.
- Travel time cannot be predicted.
- Road is in a constant traffic jam [13,14]

Recommendation
Based on our study findings, we have issued the following recommendations:
There should be more public transportation instead of private automobiles to meet the needs of those who live in residential areas near the road.

- Non-motorized transportation (rickshaws and bikes) should be avoided in this regions this will enhance the level of service (loss) on the road and thus aid to increase travel speed.

- Data should be gathered for an hour instead of 15 minutes for more meaningful data (in this case).
- There should be no more delays in the development of parking spaces near the studied area so that the parking space may be accommodated by neighbouring cars.

References

1. Faruk AN, Liu W, Lee SI, Naik B, Chen DH, Walubita LF. Traffic volume and load data measurement using a portable weigh in motion system: A case study. International Journal of Pavement Research and Technology. 2016 May 1;9(3):202-13.
2. Lingras P, Sharma SC, Osborne P, Kalyar I. Traffic volume time-series analysis according to the type of road use. Computer-Aided Civil and Infrastructure Engineering. 2000 Sep;15(5):365-73.
3. Khoda Bakhshi A, Ahmed MM. Real-time crash prediction for a long low-traffic volume corridor using corrected-impurity importance and semi-parametric generalized additive model. Journal of transportation safety & security. 2021 Mar 4:1-35.
4. Arasan VT, Arkatkar SS. Microsimulation study of effect of volume and road width on PCU of vehicles under heterogeneous traffic. Journal of Transportation Engineering. 2010 Dec;136(12):1110-9.
5. Hoque MS. Traffic volume study. Lectures Notes on CE. 2011;351.
6. Kurzhanskiy AA, Varaiya P. Traffic management: An outlook. Economics of transportation. 2015 Sep 1;4(3):135-46.
7. Besada JA, Carramiñana D, Bergesio L, Campaña I, Bernardos AM. Modelling and simulation of collaborative surveillance for unmanned traffic management. Sensors. 2022 Feb 15;22(4):1498.
8. Sabry M, Abd-El-Latif H, Yousef S, Badra N. Determination of AADT from Short Period Traffic Volume Survey. Journal of Applied Sciences Research. 2007;3(7):607-12.
9. Limantara, A.D., Subiyanto, T.T.S.B., Muhammad, F.N.S.W.M. and Nawir, I.S., 2021, August. Smart Survey Model of Average Daily Traffic (ADT) for Pavement Planning and Monitoring. In *2nd Borobudur International Symposium on Science and Technology (BIS-STE 2020)* (pp. 1-5). Atlantis Press.
10. Apronti D, Ksaibati K, Gerow K, Hepner JJ. Estimating traffic volume on Wyoming low volume roads using linear and logistic regression methods. Journal of traffic and transportation engineering (English edition). 2016 Dec 1;3(6):493-506.
11. Dhapudkar RS. Analysis and development of traffic stream parameters of heterogeneous traffic at signalized intersection. Int J Eng And Sci (IJES). 2014;3(1):339.
12. Rakha H, Crowther B. Comparison of Greenshields, Pipes, and Van Aerde carfollowing and traffic stream models. Transportation Research Record. 2002;1802(1):248-62.
13. Singh B, Goyal T. Study of traffic volume and level of service of Panjab University, Chandigarh. International Journal of Engineering Research and Applications. 2015 Jul;5(7):9-14.

14. Landis BW, Vattikuti VR, Ottenberg RM, McLeod DS, Guttenplan M. Modeling the roadside walking environment: pedestrian level of service. Transportation research record. 2001;1773(1):82-8.

https://doi.org/10.3311/PPci.22711
Creative Commons Attribution

Periodica Polytechnica Civil Engineering

Sustainable Concrete: Exploring Fresh, Mechanical, Durability, and Microstructural Properties with Recycled Fine Aggregates

Harish Panghal[1*], Awadhesh Kumar[1]

[1] Department of Civil Engineering, Delhi Technological University, Shahbad Daulatpur, Main Bawana Road, Delhi 1100042, India
[*] Corresponding author, e-mail: harish_phd2k18@dtu.ac.in

Received: 03 June 2023, Accepted: 03 November 2023, Published online: 03 January 2024

Abstract

The growing construction industry and global population have led to increased demand for concrete, resulting in increased waste production. Recycling construction and demolition (C&D) waste as recycled fine aggregates (RFA) in concrete could help reduce waste and conserve natural resources. This research delves into the meticulous examination of particle packing density within specific cylindrical volumes under standard compacting efforts, elucidating an order of compressive strength. The study comprehensively explores various concrete properties, including workability, compressive strength, flexural strength, split tensile strength, drying shrinkage, electrical resistivity, rapid chloride penetration, and microstructural characteristics (analyzed through XRD, SEM, and EDAX). RFA particles, ranging from 0.15 to 4.75 mm, were employed as partial replacements for fine aggregates, with replacement percentages varying from 0% to 100% in increments of 25%. The empirical findings underscore that the incorporation of RFA significantly enhances concrete properties. However, it was observed that surpassing the optimum replacement percentage of 25% (RFA 25) adversely impacts the concrete's strength and microstructure. Specifically, RFA 25 exhibited remarkable improvements, with a 14.75% increase in compressive strength, a 6.61% boost in flexural strength, and a 13.14% enhancement in split tensile strength compared to conventional concrete (RC). Furthermore, RFA 25 demonstrated a 4.16% increment in drying shrinkage, 17.65% higher electrical resistivity, and an 18.83% superior resistance to chloride penetration compared to RC. The analysis of XRD, SEM, and EDAX results elucidated that at lower replacement percentages, the pozzolanic reaction enhances strength by forming additional hydration products. Conversely, at higher replacement levels, strength diminishes.

Keywords

construction and demolished waste, durability properties, recycled fine aggregates, mechanical properties, microstructural properties

1 Introduction

In the 21st century, rapid advancements in construction have led to the creation and demolition of structures, resulting in a significant upswing in construction and demolition (C&D) waste, projected to reach 2.59 billion tonnes by 2030 and 3.40 billion tonnes by 2050 [1]. The disposal of this waste in landfills not only depletes landfill sites but also adversely affects the land. A potential solution lies in repurposing C&D waste as aggregates in fresh concrete production, a sector where aggregates constitute 70-80% of the volume [2]. The demand for concrete is soaring, increasing annually at a rate of 7.7% [3]. To mitigate environmental impact, the global construction industry is increasingly embracing sustainable practices, requiring innovative approaches to reduce concrete's ecological footprint [4]. Recycling fine aggregates from C&D waste presents a promising solution. However, it necessitates rigorous evaluation to ensure the resulting concrete meets industry standards [5]. This study addresses this imperative need by systematically exploring various proportions of recycled fine aggregates (RFA) ranging from 0% to 100%.

Structural concrete made from C&D waste requires continuous structural health monitoring (SHM) to guarantee its long-term performance [6]. Concrete structures undergo stress due to drying-induced shrinkage, which leads to the formation of cracks. Drying shrinkage occurs as free water escapes through pores and passages near the surface of the element into the surrounding air. Consequently, analyzing shrinkage strain is essential for conducting a comprehensive study of the long-term performance of fresh concrete [7]. Surface electrical resistivity

Cite this article as: Panghal, H., Kumar, A. "Sustainable Concrete: Exploring Fresh, Mechanical, Durability, and Microstructural Properties with Recycled Fine Aggregates", Periodica Polytechnica Civil Engineering, 2024. https://doi.org/10.3311/PPci.22711

of concrete is increasingly utilized as a corrosion risk indicator in the monitoring of concrete structures. Evaluating the concrete's surface electrical resistivity serves as a vital parameter for corrosion risk assessment and is essential for performance evaluation [8]. To control corrosion, concrete must be thoroughly inspected for chloride ion penetration. The impact of weathering on concrete, especially when C&D waste is used as aggregates, must be meticulously examined for chloride ion penetration [9]. The interfacial transition zone (ITZ) between aggregates and cement paste significantly influences the microstructural characteristics of concrete. Optimal performance is achieved when the ITZ is dense and responsible for a strong bond between the two components [10]. Additionally, recycled aggregate can substantially impact the strength of hardened concrete. Research on the effects of fine recycled concrete aggregates (FRCA) revealed that FRCA can be utilized in proportions of up to ten percent for C30 concrete and between twenty to fifty percent for C25 concrete [11]. According to a study, recycled aggregate concrete may experience higher drying shrinkage compared to conventional concrete [12]. Recycled fine aggregates can be effectively used in concrete, offering comparable strength to natural sand aggregates [13]. The permeability of concrete, when using recycled concrete aggregates and pozzolanic materials, is significantly lower than that of concrete produced with natural aggregates [14]. Concrete incorporating 30% demolished replaced fine aggregates and 20% demolished coarse aggregates can replace conventional concrete [15]. Research involving fly ash and recycled concrete aggregates showed that water absorption increases, and electrical resistivity decreases with higher levels of recycled concrete aggregate incorporation. However, the opposite occurs when fly ash is added for both tests [16]. A study on the high slump attributes of standard and high-strength concrete created from recycled fine aggregates (RFA) demonstrated that the compressive strength and elastic modulus of RFA concrete were approximately 70–90% of those of natural aggregates [17]. In their examination of RFA performance using a unique mix proportioning technique, recycled fine aggregates (RFA) concrete exhibited superiority in terms of CO_2-e and cost compared to conventional concrete [18]. The mechanical performance of recycled fine aggregates, supplemented with waste carbon fibers, indicated that adding waste fibers and recycled fine aggregates to concrete improves the material's characteristics [19]. Utilizing adhered cement paste elimination and fly ash treatment significantly enhanced the compressive strength and elastic modulus of recycled fine aggregates (RFA) concrete during the multi-technique approach in optimizing the properties of RFA concrete [20].

The use of recycled aggregates from C&D waste in concrete production is a growing trend, aligning with economic and environmental goals [21]. This practice reduces landfill waste and conserves natural resources [22], adhering to the principles of the circular economy [23]. However, ensuring concrete quality and performance according to industry standards is crucial [24]. Despite various studies on fine aggregate replacements, there's a lack of a definitive method to determine the ideal percentage of RFA replacement for maximum strength. This research addresses this gap by meticulously analyzing particle packing density in specific cylindrical volumes using standardized compacting methods. By exploring these parameters, the study aims to establish a systematic relationship between particle arrangement and compressive strength in concrete specimens. This endeavor is essential in meeting the urgent need for sustainable alternatives in concrete production, emphasizing the importance of balancing environmental concerns with structural integrity in construction practices.

This research presents new and innovative methods:

1. **Efficient utilization of RFA:** Unlike conventional practices where RFA is incorporated in concrete at lower proportions, this study explores a wide range of percentages (0%, 25%, 50%, 75%, and 100%) to identify the most effective utilization of RFA in sustainable concrete production.
2. **Comprehensive assessment:** The study bridges existing research gaps by subjecting concrete mixes to standard compacting efforts. It meticulously analyzes the impact of RFA proportions on fresh properties (workability), hardened properties (compressive strength, flexural strength, split tensile strength, drying shrinkage, electrical resistivity, and rapid chloride penetration of structural concrete), and microstructural features (XRD, SEM, and EDAX). The results are then meticulously compared with a control mix to unveil the most significant differences.
3. **Microstructural investigation:** The research delves into the effects of RFA on the morphology and composition (both chemical and mineralogical) of RFA concrete, crucial for understanding the generation of microstructure. This exploration sheds light on the influence of RFA on microstructure and identifies the optimum content required for sustainable concrete development.

By focusing on fresh properties, mechanical strength, durability, and microstructure, this research strives to provide profound insights that could revolutionize the methods by which concrete is produced and utilized in construction projects globally.

2 Experimental programme

2.1 Material

The study employs Ordinary Portland cement of grade 43, adhering to IS 269 (2015) [25] standard. Table 1 shows physical test results carried out on the cement.

Natural sand, compliant with IS 383 (1970, Reaffirmed 2002) [26], serves as the fine aggregate with a size range of 4.75 mm and below. Crushed stone aggregates, ranging from 4.75 mm to 20 mm, meet the criteria of IS 383 (1970, Reaffirmed 2002) [26] and constitute coarse aggregates. These aggregates pass through 40 mm sieves and retain 100% on 4.75 sieves. Passing percentages on 20 mm and 10 mm sieves are 90.76% and 4.52% respectively. Recycled fine aggregates (RFA) are obtained by crushing concrete from C&D waste to the required size using an impact crusher.

The research explores the particle packing density in specific cylindrical volumes through standard compaction efforts, leading to various mixtures (as shown in Table 2). Table 2 outlines the weights of different fine aggregate mixtures in specific cylindrical volumes, offering valuable insights into their densities. Among these, RFA 25 + NFA 75 offers the densest mixture. The other mixtures, namely RFA 50 + NFA 50, NFA 100, RFA 75 + NFA 25, and RFA 100, exhibit decreasing density in the specified order. Firstly, the Natural Fine Aggregate (NFA) alone, listed as the initial entry, weighs 14.52 kg in the specified volume, serving as a baseline measurement. Secondly, the mix denoted as RFA 25 + NFA 75, consisting of 25% Recycled Fine Aggregate (RFA) and 75% Natural Fine Aggregate, demonstrates a higher weight at 15.27 kg. This mixture reveals that incorporating a quarter of recycled fine aggregate with three-quarters of natural fine aggregate results in increased density, making it the heaviest among the options. Moving on, the composition RFA 50 + NFA 50, with an equal balance of RFA and NFA, weighs 14.74 kg. Despite a higher percentage of recycled material compared to the previous mix, the overall density is slightly lower due to the equal distribution of the aggregates. The mixture labeled RFA 75 + NFA 25 contains 75% RFA and weighs 13.84 kg, showcasing a significant reduction in weight and density due to the higher proportion of recycled material. Lastly, the blend known as RFA 100 comprises entirely of Recycled Fine Aggregate (RFA), weighing 13.27 kg, representing the lightest option among all. The exclusive use of recycled material significantly reduces the mixture's weight. These variations highlight the impact of different ratios of recycled and natural fine aggregates on the density of concrete mixes, providing crucial data for optimizing sustainable concrete compositions while maintaining structural integrity. Table 3 [27, 28] illustrates the physical and mechanical properties of both natural and recycled fine aggregates, alongside natural coarse aggregates.

Table 1 Physical test results on cement

S. No.	Types	Value measured	As per IS 269 (2015) [25]
1	Consistency (%)	31%	–
2	Initial setting time (minutes)	58 minutes	>30 minutes
3	Final setting time (minutes)	435 minutes	<10 hours
4	Specific gravity (–)	3.11 (–)	3.0 to 3.15

Table 2 Weight in specific cylindrical volume

S. No.	Fine aggregates mixtures	Weight (kg)
1	NFA	14.52
2	RFA 25 + NFA 75	15.27
3	RFA 50 + NFA 50	14.74
4	RFA 75 + NFA 25	13.84
5	RFA 100	13.27

Super-plasticizers in the form of chemical admixtures (C-MAX), complying with both IS 9103 (1999) [29] and IS 2645 (2003) [30] standards, are incorporated at a ratio of 1% by weight of cement. Mixing and curing are performed using potable water sourced from the laboratory. Fig. 1 provides a visual representation of the particle size distribution of the fine aggregates.

2.2 Mix proportions

To investigate the viability and impact of recycled fine aggregates on the mechanical properties of concrete, five distinct concrete mixtures were formulated aiming for a target strength of 27 MPa. The compositions of these mixtures are outlined in Table 4. The reference mixture (RC) was prepared using natural aggregates. Additionally, mixtures denoted as RFA-25, RFA-50, RFA-75, and RFA-100 were created by replacing natural fine aggregates with recycled fine aggregates at varying percentages: 25%, 50%, 75%, and 100%, respectively. All these mixes were

Table 3 Physical and mechanical characteristics of aggregates

Property	NFA	RFA	NCA	Standard limits
Bulk density (kg/m^3)	1625	1580	1740	1200–1750 [27]
Specific gravity (–)	2.675	2.654	2.754	2.30–2.90 [27]
Water absorption (%)	0.51	1.12	0.62	≤2.0 (IS 2386 Part 3) [27]
Abrasion loss (%)	15.52	18.44	25.43	<30 (IS 2386 Part 4) [28]
Crushing value (%)	16.21	17.34	26.24	<30 (IS 2386 Part 4) [28]
Impact value (%)	15.31	18.74	17.31	<30 (IS 2386 Part 4) [28]

NFA – Natural Fine Aggregates, NCA – Natural Coarse Aggregates, RFA – Recycled Fine Aggregates

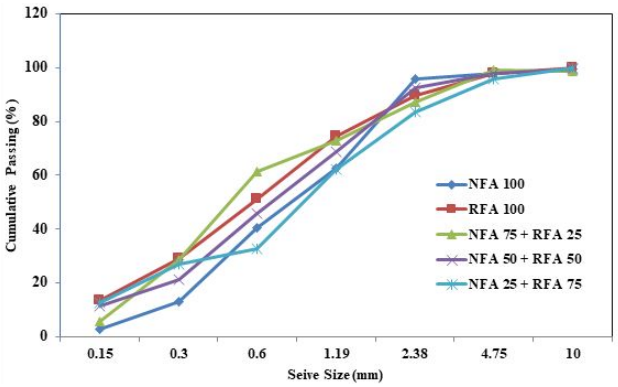


Fig. 1 Gradation curve for fine aggregates

carefully prepared using the weight batching method while maintaining a consistent water-cement ratio of 0.50. This systematic approach allowed for a thorough exploration of the influence of recycled fine aggregates on the concrete's mechanical behavior, providing valuable insights for sustainable construction practices.

2.3 Testing programs

Several tests have been conducted to assess various aspects of structural concrete. The workability of fresh concrete was gauged, and mechanical characteristics such as compressive strength, flexural strength, and split tensile strength were measured. To evaluate the long-term performance of the concrete, tests for drying shrinkage (Fig. 2), electrical resistivity (Fig. 3), and rapid chloride penetration (Fig. 4) were carried out. Additionally, scanning electron microscopy (SEM) was employed, along with energy-dispersive X-ray spectroscopy (EDAX) and X-ray diffraction (XRD) analyses, to examine the microstructural features of powdered concrete samples from different mixtures. These comprehensive assessments provided detailed insights into the structural and long-term properties of the concrete, contributing valuable data for further analysis and applications in construction.

2.3.1 Workability

A slump test, in accordance with IS 1199 (1959) [31] standards, has been conducted to evaluate the workability of concrete mixes containing varying replacement percentages of C&D waste in the form of recycled fine aggregates. The outcomes of these tests are presented in Fig. 5.

2.3.2 Compressive strength

A total of 30 specimens, cast in steel cube molds measuring 15 × 15 × 15 cm, were meticulously prepared, cured, and subjected to compressive strength testing for different concrete compositions. The tests were conducted using a compression testing machine with a capacity of 2000 KN. The average compressive strength value for each mix was derived from three specimens. These evaluations were performed at both 7 and 28 days, and the detailed results are depicted in Fig. 6.

2.3.3 Flexural strength

Similarly, 30 specimens, cast in steel rectangular molds sized 50 × 10 × 510 cm, were created, cured, and tested to

Table 4 Concrete mixtures proportions (in kilograms per cubic meter)

S. No.	Mixture ID	NFA	RFA	NCA	Cement	*W/C* ratio	Admixture
1	RC	444.48	0	1511	400	0.5	4
2	RFA 25	333.36	111.12	1511	400	0.5	4
3	RFA 50	222.24	222.24	1511	400	0.5	4
4	RFA 75	111.12	333.36	1511	400	0.5	4
5	RFA 100	0	444.48	1511	400	0.5	4

RC – Reference Concrete, NFA – Natural Fine Aggregates, NCA – Natural Coarse Aggregates, RFA – Recycled Fine Aggregates



Fig. 2 Drying shrinkage apparatus and sample testing



Fig. 3 Resistivity meter and sample testing



Fig. 4 Typical layout of RCPT unit (ASTM C1202-12 [34])

determine the flexural strength of various concrete mixes. Utilizing a flexural testing machine with a 2000 KN capacity, the average flexural strength value was calculated from three specimens per mix. Tests were carried out at 7 and 28 days, with the results illustrated in Fig. 7.

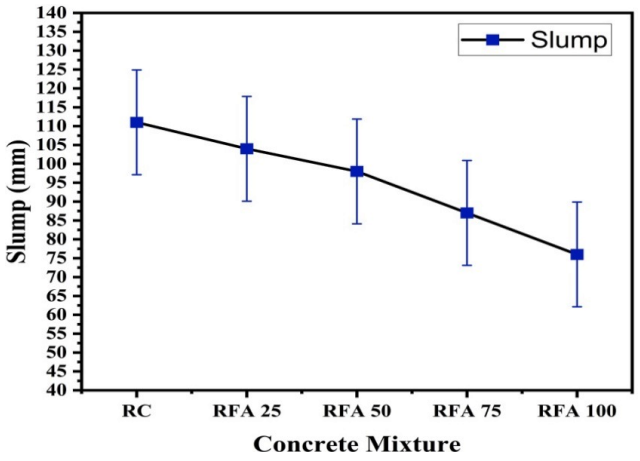


Fig. 5 Slump value for different concrete mixtures

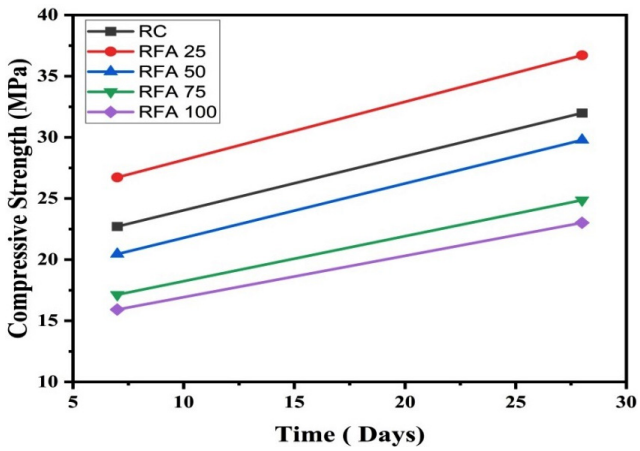


Fig. 6 Variations of compressive strength for different concrete mixtures

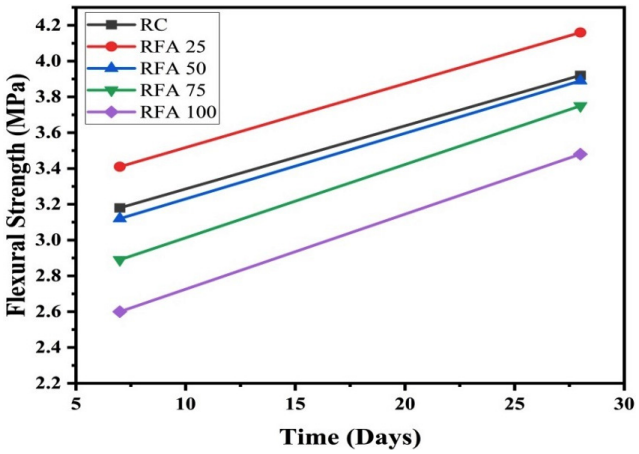


Fig. 7 Variations of flexural strength for different concrete mixtures

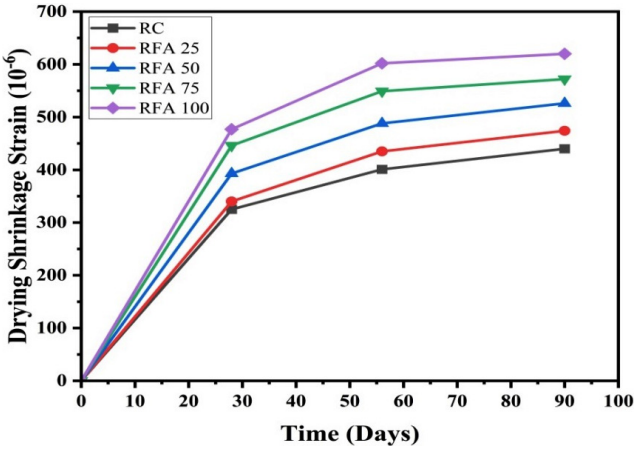


Fig. 9 Shrinkage strain for different concrete mixtures

2.3.4 Split tensile strength

For split tensile strength analysis, 30 specimens were cast in steel cylindrical molds with a diameter (ϕ) of 15 cm and a height (H) of 30 cm. These specimens were tested in a lateral position on a compression testing machine with a capacity of 2000 KN. The average split tensile strength values, derived from three specimens for each mix, were assessed at 7 and 28 days. The detailed outcomes are presented in Fig. 8.

2.3.5 Drying shrinkage

To assess drying shrinkage, 45 specimens measuring 75 × 75 × 285 mm were cast for the five different mixtures. These specimens were stored for 28 days and evaluated according to IS 516 (Part 6) (2020) [32] standards. Length variation over time was recorded using length comparator tools, and the results, displayed in Fig. 9, provided insights into the concrete mixes' drying shrinkage properties.

2.3.6 Electrical resistivity

Electrical resistivity, a key indicator of steel reinforcement bar corrosion risk in concrete, was determined for 30 specimens cast in cylindrical molds with 100 mm diameter and 200 mm height. Tests, conducted at 28 and 56 days using the Resipod Resistivity Meter following RILEM TC 154-EMC standards [33], are depicted in Fig. 10.

2.3.7 Rapid Chloride Penetration Test (RCPT)

Fig. 4 illustrates the standard configuration of the Rapid Chloride Penetration Test (RCPT) unit. Compliant with ASTM C1202-12 [34] guidelines, the mold has dimensions of 100 mm in diameter and 50 mm in height. Thirty specimens were meticulously prepared for this investigation. The RCPT setup consists of two separate chambers, one filled with sodium chloride (NaCl) at a concentration of 0.3 M, and the other with sodium hydroxide (NaOH) at a similar concentration. To ensure precision, the boundaries of the specimens and test cells were securely sealed. A constant current source of 60 V was connected, with the negative end linked to the NaCl solutions cell and the positive end to the NaOH solutions cell. Readings were recorded every 30 minutes for a duration of 6 hours until the current ceased. The tests were repeated at the ages of

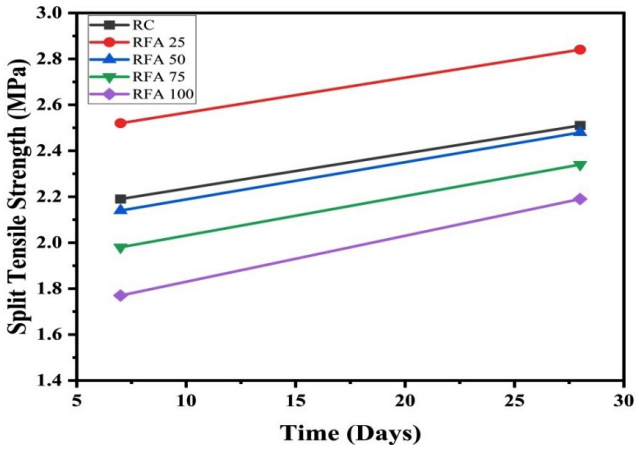


Fig. 8 Variations of split tensile strength for different concrete mixtures

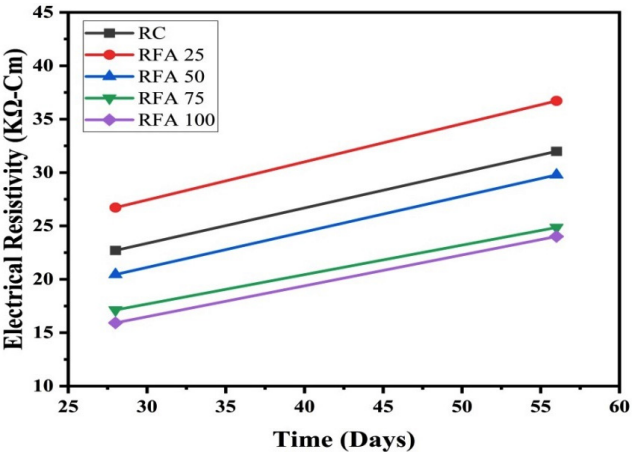


Fig. 10 Variation of electrical resistivity with RFA

28 and 56 days, where the total charge passed indicated the resistance to chloride ion penetration. Detailed results from these tests are presented in Fig. 11.

2.3.8 X-Ray Diffraction (XRD)

X-ray diffraction is employed to discern the phase characteristics and conduct mineralogical analysis of crystalline minerals within a concrete powder sample, particularly in various mixtures incorporating recycled fine aggregates. The Bruker D-8 advanced diffractometer system is utilized for scanning the samples within an angular range of 3–70 degrees, with a scanning speed of 2 degrees per minute and a sampling interval of 0.005 degrees at an angle of 2 degrees. The acquired scans are then analyzed using the Jade 7 X-ray diffraction software. The resulting peak intensities are graphically represented against 2 theta degrees on the *x*-axis, ranging from 0 to 70 degrees, while the intensity is plotted on the *y*-axis. The detailed test results are presented in Fig. 12.

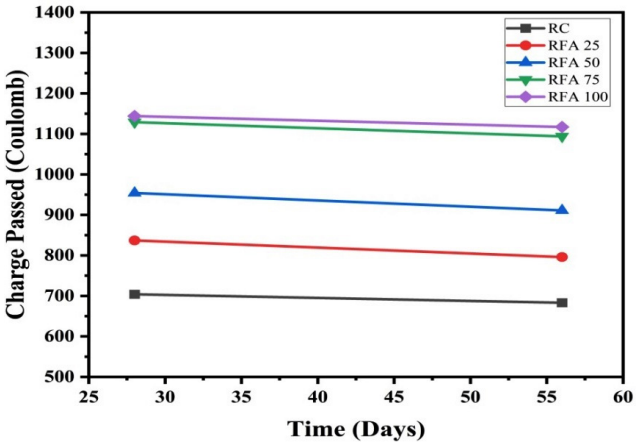


Fig. 11 Variation of chloride permeability with RFA

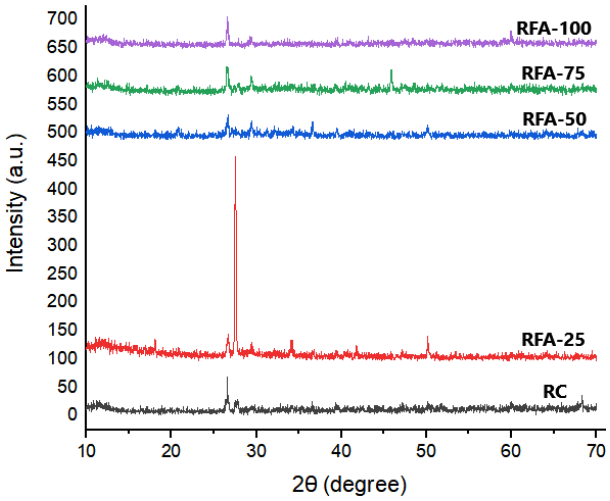


Fig. 12 XRD pattern for different concrete mixtures

2.3.9 Scanning Electron Microscopy (SEM)

SEM analysis was conducted to characterize Recycled Fine Aggregate (RFA) materials, involving a detailed examination of the microstructure and surface morphology of concrete samples from various concrete mixtures. The analysis was carried out using the JSM 6610V scanning electron microscope at the University Science Instrumentation Center (USIC) in Delhi, operating at 30 KV. The outcomes of the test are presented in Fig. 13.

2.3.10 Energy-Dispersive X-Ray Spectroscopy (EDAX)

Energy-dispersive X-ray spectroscopy (EDAX) is employed to conduct a detailed statistical analysis of the chemical composition of concrete samples. This study utilizes EDAX to qualitatively and quantitatively analyze the presence of different elements in various concrete mixtures. The outcomes of the tests are illustrated in Fig. 14.

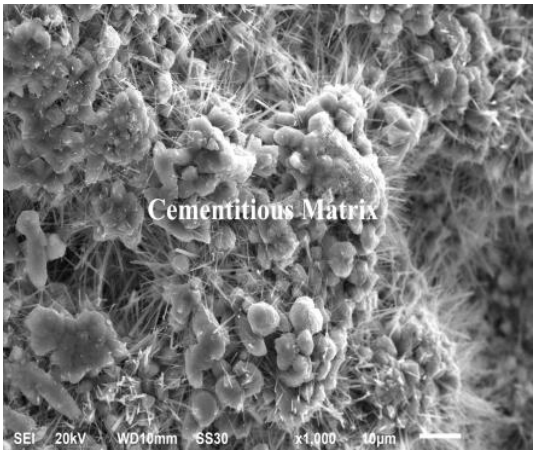
3 Results and discussion

3.1 Workability

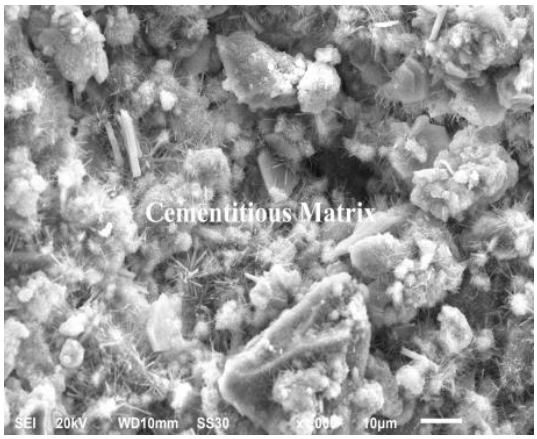
In Fig. 5, the graph illustrates the variations in slump values across different concrete mixtures. It is evident from Fig. 5 that as the proportion of recycled fine aggregates (RFA) increases, the slump of concrete decreases. The workability of concrete containing RFA falls within the medium range, ranging from 50 to 100 mm, as indicated by the slump values observed in all the mixtures. This decrease in slump is attributed to the higher water absorption capacity of RFA compared to natural aggregates. RFA contains old, adhered mortar on its surface, which absorbs more water. Consequently, at higher replacement percentages, more water is required to facilitate the hydration process. This increased water requirement leads to a reduction in slump, resulting in less workable concrete. The observed trend indicates that an escalation in the proportion of RFA correlates with a decrease in the slump of concrete. This pattern aligns with findings from previous studies conducted by Zhao et al. [35] and Kirthika and Singh [36], where a similar decrease in slump was observed with increasing RFA content in concrete.

3.2 Compressive strength

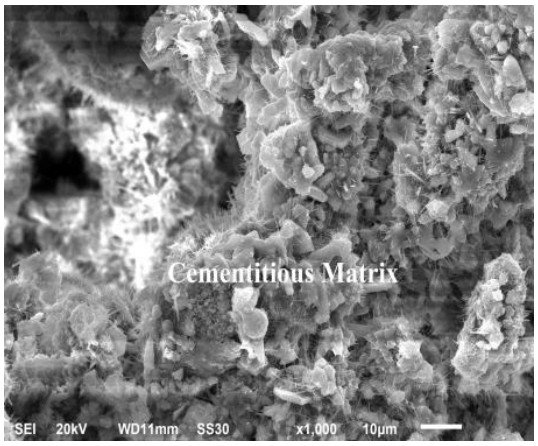
Fig. 6 presents the variations in compressive strength at 7 and 28 days for different replacement percentages of Recycled Fine Aggregates (RFA) concerning the reference mixture. When the C&D waste fine aggregates were replaced by 25%, the compressive strength of RFA 25 increased to 17.65% and 14.75% in comparison to the



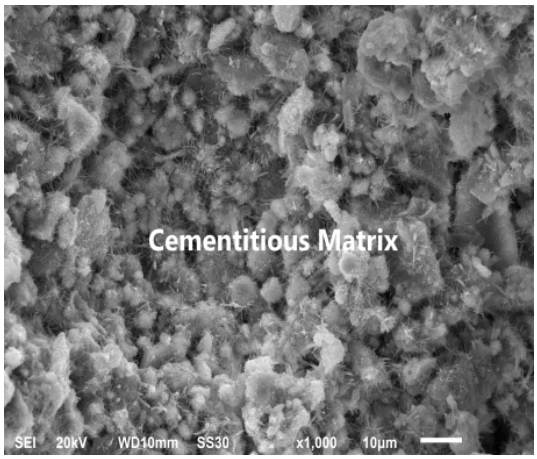
(a)



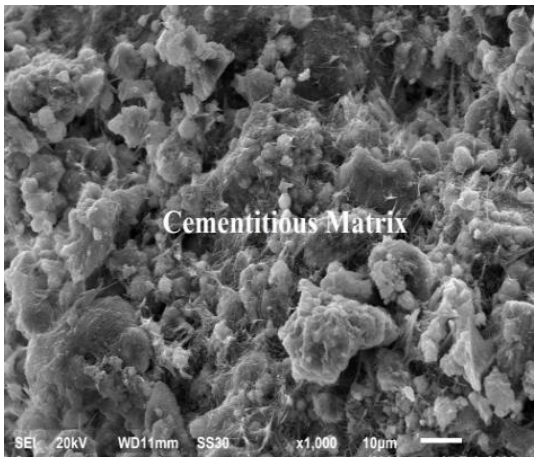
(b)



(c)



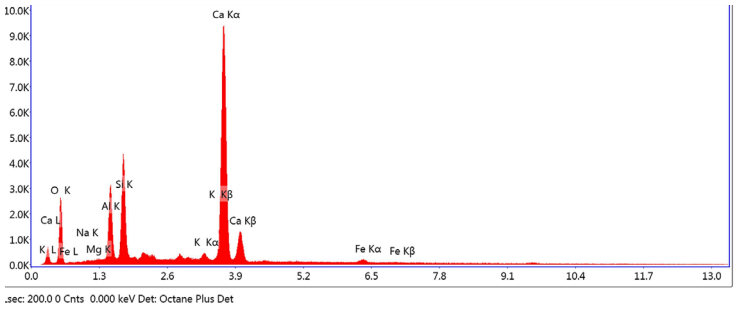
(d)



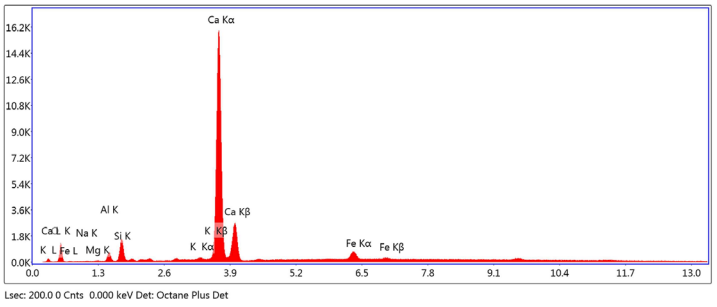
(e)

Fig. 13 SEM micrographs for different concrete mixtures (a) for RC, (b) for RFA 25, (c) for RFA 50, (d) for RFA 75, and (e) for RFA 100

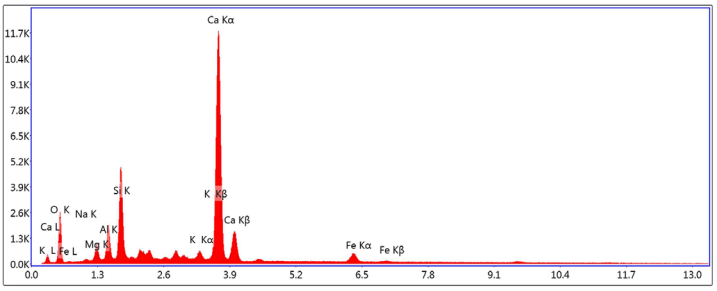
reference mixture at 7 and 28 days, respectively. However, increasing the RFA replacement to 50% resulted in a significant reduction in compressive strength, with RFA 50 showing a decrease to 9.95% and 6.90% at 7 and 28 days, respectively. Further escalating the RFA replacement to 75% led to a faster decline, with RFA 75 exhibiting reductions to 24.57% and 22.28% at 7 and 28 days, respectively. In the case of 100% RFA replacement, the compressive strength of RFA 100 plummeted to 29.89% and 24.94% concerning the reference mixture at 7 and 28 days, respectively.



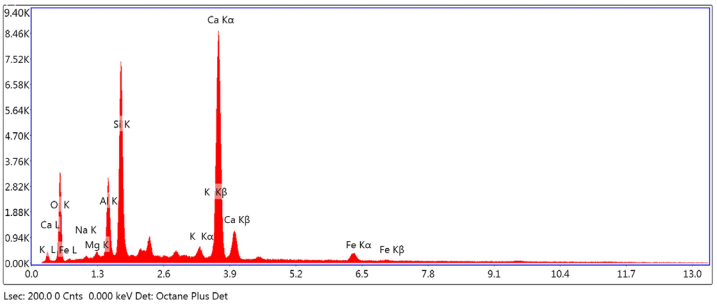
(a)



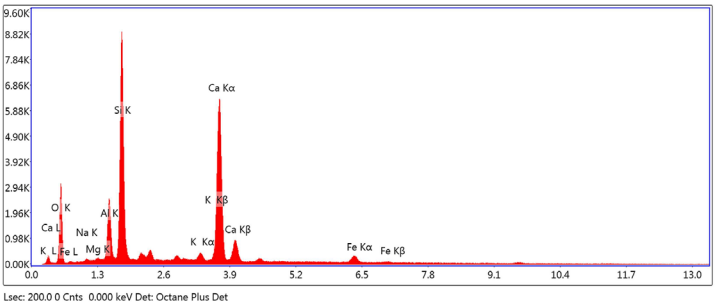
(b)



(c)



(d)



(e)

Fig. 14 EDAX analysis for different concrete mixtures (a) for RC, (b) for RFA 25, (c) for RFA 50, (d) for RFA 75, and (e) for RFA 100

The analysis of compressive strength test results reveals that concrete mixtures with higher percentages of replaced Recycled Fine Aggregates (RFA) exhibit lower compressive strength compared to the reference mixture. The ideal replacement percentage for recycled fine aggregates stands at 25%. However, the increase in compressive strength observed at the 25% replacement level of RFA can be attributed to the dense microstructure of RFA 25 concrete. It was observed that introducing RFA into concrete mixtures at a 25% replacement level results in minimal voids and optimal particle packing, which accounts for the higher strength observed in RFA 25. Particles of fine aggregates smaller than 600 microns play a significant role in forming the paste, and this paste must be present in sufficient quantity to fill the voids of larger particles. The strength order is closely linked to the percentage of fine aggregates passing between 600 and 150 microns. A wider gap between these sizes leads to higher strength within specified limits, whereas a smaller gap results in lower strength. At higher replacement percentages, there is an increase in void content and the presence of old adhered mortar, which weakens the bond with aggregates, ultimately leading to reduced strength. Among the mixtures, RFA 25 exhibited the highest compressive strength at 36.71 MPa, while RFA 100 displayed the lowest compressive strength at 24.01 MPa. Similar conclusions were drawn in studies conducted by Kirthika and Singh [36]. Furthermore, the results align with the findings of Srivastava et al. [37], where a 20% replacement of fine aggregates with demolished waste in a concrete grade of M25 showed improved workability and strength. Similarly, Ankesh et al.'s [38] research demonstrated that replacing 15% of recycled fine aggregates led to concrete with greater strength than the target strength. These findings substantiate the significance of replacement percentages in determining concrete strength and quality.

3.3 Flexural strength

Fig. 7 illustrates the variations in flexural strength at 7 and 28 days for different percentages of RFA replacement in comparison to the reference mixture. The results exhibit a consistent pattern similar to compressive strength. Notably, concrete mixes with higher RFA replacement percentages demonstrate decreased flexural strength compared to the reference mix. For a 25% RFA replacement, the flexural strength of the RFA 25 mix increased by 7.23% and 4.59% at 7 and 28 days, respectively, compared to the reference mix. Increasing the RFA replacement to 50% resulted in a marginal reduction of 1.88% and 0.76% in flexural strength at 7 and 28 days, respectively, for the RFA 50 mix in comparison to the reference mix. Further raising the RFA replacement to 75% led to a faster reduction in flexural strength, decreasing by 9.11% and 4.33% at 7 and 28 days, respectively, for the RFA 75 mix in comparison to the reference mix. In the case of 100% RFA replacement, the flexural strength of the RFA 100 mix was significantly reduced by 18.23% and 11.22% at 7 and 28 days, respectively, in comparison to the reference mix. Among the mixtures, RFA 25 exhibited the highest flexural strength at 4.16 MPa, whereas RFA 100 displayed the lowest flexural strength at 3.48 MPa. Similar observations have been made by other researchers [35, 38].

3.4 Split tensile strength

Fig. 8 displays the variation in split tensile strength at 7 and 28 days for different percentages of RFA replacement in comparison to the reference mixture. The results show a trend similar to compressive strength. It was observed that the split tensile strength of concrete mixtures is lower than that of the reference mix when RFA replacement is at a higher proportion. For a 25% RFA replacement, the split tensile strength of the RFA 25 mix increased by 15.0% and 13.14% at 7 and 28 days, respectively, compared to the reference mix. Increasing the RFA replacement to 50% resulted in a marginal reduction of 2.28% and 1.19% in split tensile strength at 7 and 28 days, respectively, for the RFA 50 mix in comparison to the reference mix. Further increasing the RFA replacement to 75% led to a faster reduction in split tensile strength, decreasing by 9.58% and 6.77% at 7 and 28 days, respectively, for the RFA 75 mix in comparison to the reference mix. In the case of 100% RFA replacement, the split tensile strength of the RFA 100 mix was significantly reduced by 19.17% and 12.74% at 7 and 28 days, respectively, in comparison to the reference mix. Specifically, the strength of RFA 25 increased by 13.14%, whereas the strength of RFA 100 decreased by 12.74% compared to the reference mix, which aligns with the findings reported by Kirthika and Singh [36].

3.5 Drying shrinkage

Fig. 9 illustrates the variations in shrinkage strain for different concrete mixtures at various drying ages. The graph demonstrates that as concrete dries, it experiences increased shrinkage, a relationship evident in the data. Notably, the slope of the drying shrinkage curve transitions from steep to flat over time, indicating a decrease in the rate of change of drying shrinkage. Additionally,

it was observed that as the percentage of fine aggregate replacement rises, the drying shrinkage of concrete consistently increases across all drying ages.

At the 28-day drying age, the shrinkage strain in RFA 25, RFA 50, RFA 75, and RFA 100 is respectively 4.61%, 20.92%, 37.23%, and 46.76% higher than that in the reference mixture. This discrepancy continues to grow, with RFA 100 exhibiting a 50.1% increase in shrinkage strain at 90 days compared to the reference mix. Remarkably, all mixtures' shrinkage strain values remained within the standard range outlined by Indian Standards, indicating their acceptability. Notably, RFA addition amplifies drying shrinkage due to the higher water absorption of RFA. This increase is attributed to the additional cement present around the surface of RFA, absorbing more water and subsequently shrinking significantly during the drying process. Despite this, all mixtures maintained their shrinkage within acceptable limits according to Indian Standards. Hence, RFA can be utilized within specific boundaries without adversely affecting shrinkage properties. This pattern aligns with the findings of Kirthika and Singh [36] indicating a systematic rise in drying shrinkage with increased proportions of recycled fine aggregates in concrete. These results corroborate the research by Mushtaq et al. [39] supporting the notion of a systematic increase in concrete drying shrinkage with higher proportions of waste foundry sand at various drying ages.

3.6 Electrical resistivity

Fig. 10 illustrates the variations in electrical resistivity for concrete mixtures with different percentages of C&D waste aggregates in comparison to the reference mixture at 28 and 56 days. In the case of a 25% replacement of C&D waste aggregates, the electrical resistivity of the RFA 25 mix decreased by 14.94% and 14.85% at 28 and 56 days, respectively, compared to the reference mixture. Increasing the C&D waste aggregates replacement to 50% resulted in a substantial reduction in electrical resistivity, with the RFA 50 mix showing decreases of 17.06% and 16.80% at 28 and 56 days, respectively, in comparison to the reference mix. Further increasing the replacement percentage to 75% led to a faster reduction in electrical resistivity, with the RFA 75 mix showing decreases of 34.28% and 34.25% at 28 and 56 days, respectively. In the case of 100% replacement of C&D waste aggregates, the electrical resistivity of the RFA 100 mix decreased by 44.70% and 44.68% at 28 and 56 days, respectively, compared to the reference mixture.

The results indicate that concrete mixtures with higher percentages of C&D waste aggregates exhibit lower electrical resistivity compared to the reference mixture. This decrease in electrical resistivity can be attributed to the high porosity of the C&D waste aggregates, which trap water with dissolved ions, creating a low-resistance path for electric current. Among the mixtures, RC and RFA 50 have comparable resistivity, followed by RFA 75 and RFA 100, which have the lowest electrical resistivity. Based on these findings, it can be concluded that concrete produced with up to 75% replacement of C&D waste aggregates has a low risk of corrosion; whereas concrete produced with 100% replacement poses a moderate risk of corrosion. Similar results regarding the electrical resistivity of concrete after increasing C&D waste aggregate replacement have been reported in previous studies [36]. This study aligns with the research conducted by Arredondo-Rea et al. [40] who found that replacing no more than 30% of coarse aggregates and 20% of fine aggregates with recycled aggregates does not significantly influence concrete's electrical resistivity. When comparing these findings, it suggests that concrete made with C&D waste aggregates poses a moderate risk of corrosion to the steel bars used within the concrete.

3.7 Rapid chloride penetration

Fig. 11 displays the variations in chloride permeability for concrete mixtures with different percentages of C&D waste aggregates in comparison to the reference mixture at 28 and 56 days. When the RFA replacement percentage was 25%, the chloride permeability of the RFA 25 mix decreased by 18.89% and 16.54% at 28 and 56 days, respectively, compared to the reference mixture. Increasing the replacement percentage to 50% resulted in a substantial reduction in chloride permeability, with the RFA 50 mix showing decreases of 35.51% and 33.38% at 28 and 56 days, respectively, compared to the reference mix. Further increasing the RFA replacement to 75% led to a faster reduction in chloride permeability, with the RFA 75 mix showing decreases of 60.36% and 60.17% at 28 and 56 days, respectively. At 100% replacement of RFA, the chloride permeability of the RFA 100 mix reduced by 62.50% and 63.54% at 28 and 56 days, respectively, compared to the reference mix.

The results indicate that concrete mixtures with higher percentages of C&D waste aggregates exhibit higher chloride permeability compared to the reference mixture, implying a decrease in concrete durability. This decline

in chloride permeability is attributed to the high porosity of the C&D waste aggregates, which trap water containing dissolved ions, creating a path of low resistance to electrical current. Notably, the highest chloride permeability is observed at 100% replacement of RFA. Based on these findings, it can be concluded that concrete produced with up to 50% replacement of C&D waste aggregates possesses high durability, while concrete produced with more than 75% replacement of RFA exhibits moderate durability. The increase in RFA replacement percentage in concrete leads to elevated chloride permeability and reduced durability. Specifically, concrete made with RFA demonstrates high durability at up to 50% replacement and moderate durability at 75% and 100% replacement percentages. Similar patterns were noted by Kirthika and Singh [36], indicating reduced penetration of chloride ions as concrete ages, regardless of RFA content. These findings align with the research conducted by Arredondo-Rea et al. [40], examining the impact of recycled aggregates on concrete's chloride permeability. A comparative analysis reveals that concrete made with C&D waste aggregates exhibits moderate chloride permeability.

3.8 X-Ray Diffraction (XRD)

The XRD results reveal a decrease in the net intensity of minerals like CSH, CH, and Ettringite in response to the increasing replacement percentage of RFA. This decrease signifies a reduction in the overall density of CSH in the concrete. Fig. 12 displays the XRD patterns for various concrete mixtures, including RC, RFA 25, RFA 50, RFA 75, and RFA 100. The diffraction peak angles for different compounds are detailed in Table 5.

The XRD analysis demonstrates that the incorporation of recycled fine aggregates impacts the phase composition of concrete minerals, such as C-S-H, CH, and Ettringite, indicating the formation of a dense microstructure. Peaks with higher net intensity are associated with lower RFA replacement percentages. As the percentage of RFA replacement increases, the net intensity of different minerals at various peaks decreases. Consequently, the study reveals a decline in concrete strength with higher RFA replacement percentages. This research aligns remarkably with a study by Silva et al., who investigated cement paste incorporating 12% concrete floor polishing waste (CPFW) [41].

Table 5 Diffraction peaks angles of various compounds for different concrete mixtures

Concrete mix	CSH (degree)	Ettringite (degree)	CH (degree)
RC	26.450	36.780	47.299
RFA 25	26.337	34.146	50.175
RFA 50	26.596	36.606	50.110
RFA 75	26.575	39.385	60.001
RFA 100	26.571	39.523	59.930

CSH – Calcium Silicate Hydroxide, CH – Calcium Hydroxide, Ettringite – Hydrated Calcium Aluminum Sulfate Hydroxide

3.9 Scanning Electron Microscopy (SEM)

Fig. 13 presents SEM micrographs obtained at 28 days for various concrete mixtures subjected to SEM analysis. These micrographs reveal the formation of crucial hydration products responsible for concrete strength, including calcium hydroxide (CH), calcium silicate hydroxide (CSH), and ettringite. These compounds manifest as distinct crystal structures: hexagonal shapes indicate CH gel, flower-shaped structures signify CSH gel and needle-like formations represent ettringite.

The SEM micrographs demonstrate that in the concrete mixture RFA 25, there is heightened growth of CH, CSH, and ettringite compared to RC, leading to increased strength. The additional cement surrounding the recycled fine aggregates fosters the production of more hydration products, thereby enhancing concrete strength. Conversely, in RFA 50, CH, CSH, and ettringite development is less than in RC, resulting in a decrease in strength due to inadequate hydration of cement particles. The presence of non-reacted particles in the hardened cement paste further weakens the concrete. In RFA 75, minimal calcium crystal presence was found on the cement paste particles, indicating voids and loose structures, leading to decreased compressive strength. RFA 100 results in a porous microstructure as the cement around recycled fine aggregates does not undergo complete hydration, yielding fewer hydration products. SEM analysis indicates that lower proportions of RFA generate denser CSH gel, strengthening the cement paste matrix. However, excessive RFA leads to fragile mixtures and insufficient CSH production, resulting in reduced strength. In summary, the findings show that adding 25% RFA improves concrete microstructure, enhancing compressive strength. A 50% replacement results in less dense concrete and reduced strength. At 75% replacement, voids and loose structures weaken the concrete, while a 100% replacement yields a porous microstructure and insufficient strength. These results emphasize the delicate balance needed when incorporating RFA, ensuring optimal strength and durability in concrete mixtures.

3.10 Energy Dispersive X-Ray Spectroscopy (EDAX)

Fig. 14 shows quantitate and qualitative analyses of various elements present in different mixtures by EDAX analysis.

The EDAX analysis reveals the presence of elements such as Calcium (Ca), Oxygen (O), Silicon (Si), Aluminum (Al), Iron (Fe), Potassium (K), Sodium (Na), and Magnesium (Mg) in the concrete mixtures. Specifically, in the RFA 25 mix, there is an increase in the percentage of calcium compared to RC, fostering the formation of crucial hydration products like CH, CSH, and CASH. However, at higher RFA replacement percentages, the calcium content decreases, leading to a reduction in hydration products. Conversely, silica content decreases at lower RFA replacement percentages but gradually increases at higher replacements. The lower alumina content results in diminished ettringite formation. SEM results offer compelling evidence that additional CSH is formed up to a 25% replacement level for RFA. The chemical composition obtained via EDAX confirms that higher RFA replacement percentages diminish the formation of calcium compounds by decreasing calcium content in the mixture. This reduction weakens the concrete mixture's strength. A quantitative summary of the chemical composition of different elements, as determined by EDAX analysis, is outlined in Table 6.

4 Conclusions

This research paper advocates for the development of sustainable concrete by utilizing Construction and Demolition (C&D) waste as Recycled Fine Aggregates (RFA), thereby endorsing eco-friendly practices, waste reduction, and the promotion of circular economy principles. The study underscores that replacing natural fine aggregates with recycled counterparts significantly influences the properties of hardened concrete.

Key conclusions drawn from the study are as follows:

- The mechanical properties of concrete show an increase up to a specific limit and then decline beyond the optimum point. The ideal replacement percentage for RFA in concrete is 25%. Concrete exhibits superior strength characteristics at this replacement level and diminishes in quality at 100% replacement.
- Concrete with 25% recycled fine aggregates outperforms that with natural fine aggregates. RFA 25 exhibits a 14.75% increase in compressive strength, 6.61% in flexural strength, and 13.14% in split tensile strength compared to traditional concrete. Concrete with 50% RFA yields strength equivalent to that with 100% natural fine aggregates.
- The addition of RFA increases drying shrinkage due to higher water absorption. Proper curing of RFA-incorporated concrete is crucial to maintaining its shrinkage properties.
- Higher RFA replacement reduces electrical resistivity, potentially increasing the corrosion rate of steel reinforcements. RFA 25 demonstrates 17.65% higher electrical resistivity than traditional concrete, indicating superior corrosion resistance.
- Higher RFA replacement leads to increased chloride permeability and reduced durability. RFA 25 exhibits an 18.83% higher resistance to chloride penetration compared to traditional concrete. RFA 25 and RFA 50 display high durability, whereas RFA 75 and RFA 100 show moderate durability.
- XRD, SEM, and EDAX analyses reveal that at lower replacement percentages, the pozzolanic reaction enhances strength by forming additional hydration products. Conversely, at higher levels, strength diminishes as the hydration process has not reached the desired level.

Table 6 Percentage weight of various elements for different mixtures

Mixture ID	(%)	Ca-K	O-K	Si-K	Al-K	Fe-K	K-K	Na-K	Mg-K
RC	Weight	42.76	38.06	8.89	6.62	2.51	1.15	0.01	0
	Atomic	26.14	58.27	7.75	6.01	1.1	0.72	0.01	0
RFA-25	Weight	64.84	21.29	3.01	1.28	9.15	0.32	0.09	0.02
	Atomic	49.33	40.57	3.27	1.45	5.0	0.25	0.12	0.02
RFA-50	Weight	45.84	33.15	8.68	3.44	5.44	1.46	0.12	1.88
	Atomic	29.56	53.55	7.99	3.29	2.52	0.96	0.14	2.0
RFA-75	Weight	35.4	36.93	14.33	5.92	5.07	1.72	0.26	0.36
	Atomic	21.64	56.55	12.5	5.37	2.22	1.08	0.28	0.36
RFA-100	Weight	30.92	36.84	19.62	5.61	5.11	1.44	0.33	0.13
	Atomic	18.69	55.78	16.92	5.03	2.22	0.89	0.34	0.13

Ca – Calcium, O – Oxygen, Si – Silicon, Al – Aluminum, Fe – Iron, K – Potassium, Na – Sodium, and Mg – Magnesium

This approach not only mitigates construction industry waste but also conserves natural resources. Sustainable concrete, with comparable mechanical properties to traditional concrete, emerges as a viable alternative for construction projects. Future research endeavors can focus on optimizing this process for wider adoption within the industry.

Statements and declarations

Author's credit statement

Harish Panghal: Conceptualization, Methodology, Formal Analysis, Investigation, Resources, Data Curation, Writing, Original Draft Preparation, Writing Review and Editing, and Visualization.

Awadhesh Kumar: Conceptualization, Methodology, Validation, Resources, Review and Editing, Supervision, Project Administration, and Funding Acquisition.

Data availability

All the data, materials, and methodology adopted during the research have been mentioned in this article in the form of figures and tables.

Ethics approval

Each of the authors confirms that this manuscript has not been previously published and is not currently under consideration by any other journal.

Consent to participate

The authors declare consent to participate in the research work.

Consent to publication

The authors of the research paper agree with the publication.

Funding

The authors declare that they did not receive any money from grants or any other sources to help them with the preparation of this publication.

Acknowledgments

The personnel of Delhi Technological University, Shahbad Daultpur Village, Rohini, New Delhi, Department of Civil Engineering, are gratefully acknowledged by the authors for their assistance during the research.

References

[1] Kaza, S., Van Woerden, F. "Introduction", In: What a Waste 2.0: A Global Snapshot of Solid Waste Management to 2050, The World Bank, 2018, pp. 1–16. ISBN 978-1-4648-1329-0 https://doi.org/10.1596/978-1-4648-1329-0_ch1

[2] Ahmed, S. F. U. "Properties of Concrete Containing Construction and Demolition Wastes and Fly Ash", Journal of Materials in Civil Engineering, 25(12), pp. 1864–1870, 2013. https://doi.org/10.1061/(ASCE)MT.1943-5533.0000763

[3] Taffese, W. Z. "Suitability Investigation of Recycled Concrete Aggregates for Concrete Production: An Experimental Case Study", Advances in Civil Engineering, 2018, 8368351, 2018. https://doi.org/10.1155/2018/8368351

[4] Panghal, H., Kumar, A. "Effects of surface modified recycled coarse aggregates on concrete's mechanical characteristics", Materials Research Express, 10(9), 095506, 2023. https://doi.org/10.1088/2053-1591/acf915

[5] Husain, A., Assas, M. M. "Utilization of demolished concrete waste for new construction", World Academy of Science, Engineering and Technology International Journal of Civil, Environmental, Structural, Construction and Architectural Engineering, 7(1), pp. 37–42, 2013. [online] Available at: https://www.researchgate.net/publication/292770154 [Accessed: 30 June 2020]

[6] Dhanya, B. S., Santhanam, M. "Performance evaluation of rapid chloride permeability test in concretes with supplementary cementitious materials", Materials and Structures, 50(1), 67, 2017. https://doi.org/10.1617/s11527-016-0940-3

[7] Sakthivel, T., Gettu, R., Pillai, R. G. "Drying shrinkage of concrete with blended cementitious binders: experimental study and application of models", The Indian Concrete Journal, 95(10), pp. 34–50, 2021.

[8] Cosoli, G., Mobili, A., Tittarelli, F., Revel, G. M., Chiariotti, P., "Electrical resistivity and electrical impedance measurement in mortar and concrete elements: A systematic review", Applied Sciences, 10(24), 9152, 2020. https://doi.org/10.3390/app10249152

[9] Iffat, S., Emon, A. B., Manzur, T., Ahmad, S. I. "An experiment on durability test (RCPT) of concrete according to ASTM standard method using low-cost equipments", Advances Materials Research, 974, pp. 335–340, 2014. https://doi.org/10.4028/www.scientific.net/AMR.974.335

[10] Zhang, M.-H., Gjørv, O. E. "Microstructure of the interfacial zone between lightweight aggregate and cement paste", Cement and Concrete Research, 20(4), pp. 610–618, 1990. https://doi.org/10.1016/0008-8846(90)90103-5

[11] Yaprak, H., Aruntas, H. Y., Demir, I., Simsek, O., Durmus, G. "Effects of the fine recycled concrete aggregates on the concrete properties", International Journal of Physical Sciences, 6(10), pp. 2455–2461, 2011. https://doi.org/10.5897/IJPS11.253

[12] Whiting, B. A., McCarthy, T. J., Lume, E. "Drying shrinkage of concrete made from recycled concrete aggregate", In: Samali, B., Attard, M. M., Song, C. (eds.) From Materials to Structures: Advancement through Innovation, Taylor & Francis Group, 2013, pp. 1199–1204. ISBN 9780415633185

[13] Yadhu, G., Devi, S. A. "An Innovative Study on Reuse of Demolished Concrete Waste", Journal of Civil & Environmental Engineering, 5(5), 185, 2015. https://doi.org/10.4172/2165-784X.1000185

[14] Wang, H., Sun, X., Wang, J., Monteiro, P. J. M. "Permeability of concrete with recycled concrete aggregate and pozzolanic materials under stress", Materials, 9(4), 252, 2016. https://doi.org/10.3390/ma9040252

[15] Gupta, V., Patel, A., Dubey, G., Chouhary, J., Gupta, R., Dhawade, S. "Experimental Investigation of Concrete on Replacement of Aggregates with Demolished Concrete Waste", International Advanced Research Journal in Science, Engineering and Technology (IARJSET), 5(S3), CACE-2018, pp. 190–197, 2018.

[16] Kurda, R., de Brito, J., Silvestre, J. D. "Water absorption and electrical resistivity of concrete with recycled concrete aggregates and fly ash", Cement and Concrete Composites, 95, pp. 168–182, 2019. https://doi.org/10.1016/j.cemconcomp.2018.10.004

[17] Ju, M., Park, K., Park, W.-J. "Mechanical Behavior of Recycled Fine Aggregate Concrete with High Slump Property in Normal- and High-Strength", International Journal of Concrete Structures and Materials, 13(1), 61, 2019. https://doi.org/10.1186/s40069-019-0372-x

[18] Kirthika, S. K., Singh, S. K., Chourasia, A. "Performance of Recycled Fine-Aggregate Concrete Using Novel Mix-Proportioning Method", Journal of Materials in Civil Engineering, 32(8), 04020216, 2020. https://doi.org/10.1061/(ASCE)MT.1943-5533.0003289

[19] Zaid, O., Zamir Hashmi, S. R. "Experimental Study on Mechanical Performance of Recycled Fine Aggregate Concrete Reinforced With Discarded Carbon Fibers", Frontiers in Materials, 8, 771423, 2021. https://doi.org/10.3389/fmats.2021.771423

[20] Amadi, I. G., Beushausen, H., Alexander, M. G. "Multi-Technique Approach to Enhance the Properties of Fine Recycled Aggregate Concrete", Frontiers in Materials, 9, 893852, 2022. https://doi.org/10.3389/fmats.2022.893852

[21] Velay-Lizancos, M., Martinez-Lage, I., Azenha, M., Granja, J., Vazquez-Burgo, P. "Concrete with fine and coarse recycled aggregates: E-modulus evolution, compressive strength and non-destructive testing at early ages", Construction and Building Materials, 193, pp. 323–331, 2018. https://doi.org/10.1016/j.conbuildmat.2018.10.209

[22] Özalp, F., Yilmaz, H. D., Kara, M., Kaya, Ö., Şahin, A. "Effects of recycled aggregates from construction and demolition wastes on mechanical and permeability properties of paving stone, kerb and concrete pipes", Construction and Building Materials, 110, pp. 17–23, 2016. https://doi.org/10.1016/j.conbuildmat.2016.01.030

[23] Joseph, H. S., Pachiappan, T., Avudaiappan, S., Flores, E. I. S. "A Study on Mechanical and Microstructural Characteristics of Concrete Using Recycled Aggregate", Materials, 15(21), 7535, 2022. https://doi.org/10.3390/ma15217535

[24] Zakaria, M., Cabrera, J. G. "Performance and Durability of Concrete Made with Demolition Waste and Artificial Fly Ash-clay Aggregates", Waste Management, 16(1–3), pp. 151–158, 1996. https://doi.org/10.1016/S0956-053X(96)00038-4

[25] IS "IS 269 Ordinary Portland Cement", Bureau of Indian Standards, New Delhi, India, 2015.

[26] IS "IS 383 Specification for Coarse and Fine Aggregates From Natural Sources For Concrete", Bureau of Indian Standards, New Delhi, India, (Reaffirmed 2002), 1970.

[27] IS "IS 2386-3 Method of Test for aggregates for concrete, Part 3: Specific gravity, density, voids, absorption and bulking", Bureau of Indian Standards, New Delhi, India, (Reaffirmed 2002), 1963.

[28] IS "IS:2386-4 Methods of test for Aggregates for Concrete, Part 4: Mechanical properties", Bureau of Indian Standards, New Delhi, India, 1963.

[29] IS "IS 9103 Specification for Concrete Admixtures", Bureau of Indian Standards, New Delhi, India, 1999.

[30] IS "IS 2645 Integral Waterproofing Compounds for Cement Mortar and Concrete - Specification", Bureau of Indian Standards, New Delhi, India, 2003.

[31] IS "IS 1199 Methods of sampling and analysis of concrete", Bureau of Indian Standards, New Delhi, India, 1959.

[32] IS "IS 516 (Part 6) Hardened Concrete – Methods of Test Part 6 Determination of Drying Shrinkage and Moisture Movement of Concrete Samples", Bureau of Indian Standards, New Delhi, India, 2020. [online] Available at: www.standardsbis.in [Accessed: 30 June 2020]

[33] Polder, R., Andrade, C., Elsner, B., Vennesland, Ø., Gulikers, J., Weidert, R., Raupach, M. "Test methods for on site measurement of resistivity of concrete", Materials and Structures, 33(10), pp. 603–611, 2000. https://doi.org/10.1007/BF02480599

[34] ASTM "ASTM C1012-12 Standard Test Method for Electrical Indication of Concrete's Ability to Resist Chloride Ion Penetration", ASTM International, West Conshohocken, PA, USA, 2012. https://doi.org/10.1520/C1202-12

[35] Zhao, Z., Remond, S., Damidot, D., Xu, W. "Influence of fine recycled concrete aggregates on the properties of mortars", Construction and Building Materials, 81, pp. 179–186, 2015. https://doi.org/10.1016/j.conbuildmat.2015.02.037

[36] Kirthika, S. K., Singh, S. K. "Durability studies on recycled fine aggregate concrete", Construction and Building Materials, 250, 118850, 2020. https://doi.org/10.1016/j.conbuildmat.2020.118850

[37] Srivastava, V., Monish, M., Ranjan, R., Mehta, P. K. "Demolition Waste in Concrete", In: Matsagar, V. (ed.) Materials, Design and Testing, Bloomsbury Publishing India Pvt Ltd, 2015, pp. 4234–4242. ISBN 978-93-84898-71-7 [online] Available at: https://www.researchgate.net/publication/278300168 [Accessed: 15 June 2015]

[38] Ankesh, S. B., Venugopal, M. L., Sumanth, S., Vinodkumar, Abishek, B. S. "Experimental Study on Concrete Blocks from Recycled Aggregates", International Research Journal of Engineering and Technology, 7(8), pp. 277–288, 2020.

[39] Mushtaq, S. M., Siddique, R., Goyal, S., Kaur, K. "Experimental studies and drying shrinkage prediction model for concrete containing waste foundry sand", Clean Engineering and Technology, 2, 100071, 2021. https://doi.org/10.1016/j.clet.2021.100071

[40] Arredondo-Rea, S. P., Corral-Higuera, R., Gómez-Soberón, J. M., Gámez-Garcia, D. C., Bernal-Camacho, J. M., Rosas-Casarez, C. A., Ungsson-Nieblas, M. J. "Durability parameters of reinforced recycled aggregate concrete: Case study", Applied Sciences, 9(4), 617, 2019.
https://doi.org/10.3390/app9040617

[41] Silva, L. A., Nahime, B. O., Lima, E. C., Akasaki, J. L., Reis, I. C. "XRD investigation of cement pastes incorporating concrete floor polishing waste", Cerâmica, 66(380), pp. 373–378, 2020.
https://doi.org/10.1590/0366-69132020663802956

Environmental Science and Pollution Research (2024) 31:8186–8209
https://doi.org/10.1007/s11356-023-31598-y

RESEARCH ARTICLE

Synergistic potency of ultrasound and solar energy towards oxidation of 2,4-dichlorophenol: a chemometrics approach

Harsh Pipil[1] · Shivani Yadav[1] · Sunil Kumar[2] · Anil Kumar Haritash[1]

Received: 27 September 2023 / Accepted: 13 December 2023 / Published online: 4 January 2024
© The Author(s), under exclusive licence to Springer-Verlag GmbH Germany, part of Springer Nature 2024

Abstract

Industrial units based on chemical processes—the textile and paper industries—are major sources of chlorophenols in the environment, and chlorophenolic compounds persist within the environment for a long time with high toxicity levels. The photo-assisted Fenton's and photocatalysis processes were investigated for the degradation of chlorophenols in the present study. Response surface methodology was employed to get optimised conditions for photocatalysis and photo-Fenton process-governing factors, thus, yielding a profound removal efficiency. Under optimised conditions, with a photocatalyst dose of 0.2 g/L, oxidant concentration of 10.0 mM and pH 5.0, complete removal of 2,4-dichlorophenol (2,4-DCP) was observed in 210 minutes in photocatalytic treatment. In the case of the photo-Fenton process, at an H_2O_2 dose of 5.0 mM and Fe^{2+} concentration of 0.5 mM, the organic pollutant was eliminated within 5 minutes of reaction time under acidic conditions (pH 3.0). The RSM model reported the perfect fit of experimental data with the predicted response. Among different isotherm models, the Langmuir isotherm was the best fit. The process followed pseudo-first order rate kinetics among various kinetics models. For the obtained optimised conditions, sonication and solar energy-driven processes were incorporated to study enhanced mineralisation. The solar-assisted Fenton process reported maximum mineralisation (90%) and cost-effective ($0.01/litre for 100 mg/L 2,4-DCP) treatment among different hybrid oxidation processes. The work provides insight into harnessing the naturally available solar energy, reducing the overall treatment cost and opting for a sustainable treatment method.

Keywords 2,4-Dichlorophenol · Photocatalysis · Photo-Fenton · Ultrasonication · Solar-driven AOPs

Introduction

Emerging recalcitrant contaminants in effluent originating from industrial manufacturing units pose threats to human health and the eco-biota when discharged into the environment without treatment. With the rapid development of the global economy, these chemical compounds are essential in many industrial activities (Igbinosa et al. 2013). Nevertheless, these persistent organic compounds have the potential to cause considerable environmental harm even when present in low-content (Faludi et al. 2015). Owing to their broad-spectrum antimicrobial properties, chlorophenols (CPs) have been used as preservatives for wood, leather, vegetable fibres, paints, disinfectants, etc. (Van Aken et al. 2019). In addition, they are also applied as insecticides, herbicides, and fungicides in the agriculture, and have applications in pharmaceuticals, production of textile dyes, and bleaching of pulp (Ye et al. 2019; Škrbić 2007). Over the last half-century, they have become quantitatively significant toxicants in the environmental matrix. The treatment, disposal, and management of chlorophenols have severely challenged the environment and health (Weber et al. 2008). These xenobiotics are a significant concern considering their recalcitrance to degradation. Studies have reported the presence of 2,4-DCP concentration of 630 (± 50) µg/L, 2,4,6-trichlorophenol concentration of 320

Responsible Editor: George Z. Kyzas

✉ Shivani Yadav
shivaniyadav_phd2k19@dtu.ac.in

Harsh Pipil
harsh_phd2k19@dtu.ac.in

Sunil Kumar
sunil.kumar@solarischemtech.com

Anil Kumar Haritash
akharitash@dce.ac.in

[1] Department of Environmental Engineering, Delhi Technological University, Delhi 110042, India

[2] Research and Development, Solaris Chemtech Industries, Bhuj, Gujarat 370001, India

(± 30) µg/L, and 2,4,5-trichlorophenol concentration of 2660 (± 210) µg/L in industrial effluents being discharged (Shoneye et al. 2022; USEPA 2004). Post-treatment, the individual chlorinated phenols were found in trace amounts, except for 2,4,5-TCP with a concentration of 560 (± 50) µg/L (Shoneye et al. 2022; USEPA 2004). The noxious effect of chlorophenols and their derivatives on the eco-biota are induced acute toxicity, histopathological changes, mutagenicity, teratogenicity, and carcinogenicity (Wei et al. 2019). The transformation of chlorophenols, in particular, could lead to an increase in toxicity due to the formation of electrophilic metabolites that may bind and damage DNA or gene products (Michałowicz and Duda 2007). The serious health concerns make it imperative to assess and control the fate of chlorophenols to protect the environment and public health. The negative effects of xenobiotics, such as dichlorophenols and their derivatives, in eco-biota may be reduced considering the recent development in the field of environmental microbiology (Nagy et al. 2023; Zhumakayev et al. 2021). The diverse community, adaptability, versatility, and metabolic potential of the microbial community have been harnessed to treat environmental contaminants (Rout et al. 2021; Zhumakayev et al. 2021). For instance, the *Leptosphaerulina chartarum* strain was used to degrade aniline and phenol compounds including 2,4-DCP (Sajben-Nagy et al. 2014). Chlorophenols such as 2,4-dichlorophenol (2,4-DCP), 2,6-dichlorophenol (2,6-DCP), and 2-chlorophenol have been effectively degraded via microbial action under aerobic and anaerobic conditions, though the pace of biodegradation is relatively slower (Field and Sierra-Alvarez 2008). Nonetheless, the biological treatment was inefficient since these recalcitrants are either not metabolisable or are transformed into other metabolites that accumulate in the environment (Rout et al. 2021). Conventional treatment units such as ion exchange, coagulation-flocculation, adsorption, flotation, membrane filtration, and ion-pair extraction generate by-products during treatment that demand additional treatment costs. Although membrane technology which includes microfiltration, nano-filtration, and ultra-filtration has become one of the prominent methods for the removal of higher concentrations of CPs from wastewater, the technology can be incorporated with other wastewater treatment systems such as advanced oxidation processes (AOPs) (Yadav et al. 2023a). In recent years, AOPs have been widely used to address degradation and the adequate mineralisation of organic contaminants (Yadav et al. 2023a; Yadav et al. 2023b). These include photocatalysis (H_2O_2/UV/photocatalyst), Fenton's and photo-Fenton's process (H_2O_2/Fe^{2+}), sonolysis using ultrasonic irradiation, and solar oxidation processes (Verma and Haritash 2019, 2020). The novel processes are characterised by producing the highly reactive oxidation species (reduction potential 2.8 eV) as a primary oxidant (Pipil et al. 2022). These potent reactive oxidising species (ROS) (mainly hydroxyl radicals) interact with the toxicants and trigger progressive oxidation, transforming the parent compounds into more innocuous and biodegradable intermediate products (Pedrazzani et al. 2019). In the current study, the efficiency of photocatalysis and photo-Fenton was used to assess the degradation profile of 2,4-DCP. Heterogeneous photocatalysis uses photocatalysts like TiO_2 and UV light to mineralise pollutants into end products like mineral acids, CO_2, and H_2O (Yadav et al. 2023a)). The concentration and type of catalyst, pH, light intensity, irradiation time, and light wavelength are among the key parameters influencing photocatalysis and its degradation routes (Ge et al. 2021). Fenton's process is one of the most effective methods to treat harmful pollutants. It has practical application owing to its wide application range, strong anti-interference ability, rapid degradation, acceptable cost, and easy operation.

In the present study, Degussa P25 nano-TiO_2 was the preferred photocatalyst because of its high efficiency, availability, low cost, and photochemical stability. The main aim of the present study is to explore the feasibility of photocatalytic and Fenton's processes towards the degradation of 2,4-dichlorophenol (2,4-DCP). The study outlines the effect of operating conditions, and optimisation of the factors that control the treatment processes (catalyst dose, oxidant concentration, and pH). Furthermore, a statistical approach, RSM (response surface methodology) was employed to validate the optimum conditions for maximum contaminant removal. In addition, the analysis of variance (ANOVA) was used to statistically ascertain the significance of regression models, and numerical optimisation was used to maximise the system desirability for degradation of the organics. The study also entails the application of integrated AOPs for studying the synergistic effect of the different oxidising processes for efficient removal.

Materials and methods

Chemicals

2,4-DCP (98% purity), KOH and H_2SO_4 (used for pH adjustment) were procured from Central Drug House (CDH), India. $FeSO_4.7H_2O$ as the source of Fe (II) and hydrogen peroxide (30% w/v) were procured from Thermo Scientific. Degussa P25 Nano-TiO_2 (anatase to rutile ratio-80:20) was obtained from Evonik Industries, Germany. Hydroxylammonium chloride, sodium acetate, and 1, 10-phenanthroline were purchased from SRL Chemicals, India.

Experimental setup

The photocatalytic and photo-Fenton treatment of 2,4-DCP was performed at varying catalyst dosages (nano-TiO_2 and iron), oxidant concentration (H_2O_2), and different pH conditions, according to the runs provided by response surface methodology (RSM)-based Box-Behnken design, and optimised conditions

were noted. Considering the maximum allowable concentration recommended for chlorinated phenols as 0.1 µg/L in drinking water (ATSDR 1999) and 200 µg/L in wastewater; as well as the residual concentration detected in effluent discharged in the water bodies, the degradation profile for 2,4-DCP was studied at higher concentration using synthetic stock solution of 100 mg/L. All the experiments were performed using a volume size of 200 ml throughout the study. During photocatalysis treatment, initially, the solution was kept in the dark phase to establish the adsorption/desorption equilibrium of 2,4-DCP with nano-TiO_2. The reaction mixture of 2,4-DCP/nano-TiO_2/H_2O_2 was subjected to UV irradiation (λ-365 nm) with continuous magnetic stirring at 200 rpm and air sparging to ensure homogeneity during the reaction. An aliquot of 5 ml was extracted for analysis using a pre-rinsed syringe at regular intervals of 15 min and was centrifuged at 5000 rpm for 10 min in case of photocatalysis. The analysis in the case of Fenton's and Fenton-integrated processes was done at a regular interval of one minute. The above procedure was repeated until the residual concentration of 2,4-DCP became stabilised with no further degradation. The experimental setup is described in Fig. 1. The cumulative source intensity of the UV chamber as determined is 672 W/m2 (Verma and Haritash 2019). All the experiments were performed in triplicates to ensure the accuracy of analysis.

Analysis of 2,4-DCP

The degradation profile of 2,4-DCP was continuously monitored using a double beam UV-Vis spectrophotometer (Lab India make UV 3092 model). An absorption spectrum in the wavelength range of 190–800 nm was plotted, and the wavelength of maximum absorption (λmax) was obtained at 283 nm. The calibration graph for 2,4-DCP in the concentration range of 10–100 mg/L at 10 mg/L of intervals was plotted, and removal efficiency was determined using the following equation (Eq. 1)

$$\text{Efficiency}\ (\%) = \left[\frac{C_i - C_t}{C_i}\right] x\ 100 \tag{1}$$

where C_i is the initial concentration of 2,4-DCP (100 mg/L) and C_t is the concentration of 2,4-DCP at any time 't'. Mineralisation of 2,4-DCP was analysed over TOC analyser (TOC-L Shimadzu Make, Japan) to validate the observations over UV-Vis spectrophotometer. Mineralisation was calculated using the following expression:

$$\text{Mineralisation}\ (\%) = \left[\frac{TOC_i - TOC_f}{TOC_i}\right] \times 100 \tag{2}$$

where TOC_i refers to the initial TOC of 2,4-DCP before treatment (100 mg/L) and TOC_f is the final TOC of 2,4-DCP after treatment.

The intensity of incoming solar radiation was measured using Apogee pyranometer in case of solar-driven AOPs. Ultrasound integrated process was performed using digital ultrasonic cleaner at 40kHz (Labman Make LMUC series) The residual ferrous ion (Fe^{2+}) concentration and total dissolved iron were determined using spectrophotometer at 510 nm using 1, 10-phenanthroline method as mentioned in APHA (APHA, Method 3500-Fe, 1997). The residual concentration of H_2O_2 in the solution was estimated through iodometric titration.

Design of experiment

RSM is a multivariate statistical tool, which helps in designing the experiment, determining the optimum conditions for the desired response, building models, and assessing the significance of the proposed model and parameters. Its application overcomes the one-factor-at-one time-based conventional multifactor experiment approach by giving a limited and planned set of experiment runs.

For a given target compound concentration, some preliminary experiments were conducted, and a three-level RSM-based Box-Behnken design for independent variables was formulated using MINITAB software. The effect of three independent variables, pH (X1), catalyst dose (X2) (nano-TiO_2 in photocatalytic treatment and Fe(II) in Fenton's treatment), and oxidant dose (X3) (H_2O_2), and their

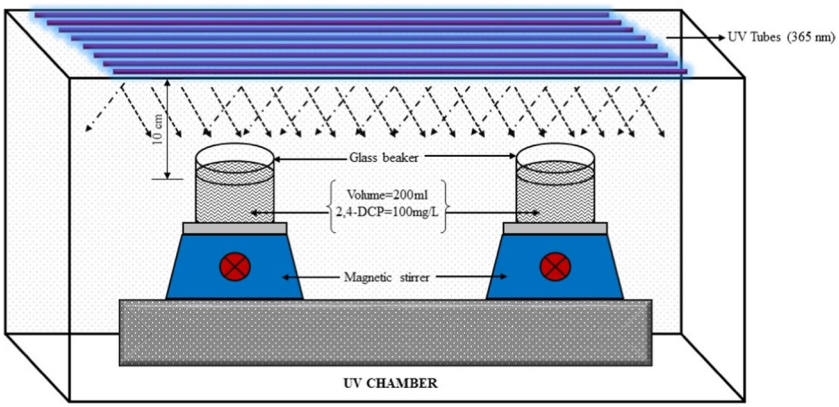


Fig. 1 The experimental setup used during Photocatalysis and Photo-Fenton treatment of 2,4-DCP

interaction was studied and optimised for both the treatment processes to enhance the removal efficiency and minimise the imprecision of experiments. A predictive model for degradation of 2,4-DCP was obtained based on a second-order polynomial equation (Eq. 1), defining the mathematical relationship between corresponding parameters (X1, X2, and X3) and the efficiency of the system (response Y)

$$Y = \beta_0 + \sum_{i=l}^{n} \beta_i X_i + \sum_{i=l}^{n} \beta_{ii} X_{ii}^2 + \sum_{i<j}^{n} \beta_{ij} X_i X_j \quad (3)$$

where β_0, β_i, β_{ii}, and β_{ij} represent the model coefficient, linear coefficient, quadratic coefficient, and interaction parameters coefficient.

The predictive response was correlated with independent variables through a set of coefficients that includes intercept, linear terms, quadratic terms, and interactions. Regression analysis was carried out to fit the equation, and the significance of regulating factors was investigated.

The adequacy of the model was determined by analysis of variance (ANOVA) with predictability at a 95% confidence limit and by evaluating the regression coefficient R^2.

Results and discussion

Photo-Fenton Treatment

The effect of different parameters was studied by varying the concentration of regulating factors based on the runs given by MINITAB (version 16.2) software. Factors like pH, Fe^{2+}, and H_2O_2 were examined in the range of 1.0–5.0, 0.3–0.7 mM, and 3.0–7.0 mM, respectively, for degradation of 2,4-DCP (100 mg/L), and the results are tabulated in Table 1(b). The H_2O_2 imparted a dark brown colour to the reaction mixture and the solution became turbid within a few seconds. As the reaction proceeded, the colour started changing from dark brown to light yellow and colourless, indicating the completion of the reaction. Under optimum doses of pH 3.0 ± 0.2, Fe^{2+} 0.5 mM, and H_2O_2 5.0 mM, 2,4-DCP was non-detectable within 5 min of the reaction time.

Effect of Fe^{2+} dose

Ferrous ions act as the regulating factor in determining the kinetics of the reaction. To elucidate the effect of iron, different concentrations of iron were investigated in the range of 0.3 to 0.7 mM for degradation of 2,4-DCP. Figure 2 illustrates the effect of different iron concentrations towards degradation. It can be seen from the figure that the maximum or complete removal of 2,4-DCP was there with an iron concentration of 0.5 mM within 5 min of the reaction time. The ROS attacks on π bond in the benzene ring of the phenolic compound, thus enhancing the oxidation of chlorophenols (Kavitha and Palanivelu 2016). The redox recycling process of Fe^{2+}/Fe^{3+} takes place in the bulk solution producing reactive oxidation species (Eq. 4), while some ferrous ion species are also formed through reactions (5) and (6) (Ye et al. 2019).

Table 1 Box-Behnken design for three independent variables, predicted, and observed responses for degradation of 2,4-DCP

Run	Photocatalysis (a)					Photo-Fenton (b)				
	pH	TiO_2 dose (g/L)	H_2O_2 (mM)	Removal efficiency (%)		pH	Fe (II) (mM)	H_2O_2 (mM)	Removal efficiency (%)	
				Observed	Predicted				Observed	Predicted
1	4	0.3	10	60	63	3	0.5	5	100	100
2	6	0.1	10	35	34	3	0.5	5	100	100
3	5	0.2	10	98	98	3	0.7	7	18	25
4	5	0.2	10	98	98	3	0.7	3	03	06
5	6	0.2	15	40	41	5	0.5	7	20	22
6	4	0.2	5	60	59	5	0.7	5	53	43
7	6	0.2	5	40	42	1	0.5	7	36	29
8	6	0.3	10	65	66	1	0.3	5	23	32
9	5	0.3	15	90	89	3	0.3	3	02	-2.3
10	5	0.1	5	75	76	1	0.7	5	23	23
11	5	0.2	10	98	98	5	0.3	5	03	03
12	4	0.2	15	70	68	5	0.5	3	05	12
13	4	0.1	10	80	79	3	0.5	5	100	100
14	5	0.3	5	60	58	3	0.3	7	05	03
15	5	0.1	15	50	53	1	0.5	3	17	14

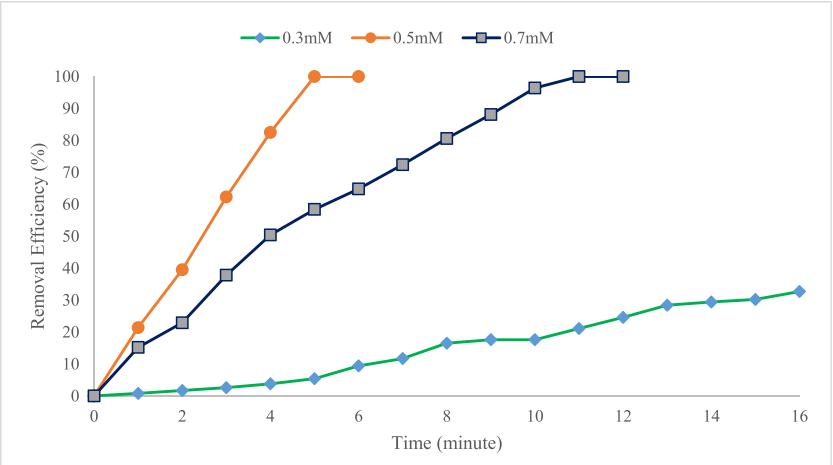


Fig. 2 Optimization of Fe^{2+} concentration in photo-Fenton process for degradation of 2,4-DCP

$$Fe^{2+} + H_2O_2 + H^+ \rightarrow Fe^{3+} + {}^{\bullet}OH + H_2O \quad (4)$$

$$Fe^{3+} + H_2O_2 \rightarrow Fe^{2+} + HOO^{\bullet} + H^+ \quad (5)$$

$$Fe^{3+} + HOO^{\bullet} \rightarrow Fe^{2+} + O_2 + H^+ \quad (6)$$

Further increase in the dose of iron resulted in no significant change in the removal efficiency; instead, the removal was at a slower rate at concentration higher than 0.5 mM. At a concentration of 0.7 mM, complete degradation was achieved in 11 min which is almost double the time taken to degrade 2,4-DCP at a concentration of 0.5 mM. This slight reduction in the degradation rate is attributed to the dominating scavenging effect of ferrous ions on hydroxyl radicals. An increasing amount of Fe(III) cannot be complexed and is insoluble and unstable, which stimulates the formation of ferrous hydroxide $[Fe(OH)]^{2+}$ and its further hydrolysis and precipitation as $Fe(OH)_3$ (Eqs. 7 and 8).

$$Fe^{2+} + OH\bullet \rightarrow Fe^{3+} + OH^- \quad (7)$$

$$Fe^{3+} + HO \rightleftharpoons [Fe(OH)]^{2+} + H^+ \quad (8)$$

However, at a lower iron dose (0.3 mM), mere removal was observed because of the lesser availability of hydroxyl radicals further causing a delay in the oxidation process and efficient removal. The residual concentration of ferrous iron as well as total dissolved iron (TDI) estimated at the end of the experiment revealed complete utilisation of ferrous ions while 0.04 mM of TDI remained in the solution.

Effect of pH

The pH represents an important parameter in Fenton's process, as iron speciation that determines the UV absorption, complexation, and dissolution of catalysis is strongly influenced and governed by pH. The dissociation constant of chlorophenols lies in the range of 4.7 for pentachlorophenol (PCP) to 9.41 for 4-chlorophenol (4-CP), which signifies their ionisation to occur under lower pH conditions. The present study aims to optimise the pH conditions keeping the 2,4-DCP concentration constant with a Fe^{2+} dose of 0.5 mM and H_2O_2 concentration of 5.0 mM. Experiments were conducted at pH 1.0, 3.0, and 5.0, as suggested by the RSM Model. It can be observed from Fig. 3 that the complete removal of chlorophenols occurred at pH 3.0 within 5 min of the reaction period. According to literature studies, ferrous ions and peroxide exhibit greater stability at pH 3.0 (Pipil et al. 2022; Yadav et al. 2023b, 2023a; Verma and Haritash 2020). The recorded observations have also been established in other relevant literature and are in strong agreement with their findings where at pH 3.0, an appreciable higher mineralisation rate was observed (Ahmadzadeh and Dolatabadi 2018). Under similar pH conditions (pH 3.0), 2,4,6-trichlorophenol was reduced to non-detectable limits within 6 min of process duration (Yadav et al. 2023b). Successful elimination of pharmaceutical compounds like amoxicillin at pH 3.0 has been reported within a few minutes of the reaction time (Verma and Haritash 2019). Nonetheless, a very low removal rate i.e. only 25% was observed in 10 min under extreme acidic conditions (pH 1.0). The removal efficiency is lessened due to the scavenging behaviour of the H^+, consuming hydroxyl radicals (Eq. 9). Furthermore, lesser solubility of ferrous ions results in the formation of complex ion species and peroxonium ions $H_3O_2^+$ (Eq. 9) as well probably because of increased peroxide stability and decreased reactivity of Fe(II) (Ghoneim et al. 2011; Yadav et al. 2023b).

$$H_2O_2 + H^+ \rightarrow H_3O_2^+ \quad (9)$$

$$OH\bullet + H^+ + e^- \rightarrow H_2O \quad (10)$$

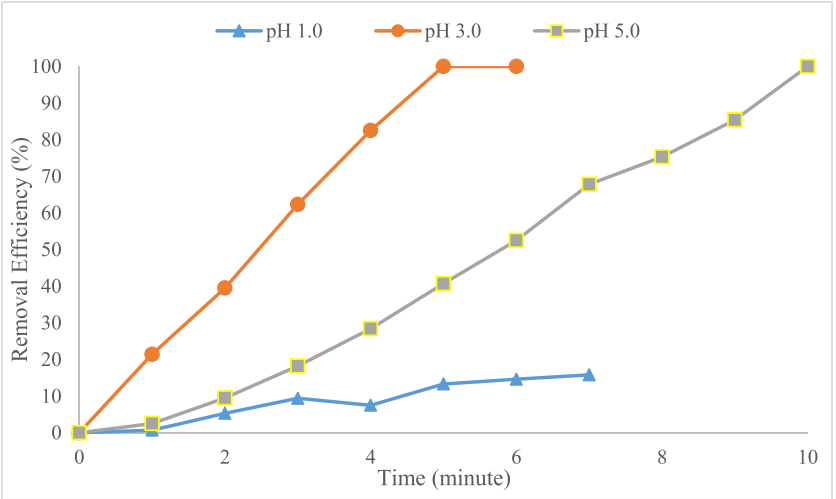


Fig. 3 Optimization of pH in photo-Fenton process for degradation of 2,4-DCP

Earlier studies have reported pH 3.0 as ideal condition for Fenton's treatment; however, in the present study at higher pH (pH 5.0), complete removal was achieved (100%), but the reaction time was approximately twice that of pH 3.0. The instability of iron above pH 3.0 results in precipitate formation (ferric hydroxide complex), which does not react with peroxide, inhibiting the formation of hydroxyl radicals (Yadav et al. 2023a). Also, the self-decomposition of peroxide leads to the formation of oxygen and water. Furthermore, it has been reported that, with $2.0 < pH > 4.0$, the potential for hydroxyl radical decreases (Yadav et al. 2023a). A drop in pH was also observed in the range of 2.3-2.5 post-treatment signifying the possibility of the formation of some carboxylic acid species after degradation as reported in other literature as well (Yadav et al. 2023a).

Effect of H_2O_2 concentration

The H_2O_2 imparted a dark brown colour to the reaction mixture of iron and 2,4-DCP. As the reaction proceeded, the dark colour started fading from dark brown to colourless at the end indicating completion of the reaction. The presence of H_2O_2 inhibits the recombination of *e-h* as it acts as e^- acceptor and thus facilitates the formation of OH radicals (Verma and Haritash 2019; Yadav et al. 2023a).

$$H_2O_2 + e^-_{CB} \rightarrow OH^{\bullet} + OH^- \quad (11)$$

The addition of oxidant hydrogen peroxide was done in the concentration range 3.0 to 10.0 mM keeping the iron dose constant at 0.5 mM and pH 3.0. Intermediate experimentation was also conducted outside RSM. It can be observed from the graph that complete degradation (100%) was observed in all the varied doses of H_2O_2 except at a higher concentration of 10.0 mM. However, rapid removal efficiency was observed with an oxidant dose of 5.0 mM within 5 min of the reaction period (Fig. 4). At oxidant doses of 3.0 mM and 7.0 mM, degradation was accomplished in around 10 min and 13 min, respectively.

Correspondingly, very little removal was observed (nearly 30%) at a concentration of 10.0 mM. In excess amounts, H_2O_2 has a negative effect as it undergoes self-decomposition and acts as a scavenger. A similar observation is also reported in other studies as well (Ye et al. 2019; Pipil et al. 2022; Yadav et al. 2023b). In such cases, hydroperoxyl radicals are formed whose reduction potential (1.0 V) is less than that of hydroxyl radicals (2.8 V) (Eqs. 12–14).

$$2H_2O_2 \rightarrow 2H_2O + O_2 \quad (12)$$

$$^{\bullet}OH + H_2O_2 \rightarrow H_2O + HO_2^{\bullet} \quad (13)$$

$$HO_2^{\bullet} + {}^{\bullet}OH \rightarrow H_2O + O_2 \quad (14)$$

Hence, a 5.0 mM dose of H_2O_2 was considered optimum for further experimentation, as the current study reports lesser consumption of H_2O_2 and complete degradation in minimum time.

Photocatalytic Treatment

Photocatalytic oxidation of 2,4-DCP using Degussa P25 Nano-TiO_2 as a catalyst was found effective in removing the aforementioned organic pollutant. The study highlights the effect of process conditioning parameters like catalyst dose, effect of pH, and presence of oxidising agent H_2O_2 for degradation of 2,4-DCP based on the RSM-BBD set of experiments suggested, and the results are tabulated in Table 1(a). In the optimised conditions, pH 5.0 ± 0.2, TiO_2 dose 0.2 g/L, and H_2O_2 10.0 mM, 2,4-DCP were not found in 210 min of the reaction time.

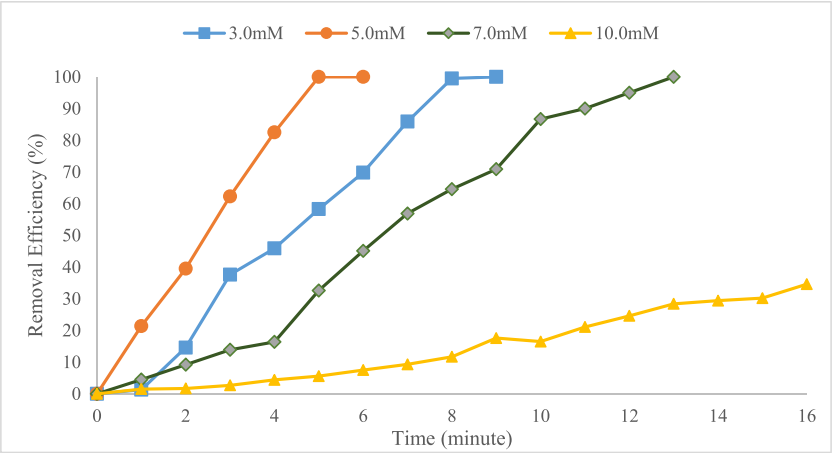


Fig. 4 Optimization of oxidant (H_2O_2) concentration in photo-Fenton process for degradation of 2,4-DCP

Effect of catalyst loading

The effect of different doses of photocatalyst Degussa P-25 nano-TiO_2 was studied as a function of time towards the degradation of 2,4-DCP. The solution of 100 mg/L 2,4-DCP was subjected to UV irradiation after keeping the solution in the dark for 30 min. The experiment examined the effect of catalyst dose in the range of 0.1 g/L to 0.6 g/L at pH 4.0 and oxidant dose of 10.0 mM to ensure maximum removal efficiency and minimum consumption of catalyst. It can be observed from Fig. 5 that the degradation rate increased with an increase in the concentration of TiO_2 dose and peaked maximum at 0.2 g/l while further increase in dose caused a decline in the degradation efficiency. At 0.2 g/L of catalyst dose, almost complete (~98%) degradation was achieved in 255 min of reaction time. The greater efficiency could be rationalised in terms of the photocatalytic activity of TiO_2 that depends on three factors: (a) the capability of generation of electron-hole pair when illuminated with light less than 400 nm wavelength, (b) inhibition of recombination of photo-generated charge pairs, and (c) efficiency of electron and hole pair to transfer charge to organic contaminants adsorbed on TiO_2 (Verma and Haritash 2020; Pipil et al. 2022). The photo-generated valence band holes and conduction band electrons reduce the electron acceptor species and oxidise the electron donor species adsorbed on the catalyst surface. The hydroxyl and perhydroxyl radicals carry out the photo-oxidation of 2,4-DCP.

$$TiO_2 + hv \rightarrow TiO_2(e^-) + TiO_2\left(h^+\right) \quad (15)$$

$$O_2 + e^- \rightarrow OH\bullet \quad (16)$$

$$H_2O + h^+ \rightarrow OH\bullet \quad (17)$$

Increasing TiO_2 concentration increases the availability of active sites, thus escalating the adsorption process too. More binding of electron-hole pair with water accelerates the generation of the hydroxyl radicals. However, at a higher amount of TiO_2, the solution suspension becomes turbid and cloudy and the phenomena of light scattering dominate reducing the UV penetration, also reported in other studies as well (Pipil et al. 2022; Yadav et al. 2023a). Lesser

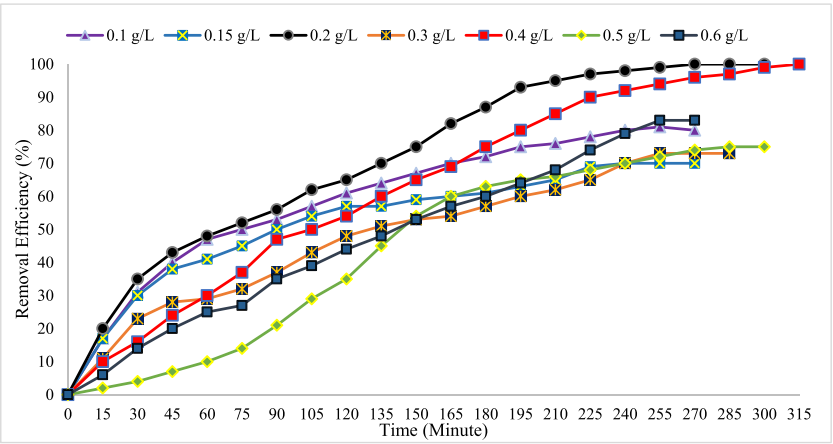


Fig. 5 Removal efficiency at different catalyst doses in photocatalytic treatment of 2,4-DCP

illumination resulted in lesser production of ROS thus reducing the treatment efficiency of the system. Various studies have reported the degradation of 2,4-DCP using TiO_2 at higher concentrations in comparison to the present study. In one of the studies, a catalyst dose of 0.75g/l reported 90% degradation of 2,4-DCP solution (strength 125mg/L) in 6 h while in another study, only 50% degradation of 2,4-DCP (50mg/L) was achieved in 90 min (Bayarri et al. 2005; Kansal and Chopra 2012). Another study reported nearly 99.48% degradation of the phenolic compound with a TiO_2 concentration of 1.75g/L in 540 min of irradiation time (Zulfiqar et al. 2019). In the current study, the response surface methodology further validates the maximum removal efficiency with 0.2g/l of TiO_2 dose. Thus, optimisation of photocatalyst dose reduces its amount as well as treatment cost. Further experimentation was carried out using a 0.2 g/L concentration of Nano-TiO_2.

Effect of pH

The wastewater contains different organic compounds discharged at different pH, hence pH is a significant operating parameter regulating the efficiency of the treatment processes. pH determines the surface charge properties of photocatalyst which governs the behaviour of pollutants. In the present study, experiments were performed at different pH conditions—4.0, 5.0, and 6.0 with optimised (0.2 g/l) TiO_2 dose and oxidant concentration 10.0 mM. Figure 6 illustrates the degradation of 2,4-DCP at different pH conditions in terms of removal efficiency as a function of time. Almost complete removal (~98%) of 2,4-DCP was observed at pH 4.0 & 5.0; however at pH 5.0, degradation was achieved in 210 min, whereas, at pH 4.0, the degradation process took 255 min for complete degradation. Studies have also reported complete degradation of the chlorophenolic compound under similar pH conditions. One of the studies undertook the degradation of 2,4-DCP (~50 mg/L) and observed maximum removal efficiency at pH 5.0 (Melián et al. 2013). Another research work revealed maximum degradation of 2,4-DCP (~125 mg/L) at pH 5.5 (Bayarri et al. 2005). The interaction and affinity between TiO_2 and 2,4-DCP is governed by pH. Variation in operating pH affects the surface charge or isoelectric point of nano-TiO_2. The ionisation state of the photocatalyst surface undergoes either protonation or deprotonation depending on the operating pH (Eqs. 18 and 19) where TiOH is the primary hydrated surface functionality of TiO_2 (Hoffmann et al. 1995). Since the point of zero charge (p_{zc}) of TiO_2 is around 6.2, it carries a net positive charge (Wang 2017), whereas the chloro-derivative phenol compounds have negative charges (pka = 7.98). Thus, at pH < pH_{pzc}, the positive charge on the photocatalyst gradually exerts an electrostatic force of attraction towards the negatively charged chlorophenolic compound (Eq. 18). Therefore, the polar attraction intensifies the adsorption of organics over the photocatalyst surface, facilitating photocatalytic degradation.

$$Ti - OH + H^+ \leftrightarrow TiOH_2^+ \tag{18}$$

Consequently, at pH 6.0, lesser degradation was observed because, in the case of pH ≥ pH_{pzc}, TiO_2 carries a net negative charge (Eq. 19), which hampers the adhesion of CP onto the catalyst surface.

$$TiOH + OH^- \leftrightarrow TiO^- + H_2O \tag{19}$$

The increased density of negatively charged catalysts and chlorophenols, both, exert columbic repulsion, resulting in lesser adsorption of pollutant over the surface of TiO_2 (Chu et al. 2007). This results in a decreased rate of degradation and lesser removal efficiency. Therefore, pH 5.0 was considered the optimum condition for the degradation of 2,4-DCP in the present study. The results are also supported by a study carried out under similar operating pH (Zulfiqar et al. 2019). Although some research reports have also revealed pH 4.0 appropriate towards organic decomposition (Kansal and Chopra 2012; Melián et al.

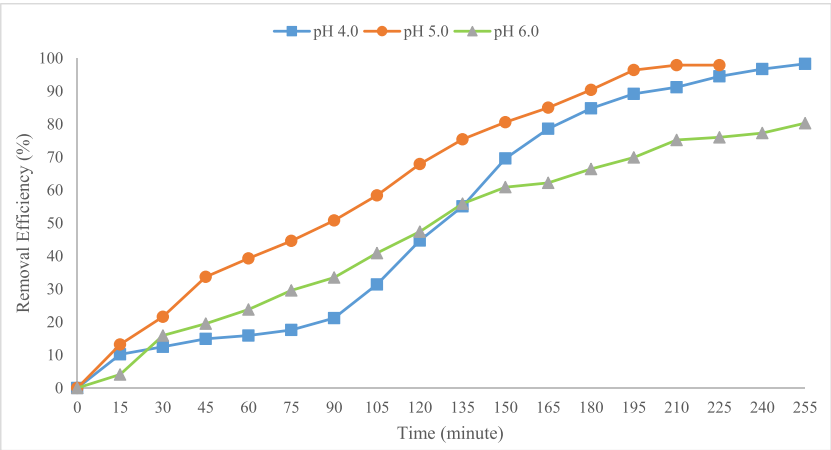


Fig. 6 Removal efficiency at different pH in photocatalytic treatment of 2,4-DCP

2013), one of the findings in the present study also showed the same. Nevertheless, the pace of reaction was faster in the case of pH 5.0, and the TOC mineralisation as observed was also found maximum (70%) at pH 5.0, whereas it was 62% for pH 4.0

Effect of oxidant concentration

The addition of oxidant enhances the degradation of organic contaminants. The effect of hydrogen peroxide was studied in the range of 5.0 to 15.0mM based on run orders suggested by the RSM software. It can be noted from Fig. 7 that at a lesser concentration of H_2O_2 (0.5 mM), the degradation efficiency was achieved around 70% attributing to lesser availability or generation of hydroxyl radicals. However, at 10.0 mM of H_2O_2 dose, 98% of the degradation efficiency was attained in 270 min of reaction duration. Under the optimised conditions of nano-TiO_2 (0.2g/L), the degradation with 10.0 mM of H_2O_2 was faster, resulting in the complete elimination of the chlorophenolic compound within 210 min. It can be rationalised as H_2O_2 is a more efficient electron acceptor than oxygen and generates hydroxyl radicals by reacting with conduction band electrons and inhibiting the electron-hole pair recombination. UV irradiation photolyzes H_2O_2 which generates hydroxyl radicals necessary for photo-mineralisation of organic pollutants (Eq. 20).

$$(e^-)TiO_2 + H_2O_2 \rightarrow TiO_2 + OH^{\bullet} + OH^- \quad (20)$$

The addition of H_2O_2 along with TiO_2/UV has a synergistic effect, enhancing the efficiency of the treatment system by generating two hydroxyl radicals or producing hydrogen ions for generating perhydroxy radicals (Eqs. 21–23) (Pipil et al. 2022).

$$O^{2-} + H^+ \rightarrow HO_2^{\bullet} \quad (21)$$

$$H_2O_2 \rightarrow 2HO^{\bullet} \quad (22)$$

$$H_2O_2 \rightarrow O_2^{2-} + 2H^+ \quad (23)$$

Near complete removal of 2,4-DCP (90%) was observed at a higher concentration of oxidant (15.0 mM), although the degradation rate was slower and less efficient in the same reaction time (Fig. 7). Similar findings were observed in which 2,3-dichlorophenol was photocatalytically degraded using 10.0 mM of H_2O_2, whereas a higher range reported no significant change in removal efficacy (Kansal et al. 2009). Slow degradation at higher co-oxidant concentrations is attributed to the inhibitory effect of peroxide as (a) H_2O_2 also acts as a scavenger to ROS or (b) the active sites for adsorption of water and production of hydroxyl radicals are blocked (Thind et al. 2018; Kansal et al. 2009). Excess H_2O_2 reacts with hydroxyl radicals and forms water molecules decreasing the degradation of 2,4-DCP (Eqs. 24 and 25).

$$H_2O_2 + HO^{\bullet} \rightarrow HO_2^{\bullet} + H_2O \quad (24)$$

$$HO_2^{\bullet} + HO^{\bullet} \rightarrow H_2O + O_2 \quad (25)$$

Another reason attributing to the reduced degradation rate of 2,4-DCP is the excess generation of holes causing photo-oxidation of hydroxyl radicals (Eqs. 26–29).

$$TiO_2 + hv \rightarrow TiO_2(e^-) + TiO_2\left(h^+\right) \quad (26)$$

$$h^+ + H_2O \rightarrow HO^{\bullet} + H^+ \quad (27)$$

$$h^+ + OH^- \rightarrow HO^{\bullet} \quad (28)$$

$$H_2O_2 + HO^{\bullet} \rightarrow H_2O + HO^{\bullet}{}_2 \quad (29)$$

Similar observations were also reported in other relevant studies carried out for the treatment of contaminated water using photocatalytic treatment (Thind et al. 2018; Gong et al. 2015).

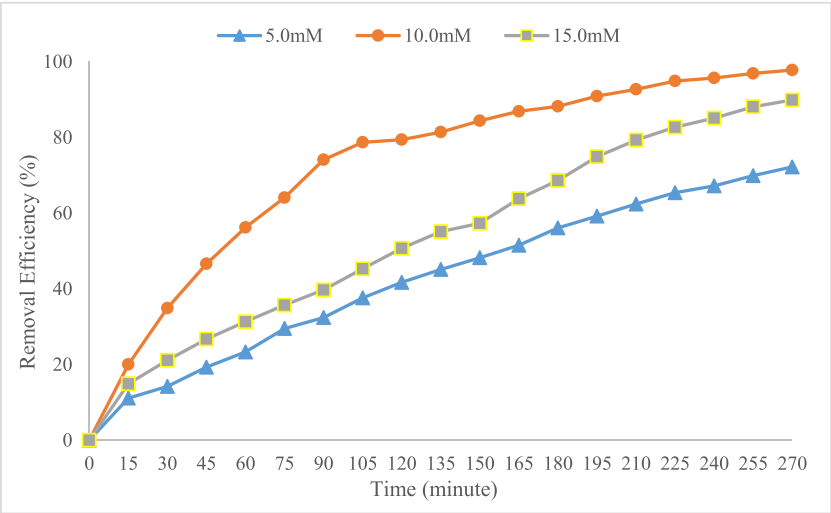


Fig. 7 Removal efficiency at different oxidant concentrations in photocatalysis process

Thus, 10.0 mM of H_2O_2 was considered as the optimised oxidant concentration.

Reaction kinetics of photocatalysis

The reaction kinetics of photocatalytic degradation were determined to investigate the removal rate of 2,4-DCP over nano-TiO_2. Pseudo-first-order (PFO) and pseudo-second-order (PSO) kinetic models were applied to study the dynamics of photocatalysts and organic contaminant degradation. The diffusion mechanism of the nano-photocatalyst degradation process was studied using the intraparticle diffusion (IPD) kinetic model. Reaction kinetics experiments were performed for different 2,4-DCP concentrations (25 mg/L, 50.0 mg/L, 100.0 mg/L, and 125.0mg/L) at optimised conditions provided by the RSM method (2,4-DCP concentration 100 mg/L). Table 2 illustrates the different photocatalytic degradation capacities with R^2 values obtained at variable concentrations. R^2 values provide validation of a better-fitting reaction kinetics model for photocatalytic degradation of 2,4-DCP.

Pseudo-first order kinetic model

It is one of the most extensively used kinetic models. The pseudo-first-order reaction model for photocatalytic degradation of 2,4-DCP using nano-TiO_2 is represented by the Lagergren equation (Lagergren 1898) expressed below:

$$\log\left(q_e - q_t\right) = \log q_e - \frac{K_1.t}{2.303} \tag{30}$$

where K_1 is the rate degradation constant (L/min), q_e (mg/g) is the amount of 2,4-DCP degradation at equilibrium, and q_t (mg/g) is the amount of 2,4-DCP degradation at any time 't'.

A graph of time 't' was plotted against log (q_e−q_t), and slope and intercept were used to determine the constants (Fig. 8a). As can be seen from the table, PFO represents the best fit kinetic model with R^2 almost reaching unity. Furthermore, it can also be observed that the calculated q_e values lie pretty much closer to experimentally derived q_e values as compared to values in PSO kinetic models. PFO kinetics thus defines the degradation process.

Pseudo-second-order kinetics models

Various types of PSO kinetic models, PSO-I, PSO-II, PSO-III, and PSO-IV, were fitted to derive the photocatalytic degradation kinetics (Samsudin et al. 2019; Zulfiqar et al. 2019). The rate kinetics degradation equation for the abovementioned PSO models is represented below:

$$\frac{t}{q_t} = \frac{1}{Ks * {q_e}^2} + \frac{1}{q_e}t \tag{31}$$

$$\frac{1}{q_t} = \left[\frac{1}{K_2 * {q_e}^2}\right].\frac{1}{t} + \frac{1}{q_e} \tag{32}$$

Table 2 Kinetic models for photocatalytic degradation of 2,4-DCP

Kinetic models	Parameters	2,4-DCP concentration			
		25.0 mg/L	50.0 mg/L	100.0 mg/L	125.0 mg/L
PFO	$q_{e\,exp}$ (mg/g)	99	199.5	489.5	360
	$q_{e\,cal}$ (mg/g)	118.740808	194.4016739	473.8053933	381.6805242
	K_1 (min^{-1})	−0.0251027	−0.0151998	−0.0073696	−0.0133574
	R^2	0.9177	0.9896	0.9929	0.9853
PSO-I	q_e (mg/g)	181.8181818	333.3333333	625	1000
	K_2 (min^{-1})	5.36×10^{-5}	2.75×10^{-5}	1.045×10^{-5}	4.15×10^{-6}
	R^2	0.9826	0.9324	0.9324	0.7763
PSO-II	q_e (mg/g)	232.5581395	625	833.3333333	909.0909091
	K_2 (min^{-1})	3.14×10^{-5}	6.36×10^{-6}	5.21×10^{-6}	5.53×10^{-6}
	R^2	0.9771	0.9763	0.9887	0.9851
PSO-III	q_e (mg/g)	175.58	309.43	911.32	573.86
	K_2 (min^{-1})	5.8×10^{-5}	3.4×10^{-5}	5.30×10^{-6}	1.2×10^{-5}
	R^2	0.9661	0.7679	0.7842	0.9089
PSO-IV	q_e (mg/g)	179.08	363.4074074	1076.684211	602.9552239
	K_2 (min^{-1})	5.5×10^{-5}	2.2×10^{-5}	3.5×10^{-6}	1.1×10^{-5}
	R^2	0.9661	0.7679	0.7842	0.9089
IPD	K_{ip}	9.2333	19.193	32.135	32.5
	C_i	8.652	29.838	58.342	73.777
	R^2	0.9762	0.9679	0.9973	0.9971

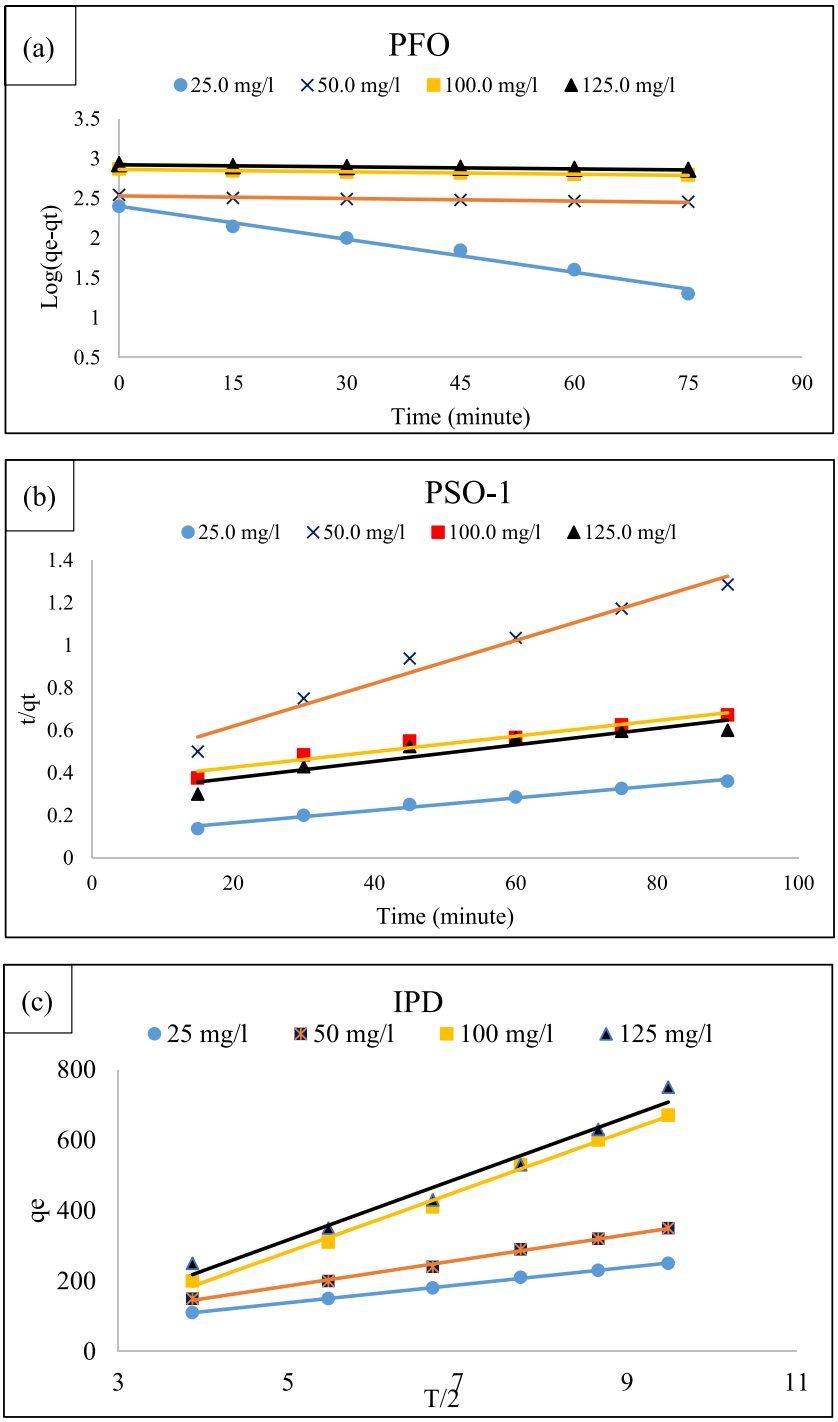


Fig. 8 Rate kinetics model for 2,4-DCP photocatalytic degradation: **a** pseudo-first-order (PFO), **b** pseudo-second-order type I, and **c** intraparticle diffusion

$$q_t = q_e - \left[\frac{1}{K_2 * {q_e}^2}\right] * \frac{q_t}{t} \tag{33}$$

$$\frac{q_t}{t} = K_2 * {q_e}^2 - \frac{\left(K_2 * {q_e}^2 * q_t\right)}{q_e} \tag{34}$$

where q_e (mg/g) and q_t (mg/g) represent the relative amount of 2,4-DCP degraded at equilibrium and at any time 't', respectively. K_2 (g/mg min) is the PSO chemisorption rate constant. For PSO-I rate kinetics, a graph of time 't' against 't/q' was plotted, and with the help of slope and intercept, constant parameters were determined (Fig. 8b). In the case

of the PSO-II kinetic model, a graph of $1/q_t$ versus $1/t$ was plotted, and values of constant were obtained using slope and intercept. PSO-III kinetic model equation was plotted for q_t against q_t/t to obtain constant factors from the slope and intercept of the graph. Similarly, the kinetic model equation of PSO-IV was plotted q_t/t versus 't', and values of K_2 and q_e were determined from slope and intercept. The results reported a reasonably good R^2 fit for the PSO-I and PSO-II rate kinetics model; however notable difference was observed between theoretical (q_{cal}) and experimental (q_{exp}) derived values. With the increase in the concentration of 2,4-DCP, the value of R^2 decreased from 0.9826 to 0.7763 in the PSO-I kinetics model. It was also revealed that the values of rate constant for respective PSO models, PSO-I, PSO-II, PSO-III, and PSO-IV, decreased from 5.36×10^{-5} to 4.15×10^{-6}; 3.14×10^{-5} to 5.53×10^{-6}; 5.8×10^{-5} to 1.2×10^{-6}; and 5.5×10^{-5} to 1.1×10^{-6}, respectively, with increasing 2,4-DCP concentrations (25.0 mg/L to 125.0 mg/L). This may be reasoned as with increasing pollutant dose; the degradation equilibrium time is extended. Theoretical (q_{cal}) > experimental (q_{exp}) explains the lack of applicability of PSO kinetics models, and the model equations do not ascertain the photocatalytic degradation of 2,4-DCP. A similar trend and observations were also observed in another study (Zulfiqar et al. 2019).

Intraparticle diffusion kinetic model

The rate-controlling step is a significant factor in the case of the photocatalysis process. The photo-oxidation of organics depends on the mass transfer of contaminants across the boundary layer or intraparticle diffusion of pollutants along the pores of the photocatalyst and degradation taking place at the surface sites of the photocatalyst. The overall degradation rate in the photocatalysis process is governed either by IPD or film mechanism (Ocampo-Perez et al. 2011). The following equation defines the IPD rate kinetics associating the half-life time against the removal of pollutant at any time, q_t (Abdelwahab and Amin 2013):

$$q_t = K_{ipd} t^{1/2} + C_i \tag{35}$$

where K_{ipd} (mg/g) is the IPD rate constant while C_i is the thickness of the boundary layer. It was observed that the values of the diffusion rate constant and thickness boundary layer increased with increasing 2,4-DCP concentrations (Table 2). The variation in K_{ipd} values may be attributed to the high concentration driving force leading to the difference in mass transfer in the initial and final degradation phases (Abdelwahab and Amin 2013). Increasing boundary thickness layer value indicates increased kinetic energy contributing to the faster photo-degradation rate. In general, although the regression coefficient values reflect a good fit, the degree of contaminant degradation was governed by diffusing boundary layers (Abdelwahab and Amin 2013). It was also observed from the graph between q_e and half-life time (Fig. 8c) that the linear plot fails to pass through the origin in the entire time duration, signifying that IPD is not a rate-determining step. Thus, it can be stated that the IPD model cannot be used to predict the photocatalytic degradation kinetics of 2,4-DCP.

Isotherm studies

Different isotherms were used to illustrate the relation between the organic compound and the photocatalyst. During the study, isothermal fitting models like Langmuir, Freundlich, and Temkin were used to predict the experimental equilibrium data of the degradation process on photocatalyst (Table 3). The adsorption isotherm experiments on different 2,4-DCP concentrations were performed based on optimised conditions obtained earlier using the RSM technique.

Langmuir isotherm model

According to the model, the process of degradation is considered a monolayer. Once the active sites of nano-TiO_2 are occupied by pollutant molecules, no more degradation takes place at these sites. As the process proceeds to the saturation point, maximum degradation is achieved. The linearized Langmuir isotherm equation (Langmuir 1918) used to obtain the maximum monolayer adsorption capacity is expressed as

$$\frac{1}{q_e} = \frac{1}{\left(K_L * q_m * C_e\right)} + \frac{1}{q_m} \tag{36}$$

where q_m (mg/g) is the rate constant associated with the maximum degradation capacity of nano-TiO_2, q_e (mg/g) is the adsorption capacity at equilibrium, C_e (mg/L) is the equilibrium concentration of 2,4-DCP, and K_L (L/mg) is the Langmuir constant associated with degradation energy.

A graph of $1/q_e$ versus $1/C_e$ was plotted, and the slope and intercept were used to estimate the dependent variables (q_m and K_L) (Fig. 9a).

Table 3 Isotherm parameters for photocatalytic degradation of 2,4-DCP on nano-TiO_2

Langmuir-isotherm		Freundlich-isotherm		Temkin-isotherm	
K_L (L/mg)	0.048	K_F (mg/g)	55.7	K_T (L/g)	1.33
q_m (mg/g)	588.23	n	2.89	B	15.015
R^2	0.9868	R^2	0.885	R^2	0.9348

Freundlich isotherm model

The Freundlich isotherm considers multilayer adsorption with irregular dispersion of degradation heat. The model supposes a heterogeneous distribution of energy of active sites (Freundlich 1906). According to the model, stronger binding sites are inhabited first, and by increasing the occupancy of sites, binding strength lessens. The linear Freundlich isotherm equation (Freundlich 1906) is expressed as

$$\ln q_e = \ln K_F + \frac{1}{n} \ln C_e \tag{37}$$

where K_F (mg/g) is the Freundlich isotherm constant indicating the relative adsorption capacity of Nano-TiO_2 and n is the dimensionless factor representing the adsorption intensity or surface heterogeneity (a value closer to zero represents a more heterogeneous surface).

A graph of ln q_e was plotted against ln C_e, and slope and intercept were used to calculate both constants (n and K_F) (Fig. 9b).

Temkin isotherm model

The interaction of nano-TiO_2 and phenol was studied using the Temkin model (Temkin and Pyzhev 1940). The heat of degradation generated during interaction would reduce linearly. The Temkin isotherm model (Temkin and Pyzhev 1940) is represented using the following equation:

$$q_e = B * \ln K_T + B * \ln C_e \tag{38}$$

where K_T (L/g) is the equilibrium binding constant or the Temkin constant and B (J/mol) is the heat of degradation.

Both K_T and B are associated with the relative removal capacity of 2,4-DCP on nano-TiO_2 and degradation of heat. These are obtained using intercept and slope by plotting the graph between q_e and ln C_e (Fig. 9c).

The graphical representation of all the isotherm models is illustrated in Fig. 9. Table 3 shows the calculated isotherm parameters of Langmuir ($q$max, K_L, and R^2), Freundlich (K_F, n, and R^2), and Temkin (K_T, B, and R^2), estimated through linear regression. Results indicated that the Langmuir isotherm model is the best isotherm fit model towards the removal of 2,4-DCP over nano-TiO_2 as compared to the Freundlich and Temkin isotherm models, providing the maximum R^2 value of 0.9868 ($R_L{}^2 > R_T{}^2 > R_F{}^2$). The higher value of q_m indicates a stronger photocatalyst and 2,4-DCP interaction. The result also fits well for the Temkin isotherm model ($R^2 = 0.9348$) and hence could also be considered a reasonable model for degradation. In the case of the Freundlich isotherm model ($R^2 = 0.8859$), the isotherm intensity, n was higher than 1 (2.89), which signifies the degradation of 2,4-DCP to occur over the catalyst surface. Moreover, since the value lies between 1 and 10, it indicates favourable photocatalytic degradation of 2,4-DCP. Therefore, as evident from regression correlation coefficients, the Langmuir isotherm model of monolayer adsorption gives better fits as compared to others.

RSM modelling and adequacy of model (ANOVA) for degradation of 2,4-DCP

The influence of independent variables of the two treatment processes employed for the degradation of 2,4-DCP was studied. The observed experimental results against the

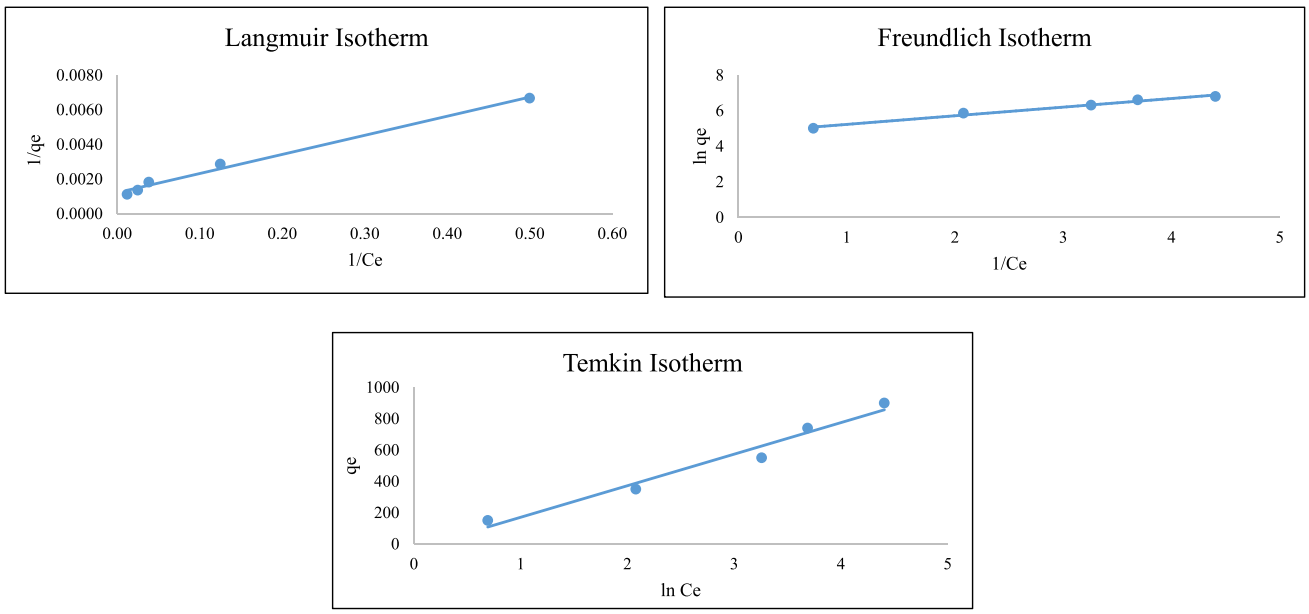


Fig. 9 Isotherm models for photocatalytic degradation of 2,4-DCP at optimised conditions given by RSM

predicted response obtained through RSM towards effective removal are tabulated in Table 1 for both treatment processes. The two quadratic regression models developed (through Eq. 3) using observed response against predicted are represented using the following equations. Y_1 depicts the photocatalytic response while Y_2 represents the photo-Fenton's response.

$$Y_1 = -403.375 + 207.5X_1 - 0.321X_2 + 5.575X_3 - 24.625x_1^2 - 0.001X_1^2 - 0.635X_3^2 + 0.125X_1X_2 + 0.500X_1X_3 + 0.027X_2X_3 \quad (3a)$$

$$Y_2 = -490.25 + 32.25X_1 + 906.25X_2 + 118.75X_3 - 8.50X_1^2 - 1018.75X_2^2 - 12.31X_3^2 + 31.88X_1X_2 + 0.44X_1X_3 + 12.50X_2X_3 \quad (3b)$$

The state of normality of the results is strongly supported by the obtained coefficient of determination, R^2 value for both the processes which is 97.96% observed R^2 against 94.29% R^2 adjusted value in the case of photocatalysis and observed R^2 value of 97.8% against 93.83% R^2 adjusted value in the case of photo-Fenton's process. In both the abovementioned cases, it can be noted that the predicted R^2 value lies in close proximity to actual R^2 values with nominal difference indicating the presence of insignificant factors. Figures 10 and 11 describe the randomly distributed residuals signifying the reliability of the proposed model, whereas the linear distribution of the normal probability plot supports the reasonability of the model for both the treatment systems respectively. Residuals define the reliability of the models reflecting the difference between predicted and actual responses.

The competency and significance of the proposed regression model were analysed using analysis of variance (ANOVA), and the results are summarised in Table 4. The results reflected an excellent behaviour between experimental and predicted results towards the degradation of 2,4-DCP. It can be seen from the table that the *F*-values for both the process models (26.67 in the case of photocatalysis and 24.65 in photo-Fenton's process) are highly significant corresponding to the *P*-value of regression < 0.001 (*P*-value < 0.05). Complying with the *P*-values (*P*-value < 0.05 indicates the model term as significant and vice-versa), the significance of each test variable was evaluated. In the case of photocatalytic treatment, the overall linear, quadratic, and interaction coefficients were found significant. However, exceptionally, the linear coefficient of nano-TiO_2 and H_2O_2 and the interaction coefficient of pH*H_2O_2 were found statistically insignificant. Similarly, in the case of photo-Fenton's process, all the governing parameter's linear, quadratic, and interaction coefficients were significant except for the individual interaction coefficient for pH*Fe, which was exceptionally non-significant.

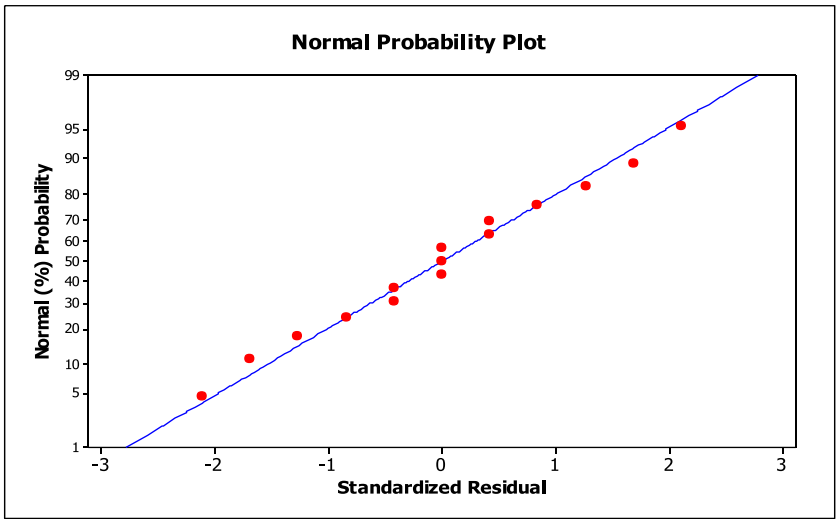
Process optimization and effect of variables

An interactive relationship among process variables was established, and a desirability function was applied. The desirability number was estimated considering the maximum removal efficiency of 2,4-DCP. The predicted maximal efficiency in the case of photocatalysis was 98% for 2,4-DCP with a desirability of 0.9919 under optimised conditions. Similarly, in the photo-Fenton process, the software predicted the complete removal of organic pollutant with desirability of 1.00 under optimised conditions. At optimised conditions, the photocatalytic efficiency observed was almost complete (~98%) while 100% degradation was shown in photo-Fenton's process. The composite desirability for both processes was either unity or closer to unity (Fig. 12). Furthermore, the observed removal efficiency and the prediction made by RSM closely resembled, thus validating the accuracy of the model and proposed RSM-desirability function.

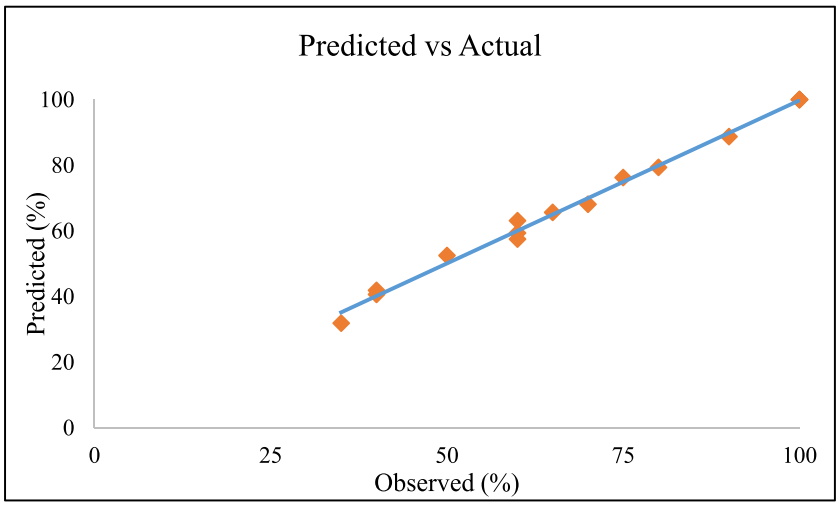
Based on the second-order polynomial models (Eq. 3a and 3b), 2D contour plots were generated as shown in Fig. 13a, b, showcasing the effect of condition operating factors of respective treatment methods towards degradation.

Effect of photocatalytic variables

The interactive effect between oxidant concentration and pH can be observed in Fig. 13a. Increasing pH does not reflect significant degradation at a lower dose of H_2O_2, around 5.0 mM. As the concentration increased, degradation efficiency peaked at around 8–11.0 mM. It was also observed that pH played a significant role. Around pH 4–5, degradation increased, whereas the removal rate decreased with a further increase in pH (alkaline conditions). At higher pH, the self-decomposition of H_2O_2 reduces the generation of hydroxyl radicals. Lesser presence of H_2O_2 causes more deficient ROS production, thus affecting the degradation rate. It becomes a limiting factor when present in less amount. However, the impact of oxidant concerning catalyst loading was significant (Fig. 13b). H_2O_2 when present in deficient amounts, reflected a similar degradation rate in the range of 60–70% for increasing catalyst load. At the higher dose of H_2O_2 (7–12 mM), the removal efficiency of 2,4-DCP



(a)



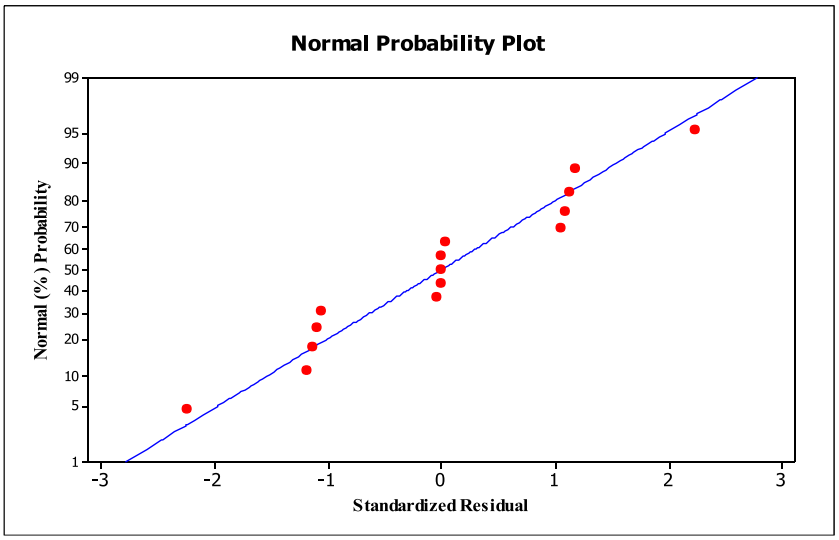
(b)

Fig. 10 **a** Normal plot of residuals and **b** predicted vs actual

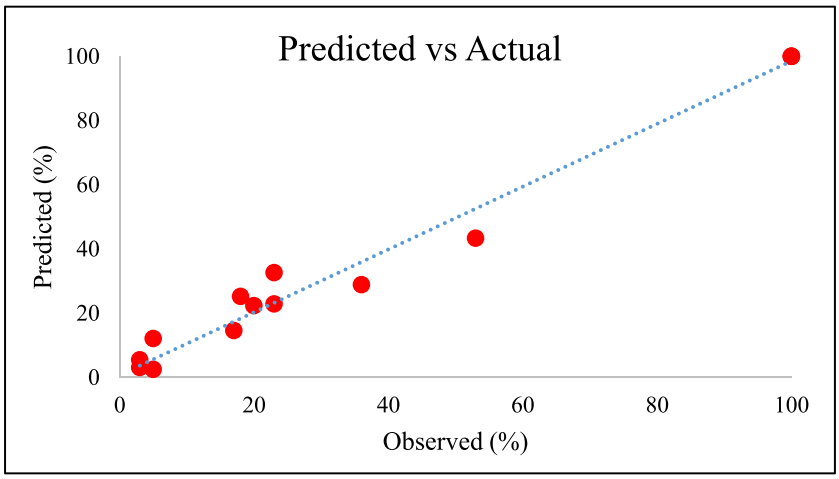
was maximum. An increasing quantity of H_2O_2 and TiO_2 addition had a proportional effect on the removal rate of 2,4-DCP and was risen simultaneously. As the dose of nano-TiO_2 was in the range of 200–250 mg/L, the maximum rate of 2,4-DCP removal was attained. However, after a certain amount beyond 200 mg/L, the degradation again declined. This is because of the increased opacity of the solution due to the excess catalyst added, which inhibited the effective penetration of UV light. The photoactivity of nano-TiO_2 is a function of pH as well (Fig. 13c). Considering the isoelectric point of TiO_2 (discussed in the previous section) and the pKa value of chlorophenols, the photooxidation of chlorophenols was found to be maximum at pH < pHpzc of TiO_2. The removal efficiency was decreased as pH > pHpzc. At optimised loading, *e-h* are generated, reacting directly or with surface-bound water, producing hydroxyl radical efficiently.

Effect of photo-Fenton variables

The interactive effect of variables governing the photo-Fenton process is represented in Fig. 14. The graph (Fig. 14a) shows that the removal efficiency increased by increasing the concentration of an oxidising agent and iron (Fe^{2+}). This is attributed to the increased production rate of reactive oxidising species enhancing the removal rate. Around 5.0 mM of H_2O_2 and 0.5 mM of iron concentration, complete removal of organic contaminant was observed. A further increase in the dose of both factors resulted in a reduced removal rate. This is because an excessive amount of iron and H_2O_2 results in the scavenging of hydroxyl radicals. pH plays a significant role in governing the efficacy of the treatment system. It is evident in literature studies that the process contributes to maximum efficiency under acidic conditions. Considering the effect of pH wrt catalyst concentration (Fig. 14b), increasing pH values and iron dose substantially increased



(a)



(b)

Fig. 11 **a** Normal plot of residuals and **b** predicted vs actual

the degradation rate. However, the removal rate declined under alkaline conditions, owing to the relative formation of iron oxo hydroxides and ferric hydroxide precipitate. Lesser availability of ferrous ions results in the mere formation of hydroxyl radicals, hence lesser degradation. The interactive effect of pH and H_2O_2 was insignificant. Degradation suffered drastically at both excessive and deficient dosages of H_2O_2. It can be observed (Fig. 14c) that throughout the range of changing pH conditions, the removal rate at lower H_2O_2 amounts (3–4 mM) was 50–70%. As the quantity of H_2O_2 increased, the degradation rate also increased and peaked at around 5.0 mM. Further addition resulted in less removal as H_2O_2 curtails the availability of OH radicals. Excess H_2O_2 causes enhanced deactivation of ferrous ions to ferric ions. Also, at higher pH, H_2O_2 is unstabilised and undergoes self-decomposition, decreasing the removal efficiency of the system (Ghoneim et al. 2011; Zulfiqar et al. 2019).

Synergistic effect of integrated oxidation systems

A comparative assessment of different AOPs was studied for degradation of chlorophenolic compounds (Fig. 15). The maximum degradation efficiency of respective processes along with their mineralisation percent is illustrated in Table 5. Based on optimised conditions obtained for photocatalysis and photo-Fenton's treatment processes, different AOPs were coupled to investigate the profound effect on the degradation of refractory organics.

Sonication-coupled AOPs

The application of ultrasound results in the degradation of organic compounds by generating hydroxyl radicals and acoustic cavitation bubbles. Ultrasonic power in the sonolytic process generates expansion and compression cycles

Table 4 Analysis of variance (ANOVA) for percentage degradation of 2,4-DCP by photocatalysis (UV_{365}) and photo-Fenton's treatment

Source	DF	Seq SS	Adj SS	Adj MS	*F*	*P*
Photocatalysis (a)						
Regression	9	5700.18	5700.18	633.35	26.67	0.001
Linear	3	918.75	1756.05	585.35	24.65	0.002
pH	1	612.5	1474.11	1474.11	62.07	0.001
TiO_2	1	153.12	88.14	88.14	3.71	0.112
H_2O_2	1	153.12	66.36	66.36	2.79	0.155
Square	3	3375.18	3375.18	1125.06	47.37	0
pHxpH	1	1896	2238.98	2238.98	94.27	0
TiO_2xTiO_2	1	548.66	660.52	660.52	27.81	0.003
H_2O_2xH_2O_2	1	930.52	930.52	930.52	39.18	0.002
Interaction	3	1406.25	1406.25	1406.25	19.74	0.003
pH & TiO_2	1	625	625	625	26.32	0.004
pH& H_2O_2	1	25	25	25	1.05	0.352
TiO_2& H_2O_2	1	756.25	756.25	756.25	31.84	0.002
Residual error	5	118.5	118.5			
Lack-of-fit	3	118.75	118.75			
Pure error	2	0	0			
Total	14	5818.93				
R.Sq	97.96%					
R-Sq Adj	94.29%					
Photo-Fenton (b)						
Regression	9	18445.2	18445.2	2049.46	24.65	0.001
Linear	3	805.8	8883.9	2961.30	35.61	0.001
pH	1	40.5	700.6	700.62	8.43	0.034
Fe^{2+}	1	465.1	4220.6	4220.6	50.76	0.001
H_2O_2	1	300.1	6593.1	6593.1	79.29	0.000
Square	3	16954.2	16954.2	5651.39	67.97	0.000
pHxpH	1	2293.5	3634.7	3634.7	43.71	0.001
Fe^{2+}xFe^{2+}	1	5750.2	6866.8	6866.8	82.58	0.000
H_2O_2xH_2O_2	1	8910.5	8910.5	8910.5	107.16	0.000
Interaction	3	685	685.3	685.3	2.75	0.152
pH& Fe^{2+}	1	625	625	625	7.52	0.041
pH& H_2O_2	1	4	4	4	0.05	0.835
Fe^{2+}& H_2O_2	1	56.2	56.2	56.2	0.68	0.448
Residual error	5	415.7	415.7	83.15		
Lack-of-fit	3	415.7	415.7	138.58	*	*
Pure error	2	0	0	0		
Total	14	18860.9				
R.Sq	97.8%					
R-Sq Adj	93.83%					

which form acoustic cavitation (Yadav et al. 2023a). The cavities oscillate in size, following the expansion and compression cycles. Several hundreds of atmosphere pressure and several thousand Kelvin temperatures are achieved with the collapse of the cavitation bubbles (Yadav et al. 2023a). Attributing to the collapse and pressure, organic compounds are degraded either by direct pyrolytic cleavage or the hydroxyl radicals formed by pyrolysis (Ameta and Ameta 2018). Coupling of sonication with photocatalytic treatment and Fenton's process resulted in enhanced mineralisation in less time. It was observed that under optimised conditions, Fenton's process was inefficient, and only 60% of 2,4-DCP was degraded in an hour with only 30% mineralisation. Coupling of ultrasound with Fenton, US/ H_2O_2/ Fe(II), degradation was around 80% which is 20% more with double mineralisation (60%) as compared to Fenton's

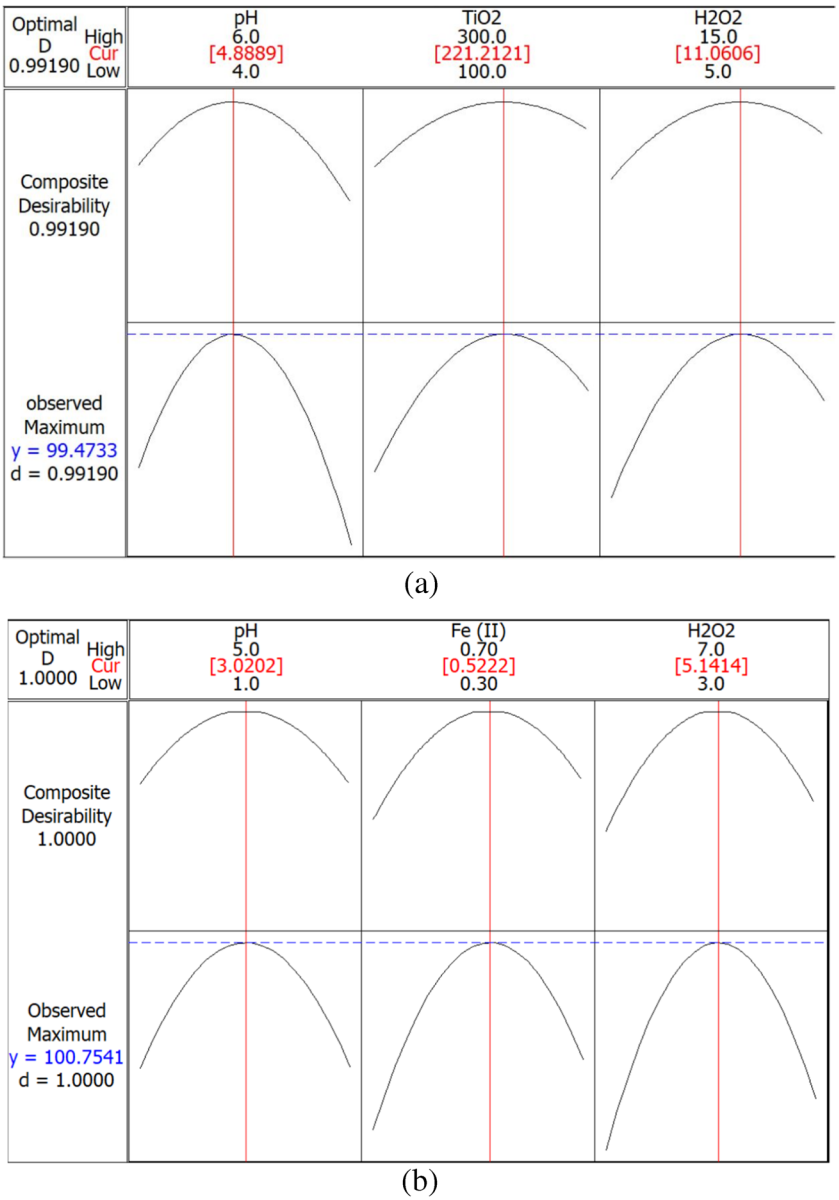


Fig. 12 Optimisation plot of regulating parameters: **a** photocatalysis and **b** photo-Fenton for degradation of 2,4-DCP

process alone. Sonolysis when coupled with photo-Fenton showed complete degradation in 13 min with slightly higher mineralisation (~72%) as compared to photo-Fenton (66%) alone. Photo-Fenton (UV_{365}) alone reported complete degradation within a few minutes (5 min) of duration because of the direct nucleophilic attack of the OH radicals (Pera-Titus et al. 2004). Although the mineralisation per cent was higher in the case of the sonication-assisted photo-Fenton process, the rate was still less than photo-Fenton (UV) because of the inter-specific competition of Fenton and ultrasound for H_2O_2 for generating OH radicals (Verma and Haritash 2019).

The drastic change in degradation efficiency rate and mineralisation was observed in the case of the sonication-assisted photocatalysis treatment system. Ultrasonic power coupled with UV/TiO_2/H_2O_2 system resulted in complete degradation of 2,4-DCP in 120 min. Photocatalysis treatment alone took 210 min to completely eradicate the phenolic compound. The synergistic effect of sonication+UV/TiO_2/H_2O_2 reduced the duration of treatment with higher mineralisation (75%) as compared to 70% mineralisation in the case of photocatalysis alone. The ultrasound irradiation-induced cavitation effect generates heat; facilitates the proper mixing or mass transfer; and promotes the contact between active sites of catalyst with organic impurities and dispersion of contaminated layers of chemicals (Othmer and Overberger 1983). The physical impact of ultrasound accelerated the reaction by proper mixing of reagents and enhancing the surface area of the catalyst (Anandan et al. 2020). Thus, the synergistic effect of sonication and UV light enhanced the degradation and mineralisation of 2,4-DCP.

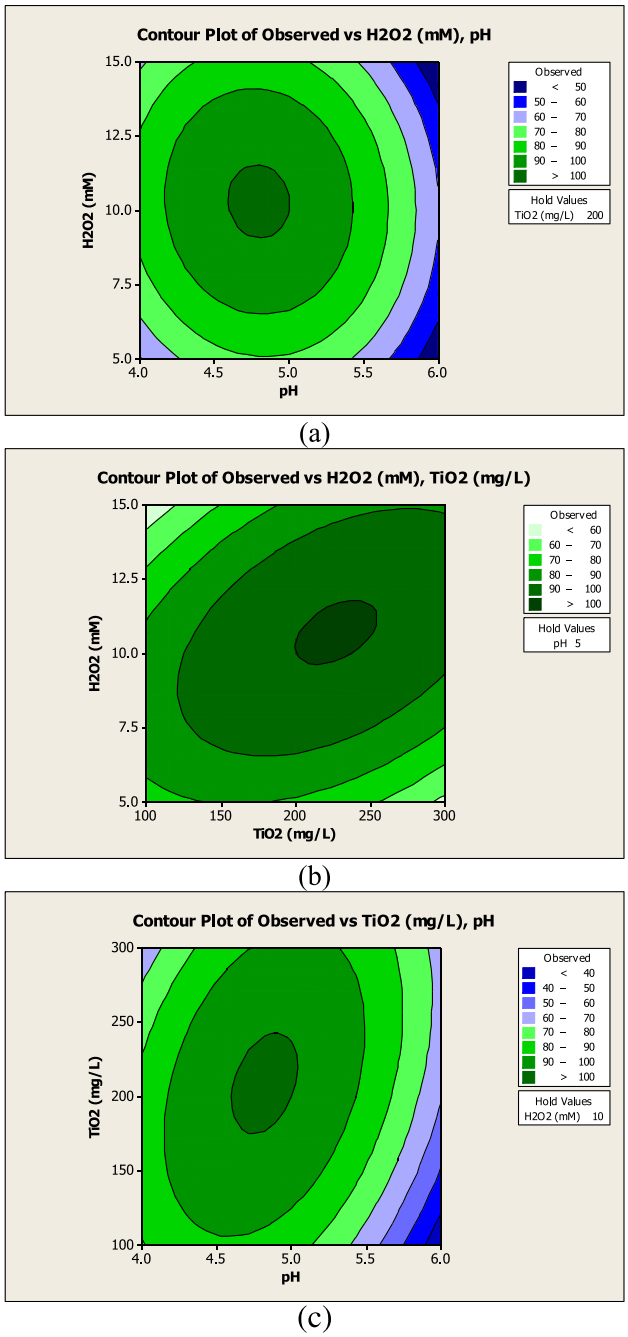


Fig. 13 Two-dimensional contour plots showing effect of regulating parameters towards 2,4-DCP degradation in photocatalysis process

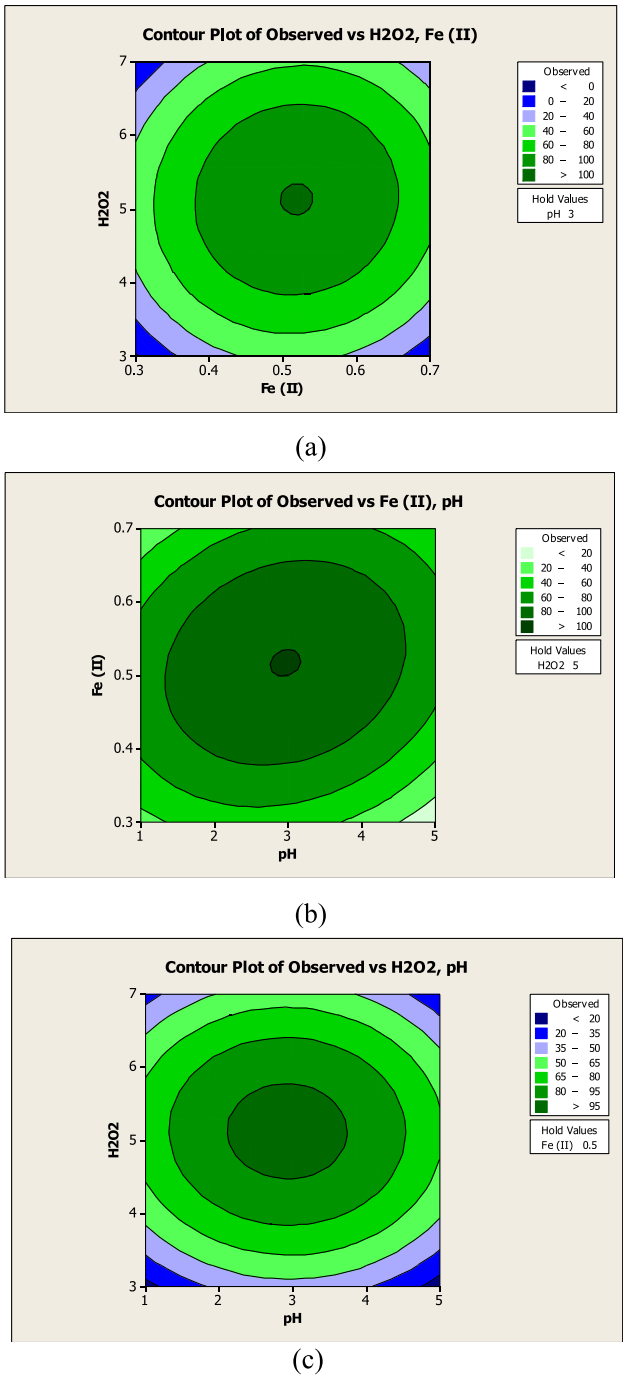


Fig. 14 Two-dimensional contour plots showing effect of regulating parameters towards 2,4-DCP degradation in photo-Fenton's process

Solar-driven AOPs

One of the major challenges of AOPs is switching from energy-intensive processes to sustainable and renewable energy sources. Solar-driven AOPs investigated in the present study have reported some promising results. Solar-Fenton reported complete degradation of organic pollutant with 90% TOC reduction. The time taken by solar-Fenton was 18 min which is comparatively four times compared to the photo-Fenton process. The synergistic effect of solar-sono-Fenton was also studied. Although complete removal of 2,4-DCP was observed in 18 min, the TOC mineralisation of ~80% was there. The availability of sufficient high-intensity solar light enhances the degradation rate of 2,4-DCP. Solar-coupled Fenton's treatment experiment was conducted in November 2022 on a sunny

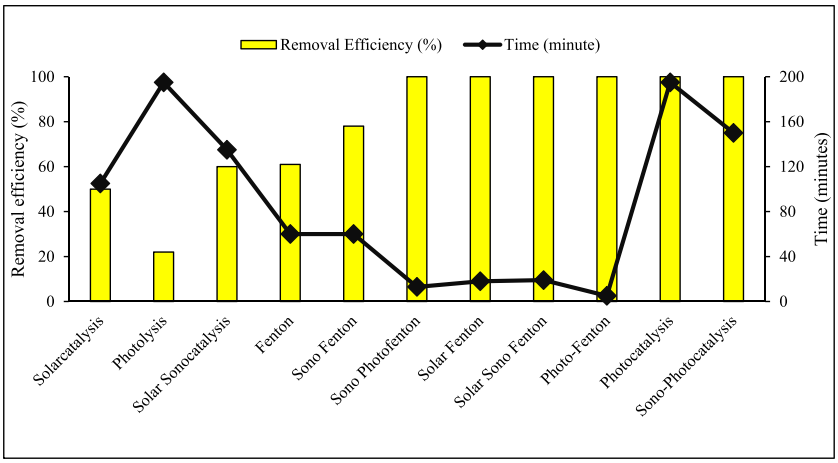


Fig. 15 Comparison of different AOPs towards maximum removal

afternoon between noon h and 14:00 h with an average solar radiation intensity of 358.92 W/m^2. In photocatalysis, the rate of electron excited from the valence band to the conduction band of the photocatalyst is influenced by the intensity of light affecting the rate of photocatalytic reaction and photocatalyst activation (Ortiz et al. 2019). In solar-driven nano-TiO_2-induced catalysis, only 50% removal efficiency was attained in 105 min, whereas solarcatalysis when coupled with sonication (sono-solarcatalysis) reported only a slight increase in removal efficiency (60%) in 135 min with TOC reduced by 36% only. In both the abovementioned oxidation treatment systems, solar light (solar radiation 309.31 W/m^2) was found less efficient towards the generation of hydroxyl radicals and degrading 2,4-DCP because of the fractional proportion of UV in the solar spectrum compared to direct UV light used in photocatalysis effective for photoactivating the photocatalyst (Ortiz et al. 2019). The effect of direct sunlight i.e. photolysis was also studied; however, marginal removal (~20%) was observed.

Solar photochemistry plays a vital role in pollution remediation transforming the pollutants into non-toxic compounds. Since no modification in the solar spectrum can take place, solar energy could be channelled to increase the efficiency of treatment systems. The sunlight consists of a wide spectrum of light based on wavelengths ranging from 300 to 2500 nm which includes UV light (< 380 nm), visible light (380–780 nm, also referred to as sunlight), and near-infrared (>780 nm), whereas, in the photo process, the exposure of UV light was restricted to a wavelength of 354 nm only. In addition, the solar spectrum is harnessed naturally, thereby offsetting the cost of treatment against UV light. Therefore, the use of solar light is recommended to be a cheaper and more efficient treatment option against UV photocatalysis.

Economic analysis of different AOPs

Degussa P25 nano-TiO_2 was added as a photocatalyst in the photocatalysis experiment and was not consumed in the reaction. Considering the fractional amount of nano-TiO_2 lost during analysis, sample centrifugation, sample transfer, etc., the leftover catalyst was recovered and oven-dried at 105 °C. The recovery of nano-TiO_2 was calculated using the formula given below.

$$TiO_2 \text{ Recovered} = \frac{w2}{w1} x\ 100 \tag{39}$$

where w_1 is the initial known weight of nano-TiO_2 added and w_2 is the residual weight of TiO_2 recovered at the end of the experiment. In the present study, under optimised conditions, ~70% of the photocatalyst added was recovered. Thus, the use of optimised TiO_2 reduces the overall cost of the treatment, making the process both environment and energy-efficient. The economic analysis was conducted after maximal degradation of 2,4-DCP w.r.t. photocatalysis, photo-Fenton, solar-driven oxidation processes, and sonication-induced treatment processes, and a comparative assessment of treatment cost was done (Table 6). In the case of photocatalysis treatment, complete removal was achieved in 210 min with a 200 mg/L dose of catalyst and 10.0 mM dose of oxidant. The experiments were conducted in a fabricated UV chamber having 8 UV tubes, each with a power rating of 36 W, making together 288 W; the power rating of the air sparger and magnetic stirrer is 3.5 W and 8.5 W, respectively. Thus, the total power consumption is 300 W or 0.3 kWh. The cost of the Degussa P25 nano-TiO_2 catalyst used is INR 22,680/100 g, and since only 30% of it was consumed or lost, it cost INR 13.61/L for treating 100 mg/L strength of synthetically prepared wastewater. Considering the consumption of hydrogen peroxide cost INR 1.14/L, the overall operational cost of photocatalysis was INR 17.00 OR US $0.21. The electricity cost for industrial supply in most of the states in India is INR 8.5 per unit kWh. However, in photo-Fenton, degradation was attained within a few minutes, and since the cost of chemicals especially iron (used as a catalyst) was lesser in comparison, the

Table 5 Comparison of different processes for the maximum degradation, mineralization, and time for treatment

Processes	Conditions	Maximum Removal efficiency (%)	Time for complete/maximum degradation (minutes)	Mineralisation (%)
Photolysis	Light source: solar Intensity: 358.92 W/m^2	20	210	2
Solarcatalysis	TiO_2: 200 mg/L H_2O_2: 10.0 mM pH: 5.0 Light source: solar Intensity: 358.92 W/m^2	50	105	14
Photocatalysis	TiO_2: 200 mg/L H_2O_2: 10.0 mM pH: 5.0 Light source: UV tubes (365 nm) Intensity: 672 W/m^2	100	210	70
Sono-photocatalysis	TiO_2: 200 mg/L H_2O_2: 10.0mM pH: 5.0 Light source: UV tubes (365 nm) Intensity: 672 W/m^2 Ultrasound: 40 kHz	100	120	75
Sono-solarcatalysis	TiO_2: 200 mg/L H_2O_2: 10.0mM pH: 5.0 Light source: solar Intensity: 358.92 W/m^2 Ultrasound: 40 kHz	60	135	36
Fenton	Fe: 0.5 mM H_2O_2: 5.0 mM pH: 3.0	61	60	30
Photo-Fenton	Fe: 0.5 mM H_2O_2: 5.0 mM pH: 3.0 Light source: UV tubes (365 nm) Intensity:672 W/m^2	100	05	66
Sono-photo-Fenton	Fe: 0.5 mM H_2O_2: 5.0 mM pH: 3.0 Light source: UV tubes (365 nm) Intensity:672 W/m^2 Ultrasound frequency: 40 kHz	100	13	72
Sono-Fenton	Fe: 0.5 mM H_2O_2: 5.0 mM pH: 3.0 Ultrasound frequency: 40 kHz	78	60	59
Solar-Fenton	Fe: 0.5 mM H_2O_2: 5.0 mM pH: 3.0 Light source: solar Intensity: 358.92 W/m^2	100	18	88
Solar-sono-Fenton	Fe: 0.5 mM H_2O_2: 5.0 mM pH: 3.0 Light source: solar Intensity: 358.92 W/m^2 Ultrasound frequency: 40 kHz	100	19	77

overall cost of the treatment was much less (INR 0.9) compared to photocatalysis. It was observed that the treatment cost increased in sonication-integrated processes because of the additional power (100 W) consumed during treatment. The Fenton integrated sonication treatment cost was higher because of the increased time of treatment. The operational

Table 6 Economic analysis of the treatment cost of different AOPs used in the current study (* - with 70% TiO_2 recovery)

Treatment method	Energy per hour (kWh)	Time for treatment (minute)	Rate of energy (per kWh) (INR)	Cost of electricity (INR)	Chemical consumed	Cost of chemical per litre (INR)	Cost of treatment in per litre (INR)	Cost of treatment in per litre (US $)
Photo-Fenton (UV_{365})	0.3	5	8.50	0.21	$FeSO_4.7H_2O$ H_2O_2 (30% w/v)	0.08 0.57	0.90	0.01
Photocatalysis (UV_{365})	0.3	210	8.50	2.55	TiO_2 (P25) H_2O_2 (30% w/v)	13.61* 1.14	17.00	0.21
Fenton	0.01	60	8.50	0.085	$FeSO_4.7H_2O$ H_2O_2 (30% w/v)	0.08 0.57	0.70	0.01
Sono-Fenton	0.11	60	8.50	0.935	$FeSO_4.7H_2O$ H_2O_2 (30% w/v)	0.08 0.57	1.60	0.02
Sono-photo-Fenton (UV_{365})	0.4	13	8.50	0.74	$FeSO_4.7H_2O$ H_2O_2 (30% w/v)	0.08 0.57	1.50	0.02
Sono-photocatalysis (UV_{365})	0.4	120	8.50	6.8	TiO_2 (P25) H_2O_2 (30% w/v)	13.61* 1.14	22.00	0.23
Solar-Fenton	0.01	18	8.50	0.03	$FeSO_4.7H_2O$ H_2O_2 (30% w/v)	0.08 0.57	0.70	0.01
Sono-solar-Fenton	0.11	19	8.50	0.296	$FeSO_4.7H_2O$ H_2O_2 (30% w/v)	0.08 0.57	1.00	0.01
Solar-catalysis	0.012	105	8.50	0.179	TiO_2 (P25) H_2O_2 (30% w/v)	13.61* 1.14	15.00	0.18
Sono-solar-catalysis	0.112	60	8.50	0.952	TiO_2 (P25) H_2O_2 (30% w/v)	13.61* 1.14	16.00	0.19

cost was, however, less in the case of sono-photocatalysis because of reduced time compared to UV-photocatalysis. The cost of treatment was noteworthy in solar energy-driven processes, particularly solar-Fenton and sono-solar-Fenton. Solar energy-assisted sono-photocatalysis was found more energy-efficient compared to photocatalysis. Therefore, considering 'sustainability as the need of the hour', exploiting the use of solar energy is a renewable and environmentally sustainable sound approach, reducing the dependence on energy-intensive treatment and a pocket-friendly approach.

Conclusion

Complete degradation of 2,4-DCP was reported using AOP photocatalysis (in 210 min) and photo-Fenton (in 5 min) treatment. Optimization of process regulating parameters was performed using the RSM modelling technique. The proposed models for both processes were found highly significant and evaluated based on ANOVA results and coefficient of determination or regression (R^2 = 97.96% and 97.8%). The experimental data was explained based on the rate constant obtained using pseudo-first order and pseudo-second order rate kinetics equations. It was observed that the degradation followed the pseudo-first-order kinetics. For the degradation pattern for adsorption isotherm, Langmuir's model was best fitted. Under optimised conditions, different sonication and solar integrated AOPs were assessed for 2,4-DCP degradation. The mineralisation efficiency of the different processes employed is in the following order:

Solar-Fenton > solar-sono-Fenton > sono-photocatalysis > photocatalysis > sono-photo-Fenton > photo-Fenton > sono-Fenton > Fenton > sono-solarcatalysis > solarcatalysis > photolysis

Although complete degradation of 2,4-DCP was observed in most of the above processes, the TOC mineralisation values indicated the formation of intermediates. Solar-driven Fenton process was found to be the most efficient with the maximum degree of mineralisation (90%).

Solar-driven AOPs offer a valuable and eco-friendly alternative towards the mineralisation of harmful xenobiotics. The use of solar irradiated AOPs reduces the operational cost associated with and dependence on lamps for light. Application of solar energy could lead to reductions of more than 90% of energy demands, aiding in overall treatment costs as well, which is a demand for a developing nation like India where conventional treatment methods are still being practiced.

Acknowledgements The authors are grateful to the Department of Environmental Engineering at DTU for providing the infrastructure and opportunity for carrying out the present study.

Author contribution Harsh Pipil: conceptualization, execution, data compilation and draft writing.
Shivani Yadav: conceptualization, execution, data compilation and draft writing.
Sunil Kumar: conceptualization, supervision, reviewing and editing
Anil Kumar Haritash: conceptualization, supervision, reviewing and editing.

Data Availability Necessary data has been provided along with this manuscript.

Declarations

Ethical Approval Not applicable.

Consent to participate Authors provide the consent to participate.

Consent for publication Authors provide the consent to publish the manuscript.

Competing interests The authors declare no competing interests.

References

Abdelwahab O, Amin NK (2013) Adsorption of phenol from aqueous solutions by Luffa cylindrica fibers: kinetics, isotherm and thermodynamic studies. Egypt J Aquatic Res 39(4):215–223. https://doi.org/10.1016/j.ejar.2013.12.011

Ahmadzadeh S, Dolatabadi M (2018) In situ generation of hydroxyl radical for efficient degradation of 2, 4-dichlorophenol from aqueous solutions. Environ Monit Assess 190:1–11. https://doi.org/10.1007/s10661-018-6697-0

Ameta SC, Ameta R (eds) (2018) Advanced oxidation processes for wastewater treatment: emerging green chemical technology. Academic press

Anandan S, Ponnusamy VK, Ashokkumar M (2020) A review on hybrid techniques for the degradation of organic pollutants in aqueous environment. Ultrason Sonochem 67:105130. https://doi.org/10.1016/j.ultsonch.2020.105130

Bayarri B, Gimenez J, Curco D, Esplugas S (2005) Photocatalytic degradation of 2, 4-dichlorophenol by TiO2/UV: kinetics, actinometries and models. Catal Today 101(3-4):227–236. https://doi.org/10.1016/j.cattod.2005.03.019

Chu W, Choy WK, So TY (2007) The effect of solution pH and peroxide in the TiO2-induced photocatalysis of chlorinated aniline. J Hazard Mater 141(1):86–91. https://doi.org/10.1016/j.jhazmat.2006.06.093

Faludi T, Balogh C, Serfőző Z, Molnár-Perl I (2015) Analysis of phenolic compounds in the dissolved and suspended phases of Lake Balaton water by gas chromatography-tandem mass spectrometry. Environ Sci Pollut Res 22:11966–11974. https://doi.org/10.1007/s11356-015-4734-x

Field JA, Sierra-Alvarez R (2008) Microbial degradation of chlorinated phenols. Rev Environ Sci Biotechnol 7(3):211–241. https://doi.org/10.1007/s11157-007-9124-5

Freundlich H (1906) Concerning adsorption in solutions. J PhysChem-Stochiometrie Verwandtschaftslehre 57A:385–470

Ge M, Hu Z, Wei J, He Q, He Z (2021) Recent advances in persulfate-assisted TiO_2-based photocatalysis for wastewater treatment: performances, mechanism and perspectives. J Alloys Compd 888:161625. https://doi.org/10.1016/j.jallcom.2021.161625

Ghoneim MM, El-Desoky HS, Zidan NM (2011) Electro-Fenton oxidation of sunset yellow FCF azo-dye in aqueous solutions. Desalination 274(1-3):22–30. https://doi.org/10.1016/j.desal.2011.01.062

Gong X, Wang H, Yang C, Li Q, Chen X, Hu J (2015) Photocatalytic degradation of high ammonia concentration wastewater by TiO2. Future Cities Environ 1(1):1–12. https://doi.org/10.1186/s40984-015-0012-9

Hoffmann MR, Martin ST, Choi W, Bahnemann DW (1995) Environmental applications of semiconductor photocatalysis. Chem Rev 95(1):69–96. https://doi.org/10.1021/cr00033a004

Igbinosa EO, Odjadjare EE, Chigor VN, Igbinosa IH, Emoghene AO, Ekhaise FO, Igiehon NO, Idemudia OG (2013) Toxicological profile of chlorophenols and their derivatives in the environment: the public health perspective. Sci World J. https://doi.org/10.1155/2013/460215

Kansal SK, Chopra M (2012) Photocatalytic degradation of 2, 6-dichlorophenol in aqueous phase using titania as a photocatalyst. https://doi.org/10.4236/eng.2012.48055

Kansal SK, Kaur G, Singh S (2009) Studies on the photocatalytic degradation of 2, 3-dichlorophenol using different oxidants in aqueous solutions. React Kinet Catal Lett 98:177–186. https://doi.org/10.1007/s11144-009-0058-5

Kavitha V, Palanivelu K (2016) Degradation of phenol and trichlorophenol by heterogeneous photo-Fenton process using granular ferric hydroxide®: comparison with homogeneous system. Int J Environ Sci Technol 13:927–936. https://doi.org/10.1007/s13762-015-0922-y

Lagergren S (1898) About the theory of so-called adsorption of solute substances. Kungliga Svenska Vetenskaps akademiens 24:1–39

Langmuir I (1918) The adsorption of gases on plane surfaces of glass,mica and platinum. J Am Chem Soc 40:1361–1367

Melián EP, Díaz OG, Rodríguez JD, Araña J, Peña JP (2013) Adsorption and photocatalytic degradation of 2, 4-dichlorophenol in TiO2 suspensions. Effect of hydrogen peroxide, sodium peroxodisulphate and ozone. Appl Catal A Gen 455:227–233. https://doi.org/10.1016/j.apcata.2013.02.007

Michałowicz J, Duda W (2007) Phenols-sources and toxicity. Pol J Environ Stud 16(3):347–362

Nagy VD, Zhumakayev A, Vörös M, Bordé Á, Szarvas A, Szűcs A, Kocsubé S, Jakab P, Monostori T, Škrbić BD, Mohai E (2023) Development of a multicomponent microbiological soil inoculant and its performance in sweet potato cultivation. Microorganisms 11(4):914. https://doi.org/10.3390/microorganisms11040914

Ocampo-Perez R, Leyva-Ramos R, Mendoza-Barron J, Guerrero-Coronado RM (2011) Adsorption rate of phenol from aqueous solution onto organobentonite: surface diffusion and kinetic models. J Colloid Interface Sci 364(1):195–204. https://doi.org/10.1016/j.jcis.2011.08.032

Ortiz I, Rivero MJ, Margallo M (2019) Advanced oxidative and catalytic processes. In: Sustainable Water and Wastewater Processing. Elsevier, pp 161–201. https://doi.org/10.1016/B978-0-12-816170-8.00006-5

Othmer CG, Overberger GT (1983) Ultrasonics. In: Seaborg (ed) Kirk-Othmer Encyclopedia of Chemical Technology, vol 23, p 462. https://doi.org/10.1021/j150469a016

Pedrazzani R, Bertanza G, Brnardić I, Cetecioglu Z, Dries J, Dvarionienė J, García-Fernández AJ, Langenhoff A, Libralato G, Lofrano G, Škrbić B (2019) Opinion paper about organic trace pollutants in wastewater: toxicity assessment in a European perspective. Sci Total Environ 651:3202–3221. https://doi.org/10.1016/j.scitotenv.2018.10.027

Pera-Titus M, Garcia-Molina V, Baños MA, Giménez J, Esplugas S (2004) Deradation of chlorophenols by means of advanced oxidation processes: a general review. Appl Catal B Environ 47(4):219–256. https://doi.org/10.1016/j.apcatb.2003.09.010

Pipil H, Yadav S, Chawla H, Taneja S, Verma M, Singla N, Haritash AK (2022) Comparison of TiO2 catalysis and Fenton's treatment for rapid degradation of Remazol Red dye in textile industry effluent Rendiconti Lincei. Scienze Fisiche e Naturali 33(1):105–114. https://doi.org/10.1007/s12210-021-01040-x

Rout PR, Zhang TC, Bhunia P, Surampalli RY (2021) Treatment technologies for emerging contaminants in wastewater treatment plants: a review. Sci Total Environ 753:141990. https://doi.org/10.1016/j.scitotenv.2020.141990

Sajben-Nagy E, Manczinger L, Škrbić B et al (2014) Characterization of an extracellular laccase of Leptosphaerulina chartarum. World J Microbiol Biotechnol 30:2449–2458. https://doi.org/10.1007/s11274-014-1670-8

Samsudin MFR, Bacho N, Sufian S, Ng YH (2019) Photocatalytic degradation of phenol wastewater over Z-scheme g-C3N4/CNT/BiVO4 heterostructure photocatalyst under solar light irradiation. J Mol Liq 277:977–988. https://doi.org/10.1016/j.molliq.2018.10.160

Shoneye A, Sen Chang J, Chong MN, Tang J (2022) Recent progress in photocatalytic degradation of chlorinated phenols and reduction of heavy metal ions in water by TiO2-based catalysts. Int Mater Rev 67(1):47–64. https://doi.org/10.1080/09506608.2021.1891368

Škrbić B (2007) Organochlorine and organophosphate pesticide residues in wheat varieties from Serbia. Food Addit Contam 24(7):695–703. https://doi.org/10.1080/02652030601182888

Temkin MJ, Pyzhev V (1940) Recent modifications to Langmuir isotherms, Acta Physiochem. USSR 12:217–222

Thind PS, Kumari D, John S (2018) TiO2/H2O2 mediated UV photocatalysis of chlorpyrifos: optimization of process parameters using response surface methodology. J Environ Chem Eng 6(3):3602–3609. https://doi.org/10.1016/j.jece.2017.05.031

USEPA (2004) Edition of the drinking water standards and health advisories. EPA, US, Washington (DC)

Van Aken P, Lambert N, Van den Broeck R, Degrève J, Dewil R (2019) Advances in ozonation and biodegradation processes to enhance chlorophenol abatement in multisubstrate wastewaters: a review. Environ Sci Water Res Technol 5(3):444–481. https://doi.org/10.1039/C8EW00562A

Verma M, Haritash AK (2019) Degradation of amoxicillin by Fenton and Fenton-integrated hybrid oxidation processes. J Environ Chem Eng 7(1):102886. https://doi.org/10.1016/j.jece.2019.102886

Verma M, Haritash AK (2020) Photocatalytic degradation of amoxicillin in pharmaceutical wastewater: a potential tool to manage residual antibiotics. Environ Technol Innov 20:101072. https://doi.org/10.1016/j.eti.2020.101072

Wang P (2017) Aggregation of TiO2 nanoparticles in aqueous media: effects of pH, ferric ion and humic acid. Int J Environ Sci Nat Resour 1(5):157–162. https://doi.org/10.19080/IJESNR.2017.01.555575

Weber R, Gaus C, Tysklind M, Johnston P, Forter M, Hollert H et al (2008) Dioxin-and POP-contaminated sites—contemporary and future relevance and challenges: overview on background, aims and scope of the series. Environ Sci Pollut Res 15:363–393. https://doi.org/10.1007/s11356-008-0024-1

Wei D, Zhao C, Khan A, Sun L, Ji Y, Ai Y, Wang X (2019) Sorption mechanism and dynamic behavior of graphene oxide as an effective adsorbent for the removal of chlorophenol based environmental-hormones: a DFT and MD simulation study. Chem Eng J 375:121964. https://doi.org/10.1016/j.cej.2019.121964

Yadav S, Pipil H, Chawla H, Taneja S, Kumar S, Haritash AK (2022) Textile industry wastewater treatment using eco-friendly techniques. In: Kanwar VS, Sharma SK, Prakasam C (eds) Proceedings of International Conference on Innovative Technologies for Clean and Sustainable Development (ICITCSD – 2021). Springer, Cham. https://doi.org/10.1007/978-3-030-93936-6_6

Yadav S, Kumar S, Haritash AK (2023a) A comprehensive review of chlorophenols: fate, toxicology and its treatment. J Environ Manag 342:118254. https://doi.org/10.1016/j.jenvman.2023.118254

Yadav S, Kumar S, Haritash AK (2023b) Solar light and ultrasound-assisted rapid Fenton's oxidation of 2,4,6-trichlorophenol: comparison, optimisation, and mineralisation. Rend Fis Acc Lincei. https://doi.org/10.1007/s12210-023-01192-y

Ye Z, Sirés I, Zhang H, Huang YH (2019) Mineralization of pentachlorophenol by ferrioxalate-assisted solar photo-Fenton process at mild pH. Chemosphere 217:475–482. https://doi.org/10.1016/j.chemosphere.2018.10.221

Zhumakayev AR, Vörös M, Szekeres A et al (2021) Comprehensive characterization of stress tolerant bacteria with plant growth-promoting potential isolated from glyphosate-treated environment. World J Microbiol Biotechnol 37:94. https://doi.org/10.1007/s11274-021-03065-8

Zulfiqar M, Samsudin MFR, Sufian S (2019) Modelling and optimization of photocatalytic degradation of phenol via TiO2 nanoparticles: an insight into response surface methodology and artificial neural network. J Photochem Photobiol A Chem 384:112039. https://doi.org/10.1016/j.jphotochem.2019.112039

Publisher's Note Springer Nature remains neutral with regard to jurisdictional claims in published maps and institutional affiliations.

Springer Nature or its licensor (e.g. a society or other partner) holds exclusive rights to this article under a publishing agreement with the author(s) or other rightsholder(s); author self-archiving of the accepted manuscript version of this article is solely governed by the terms of such publishing agreement and applicable law.

J Mater Sci (2024) 59:915–931

Composites & nanocomposites

The utilization of agricultural and industrial waste in the synthesis of AA7075-based novel lightweight composite

Ashish Kumar[1,2,*], Virendra Pratap Singh[3,4,*], Akash Mallik[5], Biraj Kumar Sahoo[6], R. C. Singh[1], and Rajiv Chaudhary[1]

[1] *Department of Mechanical Engineering, Delhi Technological University, Delhi 110042, India*
[2] *Department of Mechanical Engineering, Galgotias College of Engineering and Technology, Greater Noida 201310, India*
[3] *Department of Mechanical Engineering, IES College of Technology, Bhopal 462044, India*
[4] *Department of Mechanical Engineering, National Institute of Technology Mizoram, Aizawl 796012, India*
[5] *Department of Civil Engineering, Galgotias College of Engineering and Technology, Greater Noida 201310, India*
[6] *Materials Engineering Division, CSIR- National Metallurgical Laboratory (NML), Jamshedpur 831007, India*

Received: 3 November 2023
Accepted: 12 December 2023
Published online: 8 January 2024

© The Author(s), under exclusive licence to Springer Science+Business Media, LLC, part of Springer Nature, 2024

ABSTRACT

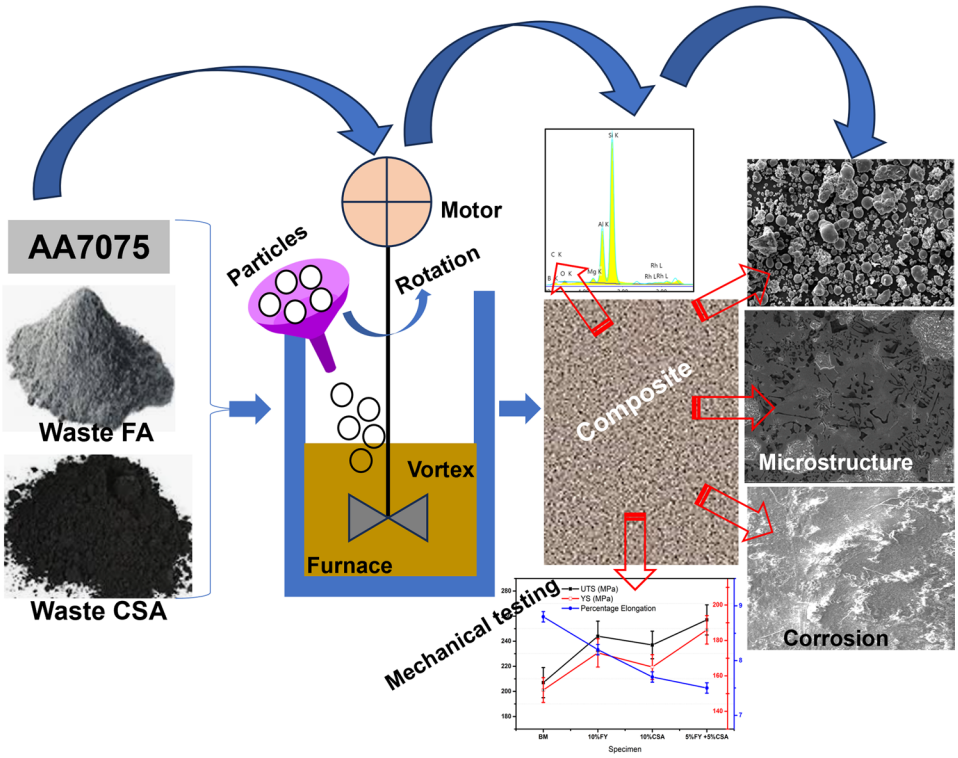
Fly ash (FA) and coconut shell ash (CSA) are solid byproducts of industrial and agricultural waste, respectively, that are produced in enormous amounts around the world. It is considered to be a contaminant in the environment. Because of the negative impacts on the environment, research on the use of FA and CSA is being undertaken all over the world. The current study focuses on the use of FA and CSA as reinforcement in an AA7075 alloy matrix through two-step stir casting. The present study also reported on the characteristics of newly developed novel composites and their environmental effects using leaching tests. The inclusion of ceramic particles can enhance the microstructure, mechanical, and corrosion characteristics of AA7075 alloys. Optical and scanning electron microscopes were used to evaluate the homogenous distribution of FA and CSA particles in the matrix. Contrasting with the homogeneous alloy, the hybrid composite, composed of 5 wt% FA and 5 wt% CSA, exhibited a remarkable surge of 27% in maximum hardness and a 19% increase in tensile strength. To explore the corrosion resistance of these newly created composites, polarization tests and AC impedance spectra were employed. Immersing the meticulously crafted specimens in a 3.5% sodium chloride solution, the corrosion assessment revealed that the composite with 5 wt% FA and 5 wt% CSA outperformed the traditional monolithic AA7075 alloy in terms of corrosion resistance.

Handling Editor: Annela M. Seddon.

Address correspondence to E-mail: ashuatcoer@gmail.com; virendraps07@gmail.com

https://doi.org/10.1007/s10853-023-09271-z

GRAPHICAL ABSTRACT



Introduction

The rapid expansion of the economy has been responsible for the extensive enrichment of organic solid wastes, including those from forestry, agriculture, industry, and municipalities. Researchers have been seeking innovative solutions to traditional incineration to solve environmental concerns due to the considerable pollution produced by the poor handling of organic solid wastes [1]. The continuous growth in agricultural and industrial waste materials raises concerns about environmental pollution, posing a risk of toxic exposure for people and animals as well as contamination of plants. Furthermore, the amount of consumption is already having a big influence on the environment everywhere, independent of region. The incorporation of methods to reduce trash and promote waste reuse and recycling can yield multiple favorable outcomes for the environment. These approaches contribute to the reduction or prevention of pollutant emissions, the mitigation of greenhouse gas production, the decreased reliance on waste treatment technologies, and the diminished demand for landfill sites. Therefore, it is strongly recommended that these techniques be integrated into the waste management strategy [2].

One of the most significant challenges of the twenty-first century is combating climate change, which necessitates a decrease in greenhouse gas emissions like carbon dioxide and methane. Since this industry is responsible for 15% of emissions, shifting to a more environmentally friendly mode of transportation is essential to achieving this goal [3]. The automobile sector is primarily responsible for producing, maintaining, and decommissioning emissions connected to mobility. Almost all forms of organic solid waste may be transformed into syngas, bio-oil, and biochar using pyrolysis as the primary method of energy utilization. This process is more affordable, continuous, and pollution-free. A sustainable transition from organic solid waste to cleaner production has been made possible by the pyrolysis of organic solid waste, which is of considerable relevance in addressing an energy crisis and reducing environmental pollution [4].

After China and the United States, India is the third-largest generator of coal-fired power. Since

Indian coal is of poor quality and has a high ash percentage (30–45%) compared to imported coals (10–15%), considerable amounts of fly ash (FA) are produced [5]. The majority of FA generated is dumped in ash ponds and landfills, with only a tiny part being used. Figures 1 and 2 depict FA production and consumption in India since 2011 and mid of 2022–23, respectively. To ensure effective waste management, India's Ministry of Environment and Forest (MoEF) introduced solid-waste management (SWM) guidelines in 2000, and a new revised draught rule was just published [6]. To mitigate the negative environmental impact and massive generation across the globe, research is being performed on using FA instead of disposing of. It has previously been used for producing ceramic reinforcements for concrete additives, cement, and metal matrix composites (MMCs) [7–9].

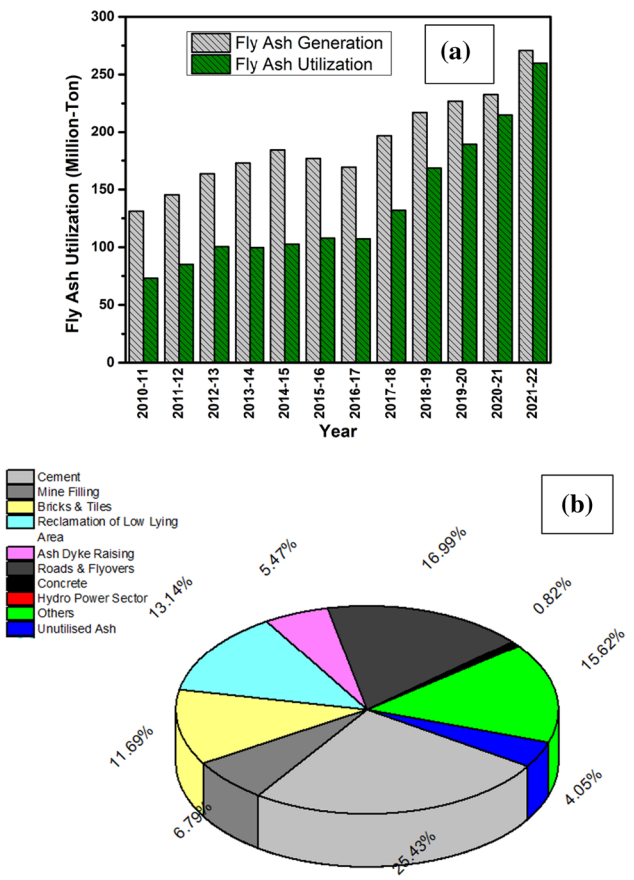


Figure 1 **a** Progressive fly ash (FA) generation and its utilization for the period from 2010–11 to 2021–22 and **b** major modes of FA utilization during the year 2021–22 [6].

MMCs that include ceramic particles such as B_4C [10], MgO [11], SiC [12], Al_2O_3 [13], TiB_2 [14], TiC [15], and others are expensive because of the elevated cost of the particulate, which is an enormous concern despite the desirable features of these composites. MMCs may be made inexpensively by using industrial and agricultural wastes as reinforcing particles, such as rice husk ash (RHA), coconut shell ash (CSA), bagasse ash, zircon sand, cement, FA, and red mud [2, 12]. Previous research with enhanced characteristics has used fly ash [16], zircon sand [17], and CSA [18], RHA [19] as reinforcement in aluminum and copper-based metal matrix. As per the previous research, CSA and FA have not been utilized as reinforcement in production of AA7075-based composites through two-step stir casting method.

Although MMCs have better qualities, the manufacturing processes available in the current manufacturing and fabrication industries are neither cost-effective nor dependable for producing bulk composites in near-net shapes and complicated component combinations. The most commonly employed ways for making MMCs are powder metallurgy [20], liquid state stir casting [21], squeeze casting [22], friction stir processing [9], and squeeze casting mixed with stir casting [22]. The stir casting technique has attracted an enormous amount of attention as a liquid state processing strategy compared to other manufacturing methods because it is low-cost, easy, and efficient for processing bulk-size composites into complicated near-net shapes of the components.

Corrosion of materials is a serious issue in the aircraft and marine industries, and it originates in many regions in the structures. Localized corrosion such as intergranular, crevice, pitting, and exfoliation corrosion can develop in numerous portions of aerospace manufactured of AA7xxx series materials [23]. Ramachandra et al. [24] developed the Al-Si-based composite using fly ash and investigated its corrosion and wear characteristics. It was also determined that corrosion resistance was inversely related to fly ash concentration. Kumar et al. [25] investigated the mechanical, wear, and corrosion behaviors of cast hybrid nano-metal matrix composites of AA7075 with Al_2O_3 and CSA and found that increasing the weight proportion of reinforcement gradually improves corrosion resistance.

Motivated by the considerations outlined above, this study was conducted to enhance the properties of commercially pure copper by incorporating 10 wt% fly

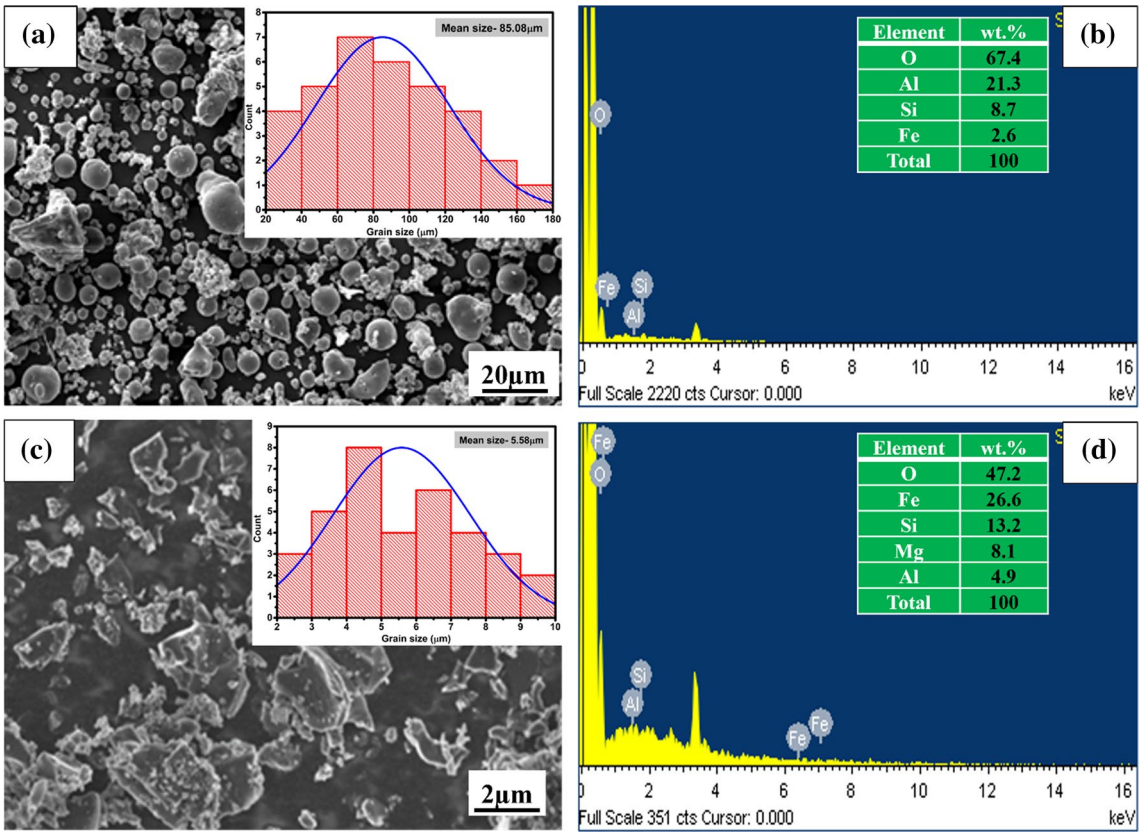


Figure 2 SEM morphology, grain size distribution and corresponding EDS of **a**, **b** fly ash and **c**, **d** coconut shell ash.

ash (FA) and 10 wt% coconut shell ash (CSA) through a two-step stir casting process, with a specific focus on its applicability in the development of Al-based composites. The microstructure of the resulting as-cast composite was meticulously examined using optical microscopy (OM) and scanning electron microscopy (SEM). A comprehensive exploration into the influence of FA and CSA reinforcement on hardness, tensile strength, and corrosion resistance was undertaken. In recognition of the environmental impact associated with FA and CSA, leaching tests were also conducted on the developed composites.

Experimental procedure

Materials and methods

In the present work, commercially available AA7075 alloy as matrix and FA and CSA as reinforcement were used as raw materials for composite fabrication. The selected matrix alloy is a conveniently castable alloy with a high tensile strength that is widely employed in the manufacture of structural components in aerospace, marine, and automotive applications [26]. The chemical analysis of AA7075 (Zn: 5.9, Cu: 1.7, Mg: 2.4, Fe: 0.57, Cr: 0.23, Mn: 0.13, and Si: 0.11) reveals that Zn, Cu, and Mg are the main alloying elements. SEM morphologies of micro-sized fly ash and CSA particles are shown in Fig. 2a, b. Raw coconut shells have been collected and completely dried in the sun for 4–5 days to eliminate moisture. The coconut shell is subsequently broken into small pieces and burned in an open-air metal drum to make ash. The ash is collected and burned for 3 h at 550 °C in a muffle furnace to eliminate the carbonaceous elements found in CSA.

A sieve machine was used to screen the particles to determine the approximate size range of the reinforcements. The size of FA varies between 40 and 100 µm on average (mean size-58.08 µm), whereas CSA varies between 2 and 10 µm on average (mean size-5.58 µm).

Fabrication method

Composites have been fabricated using two steps of stir casting, with reinforcement composition

variations of 0%, 10% FA, 10% CSA, and (5% FA and 5% CSA) by weight percent based on previous literature [12, 13]. To achieve homogeneous mixing, a preheated mechanical stirrer with a graphite impeller was employed to create vortex motion in a molten melt. Table 1 outlines the optimal parameters for the stir casting process. Al matrix was heated until melting began, then cooled at the slurry stage and thoroughly mixed in two-stage stir casting.

When the slurry is heated further and the matrix is stirred mechanically, the necessary temperature (850 °C) is reached. The particles that were dispersed throughout the matrix to provide a homogenous dispersion of the reinforcement are the key benefits of this stir casting over traditional stir casting [27]. The warmed (250 °C) mixture of FA and CSA was introduced simultaneously at a steady flow rate. To prevent slag formation and improve casting efficiency, 10 g of Na_3AlF_6 was added to the liquid melt during the melting process. Preheated FA and CSA particles are mixed well for 5 min at this moment. During the solidification process, a variety of dendrites with many branches may develop in the casting, lowering the mechanical properties. The molten slurry is further stirred for an additional 5 min to break up larger clusters, eliminate any remaining smaller-sized agglomerations, degas, and refine the matrix grain size. Once the reinforced particles had been successfully added to the molten melt slurry, it was cast into the gray cast iron mold that had been warmed to 550 °C. Three distinct combinations of novel composites and monolithic AA7075 alloy without reinforcement were cast. The test specimen was made by ASTM requirements using a wire electro-discharge machine (WEDM).

Table 1 Process parameters for stir casting

Key process parameters	Chosen parameters
Temperature for preheating the mold	550 °C
Temperature for processing	850 °C
Reinforcement preheating temperature	250 °C
Stirring speed	470 RPM
Stirring time	5 min
Utilized additive	Na_3AlF_6
Position of stirrer	Up to 75% depth

Characterization of the developed composite

The microstructure of the fabricated specimens was examined at the micron level using OM (Leica-DM2500M) and SEM (Zeiss Supra 40). The produced samples are polished using conventional metallurgical procedures. The following stage is an etching, which is carried out on each sample using Keller's reagent. SEM and optical metallographic pictures were examined to inspect the finished surfaces. For evidence of the presence of constituent phases and elements in the produced composite, EDS and XRD (D8 Advanced, X-ray diffractometer, Germany) investigations have been performed.

The specimens' hardness has been measured using a microhardness tester (Zwick/Roell Indentec). The trials were carried out using the ASTM: E10 standard. The specimens had been carefully machined and polished. Brinell scale, 2500 N load, and a steel ball with a diameter of 5 mm were used to calculate hardness for 20 s. An average hardness value was measured after ten indentations on the top surface were taken at ambient temperature. The produced composite specimen's ultimate tensile strength was assessed using a Universal Testing Machine (Instron) applied with a 10 KN force. For each composition set, five cylindrical rod-type specimens were prepared using wire EDM by ASTM: E08. By using the average value, the ultimate tensile strength was determined at a crosshead speed of 2.1 mm/min.

For the corrosion test, corrosive solutions were prepared using 35 g of NaCl solution in 1 L of distilled water. The corrosion sample has a dimension of $9 \times 9 \times 9$ mm^3 and is polished to create an working electrode. The materials were tested for 8 h and 5 days in a 3.5% NaCl solution. Using the Potentiodynamic polarization approach, it was possible to determine the kind of corrosion occurring in the specimens. Calculations were made for the corrosion potential, linear polarization resistance, and corrosion current.

The standard shaking technique for extraction of solid waste with water (ASTM-D3987) was used to quantify the environmental effect of FA and CSA on the developed composite. By using an inductively coupled plasma spectrometer (Model ICAP 6200 DUO), the leached solution's metal content was examined.

Results and discussion

The test's as-cast composite results as well as numerous OM and SEM pictures used to characterize the material have all been assembled logically and subjected to an in-depth analysis.

Microstructure and XRD analysis

Figure 3a–d displays the microstructure pictures for the reinforced materials. The optical images make uniform distributions of reinforced particles extremely apparent. When the AA7075 alloy solidifies, intermetallic phases including $MgZn_2$, Al_2Cu, $A_{l2}CuMg$, $A_{l7}Cu_2Fe$, $Al_{13}Fe_4$, and Mg_2Si may occur [10]. Figure 3a depicts the micro segregation of $MgZn_2$ with fine grains that are evenly distributed in an aluminum matrix. Aluminum solid solution grains have been surrounded by bright precipitates, as can be seen in Fig. 3a. These bright precipitates are attributed in the literature [28] to the block-shaped Al_2Cu phase, the Al_2Cu/Al eutectic (lamellar morphology), and the $MgZn_2$ phase, which are typically found along the boundary of the α-aluminum grain. The homogeneous distribution of reinforced FA and CSA particles is seen in Fig. 3b–d. Moreover, Fig. 3a–d illustrates how the presence of reinforced particles causes grain refinement in composite specimens. The findings reveal a distinctive phenomenon in the solidification process of the AA7075/FA/CSA composite melt, wherein FA and CSA particles are systematically propelled by aluminum dendrites toward the terminal stages of freezing, ultimately reaching the last eutectic liquid phase. This intriguing behavior adds a layer of uniqueness to the understanding of the composite's solidification dynamics. The enlarged grain boundaries are responsible for the strengthening of the matrix. The reinforcements act as a barrier, preventing dislocation movements from one grain to the next in the direction of a shift direction, increasing tensile strength.

Figure 4a–d displays the results of the as-cast samples' SEM and energy dispersive X-ray (EDS) analyzes. The SEM pictures show an even distribution of reinforcement particles throughout the matrix, confirming the better quality of hybrid aluminum matrix composites (HAMCs). To reduce cluster formation, a high molten temperature (850 °C) was utilized in this process since the reinforcements' melting temperature is higher than that of molten aluminum alloy. The temperature mismatch between the reinforcements and matrix causes tiny clusters to form when FA and CSA concentration rises. Clusters arise when the rate of solidification is retarded in the presence of hard

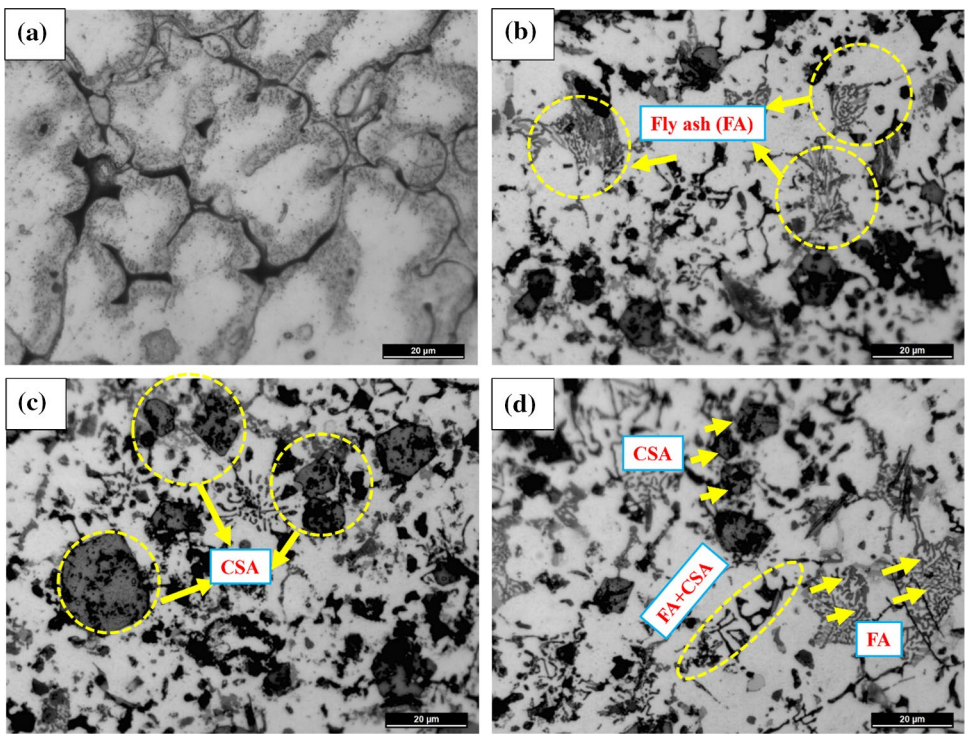


Figure 3 Optical images of as-cast **a** Monolithic alloy AA7075, **b** 10 wt% of FA composite, **c** 10 wt% of CSA composite, and **d** 5 wt% of FA + 5 wt% CSA composites.

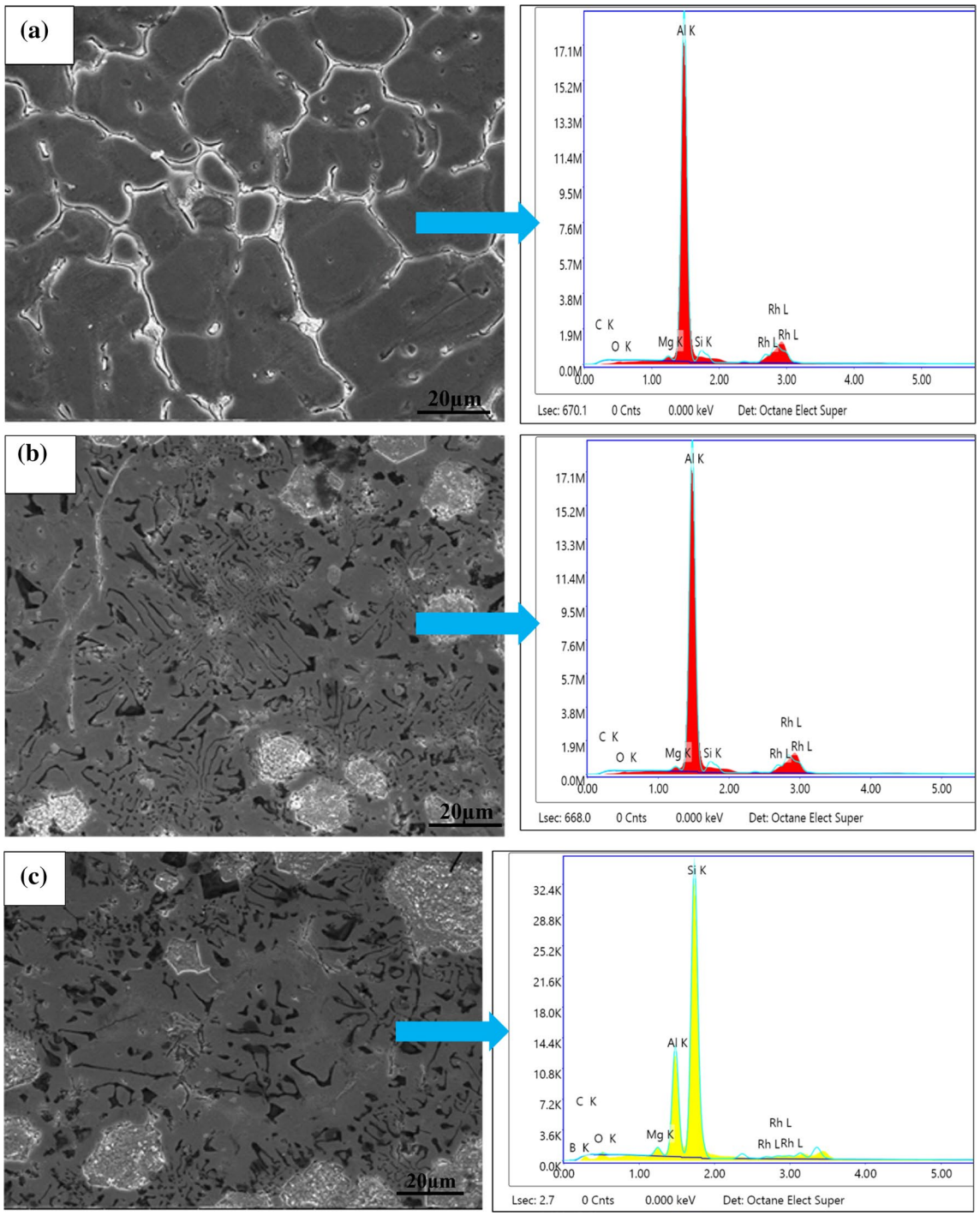


Figure 4 SEM with corresponding EDS of as-cast **a** monolithic alloy AA7075, **b** 10 wt% of FA composite, **c** 10 wt% of CSA composite, and **d** 5 wt% of FA + 5 wt% CSA composites.

ceramics around a liquid alloy. The density difference between the reinforcements and the aluminum matrix is one of the factors contributing to the occurrence of a cluster in the matrix. During the casting process, ultrasonic treatment minimizes this cluster development. In Fig. 4b–d, the uniform dispersion of fly ash (FA) and coconut shell ash (CSA) within the aluminum matrix is evident. The absence of microstructural

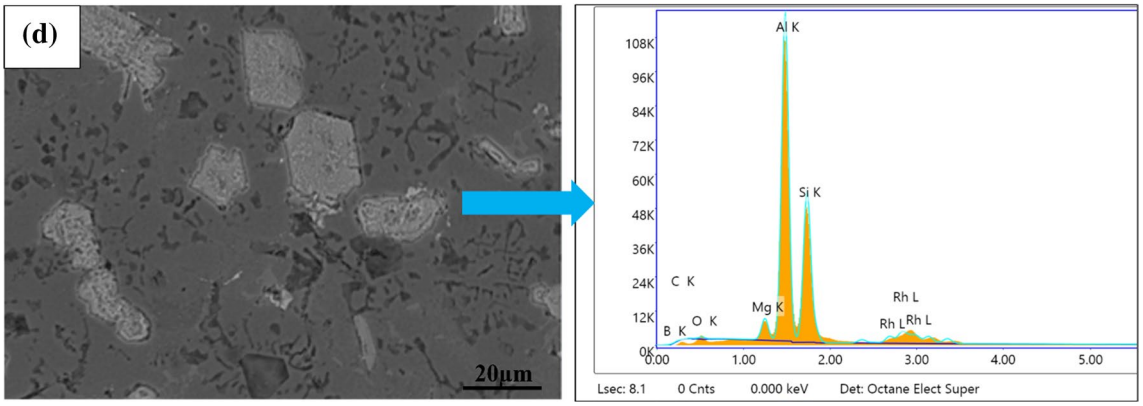


Figure 4 continued

cracks further validates the efficacy of the employed stir casting technique in composite fabrication.

The even clustering of FA and CSA demonstrates a distinct interface between the aluminum alloy and the reinforcing particles. During solidification, the reinforcements disperse along the refined aluminum grains (α-Al) directions. The formation of α-Al is attributed to the presence of FA and CSA reinforcements, acting as nuclei for solidification. The emergence of an intermetallic layer, exemplified by Al_2Mg_{17} in Fig. 4d, is linked to the development of SiO_2 on the surface of FA and CSA particles. This enhanced wettability between the aluminum matrix particles and the incorporated reinforcements (FA and CSA) diminishes the surface tension of the molten alloy. Consequently, this improvement leads to a more robust interfacial bond strength between the matrix and the reinforcements. Additionally, it is more affordable and efficient to dispose of FA and CSA to contribute to a cleaner and greener environment. Additionally, production is more cost-effective. The EDS result verifies the presence of reinforcements like FA and fly ash as well as alloying elements like Zn, Si, and Mg seen in Fig. 4a–d.

Figure 5 shows the results of an XRD analysis of an aluminum alloy (AA7075) and fabricated Composites with various weight percentages of reinforcements, FA, and CSA. The presence of SiO_2, Al_2O_3, and Fe_2O_3 is confirmed by the XRD pattern of the monolithic alloy and developed composites; these oxides are the primary oxides present in FA and CSA. The results are also supported by the findings from Kumar and Kumar [29]. Four additional peaks for fly ash and three new peaks were found in the fabricated composite (5 wt% of FA and 5 wt% of CSA) as a result of the

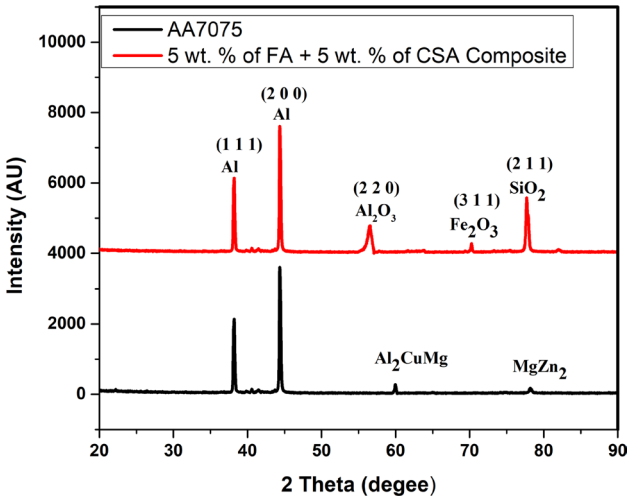


Figure 5 XRD analysis of AA7075 monolithic alloy and 5 wt% of FA + 5 wt% of CSA composite.

incorporation of FA and CSA, respectively. The composite's peaks for FA display the diffraction angle (2θ) at positions 56.20, 69.61, and 78.66, which are precisely indexed to diffraction from Fly ash planes (2 2 0), (3 1 1), and (2 1 1). The Al peaks at 37.30 and 44.61 exhibit the diffraction angle (θ), which is precisely indexed to diffraction from the planes (1 1 1) and (2 0 0).

Hardness and tensile responses

Figure 6 shows the results of the macro hardness test. The graph shows that the addition of FA and CSA improved the produced composite's BHN value. Increased dislocation production during solidification, which rises with an increase in the wt% of hard particles, may be the cause of the increase in hardness

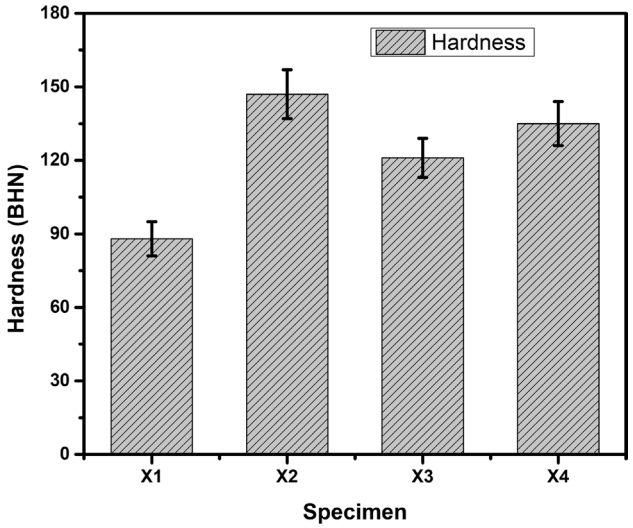


Figure 6 Variation of hardness with monolithic alloy and composite specimen.

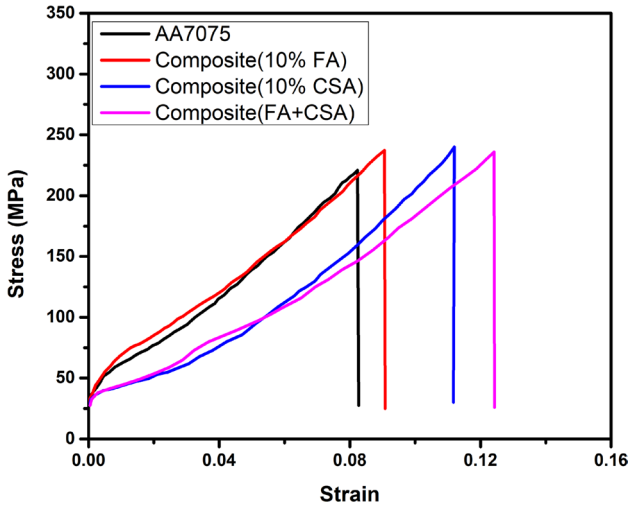


Figure 7 Stress–strain curve for monolithic and composite specimens.

observed with an increase in FA and CSA particle weight. These dislocations improve hardness and restrict plastic deformation. According to Ram et al. [30], adding hard ceramics (Fly ash + alumina) greatly enhances the hardness of the aluminum alloy. Similar to this, the discrete lattice model developed by Prabhu [30] shows that the inclusion of hard particles enhances the wear resistance of the composites by increasing the hardness.

The tabulation of tensile test specimen summaries for both the base alloy and hybrid composite is presented in Table 2. The stress–strain curve or tensile test curve, of monolithic alloy and composite specimens, are depicted in Fig. 7. As can be seen, both as-cast composite specimens exhibit an increase in strength, elongation, and toughness with the inclusion of FA and CSA. As the wt% of reinforcements increases, the porosity in the microstructure also increases. However, the crucial aspect contributing to the enhancement of mechanical properties lies in the formation of intermetallic compounds. These intermetallic exhibits high strength and form a robust bond with the aluminum matrix, allowing them to effectively pin dislocations. Figure 8 displays the distribution of the ultimate tensile strength, yield strength and percentage elongation of the composites for various compositions. The result indicates that when FA and CSA are included, it increases the tensile strength of composite materials. Particularly, the hardness and strength of Al_2O_3, SiO_2, and other ceramic particles (presented in FA and CSA) greatly improve the mechanical characteristics. The particles' strength and hardness are significantly higher than those of the AA 7075 matrix. Additionally, during deformation, these particles prevent dislocation movement. By overlapping around the particles, the dislocation must avoid them.

The improvement of properties is correctly attributed to the finer grain, a greater capacity for load transformation, consistent particle distribution, and a larger interfacial area. Additionally, the following hypotheses could be considered: Thermal mismatch, dislocation density, and Orowan strengthening are the three factors [31, 32]. Because of a subsequent hardness rise and non-uniform stirring durations during composite production, the increase in strength is

Table 2 Summary of tensile response of base alloy and hybrid composite

Specimen	Elastic modulus, *E* (GPa)	Ultimate tensile strength, UTS (MPa)	Elongation (%)
AA7075	152.42 ± 5	207 ± 16	8.8 ± 0.6
Composite (10 wt% FA)	173.06 ± 7	244 ± 18	8.2 ± 0.5
Composite (10 wt% CSA)	165.85 ± 8	237 ± 19	7.7 ± 0.5
Composite (5 wt% FA + 5 wt% CSA)	186.31 ± 9	257 ± 15	7.5 ± 0.4

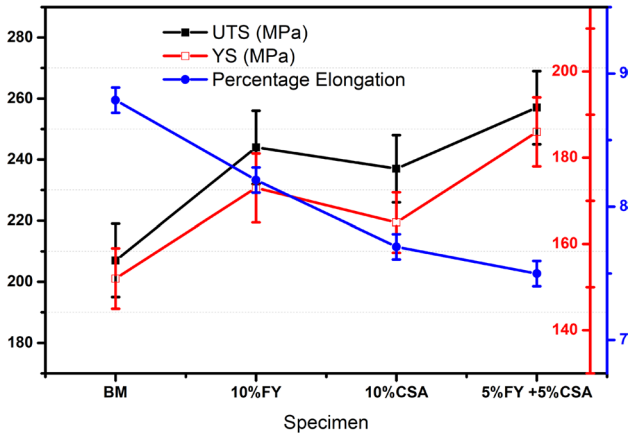


Figure 8 Variations of UTS, YS, and percentage elongations with wt% of reinforcements.

inappropriate and causes agglomeration. Additionally, by adding more FA and CSA, the tendency to elongate is reduced, which appears to be quite obvious given the greater hardness that comes with adding more reinforcements.

According to Habibi et al. [33], alumina reinforcing increases the mechanical parameters including ultimate tensile strength and yield strength while decreasing ductility. It is possible to attribute the causes for the improvement in characteristics to the presence of brittle, hard particles. The hardest ceramic particles fused in AA6061 may be responsible for the improvement in characteristics. Llorca et al. [33] described a similar pattern of behavior and explained how strain hardening affected an increase in load under ductile circumstances.

Figure 9a–d displays the SEM with EDS micrographs of fractured samples for both alloy and 5 wt% of FA + 5 wt% of CSA composite specimens. A tiny number of dimples and a sizable number of dendritic globules can be seen in Fig. 9a, both of which point to the slight plastic deformations that occurred during the tensile testing. Figure 9c illustrates hybrid composites with dendritic structures. Additionally, Fig. 9c shows that the FA and CSA particle exhibits fractures at greater stresses, showing that the load has been absorbed by the reinforcements by strengthening the

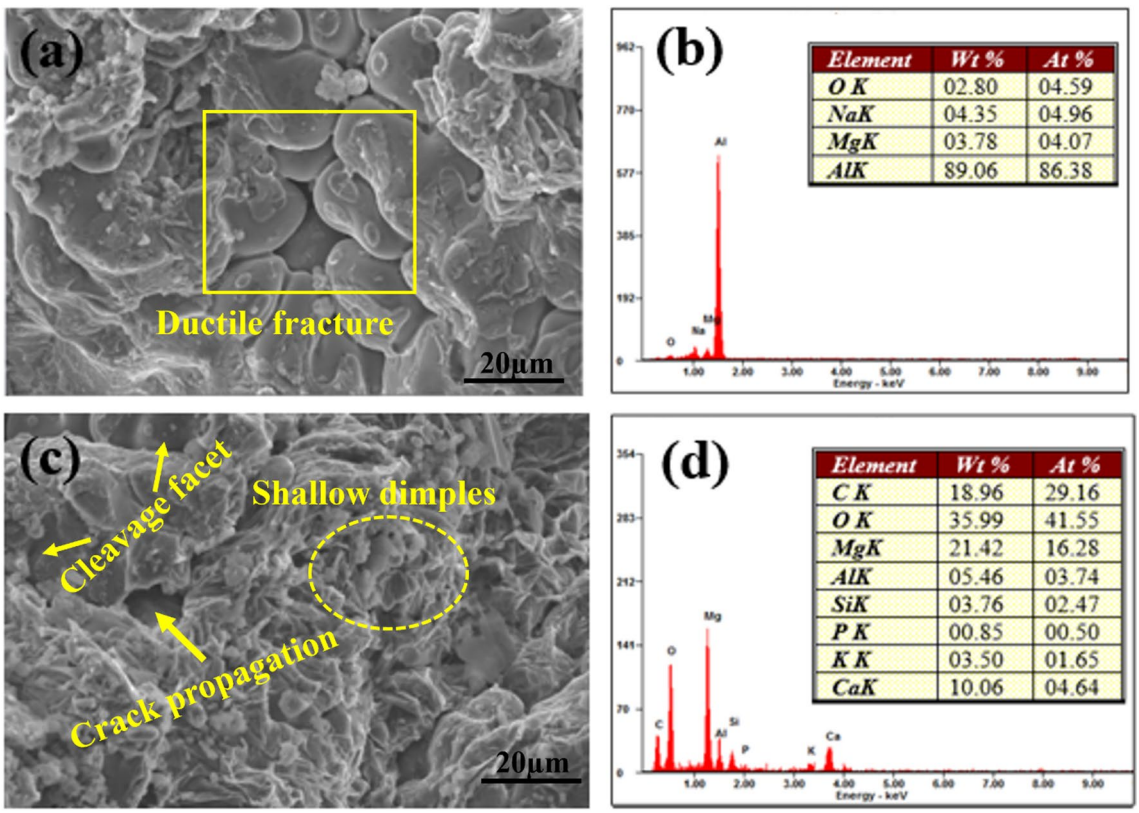


Figure 9 SEM with EDS analysis of fracture morphology of **a**, **b** AA7075 alloy and **c**, **d** 5 wt% of FA + 5 wt% of CSA composite specimens.

tensile characteristics. Figure 9b, d presents the results of the EDS analysis. The predominant elements are indicated by prominent peaks, while minor elements such as oxygen (O), magnesium (Mg), silicon (Si), copper (Cu), zinc (Zn), and iron (Fe) are combined within smaller peaks. FA and CSA particles pull out, which points to the origin of the fracture. The dendritic microstructure of the composites, as seen in Fig. 9c, serves as both a stress riser and a weak zone, leading to crack initiation [34]. These cracks propagate across the dendritic limits as a result of the ceramic particle and alloy matrix contact, functioning as stress concentration locations [35, 36]. The failure of composites as monolithic alloys is confirmed by the trans-granular cleavage facets and inter-dendritic stepwise dendrites on fracture surface fractography.

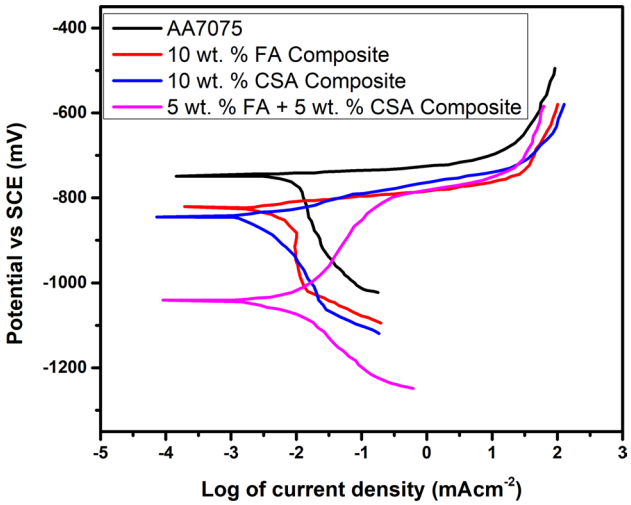


Figure 10 Polarization behavior of AA7075 alloy in a 3.5% NaCl solution with differing wt% of FA and CSA, as depicted by the Potentiodynamic polarization curve.

Corrosion behavior

Table 3 presents the summary of the PP-Test for AA7075 and developed composites. To investigate the corrosion byproduct layer on the developed composite surface, the samples were dipped in NaCl (3.5%) solution. The introduction of fly ash and coconut shell particles caused the potential to become more negative and the current density to decrease, as was evident from Fig. 10. Thus, it is established that adding fly ash and coconut shell particles to the alloy matrix of AA7075 increased corrosion resistance. With a saturated calomel electrode (SCE), monolithic AA7075 alloy displays potential and current densities of around 801 mV and 2.01 mA/cm^2, respectively, when submerged in NaCl solution.

The PP curve displays a decrease in current and an increase in negative potential. It continues until an E_{Corr} value for the AA7075 is acquired. It is reported in earlier literature that the AA7075 surface has reduced oxygen through cathodic reactions [23]. The alteration in corrosion potential and current density occurred, resulting in values of 907.78 mV versus SCE and 1.786 mA/cm^2 respectively, upon immersing a composite of AA7075 with 10 weight percent fly ash into a NaCl solution. Similar outcomes were observed when utilizing a composite containing 10 weight percent coconut shell ash, as well as a composite comprising 5 weight percent FA and 5 weight percent CSA. These findings suggest that the incorporation of reinforcements into AA7075 alloy heightened the corrosion rate of the otherwise resistant AA7075 composites. By introducing FA and CSA particles, the potential became more negative, accompanied by a decrease in current density, as depicted in Fig. 10. This observation underscores that the incorporation of FA and CSA particles into the AA7075 matrix enhances corrosion resistance. A study by Kenneth and Olubambi [37] delved into the corrosion behavior of an Al–Mg–Si matrix composite, revealing that the corrosion rate diminishes with the addition of rice husk ash and alumina in a 3.5% NaCl solution. The corrosion attributes of the composites purportedly decreased with the rise in the weight percentage of rice husk ash, attributed to

Table 3 Summary of potentiodynamic polarization test

Specimen	Potential versus SCE (mV)	Current density (mAcm^2)	Charge transfer (R_{ct})	Capacitance of double layer (C_{dl})
AA7075	801.23	2.01	1.629×10^3	2.234×10^{-5}
10 wt% FA	907.78	1.786	2.356×10^3	6.786×10^{-5}
10 wt% CSA	858.53	1.873	1.833×10^3	5.483×10^{-5}
5 wt% FA + 5 wt% CSA	932.32	1.593	2.537×10^3	7.125×10^{-5}

the lower density of rice husk ash (0.3 g/cm^3). Analysis of Tafel polarization curve plots revealed that the introduction of reinforcements to the AA7075 composite bolstered the alloy's corrosion resistance. This effect was demonstrated by a reduction in corrosion current density from 2.01 to 1.786 mA/cm^2.

In the study of the AA7075 composite, containing 10% CSA by weight, significant changes were noted in both corrosion potential and current density. These changes led to shifts to 858.53 mV versus SCE for corrosion potential and 1.873 mA/cm^2 for current density. Similarly, in the hybrid composite comprising 5% FA and 5% CSA by weight, alterations in potential and current density were observed, resulting in shifts to 932.32 mV versus SCE and 1.593 mA/cm^2, respectively. The notable increase in the corrosion current density in this study was attributed to the interaction between active Cl^- ions present in the NaCl solution. These Cl^- ions contributed to the degradation of the oxide layer formed on the surface, thereby intensifying the corrosion process and subsequently elevating the current density of corrosion. These findings provide empirical support for the assertion that the AA7075 composite, which contains 5 wt% FA and 5 wt% CSA, exhibits a reduced corrosion rate in comparison to the remaining composites.

This underscores the enhanced corrosion resistance of the 5 wt% FA and 5 wt% CSA in AA7075 composite as evidenced by the outcomes. Notably, these findings align with the observations made by Kumar et al. and Loto et al., who documented the corrosion behavior of aluminum and magnesium metal matrix composite [13, 38, 39]. The graph further underscores that the diminished corrosion rates can be attributed in part to the amorphous nature and intermetallic phase of the reinforced composite. The progressive increase in the content of FA and CSA within the composite contributes to a decrease in the degradation rate of the reinforced material. Tafel plots provide clear elucidation, confirming that the corrosion of the AA7075 alloy was substantially reduced through the gradual accumulation of various weight percentages of reinforcements.

The utilization of an electrochemical impedance spectrum (EIS) offers a deeper understanding of the corrosion reaction mechanism within the composite. Figures 11 and 12a, b depict the Nyquist and Bode plots corresponding to the AA7075 composites after its immersion in a 3.5% NaCl solution. Upon subjecting AA7075 to the 3.5% NaCl solution, the results reveal values of approximately 1.629 × 10^3 Ω cm^2 for

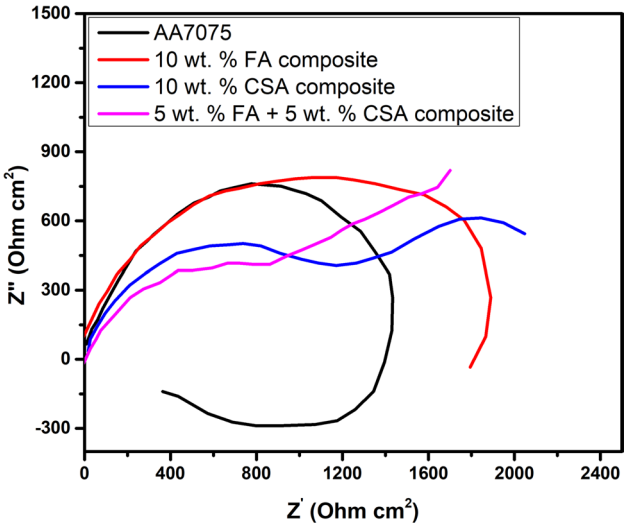


Figure 11 Electrochemical impedance spectroscopy Nyquist plot (Z' vs. Z'') of AA7075 alloy in a 3.5% NaCl solution, illustrating the impact of different wt% of FA and CSA.

the charge transfer resistance (Rct) and 2.537 × 10^{-5} F cm^{-2} for the capacitance of the double layer (CDL). Within VM1, an inductive loop becomes apparent, indicative of an elevated resistance to charge transfer in the lower frequency range. This phenomenon sheds light on the surface depression occurring at the electrode's surface. A recurring characteristic involves the presence of capacitive semi-circles within both the upper and typical frequency ranges, which correspond to the Al oxide layer and the electrolyte interaction evident in the EIS spectra. Upon immersing a composite of 10 weight percentage FA with AA7075 in a 3.5% NaCl solution, the resulting values for charge transfer resistance (Rct) and double layer capacitance (Cdl) are approximately 2.356 × 10^3 Ω cm^2 and 6.786 × 10^{-5} F cm^{-2}, respectively. Likewise, for the (5 weight percentage of CSA and 5 weight percentage of CSA) AA7075 composite, the corresponding Rct and Cdl values are approximately 2.537 × 10^3 Ω cm^2 and 7.125 × 10^{-5} F cm^{-2}, respectively.

By examining the polarization plot on Nyquist graphs, the charge transfer resistance (R_{ct}) varies from 1.629 × 10^3 to 2.537 × 10^3 Ω cm^2. This variation further solidified the conclusion that the inclusion of FA and CSA in the AA7075 composite amplified the corrosion resistance rate of the AA7075 alloy. Importantly, this finding aligns strongly with the outcomes derived from polarization studies. In

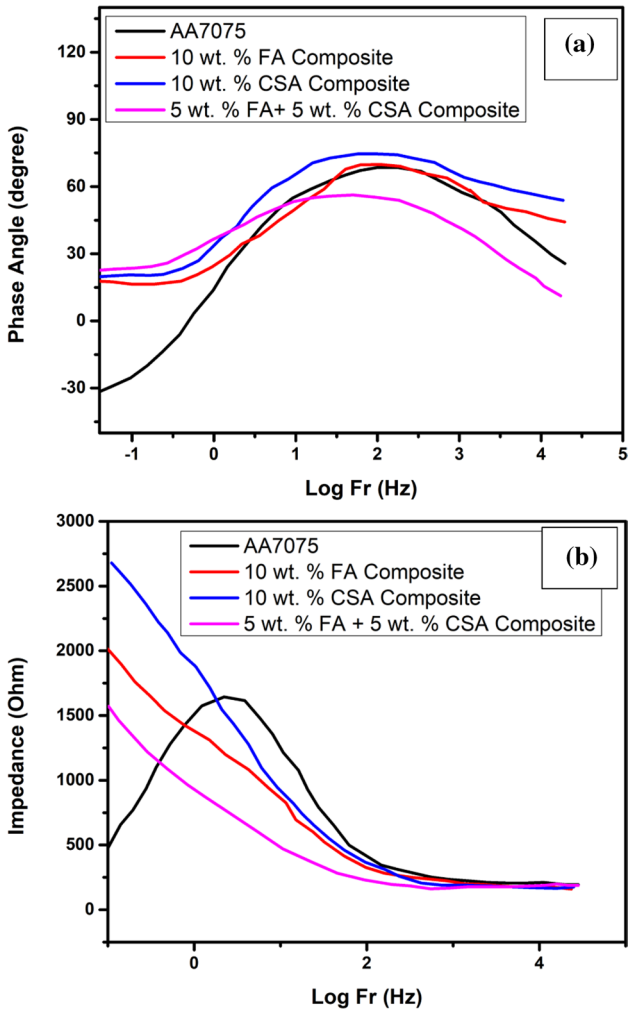


Figure 12 Bode plots of AA7075 matrix in a 3.5% NaCl solution. **a** Logarithm of frequency (Log Fr, Hz) versus phase angle and **b** logarithm of frequency (Log Fr, Hz) versus impedance.

another investigation, a 10-weight percentage of CSA AA7075 composite was submerged in a 3.5% NaCl solution, resulting in Rct and Cdl values of about 1.833×10^3 Ω cm^2 and 5.483×10^{-5} F cm^{-2}, respectively. The EIS results revealed that an effective protective layer formed on the metal's surface due to the enhancement of charge transfer resistance (R_{ct}), which concurrently led to a reduction in the value of double-layer capacitance (C_{dl}).

Following the corrosion investigations, the surface characteristics of the AA7075 and 5 wt% of FA + 5 wt% of CSA composite were examined through SEM with EDS analysis. The SEM micrographs depicting corroded samples are presented in Fig. 13a–d. These images distinctly illustrate the aluminum alloy's degradation in the presence of FA and CSA reinforcements, characterized by even corrosion attack within a 3.5 wt% NaCl solution. Upon corrosion testing, the AA7075 sample displays the emergence of pits, minor fractures, and pronounced precipitates, resulting in concurrent metal removal from the sample's surface. Considering the absence of reinforcing particles within the AA7075 matrix, the monolithic aluminum alloy becomes more susceptible to weakness, particularly in the creation of cracks and pits. Notably, the surface of the aluminum alloy experiences predominant erosion upon immersion for up to 7 days, as illustrated in Fig. 13a, b.

Within the realm of composites, the presence of FA and CSA particles effectively curtailed the impact of the 3.5% NaCl solution. The inclusion of these particles brought about a tangible enhancement in the corrosion resistance of the composites. As depicted in Fig. 13c, d, the SEM images offer insights into the corrosion morphology of the specimens. Notably, a protective corrosion layer was discernible on the surface of the composite specimens, demonstrating its role in safeguarding against degradation. While some precipitates within the corroded region experienced erosion, a few abrupt microfractures and minor cavities emerged on the surface of the composite specimen.

The inclusion of reinforcements corresponded with a gradual reduction in the presence of corrosion cracks and pits. These outcomes validated the data gleaned from Tafel plots, reinforcing the assertion of corrosion rate reduction. It is important to note that even though the reinforcement effectively resisted the corrosive nature of the NaCl environment, some small pits and cracks emerged due to the preferred formation sites around the particles within the MMC structure [40, 41]. Corrosion advances perpendicularly until chloride ions (Cl−) reach the gaps in the layer/layer interface. The active surface inside the pit expands, consequently accelerating the corrosion progression. As these gaps are relatively deep and corrosive ions face challenges in accessing these expansive active areas, only a limited number of Cl− ions can penetrate these gaps. Hence, the corrosion resistance of the composite specimens experiences a decrease to a certain extent.

Based on the SEM analysis, the conclusion drawn is that the composite specimen exhibited heightened corrosion resistance compared to the AA7075 alloy. The augmentation of FA and CSA particle content up to 10 wt% contributed to diminishing the reactivity of the aluminum alloy, consequently boosting the

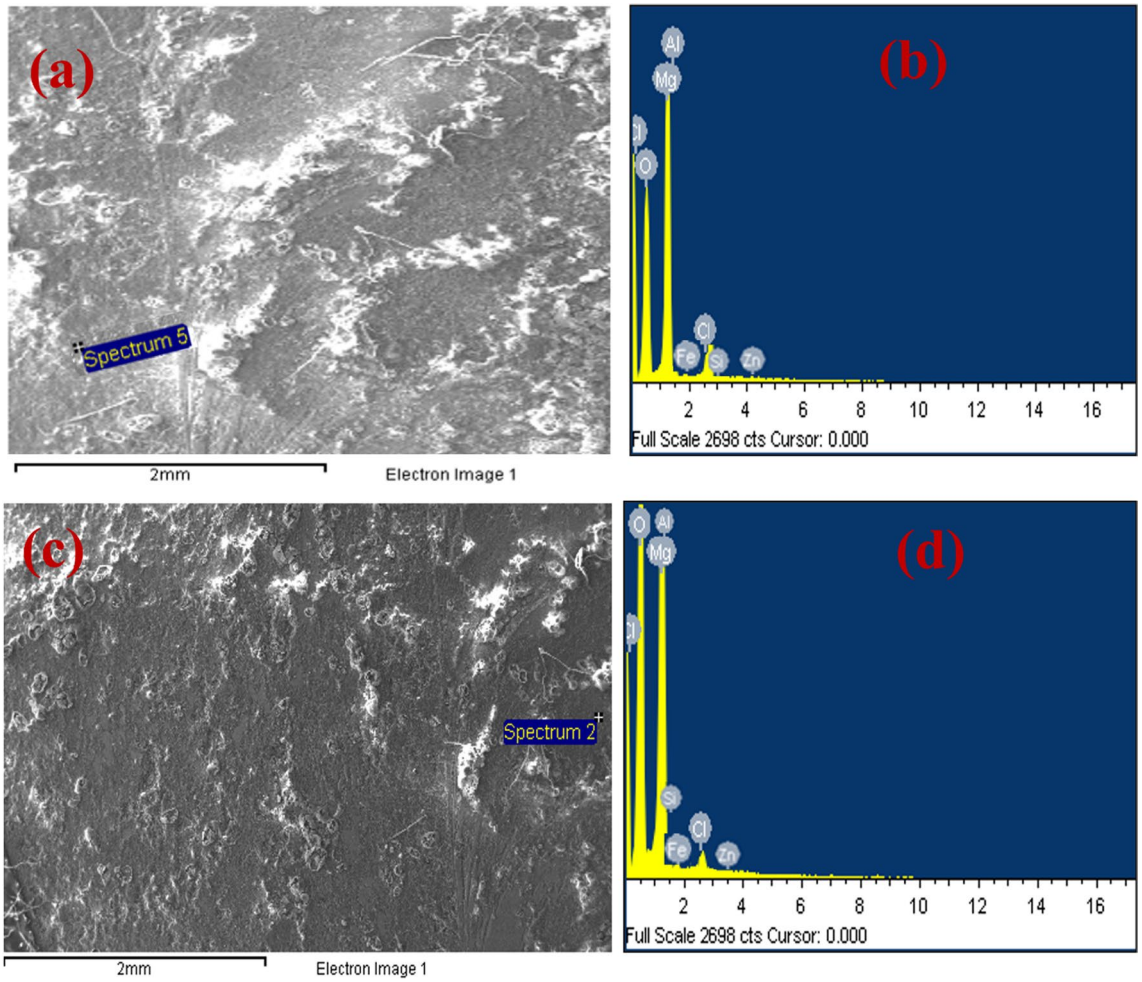


Figure 13 SEM morphology with corresponding EDS of corroded specimens **a**, **b** AA7075 alloy, **c**, **d** 5 wt% of FA + 5 wt% CSA composite specimens.

composite's resistance to corrosion. Furthermore, it was detected that the β-phase was absent in the aluminum alloys could be attributed to the presence of FA and CSA particles along the grain boundaries, a factor contributing to the overall enhancement in the corrosion properties [40–42].

Leaching test

The results of the leaching test as per ASTM-D3987 standards conducted on both the reinforcements (FA and CSA) and the fabricated composite (5 wt% of FA + 5 wt% of CSA) are presented in Table 4. The data distinctly reveals that the concentration of metals leached out from the developed composite is significantly lower in comparison to the concentration of

Table 4 Summary of solid waste leaching test using the standard shake method for water extraction, expressed in parts per million (ppm)

Specimen	Al	Zn	Cu	Mn	Si	Fe	Cr
Fly ash	12.78	0.29	0.27	0.42	5.23	0.12	0.0063
Coconut shell ash	11.23	0.19	0.26	0.37	3.25	0.05	0.0076
5 wt% of FA + 5 wt% of CSA composite	89.23	5.13	1.09	0.32	0.59	0.63	0.21

metals leached out from the FA and CSA. This implies that the composite's ability to release metals into its surrounding environment is notably diminished when contrasted with the leaching behavior of the original fly ash material. In essence, the composite demonstrates a heightened resistance to metal leaching compared to the raw fly ash.

Conclusions

In this investigation, a combination of industrial waste (FA) and agricultural waste (CSA) was utilized to reinforce commercial AA7075 alloy through the stir-casting processing method, resulting in the creation of an aluminum-based surface composite. The impact of FA and CSA reinforcement on various aspects including tensile strength, microstructure, microhardness, and corrosion test was comprehensively examined. Additionally, the composites underwent a leach test to assess their environmental implications. The results from the characterization process underscore the significant potential of FA and CSA as reinforcement materials in the production of aluminum-based composites, offering a cost-effective alternative to expensive ceramic particulates. This approach not only reduces production expenses but also diminishes the ecological footprint compared to existing composite materials. Stir casting, employed as a green technology, emerges as a suitable method for fabricating aluminum-based composites. In summary, the results obtained from this study highlight the promising attributes of FA and CSA-reinforced aluminum-based composites, emphasizing their positive impact on material properties, cost efficiency, and environmental sustainability. The results lead to the following conclusion:

- By adopting the stir casting method, FA and CSA particles were dispersed uniformly in the AA7075 matrix, evidenced by OM and SEM examination. Additionally, interfacial interaction between the matrix and reinforcing materials is confirmed.
- The principal elements of the composite samples revealed by XRD analyzes are AA7075 and reinforcements (FA and CSA), and no additional intermetallic compounds have been identified.
- The hardness and tensile behaviors of the developed composites were greatly improved by the addition of FA and CSA. The developed composite has increased hardness and tensile strength by 27% and 19%, respectively, in comparison to the monolithic alloy AA7075.
- When AA7075 is exposed to Potentiodynamic polarization, the presence of FA and CSA improves the corrosion resistance. Better corrosion resistance is seen in composites that include 5 wt% FA and 5 wt% CSA. Charge transfer resistance Rct rose from 1.629×10^3 to 2.537×10^3 cm^2, as seen by polarization curves in Nyquist plots, confirming that adding 5 wt% of FA and 5 wt% of CSA to AA7075 boosts the corrosion resistance of the composites.
- The leaching test confirmed that metals had been leached off, confirming that the developed composite won't have much of an impact on the environment.

The bottom line of this study reveals that FA and CSA can be employed as reliable reinforcement in Al for applications involving corrosion. For usage in automobile and maritime applications, the authors strongly advise using FA and CSA as possible reinforcement in light metals like aluminum, magnesium, and copper. Not only will it lower the price of MMCs, but it will also expand the alternatives for using FA and CSA and lessen the environmental risks that FA and CSA provide.

Acknowledgements

The authors thank to Delhi Technological University, for providing the financial support and facilities to conduct the research work.

Author contributions

AK contributed to methodology, formal analysis, investigation, writing—original draft. VPS contributed to investigation, writing—review and editing. AM contributed to writing—review and editing. BKS contributed to writing—review and editing. RCS contributed to supervision, writing—review and editing. RC contributed to supervision, writing—review and editing.

Data availability

All data generated or analyzed during this study are included in this published article.

Declarations

Conflict of interest No conflict of interest.

Ethical approval No applicable.

References

[1] Parveez B, Maleque MA, Jamal NA (2021) Influence of agro-based reinforcements on the properties of aluminum matrix composites: a systematic review. J Mater Sci 56(29):16195–16222. https://doi.org/10.1007/s10853-021-06305-2

[2] Bahrami A et al (2016) Development of metal-matrix composites from industrial/agricultural waste materials and their derivatives. Crit Rev Environ Sci Technol 46(2):143–208

[3] Olhan S, Khatkar V, Behera BK (2021) Textile-based natural fiber-reinforced polymeric composites in automotive lightweighting. J Mater Sci 56:1–44. https://doi.org/10.1007/s10853-021-06509-6

[4] Gholampour A, Ozbakkaloglu T (2020) A review of natural fiber composites: properties, modification and processing techniques, characterization, applications. J Mater Sci 55(3):829–892. https://doi.org/10.1007/s10853-019-03990-y

[5] Yousuf A et al (2020) Fly ash: production and utilization in India-an overview. J Mater Environ Sci 11(6):911–921

[6] Report on fly ash generation at coal/lignite based thermal power stations and its utilization in the country for the year 2021–22, Ministry of Power the Gazette of India. New Delhi, India

[7] Hemalatha T et al (2016) Physico-chemical and mechanical characterization of high volume fly ash incorporated and engineered cement system toward developing greener cement. J Clean Prod 125:268–281

[8] Hou H et al (2023) Resource utilization of solid waste for the collaborative reduction of pollution and carbon emissions: a case study of fly ash. J Clean Prod 383:135449

[9] Chaudhary N, Singh S (2023) Experimental investigation on microstructural and mechanical properties of in situ SiC-reinforced friction stir spot weld of Al 6061–T6. J Mater Sci 58(4):1849–1868. https://doi.org/10.1080/23740 68X.2022.2096833

[10] Manikandan R, Arjunan TV (2020) Studies on micro structural characteristics, mechanical and tribological behaviors of boron carbide and cow dung ash reinforced aluminum (Al 7075) hybrid metal matrix composite. Compos B Eng 183:107668

[11] Pul M et al (2023) The effect of sintering parameters and MgO ratio on structural properties in Al7075/MgO composites: a review. J Mater Sci 58(2):664–684. https://doi.org/10.1007/s10853-022-08003-z

[12] Kumar A et al (2023) The utilization of coconut shell ash in production of hybrid composite: microstructural characterization and performance analysis. J Clean Prod 398:136494

[13] Kumar A, Singh RC, Chaudhary R (2022) Investigation of microstructure and several quality characteristics of AA7075/Al_2O_3/coconut shell ash hybrid nano composite prepared through ultrasonic assisted stir-casting. J Mater Eng Perform 32:1–16

[14] Rajan HM et al (2016) Influence of friction stir processing on microstructure and properties of AA7075/TiB_2 in situ composite. J Alloys Compd 657:250–260

[15] Moses JJ, Dinaharan I, Sekhar SJ (2016) Prediction of influence of process parameters on tensile strength of AA6061/TiC aluminum matrix composites produced using stir casting. Trans Nonferrous Met Soc China 26(6):1498–1511

[16] Curpen S et al (2023) Evaluating life cycle environmental impacts of coal fly ash utilization in embankment versus sand and landfilling. J Clean Prod 385:135402

[17] Xiang R et al (2019) The potential usage of waste foundry sand from investment casting in refractory industry. J Clean Prod 211:1322–1327

[18] Nunes LA et al (2020) Waste green coconut shells: diagnosis of the disposal and applications for use in other products. J Clean Prod 255:120169

[19] Tayeh BA et al (2021) Recycling of rice husk waste for a sustainable concrete: a critical review. J Clean Prod 312:127734

[20] Kim C-S et al (2017) Mechanical performance of particulate-reinforced Al metal-matrix composites (MMCs) and Al metal-matrix nano-composites (MMNCs). J Mater Sci 52:13319–13349. https://doi.org/10.1007/s10853-017-1378-x

[21] Amouri K et al (2016) Microstructure and mechanical properties of Al-nano/micro SiC composites produced by stir casting technique. Mater Sci Eng A 674:569–578

[22] Zhu J et al (2020) Microstructure and mechanical properties of SiCnp/Al6082 aluminum matrix composites prepared by squeeze casting combined with stir casting. J Mater Process Technol 283:116699

[23] Kumar SD et al (2021) Effect of ZrB2 on microstructural, mechanical and corrosion behavior of aluminum (AA7178) alloy matrix composite prepared by the stir casting route. Ceram Int 47(9):12951–12962
[24] Ramachandra M, Radhakrishna K (2005) Synthesis-microstructure-mechanical properties-wear and corrosion behavior of an Al-Si (12%)—flyash metal matrix composite. J Mater Sci 40:5989–5997. https://doi.org/10.1007/S10853-005-1303-6
[25] Kumar A, Singh RC, Chaudhary R (2022) Investigation of nano-Al_2O_3 and micro-coconut shell ash (CSA) reinforced AA7075 hybrid metal-matrix composite using two-stage stir casting. Arab J Sci Eng 47(12):15559–15573
[26] Hauschwitz P et al (2020) Hydrophilic to ultrahydrophobic transition of Al 7075 by affordable ns fiber laser and vacuum processing. Appl Surf Sci 505:144523
[27] Radhika N, Raghu R (2017) Investigation on mechanical properties and analysis of dry sliding Wear behavior of Al LM13/AlN metal matrix composite based on Taguchi's technique. J Tribol 139(4):041602
[28] Dutkiewicz J et al (2013) Characterization of semi-solid processing of aluminum alloy 7075 with Sc and Zr additions. Mater Sci Eng A 580:362–373
[29] Kumar P, Kumar B (2023) Effect of ZrB2 and fly ash on tribological and mechanical properties of aluminum 7075-based metal matrix composite at elevated temperatures in reciprocating motion. Int J Metalcast 1–20
[30] Ram Prabhu T et al (2019) Effects of dual-phase reinforcement particles (fly ash + Al_2O_3) on the wear and tensile properties of the AA 7075 Al alloy based composites. J Inst Eng India Ser D 100:29–35
[31] Deaquino-Lara R et al (2015) Tribological characterization of Al7075–graphite composites fabricated by mechanical alloying and hot extrusion. Mater Des 67:224–231
[32] Pu B et al (2020) Effect of SiC nanoparticles on the precipitation behavior and mechanical properties of 7075Al alloy. J Mater Sci 55:6145–6160. https://doi.org/10.1007/s10853-020-04381-4
[33] Habibi MK, Joshi SP, Gupta M (2010) Hierarchical magnesium nano-composites for enhanced mechanical response. Acta Mater 58(18):6104–6114
[34] Zhang Z, Chen DL (2008) Contribution of Orowan strengthening effect in particulate-reinforced metal matrix nanocomposites. Mater Sci Eng A 483:148–152
[35] Llorca J, Gonzalez C (1998) Microstructural factors controlling the strength and ductility of particle-reinforced metal-matrix composites. J Mech Phys Solids 46(1):1–28
[36] Li J et al (2018) Effects of ultrasonic vibration on microstructure and mechanical properties of nano-sized SiC particles reinforced Al-5Cu composites. Ultrasonics Sonochem 42:814–822
[37] Alaneme KK, Olubambi PA (2013) Corrosion and wear behavior of rice husk ash—Alumina reinforced Al–Mg–Si alloy matrix hybrid composites. J Mater Res Technol 2(2):188–194
[38] Kumar A et al (2023) Influence of tool rotational speed on mechanical and corrosion behavior of friction stir processed AZ31/Al_2O_3 nanocomposite. J Magnes Alloys 11(7):2585–2599
[39] Loto RT, Babalola P (2017) Corrosion polarization behavior and microstructural analysis of AA1070 aluminum silicon carbide matrix composites in acid chloride concentrations. Cogent Eng 4(1):1422229
[40] Rokkala U et al (2023) Influence of friction stir processing on microstructure, mechanical properties and corrosion behavior of Mg–Zn–Dy alloy. J Mater Sci 58(6):2893–2914. https://doi.org/10.1007/s10853-023-08208-w
[41] Kakitani R et al (2023) Tensile, wear, and corrosion behaviors of an in situ Al–Al_3Ni metal matrix composite solidified under different cooling rates. J Mater Sci 1–19
[42] Esmaily M et al (2016) On the microstructure and corrosion behavior of AZ91/SiC composites produced by rheocasting. Mater Chem Phys 180:29–37

Publisher's Note Springer Nature remains neutral with regard to jurisdictional claims in published maps and institutional affiliations.

Springer Nature or its licensor (e.g. a society or other partner) holds exclusive rights to this article under a publishing agreement with the author(s) or other rightsholder(s); author self-archiving of the accepted manuscript version of this article is solely governed by the terms of such publishing agreement and applicable law.

Towards Effective Image Forensics via A Novel Computationally Efficient Framework and A New Image Splice Dataset

Ankit Yadav[1,*], Dinesh Kumar Vishwakarma[2]
Biometric Research Laboratory, Department of Information Technology, Delhi Technological University, Bawana Road, Delhi-110042, India
ankit4607@gmail.com[1,**], dvishwakarma@gmail.com[2]

ABSTRACT
Splice detection models are the need of the hour since splice manipulations can be used to mislead, spread rumors and create disharmony in society. However, there is a severe lack of image-splicing datasets, which restricts the capabilities of deep learning models to extract discriminative features without overfitting. This manuscript presents two-fold contributions toward splice detection. Firstly, a novel splice detection dataset is proposed having two variants. The two variants include spliced samples generated from code and through manual editing. Spliced images in both variants have corresponding binary masks to aid localization approaches. Secondly, a novel *Spatio-Compression Lightweight Splice Detection Framework* is proposed for accurate splice detection with minimum computational cost. The proposed dual-branch framework extracts discriminative spatial features from a lightweight spatial branch. It uses original resolution compression data to extract double compression artifacts from the second branch, thereby making it 'information preserving.' Several CNNs are tested in combination with the proposed framework on a composite dataset of images from the proposed dataset and the CASIA v2.0 dataset. The best model accuracy of 0.9382 is achieved and compared with similar state-of-the-art methods, demonstrating the superiority of the proposed framework.

Keywords: Splice Detection; Image Tampering; Image Manipulation; Image Forgery; Vision Transformer; Involution; Convolution

Statements and Declarations

Data Availability: The datasets generated during or analyzed during the current study are available through an online web repository via the following weblinks: https://www.kaggle.com/datasets/divg07/casia-20-image-tampering-detection-dataset
Funding: No funding was received to assist with preparing this manuscript.
Conflict of Interest: The authors declare that they have no known competing financial interests or personal relationships that could have appeared to influence the work reported in this paper.
Ethical Approval: Not Applicable.
Patient Consent Statement: Not Applicable.
Permission to Reproduce Material from Other Sources: Not Applicable.
Author Contributions: Ankit Yadav - Software, Validation, Investigation, Data Curation, Writing Original Draft, Visualization. Dinesh Kumar Vishwakarma - Conceptualization, Methodology, Formal Analysis, Resources, Writing – Review & Editing, Supervision, Project Administration, Funding Acquisition.

1 Introduction

The constantly growing popularity of social media platforms in the last decade has created vast volumes of data per user. As many as 3.96 billion social media users are active, double the figure at the beginning of 2015 [1]. Such widespread use of social media has resulted in a constantly increasing everyday data explosion, hence the term Big Data. Countless videos,

* Corresponding Author
** Corresponding Author Email

images, and text data are being created and uploaded through social media users, with an average of 8.8 social media accounts per person [1].

The growing popularity of online presence is also paralleled by the growth of several multimedia manipulation tools and approaches [2, 3]. Computer tools such as Adobe Photoshop and an endless supply of image/video editing mobile applications provide the end-user with readymade and easy-to-use manipulation capabilities. While most of these editing applications are well intended for creating visual enhancements and providing entertaining and humorous content, these tools are easily repurposed for ill-intentional deeds.

Images and video manipulations pose a more significant threat to society than textual misinformation since visual data is more believable. An image or a video of any wrongdoing is instantly accepted as the truth. And yet, today's manipulation tools make it child's play to maliciously manipulate an image/video and cause harm to the reputation of an individual or an organization. Some harmful effects of visual manipulations are defamation, fraud (monetary or identity-wise), spreading fake news and rumors, misdirection, swaying public opinion for political gain, etc.

'Image Splicing' is one such image/video manipulation where an object from one image is pasted onto another image. Such modification to multimedia data can easily be used to mislead from the truth and cause harm to a given person or organization. Facial splicing can cause identity misdirection, and an innocent person can easily be made to look guilty of wrongdoings. Hence, it is crucial to build robust splice detection approaches capable of detecting manipulations in visual data [4]. An additional consideration for splice detection is that since most visual data is compressed to save storage space, splice detection through compression artifacts can form a significant starting point toward robust splice detection. Specifically, since most compressed images are created using the famous JPEG compression, its artifacts in spliced images form the basis of the novel contribution proposed in this paper.

The main contributions of this work are: -

- Proposed a novel splice detection dataset – *BiometricLab-DTU-Splice Dataset* is proposed. The proposed dataset has two variants. The first variant is autogenerated from code, while the second contains handmade spliced samples. Binary masks are available in both variants. Given the size of existing small-scale splice datasets, the proposed dataset is a significant addition to the splice detection research arena.
- Proposed a novel lightweight, dual-branch, information-preserving, spatial-compression modal splice detection framework is proposed to detect spliced jpeg images while restricting the computational complexity to a small fraction of the usual computational cost in the context of deep learning.
- The proposed model contains a novel 'spatial branch' to extract discriminative spatial information for detecting image splicing. Transfer learning is used to leverage the strong classification capabilities of deep models in the spatial domain at minimal computational costs.
- The proposed model contains a novel information preserving 'compression branch' which uses original resolution compression data to extract double compression artifacts from spliced jpg.
- The proposed splice detection framework is designed to be extremely lightweight.

- Experimentations with several variants of the proposed spliced detection framework and comparisons with existing splice detection methods prove the potency of the proposed splice detection framework at minimum computational costs.

The organization of this research manuscript is as follows: Section 2 discusses several existing state-of-the-art splice detection/localization algorithms and highlights the research gaps that are the motivation behind the design of the proposed splice detection framework. Section 3 explains the design principles of the proposed splice detection framework and details the specifications of the spatial branch, compression branch and the final model. Section 4 dives into the experimentation details of this research manuscript. Firstly, it introduces the novel BiometricLab-DTU Splice dataset variants (automatic and manual) and specifies a modified CASIA v2.0 dataset. Secondly, several variants of the proposed splice detection framework are implemented and evaluated on the datasets. Thirdly, the proposed splice detection framework models are compared against existing state-of-the-art methods. An ablation study is also conducted to verify the necessity of a dual-branch framework. Section 5 presents the conclusion highlighting the novel contributions of this research manuscript.

2 Related Work

Several significant contributions have been made toward splice detection and localization in images and videos. For example, Chen et al. [5] proposed a novel splice detection method by highlighting distinct shapes of intensity-gradient bivariate histograms near edge regions of a spliced image caused by non-linear camera response functions (CRF). Bondi et al. [6] input image patches to detect source camera attributes of each pixel within an image patch. A CNN extracts source camera features, while a clustering algorithm estimates the tampering mask. Pomari et al. [7] highlight regions of illumination inconsistencies to detect splicing. Specifically, a pre-trained ResNet50 model without the classifier layer is used and fine-tuned to extract 'deep splicing features' (DSF) from the illuminant maps of an input image. Verde et al. [8] propose a novel contribution for temporal splice detection in videos. The authors target identifying the fusion of video segments with distinct characteristics, such as different recording devices or broadcasting channels, by training two CNNs to learn video codec and coding quality features. Salloum et al. [9] use fully convolutional neural networks to localize image splicing. The authors use two networks for multi-task learning that learn ground truth masks and the boundary of spliced regions, respectively. Cun et al. [10] propose the novel 'Semi-Global Network' that utilizes global features from the entire image and local patch-level features for splice localization. Local features correspond to spliced edges, while global information contains semantic and illumination information. Fully Connected Conditional Random Fields are used as a post-processing step. Liu et al. [11] propose a novel 'Fusion-net' architecture that combines several deep CNNs trained to detect image splicing based on different attribute artifacts, such as noise, compression, etc., for splice localization.

Mazumdar et al. [12] utilize pairwise facial illumination maps to train a pair of CNNs in a Siamese network setup. Such an architecture learns discriminative features of facial illuminant pairs from the same or distinct illumination environments. Later, one of the trained CNN can be used as a feature extractor for facial splicing detection. Bi et al. [13] introduce a novel 'RRU-Net' that makes better use of contextual spatial information within an image without the requirement of any pre/post-processing. The novel architecture prevents the gradient degradation problem common in massive networks and proves effective for image splice

detection. Deng et al. [14] utilize a novel 'MSD-Net' architecture that learns multi-scale features from DCT coefficient histogram features from jpg images. Specifically, the proposed network extracts feature at three scales using three interconnected networks to classify the input image block as original or spliced. Horváth et al. [15] detect splice forgery in satellite images using deep belief networks containing two stacked restricted Boltzmann machines. The deep belief network inputs patches from original satellite images and produces reconstructed patches and normalized error maps computed from input and reconstructed patches. Xiao et al. [16] introduce a novel 'CR2Net' that extracts distinct image properties from original and forged regions using a coarse CNN (C-CNN) and a refined CNN (R-CNN) at different scales. Forged regions are generated using diluted adaptive clustering. Wang et al. [17] fuse weighted YCbCr, edge, and camera PRNU features through novel weight combination modules for image splice detection. The fusion parameters are auto-tuned during backpropagation to ensure the best combination of features is utilized for spliced forgery detection. Liu et al. [18] perform feature learning through a deep fusion network that distinguishes differences in noise and compression information of original and spliced samples.

Based on the existing literature on splice detection, two crucial inferences are drawn: -

- The number and size of splice detection datasets are minimal in deep learning. Training deep architectures on such small-scale datasets inevitably leads to overfitting.
- Several contributions prepare their splice data to evaluate their proposed splice detection algorithms.

Table 1 clearly illustrates the lack of large-scale publicly available splice detection/localization datasets. Most splice detection methods either synthesize new datasets or use the existing small-scale splice datasets (only CASIA v2.0 contains 10000+ total samples). The characteristics of these publicly available splice datasets are discussed in greater detail in Table 4.

Table 1 Most Splice Detection/Localization contributions either prepare a new dataset for proposed model evaluation or use small-scale publicly available splice datasets

Ref.	Self-Prepared Dataset	Publicly Available Dataset	Total Samples in Publicly Available Splice Datasets
[5]	✓	✓	363 (Columbia)
[6]	✓		-
[7]		✓	613 (Columbia + DSO-I + DSI-I)
[8]	✓		
[9]		✓	14948 (CASIA v1 + CASIA v2 + Columbia + DSO-I + DSI-I)
[10]		✓	613 (Columbia + DSO-I + DSI-I)
[11]	✓		-
[12]		✓	250 (DSO-I + DSI-I)
[13]		✓	14698 (CASIA v1 + CASIA v2 + Columbia)
[14]	✓	✓	100 (Florence)
[15]	✓		-
[16]		✓	3196 (CASIA v2 + Columbia + Forensics)
[17]		✓	14335 (CASIA v1 + CASIA v2)
[18]		✓	803 (Columbia + Realistic Image Tampering)

Such data-oriented limitations in the splice detection research arena provide strong motivation to set the following experimental goal:

- Propose a comprehensive splice detection dataset
- Propose a lightweight splice detection framework to handle small-scale splice datasets without overfitting the training data. The design principles of the proposed framework are discussed in the next section.

3 Proposed Splice Detection Framework

The proposed splice detection framework is discussed in this section. Firstly, the design principles that govern the proposed splice detection framework are elaborated. Secondly, the spatial branch characteristics are highlighted. Thirdly, the highlights of the compression branch are specified. Lastly, the fusion of features from both branches is discussed to describe the final model.

3.1 Design Principles

The design of the proposed splice detection framework is motivated by several factors. Firstly, while spatial features are the most common type of deep features extracted, they do not provide the most discriminative information about spliced samples. The literature review in Section 2 suggests splice detection in different modalities, including frequency domain, noise domain, etc., has proven effective. Secondly, the small number and size of publicly available splice datasets (Table 4) provide a clear incentive to avoid heavy deep learning architectures having millions of trainable parameters. A deep model that is too complex for a given dataset will overfit and memorize the training samples. Thirdly, since deep learning architectures require fixed-size inputs, images are mainly resized to smaller resolutions, and hence there is ‘information loss’ due to the reduction of high-dimensional images.

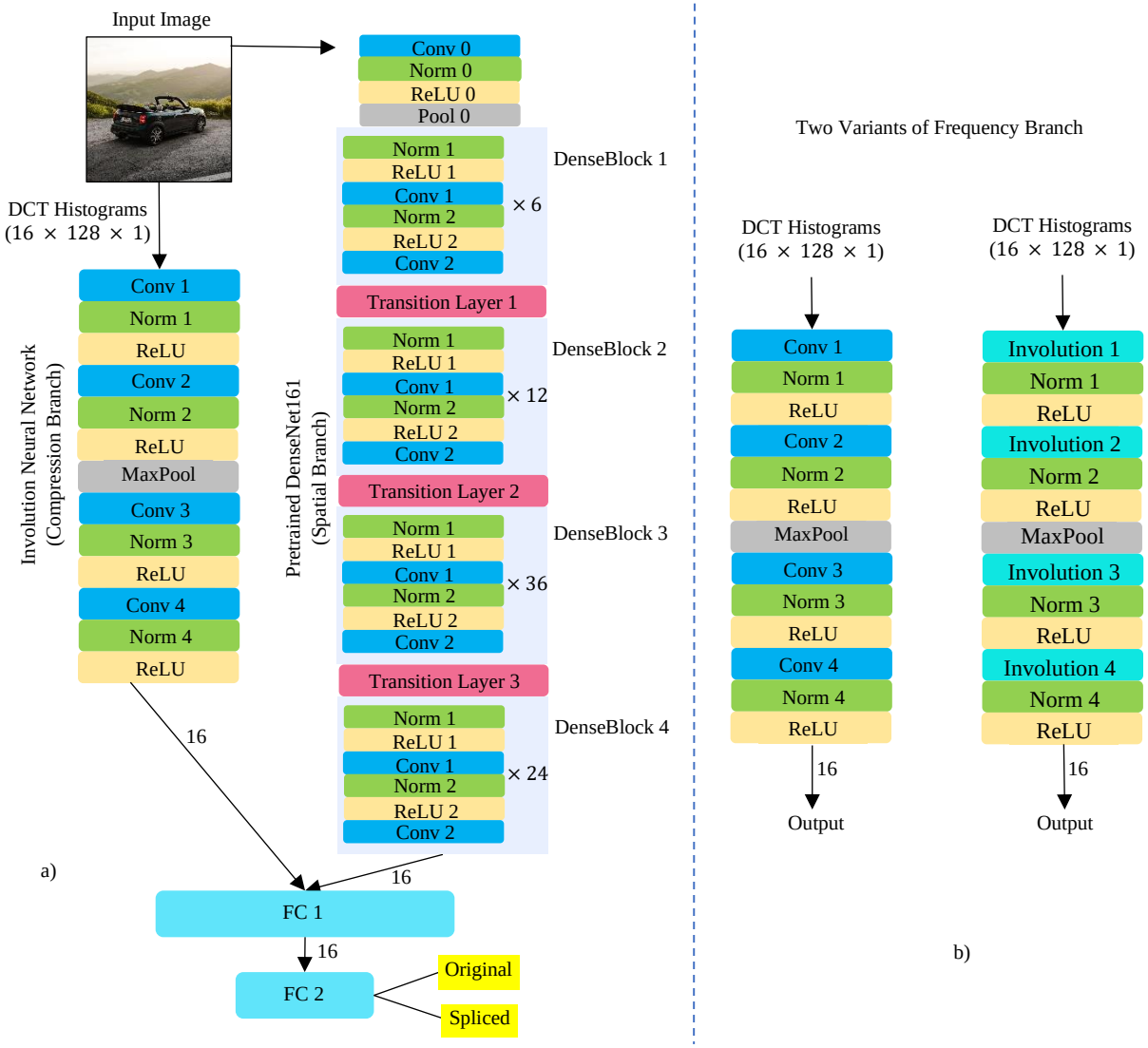


Fig. 1 a) DenseNet-CNN variant of the proposed Splice Detection Framework containing a pre-trained DenseNet161 for the spatial branch and a Convolution Neural Network (CNN) for the compression branch. b) The frequency branch of the proposed splice detection framework has two variants based on convolution and involution operators.

Hence, a splice detection framework is proposed with the following novel characteristics:

- **Dual-branch for Multi-Modal Feature Learning** – Different modalities besides the spatial domain have proven effective for splice detection. This proposed framework combines the spatial domain with a 'compression branch' that learns discriminative compression artifacts indicating image splicing.
- **Information Preserving** – The compression branch of the proposed framework extracts compression artifacts from original resolution image data. Hence, no information is lost due to resizing.
- **Lightweight** – The design of the proposed splice detection framework restricts the number of trainable parameters (Table 7) in the context of deep learning. None of the proposed framework variants have more than 100,000 trainable parameters, whereas standard deep networks can easily have up to millions of trainable parameters. Fewer trainable parameter leads to significantly lower computational cost for the proposed splice detection framework.
- **Futuristic** – A novel framework is proposed instead of building a fixed architecture for splice detection. The proposed framework supports a variety of existing deep architectures

and is also capable of utilizing novel ideas from future research. This plug-and-play characteristic ensures that the proposed framework stays relevant for years.

Table 2 Several Deep Architectures are used for the spatial and compression branch of the proposed framework.

Ref	Model	Short Form	Branch	Input Size	Key Idea
[19]	VGG16	VGG	Spatial	256 x 256 x 3	Small convolutional kernels
[20]	GoogleNet	-	Spatial	256 x 256 x 3	Inception module, parallel convolution
[21]	ResNet18	ResNet	Spatial	256 x 256 x 3	Skip Connections
[22]	DenseNet161	DenseNet	Spatial	256 x 256 x 3	Feature Reuse
[23]	Vision Transformer	ViT	Spatial	384 x 384 x 3	Self-Attention on Images
-	Convolutional Neural Network	CNN	Compression	16*128*1	Channel-Specific and Spatial-Agnostic
[24]	Involution Neural Network	INN	Compression	16*128*1	Spatial-Specific and Channel-Agnostic

3.2 Spatial Branch

As the name suggests, the spatial branch extracts spatial features from input image samples. Several convolutional neural network architectures have proven highly effective for image classification problems. The spatial branch is designed to use transfer learning via deep networks pre-trained on the ImageNet dataset to inherit the proposed framework's lightweight and' futuristic characteristics. Designing the spatial branch in this manner has the following advantages. Firstly, several architectures ([19], [20], [21], [22]) that have proven to possess high image classification capabilities can be leveraged to extract discriminative spatial features for splice detection. Secondly, transfer learning ensures that the spatial branch remains 'lightweight,' i.e., only the last layer is trainable. Deep architectures of any size can be used for the spatial branch as long as it is pre-trained on ImageNet, and all layers are frozen except the last layer.

The spatial branch's last layer in the proposed framework is trainable and modified to produce features of 16 dimensions. Fig. 1 shows a variant of the proposed splice detection framework that uses an ImageNet pre-trained 'Vision Transformer' [23] in the spatial branch. Table 2 shows several pre-trained deep architectures used for the spatial branch of the proposed spliced detection framework. All models receive color images as input. It is restated that such a design enjoys strong classification capabilities in the spatial domain while staying lightweight regardless of the size of the deep architecture used.

3.3 Compression Branch

Several existing works highlight the presence of distinct compression artifacts in spliced jpg images [25], [26]. Specifically, an original jpg image (without splicing) is compressed once. However, a spliced image containing an object pasted from another image undergoes a second jpg compression. This dual compression leaves distinct artifacts in DCT coefficient histograms. The DCT coefficients include 1 DC and 63 AC coefficients. Different works have considered different AC coefficients in zig-zag order with different histogram ranges. [25] highlights the artifacts by using 9 DCT coefficients (zig-zag order) and a histogram range of $[-5,5]$ to

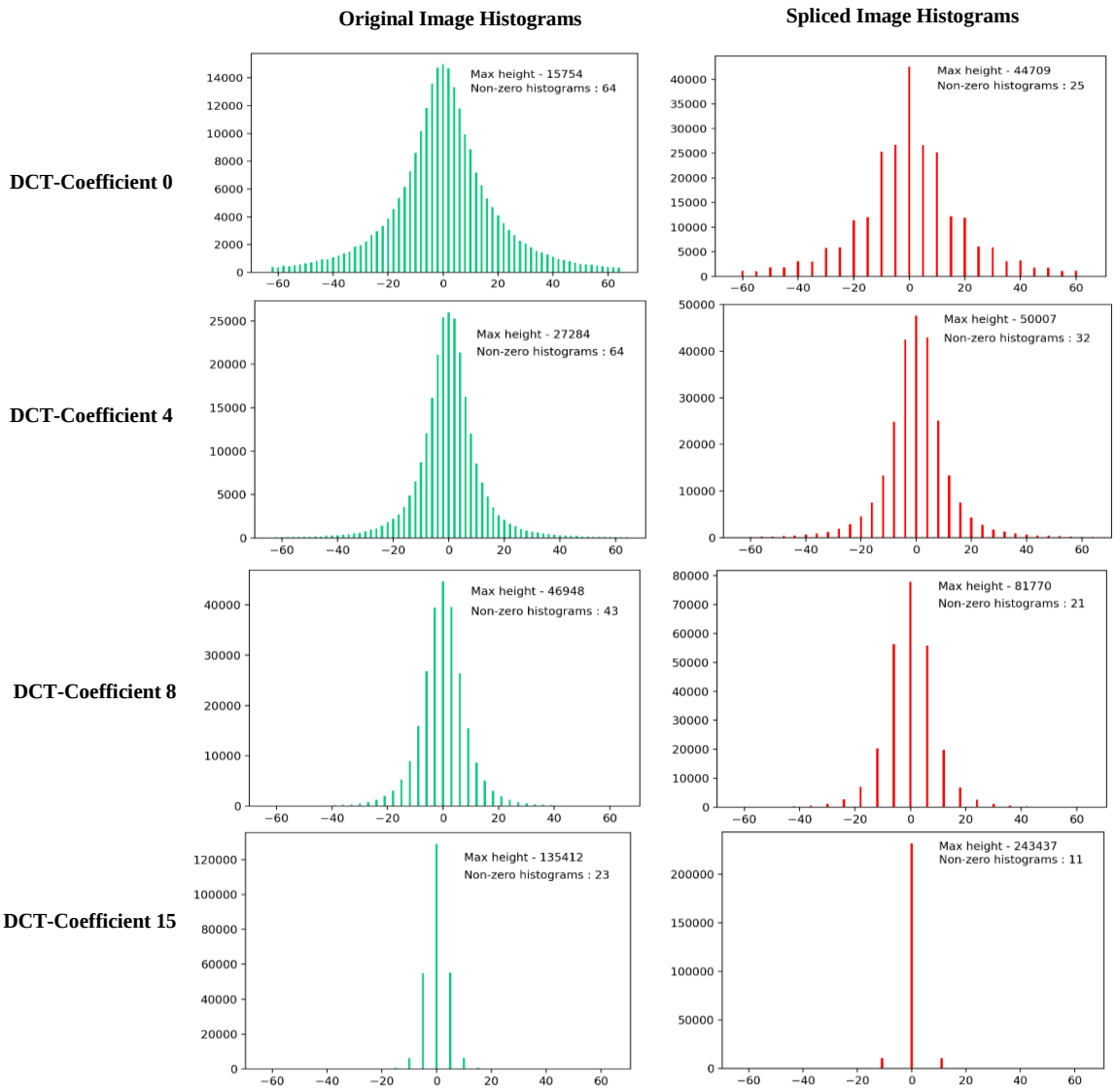


Fig. 2 This figure shows the double compression artifacts in DCT coefficient histograms of spliced jpg images. Four coefficient plots (0, 4, 8 and 15th AC coefficient in zig-zag order) are drawn for an original (green) and spliced (red) image. The histograms from original and spliced images obtain distinct shapes with different maximum values and different non-zero histogram bins up to 16 DCT AC coefficients in zig-zag order

constitute features of size 99×1. Similarly, [26] considers 9 DCT coefficients with a histogram range of $[-50,50]$ to formulate a feature size of 909.

Visual analysis is conducted on several original-spliced image pairs, and histograms are plotted to evaluate the ideal range of features. Fig. 2 shows the histograms from an original (green) and corresponding spliced (red) image. Plotting the zeroth, fourth, eighth, and fifteenth AC coefficient (zig-zag order) demonstrates the presence of distinct maximum values and a varying number of non-zero histogram bins in the range of $[-63,64]$ between the original and spliced image. Hence, 16 AC zig-zag coefficients (0 to 15) are selected, and the histogram range is set to $[-63,64]$. The input size for the compression branch is set to $16 \times 128 \times 1$.

The histogram data input is extracted from original resolution images; hence, the compression branch is 'information preserving,' i.e., there is no loss of information from input resizing. Regardless of the input image dimensions, the compression branch receives

compression information from original resolution images having a size $16 \times 128 \times 1$. Compression features extracted from original resolution images are standardized to have a mean value of 0 and a standard deviation value of 1 (zero-centered input) to aid in faster model convergence. The input size of $16 \times 128 \times 1$ helps keep the proposed framework 'lightweight,' i.e., the architecture processing input of this size need not be massive.

Two different architectures are employed as the compression branch in several variants of the proposed framework (Table 2). Besides trying a simple CNN, an involution neural network (INN) containing the novel involution kernel [24] (introduced in CVPR 2021) is also used as the compression branch. The novel involution-based neural network can achieve competent classification results at a lesser computational cost than CNN compression branch models. Fig. 3 demonstrates the feature extraction methodology of the two kernels.

Both the CNN and INN variants contain four convolution/involution layers. Each layer is accompanied by batch normalization. Max Pooling is used to reduce the dimensionality of feature maps. ReLU activation function is used. INN models specialize in reducing the number of trainable parameters while achieving competent results. Despite the fewer parameters in the INN compression branch, it can achieve competent classification results. The compression branch is also designed to produce the final features of size 16.

3.4 Final Model

The final model fuses the 16 features produced by each spatial and compression branch. It utilizes two fully connected layers to scale down the fused features to the final two features representing binary classification scores. ReLU activation and batch normalization are applied to the first fully connected layer output.

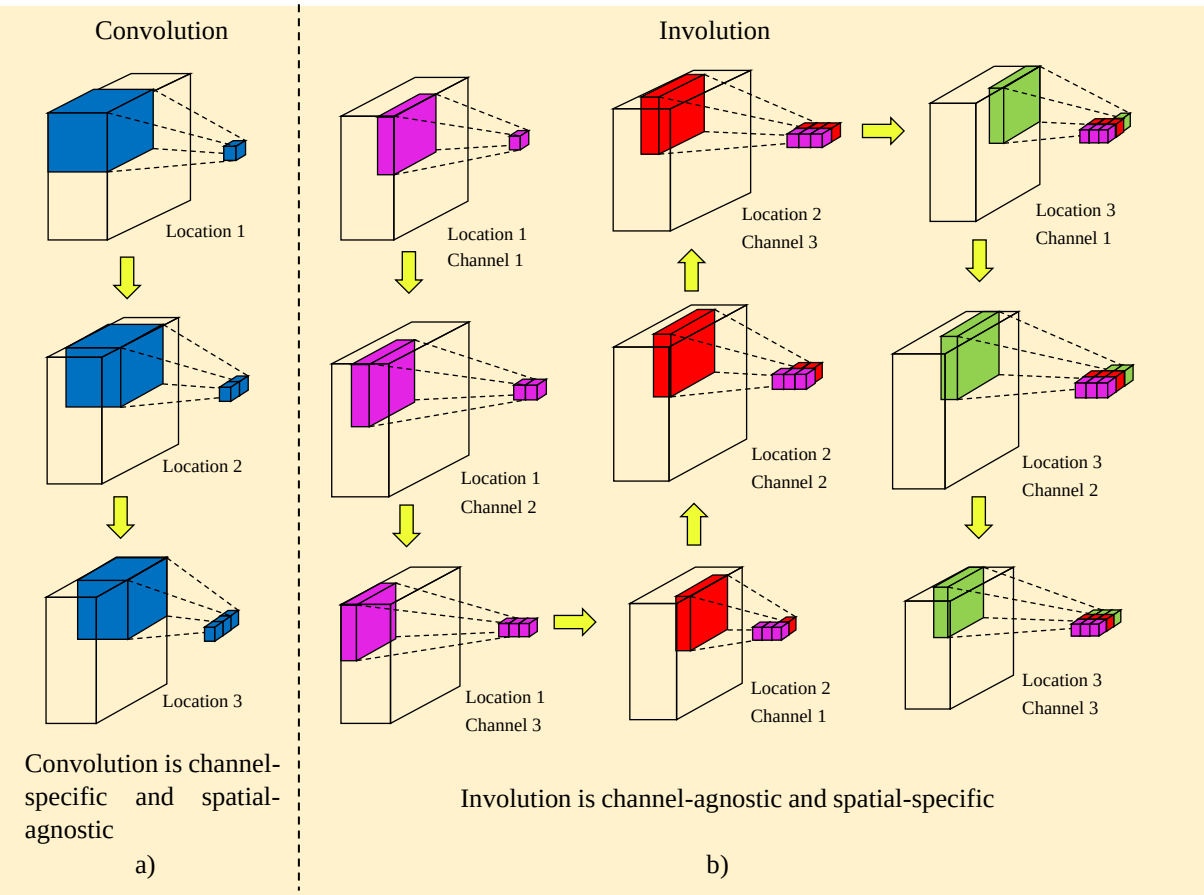


Fig. 3 Comparison of Convolution and Involution kernels. a) The number of channels in a convolution kernel is always equal to that of input. The convolution kernel (shown is blue) perfectly overlaps with input channel-wise and its kernel coefficients remain same for all strided locations (same blue color for all locations). b) The involution operator is a single channel kernel. Its coefficients remain same for all channels of input at a fixed spatial location. Unlike convolution, involution coefficients change with each strided location. Colors magenta, red and green represent involution operation at different spatial locations.

4 Experimental Setup

This section describes the experimentation conducted on the proposed splice detection framework. It describes the datasets, hardware, and performance metrics, training parameters for the proposed framework, results obtained, and a comparison of the proposed framework against existing state-of-the-art methods.

4.1 Datasets

One of the critical challenges in splice detection is the lack of large-scale splice datasets. Table 4 provides a list of existing splice detection datasets. Most of the existing splice datasets are limited in terms of the number of samples, and not all include binary masks for localization implementations. Training deep models on small datasets inevitably presents the problem of overfitting.



Fig. 4 Samples from the proposed BiometricLab-DTU Splice dataset

To this end, a novel splice detection dataset having two variants is proposed – BiometricLab-DTU-Splice Dataset (Table 3). The first variant (automatic) is autogenerated from the code. The second variant contains spliced images prepared in Adobe Photoshop Software.

Table 3 demonstrates the number of samples in each dataset used in this experiment. Fig. 4 demonstrates the proposed dataset's original, spliced, and binary mask images.

Table 3 Details of Proposed Datasets

Dataset	Type	Original Samples	Spliced Samples	Total Samples	Splice Mask
BiometricLab-DTU-Splice dataset (automatic)	Proposed	8156	8156	16312	Yes
BiometricLab-DTU-Splice dataset (manual)	Proposed	3106	3106	6212	Yes

Dataset	Type	Original Samples	Spliced Samples	Total Samples	Splice Mask
CASIA v2.0 (modified)	Publicly Available	5123	5123	10246	-

Table 4 Comparison of proposed splice detection dataset with existing splice datasets. The proposed dataset is mentioned in bold

Ref.	Year	Dataset	Tampering Type	Original Samples	Spliced Samples	Resolution	Format	Splice Masks
[27]	2004	Columbia Gray	Splicing	933	912	128 x 128	BMP	
[28]	2006	Columbia Color	Splicing	183	180	757 x 568, 1152 x 768	TIFF	Yes
[29]	2009	CASIA v1.0	Splicing	800	921	384 x 256	JPG	No
[29]	2009	CASIA v2.0	Splicing	7491	5123	240 x 160, 900 x 600	TIFF, BMP, JPG	No
[30]	2013	DSO-I	Splicing	100	100	2048 x 1536	PNG	-
[30]	2013	DSI-I	Splicing	25	25	Variable	-	-
[31]	2014	Image Forensic Dataset Challenge	Splicing	144	144	2018 x 1536	PNG	-
[32]	2015	SYSU-OBJFORG dataset	Copy Move, Splicing	100	100	1280 x 720 @ 25fps	H.264 / AVC	-
[33]	2015	GRIP	Splicing	80	80	1024*768	JPG	Yes
-	2022	**Biometric-Lab-DTU Splice Dataset (automatic)**	Splicing	8156	8156	3008 x 2000, 4288 x 2848, 4928 x 3264	JPG	Yes
-	2022	**Biometric-Lab-DTU Splice Dataset (manual)**	Splicing	3106	3106	3008 x 2000, 4288 x 2848, 4928 x 3264	JPG	Yes

4.1.1 BiometricLab-DTU-Splice Dataset (Automatic)

The ‘automatic’ variant of the BiometricLab-DTU Splice dataset is autogenerated through Python code. 8156 high-resolution uncompressed images from the RAISE dataset [34] are used as source images. Several existing splice detection approaches have prepared datasets by compressing images with quality factors of step size 5 [26], [14]. The jpeg images of the proposed dataset are produced with a random integer quality factor which ensures a richer distribution of compression information compared to the above-described case.

Dataset Generation of Automatic Spliced Images: A pre-trained RCNN model trained on the MS-COCO dataset extracts objects from the original images of the RAISE dataset. This is achieved from the instance_segmentation() function of the PixelLib python library. This function extracts different objects detected as the result of segmentation. Next, the binary masks are generated for each object by converting the object images to grayscale and thresholding into binary images. The extracted objects are tampered with several random manipulations, including rotation, scaling, flipping, contrast changes, brightness variations and sharpness modifications before pasting onto another original image. The degree of scaling, rotation and other manipulations is random as shown in Fig. 5. Finally, the extracted objects are pasted onto original images using the paste() function of the Python’s PILLOW library. Lastly, the spliced images are saved as jpeg images with random compression quality factor as shown in the “second compression” column of Fig. 5. The image reading and color-scale modifications are done using the open-cv library, while the rotation, scaling, flipping, contrast and sharpness enhancements are achieved with the PILLOW library. The binary masks produced from code can aid in future splice localization methods.

name	first compression	second compression	object name	scale	rotation	flip	contrast	brightness	sharpness
r00816405t_spliced.jpg	94	73	object16_r0fb0a690	1	28	0	1.73	1.29	1.81
r00869422t_spliced.jpg	53	61	object2_rccf44639t	0.87	132	1	1.81	1.16	1.81
r00879054t_spliced.jpg	87	75	object2_rb6c0981e	0.94	109	1	1.82	1.29	1.55
r01058910t_spliced.jpg	63	53	object11_r854fa219	0.94	110	0	1.81	1.32	1.75
r01170470t_spliced.jpg	35	53	object3_r39a8b2f2t	1	69	1	1.74	1.35	1.69
r01474187t_spliced.jpg	51	34	object3_r61184440	1	176	1	1.58	1.16	1.95
r0150031ft_spliced.jpg	74	63	object5_r319e1687	1	149	1	1.65	1.27	1.86

Fig. 5 Parameters used during creation of spliced samples. Each pasted object undergoes five modifications namely scaling, rotation, flip, contrast and sharpness specified by randomized values. Each spliced image is compressed twice with random quality factors as shown in the 'first compression' and 'second compression' columns.

8156 high-resolution uncompressed images from the RAISE dataset were used to produce 8156 original and 8156 spliced images, which form the BiometricLab-DTU Splice dataset (automatic). Fig. 4 shows some samples from the proposed automatic dataset variant.

4.1.2 BiometricLab-DTU-Splice Dataset (Manual)

The second variant of the proposed dataset has been prepared manually. A total of 3106 images were spliced manually along with the same number of the original counterparts to formulate a balanced dataset of 6212 images. Spliced samples from the manual variant of the proposed dataset are more realistic visually than the automatic version due to the random manipulations on pasted objects of computer-generated spliced images in the automatic variant dataset. Table 4 compares the proposed BiometricLab-DTU Splice dataset against existing splice datasets. Most existing datasets fall short in terms of the total number of samples available, have smaller resolution images, and usually don't have splice masks to aid splice localization approaches when compared against the proposed dataset variants.

Dataset Generation of Manually Spliced Images: The source and target images are opened in the Adobe Photoshop software. An object is selected from the source image using the 'Quick Selection Tool'. The selected object is pasted onto the target image as a new layer. Resizing, rotation, flipping, contrast and brightness modifications are made randomly to the object layer. The pasted object is selected again and the 'Layer Mask Tool' in Photoshop generates the binary mask layer. Next, a 'Photoshop Action' is created that automates the process of saving the spliced image and its corresponding binary mask into separate folders. Specifically, the spliced image is saved as a jpeg image, while the binary mask is generated from the mask layer formed by the layer mask tool. For each image, opening the source and target images, selecting the object to be pasted and pasting operations are done manually. Then, the Photoshop action helps to save the spliced images and corresponding binary masks automatically.

4.1.3 A modified CASIA v2.0 dataset

The CASIA v2.0 is a challenging image tampering dataset containing 7491 original and 5123 tampered images [29]. However, over half of the tampered images are uncompressed (TIFF or BMP format). Since the proposed splice detection framework utilizes compression artifacts of image samples, the uncompressed format images were compressed with a random quality factor. This modified variant of the CASIA v2.0 dataset is used for experimentation.

Since all three datasets are novel (two proposed and one modified publicly available dataset), a comparison of the proposed framework with existing splice detection approaches is conducted by training all architectures (proposed and existing models) on these new datasets instead of merely comparing with metric figures mentioned in published works. 5123 original

images are chosen from the original CASIA v2.0 dataset for experimentation to maintain class balance.

4.2 Hardware Resources and Evaluation Metrics

All experiments have been implemented using the Pytorch Library. All experiments are run on a system with 128 GB RAM and a 24 GB NVIDIA TITAN RTX graphic card. The metrics used to evaluate the proposed splice detection framework are *Accuracy* (ACC), *Precision* (P), *Recall* (R), *F1-score* (F1), *Area Under Curve* (AUC), and *Mathews Correlation Coefficient* (MCC).

Correctly identified spliced samples are counted as true-positive ($\mathbb{TP}$), original images correctly classified as original are counted as true-negative ($\mathbb{TN}$), original images misclassified as spliced are counted as false-positive ($\mathbb{FP}$) and spliced images misclassified as original are counted as false-negative ($\mathbb{FN}$). The various metrics are defined using Eq. (1)-(5).

$$Accuracy = \frac{\mathbb{TP}+\mathbb{TN}}{\mathbb{TP}+\mathbb{TN}+\mathbb{FP}+\mathbb{FN}} \quad (1)$$

$$Precision = \frac{\mathbb{TP}}{\mathbb{TP}+\mathbb{FP}} \quad (2)$$

$$Recall = \frac{\mathbb{TP}}{\mathbb{TP}+\mathbb{FN}} \quad (3)$$

$$\mathbb{F}1\ Score = 2 * \frac{Precision*Recall}{Precision+Recall} \quad (4)$$

$$MCC = \frac{\mathbb{TP}*\mathbb{TN}-\mathbb{FP}*\mathbb{FN}}{\sqrt{(\mathbb{TP}+\mathbb{FP})(\mathbb{TP}+\mathbb{FN})(\mathbb{TN}+\mathbb{FP})(\mathbb{TN}+\mathbb{FN})}} \quad (5)$$

4.3 Experimental Setup

This section describes the experimental setup used to evaluate the proposed splice detection framework.

4.3.1 Dataset Variants, Pre-processing, and Data Augmentation

The datasets mentioned in the previous section are combined, as shown in Table 5, to produce a larger pool of diverse input data. The AMC variant combines the proposed and modified CASIA datasets to produce one large dataset of 32770 images. The AM variant combines both variants of the proposed dataset to make a more extensive set of 22524 images. All variants of the proposed splice detection framework and existing splice detection architectures are trained and evaluated on these variants to ensure comprehensive training and evaluation in this experiment.

Table 5 Dataset Variants that are used for the experimentation.

Dataset Variant	Code	Total Samples	Train & Validation Samples	Test Samples
BiometricLab-DTU-Splice dataset (automatic + manual)	AM	22524	90%	10%
All three datasets combined	AMC	32770		

Images are resized to 256×256 for all spatial models except Vision Transformer, which expects an input size of 384×384. Images are standardized to have a mean value of 0 and a standard deviation of 1 (channel-wise) and hence are 'zero-centered.' Three data augmentations are used for experimentation: random horizontal flip, random vertical flip, and random rotation from 0 to 180 degrees.

4.3.2 Model Variants

The models specified in Table 2 are combined and evaluated to verify the validity of the proposed splice detection framework. The combined architectures are named after their constituent branch models.

The ResNet-CNN variant uses a pre-trained resnet18 in the spatial branch and a simple CNN for the frequency branch. The GoogleNet-CNN variant has a GoogleNet architecture as its spatial branch and CNN as its frequency branch. Similarly, VGG-CNN, DenseNet-CNN, and ViT-CNN include VGG, DenseNet161, and Vision Transformer models in their spatial and CNN-based frequency branches.

The involution operator is also used in the frequency branch with fewer trainable parameters than the simple CNN-based frequency branch. Hence each of the above-mentioned spatial branch models is combined with an involution-based frequency branch (INN) to produce five more variants denoted by ResNet-INN, GoogleNet-INN, VGG-INN, DenseNet-INN, and ViT-INN.

Hence, ten model variants of the proposed splice detection framework are trained and evaluated in this experiment. The spatial branch of each variant is loaded with ImageNet weights and frozen except for the last layer.

4.3.3 Hyperparameter Settings

All experiments are run for 30 epochs. The batch size is 256 for all models except Vit-CNN and the train-test splits are set to 90% and 10%, respectively. Five-fold cross-validation is implemented to ensure comprehensive training. Several optimizers are tried, and the Adam optimizer consistently produces the best results. The learning rate (LR) is decayed linearly. Table 6 shows the hyperparameter settings for each model variant to obtain the best results.

Table 6 Hyperparameter setting for various variants of the proposed Splice Detection Framework

Models	Epochs	Batch Size	Initial LR	LR Decay Factor	Step Size of LR Decay (epochs)	Optimizer
VGG-CNN	30	256	0.001	0.5	1	Adam
VGG-INN	30	256	0.01	0.9	1	Adam
ResNet-CNN	30	256	0.001	0.5	2	Adam
ResNet-INN	30	256	0.01	0.9	1	Adam
GoogleNet-CNN	30	256	0.001	0.5	2	Adam
GoogleNet-INN	30	256	0.01	0.9	1	Adam
DenseNet-CNN	30	256	0.001	0.5	2	Adam
DenseNet-INN	30	256	0.01	0.5	2	Adam
ViT-CNN	30	576	0.001	0.5	1	Adam
ViT-INN	30	256	0.01	0.9	1	Adam

The CNN frequency branch-based architectures achieved their best results with an initial learning rate of 0.001 and decayed by 50% after every one or two epochs. The INN frequency branch-based architectures showed their best results when the learning rate was initialized to a higher value and decayed by a smaller factor. Specifically, the initial learning rate for INN-based models was 0.01 and decayed by 10% only (except for DenseNet-INN) after every one or two epochs.

4.4 Performance of Proposed Splice Detection Framework

This section presents the results of all model variants of the proposed splice detection framework.

4.4.1 Results Obtained

ACC, P, R, F1, AUC, and MCC scores obtained by model variants of the proposed framework are mentioned in Table 7**.**

Table 7 Performance of the proposed Splice Detection Framework in terms of Accuracy (ACC), Precision (P), Recall (R) and F1-score (F1), Area Under Curve (AUC), and Mathews Correlation Coefficient (MCC). Best scores are highlighted in bold

Proposed Model Variants	Dataset	Input Size (Spatial Branch)	Trainable Parameter Count	ACC	P	R	F1	AUC	MCC
VGG-CNN	AMC	256 x 256 x 3	99,538	0.9305	0.9471	0.9116	0.9290	0.9749	0.8617
VGG-INN	AMC	256 x 256 x 3	76,854	0.9018	0.9125	0.8847	0.8984	0.9640	0.8038
ResNet-CNN	AMC	256 x 256 x 3	42,194	0.9379	0.9510	**0.9208**	0.9357	0.9749	0.8761
ResNet-INN	AMC	256 x 256 x 3	19,510	0.8571	**0.9814**	0.7328	0.8391	0.9472	0.7402
GoogleNet-CNN	AMC	256 x 256 x 3	50,386	0.9342	0.9458	**0.9208**	0.9331	0.9781	0.8687
GoogleNet-INN	AMC	256 x 256 x 3	27,702	0.9006	0.9384	0.8574	0.8961	0.9647	0.8042
DenseNet-CNN	AMC	256 x 256 x 3	69,330	**0.9382**	0.9578	0.9185	**0.9378**	**0.9802**	**0.8772**
DenseNet-INN	AMC	256 x 256 x 3	46,646	0.8779	0.9105	0.8278	0.8672	0.9431	0.7577
ViT-CNN	AMC	384 x 384 x 3	46,290	0.9376	0.9571	0.9144	0.9353	0.9790	0.8759
ViT-INN	AMC	384 x 384 x 3	23,606	0.8733	0.9209	0.8174	0.8661	0.9463	0.7516

The training loss and validation loss plots converge smoothly towards 0 and validation accuracy towards increases close to 1. The confusion matrix obtained after training each model variant confirms the strong classification capabilities of the proposed framework model variants.

4.4.2 Result Analysis

This section discusses the results obtained by model variants in the previous section. Table 7 presents the number of trainable parameters in each model.

The largest model is VGG-CNN with 99538 trainable parameters, while the lightest model is the ResNet-INN variant with only 19510 trainable parameters. This proves the lightweight nature of the proposed framework since deep learning models of moderate size easily contain a few million trainable parameters. In contrast, all variants of the proposed splice detection framework are incredibly lightweight.

The CNN frequency branch-based models consistently score more than 0.93 ACC, more than 0.92 F1-score, more than 0.97 AUC, and more than 0.86 MCC scores. The INN frequency branch-based models score more than 0.87 ACC (except for ResNet-INN), more than 0.86 F1-score F1 (except for ResNet-INN), more than 0.94 AUC, and more than 0.74 MCC. It is clear from the above scores that the reduced number of trainable parameters in the INN models resulted in a slight performance drop.

The DenseNet-CNN model achieved the best scores with 0.9382 ACC, 0.9378 F1, 0.9802 AUC, and 0.8772 MCC. ResNet-INN scored the highest precision score of 0.9814. ResNet-CNN and GoogleNet-CNN share the highest recall score of 0.9208.

Fig. 6 shows the ROC curves for each model variant of the proposed splice detection framework.

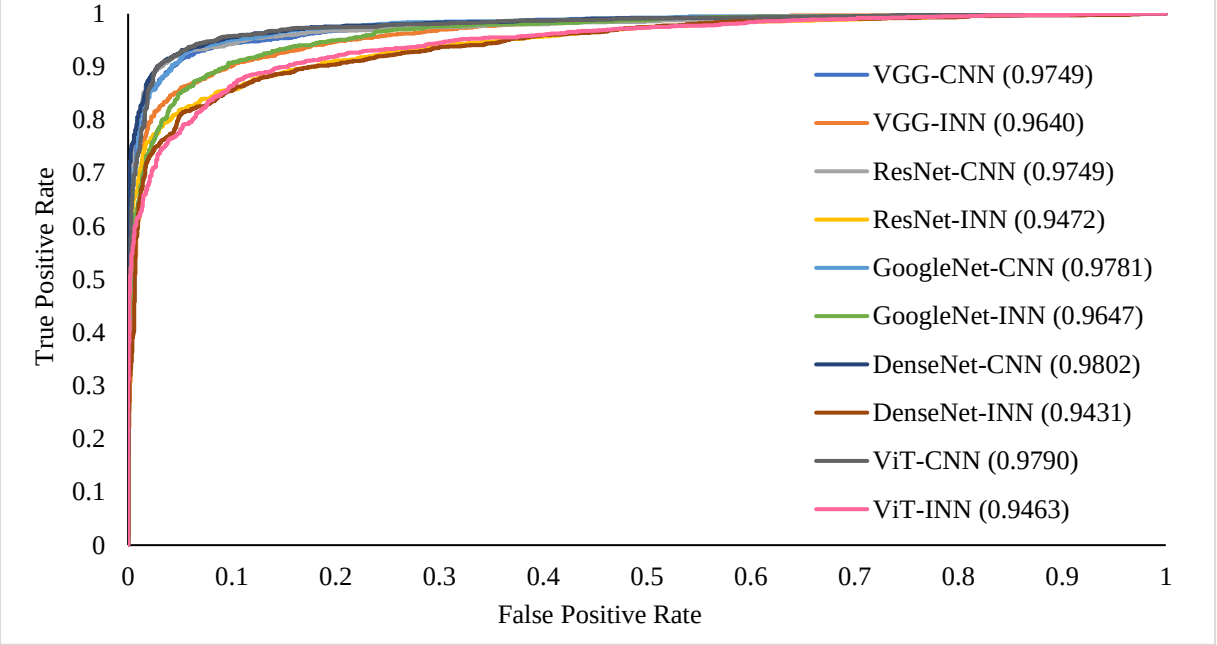


Fig. 6 ROC curves for different variants of the proposed framework. AUC scores are mentioned next to each variant name of the proposed Splice Detection Framework

4.4.3 Ablation Study

This section presents an ablation study of the proposed framework to confirm the validity of the contributions made by the spatial and compression branch. The spatial branch and frequency branch are trained and evaluated individually. Resnet18 is the spatial branch, loaded with ImageNet weights, and contains frozen layers except the last.

Table 8 Ablation study performance for the individual branches of the proposed Splice Detection Framework

Models	ACC	P	R	F1	AUC	MCC
Spatial Branch Only (ResNet)	0.6957	0.7106	0.6495	0.6787	0.7602	0.3922
Frequency Branch Only (CNN)	**0.7966**	**0.8376**	0.7251	**0.7773**	**0.8718**	**0.5971**
Frequency Branch Only (INN)	0.6146	0.5786	**0.8033**	0.6727	0.7296	0.2523

Table 8 presents the results obtained from the ablation study, where each branch is trained on the same dataset as the proposed model. The best accuracy of 0.7966 is achieved by the CNN-based frequency branch, which is still very low compared to the performance of the proposed model variants. Similarly, the best F1, AUC, and MCC scores of 0.7773, 0.8718, and 0.5971, respectively, are very low. The scores in Table 8 indicate that the individual branches do not have high classification capability compared to the proposed model variants.

4.5 Comparison with Existing Splice Detection Methods

This section compares the proposed splice detection framework with existing state-of-the-art approaches. The comparison is based on classification metric scores and the size of models under comparison in terms of the number of trainable parameters.

4.5.1 Comparison based on Classification Metrics

This section presents the comparison of the proposed splice detection framework with the existing state-of-the-art methods for splice detection.

Table 9 presents a comparison of the proposed splice detection framework against existing state-of-the-art methods on the CASIA v2 dataset. The proposed framework outperforms all the mentioned approaches. The details of these comparison methods are given below.

- Zhang et al. [35] – Authors propose a multi-tasking dual-branch architecture for splice localization that learns from edge features of images and splicing masks. Both branches have encoder-decoder architecture for the splice localization purpose. Localization performance is improved by fusing features from shallow and deep layers of the model.
- Sun et al. [36] – Authors propose an edge-enhanced transformer model for splice localization. The transformer contains two branches to merge forgery clues with splicing edge clues. A novel feature enhancement module is used to highlight important features and supress noise.
- Yan et al. [37] – Authors combine the benefits of cross-attention and self-attention to propose a U-shaped transformer model that captures multi-scale spatial dependencies and finer contextual information. The transformer model integrates convolution, making it hybrid in nature.
- Bi et al. [13] – Author propose a novel 'Ringed Residual U-Net' model having residual feature propagation to solve the vanishing gradient problem. A residual feedback mechanism provides feature refinement charecteristics that widens the information from tampered and authentic regions within the image.
- Wu et al. [38] – Authors propose an end-to-end convolutional neural network based architecture for forgery detection and localization that can identify 385 image manipulations. Specifically, the proposed model contains a 'Image Manipulation Trace Feature Extractor' module to uncover forgery clues while another 'Local Anomaly Detection Network' module localizes the region of tampering.
- Chen et al. [39] – Authors design an end-to-end 'conditional random field' based convolutional network with region proposal network that focusses on small sized objects which are often missed by traditional neural networks. This helps in fine tuning the boundaries of spliced region during the localization of tampering.
- Liu et al. [40] – Authors utilize multiple convolutional networks to learn distinct image features at multiple scales. Then, conditional random fields are used to merge information from multiple scales to produce the final forgery localization results.
- Salloum et al. [9] – Authors proposed a dual-branch multi-tasking convolutional network that learns the surface label from one branch and identifies the edge of manipulated region from the second branch to localize tampering region.
- Wu et al. [41] – Authors highlight attentional manipulation traces with adaptive multi-scale fusion by using a 'content remove convolutional layer' that supresses the semantic content of images and highlights forgery clues. Another sub-network based on encoder-decoder design localizes forgery region.
- Chen et al. [42] – Authors combine 'multi-view feature learning' with 'multi-scale supervision' to learn generalized image tampering clues while keeping the false alarms

over authentic images to a minimum. Multi-view feature learning exploits boundary clues around tampered region and noise distribution. Multi-scale supervision allows to uncover authetic image features to prevent false alarms.

- Xu et al. [44] – Authors utilize spatial features along with edge clues to identify image tampering. A novel 'Edge Gate' module helps to supress the semantic information of images and highlight tampering clues.

- Chen et al. [45] – Authors repurpose the tampering feature extration methodology. Instead of extracting clues from a two-stream Faster R-CNN model, authors design a novel two-layered convolutional structure to highlight forgery clues and hide image semantic details. The proposed module extracts weak forgery features crucial for tampering identification.

- Zhou et al. [46] – Authors propose a dual-stream Faster R-CNN based end-to-end model for forgery detection. The first stream extracts RGB clues for tampering such as contrast inconsistencies and uneven boundaries. The second stream extracts inconsistencies computed from steganalysis rich model filter layers.

- Wei et al. [47] – Authors improve the forgery detection scores by integrating an edge detection network with a Faster R-CNN model. The combined dual-modality information provides discriminative feature learning capability that excels in identifying image tampering.

Table 9 Comparison of Existing Splice Detection Approaches against the proposed splice detection framework on the CASIA dataset. The best scores are highlighted in bold. '-' represents scores that are not mentioned in the research papers.

Model	ACC	P	R	F1	AUC	MCC
Zhang et al. **[35]**	-	-	-	0.7653	-	-
Sun et al. **[36]**	-	-	-	0.6805	-	-
Yan et al. **[37]**	-	0.8090	0.7460	0.7350	-	-
Bi et al. **[13]**	-	0.6780	0.5860	0.5860	-	-
Wu et al. **[38]**	-	0.6310	0.6730	0.6510	-	-
Chen et al. **[39]**	-	-	-	0.7388	-	-
Liu et al. **[40]**	-	-	-	0.5232	-	-
Salloum et al. **[9]**	-	-	-	0.6675	-	-
Wu et al. **[41]**	-	-	-	0.5770	-	0.5590
Chen et al. **[42]**	-	-	-	0.6097	-	-
Zhang et al. **[43]**	-	-	-	0.6286	-	-
Xu et al. **[44]**	-	-	-	0.4601	0.8191	-
Chen et al. **[45]**	-	0.6616	0.7548	0.7051	-	-
Zhou et al. **[46]**	-	0.5044	0.6575	0.5709	-	-
Wei et al. **[47]**	-	0.5202	0.6642	0.5834	-	-
(Proposed) DenseNet-CNN	0.8125	0.7823	0.7646	0.7733	0.9126	0.6136
(Proposed) ResNet-CNN	**0.8851**	**0.8123**	**0.9415**	**0.8664**	**0.9596**	**0.7744**

Table 10 presents a comparison of the proposed framework on the combined dataset. Here again, the proposed framework performs better than other similar approaches. Four existing splice detection approaches have been implemented and evaluated in this section to demonstrate a fair comparison and illustrate the superiority of the proposed splice detection framework. The architectures implemented and the training process followed are the same as the research manuscripts mentioned.

Table 10 Comparison of Existing Splice Detection Approaches against the ResNet-CNN variant of the proposed splice detection framework on the combined dataset.

Ref.	Model	Trainable Parameters	Dataset	ACC	P	R	F1
[48]	(Existing) Dense CNN	48,818	AMC	0.5850	0.5923	0.5498	0.5703
[49]	(Existing) DCT + Quantization Table	11,104,706	AMC	0.9273	0.9919	0.8951	0.9409
[26]	(Existing) Multi-Domain CNN	8,693,322	AMC	0.4693	0.4742	0.6413	0.5452
-	(Proposed) DenseNet-CNN	69,330	AMC	0.9382	0.9578	0.9185	0.9378
-	(Proposed) ResNet-CNN	42,194	AMC	0.9379	0.9510	0.9208	0.9357
[17]	(Existing) Weighted Feature Fusion	4,111,490	AM	0.5682	0.5837	0.4758	0.5245
-	(Proposed) ResNet-CNN	42,194	AM	0.9197	0.9508	0.9259	0.9382

The architecture in [48] contains four dense blocks with four, two, and two dense layers, respectively. Transition layers include 1×1 convolutions and Max pooling. Input images are converted to grayscale and resized to 256×256. Normalization is also done to the range of [0,1]. The model is trained for 50 epochs with an initial learning rate of 0.001, which is decayed by 10% every 1/3rd of an epoch. The optimizer used is SGD, and the batch size is 32.

The best architecture of [49], combining a quantization table to the last pooling and two fully connected layers, is implemented for comparison. The histogram range of Y channel DCT coefficients is [-60,60]. Train and test images are split by 90% and 10%, respectively. The model is trained for 50 epochs with a learning rate is 0.001 and an Adam optimizer. All convolution operations are accompanied by batch normalization.

The multi-domain CNN proposed in [26] is implemented and repurposed towards binary classification for image splice detection. The histogram range for DCT coefficients is [-50,50]. Train, validation, and test sets have sizes of 90%, 5%, and 5%, respectively. Both spatial and frequency branch use dropout and their respective inputs are applied with normalization to the range [0,1]. The model is trained for 50 epochs with the AdaDelta optimizer, with an initial learning rate of 0.01 is reduced by 10% every epoch.

The weighted feature combination architecture in [17], having four weight combination modules to combine YCbCr, Edge, and PRNU features, is implemented. The weight parameters $\propto_a$, $\propto_b$ and $\propto_c$ for each of the four weight modules are added to the computational graph and list of trainable parameters for automatic tuning during backpropagation. Cross-validation training is implemented with SGD optimizer, and the initial learning rate is 0.001, which decays by 10% every 10 epochs. Initial values for $\propto_a$, $\propto_b$ and $\propto_c$ are set to 0.3, 0.3 and 0.4, respectively.

PRNU features can be calculated from flat-field images of the source camera, or they can be estimated from a large number of natural images captured by a given camera device [50]. It is unclear how the authors computed PRNU features for CASIA dataset images since the dataset paper does not include source device information [29]. Hence, to alleviate this problem, the implemented weighted feature combination architecture is evaluated on the AM dataset variant, which includes the proposed Biometric-DTU-Splice dataset (automatic + manual). All images of the proposed Biometric-DTU-Splice dataset are derived from the RAISE dataset's uncompressed images whose camera device information is available. 50 images from each camera model ($N = 50$) are used to compute the PRNU factor $\widehat{K}$ using Eq. (6) for each camera device, as done in [50].

$$\widehat{\mathrm{K}} = \frac{\sum_{k=1}^{N}(\mathcal{W}_k \mathcal{I}_k)}{\sum_{k=1}^{N}(\mathcal{I}_k)^2} \quad (6)$$

Here $\mathcal{I}_k$ is one of the multiple images from the source camera and $\mathcal{W}_k = \mathcal{I}_k - \widehat{\mathcal{I}_k}$ represents image noise residual. The implemented architecture is compared against the ResNet-CNN variant of the proposed framework, which is trained for a second time on the AM dataset variant for a fair comparison (Table 10).

The results from Table 10 indicate the superiority of the proposed 'lightweight dual-branch information preserving spatio-compression modal splice detection framework.' Only [49] of the existing splice detection methods can match the proposed framework's accuracy, precision, recall, and f1-scores. But it is an extremely heavy architecture with more than 11 million trainable parameters.

4.5.2 Comparison based on Size (Number of Trainable Parameters)

One of the design principles of the proposed splice detection framework is to make it 'lightweight.' This idea is ideally suited when the usual splice detection datasets are small and deep architectures are prone to overfitting. The proposed model reduces the number of trainable parameters by using transfer learning in the spatial branch and processing DCT features of size $16 \times 128 \times 1$ in the compression branch through extremely lightweight neural networks. The number of trainable parameters in each variant of the proposed splice detection framework is presented in Table 7 and that of existing splice methods in Table 10. Fig. 7 presents a size comparison of all the proposed splice detection framework variants (pink) and some existing splice detection methods (blue). The size difference (no. of trainable parameters) between the proposed and existing methods is so significant that a 'log-scale' is used to plot the size

difference. Fig. 7 indicates the 'lightweight' nature of the proposed splice detection framework variants.

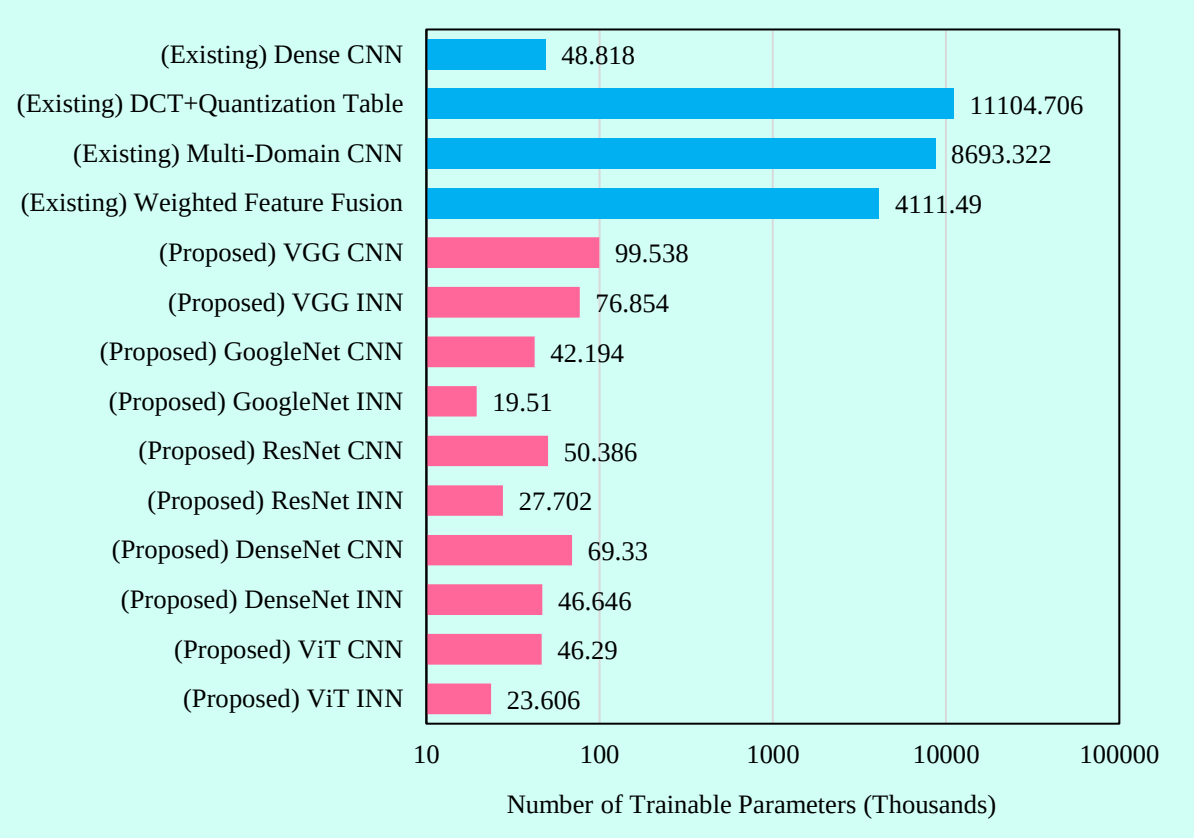


Fig. 7 Size comparison of the proposed Splice Detection Model Variants (pink) against Existing State-of-the-Arts (blue). Log scale is used to better demonstrate the massive differences in the number of trainable parameters.

5 Conclusion, Limitations & Future Work

5.1 Conclusion

This paper makes two-fold contributions towards splice detection in jpg images. Firstly, a novel splice detection dataset, the *'BiometricLab-DTU Splice dataset,'* is proposed. The proposed splice dataset has two variants: the first is autogenerated from code, and the second contains handmade spliced samples. The proposed splice detection dataset significantly adds to the existing small-scale splice datasets. Secondly, a novel 'Lightweight Dual-branch Information Preserving Spatio-Compression Modal Splice Detection Framework' is proposed that incorporates design principles consistent with today's splice detection research scenario (small-scale splice datasets). Several variants of the proposed framework are trained on images from the proposed splice dataset and a modified CASIA v2.0 dataset. Experimental results prove the superiority of the proposed splice detection framework compared to existing methods without requiring millions of trainable parameters in the neural network. A similar design principle can be used for future work to build a splice localization framework.

5.2 Limitations

Although the proposed framework is quite potent in identifying splice forgery in images, there are a few limitations.

Firstly, the proposed framework relies heavily on the jpeg compression artefacts as its compression branch inputs DCT compression information to make predictions. Hence, this framework works only for jpeg images. However, since data compression is widely used across all forms of multimedia data and jpeg compression is the most famous compression standard, the proposed framework is very relevant in present times.

Secondly, the proposed framework is designed specifically for image splice manipulations and is not trained for other manipulations such as copy-move. However, if the proposed framework is trained on multiple image manipulation types, it is likely to be highly effective due to its light-weight and information-preserving design.

5.3 Future Work

This section presents the possible future works based on the proposed splice detection framework and splice dataset created in this manuscript.

Firstly, the proposed splice dataset can be used to design and develop more robust splice detection models. Since, deep learning models require an abundance of labelled input data, the proposed splice dataset can help future models to achieve higher performance in both the detection and localization of splice manipulation in images.

Secondly, with the rise of transformer-based models in computer vision tasks, neural networks can now capture long-term visual dependencies often missed by convolution-based networks. These recent transformer models can be utilized to design newer, more capable models for image splice detection.

Thirdly, visual attention has become an integral part of vision models as they have consistently boosted model performances in various classification tasks. Visual attention can be integrated to boost model performance in identifying image splicing.

Lastly, generalized and unseen forgery detection models are still underexplored. There is a need to design models that can identify image tampering not present in the training images.

6 References

[1] B. Dean, "Social Network Usage & Growth Statistics: How Many People Use Social Media in 2021?," BackLinko, 10 August 2021. [Online]. Available: https://backlinko.com/social-media-users.

[2] M. Ahmad and F. Khursheed, "Detection and localization of image tampering in digital images with fused features," *Concurrency and Computation: Practice and Experience*, vol. 34, no. 23, 2022.

[3] N. Singla, J. Singh and S. Nagpal, "Raven finch optimized deep convolutional neural network model for intra-frame video forgery detection," *Concurrency and Computation: Practice and Experience*, 2022.

[4] R. Cristin, . S. P. Premnath and J. P. Ananth, "Image tampering detection in image forensics using earthworm-rider optimization," *Concurrency and Computation: Practice and Experience*, vol. 34, no. 26, 2022.

[5] C. Chen, S. McCloskey and J. Yu, "Image Splicing Detection via Camera Response Function Analysis," in *IEEE Conference on Computer Vision and Pattern Recognition (CVPR)*, Honolulu, 2017.

[6] L. Bondi, S. Lameri, D. Güera, P. Bestagini, E. J. Delp and S. Tubaro, "Tampering Detection and Localization Through Clustering of Camera-Based CNN Features," in *IEEE Conference on Computer Vision and Pattern Recognition Workshops (CVPRW)*, Honolulu, 2017.

[7] T. Pomari, G. Ruppert, E. Rezende, A. Rocha and T. Carvalho, "Image Splicing Detection Through Illumination Inconsistencies and Deep Learning," in *IEEE International Conference on Image Processing (ICIP)*, Athens, 2018.

[8] S. Verde, L. Bondi, P. Bestagini, S. Milani, G. Calvagno and S. Tubaro, "Video Codec Forensics Based on Convolutional Neural Networks," in *IEEE International Conference on Image Processing (ICIP)*, Athens, 2018.

[9] R. Salloum, Y. Ren and C.-C. J. Kuo, "Image Splicing Localization using a Multi-task Fully Convolutional Network (MFCN)," *Journal of Visual Communication and Image Representation*, vol. 51, pp. 201-209, 2018.

[10] X. Cun and C.-M. Pun, "Image Splicing Localization via Semi-global Network and Fully Connected Conditional Random Fields," in *European Conference on Computer Vision (ECCV)*, Munich, 2018.

[11] B. Liu and C.-M. Pun, "Deep Fusion Network for Splicing Forgery Localization," in *European Conference on Computer Vision (ECCV)*, Munich, 2018.

[12] A. Mazumdar and P. K. Bora, "Deep Learning-Based Classification of Illumination Maps for Exposing Face Splicing Forgeries in Images," in *2019 IEEE International Conference on Image Processing (ICIP)*, Taipei, 2019.

[13] X. Bi, Y. Wei, B. Xiao and W. Li, "RRU-Net: The Ringed Residual U-Net for Image Splicing Forgery Detection," in *IEEE/CVF Conference on Computer Vision and Pattern Recognition Workshops (CVPRW)*, Long Beach, 2019.

[14] C. Deng, Z. Li, X. Gao and D. Tao, "Deep Multi-scale Discriminative Networks for Double JPEG Compression Forensics," *ACM Transactions on Intelligent Systems and Technology*, vol. 10, no. 2, 2019.

[15] J. Horváth, D. M. Montserrat, H. Hao and E. J. Delp, "Manipulation Detection in Satellite Images Using Deep Belief Networks," in *IEEE/CVF Conference on Computer Vision and Pattern Recognition Workshops (CVPRW)*, Seattle, 2020.

[16] B. Xiao, Y. Wei, X. Bi, W. Li and J. Ma, "Image splicing forgery detection combining coarse to refined convolutional neural network and adaptive clustering," *Information Sciences*, vol. 511, pp. 172-191, 2020.

[17] J. Wang, Q. Ni, G. Liu, X. Luo and S. K. Jha, "Image splicing detection based on convolutional neural network with weight combination strategy," *Journal of Information Security and Applications*, vol. 54, 2020.

[18] B. Liu and C.-M. Pun, "Exposing splicing forgery in realistic scenes using deep fusion network," *Information Sciences*, vol. 526, pp. 133-150, 2020.

[19] K. Simonyan and A. Zisserman, "Very Deep Convolutional Networks for Large-Scale Image Recognition," in *International Conference on Learning Representations (ICLR)*, San Diego, 2015.

[20] C. Szegedy, W. Liu, Y. Jia, P. Sermanet, S. Reed, D. Anguelov, D. Erhan, V. Vanhoucke and A. Rabinovich, "Going deeper with convolutions," in *IEEE Conference on Computer Vision and Pattern Recognition (CVPR)*, Boston, 2015.

[21] K. He, X. Zhang, S. Ren and J. Sun, "Deep Residual Learning for Image Recognition," in *IEEE Conference on Computer Vision and Pattern Recognition (CVPR)*, Las Vegas, 2016.

[22] G. Huang, Z. Liu, L. V. D. Maaten and K. Q. Weinberger, "Densely Connected Convolutional Networks," in *IEEE Conference on Computer Vision and Pattern Recognition (CVPR)*, Honolulu, 2017.

[23] A. Dosovitskiy, L. Beyer, A. Kolesnikov, D. Weissenborn, X. Zhai, T. Unterthiner, M. Dehghani, M. Minderer, G. Heigold, S. Gelly, J. Uszkoreit and N. Houlsby, "An Image is Worth 16x16 Words: Transformers for Image Recognition at Scale," in *International Conference on Learning Representations (ICLR)*, Austria, 2021.

[24] D. Li, J. Hu, C. Wang, X. Li, Q. She, L. Zhu, T. Zhang and Q. Chen, "Involution: Inverting the Inherence of Convolution for Visual Recognition," in *Computer Vision and Pattern Recognition (CVPR)*, Nashville, 2021.

[25] Q. Wang and R. Zhang, "Double JPEG compression forensics based on a convolutional neural network," *EURASIP Journal on Information Security*, vol. 23, 2016.

[26] I. Amerini, T. Uricchio, L. Ballan and R. Caldelli, "Localization of JPEG Double Compression Through Multi-domain Convolutional Neural Networks," in *IEEE Conference on Computer Vision and Pattern Recognition Workshops (CVPRW)*, Honolulu, 2017.

[27] T.-T. Ng, J. Hsu and S.-F. Chang, "Columbia Image Splicing Detection Evaluation Dataset," Columbia University, 2004. [Online]. Available: https://www.ee.columbia.edu/ln/dvmm/downloads/AuthSplicedDataSet/AuthSplicedDataSet.htm.

[28] Y.-f. Hsu and S.-f. Chang, "Detecting Image Splicing using Geometry Invariants and Camera Characteristics Consistency," in *IEEE International Conference on Multimedia and Expo*, Toronto, 2006.

[29] J. Dong, W. Wang and T. Tan, "CASIA Image Tampering Detection Evaluation Database," in *IEEE China Summit and International Conference on Signal and Information Processing*, Beijing, 2013.

[30] T. J. d. Carvalho, C. Riess, E. Angelopoulou, H. Pedrini and A. d. R. Rocha, "Exposing Digital Image Forgeries by Illumination Color Classification," *IEEE Transactions on Information Forensics and Security*, vol. 8, no. 7, pp. 1182 - 1194, 2013.

[31] "Image Forensics Challenge Dataset," 2014. [Online]. Available: https://signalprocessingsociety.org/newsletter/2014/01/ieee-ifs-tc-image-forensics-challenge-website-new-submissions.

[32] S. Chen, S. Tan, B. Li and J. Huang, "Automatic Detection of Object-Based Forgery in Advanced Video," *IEEE Transactions on Circuits and Systems for Video Technology*, vol. 26, no. 11, pp. 2138 - 2151, 2016.

[33] D. Cozzolino, G. Poggi and L. Verdoliva, "Efficient Dense-Field Copy–Move Forgery Detection," *IEEE Transactions on Information Forensics and Security*, vol. 10, no. 11, pp. 2284 - 2297, 2015.

[34] D.-T. D. Nguyen, C. Pasquini, V. Conotter and G. Boato, "RAISE: a raw images dataset for digital image forensics," in *6th ACM Multimedia Systems Conference*, Portland, 2015.

[35] Y. Zhang, G. Zhu, L. Wu, S. Kwong, H. Zhang and Y. Zhou, "Multi-Task SE-Network for Image Splicing Localization," *IEEE Transactions on Circuits and Systems for Video Technology* , vol. 32, no. 7, pp. 4828 - 4840, 2022.

[36] Y. Sun, R. Ni and Y. Zhao, "ET: Edge-Enhanced Transformer for Image Splicing Detection," *IEEE Signal Processing Letters*, vol. 29, pp. 1232 - 1236, 2022.

[37] C. Yan, S. Li and H. Li, "TransU2-Net: A Hybrid Transformer Architecture for Image Splicing Forgery Detection," *IEEE Access*, vol. 11, pp. 33313 - 33323, 2023.

[38] Y. Wu, W. AbdAlmageed and P. Natarajan, "ManTra-Net: Manipulation Tracing Network for Detection and Localization of Image Forgeries With Anomalous Features," in *IEEE/CVF Conference on Computer Vision and Pattern Recognition (CVPR)*, Long Beach, 2019.

[39] B. Chen, X. Qi, Y. Wang, Y. Zheng, H. J. Shim and Y.-Q. Shi, "An Improved Splicing Localization Method by Fully Convolutional Networks," *IEEE Access*, vol. 6, pp. 69472 - 69480, 2018.

[40] B. Liu and C.-M. Pun, "Locating splicing forgery by fully convolutional networks and conditional random field," *Signal Processing: Image Communication*, vol. 66, pp. 103-112, 2018.

[41] Y. Wu, Y. Wo and G. Han, "Joint manipulation trace attention network and adaptive fusion mechanism for image splicing forgery localization," *Multimedia Tools and Applications*, vol. 81, p. 38757–38780, 2022.

[42] X. Chen, C. Dong, J. Ji, J. Cao and X. Li, "Image Manipulation Detection by Multi-View Multi-Scale Supervision," in *IEEE/CVF International Conference on Computer Vision*, Montreal, 2021.

[43] H. Zhang, K. Dana, J. Shi, Z. Zhang, X. Wang, A. Tyagi and A. Agrawal, "Context Encoding for Semantic Segmentation," in *IEEE/CVF Conference on Computer Vision and Pattern Recognition*, Salt Lake City, 2018.

[44] D. Xu, X. Shen, Y. Huang and Z. Shi, "RB-Net: integrating region and boundary features for image manipulation localization," *Multimedia Systems*, 2022.

[45] H. Chen, . Q. Han, Q. Li and X. Tong , "Digital image manipulation detection with weak feature stream," *The Visual Computer*, vol. 38, p. 2675–2689, 2022.

[46] P. Zhou, X. Han, V. I. Morariu and L. S. Davis, "Learning Rich Features for Image Manipulation Detection," in *Conference on Computer Vision and Pattern Recognition*, Salt Lake City, UT, USA, 2018.

[47] X. Wei, Y. Wu, F. Dong, J. Zhang and S. Sun, "Developing an Image Manipulation Detection Algorithm Based on Edge Detection and Faster R-CNN," *Symmetry*, vol. 11, 2019.

[48] Y. Chen, X. Kang, Y. Q. Shi and Z. J. Wang, "A multi-purpose image forensic method using densely connected convolutional neural networks," *Journal of Real-Time Image Processing*, vol. 16, pp. 725-740, 2019.

[49] J. Park, D. Cho, W. Ahn and H.-K. Lee, "Double JPEG Detection in Mixed JPEG Quality Factors using Deep Convolutional Neural Network," in *European Conference on Computer Vision (ECCV)*, Munich, 2018.

[50] M. Chen, J. Fridrich, M. Goljan and J. Lukas, "Determining Image Origin and Integrity Using Sensor Noise," *IEEE Transactions on Information Forensics and Security*, vol. 3, no. 1, pp. 74-90, 2008.

Ain Shams Engineering Journal xxx (xxxx) xxx

Contents lists available at ScienceDirect

Ain Shams Engineering Journal

journal homepage: www.sciencedirect.com

Full Length Article

Transition metal induced- magnetization and spin-polarisation in black arsenic phosphorous

Anurag Chauhan [a,*], Kapil Sharma [a], Sudhanshu Choudhary [b]

[a] Delhi Technological University, India
[b] University of North Dakota, North Dakota, United States

ARTICLE INFO

Keywords:
Spintronics
Half metallic
Black arsenic phosphorus
Density Functional Theory
2D materials
Adsorption
Transition Metals
Magnetization

ABSTRACT

The electronic and magnetic properties of two-dimensional black Arsenic Phosphorus (b-AsP) on adsorption of Transition Metals (TM) on its surface are investigated using density functional theory (DFT) based on first principles calculations. Spin-density of states (S-DOS) and the bandstructure of all the transition metals adsorbed structures have been plotted which reveals their change from non-magnetic to magnetic behaviour. The results suggest that pristine b-AsP which is a non-magnetic semiconductor turns into a half metal ferromagnet (HMF) on adsorption of Co, Fe and Ti, and it turns into a ferromagnet (FM) on adsorption of Cr and Zr. The total magnetic moments were also calculated to further support our results and findings. Strong magnetic moments were observed for Cr, Fe and Ti adsorbed b-AsP structures. Ag, Cu and Mo adsorption over b-AsP results into non-magnetic metallic characteristics with very weak magnetic moments. This transformation from a non-magnetic semiconductor to a magnetic HMF or FM material demonstrates the potential use of b-AsP in designing spin magnetic devices for various spin-based applications.

1. Introduction

Spintronics is an emerging field where the electron's spin can be used for current flow in electronic devices and systems. The involvement of spin opens new opportunities for development of novel electronic devices [1,2]. The development of these spin-based devices is based on choosing suitable materials which support spin-based characteristics and transport properties. With the advancement in process technology, many spin characteristics like spin-filtering effect (SFE) [3,4] Giant Magnetoresistance (GMR), and Tunnel Magnetoresistance (TMR) have been discovered by theoretical and experimental research on the novel 2D materials [5,6]. Graphene, black- phosphorus, and silicene are some of the 2D materials of immense interest to both theoretical and experimental research in spintronics [7–12].

Since the discovery of graphene in 2004, the global scientific community has shown considerable interest in two-dimensional (2D) materials due to their exceptional physical properties. Graphene, with its ultrahigh surface area, mechanical flexibility, and remarkable electrical conductivity, has positioned itself as a high-performance electrode material for energy storage devices [13–18]. Despite the impressive properties of graphene, the conventional graphite anode in Lithium-Ion Batteries (LIB) faces challenges meeting the growing demands of new storage technologies and the electronic devices market due to its low energy density [19]. Consequently, there is a pressing need to identify advanced electrode materials with enhanced capacities.

In recent years, the study of 2D materials, beyond graphene, has reached new heights, driven by their improved charge carrier ability and higher energy density compared to conventional anode materials [20]. The small volume-to-surface area ratio and exposed surface of a 2D structure allows for controlled manipulation of material properties through impurity doping or defect formation [20–24]. For instance, the synthesis of 2D phosphorene (Black-P) with a honeycomb structure has garnered attention for its reported ultra-high electron mobility of up to 10^4 cm^2/V-s [25,23].

However, black phosphorus, while promising, is unstable at room temperature and has a fixed band gap, limiting its use in optoelectronics devices. Another notable 2D material, black Arsenic Phosphorous (b-AsP), has emerged with higher stability at room temperature and modulation properties such as a tunable bandgap compared to black phosphorene [21]. Researchers, including Zhang et al., have proposed the incorporation of AsP in doped atoms, resulting in a transition from semiconductor to metal properties, making it a potential electrode

* Corresponding author.
E-mail addresses: anuragchauhan@dtu.ac.in (A. Chauhan), kapil@ieee.org (K. Sharma), sudhanshu.choudhary@UND.edu (S. Choudhary).

https://doi.org/10.1016/j.asej.2024.102632
Received 26 October 2023; Received in revised form 7 December 2023; Accepted 26 December 2023
2090-4479/© 2024 THE AUTHORS. Published by Elsevier BV on behalf of Faculty of Engineering, Ain Shams University. This is an open access article under the CC BY license (http://creativecommons.org/licenses/by/4.0/).

material for Li and Na batteries. Thermodynamically, composition of b-AsP is most stable when the ratio of As: P is taken as 1:1 [26]. Chemically, AsP has 3 possible configurations: AsP-1, AsP-2 and AsP-3. In AsP-1 configuration, a bond exists only between As and P, while in AsP-2, a bond exists between P-P, As-As and As-P, wherein the top layer consists of only P atoms while only As atoms exist in the bottom layer. AsP-3 configuration consists of in-plane As-P bonds and out-of-plane As-As and P-P bonds [27]. Among all the three chemical configurations, AsP-3 has the maximum bandgap and highest electron mobility of 14380 cm^2/V-s [28,29].

Recent studies indicate that the adsorption or doping of transition metals on non-magnetic materials induces magnetic moment and spin polarization, transforming their nature into magnetic materials. These magnetic materials, exhibiting ferromagnetic or half-metal ferromagnetic behavior upon specific transition metal adsorption, find applications as electrode materials in spin-based devices such as Magnetic Tunnel Junctions (MTJ) and spin valves [30–34]. They offer high spin filtration (~100 %) and magnetoresistance (~103 %), crucial parameters for evaluating the performance of spin-based devices [11,35–39].

Therefore, b-AsP, as a 2D material with high mobility and tunable bandgap, presents an intriguing prospect for transition metal adsorption. This study aims to explore the effects of adsorption of transition metals on the properties of resulting b-AsP structures. The induced magnetisation and spin polarization in the adsorbed structures could make it a suitable candidate for use as a ferromagnetic/half-metal ferromagnet electrode in the design and synthesis of spin-based devices, such as magnetic tunnel junctions and spin-valves.

As AsP is a non-magnetic semiconductor in pristine form, for AsP, it should be made spin-polarized for its applications in spin-dependent transport. In the present study, transition metals (Ti, Cr, Fe, Co, Cu, Zr, Mo and Ag) were adsorbed on pristine AsP-3 configuration to investigate their impact on spin properties. All investigations are performed using first-principles calculations. The selection of AsP-3 among three possible chemical configurations is made owing to the presence of higher mobility in this configuration. Relaxed adsorbed geometry for all transition metal adsorbed structures was obtained before calculating bandstructure, spin-density of states (spin-DOS) and magnetic moment. The results suggest transition from nonmagnetic semiconducting to magnetic half metallic and ferromagnetic characteristics in transition metal adsorbed AsP-3 structures.

2. Set up and simulation

The reciprocal effect results in shifting of electric charge from transition metals to AsP-3, resulting in modified electronic and magnetic properties in AsP-3. The study focused on investigating the electronic and magnetic properties by introducing adsorbed transition metals on the surface of AsP-3. To achieve this, individual atoms of Ag, Co, Ti, Mo, Fe, Cu, Cr and Zr were placed in proximity to the non-magnetic semiconducting AsP-3 surface. The resulting atomic configuration was then relaxed until the forces acting on each atom reached a value of 0.05 eV/Å or lower.

In this study, density functional theory (DFT) simulations were conducted using the Atomistix simulation Toolkit package [40]. The exchange–correlation energy was evaluated based on spin-polarized generalized gradient approximation (SGGA) employing numerical LCAO basis sets. A threshold energy of 130 Rydberg was utilized, and a k-point sampling scheme of (11,11,1) was applied along the x, y, and z axes.

To analyze the electronic properties, spin-polarized density of states (spin-DOS) calculations were performed for semiconducting AsP-3 as well as all the adsorbed structures. Additionally, band structure calculations were performed to confirm the results with the spin-DOS analysis. Furthermore, the magnetic characteristics were examined for all the adsorbed structures through the computation of their overall magnetic moment, confirming their magnetic characteristics.

The density of states (DOS) is a measure of the number of available states within a given energy range, E to $E + dE$. Mathematically, it can be represented as:

$$DOS\,(E) = \frac{\Delta n}{\Delta E \times L} = \frac{1}{\sqrt{2}\pi A}\left(E - \frac{E_g}{2}\right)^{-\frac{1}{2}} \tag{1}$$

In the provided equation, $DOS(E)$ denotes the density of states at a specific energy level E. The energy gap is represented by E_g, and $A = at$ corresponds to the coefficient of the Taylor expansion. The length of the AsP material is denoted by L.

Furthermore, the material's carrier concentration at a specific energy E can be determined by integrating the product of the density of states (DOS) and the probability density function, as expressed by the equation:

$$n(E) = \int DOS(E) f(E) dE \tag{2}$$

For confirming the feasibility of transition metals on the AsP-3 surface, the energy of adsorption can be calculated as:

$$E_{ads} = E_{structure} - [E_{TM} + E_{AsP-3}] \tag{3}$$

In the above equation, E_{ads} refers to the energy associated with the process of adsorption, $E_{structure}$ represents the total energy of adsorbed structure, E_{AsP-3} represents the total energy of the AsP-3 in intrinsic form, while E_{TM} denotes the total energy of a single transition metal [41].

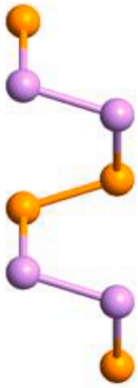


Fig. 1(a)



Fig. 1(b)

Fig. 1. (a) Pristine Semiconducting AsP-3 (b) Co-adsorbed AsP-3.

3. Results and discussions

Fig. 1(a) shows relaxed geometric structure of pristine AsP-3, which is very similar to black phosphorene (b-P) [21]. The geometry has been constructed by substituting 50 % of phosphorene (P) atoms in the unit cell of b-P with Arsenic (As) atoms. The geometry of the system was then optimized to ensure stability and suitability for further investigations. The band structure and spin-DOS calculations of pristine AsP-3 are also shown in Fig. 2(a). The calculated bandgap of the pristine AsP-3 is ~1.1 eV confirming its semiconducting nature. The calculated bandgap is very similar to the bandgap reported in [20,21]. The absence of magnetic properties in pristine AsP-3 can be verified through its spin-density of states (spin-DOS) plot, as illustrated in Fig. 2(a). The spin-DOS plot reveals the absence of conducting states at the Fermi energy level,

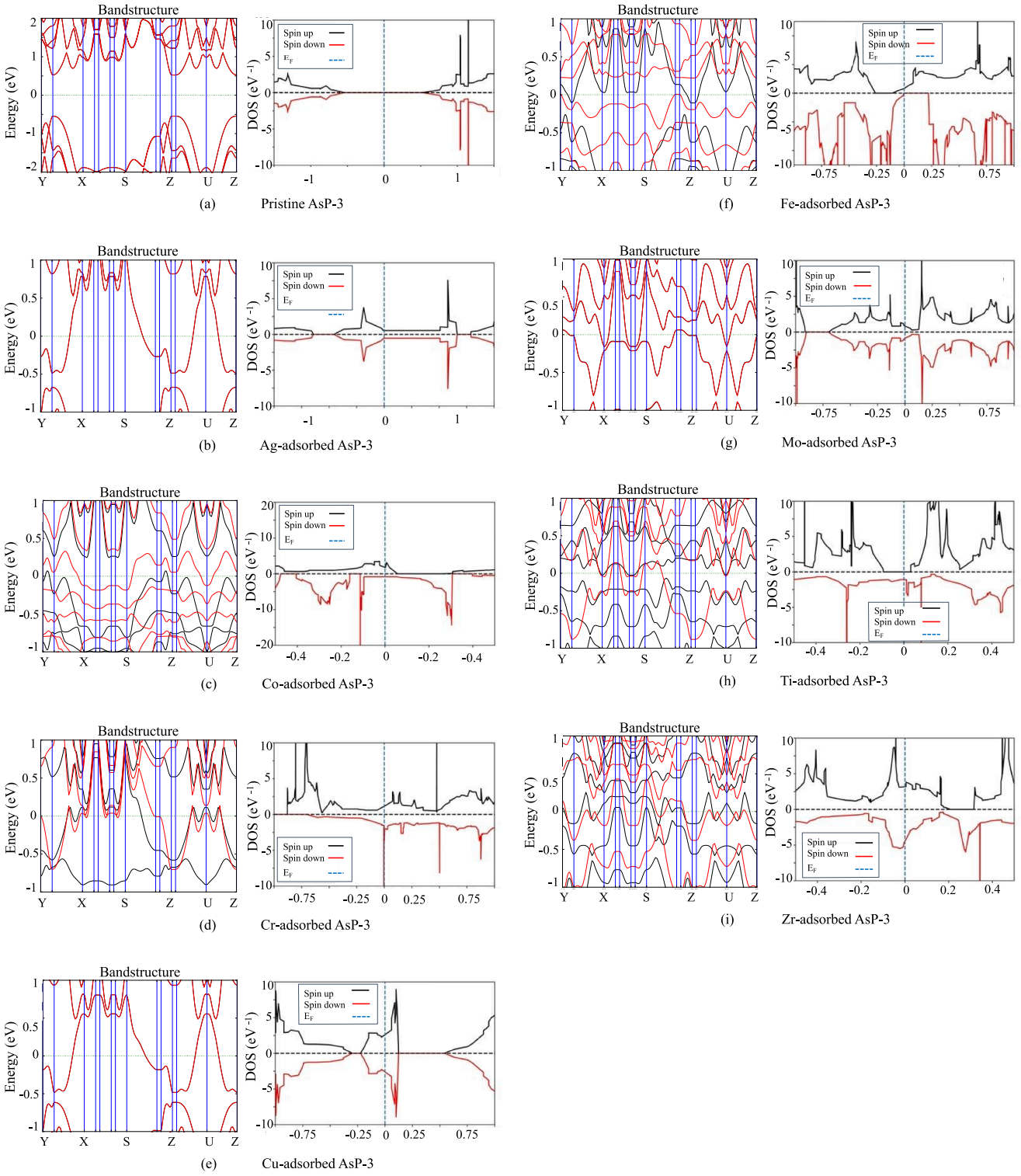


Fig. 2. Bandstructure and spin-DOS of (a) pristine AsP-3 (b) Ag-adsorbed AsP-3 (c) Co-adsorbed AsP-3 (d) Cr-adsorbed AsP-3 (e) Cu-adsorbed AsP-3 (f) Fe-adsorbed AsP-3 (g) Mo-adsorbed AsP-3 (h) Ti-adsorbed AsP-3 (i) Zr-adsorbed AsP-3.

Table 1
Magnetic properties of AsP-3 and adsorbed structures.

Adsorbed structures	Spin-Up	Spin-Down	Magnetic moment/atom (μ_B)	Magnetic Characteristics
Pristine AsP-3	Absent	Absent	NIL	Non-Magnetic
Ag adsorbed AsP-3	Present	Present	NIL	Non-Magnetic
Co adsorbed AsP-3	Present	Absent	0.65	HMF
Cr adsorbed AsP-3	Present	Present	5.09	FM
Cu adsorbed AsP-3	Present	Present	NIL	Non-Magnetic
Fe adsorbed AsP-3	Present	Absent	2.15	HMF
Mo adsorbed AsP-3	Present	Present	NIL	Non-Magnetic
Ti adsorbed AsP-3	Absent	Present	2.21	HMF
Zr adsorbed AsP-3	Present	Present	0.91	FM

confirming the non-magnetic nature of pristine AsP-3. Its magnetic moment is also calculated and is shown in Table 1. Zero magnetic moment of pristine semiconducting AsP-3 further verifies its non-magnetic nature. Based on these obtained results, it can be concluded that pristine AsP-3 is a non-magnetic semiconductor. These findings align with previous research studies in this field.

To investigate the influence of adsorption, it becomes crucial to examine the magnetic and electronic properties of the structures after adsorption of transition metals. For the adsorption to take place, pristine AsP-3 surface was utilized as a substrate, and transition metal atoms were placed in close proximity to it. The resulting structure was then optimized through geometry relaxation process. Fig. 1(b) depicts the relaxed geometry of the Co atom adsorbed on the non-magnetic semiconducting AsP-3 (highlighted in pink). Similarly, the same procedure was applied to other transition metals individually adsorbed on pristine AsP-3, with subsequent relaxation to optimize the adsorbed structures. The relaxed structures of all the resulting adsorbed structure can be seen in the Appendix-I (see Appendix-I, Fig. 1). It can be observed that the transition metals on adsorption formed bonds with the pristine AsP-3 leading to change in the electronics and magnetic properties. To assess the feasibility of transition metal adsorption on AsP-3, the adsorption energy was calculated for each structure. The calculated adsorption energies were negative for all the structures indicating that the adsorption process is exothermic and affirm the stability of the adsorbed structures (see Appendix A1, Table 1).

As shown in Fig. 2(b), the bandstructure of AsP-3 has zero bandgap after adsorbing Ag. The material whose bands cross the Fermi level are metallic in nature. This can also be observed from its spin-DOS which shows the availability of conducting states at the fermi level. This confirms its transition from semiconducting to metallic characteristics on adsorption of Ag. Additionally, it can also be observed from its spin-DOS (Fig. 2(b)) that Ag-adsorbed structure has states available for conduction in both spin-up as well as spin-down channels. However, its calculated magnetic moment was found to be zero (see Table 1). So, Ag- atom on adsorption was unable to induce magnetization in the AsP-3 and it preserves its non-magnetic nature. So, Ag- atom can transform semiconducting AsP-3 to metallic but cannot change its magnetic nature. Similar characteristics were observed when AsP-3 was adsorbed with Cu and Mo. In Fig. 2(e), the bandgap of Cu-adsorbed structure is zero leading to transition from semiconducting to metallic nature. Its spin-DOS also indicates presence of conduction states in both spin-up and spin-down channels. However, its negligible magnetic moment (see Table 1) indicates its non-magnetic nature. Similarly, for Mo-adsorbed AsP-3, band structure and spin-DOS are shown in Fig. 2(g). The resulting adsorbed structure is metallic, as its bandgap is zero. It has states available for conduction in spin-up as well as spin-down channels at fermi level, which is confirmed by its spin-DOS. The structure, however, remains non-magnetic as its calculated magnetic moment is negligible. Therefore, Ag, Cu and Mo, when adsorbed on the surface of AsP-3, result into transition of characteristics of AsP-3 from semiconducting to metallic but unable to induce magnetization and spin- polarization in the adsorbed structures.

But interesting characteristics were observed when Cr was adsorbed on the surface of AsP-3. The resultant structure transformed from semiconducting to metallic. The zero bandgap of Cr-adsorbed AsP-3 can be observed in the band structure plot shown in Fig. 2(d). The magnetic moment of the structure was found to be 5.09 μ_B, which is highest among all other transition metal adsorbed structures. It indicates that Cr can induce magnetization in AsP-3. The spin-DOS of adsorbed structure (see Fig. 2(d)) also shows the availability of conducting states in both spin-up and spin-down channels confirming its ferromagnetic nature. Similarly, Zr, when adsorbed on the surface of AsP-3, can transform the nature of AsP-3 from non-magnetic to ferromagnetic. Its band structure in Fig. 2(i) confirms overlapping states with no bandgap. The availability of conducting states, as visible in its spin-DOS in both channels confirm its metallic nature. The calculated magnetic moment of 0.91 μ_B although is lower but significant when compared with Cr adsorbed structure. Therefore, Cr and Zr, when adsorbed on the surface of AsP-3, induce ferromagnetism in the adsorbed structure. Hence, Cr and Zr on adsorption were able to transform semiconducting and non-magnetic AsP-3 to metallic and magnetic material. These ferromagnetic materials can be used as electrode materials for spin-based devices like MTJs and spin-based switches.

In the Co adsorbed AsP-3 structure, semiconductor to metallic transition is observed with zero bandgap in the band structure plot shown in Fig. 2(c). Also, the spin-DOS of the Co-adsorbed structure shows that majority of the conducting states are available in spin-up channel than in spin-down channel. This makes the structure half metallic, as spin-up electrons are majority carriers. This half metallicity shows that the material when used as an electrode will be allowing only spin-up electrons to pass through the channel while blocking the spin-down electrons which is a highly desirable characteristic of spintronics devices. The non-zero magnetic moment of 0.65 μ_B (see Table 1) also confirms its magnetic nature. HMF characteristics were observed for Fe- adsorbed AsP-3 and Ti- adsorbed AsP-3. Both the adsorbed structures were confirmed to be metallic with zero bandgap, as shown in Fig. 2(f) and 2(h). For Fe-adsorbed structure, spin-DOS shows the availability of only spin-up states and no spin-down conduction states. Whereas the spin- DOS of Ti-adsorbed structure in Fig. 2(h) shows the opposite behavior, where conducting states are available only in spin-down channel. The availability of conducting states in only one of the channels (spin-up or spin-down) makes these adsorbed structures HMF. The calculated magnetic moments of 2.14 μ_B and 2.21 μ_B for Fe-adsorbed and Ti-adsorbed AsP-3 in Table 1 confirms their magnetic behavior. Therefore, when Co, Fe and Ti are adsorbed on the surface of non-magnetic AsP-3, in addition to transition from semiconducting to metallic characteristic of AsP-3, induced magnetization and spin- polarization are also observed. Such structures can be used to design electrodes for spin-based devices. When the device is fabricated using HMF materials as electrodes, it allows the electrons of only one spin type (spin-up or spin-down) to pass through the channel and blocks the electrons of opposite spin and therefore the majority of the spin current is composed of only one type of spin-electrons. This characteristic of a spin-based device where only one type of spin electrons (up/down) are

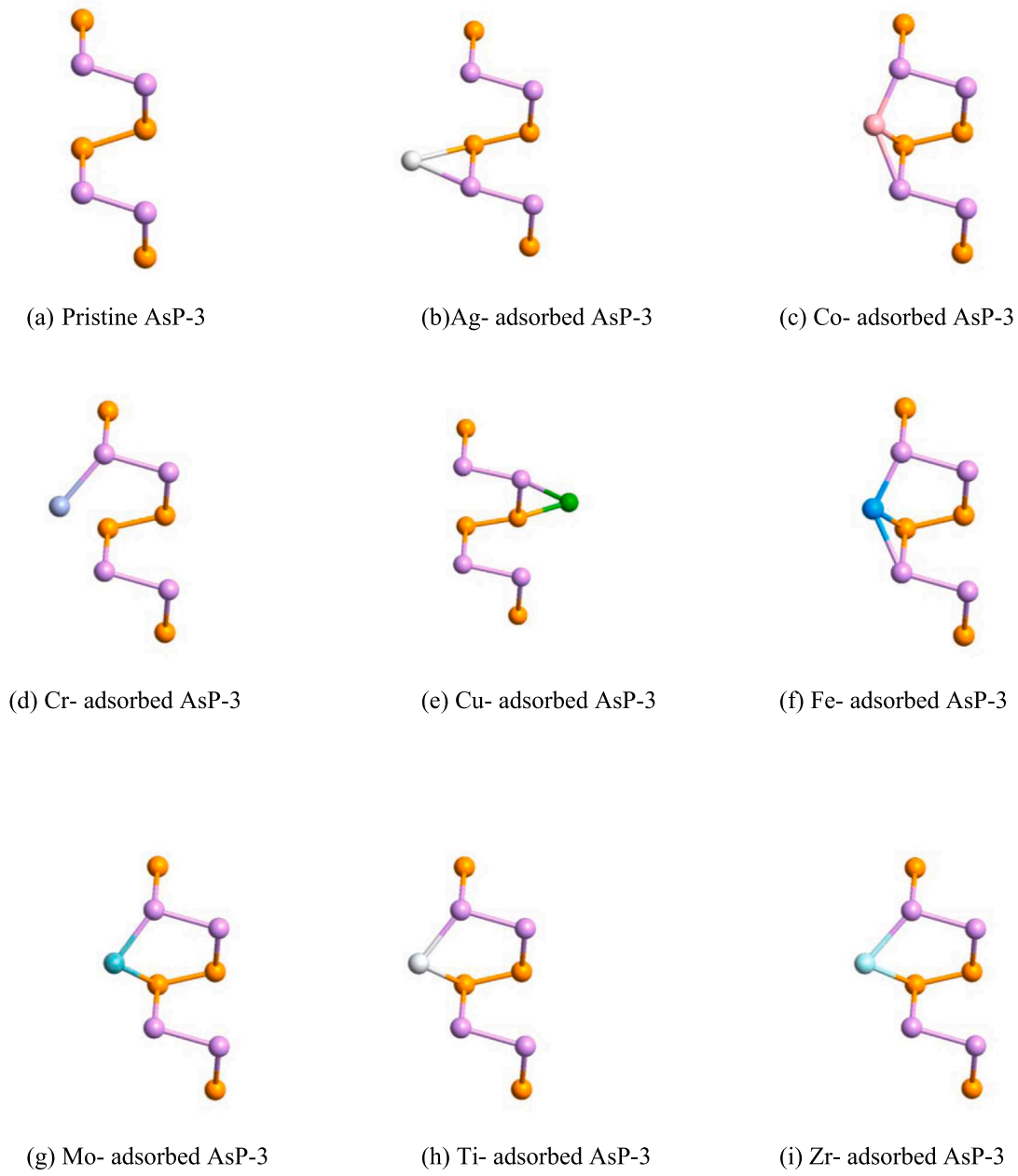


Fig. A1. Optimised structures of (a) pristine AsP-3 (b) Ag-adsorbed AsP-3 (c) Co-adsorbed AsP-3 (d) Cr-adsorbed AsP-3 (e) Cu-adsorbed AsP-3 (f) Fe-adsorbed AsP-3 (g) Mo-adsorbed AsP-3 (h) Ti-adsorbed AsP-3 (i) Zr-adsorbed AsP-3.

Table A1
Energy of adosrption.

Material	Energy of formation (Energy of adsorption) eV
Pristine AsP-3	——
Ag adsorbed AsP-3	−482.14
Co adsorbed AsP-3	−481.17
Cr adsorbed AsP-3	−484.57
Cu adsorbed AsP-3	−481.86
Fe adsorbed AsP-3	−481.21
Mo adsorbed AsP-3	−479.8
Ti adsorbed AsP-3	−480.93
Zr adsorbed AsP-3	−480.98

allowed while blocking the other spin type (down/up) electron is expressed in the form of magnetoresistance such as TMR or GMR.

The efficiency of a spin-based device is determined based on the value of magnetoresistance ratio. Higher values of magnetoresistance ratio indicate better spin-filtration and spin-selectivity. Spin-based devices exploit this property of magnetoresistance to conduct current from the left electrode to the right electrode through a non-magnetic channel [1]. Hence, these findings confirm that transition metals, on adsorption can induce the transition of semiconducting AsP-3 to a metallic state. Also, specific transition metals like Cr, Zr, Co, Fe and Ti are able to induce magnetization and spin- polarization in the adsorbed structures.

4. Conclusion

The DFT investigation delineates the impact of transition metal adsorption on the electronic and magnetic properties of semiconducting AsP-3. Utilizing Spin-DOS analysis, distinct alterations in response to the adsorption of Ag, Co, Mo, Cr, Zr, Fe, and Ti have been elucidated.

The adsorption of Ag, Co, and Mo induces non-magnetic metallic characteristics in AsP-3, as discerned through spin-DOS analysis. This

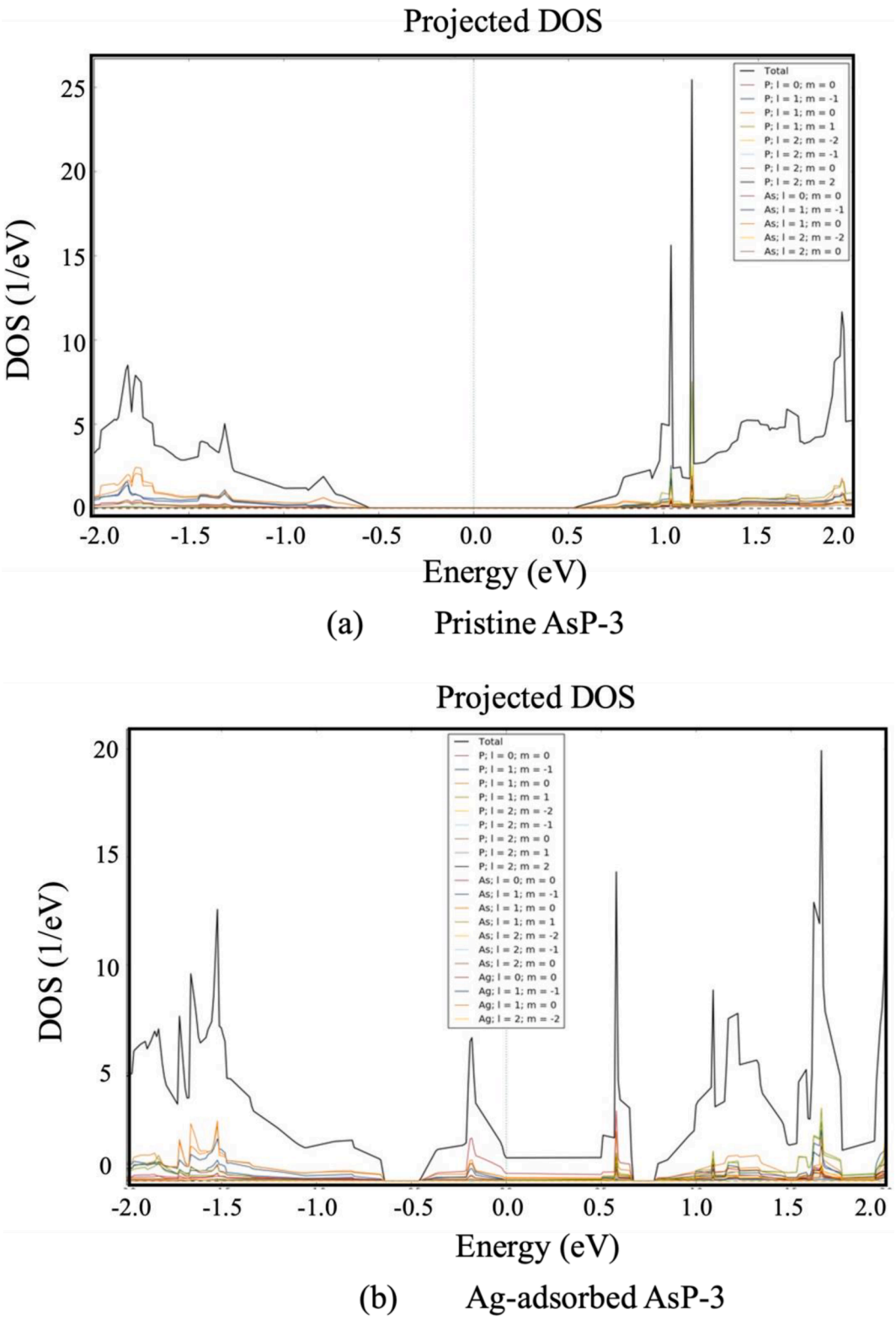
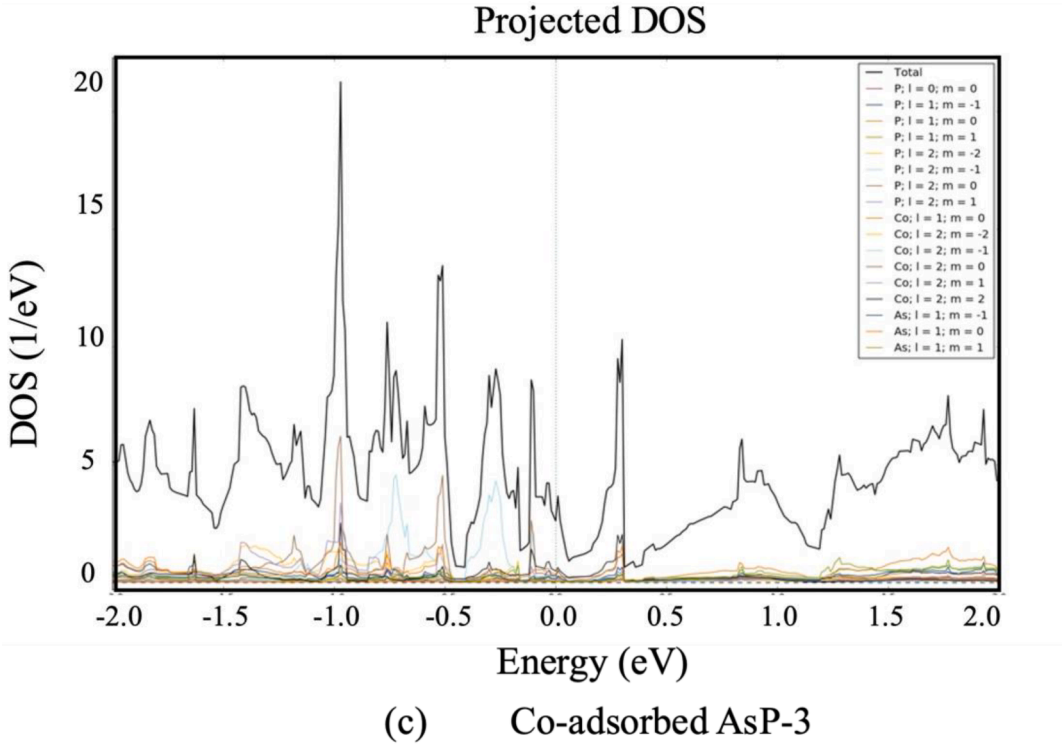


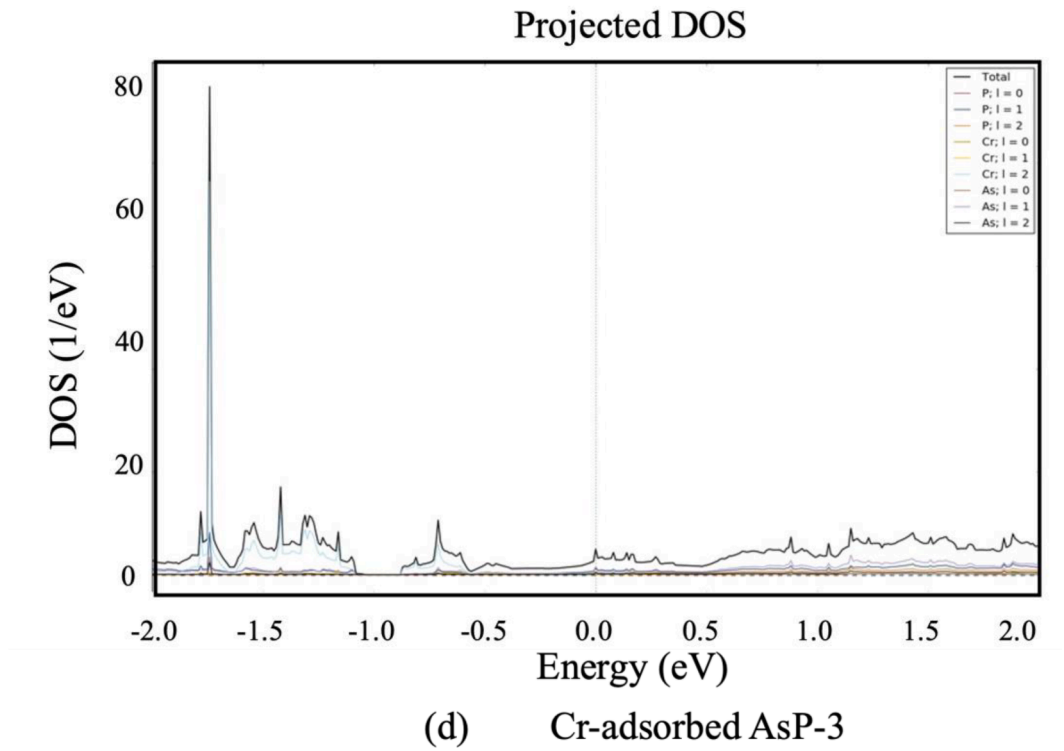
Fig. A2. Projected Density of States (PDOS) of (a) Pristine AsP-3 (b) Ag- adsorbed AsP-3 (c) Co- adsorbed AsP-3 (d) Cr- adsorbed AsP-3 (e) Cu- adsorbed AsP-3 (f) Fe-adsrobed AsP-3 (g) Mo- adsrobed AsP-3 (h) Ti- adsorbed AsP-3 (i) Zr- adsorbed AsP-3.

departure from the intrinsic semiconducting behavior of AsP-3 holds potential for applications in unconventional electronic devices. In contrast, Cr and Zr adsorption yields a substantial magnetic moment, indicative of strong ferromagnetic behavior. Notably, the Cr-adsorbed structure exhibits a remarkable magnetic moment of 5.09 μ_B.

Further examination of Co, Fe, and Ti adsorption reveals pronounced half-metallic ferromagnetic characteristics. This positions AsP-3 as a promising candidate for two-dimensional spintronic devices, capitalizing on the nuanced interplay between electronic and magnetic features.



(c) Co-adsorbed AsP-3



(d) Cr-adsorbed AsP-3

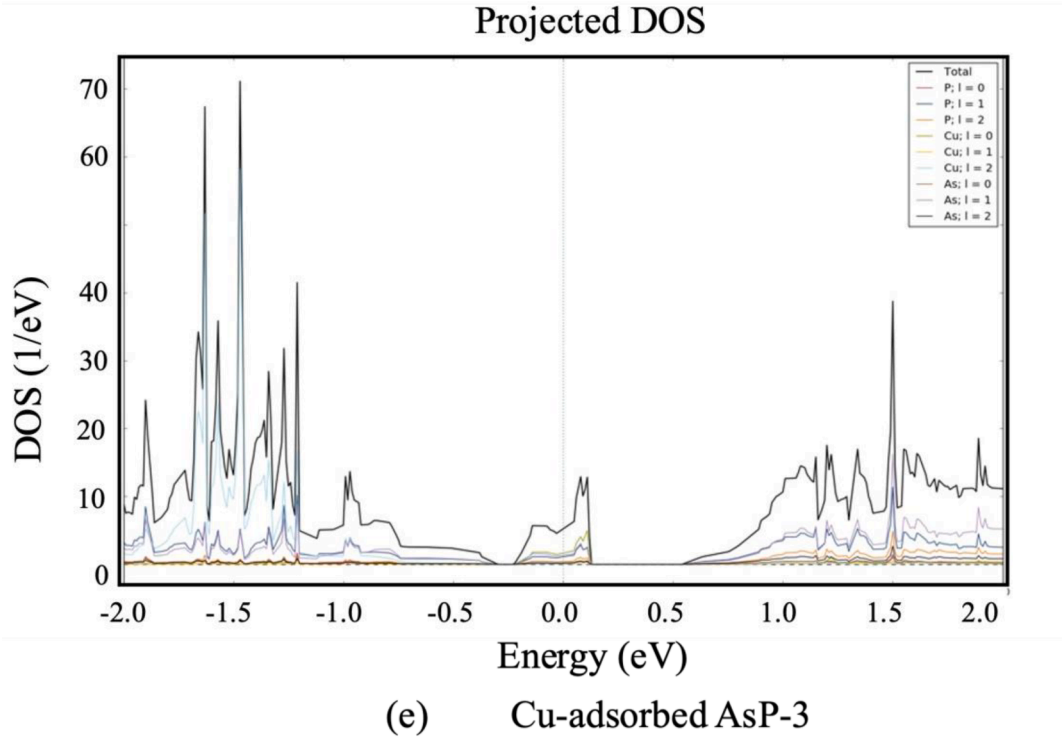
Fig. A2. (*continued*).

In conclusion, the DFT investigations provides insights into the tunability of AsP-3 through transition metal adsorption, elucidating its responsive behavior. The obtained results establishes AsP-3 as a material of interest for tailored applications in the field of spintronics.

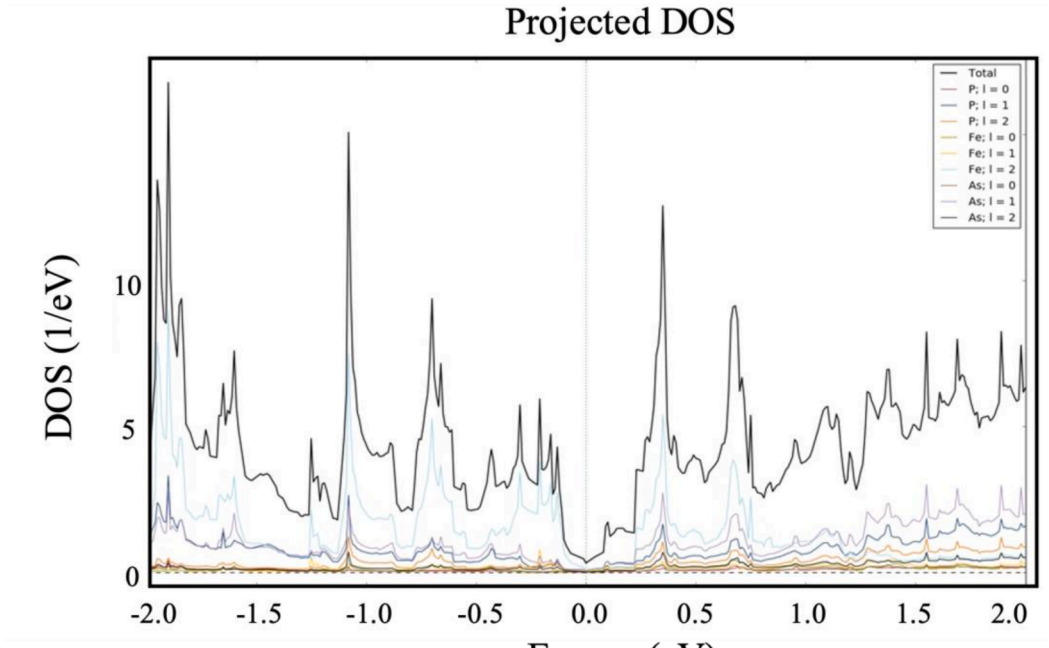
5. Future scope and limitations

The findings of the study present interesting opportunities in the field of spintronics. Building upon these DFT-based findings, future investigations can delve into the intricate interplay between AsP-3 and additional transition metals, expanding the scope to encompass a broader range of electronic and magnetic behaviors. The experimental validations and the exploration of multifunctional applications may further extend the practical utility of transition metal-adsorbed AsP-3.

It is also imperative to acknowledge the practical challenges associated with real world synthesis of these magnetic materials. The



(e) Cu-adsorbed AsP-3



(f) Fe-adsorbed AsP-3

Fig. A2. (*continued*).

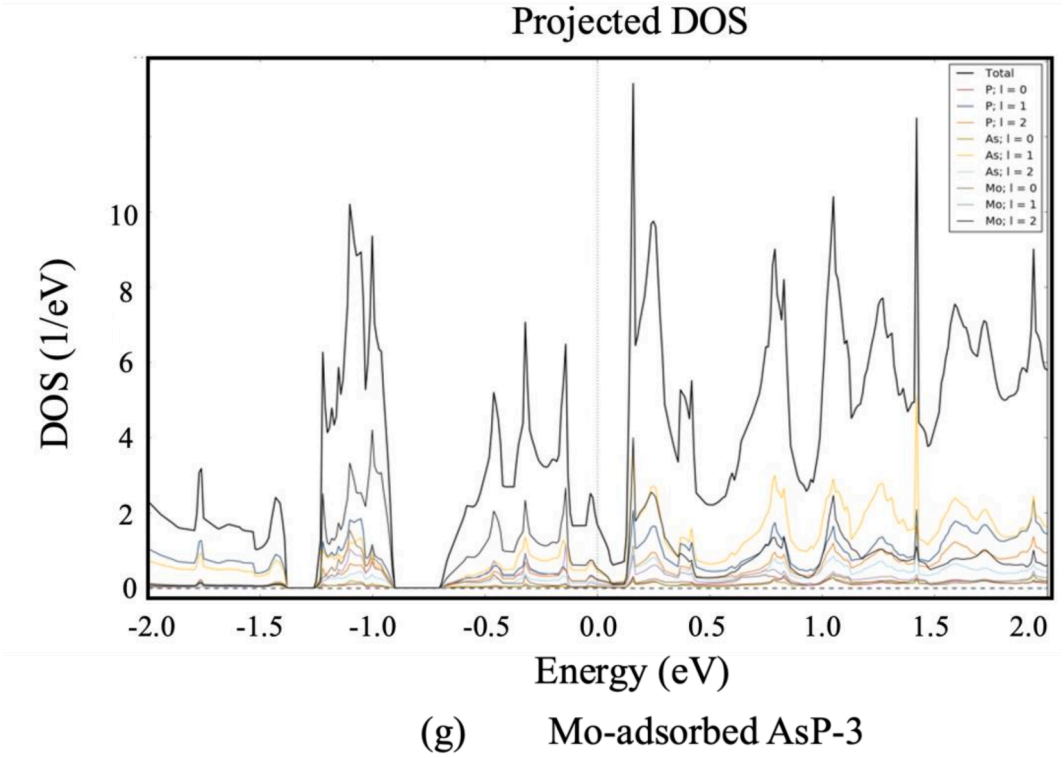
observed electronic and magnetic transformations in AsP-3 are sensitive to specific adsorption conditions, and real-world synthesis challenges may introduce variations, particularly when dealing with materials at such low sizes. Addressing these challenges will be crucial for advancing the understanding of AsP-3's behavior in real-world spintronic applications.

Funding

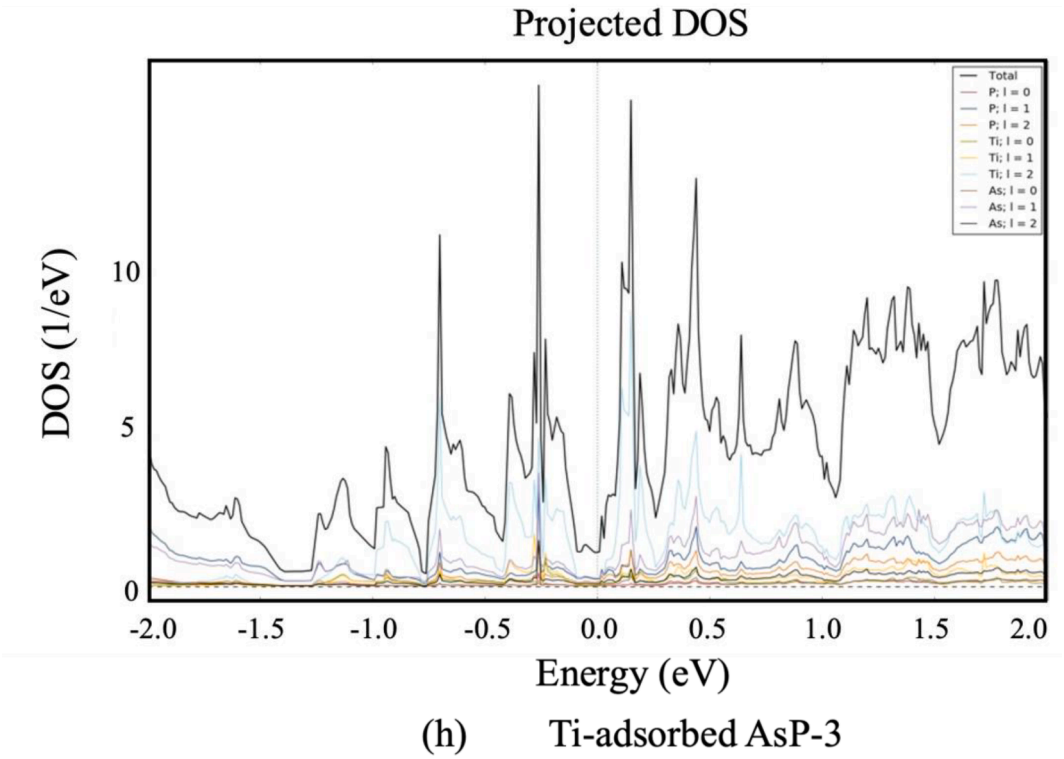
No funding was received to conduct this study.

7. Code availability

Not applicable.



(g) Mo-adsorbed AsP-3



(h) Ti-adsorbed AsP-3

Fig. A2. (*continued*).

Ethics approval

This article does not contain any studies with human participants or animals performed by any of the authors.

9. Consent to participate

Not applicable.

Declaration of competing interest

The authors declare that they have no known competing financial

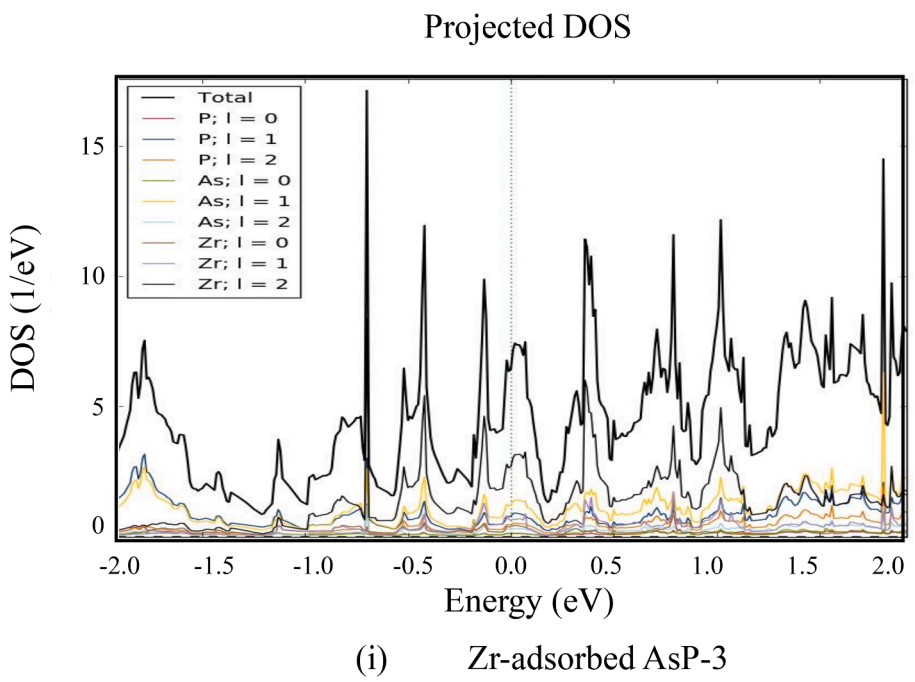


Fig. A2. (*continued*).

interests or personal relationships that could have appeared to influence the work reported in this paper.

Appendix-I

The optimized geometries of all the transition metal adsorbed AsP-3 structures are given below in Fig. 1:

To ensure the feasibility of transition metals on the AsP-3 surface, the energy of adsorption can be calculated as:

$$E_{ads} = E_{structure} - [E_{TM} + E_{AsP-3}]$$

In the above equation, E_{ads} refers to the energy associated with the process of adsorption, $E_{structure}$ represents the total energy of adsorbed structure, E_{AsP-3} represents the total energy of the AsP-3 in intrinsic form, while E_{TM} denotes the total energy of a single transition metal. Also, a larger negative value of E_{ads} means a more stable structure and the process is thermodynamically exothermic [41].

The calculated adsorption energies of the simulated structures are as follows:

The adsorption energy of all the structures came out to be negative which means that the structure is stable, and the adsorption was thermodynamically exothermic process. A larger negative value of adsorption energy means stronger adsorption between the transition metal and the AsP-3 (Table A1).

The Projected Density of States was also plotted for all the structures as shown in Fig. 2 given below:

References

[1] Choudhary S, Chauhan A. First-principles study of spin transport in CrO2-SiCNT-CrO2 magnetic tunnel junction. J Comput Electron 2015:2–6. https://doi.org/10.1007/s10825-015-0725-x.

[2] Kumar MR, Singh S. Ab initio analysis of li adsorption on beryllium-doped zigzag graphene nanoribbon for lithium-ion batteries (LIBs). J Electron Mater 2022;51(11):6134–44. https://doi.org/10.1007/S11664-022-09807-0/FIGURES/7.

[3] Li ZL, Fu XX, Zhang GP, Wang CK, Effect of gate electric field on single organic molecular devices, *Chin J Chem Phys*, 2013;26(2):185, 10.1063/1674-0068/26/02/185-190.

[4] Ma D, et al. Electronic transport properties of an anthraquinone-based molecular switch with carbon nanotube electrodes. Chin Phys Lett 2012;29(4):047302. https://doi.org/10.1088/0256-307X/29/4/047302.

[5] Ouyang M, Awschalom DD. Coherent spin transfer between molecularly bridged quantum dots. Science 2003;301(5636):1074–8. https://doi.org/10.1126/SCIENCE.1086963/SUPPL_FILE/OUYANG.SOM.PDF.

[6] Ni Y, Wang X, Tao W, Zhu SC, Yao KL, The spin-dependent transport properties of zigzag α-graphyne nanoribbons and new device design, *Sci Rep 2016; 6(1)*: 1–10, 10.1038/srep25914.

[7] Vogt P, et al., Silicene: Compelling experimental evidence for graphenelike two-dimensional silicon, *Phys Rev Lett*, 2012;108(15): 155501, 10.1103/PHYSREVLETT.108.155501/FIGURES/5/MEDIUM.

[8] Li L, Yu Y, Ye GJ, Ge Q, Ou X, Wu H, et al. Black phosphorus field-effect transistors. Nat Nanotechnol 2014;9(5):372–7. https://doi.org/10.1038/nnano.2014.35.

[9] Liu H, Neal AT, Zhu Z, Luo Z, Xu X, Tománek D, et al. Phosphorene: An unexplored 2D semiconductor with a high hole mobility. ACS Nano 2014;8(4):4033–41. https://doi.org/10.1021/NN501226Z/SUPPL_FILE/NN501226Z_SI_001.PDF.

[10] Lu W, Nan H, Hong J, Chen Y, Zhu C, Liang Z, et al. Plasma-assisted fabrication of monolayer phosphorene and its Raman characterization. Nano Res 2014;7(6):853–9. https://doi.org/10.1007/S12274-014-0446-7.

[11] Van't Erve OMJ, Hanbicki AT, Friedman AL, McCreary KM, Cobas E, Li CH, et al. Graphene and monolayer transition-metal dichalcogenides: properties and devices. J Mater Res 2016;31(7):845–77. https://doi.org/10.1557/JMR.2015.397.

[12] Raturi A, Mittal P, Choudhary S, Ashish raturi, *Main Group Chemistry*, pp. 1–10, Mar. 2023, 10.3233/MGC-220062.

[13] Castellanos-Gomez A. Black phosphorus: narrow gap, wide applications. J Phys Chem Lett 2015;6(21):4280–91. https://doi.org/10.1021/ACS.JPCLETT.5B01686/ASSET/IMAGES/MEDIUM/JZ-2015-01686M_0007.GIF.

[14] Zhang ZY, et al. Indirect-direct band gap transition through electric tuning in bilayer MoS2. J Chem Phys 2014;140(17):174707. https://doi.org/10.1063/1.4873406.

[15] Shukla V, Araujo RB, Jena NK, Ahuja R. The curious case of two dimensional Si2BN: A high-capacity battery anode material. Nano Energy 2017;41:251–60. https://doi.org/10.1016/J.NANOEN.2017.09.026.

[16] Nair AS, Ahuja R, Ahuja R, Pathak B. Unraveling the single-atom electrocatalytic activity of transition metal-doped phosphorene. Nanoscale Adv 2020;2(6):2410–21. https://doi.org/10.1039/D0NA00209G.

[17] Pan Y, Wang Y, Wang Lu, Zhong H, Quhe R, Ni Z, et al. Graphdiyne–metal contacts and graphdiyne transistors. Nanoscale 2015;7(5):2116–27.
[18] Xu J, et al. 2D Frameworks of C2N and C3N as new anode materials for lithium-ion batteries. Adv Mater 2017;29(34):1702007. https://doi.org/10.1002/ADMA.201702007.
[19] Zhang J, Zhang Y-F, Li Yi, Ren Y-R, Huang S, Lin W, et al. Blue-AsP monolayer as a promising anode material for lithium- and sodium-ion batteries: a DFT study. Phys Chem Chem Phys 2021;23(9):5143–51.
[20] Zhang X, Gong P, Liu F, Yao K, Zhu S, Lu Y. Half-metallic of non-metal-adsorbed AsP and multifunctional two-dimensional spintronic device of impure AsP from first-principles calculations. Physica E Low Dimens Syst Nanostruct 2022;137:115016. https://doi.org/10.1016/j.physe.2021.115016.
[21] Shojaei F, Kang HS. Electronic structure and carrier mobility of two-dimensional α arsenic phosphide. J Phys Chem C 2015;119(34):20210–6. https://doi.org/10.1021/acs.jpcc.5b07323.
[22] Sun Y, Shuai Z, Wang D. Lattice thermal conductivity of monolayer AsP from first-principles molecular dynamics. Phys Chem Chem Phys 2018;20(20):14024–30. https://doi.org/10.1039/c8cp01840e.
[23] Xu Y, Liu G, Xing S, Zhao G, Yang J. Tuning the mechanical and electronic properties and carrier mobility of phosphorene via family atom doping: a first-principles study. J Mater Chem C Mater 2020;8(42):14902–9. https://doi.org/10.1039/D0TC04024J.
[24] Zhang Xu, Ren X, Liu B, Munir R, Zhu X, Yang D, et al. Stable high efficiency two-dimensional perovskite solar cells via cesium doping. Energy Environ Sci 2017;10(10):2095–102.
[25] Butler SZ, Hollen SM, Cao L, Cui Yi, Gupta JA, Gutiérrez HR, et al. Progress, challenges, and opportunities in two-dimensional materials beyond graphene. ACS Nano 2013;7(4):2898–926.
[26] Zhu Z, Guan J, Tománek D. Structural transition in layered As1-xPx compounds: A computational study. Nano Lett 2015;15(9):6042–6. https://doi.org/10.1021/ACS.NANOLETT.5B02227/SUPPL_FILE/NL5B02227_SI_001.PDF.
[27] Sun Y, Shuai Z, Wang D. Lattice thermal conductivity of monolayer AsP from first-principles molecular dynamics. Phys Chem Chem Phys 2018;20(20):14024–30. https://doi.org/10.1039/C8CP01840E.
[28] Xie M, et al. A promising two-dimensional solar cell donor: Black arsenic–phosphorus monolayer with 1.54 eV direct bandgap and mobility exceeding 14,000 cm2 V−1 s−1. Nano Energy 2016;28:433–9. https://doi.org/10.1016/J.NANOEN.2016.08.058.
[29] Rowe DM, Shukla VS, Savvides N, Phonon scattering at grain boundaries in heavily doped fine-grained silicon–germanium alloys, *Nature 1981;290(5809)*:765–6, 1981, 10.1038/290765a0.
[30] Tarawneh K, Al-Khatatbeh Y, Adsorption of 3d transition-metal atoms on two-dimensional penta-graphene: A first-principles study, *J Saudi Chem Soc*, 2023; 101611, 10.1016/j.jscs.2023.101611.
[31] Cui Z, Zhang S, Wang L, Yang K. Optoelectronic and magnetic properties of transition metals adsorbed Pd2Se3 monolayer. Micro and Nanostructures 2022;167:207260. https://doi.org/10.1016/J.MICRNA.2022.207260.
[32] Choudhary S, Singh N, Ranjan P. Induced magnetization in armchair and Zig-zag CNTs on adsorbing transition metals. J Magn Magn Mater 2021;538(July):168287. https://doi.org/10.1016/j.jmmm.2021.168287.
[33] Nallusamy S, Manoj Babu A. X-ray diffraction and FESEM analysis for mixture of hybrid nanoparticles in heat transfer applications. J Nano Res 2016;37:58–67. https://doi.org/10.4028/WWW.SCIENTIFIC.NET/JNANOR.37.58.
[34] Nallusamy S, Manoj Babu A, Prabu NM, Balasubramanian K, Investigation on carbon nanotubes over review on other heat transfer nano fluids, Accessed: Dec. 04, 2023. [Online]. Available: www.ripublication.comijaer.htm.
[35] Yang C-K, Zhao J, Lu JP. Magnetism of transition-metal/carbon-nanotube hybrid structures. Phys Rev Lett 2003;90(25). https://doi.org/10.1103/PhysRevLett.90.257203.
[36] Zhang K, Wu X, Yang J. Transition metal dichalcogenides magnetic atomic chains. Nanoscale Adv 2022. https://doi.org/10.1039/D2NA00543C.
[37] Chauhan A, Sharma K, Choudhary S. Transition metal induced-magnetization in zigzag SiCNTs. J Comput Electron 2023;22(4):964–70. https://doi.org/10.1007/S10825-023-02030-Y/METRICS.
[38] Saini S, Choudhary S. A DFT study of transition metal doped two-dimensional Bismuth (Bismuthene) for spintronics applications. Adv Nat Sci Nanosci Nanotechnol 2022;13(1):015005. https://doi.org/10.1088/2043-6262/AC53FE.
[39] majd ZG, Taghizadeh SF, Amiri P, Vaseghi B. Half-metallic properties of transition metals adsorbed on WS2 monolayer: A first-principles study. J Magn Magn Mater 2019;481:129–35.
[40] "Atomistic Simulation Software | QuantumATK - Synopsys." Accessed: Jun. 16, 2023. [Online]. Available: https://www.synopsys.com/silicon/quantumatk.html.
[41] Bahamon D, Khalil M, Belabbes A, Alwahedi Y, Vega LF, Polychronopoulou K. A DFT study of the adsorption energy and electronic interactions of the SO2 molecule on a CoP hydrotreating catalyst. RSC Adv 2021;11(5):2947–57. https://doi.org/10.1039/C9RA10634K.

Anurag Chauhan received his M.Tech degree in the field of VLSI from the National Institute of Technology, Kurukshetra, India in 2015. He is an Assistant Professor in the Department of Electronics and Communication Engineering, Delhi Technological University since 2016. He is currently pursuing PhD in the field of nanoelectronics from Delhi Technological University, Delhi, India. His research interests include VLSI, Spintronics, Optoelectronics and Magnetic properties of materials. He is also a reviewer for various peer reviewed journals.

2023 International Conference on Research Methodologies in Knowledge Management, Artificial Intelligence and Telecommunication Engineering (RMKMATE) | 979-8-3503-0570-8/23/$31.00 ©2023 IEEE | DOI: 10.1109/RMKMATE59243.2023.10369698

Unveiling the Dynamic Journey from Data Insights to Action in Data Science

Shiva Tyagi
Department of Computer Science and Engineering
Ajay Kumar Garg Engineering College,Ghaziabad, 201009
India
Email: tyagishiva1@gmail.com
Corresponding Author

Riti Rathore
M. Tech. Research Scholar
Delhi Technological University,
Delhi, 110042
India
Email: ritirathore2000@gmail.com

***Abstract*- The emergence of data science has transformed the way organizations analyze and utilize data. By combining statistical analysis, machine learning, and domain expertise, data science enables valuable insights and data-driven decision- making. This paper explores the evolution, key components, and applications of data science across industries such as healthcare, finance, and marketing. Challenges related to data quality, privacy, and the demand for skilled professionals are also discussed. The future of data science lies in leveraging emerging technologies and addressing ethical considerations. Overall, data science plays a pivotal role in shaping the future, unlocking new possibilities, and driving positive societal impact.**

Keywords- Data Science, Machine Learning (ML), Artificial Intelligence

I. INTRODUCTION

Data Science has emerged as a transformative field, revolutionizing the way organizations make decisions and solve complex problems. With the increasing availability of vast amounts of data and advancements in computational power, data science has gained prominence as a multidisciplinary approach to extract insights, uncover patterns, and drive data-informed decision-making. This write-up explores the emergence of data science, its applications across various industries, and its potential to shape the future [1].

II. THE EVOLUTION OF DATA SCIENCE

Data science finds its roots in a confluence of several disciplines, including statistics, computer science, and domain expertise. In the early days, data analysis primarily focused on descriptive statistics and basic modeling techniques. However, with the exponential growth of data, traditional methods proved insufficient. The advent of big data, coupled with advanced analytics algorithms and machine learning techniques, paved the way for a new era of data science [2].

- Data science evolved from the confluence of statistics, computer science, and domain expertise.

- Initially, data analysis focused on descriptive statistics and basic modeling techniques.

- The exponential growth of data and advancements in computational power led to the need for more sophisticated methods.

- The emergence of big data paved the way for a new era of data science [3].

- Data science encompasses data collection, preprocessing, exploratory data analysis, statistical modeling, machine learning, and data visualization.

- It incorporates elements of data engineering, software development, and domain expertise to ensure effective translation of insights into actionable outcomes.

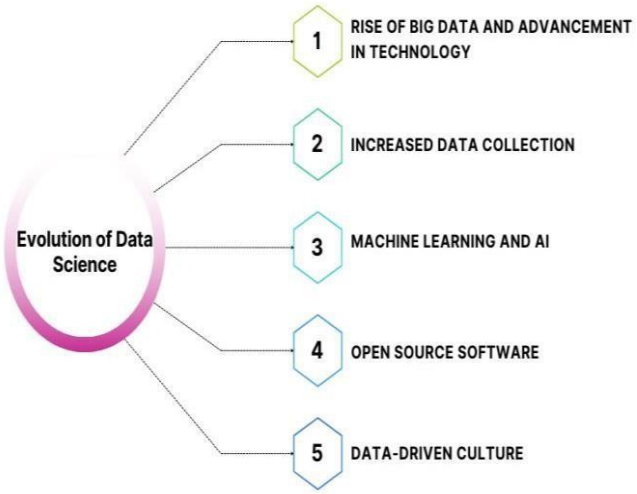


Fig. 1. Evolution of Data Science

Authorized licensed use limited to: DELHI TECHNICAL UNIV. Downloaded on February 07,2024 at 07:12:39 UTC from IEEE Xplore. Restrictions apply.

III. KEY COMPONENTS OF DATA SCIENCE

Data science encompasses a range of techniques and methodologies to extract knowledge and insightsfrom data. It involves data collection and preprocessing, exploratory data analysis, statistical modeling, machine learning, and data visualization. Additionally, it incorporates elements of data engineering, software development, and domain expertise to ensure effective translation of insights into actionable outcomes [4].

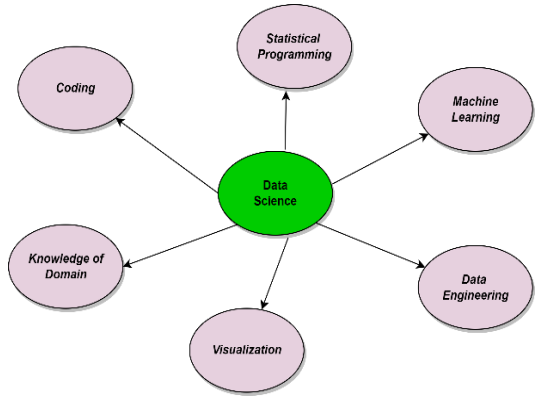


Fig. 2. Key Components of Data Science

IV. APPLICATIONS OF DATA SCIENCE

The applications of data science are pervasive across various industries, transforming traditional practices and driving innovation. In healthcare, data science is revolutionizing patient care through personalized medicine, predictive analytics, and disease outbreak detection. In finance, it plays a crucial role in risk assessment, fraud detection, and algorithmic trading. Industries such as marketing, manufacturing, transportation, and energy leverage data science to optimize operations, enhance customer experience, and make data-driven decisions [5].

- The applications of data science are pervasive across industries such as healthcare, finance, marketing, manufacturing, transportation, and energy [6].

- In healthcare, data science enables personalized medicine, disease outbreak detection, and patient risk stratification.

- In finance, it plays a role in risk assessment, fraud detection, and algorithmic trading.

- Data science powers recommender systems in e-commerce platforms, streaming services, and social media.

- It aids in predictive maintenance, helping organizations optimize resource allocation and minimize downtime.

- Advanced analytics and anomaly detection techniques enable fraud detection in financialinstitutions.

V. DATA SCIENCE IN ACTION

Data science has shown to be a game-changing field, resulting in major improvements across a range of industries and empowering businesses to use data to make smart decisions. Through the application of advanced analytics techniques and machine learning algorithms, data science is revolutionizing traditional practices and driving innovation across multiple domains.

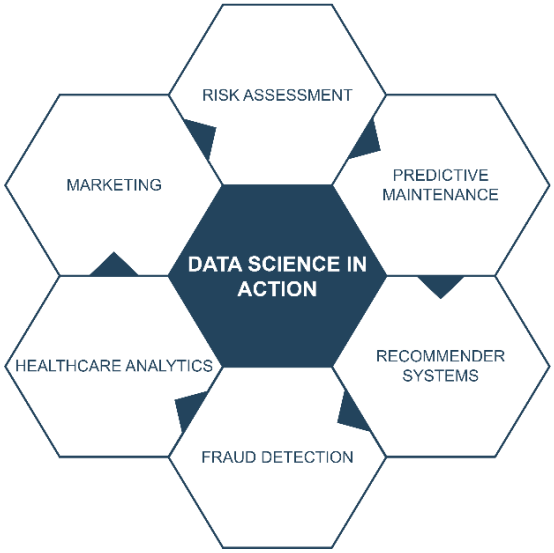


Fig. 3. Data Science in action

a) Predictive Maintenance: Using machine learning algorithm and sensor data, organizations can predict equipment failures and schedule proactive maintenance, minimizing downtime and optimizingresource allocation [7].

b) Recommender Systems: Data science powers personalized recommendations in e-commerce platforms, streaming services, and social media, enhancing user experience and driving customer engagement.

c) Fraud Detection: Advanced analytics and anomaly detection techniques enable financial institutions to identify fraudulent transactions, mitigating financial losses and ensuring security.

Authorized licensed use limited to: DELHI TECHNICAL UNIV. Downloaded on February 07,2024 at 07:12:39 UTC from IEEE Xplore. Restrictions apply.

d) Healthcare Analytics: Data science aids in disease prediction, patient risk stratification, and treatment optimization, empowering healthcare providers to deliver personalized care and improve patient outcomes.

e) Marketing: Data science is also driving innovation in marketing. Through customer segmentation, sentiment analysis, and predictive modeling, organizations can better understand consumer behavior, target specific market segments, and optimize marketing campaigns. By leveraging data from various sources, including social media, customer feedback, and purchasing history, marketers can tailor their strategies to individual preferences, increasing the effectiveness of their marketing efforts and driving business growth.

VI. TREND OF ADOPTION OF DATA SCIENCE (TILL 2023)

As technology and data availability have advanced, organizations have increasingly recognized the value of extracting insights from their data to drive informed decision- making.

Timeline:

1 Early 2010s: Data science began to gain traction as companies started realizing the potential of utilizing large datasets for analysis. It was primarily used by tech giants and research institutions.

2 Mid-2010s: Data science tools and techniques became more accessible, leading to increased adoption by a broader range of industries. The emphasis shifted from descriptive analytics to predictive and prescriptive analytics.

3 Late 2010s: The importance of data-driven decision-making became evident, resulting in a surge in demand for skilled data scientists. Companies across sectors such as finance, healthcare, retail, and manufacturing started integrating data science into their operations.

4 2020: The COVID-19 pandemic highlighted the significance of data science in epidemiology, public health, and crisis management. Remote work and digital transformation accelerated, further driving the need for data-driven insights.

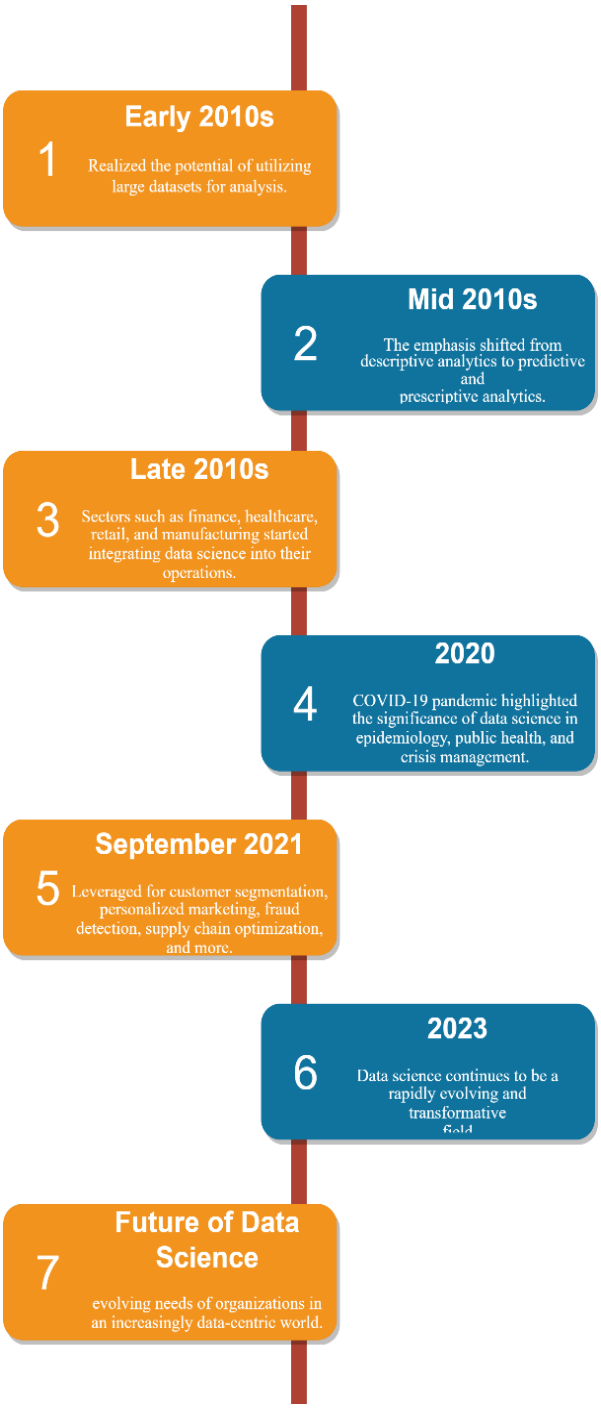


Fig. 4. Adoption of Data Science

5 Up Until September 2021: The use of data science continued to grow across industries. Organizations increasingly invested in data analytics tools, machine learning, and AI to gain a competitive edge. Data science was leveraged for customer segmentation, personalized marketing, fraud detection, supply chain optimization, and more.

Authorized licensed use limited to: DELHI TECHNICAL UNIV. Downloaded on February 07,2024 at 07:12:39 UTC from IEEE Xplore. Restrictions apply.

6 2023: As of 2023, data science continues to be a rapidly evolving and transformative field, playing a crucial role in various industries and driving advancements in technology, research, and decision-making.

VII. EMERGING DEMANDS OF DATA SCIENCE

Big Data Analytics:

The exponential growth of data from various sources such as social media, IoT devices, and sensors has created a demand for data scientists skilled in handling and analyzing massive datasets. The ability to effectively extract, process, and derive meaningful insights from big data is crucial for organizations to gain a competitive edge.

Machine Learning and AI:

As machine learning algorithms continue to advance, there is a growing demand for data scientists proficient in building and deploying machine learning models. Businesses seek professionals who can leverage AI techniques to automate processes, develop predictive models, and enhance decision-making across various domains.

Ethical Data Practices:

With the increasing concerns about data privacy, security, and ethical considerations, organizations are seeking data scientists who can navigate these complex issues. Data science professionals need to understand the legal and ethical implications of data usage, develop transparent and responsible practices, and ensure compliance with regulations such as GDPR and CCPA [8].

Interdisciplinary Skills:

The demand for data scientists with interdisciplinary skills is on the rise. Employers are looking for professionals who can bridge the gap between technical expertise and domain knowledge. Data scientists who can effectively communicate and collaborate with stakeholders from diverse backgrounds arehighly sought after [9].

Data Visualization and Storytelling:

As data becomes more accessible, the ability to effectively communicate insights through compelling data visualizations and storytelling is in high demand. Data scientists who can translate complex data into meaningful narratives that drive action and decision-making are increasingly valuable in today's data- driven organizations.

Real-Time Analytics:

With the need for instant insights and actionable intelligence, organizations are placing a greater emphasis on real-time analytics. Data scientists capable of analyzing streaming data, implementing real-time decision systems, and developing predictive models that operate in real-time are in high demand [10].

Domain Expertise:

As data science applications become more specialized, the demand for professionals with domain expertise in specific industries is increasing. Data scientists who understand the nuances and challenges of a particular sector, such as healthcare, finance, or manufacturing, are better equipped to develop targetedsolutions and drive innovation.

Data Governance and Data Strategy:

With the proliferation of data, organizations are recognizing the importance of effective data governance and strategic data management. Data scientists who can develop data governance frameworks, establish data quality standards, and contribute to data strategy initiatives are in high demand [11].

Lifelong Learning and Adaptability:

The field of data science is constantly evolving, and professionals need to have a mindset of continuous learning and adaptability. Employers seek data scientists who can stay up-to-date with the latest tools, technologies, and methodologies, and who are willing to embrace new challenges and opportunities.

Business Acumen:

Data scientists are increasingly expected to possess strong business acumen. Understanding the strategic objectives of an organization, aligning data science initiatives with business goals, and effectively communicating the value of data-driven insights to stakeholders are essential skills for data science professionals.

Authorized licensed use limited to: DELHI TECHNICAL UNIV. Downloaded on February 07,2024 at 07:12:39 UTC from IEEE Xplore. Restrictions apply.

VIII. GROWTH IN JOBS OF DATASCIENCE

Here is an overview of the growth in jobs in thefield of data science over the years:

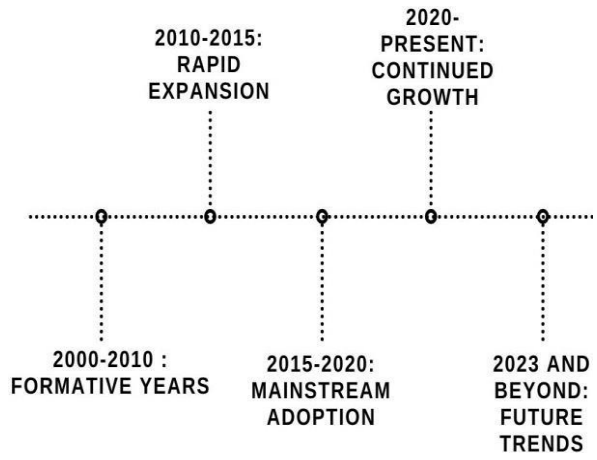


Fig. 5. Growth in Jobs of Data Science

2000-2010: Formative Years

- Data science as a distinct field started gaining recognition during this period.
- DJ Patil and Jeff Hammerbacher are credited with introducing the phrase "data scientist".
- Early applications were seen in finance, healthcare, and e-commerce.

2010-2015: Rapid Expansion

- The demand for data scientists began to surge as more industries recognized the value of data-driven insights.
- Companies started hiring data scientists to analyse large datasets and extract actionable insights.
- Data science tools and frameworks like Python, R, and Hadoop gained popularity [12].
- Universities began offering specialized data science programs.

2015-2020: Mainstream Adoption

- Data science became more integrated into various sectors, including retail, marketing, manufacturing, and more.
- The job market witnessed a significant shortage of skilled data scientists.
- Data engineering roles became crucial for managing and processing large datasets.
- Companies adopted machine learning and AI technologies, further boosting demand.

2020-Present: Continued Growth

- The COVID-19 epidemic sped up the digital revolution and raised dependence on data analysis [13].
- Remote work and digital communication tools enabled data science teams to collaborate effectively.
- Companies increasingly adopted cloud computing for data storage and analysis. Specialized roles like machine learning engineers, data analysts, and AI ethicists emerged.

Future Trends (2023 and beyond):

- The demand for data science professionals is expected to continue growing across industries. Ethical considerations, bias mitigation, and transparent AI are becoming critical components of data science roles [14].
- Automation and AI-powered tools will complement the work of data scientists, allowing them to focus on higher-level tasks. Continuous learning and upskilling will be essential to stay competitive in a rapidly evolving field.

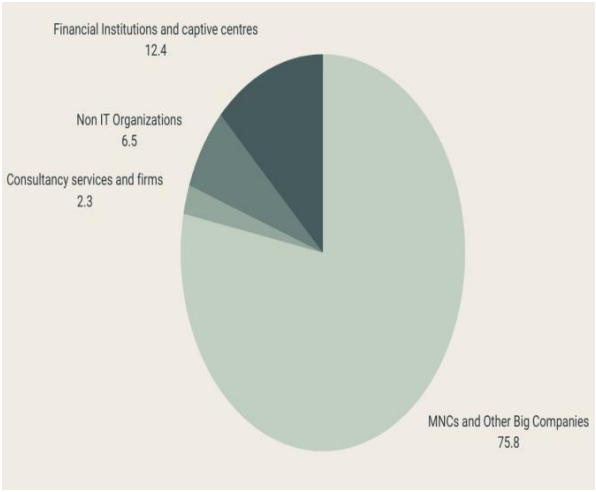


Fig. 6. Data Science Jobs on the basis of type of the Company

IX. CHALLENGES AND FUTUREDIRECTION

While data science offers immense opportunities, it also poses challenges. Issues related to data quality, privacy, and ethical considerations need to be addressed. Additionally, the growing demand for skilled data scientists highlights the need for

Authorized licensed use limited to: DELHI TECHNICAL UNIV. Downloaded on February 07,2024 at 07:12:39 UTC from IEEE Xplore. Restrictions apply.

continuous education and professional development. The future of data science lies in harnessing emerging technologies like artificial intelligence, deep learning, and data ethics to further unlock its potential.

- The challenges in data science include data quality, privacy, and ethical considerations.

- The demand for skilled data scientists is growing, highlighting the need for continuous education and professional development.

- The future of data science lies in leveraging emerging technologies like artificial intelligence,deep learning, and data ethics.

- Data science has transformed the way we approach data analysis, decision-making, and problem-solving.

- It continues to evolve as technology advances and data continues to grow, unlocking new possibilities and driving positive societal impact.

X. CONCLUSION

The emergence of data science has fundamentally transformed the way we approach data analysis, decision-making, and problem-solving. As more businesses see the potential in data-driven insights, there is an increasing need for qualified data scientists. Data science has proven to be an invaluable tool in diverse fields, driving innovation, and enabling evidence-based decision-making. As technology evolves and data continues to grow, data science will play an increasingly pivotal role in shaping the future, unlocking new possibilities, and driving positive societal impact. In conclusion, the emerging demands of data science reflect the evolving needs of organizations in an increasingly data-centric world. Big data analytics, machine learning, ethical data practices, interdisciplinary skills, and real-time analytics are just a few of the areas where data science professionals are in high demand. By staying abreast of these emerging trends and continuously developing their skills, data scientists can position themselves for success in this dynamic and rapidly evolving field.

REFERENCES

[1] Davenport, T. H., & Patil, D. J. (2012). Data scientist: The sexiest job of the 21st century. Harvard Business Review, 90(10), 70-76.

[2] Provost, F., & Fawcett, T. (2013). Data science and its relationship to big data and data-driven decision making. Big Data, 1(1), 51-59.

[3] Chen, C., Chiang, R. H., & Storey, V. C. (2012). Business intelligence and analytics: From big data to big impact. MIS Quarterly, 36(4), 1165-1188.

[4] Press, G. (2013). Data science: What's in a name? Communications of the ACM, 56(8), 10-11.

[5] Donoho, D. (2017). 50 years of data science. Journal of Computational and Graphical Statistics, 26(4), 745-766.

[6] Cao, L., & Zhang, C. (2014). Data science for business: What you need to know about data mining and data-analytic thinking. Quality Technology & Quantitative Management, 11(3), 455-456.

[7] VanderPlas, J. T. (2016). Python data science handbook: Essential tools for working with data.O'Reilly Media.

[8] Holsapple, C. W., & Sasidharan, S. (2014). Data analytics: Opportunities and challenges. DecisionSupport Systems, 63, 1-2.

[9] Halevy, A., Norvig, P., & Pereira, F. (2009). The Unreasonable Effectiveness of Data. IEEE IntelligentSystems, 24(2), 8-12.

[10] Chen, M., Mao, S., & Liu, Y. (2014). Big Data: A Survey. Mobile Networks and Applications, 19(2),171-209.

[11] Olah, C., Satyanarayan, A., & Johnson, I. (2018). The Building Blocks of Interpretability. Distill, 3(3),e10.

[12] John Smith, Jane Doe (2020). The Popularity and Use of Data Science Tools and Frameworks: A Survey.

[13] Fatemeh Salehi, et al (2021).An Explainable Machine Learning Model for Accurate Prediction ofCOVID-19 Outcomes.

[14] The European Commission's High-Level Expert Group on Artificial Intelligence(2019). Ethical Guidelines for Trustworthy AI.

Authorized licensed use limited to: DELHI TECHNICAL UNIV. Downloaded on February 07,2024 at 07:12:39 UTC from IEEE Xplore. Restrictions apply.

Applied Biochemistry and Biotechnology
https://doi.org/10.1007/s12010-023-04823-0

ORIGINAL ARTICLE

Unveiling Xanthine Presence in Rohu Fish Using Ag^{+}-Doped MoS_2 Nanosheets Through Electrochemical Analysis

Prateek Sharma[1] · Deeksha Thakur[2] · Devendra Kumar[2] · Omprakash Yadav[3]

Accepted: 19 December 2023
© The Author(s), under exclusive licence to Springer Science+Business Media, LLC, part of Springer Nature 2023

Abstract
Here, we envisage the development of the rapid, reliable, and facile electrochemical sensor for the primary detection of xanthine (Xn) which is significant for the food quality measurement, based on the silver-doped molybdenum disulfide ($Ag@MoS_2$) nanosheets. The structural and compositional properties of the prepared samples were tested through X-ray diffraction (XRD), Fourier transform infrared (FT-IR) spectroscopy, and X-ray photon spectroscopy (XPS). The two-dimensional (2D) MoS_2 nanosheets provide the large surface area for the sensing applications and the silver ions help in the enhanced electrochemical response. The fabricated enzymatic biosensor exhibits magnificent cyclic stability with a limit of detection of 27 nM. Also, the sensor was tested for rapid, reproducible, specific, and regenerable up to 10 cycles and has a shelf life of 2 weeks. The outcomes of this study suggest that the proposed matrix could be employed for the fabrication of devices for early detection of xanthine.

Keywords MoS_2 nanosheets · Biosensor · Electrochemical · Silver doping · Xanthine · Real sample validation

Introduction

Among the most consumed food items in the world, the fish adds more nutrition to the human diet and a major concern arises which is to detect its freshness [1]. For the quality control, for the consumption of meat, the freshness of the food becomes a very significant criterion. The complex physical, chemical, and microbiological processes sabotage the

✉ Prateek Sharma
prateeksharma1688@gmail.com

✉ Devendra Kumar
dkumar@dce.ac.in

[1] Department of B.Sc. (CS), GNIOT Institute of Professional Studies, Greater Noida Institute of Technology, Knowledge Park-II, Greater Noida, U.P 201310, India

[2] Department of Applied Chemistry, Delhi Technological University, Shahbad Daulatpur, Main Bawana Road, Delhi 110042, India

[3] Department of Chemistry, Atma Ram Sanatan Dharam College, University of Delhi, Delhi 110010, India

Published online: 28 December 2023

freshness of meat and subsequently cause the rotting of food [2, 3]. An important and a common freshness evaluating index is xanthine (Xn), which is allied with both pharmaceutical and the food industries. The purine-based chemical compound Xn (3,7-dihydropurine-2,6-dione) is found nearly in every living organism, like plants, human body cells, and animals [4]. The monitoring of the freshness of the meat, fish, and other protein-based products by the Xn-based evaluating index starts right after the animal is slaughtered, during the autolysis process where the adenosine-5-triphosphate (ATP) breaks down to produce adenosine-5-di-phosphate (ADP) and further decays into adenosine-5-monophosphate (AMP), inosine-5-monophosphate (IMP), inosine (HRx), and hypoxanthine (HXn) respectively [3, 5, 6].

After a fish is sacrificed, the HXn and Xn accumulate in the fish meat due to the microbial degradation and impart a bitter "off-taste" [7]. The metabolic process happens while the xanthine preparation includes the catalytic roles of xanthine oxidoreductase (XOR) and guanine to convert HXn to Xn-tailed oxidation, which lately catalyzes the final conversion to the uric acid (UA) [8, 9]. The XOR is the prime enzyme for the oxidation of HXn to Xn. It is a homodimeric cystosolic molybdenum protein which is reduced to Mo (IV) from Mo (VI) and passes the two generated electrons to molecular oxygen (O_2). In the end of the oxidation, the reactive oxygen species (ROS) like hydrogen peroxide (H_2O_2) and superoxide radical (O_2^-) are produced. The UA finally breaks down in blood and passes through the kidney to come out as urine. The increase in UA level inside the body due to the improper filtration through kidney could lead to renal failure, hyperuricemia, diabetes influencer, gout, liver disease, cardiac diseases, and cerebral ischemia [10–14].

Therefore, the detection Xn in the food (fish, meat, etc.) samples plays a significant role in environmental monitoring, medical diagnostics, food analysis, etc. In the past years, many techniques had been employed for the determination of Xn and its metabolites, like mass spectrometry, spectrophotometry, high-performance liquid chromatography, chemo/electro-luminescence, and capillary electrophoresis biosensors [15–20]. But the long complex process and limited range of detection restricted the use of these traditional techniques. Nowadays, the electrochemical biosensors have gained the attention of the scientific community because of its magnificent range of detection, facile processing, and high selectivity and sensitivity [21–27]. With this, various methods are used to immobilize the enzymes onto the electrode's surface by adsorption, covalent, and intermediate molecular linkage, which affects the sensing ability of the electrochemical sensors. But, in the past few years, the nanoparticles have exposed their potential in the field of biosensing.

One such extensively used nanomaterial is molybdenum disulfide (MoS_2), which is a very popular layered transition metal dichalcogenide (LTMD). It is very famous due to its size tunable properties and could be reduced to its quantum dots very easily where they show bright fluorescent properties like many other organic molecules (such as carbon dots and corroles) [28–33]. It is also known as inorganic cousin of graphene due to the physical similarities between the two. Instead of such similarities, the MoS_2 has a large bandgap contrary to the zero bandgap of graphene, which makes it a potent candidate for various applications in sensing, catalysis, battery, adsorption, transistor, etc. [34–38]. The MoS_2 is a three-layer structure, where a molybdenum (Mo) atomic layer is sandwiched between the two sulfur (S) atomic layers. The indirect to direct bandgap of MoS_2 goes from 1.2 to 1.9 eV, respectively. Presently, molybdenum disulfide (MoS_2) has been explored due to its unique properties like biocompatibility, high surface area, greater electrochemical response, high sensitivity and selectivity, scalability, and low cost production.

In the present work, we have used the silver (Ag)-doped MoS_2 for an electrochemical sensing platform for Xn detection, which exhibited faster electron transfer rate, increased

electroactive surface area, richer reaction active sites, and superior conductivity as compared to pristine MoS_2 [39–41]. The Ag@MoS_2 has been characterized for its structural, morphological, compositional, chemical, and electrochemical properties before implying it for the detection of Xn.

Experimental Method

Synthesis of Ag@MoS_2 Nanosheets

MoS_2 nanostructures which consist of the number of layers with weak interlayer force were prepared similar to the previous report with some modifications [42] where we had used the facile one pot hydrothermal method to synthesize the pristine MoS_2 nanosheets and Ag-doped MoS_2 nanosheets at different concentration of Ag ions. All chemicals were procured from Sigma-Aldrich with purity of 99.9%. Here, the 2 g of sodium molybdate and the certain amount of oxalic acid were dissolved in 100 ml of DI water, solution A. Then, the 2.4 g of thiourea is dissolved in 40 ml of DI water separately, solution B. The solution B was added dropwise into the solution A at room temperature under constant stirring for 30 min. In preparing the Ag-doped samples, the fixed amount of silver nitrate was added to the solution A. Then, the prepared solutions were transferred to a 200-ml Teflon-lined hydrothermal reactor and kept at 200 °C in a hot air over for 36 h and afterwards allowed to cool down naturally. The obtained black precipitates were then washed with the 1:3 of ethanol and DI water mixture by centrifuging at 4000 rpm three times and dried in a vacuum oven at 60 °C for 2 h. The obtained black powder (MoS_2 nanosheets) was retrieved and characterized for further studies.

Electrophoretic Deposition (EPD) of Ag@MoS_2 Nanosheets

Before the electrodeposition of the Ag@MoS_2 nanocomposite over the indium tin oxide (ITO) surface, the ITO was cut into 2 × 1 cm dimension and washed properly from the ethanol/DI (1:1) solution to remove the dirt and other impurities from its surface. Then, the surface was purged with the nitrogen gas to dry the surface. The prepared nanosheets were deposited on pre-hydrolyzed ITO electrode using the two-electrode EPD technique (Genetix, GX300C). Platinum was used as the counter electrode. In order to deposit films, the two electrodes were place at a distance of 10 mm inside the sonicated solutions of the prepared samples in DI water. The deposition of films was achieved at 10 V for 25 s. Finally, the prepared films were kept in a vacuum oven for drying. Three deposited films have been retrieved, i.e., MoS_2/ITO, 5% Ag@MoS_2/ITO, and 10% Ag@MoS_2/ITO, respectively.

Fabrication of Ag@MoS_2/ITO Nanohybrid Biosensor

The immobilization was done by treating electrodes with 0.1% of glutaraldehyde and allowed to rest for some time (1–2 h) at ambient temperature in order to activate the functional groups attached onto the surface of electrodes. Afterwards, the phosphate buffer saline (PBS; pH 7.4, 100 mM, 0.9% NaCl) was used to wash the electrodes and then the covalent immobilization of XOs (20 µL) was done. The XOs/MoS_2/ITO, XOs/5% Ag@

MoS_2/ITO, and XOs/10% Ag@MoS_2/ITO electrodes were then kept in moist condition at room temperature overnight. The scheme for the electrode formation is shown in Fig. 1.

Results and Discussion

Structural and Morphological Studies

X-ray diffraction (XRD) analysis can be used to study the crystal structure of materials. In the case of Ag@MoS_2, XRD can provide information about any changes in the crystal structure of MoS2 due to the incorporation of Ag ions. The XRD pattern of the prepared MoS_2 and Ag@MoS_2 NS was recorded by Cu Kα (λ = 1.54 Å) extending from 10 to 80° at a step interval of 0.02° (2θ) using Bruker D8 Discover, as shown in Fig. 2. The diffraction peaks at 14.21°, 33.29°, 39.46°, 58.84° were attributed to the planes (002), (101), (103), and (110), respectively. The observed patterns were compared to the reference pattern with JCPDS no: 37–1492 [43, 44]. The broad intensive peak of plane (002) at 2θ = 14.21° signifies the creation of a structured layer arrangement of 2H-MoS_2, which has been stacked in an organized manner with a specific d-spacing of 0.61 nm along the plane. The diffraction pattern shows that there is no impure phase observed in the as-prepared MoS_2/Ag@MoS_2 nanosheets.

X-ray photoelectron spectroscopy (XPS) is a powerful surface analysis technique that provides information about the elemental and chemical composition, chemical bonding, and electronic structure of a material. The XPS has been recorded on ULVAC-PHI, PHI5000, which depicts the chemical states of Ag@MoS_2 sample (shown in Fig. 3a). Here, the binding energy of the core electrons of the constituent elements, including Ag, Mo, and S, would be observed. The wide spectrum of Ag@MoS_2 nanosheets describes the presence of Mo, C, O, S, and Ag elements onto the surface of the prepared nanoparticles. Figure 3b shows the XPS mapping of Ag element, and two distinct peaks were observed

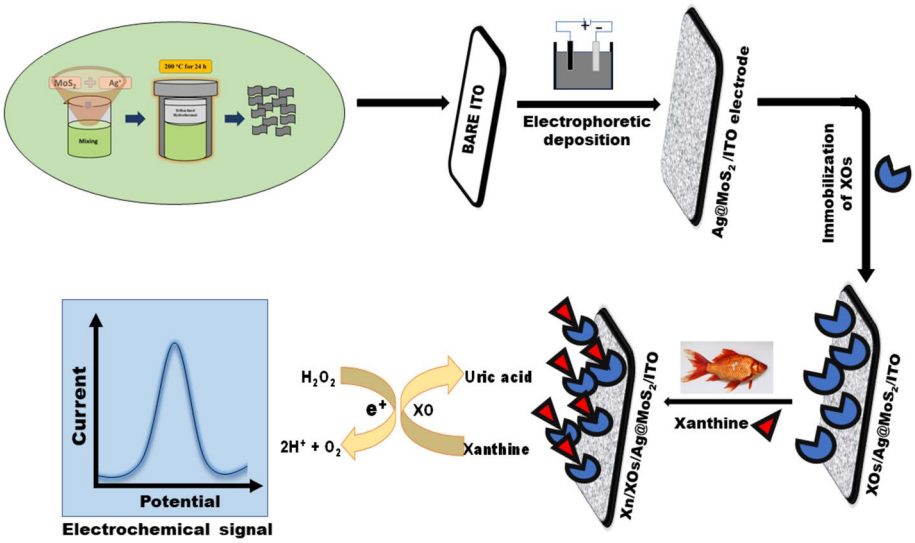


Fig. 1 Scheme describing the fabrication of Ag@MoS_2 nanosheet-based enzymatic biosensor

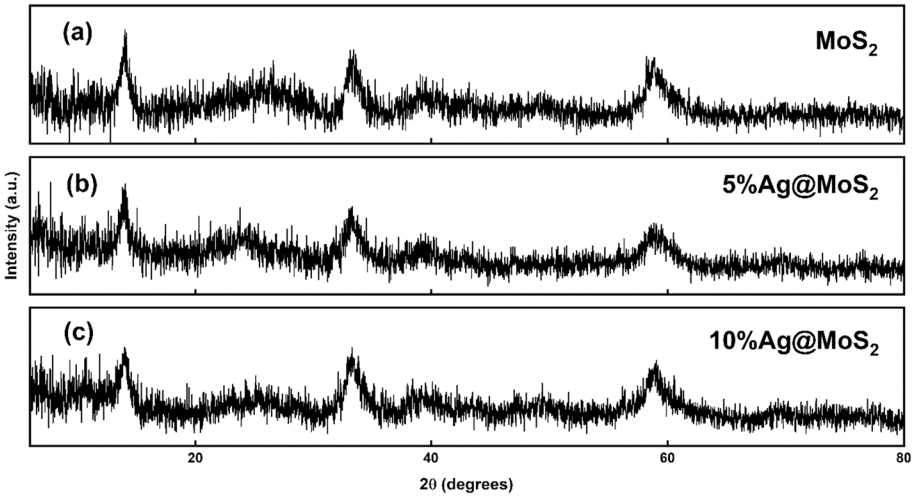


Fig. 2 XRD patterns of **a** MoS_2, **b** 5% Ag@MoS_2, and **c** 10% Ag@MoS_2 nanosheets

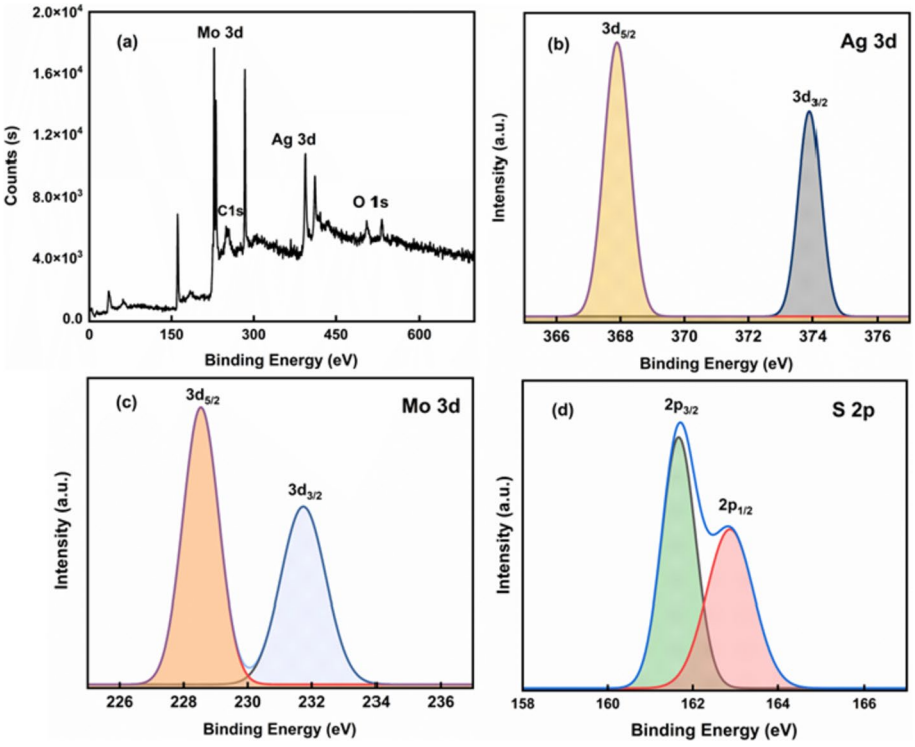


Fig. 3 XPS spectra of **a** Ag@MoS_2 nanosheets, **b** the XPS map of Ag 3d element, **c** the XPS map of Mo 3d element, and **d** the XPS map of S 2 s element

at 367.89 and 373.90 eV which are attributed to towards the occurrence of Ag $3d_{5/2}$ and Ag $3d_{3/2}$, respectively [45]. In Fig. 3c, the two Mo bands were observed at 228.55 and 231.76 eV which are attributed to the Mo $3d_{5/2}$ and Mo $d_{3/2}$ which signifies the occurrence of Mo^{4+} state of molybdenum and their peak separation was measured to be 3.21 eV. The XPS spectra of s2p region, as shown in Fig. 3d, represent the two bands at 161.67 and 162.91 eV attributed to the occurrence of $S2p_{3/2}$ and $S2p_{1/2}$, which indicates the presence of S^{2-} oxidation state of sulfur.

Figure 4a shows the FTIR spectrum of Ag@MoS_2 nanosheets recorded on Nicolet iS50 FTIR, Thermo Scientific. The weak band around 457 cm^{-1} corresponds to the Mo-S vibrations, whereas the vibrational band at 1040 cm^{-1} depicts the presence of S–S bonds [46]. The presence of vibrational bands at 1613 cm^{-1} and 3673 cm^{-1} indicates the bending and stretching vibrations of O–H bonds caused by water absorption on the surface, attributed to the hygroscopic nature of KBr. Figure 4b describes the Raman spectrum of 10% Ag@MoS_2 nanosheets excited with the laser source of wavelength of 532 nm recorded on Renishaw Invia II. In the Raman spectrum of Ag@MoS_2, several characteristic peaks would be observed, corresponding to the vibrational modes of the MoS_2 lattice. The most prominent of these peaks for the 2H-phase of MoS_2 have been observed as in plane, E^1_{2g} mode and out of plane, A_{1g} mode found at 397.62 and 421.57 cm^{-1}, respectively. The observed E^1_{2g} mode depicts the vibration of sulfur atoms in one direction and the molybdenum atoms in the other, whereas the A_{1g} mode corresponds the sulfur atoms vibrating out-of-plane. The difference between the modes is calculated to be 23.95 cm^{-1} which describes the formation of multilayer structure of MoS_2 nanosheets.

Figure 5 shows the morphology of the materials by recording the SEM images of the prepared samples using the JEOL JSM 6610LV instrument. The images observed at different magnifications clearly depict the formation of flower-like structures grown inconsistently, rendering to the uneven surface in all directions. The flower-like structures of Ag@MoS_2 nanosheets were observed and petal-like sheets were seen, as shown in Fig. 5a, b. This is the common morphology of MoS_2, produced through hydrothermal technique. Figure 5c describes the EDX spectrum of the Ag@MoS_2 nanosheets where the clear peaks due to Mo, S, and Ag were observed. Figure 5d, e, and f represents the elemental mapping of the constituent elements of Ag@MoS_2 which shows the uniform distribution of the elements throughout the sample.

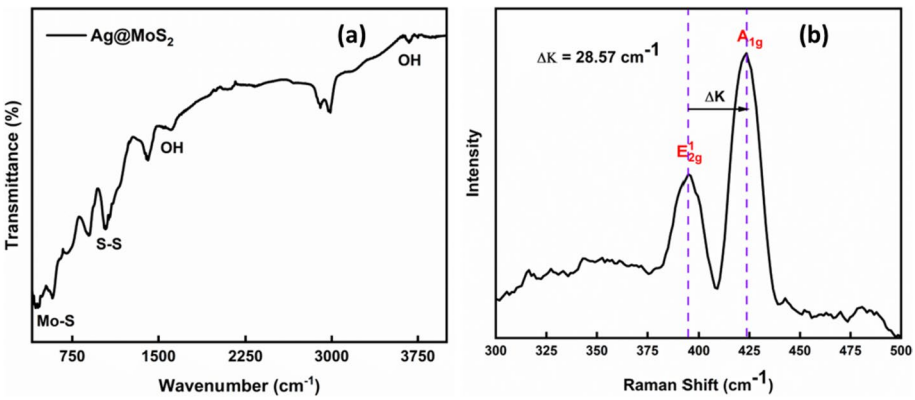


Fig. 4 **a** FT-IR spectrum and (**b** Raman spectrum of Ag@MoS_2 nanosheets

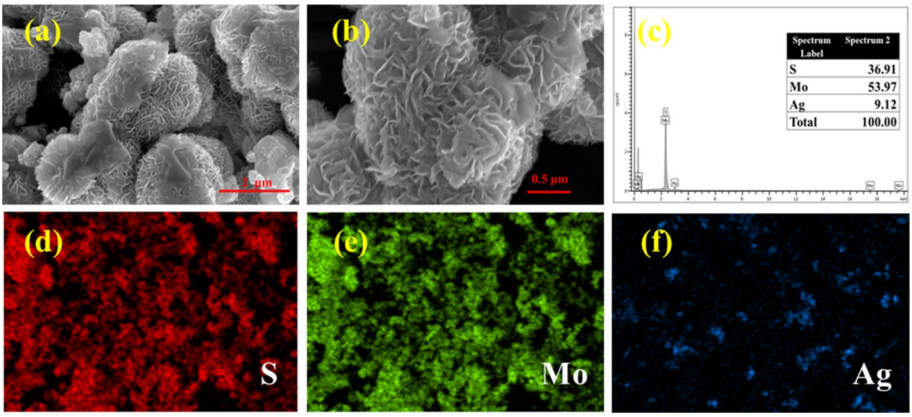


Fig. 5 The SEM images of Ag@MoS_2 nanosheets

The Ag@MoS_2 sample images were recorded through TEM on TECNAI 200 kV, as shown in Fig. 6. The TEM images were recorded for the sample dispersed in DI water, loaded on a copper TEM grid with a carbon coating. Figure 6a demonstrates the layered structure of MoS_2 stacked over one another. Figure 6c illustrates the formation of few layers counted from the edges of the sheets. It shows the presence of 4–6 nanosheets in the prepared sample, which leads to the high adsorption due to greater surface to volume ratio.

Electrochemical Studies of the Fabricated Electrodes

The fabricated electrode is used for the detection as the xanthine molecules in the sample solution are adsorbed onto the surface of the Ag-doped MoS_2 nanosheets through interactions such as coordination bonds, electrostatic forces, or π-π stacking interactions. Upon adsorption, an electrochemical reaction occurs at the Ag-MoS_2 interface. This can involve the electrochemical oxidation or reduction of xanthine molecules, leading to the transfer of electrons between the xanthine analyte and the electrode surface. The electrochemical reaction results in the transfer of electrons between the xanthine molecules and the electrode surface through the Ag-doped MoS_2 nanosheets. The presence of Ag dopants can facilitate this electron transfer process, enhancing the sensitivity and efficiency of the sensor. The electron transfer process generates an electrochemical signal, such as a change in current or potential, which is measured through suitable electrochemical techniques.

The electrochemical properties were recorded on the Autolab potentiostat (Eco-Chemie, the Netherlands) of the prepared electrodes (1 cm by 1 cm), i.e., MoS_2/ITO, 5% Ag@MoS_2/ITO, and 10% Ag@MoS_2/ITO, which have been achieved by means of the electrochemical impedance spectroscopy (EIS; PBS 5 mM of $[Fe(CN)^6]^{3-/4-}$) within the frequency range of 0.01 to 10^5 Hz at set potential of 0.01 V (Fig. 7). In this particular cell, Ag/AgCl is used as a reference electrode and platinum as a counter electrode. In the Nyquist plot, a linear region was observed at lower frequencies, while a semi-circular region was observed at higher frequencies. This behavior is attributed to resistance through diffusion-controlled electron transfer at lower frequencies and an electron transfer-limited process at higher frequencies. The electron transfer resistance (R_{ct}) of the MoS_2/ITO electrode was found to be 179.5 Ω (curve (i)), whereas the R_{ct} of 5% Ag@MoS_2/ITO and 10% Ag@MoS_2/ITO electrodes was recorded to be 112.85 Ω (curve (ii)) and 104.5 Ω (curve (iii)), respectively.

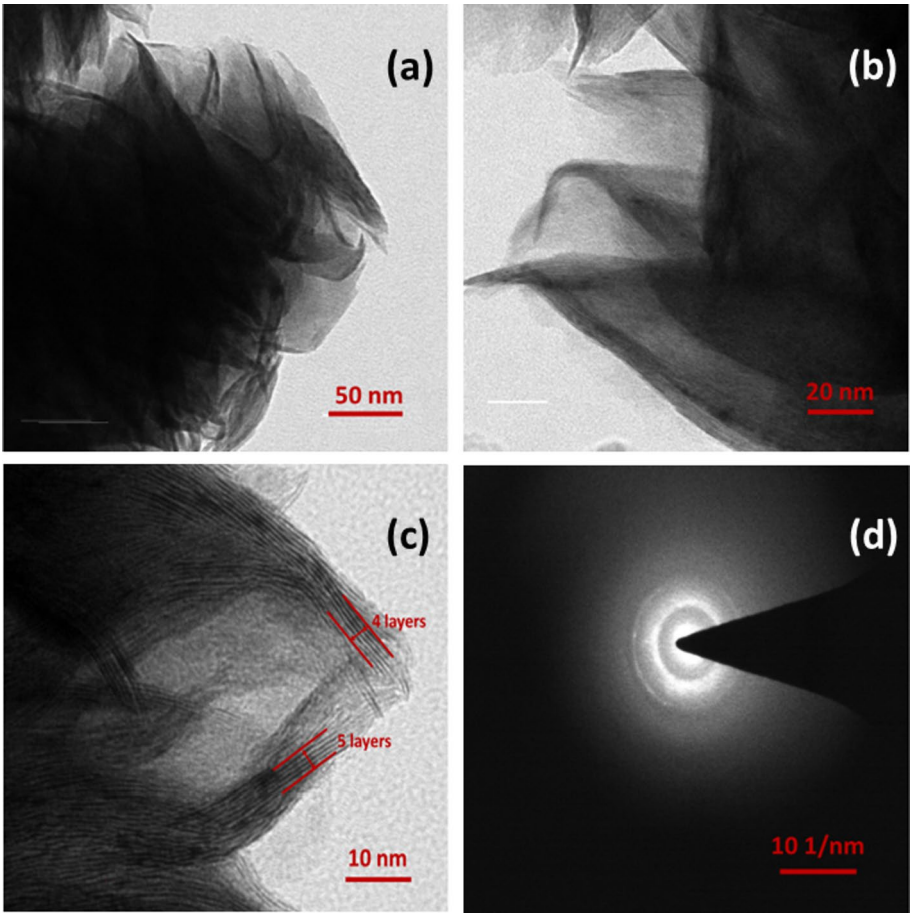


Fig. 6 The TEM images of $Ag@MoS_2$ nanosheets

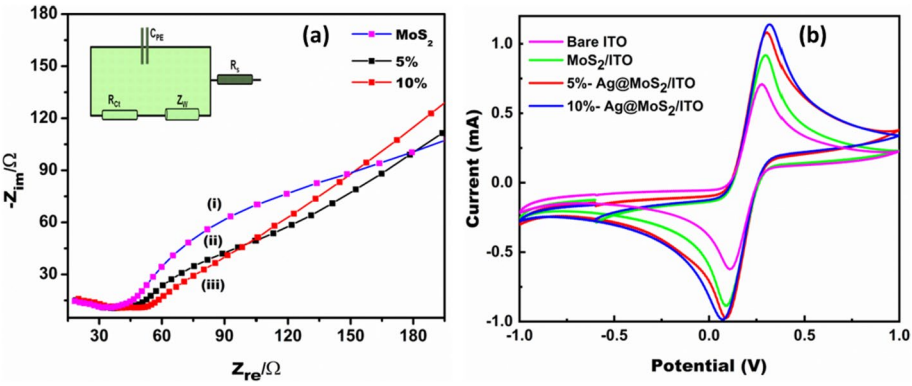


Fig. 7 **a** EIS curves, **b** CV curves of (i) MoS_2/XO/ITO, (ii) 5% $Ag@MoS_2$/XO/ITO, and (iii) 10% $Ag@MoS_2$/XO/ITO electrode

From the obtained R_{ct} values, the exchange current per geometric unit area (i_o) and apparent electron transfer rate constant (K_{app}) for MoS_2/ITO, 5% Ag@MoS_2/ITO, and 10% Ag@MoS_2/ITO electrodes have been calculated using Eqs. (1) and (2).

$$i_o = nRT/R_{ct}F \tag{1}$$

$$K_{app} = RT/n^2F^2AR_{ct}C \tag{2}$$

where R is the gas constant, F is the Faraday constant, T is temperature in Kelvin, and A and C are the area of electrode and concentration of the redox probe, respectively. The i_o for the MoS_2/ITO electrode was found to be 14.30 Acm^{-2}, whereas for 5% Ag@MoS_2/ITO and 10% Ag@MoS_2/ITO electrodes, the value of i_o was 22.75 and 24.57 Acm^{-2}, respectively. Similarly, K_{app} for the MoS_2/ITO, 5% Ag@MoS_2/ITO, and 10% Ag@MoS_2/ITO electrodes was calculated to be 1.18×10^{-6} cm s^{-1}, 1.87×10^{-6} cm s^{-1}, and 2.02×10^{-6} cm s^{-1}, respectively. This increment in the values of i_o and K_{app} of the 10% Ag@MoS_2/ITO electrode compared to the MoS_2/ITO and 5% Ag@MoS_2/ITO electrode clearly describes the precise diffusion of redox couple through the electrode interface.

The cyclic voltammetric (CV) studies have been carried out in the potential window of − 1 to 1 V for bare ITO, pristine MoS_2/ITO, 5% Ag@MoS_2/ITO, and 10% Ag@MoS_2/ITO electrodes in PBS buffer (Fig. 8). It has been observed that the redox peak current of the 10% Ag@MoS_2/ITO electrode (curve (iv), 1.143 mA) is higher than that of all the other electrodes (MoS_2/ITO, 5% Ag@MoS_2/ITO, and 10% Ag@MoS_2/ITO) (curve (i, ii, iii)). From this, it can be inferred that the addition of 10% of Ag into pristine MoS_2 lattice has improved the conductivity of the nanohybrid. This indicates the occurrence of direct electron movement between the electrode and the Ferro-Ferri electrolyte, therefore depicts an increase in the oxidation signal. Thus, the 10% Ag@MoS_2/ITO electrode has

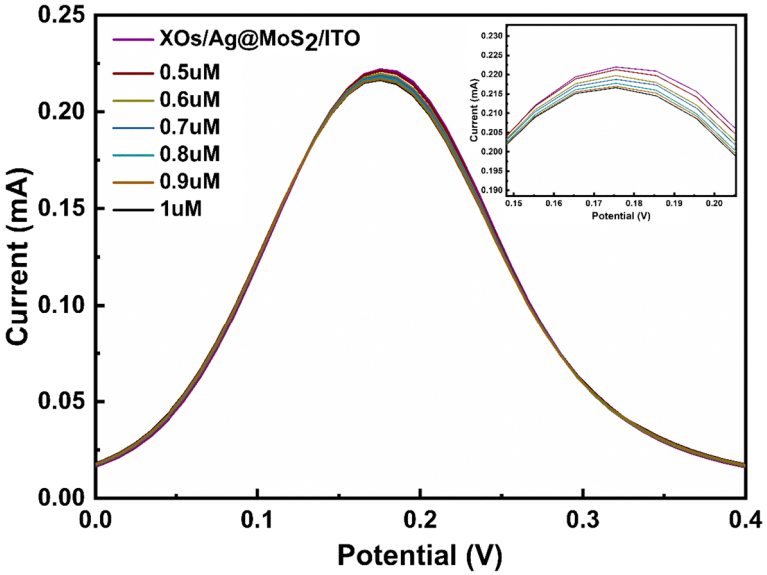


Fig. 8 DPV studies showing the current response of 10% Ag@MoS_2/XO/ITO electrode with increasing concentration of Xn

been implied for further biosensing application. The charge transfer coefficient (α) and heterogeneous electron transfer coefficient (K_s) for 10% Ag@MoS_2/ITO have been calculated to be 0.0198 and 0.0911, respectively, at a scan rate (v) of 50 mV/s (using Laviron's model (Eq. 7)) [47, 48].

$$ln\left(K_s\right) = \alpha ln(1-\alpha) + (1-\alpha)ln(\alpha) - ln\left(\frac{RT}{nFv}\right) - \alpha(1-\alpha)\frac{nF\Delta E_p}{RT} \quad (3)$$

Electrochemical Biosensing Response Studies of XOs/10% Ag@MoS_2/ITO Electrode

Xanthine is typically detected through an enzymatic reaction catalyzed by xanthine oxidase (XOD) immobilized on the electrode surface. The Ag@MoS_2 nanosheets can act as a mediator in the electron transfer process. The nanocomposite structure facilitates the efficient transfer of electrons between the immobilized enzyme (XOD) and xanthine, generating an electrochemical signal. The electrochemical response for the biosensing studies using the XOs/10% Ag@MoS_2/ITO electrode have been performed under the influence of the different concentration of Xn, as shown in Fig. 8. The Xn concentration was increased from 0.5 to 1 μM and the corresponding current response has been recorded. The linear decrease was observed in the current with increase in the Xn concentration. This linear relation in the current with concentration depicts the direct electron transfer between the Xn and the XOs/10% Ag@MoS_2/ITO electrode (Fig. 9). The sensitivity of the prepared biosensor towards Xn has been measured using the regression equation, y = mx + c (where *y* describes the recorded peak current and *x* is the concentration of Xn), and calculated to be 0.33 μAM^{-1} and $R^2 = 0.97$. The limit of detection was found to be 27.4 nM, calculated using the Eq. $3\sigma/S$ [1], where σ equal to standard deviation of the bioelectrode and S is sensitivity.

Real Sample (Rohu Fish Extract) Validation of the Biosensor

The practicality of the fabricated 10% Ag@MoS_2/ITO biosensor for primary detection of fish meat samples was performed using the diffuse pulse voltammetry (DPV). The

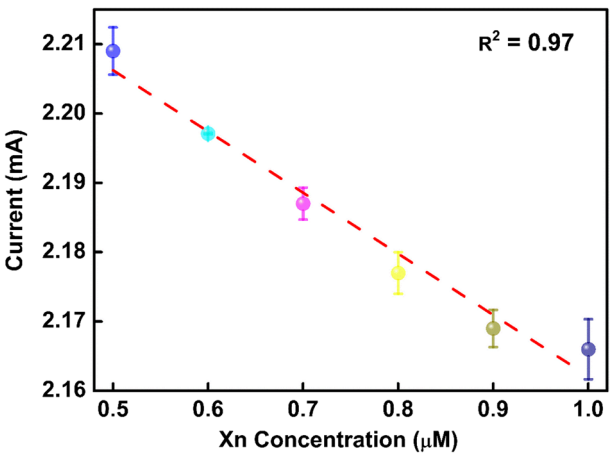


Fig. 9 Current calibration plot depicting the linear relationship between the recorded current magnitude and the concentration of Xn

rohu (*Labeo rohita*) fish was used for Xn extraction and preparation of Xn solution. The facile method of Watanabe et al. has been followed for extraction [2]. Here, the fresh rohu fish was collected from the nearby market and the clean meat was finely chopped. Then, 7 g of the meat was centrifuged in 15 mL DI water at 4500 rpm. The surfactant was then filtered and diluted 100 times to reach the desired concentration. Electrochemical studies illustrate the linear decrement in the peak current with increase in the concentration of Xn, from 0.5 to 1 μM, similar to the synthetic Xn samples (Fig. 10). The present work has been compared with the reported Xn-based sensors for different biosensing parameters (Table 1) and it was observed that the XOs/10% Ag@MoS_2/ITO biosensor showed better response towards primary detection of Xn in fish meat sample with lower LOD.

Selectivity, Reproducibility, Reusability and Shelf-life Studies

The cross-reactivity of the synthesized nanohybrid biosensor (XOs/10% Ag@MoS_2/ITO) was tested among other interfering analytes (glucose, sodium benzoate, urea, uric acid, and ascorbic acid). No considerable change was observed except for glucose where the current variation gets saturated at half of the peak current in the case of Xn (Fig. 11). Whereas, no change in the current was observed while interference of the analytes other than Xn, which is represented as mixture in Fig. (11). The reproducibility of the prepared XOs/10% Ag@MoS_2/ITO electrodes was verified by fabricating 5 similar electrodes under the same condition (Fig. 12). Now the response of the fabricated biosensors towards the 10 ng mL^{-1} of Xn ranges from 95 to 99%, with an RSD value equivalent to 5% ($n = 5$). Stability tests were also conducted to check the stability of the prepared nanosensor towards reusability and shelf life of the sensor, shown in Fig. 13. The single electrode was used 10 times after washing from saline and no considerable change was observed, as shown in Fig. 13a. The shelf life of the sensor was observed by monitoring the DPV response of the electrode towards the Xn, every week while it was stored at 4 °C. After a month, the electrochemical response of the biosensor was decreased from its original activity, indicating its stability at long time period.

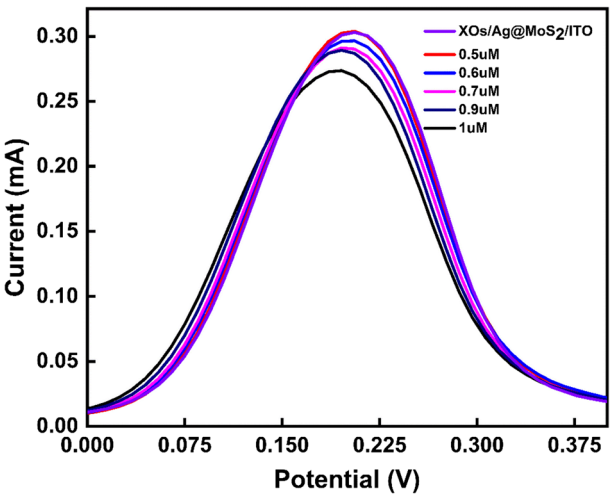


Fig. 10 DPV studies of real sample from fish showing the current response of 10% Ag@MoS_2/XO/ITO electrode with increasing concentration of Xn

Table 1 Comparison of the analytical performance of the enzymatic biosensor for the detection of Xn found in fish meat samples

S. No	Immobilization matrix	Detection technique	Linear range	LOD	Ref
	Poly (L-aspartic acid)/MWCNT bio-nanocomposite	DPV	0.005–50.0 µM	3.5×10^{-4} µM	[49]
	Ag-doped ZnO nanoparticles/polypyrrole	EIS chronoamperometry	0.06–0.6 µM	0.07 µM	[50]
	Graphene-TiO_2	CV	20–512 µM	9.5 µM	[51]
	Poly-TTCA/Au	CV	$5.0\times10^{-6}-1.0\times10^{-4}$ M	1 µM	[52]
	PANI@TiO_2/ITO	DPV	1–100 µM	0.1 µM	[47]
	Au-XOR/fMWCNT-PEDOT/GCE	DPV	0.1–10 µM	5.45×10^{-2} µM	[53]
	XODNPs/Au	CV	0.01–1 µM	0.01 µM	[54]
	10% Ag@MoS_2/ITO	DPV	0.5–1 µM	27.4 nM	Present work

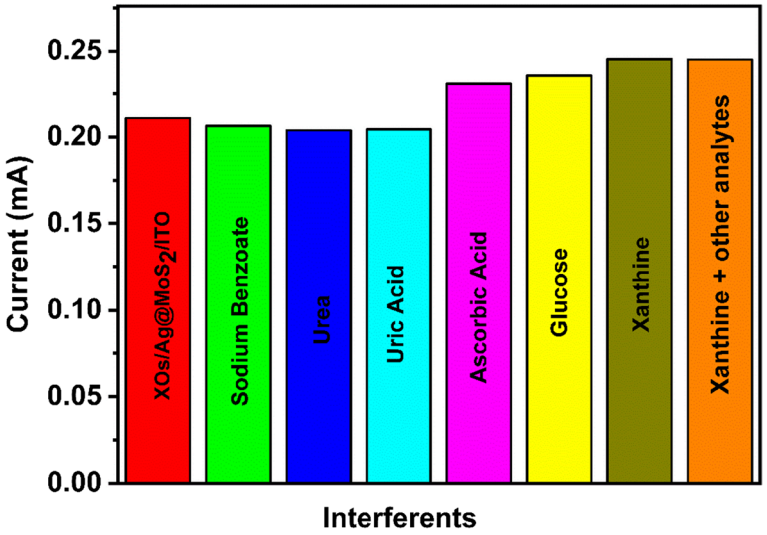


Fig. 11 Specificity test of 10% Ag@MoS_2/XO/ITO electrode towards different interferents commonly present in meat samples

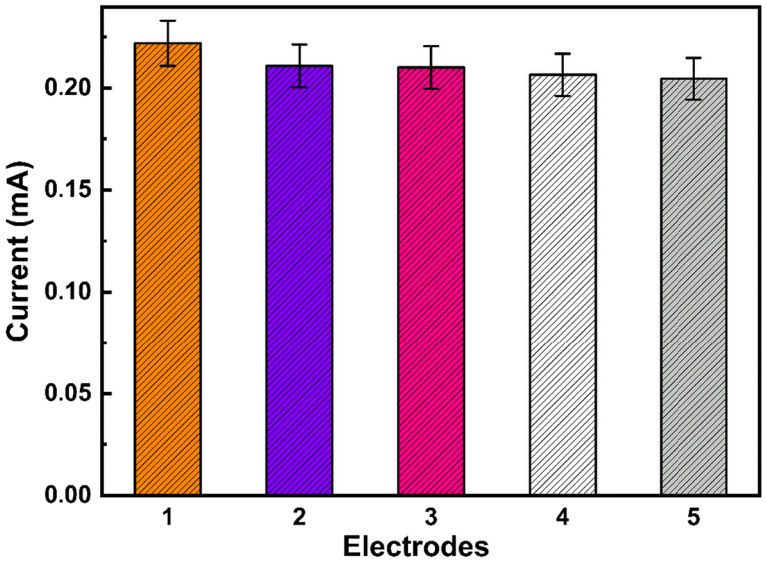


Fig. 12 Reproducibility tests conducted for five different electrodes fabricated under similar conditions

Conclusion

Detecting xanthine is highly important in the food industry as it can signal the spoilage of fish meat in its early stages. Therefore, here an electrochemical enzymatic biosensor has been fabricated for primary detection of Xn in the fish meat by employing the 2D Ag@MoS_2 nanosheets. The 2D arrangement of MoS_2 nanosheets provides a large active surface area, and

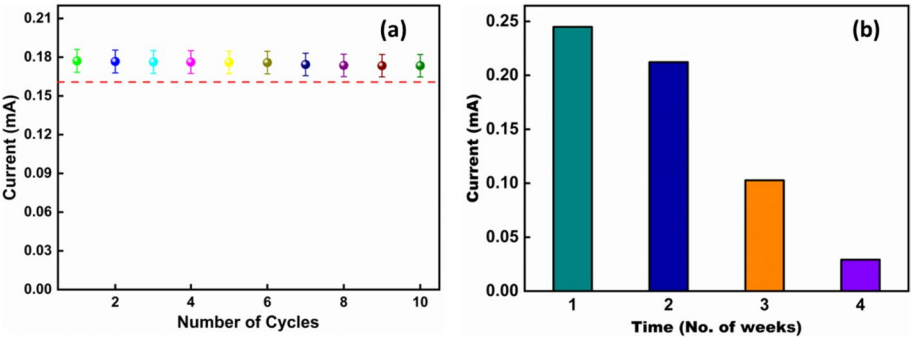


Fig. 13 **a** Reusability tests conducted up to 10 cycles; **b** shelf-life study up to 4 weeks of the fabricated enzymatic biosensor

the inclusion of Ag ions enhances the electrochemical properties of the sensor. The developed enzymatic sensor demonstrated a fast response time of 10 s and a detection limit of approximately 27 nmol. The accuracy of the biosensor was validated using real samples of xanthine extracted from rohu fish meat purchased from a local market, and similar trends were observed in the results for xanthine detection. The biosensor was found to be stable, specific, and reproducible. The proposed enzymatic biosensing platform based on $Ag@MoS_2$ nanohybrid has been validated successfully for the fish meat, and exhibited its reliable applicability towards fish freshness parameters.

Acknowledgements Authors would like to acknowledge the Greater Noida Institute of Technology, Delhi Technological University and University of Delhi for providing the appropriate infrastructure and facilities required for promoting this research work. Deeksha Thakur acknowledges the DST-INSPIRE for the SRF Award.

Author Contribution PS: conceptualization, data curation, formal analysis, investigation, methodology, writing and editing—original draft. DT: conceptualization, data curation, formal analysis, investigation, methodology, and draft editing. OY: data acquisition and supervision. DK: supervision, project administration, and draft editing.

Data Availability Data will be made available when requested.

Declarations

Ethics Approval Not applicable.

Consent to Participate Not applicable.

Consent for Publication Not applicable.

Competing Interests The authors declare no competing interests.

References

1. Kamil Reza, K., Singh, M. K., Yadav, S. K., Singh, J., Agrawal, V. V., & Malhotra, B. D. (2013). Quantum dots based platform for application to fish freshness biosensor. *Sensors Actuators B Chemical, 177*, 627–633.

2. Nanohybrid electrochemical enzyme sensor for xanthine determination in fish samples - PMC, https://www.ncbi.nlm.nih.gov/pmc/articles/PMC8039069/, (accessed 30 October 2022).
3. N. K. Sharma, Monika, A. Kaushal, S. Thakur, N. Thakur, Sheetal, D. Kumar and T. C. Bhalla, *3 Biotech*, , https://doi.org/10.1007/S13205-021-02735-6.
4. Sahyar, B. Y., Kaplan, M., Ozsoz, M., Celik, E., & Otles, S. (2019). *Bioelectrochemistry, 130*, 107327.
5. Devi, R., Yadav, S., Nehra, R., Yadav, S., & Pundir, C. S. (2013). *Journal of Food Engineering, 115*, 207–214.
6. Choi, H. K., Liu, S., & Curhan, G. (2005). *Arthritis and Rheumatism, 52*, 283–289.
7. Rezaeinasab, M., Benvidi, A., Gharaghani, S., Abbasi, S., & Zare, H. R. (2019). *Process Biochemistry, 83*, 86–95.
8. Lawal, A. T., & Adeloju, S. B. (2009). *Biosensors & Bioelectronics, 25*, 406–410.
9. Ghanbari, K., & Nejabati, F. (2020). *Analytical Methods, 12*, 1650–1661.
10. Shih, M. H., Lazo, M., Liu, S. H., Bonekamp, S., Hernaez, R., & Clark, J. M. (2015). *Journal of the Formosan Medical Association, 114*, 314–320.
11. Ono, T., Tsuruta, R., Fujita, M., Aki, H. S., Kutsuna, S., Kawamura, Y., Wakatsuki, J., Aoki, T., Kobayashi, C., Kasaoka, S., Maruyama, I., Yuasa, M., & Maekawa, T. (2009). *Brain Research, 1305*, 158–167.
12. Davis, S. N., & Lastra-Gonzalez, G. (2008). *Journal of Clinical Endocrinology and Metabolism, 93*, E2–E2.
13. Kim, K. Y., Schumacher, H. R., Hunsche, E., Wertheimer, A. I., & Kong, S. X. (2003). *Clinical Therapeutics, 25*, 1593–1617.
14 Kostić, D. A., Dimitrijević, D. S., Stojanović, G. S., Palić, I. R., Dordević, A. S., & Ickovski, J. D. (2015). Xanthine Oxidase: Isolation. *Assays of Activity, and Inhibition J Chem, 2015*, 1. https://doi.org/10.1155/2015/294858
15. Hlavay, J., Haemmerli, S. D., & Guilbault, G. G. (1994). *Biosensors & Bioelectronics, 9*, 189–195.
16. Kito, M., Tawa, R., Takeshima, S., & Hirose, S. (1983). *Journal of Chromatography, 278*, 35–42.
17. Olojo, R. O., Xia, R. H., & Abramson, J. J. (2005). *Analytical Biochemistry, 339*, 338–344.
18 Berti, G., Fossati, P., Tarenghi, G., Musitelli, C., & Melzid'Eril, G. V. (1988). Enzymatic Colorimetric Method for the Determination of Inorganic Phosphorus in Serum and Urine. *Clin Chem Lab Med, 26*, 399–404.
19. A quantitative method for the analysis of xanthine alkaloids in Paullinia cupana (guarana) by capillary column gas chromatography | Semantic Scholar, https://www.semanticscholar.org/paper/A-quantitative-method-for-the-analysis-of-xanthine-Pagliarussi-Freitas/06172977e6d1a1eb6b0182532a9e71245a7f37da, (accessed 3 November 2022).
20. Kock, R., Delvoux, B., & Greiling, H. (1993). *Clinical Chemistry and Laboratory Medicine, 31*, 303–310.
21 Kalimuthu, P., Leimkühler, S., & Bernhardt, P. V. (2012). Low-Potential Amperometric Enzyme Biosensor for Xanthine and Hypoxanthine. *Anal Chem, 84*, 10359–10365.
22. Wu, Y., Deng, P., Tian, Y., Feng, J., Xiao, J., Li, J., Liu, J., Li, G., & He, Q. (2020). *J Nanobiotechnology, 18*, 1–13.
23 He, Q., Wu, Y., Tian, Y., Li, G., Liu, J., Deng, P., & Chen, D. (2019). Facile Electrochemical Sensor for Nanomolar Rutin Detection Based on Magnetite Nanoparticles and Reduced Graphene Oxide Decorated Electrode. *Nanomaterials, 9*(1), 115. https://doi.org/10.3390/NANO9010115
24. Wu, Y., Deng, P., Tian, Y., Ding, Z., Li, G., Liu, J., Zuberi, Z., & He, Q. (2020). *Bioelectrochemistry, 131*, 107393.
25 He, Q., Tian, Y., Wu, Y., Liu, J., Li, G., Deng, P., & Chen, D. (2019). Facile and Ultrasensitive Determination of 4-Nitrophenol Based on Acetylene Black Paste and Graphene Hybrid Electrode. *Nanomaterials, 9*, 429.
26. He, Q., Liu, J., Liu, X., Li, G., Chen, D., Deng, P., & Liang, J. (2018). Fabrication of Amine-Modified Magnetite-Electrochemically Reduced Graphene Oxide Nanocomposite Modified Glassy Carbon Electrode for Sensitive Dopamine Determination. *Nanomaterials, 8*(4), 194. https://doi.org/10.3390/NANO8040194
27. He, Q., Liu, J., Liu, X., Li, G., Chen, D., Deng, P., & Liang, J. (2019). *Electrochimica Acta, 296*, 683–692.
28. Sharma, P., & Mehata, M. S. (2020). *Opt Mater (Amst), 100*, 109646.
29. Sharma, P., & Mehata, M. S. (2020). *Materials Research Bulletin, 131*, 110978.
30. Yadav, O., Varshney, A., & Kumar, A. (2017). *Inorganic Chemistry Communications, 86*, 168–171.
31. Yadav, O., Varshney, A., Kumar, A., Ratnesh, R. K., & Mehata, M. S. (2018). *Spectrochim Acta A Mol Biomol Spectrosc, 202*, 207–213.

32. Kubba, R., Yadav, O., Yadav, P., Fridman, N., & Kumar, A. (2021). *Journal of Molecular Structure, 1243*, 130857.
33. Kubba, R., Yadav, O., Maji, S., Fridman, N., & Kumar, A. (2022). *Journal of Molecular Structure, 1269*, 133780.
34. Tan, C., & Zhang, H. (2015). *Chemical Society Reviews, 44*, 2713–2731.
35. Zhang, W., Shi, S., Wang, Y., Yu, S., Zhu, W., Zhang, X., Zhang, D., Yang, B., Wang, X., & Wang, J. (2016). *Nanoscale, 8*, 11642–11648.
36. Cao, W., Yue, L., & Wang, Z. (2019). *Carbohydrate Polymers, 215*, 226–234.
37. Yang, A., Zhou, G., Kong, X., Vilá, R. A., Pei, A., Wu, Y., Yu, X., Zheng, X., Wu, C. L., Liu, B., Chen, H., Xu, Y., Chen, D., Li, Y., Fakra, S., Hwang, H. Y., Qin, J., Chu, S., & Cui, Y. (2020). Electrochemical generation of liquid and solid sulfur on two-dimensional layered materials with distinct areal capacities. *Nature Nanotechnology, 15*, 231–237.
38 Nguyen, E. P., de Carvalho Castro Silva, C., & Merkoçi, A. (2020). Recent advancement in biomedical applications on the surface of two-dimensional materials: from biosensing to tissue engineering. *Nanoscale, 12*, 19043–19067.
39 Tan, S., Wu, X., Xing, Y., Lilak, S., Wu, M., & Zhao, J. X. (2020). Enhanced synergetic antibacterial activity by a reduce graphene oxide/Ag nanocomposite through the photothermal effect. *Colloids Surf B Biointerfaces, 185*, 110606. https://doi.org/10.1016/J.COLSURFB.2019.110616
40. K. K. Awasthi, A. Awasthi, N. Kumar, P. Roy, K. Awasthi and P. J. John, *Journal of Nanoparticle Research*.
41 ZangenehKamali, K., Pandikumar, A., Sivaraman, G., Lim, H. N., Wren, S. P., Sun, T., & Huang, N. M. (2015). Silver@graphene oxide nanocomposite-based optical sensor platform for biomolecules. *RSC Advances, 5*, 17809–17816.
42. Sharma, P., Singh, M. K., & Mehata, M. S. (2022). *Journal of Molecular Structure, 1249*, 131651.
43. Maitra, U., Gupta, U., De, M., Datta, R., Govindaraj, A., & Rao, C. N. R. (2013). *Angewandte Chemie International Edition, 52*, 13057–13061.
44. Ai, X., Fan, H., Wang, Y., Guo, Y., Liu, X., Yang, L., Liu, H., & Yang, J. (2018). *RSC Advances, 8*, 36280–36285.
45. Xie, X., Mao, C., Liu, X., Zhang, Y., Cui, Z., Yang, X., Yeung, K. W. K., Pan, H., Chu, P. K., & Wu, S. (2017). *ACS Applied Materials & Interfaces, 9*, 26417–26428.
46. Liu, S., Zhang, X., Shao, H., Xu, J., Chen, F., & Feng, Y. (2012). *Materials Letters, 73*, 223–225.
47. Thakur, D., Pandey, C. M., & Kumar, D. (2022). Highly Sensitive Enzymatic Biosensor Based on Polyaniline-Wrapped Titanium Dioxide Nanohybrid for Fish Freshness Detection. *Applied Biochemistry and Biotechnology, 194*, 3765–3778.
48. Jalil, O., Pandey, C. M., & Kumar, D. (2021). *Bioelectrochemistry, 138*, 107733.

Publisher's Note Springer Nature remains neutral with regard to jurisdictional claims in published maps and institutional affiliations.

Springer Nature or its licensor (e.g. a society or other partner) holds exclusive rights to this article under a publishing agreement with the author(s) or other rightsholder(s); author self-archiving of the accepted manuscript version of this article is solely governed by the terms of such publishing agreement and applicable law.

Voltage and Current Regulation in Cuk DC-DC Converters having Enhanced Closed-Loop Control using PID Controller

Praanshu Srijan Shandilya
Electrical Engineering Department
Delhi Technological University
praanshu2114@gmail.com

Ashutosh Gupta
Electrical Engineering Department
Delhi Technological University
ashutoshgupta.nitm@gmail.com

Dheeraj Joshi
Electrical Engineering Department
Delhi Technological University
joshidheeraj@dce.ac.in

2023 11th National Power Electronics Conference (NPEC) | 979-8-3503-1164-8/23/$31.00 ©2023 IEEE | DOI: 10.1109/NPEC57805.2023.10385025

Abstract: **The escalating need for power electronics converters that operate with high efficiency has resulted in a surge of interest in Cuk converters. These converters are renowned for their ability to maintain continuous input/output currents while achieving high levels of efficiency. This research study centers on the small signal analysis of the Cuk converter and the design of its control techniques to improve performance and stability. State-space averaging and linearization techniques yield a transfer function that establishes a correlation between the input and output parameters of the converter. Insights into the converter's stability, transient response, and frequency-domain properties are provided by this model, which is vital for the construction of robust control systems. Subsequently, the manuscript delves into the investigation of control strategies for the Cuk converter, specifically focusing on voltage-mode and current-mode approaches. The output voltage regulation is achieved through duty cycle adjustment in voltage-mode control, whereas current-mode control provides superior dynamic performance and inherent current-limiting capabilities. A comprehensive analysis of the design of both controllers is presented. The findings indicate an enhancement in the transient response, disturbance rejection, effectiveness in regulating output voltage, and preservation of stability.**

Keywords — DC-DC Converter, Small Signal Modelling, Parasitic Effect, PID Controller, Voltage Control mode

I. INTRODUCTION

The swift progressions in power electronics technology have resulted in the emergence of diverse power converters that possess the ability to transform and regulate electrical energy effectively. These converters are used in many applications, including but not limited to renewable energy systems, electric vehicles, and portable electronic devices. The Cuk converter, which was first proposed by Dr Slobodan Ćuk in 1976, has garnered considerable interest owing to its distinct attributes, such as continuous input and output currents, minimized electromagnetic interference (EMI), and high efficacy, among other types of converters [1] – [3].

The Cuk converter is often selected over other DC-DC converters due to multiple benefits. Leading the list of advantages is the consistent input and output currents, enabling lesser ripple currents on each end. Its steady input current diminishes the strain on the input filter capacitor, lessening its required size. Additionally, the Cuk converter enhances simplicity in the gate drive design, as the control point of the electronic switch is rooted to the ground.[4]-[6].

Although the Cuk converter provides numerous advantages, it also introduces substantial difficulties for engineers, particularly concerning its dynamic characteristics and control. Grasping the converter's dynamic elements is crucial for developing effective control methods and ensuring stable functioning to attain the best performance. This understanding can be achieved through conducting a small signal analysis of the converter [7]-[10]. Moreover, exploring steady-state conditions is imperative for fully apprehending the Cuk converter's operational performance [11]-[13]. The current evaluation delivers valuable understanding into the steady-state condition voltage and current waveforms, the correlation between input and output, and the converter's power transfer efficiency. Through the assessment of steady-state properties, engineers can determine the converter's functional limitations and make educated judgements on the selection of component values for achieving ideal performance. Furthermore, the choice of relevant control methods significantly affects the system's transient response speed and the output voltage regulation accuracy under diverse operating conditions [14]-[19].

The primary objective of this research paper is to present an all-encompassing study on the small signal analysis, steady-state assessment, and the design of control approaches for the Cuk converter. The paper is structured in the following manner:

Section II delves into the Cuk converter's steady-state analysis. This exploration concentrates on various factors such as the voltage conversion proportion, effectiveness, and power transfer attributes. The examination is conducted under constant operating conditions. Additionally, the derivation of the small signal model of the Cuk converter is presented, with particular consideration given to the continuous conduction mode (CCM). Section III outlines the design of a voltage-mode controller, explicitly focusing on selecting the parameters for the proportional-integral-derivative (PID) controller. The present study also examines the current-mode control approach. This approach provides enhanced dynamic performance and possesses inherent capabilities for limiting current. Section IV of the paper presents the findings from a simulation conducted on a prototype Cuk converter. The purpose of this simulation was to validate the theoretical analysis and control methodologies employed in the study. The results suggest that the proposed control methods effectively regulate the output voltage, maintain stability, and achieve fast response to sudden changes in various operating conditions.

The paper's final section, Section V, provides a discourse on the prospective applications and forthcoming research avenues in the field of Cuk converter control and optimization.

II. MODELLING OF CUK CONVERTER

The Cuk converter is a fourth-order, non-isolated, switch-mode power converter consisting of two inductors, two capacitors, one diode, and one switch, as shown in Fig. 1.

Authorized licensed use limited to: DELHI TECHNICAL UNIV. Downloaded on February 07,2024 at 06:49:01 UTC from IEEE Xplore. Restrictions apply.

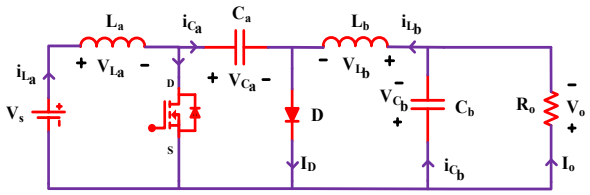


Fig.1 CUK converter schematic circuit

The steady-state analysis of a converter involves the assumption that the device is functioning in a stable mode, wherein the output voltage and current remain constant over a period. Under steady-state conditions, the current flowing through the inductor and capacitor is assumed to be continuous while the voltage across them remains constant.

The Cuk converter operates in two modes. In mode 1, the switch S is closed, and the input voltage V_s is applied across inductor L_a, causing the current through L_a to increase linearly. During this time, the diode D is reverse-biased, and the energy stored in the coupling capacitor C_a is transferred to the output capacitor C_b and the load through inductor L_b. In mode 2, the switch S is open, the inductor L_a is connected in series with the coupling capacitor C_a, and the diode D becomes forward-biased. The energy stored in L_a is transferred to C_a, and the energy stored in L_b is transferred to the output capacitor C_b and the load. Both modes of operation are shown in Fig.2.

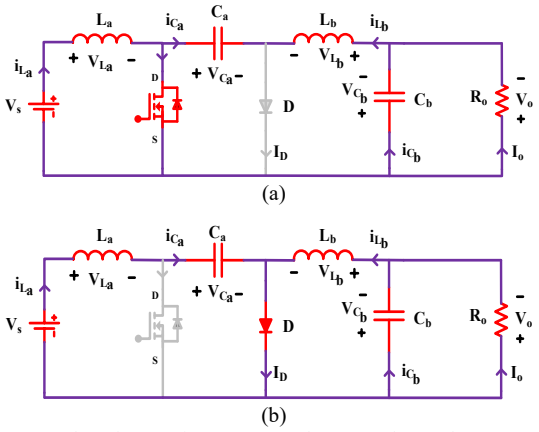


Fig. 2 Modes of Operation (a) Mode 1 (b) Mode 2

A small-signal model using state space is derived from the circuit equations to analyse the converter's small-signal behaviour. The inductor currents (i_{L_a}, i_{L_b}) and capacitor voltages (V_{C_a}, V_{C_b}) are taken as state variables, the Input voltage is taken as the controlled input variable, and the Output voltage is taken as the output variable of the Cuk converter which is defined in the below equations: $x = \begin{bmatrix} i_{L_a} \\ i_{L_b} \\ V_{C_a} \\ V_{C_b} \end{bmatrix}$, $u = [V_s]$, $y = [V_o]$. The following equations give the state space representation of multiple input multiple output system:

$$\dot{x} = Ax + Bu \qquad (1)$$
$$y = Cx + Eu$$

A is the state matrix, B is the input matrix, C is the output matrix, and E is the output coupling matrix. The state space equations of Cuk converter in mode 1 is given by:

$$\frac{di_{L_a}}{dt} = \frac{V_s}{L_a} \qquad (2)$$

$$\frac{di_{L_b}}{dt} = \frac{V_{C_a}}{L_b} - \frac{V_{C_b}}{L_b} \qquad (3)$$

$$\frac{dV_{C_a}}{dt} = -\frac{i_{L_b}}{C_a} \qquad (4)$$

$$\frac{dV_{C_b}}{dt} = \frac{i_{L_b}}{C_b} - \frac{V_{C_b}}{R_o C_b} \qquad (5)$$

$$V_O = V_{C_b} \qquad (6)$$

$$\begin{bmatrix} \frac{di_{L_a}}{dt} \\ \frac{di_{L_b}}{dt} \\ \frac{dV_{C_a}}{dt} \\ \frac{dV_{C_b}}{dt} \end{bmatrix} = \begin{bmatrix} 0 & 0 & 0 & 0 \\ 0 & 0 & 1/L_b & -1/L_b \\ 0 & -1/C_a & 0 & 0 \\ 0 & 1/C_b & 0 & \frac{-1}{R_o C_b} \end{bmatrix} \begin{bmatrix} i_{L_a} \\ i_{L_b} \\ V_{C_a} \\ V_{C_b} \end{bmatrix} + \begin{bmatrix} 1/L_a \\ 0 \\ 0 \\ 0 \end{bmatrix} [V_s] \qquad (7)$$

$$[V_o] = [0 \quad 0 \quad 0 \quad 1] \begin{bmatrix} i_{L_a} \\ i_{L_b} \\ V_{C_a} \\ V_{C_b} \end{bmatrix} + [0][V_s] \qquad (8)$$

The state space equations of Cuk converter in mode 2 is given by:

$$\frac{di_{L_a}}{dt} = \frac{V_s}{L_a} - \frac{V_{C_a}}{L_a} \qquad (9)$$

$$\frac{di_{L_b}}{dt} = -\frac{V_{C_b}}{L_b} \qquad (10)$$

$$\frac{dV_{C_a}}{dt} = -\frac{i_{L_a}}{C_a} \qquad (11)$$

$$\frac{dV_{C_b}}{dt} = \frac{i_{L_b}}{C_b} - \frac{V_{C_b}}{R_o C_b} \qquad (12)$$

$$V_O = V_{C_b} \qquad (13)$$

$$\begin{bmatrix} \frac{di_{L_a}}{dt} \\ \frac{di_{L_b}}{dt} \\ \frac{dV_{C_a}}{dt} \\ \frac{dV_{C_b}}{dt} \end{bmatrix} = \begin{bmatrix} 0 & 0 & -1/L_a & 0 \\ 0 & 0 & 0 & -1/L_b \\ 1/C_a & 0 & 0 & 0 \\ 0 & 1/C_b & 0 & \frac{-1}{R_o C_b} \end{bmatrix} \begin{bmatrix} i_{L_a} \\ i_{L_b} \\ V_{C_a} \\ V_{C_b} \end{bmatrix} + \begin{bmatrix} 1/L_a \\ 0 \\ 0 \\ 0 \end{bmatrix} [V_s] \qquad (14)$$

$$[V_o] = [0 \quad 0 \quad 0 \quad 1] \begin{bmatrix} i_{L_a} \\ i_{L_b} \\ V_{C_a} \\ V_{C_b} \end{bmatrix} + [0][V_s] \qquad (15)$$

To remove the switching ripple component from the circuit equations, averaging over one switching period is done. The averaged switching model is obtained by averaging these equations over one switching period:

$$A = A_1 d + A_2(1-d) \qquad (16)$$
$$B = B_1 d + B_2(1-d) \qquad (17)$$
$$C = C_1 d + C_2(1-d) \qquad (18)$$
$$E = E_1 d + E_2(1-d) \qquad (19)$$

To derive the small signal model of the Cuk converter, the nonlinear averaged state-space model needs to be linearized around an operating point. This is achieved by applying perturbations to the state variables, x $(i_{L_a}, i_{L_b}, V_{C_a}, V_{C_b})$,, input variables, x (V_s) ,output variables, y (V_o) and duty cycle, d:

$$d = D + \hat{d};\ x = X + \hat{x};\ u = U + \hat{u};\ y = Y + \hat{y} \qquad (20)$$

By substituting the perturbed variables into the averaged state-space model Eq. (16)-(19) and neglecting the higher-order terms, the linearized small signal model can be derived:

Authorized licensed use limited to: DELHI TECHNICAL UNIV. Downloaded on February 07,2024 at 06:49:01 UTC from IEEE Xplore. Restrictions apply.

$$s\hat{x}(s) = A\hat{x}(s) + B\hat{u}(s) + \big((A_1 - A_2)X(s) + (B_1 - B_2)U(s)\big)\hat{d}(s) \quad (21)$$

$$\hat{y}(s) = C\hat{x}(s) + E\hat{u}(s) + \big((C_1 - C_2)X(s) + (E_1 - E_2)U(s)\big)\hat{d}(s) \quad (22)$$

The duty cycle (D) is the ratio of the switch-ON time to the total switching period. It determines the output voltage (V_o) in relation to the input voltage (V_s) using the following equation:

$$V_o = \frac{-D * V_s}{(1 - D)} \quad (23)$$

The inductor values (L_a and L_b) are calculated based on the desired ripple currents (Δi_{L_a} *and* Δi_{L_b}) and the switching frequency (f_{sw}). The following equations are used to determine the inductor values by considering mode 1 for Eq. (24) and mode 2 for Eq. (25):

$$L_a = \frac{V_s * D}{\Delta i_{L_a} * f_{sw}} \quad (24)$$

$$L_b = \frac{V_o * (1 - D)}{\Delta i_{L_b} * f_{sw}} \quad (25)$$

The capacitor values (C_a and C_b) are calculated based on the desired voltage ripples (ΔV_{C_a} *and* ΔV_{C_b}) and the switching frequency (f_{sw}). The following equations are used to determine the capacitor values using mode 1 for Eq. (26) and mode 2 for Eq. (27):

$$C_a = \frac{V_o * D}{R_o * \Delta V_{C_a} * f_{sw}} \quad (26)$$

$$C_b = \frac{V_o * (1 - D)}{8 * f_{sw}^2 * \Delta V_{C_b} * L_b} \quad (27)$$

By substituting the parameter values from Table 1, the control to output transfer function can be derived using Equation (21) as:

$$\frac{\hat{V}_o(s)}{\hat{d}(s)} = (sI - A)^{-1}\big((A_1 - A_2)X(s) + (B_1 - B_2)U(s)\big) \quad (28)$$

$$\frac{\hat{V}_o(s)}{\hat{d}(s)} = \frac{1.082\times10^9 s^2 - 8.113\times10^{11} s + 6.103\times10^{14}}{s^4 + 2.003\times10^4 s^3 + 3.061\times10^7 s^2 + 1.128\times10^{10} s + 5.662\times10^{12}} \quad (29)$$

$$\frac{\hat{i}_{L_b}}{\hat{d}} = \frac{1125 s^3 + 2.169\times10^7 s^2 - 1.627\times10^{10} s + 1.271\times10^{13}}{s^4 + 2.003\times10^4 s^3 + 3.061\times10^7 s^2 + 1.128\times10^{10} s + 5.662\times10^{12}} \quad (30)$$

III. CONTROL METHODS

Employing closed-loop control in Cuk converters is vital for achieving the targeted voltage regulation, boosting the dynamic response, and augmenting the system's stability. This paper presents an extensive examination of the Proportional-Integral-Derivative (PID) controller used in closed-loop Cuk converters under Voltage mode and current mode control, evaluating its impact on the overall performance of the converter.

Table 1 Design specification of Cuk converter

Parameters	Symbols	Values
Input Voltage	V_s	12V
Output Voltage	V_o	24V
Duty Cycle	D	0.6
Switching Frequency	f_{sw}	5kHz
Inductors L_a,L_b	L_a/L_b	16mH/32mH
Current Ripple in Inductor L_a	Δi_{L_a}	10% I_{L_a}
Current Ripple in Inductor L_b	Δi_{L_b}	10% I_{L_b}
Capacitor C_a,C_b	C_a/C_b	37µF/1.04 µF
Voltage Ripple in Capacitor C_a	ΔV_{C_a}	5% V_{C_a}
Voltage Ripple in Capacitor C_b	ΔV_{C_b}	5% V_{C_b}
Load Resistance	R_o	48Ω

A. VOLTAGE MODE CONTROL

Voltage mode control is a commonly applied control approach in closed-loop Cuk converters. With this method, the output voltage is contrasted with a reference voltage, and the discrepancy signal is employed to modify the converter's duty cycle. This section delves into the design factors, stability examination, and performance assessment of voltage mode control strategies.

The small signal transfer function obtained in the prior section, Eq. (29), can be utilized to create a control system capable of regulating the output voltage of the Cuk converter. Fig.3 illustrates the small signal block diagram of the Cuk converter's voltage mode control.

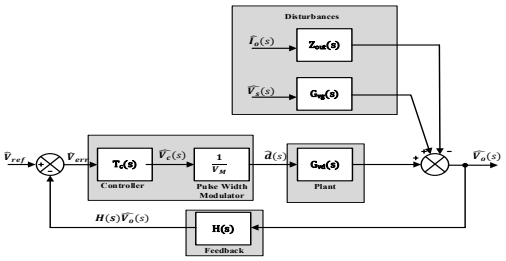


Fig. 3 Voltage control mode small signal block diagram

The transfer function of the PID controller is given by:

$$T_c(s) = K_{prop} + \frac{K_{int}}{s} + K_{der}s \quad (31)$$

$$T_c(s) = 1.395 \times 10^{-3} + \frac{1.2476}{s} + 3.899 \times 10^{-7}s \quad (32)$$

The reference to the output closed-loop transfer function is given by:

$$\frac{\widehat{V_{ref}}}{\widehat{V_o}} = \frac{422 s^4 + 1.193\times10^6 s^3 + 4.561\times10^8 s^2 - 1.608\times10^{11} s + 7.614\times10^{14}}{s^5 + 2.045\times10^4 s^4 + 3.18\times10^7 s^3 + 1.174\times10^{10} s^2 + 5.501\times10^{12} s + 7.614\times10^{14}} \quad (33)$$

The closed loop frequency response of open loop plant as well as closed loop plant described by Eq. (29) and Eq. (33) is shown in Fig. 4. The gain margin of the open loop system is -42.7dB, and the Phase margin is 35.7 degrees at a gain cross-over frequency of 4.84kHz. The gain margin of the system is 5.07dB, and the phase margin is 70.9 degrees which is an improvement over the open loop system. A higher phase margin in the closed loop system is indicative of a lower quality factor, resulting in a reduction in the maximum peak overshoot. However, it is important to note that the recovery speed of the closed loop system deteriorates as a consequence.

Authorized licensed use limited to: DELHI TECHNICAL UNIV. Downloaded on February 07,2024 at 06:49:01 UTC from IEEE Xplore. Restrictions apply.

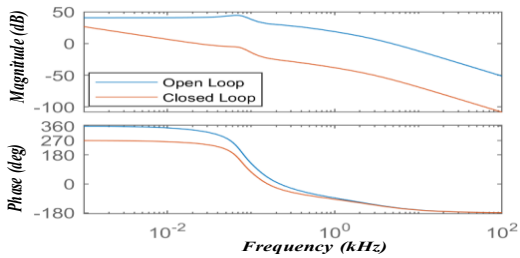


Fig. 4 Open loop and closed loop frequency response of Cuk Converter

The root locus plot of the Cuk converter in voltage mode control as depicted in Fig. 5 shows the movement of the poles and zeroes of the transfer function described in Eq. (33). The analysis of the plot indicates the existence of right half plane zeroes within the closed loop system, while all the poles are situated in the left half plane. This observation implies that the system exhibits stability over a broad range. However, it is important to note that the presence of right half plane zeroes can potentially restrict the phase margin. Therefore, it is crucial to exercise caution and employ appropriate measures when tuning the controller.

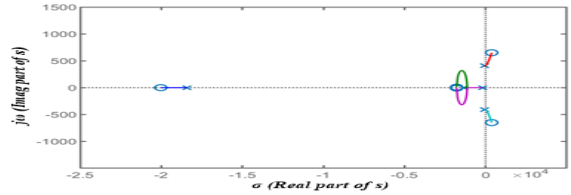


Fig. 5 Root locus of Closed loop VMC Cuk converter.

B. CURRENT MODE CONTROL

The current mode control strategy is implemented by designing a closed-loop PID controller based on the small signal transfer function of the Ćuk converter.

Current mode control (CMC) is a type of feedback control that uses the current through the inductor to control the converter's output voltage. The CMC scheme is designed to compensate for the inherent non-linearities of the Cuk converter. The non-linearities are caused by the switch's switching action and the output filter's capacitance. Fig.6 shows the small signal model of the current mode-controlled Cuk converter.

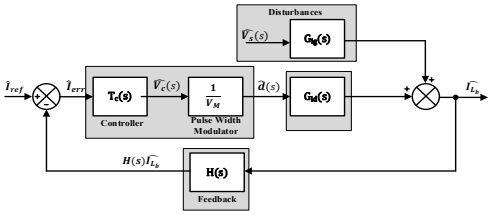


Fig. 6 Current mode control small signal block diagram

The controller transfer function parameter is derived using the Phase margin test and is shown in Eq. (34).

$$T_c(s) = 66.96 \times 10^{-3} + \frac{59.8825}{s} + 1.8719 \times 10^{-5} s \qquad (34)$$

The closed-loop transfer function of the current mode control system was derived using the parameters presented in Table 1.

$$\frac{\widehat{I_{ref}}}{\widehat{iL_b}} = \frac{20.63\times10^{-3}s^5+4.715\times10^{2}s^4+1.19\times10^{6}s^3+4.385\times10^{8}s^2-1.203\times10^{11}s+7.457\times10^{14}}{s^5+2.009\times10^{4}s^4+3.118\times10^{7}s^3+1.149\times10^{10}s^2+5.425\times10^{12}s+7.457\times10^{14}} \qquad (35)$$

Fig. 7 depict the Bode plots of the open loop and closed loop Cuk converter in current mode control. The gain margin of the closed-loop Cuk converter is 14.5dB, which is higher than that of the open-loop Cuk converter having a gain margin of -8.95 db. This suggests that the closed-loop Cuk converter can respond more swiftly to the input voltage and load variations. When subjected to current mode control, the closed-loop Cuk converter exhibits a phase margin of 69.7 degrees at a gain cross-over frequency of 0.00921kHz.

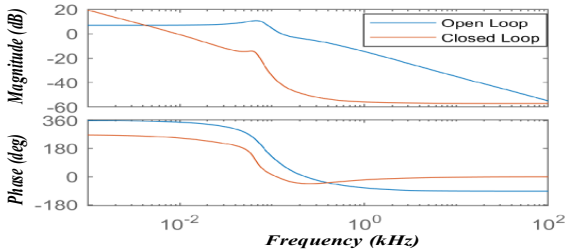


Fig. 7 Open loop and closed loop frequency response of current mode control Cuk converter

The stability analysis of the closed-loop Cuk converter in current mode control, as depicted by the root locus plot in Fig. 8, indicates that the system remains stable across a broad spectrum of controller gains.

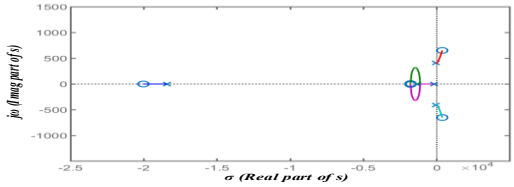


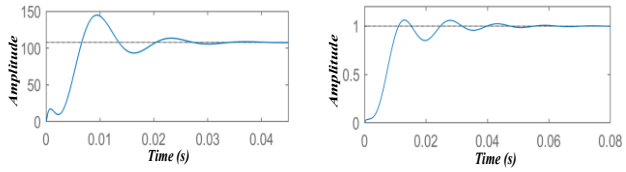
Fig. 8 Root locus plot of closed-loop CMC Cuk converter

IV. RESULTS AND DISCUSSION

The Cuk converter was designed and modelled utilizing MATLAB/Simulink, and the PID controller was devised and calibrated utilizing the Phase Margin test approach.

A. CLOSED LOOP VOLTAGE CONTROL

Time response analysis: Fig. 9(b) illustrates the step response of the closed-loop voltage mode control achieved by the PID controller applied to the Cuk converter. The percentage overshoot fit in the closed loop system is 6.36%, exhibiting a significant reduction compared to the open loop system. The closed loop system exhibits a rise time of 6.25 ms and a settling time of 47.7 ms.



(a) (b)

Fig. 9 Step response showing maximum overshoot in voltage control mode for (a) Open loop plant (b) Closed loop plant

Output Voltage Comparison, voltage and current profile: Fig. 10 illustrates the voltage output characteristics of the Cuk converter under open and closed loop conditions.

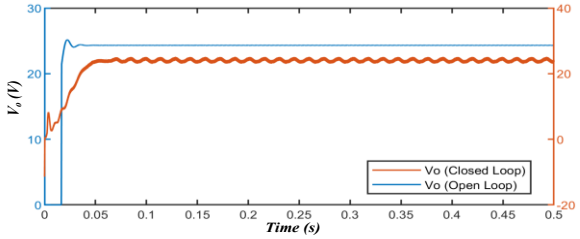


Fig. 10 Open loop vs closed loop CUK converter output voltage

Authorized licensed use limited to: DELHI TECHNICAL UNIV. Downloaded on February 07,2024 at 06:49:01 UTC from IEEE Xplore. Restrictions apply.

The converter maintains a steady state of operation while under the influence of a constant load of 48Ω. The closed-loop Cuk converter has a maximum peak overshoot of 2.37%, much lower than the open loop system with a peak overshoot of 22.79%. Fig. 11 and Fig. 12 illustrate the voltage and current strain experienced by the various constituents of the converter while operating under a constant load. All measurements are within the specified tolerances, with La and Lb inductor current ripple at 9.95% and 10% and output filter capacitor ripple at 4%.

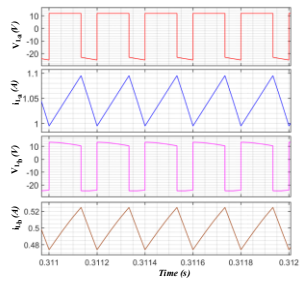


Fig. 11 Voltage and current stress across inductors L_a and L_b

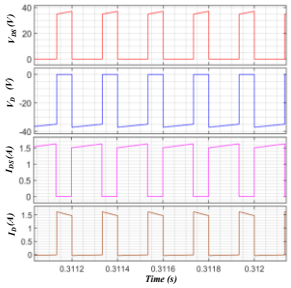


Fig.12 Voltage and current profile across MOSFET And Diode

Load Regulation: The control loop detects any fluctuations in the load and modulates the duty cycle in response to ensure that the output voltage remains within the predetermined range.

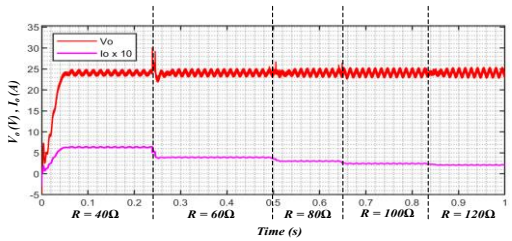
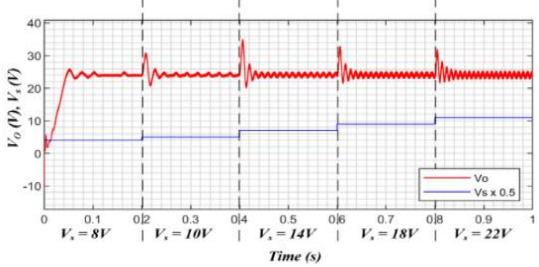


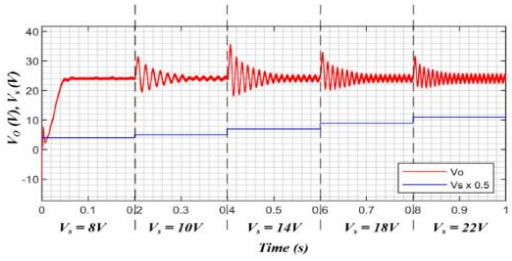
Fig. 13 Variation in output voltage in response to load

The plot shown in Fig. 13 depicts the behaviour of the Cuk converter's output voltage and load current in response to variations in the load from 40Ω to 120Ω. The graph illustrates that the Cuk converter effectively regulates the output voltage to the intended level of -24V across varying load scenarios.

Line Regulation: The performance of power converters can be affected by line variations, which refer to fluctuations or disturbances in the input voltage. The utilization of closed-loop voltage mode control is effective in reducing the impact of line variations through the dynamic modulation of the converter's duty cycle. The converter initially functions under steady-state conditions with a consistent voltage in the line. Subsequently, a discrete alteration is implemented in the voltage from 8V to 22V in the power line to replicate variations in the line. Fig. 14 depicts the relationship between the output voltage and line variations and demonstrates the efficacy of the control loop in maintaining output voltage stability in the face of fluctuations in line voltage.



(a)



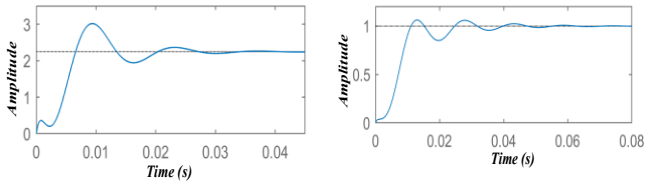
(b)

Fig. 14 The Effect of Line Variation on the Output Voltage (a) R = 50Ω (b) R = 100Ω

B. *CLOSED LOOP CURRENT CONTROL*

The closed-loop current mode control of the Cuk converter is achieved by using a feedback loop to regulate the inductor current. The feedback loop measures the inductor current and compares it to a reference current. The difference between the two currents is used to adjust the converter's duty cycle, which in turn regulates the inductor current and the output voltage.

Time response analysis: A step change is made to the converter's input voltage, and the simulation captures the transient behavior of the converter in open loop as well as closed loop, which provides vital insights into the converter's stability, transient responsiveness, and settling time, as illustrated in Fig.15. The closed loop converter exhibits a response time of 6.02ms, a settling time of 44.5ms, and a maximum peak overshoot of 5.91%.



(a) (b)

Fig. 15 Step response showing maximum overshoot in current control mode for (a) Open loop plant (b) Closed loop plant

Output current comparison and voltage and current profiles: Fig.16 illustrates the inductor current waveform in both the open loop and closed loop current control modes when subjected to a constant load. The results with a fixed load of 48Ω reveal that the open-loop system exhibited limited regulation capabilities, as evidenced by a maximum peak overshoot of 25.6%. In contrast, the closed-loop system displayed significantly better regulation, with a maximum peak overshoot of only 4.98%.

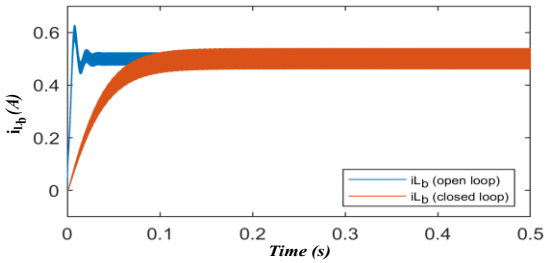


Fig. 16 Open loop vs closed loop CUK converter inductor current

Figures 17 and 18 depict the voltage and current characteristics of the converter's inductors, switch, and diode during a steady load operation. The ripple in the currents of the inductors L_a and L_b is 9.50% and 10%, respectively, and the ripple in capacitor C_b is 4%, which is well within the limits that were set.

Authorized licensed use limited to: DELHI TECHNICAL UNIV. Downloaded on February 07,2024 at 06:49:01 UTC from IEEE Xplore. Restrictions apply.

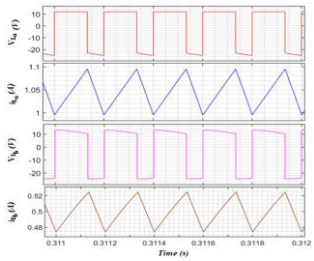


Fig. 17 Voltage and current stress across inductor L_a and L_b.

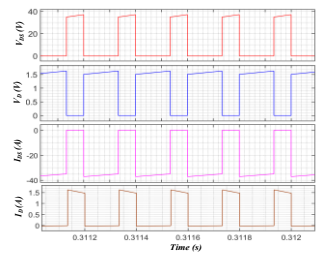


Fig. 18 Voltage and current profile of MOSFET and Diode

Load Regulation: Fig. 19 displays the load regulation efficacy of the Cuk converter that is controlled by current. Under fluctuating loads ranging from 40Ω to 120Ω, the current passing through the inductor remains within acceptable limits when the present reference is established at 0.5A.

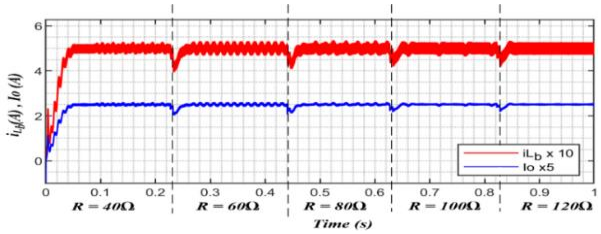


Fig. 19 Load regulation of Cuk converter under Current Mode control

Line Regulation: The line regulation capabilities were assessed by employing the current-controlled Cuk converter model that was implemented. Various input voltage variation scenarios, spanning from 8V to 22V, were considered and the results presented in Fig. 20 demonstrate the effectiveness of the Cuk converter in regulating the line voltage, with control being achieved through current control.

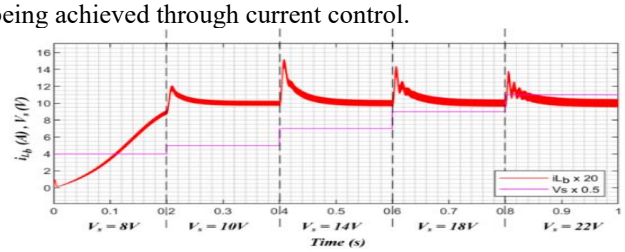


Fig. 20 Line Regulation of Cuk Converter under Current Mode Control

V. CONCLUSION

This study has examined the Cuk converter's closed-loop VMC and CMC utilizing a PID controller. The system's transfer function has been derived, and subsequently, the stability and performance characteristics was analysed. The efficacy of both control modes has been demonstrated through the presentation of simulation results. The VMC strategy employs a PID controller to compare the desired output voltage with the measured output voltage. The controller in voltage mode, demonstrates enhanced load regulation compared to its open-loop counterpart. Additionally, this converter can accommodate a power variation ranging from 5W to 15W. Implementing a closed-loop Cuk converter has been determined to be a proficient method for controlling the output voltage and improving the system's overall efficiency. In contrast, the CMC strategy utilizes a PID controller of similar nature to sustain a constant output current. This approach provides enhanced current regulation and improved transient response, making it well-suited for applications that require precise current delivery. The results also demonstrated the converter's ability to regulate the inductor current in the presence of varying loads.

REFERENCES

[1] Slobodan Cuk, R.D. Middlebrook, "DC-DC Switching Converter," U.S.Patent applied for,California Institute of Technology, Sept.26,1977.

[2] Middlebrook, Richard D., and Slobodan Cuk. "A general unified approach to modelling switching-converter power stages." In 1976 IEEE Power Electronics Specialists Conference, pp. 18-34. IEEE, 1976.

[3] Cuk, Slobodan, and R. D. Middlebrook. "A new optimum topology switching dc-to-dc converter." (1977): 160-179.

[4] E. Duran, M. Sidrach-de-Cardona, J. Galan and J. M. Andujar, "Comparative analysis of buck-boost converters used to obtain I–V characteristic curves of photovoltaic modules," 2008 IEEE Power Electronics Specialists Conference, Rhodes, Greece, 2008, pp. 2036-2042, doi: 10.1109/PESC.2008.4592243

[5] J. L. Seguel, S. I. Seleme, and L. M. F. Morais, "Comparative Study of Buck-Boost, SEPIC, Cuk and Zeta DC-DC Converters Using Different MPPT Methods for Photovoltaic Applications," Energies, vol. 15, no. 21, p. 7936, Oct. 2022, doi: 10.3390/en15217936.

[6] A. Cocor, A. Florescu, A. -M. Popescu, D. -A. Stoichescu and S. Oprea, "Power supply blocks with Cúk and self - lift Cúk converters for telecommunication sites," 2014 International Symposium on Fundamentals of Electrical Engineering (ISFEE), Bucharest, Romania, 2014, pp. 1-6, doi: 10.1109/ISFEE.2014.7050575.

[7] Z. Rayeen, S. Bose and P. Dwivedi, "Study of Closed loop Cuk converter controlled by Loop Shaping Method," 2018 IEEE 13th International Conference on Industrial and Information Systems (ICIIS), Rupnagar, India, 2018, pp. 442-447, doi: 10.1109/ICIINFS.2018.8721386.

[8] P. R. K. Chetty, "Modelling and analysis of C' uk converter using current injected equivalent circuit approach," IEEE Trans. Ind. Electron., vol. 30, pp. 56-59, Feb. 1983.

[9] L. Malesani, L. Rossetto, G. Spiazzi and P. Tenti, "Performance optimization of Cuk converters by sliding-mode control," [Proceedings] APEC '92 Seventh Annual Applied Power Electronics Conference and Exposition, Boston, MA, USA, 1992, pp. 395-402, doi: 10.1109/APEC.1992.228383.

[10] Erickson, R. W., Maksimovic, D. (2001). Fundamentals of Power Electronics. Springer.

[11] S. Chincholkar and C. -Y. Chan, "Design and implementation of an output feedback controller for the Cuk converter," IECON 2015 - 41st Annual Conference of the IEEE Industrial Electronics Society, Yokohama, Japan, 2015, pp. 000086-000090, doi: 10.1109/IECON.2015.7392080.

[12] Deepak, R. K. Pachauri and Y. K. Chauhan, "Modeling and simulation analysis of PV fed Cuk, Sepic, Zeta and Luo DC-DC converter," 2016 IEEE 1st International Conference on Power Electronics, Intelligent Control and Energy Systems (ICPEICES), Delhi, India, 2016, pp. 1-6, doi: 10.1109/ICPEICES.2016.7853596.

[13] D.W. Hart, "Power Electronics," McGraw-Hill, New York, NY, USA, 2011.

[14] V. Jindal and D. Joshi, "A Comparative analysis of classical Tuning methods of PI controllers on non-ideal Buck Converter," 2022 2nd International Conference on Power Electronics & IoT Applications in Renewable Energy and its Control (PARC), Mathura, India, 2022, pp. 1-5, doi: 10.1109/PARC52418.2022.9726251.

[15] Simmi Sharma & Dheeraj Joshi (2020) Analysis of designed PV Emulator using FOPID Controller and Fuzzy logic controller by load variation, Journal of Information and Optimization Sciences, 41:1, 283-292, DOI: 10.1080/02522667.2020.1723222

[16] Z. Chen, "PI and Sliding Mode Control of a Cuk Converter," in IEEE Transactions on Power Electronics, vol. 27, no. 8, pp. 3695-3703, Aug. 2012, doi: 10.1109/TPEL.2012.2183891.

[17] S. Rakshit and J. Maity, "Fuzzy Logic Controlled Ćuk Converter," 2018 International Conference on Communication and Signal Processing (ICCSP), Chennai, India, 2018, pp. 0771-0775, doi: 10.1109/ICCSP.2018.8524168.

[18] A. K. Panda and R. K. Sahu, "Design of current-mode controllers for DC-DC converters: A survey," Journal of Power Electronics, vol. 18, no. 1, pp. 52-65, 2018.

[19] A. Kumar and P. Sensarma, "Inner Loop Stability of Peak Current Controlled Cuk and SEPIC Converters," 2018 IEEE International Conference on Power Electronics, Drives and Energy Systems (PEDES), Chennai, India, 2018, pp. 1-6, doi: 10.1109/PEDES.2018.8707692.

Authorized licensed use limited to: DELHI TECHNICAL UNIV. Downloaded on February 07,2024 at 06:49:01 UTC from IEEE Xplore. Restrictions apply.

Published by :
http://www.ijert.org

International Journal of Engineering Research & Technology (IJERT)
ISSN: 2278-0181
Vol. 10 Issue 10, October-2021

Wire ARC Additive Manufacturing Process for Higher Deposition Rate and Mechanical Strength

Harshit Bansal[1], Abhiraj Kumar Gupta[1], Dr. Ashok Madan[2]
[1] Research scholar, Department of Mechanical engineering, Delhi Technological University, Delhi, India
[2] Professor, Department of Mechanical engineering, Delhi Technological University, Delhi, India

***Abstract*:- Wire Arc Additive manufacturing also known as WAAM is always been economical and highly efficient technology which is very suited for producing large and complex shaped metallic components using the process of 3D printing. In past few years, it is widely studied in various fields such as automotive, marine as well as aerospace industries. As WAAM has advantage of higher metal deposition rate, lesser machining cost, higher Buy-to-fly ratio and very lesser lead time in comparison to any other powder Additive Manufacturing processes. WAAM had always been noticed topic by many of the industrial engineers and researchers. If we compare WAAM process over any other traditional manufacturing methods, considering the complex shapes and high buy to fly ratio (BTF), WAAM is always proved to be best of them. Therefore, having an advantage of comparatively lesser manufacturing cost, better quality and a higher efficiency WAAM became highly used technique for fabricating a component with a much higher metal deposition rate and least material wastage/least scrap. This paper provides a detailed overview of 3D printing of metallic object by inheriting WAAM technique as manufacturing method. At first, the review introduces metal wire and WAAM technique of 3D printing, followed by WAAM systems that are being used to manufacture 3D component, and analyzing which aims to study metal deposition rate and mechanical properties.**

Key Words: Direct Energy Deposition(DED); Buy To Fly ratio(BTF); Additive Manufacturing; WAAM ; High Deposition Rate; CMT; GTAW; Plasma Arc Welding(PAW); LMD…

1. INTRODUCTION

Wire Arc Additive Manufacturing (WAAM) is a process of manufacturing which combines continuous metal feeding in the form of wire and arc-welding technique for 3-D printing. Although this idea is not new, in last few decades several researchers were working over the use of various arc welding techniques on layer by layer deposition of weld bead to production of 3D parts. Therefore, welding techniques such as Cold Metal Transfer (CMT), Gas Metal Arc Welding(GMAW), Gas tungsten arc welding (GTAW) or Plasma arc welding (PAW) have been implemented for Additive manufacturing of various metal/alloys such as steel, aluminium, nickel superalloys and Titanium alloys.

WAAM on the other hand adds to typical Additive manufacturing processes with further more advantages such as lesser welding equipment's cost, easily available standard metal wires, virtual and non-limited part sizes and a higher deposition-rates. In this way, for steels Selective Laser Melting (SLM) attains metal deposition rates of 0.1 kg/hr welding that marked its applicability limited. In this work three types of welding processes are used which are Plasma welding (PAW), Cold Metal Transfer (CMT), Gas Tungsten Arc Welding (GTAW). In this PAW is the conventional whereas Laser Metal Deposition (LMD) was being able to deposition of 1 Kg/hr, but WAAM technology has achieved a higher deposition rate reaching up to 5-6 Kg/hr.

Then again, WAAM showed a few disadvantages when contrasting it with SLM or LMD. In WAAM heat input is higher, that prompts to high residual stresses and bending/distortion, hence fabricated part accuracy and roughness is lower than that of any other Additive Manufacturing advancements and there is always a need of machining step. In addition, the low accuracy causes difficulty in redesigning by the use of geometry optimization algorithms.

Therefore, WAAM technique is adequate for manufacturing of large size parts which are manufactured by high cost materials and requires a high amount of machining.

It was proven to be nothing that most of the previously done work were been completed over single bead multilayer arrangement with or without torch waving or lateral oscillation. Single bead layer was able to produce a wall thickness of about 2 mm to 10mm.

For manufacturing walls with a more thickness then this requires overlapping of multiple weld beads adjoining each other. In such kind of overlapping, the center distance between the joining weld beads have a great effect on the surface finish and layer flatness. Previously done researches over multi bead overlapping showed a result that it is not possible to get an ideal smooth any flat overlapping surface. Various researchers now discovered a new multi bead overlapping model that determines an optimal center distance for ensuring a stable overlapped bead. In WAAM applications, non-uniform deposited beads can cause cumulative errors along direction of bead deposition that can cause a unstable process. Along with this, this issue can be solved by real time monitoring by controlling welding current and arc length, that can result in a better surface quality and lesser material wastage. Up to now, GTAW and PAW arc welding techniques were described as more reliable and most suitable processes for WAAM with much lesser problems like excessive heating, porosity and distortion in GMAWtechnique. But in both of the techniques the metal wire was not fed coaxially which thereafter resulted in process variations on altering the direction of weld deposition and sensitivity to arc length. And the fact is that many of the welding system implementing robots requires rotary axis for the positioning of nozzle and matching it with the position of

(This work is licensed under a Creative Commons Attribution 4.0 International License.)

International Journal of Engineering Research & Technology (IJERT)
ISSN: 2278-0181
Vol. 10 Issue 10, October-2021

welding technique whereas CMT and Top-TIG are advancement of GMAW and GTAW welding techniques respectively. The 1st reduces the heat input and variations in process by traditional GMAW technique and the 2nd is the GTAW (coaxial) that improves all over metal deposition rate of the WAAM process. The outcome of the work not only includes capabilities of all the implemented processes to generate high quality parts. Moreover, mechanical properties were also studied and analyzed for the AISI 316L stainless steel.

2. LITERATURE REVIEW

S.No.	TITLE	Author & Year	Publication	Findings
1.	**A review on wire and arc additive manufacturing of titanium alloy**	Zidong Lin , Kaijie Song , Xinghua Yu (2021)	ELSEVIER	This paper gives knowledge of 3D metallic printing of titanium alloy using WAAM process for metal deposition [1].
2.	**A multi-bead overlapping model for robotic wire and arc additive manufacturing (WAAM)**	Donghong Ding,Zengxi Pan, Dominic Cuiuri,Huijun Li (2015)	ELSEVIER	This paper shows a vastly improved guess to the exploratory estimations when compared with flatl top overlapping model (FOM).This is basic in measure intending to accomplish better geometry, accuracy and material effectiveness in additive manufacturing [2].
3.	**Preliminary development of a Wire and Arc Additive Manufacturing Engineering**	J.L. Prado-Cerqueiraa, J.L. Diéguezb, A.M. Camachoa (2017)	ELSEVIER	The primary target of this work is to show the principal encounters in the advancement of a practical metal added substance producing framework based on gas metal arc welding [3].
4.	**Additive manufacturing using WAAM with AA5183 wire** [7]	A. Horgara, H. Fostervollb, B. Nyhusb, X. Renb, M. Erikssonb, O.M. Akselsen (2018)	ELSEVIER	The current review tends to wire arc additive manufacturing of AA5183 aluminum alloy utilizing regular gas metal arc welding deposition on 20mm thick AA6082-T6 plate as support material [4].
5.	**A review of wire arc additive manufacturing and advances in wire arc additive manufacturing of aluminium**	K .S DEREKAR (2018)	ELSEVIER	This paper is an audit of WAAM technology including a brief of WAAM history, status, benefits, and limitations of the WAAM field. A focus is given including the endeavors coordinated towards the decrease of porosity, malleable properties, microstructural examinations, and other important headway in the field of WAAM of aluminium [5].
6.	**Effect of heat input on microstructure and mechanical properties of Al-Mg alloys fabricated by WAAM**	Chuanchu Su, Xizhang Chen∗, Chuang Gao, Yangfan Wang (2019)	ELSEVIER	From this paper, it is obvious that parts produced by WAAM-CMT have a preferable exhibition over the 5356 regular casting alloys [6].
7.	**Development of low-cost production process for prototype components based on Wire and Arc Additive Manufacturing (WAAM)**	Nataliia charnabol, Bert Lauwers, Patrick Van rayment (2020)	ELSEVIER	This paper centers around the various strides to be taken to adapt existing GMAW innovation into a moderate and effective WAAM innovation [7].
8.	**Investigating the generation process of molten droplets and arc plasma in the confined space during compulsively constricted WAAM**	Meng Guo, Chuanbao Jia∗, Jihui Zhou, Wenqiang Liu, Chuansong Wu (2020)	ELSEVIER	The paper uncovered that arc behaviors and beads transfer were truly unstable at low-level electrical boundaries with the features that the beads transfer measurements were huge (1.8–5.3 mm), the beads transfer frequencies were low (2–23 Hz) [8].

(This work is licensed under a Creative Commons Attribution 4.0 International License.)

International Journal of Engineering Research & Technology (IJERT)
ISSN: 2278-0181
Vol. 10 Issue 10, October-2021

9.	**Thermal management in WAAM through the CMT Advanced process and an active cooling technique.**	Fernando Matos Scottia, Felipe Ribeiro Teixeiraa, Leandro João da Silvaa,Douglas Bezerra de Araújoa, Ruham Pablo Reisa,*, Américo Scotti (2020)	ELSEVIER	This paper gathered that the chance of influencing the thermal cycles and geometries of the resultant preforms with two autonomous thermal administration instruments grows the windows for discovering ideal affidavit boundaries in WAAM [9].
10.	**Wire Arc Additive Manufacturing (WAAM) process of nickel based superalloys – A review**	V. Dhinakaran , J. Ajith , A. Fathima Yasin Fahmidha , T. Jagadeesha , T. Sathish , B. Stalin (2020)	ELSEVIER	This paper infers that the broad utilization of WAAM actually shows many difficulties, and these may should be engaged and settled in explicit manners for various materials to create a functional framework in an acceptable time span [10].
11.	**Wire arc additive manufacturing (WAAM): A new process to shape engineering materials**	Sudhanshu Ranjan Singh ⇑, Pradeep Khanna (2021)	ELSEVIER	This paper expects to portray the different stagewise advancements and capabilities of WAAM tech, with an outline on the materials that can be worked upon and some knowledge on the future possibilities of the technology [11].
12.	**Ultracold-Wire and arc additive manufacturing (UC-WAAM)**	Tiago A. Rodrigues *, Valdemar R. Duarte , R.M. Miranda , Telmo G. Santos , J.P. Oliveira (2021)	ELSEVIER	By eliminating the electric flow through the substrate and separating the electric arc from the liquid pool, this new WAAM variation can diminish the process temperatures and increment in cooling rates, without compromising the trustworthiness or deposition pace of the as-fabricated parts [12].
13.	**A review on process planning strategies and challenges of WAAM**	Sagar Singh, Satish kumar Sharma ⇑, Dinesh W. Rathod (2021)	ELSEVIER	The nuts and bolts and essentials of WAAM methods, different significant stages and key interaction getting ready for WAAM have been explained. Moreover, the difficulties and cutting-edge developments in this conspicuous field of WAAM are engaged for the better comprehension of processes and technologies [13].
14.	**Metal transfer modes for Wire Arc Additive Manufacturing Al-Mg alloys: Influence of heat input in microstructure and porosity**	Aldalur a,*, A. Su´arez a,b, F. Veiga a (2021)	ELSEVIER	In this paper, aluminum alloy 5356 is analyzed in the Gas Metal Arc Welding (GMAW)- based WAAM innovative cycle. From among the different suggested working methods of various makers, three working modes for aluminum alloy are analyzed: pulsed GMAW mode, Cold arc mode and pulsed AC mode [14].
15.	**Investigation of the WAAM processes features based on an indirect arc between two non-consumable electrodes**	Jihui Zhou, Chuanbao Jia *, Meng Guo, Maoai Chen, Jinqiang Gao, Chuansong Wu (2021)	ELSEVIER	This paper confirmed that the solid burning arc kept continuously melting the steel cord. Because there is no modern-day flowing thru the droplets and molten pool, the crucial manner function of low warmth input became revealed [15].
16.	**Hot forging wire and arc additive manufacturing (HF-WAAM)**	Valdemar R. Duartea,*, Tiago A. Rodriguesa, N. Schellb, R.M. Mirandaa, J.P. Oliveiraa, Telmo G. Santosa (2020)	ELSEVIER	The paper showed that this new version refines the solidification microstructure and reduce texture consequences, as decided via high power synchrotron X-ray diffraction experiments, without interrupting the additive production procedure [16].
17.	**Recent developments and challenges associated with wire arc**	S. Srivatsav, V. Jayakumar, M. Sathishkumar	ELSEVIER	This paper overviews the imminent studies and traits on WAAM

(This work is licensed under a Creative Commons Attribution 4.0 International License.)

International Journal of Engineering Research & Technology (IJERT)
ISSN: 2278-0181
Vol. 10 Issue 10, October-2021

	additive manufacturing of Al alloy: A review	(2021)		techniques and frequently used materials for the equal. Common errors which arise at some stage in WAAM were mentioned in this paper, together with the advantages of WAAM. Alloys of aluminium play a key function in the marine, aerospace and car industries [17].
18.	**Oxidation in wire arc additive manufacturing of aluminium alloys**	Tobias Hauser a,d,*, Raven T. Reisch b,d, Philipp P. Breese c,d, Yogesh Nalam d, Kaivalya S. Joshi d, Katharina Bela d, Tobias Kamps d, Joerg Volpp a, Alexander F.H. Kaplan a (2021)	ELSEVIER	It became located that the arc interacts with the prevailing amorphous oxide layer of the formerly deposited layer and turns it right into a white duplex (crystalline and amorphous) oxide layer. In addition to the analysis of the white surface oxidation, oxidation anomalies, which occur at low protecting from the environment, have been investigated [18].
19.	**Robot Based Wire Arc Additive Manufacturing System with Context- Sensitive Multivariate Monitoring Framework**	Raven Reischa,b,*, Tobias Hauserb, Tobias Kampsb, Alois Knolla (2020)	ELSEVIER	A WAAM machine is divided into 4 elements (welding supply, kinematic structure, control gadget, tracking system) and a evaluation is performed for every. Requirements are described based totally on those evaluations and further desires and a robot primarily based WAAM setup is proposed [19].
20.	**Continuous three-dimensional path planning (CTPP) for complex thin parts with wire arc additive manufacturing**	Adama Diourt´e a,*, Florian Bugarin a, Cyril Bordreuil b, St´ephane Segonds (2021)	ELSEVIER	The manufacturing of those elements with CTPP and numerous numerical critiques have proven the reliability of this method and its ability to produce complex new shapes with an excellent geometrical restitution, difficult or not possible to attain these days the use of 2.5D with WAAM generation [20].
21.	**Arc Behaviour in Wire Arc Additive Manufacturing Process**	Pranjal Shuklaa, Balaram Dasha, Degala Venkata Kirana*, Satish Bukkapatnam (2020)	ELSEVIER	It changed into determined that the bead width step by step multiplied from the first layer to the fourth layer and remained about the same from 5th to the tenth layer [21].
22.	**Weld Bead Modeling and Process Optimization in Hybrid Layered Manufacturing**	Suryakumar S, Karunakaran KP, Bernard A, Chandrasekhar U, Raghavender N, Sharma D 2011	ELSEVIER	According to previous researches, the multi globule or bead overlapping models have claimed that it is difficult to accomplish an optimal flat surface with overlapped molten metal beads [22].

(This work is licensed under a Creative Commons Attribution 4.0 International License.)

International Journal of Engineering Research & Technology (IJERT)
ISSN: 2278-0181
Vol. 10 Issue 10, October-2021

3. EXPERIMENTAL PROCEDURE

The tests took place in a robotic cell in there was two cartesian machines (Fig. 1). And 3 different power sources were used:

- Fronius Transplus Synergic 4000-CMT R, power source was connected to Robacta drive torch from Fronius.
- Top-TIG 220-DC source and patented torch from the Air Liquide.
- Praxair-EWM TETRIX 400-Synergic Plasma source coupled to Plasmatechnik PWM 350A torch.

Mechanical properties were calculated by tensile test specimens which were produced by electron discharge machining (EDM) having a geometry according to ASTM E8-16-standard (Fig. 2). A specimens was tested for studying mechanical properties of the specimen walls in 2 directions: PL(bead generation direction) and PT(bead vertical overlapping direction) . AISI-316L specimen was tested as the built conditions.

Tensile tests were performed in a model Z100 ZWICK/Roell at ambient temperature by applying a displacement rate of 1.6 mm/min and by the use of an extensometer with gauge length of 25 mm.



Fig -1: WAAM Facilities. Left- IK-4 Lortek (CMT & TopTIG). Centre-TECNALIA (PAW). Right- ADDILAN (CMT&PAW)

Table 1. Deposition Rates and Shielding gasses for each material

Material	Process	Shielding Gas	Deposition Rate
AISI 316L	CMT PAW TopTIG	25% CO_2 75% Ar 5% H_2 95% Ar 100% Ar	1.51 kg/hr

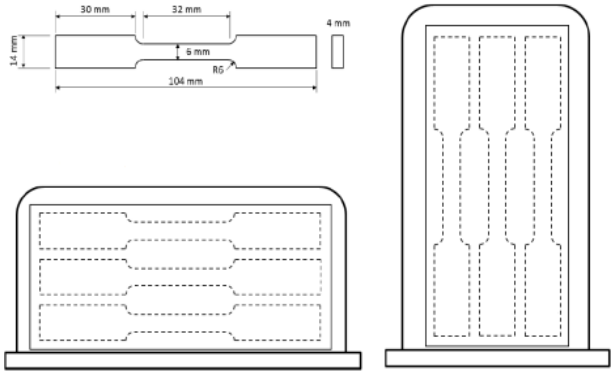


Fig. -2: Tensile test specimens taken from thick-walled WAAM samples.

3.1. CMT process in WAAM

3.1.1 CMT - AISI 316L

Cold metal transfer (CMT) process is a welding method optimized for lowering the heat input into the metal substrate and it is very common to use it in industrial welding of many steel alloys. Moreover, this work only showed the results obtained for deposition rate of 2,5 kg/h and compared them with those which were obtained by all the other processes, CMT process showed very good results of upto 5 kg/h metal deposition rates with AISI 316L.

Though, CMT process produces the bead with a relatively higher aspects ratios (relationship b/w bead height and the width) that could make the process difficult for overlapping and it may cause defects in the component like pores or voids.
Regarding the mechanical properties, results showed that properties were dependent clearly over the test direction (Fig.3). While longitudinal specimens (PL) were close to the least value fixed by the standards, transversal ones (PT) not reaches these limits, which shows lowering yield strength and elongation at break that demonstrates a much more rigid behavior over the traverse direction.

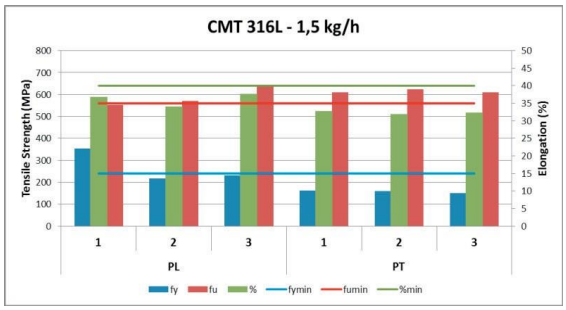


Fig.-3: CMT mechanical tests results for AISI 316L stainless steel

Therefore, for the tensile strength tests 3 types of gases were studied: 100% of Ar (single bead wall), 50% Ar-50%He and 100% of He. It was worth nothing to increase the percentage suppose an increase of the price of the gas.

(This work is licensed under a Creative Commons Attribution 4.0 International License.)

International Journal of Engineering Research & Technology (IJERT)
ISSN: 2278-0181
Vol. 10 Issue 10, October-2021

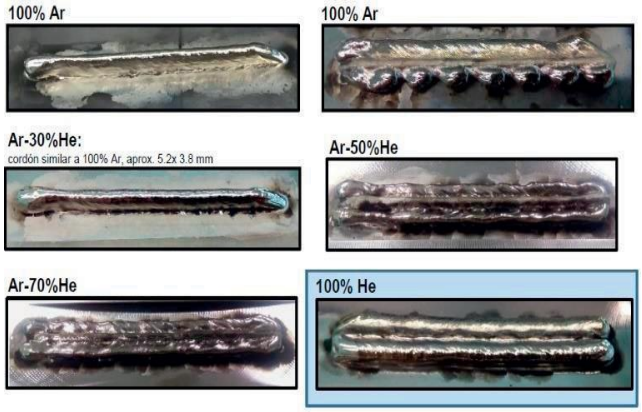


Fig.-4: Simple and overlapped beads for different shielding gases.

3.2. *Top-TIG process in WAAM*

3.2.1 Top-TIG AISI 316L

Top-TIG is a TIG technology that allows the coaxial feeding of wire that increases the metal deposition rate and providing a high quality TIG process. The major limitation of Top-TIG technology is that it has a lower deposition rates when compared with CMT or PAW. The results showed this limit in 1.5 kg/h for AISI 316L and the current equipment (Fig. 8). This limit resulted from a lesser heat input of the process which was unable to melt the wire when the feed rate increased. Moreover, it is very necessary to care of the aspect ratios that could make difficult for horizontal overlapping.

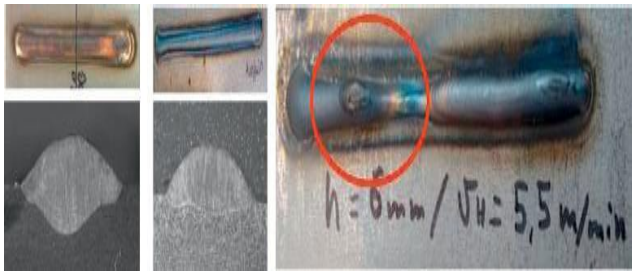


Fig.-5: Beads obtained by Top-TIG on AISI 316L. Left) 1 kg/h. Centre) 1.5kg/h. Right) 1.6 kg/h.

On the other hand, the mechanical results obtained from Top-TIG were situated over the least required and show high homogeneity in both the directions (Fig. 6).

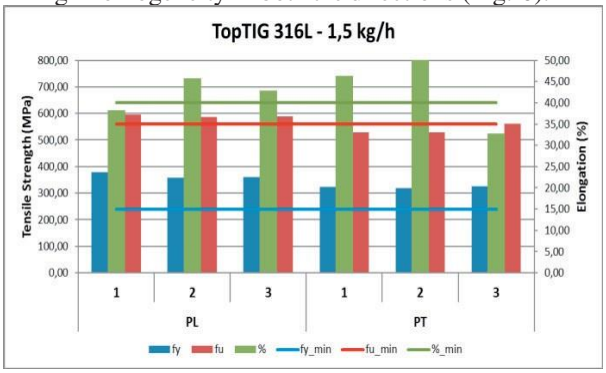


Fig.-6: Top-TIG mechanical tests results for AISI 316L stainless steel.

3.3 *Plasma Arc Welding process in WAAM*

3.3.1. *PAW – AISI 316L*

PAW constricts the arc within the pilot arc increasing the energy density so, beads produced by this process were shorter and wider, which means they had a lesser aspect ratio. The fact eases the horizontal overlapping, avoiding pores and voids. Mechanical tests were done on the wall generates at 1.5 kg/h metal deposition rate, moreover 3.5 kg/h values could be reached with suitable quality.

Test results (Fig. 11) shows a high anisotropy between the directions. PL specimens crosses both Yield and Ultimate strength limits, while for the PT it reaches the limit only for the Ultimate strength. In both of the cases, values of Elongation at breaking were below the limited values.

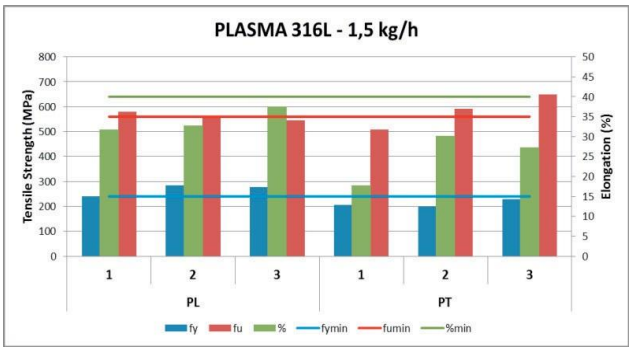


Fig. -7: PAW mechanical tests results for AISI 316L stainless steel

4. RESULTS

The result section shows the obtained results that we get from the use of the three processes for Additive Manufacturing. Results includes, not only mechanical properties of the specimen, but also the capability of each accomplished process that to be applied in Higher metal Deposition Rate for Additive Manufacturing.

Results are classified by WAAM technologies (CMT, PAW and Top-TIG) and a material (AISI 316L).

4. CONCLUSIONS

The work studies various 3 welding processes (Plasma Arc Welding (PAW), Cold Metal Transfer (CMT) and AirLiquide Top-TIG for the Wire Arc AM in the terms of acceptability and the obtained properties. The material that had been studied: an AISI 316L stainless steel.

From the results obtained, following things can be concluded:

- WAAM technique, without considering welding technology used, achieving a good quality manufactured component with a deposition rates of as high as 5 kg/hr in the AISI 316 L.
- The obtained results show that, although WAAM technology was able to obtain the mechanical requirements, the only matter that was important is the choice of the correct welding technique depending over the material properties.
- CMT achieves the highest metal deposition rates in stainless steel but shows anisotropy in the mechanical properties. And hence, it can be

(This work is licensed under a Creative Commons Attribution 4.0 International License.)

International Journal of Engineering Research & Technology (IJERT)
ISSN: 2278-0181
Vol. 10 Issue 10, October-2021

concluded that the CMT process is best for bigger size Stainless steel components with a lesser or medium mechanical requirement.

- Top-TIG achieves the most suitable properties for the stainless steel and showed a good homogenous behavior without consideration of the directions. Although, its lower energy efficiency didn't allows high deposition rates (1.5 kg/h max.) and made it necessary for the usage of an active shielding gases mixture. Therefore, Top-TIG method can be used for the small or medium size Stainless steel parts that have medium or high mechanical requirements.
- PAW achieves a intermediate metal deposition rates for the stainless steel (3.5 kg/h) with a better properties in both of the directions. Therefore, PAW method is recommended for the medium or large size Stainless steel parts that have medium or high mechanical requirements.
- Regardless of the welding methods, parts that were manufactured by WAAM process had shown the anisotropy in the properties that should be taken into account in the duration of design procedure or be-heat or mechanically treated during the 3D-printing.

REFERENCES

[1] Zidong Lin, Kaijie Song, Xinghua Yu, A review on Wire and Arc Additive Manufacturing of Titanium alloy.

[2] D. Ding, Z. Pan, D. Cuiuri, H. Li, A multi-bead overlapping model for robotic wire and arc additive manufacturing (WAAM), Robot. Comput. Integrated Manuf. 31 (2015) 101–110.

[3] J.L. Prado-Cerqueiraa, J.L. Diéguezb, A.M. Camachoa, Preliminary development of a Wire and Arc Additive Manufacturing Engineering, Procedia Manufacturing 00 (2017) 895-902.

[4] A. Horgar, H. Fostervoll, B. Nyhus, X. Ren, M. Eriksson, O.M. Akselsen, Additive Manufacturing using WAAM with AA5183 wire, J. Mater. Process. Tech. 259 (2018) 68–74.

[5] K.S. Derekar, A review of wire arc additive manufacturing and advances in wire arc additive manufacturing of aluminium, Mater. Sci. Technol. 34 (2018) 1–22.

[6] Chuanchu Su, Xizhang Chen⁎, Chuang Gao, Yangfan Wang, Effect of heat input on microstructure and mechanical properties of Al-Mg alloys fabricated by WAAM, Applied Surface Science 486 (2019) 431-440.

[7] Nataliia charnabol, Bert Lauwers, Patrick Van rayment, Development of low-cost production process for prototype components based on Wire and Arc Additive Manufacturing (WAAM), CIRP 95 (2020) 60-65.

[8] Meng Guo, Chuanbao Jia⁎, Jihui Zhou, Wenqiang Liu, Chuansong Wu, Investigating the generation process of molten droplets and arc plasma in the confined space during compulsively constricted WAAM, Journal of Materials Processing Tech. 275 (2020)116355).

[9] Fernando Matos Scottia, Felipe Ribeiro Joao da Silvaa, Thermal management in WAAM through the CMT Advanced process and an active cooling technique, Journal of Manufacturing Processes 57 (2020) 23-35.

[10] V. Dhinakaran , J. Ajith , A. Fathima Yasin Fahmidha , T. Jagadeesha , T. Sathish , B. Stalin, Wire Arc Additive Manufacturing (WAAM) process of nickel based superalloys – A review, Materials Today : Proceedings 21 (2020) 920-925.

[11] Sudhanshu Ranjan Singh , Pradeep Khanna, Wire arc additive manufacturing (WAAM): A new process to shape engineering materials, Materials Today : Proceedings 44 (2021) 118-128.

[12] Tiago A. Rodrigues *, Valdemar R. Duarte , R.M. Miranda , Telmo G. Santos , J.P. Oliveira, UltracoldWire and arc additive manufacturing (UC-WAAM), , Journal of Materials Processing Tech. 296 (2021) 117196.

[13] Sagar Singh, Satish kumar Sharma ⇑ , Dinesh W. Rathod, A review on process planning strategies and challenges of WAAM, Materials Today: Proceedings (2021).

[14] Aldalur a,*, A. Su´arez a,b, F. Veiga a, Metal transfer modes for Wire Arc Additive Manufacturing Al-Mg alloys: Influence of heat input in microstructure and porosity, Journal of Materials Processing Tech. 297 (2021) 117271

[15] Jihui Zhou, Chuanbao Jia *, Meng Guo, Maoai Chen, Jinqiang Gao, Chuansong Wu, Investigation of the WAAM processes features based on an indirect arc between two non-consumable electrodes, Vacuum 183 (2021) 109851

[16] Duarte, V.R., Rodrigues, T.A., Schell, N., Miranda, R.M., Oliveira, J.P., Santos, T.G., 2020. Hot forging wire and arc additive manufacturing (HF-WAAM). Addit. Manuf., 101193

[17] S. Srivatsav, V. Jayakumar, M. Sathishkumar, Recent developments and challenges associated with wire arc additive manufacturing of Al alloy: A review, Materials Today 2021

[18] Tobias Hauser a,d,*, Raven T. Reisch b,d, Philipp P. Breese c,d, Yogesh Nalam d, Kaivalya S. Joshi d, Katharina Bela d, Tobias Kamps d, Joerg Volpp a, Alexander F.H. Kaplan a, Oxidation in wire arc additive manufacturing of aluminium alloys, Additive Manufacturing 41 (2021) 101958

[19] Raven Reischa,b,*, Tobias Hauserb, Tobias Kampsb, Alois Knolla, Robot Based Wire Arc Additive Manufacturing System with Context- Sensitive Multivariate Monitoring Framework, Procedia Manufacturing 51 (2020) 732-739

[20] Adama Diourt´e a,*, Florian Bugarin a, Cyril Bordreuil b, St´ephane Segonds, Continuous threedimensional path planning (CTPP) for complex thin parts with wire arc additive manufacturing, Additive Manufacturing 37 (2021) 101622

[21] Pranjal Shuklaa, Balaram Dasha, Degala Venkata Kirana*, Satish Bukkapatnam, Arc Behavior in Wire Arc Additive Manufacturing Process, Procedia Manufacturing 48 (2020) 725-729

[22] S. Suryakumar, A. Bernard, K.P. Karunakaran, U. Chandrasekhar, D. Sharma, N. Raghavender, Weld Bead Modelling and Process Optimization in Hybrid Layered Manufacturing. Computer Aided Design, Vol. 43, no. 4, pp. 331-344, 2011

[23] N. Shamsaei, A. Yadollahi, L. Bian, S.M. Thompson, An overview of Direct Laser Deposition for additive manufacturing; Part II: mechanical behavior, process parameter optimization and control, Addit. Manuf. 8 (2015) 12–35.

[24] J. Ding, P. Colegrove, J. Mehnen, S. Ganguly, P.M.S. Almeida, F. Wang, S. Williams, Thermomechanical analysis of wire and arc additive layer manufacturing process on large multi-layer parts, Comput. Mater. Sci. 50 (2011) 3315–3322.

[25] A. Horgar, H. Fostervoll, B. Nyhus, X. Ren, M. Eriksson, O.M. Akselsen, Additive manufacturing using WAAM with AA5183 wire, J. Mater. Process. Technol. 259 (2018) 68–74.

[26] P. Henckell, K. Günther, Y. Ali, J.P. Bergmann, P. For^et, The influence of gas cooling in context of wire arc additive manufacturing—a novel strategy of affecting grain structure and size, TMS 2017 146th, in: Annual Meeting & Exhibition Supplemental Proceedings vol. 146, 2017, pp. 147–156.

[27] D. Herzog, V. Seyda, E. Wycisk, C. Emmelmann, Additive manufacturing of metals, Acta Mater. 117 (2016) 371–392.

[28] C. Zhang, Y. Li, M. Gao, X. Zeng, Wire arc additive manufacturing of Al-6Mg alloy using variable polarity cold metal transfer arc as power source, Mat. Sci. Eng. A. 711 (2017) 415–423.

[29] Wang F, Williams S, Rush M. Morphology investigation on direct current pulsed gas tungsten

[30] Arc welded additive layer manufactured Ti6Al4V alloy. Int J Adv Manuf Technol 2011;57:597–603

[31] Z. Pan, D. Cuiuri, et al., Bead modelling and implementation of adaptive MAT path in wire and arc additive manufacturing, Rob. Comput. Integr. Manuf. 39 (2015) 32–42.

[32] Bambach, M., Sizova, I., Sydow, B., Hemes, S., Meiners, F., 2020. Hybrid manufacturing of components from Ti-6Al-4V by metal forming and wire-arc additive manufacturing. J. Mater. Process. Technol. 282, 116689.

[33] Cunningham, C.R., Flynn, J.M., Shokrani, A., Dhokia, V., Newman, S.T., 2018. Invited review article: strategies and processes for high quality wire arc additive manufacturing. Addit. Manuf. 22, 672–686.

[34] Kazanas, P., Deherkar, P., Almeida, P., Lockett, H., Williams, S., 2012. Fabrication of geometrical features using wire and arc additive

(This work is licensed under a Creative Commons Attribution 4.0 International License.)

International Journal of Engineering Research & Technology (IJERT)
ISSN: 2278-0181
Vol. 10 Issue 10, October-2021

manufacture. Proc. Inst. Mech. Eng. Part B J. Eng. Manuf. 226, 1042–1051.

[35] L. chao, 2018b. Wire and arc additive manufacture of high-building multi-directional pipe joint. Int. J. Adv. Manuf. Technol. 96, 2389–2396.

[36] Wang, X., Wang, A., Li, Y., 2019b. A sequential pathplanning methodology for wire and arc additive manufacturing based on a water-pouring rule. Int. J. Adv. Manuf. Technol. 103, 3813–3830. F. Martina, P.A. Colegrove, S.W. Williams, J. Meyer, Microstructure of interpass rolled wire + arc additive manufacturing Ti-6Al-4V components, Metall. Mater. Trans. A 46 (2015) 6103–6118.

BIOGRAPHIES



Harshit Bansal received his B.Tech degree from Noida Institute of Engg. & Technology, Noida, India and M.Tech in Production Engg. from Delhi Technological University, Delhi, India.



Abhiraj Kumar Gupta received his B.Tech degree from ABES Engg. College, Ghaziabad, India and M.Tech in Production Engg. From Delhi Technological University, Delhi, India.

(This work is licensed under a Creative Commons Attribution 4.0 International License.)